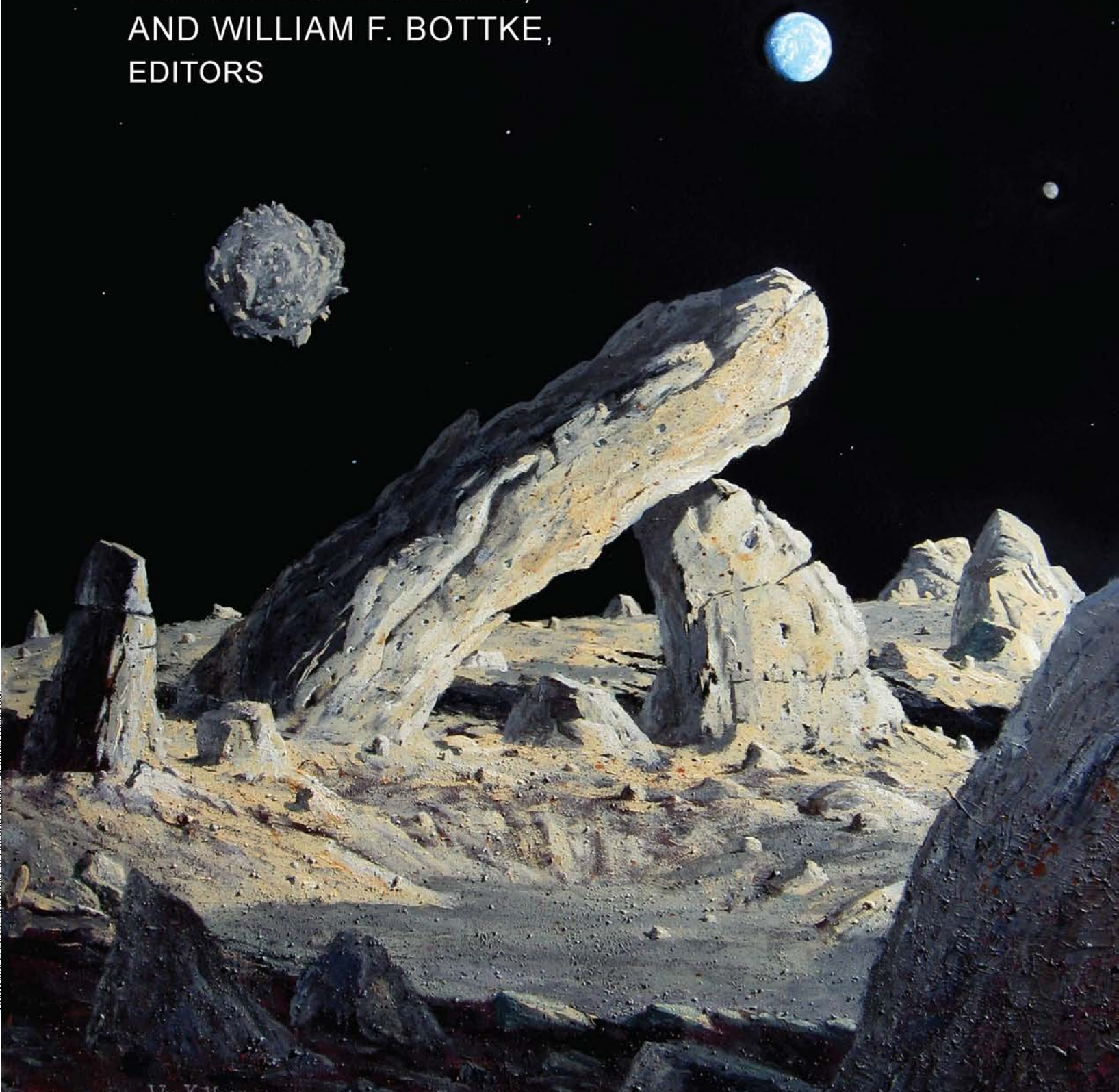


# ASTEROIDS IV

PATRICK MICHEL,  
FRANCESCA E. DEMEO,  
AND WILLIAM F. BOTTKE,  
EDITORS



**THE UNIVERSITY OF ARIZONA SPACE SCIENCE SERIES**  
RICHARD P. BINZEL, GENERAL EDITOR

**Asteroids IV**

P. Michel, F. E. DeMeo, and W. F. Bottke, editors, 2015, 895 pages

**Protostars and Planets VI**

Henrik Beuther, Ralf S. Klessen, Cornelis P. Dullemond, and Thomas Henning, editors, 2014, 914 pages

**Comparative Climatology of Terrestrial Planets**

Stephen J. Mackwell, Amy A. Simon-Miller, Jerald W. Harder, and Mark A. Bullock, editors, 2013, 610 pages

**Exoplanets**

S. Seager, editor, 2010, 526 pages

**Europa**

Robert T. Pappalardo, William B. McKinnon, and Krishan K. Khurana, editors, 2009, 727 pages

**The Solar System Beyond Neptune**

M. Antonietta Barucci, Hermann Boehnhardt, Dale P. Cruikshank, and Alessandro Morbidelli, editors, 2008, 592 pages

**Protostars and Planets V**

Bo Reipurth, David Jewitt, and Klaus Keil, editors, 2007, 951 pages

**Meteorites and the Early Solar System II**

D. S. Lauretta and H. Y. McSween, editors, 2006, 943 pages

**Comets II**

M. C. Festou, H. U. Keller, and H. A. Weaver, editors, 2004, 745 pages

**Asteroids III**

William F. Bottke Jr., Alberto Cellino, Paolo Paolicchi, and Richard P. Binzel, editors, 2002, 785 pages

TOM GEHRELS, GENERAL EDITOR

**Origin of the Earth and Moon**

R. M. Canup and K. Righter, editors, 2000, 555 pages

**Protostars and Planets IV**

Vincent Mannings, Alan P. Boss, and Sara S. Russell, editors, 2000, 1422 pages

**Pluto and Charon**

S. Alan Stern and David J. Tholen, editors, 1997, 728 pages

**Venus II—Geology, Geophysics, Atmosphere,  
and Solar Wind Environment**

S. W. Bougher, D. M. Hunten,  
and R. J. Phillips, editors, 1997, 1376 pages

**Cosmic Winds and the Heliosphere**

J. R. Jokipii, C. P. Sonett,  
and M. S. Giampapa, editors, 1997, 1013 pages

**Neptune and Triton**

Dale P. Cruikshank, editor, 1995, 1249 pages

**Hazards Due to Comets and Asteroids**

Tom Gehrels, editor, 1994, 1300 pages

**Resources of Near-Earth Space**

John S. Lewis, Mildred S. Matthews,  
and Mary L. Guerrieri, editors, 1993, 977 pages

**Protostars and Planets III**

Eugene H. Levy and Jonathan I. Lunine, editors, 1993, 1596 pages

**Mars**

Hugh H. Kieffer, Bruce M. Jakosky, Conway W. Snyder,  
and Mildred S. Matthews, editors, 1992, 1498 pages

**Solar Interior and Atmosphere**

A. N. Cox, W. C. Livingston,  
and M. S. Matthews, editors, 1991, 1416 pages

**The Sun in Time**

C. P. Sonett, M. S. Giampapa,  
and M. S. Matthews, editors, 1991, 990 pages

**Uranus**

Jay T. Bergstrahl, Ellis D. Miner,  
and Mildred S. Matthews, editors, 1991, 1076 pages

**Asteroids II**

Richard P. Binzel, Tom Gehrels,  
and Mildred S. Matthews, editors, 1989, 1258 pages

**Origin and Evolution of Planetary and Satellite Atmospheres**

S. K. Atreya, J. B. Pollack,  
and Mildred S. Matthews, editors, 1989, 1269 pages

**Mercury**

Faith Vilas, Clark R. Chapman,  
and Mildred S. Matthews, editors, 1988, 794 pages

**Meteorites and the Early Solar System**

John F. Kerridge and Mildred S. Matthews, editors, 1988, 1269 pages

**The Galaxy and the Solar System**

Roman Smoluchowski, John N. Bahcall,  
and Mildred S. Matthews, editors, 1986, 483 pages

**Satellites**

Joseph A. Burns and Mildred S. Matthews, editors, 1986, 1021 pages

**Protostars and Planets II**

David C. Black and Mildred S. Matthews, editors, 1985, 1293 pages

**Planetary Rings**

Richard Greenberg and André Brahic, editors, 1984, 784 pages

**Saturn**

Tom Gehrels and Mildred S. Matthews, editors, 1984, 968 pages

**Venus**

D. M. Hunten, L. Colin, T. M. Donahue,  
and V. I. Moroz, editors, 1983, 1143 pages

**Satellites of Jupiter**

David Morrison, editor, 1982, 972 pages

**Comets**

Laurel L. Wilkening, editor, 1982, 766 pages

**Asteroids**

Tom Gehrels, editor, 1979, 1181 pages

**Protostars and Planets**

Tom Gehrels, editor, 1978, 756 pages

**Planetary Satellites**

Joseph A. Burns, editor, 1977, 598 pages

**Jupiter**

Tom Gehrels, editor, 1976, 1254 pages

**Planets, Stars and Nebulae, Studied with Photopolarimetry**

Tom Gehrels, editor, 1974, 1133 pages



# **Asteroids IV**



# **Asteroids IV**

**Edited by**

**P. Michel  
F. E. DeMeo  
W. F. Bottke**

**With the assistance of**

**Renée Dotson**

**With 148 collaborating authors**

**THE UNIVERSITY OF ARIZONA PRESS  
Tucson**

in collaboration with

**LUNAR AND PLANETARY INSTITUTE  
Houston**

*About the front cover:*

“Riding on a Rubble Pile”

Numerical simulations of asteroid disruptions indicate that in many cases of asteroid disruption by a collision with another object, fragment ejection velocities are typically slow enough that most of the fragments reassemble, leading to the formation of rubble piles. It occurred to the artist that during such processes, various irregularly shaped rock shards could fall back at very slow velocities (centimeters per second in some cases) and pile up in grotesque formations not seen on Earth. Here, a large, narrow rock shard has come to rest at an angle on another rock at the surface of the rubble pile. This asteroid also has a rubble-pile satellite (upper left), constituting a binary system. Earth and the Moon are in the distance (upper right). Painting copyright William K. Hartmann, acrylic, mixed with basaltic soil from Tucson.

*About the back cover:*

Haulani impact crater (diameter 35 km) on asteroid (1) Ceres from Dawn’s Framing Camera with a spatial resolution of ~140 m/pixel. The color mosaic is a cut out of the global mosaic in orthographic projection, obtained in August 2015. Haulani (10°E, 6°N) is shown in colors R = 965 nm, G = 555 nm, B = 438 nm. Absolute reflectance values range between 0.025 and 0.055. This young crater, as indicated by its ray system and lack of impact craters on its floor, contrasts in various bright bluish tones sharply from the surrounding brownish background material. At its center, an irregular remnant central peak at the rim of a central pit exists. The unique colors in the crater indicate excavation and deposition of a subsurface layer of potentially hydrated materials.

The University of Arizona Press  
in collaboration with the Lunar and Planetary Institute  
© 2015 The Arizona Board of Regents  
All rights reserved  
∞ This book is printed on acid-free, archival-quality paper.  
Manufactured in the United States of America

20 19 18 17 16 15 6 5 4 3 2 1

Library of Congress Cataloging-in-Publication Data

Names: Michel, Patrick, 1970– editor. | DeMeo, Francesca E., editor. |  
Bottke, William F. (William Frederick), 1966– editor.

Title: Asteroids IV / edited by Patrick Michel, Francesca E. DeMeo, and  
William F. Bottke ; with the assistance of Renee Dotson ; with 148  
collaborating authors.

Other titles: University of Arizona space science series.

Description: Tucson : The University of Arizona Press ; Houston : Lunar and  
Planetary Institute, 2015. | Series: The University of Arizona space  
science series | Includes bibliographical references and index.

Identifiers: LCCN 2015024269 | ISBN 9780816532131 (cloth : alk. paper)

Subjects: LCSH: Asteroids.

Classification: LCC QB651 .A857 2015 | DDC 523.44—dc23 LC record available at <http://lccn.loc.gov/2015024269>

# Contents

List of Contributing Authors .....	xiii
Scientific Organizing Committee and Acknowledgment of Reviewers .....	xiv
Foreword .....	xv
Preface .....	xvii

## PART 1: INTRODUCTION

Asteroids: Recent Advances and New Perspectives <i>P. Michel, F. E. DeMeo, and W. F. Bottke</i> .....	3
--	---

## PART 2: PHYSICAL AND COMPOSITIONAL PROPERTIES

### 2.1. Asteroid Composition and Physical Properties

The Compositional Structure of the Asteroid Belt <i>F. E. DeMeo, C. M. O'D. Alexander, K. J. Walsh, C. R. Chapman, and R. P. Binzel</i> .....	13
--	----

Mineralogy and Surface Composition of Asteroids <i>V. Reddy, T. L. Dunn, C. A. Thomas, N. A. Moskovitz, and T. H. Burbine</i> .....	43
--	----

Astronomical Observations of Volatiles on Asteroids <i>A. S. Rivkin, H. Campins, J. P. Emery, E. S. Howell, J. Licandro, D. Takir, and F. Vilas</i> .....	65
--	----

Space-Based Thermal Infrared Studies of Asteroids <i>A. Mainzer, F. Usui, and D. E. Trilling</i> .....	89
---	----

Asteroid Thermophysical Modeling <i>M. Delbo, M. Mueller, J. P. Emery, B. Rozitis, and M. T. Capria</i> .....	107
--	-----

Asteroid Photometry <i>J.-Y. Li, P. Helfenstein, B. J. Buratti, D. Takir, and B. E. Clark</i> .....	129
--	-----

Asteroid Polarimetry <i>I. Belskaya, A. Cellino, R. Gil-Hutton, K. Muinonen, and Y. Shkuratov</i> .....	151
--	-----

Radar Observations of Near-Earth and Main-Belt Asteroids <i>L. A. M. Benner, M. W. Busch, J. D. Giorgini, P. A. Taylor, and J.-L. Margot</i> .....	165
---	-----

Asteroid Models from Multiple Data Sources <i>J. Ďurech, B. Carry, M. Delbo, M. Kaasalainen, and M. Viikinkoski</i> .....	183
--	-----

### 2.2. Populations

The Complex History of Trojan Asteroids <i>J. P. Emery, F. Marzari, A. Morbidelli, L. M. French, and T. Grav</i> .....	203
---	-----

The Active Asteroids <i>D. Jewitt, H. Hsieh, and J. Agarwal</i> .....	221
--	-----

The Near-Earth Object Population: Connections to Comets, Main-Belt Asteroids, and Meteorites <i>R. P. Binzel, V. Reddy, and T. L. Dunn</i> .....	243
---	-----

Small Near-Earth Asteroids as a Source of Meteorites <i>J. Borovička, P. Spurný, and P. Brown</i>	257
--	-----

Meteoroid Streams and Zodiacal Dust <i>P. Jenniskens</i>	281
---	-----

### **2.3. Families**

Identification and Dynamical Properties of Asteroid Families <i>D. Nesvorný, M. Brož, and V. Carruba</i>	297
---	-----

Asteroid Family Physical Properties <i>J. R. Masiero, F. E. DeMeo, T. Kasuga, and A. H. Parker</i>	323
---	-----

Collisional Formation and Modeling of Asteroid Families <i>P. Michel, D. C. Richardson, D. D. Durda, M. Jutzi, and E. Asphaug</i>	341
--	-----

### **2.4. Multiple Systems**

Asteroid Systems: Binaries, Triples, and Pairs <i>J.-L. Margot, P. Pravec, P. Taylor, B. Carry, and S. Jacobson</i>	355
--	-----

Formation and Evolution of Binary Asteroids <i>K. J. Walsh and S. A. Jacobson</i>	375
--	-----

## **PART 3: SPACE MISSIONS**

Hayabusa Sample Return Mission <i>M. Yoshikawa, J. Kawaguchi, A. Fujiwara, and A. Tsuchiyama</i>	397
---	-----

The Dawn Mission to Vesta and Ceres <i>C. T. Russell, H. Y. McSween, R. Jaumann, and C. A. Raymond</i>	419
---	-----

The Flybys of Asteroids (2867) Šteins, (21) Lutetia, and (4179) Toutatis <i>M. A. Barucci, M. Fulchignoni, J. Ji, S. Marchi, and N. Thomas</i>	433
---	-----

Phobos and Deimos <i>S. L. Murchie, P. C. Thomas, A. S. Rivkin, and N. L. Chabot</i>	451
---	-----

## **PART 4: EVOLUTIONARY PROCESSES**

### **4.1. Dynamical Evolution**

New Paradigms for Asteroid Formation <i>A. Johansen, E. Jacquet, J. N. Cuzzi, A. Morbidelli, and M. Gounelle</i>	471
---	-----

The Dynamical Evolution of the Asteroid Belt <i>A. Morbidelli, K. J. Walsh, D. P. O'Brien, D. A. Minton, and W. F. Bottke</i>	493
--	-----

The Yarkovsky and YORP Effects <i>D. Vokrouhlický, W. F. Bottke, S. R. Chesley, D. J. Scheeres, and T. S. Statler</i>	509
--	-----

### **4.2. Differentiation**

Asteroid Differentiation: Melting and Large-Scale Structure <i>A. Scheinberg, R. R. Fu, L. T. Elkins-Tanton, and B. P. Weiss</i>	533
---	-----

Hydrothermal and Magmatic Fluid Flow in Asteroids <i>L. Wilson, P. A. Bland, D. Buczkowski, K. Keil, and A. N. Krot</i>	553
Early Impact History and Dynamical Origin of Differentiated Meteorites and Asteroids <i>E. R. D. Scott, K. Keil, J. I. Goldstein, E. Asphaug, W. F. Bottke, and N. A. Moskovitz</i>	573
<b>4.3. Physical Evolution</b>	
Asteroid Surface Alteration by Space Weathering Processes <i>R. Brunetto, M. J. Loeffler, D. Nesvorný, S. Sasaki, and G. Strazzulla</i>	597
The Formation and Evolution of Ordinary Chondrite Parent Bodies <i>P. Vernazza, B. Zanda, T. Nakamura, E. Scott, and S. Russell</i>	617
Sources of Water and Aqueous Activity on the Chondrite Parent Asteroids <i>A. N. Krot, K. Nagashima, C. M. O'D. Alexander, F. J. Ciesla, W. Fujiya, and L. Bonal</i>	635
<b>4.4. Collisions</b>	
Global-Scale Impacts <i>E. Asphaug, G. Collins, and M. Jutzi</i>	661
Modeling Asteroid Collisions and Impact Processes <i>M. Jutzi, K. Holsapple, K. Wünneman, and P. Michel</i>	679
The Collisional Evolution of the Main Asteroid Belt <i>W. F. Bottke, M. Brož, D. P. O'Brien, A. Campo Bagatin, A. Morbidelli, and S. Marchi</i>	701
<b>4.5. Surface Geology and Geophysics</b>	
Cratering on Asteroids <i>S. Marchi, C. R. Chapman, O. S. Barnouin, J. E. Richardson, and J.-B. Vincent</i>	725
Asteroid Interiors and Morphology <i>D. J. Scheeres, D. Britt, B. Carry, and K. A. Holsapple</i>	745
Asteroid Surface Geophysics <i>N. Murdoch, P. Sánchez, S. R. Schwartz, and H. Miyamoto</i>	767
<b>PART 5: GROUNDBASED SURVEYS, HAZARDS, AND FUTURE EXPLORATION</b>	
Surveys, Astrometric Follow-Up, and Population Statistics <i>R. Jedicke, M. Granvik, M. Micheli, E. Ryan, T. Spahr, and D. K. Yeomans</i>	795
Orbits, Long-Term Predictions, and Impact Monitoring <i>D. Farnocchia, S. R. Chesley, A. Milani, G. F. Gronchi, and P. W. Chodas</i>	815
Asteroid Impacts and Modern Civilization: Can We Prevent a Catastrophe? <i>A. W. Harris, M. Boslough, C. R. Chapman, L. Drube, P. Michel, and A. W. Harris</i>	835
Human Exploration of Near-Earth Asteroids <i>P. A. Abell, B. W. Barbee, P. W. Chodas, J. Kawaguchi, R. R. Landis, D. D. Mazanek, and P. Michel</i>	855
Index	881



## List of Contributing Authors

- Abell P. A. 855  
Agarwal J. 221  
Alexander C. M. O'D. 13, 635  
Asphaug E. 341, 573, 661  
Barbee B. W. 855  
Barnouin O. S. 725  
Barucci M. A. 433  
Belskaya I. 151  
Benner L. A. M. 165  
Binzel R. P. 13, 243  
Bland P. A. 553  
Bonal L. 635  
Borovička J. 257  
Boslough M. 835  
Bottke W. F. 3, 493, 509,  
573, 701  
Britt D. 745  
Brown P. 257  
Brož M. 297, 701  
Brunetto R. 597  
Buczkowski D. 553  
Buratti B. 129  
Burbine T. H. 43  
Busch M. W. 165  
Camps H. 65  
Campo Bagatin A. 701  
Capria M. T. 107  
Carruba V. 297  
Carry B. 183, 355, 745  
Cellino A. 151  
Chabot N. L. 451  
Chapman C. R. 13, 725, 835  
Chesley S. R. 509, 815  
Chodas P. W. 815, 855  
Ciesla F. J. 635  
Clark B. E. 129  
Collins G. 661  
Cuzzi J. N. 471  
Delbo M. 107, 183  
DeMeo F. E. 3, 13, 323  
Drube L. 835  
Dunn T. L. 43, 243  
Durda D. D. 341  
Durech J. 183  
Elkins-Tanton L. T. 533  
Emery J. P. 65, 107, 203  
Farnocchia D. 815  
French L. M. 203  
Fu R. R. 533  
Fujiwara A. 397  
Fujiya W. 635  
Fulchignoni M. 433  
Gil-Hutton R. 151  
Giorgini J. D. 165  
Goldstein J. I. 573  
Gounelle M. 471  
Granvik M. 795  
Grav T. 203  
Gronchi G. F. 815  
Harris A. W. (DLR) 835  
Harris A. W. (USA) 835  
Helfenstein P. 129  
Holsapple K. A. 679, 745  
Howell E. S. 65  
Hsieh H. 221  
Jacobson J. A. 375  
Jacobson S. 355  
Jacquet E. 471  
Jaumann R. 419  
Jedicke R. 795  
Jenniskens P. 281  
Jewitt D. 221  
Ji J. 433  
Johansen A. 471  
Jutzi M. 341, 661  
Kaasalainen M. 183  
Kasuga T. 323  
Kawaguchi J. 397, 855  
Keil K. 553, 573  
Krot A. N. 553, 635  
Landis R. R. 855  
Li J.-Y. 129  
Licandro J. 65  
Loeffler M. J. 597  
Mainzer A. 89  
Marchi S. 701, 725  
Marchin S. 433  
Margot J.-L. 165, 355  
Marzari F. 203  
Masiero J. R. 323  
Mazanek D. D. 855  
McSween H. Y. 419  
Michel P. 3, 341, 679, 835, 855  
Micheli M. 795  
Milani A. 815  
Minton D. A. 493  
Miyamoto H. 767  
Morbidelli A. 203, 471, 493, 701  
Moskovitz N. A. 43, 573  
Mueller M. 107  
Muinonen K. 151  
Murchie S. L. 451  
Murdoch N. 767  
Nagashima K. 635  
Nakamura T. 617  
Nesvorný D. 297, 597  
O'Brien D. P. 493, 701  
Parker A. H. 323  
Pravec P. 355  
Raymond C. A. 419  
Reddy V. 43, 243  
Richardson D. C. 341  
Richardson J. E. 725  
Rivkin A. S. 65, 451  
Rozitis B. 107  
Russell C. T. 419  
Russell S. 617  
Ryan E. 795  
Sánchez P. 767  
Sasaki S. 597  
Scheeres D. J. 509, 745  
Scheinberg A. 533  
Schwartz S. R. 767  
Scott E. R. D. 573, 617  
Shkuratov Y. 151  
Spahr T. 795  
Spurný P. 257  
Statler T. S. 509  
Strazzulla G. 597  
Takir D. 65, 129  
Taylor P. A. 165, 355  
Thomas C. A. 43  
Thomas N. 433  
Thomas P. C. 451  
Trilling D. E. 89  
Tsuchiyama A. 397  
Usui F. 89  
Vernazza P. 617  
Viikinkoski M. 183  
Vilas F. 65  
Vincent J.-B. 725  
Vokrouhlický D. 509  
Walsh K. J. 13, 375, 493  
Weiss B. P. 533  
Wilson L. 553  
Wünneman K. 679  
Yeomans D. K. 795  
Yoshikawa M. 397  
Zanda B. 617

## Scientific Organizing Committee

*The editors thank the following for their assistance in the planning stages of this book:*

Paul Abell  
Erik Asphaug  
Olivier Barnouin  
Peter Brown  
Thomas H. Burbine  
Humberto Campins  
Clark Chapman  
Beth Clark  
Guy Consolmagno  
Linda Elkins-Tanton  
Joshua Emery

Peter Jeniskens  
Alan W. Harris (DLR)  
Alan W. Harris (USA)  
Keith Holsapple  
Amy Mainzer  
Joseph Masiero  
Alessandro Morbidelli  
Karri Muinonen  
David Nesvorný  
Michael Nolan  
David Polishook

Vishnu Reddy  
Derek C. Richardson  
Andrew Rivkin  
Daniel Scheeres  
Edward R. D. Scott  
Giovanni Valsecchi  
Joseph Veverka  
David Vokrouhlický  
Benjamin Weiss  
Donald Yeomans

## Acknowledgment of Reviewers

*The editors gratefully acknowledge the following individuals, as well as several anonymous reviewers, for their time and effort in reviewing chapters in this volume:*

Conel M. O'D. Alexander  
Erik Asphaug  
Olivier Barnouin  
Richard Binzel  
Mike Brown  
Thomas Burbine  
Bobby Bus  
Adriano Campo Bagatin  
Alberto Cellino  
Clark Chapman  
Andy Cheng  
Fred Ciesla  
Beth Clark  
Edward Cloutis  
Gareth Collins  
Guy Consolmagno  
Matija Cuk  
Julia de Leon  
Marco Delbo  
Elisabetta Dotto  
Tasha Dunn  
Sonia Fornasier  
Kathryn Gardner-Vandy  
Jerome Gattacceca  
Lee Graham  
Simon Green  
Bruce Hapke  
Paul Hardersen

Alan Harris (DLR)  
Alan Harris (USA)  
Carl Hergenrother  
Takahiro Hiroi  
Joshua Hopkins  
Kevin R. Housen  
Henry Hsieh  
Boris Ivanov  
Ralf Jaumann  
Robert Jedicke  
Klaus Keil  
Tomas Kohout  
Katherine Kretke  
Dante Lauretta  
Guy Libourel  
Anny-Chantal Levasseur-Regourd  
Dmitrij Lupishko  
Franck Marchis  
Jean-Luc Margot  
Francesco Marzari  
Joseph Masiero  
Jay McMahon  
Hap McSween  
David Minton  
David Morrison  
Nick Moskovitz  
Thomas Mueller  
Karri Muinonen

Akiko M. Nakamura  
David Nesvorný  
David O'Brien  
Alex Parker  
Jean-Marc Petit  
Carle Pieters  
Olga Popova  
Petr Pravec  
Sean Raymond  
Derek C. Richardson  
Pascal Rosenblatt  
Ben Rositzis  
Alan Rubin  
David P. Rubincam  
Gal Sarid  
Dan Scheeres  
Michael K. Shepard  
Colin Snodgrass  
Lydie Staron  
Paolo Tanga  
Kleomenis Tsiganis  
Giovanni B. Valsecchi  
Jérémie Vaubaillon  
Paul Wiegert  
Don Yeomans  
Edward Young  
Mike Zolensky

## **Foreword**

In the founding volume of what would become the Space Science Series, Tom Gehrels (1925–2011) wrote, “We are now on the threshold of a new era of asteroid studies” (*Gehrels*, 1971). These words once again trumpet the state of the field four decades later with the release of *Asteroids IV*. Yet why do asteroids captivate our curiosity in a way that so greatly exceeds their small total mass relative to the rest of our solar system? It is because asteroids matter. Now more than ever before, we realize how much asteroids matter to scientists, to explorers, and to the future of humanity. As evidenced throughout this volume, scientists across broad disciplines recognize that understanding asteroids is essential to discerning the basic processes of planetary formation, including how their current distribution bespeaks our solar system’s cataclysmic past. For explorers, the nearest asteroids beckon as the most accessible milestones in interplanetary space, offering spaceflight destinations easier to reach than the lunar surface. For futurists, the prospects of asteroids as commercial resources tantalize as a twenty-first-century gold rush, albeit with far greater challenges and less certain rewards than faced by nineteenth-century pioneers. For humanity as a whole, it is not a question of if — but when — the next major impact will occur. While the disaster probabilities are thankfully small during any one lifespan (and minuscule within the time horizons typically considered by funding agencies), fully cataloging and characterizing the potentially hazardous asteroid population remains unfinished business. While the motivation to “know thy enemy” may ultimately prompt a dedicated spacebased asteroid survey, the richness of the overall scientific return and their exploration/utilization potential will prove that these little worlds are actually our friends.

*Asteroids IV* sets the scientific foundation upon which all these topics and more will continue to be built upon for the foreseeable future. Herein our expert authors lay out what we know, how we know it, and where we go from here. Through this approach, our collective goal is to provide a gateway for new researchers and students of all ages to enter this field by ascertaining the current state. Challenge what doesn’t make sense, resolve what is contentious, and most importantly, fearlessly pursue new ideas that can break through to new paradigms in our understanding. Dare boldly enough to be wrong while being modest enough to reshape or abandon ideas that fail. Only in this way can we soar through the threshold on which we currently stand.

It is my privilege to thank the editors, scientific organizing committee, and authors who crafted this work. Leading the effort with boundless energy and enthusiasm is Patrick Michel. Shining throughout is the careful organization and integrative thinking of Francesca DeMeo. Holding this project steady by his *Asteroids III* editorial experience, Bill Bottke brought his creative thinking as the capstone. Less visible, but whose quality and presence grace every page, are Renée Dotson and colleagues at the Lunar and Planetary Institute (LPI), who brought this volume to physical reality. The ongoing success of the Space Science Series would not be possible without the unfailing support of LPI Director Dr. Stephen Mackwell and the professionalism of the University of Arizona Press.

Richard P. Binzel  
Space Science Series General Editor  
Cambridge, Massachusetts  
August 2015

## **REFERENCES**

- Gehrels T. (1971) Preface to *Physical Studies of Minor Planets* (T. Gehrels, ed.). NASA SP-267, U.S. Government Printing Office, Washington, DC. 687 pages.



## Preface

Asteroids are fascinating worlds. Considered the building blocks of our planets, many of the authors of this book have devoted their scientific careers to exploring them with the tools of our trade: ground- and spacebased observations, *in situ* space missions, and studies that run the gamut from theoretical modeling efforts to laboratory work. Like fossils for paleontologists, or DNA for geneticists, they allow us to construct a veritable time machine and provide us with tantalizing glimpses of the earliest nature of our solar system. By investigating them, we can probe what our home system was like before life or even the planets existed.

The origin and evolution of life on our planet is also intertwined with asteroids in a different way. It is believed that impacts on the primordial Earth may have delivered the basic components for life, with biology favoring attributes that could more easily survive the aftermath of such energetic events. In this fashion, asteroids may have banished many probable avenues for life to relative obscurity. Similarly, they may have also prevented our biosphere from becoming more complex until more recent eras. The full tale of asteroid impacts on the history of our world, and how human life managed to emerge from myriad possibilities, has yet to be fully told.

The hazard posed by asteroid impacts to our civilization is low but singular. The design of efficient mitigation strategies strongly relies on asteroid detection by our ground- and spacebased surveys as well as knowledge of their physical properties. A more positive motivation for asteroid discovery is that the proximity of some asteroids to Earth may allow future astronauts to harvest their water and rare mineral resources for use in exploration. A key goal of asteroid science is therefore to learn how humans and robotic probes can interact with asteroids (and extract their materials) in an efficient way. We expect that these adventures may be commonplace in the future.

Asteroids, like planets, are driven by a great variety of both dynamical and physical mechanisms. In fact, images sent back by space missions show a collection of small worlds whose characteristics seem designed to overthrow our preconceived notions. Given their wide range of sizes and surface compositions, it is clear that many formed in very different places and at different times within the solar nebula. These characteristics make them an exciting challenge for researchers who crave complex problems. The return of samples from these bodies may ultimately be needed to provide us with solutions.

In the book *Asteroids IV*, the editors and authors have taken major strides in the long journey toward a much deeper understanding of our fascinating planetary ancestors. This book reviews major advances in 43 chapters that have been written and reviewed by a team of more than 200 international authorities in asteroids. It is aimed to be as comprehensive as possible while also remaining accessible to students and researchers who are interested in learning about these small but nonetheless important worlds. We hope this volume will serve as a leading reference on the topic of asteroids for the decade to come.

We are deeply indebted to the many authors and referees for their tremendous efforts in helping us create *Asteroids IV*. We also thank the members of the *Asteroids IV* scientific organizing committee for helping us shape the structure and content of the book. The conference associated with the book, “Asteroids Comets Meteors 2014” held June 30–July 4, 2014, in Helsinki, Finland, did an outstanding job of demonstrating how much progress we have made in the field over the

last decade. We are extremely grateful to our host Karri Muinonen and his team. The editors are also grateful to the *Asteroids IV* production staff, namely Renée Dotson and her colleagues at the Lunar and Planetary Institute, for their efforts, their invaluable assistance, and their enthusiasm; they made life as easy and pleasant as possible for the editors, authors, and referees. They also thank Richard Binzel, the General Editor of the Space Science Series, for his strong support and advice during this process, as well as the staff at the University of Arizona Press.

Finally, editor Patrick Michel would like to thank his wife Delphine, who married him on June 14, 2013, almost at the birth of the book process. He is grateful that she was willing to put up with him as he spent many of his nights and weekends working on the book. Thanks to her support, their trajectories are as bounded as a perfectly stable asteroid binary system, and this was probably the best way to experience from the start what her life would be like with a researcher! Co-editor Bottke would also like to thank his wife Veronica and his children Kristina-Marie, Laura, and Julie, who make up his own favorite asteroid family. Since *Asteroids III*, the size distribution of the family members has been steadily changing, and who knows how many tiny new members it will contain by *Asteroids V*! Co-editor DeMeo would like to thank her husband Alfredo for his support and encouragement throughout the process of creating this book. They met at the beginning of her career in research, becoming an asteroid pair and now continuing on the same orbit in life.

*Patrick Michel, Francesca DeMeo, and William F. Bottke*  
*August 2015*

***Part 1:***  
***Introduction***



# Asteroids: Recent Advances and New Perspectives

Patrick Michel

Lagrange Laboratory, Université Côte d'Azur, Observatoire de la Côte d'Azur, CNRS

Francesca E. DeMeo

Massachusetts Institute of Technology

William F. Bottke

Southwest Research Institute

## 1. INTRODUCTION

Asteroids are thought to be leftover planetesimals that are closely related to the precursor bodies that formed both the terrestrial planets and the cores of the giant planets. The most primitive ones contain a record of the original composition of the solar nebula in which the planets formed. The organic matter and properties of water that some contain provide us with critical clues about how life started on Earth. Moreover, some of them cross the trajectory of our planet and therefore pose a risk to humanity.

The sizes, shapes, and rotational, internal, and surface properties of asteroids are the outcome of collisional and dynamical evolution that has molded them since they formed. Understanding the processes they experienced, how these mechanisms changed their properties, and how these factors in turn influenced their evolution can serve as a tracer to tell us the story of the solar system.

In 2005, the European Space Agency published its report *Cosmic Vision: Space Science for Europe in 2015–2025*, which contained two questions related to asteroid research: (1) what are the conditions for planet formation and the emergence of life? (2) How does the solar system work?

Similarly, in 2012, the committee on the planetary science decadal survey appointed by the U.S. National Research Council published a list of questions intimately related to asteroid research. We repeat here those that help put into context the work that is presented throughout *Asteroids IV*: (1) What were the initial stages, conditions, and processes of solar system formation and the nature of the interstellar matter that was incorporated? (2) What solar system bodies endanger Earth's biosphere, and what mechanisms shield it?

In addition, the decadal survey indicated the goals for research on primitive bodies for the next decade: (1) Decipher the record in primitive bodies of epochs and processes not obtainable elsewhere, and (2) understand the role of primitive bodies as building blocks for planets and life.

Important questions related to asteroids in various areas were then indicated, some of which include:

- Which classes of meteorites come from which classes of asteroids, and how diverse were the components from which asteroids were assembled?
- Did asteroid differentiation involve near-complete melting to form magma oceans, or modest partial melting?
- What are the internal structures of Jupiter's Trojan asteroids? Are there systematic chemical or isotopic gradients in the solar system, and if so, what do they reveal about accretion?
- Do we have meteoritic samples of the objects that formed the dominant feeding zones for the innermost planets?
- How did Earth get its water and other volatiles? What is the mechanical process of accretion up to and through the formation of meter-size bodies?
- Which classes of asteroids participated in the late heavy bombardment of the inner planets and the Moon, and how did the current population of asteroids evolve in time and space?
- What are the sources of asteroid groups (e.g., Trojans) that remain to be explored by spacecraft?

It is clear that the solutions to these questions will allow us to glean insights into many fundamental planetary science problems, in particular those connected to the formation and evolution of our solar system.

Since the last book in this series, *Asteroids III*, we have made tremendous advances in our knowledge of asteroids, thanks to the combined efforts of ground- and spacebased observations, space mission rendezvous and flybys, laboratory analysis of returned samples, and theoretical and numerical modeling. In *Asteroids IV*, major strides have been made in the long journey that will eventually lead us to a much deeper understanding of our planetary ancestors. In the words of the classic Californian science fiction radio show *Hour 25*, our progress has all of us now “standing on the verge of new worlds, new ideas, and new adventures.”

This book reviews these major advances in 42 chapters, with the aim of being as exhaustive as possible while also

remaining accessible to students and researchers who are interested to learn about these fascinating bodies and what they tell us about solar system history. Here we introduce the major concepts and topics of this book and highlight some of the major advances that have been made since *Asteroids III*. This introduction does not include references except from the chapters themselves.

## 2. ASTEROID FORMATION AND SOLAR SYSTEM EVOLUTION

Many major improvements have been achieved in solar system dynamical studies since *Asteroids III*. As discussed in the review chapter by Johansen et al., new modeling work on the very early phases of planetesimal growth, together with constraints derived from meteorites and protoplanetary disks, have inspired next-generation scenarios of how the largest asteroids originated. Simulations of the evolution of turbulent gas and dust in protoplanetary disks demonstrate that 100- to 1000-km-diameter asteroids may have formed directly from the gravitational collapse of small particles that organize themselves in dense filaments and clusters. Although many open questions remain, these models provide a potential solution to the long-standing issue regarding the passage from centimeter-sized particles to asteroidal bodies in planetary growth studies, bypassing the long-standing “meter-size barrier.”

In effect, laboratory experiments have shown that micro-meter-scale dust readily aggregates into millimeter- or even pebble-sized agglomerates. On the largest scales, impact simulations have shown that self-gravity among two colliding protoplanets ensures net growth, although the efficiency of two planetesimals combining is often less than 100% (see the chapter by Asphaug et al.). The situation is still murky for objects ranging in size from millimeters to kilometers. In fact, macroscopic dust particles (millimeter or larger) have poor sticking properties in particle-particle collisions, while gravity between the components is too low to act as a “glue” between them. Johansen et al. discuss how the self-gravity of a sufficiently massive particle clump may be capable of growing bodies in this size range.

Several dynamical scenarios have also emerged to describe the early phases of the solar system, with the observed properties of the asteroid belt acting as a constraint (see chapter by Morbidelli et al.). They indicate that the asteroid belt has been sculpted by one or possibly a series of processes, and that this evolution can be characterized by three phases.

The first phase starts during the lifetime of the gaseous protoplanetary disk when the giant planets formed. Here the giant planets may have undergone migration as they gravitationally interacted with the solar nebula. One of the new scenarios describing this phase, which involves the migration of Jupiter through the asteroid belt, is called the “Grand Tack.” It is capable of producing dynamical excitation among the existing asteroids, forcing many out of the region where the main belt currently lies, while also introducing new low-albedo asteroids into the main belt from the Jupiter-Saturn

zone. This could have left the population in a state similar to the observed main belt, with a low-mass population having a wide range of eccentricities, inclinations, and compositions.

The second phase occurs later, possibly as late as ~4 G.y. ago or nearly 500 m.y. after the removal of the gaseous protoplanetary disk. Once again, the giant planets became temporarily unstable, such that some of them may have strongly interacted with a large primordial disk of comet-like planetesimals located in the outer reaches of the solar system. This allowed the giant planets to migrate from an initial resonant and compact configuration to their current configuration. The instability may also have led to the additional loss of asteroids from the main-belt region. The so-called “Nice model” provides a description of this evolutionary phase. The strength of this model is that it naturally reproduces various observed constraints within a single model, such as the current semimajor axes, eccentricities, and inclinations of giant planets; the curious existence of Trojan asteroids, a population that is reviewed by Emery et al.; and the structure of the Kuiper belt beyond Neptune. The Nice model also provides a possible explanation to the origin of the so-called late heavy bombardment, which some argue produced numerous younger basins on the Moon and terrestrial planets.

The studies of these first two phases provide us with new insights into how and where planets formed, with implications for the dynamical history of the asteroid belt and the diversity of compositions observed in the relatively narrow ~1-AU-wide main asteroid belt, as reviewed by DeMeo et al. These new scenarios together describe an evolutionary process that could lead to a solar system with properties that are consistent with the observed one. The aforementioned constraints, however, are challenging, and it is possible that the new scenarios will founder as they are tested in detail. Therein lies the new science that will comprise *Asteroids V* in the decade or more to come.

The third phase, reviewed by Morbidelli et al., covers the interval between late giant planet migration until today. Potentially as much as half the asteroid population was lost via depletion taking place at unstable resonances with the giant and terrestrial planets, mostly during the subsequent 100 m.y. after late planet migration took place.

Additional constraints on these ideas come from models of the collisional evolution of the asteroid belt. As reviewed by Bottke et al., the latest generation of model results suggests that the main belt’s wavy size-frequency distribution describes a primordial population dominated by 100-km-diameter and larger objects (see Johansen et al.) that undergoes sufficient comminution to create much of the observed population of <100-km bodies. The shape of the size distribution created in this process can then be considered something of a fossil-like remnant of a violent early epoch. This left the main-belt size distribution in a collisional quasisteady state, and it has possibly been that way for billions of years.

Insights from collisional evolution models, however, rely strongly on our understanding of the physics of collisional disruption events. Scaling laws are needed to define the results of two-body collision results, and precise expressions are

needed to define the nature of the fragment size frequency and ejection velocity distributions. As reviewed by Asphaug et al. and Jutzi et al., numerical modeling has become an important method for studying global-scale impacts and asteroid collisions. Moreover, impact experiments remain an important activity that has greatly improved our understanding of the impact process at small scales.

Since *Asteroids III*, computational resources, numerical methods, and impact experiments have all led to a new understanding of the impact process at both large and small scales. Several material models introduced in shock physics codes, with some of their results validated by comparison with laboratory hypervelocity shot experiments, now allow us to better account for the diversity of asteroid properties that affect collision outcomes. In particular, porosity models have been introduced to account for the influence of microporosity in the fragmentation process. Porosity helps to dissipate a portion of the impact energy into the crushing of pores, which results in compaction. This makes porous asteroids more resistant to disruption against impact than expected (see Jutzi et al.). The importance of the shear strength, and its dependency on the confining pressure produced by asteroidal self-gravity, is reviewed by Asphaug et al. They find that when this kind of friction is introduced, the impact energy threshold for disruption can increase by a factor of 5 to 10. The disruption threshold further increases by a factor of 2 to 3 when the energy dissipation by compaction (pore crushing) is taken into account.

The implications of these results are that many collision events previously considered catastrophic, defined as half the combined mass of the projectile and target flying away at escape velocity, are instead more likely to produce a shattered target that remains in possession of much of its mass. As collisional evolution models begin to take these results into account, new possible evolutionary histories of the asteroid belt may reveal themselves.

### 3. ASTEROID DIFFERENTIATION

Another issue that has made major advances since *Asteroids III* is asteroid differentiation. It was originally expected that asteroids that formed early and large enough to heat up enough from the decay of short-lived radioactive isotopes such as  $^{26}\text{Al}$  and melt would eventually form an iron core, olivine-rich mantle, and basaltic crust. Thus all differentiated bodies, large or small, would look like little Vesta. Observational evidence for the mantle material among the known asteroids was lacking, thereby raising the question of “Where is the missing mantle material?” Scheinberg et al. describe differentiation models, including the possibility of partial differentiation, whereby some asteroids may have experienced enough melting to form differentiated interiors but still preserve primitive surface layers. The salient point here is that not all magmas are buoyant; some are happy to reside at depth rather than propelling themselves to the surface. Thus, the old adage that one cannot judge a book by its cover may be particularly appropriate here.

The possible sources of asteroid heating in the early solar system are summarized by Wilson et al. They describe the physical transport of magma in an asteroid during the differentiation process. Because most of our evidence of and information about asteroid differentiation comes from meteorite fragments of differentiated asteroids, these samples can be used to establish a chronology for asteroid formation, differentiation, and subsequent disruption of these differentiated bodies (see chapter by Scott et al.).

### 4. ASTEROID FAMILIES

Collisional evolution models have various constraints that they must reproduce to be validated, as Bottke et al. discuss in their review chapter. A critical one is the number and precise nature of asteroid families. An asteroid family is a group of asteroids that share similar orbital and compositional properties. They have long been thought to originate from the collisional disruption of parent asteroids. It is only in the last decade, however, that the collisional origin of asteroid families has been directly demonstrated by numerical simulations, as reviewed by Michel et al. By including both physical and dynamical effects, such as fragmentation and the gravitational self-atraction of components after a disruption, runs from these codes show that the catastrophic disruption of bodies larger than a few hundred meters in diameter will lead to reaccumulation of debris and the formation of large gravitational aggregates. This potentially solves the mystery of how very large members within asteroid families might form. Without this reaccumulation process, family members produced solely by the fragmentation phase would tend to be very small because the impact energy needed to reproduce the observed ejection speeds is too high to create large monolithic fragments.

Numerical simulations also benefit from the identification of very young families whose properties are the direct outcomes of parent body disruption events. These properties can be directly compared with numerical simulation outcomes, while the dispersion of older families is affected more by post-collision and dynamical processes. Through a careful comparison, we can obtain constraints on the internal structure of family members and the initial state of the parent body from which they came, while also probing the initial dynamical state of the new family. The results of this exercise show that the outcome of a parent body disruption depends strongly on the nature of its internal structure.

Since *Asteroids III*, the inventory of asteroid families has been steadily increasing as surveys continue to find new main-belt bodies. At the same time, several dedicated programs and sky surveys have produced an abundance of physical observations; nearly 2 orders of magnitude more asteroids have been characterized in some fashion than had been done a little more than a decade ago. This has set the stage for huge advances in our knowledge of families, as reviewed in the chapters by Nesvorný et al. and Masiero et al. Progress includes the discovery of several very young families, new data to better understand the full reach of

specific families, and new tools that allow us to determine the dynamical evolution of families by nongravitational forces and date their approximate age.

A key advance in this work has been the comprehensive measurements of asteroid colors by the Sloan Digital Sky Survey and albedos by the Wide-field Infrared Survey Explorer (WISE) infrared telescope. These spectacular datasets also allow us to search for how the surface properties of different family members might vary from object to object. This could help us identify heterogeneity in the composition of the parent body. More critically for impact simulations aiming to reproduce the initial size frequency and ejection velocity distributions of family members, diameter measurements lead to improved estimates of the size-frequency distribution of family members as well as estimates of the original parent body sizes. These data are a rich and diverse source of new information about this history of the main belt.

## 5. ACTIVE ASTEROIDS

One of the more remarkable observational discoveries of the last decade is that some main-belt bodies eject small particles that lead to transient, comet-like comae and tails. These peculiar objects are called active asteroids, and are discussed in Jewitt et al. They are particularly remarkable for being an entirely new population located in one of the closest and most intensively studied regions of the solar system.

There are many plausible causes of this activity. They include impact ejection and disruption, rotational instabilities, electrostatic repulsion, radiation pressure sweeping, dehydration stresses and thermal fracture, as well as ice sublimation. The evidence suggests that one size does not fit all, and a good physical mechanism for activity for one object may not be a good fit for another. We expect substantial advances will be made in this area over the years between the publications of *Asteroids IV* and *V*. These processes also imply that the difference between asteroids and comets in terms of surface activity may be smaller than previously thought, supporting the idea of an asteroid-comet continuum.

## 6. WATER IN ASTEROIDS

While the search for extraterrestrial water has always been a priority in solar system science, particularly with NASA's "follow the water" space mission priorities, it has only recently become a big topic in asteroid science. Even though evidence of aqueous alteration on asteroids has long been known, the direct evidence of water or ice has been limited. *Asteroids IV* has a number of chapters dedicated to recent advances in understanding the role of water on or in asteroids. As described above, the discoveries of activated asteroids covered by Jewitt et al. have great implications for better understanding the relationship between asteroids and comets. Rivkin et al. present observational evidence for water and hydration on asteroids detected from visible to mid-IR wavelengths. They also discuss possible explanations for the presence of water or hydroxyl detections on asteroid surfaces; these explana-

tions include not only the formation of those asteroids in an ice-rich environment, but also space weathering processes and the delivery of exogenic material. Among chondrites that accreted ices during formation, the chapter by Krot et al. describes the degree of aqueous alteration among chondrite types, their implications for the likely locations of the snow line early in solar system history, and the probable location of chondrite formation relative to this snow line.

## 7. ASTEROID PHYSICAL AND COMPOSITIONAL PROPERTIES

The available data on the sizes and shapes of asteroids has grown by exponentially since *Asteroids III*. Mid-infrared surveys, including WISE, have provided diameter and albedo estimates for more than 150,000 asteroids, increasing the characterized population by orders of magnitude (see the chapter by Mainzer et al.). From these data, the first "albedo map" of the main belt was created.

The abundance of thermal infrared data motivated advances in asteroid thermophysical modeling. This modeling has not only improved albedo estimates but has also constrained thermal inertia and surface roughness among different bodies. These parameters in turn constrain the grain sizes at the surface, as discussed in the chapter by Delbo et al. Moreover, a new mechanism for regolith production has been identified: thermal cracking through repeated temperature changes on an asteroid surface. We also have identified more shapes of asteroids than ever before via radar studies (chapter by Benner et al.), direct asteroid imaging, lightcurve inversion into shape models, and the combination of multiple data sources (see the chapter by Durech et al.). So far, these shapes have proven to be reliable, as demonstrated by spacecraft imaging the same targets.

In their review chapter, Reddy et al. review revised equations to constrain mineralogy and describe diagnostic features in the mid-infrared spectroscopy of asteroids, for which there were little data in previous books. Belskaya et al. discuss how our growing sample of polarimetric measurements has helped constrain the refractive index, particle size, packing density, and optical heterogeneity. Advances in photometry were led by spacecraft observations as well as theory and laboratory measurement (see the chapter by Li et al.).

For three decades we have sought to understand why the most common meteorite type, ordinary chondrites, does not spectrally match the most common asteroid taxonomic type, the so-called S-type asteroid. This has been known as the ordinary chondrite paradox. It was the Hayabusa mission returning samples from (25143) Itokawa that finally settled and resolutely revealed that these two sets are in fact a compositional match (see chapters by Yoshikawa et al. and Brunetto et al.). Significant progress has been made in understanding the primary cause of the spectral mismatch, i.e., the space weathering process. Brunetto et al. review what we have learned about space weathering over the past decade. Vernazza et al., in light of the link between ordinary chondrites and S-type asteroids, review the compositions of

ordinary chondrites and what they tell us in the context of the formation and evolution of S-type parent bodies. It has been scientifically rewarding to resolve this longstanding puzzle with the first sample return mission to an asteroid.

## 8. ASTEROID GEOPHYSICS

Before the first asteroid images were sent from space, our knowledge of asteroids relied entirely on groundbased observations, meteorite analysis, and analytical/numerical modeling studies. Now, *in situ* images from flyby and rendezvous missions have revolutionized our knowledge of their physical properties. Since *Asteroids III*, space missions have closely studied an extreme range of asteroid sizes. For example, NASA's Dawn mission, reviewed by Russell et al., orbited (4) Vesta, the second largest asteroid (530 km diameter), and is now orbiting (1) Ceres, the largest (950-km diameter). These two worlds provide potential windows into the nature of the protoplanets that accreted into the terrestrial planets and perhaps those strange large bodies found today in the Kuiper belt.

On the opposite end of the size distribution, Japan's Hayabusa mission visited a 320-m-sized near-Earth asteroid (NEA) named (25143) Itokawa, which turns out to be a rubble pile, and successfully returned a sample to Earth, as reviewed by Yoshikawa et al. The European Space Agency's (ESA) Rosetta mission performed flybys of the E-type asteroid (2867) Steins, discovering that it had the shape of a "diamond in the sky," and the M-type asteroid (21) Lutetia, which was found to have an intriguingly high density of  $3.4 \text{ g cm}^{-3}$ . Rosetta then continued on to Comet 67P/Churyumov-Gerasimenko, where it successfully performed the spectacular and successful landing of Philae. These encounters, as well as that with the contact binary (4179) Toutatis by China's Chang'e mission, are reviewed by Barucci et al.

Finally, Murchie et al. discuss what we have learned about Phobos and Deimos, two bodies in orbit around Mars. These satellites have several traits in common with low-reflectance bodies, and they arguably resemble some of the typical denizens found in the outer asteroid belt. The origins of Mars' satellites have long been debated. Some believe their physical properties point to them being captured asteroids. The problem is that the low inclinations of Phobos and Deimos are hard to match by any known capture mechanism. Instead, it can be argued they are more likely to be the byproduct of a disk of debris formed near Mars by some potential mechanism (e.g., similar to the preferred theory of the formation of Earth's Moon). Comparisons between Phobos/Deimos and what is known about low-albedo asteroids may ultimately provide us with solutions to this longstanding problem.

These missions showed us that asteroids are not only incredibly diverse in size, shape, structure, composition, and rotational properties, but have also been subjected to a wide range of processes. Each encounter/rendezvous provided us with a taste of how granular mechanics, landslides, earthquakes, faulting, and impact cratering affect worlds of

many different sizes. The way in which matter behaves on an asteroidal surface, as well as the way in which the surface material will respond to different processes, depends drastically on a body's surface gravity. It is therefore no surprise that the 34-km-long asteroid (433) Eros, the primary target of the Near Earth Asteroid Rendezvous (NEAR) mission, and the 535-m-long asteroid (25143) Itokawa have very different surface properties, despite the fact that they are the same taxonomic type.

Over the past decade, remote and *in situ* observations have revealed that the surfaces of asteroids are generally covered by loose unconsolidated material called regolith. Regolith is present on asteroids of all sizes, from the largest to those as small as a few hundreds of meters, such as Itokawa. As a result of the unique microgravity environment that the smaller (and most populous) components of the asteroid population possess, complex and varied geophysical processes have given birth to fascinating features that we are just now beginning to understand. These processes were first described through detailed spacecraft observations, but recently have been studied in detail using theoretical, numerical, and experimental methods that combine several scientific disciplines. Murdoch et al. provide a summary of what the scientific community has learned so far about granular materials on the surfaces of these small planetary bodies using both experimental techniques and numerical simulations. Studies of how regolith evolves and responds to different processes (e.g., impacts, shaking, etc.) in low-gravity environments are vital to our understanding of observations as well as the design of future space missions.

Other ubiquitous features of asteroid surfaces are impact craters. As discussed by Marchi et al., crater populations are a powerful tool to trace back an asteroid's surface history and constrain its age. Large craters excavate deep inside the asteroid and produce reverberating stresses that cause global surface modifications, massive faulting, and overturn. Of the known asteroid craters, only the ~500-km Rheasilvia and ~400-km Veneneia craters, the two largest craters on (4) Vesta (see the chapter by Russell et al.), show clear evidence for gravitational rebound and central peak formation. These two basins overlap in Vesta's southern hemisphere, providing a distinct challenge for modeling efforts (see the chapter by Asphaug et al.). Understanding the formation of these giant craters is critical to interpreting Vesta's history, the nature of its associated asteroid family, and the origin of the howardite, eucrite, and diogenite (HED) meteorites that are almost certainly samples from Vesta itself.

While many broad questions were posed in the *Asteroids III* chapter on asteroid interiors, we are now able to delve more deeply into these. In this volume, authors leverage what has been learned from observations across a huge range of asteroid sizes and from our greater understanding of the processes that contribute to their interior properties (see the chapter by Scheeres et al.). As an example, consider that giant craters act as probes of interior geology (see Asphaug et al.), while bodies smaller than 100 km in diameter may increasingly originate from cratering and disruption events

among larger bodies (see Bottke et al.). Consequently, most smaller bodies should be fractured, shattered, or rubble-pile bodies. Moreover, according to simulations, all bodies larger than a few hundred meters extracted from a larger body through a catastrophic disruption experienced reaccumulation during the ejection/gravitational phase of the collision (see Michel et al.).

Along these lines, Scheeres et al. review our current understanding of asteroid interiors and morphology. This includes a discussion of the strength of asteroid materials as inferred from meteors and meteorites, the density and porosity of asteroids as derived from remote observations, global constraints on asteroid strength and morphology based on ground- and spacebased observations, analytical theories of asteroid strength and evolution, and the current state of numerical simulation techniques of asteroid strength.

Despite these efforts, however, it is clear that many issues and questions remain. For example, we do not yet have a clear and detailed view of how to define the interior of an asteroid, even though we can approximately infer its strength based on its spin rate and on how it evolves. We are also lacking a robust theory of tidal dissipation within such rubble-pile bodies, as well as a way to characterize the critical parameters of rubble piles (e.g., rigidity, tidal Love number). Compared to the extent of knowledge at the time of *Asteroids III*, major advances have been made, but we still have a long way to go. It is here that direct measurements of asteroid interiors using techniques such as radar tomography or seismic experiments could provide us with new and strongly needed insights.

## 9. YARKOVSKY AND YORP EFFECTS

During the current and relatively calmer phase of main-belt history (i.e., the last 3 G.y. or so), we have become increasingly aware of slow but steady dynamical mechanisms that contribute to the evolution of asteroid physical properties, the modification of the orbits of asteroid family members, and the transport of asteroids from the main belt to resonances that can take them into near-Earth space. Vokrouhlický et al. review recent progress in our understanding of the Yarkovsky and Yarkovsky-O’Keefe-Radzievskii-Paddack (YORP) thermal forces that modify the orbits and spin rates of small asteroids. At the time of *Asteroids III*, the Yarkovsky effect had been explored theoretically, but it had not yet been directly detected. (6489) Golevka was the first asteroid for which an unambiguous signature of the Yarkovsky effect was detected in its orbit. Other detections, as well as upcoming possibilities, are reviewed in the chapter by Vokrouhlický et al.

Additional progress has also been made concerning the “sunlight alters spin” mechanism called the YORP effect. Analyses of small-asteroid populations indicate clear evolutionary differences due to the YORP effect, both in rotation rate and obliquity. Vokrouhlický et al. discuss the direct measurements of this effect as well as how sensitive it is to small-scale surface topography. YORP can either decrease or increase an asteroid’s spin rate. In the latter case, YORP

spinup can lead to a fission event and/or to the formation of a binary system. For such a system, a variant of the YORP effect has been proposed, called binary YORP (BYORP), that can potentially cause interesting effects to the newly formed satellite. It has not been directly observed as of yet, although some predictions stemming from this effect have been confirmed.

Both the Yarkovsky and YORP effects have many implications for asteroid properties, family structures, distribution of asteroid spin properties, transport of asteroids out of the main belt, and formation of asteroid binaries (Walsh and Jacobson), and could be an intriguing tool to probe the nature of individual asteroids.

## 10. MULTIPLE SYSTEMS

Multiple systems (e.g., binary and triple asteroids) are a nonnegligible fraction of the asteroid population. Their formation and evolution have been the subject of intensive work and discoveries over the past decade. The observational aspects of these systems are reviewed by Margot et al., while Walsh and Jacobson review how they have been modeled to date.

Since *Asteroids III*, the number of known binary NEAs has also more than quadrupled, while the number of known large main-belt asteroids with satellites has doubled. Half a dozen triple asteroids have been discovered. Moreover, populations of so-called asteroid pairs, defined as asteroids that have lost companions, have now become a flourishing field of research. Even small main-belt binaries have been identified, which is quite an achievement given how difficult it is to study small main-belt asteroids of any type.

These systems provide a natural laboratory in which to study many different types of physical processes acting on asteroids and how their dynamics provide a valuable probe of their physical properties — otherwise only possible with *in situ* spacecraft missions. Observations of small binary systems (with diameters of the primary body <10 km) have motivated theoretical work showing that YORP torques can efficiently drive the rotational disruption of small asteroids. Constraints on the dynamical evolution of those systems have also been obtained; they account for the effect of tides, thermal forces, and rigid body physics. The split pairs have then pushed theorists to explore a wide range of evolutionary end-states.

## 11. NEAR-EARTH ASTEROIDS

Asteroids that cross Earth’s trajectory pose a threat to humankind. The explosion of a 20-m bolide over Chelyabinsk in Russia on February 13, 2013, and the realization that even relatively small impact events can cause human injuries, served as a valuable reminder of this fact. The inventory of potentially hazardous asteroids (PHAs) has driven the development of mitigation strategies; there are very low probabilities of Earth impact in the near future, but if a large asteroid does hit, the impact could have major consequences for life on Earth.

The proximity of asteroids in the PHA class of bodies also offers us with the opportunity for exploration via robotic and human missions. Abell et al. review the current status of ongoing projects to fulfill the dream of a human mission to an asteroid by NASA and other space agencies. These asteroids may also be a potential source of rare minerals, although there is still much to learn and to be done before we can fully exploit them.

The recent advances in asteroid surveys are reviewed in the chapter by Jedicke et al. To date, the vast majority of the known asteroids have been discovered by dedicated surveys funded by NASA. The ability of these surveys to find small asteroids has also steadily improved, with 8× more near-Earth objects (NEOs) and 10× more main-belt asteroids found in the last 5 years than in the 5 years leading up to *Asteroids III*. In particular, the NASA directive to discover 90% of NEOs greater than 1 km in diameter is estimated to have been achieved, and now the new challenge is to do the same for the smaller NEOs, which still pose serious regional threats to Earth.

Once an object is discovered, its orbit must be computed. Despite a well-consolidated theory of orbit determination, the increasing number and ever higher quality of observational data, together with the goal of pushing forward the horizon for ephemeris predictions, pose new challenges in estimating asteroid trajectories. Farnocchia et al. review the methods currently in use to compute asteroid orbits, predict their evolutions, and assess the impact hazard to Earth. Considerable activity has taken place regarding the hazard caused by asteroids. The goals of these studies are to increase the number of identified potentially hazardous objects and better understand the efficiency of various mitigation techniques. International institutions, such as the United Nations (UN), have also begun to organize a response to this risk. These activities are reviewed in the chapter by Harris et al.

Another field that has flourished since the time of *Asteroids III* is the study of subkilometer-sized asteroids. There are more than 9000 of these that have been discovered to date among NEOs. Binzel et al. summarize the current understanding of NEO spectroscopic properties.

Another method that can be employed to study the smallest asteroids is the use of meteoroid observation networks, which detect and measure fireballs, typically centimeter- to meter-sized bodies that enter Earth's atmosphere. Emission measurements provide compositional information, and additional data is provided by the fireball's path, which can constrain the body's orbit prior to entry.

Spectacular fireballs from the past decade that have resulted in meteorite recovery include the Chelyabinsk and Almahata Sitta (2008 TC<sub>3</sub>) events (see the chapter by Borovička et al.). The case of Almahata Sitta is particularly fascinating. As reviewed by Borovička et al., in October 2008, a small asteroid with a flat (gray) spectrum at 550–800-nm wavelengths and a weak pyroxene absorption band around 900 nm — asteroid 2008 TC<sub>3</sub> — entered the atmosphere and exploded over the Nubian desert, depositing material in a strewn field in northern Sudan. Searches to date

have recovered >600 fragments, but the net collected mass is still <1% of the expected mass of the roughly 3–4-m-diameter bolide. Most of this missing mass was almost certainly lost in the atmosphere. These materials are collectively named Almahata Sitta (AHS), and represent the first recovered meteorites from a spectrally observed asteroid. The ensuing wave of work on AHS revealed an enormous diversity of components. None of this was predicted from the remote spectral observations of the asteroid in space, showing that our interpretation of asteroid physical and compositional properties from remote observations must always be treated with due caution.

Smaller bodies in the form of micrometeorites also reach Earth. Interplanetary matter falls to Earth at a rate of 10,000–40,000 tons per year, mostly in the form of meteoroids with sizes ranging from 10 μm to 1 mm. Most of this material appears to come from disrupted Jupiter-family comets, which would explain the dynamical signatures of these bodies as well as their predominately primitive compositions. Jenniskens reviews the considerable progress made in this area, as well as what we have learned in charting meteoroid streams at Earth and understanding the mechanisms of meteoroid stream formation and evolution.

Several ongoing fragmentation cascades of comets and primitive asteroids manifest themselves as multiple meteoroid streams at Earth. Evidence is mounting that recently released meteoroids fall apart on timescales of 100–10,000 years, breaking into smaller meteoroids that survive for another ~100,000 years to form the zodiacal dust cloud. Main-belt asteroids are thus thought to contribute only a small fraction of the cloud's material. For asteroid-like material, the active asteroid (3200) Phaeton is perhaps the most significant source of the infall to Earth of freshly ejected meteoroids.

## 12. PERSPECTIVES

During the next decade, our knowledge of asteroids should undergo major improvements and possibly substantial revisions, thanks to both current and future space missions, groundbased observations, and future advances in numerical and theoretical works.

Dawn's visit to (1) Ceres will be completed by the time this book is released, but most of the science learned from that part of the mission will be in the realm of *Asteroids V*.

Two sample return space missions — Hayabusa-2 and the Origins Spectral Interpretation Resource Identification and Security-Regolith Explorer (OSIRIS-REx) — will visit their respective asteroid targets at nearly the same time. The Japan Aerospace Exploration Agency's (JAXA) Hayabusa-2 mission, launched successfully on December 3, 2014, will arrive at the primitive C-type NEA 1999 JU<sub>3</sub> in 2018. It will orbit the body for approximately one year before returning a sample to Earth in 2020. A small lander, the Mobile Asteroid Surface Scout (MASCOT), will perform *in situ* investigations, while a small carry-on impactor will perform a 2 km s<sup>-1</sup> impact and will create a crater on the asteroid's surface — allowing us to test numerical impact models and

scaling laws on a real asteroid surface — in which a sample will possibly be collected in addition to at least one other sample in a different area.

The counterpart of Hayabusa-2, NASA's OSIRIS-REx mission, will be launched in September 2016 and will arrive at the primitive B-type asteroid (101955) Bennu in 2018. It will also orbit its target for nearly a year before collecting a sample. The samples will then arrive on Earth in 2023. These two missions will allow us to make huge strides in our understanding of primitive asteroids while also helping us place into context our knowledge of certain types of carbonaceous chondrite meteorites. It will also be novel to compare and contrast the physical nature and compositional properties of two different C-complex asteroids (or see if they are from the same parent family).

ESA and NASA are also now performing a Phase A study of the Asteroid Impact and Deflection Assessment (AIDA) mission. AIDA is a joint ESA-NASA cooperative project that entered into the 15-month Phase A in 2015 and aims to be the first kinetic impactor test if approved in fall 2016 for launch in 2020. The characterization of its target — the secondary of the binary NEA (65803) Didymos — by ESA and the kinetic impact test by NASA would take place in 2022 and would allow us to have a first direct measurement of an asteroid internal structure by radar tomography and an asteroid's response to an impact.

It is also hoped that a new Discovery-class mission will be selected with asteroids as a target. Several proposed projects intend to survey and discover asteroids, visit particular or several asteroids in the main belt, perform seismic experiments on a NEA, and visit Trojan or active main-belt asteroids. The Japanese are studying a sample return from a Trojan asteroid using a novel solar sail for propulsion.

The 2029 Apophis encounter at 5.6 Earth radii from Earth's center is close enough for the body's spin to be affected by tidal forces. This will be a grand experiment in asteroid seismology that nature is performing for us. It would thus be interesting to see if tidal effects are enough strong to trigger some kind of surface or interior motion. This opportunity is so unique that it may ultimately motivate a space agency or an international effort to devote a small space mission to it.

The next generation of groundbased and spacebased telescopes is also underway. The space mission Gaia (ESA)

is an all-sky astronomic space survey launched in 2013 that will measure the positions and colors of all sources down to a magnitude of V = 20. By the end of the mission in 2020, Gaia is expected to provide absolute astrometric positions for 350,000 asteroids that will be 2 orders of magnitude more precise than currently exist. We will also gain huge improvements in the accuracy of asteroid orbit determinations, and the masses of the largest 100 asteroids will be well established. Using spectra in visible wavelengths, Gaia will also provide a more refined taxonomic classification for many asteroids. Overall shapes, spins, and pole coordinates for various asteroids will also be part of the Gaia output.

The Large Synoptic Survey Telescope (LSST) also promises to discover large numbers of NEOs and other small bodies in the solar system. The James Webb Space Telescope (JWST), scheduled to launch in 2018, is the successor to the Hubble and Spitzer telescopes; it will feature a 6.5-m primary mirror. The next generations of groundbased telescopes are also in design or at early stages of construction. These include 30–40-m-class telescopes such as the Thirty Meter Telescope (TMT) to be built in Hawaii and the Giant Magellan Telescope (GMT) and European Extremely Large Telescope (E-ELT) to be built in Chile. These telescopes will provide opportunities for research on asteroids not currently possible and will allow discoveries we have not yet imagined.

Finally, our knowledge of asteroids is crucial to understanding the surroundings of other stars. We now have discovered more than 1800 confirmed extrasolar planets, plus more than 4500 Kepler planet candidates. The number of discoveries regarding exoplanets and debris disks will only increase, although we will not be able to observe the detailed properties of these systems in the near future. Asteroids carry information that is key to understanding planetary formation, as explained in several chapters of this book. They, along with comets, are the closest analog we have to the types of objects involved in planet formation. By exploring how asteroids formed and evolved, we glean insights into the history and properties of debris disks and planetary systems around other stars. Asteroids are therefore fascinating not only because they tell us about our own solar system's provenance and evolution, but also because they can help us better interpret what is going on in newly discovered planetary systems.

*Part 2:*

*Physical and  
Compositional Properties*



# The Compositional Structure of the Asteroid Belt

F. E. DeMeo

*Massachusetts Institute of Technology*

C. M. O'D. Alexander

*Carnegie Institution of Washington*

K. J. Walsh and C. R. Chapman

*Southwest Research Institute*

R. P. Binzel

*Massachusetts Institute of Technology*

---

The past decade has brought major improvements in large-scale asteroid discovery and characterization, with over half a million known asteroids, more than 100,000 of which have some measurement of physical characterization. This explosion of data has allowed us to create a new global picture of the main asteroid belt. Put in context with meteorite measurements and dynamical models, a new and more complete picture of solar system evolution has emerged. The question has changed from “What was the original compositional gradient of the asteroid belt?” to “What was the original compositional gradient of small bodies across the entire solar system?” No longer is the leading theory that two belts of planetesimals are primordial, but instead those belts were formed and sculpted through evolutionary processes after solar system formation. This chapter reviews the advancements on the fronts of asteroid compositional characterization, meteorite measurements, and dynamical theories in the context of the heliocentric distribution of asteroid compositions seen in the main belt today. This chapter also reviews the major outstanding questions relating to asteroid compositions and distributions and summarizes the progress and current state of understanding of these questions to form the big picture of the formation and evolution of asteroids in the main belt. Finally, we briefly review the relevance of asteroids and their compositions in their greater context within our solar system and beyond.

## 1. INTRODUCTION

By the early 1990s, in the era of *Asteroids II*, roughly 10,000 asteroids had been discovered, only a fraction of the total number of asteroids that are now known to exist. At that time, asteroids were discovered by visually inspecting photographic plates for light trails. In the 1990s, many of the major automated discovery surveys came online. By the year 2000, around the time of *Asteroids III*, ~20,000 asteroids were known (see Fig. 1). Today (in 2015, *Asteroids IV*) there are roughly 700,000 asteroids with known orbits, revealing much new information about the asteroid belt’s dynamic past. About 100,000 asteroids have measurements that tell us about their surface compositions (Ivezic et al., 2001; Szabo et al., 2004; Nesvorný et al., 2005; Carvano et al., 2010), providing a broader view of the asteroid belt than ever before. With the explosion of asteroid discoveries over the past decade (Fig. 1) and the conclusion of two of the largest asteroid physical measurement surveys, the Sloan Digital Sky Survey (SDSS)

(Ivezic et al., 2001) and the Wide-field Infrared Survey Explorer (WISE) (Mainzer et al., 2011), it is timely to reflect upon recent advances, leaving us well poised for the next generation of major surveys, including Gaia (Mignard, 2007) and the Large Synoptic Survey Telescope (LSST) (Ivezic et al., 2007; Jones et al., 2009).

This chapter reviews our current understanding of the compositions of asteroids in the main belt from asteroidal, meteoritic, and dynamical perspectives. Our view of the asteroid belt has changed dramatically since the “big picture” chapters from *Asteroids* and *Asteroids II* (Chapman, 1979; Gradie et al., 1989; Bell, 1989). In the context of this chapter, the use of the term “compositional trends” is more akin to taxonomic rather than mineralogical trends, and the “compositions” discussed here refer more to broad trends of observational data than any derived mineralogical information. In section 2, we review the current tools used to compositionally (taxonomically) characterize and classify asteroids and meteorites, and the dynamical tools that help us interpret the current orbital distribution of the

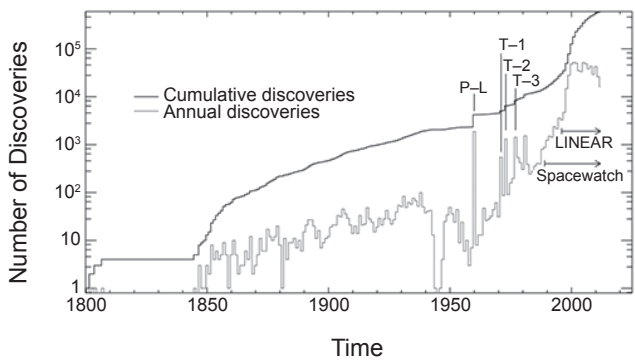


**Fig 1.** The cumulative number of known asteroids and the yearly discovery rate are plotted above. The surveys responsible for spikes in detection are marked: Palomar-Leiden (P-L), Trojan (T-1, T-2, T-3), Spacewatch, and LINEAR. Recent years have seen an explosion in asteroid discoveries due to automated telescopic surveys with advanced detection algorithms. As of the year 2015, nearly 700,000 asteroids have been discovered.

asteroids. We also review the current distribution of asteroid classes in the main asteroid belt. Section 3 focuses on how the current observational constraints strengthen or weaken leading dynamical theories. In section 4, we summarize the meteoritic evidence for asteroid compositions, as well as when and how asteroids formed. In section 5, we compile the major compositional questions in asteroid science and review the progress made toward answering many of them to provide a broad view of asteroid compositions and their locations in the belt. Section 6 looks at asteroids in their greater context for Earth, the solar system, and beyond. Appendix A lists the major outstanding questions relevant to asteroid compositions and distributions. Appendix A also briefly summarizes the current state of knowledge and suggests future work to solve these problems. Many of these questions are noted specifically in this chapter and are addressed, and most are covered in more detail in other chapters.

## 2. THE OBSERVATIONAL PERSPECTIVE

### 2.1. Asteroid Composition Tools

The surface properties (grain size, mineralogy, degree of space weathering, etc.) of an asteroid can be inferred through spectral and photometric measurements at wavelengths from the ultraviolet (UV) to the infrared (IR). Thermal emission at longer wavelengths is used to calculate surface albedos that are related to surface compositions (see the chapter by Mainzer et al. in this volume). Absorption features in reflectance spectra from UV to mid-IR wavelengths and emission features in the mid-IR range can be used to identify minerals and other compounds on the surface of an asteroid or meteorite (see the chapter by Reddy et al. in this volume). For example, olivine and pyroxene have readily identifiable absorption features located at 1  $\mu\text{m}$  and, for pyroxene, 2  $\mu\text{m}$ .

While mineralogical analysis is most appropriate for detailed studies of bodies with distinct features, relatively few asteroids have the high-quality spectra that are required for this. On the other hand, taxonomic classifications can be made using lower-quality or lower-resolution spectra, providing a rapid characterization of asteroid spectra and a common language for comparing them. Hence, taxonomic information is available for orders of magnitude more than the number of asteroids for which detailed spectra have been measured. At the time of *Asteroids III*, the majority of reflectance spectra were taken at visible wavelengths to 1  $\mu\text{m}$ , and were classified according to the Bus or Tholen taxonomies (*Bus and Binzel*, 2002b; *Tholen and Barucci*, 1989). The mafic silicate-rich asteroids with available near-IR spectra at the time were classified mineralogically by the Gaffey system (*Gaffey et al.*, 1993). By the early 2000s, near-IR spectrometers became available, such as SpeX on the NASA Infrared Telescope Facility (IRTF) (*Rayner et al.*, 2003). An extension of the Bus taxonomy, the so-called Bus-DeMeo taxonomy, was created to classify both the visible and near-IR data in such a way as to be as consistent with the Bus taxonomy as possible (*DeMeo et al.*, 2009). A comparison of each of these major taxonomies is presented in Table 1.

Asteroid spectra are traditionally divided into three major complexes and each of the complexes is divided into individual classes (also called “types”). The S-complex, originally named for its expected silicaceous composition (*Chapman et al.*, 1975), is characterized by spectra with moderate silicate absorption features at 1 and 2  $\mu\text{m}$ . The C-complex, historically named in connection with carbonaceous chondrite meteorites, has low-albedo surfaces with spectra that have flat or low slopes and are subtly featured to featureless. Subtle features have absorptions of only a few percent, one of the most notable being the 0.7- $\mu\text{m}$  feature indicating the presence of phyllosilicates likely due to aqueous alteration (*Vilas and Gaffey*, 1989). The X-complex is characterized by moderately sloped and subtly featured or featureless spectra. It has long been known that the X-complex is compositionally degenerate because it comprises the darkest and brightest surfaces of all asteroids, with albedos as low as a few percent to as high as 50%. The Tholen taxonomy distinguished the X-complex by albedo, breaking it up into the E, M, and P classes, ranging from high to low albedo.

Additionally, there are spectral classes that do not fit within these three main complexes. These spectra typically have more extreme or distinct characteristics and are much less common than the major complexes. These include the spectrally featureless and very red-sloped D-types; the spectrally olivine-dominated A-types with the broad, deep 1- $\mu\text{m}$  feature; and the spectrally pyroxene-dominated V-types with a deep, narrow 1- $\mu\text{m}$  feature and a deep, broad 2- $\mu\text{m}$  feature. Additionally, there are the K-, L-, T-, O-, Q-, and R-types. A visual summary of the visible and near-IR spectral classes is provided in Fig. 2. A description of the spectral features can be found in *Bus and Binzel* (2002b) and *DeMeo et al.* (2009).

TABLE 1. Comparison and explanation of the progression of spectral taxonomies.

Taxonomic System	Tholen (1984)	Gaffey (1993)	Bus (2002)	Bus-DeMeo (2009) (B-D)	Taxonomy Notes	Relevant Minerals and Possible Meteorite Analogs
Wavelength Range	0.33–1 μm	0.35–2.50 μm	0.45–0.90 μm	0.45–2.45 μm		
S-complex		S	SI SII SIII SIV SV SVI SVII	S Sa Sq Sr Sk Sl	 Tholen: Defined only S. Gaffey: 7 mineralogic classes based on Band I center and Band II/Band I area ratio. Primarily separates olivine to orthopyroxene ratio. Bus: Separates based on strength of 0.9-μm drop, indicative of 1-μm band. B-D: Definition largely preserved from Bus. Now includes full 1- and 2-μm feature in near-IR. Sl, Sk, and Ld are removed, Sv is added.	Minerals: olivine, pyroxene Meteorites: S(I): pallasites?, R chondrites, brachinites S(IV): many are ordinary-chondrite-like S(V): primitive achondrites? S(VII): basaltic achondrites
C-complex				B C Cb Cg Cgh Ch	 Tholen: Primarily distinguished by the 0.3–0.5-μm UV dropoff region. Bus and B-D do not cover this region, thus do not make these distinctions. Bus: Defined by UV dropoff and/or by 0.7-μm Cgh, Ch feature. B-D: Definition largely preserved from Bus. Near-IR is largely degenerate.	Minerals: opaques, carbon, phyllosilicates, some have weak features indicating olivine, pyroxene Meteorites: carbonaceous chondrites (except CV), possibly impact melts from ordinary chondrites and HEDs?
X-complex		E M P		X Xc Xe Xk	 Tholen: EMP are spectrally degenerate. Distinguished by high (E), med (M), and low (P) albedo. Bus: X class defined by shape of curve and/or 0.49-μm Xe feature. B-D: Definition largely preserved from Bus. Near-IR is largely degenerate.	Minerals: M,P: opaques, carbon, low-Fe pyroxene. E: enstatite, oldhamite Meteorites: M,P: carbonaceous chondrites (not CV). M w/high radar albedo: irons, CB chondrites, silicate-rich irons E: enstatites
Other: End members, outliers				T D Q O R V A K L Ld	 Definitions for each of these classes are relatively consistent among taxonomies as they are each spectrally distinct.	D: opaques, organics Q: mostly LL OCs O: pyroxene, olivine R: olivine, pyroxene V: HEDs, pyroxene, plagioclase feldspar A: pallasite, brachinite, R chondrites, olivine K: CO, CV, olivine L: CAI-rich, spinel-rich

A simple description of relevant minerals and meteorites for each class is presented. For meteorite and mineral details see Burbine et al. (2002).

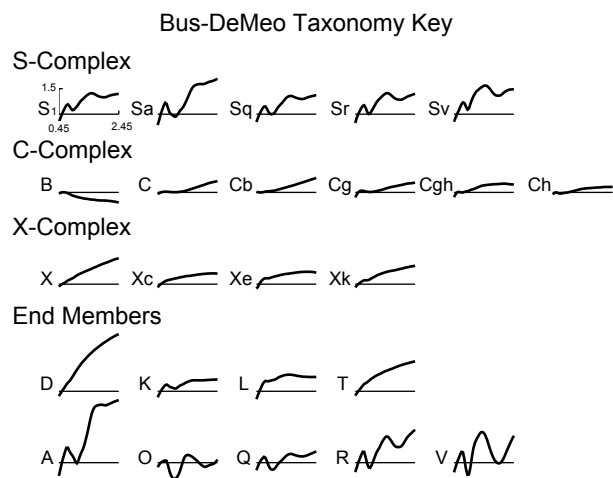


**Fig 2.** The 24 spectral classes of the Bus-DeMeo taxonomy key measured over visible and near-infrared wavelengths. Based on work from DeMeo *et al.* (2009).

The accuracy of an asteroid's classification depends on the quality of the data. Also, repeated observations of a single object may show spectral (hence perhaps taxonomic) differences that may be intrinsic (due to rare mineralogical or grain size variations on different portions of the body), may reflect real but uncorrected variations due to photometric viewing geometry, or may reflect instrumental or observational artifacts. We emphasize the advice from the chapter by *Bus et al.* (2002) in *Asteroids III*, “We should not feel compelled to decide which label is ‘correct,’ but should rather accept these distinct labels as a consequence of our growing knowledge about that object.” For example, an object classified by visible wavelength measurements alone may “change its type” when the wavelength coverage is extended to the near-IR, or when an albedo measurement becomes available. An improved answer as more information becomes available is simply the scientific method at work.

One of the biggest challenges remains how to determine surface compositions from asteroid spectra and spectral types. Most materials on an asteroid's surface do not produce distinct, identifiable features in a reflectance spectrum. Furthermore, an asteroid spectrum is not only a product of composition, but is also affected by factors such as grain size, temperature, viewing geometry, and space-weathering processes (see the chapter by Reddy *et al.* in this volume). The compositional interpretation of many asteroid classes has broadened over time. While the S-complex has been linked to ordinary chondrite meteorites and the C-complex to carbonaceous chondrites, there is strong evidence that these spectral classes are not compositionally uniform. There is a range of different types of ordinary and carbonaceous chondrites, and there are additional meteorite classes that also may comprise subsets of the S- and C-complexes. This must be accounted for when interpreting spectra.

In addition to the visible and near-IR, asteroid spectra are now also measured beyond 2.5  $\mu\text{m}$  and into the mid-IR.

Asteroid spectra at these wavelengths are categorized by the presence of and shape of a 3- $\mu\text{m}$  absorption feature indicating hydrated minerals or phyllosilicates (*Takir and Emery*, 2012; see also the chapter by Rivkin *et al.* in this volume). There are four distinct spectral groups of 3- $\mu\text{m}$  features. Beyond the 3- $\mu\text{m}$  feature, the mid-IR range (7–25  $\mu\text{m}$ ) holds a wealth of information (*Emery et al.*, 2006) because many minerals have diagnostic features at these wavelengths. There are multiple deterrents to analyzing these longer wavelengths: Instrument design sensitivity requirements are challenged by measurements taken at ambient temperatures, observations are constrained by the lower solar flux, and available laboratory experimentation to interpret the spectra is currently limited in number (e.g., *Vernazza et al.*, 2010, 2012).

## 2.2. The Historical Perspective

Initial measurements from the 1940s through the 1970s found that the surface brightness and colors of asteroids trend from medium-albedo and moderate spectral slopes (S-complex) for bodies in the inner part of the main asteroid belt to lower-albedo and neutral spectral slopes (C-complex) toward the outer part of the main belt (*Fisher*, 1941; *Kitamura*, 1959; *Wood and Kuiper*, 1963; *Chapman et al.*, 1971, 1975). The diversity was a great surprise and the trend with distance motivated further observations.

The hundreds of observations available with even greater wavelength coverage in the 1980s then revealed distinct peaks in relative abundance for each of the major classes of asteroids at certain distances throughout the belt (*Zellner et al.*, 1985; *Gradie and Tedesco*, 1982; *Gradie et al.*, 1989). Because the asteroids were grouped systematically with heliocentric distance, it was concluded that the asteroids formed close to their current locations. In the context of a relatively static solar system, where the asteroids were assumed to have formed nearly in place, the variation in the compositions of these asteroids was interpreted to represent the original thermal gradient across the main belt from the time of planetesimal formation (see question C1 of Appendix A). While this fundamental trend among the largest asteroids has remained robust, both our interpretation of surface properties and the dynamical models explaining this structure have evolved.

Two major surveys from the late 1990s to early 2000s (*Bus and Binzel*, 2002a; *Lazzaro et al.*, 2004) provided spectroscopic data for around 2000 asteroids. While much of the ensuing analysis focused on asteroid families, two works investigated taxonomic distributions with orbital properties. *Bus and Binzel* (2002b) note a more detailed distribution than Gradie and Tedesco, finding double peaks for the S- and C-complex with distance from the Sun. *Mothé-Diniz et al.* (2003) found that the distribution of C-complex objects was different for higher vs. lower inclinations. These authors were also the first to show the presence of S-complex asteroids at distances as far as 3 AU in their dataset of asteroids larger than 15 km and found a fairly even distribution of S-complex out to that distance.

### 2.3. Recent Progress

The next major survey released was the Sloan Digital Sky Survey. Although it was designed for extragalactic studies, it made crude spectral observations of more than 100,000 moving objects in the field. These data were released in several Moving Object Catalogs (*Ivezic et al.*, 2001; *Parker et al.*, 2008). Combined with the more recent Near-Earth Object Wide-field Infrared Survey Explorer (NEOWISE) survey, which produced over 100,000 diameters and albedo estimates (*Mainzer et al.*, 2011; *Masiero et al.*, 2011), there now exists a treasure trove of physical measurements to analyze. Many of the advances in understanding the compositions of asteroids in the main belt since *Asteroids III* have stemmed from these datasets, as well as targeted spectroscopic surveys or targeted follow-up studies of objects in these two large datasets. Here we describe taxonomic trends beginning in the Hungaria region and extending out to the Jupiter Trojans. Figure 3 shows the distribution of the asteroid class in each heliocentric distance region and multiple size regimes. We use the terms “inner,” “middle,” and “outer” main belt to refer to the three regions of the main belt carved by the  $v_6$  secular, 3:1, and 5:2 mean-motion resonances (the  $v_6$  starts near 2 AU and the 3:1 and 5:2 are located at 2.5 and 2.82 AU, respectively).

The Hungaria region ( $1.8\text{--}2.0$  AU,  $i \sim 20^\circ$ ) is dominated by high-albedo [ $>0.3$  (*Tholen and Barucci, 1989*)] E-type

asteroids that have moderate spectral slopes and often display a 0.49- $\mu\text{m}$  absorption feature (*Gradie and Tedesco*, 1982; *Bus and Binzel*, 2002b). These E-types are considered members of the Hungaria asteroid family (*Gaffey et al.*, 1992) with (434) Hungaria being the brightest member. In the Hungaria region, however, there are a variety of compositional types, including S- and C-complex objects (*Carvano et al.*, 2001).

In the inner main belt (2.0–2.5 AU), the dominant players are (4) Vesta (V-type) and a number of large S-complex asteroids. C-complex asteroids are rare in the inner belt at large sizes ( $D > 100$  km) where they comprise only 6% of the total mass, but they make up a quarter of the mass at medium sizes ( $20 \text{ km} < D < 100 \text{ km}$ ), and are almost equal to the S-complex by mass at the smallest sizes ( $5 \text{ km} < D < 20 \text{ km}$ ). At the same time, the fractions of medium-sloped spectral types (M and P) decrease at smaller sizes. Newly discovered in the inner main belt are D-type asteroids defined by their very red spectral slopes, which had only previously been seen at larger distances aside from a few near-Earth objects (NEOs) that have dynamical origins in the outer belt and beyond (Carvano et al., 2010; DeMeo and Carry, 2014; DeMeo and Binzel, 2008). These objects are discussed later in section 5.2.

An interesting effect of viewing the inner main belt by mass (previous analyses have viewed such statistics by number, not by mass) is the relative insignificance of the Vesta family, the products of a large collision with Vesta, in the inner belt

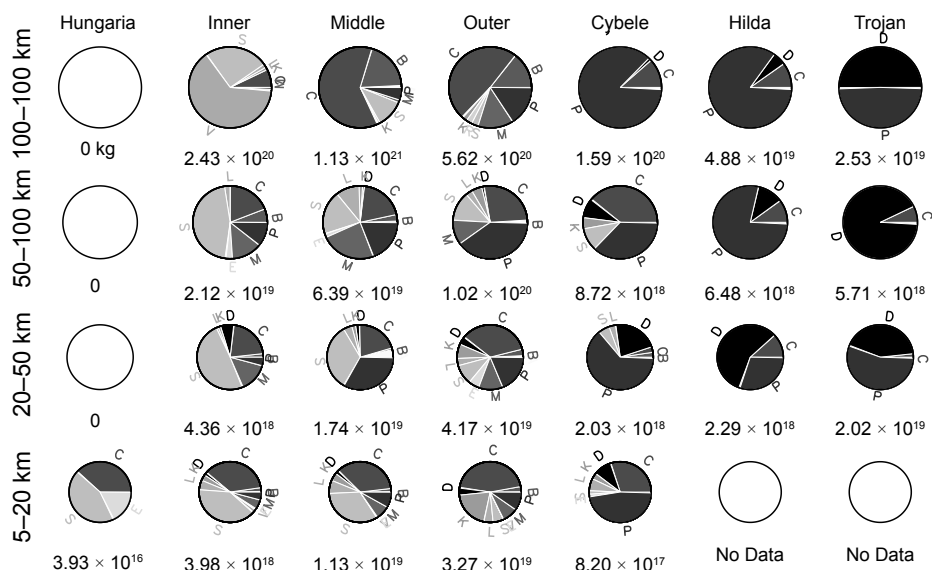


**Fig 3.** The distribution of asteroid classes by mass in distinct size ranges and distances from the Sun. Asteroid mass is grouped according to objects within four size ranges, with diameters of 100–1000 km, 50–100 km, 20–50 km, and 5–20 km. Seven zones are defined as in Fig. 1: Hungaria, inner belt, middle belt, outer belt, Cybele, Hilda, and Trojan. The total mass of each zone at each size is labeled and the pie charts mark the fractional mass contribution of each unique spectral class of asteroid. The total mass of Hildas and Trojans are underestimated because of discovery incompleteness. The top row is consistent with results from *Gradie and Tedesco* (1982) and *Gradie et al.* (1989). Figure from *DeMeo and Carry* (2014).

(Binzel and Xu, 1993). Indeed, when excluding Vesta itself, only a handful of all Vesta family members, called vestoids, are larger than 5 km, so their mass contribution even among 5–20-km-diameter bodies is minuscule [1% of that size range and region (DeMeo and Carry, 2014)]. Vestoids are significant contributors to the inner belt in terms of the total number observed (Parker et al., 2008; Masiero et al., 2013), but it is their high albedo, close distance, and spectral distinctiveness that have biased their discovery and classification.

In the middle main belt (2.5–2.82 AU), (1) Ceres (C-type in the Bus-DeMeo taxonomy) and (2) Pallas (B-type) are the largest objects and they comprise roughly 31% and 7%, respectively, of the entire main belt by mass. The broad taxonomic makeup of the inner and middle belt at the smallest sizes is essentially identical.

In the outer main belt (2.82–3.3 AU), the C-complex dominates by mass, with (10) Hygiea being the largest and most massive member. Despite the fact that the relative fraction of S-complex asteroids is small in the outer main belt, their total mass is still quite significant given that the mass in the outer belt is 2–10× greater than in the inner belt at each size range.

A- and V-types, respectively olivine-dominated and basaltic asteroids, are present in small numbers throughout the main belt, aside from those associated with Vesta (Lazzaro et al., 2000; Moskovitz et al., 2008; Sanchez et al., 2014). Their discovery in the middle and outer belts was surprising since differentiated bodies or fragments of them were not expected in the context of the classical understanding of asteroid differentiation. Significant advances have been made since *Asteroids III* in understanding the complexity of both the asteroid differentiation process and the mechanisms that displace material throughout the solar system (see the chapters by Scheinberg et al., Scott et al., and Morbidelli et al. in this volume).

Families play a very important role in the architecture and composition of the main belt. The chapter by Masiero et al. in this volume covers this topic in detail. It will be valuable for future work to incorporate the size-frequency distribution of asteroid families into studies of the radial distance distribution of asteroids in the main belt to fully interpret the results, particularly at small asteroid sizes.

The taxonomic makeup of the largest Hildas (~4 AU) and Trojans (5.2 AU) remain predominantly P-type and D-type, respectively. The trends at smaller sizes are discussed in section 5.2. The chapter by Emery et al. in this volume is dedicated to the Trojan population, covering the compositional and physical characteristics as well as the dynamical history.

### 3. THE DYNAMICAL PERSPECTIVE

#### 3.1. Dynamical Tools

Determination of an asteroid's orbit immediately tells you where it is currently spending its time in the solar system, and the combination of the distributions of known orbits and

physical properties provide powerful clues to the evolution of the solar system (questions A2 and A3 in Appendix A). However, there are many more asteroids with known orbits than there are with physical characterization, and at times we are left to gain context based on their orbits alone. The dominant perturber in the solar system is Jupiter, and its effects are made clear by the large depleted Kirkwood gaps in the asteroid population owing to its mean-motion resonances. Given the dominance of Jupiter's perturbations for asteroid orbits, one can take advantage of its similarity to the restricted three-body problem to generate some quasi-conserved quantities. The most common measure is the Tisserand parameter  $T_J$ , which is calculated with respect to Jupiter and can help to distinguish between different classes of small body orbits. This is primarily used to separate Jupiter-family comets ( $2 < T_J < 3$ ) from nearly isotropic comets ( $T_J < 2$ ), but is also commonly used to try to uncover dormant comets in the NEO population (Levison et al., 1994; Bottke et al., 2002b; DeMeo and Binzel, 2008) and separate main-belt comets from the ordinary comet population (see the chapter by Jewitt et al. in this volume).

Orbits are typically calculated and reported for what the asteroid's Keplerian orbit would be at a specific epoch in the presence only of the Sun. This calculated "osculating orbit" does not incorporate any information about short- or long-term oscillations of the orbit owing to the perturbations of the giant planets. The "proper elements" of an asteroid represent quasi-integrals of motion, meaning that they are nearly constant in time, and can be calculated or estimated using various numerical and analytical tools (Knežević et al., 2002). The difference between an asteroid's osculating and proper orbital elements can be substantial — tens of percent in  $a$ ,  $e$ , and  $i$ . The proper elements of an asteroid are representative of its long-term orbit and are essential in studies of dynamically related clusters or families of asteroids (see the chapter by Nesvorný et al. in this volume; Bendjoya et al., 2002; Zappalà, 2002).

An important dynamical process affecting the entire main asteroid belt is the Yarkovsky effect (see Bottke et al., 2002a, 2006). This is a size-dependent drift in a body's semimajor axis caused by the reemission of absorbed solar radiation. It is the main driver that pushes main-belt asteroids into resonances and they can then become NEOs or be driven to extreme orbits that could have them impact a planet or the Sun, or be ejected from the solar system. Smaller objects move more rapidly, where drift rates scale roughly as  $1/D$ , which means that where we find smaller objects now may simply be a waypoint on a drift across the asteroid belt (where a 1-km body might drift roughly  $10^{-4}$  AU in 1 m.y.). A similar point of confusion for small objects is that the collisional lifetimes are much shorter than the age of the solar system at sizes smaller than 10–30 km (see the chapter by Bottke et al. in this volume). Between the effects of the Yarkovsky drift and collisional evolution, we can really trust the orbits of only the 500 or so largest bodies ( $D > 50$  km) as tracers of the early structures of the asteroid belt.

As the Yarkovsky effect pushes asteroids around, some will inevitably reach an orbital resonance [a mean-motion resonance with Jupiter or other powerful secular resonances (see Nesvorný *et al.*, 2002)]. While the effects of this may vary, a typical response is an increase in the asteroid's orbital eccentricity. As the eccentricity increases to large values, it can cause the body to cross the orbit of Jupiter, which can easily result in its ejection from the solar system. If the asteroid first has an interaction with the terrestrial planets, it is possible that its orbit can be altered in a way to pull it out of the main asteroid belt and reside almost entirely within the inner solar system. In near-Earth space, the orbital dynamics are controlled by the chaotic interactions with the terrestrial planets and thus the population is transient, with only a 10-m.y. lifetime (Gladman *et al.*, 2000). Numerical models of the evolution from the main belt to near-Earth orbits have largely recovered the flux of bodies moving through different resonant passageways and can explain the size of the NEO population (Bottke *et al.*, 2000, 2002b). Furthermore, the NEO model of Bottke *et al.* (2002b) provides a dynamical tool to make statistical links between NEAs and the most likely resonant pathway they traveled from the main asteroid belt. Some NEOs can be probabilistically linked to specific regions of the main belt, allowing for links to be made between bodies and their regions or possible parent asteroid families (e.g., Campins *et al.*, 2010).

Even the orbits of the largest bodies have likely been altered substantially early in solar system history. As models of solar system evolution have matured, the effects of the possible "late" (after ~400 m.y. or so) movements of the giant planets have been studied in the most detail (see the chapter by Morbidelli *et al.* in this volume). Specifically, some traces of giant planet migration are still found in the main asteroid belt by way of depletions near primordial mean-motion resonances with Jupiter (Minton and Malhotra, 2009), although some types of migrations can be ruled out by clear patterns of depletion and orbital changes that would still be noticeable in today's asteroid belt (Morbidelli *et al.*, 2010). As the possible late migration of the giant planets has been studied in more detail, it is clear that many small bodies could be affected. The violent instability of the giant planets has been found to provide ideal dynamical pathways to capture the Trojan asteroids at Jupiter (Morbidelli *et al.*, 2005; Nesvorný *et al.*, 2013), capture the irregular satellites of the giant planets (Nesvorný *et al.*, 2014), implant D- and P-type asteroids from the primordial Kuiper belt into the main asteroid belt (Levison *et al.*, 2009), and sculpt the Kuiper belt (Levison *et al.*, 2008; Batygin *et al.*, 2012). An example of the effects that planetary migration would have on small bodies and the asteroid belt is shown in Fig. 4.

The distribution of asteroid orbits, their physical properties, and the total mass depletion in the asteroid-belt region are all used as constraints on early solar system evolution, as discussed below (and in more detail in the chapter by Morbidelli *et al.*).

### 3.2. Dynamical Overview of the Main Belt

The asteroid belt today is estimated to contain approximately  $\sim 5 \times 10^{-4}$  Earth masses ( $M_{\oplus}$ ), which is approximately  $3\times$  the mass of its most massive asteroid, (1) Ceres (Krasinsky *et al.*, 2002). This is in contrast to the nearly  $1 M_{\oplus}$  of material that would be expected to inhabit this region given a smooth distribution of the solid material found in the planets (Weidenschilling, 1977). Similarly, classical models of planetesimal formation suggest that the current mass in the asteroid belt today would not be enough to have grown the largest asteroids, and thus there has been a depletion of mass since the asteroid belt formed (see Weidenschilling and Jackson, 1993). As discussed in detail in the chapter by Morbidelli *et al.* (and below), there are multiple proposed methods to remove so much mass from the asteroid belt, and there are also new models for planetesimal formation that may allow the formation of large asteroids directly from small "pebbles" in the solar nebula (see the chapter by Johansen *et al.* in this volume).

The orbital distribution of the asteroid belt finds that most of the dynamically stable phase space of  $a$ ,  $e$ ,  $i$  is filled, with orbital eccentricities ranging from 0 to 0.35 and inclinations from  $0^{\circ}$  to about  $30^{\circ}$ . Meanwhile, every theory for planetesimal formation relies on the damping effects of the gaseous solar nebula to reduce relative velocities and increase accretion rates (see the chapter by Johansen *et al.*). This implies that, at least immediately following their formation, planetesimals would have been on circular and coplanar orbits and were dynamically excited into their current orbits at some later time.

The loss of mass, observed dynamical excitement, and taxonomic mixing are presumed to be closely linked to the dynamical evolution of the solar system — including the formation and migration of the terrestrial and giant planets. As described in more detail in the chapter by Morbidelli *et al.*, models typically attack all three constraints with one mechanism. Studies of sweeping secular resonances due to the dissipation of the solar nebula suffer dual problems of needing long (20 m.y.) timescales of gas dissipation to deplete enough bodies, and then typically failing to reproduce the inclination distributions (see O'Brien *et al.*, 2007). The inclination distribution is also a problem for models that invoke stranded planetary embryos that excite and deplete the primordial asteroid belt (see O'Brien *et al.*, 2006). Here there is depletion of low-inclination bodies owing to their low-velocity encounters with planetary embryos, and again a mismatch with the observed distributions. Collisional processes are also important constraints. While even very massive asteroid belts (e.g., with 1000 times more mass than today) would have collisionally ground away most mass and reached a total mass similar to that found today (Chapman and Davis, 1975), the remnants and scars of such dramatic and long-term collisional evolution would likely be more visible in our studies today (see also the chapter by Bottke *et al.*).

Partly due to the inability of models to simultaneously match constraints with the terrestrial planets (the mass of

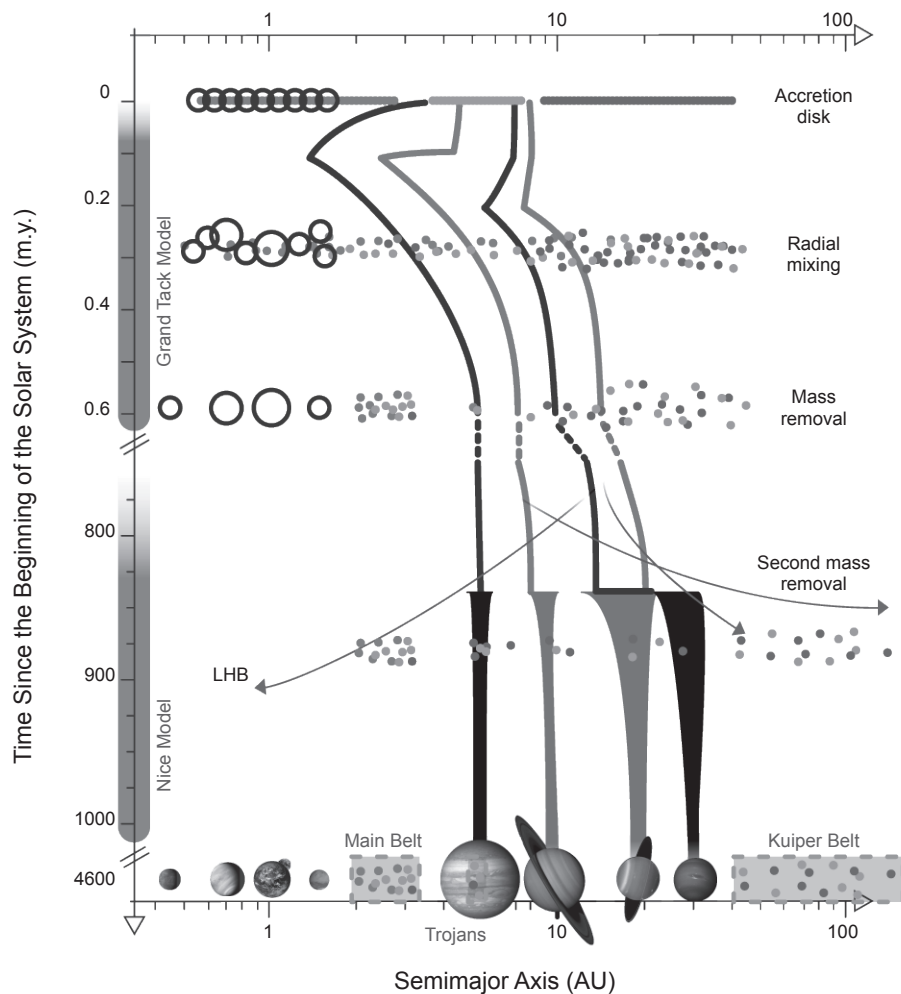


**Fig 4.** This cartoon depicts major components of the dynamical history of small bodies in the solar system based on models. These models may not represent the actual history of the solar system, but are possible histories. The figure displays periods of radial mixing, mass removal, and planet migration — ultimately arriving at the current distribution of planets and small-body populations. Figure from DeMeo and Carry (2014).

Mars) and with the asteroid belt (orbital distributions and water delivery), a recently proposed model, the Grand Tack model, invokes a scattering implantation of nearly the entire asteroid belt population from different parent populations (Walsh *et al.*, 2011). This dramatic migration of the giant planets causes widespread depletion and then mixing of remnant populations into the dynamically stable asteroid belt. When Jupiter is migrating inward, it completely depletes all objects native to the current asteroid belt. During its outward migration it scatters some remnants of this population back into the asteroid belt, and then during the outermost stretches of its migration it also scatters in bodies from more primitive reservoirs between and beyond the formation region of the giant planets. This mechanism is distinct from others as it implies separate parent populations for some of the major different compositional classes found in the asteroid belt, and also because it results in a low-mass asteroid belt from

very early on in solar system history. While it provides first-order matches to these three asteroid belt constraints (mass depletion, orbital distributions, and taxonomic distributions), they were not a prediction of the model — rather, they were a necessary constraint for the model to be viable. Going forward, each of these can be investigated more closely and hopefully limit or rule out some of the free parameters in the current Grand Tack scenario (growth and migration parameters of the giant planets).

Already, the Grand Tack model relies on some assistance from what is thought to follow in solar system history. The eccentricity distribution in the Grand Tack model is elevated compared to what is observed today (Walsh *et al.*, 2012). However, the motion of the giant planets during the “Nice model,” which might have happened roughly 400 m.y. later, will alter the orbits of the asteroid belt while having minimal affect on taxonomic distributions or total mass

[eccentricities are the primary orbital element altered, and total mass is only depleted by a factor of 2–3 (*Morbidelli et al.*, 2010), although the Nice model is credited with implanting D- and P- types bodies in the main belt]. In fact, *Minton and Malhotra* (2011) find that a very excited asteroid belt (elevated eccentricities) is a good fit when considering very simple models of giant planet migration that could come later. However, the models regarding later giant planet migration is a field of active study, and so each new iteration may require a reinvestigation of this aspect of the Grand Tack model’s asteroid belt fits.

If the Grand Tack model relies on later events, it begs the question of how much we can use different mechanisms to explain different constraints — and are there ways to mesh asteroid belt constraints with other models of planet formation? Already planet-formation models are increasingly using the asteroid belt as a constraint for their model outcomes, both for delivering water-rich asteroid material to the growing planets (*Morbidelli et al.*, 2000), and also for using their orbits to rule out other modes of planet migration (*Minton and Malhotra*, 2009; *Walsh and Morbidelli*, 2011).

Meanwhile, recent advances in planetesimal formation (see the chapter by Johansen et al. in this volume) imply the possibility of a different initial distribution of mass in the early solar system than previously considered. It is possible that planetesimal formation relies on clumps of “pebbles” collapsing, which could lead to a small number of planetesimals amid a huge number of remnant pebbles — where only a few of the formed planetesimals are large enough to rapidly accrete the remaining pebbles (see *Ormel and Klahr*, 2010). One could envision scenarios in which the asteroid belt never had much mass, and thus dynamical and taxonomic stirring would be constraints independent of mass loss.

#### 4. THE METEORITE PERSPECTIVE

##### 4.1. Meteorite Composition Tools

The parent asteroids of most meteorites would have formed at different times and/or places in an evolving solar nebula. This will have had profound effects on the initial compositions and subsequent histories of the asteroids that are reflected in the way meteorites are classified.

Radial thermal gradients in the disk will have dictated gross differences in compositions upon accretion, such as rock/ice ratios. However, it is evident from the meteorite record that more transient processes were also important in the thermal processing of dust and that radial transport brought together materials with different thermal histories. The thermal processing of dust has left its imprint on the major- and trace-element compositions that show clear variations associated with their volatility. Estimates of the relative volatilities of the elements are traditionally based on thermodynamic equilibrium calculations of their 50% condensation temperatures from a gas of solar composition at a total pressure of  $10^{-4}$  bar (e.g., *Lodders*, 2003). There

is also evidence in meteorites for the fractionation of elements in the nebula according to their chemical affinities (lithophile — rock-loving, siderophile — Fe-metal-loving, and chalcophile — sulfide-loving). Physical processes that separated solid/melt from gas and silicates from metal seem the most likely causes for these variations.

After accretion, asteroids were subject to internal heating, largely due to the decay of the short-lived radionuclide  $^{26}\text{Al}$  ( $t_{1/2} \approx 720,000$  yr) that was inherited from the protosolar molecular cloud. Thus, asteroids that formed early will tend to have been more internally heated than those that formed later, although other parameters will also have influenced internal temperatures. The least-heated meteorites ( $<150^\circ\text{C}$ ) normally exhibit varying degrees of aqueous alteration. Thermally metamorphosed meteorites have been more severely heated (up to  $800^\circ\text{--}900^\circ\text{C}$ ), which will have dehydrated them if they were not dry already, and they exhibit varying degrees of recrystallization and chemical reequilibration between minerals. Finally, there are meteorites that came from bodies that underwent melting and, in many cases, differentiation that produced metal-sulfide cores and silicate mantles.

The classification of meteorites has recently been reviewed in considerable depth (*Krot et al.*, 2014), and so is only briefly summarized here. The most basic separation of meteorites is into unmelted meteorites (chondrites) and melted meteorites (nonchondrites). The chondrites are generally assumed to come from parent bodies that were smaller and/or formed later than those of the nonchondrites, although it is possible that some chondrites are the unmelted crusts of differentiated bodies (*Weiss and Elkins-Tanton*, 2013). For further subdividing meteorites, the most useful classification tools reflect the meteorites’ nebular (primary) and parent body (secondary) characteristics — both physical and chemical. It is important to note that the causes of the variations in primary and secondary features are not always well understood, but that makes them no less useful as classification tools. Superimposed on the primary and secondary characteristics can be shock features and brecciation associated with later large impacts, as well as terrestrial weathering. A complete classification scheme must also account for these effects, but they will not be considered here.

For classification based on bulk chemistries, it is usually sufficient to use a few representative element ratios that reflect the major fractionations that influenced meteorite compositions. The CI chondrites enjoy a unique status among meteorites because their bulk compositions are identical within error to the rock-forming component of the solar photosphere. Since all objects are thought to have ultimately evolved from the solar composition, elemental compositions and ratios are usually normalized to (divided by) the CI composition.

Oxygen isotopes have proved to be a very useful classification tool because, in addition to the mass-dependent fractionations produced by most physical and chemical processes, meteorites exhibit mass-independent variations (changes in  $^{16}\text{O}$  abundance relative to  $^{17}\text{O}$  and  $^{18}\text{O}$ ).

Recently, other isotope systems, most notably Cr, have begun to be used as additional classification tools.

A significant number of meteorites do not fit easily into the established groups. Since by convention groups must be composed of five or more members, these meteorites are classified as ungrouped. Each meteorite group is generally assumed to come from a single asteroidal parent body that had a uniform composition at the time of its formation. Nevertheless, it cannot be ruled out that members of a group come from a number of asteroids that formed at similar times and places (e.g., Vernazza *et al.*, 2014) (see also question B2 in Appendix A). Assuming that a group comes from a single parent body and that ungrouped meteorites come from separate parent bodies, meteorites appear to be samples of 100–150 distinct parent bodies (Burbine *et al.*, 2002) (see also question B1 in Appendix A).

**4.1.1. Chondrites.** The chondrites are composed of three major components — refractory inclusions and chondrules, both of which formed at high temperatures, are embedded in a fine-grained matrix. Refractory inclusions are a diverse group of objects, broadly divided into calcium-aluminum-rich inclusions (CAIs) and amoeboid olivine aggregates (AOAs). The inclusions are the oldest known solar system solids and, in some cases, formed by condensation from a hot gas, while others formed by melting and evaporation of preexisting solids (MacPherson, 2014). Chondrules appear to have typically formed 1–3 m.y. after refractory inclusions as molten silicate-metal droplets in brief (hours to days) heating events in very “dust-rich” environments. Being so fine grained, the matrix is very susceptible to parent-body modification, but seems to originally have been dominated by a mix of fine-grained (<5–10 µm) crystalline and amorphous silicates. Matrix also contains the bulk of the most volatile elements in chondrites, as well as all the organic matter and presolar circumstellar grains found in them, and probably originally contained the ices accreted by most chondrite groups.

Almost all chondrites belong to one of five classes that have been further subdivided into a number of groups (Table 2). Each group is defined by a narrow range of primary physi-

cal features (e.g., chondrule sizes, abundances, types, etc.), elemental compositions, and O (and Cr) isotopic compositions.

After accretion, varying degrees of aqueous alteration and/or thermal metamorphism in the parent bodies led to the modification of the primary features of all chondrites. The extent of this modification is reflected in a chondrite’s petrologic type — a chondrite that was unaffected by either aqueous alteration or thermal metamorphism is assigned a petrologic type of 3.0, while petrologic types 3–6 reflect increasing degrees of thermal metamorphism and types 3–1 reflect increasing extents of aqueous alteration. A meteorite’s petrologic type is normally given after its chemical group (e.g., CI1, LL3.0, and H6).

**4.1.2. Nonchondrites.** As with the chondrites, the non-chondritic meteorites are classified according to the properties of their components (mineralogy, grain size, etc.), as well as by their bulk chemical and isotopic compositions (Table 3). Except for those from the Moon and Mars, it is generally assumed that nonchondritic meteorites evolved from originally chondrite-like objects. They are divided into (1) primitive achondrites that have seen very intensive metamorphism, as well as relatively low degrees of partial melting and melt extraction; and (2) differentiated meteorites that underwent extensive melting and differentiation. The differentiated meteorites are further divided on the basis of their Fe-metal contents into achondrites (metal-poor), stony-irons, and irons.

Primitive achondrites sometimes contain relict chondrules, which are chondrules that have survived metamorphism and partial melting of its host rock. However, they have not been conclusively linked to any known chondrite groups. Only one primitive achondrite, the ungrouped Tafassasset, has geochemical affinities to carbonaceous chondrites (Gardner-Vandy *et al.*, 2012). Similarly, only one achondrite, the ungrouped basaltic achondrite Northwest Africa (NWA) 011 and several paired specimens from the same fall, seems to have formed by melting of a carbonaceous chondrite-like body (Warren, 2011).

**4.1.2.1. Stony irons.** Mesosiderites are breccias composed of diverse silicate clasts that are intimately mixed with roughly equal amounts of Fe,Ni-metal and sulfide. Pallasites

TABLE 2. Summary of the recognized chondrite classes and groups.

Class	Groups	
Enstatite (E)	EH, EL	Highly reduced, metamorphosed types 3–6
Rumuruti (R)		Metamorphosed types 3–6, some OH-bearing minerals
Ordinary (O)	H, L, LL	Metamorphosed types 3–6, evidence for H <sub>2</sub> O activity
Carbonaceous (C)	CI, CM, CR CO, CV CK CH, CB	Aqueously altered types 1–3 Metamorphosed types 3, evidence for H <sub>2</sub> O activity Metamorphosed types 3–6, evidence for H <sub>2</sub> O activity Metal-rich, impact products
Kakangari (K)		

TABLE 3. Summary of the nonchondrites.

Meteorite Type	Composition
<i>Primitive achondrites</i>	
Winonaites	Related to IAB irons
Acapulcoites and lodranites	
Brachinites	
<i>Achondrites</i>	
Aubrites	Broadly basaltic compositions, related to E chondrites
Ureilites	Contain veins of graphite and diamond
Angrites	Basaltic compositions
HEDs	From (4) Vesta
Howardites	Eucrite and diogenite breccias
Eucrites*	Basaltic compositions
Diogenites	Coarse pyroxene and olivine
<i>Stony irons</i>	
Mesosiderites	Impact breccias
Pallasites	Core-mantle boundary material (?)
Main group	Related to IIIAB irons (?)
Eagle Station group	Related to C chondrites
Pyroxene group	
<i>Irons</i> <sup>†</sup>	
Magmatic	IVAs related to L/LL chondrites
IC, IIAB, IID, IIC, IIF, IIG, IIIAB, IIIE, IIIF, IVA, IVB	
Non-magmatic	IIES related to H chondrites,
IAB, IIE, IIICD	IABs related to winonaites

\* A few anomalous eucrites may not be from (4) Vesta.

† 15% of irons remain ungrouped.

are composed of Fe,Ni-metal/sulfide that is intergrown with similar proportions of relatively coarse-grained olivine and pyroxene crystals. There are three recognized subtypes that probably came from at least three different parent bodies. Traditionally, it has been assumed that pallasites are core-mantle boundary samples. However, recent studies indicate that the main-group pallasites experienced a range of cooling rates, which would not be expected if they come from the core-mantle boundary of a single body (Yang et al., 2010b).

**4.1.2.2. Irons.** Iron meteorites are divided into 14 chemical groups, although ~15% of irons remain ungrouped. The chemical groups fall into one of two categories, magmatic and nonmagmatic. The magmatic irons exhibit intragroup chemical variations that are consistent with fractionation between solid and liquid metal that presumably occurred during crystallization of planetesimal cores. The chemical variations within the nonmagmatic iron groups are more difficult to understand and they tend to contain abundant silicate clasts. These irons may have formed in melt pools during failed core formation, but are more likely the products of impacts. Many of the ungrouped irons are also probably impact melts, particularly the smaller ones.

## 4.2. When and How Big Did Asteroids Form?

As discussed in detail below, the formation of chondrites seems to have occurred between roughly 2 and 4 m.y. after CAIs (question A1 in Appendix A). Calcium-aluminum-rich inclusions are the oldest dated objects in meteorites [4567.3 ± 0.2 m.y. (Connelly et al., 2012)] and are generally considered to provide the best estimate of the time of solar system formation, although Boss et al. (2012) have suggested that most CAIs formed toward the end of the Fu Orionis outburst phase of young stellar evolution. Meteorites from differentiated objects seem to have formed slightly earlier than chondrites, although the uncertainties in their ages do allow for significant overlap with chondrite formation and it is possible that some chondrites represent the unmelted crusts of differentiated objects. Some carbonaceous chondrites, such as the CKs, formed roughly contemporaneously with the other chondrite classes, but others may have formed up to 1 m.y. later. The absence of chondrites that formed later than 3–4 m.y. after CAIs suggests that planetesimal formation effectively ceased at this time in the chondrite-forming regions, possibly marking the dissipation of the gas disk. If the carbonaceous chondrites were scattered into the asteroid belt from the outer solar system, this must have occurred after the formation of the youngest carbonaceous chondrites.

At present, there is no way to measure the accretion ages of chondrites directly, although there is evidence from their short-lived <sup>53</sup>Mn-Cr systematics that the H and EH chondrite parent bodies had formed ~2 m.y. after CAIs (Polnau and Lugmair, 2001; Shukolyukov and Lugmair, 2004). In principle, the youngest chondrules in a chondrite group provide an upper limit to the age of their parent body. Most studies have dated individual chondrules using the <sup>26</sup>Al-Mg system on the assumption that the <sup>26</sup>Al/<sup>27</sup>Al ratio of ~5 × 10<sup>-5</sup> seen in most undisturbed CAIs represents the homogeneous initial ratio of the solar system (e.g., Bizzarro et al., 2004; Hutchison et al., 2009; Jacobsen et al., 2008; Kita and Ushikubo, 2012; Ushikubo et al., 2013; Villeneuve et al., 2009). The assumption of a homogeneous <sup>26</sup>Al/<sup>27</sup>Al ratio in the solar nebula has been questioned by some (Larsen et al., 2011; Schiller et al., 2015), but at present the balance of evidence supports a homogeneous distribution (Kita et al., 2013; Wasserburg et al., 2012). A few chondrule studies have also used the <sup>53</sup>Mn-Cr (Kita et al., 2005), <sup>182</sup>Hf-W (Kleine et al., 2008), and Pb-Pb systems (Amelin and Krot, 2007; Amelin et al., 2002; Connelly et al., 2012; Krot et al., 2005) to date chondrules. Together, these studies suggest that (1) most chondrules in ordinary and CO chondrites and the ungrouped carbonaceous chondrite Acfer 094 formed between 1 and 3 m.y. after CAIs, (2) formation of CV chondrules began almost contemporaneously with CAIs and continued for >3.4 m.y., and (3) chondrules in CR chondrites began forming at about the same time as ordinary and CO chondrules, but the youngest ages are >3–4 m.y. after CAIs. Chondrules in the CB chondrites, which are different from those in other

chondrite groups, have average ages of  $4.6 \pm 0.5$  m.y. after CAIs ( $2\sigma$  standard error) and seem to have formed in an impact (Krot *et al.*, 2005; Yamashita *et al.*, 2010).

Taken at face value, these chondrule ages imply that all chondrite parent bodies formed  $>3$ – $4$  m.y. after CAIs. However, the apparent spreads in chondrule ages are problematic. Chondrules in a particular chondrite group exhibit a limited range of physical and chemical properties that vary from group to group. At the levels of turbulence that are thought to exist in disks, even in a so-called dead zone, chondrules would be mixed over many astronomical units on timescales of 1–3 m.y. (Alexander, 2005; Alexander and Ebel, 2012; Cuzzi *et al.*, 2010). Thus, either chondrite formation was dispersed over a large fraction of the solar nebula, as in the Grand Tack and Nice models, or the quoted ranges in chondrule ages are not real. The latter must be ruled out before concluding the former. Indeed, it has been suggested that most of the reported ranges in Al-Mg ages simply reflect the uncertainties in the measurements (i.e., most chondrules in a chondrite group could have the same age or a narrow range of ages) (Alexander and Ebel, 2012; Kita and Ushikubo, 2012), and that the youngest ages, indeed perhaps all chondrule ages, have been disturbed by parent-body processes (Alexander, 2005; Alexander and Ebel, 2012). It remains to be seen if the range in chondrule Pb-Pb ages also reflect parent-body disturbance.

Given that parent-body processes can disturb the radiometric systems that are used to date chondrules, it is essential to study only the least-metamorphosed and aqueously altered members of a chondrite group. Even in these chondrites, it is essential to take care to select only those chondrules that can be shown to have undergone no secondary modification. The most careful Al-Mg study of chondrule ages conducted to date has been for the ungrouped carbonaceous chondrite Acfer 094, where 9 of the 10 chondrule ages are within error of a mean of  $2.3^{+0.5}_{-0.3}$  m.y. ( $^{26}\text{Al}/^{27}\text{Al} = 5.7 \pm 1.0 \times 10^{-6}$ ) after CAIs (Ushikubo *et al.*, 2013). Selecting only similar (type I) chondrules from a previous study of a primitive CO (Kurahashi *et al.*, 2008) gives a mean age of  $2.0^{+0.3}_{-0.2}$  m.y. ( $^{26}\text{Al}/^{27}\text{Al} = 7.1 \pm 0.8 \times 10^{-6}$ ) after CAIs. The Al-Mg system is more susceptible to modification in the chondrules analyzed in Semarkona, the ordinary chondrite that has been least affected by parent-body processes, but the chondrules have a mean age of  $2.0^{+0.5}_{-0.3}$  m.y. ( $^{26}\text{Al}/^{27}\text{Al} = 7.3 \pm 1.4 \times 10^{-6}$ ) after CAIs (Kita *et al.*, 2000; Villeneuve *et al.*, 2009), which is very similar to those for CO and Acfer 094 chondrules. This Semarkona average chondrule age is consistent with an average age of  $1.7 \pm 0.7$  m.y. after CAIs for H-chondrite chondrules obtained using the  $^{182}\text{Hf}-\text{W}$  system (Kleine *et al.*, 2008).

Additional constraints on the timing of accretion can potentially come from the thermal histories of chondrites since the abundance of the radioactive heat source,  $^{26}\text{Al}$ , will have been a function of accretion time. Modeling of mineral ages with different closure temperatures during metamorphism has been used to estimate the accretion time ( $\geq 2$ – $3$  m.y. after

CAIs) and size ( $\sim 100$  km in diameter) of the H ordinary chondrite parent body (Harrison and Grimm, 2010; Henke *et al.*, 2013; Kleine *et al.*, 2008; Trieloff *et al.*, 2003). Alternatively, assuming that the maximum peak temperatures estimated for any member of a chondrite group represents the peak central temperature achieved in their parent body, along with a diameter of 60 km, Sugiura and Fujiya (2014) estimated accretion ages for all chondrite groups (Table 4), including one for the ordinary chondrites of  $\sim 2.1$  m.y. after CAIs. If this accretion age for the ordinary chondrites is approximately correct, it constitutes further evidence that many measured chondrule ages (e.g., those  $>2.1$  m.y.) are disturbed. Such estimates depend on many assumptions, not the least of which are that we have samples from all depths in the chondrite parent bodies, that the peak temperatures have been accurately determined, that accretion temperatures and initial water ice contents are known, and that the parent body sizes are known. A lack of samples from the deep interior of the CO parent body, for example, could explain why the estimated accretion age of the COs ( $\sim 2.7$  m.y. after CAIs) is younger than for the ordinary chondrites despite their average chondrule ages being so similar.

Further complicating these estimates, some have questioned the simple internal heating models and argue that at least the ordinary chondrite parent bodies are rubble piles produced by early collisions while the bodies were still hot (Ganguly *et al.*, 2013; Scott *et al.*, 2014). Also, there is the suggestion that the CV chondrites, at least, formed in the presence of magnetic fields generated by dynamos in their planetesimal cores (Weiss and Elkins-Tanton, 2013), i.e., that these chondrites are the unheated crusts of differentiated bodies. If true, the accretion age of the CV parent body would have to have been significantly earlier than estimated by Sugiura and Fujiya (2014). However, to date, no achondrites or iron meteorites have been linked to the CVs.

Constraints on the timing of aqueous alteration can be established in some chondrites because two products of alteration, fayalitic olivine and carbonates, incorporated short-lived  $^{53}\text{Mn}$ . Fayalitic olivine in ordinary chondrites formed at  $2.4^{+1.8}_{-1.3}$  after CAIs, while in CV and CO chondrites it formed at  $4.2^{+0.8}_{-0.7}$  and  $5.1^{+0.5}_{-0.4}$  after CAIs, respectively (Doyle *et al.*, 2015). Four to 5 m.y. after CAIs is also about the time that carbonates formed in CM and CI chondrites and the ungrouped chondrite Tagish Lake (Fujiya *et al.*, 2012, 2013; Jilly *et al.*, 2014). Thermal modeling suggests that the parent bodies of these meteorites formed 3–4 m.y. after CAIs.

Thermal modeling of differentiated bodies is even more problematic than for chondrites because, for instance, the initial bulk composition is not known, and how the melts segregate within the bodies can have a profound affect on thermal histories (e.g., Moskovitz and Gaidos, 2011; Neumann *et al.*, 2014). Nevertheless, models of varying degrees of sophistication have been used to estimate their accretion times. For instance, core formation on the IIAB, IIIAB, IVA, IVB, and IID iron meteorite parent bodies occurred at  $0.7 \pm 0.3$ ,  $1.2 \pm 0.3$ ,  $1.4 \pm 0.5$ ,  $2.9 \pm 0.5$ , and  $3.1 \pm 0.8$  m.y.

TABLE 4. Average ages and estimates of the accretion ages of chondrites and various nonchondrites from *Sugiura and Fujiya* (2014) unless otherwise indicated.

Group	Chondrules	Time After CV CAI	Other
<i>Chondrites</i>			
E		$1.8 \pm 0.1$	
O	$2.0 + 0.5, -0.3^*, 1.7 \pm 0.7^\dagger$	$2.1 \pm 0.1, \geq 2-3^\ddagger$	
R		$2.1 \pm 0.1$	
CK		$2.6 \pm 0.2$	
CO	$2.0 + 0.3, -0.2^\S$	$2.7 \pm 0.2$	
CV		$3.0 \pm 0.2$	
CI, CM, CR, TL		$3.5 \pm 0.5$	
<i>Nonchondrites</i>			
Angrites	—	$0.5 \pm 0.4$	$\leq 1.5^\#$
HEDs	—	$0.8 \pm 0.3$	$\leq 2.5 \pm 1^{**}, \leq 0.6 + 0.5, -0.4^{\dagger\dagger}, < 1^{\ddagger\ddagger}$
Magmatic irons	—	$0.9 \pm 0.3$	$1.0 \pm 0.6, 1.3 \pm 0.5, 1.5 \pm 0.5^{\$\$}$
Stony irons	—	$0.9 \pm 0.3$	
Ureilites	—	$1.0 \pm 0.3$	
Acapulcoites + lodranites	—	$1.3 \pm 0.3$	
Aubrites	—	$1.5 \pm 0.1$	
NWA 011	—	$1.5 \pm 0.1$	
Tafassasset	—	$1.9 \pm 0.2$	

\* See text for details.

† Kleine et al. (2008).

‡ Harrison and Grimm (2010), Henke et al. (2013), Kleine et al. (2008), and Trieloff et al. (2003).

§ See text for details.

¶ Kleine et al. (2012).

\*\* Trinquier et al. (2008).

†† Schiller et al. (2011).

‡‡ Neumann et al. (2014).

§§ Kruijer et al. (2013).

Ages are in millions of years after CV CAI formation.

after CAIs, respectively (Kruijer et al., 2014). Previous modeling suggested that the accretion of the IVA, IVB, and IID parent bodies occurred, respectively, at  $1.0 \pm 0.6$ ,  $1.3 \pm 0.5$ , and  $1.5 \pm 0.5$  m.y. after CAIs (Kruijer et al., 2013). However, Kruijer et al. (2014) have significantly revised the accretion age estimates to  $\sim 0.1$ – $0.3$  m.y. after CAIs for the parent bodies of all these iron meteorites. Estimates for the timing of differentiation and the onset of magma ocean crystallization of the HED parent body [(4) Vesta] of  $2.5 \pm 1.0$  m.y. (Lugmair and Shukolyukov, 1998, 2001; Trinquier et al., 2008) and  $\leq 0.6^{+0.5}_{-0.4}$  (Schiller et al., 2011), respectively, are broadly consistent with estimates of accretion times for Vesta of  $< 1$  m.y. after CAIs (Neumann et al., 2014). Core formation in the angrite parent body occurred  $\leq 2$  m.y. after CAIs, and its accretion must have occurred  $\leq 1.5$  m.y. after CAIs (Kleine et al., 2012).

Metallographic cooling rates have been used to argue that the iron meteorites formed in still hot cores that had been stripped of their silicate mantles by impacts (Yang et al., 2007, 2008, 2010a,b). The estimated parent-body diameters for the best-studied groups are IVA =  $300 \pm 100$  km and IVB =  $140 \pm 30$  km, and, assuming roughly chondritic compositions, the sizes of the original bodies with their silicate mantles would have been roughly twice these estimates. Thus, the formation of relatively large asteroids

began quite early. There is geochemical evidence that an even bigger object, Mars, had reached  $\sim 50\%$  of its present mass in  $\leq 1.8^{+0.9}_{-1.0}$  m.y. after CAIs (Dauphas and Pourmand, 2011; Tang and Dauphas, 2014), i.e., contemporaneously with most chondrites.

#### 4.3. How Did Asteroids Form?

Of the chondrites, only the CI chondrites lack clear evidence for chondrules, although even in these highly altered and brecciated rocks, mineral fragments suggest that some chondrules or chondrule fragments may have been present at the time of accretion. It is much harder to say if chondrules were as abundant in the parent bodies of the nonchondritic meteorites, but relict chondrules have been reported in the primitive achondrites, and in silicate inclusions in IIE irons (tentatively linked to H chondrites). Ordinary, R and enstatite chondrites only contain 10–15 vol.% matrix and refractory inclusions are rare in them. It cannot be ruled out that chondrules dominated the dust in their formation regions, but it is also possible that chondrules were preferentially concentrated during planetesimal formation, as predicted by turbulent concentration (Chambers, 2010; Cuzzi et al., 2010) and possibly streaming instability models (see the chapter by Johansen et al. in this volume).

However, the rarity of primitive meteorites with few or no chondrules suggests another intriguing possibility — that chondrule formation and planetesimal formation were linked in some way (Alexander *et al.*, 2008). Metzler (2012) has argued that chondrules in ordinary chondrites were accreted within hours of their formation while they were still hot and plastic. Such a scenario would be consistent with reaccretion of chondrules produced in hit-and-run collisions between partially molten planetesimals (Asphaug *et al.*, 2011), for instance. However, such a model must overcome some serious problems: (1) Accretion of hot chondrules is difficult to reconcile with the contemporaneous accretion of thermally labile material, such as organic matter and water ice; (2) there are a number of geochemical/petrologic objections to making chondrules this way; and (3) it is not clear why only primitive objects that formed in this way are present in our collections. Johnson *et al.* (2015) also propose that chondrules were produced in collisions, although not rapidly reaccreted, i.e., they are byproducts of planetesimal formation rather than being intimately linked to it. If correct and turbulent concentration and the streaming instability need chondrules to work, then the dominant mechanism(s) for planetesimal formation has still to be identified (question A1, Appendix A).

#### 4.4. Where Did Asteroids Form?

There is clear isotopic evidence in O, Ti, Cr, Mo, and Ru for a distinction between the carbonaceous chondrites and almost all other inner solar system objects (including Earth, Moon, and Mars) for which we have samples (Burkhardt *et al.*, 2011; Warren, 2011). With the exception of O, the subtle isotopic variations appear to be nucleosynthetic in origin. The causes of these differences are still not understood, but presumably they reflect subtle differences in the materials from which the planets/planetesimals formed (question A1, Appendix A). These differences are certainly consistent with formation of the carbonaceous chondrites in the outer solar system (beyond the initial orbit of Jupiter), as in envisioned by the Grand Tack and Nice models, but at present other explanations may also be possible.

Since objects at or beyond the orbit of Jupiter tend to be water ice-rich, water contents are a potential means for distinguishing between meteorites/asteroids with inner and outer solar system origins. Some carbonaceous chondrites (CI, CM, and Tagish Lake) were relatively water-rich when they formed, as is evident in the abundant clay minerals that they contain. Other carbonaceous chondrites seem to have accreted some water (CR and CV), but evidence for accretion of water ice in others is limited (CO) or lacking (CK, CH, CB). Further confusing this issue is that ordinary (Alexander *et al.*, 1989; Grossman *et al.*, 2000) and R chondrites (McCanta *et al.*, 2008) also seem to have accreted water ice.

If water contents cannot be used to determine whether the carbonaceous chondrite parent bodies formed at greater radial distances than other meteorite parent bodies, perhaps

the H isotopes of the water can. There is expected to have been a radial gradient in the D/H ratio of water ice in the disk that reflected mixing between interstellar water (high D/H) and water with low D/H that had reequilibrated with H<sub>2</sub> in the hot inner disk (Albertsson *et al.*, 2014; Jacquet and Robert, 2013; Yang *et al.*, 2013). The D/H ratios of water in all comets are similar to or greater than the terrestrial ratio (Lis *et al.*, 2013), and the terrestrial ratio is almost an order of magnitude higher than the bulk solar value. The only other outer solar system planetesimals with measured D/H ratios are Saturn's moons Enceladus, whose water like most comets is enriched in D relative to Earth (Waite *et al.*, 2009), and Titan, whose atmospheric methane D/H is Earth-like (Nixon *et al.*, 2012). On the other hand, the N isotopes of Titan's atmosphere are <sup>15</sup>N-enriched compared to Earth (Mandt *et al.*, 2014), like comets (Rousselot *et al.*, 2014; Shinnaka *et al.*, 2014). While it is still not certain where and how the comets and Saturn's moons formed, their compositions suggest that ice in the outer solar system had D/H ratios that were greater than or equal to terrestrial. However, except for the CR chondrites, the best estimates of the D/H ratios of water in carbonaceous chondrites at the time of accretion were subterrestrial (Alexander *et al.*, 2012). Rather surprisingly, the D/H ratios for water in ordinary and R chondrites are similar to those of the more enriched comets. This probably does not mean that they formed in the outer solar system. It more likely reflects isotopic fractionation associated with the loss of H<sub>2</sub> generated by the oxidation of metal by water in their parent bodies. The effect may have been larger in the ordinary and R chondrites because they had lower initial water/metal ratios. Nevertheless, this process should also have affected the carbonaceous chondrites, so that their initial water D/H ratios were probably somewhat lower than estimated by Alexander *et al.* (2012).

In summary, while carbonaceous chondrites and their asteroidal parent bodies are geochemically distinct from other inner solar system objects that we have samples of, at present there is no direct evidence that they formed at much greater radial distances from the Sun than other meteorite parent bodies.

### 5. ASTEROID COMPOSITIONAL TRENDS

In this section, we explore questions related to the taxonomic distribution of asteroids at both the large and small sizes. A number of questions listed in Appendix A are discussed here.

#### 5.1. What is the Source of the Compositional Gradient in the Main Belt?

For the largest asteroids ( $D > \sim 100$  km), the trend of taxonomic types as a function of distance from the Sun, in the order of S, C, P, D, remains robust. The canonical interpretation of this gradient is that it reflects the compositional variation with distance from the Sun of the dust in

the solar nebula (*Chapman et al.*, 1971, 1975; *Gradie and Tedesco*, 1982) (question C1, Appendix A). At the time, it was anticipated that (1) dynamical processes might have smeared an originally sharper division between asteroids of different composition, and (2) different materials, condensing and accreting earlier or later, might have formed at the same solar distance, also smearing the gradient (*Ruzmaikina et al.*, 1989; *Petit et al.*, 2002).

These ideas have not been ruled out entirely, but it is now apparent that other processes may have played a greater role in producing this gradient. The largest source of uncertainty is the ongoing challenge to associate many of the asteroid taxonomic types with specific types of meteorites or compositions (*Burbine et al.*, 2002). There are ~40,000 meteorites in our collections, yet only ~100–150 distinct parent bodies have been identified from the collections. There are more than 700,000 known asteroids, but only ~100 asteroids with diameters greater than 100 km and 122 notable families (see the chapter by Nesvorný et al. in this volume) that may be considered indicators of the number of parent bodies existing in the main belt today (question B1, Appendix A). It is also possible, but not yet firmly established, that more than one asteroid could be the source of a single meteorite group (e.g., *Vernazza et al.*, 2014) (question B2, Appendix A). There is certainly more work needed to understand the links between meteorites and their asteroidal sources. Next, we briefly summarize some of the known and proposed associations.

It is now clear that a fraction of S-complex objects are ordinary chondrites and that the HEDs are mostly associated with Vesta and its family, but most taxonomic types cannot be robustly associated with specific meteorites or mineralogies. Many asteroid spectra are simply not diagnostic of unique mineral assemblages. E-types have been associated with enstatite chondrites or achondrites, M-types with metallic meteorites, A-types with pallasites or olivine-rich achondrites, L-types with CAIs, etc., but these connections are not unique or robust (*Burbine et al.*, 2002). It is generally understood that some of the C-complex asteroids (including P- and D-types) are likely associated with carbonaceous chondrites, of which there are many subtypes. It is probable that many of these asteroids do not supply meteorites to Earth because their distant orbits are less likely to be perturbed into Earth-crossing, or if their fragments do enter the atmosphere, they may be too fragile and/or arrive at too high a velocity to survive as a meteorite.

A major advance toward interpreting the taxonomic gradient is the understanding of processes that move asteroids and their fragments about. Since the time of *Asteroids* and *Asteroids II*, there is far better understanding of major and minor resonances in the main belt (*Nesvorný et al.*, 2002), of how the Yarkovsky effect (and associated YORP effect) works (*Bottke et al.*, 2006), of past dynamical regimes (e.g., the Grand Tack or Nice models) that may have had profound effects on the distributions of small bodies in the inner and outer solar system (see the chapter by Morbidelli et al. in this volume), and of how asteroid families produced by

catastrophic collisions evolve. It has also been suggested that some inner belt asteroids were emplaced as debris from the terrestrial planet region (*Bottke et al.*, 2006), that comets can be implanted into the main belt, and even that Ceres might have been implanted from the outer solar system (*McKinnon*, 2008).

The gradient is less obvious for smaller main-belt asteroids than for larger ones, but this could be attributed to the fact that several processes act more readily on smaller bodies. The idea that the larger asteroids retain some element of a primordial gradient is more tenable, but clearly only one of a number of possibilities, given recent models (*Walsh et al.*, 2011, 2012). It is uncertain whether astronomical observations together with dynamical scenarios can uniquely solve this problem. We need to measure actual compositions as a function of location in the solar system, whether through better understanding from meteoritical research or from *in situ* studies, to resolve the matter. It is still not understood in any quantitative way how meteorites with different oxygen isotopes were distributed in the early solar system, nor from where they are derived in the modern epoch. Short of a wholly impractical mineralogical and isotopic assay of dozens of asteroids and comets, there does not appear to be a way for this question to be robustly resolved in the near term.

## 5.2. Distribution Changes with Size

While the smallest asteroids are the least studied due to observational biases, there are some interesting possible trends and discoveries that have been noted in the past decade (question C2, Appendix A). Among the Hildas and Trojans the relative frequency of D- and P-types changes as a function of size. *Grav et al.* (2012) find a decrease in spectral slope with decreasing size, which translates to more P-types at smaller sizes. *DeMeo and Carry* (2014) also note a change in relative fraction between the D- and P-types. The cause of this change in spectral slope as a function of size is not yet understood. Possible explanations could include space weathering (*Lantz et al.*, 2013; *Brunetto et al.*, 2014), compositional differences, or grain size effects (e.g., *Cloutis et al.*, 2011a,b).

Additionally, among the smallest asteroids ( $D < \sim 15$  km) we find very red asteroids, D-types, in the inner belt where they were previously not expected (*DeMeo et al.*, 2014). The compositional makeup of these bodies and how they arrived in their current locations are under debate. They could have been scattered farther than expected during the late-stage migration modeled by *Levison et al.* (2009). Perhaps they arrived through another mechanism such as an earlier migration, other planetary scattering, or Yarkovsky drift across the resonances. Ultimately, we cannot rule out the possibility that they are compositionally distinct from other D-types and thus do not require an implantation mechanism.

*DeMeo and Carry* (2013, 2014) reported that the relative abundance of C-complex asteroids in the inner main belt is greater at the smaller sizes. There are multiple possible explanations for asteroids of different compositional types to

have different size distributions. It could be related to the size-frequency distribution of families; for example, C-complex objects may survive longer if they have high porosity, as in the case of (253) Mathilde. Bodies with an ice component may have shorter lifetimes, as both sublimation and collisions are at play (Rivkin *et al.*, 2014). Shocked S-complex objects that have suppressed absorption features could be masquerading as other taxonomic types, including the C- or X-complex (Britt and Pieters, 1989; Reddy *et al.*, 2014; Kohout *et al.*, 2014). Differences could also be attributed to the primordial size distributions of asteroids of different compositional types.

### 5.3. What Processes Can Mix Wildly Different Meteorite Types into a Single Tiny Body?

There has been increased focus recently on asteroids in the size range for meteorite delivery, partly due to recent spectacular events such as the fall of 2008 TC<sub>3</sub> (Almahata Sitta), the airblast from the Chelyabinsk meteorite in 2013, and several asteroid close approaches, such as 2012 DA<sub>14</sub>.

Almahata Sitta presents a new puzzle to the meteorite and asteroid communities because of the diversity of meteorite types that have been mixed into a single small body (question B6, Appendix A). Almahata Sitta is predominantly made of ureilitic lithologies, but contains an unprecedentedly large fraction of a variety of other meteorite types, including enstatite chondrites, ordinary chondrites, and even carbonaceous chondrites (Zolensky *et al.*, 2010). Gayon-Markt *et al.* (2012) concluded that it could not have been assembled by low-velocity collisions among asteroids of diverse types in the Nysa-Polana family region (the suspected source region of Almahata Sitta) in the current dynamical environment. The mixture of two or three different meteorite types could be ascribed to unusual but possible coincidental encounters at the low-velocity tails of their dynamical parameters, but the variety of different materials in this case is so large that it is difficult to appeal to such low-probability events. In addition, Almahata Sitta is not a regolith breccia (it does not contain implanted solar-wind particles), so it was not lying on the surface of an asteroid for an extended period of time. Hence, Gayon-Markt *et al.* (2012) suggest that the diverse pieces must have been assembled in early times when collisional velocities were much lower.

Asteroid 2008 TC<sub>3</sub> exhibited a seemingly flat reflectance spectrum most closely, but not convincingly, resembling F-types (Jenniskens *et al.*, 2009) (F-types are from the Tholen taxonomy and would fall under the C-complex in the Bus and Bus-DeMeo taxonomies; see Table 1), where the spectral data had large error bars and did not contain diagnostic absorption features. Ureilites are fairly dark and some of the other incorporated meteorite types exhibited shock-darkening, thus a fairly featureless reflectance spectrum is not unexpected. A wide variety of mineralogies, so long as they contain a fraction of low-albedo materials or shock-darkened grains, might show such a spectrum. Thus there is no strong basis for arguing that other asteroids with

similar spectra should be similarly composed of heterogeneous materials the way Almahata Sitta is.

This mystery might be addressed if we could identify a larger proportion of meteorites that resemble Almahata Sitta. Is there a bias against finding meteorites of this type? The Sudanese desert was an especially good background for picking up pieces of the meteorite. Maybe these kinds of meteorite conglomerates are typically even weaker than Almahata Sitta and fragment even higher in the atmosphere, lessening the chance of recovery on the ground (e.g., similar to reasons for why we apparently lack samples of comets). If this is a more common kind of assemblage than we now think, we would be forced to abandon some of our ideas about asteroid family homogeneity (e.g., from the similar colors and albedos of asteroid family members) or about relative velocities among asteroids during early epochs of solar system history. Given the mismatch in scale between astronomical observation of asteroids and the centimeter-to-meter-scale heterogeneities within Almahata Sitta and other meteorites such as Kaidun (Zolensky, 2003), asteroid astronomical techniques are less likely to resolve this mystery than are techniques of meteor and fireball observation and meteorite research in the laboratory.

### 5.4. The Missing Mantle Problem

The canonical view of asteroid differentiation has been that a fully differentiated body should form an iron core, a silicate mantle, and a basalt crust. Olivine and pyroxene are the spectrally dominant materials in the mantle and crust, respectively. Meteorite collections include a diversity of iron meteorites that imply the existence of more than 60 distinct parent bodies (Wasson, 1995; Burbine *et al.*, 2002). However, the meteorite and asteroid records lack a substantial population of olivine-dominated or pyroxene-dominated bodies (Burbine *et al.*, 1996; Bus and Binzel, 2002a; Binzel *et al.*, 2004; Lazzaro *et al.*, 2004; Carvano *et al.*, 2010; DeMeo and Carry, 2013), aside from HEDs and vestoids linked to Vesta (Consolmagno and Drake, 1977; Binzel *et al.*, 1993; Prettyman *et al.*, 2012). This has been known as the “missing mantle problem,” and also as the “missing dunite problem” (question C3, Appendix A). One of the major outstanding questions in asteroid science that has existed for decades has been this perceived shortage of dunite or olivine in the asteroid belt.

Multiple solutions have been proposed to the missing mantle problem. The “battered to bits” scenario was a leading theory from the 1990s, whereby Burbine *et al.* (1996) further explored a proposal by Chapman (1986) that the mantle and crustal material of the original differentiated bodies had been ground down to pieces below the limit of our observational capabilities or even so they were too small to be delivered to Earth as meteorites. The primary weakness of this scenario is that the mantle and crustal components should not be substantially structurally weaker than undifferentiated material such as the C- and S-complexes that have

survived. Additionally, larger-scale spectroscopic surveys have placed even more stringent limits on the abundance of differentiated material and find it exceedingly rare in both the main belt and among NEOs that are sourced from the smaller (meter- to kilometer-sized) main-belt population (Bus and Binzel, 2002a; Binzel et al., 2004; Lazzaro et al., 2004; Carvano et al., 2010; DeMeo and Carry, 2013).

A more recent suggestion is that the classic view of asteroids differentiating into a pyroxene-rich crust, olivine-rich mantle, and iron core may be incorrect or uncommon (Elkins-Tanton et al., 2011). The differentiation models cause an asteroid's interior to heat and melt due to the decay of  $^{26}\text{Al}$ , but the exterior remains unheated and primitive (see the chapter by Scheinberg et al. in this volume). Thus the unheated crust would hide evidence of a differentiated interior from a remote observer. Weiss et al. (2012) propose that asteroid (21) Lutetia's high density, measured by the Rosetta spacecraft, is evidence of a core due to internal differentiation. Also, recent measurements of the primitive CV meteorite Allende find a directionally stable remnant magnetization that could be explained by the presence of a core dynamo in the parent body's past (Carporzen et al., 2011). As for rethinking the olivine-rich mantle model, the smoking gun has been the lack of appreciable olivine on the surface of Vesta from the Dawn mission (Le Corre et al., 2013). Another test of this differentiation scenario could be observations of asteroid families, whereby family members represent pieces of the parent asteroid's interior. The spectra and albedos of asteroid families tend to be very homogeneous (Parker et al., 2008; Masiero et al., 2011); however, the parent bodies of these families may not have been large enough to differentiate in the first place.

In addition to improved differentiation models, there is a new dynamical context for small bodies. It is possible, even likely, that bodies that formed iron cores formed closer to the Sun, in the terrestrial planet region (see the chapter by Scott et al. in this volume). During the tumultuous time of planet formation, these differentiated bodies were catastrophically disrupted, but their remnants were later scattered outward into their current locations in the main belt (Bottke et al., 2006). In addition, the so-called Grand Tack model (Walsh et al., 2011) proposes that within the first few million years of solar system formation, Jupiter migrated inward to the current location of Mars, then due to Saturn's presence turned course and moved back outward, scattering a significant number of bodies out to the location of the main belt today. The orbital distribution of basaltic and olivine-dominated objects spread across the main belt today are consistent with the idea that a small amount of material was scattered into their current locations (e.g., Moskovitz et al., 2008).

### 5.5. The Ordinary Chondrite Paradox

The ordinary chondrite paradox was a longstanding puzzle in asteroid science (question B7, Appendix A), whereby the most common meteorite type, the ordinary chondrites, did

not spectroscopically match the most common asteroids, the S-complex (Bell, 1989). Originally the S-complex asteroids in the inner belt were interpreted as igneous bodies that had undergone significant heating and melting, exposing iron, olivine, and pyroxene on the surface (McCord and Gaffey, 1974; Chapman, 1974). Thus, they were not considered compositionally linked to ordinary chondrites. However, the possibility of an effect, such as space weathering seen on the Moon, that altered ordinary chondrite spectra to look like S-complex asteroids could not be ruled out (Chapman 1979).

By the 1990s, the space weathering hypothesis gained traction. Spectral measurements of tens of NEOs demonstrated that the S-complex NEOs spanned the entire spectral slope range from spectrally flat ordinary chondrites to spectrally red S-complex main belt asteroids (Binzel et al., 1996, 2010). The Galileo mission data for Ida revealed that spectral differences were correlated with the age of surface features, and the discovery of Ida's moon Dactyl allowed density estimates that rejected the hypothesis of a core or other large metal components that may have been produced by large-scale melting and differentiation (Chapman 1996). Images and spectra of asteroid (433) Eros from the NEAR mission showed that dark regolith on the wall of the crater Psyche moves downslope exposing younger, brighter material (Everka et al., 1999; Murchie et al., 2002). The most important result from NEAR-Shoemaker was the conclusion from X-ray fluorescence spectroscopy that the major elemental composition of Eros was that of ordinary chondrites and that body had not differentiated (Nittler et al., 2001). Additional ground-based studies of Itokawa (Binzel et al., 2001) and an increased understanding of the effects of space weathering (Sasaki et al., 2001, Chapman 2004, Brunetto et al., 2006) further strengthened the ordinary chondrite–S-complex link. However, it was not until the sample return from Itokawa by JAXA's Hayabusa spacecraft (Nakamura et al., 2011) that conclusively proved the link. While it became clear that space weathering accounted for much of the spectral slope difference between ordinary chondrites and S-complex asteroids, other factors including grain size and observational phase angle were also determined to affect spectral slope (see chapter by Reddy et al.). For further discussion of the ordinary chondrite problem see the chapter by Brunetto et al.

The ordinary chondrite paradox case is now generally considered closed — ordinary chondrite compositions are part of the S-complex. There are two large problems remaining: (1) to determine which S-complex asteroids are not ordinary chondrites and may supply other meteorite types, and (2) to determine how many original parent bodies the ordinary chondrites come from. The S-complex encompasses a range of spectral characteristics and a diverse set of compositions (e.g., Gaffey et al., 1993; Dunn et al., 2013). Detailed mineralogical modeling of a large quantity of S-complex spectra, combined with a refined understanding of other factors that affect an asteroid's reflectance spectrum, is needed if we are to make further progress. Exploring a

broader wavelength range from the UV to mid-IR would provide additional constraints.

## 6. ASTEROIDS IN THEIR GREATER CONTEXT

Studies of asteroids and meteorites reveal their current compositions and structure as well as how and when they formed, including the conditions of the solar system at the time of planet and planetesimal formation. Asteroids, however, are more broadly relevant in our own solar system and beyond. In this section we explore asteroids and their relevance to Earth and habitability and the topic of asteroids outside our solar system. The field of exoasteroids is growing rapidly and the role asteroids play in creating the conditions for life (particularly the role in delivering water) is now being studied extensively. While these topics play a minor role in this book, one may envision these topics to be mature by the time of *Asteroids V*.

### 6.1. The Relevance of Asteroids to Earth Formation and Conditions for Life

No meteorite group or combination of groups can reproduce both the elemental and isotopic compositions of Earth, the planet for which we have the best data (*Palme and O'Neill*, 2014; *Halliday*, 2014) (question D1, Appendix A). Impact erosion and volatile loss during melting/differentiation of planetesimal precursors may explain some of the differences, but it seems that Earth was at least partially made of materials not present in our meteorite collections.

The abundances of highly siderophile elements in Earth's silicate mantle and crust are much higher than would be predicted since these elements should have gone essentially quantitatively into Earth's Fe-metal core during differentiation (*Walker*, 2009). It has been proposed that these elements were added to Earth after the last major event that enabled exchange between the core and the silicate mantle (*Chou*, 1978), which is normally taken to be the Moon-forming impact. The age of the Moon-forming impact is still uncertain — it must have been earlier than the oldest known lunar crustal rocks that formed 4.36 b.y. ago (*Borg et al.*, 2011), and could be as old as  $4.507^{+0.1}_{-0.01}$  b.y. (*Kleine et al.*, 2009; *Touboul et al.*, 2007). The isotopic composition of the highly siderophile elements Os and Ru suggest that the material responsible for this so-called late veneer was probably ordinary- or enstatite-chondrite-like (i.e., volatile-poor), rather than carbonaceous-chondrite-like (i.e., volatile-rich) (*Walker*, 2009). The fraction of Earth's mass that was accreted as a late veneer was on the order of 0.5% (*Walker*, 2009). The material accreted during the proposed late heavy bombardment (LHB), an increase in the lunar basin formation rate about 4 b.y. ago, would have been a minor component of the late veneer. However, there has been a longstanding debate about how long the LHB lasted or even whether there was a LHB (*Chapman et al.*, 2007; *Morbidelli et al.*, 2012). One model (the Nice model)

proposes that the LHB was caused by an episode of giant planet orbital migration that destabilized the inner edge of the asteroid belt (*Bottke et al.*, 2012).

The LHB, and the late veneer as a whole, was not a significant source of Earth's volatiles. Apart from the Os and Ru evidence, and model support that the LHB and the late veneer material were volatile-poor, there is evidence for oceans 4.4–4.3 b.y. ago (*Cavosie et al.*, 2005; *Mojzsis et al.*, 2001; *Wilde et al.*, 2001), i.e., 300–400 m.y. before the LHB. Earth's atmosphere is probably even older,  $\sim 4.527^{+20}_{-10}$  b.y. (*Avicen and Marty*, 2014), which is of a similar age to or possibly older than the Moon. So volatiles were accreted by Earth quite early and were not lost in any subsequent giant impacts, which is consistent with the new evidence for a wetter Moon than previously suspected (*Saal et al.*, 2013) and with the timing for water accretion measured in eucrites (*Sarafian et al.*, 2014).

It has been argued that Jupiter-family comets (JFCs) like Hartley 2 could have been the main sources of Earth's water because they have roughly terrestrial water D/H ratios (*Hartogh et al.*, 2011), although the water D/H of another JFC is roughly 3× terrestrial (*Altweegg et al.*, 2015). However, at least in the Nice model, objects from the scattered disk, the source of the JFCs, would have been scattered into the inner solar system only during the LHB (*Levison et al.*, 2009), which is too late given the evidence for an atmosphere and oceans hundreds of millions of years before the LHB. Also, as mentioned above, the isotopic compositions of Os and Ru suggest that the late veneer material was dominated by ordinary- and enstatite-chondrite-like material. Finally, it is important to remember that Earth would have accreted whole comets and not just their ice. Comets are organic-rich, and judging by the organics in meteorites and interplanetary dust particles, which may be cometary, cometary organic material is very D-rich. Consequently, the bulk D/H even of comets like Hartley 2 is probably significantly more D-rich than their ice and Earth (*Alexander et al.*, 2012). On the other hand, the bulk H and N isotopic compositions of CI and CM chondrites are quite similar to Earth's (*Alexander et al.*, 2012). In fact, the addition of ~2 wt.% of CI or ~4 wt.% of CM chondrite material can roughly reproduce not only the H and N isotopes, but also the abundances of many of Earth's most volatile elements (H, C, Cl, Br, I, Ne, Ar, and Kr) (*Alexander et al.*, 2012; *Marty*, 2012).

### 6.2. Asteroids Outside Our Solar System

Asteroids play an important role outside our solar system as well (questions D3 and D4, Appendix A). Asteroids are inferred to exist as remnants around white dwarf stars and are used as tracers of the dynamics and physical properties in these systems. Gravitational settling in cool white dwarfs causes all elements heavier than helium to sink to the star's interior. One-fourth to one-third of cool white dwarfs have heavy elements in their atmospheres that accreted from in-

falling asteroids (*Alcock et al.*, 1986; *Jura*, 2008; *Jura and Young*, 2014). These asteroids around white dwarfs are at least 85% by mass oxygen, magnesium, silicate, and iron, resembling rocky planetesimals and bulk Earth in our solar system (*Jura and Young*, 2014). This observational technique of studying white dwarf atmospheres can also detect asteroid differentiation, and evidence of water was detected in “exoasteroid” debris (*Farihi et al.*, 2011, 2013). Studies of cool white dwarfs may enable us to understand asteroid compositions, formation, and evolution in other planetary systems.

Asteroid belts are present around stars, as evidenced by the collisional dust (equivalent to our own zodiacal dust) observed around other mature stars. Debris disks are detected by the light emitted by dust grains in the disk at thermal wavelengths (e.g., *Lawler et al.*, 2009; *Lawler and Gladman*, 2012). The peak flux and wavelength of the emitted light provides an estimate for the mass of the disk and its distance from the star. While most known debris disks are Kuiper-belt-like, located at distances from tens to hundreds of astronomical units, a small number exhibit mid-IR emission indicating warm dust. Most spectral measurements of debris disks have been taken at IR wavelengths where the flux ratio of the disk to star is most favorable. Minerals can be identified by emission features (e.g., *Christensen et al.*, 2000) with silicates being the most common and easiest to identify (e.g., *Beichman et al.*, 2005; *Lisse et al.*, 2012; *Ballering et al.*, 2014). Interpretation of these spectra, however, is challenging because many grain properties other than composition (size, shape) can affect the spectrum. Continued studies of debris disks will reveal the diversity of extrasolar asteroid belt configurations and compositions that will provide context for our own solar system and for understanding the role asteroid belts play in creating the conditions for habitability on Earth-sized planets.

## 7. THE FUTURE: WHAT'S NEXT?

Potential avenues for future work on specific questions addressed in this chapter are given in Appendix A. We highlight a few avenues for future work here:

- In general, for the future of understanding the compositions and distributions of asteroids there are several techniques and topics that hold promise. While the past decades have focused primarily on the visible and near-IR wavelength ranges for spectroscopic study, extending to the UV and mid-IR could potentially provide new constraints for asteroid surfaces.
- The internal structures and geophysics of asteroids remain largely unexplored. Additional studies of

densities and differentiation processes will play an important role in understanding asteroid interiors (*Carry*, 2012).

- Studies of small asteroids (a few kilometers in the main belt and a few tens of meters among NEOs) will be a focus in future years, as there is much progress to make on the processes relevant to these size ranges. Understanding the compositional makeup and mixture of serendipitous meteorite falls is a young and developing field. The study of shock-darkening effects on the surfaces of asteroids and meteorites is another avenue of future work. While the foundations for the shocking process were established decades ago (e.g., *Britt and Pieters*, 1994), there is renewed interest as we observe the smallest asteroids.
- Ongoing and upcoming space missions will also add great value to our understanding of asteroid compositions. Dawn recently completed its study of Vesta and will have studied Ceres by the time this book is published. The Origins Spectral Interpretation Resource Identification and Security-Regolith Explorer (OSIRIS-REx) and Hayabusa-2 missions are scheduled to return samples of primitive asteroids. Gaia is actively taking visible wavelength spectra of tens to hundreds of thousands of asteroids and will provide a large new set of data to the community.

Just as important as exploring all these interesting avenues of asteroid research is exploring the connections between them. We must understand how each new discovery relates to our current body of knowledge and to the big picture of asteroids, our solar system, and beyond.

**Acknowledgments.** We would thank the following authors for fruitful discussions: B. Carry, R. Brunetto, T. Burbine, P. Vernazza, D. Polishook, M. Elvis, C. Lisse, and V. Reddy. We thank B. Carry for contributing Fig. 1. We thank N. Moskovitz and G. Libourel for helpful reviews that improved the manuscript. This material is based upon work supported by the National Aeronautics and Space Administration under Grant No. NNX12AL26G issued through the Planetary Astronomy Program and through the Hubble Fellowship grant HST-HF-51319.01-A, awarded by the Space Telescope Science Institute, which is operated by the Association of Universities for Research in Astronomy, Inc., for NASA, under contract NAS 5-26555. This material is based upon work supported by the National Science Foundation under Grant No. 0907766. C.M.O’D.A. acknowledges partial support from NASA grant NNX14AJ54G and from NASA’s Astrobiology Institute. K.J.W. was partially supported by the NASA Planetary Geology and Geophysics Program under grant NNX13AM82G.

## APPENDIX A: MAJOR OUTSTANDING ASTEROID COMPOSITIONAL QUESTIONS

Question	Possible Solutions	What Next?	Related Chapters
<b>A. Formation and Physical Evolution of Asteroids</b>			
1. Where, when, and how did they form?	<p><i>Where:</i> Links between asteroids and meteorites help constrain the conditions and location of formation. Dynamical models link where the asteroids are located now to where they originally formed.</p> <p><i>When:</i> Recent advances dating meteorites have constrained formation ages. For example, igneous meteorites have crystallization ages older than chondritic ones. So bodies that melted, melted early. Bodies that did not melt formed later. <i>How:</i> A second leading theory on formation, through streaming instability, has emerged since <i>Asteroids III</i>.</p>	Isotopic evidence points to carbonaceous chondrites being different from all others. But they are not all more water-rich, and their water H isotopes are not comet/Enceladus-like. Ages of chondrules and secondary minerals can be used to estimate chondrite formation ages. The almost ubiquitous presence of chondrules suggests that they may have played a role in planetesimal formation.	Section 4, this chapter; Johansen
2. How have they evolved physically?	Asteroid compositional changes are caused by early heating, aqueous alteration, and the external environment (space weathering). Physical changes are caused by impacts, radiation pressure (YORP spinup), and close approaches to planets (large tidal force).	Continued work on collisional and thermal modeling, studies of families, spacecraft measurements including surface (crater) observations. <i>In situ</i> measurements and sample return of non-OC-like bodies. Density measurements to understand interiors.	Brunetto, Krot, Scheinberg, Scott, Wilson, Bottke, Asphaug, Jutzi
3. How have they evolved dynamically?	Planetary migration likely plays a leading role in early solar system history. Planetary scattering, collisions, orbital drift, and orbital changes due to resonances dominate later history.	Identify the current spread in semimajor axis of each compositional group and use it to constrain the different migration scenarios. Search for and characterize interlopers for composition. Orbital and mass constraints also continue to inform dynamical history.	Section 3, this chapter; Morbidelli, Vokrouhlický, Bottke
<b>B. Asteroid and Meteorite Compositions</b>			
1. How many original parent bodies are represented in the asteroid belt?	Based on the meteorite record and the assumption that each meteorite group comes from a single parent body, there are at least 100–150 distinct parent bodies.	Meteor observation networks will provide insight on source bodies for meteorites. Continued work linking large main-belt asteroids to meteorites.	Burbine <i>et al.</i> (2002)
2. Can a single meteorite group be represented by more than one parent body?	(a) The simplest assumption is that each meteorite group comes from one parent body. (b) More than one object could have formed at a similar time and a similar distance from the Sun, in which case they might look very similar. For instance, there could be more original (>50–100 km) S-type asteroids than the three needed to explain the three ordinary chondrite groups.	Further research on meteorite composition will yield better understanding of parent bodies. For example, high-precision isotopic measurements may reveal if the OCs separate and demand more than three bodies. Sample return will provide insight, as will a review of how many primary parent bodies (those > 50–100 km) there are in each spectral class.	Burbine <i>et al.</i> (2002)

## APPENDIX A (continued)

Question	Possible Solutions	What Next?	Related Chapters
<b>B. Asteroid and Meteorite Compositions (continued)</b>			
3. How well do meteorites sample the asteroids?	<p>Comparison of meteorites with micrometeorites and breccias suggests meteorites may be fairly representative samples of the major types of asteroids. We still find new types of meteorites (and presumably parent bodies), but differences tend to be subtle. However, the inherent “top-heavy” asteroid size distribution means that rare, large collisions stochastically dominate the ejected fragments by mass, resulting in an inherent possibility of large deviations from direct representation of asteroid types by meteorite collections. If there is more diversity in the spectra of main-belt asteroids than meteorites, could much of this diversity be due to regolith processes (grain size and density sorting) and space weathering? Also, there are biases associated with delivery efficiency from different resonances and the robustness of the samples as they pass through Earth’s atmosphere.</p>	<p>Characterize asteroids at sizes relevant to meteorite falls (~5–50 m) to compare with the meteorite collection. IDPs, micrometeorites, and clasts in meteorite regoliths provide alternative samplings of the asteroid belt — how similar are they to the meteorites?</p>	Borovička, Jenniskens, Binzel
4. How robust are our asteroid-meteorite links?	<p>A few connections are robust: OCs make up part of the S class. HEDs are linked with V-types and the largest group of isotopically linked HEDs are concluded to be from Vesta. Isotopically distinct HEDs, as well as the diversity of other achondrites, point to a wide diversity of differentiation processes that remain poorly understood. The CMs may be linked with Ch and Cgh asteroids. The weaker and fewer bands present in an asteroid spectrum, the less confident we are of its composition. The C and X complexes could be extremely compositionally diverse, but observations are also affected by varying grain size, phase angle, regolith gardening, space weathering, etc. Shock darkening, which also mutes absorption bands, can also disguise the compositional identity of asteroid surfaces.</p>	<p>Dynamical study of asteroid families has the potential for addressing this question. By determining the ages of families and comparing with meteorite shock ages, and by following the plausible dynamical routes from family to Earth, current best guesses of associations of some meteorite types with families might become more robust. The mid-IR may be the next frontier for groundbased observational studies. Meteorite studies of spectral effects not related to composition are needed. Asteroid sample return will provide valuable insight for featureless asteroids. Serendipitous observation and recovery of objects such as 2008 TC<sub>3</sub> will also provide “free sample return.”</p>	Vernazza, Brunetto, Yoshikawa, Reddy, Burbine et al. (2002)

**APPENDIX A: (continued)**

Question	Possible Solutions	What Next?	Related Chapters
<b>B. Asteroid and Meteorite Compositions (continued)</b>			
5. How well do NEOs represent the main belt and beyond?	We now understand that dynamical and weathering processes can be relatively fast, suggesting that NEO flux is just a current snapshot, influenced by stochastic events like more recent disruption events. Size might also matter, and the speed at which an asteroid's orbit drifts due to the Yarkovsky effect increases with proximity to the Sun and with decreasing diameter. Yarkovsky is more effective at the small sizes (10 m or smaller) that might dominate meteorite samples. Additionally, size-dependent delivery mechanisms (Yarkovsky) mean that different size ranges could be dominated by specific asteroid families. NEO lifetimes and the NEO delivery models have helped link NEOs to their main-belt source regions.	Survey main-belt asteroids at sizes similar to NEOs (~1 km). Study dynamical and compositional links between NEOs and main-belt families and specific regions. Dynamics need to be calibrated by observations. New understanding of differentiation processes is also relevant.	Binzel
6. What is the diversity of compositions within individual small asteroids? What processes mix wildly different meteorite types into a single tiny body (e.g., Almahata Sitta, Kaidun)? When did the mixing occur?	Collisional or accretional processes (or both) could potentially bring such diverse materials together.	Implementation of ATLAST-like telescopic surveys of asteroids/meteoroids on their final approach to Earth and increased video surveillance and recovery of fall samples to understand the prevalence of and compositions of these mixes. Physical measurements of the smallest asteroids (5–100-m). Sample return of small asteroids will also provide constraints.	Section 5.3, this chapter; Borovička, Bottke?
7. The ordinary chondrite paradox: Why does the most common asteroid type, S-type, not match the most common meteorite type, OC?	Space weathering is the primary reason for the spectral mismatch. Laboratory experiments plus ground- and spacebased asteroid measurements made great progress. Hayabusa's sample return of Itokawa provided conclusive evidence. Other factors affecting spectral slope include grain properties and observational phase angle.	This question is solved. The follow up questions are: What S-type asteroids are not OCs? What meteorites do they supply? How does the space environment affect other asteroid types?	Section 5.5, this chapter; Vernazza, Brunetto, Binzel, Yoshikawa
8. What are the interior compositions of asteroids?	Density measurements and asteroid families currently provide the most information about asteroid interiors. How compositionally homogenous or differentiated the medium to large asteroids are is largely unknown.	Density measurements particularly from multiple systems. The porosity of asteroid interiors must be better constrained as well.	Margot, Scheeres, Barucci

## APPENDIX A: (continued)

Question	Possible Solutions	What Next?	Related Chapters
<b>C. Asteroid Compositional Distributions</b>			
1. What is the source of the compositional gradient in the main belt? Why are the Hildas and Trojans compositionally homogeneous compared to the main belt?	(a) It is a primordial remnant from the temperature and compositional gradient in the disk.  (b) It is the result of a transplantation of one or more groups of asteroids that formed elsewhere. (3) Hildas and Trojans actually are more compositionally diverse than they appear, but they have significant quantities of low-albedo materials that render diagnostic spectral features nearly invisible.	Progress on early solar system environment models and asteroid formation models. The best although impractical way to solve this is a mineralogical and isotopic assay of dozens of asteroids and comets.	Sections 2.2, 2.3, 5.1, this chapter; Morbidelli, Johansen, Emery
2. How does the distribution of asteroids change as a function of size? What is the significance of that distribution?	Recent work has explored the change in relative abundance of asteroid types as a function of size. Many factors still need to be taken into account, such as (1) the size-frequency distribution of families, (2) the difference in collisional lifetimes per asteroid class, and (3) the fact that some compositions are masked at smaller sizes due to processes such as collisions and “shocking.”	Additional study of the size distribution of families in the inner belt. Groundbased imaging and shape models plus mission visits to primitive bodies. Constrain how prevalent shocking is in the main belt. Larger samples of small asteroids in the main belt (1–20 km) will help determine the distribution at smaller sizes.	Section 5.2, this chapter
3. The missing mantle problem: Where is all the missing mantle material? Additional questions: Why are V- and A-types scattered throughout the entire main belt?	(a) Asteroids differentiate differently than expected — perhaps they don't form large olivine-rich mantles and pyroxene-rich crusts.  (b) The parents of these cores formed in the terrestrial planet region. They were destroyed and only the strongest metallic fragments were subsequently delivered to their current locations in the main belt.  (c) “Battered to bits” — this theory is currently less favored. Collisional modeling, crater counts, and observational evidence do not support an aggressive regime of collisional destruction and battering.  (d) Previous theories postulated olivine was hidden by weathering processes. Recent progress on space weathering disproves this hypothesis.	Further study of dynamical solutions and differentiation modeling. Continued study of meteorites to understand differentiation. Continued search for differentiation in families, including metal within large families.	Section 5.4, this chapter; Scheinberg, Wilson, Scott
4. Where is the water in the asteroid belt? How much is there? Where did these water-rich asteroids form?	Current evidence: main-belt comets, activated asteroids, water absorptions, Ceres outgassing, and possible exposures of ice on Ceres.	Discover additional active asteroids and explore asteroid-comet connections. Continue studies of extinct or dormant comets among NEOs. Visit and map surfaces such as by the Dawn, OSIRIS-REx, and Hayabusa-2 missions. Also, density measurements, radar sounding by spacecraft, etc., might reveal ice buried beneath thick surficial lag deposits.	Jewitt, Rivkin, Krot, Binzel

**APPENDIX A: (continued)**

Question	Possible Solutions	What Next?	Related Chapters
<b>D. Asteroids in Their Greater Context</b>			
1. Importance of the asteroid belt for Earth: Do we have remnants of Earth's building blocks? Do we have remnants of Earth's water source?	Arguments exist for and against enstatites or angrites being primary components of Earth. Water from Earth's oceans is argued to have been delivered from asteroids. Late veneer. Isotopic compositions show that the known chondrites were not the major building blocks of Earth, but the CI + CM-chondrite-like material may have been the sources of Earth's volatile materials as suggested by the SMOW D/H ratio.	Continued studies of D/H ratios of meteorites, comets, and asteroids. Continued theoretical studies of planet formation and dynamical studies of planet and planetary migrations.	Section 6.1, this chapter
2. Importance of the asteroid belt for the rest of our solar system?	Surface ages determined by impacts and cratering rates. Main belt and Kuiper belt orbital architecture and captured Trojans and satellites constrain giant planet migration. Study of solar corona is enabled by asteroids and comets evaporating during close approach to the Sun.	Continue with current progress on crater studies, dynamical studies including migration.	Beyond the scope of this book
3. What role do asteroids play in other planetary systems?	Collisions in massive asteroid belts create debris disks around old stars.	Identify and characterize extrasolar asteroid belts (evolved debris disks). Survey different planetary system architectures including asteroid belt distances and masses.	Section 6.2, this chapter; mostly beyond the scope of this book
4. What role do asteroids play in creating the conditions for habitability on Earth-sized planets?	Asteroids are tracers of dynamics and physical properties in dusty white dwarf systems.	Identify and characterize dusty white dwarf systems, and link those systems to the expected properties of precursor planetary systems.	Beyond the scope of this book
5. What is the importance of asteroids as hazards and resources for Earth?	Meteorites are known to contain water and organics (including amino acids), which could be precursors for life. They represent the initial conditions and compositions for forming terrestrial planets. They could be responsible for water delivery and creating oceans. They could also be responsible for destroying life through impacts.	Understand the link or the gradient between comets and wet asteroids. Measure the D/H ratio of a wider array of water-rich small bodies. Dynamical studies of delivery. Understand consequences of delivery of too much water. Studies of impact and water retention on Earth. Studies of ocean-forming mechanisms unrelated to small-body delivery.	Harris, Jedicke, Farnocchia
	Asteroids as a hazard have motivated increased attention to discovery surveys. Asteroids contain rare-Earth elements, including metals of value. Asteroids contain water or water components useful for space travel.	Discover 90% of PHAs down to 140 m. Understand the size of the small NEA population (<140 m). Evaluate and prepare for deflection strategies or evacuation plans. Continue to explore asteroids as resources.	

## REFERENCES

- Albertsson T., Semenov D., and Henning, T. (2014) Chemodynamical deuterium fractionation in the early solar nebula: The origin of water on Earth and in asteroids and comets. *Astrophys. J.*, **784**, 39.
- Alcock C., Fristrom C. C., and Siegelman R. (1986) On the number of comets around other single stars. *Astrophys. J.*, **302**, 462–476.
- Alexander C. M. O'D. (2005) From supernovae to planets: The view from meteorites and IDPs. In *Chondrites and the Protoplanetary Disk* (A. N. Krot et al., eds.), pp. 972–1002. Astronomical Society of the Pacific, San Francisco.
- Alexander C. M. O'D. and Ebel D. S. (2012) Questions, questions: Can the contradictions between the petrologic, isotopic, thermodynamic, and astrophysical constraints on chondrule formation be resolved? *Meteoritics & Planet. Sci.*, **47**, 1157–1175.
- Alexander C. M. O'D., Barber D. J., and Hutchison R. (1989) The microstructure of Semarkona and Bishunpur. *Geochim. Cosmochim. Acta.*, **53**, 3045–3057.
- Alexander C. M. O'D., Grossman J. N., Ebel D. S., and Ciesla F. J. (2008) The formation conditions of chondrules and chondrites. *Science*, **320**, 1617–1619.
- Alexander C. M. O'D., Bowden R., Fogel M. L., Howard K. T., Herd C. D. K., and Nittler L. R. (2012) The provenances of asteroids, and their contributions to the volatile inventories of the terrestrial planets. *Science*, **337**, 721–723.
- Altweig K., Balsiger H., Bar-Nun A., Berthelier J. J., Bieler A., Bochsler P., Briois C., Calmonte U., Combi M., De Keyser J., Eberhardt P., Fiethe B., Fuselier S., Gasc S., Gombosi T. I., Hansen K. C., Hässig M., Jäckel A., Kopp E., Korth A., LeRoy L., Mall U., Marty B., Mousis O., Neefs E., Owen T., Rème H., Rubin M., Sémond T., Tzou C.-Y., Waite H., and Wurz P. (2015) 67P/Churyumov-Gerasimenko, a Jupiter family comet with a high D/H ratio. *Science*, **347**, Article ID 1261952.
- Amelin Y. and Krot A. (2007) Pb isotopic age of the Allende chondrules. *Meteoritics & Planet. Sci.*, **42**, 1321–1335.
- Amelin Y., Krot A. N., Hutcheon I. D., and Ulyanov A. A. (2002) Lead isotopic ages of chondrules and calcium-aluminum-rich inclusions. *Science*, **297**, 1678–1683.
- Asphaug E., Jutzi M., and Movshovitz N. (2011) Chondrule formation during planetesimal accretion. *Earth Planet. Sci. Lett.*, **308**, 369–379.
- Avic G. and Marty B. (2014) The iodine-plutonium-xenon age of the Moon-Earth system revisited. *Philos. Trans. R. Soc., A372*, 20130260.
- Ballering N. P., Reike G. H., and Gaspar A. (2014) Probing the terrestrial regions of planetary systems: Warm debris disks with emission features. *Astrophys. J.*, **793**, Article ID 57.
- Batygin K., Brown M. E., and Betts H. (2012) Instability-driven dynamical evolution model of a primordially five-planet outer solar system. *Astrophys. J. Lett.*, **744**, Article ID L3.
- Beichman C. A. et al. (2005) An excess due to small grains around the nearby K0 V star HD 69830: Asteroid or cometary debris? *Astrophys. J.*, **626**, 1061–1069.
- Bell J. F., Davis D. R., Hartmann W. K., and Gaffey M. J. (1989) Asteroids — The big picture. In *Asteroids II* (R. P. Binzel et al., eds.), pp. 921–945. Univ. of Arizona, Tucson.
- Bendjoya P. and Zappalà V. (2002) Asteroid family identification. In *Asteroids III* (W. F. Bottke Jr. et al., eds.), pp. 613–618. Univ. of Arizona, Tucson.
- Binzel R. P. and Xu S. (1993) Chips off of asteroid 4 Vesta: Evidence for the parent body of basaltic achondrite meteorites. *Science*, **260**, 186–191.
- Binzel R. P., Bus S. J., Burbine T. H., and Sunshine J. M. (1996) Spectral properties of near-Earth asteroids: Evidence for sources of ordinary chondrite meteorites. *Science*, **273**, 946–948.
- Binzel R. P., Rivkin A. S., Bus S. J., Sunshine J. M., and Burbine T. H. (2001) MUSES-C target asteroid (25143) 1998 SF36: A reddened ordinary chondrite. *Meteoritics & Planet. Sci.*, **36**, 1167–1172.
- Binzel R. P., Rivkin A. S., Stuart J. S., Harris A. W., Bus S. J., and Burbine T. H. (2004) Observed spectral properties of near-Earth objects: Results for population distribution, source regions, and space weathering processes. *Icarus*, **170**, 259–294.
- Binzel R. P. et al. (2010) Earth encounters as the origin of fresh surfaces on near-Earth asteroids. *Nature*, **463**, 331–334.
- Bizzarro M., Baker J. A., and Haack H. (2004) Mg isotope evidence for contemporaneous formation of chondrules and refractory inclusions. *Nature*, **431**, 275–278.
- Borg L. E., Connolly J. N., Boyet M., and Carlson R. W. (2011) Chronological evidence that the Moon is either young or did not have a global magma ocean. *Nature*, **477**, 70–72.
- Boss A. P., Alexander C. M. O'D., and Podolak M. (2012) Cosmochemical consequences of particle trajectories during FU Orionis outbursts by the early Sun. *Earth Planet. Sci. Lett.*, **345**, 18–26.
- Bottke W. F., Jedicke R., Morbidelli A., Petit J. M., and Gladman B. (2000) Understanding the distribution of near-Earth asteroids. *Science*, **288**, 2190–2194.
- Bottke W. F. et al. (2002a) Debiased orbital and absolute magnitude distribution of near-Earth objects. *Icarus*, **156**, 399–433.
- Bottke W. F., Vokrouhlický D., Rubincam D. P., and Broz M. (2002b) The effect of Yarkovsky thermal forces on the dynamical evolution of asteroids and meteoroids. In *Asteroids III* (W. F. Bottke Jr. et al., eds.), pp. 395–408. Univ. of Arizona, Tucson.
- Bottke W. F., Vokrouhlický D., Rubincam D. P., and Nesvorný D. (2006) The Yarkovsky and YORP effects: Implications for asteroid dynamics. *Annu. Rev. Earth Planet. Sci.*, **34**, 157–191.
- Bottke W. F., Vokrouhlický D., Minton D., Nesvorný D., Morbidelli A., Brasser R., Simonson B., and Levison H. F. (2012) An Archaean heavy bombardment from a destabilized extension of the asteroid belt. *Nature*, **485**, 78–81.
- Britt D. T. and Pieters C. M. (1989) Black chondrite meteorites: An analysis of fall frequency and the distribution of petrologic types. *Meteoritics*, **24**, 255.
- Britt D. and Pieters C. (1994) Darkening in black and gas-rich ordinary chondrites: The spectral effects of opaque morphology and distribution. *Geochim. Cosmochim. Acta*, **58**, 3905–3919.
- Brunetto R. et al. (2006) Space weathering of silicates simulated by nanosecond pulse UV excimer laser. *Icarus*, **180**, 546–554.
- Brunetto R. et al. (2014) Ion irradiation of Allende meteorite probed by visible, IR, and Raman spectroscopies. *Icarus*, **237**, 278–292.
- Burbine T. H., Meibom A., and Binzel R. P. (1996) Mantle material in the main belt: Battered to bits? *Meteoritics & Planet. Sci.*, **31**, 607–620.
- Burbine T. H., McCoy T. J., Meibom A., Gladman B., and Keil K. (2002) Meteoritic parent bodies: Their number and identification. In *Asteroids III* (W. F. Bottke Jr. et al., eds.), pp. 653–667. Univ. of Arizona, Tucson.
- Burkhardt C., Kleine T., Oberli F., Pack A., Bourdon B., and Wieler R. (2011) Molybdenum isotope anomalies in meteorites: Constraints on solar nebula evolution and origin of the Earth. *Earth Planet. Sci. Lett.*, **312**, 390–400.
- Bus S. J. and Binzel R. P. (2002a) Phase II of the Small Main-Belt Asteroid Spectroscopic Survey: The observations. *Icarus*, **158**, 106–145.
- Bus S. J. and Binzel R. P. (2002b) Phase II of the Small Main-Belt Asteroid Spectroscopic Survey: A feature-based taxonomy. *Icarus*, **158**, 146–177.
- Bus S. J., Vilas F., and Barucci M. A. (2002) Visible-wavelength spectroscopy of asteroids. In *Asteroids III* (W. F. Bottke Jr. et al., eds.), pp. 169–182. Univ. of Arizona, Tucson.
- Camps H., Morbidelli M., Tsiganis K., de Leon J., Licandro J., and Lauretta D. (2010) The origin of asteroid 101955 (1999 RQ36). *Astrophys. J. Lett.*, **721**, L53–L57.
- Carporzen L. et al. (2011) From the cover: Magnetic evidence for a partially differentiated carbonaceous chondrite parent body. *Proc. Natl. Acad. Sci.*, **108**, 6386–6389.
- Carry B. (2012) Density of asteroids. *Planet. Space Sci.*, **73**, 98–118.
- Carvano J. M., Lazzaro D., Mothé-Diniz T., Angeli C., and Florczak M. (2001) Spectroscopic survey of the Hungaria and Phocaea dynamical groups. *Icarus*, **149**, 173–189.
- Carvano J. M., Hasselmann H., Lazzaro D., and Mothé-Diniz T. (2010) SDSS-based taxonomic classification and orbital distribution of main belt asteroids. *Astron. Astrophys.*, **510**, A43.
- Cavosie A. J., Valley J. W., and Wilde S. A. (2005) Magmatic  $\delta^{18}\text{O}$  in 4400–3900 Ma detrital zircons: A record of the alteration and recycling of crust in the Early Archean. *Earth Planet. Sci. Lett.*, **235**, 663–681.
- Chambers J. E. (2010) Planetesimal formation by turbulent concentration. *Icarus*, **208**, 505–517.
- Chapman, C. R. (1974) Asteroid size distribution: Implications for the origin of stony-iron and iron meteorites. *Geophys. Res. Lett.*, **1**, 341–344.

- Chapman C. R. (1979) The asteroids: Nature, interrelations, origins, and evolution. In *Asteroids* (T. Gehrels, ed.), pp. 25–60. Univ. of Arizona, Tucson.
- Chapman C. R. (1986) Implications of the inferred compositions of asteroids for their collisional evolution. *Mem. Soc. Astron. Ital.*, 57, 103–114.
- Chapman C. R. (1996) S-type asteroids, ordinary chondrites, and space weathering: The evidence from Galileo's fly-bys of Gaspra and Ida. *Meteoritics & Planet. Sci.*, 31, 699–725.
- Chapman C. R. (2004) Space weathering of asteroid surfaces. *Annu. Rev. Earth Planet. Sci.*, 32, 539–567.
- Chapman C. R. and Davis D. R. (1975) Asteroid collisional evolution: Evidence for a much larger early population. *Science*, 190, 553–556.
- Chapman C. R., Johnson T. V., and McCord T. B. (1971) A review of spectrophotometric studies of asteroids. In *Physical Studies of Minor Planets* (T. Gehrels, eds.), IAU Colloq. 12, NASA SP-267.
- Chapman C. R., Morrison D., and Zellner B. (1975) Surface properties of asteroids — A synthesis of polarimetry, radiometry, and spectrophotometry. *Icarus*, 25, 104–130.
- Chapman C. R., Cohen B. A., and Grinspoon D. H. (2007) What are the real constraints on the existence and magnitude of the late heavy bombardment? *Icarus*, 189, 233–245.
- Christensen P. R. et al. (2000) A thermal emission spectral library of rock-forming minerals. *J. Geophys. Res.*, 105, 9735–9740.
- Cloutis E. A., Hiroi T., Gaffey M. J., Alexander C. M. O'D., and Mann P. (2011a) Spectral reflectance properties of carbonaceous chondrites: 1. CI chondrites. *Icarus*, 212, 180–209.
- Cloutis E. A., Hudon P., Hiroi T., Gaffey M. J., and Mann P. (2011b) Spectral reflectance properties of carbonaceous chondrites: 1. CM chondrites. *Icarus*, 216, 309–346.
- Chou C.-L. (1978) Fractionation of siderophile elements in the Earth's upper mantle. *Proc. Lunar Planet. Sci. Conf. 9th*, pp. 219–230.
- Connelly J. N., Bizzarro M., Krot A. N., Nordlund Å., Wielandt D., and Ivanova M. A. (2012) The absolute chronology and thermal processing of solids in the solar protoplanetary disk. *Science*, 338, 651–655.
- Consolmagno G. J. and Drake M. J. (1977) Composition and evolution of the eucrite parent body — Evidence from rare earth elements. *Geochim. Cosmochim. Acta*, 41, 1271–1282.
- Cuzzi J., Hogan R. C., and Bottke W. F. (2010) Towards initial mass functions for asteroids and Kuiper belt objects. *Icarus*, 208, 518–538.
- Dauphas N. and Pourmand A. (2011) Hf-W-Th evidence for rapid growth of Mars and its status as a planetary embryo. *Nature*, 473, 489–492.
- DeMeo F. E. and Binzel R. P. (2008) Comets in the near-Earth object population. *Icarus*, 194, 436–449.
- DeMeo F. E. and Carry B. (2013) The taxonomic distribution of asteroids from multi-filter all-sky photometric surveys. *Icarus*, 226, 723–741.
- DeMeo F. E. and Carry B. (2014) Solar system evolution from compositional mapping of the asteroid belt. *Nature*, 505, 629–634.
- DeMeo F. E., Binzel R. P., Slivan S. M., and Bus S. J. (2009) An extension of the Bus asteroid taxonomy into the near-infrared. *Icarus*, 202, 160–180.
- DeMeo F. E., Binzel R. P., Carry B., Polishook D., and Moskovitz N. A. (2014) Unexpected D-type interlopers in the inner main belt. *Icarus*, 229, 392–399.
- Doyle P. M., Jogo K., Nagashima K., Krot A. N., Wakita S., Ciesla F. J., and Hutcheon I. D. (2015) Early aqueous activity on the ordinary and carbonaceous chondrite parent bodies recorded by fayalite. *Nature Commun.*, 6, DOI: 10.1038/ncomms8444.
- Dunn T. L., Burbine T. H., Bottke W. F., and Clark J. P. (2013) Mineralogies and source regions of near-Earth asteroids. *Icarus*, 222, 273–282.
- Elkins-Tanton L., Weiss B. P., and Zuber M. T. (2011) Chondrites as samples of differentiated planetesimals. *Earth Planet. Sci. Lett.*, 305, 1–10.
- Emery J. P., Cruikshank D. P., and Van Cleve J. (2006) Thermal emission spectroscopy (5.2–38 μm) of three Trojan asteroids with the Spitzer Space Telescope: Detection of fine-grained silicates. *Icarus*, 182, 496–512.
- Farihi J. et al. (2011) Possible signs of water and differentiation in a rocky exoplanetary body. *Astrophys. J. Lett.*, 728, L8.
- Farihi J., Gansicke B. T., and Koester D. (2013) Evidence for water in the rocky debris of a disrupted extrasolar minor planet. *Science*, 342, 218–220.
- Fisher H. (1941) Farbmessungen an kleinen planeten. *Astron. Nachr.*, 272, 127–147.
- Fujiya W., Sugiura N., Hotta H., Ichimura K., and Sano Y. (2012) Evidence for the late formation of hydrous asteroids from young meteoritic carbonates. *Nature Commun.*, 3, 627.
- Fujiya W., Sugiura N., Sano Y., and Hiyagon H. (2013) Mn-Cr ages of dolomites in CI chondrites and the Tagish Lake ungrouped carbonaceous chondrite. *Earth Planet. Sci. Lett.*, 362, 130–142.
- Gaffey M. J., Reed K. L., and Kelley M. S. (1992) Relationship of E-type Apollo asteroid 3103 (1982 BB) to the enstatite achondrite meteorites and the Hungaria asteroids. *Icarus*, 100, 95–109.
- Gaffey M. J. et al. (1993) Mineralogical variations within the S-type asteroid class. *Icarus*, 106, 573–602.
- Ganguly J., Tirone M., Chakraborty S., and Domanik K. (2013) H-chondrite parent asteroid: A multistage cooling, fragmentation and re-accretion history constrained by thermometric studies, diffusion kinetic modeling and geochronological data. *Geochim. Cosmochim. Acta*, 105, 206–220.
- Gardner-Vandy K. G. et al. (2012) The Tafassasset primitive achondrite: Insights into initial stages of planetary differentiation. *Geochim. Cosmochim. Acta*, 85, 142–159.
- Gayon-Markt J., Delbo M., Morbidelli A., and Marchi S. (2012) On the origin of the Almahata Sitta meteorite and 2008 TC<sub>3</sub> asteroid. *Mon. Not. R. Astron. Soc.*, 424, 508–518.
- Gladman B., Michel P., and Froeschle C. (2000) The near-Earth object population. *Icarus*, 146, 176–189.
- Gradie J. and Tedesco E. (1982) Compositional structure of the asteroid belt. *Science*, 216, 1405–1407.
- Gradie J. C., Chapman C. R., and Tedesco E. F. (1989) Distribution of taxonomic classes and the compositional structure of the asteroid belt. In *Asteroids II* (R. P. Binzel et al., eds.), pp. 316–335. Univ. of Arizona, Tucson.
- Grav T., Mainzer A. K., Bauer J. M., and Nugent C. R. (2012) WISE/NEOWISE observations of the jovian Trojan population: Taxonomy. *Astrophys. J.*, 759, Article ID 49.
- Grossman J. N., Alexander C. M. O'D., Wang J., and Brearley A. J. (2000) Bleached chondrules: Evidence for widespread aqueous processes on the parent asteroids of ordinary chondrites. *Meteoritics & Planet. Sci.*, 35, 467–486.
- Halliday A. N. (2014) The origin and earliest history of the Earth. In *Planets, Asteroids, Comets and the Solar System* (A. M. Davis, ed.), pp. 149–211. Elsevier, Oxford.
- Harrison K. P. and Grimm R. E. (2010) Thermal constraints on the early history of the H-chondrite parent body reconsidered. *Geochim. Cosmochim. Acta*, 74, 5410–5423.
- Hartogh P., Lis D. C., Bockelée-Morvan D., de Val-Borro M., Biver N., Küppers M., Emprechtinger M., Bergin E. A., Crovisier J., Rengel M., Moreno R., Szutowicz S., and Blake G. A. (2011) Ocean-like water in the Jupiter-family Comet 103P/Hartley 2. *Nature*, 478, 218–220.
- Henke S., Gail H. P., Trieloff M., and Schwarz W. H. (2013) Thermal evolution model for the H chondrite asteroid-instantaneous formation versus protracted accretion. *Icarus*, 226, 212–228.
- Hutcheon I. D., Marhas K. K., Krot A. N., Goswami J. N., and Jones R. H. (2009) <sup>26</sup>Al in plagioclase-rich chondrules in carbonaceous chondrites: Evidence for an extended duration of chondrule formation. *Geochim. Cosmochim. Acta*, 73, 5080–5099.
- Ivezic Z. et al. (2001) Solar system objects observed in the Sloan Digital Sky Survey commissioning data. *Astron. J.*, 122, 2740–2784.
- Ivezic Z. et al. (2007) LSST: Comprehensive NEO detection, characterization, and orbits. In *Near Earth Objects, Our Celestial Neighbors: Opportunity and Risk* (A. Milani et al., eds.), pp. 353–362. IAU Symp. 236, Cambridge Univ., Cambridge.
- Jacobsen B., Yin Q.-Z., Moynier F., Amelin Y., Krot A. N., Nagashima K., Hutcheon I. D., and Palme H. (2008) <sup>26</sup>Al–<sup>26</sup>Mg and <sup>207</sup>Pb–<sup>206</sup>Pb systematics of Allende CAIs: Canonical solar initial <sup>26</sup>Al/<sup>27</sup>Al ratio reinstated. *Earth Planet. Sci. Lett.*, 272, 353–364.
- Jacquet E. and Robert F. (2013) Water transport in protoplanetary disks and the hydrogen isotopic composition of chondrites. *Icarus*, 223, 722–732.
- Jenniskens P. et al. (2009) The impact and recovery of 2008 TC<sub>3</sub>. *Nature*, 458, 485–488.
- Jilly C. E., Huss G. R., Krot A. N., Nagashima K., Yin Q.-Z., and Sugiura N. (2014) <sup>53</sup>Mn–<sup>53</sup>Cr dating of aqueously formed carbonates in the CM2 lithology of the Sutter's Mill carbonaceous chondrite. *Meteoritics & Planet. Sci.*, 49, 2104–2117.
- Johnson B. C., Minton D. A., Melosh H. J., and Zuber M. T. (2015) Impact jetting as the origin of chondrules. *Nature*, 517, 339–341.

- Jones R. L. et al. (2009) Solar system science with LSST. *Earth Moon Planets*, *105*, 101–105.
- Jura M. (2008) Pollution of single white dwarfs by accretion of many small asteroids. *Astron. J.*, *135*, 1785–1792.
- Jura M. and Young E. D. (2014) Extrasolar cosmochemistry. *Annu. Rev. Earth Planet Sci.*, *42*, 45–67.
- Kita N. T. and Ushikubo T. (2012) Evolution of protoplanetary disk inferred from  $^{26}\text{Al}$  chronology of individual chondrules. *Meteoritics & Planet. Sci.*, *47*, 1108–1119.
- Kita N. T., Nagahara H., Togashi S., and Morishita Y. (2000) A short duration of chondrule formation in the solar nebula: Evidence from  $^{26}\text{Al}$  in Semarkona ferromagnesian chondrules. *Geochim. Cosmochim. Acta*, *64*, 3913–3922.
- Kita N. T., Huss G. R., Tachibana S., Amelin Y., Nyquist L. E., and Hutcheon I. D. (2005) Constraints on the origin of chondrules and CAIs from short-lived and long-lived radionuclides. In *Chondrites and the Protoplanetary Disk* (A. N. Krot et al., eds.), pp. 558–587. Astronomical Society of the Pacific, San Francisco.
- Kita N. T., Yin Q.-Z., MacPherson G. J., Ushikubo T., Jacobsen B., Nagashima K., Kurahashi E., Krot A. N., and Jacobsen S. B. (2013)  $^{26}\text{Al}$ - $^{26}\text{Mg}$  isotope systematics of the first solids in the early solar system. *Meteoritics & Planet. Sci.*, *48*, 1383–1400.
- Kitamura M. (1959) Photoelectric study of colors of asteroids and meteorites. *Publ. Astron. Soc. Japan*, *11*, 79.
- Kleine T. et al. (2008) Hf-W thermochronometry: Closure temperature and constraints on the accretion and cooling history of the H chondrite parent body. *Earth Planet. Sci. Lett.*, *270*, 106–118.
- Kleine T., Toublou M., Bourdon B., Nimmo F., Mezger K., Palme H., Jacobsen S. B., Yin Q.-Z., and Halliday A. N. (2009) Hf-W chronology of the accretion and early evolution of asteroids and terrestrial planets. *Geochim. Cosmochim. Acta*, *73*, 5150–5188.
- Kleine T., Hans U., Irving A. J., and Bourdon B. (2012) Chronology of the angrite parent body and implications for core formation in protoplanets. *Geochim. Cosmochim. Acta*, *84*, 186–203.
- Knežević Z., Lemaître A., and Milani A. (2002) The determination of asteroid proper elements. In *Asteroids III* (W. F. Bottke Jr. et al., eds.), pp. 603–612. Univ. of Arizona, Tucson.
- Kohout T. et al. (2014) Mineralogy, reflectance spectra, and physical properties of the Chelyabinsk LL5 chondrite — Insight into shock-induced changes in asteroid regoliths. *Icarus*, *228*, 78–85.
- Krasinsky G. A., Pitjeva E. V., Vasilyev M. V., and Yagudina E. I. (2002) Hidden mass in the asteroid belt. *Icarus*, *158*, 98–105.
- Krot A. N., Amelin Y., Cassen P., and Meibom A. (2005) Young chondrules in CB chondrites from a giant impact in the early solar system. *Nature*, *436*, 989–992.
- Krot A. N., Keil K., Scott E. R. D., Goodrich C. A., and Weisberg M. K. (2014) Classification of meteorites and their genetic relationships. In *Meteorites and Cosmochemical Processes* (A. M. Davis, ed.), pp. 1–63. Elsevier-Pergamon, Oxford.
- Kruijer T. S., Fischer-Gödde M., Kleine T., Sprung P., Leya I., and Wieler R. (2013) Neutron capture on Pt isotopes in iron meteorites and the Hf-W chronology of core formation in planetesimals. *Earth Planet. Sci. Lett.*, *361*, 162–172.
- Kruijer T. S., Kleine T., Fischer-Gödde M., Burkhardt C., and Rainer W. (2014) Nucleosynthetic W isotope anomalies and the Hf-W chronometry of Ca-Al-rich inclusions. *Earth Planet. Sci. Lett.*, *403*, 317–327.
- Kurahashi E., Kita N. T., Nagahara H., and Morishita Y. (2008)  $^{26}\text{Al}$ - $^{26}\text{Mg}$  systematics of chondrules in a primitive CO chondrite. *Geochim. Cosmochim. Acta*, *72*, 3865–3882.
- Lantz C., Clark B. E., Barucci M. A., and Lauretta D. S. (2013) Evidence for the effects of space weathering spectral signatures on low albedo asteroids. *Astron. Astrophys.*, *554*, A138.
- Larsen K. K., Trinquier A., Paton C., Schiller M., Wielandt D., Ivanova M. A., Connelly J. N., Nordlund Ö., Krot A. N., and Bizzarro M. (2011) Evidence for magnesium isotope heterogeneity in the solar protoplanetary disk. *Astrophys. J. Lett.*, *735*, L37.
- Lawler S. M. and Gladman B. (2012) Debris disks in Kepler exoplanet systems. *Astrophys. J.*, *752*, Article ID 53.
- Lawler S. M. et al. (2009) Explorations beyond the snow line: Spitzer/IRS spectra of debris disks around solar-type stars. *Astrophys. J.*, *705*, 89–111.
- Lazzaro D. et al. (2000) Discovery of a basaltic asteroid in the outer main belt. *Science*, *288*, 2033–2035.
- Lazzaro D., Angeli C. A., Carvano J. M., Mothé-Diniz T., Duffard R., and Florcza M. (2004)  $\text{S}_3\text{OS}_2$ : The visible spectroscopic survey of 820 asteroids. *Icarus*, *172*, 179–220.
- Le Corre L. et al. (2013) Olivine or impact melt: Nature of the “orange” material on Vesta from Dawn. *Icarus*, *226*, 1568–1594.
- Levison H. F. and Duncan M. J. (1994) The long-term dynamical behavior of short-period comets. *Icarus*, *108*, 18–36.
- Levison H. F., Morbidelli A., Van Laerhoven C., Gomes R., and Tsiganis K. (2008) Origin of the structure of the Kuiper belt during a dynamical instability in the orbits of Uranus and Neptune. *Icarus*, *196*, 258–273.
- Levison H. F., Bottke W. F., Gounelle M., Morbidelli A., Nesvorný D., and Tsiganis K. (2009) Contamination of the asteroid belt by primordial trans-neptunian objects. *Nature*, *460*, 364–366.
- Lis D. C. et al. (2013) A Herschel study of D/H in water in the Jupiter-family Comet 45P/Honda-Mrkos-Pajdušáková and prospects for D/H measurements with CCAT. *Astrophys. J. Lett.*, *774*, L3.
- Lisse C. M. et al. (2012) Spitzer evidence for a late-heavy bombardment and the formation of ureilites in eta Corvi at ~1 Gyr. *Astrophys. J.*, *747*, Article ID 93.
- Lodders K. (2003) Solar system abundances and condensation temperatures of the elements. *Astrophys. J.*, *591*, 1220–1247.
- Lugmair G. W. and Shukolyukov A. (1998) Early solar system timescales according to  $^{53}\text{Mn}$ - $^{53}\text{Cr}$  systematics. *Geochim. Cosmochim. Acta*, *62*, 2863–2886.
- Lugmair G. W. and Shukolyukov A. (2001) Early solar system events and timescales. *Meteoritics & Planet. Sci.*, *36*, 1017–1026.
- MacPherson G. J. (2014) Calcium-aluminum-rich inclusions in chondritic meteorites. In *Meteorites and Cosmochemical Processes* (A. M. David, ed.), pp. 139–179. Elsevier-Pergamon, Oxford.
- Mainzer A. et al. (2011) Preliminary results from NEOWISE: An enhancement to the Wide-field Infrared Survey Explorer for solar system science. *Astrophys. J.*, *731*, Article ID 53.
- Mandt K. E., Mousis O., Lunine J., and Gautier D. (2014) Protosolar ammonia as the unique source of Titan’s nitrogen. *Astrophys. J. Lett.*, *788*, L24.
- Marty B. (2012) The origins and concentrations of water, carbon, nitrogen and noble gases on Earth. *Earth Planet. Sci. Lett.*, *313*, 56–66.
- Masiero J. R. et al. (2011) Main belt asteroids with WISE/NEOWISE. I. Preliminary albedos and diameters. *Astrophys. J.*, *741*, 68.
- Masiero J. R. et al. (2013) Asteroid family identification using the hierarchical clustering method and WISE/NEOWISE physical properties. *Astrophys. J.*, *770*, 7.
- McCanta M. C., Treiman A. H., Dyar M. D., Alexander C. M. O’D., Rumble D. III, and Essene E. J. (2008) The LaPaz Icefield 04840 meteorite: Mineralogy, metamorphism, and origin of an amphibole- and biotite-bearing R chondrite. *Geochim. Cosmochim. Acta*, *72*, 5757–5780.
- McCord T. B. and Gaffey M. J. (1974) Asteroids — Surface composition from reflection spectroscopy. *Science*, *186*, 352–355.
- McKinnon W. B. (2008) Could Ceres be a refugee from the Kuiper Belt? In *Asteroids, Comets, Meteors*, Abstract #8389. LPI Contribution No. 1405, Lunar and Planetary Institute, Houston.
- Metzler K. (2012) Ultrarapid chondrite formation by hot chondrule accretion? Evidence from unequilibrated ordinary chondrites. *Meteoritics & Planet. Sci.*, *47*, 2193–2217.
- Mignard F. (2007) The Gaia mission: Expected applications to asteroid science. *Earth Moon Planets*, *101*, 97–125.
- Minton D. and Malhotra R. (2009) A record of planet migration in the main asteroid belt. *Nature*, *457*, 1109–1111.
- Minton D. and Malhotra R. (2011) Secular resonance sweeping of the main asteroid belt during planet migration. *Astrophys. J.*, *732*, 53.
- Mojzsis S. J., Harrison T. M., and Pidgeon R. T. (2001) Oxygen-isotope evidence from ancient zircons for liquid water at the Earth’s surface 4,300 Myr ago. *Nature*, *409*, 178–181.
- Morbidelli A. et al. (2000) Source regions and time scales for the delivery of water to Earth. *Meteoritics & Planet. Sci.*, *35*, 1309–1320.
- Morbidelli A., Levison H. F., Tsiganis K., and Gomes R. (2005) Chaotic capture of Jupiter’s Trojan asteroids in the early solar system. *Nature*, *435*, 462–465.
- Morbidelli A., Brasser R., Gomes R., Levison H. F., and Tsiganis K. (2010) Evidence from the asteroid belt for a violent past evolution of Jupiter’s orbit. *Astronom. J.*, *140*, 1391–1401.
- Morbidelli A., Marchi S., Bottke W. F., and Kring D. A. (2012) A sawtooth-like timeline for the first billion years of lunar bombardment. *Earth Planet. Sci. Lett.*, *355*, 144–151.

- Moskovitz N. A. et al. (2008) The distribution of basaltic asteroids in the main belt. *Icarus*, 198, 77–90.
- Moskovitz N. and Gaidos E. (2011) Differentiation of planetesimals and the thermal consequences of melt migration. *Meteoritics & Planet. Sci.*, 46, 903–918.
- Mothé-Diniz T., Carvano J., and Lazzaro D. (2003) Distribution of taxonomic classes in the main belt of asteroids. *Icarus*, 162, 10–21.
- Murchie S. et al. (2002) Color variations on Eros from NEAR multispectral imaging. *Icarus*, 155, 145–168.
- Nakamura T. et al. (2011) Itokawa dust particles: A direct link between S-type asteroids and ordinary chondrites. *Science*, 333, 1113–1115.
- Nesvorný D., Ferraz-Mello S., Holman M., and Morbidelli A. (2002) Regular and chaotic dynamics in the mean-motion resonances: Implications for the structure and evolution of the asteroid belt. In *Asteroids III* (W. F. Bottke Jr. et al., eds.), pp. 379–394. Univ. of Arizona, Tucson.
- Nesvorný D., Jedicke R., Whitely R. J., and Ivezic Z. (2005) Evidence for asteroid space weathering from the Sloan Digital Sky Survey. *Icarus*, 173, 132–152.
- Nesvorný D., Vokrouhlický D., and Morbidelli A. (2013) Capture of Trojans by jumping Jupiter. *Astrophys. J.*, 768, 45.
- Nesvorný D., Vokrouhlický D., and Deienno R. (2014) Capture of irregular satellites at Jupiter. *Astrophys. J.*, 784, 22.
- Neumann W., Breuer D., and Spohn T. (2014) Differentiation of Vesta: Implications for a shallow magma ocean. *Earth Planet. Sci. Lett.*, 395, 267–280.
- Nittler L. R. et al. (2001) X-ray fluorescence measurements of the surface elemental composition of asteroid 433 Eros. *Meteoritics & Planet. Sci.*, 36, 1673–1695.
- Nixon C. A., Temelso B., Vinatier S., Teanby N. A., Bézard B., Achterberg R. K., Mandt K. E., Sherrill C. D., Irwin P. G. J., Jennings D. E., Romani P. N., Coustenis A., and Flasar F. M. (2012) Isotopic ratios in Titan's methane: Measurements and modeling. *Astrophys. J.*, 749, 159.
- O'Brien D. P., Morbidelli A., and Levison H. F. (2006) Terrestrial planet formation with strong dynamical friction. *Icarus*, 184, 39–58.
- O'Brien D. P., Morbidelli A., and Bottke W. F. (2007) The primordial excitation and clearing of the asteroid belt — Revisited. *Icarus*, 191, 434–452.
- Ormel C. W. and Klahr H. H. (2010) The effect of gas drag on the growth of protoplanets. Analytical expressions for the accretion of small bodies in laminar disks. *Astron. Astrophys.*, 520, 43.
- Palme H. and O'Neill H. S. C. (2014) Cosmochemical estimates of mantle composition. In *Treatise on Geochemistry* (H. Holland and K. K. Turekian, eds.), pp. 1–39. Elsevier, Oxford.
- Parker A. et al. (2008) The size distributions of asteroid families in the SDSS Moving Object Catalog 4. *Icarus*, 198, 138–155.
- Petit J., Chamber J., Franklin F., and Nagasawa M. (2002) Primordial excitation and depletion of the main belt. In *Asteroids III* (W. F. Bottke Jr. et al., eds.), pp. 711–723. Univ. of Arizona, Tucson.
- Polnau E. and Lugmair G. W. (2001) Mn-Cr isotope systematics in the two ordinary chondrites Richardton (H5) and Ste. Marguerite (H4). *Lunar Planet. Sci. XXXII*, Abstract #1527. Lunar and Planetary Institute, Houston.
- Prettyman T. H. et al. (2012) Elemental mapping by Dawn reveals exogenic H in Vesta's regolith. *Science*, 338, 242–244.
- Rayner J. T. et al. (2003) SpeX: A medium-resolution 0.8–5.5 micron spectrograph and imager for the NASA Infrared Telescope Facility. *Publ. Astron. Soc. Pacific*, 115, 362–382.
- Reddy V. et al. (2014) Chelyabinsk meteorite explains unusual spectral properties of Baptistina asteroid family. *Icarus*, 237, 116–130.
- Rivkin A. S., Asphaug E., and Bottke W. F. (2014) The case of the missing Ceres family. *Icarus*, 243, 429–439.
- Rousselot P., Pirali O., Jehin E., Vervloet M., Hutsemékers D., Manfroid J., Cordier D., Martin-Drumel M.-A., Gruet S., Arpigny C., Decock A., and Mousis O. (2014) Toward a unique nitrogen isotopic ratio in cometary ices. *Astrophys. J. Lett.*, 780, L17.
- Ruzmaikina T. V., Safronov V. S., and Weidenschilling S. J. (1989) Radial mixing of material in the asteroidal zone. In *Asteroids II* (R. P. Binzel et al., eds.), pp. 681–700. Univ. of Arizona, Tucson.
- Saal A. E., Hauri E. H., Van Orman J. A., and Rutherford M. J. (2013) Hydrogen isotopes in lunar volcanic glasses and melt inclusions reveal a carbonaceous chondrite heritage. *Science*, 340, 1317–1320.
- Sanchez J. A. et al. (2014) Olivine-dominated asteroids: Mineralogy and origin. *Icarus*, 228, 288–300.
- Sarafian A. R., Nielson S. G., Marschall H. R., McCubbin F. M., and Monteleone B. D. (2014) Early accretion of water in the inner solar system from a carbonaceous chondrite-like source. *Science*, 346, 623–626.
- Sasaki S., Nakamura K., Hamabe Y., Kurahashi E., and Hiroi T. (2001) Production of iron nanoparticles by laser irradiation in a simulation of lunar-like space weathering. *Nature*, 410, 555–557.
- Schiller M., Baker J., Creech J., Paton C., Millet M.-A., Irving A., and Bizzarro M. (2011) Rapid timescales for magma ocean crystallization on the howardite-eucrite-diogenite parent body. *Astrophys. J. Lett.*, 740, L22.
- Schiller M., Paton C., and Bizzarro M. (2015) Evidence for nucleosynthetic enrichment of the protosolar molecular cloud core by multiple supernova events. *Geochim. Cosmochim. Acta*, 149, 88–102.
- Scott E. R. D., Krot T. V., Goldstein J. I., and Wakita S. (2014) Thermal and impact history of the H chondrite parent asteroid during metamorphism: Constraints from metallic Fe-Ni. *Geochim. Cosmochim. Acta*, 136, 13–37.
- Shinnaka Y., Kawakita H., Kobayashi H., Nagashima M., and Boice D. C. (2014)  $^{14}\text{NH}_2/^{15}\text{NH}_2$  ratio in Comet C/2012 S1 (ISON) observed during its outburst in 2013 November. *Astrophys. J. Lett.*, 782, L16.
- Shukolyukov A. and Lugmair G. W. (2004) Manganese-cromium isotope systematics of enstatite meteorites. *Geochim. Cosmochim. Acta*, 68, 2875–2888.
- Sugiura N. and Fujiya W. (2014) Correlated accretion ages and  $\epsilon^{54}\text{Cr}$  of meteorite parent bodies and the evolution of the solar nebula. *Meteoritics & Planet. Sci.*, 49, 772–787.
- Szabó Gy. M., Ivezic Z., Juric M., Lupton R., and Kiss L. L. (2004) Colour variability of asteroids in the Sloan Digital Sky Survey Moving Object Catalog. *Mon. Not. R. Astron. Soc.*, 348, 987–998.
- Takir D. and Emery J. P. (2012) Outer main belt asteroids: Identification and distribution of four 3- $\mu\text{m}$  spectral groups. *Icarus*, 219, 641–654.
- Tang H. and Dauphas N. (2014)  $^{60}\text{Fe}-^{60}\text{Ni}$  chronology of core formation in Mars. *Earth Planet. Sci. Lett.*, 390, 264–274.
- Tholen D. J. and Barucci M. A. (1989) Asteroid taxonomy. In *Asteroids II* (R. P. Binzel et al., eds.), pp. 298–315. Univ. of Arizona, Tucson.
- Touboul M., Kleine T., Bourdon B., Palme H., and Wieler R. (2007) Late formation and prolonged differentiation of the Moon inferred from W isotopes in lunar metals. *Nature*, 450, 1206–1209.
- Trieloff M., Jessberger E. K., Herrwerth I., Hopp J., Fieni C., Ghelis M., Bourot-Denise M., and Pellat P. (2003) Structure and thermal history of the H-chondrite parent asteroid revealed by thermochronometry. *Nature*, 422, 502–506.
- Trinquier A., Birck J. L., Allègre C. J., Göpel C., and Ulfbeck D. (2008)  $^{53}\text{Mn}-^{53}\text{Cr}$  systematics of the early solar system revisited. *Geochim. Cosmochim. Acta*, 72, 5146–5163.
- Ushikubo T., Nakashima D., Kimura M., Tenner T. J., and Kita N. T. (2013) Contemporaneous formation of chondrules in distinct oxygen isotope reservoirs. *Geochim. Cosmochim. Acta*, 109, 280–295.
- Vernazza P. et al. (2010) Mid-infrared spectral variability for compositionally similar asteroids: Implications for asteroid particle size distributions. *Icarus*, 207, 800–809.
- Vernazza P. et al. (2012) High surface porosity as the origin of emissivity features in asteroid spectra. *Icarus*, 221, 1162–1172.
- Vernazza P. et al. (2014) Multiple and fast: The accretion of ordinary chondrite parent bodies. *Astrophys. J.*, 791, Article ID 120.
- Everka J., Thomas P. C., Bell J. F. III, Bell M., Carcich B., Clark B., Harch A., Joseph J., Martin P., Robinson M., Murchie S., Izenberg N., Hawkins E., Warren J., Farquhar R., Cheng A., Dunham D., Chapman C., Merline W. J., McFadden L., Wellnitz D., Malin M., Owen W. M. Jr., Miller J. K., Williams B. G., and Yeomans D. K. (1999) Imaging of asteroid 433 Eros during NEAR's flyby reconnaissance. *Science*, 285, 562–564.
- Vilas F. and Gaffey M. J. (1989) Phyllosilicate absorption features in main-belt and outer-belt asteroid reflectance spectra. *Science*, 246, 790–792.
- Villeneuve J., Chaussidon M., and Libourel G. (2009) Homogeneous distribution of  $^{26}\text{Al}$  in the solar system from the Mg isotopic composition of chondrules. *Science*, 325, 985–988.
- Waite J. H. Jr., Lewis W. S., Magee B. A., Lunine J. I., McKinnon W. B., Glein C. R., Mousis O., Young D. T., Brockwell T., Westlake

- J., Nguyen M. J., Teolis B. D., Niemann H. B., McNutt R. L. Jr., Perry M., and Ip W. H. (2009) Liquid water on Enceladus from observations of ammonia and  $^{40}\text{Ar}$  in the plume. *Nature*, *460*, 487–490.
- Walker R. (2009) Highly siderophile elements in the Earth, Moon and Mars: Update and implications for planetary accretion and differentiation. *Chem. Erde–Geochem.*, *69*, 101–125.
- Walsh K. J. and Morbidelli A. (2011) The effect of an early planetesimal-driven migration of the giant planets on terrestrial planet formation. *Astron. Astrophys.*, *526*, 126.
- Walsh K. J., Morbidelli A., Raymond S. N., O'Brien D. P., and Mandell A. M. (2011) A low mass for Mars from Jupiter's early gas-driven migration. *Nature*, *475*, 206–209.
- Walsh K. J., Morbidelli A., Raymond S. N., O'Brien D. P., and Mandell A. M. (2012) Populating the asteroid belt from two parent source regions due to the migration of giant planets — “The Grand Tack.” *Meteoritics & Planet. Sci.*, *47*, 1941–1947.
- Warren P. H. (2011) Stable-isotopic anomalies and the accretionary assemblage of the Earth and Mars: A subordinate role for carbonaceous chondrites. *Earth Planet. Sci. Lett.*, *311*, 93–100.
- Wasserburg G. J., Wimpenny J., and Yin Q.-Z. (2012) Mg isotopic heterogeneity, Al-Mg isochrons, and canonical  $^{26}\text{Al}/^{27}\text{Al}$  in the early solar system. *Meteoritics & Planet. Sci.*, *47*, 1980–1997.
- Wasson J. T. (1995) Sampling the asteroid belt: How biases make it difficult to establish meteorite-asteroid connections. *Meteoritics*, *30*, 595.
- Weidenschilling S. J. (1977) The distribution of mass in the planetary system and solar nebula. *Astrophys. Space Sci.*, *51*, 153–158.
- Weidenschilling S. J. and Jackson A. A. (1993) Orbital resonances and Poynting-Robertson drag. *Icarus*, *104*, 244–254.
- Weiss B. P. and Elkins-Tanton L. T. (2013) Differentiated planetesimals and the parent bodies of chondrites. *Annu. Rev. Earth Planet. Sci.*, *41*, 529–560.
- Weiss B. P. et al. (2012) Possible evidence for partial differentiation of asteroid Lutetia from Rosetta. *Planet. Space Sci.*, *66*, 137–146.
- Wilde S. A., Valley J. W., Peck W. H., and Graham C. M. (2001) Evidence from detrital zircons for the existence of continental crust and oceans on Earth 4.4 Gyr ago. *Nature*, *409*, 175–178.
- Wood X. H. J. and Kuiper G. P. (1963) Photometric studies of asteroids. *Astrophys. J.*, *137*, 1279–1285.
- Yamashita K., Maruyama S., Yamakawa A., and Nakamura E. (2010)  $^{53}\text{Mn}-^{53}\text{Cr}$  chronometry of CB chondrite: Evidence for uniform distribution of  $^{53}\text{Mn}$  in the early solar system. *Astrophys. J.*, *723*, 20–24.
- Yang J., Goldstein J. I., and Scott E. R. D. (2007) Iron meteorite evidence for early formation and catastrophic disruption of protoplanets. *Nature*, *446*, 888–891.
- Yang J., Goldstein J. I., and Scott E. R. D. (2008) Metallographic cooling rates and origin of IVA iron meteorites. *Geochim. Cosmochim. Acta*, *72*, 3043–3061.
- Yang J., Goldstein J. I., Michael J. R., Kotula P. G., and Scott E. R. D. (2010a) Thermal history and origin of the IVB iron meteorites and their parent body. *Geochim. Cosmochim. Acta*, *74*, 4493–4506.
- Yang J., Goldstein J. I., and Scott E. R. D. (2010b) Main-group pallasites: Thermal history, relationship to IIIAB irons, and origin. *Geochim. Cosmochim. Acta*, *74*, 4471–4492.
- Yang L., Ciesla F. J., and Alexander C. M. O'D. (2013) The D/H ratio of water in the solar nebula during its formation and evolution. *Icarus*, *226*, 256–267.
- Zappalà V., Cellino A., dell'Oro A., and Paolicchi P. (2002) Physical and dynamical properties of asteroid families. In *Asteroids III* (W. F. Bottke Jr. et al., eds.), pp. 619–631. Univ. of Arizona, Tucson.
- Zellner B., Tholen D. J., and Tedesco E. F. (1985) The eight-color asteroid survey — Results for 589 minor planets. *Icarus*, *61*, 355–416.
- Zolensky M. (2003) The Kaidun microbreccia meteorite: A harvest from the inner and outer asteroid belt. *Chem. Erde–Geochem.*, *63*, 185–246.
- Zolensky M. et al. (2010) Mineralogy and petrography of the Almahata Sitta ureilite. *Meteoritics & Planet. Sci.*, *45*, 1618–1637.



# Mineralogy and Surface Composition of Asteroids

**Vishnu Reddy**

*Planetary Science Institute*

**Tasha L. Dunn**

*Colby College*

**Cristina A. Thomas**

*NASA Goddard Space Flight Center*

**Nicholas A. Moskovitz**

*Lowell Observatory*

**Thomas H. Burbine**

*Mount Holyoke College*

---

Methods to constrain the surface mineralogy of asteroids have seen considerable development during the last decade, with advancement in laboratory spectral calibrations and validation of interpretive methodologies by spacecraft rendezvous missions. This has enabled the accurate identification of several meteorite parent bodies in the main asteroid belt and helped constrain the mineral chemistries and abundances in ordinary chondrites and basaltic achondrites. With better quantification of spectral effects due to temperature, phase angle, and grain size, systematic discrepancies due to noncompositional factors can now be virtually eliminated for mafic silicate-bearing asteroids. Interpretation of spectrally featureless asteroids remains a challenge. This chapter presents a review of all mineralogical interpretive tools currently in use and outlines procedures for their application.

## 1. INTRODUCTION

Physical characterization of small bodies through the use of reflectance spectroscopy provides insight into the diversity of chemical compositions in the solar system and enables meteorites in our terrestrial collections to be linked to specific parent bodies in space. Since the publication of *Asteroids III*, there have been numerous advances in the mineralogical characterization of asteroid surfaces using visible/near-infrared (VIS/NIR) and mid-IR spectra. One of the most significant developments in groundbased characterization of small bodies over the last decade is the commissioning of the SpeX instrument in the NASA Infrared Telescope Facility (IRTF) on Mauna Kea, Hawai‘i. The ideal spectral resolution (~few hundred), wavelength range (0.8–5 μm), and high altitude of Mauna Kea have facilitated the mineralogical characterization of asteroids down to a visual magnitude of 19.

In addition to groundbased observations, the last decade has been witness to a series of successful spacecraft missions, including flybys of (2867) Šteins, (21) Lutetia, (4179) Toutatis, a rendezvous mission to asteroid (4) Vesta, and a sample return from near-Earth asteroid (25143) Ito-

kawa. These missions have helped study the shape, morphology, and surface composition of asteroids over a wide range of sizes, from Itokawa (535 m) to Vesta, which (at 525 km) is the second most massive object in the asteroid belt. Two more sample return missions are planned for the next decade, both of which are targeting primitive near-Earth asteroids. Hayabusa-2 calls for a sample return of C-type asteroid (162173) 1999 JU<sub>3</sub>, and the Origins Spectral Interpretation Resource Identification and Security-Regolith Explorer (OSIRIS-REx) mission will return a sample from the potentially hazardous asteroid (101955) Bennu.

Our ability to track meteorite falls back to their possible parent asteroids has benefited from increased interest in the monitoring of fireballs, the streak of light generated as a meteorite comes through the atmosphere. The Chelyabinsk meteorite, which exploded over Russia on February 15, 2013, is the most well-documented fireball in modern history. The combination of all-sky-camera data from networks such as Cameras for Allsky Meteor Surveillance, the Desert Fireball Network in Australia, and NASA’s All Sky Fireball Network with weather radar data has helped in the recovery of several meteorites with accurate orbits in the last decade

(Bland *et al.*, 2009; Fries *et al.*, 2014). Although a rare occurrence, the discovery of Earth impactors prior to impact, such as 2008 TC<sub>3</sub>, has enabled us to compare recovered meteorite samples to Earth-based telescopic observations (Jenniskens *et al.*, 2009).

Advances in the collection and quality of spectral data have necessitated improvements in our ability to interpret these data. New formulas for deriving mineralogies from VIS/NIR spectra with prominent 1- and 2-μm absorption bands have been developed (Burbine *et al.*, 2007; Dunn *et al.*, 2010b; Reddy *et al.*, 2011), and the effects of noncompositional parameters have been well characterized, allowing for more accurate interpretations of asteroid surface mineralogies (e.g., Burbine *et al.*, 2009; Sanchez *et al.*, 2012, Reddy *et al.*, 2012c). For spectra devoid of prominent absorption features at visible and near-IR wavelengths, radiative transfer models can provide insight into mineral compositions and abundances. Another area of focus is the 3-μm region, where hydrated silicates and organics have distinct absorption features. Much progress has also been made on spectroscopy of asteroids and meteorites at mid-IR wavelengths (5–25 μm).

In this chapter we review advances made over the last decade in determining mineralogy and surface composition of asteroids at wavelengths ranging from the visible to the mid-IR. We focus on asteroids showing silicate absorption features, as they have the best laboratory spectral calibrations to derive mineralogy with remote sensing data. We also examine the role that spacecraft have played in improving our understanding of asteroid surface morphology and composition. Finally, we discuss the connections between meteorite groups and potential asteroid sources that have been made as a result of these advances in the collection and interpretation of asteroid spectra.

## 2. MINERALOGICAL CHARACTERIZATION

Visible/near-infrared (VIS/NIR) spectra (0.3–2.5 μm) have been widely used to determine mafic mineral abundances and compositions of asteroids since the relationship between spectral properties (i.e., absorption features) and mineralogy in meteorites was first recognized (e.g., Adams, 1975; Burns *et al.*, 1972; Cloutis *et al.*, 1986; Cloutis and Gaffey, 1991). Most previous work examining the spectral properties of silicate minerals has focused on olivine and pyroxene, both of which have diagnostic spectral properties in the VIS/NIR.

Olivine and pyroxene are the primary mineral phases in most primitive meteorites and in many types of non-chondritic meteorites. The structure of olivine consists of individual silicon-oxygen tetrahedra linked by divalent Mg and Fe atoms that occupy the M1 and M2 structural sites. Substitution of Mg and Fe between the M1 and M2 sites results in a solid solution series defined by two compositional endmembers: the Fe-endmember fayalite ( $\text{Fe}_2\text{SiO}_4$ ) and the Mg-endmember forsterite ( $\text{Mg}_2\text{SiO}_4$ ). Pyroxenes are a group of chain silicate minerals that share the chemical formula

$(\text{M}2)(\text{M}1)(\text{Si},\text{Al})_2\text{O}_6$ . Three pyroxene subgroups have been defined based on occupancy of the M2 site. In low-Ca pyroxenes, the M2 site is occupied by Fe or Mg, in high-Ca pyroxenes by Ca, and in sodium pyroxenes by Na. Because high-Ca pyroxenes have monoclinic symmetries, they are often referred to as clinopyroxenes. The term orthopyroxenes is commonly used when referring to the orthorhombic low-Ca pyroxene endmembers, enstatite ( $\text{Mg}_2\text{Si}_2\text{O}_6$ ) and ferrosilite ( $\text{Fe}_2\text{Si}_2\text{O}_6$ ). For a more in-depth discussion of the structure and composition of the olivine and pyroxene groups, we refer the reader to Deer *et al.* (1966).

The primary diagnostic feature in olivine is a composite absorption feature at ~1 μm, which consists of three distinct absorption bands. The composite 1-μm band, which is attributed to electronic transitions of  $\text{Fe}^{2+}$  occupying both the M1 and M2 crystallographic sites (Burns, 1970), moves to longer wavelengths as FeO content increases (King and Ridley, 1987; Sunshine and Pieters, 1998). Pyroxenes have two absorption bands at ~1 μm and ~2 μm that are associated with crystal field transitions in  $\text{Fe}^{2+}$ , which preferentially occupies the M2 site (Clark, 1957; Burns, 1970) (Fig. 1). Low-calcium pyroxenes, which are conventionally defined as having less than 11 mol%  $\text{CaSiO}_3$  (wollastonite, or Wo) (Adams, 1974), show a well-defined relationship between absorption band positions and composition, as both Band I and Band II positions increase with increasing ferrous iron content (Adams, 1974; Burns *et al.*, 1972; Cloutis and Gaffey, 1991). There is also a correlation between composition and band positions in high-calcium pyroxene, although the relationship is complicated by the presence of calcium in addition to iron. In spectral type B clinopyroxenes (<Wo<sub>50</sub>), there is a positive correlation between calcium content and Band I and II position, regardless of iron content (Cloutis and Gaffey, 1991). However, there does not appear to be a systematic relationship between Band I or Band II position

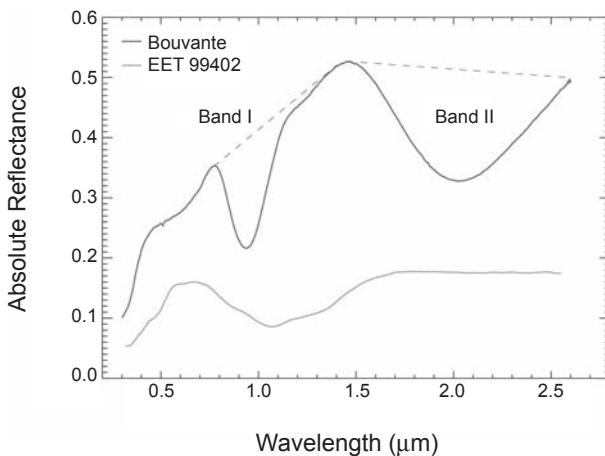


**Fig. 1.** Laboratory-measured spectra of olivine ( $\text{Fa}_{35}$ ) in the brachinitite EET 994012 (Burbine *et al.*, 2007) and pyroxene ( $\text{Fs}_{53}\text{Wo}_{14}$ ) in the eucrite Bouvante (Burbine *et al.*, 2001). The area underneath the dashed lines is the band area. The band area ratio is the area of Band II/area of Band I.

and Ca and Fe content in spectral type A clinopyroxenes ( $>\text{Wo}_{50}$ ) (Cloutis and Gaffey, 1991; Schade et al., 2004). In mixtures of orthopyroxene and clinopyroxene, spectral shape and band positions are dominated by the orthopyroxene component, as clinopyroxene only begins to affect the band positions at abundances  $>75$  wt% (Cloutis and Gaffey, 1991).

### 3. NONCOMPOSITIONAL SPECTRAL EFFECTS

Prior to mineralogical interpretation, spectral band parameters of S-type and V-type asteroids must be corrected for noncompositional effects, such as temperature, phase angle, and grain size. Phase angle is defined as the Sun-target-observer angle, and is typically less than  $25^\circ$  for main-belt asteroids but can be much higher for near-Earth asteroids. With increasing or decreasing phase angle the slope of a reflectance spectrum generally becomes redder or bluer respectively, an effect known as phase reddening. Particle size primarily affects the depth and slope of an absorption feature and overall reflectance, with absorption bands reaching the greatest depth at a grain size bin that provides maximum spectral contrast (deepest absorption bands). Larger particle size typically means deeper bands, bluer (more negative) spectral slope, and lower overall reflectance. Analysis of particles returned by the Hayabusa spacecraft from near-Earth asteroid (25143) Itokawa have shown that a majority of the 1534 particles have a size range between 3 and 40  $\mu\text{m}$ , with most of them smaller than 10  $\mu\text{m}$  (Nakamura et al., 2011). This would suggest that spectra of laboratory meteorite samples with grain sizes  $<100$   $\mu\text{m}$  would best represent spectra of asteroid regolith, although the method of sampling likely biased the grain size distribution of the collected material. Temperature differences between asteroid surfaces and room temperature measurements produce changes in absorption band centers, band depths, band widths, and band area ratios (BAR). Of these three factors, temperature corrections of band centers have a large impact on mineralogical characterization, whereas phase angle corrections are important for constraining space weathering on small bodies, as they affect spectral slope, albedo, and band depth. Ignoring these effects could lead to erroneous interpretations of asteroid surface mineralogy and space weathering effects (Sanchez et al., 2012).

#### 3.1. Temperature-Induced Spectral Effects

The rationale behind applying corrections for temperature-induced spectral effects is motivated by the fact that current laboratory spectral calibrations for the interpretation of asteroid spectra are derived using room-temperature mineral/meteorite spectra ( $\sim 300$  K). In contrast, the surface temperatures of asteroids can range from 140 to 440 K depending on the object's heliocentric distance. This temperature difference produces changes in absorption band centers, band depths, band widths, and BARs, which in turn can lead to over- or underestimation of iron/calcium content in silicates and variations in BAR. Several calibrations for correcting spectral band parameters of specific minerals or meteorite

types have been developed in recent years (e.g., Burbine et al., 2009; Reddy et al., 2012c; Sanchez et al., 2012).

The first step in temperature correction of asteroid spectral band parameters is an estimation of the subsolar equilibrium surface temperature, T (Burbine et al., 2009)

$$T = \left[ \frac{(1 - A)L_0}{16\eta\varepsilon\sigma r^2} \right]^{1/4} \quad (1)$$

where A is the bolometric Bond albedo of the asteroid,  $L_0$  is the solar luminosity ( $3.827 \times 10^{26}$  W),  $\eta$  is the beaming parameter (assumed to be unity) (e.g., Cohen et al., 1998),  $\varepsilon$  is the asteroid's infrared emissivity (assumed to be 0.9),  $\sigma$  is the Stefan-Boltzman constant ( $5.67 \times 10^{-8}$  J s $^{-1}$  m $^{-2}$  K $^{-4}$ ), and r is the asteroid's distance from the Sun in meters. If the asteroid albedo A is unknown, a value can be assumed based on its taxonomic classification. The typical variation in the calculated temperature due to changes in the assumed parameters is in the range of  $\pm 10$  K (Burbine et al., 2009).

Burbine et al. (2009) developed equations to correct for temperature-induced spectral effects in V-type asteroids using spectra of bronzite and enstatite measured at various temperatures by Moroz et al. (2000). Reddy et al. (2012c) improved those temperature corrections by developing equations based on spectra of howardite-eucrite-diogenite (HED) meteorites over a range of temperatures (equations (2)–(5) in Table 1). These equations help derive a correction factor that is added to the Band I and II centers to obtain values at 300 K. Sanchez et al. (2012) derived similar equations for ordinary chondrites using temperature series from Moroz et al. (2000) and Hinrichs and Lucey (2002). They noted that the Band I center changes due to temperature are negligible and can be essentially ignored, and derived a temperature correction for the Band II center (equation (6) in Table 1). For monomineralic-olivine or olivine-rich A-type asteroids, Sanchez et al. (2014) derived temperature corrections using data from Hinrichs and Lucey (2002). Similar to previous equations, the Band I center correction is added to the Band I center before analysis (equation (8) in Table 1).

Band depth is also affected by changing temperature and causes an increase or decrease in BAR. Sanchez et al. (2012) derived equations to correct for temperature effects on BAR of ordinary chondrites. The correction derived using the equation below must be added to the calculated BAR value (equation (7) in Table 1). For olivine-dominated asteroids, the depth of the 1- $\mu\text{m}$  band changes with temperature. We derived an equation to correct Band I depth (%) for temperature effects using data from Hinrichs and Lucey (2002) (equation (9) in Table 1).

#### 3.2. Phase-Angle-Induced Spectral Effects

Phase-angle-induced spectral effects can be exhibited as phase reddening, which is characterized by an increase in spectral slope (reddening) and variations in albedo and absorption band depth with changing phase angle (Gradie

TABLE 1. Calibrations for correcting noncompositional effects.

Effect	Analog	Operation	Equation	Equation No.
Temperature	Howardites and eucrites*	Add to Band I Center	$\Delta BI(\mu\text{m}) = 0.01656 - 0.0000552 \times T (\text{K})$	(2)
		Add to Band II Center	$\Delta BI(\mu\text{m}) = 0.05067 - 0.00017 \times T (\text{K})$	(3)
	Diogenites*	Add to Band I Center	$\Delta BI(\mu\text{m}) = 1.7 \times 10^{-9} \times T^3 (\text{K}) - 1.26 \times 10^{-6} \times T^2 (\text{K}) + 2.66 \times 10^{-4} \times T (\text{K}) - 0.0124$	(4)
		Add to Band II Center	$\Delta BI(\mu\text{m}) = 0.038544 - 0.000128 \times T (\text{K})$	(5)
	Ordinary chondrites†	Add to Band II Center	$\Delta BI(\mu\text{m}) = 0.06 - 0.0002 \times T (\text{K})$	(6)
		Add to Band Area Ratio	$\Delta BAR = 0.00075 \times T (\text{K}) - 0.23$	(7)
	Olivine-rich A-type asteroids‡	Add to Band I Center	$\Delta BI(\mu\text{m}) = -(1.18 \times 10^{-7})T^2 + (2.15 \times 10^{-5})T + 0.004$	(8)
		Add to Band I Depth	$BI_{\text{depth corr}} = 0.0057 \times T (\text{K}) - 1.71$	(9)

\*Reddy *et al.* (2012c).†Sanchez *et al.* (2012).‡Sanchez *et al.* (2014).

*et al.*, 1980; Gradie and Veverka, 1986; Clark *et al.*, 2002; Mann *et al.*, 2011; Shepard and Cloutis, 2011) (Fig. 2). This effect, caused by a wavelength dependence of the single-scattering albedo, has been observed in both groundbased (e.g., Gehrels, 1970; Millis *et al.*, 1976; Lumme and Bowell, 1981; Nathues *et al.*, 2005; Nathues, 2010; Reddy *et al.*, 2012c) and spacecraft observations (Clark *et al.*, 2002; Bell *et al.*, 2002; Kitazato *et al.*, 2008) of small bodies. Asteroid observations need to be corrected for phase-angle effects because they can influence spectral slope and band depth, which are both nondiagnostic parameters. The equations de-

veloped to correct spectral band parameters for phase angle effects normalize them to 0° phase angle.

Reddy *et al.* (2012c) observed Vesta at different phase angles and quantified the effect on spectral slope. Based on these observations, they developed an equation to correct the visible spectral slope (0.4–0.7 μm) for phase angle effects

$$S_c = S - \gamma \alpha \quad (10)$$

where  $S_c$  is the phase angle corrected spectral slope,  $S$  is the measured spectral slope,  $\gamma = 0.0198\%/\mu\text{m}/\text{deg}$ , and  $\alpha$  is the phase angle in degrees. However, data from Dawn predict a similar trend but with less phase reddening (Li *et al.*, 2013) than that observed by Reddy *et al.* (2012c).

Similarly, Reddy *et al.* (2012c) developed an equation to correct the BAR for phase reddening based on groundbased near-IR spectral observations of Vesta

$$BAR_c = BAR - \gamma_3 \alpha \quad (11)$$

where  $BAR_c$  is the phase-angle-corrected BAR,  $\gamma_3 = 0.0292/\text{deg}$ , and  $\alpha$  is the phase angle in degrees.

Sanchez *et al.* (2012) did not find any systematic changes in BAR due to phase angle for ordinary chondrites. They did develop a phase angle correction for correcting Band I and II depths of olivine-pyroxene assemblages

$$BI_{\text{dep}} = BI_{\text{dep}} - 0.066 \times (\alpha) \quad (12)$$

$$BII_{\text{dep}} = BII_{\text{dep}} - 0.093 \times (\alpha) \quad (13)$$

where  $BI_{\text{dep}}$  and  $BII_{\text{dep}}$  are the corrected band depths (%) and  $\alpha$  is the phase angle. The phase angle range in which these equations are valid are between 2° and 70° for Band I and 2° and 55° for Band II. While these equations are valid for smaller grain sizes (<45 μm), a plethora of observational data of asteroids and laboratory studies of meteorites have shown that asteroid regolith contains, at a minimum, an optically dominant amount of fine grains.

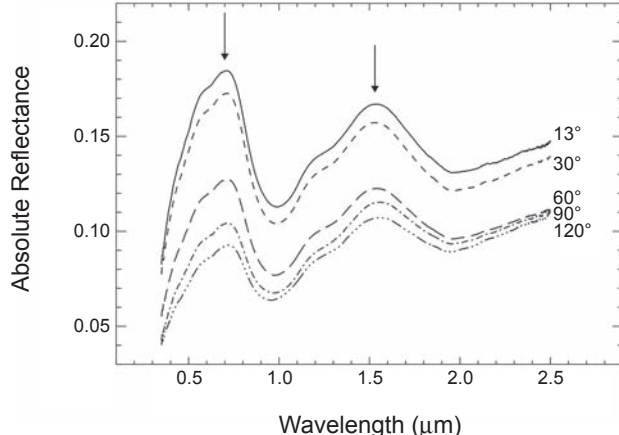


**Fig. 2.** Laboratory near-IR spectra of Dhurmsala meteorite (LL6 ordinary chondrite) at different phase angles  $\alpha = 13^\circ$  (solid line),  $30^\circ$  (short dashed line),  $60^\circ$  (long dashed line),  $90^\circ$  (dot-short dashed line), and  $120^\circ$  (dot-long dashed line) from Sanchez (2012). The figure shows spectra that are not normalized or offset from each other. As the phase angle increases the overall reflectance decreases, and the two arrows show the dramatic decrease in reflectance at the two reflectance peaks of the spectra. The reflectance in the shorter wavelength end (blue region) of the spectrum decreases faster than the longer wavelength end (red) of the spectra with increasing phase angle creating the observed red slope (phase reddening).

## 4. FORMULAE FOR DERIVING ASTEROID COMPOSITIONS

### 4.1. Mafic Mineral Compositions

The correlation between mafic silicate compositions (i.e., mol% Fa in olivine and mol% Fs in pyroxene) and band centers is commonly used to determine asteroid compositions from VIS/NIR spectra. Because of the complex nature of the composite olivine band, most work has focused on the correlation between band centers and pyroxene composition. Gaffey *et al.* (2002) devised a set of equations defining the relationships between band centers and pyroxene compositions, where compositions are expressed as the calcium endmember wollastonite (Wo) and iron endmember ferrosilite (Fs). Although both pyroxene and olivine composition affect the position of Band I, the Gaffey calibrations removed the effect of olivine, thus allowing a single pyroxene composition to be measured.

The Gaffey *et al.* (2002) calibrations, while pioneering, have recently been shown to only work on a limited range of pyroxene compositions and are restricted to mineral assemblages containing a single pyroxene (Gaffey, 2007; McCoy *et al.*, 2007). This is a limitation when attempting to use these formulas on meteorite or asteroid mineralogies. For example, no formulas are available for Fs compositions above 50 mol%, which is the range of most Fe-rich eucrites (Burbine *et al.*, 2009). Also, these formulas can greatly overestimate the Fs content in samples containing more than one pyroxene, such as the ordinary chondrites (Gaffey, 2007; McCoy *et al.*, 2007). To address the problem of derived pyroxene compositions, Gaffey (2007) developed a procedure to correct for two-pyroxene assemblages. In this procedure, the BAR is used to determine an offset for Band I. The Band II position is corrected by compensating for the presence of augite. This is accomplished by subtracting a predetermined value from the measured Band II position (0.065  $\mu\text{m}$  for H chondrites, 0.062  $\mu\text{m}$  for L, and 0.076  $\mu\text{m}$  for LL) (Gaffey, 2007). The new Band I and Band II centers are then applied to the original Gaffey *et al.* (2002) equations, resulting in a single low-Ca pyroxene composition for H, L, and LL chondrite analogs. The correct analog is selected when the derived Fs and Wo values are consistent with measured values.

We tested the Gaffey *et al.* (2002) equations and subsequent corrections using 38 ordinary chondrites with pyroxene compositions analyzed by Dunn *et al.* (2010a). As per the guidelines established by the calibration, we selected the equations that satisfied each set of constraints (in terms of Wo and Fs content). In most cases, this was equations (2b) and (3a) from Gaffey *et al.* (2002). With corrections applied, the difference between measured and derived Wo values ranges from -8.3 mol% to +9.3 mol%, and 63% of derived Wo values are negative. This would suggest the Band I position is being overcorrected. Calculated Fs values are dependent on whether one is testing for H, L, or LL chondrites. Calculated Fs values do not differ substantially between the H and L chondrites, but LL chondrites values are always lower

(due to the higher correction factor). The difference between measured Fs values and Fs values calculated using the L chondrite correction range from -7.2 mol% to 9.1 mol%. Often the Fs content is either too low or too high to correctly classify the sample as H, L, or LL. Only 30% of H chondrites, 29% of L chondrites, and 43% of LL chondrites were classified correctly.

Despite the issues associated with using the Gaffey *et al.* (2002) pyroxene calibrations on ordinary-chondrite-like mineralogies, these calibrations are well suited for single pyroxene assemblages, such as the HED meteorites (e.g., Reddy *et al.*, 2010; Hardersen *et al.*, 2011, 2014). Any calibration for deriving mafic mineral compositions is most successful when designed and implemented for a limited range of mineral assemblages, such as those developed for the HEDs (Burbine *et al.*, 2007), the ordinary chondrites (Dunn *et al.*, 2010b), and olivine-rich meteorites (Reddy *et al.*, 2011) (Table 2). Each of these sets of calibrations is designed with a specific suite of meteorites and potential asteroid analogs in mind. The Burbine *et al.* (2007) calibrations (equations (14–17) from Table 2) were developed using a suite of 13 HED meteorites [basaltic achondrites believed to originate from asteroid (4) Vesta] (McCord *et al.*, 1970). Thus, the Burbine *et al.* (2007) calibrations are useful for deriving pyroxene chemistries of Vesta-like (V-type) asteroids. These calibrations are preferable to those of Gaffey *et al.* (2002) because they are simpler, are applicable to the entire range of pyroxene compositions in HEDs (Fs<sub>23–56</sub>; Wo<sub>2–14</sub>), and are more accurate (to within 3 mol% Fs and 1 mol% Wo).

Dunn *et al.* (2010b) developed formulas for deriving pyroxene and olivine compositions of the ordinary chondrites and asteroids with similar mineralogies (primarily S-types and Q-types). These formulas, one for Fa content in olivine and one for Fs content in pyroxene (equations (18) and (19) from Table 2), have low error (<2 mol%) and were developed based on the suggestion that the Band I center in the ordinary chondrites is controlled almost entirely by the abundance of FeO in olivine and pyroxene, and can therefore serve as a proxy for bulk FeO content. This also suggests that there is no significant correlation between Band I center and CaO content (mol% Wo) in meteorites and asteroids that consist of both olivine and pyroxene. However, we would expect CaO content to have a much more significant effect on band positions in pyroxene-dominated asteroids, such as the vestoids.

Recently, Reddy *et al.* (2011) added another formula to derive forsterite (Fo) content of olivine in meteorites and asteroids composed almost entirely of olivine (equation (22) from Table 2). The relationship between band position and olivine composition was first examined by King and Ridley (1987). Reddy *et al.* (2011) improved this calibration by adding more Mg-rich olivines (Fo<sub>85–93</sub>) to the sample suite. The root mean squared (RMS) error between measured values and laboratory derived Fo content is 5 mol%. This equation is designed to be used with A-type asteroids, which have a weak or nearly absent 2- $\mu\text{m}$  feature consistent with a monomineralic olivine composition.

TABLE 2. Calibrations for various meteorite mineralogies and their asteroid analogs.

Asteroid Type	Analog	Comp. Range	Equation	Error	Equation No.
V-types	HEDs*	$Fs_{23-56}, Wo_{2-14}$	$Fs = 1023.4 \times BIC - 913.82$	$\pm 3$ mol%	(14)
			$Fs = 205.9 \times BIIC - 364.3$	$\pm 3$ mol%	(15)
			$Wo = 396.1 \times BIC - 360.55$	$\pm 1$ mol%	(16)
			$Wo = 79.91 \times BIIC - 148.3$	$\pm 1$ mol%	(17)
S-types	Ordinary chondrites†	$Fa_{17-31}$	$Fa = -1284.9 \times (BIC)^2 + 2656.5 \times (BIC) - 1342.2$	$\pm 1.3$ mol%	(18)
		$Fs_{14-26}, Wo_{1-3}$	$Fs = -879.1 \times (BIC)^2 + 1824.9 \times (BIC) - 921.7$	$\pm 1.4$ mol%	(19)
			$ol/(ol + px) = -0.242 \times BAR + 0.728$	$\pm 0.03$	(20)
A-types	Lodranites/acapulcoites‡		$px/(ol + px) = 0.417 \times BAR + 0.052$		(21)
			$Fo = -1946.6 \times (BIC) - 2139.4$	$\pm 5$ mol%	(22)
			$ol/(ol + px) = -11.27 \times BAR^2 + 0.3012 \times BAR + 0.956$	$\pm 0.003$	(23)

\*Burbine et al. (2007).

†Dunn et al. (2010b).

‡Cloutis et al. (1986).

§Reddy et al. (2011).

¶Sanchez et al. (2014).

One must use caution when applying any of these calibrations to asteroids, as inaccurate derived mineralogies can lead to misinterpretation of asteroid geologic histories. Such is the case of Itokawa, the target of the Hayabusa mission (see section 6). Abell et al. (2007) suggested that Itokawa had experienced partial melting, based on its high-Fe pyroxene content, while others argued it was compositionally similar to the ordinary chondrites (e.g., Binzel et al., 2001; Abe et al., 2006; Okada et al., 2006). Itokawa's primitive origin (as an LL chondrite) was confirmed by the Hayabusa sample return mission (Nakamura et al., 2011). However, this extremely rare case of obtaining the “ground truth” for specific asteroids is only possible via sample return or terrestrial impact and recovery of an observed asteroid, such as 2008 TC<sub>3</sub>.

Figure 3 shows a decision-making flowchart for interpretation of asteroid spectra based on mineralogical calibrations that are available. In asteroids that show only a 1-μm absorption feature, iron abundance in olivine can be constrained using its Band I center position and equations from Reddy et al. (2011). For asteroids with 1- and 2-μm bands, similar calibrations exist depending on where the asteroid spectral band parameters plot on the Band I center vs. BAR plot (Gaffey et al., 1993). This Band I center vs. BAR plot is broken into S-type subclasses with different zones marking different compositional types. Asteroids in the S(IV) region can be mineralogically characterized using Dunn et al. (2010b) calibrations. Those that fall in the basaltic achondrite zone can be interpreted using calibrations from Gaffey et al. (2002) and Burbine et al. (2009). Meteorite analogs for these three asteroid types (olivine-rich A-type asteroids, S/Q-type asteroids, and V-type asteroids) constitute 91% of all the meteorites in our terrestrial collection (see the chapter by DeMeo et al. in this volume).

## 4.2. Mafic Mineral Abundances

In spectra containing both olivine and pyroxene absorptions, the combined absorption features near 1 μm (Band I)

and 2 μm (Band II) are also sensitive to the relative proportions of olivine and pyroxene. The ratio of the areas of these two bands (Band II/Band I) is commonly used to estimate olivine and pyroxene abundances in meteorites and asteroids (Cloutis et al., 1986). The linear relationship between BAR and the ratio of pyroxene to olivine + pyroxene [px/(ol + px)] was first recognized by Cloutis et al. (1986) (equation (21) from Table 2). However, the mixtures Cloutis et al. used to derive their equation did not contain clinopyroxene. As a result, their calibrations were not well suited for determining the BARs of mixtures containing more than one pyroxene (i.e., ordinary chondrites).

The Cloutis et al. calibration was initially designed to derive BARs from mixtures of known mineral proportions. However, this relationship between mafic mineral abundances and BAR is also an important tool for determining asteroid mineralogies from VIS/NIR spectra. Gastineau-Lyons et al. (2002) used this relationship to derive mineral abundances from measured BARs of asteroid spectra. However, because the original Cloutis et al. (1986) regression was based on simple mixtures of olivine and orthopyroxene, the presence of more than one pyroxene (or other additional phases) complicated spectral interpretations of asteroids made using this calibration (Gaffey et al., 1993; Sunshine et al., 2004).

In an attempt to develop BAR calibrations that were more useful in asteroid spectroscopy, Burbine et al. (2003) used normative abundances of the ordinary chondrites (abundances calculated from measured bulk chemistry) to derive a calibration for the S-type asteroids. The most recent revision of the calibrations for S-type asteroid mineralogies was produced by Dunn et al. (2010b) (equation (20) from Table 2). Dunn et al. used measured modal abundances of ~50 ordinary chondrite powders to derive their calibrations. Modes were determined using a position-sensitive X-ray diffraction technique (Dunn et al., 2010a), which allows for measurement of phases present at abundances as low as 1 wt% (Cressey and Schofield, 1996). Using this technique, Dunn et al. (2010b) were able to account for pigeonite, the

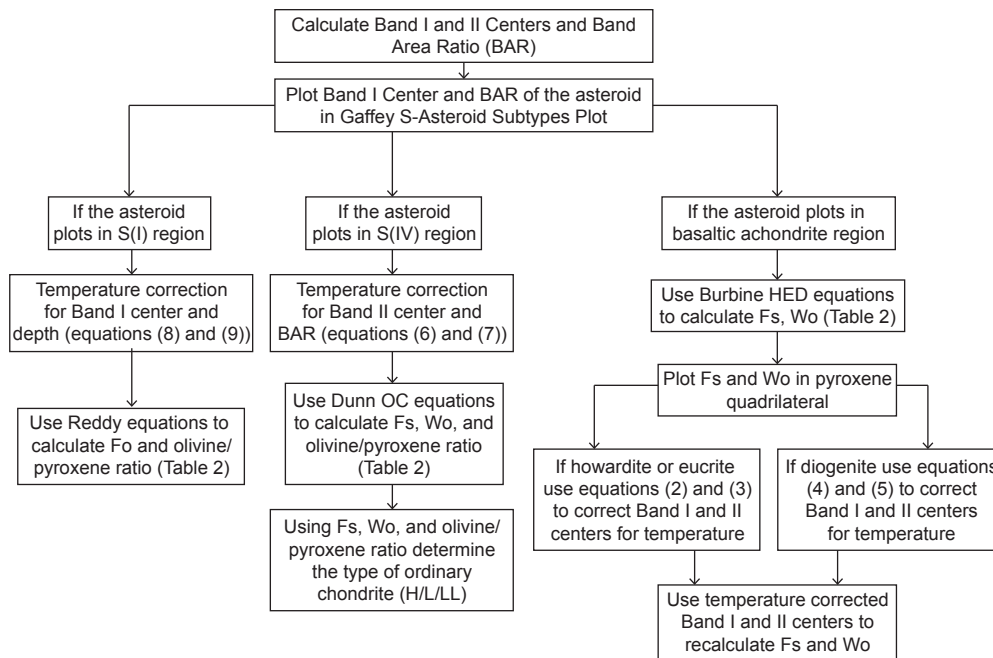


**Fig. 3.** Flowchart showing a decision making tree for mineralogical characterization of A-, S-, and V-type asteroids using equations from Reddy et al. (2011), Dunn et al. (2010b), and Burbine et al. (2007).

third pyroxene present in the ordinary chondrites. Because this regression was derived using measured abundances (as opposed to abundances calculated using CIPW norms), it provides a more accurate measure of olivine and pyroxene abundances from VIS/NIR spectra.

Gaffey et al. (2002) suggested that pyroxene abundances could be constrained even further by considering the effect of high-Ca pyroxene on Band II position, which they suggested is a linear function of the relative abundance of the two pyroxenes. This assertion requires that the cpx/(opx + cpx) ratio is well-correlated with Band II center in the range of values found in ordinary chondrites. Using XRD-measured pyroxene abundances and Band II centers, Dunn et al. (2010b) derived an equation for establishing the ratio of high-Ca pyroxene to total pyroxene. However, this equation yielded a very low  $R^2$  value of 0.15. The remarkably low  $R^2$  value indicates that there is no significant correlation between Band II position and relative pyroxene abundance in the ordinary chondrites.

Although the Dunn et al. (2010b) regression formula is well suited for asteroids with ordinary-chondrite-like compositions (e.g., some S-types and Q-types), it is not as equally well suited for asteroids with other mineralogies. For example, the original calibration of Cloutis et al. (1986) is still better suited for asteroids that are compositionally similar to primitive achondrites (lodranites and acapulcoites), which are primarily mixtures of low-Ca pyroxene and olivine (e.g., McCoy et al., 2000). The Dunn et al. (2010b) calibrations would not work well for mineralogies that are dominated by only one mafic phase (i.e., either olivine or pyroxene, but not both). Recently, Sanchez et al. (2014) developed a calibra-

tion for olivine-rich asteroids using the R chondrites (equation (23) from Table 2), which contain higher abundances of olivine than the ordinary chondrites (65–78%) (Bischoff et al., 2011). Initial tests of this calibration yield abundances in strong agreement with previous characterizations. However, it is important to note that this calibration was developed using a limited sample selection (only seven R chondrites). Also, although R chondrites provide a good spectral match with olivine-dominated asteroids, their compositions may differ (Sanchez et al., 2014). Consequently, any interpretations made using the Sanchez et al. (2014) formula should be taken with caution. Additional laboratory measurements will be necessary to improve the robustness of this calibration.

## 5. SPECTRAL MODELING

### 5.1. Modified Gaussian Model

Composite mineral absorption bands can be deconvolved into discrete mathematical functions. The modified Gaussian model (MGM) (Sunshine et al., 1990) constructs a model spectrum from one or more modified Gaussian functions to represent absorption features from individual species (Fig. 4). These modified Gaussians are physically motivated by crystal field theory and represent the relationship between the natural log of reflectance and energy (Sunshine et al., 1990). In comparison to ordinary Gaussians, these modified functions include the addition of a power law index of  $n = -1$  to their energy dependence. Each MGM band is associated with three degrees of freedom (center, width, depth). The full model includes a continuum, which is typically linear

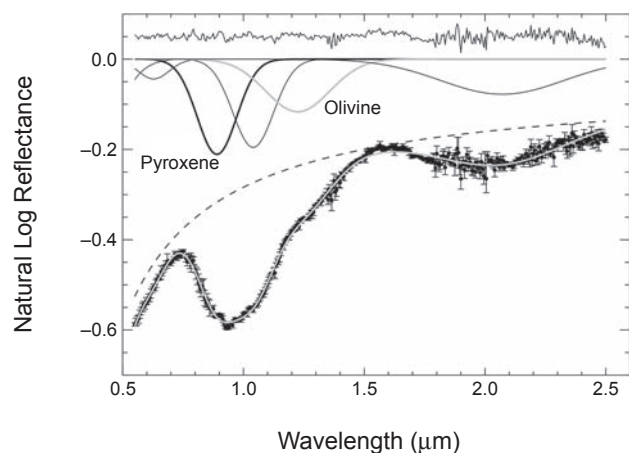


**Fig. 4.** Modified Gaussian model of asteroid (25143) Itokawa. From bottom to top: asteroid data with error bars (black), best-fit model (gray), model continuum (dashed), six Gaussian bands used in the model, and residuals from the model fit. The Gaussian band centered around 0.9  $\mu\text{m}$  (thick black line) is attributed to pyroxene (pyx), while the band around 1.2  $\mu\text{m}$  (thick gray line) is attributed to olivine (ol). The ratio of these bands' strengths provides a means for comparison to equivalent models of OC meteorite spectra. This comparison correctly predicts an LL-type composition for Itokawa (Binzel *et al.*, 2001).

in energy space and adds two free parameters for slope and offset. Initial values for all these parameters are specified at the onset of modeling and are iteratively adjusted until a best fit is determined by minimizing the RMS residuals of the difference between reflectance data and the model spectrum.

The MGM was originally employed to analyze laboratory spectra of terrestrial and meteorite samples (Sunshine *et al.*, 1990; Sunshine and Pieters, 1993) and has since been extensively applied to mafic silicate systems including the Moon (e.g., Isaacson *et al.*, 2011), Mars (e.g., Clenet *et al.*, 2013), and a variety of asteroid types. In its most basic implementation, the MGM can be used as a simple band analysis tool to measure band parameters, analogous to those discussed in section 3. Using the MGM to derive band parameters is beneficial because it can serve as a consistent analysis tool that does not vary from one implementation to the next. This is not necessarily the case with other band analysis techniques that may employ different methodologies (e.g., Cloutis *et al.*, 1986; Moskovitz *et al.*, 2010; Dunn *et al.*, 2013). Standardizing a tool like the MGM for measuring band parameters can facilitate comparisons across investigations, but does require that continua be modeled in a consistent manner.

The MGM has been employed as a band analysis tool in several studies of near-Earth asteroids. Rivkin *et al.* (2004) showed that the MGM could reliably recover Band I areas for S-type NEAs in cases where only near-IR spectra were available and the 1- $\mu\text{m}$  band was not fully resolved. These authors defined the MGM-derived ratio of band areas (RBA) parameter as an analog to BAR for spectra where visible

data were not available. Although not extensively tested, the RBA reasonably reproduces compositions for objects with well-constrained mineralogy like Itokawa and Eros. Vernazza *et al.* (2008) and Thomas and Binzel (2010) extended the use of the MGM as a band analysis tool to link H, L, and LL ordinary chondrites to their asteroidal counterparts in near-Earth space. The MGM has also been used to correlate the band parameters of V-type asteroids with subgroups of the HED meteorites (Mayne *et al.*, 2011).

In its full implementation the MGM is used to model specific mineral absorption bands. This can involve diagnosing the origin of unknown features (e.g., Hiroi *et al.*, 1996) or starting with *a priori* assumptions about composition to generate a mineralogical model (e.g., Mayne *et al.*, 2011). For example, the relative strengths of pyroxene and olivine bands in the vicinity of 1  $\mu\text{m}$  led Binzel *et al.* (2001) to correctly predict an LL-chondrite-like composition for (25143) Itokawa (Fig. 4). Analyses of other S-complex asteroids suggest that the MGM can constrain the relative abundance of high-Ca to low-Ca pyroxene. For example, Sunshine *et al.* (2004) found high-Ca pyroxene abundances >40% for the large main-belt asteroids (17) Thetis, (847) Agnia, and (808) Merxia, thus implying that these objects experienced high degrees of partial melting consistent with a history of igneous differentiation.

The three overlapping 1- $\mu\text{m}$  olivine bands, as seen in the spectra of A-type asteroids, are particularly well suited to MGM analysis, despite their sensitivity to space weathering (e.g., Brunetto *et al.*, 2007) and temperature (e.g., Lucey *et al.*, 1998). Using the MGM, Sunshine *et al.* (2007) showed that A-type asteroids segregate into two groups based on olivine composition. Those with magnesian (forsteritic) compositions suggest an igneous history involving the differentiation of ordinary chondrite precursors, whereas those with ferroan (fayalitic) compositions are more consistent with an origin tied to oxidized R-chondrite precursors. K-type asteroids in the Eos family have also been associated with an olivine-dominated composition (Mothé-Diniz *et al.*, 2008).

Due to their prominent 1- and 2- $\mu\text{m}$  absorption features, pyroxene-dominated V-type asteroids have been extensively modeled with the MGM. Traditional band analyses of these asteroids (section 3) have generally focused on deriving bulk pyroxene composition (e.g., Wo, Fs, and En numbers), whereas MGM analyses are typically used to measure the abundance ratio of high-Ca to low-Ca pyroxene. These different approaches can provide complementary insight when performed in tandem (e.g., Lim *et al.*, 2011). MGM analyses of V-type asteroids suggest that very roughly 25–40% of their total pyroxene is in the high-Ca phase (Duffard *et al.*, 2006; Mayne *et al.*, 2011), consistent with the pyroxene composition of the HED meteorites (Mittlefehldt *et al.*, 1998) and therefore supporting the generally accepted link between these asteroids and meteorites.

Like any compositional analysis tool the MGM has limitations. Perhaps its greatest weaknesses are the dependence on multiple free parameters in even relatively simple mineralogical models and the sensitivity of those parameters

to prescribed initial conditions. Without careful application these issues can produce nondiagnostic or degenerate fits.

## 5.2. Radiative Transfer Models

Models of radiative transfer on atmosphereless bodies generally involve computing reflectivity (i.e., scattering and phase-corrected single-scattering albedo) based on optical constants and particle sizes of specific mineral species. Reflectivity is computed as a function of assumed viewing geometry and is rooted in approximations of geometric optics. Radiative transfer models can provide insight into particle sizes, mineral compositions, and mineral abundances.

Various approaches have been developed to treat the presumably chaotic structure and mixture of mineral grains in planetary regoliths. The approximation of an areal or linear mixture involves computing the reflectance from mineral phases separately and then linearly combining those to represent the total reflectance. This “checkerboard” approach assumes the constituent minerals are optically separated so that multiple scattering does not occur between minerals. Intimate, nonlinear, or “salt-and-pepper” mixtures involve computing an average single-scattering albedo of the mineral constituents as input to the reflectivity calculation. The sizes of particles relative to the incident wavelength of light determine how the single-scattering albedo is calculated in such homogeneous mixtures (Shkuratov *et al.*, 1999; Poulet *et al.*, 2002).

Radiative transfer models are some of the most widely used tools for compositional analyses of planetary bodies. The theory outlined by Hapke (1981) and since improved upon in a number of subsequent publications (Hapke, 1984, 1986, 2001, 2002, 2008) was one of the first to derive the single-scattering albedo for a grain with prescribed size and optical properties. Shkuratov *et al.* (1999) developed a similar but alternative model that employs a distinct treatment of particle scattering. A detailed review and comparison of these two implementations is presented in Poulet *et al.* (2002). More recently, Lawrence and Lucey (2007) expanded upon the Hapke formalism by incorporating the spectral effects of coarse-grained Fe-Ni metal to facilitate modeling of the metal-rich assemblages frequently encountered in small-body studies, thus enabling studies of the effects of space weathering on mafic silicate bodies like the Moon, basaltic achondrites, and ordinary chondrites. Finally, Lucey and Riner (2011) introduced a new treatment of large, opaque iron agglutinates as a way to model the optical effects of weathering via impact and shock-alteration processes.

Such radiative transfer models have been used for a variety of asteroid applications. Based on spectrophotometry from the Near Earth Asteroid Rendezvous (NEAR) mission, Clark *et al.* (2001, 2002) modeled near-IR spectra of the S-type NEA (433) Eros and were able to disentangle viewing geometry, grain size, composition, and surface weathering effects as causes of color and albedo variability across the asteroid’s surface. Clark *et al.* (2004) applied the same model to E-type asteroids and found that this single taxonomic class could actually be broken into three compositional groups:

objects like (44) Nysa with enstatite-like compositions that include a low-iron orthopyroxene component, objects like (64) Angelina composed of forsterite olivine and oldhamite, and objects like (434) Hungaria, which may be linked to the enstatite-rich aubrite meteorites.

Several variants of radiative transfer models have been used to address issues related to space weathering. Employing a variant of the Shkuratov model, Vernazza *et al.* (2008) showed that the majority of S-type NEAs, in spite of their weathered appearance, have compositions most similar to LL ordinary chondrites (Fig. 5). This is surprising in light of the fact that LL chondrites are rare among ordinary chondrite meteorite falls and may be a result of selection bias influencing the delivery of meteorites from the main belt to Earth. This same model was employed to argue that the timescale of space weathering is a rapid  $\sim 10^6$  yr (Brunetto *et al.*, 2006; Vernazza *et al.*, 2009a); however, this result remains somewhat controversial (Willman and Jedicke, 2011). As such, it is currently unclear how effective these models are in connecting the timescales of space weathering to observed spectral changes.

This particular implementation of the Shkuratov model (Vernazza *et al.*, 2008) does not attempt to fit data beyond  $\sim 2 \mu\text{m}$  due to ineffectiveness of the applied space-weathering model (Fig. 5). However, this implementation has been used exclusively to derive olivine to pyroxene abundance ratios, information that is entirely contained in the 0.6–1.6- $\mu\text{m}$  spectral range and therefore is not dependent on the properties of the 2- $\mu\text{m}$  band. As such, future work to derive silicate

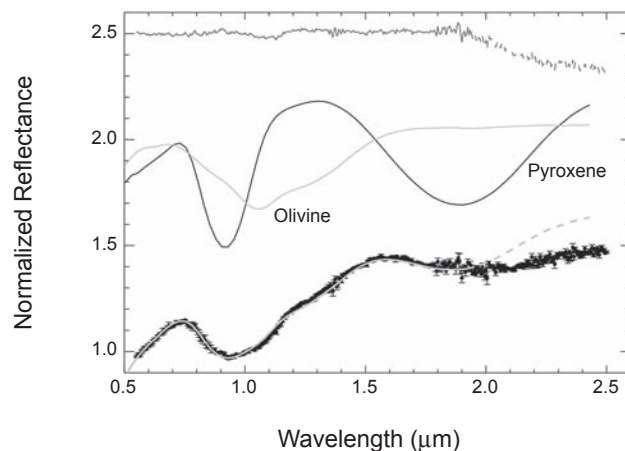


**Fig. 5.** Shkuratov model of asteroid (25143) Itokawa. From bottom to top: asteroid data with error bars (black), best fit model (gray), spectra of mineral endmembers olivine (ol) and low-Ca pyroxene (pyx) used in the model, and residuals from the model fit. This model, based on Vernazza *et al.* (2008), assumes 50% porosity on the asteroid’s surface and only fits the data between 0.55 and 2  $\mu\text{m}$  due to inaccuracy in the treatment of space weathering at longer wavelengths (for details, see Brunetto *et al.*, 2006). This model suggests a composition of  $\text{ol}/(\text{ol} + \text{low-Ca pyx}) = 76\%$ , consistent with the known LL-chondrite composition of Itokawa.

abundances could benefit from exclusive focus on spectral information contained within the 1- $\mu\text{m}$  region.

Primitive compositions have also been modeled with radiative transfer techniques. The spectra of primitive asteroid types (e.g., C- and D-types) are generally red-sloped and largely devoid of prominent absorption features, particularly at visible and near-IR wavelengths. Thus, compositional models of these objects can be less specifically diagnostic, instead providing upper limits on mineral abundances. For example, *Cruikshank et al.* (2001) argued that the surface of the Trojan asteroid (624) Hektor contained <3 wt% water ice and <40% hydrated silicates. Their models further suggested that an unknown low-albedo, spectrally neutral material, potentially analogous to elemental carbon, is responsible for the red color and low albedo of D-type asteroids. *Emery and Brown* (2004) expanded upon this work by modeling the spectra of 17 Trojans. Their results are consistent with *Cruikshank et al.* (2001), suggesting that the Trojan's red spectral slopes are unlikely due to organics and that the Trojan's overall spectral properties may be attributed to a combination of anhydrous silicates and carbonaceous material. Based on data at thermal-IR wavelengths, *Emery et al.* (2006) modeled the emissivity spectra of several Trojans to argue for compositions due to fine-grained silicates embedded within an optically transparent matrix. *Yang and Jewitt* (2011) largely corroborated this result and suggested that Trojan silicates should be iron-poor to account for spectral data at both near-IR and thermal-IR wavelengths. Finally, *Yang et al.* (2013) modeled Trojan spectra to suggest a composition with small quantities of fine-grained silicates (1–5 wt%) and a low-albedo component (2–10 wt%) embedded within a matrix of salt deposits. In spite of these advances, full compositional characterization of Trojan asteroids remains an unsolved problem.

Perhaps the best examples of featureless spectra that evade compositional characterization are those belonging to the asteroid (21) Lutetia. Even though Lutetia was the target of a spacecraft flyby (see the chapter by Barrucci et al. in this volume), radiative transfer models suggest its composition consists of weathered goethite (*Rivkin et al.*, 2011), a hydrated iron-bearing mineral, whereas spectral matching to laboratory samples suggests a very different composition, more analogous to enstatite chondrites (*Vernazza et al.*, 2009b).

Spectral data at longer wavelengths (>3  $\mu\text{m}$ ) can better diagnose specific compositions on primitive asteroids. For example, radiative transfer models have provided specific insight into the presence of hydrated minerals on primitive asteroids (e.g., *Rivkin et al.*, 2006; *Rivkin and Emery*, 2010; *Campins et al.*, 2010). Compositional analysis at mid-IR wavelengths remains a major frontier of asteroid science (see the chapter by Rivkin et al. in this volume).

## 6. COMPOSITIONAL CONSTRAINTS FROM MID-INFRARED OBSERVATIONS

In the mid-IR wavelength region spectral bands are chiefly due to vibrational and lattice modes. The resulting reflectance and emission spectra in these wavelengths are

strongly dependent on surface parameters such as grain size (e.g., *Lyon*, 1964; *Hunt and Logan*, 1972; *Salisbury et al.*, 1991a; *Le Bras and Erard*, 2003) and porosity (*Aronson et al.*, 1966; *Logan et al.*, 1973; *Salisbury et al.*, 1991b), as well as environmental conditions such as ambient pressure (*Logan et al.*, 1973; *Salisbury and Walter*, 1989).

### 6.1. Diagnostic Spectral Features in the Mid-Infrared

Laboratory studies of powdered meteorites and silicate minerals display a variety of diagnostic spectral signatures: Christiansen features, Restrahlen bands, transparency features, and absorption bands. The Christiansen feature is a reflectance minimum (emissivity maximum) located ~7.5–10  $\mu\text{m}$  in most silicates. In this wavelength region the real part of the refractive index changes rapidly (dropping through unity) and therefore may approach the refractive index of the medium surrounding the mineral grains, resulting in minimal scattering. The location where the real refractive index equals unity is the Christiansen frequency (e.g., *Logan et al.*, 1973). For silicates, the Christiansen frequency occurs at a shorter wavelength than the Restrahlen band, where scattering is minimal and the absorption coefficient is small. The resulting reflectance minimum (the Christiansen feature) is often located at longer wavelengths than the Christiansen frequency. *Hapke* (1996) interpreted this feature as occurring due to a transition between the surface and volume scattering regimes. Past work (*Conel*, 1969; *Logan et al.*, 1973; *Salisbury and Walter*, 1989) has noted that the wavelength of the Christiansen feature is an indicator of mineral composition. The wavelength of the Christiansen feature for individual minerals depends on the polymerization of the mineral with the feature occurring at shorter wavelengths for feldspars and longer wavelengths for mafic minerals such as olivine and pyroxene (*Logan et al.*, 1973). For a given asteroid or meteorite, the Christiansen feature is the combination of the characteristic Christiansen features of all the constituent minerals. Often times the principal Christiansen feature corresponds to the strongest molecular vibration band. However, in the case of some meteorites, the individual Christiansen features are far enough apart that numerous local reflectance minima are seen.

Restrahlen bands are the result of strong fundamental molecular vibrations. For silicates they appear at ~8.5–12  $\mu\text{m}$  and are the product of Si-O asymmetric stretching (e.g., *Lyon*, 1964; *Hunt*, 1982; *Salisbury et al.*, 1991b). These bands appear as peaks in reflectance and troughs in transmittance (*Vincent and Hunt*, 1968) and are centered on the short wavelength side of the maximum of the imaginary index. In this wavelength region the absorption coefficient and specular reflectance are high (*Salisbury et al.*, 1987a), causing most incident radiation not to enter the sample and instead be reflected on the first surface. *Lyon* (1964) showed that Restrahlen bands are difficult to detect in the spectra of particulate minerals because of multiple occurring reflections, which increase the proportion of photons that enter the medium and are absorbed. Therefore, the height of Restrahlen

bands decreases with decreasing grain size (*Salisbury et al.*, 1987b; *Le Bras et al.*, 2003). A second group of less intense Restrahlen bands occurs between  $\sim 16.5$  and  $25\text{ }\mu\text{m}$  and is associated with Si-O-Si bending. Restrahlen features of silicates shift to longer wavelengths when heavier cations are in the lattice structure since they slow the frequency of the molecular vibrations. Meteorite spectra (*Salisbury et al.*, 1991a) show that the Restrahlen region is dominated by olivine and pyroxene. These spectra from *Salisbury et al.* (1991a) also demonstrate the slight shift to longer wavelengths with increasing iron content that can be seen in the ordinary chondrite's progression from more forsteritic olivine (H chondrites) to more fayalitic olivine (LL chondrites).

Between the two Restrahlen bands, the spectra of particulate silicates are dominated by a broad reflectance maximum (emissivity minimum) known as the transparency feature. The absorption coefficient is low enough in this region that silicate grains are optically thin and volume scattering dominates the scattering process. The feature is dependent on the presence of small particles ( $<75\text{ }\mu\text{m}$ ) and changing optical constants (*Salisbury et al.*, 1987b; *Salisbury and Walter*, 1989; *Mustard and Hays*, 1997). Laboratory spectra of silicate minerals demonstrate that the wavelengths of the transparency peaks and Christiansen features are diagnostic of composition and are correlated with each other (*Logan et al.*, 1973; *Salisbury et al.*, 1987b; *Salisbury and Walter*, 1989; *Hapke*, 2012).

Absorption features in the mid-IR are present at various wavelengths. For primitive carbonaceous chondrites, the most prominent absorption feature is the O-H stretching vibration feature near  $3.0\text{ }\mu\text{m}$  (*Salisbury and Hunt*, 1974; *Miyamoto*, 1988). This absorption feature tends to increase in spectral contrast as particle size is reduced below  $75\text{ }\mu\text{m}$  since the continuum reflectance rises with increasing scattering (*Salisbury and Walter*, 1989; *Salisbury et al.*, 1991b).

Crystalline olivines have strong diagnostic absorption features between  $9$  and  $12\text{ }\mu\text{m}$  (due to Si-O stretches) as well as several other minor bands at longer wavelengths. All olivine bands shift to shorter wavelengths with decreasing Fe/(Fe + Mg) content (*Koike et al.*, 2003) and decreasing temperature (*Koike et al.*, 2006). Crystalline pyroxenes have absorption features at similar but slightly shorter wavelengths than the olivines. Most of these features shift to shorter wavelengths with decreasing Fe/(Fe + Mg) content, except the  $10.5$ - and  $11.5\text{-}\mu\text{m}$  bands, which shift to longer wavelengths (*Chihara et al.*, 2002). Past spectral studies of crystalline olivine and pyroxene under a variety of laboratory conditions include *Mukai and Koike* (1990), *Koike et al.* (1993), *Jager et al.* (1998), *Henning and Mutschke* (1997), *Pitman et al.* (2010), and *Lane et al.* (2011). Amorphous olivines and pyroxenes have broad absorption features near  $10\text{ }\mu\text{m}$  with a weaker band near  $20\text{ }\mu\text{m}$ . Laboratory investigations of these amorphous silicates include *Day* (1981), *Koike and Hasegawa* (1987), *Scott and Duley* (1996), and *Brucato et al.* (1999).

Mid-infrared (or thermal) reflectance spectra ( $5$ – $25\text{ }\mu\text{m}$ ) of crystalline olivines and pyroxenes with various compositions and grain sizes are available at the ASTER spectral

library (<http://speclib.jpl.nasa.gov>) (*Baldridge et al.*, 2009). Additional data, including optical constants and references, are available at JPDOC (<http://www.astro.uni-jena.de/Laboratory/Database/jpdoc/f-dbase.html>) (*Henning et al.*, 1999).

## 6.2. Astronomical Observations in the Mid-Infrared

One key difference between mid-IR spectral laboratory data and mid-IR astronomical observations of asteroids is surface pressure. *Logan et al.* (1973) first demonstrated that decreasing the atmospheric pressure for a particulate sample results in an increase in spectral contrast, a shift to shorter wavelengths of the Christiansen feature, and potential loss of the transparency feature. These spectral changes are due to the fact that the space environment introduces thermal gradients in a particulate sample that alter the spectral features. At lower pressures a sharp thermal gradient occurs, as less or almost no interstitial gas is present to convectively transport heat. In a vacuum, the sample is heated by the absorption of radiation in visible wavelengths to a depth that is dependent on the absorption coefficient in visible wavelengths, and the sample emits to a cooler background in infrared wavelengths over a depth dependent on the absorption coefficient in infrared wavelengths. For silicates, the absorption coefficient for visible wavelengths is much smaller than the absorption coefficient in near-infrared wavelengths. This results in an emitting layer of particles that is shallower than the absorbing layer. Different wavelength regions in the spectrum are effectively sampling the two different temperatures, which increases the emissivity contrast.

In addition to surface pressure, grain size effects can also hinder mid-IR astronomical observations of asteroids. Various authors (e.g., *Lyon*, 1964; *Salisbury et al.*, 1987a; *Le Bras and Erard*, 2003) have demonstrated that the prominent Restrahlen features are difficult to detect for particulate surfaces and that the strength of the Restrahlen features varies inversely proportionally to particle size. Grain size effects can also impact attempts to apply spectral deconvolution techniques to mid-IR data. Past work has demonstrated that mid-IR spectra represent linear combinations of the abundances of the individual components (*Lyon*, 1964; *Thomson and Salisbury*, 1993; *Ramsey and Christensen*, 1998; *Hamilton and Christensen*, 2000). The effectiveness of linear spectral deconvolution techniques for asteroid surfaces is dependent on the particle size of the regolith. *Ramsey and Christensen* (1998) found that linear deconvolution fails for grain sizes below  $10\text{ }\mu\text{m}$  where nonlinear volume scattering dominates.

Finally, another important factor to consider when using astronomical observations of asteroids to determine silicate mineralogy is the presence of significant Si-O absorption features in the mid-IR spectra of observed standard stars. *Cohen et al.* (1992) identified the Si-O fundamental absorption in stellar spectra. Prior to that, early work to investigate asteroids using mid-IR spectroscopy was hindered by insufficient understanding of the nature of the standard stars (e.g., *Gillet and Merrill*, 1975; *Green et al.*, 1985).

The Kuiper Airborne Observatory (KAO) and the European Space Agency's Infrared Space Observatory (ISO) observed several large asteroids in the 1990s. KAO spectra (5–14  $\mu\text{m}$ ) of (1) Ceres showed three potential emission features, but no mineralogical match was identified (Cohen *et al.*, 1998). The ISO spectra (6–12  $\mu\text{m}$ ) showed evidence of silicates on the surface (Dotto *et al.*, 2000) and made connections between (10) Hygiea and (511) Davida and the CO and CM carbonaceous chondrites (Barucci *et al.*, 2002; Dotto *et al.*, 2002).

### 6.3. Recent Advances in Mid-Infrared Asteroid Spectroscopy

Since *Asteroids III*, there have been several notable works connecting mid-IR spectroscopy of asteroids to meteorites and silicate mineralogies. Much of the work in this area has focused on the 3- $\mu\text{m}$  region where hydrated silicates have a distinct absorption feature. This spectral feature was discussed in great detail in *Asteroids III* (Rivkin *et al.*, 2002). Recent work by Takir and Emery (2012) classified 3- $\mu\text{m}$  asteroid spectra into four distinct groups, demonstrating that there was thermal stratification of outer main-belt asteroids early in the history of the solar system. The asteroids that had experienced aqueous alteration (the “sharp” group) are located in the  $2.5 < a < 3.3 \text{ AU}$  region, while those that remained unaltered (the “rounded” group) are in the  $3.3 < a < 4.0 \text{ AU}$  region.

Lim *et al.* (2005) performed a survey of 29 asteroids using 8–13- $\mu\text{m}$  spectra. Their analysis identified emissivity features for (1) Ceres, which were similar to those seen by Cohen *et al.* (1998) with KAO and Dotto *et al.* (2000) with ISO. No definitive mineralogy was established. They also noted a marginal detection of features for (4) Vesta, which matched features found in HED meteorites (Salisbury *et al.*, 1991a). Work by Lim *et al.* (2011) attempted to establish a formalism for connecting features in the emissivity spectra of the V-type asteroid (956) Elisa to those seen in the spectra of HED meteorites.

Emery *et al.* (2006) presented mid-IR (5.2–38  $\mu\text{m}$ ) spectra of three Trojan asteroids: (624) Hektor, (911) Agamemnon, and (1172) Aneas. Using spectra of fine-grained silicates from the ASTER spectral library, they concluded that the spectra are characteristic of either small silicate grains imbedded in a relatively transparent matrix or small silicate grains in a very underdense (fairy castle) surface layer. Mid-infrared (8–33  $\mu\text{m}$ ) spectra of (617) Patroclus by Mueller *et al.* (2010) showed similar emissivity features, suggesting that the object has mineralogy much like that of the other observed Trojans.

The work of Vernazza *et al.* (2010) showed spectral variability between mid-IR spectra of eight S-type asteroids, which previous analyses using visible and near-infrared spectroscopic techniques had determined were of similar compositions. The analysis concluded that the variability was due to differences in the regolith particle size and space-weathering effects. The authors indicated that the asteroids are covered with a very-fine-grained regolith ( $< 5 \mu\text{m}$ ) that conceals some spectral features.

Vernazza *et al.* (2012) noted that while emission features on asteroids in the mid-IR spectral region were common, the asteroid spectra do not always match the laboratory spectra of minerals and meteorites. The authors demonstrated that by suspending the meteorite and mineral powders in potassium bromide powder, which is transparent in the infrared, and were able to recreate the spectra of main-belt asteroids with emissivity spectra. The work suggests that these asteroids have extremely porous regolith layers.

Irradiation experiments of the Tagish Lake meteorite demonstrated a small shift to longer wavelengths of the 10- $\mu\text{m}$  silicate emission feature that is likely caused by the amorphization of the silicates (Vernazza *et al.*, 2013). They used a combination of albedo with visible, near-IR, and mid-IR spectra to determine that Tagish Lake-like objects are a very small percentage of the main-belt population and that (368) Haidea is the best match to the meteorite's spectrum and albedo.

## 7. CONSTRAINTS FROM SPACECRAFT MISSIONS

Starting with the Galileo flyby of asteroids (951) Gaspra and (243) Ida, spacecraft investigations of asteroids have provided validation for groundbased spectroscopic studies. More recently, the Japanese Hayabusa and NASA's Dawn missions have completed detailed mineralogical studies of asteroids (25143) Itokawa and (4) Vesta, respectively, from orbit. The Hayabusa mission has also brought back microscopic samples of Itokawa that have helped immensely in the confirmation of precursor telescopic observations. Initially the surface composition of Eros was ambiguous, with derived compositions ranging from H-L-LL chondrites to primitive achondrites (McFadden *et al.*, 2001; Izenberg *et al.*, 2003; McCoy *et al.*, 2002). Further analysis of spectral observations of Eros by the Near-Infrared Spectrometer (NIS) and Multispectral Imager (MIS) on NEAR suggested a surface composition consistent with a space-weathered L6 ordinary chondrite (Nittler *et al.*, 2001; McCoy *et al.*, 2002; Izenberg *et al.*, 2003). McFadden *et al.* (2005) reported evidence for partial melting based on MGM analysis of Eros reflectance spectra. This debate between partial melt vs. space-weathered L6 chondrite was further fueled by the results from the NEAR X-Ray Spectrometer (XRS) experiment, which discovered strong sulfur depletion. Nittler *et al.* (2001) argued that the best explanation for the depletion is space weathering on an ordinary-chondrite-type object.

Similar to Eros, the surface composition of near-Earth asteroid (25143) Itokawa was the subject of much debate prior to the arrival of the Hayabusa spacecraft at the target object and subsequent return of the asteroid's samples to Earth. Binzel *et al.* (2001) interpreted the surface composition of Itokawa to be a space-weathered LL chondrite with 0.05% nanophase iron on the surface. In contrast, Abell *et al.* (2007) argued that the mean pyroxene chemistry of Itokawa ( $\sim\text{Fs}_{43\pm5}\text{Wo}_{14\pm5}$ ), estimated from its spectrum using calibrations from Gaffey *et al.* (2002), indicated a surface that

experienced partial melting. Analysis of samples returned by the Hayabusa spacecraft (Nakamura et al., 2011) has shown that Itokawa is indeed an LL chondrite as suggested by Binzel et al. (2001). Mineralogical analysis of the returned samples and the availability of newer spectral calibrations from Dunn et al. (2010b) provide us with an opportunity to validate groundbased spectral interpretive tools.

We used the spectral band parameters of Itokawa from the IRTF (Binzel et al., 2001; Abell et al., 2007) to calculate its olivine and pyroxene ratios and chemistries and to compare them with laboratory-measured values from samples returned by the Hayabusa spacecraft. Figure 6 (reproduced from Nakamura et al., 2011) shows olivine iron abundance (fayalite) on the Y-axis and pyroxene iron abundance (ferrosilite) on the X-axis from laboratory measurements of ordinary chondrites (H, L, and LL), Itokawa samples returned by the Hayabusa spacecraft (black circle), and those derived from the groundbased telescopic spectrum (gray circle) using the Dunn et al. (2010b) calibrations. The difference between laboratory measured values of Itokawa samples and those from groundbased spectral data is less than 1 mol%, confirming Itokawa as an LL chondrite and attesting to the

validity of the Dunn et al. (2010b) calibrations. Similarly, we used spectral band parameters for Eros from the NIS instrument on NEAR spacecraft (Izenberg et al., 2003) and groundbased spectral data (Murchie and Pieters, 1996) to calculate its olivine and pyroxene chemistries to (1) check for consistency between the two datasets, and (2) validate the L chondrite interpretation by Izenberg et al. (2003). Figure 6 also shows fayalite and ferrosilite values for Eros calculated from NEAR and groundbased spectral data. These results validate the Izenberg et al. (2003) interpretation that Eros' surface composition is similar to an L chondrite rather than a partial melt, as proposed by McFadden et al. (2005).

NASA's Dawn spacecraft completed a year-long mission to characterize asteroid (4) Vesta (Russell et al., 2012), mapping the surface with a multi-color Framing Camera (FC) (Reddy et al., 2012a; Jaumann et al., 2012), a VIS/NIR spectrometer (VIR) (De Sanctis et al., 2012a), and a gamma-ray and neutron detector (Prettyman et al., 2012). Prior to Dawn's arrival, Vesta had been the most studied asteroid in the asteroid belt (e.g., Gaffey, 1997; Reddy et al., 2010; Thomas et al., 1997a; Binzel et al., 1997; Li et al., 2010), with nearly 100 years of spectral observations dating back to the early part of the last century (Bobrovnikoff, 1929). Many groundbased and Hubble Space Telescope (HST) observations of the vestan surface were confirmed by the Dawn mission, such as the hemispherical albedo dichotomy between the eastern and western hemisphere (Reddy et al., 2013), which was proposed based on monomodal photometric lightcurve observations of Vesta (Li et al., 2010). Like many observations, this was confirmed by comparing groundbased and HST albedo and compositional maps of Vesta (Gaffey, 1997; Binzel et al., 1997; Li et al., 2010) to multi-color camera data from the Dawn mission (Reddy et al., 2010). Figure 7 shows albedo features identified first in HST images (Binzel et al., 1997; Li et al., 2010) and then by the Dawn spacecraft. Features are annotated to show positive identification of geological features on both datasets.

While groundbased and HST observations of Vesta matched those made by Dawn, the interpretation of certain features was enhanced due to better spatial resolution of the spacecraft data. Of particular interest to the groundbased spectroscopy community was the "olivine-rich" unit named "Leslie feature" in the Gaffey (1997) IRTF map of Vesta. Rotationally resolved spectra of Vesta showed a drop in BAR when this feature rotated into view. Le Corre et al. (2013) identified this as the Oppia crater and its surrounding ejecta blanket, but suggested that this drop in BAR was due to the presence of impact melt in the ejecta blanket rather than olivine. The rotational compositional variation between the northern and southern hemispheres, where the South Pole Rheasilvia basin excavated more diogenetic material (Reddy et al., 2010), was also confirmed by Dawn FC and VIR data (Reddy et al., 2012a; De Sanctis et al., 2012a). Dawn observations also confirmed the Hasegawa et al. (2003) hypothesis that the vestan surface was contaminated by carbonaceous chondrite impactors (Reddy et al., 2012b; McCord et al., 2012; De Sanctis et al., 2012b; Prettyman et al., 2012). This

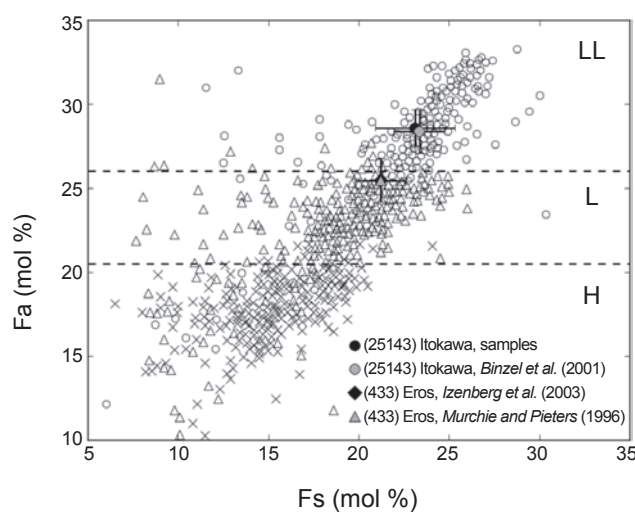


**Fig. 6.** Plot showing olivine iron content (mol% fayalite) on the Y-axis and pyroxene iron content (mol% ferrosilite) on the X-axis from laboratory measurements of ordinary chondrites (H, L, and LL). Fayalite and ferrosilite values from Itokawa samples (Nakamura et al., 2011) and spectrally derived values using Binzel et al. (2001) IRTF telescopic spectra data are also shown. Spectrally derived values were calculated using equations from Dunn et al. (2010b). The difference between the olivine and pyroxene iron content between the two datasets is less than 1 mol% and plot in the LL chondrite zone as predicted by Binzel et al. (2001). Also shown, fayalite and ferrosilite values for (433) Eros from Murchie and Pieters (1996) (groundbased spectral data) and Izenberg et al. (2003) (NEAR NIS spectral data). The Fs and Fa values for Eros are identical and fall in the L-chondrite region of the plot. Figure adapted from Nakamura et al. (2011).

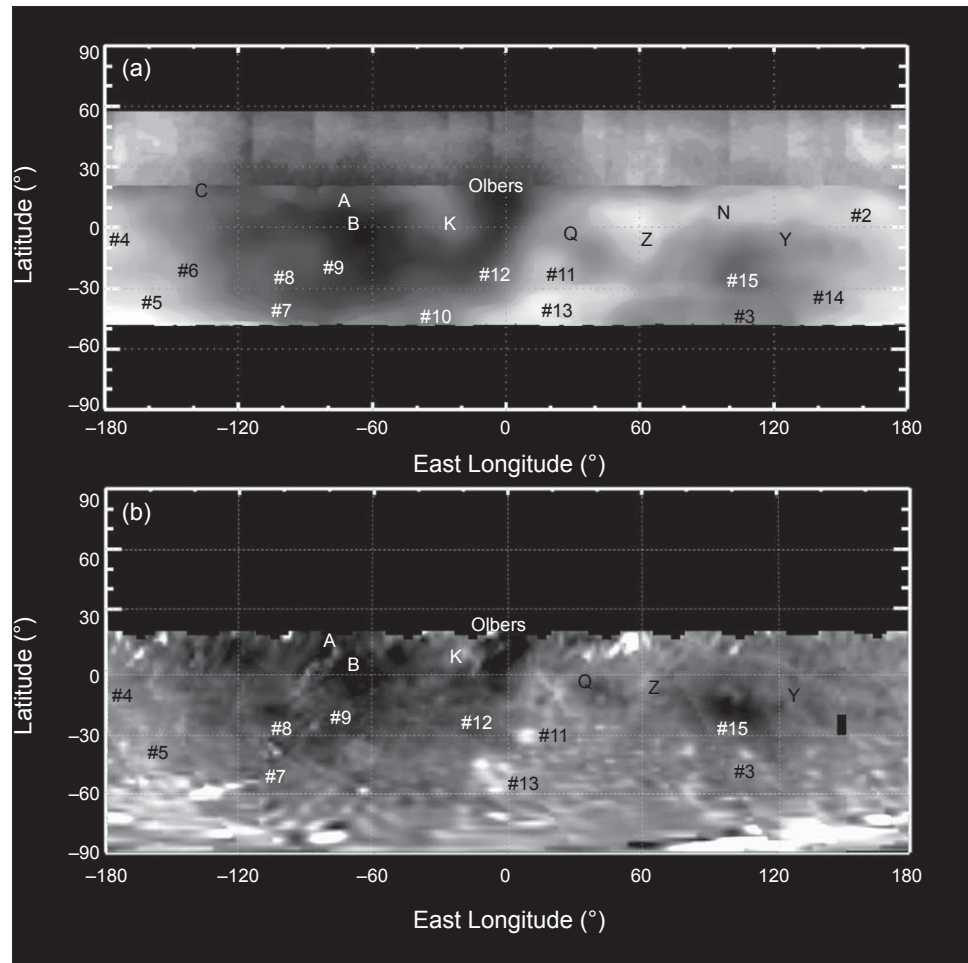


**Fig. 7.** (a) HST map of Vesta in 0.673- $\mu\text{m}$  filter projected in the Thomas *et al.* (1997a) coordinate system based on observations from 1994, 1996, and 2007 oppositions at a resolution of  $\sim$ 50 km/pixel. (b) Dawn FC map of Vesta in 0.75- $\mu\text{m}$  filter from Rotational Characterization 1 (RC1) phase at a resolution of 9.06 km/pixel with prime meridian similar to the Thomas *et al.* (1997a) coordinate system. The maps show corresponding bright features and dark features identified by Binzel *et al.* (1997) and Li *et al.* (2010). Figure reproduced from Reddy *et al.* (2013).

hypothesis was initially based on the groundbased identification of an OH absorption band at 2.8  $\mu\text{m}$ . Results from the Dawn mission have provided the groundbased spectroscopy community an opportunity to verify nearly a century of observations of Vesta.

## 8. ASTEROIDS WITH DERIVED MINERALOGIES

The challenges to link a meteorite with a particular parent body or source body are daunting. A parent body is the original body that the meteorite formed on, while the source body is a larger fragment of the original parent body that is the direct source of the meteorite. Lunar meteorites were easily identified (e.g., Marvin, 1983) due to their similarity in mineralogy and chemistry to returned Apollo samples. Martian meteorites were identified (e.g., Bogard and Johnson,

1983), in part, by the similarity of gas abundances found in meteoritic glasses and the composition of the martian atmosphere analyzed by the Viking spacecraft. The only instance in which a link between a meteorite and its asteroid source has been made with complete certainty is the Almahata Sitta meteorite and near-Earth asteroid 2008 TC<sub>3</sub>, which impacted the atmosphere in October 2008. Fragments of the asteroid “rained” down over the Sudan, then were collected and identified as a ureilites (Jenniskens *et al.*, 2009).

Apart from a compositional link, a dynamical pathway to deliver meteorites from an asteroid to Earth is needed. While challenges remain, we can now attempt to dynamically link an asteroid with a meteorite group, since the Yarkovsky effect (Bottke *et al.*, 2006) is known to be able to supply small fragments ( $<10$  km) to meteorite-supplying resonances across vast regions of the asteroid belt. Bottke *et al.* (2010) argues that the Yarkovsky effect allows asteroid families

far from meteorite-supplying resonances to dominate the meteorite flux. This allows all asteroids in the main belt to contribute meteorites to our terrestrial collection.

A few strong cases can be made for linkages between observed asteroids and meteorite types, such as those discussed in *Asteroids III*: (4) Vesta, (6) Hebe, and (3103) Eger. Asteroid (4) Vesta ( $a = 2.36$  AU) has been known since the 1970s to have visible (McCord et al., 1970) and near-IR (Larson and Fink, 1975) spectral properties similar to HEDs. This spectral similarity was confirmed by the Dawn mission and reinforced by bulk elemental composition of Vesta's surface, which are also similar to HEDs (Reddy et al., 2012a; De Sanctis et al., 2012a; Prettyman et al., 2012). Although Vesta's location in the asteroid belt makes it difficult to produce a significant flux of fragments to the 3:1 and  $v_6$  meteorite-supplying resonances (Wetherill, 1987), numerous V-type members of the Vesta family (called vestoids) populate the inner main belt between meteorite-supplying resonances ( $a = 2.22\text{--}2.49$  AU) (Binzel and Xu, 1993) and could serve as potential source bodies. Recently a number of V-types have also been identified in the outer asteroid belt (Lazarro et al., 2000; Hardersen et al., 2004). Although it is very difficult to dynamically move a body from the inner belt to the outer belt, the presence of a number of eucrites with distinctly different oxygen isotopic ratios than most HEDs implies that there could be multiple eucrite parent bodies (McSween et al., 2011), some of which could reside in the outer belt. The recovery of Bunburra Rockhole meteorite (anomalous eucrite) with an Aten-type orbit, delivered to Earth via  $v_6$  resonance from the inner main belt, serves as an additional evidence for multiple basaltic parent bodies (Bland et al., 2009).

S-type asteroid (6) Hebe ( $a = 2.43$  AU) was postulated as the parent body of the H chondrites and IIE iron meteorites based on its spectral parameters, large diameter ( $\sim 200$  km), and location near the 3:1 and  $v_6$  resonances (Gaffey and Gilbert, 1998). Recent modeling by Bottke et al. (2010) has confirmed that these resonances are probable source regions of the H chondrites. In addition, asteroid (695) Bella, located near the 3:1 resonance, has been interpreted as having a mineralogy similar to H chondrites (Fieber-Beyer et al., 2012).

E-type near-Earth asteroid (3103) Eger ( $a = 1.41$  AU) has been linked with the aubrite meteorites based on its high albedo, flat reflectance spectrum, and absorption feature at  $\sim 0.5 \mu\text{m}$  (Gaffey et al., 1992; Burbine et al., 2002). In the last decade a number of additional E-type asteroids have been observed to have spectral properties consistent with aubrites (Kelley and Gaffey, 2002; Clark et al., 2004; Fornasier et al., 2008). Many of these bodies, such as (434) Hungaria, are found among the Hungarias ( $a = 1.78\text{--}2.06$  AU) (McEarchen et al., 2010). The relatively old median cosmic-ray-exposure age of aubrites, compared to other meteorite groups, is consistent with being derived from bodies in the Hungaria region (Cuk et al., 2012). Spectra of E-type asteroid (2867) Šteins ( $a = 2.36$  AU), the target asteroid of the Rosetta mission, are also consistent with an aubrite composition (e.g., Markus et al., 2013).

Since the publication of *Asteroids III*, much of the focus on asteroid-meteorite connections has been on the L and LL chondrites. The (1272) Gefion family ( $a = 2.70\text{--}2.82$  AU) has been proposed by Bottke et al. (2005) and Nesvorný et al. (2009) to be the source of the L chondrites. The Gefion family is composed primarily of S-type objects (Bus, 1999) and has an estimated age that is consistent with the 470-Ma shock event (Korochantseva et al., 2007) found in L chondrites. Estimated cosmic-ray-exposure ages of fragments of the Gefion family, traveling through the 5:2 resonance, are consistent with L chondrites (Nesvorný et al., 2009). A few observed Gefion family members have interpreted mineralogies roughly consistent with L chondrites (Blagen, 2012; Roberts and Gaffey, 2014); however, this is not the case for all observed members (Roberts and Gaffey, 2014).

A relatively large percentage of observed near-Earth asteroids have spectral features and interpreted mineralogies similar to LL chondrites. In fact, approximately two-thirds of S- and Q-type NEAs studied by Vernazza et al. (2008) have olivine/(olivine + pyroxene) ratios similar to LL chondrites. The same is true for members of the (8) Flora family ( $a = 2.16\text{--}2.40$  AU), which is located near the  $v_6$  resonance. However, Gaffey (1984) argued that (8) Flora has a nonchondritic mineralogy due to interpreted mineralogical variations that are not consistent with an undifferentiated surface. The LL-chondrite mineralogy of at least one S-type asteroid, (25143) Itokawa, has been confirmed by the Hayabusa sample return mission (Nakamura et al., 2011). The Chelyabinsk, Russia, meteorite is also an LL chondrite, although the exact parent body is still debated. Reddy et al. (2014) suggested that it might be a fragment of the Flora asteroid family based on mineralogical analysis, while de la Fuente Marcos and de la Fuente Marcos (2013) suggested that the most likely source body was 2011 EO<sub>40</sub>, although its composition is unknown.

Another recent link has been made between the CM chondrites and Ch-type asteroids (13) Egeria ( $a = 2.58$  AU) and (19) Fortuna ( $a = 2.44$  AU) (Fornasier et al., 2014). Both objects have a distinctive spectral feature at  $0.7 \mu\text{m}$  that is only found in the spectra of CM meteorites. Vilas and Gaffey (1989) showed that spectra of dark asteroids showed diagnostic carbonaceous chondrite-like absorption bands. Burbine (1998) argued that the location of these bodies near meteorite-supplying resonances would be extremely favorable to supplying meteorites to Earth from these bodies, since the relatively fragile CM chondrites would not be expected to be able to survive long in space. However, a number of other asteroids have been classified as Ch-types (Bus and Binzel, 2002; DeMeo et al., 2009) and could also be potential CM chondrite parent bodies. Fieber-Beyer et al. (2012) identified (1358) Gaika, which is also located near the 3:1 resonance, as having an interpreted mineralogy similar to CM chondrites.

## 9. OUTSTANDING QUESTIONS AND FUTURE DIRECTIONS

Despite the advances in asteroid spectroscopy over the last decade, including our ability to constrain the mineralogies of

asteroids from which ~90% of meteorites in our terrestrial collection come, several challenges remain ahead, including our inability to identify parent bodies of iron meteorites.

1. With the addition of each new calibration for deriving asteroid mineralogy, our ability to characterize the mineralogies of asteroid surfaces improves significantly. However, because different formulas work better for different assemblages, caution must be used when applying these calibrations to any asteroid spectrum. Additional laboratory characterization of samples is necessary before a complete working inventory of calibrations for deriving mineralogies from VIS/NIR spectra can be developed.

2. Currently, we do not have a reliable method to constrain the mineralogy of most carbonaceous C-type asteroids, M-type asteroids, and primitive-achondrite-type asteroids. Our inability to treat complex mineralogies is the biggest challenge as we move ahead into the next decade of small-body characterization. Some recent advances have been made in showing that most carbonaceous chondrites (widely believed to derive from C-type asteroids) do exhibit absorption features that are diagnostic of their mafic silicates and calcium-aluminum-rich inclusions (*Cloutis et al.*, 2010, 2012).

3. Future work is needed to better establish relationships between MGM-derived bands and their corresponding mineralogical interpretations, particularly for compositions relevant to asteroids. Such calibrations exist for lunar and martian compositions, but are less common for asteroid studies.

4. Future work in radiative transfer modeling of regolith systems should continue to examine the importance of assumptions about particle sizes, shapes, compositions, and particle size distributions. For example, the treatment of complex particles such as agglutinates and impact glasses remains largely unexplored, but could be an important component of future modeling efforts. The planned sample return missions OSIRIS-REx and Hayabusa-2 will ultimately provide ground truth to improve upon the accuracy of radiative transfer models.

5. The availability (or lack) of optical constants for minerals relevant to asteroidal compositions can be a limitation of radiative transfer models. Radiative transfer methods are most effective at constraining compositions for S- and V-type asteroids (and their meteoritic counterparts) due to the wide availability of optical constants for Fe-bearing silicates (e.g., *Lucey et al.*, 1998; *Denevi et al.*, 2007; *Trang et al.*, 2013). These models are not as successful in treating Fe-poor systems such as Mercury (*Lucey and Riner*, 2011). Of potential importance to the compositional interpretation of asteroids such as M-types is the need for optical constants of opaque minerals beyond those measured for iron metal (*Cahill et al.*, 2012). There is also a need for improved optical constants at UV wavelengths (particularly for silicates), where little compositional modeling of asteroids has been conducted.

**Acknowledgments.** The authors are grateful for the comments of the editor (F. DeMeo) and two reviewers (P. S. Hardersen and E. A. Cloutis), whose comments helped to improve this chapter.

V.R. would like to thank J. A. Sanchez for valuable comments on the effects of temperature and phase angle on near-IR spectra and L. Le Corre for Vesta maps used in this chapter. N.A.M. is grateful to S. Lawrence for reviewing the Hapke modeling section. Support for V.R. to carry out this effort came from NASA Planetary Geology and Geophysics Grants NNX14AN35G (PI: Reddy) and NNX14AN05G (PI: Gaffey), as well as NASA Planetary Mission Data Analysis Program Grant NNX14AN16G (PI: Le Corre). V.R., C.A.T., N.A.M., and T.H.B. were visiting astronomers at the Infrared Telescope Facility, operated by the University of Hawai‘i under contract to the National Aeronautics and Space Administration.

## REFERENCES

- Abe M., Takagi Y., Kitazato K., Abe S., Hiroi T., Vilas F., Clark B. E., Abell P. A., Lederer S. M., Jarvis K. S., Nimura T., Ueda Y., and Fujiwara A. (2006) Near-infrared spectral results of asteroid Itokawa from the Hayabusa spacecraft. *Science*, *312*, 1334–1338.
- Abell P. A., Vilas F., Jarvis K. S., Gaffey M. J., and Kelley M. S. (2007) Mineralogical composition of (25143) Itokawa 1998 SF36 from visible and near-infrared reflectance spectroscopy: Evidence for partial melting. *Meteoritics & Planet. Sci.*, *42*, 2165–2177.
- Adams J. B. (1974) Visible and near-infrared diffuse reflectance spectra of pyroxenes as applied to remote sensing of solid objects in the solar system. *J. Geophys. Res.*, *79*, 4829–4836.
- Adams J. B. (1975) Interpretation of visible and near-infrared diffuse reflectance spectra of pyroxenes and other rock-forming minerals. In *Infrared and Raman Spectroscopy of Lunar and Terrestrial Minerals* (C. I. Karr, ed.), pp. 91–116. Academic, New York.
- Aronson J. R., Emslie A. G., and McLinden H. G. (1966) Infrared spectra from particulate surfaces. *Science*, *152*, 345–346.
- Baldridge A. M., Hook S. J., Grove C. I., and Rivera G. (2009) The ASTER Spectral Library Version 2.0. *Remote Sens. Environ.*, *113*, 711–715.
- Barucci M. A., Dotto E., Brucato J. R., Mueller T. G., Morris P., Doressoundiram A., Fulchignoni M., de Sanctis M. C., Owen T., Crovisier J., Le Bras A., Colangeli L., and Mennella V. (2002) 10 Hygiea: ISO infrared observations. *Icarus*, *156*, 202–210.
- Bell J. F., Izenberg N. I., Lucey P. G., Clark B. E., Peterson C., Gaffey M. J., Joseph J., Carcich B., Harch A., Bell M. E., Warren J., Martin P. D., McFadden L. A., Wellnitz D., Murchie S., Winter M., Veverka J., Thomas P., Robinson M. S., Malin M., and Cheng A. (2002) Near-IR reflectance spectroscopy of 433 Eros from the NIS instrument on the NEAR mission: I — Low phase angle observations. *Icarus*, *155*, 119–144.
- Binzel R. P. and Xu S. (1993) Chips off of asteroid 4 Vesta: Evidence for the parent body of basaltic achondrite meteorites. *Science*, *260*, 186–191.
- Binzel R. P., Gaffey M. J., Thomas P. T., Zellner B. H., Storrs A. D., and Wells E. N. (1997) Geologic mapping of Vesta from 1994 Hubble Space Telescope images. *Icarus*, *128*, 95–103.
- Binzel R. P., Rivkin A. S., Bus S. J., Sunshine J. M., and Burbine T. H. (2001) MUSES-C target asteroid 1998 SF36: A reddened ordinary chondrite. *Meteoritics & Planet. Sci.*, *36*, 1167–1172.
- Bischoff A., Vogel N., and Roszjar J. (2011) The Rumuruti chondrite group. *Chem. Erde-Geochem.*, *71*, 101–133.
- Blagen J. R. (2012) Testing the Gefion family as a possible parent body for the L-chondrite meteorites. M.S. thesis, University of North Dakota, Grand Forks.
- Bland P. A., Spurny P., Towner M. C., et al. (2009) An anomalous basaltic meteorite from the innermost main belt. *Science*, *325*, 1525–1527.
- Bobrovnikoff N. T. (1929) The spectra of minor planets. *Lick Obs. Bull.*, *407*, 18–27.
- Bogard D. D. and Johnson P. (1983) Martian gases in an Antarctic meteorite? *Science*, *221*, 651–654.
- Bottke W. F., Durda D. D., Nesvorný D., Jedicke R., Morbidelli A., Vokrouhlický D., and Levison H. (2005) The fossilized size distribution of the main asteroid belt. *Icarus*, *175*, 111–140.
- Bottke W. F. Jr., Vokrouhlický D., Rubincam D. P., and Nesvorný D. (2006) The Yarkovsky and YORP effects: Implications for asteroid dynamics. *Annu. Rev. Earth Planet. Sci.*, *34*, 157–191.

- Bottke W., Vokrouhlický D., Nesvorný D., and Shrbeny L. (2010) (6) Hebe really is the H chondrite parent body. *Bull. Am. Astron. Soc.*, 42, 1051.
- Brucato J. R., Colangeli L., Mennella V., Palumbo P., and Bussoletti E. (1999) Mid-infrared spectral evolution of thermally annealed amorphous pyroxene. *Astron. Astrophys.*, 348, 1012–1019.
- Brunetto R., Vernazza P., Marchi S., Birlan M., Fulchignoni M., Orofino V., and Strazzulla G. (2006) Modeling asteroid surfaces from observations and irradiation experiments: The case of 832 Karin. *Icarus*, 184, 327–337.
- Brunetto R., de Leon J., and Licandro J. (2007) Testing space weathering models on A-type asteroid (1951) Lick. *Astron. Astrophys.*, 472, 653–656.
- Burbine T. H. (1998) Could G-class asteroids be the parent bodies of the CM chondrites? *Meteoritics & Planet. Sci.*, 33, 253–258.
- Burbine T. H., Buchanan P. C., Binzel R. P., Bus S. J., Hiroi T., Hinrichs J. L., Meibom A., and McCoy T. J. (2001) Vesta, vestoids, and the howardite, eucrite, diogenite group: Relationships and the origin of spectral differences. *Meteoritics & Planet. Sci.*, 36, 761–781.
- Burbine T. H., McCoy T. J., Meibom A., Gladman B., and Keil K. (2002) Meteoritic parent bodies: Their number and identification. In *Asteroids III* (W. F. Bottke Jr. et al., eds.), pp. 653–668. Univ. of Arizona, Tucson.
- Burbine T. H., McCoy T. J., Jarosewich E., and Sunshine J. M. (2003) Deriving asteroid mineralogies from reflectance spectra: Implications for the MUSES-C target asteroid. *Antarct. Meteorite Res.*, 16, 185–195.
- Burbine T. H., Buchanan P. C., and Binzel R. P. (2007) Deriving formulas from HED spectra for determining the pyroxene mineralogy of Vesta and vestoids. *Lunar Planet. Sci. XXXVIII*, Abstract #2117. Lunar and Planetary Institute, Houston.
- Burbine T. H., Buchanan P. C., Dolkar T., and Binzel R. P. (2009) Pyroxene mineralogies of near-Earth vestoids. *Meteoritics & Planet. Sci.*, 44, 1331–1341.
- Burns R. G. (1970) Crystal field spectra and evidence of cation ordering in olivine minerals. *Am. Mineral.*, 55, 1608–1632.
- Burns R. C., Huggins F. E., and Abu-Eid R. M. (1972) Polarized absorption spectra of single crystals of lunar pyroxene and olivine. *Moon*, 4, 93–102.
- Bus S. J. (1999) Compositional structure in the asteroid belt: Results of a spectroscopic survey. Ph.D. thesis, Massachusetts Institute of Technology, Cambridge.
- Bus S. J. and Binzel R. P. (2002) Phase II of the Small Main-belt Asteroid Spectroscopic Survey: A feature-based taxonomy. *Icarus*, 158, 146–177.
- Cahill J. T. S., Blewett D. T., Nguyen N. V., Xu K., Kirillov O. A., Lawrence S. J., Denevi B. W., and Coman E. I. (2012) Determination of iron metal optical constants: Implications for ultraviolet, visible and near-infrared remote sensing of airless bodies. *Geophys. Res. Lett.*, 39, 10204.
- Camps H., Hargrove K., Pinilla-Alonso N., Howell E. S., Kelley M. S., Licandro J., Mothe-Diniz T., Fernandez Y., and Ziffer J. (2010) Water ice and organics on the surface of asteroid 24 Themis. *Nature*, 464, 1320–1321.
- Chihara H., Koike C., Tsuchiya A., Tachibana S., and Sakamoto D. (2002) Compositional dependence of infrared absorption spectra of crystalline silicates. I. Mg-Fe pyroxenes. *Astron. Astrophys.*, 391, 267–273.
- Clark B. E. and 11 colleagues (2001) Space weathering on Eros: Constraints from albedo and spectral measurements of Psyche crater. *Meteoritics & Planet. Sci.*, 36, 1617–1637.
- Clark B. E., Helfenstein P., Bell J. F. III, Peterson C., Ververka J., Izenberg N. I., Domingue D., Wellnitz D., and McFadden L. (2002) NEAR Infrared Spectrometer photometry of asteroid 433 Eros. *Icarus*, 155, 189–204.
- Clark B. E., Bus S. J., Rivkin A. S., McConnochie T., Sanders J., Shah S., Hiroi T., and Shepard M. (2004) E-type asteroid spectroscopy and compositional modeling. *J. Geophys. Res.*, 109, E02001.
- Clark S. P. Jr. (1957) Absorption spectra of some silicates in the visible and near-infrared. *Am. Mineral.*, 42, 732–742.
- Clenet H. and 9 colleagues (2013) A systematic mapping procedure based on the modified Gaussian model to characterize magmatic units from olivine/pyroxenes mixtures: Application to the Syrtis Major volcanic shield on Mars. *J. Geophys. Res.*, 118, 1632–1655.
- Cloutis E. A. and Gaffey M. J. (1991) Pyroxene spectroscopy revisited: Spectral-compositional correlations and relationships to geothermometry. *J. Geophys. Res.*, 91, 11641–11653.
- Cloutis E. A., Gaffey M. J., Jackowski T. L., and Reed K. L. (1986) Calibration of phase abundance, composition, and particle size distribution for olivine-orthopyroxene mixtures from reflectance spectra. *J. Geophys. Res.*, 91, 11641–11653.
- Cloutis E. A., Hudon P., Romanek C. S., Reddy V., Hardersen P. S., and Gaffey M. J. (2010) Spectral reflectance properties of ureilites. *Meteoritics & Planet. Sci.*, 45(10–11), 1668–1694.
- Cloutis E. A., Hudon P. A., Hiroi T., and Gaffey M. J. (2012) Spectral reflectance properties of carbonaceous chondrites 4: Aqueously altered and thermally metamorphosed meteorites. *Icarus*, 220, 586–617.
- Cohen M., Walker R. G., and Witteborn F. C. (1992) Spectral irradiance calibration in the infrared. II.  $\alpha$  Tau and the recalibration of the IRAS low resolution spectrometer. *Astron. J.*, 104, 2030–2044.
- Cohen M., Witteborn F. C., Roush T., Bregman J. D., and Wooden D. H. (1998) Spectral irradiance calibration in the infrared. VIII. 5–14 micron spectroscopy of the asteroids Ceres, Vesta, and Pallas. *Astron. J.*, 115, 1671–1679.
- Conel J. E. (1969) Infrared emissivities of silicates: Experimental results and a cloudy atmosphere model of spectral emission from condensed particle mediums. *J. Geophys. Res.*, 74, 1614–1634.
- Cressey G. and Schofield P. F. (1996) Rapid whole-pattern profile stripping methods for the quantification of multiphase samples. *Powder Diff.*, 11, 35–39.
- Cruikshank D. P., Dalle Ore C. M., Roush T. L., Geballe T. R., Owen T. C., de Bergh C., Cash M. D., and Hartmann W. K. (2001) Constraints on the composition of Trojan asteroid 624 Hektor. *Icarus*, 153, 348–360.
- Cuk M., Burn J. A., Gladman B. J., Hamilton D. P., and Nesvorný D. (2012) Hungaria family as the Source Of Aubrites. *AAS/Division for Planetary Sciences*, 44, #105.02.
- Day K. L. (1981) Infrared extinction of amorphous iron silicates. *Astrophys. J.*, 246, 110–112.
- Deer W. A., Howie R. A., and Zussman J. (1966) *An Introduction to the Rock-Forming Minerals*. Addison, Essex.
- de la Fuente Marcos C. and de la Fuente Marcos R. (2013) The Chelyabinsk superbolide: A fragment of asteroid 2011 EO40? *Mon. Not. R. Astron. Soc.*, DOI: 10.1093/mnras/slt103.
- Denevi B. W., Lucey P. G., Hochberg E. J., and Steutel D. (2007) Near-infrared optical constants of pyroxene as a function of iron and calcium content. *J. Geophys. Res.*, 112, E05009.
- De Sanctis M. C., Ammannito E., Capria M. T., Tosi F., Capaccioni F., Zambon F., Carraro F., Fonte S., Frigeri A., Jaumann R., Magni G., Marchi S., McCord T. B., McFadden L. A., McSween H. Y., Mittlefehldt D. W., Nathues A., Palomba E., Pieters C. M., Raymond C. A., Russell C. T., Toplis M. J., and Turrini D. (2012a) Spectroscopic characterization of mineralogy and its diversity across Vesta. *Science*, 336(6082), 697–700.
- De Sanctis M. C. et al. (2012b) Detection of widespread hydrated materials on Vesta by the VIR imaging spectrometer on board the Dawn mission. *Astrophys. J. Lett.*, 758, L36.
- DeMeo F. E., Binzel R. P., Slivan S. M., and Bus S. J. (2009) An extension of the Bus asteroid taxonomy into the near-infrared. *Icarus*, 202, 160–180.
- Dotto E., Mueller T. G., Barucci M. A., Encrenaz Th., Knacke R. F., Lellouch E., Doressoundiram A., Crovisier J., Brucato J. R., Colangeli L., and Mennella V. (2000) ISO results on bright main belt asteroids: PHT-S observations. *Astron. Astrophys.*, 358, 1133–1141.
- Dotto E., Barucci M. A., Müller T. G., Brucato J. R., Fulchignoni M., Mennella V., and Colangeli L. (2002) ISO observations of low and moderate albedo asteroids: PHT-P and PHT-S results. *Astron. Astrophys.*, 393, 1065–1072.
- Duffard R., de Leon J., Licandro J., Lazzaro D., and Serra-Ricart M. (2006) Basaltic asteroid in the near-Earth objects population: A mineralogical analysis. *Astron. Astrophys.*, 456, 775–781.
- Dunn T. L., Cressey G., McSween H. Y. Jr., and McCoy T. J. (2010a) Analysis of ordinary chondrites using powder X-ray diffraction: I. Modal mineral abundances. *Meteoritics & Planet. Sci.*, 45, 123–134.
- Dunn T. L., McCoy T. J., Sunshine J. M., and McSween H. Y. Jr. (2010b) A coordinated spectral, mineralogical, and compositional study of ordinary chondrites. *Icarus*, 208, 789–797.

- Dunn T. L., Burbine T. H., Bottke W. F., and Clark J. P. (2013) Mineralogies and source regions of near-Earth asteroids. *Icarus*, 222, 273–282.
- Emery J. P. and Brown R. H. (2004) The surface composition of Trojan asteroids: Constraints set by scattering theory. *Icarus*, 170, 131–152.
- Emery J. P., Cruikshank D. P., and Van Cleve J. (2006) Thermal emission spectroscopy (5.2–38 micron) of three Trojan asteroids with the Spitzer Space Telescope: Detection of fine-grained silicates. *Icarus*, 182, 496–512.
- Fiebiger-Beyer S. K., Gaffey M. J., Hardersen P. S., and Reddy V. (2012) Near-infrared spectroscopy of 3:1 Kirkwood Gap asteroids: Mineralogical diversity and plausible meteorite parent bodies. *Icarus*, 221, 593–602.
- Fornasier S., Migliorini A., Dotto E., and Barucci M. A. (2008) Visible and near infrared spectroscopic investigation of E-type asteroids, including 2867 Steins, a target of the Rosetta mission. *Icarus*, 196, 119–134.
- Fornasier S., Lantz C., Barucci M. A., and Lazzarin M. (2014) Aqueous alteration on main belt primitive asteroids: Results from visible spectroscopy. *Icarus*, 233, 163–178.
- Fries M., Le Corre L., Hankey M., Fries J., Matson R., Schaefer J. and Reddy V. (2014) Detection and rapid recovery of the Sutter's Mill meteorite fall as a model for future recoveries worldwide. *Meteoritics & Planet. Sci.*, 49(11), 1989–1996, DOI: 10.1111/maps.12249.
- Gaffey M. J. (1984) The S-type asteroids and the ordinary chondrites: The (8) Flora case. *Lunar Planet. Sci. XV*, p. 284. Lunar and Planetary Institute, Houston.
- Gaffey M. J. (1997) Surface lithologic heterogeneity of asteroid 4 Vesta. *Icarus*, 127, 130–157.
- Gaffey M. J. (2007) One pyroxene? Two pyroxenes? Three pyroxenes? Pyroxene compositions from asteroid spectra. *Lunar Planet. Sci. XXXVIII*, Abstract #1618. Lunar and Planetary Institute, Houston.
- Gaffey M. J. and Gilbert S. L. (1998) Asteroid 6 Hebe: The probable parent body of the H-type ordinary chondrites and the IIE iron meteorites. *Meteoritics & Planet. Sci.*, 33, 1281–1295.
- Gaffey M. J., Reed K. L., and Kelley M. S. (1992) Relationship of E-type Apollo asteroid 3103 (1982 BB) to the enstatite achondrite meteorites and the Hungaria asteroids. *Icarus*, 100, 95–109.
- Gaffey M. J., Bell J. F., Brown R. H., Burbine T. H., Piatek J. L., Reed K. L., and Chaky D. A. (1993) Mineralogical variations within the S-type asteroid class. *Icarus*, 10, 573–602.
- Gaffey M. J., Cloutis E. A., Kelley M. S., and Reed K. L. (2002) Mineralogy of asteroids. In *Asteroids III* (W. F. Bottke Jr. et al., eds.), pp. 83–204. Univ. of Arizona, Tucson.
- Gastineau-Lyons H. K., McSween H. Y. Jr., and Gaffey M. J. (2002) A critical evaluation of oxidation versus reduction during metamorphism of L and LL group chondrites, and implications for asteroid spectroscopy. *Meteoritics & Planet. Sci.*, 37, 75–89.
- Gehrels T. (1970) Photometry of asteroids. In *Surfaces and Interiors of Planets and Satellites* (A. Dollfus, ed.), pp. 317–375. Academic, London.
- Gillet F. C. and Merrill K. M. (1975) 7.5–13.5 micron spectra of Ceres and Vesta. *Icarus*, 26, 358–360.
- Gradie J. and Veverka J. (1986) The wavelength dependence of phase coefficients. *Icarus*, 66, 455–467.
- Gradie J., Veverka J., and Buratti B. (1980) The effects of scattering geometry on the spectrophotometric properties of powdered material. *Proc. Lunar Planet. Sci. Conf. 11th*, pp. 799–815.
- Green S. F., Eaton N., Aitken D. K., Roche P. F., and Meadows A. J. (1985) 8- to 13-micron spectra of asteroids. *Icarus*, 62, 282–288.
- Hamilton V. E. and Christensen P. R. (2000) Determining the modal mineralogy of mafic and ultramafic igneous rocks using thermal emission spectroscopy. *J. Geophys. Res.*, 105, 9717–9734.
- Hapke B. (1981) Bidirectional reflectance spectroscopy 1. Theory. *J. Geophys. Res.*, 86, 3039–3054.
- Hapke B. (1984) Bidirectional reflectance spectroscopy III. Correction for macroscopic roughness. *Icarus*, 59, 41–59.
- Hapke B. (1986) Bidirectional reflectance spectroscopy IV. The extinction coefficient and the opposition effect. *Icarus*, 67, 264–280.
- Hapke B. (1996) Applications of an energy transfer model to three problems in planetary regoliths: The solid-state greenhouse, thermal beaming, and emittance spectra. *J. Geophys. Res.*, 101, 16833–16840.
- Hapke B. (2001) Space weathering from Mercury to the asteroid belt. *J. Geophys. Res.*, 106, 10039–10073.
- Hapke B. (2002) Bidirectional reflectance spectroscopy 5. The coherent backscatter opposition effect and anisotropic scattering. *Icarus*, 157, 523–534.
- Hapke B. (2008) Bidirectional reflectance spectroscopy 6. Effects of porosity. *Icarus*, 195, 918–926.
- Hapke B. (2012) *Theory of Reflectance and Emittance Spectroscopy*, 2nd edition. Cambridge Univ., Cambridge. 528 pp.
- Hardersen P. S., Gaffey M. J., and Abell P. A. (2004) Mineralogy of asteroid 1459 Magnya and implications for its origin. *Icarus*, 167, 170–177.
- Hardersen P. A., Cloutis E. A., Gaffey M. J., and Reddy V. (2011) The M/X-asteroid menagerie: Results of an NIR spectral survey of 45 main-belt asteroids. *Meteoritics & Planet. Sci.*, 46, 1910–1938.
- Hardersen P. S., Reddy V., Roberts R., and Mainzer A. (2014) More chips off of asteroid (4) Vesta: Characterization of eight Vestaoids and their HED meteorite analogs. *Icarus*, 242, 269–282.
- Hasegawa S. et al. (2003) Evidence of hydrated and/or hydroxylated minerals on the surface of asteroid 4 Vesta. *Geophys. Res. Lett.*, 30(21), 2023.
- Henning Th. and Mutschke H. (1997) Low-temperature infrared properties of cosmic dust analogues. *Astron. Astrophys.*, 327, 743–754.
- Henning Th., Il'In V. B., Krivova N. A., Michel B., and Voshchinnikov N. V. (1999) WWW database of optical constants for astronomy. *Astron. Astrophys. Suppl. Ser.*, 136, 405–406.
- Hinrichs J. L. and Lucey P. G. (2002) Temperature-dependent near-infrared spectral properties of minerals, meteorites, and lunar soil. *Icarus*, 155, 169–180.
- Hiroi T., Vilas F., and Sunshine J. M. (1996) Discovery and analysis of minor absorption bands in S-asteroid visible reflectance spectra. *Icarus*, 119, 202–208.
- Hunt G. R. (1982) Spectroscopic properties of rocks and minerals. In *Handbook of Physical Properties of Rocks, Vol. 1* (R. S. Carmichael, ed.), pp. 295–385. CRC, Boca Raton, Florida.
- Hunt G. R. and Logan L. M. (1972) Variation of single particle mid-infrared emission spectrum with particle size. *Appl. Opt.*, 11, 142–147.
- Isaacson P. J. and 12 colleagues (2011) Remote compositional analysis of lunar olivine-rich lithologies with Moon Mineralogy Mapper (M3) spectra. *J. Geophys. Res.*, 116, E00G11.
- Izenberg N. R., Murchie S. L., Bell J. F. III, McFadden L. A., Wellnitz D. D., and Clark B. E. (2003) Spectral properties and geologic processes on Eros from combined NEAR NIS and MSI data sets. *Meteoritics & Planet. Sci.*, 38(7), 1053–1077.
- Jäger C., Molster F. J., Dorschner J., Henning Th., Mutschke H., and Waters L. B. F. M. (1998) Steps toward interstellar silicate mineralogy. IV. The crystalline revolution. *Astron. Astrophys.*, 339, 904–916.
- Jaumann R. et al. (2012) Vesta's shape and morphology. *Science*, 336, 687–690.
- Jenniskens P., Shaddad M. H., Numan D., Elsir S., Kudoda A. M., Zolensky M. E., Le L., Robinson G. A., Friedrich J. M., Rumble D., Steele A., Chesley S. R., Fitzsimmons A., Duddy S., Hsieh H. H., Ramsay G., Brown P. G., Edwards W. N., Tagliaferri E., Boslough M. B., Spalding R. E., Dantowitz R., Kozubal M., Pravec P., Borovicka J., Charvat Z., Vaubaillon J., Kuiper J., Albers J., Bishop J. L., Mancinelli R. L., Sandford S. A., Milam S. N., Nuevo M., and Worden S. P. (2009) The impact and recovery of asteroid 2008 TC3. *Nature*, 458, 485–488.
- Kelley M. S. and Gaffey M. J. (2002) High-albedo asteroid 434 Hungaria: Spectrum, composition and genetic connections. *Meteoritics & Planet. Sci.*, 37, 1815–1827.
- King T. V. and Ridley W. I. (1987) Relation of the spectroscopic reflectance of olivine to mineral chemistry and some remote sensing applications. *J. Geophys. Res.*, 92, 11457–11469.
- Kitazato K., Clark B. E., Abe M., Abe S., Takagi Y., Hiroi T., Barnouin-Jha O. S., Abell P. A., Lederer S. M., and Vilas F. (2008) Near-infrared spectrophotometry of asteroid 25143 Itokawa from NIRS on the Hayabusa spacecraft. *Icarus*, 194, 137–145.
- Koike C. and Hasegawa H. (1987) Mid-infrared extinction coefficients of amorphous silicates. *Astrophys. Space Sci.*, 134, 361–379.
- Koike C., Shibai H., and Tuchiyama A. (1993) Extinction of olivine and pyroxene in the mid- and far-infrared. *Mon. Not. R. Astron. Soc.*, 264, 654–658.
- Koike C., Chihara H., Tuchiyama A., Suto H., Sogawa H., and Okuda H. (2003) Compositional dependence of infrared absorption spectra of crystalline silicate. II. Natural and synthetic olivines. *Astron. Astrophys.*, 399, 1101–1107.

- Koike C., Mutschke H., Suto H., Naoi T., Chihara H., Henning Th., Jäger C., Tsuchiyama A., Dorschner J., and Okuda H. (2006) Temperature effects on the mid-and far-infrared spectra of olivine particles. *Astron. Astrophys.*, 449(2), 583–596.
- Korochantseva E. V., Trieloff M., Lorenz C. A., Buykin A. I., Ivanova M. A., Schwarz W. H., Hopp J., and Jessberger E. K. (2007) L-chondrite asteroid breakup tied to Ordovician meteorite shower by multiple isochron  $^{40}\text{Ar}$ - $^{39}\text{Ar}$  dating. *Meteoritics & Planet. Sci.*, 42, 113–130.
- Lane M. D., Glotch T. D., Dyar M. D., Pieters C. M., Klima R., Hiroi T., Bishop J. L., and Sunshine J. (2011) Midinfrared spectroscopy of synthetic olivines: Thermal emission, specular and diffuse reflectance, and attenuated total reflectance studies of forsterite to fayalite. *J. Geophys. Res.*, 116, E08010.
- Larson H. P. and Fink U. (1975) Infrared spectral observations of asteroid 4 Vesta. *Icarus*, 26, 420–427.
- Lawrence S. J. and Lucey P. G. (2007) Radiative transfer mixing models of meteoritic assemblages. *J. Geophys. Res.*, 112, E07005.
- Lazzaro D., Michchenko T., Carvano J. M., Binzel R. P., Bus S. J., Burbine T. H., Mothé-Diniz T., Florcak M., Angelis C. A., and Harris A. W. (2000) Discovery of a basaltic asteroid in the outer main belt. *Science*, 288, 2033–2035.
- Le Bras A. and Erard S. (2003) Reflectance spectra of regolith analogs in the mid-infrared: Effects of grain size. *Planet. Space Sci.*, 51, 281–294.
- Le Corre L., Reddy V., Schmedemann N., Becker K. J., O'Brien D. P., Yamashita N., Peplowski P. N., Prettyman T. H., Li J.-Y., Cloutis E. A., Denevi B., Kneissl T., Palmer E., Gaskell R., Nathues A., Gaffey M. J., Garry B., Sierks H., Russell C. T., and Raymond C. (2013) Nature of the orange material on (4) Vesta from Dawn observations. *Icarus*, 226(2), 1568–1594.
- Li J.-Y. et al. (2010) Photometric mapping of asteroid (4) Vesta's southern hemisphere with Hubble Space Telescope. *Icarus*, 208, 238–251.
- Li J.-Y., Le Corre L., Schröder S. E., Reddy V., Denevi B. W., Buratti B. J., Mottola S., Hoffmann M., Gutierrez-Marques P., Nathues A., Russell C., and Raymond C. A. (2013) Global photometric properties of asteroid (4) Vesta observed with Dawn Framing Camera. *Icarus*, 226, 1252–1274.
- Lim L. F., McConnochie T. H., Bell J. F. III, and Hayward T. L. (2005) Thermal infrared (8–13  $\mu\text{m}$ ) spectra of 29 asteroids: The Cornell mid-infrared asteroid spectroscopy (MIDAS) survey. *Icarus*, 173, 385–408.
- Lim L. F., Emery J. P., and Moskovitz N. A. (2011) Mineralogy and thermal properties of V-type asteroid 956 Elisa: Evidence for diogenetic material from the Spitzer IRS (5–35 micron) spectrum. *Icarus*, 213, 510–523.
- Logan L. M., Hunt G. R., Salisbury J. W., and Balsamo S. R. (1973) Compositional implications of Christiansen frequency maximums for infrared remote sensing applications. *J. Geophys. Res.*, 78, 4983–5003.
- Lucey P. G. and Riner M. A. (2011) The optical effects of small iron particles that darken but do not reddens: Evidence of intense space weathering on Mercury. *Icarus*, 212, 451–462.
- Lucey P. G., Keil K., and Whitely R. (1998) The influence of temperature on the spectra of A-asteroids and implications for their silicate chemistry. *J. Geophys. Res.*, 103, 5865–5871.
- Lumme K. and Bowell E. (1981) Radiative transfer in the surfaces of atmosphereless bodies: I — Theory. II — Interpretation of phase curves. *Astron. J.*, 86, 1694–1721.
- Lyon R. J. P. (1964) *Evaluation of Infrared Spectrophotometry for Compositional Analysis of Lunar and Planetary Soils. Part II: Rough and Powdered Surfaces*. NASA-CR-100, Washington, DC.
- Mann P., Cloutis E. A., and Reddy V. (2011) The effect of changing viewing geometry on pyroxene and eucrite reflectance spectra. *Lunar Planet. Sci. XLII*, Abstract #2268. Lunar and Planetary Institute, Houston.
- Markus K., Arnold G., Hiesinger H., Capaccioni F., Filacchione G., Tosi F., De Sanctis M. C., Capria M. T., Ammannito E., and Erard S. (2013) Comparison of ground-based and VIRTIS-M/ROSETTA reflectance spectra of asteroid 2867 Šteins with laboratory reflectance spectra in the VIS and IR. *EGU General Assembly*, EGU2013-11287.
- Marvin U. B. (1983) The discovery and initial characterization of Allan Hills 81005: The first lunar meteorite. *Geophys. Res. Lett.*, 10, 775–778.
- Mayne R. G., Sunshine J. M., McSween H. Y. Jr., Bus S. J., and McCoy T. J. (2011) The origin of Vesta's crust: Insights from spectroscopy of the vestoids. *Icarus*, 214, 147–160.
- McCord T. B., Adams J. B., and Johnson T. V. (1970) Asteroid Vesta: Spectral reflectivity and compositional implications. *Science*, 168, 1445–1447.
- McCord T. et al. (2012) Dark material on Vesta: Adding carbonaceous volatile-rich materials to planetary surfaces. *Nature*, 491, 83–86.
- McCoy T. J., Nittler L. R., Burbine T. H., Trombka J. I., Clark P. E., and Murphy M. E. (2000) Anatomy of a partially-differentiated asteroid: A “NEAR”-sighted view of acapulcoites and lodranites. *Icarus*, 148, 29–36.
- McCoy T. J., Robinson M. S., Nittler L. R., and Burbine T. H. (2002) The Near Earth Asteroid Rendezvous mission to asteroid 433 Eros: A milestone in the study of asteroids and their relationship to meteorites. *Chem. Erde*, 62, 89–121.
- McCoy T. J., Corrigan C. M., Sunshine J. M., Bus S. J., and Gale A. (2007) Does spectroscopy provide evidence for widespread partial melting of asteroids? II. Pyroxene compositions. *Lunar Planet. Sci. XXXVIII*, Abstract #1631. Lunar and Planetary Institute, Houston.
- McEachern F. M., Čuk M., and Stewart S. T. (2010) Dynamical evolution of the Hungaria asteroids. *Icarus*, 210, 644–654.
- McFadden L. A., Wellnitz D. D., Shnaubelt M., Gaffey M. J., Bell J. F. III, Izenberg N. R., Murchie S. L., and Chapman C. R. (2001) Mineralogical interpretation of Eros from NEAR near-infrared spectrometer low phase flyby. *Meteoritics & Planet. Sci.*, 36, 1711–1726.
- McFadden L. A., Goldman N. J., Gaffey M. J., and Izenberg N. R. (2005) Evidence for partial melting in reflectance spectra of 433 Eros. *Lunar Planet. Sci. XXXVI*, Abstract #1561. Lunar and Planetary Institute, Houston.
- McSween H. Y., Mittlefehldt D. W., Beck A. W., Mayne R. G., and McCoy T. J. (2011) HED meteorites and their relationship to the geology of Vesta and the Dawn mission. *Space Sci. Rev.*, 163, 141–174.
- Millis R. L., Bowell E., and Thompson D. T. (1976) UVB photometry of asteroid 433 Eros. *Icarus*, 28, 53–67.
- Mittlefehldt D. W., McCoy T. J., Goodrich C. A., and Kracher A. (1998) Non-chondritic meteorites from asteroidal bodies. In *Planetary Materials* (J. J. Papike, ed.), pp. 4-1 to 4-195. Reviews in Mineralogy, Vol. 36, Mineralogical Society of America, Washington.
- Miyamoto M. (1988) Hydration bands near 3  $\mu\text{m}$  and weathering of some Antarctic meteorites. *Earth Planet. Sci. Lett.*, 88, 398–402.
- Moroz L., Schade U., and Wächter R. (2000) Reflectance spectra of olivine-orthopyroxene-bearing assemblages at decreased temperatures: Implications for remote sensing of asteroids. *Icarus*, 147, 79–93.
- Moskovitz N. A., Willman M., Burbine T. H., Binzel R. P., and Bus S. J. (2010) A spectroscopic comparison of HED meteorites and V-type asteroids in the inner main belt. *Icarus*, 208, 773–788.
- Mothé-Diniz T., Carvano J. M., Bus S. J., Duffard R., and Burbine T. H. (2008) Mineralogical analysis of the Eos family from near-infrared spectra. *Icarus*, 195, 277–294.
- Mueller M., Marchis F., Emery J. P., Harris A. W., Mottola S., Hestroffer D., Berthier J., and di Martino M. (2010) Eclipsing binary Trojan asteroid Patroclus: Thermal inertia from Spitzer observations. *Icarus*, 205, 505–515.
- Mukai T. and Koike C. (1990) Optical constants of olivine particles between wavelengths of 7 and 200 microns. *Icarus*, 87, 180–187.
- Murchie S. L. and Pieters C. M. (1996) Spectral properties and rotational spectral heterogeneity of 433 Eros. *J. Geophys. Res.*, 101, 2201–2214.
- Mustard J. F. and Hays J. E. (1997) Effects of hyperfine particles on reflectance spectra from 0.3–25  $\mu\text{m}$ . *Icarus*, 125, 145–163.
- Nakamura T., Noguchi T., Tanaka M., Zolensky M. E., Kimura M., Tsuchiyama A., Nakato A., Ogami T., Ishida H., Uesugi M., Yada T., Shirai K., Fujimura A., Okazaki R., Sandford S., Wakita S., Ishibashi Y., Abe M., Okada T., Ueno M., Mukai T., Yoshikawa M., and Kawaguchi J. (2011) Itokawa dust particles: A direct link between S-type asteroids and ordinary chondrites. *Science*, 333, 1113–1116.
- Nathues A. (2010) Spectral study of the Eunomia asteroid family. Part II: The small bodies. *Icarus*, 208, 252–275.
- Nathues A., Mottola S., Kaasalainen M., and Neukum G. (2005) Spectral study of the Eunomia asteroid family I. Eunomia. *Icarus*, 175, 452–463.
- Nesvorný D., Vokrouhlický D., Morbidelli A., and Bottke W. F. (2009) Asteroidal source of L chondrite meteorites. *Icarus*, 200, 698–701.

- Nittler L. R. and 14 colleagues (2001) X-ray fluorescence measurements of the surface elemental composition of asteroid 433 Eros. *Meteoritics & Planet. Sci.*, 36, 1673–1695.
- Okada T., Shirai K., Yamamoto Y., Arai T., Ogawa K., Hosono K., and Kata M. (2006) X-ray fluorescence spectrometry of asteroid Itokawa by Hayabusa. *Science*, 312, 1338–1341.
- Pitman K. M., Dijkstra C., Hofmeister A. M., and Speck A. K. (2010) Infrared laboratory absorbance spectra of olivine: Using classical dispersion analysis to extract peak parameters. *Mon. Not. R. Astron. Soc.*, 406, 460–481.
- Poulet F., Cuzzi J. N., Cruikshank D. P., Roush T., and Dalle Ore C. M. (2002) Comparison between the Shkuratov and Hapke scattering theories for solid planetary surfaces: Application to the surface composition of two Centaurs. *Icarus*, 160, 313–324.
- Prettyman T. H. et al. (2012) Elemental mapping by Dawn reveals exogenic H in Vesta's howarditic regolith. *Science*, 338(6104), 242–246.
- Ramsey M. S. and Christensen P. R. (1998) Mineral abundance determination: Quantitative deconvolution of thermal emission spectra. *J. Geophys. Res.*, 103, 577–596.
- Reddy V., Gaffey M. J., Kelley M. S., Nathues A., Li J-Y., and Yarbrough R. (2010) Compositional heterogeneity of asteroid 4 Vesta's southern hemisphere: Implications for the Dawn Mission. *Icarus*, 210, 693–706.
- Reddy V., Nathues A., Gaffey M. J., and Schaeff S. (2011) Mineralogical characterization of potential targets for the ASTEX mission scenario. *Planet. Space. Sci.*, 59, 772–778.
- Reddy V., Nathues A., Le Corre L., Sierks H., Li J-Y., Gaskell R., McCoy T., Beck A., Schröder S. E., Pieters C. M., Becker K. J., Buratti B. J., Denesi B., Blewett D. T., Christensen U., Gaffey M. J., Gutierrez-Marques P., Hicks M., Keller H. U., Maue T., Mottola S., McFadden L. A., McSween H. Y., Mittlefehldt D., O'Brien D. P., Raymond C., and Russell C. T. (2012a) Color and albedo heterogeneity of Vesta from Dawn. *Science*, 336, 700–704.
- Reddy V., Le Corre L., O'Brien D. P., Nathues A., Cloutis E. A., Durda D. D., Bottke W. F., Bhatt M. U., Nesvorný D., Buczkowski D., Scully J. E. C., Palmer E. M., Sierks H., Mann P. J., Becker K. J., Beck A. W., Mittlefehldt D., Li J-Y., Gaskell R., Russell C. T., Gaffey M. J., McSween H. Y., McCord T. B., Combe J-P., and Blewett D. (2012b) Delivery of dark material to Vesta via carbonaceous chondritic impacts. *Icarus*, 221, 544–559.
- Reddy V., Sanchez J. A., Nathues A., Moskovitz N. A., Li J-Y., Cloutis E. A., Archer K., Tucker R. A., Gaffey M. J., Mann J. P., Sierks H., and Schade U. (2012c) Photometric, spectral phase and temperature effects on Vesta and HED meteorites: Implications for Dawn mission. *Icarus*, 217, 153–168.
- Reddy V., Li J.-Y., Le Corre L., Scully J. E., Gaskell R., Russell C. T., Park R. S., Nathues A. N., Raymond C. R., Gaffey M. J., Becker K. J., and McFadden L. A. (2013) Comparing Dawn, Hubble Space Telescope and ground-based interpretations of (4) Vesta. *Icarus*, 226, 1103–1114.
- Reddy V., Sanchez J., Bottke W., Cloutis E., Izawa M., O'Brien D., Mann P., Cuddy M., Le Corre L., Gaffey M., and Fujihara G. (2014) Chelyabinsk meteorite explains unusual spectral properties of Baptistina asteroid family. *Icarus*, 237, 116–130.
- Rivkin A. S. and Emery J. P. (2010) Detection of ice and organics on an asteroidal surface. *Nature*, 464, 1322–1323.
- Rivkin A. S., Howell E. S., Vilas F., and Lebofsky L. A. (2002) Hydrated minerals on asteroids: The astronomical record. In *Asteroids III* (W. F. Bottke Jr. et al., eds.), pp. 235–253. Univ. of Arizona, Tucson.
- Rivkin A. S., Binzel R. P., Sunshine J., Bus S. J., Burbine T. H., and Saxena A. (2004) Infrared spectroscopic observations of 69230 Hermes (1937 UB): Possible unweathered endmember among ordinary chondrite analogs. *Icarus*, 172, 408–414.
- Rivkin A. S., Volquardsen E. L., and Clark B. E. (2006) The surface composition of Ceres: Discovery of carbonates and iron-rich clays. *Icarus*, 185, 563–567.
- Rivkin A. S., Clark B. E., Ockert-Bell M., Volquardsen E., Howell E. S., Bus S., Thomas C. A., and Shepard M. (2011) Asteroid 21 Lutetia at 3 microns: Observations with IRTF SpeX. *Icarus*, 216, 62–68.
- Roberts R. V. and Gaffey M. J. (2014) Update on testing the Gefion dynamical family as a possible source of the L-chondrites. *Lunar Planet. Sci. XLV*, Abstract #1263. Lunar and Planetary Institute, Houston.
- Russell C.T. et al. (2012) Dawn at Vesta: Testing the protoplanetary paradigm. *Science*, 336, 684–686.
- Salisbury J. W. and Hunt G. R. (1974) Meteorite spectra and weathering. *J. Geophys. Res.*, 79, 4439–4441.
- Salisbury J. W. and Walter L. S. (1989) Thermal infrared (2.5–13.5 μm) spectroscopic remote sensing of igneous rock types on particulate planetary surfaces. *J. Geophys. Res.*, 94, 9192–9202.
- Salisbury J. W., Hapke B., and Eastes J. W. (1987a) Usefulness of weak bands in midinfrared remote sensing of particulate planetary surfaces. *J. Geophys. Res.*, 92, 702–710.
- Salisbury J. W., Walter L. S., and Vergo N. (1987b) *Mid-Infrared (2.1–25 mm) Spectra of Minerals, 1st edition*. U.S. Geol. Surv. Open File Rept. 87–263.
- Salisbury J. W., D'Aria D. M., and Jarosewich E. (1991a) Mid infrared (2.5–13.5 μm) reflectance spectra of powdered stony meteorites. *Icarus*, 92, 280–297.
- Salisbury J. W., Walter L. S., Vergo N., and D'Aria D. M. (1991b) *Infrared (2.5–25 μm) Spectra of Minerals*. Johns Hopkins Univ., Laurel, Maryland. 294 pp.
- Sanchez J. A., Reddy V., Nathues A., Cloutis E. A., Mann P., and Hiesinger H. (2012) Phase reddening on near-Earth asteroids: Implications for mineralogical analysis, space weathering and taxonomic classification. *Icarus*, 220, 36–50.
- Sanchez J. A., Reddy V., Kelley M. S., Cloutis E. A., Bottke W. F., Nesvorný D., Lucas M. P., Hardersen P. S., Gaffey M. J., Abell P. A., and Le Corre L. (2014) Olivine-dominated asteroids: Mineralogy and origin. *Icarus*, 228(1), 288–300.
- Schade U., Wäsch R., and Moroz L. (2004) Near-infrared reflectance spectroscopy of Ca-rich clinopyroxenes and prospects for remote spectral characterization of planetary surfaces. *Icarus*, 168, 80–92.
- Scott A. and Duley W. W. (1996) Ultraviolet and infrared refractive indices of amorphous silicates. *Astrophys. J. Suppl. Ser.*, 105, 401–405.
- Shepard M. K. and Cloutis E. (2011) Laboratory measurements of band depth variation with observed geometry. *Lunar Planet. Sci. XLII*, Abstract #1043. Lunar and Planetary Institute, Houston.
- Shkuratov Y., Starukhina L., Hoffmann H., and Arnold G. (1999) A model of spectral albedo of particulate surfaces: Implications for optical properties of the Moon. *Icarus*, 137, 235–246.
- Sunshine J. M. and Pieters C. M. (1993) Estimating modal abundances from the spectra of natural and laboratory pyroxene mixtures using the modified Gaussian model. *J. Geophys. Res.*, 98, 9075–9087.
- Sunshine J. M. and Pieters C. M. (1998) Determining the composition of olivine from reflectance spectroscopy. *J. Geophys. Res.*, 103, 13675–13688.
- Sunshine J. M., Pieters C. M., and Pratt S. F. (1990) Deconvolution of mineral absorption bands: An improved approach. *J. Geophys. Res.*, 95, 6955–6966.
- Sunshine J. M., Bus S. J., McCoy T. J., Burbine T. H., Corrigan C. M., and Binzel R. P. (2004) High-calcium pyroxene as an indicator of igneous differentiation in asteroids and meteorites. *Meteoritics & Planet. Sci.*, 39, 1343–1357.
- Sunshine J. M., Bus S. J., Corrigan C. M., McCoy T. J., and Burbine T. H. (2007) Olivine-dominated asteroids and meteorites: Distinguishing nebular and igneous histories. *Meteoritics & Planet. Sci.*, 42, 155–170.
- Takir D. and Emery J. P. (2012) Outer main belt asteroids: Identification and distribution of four 3-μm spectral groups. *Icarus*, 219, 641–654.
- Thomas C. A. and Binzel R. P. (2010) Identifying meteorite source regions through near-Earth object spectroscopy. *Icarus*, 205, 419–429.
- Thomas P. C., Binzel R. P., Gaffey M. J., Zellner B. H., Storrs A. D., and Wells E. (1997a) Vesta: Spin pole, size, and shape from HST images. *Icarus*, 128, 88–94.
- Thomson J. L. and Salisbury J. W. (1993) The mid-infrared reflectance of mineral mixtures (7–14 μm). *Remote Sens. Environ.*, 45, 1–13.
- Trang D., Lucey P. G., Gilliss-Davis J. J., Cahill J. T. S., Klima R. L., and Isaacson P. J. (2013) Near-infrared optical constants of naturally occurring olivine and synthetic pyroxene as a function of mineral composition. *J. Geophys. Res.*, 118, 708–732.
- Vernazza P., Binzel R. P., Thomas C. A., DeMeo F. E., Bus S. J., Rivkin A. S., and Tokunaga A. T. (2008) Compositional differences between meteorites and near-Earth asteroids. *Nature*, 454, 858–860.
- Vernazza P., Binzel R. P., Rossi A., Fulchignoni M., and Birlan M. (2009a) Solar wind as the origin of rapid reddening of asteroid surfaces. *Nature*, 458, 993–995.

- Vernazza P., Brunetto R., Binzel R. P., Perron C., Fulvio D., Strazzulla G., and Fulchignoni M. (2009b) Plausible parent bodies for enstatite chondrites and mesosiderites: Implications for Lutetia's fly-by. *Icarus*, 202, 477–486.
- Vernazza P., Carry B., Emery J., Hora J. L., Cruikshank D., Binzel R. P., Jackson J., Helbert J., and Maturilli A. (2010) Mid-infrared spectral variability for compositionally similar asteroids: Implications for asteroid particle size distributions. *Icarus*, 207, 800–809.
- Vernazza P., Delbo M., King P. L., Izawa M. R. M., Olofsson J., Lamy P., Cipriani F., Binzel R. P., Marchis F., Merín B., and Tamani A. (2012) High surface porosity as the origin of emissivity features in asteroid spectra. *Icarus*, 221, 1162–1172.
- Vernazza P., Fulvio D., Brunetto R., Emery J. P., Dukes C. A., Cipriani F., Witasse O., Schaible M. J., Zanda B., Strazzula G., and Baragiola R. A. (2013) Paucity of Tagish Lake-like parent bodies in the asteroid belt and among Jupiter Trojans. *Icarus*, 225, 517–525.
- Vincent R. K. and Hunt G. R. (1968) Infrared reflectance from mat surfaces. *Appl. Opt.*, 7, 53–59.
- Vilas F. and Gaffey M. J. (1989) Identification of phyllosilicate absorption features in main-belt and outer-belt asteroid reflectance spectra. *Science*, 246, 790–792.
- Wetherill G. W. (1987) Dynamical relations between asteroids, meteorites and Apollo-Amor objects. *Philos. Trans. R. Soc. London*, A323, 323–337.
- Willman M. and Jedicke R. (2011) Asteroid age distributions determined by space weathering and collisional evolution models. *Icarus*, 211, 504–510.
- Yang B. and Jewitt D. (2011) A near-infrared search for silicates in jovian Trojan asteroids. *Astron. J.*, 141, 95.
- Yang B., Lucey P., and Glotch T. (2013) Are large Trojan asteroids salty? An observational, theoretical, and experimental study. *Icarus*, 223, 359–366.



# Astronomical Observations of Volatiles on Asteroids

**Andrew S. Rivkin**

*The Johns Hopkins University Applied Physics Laboratory*

**Humberto Campins**

*University of Central Florida*

**Joshua P. Emery**

*University of Tennessee*

**Ellen S. Howell**

*Arecibo Observatory/Universities Space Research Association*

**Javier Licandro**

*Instituto de Astrofísica de Canarias/Departamento de Astrofísica, Universidad de La Laguna*

**Driss Takir**

*Astrogeology Science Center, U.S. Geological Survey*

**Faith Vilas**

*Planetary Science Institute*

---

We have long known that water and hydroxyl are important components in meteorites and asteroids. However, in the time since the publication of *Asteroids III*, evolution of astronomical instrumentation, laboratory capabilities, and theoretical models have led to great advances in our understanding of H<sub>2</sub>O/OH on small bodies, and spacecraft observations of the Moon and Vesta have important implications for our interpretations of the asteroidal population. We begin this chapter with the importance of water/OH in asteroids, after which we will discuss their spectral features throughout the visible and near-infrared (IR). We continue with an overview of the findings in meteorites and asteroids, closing with a discussion of future opportunities, the results from which we can anticipate reading in *Asteroids V*. Because this topic is of broad importance to asteroids, we also point to relevant in-depth discussions elsewhere in this volume.

## 1. WATER ICE SUBLIMATION AND PROCESSES THAT CREATE, INCORPORATE, OR DELIVER VOLATILES TO THE ASTEROID BELT

### 1.1. Accretion/Solar System Formation

The concept of the “snow line” (also known as the “water-frost line”) is often used in discussing the water inventory of small bodies in our solar system. The snow line is the heliocentric distance at which water ice is stable enough to be accreted into planetesimals. The placement of the snow line has varied in different models. A location just inside Jupiter helps explain the greater mass of the giant planets as they accrete a larger fraction of the mass in the solar nebula. Although the location of the snow line before and during planet formation

is uncertain, some studies show it may have fallen within the asteroid belt (*Lunine and Reid*, 2006). The location of the snow line in our solar system coinciding with the asteroid belt is consistent with observations of disks around other stars (e.g., *Su et al.*, 2013), where planetesimal rings tend to coincide with the snow line around those stars. However, it seems the relatively simple concept of a static snow line requires revisions in light of new results on several fronts. For instance, the snow line likely moved with time as the Sun’s luminosity changed early in solar system history (e.g., *Martin and Livio*, 2012). Even though there is no agreement on the details of planetesimal formation and growth, some models favor the growth of ~100-km-scale planetesimals directly from centimeter-scale pieces (*Morbidelli et al.*, 2009; *Cuzzi et al.*, 2010; for a dissenting view see *Weidenschilling*, 2011). Hence the timing of those assemblies as conditions change

could have a strong influence on the amount of radioactive elements present in a planetesimal's interior and on its rock-to-ice ratio, further complicating the concept of a snow line. Recent observations also point to a more complex picture. For example, the concept of an asteroid-comet continuum, where there is no clear boundary between primitive asteroids and cometary nuclei (e.g., *Gounelle*, 2011), is gaining support and is consistent with the intermittent cometary behavior of some main-belt and near-Earth asteroids (NEAs) (e.g., *Hsieh and Jewitt*, 2006; *Licandro et al.*, 2007, 2011b; *Jewitt et al.*, 2013; *Mommert et al.*, 2014), which will be discussed in more detail in section 1.3 below. The chapter by Johansen et al. in this volume summarizes the current state of thought about asteroid formation.

## 1.2. Grand Tack/Nice Model Delivery of Outer Solar System Material

One of the main motivations for studying the asteroid belt is to better understand the conditions in the solar nebula and the material that formed the terrestrial planets. The distribution of spectroscopic asteroid types is not randomly mixed, but instead follows a trend with heliocentric distance (*Chapman et al.*, 1975; *Gradie and Tedesco*, 1982), which has long been interpreted as a remnant property of the solar nebula. However, discoveries of extrasolar planets and other planetary systems have greatly broadened our notions of what is “normal” and “typical.” Also, increasing computational capabilities have allowed ever more realistic and detailed models of accretion, and are now challenging long-held ideas of what we thought we knew about solar system formation. The asteroid belt is an important key to constraining and testing these models.

Dynamical models suggest the asteroid belt of today may be very different from when it formed. *Bottke et al.* (2012) argue that the asteroid belt once extended significantly sunward compared with today, with the Hungaria region the eroded remnant of a once-larger population. Similarly, there are arguments that Vesta formed closer to the Sun and was later transported into the main asteroid belt (*Bottke et al.*, 2006). More importantly for the discussion here, the “Nice Model” (*Gomes et al.*, 2005; *Morbidelli et al.*, 2005; *Tsiganis et al.*, 2005), which has gained wide acceptance, predicts a large influx of volatile-rich objects from the outer solar system to the inner solar system and the insertion of primitive transneptunian objects (TNOs) into the outer belt (*Levison et al.*, 2009).

The related “Grand Tack” model (*Morbidelli et al.*, 2010; *Walsh et al.*, 2011) interprets the low-albedo asteroids as originating among the giant planets, with later delivery to their current positions in the main asteroid belt by the migration of Jupiter. *Walsh et al.* (2011) and references therein describe how the original material in the asteroid belt would be disturbed by inward migration of Jupiter, leaving only the inner asteroid belt intact, scattering some of these objects outward behind it as it moves. After Saturn moves into resonance with Jupiter, both begin to migrate

outward, and some of the previously scattered objects are scattered back into the asteroid belt region, along with other more volatile-rich objects (perhaps the antecedents of the C-complex asteroids) that may have formed closer to 5 AU.

This scenario solves the problem of having both high- and low-temperature materials side by side in the asteroid belt. However, it means that the compositional gradient with heliocentric distance is not primordial, and allows a larger amount of radial mixing than previously considered. The problem of linking meteorites to their asteroid parent bodies also becomes more complex, since the current position of the asteroids may be unrelated to where those bodies formed. However, asteroid families, collisional fragments of once intact parent bodies, are nearly all spectrally uniform, while many meteorites clearly show that differentiation has occurred. Differentiated objects can form closer to the Sun, and be emplaced in the asteroid belt by Jupiter during its migration. Undifferentiated objects form farther out, and are scattered inward by Jupiter. Both can now exist side by side, but neither is necessarily representative of material that condensed at 2–4 AU.

## 1.3. Hydroxyl/Water Creation Via Space Weathering

Although the term “space weathering” is usually associated with nanophase iron (or iron sulfide) embedded in glassy rims of silicate grains and the links between S-class asteroids and ordinary chondrites, the processes that form these rims (and npFe<sup>0</sup> particles) can also involve water and OH.

*Starukhina* (2001), modeling the interaction of solar wind protons with regolith, predicted that OH and its diagnostic 3-μm absorption band should always be present on airless bodies. While the quantitative results have not been borne out [for instance, Vesta has a 3-μm band depth ~2% at its deepest (*De Sanctis et al.*, 2012a), compared to the ~20–70% depth predicted by Starukhina], it was one of the first treatments attempting to predict the effects of space weathering in that spectral region. Thoughts on how the spectrum of airless bodies might change near 3 μm with exposure to typical regolith processes have varied from a prediction of dehydration (Pieters, personal communication) to the creation of bands (e.g., *Starukhina*, 2001) to no appreciable effect (*Rivkin et al.*, 2003).

The spectral models by Starukhina followed decades of lunar-centered work by other researchers. *Arnold* (1979) investigated ice survivability on the Moon, following up the work of *Watson et al.* (1961). Arnold proposed that solar wind reduction of iron in the lunar regolith, such as is now implicated in space weathering (*Noble et al.*, 2001), could create significant amounts of water, which could then potentially make its way to cold traps in permanently shadowed craters near the lunar poles. Lunar Prospector data shows a hydrogen enhancement near the lunar poles, interpreted as due to ice (*Feldman et al.*, 2001). The independent observation of 3-μm bands on the Moon by three spacecraft [Visible and Infrared Mapping Spectrometer (VIMS) on Cassini (*Clark*, 2009), High Resolution Instrument (HIR) on

the Deep Impact (DI) spacecraft (*Sunshine et al.*, 2009), the Moon Mineralogy Mapper (M<sup>3</sup>) on Chandrayaan-1 (*Pieters et al.*, 2009)] provided convincing evidence of OH on the Moon. While interpretations are continuing to evolve, the early consensus seems to be that the band is due, at least in part, to adsorbed water and OH likely created by the interaction of solar wind protons and silicates in the lunar regolith. The presence of ice at the lunar poles is consistent with formation of water in the regolith via solar wind interactions, but other potential water sources have been identified [such as retention and migration of cometary volatiles after impacts (e.g., *Stewart et al.* 2011)], and solar wind interaction is not the only possible origin for lunar water. The relative contribution and importance of any solar-wind-created water to any ice deposits is not yet fully understood.

The presence of water on the lunar surface potentially reopens interpretations of asteroidal (and other small body) surfaces. However, the small bodies also provide an opportunity to better understand the lunar results. If the 3-μm band seen on the Moon is due to the implantation of solar wind protons in the lunar regolith, this absorption band should also be present on other small body surfaces, with allowances made for the increased distance from the Sun and other factors. If independent of local composition, as suggested by the high-spatial-resolution M<sup>3</sup> data, most asteroids should have similar effects when under similar conditions. If temperature sensitive, as suggested by the DI data, differences may be seen with solar distance. If due to photometric effects but not temperature, a well-conceived program of NEA observations should be able to separate those effects. These are still active areas of research, with a better understanding of the relationship between regolith processes and hydroxyl/water content likely over the next decade.

In addition to the possibility of solar wind protons creating water or hydroxyl, space weathering processes may have additional effects on asteroidal surfaces. *Britt et al.* (2014) argued that the micrometeorite and ultraviolet (UV) processes that create nanophase iron in silicates would, given their different mineralogies, instead create amino acids on carbonaceous bodies like the C asteroids. They suggest that space weathering, when viewed from a thermodynamic standpoint, involves decomposition of rock-forming minerals with results depending on specific composition. In their view, this decomposition is only the first stage of space weathering, with a second stage using the results of that decomposition as catalysts. For the volatile-rich carbonaceous chondrites and their parent asteroids, not only silicates but water, carbon monoxide, and other volatiles can interact via Fischer-Tropsch reactions to create ever-longer carbon chains and kerogen-like insoluble organic matter, as is seen in carbonaceous chondrites. This line of research is still in its infancy, and the observational consequences and predictions are not yet fully understood, particularly in the context of water. Previous work on space weathering of carbonaceous chondrites and/or low-albedo asteroids has focused on changes in spectral slope rather than how it may alter absorptions associated with hydrated minerals.

#### 1.4. Delivery of Exogenic Hydrated Material

It has been proposed that dark material identified on the surface of asteroid (4) Vesta by NASA's Dawn spacecraft was delivered by low-velocity impacts with carbonaceous chondritic material (*Reddy et al.*, 2012). Several lines of evidence support this interpretation, including elemental composition (*Prettyman et al.*, 2012), near-infrared (IR) spectra (*McCord et al.*, 2012), geomorphology (*Denevi et al.*, 2012), and analogy with HED meteorites, especially howardites (*Reddy et al.*, 2012, and references therein). These findings confirm reports of a weak absorption near 3 μm in groundbased spectroscopy of Vesta by *Hasegawa et al.* (2003) and *Rivkin et al.* (2006), who suggested that impacts with carbonaceous objects could have added to the original igneous surface composition.

Visible images from the Dawn spacecraft place most of the dark material in the oldest regions of Vesta's surface. Initially two sources for this dark material were considered: ancient volcanic activity or exogenic material. However, convergence among the different observational constraints points to an exogenic origin for the dark material; further details appear in the chapter by Russell et al. in this volume.

The same exogenic source of hydrated carbonaceous chondritic material on Vesta is proposed by *Shepard et al.* (2015) to explain a 3-μm absorption feature, often attributed to the presence of hydrated minerals (*Rivkin et al.*, 2000), on a number of M-class asteroids with the high radar reflectivity suggestive of a high metal content. In a related result, *Landsman et al.* (2013) reported the detection of 3-μm absorption features on five M-class asteroids recently observed at these wavelengths. *Landsman et al.* (2013) also report considerable diversity in the shape of the hydrated mineral feature in their M-class asteroid sample. However, the M class in general contains a great deal of variety, and objects with low radar reflectivity and 3-μm bands also appear in this class. It seems likely that at least some M asteroids do not have high metal content. Further discussion of the M-class asteroids is found in section 3.3.4.

Interestingly, exogenic processes have also been invoked by *Bottke et al.* (2010, 2013), who argued that impact debris from the irregular satellites of the jovian planets should be driven onto the regular satellites of those systems, and could have accumulated to a depth of tens or even hundreds of meters on the Galilean satellites. The irregular satellites are further discussed below.

## 2. DISCUSSION OF SPECTRAL FEATURES ON ASTEROIDS AND METEORITES

While two sample returns to low-albedo asteroids are slated for the next decade (section 6.2), remote sensing will by necessity remain the primary method for detecting and characterizing the hydrated mineralogies of large numbers of small bodies. Three wavelength regions are primarily used for this purpose, each with their own strengths and limitations: the visible and near-IR spectral region (~0.4–0.8 μm),

the 3- $\mu\text{m}$  region, and the mid-IR (5–13  $\mu\text{m}$ ). An overview table of the most important absorption bands is presented in Table 1. Other wavelengths are used in cometary studies, for instance, but have not been used at asteroids due to an expectation of very low contrast and very meager gas production rates from asteroids. Other techniques, such as groundbased radar or submillimeter observations, may give indirect evidence for the presence of hydrated minerals (Hanson *et al.*, 2006), but our understanding of the relationship between radar albedo and hydrated minerals is incomplete. The meteorites have given us most of our information about the specific minerals present in the asteroids and the aqueous alteration processes that occurred early in solar system history. We discuss the spectral properties of the hydrated minerals and aqueous alteration products below, but details of the minerals in and processes experienced by the meteorites themselves, and the conditions under which they were created and operated, are discussed in detail in the chapter by Krot *et al.* in this volume.

We note that there are additional ways to detect water/OH and other volatiles, such as neutron spectrometers like the one carried by Dawn, or via sounding with radar instruments like the Shallow Radar (SHARAD) instrument on the Mars Reconnaissance Orbiter (MRO) (Seu *et al.*, 2004). These may be the only methods for directly detecting volatiles on some objects, particularly those for which surface volatiles are unstable. We acknowledge that such measurements are particularly valuable, but are out of the scope of discussion in a chapter devoted to “astronomical observations.”

## 2.1. Visible/Near-Infrared

An absorption band centered near 0.7  $\mu\text{m}$  is seen in asteroids as well as the CM meteorites. The absorption has classically been attributed to  $\text{Fe}^{2+}$ - $\text{Fe}^{3+}$  intervalence charge transfer, associated with phyllosilicates but not diagnostic of them (Vilas and Gaffey, 1989; Vilas, 1994; King and Clark, 1997). Cloutis *et al.* (2011a) attributes bands near 0.7  $\mu\text{m}$  to saponite group phyllosilicates (band centers 0.59–0.67  $\mu\text{m}$ ) and “mixed valence Fe-bearing serpentine group phyllosilicates” (band centers 0.70–0.75  $\mu\text{m}$ ). Unlike

the Ch asteroids, for which the 0.7- $\mu\text{m}$  band is a defining characteristic (section 3.3.1), some CM meteorites have no absorption band at these wavelengths. In addition, while a few thermally metamorphosed, non-CM meteorites also have the band (B-7904: C2-ung; Y-86029: CI1), such samples discussed in Cloutis *et al.* (2012) can be grouped with the CM meteorites for our purposes.

Combination bands involving the OH fundamental stretching mode appear in the 2.2–2.4  $\mu\text{m}$  region, generally in pairs (Hunt, 1977). These bands are commonly used to identify phyllosilicates on Earth and Mars, with the band positions providing the Al and/or Mg composition of the minerals. The presence of opaques strongly masks these bands (Clark, 1983), and there is only “occasional evidence” for them in spectra of CM chondrites (Cloutis *et al.*, 2011a) and they are only weakly found in “a few” CI chondrites (Cloutis *et al.*, 2011b). It is not surprising, then, that telescopic spectra of asteroids have not shown conclusive evidence of these bands. However, their presence in the meteorite data suggests that sufficiently high-quality data could be capable of capturing the bands, providing an additional way of measuring the composition of low-albedo asteroids.

Two additional near-IR bands of possible interest are at 1.4 and 1.9  $\mu\text{m}$ . These are overtones of longer-wavelength bands: the 1.4- $\mu\text{m}$  absorption is the first overtone of the OH band at ~2.7–2.8  $\mu\text{m}$  (see below), while the 1.9- $\mu\text{m}$  band is due to a combination of an  $\text{H}_2\text{O}$  bending mode and the OH stretching modes (Clark, 1999). As with the phyllosilicate bands above, these absorptions are of great use in terrestrial studies, but are much more difficult to use in asteroidal studies. In addition to their susceptibility to masking by opaque components, their association with water *per se* makes them difficult to observe through Earth’s atmosphere and in laboratory measurements at ambient conditions [see, e.g., Bishop and Pieters (1995) for spectral changes between Earth ambient and Mars ambient conditions]. Because of these limitations, the 1.4- and 1.9- $\mu\text{m}$  bands are unlikely to be utilized for observations of asteroidal volatiles in the near future.

There have also been investigations at wavelengths shorter than 0.5  $\mu\text{m}$ , most notably focusing on an absorption at 0.43  $\mu\text{m}$  that Vilas *et al.* (1993) attributed to ferric iron

TABLE 1. Characteristics of the main absorption bands discussed in this chapter.

Absorption Band	Composition	Notes
~0.6–0.67 $\mu\text{m}$	Saponite	Caused by $\text{Fe}^{3+}$ - $\text{Fe}^{2+}$ charge transfer
~0.7–0.75 $\mu\text{m}$	Serpentine	
~2.7–2.8 $\mu\text{m}$	Hydroxyl (OH)	Position can vary from 2.67 to 2.94 $\mu\text{m}$ in phyllosilicates
~2.95 $\mu\text{m}$	Water in minerals	Position can vary
~3.1–3.2 $\mu\text{m}$	Water ice	Positions vary depending on crystalline vs. amorphous nature, temperature
~10–12.5 $\mu\text{m}$	Aluminum, magnesium, iron hydroxides	$\text{Mg}_2\text{OH}$ center wavelengths 15–17 $\mu\text{m}$

Specific positions depend upon many factors, including temperature and specific mineral composition. Information taken from Clark *et al.* (1990), Cloutis *et al.* (2011a,b), and Dyar *et al.* (2010) and references therein.

in aqueously altered minerals and the U–B color index (an indication of oxidized iron), which *Feierberg et al.* (1985) suggested was correlated to 3-μm band depth in a sample of 14 low-albedo asteroids. *Vilas* (1995) found no correlation between U–B color and 3-μm absorption in higher-albedo objects, suggesting little oxidized iron on their surfaces. *Rivkin* (2012) found that the u'–g' color in the Sloan Digital Sky Survey (SDSS) did not differ between the C-complex asteroids with and without a 0.7-μm band, suggesting it was not diagnostic for hydrated minerals. While the rise of charge-coupled devices (CCDs) has led to relatively few UV observations of asteroids in the past decade, the UV capabilities of spacecraft like Rosetta (*Coradini et al.*, 1999; *Stern et al.*, 2011), New Horizons (*Stern et al.*, 2008), and Dawn (*De Sanctis et al.*, 2012b) may spur more small-bodies work in this wavelength region.

## 2.2. 3-μm Region

Water and hydroxyl both have strong absorptions in the 3-μm region. Hydroxyl has a band position that varies depending on specific composition but is generally expected in the 2.7–2.8-μm region (*Clark et al.*, 1990). However, the band's position can also vary with other factors: *Farmer* (1974) cites positions from 2.67 to 2.94 μm in layer silicates, and *Ryskin* (1974) finds a band position at wavelengths as long as 3.45 μm in some materials. The 3-μm region also hosts other volatile species: Methane and other organic materials have absorptions in the 3.3–3.4-μm region, and while ammonia is not expected on asteroidal surfaces, the ammonium ( $\text{NH}_4^+$ ) ion has a band center near 3.1 μm and was interpreted as present in Ceres' spectrum (*King et al.*, 1992). Several studies have established that the carbonaceous chondrite meteorites in our collections share particular band shapes (Fig. 1), with a strong absorption edge near 2.7 μm due to hydroxyl followed by a relatively linear return to continuum behavior as wavelengths increase. Earlier studies (*Hiroi et al.*, 1996; *Jones*, 1989) unavoidably retained some telluric water in their laboratory spectra, but similar spectral behavior is seen in samples in which telluric water has been removed (*Beck et al.*, 2010; *Takir et al.*, 2013) (see also section 3 below). However, in those cases where terrestrial adsorbed water is still present, the absorption band is deeper and wider. Studies have shown that the band minimum in the 2.7–2.8-μm region in carbonaceous chondrites is indicative of phyllosilicate composition and degree of aqueous alteration (*Sato et al.*, 1997; *Osawa et al.*, 2005; *Beck et al.*, 2010; *Takir et al.*, 2013).

The benefits derived from observing absorptions due to water and OH *per se* rather than indirectly via associated absorptions are partially offset due to the difficulties associated with observing at these wavelengths. Transmission through Earth's atmosphere is closely related to the spectrum of water vapor, and the wavelengths with the strongest absorptions in hydrated and hydroxylated minerals typically have low atmospheric transmission. Indeed, most researchers will simply omit data obtained in the 2.5–2.8-μm spectral region as compromised beyond recovery. Furthermore, detailed below,

laboratory measurements of materials are not immune to interference from terrestrial water. Early researchers found that atmospheric water quickly affected samples measured in ambient conditions, with atmospheric water readsorbing on samples between the time they were removed from a dry nitrogen atmosphere and the time they were measured in the spectrometer, and some adsorbed water remained even under a strong vacuum at room temperatures (*Clark et al.*, 1993).

Comparing meteorite and asteroid reflectance spectra in the 3-μm region can therefore be challenging because meteorite spectra have usually been acquired under ambient terrestrial conditions where atmospheric water is dominant (see above), but advances in laboratory spectroscopy allow samples to be heated and/or put into vacuum to remove terrestrial water and spectra to be collected without exposing the sample to ambient conditions.

In addition to the measures to improve laboratory data, techniques for asteroid observations in this wavelength region have also been developed. The absorption bands seen in minerals in the 3-μm spectral region are broader than those seen in the atmosphere, and with care and effort the difficulties can be limited or minimized. The vast majority of observations in this wavelength region are obtained at Mauna Kea, with precipitable water vapor values commonly less than 10% of the mean U.S value of 20 mm (*Shands*, 1949), and reduction techniques have been developed to fit and remove atmospheric lines from object and standard spectra, minimizing the effects of airmass mismatch and increasing the number of calibration stars that can be fruitfully used for a given object (*Volquardsen et al.*, 2007).

Water *per se* has a different band shape and band position than hydroxyl. Water ice has three separate bands due to molecular vibrations in the 3-μm region, at ~3.2, ~3.1, and ~3.0 μm, with shifts in center depending on whether the ice is crystalline or amorphous, and as a function of temperature (*Mastrappa et al.*, 2009). The strength and proximity of these bands results in a broad “3-μm band” due to their overlap. The strength of the water band is such that thicknesses of more than ~100 nm result in band saturation. This is inevitably the case on icy satellites, but ices of this thickness or less have been reported on asteroids (*Rivkin and Emery*, 2010; *Campins et al.*, 2010).

In both the 3-μm region and the mid-IR (section 2.3), contributions by thermal emission from the asteroid to the measured spectrum can be important — indeed, by 4–5 μm thermal emission dominates over reflected light throughout the main asteroid belt. In order to make useful comparisons to laboratory data, this thermal flux must be modeled and removed. The techniques for doing so typically use the Standard Thermal Model (STM) or Near Earth Asteroid Thermal Model (NEATM). While beyond the scope of this chapter, details of these models can be found in *Lebofsky and Spencer* (1989) and *Harris and Lagerros* (2002), and in the chapter by Delbo et al. in this volume.

Thermal flux can also, in some circumstances, “fill in” an absorption band. Because these circumstances can arise in the 3-μm spectral region, of particular interest for hydrated

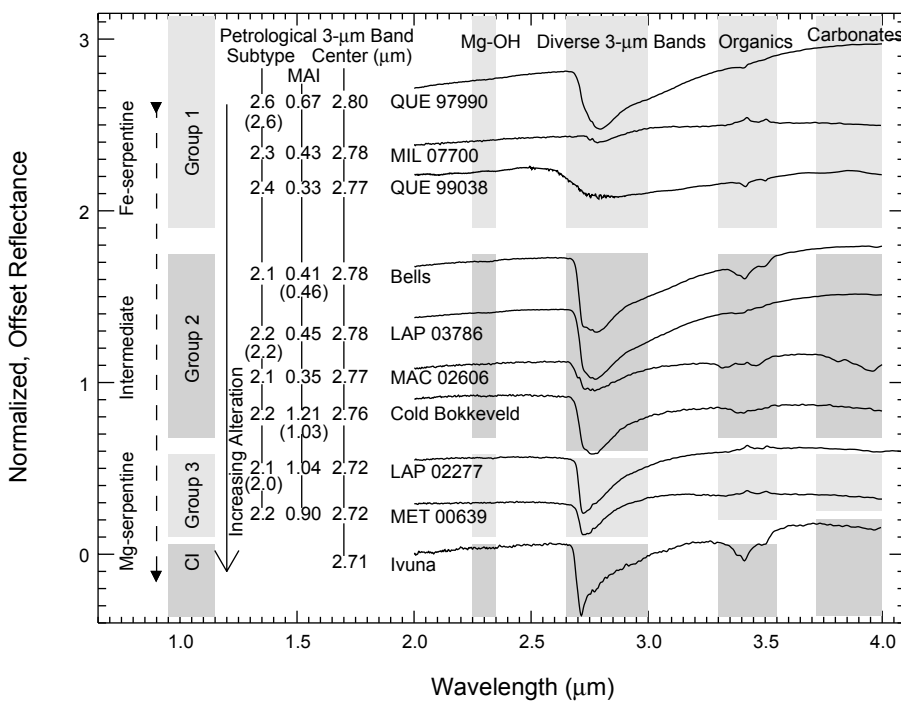


**Fig. 1.** Infrared reflectance spectra of CM and CI carbonaceous chondrites measured under dry and vacuum conditions. The MAI and the petrologic subtype were determined applying the alteration scales of Browning *et al.* (1996) and Rubin *et al.* (2007), respectively. Our spectral investigation revealed distinct groups among CM chondrites: group 1 (QUE 97990, QUE 99038, and MIL 07700), group 2 (Bells, LAP 03786, MAC 02606, and Cold Bokkeveld), and group 3 (LAP 02277 and MET 00639). Ivuna is the only CI chondrite analyzed. The 3- $\mu\text{m}$  band center decreases with increasing alteration. Adopted from Takir *et al.* (2013).

asteroid studies, here we discuss those circumstances and the consequences for astronomical observations following the logic presented by Rivkin *et al.* (2013a) and Clark (1979). In an absorption band, the emissivity increases relative to that outside the band because the reflectance decreases in the band. The increased emissivity leads to an increase in thermal flux inside the band, potentially enough to “fill in” the absorption at sufficiently high temperatures. It can easily be shown that halving the band depth (or doubling it) would similarly halve (or double) the change in emissivity, leading to the same level of fill-in at a given temperature regardless of band depth. Roughly speaking, to erase an absorption band, the thermal flux times the continuum reflectance at the wavelength of interest needs to be about the reflected flux. This condition does not occur in the 3- $\mu\text{m}$  region for main-belt asteroids, but can be reached by 3.5  $\mu\text{m}$  or shortward in near-Earth objects (NEOs) (Rivkin *et al.*, 2013b), and partial filling can occur at shorter wavelengths.

This treatment of thermal fill-in only formally holds in situations where Kirchhoff’s Law is valid. The bidirectional nature of the reflectance data collected for asteroids vs. the hemispherical-directional nature of the emission data collected means that Kirchhoff’s Law does not fully hold, and Hapke modeling of organic and carbon dioxide bands sug-

gests fill-in may occur for thermal fluxes ~30–50% of what the rule of thumb above would suggest. It is likely that the Origins Spectral Interpretation Resource Identification and Security-Regolith Explorer (OSIRIS-REx) mission will see band depths appear to change with time of day as surfaces on Bennu heat and cool, and it is possible that some observations of organic materials may be difficult or impossible at some times of day due to this effect. Such observations, however, will be useful for more rigorously understanding the conditions under which thermal fill-in is important.

### 2.3. Mid-Infrared Region

The mid-IR (5–50  $\mu\text{m}$ ) spectral region has not been widely used to measure asteroid mineralogy, including hydration state. The main reasons for this neglect are (1) spectral contrast is generally quite low and (2) the high flux and rapid variability of thermal emission from Earth’s atmosphere has made it difficult to obtain spectra of sufficient sensitivity. Nevertheless, several mid-IR spectral features offer the opportunity for evaluating hydration state, and space platforms and large groundbased telescopes have produced very-high-quality mid-IR data (see the chapter by Reddy *et al.* in this volume).

The primary feature for direct detection of hydration in the mid-IR is the H-O-H (or X-O-H) bending vibration near 6.25  $\mu\text{m}$ . For typical planetary materials, the strongest features in this wavelength range are the Si-O stretch and bend vibrational modes of silicates near 8–12  $\mu\text{m}$  and 15–25  $\mu\text{m}$ , respectively. Since bond strengths (and therefore vibrations) are sensitive to molecular structure, silicates express a rich diversity of mid-IR spectra that are diagnostic not only of silicate class, but also of compositions. Phyllosilicates, particularly those typically found in carbonaceous meteorites, tend to have a single-peaked absorption in the Si-O stretch region near 10  $\mu\text{m}$ . *Beck et al.* (2014), using transmission spectra, find a consistent anticorrelation between the location of this absorption and the presence of an olivine peak near 11.2  $\mu\text{m}$  for CI and CM meteorites, which they interpret as an indication of degree of hydration. The 6.25- $\mu\text{m}$  feature is not generally present in their spectra, but the transmission pathlengths may have been insufficient. It is not clear whether reflectance or emittance spectra would show such a trend, but mid-IR reflectance spectra of several CI and CM meteorites published by *Salisbury et al.* (1991) show indications of similar behavior. The reflectance spectra also contain a ~6.15- $\mu\text{m}$  feature, particularly in the more heavily hydrated meteorites, but the spectra were measured in air, so contamination by adsorbed  $\text{H}_2\text{O}$  is likely. Other phases associated with aqueous alteration (e.g., carbonates) also have spectral features in the mid-IR (e.g., *Clark et al.*, 2007).

Only a few applications of telescopic mid-IR data to identify hydration on asteroids have been published. *Milliken and Rivkin* (2009) show that a 6–14- $\mu\text{m}$  spectrum of Ceres obtained from the Kuiper Airborne Observatory by *Cohen et al.* (1998) is well-matched by linear-mixing models that were developed for the 2–4- $\mu\text{m}$  spectral region and that include brucite ( $\text{Mg}(\text{OH})_2$ ) and cronstedtite (Fe-rich serpentine). *Vernazza et al.* (2013) note that (368) Haidea is the only asteroid in the Spitzer Space Telescope (SST) spectral database (of 87 asteroids searched) that shows a single emissivity peak in the Si-O stretch region. The spectrum of Haidea is well-matched in the visible–near-IR and the mid-IR by the Tagish Lake meteorite, which is a heavily hydrated meteorite (*Zolensky et al.*, 2002), from which *Vernazza et al.* (2013) conclude that Haidea too is hydrated. SST spectra of other D-type asteroids (e.g., *Emery et al.*, 2006) show clear olivine peaks, quite distinct from Haidea and Tagish Lake, supporting the view that D-type asteroids are composed of anhydrous, primitive material and suggesting that both Tagish Lake and Haidea are somewhat anomalous. Using laboratory spectra of CM meteorites and SST spectra of three C-type asteroids, *McAdam et al.* (2013) suggest that some subfeatures at ~12–14  $\mu\text{m}$  in phyllosilicates may also be diagnostic of hydration. These are within the broader “transparency feature” found at those wavelengths, where the emissivity is at its lowest (see the Reddy et al. chapter in this volume for a fuller discussion of mid-IR spectral features).

With no active mid-IR space telescopes, with many of the mid-IR spectrometers on large groundbased telescopes not offered in recent calls, and with the future of the Stratospher-

ic Observatory for Infrared Astronomy (SOFIA) uncertain, the immediate future for exploring hydration in the mid-IR might seem challenging. However, CanariCam, a mid-IR camera/spectrometer on the recently built 10-m Gran Telescopio Canarias (GTC) is demonstrating that high-sensitivity mid-IR spectra of asteroids can be obtained from the ground (*Licandro et al.*, 2014). The James Webb Space Telescope (JWST), with spectral capability from 1 to 28  $\mu\text{m}$  (<http://jwst.nasa.gov/about.html>), should be an excellent facility for studying hydration on asteroids. And lastly, near- and mid-IR instrument payloads are becoming more common on proposed and in-development spacecraft missions, including the OSIRIS-REx Visible and IR Spectrometer (OVIRS) and OSIRIS-REx Thermal Emission Spectrometer (OTES) instruments, which will map the presumably hydrous (e.g., *Clark et al.*, 2011) asteroid Bennu from 0.4 to 50  $\mu\text{m}$  down to spatial scales of ~24 cm. These and other future opportunities are further discussed in section 6.

### 3. RESULTS AND INTERPRETATIONS FOR ASTEROIDS AND METEORITES

The spectral analysis of water and OH in meteorites has taken several large strides in the past decade. A series of papers by Cloutis et al. focused on the visible and near-IR spectra of carbonaceous chondrites. Increased laboratory capabilities, including the ability to drive off terrestrial water and take spectra without breaking vacuum, have led to a much better sense of the spectral properties of hydroxyl in carbonaceous chondrites (section 2.2 and below), and mapped out OH band centers with mineralogy. Work by *Milliken et al.* (2007) in the context of martian studies provides a potential way to remotely measure water in meteorites through calculation of spectral parameters such as band depth and integrated band depth, integrated band area, mean and normalized optical path length, and effective single-particle absorption thickness, although to this point these have not been applied to estimating hydroxyl amounts, nor have they been used on carbonaceous chondrites in the published literature.

CM (Mighei-like) and CI (Ivuna-like) carbonaceous chondrite meteorites are widely thought to be the possible analogs for dark and primitive asteroids [e.g., C-, D-, G-, K-, F-, and B-types in the Tholen taxonomy, C-complex in the Bus taxonomy (e.g., *Burbine et al.*, 2002)]. These meteorites experienced varying degrees of fluid-assisted alteration on their parent bodies (*McSween*, 1979). Spectroscopic, mineralogic, oxygen and hydrogen isotopic, and textural analyses of CM and CI carbonaceous chondrites have revealed that these meteorites contain aqueously altered materials (*Takir et al.*, 2013; *Hiroi et al.*, 1996; *Beck et al.*, 2010; *Zolensky et al.*, 1993; *Clayton and Mayeda*, 1999; *Lee*, 1993; and others). Laboratory analyses of carbonaceous chondrites combined with astronomical observations of hydrated asteroids can lead to important clues about abundance and distribution of  $\text{H}_2\text{O}$  in the early solar system.

*Takir et al.* (2013) measured meteorite spectra under dry (elevated temperatures) and vacuum ( $10^{-8}$ – $10^{-7}$  torr)

conditions to minimize the effect of adsorbed water and mimic the asteroid-like environment. *Beck et al.* (2010) previously measured carbonaceous chondrite transmission spectra; however, absorption features in transmission do not always have the same shape or position as they do when measured in reflectance, due to the scattering of reflected illumination by granular particles. *Takir et al.* (2013) also investigated the degree of hydration in CM and CI chondrites, using the previously defined alteration scales of *Browning et al.* (1996) (Mineralogical Alteration Index) and *Rubin et al.* (2007) (Petrological Subtype). *Takir et al.* (2013) identified three spectral groups of CM chondrites (plus the CI chondrite Ivuna), using the 3- $\mu\text{m}$  band center and shape of IR reflectance spectra (Fig. 1). The diversity in the 3- $\mu\text{m}$  band demonstrates that distinct parent body aqueous alteration environments experienced by carbonaceous chondrites can be distinguished using reflectance spectroscopy. The first group (Group 1) shows the lowest degree of aqueous alteration and is characterized by 3- $\mu\text{m}$  band centers at longer wavelengths than other groups. Group 1 is consistent with the occurrence of Fe-rich serpentine (cronstetite). Group 3, which exhibits the highest degree of aqueous alteration, is characterized by 3- $\mu\text{m}$  band centers at shorter wavelengths and is consistent with Mg-rich serpentine (antigorite). The third group, Group 2, is intermediate between Groups 1 and 3 and more likely includes both types of serpentine minerals.

Along with the advances in meteorite spectroscopy, observations of asteroids have flowered in the past decade. The majority of telescopic observations in the 3- $\mu\text{m}$  region have been obtained at the Infrared Telescope Facility (IRTF) using the SpeX instrument, but observations at other wavelengths have been made using other telescopes across the world, with orbiting telescopes, and *in situ* orbiting Vesta and flying past Lutetia. Asteroid researchers have also made use of datasets acquired for astrophysical projects such as the SDSS. The use

of all these observations has led to a fuller characterization of several individual objects and an understanding of the hydrated mineralogy present in the asteroid belt and beyond.

### 3.1. Correlation of 0.7- $\mu\text{m}$ Band and 3- $\mu\text{m}$ Band

A growing database of asteroidal spectra available at both 0.7 and 3  $\mu\text{m}$  has been accumulating in order to understand the relationship between these bands. *Vilas* (1994) showed that the 0.7- $\mu\text{m}$  band is present when the 3- $\mu\text{m}$  band is seen in ~85% of a sample of 31 CCD reflectance spectra and IR multicolor photometry observations of low-albedo asteroids, and applied this correlation to the larger Eight Color Asteroid Survey (ECAS) photometry database to identify potentially aqueously altered asteroids. While this is good evidence that the bands are related, it is also important to understand why the bands sometimes are not correlated. *Howell et al.* (2011) show that, upon closer examination using simultaneous observations, the 3- $\mu\text{m}$  band is often variable with rotation of an asteroid, and that whenever the 0.7- $\mu\text{m}$  band is present, the 3- $\mu\text{m}$  band is also seen. However, the 3- $\mu\text{m}$  band can be present without the 0.7- $\mu\text{m}$  band, and indeed is seen in about half the objects observed at 3- $\mu\text{m}$  for which the 0.7  $\mu\text{m}$  band is absent. This makes the 0.7- $\mu\text{m}$  absorption a reliable proxy for hydration, but the 0.7- $\mu\text{m}$  absorption is limited to only establishing a lower bound on the total number of hydrated objects. Table 2 shows the correlation of the 156 objects in the literature that have been observed at both wavelengths.

### 3.2. 3- $\mu\text{m}$ Band Shapes

Using high-quality near-IR (0.7–4.0  $\mu\text{m}$ ) spectra of 35 outer main-belt asteroids ( $2.5 < a < 4.0$  AU), *Takir and Emery* (2012) identified four 3- $\mu\text{m}$  spectral and orbital groups, each of which is presumably linked to distinct surface mineralogy (Figs. 2 and 3). Table 3 shows these groups, examples

TABLE 2. Correlation between the 0.7- and 3- $\mu\text{m}$  bands in the total sample of available main-belt asteroid spectra and the sample of C-complex asteroids.

		All Asteroids		C-Complex Asteroids	
		3- $\mu\text{m}$	3- $\mu\text{m}$	3- $\mu\text{m}$	3- $\mu\text{m}$
		Band	Band	Band	Band
		Absent	Present	Absent	Present
0.7- $\mu\text{m}$ band present	Number of objects	0	56	0	44
0.7- $\mu\text{m}$ band absent	Percent of objects	0%	35%	0%	63%
	Number of objects	57	47	9	17
	Percent of objects	37%	29%	13%	24%

A total of 160 main-belt asteroids have been observed at both 0.7 and 3  $\mu\text{m}$  to investigate the hydration state. The bands are correlated for 113 objects, or 70% of the sample. The remaining objects have a 3- $\mu\text{m}$  band, but no 0.7- $\mu\text{m}$  band. No objects are found to have a 0.7- $\mu\text{m}$  band, and lacking a 3- $\mu\text{m}$  band, making the presence of the 0.7- $\mu\text{m}$  band a good proxy for hydration, but only a lower limit on the number of hydrated objects. The correlation for 70 C-complex objects is shown in the right two columns. In cases where insufficient data exists to determine the Bus-DeMeo taxonomic class, we include Tholen C, B, F, and G taxonomic classes as well as CP and PC, but not those classified as P. Data sources for this table are *Zellner et al.* (1985), *Lazzaro et al.* (2004), *Sawyer* (1991), *Vilas* (1994), *Lebofsky* (1980), *Lebofsky et al.* (1990), *Feierberg et al.* (1985), *Rivkin et al.* (2000, 2002b, 2012), *Fornasier et al.* (2011, 2014), and *Howell et al.* (2011).

of each, alternate names, and compositional interpretation. The sharp group (or Pallas types) exhibits a characteristically sharp 3- $\mu\text{m}$  feature, reflectance decreasing with decreasing wavelength into the 2.5–2.85- $\mu\text{m}$  spectral region, attributed to OH-stretching in hydrated minerals (e.g., phyllosilicates) (Rivkin et al., 2002b). The majority of asteroids in this group are concentrated in the  $2.5 < a < 3.3$ -AU region. The second group, the rounded group (or Themis types), exhibits a rounded 3- $\mu\text{m}$  band (reflectance increases with decreasing wavelength shortward of  $\sim 3.07$   $\mu\text{m}$ ), attributed to H<sub>2</sub>O ice (e.g., Rivkin and Emery, 2010). Asteroids in this group are located in  $3.4 < a < 4.0$ -AU region. The third group, the (1) Ceres-like group, is located in the 2.5–3.3-AU region and characterized by a narrow 3- $\mu\text{m}$  band center at  $\sim 3.05$   $\mu\text{m}$  superposed on a much wider absorption from 2.8 to 3.7  $\mu\text{m}$  that is consistent with brucite (Milliken and Rivkin, 2009). The fourth group, the 52 Europa-like group [grouped into

the Themis types by Rivkin et al. (2012)] exhibits a 3- $\mu\text{m}$  band centered around 3.15  $\mu\text{m}$  with longer wavelength band minimum and steeper rise on the long-wavelength edge of the absorption.

On the basis of the 3- $\mu\text{m}$  band shape and center, Takir et al. (2015) found that the sharp asteroids possibly have similar phyllosilicate mineralogy as CM Group 2 and Ivuna, suggesting that these asteroids and meteorites experienced similar aqueous alteration processes. These results suggest that CM and CI chondrites are possibly the meteorite analogs for the sharp group (Fig. 4). The authors found Ivuna to have a spectrum consistent with lizardite and chrysotile. No meteorite match was found either for the rounded group, Ceres-like group, or Europa-like group.

Differences within each of these groups are still to be fully understood. For instance, the relationship between the Europa, Ceres, and rounded groups is not entirely clear — the

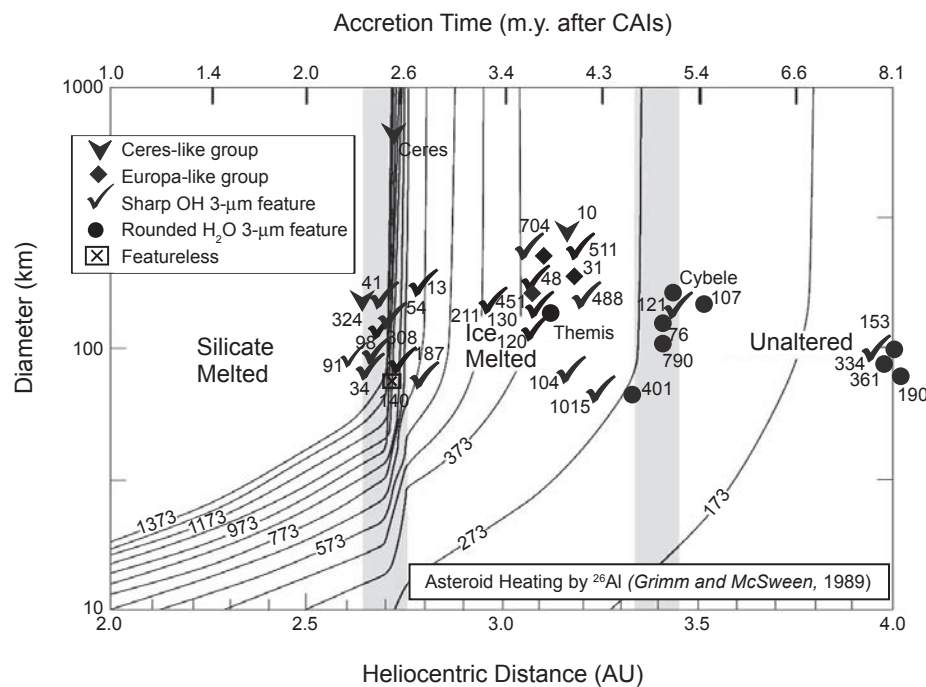


**Fig. 2.** Asteroids classified according to the Takir 3- $\mu\text{m}$  classes are plotted in the context of the thermal model of Grimm and McSween (1993). Adopted from Takir and Emery (2012).

TABLE 3. Potential major groupings for objects in the 3- $\mu\text{m}$  spectral region.

Example Body	Takir Class	Rivkin Class	Interpretation
511 Davida	Sharp	Pallas	CM-like phyllosilicates
24 Themis	Rounded	Themis	Water-ice frost, organics
52 Europa	Europa	Themis	Water-ice frost, organics
1 Ceres	Ceres	Ceres	Brucite, carbonates
21 Lutetia	—	Lutetia	Goethite?

While a formal taxonomy has not yet been developed for objects in the 3- $\mu\text{m}$  spectral region, presented here are the potential classes as defined by Takir et al. (2012) and Rivkin et al. (2012), with type examples and possible compositions for each group (also from these cited works).

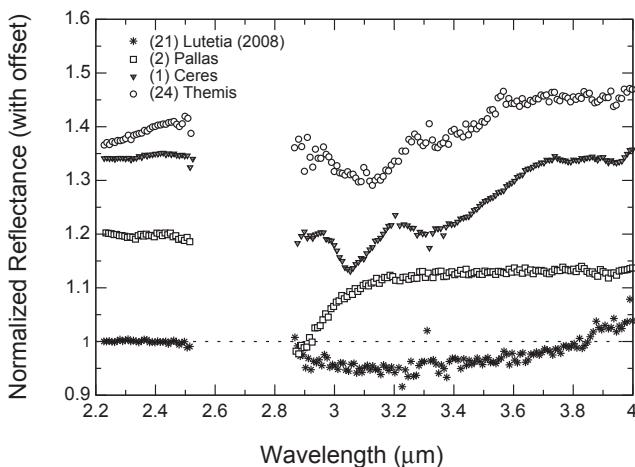


**Fig. 3.** The diversity of asteroids in the 3- $\mu\text{m}$  spectral region can be seen by comparing several of the largest objects. Each of these bodies shows evidence of different mineralogies, although the specific minerals in each case may still be under debate. Figure from Rivkin *et al.* (2011).

Ceres types are interpreted very differently from the rounded group, but there may be objects that appear spectrally intermediate between the groups. It is apparent that there is variation within the sharp group, with some structure visible within the main absorption on some objects. It is also not certain whether the same object can vary between different band shapes on its surface; for example, 704 Interamnia is classified differently in Takir and Emery (2012) and Rivkin *et al.* (2012). Further work is necessary to better establish the compositions found in these groups: Beck *et al.* (2010) proposed goethite as an alternate to ice frost in the Themis-type asteroids based in part on the thermodynamic difficulty of keeping frost on these asteroid surfaces. Nonetheless, while other closely related minerals have been found in both meteorite and asteroid spectra, extraterrestrial goethite has never been identified within the meteorite inventory. Jewitt (2012), considering ice vs. goethite, preferred ice as a simpler interpretation for this reason. Also, goethite is a poor match for the spectrum of (24) Themis at wavelengths shortward of 3  $\mu\text{m}$  (Pinilla-Alonso, 2011). The interpretation of brucite and carbonates on Ceres will be tested and honed by Dawn's visit to that object, with consequences for the interpretation of other Ceres types.

Additional groups beyond those identified in Takir *et al.* and mentioned above appear to be present. Rivkin *et al.* (2011) found the band shape on Lutetia to be unlike Pallas, Ceres, or Themis (Fig. 4) and proposed a fit to goethite, inspired by Beck *et al.* (2011). Yang *et al.* (2009) observed a flat-floored 3- $\mu\text{m}$  band on Comet Holmes due to ice grains, which may theoretically be present on portions of asteroid surfaces, although such a spectrum has not yet been found on asteroids. Finally, some objects appear to have no absorption band in the 3- $\mu\text{m}$  region. In some cases, like the Trojan asteroids, this may be because only relatively poor-quality data is available and significant absorptions may be hidden

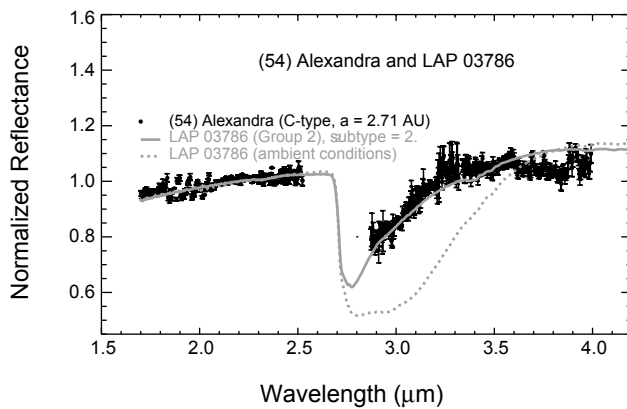


**Fig. 4.** Meteorite LAP 03786 and (54) Alexandra, showing an example of the comparison between CM and CI chondrites and asteroids with the sharp/Pallas-type 3- $\mu\text{m}$  feature. While asteroid spectra have been poor matches for meteorite spectra taken in ambient conditions (dotted line), meteorite spectra with terrestrial water removed (solid line) are much better matches. Figure from Takir *et al.* (2015).

in the uncertainties. However, resolved observations of Comets 9P/Tempel 1 and 103P/Hartley 2 by Groussin *et al.* (2013) showed spectra were very well fit by a sum of reflected and thermally emitted flux, showing no 3- $\mu\text{m}$  absorption within ~2% (although H<sub>2</sub>O emission was seen in some cases).

Preliminary results from the LXD-mode Main belt and NEO Observing Program (LMNOP) (Rivkin *et al.*, 2012, 2014b) are consistent with Takir *et al.*, with some additional insights available from a larger sample size. The different 3- $\mu\text{m}$  types can be found in most of the C-complex component classes, other than the Ch class as discussed below. When the Ch class is excluded, Pallas/sharp types make up 44% of the 48 C-complex asteroids in the LMNOP for which band shapes can be assigned, while Themis types make up 42%. This is similar to the (smaller) X-complex sample of 13, including 7 Pallas types and 5 Themis types. The four Ceres types in the LMNOP sample are all found in the C complex.

The sample of low-albedo (but non-Ch) asteroids shows a correlation between 3- $\mu\text{m}$  band shape and size as well as with solar distance: Pallas types make up 27% of the H < 7 sample (corresponding roughly to D > 200 km), but 69% of the H < 8.5 sample (D < 100 km). The Themis types start at ~36% of the largest-sized sample, peaking at 55% of the 150–200-km sample before declining to 40% of the H < 8.5 group. The Ceres types are found only in the H < 7 group. Turning to solar distance (and again excluding the Ch asteroids) shows the inner belt (a < 2.82 AU) dominated by the Pallas types (63%), while in the outer belt (a > 2.82 AU) the Themis types are more numerous, outnumbering the Pallas types 48% to 33%.

The observation that Ch asteroids are overwhelmingly (perhaps unanimously) Pallas-type objects means that the former can be used as a proxy for the latter, even if only providing a lower limit on their numbers. The work of

Rivkin (2012) using the SDSS to study the 0.7- $\mu\text{m}$  band is consistent with the LMNOP findings and is discussed below.

### 3.3. Connections with Taxonomy

**3.3.1. C-complex asteroids.** The majority of work on hydrated asteroids has focused on the C-complex asteroids, a group that comprises the B, C, Cb, Cg, Ch, and Cgh classes in the Bus taxonomy (Bus and Binzel, 2002a). These asteroids, as described elsewhere in this volume, have low albedos and are generally associated with the carbonaceous chondrite meteorites. Most of the largest bodies in the asteroid belt are C-complex asteroids, including Ceres, Pallas, Hygiea, Interamnia, and Europa.

In the Bus asteroid taxonomy, the Cgh and Ch asteroid classes are defined as those with 0.7- $\mu\text{m}$  bands, with behavior shortward of 0.55  $\mu\text{m}$  discriminating between the Cgh and Ch classes. The extension of the Bus taxonomy to 2.5  $\mu\text{m}$  by DeMeo et al. (2009) maintained those two classes, with similar definitions. The Cgh class is relatively rare, with Ch asteroids in the Small Main-Belt Asteroid Spectroscopic Survey (SMASS) dataset outnumbering them 9:1. While the shared characteristic of these classes is the 0.7- $\mu\text{m}$  band, the exact band minimum varies from roughly 0.687–0.740  $\mu\text{m}$  in a sample of Ch asteroids studied by Rivkin et al. (2013b). Vilas (1994) noted the difference in 0.7- $\mu\text{m}$  band center between the C-class asteroids and the CM2 carbonaceous chondrites, where it is nearer to 0.72–0.73  $\mu\text{m}$ , and suggested that this difference could be due to a shift in temperature between asteroid surfaces and laboratory reflectance studies, but found no laboratory studies to confirm this. Vilas reported three main-belt asteroids, a Cybele, and a Hilda asteroid with absorption bands in the 0.6–0.65- $\mu\text{m}$  and 0.8–0.9- $\mu\text{m}$  ranges, which could be attributed to saponites (Cloutis et al., 2011a,b). Only one of these objects, (165) Loreley, was observed by the SMASS survey, where it was classified as a Cb and these features were not reported (Bus and Binzel, 2002a,b). None of the objects were observed by the Small Solar System Objects Spectroscopic Survey (S<sup>3</sup>OS<sup>2</sup>) survey (Lazzaro et al. 2004), and so confirmation awaits future studies.

The presence of a band near 0.7  $\mu\text{m}$  provides a partial link between the Ch asteroids and CM meteorites: They are the only asteroids and only meteorites that have identified absorption bands at those wavelengths. Carvano et al. (2003) performed least-squares comparisons of the asteroidal spectra in the S<sup>3</sup>OS<sup>2</sup> to laboratory spectra of meteorites and concluded that most asteroids with 0.7- $\mu\text{m}$  bands were “very likely” to be related to the CM2 meteorites. The connection between the Ch asteroids and the Pallas-type 3- $\mu\text{m}$  bands is discussed in section 3.2.

Fornasier et al. (2014) analyzed the visible–near-IR spectra of 600 low-albedo asteroids (C, G, B, F, P in the Tholen taxonomy), including 80 that were newly obtained. They found roughly 50% of the 454 C-class asteroids in their sample have the 0.7- $\mu\text{m}$  absorption, compared to only 10% of the 92 B-class asteroids they studied. The F, G, and

P asteroids have far fewer objects in their samples (13, 18, and 23, respectively) but all have strong tendencies to either lack the band (~8% of F asteroids and 4% of P asteroids) or have it (100% of G asteroids). They did not separate the P asteroids from the C-complex asteroids for most of their analysis, but the P asteroids are a small enough fraction of the overall sample that they should not skew the results. Fornasier et al. found that the fraction of hydrated asteroids decreased with decreasing size, although the decrease was not monotonic. They found no correlation between fraction of hydrated asteroids and geometric albedo. However, they concluded that the 0.7- $\mu\text{m}$  band centers for the meteorites are generally at longer wavelengths than for the asteroids, although no conclusion was reached as to why that is the case. They suggested that spectral differences may be attributed to different mineral abundances between CM chondrites and the asteroids, to possible effects due to grain size, or because the meteorite collection may not be fully representative of the aqueously altered asteroid population.

Rivkin (2012) used the SDSS to measure the fraction of objects with a 0.7- $\mu\text{m}$  band, first filtering the large set of objects in the *Third Release of the Moving Object Catalog* to include only those objects with C-like color indices, with a resulting sample size of 3724 observations of 3124 objects. He used two independent techniques, performing a best fit to the average of each C-complex component class convolved to SDSS resolution, as well as fitting the distribution of 0.7- $\mu\text{m}$  band depths to two Gaussians (one with zero band depth representing the C asteroids, one with a nonzero band depth representing the Ch asteroids). He estimated 30% of all C-complex asteroids have a band at 0.7  $\mu\text{m}$ , with some evidence of a higher fraction in the middle asteroid belt (2.50–2.82 AU) compared to the inner or outer belt. When including the SMASS and S<sup>3</sup>OS<sup>2</sup> datasets, it appears the Ch fraction of the C complex reaches an overall minimum near H  $\sim$  12–14. Fornasier et al. (2014) noted some of the differing conclusions between their work and that of Rivkin (2012), suggesting that some of the differences may be due to the non-optimal filter placement in the SDSS observations compared to the placement and width of the 0.7- $\mu\text{m}$  band.

All the 3- $\mu\text{m}$  band shapes discussed above are found in the C-complex population. Rivkin et al. (2013b) reports that all their samples of more than 30 Ch class asteroids have 3- $\mu\text{m}$  bands consistent with being all “sharp” (or “Pallas”) types, with the few possible exceptions attributable to low-quality data or misclassified asteroids. However, Pallas types are also present among other C-complex classes, as well as non-C classes.

The Japanese AKARI satellite conducted the first space-borne asteroid spectroscopic survey in the 3- $\mu\text{m}$  region, observing 33 low-albedo asteroids (Okamura et al., 2014a). Okamura et al. (2014b) performed principal component analysis (PCA) on these data as well as meteorite and mineral data. While some good matches were found, in general close matches between the AKARI observations and meteorite spectra were not found. However, the depth of the 2.7- $\mu\text{m}$  absorption was found to correlate with the

depth of the 0.7- $\mu\text{m}$  absorption, interpreted as meaning that the 2.7- $\mu\text{m}$  absorption is controlled by serpentine abundance.

Work at longer wavelengths has been more limited. However, *McAdam et al.* (2013) analyzed SST data for the 10–12- $\mu\text{m}$  feature discussed above, finding it in seven C-complex asteroids but absent from three D-class Trojan asteroids. *Licandro et al.* (2012) reported SST spectra covering the 5–14- $\mu\text{m}$  region for eight Themis family asteroids [including members of several classes in the C and X complexes (*Bus and Binzel*, 2002b; *Lazzaro et al.*, 2004)], finding broad emission features of  $\sim$ 2–4%. However, these were not interpreted in terms of phyllosilicate content. Spectroscopic observations of the OSIRIS-REx target asteroid (101955) Bennu from 5 to 38  $\mu\text{m}$  by *Emery et al.* (2014) showed no spectral features outside of observational uncertainties.

**3.3.2. B-class asteroids.** *Ali-Lagoa et al.* (2013) studied the physical properties of B-class asteroids, derived by fitting a thermal model to Wide-field Infrared Survey Explorer (WISE) observations, i.e., effective diameter, beaming parameter, and the albedo ratio  $p_{\text{IR}}/p_{\text{V}}$ , where  $p_{\text{IR}}$  is the albedo at 3.4  $\mu\text{m}$  as defined in *Mainzer et al.* (2011). *Ali-Lagoa et al.* (2013) include in their B-class sample all objects that have a published flat to slightly blue spectral slope in the visible range, i.e., any object that has ever been classified as B-class, including Tholen's F-types, and ambiguous designations, following *Clark et al.* (2010) and *de León et al.* (2012).

By combining the IR and visible albedos with 2.5- $\mu\text{m}$  reflectances from the literature (*Clark et al.*, 2010; *de León et al.*, 2012), *Ali-Lagoa et al.* (2013) obtained the ratio of reflectances at 3.4 and 2.5  $\mu\text{m}$ , from which they find statistically significant indications that the presence of a 3- $\mu\text{m}$  absorption band related to water may be commonplace among the B-types. Using Tholen's B-type ECAS classification, *Villas* (1994) concluded that 30% of those asteroids showed a 0.7- $\mu\text{m}$  absorption, which — using *Howell et al.*'s (2011) correlation — sets a significant lower limit on the presence of water in the B-types.

**3.3.3. P-class asteroids.** The X-complex asteroids span a range of albedos, as has been known since the 1980s when the Tholen taxonomy recognized that the E, M, and P classes were indistinguishable without albedo information and created the X class to hold such objects. The Bus taxonomy (and later Bus-DeMeo taxonomy) does not use albedo information, and has divided the X complex into several classes (Xe, Xk, Xc, X) based on spectral features alone, with imperfect correlations to the Tholen classes. While the Bus classes in the C complex are well suited to a discussion of hydrated minerals, the Tholen classes provide more convenient discussion of hydrated minerals in the X complex. Therefore, at the risk of some confusion, and understanding that several asteroids are classified in either the X or C complex depending on the specific spectrum analyzed, we use the E/M/P classes defined by Tholen in this section rather than the Bus classes.

The low-albedo X/P-class asteroids fit neatly into the discussion of the C-class asteroids above and, as noted, the work of *Fornasier et al.* (2014), following the work of

others, concluded that they belonged to the same alteration sequence as the C-complex asteroids. The largest P-class asteroid, (65) Cybele, has been found to have a Themis-like 3- $\mu\text{m}$  band, interpreted as due to surface ice frost (*Licandro et al.*, 2011a). The asteroid set analyzed by *Takir and Emery* (2012) included five P-class asteroids, including two in the Cybele region and two in the Hilda region. These four objects all have rounded 3- $\mu\text{m}$  bands, while the final P asteroid [(140) Siwa] did not show any absorption above the noise. The three Cybele/Hilda group C-class asteroids studied by Takir and Emery included both rounded and sharp members, providing further evidence that spectral slope and 3- $\mu\text{m}$  band shape are correlated, and perhaps connected.

**3.3.4. M-class asteroids.** Our understanding of M-class asteroids continues to evolve. While the presence of a 3- $\mu\text{m}$  band on several M asteroids (which led to their proposed reclassification as “W-class asteroids” by *Rivkin et al.*) was established late last century (*Jones et al.*, 1990; *Rivkin et al.*, 2000), no consensus on interpretations was reached. The discovery of objects with both a 3- $\mu\text{m}$  band and high radar albedo (*Shepard et al.*, 2015) has led to the consideration of impactor contamination as a cause of the 3- $\mu\text{m}$  band on these objects, as noted in section 1.4, but the band depths on some objects seem too deep to be caused by this process or are on objects with low radar albedo. While work is ongoing in general, we note that some objects have been reclassified into or out of the M-asteroid class based on additional spectra or new albedos [e.g., (785) Zwetana was classified as an M by *Zellner et al.* (1985), but as a Cb by *Bus and Binzel* (2002a)] and that the Lutetia-type 3- $\mu\text{m}$  band shape has only been seen in E- or M-class objects, suggesting that it is not simply caused by contamination by common carbonaceous material in all cases.

Several studies focused on the M-class asteroid (21) Lutetia, a Rosetta flyby target. *Rivkin et al.* (2011) compiled 3- $\mu\text{m}$  observations over several years to conclude Lutetia had a deeper 3- $\mu\text{m}$  band (3–5%) in its southern hemisphere than its northern hemisphere (<2%), and that goethite appeared to be a plausible surface constituent. The variation observed is consistent with the hemispheric-level variation seen at shorter wavelengths (*Nedelcu et al.*, 2007), where Lutetia's spectral slope varies from X-like to C-like. Two papers by *Birlan et al.* taken together also reported spectral variation on Lutetia consistent with what was seen by *Rivkin et al.* (2011), with *Birlan et al.* (2010) reporting an upper limit of 0.5% for any 3- $\mu\text{m}$  band depth from observations in 2010 compared to a band depth of several percent in 2003–2004 (*Birlan et al.*, 2006). The Rosetta flyby passed the northern hemisphere of Lutetia in July 2010, and found no absorption in the 3- $\mu\text{m}$  region, although instrumental artifacts make it difficult to judge the actual upper limit value. *Barucci et al.* (2012), considering all published data, concluded that Lutetia had a chondritic surface, possibly a mixture of enstatite and carbonaceous chondrite. The northern hemisphere of Lutetia stands as a cautionary tale about the difficulties of interpreting featureless spectra. Interestingly, the Alice instrument on Rosetta found a significantly lower UV albedo near

180 nm than 550 nm, and strong reflectance drop from 180 to 160 nm (Stern et al., 2011). The possible interpretations include water ice frost, although there are other possible interpretations, and the survival of frost on Lutetia's surface would be unexpected.

### 3.4. Near-Earth Asteroids

While the NEAs are derived from the main belt, we are aware that the populations are not exact mirrors of one another. The most important difference relevant to this chapter is the relative lack of Ch asteroids in the NEA population relative to their numbers in the main asteroid belt. As we have seen, estimates of the fraction of main-belt C-complex asteroids with 0.7-μm bands (i.e., the “Ch fraction”) range from ~30 to 45% (Rivkin, 2012; Fornasier et al., 2014). For comparison, Binzel et al. (2004) only found one Ch asteroid in their sample of 24 C-complex NEAs. Updated data from the Massachusetts Institute of Technology (MIT)-University of Hawaii (UH)-IRTF “Joint Campaign” finds 6 Ch or Cgh asteroids in a sample of 88 NEOs for which they have data covering the 0.7-μm region [(144901) 2004 WG<sub>1</sub>, (285263) 1998 QE<sub>2</sub>, (365246) 2009 NE, 2002 DH<sub>2</sub>, 2007 YB<sub>2</sub>, 2012 EG<sub>5</sub> (R. Binzel and F. DeMeo, personal communication)], a similar (if slightly larger) fraction as found in the 2004 work. This does not seem to be a size effect — the Mars-crossers in the Binzel et al. (2004) sample have a Ch fraction similar to the main-belt value (although the larger Joint Campaign dataset finds a much smaller Ch fraction), and Rivkin (2012) found a Ch fraction of 25–40% for the smallest size bin (H of 16–18) in the SDSS data, of similar size to the NEAs. Perhaps surprisingly, the small fraction of Ch-class NEAs is also inconsistent with the fraction of hydrated meteorites — while it is not obvious how best to compare numbers of meteorites in a consistent way, the fraction of carbonaceous chondrite meteorite falls of the CM group (in which the 0.7-μm band is prevalent; see section 3) is roughly 33%, again much higher than the 5% seen in the NEO population. A possible explanation for this can be found in the work of Marchi et al. (2009), who noted that the chaotic evolution of NEA orbits can lead to low-perihelion eras where surface temperatures exceed the stability temperatures of phyllosilicates. Given the factor of 4–8 difference between the Ch fraction of NEAs vs. main-belt asteroids and meteorites, Rivkin (2012) estimated ~75–88% of NEOs have experienced such eras, although this is perhaps a simplistic approach.

Observations of NEAs in the 3-μm region have been rare, with the vast majority of objects too faint to observe. However, absorptions have been found on two NEOs, 1992 UY<sub>4</sub> (Volquardsen et al., 2007) and 1996 FG<sub>3</sub> (Rivkin et al., 2013a). The band shapes for these objects are not as well-measured as those of brighter asteroids, but 1996 FG<sub>3</sub> appears to have a Pallas-type/sharp band. Volquardsen et al. (2007) interpreted the band shape of 1992 UY<sub>4</sub> as similar to that of (375) Ursula, which is a Ceres- or Themis-type, but the observational uncertainties do not rule out a Pallas-type spectrum at the 1σ level.

Absorptions in the 3-μm region have also been detected on the S-class asteroids (433) Eros and (1036) Ganymed (Rivkin et al., 2013c), with Wigton et al. (2014) also detecting a 3-μm band on (3122) Florence. At this writing, it is not yet clear whether these bands are caused by native material like the phyllosilicates found in the LL chondrite Semarkona; whether they are caused by solar wind interactions with regolith, like what is discussed in section 1.5 above; or whether they are due to some other process.

### 3.5. Main-Belt Comets (aka Active Asteroids) and Ceres

The discovery of “main-belt comets” (MBCs) (Hsieh and Jewitt, 2006; see also the chapter by Jewitt et al. in this volume), also known as “active asteroids,” suggests that ice persists near the surfaces of objects in the asteroid belt. Active asteroids are members of the NEA or main-belt asteroid populations that present comet-like tails, but have orbits that are unlikely to originate from the known comet reservoirs, e.g., the transneptunian belt and the Oort cloud, and are thought to have formed in the main belt instead. These objects eject dust, producing transient comet-like comae and tails. Several dust ejection mechanisms have been proposed: sublimation of ice, rotational fission, ejection by collisions, electrostatic repulsion, thermal fracture, dehydration stresses, and radiation pressure sweeping (e.g., Bertini, 2011; Jewitt, 2012; Jewitt et al., this volume), and at least some of the objects are best explained as experiencing processes unrelated to volatiles (e.g., Jewitt et al., 2015). Currently, 15 active asteroids are known, two of which are NEAs [(3200) Phaethon and (4015) Wilson-Harrington] while the other 13 are in the main belt.

The detection of repetitive dust ejection events in some MBCs [e.g., 133P/Elst-Pizarro and 238P/Read (see Hsieh et al., 2004; Jewitt et al., this volume, and references therein)] and the indication that in these and other MBCs [e.g., 238P, (300163) 2006 VW<sub>139</sub>, P/2010 R<sub>2</sub> (La Sagra), and P/2012 T<sub>1</sub> (PANSTARRS) (see Jewitt et al., this volume)] dust ejection lasted for several months strongly suggests that ice sublimation is their preferred ejection mechanism (Hsieh et al., 2004). Interestingly, three MBCs, 133P, 176P, and 238P, are members of the Themis dynamical family and share spectral properties with other asteroids in this family (see Licandro et al., 2011b, 2013; Hsieh et al., 2012), indicating they have a common origin. Furthermore, water ice was discovered on the surface of the largest member of this family, (24) Themis (Campins et al., 2010; Rivkin and Emery, 2010). Because the water ice on the surface of Themis is short-lived, it likely is resupplied from its interior, and this also supports the hypothesis that there is a water ice reservoir below the surface of some MBCs. Thermal models are consistent with the survival of very shallow subsurface water ice over the age of the solar system in main-belt asteroids (Schorghofer, 2008).

One interesting question regarding Themis family MBCs is, “Why are only some Themis family asteroids active?” If

activity in MBCs is indeed driven by ice sublimation, this ice may normally be protected from sunlight by a poorly conducting surface layer and activity could start with a collision penetrating this layer, exposing the ice to sunlight (*Hsieh and Jewitt*, 2006; *Schorghofer*, 2008; *Capria et al.*, 2012). Recent dynamical results are consistent with this proposed mechanism; more specifically, the discovery of a very young subfamily within the Themis family, called the Beagle family, and the fact that MBC 133P is also a member of the Beagle subfamily (*Nesvorný et al.*, 2008). The relatively recent formation event of the Beagle family may have produced fragments, such as 133P, with shallow ice that can be exposed by small (and thus more frequent) collisions. However, since the other MBC in the Themis family, 176P, is *not* a member of the Beagle family, multiple collisional events or perhaps surface disruption following YORP spin-up are needed to explain their activity (*Campins et al.*, 2012). Another factor that may help explain why only a few Themis family members show activity is a heterogeneous set of compositions among small Themis fragments. This issue can be addressed by focused spectroscopic studies of this family (section 4.7).

It is also suggestive that all the MBCs with known spectra are primitive asteroids. More specifically, 133P, 176P, 238P, (3200) Phaethon and (4015) Wilson-Harrington all belong to the C-complex population in the Tholen taxonomy (*Licandro et al.*, 2007, 2011b, 2013), and (596) Scheila [whose activity is attributed to an impulsive event like a collision (e.g., *Moreno et al.*, 2011)] is a D-type asteroid (*Licandro et al.*, 2011c).

A particularly interesting and related result is the detection by the Herschel Space Telescope of water vapor emission around asteroid (1) Ceres (*Kuipers et al.*, 2014). Models of Ceres' interior include a near-surface ice mantle above a rocky core (*Thomas et al.*, 2005; *McCord and Sotin*, 2005), with the ice separated from the vacuum of space by either a lag deposit similar to comets or a primordial crust. The water emission seen by Herschel is variable, suggesting a connection with surface features, and correlated with solar distance. While Ceres is not considered an MBC (no dust emission or tail has ever been seen), it is possible that MBCs and Themis originated in Ceres-like bodies that were catastrophically disrupted (*Castillo-Rogez and Schmidt*, 2010). Such a scenario could increase the ice fraction among some fragments and also maintain it near the surface in small objects like the MBCs, while still leaving it accessible for activation and sublimation via impacts.

### 3.6. Related Populations

The Trojan asteroids and satellites of Mars are discussed in detail in the chapters by Emery et al. and Murchie et al. in this volume. However, it is worth briefly discussing them again here, along with the irregular satellites of Jupiter, in the context of their hydrated or icy mineralogy. The Cybele and Hilda asteroids are considered in the context of the main-belt asteroids throughout this chapter, although dynamical studies

suggest their origins may lie outside the main belt and with the other objects discussed below.

The Trojan asteroids of Jupiter are dominated by members of the low-albedo P and D classes in the Tholen taxonomy: *DeMeo and Carry* (2013) estimate the Trojan population is two-thirds D-class asteroids by mass, with P-class asteroids making up the vast majority of the remainder. In a follow-up, *DeMeo and Carry* (2014) looked at the mass distribution with size, finding the D:P:C ratio varies wildly in the Trojan population, with Ds dominant in the 50–100-km size range but the D:P fraction more equal outside that range. Focused studies of Trojan asteroids by *Dotto et al.* (2006), *Fornasier et al.* (2007), and *De Luise et al.* (2010) found no objects with the 0.7-μm band seen in CM meteorites and Ch asteroids (section 2.1), even among objects with spectral slopes that place them in the C complex. *Emery and Brown* (2003) studied 20 Trojan asteroids in the 3-μm region, also finding them featureless. This is consistent with a lack of hydrated minerals, but the available spectra are necessarily of lower quality than main-belt objects of similar size. *Emery and Brown* (2004) find that the absence of absorptions in the 3-μm region limits the abundance of H<sub>2</sub>O ice to a few weight percent (at the surfaces), but up to 10–20 wt% hydrated minerals could be present and not seen in those data. *Cruikshank et al.* (2001) noted that 624 Hektor, the largest Trojan, could have 3 wt% ice or 40% hydrated minerals on its surface given observational uncertainties. If hydrated minerals are present on Trojan asteroids, their detection awaits observations from spacecraft visits or with larger or more capable telescopes than have been available to this point.

*Vilas et al.* (2006) compiled BVRI photometry, ECAS filter photometry, narrowband photometry, and CCD reflectance spectra of jovian irregular satellites, determining whether a 0.7-μm band was present. Of their sample of 16 targets, 11 tested positive for a 0.7-μm band. However, each of the groupings represented (Himalia prograde, Pasiphae retrograde, Carme retrograde) had members that tested both positive and negative. The sample also contained C types that tested both positive and negative and P/D types that tested both positive and negative. New CCD reflectance spectra (*Vilas*, 2010, 2013) confirm that the 0.7-μm feature is present in all Himalia group objects in their sample as well as some objects from the Pasiphae group.

Himalia, the largest of the jovian irregular satellites, has been observed from the ground and space. *Jarvis et al.* (2000) interpreted spectral and spectrophotometric data for Himalia to include a 0.7-μm band, although observational uncertainties were large. *Chamberlain and Brown* (2004) analyzed Cassini VIMS observations of Himalia, finding the “suggestion” of a 3-μm band, although large uncertainties frustrated a detailed spectral fit. More recently, *Brown and Rhoden* (2014) detected a 3-μm absorption on Himalia using the Keck telescope, finding a spectral shape that is a good match to the Themis/rounded type found in main-belt asteroids. While the *Vilas et al.* (2006) and *Jarvis et al.* (2000) findings of a 0.7-μm band would lead one to expect a 3-μm band on Himalia, a Pallas-type/sharp band

shape would be expected (see section 3.2). The finding of a Themis-type band shape led *Brown and Rhoden* (2014) to suggest additional observations of Himalia were needed to confirm the presence of a 0.7- $\mu\text{m}$  band. An additional possible explanation for the mismatch between the 3- $\mu\text{m}$  band shape seen on Himalia based on expectations from main-belt asteroids may be found in the work of *Clark et al.* (2012). They suggest that a band at 0.67  $\mu\text{m}$  seen on Iapetus by *Vilas et al.* (1996) may be due to nanophase hematite and/or iron. This may be a way of explaining a co-occurrence of the 0.7- $\mu\text{m}$  and non-Pallas-type 3- $\mu\text{m}$  bands, although obviously more work is needed.

Finally, *Fraeman et al.* (2014) used data from MRO's Compact Reconnaissance Imaging Spectrometer for Mars (CRISM) to detect absorptions centered near 0.65 and 2.8  $\mu\text{m}$  on Phobos and Deimos, the latter interpreted as due to hydrated minerals and with a band shape similar to the Pallas/sharp types. The band at 0.65  $\mu\text{m}$  was interpreted as either due to hydrated minerals (and the equivalent of the 0.7- $\mu\text{m}$  band discussed above) or, again, as due to nanophase materials. It is worth noting that while all of Deimos' surface and most of Phobos' surface had these absorptions, the areas of Phobos associated with Stickney and its ejecta have a more shallow spectral slope than the rest of Phobos and lack these absorptions, and are apparently anhydrous. Previous Earth- and spacebased observations of Phobos and Deimos did not find convincing evidence for hydrated minerals (*Murchie and Erard*, 1996; *Rivkin et al.*, 2002a; *Gendrin et al.*, 2005).

The Trojan asteroids, irregular satellites of the giant planets, and perhaps even Phobos and Deimos are thought to derive from the TNO population in Nice Model interpretations. Transneptunian objects are well known for having icy surfaces and a variety of spectral slopes similar to primitive asteroids. Other than Pluto, however, they are too faint to be observed in the 3- $\mu\text{m}$  region to study non-ice-hydrated minerals. Aqueous alteration products have been reported in the 0.7- $\mu\text{m}$  region on some TNOs and the related Centaur population (*De Bergh et al.*, 2004), although these interpretations have not been confirmed (*Fornasier et al.*, 2009) and band centers are different from what is seen on Ch asteroids (perhaps they are due to nanophase materials rather than phyllosilicates, as suggested above for Himalia). *Barucci et al.* (2008) reviews the evidence for TNO aqueous alteration from visible spectra.

### 3.7. Rotational Variation

To investigate the correlation of the 0.7- and 3- $\mu\text{m}$  absorption bands, *Howell et al.* (2005) reported rotationally resolved spectra of several asteroids to test whether variability with rotation could explain previous inconsistent observations. When simultaneous observations were not possible, full rotational coverage was obtained to explore whether spectral variation was present. The sample was not unbiased, since objects with inconsistent spectral observations were specifically targeted, so the rate of variability seen may not be typical. However, band depth variations ranging from 1% to 5% were found

in most of the objects studied, suggesting that variation is common, if not ubiquitous. Variation in band depth is now thought to explain all the cases where an asteroid with a 0.7- $\mu\text{m}$  band was not seen to have a corresponding 3- $\mu\text{m}$  band. For instance, *Lebofsky* (1980) found that the Ch asteroid (554) Peraga did not have a 3- $\mu\text{m}$  absorption, but due to the wavelength he used as the continuum to define the band, and the low spectral resolution of their photometry, those observations did not have the precision required to detect the band that is now seen.

*Rivkin and Volquardsen* (2010) observed Ceres over its entire rotation, finding band depths to be shallower at the longitudes associated with bright regions in the Hubble Space Telescope (HST) maps. This could be due to a smaller concentration of brucite and carbonates, or plausibly consistent with a variation in particle size. The variation seen and the precision of the data led to an estimate that brucite-free areas 200 km in diameter (at the equator) or larger would have been detected, and that if the ~3% variation in band depth were entirely due to the bright regions, those bright regions would have band depths of ~15–17% compared to the ~20–21% global average band depth.

Improved instrumentation has greatly expanded the number of asteroids observable at 3  $\mu\text{m}$ , and the sensitivity of the band depth that is detectable. However, the interpretation of the Vesta low-albedo surface material as impactor ejecta (section 1.6) might lead one to think that contamination may be a common occurrence and explains most if not all observations of variation. The nature and depth of the 3- $\mu\text{m}$  band that is observed suggests that this is not the case. Groundbased observations of Vesta show a much weaker band than the 10–20% band seen on most Ch asteroids. While other bright S-type objects (and members of other taxonomic classes not expected to have abundant hydrated surface materials) may show possible bands of a few percent, none show the deep, obvious bands of the Ch or even many of the W-class objects. More work certainly needs to be done to clarify this issue, but the current evidence suggests that there are asteroids composed of abundant hydrated silicates, formed in place, parents of CM and CI chondrites, among others. There may also be traces of impactor material detectable on asteroids without native hydrated silicates in their interiors, but careful groundbased spectroscopy can often distinguish them from each other. Improving these methods and finding robust tests of hydrated composition will certainly be a high priority in the future and an important goal of future missions.

### 3.8. Family Studies

Members of asteroid families are the fragments of larger, collisionally disrupted or cratered parent bodies; spectroscopic studies of family members provide information about the interior of the parent body. Three chapters in this volume (by Nesvorný et al., Masiero et al., and Michel et al.) address various aspects of asteroid family studies. Observations of the Themis family serve to illustrate the benefits of characterizing

hydration and other properties of family members. The Themis family is one of the most numerous and statistically reliable in the asteroid belt. It is approximately 3.2 AU from the Sun in low-inclination orbits and, as discussed in section 3.5, contains three MBCs. Spectroscopic studies of this family reveal an interesting picture. *Florczak et al.* (1999) obtained visible spectra (0.49–0.92 μm) of 36 members of this family, and found that about 50% of their sample showed evidence of aqueous alteration, indicating that the parent body was sufficiently warm to mobilize water. Their results also suggest that the percentage of asteroids showing aqueous alteration may decrease with the diameter of the objects; however, this needs confirmation as it could be due to observational biases, including the difficulty of detecting the 0.7-μm band in the fainter targets. In addition, *Campins* (2014) pointed out that Themis family fragments show clear spectral diversity in the near-IR (1–2.5 μm), with individual objects falling in four of the five groups of B-type near-IR spectra identified by *de León et al.* (2012). Wide variety in spectral slopes was also seen in the Themis family by *Fornasier et al.* (2014). Moreover, the 3-μm band on (24) Themis itself is indicative of water ice as opposed to hydrated minerals, as noted. The above results support at least some compositional diversity in the parent body of the Themis family and the distribution of compositions could be attributed to fragments coming from different depths in the original parent body. This tantalizing result and other aspects of family structure and composition can be addressed by new spectroscopic surveys, such as the European Space Agency's Gaia mission (*Campins et al.*, 2012) and targeted ground- and spacebased studies.

Family studies will also be important for understanding the nature of the different 3-μm types. While families are known to be relatively homogeneous in terms of their Tholen or Bus-DeMeo classifications, it is not yet clear how homogeneous they will be in terms of their hydrated mineralogies. The Hygiea family in particular should provide an interesting test: *Rivkin et al.* (2014a) argued that the lack of a Ceres family is supporting evidence that it has an icy shell covered by a lag deposit so that any collisional debris would quickly sublime away. It is tempting to assign a similar interior structure to Hygiea given its surface similarity to Ceres, but the existence of a Hygiea collisional family is at odds with the Ceres family scenario. Observations to determine whether Hygiea family members share a similar 3-μm band shape or not will be critical in interpreting whether Hygiea is an interloper in its own family.

#### 4. DISCUSSION

While much work is still to be done, and some key datasets are not yet in the literature or in some cases even yet obtained, the outlines of an overall scenario can be discerned. The strong correlation between the 0.7-μm band and the Sharp/Pallas-type 3-μm band shape suggests that the process creating the minerals responsible for the former also creates minerals responsible for the latter. However, because some Pallas types can be found without a 0.7-μm

band, the situation is likely not as simple as one mineral being responsible for both bands in all cases. Similarly, the presence of Themis-type band shapes in members of the C, P, and B classes suggests that whatever is causing the different spectral slopes of these objects is independent of the hydrated mineral composition, and the apparent concentration of the Ceres-type bands in large asteroids, if not related to poorer-quality data for smaller (and on average fainter) objects, is suggestive of similar histories for those objects (although see section 3.8). Furthermore, the fact that only Pallas-type bands are found in the meteorite collection is also likely an important clue.

The process or processes that changed aggregations of pebbles and dust (with or without ice) into solid rock is not well understood (*Consolmagno et al.*, 2003; H. Connolly, personal communication). Indeed, the process by which planetesimals are assembled has been a subject of much recent interest, with recent evidence suggesting that 100-km-scale objects are created directly from centimeter-sized building blocks, without intermediate stages (*Morbidelli et al.*, 2009).

One can imagine scenarios that, while at this point provisional, account for all of these factors: Carbonaceous/low-albedo 100-km-scale objects form as dust/pebble/ice aggregates into objects we would now call Themis types. The objects that have internal heat sufficient to melt ice undergo aqueous alteration, which can include exothermic reactions that lead to a self-perpetuating process. The aqueous alteration process lithifies bodies, and creates the minerals that exhibit Pallas-type bands. Objects that are sufficiently large and/or contain sufficient heat can differentiate with an icy crust/mantle over a rocky core. The alteration processes associated with this pathway may create the brucite and carbonates seen on the Ceres types. The Themis types remain as they were at formation, unlithified and therefore unable to generate meteorites. The Ceres types may not create meteorites because they have near-surface ice, and large impacts may only create icy families that are short-lived against sublimation instead of the rocky families created by other parent bodies (see *Rivkin et al.*, 2014a). In this scenario, only the Pallas types, lithified by aqueous alteration, can generate low-albedo, carbonaceous material strong enough to survive passage through Earth's atmosphere to be collected as meteorites.

This scenario has potential inconsistencies — for instance, it's not clear if dynamical families can be created in situations where meteorites are not predicted (for instance, with the Themis family), and it's not obvious that Hygiea and Ceres, both of which have very similar spectra in the 3-μm region, will necessarily have had similar histories and have similar interiors. Nevertheless, the ongoing work in understanding the hydrated mineralogies of the asteroids seem likely lead to paradigms at least broadly similar to what is outlined above.

#### 5. FUTURE WORK

We have spent the previous pages discussing the current state of affairs with regard to water/hydroxyl in the

asteroid and meteorite populations. The upcoming decade promises further progress on many fronts, from Earth-based observations using new capabilities and facilities to *in situ* observations by spacecraft and sample returns.

### 5.1. Observing from the Stratosphere and Above

As noted above, Earth's atmosphere places limitations on groundbased studies of asteroidal water/OH, making some wavelengths basically unobservable. The capability to observe from above Earth's atmosphere would revolutionize the work presented here, allowing OH band depths and band centers to be directly measured instead of inferred or modeled. The spaceborne telescopes of the late twentieth and early twenty-first century generally did not cover the 3- $\mu\text{m}$  region, or had broadband filters that only allowed indirect measurements, but the next generation of facilities should provide improved coverage.

**5.1.1. Stratospheric Observatory for Infrared Astronomy.** The SOFIA project has been fully commissioned, with the First Light Infrared TEst CAMera (FLITECAM) instrument providing spectroscopic data with spectral resolution ( $\lambda/\Delta\lambda$ ) of 1300 from wavelengths 1.14–4.07  $\mu\text{m}$ , with some gaps in coverage. Its typical flight altitude of 11–14 km puts it above 99% of Earth's water vapor, making it well suited to observations in the 3- $\mu\text{m}$  region. However, it is unclear how many asteroids will be observable due to proposal pressure over SOFIA's planned lifetime, and budget pressures threaten to shorten the mission lifetime to a much shorter one than originally expected.

**5.1.2. Balloon-borne observations and suborbital flights.** New efforts to use balloon-borne telescopes to study small bodies began with the effort mounted to observe Comet ISON in 2013 ("BRRISON"). Very high-altitude balloons show the promise of providing a long-term platform to study astronomical phenomena above much of Earth's atmosphere, thus reducing, if not quite fully eliminating, the effects of Earth's atmosphere on IR observations (Young *et al.*, 2013), although pointing stability of the balloons remains an ongoing concern. The BRRISON and BOPPS missions included asteroids in their observing plans, and Ceres was observed with UV/visible and IR instruments during the BOPPS flight, which occurred as this was being written.

Concurrently, telescopes are being developed for commercial suborbital spacecraft that will operate above Earth's atmosphere. These should be capable of making rapid timescale observations, and can sample UV through the NIR spectral region (Vilas *et al.*, 2013), eliminating atmospheric contamination effects, but are more limited in observational duration. These techniques also hold the promise of expanding observations of water-bearing asteroids while minimizing atmospheric contamination.

**5.1.3. James Webb Space Telescope.** The James Webb Space Telescope (JWST) has similar potential to revolutionize asteroidal studies. Its Near-Infrared Spectrograph (NIRSPEC) instrument has spectroscopic capabilities in the 1–5- $\mu\text{m}$  spectral region, and the Mid-Infrared Instrument

(MIRI) provides low-resolution spectroscopy ( $\lambda/\Delta\lambda \sim 100$ ) from 5 to 14  $\mu\text{m}$  and medium-resolution spectroscopy ( $\lambda/\Delta\lambda \sim 2200$ –3500) and imaging in nine bands from 5 to 28  $\mu\text{m}$ . The anticipated sensitivity for JWST should allow high-quality ( $S/N > 30$  in 10<sup>4</sup> s) measurements in the 3- $\mu\text{m}$  region to be made for low-albedo main-belt asteroids of ~3 km diameter, with the size rising to ~10 km in the Trojan clouds (or for the irregular satellites of Jupiter). Unfortunately, the current capabilities planned for JWST do not include the ability to track objects moving faster than Mars, which precludes observations of NEOs at arbitrary times (for instance, near perihelion and/or away from quadrature). It is possible, however, that certain NEOs of interest can be observed at specific times when their apparent rates of motion are slower (if such times exist). As with SOFIA, proposal pressure for JWST may be the greatest impediment to asteroidal studies.

### 5.2. Spacecraft Visits to Asteroids

In addition to spacecraft telescopically observing asteroids, at least three spacecraft will be visiting asteroids and making close-up observations. Dawn, mentioned above in the context of Vesta, will be visiting Ceres by the time this book is published. We expect it to make great progress toward answering several of the questions posed here. The other two spacecraft, Hayabusa-2 and OSIRIS-REx, are intended as sample return missions to primitive asteroids. However, both missions also carry IR spectrometers that will allow observations in the wavelength regions discussed above to provide context for the samples.

**5.2.1. Dawn at Ceres.** The Dawn mission team has contrasted the water-rich nature of Ceres to the water-poor nature of Vesta, and several of the mission goals at Ceres relate to water, including mapping hydrogen abundance using the neutron spectrometer. More pertinent to this chapter, the VIR visible and near-IR spectrometer covers the 0.25–5- $\mu\text{m}$  spectral range, including both the 0.7- $\mu\text{m}$  and 3- $\mu\text{m}$  region. The mission plan includes obtaining half of the VIR frames with a spatial resolution of 400 m or better, with the remainder at a spatial resolution of 1.6 km or better. While Earth-based observations have not detected ice on Ceres' surface, the higher spatial resolution available in the Dawn data will be able to detect much smaller amounts of surface ice (stable at very high latitudes) or place much stronger upper limits on ice abundance than are currently available. It will also provide context for the Herschel observations of water sublimation from Ceres (Kippers *et al.*, 2014), perhaps by identifying surface features related to sublimation.

**5.2.2. Hayabusa-2.** The Hayabusa-2 mission was launched in 2015 by the Japanese space agency JAXA, targeting the low-albedo asteroid 1999 JU<sub>3</sub> for a sample return mission. Observations of 1999 JU<sub>3</sub> place it in the C class (Pinilla-Alonso *et al.*, 2013). Besides the returned sample, Hayabusa-2 carries two instruments that will be able to detect and characterize hydrated minerals on the asteroidal surface: a multiband imager (ONC-T), which would allow measurement of the 0.7- $\mu\text{m}$  band if present at

spatial resolution of 2 m/pixel, and a near-IR spectrometer (NIRS3), which covers a wavelength range of 1.8–3.2 μm. The goal of NIRS3 is to allow hydrated mineral quantities to be estimated to ~1–2% (Iwata *et al.*, 2013), and the spatial sampling is ~40 m/spectrum at the 20-km “home position” altitude, improving to 2 m/spectrum during one low-altitude mission phase.

**5.2.3. Origins Spectral Interpretation Resource Identification and Security-Regolith Explorer.** As noted above, NASA’s OSIRIS-REx mission will return samples to Earth from the NEA 101955 Bennu (Lauretta *et al.*, 2015). The OSIRIS-REx spacecraft will be well instrumented to carry out a year-long campaign to characterize Bennu and select a sampling site. OVIRS will map the spectrum of the asteroid from 0.4 to 4.2 μm. These data will be well suited for direct searches for the 0.7- and 3-μm hydration features. OTES will similarly map Bennu from 6 to 50 μm, providing complementary spectral information in the mid-IR for mineralogical characterization. Thermal mapping at different times of day and points in the orbit around the Sun will enable monitoring of temperatures and derivation of spatially resolved thermal inertias, which can both be used to understand the stability of water (in its various forms) on and below Bennu’s surface as well as measure mid-IR bands associated with phyllosilicates (section 2.3). The imagers will be used for sensitive searches for extended emission and/or plumes, which, if present, could suggest either thermal fatigue- or volatile-related release of dust. Most importantly, the samples returned to Earth will be analyzed in detail, providing a window into the make-up of primitive solar system material and excellent ground truth for the interpretation of remote observations.

### 5.3. Large Groundbased Telescopes

The prospects for larger groundbased telescopes provide additional opportunities for observing smaller and more distant asteroids in the future. Planned telescopes in the 20-m and larger class like the Giant Magellan Telescope (GMT) (25 m), Thirty Meter Telescope (TMT) (30 m), and European Extremely Large Telescope (E-ELT) (39 m) will begin operation late this decade and early next decade. Instrumentation on the TMT and GMT, expected to be the first ones completed, will not cover the 3-μm region at first and will only cover the 0.7-μm region at very high spectral resolution (<http://tmt.org/sites/default/files/TMT-Instrumentation-and-Performance-Handbook.pdf>, <http://www.eso.org/sci/meetings/2013/EELT2013/talks/Jacoby.pdf>). Instrumentation at the E-ELT is yet to be finalized. Despite this, we expect members of the community to make use of these facilities in ways that are not necessarily obvious at the moment.

## 6. OPEN QUESTIONS

1. *Can the different 3-μm types be found on a single body?* Did the aqueous alteration process create spectrally distinct minerals at different times? Were some minerals more

commonly created with depth? Is the 3-μm type a function of starting material?

2. *To what extent is impactor contamination important on small bodies?* If contamination by carbonaceous impactors has caused the 3-μm band on Vesta, is it also potentially important on large (or small) S-class asteroids? What does the existence of different 3-μm types and the correlation of the 0.7-μm band and the Pallas-type 3-μm band tell us about how widespread impactor contamination may be? Can we identify this process on low-albedo objects as well, and should contamination by ordinary chondrite impactors also be expected?

3. *How do the outer solar system small-body populations (Trojans, irregular satellites, comets) fit into the overall picture?* At the time of *Asteroids III*, it was thought that asteroids and comets were disjunct sets and the Hilda and Trojan asteroids were in effect an outward extension of the asteroid belt. At this writing, there appear to be ample objects with physical natures that are partially cometary and partially asteroidal. Do the Trojans and irregular satellites represent material that is distinct from both asteroids and comets, or are they simply typical comets that experienced transport early in solar system history?

4. *Does the solar wind create appreciable amounts of OH on small-body surfaces?* The water brought to Earth by asteroidal impacts may not only have come on carbonaceous bodies — if significant amounts of OH can be created by the solar wind, most asteroidal impactors regardless of composition will have brought in some water, if only a trace. In addition, while the timescale for mining water from asteroids commercially is likely decades away, the techniques needed to identify good targets will be critically dependent upon knowing whether any OH detected is on the very surface or likely to be representative of the interior.

5. *What is responsible for the varying appearance of the 0.7-μm band in asteroids/meteorites that otherwise appear similar at 3 μm?* The frequent presence of 0.7-μm bands in CM meteorite spectra leads to a reasonable linkage between that meteorite group and the Ch asteroids, as discussed several times above. However, there is a significant fraction of C-complex asteroids without the 0.7-μm band but with a Pallas-type 3-μm band. What is their association with the Ch asteroids?

6. *What variation in band shape is present in each of the 3-μm types, and what is causing that variability?* Are the differences in band position in the Themis types, or the presence/absence of shoulders in Pallas-type bands, indicative of important compositional differences?

7. *How can we best account for volatiles hidden from the surface?* The MBCs offer examples of the importance of indirect measurements of water ice when targets are faint. Similarly, the lack of any water or hydroxyl absorption in Rosetta measurements of Comet 67P (Capaccioni *et al.*, 2015) indicates that spectral evidence for volatiles may be absent even if high-spatial-resolution and high-quality data are available. It is possible that many (most?) undifferentiated low-albedo objects in the outer asteroid and beyond

have much more ice than their surface spectra betray, and depending on surface conditions any ice table may be deeper than even neutron spectroscopy can reach.

## 7. CONCLUSIONS

Since the publication of *Asteroids III*, the water content of small bodies has been recognized as of great importance to their study, with robotic and human exploration of water-rich asteroids assigned high priority by the international planetary science community. New instruments and capabilities in laboratories and at telescopes have allowed better data to be obtained and the interfering effects of Earth's water to be minimized. The discovery of the “activated asteroids” and of ice at asteroidal surfaces has demonstrated that free water is still present today in significant amounts. Work by many authors has linked the Ch asteroid class to the CM meteorite group sufficiently firmly that the type of statistical and mineralogical analysis that has been commonplace for ordinary chondrite and basaltic achondrite analogs can now begin for the carbonaceous chondrites. Variety in the hydrated mineralogy of asteroids has been seen, and we are starting to associate that variety with particular asteroid sizes and locations, with an apparent path toward divining their histories. Toward this effort, the groundbased remote sensing that we have historically used to study asteroids will be augmented in the near future with observations by airborne and spaceborne platforms, visits to hydrated asteroids, and ground truth via sample return. By the time *Asteroids V* is released, presumably sometime in the 2020s or early 2030s, it seems likely that the state of knowledge of the hydrated minerals on asteroids will not be containable in a single chapter.

**Acknowledgments.** A.S.R. acknowledges the long-standing support of the NSF and NASA Planetary Astronomy programs and the NASA NEO Observations program. H.C. acknowledges support through the NASA NEOO and Solar System Observations programs and NASA's OSIRIS-REx mission through a contract with the University of Arizona. J.P.E. and D.T. acknowledge NASA Planetary Astronomy grant NNX08AV93G, and D.T. additionally acknowledges support from NASA Cosmochemistry grant NNX10AH48G (Harry Y. McSween Jr., PI). We all thank NASA IRTF staff for their assistance with asteroid observations, and note the IRTF is operated by the University of Hawaii under Cooperative Agreement No. NCC 5-538 with the National Aeronautics and Space Administration, Office of Space Science, Planetary Astronomy Program. Thanks to the people of Hawai'i for allowing observers to visit and build upon the sacred mountain of Mauna Kea for the purposes of advancing science.

## REFERENCES

- Ali-Lagoa V., de León J., Licandro J., Delbó M., Campins H., Pinilla-Alonso N., and Kelley M. S. (2013) Physical properties of B-type asteroids from WISE data. *Astron. Astrophys.*, **554**, A71.
- Arnold S. M. (1979) Rapid photometry of cataclysmic variable stars. Ph.D. thesis, Rochester Univ., New York.
- Barucci M. A., Brown M. E., Emery J. P., and Merlin F. (2008) Composition and surface properties of transneptunian objects and centaurs. In *The Solar System Beyond Neptune* (M. A. Barucci et al., eds.), p. 143. Univ. of Arizona, Tucson.
- Barucci M. A., Belskaya I. N., Fornasier S., Fulchignoni M., Clark B. E., Coradini A., Capaccioni F., Dotto E., Birlan M., and Leyrat C. (2012) Overview of Lutetia's surface composition. *Planet. Space Sci.*, **66**, 23–30.
- Beck P., Quirico E., Montes-Hernandez G., Bonal L., Bolland J., Orthous-Daunay F.-R., Howard K. T., Schmitt B., Brissaud O., Deschamps F., Wunder B., and Guillot S. (2010) Hydrous mineralogy of CM and CI chondrites from infrared spectroscopy and their relationship with low albedo asteroids. *Geochim. Cosmochim. Acta*, **74**, 4881–4892.
- Beck P., Quirico E., Sevestre D., Montes-Hernandez G., Pommerol A., and Schmitt B. (2011) Goethite as an alternative origin of the 3.1 μm band on dark asteroids. *Astron. Astrophys.*, **526**, A85.
- Beck P., Garenne A., Quirico E., Bonal L., Montes-Hernandez G., Moynier F., and Schmitt B. (2014) Transmission infrared spectra (2–25 μm) of carbonaceous chondrites (CI, CM, CV-CK, CR, C2 ungrouped): Mineralogy, water, and asteroidal processes. *Icarus*, **229**, 263–277.
- Bertini I. (2011) Main belt comets: A new class of small bodies in the solar system. *Planet. Space Sci.*, **59**, 365–377.
- Binzel R. P., Rivkin A. S., Stuart J. S., Harris A. W., Bus S. J., and Burbine T. H. (2004) Observed spectral properties of near-Earth objects: Results for population distribution, source regions, and space weathering processes. *Icarus*, **170**, 259–294.
- Birlan M., Vernazza P., Fulchignoni M., Barucci M. A., Descamps P., Binzel R. P., and Bus S. J. (2006) Near infrared spectroscopy of the asteroid 21 Lutetia. I. New results of long-term campaign. *Astron. Astrophys.*, **454**, 677–681.
- Birlan M., Nedelcu A., Vernazza P., Binzel R., Carry B., DeMeo F., Barucci A., and Fulchignoni M. (2010) 21 Lutetia: Groundbased near-infrared spectroscopy prior to the Rosetta flyby. *Bull. Am. Astron. Soc.*, **42**, 1050.
- Bishop J. L. and Pieters C. M. (1995) Low-temperature and low atmospheric pressure infrared reflectance spectroscopy of Mars soil analog materials. *J. Geophys. Res.—Planets*, **100**, 5369–5379.
- Bottke W. F., Nesvorný D., Grimm R. E., Morbidelli A., and O'Brien D. P. (2006) Iron meteorites as remnants of planetesimals formed in the terrestrial planet region. *Nature*, **439**, 821–824.
- Bottke W. F., Nesvorný D., Vokrouhlický D., and Morbidelli A. (2010) Collisional evolution of the irregular satellites. *Astron. J.*, **139**, 994–1014.
- Bottke W. F., Vokrouhlický D., Minton D., Nesvorný D., Morbidelli A., Brasser R., Simonson B., and Levison H. F. (2012) An Archean heavy bombardment from a destabilized extension of the asteroid belt. *Nature*, **485**, 78–81.
- Bottke W. F., Vokrouhlický D., Nesvorný D., and Moore J. M. (2013) Black rain: The burial of the Galilean satellites in irregular satellite debris. *Icarus*, **223**(2), 775–795.
- Britt D., Schelling P., Consolmagno G., and Bradley T. (2014) Space weathering on volatile rich asteroids. *Lunar Planet. Sci. XLV*, Abstract #2067. Lunar and Planetary Institute, Houston.
- Brown M. E. and Rhoden A. R. (2014) The 3 μm spectrum of Jupiter's irregular satellite Himalia. *Astrophys. J. Lett.*, **793**, L44.
- Browning L. B., McSween H. Y., and Zolensky M. E. (1996) Correlated alteration effects in CM carbonaceous chondrites. *Geochim. Cosmochim. Acta*, **60**, 2621–2633.
- Burbine T. H., McCoy T. J., Meibom A., Gladman B., and Keil K. (2002) Meteoritic parent bodies: Their number and identification. In *Asteroids III* (W. F. Bottke Jr. et al., eds.), pp. 653–667. Univ. of Arizona, Tucson.
- Bus S. J. and Binzel R. P. (2002a) Phase II of the Small Main-Belt Asteroid Spectroscopic Survey: A feature-based taxonomy. *Icarus*, **158**, 146–177.
- Bus S. J. and Binzel R. P. (2002b) Phase II of the Small Main-Belt Asteroid Spectroscopic Survey: The observations. *Icarus*, **158**, 106–145.
- Campins H. (2014) Volatiles in asteroids. In *Asteroids, Comets, Meteors* (K. Muinonen et al., eds.), p. 94. Helsinki, Finland.
- Campins H., Hargrove K., Pinilla-Alonso N., Howell E. S., Kelley M. S., Licandro J., Mothé-Diniz T., Fernández Y., and Ziffer J. (2010) Water ice and organics on the surface of the asteroid 24 Themis. *Nature*, **464**, 1320–1321.

- Camps H., de León J., Licandro J., Kelley M. S., Fernández Y., Ziffer J., and Nesvorný D. (2012) Spectra of asteroid families in support of Gaia. *Planet. Space Sci.*, 73, 95–97.
- Capaccioni F., Coradini A., Filacchione G., et al. (2015) The organic-rich surface of Comet 67P/Churyumov-Gerasimenko as seen by VIRTIS/Rosetta. *Science*, 347(6220), aaa0628.
- Capria M. T., Marchi S., de Sanctis M. C., Coradini A., and Ammannito E. (2012) The activity of main belt comets. *Astron. Astrophys.*, 537A, 82C.
- Carvano J. M., Mothé-Diniz T., and Lazzaro D. (2003) Search for relations among a sample of 460 asteroids with featureless spectra. *Icarus*, 161, 356–382.
- Castillo-Rogez J. C. and Schmidt B. E. (2010) Geophysical evolution of the Themis family parent body. *Geophys. Res. Lett.*, 37, 10202.
- Chamberlain M. A. and Brown R. H. (2004) Near-infrared spectroscopy of Himalia. *Icarus*, 172, 163–169.
- Chapman C. R., Morrison D., and Zellner B. H. (1975) Surface properties of asteroids — A synthesis of polarimetry, radiometry, and spectrophotometry. *Icarus*, 25, 104–130.
- Clark B. E., Ziffer J., Nesvorný D., Campins H., Rivkin A. S., Hiroi T., Barucci M. A., Fulchignoni M., Binzel R. P., Fornasier S., DeMeo F., Ockert-Bell M. E., Licandro J., and Mothé-Diniz T. (2010) Spectroscopy of B-type asteroids: Subgroups and meteorite analogs. *J. Geophys. Res.–Planets*, 115, 6005.
- Clark B. E. and 14 co-authors (2011) Asteroid (101955) 1999 RQ36: Spectroscopy from 0.4 to 2.4  $\mu\text{m}$  and meteorite analogs. *Icarus*, 216, 462–475.
- Clark R. (1979) Planetary reflectance measurements in the region of planetary thermal emission. *Icarus*, 40(1), 94–103.
- Clark R. N. (1983) Spectral properties of mixtures of montmorillonite and dark carbon grains: Implications for remote sensing minerals containing chemically and physically adsorbed water. *J. Geophys. Res.*, 88, 10635–10644.
- Clark R. N. (1999) *Spectroscopy of Rocks and Minerals, and Principles of Spectroscopy*. Available online at <http://speclab.cr.usgs.gov/PAPERS.refl-mrs/refl4.html>.
- Clark R. N. (2009) Detection of adsorbed water and hydroxyl on the Moon. *Science*, 326, 562.
- Clark R. N., King T. V., Klejwa M., Swayze G. A., and Vergo N. (1990) High spectral resolution reflectance spectroscopy of minerals. *J. Geophys. Res.–Solid Earth*, 95(B8), 12653–12680.
- Clark R. N., Swayze G. A., Gallagher A. J., King T. V. V., and Calvin W. M. (1993) *The U.S. Geological Survey, Digital Spectral Library: Version 1 (0.2 to 3.0  $\mu\text{m}$ )*. U.S. Geological Survey Open File Report 93–592.
- Clark R. N., Swayze G. A., Wise R., Livo K. E., Hoefen T. M., Kokaly R. F., and Sutley S. J. (2007) *USGS Digital Spectral Library splib06a*. U.S. Geological Survey Data Series 231.
- Clark R. N., Cruikshank D. P., Jaumann R., Brown R. H., Stephan K., Dalle Ore C. M., Eric Livo K., Pearson N., Curchin J. M., Hoefen T. M., Buratti B. J., Filacchione G., Baines K. H., and Nicholson P. D. (2012) The surface composition of Iapetus: Mapping results from Cassini VIMS. *Icarus*, 218, 831–860.
- Clayton R. N. and Mayeda T. K. (1999) Oxygen isotope studies of carbonaceous chondrites. *Geochim. Cosmochim. Acta*, 63, 2089–2104.
- Cloutis E. A., Hiroi T., Gaffey M. J., Alexander C. M. O'D., and Mann P. (2011a) Spectral reflectance properties of carbonaceous chondrites: 1. CI chondrites. *Icarus*, 212, 180–209.
- Cloutis E. A., Hudon P., Hiroi T., Gaffey M. J., and Mann P. (2011b) Spectral reflectance properties of carbonaceous chondrites: 2. CM chondrites. *Icarus*, 216, 309–346.
- Cloutis E., Hudon P., Hiroi T., and Gaffey M. (2012) Spectral reflectance properties of carbonaceous chondrites 4: Aqueously altered and thermally metamorphosed meteorites. *Icarus*, 220(2), 586–617.
- Consolmagno G. J., Weidenschilling S. J., and Britt D. T. (2003) Forming well-compacted meteorites by shock events in the solar nebula. *Meteoritics & Planet. Sci. Suppl.*, 38, 5247.
- Cohen M., Witteborn F. C., Roush T., Bregman J., and Wooden D. (1998) Spectral irradiance calibration in the infrared. VIII. 5–14 micron spectroscopy of the asteroids Ceres, Vesta, and Pallas. *Astron. J.*, 115, 1671–1679.
- Coradini A., Capaccioni F., Drossart P., Semery A., Arnold G., and Schade U. (1999) VIRTIS: The imaging spectrometer of the Rosetta mission. *Adv. Space Res.*, 24, 1105–1114.
- Cruikshank D., Dalle Ore C., Roush T., Geballe T., Owen T., de Bergh C., Cash M., and Hartmann W. (2001) Constraints on the composition of Trojan asteroid 624 Hektor. *Icarus*, 153(2), 348–360.
- Cuzzi J. N., Hogan R. C., and Bottke W. F. (2010) Towards initial mass functions for asteroids and Kuiper belt objects. *Icarus* 208, 518–538.
- De Bergh C., Boehnhardt H., Barucci M., Lazzarin M., Fornasier S., Romon-Martin J., Tozzi G., Doressoundiram A., and Dotto E. (2004) Aqueous altered silicates at the surface of two Plutinos? *Astron. Astrophys.*, 416(2), 791–798.
- de León J., Pinilla-Alonso N., Campins H., Licandro J., and Marzo G. A. (2012) Near-infrared spectroscopic survey of B-type asteroids: Compositional analysis. *Icarus*, 218, 196–206.
- De Luise F., Dotto E., Fornasier S., Barucci M. A., Pinilla-Alonso N., Perna D., and Marzari F. (2010) A peculiar family of Jupiter Trojans: The Eurybates. *Icarus*, 209, 586–590.
- DeMeo F. E. and Carry B. (2013) The taxonomic distribution of asteroids from multi-filter all-sky photometric surveys. *Icarus*, 226, 723–741.
- DeMeo F. E. and Carry B. (2014) Solar system evolution from compositional mapping of the asteroid belt. *Nature*, 505, 629–634.
- DeMeo F. E., Binzel R. P., Slivan S. M., and Bus S. J. (2009) An extension of the Bus asteroid taxonomy into the near-infrared. *Icarus*, 202, 160–180.
- Denevi B. W., Blewett D. T., Buczkowski D. L., Capaccioni F., Capria M. T., De Sanctis M. C., Garry W. B., Gaskell R. W., Le Corre L., and Li J.-Y. (2012) Pitted terrain on Vesta and implications for the presence of volatiles. *Science*, 338, 246.
- De Sanctis M. C., Combe J.-P., Ammannito E., Palomba E., Longobardo A., McCord T. B., Marchi S., Capaccioni F., Capria M. T., Mittlefehldt D. W., Pieters C. M., Sunshine J., Tosi F., Zambon F., Carraro F., Fonte S., Frigeri A., Magni G., Raymond C. A., Russell C. T., and Turrini D. (2012a) Detection of widespread hydrated materials on Vesta by the VIR imaging spectrometer on board the Dawn mission. *Astrophys. J. Lett.*, 758, L36.
- De Sanctis M., Coradini A., Ammannito E., Filacchione G., Capria M., Fonte S., Magni G., Barbis A., Bini A., Dami M., et al. (2012b) The VIR spectrometer. In *The Dawn Mission to Minor Planets 4 Vesta and 1 Ceres* (C. Russell and C. Raymond, eds.), pp. 329–369. Springer, Berlin.
- Dotto E., Fornasier S., Barucci M. A., Licandro J., Boehnhardt H., Hainaut O., Marzari F., de Bergh C., and De Luise F. (2006) The surface composition of Jupiter Trojans: Visible and near-infrared survey of dynamical families. *Icarus*, 183, 420–434.
- Dyar M. D., Hibbitts C. A., and Orlando T. M. (2010) Mechanisms for incorporation of hydrogen in and on terrestrial planetary surfaces. *Icarus*, 208, 425–437.
- Emery J. P. and Brown R. H. (2003) Constraints on the surface composition of Trojan asteroids from near-infrared (0.8–4.0  $\mu\text{m}$ ) spectroscopy. *Icarus*, 164, 104–121.
- Emery J. P. and Brown R. H. (2004) The surface composition of Trojan asteroids: Constraints set by scattering theory. *Icarus*, 170, 131–152.
- Emery J., Cruikshank D. P., and Van Cleve J. (2006) Thermal emission spectroscopy (5.2–38  $\mu\text{m}$ ) of three Trojan asteroids with the Spitzer Space Telescope: Detection of fine-grained silicates. *Icarus*, 182, 496–512.
- Emery J. P., Fernández Y. R., Kelley M. S. P., Warden (née Crane) K. T., Hergenrother C., Lauretta D. S., Drake M. J., Campins H., and Ziffer J. (2014) Thermal infrared observations and thermophysical characterization of OSIRIS-REx target asteroid (101955) Bennu. *Icarus*, 234, 17–35.
- Farmer V. (1974) The layer silicates. In *The Infrared Spectra of Minerals* (V. C. Farmer, ed.), pp. 331–363. Mineralogical Society of America, Monograph 4.
- Feierberg M. A., Lebofsky L. A., and Tholen D. J. (1985) The nature of C-class asteroids from 3- $\mu\text{m}$  spectrophotometry. *Icarus*, 63, 183–191.
- Feldman W., Maurice S., Lawrence D., Little R., Lawson S., Gasnault O., Wiens R., Barraclough B., Elphic R., and Prettyman H. (2001) Evidence for water ice near the lunar poles. *J. Geophys. Res.*, 106, 23231–23252.
- Florczak M., Lazzaro D., Mothé-Diniz T., Angeli C. A., and Betzler A. S. (1999) A spectroscopic study of the Themis family. *Astron. Astrophys. Suppl.*, 134, 463–471.
- Fornasier S., Dotto E., Hainaut O., Marzari F., Boehnhardt H., De Luise F., and Barucci M. A. (2007) Visible spectroscopic and photometric survey of Jupiter Trojans: Final results on dynamical families. *Icarus*, 190(2), 622–642.

- Fornasier S., Barucci M., De Bergh C., Alvarez-Candal A., DeMeo F., Merlin F., Perna D., Guibert A., Delsanti A., Dotto E., et al. (2009) Visible spectroscopy of the new ESO large programme on trans-neptunian objects and Centaurs: Final results. *Astron. Astrophys.*, 508(1), 457–465.
- Fornasier S., Clark B. E., and Dotto E. (2011) Spectroscopic survey of X-type asteroids. *Icarus*, 214(1), 131–146.
- Fornasier S., Lantz C., Barucci M. A., and Lazzarin M. (2014) Aqueous alteration on main belt primitive asteroids: Results from visible spectroscopy. *Icarus*, 233, 163–178.
- Fraeman A. A., Murchie S. L., Arvidson R. E., Clark R. N., Morris R. V., and Rivkin A. S. (2014) Spectral absorptions on Phobos and Deimos in the visible/near infrared wavelengths and their compositional constraints. *Icarus*, 229, 196–205.
- Gendrin A., Langevin Y., and Erard S. (2005) ISM observation of phobos reinvestigated: Identification of a mixture of olivine and low-calcium pyroxene. *J. Geophys. Res.–Planets*, 110, DOI: 10.1029/2004JE002245.
- Gomes R., Levison H. F., Tsiganis K., and Morbidelli A. (2005) Origin of the cataclysmic late heavy bombardment period of the terrestrial planets. *Nature*, 435, 466–469.
- Gounelle M. (2011) The asteroid-comet continuum: In search of lost primitivity. *Elements*, 7, 29–34.
- Gradie J. and Tedesco E. (1982) Compositional structure of the asteroid belt. *Science*, 216, 1405–1407.
- Grimm R. E. and McSween H. Y. Jr. (1993) Heliocentric zoning of the asteroid belt by aluminum-26 heating. *Science*, 259, 653–655.
- Groussin O., Sunshine J. M., Feaga L. M., Jorda L., Thomas P. C., Li J.-Y., A'Hearn M. F., Belton M. J. S., Besse S., and Carcich B. (2013) The temperature, thermal inertia, roughness and color of the nuclei of Comets 103P/Hartley 2 and 9P/Tempel 1. *Icarus*, 222, 580–594.
- Hanson H. M., Howell E., Magri C., and Nolan M. (2006) Correlating Arecibo radar and IRTF near-infrared spectral observations of 105 Artemis. *Bull. Am. Astron. Soc.*, 38, 933.
- Harris A. W. and Lagerros J. S. V. (2002) Asteroids in the thermal infrared. In *Asteroids III* (W. F. Bottke Jr. et al., eds.), pp. 205–218. Univ. of Arizona, Tucson.
- Hasegawa S., Murakawa K., Ishiguro M., Nonaka H., Takato N., Davis C. J., Ueno M., and Hiroi T. (2003) Evidence of hydrated and/or hydroxylated minerals on the surface of asteroid 4 Vesta. *Geophys. Res. Lett.*, 30, DOI: 10.1029/2003GL01862.
- Hiroi T., Zolensky M. E., Pieters C. M., and Lipschutz M. E. (1996) Thermal metamorphism of the C, G, B, and F asteroids seen from the 0.7 μm, 3 μm and UV absorption strengths in comparison with carbonaceous chondrites. *Meteoritics & Planet. Sci.*, 31, 321–327.
- Howell E. S., Rivkin A. S., and Vilas F. (2005) Water distribution in the asteroid belt. In *Workshop on Oxygen in Asteroids and Meteorites*, p. 18. LPI Contribution No. 1267, Lunar and Planetary Institute, Houston.
- Howell E. S., Rivkin A. S., Vilas F., Magri C., Nolan M. C., Vervack R. J. Jr., and Fernandez Y. R. (2011) Hydrated silicates on main-belt asteroids: Correlation of the 0.7- and 3-micron absorption bands. *EPSC-DPS Joint Meeting 2011*, 637.
- Hsieh H. H. and Jewitt D. (2006) A population of comets in the main asteroid belt. *Science*, 312, 561–563.
- Hsieh H. H., Jewitt D. C., and Fernandez Y. R. (2004) The strange case of 133P/Elst-Pizarro: A comet among the asteroids. *Astron. J.*, 127(5), 2997–3017.
- Hsieh H. H., Yang B., Haghighipour N., et al. (2012) Discovery of main-belt Comet P/2006 VW<sub>139</sub> by Pan-STARRS1. *Astrophys. J. Lett.*, 748, L15.
- Hunt G. R. (1977) Spectral signatures of particulate minerals in the visible and near infrared. *Geophysics*, 42(3), 501–513.
- Iwata T., Kitazato K., Abe M., Ohtake M., Matsuura S., Tsumura K., Hirata N., Honda C., Takagi Y., Nakuchi Y., Hiroi T., Senshu H., Arai T., Nakamura T., Matsunaga T., Komatsu M., Takato N., and Watanabe S. (2013) Results of the critical design for NIR3: The Near Infrared Spectrometer on Hayabusa-2. *Lunar Planet. Sci. XLIV*, Abstract #1908. Lunar and Planetary Institute, Houston.
- Jarvis K. S., Vilas F., Larson S. M., and Gaffey M. J. (2000) JV1 Himalia: New compositional evidence and interpretations for the origin of Jupiter's small satellites. *Icarus*, 145, 445–453.
- Jewitt D. (2012) The active asteroids. *Astron. J.*, 143(3), 66.
- Jewitt D., Li J., and Agarwal J. (2013) The dust tail of asteroid (3200) Phaethon. *Astrophys. J. Lett.*, 771(2), L36.
- Jewitt D., Agarwal J., Weaver H., Mutchler M., and Larson S. (2015) Episodic ejection from active asteroid 311P/PANSTARRS. *Astrophys. J.*, 798, Article ID 109.
- Jones T. D. (1989) An infrared reflectance study of water in outer belt asteroids: Clues to composition and origin. Ph.D. dissertation, Univ. of Arizona, Tucson.
- Jones T. D., Lebofsky L. A., Lewis J. S., and Marley M. S. (1990) The composition and origin of the C, P, and D asteroids: Water as a tracer of thermal evolution in the outer belt. *Icarus*, 88, 172–192.
- King T. V. V. and Clark R. N. (1997) The presence of a single absorption feature: What it does and doesn't imply. *Lunar Planet. Sci. XXVIII*, pp. 727–728. Lunar and Planetary Institute, Houston.
- King T. V. V., Clark R. N., Calvin W. M., Sherman D. M., and Brown R. H. (1992) Evidence for ammonium-bearing minerals on Ceres. *Science*, 257, 1551–1553.
- Küppers M., O'Rourke L., Bockelée-Morvan D., Zakharov V., Lee S., von Allmen P., Carry B., Teyssier D., Marston A., and Müller T. (2014) Localized sources of water vapour on the dwarf planet (1) Ceres. *Nature*, 505, 525–527.
- Landsman Z. A., Campins H., Hargrove K., Pinilla-Alonso N., Emery J., and Ziffer J. (2013) An investigation of the 3-μm feature in M-type asteroids. In *45th AAS/Division for Planetary Sciences Meeting Abstracts*, #208.15.
- Lauretta D. S. and 28 co-authors (2015) The OSIRIS-REx target asteroid 101955 Bennu: Constraints on its physical, geological, and dynamical nature from astronomical observations. *Meteoritics & Planet. Sci.*, 50, 834–849.
- Lazzaro D., Angelil C. A., Carvano J. M., Mothé-Diniz T., Duffard R., and Florczak M. (2004) S3OS2: The visible spectroscopic survey of 820 asteroids. *Icarus*, 172, 179–220.
- Lebofsky L. A. (1980) Infrared reflectance spectra of asteroids: A search for water of hydration. *Astron. J.*, 85, 573–585.
- Lebofsky L. A. and Spencer J. R. (1989) Radiometry and thermal modeling of asteroids. In *Asteroids II* (R. P. Binzel et al., eds.), pp. 128–147. Univ. of Arizona, Tucson.
- Lebofsky L. A., Jones T. D., Owensby P. D., Feierberg M. A., and Consolmagno G. J. (1990) The nature of low albedo asteroids from 3-μm spectrophotometry. *Icarus*, 83, 12–26.
- Lee M. (1993) The petrography, mineralogy and origins of calcium sulphate within the Cold Bokkeveld CM carbonaceous chondrite. *Meteoritics*, 28, 53–62.
- Levison H. F., Bottke W. F., Gounelle M., Morbidelli A., Nesvorný D., and Tsiganis K. (2009) Contamination of the asteroid belt by primordial trans-neptunian objects. *Nature*, 460, 364–366.
- Licandro J., Campins H., Mothé-Diniz T., Pinilla-Alonso N., and de León J. (2007) The nature of comet-asteroid transition object (3200) Phaethon. *Astron. Astrophys.*, 461, 751–757.
- Licandro J., Campins H., Kelley M., Hargrove K., Pinilla-Alonso N., Cruikshank D., Rivkin A. S., and Emery J. (2011a) (65) Cybele: Detection of small silicate grains, water-ice, and organics. *Astron. Astrophys.*, 525, A34.
- Licandro J., Campins H., Tozzi G. P., de León J., Pinilla-Alonso N., Boehnhardt H., and Hainaut O. R. (2011b) Testing the comet nature of main belt comets. The spectra of 133P/Elst-Pizarro and 176P/LINEAR. *Astron. Astrophys.*, 532, 65.
- Licandro J., de León J., Kelley M. S., Emery J., Rivkin A., Pinilla-Alonso N., Mothé-Diniz T., Campins H., and Ali-Lagoa V. (2011c) Multi-wavelength study of activated asteroid (596) Scheila. *European Planet. Sci. Congr.*, 6, EPSC-DPS2011-1109-1.
- Licandro J., Hargrove K., Kelley M., Campins H., Ziffer J., Ali-Lagoa V., Fernández Y., and Rivkin A. (2012) 5–14 μm Spitzer spectra of Themis family asteroids. *Astron. Astrophys.*, 537, A73.
- Licandro J., Moreno F., de León J., Tozzi G. P., Lara L. M., Cabrera-Lavers A. (2013) Exploring the nature of new main-belt comets with the 10.4 m GTC telescope: (300163) 2006 VW<sub>139</sub>. *Astron. Astrophys.*, 550, 7.
- Licandro J., Alvarez-Iglesias C., Cabrera-Lavers A., Ali-Lagoa V., Pinilla-Alonso N., Campins H., de León J., and Kelley M. (2014) The GTC mid-infrared spectroscopic program of primitive outer-belt asteroids. In *Asteroids, Comets, Meteors 2014* (K. Muinonen et al., eds.), p. 338. Helsinki, Finland.
- Lunine J. and Reid I. (2006) Astrobiology: A multidisciplinary approach. *Phys. Today*, 59, 58.

- Mainzer A., Grav T., Masiero J., Bauer J., Wright E., Cutri R., Walker R., and McMillan R. (2011) Thermal model calibration for minor planets observed with wise/neowise: Comparison with infrared astronomical satellite. *Astrophys. J. Lett.*, 737(1), L9.
- Marchi S., Delbo M., Morbidelli A., Paolicchi P., and Lazzarin M. (2009) Heating of near-Earth objects and meteoroids due to close approaches to the Sun. *Mon. Not. R. Astron. Soc.*, 400, 147–153.
- Martin R. and Livio M. (2012) On the evolution of the snow line in protoplanetary discs. *Mon. Not. R. Astron. Soc. Lett.*, 425, L6–L9.
- Mastrapa R. M., Sandford S. A., Roush T. L., Cruikshank D. P., and Dalle Ore C. M. (2009) Optical constants of amorphous and crystalline H<sub>2</sub>O-ice: 2.5–22 μm (4000–455 cm<sup>-1</sup>) optical constants of H<sub>2</sub>O-ice. *Astrophys. J.*, 701, 1347–1356.
- McAdam M., Sunshine J. M., Kelley M. S. (2013) Composition and degree of alteration of dark asteroids. *AAS/Division for Planetary Sciences*, 45, #205.10.
- McCord T. B. and Sotin C. (2005) Ceres: Evolution and current state. *J. Geophys. Res.–Planets*, 110, E5.
- McCord T. B., Li J.-Y., Combe J.-P., McSween H. Y., Jaumann R., Reddy V., Tosi F., Williams D. A., Blewett D. T., and Turrini D. (2012) Dark material on Vesta from the infall of carbonaceous volatile-rich material. *Nature*, 491, 83–86.
- McSween H. Y. (1979) Alteration in CM carbonaceous chondrites inferred from modal and chemical variations in matrix. *Geochim. Cosmochim. Acta*, 43, 1761–1770.
- Milliken R. E. and Rivkin A. S. (2009) Brucite and carbonate assemblages from altered olivine-rich materials on Ceres. *Nature Geosci.*, 2, 258–261.
- Milliken R. E., Mustard J. F., Poulet F., Jouget D., Bibring J.-P., Gondet B., and Langevin Y. (2007) Hydration state of the martian surface as seen by Mars Express Omega: 2. H<sub>2</sub>O content of the surface. *J. Geophys. Res.–Planets*, 112, E8.
- Mommert M., Farnocchia D., Hora J. L., Chesley S. R., Trilling D. E., Chodas P. W., Mueller M., Harris A. W., Smith H. A., and Fazio G. G. (2014) The discovery of cometary activity in near-Earth asteroid (3552) Don Quixote by Mommert et al. *Astron. J.*, 781, Article ID 25.
- Morbidelli A., Levison H. F., Tsiganis K., and Gomes R. (2005) Chaotic capture of Jupiter's Trojan asteroids in the early solar system. *Nature*, 435, 462–465.
- Morbidelli A., Bottke W. F., Nesvorný D., and Levison H. F. (2009) Asteroids were born big. *Icarus*, 204(2), 558–573.
- Morbidelli A., Brasser R., Gomes R., Levison H. F., and Tsiganis K. (2010) Evidence from the asteroid belt for a violent past evolution of Jupiter's orbit. *Astron. J.*, 140, 1391–1401.
- Moreno F., Licandro J., Ortiz J., Lara L. M., Ali-Lagoa V., Vaduvescu O., Morales N., Molina A., and Lin Z.-Y. (2011) (596) Scheila in outburst: A probable collision event in the main asteroid belt. *Astrophys. J.*, 738(2), 130.
- Murchie S. and Erard S. (1996) Spectral properties and heterogeneity of Phobos from measurements by Phobos 2. *Icarus*, 123, 63–86.
- Nedelcu D. A., Birlan M., Vernazza P., Descamps P., Binzel R. P., Colas F., Kryszczynska A., and Bus S. J. (2007) Near infrared spectroscopy of the asteroid 21 Lutetia. II. Rotationally resolved spectroscopy of the surface. *Astron. Astrophys.*, 470, 1157–1164.
- Nesvorný D., Bottke W., Vokrouhlický D., Sykes M., Lien D., and Stansberry J. (2008) Origin of the near-ecliptic circumsolar dust band. *Astrophys. J.*, 679, L143–L146.
- Noble S. K., Pieters C., Taylor L. A., Morris R. V., Allen C. C., McKay D. S., and Keller L. P. (2001) The optical properties of the finest fraction of lunar soil: Implications for space weathering. *Meteoritics & Planet. Sci.*, 36, 31–42.
- Okamura N., Hasegawa S., Usui F., Hiroi T., Ootsubo T., Müller T. G., and Sugita S. (2014a) Spectroscopic observations of dark main-belt asteroids in the 2.5–3.1 μm range. *Lunar Planet. Sci. XLV*, Abstract #1375. Lunar and Planetary Institute, Houston.
- Okamura N., Sugita S., Kamata S., Usui F., Hiroi T., Ootsubo T., Müller T. G., Sakon I., and Hasegawa S. (2014b) Principal-component analysis of the continuous 3-μm spectra of low-albedo asteroids observed with the AKARI satellite. *Lunar Planet. Sci. XLV*, Abstract #2446. Lunar and Planetary Institute, Houston.
- Osawa T., Kagi H., Nakamura T., and Noguchi T. (2005) Infrared spectroscopic taxonomy for carbonaceous chondrites from speciation of hydrous components. *Meteoritics & Planet. Sci.*, 40, 71–86.
- Pieters C. M., Goswami J. N., Clark R. N., Annadurai M., Boardman J., Buratti B., Combe J., Dyar M. D., Green R., Head J. W., Hibbits C., Hicks M., Isaacson P., Klima R., Kramer G., Kumar S., Livo E., Lundein S., Malarct E., McCord T., Mustard J., Nettles J., Petro N., Runyon C., Staid M., Sunshine J., Taylor L. A., Tompkins S., and Varanasi P. (2009) Character and spatial distribution of OH/H<sub>2</sub>O on the surface of the Moon Seen by M<sup>3</sup> on Chandrayaan-1. *Science*, 326, 568.
- Pinilla-Alonso N. (2011) Ice vs. goethite on Themis. In *Workshop on Water in Asteroids and Meteorites*, Observatoire de Paris, Paris, France.
- Pinilla-Alonso N., Lorenzi V., Campins H., de Leon J., and Licandro J. (2013) Near-infrared spectroscopy of 1999 JU<sub>3</sub>, the target of the Hayabusa 2 mission. *Astron. Astrophys.*, 552, A79.
- Prettyman T., Mittlefehldt D., Yamashita N., Lawrence D., Beck A., Feldman W., McCoy T., McSween H., Toplis M., and Titus T. (2012) Elemental mapping by Dawn reveals exogenic H in Vesta's regolith. *Science*, 338, 242.
- Reddy V., Le Corre L., O'Brien D. P., Nathues A., Cloutis E. A., Durda D., Bottke W., Bhatt M., Nesvorný D., and Buczkowski D. (2012) Delivery of dark material to Vesta via carbonaceous chondritic impacts. *Icarus*, 221, 544–559.
- Rivkin A. (2012) The fraction of hydrated C-complex asteroids in the asteroid belt from SDSS data. *Icarus*, 221(2), 744–752.
- Rivkin A. S. and Emery J. P. (2010) Detection of ice and organics on an asteroidal surface. *Nature*, 464, 1322–1323.
- Rivkin A. S. and Volquardsen E. L. (2010) Rotationally-resolved spectra of Ceres in the 3-μm region. *Icarus*, 206(1), 327–333.
- Rivkin A. S., Lebofsky L. A., Clark B. E., Howell E. S., and Britt D. T. (2000) The nature of M-class asteroids in the 3-μm region. *Icarus*, 145, 351–368.
- Rivkin A. S., Brown R. H., Trilling D. E., Bell J. F., and Plassmann J. H. (2002a) Infrared spectrophotometry of Phobos and Deimos. *Icarus*, 156, 64–75.
- Rivkin A. S., Howell E. S., Vilas F., and Lebofsky L. A. (2002b) Hydrated minerals on asteroids: The astronomical record. In *Asteroids III* (W. F. Bottke Jr. et al., eds.), pp. 235–253. Univ. of Arizona, Tucson.
- Rivkin A. S., Davies J. K., Johnson J. R., Ellison S. L., Trilling D. E., Brown R. H., and Lebofsky L. A. (2003) Hydrogen concentrations on C-class asteroids derived from remote sensing. *Meteoritics & Planet. Sci.*, 38, 1383–1398.
- Rivkin A. S., McFadden L. A., Binzel R. P., and Sykes M. (2006) Rotationally-resolved spectroscopy of Vesta I: 2–4 μm region. *Icarus*, 180, 464–472.
- Rivkin A. S., Clark B. E., Ockert-Bell M. E., Shepard M. K., Volquardsen E. L., Howell E. S., and Bus S. J. (2011) Asteroid 21 Lutetia at 3 μm: Observations with IRTF SpeX. *Icarus*, 216, 62–68.
- Rivkin A. S., Howell E. S., Emery J. P., Volquardsen E. L., and DeMeo F. E. (2012) Toward a taxonomy of asteroid spectra in the 3-μm region. In *European Planet. Sci. Congr. 2012*, p. 359.
- Rivkin A. S., Howell E. S., Vervack R. J. Jr., Magri C., Nolan M. C., Fernandez Y. R., Cheng A. F., Barucci M. A., and Michel P. (2013a) The NEO (175706) 1996 FG<sub>3</sub> in the 2–4 μm spectral region: Evidence for an aqueously altered surface. *Icarus*, 223, 493–498.
- Rivkin A. S., Howell E., Emery J., and Volquardsen E. (2013b) The Ch asteroids: Connecting a visible taxonomic class to a 3-μm spectral shape. In *AAS/Division for Planetary Sciences Meeting Abstracts*, 45, #205.11.
- Rivkin A. S., Howell E. S., Emery J. P., and Sunshine J. M. (2013c) Does the solar wind create OH on NEO surfaces?: Observations of 433 Eros and 1036 Ganymed. *Lunar Planet. Sci. XLIV*, Abstract #2070. Lunar and Planetary Institute, Houston.
- Rivkin A. S., Asphaug E., and Bottke W. F. (2014a) The case of the missing Ceres family. *Icarus*, 243, 429–439.
- Rivkin A. S., Howell E., and Emery J. (2014b) The LXD-mode Main-belt/NEO Observing Program (LMNOP): Results. In *Asteroids, Comets, Meteors 2014* (K. Muinonen et al., eds.), p. 469. Helsinki, Finland.
- Rubin A. E., Trigo-Rodriguez J. M., Huber H., and Wasson J. T. (2007) Progressive aqueous alteration of CM carbonaceous chondrites. *Geochim. Cosmochim. Acta*, 71(9), 2361–2382.
- Ryskin Y. I. (1974) The vibrations of protons in minerals: Hydroxyl, water and ammonium. In *The Infrared Spectra of Minerals* (V. C.

- Farmer, ed.), pp. 137–181. Mineralogical Society of America, Monograph 4.
- Salisbury J. W., D’Aria D. M., and Jarosewich E. (1991) Midinfrared (2.5–13.5  $\mu\text{m}$ ) reflectance spectra of powdered stony meteorites. *Icarus*, 92, 280–297.
- Sato K., Miyamoto M., and Zolensky M. E. (1997) Absorption bands near three micrometers in diffuse reflectance spectra of carbonaceous chondrites: Comparison with asteroids. *Meteoritics*, 32, 503–507.
- Sawyer S. R. (1991) A high resolution CCD spectroscopic survey of low-albedo main belt asteroids. Ph.D. dissertation, Univ. of Texas, Austin.
- Schorghofer N. (2008) The lifetime of ice on main belt asteroids. *Astrophys. J.*, 682, 697–705.
- Seu R., Biccari D., Orosei R., Lorenzoni L., Phillips R., Marinangeli L., Picardi G., Masdea A., and Zampolini E. (2004) SHARAD: The MRO 2005 shallow radar. *Planet. Space Sci.*, 52(1), 157–166.
- Shands A. L. (1949) *Mean Precipitable Water in the United States*. U.S. Department of Commerce Division of Climatological and Hydrologic Services, Technical Paper No. 10.
- Shepard M. K., Taylor P. A., Nolan M. C., Howell E. S., Springmann A., Giorgini J. D., Warner B. D., Harris A. W., Stephens R., Merline W. J., et al. (2015) A radar survey of M- and X-class asteroids. III. Insights into their composition, hydration state, and structure. *Icarus*, 245, 38–55.
- Starukhina L. (2001) Water detection on atmosphereless celestial bodies: Alternative explanations of the observations. *J. Geophys. Res.*, 106(E7), 14701–14710.
- Stern S. A., Slater D. C., Scherrer J., Stone J., Dirks G., Versteeg M., Davis M., Gladstone G. R., Parker J. W., Young L. A., et al. (2008) Alice: The ultraviolet imaging spectrograph aboard the New Horizons Pluto-Kuiper belt mission. *Space Sci. Rev.*, 140(1–4), 155–187.
- Stern S. A., Parker J. Wm., Feldman P. D., Weaver H. A., Steffl A., A’Hearn M. F., Feaga L., Birath E., Graps A., and Bertaux J.-L. (2011) Ultraviolet discoveries at asteroid (21) Lutetia by the Rosetta Alice ultraviolet spectrograph. *Astron. J.*, 141, 3.
- Stewart B. D., Pierazzo E., Goldstein D. B., Varghese P. L., and Trafton L. M. (2011) Simulations of a comet impact on the Moon and associated ice deposition in polar cold traps. *Icarus*, 216, 1–16.
- Su K. Y., Rieke G. H., Malhotra R., Stapelfeldt K. R., Hughes A. M., Bonsor A., Wilner D. J., Balog Z., Watson D. M., Werner M. W., et al. (2013) Asteroid belts in debris disk twins: Vega and Fomalhaut. *Astrophys. J.*, 763(2), 118.
- Sunshine J. M., Farnham T. L., Feaga L. M., Groussin O., Merlin F., Milliken R. E., and A’Hearn M. F. (2009) Temporal and spatial variability of lunar hydration as observed by the Deep Impact spacecraft. *Science*, 326, 565.
- Takir D. and Emery J. (2012) Outer main belt asteroids: Identification and distribution of four 3- $\mu\text{m}$  spectral groups. *Icarus*, 219, 641–654.
- Takir D., Emery J. P., McSween H. Y., Hibbitts C. A., Clark R. N., Pearson N., and Wang A. (2013) Nature and degree of aqueous alteration in CM and CI carbonaceous chondrites. *Meteoritics & Planet. Sci.*, 48(9), 1618–1637.
- Takir D., Emery J., and McSween H. (2015) Toward an understanding of phyllosilicate mineralogy in the outer main belt region. *Icarus*, 257, 185–193.
- Thomas P. C., Parker J. W., McFadden L. A., Russell C. T., Stern S. A., Sykes M. V., and Young E. F. (2005) Differentiation of the asteroid Ceres as revealed by its shape. *Nature*, 437(7056), 224–226.
- Tsiganis K., Gomes R., Morbidelli A., and Levison H. (2005) Origin of the orbital architecture of the giant planets of the solar system. *Nature*, 435, 459–461.
- Vernazza P., Fulvio D., Brunetto R., Emery J. P., Dukes C. A., Cipriani F., Witasse O., Schaible M. J., Zanda B., Strazzulla G., and Baragiola R. A. (2013) Paucity of Tagish Lake-like parent bodies in the asteroid belt and among Jupiter Trojans. *Icarus*, 225, 517–525.
- Vilas F. (1994) A cheaper, faster, better way to detect water of hydration on solar system bodies. *Icarus*, 111, 456–467.
- Vilas F. (1995) Is the U-B color sufficient for identifying water of hydration on solar system bodies? *Icarus*, 115, 217–218.
- Vilas F. (2010) Composition of jovian outer irregular satellites from reflectance spectrophotometry: New MMT data. *Bull. Am. Astron. Soc.*, 42, 951.
- Vilas F. (2013) Reflectance spectrophotometry of the irregular outer jovian satellites as insight to solar system history. *Lunar Planet. Sci. XLIV*, Abstract #2900. Lunar and Planetary Institute, Houston.
- Vilas F. and Gaffey M. J. (1989) Phyllosilicate absorption features in main-belt and outer-belt asteroid reflectance spectra. *Science*, 246, 790–792.
- Vilas F., Hatch E. C., Larson S. M., Sawyer S. R., and Gaffey M. J. (1993) Ferric iron in primitive asteroids — A 0.43-micron absorption feature. *Icarus*, 102, 225–231.
- Vilas F., Larson S. M., Stockstill K. R., and Gaffey M. J. (1996) Unraveling the zebra: Clues to the Iapetus dark material composition. *Icarus*, 124, 262–267.
- Vilas F., Lederer S. M., Gill S. L., Jarvis K. S., and Thomas-Osip J. E. (2006) Aqueous alteration affecting the irregular outer planets satellites: Evidence from spectral reflectance. *Icarus*, 180, 453–463.
- Vilas F., Sollitt L., and Sykes M. V. (2013) Progress toward the operational ATSA Suborbital Observatory. In *Next Generation Suborbital Researcher’s Conference 2013*, Broomfield, Colorado.
- Volquardsen E. L., Rivkin A. S., and Bus S. J. (2007) Composition of hydrated near-Earth object (100085) 1992 UY<sub>4</sub>. *Icarus*, 187, 464–468.
- Walsh K. J., Morbidelli A., Raymond S. N., O’Brien D. P., and Mandell A. M. (2011) A low mass for Mars from Jupiter’s early gas-driven migration. *Nature*, 475, 206–209.
- Watson K., Murray B., and Brown H. (1961) On the possible presence of ice on the Moon. *J. Geophys. Res.*, 66(5), 1598–1600.
- Weidenschilling S. (2011) Initial sizes of planetesimals and accretion of the asteroids. *Icarus*, 214(2), 671–684.
- Wigton N., Emery J. P., Rivkin A. S., and Thomas C. A. (2014) Near-infrared (2–4  $\mu\text{m}$ ) spectroscopy of near-Earth asteroids: Searching for OH/H<sub>2</sub>O on small planetary bodies. In *AAS/Division for Planetary Sciences Meeting*, 46, #213.16.
- Yang B., Jewitt D., and Bus S. J. (2009) Comet 17P/Holmes in outburst: The near infrared spectrum. *Astron. J.*, 137(5), 4538.
- Young E. F., Osterman S., Woodruff R., Germann L., Diller J., Dinkel K., Dischner Z., and Truesdale N. (2013) Beyond HST: High acuity imaging from the Earth’s stratosphere. In *Next Generation Suborbital Researcher’s Conference 2013*, Broomfield, Colorado.
- Zellner B., Tholen D. J., and Tedesco E. F. (1985) The eight-color asteroid survey — Results for 589 minor planets. *Icarus*, 61, 335–416.
- Zolensky M. E., Barrett R., and Browning L. (1993) Mineralogy and composition of matrix and chondrule rims in carbonaceous chondrites. *Geochim. Cosmochim. Acta*, 57, 3123–3148.
- Zolensky M. E., Nakamura K., Gounelle M., Mikouchi T., Kasama T., Tachikawa O., and Tonui E. (2002) Mineralogy of Tagish Lake: An ungrouped type-2 carbonaceous chondrite. *Meteoritics & Planet. Sci.*, 37, 737–761.



# Space-Based Thermal Infrared Studies of Asteroids

**Amy Mainzer**

*Jet Propulsion Laboratory, California Institute of Technology*

**Fumihiko Usui**

*The University of Tokyo*

**David E. Trilling**

*Northern Arizona University*

---

Large-area surveys operating at mid-infrared wavelengths have proven to be a valuable means of discovering and characterizing minor planets. Through the use of radiometric models, it is possible to derive physical properties such as diameters, albedos, and thermal inertia for large numbers of objects. Modern detector array technology has resulted in a significant improvement in spatial resolution and sensitivity compared with previous generations of spacebased infrared telescopes, giving rise to a commensurate increase in the number of objects that have been observed at these wavelengths. Spacebased infrared surveys of asteroids therefore offer an effective method of rapidly gathering information about the orbital and physical properties of small-body populations. The AKARI, Wide-field Infrared Survey Explorer (WISE)/ Near-Earth Object Wide-field Infrared Survey Explorer (NEOWISE), Spitzer Space Telescope, and Herschel Space Observatory missions have significantly increased the number of minor planets with well-determined diameters and albedos.

## 1. INTRODUCTION

A variety of remote-sensing techniques have given rise to much of our understanding of the small-body populations in our solar system. Groundbased surveys operating at visible wavelengths have discovered most of the minor planets that are known today. At present, roughly 700,000 asteroids have been discovered in the main belt between Mars and Jupiter, ~13,000 near-Earth objects (NEOs) are known at all sizes, and some 5000 jovian Trojans have been found. While these numbers are thought to represent only a tiny fraction of the small bodies believed to exist in our solar system, much can be learned about these populations by studying the physical and dynamical properties of representative samples (e.g., Bottke et al., 2005; Mainzer et al., 2011b; Grav et al., 2011a; see also the chapter by Jedicke et al. in this volume). Moreover, information about the probable composition and mineralogy of asteroids can be learned from visible and near-infrared (VNIR) spectroscopy and spectrophotometry. Such studies have been carried out for ~2500 asteroids [e.g., the Massachusetts Institute of Technology (MIT)-University of Hawaii (UH)-Infrared Telescope Facility (IRTF) Joint Campaign for NEO Spectral Reconnaissance (*Tholen and Barucci*, 1989; *Xu* et al., 1995; *Bus and Binzel*, 2002; *DeMeo* et al., 2009; *Reddy*, 2010; *Kuroda* et al., 2014; and many others)]. Compared to broadband imaging, spectrally resolved observations require brighter sources for the same signal-to-

noise ratio, which limits the number of targets observable. The fourth release of the Sloan Digital Sky Survey (SDSS) Moving Object Catalog (*Stoughton* et al., 2002; *Abazajian* et al., 2003) provided ~100,000 observations in u, g, r, i, and z filters, leading to taxonomic classifications for ~64,000 asteroids (*Carvano* et al., 2010).

Asteroid lightcurves, sometimes combined with stellar occultation data, have been inverted to obtain models of shapes and rotational states for hundreds of objects (*Kaasalainen* et al., 2001; *Durech* et al., 2010; see also the chapter by Durech et al. in this volume). Radar observations can produce the most detailed information about shape, size, orbit, and spin state short of visiting a body with spacecraft (e.g., *Ostro* et al., 2002; see the chapter by Benner et al. in this volume). Since radar echoes must be sent to and received from a body, sensitivity drops as distance to the fourth power, so objects must make fairly close approaches in order to be detected. Approximately 600 asteroids have been observed with radar to date (<http://echo.jpl.nasa.gov/asteroids/index.html>). Polarimetry offers a means of studying asteroid surface properties, but since only a small fraction of the total luminosity is polarized, this technique has been applied to ~300 asteroids thus far (*Lupishko and Vasilyev*, 2012; *Gil-Hutton and Canada-Assani*, 2012).

While powerful, these techniques have only been employed on a small fraction of asteroids. Until recently, for the vast majority of asteroids, nothing was known except

for absolute visible magnitudes (denoted H) and orbital parameters. Observing small bodies at thermal infrared (IR) wavelengths with space telescopes complements other techniques such as visible-light groundbased surveys, VNIR spectroscopy and spectrophotometry, radar studies, and *in situ* spacecraft visits. If a telescope can be cryogenically cooled such that its sensitivity is limited by the natural backgrounds in space, rather than by self-emission, it is possible to obtain measurements of physical properties such as diameters and albedos very rapidly for a large number of asteroids. Advances in IR detector technology have made it possible to achieve diffraction-limited imaging and orders-of-magnitude improvement in sensitivity compared to previous generations of IR space telescopes such as the Infrared Astronomical Satellite (IRAS) (Neugebauer *et al.*, 1984; Tedesco *et al.*, 2002b), the Mid-Course Space Experiment (MSX) (Mill *et al.*, 1994; Price *et al.*, 2001; Tedesco *et al.*, 2002a), and the Infrared Space Observatory (ISO) (Kessler *et al.*, 1996). More recent surveys have now observed a substantial fraction of the known asteroids at thermal-IR wavelengths, allowing for robust determinations of their diameters and (where corresponding visible light observations are available) albedos. These measurements in turn inform the understanding of the dynamical and collisional history of the asteroids, their probable compositions and structure, and the impact hazard they pose to Earth.

Groundbased thermal-IR observations began to play an important role in the physical characterization of the largest asteroids beginning in the 1970s with the advent of IR detectors (e.g., Allen, 1970, 1971; Matson, 1971). These observations require the largest groundbased telescopes due to the enormous thermal background from Earth's atmosphere and the telescope itself (backgrounds  $\sim 10^6$  lower between  $\sim 4$  and  $200\text{ }\mu\text{m}$  are achievable with a spacebased cooled telescope). Moreover, Earth's atmospheric opacity restricts groundbased observations to selected wavelengths. Some mid-IR instruments are available on groundbased telescopes, especially at high-altitude observatories in Hawaii and Chile, leading to observations of several hundred objects to date (e.g., Hansen, 1976; Cruikshank, 1977; Lebofsky *et al.*, 1978; Morrison and Lebofsky, 1979; Delbó *et al.*, 2003, 2011; Matter *et al.*, 2011; Müller *et al.*, 2012, 2013; Wolters *et al.*, 2005, 2008).

Thermal IR fluxes can be used to derive physical properties such as effective spherical diameter (defined as the diameter of a spherical thermal model asteroid emitting the same IR flux as that observed) through the use of radiometric models. Section 3 below and the chapter by Delbó *et al.* in this volume give a more detailed description of common thermal models (see also Harris and Lagerros, 2002). Small-body spectral energy distributions consist of the sum of blackbody curves produced by reflected sunlight, centered at visible wavelengths, and blackbody curves generated by thermal emission from areas at different temperatures. The central wavelength of the thermal peak depends on an object's heliocentric distance and thermal properties but usually lies somewhere between 5 and  $20\text{ }\mu\text{m}$  for most aster-

oids interior to Saturn's orbit. Hence, by combining orbital information with thermal-IR observations that bracket an object's rotational lightcurve, it is possible to constrain the total energy being emitted by an asteroid and convert this into an effective spherical diameter. With only a single IR measurement, it is possible to compute a projected size, but this does not necessarily correspond to the effective spherical diameter if the object is elongated. Diameters derived from good-quality thermal-IR measurements are considerably more accurate than those estimated from visible-light observations alone, since an asteroid's visible flux depends strongly on its albedo. With multiple thermally dominated IR bands that adequately sample rotational phase, effective spherical diameters can be determined to within  $\pm 10\%$  (Mainzer *et al.*, 2011c) (see section 3 for a more detailed discussion). However, since asteroid albedos range from a few percent to  $\sim 50\%$  (e.g., Binzel *et al.*, 2004; Mainzer *et al.*, 2011b), effective spherical diameters derived from only visible light measurements are typically uncertain by factors of 2–3. If both IR and visible observations are available, it is possible to solve for albedo as well.

Spacebased thermal-IR surveys therefore offer a number of advantages for understanding small-body populations. Since an asteroid's visible flux is a strong function of its albedo, visible-light surveys are preferentially biased against low-albedo objects, which are intrinsically dimmer than higher-albedo asteroids. By contrast, surveys that independently detect asteroids (whether previously known or new) based solely on their thermal-IR flux are approximately equally sensitive to low- and high-albedo asteroids. Infrared-selected samples directly measure diameter and are insensitive to albedo, allowing for direct determination of a population's size-frequency distribution rather than its H-magnitude distribution. An IR-selected sample can therefore be readily extrapolated to determine the orbital and physical properties of the underlying population.

In addition, albedos derived from the combination of visible and IR observations offer clues to an object's probable composition. Accurate measurements of asteroid diameters are needed to constrain the impact energy of potentially hazardous objects and inform mitigation strategies. Spacebased telescopes can, depending on their design, observe regions of sky that are inaccessible to groundbased observers. All-sky surveys offer the additional benefit of sampling the population of objects with high inclinations more thoroughly. Thermal-IR observations can be used to determine thermal inertia, a key parameter for understanding the nature of asteroid regoliths (see the chapter by Delbó *et al.* in this volume). Depending on wavelength and spectral resolution, spacebased IR instruments can allow for measurement of emission and absorption features that are difficult or impossible to access from groundbased facilities.

## 2. THE MISSIONS

The IRAS space telescope was the first space mission to survey the minor planets at thermal-IR wavelengths in 1983,

followed by MSX and ISO in 1995–1998 and 1996–1997, respectively. With 62 pixels and a 60-cm telescope, the IRAS mission observed ~2200 asteroids (Matson et al., 1989; Veecher et al., 1989; Tedesco et al., 2002b). ISO observed ~40 different asteroids in targeted mode (Dotto et al., 2002), and MSX observed an additional ~30 objects not detected by IRAS (Tedesco et al., 2002a). IRAS was not diffraction limited due to the large physical size of its pixels; its minimum spatial resolution was ~30 arcsec. IRAS discovered six asteroids, including (3200) Phaethon, the parent body of the Geminid meteor stream (Whipple, 1983; Green et al., 1985), and five comets.

As larger-format IR arrays with smaller pixels and lower noise became available, they were incorporated into next-generation observatories such as the Spitzer Space Telescope (hereafter Spitzer) (Werner et al., 2004), the AKARI mission (Murakami et al., 2007), WISE (Wright et al., 2010), and the Herschel Space Observatory (hereafter Herschel) (Pilbratt et al., 2010). These new arrays allowed for Nyquist-sampled images (i.e. the pixel width is less than half the size of the point spread function produced by the telescope), improving spatial resolution and sensitivity by orders of magnitude over IRAS and MSX.

The advances in microelectronics, visible-light camera chips, and tactical sensors are directly responsible for the vast improvement in sensitivity and miniaturization from the IRAS mission to today. The 62 IRAS detectors were individually manufactured and hand-assembled; each pixel was ~1–2 mm across (Young, 1993). Major developments since IRAS include the advent of monolithically fabricated arrays of pixels and the ability to produce semiconductor material with extremely low levels of impurities. The result is the development of megapixel IR arrays capable of achieving low read noise and dark currents well below the natural zodiacal background at thermal-IR wavelengths. For example, the WISE mission included four 1024<sup>2</sup> detector arrays, each with 18-μm pixels (Mainzer et al., 2005). Recent developments include the fabrication of megapixel mid-IR detectors capable of operating at higher temperatures, which will ease the burden on cryogenic systems for future missions (McMurtry et al., 2013).

Spitzer, AKARI, WISE, and Herschel were cryogenically cooled during their prime mission phases, and all but Herschel continued to operate using the wavelengths that remained available following depletion of their liquid or solid cryogens. Table 1 summarizes the key technical and operational differences between them. Spitzer and Herschel functioned as general-purpose observatories, with a wide range of observing modes employed during their fully cryogenic missions. Both performed targeted observations of previously known objects; neither mission has been widely used for asteroid discovery. WISE operated in a single-survey mode, covering the entire sky in six months. Modifications to its science data processing pipeline allowed new discoveries of minor planets to be made. The primary objective of the AKARI mission was to carry out an all-sky survey; AKARI also had the capability of performing targeted spectroscopic

and imaging observations. After the liquid cryogen boiled off, only near-IR observations in a targeted mode were carried out. AKARI did not discover new asteroids; the all-sky observing cadence did not support the multiple observations needed to discover new moving objects.

In this chapter, we review only spacebased asteroid studies from remote telescopic observations. For a detailed discussion of the results from mid-IR observations of small bodies carried out by *in situ* missions such as Dawn and Rosetta, the reader is referred to the chapters by Barucci et al. and Russell et al. in this volume. These missions gathered thermal-IR maps of bodies such as (2867) Šteins (Leyrat et al., 2011), (21) Lutetia, and (4) Vesta (Keihm et al., 2012; Tosi et al., 2014; Capria et al., 2014).

## 2.1. Spitzer Space Telescope

Spitzer was launched on August 25, 2003, into an Earth-trailing orbit (Werner et al., 2004). As a NASA “Great Observatory,” it was designed to function as a facility observatory for the astrophysics and planetary communities. The 85-cm telescope was launched warm, sitting atop a ~350-L superfluid helium cryostat that enclosed the instruments and fine guidance sensor. During its 5.5-year fully cryogenic mission, three instruments were available: the Infrared Array Camera (IRAC), an imager operating at 3.6, 4.5, 5.8, and 8 μm (Fazio et al., 2004); the Multiband Imaging Photometer for Spitzer (MIPS), which provided imaging and spectroscopy covering the wavelength range 24–160 μm (Rieke et al., 2004); and the Infrared Spectrograph (IRS), which provided low- and medium-resolution spectroscopy between 5 and 35 μm and imaging at 16 and 22 μm (Houck et al., 2004). The IRAC instrument observed the 3.4- and 5.8-μm channels simultaneously, and the 4.5- and 8-μm channels simultaneously. During the fully cryogenic portion of the Spitzer mission, the telescope temperature was maintained below 8 K using vapor escaping from the superfluid helium cryostat; focal planes were maintained at 1.4 K to support operation of the longest wavelengths.

In 2008, the liquid helium was depleted; at this point, the focal planes and telescope reached an equilibrium temperature near 29 K. The 3.6- and 4.5-μm channels of IRAC continued to operate via passive cooling in an extended “warm mission” phase (Storrie-Lombardi and Dodd, 2012). Asteroids throughout the solar system were targeted using all three Spitzer instruments during the fully cryogenic and warm mission phases (e.g., Emery et al., 2006, 2014; Trilling et al., 2010; Licandro et al., 2012; Bhattacharya et al., 2010; Mommert et al., 2015; Ryan et al., 2015).

Data from Spitzer can be accessed through the Spitzer Heritage Archive (<http://sha.ipac.caltech.edu>). In general, proprietary periods are one year for Guest Observer programs.

## 2.2. AKARI

Consisting of a 68.5-cm telescope, the AKARI satellite (meaning “light” as opposed to representing an acronym)

TABLE 1. Summary of recent spacebased IR telescope capabilities (as of March 2015).

Mission	Date	Wavelengths	Field of View (arcmin)	Observing Modes
Spitzer	2003–2008	IRAC: Imaging 3.6, 4.5, 5.8, 8 $\mu\text{m}$ IRS: Spectroscopy 5–35 $\mu\text{m}$ IRS: Imaging 16, 22 $\mu\text{m}$ MIPS: Imaging 24, 70, 160 $\mu\text{m}$ MIPS: Spectroscopy 55–95 $\mu\text{m}$	IRAC: 5 $\times$ 5 IRS: $\sim$ 0.9 $\times$ 1.35 MIPS: 5 $\times$ 5	Targeted
Spitzer	2008–present	IRAC: Imaging 3.6 and 4.5 $\mu\text{m}$	IRAC: 5 $\times$ 5	Targeted
AKARI	2006–2007	IRC: Imaging 9, 18 $\mu\text{m}$ FIS: Imaging 65, 90, 140, 160 $\mu\text{m}$	IRC: 10 (cross-scan direction) FIS: 8–12 (cross-scan direction)	Survey
AKARI	2006–2007	IRC: Imaging 2.4, 3.2, 4.1, 7, 9, 11, 15, 18, 24 $\mu\text{m}$ IRC: Spectroscopy 1.8–5.2, 5.4–12.9, 17.5–25.7 $\mu\text{m}$ FIS: Imaging 65, 90, 140, 160 $\mu\text{m}$ FIS: Spectroscopy 60–180 $\mu\text{m}$	IRC imaging: 10 $\times$ 10 FIS imaging: 8–12 (cross-scan direction)	Targeted
AKARI	2008–2001	IRC: Imaging 2.4, 3.2, 4.1 $\mu\text{m}$ IRC: Spectroscopy 2.5–5 $\mu\text{m}$	IRC imaging: 10 $\times$ 10	Targeted
WISE	2010–2011	Imaging 3.1, 4.6, 12, 22 $\mu\text{m}$	47 $\times$ 47	Survey
NEOWISE	2013–present	Imaging 3.4 and 4.6 $\mu\text{m}$	47 $\times$ 47	Survey
Herschel	2009–2013	HIFI: Spectroscopy 157–212 and 240–625 $\mu\text{m}$ PACS: Imaging at 70, 100, 160 $\mu\text{m}$ PACS: Spectroscopy 55–210 $\mu\text{m}$ SPIRE: Imaging 250, 350, 500 $\mu\text{m}$ SPIRE: Spectroscopy 194–617 $\mu\text{m}$	PACS Imager: 1.75 $\times$ 3.5 PACS Spectrometer: 47 $\times$ 47 SPIRE Imager: 4 $\times$ 8 Spectrometer: 2.6	Targeted

launched on February 21, 2006, into a Sun-synchronous polar orbit at 700 km altitude (*Murakami et al.*, 2007). AKARI carried two instruments, the InfraRed Camera (IRC) (*Onaka et al.*, 2007) and the Far-Infrared Surveyor (FIS) (*Kawada et al.*, 2007), covering the spectral ranges of 2–26  $\mu\text{m}$  and 50–180  $\mu\text{m}$ , respectively. The whole telescope and instruments were cooled down to  $\sim$ 6 K using 180 L of superfluid helium and two sets of two-stage Stirling cycle mechanical coolers (*Nakagawa et al.*, 2007). AKARI’s liquid helium supply lasted until August 26, 2007, and enabled 550 days of fully cryogenic operations (the AKARI “cold mission”).

During the cold mission phase, AKARI completed an all-sky survey at six bands: 9, 18, 65, 90, 140, and 160  $\mu\text{m}$  (*Ishihara et al.*, 2010; *Yamamura et al.*, 2010). The mid-IR part of the all-sky survey was conducted at two broadbands centered at 9 and 18  $\mu\text{m}$  with the IRC. More than 90% of the sky was observed with both bands, and a large portion of the sky was observed more than three times. The point source catalog of  $\sim$ 877,000 objects was produced from the mid-IR images of the all-sky survey data (*Ishihara et al.*, 2010). An asteroid catalog was also constructed from the mid-IR survey data (*Usui et al.*, 2011). The 16-month cold mission allowed the inner edge of the main belt to be observed at least once (*Usui et al.*, 2013). AKARI detected point sources by identifying objects that were detected at least twice at the same fixed point on the sky, leaving transient sources to

be identified with the list of solar system bodies known at the time of data processing. Most asteroids in the AKARI catalog were detected fewer than five times, with  $\sim$ 25% having one detection (*Usui et al.*, 2011). The two mid-IR bands observed different regions of the sky, separated by  $\sim$ 25' in the cross-scan direction; thus solar system objects were not observed simultaneously in both bands. In total, 5120 known asteroids were identified with AKARI detections. The list of derived sizes and albedos, known as the Asteroid Catalog Using AKARI (AcuA), is publicly available (<http://darts.isas.jaxa.jp/ir/akari/catalogue/AcuA.html>). The IR fluxes of individual asteroids observed with AKARI will also be released in the near future.

The instruments onboard AKARI performed both deep imaging and spectroscopy in the targeted observation mode, occasionally inserted into a continuous survey operation. The targeted observations were planned in advance to maximize the all-sky survey coverage and efficiency. A number of observations for a wide variety of astrophysical targets ranging from solar system objects to galaxies at cosmological distances were carried out in the targeted mode. During the cold mission, AKARI made more than 5000 targeted observations, including a small serendipitous survey of asteroids (*Hasegawa et al.*, 2013), thermal-IR photometric observations of (25143) Itokawa (*Müller et al.*, 2014b) and (162173) 1999 JU<sub>3</sub> (*Hasegawa et al.*, 2008), the targets of

the Japan Aerospace Exploration Agency (JAXA) Hayabusa and Hayabusa-2 sample return missions (see the chapter by Yoshikawa et al. in this volume).

After the exhaustion of AKARI's liquid helium, the telescope and instruments remained at sufficiently low temperatures (below 50 K) owing to the mechanical cooler. Targeted near-IR observations with the IRC were therefore able to be carried out in the AKARI "warm mission" phase. Low-resolution spectroscopy was performed using the near-IR channel of the IRC from 2–5  $\mu\text{m}$ . The AKARI warm mission's science observations began in June 2008 and continued until May 2011. The IRC carried out more than 12,000 targeted observations during the warm mission, including spectroscopy of 70 asteroids. The AKARI data are available from the Institute of Space and Astronautical Science (ISAS)/JAXA (<http://www.ir.isas.jaxa.jp/AKARI/Observation/>).

### 2.3. Wide-Field Infrared Survey Explorer/Near-Earth Object Wide-Field Infrared Survey Explorer

Launched on December 14, 2009, into a 525-km Sun-synchronous orbit, the WISE mission surveyed the entire sky at four infrared wavelengths (3.4, 4.6, 12 and 22  $\mu\text{m}$ ; denoted W1, W2, W3, and W4 respectively) using a 40-cm telescope (Wright et al., 2010). The survey's scientific objectives were to find the cool stars and luminous galaxies using a single operational mode. The survey strategy was designed for rapid sky coverage, resulting in observations of the entire sky with an average depth of  $\sim$ 10 exposures on the ecliptic plane (rising to thousands at the ecliptic poles) after six months. All four wavelengths were imaged simultaneously using beam splitters. Augmentations to the WISE science data processing pipeline allowed for archiving of the individual single-frame exposures as well as mining of moving objects from the images in real time (Mainzer et al., 2011a). The fully cryogenic baseline mission was completed in July 2010, and the solid hydrogen cryogen used to cool the W3 and W4 detectors was partially exhausted on August 5, 2010, resulting in the loss of the W4 channel. Operations continued using the W1, W2, and W3 arrays until the cryogen was fully exhausted on September 30, 2010. The mission continued in a post-cryogenic phase with the goal of observing NEOs (asteroids and comets with perihelia  $<1.3$  AU) until February 1, 2011, using the passively cooled W1 and W2 channels. After this, it was placed into hibernation for 32 months. During all phases of the prime mission,  $>158,000$  asteroids were detected, including  $\sim$ 34,000 new discoveries.

The spacecraft was reawakened in August 2013 to begin an extended mission, known as NEOWISE, to discover and characterize the NEO population using the 3.4- and 4.6- $\mu\text{m}$  channels, which remain operational via passive cooling to  $\sim$ 75 K. Survey operations resumed on December 21, 2013, and are expected to continue until early 2017. To date, the spacecraft has observed  $\sim$ 15,600 minor planets, including 391 NEOs, a rate of  $\sim$ 0.7–0.8 NEOs per day (Mainzer et al., 2014b; Nugent et al., 2015).

The WISE observational strategy typically resulted in  $\sim$ 10–12 observations of most asteroids spaced over  $\sim$ 36 hours. However, the short length of the observational arc means that groundbased follow-up is necessary to secure orbits for new discoveries. The worldwide community of professional and amateur observers has contributed to follow-up for NEOWISE NEO candidate discoveries, which are typically found with  $R \sim 22$  mag. As an all-sky survey, NEOWISE candidates are frequently found at high declinations, regardless of weather or lunar phase, posing unique challenges for follow-up observers.

All data from the WISE prime mission and the first year of the NEOWISE reactivation have been publicly released and are available through NASA's Infrared Science Archive (IRSA) (<http://irsa.ipac.caltech.edu/Missions/wise.html>). Derived physical properties for minor planets are being prepared for submission to NASA's Planetary Data System; until then, they are available through the individual NEOWISE team publications, i.e., Mainzer et al. (2011b, 2012a, 2014a,b) for the NEOs; Masiero et al. (2011, 2012a, 2014) for the main-belt asteroids (MBAs); Grav et al. (2011b, 2012a,b) for the Hilda group and jovian Trojans; and Bauer et al. (2013) for the scattered-disk objects and Centaur populations.

### 2.4. Herschel Space Observatory

Herschel launched on May 14, 2009, carrying a 3.5-m telescope into orbit around the Earth-Sun L<sub>2</sub> Lagrange point (Pilbratt et al., 2010). Herschel's telescope was passively cooled, and a Dewar containing  $\sim$ 2370 L of superfluid liquid helium was used to cool its far-IR instruments, the Photodetector Array Camera and Spectrometer (PACS) (Poglitsch et al., 2010), the Spectral and Photometric Imaging REceiver (SPIRE) (Griffin et al., 2010), and the Heterodyne Instrument for the Far Infrared (HIFI) (de Graauw et al., 2010). Owing to its longer wavelengths, spanning 55–671  $\mu\text{m}$ , Herschel was primarily used to observe the more distant minor planets (which are cooler and therefore emit strongly at far-IR) such as transneptunian and Kuiper belt objects by the open-time key program entitled "TNOs are cool: A survey of the transneptunian region" (Müller et al., 2010). However, MBAs were used as calibration sources (Müller et al., 2014a), and measurements of individual targets of interest were made for  $\sim$ 10 asteroids (e.g., Leyrat et al., 2012; O'Rourke et al., 2012; Müller et al., 2013, 2014b,c).

Herschel data may be accessed through the Herschel Science Archive (HSA) maintained by the European Space Agency (ESA) (<http://www.cosmos.esa.int/web/herschel/science-archive>). It is also possible to query the HSA through NASA's Herschel Science Center (<http://irsa.ipac.caltech.edu/applications/Herschel/>).

## 3. THERMAL MODELING

Thermal models range in sophistication and complexity; different models are used depending on data quality,

computing resources, and the availability of ancillary data such as shape models and rotational states. All models begin by solving the energy balance between incident solar radiation, reflected sunlight, and thermal emission (e.g., *Lebofsky et al.*, 1986). For a spherical, airless body, this is given by

$$A_p S = L_r + L_e \quad (1)$$

where  $A_p$  is the object's projected area,  $S$  is the solar flux at the distance of the asteroid, and  $L_r$  and  $L_e$  are the reflected and emitted radiation, respectively, and  $L_r/L_e = A/(1-A)$ , where  $A$  is the bolometric Bond albedo. In essence, the purpose of thermal modeling is to determine  $L_e$  from the observed flux in one direction (or a few directions for objects observed at multiple viewing geometries), and one or a few thermally dominated bandpasses. The extrapolation to all directions and the bolometric emitted radiation are what the model provides. The total thermal emission is given by

$$L_e = \varepsilon \eta \sigma R^2 \int_{-\pi}^{\pi} \int_{-\pi/2}^{\pi/2} T^4(\theta, \phi) \cos(\phi) d\phi d\theta \quad (2)$$

where  $\varepsilon$  is the emissivity as a function of wavelength,  $\eta$  is the so-called beaming parameter (described in more detail below),  $\sigma$  is the Stefan-Boltzmann constant,  $R$  is the object's radius, and  $T$  is the object's temperature distribution as a function of longitude ( $\theta$ ) and latitude ( $\phi$ ), measured from the subsolar point.

The standard thermal model (STM) (*Lebofsky et al.*, 1986, and references therein) and the popular near-Earth asteroid thermal model (NEATM) (*Harris*, 1998) adopt the following temperature distribution across the asteroid's surface

$$T(\theta, \phi) = \begin{cases} T_{ss} \cos^{1/4} \zeta & \text{if } \zeta < \pi/2 \\ 0 & \text{if } \zeta \geq \pi/2 \end{cases} \quad (3)$$

where the angular distance from the subsolar point is  $\zeta$  and the temperature at the subsolar point ( $T_{ss}$ ) is

$$T_{ss} = \left[ \frac{S(1-A)}{\eta \varepsilon \sigma} \right]^{1/4} \quad (4)$$

Since the peak of the Sun's spectral energy distribution occurs at visible wavelengths, the Bond albedo is customarily assumed to be equal to the total Bond albedo at V band ( $\sim 0.56 \mu\text{m}$ ),  $A_v$ . In the system of *Bowell et al.* (1989), the Bond albedo is related to the more readily measured visible geometric albedo  $p_V$  by

$$A \sim A_v = p_V q = p_V (0.29 + 0.684G) \quad (5)$$

where  $G$  is the so-called phase slope parameter that ranges from  $\sim -0.1$  to  $0.4$  (*Bowell et al.*, 1989; *Harris et al.*, 1989).

Since  $p_V$  is generally  $< 1$ ,  $A$  is usually  $\ll 1$ . We therefore have a direct relationship between the asteroid's thermal flux

and its diameter  $D$ :  $L_e \propto D^2(1-A) \rightarrow D^2$ . However, since the asteroid's reflected sunlight goes as  $L_r = A_p AS \propto AD^2$ , diameter and albedo cannot be easily disentangled if only  $L_r$  is measured. This results in a much larger uncertainty in the derived diameter unless  $p_V$  is already known, given the large range of asteroid albedos ( $\sim 0.02$  to  $> 0.5$ ) (*Binzel et al.*, 2004; *Mainzer et al.*, 2011b; *Masiero et al.*, 2011).

If only the absolute visible magnitude  $H$  of the asteroid is available, corresponding to its V-band magnitude measured or extrapolated at  $\alpha = 0^\circ$  and object-to-observer and heliocentric distances of 1 AU, a frequently used empirical relationship for diameter is given by

$$D = \frac{1329}{\sqrt{p_V}} 10^{-H/5} \quad (6)$$

where  $D$  is the diameter in kilometers (*Bowell et al.*, 1989; *Harris and Lagerros* 2002). This relationship also demonstrates that diameter derived from visible-light observations alone is a sensitive function of an asteroid's albedo, underscoring the value of obtaining diameters obtained radiometrically.

Thermal models offer the possibility of deriving physical properties for large numbers of asteroids, with increasingly sophisticated models and better data allowing for more and improved constraints on parameters such as diameter, geometric visible albedo ( $p_V$ ), infrared albedo ( $p_{IR}$ ), emissivity, shape, rotational state, and thermal inertia. The STM corresponds to the case of a nonrotating spherical body, or one with zero thermal inertia and no nightside emission, observed at  $0^\circ$  solar phase angle. The beaming parameter  $\eta$ , which takes into account surface roughness and the "beaming" of thermal emission in the direction of the Sun, is often set to 0.756 in the STM based on empirical fits to the diameters of (1) Ceres and (2) Pallas derived from stellar occultations. The fast rotating model (FRM) (*Lebofsky et al.*, 1978; *Veeder et al.*, 1989; *Lebofsky and Spencer*, 1989), by contrast, is more appropriate for an object that rotates rapidly or has high thermal inertia/high thermal conductivity; effectively,  $\eta$  is set to  $\pi$ , and the nightside emits flux and does not follow equation (3). The NEATM assumes a hybrid approach that still assumes zero contribution from the nightside, but allows  $\eta$  to be fit as a free parameter if observations from more than one thermal-IR band are available.

NEATM-derived diameters generally reproduce measurements from radar, stellar occultations, and *in situ* spacecraft visits to within  $\pm 10\%$ , given multiple thermally dominated IR measurements that adequately sample an asteroid's rotational light curve with good signal-to-noise ratio (SNR) and an accurate determination of distance from knowledge of its orbit (*Mainzer et al.*, 2011c). It is worth noting that the accuracy of the diameters of objects used to confirm the performance of radiometric thermal models (such as radar or stellar occultations) is typically  $\sim 10\%$ . With these caveats, albedos can be determined to within  $\pm 25\%$  of their value (i.e.,  $p_V = 0.04 \pm 0.01$ ) if good-quality visible-light observations are available. The accuracy of the derived albedo

depends critically on the accuracy of H (see below). If only observations at a single band centered near 4.6  $\mu\text{m}$  are available (as is the case for some WISE/NEOWISE and Spitzer targets), diameter errors typically degrade to  $\pm 20\text{--}25\%$ , and albedos can only be known to within  $\pm 40\text{--}50\%$  of their value (Mueller et al., 2007; Harris et al., 2011; Mainzer et al., 2012a; Masiero et al., 2012a).

While diameter determinations from thermal-IR observations are relatively insensitive to visible light measurements, the latter are required to determine  $p_V$ . Obtaining good-quality H and G measurements (Bowell et al., 1989) is a persistent difficulty. Most of the time, visible observations collected simultaneously with IR fluxes are not available, so the absolute magnitude H and phase curve slope parameter G must be used to extrapolate the apparent visible magnitude at the time the IR observations were taken. Most asteroid observations come from the visible-light surveys that discover them, such as the Catalina Sky Survey, Lincoln Near Earth Asteroid Research (LINEAR), and Panoramic Survey Telescope and Rapid Response System (PanSTARRS). Typically, discovery observations are made with broadband V + R band filters to maximize sensitivity to NEOs, and while astrometric calibrations can be very accurate, photometric measurements can be considerably more variable. Moreover, G is known to vary with asteroid taxonomic type (e.g., Harris and Young, 1989). Williams (2012) recomputed H and G values for the entire Minor Planet Center catalog on a survey-by-survey basis and found that H offsets peak at +0.4 mag in the range H = 14.2–14.5 mag, but decrease to +0.1 mag for H > 20 mag, significantly expanding on the work of Pravec et al. (2012), who measured H values for 583 minor planets. Williams (2012) recomputed photometric magnitudes to account for the various surveys' filters. NEOWISE thermal model fits were performed assuming large ( $\pm 0.3$  mag or more) errors for H if no direct measurements of these parameters were available (e.g., from Warner et al., 2009; Pravec et al., 2012) at the time of publication. Future work will incorporate the Williams (2012) H and G values into thermal models from NEOWISE. If H values are well known, albedo can be determined to within 25%, but if H is poorly known, then the accuracy of the albedo degrades accordingly.

In bands where reflected sunlight contributes a non-negligible fraction of the total flux, the albedo at that wavelength ( $p_{\text{IR}}$ ) must also be treated as a free parameter in thermal models. For NEOs with subsolar temperatures

close to  $\sim 300$  K, peak thermal emission occurs near  $\sim 10 \mu\text{m}$ . Wavelengths longer than  $\sim 4 \mu\text{m}$  are typically thermally dominated for asteroids at heliocentric distances less than  $\sim 4$  AU; shorter wavelengths are a mix of reflected sunlight and thermal emission.

The infrared albedo at  $\sim 3 \mu\text{m}$  is not necessarily equal to the visible albedo, and it is correlated with taxonomic type. The trends for each taxonomic type are (Mainzer et al., 2011d, 2012c)  $p_{\text{IR}}/p_V \sim 1$  for C-complex asteroids (except for D-types),  $p_{\text{IR}}/p_V \sim 1.7$  for S-complex asteroids,  $p_{\text{IR}}/p_V \sim 2.2$  for D-types, and  $p_{\text{IR}}/p_V \lesssim 1$  for B-types. The differences between  $p_{\text{IR}}/p_V$  for all of these taxonomic types is likely due to the fact that their VNIR slopes are either blue (as is the case for the B-types), flat (C-complex), red (S-complex), or very red (D-types), and the trend of these slopes continues out to  $\sim 3 \mu\text{m}$ . Consequently, if  $p_{\text{IR}}$  can be determined, it can be used as a proxy for distinguishing between taxonomic types that otherwise have nearly identical visible albedos (Grav et al., 2012a,b, 2015; Alí-Lagoa et al., 2013; Masiero et al., 2014).

While STM, FRM, and NEATM are useful tools for rapidly determining effective spherical diameter,  $p_V$ , and  $p_{\text{IR}}$  for large numbers of asteroids, they are of limited use for determining additional parameters such as emissivity and thermal inertia. To extract these parameters, *thermophysical* models are needed; see the chapter by Delbó et al. in this volume for a detailed discussion of their theory and application.

## 4. RESULTS

Table 2 summarizes the numbers of asteroids that are known to have been observed to date by Spitzer, WISE/NEOWISE, AKARI, and Herschel for NEOs, MBAs, jovian Trojans, and Centaurs. Given the capabilities of each mission's survey data and selection methods, much can be learned about the properties of the various asteroid populations.

### 4.1. Infrared-Selected and Optically Selected Population Studies

Samples of asteroids imaged by spacebased IR telescopes can be selected in two ways. In an independent survey, all small-body candidates are treated identically regardless of whether they are previously known or might be new discoveries (assuming the survey's cadence allows for an

TABLE 2. Summary of recent spacebased asteroid observations and discoveries.

Mission	NEOs	MBAs	Cybeles	Hildas	Jovian Trojans	Centaurs	Asteroid Discoveries
Spitzer	<10	~2000	1	62	~70	42	0
Spitzer Warm Mission	~600	0	0	0	0	28	0
AKARI	90	4806	106	86	110	7	0
WISE	~700	~158,000	1342	1023	~2000	52	~34,000
NEOWISE	391	~15,600	100	50	50	1	215
Herschel	~7	~8	1	0	0	18	0

observational arc sufficient to enable the discovery of new moving objects). In a targeted sample, the telescope observes previously known asteroids and cannot independently discover new ones.

In an independent survey, asteroids are selected based on their IR fluxes, whereas in a targeted survey, asteroids are drawn from the catalog of objects discovered by other observers, almost all of whom operate at visible wavelengths. Understanding the selection biases of the sample is critical when probing population properties below the size regime for which the sample is observationally complete.

Since IR flux is insensitive to albedo, IR surveys are less biased against low-albedo objects than surveys that select targets based on their visible flux alone. Visible-light surveys are less likely to discover low-albedo objects, particularly at smaller sizes, due to their intrinsic faintness. Moreover, since diameter is determined directly from IR fluxes, no conversion between H and diameter is needed, eliminating the uncertainty associated with the large range of possible asteroid albedos. Infrared-selected samples can be extrapolated to determine the size-frequency distribution of the underlying population they represent, since the sample selection method is insensitive to albedo.

The NEOWISE project operated as an independent survey, using data processing methods to select moving object objects based on their IR fluxes. Known and new candidates were treated identically by the WISE Moving Object Processing System (WMOPS), which required all moving object candidates to be detected a minimum of 5 times over  $\sim 15$  hours (Mainzer et al., 2011a; Cutri et al., 2012). A detailed description of WMOPS can be found in the WISE Explanatory Supplement, section IV.5. Most objects were observed an average of  $\sim 12$  times over  $\sim 36$  hours. Over the course of the year-long prime mission,  $\sim 158,000$  asteroids were detected, including  $\sim 34,000$  new discoveries. During the 8.5-month fully cryogenic portion of the mission, asteroids were selected by WMOPS based on their 12- $\mu\text{m}$  flux; after the cryogen depleted, the primary band for asteroid selection became the 4.6- $\mu\text{m}$  channel.

One of the main results of the WMOPS-selected sample was the discovery that asteroid albedo distributions appear to remain constant over a wide range of diameters. An example of this can be seen in Fig. 1, which compares the albedo-size relationship for a sample of 44 optically selected jovian Trojans observed with Spitzer (Fernández et al., 2009) to a sample of 1739 Trojans found using WMOPS (Grav et al., 2011a). While the optically selected sample shows a strong trend of increasing albedo with decreasing size, no strong trend is apparent in the IR-selected, albedo-insensitive sample. A similar effect is observed when the diameter-albedo relationship for NEO samples is examined (Fig. 2) (Delbó et al., 2003; Binzel et al., 2004; Trilling et al., 2010). For the small NEOs, a real increase in albedo with decreasing diameter cannot be ruled out, but because the sample was selected on the basis of its visible flux, any real trend is entangled with the optical surveys' bias against discovery of small, dark NEOs (Mainzer et al., 2014a). The

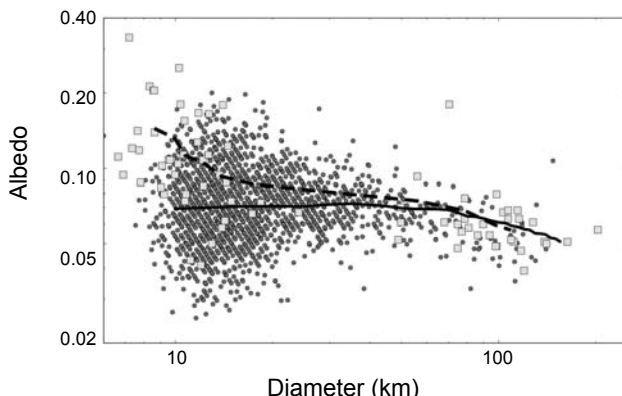


**Fig. 1.** Comparison of the IR-selected NEOWISE sample of 1739 jovian Trojans (filled gray circles) (Grav et al., 2011a, 2012b) to the optically selected sample observed by Spitzer (light gray squares) (Fernández et al., 2009); the solid and dashed lines give the running medians for the NEOWISE and Spitzer samples, respectively.

NEOWISE-discovered NEOs have lower albedos than those discovered by optical surveys (Fig. 3).

Using the IR-selected sample from NEOWISE, survey biases were estimated in order to determine the orbital properties, numbers, and physical properties of various asteroid populations. Survey biases were computed as a function of orbital and physical properties using the complete survey pointing list and the sensitivity in each wavelength, which derives from observations of asteroids with well-determined orbits [see Mainzer et al. (2011b) and Grav et al. (2011a) for an expanded description of the debiasing methodology as applied to WISE data]. The process of removing the survey bias signatures from the observed sample is known as debiasing (cf. Bottke et al., 2002; Jedicke and Metcalfe, 1998; Spahr, 1998).

Mainzer et al. (2011b) found that there are  $\sim 20,500 \pm 3000$  near-Earth asteroids larger than 100 m in diameter, of which  $\sim 25\%$  had been discovered as of 2011. That work verified that  $>90\%$  of NEAs larger than 1 km had been discovered, fulfilling the 1998 “Spaceguard” goal given to NASA. The subpopulations of the NEAs, including potentially hazardous asteroids (PHAs) (asteroids whose minimum orbit intersection distances are  $<0.05$  AU and  $H < 22$  mag) were studied by Mainzer et al. (2012b). However, since WISE measures diameter, rather than H, the authors recommended a change to a diameter-based definition for PHAs and concluded that there are  $\sim 4700 \pm 1500$  PHAs larger than  $\sim 100$  m (Mainzer et al., 2012b). Matches to the orbital-element models of Bottke et al. (2002) and Greenstreet and Gladman (2013) are generally in good agreement. Approximately twice as many PHAs were found occupying orbits with the lowest inclinations as compared with the model of Bottke et al. (2002); however, by recomputing the evolutionary models of NEOs with a finer orbital-element grid, Greenstreet and Gladman (2013) found similar results for the lowest-inclination bins. NEOWISE did not effectively probe the NEA population below 100 m,

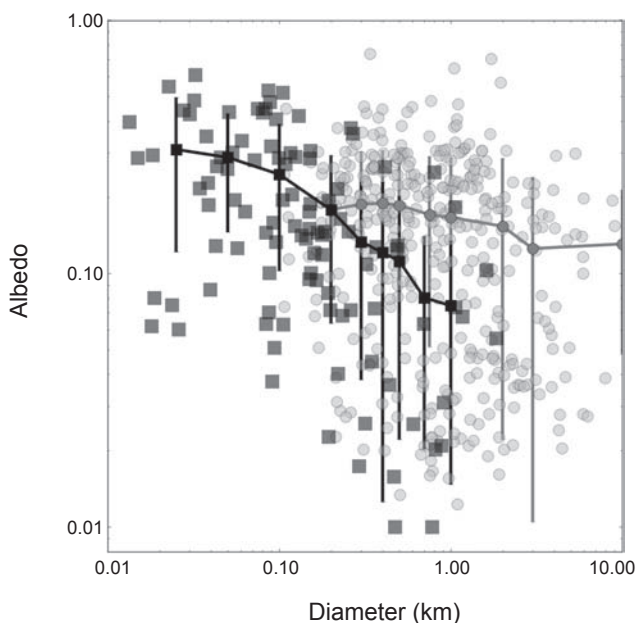


**Fig. 2.** The IR-selected sample of NEOs from NEOWISE (gray points; running median shown as gray line) shows little change in albedo with diameter, whereas a sample of asteroids selected based on their visible magnitudes (black points and line) shows an increase in albedo with decreasing diameter (Mainzer *et al.*, 2014a).

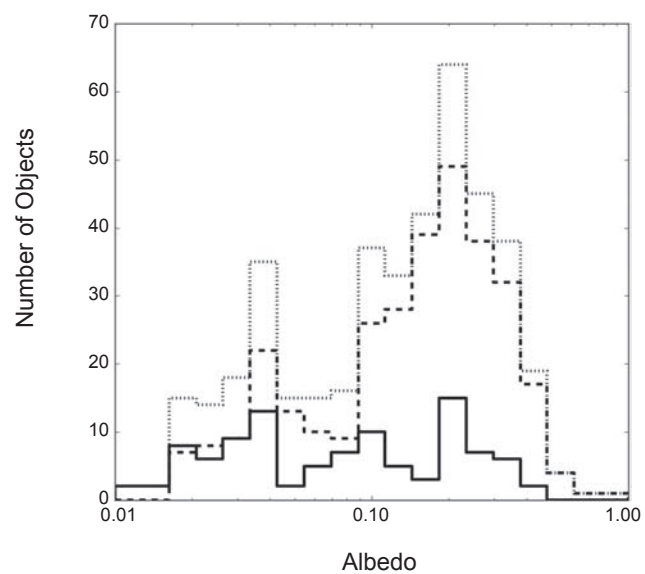


**Fig. 3.** The albedo distribution of the NEOs discovered by WISE during its prime mission (black) has relatively more low-albedo NEOs than the objects discovered by visible light surveys (dot-dashed line). The albedo distribution for the entire NEO sample from the WISE prime mission is shown as a finely dashed line; 36% of NEOs have albedos <0.1 (Mainzer et al., 2011b).

with the exception of the optically selected sample shown in Fig. 3. Debiasing for this sample requires accounting for the optical survey selection effects in addition to the NEOWISE sample biases, a more complicated undertaking.

*Grav et al.* (2011b) and *Grav et al.* (2012a) debiased the NEOWISE jovian Trojan and Hilda samples, respectively, facilitating comparison between the leading and trailing Trojan clouds and leading to estimates of their numbers, size, and albedo distributions. Infrared observations have revealed key attributes of the jovian Trojans, Hildas, and Cybele asteroids. These results indicate that Trojans in the leading and trailing clouds are extremely similar in terms of albedos, taxonomic types, and size distributions; the major difference is that Trojans in the leading ( $L_4$ ) cloud outnumber the trailing ( $L_5$ ) by a factor of  $1.4 \pm 0.2$  (*Grav et al.*, 2011a). Theories of early giant planet migration must account for these observational constraints. *Marsset et al.* (2014) obtained visible and near-IR spectra of eight jovian Trojans found by WISE and Spitzer to have relatively high albedos and found that these objects had taxonomic types consistent with other primitive, low-albedo Trojans. One likely explanation is that when determining albedos for thousands of objects, normal statistical fluctuations will scatter a small fraction of the observations in favor of brighter albedos. See the chapter by Emery et al. in this volume for a more comprehensive discussion of the jovian Trojans.

Spitzer observed an optically selected sample of ~600 NEOs during its warm mission at 3.6 and 4.5  $\mu\text{m}$  (*Trilling et al., 2010; Mueller et al., 2011*). Improved diameter con-

straints assist with assessments of impact hazard. Targets of interest, such as (101955) Bennu, the target of the upcoming Origins Spectral Interpretation Resource Identification and Security-Regolith Explorer (OSIRIS-REx) mission, have also been observed with Spitzer and Herschel to determine size, albedo, and thermal inertia (*Emery et al.*, 2014; *Yu et al.*, 2014; *Mommert et al.*, 2014a,b; see also the chapter by Delb o et al. in this volume). The target of the Hayabusa-2 mission, (162173) 1999 JU<sub>3</sub>, has been intensively observed with AKARI, Spitzer, and Herschel, as well as groundbased facilities such as Subaru (*Hasegawa et al.*, 2008; *Mueller et al.*, 2011). WISE, Spitzer, and Herschel have been used to study Centaurs, a transitional population between transneptunian objects and Jupiter-family comets (*Bauer et al.*, 2013; *Duffard et al.*, 2014). Measurements from IRAS, AKARI, and WISE have been used to identify NEOs likely to be of cometary origin by performing follow-up observations of objects with low albedos and comet-like orbits (*Kim et al.*, 2014). This work builds on the work of *DeMeo and Binzel* (2008) and *Fern ndez et al.* (2005), who estimated the fraction of NEOs likely to be of cometary origins as 8% and 4%, respectively. *Mommert et al.* (2015) debiased the sample of large NEOs detected during the fully cryogenic portion of the WISE mission and found that 9% are likely to be dormant short-period comets.

The albedo-insensitive sample from *Mainzer et al.* (2012c) suggests a paucity of NEOs with low albedos at low perihelion distances, although the sample size is small. *Delb  * et al. (2014) posit that thermal cracking plays a key role in

regolith production, with an erosion and destruction process that preferentially affects more fragile, low-albedo, carbonaceous objects as they approach the Sun; see also Čapek and Vokrouhlický (2010, 2012).

#### 4.2. Main-Belt Asteroid Studies

The MBAs have now been extensively studied at thermal-IR wavelengths, with >155,000 having been observed by WISE and 4806 objects by AKARI (Masiero et al., 2011, 2012a; Usui et al., 2011; Hasegawa et al., 2013). Usui et al. (2014) shows the comparison of diameters and albedos derived for the ~1900 MBAs observed in common between AKARI and WISE. Diameters between the two datasets match to within  $\pm 10\%$ , and albedos to within  $\pm 22\%$ ; these results are in good agreement with the error bars described above. Figure 4 shows that, as found by IRAS, the asteroids within the main belt become darker with increasing heliocentric distance (Masiero et al., 2011).

Radiometrically derived diameters and albedos are valuable for improving determinations of asteroid collisional family ages and membership; in most cases, calculations prior to the recent IR missions described here have relied on sizes estimated from H and an assumed albedo (cf. Marzari et al., 1995). By combining albedos and colors with orbital information, it is possible to identify probable family members at velocity limits that would otherwise be indistinguishable from background objects, assuming that collisional family members have similar albedos and colors. Furthermore, families that overlap in velocity space can be disentangled on the basis of their albedos and colors (Masiero et al., 2013; Walsh et al., 2013; Carruba et al., 2013;

Milani et al., 2014). With improved and expanded family membership lists down to smaller sizes, the timing of collisions can be determined with greater precision, since the age-determination technique relies upon the strength of non-gravitational forces such as the Yarkovsky and Yarkovsky-O'Keefe-Radzievskii-Paddack (YORP) effects, which in turn depends on the size and mass of an object (Masiero et al., 2012b). Asteroid collisional families are discussed in greater depth in the chapters by Nesvorný et al., Michel et al., and Masiero et al. in this volume.

Diameters and albedos play a role in understanding which source reservoirs among the MBAs and comets are most likely to have produced NEOs. While it is difficult to associate the origins of an individual asteroid with a specific source region, associations can sometimes be inferred by comparing source region albedos to the object of interest and by using diameters to constrain migration timescales due to nongravitational forces (e.g., Campins et al., 2013; Masiero et al., 2015). Gathering measurements of albedos and diameters for larger numbers of asteroids down to smaller sizes will facilitate improved understanding of NEO origins and subsequent evolution, since nongravitational forces depend strongly on asteroid sizes (see the chapter by Vokrouhlický et al. in this volume).

#### 4.3. Taxonomy, Albedo, and Beaming

Albedos and diameters derived from IR observations have proven useful for studies of the compositional diversity of asteroids throughout the main belt. Previous measurements of the asteroids in the main belt suggested a uniform, smooth change in composition from more highly reflective, stony asteroids closer to the Sun to dark, carbon-rich objects that were barely altered by solar heating in its more distant regions. However, data from the WISE mission and the SDSS have shown that while there is an overall gradient, the true picture is much more jumbled, with a wide range of different compositions scattered throughout the belt. Asteroids rich in minerals that require high temperatures to form have been found in the outer belt, while primitive objects are found close to its inner edge. These results suggest that the early migration of the giant planets may have turbulently scrambled the asteroids and show at the very least that the early solar system was more dynamic than previously believed (DeMeo and Carry, 2013, 2014); see also the chapter by DeMeo et al. in this volume.

Comparisons between albedos derived from infrared data and taxonomic classifications derived from VNIR spectroscopy and spectrophotometry indicate a strong but not universal correlation between taxonomic types and albedos (Mainzer et al., 2011a,b; Thomas et al., 2011). Asteroids with neutral or blue spectra at VNIR wavelengths tend to have low visible albedos, and most red objects are associated with higher visible albedos (with the exception of classes such as D-types, which despite their red VNIR spectra have low albedos). However, as described above, even though average  $p_V$  values may be nearly identical for some taxonomic types such as

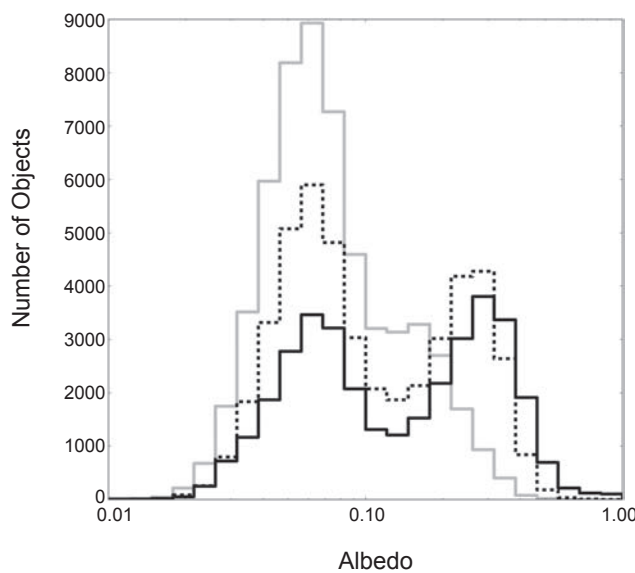


**Fig. 4.** The albedo distribution for asteroids in the inner (solid line; defined as semimajor axes between 1.8 and 2.5 AU), middle (dashed line; 2.5–2.82 AU), and outer (dotted line;  $2.82 < 3.6$  AU) regions of the main belt from Masiero et al. (2011).

C-, P-, and D-types, their 3  $\mu\text{m}$  albedos ( $p_{\text{IR}}$ ) are distinctly different. Therefore,  $p_{\text{IR}}$  can be used to distinguish between C/P-types and D-types (Grav et al., 2012b) when VNIR spectra are unavailable. Albedos have been used to identify candidate V-type asteroids throughout the main belt that have been subsequently observed spectroscopically to confirm their taxonomic type (Hardersen et al., 2014). Moreover, objects with extremely low albedos ( $p_V \sim 0.02$ ) in the main belt have been identified as the possible progenitors of the Tagish Lake meteorite, one of the darkest and most primitive carbonaceous chondrites ever found (Vernazza et al., 2013).

The beaming parameter  $\eta$  has also been shown to correlate with thermal inertia and rotation rate (Harris, 1998; Spencer et al., 1989; Delbó, 2004; Delbó et al., 2007). However, caution must be used in the interpretation of beaming values, since  $\eta$  also correlates with the phase angle at which an object is observed (Delbó et al., 2003, 2007; Wolters et al., 2008; Mainzer et al., 2011b). The NEATM assumes a temperature distribution that drops to zero at the terminator. For rotating bodies with anything other than low thermal inertias, the temperature distribution is likely to be nonzero past the terminator; when these bodies are observed at high phase angle, some portion of the nightside flux is seen, resulting in changes to  $\eta$  to conserve energy. Moreover, increased surface roughness can increase the sunward beaming of radiation, and  $\eta$  also depends on the spin axis orientation with respect to the Sun.

With these caveats, objects with extremely high values of  $\eta$  are good candidates for high thermal inertias or rapid rotation rates. Harris and Drube (2014) found 18 NEOs with high  $\eta$  values ( $>2$ ) and albedos that may indicate a metallic composition consistent with the fragmented cores of differentiated bodies. Since high radar albedos can correspond to high metal content, follow-up radar observations are desirable to confirm their nature. NEOs tend to have higher  $\eta$  values than MBAs and jovian Trojans; this may indicate higher thermal inertia, although they are often observed at higher phase angles than MBAs (Delbó et al., 2007; Mainzer et al., 2011b; Masiero et al., 2011; Grav et al., 2011b). Bauer et al. (2013) used WISE to perform thermal modeling on 52 Centaurs and scattered disk objects, finding that most  $\eta$  values were low and similar to those of bare cometary nuclei, suggesting a common origin. Observations of 85 transneptunian objects by Lellouch et al. (2013) showed that high  $\eta$  values were rare at low heliocentric distances, which they interpret as evidence of decreasing thermal inertia. The advent of new mid-IR data from WISE, Spitzer, AKARI, and Herschel promises to shed further light on thermal inertia trends as thermophysical models are applied to many more objects (see recent results from, e.g., Hanus et al., 2015; Koren et al., 2015; and the chapter by Delbó et al. in this volume).

#### 4.4. Activated Asteroids and Comets

The boundary between asteroids and comets is now considerably more permeable than previously suspected. Objects with low albedos and cometary orbits (often telltale

signatures of comets) have stubbornly resisted attempts to find evidence of cometary activity such as comae or tails, and asteroids are sometimes revealed upon further inspection to have become active. Thermal IR imaging surveys have been used to constrain cometary nucleus sizes during periods of inactivity when dust and gas do not obscure them, allowing for determinations of comet size frequency distributions (e.g., Bauer et al., 2011; Fernández et al., 2013). Thermal-IR imaging can also discover cometary activity around objects previously thought to be asteroidal. For example, WISE observed extended emission around three asteroids during its prime mission, which were subsequently redesignated as comets (237/P LINEAR, 233/P La Sagra, and P/2009 WX51 Catalina), and Spitzer found evidence for activity on (3552) Don Quixote (Mommert et al., 2014c). Since dust emits strongly at thermal-IR wavelengths when comets reach the inner solar system, IR surveys can be used to discover new comets. IRAS discovered five comets, and NEOWISE has discovered 24 to date.

Although a detailed discussion of comets is outside the scope of this book, thermal-IR data can also constrain the sizes and quantities of the dust particles produced by comets (Bauer et al., 2012a). The slope of the particle size distributions in turn can be used to determine whether the dust was produced by a collision between two asteroids or driven off the surface by volatiles such as CO and CO<sub>2</sub>, a key signature of cometary activity. This technique is useful for understanding the nature of activity observed in some MBAs (Bauer et al., 2012b; Stevenson et al., 2012); see the chapter by Jewitt et al. in this volume for a detailed discussion of these objects.

#### 4.5. Mid-Infrared Spectroscopy of Asteroids

A number of key spectral features that vary depending on a surface's composition, grain size, and porosity can be observed at mid-IR wavelengths. Laboratory studies of meteorites indicate the presence of absorption and emission features caused by vibrational and lattice modes; for example, crystalline and amorphous silicates show broad absorption features near  $\sim 10 \mu\text{m}$ .

AKARI, Spitzer, and Herschel all carried spectrographs operating at mid-IR wavelengths during their fully cryogenic mission phases. Spectra have been collected for  $\sim 87$  asteroids using the Spitzer IRS and MIPS instruments (e.g., Cruikshank et al., 2006; Campins et al., 2009a,b; Lim et al., 2011; Marchis et al., 2012). Spitzer IRS spectra covering 5–38  $\mu\text{m}$  revealed broad emission features near 10 and 20  $\mu\text{m}$  on three jovian Trojans, consistent with the presence of fine-grained silicates (Emery et al., 2006; Cruikshank, 2005). Similar but smaller emission plateaus were observed between 9 and 12  $\mu\text{m}$  on eight Themis-family asteroids and (65) Cybele, indicating that these bodies may also be covered with small silicate grains (Licandro et al., 2011, 2012); see also the chapters by Delbó et al. and Emery et al. in this volume. Moreover, Vernazza et al. (2012) showed that mid-IR spectra meteorite samples diluted with IR-transparent KBr powder matched observed emissivity features in MBAs, suggesting

that surface porosity can also be constrained. *Marchis et al.* (2012) used Spitzer IRS spectroscopy of binary asteroids to constrain their bulk densities, thermal inertia, and surface grain properties. The chapter by Reddy et al. in this volume provides a more comprehensive discussion of mid-IR spectroscopy, including theory and observations.

Mid-IR spectra have also proven useful for constraining the abundance of volatiles on small bodies; for example, many species such as CO and CO<sub>2</sub> have been identified on comets photometrically through excess flux above their thermal emission (e.g., *Bauer et al.*, 2011; *Reach et al.*, 2013). Recently, Herschel heterodyne spectroscopy of the largest object in the main belt, (1) Ceres, has revealed the presence of water vapor as the dwarf planet approached perihelion (*Küppers et al.*, 2014). The water vapor line was detected at three separate epochs at 557 GHz ( $\lambda = 540\mu\text{m}$ ), further illustrating that the distinction between dark asteroids and comets is sometimes blurred (*Briani et al.*, 2011). See the chapter by Rivkin et al. in this volume for a discussion of the implications of this result.

#### 4.6. Earth Co-Orbitals

Among the near-Earth objects discovered by NEOWISE during its post-cryogenic mission is the first known Earth Trojan, 2010 TK<sub>7</sub>, and an object in a so-called “horseshoe” orbit co-orbital with Earth, 2010 SO<sub>16</sub> (*Connors et al.*, 2011; *Christou and Asher*, 2011; *Mainzer et al.*, 2012a). 2010 TK<sub>7</sub> was discovered by NEOWISE because its  $\sim$ 395-year libration period caused it to move to the region near 90° solar elongation where the satellite continually observes. Because Earth Trojans are thought to be dynamically constrained to remain more than  $\sim$ 24° away from Earth in mean anomaly (*Tabachnik and Evans*, 2000), they spend most of their time in regions of the sky that are difficult or impossible for groundbased telescopes to observe. Infrared measurements from NEOWISE have provided preliminary estimates of diameters and albedos (*Mainzer et al.*, 2012a). 2010 TK<sub>7</sub> is thought to be temporarily captured by Earth, with a dynamical stability timescale of  $\sim$ 7000 years (*Connors et al.*, 2011; *Marzari and Scholl*, 2013). By contrast, 2010 SO<sub>16</sub> librates across the L<sub>3</sub> Earth-Sun Lagrange point in a horseshoe pattern that has the longest known stability of any Earth co-orbital, several hundred thousand years (*Christou and Asher*, 2011).

Although approximately half a dozen horseshoe and quasisatellite co-orbitals are known at present, 2010 TK<sub>7</sub> remains the sole Earth Trojan found to date. These objects may represent a much larger population that remains undiscovered because they spend the majority of their time in the daytime sky on Earth. Future surveys designed to survey at low solar elongations may be able to find more of these unusual objects.

### 5. CONCLUSIONS

Spacebased infrared studies of asteroids offer a valuable means of rapidly determining the physical and orbital proper-

ties of large numbers of objects. Modern detector arrays have allowed recent space missions to reach background-limited sensitivities that are improved by orders of magnitude compared to prior generations of IR telescopes. These capabilities have opened a new window into the nature of our solar system’s small bodies. Future generations of spacebased IR telescopes using new large-format detectors (e.g., *McMurtry et al.*, 2013) will further improve our understanding.

**Acknowledgments.** This study is based on observations with AKARI, a JAXA project with the participation of ESA. This work is based in part on observations made with the Spitzer Space Telescope, which is operated by the Jet Propulsion Laboratory/California Institute of Technology under a contract with NASA. This publication makes use of data products from NEOWISE, which is a project of the Jet Propulsion Laboratory/California Institute of Technology funded by the National Aeronautics and Space Administration. This publication makes use of data products from the Wide-field Infrared Survey Explorer, which is a joint project of the University of California, Los Angeles, and the Jet Propulsion Laboratory/California Institute of Technology, funded by the National Aeronautics and Space Administration. Herschel is an ESA space observatory with science instruments provided by European-led Principal Investigator consortia and with important participation from NASA. We gratefully acknowledge the helpful input from referees M. Delbó and A. Harris of DLR.

### REFERENCES

- Abazajian K., Adelman-McCarthy J. K., Agüeros M. A., Allam S. S., Anderson S. F., Annis J., Bahcall N. A., Baldry I. K., Bastian S., Berlind A., Bernardi M., Blanton M. R., Blythe N., Bochanski J. J. Jr., Boroski W. N., Brewington H., Briggs J. W., Brinkmann J., Brunner R. J., Budavári T., Carey L. N., Carr M. A., Castander F. J., Chiu K., Collinge M. J., Connolly A. J., Covey K. R., Csabai I., Dalcanton J. J., Dodelson S., Doi M., Dong F., Eisenstein D. J., Evans M. L., Fan X., Feldman P. D., Finkbeiner D. P., Friedman S. D., Frieman J. A., Fukugita M., Gal R. R., Gillespie B., Glazebrook K., Gonzalez C. F., Gray J., Grebel E. K., Grodnicki L., Gunn J. E., Gurbani V. K., Hall P. B., Hao L., Harbeck D., Harris F. H., Harris H. C., Harvanek M., Hawley S. L., Heckman T. M., Helmboldt J. F., Hendry J. S., Hennessy G. S., Hindsley R. B., Hogg D. W., Holmgren D. J., Holtzman J. A., Homer L., Hui L., Ichikawa S.-I., Ichikawa T., Inkman J. P., Ivezíć Ž., Jester S., Johnston D. E., Jordan B., Jordan W. P., Jorgensen A. M., Jurić M., Kauffmann G., Kent S. M., Kleinman S. J., Knapp G. R., Kniazev A. Y., Kron R. G., Krzesiński J., Kunszt P. Z., Kuropatkin N., Lamb D. Q., Lampeitl H., Laubscher B. E., Lee B. C., Leger R. F., Li N., Lidz A., Lin H., Loh Y.-S., Long D. C., Loveday J., Lupton R. H., Malik T., Margon B., McGehee P. M., McKay T. A., Meiksin A., Miknaitis G. A., Moorthy B. K., Munn J. A., Murphy T., Nakajima R., Narayanan V. K., Nash T., Neilsen E. H. Jr., Newberg H. J., Newman P. R., Nichol R. C., Nicinski T., Nieto-Santisteban M., Nitta A., Odenkirchen M., Okamura S., Ostriker J. P., Owen R., Padmanabhan N., Peoples J., Pier J. R., Pindor B., Pope A. C., Quinn T. R., Rafikov R. R., Raymond S. N., Richards G. T., Richmond M. W., Rix H.-W., Rockosi C. M., Schaye J., Schlegel D. J., Schneider D. P., Schroeder J., Scranton R., Sekiguchi M., Seljak U., Sergey G., Sesar B., Sheldon E., Shimasaku K., Siegmund W. A., Silvestri N. M., Sinisgalli A. J., Sirko E., Smith J. A., Smolčić V., Snedden S. A., Stebbins A., Steinhardt C., Stinson G., Stoughton C., Strateva I. V., Strauss M. A., SubbaRao M., Szalay A. S., Szapudi I., Szkody P., Tasca L., Tegmark M., Thakar A. R., Tremonti C., Tucker D. L., Uomoto A., Vandenberg Berk D. E., Vandenberg J., Vogeley M. S., Voges W., Vogt N. P., Walkowicz L. M., Weinberg D. H., West A. A., White S. D. M., Wilhite B. C., Willman B., Xu Y., Yanny B., Yarger J., Yasuda N., Yip C.-W., Yocom D. R., York D. G., Zakamska N. L., Zehavi I., Zheng W., Zibetti S., and Zucker D. B. (2003) The first data release of the Sloan digital sky survey. *Astron. J.*, 126, 2081–2086.

- Alí-Lagoa V., de León J., Licandro J., Delbó M., Campins H., Pinilla-Alonso N., and Kelley M. S. (2013) Physical properties of B-type asteroids from WISE data. *Astron. Astrophys.*, 554, A71.
- Allen D. A. (1970) Infrared diameter of Vesta. *Nature*, 227, 158–159.
- Allen D. A. (1971) The method of determining infrared diameters. In *Physical Studies of the Minor Planets* (T. Gehrels, ed.), p. 41. NASA SP-267, Washington, DC.
- Bauer J. M., Walker R. G., Mainzer A. K., Masiero J. R., Grav T., Dailey J. W., McMillan R. S., Lisse C. M., Fernández Y. R., Meech K. J., Pittichova J., Blauvelt E. K., Masci F. J., A'Hearn M. F., Cutri R. M., Scotti J. V., Tholen D. J., DeBaun E., Wilkins A., Hand E., Wright E. L., and the WISE Team (2011) WISE/NEOWISE observations of Comet 103P/Hartley 2. *Astrophys. J.*, 738, 171.
- Bauer J. M., Kramer E., Mainzer A. K., Stevenson R., Grav T., Masiero J. R., Walker R. G., Fernández Y. R., Meech K. J., Lisse C. M., Weissman P. R., Cutri R. M., Dailey J. W., Masci F. J., Tholen D. J., Pearman G., Wright E. L., and the WISE Team (2012a) WISE/NEOWISE preliminary analysis and highlights of the 67P/Churyumov-Gerasimenko near nucleus environs. *Astrophys. J.*, 758, 18.
- Bauer J. M., Mainzer A. K., Grav T., Walker R. G., Masiero J. R., Blauvelt E. K., McMillan R. S., Fernández Y. R., Meech K. J., Lisse C. M., Cutri R. M., Dailey J. W., Tholen D. J., Riesen T., Urban L., Khayat A., Pearman G., Scotti J. V., Kramer E., Cherry D., Gautier T., Gomillion S., Watkins J., Wright E. L., and the WISE Team (2012b) WISE/NEOWISE observations of active bodies in the main belt. *Astrophys. J.*, 747, 49.
- Bauer J. M., Grav T., Blauvelt E., Mainzer A. K., Masiero J. R., Stevenson R., Kramer E., Fernández Y. R., Lisse C. M., Cutri R. M., Weissman P. R., Dailey J. W., Masci F. J., Walker R., Waszczak A., Nugent C. R., Meech K. J., Lucas A., Pearman G., Wilkins A., Watkins J., Kulkarni S., Wright E. L., the WISE Team, and the PTF Team (2013) Centaurs and scattered disk objects in the thermal infrared: Analysis of WISE/NEOWISE observations. *Astrophys. J.*, 773, 22.
- Bhattacharya B., Noriega-Crespo A., Penprase B. E., Meadows V. S., Salvato M., Aussel H., Frayer D., Ilbert O., Le Floch E.,Looper D., Surace J., Capak P., Giorgini J. D., Granvik M., Grillmair C., Hagen A., Helou G., Reach W. T., Rebull L. M., Sanders, D. B., Scoville N., Sheth K., and Yan L. (2010) Mid-infrared photometric analysis of main belt asteroids: A technique for color-color differentiation from background astrophysical sources. *Astrophys. J.*, 720, 114.
- Binzel R. P., Rivkin A. S., Stuart J. S., Harris A. W., Bus S. J., and Burbine T. H. (2004) Observed spectral properties of near-Earth objects: Results for population distribution, source regions, and space weathering processes. *Icarus*, 170, 259–294.
- Bottke W. F., Morbidelli A., Jedicke R., Petit J.-M., Levison H. F., Michel P., and Metcalfe T. S. (2002) Debiased orbital and absolute magnitude distribution of the near-Earth objects. *Icarus*, 156, 399–433.
- Bottke W. F., Durda D. D., Nesvorný D., Jedicke R., Morbidelli A., Vokrouhlický D., and Levison H. (2005) The fossilized size distribution of the main asteroid belt. *Icarus*, 175, 111–140.
- Bowell E., Hapke B., Domingue D., Lumme K., Peltoniemi J., and Harris A. W. (1989) Application of photometric models to asteroids. In *Asteroids II* (R. P. Binzel et al., eds), pp. 524–556. Univ. of Arizona, Tucson.
- Briani G., Morbidelli A., Gounelle M., and Nesvorný D. (2011) Evidence for an asteroid-comet continuum from simulations of carbonaceous microxenolith dynamical evolution. *Meteoritics & Planet. Sci.*, 46, 1863–1877.
- Bus S. J. and Binzel R. P. (2002) Phase II of the Small Main-Belt Asteroid Spectroscopic Survey: A feature-based taxonomy. *Icarus*, 158, 146–177.
- Camps H., Emery J. P., Kelley M., Fernández Y., Licandro J., Delbó M., Barucci A., and Dotto E. (2009a) Spitzer observations of spacecraft target 162173 (1999 JU<sub>3</sub>). *Astron. Astrophys.*, 503, L17–L20.
- Camps H., Kelley M. S., Fernández Y., Licandro J., and Hargrove K. (2009b) Low perihelion near-Earth asteroids. *Earth Moon Planets*, 105, 159–165.
- Camps H., de León J., Morbidelli A., Licandro J., Gayon-Markt J., Delbó M., and Michel P. (2013) The origin of asteroid 162173 (1999 JU<sub>3</sub>). *Astron. J.*, 146, 26.
- Čapek D. and Vokrouhlický D. (2010) Thermal stresses in small meteoroids. *Astron. Astrophys.*, 519, A75.
- Čapek D. and Vokrouhlický D. (2012) Thermal stresses in small meteoroids II. Effects of an insulating surface layer. *Astron. Astrophys.*, 539, A25.
- Capria M. T., Tosi F., De Sanctis M. C., Capaccioni F., Ammannito E., Frigeri A., Zambon F., Fonte S., Palomba E., Turriti D., Titus T. N., Schröder S. E., Toplis M., Li J.-Y., Combe J.-P., Raymond C. A., and Russell C. T. (2014) Vesta surface thermal properties map. *Geophys. Res. Lett.*, 41, 1438–1443.
- Carruba V., Domingos R. C., Nesvorný D., Roig F., Huaman M. E., and Souami D. (2013) A multidomain approach to asteroid families' identification. *Mon. Not. R. Astron. Soc.*, 433, 2075–2096.
- Carvano J. M., Hasselmann P. H., Lazzaro D., and Mothé-Diniz T. (2010) SDSS-based taxonomic classification and orbital distribution of main belt asteroids. *Astron. Astrophys.*, 510, A43.
- Christou A. A. and Asher D. J. (2011) A long-lived horseshoe companion to the Earth. *Mon. Not. R. Astron. Soc.*, 414, 2965–2969.
- Connors M., Wiegert P., and Veillet C. (2011) Earth's Trojan asteroid. *Nature*, 475, 481–483.
- Cruikshank D. P. (1977) Radii and albedos of four Trojan asteroids and jovian satellites 6 and 7. *Icarus*, 30, 224–230.
- Cruikshank D. P. (2005) Solar system observations with Spitzer Space Telescope: Preliminary results. *Adv. Space Res.*, 36, 1070–1073.
- Cruikshank D. P., Stansberry J. A., Emery J. P., van Cleve J., Fernández Y. R., Werner M. W., Reike G. H., and Trilling D. E. (2006) Solar system observations with Spitzer Space Telescope. In *The Spitzer Space Telescope: New Views of the Cosmos* (L. Armus and W. T. Reach, eds.), p. 23. ASP Conf. Ser. 357, Astronomical Society of the Pacific, San Francisco.
- Cutri R. M., Wright E. L., Conrow T., Bauer J., Benford D., Brandenburg H., Dailey J., Eisenhardt P. R. M., Evans T., Fajardo-Acosta S., Fowler J., Gelino C., Grillmair C., Harbut M., Hoffman D., Jarrett T., Kirkpatrick J. D., Leisawitz D., Liu W., Mainzer A., Marsh K., Masci F., McCallon H., Padgett D., Ressler M. E., Royer D., Skrutskie M. F., Stanford S. A., Wyatt P. L., Tholen D., Tsai C. W., Wachter S., Wheelock S. L., Yan L., Alles R., Beck R., Grav T., Masiero J., McCollum B., McGehee P., Papin M., and Wittman M. (2012) *Explanatory Supplement to the WISE All-Sky Data Release Products*, p. 1. Available online at <http://wise2.ipac.caltech.edu/docs/release/allsky/expsup/>.
- de Graauw T., Helmich F. P., Phillips T. G., Stutzki J., Caux E., Whyborn N. D., Dieleman P., Roelfsema P. R., Aarts H., Assendorp R., Bachiller R., Baechtold W., Barcia A., Beintema D. A., Belitsky V., Benz A. O., Bieber R., Boogert A., Borys C., Bumble B., Cais P., Caris M., Cerulli-Irelli P., Chattopadhyay G., Cherednichenko S., Ciechanowicz M., Coeur-Joly O., Comito C., Cros A., de Jonge A., de Lange G., Delforges B., Delorme Y., den Bogerdene T., Desbat J.-M., Diez-González C., di Giorgio A. M., Dubbeldam L., Edwards K., Eggens M., Erickson N., Evers J., Fich M., Finn T., Franke B., Gaier T., Gal C., Gao J. R., Gallego J.-D., Gauffre S., Gill J. J., Glenz S., Golstein H., Goulooze H., Gunsing T., Güsten R., Hartogh P., Hatch W. A., Higgins R., Honingh E. C., Huisman R., Jackson B. D., Jacobs H., Jacobs K., Jarchow C., Javadi H., Jellema W., Justen M., Karpov A., Kasemann C., Kawamura J., Keizer G., Kester D., Klapwijk T. M., Klein T., Kollberg E., Kooij J., Kooiman P.-P., Kopf B., Krause M., Krieg J.-M., Kramer C., Kruizinga B., Kuhn T., Laauwen W., Lai R., Larsson B., Leduc H. G., Leinz C., Lin R. H., Liseau R., Liu G. S., Loose A., López-Fernandez I., Lord S., Luinge W., Marston A., Martín-Pintado J., Maestrini A., Maiwald F. W., McCoey C., Mehdi I., Megej A., Melchior M., Meinsma L., Merkel H., Michalska M., Monstein C., Moratschke D., Morris P., Muller H., Murphy J. A., Naber A., Natale E., Nowosielski W., Nuzzolo F., Olberg M., Olbrich M., Orfei R., Orleanski P., Ossenkopf V., Peacock T., Pearson J. C., Peron I., Phillip-May S., Piazzo L., Planesas P., Rataj M., Ravera L., Risacher C., Salcez M., Samoska L. A., Saraceno P., Schieder R., Schlecht E., Schlöder F., Schmülling F., Schultz M., Schuster K., Siebertz O., Smit H., Szczepański R., Shipman R., Steinmetz E., Stern J. A., Stokroos M., Teipen R., Teyssier D., Tils T., Trappe N., van Baaren C., van Leeuwen B.-J., van de Stadt H., Visser H., Wildeman K. J., Wafelbakker C. K., Ward J. S., Wesselius P., Wild W., Wulff S., Wunsch H.-J., Tiemens X., Zaai P., Zirath H., Zmuidzinis J., and Zwart F. (2010) The Herschel-Heterodyne Instrument for the Far-Infrared (HIFI). *Astron. Astrophys.*, 518, L6.
- Delbó M. (2004) The nature of near-Earth asteroids from the study of their thermal infrared emission. Ph.D. thesis, Freie Universität, Berlin.

- Delb   M., Harris A. W., Binzel R. P., Pravec P., and Davies J. K. (2003) Keck observations of near-Earth asteroids in the thermal infrared. *Icarus*, 166, 116–130.
- Delb   M., Dell’Oro A., Harris A. W., Mottola S., and Mueller M. (2007) Thermal inertia of near-Earth asteroids and implications for the magnitude of the Yarkovsky effect. *Icarus*, 190, 236–249.
- Delb   M., Walsh K., Mueller M., Harris A. W., and Howell E. S. (2011) The cool surfaces of binary near-Earth asteroids. *Icarus*, 212, 138–148.
- Delb   M., Libourel G., Wilkerson J., Murdoch N., Michel P., Ramesh R., Ganino C., Verati C., and Marchi S. (2014) Thermal fatigue as the origin of regolith on small asteroids. *Nature*, 508, 233–236.
- DeMeo F. and Binzel R. P. (2008) Comets in the near-Earth object population. *Icarus*, 194, 436–449.
- DeMeo F. E. and Carry B. (2013) The taxonomic distribution of asteroids from multi-filter all-sky photometric surveys. *Icarus*, 226, 723–741.
- DeMeo F. E. and Carry B. (2014) Solar system evolution from compositional mapping of the asteroid belt. *Nature*, 505, 629–634.
- DeMeo F. E., Binzel R. P., Slivan S. M., and Bus S. J. (2009) An extension of the Bus asteroid taxonomy into the near-infrared. *Icarus*, 202, 160–180.
- Dotto E., Barucci M. A., M  ller T. G., Storrs A. D., and Tanga P. (2002) Observations from orbiting platforms. In *Asteroids III* (W. F. Bottke Jr. et al., eds.), pp. 219–234. Univ. of Arizona, Tucson.
- Duffard R., Pinilla-Alonso N., Santos-Sanz P., Vilenius E., Ortiz J. L., Mueller T., Fornasier S., Lellouch E., Mommert M., Pal A., Kiss C., Mueller M., Stansberry J., Delsanti A., Peixinho N., and Trilling D. (2014) “TNOs are cool”: A survey of the trans-neptunian region. XI. A Herschel-PACS view of 16 Centaurs. *Astron. Astrophys.*, 564, A92.
- Durech J., Sidorin V., and Kaasalainen M. (2010) DAMIT: A database of asteroid models. *Astron. Astrophys.*, 513, A46.
- Emery J. P., Cruikshank D. P., and Van Cleve J. (2006) Thermal emission spectroscopy (5.2–38 µm) of three Trojan asteroids with the Spitzer Space Telescope: Detection of fine-grained silicates. *Icarus*, 182, 496–512.
- Emery J. P., Fern  ndez Y. R., Kelley M. S. P., Warden (n  e Crane) K. T., Hergenrother C., Lauretta D. S., Drake M. J., Campins H., and Ziffer J. (2014) Thermal infrared observations and thermophysical characterization of OSIRIS-REx target asteroid (101955) Bennu. *Icarus*, 234, 17–35.
- Fazio G. G., Hora J. L., Allen L. E., Ashby M. L. N., Barmby P., Deutsch L. K., Huang J.-S., Kleiner S., Marengo M., Megeath S. T., Melnick G. J., Pahre M. A., Patten B. M., Polizotti J., Smith H. A., Taylor R. S., Wang Z., Willner S. P., Hoffmann W. F., Pipher J. L., Forrest W. J., McMurry C. W., McCreight C. R., McKelvey M. E., McMurray R. E., Koch D. G., Moseley S. H., Arendt R. G., Mentzell J. E., Marx C. T., Losch P., Mayman P., Eichhorn W., Krebs D., Jhabvala M., Gezari D. Y., Fixsen D. J., Flores J., Shakoordzadeh K., Jungo R., Hakun C., Workman L., Karpati G., Kichak R., Whitley R., Mann S., Tolstrup E. V., Eisenhardt P., Stern D., Gorjian V., Bhattacharya B., Carey S., Nelson B. O., Glaccum W. J., Lacy M., Lowrance P. J., Laine S., Reach W. T., Stauffer J. A., Surace J. A., Wilson G., Wright E. L., Hoffman A., Domingo G., and Cohen M. (2004) The Infrared Array Camera (IRAC) for the Spitzer Space Telescope. *Astrophys. J. Suppl.*, 154, 10–17.
- Fern  ndez Y. R., Jewitt D. C., and Sheppard S. S. (2005) Albedos of asteroids in comet-like orbits. *Astron. J.*, 130, 308–318.
- Fern  ndez Y. R., Jewitt D., and Ziffer J. E. (2009) Albedos of small jovian Trojans. *Astron. J.*, 138, 240–250.
- Fern  ndez Y. R., Kelley M. S., Lamy P. L., Toth I., Groussin O., Lisse C. M., A’Hearn M. F., Bauer J. M., Campins H., Fitzsimmons A., Licandro J., Lowry S. C., Meech K. J., Pittichov   J., Reach W. T., Snodgrass C., and Weaver H. A. (2013) Thermal properties, sizes, and size distribution of Jupiter-family cometary nuclei. *Icarus*, 226, 1138–1170.
- Gil-Hutton R. and Ca  nada-Assandri M. (2012) Polarimetric survey of main-belt asteroids. II. Results for 58 B- and C-type objects. *Astron. Astrophys.*, 539, A115.
- Grav T., Jedicke R., Denneau L., Chesley S., Holman M. J., and Spahr T. B. (2011a) The Pan-STARRS synthetic solar system model: A tool for testing and efficiency determination of the moving object processing system. *Publ. Astron. Soc. Pac.*, 123, 423–447.
- Grav T., Mainzer A. K., Bauer J., Masiero J., Spahr T., McMillan R. S., Walker R., Cutri R., Wright E., Eisenhardt P. R. M., Blauvelt E., DeBaun E., Elsbury D., Gautier T. IV, Gomillion S., Hand E., and Wilkins A. (2011b) WISE/NEOWISE observations of the jovian Trojans: Preliminary results. *Astrophys. J.*, 742, 40.
- Grav T., Mainzer A. K., Bauer J., Masiero J., Spahr T., McMillan R. S., Walker R., Cutri R., Wright E., Eisenhardt P. R., Blauvelt E., DeBaun E., Elsbury D., Gautier T., Gomillion S., Hand E., and Wilkins A. (2012a) WISE/NEOWISE observations of the Hilda population: Preliminary results. *Astrophys. J.*, 744, 197.
- Grav T., Mainzer A. K., Bauer J. M., Masiero J. R., and Nugent C. R. (2012b) WISE/NEOWISE observations of the jovian Trojan population: Taxonomy. *Astrophys. J.*, 759, 49.
- Grav T., Bauer J. M., Mainzer A. K., Masiero J. R., Nugent C. R., Cutri R. M., Sonnett S., and Kramer E. (2015) NEOWISE: Observations of the irregular satellites of Jupiter and Saturn. *Astrophys. J.*, 809, 3.
- Green S. F., Meadows A. J., and Davies J. K. (1985) Infrared observations of the extinct cometary candidate minor planet (3200) 1983 TB. *Mon. Not. R. Astron. Soc.*, 214, 29P–36P.
- Greenstreet S. and Gladman B. (2013) High-inclination Atens are indeed rare. *Astrophys. J. Lett.*, 767, L18.
- Griffin M. J., Aberget A., Abreu A., Ade P. A. R., Andr   P., Augueres J.-L., Babbedge T., Bae Y., Baillie T., Baluteau J.-P., Barlow M. J., Bendo G., Benielli D., Bock J. J., Bonhomme P., Brisbin D., Brockley-Blatt C., Caldwell M., Cara C., Castro-Rodriguez N., Cerulli R., Chanial P., Chen S., Clark E., Clements D. L., Clerc L., Coker J., Communal D., Conversi L., Cox P., Crumb D., Cunningham C., Daly F., Davis G. R., de Antoni P., Delderfield J., Devin N., di Giorgio A., Didschuns I., Dohlen K., Donati M., Dowell A., Dowell C. D., Duband L., Dumaye L., Emery R. J., Ferlet M., Ferrand D., Fontignie J., Fox M., Franceschini A., Frerking M., Fulton T., Garcia J., Gastaud R., Gear W. K., Glenn J., Goizel A., Griffin D. K., Grundy T., Guest S., Guillemet L., Hargrave P. C., Harwit M., Hastings P., Hatziminaoglou E., Herman M., Hinde B., Hristov V., Huang M., Imhof P., Isaak K. J., Israelsson U., Ivison R. J., Jennings D., Kiernan B., King K. J., Lange A. E., Latter W., Laurent G., Laurent P., Leeks S. J., Lellouch E., Levenson L., Li B., Li J., Lilienthal J., Lim T., Liu S. J., Lu N., Madden S., Mainetti G., Marlani P., McKay D., Mercier K., Molinari S., Morris H., Moseley H., Mulder J., Mur M., Naylor D. A., Nguyen H., O’Halloran B., Oliver S., Olofsson G., Olofsson H.-G., Orfei R., Page M. J., Pain I., Panuzzo P., Papageorgiou A., Parks G., Parr-Burman P., Pearce A., Pearson C., P  rez-Fournon I., Pinsard F., Pisano G., Podosek J., Pohlen M., Polehampton E. T., Pouliquen D., Rigopoulou D., Rizzo D., Roseboom I. G., Roussel H., Rowan-Robinson M., Rownd B., Saraceno P., Sauvage M., Savage R., Savini G., Sawyer E., Scharberg C., Schmitt D., Schneider N., Schulz B., Schwartz A., Shafer R., Shupe D. L., Sibthorpe B., Sidher S., Smith A., Smith A. J., Smith D., Spencer L., Stobie B., Sudwala R., Sukhatme K., Surace C., Stevens J. A., Swinyard B. M., Trichas M., Tourette T., Triou H., Tseng S., Tucker C., Turner A., Vaccari M., Valtchanov I., Vigroux L., Virique E., Voellmer G., Walker H., Ward R., Waskett T., Weilert M., Wesson R., White G. J., Whitehouse N., Wilson C. D., Winter B., Woodcraft A. L., Wright G. S., Xu C. K., Zavagno A., Zemcov M., Zhang L., and Zonca E. (2010) The Herschel-SPIRE instrument and its in-flight performance. *Astron. Astrophys.*, 518, L3.
- Hansen O. L. (1976) Radii and albedos of 84 asteroids from visual and infrared photometry. *Astron. J.*, 81, 74–84.
- Hanus J., Delbo M., Durech J., and Ali-Lagoa V. (2015) Thermo-physical modeling of asteroids from WISE thermal infrared data — Significance of the shape model and the pole orientation uncertainties. *Icarus*, 256, 101.
- Hardersen P. S., Reddy V., Roberts R., and Mainzer A. (2014) More chips off of asteroid (4) Vesta: Characterization of eight Vestaoids and their HED meteorite analogs. *Icarus*, 242, 269–282.
- Harris A. W. (1998) A thermal model for near-Earth asteroids. *Icarus*, 131, 291–301.
- Harris A. W. and Drube L. (2014) How to find metal-rich asteroids. *Astrophys. J. Lett.*, 785, L4.
- Harris A. W. and Lagerros J. S. V. (2002) Asteroids in the thermal infrared. In *Asteroids III* (W. F. Bottke Jr. et al., eds.), pp. 205–218. Univ. of Arizona, Tucson.
- Harris A. W. and Young J. W. (1989) Asteroid lightcurve observations from 1979–1981. *Icarus*, 81, 314–364.
- Harris A. W., Young J. W., Contreiras L., Dockweiler T., Belkora L., Salo H., Harris W. D., Bowell E., Poutanen M., Binzel R. P.,

- Tholen D. J., and Wang S. (1989) Phase relations of high albedo asteroids — The unusual opposition brightening of 44 Nysa and 64 Angelina. *Icarus*, 81, 365–374.
- Harris A. W., Mommert M., Hora J. L., Mueller M., Trilling D. E., Bhattacharya B., Bottke W. F., Chesley S., Delbo M., Emery J. P., Fazio G., Mainzer A., Penprase B., Smith H. A., Spahr T. B., Stansberry J. A., and Thomas C. A. (2011) Explore NEOs. II. The accuracy of the warm Spitzer near-Earth object survey. *Astron. J.*, 141, 75.
- Hasegawa S., Müller T. G., Kawakami K., Kasuga T., Wada T., Ita Y., Takato N., Terada H., Fujiyoshi T., and Abe M. (2008) Albedo, size, and surface characteristics of Hayabusa-2 sample-return target 162173 1999 JU<sub>3</sub> from AKARI. *Publ. Astron. Soc. Japan*, 60, 399.
- Hasegawa S., Müller T. G., Kuroda D., Takita S., and Usui F. (2013) The asteroid catalog using AKARI IRC slow-scan observations. *Publ. Astron. Soc. Japan*, 65, 34.
- Houck J. R., Roellig T. L., van Cleve J., Forrest W. J., Herter T., Lawrence C. R., Matthews K., Reitsema H. J., Soifer B. T., Watson D. M., Weedman D., Huisjen M., Troeltzsch J., Barry D. J., Bernard-Salas J., Blacken C. E., Brandl B. R., Charmandaris V., Devost D., Gull G. E., Hall P., Henderson C. P., Higdon S. J. U., Pirger B. E., Schoenwald J., Sloan G. C., Uchida K. I., Appleton P. N., Armus L., Burgdorf M. J., Fajardo-Acosta S. B., Grillmair C. J., Ingalls J. G., Morris P. W., and Teplitz H. I. (2004) The Infrared Spectrograph (IRS) on the Spitzer Space Telescope. *Astrophys. J. Suppl.*, 154, 18–24.
- Ishihara D., Onaka T., Kataza H., Salama A., Alfageme C., Cassatella A., Cox N., García-Lario P., Stephenson C., Cohen M., Fujishiro N., Fujiwara H., Hasegawa S., Ita Y., Kim W., Matsuhara H., Murakami H., Müller T. G., Nakagawa T., Ohyama Y., Oyabu S., Pyo J., Sakon I., Shibai H., Takita S., Tanabé T., Uemizu K., Ueno M., Usui F., Wada T., Watarai H., Yamamura I., and Yamauchi C. (2010) The AKARI/IRC mid-infrared all-sky survey. *Astron. Astrophys.*, 514, A1.
- Jedicke R. and Metcalfe T. S. (1998) The orbital and absolute magnitude distributions of main belt asteroids. *Icarus*, 131, 245–260.
- Kaasalainen M., Torppa J., and Muinonen K. (2001) Optimization methods for asteroid lightcurve inversion. II. The complete inverse problem. *Icarus*, 153, 37–51.
- Kawada M., Baba H., Barthel P. D., Clements D., Cohen M., Doi Y., Figueiredo E., Fujiwara M., Goto T., Hasegawa S., Hibi Y., Hirao T., Hiromoto N., Jeong W.-S., Kaneda H., Kawai T., Kawamura A., Kester D., Kii T., Kobayashi H., Kwon S. M., Lee H. M., Makiuti S., Matsuo H., Matsuura S., Müller T. G., Murakami N., Nagata H., Nakagawa T., Narita M., Noda M., Oh S. H., Okada Y., Okuda H., Oliver S., Ootsubo T., Pak S., Park Y.-S., Pearson C. P., Rowan-Robinson M., Saito T., Salama A., Sato S., Savage R. S., Serjeant S., Shibai H., Shirahata M., Sohn J., Suzuki T., Takagi T., Takahashi H., Thomson M., Usui F., Verdugo E., Watabe T., White G. J., Wang L., Yamamura I., Yamauchi C., and Yasuda A. (2007) The Far-Infrared Surveyor (FIS) for AKARI. *Publ. Astron. Soc. Japan*, 59, 389.
- Keihm S., Tosi F., Kamp L., Capaccioni F., Gulkis S., Grassi D., Hofstaedter M., Filacchione G., Lee S., Giuppi S., Janssen M., and Capria M. (2012) Interpretation of combined infrared, submillimeter, and millimeter thermal flux data obtained during the Rosetta fly-by of asteroid (21) Lutetia. *Icarus*, 221, 395–404.
- Kessler M. F., Steinz J. A., Anderegg M. E., Clavel J., Drechsel G., Estaria P., Faelker J., Riedinger J. R., Robson A., Taylor B. G., and Ximénez de Ferrán S. (1996) The Infrared Space Observatory (ISO) mission. *Astron. Astrophys.*, 315, L27–L31.
- Kim Y., Ishiguro M., and Usui F. (2014) Physical properties of asteroids in comet-like orbits in infrared asteroid survey catalogs. *Astrophys. J.*, 789, 151.
- Koren S., Wright E. L., and Mainzer A. (2015) Characterizing asteroids multiply-observed at infrared wavelengths. *Icarus*, 258, 82.
- Küppers M., O'Rourke L., Bockelée-Morvan D., Zakharov V., Lee S., von Allmen P., Carry B., Teyssier D., Marston A., Müller T., Crovisier J., Barucci M. A., and Moreno R. (2014) Localized sources of water vapour on the dwarf planet (1) Ceres. *Nature*, 505, 525–527.
- Kuroda D., Ishiguro M., Takato N., Hasegawa S., Abe M., Tsuda Y., Sugita S., Usui F., Hattori T., Iwata I., Imanishi M., Terada H., Choi Y.-J., Watanabe S.-I., and Yoshikawa M. (2014) Visible-wavelength spectroscopy of subkilometer-sized near-Earth asteroids with a low delta-v. *Publ. Astron. Soc. Japan*, 66, 51.
- Lebofsky L. A. and Spencer J. R. (1989) Radiometry and a thermal modeling of asteroids. In *Asteroids II* (R. P. Binzel et al., eds.), pp. 128–147. Univ. of Arizona, Tucson.
- Lebofsky L. A., Veeder G. J., Lebofsky M. J., and Matson D. L. (1978) Visual and radiometric photometry of 1580 Betulia. *Icarus*, 35, 336–343.
- Lebofsky L. A., Sykes M. V., Tedesco E. F., Veeder G. J., Matson D. L., Brown R. H., Gradić J. C., Feierberg M. A., and Rudy R. J. (1986) A refined ‘standard’ thermal model for asteroids based on observations of 1 Ceres and 2 Pallas. *Icarus*, 68, 239–251.
- Lellouch E., Santos-Sanz P., Lacerda P., Mommert M., Duffard R., Ortiz J. L., Müller T. G., Fornasier S., Stansberry J., Kiss C., Vilenius E., Mueller M., Peixinho N., Moreno R., Grousson O., Delsanti A., and Harris A. W. (2013) “TNOs are cool”: A survey of the trans-neptunian region. IX. Thermal properties of Kuiper belt objects and Centaurs from combined Herschel and Spitzer observations. *Astron. Astrophys.*, 557, A60.
- Leyrat C., Coradini A., Erard S., Capaccioni F., Capria M. T., Drossart P., de Sanctis M. C., Tosi F., and the VIRTIS Team (2011) Thermal properties of the asteroid (2867) Steins as observed by VIRTIS/Rosetta. *Astron. Astrophys.*, 531, A168.
- Leyrat C., Barucci A., Mueller T., O'Rourke L., Valtchanov I., and Fornasier S. (2012) Thermal properties of (4) Vesta derived from Herschel measurements. *Astron. Astrophys.*, 539, A154.
- Licandro J., Campins H., Kelley M., Hargrove K., Pinilla-Alonso N., Cruikshank D., Rivkin A. S., and Emery J. (2011) (65) Cybele: Detection of small silicate grains, water-ice, and organics. *Astron. Astrophys.*, 525, A34.
- Licandro J., Hargrove K., Kelley M., Campins H., Ziffer J., Ali-Lagoa V., Fernández Y., and Rivkin A. (2012) 5–14 μm Spitzer spectra of Themis family asteroids. *Astron. Astrophys.*, 537, A73.
- Lim L. F., Emery J. P., and Moskovitz N. A. (2011) Mineralogy and thermal properties of V-type asteroid 956 Elisa: Evidence for diogenitic material from the Spitzer IRS (5–35 μm) spectrum. *Icarus*, 213, 510–523.
- Lupishko D. F. and Vasilyev S. V. (2012) *Asteroid Polarimetric Database V7.0*. NASA Planetary Data System, EAR-A-3-RDR-APD-POLARIMETRY-V7.0.
- Mainzer A. K., Eisenhardt P., Wright E. L., Liu F.-C., Irace W., Heinrichsen I., Cutri R., and Duval V. (2005) Preliminary design of the Wide-Field Infrared Survey Explorer (WISE). In *UV/Optical/IR Space Telescopes: Innovative Technologies and Concepts II* (H. A. MacEwen, ed.), pp. 262–273. SPIE Conf. Ser. 5899, Bellingham, Washington.
- Mainzer A., Bauer J., Grav T., Masiero J., Cutri R. M., Dailey J., Eisenhardt P., McMillan R. S., Wright E., Walker R., Jedicke R., Spahr T., Tholen D., Alles R., Beck R., Brandenburg H., Conrow T., Evans T., Fowler J., Jarrett T., Marsh K., Masci F., McCallon H., Wheelock S., Wittman M., Wyatt P., DeBaun E., Elliott G., Elsbury D., Gautier T. IV, Gomillion S., Leisawitz D., Maleszewski C., Micheli M., and Wilkins A. (2011a) Preliminary results from NEOWISE: An enhancement to the Wide-field Infrared Survey Explorer for solar system science. *Astrophys. J.*, 731, 53.
- Mainzer A., Grav T., Bauer J., Masiero J., McMillan R. S., Cutri R. M., Walker R., Wright E., Eisenhardt P., Tholen D. J., Spahr T., Jedicke R., Denneau L., DeBaun E., Elsbury D., Gautier T., Gomillion S., Hand E., Mo W., Watkins J., Wilkins A., Bryngelson G. L., Del Pino Molina A., Desai S., Gómez Camus M., Hidalgo S. L., Konstantopoulos I., Larsen J. A., Maleszewski C., Malkan M. A., Mauduit J.-C., Mullan B. L., Olszewski E. W., Pforr J., Saro A., Scotti J. V., and Wasserman L. H. (2011b) NEOWISE observations of near-Earth objects: Preliminary results. *Astrophys. J.*, 743, 156.
- Mainzer A., Grav T., Masiero J., Bauer J., Wright E., Cutri R. M., McMillan R. S., Cohen M., Ressler M., and Eisenhardt P. (2011c) Thermal model calibration for minor planets observed with Wide-field Infrared Survey Explorer/NEOWISE. *Astrophys. J.*, 736, 100.
- Mainzer A., Grav T., Masiero J., Hand E., Bauer J., Tholen D., McMillan R. S., Spahr T., Cutri R. M., Wright E., Watkins J., Mo W., and Maleszewski C. (2011d) NEOWISE studies of spectrophotometrically classified asteroids: Preliminary results. *Astrophys. J.*, 741, 90.
- Mainzer A., Grav T., Masiero J., Bauer J., Cutri R. M., McMillan R. S., Nugent C. R., Tholen D., Walker R., and Wright E. L. (2012a) Physical parameters of asteroids estimated from the WISE 3-band data and NEOWISE post-cryogenic survey. *Astrophys. J. Lett.*, 760, L12.
- Mainzer A., Grav T., Masiero J., Bauer J., McMillan R. S., Giorgini J., Spahr T., Cutri R. M., Tholen D. J., Jedicke R., Walker R., Wright E., and Nugent C. R. (2012b) Characterizing subpopulations within the near-Earth objects with NEOWISE: Preliminary results. *Astrophys. J.*, 752, 110.

- Mainzer A., Masiero J., Grav T., Bauer J., Tholen D. J., McMillan R. S., Wright E., Spahr T., Cutri R. M., Walker R., Mo W., Watkins J., Hand E., and Maleszewski C. (2012c) NEOWISE studies of asteroids with Sloan photometry: Preliminary results. *Astrophys. J.*, 745, 7.
- Mainzer A., Bauer J., Grav T., Masiero J., Cutri R. M., Wright E., Nugent C. R., Stevenson R., Clyne E., Cukrov G., and Masci F. (2014a) The population of tiny near-Earth objects observed by NEOWISE. *Astrophys. J.*, 784, 100.
- Mainzer A., Bauer J., Cutri R. M., Grav T., Masiero J., Beck R., Clarkson P., Conrow T., Dailey J., Eisenhardt P., Fabinsky B., Fajardo-Acosta S., Fowler J., Gelino C., Grillmair C., Heinrichsen I., Kendall M., Kirkpatrick J. D., Liu F., Masci F., McCallon H., Nugent C. R., Papin M., Rice E., Royer D., Ryan T., Sevilla P., Sonnett S., Stevenson R., Thompson D. B., Wheelock S., Wiemer D., Wittman M., Wright E., and Yan L. (2014b) Initial performance of the NEOWISE reactivation mission. *Astrophys. J.*, 792, 30.
- Marchis F., Enriquez J. E., Emery J. P., Mueller M., Baek M., Pollock J., Assafin M., Vieira Martins R., Berthier J., Vachier F., Cruikshank D. P., Lim L. F., Reichart D. E., Ivansen K. M., Haislip J. B., and LaCluyze A. P. (2012) Multiple asteroid systems: Dimensions and thermal properties from Spitzer Space Telescope and groundbased observations. *Icarus*, 221, 1130–1161.
- Marsset M., Vernazza P., Gourgeot F., Dumas C., Birlan M., Lamy P., and Binzel R. P. (2014) Similar origin for low- and high-albedo jovian Trojans and Hilda asteroids? *Astron. Astrophys.*, 568, L7.
- Marzari F. and Scholl H. (2013) Long term stability of Earth Trojans. *Cel. Mech. Dyn. Astron.*, 117, 91–100.
- Marzari F., Davis D., and Vanzani V. (1995) Collisional evolution of asteroid families. *Icarus*, 113, 168–187.
- Masiero J. R., Mainzer A. K., Grav T., Bauer J. M., Cutri R. M., Dailey J., Eisenhardt P. R. M., McMillan R. S., Spahr T. B., Skrutskie M. F., Tholen D., Walker R. G., Wright E. L., DeBaun E., Elsbury D., Gautier T. IV, Gomillion S., and Wilkins A. (2011) Main belt asteroids with WISE/NEOWISE. I. Preliminary albedos and diameters. *Astrophys. J.*, 741, 68.
- Masiero J. R., Mainzer A. K., Grav T., Bauer J. M., Cutri R. M., Nugent C., and Cabrera M. S. (2012a) Preliminary analysis of WISE/NEOWISE 3-band cryogenic and post-cryogenic observations of main belt asteroids. *Astrophys. J. Lett.*, 759, L8.
- Masiero J. R., Mainzer A. K., Grav T., Bauer J. M., and Jedicke R. (2012b) Revising the age for the Baptistina asteroid family using WISE/NEOWISE data. *Astrophys. J.*, 759, 14.
- Masiero J. R., Mainzer A. K., Bauer J. M., Grav T., Nugent C. R., and Stevenson R. (2013) Asteroid family identification using the hierarchical clustering method and WISE/NEOWISE physical properties. *Astrophys. J.*, 770, 7.
- Masiero J. R., Grav T., Mainzer A. K., Nugent C. R., Bauer J. M., Stevenson R., and Sonnett S. (2014) Main belt asteroids with WISE/NEOWISE: Near-infrared albedos. *Astrophys. J.*, 791, 121.
- Masiero J. R., Carruba V., Mainzer A., Bauer J. M., and Nugent C. (2015) The Euphyrosyne family's contribution to the low albedo near-Earth asteroids. *Astrophys. J.*, 809, 179.
- Matson D. L. (1971) Infrared observations of asteroids. In *Physical Studies of the Minor Planets* (T. Gehrels, ed.), pp. 45–50. NASA SP-267, Washington, DC.
- Matson D. L., Veverka J., Tedesco E. F., and Lebofsky L. A. (1989) The IRAS asteroid and comet survey. In *Asteroids II* (R. P. Binzel et al., eds.), pp. 269–281. Univ. of Arizona, Tucson.
- Matter A., Delbó M., Ligori S., Crouzet N., and Tanga P. (2011) Determination of physical properties of the asteroid (41) Daphne from interferometric observations in the thermal infrared. *Icarus*, 215, 47–56.
- McMurtry C., Lee D., Beletic J., Chen C.-Y. A., Demers R. T., Dorn M., Edwall D., Fazar C. B., Forrest W. J., Liu F., Mainzer A. K., Pipher J. L., and Julius A. (2013) Development of sensitive long-wave infrared detector arrays for passively cooled space missions. *Optical Eng.*, 52(9), 091804.
- Milani A., Cellino A., Knežević Z., Novaković B., Spoto F., and Paolicchi P. (2014) Asteroid families classification: Exploiting very large datasets. *Icarus*, 239, 46–73.
- Mill J. D., O'Neil R. R., Price S., Romick G. J., Uy O. M., Gaposchkin E. M., Light G. C., Moore W. W. Jr., Murdock T. L., and Stair A. T. Jr. (1994) Mid-course space experiment: Introduction to the spacecraft, instruments, and scientific objectives. *J. Spacecraft Rockets*, 31, 900–907.
- Mommert M., Farnocchia D., Hora J. L., Chesley S. R., Trilling D. E., Chodas P. W., Mueller M., Harris A. W., Smith H. A., and Fazio G. G. (2014a) Physical properties of near-Earth asteroid 2011 MD. *Astrophys. J. Lett.*, 789, L22.
- Mommert M., Hora J. L., Farnocchia D., Chesley S. R., Vokrouhlický D., Trilling D. E., Mueller M., Harris A. W., Smith H. A., and Fazio G. G. (2014b) Constraining the physical properties of near-Earth object 2009 BD. *Astrophys. J.*, 786, 148.
- Mommert M., Hora J. L., Harris A. W., Reach W. T., Emery J. P., Thomas C. A., Mueller M., Cruikshank D. P., Trilling D. E., Delbó M., and Smith H. A. (2014c) The discovery of cometary activity in near-Earth asteroid (3552) Don Quixote. *Astrophys. J.*, 781, 25.
- Mommert M., Harris A. W., Mueller M., Hora J. L., Trilling D. E., Bottke W. F., Thomas C. A., Delbo M., Emery J. P., Fazio G., and Smith H. A. (2015) ExploreNEOs. VIII. Dormant short-period comets in the near-Earth asteroid population. *Astron. J.*, 150, 106.
- Morrison D. and Lebofsky L. (1979) Radiometry of asteroids. In *Asteroids* (T. Gehrels, ed.), pp. 184–205. Univ. of Arizona, Tucson.
- Mueller M., Harris A. W., and Fitzsimmons A. (2007) Size, albedo, and taxonomic type of potential spacecraft target asteroid (10302) 1989 ML. *Icarus*, 187, 611–615.
- Mueller M., Delbó M., Hora J. L., Trilling D. E., Bhattacharya B., Bottke W. F., Chesley S., Emery J. P., Fazio G., Harris A. W., Mainzer A., Mommert M., Penprase B., Smith H. A., Spahr T. B., Stansberry J. A., and Thomas C. A. (2011) Explore NEOs. III. Physical characterization of 65 potential spacecraft target asteroids. *Astron. J.*, 141, 109.
- Müller T. G., Lellouch E., Stansberry J., Kiss C., Santos-Sanz P., Vilenius E., Protopapa S., Moreno R., Mueller M., Delsanti A., Duffard R., Fornasier S., Groussin O., Harris A. W., Henry F., Horner J., Lacerda P., Lim T., Mommert M., Ortiz J. L., Rengel M., Thirouin A., Trilling D., Barucci A., Crovisier J., Doressoundiram A., Dotto E., Gutiérrez P. J., Hainaut O. R., Hartogh P., Hestroffer D., Kidger M., Lara L., Swinyard B., and Thomas N. (2010) “TNOS are cool”: A survey of the trans-neptunian region. I. Results from the Herschel science demonstration phase (SDP). *Astron. Astrophys.*, 518, L146.
- Müller T. G., O'Rourke L., Barucci A. M., Pál A., Kiss C., Zeidler P., Altieri B., González-García B. M., and Küppers M. (2012) Physical properties of OSIRIS-REx target asteroid (101955) 1999 RQ<sub>36</sub>. Derived from Herschel, VLT/VISIR, and Spitzer observations. *Astron. Astrophys.*, 548, A36.
- Müller T. G., Miyata T., Kiss C., Gurwell M. A., Hasegawa S., Vilenius E., Sako S., Kamizuka T., Nakamura T., Asano K., Uchiyama M., Konishi M., Yoneda M., Ootsubo T., Usui F., Yoshii Y., Kidger M., Altieri B., Lorente R., Pál A., O'Rourke L., and Metcalfe L. (2013) Physical properties of asteroid 308635 (2005 YU<sub>55</sub>) derived from multi-instrument infrared observations during a very close Earth approach. *Astron. Astrophys.*, 558, A97.
- Müller T., Balog Z., Nielbock M., Lim T., Teyssier D., Olberg M., Klaas U., Linz H., Altieri B., Pearson C., Bendo G., and Vilenius E. (2014a) Herschel celestial calibration sources. Four large main-belt asteroids as prime flux calibrators for the far-IR/sub-mm range. *Exp. Astron.*, 37, 253–330.
- Müller T. G., Hasegawa S., and Usui F. (2014b) (25143) Itokawa: The power of radiometric techniques for the interpretation of remote thermal observations in the light of the Hayabusa rendezvous results. *Publ. Astron. Soc. Japan*, 66, 52.
- Müller T. G., Kiss C., Scheirich P., Pravec P., O'Rourke L., Vilenius E., and Altieri B. (2014c) Thermal infrared observations of asteroid (99942) Apophis with Herschel. *Astron. Astrophys.*, 566, A22.
- Murakami H., Baba H., Barthel P., Clements D. L., Cohen M., Doi Y., Enya K., Figueredo E., Fujishiro N., Fujiwara H., Fujiwara M., Garcia-Lario P., Goto T., Hasegawa S., Hibi Y., Hirao T., Hiromoto N., Hong S. S., Imai K., Ishigaki M., Ishiguro M., Ishihara D., Ita Y., Jeong W.-S., Jeong K. S., Kaneda H., Kataza H., Kawada M., Kawai T., Kawamura A., Kessler M. F., Kester D., Kii T., Kim D. C., Kim W., Kobayashi H., Koo B. C., Kwon S. M., Lee H. M., Lorente R., Makita S., Matsuhara H., Matsumoto T., Matsuo H., Matsuura S., Müller T. G., Murakami N., Nagata H., Nakagawa T., Naoi T., Narita M., Noda M., Oh S. H., Ohnishi A., Ohyama Y., Okada Y., Okuda H., Oliver S., Onaka T., Ootsubo T., Oyabu S., Pak S., Park Y.-S., Pearson C. P., Rowan-Robinson M., Saito T., Sakon I., Salama A., Sato S., Savage R. S., Serjeant S., Shibai H., Shirahata M., Sohn J., Suzuki T., Takagi T., Takahashi H., Tanabé T., Takeuchi T. T., Takita S., Thomson M., Uemizu K., Ueno M., Usui F., Verdugo E., Wada T., Wang L., Watabe T., Watarai H., White G. J., Yamamura I., Yamauchi C., and Yasuda A. (2007) The infrared astronomical mission AKARI. *Publ. Astron. Soc. Japan*, 59, 369.

- Nakagawa T., Enya K., Hirabayashi M., Kaneda H., Kii T., Kimura Y., Matsumoto T., Murakami H., Murakami M., Narasaki K., Narita M., Ohnishi A., Tsunematsu S., and Yoshida S. (2007) Flight performance of the AKARI cryogenic system. *Publ. Astron. Soc. Japan*, **59**, 377.
- Neugebauer G., Habing H. J., van Duinen R., Aumann H. H., Baud B., Beichman C. A., Beintema D. A., Boggess N., Clegg P. E., de Jong T., Emerson J. P., Gautier T. N., Gillett F. C., Harris S., Hauser M. G., Houck J. R., Jennings R. E., Low F. J., Marsden P. L., Miley G., Olmon F. M., Pottasch S. R., Raimond E., Rowan-Robinson M., Soifer B. T., Walker R. G., Wesselius P. R., and Young E. (1984) The Infrared Astronomical Satellite (IRAS) mission. *Astrophys. J. Lett.*, **278**, L1–L6.
- Nugent C. R., Mainzer A., Masiero J., Bauer J., Cutri R. M., Grav T., Kramer E., Sonnett S., Stevenson R., and Wright E. L. (2015) NEOWISE Reactivation Mission Year One: Preliminary asteroid diameters and albedos. *Astrophys. J.*, in press.
- Onaka T., Matsuhara H., Wada T., Fujishiro N., Fujiwara H., Ishigaki M., Ishihara D., Ita Y., Kataza H., Kim W., Matsumoto T., Murakami H., Ohyama Y., Oyabu S., Sakon I., Tanabé T., Takagi T., Uemizu K., Ueno M., Usui F., Watarai H., Cohen M., Enya K., Ootsubo T., Pearson C. P., Takeyama N., Yamamoto T., and Ikeda Y. (2007) The Infrared Camera (IRC) for AKARI — Design and imaging performance. *Publ. Astron. Soc. Japan*, **59**, 401.
- O'Rourke L., Müller T., Valtchanov I., Altieri B., González-García B. M., Bhattacharya B., Jorda L., Carry B., Küppers M., Groussin O., Altwegg K., Barucci M. A., Bockelee-Morvan D., Crovisier J., Dotto E., García-Lario P., Kidger M., Llorente A., Lorente R., Marston A. P., Sanchez Portal M., Schulz R., Sierra M., Teyssier D., and Vavrek R. (2012) Thermal and shape properties of asteroid (21) Lutetia from Herschel observations around the Rosetta flyby. *Planet. Space Sci.*, **66**, 192–199.
- Ostro S. J., Hudson R. S., Benner L. A. M., Giorgini J. D., Magri C., Margot J. L., and Nolan M. C. (2002) Asteroid radar astronomy. In *Asteroids III* (W. F. Bottke Jr. et al., eds.), pp. 151–168. Univ. of Arizona, Tucson.
- Pilbratt G. L., Riedinger J. R., Passvogel T., Crone G., Doyle D., Gageur U., Heras A. M., Jewell C., Metcalfe L., Ott S., and Schmidt M. (2010) Herschel Space Observatory. An ESA facility for far-infrared and submillimetre astronomy. *Astron. Astrophys.*, **518**, L1.
- Poglitsch A., Waelkens C., Geis N., Feuchtgruber H., Vandenbussche B., Rodriguez L., Krause O., Renotte E., van Hoof C., Saraceno P., Cepa J., Kerschbaum F., Agnès P., Ali B., Altieri B., Andreani P., Auguera J.-L., Balog Z., Barl L., Bauer O. H., Belbachir N., Benedettini M., Billot N., Boulade O., Bischof H., Blommaert J., Callut E., Cara C., Cerulli R., Cesarsky D., Contursi A., Creten Y., De Meester W., Doublier V., Doumayerou E., Duband L., Exter K., Genzel R., Gillis J.-M., Grözinger U., Henning T., Herreros J., Huygen R., Inguscio M., Jakob G., Jamar C., Jean C., de Jong J., Katterhofer R., Kiss C., Klaas U., Lemke D., Lutz D., Madden S., Marquet B., Martignac J., Mazy A., Merken P., Montfort F., Morbidelli L., Müller T., Nielbock M., Okumura K., Orfei R., Ottensamer R., Pezzuto S., Popesso P., Putzeys J., Regibo S., Reveret V., Royer P., Sauvage M., Schreiber J., Stegmaier J., Schmitt D., Schubert J., Sturm E., Thiel M., Tofani G., Vavrek R., Wetzstein M., Wieprecht E., and Wieszorek E. (2010) The Photodetector Array Camera and Spectrometer (PACS) on the Herschel Space Observatory. *Astron. Astrophys.*, **518**, L2.
- Pravec P., Harris A. W., Kušnírák P., Galád A., and Horoch K. (2012) Absolute magnitudes of asteroids and a revision of asteroid albedo estimates from WISE thermal observations. *Icarus*, **221**, 365–387.
- Price S. D., Egan M. P., Carey S. J., Mizuno D. R., and Kuchar T. A. (2001) Midcourse space experiment survey of the galactic plane. *Astron. J.*, **121**, 2819–2842.
- Reach W. T., Kelley M. S., and Vaubaillon J. (2013) Survey of cometary CO<sub>2</sub>, CO, and particulate emissions using the Spitzer Space Telescope. *Icarus*, **226**, 777–797.
- Reddy V. (2010) Reddy IRTF Near-Earth Asteroid Spectra V1.0. EAR-A-10046-5-REDDYSPEC-V1.0, NASA Planetary Data System.
- Rieke G. H., Young E. T., Engelbracht C. W., Kelly D. M., Low F. J., Haller E. E., Beeman J. W., Gordon K. D., Stansberry J. A., Misselt K. A., Cadieu J., Morrison J. E., Rivlis G., Latter W. B., Noriega-Crespo A., Padgett D. L., Stapelfeldt K. R., Hines D. C., Egami E., Muzerolle J., Alonso-Herrero A., Blaylock M., Dole H., Hinz J. L., Le Floch E., Papovich C., Pérez-González P. G., Smith P. S., Su K. Y. L., Bennett L., Frayer D. T., Henderson D., Lu N., Masci F., Pesenson M., Rebull L., Rho J., Keene J., Stolovy S., Wachter S., Wheaton W., Werner M. W., and Richards P. L. (2004) The Multiband Imaging Photometer for Spitzer (MIPS). *Astrophys. J. Suppl.*, **154**, 25–29.
- Ryan E. L., Mizuno D. R., Shenoy S. S., Woodward C. E., Carey S. J., Noriega-Crespo A., Kraemer K. E., and Price S. D. (2015) The kilometer-sized main belt asteroid population revealed by Spitzer. *Astron. Astrophys.*, **578**, 42.
- Sphaer T. B. (1998) Debiasing the main-belt asteroid population. Ph.D. thesis, University of Florida, Gainesville.
- Spencer J. R., Lebofsky L. A., and Sykes M. V. (1989) Systematic biases in radiometric diameter determinations. *Icarus*, **78**, 337–354.
- Stevenson R., Kramer E. A., Bauer J. M., Masiero J. R., and Mainzer A. K. (2012) Characterization of active main belt object P/2012 F5 (Gibbs): A possible impacted asteroid. *Astrophys. J.*, **759**, 142.
- Storrie-Lombardi L. J. and Dodd S. R. (2012) Spitzer warm mission: Maximizing the science return in the extended mission phase. In *Observatory Operations: Strategies, Processes, and Systems IV* (A. B. Peck et al., eds.), 84481E. SPIE Conf. Ser. 8448, Bellingham, Washington.
- Stoughton C., Lupton R. H., Bernardi M., Blanton M. R., Burles S., Castander F. J., Connolly A. J., Eisenstein D. J., Frieman J. A., Hennessy G. S., Hindsley R. B., Ivezić Ž., Kent S., Kunszt P. Z., Lee B. C., Meiksin A., Munn J. A., Newberg H. J., Nichol R. C., Nicinski T., Pier J. R., Richards G. T., Richmond M. W., Schlegel D. J., Smith J. A., Strauss M. A., SubbaRao M., Szalay A. S., Thakar A. R., Tucker D. L., Vanden Berk D. E., Yanny B., Adelman J. K., Anderson J. E. Jr., Anderson S. F., Annis J., Bahcall N. A., Bakken J. A., Bartelmann M., Bastian S., Bauer A., Berman E., Böhringer H., Boroski W. N., Bracker S., Briegel C., Briggs J. W., Brinkmann J., Brunner R., Carey L., Carr M. A., Chen B., Christian D., Colestock P. L., Crocker J. H., Csabai I., Czarapata P. C., Dalcanton J., Davidsen A. F., Davis J. E., Dehnen W., Dodelson S., Doi M., Dombeck T., Donahue M., Ellman N., Elms B. R., Evans M. L., Eyer L., Fan X., Federwitz G. R., Friedman S., Fukugita M., Gal R., Gillespie B., Glazebrook K., Gray J., Grebel E. K., Greenawalt B., Greene G., Gunn J. E., de Haas Ē., Haiman Z., Haldeman M., Hall P. B., Hamabe M., Hansen B., Harris F. H., Harris H., Harvanek M., Hawley S. L., Hayes J. J. E., Heckman T. M., Helmi A., Henden A., Hogan C. J., Hogg D. W., Holmgren D. J., Holtzman J., Huang C.-H., Hull C., Ichikawa S.-I., Ichikawa T., Johnston D. E., Kauffmann G., Kim R. S. J., Kimball T., Kinney E., Klaene M., Kleinman S. J., Klypin A., Knapp G. R., Korennek J., Krolik J., Kron R. G., Krzesiński J., Lamb D. Q., Leger R. F., Limmongkol S., Lindenmeyer C., Long D. C., Loomis C., Loveday J., MacKinnon B., Mannery E. J., Mantsch P. M., Margon B., McGehee P., McKay T. A., McLean B., Menou K., Merelli A., Mo H. J., Monet D. G., Nakamura O., Narayanan V. K., Nash T., Neilsen E. H. Jr., Newman P. R., Nitta A., Odenkirchen M., Okada N., Okamura S., Ostriker J. P., Owen R., Pauls A. G., Peoples J., Peterson R. S., Petrvick D., Pope A., Pordes R., Postman M., Prosaipio A., Quinn T. R., Rechenmacher R., Rivetta C. H., Rix H.-W., Rockosi C. M., Rosner R., Ruthmansdorfer K., Sandford D., Schneider D. P., Scranton R., Sekiguchi M., Sergey G., Sheth R., Shimasaku K., Smee S., Sneden S. A., Stebbins A., Stubbs C., Szapudi I., Szkody P., Szokoly G. P., Tabachnik S., Tsvetanov Z., Uomoto A., Vogeley M. S., Voges W., Waddell P., Walterbos R., Wang S.-I., Watanabe M., Weinberg D. H., White R. L., White S. D. M., Wilhite B., Wolfe D., Yasuda N., York D. G., Zehavi I., and Zheng W. (2002) Sloan Digital Sky Survey: Early data release. *Astron. J.*, **123**, 485–548.
- Tabachnik S. A. and Evans N. W. (2000) Asteroids in the inner solar system — I. Existence. *Mon. Not. R. Astron. Soc.*, **319**, 63–79.
- Tedesco E. F., Egan M. P., and Price S. D. (2002a) The Midcourse Space Experiment Infrared Minor Planet Survey. *Astron. J.*, **124**, 583–591.
- Tedesco E. F., Noah P. V., Noah M., and Price S. D. (2002b) The Supplemental IRAS Minor Planet Survey. *Astron. J.*, **123**, 1056–1085.
- Tholen D. and Barucci M. (1989) Asteroid taxonomy. In *Asteroids II* (R. P. Binzel et al., eds.), pp. 298–315. Univ. of Arizona, Tucson.
- Thomas C. A., Trilling D. E., Emery J. P., Mueller M., Hora J. L., Benner L. A. M., Bhattacharya B., Bottke W. F., Chesley S., Delbó M., Fazio G., Harris A. W., Mainzer A., Mommert M., Morbidelli A., Penprase B., Smith H. A., Sphaer T. B., and Stansberry J. A. (2011) ExploreNEOs. V. Average albedo by taxonomic complex in the near-Earth asteroid population. *Astron. J.*, **142**, 85.

- Tosi F., Capria M. T., De Sanctis M. C., Combe J.-P., Zambon F., Nathues A., Schröder S. E., Li J.-Y., Palomba E., Longobardo A., Blewett D. T., Denevi B. W., Palmer E., Capaccioni F., Ammannito E., Titus T. M., Mittlefehldt D. W., Sunshine J. M., Russell C. T., and Raymond C. A. (2014) Thermal measurements of dark and bright surface features on Vesta as derived from Dawn/VIR. *Icarus*, 240, 36–57.
- Trilling D. E., Mueller M., Hora J. L., Harris A. W., Bhattacharya B., Bottke W. F., Chesley S., Delbó M., Emery J. P., Fazio G., Mainzer A., Penprase B., Smith H. A., Spahr T. B., Stansberry J. A., and Thomas C. A. (2010) ExploreNEOs. I. Description and first results from the Warm Spitzer Near-Earth Object Survey. *Astron. J.*, 140, 770–784.
- Usui F., Kuroda D., Müller T. G., Hasegawa S., Ishiguro M., Ootsubo T., Ishihara D., Kataza H., Takita S., Oyabu S., Ueno M., Matsuhara H., and Onaka T. (2011) Asteroid catalog using AKARI: AKARI/IRC mid-infrared asteroid survey. *Publ. Astron. Soc. Japan*, 63, 1117–1138.
- Usui F., Kasuga T., Hasegawa S., Ishiguro M., Kuroda D., Müller T. G., Ootsubo T., and Matsuhara H. (2013) Albedo properties of main belt asteroids based on the all-sky survey of the infrared astronomical satellite AKARI. *Astrophys. J.*, 762, 56.
- Usui F., Hasegawa S., Ishiguro M., Müller T. G., and Ootsubo T. (2014) A comparative study of infrared asteroid surveys: IRAS, AKARI, and WISE. *Publ. Astron. Soc. Japan*, 66, 5611.
- Veeder G. J., Tedesco E. F., and Matson D. L. (1989) Asteroid results from the IRAS survey. In *Asteroids II* (R. P. Binzel et al., eds.), pp. 282–289. Univ. of Arizona, Tucson.
- Vernazza P., Delbó M., King P. L., Izawa M. R. M., Olofsson J., Lamy P., Cipriani F., Binzel R. P., Marchis F., Merin B., and Tamanai A. (2012) High surface porosity as the origin of emissivity features in asteroid spectra. *Icarus*, 221, 1162–1172.
- Vernazza P., Fulvio D., Brunetto R., Emery J. P., Dukes C. A., Cipriani F., Witasse O., Schaible M. J., Zanda B., Strazzulla G., and Baragiola R. A. (2013) Paucity of Tagish Lake-like parent bodies in the asteroid belt and among Jupiter Trojans. *Icarus*, 225, 517–525.
- Walsh K. J., Delbó M., Bottke W. F., Vokrouhlický D., and Lauretta D. S. (2013) Introducing the Eulalia and new Polana asteroid families: Re-assessing primitive asteroid families in the inner main belt. *Icarus*, 225, 283–297.
- Warner B. D., Harris A. W., and Pravec P. (2009) The asteroid lightcurve database. *Icarus*, 202, 134–146.
- Werner M. W., Roellig T. L., Low F. J., Rieke G. H., Rieke M., Hoffmann W. F., Young E., Houck J. R., Brandl B., Fazio G. G., Hora J. L., Gehrz R. D., Helou G., Soifer B. T., Stauffer J., Keene J., Eisenhardt P., Gallagher D., Gautier T. N., Irace W., Lawrence C. R., Simmons L., Van Cleve J. E., Jura M., Wright E. L., and Cruikshank D. P. (2004) The Spitzer Space Telescope mission. *Astrophys. J. Suppl.*, 154, 1–9.
- Whipple F. L. (1983) 1983 TB and the Geminid meteors. *IAU Circular* 3881.
- Williams G. V. (2012) Minor planet astrophotometry. Ph.D. thesis, Open University, Milton Keynes.
- Wolters S. D., Green S. F., McBride N., and Davies J. K. (2005) Optical and thermal infrared observations of six near-Earth asteroids in 2002. *Icarus*, 175, 92–110.
- Wolters S. D., Green S. F., McBride N., and Davies J. K. (2008) Thermal infrared and optical observations of four near-Earth asteroids. *Icarus*, 193, 535–552.
- Wright E. L., Eisenhardt P. R. M., Mainzer A. K., Ressler M. E., Cutri R. M., Jarrett T., Kirkpatrick J. D., Padgett D., McMillan R. S., Skrutskie M., Stanford S. A., Cohen M., Walker R. G., Mather J. C., Leisawitz D., Gautier T. N. III, McLean I., Benford D., Lonsdale C. J., Blain A., Mendez B., Irace W. R., Duval V., Liu F., Royer D., Heinrichsen I., Howard J., Shannon M., Kendall M., Walsh A. L., Larsen M., Cardon J. G., Schick S., Schwalm M., Abid M., Fabinsky B., Naes L., and Tsai C.-W. (2010) The Wide-field Infrared Survey Explorer (WISE): Mission description and initial on-orbit performance. *Astron. J.*, 140, 1868–1881.
- Xu S., Binzel R. P., Burbine T. H., and Bus S. J. (1995) Small Main-belt Asteroid Spectroscopic Survey: Initial results. *Icarus*, 115, 1–35.
- Yamamura I., Makuti S., Ikeda N., Fukuda Y., Oyabu S., Koga T., and White G. J. (2010) *VizieR Online Data Catalog: AKARI/FIS All-Sky Survey Point Source Catalogues*. Institute of Space and Astronautical Science, JAXA.
- Young E. T. (1993) Space infrared detectors from IRAS to SIRTF. In *Infrared Spaceborne Remote Sensing* (M. S. Scholl, ed.), pp. 96–108. SPIE Conf. Ser. 2019, Bellingham, Washington.
- Yu L., Ji J., and Wang S. (2014) Shape, thermal and surface properties determination of a candidate spacecraft target asteroid (175706) 1996 FG<sub>3</sub>. *Mon. Not. R. Astron. Soc.*, 439, 3357–3370.

# Asteroid Thermophysical Modeling

Marco Delbo

Lagrange Laboratory, Université Côte d'Azur, Observatoire de la Côte d'Azur, CNRS

Michael Mueller

SRON Netherlands Institute for Space Research

Joshua P. Emery and Ben Rozitis

University of Tennessee

Maria Teresa Capria

Istituto di Astrofisica e Planetologia Spaziali

---

The field of asteroid thermophysical modeling has experienced an extraordinary growth in the last 10 years, as new thermal-infrared data became available for hundreds of thousands of asteroids. The infrared emission of asteroids depends on the body's size, shape, albedo, thermal inertia, roughness, and rotational properties. These parameters can therefore be derived by thermophysical modeling of infrared data. Thermophysical modeling led to asteroid size estimates that were confirmed at the few-percent level by later spacecraft visits. We discuss how instrumentation advances now allow mid-infrared interferometric observations as well as high-accuracy spectrophotometry, posing their own set of thermal-modeling challenges. We present major breakthroughs achieved in studies of the thermal inertia, a sensitive indicator for the nature of asteroids soils, allowing us to, e.g., determine the grain size of asteroidal regoliths. Thermal inertia also governs nongravitational effects on asteroid orbits, requiring thermophysical modeling for precise asteroid dynamical studies. The radiative heating of asteroids, meteoroids, and comets from the Sun also governs the thermal stress in surface material; only recently has it been recognized as a significant weathering process. Asteroid space missions with thermal-infrared instruments are currently undergoing study at all major space agencies. This will require a high level of sophistication of thermophysical models in order to analyze high-quality spacecraft data.

## 1. INTRODUCTION

Asteroid thermophysical modeling is about calculating the temperature of asteroids' surface and immediate subsurface, which depend on absorption of sunlight, multiple scattering of reflected and thermally emitted photons, and heat conduction. Physical parameters such as albedo (or reflectivity), thermal conductivity, heat capacity, emissivity, density and roughness, along with the shape (e.g., elevation model) of the body, its orientation in space, and its previous thermal history are taken into account. From the synthetic surface temperatures, thermally emitted fluxes (typically in the infrared) can be calculated. Physical properties are constrained by fitting model fluxes to observational data.

It is important to differentiate between sophisticated *thermophysical models* (TPMs) (Lebofsky and Spencer, 1989; Spencer, 1990; Spencer et al., 1989; Lagerros, 1997, 1996a, 1998; Delbo, 2004; Mueller, 2007; Rozitis and Green, 2011) and *simple thermal models*, which typically assume spherical

shape, neglect heat conduction (or simplify its treatment), and do not treat surface roughness (for reviews, see Harris and Lagerros, 2002; Delbo and Harris, 2002). In the past, the use of TPMs was reserved to the few exceptional asteroids for which detailed shape models and high-quality thermal-infrared data existed (Harris and Lagerros, 2002). In the last 10 years, however, TPMs became significantly more applicable (see section 6), thanks both to new spaceborne infrared telescopes [the Spitzer Space Telescope (Spitzer), Wide-field Infrared Survey Explorer (WISE), and AKARI] (see the chapter by Mainzer et al. in this volume) and to the availability of an ever-growing number of asteroid shape models (see the chapter by Durech et al. in this volume).

After introducing the motivations and the different contexts for calculating asteroid temperatures (section 2), we provide an overview of simple thermal models (section 3) and of TPMs (section 4). We describe data analysis techniques based on TPMs (section 5), then we present the latest results and implications on the physics of asteroids (section 6). In

section 7, we discuss temperature-induced surface changes on asteroids (see also the chapter by Murdoch et al. in this volume). All symbols used in this chapter are detailed in Table 1.

Note that we do not discuss here the so-called asteroid thermal evolution models that are generally used to compute

the temperature throughout the body as a function of time, typically taking into account internal heat sources such as the decay of radiogenic  $^{26}\text{Al}$ . Such models allow estimates of the degree of metamorphism, aqueous alteration, melting, and differentiation that asteroids experienced during the early phases of the solar system formation (for a review, see McSween et al., 2002).

## 2. MOTIVATIONS AND APPLICATIONS OF THERMOPHYSICAL MODELS

Thermophysical modeling of observations of asteroids in the thermal infrared ( $\lambda \geq 4 \mu\text{m}$ ) is a powerful technique to determine the values of physical parameters of asteroids, such as their sizes (e.g., Müller et al., 2014a), thermal inertia, and roughness of their soils (e.g., Müller and Lagerros, 1998; Mueller, 2007; Delbo and Tanga, 2009; Matter et al., 2011; Rozitis and Green, 2014; Capria et al., 2014), and in certain cases their bulk density and bulk porosity as well (Rozitis et al., 2013, 2014; Emery et al., 2014; Chesley et al., 2014).

Knowledge of physical properties is crucial to understand asteroids. For example, size information is fundamental to constrain the asteroid size frequency distribution, which informs us about the collisional evolution of these bodies (Bottke et al., 2005), and is of paramount importance for the study of asteroid families, Earth-impact risk assessment of near-Earth asteroids (NEAs) (for a review, see the chapter by Harris et al. in this volume), and development of asteroid space mission scenarios (section 5.7). Accurate sizes are also a prerequisite for calculating the volumes of asteroids for which we know the mass, allowing us to derive the bulk density, which informs us about the internal structure of these bodies (e.g., Carry, 2012).

Thermal inertia, the resistance of a material to temperature change (section 5.2), is a sensitive indicator for the properties of the grainy soil (regolith) (see the chapter by Murdoch et al. in this volume) on asteroids; e.g., the typical grain size (Gundlach and Blum, 2013) and degree of cementation (Piqueux and Christensen, 2009a,b) can be inferred from thermal-inertia measurements. In general, the regolith is what we study by means of remote-sensing observations. Understanding the regolith is therefore crucial to infer the nature of the underlying body. Regolith informs us about the geological processes occurring on asteroids (see the chapter by Murdoch et al. in this volume), such as impacts, micrometeoroid bombardment (Hörz and Cintala, 1997), and thermal cracking (Delbo et al., 2014). Regolith contains records of elements implanted by the solar wind and cosmic radiation, and therefore informs us about the sources of those materials (Lucey, 2006). Regolith porosity can shed light on the role of electrostatic and van der Waals forces acting on the surface of these bodies (e.g., Rozitis et al., 2014; Vernazza et al., 2012).

Knowledge of surface temperatures is also essential for the design of the instruments and for the near-surface operation of space missions, as in the case of the sample return missions Hayabusa-2 [Japan Aerospace Exploration Agency (JAXA)] and Origins, Spectral Interpretation, Resource Identification,

TABLE 1. Nomenclature.

Symbol	Quantity	Unit
T	Temperature	K
$T_{\text{SS}}$	Subsolar temperature	K
$\sigma$	Stefan-Boltzmann constant	(5.67051 $10^{-8}$ ) $\text{W m}^{-2} \text{K}^{-4}$
$S_{\odot}$	Solar constant at $r = 1 \text{ AU}$	(1329) $\text{W m}^{-1}$
r	Distance to the Sun	AU
$\vec{r}$	Vector to the Sun	m
$\Delta$	Distance to the observer	AU
$\epsilon$	Emissivity	—
$\eta$	Beaming parameter	—
$\kappa$	Thermal conductivity	$\text{W m}^{-1} \text{K}^{-1}$
C	Heat capacity	$\text{J kg}^{-1} \text{K}^{-1}$
$\Gamma$	Thermal inertia	$\text{J m}^{-2} \text{s}^{-1/2} \text{K}^{-1}$
$\Theta$	Thermal parameter	—
$\rho$	Material density	$\text{kg m}^{-3}$
H	Absolute magnitude of the H,G system	
G	Slope parameter of the H,G system	
V	Actual magnitude in the V-band	
D	Diameter	m (or km)
A	Bolometric Bond albedo	—
$p_V$	Geometric visible albedo	—
z	Depth in the subsoil	m
t	Time	s
$r_p$	Pore radius of regolith	m
$\bar{\theta}$	Mean surface slope	deg
$l_s$	Thermal skin depth	m
P	Rotation period	s
$\omega$	$= 2\pi/P$	$\text{s}^{-1}$
$\lambda_p$	ecliptic longitude of the pole	deg
$\beta_p$	ecliptic latitude of the pole	deg
$\phi_0$	Initial rotational phase at epoch	deg
$\alpha$	(Phase) angle between asteroid-Sun-observer	deg
a	Area of a facet	$\text{m}^2$
S	Shadowing function	
$F_{\vec{i},\vec{j}}$	View factor	
$J_V(j)$	Visible radiosity	
$J_{IR}(j)$	Infrared radiosity	
$\hat{n}$	Local normal	m
$\vec{i}$	Vector to the local facet	m
$\vec{j}$	Vector to the remote facet	m
$\gamma_c$	Crater opening angle	deg
$\rho_c$ or $f$	Area density of craters	
$\phi$	Emission angle	rad
$f_{\lambda}(\tau)$	Infrared flux	$\text{W m}^{-2} \mu\text{m}^{-1}$
$\lambda$	Wavelength	$\mu\text{m}$

Security, Regolith Explorer (OSIRIS-REx) (NASA). In the future, knowledge of asteroid temperatures will be crucial for planning human interaction with asteroids.

Another reason to model asteroid surface temperatures is that they affect the orbital and spin-state evolution via the Yarkovsky and Yarkovsky-O'Keefe-Radzievskii-Paddack (YORP) effects, respectively (see section 5.8 and the chapter by Vokrouhlický et al. in this volume). In particular, thermal inertia dictates the strength of the asteroid Yarkovsky effect. This influences the dispersion of members of asteroid families, the orbital evolution of potentially hazardous asteroids, and the delivery of  $D \leq 40$  km asteroids and meteoroids from the main belt into dynamical resonance zones capable of transporting them to Earth-crossing orbits (see chapter by Vokrouhlický et al. in this volume and references therein).

The YORP effect is believed to be shaping the distribution of rotation rates (Bottke et al., 2006) and spin-vector orientation (Vokrouhlický et al., 2003; Hanuš et al., 2011, 2013); small gravitationally bound aggregates could be spun up so fast (Vokrouhlický et al., this volume; Bottke et al., 2006, and references therein) that they are forced to change shape and/or undergo mass shedding (Holsapple, 2010). Approximately 15% of NEAs are observed to be binaries (Pravec et al., 2006), and YORP spinup is proposed as a viable formation mechanism (Walsh et al., 2008; Scheeres, 2007; Jacobson and Scheeres, 2011).

A further motivation to apply TPM techniques is to constrain the spin-axis orientation and the sense of rotation of asteroids [examples are 101955 Bennu and 2005 YU<sub>55</sub> (Müller et al., 2012, 2013)]. The chapter by Durech et al. in this volume describes how to use optical and thermal-infrared data simultaneously to derive more reliable asteroid shapes and spin properties.

The temperature and its evolution through the entire life of an asteroid can alter its surface composition and nature of the regolith (section 7). For example, when the temperature rises above a certain threshold for a sustained period, certain volatiles can be lost via sublimation (Schorghofer, 2008; Capria et al., 2012), dehydration (Marchi et al., 2009), or desiccation (Delbo and Michel, 2011; chapter by Jewitt et al. in this volume, and references therein).

There can be pronounced and fast temperature variations between day and night. Modeling these temperature variations is fundamental to studying the effect of thermal cracking of asteroid surface material (section 7.1), which was found to be an important source of fresh regolith production (Delbo et al., 2014).

### 3. SIMPLE THERMAL MODELS

We start by introducing the Near-Earth Asteroid Thermal Model (NEATM) (Harris, 1998), which is typically used where the data quality and/or the available knowledge about asteroid shape and spin preclude the usage of TPMs. Typically, the NEATM allows a robust estimation of asteroid diameter and albedo, but does not provide any direct information on thermal inertia or surface roughness

(for a review, see Harris and Lagerros, 2002). The recent large-scale thermal-emission surveys of asteroids and trans-neptunian objects (TNOs) (see Mainzer et al., this volume; Lellouch et al., 2013, and references therein) typically use the NEATM in their data analysis, thereby establishing it as the de facto default among the simple thermal models. The typical NEATM accuracy is 15% in diameter and roughly 30% in albedo (Harris, 2006). Other simple thermal models are the standard thermal model (STM) (Lebofsky et al., 1986), isothermal latitude model (ILM) [also known as the fast rotating model (FRM)] (Lebofsky and Spencer, 1989), and the night emission simulated thermal model (NESTM) (Wolters and Green, 2009). The STM and the ILM [reviewed by, e.g., Harris and Lagerros (2002)] have largely fallen out of use.

The NEATM assumes that the asteroid has a spherical shape and does not directly account for thermal inertia nor surface roughness. The surface temperature is given by the instantaneous equilibrium with the insolation, which is proportional to the cosine of the angular distance between local zenith and the Sun and zero at the nightside. The maximum temperature occurs at the subsolar point and it reads

$$(1 - A)S_{\odot}r^{-2} = \eta\sigma\epsilon T_{SS}^4 \quad (1)$$

(nomenclature is defined in Table 1). The parameter  $\eta$  was introduced in the STM of Lebofsky et al. (1986) as a means of changing the model temperature distribution to take into account the observed enhancement of thermal emission at small solar phase angles due to surface roughness. This is known as the beaming effect, and for this reason,  $\eta$  is also called the *beaming parameter*. The  $\eta$  formalism, in the NEATM, allows a first-order description of the effect of a number of geometrical and physical parameters, in particular the thermal inertia and surface roughness on the spectral energy distribution of an asteroid (Delbo et al., 2007). For a large thermal inertia, one would expect  $\eta$  values significantly larger than unity [e.g., 1.5–3, with theoretical maximum values around 3.5 (Delbo et al., 2007)], whereas for low thermal inertia  $\eta \approx 1$  (for  $\Gamma = 0$  and zero surface roughness). Roughness, on the other hand, tends to lower the value of  $\eta$  (for observations at low or moderate phase angles). For instance, a value of  $\eta \sim 0.8$  for a main-belt asteroid (MBA) indicates that this body has low thermal inertia and significant roughness [with minimum theoretical values of 0.6–0.7 (Spencer, 1990; Delbo et al., 2007)]. We note, however, that  $\eta$  is not a physical property of an asteroid, as it can vary due to changing observing and illumination geometry, aspect angle, heliocentric distance of the body, phase angle, and wavelength of observation.

## 4. THERMOPHYSICAL MODELS

### 4.1. Overview

Different TPMs have been proposed to study the thermal emission of asteroids, comets, planets, and satellites. The first models were motivated by thermal observations of the lunar surface, which revealed an almost thermally insulating

surface that emits thermal radiation in a non-Lambertian way (Pettit and Nicholson, 1930; Wesselink, 1948). Heat conduction and radiation scattering models of various rough surfaces were able to reproduce the lunar observations to a good degree (e.g., Smith, 1967; Buhl *et al.*, 1968a,b; Sexl *et al.*, 1971; Winter and Krupp, 1971), and the derived thermal inertia and surface roughness values matched *in situ* measurements by Apollo astronauts (see Rozitis and Green, 2011, and references therein). These early lunar models were adapted to general planetary bodies, albeit with an assumed spherical shape, by Spencer *et al.* (1989) and Spencer (1990). The most commonly used asteroid TPMs of Lagerros (1996a, 1997, 1998), Delbo (2004), Mueller (2007), and Rozitis and Green (2011) are all based on Spencer *et al.* (1989) and Spencer (1990). Here we present the basic principles utilized in TPMs; for implementation details, the reader is referred to the cited works.

All TPMs represent the global asteroid shape as a mesh of (triangular) facets (see Fig. 1) that rotates around a given spin vector with rotation period P. In general, utilized shape models are derived from radar observations, inversion of optical light curves, *in situ* spacecraft images, or stellar occultation timing (for a review of asteroid shape modeling, see the chapter by Durech *et al.* in this volume). If no shape model is available, one typically falls back to a sphere or an ellipsoid (e.g., Müller *et al.*, 2013, 2014a; Emery *et al.*, 2014).

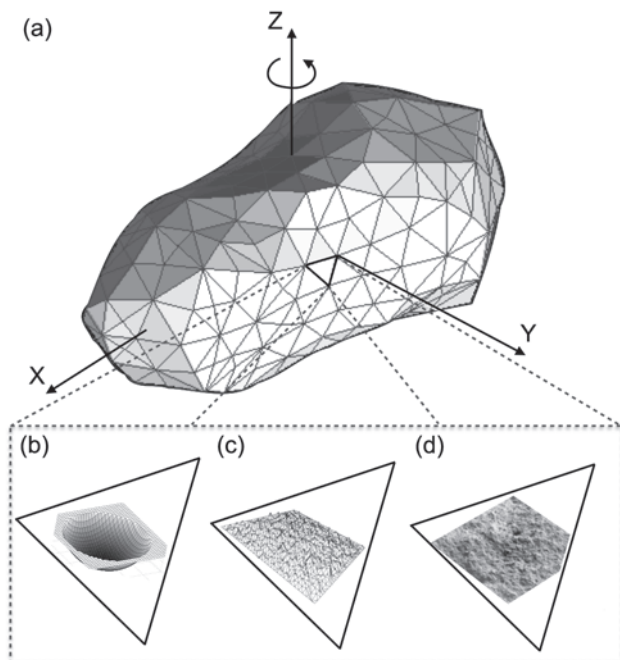


**Fig. 1.** (a) Example of a triangulated three-dimensional shape model as typically used in TPMs [asteroid (2063) Bacchus from <http://echo.jpl.nasa.gov/asteroids/shapes/shapes.html>]. Temperatures are color coded: white corresponds to the maximum and dark gray corresponds to minimum temperature. The three different roughness models sketched at the bottom are (b) hemispherical section craters (Davidsson *et al.*, 2015), (c) Gaussian surface (Rozitis and Green, 2011), and (d) fractal surface (Davidsson *et al.*, 2015).

The goal is to calculate the thermal emission of each facet of the shape model at a given illumination and observation geometry. To this end, the temperature of the surface and, in the presence of thermal inertia, the immediate subsurface need to be calculated. Generally, lateral heat conduction can be neglected as the shape model facets are much larger than the penetration depth of the diurnal heat wave (i.e., the thermal skin depth), and only one-dimensional heat conduction perpendicular to and into the surface needs to be considered. For temperature T, time t, and depth z, one-dimensional heat conduction is described by

$$\rho C \frac{\partial T}{\partial t} = \frac{\partial}{\partial z} \kappa \frac{\partial T}{\partial z} \quad (2)$$

where  $\kappa$  is the thermal conductivity,  $\rho$  is the material density, and C is the heat capacity. If  $\kappa$  is independent of depth (and, implicitly, temperature independent, see section 5.3), equation (2) reduces to the diffusion equation

$$\frac{\partial T}{\partial t} = \frac{\kappa}{\rho C} \frac{\partial^2 T}{\partial z^2} \quad (3)$$

It is useful to define the thermal inertia  $\Gamma$  and the thermal skin depth  $l_s$

$$\Gamma = \sqrt{\kappa \rho C} \quad (4)$$

$$l_s = \sqrt{\kappa P / 2\pi\rho C} \quad (5)$$

These material properties are generally assumed to be constant with depth and temperature in asteroid TPMs, but varying properties have been considered in some Moon, Mars, planetary satellites, and asteroid models (e.g., Giese and Kuehrt, 1990; Urquhart and Jakosky, 1997; Piqueux and Christensen, 2011; Keihm, 1984; Keihm *et al.*, 2012; Capria *et al.*, 2014, see also section 5.3).

Thermophysical model implementations typically employ dimensionless time and depth variables:  $\tau = 2\pi t/P$  and  $Z = z/l_s$ . Then, the only remaining free parameter is the dimensionless thermal parameter [ $\Theta = \Gamma \sqrt{\omega} / \epsilon \sigma T_{ss}^3$  (Spencer, 1990)] describing the combined effect of thermal inertia, rotation period, and heat emission into space on the surface temperature distribution (see Fig. 2).

A numerical finite-difference technique is used to solve the one-dimensional heat conduction equation, and an iterative technique is used to solve the surface boundary condition. This requires a suitable number of time and depth steps to fully resolve the temperature variations and to ensure model stability (typically, at least 360 time steps and 40 depth steps over 8 thermal skin depths are required). Thermophysical models are run until specified convergence criteria are met (e.g., until temperature variations between successive model iterations are below a specified level) and/or until a specified number of model iterations have been made.

For applications such as the study of the sublimation of water ice from the shallow subsurface of asteroids [e.g., the main-belt comets (MBCs) or 24 Themis], the heat conduction equation must be coupled with a gas diffusion equation (Schorghofer, 2008; Capria et al., 2012; Prialnik and Rosenberg, 2009) (for a review, see also Huebner et al., 2006).

The one-dimensional heat conduction equation is solved with internal and surface boundary conditions to ensure conservation of energy. Since the amplitude of subsurface temperature variations decreases exponentially with depth, an internal boundary condition is required to give zero temperature gradient at a specified large depth

$$\left( \frac{\partial T}{\partial z} \right)_{z \gg l_s} = 0 \quad (6)$$

A typical surface boundary condition for a facet at point  $\bar{r}$  with respect to the asteroid origin, at point  $\bar{r}$  with respect to the Sun, and with surface normal  $\hat{n}$  is then given by

$$\begin{aligned} \varepsilon\sigma T^4(\bar{r}, t) - \left( \frac{\partial T(\bar{r}, t)}{\partial z} \right)_{z=0} &= \\ \frac{(1-A)S_\odot(\bar{r} \cdot \hat{n})(1-S(\bar{r}, \bar{t}))}{\bar{r}^3} + & \\ (1-A) \int J_V(\bar{j}) F_{\bar{r}, \bar{j}} d\alpha' + & \\ \varepsilon\sigma(1-\varepsilon) \int J_{IR}(\bar{j}) F_{\bar{r}, \bar{j}} d\alpha' & \end{aligned} \quad (7)$$

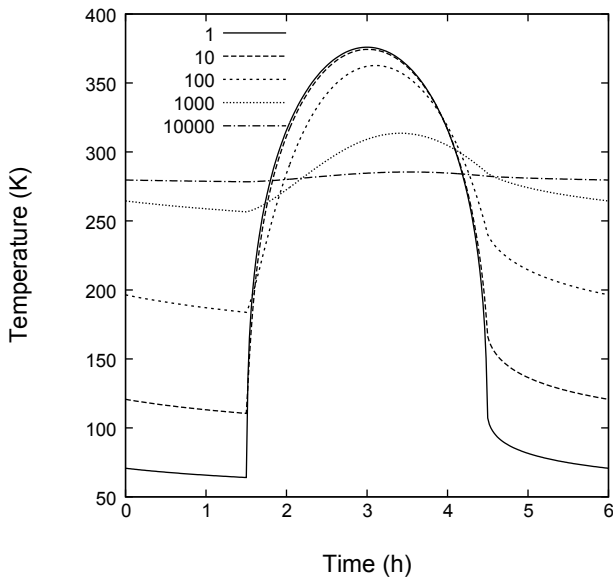


**Fig. 2.** Synthetic diurnal temperature curves on the equator of a model asteroid for different values of thermal inertia (in units of  $J \text{ m}^{-2} \text{ s}^{-1/2} \text{ K}^{-1}$ ). Increasing thermal inertia smooths temperature contrasts and causes the temperature peak to occur after the insolation peak at 3 h. The asteroid is situated at a heliocentric distance of  $r = 1.1 \text{ AU}$ , has a spin period of 6 h, Bond albedo of  $A = 0.1$ , and its spin axis is perpendicular to the orbital plane.

The lefthand side of equation (7) gives the thermal energy radiated to space and the heat conducted into the subsurface, and the righthand side gives the input radiation from three different sources: direct solar radiation, multiply scattered solar radiation (i.e., self-illumination), and reabsorbed thermal radiation (i.e., self-irradiation). The two last components are also known as mutual heating (see Fig. 3).

The amount of solar radiation absorbed by a facet depends on the Bond albedo  $A$  and any shadows projected on it, which is dictated by  $S(\bar{r}, \bar{t})$  [i.e.,  $S(\bar{r}, \bar{t}) = 1$  or 0, depending on the presence or absence of a shadow]. Projected shadows occur on globally nonconvex shapes only, which can be determined by ray-triangle intersection tests of the solar illumination ray (e.g., Rozitis and Green, 2011) or by local horizon mapping (e.g., Statler, 2009). Related to shadowing are the self-heating effects arising from interfacing facets, which tend to reduce the temperature contrast produced inside concavities. The problem here is to determine which facets see other facets, and to calculate the amount of radiation exchanged between them. The former can be determined by ray-triangle intersection tests again, and the latter can be solved using view factors. The view factor  $F_{\bar{r}, \bar{j}}$  is defined as the fraction of the radiative energy leaving the local facet  $\bar{r}$  that is received by the remote facet  $\bar{j}$  assuming Lambertian emission (Lagerros, 1998).  $J_V(\bar{j})$  and  $J_{IR}(\bar{j})$  are then the visible and thermal-infrared radiosities of remote facet  $\bar{j}$ . Either single or multiple scattering can be taken into account, and the latter can be efficiently solved using Gauss-Seidel iterations (Vasavada et al., 1999). Most TPMs neglect shadowing and self-heating effects resulting from the global shape for simplicity, but they can be significant on asteroids with large shape concavities [e.g., the south pole of (6489) Golevka (Rozitis and Green, 2013)].

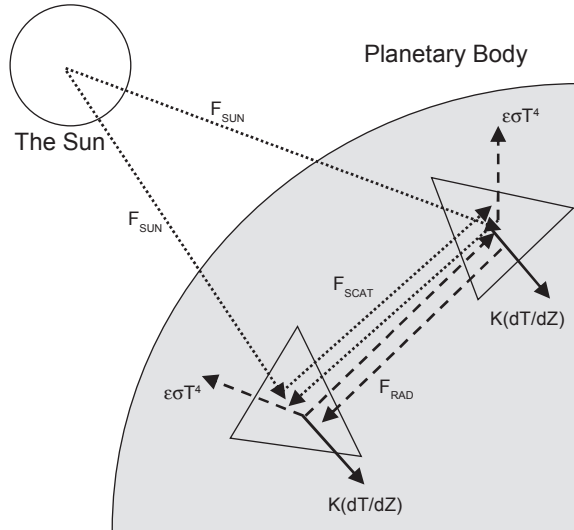


**Fig. 3.** Diagram illustrating the energy balance and radiation transfer between facets (from Rozitis and Green, 2011). The terms  $F_{\text{SUN}}$ ,  $F_{\text{SCAT}}$ ,  $F_{\text{RAD}}$ ,  $k(dT/dx)$ , and  $\varepsilon\sigma T^4$  are direct sunlight, multiply scattered sunlight, reabsorbed thermal radiation, conducted heat, and thermal radiation lost to space, respectively.

## 4.2. Modeling Asteroid Thermal Emission

Once the surface temperature distribution across an asteroid surface has been computed, the emission spectrum (Fig. 4) at a given observation geometry and a specified time can be calculated. The monochromatic flux density, also known as spectral energy distribution (SED), can also be calculated at wavelengths of interest. When these model fluxes are plotted as a function of the asteroid rotational phase, one obtains the so-called thermal light curves (e.g., Fig. 5), which can be used to test the fidelity of shape and albedo models typically used as input in the TPM.

When the temperature for a facet is known, the intensity  $I_\lambda(\tau)$  at which it emits at wavelength  $\lambda$  is given by the Planck function. Assuming Lambertian emission, the spectral flux of the facet seen by an observer is then

$$f_\lambda(\tau) = I_\lambda(\tau) \frac{a}{\Delta^2} \cos \phi \quad (8)$$

where  $a$  is area of the facet,  $\Delta$  is the distance to the observer, and  $\phi$  is the emission angle. The total observed flux is obtained by summing the thermal fluxes of all visible shape model facets, including any contributions from surface roughness elements contained within them. For disk-integrated measurements, this summation is performed across the entire visible side of the asteroid, while for spatially resolved measurements it is summed across facets contained within the detector pixel's field of view.

The assumption of Lambertian emission depends on no directionality induced by surface irregularities at scales below the thermal skin depth. Davidsson and Rickman (2014)

show that surface roughness at subthermal-skin-depth scales is quasi-isothermal and is therefore not likely to deviate from Lambertian emission overall. However, radiative transfer processes between the regolith grains could contribute up to 20% of the observed beaming effects (Hapke, 1996). Rozitis and Green (2011, 2012) investigated combined microscopic (regolith grain induced) and macroscopic (surface roughness induced) beaming effects, and demonstrated that the macroscopic effects dominated overall. This was previously found to be the case in directional thermal emission measurements of lava flows on Earth (Jakosky et al., 1990).

As wavelengths increase to the submillimeter range and above, asteroid regolith becomes increasingly transparent and the observed flux is integrated over increasing depths (Chamberlain et al., 2009; Keihm et al., 2013). Modeling such fluxes with typical thermal models (which derive fluxes from surface temperatures only) requires a significant reduction in effective spectral emissivity. For example, 3.2-mm flux measurements of (4) Vesta require an emissivity of  $\sim 0.6$  to match model predictions (Müller and Barnes, 2007). The reduction in emissivity can be explained by lower subsurface emission temperatures (Lagerros, 1996b) and by different subsurface scattering processes dependent on grain size (Redman et al., 1992; Müller and Lagerros, 1998). Keihm et al. (2012, 2013) attribute the reduced emissivity at submillimeter/millimeter wavelengths to a higher thermal inertia value of the subsurface layers. Reduction in emissivity has also been determined at wavelengths shorter than  $4.9 \mu\text{m}$  for disk-resolved regions of (4) Vesta (Tosi et al., 2014).

## 4.3. Surface Roughness

Roughness causes an asteroid surface to thermally emit in a non-Lambertian way with a tendency to reradiate the absorbed solar radiation back toward the Sun, an effect

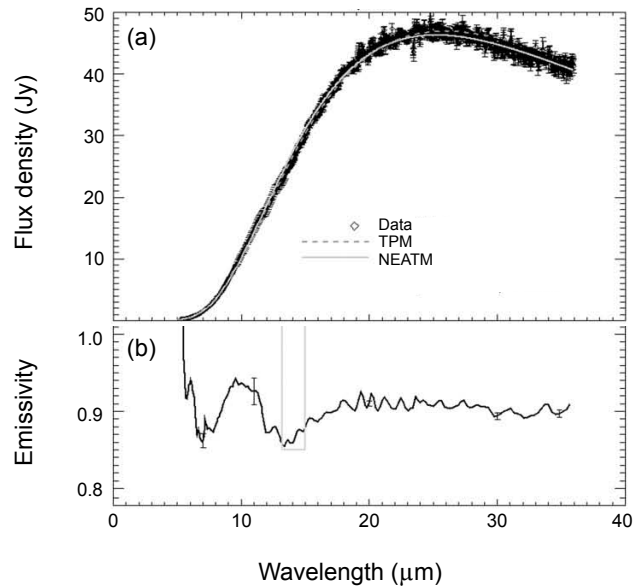


**Fig. 4.** (a) Example of SED calculated from a TPM and the NEATM compared to Spitzer spectrum of (87) Sylvia. (b) Spectral emissivity derived from the above; data divided by the NEATM continuum. From Marchis et al. (2012).

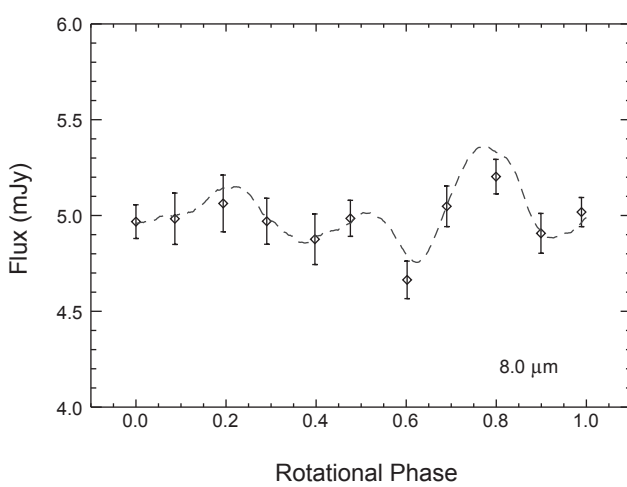


**Fig. 5.** Example of a TPM-generated thermal lightcurve (dashed line) and real data for (101955) Bennu. From Emery et al. (2014).

known as thermal-infrared beaming (*Lagerros*, 1998; *Rozitis and Green*, 2011). It is thought to be the result of two different processes: A rough surface will have elements oriented toward the Sun that become significantly hotter than a flat surface, and multiple scattering of radiation between rough surface elements increases the total amount of solar radiation absorbed by the surface. The relevant size scale ranges from the thermal skin depth to the linear size of the facets in the shape model. It is included in thermophysical models by typically modeling an areal fractional coverage ( $f$ ) of spherical-section craters (of opening angle  $\gamma_C$ ) within each shape model facet. Other more complex forms have been considered, such as Gaussian random (*Lagerros*, 1998) or fractal (*Groussin et al.*, 2013) surfaces or parallel sinusoidal trenches (see Fig. 1), but the spherical-section crater produces similar results [in terms of the disk-integrated beaming effect (*Lagerros*, 1998)] and accurately reproduces the directionality of the lunar thermal-infrared beaming effect (*Rozitis and Green*, 2011). However, it has been shown that for disk-resolved data, thermal emission depends on roughness type as well as roughness level (*Davidsson et al.*, 2015).

Spherical-section craters are typically implemented, as the required shadowing and view-factor calculations can be performed analytically (*Emery et al.*, 1998; *Lagerros*, 1998). Heat conduction can be included by dividing the crater into several tens of surface elements for which the same equations listed above can be applied. Alternatively, the temperature distribution within the crater resulting from heat conduction,  $T_{\text{crater}}(\Gamma)$ , can be approximated using

$$\frac{T_{\text{rough}}(\Gamma)}{T_{\text{rough}}(0)} = \frac{T_{\text{smooth}}(\Gamma)}{T_{\text{smooth}}(0)} \quad (9)$$

where  $T_{\text{rough}}(0)$  can be calculated analytically assuming instantaneous equilibrium (*Lagerros*, 1998).  $T_{\text{smooth}}(0)$  and  $T_{\text{smooth}}(\Gamma)$  are the corresponding smooth-surface temperatures, which can be calculated exactly. This approximation is computationally much cheaper than the full implementation. However, it does not work on the nightside of the asteroid, and temperature ratios diverge near the terminator (*Mueller*, 2007). An even simpler alternative is to multiply the smooth-surface temperatures by a NEATM-like  $\eta$  value (e.g., *Groussin et al.*, 2011). While this alternative might produce the correct disk-integrated color temperature of the asteroid, it does not reproduce the directionality of the beaming effect. Indeed, roughness models predict a limb-brightening effect (*Rozitis and Green*, 2011), which is seen in spatially-resolved measurements of (21) Lutetia by Rosetta (*Keihm et al.*, 2012).

The above implementations neglect lateral heat conduction, although the spatial scales representing surface roughness can, in some cases, become comparable to the thermal skin depth. Modeling of three-dimensional heat conduction inside rocks the size of the thermal skin depth has demonstrated that their western sides (for a prograde rotator; eastern sides for a retrograde rotator) are gener-

ally warmer than their eastern sides, which could result in a tangential-YORP effect that predominantly spins up asteroids (*Golubov and Krugly*, 2012). Other than this, it appears that the one-dimensional heat conduction approximation still produces satisfactory results.

In thermophysical models, the degree of surface roughness can be quantified in terms of the Hapke mean surface slope

$$\tan \bar{\theta} = \frac{2}{\pi} \int_0^{\pi/2} a(\theta) \tan \theta \, d\theta \quad (10)$$

where  $\theta$  is the angle of a given facet from horizontal, and  $a(\theta)$  is the distribution of surface slopes (Hapke, 1984). Alternatively, it can be measured in terms of the root mean square (RMS) surface slope (Spencer, 1990). This then allows comparison of results derived using different surface roughness representations [e.g., craters of different opening angles and fractional coverages, or different Gaussian random surfaces (*Davidsson et al.*, 2015)], and comparison against roughness measured by other means. It has been demonstrated that different roughness representations produce similar degrees of thermal-infrared beaming when they have the same degree of roughness measured in terms of these values (Spencer, 1990; *Emery et al.*, 1998; *Lagerros*, 1998; *Rozitis and Green*, 2011).

## 5. DATA ANALYSIS USING A THERMOPHYSICAL MODEL

### 5.1. Thermal Infrared Spectrophotometry

Physical properties that can be derived from TPM fits to disk-integrated thermal observations include diameter, geometric albedo, thermal inertia, and roughness. In practically all cases, the absolute visual magnitude  $H$  is known, establishing a link between  $D$  and  $p_V$  and reducing the number of TPM fit parameters by one

$$D(\text{km}) = 1329 p_V^{-1/2} 10^{-H/5} \quad (11)$$

(*Fowler and Chillemi*, 1992; *Vilenius et al.*, 2012). Frequently, the rotational phase during the thermal observations is not sufficiently well known and has to be fitted to the thermal data (e.g., *Harris et al.*, 2005; *Ali-Lagoa et al.*, 2014). In some cases, TPMs can be used to constrain the orientation of the spin vector of an asteroid, with  $\lambda_p$  and  $\beta_p$  treated as free parameters [as demonstrated by, e.g., *Müller et al.* (2013, 2012); note that in the case of (101955) Bennu the radar-constrained pole solution was not yet known]. Moreover, *Müller et al.* (2014b) successfully performed a TPM analysis of an asteroid [(99942) Apophis] in a non-principal axis rotation state for the first time.

The thermal effects of thermal inertia and surface roughness are difficult to tell apart. A commonly used approach is to use four different roughness models corresponding to no, low, medium, and high roughness, with each model leading

to a different thermal-inertia fit (*Mueller*, 2007; *Delbo* and *Tanga*, 2009); frequently, the scatter between these four solutions accounts for the bulk of the uncertainty in thermal inertia. However, in some lucky cases, data do allow the effects of roughness and thermal inertia to be disentangled. This requires good wavelength coverage straddling the thermal emission peak and good coverage in solar phase angle, such that both the morning and afternoon sides of the asteroid are seen (see Fig. 6 for an illustration).

The best-fitting model parameters are those that minimize  $\chi^2$ . Their uncertainty range is spanned by the values that lead to  $\chi^2$  within a specified threshold of the best fit, depending on the number of free fit parameters. Ideally, the reduced  $\chi^2$  of the best fit should be around unity. However, due to systematic uncertainties introduced in thermal-infrared observations (e.g., flux offsets between different instruments), and/or in the thermophysical modeling, it is not uncommon to get large reduced  $\chi^2$  values. Large  $\chi^2$  values are also obtained when the assumed shape model differs significantly from the asteroid's true shape (*Rozitis* and *Green*, 2014). In particular, if the spatial extent of the shape model's z-axis is wrong, this can lead to diameter determinations that are inconsistent with radar observations [e.g., for 2002 NY<sub>40</sub> and (308635) 2005 YU<sub>55</sub> in *Müller et al.* (2004, 2013), respectively], and/or two different thermal inertia determinations [e.g., the two different results produced for (101955) Bennu by *Emery et al.* (2014) and *Müller et al.* (2012)]. In some works, the asteroid shape model has also been optimized during the thermophysical fitting to resolve inconsistencies with radar observations [e.g., (1862) Apollo and (1620) Geographos in *Rozitis et al.* (2013) and *Rozitis and Green* (2014), respectively].

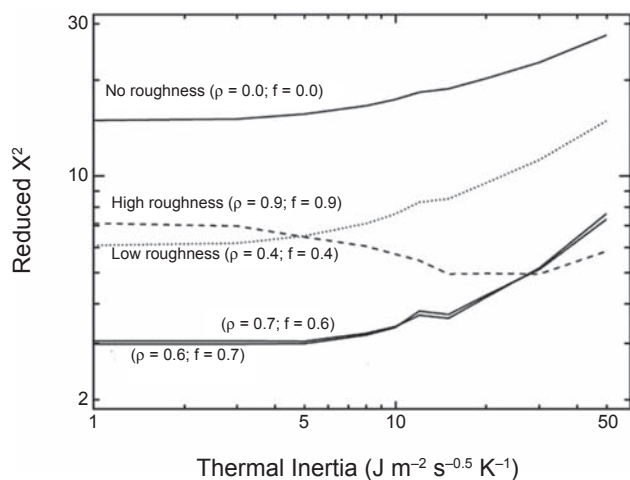


**Fig. 6.** (21) Lutetia: TPM fit that allows surface roughness to be constrained. The quantity  $\rho$  here is not the bulk density of the body, but the r.m.s. of the slopes on the surface. It is related to the ratio between the diameter and the depth of spherical section craters (*Lagerros*, 1998) in this particular case.  $f$  is the areal fraction of each facet covered with craters. From *O'Rourke et al.* (2012).

We remind the reader that the accuracy of the physical properties (in particular the value of  $\Gamma$ ) of asteroids derived from TPM depends on the quality of the thermal-infrared data and coverage in wavelength, phase, rotational, and aspect angle. The accuracy of the shape model and the H and G values are also important (see, e.g., *Rozitis and Green*, 2014). The derived thermal inertia value often depends on the assumed degree of roughness and it is usually affected by large errors (e.g., 50% or 100%; see Table 2). Care must be used in accepting TPM solutions purely based on the goodness of fit (e.g., the value of the  $\chi^2$ ), as they can be dominated by one or few measurements with unreliable small errors or calibration offsets between measurements from different sources.

## 5.2. Thermal Inertia and Thermal Conductivity

As asteroids rotate, the alternance of day and night causes cyclic temperature variations that are controlled by the thermal inertia [defined by equation (4)] of the soil and the rotation rate of the body. In the limit of vanishing thermal inertia, the surface temperature would be in instantaneous equilibrium with the incoming solar flux, depending only on the solar incidence angle (as long as self-heating can be neglected); surface temperatures would peak at local noon and would be zero at night. In reality, thermal conduction into and from the subsoil causes a certain thermal memory, referred to as *thermal inertia*. This smoothens the diurnal temperature profile, leads to nonzero nightside temperatures, and causes the surface temperature to peak on the afternoon side, as shown in Fig. 2, thereby also causing the Yarkovsky effect (section 5.8).

The mass density  $\rho$ , the specific heat capacity  $c$ , and the thermal conductivity  $\kappa$  — and correspondingly  $\Gamma$  itself — must be thought of as effective values representative of the depth range sampled by the heat wave, which is typically in the range of a few centimeters. In turn, thermal-inertia values inform us about the physical properties of the top few centimeters of the surface, not about bulk properties of the object.

As will be discussed below (section 6.5),  $\rho$  and  $c$  of an asteroid surface can plausibly vary within a factor of several, while plausible values of  $\kappa$  span a range of more than 4 orders of magnitude. It is therefore not unjustified to convert from  $\Gamma$  to  $\kappa$  and back using reference values for  $\rho$  and  $c$  (note that Yarkovsky/YORP models tend to phrase the thermal conduction problem in units of  $\kappa$ , while TPMs tend to be formulated in units of  $\Gamma$ , which is the observable quantity).

Importantly, the  $\kappa$  of finely powdered lunar regolith is 3 orders of magnitude lower than that of compact rock (compact metal is even more conductive, by another order of magnitude). This is because radiative thermal conduction between regolith grains is significantly less efficient than phononic heat transfer within a grain. A fine regolith, an aggregate of very small grains, is a poor thermal conductor and displays a low  $\Gamma$ . Thermal inertia can therefore be used to infer the presence or absence of thermally insulating powdered surface material. In extension, thermal inertia can be

TABLE 2. Published thermal inertia values.

Number	Name	D (km)	$\Delta_D$ (km)	$\Gamma$ (SI)	$\Delta_\Gamma$ (SI)	Tax	r (AU)	Ref.	Number	Name	D (km)	$\Delta_D$ (km)	$\Gamma$ (SI)	$\Delta_\Gamma$ (SI)	Tax	r (AU)	Ref.
1	Ceres	923	20	10	10	C	2.767	1	1620	Geographos	5.04	0.07	340	120	S	1.1	12
2	Pallas	544	43	10	10	B	2.772	1	1862	Apollo	1.55	0.07	140	100	Q	1.0	13
3	Juno	234	11	5	5	S	2.671	1	2060	Chiron	142	10	4	4	B/Cb	8–15	14
4	Vesta	525	1	20	15	V	2.3	2	2060	Chiron	218	20	5	5	B/Cb	13	15
16	Psyche	244	25	125	40	M	2.7	3	2363	Cebrenes	82	5	7	7	D	5.2	16
21	Lutetia	96	1	5	5	M	2.8	4	2867	Steins	4.92	0.4	150	60	E	2.1	17
22	Kalliope	167	17	125	125	M	2.3	5	2867	Steins	5.2	1	210	30	E	2.1	18
32	Pomona	85	1	70	50	S	2.8	6	8405	Asbolus	66	4	5	5	—	7.9	19
41	Daphne	202	7	25	25	Ch	2.1	7	3063	Makhaon	116	4	15	15	D	4.7	16
44	Nysa	81	1	120	40	E	2.5	6	10199	Chariklo	236	12	1	1	D	13	14
45	Eugenia	198	20	45	45	C	2.6	5	10199	Chariklo	248	18	16	14	D	13	13
87	Sylvia	300	30	70	60	P	2.7	5	25143	Itokawa	0.32	0.03	700	100	S	1.1	8
107	Camilla	245	25	25	10	P	3.2	5	25143	Itokawa	0.320	0.029	700	200	S	1.1	20
110	Lydia	93.5	3.5	135	65	M	2.9	6	29075	1950 DA	1.30	0.13	24	20	M	1.7	21
115	Thyra	92	2	62	38	S	2.5	6	33342	1998 WT <sub>24</sub>	0.35	0.04	200	100	E	1.0	8
121	Hermione	220	22	30	25	Ch	2.9	5	50000	Quaoar	1082	67	6	4	—	43	15
130	Elektra	197	20	30	30	Ch	2.9	5	54509	YORP	0.092	0.010	700	500	S	1.1	8
277	Elvira	38	2	250	150	S	2.6	6	55565	2002 AW <sub>197</sub>	700	50	10	10	—	47	22
283	Emma	135	14	105	100	P	2.6	5	90377	Sedna	995	80	0.1	0.1	—	87	23
306	Unitas	56	1	180	80	S	2.2	6	90482	Orcus	968	63	1	1	—	48	13
382	Dodona	75	1	80	65	M	2.6	6	99942	Apophis	0.375	0.014	600	300	Sq	1.05	24
433	Eros	17.8	1	150	50	S	1.6	8	101955	Bennu	0.495	0.015	650	300	B	1.1	25
532	Herculina	203	14	10	10	S	2.772	1	101955	Bennu	0.49	0.02	310	70	B	1.1	26
617	Patroclus	106	11	20	15	P	5.9	9	136108	Haumea	1240	70	0.3	0.2	—	51	27
694	Ekard	109.5	1.5	120	20	—	1.8	6	162173	1999 JU <sub>3</sub>	0.87	0.03	400	200	C	1.4	28
720	Bohlinia	41	1	135	65	S	2.9	6	175706	1996 FG <sub>3</sub>	1.71	0.07	120	50	C	1.4	29
956	Elisa	10.4	0.8	90	60	—	1.8	10	208996	2003 AZ <sub>84</sub>	480	20	1.2	0.6	—	45	27
1173	Anchises	136	15	50	20	P	5.0	11	308635	2005 YU <sub>55</sub>	0.306	0.006	575	225	C	1.0	30
1580	Betulia	4.57	0.46	180	50	C	1.1	8	341843	2008 EV <sub>5</sub>	0.370	0.006	450	60	C	1.0	31

References: [1] Müller and Lagerros (1998); [2] Leyrat et al. (2012); [3] Matter et al. (2013); [4] O'Rourke et al. (2012); [5] Marchis et al. (2012); [6] Delbo and Tanga (2009); [7] Matter et al. (2011); [8] Mueller (2007); [9] Mueller et al. (2010); [10] Lim et al. (2011); [11] Horner et al. (2012); [12] Rozitis and Green (2014); [13] Rozitis et al. (2013); [14] Groussin et al. (2004); [15] Fornasier et al. (2013); [16] Fernández et al. (2003); [17] Lamy et al. (2008); [18] Leyrat et al. (2011); [19] Fernández et al. (2002); [20] Müller et al. (2014a); [21] Rozitis et al. (2014); [22] Cruikshank et al. (2005); [23] Pál et al. (2012); [24] Müller et al. (2014b); [25] Müller et al. (2012); [26] Emery et al. (2014); [27] Lellouch et al. (2013); [28] Müller et al. (2011); [29] Wolters et al. (2011); [30] Müller et al. (2013); [31] Ali-Lagoa et al. (2014). Note: For Ceres, Pallas, Juno, and Herculina, r is assumed equal to the semimajor axis of the orbit.

used as a proxy of regolith grain size. The required calibration under Mars conditions (where the tenuous atmosphere enhances thermal conduction within pores compared to a vacuum) was obtained by Presley and Christensen (1997a,b) and used in the analysis of thermal-inertia maps of Mars (see Mellon et al., 2000; Putzig and Mellon, 2007). Similar progress in asteroid science was slowed down by the lack of corresponding laboratory measurements under vacuum conditions (but see below for recent laboratory measurements of meteorites). However, Gundlach and Blum (2013) provided a calibration relation based on heat-transfer modeling in a granular medium.

### 5.3. Temperature Dependence of Thermal Inertia

Thermal inertia is a function of temperature (Keihm, 1984), chiefly because the thermal conductivity is. In general, for a lunar-like regolith, the thermal conductivity is given by

$$\kappa = \kappa_b + 4\sigma r_p T^3 \quad (12)$$

where  $\kappa_b$  is the solid-state thermal conductivity (heat conduction by phonons) and  $r_p$  is the radius of the pores of the regolith. The term proportional to  $T^3$  is due to the heat conduction by photons. Equation (12) is often written in the form  $\kappa = \kappa_0(1 + \chi T^3)$  (e.g., Vasavada et al., 1999). Note that  $\kappa_b$  is itself a function of T (Opeil et al., 2010). There is extensive literature on the T-dependence of the conductivity of lunar regolith (e.g., Vasavada et al., 1999, and references therein). A theoretical description of the temperature dependence of  $\kappa$  in regoliths is given by Gundlach and Blum (2013).

Asteroid TPMs typically neglect the temperature dependence of  $\Gamma$ . This is not critical for typical remote observations, which are dominated by the warm sunlit hemisphere (see Fig. 7) (Capria et al., 2014; Vasavada et al., 2012). In the analysis of highly spatially resolved observations, however, the temperature dependence must be considered,

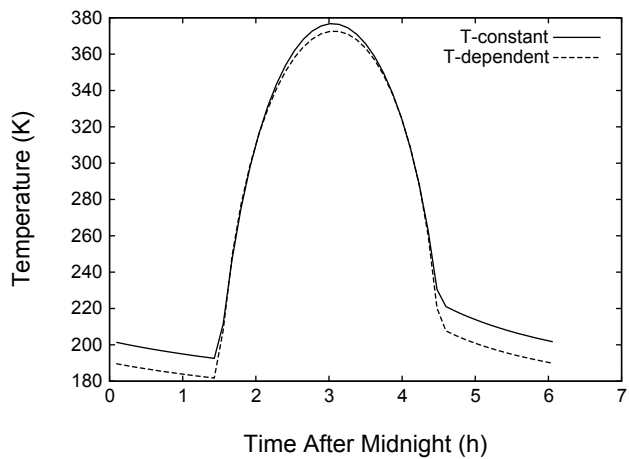


**Fig. 7.** Diurnal temperature curves at the equator of an asteroid with  $A = 0.1$ ,  $P = 6$  h,  $\epsilon = 1.0$  at a heliocentric distance of 1.0 AU. Solid curve: constant thermal conductivity  $\kappa = 0.02$  W K $^{-1}$  m $^{-1}$ . Dashed curve: temperature-dependent heat conductivity  $\kappa = 10^{-2}[1 + 0.5(T/250)^3]$  W K $^{-1}$  m $^{-1}$ .

certainly when analyzing nighttime observations on low- $\Gamma$  asteroids. Note that for temperature-dependent  $\kappa$ , equation (2) must be used instead of equation (3) (see, e.g., Capria *et al.*, 2014).

Caution must be exercised when comparing thermal-inertia results obtained at different heliocentric distances  $r$ , i.e., at different temperatures. All other things being equal,  $T^4 \propto r^{-2}$ . Assuming that the  $T^3$  term dominates in equation (12), the thermal inertia of a test object scales with (see also Mueller *et al.*, 2010)

$$\Gamma \propto \sqrt{\kappa} \propto T^{3/2} \propto r^{-3/4} \quad (13)$$

#### 5.4. Binary Asteroid Thermophysical Models

A rather direct determination of thermal inertia can be obtained by observing the thermal response to eclipses and their aftermath, allowing one to see temperature changes in real time. Such observations have been carried out for planetary satellites such as the Galilean satellites (Morrison and Cruikshank, 1973) and Earth's Moon (Pettit, 1940; Shorthill, 1973; Lawson *et al.*, 2003; Lucey, 2000; Fountain *et al.*, 1976). Mueller *et al.* (2010) report the first thermal observations of eclipse events in a binary Trojan asteroid system, (617) Patroclus, where one component casts shadow on the other while not blocking the line of sight toward the observer.

The thermophysical modeling of eclipse events is relatively straightforward, assuming the system is in a tidally locked rotation state typical of evolved binary systems. In that case, the components' spin rates match one another, and their spin axes are aligned with that of the mutual orbit. The system is therefore at rest in a co-rotating frame and can be modeled like a single object with a nonconvex

(disjointed) global shape. Eclipse effects are fully captured, provided that shadowing between facets is accounted for. The two hemispheres that face one another can, in principle, exchange heat radiatively. This is negligible for typical binary systems, however.

As discussed above, the thermal effects of roughness and thermal inertia can be hard to disentangle. In the case of eclipse measurements, which happen at essentially constant solar phase angle, the effect of surface roughness is much less of a confounding factor. This is because the variation in the thermal signal is dominated by the temperature change induced by the passing shadow, which is a strong function of thermal inertia.

It must be kept in mind that the duration of an eclipse event is short compared to the rotation period. The eclipse-induced heat wave therefore probes the subsoil less deeply than the diurnal heat wave does (the typical heat penetration depth is given by equation (5) with  $P$  equal to the duration of the eclipse event). A depth dependence of thermal inertia (see section 6.6) could manifest itself in different thermal-inertia determinations using the two different measurement methods.

#### 5.5. Thermal-Infrared Interferometry

Interferometric observations of asteroids in the thermal infrared measure the spatial distribution of the thermal emission along different directions on the plane of sky, thereby constraining the distribution in surface temperature and hence thermal inertia and roughness. Provided the asteroid shape is known, interferometry can be used to break the aforementioned degeneracy between thermal inertia and roughness from a single-epoch observation (Matter *et al.*, 2011, 2013). Interferometry also allows precise determination of the size of an asteroid (Delbo *et al.*, 2009).

Spatial resolutions between 20 and 200 milliarcseconds can be obtained from the ground (see the chapter by Durech *et al.* in this volume for a review and future perspectives of the application of this technique). While for the determination of asteroid sizes and shapes from interferometric observations in the thermal infrared, simple thermal models can be used (Delbo *et al.*, 2009; Carry *et al.*, 2015), a TPM was utilized to calculate interferometric visibilities of asteroids in the thermal infrared for the observations of (41) Daphne (Matter *et al.*, 2011) and (16) Psyche (Matter *et al.*, 2013).

Mid-infrared interferometric instruments measure the total flux and the visibility of a source, the latter related to the intensity of the Fourier transform (FT) of the spatial flux distribution along the interferometer's baseline projected on the plane of sky. Thus, the data analysis procedure consisted of generating images of the thermal-infrared emission of the asteroids at different wavelengths as viewed by the interferometer and then obtaining the model visibility and flux for each image. The former is related to the FT of the image, the latter is simply the sum of the pixels. The free parameters of the TPM (size, thermal-inertia value, and roughness) are adjusted in order to minimize the distance between the disk-integrated flux and visibility of the model,

and the corresponding observed quantities (see *Matter et al.*, 2011, 2013; see also the chapter by Durech et al.). Some results from these observational programs are discussed in section 6 and in the chapter by Durech et al.

### 5.6. Disk-Resolved Data and Retrieval of Temperatures

The availability of disk-resolved thermal-infrared observation has been steadily increasing over the years. The European Space Agency's (ESA) Rosetta mission performed successful flybys of the asteroids (2867) Steins (in 2008) and (21) Lutetia (in 2010) (see the chapter by Barucci et al. in this volume). In 2011, NASA's Dawn mission began its one-year orbit of (4) Vesta (*Russell et al.*, 2012), and is reaching (1) Ceres at the time of this writing. JAXA's Hayabusa-2 sample-return mission will map its target asteroid (162173) Ryugu (1999 JU<sub>3</sub>) using the thermal infrared imager (TIR) onboard the spacecraft (*Okada et al.*, 2013); NASA's OSIRIS-REx mission and its thermal spectrometer (OTES) will do likewise for its target asteroid (101955) Bennu (in 2018–2019). These data can be used to derive surface-temperature maps, from which maps of thermal inertia and roughness can be derived.

Three different methods are used to measure surface temperatures from orbiting spacecraft: bolometry, mid-infrared spectroscopy, and near-infrared spectroscopy. In the following, we will elaborate on the challenges posed by these different methods, and on their dependence on spectral features, surface roughness, illumination geometry, and viewing geometry.

Bolometers measure thermal flux within a broad bandpass in the infrared, approximating the integral of the Planck function,  $U = \sigma T_e^4$  (e.g., *Kieffer et al.*, 1977; *Paige et al.*, 2010). The temperature derived in this way (*effective temperature*) is directly relevant to the energy balance on the surface. Since the bolometric flux is spectrally integrated, the resulting temperature is fairly insensitive to spectral emissivity variations, as long as the bolometric emissivity (weighted spectrally averaged emissivity) is known or can be reasonably approximated.

Temperatures derived from mid-infrared spectrometry, on the other hand, are typically *brightness temperatures*, i.e., the temperature of a black body emitting at the wavelength in question. It is generally assumed that at some wavelength, the spectral emissivity is very close to 1.0, and the brightness temperature at this wavelength is taken as the surface temperature.

Spacecraft sent to asteroids (and/or comets) have more commonly been instrumented with near-infrared spectrometers (e.g.,  $\lambda < 5 \mu\text{m}$ ) rather than mid-infrared spectrometers. The long-wavelength ends of these spectrometers often extend into the range where thermal emission dominates the measured flux (for the daytime surface temperatures of most asteroids). At these wavelengths, one cannot assume that the emissivity is close to 1.0. It is therefore not practical to derive brightness temperatures. Instead, the *color temperature* is derived, i.e., the temperature of a blackbody

that emits with the same spectral shape. Such derivations have to separate temperature from spectral emissivity. The problem is underconstrained ( $N + 1$  unknowns, but only  $N$  data points), so there is no deterministic solution. Spectral emissivities for fine-grained silicates trend in the same direction as the blackbody curve, so it would be very easy to mistake spectral emissivity variations for different temperatures. The most statistically rigorous approach that has been applied to separating temperature and spectral emissivity in the 3–5-μm region is that of *Keihm et al.* (2012) and *Tosi et al.* (2014) for Rosetta's Visible and Infrared Thermal Imaging Spectrometer (VIRTIS) data of Lutetia and Dawn's Visual and Infrared Spectrometer (VIR) data of Vesta.

Temperatures thus measured represent an average temperature in the field of view of a given pixel: Illuminated hot zones and shadowed colder parts will both contribute. They do not directly correspond to a physical temperature of the soil; rather, they depend sensitively on the observation and illumination geometry (see *Rozitis and Green*, 2011, in particular their Fig. 9), especially in the case of large illumination angles.

Microwave spectrometers such as the Microwave Instrument for Rosetta Orbiter (MIRO) (*Gulkis et al.*, 2007) can provide both day- and nightside thermal flux measurements. At submillimeter, millimeter, and longer wavelengths, asteroid soils become moderately transparent. Subsurface layers contribute significantly to the observable thermal emission, thus providing information on the subsurface temperature. Observable fluxes depend on the subsurface temperature profile, weighted by the wavelength-dependent electrical skin depths, so both a thermal and an electrical model are required to interpret such data (*Keihm et al.*, 2012).

We remind the reader here that thermal-infrared fluxes should be used as input data for TPMs and not (effective, color, or brightness) temperatures derived from radiometric methods, because of their dependence on illumination and observation angles.

### 5.7. Sample Return Missions

Space agencies across the planet are developing space missions to asteroids, notably sample return missions to primitive (C- and B-type) NEAs: Hayabusa-2 was launched by JAXA toward (162173) 1999 JU<sub>3</sub> on December 3, 2014, and OSIRIS-REx is to be launched by NASA in 2016 (*Lauretta et al.*, 2012). A good understanding of the expected thermal environment, which is governed by thermal inertia, is a key factor in planning spacecraft operations on or near asteroid surfaces. For example, OSIRIS-REx is constrained to sampling a regolith no hotter than 350 K, severely constraining the choice of the latitude of the sample selection area on the body, the local time, and the arrival date on the asteroid.

Both Hayabusa-2 and OSIRIS-REx are required to take regolith samples from the asteroid surface back to Earth. Obviously, this requires that regolith be present in the first place, which needs to be ascertained by means of groundbased thermal-inertia measurements. The sampling

mechanism of OSIRIS-REx, in particular, requires relatively fine (centimeter-sized or smaller) regolith.

### 5.8. Accurate Yarkovsky and YORP Modeling from Thermophysical Models

Scattered and thermally emitted photons carry momentum. Any asymmetry in the distribution of outgoing photons can, after averaging over an orbital period, impart a net recoil force (Yarkovsky effect) and/or a net torque (YORP effect) on the asteroid. Both effects are more noticeable as the object gets smaller. For objects that are small enough, the orbits can be significantly affected by the Yarkovsky effect, and their rotation state can be significantly affected by the YORP effect (*Bottke et al.*, 2006; see also the chapter by Vokrouhlický et al. in this volume).

The strength of the Yarkovsky effect is strongly influenced by thermal inertia (*Bottke et al.*, 2006, and references therein) and by the degree of surface roughness (*Rozitis and Green*, 2012). However, the strength and sign of the YORP rotational acceleration on an asteroid is independent of thermal inertia (*Čapek and Vokrouhlický*, 2004), but it is highly sensitive to the shadowing (*Breiter et al.*, 2009), self-heating (*Rozitis and Green*, 2013), and surface roughness effects (*Rozitis and Green*, 2013) that are incorporated in TPMs.

Accurate calculations of the instantaneous recoil forces and torques require an accurate calculation of surface temperatures as afforded by TPMs; *Rozitis and Green* (2012, 2013) report on such models. Other than on thermal inertia, the Yarkovsky-induced orbital drift depends on the bulk mass density. Therefore, Yarkovsky measurements combined with thermal-inertia measurements can be used to infer the elusive mass density (*Mommert et al.*, 2014a,b; *Rozitis and Green*, 2014; *Rozitis et al.*, 2013, 2014). In the case of (101955) Bennu, the uncertainties in published values of thermal inertia (*Emery et al.*, 2014) and measured Yarkovsky drift (*Chesley et al.*, 2014) are so small that the accuracy of the inferred mass density rivals that of the expected *in situ* spacecraft result ( $1260 \pm 70 \text{ kg m}^{-3}$ , i.e., a nominal uncertainty of only 6%). *Rozitis et al.* (2014) derived the bulk density of (29075) 1950 DA and used it to reveal the presence of cohesive forces stabilizing the object against the centrifugal force.

In turn, the measured Yarkovsky drift can be used to infer constraints on thermal inertia. This was first done by *Chesley et al.* (2003), studying the Yarkovsky effect on (6489) Golevka, and by *Bottke et al.* (2001), studying the Koronis family in the main asteroid belt; both studies revealed thermal inertias consistent with expectations based on the observed correlation between thermal inertia and diameter (see section 6.2).

While the YORP effect is highly sensitive to small-scale uncertainties in an asteroid's shape model (*Statler*, 2009), it can be used to place constraints on the internal bulk density distribution of an asteroid (*Scheeres and Gaskell*, 2008). For instance, *Lowry et al.* (2014) explain the YORP detection on (25143) Itokawa — which was opposite in sign to that

predicted — by Itokawa's two lobes having substantially different bulk densities. However, unaccounted lateral heat conduction in thermal-skin-depth-sized rocks could also explain, at least partially, this opposite sign result (*Golubov and Krugly*, 2012).

## 6. LATEST RESULTS FROM THERMOPHYSICAL MODELS

In the *Asteroids III* era, thermal properties were known for only a few asteroids, i.e., (1) Ceres, (2) Pallas, (3) Juno, (4) Vesta, (532) Herculina from *Müller and Lagerros* (2002), and (433) Eros from *Lebofsky and Rieke* (1979). Since then, the number of asteroids with known thermal properties has increased steadily. We count 59 minor bodies with known value of  $\Gamma$  (see Table 2). Of these, 16 are NEAs, 27 are MBAs, 4 are Jupiter Trojans, 5 are Centaurs, and 7 are TNOs.

These classes of objects present very different physical properties, such as size, regolith grain size, average value of the thermal inertia, and composition. Other important differences are their average surface temperatures, due to their very different heliocentric distances and orbital elements. The illumination and observation geometry are also diverse for different classes of objects. For instance, for TNOs and MBAs the phase angle of observation from Earth and Earth-like orbits is typically between a few and a few tens of degrees, respectively. On the other hand, NEAs can be observed under a much wider range of phase angles that can approach  $100^\circ$  or more (see also *Müller*, 2002). Special care should be used in these cases to explicitly calculate the heat diffusion in craters instead of using the approximation of equation (9).

### 6.1. Ground Truth from Space Missions to Asteroids

A number of asteroids have been, or will be, visited by spacecraft, providing ground-truth for the application of TPMs to remote sensing thermal-infrared data.

(21) *Lutetia*: Based on groundbased data and a TPM, *Müller et al.* (2006) measured Lutetia's effective diameter and  $p_V$  to within a few percent of the later Rosetta result (*Sierks et al.*, 2011). Their thermal-inertia constraint ( $\Gamma < 50 \text{ J m}^{-2} \text{ s}^{-1/2} \text{ K}^{-1}$ ) was refined by *O'Rourke et al.* (2012) based on the Rosetta shape model and more than 70 thermal-infrared observations obtained from the ground and by Spitzer, AKARI, and Herschel:  $\Gamma = 5 \text{ J m}^{-2} \text{ s}^{-1/2} \text{ K}^{-1}$  with a high degree of surface roughness. *Keihm et al.* (2012) used MIRO onboard Rosetta to obtain a surface thermal inertia  $\leq 30 \text{ J m}^{-2} \text{ s}^{-1/2} \text{ K}^{-1}$ . The low thermal inertia can be explained by a surface covered in fine regolith; *Gundlach and Blum* (2013) infer a regolith grain size of about  $200 \mu\text{m}$ . The study of the morphology of craters by *Vincent et al.* (2012) indicates abundant, thick (600 m), and very fine regolith, confirming the TPM results.

(433) *Eros* was studied by the NASA Near Earth Asteroid Rendezvous (NEAR)-Shoemaker space mission, which allowed determination of the shape and size of this

asteroid [mean radius of 8.46 km with a mean error of 16 m (*Thomas et al.*, 2002)]. *Mueller* (2007) performed a TPM analysis of the groundbased thermal-infrared data by *Harris and Davies* (1999), obtaining a best-fit diameter of 17.8 km that is within 5% of the *Thomas et al.* (2002) result of 16.9 km, and  $\Gamma$  in the range  $100\text{--}200 \text{ J m}^{-2} \text{ s}^{-1/2} \text{ K}^{-1}$ . The latter value, in agreement with TPM results of *Lebofsky and Rieke* (1979), implies coarser surface regolith than that on the Moon and larger asteroids (see, e.g., *Mueller*, 2007; *Delbo et al.*, 2007). From the value of  $\Gamma$  of *Mueller* (2007), *Gundlach and Blum* (2013) calculated a 1–3-mm typical regolith grain size for Eros. Optical images of the NEAR-Shoemaker landing site at a resolution of about 1 cm/pixel (*Everka et al.*, 2001) show very smooth areas at the scale of the camera spatial resolution (Fig. 8), likely implying millimeter or submillimeter grain size regolith, consistent with TPM results.

(25143) *Itokawa* physical properties were derived *in situ* by the JAXA sample-return mission Hayabusa, allowing us to compare the size, albedo, and regolith nature derived from the TPMs with spacecraft results. *Müller et al.* (2014a) show an agreement within 2% between the size and the geometric visible albedo inferred from TPM analysis of thermal-infrared data and the value of the corresponding parameters from Hayabusa data. The TPM thermal inertia value for Itokawa is around  $750 \text{ J m}^{-2} \text{ s}^{-1/2} \text{ K}^{-1}$ , significantly higher than the value of Earth's Moon (about  $50 \text{ J m}^{-2} \text{ s}^{-1/2} \text{ K}^{-1}$ ) and of other large MBAs, including (21) Lutetia, implying a coarser regolith on this small NEA. The corresponding average regolith grain size according to *Gundlach and Blum* (2013) is ~2 cm. Hayabusa observations from the optical navigation camera (ONC-T), obtained during the descent of the spacecraft to the "Muses Sea" region of the asteroid, reveal similar grain sizes, at a spatial resolution of up to 6 mm/pixel. In particular, *Yano et al.* (2006) describe "Muses Sea" as composed of numerous size-sorted granular materials ranging from several centime-

ters to subcentimeter scales. Itokawa's regolith material can be classified as "gravel," larger than submillimeter regolith powders filling in ponds on (433) Eros (Fig. 8).

It is worth pointing out, however, that "Muses Sea" is not representative of Itokawa's surface as a whole. Rather, it was selected as a touchdown site because, in earlier images of Hayabusa, it appeared as particularly smooth (minimizing operational danger for the spacecraft upon touchdown) and apparently rich in regolith (maximizing the chance of sampling regolith). Grain sizes measured at "Muses Sea" are therefore lower limits on typical grain sizes rather than values typical for the surface as a whole.

## 6.2. Thermal Inertia of Large and Small Asteroids

An inverse correlation between  $\Gamma$  and D was noticed by *Delbo et al.* (2007), then updated by *Delbo and Tanga* (2009) and *Capria et al.* (2014). This supported the intuitive view that large asteroids have, over many hundreds of millions of years, developed substantial insulating regolith layers, responsible for the low values of their surface thermal inertia. On the other hand, much smaller bodies, with shorter collisional lifetimes (*Marchi et al.*, 2006; *Bottke et al.*, 2005, and references therein), have less regolith and/or larger regolith grains (less mature regolith), and therefore display a larger thermal inertia.

In light of the recently published values of  $\Gamma$  (Table 2), the said inversion correlation between  $\Gamma$  and D is less clear, in particular when the values of the thermal inertia are temperature corrected (Fig. 9). However, the  $\Gamma$  vs. D distribution of  $D > 100 \text{ km}$  (large) asteroids is different than that of  $D < 100 \text{ km}$  (small) asteroids. Small asteroids typically have higher  $\Gamma$  values than large asteroids, which present a large scatter of  $\Gamma$  values, ranging from a few to a few hundreds of  $\text{J m}^{-2} \text{ s}^{-1/2} \text{ K}^{-1}$ . This is a clear indication of a diverse regolith nature among these large bodies. A shortage of low  $\Gamma$  values for small asteroids is also clear, with the notable exception of 1950 DA, which has an anomalously low  $\Gamma$  value compared to other NEAs of similar size (*Rozitis et al.*, 2014).

Figure 9 also shows previously unnoticed high-thermal-inertia C types, perhaps related to CR carbonaceous chondrites, which contain abundant metal phases. We also note that all E types in our sample appear to have a size-independent thermal inertia.

## 6.3. Very Low $\Gamma$ Values

We also note that some of the C-complex outer MBAs and Jupiter Trojans have very low thermal inertia, in the range between a few and a few tens of  $\text{J m}^{-2} \text{ s}^{-1/2} \text{ K}^{-1}$ . In order to reduce the thermal inertia of a material by at least 1 order of magnitude [from the lowest measured thermal inertia of a meteorite,  $\sim 650 \text{ J m}^{-2} \text{ s}^{-1/2} \text{ K}^{-1}$  at 200 K (*Opeil et al.*, 2010)] to the typical values for these large asteroids (Table 2 and Fig. 9), a very large porosity (>90%) of the first few millimeters of the regolith is required (*Vernazza et al.*,

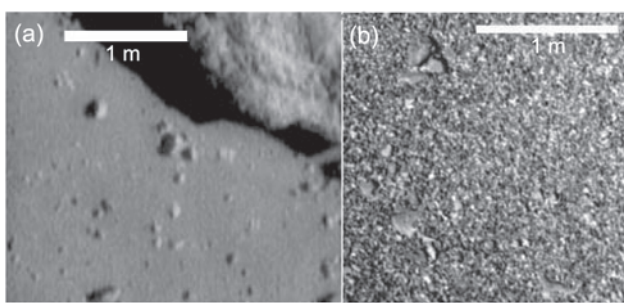


**Fig. 8.** Higher  $\Gamma$ -values correspond to coarser regoliths. (a) Close-up image of (433) Eros from the NASA NEAR Shoemaker mission reveals coarse regolith with grain size in the millimeter range (adapted from *Everka et al.*, 2001). The value of  $\Gamma$  is  $\sim 150 \text{ J m}^{-2} \text{ s}^{-1/2} \text{ K}^{-1}$  for Eros. (b) Image from the JAXA Hayabusa mission of the surface of (25143) Itokawa displaying gravel-like regolith (from *Yano et al.*, 2006). The value of  $\Gamma$  is  $\sim 750 \text{ J m}^{-2} \text{ s}^{-1/2} \text{ K}^{-1}$  for Itokawa.

2012). This is consistent with the discovery that emission features in the mid-infrared domain (7–25  $\mu\text{m}$ , Fig. 4) are rather universal among large asteroids and Jupiter Trojans (Vernazza *et al.*, 2012), and that said features can be reproduced in the laboratory by suspending meteorite and/or mineral powder (with grain sizes  $<30\ \mu\text{m}$ ) in infrared-transparent potassium bromide (KBr) powder (Vernazza *et al.*, 2012). As KBr is not supposed to be present on the surfaces of these minor bodies, regolith grains must be “suspended” in void space, likely due to cohesive forces and/or dust levitation. On the other hand, radar data indicate a significant porosity (40–50%) of the first  $\sim 1\ \text{m}$  of regolith (Magri *et al.*, 2001; Vernazza *et al.*, 2012), indicating decreasing porosity with increasing depth (see Fig. 5 of Vernazza *et al.*, 2012, for a regolith schematic).

#### 6.4. Average Thermal Inertia of Asteroid Populations

As described previously, the thermal inertia of an asteroid can be directly derived by comparing measurements of its thermal-infrared emission to model fluxes generated by means of a TPM. Typically, more than one observation epoch is required to derive the thermal inertia, in order to “see” the thermal emission from different parts of the asteroid’s diurnal temperature distribution. Unfortunately, the large majority of minor bodies for which we have thermal-infrared observations have been observed at a single epoch and/or information about their gross shape and pole orientation is not available, precluding the use of TPMs. However, if one assumes the thermal inertia to be roughly constant within a population of asteroids (e.g., NEAs) one can use observations of different asteroids under non-identical illumination and viewing geometries, as if they were from a unique object. Delbo *et al.* (2003) noted that qualitative information about the average thermal

properties of a sample of NEAs could be obtained from the distribution of the  $\eta$  values of the sample as a function of the phase angle,  $\alpha$ . Delbo *et al.* (2007) and Lellouch *et al.* (2013) developed a rigorous statistical inversion method, based on the comparison of the distributions of published NEATM  $\eta$  values vs.  $\alpha$  (or vs.  $r$ ) with that of a synthetic population of asteroids generated through a TPM, using realistic distributions of the input TPM parameters such as the rotation period, aspect angle, etc. Delbo *et al.* (2007) found that the average thermal inertia value for kilometer-sized NEAs is around  $200\ \text{J m}^{-2}\ \text{s}^{-1/2}\ \text{K}^{-1}$ . The average thermal inertia of binary NEAs is higher than that of nonbinary NEAs, possibly indicating a regolith-depriving mechanism for the formation of these bodies (Delbo *et al.*, 2011). The same authors also found that NEAs with slow rotational periods ( $P > 10\ \text{h}$ ) have higher-than-average thermal inertia. From a sample of 85 Centaurs and TNOs observed with the Multi-Band Imaging Photometer for Spitzer (MIPS) and Herschel’s Photodetector Array Camera and Spectrometer (PACS), Lellouch *et al.* (2013) found that surface roughness is significant, a mean thermal inertia  $\Gamma = 2.5 \pm 0.5\ \text{J m}^{-2}\ \text{s}^{-1/2}\ \text{K}^{-1}$ , and a trend toward decreasing  $\Gamma$  with increasing heliocentric distance. The thermal inertias derived by Lellouch *et al.* (2013) are 2–3 orders of magnitude lower than expected for compact ices, and generally lower than on Saturn’s satellites or in the Pluto/Charon system. These results are suggestive of highly porous surfaces.

#### 6.5. Relevant Astronomical and Laboratory Data

Physical interpretations of thermal-inertia estimates depend strongly on laboratory and ground-truth measurements of relevant material properties. While in the *Asteroids III* era we based interpretation of thermal inertia on Earth analog materials, in the last few years laboratory measurements

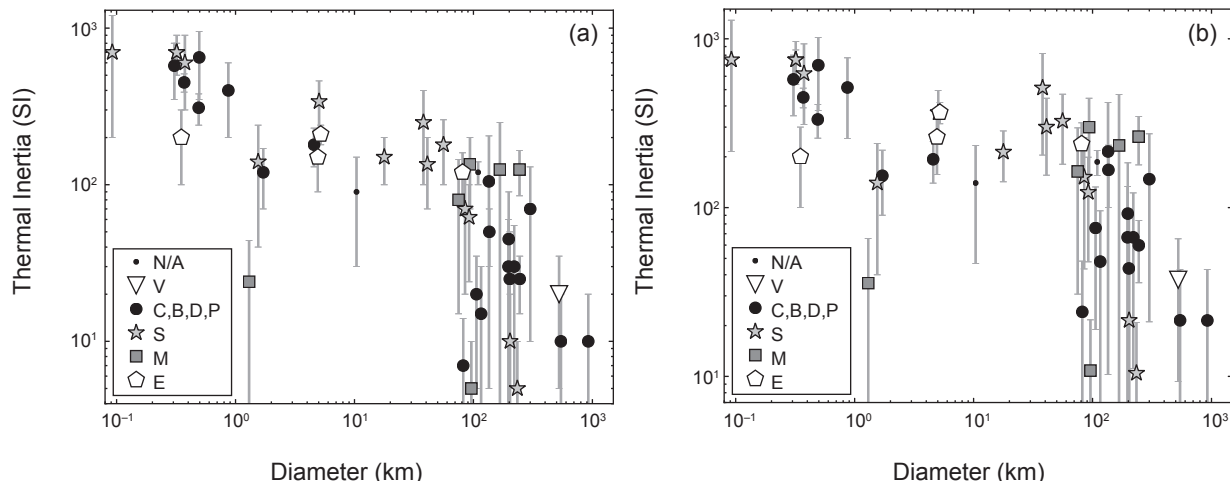


**Fig. 9.**  $\Gamma$  values vs.  $D$  from Table 2 for different taxonomic types (see key). **(a)** Original measurements; **(b)**  $\Gamma$  corrected to 1 AU heliocentric distance for temperature-dependent thermal inertia assuming equation (13) and the heliocentric distance at the time of thermal infrared observations reported in Table 2. Trojans, Centaurs, and transneptunian objects are not displayed.

were performed on asteroid analog materials, i.e., meteorites. Meteorite grain densities range from  $\sim 2800 \text{ kg m}^{-3}$  for CM carbonaceous chondrites to  $\sim 3700 \text{ kg m}^{-3}$  for enstatite chondrites (*Consolmagno et al.*, 2006; *Macke et al.*, 2010, 2011a,b). Heat capacities have been measured for a wide sampling of meteorites by *Consolmagno et al.* (2013), who find that values for stony meteorites are between 450 and  $550 \text{ J kg}^{-2} \text{ K}^{-1}$ , whereas C for irons tends to be smaller ( $330\text{--}380 \text{ J kg}^{-2} \text{ K}^{-1}$ ). *Opeil et al.* (2010, 2012) present thermal conductivity measurements of stony meteorites, finding values of  $0.5 \text{ W K}^{-1} \text{ m}^{-1}$  for the carbonaceous chondrite Cold Bokkeveld to  $5.5 \text{ W K}^{-1} \text{ m}^{-1}$  for the enstatite chondrite Pillistfer. Their one iron meteorite sample has a  $\kappa$  of  $22.4 \text{ W K}^{-1} \text{ m}^{-1}$ . They also find a linear correlation between and the inverse of the porosity, from which *Opeil et al.* (2012) conclude that the measured  $\kappa$  of the samples is controlled more by microfractures than by composition.

Grain size and packing, more than compositional heterogeneity, are responsible for different thermal inertias of different surfaces. This also explains why TPMs are capable of deriving asteroid physical parameters independently of the asteroid mineralogy. Conduction between grains is limited by the area of the grain contact (*Piqueux and Christensen*, 2009a,b). As grain size decreases to diameters less than about a thermal skin depth (a few centimeters on most asteroids), conduction is more and more limited (e.g., *Presley and Christensen*, 1997b). On bodies with atmospheres, conduction through the air in pores can often efficiently transport heat. On airless bodies, however, radiation between grains, which is not very efficient, particularly at low T (e.g., *Gundlach and Blum*, 2012), is the only alternative to conduction across contacts (Fig. 10). Considering these two modes of energy transport and their dependence on grain size, *Gundlach and Blum* (2013) developed an analytical approach for determining grain size from thermal inertia measurements. They incorporated the measurements of material properties of meteorites measured above along with results of their own laboratory studies of heat transport in dusty layers. Additional laboratory measurements of conductivities of powdered meteorites under high vacuum would be valuable for more precise interpretation of asteroid thermal inertias.

The classic opportunity for ground-truth thermal measurements came with the Apollo missions. Astronauts on Apollos 15 and 17 carried out bore-hole-style temperature measurements to depths of 1.4 m below the surface on Apollo 15 and 2.3 m below the surface on Apollo 17 (*Langeseth and Keihm*, 1977; *Vaniman et al.*, 1991). Thermal conductivity of about  $0.001 \text{ W K}^{-1} \text{ m}^{-1}$  was found in the top 2 to 3 cm of the lunar regolith, increasing to about  $0.01 \text{ W K}^{-1} \text{ m}^{-1}$  over the next few centimeters, then to values as high as  $2 \text{ W K}^{-1} \text{ m}^{-1}$  deeper into the surface where the regolith appears to have been very compacted (*Langeseth and Keihm*, 1977). Low thermal inertias derived from remote thermal-infrared measurements (e.g., *Wesselink*, 1948; *Vasavada et al.*, 2012) agree with the very low  $\kappa$  in the topmost few centimeters of the lunar

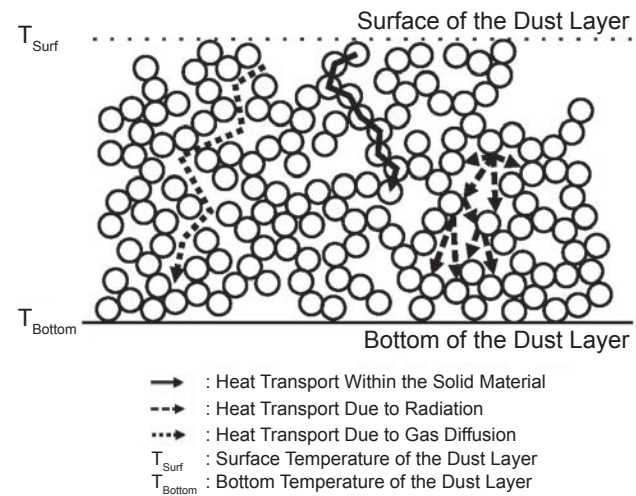


**Fig. 10.** Diagram of the modes of heat transport in regoliths. On airless bodies, heat can flow by conduction through grain boundaries (solid line) or by radiation between grains (dashed line). The dotted line showing transport by gas diffusion is not relevant to asteroid surfaces. From Gundlach and Blum (2012).

surface, and the Apollo measurements provide the necessary ground-truth for interpreting such low thermal inertias as very fine-grained, “fluffy” regolith. These measurements fostered, for instance, development of detailed models of lunar regolith (Keihm, 1984). Detailed thermal-infrared observations and thermal models of the lunar regolith today allows estimating the subsurface rock abundance (e.g., Bandfield *et al.*, 2011), which allows geological studies of the regolith production rate.

## 6.6. Dependence of $\Gamma$ with Depth

The depth dependence of typical asteroid regolith properties is poorly constrained at this point, which is why physical constants are typically assumed to be constant with depth. MIRO observations of (21) Lutetia, however, showed the existence of a top layer with  $\Gamma < 30 \text{ J m}^{-2} \text{ s}^{-1/2} \text{ K}^{-1}$ , while the thermal inertia of subsurface material appears to increase with depth, much like on the Moon (*Keihm et al.*, 2012) (see also section 5.3).

### 6.7. Infrared Limb Brightening

Recent modeling and observations show that, contrary to expectations, the flux enhancement measured in disk-integrated observations of the sunlit side of an asteroid (e.g., Lebofsky *et al.*, 1986) is dominated by limb surfaces rather than the subsolar region (Rozitis and Green, 2011; Keihm *et al.*, 2012). This suggests that for the sunlit side of an asteroid, sunlit surfaces directly facing the observer in situations where they would not be if the surface was a smooth flat one are more important than mutual self-heating between interfacing facets raising their temperatures. Figure 9 of

*Rozitis and Green* (2011) pictures this effect for a Gaussian random surface during sunrise viewed from different directions. The thermal flux observed is enhanced when viewing hot sunlit surfaces (i.e., Sun behind the observer), and is reduced when viewing cold shadowed surfaces (i.e., Sun in front of the observer).

*Jakosky et al.* (1990) also studied the directional thermal emission of Earth-based lava flows exhibiting macroscopic roughness. They found that enhancements in thermal emission were caused by viewing hot sunlit sides of rocks and reductions were caused by viewing cold shadowed sides of rocks. This agrees precisely with the model and adds further evidence that thermal-infrared beaming is caused by macroscopic roughness rather than microscopic roughness.

The effect of limb brightening has also been measured from disk-resolved thermal-infrared data ( $<5\text{ }\mu\text{m}$ ) acquired during sunrise on the nucleus of Comet 9P/Tempel 1 by NASA's Deep Impact mission (*Davidsson et al.*, 2013), and from VIRTIS and MIRO measurements of the asteroid (21) Lutetia (*Keihm et al.*, 2012).

## 6.8. Asteroid Thermal Inertia Maps

Disk-resolved thermal-infrared observations, in the range between 4.5 and  $5.1\text{ }\mu\text{m}$ , were provided by the VIR instrument (*De Sanctis et al.*, 2012) onboard NASA's Dawn (*Russell et al.*, 2012) spacecraft (*Capria et al.*, 2014, and references therein). From TPM analysis of VIR measurements, *Capria et al.* obtained a map of the roughness and the thermal inertia of Vesta. The average thermal inertia of Vesta is  $30 \pm 10\text{ J m}^{-2}\text{ s}^{-1/2}\text{ K}^{-1}$ , which is in good agreement with the values found by groundbased observations (*Müller and Lagerros*, 1998; *Chamberlain et al.*, 2007; *Leyrat et al.*, 2012). The best analog is probably the surface of the Moon, as depicted by *Vasavada et al.* (2012) and *Bandfield et al.* (2011): A surface whose thermal response is determined by a widespread layer of dust and regolith with different grain sizes and density increasing toward the interior. Exposed rocks are probably scarce or even absent. *Capria et al.* (2014) also show that Vesta cannot be considered uniform from the point of view of thermal properties. In particular, they found that the thermal inertia spatial distribution follows the global surface exposure age distribution as determined by crater counting in *Raymond et al.* (2011), with higher thermal inertia displayed by younger terrains and lower thermal inertia in older soils.

*Capria et al.* (2014) also found higher-than-average thermal-inertia terrain units located in low-albedo regions that contain the highest abundance of OH, as determined by the  $2.8\text{-}\mu\text{m}$  band depth (*De Sanctis et al.*, 2012). These terrains are associated with the dark material, thought to be delivered by carbonaceous-chondrite-like asteroids that have impacted Vesta at low velocity. Note that in general carbonaceous chondrites have lower densities and lower thermal conductivity (*Opeil et al.*, 2010) than basaltic material, which constitute the average vestan terrain. This consideration would point to a lower thermal inertia rather than a higher one, as observed on Vesta. *Capria et*

*al.* (2014) conclude that the factor controlling the thermal inertia in these areas could be the degree of compaction of the uppermost surface layers, which is higher than in other parts of the surface.

## 6.9. Thermal Inertia of Metal-Rich Regoliths

In principle, the composition of the regolith and not only its average grain size, but also the degree of compaction, also affects the thermal inertia of the soil (*Gundlach and Blum*, 2013). For instance, iron meteorites have a higher thermal conductivity than ordinary and carbonaceous chondrites (*Opeil et al.*, 2010). We thus expect that a metal-iron-rich regolith would display a higher thermal inertia than a soil with a deficiency of this component. *Harris and Drube* (2014) compared values of the NEATM  $\eta$  parameter derived from WISE data with asteroid taxonomic classifications and radar data, and showed that the  $\eta$  value appears to be a useful indicator of asteroids containing metal. *Matter et al.* (2013) performed interferometric observations with the MID-infrared Interferometric instrument (MIDI) of the European Southern Observatory's (ESO) Very Large Telescope Interferometer (VLTI) in thermal infrared of (16) Psyche and showed that Psyche has a low surface roughness and a thermal inertia value around  $120 \pm 40\text{ J m}^{-2}\text{ s}^{-1/2}\text{ K}^{-1}$ , which is one of the higher values for an asteroid of the size of Psyche ( $\sim 200\text{ km}$ ). This higher-than-average thermal inertia supports the evidence of a metal-rich surface for this body.

## 7. EFFECTS OF TEMPERATURES ON THE SURFACE OF ASTEROIDS

### 7.1. Thermal Cracking

The surface temperature of asteroids follows a diurnal cycle (see Fig. 2) with typically dramatic temperature changes as the Sun rises or sets. The resulting, repeated thermal stress can produce cumulative damage on surface material due to opening and extension of microscopic cracks. This phenomenon is known as *thermal fatigue* (*Delbo et al.*, 2014).

Growing cracks can lead to rock breakup when the number of temperature cycles is large enough. For typical asteroid properties, this process is a very effective mechanism for comminuting rocks and to form fresh regolith (*Delbo et al.*, 2014). For centimeter-sized rocks on an asteroid at 1 AU from the Sun, thermal fragmentation is at least an order of magnitude faster than comminution by micrometeoroid impacts, the only regolith-production mechanism previously considered relevant (*Hörz and Cintala*, 1997; *Hoerz et al.*, 1975).

The efficiency of thermal fragmentation is dominated by the amplitude of the temperature cycles and by the temperature change rate (*Hall and André*, 2001), which in turn depends on heliocentric distance, rotation period, and the surface thermal inertia. The rate of thermal fragmentation increases with decreasing perihelion distance: At 0.14 AU from the Sun, thermal fragmentation may erode asteroids such as (3200) Phaethon and produce the Geminids (*Jewitt*

and Li, 2010), whereas in the outer main belt, this process might be irrelevant. Thermal fragmentation of surface boulders is claimed by Dombard et al. (2010) to be the source of fine regolith in the so-called “ponds” on the asteroid (433) Eros. Production of fresh regolith originating in thermal fatigue fragmentation may be an important process for the rejuvenation of the surfaces of NEAs (Delbo et al., 2014).

Thermal cracking is reported on other bodies as well: on Earth, particularly in super-arid environments (Hall, 1999; Hall and André, 2001); the Moon (Levi, 1973; Duennbier and Sutton, 1974); Mercury (Molaro and Byrne, 2012); Mars (Viles et al., 2010); and meteorites (Levi, 1973). Moreover, Tambovtseva and Shestakova (1999) suggest that thermal cracking could be an important process in the fragmentation and splitting of kilometer-sized comets while in the inner solar system. Furthermore, Čapek and Vokrouhlický (2010) initially proposed that slowly rotating meteoroids or meteoroids with spin vectors pointing toward the Sun can be broken up by thermal cracking. In a further development of their model, Čapek and Vokrouhlický (2012) showed that as the meteoroid approaches the Sun, the stresses first exceed the material strength at the surface and create a fractured layer. If intermolecular forces (e.g., Rozitis et al., 2014) are able to retain the surface layer, despite the competing effects of thermal lifting and centrifugal forces, the particulate surface layer is able to thermally shield the core, preventing any further damage by thermal stresses.

## 7.2. Sun-Driven Heating of Near-Earth Asteroids and Meteoroids

It is known that heating processes can affect the physical properties of asteroids and their fragments, the meteorites (see, e.g., Keil, 2000). Internal heating due to the decay of short-lived radionuclides was considered early on (Grimm and McSween, 1993). Marchi et al. (2009) discuss close approaches to the Sun as an additional surface-altering heating mechanism. In the present NEA population, the fraction of bodies with relatively small perihelion ( $q$ ) is very small: About 1/2, 1/10, and 1/100 of the population of currently known NEOs (11,000 as of the time of this writing) have a perihelion distance below 1, 0.5, and 0.25 AU, where maximum temperatures exceed 400, 550, and 780 K, respectively (see Fig. 11). However, dynamical simulations show that a much larger fraction of asteroids had small perihelion distances for some time, hence experiencing episodes of strong heating in their past (Marchi et al., 2009). For instance, the asteroid 2004 LG was approaching the Sun to within only  $\sim$ 5.6 solar radii some 3 k.y. ago, and its surface was baked at temperatures of 2500 K (Vokrouhlický and Nesvorný, 2012).

Solar heating has a penetration depth of typically a few centimeters (see equation (5) and Spencer et al., 1989). Organic components found on meteorites break up at temperatures as low as 300–670 K (see Fig. 11 and Kebukawa et al., 2010; Frost et al., 2000; Huang et al., 1994), thus solar heating can remove these components from asteroid surfaces.

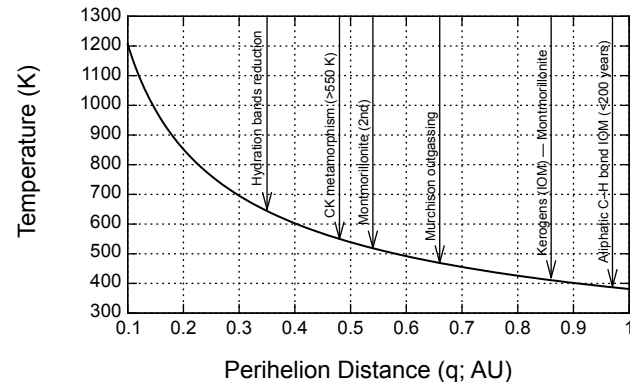


**Fig. 11.** Surface temperature of an asteroid or meteoroid as a function of the distance from the Sun. Vertical arrows indicate the threshold temperature for the thermal alteration/desiccation for a variety of chemical compounds discussed in the text (for additional information, see Delbo and Michel, 2011, and references therein). The temperature range for thermal metamorphism of the CK chondrites is from Chaumard et al. (2012).

## 7.3. Thermal Metamorphism of Meteorites

Radiative heating from the Sun has been invoked as a mechanism for the thermal metamorphism of meteoritic CK carbonaceous chondrites (Chaumard et al., 2012). The matrix of these chondrites shows textures consistent with a transient thermal event during which temperatures rose between 550 and 950 K. The inferred duration of these events is on the order of days to years, much longer than the timescale of shock events but shorter than the timescale for heating by the decay of radiogenic species such as  $^{26}\text{Al}$  (e.g., Kalleymen et al., 1991).

## 7.4. Subsurface Ice Sublimation

Observational evidence for the presence of ice on asteroid surfaces stems from the discovery of MBCs (Hsieh and Jewitt, 2006), the localized release of water vapor from the surface of (1) Ceres (Küppers et al., 2014), and the detection of spectroscopic signatures interpreted as water ice frost on the surfaces of (24) Themis (Rivkin and Emery, 2010; Campins et al., 2010) and (65) Cybele (Licandro et al., 2011).

The lifetime of ices on the surface and in the subsurface depends strongly on temperature. Thermophysical models have been used to estimate these temperatures. This requires a modification of the “classical” TPM as presented in section 4, such that heat conduction is coupled with gas diffusion (Schorghofer, 2008; Capria et al., 2012; Prialnik and Rosenberg, 2009). The referenced models assume a spherical shape. As for the interior structure, Capria et al. (2012) and Prialnik and Rosenberg (2009) assume a comet-like structure, i.e., an intimate mixture of ice and dust throughout the entire body, while Schorghofer (2008) consider an ice layer underneath a rocky regolith cover.

Sublimation of ice and the transport of water molecules through the fine-grained regolith is modeled in all cases.

All authors agree that water ice exposed on asteroid surfaces sublimates completely on timescales much shorter than the age of the solar system. Asteroid surfaces were therefore expected to be devoid of water ice, contrary to the observational evidence quoted above. However, water ice can be stable over 4.5 G.y. in the shallow subsurface, at a depth of ~1–10 m. In particular, *Fanale and Salvail* (1989) showed that ice could have survived in the subsurface at the polar regions of Ceres. Large heliocentric distances, slow rotation, and a fine-grained regolith leading to low thermal conductivity and short molecular free path all favor the stabilization of subsurface water ice (*Schorghofer*, 2008). The same authors conclude that rocky surfaces, in contrast to dusty surfaces, are rarely able to retain ice in the shallow subsurface.

To be observable on the surface, buried ice must be exposed. *Campins et al.* (2010) describe several plausible mechanisms such as impacts, recent change in the obliquity of the spin pole, and daily or orbital thermal pulses reaching a subsurface ice layer.

## 8. FUTURE CHALLENGES FOR THERMOPHYSICAL MODELS

The Spitzer and WISE telescopes have opened up a new era of asteroid thermal-infrared observations, and the exploitation of their data through TPMs has just begun (e.g., *Ali-Lagoa et al.*, 2014; *Rozitis et al.*, 2014; *Emery et al.*, 2014). At the moment, the limiting factor is the availability of accurate asteroid shape models. However, optical-wavelength all-sky surveys such as the Panoramic Survey Telescope and Rapid Response System (Pan-STARRS), Large Synoptic Survey Telescope (LSST), and Gaia are expected to produce enormous photometric datasets leading to thousands of asteroid models. We envision the availability of thousands of thermal-inertia values in some years from now, enabling more statistically robust studies of thermal inertia as a function of asteroid size, spectral class, albedo, rotation period, etc.

For instance, the distribution of  $\Gamma$  within asteroid families will be crucial in the search of evidence of asteroid differentiation: Asteroid formation models and meteorite studies suggest that hundreds of planetesimals experienced complete or partial differentiation. An asteroid family formed from the catastrophic disruption of such a differentiated asteroid should contain members corresponding to the crust, the mantle, and the iron core. However, the observed spectra and albedos are very homogeneous across asteroid families. Thermal inertia might help in separating iron-rich from iron-poor family members, supposedly originating respectively from the core and mantle of the differentiated parent body (e.g., *Matter et al.*, 2013; *Harris and Drube*, 2014).

At any size range, Fig. 9 shows an almost tenfold variability in thermal inertia, corresponding to differences in average regolith grain size of almost 2 orders of magnitude

(*Gundlach and Blum*, 2013). For small NEAs, this could be due to a combination of thermal cracking (*Delbo et al.*, 2014), regolith motion (see the chapter by Murdoch et al. in this volume), and cohesive forces (*Rozitis et al.*, 2014). Faster rotation periods allow more thermal cycles, which then enhances thermal fracturing. It also encourages regolith to move toward the equator where the gravitational potential is at its lowest (*Walsh et al.*, 2008). And for the extremely fast rotators, large boulders/rocks could be selectively lofted away, because they do not stick as well to the surface as smaller particles. For  $D > 100$ -km-sized asteroids,  $\Gamma$  values might be help to distinguish between primordial and more recently reaccumulated asteroids. The former had ~4 G.y. of regolith evolution, while the latter have a less-developed and therefore coarser regolith.

The high-precision thermal-infrared data of WISE and Spitzer pose new challenges to TPMs, as model uncertainties are now comparable to the uncertainty of the measured flux. This will become even more important with the launch of the James Webb Space Telescope (JWST). In particular, the accuracy of the shape models might represent a limiting factor (e.g., *Rozitis and Green*, 2014). The next challenge will be to allow TPMs to optimize the asteroid shape. This seems to be possible, as infrared photometry is also sensitive to shape, provided good-quality thermal data are available (see the chapter by Durech et al. in this volume).

New interferometric facilities, such as the Multi AperTure mid-Infrared SpectroScopic Experiment (MATISSE), Large Binocular Telescope Interferometer (LBTI), and Atacama Large Millimeter Array (ALMA), will become available in the next few years, requiring TPMs to calculate precise disk-resolved thermal fluxes (see chapter by Durech et al. in this volume). The wavelengths of ALMA, similar to those of MIRO, will allow measurement of thermal-infrared radiation from the subsoil of asteroids, thus providing further information about how thermal inertia varies with depth.

Certainly, constraining roughness is one of the future challenges for TPMs. To do so from disk-integrated data requires a range of wavelengths and solar phase angles. Low-phase-angle measurements are enhanced by beaming, while high-phase-angle measurements are reduced by beaming. In particular, shorter wavelengths are affected more than longer wavelengths.

Moreover, the future availability of precise sizes and cross sections of asteroids from stellar occultation timing (*Tanga and Delbo*, 2007), combined with shape information derived from lightcurve inversion (chapter by Durech et al. in this volume) will allow elimination of the necessity of constraining the object size from TPM analysis. Infrared fluxes will therefore be converted into highly reliable thermal inertia and roughness values.

**Acknowledgments.** We are grateful to S. Green and to an anonymous referee for their thorough reviews. M.D. thanks J. Hanus and the support from the French Agence National de la Recherche (ANR) SHOCKS.

## REFERENCES

- Alí-Lagoa V., Lionni L., Delbo M., et al. (2014) Thermophysical properties of near-Earth asteroid (341843) 2008 EV5 from WISE data. *Astron. Astrophys.*, 561, A45.
- Bandfield J. L., Ghent R. R., Vasavada A. R., et al. (2011) Lunar surface rock abundance and regolith fines temperatures derived from LRO Diviner Radiometer data. *J. Geophys. Res.*, 116, E00H02.
- Bottke W. F., Vokrouhlický D., Broz M., et al. (2001) Dynamical spreading of asteroid families by the Yarkovsky effect. *Science*, 294, 1693–1696.
- Bottke W. F., Durda D. D., Nesvorný D., et al. (2005) The fossilized size distribution of the main asteroid belt. *Icarus*, 175, 111–140.
- Bottke W. F. J., Vokrouhlický D., Rubincam D. P., et al. (2006) The Yarkovsky and YORP effects: Implications for asteroid dynamics. *Annu. Rev. Earth Planet. Sci.*, 34, 157–191.
- Breiter S., Bartczak P., Czekaj M., et al. (2009) The YORP effect on 25143 Itokawa. *Astron. Astrophys.*, 507, 1073–1081.
- Buhl D., Welch W. J., and Rea D. G. (1968a) Anomalous cooling of a cratered lunar surface. *J. Geophys. Res.*, 73, 7593–7608.
- Buhl D., Welch W. J., and Rea D. G. (1968b) Reradiation and thermal emission from illuminated craters on the lunar surface. *J. Geophys. Res.*, 73, 5281–5295.
- Camps H., Hargrove K., Pinilla-Alonso N., et al. (2010) Water ice and organics on the surface of the asteroid 24 Themis. *Nature*, 464, 1320–1321.
- Čapek D. and Vokrouhlický D. (2004) The YORP effect with finite thermal conductivity. *Icarus*, 172, 526–536.
- Čapek D. and Vokrouhlický D. (2010) Thermal stresses in small meteoroids. *Astron. Astrophys.*, 519, A75.
- Čapek D. and Vokrouhlický D. (2012) Thermal stresses in small meteoroids. II. Effects of an insulating surface layer. *Astron. Astrophys.*, 539, A25.
- Capria M. T., Marchi S., De Sanctis M. C., et al. (2012) The activity of main belt comets. *Astron. Astrophys.*, 537, A71.
- Capria M. T., Tosi F., De Sanctis M. C., et al. (2014) Vesta surface thermal properties map. *Geophys. Res. Lett.*, 41, 1438–1443.
- Carry B. (2012) Density of asteroids. *Planet. Space Sci.*, 73, 98–118.
- Carry B., Matter A., Scheirich P., et al. (2015) The small binary asteroid (939) Isberga. *Icarus*, 248, 516–525.
- Chamberlain M. A., Lovell A. J., and Sykes M. V. (2007) Submillimeter lightcurves of Vesta. *Icarus*, 192, 448–459.
- Chamberlain M. A., Lovell A. J., and Sykes M. V. (2009) Submillimeter photometry and lightcurves of Ceres and other large asteroids. *Icarus*, 202, 487–501.
- Chaumard N., Devouard B., Delbo M., et al. (2012) Radiative heating of carbonaceous near-Earth objects as a cause of thermal metamorphism for CK chondrites. *Icarus*, 220, 65–73.
- Chesley S. R., Ostro S. J., Vokrouhlický D., et al. (2003) Direct detection of the Yarkovsky effect by radar ranging to asteroid 6489 Golevka. *Science*, 302, 1739–1742.
- Chesley S. R., Farnocchia D., Nolan M. C., et al. (2014) Orbit and bulk density of the OSIRIS-REx target asteroid (101955) Bennu. *Icarus*, 235, 5–22.
- Consolmagno G. J., Macke R. J., Rochette P., et al. (2006) Density, magnetic susceptibility, and the characterization of ordinary chondrite falls and showers. *Meteoritics & Planet. Sci.*, 41, 331–342.
- Consolmagno G. J., Schaefer M. W., Schaefer B. E., et al. (2013) The measurement of meteorite heat capacity at low temperatures using liquid nitrogen vaporization. *Planet. Space Sci.*, 87, 146–156.
- Cruikshank D. P., Stansberry J. A., Emery J. P., et al. (2005) The high-albedo Kuiper belt object (55565) 2002 AW197. *Astrophys. J. Lett.*, 624, L53–L56.
- Davidsson B. J. R. and Rickman H. (2014) Surface roughness and three-dimensional heat conduction in thermophysical models. *Icarus*, 243, 58–77.
- Davidsson B. J. R., Gutiérrez P. J., Groussin O., et al. (2013) Thermal inertia and surface roughness of Comet 9P/Tempel 1. *Icarus*, 224, 154–171.
- Davidsson B., Rickman H., Bandfield J. L., et al. (2015) Interpretation of thermal emission. I. The effect of roughness for spatially resolved atmosphereless bodies. *Icarus*, 252, 1–21.
- Delbo M. (2004) The nature of near-Earth asteroids from the study of their thermal infrared emission. Ph.D. thesis, Free University of Berlin, Berlin, Germany. 210 pp.
- Delbo M. and Harris A. W. (2002) Physical properties of near-Earth asteroids from thermal infrared observations and thermal modeling. *Meteoritics & Planet. Sci.*, 37, 1929–1936.
- Delbo M. and Michel P. (2011) Temperature history and dynamical evolution of (101955) 1999 RQ36: A potential target for sample return from a primitive asteroid. *Astrophys. J. Lett.*, 728, L42.
- Delbo M. and Tanga P. (2009) Thermal inertia of main belt asteroids smaller than 100 km from IRAS data. *Planet. Space Sci.*, 57, 259–265.
- Delbo M., Harris A. W., Binzel R. P., et al. (2003) Keck observations of near-Earth asteroids in the thermal infrared. *Icarus*, 166, 116–130.
- Delbo M., dell’Oro A., Harris A. W., et al. (2007) Thermal inertia of near-Earth asteroids and implications for the magnitude of the Yarkovsky effect. *Icarus*, 190, 236–249.
- Delbo M., Ligori S., Matter A., et al. (2009) First VLTI-MIDI direct determinations of asteroid sizes. *Astrophys. J.*, 694, 1228–1236.
- Delbo M., Walsh K., Mueller M., et al. (2011) The cool surfaces of binary near-Earth asteroids. *Icarus*, 212, 138–148.
- Delbo M., Libourel G., Wilkerson J., et al. (2014) Thermal fatigue as the origin of regolith on small asteroids. *Nature*, 508, 233–236.
- De Sanctis M. C., Ammannito E., Capria M. T., et al. (2012) Spectroscopic characterization of mineralogy and its diversity across Vesta. *Science*, 336, 697–700.
- Dombard A. J., Barnouin O. S., Prockter L. M., et al. (2010) Boulders and ponds on the asteroid 433 Eros. *Icarus*, 210, 713–721.
- Duennbier F. and Sutton G. H. (1974) Thermal moonquakes. *J. Geophys. Res.*, 79, 4351–4363.
- Emery J. P., Sprague A. L., Witteborn F. C., et al. (1998) Mercury: Thermal modeling and mid-infrared (5–12 μm) observations. *Icarus*, 136, 104–123.
- Emery J. P., Fernández Y. R., Kelley M. S. P., et al. (2014) Thermal infrared observations and thermophysical characterization of OSIRIS-REx target asteroid (101955) Bennu. *Icarus*, 234, 17–35.
- Fanale F. P. and Salvail J. R. (1989) The water regime of asteroid (1) Ceres. *Icarus*, 82, 97–110.
- Fernández Y. R., Jewitt D. C., and Sheppard S. S. (2002) Thermal properties of Centaurs Asbolus and Chiron. *Astron. J.*, 123, 1050–1055.
- Fernández Y. R., Sheppard S. S., and Jewitt D. C. (2003) The albedo distribution of jovian Trojan asteroids. *Astron. J.*, 126, 1563–1574.
- Fornasier S., Lellouch E., Müller T., et al. (2013) TNOs are cool: A survey of the trans-neptunian region. VIII. Combined Herschel PACS and SPIRE observations of nine bright targets at 70–500 μm. *Astron. Astrophys.*, 555, A15.
- Fountain W. F., Fountain J. A., Jones B. P., et al. (1976) Observational and theoretical temperatures for a total lunar eclipse. *Moon*, 15, 421–437.
- Fowler J. W. and Chillemi J. R. (1992) IRAS asteroid data processing. In *The IRAS Minor Planet Survey* (E. F. Tedesco, ed.), pp. 17–43. Tech. Rep. PL-TR-92-2049, Phillips Laboratory, Hanscom Air Force Base, Massachusetts.
- Frost R. L., Ruan H., Kloprogge J. T., et al. (2000) Dehydration and dehydroxylation of nontronites and ferruginous smectite. *Thermochim. Acta*, 346, 63–72.
- Giese B. and Kuehrt E. (1990) Theoretical interpretation of infrared measurements at Deimos in the framework of crater radiation. *Icarus*, 88, 372–379.
- Golubov O. and Krugly Y. N. (2012) Tangential component of the YORP effect. *Astrophys. J. Lett.*, 752, L11.
- Grimm R. E. and McSween H. Y. (1993) Heliocentric zoning of the asteroid belt by aluminum-26 heating. *Science*, 259, 653–655.
- Groussin O., Lamy P., and Jorda L. (2004) Properties of the nuclei of Centaurs Chiron and Chariklo. *Astron. Astrophys.*, 413, 1163–1175.
- Groussin O., Lamy P., Fornasier S., et al. (2011) The properties of asteroid (2867) Steins from Spitzer Space Telescope observations and OSIRIS shape reconstruction. *Astron. Astrophys.*, 529, A73.
- Groussin O., Sunshine J. M., Feaga L. M., et al. (2013) The temperature, thermal inertia, roughness and color of the nuclei of Comets 103P/Hartley 2 and 9P/Tempel 1. *Icarus*, 222, 580–594.
- Gulkis S., Frerking M., Crovisier J., et al. (2007) MIRO: Microwave Instrument for Rosetta Orbiter. *Space Sci. Rev.*, 128, 561–597.

- Gundlach B. and Blum J. (2012) Outgassing of icy bodies in the solar system — II: Heat transport in dry, porous surface dust layers. *Icarus*, 219, 618–629.
- Gundlach B. and Blum J. (2013) A new method to determine the grain size of planetary regolith. *Icarus*, 223, 479–492.
- Hall K. (1999) The role of thermal stress fatigue in the breakdown of rock in cold regions. *Geomorphology*, 31, 47–63.
- Hall K. and André M.-F. (2001) New insights into rock weathering from high-frequency rock temperature data: An Antarctic study of weathering by thermal stress. *Geomorphology*, 41, 23–35.
- Hanuš J., Durech J., Brož M., et al. (2011) A study of asteroid pole-latitude distribution based on an extended set of shape models derived by the lightcurve inversion method. *Astron. Astrophys.*, 530, 134.
- Hanuš J., Brož M., Durech J., et al. (2013) An anisotropic distribution of spin vectors in asteroid families. *Astron. Astrophys.*, 559, A134.
- Hapke B. (1984) Bidirectional reflectance spectroscopy. III — Correction for macroscopic roughness. *Icarus*, 59, 41–59.
- Hapke B. (1996) A model of radiative and conductive energy transfer in planetary regoliths. *J. Geophys. Res.*, 101, 16817–16832.
- Harris A. W. (1998) A thermal model for near-Earth asteroids. *Icarus*, 131, 291–301.
- Harris A. W. (2006) The surface properties of small asteroids from thermal-infrared observations. In *Asteroids, Comets, Meteors* (D. Lazzaro et al., eds.), pp. 449–463. IAU Symp. 229, Cambridge Univ., Cambridge.
- Harris A. W. and Davies J. K. (1999) Physical characteristics of near-Earth asteroids from thermal infrared spectrophotometry. *Icarus*, 142, 464–475.
- Harris A. W. and Drube L. (2014) How to find metal-rich asteroids. *Astrophys. J. Lett.*, 785, L4.
- Harris A. W. and Lagerros J. S. V. (2002) Asteroids in the thermal infrared. In *Asteroids III* (W. F. Bottke Jr. et al., eds.), pp. 205–218. Univ. of Arizona, Tucson.
- Harris A. W., Mueller M., Delbo M., et al. (2005) The surface properties of small asteroids: Peculiar Betulia — A case study. *Icarus*, 179, 95–108.
- Hoerz F., Schneider E., Gault D. E., et al. (1975) Catastrophic rupture of lunar rocks — A Monte Carlo simulation. *Moon*, 13, 235–258.
- Holsapple K. A. (2010) On YORP-induced spin deformations of asteroids. *Icarus*, 205, 430–442.
- Horner J., Müller T. G., and Lykawka P. S. (2012) (1173) Anchises — thermophysical and dynamical studies of a dynamically unstable jovian Trojan. *Mon. Not. R. Astron. Soc.*, 423, 2587–2596.
- Hörz F. and Cintala M. (1997) Impact experiments related to the evolution of planetary regoliths. *Meteoritics & Planet. Sci.*, 32, 179–209.
- Hsieh H. H. and Jewitt D. (2006) A population of comets in the main asteroid belt. *Science*, 312, 561–563.
- Huang W. L., Bassett W. A., and Wu T. C. (1994) Dehydration and hydration of montmorillonite at elevated temperatures and pressures monitored using synchrotron radiation. *Am. Mineral.*, 79, 683–691.
- Huebner W. F., Benkhoff J., Capria M. T., et al., eds. (2006) *Heat and Gas Diffusion in Comet Nuclei*. ISSI Scientific Report SR-004, Vol. 4, International Space Science Institute.
- Jacobson S. A. and Scheeres D. J. (2011) Dynamics of rotationally fissioned asteroids: Source of observed small asteroid systems. *Icarus*, 214, 161–178.
- Jakosky B. M., Finiol G. W., and Henderson B. G. (1990) Directional variations in thermal emission from geologic surfaces. *Geophys. Res. Lett.*, 17, 985–988.
- Jewitt D. and Li J. (2010) Activity in geminid parent (3200) Phaethon. *Astron. J.*, 140, 1519–1527.
- Kalleymen G.W., Rubin A. E., and Wasson J. T. (1991) The compositional classification of chondrites. V — The Karoonda (CK) group of carbonaceous chondrites. *Geochim. Cosmochim. Acta*, 55, 881–892.
- Kebukawa Y., Nakashima S., and Zolensky M. E. (2010) Kinetics of organic matter degradation in the Murchison meteorite for the evaluation of parent-body temperature history. *Meteoritics & Planet. Sci.*, 45, 99–113.
- Keihm S. J. (1984) Interpretation of the lunar microwave brightness temperature spectrum — Feasibility of orbital heat flow mapping. *Icarus*, 60, 568–589.
- Keihm S., Tosi F., Kamp L., et al. (2012) Interpretation of combined infrared, submillimeter, and millimeter thermal flux data obtained during the Rosetta fly-by of asteroid (21) Lutetia. *Icarus*, 221, 395–404.
- Keihm S., Kamp L., Gulkis S., et al. (2013) Reconciling main belt asteroid spectral flux density measurements with a self-consistent thermophysical model. *Icarus*, 226, 1086–1102.
- Keil K. (2000) Thermal alteration of asteroids: Evidence from meteorites. *Planet. Space Sci.*, 48, 887–903.
- Kieffer H. H., Martin T. Z., Peterfreund A. R., et al. (1977) Thermal and albedo mapping of Mars during the Viking primary mission. *J. Geophys. Res.*, 82, 4249–4291.
- Küppers M., O'Rourke L., Bockelée-Morvan D., et al. (2014) Localized sources of water vapour on the dwarf planet (1) Ceres. *Nature*, 505, 525–527.
- Lagerros J. S. V. (1996a) Thermal physics of asteroids. I. Effects of shape, heat conduction and beaming. *Astron. Astrophys.*, 310, 1011–1020.
- Lagerros J. S. V. (1996b) Thermal physics of asteroids. II. Polarization of the thermal microwave emission from asteroids. *Astron. Astrophys.*, 315, 625–632.
- Lagerros J. S. V. (1997) Thermal physics of asteroids. III. Irregular shapes and albedo variegations. *Astron. Astrophys.*, 325, 1226–1236.
- Lagerros J. S. V. (1998) Thermal physics of asteroids. IV. Thermal infrared beaming. *Astron. Astrophys.*, 332, 1123–1132.
- Lamy P. L., Jorda L., Fornasier S., et al. (2008) Asteroid 2867 Steins. III. Spitzer Space Telescope observations, size determination, and thermal properties. *Astron. Astrophys.*, 487, 1187–1193.
- Langeseth M. G. and Keihm S. J. (1977) *Lunar Heat-Flow Experiment*, pp. 1–289. NASA Tech. Rept. NASA-CR-151619, CU-4-77. U.S. Govt. Printing Office, Washington, DC.
- Lauretta D. S., Barucci M. A., Bierhaus E. B., et al. (2012) The OSIRIS-REx mission — Sample acquisition strategy and evidence for the nature of regolith on asteroid (101955) 1999 RQ36. In *Asteroids, Comets, Meteors* (D. Lazzaro et al., eds.), p. 1667. IAU Symp. 229, Cambridge Univ., Cambridge.
- Lawson S. L. S. L., Rodger A. P. A. P., Bender S. C. S. C., et al. (2003) Multispectral thermal imager observations of the Moon during total eclipse. In *Lunar Planet. Sci. XXXIV*, Abstract #1761. Lunar and Planetary Institute, Houston.
- Lebofsky L. A. and Rieke G. H. (1979) Thermal properties of 433 Eros. *Icarus*, 40, 297–308.
- Lebofsky L. A. and Spencer J. R. (1989) Radiometry and a thermal modeling of asteroids. In *Asteroids II* (R. P. Binzel et al., eds.), pp. 128–147. Univ. of Arizona, Tucson.
- Lebofsky L. A., Sykes M. V., Tedesco E. F., et al. (1986) A refined “standard” thermal model for asteroids based on observations of 1 Ceres and 2 Pallas. *Icarus*, 68, 239–251.
- Lellouch E., Santos-Sanz P., Lacerda P., et al. (2013) TNOs are cool: A survey of the trans-neptunian region. IX. Thermal properties of Kuiper belt objects and Centaurs from combined Herschel and Spitzer observations. *Astron. Astrophys.*, 557, 60.
- Levi F. A. (1973) Thermal fatigue: A possible source of structural modifications in meteorites. *Meteoritics & Planet. Sci.*, 8, 209–221.
- Leyrat C., Coradini A., Erard S., et al. (2011) Thermal properties of the asteroid (2867) Steins as observed by VIRTIS/Rosetta. *Astron. Astrophys.*, 531, A168.
- Leyrat C., Barucci A., Mueller T., et al. (2012) Thermal properties of (4) Vesta derived from Herschel measurements. *Astron. Astrophys.*, 539, A154.
- Licandro J., Campins H., Kelley M., et al. (2011) (65) Cybele: Detection of small silicate grains, water-ice, and organics. *Astron. Astrophys.*, 525, A34.
- Lim L. F., Emery J. P., and Moskovitz N. A. (2011) Mineralogy and thermal properties of V-type asteroid 956 Elisa: Evidence for diogenitic material from the Spitzer IRS (5–35  $\mu\text{m}$ ) spectrum. *Icarus*, 213, 510–523.
- Lowry S. C., Weissman P. R., Duddy S. R., et al. (2014) The internal structure of asteroid (25143) Itokawa as revealed by detection of YORP spin-up. *Astron. Astrophys.*, 562, A48.
- Lucey P. G. (2000) Observations of the Moon using the Air Force Maui Space Surveillance Complex. In *Imaging Technology and Telescopes* (J. B. Breckenridge et al., eds.), pp. 216–224. SPIE Conf. Ser. 4091, Bellingham, Washington.
- Lucey P. G. (2006) Radiative transfer modeling of the effect of mineralogy on some empirical methods for estimating iron concentration from multispectral imaging of the Moon. *J. Geophys. Res.*, 111, 8003.
- Macke R. J., Consolmagno G. J., Britt D. T., et al. (2010) Enstatite chondrite density, magnetic susceptibility, and porosity. *Meteoritics & Planet. Sci.*, 45, 1513–1526.

- Macke R. J., Britt D. T., and Consolmagno G. J. (2011a) Density, porosity, and magnetic susceptibility of achondritic meteorites. *Meteoritics & Planet. Sci.*, *46*, 311–326.
- Macke R. J., Consolmagno G. J., and Britt D. T. (2011b) Density, porosity, and magnetic susceptibility of carbonaceous chondrites. *Meteoritics & Planet. Sci.*, *46*, 1842–1862.
- Magri C., Consolmagno G. J., Ostro S. J., et al. (2001) Radar constraints on asteroid regolith compositions using 433 Eros as ground truth. *Meteoritics & Planet. Sci.*, *36*, 1697–1709.
- Marchi S., Paolicchi P., Lazzarin M., et al. (2006) A general spectral slope-exposure relation for S-type main belt and near-Earth asteroids. *Astron. J.*, *131*, 1138–1141.
- Marchi S., Delbo M., Morbidelli A., et al. (2009) Heating of near-Earth objects and meteoroids due to close approaches to the Sun. *Mon. Not. R. Astron. Soc.*, *400*, 147–153.
- Marchis F., Enriquez J. E., Emery J. P., et al. (2012) Multiple asteroid systems: Dimensions and thermal properties from Spitzer Space Telescope and ground-based observations. *Icarus*, *221*, 1130–1161.
- Matter A., Delbo M., Ligori S., et al. (2011) Determination of physical properties of the asteroid (41) Daphne from interferometric observations in the thermal infrared. *Icarus*, *215*, 47–56.
- Matter A., Delbo M., Carry B., et al. (2013) Evidence of a metalrich surface for the asteroid (16) Psyche from interferometric observations in the thermal infrared. *Icarus*, *226*, 419–427.
- McSween H. Y. Jr., Ghosh A., Grimm R. E., et al. (2002) Thermal evolution models of asteroids. In *Asteroids III* (W. F. Bottke Jr. et al., eds.), pp. 559–571. Univ. of Arizona, Tucson.
- Mellon M. T., Jakosky B. M., Kieffer H. H., et al. (2000) High-resolution thermal inertia mapping from the Mars Global Surveyor Thermal Emission Spectrometer. *Icarus*, *148*, 437–455.
- Molaro J. and Byrne S. (2012) Rates of temperature change of airless landscapes and implications for thermal stress weathering. *J. Geophys. Res.*, *117*, 10011.
- Mommert M., Farnocchia D., Hora J. L., et al. (2014a) Physical properties of near-Earth asteroid 2011 MD. *Astrophys. J. Lett.*, *789*, L22.
- Mommert M., Hora J. L., Farnocchia D., et al. (2014b) Constraining the physical properties of near-Earth object 2009 BD. *Astrophys. J.*, *786*, 148.
- Morrison D. and Cruikshank D. P. (1973) Thermal properties of the Galilean satellites. *Icarus*, *18*, 224–236.
- Mueller M. (2007) Surface properties of asteroids from mid-infrared observations and thermophysical modeling. Ph.D. thesis, Freie Universitaet, Berlin, arXiv:1208.3993.
- Mueller M., Harris A. W., Bus S. J., et al. (2006) The size and albedo of Rosetta fly-by target 21 Lutetia from new IRTF measurements and thermal modeling. *Astron. Astrophys.*, *447*, 1153–1158.
- Mueller M., Marchis F., Emery J. P., et al. (2010) Eclipsing binary Trojan asteroid Patroclus: Thermal inertia from Spitzer observations. *Icarus*, *205*, 505–515.
- Müller T. G. (2002) Thermophysical analysis of infrared observations of asteroids. *Meteoritics & Planet. Sci.*, *37*, 1919–1928.
- Müller T. G. and Barnes P. J. (2007) 3.2 mm lightcurve observations of (4) Vesta and (9) Metis with the Australia Telescope Compact Array. *Astron. Astrophys.*, *467*, 737–747.
- Müller T. G. and Lagerros J. S. V. (1998) Asteroids as far-infrared photometric standards for ISOPHOT. *Astron. Astrophys.*, *338*, 340–352.
- Müller T. G. and Lagerros J. S. V. (2002) Asteroids as calibration standards in the thermal infrared for space observatories. *Astron. Astrophys.*, *381*, 324–339.
- Müller T. G., Sterzik M. F., Schütz O., et al. (2004) Thermal infrared observations of near-Earth asteroid 2002 NY40. *Astron. Astrophys.*, *424*, 1075–1080.
- Müller T. G., Durech J., Hasegawa S., et al. (2011) Thermophysical properties of 162173 (1999 JU3), a potential flyby and rendezvous target for interplanetary missions. *Astron. Astrophys.*, *525*, 145.
- Müller T. G., O'Rourke L., Barucci A. M., et al. (2012) Physical properties of OSIRIS-REx target asteroid (101955) 1999 RQ36. Derived from Herschel, VLT/ VISIR, and Spitzer observations. *Astron. Astrophys.*, *548*, A36.
- Müller T. G., Miyata T., Kiss C., et al. (2013) Physical properties of asteroid 308635 (2005 YU55) derived from multiinstrument infrared observations during a very close Earth approach. *Astron. Astrophys.*, *558*, A97.
- Müller T. G., Hasegawa S., and Usui F. (2014a) (25143) Itokawa: The power of radiometric techniques for the interpretation of remote thermal observations in the light of the Hayabusa rendezvous results. *Publ. Astron. Soc. Japan*, *66*, 52.
- Müller T. G., Kiss C., Scheirich P., et al. (2014b) Thermal infrared observations of asteroid (99942) Apophis with Herschel. *Astron. Astrophys.*, *566*, A22.
- Okada T., Fukuhara T., Tanaka S., et al. (2013) Thermal-Infrared Imager (TIR) on Hayabusa 2: Science and instrumentation. In *Lunar Planet. Sci. XLIV*, Abstract #1954. Lunar and Planetary Institute, Houston.
- Opeil C. P., Consolmagno G. J., and Britt D. T. (2010) The thermal conductivity of meteorites: New measurements and analysis. *Icarus*, *208*, 449–454.
- Opeil C. P., Consolmagno G. J., Safarik D. J., et al. (2012) Stony meteorite thermal properties and their relationship with meteorite chemical and physical states. *Meteoritics & Planet. Sci.*, *47*, 319–329.
- O'Rourke L., Müller T., Valtchanov I., et al. (2012) Thermal and shape properties of asteroid (21) Lutetia from Herschel observations around the Rosetta flyby. *Planet. Space Sci.*, *66*, 192–199.
- Paige D. A., Foote M. C., Greenhagen B. T., et al. (2010) The Lunar Reconnaissance Orbiter Diviner Lunar Radiometer Experiment. *Space Sci. Rev.*, *150*, 125–160.
- Pál A., Kiss C., Müller T. G., et al. (2012) TNOs are cool: A survey of the trans-Neptunian region. VII. Size and surface characteristics of (90377) Sedna and 2010 EK139. *Astron. Astrophys.*, *541*, L6.
- Pettit E. (1940) Radiation measurements on the eclipsed Moon. *Astrophys. J.*, *91*, 408–421.
- Pettit E. and Nicholson S. B. (1930) Lunar radiation and temperatures. *Astrophys. J.*, *71*, 102–135.
- Piqueux S. and Christensen P. R. (2009a) A model of thermal conductivity for planetary soils: 1. Theory for unconsolidated soils. *J. Geophys. Res.*, *114*, 9005.
- Piqueux S. and Christensen P. R. (2009b) A model of thermal conductivity for planetary soils: 2. Theory for cemented soils. *J. Geophys. Res.*, *114*, 9006.
- Piqueux S. and Christensen P. R. (2011) Temperature-dependent thermal inertia of homogeneous martian regolith. *J. Geophys. Res.*, *116*, 7004.
- Pravec P., Scheirich P., Kusnirak P., et al. (2006) Photometric survey of binary near-Earth asteroids. *Icarus*, *181*, 63–93.
- Presley M. A. and Christensen P. R. (1997a) Thermal conductivity measurements of particulate materials 1. A review. *J. Geophys. Res.*, *102*, 6535–6550.
- Presley M. A. and Christensen P. R. (1997b) Thermal conductivity measurements of particulate materials 2. Results. *J. Geophys. Res.*, *102*, 6551–6566.
- Prialnik D. and Rosenberg E. D. (2009) Can ice survive in main-belt comets? Long-term evolution models of Comet 133P/Elst-Pizarro. *Mon. Not. R. Astron. Soc.*, *399*, L79–L83.
- Putzig N. E. and Mellon M. T. (2007) Apparent thermal inertia and the surface heterogeneity of Mars. *Icarus*, *191*, 68–94.
- Raymond C. A., Jaumann R., Nathues A., et al. (2011) The Dawn topography investigation. *Space Sci. Rev.*, *163*, 487–510.
- Redman R. O., Feldman P. A., Matthews H. E., et al. (1992) Millimeter and submillimeter observations of the asteroid 4 Vesta. *Astron. J.*, *104*, 405–411.
- Rivkin A. S. and Emery J. P. (2010) Detection of ice and organics on an asteroidal surface. *Nature*, *464*, 1322–1323.
- Rozitis B. and Green S. F. (2011) Directional characteristics of thermal-infrared beaming from atmosphereless planetary surfaces — a new thermophysical model. *Mon. Not. R. Astron. Soc.*, *415*, 2042–2062.
- Rozitis B. and Green S. F. (2012) The influence of rough surface thermal-infrared beaming on the Yarkovsky and YORP effects. *Mon. Not. R. Astron. Soc.*, *423*, 367–388.
- Rozitis B. and Green S. F. (2013) The influence of global self heating on the Yarkovsky and YORP effects. *Mon. Not. R. Astron. Soc.*, *433*, 603–621.
- Rozitis B. and Green S. F. (2014) Physical characterization of near-Earth asteroid (1620) Geographos. Reconciling radar and thermal-infrared observations. *Astron. Astrophys.*, *568*, A43.
- Rozitis B., Duddy S. R., Green S. F., et al. (2013) A thermophysical analysis of the (1862) Apollo Yarkovsky and YORP effects. *Astron. Astrophys.*, *555*, A20.
- Rozitis B., MacLennan E., and Emery J. P. (2014) Cohesive forces prevent the rotational breakup of rubble-pile asteroid (29075) 1950 DA. *Nature*, *512*, 174–176.
- Russell C. T., Raymond C. A., Coradini A., et al. (2012) Dawn at Vesta: Testing the protoplanetary paradigm. *Science*, *336*, 684–686.

- Scheeres D. J. (2007) Rotational fission of contact binary asteroids. *Icarus*, 189, 370–385.
- Scheeres D. J. and Gaskell R. W. (2008) Effect of density inhomogeneity on YORP: The case of Itokawa. *Icarus*, 198, 125–129.
- Schorghofer N. (2008) The lifetime of ice on main belt asteroids. *Astrophys. J.*, 682, 697–705.
- Sexl R. U., Sexl H., Stremnitzer H., et al. (1971) The directional characteristics of lunar infrared radiation. *Moon*, 3, 189–213.
- Shorthill R. W. (1973) Infrared atlas charts of the eclipsed Moon. *Moon*, 7, 22–45.
- Sierks H., Lamy P., Barbieri C., et al. (2011) Images of asteroid 21 Lutetia: A remnant planetesimal from the early solar system. *Science*, 334, 487–490.
- Smith B. G. (1967) Lunar surface roughness: Shadowing and thermal emission. *J. Geophys. Res.*, 72, 4059–4067.
- Spencer J. R. (1990) A rough-surface thermophysical model for airless planets. *Icarus*, 83, 27–38.
- Spencer J. R., Lebofsky L. A., and Sykes M. V. (1989) Systematic biases in radiometric diameter determinations. *Icarus*, 78, 337–354.
- Statler T. S. (2009) Extreme sensitivity of the YORP effect to small-scale topography. *Icarus*, 202, 502–513.
- Tambovtseva L. V. and Shestakova L. I. (1999) Cometary splitting due to thermal stresses. *Planet. Space Sci.*, 47, 319–326.
- Tanga P. and Delbo M. (2007) Asteroid occultations today and tomorrow: Toward the Gaia era. *Astron. Astrophys.*, 474, 1015–1022.
- Thomas P. C., Joseph J., Carcich B., et al. (2002) Eros: Shape, topography, and slope processes. *Icarus*, 155, 18–37.
- Tosi F., Capria M. T., De Sanctis M. C., et al. (2014) Thermal measurements of dark and bright surface features on Vesta as derived from Dawn/VIR. *Icarus*, 240, 36–57.
- Urquhart M. L. and Jakosky B. M. (1997) Lunar thermal emission and remote determination of surface properties. *J. Geophys. Res.*, 102, 10959–10970.
- Vaniman D., Reddy R., Heiken G., et al. (1991) The lunar environment. In *Lunar Sourcebook* (G. H. Heiken et al., eds.), pp. 27–60. Cambridge Univ., Cambridge.
- Vasavada A. R., Paige D. A., and Wood S. E. (1999) Near-surface temperatures on Mercury and the Moon and the stability of polar ice deposits. *Icarus*, 141, 179–193.
- Vasavada A. R., Bandfield J. L., Greenhagen B. T., et al. (2012) Lunar equatorial surface temperatures and regolith properties from the Diviner Lunar Radiometer Experiment. *J. Geophys. Res.–Planets*, 117, DOI: 10.1029/2011JE003987.
- Vernazza P., Delbo M., King P. L., et al. (2012) High surface porosity as the origin of emissivity features in asteroid spectra. *Icarus*, 221, 1162–1172.
- Everka J., Farquhar B., Robinson M., et al. (2001) The landing of the NEAR-Shoemaker spacecraft on asteroid 433 Eros. *Nature*, 413, 390–393.
- Vilenius E., Kiss C., Mommert M., et al. (2012) TNOs are cool: A survey of the trans-neptunian region. VI. Herschel/PACS observations and thermal modeling of 19 classical Kuiper belt objects. *Astron. Astrophys.*, 541, A94.
- Viles H., Ehlmann B., Wilson C. F., et al. (2010) Simulating weathering of basalt on Mars and Earth by thermal cycling. *Geophys. Res. Lett.*, 37, 18201.
- Vincent J.-B., Besse S., Marchi S., et al. (2012) Physical properties of craters on asteroid (21) Lutetia. *Planet. Space Sci.*, 66, 79–86.
- Vokrouhlický D. and Nesvorný D. (2012) Sun-grazing orbit of the unusual near-Earth object 2004 LG. *Astron. Astrophys.*, 541, A109.
- Vokrouhlický D., Nesvorný D., and Bottke W. F. (2003) The vector alignments of asteroid spins by thermal torques. *Nature*, 425, 147–151.
- Walsh K. J., Richardson D. C., and Michel P. (2008) Rotational breakup as the origin of small binary asteroids. *Nature*, 454, 188–191.
- Wesselink A. J. (1948) Heat conductivity and nature of the lunar surface material. *Bull. Astron. Inst. Netherlands*, 10, 351–363.
- Winter D. F. and Krupp J. A. (1971) Directional characteristics of infrared emission from the Moon. *Moon*, 2, 279–292.
- Wolters S. D. and Green S. F. (2009) Investigation of systematic bias in radiometric diameter determination of near-Earth asteroids: The night emission simulated thermal model (NESTM). *Mon. Not. R. Astron. Soc.*, 400, 204–218.
- Wolters S. D., Rozitis B., Duddy S. R., et al. (2011) Physical characterization of low delta-V asteroid (175706) 1996 FG3. *Mon. Not. R. Astron. Soc.*, 418, 1246–1257.
- Yano H., Kubota T., Miyamoto H., et al. (2006) Touchdown of the Hayabusa spacecraft at the Muses Sea on Itokawa. *Science*, 312, 1350–1353.

# Asteroid Photometry

Jian-Yang Li

*Planetary Science Institute*

Paul Helfenstein

*Cornell University*

Bonnie J. Buratti

*California Institute of Technology, Jet Propulsion Laboratory*

Driss Takir

*Astrogeology Science Center, U.S. Geological Survey*

Beth Ellen Clark

*Ithaca College*

---

Asteroid photometry has three major applications: providing clues about asteroid surface physical properties and compositions, facilitating photometric corrections, and helping design and plan groundbased and spacecraft observations. The most significant advances in asteroid photometry in the past decade were driven by spacecraft observations that collected spatially resolved imaging and spectroscopy data. In the meantime, laboratory measurements and theoretical developments are revealing controversies regarding the physical interpretations of models and model parameter values. We will review the new developments in asteroid photometry that have occurred over the past decade in the three complementary areas of observations, laboratory work, and theory. Finally, we will summarize and discuss the implications of recent findings.

## 1. INTRODUCTION

### 1.1. Importance of Planetary Photometry

Planetary photometry concerns how the brightness of a planetary surface depends on the illumination and observing geometry. Figure 1 shows the scattering geometry and definition of terms that will be important for the rest of this chapter. The angle between the light source and local surface normal is incidence angle,  $i$ ; the angle between the observer and the local surface normal is emission angle,  $e$ ; and the angle between light source and observer, as seen from the object, is phase angle,  $\alpha$ . The dependence of the brightness of the surface on ( $i, e, \alpha$ ) is determined by the optical and mechanical properties of the surface.

Why is asteroid photometry important? We broadly divide the applications of planetary photometry, especially with spatially resolved data, into three major aspects.

First, it provides clues about the physical properties and compositions of asteroidal surfaces. How the reflectance of a particulate surface responds to the illumination and viewing geometry is fully determined by the optical and mechani-

cal properties of a surface, such as particle size, porosity, roughness, complex refractive index, etc. The ultimate goal of photometric modeling is to derive these fundamental properties of a surface by measuring the reflectance under various light-scattering geometries. Despite the development of various theoretical models, empirical or semiphysical, over the past several decades, we are still far from being able to determine all surface physical conditions from photometric observations and modeling of asteroids. The major reason is that real asteroidal surfaces have complex physical conditions that are difficult to fully parameterize. We still do not fully understand the light-scattering effects of some physical conditions, such as roughness, porosity, etc. Therefore it is nearly impossible to find exact, unique solutions of radiative transfer equations that describe real asteroidal surfaces. Some assumptions and approximations have to be made in order to derive practical analytical models, such as the Hapke model (Hapke, 1981, 1984, 1986, 2002, 2008, 2012a), the Shkuratov model (Shkuratov et al., 1999), etc. Observationally, due to the limited observing geometries available for groundbased and spacecraft observations of any asteroid, it is often difficult to fully constrain a photometric model for a particular object.

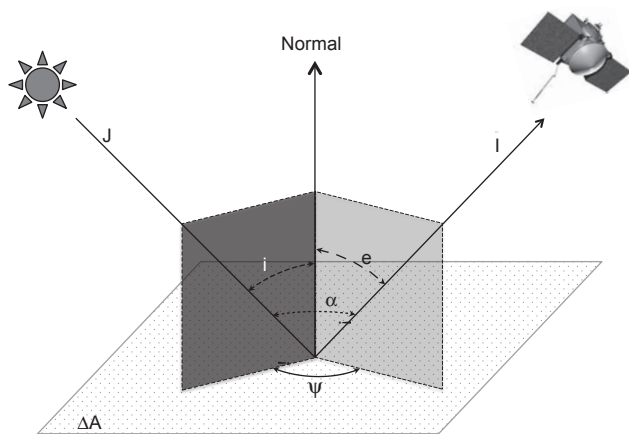


**Fig. 1.** Schematic diagram of bidirectional reflectance from a surface element  $\Delta A$ , showing the various angles. The plane containing  $J$  and  $I$  is the scattering plane. If the scattering plane also contains  $N$ , it is called the principal plane.  $\psi$  is the azimuthal angle between the planes of incidence and emission [ $\cos(\alpha) = \cos(i)\cos(e) + \sin(i)\sin(e)\cos(\psi)$ ].

Second, because the spectral reflectance of a surface depends on illumination and viewing geometry, it is necessary to correct observations (imaging or spectral) to a common (reference) geometry in order to make comparisons between different areas on an asteroid, between different asteroid surfaces, and with laboratory measurements. Photometric modeling provides such a means for this purpose. For example, phase reddening is a common phenomenon, first reported by Gehrels *et al.* (1964) and recognized on many asteroids for a long time (e.g., Clark *et al.*, 2002, and references therein; Reddy *et al.*, 2012a; Li *et al.*, 2013a) (see also section 4.1.2), that causes the spectrum of a surface to have redder slopes and stronger spectral absorptions at higher phase angles. One has to correct for this in order to make meaningful mineralogical interpretations of reflectance spectra. Other examples include mosaicking albedo and color maps of the whole surface of an asteroid from spacecraft data taken at vastly different illumination geometries (e.g., Li *et al.*, 2013a). In addition, photometric correction makes it possible to compare asteroid observations with laboratory measurements, which are usually made at a standard geometry. The general procedure of photometric correction is to fit a photometric model,  $r_{\text{model}}(i, e, \alpha)$ , to the observations,  $r(i, e, \alpha)$ , then follow equation (1) below to calculate the corrected reflectance under a reference geometry  $r(i_0, e_0, \alpha_0)$

$$r(i_0, e_0, \alpha_0) = \frac{r(i_{\text{measure}}, e_{\text{measure}}, \alpha_{\text{measure}})}{r_{\text{model}}(i_{\text{measure}}, e_{\text{measure}}, \alpha_{\text{measure}})} \times r_{\text{model}}(i_0, e_0, \alpha_0) \quad (1)$$

where  $(i_{\text{measure}}, e_{\text{measure}}, \alpha_{\text{measure}})$  is the scattering geometry of measured reflectance. The most commonly used reference

geometries for correction are  $(i_0, e_0, \alpha_0) = (0^\circ, 0^\circ, 0^\circ)$ , which corresponds to the normal reflectance, and  $(i_0, e_0, \alpha_0) = (30^\circ, 0^\circ, 30^\circ)$ , which is a common laboratory setting.

The third application of photometry (that we consider) is to predict the reflectance of an asteroidal surface at arbitrary illumination and viewing geometries for designing and planning observations, especially for asteroid spacecraft exploration missions. Spacecraft generally observe target asteroids at substantially different viewing geometries from groundbased observers. It is therefore necessary to extrapolate or interpolate the photometric measurements from the ground to calculate the nominal brightness of a target for planning purposes. For spatially resolved images, it is necessary to know the dependence of reflectance on local scattering geometry. This practical application is important for essentially all spacecraft missions with imaging or spectroscopy components.

## 1.2. Scope of This Chapter

Except for several of the largest asteroids, most asteroids appear to be point sources when observed from the ground, and the dependence of reflectance on local scattering geometry is unavailable. Therefore, up until the first asteroid flyby of (951) Gaspra by the Galileo spacecraft *en route* to the Jupiter system in 1991 (Belton *et al.*, 1992), asteroid photometry focused only on studying the dependence of total brightness of an object on solar phase angle, the so-called phase function (Fig. 2). In order to retrieve physical properties of the surface from photometric phase functions, empirical and experimental models have been developed (cf. Muinonen *et al.*, 2002, and references therein). For example, it has long been recognized that the brightness of dark objects generally decreases with phase angle faster than bright objects, resulting in relatively steeper slopes of their phase functions, a phenomenon attributed to relatively stronger multiple scattering in brighter objects (cf. Bowell and Lumme, 1979, and references therein). In addition, higher surface roughness also contributes to the steeper slope of a phase function (e.g., Veverka, 1971), although it is not possible to entirely disentangle the effects of multiple scattering and surface roughness from a disk-integrated phase function.

The most significant development in observational studies of the photometric properties of asteroids over the past decade has come from the availability of high-resolution, spatially resolved images of the surfaces of many more asteroids from flyby and rendezvous missions with asteroids (e.g., Li *et al.*, 2006, 2013a; Kitazato *et al.*, 2008; Spjuth *et al.*, 2012; Magrin *et al.*, 2012; Schröder *et al.*, 2013). From these data, we can observe how the reflectance of an asteroidal surface depends on local scattering geometries. This additional information is more powerful for retrieving the physical properties of a surface than the disk-integrated solar phase function only. The most notable advantage is to resolve the ambiguity between fitting the surface roughness and the phase function, because the effect of roughness is especially important at phase angles  $>40^\circ$  (Helfenstein, 1988).

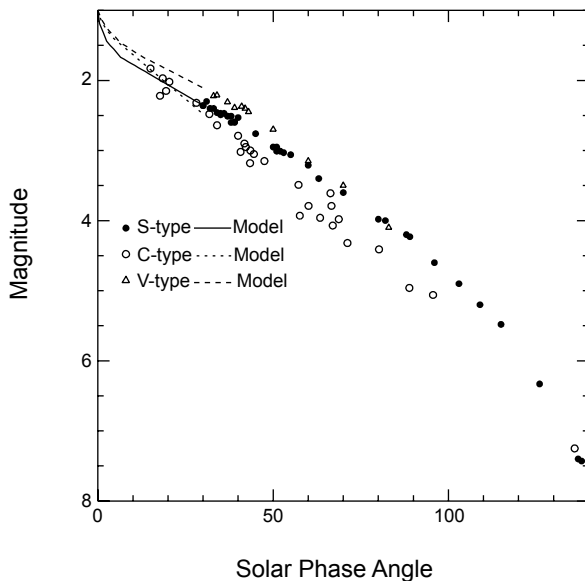


**Fig. 2.** The phase functions of three asteroid classes, all normalized at zero degree phase angle. The lines at phase angles less than  $\sim 30^\circ$  are the respective best-fit models using the data from Helfenstein and Veverka (1989) for S and C types (*Asteroids II* book), and a composite Vesta curve from Hicks et al. (2014) for V types. Data from Mathilde (Clark et al., 1999) and Bennu (B-type) (Takir et al., 2015) are used for additional C types beyond  $30^\circ$  phase angle. Data for Gaspra (Helfenstein et al., 1994), Lutetia (Masoumzadeh et al., 2014), and Eros (Li et al., 2004) are used for S types beyond  $30^\circ$  phase angle.

In this chapter, we will focus on disk-resolved photometric studies of asteroids based on photometric theories and high-resolution data returned by asteroid exploration missions. Photometric modeling based primarily on ground-based photometric surveys have been thoroughly reviewed in previous *Asteroids* books in this series (Bowell and Lumme, 1979; Bowell et al., 1989; Helfenstein and Veverka, 1989; Muinonen et al., 2002). It is important to keep in mind that physical laws dictate that the photometric signatures from planetary surfaces necessarily correlate with polarimetric signatures. In this chapter we strictly limit the scope of our discussion to asteroid photometry, and readers are referred to a companion chapter in this volume by Belskaya et al. for a comprehensive review on asteroid polarimetry. In section 2, we will review the basic concepts of photometric measurements and models, the most recent developments in theoretical models, and the controversy about several analytical models. In section 3, we will summarize observational results reported over the past decade, focusing on disk-resolved photometry based on spacecraft observations. We will then discuss applications and implications of photometric modeling to the study of general asteroid properties in section 4. In section 5, we provide a summary and a perspective on the future of asteroid photometry for the next decade to come.

## 2. OVERVIEW OF THEORIES

### 2.1. Basic Concepts

The fundamental quantity of light-scattering characteristics of a surface is reflectance. Several different quantities of reflectance and albedo exist under various illumination and observing conditions. Here we follow the definitions and conventions described in Hapke (2012b). Generally, reflectance is defined by the ratio of scattered radiance (or intensity) to incident irradiance (or flux), while albedo is defined with respect to an ideal surface that scatters all incident light isotropically (or a perfectly scattering Lambert surface). Reflectance quantities use two adjectives as prefixes to specify the collimation of incident light and the measurement conditions for scattered light, such as *directional-directional* reflectance, *directional-hemispherical* reflectance, etc. In the case where the two adjectives are the same, a prefix *bi-* is used, e.g., *bidirectional* reflectance. The most commonly used quantities in light-scattering theories and measurements are listed in Table 1. Here we describe a few of the most important quantities.

*Bidirectional reflectance*,  $r$ , is an idealized quantity, because the incident irradiance,  $J$ , is assumed to be strictly collimated (Fig. 1). For observations of most asteroids, the apparent angular size of the Sun is  $<0.5^\circ$  (at  $>1$  AU from the Sun), so the collimation assumption for incident irradiance is a good approximation except for at near-zero phase angle, where the finite size of the Sun rounds off the peak. The measurements of scattered intensity are made at the pixel scale of the camera or spectrometer, which is typically less than a few tens of milliradians per pixel.  $J$  has a unit of [ $\text{W m}^{-2}$ ] or [ $\text{W m}^{-2}$  per unit wavelength or per unit frequency]. The scattered radiance,  $I$ , has a unit of [ $\text{W m}^{-2} \text{ sr}^{-1}$ ] or [ $\text{W m}^{-2} \text{ sr}^{-1}$  per unit wavelength or unit frequency]. Therefore, bidirectional reflectance has a unit of [ $\text{sr}^{-1}$ ].

*Radiance factor* (or RADF),  $R$ , and *reflectance factor* (or REFF) are often used in laboratory measurement by ratioing the reflected light from the sample to that from a reference surface, which is usually close to a Lambert disk. A Lambert surface has a bidirectional reflectance  $r_L(0,e,e) = 1/\pi$  in any direction, with a unit of [ $\text{sr}^{-1}$ ]. Therefore, both RADF and REFF are dimensionless. Note that non-isotropic scattering, especially a phenomenon known as the “opposition effect” near zero phase (a nonlinear increase of reflectance as phase angle approaches  $0^\circ$ ; see section 2.3), can make a surface brighter than a perfectly scattering Lambert surface, producing RADFs greater than unity.

RADF is equivalent to the commonly used but often confusing notation  $I/F$ , which is usually annotated in the literature as “ $I$  is the scattered radiance, and  $\pi F$  is the incident solar irradiance.” Note, however, that the  $\pi$  here originates from the division of the bidirectional reflectance quantity of a perfectly scattering Lambert surface, which is  $1/\pi$  with a unit of [ $\text{sr}^{-1}$ ]. As such, the  $\pi$  actually has a unit of [sr]. Therefore,  $F$  has a unit of radiance rather than irradiance, making  $I/F$  dimensionless.

TABLE 1. The definitions of some commonly used reflectance quantities.

Quantity	Definition	Formula	Ref.*
Bidirectional reflectance	Ratio of the scattered radiance toward $(i, e, \alpha)$ to the collimated incident irradiance	$r(i,e,\alpha) = I(i,e,\alpha)/J [\text{ster}^{-1}]$	p. 195
Bidirectional reflectance distribution function (BRDF)	Ratio of the scattered radiance toward $(i, e, \alpha)$ to the collimated power incident on a unit area of the surface	$\text{BRDF} = I(i,e,\alpha)/J\mu_0 = r/\mu_0 [\text{ster}^{-1}]$	p. 263
Radiance factor (RADF)	Ratio of the bidirectional reflectance of a surface to that of a perfectly scattering surface <sup>†</sup> illuminated at normal direction	$\text{RADF} = \pi r(i,e,\alpha) = [I/F]$	p. 264
Reflectance factor (or reflectance coefficient, REFF)	Ratio of the reflectance of a surface to that of a perfectly diffused surface under the same conditions of illumination and viewing	$\text{REFF} = \pi r/\mu_0 = [I/F]/\mu_0$	p. 263
Lambertian albedo	Ratio of the total scattered irradiance toward all directions from a Lambert surface to incident power per unit area	$A_L = P_L/J\mu_0$ Perfectly scattering surface has $A_L = 1$	p. 187
Normal albedo	Ratio of the reflectance of a surface observed at zero phase angle from an arbitrary direction to that of a perfectly diffuse surface located at the same position, but illuminated and observed perpendicularly	$A_n = \pi r(e,e,0)$	p. 296
Geometric albedo (physical albedo)	Ratio of the integral brightness of a body at zero phase angle to the brightness of a perfect Lambert disk of the same size and at the same distance, but illuminated and observed perpendicularly. It is the weighted average of the normal albedo over the illuminated area of the body	$A_p = \int_{2\pi} r(e,e,0)\mu d\Omega^{\ddagger}$	p. 298
Bond albedo (spherical albedo, or global albedo)	Total fraction of incident irradiance scattered by a body into all directions	$A_s = \frac{1}{\pi} \int_{2\pi} \int_{2\pi} r(i,e,\alpha)\mu d\Omega_e d\Omega_i$	p. 301
Bolometric albedo (radiometric albedo)	Average of the spectral albedo $A_s(\lambda)$ weighted by the spectral irradiance of the Sun $J_s(\lambda)$	$A_b = \frac{\int_0^\infty A_s(\lambda) J_s(\lambda) d\lambda}{\int_0^\infty J_s(\lambda) d\lambda}$	p. 302
Phase integral		$q = 2 \int_0^\pi \Phi_p(\alpha) \sin \alpha d\alpha$	p. 302

<sup>\*</sup> Page numbers in Hapke (2012b).<sup>†</sup> Perfectly scattering Lambert surface has  $r = \frac{1}{\pi}\mu_0$ .<sup>‡</sup>  $d\Omega = 2\pi \sin e de = -2\pi d\mu$ .

Other important concepts include geometric albedo (or physical albedo) and Bond albedo (or spherical albedo). Similar to RADF, *geometric albedo*,  $A_p$ , is defined with respect to a perfectly scattering Lambert surface. The use of geometric albedo simplifies the modeling of the disk-integrated brightness of an object at any phase angle, which can now be expressed as the product of  $A_p$  and its disk-integrated phase function,  $\Phi(\alpha)$ , normalized to unity at zero phase angle. Note that, similar to RADF, for extremely bright and strongly backscattering objects, the geometric albedo can approach or exceed unity. For example, the geometric albedo of Enceladus is 1.38, Tethys 1.23, and Dione 1.00 (Verbiscer *et al.*, 2007).

*Bond albedo*,  $A_B$  (also known as the spherical Bond albedo), is a key quantity to measure the ability of an object to absorb incident energy, therefore critical for understanding energy balance and volatile transport on a planetary body. By definition, Bond albedo cannot exceed unity. Since Bond albedo is an integrated quantity of the disk-averaged reflectance, it can be expressed as

$$A_B = A_p q \quad (2)$$

where  $q$  is the phase integral, defined as

$$q = 2 \int_0^\pi \Phi(\alpha) \sin \alpha d\alpha \quad (3)$$

Important for thermal modeling is the bolometric Bond albedo, which is the average Bond albedo over wavelength, weighted by the solar spectrum,  $F_{\odot}(\lambda)$

$$A_B = \frac{\int_0^{\infty} A_B(\lambda) F_{\odot}(\lambda) d\lambda}{\int_0^{\infty} F_{\odot}(\lambda) d\lambda} \quad (4)$$

Because the solar spectrum peaks at about 500 nm with about half of the total flux in the visible wavelengths, the V-band Bond albedo is often taken as an approximation to the bolometric Bond albedo for asteroids.

## 2.2. Empirical Models

Sophisticated modern photometric models need to describe two types of photometric data: “whole-disk” or “disk-integrated” observations and “disk-resolved” or “surface-resolved” reflectance measurements when they are available; the latter most often obtained from spacecraft-borne instruments. Disk-resolved photometric measurements provided a new ability to detect the photometric effects of physical phenomena like macroscopic surface texture much more reliably and unambiguously than could be achieved with whole-disk data.

Surface-resolved photometric models that are applied to asteroid observations seek to relate the local scene viewing and illumination geometry to the radiance factor, RADF, or, more simply, R. In the simplified treatment of the empirical equations to model R, such as that of *Lambert* (1759) and *Minnaert* (1941), the dependence of reflectance on i and e, usually called the *disk-function* or *limb-darkening function*,  $d(i, e)$ , is often separated from the dependence on phase angle, called the *surface phase function*,  $f(\alpha)$ . The RADF of a surface is expressed as

$$R = d(i, e) f(\alpha) \quad (5)$$

Sometimes a scaling factor is added to equation (5), so that the surface phase function can be normalized, e.g., to unity at zero phase angle. Generally, the disk-function is affected by the amount of multiple scattering (therefore albedo) and surface roughness. The phase function includes the effects of single-scattering phase function, opposition surge (see section 2.3), roughness, and multiple scattering. Historically, this separation is a result of the lack of surface-resolved data before spacecraft missions, where the only available geometric variable was phase angle. Modern photometric theories indicate that when multiple scattering is not significant (i.e., for relatively dark surfaces), the disk-function and phase function can be separated in functional forms.

The most commonly used empirical photometric models are listed in Table 2. Most empirical photometric models specify the disk-function, including the Lambert model (*Lambert*, 1759), the Lommel-Seeliger (LS) model (*Seeliger*, 1887), the Minnaert model (*Minnaert*, 1941), and the lunar-Lambert model (e.g., *Buratti* and *Vercka*, 1983; *McEwen*, 1991, 1996), while leaving the phase function implicit or

unspecified. These models can describe surfaces with a wide range of different albedos. Generally, high-reflectance objects with geometric albedo close to or greater than unity are well described by the Lambert model, although essentially no asteroids scatter light following the Lambert law because the majority have albedos <0.5 (*Masiero et al.*, 2011). On the other hand, low-reflectance objects with geometric albedo <0.2 generally follow an LS scattering law. All primitive asteroids (C-, D-, P-types) and most S-type asteroids are in this category. For the highest-albedo S-type asteroids and high-albedo asteroid classes such as V- and E-types, the hybrid lunar-Lambert model is a good disk-function. The higher the albedo, the greater the partition to the Lambertian term. The Minnaert model can also describe surfaces with a wide range of albedos. The two Minnaert parameters  $A_M$  and k depend on phase angle. For a dark surface where multiple scattering is negligible, k = 0.5; for a Lambert scattering law, k = 1; and in general the higher the albedo of the surface, the higher the value of k (*McEwen*, 1991). *Buratti* (1984) showed that k = 0.5 applied to normal reflectances  $\leq 0.6$ , which include most asteroids.

The surface phase function is often expressed in various empirical forms in the literature (Table 3), including the combination of an exponential term and a polynomial term (*Hillier et al.*, 1999; *Buratti et al.*, 2011), or a linear-exponential function (*Piironen*, 1994; *Kaasalainen et al.*, 2001, 2003; *Muinonen et al.*, 2009), or a linear function in magnitude scale ( $-2.5\log(r)$ ) (*Li et al.*, 2009, 2013b), or exponentials and a polynomial in a magnitude scale (*Takir et al.*, 2015).

Disk-integrated photometric models, as the name implies, compute the whole-disk brightness of an asteroid at a given apparition by integrating the predicted surface-resolved radiance factors over the fraction of the surface that is both illuminated and visible to the observer. A *disk-integrated phase function*,  $\Phi(\alpha)$ , can be calculated as

$$\Phi(\alpha) = \frac{f(\alpha)}{\pi} \int_{\Omega(i,v)} d(i, e) \mu d\Omega \quad (6)$$

$\Phi(\alpha)$  is generally normalized to unity at zero phase angle (note that equation (6) is not normalized), and constrained by observational data spanning a range of phase angles. The disk-integrated phase function is therefore different from the surface phase function by including the integral term in equation (6) that also depends on phase angle. For simplicity and in the absence of information about the actual shape of an asteroid, the whole-disk brightness is often analytically evaluated for a sphere that has the same equivalent dimensions assumed for the asteroid. The disk-integrated phase functions calculated based on the commonly used photometric models are listed in Table 4.

Another form of empirical disk-integrated photometric model simply parameterizes the total brightness of an object measured at a range of phase angles, such as the International Astronomical Union (IAU) H-G model (next section). In addition, the three-parameter model of *Shevchenko* (1996)

TABLE 2. Commonly used empirical photometric models.

Model	RADF*	Normal Albedo ( $A_n$ )	Geometric Albedo ( $A_p$ )	Reference
Lambert	$A_L \mu_0 f(\alpha)$	$A_L f(0)$	$\frac{2}{3} A_L f(0)$	
Lommel-Seeliger	$A_{LS} \frac{\mu_0}{\mu_0 + \mu} f(\alpha)$	$\frac{1}{2} A_{LS} f(0)$	$\frac{1}{2} A_{LS} f(0)$	
Lunar-Lambert	$A_{LL} \left[ L(\alpha) \frac{2\mu_0}{\mu_0 + \mu} + (1 - L(\alpha)) \mu_0 \right] f(\alpha)^{\dagger}$ $L(\alpha) = 1 + A_1 \alpha + A_2 \alpha^2 + A_3 \alpha^3$	$A_{LL} f(0)$	$A_{LL} f(0)$	<i>McEwen</i> (1991, 1996)
Minnaert	$A_M \mu_0^{k(\alpha)} \mu^{k(\alpha)-1} f(\alpha)^{\ddagger}$ $k(\alpha) = k_0 + b\alpha$	$A_M \mu_0^{2k_0-1} f(0)$	$\frac{2}{2k+1} A_M f(0)$	<i>Minnaert</i> (1941), <i>Li et al.</i> (2009, 2013b)
Akimov	$A_n \cos \frac{\alpha}{2} \cos \left( \frac{\pi}{\pi - \alpha} \left( \Lambda - \frac{\alpha}{2} \right) \right) \frac{\cos^{\frac{\alpha}{\pi-\alpha}} \beta}{\cos \Lambda} f(\alpha)$	$A_n f(0)$	$A_n f(0)$	<i>Shkuratov et al.</i> (2011)

\*  $f(\alpha)$  is a surface phase function, generally normalized to unity at zero phase angle.  $A$  with various subscripts are constants that are directly proportional to the normal albedo and geometric albedo of the surface. Therefore, the RADF can also be expressed in terms of normal albedo or geometric albedo.

†  $L(\alpha)$  is a partition parameter between the LS term and the Lambert term. It usually depends on phase angle.

‡ This is an empirical model of  $k(\alpha)$  as adopted by *Li et al.* (2009, 2013a). *Masoumzadeh et al.* (2014) show, from their work on asteroid Lutetia using Rosetta flyby data, that the phase angle dependence of  $k$  might be better described with a second-order polynomial.

has recently been used to describe the opposition effect of (4) Vesta (*Hasegawa et al.*, 2014). This model, like the IAU H-G one, is expressed in terms of reduced magnitude

$$M(\alpha) = M(0^\circ) + \frac{a\alpha}{1+\alpha} + b\alpha \quad (7)$$

where the model parameters are  $M(0^\circ)$ , the reduced magnitude at zero phase;  $a$  characterizes the opposition effect, and  $b_\lambda$  describes the slope of the linear part of the phase curve, analogous to the phase coefficient.

### 2.3. Physically Motivated Models

Physically motivated models (e.g., *Hapke*, 1963, 1981, 1984, 1986, 2002, 2008, 2012a; *Goguen*, 1981; *Lumme and Bowell*, 1981a, 1985; *Shkuratov et al.*, 1999) approximate the solution for radiative transfer from a rough, particulate surface. A typical modern analytical photometric model can be best considered as an assemblage of mathematical components, each of which describes a functional dependence of directional light scattering on a different parameterized quasiphysical property, or a group of related properties that act in concert. The main functional components of typical models rely on (1) a component to describe albedo and directional singly scattered light by an average regolith grain,

(2) a component to describe how wave fronts are multiply scattered among and from an aggregate volume of average grains, (3) a parameterized component to describe the effects of macroscopic surface texture on reflected light, and (4) component functions to describe the opposition effect — a conspicuous nonlinear surge in brightness with decreasing phase angle that is observed at small phase angles on particulate-covered bodies. So complex are the interactions between these components that even the best available analytical models are still in development. They have continued to evolve over a span of at least three decades as laboratory testing and refinement of theory identify new deficiencies and new corrections, respectively.

Among the analytical models used for asteroid work, the *Hapke* (1981, 1984, 1986, 2002, 2008, 2012a) model, the *Shkuratov* (1999) model, and the *Lumme-Bowell* model (*Lumme and Bowell*, 1981a,b; *Bowell et al.*, 1989) have seen the widest application to both photometric and spectroscopic data. The *Lumme-Bowell* (*Lumme and Bowell*, 1981a,b) model is described in detail and discussed in the *Asteroids II* volume in this series (*Bowell et al.*, 1989) and later discussion was given in *Asteroids III* (*Muinonen et al.*, 2002). In all cases, there are both a surface-resolved expression and a disk-integrated expression in the model. In the case of the *Hapke* model, there are many variants. So in practice, whole-disk modeling is done by numerical integration over an assumed spherical or triaxial-shape, or

TABLE 3. List of empirical surface phase functions.

Model	Empirical Phase Function	References
Exponential	$f(\alpha) = e^{\beta\alpha + \gamma\alpha^2 + \delta\alpha^3}$	Takir et al. (2015)
Linear-magnitude	$f(\alpha) = 10^{-0.4\beta\alpha}$	Li et al. (2009, 2013a)
Polynomial-magnitude	$f(\alpha) = 10^{-0.4(\beta\alpha + \gamma\alpha^2 + \delta\alpha^3)}$	Takir et al. (2015)
Lunar/ROLO	$f(\alpha) = C_0 e^{-C_1\alpha} + A_0 + A_1\alpha + A_2\alpha^2 + A_3\alpha^3 + A_4\alpha^4$	Hillier et al. (1999), Buratti et al. (2011)
Linear-Exponential	$f(\alpha) = \alpha e^{-\alpha/d} + b + k\alpha$	Piironen (1994), Kaasalainen et al. (2001, 2003)
Akimov	$f(\alpha) = \frac{e^{-\mu_1\alpha} + m e^{-\mu_2\alpha}}{1+m}$	Akimov (1988)

\*  $\mu_1$  and  $\mu_2$  are model parameters, not to be confused with  $\mu_0$  and  $\mu$ , which are the cosines of incidence angle and emission angle, respectively.

TABLE 4. Disk-integrated phase functions for various commonly used photometric models.

Model	Disk-Integrated Phase Function *	References
Lambert	$\Phi(\alpha) = [\sin \alpha + (\pi - \alpha) \cos \alpha] \frac{f(\alpha)}{\pi f(0)}$	Hapke (2012b), p. 107, Equation (6.13)
Lommel-Seeliger	$\Phi(\alpha) = \left(1 - \sin \frac{\alpha}{2} \tan \frac{\alpha}{2} \ln \cot \frac{\alpha}{4}\right) \frac{f(\alpha)}{f(0)}$	Hapke (2012b), p. 108, Equation (6.14)
Lunar-Lambert	$\Phi(\alpha) = \frac{\frac{2}{3}\pi[1 - L(0)][\sin \alpha + (\pi - \alpha) \cos \alpha] + L(0)f(\alpha)\left(1 - \sin \frac{\alpha}{2} \tan \frac{\alpha}{2} \ln \cot \frac{\alpha}{4}\right)}{\frac{2}{3}[1 - L(0)] + L(0)f(0)}$	Buratti and Veverka (1983)
Hapke	$\begin{aligned} \Phi(\alpha) = & \frac{r_0}{2A_p} \left[ \left\{ \frac{(1+\gamma)^2}{4} \{ [1 + B_{S0}B_S(\alpha)]p(\alpha) - 1 \} + [1 - r_0] \right\} \right. \\ & \left. \left( 1 - \sin \frac{\alpha}{2} \tan \frac{\alpha}{2} \ln \cot \frac{\alpha}{4} \right) + \frac{4}{3} r_0 \frac{\sin \alpha + (\pi - \alpha) \cos \alpha}{\pi} \right\} [1 + B_{C0}B_C(\alpha)] \end{aligned}$	Hapke (2012b), p. 300, Equation (11.42)

\* All phase functions are normalized to unity at zero degree phase angle.

a three-dimensional shape model, any of which is oriented at the appropriate geometry to match the observation. We discuss below recent advances in these models.

**2.3.1. Hapke models.** The Hapke (1981, 1984, 1986) model was discussed in detail in the *Asteroids II* volume (Bowell et al., 1989; Helfenstein and Veverka, 1989). Since then, the model has continued to evolve through experimental variants (cf. Helfenstein et al., 1997), diverse choices in the particle phase functions used in the model, and numerous improvements introduced by Hapke (2002, 2008, 2012a) and others. Hapke (2002) improved his treatment of multiple scattering by grains with anisotropic phase functions and added

the coherent backscattering as a mechanism to account for a narrow (less than a few degrees) opposition spike that acts in addition to the shadow hiding mechanism. By far, the most significant improvement is in Hapke (2008), which identifies and corrects a serious error in how the effects of porosity and compaction are treated in nearly all similar models.

Although Hapke provides analytical expressions for the whole-disk behavior (cf. Hapke, 2012b), because of the many variants of the model in use, whole-disk phase curves predicted by the Hapke model are often obtained by numerical integration of RADF over the illuminated portion of the planetary disk or asteroid shape model.

The current form of Hapke's radiance factor equation can be expressed as

$$R(\mu_0, \mu, \alpha) = K \frac{\bar{\omega}_0}{4} \frac{\mu'_0}{\mu'_0 + \mu'} \left[ (1 + B_{SH}(\alpha)) P(\alpha) + M\left(\frac{\mu'_0}{K}, \frac{\mu'}{K}, \alpha\right) \right] (8)$$

$$(1 + B_{CB}(\alpha)) S(\mu_0, \mu, \alpha)$$

where  $\mu'_0$  and  $\mu'$  are the cosines, respectively, of the *effective* angles of incidence and emission angles after adjustment for the average slope angle of macroscopic scale topographic roughness (Hapke, 1984),  $\alpha$  is the phase angle, and  $\bar{\omega}_0$  is the average particle single-scattering albedo. The function,  $S(\mu'_0, \mu', \alpha)$  describes the shadowing and occlusion effects of macroscopic roughness,  $P(\alpha)$  is the average particle single-scattering phase function (also known as the single particle phase function, SPPF),  $(1 + B_{SH}(\alpha))$  describes the shadow-hiding opposition effect (Hapke, 1986),  $M(\mu'_0, \mu', \alpha)$  describes multiply scattered light between particles (Hapke, 2002), and  $1 + B_{CB}(\alpha)$  models the coherent backscatter opposition effect (Hapke, 2002). The porosity coefficient,  $K$ , was introduced in Hapke (2008) as an explicit adjustable parameter to more realistically model how the areal fraction of light that is blocked by grains within a quasicontinuous particulate medium increases as the particle arrangement converges to a closely packed state.

**2.3.1.1. Single scattering by average regolith grains:** Light that is scattered once by an average regolith grain is generally described by the product  $\bar{\omega}_0 P(\alpha)$  where  $\bar{\omega}_0$  is the average particle single-scattering albedo and  $P(\alpha)$  is known as the average particle single-scattering phase function. The latter describes the directional scattering behavior of average regolith grains. Since the first models of Hapke (1963, 1966), a wide variety of particle phase function expressions have been introduced to the Hapke equations (Table 5), many of which are still in use.

Currently, the most often used representation is that from McGuire and Hapke (1995). Hapke (2012a) recently introduced a simplification of the 2PHG, and found from laboratory studies that the  $b$  and  $c$  parameters could be defined in terms of one another using an empirical "hockey-stick relation" (Hapke, 2012a) so named because of the shape defined in  $b$  vs.  $c$  plots of model fits to laboratory data. The hockey-stick diagram (i.e., plot of the  $c$  vs.  $b$ ) is particularly useful for interpreting the physical structure of regolith particles from their particle phase functions with respect to the complexity of the particle shape and the density of internal scatterers (cf. McGuire and Hapke, 1995; Souchon et al., 2011).

**2.3.1.2. Opposition Surge: Shadow Hiding Opposition Effect (SHOE):** The treatment of Hapke (1986) is most widely in current use. This model uses two adjustable parameters, here called  $h_{SH}$  and  $B_{0,SH}$ , to describe the angular width and amplitude of the SHOE, respectively. It takes

into account how non-uniform states of compaction with depth can influence the angular width of SHOE and how the transparency of regolith grains affects the strength of SHOE. The angular half-width of the SHOE is  $\Delta\alpha_{SH} \approx 2 h_{SH}$  (in radians). While the Hapke model can describe SHOE for many different gradients in compaction state and particle size-distributions, most workers assume a uniform distribution of particles and compaction. In this case  $h_{SH}$  can be easily related to the regolith porosity,  $p$ , in terms of the packing factor  $\phi = (1-p)$ . Then,  $h_{SH} = -0.375 \ln(1-\phi)$ .

However, in a related paper, Hapke (2008) identified a fundamental error in the way that his own and almost all other radiative transfer approximations for regolith surfaces. Nearly all these models fail to account for the increase in reflectance seen in laboratory experiments when particulate surfaces are compacted from a more fluffy state. Hapke (2008) corrects for this effect of porosity at the expense of adding an explicit model parameter called the porosity coefficient,  $K$ , where

$$K = -\frac{\ln(1 - 1.209\phi^{2/3})}{1.209\phi^{2/3}} \quad (9)$$

A less rigorous version of  $K$  figured in earlier versions of Hapke's model where it is called the porosity factor. The porosity factor figures in Hapke's (1986) derivation of the SHOE function, which strongly depends on porosity. Helfenstein and Shepard (2011) introduced a correction to the Hapke (1986) SHOE model to make it consistent with Hapke (2008). However, it is important to note that the Hapke (2008) correction is strictly valid only for porosities in the range  $0.248 < p < 1.0$ .

**2.3.1.3. Opposition Surge: Coherent-Backscatter Opposition Effect (CBOE):** Coherent-backscatter is now known to cause the prominent, very narrow phase-curve spike that is observed most often within a few degrees of opposition (Muinonen et al., 2012). How the mechanism operates in the complex architecture of planet, satellite, and asteroid regoliths is still not fully understood (cf. Hapke et al., 2012). [Muinonen et al. (2012) have recently derived a coherent-backscatter model on the basis of a rigorous solution of Maxwell's equation (see section 2.3.3).] In his most recent treatment (Hapke, 2012a), the approximation is updated to include the dependence on the porosity factor

$$B_{CB}(\alpha) = \frac{B_{0,CB}}{1 + 1.42K} \left[ \frac{1 + \frac{1 - e^{-(1.42K/h_{CB})\tan(\alpha/2)}}{(1/h_{CB})\tan(\alpha/2)}}{\left[ 1 + (1/h_{CB})\tan(\alpha/2) \right]^2} \right] \quad (10)$$

where  $B_{0,CB}$  is the amplitude of the CBOE,  $h_{CB} = \lambda/4\pi L_T$ ,  $\lambda$  is wavelength, and  $L_T$  is the photon transport mean free path length in the medium. The angular half-width of the CBOE in radians is  $\Delta\alpha_{CB} = 0.36\lambda/2\pi L_T$ . While it is explicitly proportional to the spectral wavelength, it is important to note that

TABLE 5. Particle single-scattering phase functions.

Name	Expression	Parameters	Reference
Modified Schoenberg	$P(\alpha) = \left[ \sin \alpha  + (\pi \alpha ) \cos( \alpha ) / \pi + 0.1(1 - \cos( \alpha ))^2 \right]$		Hapke (1963, 1966)
Two-Parameter Legendre Polynomial (2PLP)	$P(\alpha) = 1 + b \cos(\alpha) + c \left( \frac{3}{2} \cos^2(\alpha) - \frac{1}{2} \right)$	b,c	Hapke (1981)
One-Parameter Henyey-Greenstein (1PHG)	$P(\alpha) = (1 - g^2) / (1 + 2g \cos(\alpha) + g^2)^{3/2}$	g	Buratti and Veranka (1983)
Two-Parameter Henyey-Greenstein (2PHG, form #1)	$P(\alpha) = \frac{(1+c)}{2} \frac{(1-b^2)}{(1-2b \cos(\alpha) + b^2)^{3/2}} + \frac{(1-c)}{2} \frac{(1-b^2)}{(1+2b \cos(\alpha) + b^2)^{3/2}}$	b,c	McGuire and Hapke (1995)
Two-Parameter Henyey-Greenstein (2PHG, form #2)	$P(\alpha) = (1-c) \frac{(1-b^2)}{(1+2b \cos(\alpha) + b^2)^{3/2}} + c \frac{(1-b^2)}{(1-2b \cos(\alpha) + b^2)^{3/2}}$	b,c	Hartman and Domingue (1998)
Three-Parameter Henyey-Greenstein (3PHG, form #1)	$P(\alpha) = (1-f) \frac{(1-g_1^2)}{(1+2g_1 \cos(\alpha) + g_1^2)^{3/2}} + (f) \frac{(1-g_2^2)}{(1+2g_2 \cos(\alpha) + g_2^2)^{3/2}}$	g <sub>1</sub> ,g <sub>2</sub> ,f	Helfenstein et al. (1991)
Three-Parameter Henyey-Greenstein (3PHG, form #2)	$P(\alpha) = (f) \frac{(1-g_1^2)}{(1+2g_1 \cos(\alpha) + g_1^2)^{3/2}} + (1-f) \frac{(1-g_2^2)}{(1-2g_2 \cos(\alpha) + g_2^2)^{3/2}}$	g <sub>1</sub> ,g <sub>2</sub> ,f	Deau and Helfenstein (2015)
Lumme-Bowell	$P(\alpha) = 0.95e^{-0.4\alpha} + 16.15e^{-4.0\alpha}$		Lumme and Bowell (1981b)

the transport mean free path length in the medium is often strongly wavelength-dependent. Hence, the angular width of the CBOE in a complex regolith can be difficult to predict.

**2.3.1.4. Multiple-scattering of light:** Hapke's (1981, 1984, 1986) model approximated multiple scattering with an analytical simplification of Chandrasekhar's (1960) H-functions for isotropically scattering grains (known as the isotropic multiple scattering approximation, or IMSA). This approximation has long been assumed to be adequate for relatively low- to moderate-albedo bodies where the contribution of multiply scattered light was small compared with the emitted singly scattered signal. For relatively high-albedo objects where multiple-scattering contributes significantly, some workers replace the approximation with the exact numerical calculation for isotropic scatterers (cf. Verbiscer, 1991) and first-order anisotropic scatterers (cf. Verbiscer and Veranka, 1992, 1994). To account for the possible strongly anisotropic scatterers, Hapke (2002) ultimately introduced an expansive treatment of multiple scattering (anisotropic multiple scattering approximation, or AMSA) that can be applied to strongly anisotropic grains.

**2.3.2. Shkuratov model.** The Shkuratov model (Shkuratov et al., 1999) is also physically motivated and describes a macroscopically fractal-like surface, and it includes a

description of both SHOE and CBOE. Unlike the Hapke and Lumme-Bowell models, in which the single-scattering and multiple-scattering contributions can be separated, the Shkuratov model is the product of three component functions and a normal reflectance coefficient  $A_n$ . In terms of the radiance factor

$$R(\mu_0, \mu, \alpha) = A_n f_{\text{SHOE}}(\alpha) f_{\text{CBOE}}(\alpha) d(\Lambda, \beta, \alpha) \quad (11)$$

where the  $f_{\text{SHOE}}$  describes the shadow-hiding opposition effect,  $f_{\text{CBOE}}$  the coherent-backscatter opposition effect, and  $d(\Lambda, \beta, \alpha)$  is the Akimov disk-distribution function that describes how the brightness of the surface at any given phase angle varies with photometric longitude,  $\Lambda$ , and photometric latitude,  $\beta$ . The Shkuratov model has four adjustable parameters. The coefficient  $A_n$  is the normal albedo. The function  $f_{\text{SHOE}} = \exp(-\kappa\alpha)$ , where  $\kappa$  is a parameter that decreases with increasing albedo to model the attenuation of projected shadows by multiple-scattering. The  $f_{\text{CBOE}}$  function has two parameters:  $\Delta_E$ , the extinction mean free path of a photon; and  $d$ , a size-scale parameter that defines the separation distance of scatterers that contribute to coherent backscatter interactions. The Akimov disk-distribution of brightness has no model parameters (Table 2).

**2.3.3. Muinonen radiative transfer-coherent backscatter model.** Many of the recent efforts to improve physically motivated photometric models have focused on incorporating a description of the coherent backscatter opposition effect. In the analytical models above, the treatment of coherent backscatter is made tractable through the use of physically reasonable simplifying assumptions and mathematical approximations — none represent exact solutions of Maxwell's equations. At present, numerical methods provide the most rigorous approach to test and model how coherent backscatter operates in the context of planetary regoliths.

A breakthrough was achieved by *Muinonen et al.* (2012), who developed a Monte Carlo integration approach that combines radiative transfer and coherent backscatter (RT + CB) from an assumed spherical assemblage of randomly distributed spherical scatterers of known size, packing, and optical constants. A particularly important aspect of this approach is that it can be independently verified by direct computer solution of Maxwell's equations (*Mackowski and Mishchenko*, 1996, 2011). While earlier works demonstrated the behavior of coherent backscatter among widely dispersed scatterers, the recent work of *Muinonen et al.* (2012) has definitively verified how the mechanism operates within loosely packed aggregates of scatterers. Their Monte Carlo simulation accurately predicts not only the contribution of coherent backscatter to the photometric opposition effect, but also accurately models the polarization behavior at small phase angles (known as the polarization opposition effect) and the circular polarization. While most tests were done assuming uniformly sized scatterers, in a preliminary experiment in which a size-distribution of scatterers was used, the results qualitatively matched the opposition behavior seen in high-albedo planetary objects, such as bright icy satellites.

The studies in *Muinonen et al.* (2012) were limited to sparsely packed arrangements of scatterers (packing factors only as large as 6.25%). To be more directly applicable to regolith-covered bodies, more work will be needed to determine the method's applicability to densely packed arrangements of scatterers.

Further numerical modeling techniques were developed by *Muinonen et al.* (2011) and *Wilkman et al.* (2014a) with the lunar mare data acquired by the Advanced Moon micro-Imager Experiment (AMIE) on the European Space Agency's Small Missions for Advanced Research in Technology-1 (SMART-1) mission. They employed a numerical approach to solve for the shadowing function resulted from the surface roughness using ray-tracking technique with the LS sphere as the auxiliary tool. Combining the numerical shadowing function solution and the RT-CB model with the classic 2PHG function and LS phase function as the volume phase function, *Wilkman et al.* (2014a) achieved good fit to the lunar mare data using Bayesian techniques and Markov chain Monte Carlo. *Wilkman et al.* (2014b) provided a numerical representation of the shadowing function for close-packed spherical volume of LS particles to facilitate the photometric modeling of low-albedo surfaces.

**2.3.4. IAU magnitude phase curve system.** The Lumme-Bowell model (*Lumme and Bowell*, 1981b) is of special

importance to asteroid studies because it was the original basis of the official IAU magnitude system for classifying and modeling the albedos and photometric behavior of whole-disk phase curves. Details of the Lumme-Bowell model and its adaptation to the H-G system are given in the *Asteroids II* volume (*Bowell et al.*, 1989). This long-used model was derived prior to the recognition of a narrow “opposition spike” that is caused by coherent backscatter and typically observed on airless bodies at phase angles less than a couple of degrees. *Muinonen et al.* (2010) developed a three-parameter model, called the H-G<sub>1</sub>-G<sub>2</sub> model, that is similar to the H-G model above but that significantly improves fits to asteroid phase curves that have a detectable opposition spike. In this model, that now officially replaces the previous IAU system, the reduced magnitude of an asteroid, V(α), is expressed as

$$V(\alpha) = H - 2.5 \log_{10} \left[ G_1 \Phi_1(\alpha) + G_2 \Phi_2(\alpha) + (1 - G_1 - G_2) \Phi_3(\alpha) \right] \quad (12)$$

where two numerically optimized, cubic-spline basis functions,  $\Phi_1(\alpha)$  and  $\Phi_2(\alpha)$  replace the basis functions of the H-G model, and a third basis function,  $\Phi_3(\alpha)$ , is introduced to describe the opposition effect. These basis functions are numerically defined by their values at their phase angle grids and the first derivatives at the two ends, as given in Tables 3 and 4 of *Muinonen et al.* (2010). The definition of H remains the same as in the H-G model. A few characteristic parameters of a phase function can now be expressed in terms of G<sub>1</sub> and G<sub>2</sub>, including the phase integral, q = 0.009082 + 0.4061G<sub>1</sub> + 0.8092G<sub>2</sub>, the photometric phase coefficient, k =  $\frac{1}{5\pi} \frac{30G_1 + 9G_2}{G_1 + G_2}$ , and the amplitude of the opposition effect, ζ - 1 = (1 - G<sub>1</sub> - G<sub>2</sub>)/(G<sub>1</sub> + G<sub>2</sub>). Since the G<sub>1</sub> and G<sub>2</sub> parameters of many asteroids appear to be somehow correlated, and can be described by a two-segment linear function (*Muinonen et al.*, 2010; *Oszkiewicz et al.*, 2011), the three-parameter model can be further reduced to a two-parameter model, parameterized by H and G<sub>12</sub>. These new phase function models significantly improve the fits to existing asteroid phase function data over a wide range of phase angles up to 140°. It has been shown that asteroid taxonomy classes generally have their G<sub>1</sub>, G<sub>2</sub> parameters, and therefore G<sub>12</sub> parameters as well, clustered in parameter space (*Oszkiewicz et al.*, 2011, 2012). For example, the G<sub>12</sub> parameters of the C complex peak at ~0.65, while that of S complex peak at ~0.45.

## 2.4. Effects of Shape Models on Photometric Modeling

Among the most important photometry-related innovations in recent years has been the development and standardization of three-dimensional digital shape models for asteroids, comets, and irregularly shaped moons of the outer planets. With the advent of close-up imaging of asteroids and

other irregularly shaped bodies by spacecraft, radar observations and shape reconstruction from Earth, and sophisticated computer modeling of telescopic rotational lightcurves, it has become possible to measure the non-uniform topography of these objects and represent them in digital form. Details of these models and how they are derived can be found in the chapter by Ďurech et al. in this volume.

In photometric studies of asteroids from spacecraft missions, shape models play a critical role in the sampling of disk-resolved photometric observations from imaging data and spectrometers. That is, for disk-resolved observations, it is important to determine the photometric geometry (i.e., local angles of incidence, emission, and phase) for each point on the surface for which a corresponding brightness (i.e., radiance factor) is to be sampled. At any such point, the shape model, ephemeris, and spacecraft navigation and pointing data provide the means for computing the orientation of the local vector surface normal from which photometric angles are measured (Fig. 1).

A pitfall in the use of shape models is that, at large incidence angles (to which properties like macroscopic roughness are very sensitive), even tiny errors in the estimated angle of incidence derived from the model can lead to large errors in photometric model fits. The presence of inaccurately represented topography, e.g., small craters or ridges that are not below the spatial resolution of the topographic model, almost invariably introduce errors in the measured photometric angles. Consequently, it is common practice to exclude or otherwise apply weak statistical weighting to observations at large incidence angles from fits of photometric models to disk-resolved asteroid data.

## 2.5. Testing of Physically Motivated Models

**2.5.1. Hapke model controversy.** Shkuratov et al. (2012, 2013; see also Zhang and Voss, 2011) criticized Hapke's model on the basis of 15 alleged failures and deficiencies. While it is beyond the scope of this chapter to provide a point-by-point discussion, these criticisms about Hapke's model fall into four categories: (1) it is not rigorous in its application of electromagnetic theory and violates conservation of energy; (2) it makes unrealistic assumptions about light scattering by natural, particulate regolith surfaces and incompletely describes the dependence of scattering on photometric geometry; (3) it employs too many adjustable parameters, some of which are not truly independent variables, making it cumbersome and ambiguous to use; and (4) in the authors' tests the model exhibits unrealistic behavior in comparison to their ray-tracing predictions, showing that parameter values retrieved from fits of the model to the laboratory and lunar photometric data are unreliable.

Hapke (2013) argued that 9 of the 15 criticisms are invalid because they are based on a profound misunderstanding of his model and the assumptions that he made in deriving its components. He acknowledged that the greatest weakness in his model is that CBOE as it applies to regolith surfaces is poorly understood and consequently its treatment in his

model is imperfect and necessarily preliminary. He notes that CBOE is known to occur in regolith surfaces and it was necessary to include at least a preliminary description to model observed regolith opposition effects. Hapke does not dispute that his model is not rigorously derivable from Maxwell's equations. He argues, however, that his model is nonetheless useful when it is applied and interpreted within the limitations that are imposed by his simplifying assumptions, all of which are stated in his published derivations. In response to one criticism, Hapke acknowledged that his recent porosity correction indeed violates the conservation of energy at distances that are smaller than the interparticle separation distance. However, he points out that the violation is irrelevant because the definitions in his model are specifically made such that energy is conserved over all distances larger than the interparticle separation, which is the minimum distance over which the radiative transfer equation is applicable.

In practice, the most difficult criticism for users of the Hapke model to overcome is that its numerous coupled (i.e., non-independent) model parameters can lead to ambiguous or unreliable parameter value retrievals when applied to observations of planetary regoliths (see below). Hapke attributes the mutual dependence of the modeled regolith properties to a true property of nature and not a failure of his model. The ability to reliably retrieve meaningful values of model parameters first and necessarily depends on the availability of sufficient photometric data coverage to fully constrain the model parameters — coverage that is often neither fully available from photometric observations of planetary surfaces, nor is adequate to constrain the Hapke model fits often tested by practitioners before application. Second, judiciously chosen fitting methods can often overcome difficulties with potentially ambiguous model retrievals (cf. Hapke, 2012a; Hapke et al., 2012). In addition, it is sometimes possible to constrain some of the model parameters, even when data are insufficient to simultaneously constrain all of them by exploiting ranges of photometric angles for which the unconstrained parameters have insignificant effect (cf. Souchon et al., 2011). Finally, as discussed in Helfenstein and Shepard (2011), it is critically important to perform a thorough error analysis on the results so that ambiguous or unreliable values can be identified.

**2.5.2. Recent tests.** Investigations to validate the fidelity and physical interpretability of physically motivated photometric models fall into three broad categories: laboratory studies, computer modeling studies, and *in situ* studies. The focus of many laboratory studies has been to test and validate the Hapke model (Buratti and Veverka, 1985; Kamei and Nakamura, 2002; Cord et al., 2003, 2005; Gunderson et al., 2005; Shkuratov et al., 2007; Shepard and Helfenstein, 2007, 2011; Helfenstein and Shepard, 2011; Hapke et al., 2009; Souchon et al., 2011), as well as compare the predictions of Hapke's model to numerical light-scattering simulations (Helfenstein, 1988; Shepard and Campbell, 1998; Ciarniello et al., 2014). Finally, *in situ* studies rely on using well-sampled planetary observation datasets to derive information about the validity of Hapke's model (cf. Guiness et al., 1997;

*Verbiscer and Veverka, 1990; Domingue et al., 1997; Helfenstein et al., 1997; Helfenstein and Shepard, 1999; Hapke et al., 2012; Shepard et al., 2001, 1993.*

Studies that exploit *a priori* knowledge of the optical properties of soil components to perform forward-modeling of surface reflectance are often (but not always) more successful than efforts that aim to invert the Hapke model to assess properties of particulate surfaces from photometric observations. Forward-modeling of remotely sensed reflectance spectra with Hapke theory has been routinely accomplished for many years for a wide range of planetary objects (cf. Roush et al., 1990; Calvin and Clark, 1991; Lucey, 1998; Verbiscer et al., 2006; Wilcox et al., 2006; Denevi et al., 2008; Warell and Davidsson, 2010). The model successfully predicts the scattering behavior of idealized soil samples (Hapke et al., 2009; Hapke and Wells, 1981; Hapke, 2012b). Computer simulation studies have investigated the geological interpretation of Hapke's (1984) correction for macroscopic roughness (Helfenstein, 1988; Shepard and Campbell, 1998). More recently, for lunar soils and laboratory analog materials, photometric roughness best matches lunar regolith relief at submillimeter size scales (Helfenstein and Shepard, 1999; Cord et al., 2003; Goguen et al., 2010). Buratti and Veverka (1985) showed that photometrically detected roughness is sensitive to the albedo of the surface, with high albedos causing dilution of shadows via multiple-scattering. Tests of the opposition surge model conclude that both coherent backscatter and shadow hiding contribute to the opposition effect (Helfenstein et al., 1997; Hapke, 1998; Hapke et al., 2012). Hapke et al. (2012) found that the angular width of the lunar opposition effect does not significantly vary with optical wavelength, contrary to the current analytical treatments of coherent backscatter, which, for the Moon, predict that the width should be proportional to the square of the wavelength. In combination with experimental evidence, the observed absence of a wavelength dependence to the opposition effect suggests that our current understanding of coherent backscatter is deficient. In Monte Carlo simulation experiments verified by direct solution of Maxwell's equations, Muinonen et al. (2012) modeled scattering from a spherical volume of sparsely distributed smaller spherical scatterers (see section 2.3.4). They found that the angular width of the CBOE was independent of the packing density of small scatterers, which is best explained if the mean length of the interference base is controlled by the size-parameter of the spherical scattering volume rather than the transport mean free path that is often assumed in analytical approximations.

Attempts to validate Hapke's (1981, 1984, 1986, 2002) theory by comparing the known characteristics of laboratory samples to those predicted by fits of the model parameters to photometric observations of the samples found no compelling evidence that individual photometric parameters could be uniquely interpreted to reveal the physical state of the samples, either in an absolute or relative sense. Instead, combinations of physical properties such as particle single-scattering albedo, roughness, and porosity were convolved within each retrieved photometric parameter (Gunderson et

al., 2005; Shepard and Helfenstein, 2007; Shkuratov et al., 2007, 2012; Souchon et al., 2011). In general, the best agreement was found, at least qualitatively, between the observed microstructure of natural soil grains and the physical interpretation of retrieved particle phase function model parameters (Souchon et al., 2011; Shepard and Helfenstein, 2007).

Only recently have tests of Hapke's (2008) correction for the effects of porosity been published (see also section 2.5.1). Helfenstein and Shepard (2011) performed a preliminary test of the model by applying it to analyze laboratory analog samples from their 2007 suite of measurements (Shepard and Helfenstein, 2007). Their results suggest that Hapke's porosity correction improves the fidelity of fits to samples composed of low- and moderate-albedo particles and may allow for more reliable retrieval of porosity estimates in these materials. However, the test also suggested that in high-albedo surfaces, the effects of porosity may be difficult to detect. More recently, Ciarniello et al. (2014) use Monte Carlo simulations of ray-tracing in particulate media to test three formulations of Hapke's model: the multiple-scattering IMSA, AMSA, and an updated version of Hapke (2008). They found that, excluding the opposition effect, the Hapke (2008) model is the most accurate to describe the reflectance behaviors of particulate media with arbitrary porosities. It is also able to characterize anisotropic scattering, unless the medium exhibits a strongly forward-scattering behavior. The IMSA and AMSA models were effective only for soils with extremely large porosities.

### 3. OBSERVATIONAL DEVELOPMENTS

Prior to the advent of interplanetary space probes, all photometric observations of asteroids were telescopic, in which objects were seen only as point sources. Thus, only disk-integrated data were available. Except for Earth-crossing asteroids, the observable phase angle range was generally limited to less than 25°–30°. When spacecraft encounters with asteroids became reality, it was possible to measure an asteroid's three-dimensional shape, to observe how the brightness of the asteroid's surface varied with local photometric geometry, and to detect terrain-dependent albedo and color heterogeneities.

Spacecraft data have their own limitations in photometric modeling, too. For some orbit missions, such as Dawn (Russell et al., 2012; see also the Russell et al. chapter in this volume) that use polar orbits, there may be a correlation between latitude and phase angle since the cameras observe the surface in the nadir direction ( $e \approx 0^\circ$ ) (e.g., Li et al., 2013a). When the field-of-view of the camera is small compared to the angular size of the target, this can introduce a bias to the observations. For fast flyby observations, the illumination geometry does not change much from image to image taken within a short duration (typically  $<1$  h), which is much shorter than the rotation period of most asteroids, and the flyby. Derivation of a shape model may then be restricted by very limited illumination and surface coverage, and the photometric analysis would be subject to

the same limitations. Spatial resolution and uncertainties in shape can also limit the accuracy of photometric models. These limitations should be considered in the modeling and interpretation of disk-resolved photometric data.

Since the first asteroid flyby of (951) Gaspra by the Galileo spacecraft in 1991 (Belton et al., 1992; Veverka et al., 1994), 13 asteroids have been imaged by spacecraft either from flybys or rendezvous. Seven asteroids were visited since the publication of *Asteroids III*, and (1) Ceres is being visited by Dawn as of early 2015. Of the seven newly imaged asteroids, the data of (25143) Itokawa (see the chapter by Yoshikawa et al. in this volume; Kitazato et al., 2008), (2867) Šteins (Barucci et al., this volume; Spjuth et al., 2012), (21) Lutetia (Barucci et al., this volume; Magrin et al., 2012; Masoumzadeh et al., 2014), and (4) Vesta (Russell et al., this volume; Li et al., 2013a; Schröder et al., 2013; Longobardo et al., 2014) are of sufficient resolution and quality to perform detailed, disk-resolved photometric studies. The images of (5535) Annefrank from the Stardust flyby were of low resolution, and only disk-integrated analysis has been performed from the spacecraft data (Hillier et al., 2011). The flyby of (132524) APL by New Horizons was serendipitous at a large distance and the returned images resemble point sources, and therefore no photometric modeling was performed. No report about the photometric properties of (4179) Toutatis from the Chinese Chang'e 2 flyby images (Huang et al., 2013; Barucci et al., this volume) has yet become available. (1) Ceres was observed by the Hubble Space Telescope (HST) in 2003/2004 with the Advanced Camera for Surveys (ACS) High Resolution Channel (HRC), and resolved to  $\sim 30$  km/pixel, facilitating the study of its disk-resolved photometric properties (Li et al., 2006). In this section, we will summarize the photometric results for Ceres, Itokawa, Šteins, Lutetia, Vesta, and Annefrank.

### 3.1. (1) Ceres

Ceres represents a thus-far unique category of asteroids or dwarf planets (cf. Rivkin et al., 2011). Ample evidence suggests that water must have played an important role in its evolutionary history and its current status (Rivkin et al., 2011). The recent unambiguous discovery of water vapor associated with localized sources on Ceres indicates a possibly active surface at the present (Küppers et al., 2014).

Li et al. (2006) reported a detailed photometric analysis of Ceres based on the images collected by the HST/ACS through three broadband filters centered at 535, 335, and 223 nm obtained in 2003/2004 at a narrow range of phase angles of  $5^\circ$ – $7^\circ$ . The disk-resolved analysis focused on studying the limb-darkening behavior to derive the roughness, and determining the single-scattering albedo. Li et al. reported a Hapke roughness parameter of  $44^\circ \pm 5^\circ$  for Ceres, much higher than those of all other objects that have been modeled with Hapke functions that include roughness (Table 6). Given that the roughness of all other objects were derived from images with much higher spatial resolution than those of Ceres, it is a question whether this high roughness is real

or an observational artifact. Indeed, the small angular size of Ceres ( $\sim 30$  pixels across) and the point spread function of the optical system could blur the edge of Ceres' disk, so that the brightness decreases toward the limb are much faster than the real surface, yielding higher roughness in the modeling. This effect probably also explains the fact that the Hapke and Minnaert model could only fit Ceres' disk within  $40^\circ$ – $50^\circ$  photometric longitude/latitude as shown by Li et al. On the other hand, the high photometric roughness of Ceres is consistent with its high radar roughness of  $20^\circ$ – $50^\circ$  (Mitchell et al., 1996), although the same radar observations also indicate that the surface of Ceres is very smooth at centimeter to decimeter scales, probably indicating different roughness at different scale sizes.

The photometric analysis in the visible and near-infrared wavelengths suggested a remarkably uniform surface of Ceres in its albedo and color (Li et al., 2006; Carry et al., 2008, 2012). The albedo maps at all three wavelengths show variations of only 4% full-width-at-half-maximum (FWHM), and about  $\pm 6\%$  peak-to-peak. Compared with other solar system objects with their surface photometric variations determined, Ceres certainly has the most uniform surface so far (Li et al., 2006). Of course, with much higher spatial resolutions in the data to be collected by Dawn, it cannot be excluded that some local areas on Ceres that are much smaller than the HST image resolution have larger albedo and/or color variations from the global average. But those small areas should not dramatically change the overall distribution of the surface albedo and color on Ceres.

### 3.2. (25143) Itokawa

Lederer et al. (2005) used broadband BVRI photometry of the S-type asteroid Itokawa between  $4^\circ$  and  $90^\circ$  phase angles obtained from the ground to characterize this target asteroid of Hayabusa prior to its launch. The authors used a Hapke model to derive a single-scattering albedo of 0.36, and a highly backscattering single particle phase function with  $g = -0.51$ , although the roughness and opposition surge parameters were assumed and could have driven this number to be large. Lederer et al. found that Itokawa has a higher albedo than average main-belt S-class asteroids. However, limited by disk-integrated observations and the lack of data at small phase angles, their models have to assume an opposition surge and the common values of roughness of  $20^\circ$  and  $36^\circ$ .

The Japanese Hayabusa spacecraft visited Itokawa in 2005 (see chapter by Yoshikawa et al. in this volume; Fujiwara et al., 2006). Kitazato et al. (2008) conducted a photometric analysis of Itokawa using disk-resolved reflectance spectra measured by the Near-infrared Spectrometer (NIRS) over multiple wavelengths ranging from 0.85 to  $2.10\text{ }\mu\text{m}$  covering phase angles from near  $0^\circ$  to  $38^\circ$ . Using a Hapke photometric model analysis, the authors found that Itokawa has a single-scattering albedo that is 35–40% less than that of asteroid (433) Eros, consistent with the results of Lederer et al. (2005). The data at low phase angles enables modeling of opposition effect. While Kitazato et al. (2008) only included

TABLE 6. Comparison of the Hapke photometric parameters of asteroids.

Object	Type	$\pi$ (visible)	h	$B_0$	g	$\theta(^{\circ})$	Reference
Average S		0.23	0.08	1.6	-0.27	20	Helfenstein and Veverka (1989)
Average C		0.037	0.025	1.03	-0.47	20	Helfenstein and Veverka (1989)
Average V (NEOs and Vesta)		0.51	0.098	1.0	-0.26	32	Hicks et al. (2014)
(4) Vesta	V	0.51	0.07	1.7	-0.24	18	Li et al. (2013a)
(951) Gaspra	S	0.36	0.06	1.63	-0.18	29	Helfenstein et al. (1994)
(243) Ida	S	0.22	0.02	1.53	-0.33	18	Helfenstein et al. (1996)
Dactyl	S	0.21	(0.020)	(1.53)	-0.33	23	Helfenstein et al. (1996)
(433) Eros	S	0.43	0.022	1.0	-0.29	28	Li et al. (2004)
(25143) Itokawa	S	0.36	(0.022)	(1.0)	-0.51	(20)	Lederer et al. (2005)
(25143) Itokawa	S	0.42	0.01	0.87	-0.35	26	Kitazato et al. (2008)
(5535) Annefrank	S	0.41	0.015	1.32	-0.19	20	Hillier et al. (2011)
(1862) Apollo	S						Helfenstein and Veverka (1989)
(253) Mathilde	C	0.034	0.094	3.18	-0.27 (two-term fit)	25	Clark et al. (1999)
(1) Ceres	C	0.070	0.06	1.6	-0.4	44	Helfenstein and Veverka (1989), Li et al. (2006)
(2867) Šteins	E	0.57	0.062	0.60	-0.30	28	Spjuth et al. (2012)
(21) Lutetia	M	0.23	0.044	1.93	-0.25	25	Masoumzadeh et al. (2014)

Values inside parentheses are assumed.

SHOE but not CBOE in the Hapke modeling, they observed wavelength dependence of the width of opposition effect, and attributed it to coherent backscattering. Compared to Eros, the lower-opposition amplitude indicates weaker contribution of the SHOE component, and the narrower width is consistent with relatively more densely packed particles in the regolith of Itokawa. The roughness parameter for Itokawa was estimated to be  $26^{\circ}$ , similar to that of Eros'. The modeled parameters of opposition effect and roughness justify the assumptions made in Lederer et al.'s (2005) work, although those studies were performed at a different wavelength regime.

### 3.3. (2867) Šteins

Spjuth et al. (2012) performed detailed photometric analyses of asteroid Šteins, the first E-type asteroid visited by spacecraft, using multi-spectral images acquired by the OSIRIS Wide Angle Camera (WAC) onboard the Rosetta spacecraft (Keller et al., 2007). An extremely wide range of phase angles from  $0.36^{\circ}$  to  $130^{\circ}$  was achieved through one filter centered at 630 nm, allowing for modeling of the opposition effect. The authors estimated the single-scattering albedo to be 0.57, the highest ever found for small bodies visited by spacecraft. The roughness is  $28^{\circ}$ , and the asymmetry factor of the 1PHG single-particle phase function is -0.27. The geometric and Bond albedos of Šteins were derived to be  $0.39 \pm 0.02$  and  $0.24 \pm 0.01$ , respectively. The high albedo of Šteins is consistent with the iron-poor

surface composition of the asteroid (Barucci et al., 2012). To study the photometric variations across the surface of Šteins, Spjuth et al. (2012) generated maps of Hapke photometric parameters, including the single-scattering albedo, roughness, and asymmetry factor of the 1PHG function, by assuming that the reflectance variation is entirely caused by one single parameter while keeping the others fixed at their respective global averages. These maps probably represent the highest possible variations in each single photometric parameter. As indicated by these maps, the surface of Šteins seems to be highly homogeneous, with a standard deviation of 0.01 for its single-scattering albedo,  $3.4^{\circ}$  for roughness, and 0.003 for the asymmetry factor. The uniform surface of Šteins is consistent with the results reported by Leyrat et al. (2010), who applied photometric correction to the flyby images with a Hapke (2002) model and performed a statistical analysis, and find no surface inhomogeneities larger than 4% at the 95% confidence level.

The photometric properties of Šteins are interpreted as the consequence of its regolith properties (Spjuth et al., 2012). The strong opposition effect and high albedo are consistent with porous, fine-grained regolith, which is consistent with the studies of aubrite meteorites, which are considered to be analog to E-type asteroids, and laboratory work (Gaffey et al., 1989; Shepard and Helfenstein, 2007). The low amplitude of SHOE indicates relatively transparent regolith particles, and/or a large density of internal scatterers of opaques. The width of opposition effect is also consistent with a high porosity of ~84% for the regolith particles.

### 3.4. (21) Lutetia

*Belskaya et al.* (2010) obtained groundbased BVRI photometric and V-band polarimetric measurements of Lutetia over a wide range of phase angles ( $0.5^\circ$ – $22.2^\circ$ ). The authors found that Lutetia has a nonconvex shape and heterogeneous surface properties, due possibly to a large crater and the variations in the texture and/or mineralogy, respectively. The polarimetric properties of Lutetia suggest a fine-grained regolith with a mean grain size smaller than  $20\text{ }\mu\text{m}$ , and a carbonaceous composition (CO, CV, CH). The Rosetta spacecraft flew by Lutetia at a close encounter distance of  $\sim 3200\text{ km}$  on July 10, 2010. The flyby geometry at Lutetia is similar to that at Šteins, while multicolor images were acquired through both WAC and the narrow angle camera (NAC) throughout the flyby, providing phase angle coverage from less than  $1^\circ$  to  $130^\circ$  at multiple wavelengths. Based on these data, *La Forgia* (2014) conducted a photometric analysis of Lutetia with a disk-integrated Hapke model. They showed that all the modeled parameters depend on wavelength. However, it has to be noted that their modeling is based on disk-integrated phase functions, and therefore strong coupling exists between at least the roughness parameter and the phase function. The photometric analysis of Lutetia showed that the asteroid's surface is composed of particles that have high reflectivity. *La Forgia* also found that Lutetia's surface is generally smooth and characterized by a low porosity. These results are consistent with the conclusion that Lutetia is an ancient planetesimal rather than a reaccumulated object, as indicated by its large diameter of  $98 \pm 2\text{ km}$  (*Sierks et al.*, 2011a) and its high density of  $3.4 \pm 0.3 \times 10^3\text{ kg m}^{-3}$  (*Pätzold et al.*, 2011). *Masoumzadeh et al.* (2014) performed a disk-resolved photometric analysis with the Hapke model and the Minnaert model using the Rosetta flyby data. They reported no wavelength dependence on the Minnaert k parameters, which is different from the *La Forgia* (2014) results. In addition, in their Hapke modeling, they derived very different single-scattering albedo with 1PHG and 2PHG single-particle phase function (0.26 vs. 0.49, respectively).

### 3.5. (4) Vesta

Dawn's rendezvous with Vesta provided us with high-resolution imaging data (*Russell et al.*, 2012, 2013; see also the chapter by Russell et al. in this volume). *Li et al.* (2013a) performed a thorough analysis of the global photometric properties of Vesta using Dawn Framing Camera (FC) (*Sierks et al.*, 2011b) images with pixel scale  $>0.25\text{ km/pixel}$  through all filters, including one clear filter and seven mid-band ( $\sim 100\text{-nm bandpass}$ ) color filters with center wavelengths from 440 nm to 960 nm. Dawn data cover a range of phase angles from  $\sim 7^\circ$  to  $\sim 90^\circ$  for disk-resolved data in all filters, and from  $\sim 24^\circ$  to  $\sim 108^\circ$  for disk-resolved data through the clear filter. *Li et al.* (2013a) found that the photometric behavior of the surface of Vesta is well described by a Hapke model and a Minnaert model, but the LS model cannot reproduce the limb-to-terminator brightness trends. The phase

functions of Vesta show weak dependence on wavelength, qualitatively consistent with previous groundbased observations (*Reddy et al.*, 2012a), but about a factor of 0.5 weaker (*Li et al.*, 2013a). The phase reddening of Vesta as observed by Dawn is similar to, or slightly stronger than, that of Eros observed by the Near Earth Asteroid Rendezvous (NEAR) mission (*Clark et al.*, 2002). The Hapke roughness parameter of Vesta is consistent at all wavelengths studied. While roughness parameter is a geometric parameter and is not supposed to depend on wavelength, for high-albedo surfaces, multiple scattering into shadows could in principle wash out shadows and result in lower modeled roughness. The lack of such effects on Vesta suggests that this effect is small for a single-shattering albedo of  $<0.55$  and a roughness of  $\sim 20^\circ$ . Compared with other asteroids studied so far, the globally averaged photometric properties of Vesta are similar to those of S-type asteroids, except for its albedo, which is about twice the average albedo of S-types.

Vesta has a highly heterogeneous surface in almost all aspects (*Reddy et al.*, 2012b; *Jaumann et al.*, 2012; *Prettyman et al.*, 2012; *De Sanctis et al.*, 2012a, 2013; *Ammanito et al.*, 2013). Its albedo and color variations have been recognized previously from groundbased and HST observations (*Gaffey*, 1997; *Binzel et al.*, 1997; *Li et al.*, 2010; *Reddy et al.*, 2013). The albedo and color maps generated from Dawn FC data further show that such heterogeneity is at almost all scale sizes, and reveal many localized areas with distinctly high and low albedos (*McCord et al.*, 2012). The overall distribution of albedo on Vesta has a FWHM of  $\sim 17\%$ , but the localized bright and dark areas have albedos from about one-half to greater than twice the average (*Li et al.*, 2013a). The single-peaked albedo distribution on Vesta is presumably a result of strong regolith mixing on Vesta caused by the complicated impact history of Vesta (*Pieters et al.*, 2012), different from the bimodal distribution on the Moon as dominated by compositional heterogeneity (e.g., *Helfenstein and Veverka*, 1987; *Hillier et al.*, 1999; *Yokota et al.*, 2011).

*Schröder et al.* (2013) reported correlations between the spatial variations in the surface phase function of Vesta and geology. After correcting the limb-to-terminator brightness trend on Vesta, they were able to map out the slopes of the surface phase functions over the whole illuminated surface of Vesta. The slope of phase function shows clear global distribution correlated with albedo and mineralogical units. Eucrite-dominated regions (*Ammanito et al.*, 2013) have relatively steeper phase functions. Since those regions are also correlated with the enriched distribution of dark material, which is interpreted as exogenous carbonaceous material delivered by impactors (*McCord et al.*, 2012; *Reddy et al.*, 2012c; *Prettyman et al.*, 2012; *De Sanctis et al.*, 2012b; *Turrini et al.*, 2014), such correlation between albedo and phase function on Vesta probably manifests the general correlation in the asteroid belt (e.g., *Bowell and Lumme*, 1979). Furthermore, on local scales, the phase function slopes are steeper on crater floors than on crater walls, interpreted as a variation in roughness due to the accumulation of loose material inside craters causing higher roughness.

*Longobardo et al.* (2014) and *Li et al.* (2013c) analyzed the visible and NIR data collected by Dawn's Visible and Infrared (VIR) instrument (*De Sanctis et al.*, 2011), but this work is still ongoing as of the writing of this chapter. The preliminary results reported by *Li et al.* (2013c) using VIR data were inconsistent in the overlapping wavelengths with those derived from the FC data taken at similar mission phases, tentatively attributed to instrumental effects. *Longobardo et al.* (2014) took a completely empirical approach with the Akimov model to fit VIR data and study the dependence of pyroxene band parameters on scattering geometry with the focus on bright and dark regions on Vesta. Their results should be less dependent on instrumental effects. The trend of band parameters with respect to scattering geometry derived from VIR data is shown to be consistent with previous observations from the ground (*Reddy et al.*, 2012a).

### 3.6. (5535) Annefrank

Disk-integrated Stardust observations of Annefrank obtained between  $47^\circ$  and  $135^\circ$  were combined with ground-based measurements obtained between  $2^\circ$  and  $18^\circ$  and analyzed by *Hillier et al.* (2011). This asteroid exhibits a steep phase curve, resulting in a very large roughness parameter of  $49^\circ$ , an unusually large single-particle-scattering albedo of 0.62, and a Henyey-Greenstein phase function,  $g$ , of  $-0.09$ , which is more isotropic than the usual strongly backscattering S-type asteroids. The shadow-hiding opposition surge width  $h = 0.015$  is more typical of the S-types. Because the shape of Annefrank is irregular, these fits to a full excursion in solar phase angle may not be unique, especially with disk-integrated data only. *Li et al.* (2004) have shown that the assumption of sphericity can lead to an overestimate of both the single-scattering albedo and the roughness parameter and a more isotropic phase function, particularly if measurements at large solar phase angles are included in modeling. *Hillier et al.* (2011) restricted their fits to  $90^\circ$  and found more typical parameters of  $20^\circ$  for the roughness parameter, 0.41 for the single-scattering albedo, and  $-0.19$  for  $g$ . Still, the single-scattering albedo of Annefrank is high.

## 4. APPLICATIONS AND INTERPRETATIONS

### 4.1. Correction for Spectral Analysis

**4.1.1. Photometric correction.** Most of the changes in the reflectance of an asteroid surface are not intrinsic but rather due to variations in viewing geometry. With a description of the photometric functions of the surface, all the non-intrinsic variations can be removed and a map of the normal reflectance or a physical parameter such as the single-scattering albedo can be produced. Since the three geometric parameters for the scattering,  $i$ ,  $e$ , and  $\alpha$ , are known *a priori* (if one possesses an accurate shape model for nonspherical bodies, which is often a requirement for asteroids), fitting a photometric function or model to space-

craft or groundbased images provides all the information needed to perform photometric corrections.

The usual procedure for photometric correction as in equation (1) is to (1) use the observed data to fit a global average photometric model, (2) calculate the ratio of the measured reflectance over the model reflectance for each surface element, and (3) multiply the ratio by the model reflectance at the desired reference geometry. In this procedure, the ratio calculated is a measure of the deviation between the actual surface reflectance and the best-fit model, and the user has a choice of reference geometries for the correction. The implicit assumptions behind the photometric correction are that (1) any deviation between the measured reflectance and the best-fit model must be real, and not due to imperfections in the photometric model or the shape model; and (2) the deviation factor is independent of scattering geometry. We shall now discuss the implications of these two assumptions.

The first assumption can sometimes be verified by fitting several different models to the same data and comparing the resultant photometric corrections, but this is often limited by data availability. Therefore, one has to judge what features in the photometrically corrected maps are real and what are artifacts based on the magnitude, scale size and shape, geologic and compositional context, etc., on a case-by-case basis. In our discussion about the second assumption (next), we will assume that the first assumption is true.

For the second assumption, two different cases exist. The first case is that the reflectance variation from the best-fit model prediction is dominated by the single-scattering albedo variation rather than variations in other photometric properties such as phase function or roughness. If albedo is low and multiple scattering is insignificant, then the reflectance is approximately proportional to the single-scattering albedo (see section 2). Thus, the deviation factor represents how much the albedo at a particular surface location deviates from the global average, and should not depend on scattering geometry. The assumption is justified. On the other hand, for high-albedo cases where multiple scattering is significant, the proportionality between single-scattering albedo and reflectance is broken, and photometric correction needs to be performed taking into account the nonlinear effect. This is a complicated process but feasible. The second case is the opposite of the first case: The variation in phase function and/or roughness dominates the deviation factors. Since the effects of phase function and roughness always depend on phase angle, so does the deviation factor. In this case, photometric correction cannot be reliably applied. For example, it is well known that variations in photometric properties other than albedo exist on the Moon, where multiple photometric models are derived for different regions based on their albedos, and photometric corrections are performed based on the corresponding models (e.g., *Yokota et al.*, 2011; *Besse et al.*, 2013; *Wu et al.*, 2013). The work of *Schröder et al.* (2013) also shows that this case exists on Vesta. One has to be aware of this constraint when interpreting data products that involve a photometric correction of a bright surface.

The selection of an appropriate photometric model for the surface is important when performing a photometric correction. In principle, any photometric model that can describe the photometric behavior of the target asteroid surface sufficiently well can be used for photometric correction, whether or not physical interpretations of model parameters are possible. Although radiative transfer models can be used to derive intrinsic physical parameters such as the single-scattering albedo or normal reflectance, unless a wide range in solar phase angles is available, unique fits to parameters in Hapke-type models are not possible (Helfenstein *et al.*, 1988). For practical photometry, empirical functions are often preferred due to their simple mathematical forms and fewer free parameters.

**4.1.2. Phase reddening.** It is well known that spectra of asteroids, and many other airless bodies, become redder as the solar phase angle increases (see review in Gehrels, 1970; Gradie and Veverka, 1986). This phenomenon of “phase reddening” is most pronounced in S-type asteroids: Bowell and Lumme (1979) found that between 0.35  $\mu\text{m}$  and 0.55  $\mu\text{m}$  the effect was 2–3 $\times$  greater for S-type asteroids than for C- or M-types. It is generally considered that phase reddening is related to the increase in spectral reflectance with wavelength. For example, the albedo of S-type asteroids doubles between 0.35  $\mu\text{m}$  and 0.8  $\mu\text{m}$  (Tedesco *et al.*, 1989). The physical reason for the reddening probably lies in the relative importance of multiple scattering: As the albedo increases, the amount of radiation that has been multiply scattered also increases. The singly scattered radiation is backscattering, while the multiply scattered radiation tends to be isotropic. Thus, at large solar phase angles, in the forward-scattered direction, the multiply scattered photons are relatively more important. Since there are more such photons as the albedo increases, the reflectance becomes redder at large phase angles. The spectra of S-type and A-type asteroids exhibit the most significant changes in albedo through the visible range of the spectrum, so they should exhibit more phase reddening than the flat C- or M-types. The spectrally unique C-class asteroid Ceres has an almost featureless spectrum between 0.4  $\mu\text{m}$  and 2.4  $\mu\text{m}$  and it exhibits no phase reddening (Tedesco *et al.*, 1983). But the connection between phase reddening and albedo is not straightforward. For example, the bright V-type asteroids, for which a composite solar phase curve was constructed from near-Earth objects (NEOs), exhibit phase reddening of only 0.002 mag/deg in B-R and 0.0016 mag/deg in I-R, even though this class of asteroids typically changes in albedo by a factor of 2 between the B and I filters (Hicks *et al.*, 2014).

Even with a spectrally flat body it is possible to get phase reddening. At larger solar phase angles, shadows cast by rough features occupy an increasing fraction of the face of the object as seen by an observer. Although these shadows are dark shadows for low-albedo surfaces, they are partly illuminated by multiply scattered photons for high-albedo objects. Thus, only low-albedo objects with flat spectra should exhibit no solar phase reddening, which is the case for Ceres, which has a visible geometric albedo of 0.09.

## 4.2. Taxonomic Classes

The application of photometric models to spacecraft images, coupled with the acquisition of measurements of near-Earth asteroids (NEAs) at large solar phase angles not attainable from the ground for asteroids in the main belt, has led to the robust modeling of a sufficient number of asteroids so that trends among the various classes of asteroids can be studied. Asteroid spacecraft observations that have been fit with photometric models are listed in Table 6, together with the modeling results. Photometric modeling of groundbased measurements of NEAs has been done for (1862) Apollo, a rare Q-type asteroid (Helfenstein and Veverka, 1989). In addition, a composite solar phase curve of V-type asteroids was created from NEA observations and fit with both Hapke and Lumme-Bowell models (Hicks *et al.*, 2014). The phase functions of C-, S-, and V-type asteroids are plotted in Fig. 2.

Asteroid (1862) Apollo, an NEA that is a member of the rare Q-type class, was observed extensively during its apparitions in 1980 and 1982 (Harris *et al.*, 1987). Q-types are similar to S-types, but have higher albedos and are consistent with non-space-weathered materials, relative to the S-types (Binzel *et al.*, 2010). The Q-types have a slightly more isotropic phase function, due possibly to this higher albedo: Multiply scattered photons tend to be more isotropic than singly scattered photons. The smaller roughness parameter may also be the result of the asteroid’s higher albedo, as multiply scattered photons partly illuminate shadows cast by rough features and lead to an underestimate of the roughness parameter.

Helfenstein and Veverka (1989) derived an average S- and C-type asteroid over the range of solar phase angles for the main belt ( $\sim 0^\circ$ – $30^\circ$ ). The small number of S-type asteroids that have been observed with spacecraft, and thus over a larger excursion in solar phase angles, have not shown a strong correlation in derived Hapke parameters (Table 6). This lack of correlation may be due to different solar phase angle sampling, or to non-unique fits, or to the models not fully accounting for the effects of multiple scattering, which partly illuminate primary shadows for both the roughness model and for the opposition surge shadow-hiding model. Or perhaps it is due to the lack of correlations between Hapke parameters and physical properties (Shepard and Helfenstein, 2007). It is also important to separate NEA and main-belt populations because the NEAs are not as weathered and are smaller and thus expected to have less substantial regoliths.

Nevertheless, Belskaya and Shevchenko (2000) noted the correlations in Fig. 3 of the Lumme-Bowell two-parameter IAU convention. Higher-albedo asteroids have larger single-scattering albedos and larger slope parameters (G-parameter). The Henyey-Greenstein parameter is slightly more forward scattering for high-albedo asteroids, which is to be expected if they are more isotropic. The opposition surge parameter also tends to decrease as the albedo increases, with a slight decrease in the compaction state. The only C-type asteroid modeled (Mathilde) seems to confirm this trend: Its

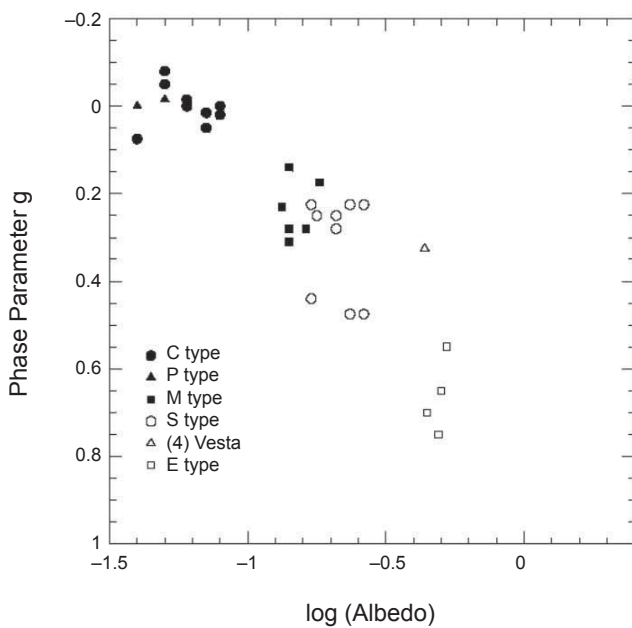


**Fig. 3.** The H and G parameters of the Lumme-Bowell model correlate well with asteroid class. The low-albedo primitive type have lower phase parameters G, while the higher-albedo asteroids have larger G. Figure based on Belskaya and Shevchenko (2000) and Hicks et al. (2014).

opposition surge amplitude of  $3.18 \pm 1.0$  (Clark et al., 1999) is significantly higher than the typical S-type of 1–2. Whether this effect is due to actual physical changes or a decrease in multiple scattering, which is not fully accounted for in Hapke's models, remains to be seen as more asteroids are studied using radiative transfer models over more uniform phase angle sampling. Ceres, an atypical asteroid that is difficult to classify but is akin to the C-types, has an amplitude of only 1.6, so perhaps as more observations are gathered, Mathilde will be shown to be anomalous.

Benner et al. (2008) found a correlation between the roughness of NEA asteroid classes at radar wavelengths and asteroid class, with E- and V-types being the roughest. However, in visible wavelength imaging data, Vesta appears to have a typical (not unusually rough) surface (Li et al., 2013a). This could be explained by the infilling of facets and asperities on the surface by fine particles, similar to the “ponding” seen on Itokawa and Eros, but on a smaller scale, so as not to be detected by radar wavelengths. With the larger gravity field of Vesta, small particles would be more likely to be retained than on the smaller asteroids.

#### 4.3. Context of Geological Process

**4.3.1. Roughness.** The roughness and size scale of features on planetary surfaces yield clues to a wide range of geophysical processes. Heavily cratered surfaces tend to exhibit large slope angles, while bodies that have undergone resurfacing due to volcanism are smoother. The accretion of

dust or volatiles onto a surface could also infill facets to form a smooth surface. For example, the low-albedo hemisphere of Iapetus is smooth because features have been infilled with dust from Saturn's Phoebe ring (Lee et al., 2009). Regions with low surface roughness could be indicative of recent activity involving possible debris flows or ponding (Veverka et al., 2006; Robinson et al., 2001). On Vesta, crater walls tend to be smoother than crater floors due to the accumulation of mass-wasted materials in the crater (Schröder et al., 2013). Differences in roughness also provide a basis for chronology of various terrains, as rougher surfaces have been subjected to more impacts. Global roughness is also affected by the mass of the body: Stronger gravitational wells tend to hold particles that are the result of meteoritic bombardment and that infill surface asperities. Viscous relaxation, which is a function of surface temperature and composition, can also smooth out a surface.

**4.3.2. Particle size and packing status.** Irvine's (1966) model of the opposition shadow hiding effect assumes that particles comprising the regolith are in the geometric optics limit ( $r \gg \lambda$ ), spherical, single-sized, and sufficiently low in albedo so that multiple scattering can be neglected. The amplitude of the surge is determined primarily by a compaction parameter, defined by  $(3/4\pi)(\rho/\rho_0)$ , where  $\rho$  is the bulk density of the regolith particles and  $\rho_0$  is the density of an individual particle. Irvine's model is an analytical one that keeps track of shadows cast by regolith particles, as well as the fraction of individual particles that are visible to the observer and illuminated, as a function of solar phase angle. As compaction parameter increases and the surface becomes less porous, the amplitude of the opposition surge decreases. For Hapke's model of shadow hiding the amplitude of the opposition effect,  $B_{0,SH}$  depends on the transparency of regolith grains;  $B_{0,SH} = 0$  for ideally transparent grains, and  $B_{0,SH} = 1$  for opaque ones. In a collection of uniform particles with no multiple scattering, the angular width parameter  $h_{SH}$  is equal to  $(3/8)K(1-\rho/\rho_0)$  (Hapke, 2012b). As the voids increase,  $h_{SH}$  decreases. In addition, Hapke's latest model (Hapke, 2008, 2012a) presents a more complicated picture where, in general, increasing filling factor (decreasing the porosity) increases the reflectance of low- and medium-albedo powders, but decreases reflectance for those with very high albedos.

Geophysical processes that cause porous surfaces include micrometeoritic bombardment, fallout of frost or dust from volcanic processes, and infall of ambient dust from interplanetary space or from rings. Mechanisms causing more compacted surfaces include annealing by high-energy particles, extrusion of fluids or dust-laden slurries, and viscous slumping. Intermediate porosities are caused by processes such as fluid-like flow of dust and “ponding” of regolith particles.

In the geometric optics limit it is difficult to derive particle sizes, not only because the shadowing process is scale invariant, but also because different combinations of size distributions give similar porosities. The current shadow-hiding models also do not fully account for the effect of multiply scattered photons. These photons will partly illuminate primary shadows so that additional photons are

scattered back into the direction of the observer with the result that the porosity will be underestimated.

## 5. SUMMARY AND FUTURE PERSPECTIVES

In conclusion, we have summarized the most recent developments in asteroid photometry since the publication of *Asteroids III*. Advancements have been made in all three areas of theory, laboratory measurement, and spacecraft observation.

We have shown that photometric modeling is important for understanding what the light-scattering behavior of an asteroid surface can tell us about the physical and compositional properties of the asteroid. We have shown that photometric modeling is important for “correcting” all spectral and imaging data to a common reference viewing geometry before intercomparisons can be made between spectral and imaging observations. And, finally, we have shown that photometric modeling is important for extrapolating specific reflectance calculations to yet-unobserved viewing geometries for the purposes of observation planning, either from the ground or from spacecraft platforms.

As discussed earlier, the past decade has seen improvements in the ability of physically motivated photometric models to accurately relate the observed photometric behavior of a regolith-covered body to the physical properties of the surface and the optical properties of its constituents. Studies suggest that, in particular, the Hapke model is realistic when macroscopic surface relief and complex particle shapes can be ignored (Hapke et al., 2009). However the approach is not entirely reliable and work is especially needed to better understand the opposition effect. In particular, the roles of coherent-backscatter, shadow-hiding, and macroscopic surface roughness need to be clearly resolved and tested. Hapke et al. (2012), for example, found no wavelength dependence of the opposition effect for lunar terrains — a result that conflicts with his model for the CBOE (Hapke, 2002, 2012). The relative contributions of CBOE and SHOE have yet to be clearly resolved in photometric studies. When both opposition effects are fit to planetary data, CBOE typically models a very narrow “opposition spike” at phase angles less than a few degrees, while SHOE, which was formerly invoked to model the entire opposition effect, now typically describes a broader angular component that may extend to a few tens of degrees in width (cf. Helfenstein et al., 1997). This range overlaps with the predicted phase angle effects from macroscopic surface roughness (Hapke, 1984). It may turn out that the individual contributions of each mechanism cannot be uniquely identified by photometric observation alone, and that polarimetric modeling may provide important missing clues (see the chapter by Belskaya et al. in this volume). Furthermore, theoretical models have been tested to the point that the viewing geometry conditions necessary for the retrieval of important physical properties (porosity, and average particle phase functions) of the asteroid surface are now defined (Hapke, 2008; Souchon et al., 2011; Helfenstein and

Shepard, 2011). These developments should be considered in future investigations, specifically from spacecraft platforms.

Laboratory measurements have been critical to the advancement of the theory and the interpretation of spacecraft measurements (e.g., Helfenstein and Shepard, 2011 and references therein).

Finally, spacecraft measurements have been obtained of Ceres, Itokawa, Šteins, Lutetia, Annefrank, and Vesta, and all these data have been fit with photometric models that have deepened our understanding of both asteroid surfaces and the photometric modeling process. We have reviewed how these additional observations can be compared with the existing observations of Gaspra, Ida, and Eros to form the basis of a developing dataset of asteroid light-scattering studies as a function of asteroid spectroscopic classification and mineralogical composition.

Future work should be informed by the need for observations at a wide range of solar phase angles, including near opposition and near or greater than 100° — for the purposes of determining asteroid surface physical characteristics. Future work should also increase the sampling of the spectral classes in observations obtained from spacecraft platforms. Finally, future work should synthesize spacecraft, laboratory, and groundbased surveys of asteroid surface physical properties and their compositional dependence.

Other future work in asteroid photometry might result in sufficient sampling of spatially resolved scattering behavior such that actual physically meaningful scattering model parameters can be mapped across the surface, such as in the work of Sato et al. (2014), who present and interpret Hapke model parameter maps of the lunar surface. These workers find decreased backscattering in the maria relative to the lunar highlands, consistent with known compositional and space weathering differences between maria and highlands, and suggesting powerful new ways to potentially study variations across the surface of an asteroid. For example, the near-future Origins Spectral Interpretation Resource Identification and Security-Regolith Explorer (OSIRIS-REx) mission will obtain large numbers of repeated observations of the surface of asteroid (101955) Bennu, sampling a wide range of viewing angles for each surface facet, conceivably enabling the first Hapke model parameter maps of an asteroid surface.

**Acknowledgments.** Support for J.-Y. L. is partly from NASA Dawn at Vesta Participating Scientist Program grant NNX-13AB82G. P.H. gratefully acknowledges support from NASA Planetary Geology and Geophysics Program grant NNX14AN04G. The thoughtful reviews from Dr. Karri Muinonen and Dr. Bruce Hapke have helped us greatly improve the manuscript.

## REFERENCES

- Akimov L. A. (1988) Light reflection by the Moon. I. *Kinem. Phys. Celest. Bodies*, 4, 3–10.
- Ammannito E. et al. (2013) Vestan lithologies mapped by the visual and infrared spectrometer on Dawn. *Meteoritics & Planet. Sci.*, 48, 2185–2198.

- Barucci M. A. et al. (2012) Overview of Lutetia's surface composition. *Planet. Space Sci.*, 66, 23–30.
- Belskaya I. N. and Shevchenko V. G. (2000) Opposition effect of asteroids. *Icarus*, 147, 94–105.
- Belskaya I. N. et al. (2010) Puzzling asteroid 21 Lutetia: Our knowledge prior to the Rosetta fly-by. *Astron. Astrophys.*, 515, Article ID A29.
- Belton M. J. S. et al. (1992) Galileo encounter with 951 Gaspra: First picture of an asteroid. *Science*, 257, 1647–1652.
- Benner L. A. et al. (2008) Near-Earth asteroid surface roughness depends on compositional class. *Icarus*, 198, 294–304.
- Besse S. et al. (2013) A visible and near-infrared photometric correction for Moon Mineralogy Mapper (M<sup>3</sup>). *Icarus*, 222, 229–242.
- Binzel R. P., Gaffey M. J., Thomas P. C., Zellner B. H., Storrs A. D., and Wells E. N. (1997) Geologic mapping of Vesta from 1994 Hubble Space Telescope images. *Icarus*, 128, 95–103.
- Binzel R. P. et al. (2010) Earth encounters as the origin of fresh surfaces on near-Earth asteroids. *Nature*, 463, 331–334.
- Bowell E. and Lumme K. (1979) Colorimetry and magnitudes of asteroids. In *Asteroids* (T. Gehrels, ed.), pp. 132–169. Univ. of Arizona, Tucson.
- Bowell E., Hapke B., Domingue D., Lumme K., Peltoniemi J., and Harris A. W. (1989) Application of photometric models to asteroids. In *Asteroids II* (R. P. Binzel et al., eds.), pp. 524–556. Univ. of Arizona, Tucson.
- Buratti B. J. (1984) Voyager disk resolved photometry of the saturnian satellites. *Icarus*, 59, 392–405.
- Buratti B. J. and Veverka J. (1983) Voyager photometry of Europa. *Icarus*, 55, 93–110.
- Buratti B. J. and Veverka J. (1985) Photometry of rough planetary surfaces: The role of multiple scattering. *Icarus*, 64, 320–328.
- Buratti B. J. et al. (2011) A wavelength-dependent visible and infrared spectrophotometric function for the Moon based on ROLO data. *J. Geophys. Res.*, 116, E00G03.
- Calvin W. M. and Clark R. N. (1991) Modeling the reflectance spectrum of Callisto 0.25 to 4.1 microns. *Icarus*, 89, 305–317.
- Carry B. et al. (2008) Near-infrared mapping and physical properties of the dwarf-planet Ceres. *Astron. Astrophys.*, 478, 235–244.
- Carry B. et al. (2012) The remarkable surface homogeneity of the Dawn mission target (1) Ceres. *Icarus*, 217, 20–26.
- Chandrasekhar S. (1960) *Radiative Transfer*. Dover, New York.
- Ciarniello M., Capaccioni F., and Filacchione G. (2014) A test of Hapke's model by means of Monte Carlo ray-tracing. *Icarus*, 237, 293–305.
- Clark B. E. et al. (1999) NEAR photometry of asteroid 253 Mathilde. *Icarus*, 140, 53–65.
- Clark B. E. et al. (2002) NEAR infrared spectrometer photometry of asteroid 433 Eros. *Icarus*, 155, 189–204.
- Cord A., Pinet P., Daydou Y., and Chevrel S. (2003) Planetary regolith surface analogs: Optimized determination of Hapke parameters using multi-angular spectroimaging laboratory data. *Icarus*, 165, 414–427.
- Cord A., Pinet P. C., Daydou Y., and Chevrel S. D. (2005) Experimental determination of the surface photometric contribution in the spectral reflectance deconvolution processes for a simulated martian crater-like regolithic target. *Icarus*, 175, 78–91.
- Deau E. and Helfenstein P. (2015) Cassini ISS broadband photometry of Saturn's main rings: I. Corrections of scattering properties with ring optical depth. *J. Geophys. Res.*, in press.
- Denevi B. W., Lucey P. G., and Sherman S. B. (2008) Radiative transfer modeling of near-infrared spectra of lunar mare soils: Theory and measurement. *J. Geophys. Res.*, 113(E2), E02003.
- De Sanctis M. C. et al. (2011) The VIR spectrometer. *Space Sci. Rev.*, 163, 329–369.
- De Sanctis M. C. et al. (2012a) Spectroscopic characterization of mineralogy and its diversity across Vesta. *Science*, 336, 697–700.
- De Sanctis M. C. et al. (2012b) Detection of widespread hydrated materials on Vesta by the VIR imaging spectrometer on board the Dawn mission. *Astrophys. J. Lett.*, 758, L36.
- De Sanctis M. C. et al. (2013) Vesta's mineralogical composition as revealed by the visible and infrared spectrometer on Dawn. *Meteoritics & Planet. Sci.*, 48, 2166–2184.
- Domingue D., Hartman W., and Verbiscer A. (1997) The scattering properties of natural terrestrial snows versus icy satellite surfaces. *Icarus*, 128, 28–48.
- Fujiwara A. et al. (2006) The rubble-pile asteroid Itokawa as observed by Hayabusa. *Science*, 312(5778), 1330–1334.
- Gaffey M. J. (1997) Surface lithologic heterogeneity of asteroid 4 Vesta. *Icarus*, 127, 130–157.
- Gaffey M. J., Bell J. F., and Cruikshank D. P. (1989) Reflectance spectroscopy and asteroid surface mineralogy. In *Asteroids II* (R. P. Binzel et al., eds.), pp. 98–127. Univ. of Arizona, Tucson.
- Gehrels T. (1970) Photometry of asteroids. In *Surface and Interiors of Planets and Satellites* (A. Dollfus, ed.), pp. 317–375. Academic, New York.
- Gehrels T., Coffeen T., and Owings D. (1964) Wavelength dependence of polarization. III. The lunar surface. *Astron. J.*, 69, 826–852.
- Goguen J. D. (1981) A theoretical and experimental investigation of the photometric functions of particulate surfaces. Ph.D. thesis, Cornell Univ., Ithaca, New York.
- Goguen J. D., Stone T. C., Kieffer H. H., and Buratti B. J. (2010) A new look at photometry of the Moon. *Icarus*, 208, 548–557.
- Gradie J. and Veverka J. (1986) The wavelength dependence of phase coefficients. *Icarus*, 66(3), 455–467.
- Guinness E. A., Arvidson R. E., Clark I. H. D., and Shepard M. K. (1997) Optical scattering properties of terrestrial varnished basalts compared with rocks and soils at the Viking Lander sites. *J. Geophys. Res.*, 102, 28687–28704.
- Gunderson K., Thomas N., and Whitby J. A. (2005) First measurements with the Physikalisch Institut Radiometric Experiment (PHIRE). *Planet. Space Sci.*, 54, 1046–1056.
- Harris A. W., Young J. W., Goguen J., Hammel H. B., Hahn G., Tedesco E. F., and Tholen D. J. (1987) Photoelectric lightcurves of the asteroid 1862 Apollo. *Icarus*, 70, 246–256.
- Hapke B. (1963) A theoretical photometric function for the lunar surface. *J. Geophys. Res.*, 68, 4571–4586.
- Hapke B. (1966) An improved theoretical lunar photometric model. *Astron. J.*, 71, 333–339.
- Hapke B. (1981) Bidirectional reflectance spectroscopy. 1. Theory. *J. Geophys. Res.*, 86, 3039–3054.
- Hapke B. (1984) Bidirectional reflectance spectroscopy. 3. Correction for macroscopic roughness. *Icarus*, 59, 41–59.
- Hapke B. (1986) Bidirectional reflectance spectroscopy. 4. The extinction coefficient and opposition effect. *Icarus*, 67, 264–280.
- Hapke B. (1998) A revised bidirectional reflectance function for planetary regolith. *Bull. Am. Astron. Soc.*, 30, 1080.
- Hapke B. (2002) Bidirectional reflectance spectroscopy. 5. The coherent backscatter opposition effect and anisotropic scattering. *Icarus*, 157, 523–534.
- Hapke B. (2008) Bidirectional reflectance spectroscopy. 6. Effects of porosity. *Icarus*, 195, 918–926.
- Hapke B. (2012a) Bidirectional reflectance spectroscopy. 7. The single particle phase function hockey stick relation. *Icarus*, 221, 1079–1083.
- Hapke B. (2012b) *Theory of Reflectance and Emittance Spectroscopy, second edition*. Cambridge Univ., Cambridge.
- Hapke B. (2013) Comment on "A critical assessment of the Hapke photometric model" by Y. Shkuratov, et al. *J. Quant. Spectrosc. Radiat. Transfer*, 116, 184–190.
- Hapke B. and Wells E. (1981) Bidirectional reflectance spectroscopy 2. Experiments and observations. *J. Geophys. Res.*, 86, 3055–3060.
- Hapke B. W., Shepard M. K., Nelson R. M., Smythe W. D., and Piatek J. (2009) A quantitative test of the ability of models based on the equation of radiative transfer to predict the bidirectional reflectance of a well-characterized medium. *Icarus*, 199, 210–218.
- Hapke B., Denevi B., Sato H., Braden S., and Robinson M. (2012) The wavelength dependence of the lunar phase curve as seen by the Lunar Reconnaissance Orbiter wide-angle camera. *J. Geophys. Res.*, 117, E00H15.
- Hartman B. and Domingue D. (1998) Scattering of light by individual particles and the implications for models of planetary surfaces. *Icarus*, 131, 421–448.
- Hasegawa S. et al. (2014) The opposition effect of the asteroid 4 Vesta. *Publ. Astron. Soc. Japan*, 66, 89.
- Helfenstein P. (1988) The geological interpretation of photometric surface roughness. *Icarus*, 73, 462–481.
- Helfenstein P. and Shepard M. K. (1999) Submillimeter-scale topography of the lunar regolith. *Icarus*, 14, 107–131.
- Helfenstein P. and Shepard M. K. (2011) Testing the Hapke photometric model: Improved inversion and the porosity correction. *Icarus*, 215, 83–100.
- Helfenstein P. and Veverka J. (1987) Photometric properties of lunar terrains derived from Hapke's equation. *Icarus*, 72, 342–357.
- Helfenstein P. and Veverka J. (1989) Physical characterization of asteroid surfaces from photometric analysis. In *Asteroids II* (R. P. Binzel et al., eds.), pp. 557–593. Univ. of Arizona, Tucson.

- Helfenstein P., Veverka J., and Thomas P. C. (1988) Uranus satellites: Hapke parameters from Voyager disk integrated photometry. *Icarus*, 74, 231.
- Helfenstein P., Bonne U. A., Stolovy S., and Veverka J. (1991) Laboratory photometric measurement of particulate soils out to very large phase angles. In *Reports of Planetary Geology and Geophysics Program, 1990*, pp. 280–282. NASA, Washington, DC.
- Helfenstein P. et al. (1994) Galileo photometry of asteroid 951 Gaspra. *Icarus*, 107, 37–60.
- Helfenstein P. et al. (1996) Galileo photometry of asteroid 243 Ida. *Icarus*, 120, 48–65.
- Helfenstein P., Veverka J., and Hillier J. K. (1997) The lunar opposition effect: A test of alternate models. *Icarus*, 128, 2–14.
- Hicks M. et al. (2014) Spectral diversity and photometric behavior of main-belt and near-Earth asteroids and (4) Vesta: A study in preparation for the Dawn encounter. *Icarus*, 235, 60–74.
- Hillier J. K., Buratti B. J., and Hill K. (1999) Multispectral photometry of the Moon and absolute calibration of the Clementine UV/Vis camera. *Icarus*, 141, 205–225.
- Hillier J. K., Bauer J. M., and Buratti B. J. (2011) Photometric modeling of asteroid 5535 Annefrank from Stardust observations. *Icarus*, 211, 546–552.
- Huang J. et al. (2013) The ginger-shaped asteroid 4179 Toutatis: New observations from a successful flyby of Chang'e-2. *Sci. Rept.*, 3, 3411.
- Irvine W. (1966) The shadowing effect in diffuse reflection. *J. Geophys. Res.*, 71, 2931.
- Jaumann R. et al. (2012) Vesta's shape and morphology. *Science*, 336, 687–690.
- Kaasalainen S., Muinonen K., and Piironen J. (2001) Comparative study of opposition effect of icy solar system objects. *J. Quant. Spectrosc. Radiat. Transfer*, 70, 529–543.
- Kaasalainen S., Piironen J., Kaasalainen M., Harris A. W., Muinonen K., and Cellino A. (2003) Asteroid photometric and polarimetric phase curves: Empirical interpretation. *Icarus*, 161, 34–46.
- Kamei A. and Nakamura A. (2002) Laboratory study of the bidirectional reflectance of powdered surfaces: On the asymmetry parameter of asteroid photometric data. *Icarus*, 156, 551–561.
- Keller H. U. et al. (2007) OSIRIS the scientific camera system onboard Rosetta. *Space Sci. Rev.*, 128, 433–506.
- Kitazato K. et al. (2008) Near-infrared spectrophotometry of asteroid 25143 Itokawa from NIRS on the Hayabusa spacecraft. *Icarus*, 194, 137–145.
- Küppers M. et al. (2014) Localized sources of water vapour on the dwarf planet (1) Ceres. *Nature*, 505, 525–527.
- La Forgia F. (2014) Photometric analysis of asteroids and comets from space observations. Ph.D. dissertation, Università Degli Studi Di Padova.
- Lambert J. H. (1759) *La perspective affranchie de l'embaras du plan géometrical*. Heidegguer, Zurich. 192 pp.
- Lederer S. et al. (2005) Physical characteristics of Hayabusa target asteroid 25143 Itokawa. *Icarus*, 173, 153–165.
- Lee J., Buratti B. J., Hicks M., and Mosher J. A. (2009) The roughness of the dark side of Iapetus from the 2004 and 2005 flyby. *Icarus*, 206, 623–630.
- Leyrat C. et al. (2010) Search for Steins' surface inhomogeneities from OSIRIS Rosetta images. *Planet. Space Sci.*, 58, 1097–1106.
- Li J.-Y., A'Hearn M. F., and McFadden L. A. (2004) Photometric analysis of Eros from NEAR data. *Icarus*, 172, 415–431.
- Li J.-Y. et al. (2006) Photometric analysis of 1 Ceres and surface mapping from HST observations. *Icarus*, 182, 143–160.
- Li J.-Y., A'Hearn M. F., Farnham T. L., and McFadden L. A. (2009) Photometric analysis of the nucleus of Comet 81P/Wild 2 from Stardust images. *Icarus*, 204, 209–226.
- Li J.-Y. et al. (2010) Photometric mapping of asteroid (4) Vesta's southern hemisphere with Hubble Space Telescope. *Icarus*, 208, 238–251.
- Li J.-Y. et al. (2013a) Global photometric properties of asteroid (4) Vesta observed with Dawn Framing Camera. *Icarus*, 226, 1252–1274.
- Li J.-Y. et al. (2013b) Photometry of the nucleus of Comet 9P/Tempel 1 from Stardust-NExT flyby and the implications. *Icarus*, 222, 467–476.
- Li J.-Y. et al. (2013c) The photometric properties of Vesta in visible and near-infrared from Dawn VIR instrument. *Lunar Planet. Sci. XLIV*, Abstract #2343. Lunar and Planetary Institute, Houston.
- Longobardo A. et al. (2014) Photometric behavior of spectral parameters in Vesta dark and bright regions as inferred by the Dawn VIR spectrometer. *Icarus*, 240, 20–35.
- Lucey P. G. (1998) Model near-infrared optical constants of olivine and pyroxene as a function of iron content. *J. Geophys. Res.*, 103, 1703–1714.
- Lumme K. and Bowell E. (1981a) Radiative transfer in the surfaces of atmosphereless bodies. I. Theory. *Astron. J.*, 86, 1694–1704.
- Lumme K. and Bowell E. (1981b) Radiative transfer in the surfaces of atmosphereless bodies. II Interpretation of phase curves. *Astron. J.*, 86, 1705–1712.
- Lumme K. and Bowell E. (1985) Photometric properties of zodiacal light particles. *Icarus*, 62, 54–71.
- Mackowski D. W. and Mishchenko M. I. (1996) Calculation of the T matrix and the scattering matrix for ensembles of spheres. *J. Optical Soc. Am.*, A13, 2266–2278.
- Mackowski D. W. and Mishchenko M. I. (2011) A multiple sphere T-matrix Fortran code for use on parallel computer clusters. *J. Quant. Spectrosc. Radiat. Transfer*, 112, 2182–2192.
- Magrin S. et al. (2012) (21) Lutetia spectrophotometry from Rosetta-OSIRIS images and comparison to ground-based observations. *Planet. Space Sci.*, 66, 43–53.
- Masiero J. R. et al. (2011) Main belt asteroids with WISE/NEOWISE. I. Preliminary albedos and diameters. *Astrophys. J.*, 741, 60.
- Masoumzadeh N., Boehnhardt H., Li J.-Y., and Vincent J.-B. (2014) Photometric analysis of asteroid (21) Lutetia from Rosetta OSIRIS images. *Icarus*, 257, 239–250.
- McCord T. B. et al. (2012) Dark material on Vesta from the infall of carbonaceous volatile-rich material. *Nature*, 490, 83–86.
- McEwen A. S. (1991) Photometric functions for photoclinometry and other applications. *Icarus*, 92, 298–311.
- McEwen A. S. (1996) A precise lunar photometric function. *Lunar Planet. Sci. XXVII*, pp. 841–842. Lunar and Planetary Institute, Houston,
- McGuire A. and Hapke B. (1995) An experimental study of light scattering by large irregular particles. *Icarus*, 113, 134–155.
- Minnaert M. (1941) The reciprocity principle in lunar photometry. *Astrophys. J.*, 93, 403–410.
- Mitchell D. L. et al. (1996) Radar observations of asteroids 1 Ceres, 2 Pallas, and 4 Vesta. *Icarus*, 124, 113–133.
- Muinonen K., Piironen J., Shkuratov Y. G., Ovcharenko A., and Clark B. E. (2002) Asteroid photometric and polarimetric phase effects. In *Asteroids III* (W. F. Bottke Jr. et al., eds.), pp. 123–138. Univ. of Arizona, Tucson.
- Muinonen K. et al. (2009) Asteroid photometric and polarimetric phase curves: Joint linear-exponential modeling. *Meteoritics & Planet. Sci.*, 44, 1937–1946.
- Muinonen K., Belskaya I. N., Cellino A., Delbò M., Levasseur-Regourd A.-C., Penttilä A., and Tedesco E. F. (2010) A three-parameter magnitude phase function for asteroids. *Icarus*, 209, 542–555.
- Muinonen K. et al. (2011) Lunar mare single-scattering, porosity, and surface-roughness properties with SMART-1 AMIE. *Astron. Astrophys.*, 531, A150.
- Muinonen K., Mishchenko M. I., Drugach J. M., Zubko E., Penttilä A., and Videen G. (2012) Coherent backscattering verified numerically for finite volume of spherical particles. *Astrophys. J.*, 760, 118.
- Oszkiewicz D. A., Muinonen K., Bowell E., Trilling D., Penttilä A., Pieniluoma T., Wasserman L. H., and Enga M.-T. (2011) Online multi-parameter phase-curve fitting and application to a large corpus of asteroid photometric data. *J. Quant. Spectrosc. Radiat. Transfer*, 112, 1919–1929.
- Oszkiewicz D. A., Bowell E., Wasserman L. H., Muinonen K., Penttilä A., Pieniluoma T., Trilling D. E., and Thomas C. A. (2012) Asteroid taxonomic signatures from photometric phase curves. *Icarus*, 219, 283–296.
- Pätzold A. et al. (2011) Asteroid 21 Lutetia: Low mass, high density. *Science*, 334, 491–492.
- Pietras C. M. et al. (2012) Distinctive space weathering on Vesta from regolith mixing processes. *Nature*, 490, 79–82.
- Piironen J. (1994) Oppositiokirkastuminen laboratoriomittauksissa ja planeettakunnan kaasukehättömillä kappaleilla. Ph.D. thesis, University of Helsinki, Finland.
- Prettyman T. H. et al. (2012) Elemental mapping by Dawn reveals exogenic H in Vesta's regolith. *Science*, 338, 242–246.
- Reddy V. et al. (2012a) Photometric, spectral phase and temperature effects on 4 Vesta and HED meteorites: Implications for the Dawn mission. *Icarus*, 217, 153–168.
- Reddy V. et al. (2012b) Color and albedo heterogeneity of Vesta from Dawn. *Science*, 336, 700–704.

- Reddy V. et al. (2012c) Delivery of dark material to Vesta via carbonaceous chondritic impacts. *Icarus*, 221, 544–559.
- Reddy V. et al. (2013) Comparing Dawn, Hubble Space Telescope, and ground-based interpretations of (4) Vesta. *Icarus*, 226, 1103–1114.
- Rivkin A. S. et al. (2011) The surface composition of Ceres. *Space Sci. Rev.*, 163, 95–116.
- Robinson M. S., Thomas P. C., Neverka J., Murchie S., and Carcich B. (2001) The nature of ponded deposits on Eros. *Nature*, 423, 396–400.
- Roush T. L., Pollack J. B., Witteborn F. C., Bregman J. D., and Simpson J. P. (1990) Ice and minerals on Callisto — A reassessment of the reflectance spectra. *Icarus*, 86, 355–382.
- Russell C. T. et al. (2012) Dawn at Vesta: Testing the protoplanetary paradigm. *Science*, 336, 684–686.
- Russell C. T. et al. (2013) Dawn completes its mission at 4 Vesta. *Meteoritics & Planet. Sci.*, 48, 2076–2089.
- Sato H., Robinson M. S., Hapke B., Denevi B. W., and Boyd A. K. (2014) Resolved Hapke parameter maps of the Moon. *J. Geophys. Res.*, 119, 1775–1805.
- Schröder S. E., Mottola S., and Keller H. U. (2013) Resolved photometry of Vesta reveals physical properties of crater regolith. *Planet. Space Sci.*, 85, 198–213.
- Seeliger H. (1887) Zur theorie der Beleuchtung der grossen Planeten insbesondere Saturn. *Abh. Bayer. Akad. Wiss. Math. Naturw. Kl. II*, 16, 405–516.
- Shepard M. K. and Campbell B. (1998) Shadows on a planetary surface and implications for photometric roughness. *Icarus*, 134, 279–291.
- Shepard M. and Helfenstein P. (2007) A test of the Hapke photometric model. *J. Geophys. Res.*, 112, E03001.
- Shepard M. K. and Helfenstein P. (2011) A laboratory study of the bidirectional reflectance from particulate samples. *Icarus*, 215, 526–533.
- Shepard M. K., Arvidson R. E., and Guinness E. A. (1993) Specular scattering on a terrestrial playa and implications for planetary surface studies. *J. Geophys. Res.*, 98, 18707–18718.
- Shepard M. K., Campbell B. A., Bulmer M. H., Farr T. G., Gaddis L. R., and Plaut J. J. (2001) The roughness of natural terrain: A planetary and remote sensing perspective. *J. Geophys. Res.*, 106, 32777–32796.
- Shevchenko V. G. (1996) Analysis of the asteroid phase dependences of brightness. *Lunar Planet. Sci. XXVII*, p. 1193. Lunar and Planetary Institute, Houston.
- Shkuratov Y., Kreslavsky M. A., Ovcharenko A. A., Stankevich D. G., Zubko E. S., Pieters C., and Arnold G. (1999) Opposition effect from Clementine data and mechanisms of backscatter. *Icarus*, 141, 132–155.
- Shkuratov Y., Bondarenko S., Kaydash V., Videen G., Munoz O., and Volten H. (2007) Photometry and polarimetry of particulate surfaces and aerosol particles over a wide range of phase angles. *J. Quant. Spectrosc. Radiat. Transfer*, 106, 487–508.
- Shkuratov Y., Kaydash V., Korokhin V., Velikodsky Y., Opanasenko N., and Videen G. (2011) Optical measurements of the Moon as a tool to study its surface. *Planet. Space Sci.*, 59, 1326–1371.
- Shkuratov Y., Kaydash V., Korokhin V., Velikodsky Y., Petrov D., Zubko E., Standevich D., and Videen G. (2012) A critical assessment of the Hapke photometric model. *J. Quant. Spectrosc. Radiat. Transfer*, 113, 2431–2456.
- Shkuratov Y., Kaydash V., Korokhin V., Velikodsky Y., Petrov D., Zubko E., Stankevich D., and Videen G. (2013) Response to the comment by B. Hapke on “A critical assessment of the Hapke photometric model.” *J. Quant. Spectrosc. Radiat. Transfer*, 116, 191–195.
- Sierks H. et al. (2011a) Images of asteroid 21 Lutetia: A remnant planetesimal from the early solar system. *Science*, 334, 487–490.
- Sierks H. et al. (2011b) The Dawn Framing Camera. *Space Sci. Rev.*, 163, 263–327.
- Souchon A. L. et al. (2011) An experimental study of Hapke’s modeling of natural granular surface samples. *Icarus*, 215, 313–331.
- Spjuth S., Jorda L., Lamy P. L., Keller H. U., and Li J.-Y. (2012) Disk-resolved photometry of asteroid (2867) Steins. *Icarus*, 221, 1101–1118.
- Takir D. et al. (2015) Photometric models of disk-integrated observations of the OSIRIS-REx target asteroid (101955) Bennu. *Icarus*, 252, 393–399.
- Tedesco E. F., Taylor R. C., Drummond J., Harwood D., Nickoloff I., Scaltriti F., Schober H. J., and Zappala V. (1983) Worldwide photometry and lightcurve observations of 1 Ceres during the 1975–1976 apparition. *Icarus*, 54, 23–29.
- Tedesco E. F., Williams J. G., Matson D. L., Veeder G. J., Gradie J. C., and Lebofsky L. (1989) A three-parameter asteroid taxonomy. *Astron. J.*, 97, 580–606.
- Turri D. et al. (2014) The contamination of the surface of Vesta by impacts and the delivery of the dark material. *Icarus*, 240, 86–102.
- Verbiscer A. J. (1991) Photometry of icy satellite surfaces. Ph.D. thesis, Cornell Univ., Ithaca, New York.
- Verbiscer A. J. and Neverka J. (1990) Scattering properties of natural snow and frost — Comparison with icy satellite photometry. *Icarus*, 175, 78–91.
- Verbiscer A. J. and Neverka J. (1992) Mimas — photometric roughness and albedo map. *Icarus*, 99, 63–69.
- Verbiscer A. J. and Neverka J. (1994) A photometric study of Enceladus. *Icarus*, 110, 155–164.
- Verbiscer A. J. et al. (2006) Near-infrared spectra of the leading and trailing hemispheres of Enceladus. *Icarus*, 182, 211–223.
- Verbiscer A., French R., Showalter M., and Helfenstein P. (2007) Enceladus: Cosmic graffiti artist caught in the act. *Science*, 315, 815.
- Neverka J. (1971) The physical meaning of phase coefficients. In *Physical Studies of Minor Planets* (T. Gehrels, ed.), p. 79. IAU Colloq. 12, NASA SP 267, Washington, DC.
- Neverka J., Belton M., Klaasen K., and Chapman C. (1994) Galileo’s encounter with 951 Gaspra: Overview. *Icarus*, 107, 2–17.
- Neverka J., Thomas P., and Hidy A. (2006) Tempel 1: Surface processes and the origin of smooth terrains. *Lunar Planet. Sci. XXXVII*, Abstract #1364. Lunar and Planetary Institute, Houston.
- Warell J. and Davidsson B. J. R. (2010) A Hapke model implementation for compositional analysis of VNIR spectra of Mercury. *Icarus*, 209, 164–178.
- Wilcox B. B., Lucey P. G., and Hawke B. R. (2006) Radiative transfer modeling of compositions of lunar pyroclastic deposits. *J. Geophys. Res.*, 111(E9), E09001.
- Wilkman O., Muinonen K., Videen G., Josset J.-L., Souchon A., and the SMART-1/AMIE Team (2014a) Lunar photometric modeling with SMART-1/AMIE imaging data. *J. Quant. Spectrosc. Radiat. Transfer*, 146, 529–539.
- Wilkman O., Muinonen K., Penttilä A., and Peltoniemi J. (2014b) Numerical surface-scattering laws for asteroid applications. In *Asteroids, Comets, Meteors 2014, Book of Abstracts* (K. Muinonen et al., eds.), p. 606. Univ. of Helsinki, Finland.
- Wu Y., Besse S., Li J.-Y., Combe J.-P., Wang Z., Zhou X., and Wang C. (2013) Photometric correction and in-flight calibration of Chang’e-1 Interference Imaging Spectrometer (IIM) data. *Icarus*, 222, 283–295.
- Yokota Y. et al. (2011) Lunar photometric properties at wavelengths 0.5–1.6 μm acquired by SELENE Spectral Profiler and their dependency on local albedo and latitudinal zones. *Icarus*, 215, 539–660.
- Zhang H. and Voss K. J. (2011) On Hapke photometric model predictions on the reflectance of closely packed particulate surface. *Icarus*, 215, 27–33.

# Asteroid Polarimetry

Irina Belskaya

*Kharkiv Karazin National University*

Alberto Cellino

*INAF-Osservatorio Astrofisico di Torino*

Ricardo Gil-Hutton

*Complejo Astronomico El Leoncito*

Karri Muinonen

*University of Helsinki and Finnish Geospatial Research Institute*

Yuriy Shkuratov

*Kharkiv Karazin National University*

---

The application of the polarimetric technique to asteroid studies progressed significantly during the last decade. The most interesting results were the discovery of asteroids with peculiar polarimetric properties, new findings on wavelength dependence of polarization, and some improvements in the polarimetric method of albedo determination. We review instruments that have been and are currently used for asteroid optical polarimetry and summarize the main results of observational surveys. Recent advances in theoretical and laboratory modeling of polarization phase effects and their implications are discussed. We focus on the most important open questions and identify promising avenues for future polarimetric investigations.

## 1. INTRODUCTION

Polarimetry is a powerful tool to study surface properties, putting constraints on albedo and surface texture. The state of partial linear polarization of the sunlight scattered by planetary surfaces in different illumination conditions is diagnostic of refractive index, particle size, packing density, optical heterogeneity, etc.

The application of the polarimetric technique to asteroid studies has a long history beginning in 1934, when the first polarization measurements of bright asteroids were obtained by B. Lyot using a photographic polarimeter. Since 1954, photoelectric polarimeters have been used to measure asteroid polarization with better accuracy. Results of polarimetric observations of six asteroids were discussed by A. Dollfus in the first review devoted to polarimetry of asteroids (Dollfus *et al.*, 1971). In the first *Asteroids* book, the chapter on optical polarimetry included a review of polarimetric observations for about 100 asteroids and their interpretation based on laboratory studies (Dollfus and Zellner, 1979). All measured asteroids were found to show so-called negative polarization at small phase angles. This is better expressed using, as a fundamental parameter, the polarization degree

$P_p$  defined in terms of the intensities of the scattered light polarized along the planes perpendicular  $I_{\perp}$  and parallel  $I_{\parallel}$  to the scattering plane

$$P_p = \frac{I_{\perp} - I_{\parallel}}{I_{\perp} + I_{\parallel}}$$

Such a definition means that the sign of the polarization degree  $P_p$  can be negative when the component  $I_{\parallel}$  with the electric vector parallel to the scattering plane predominates over the perpendicular component  $I_{\perp}$ . To achieve a detailed physical explanation of the phenomenon of negative polarization is a challenging task. In the *Asteroids II* volume, Dollfus *et al.* (1989) reviewed the first attempts of theoretical modeling of negative polarization, but these were later found to give unrealistic results (Shkuratov *et al.*, 1994). Dollfus *et al.* (1989) also described telescopic observations of asteroids and relevant laboratory data obtained after the review published in the first *Asteroids* book (Dollfus and Zellner, 1979).

In *Asteroids III*, Muinonen *et al.* (2002) reviewed some new theoretical and experimental findings on both photometric and polarimetric phase effects, and reported significant progress in understanding the physical nature of negative

polarization in terms of the multiple-scattering mechanism of coherent backscattering.

Detailed reviews on various aspects of the application of the polarimetric technique to study solar system bodies can also be found in the books by *Mishchenko et al.* (2010) and *Kolokolova et al.* (2015). In the latter, the chapters by *Cellino et al.* (2015a), *Muinonen et al.* (2015), and *Levasseur-Regourd et al.* (2015) summarize the role of polarimetric investigations in asteroid science and the status of theoretical modeling and laboratory measurements, respectively.

In the present chapter, we focus on the achievements in optical polarimetry of asteroids since *Asteroids III*. In section 2, we review the instruments and telescopes available for asteroid polarimetry. Section 3 summarizes the new findings obtained from recent observational surveys. A review of progress in analytical, numerical, and laboratory modeling of polarization phase effects is given in section 4. We discuss the main applications of the polarimetric observations to study asteroid surfaces in section 5. Finally, in section 6, we outline the future prospects for polarimetric studies.

## 2. TELESCOPES AND INSTRUMENTS

In the 1980s, and up to the end of the 1990s, the majority of the asteroid polarimetric observations were made using multichannel photopolarimeters of a kind originally designed by *Pirola* (1973). These instruments allowed simultaneous measurements in the UBVRI bands using five separate photomultipliers. One such instrument has been operated at the 1.25-m telescope of the Crimean Astrophysical Observatory in Ukraine since 1983. A detailed description of this instrument and a review of the obtained results are given by *Mishchenko et al.* (2010).

Another essentially identical instrument, built at the Astronomical Observatory of Torino in Italy (*Scaltriti et al.*, 1989), began operations in 1994 at the 2.1-m telescope of the Complejo Astronómico El Leoncito (CASLEO) in Argentina (*Cellino et al.*, 1999, 2005a). These two instruments, often used for joint observational programs, provided a large set of multi-band polarimetric observations of main-belt asteroids (*Belskaya et al.*, 2009a). The main limitation was a bright magnitude limit ( $V \sim 13$  mag). Since 2000, a new double-hole aperture polarimeter with rapid modulation provided by a rotating achromatic half-wave retarder and a Wollaston prism beam-splitter started operations at CASLEO (*Gil-Hutton et al.*, 2008), and allowed the observers to reach fainter magnitudes ( $V \sim 15$  mag). The CASLEO instruments were used for a long-term observational survey that provided polarimetric observations of more than 250 main-belt asteroids (see, e.g., *Gil-Hutton et al.*, 2014).

A new epoch in asteroid polarimetric observations has begun with new polarimeters developed around CCD detectors and the use of modern multi-mode instruments in polarimetric mode. In the period 2002–2006, a polarimetric survey of about 40 asteroids was carried out using the polarimetric mode of the Faint Object Spectrographic Camera (AFOSC) mounted at the 1.8-m telescope of the Astrophysical Ob-

servatory of Asiago in Italy (*Fornasier et al.*, 2006a). This polarimeter allows simultaneous measurements of the polarized flux at angles  $0^\circ$ ,  $45^\circ$ ,  $90^\circ$ , and  $135^\circ$  using a wedged double Wollaston prism (*Oliva*, 1997). These four beams are sufficient to determine the linear polarization parameters I, Q, and U with a single exposure. The great advantage of the instrument is that the obtained data do not depend on atmospheric changes as in the case of multiple exposures. The Asiago polarimeter has been moved to the Nordic Optical Telescope (NOT) in La Palma (Canary Islands, Spain) in 2010 and continued to be used for asteroid polarimetry (*Fornasier et al.*, 2015). An identical instrument has been recently built at the Torino observatory, and attached to a 1-m telescope of the observatory of Nice (France), located in Calern (*Pernechele et al.*, 2012). At the same time, the old polarimeters at CASLEO based on photomultiplier tubes were recently replaced by a new dual-beam imaging polarimeter, CASPOL (*Gil-Hutton et al.*, 2014), allowing a gain of about 2–3 mag over the previous instruments.

There are also other instruments that have been used for asteroid polarimetry during the last decade, including the dual-beam imaging polarimeter installed at the 2.2-m telescope of the University of Hawaii at Mauna Kea (*Masiero et al.*, 2007) and the Bologna Faint Object Spectrograph and Camera (BFOSC) in the imaging-polarimetry mode at the 1.52-m Cassini telescope of the Astronomical Observatory of Bologna, Italy. Recently, polarimetry of asteroids started with the SPOL spectropolarimeter at the Steward Observatory 2.3-m and 1.54-m telescopes (*Maleszewski et al.*, 2013).

Major part of the polarimetric observations of asteroids have been obtained using telescopes up to  $\sim 2$  m in diameter, allowing measurement of only relatively bright objects. The first polarimetric observations using large telescopes took place in 2005 when one of the 8.2-m units of the Very Large Telescope (VLT) at the European Southern Observatory's (ESO) Cerro Paranal observatory in Chile was used to study the asteroid (2867) Steins. This object, a target of the European Space Agency (ESA) Rosetta mission, was observed with the Focal Reducer/Low Dispersion spectrograph (FORS) in polarimetric mode (*Fornasier et al.*, 2006b). The mode uses a half-wave phase retarder and a Wollaston prism as a beam splitter (*Appenzeller et al.*, 1998; *Bagnulo et al.*, 2011). In the following years, new VLT observations were devoted to studies of the potentially hazardous near-Earth asteroids (NEAs) (*Delbò et al.*, 2007; *De Luise et al.*, 2007), some selected main-belt asteroids (*Cellino et al.*, 2010, 2014), and Jupiter Trojans (*Belskaya et al.*, 2014). To start an observing program on spectropolarimetry of asteroids, *Bagnulo et al.* (2015) used FORS at VLT and the ISIS instrument of the 4.2-m William Herschel Telescope (WHT) of the Isaac Newton Group of Telescopes. In spite of the different instruments used at different observing sites, asteroid polarimetric data have always been found to be in very good mutual agreement.

A comprehensive review on various techniques and devices used in optical and near-infrared polarimetry is given by *Hough* (2005). Modern approaches to the design of

astronomical polarimeters and a list of currently available polarimeters at ground-based telescopes can be found in the review by *Keller et al.* (2015).

### 3. NEW FINDINGS FROM OBSERVATIONS

During the last decade, polarimetric observations of asteroids have become more frequent. Several observing campaigns have been carried out to characterize the polarimetric behavior of asteroids of different composition types (*Belskaya et al.*, 2003, 2005; *Fornasier et al.*, 2006a; *Gil-Hutton*, 2007; *Gil-Hutton et al.*, 2008, 2014; *Gil-Hutton and Cañada-Assandri*, 2011; *Cañada-Assandri et al.*, 2012). Many observing projects have been devoted to the study of specifically selected targets, including near-Earth asteroids (*Kiselev et al.*, 2002; *De Luise et al.*, 2007; *Delbò et al.*, 2007; *Belskaya et al.*, 2009b; *Masiero*, 2010), members of dynamical families (*Cellino et al.*, 2010), Trojans (*Belskaya et al.*, 2014), targets of space missions (*Cellino et al.*, 2005b; *Fornasier et al.*, 2006b; *Belskaya et al.*, 2010; *Hadamcik et al.*, 2011), and several individual objects (*Antonyuk and Kiselev*, 2012; *Bagnulo et al.*, 2010; *Cellino et al.*, 2006; *Masiero and Cellino*, 2009). Observations in order to investigate polarimetric behavior at very small phase angles were carried out by *Belskaya et al.* (2003), *Rosenbush et al.* (2005, 2009), and *Cellino et al.* (2005a). The latter paper aimed at providing an independent estimate of the albedos of small asteroids previously observed at thermal IR wavelengths by the Infrared Astronomical Satellite (IRAS). The wavelength dependence of asteroid polarization has been the subject of papers published by *Belskaya et al.* (2009a), *Gil-Hutton et al.* (2014), and *Bagnulo et al.* (2015).

The number of asteroids for which polarimetric measurements are available reaches now  $\sim 350$ , almost  $3 \times$  the number at the time of the original *Asteroids* volume (*Dollfus and Zellner*, 1979). However, the number of asteroids with well-defined polarization phase curves did not increase substantially. For most asteroids, we have at our disposal measurements obtained at only few phase angles, which is not enough for an accurate determination of the main polarimetric parameters. To measure the depth and width of the polarization branch of an asteroid, observations at least at 5–6 different phase angles distributed from  $5^\circ$  to  $7^\circ$  to  $25^\circ$  to  $30^\circ$  are needed.

There are asteroids for which we have polarimetric observations obtained during several oppositions. For example, Fig. 1 shows a detailed polarization phase curve measured for the asteroid (21) Lutetia, a target of the Rosetta mission. The data were obtained during 10 apparitions in 1973–2011 by different authors (*Zellner and Gradie*, 1976; *Belskaya et al.*, 2010, and references therein; *Gil-Hutton et al.*, 2014). The scatter of the data for this asteroid may be a consequence of its surface heterogeneity (*Belskaya et al.*, 2010).

The behavior of the polarization phase curve is characterized by several parameters: the extreme value of the negative polarization branch  $P_{\min}$ , which occurred at the phase angle  $\alpha_{\min}$ ; the inversion angle  $\alpha_{\text{inv}}$  at which the polarization degree

changes its sign; and the polarimetric slope of the ascending branch  $h$  (Fig. 1). These parameters are typically derived by using the so-called trigonometric fit (*Lumme and Muinonen*, 1993) or the linear-exponential function (*Kaasalainen et al.*, 2003; *Muinonen et al.*, 2009). The trigonometric fit, using four free parameters (two of them can be fixed), provides a physically reasonable behavior of the polarization-phase dependence in a wide range of phase angles up to the polarization maximum  $P_{\max}$  at  $\alpha_{\max} \sim 100^\circ$  (see *Penttilä et al.*, 2005). The four-parameter linear-exponential function fits well the phase curve up to  $\alpha \sim 30^\circ$  and can be used for a joint fit of polarimetric and photometric phase curves (see *Muinonen et al.*, 2009). For a well-sampled phase curve, both fits give almost identical results (Fig. 1).

The polarimetric observations available are collected in the Asteroid Polarimetric Database (APD) at the Small Bodies Node of the Planetary Data System. The database has been compiled by *Lupishko and Vasiliev* (1997) and is updated annually (*Lupishko*, 2014). There are also other databases that include polarimetric data obtained in the specific papers (e.g., *Belskaya et al.*, 2009a,b; *Cellino et al.*, 2006; *Gil-Hutton et al.*, 2008). Below, we have summarized the most interesting recent findings on the polarimetric properties of asteroids.

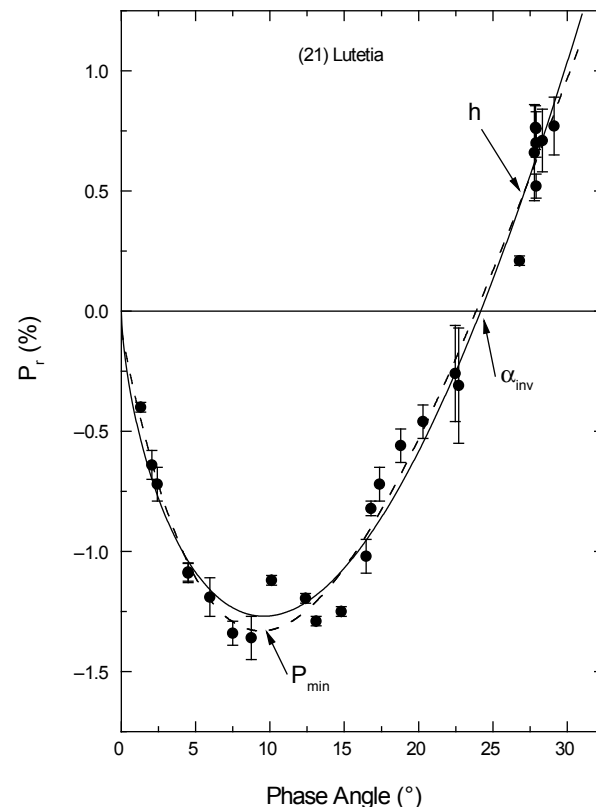


**Fig. 1.** Polarization phase-angle dependence of asteroid (21) Lutetia measured in 1973–2011 in the V-band (see text for references). The main polarimetric parameters  $P_{\min}$ ,  $\alpha_{\text{inv}}$ , and the polarimetric slope  $h$  are indicated by arrows. The solid line shows the trigonometric fit and the dashed line corresponds to the linear-exponential fit (see text).

### 3.1. Asteroids with Small Inversion Angles

In the first polarimetric survey of asteroids (Zellner and Gradie, 1976), the asteroid (704) Interamnia was found to have an unusually small inversion angle of about  $16^\circ$ . Small inversion angles typically indicate a bare rock surface (see Fig. 5). Dollfus and Zellner (1979) pointed out that it is unlikely that (704) Interamnia is the only dust-free asteroid, and assumed some peculiar surface composition of this asteroid. Belskaya *et al.* (2005) measured an even smaller inversion angle of about  $14^\circ$  for the asteroid (419) Aurelia. Both of these asteroids had been previously classified by Tholen (1989) as belonging to the rare F taxonomic class. In order to assess whether a small inversion angle could be a characteristic feature of F-class asteroids, observations of these asteroids were continued (Belskaya *et al.*, 2005; Fornasier *et al.*, 2006a; Gil-Hutton *et al.*, 2012, 2014). As a result, four more F-type asteroids, (213) Lilaea, (302) Clarissa, (325) Roberta, and (1021) Flammario, were found to have small inversion angles. The polarization phase curve of the above-mentioned asteroids is shown in Fig. 2. Their inversion angles do not exceed  $17^\circ$ .

Up to now, all known cases of asteroids exhibiting small inversion angles concern the F class. The most distinctive spectral feature of these asteroids, as compared to the other taxonomic classes, is the absence of UV absorption features at short wavelengths. More recent taxonomic classifications (Bus and Binzel, 2002; DeMeo *et al.*, 2009) use reflectance spectra covering only the visible and near-IR wavelengths and they can no longer identify a separate F class. Asteroids previously classified as F belong today mostly to the larger B or C classes. Gil-Hutton and Cañada-Assandri (2012) analyzed data obtained for 58 B- and C-type objects and found an indication of smaller inversion angles for several objects previously classified as F type.

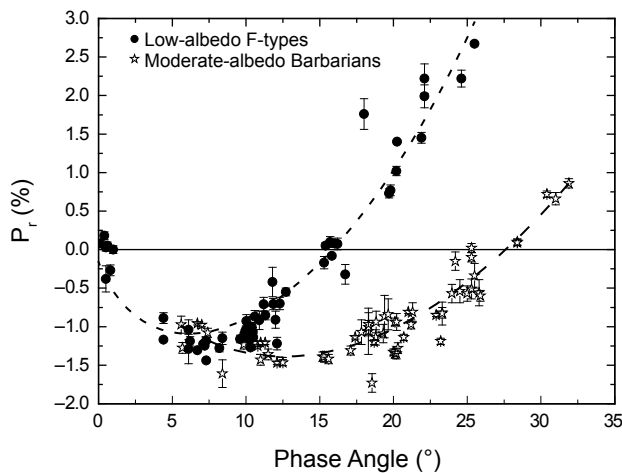


**Fig. 2.** Extreme cases of asteroid polarization phase curves (see text for references). Data for the low-albedo F-type asteroids are shown by black circles. Polarization measurements of the moderate-albedo Barbarians are shown by asterisks. The dash and dotted lines display the fits using the trigonometric function (Lumme and Muinonen, 1993).

Unlike other very dark primitive asteroids, F-class objects are relatively abundant in the inner asteroid belt, a large fraction of them being associated with the Polana family (Cellino *et al.*, 2001; Milani *et al.*, 2014). At the same time, they may be also related to extinct cometary nuclei (Kolokolova and Jockers, 1997). Polarimetric observations of two cometary nuclei, 2P/Encke (Boehnhardt *et al.*, 2008) and 133P/Elst-Pizarro (Bagnulo *et al.*, 2010), also suggest a small inversion angle similar to the F-type asteroids.

Belskaya *et al.* (2005) proposed a possible interpretation of the particular polarimetric properties of the asteroid (419) Aurelia and the other F-class asteroids. It was shown that an optical homogeneity of asteroid regolith microstructure at scales on the order of visible light wavelengths may be responsible for relatively small values of the depth of the negative polarization branch and the inversion angle (Belskaya *et al.*, 2005). One of the feasible mechanisms can be the existence of carbon deposits on the regolith particles of F-class asteroids, making them optically more homogeneous than other classes of low-albedo asteroids. This assumption is in agreement with the almost flat spectra characterizing the F class.

Polarimetric observations can therefore be crucial in the identification of new F-type objects among asteroids recently classified as B class, and possibly to strengthen the preliminary indications of analogies with the polarimetric behavior of comets.

### 3.2. Asteroids with Large Inversion Angles

Polarimetric observations of the moderate-albedo asteroid (234) Barbara unexpectedly revealed considerable negative polarization  $P_r \sim -1.2\%$  at phase angles  $\alpha \geq 20^\circ$  (Cellino *et al.*, 2006). This result was surprising, because all other asteroids previously observed have zero or positive polarization at such large phase angles, which are close to the typical inversion angle of “normal” asteroids. Further observations of (234) Barbara confirmed a wide branch of negative polarization with an inversion angle  $\alpha_{inv} \sim 28^\circ$  (Gil-Hutton *et al.*, 2008; Masiero *et al.*, 2009). Apart from the large inversion angle, the polarization phase curve of asteroid (234) Barbara is characterized by a fairly deep branch of negative polarization (see Fig. 2). Cellino *et al.* (2006) suggested that such atypical polarimetric behavior for a moderate-albedo surface might be due to some unusual surface properties related to the rare Ld taxonomic classification of (234) Barbara (Bus and Binzel, 2002). Asteroids of the Ld class are characterized by a particularly reddish reflectance spectrum (Bus and Binzel, 2002), and had not been observed previously in polarimetry. Gil-Hutton *et al.* (2008) later found four more asteroids displaying the same Barbara-like polarimetric behavior. They are the L-class asteroids (172) Baucis, (236) Honoria, and (980) Anacostia, and the K-class asteroid (679) Pax. It was then also noticed that at least two asteroids with particular polarimetric behavior, Barbara and Anacostia, had in their spectra strong spinel features (Sunshine *et al.*, 2007). According to Burbine *et al.* (1992), the asteroids (980) Anacostia and (387) Aquitania,

which have quite similar orbits, share the property of being spinel-rich, suggesting that they could be fragments of the breakup of a spinel-rich parent body with affinities to carbonaceous CO3/CV3 chondrites. Subsequent observations of (387) Aquitania also revealed a Barbara-like polarimetric behavior, confirming the existence of a relation between the unusual mineralogical and polarimetric properties of these asteroids (*Masiero and Cellino*, 2009). *Gil-Hutton et al.* (2014) later found two more “Barbarians,” the K-type asteroid (402) Chloe and the L-type (729) Watsonia.

Among the eight asteroids with large inversion angles that were known at the beginning of 2014, at least two were members of the Watsonia family identified by *Novaković et al.* (2011). This fact raised the question of polarimetric properties of other Watsonia family members. *Cellino et al.* (2014) carried out observations of a sample of nine objects belonging to the Watsonia family and found that seven of them are characterized by polarization curves with large inversion angles. These authors concluded that the Watsonia family is a repository of Barbarians. This strengthens the hypothesis that the peculiar mineralogical composition of these objects should be responsible for their unusual polarization properties.

A common characteristic of the Barbarians is their classification as L, Ld, or K types according to taxonomic classifications based on visible wavelength data (*Bus and Binzel*, 2002). On the other hand, not all the asteroids belonging to these taxonomic classes show large inversion angles (e.g., *Gil-Hutton et al.*, 2014). Some misclassification due to similar spectroscopic properties in the visible may be present. This is confirmed by the fact that, if one looks at the more recent taxonomic classification by *DeMeo et al.* (2009), which is based on data that also includes the near-IR, all Barbarians currently known for which a DeMeo classification is available belong to the same class (L).

A possible interpretation of the peculiar polarimetric properties of Barbarians is related to the presence of spinel in calcium-aluminum-rich inclusions (CAIs) at their surfaces. Spinel is characterized by an unusually high refractive index, which might be related to the unusual polarimetric behavior of these objects (*Sunshine et al.*, 2007; *Gil-Hutton et al.*, 2008; *Masiero et al.*, 2009).

The search for new asteroids with large inversion angles continues. They can be easily identified by polarimetric observations at phase angles around 20°.

### 3.3. Polarization Behavior at Small Phase Angles

The interest in obtaining polarimetric observations at small phase angles is related to the understanding of the coherent-backscattering mechanism. This contributes to photometric and polarimetric phase dependences producing sharp features near opposition (see *Muinonen et al.*, 2002, for a review). The first pieces of evidence for the existence of polarization opposition peaks were found for high-albedo Galilean satellites of Jupiter by *Rosenbush et al.* (1997). After this discovery, extensive observations of the high-albedo

asteroids were made to search for a possible polarization opposition surge. *Rosenbush et al.* (2005) presented UBVRI polarimetric observations of the E-type asteroid (64) Angelina made in three apparitions with detailed coverage of small phase angles up to 0.4°. These authors claimed the discovery of a sharp peak of negative polarization superimposed on the regular branch. The peak has an amplitude of ~0.4% centered at a phase angle  $\alpha \sim 1.8^\circ$  (*Rosenbush et al.*, 2005). The authors found that the amplitude and position of the polarization peak was slightly different before and after opposition and at different apparitions. New observations by *Zaitsev et al.* (2014) revealed a secondary minimum at  $\alpha \sim 1.5^\circ$ . They underscored that further polarimetric observations of Angelina at  $\alpha \sim 3^\circ$ – $5^\circ$  are needed to reach a final conclusion on the shape of the phase dependence near opposition. *Rosenbush et al.* (2009) carried out observations of another high-albedo asteroid, (44) Nysa, at very small phase angles down to 0.4°. A polarization opposition effect with an amplitude of ~0.3% centered at  $\alpha \sim 0.8^\circ$  was found. *Rosenbush et al.* (2009) put together all polarimetric measurements for the E-type asteroids and concluded that a sharp secondary minimum is present at  $\alpha \sim 1^\circ$ .

Polarimetric measurements of the V-type asteroid (4) Vesta (*Mishchenko et al.*, 2010) and the S-type asteroid (20) Massalia (*Belskaya et al.*, 2003) did not reveal any sharp features at small phase angles.

We compare the polarization behavior at small phase angles for high- and moderate-albedo asteroids in Fig. 3. We plotted together all available measurements in the V and R bands having an accuracy of  $\sigma_p < 0.1\%$ . The moderate-albedo asteroids show a deeper negative branch down to very small phase angles. To confirm the existence of a secondary peak of negative polarization for high-albedo asteroids, more detailed and accurate measurements at  $\alpha \sim 1^\circ$ – $2^\circ$  seem to be required.

Among low-albedo asteroids, detailed observations at small phase angles were obtained for the F-type asteroid (1021) Flammario (*Fornasier et al.*, 2006a). The VRI observations at the phase-angle range of 0.1°–1° show zero or slightly positive polarization in all filters, both before and after opposition. *Fornasier et al.* (2006a) suggested a possible explanation related to the effect of surface anisotropy. Further observations of this asteroid are needed to conclude whether or not the measured peculiarity is real.

### 3.4. Spectral Dependence of Polarization Parameters

The first pioneering studies of the spectral dependence of linear polarization for the asteroids were based on broadband multi-color measurements. *Belskaya et al.* (2009a) analyzed the observations available in UBVRI colors for 52 main-belt asteroids. Within the accuracy of the measurements, the dependence of the degree of linear polarization upon wavelength in the spectral range of 0.37–0.83 μm was generally found to be rather weak and well described by a linear trend. It was also shown that moderate- and low-albedo asteroids exhibit opposite trends. This behavior, previously

found for several C- and S-type asteroids (*Belskaya et al.*, 1987; *Lupishko and Kiselev*, 1995), was confirmed with better statistics.

More recently, *Bagnulo et al.* (2015) have published the first example of full-fledged spectropolarimetric measurements of asteroids for a sample of 12 asteroids. The obtained results are in agreement with the *Belskaya et al.* (2009a) findings. Polarization data covering the spectral range of 0.39–0.93  $\mu\text{m}$  have a positive linear slope as a function of wavelength in the case of low-albedo asteroids, whereas moderate-albedo asteroids show a negative linear slope. We note that the values of polarization degree were considered with their signs, i.e., a *negative* spectropolarimetric slope means, for increasing wavelength, *more* polarization in the red in the negative branch and *less* polarization in the red in the positive branch. Conversely, if one considers the spectral behavior of the absolute value of  $P_r$ , the sign of the spectral gradients  $|\Delta P_r|/\Delta \lambda$  for the negative and positive branches is found to have opposite values. The latter approach had been previously adopted by *Lupishko and Kiselev* (1995), who discussed the inversion of the polarization spectral dependence for the S-class asteroids. Differences in the definition of the spectropolarimetric slopes, however, do not influence the interesting conclusion about the occurrence of opposite spectropolarimetric behavior for moderate- and low-albedo asteroids. For increasing wavelength, the negative branch of moderate-albedo asteroids becomes deeper, whereas the positive polarization becomes shallower. Low-albedo asteroids exhibit exactly an opposite behavior (*Belskaya et al.*, 2009a; *Bagnulo et al.*, 2015).

Several exceptions exist, however. Two moderate-albedo asteroids with large inversion angles, (234) Barbara and (599) Luisa, showed a shallower negative branch for increasing wavelength, while another Barbarian, (236) Honoria, has

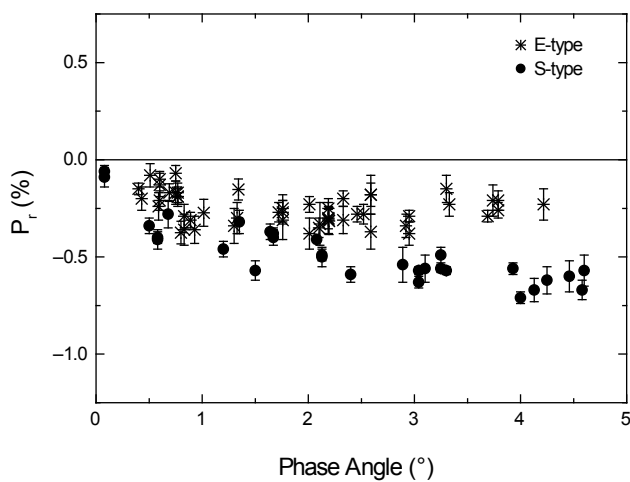


**Fig. 3.** Polarization dependence at small phase angles for the high-albedo E-type (*Zellner and Gradie*, 1976; *Rosenbush et al.*, 2005, 2009; *Zaitsev et al.*, 2014) and the moderate-albedo S-type asteroids (*Zellner and Gradie*, 1976; *Belskaya et al.*, 2003; *Fornasier et al.*, 2006a; *Gill-Hutton et al.*, 2014).

an opposite trend, typical for moderate-albedo asteroids (*Belskaya et al.*, 2009a; *Bagnulo et al.*, 2015). Among low-albedo asteroids, (87) Sylvia and (386) Siegena were mentioned as having atypical wavelength behavior (*Belskaya et al.*, 2009a). New and more accurate polarimetric measurements of these objects are needed to clarify the situation.

Note that the study of the spectral dependence of positive polarization for low-albedo asteroids is still based on a small amount of data. What seems reasonably certain is that the polarization spectra of Ceres and Pallas measured at  $\alpha \sim 22^\circ$ – $23^\circ$  are characterized by a similar increase of polarization degree with wavelength (*Bagnulo et al.*, 2015).

As for moderate-albedo asteroids, some spectral gradients of positive polarization have been reliably measured so far for several NEAs. The BVRI polarimetry of the Q-type NEA 214869 (2007 PA<sub>8</sub>) close to  $P_{\max}$  shows a nonlinear wavelength dependence of polarization (*Fornasier et al.*, 2015) that is similar to that of other moderate-albedo asteroids measured at large phase angles (Fig. 4). A similar nonlinear polarization spectrum was measured for the S-type asteroid (433) Eros at a phase angle of  $42^\circ$  (*Bagnulo et al.*, 2015). The spectropolarimetric behavior of these S- or Q-type NEAs shows an inverse correlation with the reflectance spectra in accordance with the Umov effect (*Umov*, 1905). A decrease of reflectance due to the 1- $\mu\text{m}$  absorption feature results in an increase of polarization degree at  $\lambda > 0.8 \mu\text{m}$ .

For the negative branch, the correlation between the spectropolarimetric spectrum and the spectral reflectance is more complex. *Bagnulo et al.* (2015) have shown that some asteroids with similar reflectance spectra exhibit totally different polarization spectra. As a rule, the negative polarization of S-type asteroids becomes stronger at longer wavelengths for increasing albedo, i.e., a higher albedo corresponds to a deeper  $|P_{\min}|$ . This contradicts the well-known

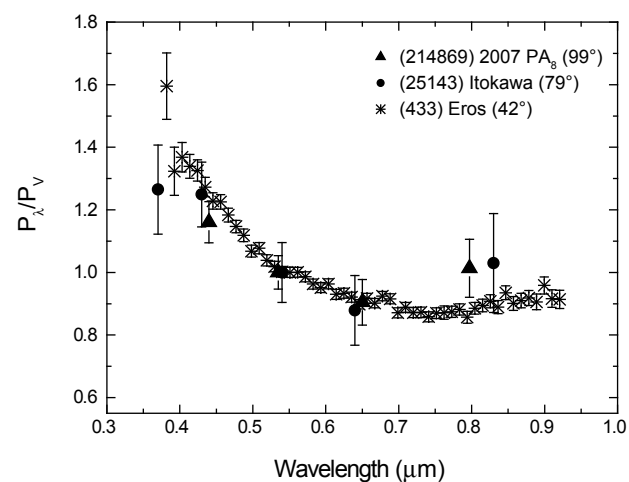


**Fig. 4.** Wavelength dependence of moderate-albedo NEAs (433) Eros (*Bagnulo et al.*, 2015), (25143) Itokawa (*Celilino et al.*, 2005b), and (214869) 2007 PA<sub>8</sub> (*Fornasier et al.*, 2015). The phase angle at which the dependence was measured is shown in parentheses.

inverse correlation of  $|P_{\min}|$  and albedo used for asteroid albedo estimations. Low-albedo asteroids tend to follow the more usual inverse correlation of  $|P_{\min}|$  and albedo.

More in general, it seems that asteroid spectropolarimetry promises to be a very important tool for the physical characterization of asteroids. The reason is that one single spectropolarimetric measurement is able to provide, at the same time, the information usually included separately in spectroscopic and polarimetric data, complemented with the dependence of polarization upon wavelength, another piece of information needed to classify asteroid behavior.

#### 4. ADVANCES IN THEORETICAL AND EXPERIMENTAL MODELING

##### 4.1. Theoretical Modeling

The understanding of the physical mechanisms responsible for the formation of the negative branch of polarization continues to improve. The role of the coherent-backscattering mechanism (CBM) was discussed in detail in *Asteroids III* by Muinonen et al. (2002). The CBM contributes both to the photometric and polarimetric phase dependences, producing sharp features near opposition. To explain broad negative branches, the contribution of single-particle scattering becomes important (e.g., Shkuratov et al., 1994, 2006; Lumme and Rahola, 1998). Recently, a standing-wave polarization mechanism (SWM) has been proposed for the negative linear polarization of single spherical and nonspherical particles (Muinonen et al., 2011). The SWM for negative polarization relies on the generation of forward- and backward-propagating internal waves within the single-scattering particles. Near the particle perimeter, these wave components form a standing wave that constitutes itself as an interference dial (Muinonen et al., 2011). For a linearly polarized incident wave, the internal standing wave, partially linearly polarized as the incident wave, tends to be stronger in the central plane perpendicular to the incident polarization. Due to an interference effect largely resembling that of the CBM, the backward-propagating wave component gives rise to negative polarization.

Several attempts were made to simulate the negative polarization of particulate surfaces. Computer modeling has been carried out by Shkuratov et al. (2002) and Stankevich et al. (2007), and applied to explain some systematic trends observed in laboratory measurements.

The successful application of the discrete dipole approximation (DDA) method to the interpretation of the polarization properties of cometary dust (e.g., Zubko et al., 2008; Lasue et al., 2009) is also noted. In particular, an analog of the Umov effect was found for single-particle scattering (Zubko et al., 2011).

Mishchenko et al. (2009) used numerically exact computer solutions of the Maxwell equations to simulate electromagnetic scattering by realistic models consisting of large numbers of randomly positioned, densely packed particles. They have shown that the negative polarization produced by

the coherent-backscattering effect is remarkably immune to packing-density effects. In this case, the negative polarization branch may become rather wide. The branch survives the increasing density, even if the characteristic distances between particles are on the order of the wavelength.

Petrov et al. (2011) developed Sh-matrix methods within the T-matrix formalism, which allows for the derivation of analytic solutions to the light scattering by nonspherical particles. This allows for a more efficient study of scattering by irregularly shaped particles.

Quantitative agreement was documented between the computations by the radiative-transfer coherent-backscattering method (RT-CB) (Muinonen, 2004) and the superposition T-matrix method (STMM) based on a direct computer solver of the Maxwell equations (Muinonen et al., 2012). The RT-CB method can make use of so-called phenomenological fundamental single scatterers (Muinonen and Videen, 2012). An extension of the RT-CB method to a realistic particulate model for an asteroid's surface is in progress.

##### 4.2. Laboratory Experiments

Laboratory measurements devoted to the interpretation of asteroid polarimetry were rather scarce last decade (e.g., Shkuratov et al., 2008). Measurements of possible meteorite analogs of the surfaces of asteroids (21) Lutetia and (2867) Steins, the targets of the Rosetta mission, were made by Hadamcik et al. (2010, 2011). An average size of regolith grains smaller than 50  $\mu\text{m}$  was suggested from the measurements.

The influence of particle size on the polarization phase curve was studied on particle-size separates of bright and absorbing powders (Ovcharenko et al., 2006; Shkuratov et al., 2008). They showed that the contributions of both the CBM and single-particle scatter are functions of particle size.

Several experiments were made to compare polarimetric properties of single particles and powdered surfaces (see Levasseur-Regourd et al., 2015, for a review). Shkuratov et al. (2007, 2008) showed that the negative polarization strengthened and the polarization degree at large phase angles increased with surface compression. The number density of the particles was found to have a major effect on the polarization maximum (Hadamcik et al., 2009).

Promising results were obtained when comparing laboratory measurements and results of numerical DDA simulations: Zubko et al. (2013) used experimentally measured refractive-index and size-distribution data for irregular feldspar particles to compute Mueller-matrix elements, obtaining highly consistent results.

Laboratory studies of structural analogs of asteroid regoliths remains in great need of further progress in interpreting polarimetric measurements of asteroids.

#### 5. POLARIMETRIC MEASUREMENTS AS A TOOL TO ASSESS SURFACE PROPERTIES

The interpretation of polarimetric observations of asteroids in terms of physical parameters is still not straightforward.

The main conclusions about asteroid surface properties as derived from polarimetric measurements are mostly based on empirical relationships. Particular importance has been paid to the relation between polarimetric parameters and albedo, and the analysis of similarities and differences in the polarization behavior of various objects.

### 5.1. Polarimetric Method of Asteroid Albedo Determination

Polarimetry is one of the best available techniques to derive the albedo from remote observations. An advantage is that an estimate of the albedo can be derived directly from polarimetric measurements without any need of ancillary information from other sources (*Bowell and Zellner*, 1974; *Zellner and Gradie*, 1976; *Zellner et al.*, 1977). This is in contrast with other possible methods of albedo determination, primarily from thermal radiometry, for which the accuracy is limited by the uncertainties in the adopted values of the absolute magnitude. In fact, a few single measurements of polarization degree at a phase angle within 7°–10° (near the extreme values of negative polarization) or even one single measurement at phase angles larger than 30° (in the positive branch of polarization) can be enough to conclude whether an asteroid has a low-, moderate-, or high-albedo surface. In order to determine a more precise value for the albedo (geometric albedo), the observations should cover at least four different phase angles to measure the polarimetric slope  $h$  with good accuracy. This number of observations is a minimum to reach a reliable result. This also constitutes a practical problem, due to the effort needed to observe the target in several observing runs, to allow the necessary change in the phase angle.

Another problem is the one of producing a reliable calibration of the empirical relationships “albedo–polarimetric slope” and “albedo– $P_{\min}$ ” used to determine the albedos of asteroids. Historically, these relations were derived from laboratory measurements of meteorites and then used to determine asteroid albedos (*Zellner and Gradie*, 1976).

Several attempts have been made since then to better calibrate the relationship using the albedos of asteroids available from radiometry and/or from stellar occultations (*Lupishko and Mohamed*, 1996; *Cellino et al.*, 1999, 2012; *Masiero et al.*, 2012). Most recently, *Cellino et al.* (2015b) performed a new, detailed analysis of the calibration problem of the relations between the geometric albedo and the polarization parameters of the asteroids.

In all the above mentioned papers, the authors derived their own values for the constant parameters  $C_1$  and  $C_2$  of the commonly adopted relationship between the geometric albedo  $A_g$  and polarimetric slope  $h$ , namely

$$\log(A_g) = C_1 \log(h) + C_2 \quad (1)$$

We have analyzed how adopting different published calibrations influences the derived values of albedo. Table 1 lists

the available sets of constants  $C_1$  and  $C_2$  found by different authors and the references to the corresponding papers. We also give the albedos calculated from equation (1) for three fixed values of the polarimetric slopes  $h$  corresponding to low-, moderate-, and high-albedo asteroids. For low- and moderate-albedo surfaces, the uncertainties in the polarimetric albedos due to different calibrations are comparable with the uncertainties caused by the errors in the measurements of the polarimetric slope  $h$ . A noticeable discrepancy appears in the case of high-albedo surfaces. Further investigation of the relationship of polarimetric slope and albedo for high-albedo asteroids is crucial to choose the best calibration.

The use of  $P_{\min}$  for albedo determination gives less-confident results. For example, in Fig. 2 the polarization phase curve of the F-type objects and that of the Barbarians show similar values of  $P_{\min}$  in spite of these objects having very different albedos. *Cellino et al.* (2015b) found large discrepancies between  $P_{\min}$ -derived albedos and those obtained from other data and recommend avoiding the use of  $P_{\min}$  for the albedo estimation.

There were also some attempts to find new polarimetric parameters that better correlate with albedo. *Masiero et al.* (2012) introduced a new polarimetric quantity  $p^*$  combining  $\log(h)$  and  $\log(P_{\min})$  in order to describe the maximum polarimetric variation when compared with the albedo and presented the albedo– $p^*$  relation. *Cellino et al.* (2015b) proposed using the difference in polarization degree at  $\alpha = 30^\circ$  and  $\alpha = 10^\circ$  as a new parameter. The comparison of albedos derived from different polarimetric parameters was generally in favor of the polarimetric slope  $h$ , mainly in cases when the coverage of the phase-polarization curve is not optimal. In these cases, a simple linear fit of observations around the inversion angle gives often reasonably accurate results (*Cellino et al.*, 2015b).

Over the last decade, numerous polarimetric measurements were carried out to determine albedos of particularly interesting asteroids, such as potentially hazardous near-Earth objects (*Belskaya et al.*, 2009b; *Fornasier et al.*, 2015; *Delbò et al.*, 2007; *De Luise et al.*, 2007) and targets of space missions (*Cellino et al.*, 2005b; *Fornasier et al.*, 2006b). In general, albedos derived from the polarimetric slope are consistent with the data of direct *in situ* measurements (e.g., *Fornasier et al.*, 2006b).

### 5.2. Regolith Properties Derived from Polarimetry

The relationship between the two parameters characterizing the negative polarization branch  $P_{\min}$  and  $\alpha_{\text{inv}}$  has long been considered as diagnostic of the surface texture (*Dollfus et al.*, 1989). According to laboratory measurements, the bare silicate rocks and fine-grained lunar samples occupy two distinct domains in the plot  $P_{\min}$  vs.  $\alpha_{\text{inv}}$ . The pulverized rocks and meteorites with grain sizes typically between 30 and 300  $\mu\text{m}$ , as well as asteroid data, lie generally in between these two domains. The general agreement of asteroid polarization phase curves with those of pulverized meteorites is considered as an indication of their similar texture.

TABLE 1. List of the constants  $C_1$  and  $C_2$  for the relationship between the geometric albedo and the polarimetric slope  $h$  used for asteroid albedo estimation.

Source of albedo data used for calibration	$C_1$	$C_2$	Albedo			References
			$h = 0.04$	$h = 0.10$	$h = 0.30$	
Meteorites	-1.00	-1.78	0.415	0.166	0.055	Bowell and Zellner (1974)
Meteorites	-0.92	-1.72	0.368	0.158	0.058	Zellner et al. (1977)
IRAS/	$-0.983 \pm 0.082$	$-1.731 \pm 0.066$	0.440	0.179	0.061	Lupishko and Mohamed (1996)
Occultations/ Spacebased						
IRAS	$-1.118 \pm 0.071$	$-1.779 \pm 0.062$	0.608	0.218	0.064	Cellino et al. (1999)
Occultations	$-0.970 \pm 0.071$	$-1.667 \pm 0.083$	0.489	0.201	0.069	Cellino et al. (2012)
WISE	$-1.207 \pm 0.067$	$-1.892 \pm 0.141$	0.624	0.207	0.055	Masiero et al. (2012)
Occultations	$-1.124 \pm 0.032$	$-1.789 \pm 0.025$	0.606	0.216	0.063	Cellino et al. (2015b)

An updated relationship between  $P_{\min}$  vs.  $\alpha_{\text{inv}}$  for asteroids is shown in Fig. 5. The domains for bare rocks and lunar fines as plotted by Dollfus et al. (1989) are also indicated. With new data, the range of inversion angles inherent for asteroid surfaces was found to be wider than previously considered. The F-class asteroids with small inversion angles occupy the domain for bare rocks, while Barbarians lie behind the domain for lunar fines. Asteroid (21) Lutetia, for which the composition is still under debate (see Barucci et al., 2012), belongs to the domain for lunar fines. The asteroids of the same composition class have a tendency to group in the plot of  $P_{\min}$  vs.  $\alpha_{\text{inv}}$ . This result suggests that a wide range of the inversion angles is most probably related to surface mineralogy rather than to variations of particle size of the regolith.

Penttilä et al. (2005) made a statistical analysis of the published polarimetric data of 100 asteroids in order to find relationships with Tholen's taxonomy (Tholen, 1984). They found groups among phase-polarization curves that agree with the published taxonomic classifications and concluded that polarimetry may provide a complementary approach for classification. Subsequent observations have confirmed that asteroids of the same taxonomic class exhibit a similar polarization phase behavior.

Fornasier et al. (2006a) showed that polarimetric values obtained for 36 asteroids of different classes are typically within the range of average polarization-phase curves of a corresponding taxonomic class. Only five asteroids in the dataset were outside the typical values of their classes, which may be due to either an erroneous taxonomic classification or their particular surface properties.

Gil-Hutton and Cañada-Assandri (2011) carried out polarimetric measurements for 56 S-, L-, Ld-, and K-type asteroids and found clear differences between their mean polarization phase curves. Polarimetry of 58 B- and C-type objects was presented by Gil-Hutton and Cañada-Assandri (2012). They found that Ch- and C-type objects show deeper negative branches than Cb or B types. Cañada-Assandri et al. (2012) observed 33 X-type objects and demonstrated clear differences in the average phase-polarization curve for objects classified as M and P type by Tholen (1984).

A large polarimetric survey of 129 main-belt asteroids has shown that the obtained data well agree with the average polarization phase curves of the corresponding types (Gil-Hutton et al., 2014).

The fact that the polarimetric properties of asteroids belonging to the same taxonomic classes are essentially identical suggests that they have similar regolith microtextures. Two extreme cases of inversion angles can be explained by optically homogeneous regolith microstructure in the case of

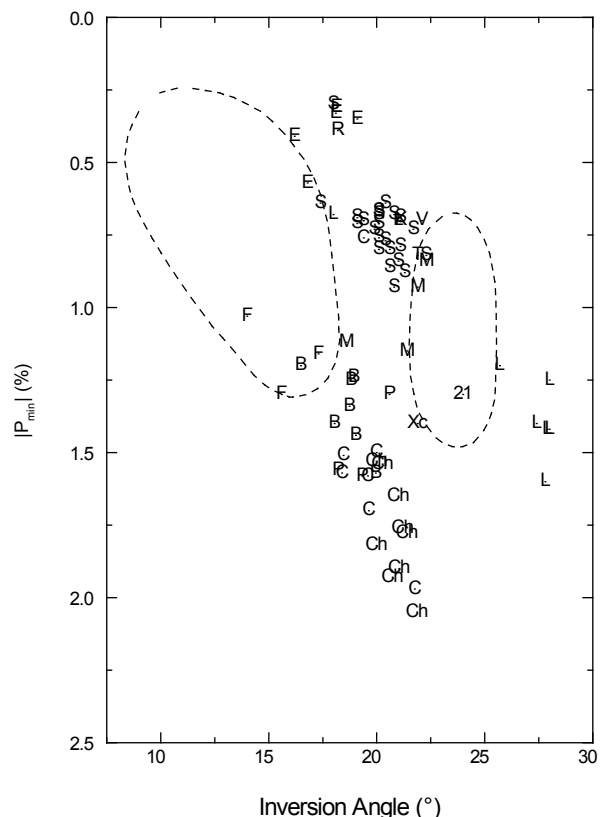


Fig. 5. Relationship between  $P_{\min}$  vs.  $\alpha_{\text{inv}}$  for asteroids of different taxonomic types (shown by letters). The domains for bare rocks and lunar fines as indicated by Dollfus et al. (1989) are also shown.

small  $\alpha_{\text{inv}}$  (Belskaya *et al.*, 2005), and heterogeneous regolith formed by a mixture of components with highly different optical properties in the case of large  $\alpha_{\text{inv}}$  (Gil-Hutton *et al.*, 2008). To understand interrelations of the surface mineralogy and texture, more laboratory and numerical modeling is needed.

### 5.3. Application to Study Near-Earth Asteroids

Observations of NEAs provide the unique possibility of investigating polarization phase dependence at large phase angles close to polarization maximum.

Recent polarimetric observations of the NEA (23187) 2000 PN<sub>9</sub> were made at the largest phase angle  $\alpha = 115^\circ$  ever observed in asteroid polarimetry (Belskaya *et al.*, 2009b). The value of maximum polarization was estimated to be  $P_{\text{max}} \sim 7.7\%$  at  $\alpha_{\text{max}} \sim 103^\circ$ , which is close to the previous estimations for the moderate-albedo NEAs. The Q-type NEA 214869 (2007 PA<sub>8</sub>) showed smaller positive polarization with  $P_{\text{max}} \sim 6\%$  at  $\alpha_{\text{max}} \sim 100^\circ$  in the V band (Fornasier *et al.*, 2015). The polarimetric properties of the asteroid 214869 (2007 PA<sub>8</sub>) are very close to those of the asteroid (25143) Itokawa (Cellino *et al.*, 2005b), suggesting possible similarity of their surface properties.

Two E-type asteroids measured at large phase angles (Kiselev *et al.*, 2002; De Luise *et al.*, 2007) provided a preliminary estimation of  $P_{\text{max}} \sim 2.3\%$  at  $\alpha_{\text{max}} \sim 80^\circ$  for a high-albedo object.

For low-albedo asteroids, no value of  $P_{\text{max}}$  has been measured so far. The single observation at large phase angle for (2100) Ra-Shalom gave  $P \sim 11\%$  at  $\alpha_{\text{max}} \sim 60^\circ$  (Kiselev *et al.*, 1999).

Large differences in the polarization degree for high-, moderate-, and low-albedo asteroids provide a unique way to select primitive low-albedo NEAs by a single polarimetric measurement at  $\alpha > 40^\circ$ . Estimations of albedo of potentially hazardous NEAs are another important application of polarimetric observations. Using instruments like the ESO 8-m VLT telescope, it is possible to obtain albedos and sizes of hazardous objects, as demonstrated by the recent observations of (99942) Apophis (Delbò *et al.*, 2007).

## 6. CONCLUSIONS AND FUTURE WORK

Extensive observational campaigns in the last decade considerably increased the number of asteroids with published polarimetric measurements. These campaigns led to the discovery of asteroids with peculiar polarimetric properties, characterized by narrow negative polarization branches with small inversion angles and wide negative branches with large inversion angles. Further observations have shown that these properties are related to surface mineralogy. All asteroids showing small inversion angles belong to the F-class asteroids, which currently are no longer identified as a separate class. Asteroids with large inversion angles, called Barbarians, seem to belong to the

L class identified by DeMeo *et al.* (2009), using both visible and near-IR spectral data. A possible interpretation of their peculiar polarimetric properties is the presence of spinel in CAIs in their surfaces. These are cases in which even a single polarimetric measurement at a suitable phase angle can be sufficient to provide a classification, something that is not always possible based on spectroscopic data at visible wavelengths. Polarimetric measurements can be an effective tool for asteroid taxonomy.

Traditional application of polarimetry to determine asteroid albedos is especially efficient in the study of NEAs. Polarimetry has been successfully used to estimate the size and albedo of potentially hazardous NEAs. Even a single polarimetric measurement at large phase angles can provide a prompt assessment of an asteroid's geometric albedo.

In the coming years the use of new polarimeters based on CCD detectors will extend available data to increasingly smaller objects and will allow the study of different groups that are important for the understanding of the physical evolution of the asteroid belt. Polarimetric observations of several asteroid family members will shed some light on their surface properties and will also be used to detect interlopers (Milani *et al.*, 2014). On the other hand, the knowledge of the polarization phase curve and polarimetric parameters of different taxonomic classes not yet studied will provide information about the relation between polarimetry and taxonomic classification. Finally, the analysis of larger numbers of spectropolarimetric observations will be used as a tool to reach more robust conclusions about the relation between polarimetric parameters and mineralogy.

In the theoretical modeling of asteroid polarimetry, there are remarkable future prospects for a rigorous, numerical multiple-scattering model where the limitations of the far-field interactions in the RT-CB method will be removed. Prior to this advance, it is plausible that an approximate RT-CB method will be extended to depolarizing, nonspherical single scatterers. Such an advance will allow for the ensemble-averaged, either experimentally measured or numerically computed, scattering matrices to be fully utilized in the interpretation of asteroid polarimetry.

Great progress in polarimetric instrumentation significantly expands the opportunities for polarimetric observations of asteroids. With the improvement of interpretation models and theory, we will enter a new era of extensive application of the polarimetric technique to the study of asteroids.

**Acknowledgments.** Part of this work has been supported by the COST Action MP1104 “Polarization as a Tool to Study the Solar System and Beyond,” ERC Advanced Grant No. 320773 entitled “Scattering and Absorption of Electromagnetic Waves in Particulate Media” (SAEMPL), and the Academy of Finland (contract 257966). R.G.H. gratefully acknowledges financial support by CONICET through PIP 114-200801-00205 and PIP 114-201101-00358. We are grateful to D. Lupishko and A.-C. Levasseur-Regourd for useful comments.

## REFERENCES

- Antonyuk K. A. and Kiselev N. N. (2012) 554 Peraga — an asteroid with unusual polarization properties? *Solar System Res.*, **46**(1), 54–56.
- Appenzeller I., Fricke K., Furtig W., et al. (1998) Successful commissioning of FORS1 — the first optical instrument on the VLT. *The Messenger*, **94**, 1–6.
- Bagnulo S., Tozzi G. P., Boehnhardt H., Vincent J.-B., and Muinonen K. (2010) Polarimetry and photometry of the peculiar main-belt object 7968 = 133P/Elst-Pizarro. *Astron. Astrophys.*, **514**, Article ID A99.
- Bagnulo S., Belskaya I. N., Boehnhardt H., Kolokolova L., Muinonen K., Sterzik M., and Tozzi G.-P. (2011) Polarimetry of small bodies of the solar system with large telescopes. *J. Quant. Spectrosc. Radiat. Transfer*, **112**, 2059–2067.
- Bagnulo S., Cellino A., and Sterzik M. (2015) Linear spectro-polarimetry: A new diagnostic tool for the classification and characterisation of asteroids. *Mon. Not. R. Astron. Soc. Lett.*, **446**, L11–L15.
- Barucci M. A., Belskaya I. N., Fornasier S., et al. (2012) Overview of Lutetia's surface composition. *Planet. Space Sci.*, **66**, 23–30.
- Belskaya I. N., Lupishko D. F., and Shakhovskoy N. M. (1987) Negative polarization spectra for five asteroids. *Soviet Astron. Lett.*, **13**, 219–220.
- Belskaya I. N., Shevchenko V.G., Kiselev N.N., Krugly Yu. N., Shakhovskoy N. M., Efimov Yu. S., Gaftonyuk N. M., Cellino A., and Gil-Hutton R. (2003) Opposition polarimetry and photometry of S- and E-type asteroids. *Icarus*, **166**, 276–284.
- Belskaya I. N., Shkuratov Y. G., Efimov Yu. S., Shakhovskoy N. M., Gil-Hutton R., Cellino A., Zubko E. S., Ovcharenko A. A., Bondarenko S. Y., Shevchenko V. G., Fornasier S., and Barbieri C. (2005) The F-type asteroids with small inversion angles of polarization. *Icarus*, **178**, 213–221.
- Belskaya I. N., Levasseur-Regourd A. C., Cellino A., Efimov Y. S., Shakhovskoy N. M., Hadamcik E., and Bendjoya Ph. (2009a) Polarimetry of main belt asteroids: Wavelength dependence. *Icarus*, **199**, 97–105.
- Belskaya I. N., Fornasier S., and Krugly Y. N. (2009b) Polarimetry and BVRI photometry of the potentially hazardous near-Earth asteroid (23187) 2000 PN<sub>9</sub>. *Icarus*, **201**, 167–171.
- Belskaya I. N., Fornasier S., Krugly Y. N., Shevchenko V. G., Gaftonyuk N. M., Barucci M. A., and Fulchignoni M. (2010) Puzzling asteroid 21 Lutetia: Our knowledge prior to the Rosetta fly-by. *Astron. Astrophys.*, **515**, A29.
- Belskaya I. N., Stinson A., Bagnulo S., Christou A., and Muinonen K. (2014) Polarimetric observations of Jupiter Trojans. In *European Planetary Science Congress 2014*, Abstract #EPS2014-727.
- Boehnhardt H., Tozzi G. P., Bagnulo S., Muinonen K., Nathues A., and Kolokolova L. (2008) Photometry and polarimetry of the nucleus of Comet 2P/Encke. *Astron. Astrophys.*, **489**, 1337–1343.
- Bowell E. and Zellner B. (1974) Polarization of asteroids and satellites. In *Planets, Stars, and Nebulae Studied with Photopolarimetry* (T. Gehrels, ed.), pp. 381–404. Univ. of Arizona, Tucson.
- Burbine T. H., Gaffey M. J., and Bell J. F. (1992) S-asteroids 387 Aquitania and 980 Anacostia — Possible fragments of the breakup of a spinel-bearing parent body with CO<sub>3</sub>/CV<sub>3</sub> affinities. *Meteoritics*, **27**, 424–434.
- Bus S. J. and Binzel R. P. (2002) Phase II of the Small Main-Belt Asteroid Spectroscopic Survey: A feature-based taxonomy. *Icarus*, **158**, 146–177.
- Cañada-Assandri M., Gil-Hutton R., and Benavidez P. (2012) Polarimetric survey of main-belt asteroids. III. Results for 33 X-type objects. *Astron. Astrophys.*, **542**, A11.
- Cellino A., Gil Hutton R., Tedesco E. F., Di Martino M., and Brunini A. (1999) Polarimetric observations of small asteroids: Preliminary results. *Icarus*, **138**, 129–140.
- Cellino A., Zappalà V., Dorelsoundiram A., Di Martino M., Bendjoya Ph., Dotto E., and Migliorini F. (2001) The puzzling case of the Nysa-Polana family. *Icarus*, **152**, 225–237.
- Cellino A., Gil-Hutton R., di Martino M., Bendjoya Ph., Belskaya I. N., and Tedesco E. F. (2005a) Asteroid polarimetric observations using the Torino UVBVI photopolarimeter. *Icarus*, **179**, 304–324.
- Cellino A., Yoshida F., Anderlucci E., Bendjoya Ph., Di Martino M., Ishiguro M., Nakamura A. M., and Saito J. (2005b) A polarimetric study of asteroid 25143 Itokawa. *Icarus*, **179**, 297–303.
- Cellino A., Belskaya I. N., Bendjoya Ph., Di Martino M., Gil-Hutton R., Muinonen K., and Tedesco E. F. (2006) The strange polarimetric behavior of asteroid (234) Barbara. *Icarus*, **180**, 565–567.
- Cellino A., Delbò M., Bendjoya Ph., and Tedesco E. F. (2010) Polarimetric evidence of close similarity between members of the Karin and Koronis dynamical families. *Icarus*, **209**, 556–563.
- Cellino A., Dell'Oro A., Bendjoya Ph., Cañada-Assandri M., and Di Martino M. (2012) A new calibration of the albedo-polarization relation for the asteroids. *J. Quant. Spectrosc. Radiat. Transfer*, **113**, 2552–2560.
- Cellino A., Bagnulo S., Tanga P., Novakovic B., and Delbò M. (2014) A successful search for hidden Barbarians in the Watsonia asteroid family. *Mon. Not. R. Astron. Soc.*, **439**, L75–L79.
- Cellino A., Gil-Hutton R., and Belskaya I. (2015a) Asteroids. In *Polarimetry of Stars and Planetary Systems* (L. Kolokolova et al., eds.), pp. 360–378. Cambridge Univ., Cambridge.
- Cellino A., Bagnulo S., Gil-Hutton R., Tanga P., and Cañada-Assandri M. (2015b) On the calibration of the relation between geometric albedo and polarimetric properties for the asteroids. *Mon. Not. R. Astron. Soc.*, **451**, 3473–3488.
- Delbò M., Cellino A., and Tedesco E. F. (2007) Albedo and size determination of potentially hazardous asteroids: (99942) Apophis. *Icarus*, **188**, 266–269.
- De Luise F., Perna D., Dotto E., Fornasier S., Belskaya I. N., Boatini A., Valsecchi G., Milani A., Rossi A., Lazzarin M., Paolicchi P., and Fulchignoni M. (2007) Physical investigation of the potentially hazardous asteroid (144898) 2004 VD<sub>17</sub>. *Icarus*, **191**, 628–635.
- DeMeo F. E., Binzel R. P., Slivan S. M., and Bus S. J. (2009) An extension of the Bus asteroid taxonomy into the near-infrared. *Icarus*, **202**, 160–180.
- Dollfus A. (1971) Physical studies of asteroids by polarization of the light. In *Physical Studies of Minor Planets* (T. Gehrels, ed.), pp. 95–116. NASA SP-267, Washington, DC.
- Dollfus A. and Zellner B. (1979) Optical polarimetry of asteroids and laboratory samples. In *Asteroids* (T. Gehrels, ed.), pp. 170–183. Univ. of Arizona, Tucson.
- Dollfus A., Wolff M., Geake J. E., Lupishko D. F., and Dougherty L. M. (1989) Photo-polarimetry of asteroids. In *Asteroids II* (R. P. Binzel et al., eds.), pp. 594–616. Univ. of Arizona, Tucson.
- Fornasier S., Beskaya I. N., Shkuratov Yu. G., Pernechele C., Barbieri C., Giro E., and Navasardyan H. (2006a) Polarimetric survey of asteroids with the Asiago telescope. *Astron. Astrophys.*, **455**, 371–377.
- Fornasier S., Belskaya I. N., Fulchignoni M., Barucci M. A., and Barbieri C. (2006b) First albedo determination of 2867 Steins, target of the Rosetta mission. *Astron. Astrophys.*, **449**, L9–L12.
- Fornasier S., Beskaya I. N., and Perna D. (2015) The potentially hazardous asteroid 2007 PA<sub>8</sub>: An unweathered L chondrite analogue surface. *Icarus*, **250**, 280–286.
- Gil-Hutton R. (2007) Polarimetry of M-type asteroids. *Astron. Astrophys.*, **464**, 1127–1132.
- Gil-Hutton R. and Cañada-Assandri M. (2011) Polarimetric survey of main-belt asteroids. I. Results for fifty-seven S-, L-, and K-type objects. *Astron. Astrophys.*, **529**, A86.
- Gil-Hutton R. and Cañada-Assandri M. (2012) Polarimetric survey of main-belt asteroids. II. Results for 58 B- and C-type objects. *Astron. Astrophys.*, **539**, A115.
- Gil-Hutton R., Mesa V., Cellino A., Bendjoya Ph., Peñaloza L., and Lovos F. (2008) New cases of unusual polarimetric behavior in asteroids. *Astron. Astrophys.*, **482**, 309–314.
- Gil-Hutton R., Cellino A., and Bendjoya Ph. (2014) Polarimetric survey of main-belt asteroids. IV. New results from the first epoch of the CASLEO survey. *Astron. Astrophys.*, **569**, A122.
- Hadamcik E., Renard J.-B., Levasseur-Regourd A. C., and Worms J. C. (2009) Laboratory measurements of the light scattered by clouds of solid particles by imaging technique. In *Light Scattering Reviews 4* (A. A. Kokhanovsky, ed.), pp. 31–70. Springer, Berlin.
- Hadamcik E., Levasseur-Regourd A. C., and Renard J.-B. (2010) Observations and laboratory simulations of asteroids by polarization measurements. In *Electro-Magnetic and Light Scattering XII* (K. Muinonen et al., eds.), pp. 70–73. Univ. of Helsinki, Helsinki.
- Hadamcik E., Levasseur-Regourd A. C., Renard J.-B., Lasue J., and Sen A. K. (2011) Polarimetric observations and laboratory simulations of asteroidal surfaces: The case of 21 Lutetia. *J. Quant. Spectrosc. Radiat. Transfer*, **112**, 1881–1890.
- Hough J. H. (2005) Polarimetry techniques at optical and infrared wavelengths. In *Astronomical Polarimetry: Current Status and*

- Future Directions* (A. Adamson et al., eds.), pp. 3–14. ASP Conf. Ser. 343, Astronomical Society of the Pacific, San Francisco.
- Kaasalainen S., Piironen J., Kaasalainen M., Harris A. W., Muinonen K., and Cellino A. (2003) Asteroid photometric and polarimetric phase curves: Empirical interpretation. *Icarus*, 161, 34–46.
- Keller C. U., Snik F., Harrington D. M., and Packham C. (2015) Instrumentation. In *Polarimetry of Stars and Planetary Systems* (L. Kolokolova et al., eds.), pp. 35–61. Cambridge Univ., Cambridge.
- Kiselev N. N., Rosenbush V. K., and Jockers K. (1999) NOTE: Polarimetry of asteroid 2100 Ra-Shalom at large phase angle. *Icarus*, 140, 464–466.
- Kiselev N. N., Rosenbush V. K., Jockers K., Velichko F. P., Shakhevskoy N. M., Efimov Y. S., Lupishko D. F., and Rumyantsev V. V. (2002) Polarimetry of near-Earth asteroid 33342 (1998 WT<sub>24</sub>). Synthetic phase angle dependence of polarization for the E-type asteroids. In *Proceedings of Asteroids, Comets, Meteors — ACM 2002* (B. Warmbein, ed.), pp. 887–890. ESA SP-500, Noordwijk, Netherlands.
- Kolokolova L. and Jockers K. (1997) Composition of cometary dust from polarization spectra. *Planet. Space Sci.*, 45, 1543–1550.
- Kolokolova L., Hough J., Levasseur-Regourd A. C., eds. (2015) *Polarimetry of Stars and Planetary Systems*. Cambridge Univ., Cambridge. 503 pp.
- Lasue J., Levasseur-Regourd A. C., Hadamcik E., and Alcouffe G. (2009) Cometary dust properties retrieved from polarization observations: Application to C/1995 O1 Hale-Bopp and 1P/Halley. *Icarus*, 199, 129–144.
- Levasseur-Regourd A. C., Renard J.-B., Shkuratov Y., and Hadamcik E. (2015) Laboratory studies. In *Polarimetry of Stars and Planetary Systems* (L. Kolokolova et al., eds.), pp. 62–80. Cambridge Univ., Cambridge.
- Lumme K. and Muinonen K. (1993) A two-parameter system for linear polarization of some solar system objects. In *Asteroids, Comets, Meteors 1993* (A. Milani et al., eds.), p. 194. IAU Symp. 160, Kluwer, Dordrecht.
- Lumme K. and Rahola J. (1998) Comparison of light scattering by stochastically rough spheres, best-fit spheroids and spheres. *J. Quant. Spectrosc. Radiat. Transfer*, 60, 439–450.
- Lupishko D. F. (2014) *Asteroid Polarimetric Database V8.0*. NASA Planetary Data System, EAR-A-3-RDR-APD-POLARIMETRY-V8.0.
- Lupishko D. F. and Kiselev N. N. (1995) Inversion effect of spectral dependence of asteroid polarization. *Bull. Am. Astron. Soc.*, 27, 1064.
- Lupishko D. F. and Mohamed R. A. (1996) A new calibration of the polarimetric albedo scale of asteroids. *Icarus*, 119, 209–213.
- Lupishko D. F. and Vasiliev S. V. (1997) Asteroid polarimetric database. *Kinematics Phys. Cel. Bodies*, 13(3), 17–23.
- Maleszewski C., McMillan R. S., and Smith P. S. (2013) Contrasting Q-type asteroid regolith from the S-complex through polarimetry. In *AAS/Division for Planetary Sciences Meeting Abstracts*, 45, #208.14.
- Masiero J. (2010) Albedo heterogeneity on the surface of (1943) Anteros. *Icarus*, 207, 795–799.
- Masiero J. and Cellino A. (2009) Polarization of asteroid (387) Aquitania: The newest member of a class of large inversion angle asteroids. *Icarus*, 199, 333–337.
- Masiero J., Hodapp K., Harrington D., and Lin H. S. (2007) Commissioning of the dual-beam imaging polarimeter for the University of Hawaii 88 inch telescope. *Publ. Astron. Soc. Pac.*, 119, 1126–1132.
- Masiero J., Hartzell C., and Scheers D. J. (2009) The effect of the dust size distribution on asteroid polarization. *Astron. J.*, 138, 1557–1562.
- Masiero J. R., Mainzer A. K., Gray T., Bauer J. M., Wright E. L., Mc Millan R. S., Tholen D. J., and Blain A. W. (2012) A revised asteroid polarization-albedo relationship using WISE/NEOWISE data. *Astrophys. J.*, 749, Article ID 104.
- Milani A., Cellino A., Knežević Z., Novaković B., Spoto F., and Paolicchi P. (2014) Asteroid families classification: Exploiting very large datasets. *Icarus*, 239, 46–73.
- Mishchenko M., Dlugach J., Liu L., Rosenbush V., Kiselev N., and Shkuratov Y. (2009) Direct solutions of the Maxwell equations explain opposition phenomena observed for high-albedo solar system objects. *Astrophys. J. Lett.*, 705, L118–L122.
- Mishchenko M. I., Rosenbush V. K., Kiselev N. N., Lupishko D. F., Tishkovets V. P., Kaydash V. G., Belskaya I. N., Efimov Y. S., and Shakhevskoy N. M. (2010) *Polarimetric Remote Sensing of Solar System Objects*. Akademperiodyka, Kyiv. 291 pp.
- Muinonen K. (2004) Coherent backscattering of light by complex random media of spherical scatterers: Numerical solution. *Waves in Random Media*, 14(3), 365–388.
- Muinonen K. and Videen G. (2012) A phenomenological single scatterer for studies of complex particulate media. *J. Quant. Spectrosc. Radiat. Transfer*, 113, 2385–2390.
- Muinonen K., Piironen J., Shkuratov Y. G., Ovcharenko A. A., and Clark B. E. (2002) Asteroid photometric and polarimetric phase effects. In *Asteroids III* (W. F. Bottke Jr. et al., eds.), pp. 123–138. Univ. of Arizona, Tucson.
- Muinonen K., Penttilä A., Cellino A., Belskaya I. N., Delbò M., Levasseur-Regourd A. C., and Tedesco E. F. (2009) Asteroid photometric and polarimetric phase curves: Joint linear-exponential modeling. *Meteoritics & Planet. Sci.*, 44, 1937–1946.
- Muinonen K., Tyynelä J., Zubko E., Lindqvist H., Penttilä A., and Videen G. (2011) Polarization of light backscattered by small particles. *J. Quant. Spectrosc. Radiat. Transfer*, 112, 2193–2212.
- Muinonen K., Mishchenko M. I., Dlugach J. M., Zubko E., Penttilä A., and Videen G. (2012) Coherent backscattering numerically verified for a finite volume of spherical particles. *Astrophys. J.*, 760, 118.
- Muinonen K., Penttilä A., and Videen G. (2015) Multiple scattering of light in particulate planetary media. In *Polarimetry of Stars and Planetary Systems* (L. Kolokolova et al., eds.), pp. 114–129. Cambridge Univ., Cambridge.
- Novaković B., Cellino A., and Knežević Z. (2011) Families among high-inclination asteroids. *Icarus*, 216, 69–81.
- Oliva T. (1997) Wedged double Wollaston, a device for single shot polarimetric measurements. *Astron. Astrophys.*, 123, 589–592.
- Ovcharenko A. A., Bondarenko S. Y., Zubko E. S., Shkuratov Y. G., Videen G., and Nelson R. (2006) Particle size effect on the opposition spike and negative polarization. *J. Quant. Spectrosc. Radiat. Transfer*, 101, 394–403.
- Penttilä A., Lumme K., Hadamcik E., and Levasseur-Regourd A.-C. (2005) Statistical analysis of asteroidal and cometary polarization phase curves. *Astron. Astrophys.*, 432, 1081–1090.
- Pernechele C., Abe L., Bendjoya Ph., Cellino A., Massone G., Rivet J. P., and Tanga P. (2012) A single-shot optical linear polarimeter for asteroid studies. In *Ground-Based and Airborne Instrumentation for Astronomy IV* (I. S. McLean et al., eds.), p. 84462H. SPIE Conf. Ser. 8446, Bellingham, Washington.
- Petrov D., Shkuratov Y., and Videen G. (2011) An analytical approach to electromagnetic wave scattering from particles of arbitrary shapes. *J. Quant. Spectrosc. Radiat. Transfer*, 112(II), 1636–1645.
- Pirola V. (1973) A double image chopping polarimeter. *Astron. Astrophys.*, 27, 383–388.
- Rosenbush V. K., Avramchuk V. V., Rosenbush A. E., and Mishchenko M. I. (1997) Polarization properties of the Galilean satellites of Jupiter: Observations and preliminary analysis. *Astrophys. J.*, 487, 402–414.
- Rosenbush V. K., Kiselev N. N., Shevchenko V. G., Jockers K., Shakhevskoy N. M., and Efimov Y. F. (2005) Polarization and brightness opposition effects for the E-type asteroid 64 Angelina. *Icarus*, 178, 222–234.
- Rosenbush V. K., Shevchenko V. G., Kiselev N. N., Sergeev A. V., Shakhevskoy N. M., Velichko F. P., Kolesnikov S. V., and Karpov N. V. (2009) Polarization and brightness opposition effects for the E-type asteroid 44 Nysa. *Icarus*, 201, 655–665.
- Scaltriti F., Pirola V., Cellino A., Anderlucci E., Corcione L., Massone G., Racioppi F., and Porcu F. (1989) The UVBVR photopolarimeter of the Torino Astronomical Observatory. *Mem. Soc. Astron. Ital.*, 60, 243–246.
- Shkuratov Y. G., Muinonen K., Bowell E., et al. (1994) A critical review of theoretical models for the negative polarization of light scattered by atmosphereless solar system bodies. *Earth Moon Planets*, 65, 201–246.
- Shkuratov Yu., Ovcharenko A., Zubko E., Miloslavskaya O., Nelson R., Smythe W., Muinonen K., Piironen J., Rosenbush V., and Helfenstein P. (2002) The opposition effect and negative polarization of structurally simulated planetary regoliths. *Icarus*, 159, 396–416.
- Shkuratov Y., Bondarenko S., Ovcharenko A., Videen G., Pieters C., Hiroi T., Volten H., Hovenier J., and Munos O. (2006) Comparative studies of the reflectance and degree of linear polarization of particulate surfaces and independently scattering particles. *J. Quant. Spectrosc. Radiat. Transfer*, 100, 340–358.

- Shkuratov Y., Bondarenko S., Kaydash V., Videen G., Munos O., and Volten H. (2007) Photometry and polarimetry of particulate surfaces and aerosol particles over a wide range of phase angles *J. Quant. Spectrosc. Radiat. Transfer*, *106*, 487–508.
- Shkuratov Y., Ovcharenko A., Psarev V., and Bondarenko S. (2008) Laboratory measurements of reflected light intensity and polarization for selected particulate surfaces. In *Light Scattering Reviews 3: Light Scattering and Reflection* (A. A. Kokhanovsky, ed.), pp. 383–402. Praxis, Chichester.
- Stankevich D., Istomina L., Shkuratov Yu., and Videen G. (2007) The coherent backscattering effects in a random medium as calculated using a ray tracing technique for large non-transparent spheres. *J. Quant. Spectrosc. Radiat. Transfer*, *106*, 509–519.
- Sunshine J., Connolly H. C., McCoy T. J., and Bus S. J. (2007) Refractory-rich asteroids: Concentrations of the most ancient materials in the solar system. *Bull. Am. Astron. Soc.*, *39*, 476.
- Tholen D. (1984) Asteroid taxonomy from cluster analysis of photometry. Ph.D. thesis, Univ. of Arizona, Tucson.
- Tholen D. (1989) Asteroid taxonomic classifications. In *Asteroids II* (R. P. Binzel et al., eds.), pp. 1139–1150. Univ. of Arizona, Tucson.
- Umov N. (1905) Chromatische depolarisation durch Lichtzerstreuung. *Phys. Zeit.*, *6*, 674–676.
- Zaitsev S. V., Kiselev N. N., Rosenbush V. K., Kolesnikov S. V., and Antonyuk K. A. (2014) Polarimetry of the E-type asteroid 64 Angelina. *Kinematics Phys. Cel. Bodies*, *30*(3), 155–160.
- Zellner B. and Gradie J. (1976) Minor planets and related objects. XX. Polarimetric evidence for the albedos and compositions of 94 asteroids. *Astron. J.*, *81*, 262–280.
- Zellner B., Leake M., Lebertre T., Duseaux M., and Dollfus A. (1977) The asteroid albedo scale. I. Laboratory polarimetry of meteorites. *Proc. Lunar Sci. Conf. 8th*, p. 1110.
- Zubko E., Shkuratov Y., Mishchenko M., and Videen G. (2008) Light scattering in a finite multi-particle system. *J. Quant. Spectrosc. Radiat. Transfer*, *109*, 2195–2206.
- Zubko E., Videen G., Shkuratov Y., Muinonen K., and Yamamoto T. (2011) The Umov effect for single irregularly shaped particles with size comparable with wavelength. *Icarus*, *212*, 403–415.
- Zubko E., Videen G., Muinonen K., Muñoz O., Nousiainen T., Shkuratov Y., and Sun W. (2013) Light scattering by feldspar particles: Comparison of model agglomerate debris particles. *J. Quant. Spectrosc. Radiat. Transfer*, *131*, 175–187.



# Radar Observations of Near-Earth and Main-Belt Asteroids

Lance A. M. Benner

*Jet Propulsion Laboratory, California Institute of Technology*

Michael W. Busch

*SETI Institute*

Jon D. Giorgini

*Jet Propulsion Laboratory, California Institute of Technology*

Patrick A. Taylor

*Arecibo Observatory*

Jean-Luc Margot

*University of California, Los Angeles*

---

Radar is a very powerful technique for characterizing near-Earth and main-belt asteroids and for improving their orbits. This results from radar's ability to spatially resolve objects that often cannot be resolved at comparable resolutions by other groundbased techniques. Radar has revealed binary and contact binary objects, at least two triple systems, non-principal-axis rotators, objects whose radar reflectivity and circular polarization ratio have longitudinal variation, irregularly shaped near-Earth asteroids, objects with metallic compositions, objects with rubble-pile structures, and detailed radar images of main-belt asteroids that reveal complicated surfaces and substantial topographic relief. This chapter concentrates on the most significant advances in the field since publication of the radar chapter by Ostro *et al.* (2002) in *Asteroids III*. Detailed descriptions of asteroid radar observing techniques and terminology have appeared in Ostro (1993) and Ostro *et al.* (2002) (*Asteroids III*), so we refer readers to those papers for background information. This chapter emphasizes the first ground-truth tests of asteroid shape models by spacecraft encounters, population trends among near-Earth and main-belt asteroids, results for selected objects, new observing techniques, improved capabilities at radar telescopes, and improvements in three-dimensional shape modeling. We conclude with a discussion of future prospects.

## 1. INTRODUCTION

Planetary radar astronomy is an active form of observation in which the observer illuminates the target with radio waves having known properties and measures the reflected signal in order to investigate the physical properties of the target and to improve its orbit. Radar observations can occur during the day, in cloudy weather, during rain, and in a real sense represent a laboratory experiment on objects at distances of up to hundreds of millions of kilometers.

The world's most sensitive facilities for radar observations of asteroids are the Arecibo Observatory and the Goldstone Solar System Radar. Arecibo has a diameter of 305 m and is the world's largest operational single-dish radio telescope. Arecibo's S-band system operates at a frequency of 2380 MHz ( $\lambda = 12.6$  cm) and has a transmitter power of 900 kW. The dish is built into a sinkhole and cannot move; to point, the transmitters and receivers are suspended above

the dish on azimuth and elevation rails that permit tracking of objects 360° in azimuth and within 20° of zenith. Arecibo is located in Puerto Rico at a latitude of +18°, so it is able to observe objects at declinations from -1° to +38° and see approximately one-third of the sky. Due to its pointing restrictions, Arecibo can track a given object for a maximum of 2.9 h/day. The highest range resolution currently available at Arecibo is 7.5 m/pixel.

The Goldstone Solar System Radar is located on the DSS-14 antenna at the National Aeronautics and Space Administration's (NASA) Goldstone Deep Space Communications Complex. DSS-14, hereafter referred to as "Goldstone," is part of the Deep Space Network (DSN). Goldstone has a diameter of 70 m, operates at a transmitter frequency of 8560 MHz ( $\lambda = 3.5$  cm), and has a transmitter power of 450 kW. Goldstone is fully steerable and can track objects north of -35°, providing coverage for ~80% of the sky. The finest range resolution available at Goldstone is 3.75 m/pixel.

Due to its higher transmitter frequency, Goldstone can provide  $3.6\times$  finer Doppler resolution than Arecibo in high signal-to-noise ratio (SNR) situations, which can be helpful for resolving small and/or slowly rotating objects.

The capabilities of Arecibo and Goldstone are complementary: Arecibo is about  $20\times$  more sensitive and can detect objects to twice the distance, but Goldstone can track objects for several times longer, much farther north and south, and achieve higher resolutions in range and Doppler frequency. Arecibo is designed as an astronomical observatory and is easier to use and schedule on short notice. The primary mission at Goldstone is spacecraft communication, and the facility is currently available for astronomical observations for  $<10\%$  of the time. Target-of-opportunity observations are possible at Goldstone but more challenging to schedule than targets identified well in advance. For many of the best targets, both observatories are utilized to maximize the return on scientific investment. Due to the time it takes equipment to switch from transmitting to receiving, Arecibo can observe objects as close as 0.008 AU and Goldstone can observe objects as close as 0.005 AU. For closer objects, the 34-m DSS-13 antenna is often used to receive echoes from Goldstone transmissions, although that bistatic configuration reduces the SNRs by a factor of  $\sim 6$ . The 100-m Green Bank Telescope is also available for bistatic observations using both Arecibo and Goldstone to transmit.

In practice, due to its greater sensitivity, Arecibo can detect significantly more near-Earth asteroids (NEAs) than is possible at Goldstone despite Arecibo's restricted pointing capabilities. The principal reason is that many near-Earth objects traverse Arecibo's declination window when they are still close enough for Arecibo to detect. The fraction of NEAs observable by Goldstone that are too far north or south for Arecibo to detect is  $\sim 5\%$  (S. P. Naidu, personal communication).

Radar astrometry can produce dramatic improvements in asteroid orbits for recently discovered objects due to radar's high fractional precision of up to 1 part in  $10^8$ . For example, for a single opposition object, including radar astrometry in the orbit solution typically increases the interval of Earth encounter statistical predictability by a factor of 5 from 80 to 400 years, on average, compared to a solution based only on optical measurements (*Ostro and Giorgini, 2004*). The effects of radar astrometry on asteroid orbit determination have been discussed in several papers; for a detailed summary see *Ostro and Giorgini (2004)*.

## 2. RECENT RADAR DETECTION HISTORY

The number of NEAs observed with radar has increased dramatically since publication of *Asteroids III*, from 120 at the end of 2002 to 508 at the end of 2014 (Fig. 1 and tabulated online at <http://echo.jpl.nasa.gov/asteroids/PDS.asteroid.radar.history.html>). This is due largely to a six-fold increase in the number of NEA discoveries. During the decade after completion of the upgrade at Arecibo in the late 1990s, the average number of NEA radar detections was 20–30

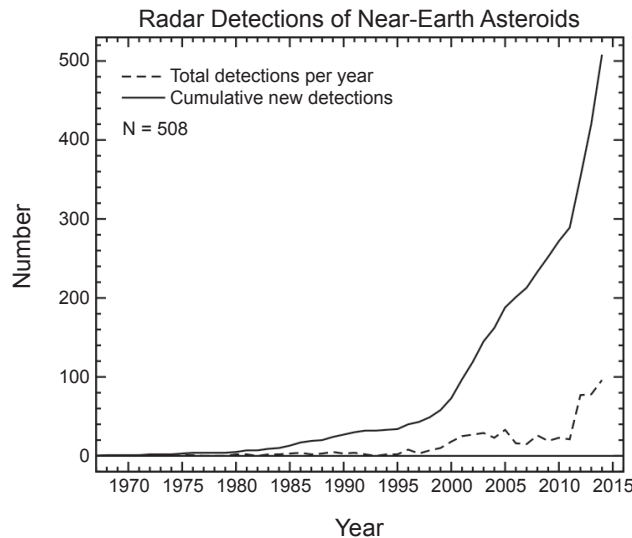


**Fig. 1.** Number of NEA radar detections through the end of 2014. The increase in cumulative detections in 1999–2000 was caused in part by a surge of discoveries by LINEAR and by the order-of-magnitude increase in sensitivity at Arecibo after the upgrade. The increase in 2012 was the result of increased funding for Arecibo and greater access to telescope time at Arecibo and Goldstone.

annually. This jumped by a factor of  $\sim 3$  in 2012 following increased NASA funding at Arecibo (and to a lesser extent at Goldstone) and due to greater access to telescope time for targets known well in advance. Many weak targets that had previously been ignored are now being observed. The minimum SNR threshold adopted for scheduling an asteroid for radar observations is typically  $\sim 30/\text{day}$  at Goldstone and  $\sim 15/\text{day}$  at Arecibo, although there are many instances where observations are attempted for weaker targets.

Obtaining time for target-of-opportunity observations at Goldstone has long been much more cumbersome than at Arecibo. At Arecibo, submission of an urgent proposal can lead to scheduling observations within one day. At Goldstone it is necessary to coordinate radiation clearance with more than 25 government organizations whose airspace surrounds DSS-14; this process used to take up to several days, but recent improvements have shrunk this to  $<2$  days. It is also possible to observe objects on very short notice without radiation clearance by reducing the transmitter power to 110 kW. Many targets of opportunity have been observed recently at both observatories by redirecting time previously scheduled for other asteroids. Radar delay-Doppler astrometry is used to update the orbit solution during the observations and is posted online shortly after the experiment is complete at <http://ssd.jpl.nasa.gov/?radar>.

### 2.1. Technological Developments

**2.1.1. Arecibo.** One of the most significant developments at Arecibo has been an upgrade in the highest resolu-

tion available for delay-Doppler imaging. Shortly after the upgrade in 1999, the highest range resolution was 15 m/pixel by taking data with the Caltech Baseband Recorder (CBR), equipment originally designed for observing pulsars. However, the CBR was complicated to use, it did not permit real-time monitoring of the data (so the user did not know if there were echoes or problems until much later), and it didn't utilize the full bandwidth available from Arecibo's klystron amplifiers. In 2004, the "Portable Fast Sampler" (PFS) data-taking system designed and built by J. L. Margot became fully operational and provided range resolutions up to 7.5 m/pixel. The PFS is much more straightforward to use, can write data directly to disk rather than using striped tape drives, permits the user to check the data in near-real time, and has been upgraded, cloned, and installed at Goldstone and Green Bank. The 7.5-m resolution is close to the theoretical limit of  $\sim 6$  m imposed by the bandwidth of Arecibo's klystrons. A factor of 2 in range resolution yields pronounced differences in the detail visible in delay-Doppler radar images, and nearly all the strongest SNR targets observed at Arecibo now use 7.5-m resolution.

**2.1.2. Goldstone.** The most important improvement at Goldstone during the last decade has been the development of finer-resolution delay-Doppler imaging using chirp waveforms. From 1992 to 2010, the finest range resolution at Goldstone was 18.75 m achieved by using binary phase-coded waveforms. Although Goldstone's klystron amplifiers could be modulated at higher frequencies and in principle obtain higher resolutions, 18.75 m (with the frequency side lobes of binary phase-coded waveforms) is the finest resolution possible without violating Goldstone's frequency license. To achieve higher resolution without violating the license, linear frequency modulation (also known as chirping) was implemented (Slade et al., 2011). The chirp system improved the resolution at Goldstone by a factor of 5 from 18.75 m to 3.75 m, a resolution twice as fine as the highest resolution available at Arecibo. This illustrates another way in which the capabilities of Arecibo and Goldstone are complementary. The first asteroid observed with a range resolution of 3.75 m was 2010 AL<sub>30</sub> (Slade et al., 2010), an object  $\sim 30$  m in diameter that approached within 0.00086 AU (0.3 lunar distances) in January 2010.

A five-fold improvement in resolution reveals considerably more detail than was previously possible and has yielded dramatic images of several objects a few hundred meters in diameter (or larger), such as (308635) 2005 YU<sub>55</sub>, (214869) 2007 PA<sub>8</sub>, (4179) Toutatis, 2014 HQ<sub>124</sub>, and (357439) 2004 BL<sub>86</sub>. For example, numerous impact craters and boulders are visible on the surface of 2005 YU<sub>55</sub> (Fig. 2). In addition, a new digital receiver system has been acquired that can obtain dual-polarization delay-Doppler images at resolutions as fine as 1.25 m/pixel, 3 $\times$  finer than Goldstone can transmit, in preparation for possible use of higher-resolution waveforms in the future.

With the new chirp/digital receiver system, it is now possible to spatially resolve NEAs  $\sim 30$  m in diameter and estimate their three-dimensional shapes. The chirp imaging system

also enables finer precision ranging astrometry, particularly for tiny objects, with uncertainties of  $\sim 10$  m.

Clones of the new digital receiver equipment were installed at Arecibo and Green Bank in 2014. Using Goldstone to transmit, Arecibo can now acquire images with a resolution of 3.75 m, which is twice as fine as Arecibo can achieve monostatically. The new equipment was successfully tested at Arecibo with observations of NEA 2014 HQ<sub>124</sub> (Fig. 3) in June 2014 and at Green Bank with observations of 2005 YQ<sub>96</sub> and 2004 BL<sub>86</sub> in January 2015. When used in bistatic mode with Goldstone transmitting and Arecibo receiving, the SNRs are about 5 $\times$  stronger relative to those obtainable with monostatic observations at Goldstone. Reception at Green Bank increases the SNRs by a factor of  $\sim 2$  relative to monostatic observations due to Green Bank's larger diameter (100 m) and the doubling of the integration time.

## 2.2. Radar Speckle Tracking

Development of the radar speckle technique for estimation of asteroid spin vectors (Busch et al., 2010) is a major new capability since publication of *Asteroids III*. When illuminated with a monochromatic coherent uncoded radar waveform [continuous-wave (CW) observations], each point on a target reradiates with a random phase determined by its distance from the transmitter and the radar scattering properties of the surface. These wavefronts combine, producing a

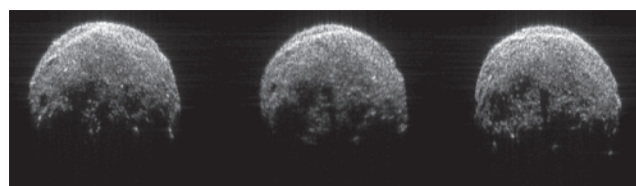


**Fig. 2.** Bistatic Goldstone DSS-14/DSS-13 radar images of near-Earth asteroid 2005 YU<sub>55</sub> obtained on November 9, 2011. Range increases down and Doppler frequency increases to the left, so rotation is clockwise. Range resolution is 3.75 m/row, but the data were double sampled, so each row corresponds to 1.875 m.

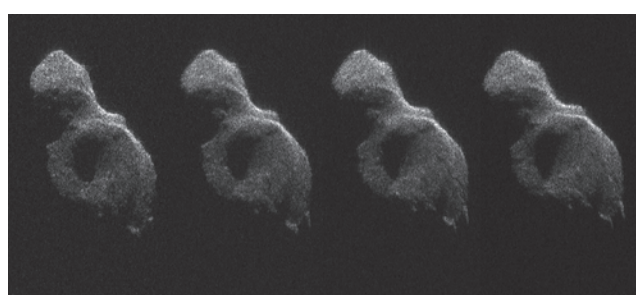


**Fig. 3.** Bistatic Goldstone-Arecibo images of near-Earth asteroid 2014 HQ<sub>124</sub> obtained on June 8, 2014. Each pixel has dimensions of 1.875 m  $\times$  0.00625 Hz.

pattern of constructive and destructive interference that project onto Earth as high- and low-intensity splotches known as radar speckles. The speckles have a characteristic length scale of  $L_{\text{speckle}} = D\lambda/d$ , where  $D$  is the distance to the target,  $d$  is its diameter, and  $\lambda$  is the radar wavelength. For NEA radar targets,  $L_{\text{speckle}}$  is usually  $>100$  km and  $<10,000$  km.

As the target rotates, the speckle pattern moves in the same direction as the target's surface. By tracking the speckle motion, it is possible to estimate the pole direction, sense of rotation, and rotation rate (Margot *et al.*, 2007, 2012). For objects with unknown spin states, the antennas must be separated by less than the speckle scale (Busch *et al.*, 2010). Near-Earth asteroids can be observed with speckle tracking by transmitting from Arecibo or Goldstone and receiving with elements of the Very Long Baseline Array (VLBA) or Very Large Array (VLA).

The current discovery rate of NEAs is  $\sim 1500$  per year, of which  $\sim 5$ – $10$  are suitable for speckle tracking. This technique has been applied to a number of NEAs and has resolved spin-state ambiguities for (341843) 2008 EV<sub>5</sub> (Busch *et al.*, 2011) and 2005 YU<sub>55</sub> (Busch *et al.*, 2012).

### 2.3. Shape Modeling Improvements

The three-dimensional shape reconstruction software was originally written by R. S. Hudson (Hudson, 1993), who used it to produce detailed shape models of contact binary (4769) Castalia (Hudson and Ostro, 1994), non-principal-axis rotator (4179) Toutatis (Hudson and Ostro, 1995; Hudson *et al.*, 2003), angular asteroid (6489) Golevka (Hudson *et al.*, 2000), and less-detailed models of several other NEAs.

When *Asteroids III* was published in 2002, the software was capable of handling 24 parameters describing the spin, shape, and reflectivity of asteroids, and 11 types of penalties designed to guide the optimization routine. Since then, C. Magri has overseen most of the development and maintenance of the software and documentation (Magri *et al.*, 2007b), with contributions from others starting in 2005 when the software was released more widely. The software is now more capable and easier to use. A number of graphical capabilities and penalty functions have been added, and the software can now handle a greater variety of input formats, coding schemes, and sampling modes. The modeling of photometric properties has also been significantly expanded. Ovoid shapes are now supported in addition to the original ellipsoid, spherical harmonic, and vertex shape representations. The user can also specify pixel masks to vignette one component of a binary asteroid when modeling the other component (Ostro *et al.*, 2006) or to assign weights to different parts of an image (Nolan *et al.*, 2013). The software can handle time-variable spin rates and spin impulses. The former was instrumental in establishing the first Yarkovsky-O'Keefe-Radzievskii-Paddack (YORP) detection (Taylor *et al.*, 2007), and the latter is important in representing spin-state changes during close planetary encounters (Takahashi *et al.*, 2013). A libration model has also been incorporated to properly represent the dynamics of asteroid satellites (Naidu and

Margot, 2015). The current version allows for 243 adjustable parameters and 24 penalties to the objective function. This makes it a rather specialized tool with a substantial learning curve, but also an invaluable asset that has transformed the depth and breadth of asteroid radar data analysis.

## 3. SCIENCE RESULTS SINCE ASTEROIDS III

### 3.1. Ground-Truth of Radar Shape Models by Spacecraft Missions: (25143) Itokawa and (4179) Toutatis

**3.1.1. (25143) Itokawa.** Itokawa was the first NEA visited by a spacecraft for which a three-dimensional model from inversion of radar images was also available. Ostro *et al.* (2004) reported radar observations and a physical model from extensive imaging in 2001, and Ostro *et al.* (2005) incorporated additional radar images obtained in 2004 to estimate improved models.

The radar observations provided repeated coverage over a restricted range of longitudes in Itokawa's northern hemisphere in 2001 and sparse coverage of other longitudes on three days in 2004. Due to the nearly 12-h rotation period, radar images obtained in 2001 sampled very similar orientations day after day, although two weeks of sky motion ultimately extended the rotational coverage somewhat (see Fig. 1 of Ostro *et al.*, 2005). The asteroid's pole direction and sky positions in 2001 precluded seeing the bend between Itokawa's "head" and "body." In 2004, the sky positions were very different, and the concavity between the components was conspicuous. Unfortunately, in 2004 radar imaging occurred on far fewer days than in 2001, so a significant fraction of the surface was never seen at high resolution, and this propagated into limitations for the shape model. The highest range resolutions in 2001 and 2004 were 15 m/pixel at Arecibo and 19 m/pixel at Goldstone.

In 2005, the Hayabusa spacecraft began an extended encounter with Itokawa (Saito *et al.*, 2006; see also the chapters by Yoshikawa *et al.* and Scheeres *et al.* in this volume). The Hayabusa images reveal zeroth-order agreement with the Ostro *et al.* (2005) smooth model's shape and dimensions, but the spacecraft data also revealed obvious differences. Figure 4 compares the three-dimensional models estimated from the radar and spacecraft images. The Ostro *et al.* radar model has principal axes within 10% of 594  $\times$  320  $\times$  288 m. The dimensions reported by Saito *et al.* (2006) were 535  $\times$  294  $\times$  209 m with uncertainties of  $\sim 1$  m. Thus, within their stated uncertainties, the long and intermediate axes are consistent but the short axis is not. The mismatch of the short axis is probably a consequence of significant gaps in latitude coverage in the radar images. The subradar latitudes during radar imaging were never within 45° of the poles and they occurred over a relatively narrow range of longitudes.

Ostro *et al.*'s (2005) smooth model shows a bend between the head and body but it underestimated the depth of the neck, a discrepancy noted in the paper. In practice, during the modeling process it is often difficult to fit every feature

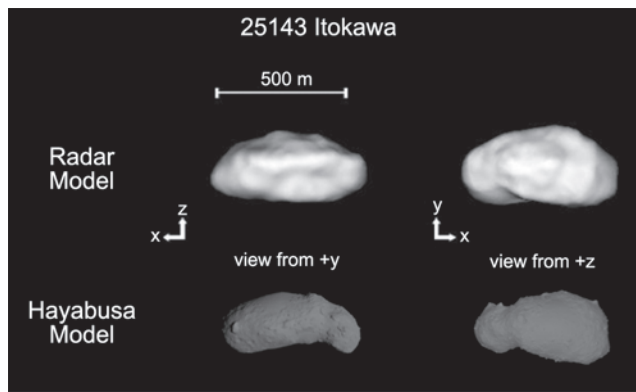


**Fig. 4.** Two principal axis views of the (25143) Itokawa models estimated from inversion of radar images [top row, adapted from Ostro et al. (2005)] and from Hayabusa spacecraft images [bottom row, adapted from Gaskell et al. (2008)]. The renderings are shown at the same orientations and approximately to scale. The lower hemisphere in the renderings on the left was not imaged by radar.

visible in the images with the shape reconstruction algorithm currently in use. For example, the fits to the narrow end were not as tapered as indicated by the data from 2001 even though various approaches were attempted to improve them. The bend between the head and the body in the synthetic images reported by Ostro et al. is not as deep as it appears in the radar images. The shape modeling started with a single-component; in retrospect, the modeling could have produced better fits had it started with two overlapping ellipsoids (S. J. Ostro, personal communication), an approach that was not in use in 2005. For example, Magri et al. (2011) started modeling deeply bifurcated contact binary (8567) 1996 HW<sub>1</sub> with overlapping ellipsoids and obtained excellent fits. The radar model of Itokawa also has an equatorial ridge that is not present on the asteroid; this was noted by Ostro et al. (2005), and is probably an artifact due to the combination of penalties against rough or concave surfaces, and also due to the *Shape* software's default vertex adjustment order from south to north in a spiral pattern. The effects of the order of vertex adjustment were explored by modeling 2008 EV<sub>5</sub> by Busch et al. (2011), who found that when the adjustment pattern was randomized, the sharpness of the equatorial ridge was reduced.

Boulders are ubiquitous in spacecraft images of Itokawa, but were any visible in the radar data? Hints of small-scale topography at the resolution limit are visible in Arecibo images near the neck in an area where Hayabusa images show several decameter-scale boulders, but the resolution in the radar images was insufficient to make statements about the origin of the radar features. Yoshinodai, the largest boulder, was not visible due to gaps in the radar latitude and longitude coverage. Inspection of the 2001 radar images shows a cluster of radar-bright pixels corresponding to a ridge several tens of meters in extent in the spacecraft images of

the northern hemisphere between the “head” and the broad smooth region known as Sagamihara.

**3.1.2. (4179) Toutatis.** Toutatis was imaged with radar during close Earth approaches in 1992, 1996, 2000, 2004, 2008, and 2012. Hudson and Ostro (1995) estimated the first three-dimensional model of Toutatis using the 1992 images with a resolution of 75 m/pixel; Hudson et al. (2003) estimated a high-resolution model utilizing images from 1992 and 1996 with resolutions as fine as 18.75 m/pixel. The Hudson et al. (2003) high-resolution model is among the most detailed published to date.

Toutatis is the second asteroid imaged in detail by radar that has also been visited by a spacecraft, and it therefore provides an important “ground-truth” test of the shape modeling process (see also the chapter by Barucci et al. in this volume). The Chang'e-2 spacecraft flew by Toutatis on December 13, 2012, and acquired a series of images at resolutions as high as ~2 m/pixel. Due to the asteroid's slow rotation and the spacecraft's velocity, the Chang'e-2 images show only one side.

Huang et al. (2013) and Zou et al. (2014) describe images obtained by the spacecraft and compare them with the Hudson et al. (2003) model. The Chang'e-2 images match the asteroid's orientation as predicted by the radar-derived spin state model (Takahashi et al., 2013), and show many of the features in the radar-derived Toutatis shape model presented in Hudson et al. (2003): the large and small lobes of the asteroid, the neck between them, and ridgelines and depressions on both lobes (Fig. 5). The spacecraft images yield estimates of the asteroid's dimensions that are consistent within their stated uncertainties: Hudson and Ostro (1995) reported major axes within 0.1 km of 4.60 × 2.29 × 1.92 km; Huang et al. (2013) estimated “Toutatis’ maximum physical length and width” to be within 10% of 4.75 × 1.95 km.

However, the Chang'e-2 images also show mismatches that reflect limitations of early radar shape modeling techniques and of the 1992 and 1996 Toutatis radar data. The most pronounced differences appear in the model's large end, which is more tapered than in spacecraft images, and the region between the two lobes, which is more angular in the Chang'e-2 images. The differences at the wide end originate primarily because previous radar observations did not have detailed coverage of that region. Although Toutatis was observed with radar in 2000, 2004, and 2008, those observations were restricted to no more than four days during each apparition and did not achieve thorough coverage due to the asteroid's slow rotation.

The true structure of the neck between the small and large components is more angular than in the Hudson et al. (2003) shape model. This is partly an artifact of the fitting procedure: The Hudson et al. shape model was rendered as a single surface, with a penalty function incorporated in the shape inversion that favored smooth shapes to prevent fitting noise. In this case, that procedure smoothed over the real structure. Better results could have been obtained by using a two-component shape model, one for each of the two lobes, and by having higher-resolution radar data.

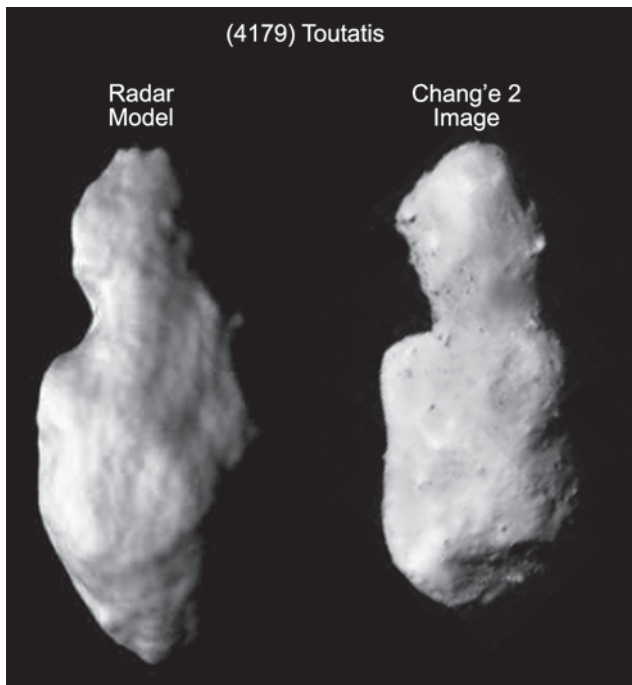


**Fig. 5.** Comparison between the *Hudson et al.* (2003) radar-derived shape model of (4179) Toutatis and a representative image obtained by the Chang'e-2 spacecraft (adapted from *Huang et al.*, 2013). The orientations and scales are approximate and were estimated by eye. Illumination directions are similar.

*Hudson et al.* (2003) adopted a conservative modeling approach and stated “In penalizing relief in our shape reconstruction, we chose to suppress features rather than to risk showing features that might not be present on Toutatis.” Although the match between the *Hudson et al.* shape model and Toutatis’ shape as seen by Chang’e-2 is not perfect, it validates the use of radar shape modeling in understanding asteroid shapes and spin states.

During the 2012 encounter, Toutatis was imaged with radar at resolutions up to 3.75 m/pixel, the highest-resolution radar images ever obtained for this object. The images placed tens of thousands of pixels on the asteroid, covered the wide end more extensively than previously, and revealed a number of small radar-bright spots that Busch et al. (in preparation) linked with boulders in the Chang’e-2 images.

Propagation of Toutatis’ spin vector from 1992 to 1996 and 2000 showed orientation differences that were within the uncertainties of the *Hudson and Ostro* (1995) spin state, but images obtained in 2004 and 2008 clearly revealed discrepancies that were much larger. *Takahashi et al.* (2013) fit the images using an updated model for the shape and spin state that incorporated radar images obtained through 2008 and integrations that explicitly included gravitational perturbations experienced by Toutatis throughout its heliocentric orbit. They were able to successfully reproduce the orientation during each apparition imaged by radar. They found that the spin state changed during each flyby, with

the most pronounced changes occurring during the closest encounter within 0.01 AU ( $\sim$ 4 lunar distances) in 2004. This is one of the first instances where changes to a NEA’s spin state during close Earth flybys have been detected. Similar changes are likely to become evident for an increasing number of NEAs as future radar observations occur; for example, *Scheeres et al.* (2005) predicted that spin-state changes should be obvious with (99942) Apophis after its approach within 5.1 Earth radii in 2029.

### 3.2. Main-Belt Asteroids

Many main-belt asteroids (MBAs) have been observed with radar since publication of *Asteroids III*, but less work has been done with this population because far fewer MBAs are suitable for detailed imaging and the SNRs of the best targets are much lower than they are for NEAs. Most MBAs observed recently have been CW detections at moderate to weak SNRs and all have been at Arecibo. However, a number of MBAs have been imaged, most notably (4) Vesta, (5) Astraea, (7) Iris, (12) Victoria, (216) Kleopatra, and (654) Zelinda. In principle, Arecibo is so sensitive that several MBAs could be detected with radar on any night of the year.

*Magri et al.* (2007a) presented detailed statistical analyses of the radar albedo and circular polarization ratio at 12.6 cm wavelength of 84 MBAs, 55 of which were observed by radar for the first time. Some conclusions from an earlier study (with a smaller sample size) by *Magri et al.* (1999) were strengthened: M asteroids have higher mean radar albedos and a wider range of albedos than other MBAs, suggesting that both metal-rich and metal-poor M-class objects exist; C- and S-class MBAs have indistinguishable radar albedo distributions; and the F, G, P, and D classes are not as radar-bright as C and S objects (but a convincing statistical test requires larger sample sizes). In contrast with earlier work, *Magri et al.* (2007a) found that S-class MBAs have higher circular polarization ratios at 12.6 cm wavelength than other MBAs, indicating greater near-surface structural complexity at decimeter scales.

*Shepard et al.* (2008a, 2011) report that circular polarization ratios at 12.6 cm wavelength for E-class MBAs (44) Nysa, (64) Angelina, and (434) Hungaria are significantly higher than for most other taxonomic classes but somewhat lower than the polarization ratios reported among E-class NEAs (*Benner et al.*, 2008). The E-class MBAs are up to several tens of kilometers in diameter, so the difference in the circular polarization ratios relative to those seen among NEAs suggests that the circular polarization ratio has an inverse gravitational dependence.

*Shepard et al.* (2008a, 2010, 2011, 2015) estimated radar albedos for most of the X- and M-class MBAs that are detectable at Arecibo. This indicated high radar albedos for (16) Psyche, (216) Kleopatra, (758) Mancunia, and (785) Zwetana, suggesting that they are almost certainly metallic; established evidence for wide variations in radar albedo as a function of rotation on (16) Psyche, (129) Antigone, (135) Hertha, (758) Mancunia, and (785) Zwetana;

suggested deep concavities on numerous objects; and showed that more than 60% of M-class asteroids with 3- $\mu\text{m}$  hydration features reported from infrared spectroscopic observations (*Rivkin et al.*, 2000) have high radar albedos that are consistent with largely metallic surfaces. The presence of hydration features associated with these M-class asteroids is puzzling; *Shepard et al.* (2015) suggest that these may be the results of material delivered via impacts. Variations in the radar albedos also suggest compositional and/or structural complexity on large scales (*Shepard et al.*, 2015).

**3.2.1. (21) Lutetia.** *Shepard et al.* (2008a) reported delay-Doppler images of Lutetia prior to the Rosetta flyby in 2010. The images viewed Lutetia along the polar axis and were not sufficient for three-dimensional shape estimation, but they suggested a polar dimension of  $84 \pm 12$  km that was consistent with later observations by the Rosetta spacecraft (*Sierks et al.*, 2011; see also the chapter by Barucci et al. in this volume).

**3.2.2. (7) Iris.** Arecibo radar images of Iris obtained in November 2006 reveal a topographically complex object whose gross shape is approximately ellipsoidal with equatorial dimensions within 15% of  $253 \times 228$  km (*Ostro et al.*, 2010). The most prominent features are three  $\sim 50$ -km-diameter concavities almost equally spaced in longitude around the south pole that are probably impact craters.

**3.2.3. (216) Kleopatra.** Kleopatra has been observed at Arecibo in 1999 (*Ostro et al.*, 2000), 2008, and 2013. The 2008 and 2013 delay-Doppler images confirm the “dogbone” shape reported by *Ostro et al.* (2000) but hint that the radar albedo may be somewhat lower than previously reported. The shape reported by *Ostro et al.* (2000) has been confirmed by adaptive optics imaging reported by *Descamps et al.* (2011), who also discovered that Kleopatra has two small moons. The SNRs of the radar observations spatially resolve the primary but are not strong enough to reveal echoes from the satellites. Additional information about Kleopatra appears in the chapter by Scheeres et al. in this volume.

### 3.3. Yarkovsky Effect Detections Enabled by Radar Astrometry

The Yarkovsky effect is a key mechanism for the delivery of NEAs from the main belt to the near-Earth region and it has been the subject of extensive theoretical investigations (*Bottke et al.*, 2002, 2006). A description of the Yarkovsky effect appears in the chapter by Vokrouhlický et al. in this volume, so here we will concentrate on the role that radar can play in its detection and the implications it has for constraining the physical properties of NEAs.

Radar observations of NEAs provide important opportunities to measure the Yarkovsky orbital drift. This effect has been detected with Arecibo radar data for (6489) Golevka (*Chesley et al.*, 2003) and is the dominant source of uncertainty in some NEA trajectory predictions (*Giorgini et al.*, 2002; *Farnocchia et al.*, 2013a,b) for bodies smaller than  $\sim 2$  km. The Yarkovsky effect acts on the semimajor axis linearly with time and the mean anomaly quadratically

with time as a function of an object’s spin, shape, thermal inertia, other material properties, and orbit. For asteroids of known sizes and spins, a measurement of the Yarkovsky drift rate can be interpreted in terms of bulk density and thermal inertia (*Chesley et al.*, 2003; *Nugent et al.*, 2012). If independent measurements of the thermal inertia exist, then it is possible to estimate the bulk density of the object (*Chesley et al.*, 2014) and thus constrain its internal structure. Although the Yarkovsky drift can be estimated in some cases with optical astrometry alone (*Nugent et al.*, 2012; *Farnocchia et al.*, 2013a), the uncertainties associated with these orbital drift determinations are typically reduced by an order of magnitude when radar data are included.

*Giorgini et al.* (2002) established the long-term coupling between the orbital evolution of (29075) 1950 DA (and NEAs in general) and physical properties such as spin state, shape, thermal inertia, and bulk density through the action of the Yarkovsky effect. The Yarkovsky effect is a major source of uncertainty for the future motion of Apophis (*Giorgini et al.*, 2008) and Bennu (*Chesley et al.*, 2014) and can lead to resonant returns and potential Earth impacts via deflection through keyholes.

*Vokrouhlický et al.* (2000) predicted that the Yarkovsky effect could be detected for several NEAs with future radar ranging measurements. This was confirmed by *Chesley et al.* (2003) for Golevka through a combination of Arecibo and Goldstone radar astrometry obtained in 1991, 1995, and 2003, and utilization of the three-dimensional model published by *Hudson et al.* (2000). This yielded a bulk density of  $2.7 \text{ g cm}^{-3}$  and was the first detection of the Yarkovsky effect for a solar system object. Predictions for detecting the Yarkovsky effect for other NEAs appeared in *Vokrouhlický et al.* (2005a,b). In general, three radar detections spread out over at least several years are necessary, although due to the dependence on the mass, a longer baseline may be required for more massive objects and a shorter baseline could suffice for smaller ones.

*Chesley et al.* (2014) report a Yarkovsky effect detection for (101955) Bennu based on a weak ranging detection at Arecibo in 2011 coupled with radar astrometry obtained in 1999 and 2005 (*Nolan et al.*, 2013). The thermal inertia was already available (*Emery et al.*, 2013), enabling direct estimation of the asteroid’s mass and bulk density, information that is invaluable for the Origins Spectral Interpretation Resource Identification and Security-Regolith Explorer (OSIRIS-REx) mission that will arrive at Bennu in 2018.

*Vokrouhlický et al.* (2005b) described binary NEAs for which detection of the Yarkovsky effect could soon be possible. Masses of binary systems can be estimated by fitting range-Doppler measurements between the components of binary system and application of Kepler’s third law (*Margot et al.*, 2002), so a Yarkovsky effect detection enables estimating the mass from an independent technique (although one that often requires numerous assumptions and is less robust than direct fitting of the mutual orbit of a binary system). The first binary where both approaches provided mass estimates is (1862) Apollo, whose bulk density estimated from

the orbit of  $\sim 2.6 \text{ g cm}^{-3}$  (T. Ford, personal communication) is consistent (to within the uncertainties) with the value of  $2.86^{+0.48}_{-0.68} \text{ g cm}^{-3}$  estimated by *Rozitis et al.* (2013) from the Yarkovsky effect detection (*Farnocchia et al.*, 2013a).

To facilitate future Yarkovsky effect detections, NEAs previously detected by radar are now observed at every opportunity when the SNRs are expected to be strong enough for ranging measurements. During the coming decade, this could increase the number of NEA mass and bulk density estimates by a factor of several. Among these is (99942) Apophis, which will approach within 0.113 AU in 2021, when radar astrometry is likely to yield a strong Yarkovsky effect detection and estimates of the asteroid's shape, mass, and density (*Giorgini et al.*, 2008; *Farnocchia and Chesley*, 2014).

### 3.4. Radar Detection of the YORP Effect

**3.4.1. (54509) YORP.** The YORP effect is a torque on the spin state of an asteroid due to the absorption and anisotropic reemission of sunlight (*Rubincam*, 2000; see also the chapter by Vokrouhlický et al. in this volume). The first direct evidence of the YORP effect came from combined radar and optical observations of asteroid (54509) YORP (*Taylor et al.*, 2007; *Lowry et al.*, 2007), and optical observations of (1862) Apollo (*Kaasalainen et al.*, 2007).

By virtue of its nearly 1:1 orbital resonance with Earth and a moderate heliocentric eccentricity, (54509) YORP made annual close approaches to Earth from 2001 to 2005. In 2001, Goldstone images and optical light curves established a rapid rotation period of 12.2 minutes. Additional light curves were obtained annually, as were radar observations at Arecibo in 2004 and 2005. Under the assumption of an unchanging spin state, neither the radar images from 2001 and 2004 nor the light curves from 2001 to 2005 could be linked self-consistently. Combining the radar-derived spin-axis orientation with the optical data showed clear evidence for a discrete change in the sidereal spin period from year to year (*Lowry et al.*, 2007), and applying the three-dimensional shape model from inversion of the radar images revealed that a continuously increasing correction to the rotational phase was required to simultaneously fit the light curves over multiple years (*Taylor et al.*, 2007). Both methods revealed a change in spin rate of  $(2.0 \pm 0.2) \times 10^{-4} \text{ deg d}^{-2}$ , amounting to more than a  $200^\circ$  of drift in rotation phase when trying to link light curves obtained over four years. The observation of YORP accelerations on the rotations of objects spanning from 100-m-sized (54509) YORP to multi-kilometer NEA (1620) Geographos (*Durech et al.*, 2008) suggests that the YORP effect is capable of altering the spin of most NEAs. Furthermore, the YORP effect is mass dependent, and if detected, can provide a useful constraint on an asteroid's mass (*Capek and Vokrouhlický*, 2004).

**3.4.2. (99942) Apophis.** When discovered in December of 2004, Apophis was briefly estimated to have a 2.7% chance of impacting Earth in 2029. Additional optical measurements quickly showed there was no impact risk at that time. However, there will be an extremely close approach

to the Earth in 2029, estimated to be a 1-in-800-year event for an object of that size.

Arecibo subsequently detected Apophis at distances of 0.192–0.268 AU in 2005 and 2006, with CW echo power spectra and ranging (*Giorgini et al.*, 2008). The first radar echoes acquired on January 27, 2005, were  $4.8\sigma$  off the frequency predicted by the optical-only solution. Including the radar measurements in a new orbit solution revealed a 1.4-arcsec systematic bias in the prediscovery optical measurements and moved the April 13, 2029, encounter prediction 4.4 Earth radii closer to Earth while reducing the uncertainty in Apophis' location during the encounter by 98%. This was a  $5\sigma$  trajectory correction.

The new radar-corrected orbit had better predictability through the 2029 encounter, but degraded rapidly thereafter. This was due to the new solution's deeper entry into Earth's gravity field in 2029, an approach 45% closer than predicted prior to the debiasing enabled by radar observations. The steeper gravity gradient differentially pulls on and elongates the statistical uncertainty space to a greater extent than the more distant uncorrected preradar encounter.

Echo power spectra, ranging measurements, and coarse-resolution images of Apophis were obtained at Goldstone and Arecibo from December 2012 through March 2013. The images and echo bandwidths suggest an elongated object but are insufficient for estimation of a detailed three-dimensional model. There had been some potential for the Yarkovsky effect to be detected if Apophis was on the low-mass side of what was possible, with a spin pole perpendicular to its orbit plane, in concert with favorable thermal properties. However, the new radar astrometry excluded that extreme combination of properties, showing no significant evidence of Yarkovsky effect motion over 2004–2013 [as predicted by *Farnocchia et al.* (2013b)], and effectively ruled out the remaining impact potential in 2036. Reliable orbit prediction is now possible into the 2060s but the orbital uncertainties grow rapidly afterward.

### 3.5. Near-Earth Asteroid Population Trends

**3.5.1. Overview of the near-Earth asteroid shape and spin distributions.** Radar observations of NEAs have revealed a heterogeneous population with a wide range of shapes and spin characteristics. Near-Earth asteroids detected by radar range over roughly 4 orders of magnitude in size from meter-scale objects 2006 RH<sub>120</sub> and 2013 EC<sub>20</sub> to the largest NEA, (1036) Ganymed, at over 30 km in effective diameter. Their rotation periods span at least 4 orders of magnitude as well, from 16 seconds to more than one week. The radar-determined shapes of NEAs are similarly diverse, from simple spheroids and ellipsoids to multiple-component (binary and triple) systems to double-lobed contact binaries and extremely irregular angular bodies.

*Taylor et al.* (2012) examined the shape and spin distributions of the NEA population observed with the Arecibo radar system since 1998. They found that radar-detected NEAs with diameters larger than  $\sim 200$  m (with a sample size of over 100 objects) are not dominated by a single category of

shape. A radar-observed multiplicity fraction of  $\sim 17\%$  among NEAs with  $H < 21$  is in agreement with optical observations (Pravec et al., 2006; see also the chapter by Margot et al. in this volume), while, perhaps surprisingly, contact binaries account for a similar fraction at  $\sim 14\%$ , roughly 50% larger than reported in earlier estimates (Benner et al., 2006). At smaller sizes, binaries and contact binaries are much less common, with only three binaries and one contact binary known with  $H > 21$  and none with  $H > 22$ . Furthermore, only about one in four objects with  $H > 21$  are assigned basic shapes due to the difficulty in obtaining sufficient resolution in radar images. Those with shapes assigned often appear irregular either with angular shapes or highly specular reflections from facets.

The spin distribution of NEAs estimated from radar observations closely matches the spin distribution determined from optical light curves (Fig. 6; see the chapter by Scheeres et al. in this volume for a different version of this figure). Light curves are biased against small, slowly rotating bodies because of their inherent faintness, which often limits their observability and hence the opportunity to confidently record an entire rotation period on the scale of many tens of hours. Radar observations detect an apparent spin rate based on the instantaneous echo bandwidth, which does not require one to observe an entire rotation. Thus, radar should detect a small, slowly rotating body as a narrow echo.

The distinct change in the shape and spin distributions of the NEA population at  $H = 21$  or 22 (100- to 200-m diameters) may indicate fundamental structural changes at this scale.

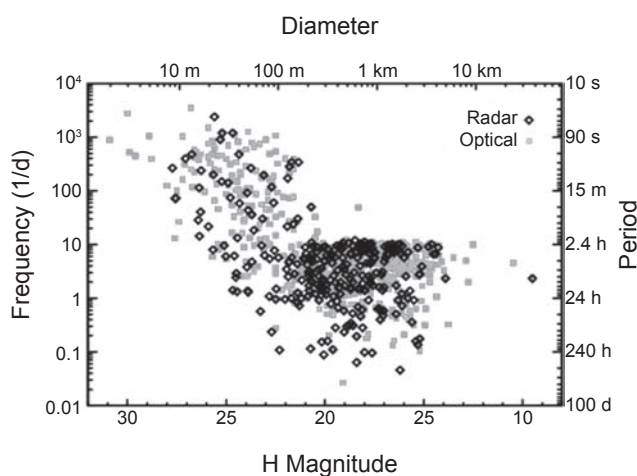


**Fig. 6.** Spin-rate distribution of near-Earth asteroids as determined by optical and radar techniques (Taylor et al., 2012). Optical data (gray squares) are periods from the Warner lightcurve database [Warner et al. (2009), September 2014 update] with quality factors  $U \geq 2$ ; radar data (black diamonds) are estimated from echo bandwidths observed at Arecibo. There is broad agreement between the two techniques despite different observational biases, including the lack of slowly rotating small bodies. Diameters are computed from absolute magnitudes by assuming an optical albedo of 0.2.

**3.5.2. Abundance of contact binary near-Earth asteroids.** Radar imaging since completion of the upgrade at Arecibo in 1999 revealed more than 30 NEAs that are deeply bifurcated (Benner et al., 2006; Brozovic et al., 2010; Magri et al., 2011). Benner et al. (2006) found that at least  $\sim 10\%$  of NEAs  $> 200$  m in diameter are candidate contact binaries, where a contact binary is defined as “an asteroid consisting of two lobes that are in contact, [and] have a bimodal mass distribution, that may once have been separate.” By this definition, objects such as Itokawa and Toutatis that have two components with substantial size differences, and thus lack bimodal mass distributions, were not classified as contact binaries. The definition of a contact binary is necessarily subjective, and due to considerable subsequent research on the formation and evolution of Itokawa and radar imaging of hundreds of additional NEAs, we now relax the definition to include objects that are obviously bifurcated, have components that can be significantly different in size (with size ratios of at least 4:1), and mass distributions that aren’t bimodal. With this revised definition, the fraction of candidate contact binaries imaged by radar has grown to  $\sim 14\%$  (Taylor et al., 2012). Given that true binaries comprise  $\sim 16\%$  of the NEA population above  $\sim 200$  m in diameter (Margot et al., 2002), this implies that the abundances of contact binaries and true binaries are comparable and that these objects together constitute  $\sim 30\%$  of the NEA population  $> 200$  m in diameter. Figure 7 shows an example: the three-dimensional model of 1996 HW<sub>1</sub>, which was imaged at Arecibo in 2008 and is one of the most deeply bifurcated NEAs observed to date (Magri et al., 2011).

These contact binary objects display considerable dynamic range in long axis lengths, spectral classes, and spin states. The largest is (192642) 1999 RD<sub>32</sub>, with a long axis of  $\sim 6$  km, and the smallest is 2013 JR<sub>28</sub>, with a long axis of  $\sim 100$  m. The fastest rotator is (4769) Castalia with a rotation period of 4 h, and the slowest, 2002 FC and 2004 RF<sub>84</sub>, have unknown rotation periods of days to weeks. None of the contact binaries rotate as fast as the rapidly spinning primaries of most NEA binaries and triples (see the chapter by Margot et al. in this volume). Some of the contact binaries rotate at rates close to where they could separate if spun up slightly (Benner et al., 2006; Scheeres, 2007). A significant (but not yet quantified) fraction are non-principal-axis rotators.

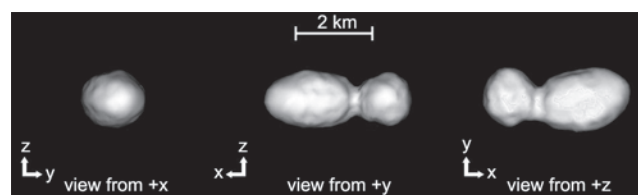


**Fig. 7.** Principal axis views of the 1996 HW<sub>1</sub> shape model (adapted from Magri et al., 2011). This is one of the most bifurcated NEAs modeled to date using delay-Doppler radar images.

How did such objects form and why are they so abundant? Plausible formation mechanisms are by low-velocity collisions; collapse of true binaries through tidal friction or as a result of orbital perturbations during close planetary encounters; by spinup due to YORP; or by partial disruption during close planetary flybys. Combinations of the factors above may be necessary to explain the slowest rotators.

**3.5.3. Binary near-Earth asteroids.** Binary asteroids are a field of vigorous research and are treated in considerable detail in the chapter by Margot et al. in this volume. In this chapter we mention them only to illustrate points that also apply to broader trends within the NEA population.

**3.5.4. Equatorial ridges.** Evidence for equatorial bulges appears in radar images for many rapidly rotating NEAs  $>200$  m in diameter, some relatively slow rotators, and for most of the primaries in binary and triple NEA systems. The first clear case was the primary of binary (66391) 1999 KW<sub>4</sub> (Ostro et al., 2006), which exhibited a “double exposure” appearance at its leading edge that corresponded to the sharp edge of its ridge. Bulges have since been seen in models for (311066) 2004 DC (Taylor, 2009), 2008 EV<sub>5</sub> (Busch et al., 2011), (136617) 1994 CC (Brozovic et al., 2011), 2005 YU<sub>55</sub> (Busch et al., 2012), the primary of (185851) 2000 DP<sub>107</sub> (Naidu et al., 2015), and in radar images of numerous other NEAs for which shape models are not yet available. Figure 8 shows renderings of shape models for selected objects with bulges. The ridges are thought to form via YORP-induced spinup acting on an object with a rubble-pile internal structure (Harris et al., 2009; Walsh et al., 2008; see also the chapter by Scheeres et al. in this volume). Although no formal estimate of their abundance is available, radar observations and three-dimensional modeling indicate that NEAs with equatorial ridges are relatively common. In more detail, the delay-Doppler signature of objects with oblate vs. spheroidal shapes are discussed by Busch et al. (2011) and applied to 2008 EV<sub>5</sub>.

In addition to the appearance of shape models, direct evidence for oblate shapes comes from images of 2013 WT<sub>44</sub>, which was observed at a subradar latitude close to a pole.

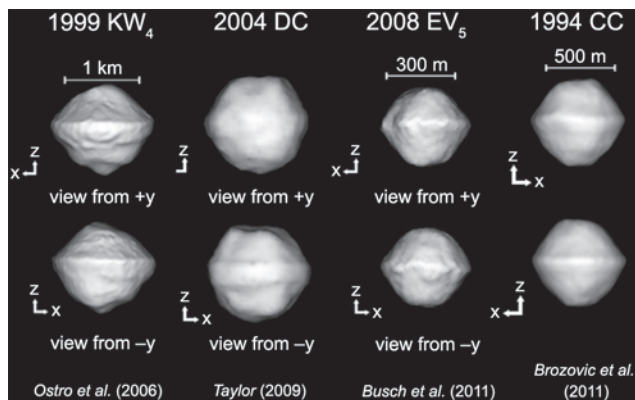


**Fig. 8.** Model renderings of four NEAs with evidence for oblate shapes. Each model is viewed along the + and - y-axes.

Figure 9 compares the radar images of 2013 WT<sub>44</sub> with a high-latitude view of the 1999 KW<sub>4</sub> model (Ostro et al., 2006) to illustrate the appearance of the equatorial ridge from a nearly pole-on perspective. The 2013 WT<sub>44</sub> images show a flat polar region, a roughly cone-shaped hemisphere, and a “doubly curved” trailing edge region that shows the entire circumference of an equatorial ridge tilted relative to the radar line-of-sight.

**3.5.5. Radar evidence for impact craters.** Features suggesting impact craters have been seen on numerous NEAs imaged by radar starting with (4179) Toutatis in 1992 (Ostro et al., 1995; see also Hudson et al., 2003). The candidate craters generally take the form of circular to ellipsoidal radar-dark features from tens of meters to more than 2 km in extent. Interpretation of radar-dark features is hampered by the counterintuitive nature of delay-Doppler images, the resolution, SNRs, and rotational coverage of the data. Deep concavities are visible along the leading edges of other objects, but do not appear as radar-dark regions. Concavities are also evident in some shape models and may represent craters but their origins are not clear. Candidate craters appear in radar images of many objects such as (4183) Cuno, (33342) 1998 WT<sub>24</sub> (Busch et al., 2008), (53319) 1999 JM<sub>8</sub> (Benner et al., 2002), and (185851) 2000 DP<sub>107</sub> (Naidu et al., 2015). Table 1 lists NEAs imaged by radar that show evidence for impact craters. Figure 10 shows Arecibo images of (136849) 1998 CS<sub>1</sub>, which has a number of radar-dark features suggesting impact craters, and Fig. 2 shows images of 2005 YU<sub>55</sub>, which has several small ellipsoidal radar-dark regions and a small concavity on its leading edge. Craters are conspicuously absent in radar images of many other NEAs, perhaps because such features are not present, due to limited viewing geometry, or perhaps because the SNRs and resolution are insufficient.

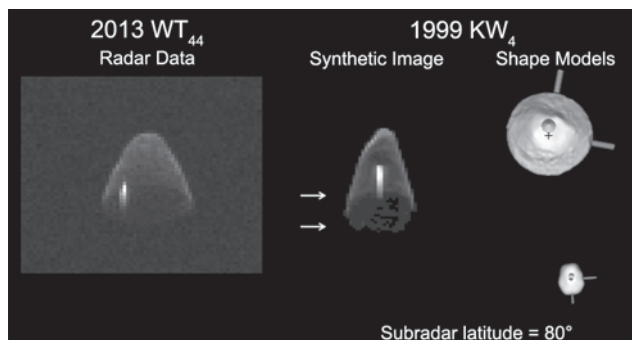


**Fig. 9.** Comparison between observations of binary NEA 2013 WT<sub>44</sub> and a synthetic radar image of binary 1999 KW<sub>4</sub> viewed at a high subradar latitude. *Left:* Goldstone delay-Doppler image of 2013 WT<sub>44</sub> obtained on March 20, 2014. Resolution = 18.75 m  $\times$  0.5 Hz. *Middle:* Synthetic radar image of 1999 KW<sub>4</sub> generated using the geometry of the models shown on the right. In the synthetic image, upper and lower arrows point to echoes from the near and far edges of the equatorial bulge.

TABLE 1. NEAs with radar-detected craters.

Asteroid	H
(1580) Betulia	14.5
(4179) Toutatis	15.3
(4183) Cuno	14.4
(33342) 1998 WT <sub>24</sub>	17.9
(52760) 1998 ML <sub>14</sub>	17.5
(53319) 1999 JM <sub>8</sub>	15.2
(136849) 1998 CS <sub>1</sub>	17.6
(185851) 2000 DP <sub>107</sub>	18.2
(304330) 2006 SX <sub>217</sub>	18.9
(308635) 2005 YU <sub>55</sub>	21.9
(388188) 2006 DP <sub>14</sub>	18.9
2010 JL <sub>33</sub>	17.7

**3.5.6. Radar evidence for boulders on near-Earth asteroid surfaces.** Delay-Doppler radar observations of numerous NEAs have revealed many small clusters of radar-bright pixels in some of the highest SNR images obtained at Arecibo and Goldstone. Many of the spots persist as the asteroids rotate, so the bright pixels are not receiver noise, self noise, or artifacts. Clusters of bright pixels appear primarily in high-resolution radar images with resolutions of 4–19 m/pixel and suggest that these are features a few tens of meters in extent or smaller. Many spots appear near the trailing edges of the images and are uprange from radar shadows, implying that the source for some of the features is small-scale topography. Figures 2 and 3 show images of 2005 YU<sub>55</sub> and 2014 HQ<sub>124</sub>, NEAs that have conspicuous and widespread radar-bright spots. To date, small groups of bright pixels have been seen on at least 14 NEAs, establishing that these features are relatively common.

Benner et al. (2014a) suggest that the bright pixels are echoes from surface and near-surface boulders, which have also been seen on each of the three NEAs imaged at close range by spacecraft: (433) Eros [Near Earth Asteroid Rendezvous (NEAR)], (25143) Itokawa (Hayabusa), and (4179) Toutatis (Chang'e-2). These asteroids have also been imaged by radar, but the SNRs and/or resolutions were insufficient to reveal boulders with Eros and Itokawa. However,

radar images of Toutatis obtained in 2012 reveal spots that can be linked with boulders in the Chang'e-2 spacecraft images. Of the objects with evidence for boulders, 1999 RD<sub>32</sub> is the largest, with a long axis of ~6 km, and 2014 BR<sub>57</sub> is the smallest, with a diameter of about 80 m.

**3.5.7. Circular polarization ratio correlations with spectral class.** Benner et al. (2008) conducted a survey of more than 200 NEAs detected by radar and found distinct correlations between their circular polarization ratios (abbreviated as “SC/OC”) and some spectral classes. E- and V-class NEAs have high SC/OC values, a trend that is mirrored among the handful of E-class MBAs that have also been detected to date by radar (Shepard et al., 2008b, 2011). In contrast, SQ-class and optically dark NEAs show circular polarization ratios that vary from ~0.1 to ~0.5 but otherwise show no obvious trends. Fifty-six percent of the NEAs in which SC/OC > 0.5 in the sample have unknown spectral classes, and if all of them turn out to be E- or V-class objects, that implies that EV-class NEAs are much more abundant in the near-Earth population than has been previously realized. Since the study by Benner et al. (2008) was published, the sample of NEAs observed by radar has more than doubled and the pattern of high SC/OC values among E- and V-class objects has persisted (Springmann et al., 2013).

How are we to understand these correlations? Benner et al. (2008) speculated that this could possibly “be due to the intrinsic mechanical properties of different mineralogical assemblages but also may reflect very different formation ages and collisional histories.” The fact that the trend of high SC/OC appears to remain across a wide range of diameters, including inner MBAs up to several tens of kilometers in diameter, suggests that there is at least a component due to composition.

Virkki et al. (2014) modeled the effects of electric permittivity and the size of surface structure on asteroid radar circular polarization ratios and radar albedos. They find that obtaining SC/OC > 1 at 3.5 and 13 cm wavelengths requires a high refractive index ( $n > 2$ ), which may explain the high polarization ratios observed among basaltic V-class objects because basalt has a relatively high refractive index. In general, SC/OC > 0.5 occurs from surfaces with scatterers from one to a few times larger than the radar wavelength, although this is also a function of the refractive index and thus composition. Fundamentally, though, asteroid surfaces with high SC/OC are still not well understood.

## 4. RESULTS FOR SELECTED ASTEROIDS

### 4.1. (101955) Bennu

Nolan et al. (2013) estimated the shape of Bennu based on Arecibo and Goldstone imaging in 1999 and 2005 (Fig. 11). Bennu is an optically dark spheroid with major axes of 565 × 535 × 508 m, a sidereal rotation period of 4.3 h, a modest equatorial ridge, evidence for a relatively large boulder in the southern hemisphere, and broad-scale near-surface roughness features.

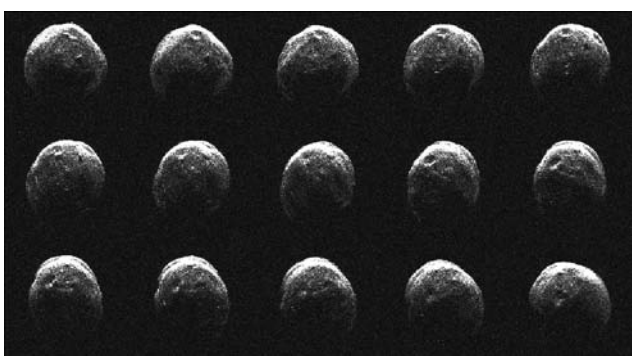


**Fig. 10.** Arecibo images of (136849) 1998 CS<sub>1</sub> obtained on January 18, 2009. Resolution is 7.5 m × 0.09 Hz. Rotation is counterclockwise.

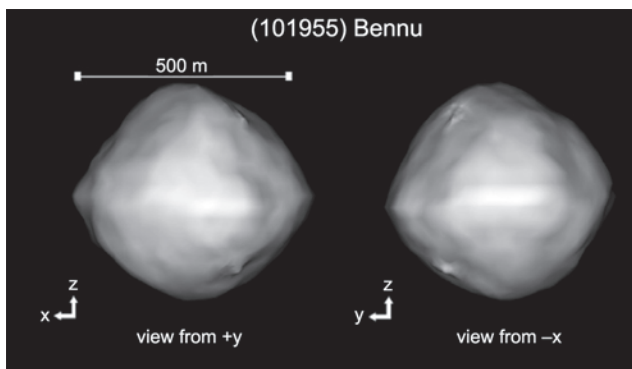


**Fig. 11.** Renderings of the three-dimensional model of (101955) Bennu (adapted from Nolan *et al.*, 2013) viewed along the x- and y-axes.

Bennu is the target of the OSIRIS-REx mission, which will provide a stringent test for the shape-modeling process when the spacecraft arrives in October 2018.

Chesley *et al.* (2014) report detection of the Yarkovsky effect for Bennu through radar astrometry obtained in 1999, 2005, and 2011 and optical astrometry from 1999 to 2013. This yields estimates of the mass and bulk density that are invaluable for planning the OSIRIS-REx mission. The density,  $\rho = 1.3 \text{ kg m}^{-3}$ , implies a macroporosity of  $\sim 40\%$  and suggests a rubble-pile internal structure. Bennu has one of the highest impact probabilities known, and, due to frequent close Earth encounters, will probably require orbital monitoring indefinitely (Milani *et al.*, 2009).

#### 4.2. (4660) Nereus

Nereus had been identified as a potential spacecraft target since its discovery because of the low  $\Delta V$  required for a rendezvous. Nereus was an early target for the NEAR mission and the original target for the Hayabusa mission. Arecibo and Goldstone images of Nereus obtained in 2002 enabled Brozovic *et al.* (2009) to reconstruct a three-dimensional model, which resembles an ellipsoid with principal axis dimensions  $X = 510 \pm 20 \text{ m}$ ,  $Y = 330 \pm 20 \text{ m}$ , and  $Z = 241^{+80}_{-10} \text{ m}$ , and features two prominent facets.

#### 4.3. (214869) 2007 PA<sub>8</sub>

Goldstone imaged 2007 PA<sub>8</sub> on 16 days in 2012. The images achieved range resolutions as fine as 3.75 m, placed thousands of pixels on the asteroid, and revealed an elongated, asymmetric object (Fig. 12) (Brozovic *et al.*, in preparation). The surface has angularities, facets, and a concavity  $> 200 \text{ m}$  in diameter. Shape modeling yields an effective diameter of  $1.35 \pm 0.05 \text{ km}$ , and elongation (long/intermediate axis ratio) = 1.4. The modeling revealed that 2007 PA<sub>8</sub> is a non-principal-axis rotator in short-axis mode with an average period of precession by the long axis around the angular momentum vector of  $4.26 \pm 0.02 \text{ d}$  and an oscillatory period

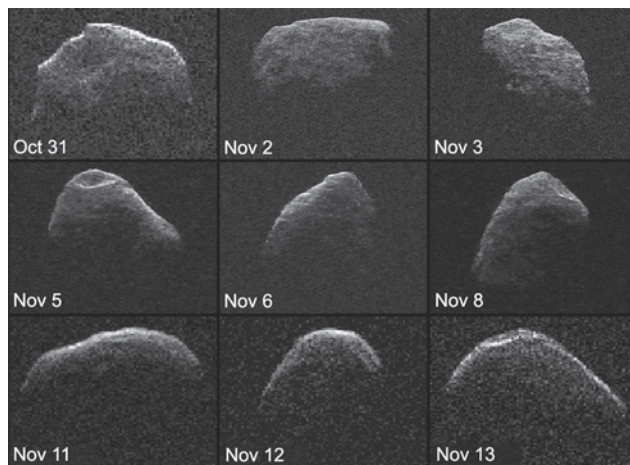


**Fig. 12.** Images of (214869) 2007 PA<sub>8</sub> obtained at Goldstone during October–November 2012. Range resolutions are 18.75 m on October 31 and November 11–13; 7.5 m on November 2, 3, and 8; and 3.75 m on November 5 and 6. The highest resolutions were obtained on dates when the asteroid was closest to Earth and the signal-to-noise ratios were strongest. Each panel has the same delay-Doppler dimensions.

around the long axis of  $20.55 \pm 3.75 \text{ d}$ . The amplitude of rolling around the long axis is  $42 \pm 7^\circ$ . 2007 PA<sub>8</sub> is the second confirmed short-axis mode non-principal-axis rotator found in the NEA population, after Apophis (Pravec *et al.*, 2014).

#### 4.4. (162421) 2000 ET<sub>70</sub>

Arecibo images of 2000 ET<sub>70</sub> place thousands of pixels on the object (Fig. 13) (Naidu *et al.*, 2013). The three-dimensional physical model has dimensions of  $2.6 \times 2.2 \times 2.1 \text{ km}$ , a retrograde spin state with a 9-h period, and an unusually low optical albedo of  $\sim 2\%$ . The northern hemisphere has dramatic ridges oriented approximately perpendicular to the long axis, but the southern hemisphere is much more rounded, a global shape dichotomy that is uncommon among NEAs imaged by radar to date.

#### 4.5. (308635) 2005 YU<sub>55</sub>

2005 YU<sub>55</sub> approached within 0.0022 AU (0.85 lunar distances) in November 2011, the closest approach of a known asteroid  $> 300 \text{ m}$  in diameter since 1982 (2012 TY<sub>52</sub>) and until 2028 (2001 WN<sub>5</sub>). This provided an extraordinary opportunity for radar imaging, and extensive observations were obtained at Goldstone, Arecibo, the Green Bank Telescope, and elements of the VLBA over two weeks (Busch *et al.*, 2012). The SNRs were among the highest ever obtained for any NEA and resulted in radar images with resolutions as fine as 3.75 m in range (Fig. 2). The images reveal a rounded object whose surface has many small radar-bright spots, suggesting numerous boulders, and radar-dark regions that may be impact craters. Modeling indicates that the shape

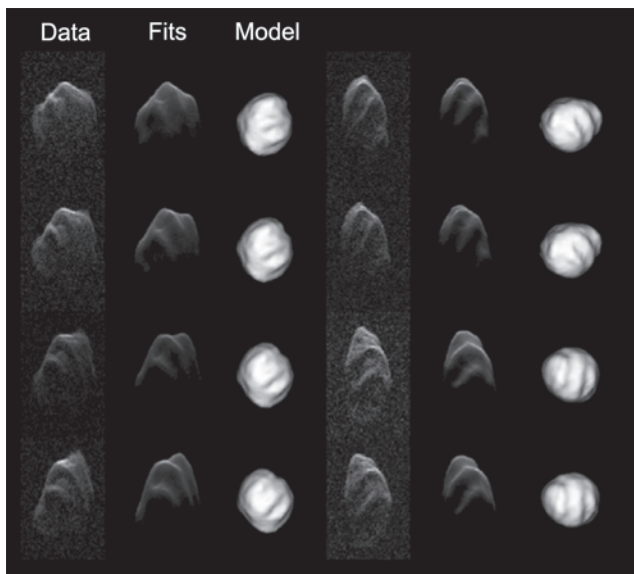


**Fig. 13.** Selected Arecibo images, fits, and plane-of-sky views of the 2000 ET<sub>70</sub> shape model (Naidu et al., 2013).

is close to spheroidal with maximum dimensions of  $360 \pm 40$  m in all directions. The shape has a ridge roughly parallel to the equator that resembles ridges seen on other rapidly rotating spheroidal NEAs imaged by radar, but unlike those other objects, 2005 YU<sub>55</sub> is a relatively slow rotator with a period of  $\sim 19$  h.

#### 4.6. 2014 HQ<sub>124</sub>

Bistatic Goldstone-Arecibo X-band images of 2014 HQ<sub>124</sub> achieve a resolution of  $3.75$  m  $\times$   $0.00625$  Hz (Fig. 3) and provide some of the most detailed radar views obtained for any near-Earth object (Benner et al., 2014b). 2014 HQ<sub>124</sub> is a slowly rotating object that is elongated, bifurcated, and angular with a long axis of at least 400 m. The larger lobe has a narrow, sinuous,  $\sim 100$ -m-long radar-dark feature that may be a scarp or perhaps a fault. These observations were the first test of new data-taking equipment at Arecibo that can acquire images at 3.75 m resolution using transmissions from Goldstone. Radar astrometry increased the interval of reliable Earth encounter predictability by a factor of 2 to  $\sim 900$  years.

#### 4.7. (341843) 2008 EV<sub>5</sub>

Busch et al. (2011) observed 2008 EV<sub>5</sub> with Arecibo, Goldstone, and the VLBA during the asteroid's passage within 0.022 AU in December 2008. Radar speckle tracking indicates retrograde rotation; this is the first NEA where that technique was used successfully. The object has a diameter of  $400 \pm 50$  m, a prominent ridge parallel to its equator, and a concavity about 150 m in diameter (Fig. 8). The concavity may be an impact crater; if so, then its ejecta may have produced some of the numerous boulders that are suggested by radar bright spots near the south pole. This object was

the target for the proposed European Space Agency's Marco Polo-R mission and is a leading candidate for NASA's proposed Asteroid Redirect Mission.

#### 4.8. (33342) 1998 WT<sub>24</sub>

1998 WT<sub>24</sub> approached within five lunar distances (0.0125 AU) in December 2001, when it was the strongest asteroid radar target ever observed up to that point. This asteroid was observed extensively at Goldstone and Arecibo and yielded a detailed three-dimensional model (Busch et al., 2008). The images show a rounded object with a conspicuous radar-bright spot several pixels in extent that persists over multiple rotations. The asteroid has a diameter of  $415 \pm 40$  m and the shape is dominated by three large basins that may be impact craters.

#### 4.9. (29075) 1950 DA

1950 DA is a type case highlighting the importance of radar astrometry and shape modeling for predicting asteroid trajectories and the interaction between orbits, shapes, and spin states due to the Yarkovsky effect.

1950 DA was discovered in 1950, lost until 2000, and then observed extensively at Arecibo and Goldstone during a close approach in March 2001. Radar astrometry indicated that 1950 DA will approach Earth in 2880, and the outcome of this approach depends on the magnitude and direction of the Yarkovsky acceleration. Due to the uncertainties in unmeasured physical parameters, Giorgini et al. (2002) included uncertainties in the Earth impact probability by expressing it as an interval, concluding that "the maximum probability of impact is best expressed as being between 0 and 0.33%."

Shape modeling by Busch et al. (2007) generated two pole solutions and two corresponding shapes: one that is roughly spheroidal and  $\sim 1.2$  km in diameter, and a second that is oblate,  $\sim 1.2$  km from pole to pole, and  $\sim 1.6$  km across at the equator (Busch et al., 2007). The data were insufficient to determine if 1950 DA spins prograde or retrograde, producing an ambiguity in the asteroid's future trajectory and thus in the impact probability.

Farnocchia and Chesley (2014) utilized additional optical astrometry, and remeasured radar astrometry from 2001 and new radar ranging from Arecibo in 2012 to further improve the orbit. The main source of uncertainty remains the Yarkovsky effect, which was detected at the  $\sim 5\sigma$  level. Utilizing a statistical model of the Yarkovsky effect, they found that, due to the sign of the orbital drift, prograde rotation is ruled out. This appears to be the first time that a pole direction ambiguity has been resolved by detection of the Yarkovsky effect, which was predicted by Busch et al. (2007).

Rozitis et al. (2014) adopted the retrograde shape model from Busch et al. (2007) and used thermal modeling of Wide-field Infrared Survey Explorer (WISE) spacecraft data to estimate 1950 DA's thermal inertia and bulk density. They state that the asteroid's rapid spin (2.1 h) implies a need

for cohesive forces to prevent rotational breakup. *Rozitis et al.*'s (2014) work hinges on the  $5\sigma$  Yarkovsky effect detection reported by *Farnocchia and Chesley* (2014) and on the retrograde shape model without regard to the uncertainties in that model. However, more recently, *Hirabayashi and Scheeres* (2015) find that cohesion is necessary over a much wider range of densities, indicating that a change in density estimate will not substantively impact the main conclusions of *Rozitis et al.* (2014) (see the chapter by Scheeres et al. in this volume).

Future radar and optical astrometry can refine estimates of 1950 DA's Yarkovsky effect drift, improve estimates of the asteroid's future trajectory, and improve estimates of its bulk density and constraints on its internal structure. The next opportunity for radar observations of 1950 DA is in 2032, when an extensive imaging campaign at Arecibo and Goldstone could provide higher-resolution images than were obtained in 2001.

#### 4.10. (1580) Betulia

*Magri et al.* (2007b) modeled the shape and spin state of Betulia using Arecibo data obtained in 2002 and light curves obtained in 1976 and 1989. They obtain a model that resembles the *Kaasalainen et al.* (2004) convex-definite shape reconstructed from light curves but is dominated by a prominent concavity in the southern hemisphere. Betulia has an effective diameter of  $5.39 \pm 0.54$  km and a shape that is roughly triangular when viewed along its polar axis.

#### 4.11. (100085) 1992 UY<sub>4</sub>

Goldstone and Arecibo radar images of 1992 UY<sub>4</sub> obtained in 2005 reveal a lumpy, modestly asymmetric, 2-km-diameter object. The surface is characterized by gently undulating topography with many modest concavities. Numerous fine-scale, radar-bright features are evident at the trailing edges and limbs; one of the most prominent has a visible extent of about 100 m and juts out abruptly from the approaching limb, suggesting a large block similar to the boulder Yoshinodai seen on (25143) Itokawa by the Hayabusa spacecraft (*Saito et al.*, 2006).

#### 4.12. Tiny Near-Earth Asteroids

Near-Earth asteroids with diameters  $<140$  m (corresponding to  $H > 22$ ) comprise approximately one-fourth of all NEAs observed with radar. The fraction of such objects observed by radar has increased  $\sim 50\%$  since publication of *Asteroids III* because more of these objects are being discovered with sufficient advance notice to schedule radar observations, due to greater access to telescope time, and due to more rapid response protocols. Several have been observed within one lunar distance, and one, 2006 RH<sub>120</sub>, was a temporarily captured satellite of Earth. A further motivation has been acute interest since 2011 in tiny NEAs that could be targets for human missions. To that end, as many

objects on the NASA Near-Earth Object Human Spaceflight Accessible Targets Study list (NHATS) (<http://neo.jpl.nasa.gov/nhats/>) are observed with radar as possible even if the SNRs are very weak.

Due to development of the 3.75-m resolution imaging system at Goldstone, it has become possible to obtain delay-Doppler images that can spatially resolve NEAs as small as  $\sim 30$  m in diameter. This opens up a new capability to investigate the physical properties of a much smaller subset of the NEA population than was previously possible. The first object imaged at 4-m resolution was 2010 AL<sub>30</sub> (*Slade et al.*, 2010). More recently, several NEAs such as (367943) Duende (2012 DA<sub>14</sub>), 2013 ET, and 2014 BR<sub>57</sub> have been imaged, revealing a suite of irregular to spheroidal shapes (Fig. 14).

Ranging astrometry from tiny NEAs can yield orbits with sufficient precision to detect nongravitational perturbations from solar radiation pressure. If detected, this perturbation yields an estimate of the area/mass ratio. To date, solar radiation pressure perturbations have been detected in the

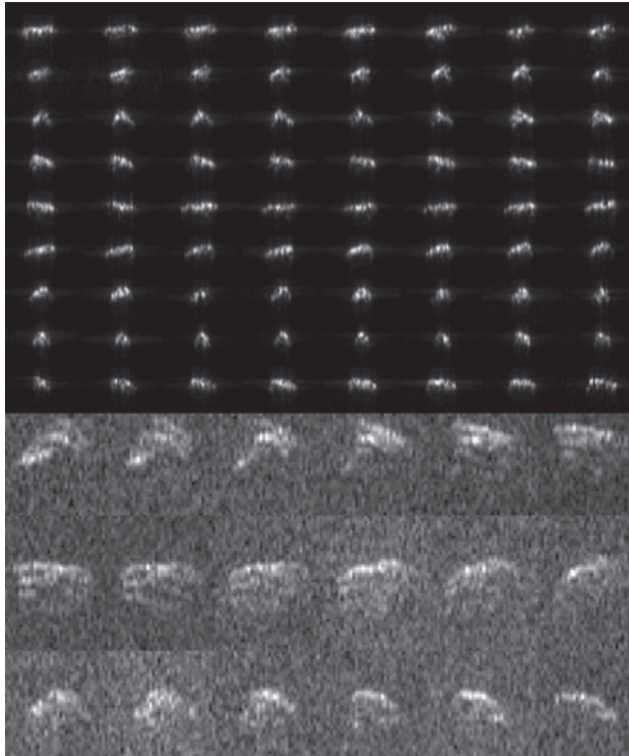


**Fig. 14.** Goldstone images of two NEAs that are less than 100 m in diameter. *Top:* (367943) Duende (2012 DA<sub>14</sub>) imaged on February 16, 2013. Duende has major axes of  $\sim 40 \times 20$  m, an angular shape, and is a non-principal-axis rotator (*Moskovitz et al.*, 2013). *Bottom:* 2013 ET images from March 10, 2013. 2013 ET appears structurally complex, has a long axis of at least 40 m, and has alternating radar-dark and radar-bright regions. In each collage, the range resolution is 3.75 m, but the data were double sampled, so each row corresponds to 1.875 m.

motion of one NEA observed by radar: 2006 RH<sub>120</sub> in 2007 (P. W. Chodas, personal communication).

## 5. THE FUTURE

The future for asteroid radar observations is potentially very bright if capabilities at least equal to those currently available at Arecibo and Goldstone are maintained. As the number of NEAs discovered has grown rapidly in the last decade, so too have the number of short-term targets of opportunity and targets known well in advance. This trend will only continue as existing surveys upgrade and as new surveys begin.

The Large Synoptic Survey Telescope (LSST) could yield vastly more NEA discoveries when it begins routine operations in the 2020s, and with it could come a dramatic increase in radar targets. Due to its sensitivity, it seems likely that many NEAs larger than a few tens of meters in diameter found by LSST will be discovered months or even years before they will be detectable by radar.

The number of NEAs observed annually with radar is a fraction of what could be done if a dedicated radar facility were available. Schedules and equipment problems continue to be obstacles for observing on short notice but are less cumbersome than only a few years ago. The net effect is that roughly one-third of NEAs that are potentially detectable with radar are actually being observed.

Arecibo could observe many more asteroids if additional telescope time and funding were available. The observatory is already operating the S-band radar at close to the legal limit imposed by local air pollution laws, and a significant increase would require new, lower-emission generators. Due to its extraordinary sensitivity, though, the most effective way to increase the number of NEA radar detections is to augment the number of observations at Arecibo.

Demand at Goldstone for spacecraft communications is expected to diminish over the next several years as existing spacecraft cease operations and as future spacecraft switch to NASA's 34-m antennas for tracking. This could provide an opportunity to observe significantly more asteroids. Although most requests at Goldstone to observe NEAs known well in advance are scheduled, obtaining time on short notice remains challenging because schedules for flight projects are arranged many weeks in advance, and changing schedules on short notice has effects that ripple through the DSN.

### 5.1. Other Radar Facilities

Are there other existing radar facilities that could be utilized to observe NEAs? The 70-m Evpatoria antenna in Crimea has conducted bistatic NEA radar observations utilizing radio telescopes at Effelsberg (Germany), Medicina (Italy), and Irbene (Latvia) as receivers. Evpatoria has also acted as a receiver for Goldstone X-band transmissions of (6489) Golevka (Zaitsev et al., 1997), 1998 WT<sub>24</sub> (Di Martino et al., 2004), and 2004 XP<sub>14</sub> and could be used for monostatic observations of very close targets if the system

were modernized (B. Shustov, personal communication). Installation of a high-power planetary radar was considered for the new 64-m Sardinia Radio Telescope (Saba et al., 2005) but was not implemented due to the cost.

In February 2013, J. Vierinen (personal communication) detected radar echoes from (367943) Duende with the European Incoherent Scatter Scientific Association (EISCAT) facility near Tromso, Norway; this was the first time EISCAT was used for asteroid observations. Nechaeva et al. (2013) observed Duende by using Evpatoria to transmit and Irbene and Medicina to receive. The 37-m X-band and 46-m ultra-high-frequency (UHF) antennas at Haystack Observatory also detected Duende (P. Erickson and M. Hecht, personal communication). Radar observations of Duende were scheduled at the 35-m Tracking and Imaging Radar (TIRA) facility in Germany, but those observations were canceled due to logistical problems (D. Koschny, personal communication). Although orders of magnitude less sensitive than Goldstone, these facilities could detect a modest number of near-Earth objects annually during very close flybys.

### 5.2. Future Radar Capabilities

A new radar facility began operations in January 2015 on the 34-m DSS-13 antenna at the Goldstone Deep Space Communications Complex. DSS-13 is an experimental test bed that has been equipped with an 80-kW klystron that transmits at C-band (7190 MHz, 4.2 cm). The klystron has a bandwidth of 80 MHz and can achieve a range resolution of up to 1.875 m/pixel, which is twice as fine as the highest resolution at the 70-m DSS-14 Goldstone antenna and four times finer than at Arecibo. DSS-13 is not equipped to receive its own radar echoes, so reception must occur at another facility such as Green Bank, Arecibo, or the 34-m DSS-28 antenna at Goldstone. Bistatic DSS-13/Arecibo and DSS-13/Green Bank observations are significantly less sensitive than observations at DSS-14, but for very strong targets such as 2005 YU<sub>55</sub>, (367943) Duende, and 2014 HQ<sub>124</sub>, where the SNR is not a limiting factor, DSS-13 would have been ideal. The new radar at DSS-13 is in its commissioning phase and routine operations are planned by the end of 2015.

The 70-m DSS-43 antenna at the Canberra Deep Space Communication Complex in Australia and the 64-m Parkes Radio Telescope could in principle be configured as a bistatic radar system using an existing S-band transmitter on DSS-43 that can radiate 400 kW. This bistatic system might achieve SNRs perhaps ~4% as strong as those at Goldstone and could enable radar observations of very close NEAs at southern declinations that are inaccessible to Goldstone and Arecibo. Proof-of-concept tests are planned in late 2015. Farther into the future, one of the 34-m DSN antennas at Canberra could be equipped with an 80-kW, 80-MHz klystron and transmitter identical to the system at DSS-13 (Davarian, 2011).

Another concept in the early stages of development is the Ka-Band Objects Observations and Monitoring (KaBOOM) phased-array radar test bed at the Kennedy Space Center (<http://www.nasa.gov/directorates/heo/scan/engineering/>

technology/*KaBOOM.html*). KaBOOM is a three-element array with antennas 12 m in diameter. The effective radiated power of an array of transmitters is proportional to  $N^2$ , where  $N$  is the number of array elements (Davarian, 2011), so in principle it is possible use a large number of small antennas radiating low power ( $\sim 5$  kW) to achieve much higher sensitivity than with a single, large dish. The engineering challenges are formidable and it is not yet known if this technique is feasible.

### 5.3. Greater Automation

Observing NEAs with radar remains a labor-intensive process that requires at least three people at the observatory to operate the telescope and transmitter, adjust cables, take data, make key decisions, and update ephemerides. At Arecibo it is still necessary to switch cables and adjust voltage gains when changing setups, a process that in principle could be automated with one electronics box. In the future, one can envision a situation with a nightly queue where the telescope automatically moves from target to target, where software automatically processes the data to determine when a detection has occurred, estimates and reports range-Doppler corrections to the ephemerides, and then slews to the next target. Imaging of high-SNR targets would require more direct human control to maximize the scientific return, but weaker targets could be observed in the automated manner described above.

### 5.4. Shape Modeling

The shape models discussed above demonstrate a clear need for improvements to the shape-modeling procedure. A better estimation algorithm that can fit topographically rugged objects is particularly desirable because features are often visible in radar images that the fits do not adequately reproduce. It would be helpful if a straightforward method of manually adjusting specific vertices on a model were possible in order to fit fine-scale features. Coupled estimation of the shapes and orbits of binaries would also be helpful.

Although increasing computer speed is useful, the limiting factor for estimating three-dimensional models is actually the ability of the user to assess the fits. Experience has shown that the human eye is more reliable than the  $\chi^2$  statistic for assessing the quality of fits, but this requires time-consuming visual inspection of many images.

Another impediment for augmenting the number of asteroid shape models is the paucity of NEA pole directions. Knowledge of the pole direction dramatically shrinks the time to estimate three-dimensional shapes. Otherwise, pole estimation requires a lengthy grid search may that not yield a unique solution. Radar speckle observations can provide pole directions for the subset of targets with very strong SNRs, and increasing the number of days of radar observations to extend sky motion can help, but the biggest contribution will probably come from obtaining more light curves. Light curves can often provide pole directions when

radar observations cannot, but obtaining light curves can be a major logistical challenge and they are often not available for many NEAs observed by radar.

## 6. SUMMARY

The number of NEAs being observed annually with radar is approaching 100, but that is still only a fraction of the number that could be observed if telescope time, funding, personnel, equipment problems, and the ability to respond to targets of opportunity very rapidly were not issues.

Asteroid radar astronomy has made dramatic strides forward since publication of *Asteroids III*; the field is growing, and it has considerable scientific potential. New discoveries occur frequently, imaging resolutions are approaching the realm of planetary geology, and radar observations have become important in ways that were never imagined only a decade ago.

**Acknowledgments.** We thank D. J. Scheeres and an anonymous reviewer for comments that improved this manuscript. Part of this work was performed at the Jet Propulsion Laboratory, California Institute of Technology, under contract with the National Aeronautics and Space Administration (NASA). This material is based in part upon work supported by NASA under the Science Mission Directorate Research and Analysis Programs.

## REFERENCES

- Benner L. A. M. and 10 colleagues (2002) Radar observations of asteroid 1999 JM8. *Meteoritics & Planet. Sci.*, **37**, 779–792.
- Benner L. A. M. and 5 colleagues (2006) Near-Earth asteroid 2005 CR37: Radar images of a candidate contact binary. *Icarus*, **182**, 474–481.
- Benner L. A. M. and 10 colleagues (2008) Near-Earth asteroid surface roughness depends on compositional class. *Icarus*, **198**, 294–304.
- Benner L. and 11 colleagues (2014a) Arecibo and Goldstone radar evidence for boulders on near-Earth asteroids. In *Asteroids, Comets, Meteors 2014 Book of Abstracts* (K. Muinonen et al., eds.), p. 59. Univ. of Helsinki, Finland.
- Benner L. A. M. and 16 colleagues (2014b) Goldstone and Arecibo radar images of near-Earth asteroid 2014 HQ124. *Bull. Am. Astron. Soc.*, **46**, #49.01.
- Bottke W. F. and 3 colleagues (2002) The effect of Yarkovsky thermal forces on the dynamical evolution of asteroids and meteoroids. In *Asteroids III* (W. F. Bottke Jr. et al., eds.), pp. 395–408. Univ. of Arizona, Tucson.
- Bottke W. F. and 3 colleagues (2006) The Yarkovsky and YORP effects: Implications for asteroid dynamics. *Annu. Rev. Earth Planet. Sci.*, **34**, 157–191.
- Brozovic M. and 10 colleagues (2009) Radar observations and a physical model of asteroid 4660 Nereus, a prime space mission target. *Icarus*, **201**, 153–166.
- Brozovic M. and 9 colleagues (2010) Radar observations and a physical model of contact binary asteroid 4486 Mithra. *Icarus*, **208**, 207–220.
- Brozovic M. and 21 colleagues (2011) Radar observations and physical modeling of triple near-Earth asteroid (136617) 1994 CC. *Icarus*, **216**, 241–256.
- Busch M. W. and 14 colleagues (2007) Physical modeling of near-Earth asteroid (29075) 1950 DA. *Icarus*, **190**, 608–621.
- Busch M. W. and 9 colleagues (2008) Physical properties of near-Earth asteroid (33342) 1998 WT24. *Icarus*, **195**, 614–621.
- Busch M. W. and 6 colleagues (2010) Determining asteroid spin states using radar speckles. *Icarus*, **209**, 535–541.
- Busch M. W. and 12 colleagues (2011) Radar observations and the shape of near-Earth asteroid 2008 EV5. *Icarus*, **212**, 649–660.

- Busch M. W. and 16 colleagues (2012) Shape and spin of near-Earth asteroid 308635 (2005 YU55) from radar images and speckle tracking. *Asteroids, Comets, Meteors 2012*, Abstract #6179. Lunar and Planetary Institute, Houston.
- Capek D. and Vokrouhlický D. (2004) The YORP effect with finite thermal conductivity. *Icarus*, 172, 526–536.
- Chesley S. R. and 9 colleagues (2003) Direct detection of the Yarkovsky effect via radar ranging to asteroid 6489 Golevka. *Science*, 302, 1739–1742.
- Chesley S. R. and 15 colleagues (2014) Orbit and bulk density of the OSIRIS-REx target asteroid (101955) Bennu. *Icarus*, 235, 5–22.
- Davarian F. (2011) Uplink arraying for solar system radar and radio science. *Proc. IEEE*, 99, 783–793.
- Descamps P. and 18 colleagues (2011) Triplicity and physical characteristics of asteroid (216) Kleopatra. *Icarus*, 211, 1022–1033.
- Di Martino M. and 13 colleagues (2004) Results of the first Italian planetary radar experiment. *Planet. Space Sci.*, 52, 325–330.
- Durech J. and 11 colleagues (2008) Detection of the YORP effect in the asteroid (1620) Geographos. *Astron. Astrophys.*, 489, L25–L28.
- Emery J. P. and 8 colleagues (2014) Thermal infrared observations and thermophysical characterization of OSIRIS-REx target asteroid (101955) Bennu. *Icarus*, 234, 17–35.
- Farnocchia D. and Chesley S. R. (2014) Assessment of the 2880 impact threat from asteroid (29075) 1950 DA. *Icarus*, 229, 321–327.
- Farnocchia D. and 5 colleagues (2013a) Near Earth asteroids with measureable Yarkovsky effect. *Icarus*, 224, 1–13.
- Farnocchia D. and 7 colleagues (2013b) Yarkovsky-driven impact risk analysis for asteroid (99942) Apophis. *Icarus*, 224, 192–200.
- Gaskell R. and 8 colleagues (2008) *Gaskell Itokawa Shape Model V1.0*. HAY-A-AMICA-5-ITOKAWASHAPE-V1.0, NASA Planetary Data System.
- Giorgini J. D. and 13 colleagues (2002) Asteroid 1950 DA's encounter with Earth: Physical limits of collision probability prediction. *Science*, 296, 132–136.
- Giorgini J. D. and 4 colleagues (2008) Predicting the Earth encounters of (99942) Apophis. *Icarus*, 193, 1–19.
- Harris A. W., Fahnestock E. G., and Pravec P. (2009) On the shapes and spins of rubble pile asteroids. *Icarus*, 199, 310–318.
- Hirabayashi M. and Scheeres D. (2015) Stress and failure analysis of rapidly rotating asteroid (29075) 1950 DA. *Astrophys. J. Lett.*, in press.
- Huang J. and 27 colleagues (2013) The ginger-shaped asteroid 4179 Toutatis: New observations from a successful flyby of Chang'e-2. *Nature Sci. Rept.*, 3, 3411.
- Hudson S. (1993) Three-dimensional reconstruction of asteroids from radar observations. *Remote Sensing Rev.*, 8, 195–203.
- Hudson R. S. and Ostro S. J. (1994) Shape of asteroid 4769 Castalia (1989 PB) from inversion of radar images. *Science*, 263, 940–943.
- Hudson R. S. and Ostro S. J. (1995) Shape and non-principal axis spin state of asteroid 4179 Toutatis. *Science*, 270, 84–86.
- Hudson R. S. and 26 colleagues (2000) Radar observations and physical model of asteroid 6489 Golevka. *Icarus*, 148, 37–51.
- Hudson R. S., Ostro S. J., and Scheeres D. J. (2003) High-resolution model of asteroid 4179 Toutatis. *Icarus*, 161, 346–355.
- Kaasalainen M. and 21 colleagues (2004) Photometry and models of eight near-Earth asteroids. *Icarus*, 167, 178–196.
- Kaasalainen M. and 4 colleagues (2007) Acceleration of the rotation of asteroid 1862 Apollo by radiation torques. *Nature*, 446, 420–422.
- Lowry S. C. and 10 colleagues (2007) Direct detection of the asteroidal YORP effect. *Science*, 316, 272–274.
- Magri C. and 9 colleagues (1999) Mainbelt asteroids: Results of Arecibo and Goldstone radar observations of 37 objects during 1980–1995. *Icarus*, 140, 379–407.
- Magri C. and 3 colleagues (2007a) A radar survey of main-belt asteroids: Arecibo observations of 55 objects during 1999–2003. *Icarus*, 186, 126–151.
- Magri C. and 6 colleagues (2007b) Radar observations and a physical model of asteroid 1580 Betulia. *Icarus*, 186, 152–177.
- Magri C. and 25 colleagues (2011) Radar and photometric observations and shape modeling of contact binary near-Earth asteroid (8567) 1996 HW1. *Icarus*, 214, 210–227.
- Margot J. L. and 7 colleagues (2002) Binary asteroids in the near-Earth object population. *Science*, 296, 1445–1448.
- Margot J. L. and 4 colleagues (2007) Large longitude libration of Mercury reveals a molten core. *Science*, 316, 710–714.
- Margot J. L. and 9 colleagues (2012) Mercury's moment of inertia from spin and gravity data. *J. Geophys. Res.*, 117, E00L09.
- Milani A. and 5 colleagues (2009) Long term impact risk for (101955) 1999 RQ36. *Icarus*, 203, 460–471.
- Moskovitz N. and 19 colleagues (2013) The near-Earth asteroid 2012 DA14. *Bull. Am. Astron. Soc.*, 45, #101.03.
- Naidu S. P. and Margot J. L. (2015) Near-Earth asteroid satellite spins under spin-orbit coupling. *Astron. J.*, 149, 80.
- Naidu S. P. and 9 colleagues (2013) Radar imaging and physical characterization of near-Earth asteroid (162421) 2000 ET70. *Icarus*, 226, 323–335.
- Naidu S. P. and 9 colleagues (2015) Radar imaging and characterization of binary near-Earth asteroid (185851) 2000 DP107. *Astron. J.*, 150, 54.
- Nechaeva M. and 19 colleagues (2013) First results of the VLBI experiment on radar location of the asteroid 2012 DA14. *Baltic Astron.*, 22, 341–346.
- Nolan M. C. and 10 colleagues (2013) Shape model and surface properties of the OSIRIS-REx target asteroid (101955) 1999 RQ36 from radar and lightcurve observations. *Icarus*, 226, 629–640.
- Nugent C. R. and 3 colleagues (2012) Detection of semi-major axis drifts in 54 near-Earth asteroids: New measurements of the Yarkovsky effect. *Astron. J.*, 144, 60–72.
- Ostro S. J. (1993) Planetary radar astronomy. *Rev. Mod. Phys.*, 65, 1235–1279.
- Ostro S. J. and Giorgini J. D. (2004) The role of radar in predicting and preventing asteroid and comet collisions with Earth. In *Mitigation of Hazardous Comets and Asteroids* (M. J. S. Belton et al., eds.), pp. 38–65. Cambridge Univ., Cambridge.
- Ostro S. J. and 13 colleagues (1995) Radar images of asteroid 4179 Toutatis. *Science*, 270, 80–84.
- Ostro S. J. and 8 colleagues (2000) Radar observations of asteroid 216 Kleopatra. *Science*, 288, 836–839.
- Ostro S. J. and 6 colleagues (2002) Asteroid radar astronomy. In *Asteroids III* (W. F. Bottke Jr. et al., eds.), pp. 151–168. Univ. of Arizona, Tucson.
- Ostro S. J. and 15 colleagues (2004) Radar observations of asteroid 25143 Itokawa (1998 SF36). *Meteoritics & Planet. Sci.*, 39, 407–424.
- Ostro S. J. and 12 colleagues (2005) Radar observations of Itokawa in 2004 and improved shape estimation. *Meteoritics & Planet. Sci.*, 40, 1563–1574.
- Ostro S. J. and 15 colleagues (2006) Radar imaging of binary near-Earth asteroid (66391) 1999 KW4. *Science*, 314, 1276–1280.
- Ostro S. J. and 7 colleagues (2010) Radar imaging of asteroid 7 Iris. *Icarus*, 207, 285–294.
- Pravec P. and 58 colleagues (2006) Photometric survey of binary near-Earth asteroids. *Icarus*, 181, 63–93.
- Pravec P. and 19 colleagues (2014) The tumbling spin state of (99942) Apophis. *Icarus*, 233, 48–60.
- Rivkin A. S. and 4 colleagues (2000) The nature of M-class asteroids from 3 μm observations. *Icarus*, 145, 351–368.
- Rozitis B. and 3 colleagues (2013) A thermophysical analysis of the (1862) Apollo Yarkovsky and YORP effects. *Astron. Astrophys.*, 555, A20.
- Rozitis B., MacLennan E., and Emery J. P. (2014) Cohesive forces prevent the rotational breakup of rubble-pile asteroid (29075) 1950 DA. *Nature*, 512, 174–176.
- Rubincam D. P. (2000) Radiative spin-up and spin-down of small asteroids. *Icarus*, 148, 2–11.
- Saba L. and 15 colleagues (2005) The Sardinia Radio Telescope as a radar for the study of near-Earth objects and space debris. *Mem. Soc. Astron. Ital. Suppl.*, 6, 104–109.
- Saito J. and 33 colleagues (2006) Detailed images of asteroid 25143 Itokawa from Hayabusa. *Science*, 312, 1341–1344.
- Scheeres D. J. (2007) Rotational fission of contact binary asteroids. *Icarus*, 189, 370–385.
- Scheeres D. J. and 5 colleagues (2005) Abrupt alteration of asteroid 2004 MN4's spin state during its 2029 Earth flyby. *Icarus*, 178, 281–283.
- Shepard M. K. and 18 colleagues (2008a) A radar survey of X- and M-class asteroids. *Icarus*, 195, 184–205.
- Shepard M. K. and 9 colleagues (2008b) Radar observations of E-class asteroids 44 Nysa and 434 Hungaria. *Icarus*, 195, 220–225.
- Shepard M. K. and 12 colleagues (2010) A radar survey of M- and X-class asteroids. II. Summary and synthesis. *Icarus*, 208, 221–237.
- Shepard M. K. and 9 colleagues (2011) Radar observations of asteroids 64 Angelina and 69 Hesperia. *Icarus*, 215, 547–551.
- Shepard M. K. and 15 colleagues (2015) A radar survey of M- and X-class asteroids. III. Insights into their compositions, hydration state, and structure. *Icarus*, 245, 38–55.

- Sierks H. and 57 colleagues (2011) Images of asteroid 21 Lutetia: A remnant planetesimal from the early solar system. *Science*, *334*, 487–490.
- Slade M. A. and 6 colleagues (2010) First results of the new Goldstone delay-Doppler radar chirp imaging system. *Bull. Am. Astron. Soc.*, *42*, 1080.
- Slade M. A., Benner L.A.M., and Silva A. (2011) Goldstone Solar System Radar Observatory: Earth-based planetary mission support and unique science results. *Proc. IEEE*, *99*, 757–769.
- Springmann A. and 3 colleagues (2013) Are the radar scattering properties of near-Earth asteroids correlated with size, shape, or spin? *Lunar Planet. Sci. XLIV*, Abstract #2915. Lunar and Planetary Institute, Houston.
- Takahashi Y., Busch M. W., and Scheeres D. J. (2013) Spin state and moment of inertia characterization of 4179 Toutatis. *Astron. J.*, *146*, 95.
- Taylor P. A. (2009) Tidal interactions in binary asteroid systems. Ph.D. thesis, Cornell Univ., Ithaca.
- Taylor P. A. and 11 colleagues (2007) Increasing spin rate of asteroid 54509 (2000 PH5) a result of the YORP effect. *Science*, *316*, 274–277.
- Taylor P. A. and 3 colleagues (2012) The shape and spin distributions of near-Earth asteroids observed with the Arecibo radar system. *Bull. Am. Astron. Soc.*, *44*, #302.07.
- Virkki A., Muinonen K., and Penttila A. (2014) Inferring asteroid surface properties from radar albedos and circular polarization ratios. *Meteoritics & Planet. Sci.*, *59*, 86–94.
- Vokrouhlický D., Milani A., and Chesley S. R. (2000) Yarkovsky effect on small near-Earth asteroids: Formulation and examples. *Icarus*, *148*, 118–138.
- Vokrouhlický D. and 3 colleagues (2005a) Yarkovsky effect opportunities. I. Solitary asteroids. *Icarus*, *173*, 166–184.
- Vokrouhlický D. and 3 colleagues (2005b) Yarkovsky effect opportunities. II. Binary systems. *Icarus*, *179*, 128–138.
- Walsh K. J., Richardson D. C., and Michel P. (2008) Rotational breakup as the origin of small binary asteroids. *Nature*, *454*, 188–191.
- Warner B. D., Harris A. W., and Pravec P. (2009) Asteroid lightcurve database. *Icarus*, *202*, 134–146.
- Zaitsev A. and 24 colleagues (1997) Intercontinental bistatic radar observations of 6489 Golevka (1991 JX). *Planet. Space Sci.*, *45*, 771–778.
- Zou X. and 5 colleagues (2014) The preliminary analysis of the 4179 Toutatis snapshots of the Chang'e-2 flyby. *Icarus*, *229*, 348–354.

# Asteroid Models from Multiple Data Sources

Josef Ďurech

*Charles University in Prague*

Benoît Carry

*Institut de Mécanique Céleste et de Calcul des Éphémérides*

Marco Delbo

*Lagrange Laboratory, Université Côte d'Azur, Observatoire de la Côte d'Azur, CNRS*

Mikko Kaasalainen and Matti Viikinkoski

*Tampere University of Technology*

---

In the past decade, hundreds of asteroid shape models have been derived using the lightcurve inversion method. At the same time, a new framework of three-dimensional shape modeling based on the combined analysis of widely different data sources — such as optical lightcurves, disk-resolved images, stellar occultation timings, mid-infrared thermal radiometry, optical interferometry, and radar delay-Doppler data — has been developed. This multi-data approach allows the determination of most of the physical and surface properties of asteroids in a single, coherent inversion, with spectacular results. We review the main results of asteroid lightcurve inversion and also recent advances in multi-data modeling. We show that models based on remote sensing data were confirmed by spacecraft encounters with asteroids, and we discuss how the multiplication of highly detailed three-dimensional models will help to refine our general knowledge of the asteroid population. The physical and surface properties of asteroids, i.e., their spin, three-dimensional shape, density, thermal inertia, and surface roughness, are among the least known of all asteroid properties. Apart from the albedo and diameter, we have access to the whole picture for only a few hundreds of asteroids. These quantities are nevertheless very important to understand, as they affect the nongravitational Yarkovsky effect responsible for meteorite delivery to Earth, as well as the bulk composition and internal structure of asteroids.

## 1. INTRODUCTION

The determination of asteroid physical properties is an essential part of the complex process of revealing the nature of the asteroid population. In many cases, this process starts with obtaining observational data, continues with creating a model of the asteroid (i.e., its size, three-dimensional shape, and spin state, in the first approximation), and ends with interpreting new facts based on the model or a set of these. In this sense, modeling is a crucial mid-step between observations and theory. Results based on individual well-studied asteroids can be generalized to other members of the population. On the other hand, a statistically large sample of asteroids with known properties can reveal physical effects that play an important role for the whole population.

In this chapter, we will build on the content of the *Asteroids III* chapter by Kaasalainen *et al.* (2002a) about asteroid models reconstructed from *disk-integrated* photometry. Although visual photometry still remains the most important data source of the modeling, the main progress in this field

since *Asteroids III* has been the addition of *complementary data sources*. Many of these data sources are *disk-resolved*, thus containing much more information than disk-integrated data. This shift in paradigm — using photometry not alone but simultaneously with complementary data — was mentioned in the last paragraph of the *Asteroids III* chapter as “perhaps the most interesting future prospect,” and we are now at this stage. In the following, we will review all data types suitable for inversion, their sources, uncertainties, and how they can be used in modeling.

When describing the methods of data inversion and the results obtained by these methods, it is also important to emphasize caveats, ambiguities, and possible sources of errors. Although the description of what can be obtained from different data sources is exciting, the knowledge of what cannot, i.e., the limitations of our datasets, is of the same importance. Omitting this may lead to overinterpretation of results.

This chapter is structured as follows. First, we review the main principles of the multimodal inverse problem in

section 2. Then, in section 3, we discuss each data type and their contribution to model characteristics and details, and we describe some extensions of the predominant model. In section 4, we discuss the main results based on lightcurve inversion and multimodal asteroid reconstruction. We conclude with prospects for the future in section 5.

## 2. THEORETICAL ASPECTS OF INVERSION AND DATA FUSION

Asteroid physical model reconstruction from multimodal data is, by its very nature, a mathematical inverse problem. It is ill-posed; i.e., the uniqueness and stability properties of the solution are usually not very good unless the data are supported by a number of prior constraints. Furthermore, it is not sufficient just to fit some model to the data numerically and try to probe the solution space with some scheme. Although there are more approaches to the problem of asteroid shape reconstruction, they are usually dealing with only one data type and we mention them in the next section. Here, we describe the problem in a general way in the framework of *generalized projections*: Our data are various one- or two-dimensional projection types of a three-dimensional model, and understanding the fundamental mathematical properties of the inverse projection mapping is essential. This includes a number of theorems on uniqueness, information content, and stability properties (Kaasalainen and Lamberg, 2006; Kaasalainen, 2011; Viikinkoski and Kaasalainen, 2014).

Let the projection point  $\xi_0$  in the image plane (plane-of-sky or range-Doppler) of the point  $\mathbf{x}_0$  on the body be mapped by the matrix  $\mathbf{A}$ :  $\xi_0 = \mathbf{Ax}_0$ . Define the set  $I(\xi)$  for any  $\xi$  as

$$I(\xi) = \{\mathbf{x} | g(\xi, \mathbf{x}; R, t) h(\mathbf{x}; M, R, t) = 1\} \quad (1)$$

where we have explicitly shown the time  $t$  and the adjustable parameters:  $M$  for the shape and  $R$  for the rotation. The projection point function  $g(\xi; \mathbf{x}) = 1$  if  $\mathbf{A}(R, t)\mathbf{x} = \xi$ , and  $g = 0$  otherwise. The ray-tracing function  $h = 1$  if  $\mathbf{x}$  is visible (for occultation, thermal, and radar data), or visible and illuminated (for disk-resolved imaging and photometry in the optical); otherwise  $h = 0$ . The set  $I(\xi)$  is numerable and finite. The number of elements in  $I(\xi)$  is at most one for plane-of-sky projections (each point on the projection corresponds to at most one point of the asteroid's surface); for range-Doppler, it can be more (more points on an asteroid's surface can have the same distance to the observer and the same relative radial velocity). Generalized projections, i.e., all the data modes presented in section 3, can now be presented as scalar values  $p(\xi)$  in the image field  $\Omega$

$$p(\xi; t) = \int_{\Omega} f(\xi, \eta) \sum_{x \in I(\eta)} S(x; M, R, L, t) d\eta \quad (2)$$

where  $L$  denotes the luminosity parameters (for scattering or thermal properties), and the luminosity function is denoted by  $S$ . The function  $f$  is the point-spread, pixellation,

or other transfer function of the image field. For interferometry, it is typically the Fourier transform kernel. In fact, the reconstruction process works efficiently by taking the Fourier transform of any image type rather than using the original pixels (Viikinkoski and Kaasalainen, 2014). For lightcurves,  $f = 1$  [and  $\xi$  is irrelevant,  $p(\xi)$  is constant]. The surface albedo is usually assumed to be constant, although its variegation can be included in  $S$  by the parameters  $L$  if there are high-quality disk-resolved data. In the case of lightcurves only, we can get an indication of non-uniform albedo and compensate for this with a (non-unique) spot model (Kaasalainen *et al.*, 2001).

The multimodal inverse problem can be expressed as follows. Let us choose as goodness-of-fit measures some functions  $\delta_i$ ,  $i = 1, \dots, n$ , of  $n$  data modalities. Typically,  $\delta$  is the usual  $\chi^2$ -fit form between  $p_{\text{model}}$  and  $p_{\text{obs}}$ . Our task is to construct a joint  $\delta_{\text{tot}}$  with weighting for each data mode

$$\delta_{\text{tot}}(P, D) = \delta_1(P, D_1) + \sum_{i=2}^n \lambda_{i-1} \delta_i(P, D_i), \quad D = \{D_i\} \quad (3)$$

where  $D_i$  denotes the data from the source  $i$ ,  $\lambda_{i-1}$  is the weight of the source  $i$ , and  $P = \{M, R, L\}$  is the set of model parameter values. The best-fit result is obtained by minimizing  $\delta_{\text{tot}}$  with nonlinear techniques, typically Levenberg-Marquardt for efficient convergence. Regularization functions  $r(P)$  can be added to the sum; these constrain, for instance, the smoothness of the surface to suppress large variations at small scales, the deviation from principal-axis rotation to force the model to rotate around the shortest inertia axis (assuming uniform density), or the gravitational slope, etc. (Kaasalainen and Viikinkoski, 2012).

The modality (and regularization) weights  $\lambda_i$  are determined using the maximum compatibility estimate (MCE) principle (Kaasalainen, 2011; Kaasalainen and Viikinkoski, 2012). This yields well-defined unique values that are, in essence, the best compromise between the different datasets that often tend to draw the solution in different directions. Moreover, MCE values of weighting parameters are objective, not dependent on the user's choice, although their values are usually close to those determined subjectively based on experience. Plotting various choices of weights typically results in an L-shaped curve shown in Fig. 1; the best solution is at the corner of the curve. In this way, the reconstruction from complementary data sources is possible even if no single data mode is sufficient for modeling alone.

For practical computations, the surface is rendered as a polyhedron, and  $S$  and  $h$  are computed accordingly with ray-tracing (Kaasalainen *et al.*, 2001). Rather than using each vertex as a free parameter, the surface can be represented in a more compact form with spherical harmonics series (for starlike or octantoid shapes) or subdivision control points (Kaasalainen and Viikinkoski, 2012; Viikinkoski *et al.*, 2015). These *shape supports* are essential for convergence: They allow flexible modifications of the surface with a moderate number of parameters while not getting stuck in local minima

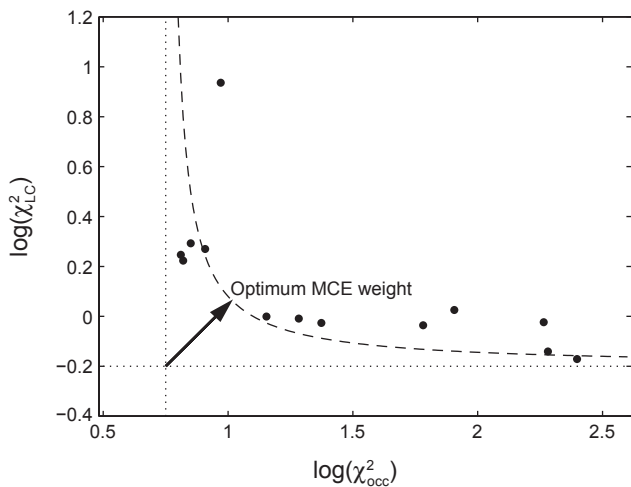


**Fig. 1.** The level of fit for lightcurves and occultation data for different weighting between the two data types. The optimum weight is around the “corner” of the L-curve. Each dot corresponds to an inversion with a different weight  $\lambda$ .

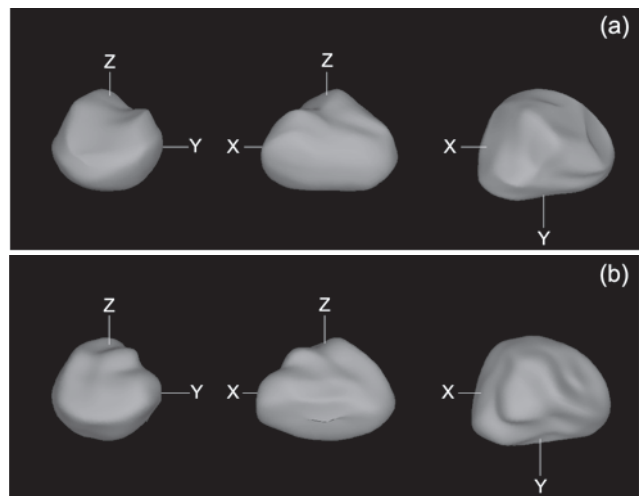


**Fig. 2.** Model of (41) Daphne reconstructed from lightcurves and adaptive-optics images using (a) subdivision surfaces and (b) octantoids. The general shape remains stable, even if small-scale features slightly change.

or overemphasizing the role of regularization functions when searching for the best-fit solution. Each shape support has its own characteristic way of representing global and local features. For example, the octantoid parameterization

$$\mathbf{x}(\theta, \varphi) = \begin{cases} x(\theta, \varphi) = e^{a(\theta, \varphi)} \sin \theta \cos \varphi \\ y(\theta, \varphi) = e^{a(\theta, \varphi)+b(\theta, \varphi)} \sin \theta \sin \varphi \\ z(\theta, \varphi) = e^{a(\theta, \varphi)+c(\theta, \varphi)} \cos \theta \end{cases} \quad (4)$$

where  $a$ ,  $b$ , and  $c$  are linear combinations of the (real) spherical harmonic functions  $Y_l^m(\theta, \varphi)$ , with coefficients  $\{a_{lm}\}$ ,  $\{b_{lm}\}$ , and  $\{c_{lm}\}$ , respectively, are easy to regularize globally while retaining the ability to produce local details. The coordinates  $(\theta, \varphi)$ ,  $0 \leq \theta \leq \pi$ ,  $0 \leq \varphi < 2\pi$ , parameterize the surface on the unit sphere  $S^2$  but do not represent any physical directions such as polar coordinates.

This inverse problem is a typical example of a case where model and systematic errors dominate over random measurement errors. Thus the stability and error estimation of the solution are best examined by using different model types (Fig. 2). In the case of shape, for example, the reliability of the features on the solution can be checked by comparing the results obtained with two or more shape supports [star-like, octantoid, subdivision (Viikinkoski et al., 2015)]. This yields better estimates than, e.g., Markov chain Monte Carlo sequences that only investigate random error effects within a single model type.

A particular feature of the model reconstruction from disk-resolved data is that the result is dominated by the target image boundaries rather than the pixel brightness distribution within the target image. This is because the information is contained in the pixel contrast, which is the largest on the

boundary (occultations are special cases of this as they are samples of the boundary contour). This is very advantageous when considering the effect of model errors in luminosity properties (scattering or thermal models): It is sufficient to have a reasonable model, and the result is not sensitive to the parameters  $L$ . Thus, for example, Atacama Large Millimeter Array (ALMA) data can be used for efficient reconstruction even with a very approximate semi-analytical Fourier-series thermal model — more detailed models have hardly any effect on the shape solution (section 3.5) (Viikinkoski and Kaasalainen, 2014; Viikinkoski et al., 2015).

### 3. DATA AND MODELING

We describe all data types that can be used, the various ways of collecting data and their accuracy, the typical number of asteroids for which data exist, and expectations for the future. We also discuss a typical result of inversion — the resolution of the model and how many targets can be modeled (Table 1).

#### 3.1. Photometry

Disk-integrated photometry is, and will always be, the most abundant source of data, because it is available for essentially every single known asteroid. Because asteroid brightness periodically changes with its rotation, frequency analysis of asteroid lightcurves provides asteroid rotation periods — the basic physical property derivable from time-resolved photometry. The regularly updated Asteroid Lightcurve Database of Warner et al. (2009) (available at <http://www.minorplanet.info/lightcurvedatabase.html>) now contains rotation periods and other physical parameters for almost 7000 objects, about half of which have a rotation

TABLE 1. List of observation techniques and derivable physical properties.

Technique	Period	Spin	Size	Shape	Thermal Inertia	Number of Models		
						Asteroids III	Asteroids IV	Asteroids V
Photometry	X	X		X		30	500	$10^4$
Images		X	X	X		5	50	$10^2$
Occultation		X	X	X		$5^*$	50	$10^2$
Radar	X	X	X	X		10	30	$10^2$
Radiometry			X		X	$10^*$	20	$10^4$
Interferometry		X	X	X		$5^\dagger$	<10	$10^2$
Flyby	X	X	X	X	X	6	10	<15

\*Ellipsoidal models.

†HST/FGS.

The “X” indicates which physical properties are derivable from which technique. The number of models available at the time of the *Asteroids III* book (Asteroids III) and now (Asteroids IV) is only approximate. The Asteroids V column is an order-of-magnitude estimate for the next decade.

period that is secure and unambiguous. The role of amateur astronomers in this field is traditionally strong, and growing even stronger with increasing levels of their technical and software equipment. Hundreds of asteroid lightcurves are published quarterly in the *Minor Planet Bulletin*; most of them are then archived in the Asteroid Light Curve Database at the Minor Planet Center site ([http://www.minorplanetcenter.net/light\\_curve2/light\\_curve.php](http://www.minorplanetcenter.net/light_curve2/light_curve.php)) in the ALCDEF standard (Warner et al., 2011). The efficiency of lightcurve production can be increased by dedicated wide-field photometric surveys (e.g., Masiero et al., 2009; Polishook et al., 2012), although the period determination from undersampled lightcurves is often ambiguous (Harris et al., 2012).

For period determination, a single lightcurve covering the full rotation is sufficient. However, a set of such lightcurves observed at different geometries (asteroid illuminated and seen from various directions) is needed to reconstruct the shape and spin state of an asteroid. The *lightcurve inversion* method of Kaasalainen and Torppa (2001) and Kaasalainen et al. (2001) was already reviewed in *Asteroids III* (Kaasalainen et al., 2002a). Since then, the method has been widely used and hundreds of asteroid models have been derived. They are publicly available at the Database of Asteroid Models from Inversion Techniques (DAMIT) (<http://astro.troja.mff.cuni.cz/projects/asteroids3D>). The reliability of the method was proved by comparing its results with independent data such as laboratory asteroid models (Kaasalainen et al., 2005), adaptive-optics (AO) images (Marchis et al., 2006), stellar occultations (Durech et al., 2011), or spacecraft images of asteroids (2867) Šteins (Keller et al., 2010) and (433) Eros (Kaasalainen et al., 2002a).

From disk-integrated photometry alone, only a global shape without any small-scale details can be derived. Because the reflectivity of the surface is not known, the models are not scaled and the information about the size has to come from complementary data. To avoid overinterpretation and artifacts of the modeling, the shapes are usually represented by a *convex* model. This allows working not in the obvious

radius parameter space but instead in the Gaussian image space (describing a convex body by the curvature of its surface). This is less intuitive, but it makes the inverse problem less vulnerable to errors of data and model because of the Minkowski stability (Lamberg and Kaasalainen, 2001): Even if the areas of individual surface facets may change significantly for slightly different datasets, the global convex shape changes very little.

From the practical point of view, we are interested in finding a *unique solution* for the inverse problem. To guarantee this, observations covering a sufficiently wide range of viewing and illumination geometries are needed. For a typical main-belt asteroid, this means observations during several apparitions. For a close-approaching near-Earth asteroid, several months could be sufficient. For more distant objects, we can in principle observe changing lightcurve amplitude because of changing aspect, but this would take many decades. Nevertheless, transneptunian objects (TNOs) and Centaurs can be never observed from Earth at geometry significantly different from opposition, which is not sufficient to reconstruct a unique convex model (Russell, 1906). If the lightcurves observed in various filters are different, there is some spectral/color variegation over the surface, and a crude color map can be reconstructed (Nathues et al., 2005).

A typical outcome of lightcurve inversion is a convex shape model that describes the global characteristics of the real asteroid. It is also easy to obtain nonconvex versions with the general inversion procedures (see section 2), but then one should produce several solutions with various model types and parameters, and be very cautious about the results (Viikinkoski et al., 2015). In general, disk-integrated photometry contains very little information about nonconvexities unless they are very pronounced or observed at very high phase angles where shadowing effects play an important role (Durech and Kaasalainen, 2003). Nonconvex models seldom fit lightcurves better than convex ones simply because the latter typically already fit the data down to noise level. This sets the resolution limit of photometry (see discussion in

Kaasalainen et al., 2001, 2002a; Viikinkoski et al., 2015, and references therein).

The relative accuracy of the sidereal rotation period determined from lightcurves is on the order of  $10^{-5}$  or better, depending mainly on the time span of observations. The direction of the spin axis can be determined with an accuracy from a couple of degrees for the models based on many decades of observations with many dense lightcurves, to more than  $20^\circ$  for models based on limited and noisy data. For asteroids orbiting in the ecliptic plane, the geometry for an Earth-based observer is limited to that plane. Then the disk-integrated brightness of a body with surface described by radius vector  $(x, y, z)$  and pole direction  $(\lambda, \beta)$  in ecliptic coordinates is the same as for a body  $(x, y, -z)$  with the spin axis direction  $(\lambda + 180^\circ, \beta)$  (Kaasalainen and Lamberg, 2006). That is why for a typical main-belt asteroid, there are usually two equally good mirror shape solutions with about the same pole latitude and pole longitude difference of about  $180^\circ$ . This ambiguity can be removed with disk-resolved plane-of-sky projections (e.g., images, stellar occultations; see sections 3.2 and 3.4).

Apart from “classical” lightcurves where the sampling of brightness variations is dense with respect to the rotation period, there are also data that are *sparse in time*. Such datasets typically consist of only a single to a few brightness measurements per night. Provided the whole sparse dataset is internally calibrated, it can be used the same way as a standard lightcurve that would be extremely long and very sparsely sampled (Kaasalainen, 2004). These data are routinely provided by all-sky astrometric surveys with various — usually poor — photometric quality. Current surveys provide data of accuracy scarcely better than 0.1 mag. Given a typical lightcurve amplitude of 0.3 mag, the signal is often drowned in noise and systematic errors. This leads to many physically acceptable models fitting the data to the noise level (Durech et al., 2005). However, the total amount of data is huge and it has been shown that at least for some asteroids, models can be successfully derived from these data or from their combination with dense lightcurves (Durech et al., 2009; Hanuš et al., 2011).

As an example, we show sparse photometry for asteroid (21) Lutetia from the U.S. Naval Observatory (260 points covering 10 years) in Fig. 3 and the period search results in Fig. 4. The best-fit model based on this dataset has the same rotation period and a similar spin-axis direction as the models based on much larger and multiple datasets (Fig. 6).

When using noisy sparse data or only a limited number of data points, a simple shape model of a triaxial ellipsoid is usually sufficient to model the data and to derive the correct period and spin vector orientation (Cellino et al., 2009; Cellino and Dell’Oro, 2012; Carbognani et al., 2012). The advantage of this approach is that the shape is described by only two parameters (axes ratios) and the scanning of the period parameter space is much faster than with general shapes.

The ongoing [Panoramic Survey Telescope and Rapid Response System (Pan-STARRS), Catalina, Gaia] and future [Asteroid Terrestrial-impact Last Alert System (ATLAS),

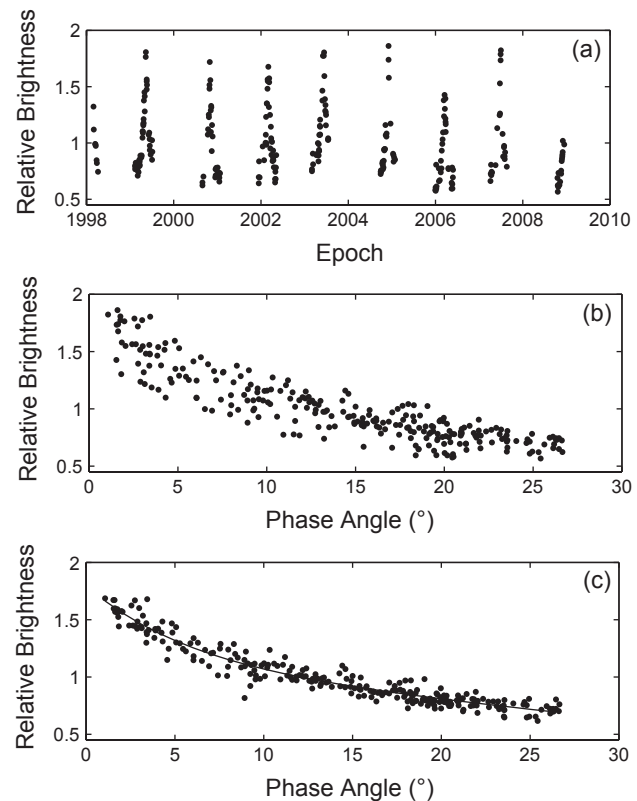


**Fig. 3.** Sparse-in-time photometry of (21) Lutetia obtained at the U.S. Naval Observatory plotted as a function of (a) time and (b) phase angle. The brightness was reduced to the unit distance from Earth and the Sun. The scatter in the phase plot is caused by the intrinsic noise of the data and the rotational and aspect effects. (c) Residuals for the best-fit model (Fig. 6) plotted over the phase curve (solid curve).

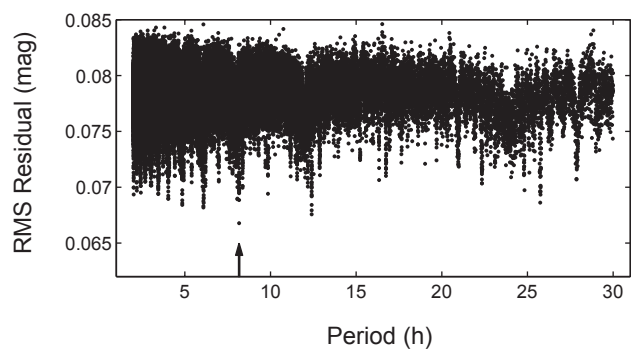


**Fig. 4.** Period search for (21) Lutetia. Each point represents a local minimum in the parameter space to which the optimization algorithm converged. The lowest RMS residual (arrow) corresponds to the best-fit model shown in Fig. 6.

Large Synoptic Survey Telescope (LSST)] surveys will provide new data every night for essentially every known asteroid. Using this data for automated lightcurve inversion with well-mastered treatment of systematic effects,

recognition of the best-fit models, definition of uniqueness of the solution, etc., is the main challenge for the future lightcurve inversion.

### 3.2. Remote Sensing Disk-Resolved Images

The most direct way to obtain information on the shape of an asteroid is to take pictures of it. The apparent shape as visible on the plane of the sky is delimited by the limb and the terminator, and multiple views obtained while the target rotates can fully characterize its three-dimensional shape. However, to resolve the small angular diameter ( $<0.5''$ ) sustained by asteroids, large facilities are required.

In the 1980s, speckle imaging or speckle interferometry provided “the first glimpses of an asteroid’s surface” [i.e., (4) Vesta by *Drummond et al.* (1988)]. This technique is based on the analysis of the speckle pattern in the images of astronomical sources obtained through large telescopes at high magnification power and very short integration time. The aim is to overcome the blurring effects due to the astronomical seeing and to attain diffraction-limited resolution images. Speckle interferometry has been commonly used to study the size, shapes, and surface features of the largest asteroids (*Drummond et al.*, 1985, 1988; *Ragazzoni et al.*, 2000; *Cellino et al.*, 2003). With the launch of the Hubble Space Telescope (HST) in orbit and the first light of the large (10-m class) groundbased telescopes equipped with AO-fed cameras [e.g., W. M. Keck, European Southern Observatory (ESO) Very Large Telescope (VLT), Geminis, Subaru], the importance of speckle interferometry has decreased.

The critical issue in direct imaging is of course the angular resolution. Any image is the result of the convolution of the object on the plane of the sky with the instrument response, the point spread function (PSF). In space, the PSF is stable and corresponds to the diffraction pattern of the telescope. From the ground, the atmospheric turbulence constantly deforms the PSF and blurs the images, hence the need for real-time correction of the PSF by AO. The technical challenges of sending a large telescope to space and of building deformable mirrors explain why the first disk-resolved images in the 1990s were still limited in resolution and only the largest asteroids — (1) Ceres, (2) Pallas, and (4) Vesta — have been imaged. In the decade since *Asteroids III*, numerous studies have been based on direct imaging of asteroids (e.g., *Thomas et al.*, 2005; *Carry et al.*, 2008; *Descamps et al.*, 2008; *Schmidt et al.*, 2009; *Marchis et al.*, 2013).

Both from space or with AO on the ground, however, the contrast and angular resolution can be improved by deconvolution of the image by the PSF. This is particularly true for images acquired from the ground with residuals from nonperfect AO correction. Deconvolution is an ill-posed problem, but robust algorithms adapted to planetary images are available (*Conan et al.*, 2000; *Mugnier et al.*, 2004; *Hom et al.*, 2007) and have been validated on-sky (*Witasse et al.*, 2006). It is nevertheless the most critical part of the post-processing, as an incorrect deconvolution can introduce a systematic error on the apparent size. An example of an

AO image and the reconstructed shape model for asteroid (41) Daphne is shown in Fig. 5.

Current facilities deliver an angular resolution of about 30 to 50 milliarcseconds (mas), depending on the wavelength. The apparent shape can therefore be measured for asteroids with an apparent diameter larger than  $\approx 80$ –100 mas, i.e., a couple of hundred targets. Simulations and observations of known targets such as the satellites of Saturn (*Marchis et al.*, 2006; *Drummond et al.*, 2009; *Carry*, 2009) have shown that a precision of a few milliarcseconds can be derived on the two-dimensional profile on the plane of the sky, corresponding to only a few kilometers for main-belt asteroids. With upcoming large telescopes (30+ m, such as the Thirty Meter Telescope or the European Extremely Large Telescope), the angular resolution will be improved by a factor of 3–4, providing more than 500 targets. Second-generation instruments with extreme AO foreseen on these telescopes should allow the observation of about 7000 asteroids, with sizes of only a few kilometers (*Merline et al.*, 2013).

Using disk-resolved images, giant craters have been discovered (*Thomas et al.*, 1997; *Conrad et al.*, 2007), ambiguity in spin solutions have been solved (*Marchis et al.*, 2006; *Carry et al.*, 2010a), albedo maps have been constructed (*Li et al.*, 2006; *Carry et al.*, 2008), convex three-dimensional shape models from lightcurves have been set to scale (*Hanuš et al.*, 2013a), and full three-dimensional shape models have been determined (*Carry et al.*, 2010b; *Descamps et al.*, 2011).

### 3.3. Flybys

Asteroid imaging and mapping *in situ* is essentially an extreme example of disk-resolved images. The modeling in such cases is more a cartographic than an inverse problem as the data are abundant, directly usable (containing identification points on the surface, etc.), and high-resolution (there is no ill-posedness). However, asteroid flybys, during which roughly half the target is likely to remain unseen (not visible and illuminated), pose a special problem: how to see the dark side. The principle here is to use the high-resolution map of the nearside, constructed with a number



**Fig. 5. (a)** Deconvoluted adaptive optics image of asteroid (41) Daphne; **(b)** corresponding image of the reconstructed model (projection of the octantoid model from Fig. 2). The model is shown under artificial illumination that enhances its three-dimensional shape and is different from the simple light-scattering model used for the inversion. The AO image has resolution of 10 mas/pixel. The model was reconstructed from 14 AO images obtained with the ESO VLT and several lightcurves.

of methods of photoclinometry, photogrammetry, and image fitting (Preusker et al., 2012; Gaskell et al., 2008; Jorda et al., 2012), as a constraint in the otherwise same multi-mode inverse problem as with groundbased observations. The procedure is described in Kaasalainen and Viikinkoski (2012); with it, reconstructions of the dark side, such as those of (2867) Šteins (Keller et al., 2010) or (21) Lutetia (Sierks et al., 2011) (see also Fig. 6), are more detailed than from, e.g., lightcurves alone. This is because half the target is accurately reconstructed, with practically no error margin, and therefore the fluctuation margin of the darkside is considerably smaller as well.

### 3.4. Stellar Occultations

The observation of a stellar occultation consists in recording the duration of the disappearance of a star behind the asteroid. Knowing the apparent motion of the asteroid on the plane of the sky, obtained from its ephemeris, this duration can be converted in a physical length on the disk

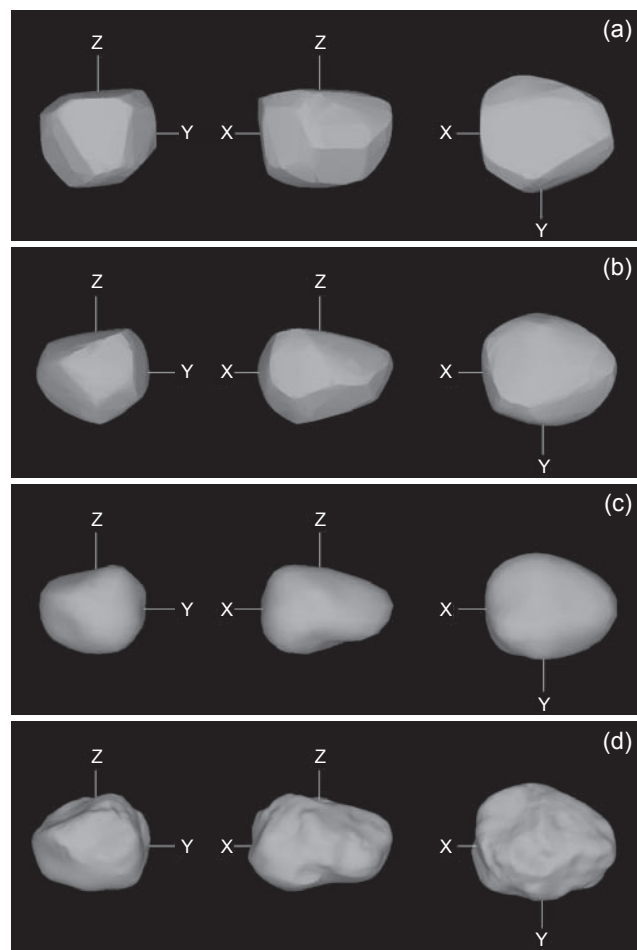


**Fig. 6.** Different shape models for (21) Lutetia derived from different sets of data. The level of detail increases with more data: **(a)** sparse photometry (section 3.1), **(b)** dense lightcurves (Torppa et al., 2003), **(c)** lightcurves and AO (Carry et al., 2010b), and **(d)** Rosetta flyby (Sierks et al., 2011).

of the asteroid, called a chord. Provided several observers record the same event from different locations on Earth, the two-dimensional profile of the asteroid is drawn on the plane of the sky (Millis and Dunham, 1989). The main difference with disk-resolved imaging resides in the profile, made by only the limb for occultations, and the limb + terminator for imaging. Both techniques provide the two-dimensional profile of the target as projected on the plane of the sky at the epoch of observations (Fig. 7).

Disk-resolved imaging and stellar occultation are, however, radically different in terms of facilities, data processing, potential targets, reproducibility, and achievable precision. For stellar occultations, the properties of the occulted star generally matter more than the actual target: the asteroid. If the occulted star is bright enough, its occultation, even by a very small asteroid, can be detected with small-aperture telescopes. This is of course the main advantage of stellar occultations, where the apparent size and shape of potentially any asteroid can be measured. Moreover, this technique can also be successfully used for distant TNOs, which have angular sizes too small to be resolved by imaging (Sicardy et al., 2011). In practice, however, a given asteroid will seldomly occult bright stars. Measurements are thus hard, if not impossible, to reproduce.

Stellar occultations are nevertheless extremely valuable. The accuracy of the timing is dictated by time-series

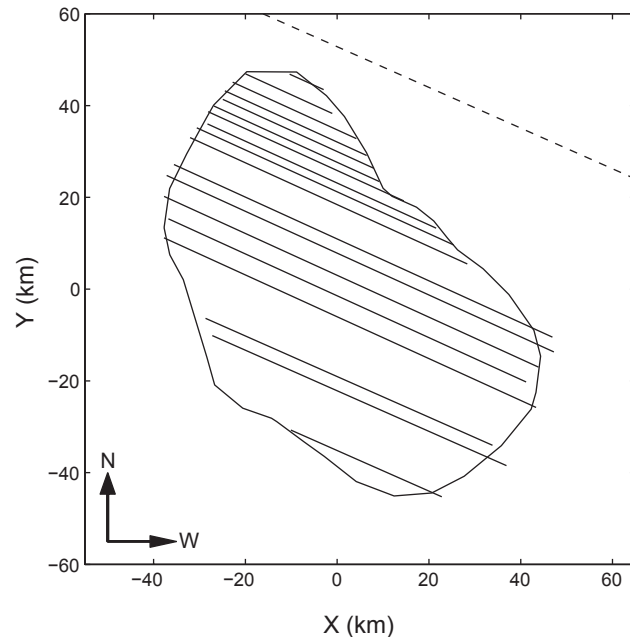


**Fig. 7.** An example of a well-covered occultation that provides almost an “image” of the projected asteroid (135) Hertha (Timerson et al., 2009). The model of Hertha based on its lightcurves and occultation data is overplotted. The dashed line is a negative observation constraining the northern part of the model’s projection. Formal timing uncertainties are between 0.02 and 0.2 s, corresponding to 0.12–1.2 km in the projection, which is below the resolution of the model. The RMS of the fit is 1.9 km.

photometry, and can therefore be extremely precise. An uncertainty of 50 ms in timings converts into only a 300-m uncertainty in the length of the chord, typical for a main-belt asteroid (at 1.5 AU from Earth with an apparent motion of  $10''/h$ ). The main source of uncertainty is, however, the absolute timing of each chord, required to align them on the plane of the sky. Occultations observed by the naked eye suffered from the fact that the absolute timing was poor. Since a decade ago, thanks to the availability of low-cost positioning and timing systems [e.g., the Global Positioning System (GPS)], stellar occultations are becoming more and more valuable.

The main contributors to the field are currently amateur astronomers: For a given event, observers have to move to set themselves on the predicted occultation path on Earth. Small-aperture ( $<20$  cm) mobile stations are therefore ideal for recording stellar occultations. Because of the uncertainties of the star and asteroid positions on sky, there is generally an uncertainty of a few tens of kilometers in the location of the occultation path on Earth, requiring observers to spread over a large area to cover the event. This usually prohibits dense coverage of the asteroid profile. When only a couple of chords are available, the event provides limited information on the size, and little if any on the shape. Current occultation predictions of sufficient accuracy concern only stars in the Hipparcos catalog and large (at least tens of kilometers) asteroids. With the upcoming publication of the European Space Agency (ESA) Gaia stellar catalog and update of asteroid orbits, this uncertainty about position is expected to drop significantly, making future occultations easier to predict, and therefore observe (Tanga and Delbo, 2007).

Overall, stellar occultations can provide precise measurements of the size and shape of an asteroid, as projected on the plane of the sky. However, events are rare for a given target. Occultations are therefore very valuable in combined datasets, e.g., to set scale to otherwise dimensionless three-dimensional shape models (e.g., Ďurech *et al.*, 2011; Hanuš *et al.*, 2011). From almost 2500 occultations compiled by Dunham *et al.* (2014), there are about 160 “good” ones that allow a reliable determination of an asteroid’s size and about 40 “excellent” ones that show details regarding an asteroid’s profile.

### 3.5. Interferometry

Inferometry is another technique that can be used to overcome the limitations of small angular sizes of asteroids, in order to measure their sizes, shapes, and the possible presence of satellites. An astronomical interferometer coherently combines (i.e., conserving phase information) the light from two or more apertures of the same telescope or of distinct telescopes spaced by a distance  $B$ . The spatial resolution (in radians) is on the order of  $\lambda/B$  where  $\lambda$  is the wavelength.

In the following, we give a basic introduction to interferometry of asteroids. Further details can be found in the following works: Jankov (2010) and Matter *et al.* (2013) for a broad introduction to astronomical optical interferometry,

methods and instrumentation; Delbo *et al.* (2009) for a description of the techniques, and the models for deriving the size and basic shape proprieties of asteroids from the ESO Very Large Telescope Interferometer (VLTI) MID-infrared Interferometric instrument (MIDI) data; Carry *et al.* (2015) for an extension of the technique of Delbo *et al.* (2009) to the determination of the sizes and the separation of binary asteroids; and Matter *et al.* (2011) for a description and the extension of a thermophysical model to the analysis of interferometric data of asteroids with the aim of obtaining surface properties such as the thermal inertia.

Interferometers measure the coherence function of the source, also called the interferometric visibility, which is given by the ratio between the correlated and total flux. The correlated flux is the amount of flux in the interferometric fringes. More precisely, the correlated flux is the Fourier transform of the brightness distribution of the source measured on the interferometer’s baseline projected on the plane of the sky (e.g., see Delbo *et al.*, 2009, and references therein).

The Fine Guidance Sensors (FGS) onboard the Hubble Space Telescope (HST) are optical white-light shearing interferometers (Nelan *et al.*, 1998) that combine the light from distinct apertures of the HST primary mirror and have been used to measure the size and basic shape properties of asteroids (Hestroffer *et al.*, 2002; Tanga *et al.*, 2003). HST/FGS data have clearly demonstrated the bi-lobed nature of some bodies such as (216) Kleopatra (Tanga *et al.*, 2001) and (624) Hektor (Tanga *et al.*, 2003), but were not able to detect the presence of the little moons orbiting these asteroids (Descamps *et al.*, 2011; Marchis *et al.*, 2014), due to the large-magnitude difference between the asteroids and their respective moons. Despite the impressive angular resolution of a few milliarcseconds, corresponding to a few kilometers at a distance of 1.2–1.5 AU, a clear limitation of HST/FGS asteroid studies is the bright limiting magnitude of the instrument of about  $V \sim 13\text{--}14$  mag (Tanga *et al.*, 2003). A recapitulation of the HST/FGS asteroids results can be found in Dotto *et al.* (2002).

Groundbased interferometry is limited to observation of bright targets because of the requirement to take exposures shorter than the atmospheric coherence time of a few milliseconds. The limiting magnitudes of groundbased long-baseline interferometers and the intrinsic low surface brightness of asteroids have prevented the use of these instruments for the studies of small solar system bodies until the availability of the VLTI.

Interferometry in the mid-infrared was proven to be also very sensitive to the global shape of asteroids as well as their surface characteristics (Matter *et al.*, 2011, 2013). In particular, since observations are typically carried out in the thermal infrared (8–13  $\mu\text{m}$ ), MIDI data are sensitive to the surface temperature distribution, which is strongly affected by the value of the thermal inertia (see the chapter by Delbo *et al.* in this volume).

Figure 8 shows the visibility and the total flux as a function of the angular diameter of an asteroid at 2.5 AU from the Sun and at 1.5 AU from Earth, where 1 mas roughly

corresponds to 1 km on the asteroid. Note that main-belt asteroids smaller than  $\sim 20$  km cannot be easily observed with MIDI at the VLTI. There are about 1000 known asteroids  $< 20$  km in diameter, implying that interferometry is potentially an interesting technique for shape modeling. On the other hand, as interferometry in the thermal infrared is sensitive to the spatial distribution of the temperature on the asteroid surface, this technique can be used to determine thermophysical properties of asteroids when the body shapes are known, as demonstrated by Matter *et al.* (2011, 2013).

Each VLTI baseline can only be used one at a time with MIDI. MIDI will likely be decommissioned in the near future, to be replaced after 2016 by the Multi AperTure mid-Infrared SpectroScopic Experiment (MATISSE). This instrument will combine up to four unit telescopes (UTs) or auxiliary telescopes (ATs), allowing six simultaneous baselines. This feature will enable measurement of the spatial distribution of the infrared flux along different directions. MATISSE will also measure closure phase relations and thus offer an efficient capability for image reconstruction. In ad-

dition to the N band, the MATISSE will also operate in the L and M bands. Unfortunately, MATISSE is not expected to be any more sensitive than MIDI.

Another second-generation instrument at the VLTI, GRAVITY, will combine the light from all four UTs, offering further improvements in spatial resolution compared to MIDI and MATISSE (although with more a more stringent  $V \leq 11$  limiting magnitude). It will provide near-infrared AO-assisted precision narrow-angle ( $\sim 4''$ ) astrometry at the 10  $\mu\text{as}$  level in the K band (2.2  $\mu\text{m}$ ). Both the reference star and the science object have to lie within the  $\sim 4''$  field of view. In imaging mode, GRAVITY can achieve a resolution of  $\sim 3$  mas in the near-IR (Eisenhauer *et al.*, 2008). The imaging mode can be used to precisely measure the sizes and the orbits of the satellites of large asteroids, the latter with  $V \leq 11$  mag.

AMBER is the current near-infrared focal instrument of the VLTI. It operates in the J, H, and K bands (i.e., from 1.0 to 2.4  $\mu\text{m}$ ). The AMBER limiting magnitude for asteroid observations is  $V \sim 9$  mag. There are only a handful of asteroids brighter than this limit. These bodies are also the largest ones with angular extensions generally  $> 100$  mas, implying a very low visibility in the J-H-K with the UT baselines. Although the photometric flux of these few asteroids is such that  $H < 7.5$  mag, their correlated magnitudes due to the low visibilities are much higher than 7.5 mag, preventing their fringe detection and tracking in the near-IR.

However, one of the most interesting instruments for asteroid groundbased interferometry is the Large Binocular Telescope Interferometer (LBTI). It consists of two 8.4-m telescopes mounted side by side in a single mount, with a 14.4-m center-to-center spacing. This configuration offers a unique capability for interferometry of a Fizeau beam combination. This offers a wide field of view ( $\sim 10\text{--}20''$ ) and low thermal background. For example, the LINC-NIRVANA instrument can — in principle — be able to resolve binary asteroids whose components are separated  $> 20$  mas. This will allow splitting many binary asteroids.

Another important source of interferometric data in the near future is ALMA. It will provide resolution  $\sim 5$  mas at 0.3 mm and a dense mesh of baselines, thus enabling “imaging” of hundreds of asteroids in the main belt (Busch, 2009). A useful feature of the multimodal inversion is that the raw ALMA (and any other interferometric) data can be used directly as the original Fourier transform: There is no need to reconstruct the image estimate. Furthermore, the reconstruction of the overall shape is insensitive to inaccuracies and uncertainties in the thermal model used because the model is determined mainly by the boundary of the projection; the distribution of brightness inside the boundary is much less important (Viikinkoski and Kaasalainen, 2014; Viikinkoski *et al.*, 2015). An example of inversion of simulated ALMA data is shown in Fig. 9.

Long-baseline interferometry can also represent a novel approach to determine the masses and the densities of asteroids in a range of sizes and distances never studied before. In particular, modern interferometers such as the VLTI, LBTI, and Magdalena Ridge Observatory Interferometer can

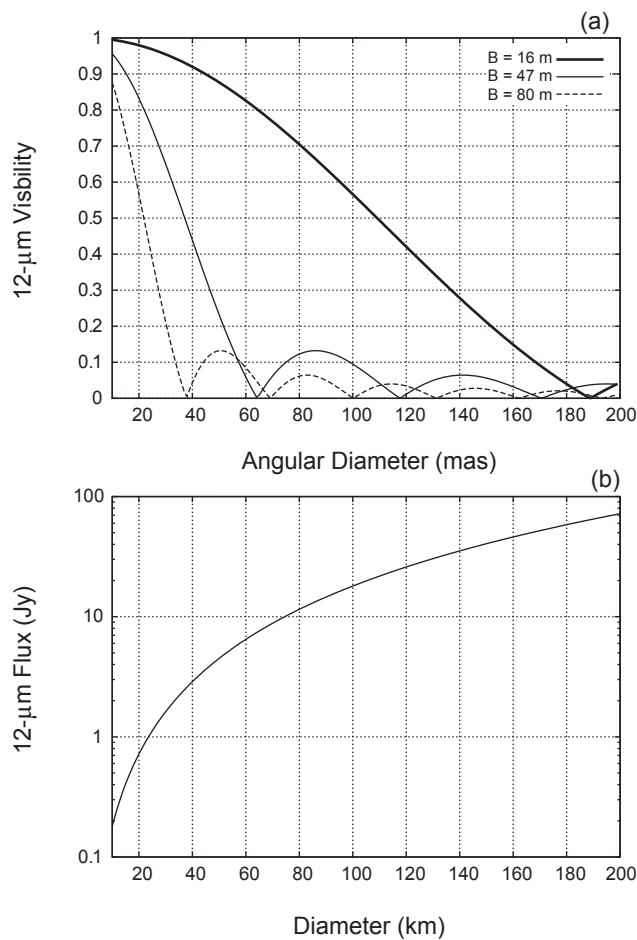


**Fig. 8.** (a) Visibility and (b) total flux for an asteroid at 2.5 AU from the Sun and 1.5 AU from Earth as a function of its diameter for different values of the baseline. The MIDI limiting correlated flux (flux times visibility) is 0.5–1 Jy and 10–20 Jy for the UTs and ATs respectively. Similar limiting fluxes are expected for MATISSE. See text for further details.

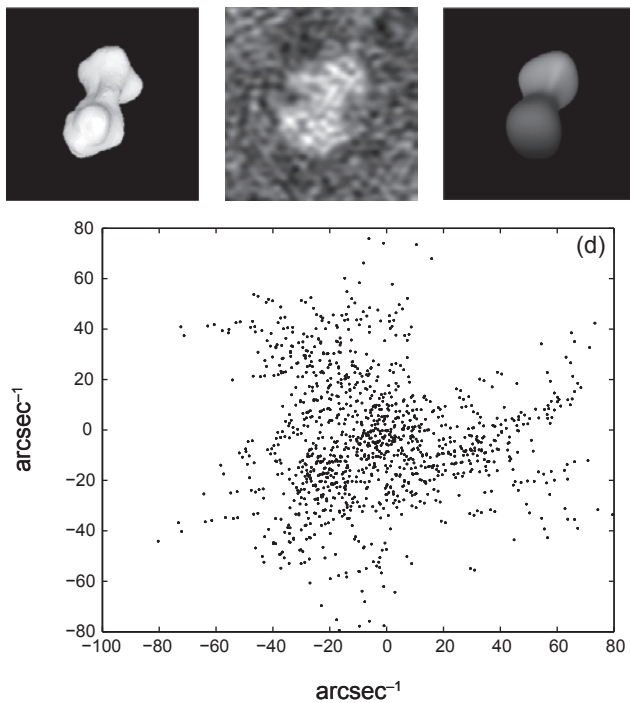


**Fig. 9.** Simulated infrared flux from an asteroid **(a)** radar shape model of Kleopatra by Ostro *et al.* (2000) and **(b)** a “dirty image” with atmospheric noise, obtained by transforming the incompletely sampled frequency plane **[(d)]**, 6000 points, 50 antennas]. The smallest resolvable detail is approximately 10 mas. Provided enough observations at different geometries are available (here eight observation runs were used), a shape model **[(c)]** can be constructed directly from the raw interferometric data.

spatially resolve binary asteroids discovered by photometric lightcurves in the main belt (Carry *et al.*, 2015). The separation of the components of these systems is too narrow for traditional observational techniques such as AO used with 10-m-class telescopes.

### 3.6. Direct Size Measurement with Gaia

The ESA Gaia mission, whose operations started in 2014, will provide accurate astrometry and photometry of asteroids. Photometric data can be used the same way as sparse photometry from groundbased observatories (section 3.1). The potential of Gaia-like data was demonstrated by Cellino *et al.* (2009) on data from the Hipparcos satellite. Apart from disk-integrated brightness, Gaia will provide also direct measurements of asteroid sizes, in a way very similar to interferometry. Being designed as an astrometry mission at the microarcsecond level, the PSF of Gaia is accurately known and stable. Deviations of the PSF from that of a point-like source can thus be measured and used to estimate the apparent size of asteroids.

Owing to the amount of sources observed by Gaia, the satellite does not download images to Earth, but only

one-dimensional flux profiles, corresponding to small two-dimensional windows centered on targets, stacked along one direction, similar to interferometry in that respect. Interpretation of this one-dimensional profile relies therefore on the *a priori* knowledge of the two-dimensional flux distribution on the plane of the sky. In the creation of the Gaia catalog, this will be done iteratively, starting from simple spheres at zero phase angle to finally the spin and triaxial ellipsoid solutions determined otherwise from Gaia photometry (Mignard *et al.*, 2007; Cellino *et al.*, 2007).

These measurements represent a great opportunity for multi-data inversion algorithms: The measurement of the extension is direct, but clearly requires a realistic description of the projected shape on the plane of the sky. Considering Gaia specifications and observing geometry, Mignard *et al.* (2007) have estimated the fraction of asteroids for which one-dimensional dimension will be measured with a precision better than 10%. This fraction is highly dependent on diameter, and 20% of asteroids between 20 and 30 km will be measured at least once, while all asteroids larger than  $\sim 80$  km will be measured repeatedly.

### 3.7. Disk-Integrated Radiometry

Measurements of asteroids emission in the thermal infrared — in general at wavelengths between 4–5 and 20–30  $\mu\text{m}$  — are mostly used to determine the sizes of these bodies (Delbo and Harris, 2002; Harris and Lagerros, 2002; see also the chapters by Mainzer *et al.* and Delbo *et al.* in this volume). Groundbased telescopes can only observe in specific windows of the electromagnetic spectrum where the atmosphere is relatively transparent: i.e., the L, M, N, and Q bands at 3, 5, 10, and 20  $\mu\text{m}$ , respectively. However, such observations are strongly affected by the variability of the transparency of the atmosphere and its thermal background. The background also receives contribution from the telescope and the optics. Hence, the thermal infrared observation of asteroids from the ground is limited to relatively bright asteroids ( $V \leq 18$  mag with 10-m-class telescopes). Absolute calibration of the flux is rarely better than 5–10%. On the other hand, in space the instrument calibration is usually stable and there is no need to reduce the thermal background from the atmosphere. As a consequence, spacebased telescopes such as Spitzer can observe much fainter and smaller asteroids (Mommert *et al.*, 2014), with uncertainties in the calibration that can reach  $\sim 1\%$  error. Also, from space the range of the observational wavelength is limited only by the detector technology, typically  $\sim 3.5$ – $50$   $\mu\text{m}$ . At longer wavelengths, the telescope optics require cooling and the observation of faint objects is confronted with the background from solar system dust cloud and infrared cirrus.

In the *Asteroids III* era, the main source of thermal infrared observations of asteroids has been the Infrared Astronomical Satellite (IRAS) Minor Planet Survey, which collected observations of more than 2200 asteroids (Tedesco *et al.*, 2002). Since then, the NASA Wide-field Infrared Survey Explorer (WISE) has observed more than 130,000 main-belt asteroids

(*Masiero et al.*, 2011, 2012; see also the chapter by Mainzer et al. in this volume), about 500 near-Earth asteroids (*Mainzer et al.*, 2011, 2012a,b), about 1100 Hilda asteroids (*Grav et al.*, 2012a), and almost 2000 Jupiter-Trojan asteroids (*Grav et al.*, 2011, 2012b) in four infrared wavelengths at 3.4, 4.6, 12, and 22  $\mu\text{m}$ ; the AKARI space telescope observed more than 5000 asteroids during its mission (*Usui et al.*, 2011, 2013; *Hasegawa et al.*, 2013); the Spitzer space telescope observed hundreds of asteroids (e.g., *Emery et al.*, 2006; *Trilling et al.*, 2010; *Licandro et al.*, 2012); and the Herschel Space Observatory, due to its longer wavelengths, spanning 55–671  $\mu\text{m}$ , was primarily used to observe transneptunian objects (*Müller et al.*, 2010). For a review of all these missions and their results, see the chapter by Mainzer et al. in this volume.

The thermal infrared spectrum of asteroids carries information about their size and surface properties, such as the thermal inertia, roughness, and emissivity. These properties are typically derived by interpreting thermal infrared data by means of thermal models (*Delbo and Harris*, 2002; *Harris and Lagerros*, 2002; chapters by Mainzer et al. and Delbo et al. in this volume). The “simple” thermal models that assume a spherical shape, a Lambertian emission of the surface, and a simplified calculation of the surface temperature distribution are used when we lack knowledge of the asteroid global shape, spin vector, and rotation period, which is the majority of the cases. Widely used are, for example, the Near-Earth Asteroid Thermal Model (*Harris*, 1998) or the Standard Thermal Model (*Lebofsky et al.*, 1986).

However, in order to derive the thermal inertia of an asteroid from measurements of its thermal infrared emission, more sophisticated models, called thermophysical models (TPMs), are needed (*Spencer*, 1990; *Spencer et al.*, 1989; *Lagerros*, 1996, 1997, 1998; *Rozitis and Green*, 2011; *Müller*, 2007; *Delbo*, 2004). Such models are used to calculate the temperature distribution over the body’s surface as a function of different parameters, including the thermal inertia. In these models, the asteroid shape is usually fixed and is modeled as a mesh of planar facets. The temperature of each facet is determined by numerically solving the one-dimensional heat diffusion equation using assumed values of the thermal inertia, with the boundary condition given by the time-dependent solar energy absorbed at the surface of the facet (for a review, see the chapter by Delbo et al. in this volume). This latter quantity is calculated from the heliocentric distance of the asteroid, the value assumed for the albedo, and the solar incident angle. Macroscopic surface roughness is usually modeled by adding hemispherical section craters of variable opening angle and variable surface density to each facet. Shadowing and multiple reflections of incident solar and thermally emitted radiation inside craters as described by *Spencer* (1990), *Emery et al.* (1998), *Rozitis and Green* (2011), and *Lagerros* (1998) are taken into account. Heat conduction is also accounted for within craters (*Spencer et al.*, 1989; *Spencer*, 1990; *Lagerros*, 1996; *Delbo*, 2004). Surface roughness can be adjusted by changing the opening angle of the craters, the density of the crater distribution, or

a combination of both (*Müller*, 2007). The total observable thermal emission is calculated by summing the contributions from each facet visible to the observer. Model parameters are adjusted until the best agreement with observational data is obtained, i.e., the least-squares residual of the fit is minimized, thereby constraining the physical properties (albedo, size, macroscopic roughness, and thermal inertia) of the asteroid.

From the point of view of multi-data inversion, however, the optimization of thermophysical parameters as described above is a two-step process: First, the spin and shape model is derived from one data type (photometry, radar, etc.), then this model is fixed and used for deriving thermophysical parameters from another data type (thermal infrared). This approach lacks the possibility of weighting the two data types with respect to each other. Moreover, the thermophysical parameters can be very sensitive to small modifications of the input shape and spin, so various modifications of the shape should be tested to see how stable the solution is (*Hanuš et al.*, 2015). Ideally, one should model shape and spin parameters together with thermal parameters. This multi-data approach using lightcurves and thermal infrared data simultaneously was successfully tested by *Durech et al.* (2012, 2014), and in principle it can also be used with data that are sparse in time.

### 3.8. Radar

Radar observations that measure the distribution of echo power in time delay and Doppler frequency (so-called range-Doppler or delay-Doppler measurements) are discussed in detail in *Ostro et al.* (2002) and in the chapter by Benner et al. in this volume. The delay-Doppler projection is many-to-one mapping of a three-dimensional surface of the target into a two-dimensional “image.” Each pixel on the image represents a bin containing integrated echo power from surface elements that have the same distance from the radar and the same relative speed (due to the rotation of the asteroid). From the point of view of inversion, images in the range-Doppler plane are generalized projections that can automatically be handled with the general procedure discussed in section 2 and in detail in *Viikinkoski and Kaasalainen* (2014) and *Viikinkoski et al.* (2015). In this approach, the multi-mode reconstruction is tuned to produce models with intermediate-scale resolution ( $\sim 1/10$  of the diameter) since these are computationally inexpensive (can be obtained in a few minutes with a laptop), and data sources other than radar do not contain more detailed information. An example of radar range-Doppler data of asteroid 2000 ET<sub>70</sub> is shown in Fig. 10 and the corresponding reconstructed shape model in Fig. 11. If detailed radar data are available, such models can then be further refined (*Naidu et al.*, 2013) with the radar techniques described in the chapter by Benner et al. in this volume.

Due to the steep decrease of echo power with the distance to the object (the fourth power of the distance), asteroids imaged by current radar facilities Arecibo and Goldstone are only close-approaching near-Earth asteroids or the largest

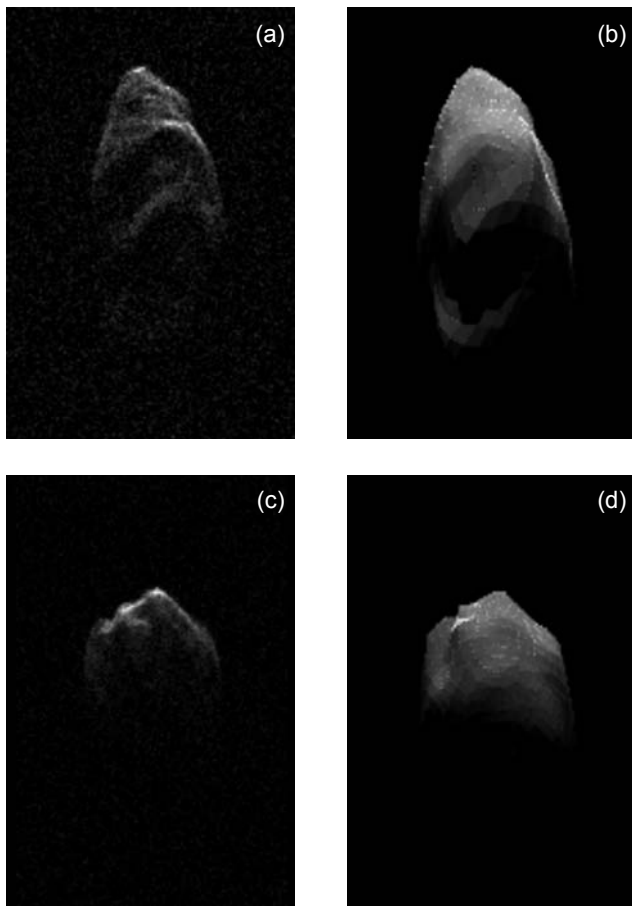


**Fig. 10.** (a), (c) Example range-Doppler radar images of asteroid 2000 ET<sub>70</sub> observed at Arecibo observatory (Naidu *et al.*, 2013). Range and frequency resolutions are 15 m and 0.075 Hz, respectively. Range increases toward the bottom, Doppler frequency increases to the right. (b), (d) The simulated images correspond to the reconstructed shape model in Fig. 11.

members of the main belt. A number of examples of what can be reconstructed from radar data is given in the chapter by Benner *et al.*

### 3.9. Asteroid Interior

We briefly discuss here the interesting possibility of peering into an asteroid. This is somewhat separate from the remote sensing framework as the data can only be obtained *in situ*; on the other hand, such data can be acquired with future space missions. The most practical option is to plant radio transmitters/receivers on the surface of a kilometer-sized asteroid and measure low-frequency ( $\sim$ 100 MHz) signals between these devices and an orbiter when the signals pass through the interior of the target.

The most robust observables are simply signal travel-time data (Pursiainen and Kaasalainen, 2013). These allow an efficient formulation of the inverse problem via the refraction index and are relatively insensitive to noise and model error.

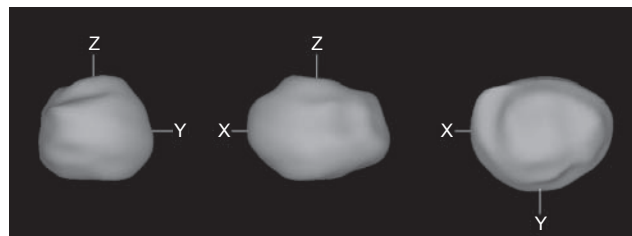


**Fig. 11.** Shape model of the asteroid 2000 ET<sub>70</sub> reconstructed from Arecibo and Goldstone delay-Doppler radar images with ADAM (section 3.11).

Nevertheless, they suffice to give a coarse-scale picture of the general distribution of permittivity inside the asteroid, as well as the locations and sizes of large anomalies (sudden low- or high-density regions such as voids or heavier minerals). This approach has also been robustly tested in laboratory conditions (Pursiainen and Kaasalainen, 2014b). A more refined possibility is to measure changes in the pulse profile, although this is more prone to errors (Pursiainen and Kaasalainen, 2014a). The interior of the asteroid is practically impossible to model accurately in three dimensions since it is supposed to have a number of cracks, voids, discontinuities, etc., all refracting and reflecting the radio waves in complicated ways. Thus a very robust scheme is essential for extracting the available information with stability. Regardless of the data type, one or two transmitters on the surface are not sufficient for a unique solution. A tetrahedral configuration of four transmitters would be ideal, but this places heavy demands on the payload design.

### 3.10. Extension of the Model

So far, we assumed that the asteroid can be described as a solid single body with constant spin vector, i.e., rotating along the axis with the maximum moment of inertia with a constant rotation rate. Although this model represents a typical asteroid, there are other configurations that can be also treated with an extension of the simple model.

**3.10.1. Binaries.** Binary asteroids form a significant part of the population of small asteroids. Pravec *et al.* (2006) estimated that the fraction of binaries is 15% for the near-Earth population and a similar fraction is assumed for the main-belt population in the same size range (see chapter by Margot *et al.* in this volume). The formation, dynamics, and physical properties of binary and multiple asteroid systems are discussed in detail in other chapters of this volume (Walsh *et al.*, Margot *et al.*). In general, modeling of such systems is more complex because the dynamics have to be taken into account. However, in some cases described below, the technique used for modeling single asteroids can be used also for multiple systems or at least their primary components.

For binary (or multiple) systems where the primary component is much larger than the satellite, the photometric signal from the satellite can be neglected and the primary can be

modeled as a single body. For such systems, the shape of the primary and the constraints on its gravitational quadrupole  $J_2$  from the orbit analysis of the secondary can be used to investigate the distribution of the density (Berthier et al., 2014; Takahashi and Scheeres, 2014).

For systems with comparable sizes, the problem becomes complicated when the system is asynchronous, i.e., when the rotation period of the primary is different from the orbital period of the secondary. Such systems are usually modeled as two ellipsoids (Scheirich and Pravec, 2009), although more general models were created from radar observation [e.g., 1999 KW<sub>4</sub>; see Ostro et al. (2006)].

Fully synchronous binaries can be approximated by single bodies if the separation of their components is not large. Even a convex model can provide a good fit to the lightcurves (Durech and Kaasalainen, 2003). Such a model does not represent the true configuration of the system, of course, but it provides the correct rotation period and orientation of the orbital plane.

When the separation of components is larger, the system has to be modeled as a two-component system. However, from the modeling point of view, it is just a moderate modification of the nonconvex problem, where the system is described by only one rotation/orbital period and orientation of the normal of the orbital plane (parallel to the spins of the bodies). If the model is based on lightcurves only, the spin and period parameters can be reconstructed accurately, but the uncertainty in shapes is large. As has been shown by Marchis et al. (2014) on (624) Hektor, the distinction between a highly nonconvex single body, two bodies in contact, or two bodies orbiting each other is difficult to make.

An example of reconstruction of a doubly synchronous binary system (90) Antiope from lightcurves and occultations is shown in Fig. 12, where the model is shown together with the silhouettes from occultations. Tens of chords observed during the occultation in 2011 (Colas et al., 2012) portray the two components to details unattainable by any other observational technique, and the large set of lightcurves observed over many apparitions constrains the rotational parameters. A similar model can be obtained by using lightcurves separately to create a scale-free model that is then scaled by occultation data [the Shaping Asteroids with Genetic Evolution algorithm (Bartczak et al., 2014)]. However, this two-step approach lacks the advantages of simultaneous inversion, where the two data types can be weighted with respect to each other.

### 3.10.2. Yarkovsky-O'Keefe-Radzievskii-Paddack (YORP) effect.

As described in detail in the chapter by Vokrouhlický in this volume, the rotation state of small asteroids is affected by the anisotropic recoil of scattered sunlight and thermal radiation, which causes a net torque called the YORP effect. This effect secularly changes the obliquity of the spin vector and the rotation period. Whereas the former is too small to be measured with current data, the latter has been measured on several asteroids (see Table 3 in the chapter by Vokrouhlický in this volume). If the change of the rotation period is larger than the uncertainty of the period, the

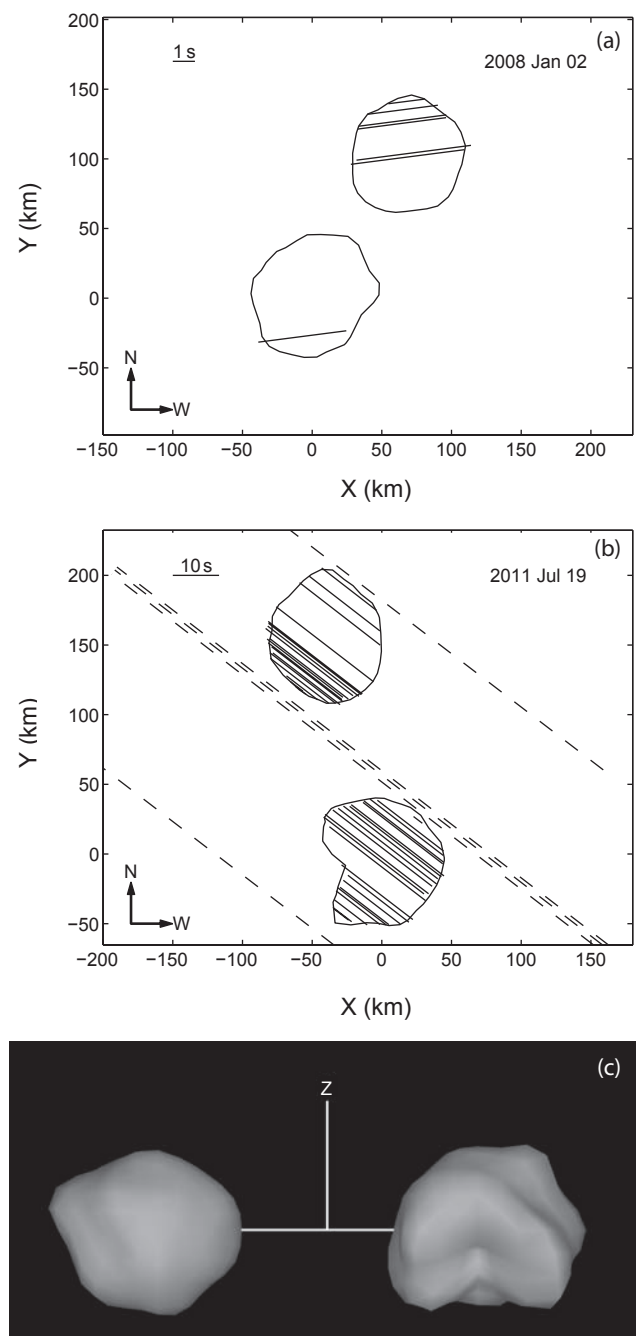


**Fig. 12.** Occultations of (90) Antiope observed in (a) 2008 and (b) 2011. The model silhouette is projected on the plane of the sky; solid lines are positive chords, dashed lines are negative observations. (c) Shape model of (90) Antiope seen from its equator reconstructed from lightcurves and the 2008 and 2011 occultations.

change can be traced from apparition to apparition, as was the case for (54509) YORP (Lowry et al., 2007). In other cases, the effect was much smaller and it revealed itself by the discrepancy between the data and the model, assuming the period to be constant (Kaasalainen et al., 2007; Durech et al., 2008, 2012; Lowry et al., 2014).

The YORP effect is easy to include in the model. We assume that the rotation rate  $\omega$  changes linearly in time  $t$  as  $d\omega/dt = v$ . Then the parameter  $v$  is another free parameter of the modeling. Because the shift in the rotation phase increases quadratically in time as  $\phi = \omega t + 1/2vt^2$ , even small changes  $d\omega/dt$  on the order of  $10^{-8}$  rad/d $^2$  can be detected with datasets covering tens of years.

In principle, the measured value of  $v$  can be compared with the theoretical value computed from the spin state, shape, size, and thermal parameters of the surface with the density as a free parameter. However, due to the sensitivity of YORP on small-scale details of the shape that are far below the resolution of the model (Statler, 2009; Kaasalainen and Nortunen, 2013), as well as the problem of transverse heat diffusion (Golubov and Krugly, 2012; Golubov et al., 2014; Ševeček et al., 2015), this can hardly be more than a rough comparison.

Because the YORP effect scales as the inverse of the square of the size of the asteroid, it becomes more important for small bodies, where it might be necessary to include it in the modeling if the data cover a wider span of time. YORP is assumed to play an important role in many dynamical processes — e.g., the distribution of rotation periods and spin obliquities of small asteroids (Pravec et al., 2008; Hanuš et al., 2013b) or the creation of asteroid binaries and asteroid pairs (Pravec et al., 2010). It is important to have more asteroids with YORP detection. Better statistics of values of period change will help to constrain theories of the YORP evolution of small asteroids.

**3.10.3. Excited rotation.** Asteroids rotating in the relaxed mode are fully described by the spin axis direction, rotation rate, and initial orientation. However, some asteroids are in an excited rotation state, which can be described as a rotating free top. More parameters are needed to describe this tumbling motion (Kaasalainen, 2001). The reason why some asteroids are in this state can be (1) primordial, (2) collisional excitation (Henych and Pravec, 2013), or (3) end state of YORP-driven spindown. The approach to the modeling is in principle the same as for asteroids in principal axis rotation, only the orientation for a given time is given by solving differential equations. From lightcurves, models of asteroids 2008 TC<sub>3</sub> (Scheirich et al., 2010) and (99942) Apophis (Pravec et al., 2014) have been derived. A model of asteroid (4179) Toutatis (Hudson et al., 2003) was derived from radar data and lightcurves. This model was later compared with the flyby images of the Chang'e-2 mission — the general shape was in agreement, although there were some minor discrepancies (Zou et al., 2014).

### 3.11. Procedures: Convexinv, Knitted Occultation, Adaptive Optics and Lightcurve Analysis (KOALA), and All-Data Asteroid Modeling (ADAM)

Software for inverse problems is available at the Database of Asteroid Models from Inversion Techniques (DAMIT) (<http://astro.troja.mff.cuni.cz/projects/asteroids3D>). Convexinv is a procedure for lightcurve inversion, while All-Data

Asteroid Modeling (ADAM) is a collection of functions from which one can tailor an inversion procedure for any data sources (Viikinkoski et al., 2015). An earlier version of this is called Knitted Occultation, Adaptive optics and Lightcurve Analysis (KOALA) (Carry et al., 2012); this is based on lightcurves and silhouette contours obtainable from images and occultations (Kaasalainen, 2011; Kaasalainen and Viikinkoski, 2012). KOALA is especially suitable for lightcurve and occultation data, while ADAM allows the use of any images (camera, radar, or interferometry) with or without lightcurves without having to process them to extract contours or other information. Both KOALA and ADAM can be used for lightcurves only but, as discussed earlier, this is not reliable. Any resulting shape should only be taken in the global sense (as a more realistic-looking rendering of a convex solution), and the details or nonconvex features are seldom likely to be real (Viikinkoski et al., 2015).

## 4. WHAT HAVE WE LEARNED FROM THREE-DIMENSIONAL SHAPES?

The purpose of the modeling methods described in previous sections is to reveal new facts about the nature of asteroids. The approach is made on two fronts: The first strategy is to use the most abundant data sources (photometry in visual and thermal IR) to produce many low-resolution models that will be a statistically significant sample of the whole asteroid population from which conclusions about the physical properties can be drawn. The second approach is to concentrate on selected targets, obtain as many different data types as possible, create detailed models of these asteroids, and extrapolate the obtained results to the whole class of similar objects. We describe in this section new research areas that directly benefit from the availability of spin solutions and three-dimensional shape models.

### 4.1. Spin-Axis Distribution and Evolution

One of the main results of the lightcurve inversion is the increasing sample of asteroids with known orientation of the spin axis. For main-belt asteroids, the long-known lack of asteroids with poles close to the ecliptic (Kryszczyńska et al., 2007) was confirmed and it was shown that it is more pronounced for smaller asteroids (Hanuš et al., 2011). In Fig. 13, we plot the distribution of pole latitudes for ~800 asteroid models with respect to their size [an updated version of Fig. 5 in Hanuš et al. (2011)]. The size-dependent structure can be explained by the YORP effect, which is more effective on smaller asteroids ( $\leq 30$  km) and pushes them into extreme values of obliquity ( $0^\circ$  or  $180^\circ$ ). This corresponds to the clustering of pole latitudes toward values of  $\pm 90^\circ$ . Although there are observation and modeling biases that affect the distribution of poles in the sample of available models, their effect is only marginal compared to the strong anisotropy seen in Fig. 13 (Hanuš et al., 2011). The spin-axis orientation of even smaller asteroids ( $\leq 5$  km) is still not known due to the lack of models. For the largest asteroids ( $\geq 60$  km), there

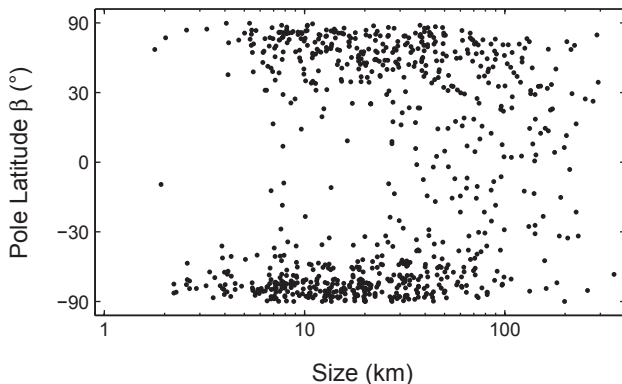


**Fig. 13.** Distribution of pole ecliptic latitude  $\beta$  with respect to the size of the asteroid for  $\sim 800$  asteroids. The scale on the vertical axis is linear in  $\sin \beta$ , which makes the vertical distribution of points in this plot uniform for an isotropic distribution of spin vectors.

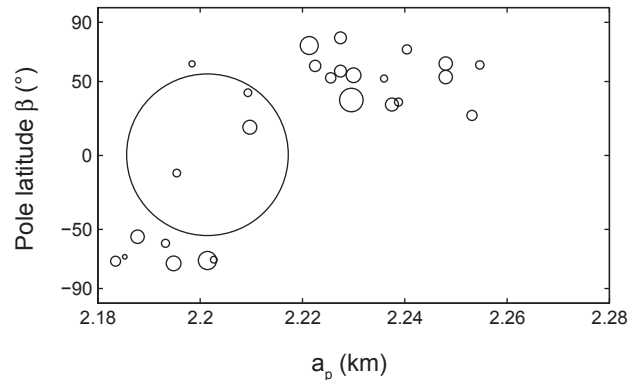


**Fig. 14.** Distribution of pole ecliptic latitude  $\beta$  with respect to the proper semimajor axis  $a_p$  of the Flora family members. The relative size of each circle corresponds to the size of the asteroid.

is a statistically significant increase of prograde rotators (98 prograde vs. 63 retrograde in Fig. 13), probably of primordial origin (Johansen and Lacerda, 2010).

A different approach to the problem of spin-axis distribution was used by Bowell et al. (2014). They analyzed variations of the mean brightness with the ecliptic longitude, from which they estimated ecliptic longitudes of spin axis for about 350,000 asteroids and revealed a clearly non-uniform distribution. However, the explanation of the cause for this non-uniformity is still unknown.

With an increasing sample of models, it is also possible to study the distribution of spin axes of members of collisional families. The results of Hanuš et al. (2013a) agree with theoretical expectations: If the spread in proper semimajor axis increases with decreasing size due to the Yarkovsky effect (see chapters by Nesvorný et al. and Vokrouhlický et al. in this volume), asteroids closer to the Sun than the center of the family should rotate retrograde, and those farther should rotate prograde. This behavior is shown in Fig. 14 for the Flora family.

#### 4.2. A Prerequisite in Many Cases

Unlike most astronomical objects, the viewing geometry of asteroids continuously changes due to their motion relative to the observer. As a corollary, knowing their rotation period and spin-vector coordinates is crucial to interpret projected size measurements and tie together observations.

As already described in section 3, the spin and three-dimensional shape are required to interpret thermal infrared radiometry, stellar occultations, or apparent sizes measured by Gaia without biases. Similarly, there have been long-running discussions to explain inconsistent spectral measurements of asteroids, which can be easily solved once the spin properties (period and orientation) are known; see, e.g., the discussion on (832) Karin by Sasaki et al. (2004), Vernazza

et al. (2007), and Chapman et al. (2007), or on (21) Lutetia by Barucci et al. (2012).

#### 4.3. Density, Composition, and Internal Structure

Density is one of the most fundamental properties to constrain the composition of asteroids and investigate their internal structure (see the chapter by Scheeres et al. in this volume). With the exception of binary asteroids with observable mutual eclipses (chapter by Margot et al. in this volume), both mass and volume are required to determine the density of an asteroid. Estimating the mass of an asteroid by measuring its gravitational influence on other objects is a challenge because of the relative low mass of asteroids compared to other planetary objects. The number of mass determinations thus limits the number of density estimates. Although there are diameter, and hence volume, estimates for all asteroids with a mass determination, the uncertainty in volume generally dominates the balance on density uncertainty (Carry, 2012).

In this respect, three-dimensional shape models are required to determine accurate volume. The level of potential biases increases with stronger assumptions on the shape, and accuracy accounting for systematics improves from sphere, to ellipsoid, to convex model, to the real shape. In the decade since *Asteroids III*, the number of density estimates has increased from 20 to 300 objects (Britt et al., 2002; Carry, 2012). Among these, the most reliable are derived from binary systems for which the volume of the primary was determined after shape modeling (e.g., Ostro et al., 2006; Shepard et al., 2006; Descamps et al., 2009, 2011; Fang et al., 2011; Marchis et al., 2013).

A detailed description of the density of asteroids and their internal structure can be found in the chapter by Scheeres et al. in this volume, from underdense asteroids, hosting large voids, to overdense asteroids, likely differentiated. In the

context of this chapter, it is important to highlight that only density estimates more precise than 10–20% can be used to discriminate between different analog meteorites and provide insights on the internal structure. Such accuracy can only be achieved with volume known to 5–10% or better, which means that a proper description of the three-dimensional shape is needed.

#### 4.4. Determination of Surface Properties by Means of Thermophysical Models

The spin state and shape model of an asteroid is input information for the TPMs. While in the *Asteroids III* era, shape and spin information were available only for a handful of asteroids, preventing application of TPMs to a large number of these bodies, this situation has drastically changed in the last few years. Physical properties (such as the value of the surface thermal inertia) of about 60 asteroids are now available thanks to the application of TPMs (see the chapter by Delbo et al. in this volume). A remarkable improvement in this field is also represented by the availability of high-quality thermal infrared data, such as those produced by the WISE and the Spitzer space telescopes. In the next few years we expect the number of asteroids with known thermal inertia values to grow, thanks to the availability of more shape and spin-state models.

#### 4.5. Surface Rearrangement

From the spin, three-dimensional shape, and density, the local gravity at the surface can be computed. Unsuspected physics has been unveiled with the modeling of the near-Earth asteroid (66391) 1999 KW<sub>4</sub> by Ostro et al. (2006). Some small asteroids present an equatorial bulge, presumably generated by regolith migration toward lower-gravity regions. This process can even form binary systems if the asteroids spin fast enough (Walsh et al., 2008; Harris et al., 2009).

#### 4.6. Cratering Events

An evident outcome of shape modeling is the capability to detect large impact craters and basins. Aside from the spacecraft encounters, the first detection was the large impact basin on Vesta, progenitor of the vestoids (Binzel and Xu, 1993), detected with the HST (Thomas et al., 1997) and confirmed by NASA's Dawn spacecraft (Russell et al., 2012). Another case is the recent impact suffered by asteroid (596) Scheila, detected by the presence of a dust tail (Bodewits et al., 2011). Lightcurves obtained before and after the impact under similar geometries are different, revealing different surface properties (Bodewits et al., 2014).

#### 4.7. Mass Distribution

Because some asteroids are less or more dense than their most-likely constituents, the question of the mass

distribution (denser material or voids) in their interior can be asked. This question is intrinsically tied with the study of the gravity field around the asteroid. The latter has been measured during spacecraft encounters (e.g., see Miller et al., 2002), but studies from Earth-bound observations have recently appeared. By comparing the spherical harmonics of the gravity field as determined from the orbit of a natural satellite, with the expected coefficients resulting from the three-dimensional shape model, the hypothesis of homogeneous mass distribution can be tested (Vachier et al., 2012; Berthier et al., 2014; Takahashi and Scheeres, 2014).

### 5. FUTURE

In the decade since *Asteroids III*, in which the principles of lightcurve inversion based on dense-in-time series were presented (Kaasalainen et al., 2002b), the number of models has seen a tenfold increase — from a few tens to a few hundreds (Table 1). The increasing availability of sparse in-time photometry and its appropriate handling in the inversion, coupled with a dramatic increase of computer time (thanks to projects like Asteroids@Home), have made this possible. Upcoming all-sky surveys such as Pan-STARRS, LSST, and Gaia are expected to produce enormous datasets, and there is little doubt that thousands of models will be derived in the next decade. Our knowledge of nongravitational effects such as YORP and Yarkovsky will directly benefit from this larger sample.

With the large number of data and models, new challenges will arise — how to extract scientifically interesting information from a large set of models of asteroids. With big data flows, the processing has to be automated, with effective data processing. The obvious search for correlations has to be done with care because of large biases in the set of models. Although the importance of detailed models of individual well-studied asteroids will be important, the main shift in paradigm and probably the primary source of interesting findings will be in tens of thousands of asteroid models derived from photometry in optical and thermal infrared wavelengths. As recent as a few years ago, only photometry in the visible was available for a large number of asteroids. The situation drastically changed with the WISE catalog of thermal fluxes for 150,000 asteroids. Automated procedures capable of dealing with photometry in the visible and thermal infrared will yield not only three-dimensional shape and spin state for thousands of asteroids, but also their diameter, their albedo, and the thermal inertia of their surface. The latter will be crucial in interpreting asteroid mineralogy, once coupled with spectroscopy (see the chapter by Reddy et al. in this volume). Understanding of observational and modeling biases will be crucial for correct interpretation of the results. Connecting spin and shape distribution of asteroids with their orbital and spin evolution will hopefully lead to a clear picture of the evolution of the main asteroid belt. The ultimate goal here is the connection of models of evolution of the main belt with spin-axis evolution and current distribution of asteroid physical properties.

Another approach that is complementary to modeling individual objects is modeling distribution functions of parameters of interest. With any inversion technique and photometric data quality, the number of models will be always much lower than the number of known asteroids just because it takes time to collect enough data at different geometries. So instead of aiming to create unique models for a statistically significant sample of the (sub)populations with known observational and modeling bias, one can use other observables than the time-brightness pairs. With this approach, there is almost no “wasting” of data because essentially all photometric points are used in the statistical approach. The aim is to model characteristics of a given asteroid population as a whole when there are not enough data to model individual members. For example, one of the observables can be the mean brightness over one apparition (Bowell *et al.*, 2014) and its dispersion, which correlates with lightcurve amplitude. If there are not enough data points to estimate mean brightness and its variance, the statistics of scatter of individual pairs of observations can be used (Szabó and Kiss, 2008). If the data come in pairs of observations separated by a constant time interval (like with Pan-STARRS), the rotation period can be estimated (Ďurech *et al.*, 2007).

Another challenge for the next decade resides in the derivation of a large sample of higher-resolution models, based on multiple data sources. Building inversion techniques capable of handling different data sources had been highlighted in *Asteroids III* as the next step, and this became reality over the past few years. The models based on multiple data sources are more realistic, more reliable, and more precise than the independent analysis of individual datasets. If practical issues of merging datasets arise, mathematical solutions have been uncovered, and algorithms and software are ready and freely available. The current sample of models derived by such methods is nevertheless still limited. If multi-data analysis is more efficient than independent analysis of the individual datasets, the practical problem of data sharing arises. Although the tools to invert multiple data sources are ready and freely available, the data are still hard to get and harder to share. To maximize the scientific output, it is necessary to combine all available data sources.

The other observing techniques (i.e., disk-resolved imaging, stellar occultations, Gaia size measurements, or radar echoes) will never provide data for more than a few thousand asteroids. However, the apparent sizes by Gaia will be measured with high precision, and will cover a decent-sized sample. Because the data will be made public, they should be used on a regular basis for modeling. The number and quality of profiles derived from stellar occultations have always been restricted due to the intrinsic complexity of prediction and the cost of equipment. The parallel availability of low-cost telescopes and cameras, together with the publication of the Gaia stellar catalog and asteroid orbits, will open a new age for stellar occultations. Any mass-production procedure of asteroid models should therefore be able to deal not only with photometry (visible and infrared) but also with stellar occultations.

Finally, if the bulk of asteroids are single objects, rotating along their shortest axis, a small fraction will either be in a tumbling state or will have satellites. Automatic modeling procedures should be able to detect such cases, triggering detailed analysis of these peculiar targets.

The rising interest of private companies in near-Earth objects as mining resources will inevitably lead to further development of the analysis of remote sensing data, building dedicated groundbased or space telescopes, and eventually moving from asteroids’ surfaces into their interiors.

**Acknowledgments.** The work of J.Ď. was supported by grant GACR P209/10/0537 from the Czech Science Foundation. M.D. acknowledges support from grant ANR-11-BS56-008 SHOCKS from the French National Research Agency.

## REFERENCES

- Bartczak P., Michałowski T., Santana-Ros T., et al. (2014) A new non-convex model of the binary asteroid 90 Antiope obtained with the SAGE modelling technique. *Mon. Not. R. Astron. Soc.*, 443, 1802–1809.
- Barucci M. A., Belskaya I. N., Fornasier S., et al. (2012) Overview of Lutetia’s surface composition. *Planet. Space Sci.*, 66, 23–30.
- Berthier J., Vachier F., Marchis F., et al. (2014) Physical and dynamical properties of the main belt triple asteroid (87) Sylvia. *Icarus*, 239, 118–130.
- Binzel R. P. and Xu S. (1993) Chips off of asteroid 4 Vesta: Evidence for the parent body of basaltic achondrite meteorites. *Science*, 260, 186–191.
- Bodewits D., Kelley M. S., Li J.-Y., et al. (2011) Collisional excavation of asteroid (596) Scheila. *Astrophys. J. Lett.*, 733, L3.
- Bodewits D., Vincent J.-B., and Kelley M. S. P. (2014) Scheila’s scar: Direct evidence of impact surface alteration on a primitive asteroid. *Icarus*, 229, 190–195.
- Bowell E., Oszkiewicz D. A., Wasserman L. H., et al. (2014) Asteroid spin-axis longitudes from the Lowell Observatory database. *Meteoritics & Planet. Sci.*, 49, 95–102.
- Britt D. T., Yeomans D. K., Housen K. R., et al. (2002) Asteroid density, porosity, and structure. In *Asteroids III* (W. F. Bottke Jr. *et al.*, eds.), pp. 485–500. Univ. of Arizona, Tucson.
- Busch M. W. (2009) ALMA and asteroid science. *Icarus*, 200, 347–349.
- Carbognani A., Tanga P., Cellino A., et al. (2012) The representation of asteroid shapes: A test for the inversion of Gaia photometry. *Planet. Space Sci.*, 73, 80–85.
- Carry B. (2009) Asteroids physical properties from high angular resolution imaging. Ph.D. thesis, Observatoire de Paris.
- Carry B. (2012) Density of asteroids. *Planet. Space Sci.*, 73, 98–118.
- Carry B., Dumas C., Fulchignoni M., et al. (2008) Near-infrared mapping and physical properties of the dwarf-planet Ceres. *Astron. Astrophys.*, 478, 235–244.
- Carry B., Dumas C., Kaasalainen M., et al. (2010a) Physical properties of (2) Pallas. *Icarus*, 205, 460–472.
- Carry B., Kaasalainen M., Leyrat C., et al. (2010b) Physical properties of the ESA Rosetta target asteroid (21) Lutetia. II. Shape and flyby geometry. *Astron. Astrophys.*, 523, A94.
- Carry B., Kaasalainen M., Merline W. J., et al. (2012) Shape modeling technique KOALA validated by ESA Rosetta at (21) Lutetia. *Planet. Space Sci.*, 66, 200–212.
- Carry B., Matter A., Scheirich P., et al. (2015) The small binary asteroid (939) Isberga. *Icarus*, 248, 516–525.
- Cellino A. and Dell’Oro A. (2012) The derivation of asteroid physical properties from Gaia observations. *Planet. Space Sci.*, 73, 52–55.
- Cellino A., Diolaiti E., Ragazzoni R., et al. (2003) Speckle interferometry observations of asteroids at TNG. *Icarus*, 162, 278–284.
- Cellino A., Tanga P., Dell’Oro A., et al. (2007) Asteroid science with Gaia: Sizes, spin properties, overall shapes and taxonomy. *Adv. Space Res.*, 40, 202–208.

- Cellino A., Hestroffer D., Tanga P., et al. (2009) Genetic inversion of sparse disk-integrated photometric data of asteroids: Application to Hipparcos data. *Astron. Astrophys.*, **506**, 935–954.
- Chapman C. R., Enke B., Merline W. J., et al. (2007) Young asteroid 832 Karin shows no rotational spectral variations. *Icarus*, **191**, 323–329.
- Colas F., Berthier J., Vachier F., et al. (2012) Shape and size of (90) Antiope derived from an exceptional stellar occultation on July 19, 2011. *Asteroids, Comets, Meteors (ACM) 2012*, Abstract #6427. LPI Contribution No. 1667, Lunar and Planetary Institute, Houston.
- Conan J.-M., Fusco T., Mugnier L. M., et al. (2000) MISTRAL: Myopic deconvolution method applied to ADONIS and to simulated VLT-NAOS images. *The Messenger*, **99**, 38–45.
- Conrad A. R., Dumas C., Merline W. J., et al. (2007) Direct measurement of the size, shape, and pole of 511 Davida with Keck AO in a single night. *Icarus*, **191**, 616–627.
- Delbo M. (2004) The nature of near-Earth asteroids from the study of their thermal infrared emission. Ph.D. thesis, Freie Universität, Berlin, 210 pp.
- Delbo M. and Harris A. W. (2002) Physical properties of near-Earth asteroids from thermal infrared observations and thermal modeling. *Meteoritics & Planet. Sci.*, **37**, 1929–1936.
- Delbo M., Ligori S., Matter A., et al. (2009) First VLTI-MIDI direct determinations of asteroid sizes. *Astrophys. J.*, **694**, 1228–1236.
- Descamps P., Marchis F., Pollock J., et al. (2008) New determination of the size and bulk density of the binary asteroid 22 Kalliope from observations of mutual eclipses. *Icarus*, **196**, 578–600.
- Descamps P., Marchis F., Ďurech J., et al. (2009) New insights on the binary asteroid 121 Hermione. *Icarus*, **203**, 88–101.
- Descamps P., Marchis F., Berthier J., et al. (2011) TriPLICITY and physical characteristics of asteroid (216) Kleopatra. *Icarus*, **211**, 1022–1033.
- Dotto E., Barucci M. A., Müller T. G., et al. (2002) Observations from orbiting platforms. In *Asteroids III* (W. F. Bottke Jr. et al., eds.), pp. 219–234. Univ. of Arizona, Tucson.
- Drummond J. D., Cocke W. J., Hege E. K., et al. (1985) Speckle interferometry of asteroids. I — 433 Eros. *Icarus*, **61**, 132–151.
- Drummond J., Eckart A., and Hege E. K. (1988) Speckle interferometry of asteroids. IV — Reconstructed images of 4 Vesta. *Icarus*, **73**, 1–14.
- Drummond J. D., Conrad A., Merline W., et al. (2009) The dimensions and pole of asteroid (21) Lutetia from adaptive optics images. *AAS/Division for Planetary Sciences Meeting Abstracts*, **41**, #59.07.
- Dunham D. W., Herald D., Frappa E., et al. (2014) *Asteroid Occultations V12.0*. NASA Planetary Data System, 216.
- Bartczak P., Michałowski T., Santana-Ros T., et al. (2014) A new Ďurech J. and Kaasalainen M. (2003) Photometric signatures of highly nonconvex and binary asteroids. *Astron. Astrophys.*, **404**, 709–714.
- Ďurech J., Grav T., Jedicek R., et al. (2005) Asteroid models from the Pan-STARRS photometry. *Earth Moon Planets*, **97**, 179–187.
- Ďurech J., Scheirich P., Kaasalainen M., et al. (2007) Physical models of asteroid from sparse photometric data. In *Near Earth Objects, Our Celestial Neighbors: Opportunity and Risk* (A. Milani et al., eds.), p. 191. Cambridge Univ., Cambridge.
- Ďurech J., Vokrouhlický D., Kaasalainen M., et al. (2008) Detection of the YORP effect in asteroid (1620) Geographos. *Astron. Astrophys.*, **489**, L25–L28.
- Ďurech J., Kaasalainen M., Warner B. D., et al. (2009) Asteroid models from combined sparse and dense photometric data. *Astron. Astrophys.*, **493**, 291–297.
- Ďurech J., Kaasalainen M., Herald D., et al. (2011) Combining asteroid models derived by lightcurve inversion with asteroidal occultation silhouettes. *Icarus*, **214**, 652–670.
- Ďurech J., Delbo M., and Carry B. (2012) Asteroid models derived from thermal infrared data and optical lightcurves. In *Asteroids, Comets, Meteors (ACM) 2012*, Abstract #6118. LPI Contribution No. 1667, Lunar and Planetary Institute, Houston.
- Ďurech J., Vokrouhlický D., Baransky A. R., et al. (2012) Analysis of the rotation period of asteroids (1865) Cerberus, (2100) Ra-Shalom, and (3103) Eger — search for the YORP effect. *Astron. Astrophys.*, **547**, A10.
- Ďurech J., Hanuš J., Delbo M., et al. (2014) Physical properties of asteroids derived from a novel approach to modeling of optical lightcurves and WISE thermal infrared data. In *AAS/Division for Planetary Sciences Meeting Abstracts*, **46**, #509.11.
- Eisenhauer F., Perrin G., Brandner W., et al. (2008) GRAVITY: Getting to the event horizon of Sgr A\*. In *Optical and Infrared Interferometry* (M. Schöller et al., eds.), p. 70132A. SPIE Conf. Ser. 7013, Bellingham, Washington.
- Emery J. P., Cruikshank D. P., and Van Cleve J. (2006) Thermal emission spectroscopy (5.2–38 μm) of three Trojan asteroids with the Spitzer Space Telescope: Detection of fine-grained silicates. *Icarus*, **182**, 496–512.
- Emery J. P., Sprague A. L., Witteborn F. C., et al. (1998) Mercury: Thermal modeling and mid-infrared (5–12 μm) observations. *Icarus*, **136**, 104–123.
- Fang J., Margot J.-L., Brozovic M., et al. (2011) Orbits of near-Earth asteroid triples 2001 SN263 and 1994 CC: Properties, origin, and evolution. *Astron. J.*, **141**, 154–169.
- Gaskell R. W., Barnouin-Jha O. S., Scheeres D. J., et al. (2008) Characterizing and navigating small bodies with imaging data. *Meteoritics & Planet. Sci.*, **43**, 1049–1061.
- Golubov O. and Krugly Y. N. (2012) Tangential component of the YORP effect. *Astrophys. J. Lett.*, **752**, L11.
- Golubov O., Scheeres D. J., and Krugly Y. N. (2014) A three-dimensional model of tangential YORP. *Astrophys. J.*, **794**, 22.
- Grav T., Mainzer A. K., Bauer J., et al. (2012a) WISE/NEOWISE observations of the Hilda population: Preliminary results. *Astrophys. J.*, **744**, 197.
- Grav T., Mainzer A. K., Bauer J., et al. (2011) WISE/NEOWISE observations of the Jovian Trojans: Preliminary results. *Astrophys. J.*, **742**, 40.
- Grav T., Mainzer A. K., Bauer J. M., et al. (2012b) WISE/NEOWISE observations of the jovian Trojan population: Taxonomy. *Astrophys. J.*, **759**, 49.
- Hanuš J., Marchis F., and Ďurech J. (2013a) Sizes of main-belt asteroids by combining shape models and Keck adaptive optics observations. *Icarus*, **226**, 1045–1057.
- Hanuš J., Ďurech J., Brož M., et al. (2013b) Asteroids' physical models from combined dense and sparse photometry and scaling of the YORP effect by the observed obliquity distribution. *Astron. Astrophys.*, **551**, A67.
- Hanuš J., Ďurech J., Brož M., et al. (2011) A study of asteroid pole-latitude distribution based on an extended set of shape models derived by the lightcurve inversion method. *Astron. Astrophys.*, **530**, A134.
- Harris A. W. (1998) A thermal model for near-Earth asteroids. *Icarus*, **131**, 291–301.
- Harris A. W., Fahnestock E. G., and Pravec P. (2009) On the shapes and spins of “rubble pile” asteroids. *Icarus*, **199**, 310–318.
- Harris A. W. and Lagerros J. S. V. (2002) Asteroids in the thermal infrared. In *Asteroids III* (W. F. Bottke Jr. et al., eds.), pp. 139–150. Univ. of Arizona, Tucson.
- Harris A. W., Pravec P., and Warner B. D. (2012) Looking a gift horse in the mouth: Evaluation of wide-field asteroid photometric surveys. In *Asteroids, Comets, Meteors (ACM) 2012*, Abstract #6069. LPI Contribution No. 1667, Lunar and Planetary Institute, Houston.
- Hasegawa S., Müller T. G., Kuroda D., et al. (2013) The asteroid catalog using AKARI IRC slow-scan observations. *Publ. Astron. Soc. Japan*, **65**, 34.
- Henych T. and Pravec P. (2013) Asteroid rotation excitation by subcatastrophic impacts. *Mon. Not. R. Astron. Soc.*, **432**, 1623–1631.
- Hestroffer D., Tanga P., Cellino A., et al. (2002) Asteroids observations with the Hubble Space Telescope. I. Observing strategy, and data analysis and modeling process. *Astron. Astrophys.*, **391**, 1123–1132.
- Hom E. F. Y., Marchis F., Lee T. K., et al. (2007) AIDA: An adaptive image deconvolution algorithm with application to multi-frame and three-dimensional data. *J. Optical Soc. Am. A*, **24**, 1580–1600.
- Hudson R. S., Ostro S. J., and Scheeres D. J. (2003) High-resolution model of asteroid 4179 Toutatis. *Icarus*, **161**, 346–355.
- Jankov S. (2010) Astronomical optical interferometry. I. Methods and instrumentation. *Serbian Astron. J.*, **181**, 1–17.
- Johansen A. and Lacerda P. (2010) Prograde rotation of protoplanets by accretion of pebbles in a gaseous environment. *Mon. Not. R. Astron. Soc.*, **404**, 475–485.
- Jorda L., Lamy P. L., Gaskell R. W., et al. (2012) Asteroid (2867) Steins: Shape, topography and global physical properties from OSIRIS observations. *Icarus*, **221**, 1089–1100.
- Kaasalainen M. (2001) Interpretation of lightcurves of precessing asteroids. *Astron. Astrophys.*, **376**, 302–309.
- Kaasalainen M. (2004) Physical models of large number of asteroids from calibrated photometry sparse in time. *Astron. Astrophys.*, **422**, L39–L42.

- Kaasalainen M. (2011) Maximum compatibility estimates and shape reconstruction with boundary curves and volumes of generalized projections. *Inverse Problems and Imaging*, 5, 37–57.
- Kaasalainen M. and Lamborg L. (2006) Inverse problems of generalized projection operators. *Inverse Problems*, 22, 749–769.
- Kaasalainen M., Mottola S., and Fulchignoni M. (2002a) Asteroid models from disk-integrated data. In *Asteroids III* (W. F. Bottke Jr. et al., eds.), pp. 139–150. Univ. of Arizona, Tucson.
- Kaasalainen M. and Nortunen H. (2013) Compact YORP formulation and stability analysis. *Astron. Astrophys.*, 558, A104.
- Kaasalainen M. and Torppa J. (2001) Optimization methods for asteroid lightcurve inversion. I. Shape determination. *Icarus*, 153, 24–36.
- Kaasalainen M., Torppa J., and Muinonen K. (2001) Optimization methods for asteroid lightcurve inversion. II. The complete inverse problem. *Icarus*, 153, 37–51.
- Kaasalainen M., Torppa J., and Piironen J. (2002b) Models of twenty asteroids from photometric data. *Icarus*, 159, 369–395.
- Kaasalainen M., Durech J., Warner B. D., et al. (2007) Acceleration of the rotation of asteroid 1862 Apollo by radiation torques. *Nature*, 446, 420–422.
- Kaasalainen M. and Viikinkoski M. (2012) Shape reconstruction of irregular bodies with multiple complementary data sources. *Astron. Astrophys.*, 543, A97.
- Kaasalainen S., Kaasalainen M., and Piironen J. (2005) Ground reference for space remote sensing. Laboratory photometry of an asteroid model. *Astron. Astrophys.*, 440, 1177–1182.
- Keller H. U., Barbieri C., Koschny D., et al. (2010) E-type asteroid (2867) Steins as imaged by OSIRIS on board Rosetta. *Science*, 327, 190–193.
- Kryszczynska A., La Spina A., Paolicchi P., et al. (2007) New findings on asteroid spin-vector distributions. *Icarus*, 192, 223–237.
- Lagerros J. S. V. (1996) Thermal physics of asteroids. I. Effects of shape, heat conduction and beaming. *Astron. Astrophys.*, 310, 1011–1020.
- Lagerros J. S. V. (1997) Thermal physics of asteroids. III. Irregular shapes and albedo variegations. *Astron. Astrophys.*, 325, 1226–1236.
- Lagerros J. S. V. (1998) Thermal physics of asteroids. IV. Thermal infrared beaming. *Astron. Astrophys.*, 332, 1123–1132.
- Lamberg L. and Kaasalainen M. (2001) Numerical solution of the Minkowski problem. *J. Comp. Appl. Math.*, 137, 213–227.
- Lebofsky L. A., Sykes M. V., Tedesco E. F., et al. (1986) A refined ‘standard’ thermal model for asteroids based on observations of 1 Ceres and 2 Pallas. *Icarus*, 68, 239–251.
- Li J.-Y., McFadden L. A., Parker J. W., et al. (2006) Photometric analysis of 1 Ceres and surface mapping from HST observations. *Icarus*, 182, 143–160.
- Licandro J., Hargrove K., Kelley M., et al. (2012) 5–14 μm Spitzer spectra of Themis family asteroids. *Astron. Astrophys.*, 537, A73.
- Lowry S. C., Fitzsimmons A., Pravec P., et al. (2007) Direct detection of the asteroidal YORP effect. *Science*, 316, 272–274.
- Lowry S. C., Weissman P. R., Duddy S. R., et al. (2014) The internal structure of asteroid (25143) Itokawa as revealed by detection of YORP spin-up. *Astron. Astrophys.*, 562, A48.
- Mainzer A., Grav T., Bauer J., et al. (2011) NEOWISE observations of near-Earth objects: Preliminary results. *Astrophys. J.*, 743, 156.
- Mainzer A., Grav T., Masiero J., et al. (2012a) Physical parameters of asteroids estimated from the WISE 3-band data and NEOWISE post-cryogenic survey. *Astrophys. J. Lett.*, 760, L12.
- Mainzer A., Grav T., Masiero J., et al. (2012b) Characterizing subpopulations within the near-Earth objects with NEOWISE: Preliminary results. *Astrophys. J.*, 752, 110.
- Marchis F., Durech J., Castillo-Rogez J., et al. (2014) The puzzling mutual orbit of the binary Trojan asteroid (624) Hektor. *Astrophys. J. Lett.*, 783, L37.
- Marchis F., Kaasalainen M., Horne E. F. Y., et al. (2006) Shape, size and multiplicity of main-belt asteroids. *Icarus*, 185, 39–63.
- Marchis F., Vachier F., Durech J., et al. (2013) Characteristics and large bulk density of the C-type main-belt triple asteroid (93) Minerva. *Icarus*, 224, 178–191.
- Masiero J., Jedicke R., Durech J., et al. (2009) The thousand asteroid light curve survey. *Icarus*, 204, 145–171.
- Masiero J. R., Mainzer A. K., Grav T., et al. (2011) Main belt asteroids with WISE/NEOWISE. I. Preliminary albedos and diameters. *Astrophys. J.*, 741, 68.
- Masiero J. R., Mainzer A. K., Grav T., et al. (2012) Preliminary analysis of WISE/NEOWISE 3-band cryogenic and postcryogenic observations of main belt asteroids. *Astrophys. J. Lett.*, 759, L8.
- Matter A., Delbo M., Ligori S., et al. (2011) Determination of physical properties of the asteroid (41) Daphne from interferometric observations in the thermal infrared. *Icarus*, 215, 47–56.
- Matter A., Delbo M., Carry B., et al. (2013) Evidence of a metal-rich surface for the asteroid (16) Psyche from interferometric observations in the thermal infrared. *Icarus*, 226, 419–427.
- Merline W. J., Drummond J. D., Carry B., et al. (2013) The Resolved Asteroid Program — Size, shape, and pole of (52) Europa. *Icarus*, 225, 794–805.
- Mignard F., Cellino A., Muinonen K., et al. (2007) The Gaia mission: Expected applications to asteroid science. *Earth Moon Planets*, 101, 97–125.
- Miller J. K., Konopliv A. S., Antreasyan P. G., et al. (2002) Determination of shape, gravity, and rotational state of asteroid 433 Eros. *Icarus*, 155, 3–17.
- Millis R. L. and Dunham D. W. (1989) Precise measurement of asteroid sizes and shapes from occultations. In *Asteroids II* (R. P. Binzel et al., eds.), pp. 148–170. Univ. of Arizona, Tucson.
- Mommert M., Farnocchia D., Hora J. L., et al. (2014) Physical properties of near-Earth asteroid 2011 MD. *Astrophys. J. Lett.*, 789, L22.
- Mueller M. (2007) Surface properties of asteroids from mid-infrared observations and thermophysical modeling. Ph.D. thesis, Freie Universität, Berlin.
- Mugnier L. M., Fusco T., and Conan J.-M. (2004) MISTRAL: A myopic edge-preserving image restoration method, with application to astronomical adaptive-optics-corrected longexposure images. *J. Optical Soc. Am. A*, 21, 1841–1854.
- Müller T. G., Lellouch E., Stansberry J., et al. (2010) “TNOs are Cool”: A survey of the trans-Neptunian region. I. Results from the Herschel science demonstration phase (SDP). *Astron. Astrophys.*, 518, L146.
- Naidu S. P., Margot J.-L., Busch M. W., et al. (2013) Radar imaging and physical characterization of near-Earth asteroid (162421) 2000 ET70. *Icarus*, 226, 323–335.
- Nathues A., Mottola S., Kaasalainen M., et al. (2005) Spectral study of the Eunomia asteroid family. I. Eunomia. *Icarus*, 175, 452–463.
- Nelan E. P., Lupie O. L., McArthur B., et al. (1998) Fine guidance sensors aboard the Hubble Space Telescope: The scientific capabilities of these interferometers. In *Astronomical Interferometry* (R. D. Reasenberg, ed.), pp. 237–247. SPIE Conf. Ser. 3350, Bellingham, Washington.
- Ostro S. J., Hudson R. S., Nolan M. C., et al. (2000) Radar observations of asteroid 216 Kleopatra. *Science*, 288, 836–839.
- Ostro S. J., Margot J.-L., Benner L. A. M., et al. (2006) Radar imaging of binary near-Earth asteroid (66391) 1999 KW4. *Science*, 314, 1276–1280.
- Ostro S. J., Rosema K. D., Campbell D. B., et al. (2002) Note: Radar observations of asteroid 1862 Apollo. *Icarus*, 156, 580–583.
- Polishook D., Ofek E. O., Waszczak A., et al. (2012) Asteroid rotation periods from the Palomar Transient Factory survey. *Mon. Not. R. Astron. Soc.*, 421, 2094–2108.
- Pravec P., Harris A. W., Vokrouhlický D., et al. (2008) Spin rate distribution of small asteroids. *Icarus*, 197, 497–504.
- Pravec P., Scheirich P., Kušnárik P., et al. (2006) Photometric survey of binary near-Earth asteroids. *Icarus*, 181, 63–93.
- Pravec P., Scheirich P., Durech J., et al. (2014) The tumbling spin state of (99942) Apophis. *Icarus*, 233, 48–60.
- Pravec P., Vokrouhlický D., Polishook D., et al. (2010) Formation of asteroid pairs by rotational fission. *Nature*, 466, 1085–1088.
- Preusker F., Scholten F., Knollenberg J., et al. (2012) The northern hemisphere of asteroid (21) Lutetia — topography and orthoimages from Rosetta OSIRIS NAC image data. *Planet. Space Sci.*, 66, 54–63.
- Pursiainen S. and Kaasalainen M. (2013) Iterative alternating sequential (IAS) method for radio tomography of asteroids in 3D. *Planet. Space Sci.*, 82, 84–98.
- Pursiainen S. and Kaasalainen M. (2014a) Detection of anomalies in radio tomography of asteroids: Source count and forward errors. *Planet. Space Sci.*, 99, 36–37.
- Pursiainen S. and Kaasalainen M. (2014b) Sparse source travel-time tomography of a laboratory target: Accuracy and robustness of anomaly detection. *Inverse Problems*, 30, 114016.
- Ragazzoni R., Baruffolo A., Marchetti E., et al. (2000) Speckle interferometry measurements of the asteroids 10-Hygia and 15-Eunomia. *Astron. Astrophys.*, 354, 315–320.

- Rozitis B. and Green S. F. (2011) Directional characteristics of thermal-infrared beaming from atmosphereless planetary surfaces — a new thermophysical model. *Mon. Not. R. Astron. Soc.*, *415*, 2042–2062.
- Russell C. T., Raymond C. A., Coradini A., et al. (2012) Dawn at Vesta: Testing the protoplanetary paradigm. *Science*, *336*, 684–686.
- Russell H. N. (1906) On the light variations of asteroids and satellites. *Astrophys. J.*, *24*, 1–18.
- Sasaki T., Sasaki S., Watanabe J.-i., et al. (2004) Mature and fresh surfaces on the newborn asteroid Karin. *Astrophys. J. Lett.*, *615*, L161–L164.
- Scheirich P., Ďurech J., Pravec P., et al. (2010) The shape and rotation of asteroid 2008 TC<sub>3</sub>. *Meteoritics & Planet. Sci.*, *45*, 1804–1811.
- Scheirich P. and Pravec P. (2009) Modeling of lightcurves of binary asteroids. *Icarus*, *200*, 531–547.
- Schmidt B. E., Thomas P. C., Bauer J. M., et al. (2009) The shape and surface variation of 2 Pallas from the Hubble Space Telescope. *Science*, *326*, 275–278.
- Ševeček P., Brož M., Čapek D., et al. (2015) The thermal emission from boulders on (25143) Itokawa and general implications for the YORP effect. *Mon. Not. R. Astron. Soc.*, *450*, 2104–2115.
- Shepard M. K., Margot J.-L., Magri C., et al. (2006) Radar and infrared observations of binary near-Earth asteroid 2002 CE26. *Icarus*, *184*, 198–210.
- Sicardy B., Ortiz J. L., Assafin M., et al. (2011) A Pluto-like radius and a high albedo for the dwarf planet Eris from an occultation. *Nature*, *478*, 493–496.
- Sierks H., Lamy P., Barbieri C., et al. (2011) Images of asteroid 21 Lutetia: A remnant planetesimal from the early solar system. *Science*, *334*, 487–490.
- Spencer J. R. (1990) A rough-surface thermophysical model for airless planets. *Icarus*, *83*, 27–38.
- Spencer J. R., Lebofsky L. A., and Sykes M. V. (1989) Systematic biases in radiometric diameter determinations. *Icarus*, *78*, 337–354.
- Statler T. S. (2009) Extreme sensitivity of the YORP effect to small-scale topography. *Icarus*, *202*, 502–513.
- Szabó G. M. and Kiss L. L. (2008) The shape distribution of asteroid families: Evidence for evolution driven by small impacts. *Icarus*, *196*, 135–143.
- Takahashi Y. and Scheeres D. J. (2014) Morphology driven density distribution estimation for small bodies. *Icarus*, *233*, 179–193.
- Tanga P. and Delbo M. (2007) Asteroid occultations today and tomorrow: Toward the GAIA era. *Astron. Astrophys.*, *474*, 1015–1022.
- Tanga P., Hestroffer D., Berthier J., et al. (2001) NOTE: HST/FGS observations of the asteroid (216) Kleopatra. *Icarus*, *153*, 451–454.
- Tanga P., Hestroffer D., Cellino A., et al. (2003) Asteroid observations with the Hubble Space Telescope. II. Duplicity search and size measurements for 6 asteroids. *Astron. Astrophys.*, *401*, 733–741.
- Tedesco E. F., Noah P. V., Noah M., et al. (2002) The Supplemental IRAS Minor Planet Survey. *Astron. J.*, *123*, 1056–1085.
- Thomas P. C., Binzel R. P., Gaffey M. J., et al. (1997) Impact excavation on asteroid 4 Vesta: Hubble Space Telescope results. *Science*, *277*, 1492–1495.
- Thomas P. C., Parker J. W., McFadden L. A., et al. (2005) Differentiation of the asteroid Ceres as revealed by its shape. *Nature*, *437*, 224–226.
- Timerson B., Ďurech J., Aguirre S., et al. (2009) A trio of well-observed asteroid occultations in 2008. *Minor Planet Bull.*, *36*, 98–100.
- Torppa J., Kaasalainen M., Michalowski T., et al. (2003) Shapes and rotational properties of thirty asteroids from photometric data. *Icarus*, *164*, 346–383.
- Trilling D. E., Mueller M., Hora J. L., et al. (2010) Explore-NEOs. I. Description and first results from the warm Spitzer near-Earth object survey. *Astron. J.*, *140*, 770–784.
- Usui F., Kasuga T., Hasegawa S., et al. (2013) Albedo properties of main belt asteroids based on the all-sky survey of the infrared astronomical satellite AKARI. *Astrophys. J.*, *762*, 56.
- Usui F., Kuroda D., Müller T. G., et al. (2011) Asteroid catalog using Akari: AKARI/IRC mid-infrared asteroid survey. *Publ. Astron. Soc. Japan*, *63*, 1117–1138.
- Vachier F., Berthier J., and Marchis F. (2012) Determination of binary asteroid orbits with a genetic-based algorithm. *Astron. Astrophys.*, *543*, A68.
- Vernazza P., Rossi A., Birlan M., et al. (2007) 832 Karin: Absence of rotational spectral variations. *Icarus*, *191*, 330–336.
- Viikinkoski M. and Kaasalainen M. (2014) Shape reconstruction from images: Pixel fields and Fourier transform. *Inverse Problems and Imaging*, *8*, 885–900.
- Viikinkoski M., Kaasalainen M., and Ďurech J. (2015) ADAM: A general method of including any data types in asteroid reconstruction. *Astron. Astrophys.*, *576*, A8.
- Walsh K. J., Richardson D. C., and Michel P. (2008) Rotational breakup as the origin of small binary asteroids. *Nature*, *454*, 188–191.
- Warner B. D., Harris A. W., and Pravec P. (2009) The asteroid lightcurve database. *Icarus*, *202*, 134–146.
- Warner B. D., Stephens R. D., and Harris A. W. (2011) Save the lightcurves. *Minor Planet Bull.*, *38*, 172–174.
- Witasse O., Lebreton J.-P., Bird M. K., et al. (2006) Overview of the coordinated ground-based observations of Titan during the Huygens mission. *J. Geophys. Res.–Planets*, *111*, 7–19.
- Zou X., Li C., Liu J., et al. (2014) The preliminary analysis of the 4179 Toutatis snapshots of the Chang'e-2 flyby. *Icarus*, *229*, 348–354.

# The Complex History of Trojan Asteroids

**Joshua P. Emery**  
*University of Tennessee*

**Francesco Marzari**  
*Università di Padova*

**Alessandro Morbidelli**  
*Lagrange Laboratory, Université Côte d'Azur, Observatoire de la Côte d'Azur, CNRS*

**Linda M. French**  
*Illinois Wesleyan University*

**Tommy Grav**  
*Planetary Science Institute*

---

The Trojan asteroids, orbiting the Sun in Jupiter's stable Lagrange points, provide a unique perspective on the history of our solar system. As a large population of small bodies, they record important gravitational interactions in the dynamical evolution of the solar system. As primitive bodies, their compositions and physical properties provide windows into the conditions in the solar nebula in the region in which they formed. In the past decade, significant advances have been made in understanding their physical properties, and there has been a revolution in thinking about the origin of Trojans. The ice and organics generally presumed to be a significant part of Trojan composition have yet to be detected directly, although the low density of the binary system Patroclus (and possibly low density of the binary/moonlet system Hektor) is consistent with an interior ice component. By contrast, fine-grained silicates that appear to be similar to cometary silicates in composition have been detected, and a color bimodality may indicate distinct compositional groups among the Trojans. Whereas Trojans had traditionally been thought to have formed near 5 AU, a new paradigm has developed in which the Trojans formed in the proto-Kuiper belt, and were scattered inward and captured in the Trojan swarms as a result of resonant interactions of the giant planets. Whereas the orbital and population distributions of current Trojans are consistent with this origin scenario, there are significant differences between current physical properties of Trojans and those of Kuiper belt objects. These differences may be indicative of surface modification due to the inward migration of objects that became the Trojans, but understanding of appropriate modification mechanisms is poor and would benefit from additional laboratory studies. Many open questions about this intriguing population remain, and the future promises significant strides in our understanding of Trojans. The time is ripe for a spacecraft mission to the Trojans, to transform these objects into geologic worlds that can be studied in detail to unravel their complex history.

## 1. INTRODUCTION

Originally considered as simply an extension of the main belt, Trojan asteroids have become recognized as a large and important population of small bodies. Trojans share Jupiter's orbit around the Sun, residing in the L<sub>4</sub> and L<sub>5</sub> stable Lagrange regions. Leading and trailing Jupiter by 60°, these are regions of stable equilibrium in the Sun-Jupiter-asteroid three-body gravitational system. The moniker "Trojan" is an artifact of history — the first three objects discovered in Jupiter's Lagrange regions were named after heroes from the *Iliad*. The naming convention stuck for Jupiter's swarms, and

the term Trojan eventually came to be used for any object trapped in the L<sub>4</sub> or L<sub>5</sub> region of any body. Nevertheless, only Jupiter Trojans are named from the *Iliad*, and when used without a designator, "Trojan" refers either specifically to Jupiter Trojans or sometimes to the collection of all bodies in stable Lagrange points. Several other solar system bodies also support stable Trojan populations, including Mars, Neptune, and two satellites of Saturn (Tethys and Dione). The populations coorbiting with Mars and the two saturnian moons appear to be quite small, but Neptune's family of Trojans is thought to be extensive (e.g., Sheppard and Trujillo, 2010). Planets can destabilize each other's Lagrange regions. For instance,

Saturn and Uranus do not have stable Trojan populations because the other planets perturb the orbits on timescales that are short relative to the age of the solar system. The Jupiter Trojans, which are the focus of this chapter, are estimated to be nearly as populous as the main belt and have stability timescales that exceed the age of the solar system.

The history of the exploration of Trojan asteroids begins with Max Wolf, who, in the late nineteenth century, was the first to turn to wide-field astrophotography for asteroid discovery (Tenn, 1994). In early 1906 he detected an object near Jupiter's L<sub>4</sub> point, marking the first observational confirmation of Lagrange's three-body solution. An object was detected near L<sub>5</sub> later in 1906 by August Kopf, then another near L<sub>4</sub> in early 1907. These were later named (588) Achilles, (617) Patroclus, and (624) Hektor, respectively (Nicholson, 1961). As physical studies of asteroids accelerated in the 1970s and 1980s, the Trojans were included, and the first sizes, albedos, rotation periods, and (visible wavelength) spectra were published (e.g., Dunlap and Gehrels, 1969; Cruikshank, 1977; Hartmann and Cruikshank, 1978; Chapman and Gaffey, 1979). Gradie and Everka (1980) established the paradigm, which is still commonly invoked, that the low albedo and red spectral slopes are due to the presence of complex organic molecules on Trojan surfaces. By 1989, when the *Asteroids II* book was published, 157 Trojans were known, from which Shoemaker et al. (1989) estimated a total population comparable to that of the main belt — an estimate that still stands, to within a factor of a few. Discovery and characterization accelerated rapidly for Trojans (as with all asteroids) through the end of the twentieth century, and by the time of *Asteroids III* in 2002, 993 Trojans had been discovered. The number now stands at 6073.

Summarizing the state of knowledge of the physical properties of Trojans at the turn of the twenty-first century, Barucci et al. (2002) describe a population that is far more homogeneous than the main belt, with uniformly low albedos ( $p_v \sim 0.03$  to 0.07) and featureless, red-sloped spectra at visible and near-infrared (VNIR) wavelengths (0.4–2.5  $\mu\text{m}$ ). A later review by Dotto et al. (2008) reports additional spectral observations, particularly of members of potential collisional families (Dotto et al., 2006; Fornasier et al., 2007), the detection of signatures of fine-grained silicates (Emery et al., 2006), and the first bulk-density measurement (Marchis et al., 2006). From these properties and their locations at 5.2 AU, Trojans have generally been inferred to contain a large fraction of H<sub>2</sub>O ice hidden from view by a refractory mantle, and a higher abundance of complex organic molecules than most main-belt asteroids (MBAs). Since those reviews, significant strides have been made in the physical characterization of Trojans, which in turn provide new insights into the nature of these enigmatic bodies.

Marzari et al. (2002a) review models for the capture of Trojans and the stability of the Lagrange regions that had developed up to that point. Although some analytical work suggested stability regions that did not match observations, numerical work by Levison et al. (1997) showed a wide region of stability for the age of the solar system. Efforts

to explain the capture of Trojans settled on two potential mechanisms as most likely: gas drag in the early nebula (e.g., Peale, 1993) and capture during the growth of Jupiter (Marzari and Scholl, 1998a). Both mechanisms predict that the present-day Trojans formed in the middle of the solar nebula, near where they currently reside. Since there is no other reservoir of material available for study from this region, the Trojans would, in this case, be an exciting window into the conditions of the solar nebula near the snow line and near Jupiter's formation region. However, neither mechanism fully explains the current orbital properties of Trojans, particularly the high inclinations.

More recently, Morbidelli et al. (2005) proposed the capture of Trojans from the same population from which the Kuiper belt originated. The Nice model postulates that resonant interactions between Jupiter and Saturn temporarily destabilize the orbits of Uranus and Neptune, which move into the primordial Kuiper belt, scattering material widely across the solar system. In this framework, Jupiter's primordial Trojan population is lost and the Lagrange regions are repopulated with this scattered Kuiper belt material. Dotto et al. (2008) include a description of this capture scenario and a discussion of the implications for Trojans. This mechanism predicts that Trojans formed much farther out in the solar nebula (~20–35 AU). In this case, the Trojans would represent the most readily accessible repository of Kuiper belt material. In the years since those reviews, some aspects of the Nice model have been reworked, and refinements to this newer mechanism for Trojan capture have been made.

Unraveling the complex history of the Trojans promises key insight into solar system evolution. As primitive objects, Trojan compositions provide direct indicators of the conditions of the nebula in the region(s) in which they formed. As a population of small bodies, Trojans act as unique probes of the history, interaction, and physical processing of the solar system. In this chapter, we review the physical properties of Trojan asteroids and scenarios for their origin and evolution. We rely heavily on previous reviews for much of the early work (Shoemaker et al., 1989; Barucci et al., 2002; Marzari et al., 2002a; Dotto et al., 2008; Slyusarev and Belskaya, 2014), focusing here on new observations and recent advances in the knowledge of Trojans.

## 2. PHYSICAL PROPERTIES

### 2.1. Size Distribution

Most asteroid surveys are conducted in visible (reflected) light, from which it is not possible to derive the size unless the albedo is known. Studies of size distributions, therefore, often use absolute magnitude ( $H_v$ ) as a proxy for size. For a population like the Trojans, where the albedo distribution is very uniform (see section 2.2), the  $H_v$  distribution should closely match the actual size distribution. Shoemaker et al. (1989) pointed out that the largest Trojans have a fairly steeply sloped cumulative  $H_v$  distribution (see Fig. 1). Jewitt et al. (2000) measured the  $H_v$  distribution for smaller Trojans, find-

ing a shallower slope for their sample of objects with  $H_v \geq 10.5$ . They interpreted this as a break between a primordial population at larger sizes and a collisionally evolved population at smaller sizes. Trojan discoveries are now complete to a bit fainter than this [ $H_v \sim 11.5$  (Karlsson, 2010)], so it is now possible to see the break in slope clearly at  $H_v \sim 9$  by downloading and plotting data from the International Astronomical Union (IAU) Minor Planet Center (MPC). Yoshida and Nakamura (2005) conducted their own survey of small Trojans in  $L_4$ . They confirmed the shallower slope for small Trojans found by Jewitt et al. (2000) and found a second break in the  $H_v$  distribution at  $H_v \sim 16$  ( $D \sim 5$  km). In a follow-up study, Yoshida and Nakamura (2008) measured a similar slope in  $L_5$  as the intermediate ( $9 \leq H_v \leq 16$ ) size range for  $L_4$ , but no break for the smallest sizes. From the same survey, Nakamura and Yoshida (2008) confirm the previously recognized population asymmetry between the two swarms.

The Near-Earth Object Wide-field Infrared Survey Explorer (NEOWISE) project, an all-sky infrared survey (Grav et al., 2011), allows for the direct derivation of diameters, since the Trojans were detected in thermal emission. This alleviates any uncertainty in converting from absolute magnitude to diameter. Figure 1 shows the cumulative size distribution of the NEOWISE sample compared to the known population of jovian Trojans. The diameters of known objects that are not in the NEOWISE sample have been estimated using an albedo of 7% (average Trojan albedo from NEOWISE, see section 2.2) and their published absolute magnitudes from the MPC catalog. The NEOWISE sample is nearly complete for diameters larger than  $\sim 20$  km, whereas the known sample dominated by optical discoveries effectively reaches to objects with diameters of about 8–10 km. Grav et al. (2011) performed preliminary debiasing that showed a size distribution that is consistent with a cumulative power law of the form  $N(>D) \sim D^{-a}$ , where the power law index  $a = 2$ , when looking at the sample with diameters from 10 to 100 km. This is consistent with the earlier estimates by Jewitt et al. (2000), which investigated the size distribution of the smaller jovian Trojans. They surveyed a 20 degree<sup>2</sup> field in the  $L_4$  cloud reaching a limiting magnitude of  $V = 22.5$  and detected 93 jovian Trojans with diameters from 4 to 40 km (where they assumed a visual albedo of 4%). They derived a power-law index of  $2.0 \pm 0.3$  for the absolute magnitude distribution in this size range.

At diameters larger than  $\sim 80$  km the distribution is significantly steeper, but the sample is limited with only 34 objects. Shoemaker et al. (1989) estimated the cumulative power law index at  $4.5 \pm 0.9$  for objects with diameters larger than 84 km. The NEOWISE results show that the slope is even steeper than that for the largest jovian Trojans. Fraser et al. (2014) reexamined the absolute magnitude distribution of bright Trojans to compare it with that of Kuiper belt objects (KBOs). They fit the observed  $H$  distribution with an exponential law  $N(H) = 10^{\alpha H}$  in different  $H$  ranges. The best-fit for bright objects was found to be  $\alpha_1 = 1.0 \pm 0.2$ , similar to the value found by Jewitt et al. (2000) and consistent with the size distribution exponent estimated in Shoemaker

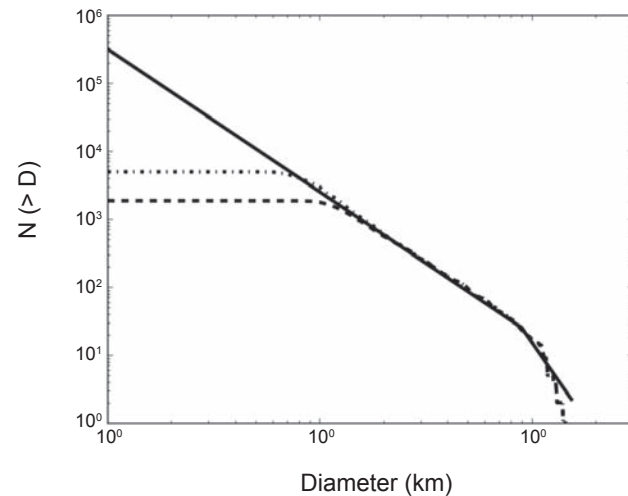


**Fig. 1.** The size distribution of the jovian Trojan population from the NEOWISE sample (dashed line) is complete for diameters larger than 20 km, while optical surveys currently sample to below 10 km (dotted line). Both samples show a size distribution with a cumulative power law index of  $\sim 2$  (solid line) for diameters between 20 and 80 km. Modified from Grav et al. (2011).

et al. (1989) and Grav et al. (2011). This fit is valid only up to a ( $r'$ -band) magnitude  $H_{\text{Break}} = 8.4^{+0.2}_{-0.1}$  beyond which the exponent changes to  $\alpha_2 = 0.36 \pm 0.01$ , compatible with the slope found by Yoshida and Nakamura (2008) and the slope of the size distribution found by the NEOWISE survey.

Comparing the size distributions of Trojans and KBOs is very important in order to test the hypothesis that Trojans are KBOs that were captured during the phase of giant planet dynamical instability (see section 4.1). Fraser et al. (2014) took into account that the albedos of Trojans and KBOs are different on average and that the albedos of red and blue KBOs are different from each other as well. In summary, they found that the parent populations of the hot classical KBOs and Trojans are statistically indistinguishable. Given that the Trojan and hot classical size distributions are distinct from other analog populations (MBAs and cold classical KBOs, respectively), Fraser et al. conclude that Trojan asteroids are derived from the hot classical Kuiper belt. The same comparison between Trojans and cold classical KBOs revealed that there is a less than 1 in 1000 probability that those two populations are drawn from the same parent distribution. This is driven by the much steeper large object slope of the cold Kuiper belt magnitude distribution (with  $\alpha_1 = 1.6 \pm 0.3$ ). According to models of dynamical capture of Trojans in the context of the Nice model (Morbidelli et al., 2005; Nesvorný et al., 2013), the bodies that are captured originate from whatever portion of the original Kuiper belt is scattered. It is now considered most likely that the hot classical population is the relic of the planetesimal disk that was scattered all over the solar system at the time of the giant planet instability (e.g., Parker et al., 2011; Morbidelli et al., 2008), part of which was captured in the Trojan region.

Thus the statistical match between the size distributions of Trojans and hot classical KBOs is important observational support of the prediction of the Nice model.

*Grav et al.* (2011) detected no significant difference in the size distributions of the leading and trailing cloud, beyond the well-established observation that the leading cloud has significantly more objects than the trailing cloud, but they did not sample the small sizes at which *Yoshida and Nakamura* (2008) noticed the difference between the two swarms. *Grav et al.* (2011) estimated the fraction of objects with diameter larger than 10 km to be  $N(\text{leading})/N(\text{trailing}) = 1.4 \pm 0.2$ , which is lower than but consistent with previous estimates of  $1.6 \pm 0.1$  derived by *Szabó et al.* (2007).

As discussed below (section 2.4), Trojans separate spectrally into two groups: a “redder” group with a steep red spectral slope and a “less-red” group with a shallower spectral slope. Using absolute magnitudes ( $H$ ) from the MPC online list of Jupiter Trojans and colors from the Sloan Digital Sky Survey (SDSS) for objects with  $H < 12.3$ , *Wong et al.* (2014) found that the two spectral groups have distinct magnitude distributions (and therefore likely distinct size distributions, given the relatively uniform albedos among Trojans). Both distributions have a break in slope near  $H \sim 8.5$ , just like the total Trojan population. The redder spectral group, however, has a shallower power-law slope on both the bright (large) and faint (small) side of the break than the less-red group, but the difference is greatest on the faint (small) side. *Grav et al.* (2012) also point out a potential trend in fraction of the two spectral/color groups with size from Wide-field Infrared Survey Explorer (WISE) data, and *DeMeo and Carry* (2014) report similar changes in abundances of the two spectral groups in their SDSS taxonomy. *Wong et al.* (2014) suggest that the different power-law slopes indicate that the two spectral groups formed in different regions of the solar nebula, and likely also point to different collisional evolutions before being captured into Jupiter’s Lagrange regions. Alternatively, a scenario in which redder objects are collisionally modified into less-red objects may also be consistent with the data.

## 2.2. Albedos

Over the first few decades of physical studies of the Trojan asteroids, thermal-infrared radiometric observations of a handful of large Trojans ( $D \geq 70$  km) from groundbased telescopes (*Cruikshank*, 1977; *Fernandez et al.*, 2003) and spacebased surveys [Infrared Astronomical Satellite (IRAS) (*Tedesco et al.*, 2002), AKARI (*Usui et al.*, 2011)] revealed visible geometric albedos ( $p_v$ ) of only a few percent, making them among the darkest objects in the solar system. The NEOWISE project (*Mainzer et al.*, 2011) obtained thermal measurements of more than 1700 known Trojan asteroids during its main cryogenic operations from January to October 2010 (Fig. 2) (*Grav et al.*, 2011, 2012). This represented an order of magnitude increase over all previous publications. The NEOWISE observed sample covers almost all the largest objects, providing a sample that is more than 80% complete down to about 10 km. The albedo distribution derived from

NEOWISE over this size range is remarkably stable, having a mean albedo of  $0.07 \pm 0.03$  across all sizes, consistent with C, P, and D taxonomic classes (see section 2.4). This average albedo is somewhat higher than found by previous studies, likely a result of different observing and analysis techniques. Nevertheless, the jovian Trojan population is one of the darkest populations in the solar system. NEOWISE detected no difference evident in the albedo distribution of the leading and trailing clouds. There is also no statistical difference in the albedo distributions of the two spectral groups described below (*Grav et al.*, 2012; *Emery et al.*, 2011).

Whereas the Spitzer Space Telescope-based observations of *Fernandez* (2009) suggested an increase in albedo at sizes smaller than 20 km, the NEOWISE observations revealed no such trend. The average albedo of Trojans remains constant down to the smallest objects observed by NEOWISE ( $\sim 10$  km). Higher albedo points in Fig. 2 represent the tail end of what appears to be a Gaussian distribution of uncertainties centered on the mean albedo of the entire population (*Grav et al.*, 2011, 2012). It is not expected that any of the small objects really have high albedos.

Note that the NEOWISE-derived albedo of the largest Trojan, (624) Hektor, is significantly higher ( $0.107 \pm 0.011$ ) than derived previously (0.022 to 0.057) using simultaneous visible and infrared photometry (*Hartmann and Cruikshank*, 1978, 1980; *Fernandez et al.*, 2003) and Spitzer Space Telescope infrared spectroscopy (*Emery et al.*, 2006). Hektor is known to be either an elongated body or contact binary, and the NEOWISE observations showed peak-to-peak amplitude of  $\sim 1$  mag over the 27 h from first to last observation. Caution should be used in radiometric interpretations of albedo without simultaneous visible photometry, particularly for objects like Hektor that are highly elongated and have large obliquities. If the NEOWISE albedo turns out to be correct, then Hektor would be remarkable not only as a contact binary with moonlets (*Marchis et al.*, 2014), but also as having an anomalously high albedo among the large Trojans.

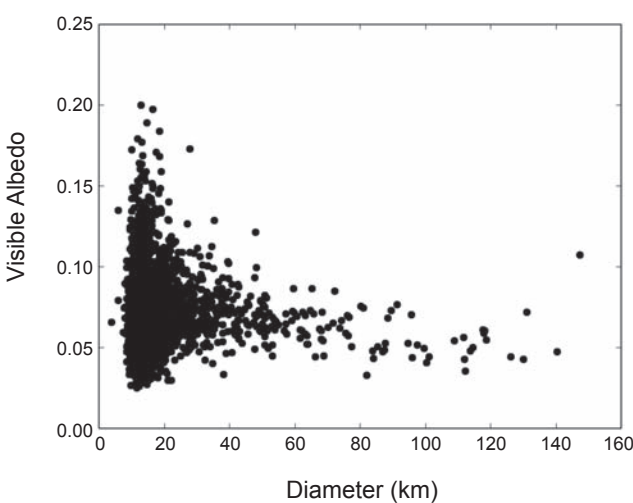


**Fig. 2.** The diameter vs. albedo distribution of the jovian Trojan population. From *Grav et al.* (2012).

*Fernandez et al.* (2003) reported an anomalously high albedo of 0.13–0.18 (depending on model parameters) for (4709) Ennomos, which they suggested might be from a recent impact excavating down to a subsurface ice layer. NEOWISE, AKARI, and IRAS all report radiometric albedos of around 0.075 for Ennomos, and *Shevchenko et al.* (2014) report occultation and phase curve observations from which they derive an albedo of 0.054. *Yang and Jewitt* (2007) see no evidence for absorptions due to H<sub>2</sub>O in near-infrared (NIR) spectra of Ennomos observed on three different nights. Unfortunately, since the rotation period is very close to 12 h [ $12.2696 \pm 0.0005$  h (*Shevchenko et al.*, 2014)], they would have been observing nearly the same hemisphere each night. It remains an open question whether Ennomos has a bright spot on its surface.

### 2.3. Rotational States and Phase Curves

Studies of asteroid light curves provide information about important properties such as rotation rates, shape, pole orientation, and surface characteristics. Rotation properties of MBAs have been shown to vary dramatically with size (*Pravec and Harris*, 2000; *Warner et al.*, 2009). The rotation of MBAs larger than ~50 km in diameter seems to be determined largely by collisions, while that of smaller bodies is shaped primarily by Yarkovsky-O'Keefe-Radzievskii-Paddack (YORP) forces and torques (*Pravec et al.*, 2008). Rotation rates of MBAs between ~0.4 and 10 km exhibit a “spin barrier” corresponding to a rotation period of ~2.2 h (summarized by *Warner et al.*, 2009). Because of their greater heliocentric distance and low geometric albedos, the Trojans have been less studied until recently.

The orbital eccentricities of the jovian asteroids are low, with a mean value of  $0.074 \pm 0.04$  (*Mottola et al.*, 2014). They are thus physically isolated from frequent dynamical interactions with other major asteroid groups. While collisions dominate the rotation periods and shapes of large MBAs, factors such as cometary outgassing, tidal braking, and YORP may be significant for the Trojans. Early work by *French* (1987), *Hartmann et al.* (1988), *Zappala et al.* (1989), and *Binzel and Sauter* (1992) suggested that larger Trojans might have, on average, higher-amplitude light curves (meaning more elongated shapes) than MBAs of a similar size. All these studies, however, were limited to different degrees either by small sample size or by observational biases favoring large amplitudes and short periods. Because determination of the true shape, surface scattering properties, and pole direction of an asteroid requires observations at many aspect angles, most recent studies have focused on rotation periods rather than systematic coverage of light-curve amplitudes and determination of pole directions. We focus first on studies of rotation periods, and will conclude with what is known about amplitudes and surface properties.

The past decade has brought the publication of several studies dedicated to eliminating observational bias in Trojan rotation data. *Molnar et al.* (2008) and *Mottola et al.* (2010) investigated medium to large Trojans (60–180 km in diam-

eter), while *French et al.* (2011, 2012, 2013), *Stephens et al.* (2012, 2014), and *Melita et al.* (2010) have focused on Trojans less than 60 km in diameter. All investigators have concluded that a significant population of Trojans rotates slowly, with periods greater than 24 h. *Mottola et al.* (2014) compared Trojan and MBAs in the size range 60–180 km, and a Kuiper nonparametric statistical test rejects the hypothesis that the two samples belong to the same population at the 5% significance level. For smaller Trojans, the overabundance of slow rotators is even more pronounced. Figure 3, from *French et al.* (2015), shows the distribution of rotation rates for Trojans less than 30 km in diameter, along with the best-fit Maxwellian curve. The Maxwellian is the distribution that would be expected if the spin vectors were oriented isotropically, with each component of the angular velocity following a Gaussian distribution. The curve has been normalized to 1 at the geometric mean rotation frequency for the sample of  $f = 1.22$  revolutions/day ( $P = 19.7$  h). The excess of slow rotators is obvious.

The presence of large numbers of slow and fast rotators has already been observed in MBAs, particularly at small diameters. *Pravec et al.* (2008), in their study of 268 small MBAs, demonstrated that the observed distribution of rotation frequencies is consistent with the YORP effect as the controlling mechanism (*Rubincam*, 2000). The YORP effect causes a prograde-rotating asteroid to speed up in its rotation and a retrograde rotator's rotation to slow. Because the YORP effect scales as  $(R^2/a^2)$ , where  $R$  is the radius of the asteroid and  $a$  is the semimajor axis of its orbit, a Trojan asteroid would be affected by YORP to a similar degree as an MBA that is about twice as large. The slow rotation of MBAs as large as (253) Mathilde, at  $R = 26$  km, has been suggested to be caused by YORP (*Rubincam*, 2000; *Harris*, 2004). Thus, Trojans with radii in the 10–15-km range ( $D = 20$ –30 km) might be expected to show evidence of YORP,

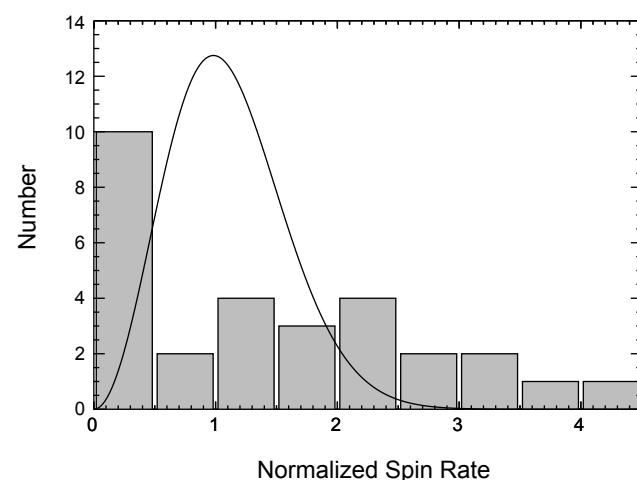


**Fig. 3.** Distribution of rotation frequencies of 31 Trojan asteroids with  $D < 30$  km vs. the best-fit Maxwellian curve. Frequencies have been normalized to the geometric mean for this group of  $\langle f \rangle = 1.22$  rotations per day ( $\langle P \rangle = 19.8$  h). From *French et al.* (2015).

and the large numbers of slow rotators in the leftmost bin of Fig. 3 suggest that they are.

What about fast rotators? The presence of a “spin barrier” at  $P \sim 2.2$  h has been well documented for MBAs. This represents the critical rotation period,  $P_C$ , at which a body without internal material strength — a rubble pile — would be spun apart by its centripetal acceleration. This period is

$$P_C \sim 3.3 \sqrt{\frac{(1+A)}{\rho}}$$

where  $P_C$  is in hours, A is the light-curve amplitude in magnitudes, and  $\rho$  is the bulk density of the body (Pravec and Harris, 2000). Figure 2 of Mottola *et al.* (2014) shows some evidence for an excess of fast rotators among Trojans as compared to the MBA population in the 60–180-km range. The French *et al.* (2015) study includes 31 well-determined light curves for sub-30-km Trojans. Currently, no Trojan has been found with a period shorter than that of (129602) 1997 WA<sub>12</sub> ( $D = 12.5$  km) at 4.84 h (French *et al.*, 2015). Several other Trojans have periods in the ~5-h range (Mottola *et al.*, 2014; French *et al.*, 2015). The observed light-curve amplitudes give density estimates of ~0.5 g cm<sup>-3</sup> if the objects are spinning at the critical period. This value would be consistent with observed comet densities (Lamy *et al.*, 2004). More observations of Trojan rotation periods are encouraged in order to locate the Trojan spin barrier, setting a limit on Trojan densities.

The most recent survey of Trojan asteroid light-curve amplitudes remains that of Binzel and Sauter (1992). After correcting for the likely bias in published light curves due to incomplete sampling at all viewing angles, they concluded that the larger Trojans ( $D > 90$  km) have higher average amplitudes, implying a more elongated shape than MBAs in the same size range. What this means in terms of the evolutionary and collisional history of the Trojans is as yet unexplained.

Most solar system bodies without atmospheres show an opposition effect (OE) — a sharp, nonlinear brightening near zero phase angle. (The phase angle is the angle between the Sun and Earth, as seen from the object. For Earth’s Moon this corresponds to a full Moon.) High-quality asteroid phase curves generally show a linear slope between phase angles of 5° and 25°, with differing slopes for different albedo asteroids (Belskaya and Shevchenko, 2000). At phase angles less than 5°, an opposition surge is observed; this is now understood as due to coherent backscattering, as it is stronger for higher-albedo surfaces (Muinonen *et al.*, 2002). Phase curves for Trojan asteroids are linear down to phase angles of ~0.1°–0.2° (Shevchenko *et al.*, 2012). This linear behavior differs dramatically from the sharp opposition spikes seen in several Centaurs, and is similar to what is observed for dark outer MBAs and Hilda asteroids (Shevchenko *et al.*, 2012). Shevchenko *et al.* (2012) attribute the absence of a strong opposition surge to the low albedos of Trojan asteroids. For such low albedos, multiply scattered light, which is required for the coherent-backscatter opposition effect to occur, does not provide a significant contribution to the reflected flux.

## 2.4. Spectral Properties

The first visible-wavelength reflectance spectra of Trojan asteroids were featureless, but the relatively steep, red spectral slopes were excitingly interpreted to indicate the presence of abundant complex organic molecules on the surfaces, masking an ice-rich interior (Gradie and Everka, 1980). Over the following two decades, reflectance spectroscopy at VNIR wavelengths continued to show a range of spectral slopes, but no absorption features (see Dotto *et al.*, 2008), placing strong constraints on the presence of ice near the surfaces and on the presence and form of organic material. Recent dedicated spectral searches for ices in the Eurybates family (DeLuise *et al.*, 2010), on several large Trojans, including Ennomos (Yang and Jewitt, 2007), and on several of the smaller ( $D \sim 10$ –30 km) Trojans for which the NEOWISE survey suggests high albedos (Marsset *et al.*, 2014), as well as a general NIR survey [0.7–2.5 μm (Emery *et al.*, 2011)] still reveal no spectral absorption bands. Yang and Jewitt (2011) reobserved seven large Trojans whose spectra had hinted at a possible broad 1-μm silicate band, but those also turned out to be featureless.

Statistical analyses of VNIR colors and spectra have revealed the presence of two distinct spectral groups (Fig. 4), a “red” group consistent with the asteroidal D-type taxonomic class and a “less-red” group consistent with the asteroidal P-type classification (Szabó *et al.*, 2007; Roig *et al.*, 2008; Emery *et al.*, 2011; Grav *et al.*, 2012). Emery *et al.* (2013) supplemented the NIR sample with 20 additional L<sub>5</sub> Trojans, showing that the two spectral groups appear to be equally distributed in the two swarms. The NIR sample is restricted to objects larger than ~70 km, and it is not yet clear if the bimodality extends to smaller sizes (e.g., Karlsson *et al.*, 2009). Emery *et al.* (2011) suggest that the spectral groups represent two compositional classes that potentially formed in different regions of the solar nebula. Otherwise, no strong correlations between spectral and any physical or orbital parameter are present (Fornasier *et al.*, 2007; Melita *et al.*, 2008; Emery *et al.*, 2011), although Szabó *et al.* (2007) suggest a weak correlation of color with orbital inclination in the L<sub>4</sub> swarm that Fornasier *et al.* (2007) attribute to the presence of the Eurybates family. Brown *et al.* (2014) presented spectra in the 2.85–4.0-μm region showing a possible absorption for a few “less-red” Trojans similar to that seen on (24) Themis (Campins *et al.*, 2010; Rivkin and Emery, 2010). The objects that Brown *et al.* (2014) observed from the “red” group showed no absorption.

Mid-infrared (MIR) (5–38 μm) emissivity spectra have been published of four Trojan asteroids [(624) Hektor, (911) Agamemnon, (1172) Aneas, and (617) Patroclus], and all four show strong emissivity peaks near 10 and 20 μm (Emery *et al.*, 2006; Mueller *et al.*, 2010). It is interesting to note that although the emissivity features seen in Patroclus, the only “less-red” object among the four, are in the same location as for the other three Trojans, the spectral contrast is significantly weaker. Whether this is a trend that follows the spectral groups remains to be discovered. From mutual eclipses of the binary

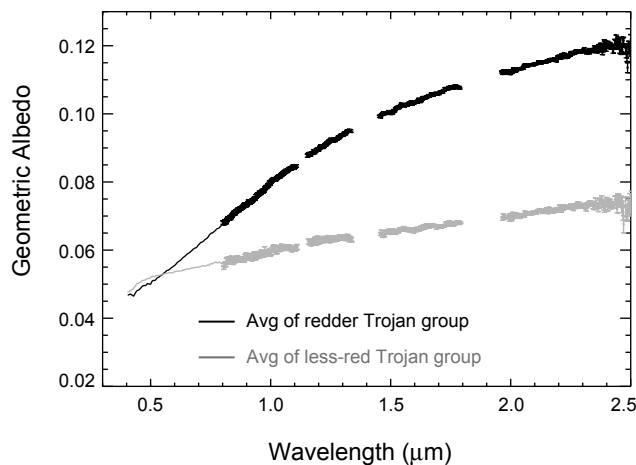


**Fig. 4.** Combined visible and NIR average spectra of the two spectral groups. The spectral groups are separated more clearly when both visible and NIR wavelength ranges are considered. These spectra have been scaled to  $p_v = 0.055$ . From Emery et al. (2011).

components, Mueller et al. (2010) derived a very low thermal inertia ( $\sim 6\text{--}20 \text{ J m}^{-2} \text{ K}^{-1} \text{ s}^{-1/2}$ ) for Patroclus. Thermal spectral energy distributions of other (large) Trojans are also consistent with very low thermal inertia surfaces (e.g., Fernandez et al., 2003; Emery et al., 2006), suggesting very fine grained, porous regoliths. Horner et al. (2012) computed a slightly higher thermal inertia of  $25\text{--}100 \text{ m}^{-2} \text{ K}^{-1} \text{ s}^{-1/2}$  for (1173) Anchises, but still consistent with a “fluffy” regolith.

## 2.5. Binarity/Densities

Binaries provide invaluable data about the physical nature of asteroids. Two are presently known among the Trojans, and they present intriguing comparisons. (617) Patroclus has a less-red surface, and the two components are nearly equal in size (Merline et al., 2002). The bulk density of the components is  $1.08 \pm 0.33 \text{ g cm}^{-3}$  (Marchis et al., 2006). The orbit is nearly circular, and the rotation periods appear to be synchronized with the orbital motion, implying that the bodies are in a principal-axis rotation state (Mueller et al., 2010). The 102.5-h period is well explained by tidal braking. (624) Hektor, on the other hand, has a rotation period of 6.924 h and appears to be either a contact binary or one extremely elongated object with a small moon  $\sim 12 \text{ km}$  in diameter (Marchis et al., 2014). Its bulk density has been determined to be  $1.0 \pm 0.3 \text{ g cm}^{-3}$  (Marchis et al., 2014), very close to that of the Patroclus system. Hektor has a redder spectrum (Emery et al., 2011), suggesting a possible difference in composition. Analysis of the Hektor system suggests a high-inclination ( $\sim 166^\circ$ ) and high-eccentricity ( $\sim 0.3$ ) orbit for the satellite, with an orbital period just between two spin-orbit resonances. This implies that the orbit has not evolved significantly since the formation of the system and is therefore primordial (Marchis et al., 2014). Most recently, Descamps (2015) reanalyzed light-curve data and adaptive

optics images of the Hektor contact binary in terms of a dumbbell shape, finding a better fit to the data and a smaller volume than the previous shape model. This smaller volume results in a higher density estimate of  $2.43 \pm 0.35 \text{ g cm}^{-3}$ . Hektor and Patroclus may therefore have different internal structures as well as belonging to different spectral groups.

Searches for other Trojan binaries have been undertaken by several researchers. In a study of light-curve amplitudes, Mann et al. (2007) report two objects with light-curve amplitudes of  $\sim 1 \text{ mag}$  [(17365) 1978 VF<sub>11</sub> and (29314) Eurydamas] and suggest these might be contact binaries. From their survey of 114 Trojans, they estimate that 6–10% of Trojans might be contact binaries. While observing a stellar occultation by (911) Agamemnon, Timerson et al. (2013) detected a brief dip after the main occultation, which they interpret as a potential moonlet. Most recently, Noll et al. (2013) observed eight outer main belt and Trojan asteroids with long rotational periods. No binaries were found, and those authors concluded that binaries are less frequent in the outer main belt and Trojan regions than in the Kuiper belt.

## 2.6. Physical Interpretation of Observations

In some ways, it seems that the Trojans are conspiring to keep the secret of their compositions and physical structure hidden. Nevertheless, the persistent effort of characterization described in the previous sections is paying off. The clearest indication of internal structure comes from the determination that (617) Patroclus and (624) Hektor both have bulk densities near  $1 \text{ g cm}^{-3}$ . This low density, relative to rock and even carbonaceous chondrites, indicates either a significant low-density component (i.e., ice), a large macroporosity, or, more likely, a combination of the two. However, the interpretation for Hektor’s interior will differ if the latest, higher-density estimate is correct. The distribution of rotation rates and sizes have both been used to argue for a division in which the largest Trojans ( $D > 80\text{--}130 \text{ km}$ ) are intact, primordial planetesimals, whereas the smaller bodies are collisional fragments (Binzel and Sauer, 1992; Jewitt et al., 2000; Yoshida and Nakamura, 2005, 2008; Grav et al., 2011; Fraser et al., 2014). If the internal compositions are distinct from surface compositions (i.e., if a surface crust hides an ice-rich interior), one would expect the properties of smaller Trojans to be systematically different from those of larger Trojans. The small Trojans are at the limit of current observing capabilities from most characterization techniques, but there does not appear to be a systematic difference between large and small Trojans.

The featureless VNIR spectra can be used to assess what is *not* on Trojan surfaces, but do not give a clear indication of what *is* on these surfaces. The red VNIR slopes have often been cited as suggestive of abundant organic material. However, Emery and Brown (2003, 2004) argue that the absence of strong absorptions in the  $2.85\text{--}4.0 \mu\text{m}$  spectral range strongly limits the types and abundance of organics, and therefore the spectral slopes cannot be due to organics. Rather, they and Emery et al. (2011) demonstrate that the

featureless, low-albedo, red-sloped VNIR spectra can be fit by amorphous and/or space-weathered silicates. Spectral models have been used to place upper limits of only a few weight % of H<sub>2</sub>O ice on the surfaces (e.g., *Emery and Brown*, 2004; *Yang and Jewitt*, 2007).

The MIR emissivity spectra that have been published demonstrate convincingly that Trojan surfaces are populated by silicate dust. The large spectral contrast and positive polarity (i.e., that the features appear as peaks rather than valleys) indicate that the dust is very fine-grained ( $\leq 10\text{-}\mu\text{m}$ -sized grains) and that the grains are fairly well separated (*Emery et al.*, 2006). No cometary (extended) emission has been detected around Trojans, so these spectra provide constraints on the surface structure. *Vernazza et al.* (2012) investigated a model in which the regolith is very porous (i.e., an extreme “fairy-castle” structure; Fig. 5a) using laboratory measurements of meteorite powders mixed with KBr. Their experiments demonstrate the viability of reproducing the MIR spectra, and they find that the features indicate dust composed primarily of amorphous forsteritic olivine, but with a nonnegligible crystalline fraction as well. This model is consistent with the very low thermal inertias measured for Trojans. *Yang et al.* (2013), on the other hand, envision a surface where silicates are embedded in a transparent matrix. They demonstrate, with laboratory measurements and spectral modeling, that salts could provide the matrix, and discuss possible evolutionary scenarios (Fig 5b). In either case, the MIR emissivity spectra point to a silicate fraction that is compositionally similar to cometary silicates (*Emery et al.*, 2006; *Vernazza et al.*, 2012).

### 3. ORIGIN AND EVOLUTION

#### 3.1. Origin of Jupiter Trojans

The capture mechanisms proposed so far for explaining the presence of Trojan populations in the Lagrange regions of the planets can be broadly divided into two main classes:

1. Trapping due to nongravitational perturbations on primordial planetesimals passing by the planet. Trapping can occur because of:

- Drift into the Trojan region due to the action of a dissipative force like gas drag (*Yoder*, 1979; *Peale*, 1993) or the Yarkovsky effect. These processes affect small bodies, which could have subsequently grown into larger asteroids once trapped in tadpole orbits.
- Collisions occurring close to the resonance border that can inject fragments into Trojans orbits (*Shoemaker et al.*, 1989).

2. Changes in the physical and orbital parameters of the planet, which can lead to a shift in the position of the Lagrange points, causing the capture of local planetesimals. Four specific mechanisms have been proposed:

- Mass growth of the planet, which causes an expansion of the resonant area, capturing close-by planetesimals as Trojans (*Marzari and Scholl*, 1998a,b; *Fleming and Hamilton*, 2000).

- Smooth migration of the planet, during which objects are swept into the Lagrange regions (*Lykawka et al.*, 2009).
- Crossing of a mean-motion resonance of the planet with another planet. A chaotic path can be opened during the evolution due to secular resonance sweeping and the superposition of secondary resonances between harmonics of the Trojan libration frequency and the critical argument of mean-motion planetary resonance. Planetesimals can be trapped in tadpole orbits via this chaotic path, which is closed once the resonance crossing has taken place (*Morbidelli et al.*, 2005; *Marzari and Scholl*, 2007). The crossing of the 2:1 resonance between Jupiter and Saturn has been invoked in the Nice model to explain the capture of the Jupiter Trojans.
- “Jumping Jupiter,” which is a period of instability of the planet orbit due to close encounters with a second planet, causing steps in semimajor axis that may lead to the capture of leftover planetesimals due to their sudden dislocation within the stable tadpole regions of the planet (*Nesvorný et al.*, 2013). This might explain an asymmetry between L<sub>4</sub> and L<sub>5</sub> since the perturbing planet may temporarily cross the Trojan region, dispersing a fraction of the local population.

The early models of the origin of Jupiter Trojans are reviewed in *Marzari et al.* (2002a). In essence, they considered capture by gas drag or the pull-down process, which is due to the broadening of the tadpole region around the Lagrange triangular points occurring during the increase of the mass of the planet. Both of these models have several problems in reproducing the observations, the most severe of which is the inclination distribution. Jupiter’s Trojans cover the inclination range 0°–35°, with a median inclination of 10° (which becomes 18° for bright Trojans with H < 12, for which our knowledge of the population is bias free), and the aforementioned capture models had problems explaining any significant inclination excitation.

It is worth noting that for the Trojan population the eccentricity excitation is much less than twice the inclination excitation (the relationship expected for a randomly excited disk). In fact, the eccentricities are smaller than 0.15, with a few exceptions. But this is due to the boundaries of the stability region. *Levison et al.* (1997) mapped these boundaries with long-term numerical simulations and demonstrated that the Trojans fill the entire region that is stable over the age of the solar system.

A decade ago, *Morbidelli et al.* (2005) proposed a radically different model for the origin of the Trojans, developed in the framework of a scenario later named the “Nice model.” In the original version of the Nice model, the giant planets formed in a more compact configuration on quasicircular and coplanar orbits. The planets migrated slowly in divergent directions as they scattered planetesimals, originally located beyond Neptune’s orbit. As the initial ratio of the orbital periods of Saturn and Jupiter was postulated to be slightly less than 2, the divergent migration brought these planets to

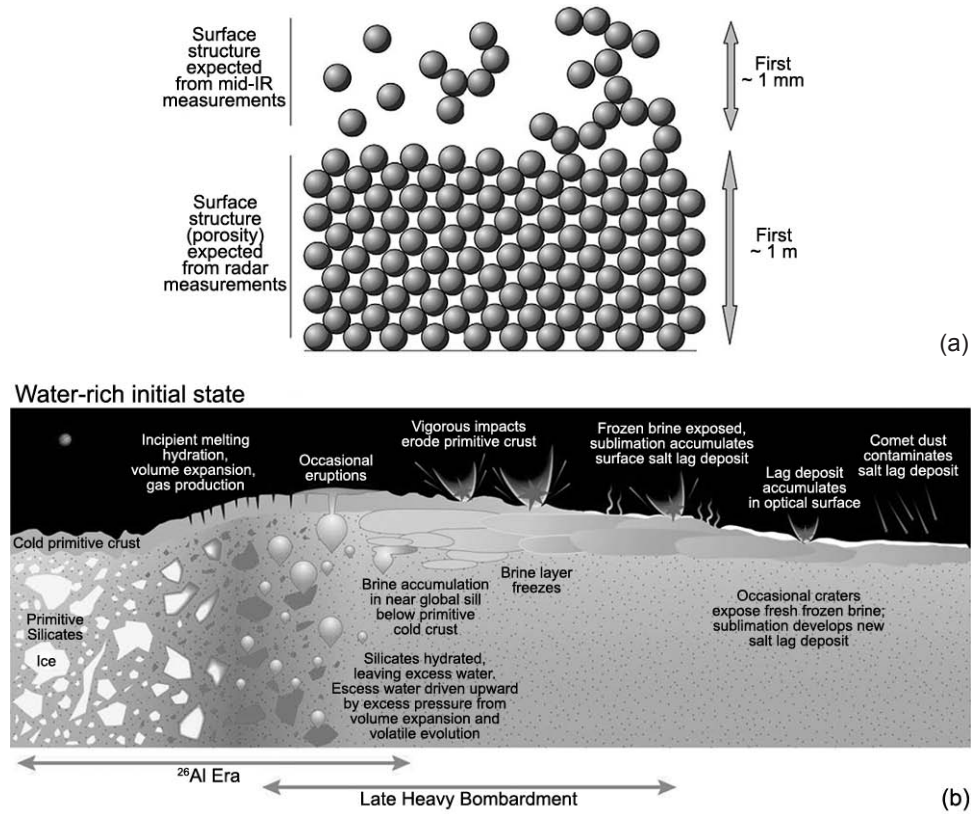


**Fig. 5.** See Plate 1 for color version. (a) Schematic model of an underdense, “fairy-castle” regolith on Trojan asteroids deduced from comparisons between MIR emissivity spectra of Trojans and laboratory measurements of powdered meteorites mixed with KBr. From Vernazza et al. (2012). (b) Evolutionary scenario that might produce salt-rich surfaces, in which embedded fine-grained silicate dust could explain measured MIR emissivity spectra of Trojans. From Yang et al. (2013).

cross their mutual 1:2 mean-motion resonance. This resonance crossing excited the eccentricities of Jupiter and Saturn and destabilized the planetary system as a whole. A phase of close encounters among the planets followed, with Uranus and Neptune scattered outward onto large-eccentricity orbits. Thus Uranus and Neptune dispersed the original transneptunian disk and, by a feedback process, all planetary eccentricities were damped to moderate values, consistent with the current ones, and the giant planet system eventually developed the current orbital configuration. In this model, the capture of Trojans occurred during the 1:2 resonance crossing. In fact, the tadpole region becomes fully unstable when the planets are near this resonance. This means that the planetesimals scattered from the transneptunian region can enter and exit the tadpole region. But when Jupiter and Saturn migrate far enough from the 1:2 resonance, the tadpole region suddenly becomes stable. The planetesimals that are there at that time are then trapped forever. A detailed map of the stability of the tadpole region as a function of the Saturn/Jupiter period ratio can be found in Robutel and Bodossian (2009).

Thus, the Morbidelli et al. (2005) paper was the first prediction of capture of Jupiter Trojans from the transneptunian disk. The simulations allowed reproducing, at least

qualitatively, the distribution of the observed Trojans in eccentricity, inclination, and libration amplitude. The capture probability into the Trojan region was shown to be large enough to justify the currently observed population, starting from a primordial transneptunian disk of  $50 M_{\oplus}$ , with a Kuiper-belt-like size-frequency distribution.

The original version of the Nice model, however, proved to be not entirely satisfactory. Further investigation of the dynamics of the giant planets in the primordial disk of gas showed that the giant planets should have emerged from the gas-disk phase locked in mean-motion resonances with each other (Morbidelli et al., 2007; Walsh et al., 2011; see Morbidelli, 2013, for a review). The instability of the planetary system then occurred when two planets fell off resonance, under the perturbations of the planetesimal disk and not when Jupiter and Saturn crossed their 1:2 mean-motion resonance (Levison et al., 2011). Also, of all the possible evolutions that the giant planets can follow during the instability phase, it was shown that the only acceptable ones are the “jumping Jupiter type,” which are evolutions in which Jupiter scatters outward a planet (Uranus, Neptune, or a rogue fifth planet of comparable mass) that had been previously scattered inward by Saturn. In this case, the

period ratio between Saturn and Jupiter impulsively jumps up. This is needed because otherwise the slow increase in the orbital separation between Saturn and Jupiter drives secular resonances across the asteroid belt (*Morbidelli et al.*, 2010) and the terrestrial planet region (*Brasser et al.*, 2009), leaving both populations on orbits inconsistent with the current ones. For this not to happen, the period ratio between Saturn and Jupiter has to jump from the original value of  $\sim 1.5$  (the 2:3 mean-motion resonance) to more than 2.3. This has become a basic requirement of success for the modern Nice model simulations (see, e.g., *Nesvorný and Morbidelli*, 2012). In this case, however, there is no 1:2 resonance crossing and the original Trojan capture model of *Morbidelli et al.* (2005) is invalidated.

*Nesvorný et al.* (2013) have reinvestigated the possibility of capture of Jupiter Trojans in the framework of the jumping-Jupiter scenario. They did this using three simulations of evolution of the giant planets [all starting initially with five planets (see *Nesvorný and Morbidelli*, 2012)] satisfying all constraints, particularly the jump of the period ratio to a value larger than 2.3, with a residual migration not driving the period ratio beyond 2.5 (the 2:5 resonance). These planetary evolutions are shown in Fig. 6.

They found that Trojans can be captured during Jupiter's jump. In essence, the captured planetesimals are those that, by chance, are on a moderate eccentricity orbit just inward of Jupiter's location at the time of the jump. When Jupiter jumps inward, these planetesimals can then fortuitously find themselves in the tadpole region. This mechanism is illustrated in Fig. 7.

Most of the captured planetesimals turned out to be only temporarily stable, so *Nesvorný et al.* (2013) continued the simulations of the captured bodies over 4 G.y. and finally they analyzed the orbits of the Trojans surviving in the tadpole region until the end. The resulting orbital distribution turned out to be remarkably similar to that observed. This is illustrated in Fig. 8 through cumulative distributions. Only the inclination distribution seems inaccurate, the observed one being less excited than the synthetic one. However, the Trojans' observed distribution is biased toward low inclinations. To remove the bias, *Nesvorný et al.* also considered the Trojans with  $H < 12$ , which constitute a complete set (*Szabó et al.*, 2007). The match becomes excellent. This model reproduces the observed distribution even better than the original 2005 model.

In addition to the orbital distribution, there are two qualitative advantages of the new model over the previous one. First, this model has the potential to explain the  $\sim 30\%$  asymmetry between the  $L_4$  and  $L_5$  populations. In fact, unlike the previous model, which was strictly symmetric for the two tadpole regions, the new model can capture more or fewer bodies in one of the two clouds depending on the specific geometry of the planetary encounter that causes the jump in Jupiter's orbit. Imagine, for instance, that the rogue planet passes through one of the two tadpole regions coming out of its last encounter with Jupiter, and it is intuitive to understand that fewer bodies will remain stable there. Indeed, the three simulations presented in *Nesvorný et al.* (2013) produced asymmetries at the 30–80% level (not necessarily in favor of  $L_4$ ).

The second advantage is that in the new model, the capture of Trojans occurs with some time-lag relative to

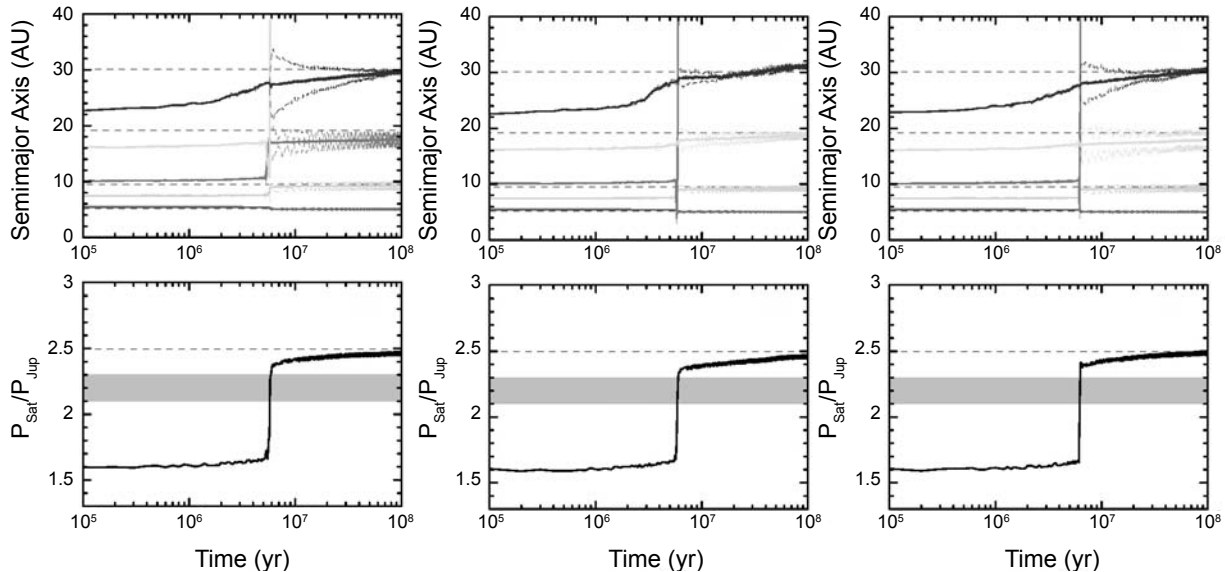


**Fig. 6.** The evolution of the giant planets in the three simulations considered in *Nesvorný et al.* (2013) for the capture of Jupiter's Trojans. The top panels show the evolution of semimajor axis (solid), perihelion and aphelion distances (dashed) for Jupiter (bottom, dark gray), Saturn (second from bottom, light gray), Uranus (middle, dark, or light gray, depending on which remains), Neptune (top, dark gray), and the planet ultimately ejected from the system (middle, light or dark gray, depending on which is ejected). The lower panels show the evolution of the period ratio between Jupiter and Saturn. The gray band shows the forbidden region, corresponding to secular resonances in the asteroid belt or in the terrestrial planet region.

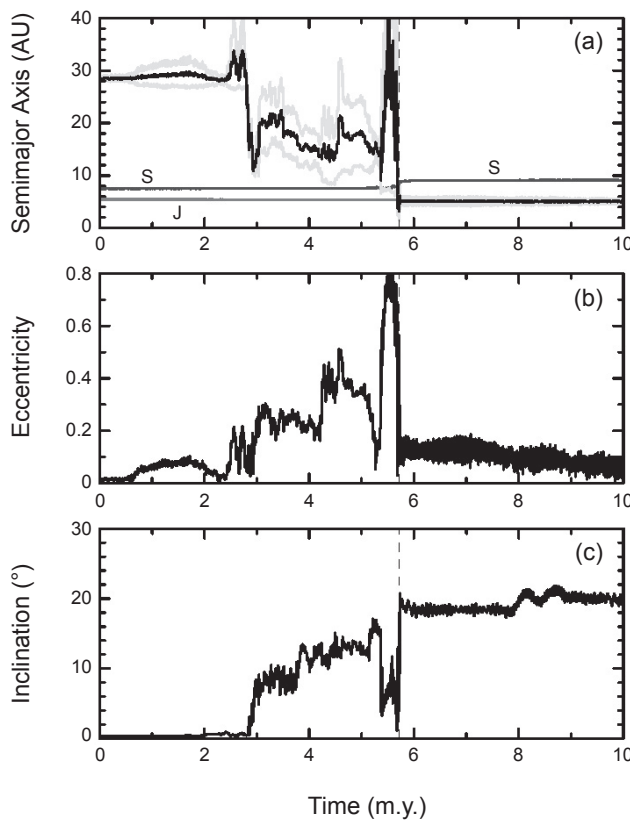


**Fig. 7.** An example of capture of a Trojan body. **(a)** Evolution of semimajor axis of the body in black and of its perihelion and aphelion distances (light gray), together with the semimajor axes of Jupiter (bottom gray curve marked “J”) and Saturn (dark gray curve marked “S”). Notice the perfect overlapping of the particle’s semimajor axis, perihelion, and aphelion and Jupiter’s semimajor axis at the end, proving the capture of a low-eccentricity Trojan. **(b)** Evolution of the eccentricity of the captured particle. **(c)** Evolution of the inclination of the captured particle. From Nesvorný et al. (2013).

the onset of the instability of the giant planets. The latter occurs when two planets fall out of resonance, whereas the capture of Trojans occurs during the last encounter of Jupiter with the scattered planet, which can only take place once the unstable phase is occurring. By contrast, in the original model the capture occurred at the 1:2 resonance crossing, which triggered the instability. The difference may be important for the capture of asteroids into Lagrange regions. If the capture of Trojans occurs at the beginning of the planet instability, the asteroid belt does not have the time to be partially destabilized and therefore asteroids cannot be captured in the Trojan region. However, this can occur in the new model. Thus, this opens the possibility that some Trojans, for instance, those consistent with the asteroidal C-types, which are a minority of the Trojan population, may come from the outer asteroid belt.

Nesvorný et al. (2013) found that the probability of an original transneptunian object to be captured over the age of the solar system as a Trojan is  $6\text{--}8 \times 10^{-7}$ . This implies  $3\text{--}4 \times 10^7$  planetesimals with  $H < 9$  ( $D > 80$  km for  $a = 7\%$  albedo) in the original transneptunian disk. With a Kuiper-belt-like size frequency distribution, this is consistent with the mass needed in the new version of the Nice model (Nesvorný and Morbidelli, 2012). This disk population is also consistent with the crater record on Iapetus (Rivera-Valentin et al., 2014), showing the overall consistency of the new Nice/jumping-Jupiter model.

Thus, the Nesvorný et al. (2013) model reinforces the idea that most Trojans are objects captured from the transneptunian disk. The same disk also gave origin to the hot Kuiper belt population and the scattered disk (Levison et al., 2008), whereas the cold Kuiper belt population might have been a separate population not significantly affected during the giant planet instability (Parker and Kavelaars, 2012; Batygin et al., 2011; Fraser et al., 2014). Because both the hot population and the Trojan population should not have suffered any significant collisional evolution at large sizes since the time

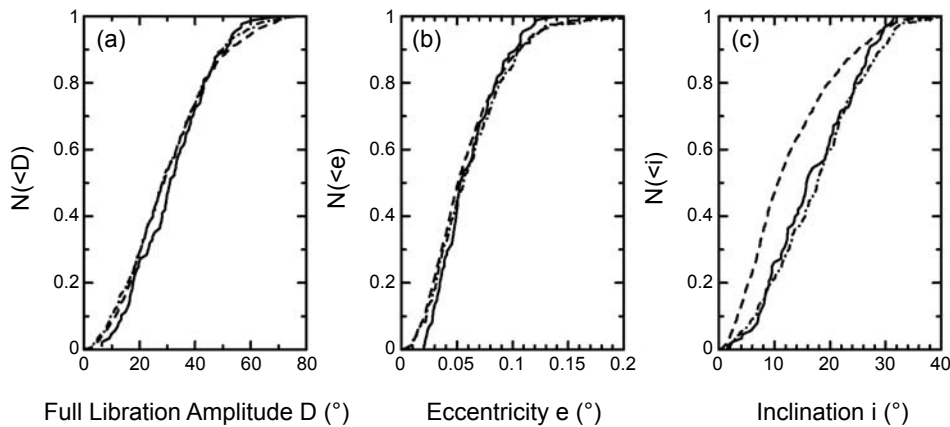


**Fig. 8.** The cumulative distribution of real (dashed) and captured Trojans (solid) in **(a)** libration amplitude, **(b)** eccentricity, and **(c)** inclination. In **(c)**, the dash-dotted curve shows the observed inclination distribution of Trojans with  $H < 12$ . Unlike the dashed distribution, the latter should be bias free. From Nesvorný et al. (2013).

of giant planet instability (Levison *et al.*, 2009), Morbidelli *et al.* (2009) predicted that size distributions of the Trojans and of the hot population should have been the same. At the time, this was a real prediction, because the size distribution of the hot population was known only for sizes much larger than the largest Trojan, and it looked much shallower. So, the prediction was that at sizes comparable to those of the Trojans (less than 200 km in diameter), the size distribution of the hot population would steepen up and look like that of the Trojans. This prediction has been recently supported by Fraser *et al.* (2014) and confirmed by Adams *et al.* (2014). We refer the reader to section 2.1 for a more detailed discussion of the Trojans' size distribution.

### 3.2. Stability Properties

The dynamical stability of Trojans is affected by different types of resonances that influence their survival in the present solar system and may have even played a significant role during the potential migration of planets in early solar system evolution. These resonances involve the fundamental frequencies of the Trojan motion, which can be related by a ratio of two small integers to those of the planetary system. Approximate analytical expressions have been derived for the frequencies of the Trojan motion within the simplified elliptical restricted three-body problem (ERTBP). The libration motion around either  $L_4$  or  $L_5$  is characterized by a long-period frequency given by  $v_l = \frac{1}{2} [1 - \sqrt{1 - 27\mu(1 - \mu)}]^{\frac{1}{2}} n_p = \sqrt{27/4\mu} n_p$  and a short-period frequency  $v_s = \frac{1}{2} [1 + \sqrt{1 - 27\mu(1 - \mu)}]^{\frac{1}{2}} n_p \approx \sqrt{1 - 27/4\mu} n_p$  (Erdi *et al.*, 2007, 2009), where  $\mu = \frac{m_p}{m_s + m_p}$  is the mass ratio and  $n_p$  is the planet mean motion. As an example, for Jupiter's Trojans  $T_l \approx 147.8$  yr and  $T_s \approx 11.9$  yr. The secular frequency of the perihelion longitude precession  $g^{\text{ERTBP}}$  is analytically given, at the second order in the libration amplitude  $d$ , as  $g^{\text{ERTBP}} = (27/8 + (129/2^6)d^2)\mu n_p$  (Erdi, 1988), while the precession frequency of the nodes is computed as  $s^{\text{ERTBP}} = 3/4d^2\mu n_p$ . In the more general problem of the Trojan motion in the full planetary system, the values of the frequencies  $v_{ls}$ ,  $g$ , and  $s$  depend on the orbital elements of the Trojan orbit and of the planets. In particular, the secular frequencies  $g$  and  $s$  include the contribution of the planets, becoming  $g = g^{\text{ERTBP}} + \sum_{j \neq p} g_j$  and  $s = s^{\text{ERTBP}} + \sum_{j \neq p} s_j$ , where  $g_j$  and  $s_j$  are the eigenfrequencies of the classical Lagrange-Laplace solution of the secular problem. Precise semi-empirical expressions have been derived for  $g$  and  $s$  as a function of the Trojan orbital parameters, fitting the outcomes of direct numerical integrations of Trojan trajectories and of all the planets of the solar system (Marzari *et al.*, 2002b, 2003a,b; Scholl *et al.*, 2005b). An integer, or near integer, relation between a frequency of the Trojan motion and one or more frequencies of the planets leads to a resonant interaction that can destabilize the tadpole motion. The possible different types of resonances have been grouped (Robutel and Gabern, 2006; Erdi *et al.*, 2007; Robutel and Bodossian, 2009) into four families:

*Family I:* Commensurabilities between the orbital frequency of the planet  $n_p$  and the libration frequencies of the Trojan

motion  $v_l$  and  $v_s$  enriched by additional secular frequencies of the planetary system. They are defined by the expression  $iv_{ls} + jn_p = -(kg + ls + \sum_n k_n g_n + \sum_n l_n s_n)$  where  $i, j, k, l, k_n, l_n$  are integers satisfying the relation  $j + k + l + \sum_n k_n + \sum_n l_n = 0$  imposed by the d'Alembert rules.

*Family II:* Commensurabilities between  $v_l$ ,  $v_s$  and the libration frequency  $\psi_{p,q}$  of the critical angle  $\theta = p\lambda_m - q\lambda_n + \dots$  of a  $p:q$  mean-motion resonance between two planets,  $n$  and  $m$ , defined as  $\psi_{p,q} = pn - qn_m$ . In this case the relation among the frequencies becomes  $iv_{ls} - j\psi_{p,q} = -(kg + ls + \sum_n k_n g_n + \sum_n l_n s_n)$ , with  $j(q-p) + k + l + \sum_n k_n + \sum_n l_n = 0$ . In the solar system, an important almost-resonance between Jupiter and Saturn is the so-called "great inequality 5:2."

*Family III:* Secular resonances between  $g$ ,  $s$ , and the eigenfrequencies of the solar system, defined by the condition  $kg + ls = -(\sum_n k_n g_n + \sum_n l_n s_n)$  and  $k + l + \sum_n k_n + \sum_n l_n = 0$ .

*Family IV:* Commensurabilities between the libration frequency of the planetary resonance  $p:q$  and the secular frequency of the Trojan motion  $g$  defined as  $ig + j\psi_{p,q} = -(ls + \sum_n k_n g_n + \sum_n l_n s_n)$  with  $i + j(q-p) + l + \sum_n k_n + \sum_n l_n = 0$ .

Present Jupiter Trojans are perturbed by all these families of resonances. Overlap of these resonances generates extended chaotic regions, which limits the extent of the phase space populated by stable orbits. In Fig. 9, a diffusion map (Robutel and Gabern, 2006) shows the stability properties of fictitious Trojan orbits of Jupiter as a function of their initial semimajor axis and eccentricity. The color coding measures the diffusion rate in the phase space computed by means of frequency map analysis (FMA) (Laskar, 1990), a powerful numerical tool for the detection of chaos from numerical integration. The color scale ranges from blue, corresponding to stable regions, to red for highly chaotic orbits, while in black are displayed those test bodies that are ejected on a short timescale. The red arch limiting the stable region from above is due to the family III nodal secular resonance  $s - s_6$ , as clearly shown in the power spectrum of a Trojan orbit lying close to the arch (Fig. 10) (Marzari *et al.*, 2003a). For higher inclinations of the test Trojan orbits, additional secular resonances such as  $s - 2s_6 + s_7$ ,  $3s - 4s_6 + s_7$ ,  $2s - 3s_5 + g_6$ ,  $3s - s_6 - 2g_5$ , and others come into play, reducing the size of the stable region. Superposition of family I resonances is responsible for the large chaotic zone extending beyond 5.35 AU, limiting the libration amplitude of Trojan orbits. The  $i = 13$  and  $i = 14$  family I resonances generate the two main v-shaped unstable yellow structures within 5.25 AU. Family II resonances, whose influence was also argued by Nesvorný and Dones (2002), are responsible for the finger-like structures extending from the outer layer of the stable region toward small eccentricities in between 5.25 and 5.35 AU. Finally, the thin yellow structures in the small libration region for  $a \leq 5.27$  are due to family IV resonances. When the initial inclination of the orbits is varied, all resonances change location since the main frequencies of the Trojan motion ( $v$ ,  $g$ , and  $s$ ) depend on inclination, but they are still responsible for the main features of the stable regions.

The resonant structure described above evolves during planet migration and can explain the chaotic capture of

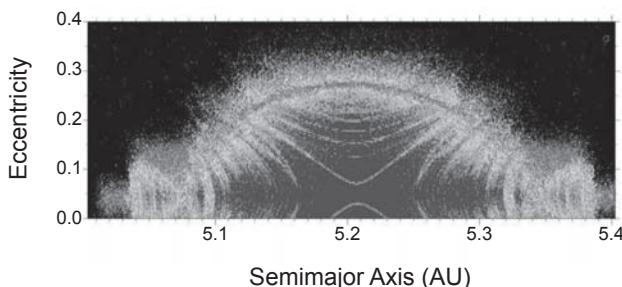


**Fig. 9.** See Plate 2 for color version. Diffusion map around  $L_4$  for an N-body model including the outer four planets. Blue indicates stable orbits while red corresponds to highly chaotic motion. The black zone marks trajectories that lead to ejection from  $L_4$  on a short timescale. From Robutel and Gabern (2006).

primordial Trojans in the original version of the Nice model (Morbidelli *et al.*, 2005). In a simplified four-body model with Jupiter and Saturn migrating through the 1:2 mean-motion resonance, Marzari and Scholl (2007) showed that a secular resonance (family III) between  $g$  and one of the two eigenfrequencies of the planetary system sweeps the Trojan region, leading to a chaotic evolution. This instability is reinforced by the sweeping of family II and family IV resonances (Morbidelli *et al.*, 2005; Robutel and Bodossian, 2009), with family IV resonances being more effective close to the resonance. Family II resonances with  $\psi_{2,1}$ ,  $\psi_{3,1}$ ,  $\psi_{4,1}$ , and  $\psi_{5,2}$  contribute to instability with different strengths during the migration of Jupiter and Saturn through the 1:2 and toward the 2:5 mean-motion resonances.

According to the numerical explorations of Nesvorný and Dones (2002) and Marzari *et al.* (2002b) with chaos detection tools, Saturn Trojans are mostly unstable and any primordial population should have been severely depleted at present. The fast diffusion in the phase space is due to family III secular resonances like the  $2g_6 - g_5$  and family II resonances with  $\psi_{5,2} = 5n_J - 2n_s$ . The same fate is shared by Uranus Trojans, which are affected by secular resonances with  $s_7$ ,  $g_7$ , and  $g_5$  (Marzari *et al.*, 2003b) and by family II resonances with  $\psi_{2,1} = 2n_U - 1n_N$  (Nesvorný and Dones, 2002). The situation is different for Neptune Trojans, which, in spite of some perturbations from the  $s_8$ , have large regions of stability with low diffusion speed (Marzari *et al.*, 2003b; Nesvorný and Dones, 2002).

The long-term stability of Venus, Earth, and Mars Trojans have been investigated mostly with Laskar's FMA (Scholl *et al.*, 2005a,b; Dvorak *et al.*, 2012; Marzari and Scholl, 2013). These studies show that Trojans of the terrestrial planets are predominantly perturbed by family III secular resonances with the eigenfrequencies  $g_2$ ,  $g_3$ ,  $g_4$ ,  $g_5$  (V, E, M) and  $s_3$ ,  $s_4$  (M). Due to the influence of these resonances, Venus Trojans are unstable with a half-life of about  $6 \times 10^8$  yr, which is further reduced when the Yarkovsky effect is included in the numerical integration of fictitious populations of tadpole orbits. Earth Trojans have, by contrast, large stability regions up to  $40^\circ$  in inclination, with the peculiarity of favoring

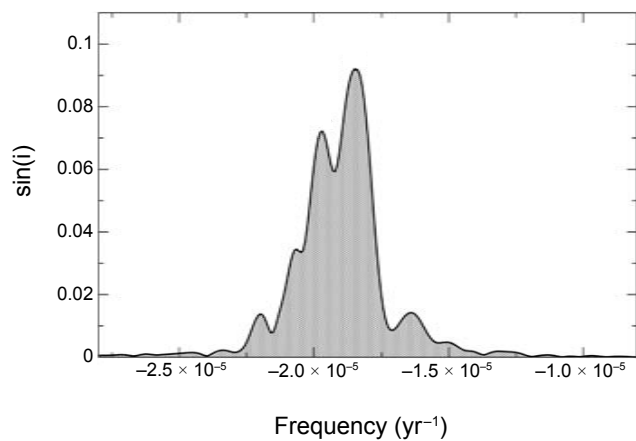


**Fig. 10.** Power spectrum of the  $p, q$  nonsingular variables for a Trojan orbit close to the  $s_6$  secular resonance. The forced component due to  $s_6$  is comparable to the proper frequency  $s$ . From Marzari *et al.* (2003a).

middle- to large-libration amplitude orbits for long-term survival, contrary to what is observed for Trojans of the outer planets. The dynamical stability of Mars Trojans is granted only for inclinations between  $15^\circ$  and  $30^\circ$  and, even in this case, the Yarkovsky force has some perturbing effect when very small bodies (in the meter size range) are considered.

### 3.3. Collisional Evolution

The collisional evolution of Trojan asteroids, initially explored by Marzari *et al.* (1997), has been recently revisited by De Elia and Brunini (2007, 2010). The newer work employs a refined collisional model that includes an updated treatment of the fragmentation physics, the escape of bodies suffering impacts that eject them out of the Trojan swarm, and the effects of Poynting-Robertson drag on small particles in the micrometer size range.

They find that the size distribution for diameters larger than about 60 km has a power-law slope that is substantially unaltered after 4.5 G.y. of evolution. The measured slope would therefore be primordial, reflecting the size distribution of the planetesimals that were trapped as Trojans during the early evolution of the solar system. This result is agreement with the suggestion of Morbidelli *et al.* (2009) that Trojans and KBOs share a common origin not only on dynamical grounds, but also because they have similar slopes to their size distributions, indicating a common origin.

Below 60 km, collisions dominate the evolution, and the slope of the size distribution relaxes toward the Dohnanyi's equilibrium value. The primordial population inferred by the models of De Elia and Brunini (2007, 2010) would include about  $1 \times 10^8$  bodies larger than 1 km, of which  $1 \times 10^6$  would survive at present. The erosion of the Trojan population leads to the formation of families, injection of bodies into Centaur and Jupiter-family comet (JFC) trajectories (Marzari *et al.*, 1995; Levison *et al.*, 1997), and the formation of a dusty ring around the orbit of Jupiter. According

to *De Elia and Brunini* (2007), the flux of Trojans into the current population of Centaurs and JFCs is negligible, with about 50 objects larger than 1 km in diameter per million years from the L<sub>4</sub> swarm. The flux from L<sub>5</sub> is expected to be even lower due to the reduced number of Trojans populating the L<sub>5</sub> swarm. This estimate is about 2 orders of magnitude smaller than that given by *Marzari et al.* (1997), and the difference can mostly be ascribed to the different scaling laws adopted in the collisional models.

A few family-forming events are expected for bodies larger than 50 km, which would produce the largest families predicted by *Beaugé and Roig* (2001) and observed by *Dotto et al.* (2006) and *Fornasier et al.* (2007). The robustness of the families identified by *Beaugé and Roig* (2001) have been recently questioned by *Broz and Rozehnal* (2011) on the grounds that the newly discovered Trojans dilute the clusters, interpreted as families, into the background. They claim that only the large family Eurybates is a real outcome of a breakup event, and the Ennomos group may be real. Family membership is based on proper elements, and *Di Sisto et al.* (2014) found that computation of proper elements for nonnumbered Trojans may not be reliable, even if observations are available over multiple oppositions. Caution is therefore advised in using nonnumbered asteroids in the family identification process.

*De Elia and Brunini* (2010) also explored the production of dust by collisions within the L<sub>4</sub> swarm and its lifetime against the Poynting-Robertson drag erosion. They estimate that the present thermal emission in the L<sub>4</sub> jovian swarm could be as high as  $\sim 3.2 \times 10^{-8}$ – $3.4 \times 10^{-8}$  L<sub>⊙</sub>, comparable to the luminosity of the inner solar system dust produced by asteroid collisions and cometary activity. This interesting prediction suggests that extrasolar giant planets could also be detected by the emission of a dusty ring produced by collisions of putative Trojans.

#### 4. DISCUSSION AND FUTURE DIRECTIONS

The Trojan asteroids remain one of the most fascinating and enigmatic group of small bodies in the solar system. Perhaps the best established property of the Trojans is their dynamical stability. Although several mechanisms are capable of capturing Trojans, the “jumping-Jupiter” version of the Nice model does the best job of matching the orbital distributions and, at the same time, fits the total population, size distribution, and L<sub>4</sub>/L<sub>5</sub> population asymmetry in a way that is consistent with the overall dynamical evolution of the outer solar system. As a result, it has become widely accepted that the majority of Trojan asteroids are likely refugees from the primordial Kuiper belt, and therefore have genetic affinities to the scattered (or scattering) and hot classical KBOs.

Studies of the physical properties of Trojans, however, do not paint such a clear picture. The low albedos and featureless spectra leave the interpretation of surface compositions open. Direct spectral comparisons with KBOs show significant differences between the two populations. Kuiper belt objects have a much wider range of albedos than

Trojans, extending in particular to higher albedos. Whereas the Trojans and small KBOs (and Centaurs) both exhibit color bimodalities, the color groups do not overlap. The “ultra-red” (RR) (*Barucci et al.*, 2005) spectral group of KBOs are completely absent from the Trojan swarms. The “red” Trojan group overlaps with the moderately red (BR) spectral group of KBOs and Centaurs, and the “less-red” Trojan group does not have a clear analog among KBOs, although some KBOs do overlap this group spectrally.

The possibility that surface compositions may have been modified by the changing irradiation and thermal environments as KBOs migrated inward is intriguing. The presence of ultra-red slopes, strong, broad absorptions at 3.6 and 4.5 μm, and a feature near 2.35 μm attributed to methanol suggest the presence of complex organics on at least some KBOs and Centaurs (e.g., *Cruikshank et al.*, 1998; *Barucci et al.*, 2006; *Emery et al.*, 2007; *Dalle Ore et al.*, 2013, 2015). Irradiation of these materials could lead to a decrease in spectral slope (e.g., *Moroz et al.*, 2004). Nevertheless, the absence of any organic absorptions, combined with clear signatures of silicate dust on Trojans, challenges any simple irradiation hypothesis (e.g., *Jewitt*, 2002; *Melita et al.*, 2009). Periods of cometary activity are likely involved (*Melita and Licandro*, 2012), especially if, as *Morbidelli et al.* (2005) discuss, the KBOs that migrated into the Trojan swarms spent significant time in orbits that brought them close to the Sun, but no satisfactory surface evolution scenario has yet been put forth that could explain the two Trojan spectral groups from a single parent population.

*Guilbert-Lepoutre* (2014) demonstrated that H<sub>2</sub>O ice can be stable on Trojans for the lifetime of the solar system if covered by ~10 m of dust at the equator (~10 cm near the poles). We might therefore expect to see some evidence for exposure by impact, particularly for smaller Trojans. Nevertheless, there is no indication that albedos increase even for the smallest Trojans currently observable. On the other hand, the very weak 3-μm absorption reported by *Brown* (2014) may be the first hint of a subsurface ice reservoir. Whether Trojans formed near 5 AU or in the Kuiper belt, they should have accreted abundant H<sub>2</sub>O ice, so the absence of any spectral signature of ice among the Trojans is curious.

Very little is known about the interior structure of Trojan asteroids. The only direct constraint comes from the densities that have been derived for a few Trojans. The low density of (617) Patroclus suggests a porous, ice-rich interior. Conflicting reports regarding (624) Hektor’s density make it difficult to assess the potential interior structure. Potential geochemical evolution of the interiors is also an open question. The apparently comet-like silicate dust reported by *Emery et al.* (2006) may suggest very little parent-body processing. On the other hand, the model of a salt-rich surface described by *Yang et al.* (2013) would require a significant amount of thermal processing of original primitive ices and silicates. Without detailed models of the thermal and chemical evolution of Trojan asteroids, it is difficult to interpret present surface compositions in terms of possible interior structures and evolutionary scenarios.

The two primary questions about the Trojans remain (1) where did they form, and (2) what are they made of? As described above, the past decade has seen advances in dynamical simulations and observations of physical properties that have drawn us significantly closer to the answers to these questions, but several particular areas are ripe for future investigations:

- What is the size distribution at small sizes?
  - How different is it for the two spectral groups?
  - What is the significance of the difference between L<sub>4</sub> and L<sub>5</sub> at small sizes?
- Why is the one robust family (Eurybates) spectrally anomalous?
- Does the capture mechanism preferentially select any original population?
  - What fraction, if any, might be from the Jupiter region (or closer)?
- Is the dust environment as predicted?
- How is Kuiper belt material (simple ices, organics, cometary silicates) modified as a body migrates inward to the thermal and irradiation environment of the Trojans?
- What is the ice fraction in the interiors of Trojans?
  - How deep is any extant ice buried?
  - Are any ices aside from H<sub>2</sub>O present?
- What is the nature of the low-albedo material on Trojan surfaces?
  - Are organic materials present on the surfaces? If so, what are its structural and chemical forms?
- Are smaller Trojans different in spectra and/or albedo from their larger siblings?
- Are Trojan silicates (and ices, if present) more similar to cometary or asteroidal material?
- Geologically, do Trojans resemble asteroids, comets, or irregular satellites (e.g., Pheobe)?
- Is there any outgassing or other source of extended emission on Trojans?
- Is the surface structure extremely porous (“fluffy”), or are the fine-grained silicates embedded in some matrix, such as a salt?
- What are the ranges of possible thermal and chemical histories for the interiors of Trojans, and how can current or future observations constrain those possible histories?

Fortunately, exciting prospects are on the horizon for learning more about Trojan asteroids and answering some of these important questions. In the nearest term, recent work by, e.g., Marsset et al. (2014), Brown (2014), and Wong et al. (2014) demonstrate the possibility of pushing spectral studies to smaller sizes with existing telescopes and instrumentation. Such observations will continue to test the hypothesis that the interiors of Trojans are distinct from their surfaces and, if the Brown (2014) and Wong et al. (2014) studies are indicative, may well surprise. Rotation properties of Trojans have long been uncertain, and the new works revealing such flat period distributions are important for understanding nongravitational torques at large distances

from the Sun. Additional information on amplitudes and spin-pole orientations will provide important constraints on these torques as well as the collisional environment. Extending spectral studies to the UV, which is currently possible with the Hubble Space Telescope, would also provide new insight into the silicates (and any ices) on the surfaces.

Through a series of workshops focused on “*In Situ* Science and Instrumentation for Primitive Bodies” that included scientists of diverse backgrounds (observers, laboratory cosmochemists, dynamical modelers), supported by the Keck Institute for Space Studies, Blacksberg et al. (2013) concluded that devising advances in instrumentation for surface science on primitive bodies, particularly the Trojan asteroids, is premature because of the fundamental uncertainties that remain in what chemical, mineralogical, and isotopic compositions to expect on the surfaces. They instead recommended a program of laboratory study to investigate the potential alteration pathways that KBO surface materials might go through on their journey to the Trojan swarms (or closer). Such laboratory work has the potential to enable direct tests of potential dynamical pathways by linking them to expected compositional changes and would thereby lead to significant advances in understanding Trojan surfaces even from the current observational dataset.

Several planned and potential groundbased and space-based survey programs are expected to lead to significant improvements in discovery and characterization of Trojans. The European Space Agency’s (ESA) Gaia mission, which started its science observations in mid-2014, will provide spectral characterization at visible wavelengths of asteroids down to V ~ 20. The Large Synoptic Survey Telescope (LSST) and the Panoramic Survey Telescope and Rapid Response System (Pan-STARRS), when fully operational, are anticipated to discover and record colors of hundreds of thousands of Trojan asteroids. Significant interest has been expressed recently in an infrared space telescope for asteroid discovery, for hazard mitigation, to support human exploration, and for science. The benefit of infrared discovery, particularly with at least two infrared pass-bands, as with the NEOWISE survey (Mainzer et al., 2011), is that the discovery data directly provide sizes. Such a mission would likely discover, and measure sizes of, large number of Trojans, and it is also likely that temporal coverage would enable estimates of thermophysical properties of the surfaces.

In terms of surface characterization, the next leap forward in terms of Trojan asteroids will probably come from the James Webb Space Telescope (JWST). With spectral coverage from 1 to 28 μm, JWST is ideally suited for searches for ices and organics, characterization of silicates, and determination of thermophysical properties. The sensitivities of JWST at wavelengths longward of 2.5 μm will significantly exceed those of current groundbased telescopes, and will enable observations of much smaller Trojans than is now possible.

Perhaps the most exciting future prospect for advances in our understanding of Trojans is the possibility of spacecraft missions to observe this population close-up. Because Trojans are, in many ways, key to understanding the evolution

of the solar system, there has been significant international interest in targeting the Trojan asteroids with an upcoming mission. The Trojans have been called out in each of the two last decadal surveys for NASA planetary science, making the short list for desired missions in the New Frontiers class. Lamy *et al.* (2012) make the case for a mission to the Trojans in the context of ESA's program of solar system exploration. Diniega *et al.* (2013) report the results of a Jet Propulsion Laboratory (JPL) Planetary Science Summer School design exercise for a mission to the Trojans. The Japan Aerospace Exploration Agency (JAXA) has been developing solar sail technology that may be well suited to provide propulsion for a deep space mission to the Trojan asteroids (e.g., Yano, 2013).

The details of a spacecraft mission to the Trojans could take many forms. A mission that includes flybys of several objects would provide important information on diversity among the Trojan swarms. An orbiter mission could return detailed geologic and spectral maps, as well as information on the interior structure and chemical composition of the body. A coordinated orbiter and lander could provide even more detailed "ground truth" for the orbital investigation. The key is to get close enough to one, or better yet several, Trojans to reveal them as geologic bodies rather than the point sources we know them as from Earth.

There is growing momentum behind determining the nature of this large, enigmatic population of primitive bodies, and it would be reasonable to expect, by whatever avenue the information may come, a revolution in the understanding of Trojan asteroids by the time *Asteroids V* goes to press.

## REFERENCES

- Adams E. R., Gulbis A. A. S., Elliot J. L., Benecchi S. D., Buie M. W., Trilling D. E., and Wasserman L. H. (2014) De-biased populations of Kuiper belt objects from the Deep Ecliptic Survey. *Astron. J.*, **148**, 55.
- Barucci M. A., Cruikshank D. P., Mottola S., and Lazzarin M. (2002) Physical properties of Trojan and Centaur asteroids. In *Asteroids III* (W. F. Bottke Jr. *et al.*, eds.), pp. 273–287. Univ. of Arizona, Tucson.
- Barucci M. A., Belskaya I. N., Fulchignoni M., and Birlan M. (2005) Taxonomy of Centaurs and trans-neptunian objects. *Astron. J.*, **130**, 1291–1298.
- Barucci M. A., Merlin F., Dotto E., Doressoundiram A., and de Bergh C. (2006) TNO surface ices. Observations of the TNO 55638 (2002 VE<sub>95</sub>) and analysis of the population's spectral properties. *Astron. Astrophys.*, **455**, 725–730.
- Batygin K., Brown M. E., and Fraser W. C. (2011) Retention of a primordial cold classical Kuiper belt in an instability-driven model of solar system formation. *Astrophys. J.*, **738**, 13.
- Beauge C. and Roig F. (2001) A semianalytical model for the motion of the Trojan asteroids: Proper elements and families. *Icarus*, **153**, 391–415.
- Belskaya I. N. and Shevchenko V. G. (2000) Opposition effect of asteroids. *Icarus*, **147**, 94–105.
- Binzel R. P. and Sauer L. M. (1992) Trojan, Hilda, and Cybele asteroids: New lightcurve observations and analysis. *Icarus*, **95**, 222–238.
- Blacksburg J., Eiler J., and Dankanich J. (2013) *In Situ Science and Instrumentation for Primitive Bodies: Final Report*. Keck Institute for Space Studies, available online at <http://kiss.caltech.edu/study/primitive-bodies/>.
- Brasser R., Morbidelli A., Gomes R., Tsiganis K., and Levison H. F. (2009) Constructing the secular architecture of the solar system II: The terrestrial planets. *Astron. Astrophys.*, **507**, 1053–1065.
- Brown M. (2014) Three-micron survey of Jupiter Trojan asteroids. In *Asteroids, Comets, Meteors 2014, Book of Abstracts* (K. Muinonen *et al.*, eds.), University of Helsinki, Finland.
- Broz M. and Rozehnal J. (2011) Eurybates — the only asteroid family among Trojans? *Mon. Not. R. Astron. Soc.*, **414**, 565–574.
- Campins H., Hargrove K., Pinilla-Alonso N., Howell E., Kelley M., Licandro J., Mothé-Diniz T., Fernandez Y., and Ziffer J. (2010) Water ice and organics on the surface of the asteroid 24 Themis. *Nature*, **464**, 1320–1321.
- Chapman C. R. and Gaffey M. J. (1979) Reflectance spectra for 277 asteroids. In *Asteroids* (T. Gehrels, ed.), pp. 655–687. Univ. of Arizona, Tucson.
- Cruikshank D. P. (1977) Radii and albedos of four Trojan asteroids and jovian satellites 6 and 7. *Icarus*, **30**, 224–230.
- Cruikshank D. P., Roush T. L., Bartholomew M. J., et al. (1998) The composition of Centaur 5145 Pholus. *Icarus*, **135**, 389–407.
- Dalle Ore C. M., Dalle Ore L. V., Roush T. L., Cruikshank D. P., Emery J. P., Pinilla-Alonso N., and Marzo G. A. (2013) A compositional interpretation of trans-neptunian objects taxonomies. *Icarus*, **222**, 307–322.
- Dalle Ore C. M., Barucci M. A., Emery J. P., et al. (2015) The composition of "ultra-red" TNOs and Centaurs. *Icarus*, **252**, 311–326.
- De Elia G. C. and Brunini A. (2007) Collisional and dynamical evolution of the L<sub>4</sub> Trojan asteroids. *Astron. Astrophys.*, **475**, 375–389.
- De Elia G. C. and Brunini A. (2010) Studying the jovian Trojan dust. *Astron. Astrophys.*, **512**, A65.
- De Luise F., Dotto E., Fornasier S., Barucci M. A., Pinilla-Alonso N., Perna D., and Marzari F. (2010) A peculiar family of Jupiter Trojans: The Eurybates? *Icarus*, **209**, 586–590.
- DeMeo F. E. and Carry B. (2014) Solar system evolution from compositional mapping of the asteroid belt. *Nature*, **505**, 629–634.
- Descamps P. (2015) Dumb-bell-shaped equilibrium figures for fiducial contact-binary asteroids and EKBOs. *Icarus*, **245**, 64–79.
- Di Sisto R., Ramos X. S., and Beaugé C. (2014) Giga-year evolution of Trojans and the asymmetry problem. *Icarus*, **243**, 287–295.
- Diniega S., Sayanagi K. M., Balcerski J., et al. (2013) Mission to the Trojan asteroids: Lessons learned during a JPL Planetary Science Summer School mission design exercise. *Planet. Space. Sci.*, **76**, 68–82.
- Dotto E., Fornasier S., Barucci M. A., et al. (2006) The surface composition of Jupiter Trojans: Visible and near-infrared survey of dynamical families. *Icarus*, **183**, 420–434.
- Dotto E., Emery J. P., Barucci M. A., Morbidelli A., and Cruikshank D. P. (2008) *De Troianis: The Trojans in the planetary system. In The Solar System Beyond Neptune* (M. A. Barucci *et al.*, eds.), pp. 383–396. Univ. of Arizona, Tucson.
- Dunlap J. L. and Gehrels T. (1969) Minor planets III. Lightcurves of a Trojan asteroid. *Astron. J.*, **74**, 796–803.
- Dvorak R., Lhotka C., and Zhou L. (2012) The orbit of 2010 TK7: Possible regions of stability for other Earth Trojan asteroids. *Astron. Astrophys.*, **541**, A127.
- Emery J. P. and Brown R. H. (2003) Constraints on the surface composition of Trojan asteroids from near infrared (0.8–4.0 μm) spectroscopy. *Icarus*, **164**, 104–121.
- Emery J. P. and Brown R. H. (2004) Surfaces of Trojan asteroids: Constraints from spectral modeling. *Icarus*, **170**, 131–152.
- Emery J. P., Cruikshank D. P., and Van Cleve J. (2006) Thermal emission spectroscopy (5.2–38 μm) of three Trojan asteroids with the Spitzer Space Telescope: Detection of fine-grained silicates. *Icarus*, **182**, 496–512.
- Emery J. P., Dalle Ore C. M., Cruikshank D. P., et al. (2007) Ices on (90377) Sedna: Confirmation and compositional constraints. *Astron. Astrophys.*, **466**, 395–398.
- Emery J. P., Burr D. M., and Cruikshank D. P. (2011) Near-infrared spectroscopy of Trojan asteroids: Evidence for two compositional groups. *Astron. J.*, **141**, 25.
- Emery J. P., Ness R. G., and Lucas M. P. (2013) A search for volatiles and spectral variation on the surfaces of Trojan asteroids. *AAS/Division for Planetary Sciences Meeting Abstracts*, **45**, #208.31.
- Érdi B. (1988) Long periodic perturbations of Trojan asteroids. *Cel. Mech.*, **43**, 303–308.
- Érdi B., Nagy I., Sandor A., Suli A., and Frohlich G. (2007) Secondary resonances of co-orbital motions. *Mon. Not. R. Astron. Soc.*, **381**, 33–40.
- Érdi B., Forgács-Dajka E., Nagy I., and Rajnai R. (2009) A parametric study of stability and resonances around L<sub>4</sub> in the elliptic restricted three-body problem. *Cel. Mech. Dynam. Astron.*, **104**, 145–158.
- Fernández Y. R., Sheppard S. S., and Jewitt D. C. (2003) The albedo distribution of jovian Trojan asteroids. *Astron. J.*, **126**, 1563–1574.

- Fernández Y. R., Jewitt D., and Ziffer J. E. (2009) Albedos of small jovian Trojans. *Astron. J.*, **138**, 240–250.
- Fleming H. J. and Hamilton D. P. (2000) On the origin of the Trojan asteroids: Effects of Jupiter's mass accretion and radial migration. *Icarus*, **148**, 479–493.
- Fornasier S., Dotto E., Hainaut O., Marzari F., Boehnhardt H., De Luise F., and Barucci M. A. (2007) Visible spectroscopic and photometric survey of Jupiter Trojans: Final results on dynamical families. *Icarus*, **190**, 622–642.
- Fraser W. C., Brown M. E., Morbidelli A., Parker A., and Batygin K. (2014) The absolute magnitude distribution of Kuiper belt objects. *Astrophys. J.*, **782**, 100.
- French L. M. (1987) Rotational properties of four L5 Trojan asteroids from CCD photometry. *Icarus*, **72**, 325–341.
- French L. M., Stephens R. D., Lederer S. M., Coley D. R., and Rohr D. A. (2011) Preliminary results from a study of Trojan asteroids. *Minor Planet Bull.*, **38**, 116–120.
- French L. M., Stephens R. D., Coley D. R., Megna R., and Wasserman L. H. (2012) Photometry of 17 jovian Trojan asteroids. *Minor Planet Bull.*, **39**, 183–187.
- French L. M., Stephens R. D., Coley D. R., Wasserman L. H., Vilas F., and La Rocca D. (2013) A troop of Trojans: Photometry of 24 jovian Trojan asteroids. *Minor Planet Bull.*, **40**, 198–203.
- French L. M., Stephens R. D., Coley D. R., Wasserman L. H., and Sieben J. (2015) Rotation lightcurves of small jovian Trojan asteroids. *Icarus*, **254**, 1–17.
- Gradie J. and Veverka J. (1980) The composition of the Trojan asteroids. *Nature*, **283**, 840–842.
- Grav T., Mainzer A. K., Bauer J., et al. (2011) WISE/NEOWISE observations of the jovian Trojans: Preliminary results. *Astrophys. J.*, **742**, 40.
- Grav T., Mainzer A. K., Bauer J. M., Masiero J. R., and Nugent C. R. (2012) WISE/NEOWISE observations of the jovian Trojan population: Taxonomy. *Astrophys. J.*, **759**, 49.
- Guilbert-Lepoutre A. (2014) Survival of water ice in Jupiter Trojans. *Icarus*, **231**, 232–238.
- Harris A. W. (2004) YORP alteration of asteroid spins: Why are slow rotators tumbling and not synchronized? *Bull. Am. Astron. Soc.*, **36**, 1185.
- Hartmann W. K. and Cruikshank D. P. (1978) The nature of Trojan asteroid 624 Hektor. *Icarus*, **36**, 353–366.
- Hartmann W. K. and Cruikshank D. P. (1980) Hektor: The largest highly elongated asteroid. *Science*, **207**, 976–977.
- Hartmann W. K., Tholen D. J., Goguen J., Binzel R. P., and Cruikshank D. P. (1988) Trojan and Hilda asteroid lightcurves I. Anomalously elongated shapes among Trojans (and Hildas?). *Icarus*, **73**, 487–498.
- Horner J., Müller T. G., and Lykawka P. S. (2012) Anchises — Thermophysical and dynamical studies of a dynamically unstable jovian Trojan. *Mon. Not. R. Astron. Soc.*, **423**, 2587–2596.
- Jewitt D. C. (2002) From Kuiper belt object to cometary nucleus: The missing ultrared matter. *Astron. J.*, **123**, 1039–1049.
- Jewitt D. C., Trujillo C. A., and Luu J. X. (2000) Population and size distribution of small jovian Trojan asteroids. *Astron. J.*, **120**, 1140–1147.
- Karlsson O. (2010) On the observational bias of the Trojan swarms. *Astron. Astrophys.*, **516**, A22.
- Karlsson O., Lagerkvist C.-I., and Davidsson B. (2009) (U)BVRI photometry of Trojan L<sub>5</sub> asteroids. *Icarus*, **199**, 106–118.
- Lamy P. L., Toth I., Fernández Y. R., and Weaver H. A. (2004) The sizes, shapes, albedos, and colors of cometary nebulae. In *Comets II* (M. C. Festou et al., eds.), pp. 223–264. Univ. of Arizona, Tucson.
- Lamy P., Vernazza P., Poncy J., et al. (2012) Trojans' odyssey: Unveiling the early history of the solar system. *Exp. Astron.*, **33**, 685–721.
- Laskar J. (1990) The chaotic motion of the solar system — A numerical estimate of the size of the chaotic zones. *Icarus*, **88**, 266–291.
- Levison H. F., Shoemaker E. M., and Shoemaker C. S. (1997) Dynamical evolution of Jupiter's Trojan asteroids. *Nature*, **385**, 42–44.
- Levison H. F., Morbidelli A., Van Laerhoven C., Gomes R., and Tsiganis K. (2008) Origin of the structure of the Kuiper belt during a dynamical instability in the orbits of Uranus and Neptune. *Icarus*, **196**, 258–273.
- Levison H. F., Bottke W. F., Gounelle M., Morbidelli A., Nesvorný D., and Tsiganis K. (2009) Contamination of the asteroid belt by primordial trans-neptunian objects. *Nature*, **460**, 364–366.
- Levison H. F., Morbidelli A., Tsiganis K., Nesvorný D., and Gomes R. (2011) Late orbital instabilities in the outer planets induced by interaction with a self-gravitating planetesimal disk. *Astron. J.*, **142**, 152.
- Lykawka P. S., Horner J., Jones B. W., and Mukai T. (2009) Origin and dynamical evolution of Neptune Trojans — I. Formation and planetary migration. *Mon. Not. R. Astron. Soc.*, **398**, 1715–1729.
- Mainzer A., Bauer J., Grav T., et al. (2011) Preliminary results from NEOWISE: An enhancement to the Wide-Field Infrared Survey Explorer for solar system science. *Astrophys. J.*, **731**, 53.
- Mann R. K., Jewitt D., and Lacerda P. (2007) Fraction of contact binary Trojan asteroids. *Astron. J.*, **134**, 1133–1144.
- Marchis F., Hestroffer D., Descamps P., et al. (2006) A low density of 0.8 g cm<sup>-3</sup> for the Trojan binary asteroid (617) Patroclus. *Nature*, **439**, 565–567.
- Marchis F., Durech J., Castillo-Rogez J., Vachier F., Cuk M., Berthier J., Wong M. H., Kalas P., Duchene G., van Dam M. A., Hamanowa H., and Viikinkoski M. (2014) The puzzling mutual orbit of the binary Trojan asteroid (624) Hektor. *Astrophys. J. Lett.*, **783**, L37.
- Marsset M., Vernazza P., Gourgeot F., Dumas C., Birlan M., Lamy P., and Binzel R. P. (2014) Similar origin for low- and high-albedo jovian Trojans and Hilda asteroids? *Astron. Astrophys.*, **568**, L7.
- Marzari F. and Scholl H. (1998a) The capture of Trojans by a growing proto-Jupiter. *Icarus*, **131**, 41–51.
- Marzari F. and Scholl H. (1998b) The growth of Jupiter and Saturn and the capture of Trojans. *Astron. Astrophys.*, **339**, 278–285.
- Marzari F. and Scholl H. (2007) Dynamics of Jupiter Trojans during the 2:1 mean motion resonance crossing of Jupiter and Saturn. *Mon. Not. R. Astron. Soc.*, **380**, 479–488.
- Marzari F. and Scholl H. (2013) Long-term stability of Earth Trojans. *Cel. Mech. Dynam. Astron.*, **117**, 91–100.
- Marzari F., Farinella P., and Vanzani V. (1995) Are Trojan collisional families a source for short period comets? *Astron. Astrophys.*, **299**, 267–276.
- Marzari F., Farinella P., Davis D. R., Scholl H., and Campo Bagatin A. (1997) Collisional evolution of Trojan asteroids. *Icarus*, **125**, 39–49.
- Marzari F., Scholl H., Murray C., and Lagerkvist C. (2002a) Origin and evolution of Trojan asteroids. In *Asteroids III* (W. F. Bottke Jr. et al., eds.), pp. 725–738. Univ. of Arizona, Tucson.
- Marzari F., Tricarico P., and Scholl H. (2002b) Saturn Trojans: Stability regions in the phase space. *Astrophys. J.*, **579**, 905–913.
- Marzari F., Tricarico P., and Scholl H. (2003a) Stability of Jupiter Trojans investigated using frequency map analysis: The MATROS project. *Mon. Not. R. Astron. Soc.*, **345**, 1091–1100.
- Marzari F., Tricarico P., and Scholl H. (2003b) The MATROS project: Stability of Uranus and Neptune Trojans. The case of 2001 QR<sub>322</sub>. *Astron. Astrophys.*, **410**, 725–734.
- Melita M. D. and Licandro J. (2012) Links between the dynamical evolution and the surface color of the Centaurs. *Astron. Astrophys.*, **539**, A114.
- Melita M. D., Licandro J., Jones D. C., and William I. P. (2008) Physical properties and orbital stability of the Trojan asteroids. *Icarus*, **195**, 686–697.
- Melita M. D., Strazzulla G., and Bar-Nun A. (2009) Collisions, cosmic radiation, and the colors of the Trojan asteroids. *Icarus*, **203**, 134–139.
- Melita M. D., Dufard R., Williams I. P., Jones D. C., Licandro J., and Ortiz J. L. (2010) Lightcurves of 6 Jupiter Trojan asteroids. *Planet. Space Sci.*, **58**, 1035–1039.
- Merline W. J., Weidenschilling S. J., Durda D. D., Margot J. L., Pravec P., and Storrs A. D. (2002) Asteroids do have satellites. In *Asteroids III* (W. F. Bottke Jr. et al., eds.), pp. 298–312. Univ. of Arizona, Tucson.
- Molnar L. A., Haegert M. J., and Hoogeboom K. M. (2008) Lightcurve analysis of an unbiased sample of Trojan asteroids. *Minor Planet Bull.*, **35**(2), 82–84.
- Morbidelli A. (2013) Dynamical evolution of planetary systems. In *Planets, Stars and Stellar Systems, Volume 3: Solar and Stellar Planetary Systems* (T. Oswalt et al., eds.) pp. 63–109. Springer-Verlag, Berlin.
- Morbidelli A., Levison H. F., Tsiganis K., and Gomes R. (2005) Chaotic capture of Jupiter's Trojan asteroids in the early solar system. *Nature*, **435**, 462–465.
- Morbidelli A., Tsiganis K., Crida A., Levison H. F., and Gomes R. (2007) Dynamics of the giant planets of the solar system in the gaseous protoplanetary disk and their relationship to the current orbital architecture. *Astron. J.*, **134**, 1790–1798.
- Morbidelli A., Levison H., Bottke W. F., Dones L., and Nesvorný D. (2009) Considerations on the magnitude distributions of the Kuiper belt and of the Jupiter Trojans. *Icarus*, **202**, 310–315.

- Morbidelli A., Levison H. F., and Gomes R. (2008) The dynamical structure of the Kuiper belt and its primordial origins. In *The Solar System Beyond Neptune* (M. A. Barucci et al., eds.), pp. 275–292. Univ. of Arizona, Tucson.
- Morbidelli A., Brasser R., Gomes R., Levison H. F., and Tsiganis K. (2010) Evidence from the asteroid belt for a violent past evolution of Jupiter's orbit. *Astron. J.*, *140*, 1391–1401.
- Moroz L., Baratta G., Strazzula G., et al. (2004) Optical alteration of complex organics induced by ion irradiation: I. Laboratory experiments suggest unusual space weathering trend. *Icarus*, *170*, 214–228.
- Mottola S. and 10 colleagues (2010) Rotational properties of Jupiter Trojans. I. Light curves of 80 objects. *Astron. J.*, *141*, 170.
- Mottola S., Di Martino M., and Carbognani A. (2014) The spin rate distribution of Jupiter Trojans. *Mem. Soc. Astron. Ital. Suppl.*, *26*, 47–51.
- Mueller M., Marchis F., Emery J. P., Harris A. W., Mottola S., Hestroffer D., Berthier J., and Di Martino M. (2010) Eclipsing binary Trojan asteroid Patroclus: Thermal inertia from Spitzer observations. *Icarus*, *205*, 505–515.
- Muinonin K., Piironen J., Shkuratov Y. G., Ovcharenko A., and Clark B. E. (2002) Asteroid photometric and polarimetric phase effects. In *Asteroids III* (W. F. Bottke Jr. et al., eds.), pp. 123–138. Univ. of Arizona, Tucson.
- Nakamura T. and Yoshida F. (2008) A new surface density model of jovian Trojans around triangular libration points. *Publ. Astron. Soc. Japan*, *60*, 293–296.
- Nesvorný D. and Dones L. (2002) How long-lived are the hypothetical Trojan populations of Saturn, Uranus, and Neptune? *Icarus*, *160*, 271–288.
- Nesvorný D. and Morbidelli A. (2012) Statistical study of the early solar system's instability with four, five, and six giant planets. *Astron. J.*, *144*, 117.
- Nesvorný D., Vokrouhlický D., and Morbidelli A. (2013) Capture of Trojans by jumping Jupiter. *Astrophys. J.*, *768*, 45.
- Nicholson S. B. (1961) The Trojan asteroids. *Astron. Soc. Pac. Leaflets*, *8(38)*, 239.
- Noll K. S., Benecchi S. D., Ryan E. L., and Grundy W. M. (2013) Ultra-slow rotating outer main belt and Trojan asteroids: Search for binaries. *AAS/Division for Planetary Sciences Meeting Abstracts*, *45*, #304.03.
- Parker A. H. and Kavelaars J. J. (2012) Collisional evolution of ultra-wide trans-neptunian binaries. *Astrophys. J.*, *744*, 139.
- Parker A. H., Kavelaars J. J., Petit, J.-M., Jones L., Gladman B., and Parker J. (2011) Characterization of seven ultra-wide trans-neptunian binaries. *Astrophys. J.*, *743*, 1.
- Peale S. J. (1993) The effect of the nebula on the Trojan precursors. *Icarus*, *106*, 308.
- Pravec P. and Harris A. W. (2000) Fast and slow rotation of asteroids. *Icarus*, *148*, 12–20.
- Pravec P. and 28 colleagues (2008) Spin rate distribution of small asteroids. *Icarus*, *197*, 497–504.
- Rivkin A. S. and Emery J. P. (2010) Detection of ice and organics on an asteroidal surface. *Nature*, *64*, 1322–1323.
- Rivera-Valentin E. G., Barr A. C., Lopez Garcia E. J., Kirchoff M. R., and Schenk P. M. (2014) Constraints on planetesimal disk mass from the cratering record and equatorial ridge on Iapetus. *Astrophys. J.*, *792*, 127.
- Robutel P. and Bodossian J. (2009) The resonant structure of Jupiter's Trojan asteroids II. What happens for different configurations of the planetary system. *Mon. Not. R. Astron. Soc.*, *399*, 69–87.
- Robutel P. and Gabern F. (2006) The resonant structure of Jupiter's Trojan asteroids — I. Long-term stability and diffusion. *Mon. Not. R. Astron. Soc.*, *372*, 1463–1482.
- Roig F., Ribeiro A. O., and Gil-Hutton R. (2008) Taxonomy of asteroid families among the Jupiter Trojans: Comparison between spectroscopic data and the Sloan Digital Sky Survey colors. *Astron. Astrophys.*, *483*, 911–931.
- Rubincam D. P. (2000) Radiative spin-up and spin-down of small asteroids. *Icarus*, *148*, 2–11.
- Scholl H., Marzari F., and Tricarico P. (2005a) Dynamics of Mars Trojans. *Icarus*, *175*, 397–408.
- Scholl H., Marzari F., and Tricarico P. (2005b) The instability of Venus Trojans. *Astron. J.*, *130*, 2912–2915.
- Sheppard S. S. and Trujillo C. A. (2010) The size distribution of the Neptune Trojans and the missing intermediate-sized planetesimals. *Astrophys. J. Lett.*, *723*, L233–L237.
- Shevchenko V. G., Belskaya I. N., Slyusarev I. G., et al. (2012) Opposition effect of Trojan asteroids. *Icarus*, *212*, 202–208.
- Shevchenko V. G., Slyusarev I. G., and Belskaya I. N. (2014) Revised albedos of Trojan asteroids (911) Agamemnon and (4709) Ennomos. *Meteoritics & Planet. Sci.*, *49*, 103–108.
- Shoemaker E. M., Shoemaker C. S., and Wolfe R. F. (1989) Trojan asteroids: Populations, dynamical structure and origin of the L4 and L5 swarms. In *Asteroids II* (R. P. Binzel et al., eds.), pp. 487–523. Univ. of Arizona, Tucson.
- Slyusarev I. G. and Belskaya I. N. (2014) Jupiter's Trojans: Physical properties and origin. *Solar System Res.*, *48*, 139–157.
- Stephens R. D., French L. M., Coley D. R., Megna R., and Wasserman L. H. (2012) Photometry of 10 jovian Trojan asteroids. *AAS/Division for Planetary Sciences Meeting Abstracts*, *44*, #110.14.
- Stephens R. D., French L. M., Davitt C., and Coley D. R. (2014) At the Scaeum gates: Observations of jovian Trojan asteroids, July–December 2013. *Minor Planet Bull.*, *41*, 95–100.
- Szabó G. M., Ivezić Ž., Jurić M., and Lupton R. (2007) The properties of jovian Trojan asteroids listed in SDSS Moving Object Catalogue 3. *Mon. Not. R. Astron. Soc.*, *377*, 1393–1406.
- Tedesco E. F., Noah P. V., Noah M., and Price S. D. (2002) The supplemental IRAS minor planet survey. *Astron. J.*, *123*, 1056–1085.
- Tenn J. S. (1994) Max Wolf: The twenty-fifth Bruce medalist. *Mercury*, *23*(3), 27–28.
- Timerson B., Brooks J., Conard S., Dunham D. W., Herald D., Tolea A., and Marchis F. (2013) Occultation evidence for a satellite of the Trojan asteroid (911) Agamemnon. *Planet. Space Sci.*, *87*, 78–84.
- Usui F., Kuroda D., Müller T. G., et al. (2011) Asteroid catalog using Akari: AKARI/IRC mid-infrared asteroid survey. *Publ. Astron. Soc. Japan*, *63*, 1117–1138.
- Vernazza P., Delbó M., King P. L., et al. (2012) High surface porosity as the origin of emissivity features in asteroid spectra. *Icarus*, *221*, 1162–1172.
- Walsh K. J., Morbidelli A., Raymond S. N., O'Brien D. P., and Mandell A. M. (2011) A low mass for Mars from Jupiter's early gas-driven migration. *Nature*, *475*, 206–209.
- Warner B. D., Harris A. W., and Pravec, P. (2009) The asteroid lightcurve database. *Icarus*, *202*, 134–146 (update of February 18, 2014, available online at <http://www.minorplanetinfo/lightcurvedatabase.html>).
- Wong I., Brown M., and Emery J. P. (2014) The differing magnitude distributions of the two Jupiter Trojan color populations. *Astron. J.*, *148*, 112.
- Yang B. and Jewitt D. (2007) Spectroscopic search for water ice on jovian Trojan asteroids. *Astron. J.*, *134*, 223–228.
- Yang B. and Jewitt D. (2011) A near-infrared search for silicates in jovian Trojan asteroids. *Astron. J.*, *141*, 95.
- Yang B., Lucey P., and Glotch T. (2013) Are large Trojan asteroids salty? An observational, theoretical, and experimental study. *Icarus*, *223*, 359–366.
- Yano H. (2013) Japanese exploration to solar system small bodies: Rewriting a planetary formation theory with astromaterial connection. *AGU Fall Meeting 2013*, #P22A-01.
- Yoder C. F. (1979) Notes on the origin of the Trojan asteroids. *Icarus*, *40*, 341–344.
- Yoshida F. and Nakamura T. (2005) Size distribution of faint jovian L<sub>4</sub> Trojan asteroids. *Astron. J.*, *130*, 2900–2911.
- Yoshida F. and Nakamura T. (2008) A comparative study of size distributions for small L4 and L5 jovian Trojans. *Publ. Astron. Soc. Japan*, *60*, 297–301.
- Zappalà V. F., Di Martino M., Cellino A., Farinella P., De Sanctis G., and Ferreri W. (1989) Rotational properties of outer belt asteroids. *Icarus*, *82*, 354–368.

# The Active Asteroids

David Jewitt

*University of California at Los Angeles*

Henry Hsieh

*Academia Sinica*

Jessica Agarwal

*Max Planck Institute for Solar System Research*

---

Some asteroids eject dust, producing transient, comet-like comae and tails; these are the active asteroids. The causes of activity in this newly identified population are many and varied. They include impact ejection and disruption, rotational instabilities, electrostatic repulsion, radiation pressure sweeping, dehydration stresses, and thermal fracture, in addition to the sublimation of asteroidal ice. These processes were either unsuspected or thought to lie beyond the realm of observation before the discovery of asteroid activity. Scientific interest in the active asteroids lies in their promise to open new avenues into the direct study of asteroid destruction, the production of interplanetary debris, the abundance of asteroid ice, and the origin of terrestrial planet volatiles.

## 1. INTRODUCTION

Small solar system bodies are conventionally labeled as either asteroids or comets, based on three distinct properties: (1) Observationally, small bodies with unbound atmospheres (“comae”) are known as comets, while objects lacking such atmospheres are called asteroids. (2) Dynamically, comets and asteroids are broadly distinguished by the use of a dynamical parameter, most commonly the Tisserand parameter measured with respect to Jupiter (*Kresak*, 1982; *Kosai*, 1992). It is defined by

$$T_J = \frac{a_J}{a} + 2 \left[ \left(1 - e^2\right) \frac{a}{a_J} \right]^{1/2} \cos(i) \quad (1)$$

where  $a$ ,  $e$ , and  $i$  are the semimajor axis, eccentricity, and inclination of the orbit (relative to Jupiter’s orbit), while  $a_J = 5.2$  AU is the semimajor axis of the orbit of Jupiter. This parameter, which is conserved in the circular, restricted three-body problem, provides a measure of the close-approach speed to Jupiter. Jupiter itself has  $T_J = 3$ . Main-belt asteroids have  $a < a_J$  and  $T_J > 3$ , while dynamical comets (from the Kuiper belt and Oort cloud) have  $T_J < 3$ . (3) Compositionally, comets are ice-rich small bodies formed beyond the snow line in the protoplanetary disk, while the asteroids are ice-free and formed inside it.

While there is often a reassuring concordance among these classification systems, all three are potentially fallible. For instance, the ability to detect a low surface brightness coma or tail is, in part, a function of instrumental parameters and observing conditions. The utility of equation (1)

is limited for objects with  $T_J$  very close to 3 because the underlying criterion is based on an idealized representation of the solar system (e.g., Jupiter’s orbit is not a circle, the gravity of other planets is not negligible, and nongravitational forces due to outgassing and photon momentum can be important). The least useful metric is the composition because, except in special cases, we have neither any practical way to measure the composition of a small body nor can we determine its formation location.

Taken together, the observational and dynamical classifications suggest a simple two-parameter schematic that usefully describes the solar system’s small body populations (Fig. 1). The four quadrants in Fig. 1 conveniently separate comets (upper left) from asteroids (lower right) and distinguish likely defunct comets (lower left) in which there is no activity, presumably due to the past depletion of near-surface volatiles (*Hartmann et al.*, 1987), from the newly recognized active asteroid class (upper right).

The working definition employed here is that active asteroids are small bodies that (1) have semimajor axis  $a < a_J$ , (2) have  $T_J > 3.08$ , and (3) show evidence for mass loss, e.g., in the form of a resolved coma or tail. In defining the critical Tisserand parameter separating asteroids from comets as  $T_J = 3.08$ , rather than 3.0, we avoid many ambiguous cases caused by deviations of the real solar system from the circular, restricted three-body approximation. This definition also excludes Encke-type comets (2P/Encke has  $T_J = 3.02$ ), and the quasi-Hilda comets ( $T_J \sim 2.9$ –3.04). The orbital distribution of the currently known active asteroids is shown in Fig. 2. Three objects occupy planet-crossing orbits while the remaining 15 orbit in the main belt.

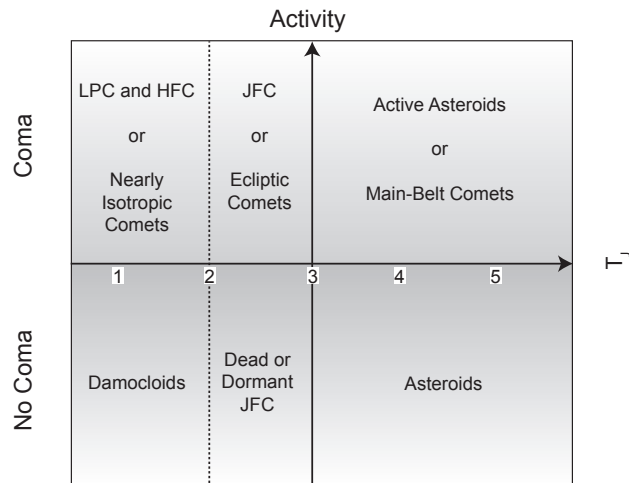


**Fig. 1.** See Plate 3 for color version. Empirical classification of small bodies based on the Tisserand parameter,  $T_J$  (x-axis), and the presence or absence of coma (y-axis). JFC, LPC, and HFC are the Jupiter-family, long-period, and Halley-family comet subtypes, distinguished by their dynamics. From Jewitt (2012).

The active asteroids are remarkable for being an entirely new population located in one of the closest and most intensively studied regions of the solar system. Their activity is driven by a surprisingly diverse set of physical processes. Reported examples include hypervelocity impact [e.g., (596) Scheila], rotational instability probably driven by Yarkovsky-O’Keefe-Radzievskii-Paddack (YORP) torques (e.g., 311P, P/2013 R3), thermal disintegration driven by intense solar heating of minerals [(3200) Phaethon] and the sublimation of ice [(1) Ceres, 133P, 238P, 313P, and 324P are the strongest examples]. Impact and rotational disruptions are primary sources of meteorites and larger planet impactors. Observations promise to improve our understanding of the physics, and of the rates, of both asteroid destruction processes and meteoroid production. Analogous disruptions occurring around other stars are likely responsible for the creation of debris disks (e.g., *Shannon and Wu*, 2011). A common dynamical end-fate of planet-crossing bodies is to strike the Sun; a better understanding of the role of thermal disintegration will be important both in the solar system and in the context of photospheric impactors in polluted white dwarf systems (*Jura and Xu*, 2013). Finally, the survival of primordial ice in the asteroids may offer the opportunity to sample volatiles from a region of the protoplanetary disk different from that in which the Kuiper belt and Oort cloud comets formed. The outer asteroid belt is also a likely source region for the volatile inventory of Earth (*Morbidelli et al.*, 2000; *O’Brien and Greenberg*, 2005), giving new relevance to the origin of the oceans.

The active asteroids were called “main-belt comets” by *Hsieh and Jewitt* (2006), while *Hsieh et al.* (2012a) employed the term “disrupted asteroids” to refer to objects that exhibit comet-like activity believed to be non-sublimation-

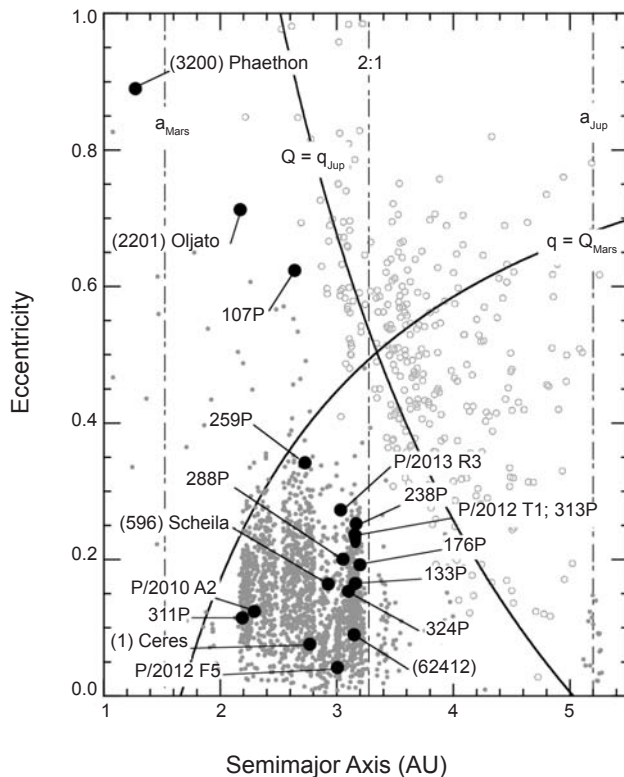


**Fig. 2.** See Plate 4 for color version. Distribution of the active asteroids in the semimajor axis vs. orbital eccentricity plane. Dynamical asteroids are shown as filled gray circles, comets as empty circles, and the active asteroids as black circles, each labeled with the object name (cf. Table 1). Objects plotted above the diagonal arcs cross either the orbit of Mars or Jupiter.

driven. We use the more general term “active asteroids” both because some of the known examples are not in the main belt (cf. Fig. 2), and because this nomenclature implies no supposition about the cause of the activity.

The active asteroids were reviewed by *Bertini* (2011) and, in more detail, by *Jewitt* (2012). This chapter updates the latter paper with many new observations and examples of asteroid activity and adopts a tutorial style in the interests of clarity.

## 2. CURRENTLY KNOWN ACTIVE ASTEROIDS

We list the active asteroids in the order of decreasing Tisserand parameter in Table 1 and discuss them briefly here.

### 2.1. (3200) Phaethon, $T_J = 4.508$

Phaethon is a B-type asteroid with a 0.14-AU perihelion distance, a dynamical lifetime to scattering by the terrestrial planets  $\sim 100$  m.y., and a source in the main asteroid belt that may be related to (2) Pallas (*de Leon et al.*, 2010). This 5-km-diameter body is the source of the Geminid meteor stream (e.g., *Williams and Wu*, 1993) and is dynamically related to kilometer-sized asteroids 2005 UD (*Ohtsuka et al.*,

TABLE 1. Summary of orbital properties.

Name	$T_J^*$	$a^\dagger$	$e^\ddagger$	$i^\S$	$q^\P$	$Q^{**}$
(3200) Phaethon	4.508	1.271	0.890	22.17	0.140	2.402
311P/PANSTARRS (P/2013 P5)	3.662	2.189	0.115	4.97	1.936	2.441
P/2010 A2 (LINEAR)	3.582	2.291	0.124	5.26	2.007	2.575
(1) Ceres	3.309	2.768	0.076	10.60	2.556	2.979
(2201) Oljato	3.299	2.172	0.713	2.52	0.623	3.721
P/2012 F5 (Gibbs)	3.228	3.004	0.042	9.73	2.877	3.129
259P/Garradd (P/2008 R1)	3.216	2.726	0.342	15.90	1.794	3.658
(596) Scheila	3.208	2.928	0.165	14.66	2.445	3.411
288P/(300163) 2006 VW <sub>139</sub>	3.203	3.050	0.200	3.24	2.441	3.659
(62412) 2000 SY <sub>178</sub>	3.197	3.146	0.090	4.76	2.864	3.445
P/2013 R3 (Catalina-PANSTARRS)	3.185	3.033	0.273	0.90	2.204	3.862
133P/(7968) Elst-Pizarro	3.184	3.157	0.165	1.39	2.636	3.678
176P/(118401) LINEAR	3.167	3.196	0.192	0.24	2.582	3.810
238P/Read (P/2005 U1)	3.152	3.165	0.253	1.27	2.364	3.966
P/2012 T1 (PANSTARRS)	3.134	3.154	0.236	11.06	2.411	3.897
313P/Gibbs (P/2014 S4)	3.132	3.156	0.242	10.97	2.391	3.920
324P/2010 R2 (La Sagra)	3.098	3.099	0.154	21.39	2.622	3.576
107P/(4015) Wilson-Harrington	3.083	2.638	0.624	2.79	0.993	4.284

\* Tisserand parameter with respect to Jupiter.

† Semimajor axis (AU).

‡ Orbital eccentricity.

§ Orbital inclination (degrees).

¶ Perihelion distance (AU).

\*\* Aphelion distance (AU).

2006; Jewitt and Hsieh, 2006; Kinoshita et al., 2007) and 1999 YC (Kasuga and Jewitt, 2008). The dispersion age of the Geminid stream is  $t \sim 10^3$  yr (Ohtsuka et al., 2006), meaning that Phaethon is active on this or a shorter timescale. The timescale for the separation of 2005 UD and 1999 YC is not known but presumably is much longer. No gas has been reported in optical spectra (Chamberlin et al., 1996), but near-Sun brightening of Phaethon by a factor of 2 was detected in Solar Terrestrial Relations Observatory (STEREO) spacecraft data in 2009 (Jewitt and Li, 2010) and 2012 (Li and Jewitt, 2013), while the ejected dust has also been resolved (Jewitt et al., 2013a) (cf. Fig. 3). However, the sudden appearance and position angle of the Phaethon dust tail indicate that the ejected particles are small, with an effective radius  $\sim 1\text{ }\mu\text{m}$  and a combined mass  $\sim 3 \times 10^5\text{ kg}$  (Jewitt et al., 2013a). This is tiny compared to the  $M_s \sim 10^{12}\text{--}10^{13}\text{ kg}$  Geminid stream mass (Hughes and McBride, 1989; Jenniskens, 1994) and suggests that the Geminids are produced by a different process. In any case, 1- $\mu\text{m}$  particles are quickly accelerated by solar radiation pressure to faster than the solar system escape speed, and cannot contribute to the Geminid stream. Larger particles evidently contribute too little to the optical scattering cross-section to be discerned in STEREO near-Sun observations taken against the bright coronal background. However, particles with sizes  $>10\text{ }\mu\text{m}$  were recently reported in thermal emission at  $25\text{ }\mu\text{m}$  (Arendt, 2014), while kilogram-mass Geminids have been recorded striking the nightside of the Moon (Yanagisawa et al., 2008). Some such bodies might survive passage through Earth's atmosphere (Madiedo et al., 2013) and could already be present, but unrecognized, in terrestrial meteorite collections.

The Geminid stream mass and dynamical age together could imply ejection of debris from Phaethon, if in steady-state, at rates  $30 \leq M_s/t \leq 300\text{ kg s}^{-1}$ . More likely, mass loss from Phaethon is highly variable, with dramatic bursts interspersed with long periods of quiescence. Continued observations of Phaethon, especially at long wavelengths sensitive to large particles, are needed.

## 2.2. 311P/PanSTARRS (P/2013 P5), $T_J = 3.662$

311P is an inner-belt asteroid (Table 1) that ejected dust episodically over at least nine months in 2013, creating a remarkable multi-tail appearance (Jewitt et al., 2013c, 2014c; Hainaut et al., 2014; Moreno et al., 2014) (cf. Fig. 4). Interpreted as synchrones (the sky-plane projected positions of dust particles of different sizes released simultaneously from the nucleus), each tail has a position angle linked to the ejection date. The intervals between ejections appear random.

The episodic mass loss is unlike that seen in any previously observed comet. This fact alone argues against ice sublimation as the driving agent. An additional consideration is that the orbit of 311P lies near the inner edge of the asteroid belt, in the vicinity of the Flora family. The Floras have been associated with the LL chondrites (Vernazza et al., 2008), which themselves reflect metamorphism to temperatures  $\sim 800^\circ\text{C}$  to  $960^\circ\text{C}$  (Keil, 2000). It is improbable that water ice could survive in such a body. Impact likewise offers an untenable explanation for activity that occurs episodically over many months.

The color of 311P indicates an S-type classification (Jewitt et al., 2013c; Hainaut et al., 2014), consistent with its

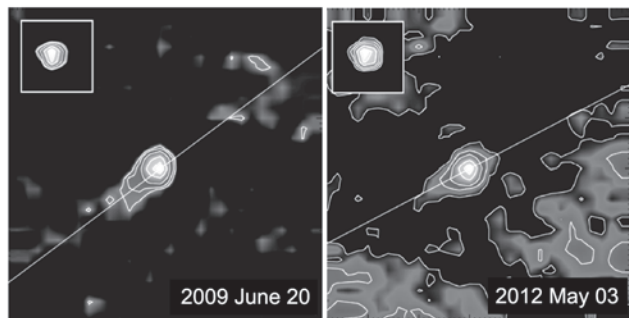


**Fig. 3.** (3200) Phaethon at perihelion in 2009 and 2012 showing extended emission along the projected Sun-comet line. The insets show the point-spread function of the STEREO camera. Each panel shows a region  $490''$  square and is the median of  $\sim 30$  images taken over a one-day period. From Jewitt *et al.* (2013a).

inner-belt orbit and with the Floras. Flora-family asteroids have a mean visual geometric albedo  $0.29 \pm 0.09$  (Masiero *et al.*, 2013). With this assumed albedo, the nucleus of 311P has a radius  $r_n \leq 240 \pm 40$  m (Jewitt *et al.*, 2013c). This small size, combined with the inner-belt location, renders 311P susceptible to spinup by radiation forces. Specifically, the YORP timescale for 311P is  $< 10^6$  yr, shorter than the collisional lifetime. Therefore, it is reasonable to conjecture that episodic mass loss from 311P results from a rotational instability in which regolith is locally unstable and occasionally avalanches off the surface in response to rapid spin (Jewitt *et al.*, 2013c). This “rotational mass shedding” qualitatively accounts for the nonsteady tail formation and the success of synchrone models, which assume ejection from the nucleus at zero initial velocity. Unstable material on 311P would depart at the gravitational escape speed,  $v_e \sim 0.3$  m s $^{-1}$  for a body with  $\rho = 3300$  kg m $^{-3}$ , the density of the LL chondrites, or less. Hainaut *et al.* (2014) suggest an alternative model in which dust production results from friction between two oscillating components of a contact binary nucleus.

### 2.3. P/2010 A2 (LINEAR), $T_J = 3.582$

P/2010 A2 showed a distinctive morphology with a leading, point-like nucleus about 120 m in diameter (Table 2), trailed by an extended tail of dust in which are embedded ribbon-like structures (Jewitt *et al.*, 2010) (see Fig. 5). The position angle of the tail and its variation with time are consistent with the action of radiation pressure on millimeter- to centimeter-sized dust particles, following impulsive ejection at very low speeds ( $\sim 0.2$  m s $^{-1}$ ) in February–March 2009, nearly a year before discovery (Jewitt *et al.*, 2010; Snodgrass *et al.*, 2010). Prediscovery observations were found as early as November 22, 2009 (UT), while detection in the first  $\sim 6$  months after the dust ejection event was impeded by the angular proximity of P/2010 A2 to the Sun (Jewitt *et al.*, 2011a). Before discovery, a large quantity of fast-moving particles are presumed to have left the vicinity of the main nucleus. The mass of particles remaining in the tail

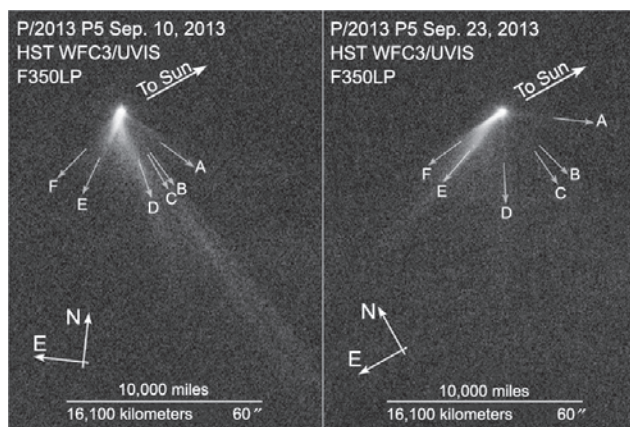


**Fig. 4.** 311P observed on two epochs showing the distinctive evolving, multiple tail structure. From Jewitt *et al.* (2013c).

at discovery is estimated to be in the range  $(6\text{--}60) \times 10^7$  kg (Jewitt *et al.*, 2010; Moreno *et al.*, 2010; Snodgrass *et al.*, 2010). Observations in October 2012 reveal a surviving trail of particles up to 20 cm in radius and a differential power-law size distribution index  $3.5 \pm 0.1$  (Jewitt *et al.*, 2013b). Kim *et al.* (2012) found that the colors most closely resemble those of an H5 chondrite. The estimated total debris mass is  $\sim 5 \times 10^8$  kg, about 10% of the mass of the nucleus.

The properties of P/2010 A2 appear consistent both with an impact origin (with a meter-scale projectile striking at  $5$  km s $^{-1}$ ) and with rotational instability (Jewitt *et al.*, 2010), although an impact origin is often assumed (Snodgrass *et al.*, 2010; Hainaut *et al.*, 2012). In the former interpretation, the distinctive arms seen in Fig. 5 are projections of the impact cone (Kleyna *et al.*, 2013), while in the latter they are ribbons of debris shed in the rotational equator (Agarwal *et al.*, 2013).

### 2.4. (1) Ceres, $T_J = 3.309$

Ceres is unique among the known active asteroids in that it is the only object for which water sublimation has been spectroscopically detected. The 556.936-GHz water ground-state line was reported in absorption by Küppers *et al.* (2014). The line area is time-variable, and can be fitted by a model-dependent water production rate  $dM/dt \sim 6$  kg s $^{-1}$ . Unlike other active asteroids, however, no dust emission has ever been reported for Ceres.

At the subsolar point on Ceres (heliocentric distance 2.6 AU), a perfectly absorbing water ice surface would sublimate in equilibrium with sunlight at the specific rate  $f_s = 5 \times 10^{-5}$  kg m $^{-2}$  s $^{-1}$  (cf. section 3.4). An exposed, subsolar ice patch of area  $(dM/dt)/f_s = 0.12$  km $^2$ , corresponding to a circle of radius 200 m, could supply water vapor. A larger area of exposed ice would be needed if the ice were more reflective, or if it were located away from the subsolar point. One possibility is that ice has been recently exposed on Ceres by a surface disturbance, possibly by the formation of a small impact crater or other geological instability. Alternatively, the

TABLE 2. Physical properties.

Name	D*	$p_V^{\dagger}$	P‡	B–V§	$dm/dt^{\ddagger}$	Ref.
(3200) Phaethon	5–7	0.08–0.17	3.603	$0.58 \pm 0.01$	N/A	[1]
311P/2013 P5 (PANSTARRS)	<0.5	0.29**	?	$0.77 \pm 0.03$	?	[2]
P/2010 A2 (LINEAR)	0.12	0.1**	?	?	N/A	[3]
(1) Ceres	975	$0.090 \pm 0.003$	9.07	?	~6	[2]
(2201) Oljato	1.8	$0.43 \pm 0.03$	?	$0.83 \pm 0.02$	5? (gas)	[3]
P/2012 F5 (Gibbs)	1.8	0.05**	$3.24 \pm 0.01$	–	–	[4]
259P/Garradd	$0.30 \pm 0.02$	0.05**	?	$0.63 \pm 0.03$	$\leq 1.5$ (gas), 0.01	[5]
(596) Scheila	$113 \pm 2$	$0.038 \pm 0.004$	15.848	$0.71 \pm 0.03$	$\leq 3$ (gas)	[6]
288P/(300163) 2006 VW139	3	0.04**	?	?	?	[7]
(62412) 2000 SY178	$7.8 \pm 0.6$	$0.065 \pm 0.010$	$3.33 \pm 0.01$	$0.64 \pm 0.03$	?	[8]
P/2013 R3 (Catalina-PANSTARRS)	<0.4 (multiple)	0.05**	?	$0.66 \pm 0.04$	?	[9]
133P/(7968) Elst-Pizarro	$3.8 \pm 0.6$	$0.05 \pm 0.02$	$3.471 \pm 0.001$	$0.65 \pm 0.03$	$<0.04$ (gas), 0.01, 0.7–1.6	[12]
176P/(118401) LINEAR	$4.0 \pm 0.4$	$0.06 \pm 0.02$	$22.23 \pm 0.01$	$0.63 \pm 0.02$	0.1	[13]
238P/Read	0.8	0.05**	?	$0.63 \pm 0.05$	0.2	[14]
P/2012 T1 (PANSTARRS)	2.4	0.05**	–	$0.65 \pm 0.07$	–	[15]
313P/2014 S4 (Gibbs)	1.0	0.05**	?	$0.72 \pm 0.02$	0.2–0.4	[16]
324P/2010 R2 (La Sagra)	1.1	0.04**	?	?	4	[17]
107P/(4015) Wilson-Harrington	$3.5 \pm 0.3$	$0.06 \pm 0.01$	7.15	?	$\leq 150$ (gas)	[18]

\* Effective diameter (km).

† Geometric albedo.

‡ Rotation period.

§ Color index. Solar color is B–V = 0.64 ± 0.02.

¶ Inferred mass loss rate in kg s<sup>-1</sup>. Unless otherwise stated, the estimates are based on continuum measurements and refer to dust. N/A means that no mass loss rate can be specified because the loss is not in steady state, or for some other reason.

\*\* Value is assumed, not measured.

References: [1] Ansdell et al. (2014); [2] Jewitt et al. (2013c, 2014c), Hainaut et al. (2014); [3] Jewitt et al. (2010, 2011a); [4] Kuppers et al. (2014); [5] Tedesco et al. (2002), McFadden et al. (1993), Russell et al. (1984); [6] Stevenson et al. (2012), Moreno et al. (2012), Novakovic et al. (2014), Drahus et al. (2015); [7] Jewitt et al. (2009); [8] Tedesco et al. (2002), Warner et al. (2009); [9] Hsieh et al. (2012b); [10] Sheppard and Trujillo (2015); [11] Jewitt et al. (2014b); [12] Hsieh et al. (2004, 2009, 2011a); [13] Hsieh et al. (2011a), Licandro et al. (2011a); [14] Hsieh et al. (2011b); [15] Moreno et al. (2013), Hsieh et al. (2013), O'Rourke et al. (2013); [16] Jewitt et al. (2015), Hui and Jewitt (2015); [17] Moreno et al. (2011b), Hsieh et al. (2012c), Hsieh (2014); [18] Veeder et al. (1984), Fernández et al. (1997), Licandro et al. (2009), Urakawa et al. (2011), Ishiguro et al. (2011b).

water vapor might not be produced by sublimation in sunlight, but by subsurface heating followed by escape through a vent (cf. Enceladus) (Porco et al., 2014), since Ceres is potentially large enough to maintain significant internal heat (Castillo-Rogez and McCord, 2010). Additional measure-

ments, presumably from the Dawn mission, will be needed to distinguish between these possibilities.

## 2.5. (2201) Oljato, $T_J = 3.299$

In the 1980s, magnetometers on the Pioneer Venus spacecraft revealed multiple, symmetric interplanetary magnetic field enhancements, clumped nonrandomly in time (Russell et al., 1984). About 25% of these events are associated with planet-crossing asteroid (2201) Oljato, whose orbit lies interior to Venus' when near perihelion. Russell et al. suggested that the magnetic disturbances result from deceleration of the solar wind, perhaps caused by mass loading from ionized gases released by an unknown process from debris distributed along Oljato's orbit. A mass-loading rate of only ~5 kg s<sup>-1</sup> is reportedly needed. Observations in 2006–2012 with the Venus Express under a similar geometry reveal no events related with Oljato. Lai et al. (2014) argue that the field enhancements were due to loading of the interplanetary wind by charged nanoscale dust in Oljato's orbit, and that the quantity of this dust decreased between the Pioneer and Venus Express missions. A spectroscopic search for gas produced by Oljato itself proved negative (Chamberlin et al., 1996), with upper limits to the CN production rate near  $10^{23}$  s<sup>-1</sup>. With a



**Fig. 5.** Trailing structures in P/2010 A2 observed January 29, 2010 (UT). The full image width is ~1' while the inset width is ~12''. From Jewitt et al. (2010).

standard H<sub>2</sub>O/CN mixing ratio of 360 (*A'Hearn et al.*, 1995), the corresponding limit to the mass production rate in water is  $\leq 1.5 \text{ kg s}^{-1}$ . Whatever the cause of the repetitive magnetic disturbances, they are not products of an inert asteroid and imply mass loss from Oljato. A dynamical simulation indicates that (2201) Oljato has negligible chance of being a captured Jupiter-family comet (*Bottke et al.*, 2002).

## 2.6. P/2012 F5 (Gibbs), T<sub>J</sub> = 3.228

P/2012 F5 was observed on September 18, 2012, to exhibit a dust trail extending  $>15'$  in the plane of the sky while at a heliocentric distance of R  $\sim 3.1$  AU. Follow-up observations in 2013 showed the object to be largely inactive and set an upper limit on the diameter of the nucleus of  $\sim 2$  km, although residual dust contamination of the nucleus photometry at the time could not be completely ruled out (*Novaković et al.*, 2014). A series of deep images in 2014 showed rapid nucleus rotation (period 3.24 h) and revealed four condensations in an orbit-aligned dust trail (Fig. 6). Dynamical analysis of the object found it to be dynamically stable over at least 1 G.y., and therefore unlikely to be recently implanted from elsewhere in the solar system (*Stevenson et al.*, 2012), although it was also found to be a member of an extremely compact asteroid cluster determined to be just  $1.5 \pm 0.1$  m.y. in age (*Novaković et al.*, 2014).

The origin of the mass loss is unclear, with evidence consistent both with impact and rotational instability. The dust trail was determined via numerical modeling to consist of particles ejected in a single impulsive event, consistent with impact, roughly nine months prior to the discovery of activity (*Moreno et al.*, 2012; *Stevenson et al.*, 2012). In

contrast, the rapid rotation suggests that material may have been lost from F5 by rotational instability. Future observations are needed to determine the ejection times and fates of the trail condensations.

## 2.7. 259P/(Garradd) (P/2008 R1), T<sub>J</sub> = 3.216

259P was observed over a  $\sim 45$ -day interval in 2008 to have the appearance of an active comet with a typical flared tail while at a heliocentric distance of R  $\sim 2$  AU (*Jewitt et al.*, 2009). The object's intrinsic brightness decreased by a factor of about 2 over the course of those observations, corresponding to a mass loss rate on the order of  $\sim 10^{-2} \text{ kg s}^{-1}$ , assuming mean grain radii of 10  $\mu\text{m}$  and bulk densities of  $\rho = 1300 \text{ kg m}^{-3}$  (*MacLennan and Hsieh*, 2012). Subsequent observations of the inactive nucleus found an effective nucleus radius of  $r = 0.30 \pm 0.02$  km (Table 2) (*MacLennan and Hsieh*, 2012), assuming a red geometric albedo of 0.05. Spectral observations limited the production of the CN radical to  $Q_{\text{CN}} \leq 1.4 \times 10^{23} \text{ s}^{-1}$ , corresponding to a water production rate  $\leq 1.5 \text{ kg s}^{-1}$  assuming H<sub>2</sub>O/CN = 360. 259P is located near the 8:3 mean-motion resonance with Jupiter and is also affected by the v<sub>6</sub> secular resonance. The dynamical lifetime in this orbit is short (20–30 m.y.) compared to the age of the solar system, suggesting that 259P was scattered into its present location from elsewhere in the asteroid belt, or possibly even from elsewhere in the solar system.

## 2.8. (596) Scheila, T<sub>J</sub> = 3.208

(596) Scheila, a 113-km-diameter object with red geometric albedo  $\sim 0.04$  (Table 2), developed a comet-like appearance in late 2010 in the form of two prominent dust plumes. Over the course of a month, dust in these plumes dispersed from the nucleus due to solar radiation pressure, apparently without any continued replenishment of particles from the nucleus (*Bodewits et al.*, 2011; *Jewitt et al.*, 2011b; *Moreno et al.*, 2011a). Dust modeling by *Ishiguro et al.* (2011a,b) demonstrated that the morphology of the observed dust plumes was consistent with the results of an impact-driven ejecta cloud consisting of a circularly symmetric ejecta cone (subsequently inverted by radiation pressure) and a down-range plume (Fig. 7). *Bodewits et al.* (2014) subsequently reported a change in the rotational lightcurve, which they attributed to the signature of the impact scar.

Upper limits to the gas production from the nucleus of  $Q_{\text{OH}} \leq 10^{26} \text{ s}^{-1}$  [corresponding to a water production rate of  $< 3 \text{ kg s}^{-1}$  (*Howell and Lovell*, 2011)] and  $Q_{\text{CN}} < 9 \times 10^{23}$  [corresponding to  $Q_{\text{H}_2\text{O}} \leq 10 \text{ kg s}^{-1}$  (*Hsieh et al.*, 2012a)] were found, though the meaning of these limits is unclear given the apparently impulsive nature of the mass loss event from Scheila. *Jewitt et al.* (2011b) calculated the mass of dust in micrometer-sized grains to be  $4 \times 10^7 \text{ kg}$ , while more model-dependent attempts to account for larger particles gave total dust masses of  $\sim 10^8$ – $10^{10} \text{ kg}$  (*Bodewits et al.*, 2011; *Ishiguro et al.*, 2011a; *Moreno et al.*, 2011a). No ice was observed in the coma (*Yang and Hsieh*, 2011).

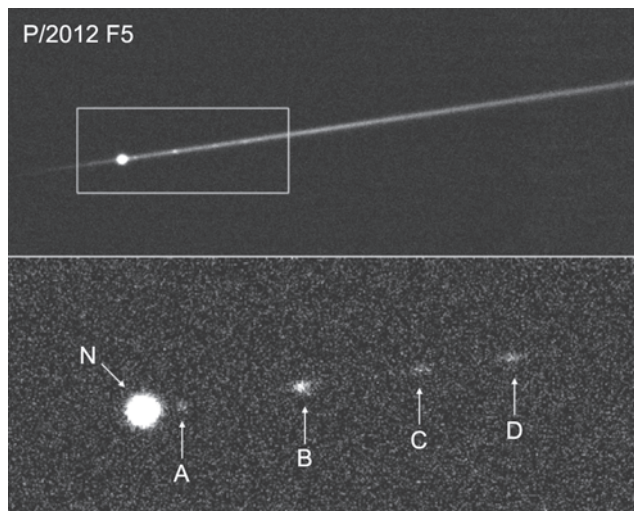


**Fig. 6.** Keck telescope images of P/2012 F5 on August 26, 2014 (UT). The region shown is  $1.0 \times 2.5'$ . The rectangular box in the top panel shows the region enlarged in the bottom panel, where a model of the trail has also been subtracted. Letters mark the primary nucleus, N, and tail condensations, A–D. From *Drahus et al.* (2015).

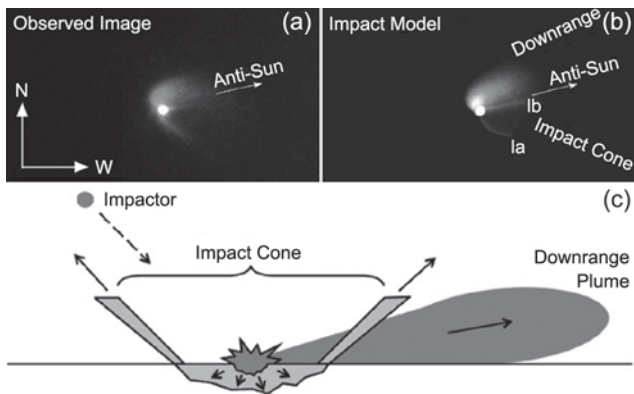


**Fig. 7.** (a) Observed image of (596) Scheila on December 12, 2010; (b) simulated image of dust ejecta consisting of an impact cone and downrange plume; and (c) diagram of the modeled impact scenario. From Ishiguro et al. (2011b).

### 2.9. 288P/(300163) 2006 VW<sub>139</sub>, T<sub>J</sub> = 3.203

Discovered in 2006 as an inactive asteroid, 288P was found to be cometary in 2011 by the Pan-STARRS1 survey telescope (Hsieh et al., 2012b) (cf. Fig. 8). A short ( $\sim 10''$ ) antisolar dust tail and a longer ( $\sim 60''$ ) dust trail aligned with the object's orbit plane were seen in deep follow-up images, indicating the simultaneous presence of both recent and months-old dust emission, strongly suggesting that the observed activity was due to a long-duration emission event, consistent with sublimation. Photometric monitoring showed that intrinsic brightness of the near-nucleus coma remained constant for at least one month, before then declining by 40% over the next month, again consistent with a long-duration emission event where the coma was continually replenished by fast-dissipating small dust particles over its period of constant brightness, and then faded quickly once the replenishment rate slowed.

Spectroscopic observations did not detect any gaseous sublimation products, setting an upper limit to the CN production rate of  $Q_{\text{CN}} < 10^{24} \text{ mol s}^{-1}$  (Hsieh et al., 2012b; Licandro et al., 2013). However, dust modeling found that the onset of activity occurred shortly after perihelion, and persisted for about 100 d (Licandro et al., 2013). A dynamical analysis by Novaković et al. (2012) found that 288P belongs to a compact cluster of 24 asteroids believed to originate from the fragmentation of a  $\sim 11\text{-km-diameter}$  parent body  $7.5 \pm 0.3$  m.y. ago.

### 2.10. (62412) 2000 SY<sub>178</sub>, T<sub>J</sub> = 3.197

(62412) 2000 SY<sub>178</sub> has diameter  $7.8 \pm 0.6$  km, geometric albedo  $0.065 \pm 0.010$ , and is a probable C-type (Sheppard and Trujillo, 2015). The nearly circular orbit at 3.146 AU is consistent with membership of the 2–3-G.y.-old Hygiea family. While the origin of the activity is unknown, the 3.33-h rotation period and 0.45-mag light curve range suggest, by analogy with 133P (Jewitt et al., 2014a), that rotation may play a role.

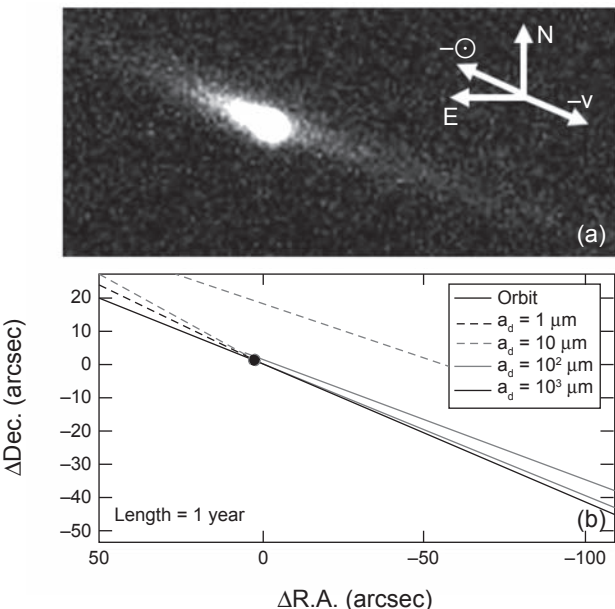


**Fig. 8.** (a) Image of 288P and (b) corresponding syndyne plot. A syndyne is the locus of positions of particles of one size released from the nucleus at zero speed over a range of times. From Hsieh et al. (2012b).

### 2.11. P/2013 R3 (Catalina-PanSTARRS), T<sub>J</sub> = 3.185

P/2013 R3 is a dust enshrouded outer-belt asteroid observed in a state of disintegration (Jewitt et al., 2014b) (cf. Fig. 9). Ten distinct components were detected in the interval from October to December 2014, with a velocity dispersion between fragments on the order of  $0.3\text{--}0.5 \text{ m s}^{-1}$ . Because of dust contamination in 2014 it is only possible to set upper limits to the size of the fragments. Assuming geometric albedo 0.05, the four largest have radii  $\leq 200$  m. The gravitational escape velocities of the largest fragments (assuming density  $\rho = 1000\text{--}3000 \text{ kg m}^{-3}$ ) are  $0.15\text{--}0.25 \text{ m s}^{-1}$ , comparable to the measured fragment-velocity dispersion. The fragmentation took place successively over a period of several months at least, excluding an impact as the cause. Disruption due to the pressure of a subsurface volatile reservoir was also excluded, although the continued dust activity of the fragments may have been caused by the sublimation of newly exposed ice. Rotational breakup seems the most likely cause of the catastrophic disruption of R3, supported by the close-to-escape-speed relative velocities of the fragments (Hirabayashi et al., 2014).

### 2.12. 133P/(7968) Elst-Pizarro, T<sub>J</sub> = 3.184

133P was first observed to be active in 1996, exhibiting a long, narrow dust trail with no visible coma, making it the first known (and currently best characterized) active asteroid in the main asteroid belt. At first suspected to be the product of a collision (Boehnhardt et al., 1998; Toth, 2000), it has since been observed to be active on three additional

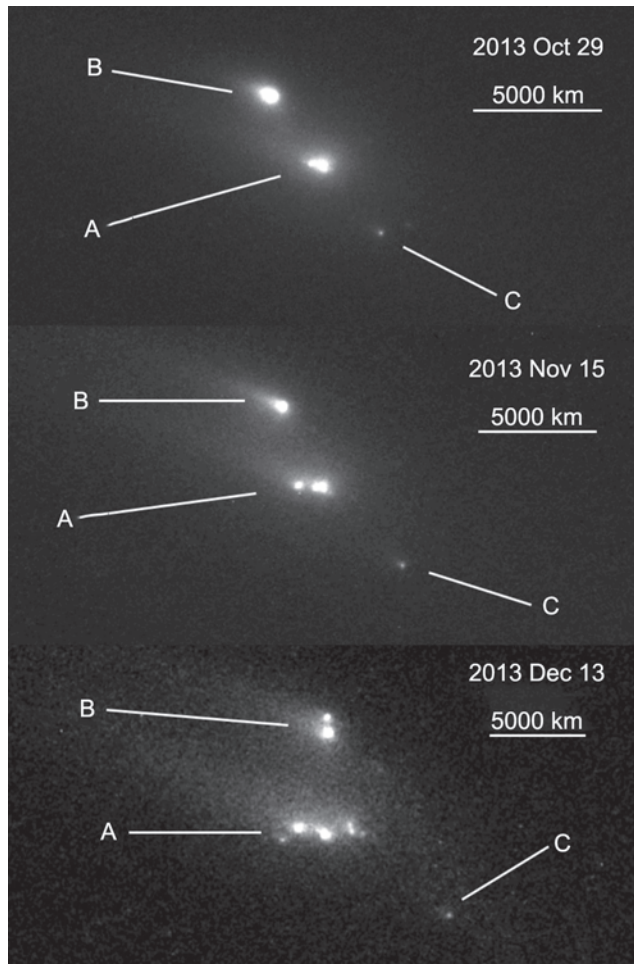


**Fig. 9.** Evolution of the components of P/2013 R3 over six weeks in 2014. The components, labeled A, B, and C, show progressive splitting and are enveloped in a  $10^8$ -kg debris cloud. Scale bars mark 5000 km at the distance of the object. Adapted from Jewitt *et al.* (2014b).

occasions in 2002, 2007, and 2013, and inactive in between (e.g., Hsieh *et al.*, 2004, 2010; Jewitt *et al.*, 2014a).

The appearance of 133P when active is typically that of a point-like nucleus with a thin tail (or “trail”) of dust following in the projected orbit (Fig. 10). Order-of-magnitude dust mass loss rates, inferred from surface photometry of the tail (Hsieh *et al.*, 2004), reach  $\sim 0.02 \text{ kg s}^{-1}$ , while comparable upper limits in gas are inferred from spectroscopy (Licandro *et al.*, 2011a). The thin tail indicates that particles are ejected very slowly from the nucleus with characteristic speeds  $\sim 1.8 a_{\mu\text{m}}^{-1/2} \text{ m s}^{-1}$ , where  $a_{\mu\text{m}}$  is the grain radius expressed in micrometers (Jewitt *et al.*, 2014a). Curiously, particles larger than a few micrometers leave the nucleus at speeds below the  $\sim 2 \text{ m s}^{-1}$  gravitational escape speed (e.g., millimeter-sized particles have  $v \sim 6 \text{ cm s}^{-1}$ ). This is inconsistent with a pure sublimation origin, and appears to require centripetal assistance and a spatially subdivided sublimating surface (Jewitt *et al.*, 2014a).

The nucleus has a rotation period of  $3.471 \pm 0.001 \text{ h}$  (Hsieh *et al.*, 2004), a spectrum similar to those of B- or

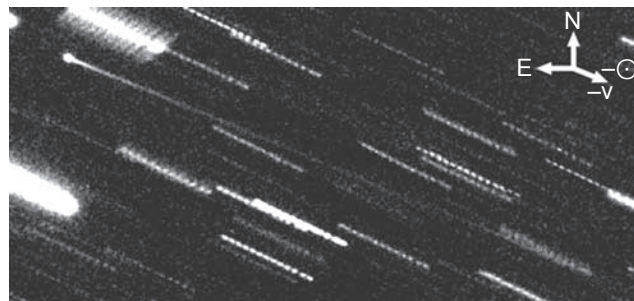


**Fig. 10.** 133P imaged September 7 2002 (UT). From Hsieh *et al.* (2004).

F-type asteroids (e.g., Bagnulo *et al.*, 2010; Licandro *et al.*, 2011a), and an optical albedo of  $p_R \sim p_V \sim 0.05$  (Hsieh *et al.*, 2009; Bauer *et al.*, 2012).

### 2.13. 176P/(118401) LINEAR, $T_J = 3.167$

176P/LINEAR was observed to exhibit a short fan-shaped tail over a single, month-long interval in 2005 (Hsieh *et al.*, 2011a). During this time, the object was about 30% brighter than the bare nucleus, leading to an implied dust mass  $\sim 10^5 \text{ kg}$ . The properties of the dust can be approximately matched by models in which the characteristic particle size is  $10 \mu\text{m}$ , the ejection speed  $\sim 5 \text{ m s}^{-1}$ , and the dust production rate  $\sim 0.07 \text{ kg s}^{-1}$ , all similar to values inferred in 133P. Activity was sought but not detected in 2011 (Hsieh *et al.*, 2014), and the water-production rate was spectroscopically limited to  $Q_{\text{H}_2\text{O}} \leq 4 \times 10^{25} \text{ s}^{-1}$  ( $\leq 1.0 \text{ kg s}^{-1}$ ) in Herschel observations 40 days after perihelion on August 8, 2011 (UT) (de Val-Borro, 2012). The  $4.0 \pm 0.4$ -km-diameter nucleus rotates with a period near 22.2 h (Table 2).

### 2.14. 238P/Read, $T_J = 3.152$

The second active asteroid in the main belt, 238P, exhibited a strong coma and dust tail when discovered in October 2005 at a heliocentric distance of  $R \sim 2.4 \text{ AU}$  (Fig. 11). Like 259P, the nucleus of 238P is tiny, with a diameter of  $\sim 0.8 \text{ km}$  (Hsieh *et al.*, 2011b). It was observed to be active in both 2005 and 2010, with a period of inactivity in between, with a coma dust mass on the order of  $10^5 \text{ kg}$  and a production rate estimated (from published photometry) near  $\sim 0.1 \text{ kg s}^{-1}$ . Also like 259P, 238P is dynamically unstable, with a survival time on the order of 20 m.y., although unlike 259P, which may have been recently implanted at its current location, 238P is hypothesized to have diffused in eccentricity from its original location within the Themis family (which also contains 133P, 176P, and 288P) due to its proximity to the 2:1 mean-motion resonance with Jupiter (Haghishipour, 2009).

### 2.15. P/2012 T1 (PanSTARRS), $T_J = 3.134$

P/2012 T1 was discovered to exhibit a diffuse coma and a featureless fan-shaped antisolar tail in October 2012.

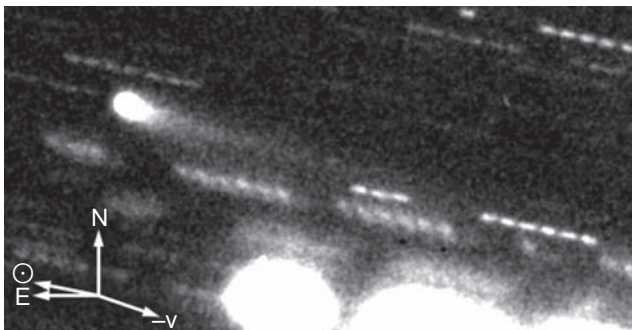


**Fig. 11.** 238P imaged on November 10, 2005 (UT). From Hsieh et al. (2009).

Photometric monitoring showed that the total scattering cross-section of the comet's coma and tail doubled over a period of about a month, remained approximately constant for another 1.5 months, and then declined by ~60% over the next 1.5 months (Hsieh et al., 2013). Spectroscopic observations using the Keck I telescope found an upper limit CN production rate of  $Q_{\text{CN}} < 1.5 \times 10^{23} \text{ mol s}^{-1}$ , and no evidence of absorption at  $0.7 \mu\text{m}$  that would indicate the presence of hydrated minerals (Hsieh et al., 2013), while Herschel Space Telescope observations were used to set an upper limit  $\text{H}_2\text{O}$  production rate of  $Q_{\text{H}_2\text{O}} < 7.6 \times 10^{25} \text{ mol s}^{-1}$  (O'Rourke et al., 2013). Dust modeling by Moreno et al. (2013) indicated that dust production began near perihelion and lasted for a period of ~4–6 months, with a total ejected dust mass on the order of  $10^7 \text{ kg}$  for maximum grain sizes of  $a = 1\text{--}10 \text{ cm}$ .

### 2.16. 313P/Gibbs (2014 S<sub>4</sub>), $T_J = 3.132$

Discovered September 24, 2014 (UT), this object has a semimajor axis 3.156 AU and is located near at least eight other active asteroids in the outer belt (Fig. 2). The nucleus radius is 500 m (albedo 0.04 assumed). Prediscovery observations from 2003 (Fig. 12) reveal 313P as only the third object, after 133P and 238P, to be active in more than one orbit, consistent with mass loss driven by the sublimation of ice. It displays a fan-shaped dust tail in both 2003 and 2014 that is well approximated by syndyne dust emission models, indicating that the dust is ejected over a period of at least three months during each active episode (Jewitt et al., 2015; Hsieh et al., 2015b; Hui and Jewitt, 2015). The object is found near two three-body mean-motion resonances with Jupiter and Saturn (11J-1S-5A and 10J+12S-7A), and its orbit has been found to be intrinsically chaotic with a Lyapunov time of  $T_L = 12,000 \text{ yr}$ , yet numerical simulations show that it is stable over at least 50 m.y. 313P is the second active asteroid, after P/2012 T1, to be associated with the ~155-m.y.-old Lixiaohua asteroid family (Hsieh et al., 2015b).

### 2.17. 324P/2010 R2 (La Sagra), $T_J = 3.098$

324P/2010 R2 was observed to be active from September 2010 to January 2011, at  $R = 2.6$  to  $2.7 \text{ AU}$ , and has a mea-

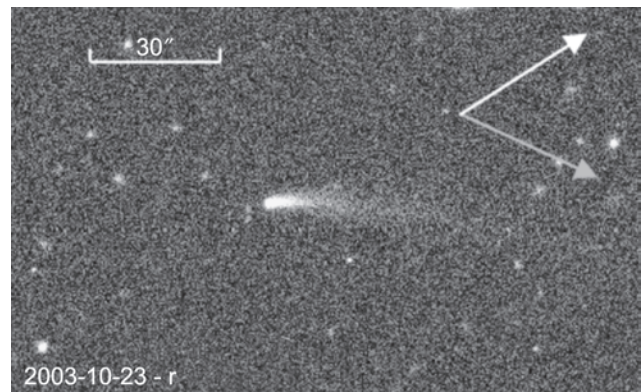


**Fig. 12.** Prediscovery image of 313P at 2.47 AU on October 23, 2003 (UT). White and gray arrows show the directions of the projected anti-solar and heliocentric velocity vectors, respectively. From Hui and Jewitt (2015).

sured nucleus size of  $r = 0.55 \pm 0.05 \text{ km}$  (Hsieh, 2012c). Moreno et al. (2011b) inferred dust production at the peak rate of  $\sim 4 \text{ kg s}^{-1}$ , with centimeter-sized particles ejected at about  $0.1\text{--}0.2 \text{ m s}^{-1}$ . A limit to the outgassing rate  $Q_{\text{CN}} \leq 3 \times 10^{23} \text{ s}^{-1}$  (corresponding to  $\sim 3 \text{ kg s}^{-1}$  in water) was placed spectroscopically (Hsieh et al., 2012c). The latter authors found (neglecting possible nongravitational forces due to outgassing) that the orbit of 324P/2010 R2 is stable on timescales  $\sim 100 \text{ m.y.}$  and argue that this object was likely formed *in situ*. Reactivation of 324P was reported in the summer of 2015, suggesting that the activity is driven by sublimation and ruling out impact as a likely cause (Hsieh and Sheppard, 2015).

### 2.18. 107P/(4015) Wilson-Harrington, $T_J = 3.083$

107P showed a prominent diffuse tail about  $2'$  in length on a blue-sensitive photographic plate taken November 19, 1949, when at  $R = 1.148 \text{ AU}$  (Fernandez et al., 1997). A red-sensitive plate taken nearly simultaneously shows only a hint of this tail. 107P appears strongly trailed on both plates owing to its noncircular motion. The tail color ( $B-R = -1$ ) is too blue to be caused by scattering from dust, and the tail position angle ( $\sim 15^\circ$  from radial to the Sun) is also inconsistent with the expected direction of a dust tail blown by radiation pressure. 107P was reobserved on November 22 and 25 but then showed no trace of a tail (Cunningham, 1950), and no comet-like activity has been reported since (Chamberlin et al., 1996; Ishiguro et al., 2011c). We regard 107P as the least convincing example of the active asteroids, both because the observations are old and unrepeated and because 107P lies very near the  $T_J > 3.08$  cut-off. Bottke et al. (2002) used a statistical dynamical model to conclude that there is a 4% chance that 107P is a captured Jupiter-family comet.

### 2.19. Related Observations

Features in the 3.0–3.5- $\mu\text{m}$  reflection spectra of large main-belt asteroids (24) Themis (diameter  $198 \pm 20 \text{ km}$ )

and (65) Cybele ( $273 \pm 12$  km) have been interpreted as absorptions due to O-H stretch in water ice and C-H stretch in an unidentified organic molecule (Campins *et al.*, 2010; Rivkin and Emery, 2010; Licandro *et al.*, 2011b). The shape of the band in Themis requires a thin, widespread, or global ice film (“frost”) only 100 Å to 1000 Å thick (Rivkin and Emery, 2010). However, such a thin film would be highly unstable to sublimation and would lead to gas production rates  $10^5$ – $10^6$  kg s $^{-1}$ , violating observational limits set spectroscopically [ $\leq 400$  kg s $^{-1}$  (Jewitt and Guillet-Lepoutre, 2012)]. The latter authors showed that, if water ice exists on these asteroids, it must be of high albedo ( $>0.3$ ) and spatially confined to regions far from the subsolar point (e.g., near the poles on objects having small obliquity) in order to keep sublimation below observational limits. The spectra of Themis and Cybele are similar to that of the iron-rich mineral goethite (Beck *et al.*, 2011), but this offers a less plausible explanation because goethite is rare in meteorites and normally attributed to weathering of the meteorites once fallen on Earth.

### 3. MECHANISMS

In this section we discuss possible mechanisms able to eject dust from asteroids. The group properties offer few clues, given the modest size of the active asteroids sample (cf. Table 2). Licandro *et al.* (2011a), for example, suggest that the color distribution of active asteroids is different from that of classical cometary nuclei. Even if future measurements prove this to be true, its significance is unclear given that a wide range of mechanisms are known to drive the observed activity in these bodies (Jewitt, 2012). Furthermore, while they are discussed separately for clarity, it is likely that different mechanisms operate together in real objects. For example, the loss of particles produced in (3200) Phaethon by thermal disintegration is likely assisted by rotation and radiation pressure sweeping. Sublimation driven mass loss from 133P is probably also rotation assisted.

#### 3.1. Rotational Mass Loss

For a sphere of density  $\rho$  the critical period at which the gravitational acceleration equals the centripetal acceleration at the equator is

$$P_c = \left( \frac{3\pi}{G\rho} \right)^{1/2} \quad (2)$$

where G is the gravitational constant. For example, with  $\rho = 1000$  kg m $^{-3}$ ,  $P_c = 3.3$  h. The critical period is independent of the asteroid size, is shorter for higher densities, and is longer for elongated spheroids in rotation about a minor axis (by a factor approximately equal to the ratio of the long to short axes of the body). The rotation and the shape of a fluid body are related, in equilibrium, by the classic MacLaurin and Jacobi ellipsoid series. However, while most asteroids may have been severely weakened by repeated impact fracturing and the formation of a rubble-pile structure, they are

not strengthless. van der Waals and other weak forces can imbue a rubble pile with a cohesive strength, while friction can provide resistance to deformation even in the absence of cohesion, and critical periods much shorter than given by equation (2) are possible (Holsapple, 2007; Sanchez and Scheeres, 2014). Calculation of the rotational stability of rubble piles remains an important but challenging and underconstrained problem in asteroid science.

Evidence for rotational instability comes from the observation that most asteroids larger than a few hundred meters in size rotate more slowly than a “barrier” period at about 2.2 h (Warner *et al.*, 2009). This is widely interpreted as meaning that faster-rotating asteroids have lost mass or have even disrupted due to centripetal forces. Recent observations of active asteroids 311P and P/2013 R3 (and possibly P/2010 A2) appear to show asteroids losing mass rotationally, so that we can begin to study this process as it happens.

In principle, the rotation rates of asteroids can be driven to critical values by external torques exerted by the gravity of other objects, by chance impacts, by outgassing, and by electromagnetic radiation. In the main belt, gravitational torques are negligible (except within binary and other multiple systems). Collisions add angular momentum stochastically, leading to a slow random walk toward larger angular momenta. Outgassing from icy asteroids can be very efficient in changing the spin but, for ice-free asteroids, radiation torques offer the most potential for driving the rotation steadily up to critical values.

Power absorbed from the Sun by the surface of an asteroid is reradiated to space as heat. Asteroids are aspherical and anisothermal, causing the radiated infrared photons to be emitted anisotropically. The angle-averaged momentum carried by thermal photons per second corresponds to a net reaction thrust on the asteroid, known as the Yarkovsky force. It has important dynamical consequences on small main-belt asteroids. If the vector representing the net force does not pass through the center of mass of the asteroid, the result is the so-called YORP torque, which can change the magnitude of the spin and excite precession (see the chapter by Vokrouhlický *et al.* in this volume).

We focus on changes in the magnitude of the spin, and estimate the relevant timescale from the ratio of the rotational angular momentum, L, to the torque, T. Ignoring the vector nature of these quantities, for simplicity, the torque is proportional to the number of photons radiated per second, which varies in proportion to  $r_n^2/R^2$ , where  $r_n$  is the asteroid radius and R is the distance from the Sun. Torque also depends on the moment-arm, defined as the perpendicular distance between the instantaneous direction of the net force and the center of mass. Statistically, at least, we expect the moment arm  $\propto r_n$ . Together, these dependences give  $T \propto r_n^3/R^2$ . Meanwhile, the spin angular momentum is  $L \propto Mr_n^2\omega$ , where M is the body mass and  $\omega$  the angular rotation rate, related to the rotational period, P, by  $\omega = 2\pi/P$ . Substituting  $M \propto pr_n^3$  gives  $L \propto pr_n^5\omega$ . Finally, the timescale for YORP to change the angular momentum is  $\tau_y = L/T$ , or  $\tau_y = K pr_n^2R^2\omega$ , where K is a constant.

The value of constant K depends sensitively on the body shape, surface texture, thermal properties, and spin vector of the asteroid. We estimate its magnitude from measurements of YORP acceleration in five asteroids (*Rozitis and Green*, 2013; *Lowry et al.*, 2014), scaled to assumed density  $\rho = 2000 \text{ kg m}^{-3}$  and spin period  $P = 5 \text{ h}$ , to obtain

$$\tau_y (\text{m.y.}) \sim 4 \left[ \frac{r_n}{1 \text{ km}} \right]^2 \left[ \frac{R}{3 \text{ AU}} \right]^2 \quad (3)$$

Order-of-magnitude deviations from equation (3) can result from peculiarities of the asteroid shape, texture, thermal properties, and spin. Still, equation (3) gives a crude but useful estimate, by showing that the angular momentum of a 1-km-radius asteroid at 3 AU can be modified significantly on timescales of just a few million years. A sustained YORP torque can drive a kilometer-scale body to rotational instability in a few times  $\tau_y$ , and the spins of subkilometer, low-density, near-Sun asteroids should be particularly susceptible to YORP torques. Setting  $\tau_y < 4.5 \times 10^9 \text{ yr}$  in equation (3) shows that asteroids as large as  $r_n \sim 30 \text{ km}$  can be affected by YORP in the age of the solar system, provided they survive against collisions for such a long time. Most of the objects in Table 2 are small enough to be potentially affected by YORP.

A major complication is that YORP torques can change not just the rotation state but the shape of an asteroid, as material slides, bounces, or rolls toward the rotational equator on its way to escape (e.g., *Harris et al.*, 2009; *Statler*, 2009). Changing the shape affects the magnitude and possibly the direction of the YORP torque (*Cotto-Figueroa et al.*, 2015), creating a feedback loop that can change the timescale for spinup relative to the value in equation (3). Evidence for equatorial accumulation of particulate matter is present in images of UFO-shaped saturnian satellites (cf. Fig. 13) and in the shapes of some rapidly rotating near-Earth asteroids, as determined by radar (*Ostro et al.*, 2006).

In part because of the complex interplay between torque, spin, material properties, shape, and mass loss, no comprehensive models of asteroid evolution and disruption by rotation have been computed, although many interesting approximations exist (*Holsapple*, 2007, 2010; *Walsh et al.*, 2008, 2012; *Jacobson and Scheeres*, 2011; *Marzari et al.*, 2011; *Hirabayashi and Scheeres*, 2014; *Sánchez and Scheeres*, 2012, 2014; *Cotto-Figueroa et al.*, 2015; *Scheeres*, 2015). These models, not always in agreement with one another, attempt to investigate the role of small torques in the production of distinctive body spins and shapes, in mass-shedding and structural failure (cf. Fig. 14), and in the formation of both binaries and unbound pairs (*Pravec et al.*, 2010; *Moskovitz*, 2012; *Polishook*, 2014).

The cohesive strength is a key parameter in all such models because, given sufficient cohesive strength, an asteroid can resist rotational forces at an arbitrarily high rotation rate (e.g., *Rozitis et al.*, 2014). Fortunately, new observations of active asteroids allow us to obtain a useful estimate of the cohesive strength.

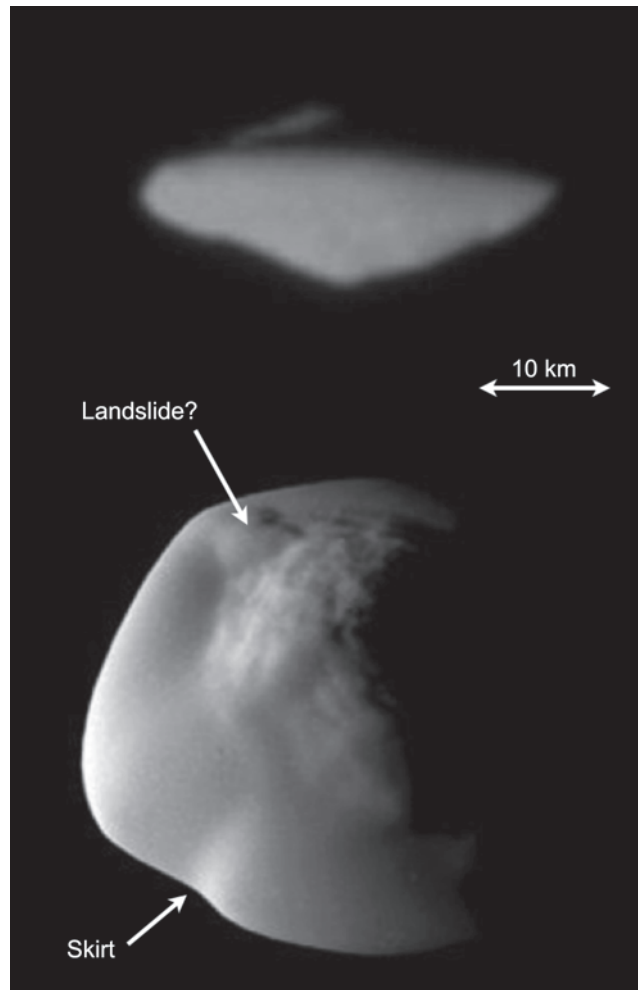


**Fig. 13.** Two views of UFO-shaped saturnian satellite Atlas showing a dust skirt around the equator where the effective gravitational attraction to the body approaches zero. Atlas is a slow rotator (period 14 hr), but it fills its Roche lobe within the saturnian system, making it a suitable analog for a body at the stability limit (*Minton* 2008). The paucity of craters indicates youth, which results from the mobility of surface dust. A possible landslide is visible on the dust skirt; corresponding landslides or avalanches leading to escape are likely responsible for the impulsive tail ejections in 311P (cf. Fig. 4). The bulk density is  $\sim 400 \text{ kg m}^{-3}$ . Credit: NASA/JPL/SSI.

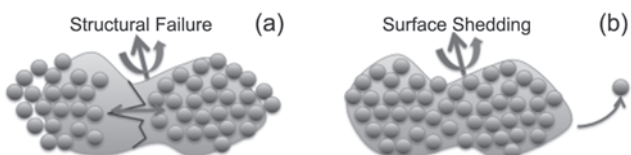


**Fig. 14.** Schematic diagram distinguishing (a) structural failure, as may be seen in P/2013 R3, from (b) surface shedding (for which 311P is a candidate). From *Hirabayashi and Scheeres* (2014).

First, we consider a toy model of two bodies in contact, both of density  $\rho$  and having dimensions  $r_p$  and  $r_s$ , with  $r_p \gg r_s$ . Assume that the smaller body sits on the rotational equator of the larger body and take the area of contact between them to be  $\sim r_s^2$ . Let the critical frequency of rotation at which gravitational attraction is balanced by centripetal acceleration be  $\omega_c$ . Then, when rotating with an angular frequency  $\omega > \omega_c$ , the minimum cohesive strength needed to bind the two bodies together may be written

$$S \sim \frac{m_s r_p (\omega^2 - \omega_c^2)}{r_s^2} \quad (4)$$

where  $m_s$  is the mass of the smaller component. If detachment occurs when  $\omega^2 \gg \omega_c^2$ , the smaller mass  $m_s$  will leave with a relative velocity,  $\Delta V$ , comparable to the instantaneous equatorial velocity of the primary, namely  $\Delta V = r_p \omega$ . Substituting for  $\Delta V$  and  $m_s = \rho r_s^3$  into equation (4), we obtain

$$S \sim \rho \left( \frac{r_s}{r_p} \right) (\Delta V)^2 \quad (5)$$

The six measured components of P/2013 R3 (Table 2 of Jewitt *et al.*, 2014b) are equivalent in volume to a single precursor body of dimension  $r_p = 350$  m. Four of these six nuclei have  $r_s \sim 200$  m and are separating at characteristic speeds  $0.2 \leq \Delta V \leq 0.5$  m s $^{-1}$ . Assuming density  $\rho = 1000$  kg m $^{-3}$  (equation (5)) gives an estimate of the cohesive strength as  $16 \leq S \leq 140$  N m $^{-2}$ . A mathematically more refined analysis, in which the initial body shape is represented by a rotational ellipsoid, gives  $40 \leq S \leq 210$  N m $^{-2}$  (Hirabayashi *et al.*, 2014). In both cases, these very small cohesive strengths are comparable to the  $\sim 25$  N m $^{-2}$  strength expected of a rubble pile bound by van der Waals forces acting on the smallest particles (Sanchez and Scheeres, 2014). The small size of the P/2013 R3 precursor body is compatible with a short YORP timescale ( $\tau_y \sim 0.5$  m.y. by equation (3)), lending credibility to the YORP spinup hypothesis for this object. Active asteroid 311P has also been interpreted (Jewitt *et al.*, 2013c, 2014c) as rotational instability of a different sort, in which only surface particulates escape from the rotating central body (Hirabayashi *et al.*, 2014).

This first determination of the cohesive strength, if broadly applicable, shows that rotation of asteroids can play a major disruptive role. Indeed, the rotational disruption rate may exceed the impact destruction rate for asteroids  $\leq 1$  km in diameter (Fig. 15). However, many questions remain about the process. In 311P, what determines the intervals between successive dust releases, and for how long will they continue? More specifically, does the distribution of dust releases resemble the power-law spectra of self-organized critical sandpiles (Laurson *et al.*, 2005), as might be expected if avalanches are responsible? Could this object be in the process of forming a binary (cf. Walsh *et al.*, 2008; Jacobson and Scheeres, 2011), or has it already formed one? Will the nucleus eventually be driven to structural instability, as has

occurred in P/2013 R3? Or could 311P be a fragment of a rotationally disrupted precursor body whose components are so widely spread as to have escaped notice?

### 3.2. Impacts

The average velocity dispersion among main-belt asteroids is  $U \sim 5$  km s $^{-1}$ , enough to cause vaporization as well as shattering and, potentially, disruption upon impact. Experiments at laboratory scales show that the ratio of  $m_e$ , the mass ejected faster than speed  $v$ , to the projectile mass,  $M$ , is

$$\frac{m_e}{M} = A \left( \frac{v}{U} \right)^\alpha \quad (6)$$

with  $A \sim 0.01$  and, very roughly,  $\alpha \sim -1.5$  (Housen and Holsapple, 2011). For an assumed spherical projectile, the mass is  $M = 4\pi\rho r_p^3/3$ , where  $r_p$  is the radius. Equation (6) is valid provided the impact does not have enough energy to completely disrupt the target asteroid. For example, an impact at 5 km s $^{-1}$  into a 1-km-radius body, with escape velocity  $v_e \sim 1$  m s $^{-1}$ , would have an ejecta to projectile mass ratio  $m_e/M \sim 3500$  by equation (6). The mass of ejecta and the scattering cross-section,  $C$ , are related by

$$m_e = \chi \rho \bar{a} C \quad (7)$$

where  $\bar{a}$  is the weighted mean particle size in the ejecta and  $\chi$  is a dimensionless constant on the order of unity. Very modest projectiles are capable of creating ejecta with a substantial cross-section. We write  $C = f\pi r_n^2$ , where  $r_n$  is the radius of the target asteroid and  $f$  is a constant. The case  $f = 1$  corresponds to ejecta with a cross-section equal to that of the target asteroid. Such an impact would result in a doubling of the asteroid brightness, and therefore should be readily detected. We set  $v = (8\pi G \rho / 3)^{1/2} r_n$ , the gravitational escape speed from the target asteroid, and combine equations (6) and (7) to obtain

$$r_p = \left( \frac{3\bar{a}f}{4A} \right)^{1/3} \left( \frac{8\pi G \rho}{3} \right)^{-\alpha/6} U^{\alpha/3} r_n^{[(2-\alpha)/3]} \quad (8)$$

Equation (8) assumes that the densities of the target and projectile are equal. Substituting the above parameters, equation (8) reduces to

$$r_p = 0.29 f^{1/3} r_n^{7/6} \quad (9)$$

Equation (9) is plotted in Fig. 16 for  $f = 0.1, 1, 10$ , and  $100$ , corresponding to changes in the apparent magnitude due to impact of  $\Delta m \sim 2.5 \log_{10} f = 0.1, 0.7, 2.5$ , and  $5$  mag, respectively. The figure shows that a 20-cm projectile striking a 1-km asteroid would eject enough material to double the total cross-section and brightness. Very modest impacts should create observable ejecta signatures.

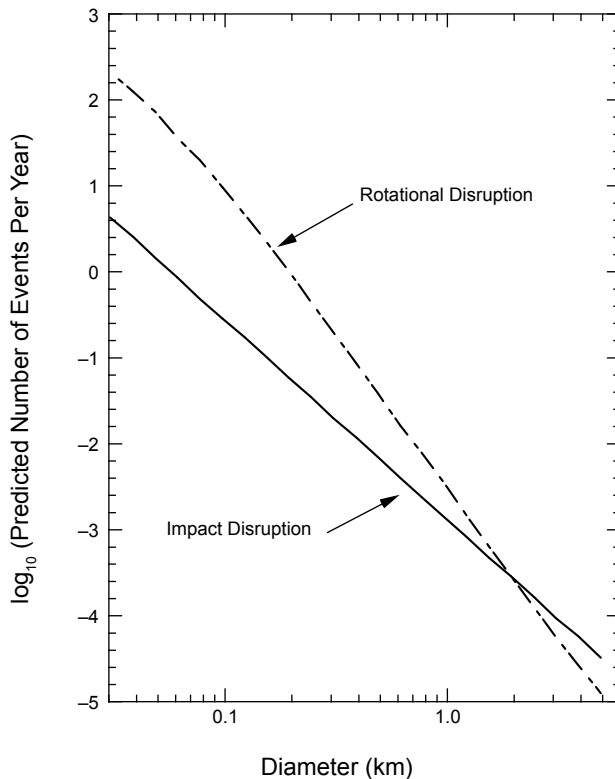


**Fig. 15.** Model rates of asteroid disruption due to impact and rotational bursting as a function of asteroid diameter. From Marzari et al. (2011).

The number of boulders in the asteroid belt is very uncertain, because these small objects are too faint to be observed directly from Earth. Models extrapolating from larger sizes suggest that the number of objects with  $r_p > 1$  m is roughly  $10^{13 \pm 1}$  (O'Brien and Greenberg, 2005). The rates at which small-scale impacts occur is correspondingly uncertain by at least an order of magnitude.

Survey observations by Denneau et al. (2015) have been interpreted, through a simple model, to show a discrepancy with the rate of asteroid disruption predicted by Bottke et al. (2005).

### 3.3. Thermal Disintegration

Forces caused by thermal expansion can exceed the fracture strength of a material, leading to cracking and the production of dust. On a low-gravity body, excess thermal strain energy can eject fragments faster than the gravitational escape speed, leading to a net loss of material (Jewitt, 2012). In a uniform material, stresses arise from differential thermal expansion across a temperature gradient. Most minerals are non-uniform in structure, consisting of compositionally distinct grains. Non-uniform materials are susceptible to fracture because of differential expansion between the component materials, with or without a temperature gradient. The thermal skin depth in the material (across which temperature gradients are particularly marked, and variable) is related to the period of

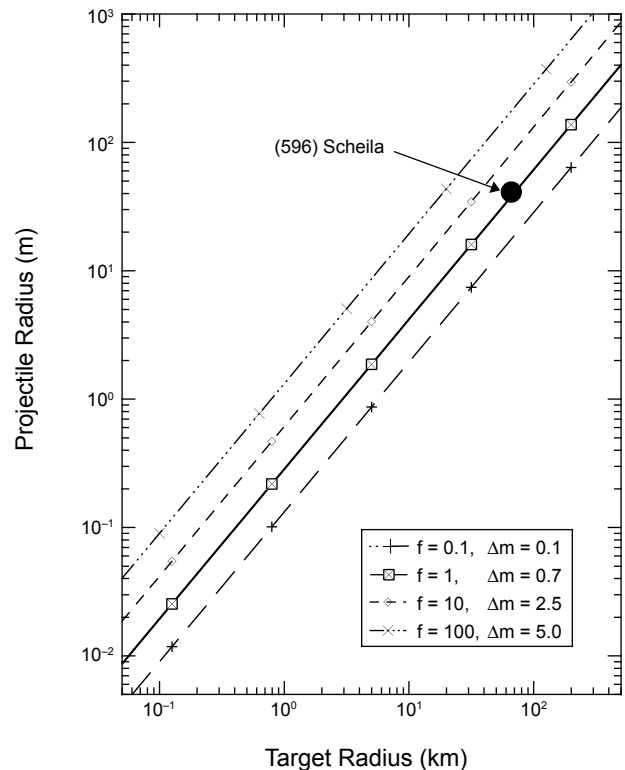


**Fig. 16.** Projectile radius (y-axis) needed to generate ejecta with cross-section  $f = 0.1, 1, 10$ , and  $100 \times$  the geometric cross-section of the target asteroid, whose radius is plotted on the x-axis (cf. equation (9)). Impacted asteroid (596) Scheila ( $r_p = 65$  km) brightened by about 1 mag following impact. The figure shows that the projectile radius was several tens of meters.

the temperature variation,  $\tau$ , and to the thermal diffusivity,  $\kappa$ , by  $\ell \sim (\kappa\tau)^{1/2}$ . For example, an asteroid with diffusivity  $\kappa = 10^{-6} \text{ m}^2 \text{ s}^{-1}$ , rotating with period  $\tau = 5$  h, would have a skin depth  $\ell \sim 0.1$  m. Thermal fracture occurring within a thermal skin depth of the physical surface may contribute to the production of regolith (Delbo et al., 2014). Desiccation (the loss of bound water from a hydrated mineral) is a separate process leading to fracture and dust production when the stresses induced by shrinkage exceed the material strength. On Earth, mudcracks in dry lake beds made of clay minerals are the most easily recognized examples of desiccation cracking.

Among the active asteroids, the most convincing evidence for thermal disintegration is from (3200) Phaethon (Li and Jewitt, 2013; Jewitt and Li, 2010; Jewitt et al., 2013a). The eccentric orbit and high obliquity [Phaethon's pole is at ecliptic coordinates  $\lambda, \beta = 85^\circ \pm 14^\circ, -20^\circ \pm 10^\circ$  (Ansdel et al., 2014)] lead to highly non-uniform surface heating, with peak temperatures near 1000 K at perihelion (Ohtsuka et al., 2009). The temperature is further modulated by Phaethon's rapid rotation (3.6-h period), with a diurnal variation of hundreds of Kelvin. Furthermore, the escape speed from the ~5-km-diameter nucleus is a few meters per second, sufficiently

small that grains produced by fracture can easily be ejected (Jewitt, 2012). While Phaethon's composition is unknown, hydrated mineralogies (montmorillonite clays) have been suggested based on the blue optical/near-infrared reflection spectrum (Licandro *et al.*, 2007). Hydrated materials, if present, would be highly susceptible to desiccation, shrinkage, and fracture. Nine asteroids with perihelia  $\leq 0.25$  AU (subsolar temperatures  $\geq 800$  K) have been searched for activity, setting upper limits to the mass loss rate from  $\leq 0.1$  to  $1 \text{ kg s}^{-1}$  (Jewitt, 2013).

On a larger scale, thermal disintegration may be important in dust disks surrounding white dwarf stars. Such disks are inferred from photospheric, heavy-element pollution (Jura and Xu, 2013).

### 3.4. Sublimation of Ice

Ice exposed at the surface of an asteroid at distance  $R$  AU from the Sun will sublimate, in equilibrium, at a specific rate  $dm/dt$  ( $\text{kg m}^{-2} \text{s}^{-1}$ ), given by the solution to

$$\frac{F_{\odot}(1-A)}{R^2} \cos(\theta) = \varepsilon\sigma T^4 + L(T) \frac{dm}{dt} \quad (10)$$

where the term on the left represents the absorbed solar power per unit area, the first term on the right represents thermal radiation to space per unit area, and the second term represents the power used per unit area in breaking bonds to sublime ice.  $F_{\odot} = 1360 \text{ W m}^{-2}$  is the solar constant,  $A$  is the Bond albedo,  $\varepsilon$  is the emissivity of the asteroid, and  $L(T)$  is the latent heat of sublimation of ice at temperature  $T$ . Here  $\theta$  is the angle between the Sun and the surface normal as seen from the sublimating surface. Values of  $\cos(\theta)$  range from 1/4 (the isothermal case, corresponding to the lowest possible temperatures) to 1 (for normal illumination at the subsolar point, the maximum-temperature case). Conduction is ignored for simplicity — its effect will be to reduce  $dm/dt$  relative to the value computed from equation (10) by an amount that depends on the conductivity (measurements of small-body regoliths suggest that the conductivity is very small, so that the error incurred by its neglect should be minor). Equation (10) can be solved in combination with the Clausius-Clapeyron relation for water ice, to evaluate  $dm/dt(R)$ , as in Fig. 17. The figure also shows (on the right-hand axis) the rate of recession of the sublimating surface due to mass loss, given by  $dr/dt = \rho^{-1} dm/dt$  ( $\text{m s}^{-1}$ ).

Maximum sublimation rates vary by nearly an order of magnitude from  $\sim 10^{-4} \text{ kg m}^{-2} \text{s}^{-1}$  at 2 AU to  $\sim 10^{-5} \text{ kg m}^{-2} \text{s}^{-1}$  at 3.5 AU, corresponding to the inner and outer edges of the main belt. The corresponding surface recession rates are from a few meters to a few  $\times 0.1$  meters per year. Water ice is thermodynamically unstable when exposed to sunlight at asteroid belt distances, but can be preserved on billion-year timescales beneath meter-thick or greater layers of porous refractory debris (Fanale and Salvail, 1989; Schorghofer, 2008). Sublimation at rates sufficient to launch dust from a small body would then require that the protective regolith be removed, perhaps

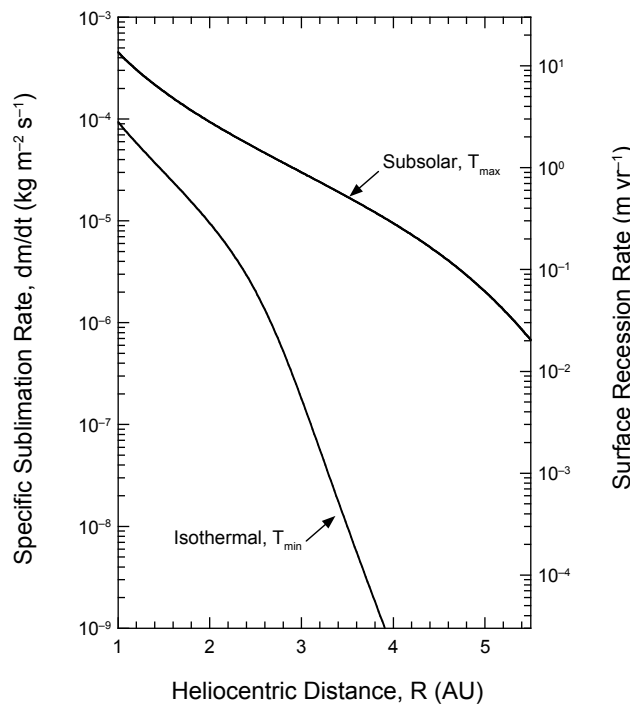


**Fig. 17.** Solutions to equation (10) for the extreme cases of subsolar sublimation ( $\theta = 0^\circ$ ) and for isothermal sublimation. The righthand axis shows the rate of recession of the sublimating surface due to mass loss, given by  $dr/dt = \rho^{-1} dm/dt$  ( $\text{m s}^{-1}$ ), where  $\rho$  is the density, taken here to be  $1000 \text{ kg m}^{-3}$ . From Jewitt (2012).

by a small impact or some other disturbance of the surface. In this scenario, sublimation would proceed from an exposed region until a new refractory covering, consisting of particles too large to be lifted by gas drag (a so-called “rubble mantle”), chokes off the flow. The ratio of the lifetime of the sublimating surface patch to the interval between successive impacts (or other surface disturbances) defines the “duty cycle”,  $f_d$ . For example, the timescale for formation of a rubble mantle on a kilometer-scale body at 3 AU is estimated from a simple model (Fig. 4 of Jewitt, 2002) at  $\sim 1$  yr, increasing to 10 yr at 4 AU. The interval between impacts of meter-scale projectiles (needed to expose ice sufficient to account for the mass loss) onto this body is perhaps  $t \sim 10^4$  yr, giving  $f_d \sim 10^{-4}-10^{-3}$ . Neither the rescaling timescale nor the excavation timescale can be specified with confidence, but  $f_d \ll 1$  is assured. As noted in section 3.2, impacts at  $5 \text{ km s}^{-1}$  are highly erosive, with an ejecta to projectile mass ratio  $m_e/M \sim 3500$  for a 1-km target asteroid (equation (6)). At this rate, the asteroid can survive for  $\sim 10^9$  yr.

### 3.5. Radiation Pressure Sweeping

Particles lifted above the surface of an asteroid are susceptible to solar radiation pressure and, if sufficiently small, can be blown away. The critical size for radiation pressure sweeping on a nonrotating asteroid is (Jewitt, 2012)

$$a_\beta (\mu\text{m}) = 10 \left( \frac{1 \text{ km}}{r_n} \right) \left( \frac{1 \text{ AU}}{R} \right)^2 \quad (11)$$

At  $R = 3 \text{ AU}$ , a 1-μm-radius grain detached from the surface (by any process) can be blown away from a nonrotating asteroid 1 km in radius.

### 3.6. Electrostatics and Gardening

Dielectric surfaces exposed to ionizing (UV and X-ray) solar radiation develop a positive electric potential (of perhaps 5 to 10 V) through the loss of photoelectrons. Conversely, electrons impacting in shadowed regions imbue a locally negative potential. The resulting electric fields near shadow boundaries can grow large enough ( $\sim 10 \text{ V m}^{-1}$  to  $100 \text{ V m}^{-1}$ ) to mobilize dust. On the Moon, horizon glow (Rennilson and Criswell, 1974) and dust impact counter experiments (Berg et al., 1976) show that charging effects near the terminator lift 10-μm-sized dust particles to meter heights and greater, at implied ejection speeds,  $\sim 1 \text{ m s}^{-1}$ . Smooth dust ponds on asteroids strongly suggest electrostatic mobilization (but not ejection) of grains in a much-lower-gravity environment (Poppe et al., 2012; see also the chapter by Murdoch et al. in this volume).

On small asteroids, electrostatic forces can potentially accelerate particles to speeds exceeding the gravitational escape speed. To within a numerical factor on the order of unity, particles smaller than a critical radius

$$a_e (\mu\text{m}) \sim 2 \left( \frac{1 \text{ km}}{r_n} \right) \quad (12)$$

can be electrostatically ejected against gravity from a nonrotating body of radius  $r_n$  (Jewitt 2012).

Larger particles are too heavy to lift against gravity, at least on a nonrotating body, whereas smaller particles are trapped by cohesive forces on the surface (Hartzell and Scheeres, 2011). Electrostatically ejected particles should therefore be confined to a narrow range of sizes near  $a_e$ . Note that equation (12) is independent of the heliocentric distance because the potential,  $V$ , depends on photon energy, not flux. Since, in the asteroid belt at 2–3 AU,  $a_e \leq a_\beta$ , particles launched electrostatically should be picked up by solar radiation pressure and propelled into comet-like dust tails.

Although electrostatic ejection must operate at some level, in practice the rate of loss of small particles from an asteroid will be limited by the rate of their production, presumably by micrometeorite bombardment. This distinguishes the role of electrostatics on the asteroids from the circumstance on the Moon, where ejected particles fall back to the surface under the high lunar gravity, to be repeatedly relaunched at each terminator crossing (Berg et al., 1976).

We crudely limit the ejected mass flux from asteroids as follows. On the Moon, impact overturn of the regolith (“gardening”) reaches to depths  $\delta r \leq 1 \text{ m}$  on timescale  $t = 1 \text{ G.y.}$  (Gault et al., 1974). Impact-produced fragments that

are largely retained on the Moon by gravity will, on the small asteroids, be immediately lost. Therefore, a strong upper limit to the electrostatic mass loss from asteroids can be obtained by assuming that the gardening rates are comparable and that none of the gardened layer is retained. The mass loss rate from a spherical asteroid is  $dM/dt \sim 4\pi r_n^2 \rho \delta r/t$ , where  $r_n$  is the radius and  $\rho$  is the density. For an  $r_n = 1\text{-km}$  asteroid with  $\rho = 2000 \text{ kg m}^{-3}$  and  $\delta r = 1 \text{ m}$ , this gives  $dM/dt \leq 10^{-6} \text{ kg s}^{-1}$ . This is 4 to 6 orders of magnitude smaller than the mass loss rates inferred from observations of active asteroids (Table 2). Of course, we cannot exclude spatially or temporally enhanced micrometeorite impact fluxes in the asteroid belt, but enhancements sufficient to bring the mass loss rates up to those in Table 2 seem unlikely. The only observation possibly supporting the existence of widespread, very low level mass loss is by Sonnett et al. (2011). If this observation is confirmed, it might be evidence for very low level ejection of dust owing to gardening losses, possibly assisted by electrostatic effects.

### 3.7. Observational Diagnostics

Diagnosing the cause of mass loss from any particular object is difficult, both because of limitations of the data and because of uncertainties in models of the mass loss mechanisms. It is often easier to rule out possible explanations than to rule them in. Spectroscopic detections of water vapor or another sublimation product would provide the most solid evidence of sublimation-driven activity, but such evidence has only been obtained for Ceres (Küppers et al., 2014). Unsuccessful attempts have been made to detect water vapor or CN emission from several other active asteroids (e.g., Jewitt et al., 2009; Licandro et al., 2011a, 2013; Hsieh et al., 2012a,b,c, 2013; de Val-Borro et al., 2012; O’Rourke et al., 2013). Typical derived upper limits to gas loss rates are  $\leq 1 \text{ kg s}^{-1}$ . Unfortunately, the significance of these nondetections is inconclusive, for two reasons. First, CN is a prominent trace species in the spectra of Kuiper belt and Oort cloud comets (with  $\text{H}_2\text{O}/\text{CN} \sim 360$ ); it might be strongly depleted in icy asteroids. Second, spectra are typically obtained long after continuum observations have revealed the mass loss — the gas could simply have escaped on a timescale short compared to the radiation pressure sweeping time for dust.

Another potential indicator is the recoil (or “rocket”) acceleration produced on the nucleus by anisotropic sublimation. Specifically, a nongravitational acceleration,  $\alpha$ , implies a mass loss rate

$$\frac{dM}{dt} = \frac{\alpha M_n}{f_\theta v_0} \quad (13)$$

where  $M_n$  is the mass of the nucleus and  $v_0$  is the velocity of the material ejected. Dimensionless parameter  $f_\theta$  accounts for the directional pattern of the mass loss, with  $f_\theta = 0$  and 1 corresponding to isotropic and perfectly collimated ejection, respectively. In fact, nongravitational acceleration of 133P at  $\alpha = 2.5 \times 10^{-10} \text{ m s}^{-2}$  has been reported (Chesley

*et al.*, 2010), albeit with only  $3\sigma$  statistical significance. To obtain the smallest possible estimate of  $dM/dt$  from equation (13), we maximize  $f_0 = 1$  and use the sound speed in H<sub>2</sub>O gas at the blackbody temperature appropriate to 3 AU, namely  $v_0 = 500$  m s<sup>-1</sup>. Approximated as a sphere of radius 2.2 km and density 1000 kg m<sup>-3</sup>, the nucleus mass is  $M_n = 4 \times 10^{13}$  kg, giving  $dM/dt \sim 20$  kg s<sup>-1</sup>. This rate exceeds the dust production rates measured in 133P by 2 to 3 orders of magnitude, forcing us to conclude either that  $\alpha$  has another cause or that the reported value should be considered only as an upper limit. *Nugent et al.* (2012) measured small semi-major axis drift rates in 42 near-Earth asteroids consistent with the Yarkovsky (radiation) acceleration. An additional 12 asteroids showed drift rates too large to be explained by the Yarkovsky effect. If confirmed, the accelerations of these asteroids, none of which is a known active asteroid, might suggest anisotropic mass loss.

Less-direct inferences can be made in the absence of spectroscopic detection of gas. Activity that repeats on the orbital timescale, as in 133P and 238P, is naturally explained only by sublimation. A prolonged period of dust emission is also suggestive of sublimation and difficult to explain as the result of a simple impact. However, prolonged emission may not be unique to sublimation. Evidence from 311P shows that mass shedding can continue for months, raising the potential for confusion with protracted emission caused by sublimation. The size vs. velocity relation for ejected dust particles also differs between mechanisms, with gas drag giving  $v \propto a^{-1/2}$ , where  $a$  is the dust radius, and rotational instabilities and impact giving a flatter dependence (Fig. 18).

Sublimation will preferentially lift small, micrometer-sized particles that are quickly dispersed by radiation pressure. Objects typically have a bright coma and tail for a few months, as long as the sublimation is ongoing, followed by a rapid fading and return to the appearance of a point source. During rotational breakup, the ejecta sizes are not constrained at all, due to the compensation of gravity by the centrifugal force. Also, impacts are expected to excavate much larger pieces of debris, depending on the escape speed from the parent body. Characteristically, small objects suspected to have undergone an impact or rotational breakup display long-lived trails of centimeter- to meter-sized debris along their orbits for many years after the event, because such large grains are not efficiently removed by radiation pressure. (596) Scheila, although clearly impacted, did not develop a debris trail because the high escape speed prevented the ejection of large debris. The absence of debris trails in sublimation-driven active asteroids is different from comets, likely because cometary sublimation is much stronger and is also able to lift large debris.

Numerical modeling is necessary because the appearance of long-lived activity can be produced either by the lingering of large, slow-dissipating dust grains, or the ongoing replenishment of small, fast-dissipating dust grains. Under the right conditions, however, dust modeling can break this degeneracy and give us insights into the origin of active asteroid activity (e.g., *Hsieh et al.*, 2004; *Ishiguro et al.*, 2011b; *Agarwal et al.*, 2013).

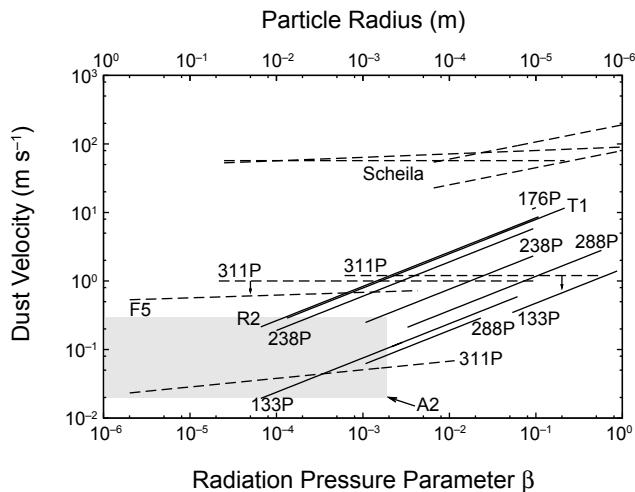


**Fig. 18.** Dust ejection velocities as function of the radiation pressure coefficient  $\beta$  or particle size. The plot is a compilation of published models for individual objects. Such models typically simulate the motion of dust grains ejected from the nucleus over a range of times, particle sizes, and velocities. The best-fitting parameters are determined from comparison with the observed shapes of the dust tails. Solid lines indicate objects with protracted, likely sublimation-driven dust emission; dashed lines and the shaded area for P/2010 A2 refer to objects with impulsive emission. Arrows indicate upper limits; the shaded area for P/2010 A2 illustrates that particles of all sizes were ejected with the same range of velocities.

Pinpointing cases of rotational instability can be difficult because there are few clear predictions about the likely appearances of such bodies. The repeated dust ejections from 311P, for example, can be reconciled with a rotational shedding instability, but it is quite likely that a range of morphologies and time-dependent emission profiles can be produced by this mechanism. Significantly, other mechanisms seem incompatible with the observations. The multiple object P/2013 R3 is self-evidently a result of breakup, with rotation as the likely cause.

Table 3 summarizes our conclusions about the mechanisms driving activity in each object. For many objects, we can eliminate several processes but cannot isolate a unique cause. This partly reflects the inadequacies of the data, but is also a true consequence of the nature of the activity. For example, in those cases where sublimation is believed to be the primary activity driver, an impact (or other disturbance) may be needed to excavate buried ice to trigger sublimation, and mass loss may be assisted by rapid rotation. We emphasize that, in many cases, the entries in Table 3 are expected to change with the acquisition of new data.

### 3.8. Distribution

The orbital distribution of the active asteroids may provide a clue as to the activity mechanisms. There is apparent clustering of active asteroids in Fig. 2 in the outer belt near

TABLE 3. Summary of mechanisms.

Name	Sublimation	Impact	Electrostatics	Rotation	Thermal
(3200) Phaethon	×	?	?	?	✓
311P/PANSTARRS (P/2013 P5)	×	×	×	✓	✗
P/2010 A2 (LINEAR)	×	✓	×	✓	✗
(1) Ceres	✓	✗	✗	✗	✗
(2201) Oljato	?	?	?	?	✗
P/2012 F5 (Gibbs)	✓	✗	✗	✓	✗
259P/Garradd (P/2008 R1)	?	?	?	?	✗
(596) Scheila	✗	✓	✗	✗	✗
288P/(300163) 2006 VW <sub>139</sub>	✓	?	?	?	✗
(62412) 2000 SY <sub>178</sub>	?	✓	?	✓	✗
P/2013 R3 (Catalina-PANSTARRS)	?	✗	✗	✓	✗
133P/(7968) Elst-Pizarro	✓	✗	?	✓	✗
176P/(118401) LINEAR	✓	?	?	✗	✗
238P/Read (P/2005 U1)	✓	✗	✗	?	✗
P/2012 T1 (PANSTARRS)	✓	✗	✗	?	✗
313P/Gibbs (P/2014 S4)	✓	✗	✗	?	✗
324P/2010 R2 (La Sagra)	✓	✗	✗	?	✗
107P/(4015) Wilson-Harrington	?	?	?	✗	✗

✓ – Evidence exists consistent with the process.

✗ – Evidence exists inconsistent with the process.

? – Insufficient or mixed evidence exists.

a  $\sim 3.1 \pm 0.1$  AU. Of the 13 active asteroids orbiting in the main belt, only two (P/2010 A2 and 311P) are located inside the 3:1 mean-motion resonance with Jupiter ( $a = 2.5$  AU), corresponding to  $\sim 15\%$  of the total, while for the asteroids as a whole, this ratio is  $\sim 35\%$ . However, the difference between these distributions is not significant. A Kolmogorov-Smirnov (K-S) test applied to compare the semimajor axes of the active asteroids and the first 500 numbered asteroids shows that the distributions have a 17% probability of being drawn from the same parent distribution and therefore are consistent. However, when the comparison is made between the distribution of the semimajor axes of active asteroids and of main-belt asteroids of comparable size, the difference instead becomes highly significant. Specifically, there is  $<0.1\%$  likelihood that active asteroids and main-belt asteroids with absolute magnitude  $H > 18$  are drawn from the same parent population, according to the K-S test. This different result occurs because of observational bias in magnitude-limited sky survey data, which strongly inhibits the detection of small asteroids in the outer belt. While the active asteroids are subject to this same bias, their detectability is also influenced by their activity, as is evident from the fact that many objects (e.g., P/2010 A2, 311P, P/2013 R3) were unknown before being discovered in an active state. We conclude that the relative paucity of active asteroids in the inner belt and the concentration near 3.1 AU are real, but larger samples from quantitative sky surveys will be important to better assess the biases. Clustering could suggest an origin as collisionally produced fragments of an ice-rich precursor (Novacović et al., 2012, 2014).

#### 4. DYNAMICS

Numerical simulations have been conducted to assess the long-term dynamical stability of many of the known active asteroids (e.g., Jewitt et al., 2009; Haghishipour, 2009; Hsieh et al., 2012a,b,c, 2013; Stevenson et al., 2012). This is of particular interest in the context of understanding whether ice-bearing main-belt comets are native to the asteroid belt or are implanted interlopers from the outer solar system. In most cases, while the median dynamical lifetime of short-period comets before ejection from the solar system or collision with the Sun was found to be  $\sim 5 \times 10^5$  yr (Levison and Duncan, 1994), active asteroids in the asteroid belt have been found to be stable over timescales of  $10^8$  yr or longer. 238P and 259P are notable exceptions, however, having been found to be unstable on timescales on the order of  $\sim 10^7$  yr (Jewitt et al., 2009; Haghishipour, 2009).

Fernández et al. (2002) forward-integrated the orbits of test particles representing the 202 Jupiter-family comets (JFCs) known at the time and several dynamical clones of each comet (using purely gravitational computations). None ended up on orbits with both low eccentricity and low inclination like that of 133P. Comet 503D/Pigott was seen to evolve onto a main-belt orbit, but with high inclination. Interestingly, we know now of active asteroids in the main belt with high inclinations (e.g., 259P and P/2010 R2), and so the possibility that these could be JFC interlopers cannot be excluded. In the same work, it was shown that detaching objects from the JFC population was possible with the inclusion of nongravitational forces in the simulations, but

such large forces were needed as to be unrealistic. The size dependence of nongravitational forces plays a role in this, since nongravitational forces should be far less effective for larger objects, while smaller objects may not be able to sustain such large nongravitational forces for very long without disintegrating or exhausting their volatile content.

The aforementioned simulations assume the modern-day architecture of the solar system. Some dynamical models of the early solar system suggest that planet migration could have resulted in the emplacement of icy outer solar system objects in what is now the main asteroid belt (e.g., Levison *et al.*, 2009; Walsh *et al.*, 2011), although probably not in low-inclination orbits like those of many active asteroids. Therefore, particularly when assessing the astrobiological significance of icy active asteroids as indicators of the composition of the inner protosolar disk, the possibility that these objects could have been implanted at early times must continue to be considered (see the chapter by Morbidelli *et al.* in this volume).

Several active asteroids are associated with collisional asteroid families and clusters. For example, four active asteroids (133P, 176P, 238P, and 288P) have been linked to the Themis family either currently or in the past (Tóth, 2000; Hsieh, 2009; Haghjipour, 2009; Hsieh *et al.*, 2012c), while P/2010 A2 and 311P are associated with the Flora family (Moreno *et al.*, 2010; Jewitt *et al.*, 2013c) and P/2012 T1 and 313P with the Lixiaohua family (Hsieh *et al.*, 2013, 2015b). The dynamical associations are consistent with photometry showing, for example, that the colors of 133P, 176P, and 238P are close to those of the Themis family (Licandro *et al.*, 2011a), while those of 311P are consistent with membership in the Flora family (Jewitt *et al.*, 2013c). However, dynamical associations are unsurprising, given that many asteroids are family members, and a causal relationship between family membership and activity cannot be assumed. The color relationships could also be coincidental, since S-types are common in the inner belt where P/2010 A2 and 311P are found, and C-types in the outer belt where 133P, 176P, 238P, and 288P orbit. However, several active objects have also been linked to much smaller, young asteroid clusters, including 133P [part of the <10-m.y.-old Beagle family (Nesvorný *et al.*, 2008)], 288P [part of a newly discovered  $7.5 \pm 0.3$ -m.y.-old cluster (Novaković *et al.*, 2012)], and P/2012 F5 [part of a  $1.5 \pm 0.1$ -m.y.-old cluster (Novaković *et al.*, 2014)]. In the case of active asteroids exhibiting sublimation-driven activity, membership in a young cluster suggests a natural mechanism by which ice could have been preserved over long timescales (i.e., within the interior of a larger parent body) and only recently exposed to more direct solar heating. In the case of objects exhibiting impact-induced activity, an associated young cluster could represent both a source of potential impactors (given that cluster members will share very similar orbits) and possibly a consequence of residing in a region of the asteroid belt characterized by high collision rates (e.g., Novaković *et al.*, 2014).

## 5. SURVEYS AND RATES

About 10 of the known active asteroids (Table 1) and  $\sim 10^6$  main-belt asteroids (Jedicke and Metcalfe, 1998) are larger than 1 km. The ratio of these numbers gives an active fraction, for all types of activity-driving mechanism,  $f \sim 10^{-5}$ . However, most asteroids fall near the limiting magnitudes of the surveys in which they are discovered and so are never effectively searched for dust emission. Therefore,  $f \sim 10^{-5}$  sets a strong lower limit to the active fraction, since many active objects must go undetected. Recent, dedicated surveys have attempted to remedy this situation by searching for comae in well-defined sky surveys. Unfortunately, most of these surveys are so small in scale that they detect no active objects [of the known active asteroids, only (118401) LINEAR (1999 RE<sub>70</sub>) was discovered as the result of a targeted survey], allowing  $3\sigma$  upper limits,  $f_{3\sigma}$ , to be determined. These include  $f_{3\sigma} \leq 54$  per million (Gilbert and Wiegert, 2009, 2010),  $f_{3\sigma} \leq 6000$  per million (Sonnett *et al.*, 2011), and  $f_{3\sigma} \leq 50$  per million (Waszczak *et al.*, 2013). These surveys were based on the attempted detection of spatially resolved coma. Cikota *et al.* (2014) instead used photometry to search for the brightening produced by the ejection of dust, finding five candidates from a search of  $\sim 75$  million observations of  $\sim 300,000$  asteroids. These candidates remain unconfirmed and it is not clear which method, resolved imaging vs. integrated photometry, offers the better sensitivity to mass loss.

Hsieh *et al.* (2015a) concluded from a sample of 30,000 objects observed near perihelion (giving two detections) that  $f \sim 100$  per million (in the outer belt), which we take as the best current estimate of the fraction of asteroids that are measurably active at any instant. This is still a lower limit to the true active fraction, in the sense that the surveys are sensitivity limited, and it is likely that more evidence for mass loss could be found by increasing the sensitivity. Sonnett *et al.* (2011) hint at this possibility by finding statistical evidence for comae in the averaged profiles of many asteroids, although not in any individual object. If real, their detection may point to electrostatic or gardening dust losses, or some other process acting broadly across the asteroid belt.

Of the present sample, at least four active asteroids are likely to be driven by outgassing (133P, 238P, 313P, and 324P), based on activity repeated in different orbits, corresponding to a fraction  $\geq 20\%$ . The fraction of sublimation-driven objects is therefore on the order of  $f \geq 20$  per million. The fraction of asteroids that contain ice,  $f_{ice}$ , could be much larger. We write  $f_{ice} = f/f_d$ , where  $f_d$  is the duty cycle, equal to the fraction of time for which the average asteroid loses mass. In the ice-excavation model described earlier,  $f_d$  is the ratio of the lifetime of an exposed ice patch to the interval between exposures (caused by boulder impacts?) on the same body. The present level of ignorance about  $f_d$  allows the possibility that  $f_{ice} = 1$ , meaning that potentially all asteroids could contain ice without violating the survey

limits. This surprising result indicates that the dividing line between comets and asteroids may be considerably less sharp than once supposed.

**Acknowledgments.** Partial support for this work was provided by NASA through grants from the Space Telescope Science Institute, which is operated by the Association of Universities for Research in Astronomy (AURA) for NASA, and through their Solar System Observations program.

## REFERENCES

- Agarwal J., Jewitt D., and Weaver H. (2013) Dynamics of large fragments in the tail of active asteroid P/2010 A2. *Astrophys. J.*, **769**, 46.
- A'Hearn M. F., Millis R. C., Schleicher D. O., Osip D. J., and Birch P. V. (1995) The ensemble properties of comets: Results from narrowband photometry of 85 comets, 1976–1992. *Icarus*, **118**, 223.
- Ansdell M., Meech K. J., Hainaut O., et al. (2014) Refined rotational period, pole solution and shape model for (3200) Phaethon. *Astrophys. J.*, **793**, 50.
- Arendt R. G. (2014) DIRBE comet trails. *Astron. J.*, **148**, 135.
- Bagnulo S., Tozzi G. P., Boehnhardt H., Vincent J.-B., and Muinonen K. (2010) Polarimetry and photometry of the peculiar main-belt object 7968 = 133P/Elst-Pizarro. *Astron. Astrophys.*, **514**, A99.
- Bauer J. M., Mainzer A. K., Grav T., et al. (2012) WISE/NEOWISE observations of active bodies in the main belt. *Astrophys. J.*, **747**, 49.
- Beck P., Quirico E., Sevestre D., et al. (2011) Goethite as an alternative origin of the 3.1  $\mu\text{m}$  band on dark asteroids. *Astron. Astrophys.*, **526**, A85.
- Berg O. E., Wolf H., and Rhee J. (1976) Lunar soil movement registered by the Apollo 17 cosmic dust experiment. In *Interplanetary Dust and Zodiacal Light* (H. Elsässer and H. Fechtig, eds.), pp. 233–237. Lecture Notes in Physics, Vol. 48, Proc. IAU Colloq. 31, Springer-Verlag, Berlin.
- Bertini I. (2011) Main belt comets: A new class of small bodies in the solar system. *Planet. Space Sci.*, **59**, 365.
- Bodewits D., Kelley M. S., Li J.-Y., et al. (2011) Collisional excavation of asteroid (596) Scheila. *Astrophys. J. Lett.*, **733**, L3.
- Bodewits D., Vincent J.-B., and Kelley M. S. P. (2014) Scheila's scar: Direct evidence of impact surface alteration on a primitive asteroid. *Icarus*, **229**, 190.
- Boehnhardt H., Sekanina Z., Fiedler A., et al. (1998) Impact-induced activity of the asteroid-Comet P/1996N2 Elst-Pizarro: Yes or no? *Highlights Astron.*, **11**, 233.
- Bottke W. F., Morbidelli A., Jedicke R., et al. (2002) Debiased orbital and absolute magnitude distribution of the near-Earth objects. *Icarus*, **156**, 399.
- Bottke W. F., Durda D. D., Nesvorný D., et al. (2005) Linking the collisional history of the main asteroid belt to its dynamical excitation and depletion. *Icarus*, **179**, 63.
- Campins H., Hargrove K., Pinilla-Alonso N., et al. (2010) Water ice and organics on the surface of the asteroid 24 Themis. *Nature*, **464**, 1320.
- Castillo-Rogez J. C. and McCord T. B. (2010) Ceres' evolution and present state constrained by shape data. *Icarus*, **205**, 443.
- Chamberlin A. B., McFadden L.-A., Schulz R., Schleicher D. G., and Bus S. J. (1996) 4015 Wilson-Harrington, 2201 Oljato, and 3200 Phaethon: Search for CN emission. *Icarus*, **119**, 173.
- Chesley S. R., Kaluna H., Kleyna J., et al. (2010) Detection of nongravitational accelerations on Comet 133P/Elst-Pizarro. *Bull. Am. Astron. Soc.*, **42**, 950.
- Cikota S., Ortiz J. L., Cikota A., Morales N., and Tancredi G. (2014) A photometric search for active main belt asteroids. *Astron. Astrophys.*, **562**, A94.
- Cotto-Figueroa D., Statler T. S., Richardson D. C., and Tanga P. (2015) Coupled spin and shape evolution of small rubble-pile asteroids: Self-limitation of the YORP effect. *Astrophys. J.*, **803**, 25.
- Cunningham L. E. (1950) Periodic comet Wilson-Harrington (1949g). *IAU Circular* **1250**, 3.
- de León J., Campins H., Tsiganis K., Morbidelli A., and Licandro J. (2010) Origin of the near-Earth asteroid Phaethon and the Geminids meteor shower. *Astron. Astrophys.*, **513**, A26.
- Denneau L., Jedicke R., Fitzsimmons A., et al. (2015) Observational constraints on the catastrophic disruption rate of small main belt asteroids. *Icarus*, **245**, 1–15.
- Delbo M., Libourel G., Wilkerson J., et al. (2014) Thermal fatigue as the origin of regolith on small asteroids. *Nature*, **508**, 233.
- de Val-Borro M., Rezac L., Hartogh P., et al. (2012) An upper limit for the water outgassing rate of the main-belt comet 176P/LINEAR observed with Herschel/HIFI. *Astron. Astrophys.*, **546**, L4.
- Drahus M., Waniak W., Tendulkar S., Agarwal J., Jewitt D., and Sheppard S. (2015) Fast rotation and trailing fragments of active asteroid P/2012 F5 (Gibbs). *Astrophys. J. Lett.*, **802**, L8.
- Fanale F. P. and Salvail J. R. (1989) The water regime of asteroid (1) Ceres. *Icarus*, **82**, 97.
- Fernández J. A., Gallardo T., and Brunini A. (2002) Are there many inactive Jupiter-family comets among the near-Earth asteroid population? *Icarus*, **159**, 358–368.
- Fernández Y. R., McFadden L. A., Lisie C. M., Helin E. F., and Chamberlin A. B. (1997) Analysis of POSS images of comet-asteroid transition object 107P/1949 W1 (Wilson-Harrington). *Icarus*, **128**, 114.
- Gault D. E., Hoerz F., Brownlee D. E., and Hartung J. B. (1974) Mixing of the lunar regolith. *Proc. Lunar Sci. Conf. 5th*, p. 2365.
- Gilbert A. M. and Wiegert P. A. (2009) Searching for main-belt comets using the Canada-France-Hawaii telescope legacy survey. *Icarus*, **201**, 714.
- Gilbert A. M. and Wiegert P. A. (2010) Updated results of a search for main-belt comets using the Canada-France-Hawaii telescope legacy survey. *Icarus*, **210**, 998.
- Haghighipour N. (2009) Dynamical constraints on the origin of main belt comets. *Meteoritics & Planet. Sci.*, **44**, 1863.
- Hainaut O. R., Kleyna J., Sarid G., et al. (2012) P/2010 A2 LINEAR. I. An impact in the asteroid main belt. *Astron. Astrophys.*, **537**, A69.
- Hainaut O. R., Boehnhardt H., Snodgrass C., et al. (2014) Continued activity in P/2013 P5 PANSTARRS. Unexpected comet, rotational break-up, or rubbing binary asteroid? *Astron. Astrophys.*, **563**, A75.
- Harris A. W., Fahnestock E. G., and Pravec P. (2009) On the shapes and spins of rubble pile asteroids. *Icarus*, **199**, 310.
- Hartmann W. K., Tholen D. J., and Cruikshank D. P. (1987) The relationship of active comets, 'extinct' comets, and dark asteroids. *Icarus*, **69**, 33.
- Hartzell C. M. and Scheeres D. J. (2011) The role of cohesive forces in particle launching on the Moon and asteroids. *Planet. Space Sci.*, **59**, 1758.
- Hirabayashi M. and Scheeres D. J. (2014) Analysis of asteroid (216) Kleopatra using dynamical and structural constraints. *Astrophys. J.*, **780**, 160.
- Hirabayashi M., Scheeres D. J., Sánchez D. P., and Gabriel T. (2014) Constraints on the physical properties of main belt comet P/2013 R3 from its breakup event. *Astrophys. J. Lett.*, **789**, L12.
- Holsapple K. A. (2007) Spin limits of solar system bodies: From the small fast-rotators to 2003 EL61. *Icarus*, **187**, 500.
- Holsapple K. A. (2010) On YORP-induced spin deformations of asteroids. *Icarus*, **205**, 430.
- Housen K. R. and Holsapple K. A. (2011) Ejecta from impact craters. *Icarus*, **211**, 856.
- Howell E. S. and Lovell A. J. (2011) (596) Scheila. *IAU Circular* **9191**, 2.
- Hsieh H. H. (2009) The Hawaii Trails Project: Comet-hunting in the main asteroid belt. *Astron. Astrophys.*, **505**, 1297.
- Hsieh H. H. (2014) The nucleus of main-belt comet P/2010 R2 (La Sagra). *Icarus*, **243**, 16.
- Hsieh H. H. and Jewitt D. (2006) A population of comets in the main asteroid belt. *Science*, **312**, 561.
- Hsieh H. and Sheppard S. (2015) Reactivation of 324P/La Sagra (P/2010 R2). *Mon. Not. R. Astron. Soc. Lett.*, **454**, L81–L85.
- Hsieh H. H., Jewitt D., and Fernández Y. R. (2004) The strange case of 133P/Elst-Pizarro: A comet among the asteroids. *Astron. J.*, **127**, 2997.
- Hsieh H. H., Jewitt D., and Fernández Y. R. (2009) Albedos of main-belt comets 133P/Elst-Pizarro and 176P/LINEAR. *Astrophys. J. Lett.*, **694**, L111.

- Hsieh H., Jewitt D., and Ishiguro M. (2009) Properties of P/2005U1 (Read). *Astron. J.*, 137, 157.
- Hsieh H. H., Jewitt D., Lacerda P., Lowry S. C., and Snodgrass C. (2010) The return of activity in main-belt comet 133P/Elst-Pizarro. *Mon. Not. R. Astron. Soc.*, 403, 363.
- Hsieh H. H., Ishiguro M., Lacerda P., and Jewitt D. (2011a) Physical properties of main-belt comet 176P/LINEAR. *Astron. J.*, 142, 29.
- Hsieh H. H., Meech K. J., and Pittichová J. (2011b) Main-belt comet 238P/Read revisited. *Astrophys. J. Lett.*, 736, L18.
- Hsieh H. H., Yang B., and Haghighipour N. (2012a) Optical and dynamical characterization of comet-like main-belt asteroid (596) Scheila. *Astrophys. J.*, 744, 9.
- Hsieh H. H., Yang B., Haghighipour N., et al. (2012b) Discovery of main-belt comet P/2006 VW139 by Pan-STARRS1. *Astrophys. J. Lett.*, 748, L15.
- Hsieh H. H., Yang B., Haghighipour N., et al. (2012c) Observational and dynamical characterization of main-belt comet P/2010 R2 (La Sagra). *Astron. J.*, 143, 104.
- Hsieh H. H., Kaluna H. M., Novaković B., et al. (2013) Main-belt comet P/2012 T1 (PANSTARRS). *Astrophys. J. Lett.*, 771, L1.
- Hsieh H. H., Denneau L., Fitzsimmons A., et al. (2014) Search for the return of activity in active asteroid 176P/LINEAR. *Astron. J.*, 147, 89.
- Hsieh H. H., Denneau L., Wainscoat R. J., et al. (2015a) The main-belt comets: The Pan-STARRS1 perspective. *Icarus*, 248, 289.
- Hsieh H. H., Hainaut O., Novaković B., et al. (2015b) Sublimation-driven activity in main-belt comet 313P/Gibbs. *Astrophys. J. Lett.*, 800, L16.
- Hughes D. W. and McBride N. (1989) The mass of meteoroid streams. *Mon. Not. R. Astron. Soc.*, 240, 73.
- Hui M. and Jewitt D. (2015) Archival observations of active asteroid 313P/Gibbs. *Astron. J.*, 149, 134.
- Ishiguro M., Hanayama H., Hasegawa S., et al. (2011a) Observational evidence for an impact on the main-belt asteroid (596) Scheila. *Astrophys. J. Lett.*, 740, L11.
- Ishiguro M., Hanayama H., Hasegawa S., et al. (2011b) Interpretation of (596) Scheila's triple dust tails. *Astrophys. J. Lett.*, 741, L24.
- Ishiguro M., Ham J.-B., Tholen D. J., et al. (2011c) Search for the comet activity of 107P/(4015) Wilson-Harrington during 2009/2010 apparition. *Astrophys. J.*, 726, 101.
- Jacobson S. A. and Scheeres D. J. (2011) Dynamics of rotationally fissioned asteroids: Source of observed small asteroid systems. *Icarus*, 214, 161.
- Jedicke R. and Metcalfe T. S. (1998) The orbital and absolute magnitude distributions of main belt asteroids. *Icarus*, 131, 245.
- Jenniskens P. (1994) Meteor stream activity I. The annual streams. *Astron. Astrophys.*, 287, 990.
- Jewitt D. C. (2002) From Kuiper belt object to cometary nucleus: The missing ultrared matter. *Astron. J.*, 123, 1039.
- Jewitt D. (2012) The active asteroids. *Astron. J.*, 143, 66.
- Jewitt D. (2013) Properties of near-Sun asteroids. *Astron. J.*, 145, 133.
- Jewitt D. and Guillet-Lepoutre A. (2012) Limits to ice on asteroids (24) Themis and (65) Cybele. *Astron. J.*, 143, 21.
- Jewitt D. and Hsieh H. (2006) Physical observations of 2005 UD: A mini-Phaethon. *Astron. J.*, 132, 1624.
- Jewitt D. and Li J. (2010) Activity in Geminid parent (3200) Phaethon. *Astron. J.*, 140, 1519.
- Jewitt D., Yang B., and Haghighipour N. (2009) Main-belt comet P/2008 R1 (Garradd). *Astron. J.*, 137, 4313.
- Jewitt D., Weaver H., Agarwal J., Mutchler M., and Drahos M. (2010) A recent disruption of the main-belt asteroid P/2010A2. *Nature*, 467, 817.
- Jewitt D., Stuart J. S., and Li J. (2011a) Pre-discovery observations of disrupting asteroid P/2010 A2. *Astron. J.*, 142, 28.
- Jewitt D., Weaver H., Mutchler M., Larson S., and Agarwal J. (2011b) Hubble Space Telescope observations of main-belt comet (596) Scheila. *Astrophys. J. Lett.*, 733, L4.
- Jewitt D., Li J., and Agarwal J. (2013a) The dust tail of asteroid (3200) Phaethon. *Astrophys. J. Lett.*, 771, L36.
- Jewitt D., Ishiguro M., and Agarwal J. (2013b) Large particles in active asteroid P/2010 A2. *Astrophys. J. Lett.*, 764, L5.
- Jewitt D., Agarwal J., Weaver H., Mutchler M., and Larson S. (2013c) The extraordinary multi-tailed main-belt comet P/2013 P5. *Astrophys. J. Lett.*, 778, L21.
- Jewitt D., Ishiguro M., Weaver H., et al. (2014a) Hubble Space Telescope investigation of main-belt comet 133P/Elst-Pizarro. *Astron. J.*, 147, 117.
- Jewitt D., Agarwal J., Li J., et al. (2014b) Disintegrating asteroid P/2013 R3. *Astrophys. J. Lett.*, 784, L8.
- Jewitt D., Agarwal J., Weaver H., Mutchler M., and Larson S. (2014c) Episodic ejection from active asteroid 311P/PANSTARRS. *Astrophys. J.*, 798, 109.
- Jewitt D., Agarwal J., Peixinho N., Weaver H., Mutchler M., Hui M., Li J., and Larson S. (2015) New active asteroid 313P/Gibbs. *Astron. J.*, 149, 81.
- Jura M. and Xu S. (2013) Extrasolar refractory-dominated planetesimals: An assessment. *Astron. J.*, 145, 30.
- Kasuga T. and Jewitt D. (2008) Observations of 1999 YC and the breakup of the Geminid stream parent. *Astron. J.*, 136, 881.
- Keil K. (2000) Thermal alteration of asteroids: Evidence from meteorites. *Planet. Space Sci.*, 48, 887.
- Kim J., Ishiguro M., Hanayama H., et al. (2012) Multi-band optical observation of the P/2010 A2 dust tail. *Astrophys. J. Lett.*, 746, L11.
- Kinoshita D., Ohtsuka K., Sekiguchi T., et al. (2007) Surface heterogeneity of 2005 UD from photometric observations. *Astron. Astrophys.*, 466, 1153.
- Kleyne J., Hainaut O. R., and Meech K. J. (2013) P/2010 A2 LINEAR. II. Dynamical dust modelling. *Astron. Astrophys.*, 549, A13.
- Kosai H. (1992) Short-period comets and Apollo-Amor-Aten type asteroids in view of Tisserand invariant. *Cel. Mech. Dyn. Astron.*, 54, 237.
- Kresak L. (1982) On the similarity of orbits of associated comets, asteroids and meteoroids. *Bull. Astron. Inst. Czechoslovakia*, 33, 104.
- Küppers M., O'Rourke L., Bockelée-Morvan D., et al. (2014) Localized sources of water vapour on the dwarf planet (1) Ceres. *Nature*, 505, 525.
- Lai H., Russell C. T., Wei H., and Zhang T. (2014) The evolution of co-orbiting material in the orbit of 2201 Oljato from 1980 to 2012 as deduced from Pioneer Venus Orbiter and Venus Express magnetic records. *Meteoritics & Planet. Sci.*, 49, 28.
- Laurson L., Alava M., and Zappetti S. (2005) Power spectra of self-organized critical sandpiles. *J. Stat. Mech.-Theory Exper.*, 2005, L11001, DOI: 10.1088/1742-5468/2005/11/L11001.
- Levison H. F. and Duncan M. J. (1994) The long-term dynamical behavior of short-period comets. *Icarus*, 108, 18.
- Levison H. F., Bottke W. F., Gounelle M., et al. (2009) Contamination of the asteroid belt by primordial trans-Neptunian objects. *Nature*, 460, 364.
- Li J. and Jewitt D. (2013) Recurrent perihelion activity in (3200) Phaethon. *Astron. J.*, 145, 154.
- Licandro J., Campins H., Mothé-Diniz T., Pinilla-Alonso N., and de León J. (2007) The nature of comet-asteroid transition object (3200) Phaethon. *Astron. Astrophys.*, 461, 751.
- Licandro J., Campins H., Kelley M., et al. (2009) Spitzer observations of the asteroid-comet transition object and potential spacecraft target 107P (4015) Wilson-Harrington. *Astron. Astrophys.*, 507, 1667.
- Licandro J., Campins H., Tozzi G. P., et al. (2011a) Testing the comet nature of main belt comets. The spectra of 133P/Elst-Pizarro and 176P/LINEAR. *Astron. Astrophys.*, 532, A65.
- Licandro J., Campins H., Kelley M., et al. (2011b) (65) Cybele: Detection of small silicate grains, water-ice, and organics. *Astron. Astrophys.*, 525, A34.
- Licandro J., Moreno F., de León J., et al. (2013) Exploring the nature of new main-belt comets with the 10.4 m GTC telescope: (300163) 2006 VW139. *Astron. Astrophys.*, 550, A17.
- Lowry S. C., Weissman P. R., Duddy S. R., et al. (2014) The internal structure of asteroid (25143) Itokawa as revealed by detection of YORP spin-up. *Astron. Astrophys.*, 562, A48.
- MacLennan E. M. and Hsieh H. H. (2012) The nucleus of main-belt comet 259P/Garradd. *Astrophys. J. Lett.*, 758, L3.
- Madiedo J. M., Trigo-Rodríguez J. M., Castro-Tirado A. J., Ortiz J. L., and Cabrera-Caño J. (2013) The Geminid meteoroid stream as a potential meteorite dropper: A case study. *Mon. Not. R. Astron. Soc.*, 436, 2818.

- Marzari F., Rossi A., and Scheeres D. J. (2011) Combined effect of YORP and collisions on the rotation rate of small main belt asteroids. *Icarus*, 214, 622.
- Masiero J. R., Mainzer A. K., Bauer J. M., et al. (2013) Asteroid family identification using the hierarchical clustering method and WISE/NEOWISE physical properties. *Astrophys. J.*, 770, 7.
- McFadden L. A., Cochran A. L., Barker E. S., Cruikshank D. P., and Hartmann W. K. (1993) The enigmatic object 2201 Oljato — Is it an asteroid or an evolved comet? *J. Geophys. Res.*, 98, 3031.
- Minton D. A. (2008) The topographic limits of gravitationally bound, rotating sand piles. *Icarus*, 195, 698.
- Morbidelli A., Chambers J., Lunine J. I., et al. (2000) Source regions and time scales for the delivery of water to Earth. *Meteoritics & Planet. Sci.*, 35, 1309.
- Moreno F., Licandro J., Tozzi G.-P., et al. (2010) Water-ice-driven activity on main-belt comet P/2010 A2 (LINEAR)? *Astrophys. J. Lett.*, 718, L132.
- Moreno F., Licandro J., Ortiz J. L., et al. (2011a) (596) Scheila in outburst. *Astrophys. J.*, 738, 130.
- Moreno F., Lara L. M., Licandro J., et al. (2011b) The dust environment of main-belt comet P/2010 R2 (La Sagra). *Astrophys. J. Lett.*, 738, L16.
- Moreno F., Licandro J., and Cabrera-Lavers A. (2012) A short-duration event as the cause of dust ejection from main-belt comet P/2012 F5 (Gibbs). *Astrophys. J. Lett.*, 761, L12.
- Moreno F., Cabrera-Lavers A., Vaduvescu O., Licandro J., and Pozuelos F. (2013) The dust environment of main-belt comet P/2012 T1 (PANSTARRS). *Astrophys. J. Lett.*, 770, L30.
- Moreno F., Licandro J., Alvarez-Iglesias C., Cabrera-Lavers A., and Pozuelos F. (2014) Intermittent dust mass loss from activated asteroid P/2013 P5 (PANSTARRS). *Astrophys. J.*, 781, 118.
- Moskovitz N. A. (2012) Colors of dynamically associated asteroid pairs. *Icarus*, 221, 63.
- Nesvorný D., Bottke W. F., Vokrouhlický D., et al. (2008) Origin of the near-ecliptic circumsolar dust band. *Astrophys. J. Lett.*, 679, L143.
- Novaković B., Hsieh H. H., and Cellino A. (2012) P/2006 VW139: A main-belt comet born in an asteroid collision? *Mon. Not. R. Astron. Soc.*, 424, 1432.
- Novaković B., Hsieh H. H., Cellino A., Micheli M., and Pedani M. (2014) Discovery of a young asteroid cluster associated with P/2012 F5 (Gibbs). *Icarus*, 231, 300.
- Nugent C. R., Margot J. L., Chesley S. R., and Vokrouhlický D. (2012) Detection of semimajor axis drifts in 54 near-Earth asteroids: New measurements of the Yarkovsky effect. *Astron. J.*, 144, 60.
- O'Brien D. P., and Greenberg R. (2005) The collisional and dynamical evolution of the main-belt and NEA size distributions. *Icarus*, 178, 179.
- Ohtsuka K., Sekiguchi T., Kinoshita D., et al. (2006) Apollo asteroid 2005 UD: Split nucleus of (3200) Phaethon? *Astron. Astrophys.*, 450, L25.
- Ohtsuka K., Nakato A., Nakamura T., et al. (2009) Solar-radiation heating effects on 3200 Phaethon. *Publ. Astron. Soc. Japan*, 61, 1375.
- O'Rourke L., Snodgrass C., de Val-Borro M., et al. (2013) Determination of an upper limit for the water outgassing rate of main-belt comet P/2012 T1 (PANSTARRS). *Astrophys. J. Lett.*, 774, L13.
- Ostro S. J., Margot J.-L., Benner L. A. M., et al. (2006) Radar imaging of binary near-Earth asteroid (66391) 1999 KW4. *Science*, 314, 1276.
- Polishook D. (2014) Spin axes and shape models of asteroid pairs. *Icarus*, 241, 79.
- Poppe A. R., Piquette M., Likhanskii A., and Horányi M. (2012) The effect of surface topography on the lunar photoelectron sheath and electrostatic dust transport. *Icarus*, 221, 135.
- Porco C., DiNino D., and Nimmo F. (2014) How the geysers, tidal stresses, and thermal emission across the south polar terrain of Enceladus are related. *Astron. J.*, 148, 45.
- Pravec P., Vokrouhlický D., Polishook D., et al. (2010) Formation of asteroid pairs by rotational fission. *Nature*, 466, 1085.
- Rennilson J. J. and Criswell D. R. (1974) Surveyor observations of lunar horizon-glow. *Moon*, 10, 121.
- Rivkin A. S. and Emery J. P. (2010) Detection of ice and organics on an asteroidal surface. *Nature*, 464, 1322.
- Rozitis B. and Green S. F. (2013) The strength and detectability of the YORP effect in near-Earth asteroids. *Mon. Not. R. Astron. Soc.*, 430, 1376.
- Rozitis B., MacLennan E., and Emery J. P. (2014) Cohesive forces prevent the rotational breakup of rubble-pile asteroid (29075) 1950 DA. *Nature*, 512, 174.
- Russell C. T., Aroian R., Arghavani M., and Nock K. (1984) Interplanetary magnetic field enhancements and their association with the asteroid 2201 Oljato. *Science*, 226, 43.
- Sánchez D. P. and Scheeres D. J. (2012) DEM simulation of rotation-induced reshaping and disruption of rubble-pile asteroids. *Icarus*, 218, 876.
- Sánchez P. and Scheeres D. J. (2014) The strength of regolith and rubble pile asteroids. *Meteoritics & Planet. Sci.*, 49, 788.
- Scheeres D. J. (2015) Landslides and mass shedding on spinning spheroidal asteroids. *Icarus*, 247, 1.
- Schorghofer N. (2008) The lifetime of ice on main belt asteroids. *Astrophys. J.*, 682, 697.
- Shannon A. and Wu Y. (2011) Planetesimals in debris disks of Sun-like stars. *Astrophys. J.*, 739, 36.
- Sheppard S. and Trujillo C. (2015) Discovery and characteristics of the rapidly rotating active asteroid (62412) 2000 SY178 in the main belt. *Astron. J.*, 149, 44.
- Snodgrass C., Tubiana C., Vincent J.-B., et al. (2010) A collision in 2009 as the origin of the debris trail of asteroid P/2010 A2. *Nature*, 467, 814.
- Sonnett S., Kleyna J., Jedecke R., and Masiero J. (2011) Limits on the size and orbit distribution of main belt comets. *Icarus*, 215, 534.
- Statler T. S. (2009) Extreme sensitivity of the YORP effect to small-scale topography. *Icarus*, 202, 502.
- Stevenson R., Kramer E. A., Bauer J. M., Masiero J. R., and Mainzer A. K. (2012) Characterization of active main belt object P/2012 F5 (Gibbs): A possible impacted asteroid. *Astrophys. J.*, 759, 142.
- Tedesco E. F., Noah P. V., Noah M., and Price S. D. (2002) The Supplemental IRAS Minor Planet Survey. *Astron. J.*, 123, 1056.
- Toth I. (2000) Impact-generated activity period of the asteroid 7968 Elst-Pizarro in 1996. *Astron. Astrophys.*, 360, 375.
- Urakawa S., Okumura S.-i., Nishiyama K., et al. (2011) Photometric observations of 107P/Wilson-Harrington. *Icarus*, 215, 17.
- Veeder G. J., Kowal C., and Matson D. L. (1984) The Earth-crossing asteroid 1983 TB. *Lunar Planet. Sci. XV*, p. 878. Lunar and Planetary Institute, Houston.
- Vernazza P., Binzel R. P., Thomas C. A., et al. (2008) Compositional differences between meteorites and near-Earth asteroids. *Nature*, 454, 858.
- Walsh K. J., Richardson D. C., and Michel P. (2008) Rotational breakup as the origin of small binary asteroids. *Nature*, 454, 188.
- Walsh K. J., Morbidelli A., Raymond S. N., O'Brien D. P., and Mandell A. M. (2011) A low mass for Mars from Jupiter's early gas-driven migration. *Nature*, 475, 206–209.
- Walsh K. J., Richardson D. C., and Michel P. (2012) Spin-up of rubble-pile asteroids: Disruption, satellite formation, and equilibrium shapes. *Icarus*, 220, 514.
- Warner B. D., Harris A. W., and Pravec P. (2009) The asteroid lightcurve database. *Icarus*, 202, 134.
- Waszczak A., Ofek E. O., Aharonson O., et al. (2013) Main-belt comets in the Palomar Transient Factory survey — I. The search for extendedness. *Mon. Not. R. Astron. Soc.*, 433, 3115.
- Williams I. P. and Wu Z. (1993) The Geminid meteor stream and asteroid 3200 Phaethon. *Mon. Not. R. Astron. Soc.*, 262, 231.
- Yanagisawa M., Ikegami H., Ishida M., et al. (2008) Lunar impact flashes by Geminid meteoroids in (2007). *Meteoritics & Planet. Sci. Suppl.*, 43, 5169.
- Yang B. and Hsieh H. (2011) Near-infrared observations of comet-like asteroid (596) Scheila. *Astrophys. J. Lett.*, 737, LL39.



# The Near-Earth Object Population: Connections to Comets, Main-Belt Asteroids, and Meteorites

**Richard P. Binzel**

*Massachusetts Institute of Technology*

**Vishnu Reddy**

*Planetary Science Institute*

**Tasha Dunn**

*Colby College*

---

Near-Earth objects (NEOs) owe their origins to both the main-belt asteroids and comets. They include (by definition) precursors for all meteorite samples. Thus understanding NEO connections is central to the modern study of small bodies in our solar system and serves as the principal focus of this chapter. Herein we also briefly highlight how the proximity of near-Earth objects enables detailed study of the smallest known and most accessible natural objects in space, and we provide links to other chapters addressing these aspects more fully. The success of Japan's Hayabusa mission sample return yields a definitive link between the most common class of near-Earth asteroids and one of the most common meteorites, a watershed whose ground truth enables a deeper level of understanding and new questions. We can now investigate the near-Earth population to pinpoint specific main-belt source regions for broad taxonomic classes and specific meteorite types in addition to estimating the extinct comet contribution. Spectral properties combined with long-term orbital modeling reveal a strong role played by planetary encounters to resurface (and likely reshape) many objects. Outstanding puzzles remain for many of the newly revealed details; their resolution will generate new insights to the basic physical processes governing small bodies.

## 1. INTRODUCTION

Few topics within the field of asteroid studies garner more widespread attention than the near-Earth population. Many reasons motivate this attention, including: (1) These are the objects that (by definition) are capable of impacting Earth, thereby delivering meteorites (many times annually) and civilization-threatening impacts (centuries to geologic time-scales). (2) These are the most accessible spaceflight destinations for both robotic and human missions, including foreseeable in-space resource utilization. (3) The population is dynamic in terms of its ongoing resupply from both main-belt asteroid and comet sources, where such resupply must occur because planetary encounters have long ago depleted the initial population. (4) Individual objects, ranging from meter-scale to tens of kilometers (12 orders of magnitude in mass), find themselves susceptible to a diverse range of physical processes involving their response to external factors such as solar flux and impacts. (5) Their proximity to Earth observers allows a variety of observational techniques through which their resolved shapes, surface properties, and diverse physical configurations can be revealed.

In the most general terms, we refer to this population as near-Earth objects (NEOs) rather than near-Earth asteroids (NEAs) to recognize that both asteroid and comet origins are possible. NEAs is an applicable term when considering them as inert bodies (not outgassing), recognizing that a dormant or extinct comet can masquerade as an "asteroid." As discussed in the chapter by Jewitt et al. in this volume, the reality is likely a continuum of properties spanning from volatile-rich to volatile-poor objects for which defining their provenance may be extraordinarily complex (see the chapter by Morbidelli et al. in this volume). Thus the simple label of "asteroid" or "comet" is inadequate for the intricacy of the problem. Nevertheless, the opportunity remains wide open for ongoing descriptive investigations.

The basics, what one might call the ABCs of NEOs, are described in many sources (e.g., Binzel et al., 2002; Morbidelli et al., 2002; see the chapter by Morbidelli et al. in this volume). Here we summarize for convenience that the population is often subdivided in terms of its orbital properties (Shoemaker et al., 1979), where these orbital categories are depicted in Fig. 1. (Each category is typically named for one of the earliest discovered and named objects

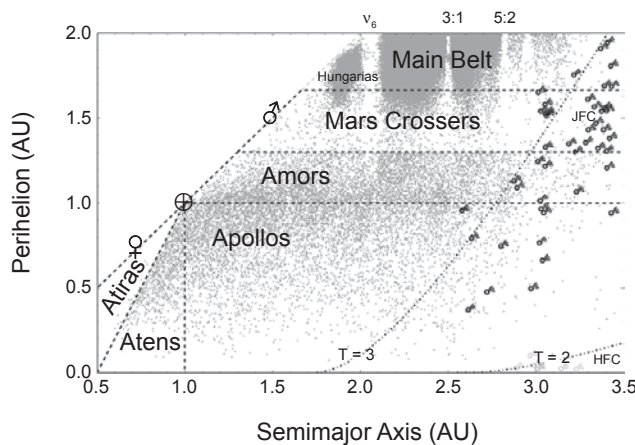


**Fig. 1.** Orbital distribution of the near-Earth object population delineating the boundaries for traditionally named regions, defined in section 1. Symbols for the planets Venus, Earth, and Mars are plotted at their locations for circular orbits. Curved lines correspond to Tisserand parameter ( $T$ ) values equal to 2 and 3, respectively, for the case of zero orbital inclination. Symbols plotting near  $T = 3$  indicate low inclination ( $<10^\circ$ ) Jupiter-family comets (JFC), while those near  $T = 2$  are Halley-family comets (HFC). The main-belt and Mars-crossing objects plotted correspond to numbered objects, while all  $\sim 12,000$  presently known near-Earth objects are depicted. Additional labels along the top of the figure denote main-belt locations described in section 3 that may be source regions for the near-Earth population, including meteorites. (The  $v_6$  resonance location is for the case of zero orbital inclination.)

therein.) Earth's orbit serves as the dividing line among the categories, taking into account its 1.7% noncircularity (eccentricity,  $e$ ). Amor asteroids are those whose perihelia ( $q$ ) are greater than 1.017 AU but less than 1.3 AU, thus at all times orbiting beyond Earth. Apollo asteroids do intersect Earth's orbit by having semimajor axes ( $a$ ) greater than 1 AU with  $q \leq 1.017$  AU, noting the relationship  $q = a[1-e]$ . About 90% of all discovered NEOs are in the Amor and Apollo categories. Aten asteroids intersect with Earth's orbit from "the inside out" by having  $a < 1$  AU and aphelia ( $Q$ , where  $Q = a[1+e] > 0.983$  AU). For asteroids entirely interior to Earth's orbit (IEOs), the category "Atira" is often applied. Tholen and Whiteley (1998) originally called these "Apohelia" objects; the first discovered is now numbered and named (163693) Atira. One additional class, not yet discovered but possibly residing entirely interior to Venus' orbit, are called "Vatiras" by Greenstreet *et al.* (2012). Less strictly defined are the Mars-crossing asteroids, but generally denoted as objects having  $a > 1.3$  and  $1.3 \leq q < 1.665$  AU, where the larger value is roughly the aphelion distance of Mars.

Closer to home, "co-orbitals" is the name given to NEOs in similar orbits to Earth (having  $a \approx 1$ ), where the largest example object is (3753) Cruithne (Wiegert *et al.*, 1997). In a rotating coordinate frame (keeping the Earth-Sun line fixed),

co-orbitals appear to move in a "horseshoe-like" pattern relative to Earth. Occasionally these objects are temporarily captured as natural satellites of Earth, in which case they are colloquially called "mini-Moons" (Granvik *et al.*, 2012; Bolin *et al.*, 2014). To date only one object, 2006 RH<sub>120</sub>, is known to have been temporarily captured. Longer-term stability is possible near the Earth-Sun Lagrange points in a 1:1 orbital resonance with Earth, where 2010 TK<sub>7</sub> is the first (and at present only) known "Earth Trojan" (Connors *et al.*, 2011). Mainzer *et al.* (in this volume) describe the advantages of spacebased satellites for the ongoing discovery and characterization of Earth co-orbitals. As discussed by in the chapter by Abell *et al.* in this volume, the proximity and easy accessibility in terms of low rocket propulsion requirements make co-orbital objects of particular interest for future human exploration and possible space resource utilization.

In this chapter we focus on the ways in which the near-Earth population intersects with asteroid, comet, and meteorite studies in terms of compositional understanding. In particular, we investigate whether the current data provide a coherent picture for how meteorites link to NEOs, and in turn, how NEOs link to their main-belt and comet origins. In many cases over the past decade or longer, increasing the available data has seemed to confound the questions rather than illuminate their solution. Yet the successful near-Earth asteroid sample return by the Japanese Hayabusa mission (Nakamura *et al.*, 2011; see the chapter by Yoshikawa *et al.* in this volume) has been the singular most important achievement for advancing asteroid-meteorite connections in the last decade and for sharpening where significant questions remain. Table 1 presents a summary of the current status for a few of these overarching questions.

Our focus on the interrelationships of the near-Earth population leaves to other chapters many of the topics outlined at the top of this section. For example, impact hazards are addressed by in the chapter by Harris *et al.* in this volume, and the role of NEAs toward the future of human spacefaring is covered in the chapter by Abell *et al.* in this volume. Physical properties of NEOs, whose proximity makes them the currently available sample of observable solar system bodies at sizes below  $\sim 1$  km (and as small as a few meters), are addressed throughout this volume. Close range is an enormous advantage for the study of objects by radar, where the application of radar to asteroid science was pioneered by S. J. Ostro. As detailed in the fundamentals given by Ostro *et al.* (2002), the measured radar signal strength has a  $R^{-4}$  dependence, where  $R$  is the observer-to-target distance. As described in the chapter by Benner *et al.* in this volume, more than 500 members of the NEO population have been observed to date using radar (a total that has dramatically increased since the time of *Asteroids III*). Radar results corroborate the diversity of properties we describe here. Particularly interesting are indications that surface roughness (as measured by radar circular polarization ratios) shows some correlation with an asteroid's taxonomic class (Benner *et al.*, 2008).

Studies of the thermal properties of the smallest bodies observable among NEOs (see the chapter by Delbo *et al.* in

TABLE 1. Resolved and outstanding questions for linking the near-Earth object population.

Question	Status	Next Steps	Section
Do NEOs represent the main belt as their predominant source region?	Yes. Confirmed by comparing the distribution of taxonomic types and by specific mineralogical links to the main belt, including asteroid families.	Further investigate the delivery efficiencies of different main-belt regions and how they are reflected in the NEO population.	2.1, 3.1, 3.2, Fig. 2, Fig. 3, Fig. 5
Are the most common meteorites (ordinary chondrites) related to the most common S-type NEOs?	Yes. Confirmed by Hayabusa sample return.	Further investigate whether the H, L, and LL ordinary chondrite fall statistics can be reconciled with the observed NEO population.	2.2, 3.1, Fig. 3, Fig. 4
Does space weathering exist as a significant spectral alteration process on NEOs?	Yes. Confirmed by Hayabusa sample return.	Clarify the timescale for space weathering and how its effects depend on composition.	2.2, 2.3, Fig. 4
Are planetary encounters a major factor in NEO physical evolution?	Yes. Confirmed by spectral correlation with encounter probability.	Further advance the studies of geophysical and seismic responses to tidal and impact stresses in small bodies as a tool for deducing NEO internal structures. Further advance understanding of the role of thermal spin-up for frequent resurfacing.	2.3
Does our current census of the NEO population accurately account for the abundance of low-albedo objects?	Not yet. Results appear to be converging toward ~35% for the low-albedo proportion.	Future infrared surveys. Further analysis of the efficiency for delivery of bodies from the inner and outer asteroid belt. Full consideration of the effects of shock darkening.	3.2
Are extinct (inactive) comets present in the NEO population?	Likely, as evidenced by the apparently “primitive” (low-albedo and assumed carbon-rich) compositions dominating “asteroids” in comet-like NEO orbits.	Achieve sample returns from apparently primitive NEOs. Further advancements in spectral studies evaluating the volatile content of comet candidates.	3.4, Fig. 5
Can discovery surveys and fireball networks augment asteroid-meteorite and asteroid-comet links?	Almost certainly. One pre-atmospheric example to date: 2008 TC <sub>3</sub> yielded Almahatta Sita meteorites. Sutter Mill meteorite orbit similar to Jupiter-family comets.	Rapid telescopic reconnaissance response to future “incoming” discoveries in concert with dedicated meteorite recovery efforts. Further advance the debiased discovery of low-albedo NEOs to inform the comet fraction.	4

this volume) reveal their tendency to have relatively high thermal inertias. This increased thermal inertia (meaning a slower rate of surface temperature rise or fall) is attributed to the diminished ability to retain regolith in their lower-gravity regimes. (Ejection velocities of excavated material from cratering impacts easily exceed the low escape velocity.) Thus the increased thermal inertia results because the “bare rock” has more mass than any individual fine grain, and consequently requires a longer time to absorb enough solar energy to raise its temperature. The corresponding thermal reradiation to cool the surface (and reach an equilibrium temperature) has significant consequences for both the rotational and orbital evolution of small bodies (see the

chapter by Vokrouhlický et al. in this volume). In fact, the rotations and spin vectors of these smallest asteroids appear to be driven by thermal reradiation, where their maximum spin rate [the so-called “spin barrier” described by Pravec and Harris (2000); see the chapter by Scheeres et al. in this volume] is indicative of their limiting strength. What’s more, the rotational evolution history of experiencing a rapid rotation at some prior epoch appears to strongly influence the shape and configuration of small bodies. This is evidenced by the presence of equatorial ridges revealed by radar (see the chapter by Benner et al. in this volume) and the abundance of binaries within the NEA population (see the chapters by Margot et al. and Walsh and Jacobson in this volume).

## 2. OVERVIEW OF NEAR-EARTH OBJECT OBSERVATIONS

Asteroid studies have entered a new age since the epoch of *Asteroids III*, perhaps most profoundly exemplified by the order of magnitude growth in the discovered NEO population from ~1200 objects in 2001 to ~12,000 in 2015 (see the chapter by Jedicke et al. in this volume). Spacebased surveys have similarly shown their potential for the coming decades by yielding albedos and diameters for nearly 1000 NEOs (see the chapter by Mainzer et al. in this volume). The turn of the millennium also coincided with a turning point in astronomical instrumentation for measuring asteroids in reflected and thermally reemitted solar flux. This turning point includes the advent of near-infrared array spectrometers (for example, as developed by Rayner et al., 2003) with high quantum efficiency sensitivity over the range ~0.7–2.5 μm, the spectral region containing absorption bands diagnostic of pyroxene and olivine mineralogies common in asteroids and meteorites (see the chapter by Reddy et al. in this volume). The first broadscale outcome was the expansion and refinement of asteroid taxonomy that began with U, B, V filter photometry (Bowell and Lumme, 1979; *Asteroids*), continuing with eight-color filter photometry (Tholen and Barucci, 1989; *Asteroids II*), visible wavelength CCD spectroscopy (Bus et al., 2002; *Asteroids III*), and then extended to the near-infrared in the Bus-DeMeo taxonomy system (DeMeo et al., 2009; see the chapter by DeMeo et al. in this volume). A second major outcome ushered in by the availability of near-infrared measurements was the extensive application of mineralogical modeling and interpretation to the near-Earth asteroid population (e.g., Vernazza et al., 2008; Thomas and Binzel, 2010; Dunn et al., 2013). We review the taxonomic distribution of the NEO population in section 2.1 and describe the results and current challenges in their mineralogical modeling in section 2.2. The detector advances enabling ground-based and spacebased thermal flux measurements (yielding albedos and diameters) as a part of the “new millennium turning point” further illuminating our understanding of the NEO population are discussed in section 3.2 and detailed in the chapter by Mainzer et al. in this volume.

### 2.1. TAXONOMIC DISTRIBUTION OF THE NEAR-EARTH OBJECT POPULATION

Apart from an asteroid’s measured brightness (see the chapter by Li et al. in this volume), the “color” of an asteroid is the most common physical parameter to be determined. For the near-Earth population, sufficient filter photometry or spectroscopic information is available to characterize about 10% of all currently catalogued objects, no small feat given the expanding rate of discovery (Galache et al., 2015). Binzel et al. (in preparation, 2015) summarize one of many spectroscopic survey efforts conducted using the NASA Infrared Telescope Facility (IRTF). They include in their tabulation results many other substantial characterization efforts focused towards NEOs (e.g., Tholen and Barucci, 1989;

Whiteley, 2001; Angeli and Lazzaro, 2002; Rivkin et al., 2005; Fevig and Fink, 2007; Licandro et al., 2008; de Leon et al., 2010; Lazzarin et al., 2008; Somers et al., 2010; Ye, 2011; Hasselmann et al., 2012; Hicks et al., 2012; Reddy et al., 2012; Sanchez et al., 2013; Kuroda et al., 2014; Thomas et al., 2014.). An online database of published NEO physical properties is maintained at <http://earn.dlr.de/neal/> and is an excellent resource for determining the original citation for specific characterization results. All totaled, more than 1000 taxonomic classifications are currently available, tripling the *Asteroids III* summary (Binzel et al., 2002). As discussed in the chapter by Reddy et al. in this volume, the taxonomic classification produced by these measurements is only a first step toward understanding an object’s composition. Herein we affirm that any compositional suggestion from taxonomy is an interpretation, not a certainty; taxonomy is not a substitute for detailed mineralogical analysis.

With this caveat, we first look at the observed distribution of NEO taxonomic classes and explore their potential sources. As depicted in Fig. 2, NEOs do in fact represent the full range of classes observed across the main belt, presenting the strongest circumstantial evidence for this transitional region of our solar system being the predominant supplier of the near-Earth population. The broad proportions of the NEO distribution matches the inner main-belt asteroids as well (Gradie and Tedesco, 1982), where in both cases the S-class asteroids are the most commonly observed. Including all the S-type subclasses, more than half of all measured NEOs fall into the broad “S-complex” (DeMeo et al., 2009). Other broad categories, the C- and X-complexes, account for ~15% and 10% of the observations. These latter values are surprisingly low proportions compared with the main belt, but this is due to observational bias that comes from magnitude-limited surveys: Higher-albedo objects are the easiest to detect and measure even if they are relatively small. Bias effects are discussed below.

The longstanding outlier between the main-belt and near-Earth populations is the Q-class, which to date remains rarely observed in the main belt (Mothé-Diniz and Nesvorný, 2008; Thomas et al., 2012). Initially recognized as unique to (1862) Apollo yet spectrally similar to the most commonly falling meteorites [ordinary chondrites (McFadden et al., 1985)], Q-class NEOs now comprise about 10% of the observed population. As discussed below (sections 2.2 and 2.3) and outlined in Table 1, the relative proportions of S- and Q-class asteroids and their meteorite relationship has been one of the longest-standing questions in asteroid science.

Essential to any discussion of an observed distribution (Fig. 2) is the question of what bias effects lurk within. For example, both discovery and spectroscopic surveys employ astronomical techniques and are thus magnitude limited. For the power-law distribution of asteroids (greater numbers with decreasing sizes; see the chapter by Bottke et al. in this volume), at any magnitude limit there are (for example) substantially more high-albedo S-type asteroids accessible for sampling than lower-albedo classes. For NEOs, the most direct consequence is the underrepresentation of C-type (and

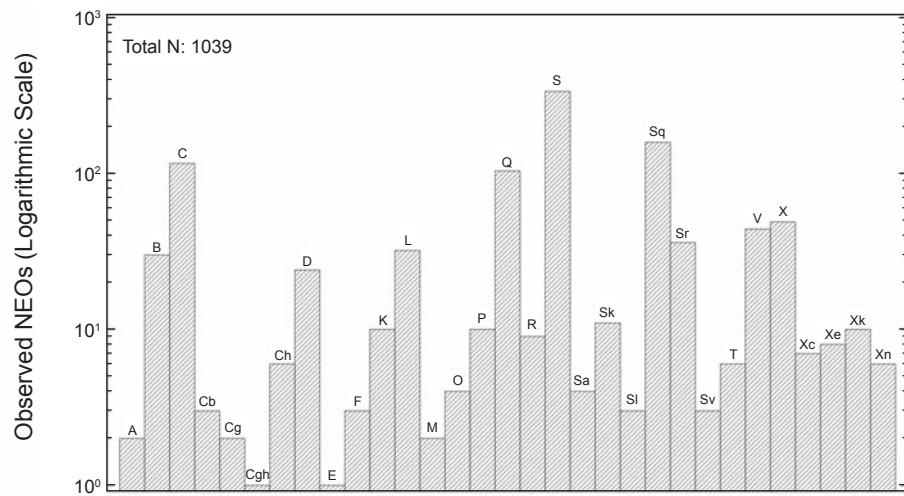


**Fig. 2.** Histogram distribution of taxonomic classes for more than 1000 near-Earth objects tabulated by Binzel et al. (in preparation, 2015) (see section 2.1 for contributing observers). Each and every one of the classes known to be present in the main belt is represented within the near-Earth population. (Note: The vertical scale is logarithmic.)

other low-albedo) asteroids in the known population. Here we attempt to overcome bias effects by considering mass distributions in the manner of DeMeo and Carry (2013). (A mass distribution provides a more debiased view owing to the fact that the largest, and most readily discovered, objects dominate the total mass of the sample; smaller members for which biased discoveries may be incomplete contribute minimal “weight” to the analysis.) Using the dataset from Binzel et al. (in preparation, 2015), we perform a mass distribution analysis of the NEO population with the results shown in Fig. 3. Compared with the mass abundance fraction of C-types in the inner main belt (DeMeo and Carry, 2014), both near-Earth asteroids and (their presumed analog) carbonaceous meteorites show considerably lower abundances. This underrepresentation of C-types among

NEOs has been previously realized (e.g., Luu and Jewitt, 1989; Stuart and Binzel, 2004) but is brought to focus by the unbiased nature of the mass distribution. We address this further in section 3.2.

## 2.2. Mineralogical Interpretation of Near-Earth Asteroids: Relationship to Meteorites

Establishing a correlation between the most commonly observed near-Earth asteroids (S-class) and the most common meteorites (ordinary chondrites comprise >80% of all falls; see the chapter by Borovička et al. in this volume) has been a vexing problem for decades (Wetherill and Chapman, 1988). Spectral interpretation of S-class asteroids and understanding their compatibility with the olivine/pyroxene mineralogy of

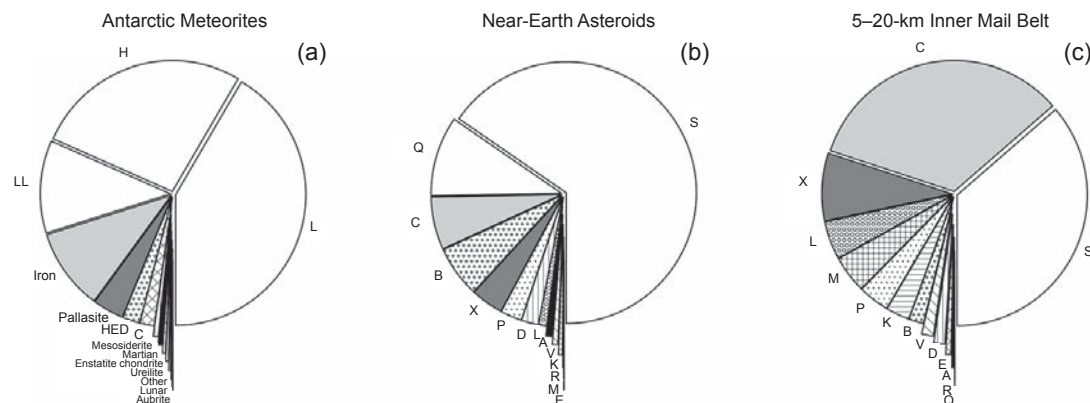


**Fig. 3.** Mass distribution for the near-Earth asteroids, Antarctic meteorites, and inner main asteroid belt. Asteroid data are from Binzel et al. (in preparation, 2015), Antarctic data are from the *Meteoritical Bulletin* database, and the comparably sized main-belt data are from DeMeo and Carry (2014). The two largest near-Earth asteroids, S-types (433) Eros and (1036) Ganymed, dominate the population mass and are not included.

ordinary chondrite meteorites has as its strongest roots the pioneering work by M. J. Gaffey (e.g., *Gaffey*, 1976; *Gaffey et al.*, 1993; see the chapter by Reddy et al. in this volume) as well as the underlying atomic structure revealed by R. G. Burns (*Burns*, 1970). In spite of discovering the mineralogical compatibility of these two groups, direct comparison of S-type asteroid spectra with laboratory spectra of ordinary chondrite meteorites shows a distinct mismatch owing to redder slopes and muted absorption bands displayed by the asteroids. Only the Q-type asteroids (*McFadden et al.*, 1985) (see section 2.1) display a compatible spectral match in slope and absorption band strengths. Finding that Q- to S-type spectral classes display a continuum in their transition [*Binzel et al.* (1996), updated in Fig. 4] bolstered the proposition that some sort of “space-weathering” process (see the chapter by Brunetto et al. in this volume) works to progressively disguise the spectral surface of a “fresh” ordinary chondrite asteroid. The Near-Earth Asteroid Rendezvous mission to the S-type asteroid (433) Eros (*Veverka et al.*, 2000) bolstered the space-weathering interpretation. Elemental abundance measurements of Eros (*Trombka et al.*, 2000) yielded evidence for its likely composition as an ordinary chondrite subject to space-weathering processes (*Chapman*, 2004). Certainly the mass distributions (Fig. 3) strongly support the S- and Q-type asteroid correspondence with ordinary chondrite meteorites. Ignoring the dominating mass of the two largest NEOs [(1036) Ganymed and (433) Eros are both S-types, and themselves make up 75% of the total mass], S- and Q-type asteroids account for 75%

of the NEO mass. In turn, ordinary chondrite meteorites (the sum of H + L + LL classes) are nearly identical in abundance at 80% of the total mass. Yet accepting this concordance as more than just a coincidence requires a definitive answer to the decades-old lingering question: Are some S-type (and Q-type) asteroids truly compositionally compatible with most ordinary chondrite meteorites?

The space engineering triumph of returning a sample from the S-type asteroid (25143) Itokawa by the Japanese Hayabusa mission (see the chapter by Yoshikawa et al. in this volume) cut the Gordian knot. Interpretation of telescopic spectra of Itokawa (then known by its provisional designation 1998 SF<sub>36</sub>) in advance of the “MUSES-C” mission (e.g., *Abell et al.*, 2007) included the specific prediction for Itokawa being a space-weathered LL ordinary chondrite (*Binzel et al.*, 2001). Hayabusa’s findings (*Nakamura et al.*, 2011) not only confirmed the 2001 prelaunch LL-chondrite prediction (see the chapter by Reddy et al. in this volume), but also revealed the details of the space-weathering process (*Noguchi et al.*, 2011) being due to nanophase iron, as predicted by *Pieters et al.* (2000).

Emboldened by this predictive success forged by Hayabusa’s ground truth link, mineralogical modeling of the near-Earth asteroid population has proceeded with new confidence. These models have taken differing approaches, including band area analysis (*Gaffey et al.*, 1993, 2002) and mixing models using optical constants for the constituent minerals (*Shkuratov et al.*, 1999). In an assuring way these approaches have yielded consistent, albeit surprising results. Most notably surprising, S-type near-Earth asteroid spectra (after correction for space weathering) are most often analogous to the LL subgroup of the ordinary chondrite meteorite population (*Vernazza et al.*, 2008; *Thomas and Binzel*, 2010; *de Leon et al.*, 2010; *Dunn et al.*, 2013). While this ordinary chondrite interpretation of asteroid spectra is overall consistent with the predominance of ordinary chondrites among all meteorite falls, the proportion is discordant. From highest-to-lowest metallic iron content, the fall percentages by mass for ordinary chondrite subgroups are H, 27%; L, 42%; LL, 12% of all meteorites (Fig. 3). Thus the epoch of *Asteroids IV* has its own new problem to solve: Why does the least-common subgroup of ordinary chondrites (LL) dominate the compositions interpreted by asteroid spectral analysis? Significant to the puzzle is that LL chondrites contain the highest proportion of olivine among the three classes, where olivine has a strong signature effect in broadening the absorption feature near 1 μm (see Fig. 4). Thus identifying and modeling olivine abundance from the spectral data would seem to be a secure art. Preferential delivery of the largest NEOs from the olivine-rich Flora region of the inner asteroid belt has been proposed as one explanation (*Vernazza et al.*, 2008) (see section 3). As addressed in the chapter by Reddy et al. in this volume, an explanation may also come through better modeling of space-weathering effects, better understanding of the role of impact shocks in altering spectral properties, or better understanding of temperature or phase-angle effects on asteroid spectra. These

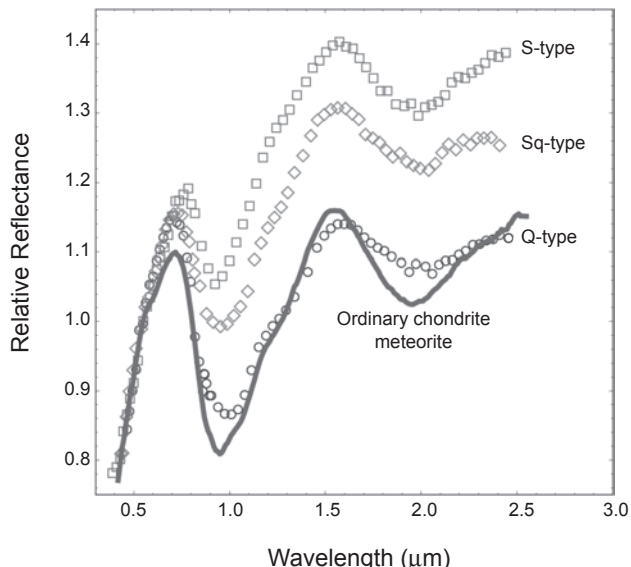


**Fig. 4.** Asteroid reflectance spectral properties display an apparent continuum of increasing slope with decreasing absorption band depth as they transition between Q-, Sq-, and S-types, where this progression is thought to be consistent with the increasing effects of space weathering on ordinary chondrite-like asteroid surfaces. Figure adapted from *Binzel et al.* (2010).

noncompositional effects are particularly relevant because olivine-dominated LL chondrites are more likely to show space-weathering effects than L or H chondrites. In addition, significant work remains to be done to clarify space-weathering effects (and their consequences) across the full range of asteroid taxonomic classes and compositions (see the chapter by Brunetto et al. in this volume).

### 2.3. Linking Observable Properties to Planetary Encounters

With Hayabusa's returned sample demonstrating space weathering as both a real and significant process affecting asteroid spectra (most notably S-type spectra; see the chapter by Brunetto et al. in this volume), a key question is the timescale for this process. Near-Earth asteroids are particularly diagnostic because the population shows the full range from "fresh" to "weathered" objects (Fig. 4). Binzel et al. (2004; see their Fig. 7) proposed a size-dependence to explain this spectral range in terms of space weathering, where size is a proxy for the surface age. Their explanation: Smaller objects have shorter collision survival lifetimes and hence (on average) younger surface ages. By corollary, a smaller object could have its surface age reset more often as even more frequent significant (even if noncatastrophic) collisions could either recoat the surface with fresh regolith or seismically reset the surface entirely.

Under this collisional hypothesis, spectral studies turned to young asteroid families (e.g., Nesvorný et al., 2002; see the chapter by Nesvorný et al. in this volume) and the smallest (and hence youngest) measured main-belt objects (Nesvorný et al., 2005; Mothé-Diniz and Nesvorný, 2008; Thomas et al., 2012). Progressively these studies have found evidence for space weathering taking hold rapidly, with indications for the timescale being shorter than  $10^6$  yr (Vernazza et al., 2009). Such short timescales pose a problem for the near-Earth asteroid population: If space weathering is so rapid, how does one explain that 10% of NEAs (the Q-types; see section 2.1 and Fig. 4) appear completely unweathered? In other words, how and why do NEAs get resurfaced at a rate that occurs more frequently than in the main belt — especially when mutual collisions (if this is the responsible resurfacing mechanism) occur more often in the main belt?

Nesvorný et al. (2005) insightfully noted that NEAs undergo planetary encounters on a timescale that is even more frequent than their mutual collisions, such that in the face of rapid space-weathering timescales, encounters would play a more important role than collisions for resurfacing. For a sample of nearly 100 S- and Q-type NEAs, Binzel et al. (2010) treated the dynamical history of each object and its spectral properties as independent variables and found a distinct correlation: All fresh "unweathered" Q-types in the sample had the possibility of a recent (within the past  $10^5$  yr) Earth encounter, while weathered S-types (having no fresh resurfacing) fully populated the sample whose orbits had no recent Earth encounters. Thus telescopic measurements of near-Earth asteroids yield a geophysical and seismological in-

terpretation that planetary encounters induce tidal distortions and/or seismic shaking processes sufficient to resurface, if not fully reshape, Earth-close-encounter objects (Richardson et al., 1998; see the chapter by Scheeres et al. in this volume). The critical distance or "seismic limit" (residing somewhere beyond the Roche limit and perhaps reaching out to more than 10 Earth radii) at which planetary close encounters could possibly create a detectable surface changing effect remains uncertain: Binzel et al. (2010) interprets a further limit than that calculated by Nesvorný et al. (2010). Thus continuing studies represent a fruitful area for new insights into the bulk geophysical properties of small asteroids and their response to tidal forces (see the chapter by Murdoch et al. in this volume). For example, Binzel et al. (2010) advocate the detailed study (Rosetta-like reconnoitering) of the 2029 Earth encounter by (99942) Apophis at 6 Earth radii; substantial tidal torques altering its rotation are predicted (Scheeres et al., 2005). Yu et al. (2014) estimate that small-scale landslides may occur. However, the overall observable consequences (small scale or large scale) of the tidal effects remain highly uncertain. Here we reemphasize that the 2029 Apophis encounter is a grand experiment in asteroid seismology that *nature is performing for us*; no other currently foreseen naturally performed case study of asteroid interiors is availing itself so opportunistically. Looking for similar tidal effects beyond Earth, ongoing studies (DeMeo et al., 2014b) indicate that Mars encounters also appear effective. Venus encounters must be similarly effective, but our sample set of "Venus only" encountering objects is presently null owing to the limitations of our Earth-based vantage point for asteroid search programs.

Even with the apparent physical evidence for tidal effects in resurfacing, it remains an open question as to how the frequency of "seismic resurfacing" by planetary encounters compares with the frequency at which rapid spin-up due to thermal reradiation (e.g., Walsh et al., 2008; see the chapter by Vokrouhlický et al. in this volume) creates "refreshed" surfaces through mass shedding. What's more, it is possible that under the conditions of frequent tidal close encounters or thermal reradiation spin-up events, frequent overturn of the surface grains could effectively allow the grains to be "sautéed," i.e., fully "cooked" by space weathering on all sides. Thus there can be no guarantee that a given surface-shaking event will expose underlying fresh unweathered material.

## 3. SOURCE REGIONS FOR NEAR-EARTH OBJECTS AND METEORITES

With increasing numbers of NEOs and main-belt asteroids having compositional characterization, preliminary attempts at unraveling the source regions for the near-Earth population (including meteorites) are becoming possible. In this section we describe the "Asteroids IV Scenario," summarized in Table 2, as a framework to be augmented or refuted as future understanding evolves. Essential to this framework is the mineralogical modeling outlined in section 2.2 (see the chapter by Reddy et al. in this volume) and dynamical modeling for asteroid orbital evolution (see the chapter by

Morbidelli et al. in this volume). Here we particularly utilize the dynamical model developed by Bottke et al. (2002) that receives as input the current orbital elements for an individual NEO and evaluates the probability for its origin from each of five source regions: the  $v_6$  secular resonance with Saturn, the intermediate-source Mars-crossing region (IMC), the 3:1 mean-motion resonance at 2.5 AU, the outer belt region (OB) near the 5:2 resonance at 2.82 AU, and the Jupiter-family comet (JFC) region. (The sum of all model output probabilities for any set of input orbital elements is equal to unity.) Each of these locations is depicted in Fig. 1. Using this model, Bottke et al. (2002) predicted that ~61% of the NEO population comes from the inner main belt ( $a < 2.5$  AU), ~24% from the central main belt ( $2.5 < a < 2.8$  AU), ~8% from the outer main belt ( $a > 2.8$  AU), and ~6% from Jupiter-family comets.

In an attempt to reveal source regions for the NEO population, Binzel et al. (2004) evaluated the Bottke source prob-

abilities for ~400 NEOs and Mars-crossing (MC) objects for which visible and near-infrared spectra had been obtained. For their sample, they found the  $v_6$  resonance contributed 46% of NEOs, the IMC 27%, the 3:1 resonance 19%, the OB 6%, and the JFC 2%. The vast majority of measured objects (~90%) were classified as S-, Q-, X-, and C-complex bodies within the Bus and Binzel (2002) taxonomy. Figure 5 illustrates their results for correlating the taxonomic classes with source regions, where results for major classes are summarized below.

### 3.1. S-Types, Q-Types, and Ordinary Chondrite Meteorites

In comparing the histogram profiles (see Fig. 5) for S- and Q-types, both have very similar distributions across the inner main belt. (For “S-type” we specifically include in this discussion the related subclasses, such as Sq-types.) An

TABLE 2. Specifics for near-Earth object and meteorite sources: The *Asteroids IV* Scenario.

Link	Evidence	Key References
LL ordinary chondrites originate from the Flora region of the inner main belt.	Flora family shows similar olivine-rich compositions. Strong dynamical link of LL-compatible NEOs favor inner main belt source.	Vernazza et al. (2009); Dunn et al. (2013); section 3.1
H ordinary chondrites originate from the mid-region of the asteroid belt.	Hebe argued as a source, but compatible asteroid compositions are broadly abundant from the 3:1 region out to, and spanning, the 5:2 resonance. H-compatible NEOs show 3:1 and 5:2 resonance source region signatures.	Gaffey and Gilbert (1998); Thomas and Binzel (2010); Vernazza et al. (2014); Nedelcu et al. (2014); section 3.1.
Less certain, but emerging ideas for the L ordinary chondrites originating from the Gefion family in the outer main belt.	Gefion family spectra compatible with L chondrites. L-compatible NEOs favor 5:2 region source.	Nesvorný et al. (2009); Binzel et al. (2014, 2015); section 3.1
“Primitive” meteorite classes sample from the outer main belt. Unresolved is the contribution from inner belt C-types.	Interpreted primitive taxonomic C- and D-classes show outer main-belt source region signatures.	Brown et al. (2000); Hiroi et al. (2001); Binzel et al. (2004); Vernazza et al. (2013); section 3.2.
Most V-type NEOs linked to Vesta and to HED meteorites. Isotopically distinct HEDs (rare) and other achondrites indicate multiple differentiated source bodies.	Spectral and dynamical links to Vesta; Dawn <i>in situ</i> measurements. Other small basaltic asteroids in outer belt. Achondrite meteorites are diverse.	McCord et al. (1970); Cruikshank et al. (1991); Binzel and Xu (1993); Lazzaro et al. (2000); Scott et al. (2009); Prettyman et al. (2012); Lucas and Emery (2014); section 3.3
Enstatite achondrites (aubrites) originate from the Hungaria region of the inner main belt.	E- and Xe-type asteroids are spectrally distinct. They show strong orbital and dynamical links to the inner main belt.	Gaffey et al. (1992); Binzel et al. (2004); section 3.3
Extinct Jupiter-family comets reside in NEO orbits having Tisserand ( $T$ ) values $< 3$ .	$T < 3$ indicates dynamical link to Jupiter; dominated by low-albedo objects.	Wetherill (1988); Fernandez et al. (2001); DeMeo and Binzel (2008); Kim et al. (2014); section 3.4

identical source region signature for both is not unexpected due to the relationship between the two groups [e.g., S-types are believed to be weathered Q-types as discussed in section 2.2 (Binzel et al., 1996)]. As discussed in section 2.2, mineralogic analyses of S- and Q-type NEAs have most often found their spectral properties to be similar to LL chondrites. Vernazza et al. (2008) suggested that the olivine-rich Flora family (near the  $v_6$  resonance) was the source region for the subset of S- and Q-type NEOs whose spectral analysis yielded results most similar to LL compositions; de León et al. (2010) independently find the same result. Dunn et al. (2013) also calculated mineralogies from individual NEO spectra to analyze the source regions based on the Bottke et al. (2002) probability models. For their sample of 47 NEOs with ordinary chondrite spectral parameters, LL chondrites again showed their familiar predominance (60% of the sample), while 15% and 10% had H- and L-chondrite mineralogies, respectively. (The remaining 15% had mineralogies that could not easily be distinguished between L or LL chondrites.) For 75% of the Dunn et al. (2013) sample, the  $v_6$  resonance was the most probable source region and the LL-chondrite mineralogies were preferentially derived from there, similarly consistent with Vernazza et al. (2008) as originating in the nearby Flora family. Results from Dunn et al. (2013) did not establish a distinct source region for NEOs with H- or L-chondrite mineralogies. While these first steps toward definitive correlations are emerging, caution is still warranted as the role of shock effects in altering spectral properties, with possible consequences for mineralogical interpretations, remains an open and emerging area for study (see the chapter by Reddy et al. in this volume).

As an example, a fruitful result of considering shock effects may be the compositional diversity displayed among members of the Baptistina asteroid family; Reddy et al. (2014) suggests them to be the source of shock-darkened LL chondrites.

Thomas and Binzel (2010) used modified Gaussian modeling (MGM) (Sunshine et al., 1990) to determine meteorite analogs and source region probabilities (model of Bottke et al., 2002) and found NEAs most closely matching H chondrites have a higher-than-average delivery preference through the 3:1 mean-motion resonance. A 3:1 resonance source preference for H-chondrite-like NEAs persists in the substantially larger sample presented by Binzel et al. (2014), with the 5:2 resonance also showing a signature for being a strong contributor of the H chondrites. The 3:1 resonance being a source for the H chondrites is consistent with Gaffey and Gilbert (1998), who suggested that asteroid (6) Hebe, which is located adjacent to the  $v_6$  and 3:1 resonances, is the parent body of the H chondrites. Vernazza et al. (2014) note that abundant main-belt asteroids having H-chondrite-like spectral properties are common in the 3:1 region, consistent with this provenance for H chondrites, but also lessening any requirement for linking specifically to Hebe. Similarly, Vernazza et al. (2014) find the provenance for H chondrites extends from the 3:1 to 5:2 resonance, spanning across the 5:2 resonance as well. Nedelcu et al. (2014) and Sanchez et al. (2015) also illustrate the case of an “H chondrite-like” NEA (2007 PA<sub>8</sub>) being derived from the 5:2 resonance, although this same object is interpreted to have an L-chondrite-like composition by Fornasier et al. (2015) (consistent with

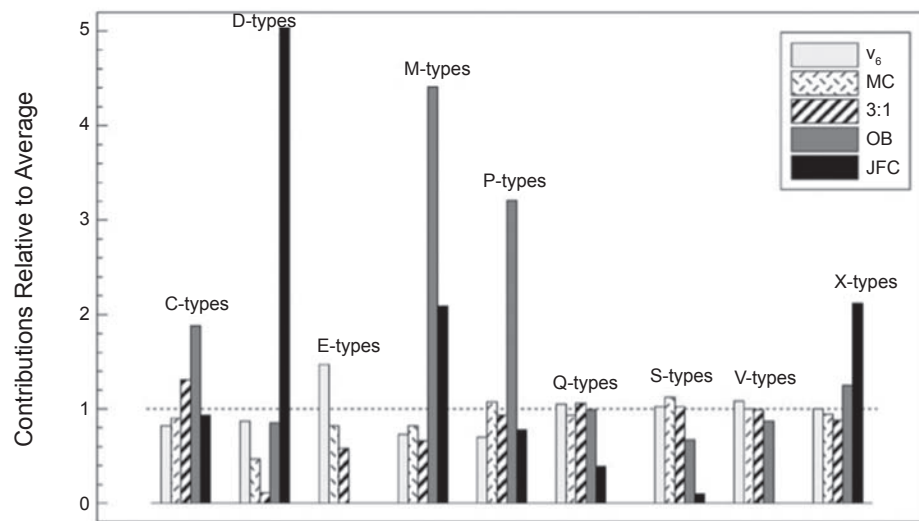


**Fig. 5.** Histogram distribution for source regions of near-Earth asteroids based on the orbital evolution model of Bottke et al. (2002). Each ratio is relative to the overall flux from each source, thus any significant deviation from unity indicates a strong signature (or relative deficiency) for that source region contributing objects in that taxonomic class to near-Earth space. Figure adapted from Binzel et al. (2004).

the L-chondrite discussion below). Thus the current evidence (see the chapter by Vernazza et al. in this volume) indicates the source region for the H-chondrite meteorites may be broad across the central region of the main belt involving both the 3:1 and 5:2 resonances.

L chondrites are increasingly being pinpointed toward an outer belt (5:2 resonance) source region, as proposed by Nesvorný et al. (2009) based on dynamical considerations for the origin of the Gefion family located nearby. Spectral interpretation of Gefion family asteroids has been found to be consistent with L chondrites (Blagén, 2012). Supporting this result is the analysis of the largest datasets for NEAs (Binzel et al., 2014; Binzel et al., in preparation, 2015) finding an outer belt preference for objects whose spectral properties are interpreted as being most similar to L chondrites. We do not consider any conclusion regarding the L chondrites to be definitive at this time: Confirming or refuting a link of L chondrites to the outer belt remains an area of active current investigation.

### 3.2. C-Types and Carbonaceous Chondrite Meteorites

As described in section 2.1, accurately quantifying the abundance of C-type NEOs has been a long-standing problem owing to the difficulty of their detection through surveys relying on visible reflected light. This difficulty is the same for all asteroid classes having low albedos, such as D- and P-types (noting that for this discussion “C-type” includes the subclasses such as B-types). As we discuss below, and as extensively addressed in the chapter by Mainzer et al. in this volume, surveys operating in the thermal infrared overcome this bias as a consequence of dark surfaces having higher relative temperatures (absorbing rather than reflecting nearly all sunlight).

As shown in Fig. 3c, the inner main belt is now more clearly revealed to have an abundance of low-albedo members [roughly 40% by mass are C-, D-, and P-types (DeMeo and Carry, 2014; DeMeo et al., 2014a)]. Yet a sharp discordance remains: These low-albedo classes comprise scarcely 20% among characterized NEOs (Fig. 3b). While this 20% value is by mass, and *should* be less subject to bias than raw discovery statistics (see section 2.1), spectroscopic reconnaissance is nonetheless subject to the same magnitude-limiting effects as visible-light discovery surveys. Thus we can have confidence that the characterized NEO population of 20% low-albedo objects represents a lower limit. As noted immediately above, reconciliation may be emerging from thermal infrared surveys that are yielding ~35% as the low albedo fraction (see Fig. 3 of the chapter by Mainzer et al. in this volume).

As work on this topic progresses in the future, there is an orbital distribution factor that might account for an ongoing deficit remaining for the abundance of low-albedo NEOs relative to the overall main belt. Specifically, the inner edge of the main belt ( $v_6$  secular resonance and the Mars-crossers evolving deeper in to near-Earth space) may overwhelmingly dominate the total NEO flux. As shown

by DeMeo and Carry (2014; see their Fig. 4), the  $v_6$  inner edge is itself dominated by S-types. Thus if the  $v_6$  inner edge specifically dominates the NEO flux, then C-types (for example) do not have equal access to this highly efficient “resonance escape hatch” for delivery into the inner solar system. This effect may be presenting itself in the source region histograms for C-types shown in Fig. 5, where the 3:1 resonance does show a stronger contribution than the  $v_6$  resonance. Overall, this figure shows a distinctly clear signature for C-type NEOs being delivered from the outer main belt, where this class most thoroughly dominates.

The minuscule fraction of carbonaceous chondrite meteorite falls (~2% in Fig. 3a) remains an enigma compared to any assessment (20–35%) for the low-albedo NEO population. Historically this factor of 10 underrepresentation of carbonaceous chondrite falls compared with the NEO population is attributed to a strong selection effect against surviving atmospheric entry (Baldwin and Sheaffer, 1971; Sears, 1998). The canonical explanation is that the lower-strength carbonaceous materials have a lower likelihood of surviving (at sizes larger than dust) and yielding recoverable fragments (Love and Brownlee, 1993; Taylor et al., 2000; Love and Alton, 2006).

Finally, when reconciling the low-albedo population of NEOs relative to the main belt and meteorite fractions, there is a reemerging consideration of a process that may be significantly important to the census: shock darkening of asteroid regoliths due to impacts. While the fundamental work revealing this process was performed more than two decades ago (Britt and Pieters, 1991, 1994), it has been brought back to the foreground by extensive studies of the Chelyabinsk meteorite (Kohout et al., 2014; Reddy et al., 2014; see the chapter by Reddy et al. in this volume). Shock darkening could factor into the equation if a significant fraction of low-albedo NEOs or main-belt objects are not carbonaceous in composition, but are instead shock-darkened ordinary chondrites. This reemerging consideration presents a possible paradox and certainly an opportunity for ongoing study.

### 3.3. Other Asteroid Classes and Possible Meteorite Source Relationships

Near-Earth asteroids having Vesta-like (V-type) spectra among the NEOs were first reported by Cruikshank et al. (1991). Examining the V-type source region histogram in Fig. 5 shows a particularly flat distribution for their origin among all inner main-belt sources, with equal preference between the  $v_6$  and 3:1 resonances. This equal source distribution mimics the broad extent of the Vesta family across the inner belt (see the chapter by Masiero et al. in this volume), yielding the conclusion that the NEO source for V-types is consistent with an origin from (4) Vesta (McCord et al., 1970; Cruikshank et al., 1991; Binzel and Xu, 1993). *In situ* elemental abundance characterization of Vesta by the Dawn mission (Prettyman et al., 2012) provides the “golden spike” for the connection between Vesta, the V-type asteroids, and the howardite-eucrite-diogenite (HED) meteorites (Consolmagno and Drake, 1977; Binzel, 2012). As a mark

of progress, it is now recognized that Vesta is likely not the only source for HED meteorites. Apart from what might be called the “main-group HEDs” is a small set (approximately five known) of isotopically anomalous meteorites that likely originated on another parent body (Scott et al., 2009). V-type asteroids that are dynamically independent of Vesta in the outer main belt (Lazzaro et al., 2000; Moskovitz et al., 2008) and perhaps 100 parent bodies being represented by iron meteorites are consistent with the previous existence of other differentiated asteroids with Vesta as a unique “intact” survivor (see the chapter by Scott et al. in this volume).

D- and X-types show source region signatures (Fig. 5) indicating they are predominantly derived from the outer belt and Jupiter-family comets, as discussed below in section 3.4. These X-types most likely have low albedos, in which case their ambiguous X classification would be resolved to being labeled as P-types. The taxonomically rare A- and E-types are uncommon in the overall NEO population (<1%), but are more common among observed Mars-crossing objects (5%). Sanchez et al. (2014) found no distinct link between known A-type asteroids and an asteroid family. Binzel et al. (2004) suggested that this was indicative of slow diffusion into Mars-crossing orbits from the Flora or Hungaria regions. Such an origin is also consistent with previous observations by Gaffey et al. (1992), who linked E-type Apollo asteroid (3103) Eger to the Hungaria region.

### 3.4. Cometary Contribution to the Near-Earth Object Population

Identifying potential cometary objects in the NEO population is in some ways more straightforward and in other ways more enigmatic than linking to main-belt source regions and to specific meteorite types. As noted in section 1, the label of “asteroid” or “comet” can be a hindrance to the problem as clearly there is a continuum in the distribution between volatile-rich and volatile-poor objects in the solar system. What’s more, the volatile-free characteristics of an object’s surface can belie the nature of a possibly volatile-rich interior. We sidestep the issue in the following way: We consider an object to be “cometary” in the sense that it is interpreted to have a “primitive” (low-albedo and carbonaceous-chondrite-like) composition and a dynamical origin from the outer belt or beyond, most notably being in an orbit similar to Jupiter-family comets (Wetherill, 1988). A superb and convincing illustration of the comet contribution to the NEO population was made by Fernandez et al. (2001, 2005), who found that “asteroids” having Tisserand values less than 3 (an orbital parameter indicating a gravitational link to Jupiter that is common to all Jupiter-family comets) display comet-nucleus-like low albedos. Outer-belt and Jupiter-family-comet links for presumed “primitive” C-, D-, and P-type asteroids are also clearly revealed in the source region analysis performed by Binzel et al. (2004) and illustrated here in Fig. 5. Follow-on analyses that have sought to quantify the currently contributed fraction of cometary material to the inner solar system (DeMeo and Binzel, 2008; Kim et al., 2014) have adopted

the same low-albedo and taxonomic criteria. DeMeo and Binzel (2008) estimate that  $8 \pm 5\%$  of the NEO population is contributed by comets, not inconsistent with the estimate of 4% given by Fernandez et al. (2005). In their recent work, Kim et al. (2014) find some cases of higher-albedo objects in the “comet-like” orbits, which they attribute to possible Yarkovsky drift of “asteroids” into those dynamical states. If Yarkovsky mixing proves to be a significant factor in pushing “asteroids” into comet-like orbits, that must lower the estimates for the comet contribution to NEOs that have relied on orbital properties as a discriminating parameter. Ongoing discoveries of the low-albedo component of the near-Earth population (see the chapter by Mainzer et al. in this volume) promise to provide the most critical new constraints for the comet fraction.

## 4. SUMMARY

In this concluding section, we attempt to “put it all together” and to look at the path ahead by pointing to our summaries in Tables 1 and 2 for the current status of key questions for the NEO population and the current scenarios for our understanding of myriad interrelationships. Exposing gaps and critical new details in all these areas — and most especially, revealing the flaws in our current thinking — should be the goal of every new student venturing into this corner of the field. Most traditionally, making advancements implies devising new observational strategies or computational models. We particularly emphasize that ongoing laboratory work using meteorites as “ground truth” is one of our field’s greatest strengths.

Ongoing advancements will certainly come through the link between remote sensing measurements (available for thousands of objects) to laboratory analysis of returned samples. As conceptualized in the pyramid of planetary exploration (Binzel, 2012), spacecraft exploration and sample return are the most specialized opportunities that maximize their yield when designed toward addressing specific and highly refined science questions. Understanding the nature of primitive C-complex asteroids and their meteorite link(s) are the goals for the Hayabusa-2 (Abe et al., 2012) and Origins Spectral Interpretation Resource Identification and Security-Regolith Explorer (OSIRIS-REx) (Lauretta et al., 2015) sample return missions.

As discovery surveys advance in their detection thresholds and cadence, future “incoming” object discoveries are sure to occur as presaged by the detection of 2008 TC<sub>3</sub> and the recovery of its fragments as Almahata Sitta meteorites (Jenniskens et al., 2010). Alas, this first example of discovering a body in space prior to its “free” sample collection proves the difficulty of remote sensing interpretation: The rare class of ureilite meteorites to which Almahata Sitta belongs has nearly featureless spectral reflectance characteristics (Cloutis et al., 2010). If not discovered prior to arrival, the detailed tracking of the entry trajectories for arriving meteorites can also enable estimates of their orbits (and source regions). Recent examples of the Sutter Mill [CM

carbonaceous chondrite (*Jenniskens et al.*, 2012; also see the chapter by Jenniskens in this volume)] and Chelyabinsk [LL ordinary chondrite (*Reddy et al.*, 2014)] recovered falls point to possible Jupiter-family comet and inner-main-belt (Baptistina family) origins. Direct samples, of course, have the enormous advantage of obviating the difficulties of mineralogic interpretation from remote sensing.

The scientific riddles and rewards offered by NEO studies, coupled with the pragmatic motivations for their investigation arising from impact hazards and exploration potential, all point to a propitious path ahead. In many ways, they all point toward the same path. Optimizing the synergies between science, human exploration, and resource utilization is the ultimate grand challenge *and opportunity* for asteroids in the twenty-first century (*Binzel*, 2014). Abundant knowledge of the population, achieved through discovery, characterization, and unraveling their interrelationships, is the enabling pathway to convergence that will deliver the most productive future for all stakeholders having interests in near-Earth objects.

**Acknowledgments.** Preparation of this chapter was supported by the National Science Foundation under Grant No. 0907766 (R.P.B.) and the NASA Near-Earth Object Observations Program grant NNX14AL06G (V.R.). We are grateful to B. J. Burt and T. H. Burbine for assistance with the figures and to J. de Leon and J. Masiero for their careful reviews. The authors unanimously acknowledge the scientific progress in asteroid spectroscopy that has been enabled by the dedicated staff of the NASA Infrared Telescope Facility and its commitment to advanced instrumentation, exemplified by the SpeX instrument (*Rayner et al.*, 2003).

## REFERENCES

- Abe M., Yano H., Okada T., Yoshikawa M., Shirai K., Hirata N., Kadono T., Ogawa K., Ohtake M., Demura H., Kitazato K., Saiki T., Mitani T., Iijima Y., Kobayashi N., Fukuhara T., and Tanaka S. (2012) Hayabusa 2, C-type asteroid sample return mission, scientific objective and instruments. *39th COSPAR Scientific Assembly*, Abstract #H0.2-7-12.
- Abell P. A., Vilas F., Jarvis K. S., Gaffey M. J., and Kelley M. S. (2007) Mineralogical composition of (25143) Itokawa 1998 SF<sub>36</sub> from visible and near-infrared reflectance spectroscopy: Evidence for partial melting. *Meteoritics & Planet. Sci.*, *42*, 2165–2177.
- Angeli C. A. and Lazzaro D. (2002) Spectral properties of Mars-crossers and near-Earth objects. Results of the S3OS2 survey. *Astron. Astrophys.*, *391*, 757–765.
- Baldwin B. and Sheaffer Y. (1971) Ablation and breakup of large meteoroids during atmospheric entry. *J. Geophys. Res.*, *76*, 4653.
- Benner L. A. M., Ostro S. J., Magri C., Nolan M. C., Howell E. S., Giorgini J. D., Jurgens R. F., Margot J.-L., Taylor P. A., Busch M. W., and Shepard M. K. (2008) Near-Earth asteroid surface roughness depends on compositional class. *Icarus*, *198*, 294–304.
- Binzel R. P. (2012) A golden spike for planetary science. *Science*, *338*, 203–204.
- Binzel R. P. (2014) Find asteroids to get to Mars. *Nature*, *514*, 559–561.
- Binzel R. P. and Xu S. (1993) Chips off of asteroid 4 Vesta — Evidence for the parent body of basaltic achondrite meteorites. *Science*, *260*, 186–191.
- Binzel R. P., Bus S. J., Burbine T. H., and Sunshine J. M. (1996) Spectral properties of near-Earth asteroids: Evidence for sources of ordinary chondrite meteorites. *Science*, *273*, 946–948.
- Binzel R. P., Rivkin A. S., Bus S. J., Sunshine J. M., and Burbine T. H. (2001) MUSES-C target asteroid 1998 SF<sub>36</sub>: A reddened ordinary chondrite. *Meteoritics & Planet. Sci.*, *36*, A20.
- Binzel R. P., Lupishko D. F., Di Martino M., Whiteley R. J., and Hahn G. J. (2002) Physical properties of near-Earth objects. In *Asteroids III* (W. F. Bottke Jr. et al., eds.), pp. 255–271. Univ. of Arizona, Tucson.
- Binzel R. P., Rivkin A. S., Stuart J. S., Harris A. W., Bus S. J., and Burbine T. H. (2004) Observed spectral properties of near-Earth objects: Results for population distribution, source regions, and space weathering processes. *Icarus*, *170*, 259–294.
- Binzel R. P., Morbidelli A., Merouane S., DeMeo F. E., Birlan M., Vernazza P., Thomas C. A., Rivkin A. S., Bus S. J., and Tokunaga A. T. (2010) Earth encounters as the origin of fresh surfaces on near-Earth asteroids. *Nature*, *463*, 331–334.
- Binzel R. P., DeMeo F. E., Burt B. J., Polishook D., Burbine T. H., Bus S. J., Tokunaga A., and Birlan M. (2014) Meteorite source regions as revealed by the near-Earth object population. *AAS/Division for Planetary Sciences Meeting Abstracts*, *46*, #213.06.
- Blagen J. R. (2012) Testing the Gefion family as a possible parent body for the L-chondrite meteorites. M.S. thesis, Univ. of North Dakota, Grand Forks.
- Bolin B., Jedicke R., Granvik M., Brown P., Howell E., Nolan M. C., Jenniskens P., Chyba M., Patterson G., and Wainscoat R. (2014) Detecting Earth's temporarily-captured natural satellites — Minimoons. *Icarus*, *241*, 280–297.
- Bottke W. F., Morbidelli A., Jedicke R., Petit J., Levison H. F., Michel P., and Metcalfe T. S. (2002) Debaised orbital and absolute magnitude distribution of the near-Earth objects. *Icarus*, *156*, 399–433.
- Bowell E. and Lumme K. (1979) Colorimetry and magnitudes of asteroids. In *Asteroids* (T. Gehrels, ed.), pp. 132–169. Univ. of Arizona, Tucson.
- Britt D. T. and Pieters C. M. (1991) Black ordinary chondrites — an analysis of abundance and fall frequency. *Meteoritics*, *26*, 279–285.
- Britt D. T. and Pieters C. M. (1994) Darkening in black and gas-rich ordinary chondrites: The spectral effects of opaque morphology and distribution. *Geochim. Cosmochim. Acta*, *58*, 3905–3919.
- Brown P. G., Hildebrand A. R., Zolensky M. E., Grady M., Clayton R. N., Mayeda T. K., Tagliaferri E., Spalding R., MacRae N. D., Hoffman E. L., Mittlefehldt D. W., Wacker J. F., Bird J. A., Campbell M. D., Carpenter R., Gingerich H., Glatiotis M., Greiner E., Mazur M. J., McCausland P. J., Plotkin H., and Rubak Mazur T. (2000) The fall, recovery, orbit, and composition of the Tagish Lake meteorite: A new type of carbonaceous chondrite. *Science*, *290*, 320–325.
- Burns R. G. (1970) *Mineralogical Applications of Crystal Field Theory*. Cambridge Univ., Cambridge.
- Bus S. J. and Binzel R. P. (2002) Phase II of the Small Main-Belt Asteroid Spectroscopic Survey. A feature-based taxonomy. *Icarus*, *158*, 146–177.
- Bus S. J., Vilas F., and Barucci M. A. (2002) Visible-wavelength spectroscopy of asteroids. In *Asteroids III* (W. F. Bottke Jr. et al., eds.), pp. 169–182. Univ. of Arizona, Tucson.
- Chapman C. R. (2004) Space weathering of asteroid surfaces. *Annu. Rev. Earth Planet. Sci.*, *32*, 539–567.
- Cloutis E. A., Hudon P., Romanek C. S., Bishop J. L., Reddy V., Gaffey M. J., and Hardersen P. S. (2010) Spectral reflectance properties of ureilites. *Meteoritics & Planet. Sci.*, *45*, 1668–1694.
- Connors M., Wiegert P., and Veillet C. (2011) Earth's Trojan asteroid. *Nature*, *475*, 481–483.
- Consolmagno G. J. and Drake M. J. (1977) Composition and evolution of the eucrite parent body: Evidence from rare earth elements. *Geochim. Cosmochim. Acta*, *41*, 1271–1282.
- Cruikshank D. P., Tholen D. J., Bell J. F., Hartmann W. K., and Brown R. H. (1991) Three basaltic Earth-approaching asteroids and the source of the basaltic meteorites. *Icarus*, *89*, 1–13.
- de León J., Licandro J., Serra-Ricart M., Pinilla-Alonso N., and Campins H. (2010) Observations, compositional, and physical characterization of near-Earth and Mars-crosser asteroids from a spectroscopic survey. *Astron. Astrophys.*, *517*, 23–45.
- DeMeo F. and Binzel R. P. (2008) Comets in the near-Earth object population. *Icarus*, *194*, 436–449.
- DeMeo F. E. and Carry B. (2013) The taxonomic distribution of asteroids from multi-filter all-sky photometric surveys. *Icarus*, *226*, 723–741.
- DeMeo F. E. and Carry B. (2014) Solar system evolution from compositional mapping of the asteroid belt. *Nature*, *505*, 629–634.
- DeMeo F. E., Binzel R. P., Slivan S. M., and Bus S. J. (2009) An extension of the Bus asteroid taxonomy into the near-infrared. *Icarus*, *202*, 160–180.

- DeMeo F. E., Binzel R. P., Carry B., Polishook D., and Moskovitz N. A. (2014a) Unexpected D-type interlopers in the inner main belt. *Icarus*, 229, 392–399.
- DeMeo F. E., Binzel R. P., and Lockhart M. (2014b) Mars encounters cause fresh surfaces on some near-Earth asteroids. *Icarus*, 227, 112–122.
- Dunn T. L., Burbine T. H., Bottke W. F., and Clark J. P. (2013) Mineralogies and source regions of near-Earth asteroids. *Icarus*, 222, 273–282.
- Fernández Y. R., Jewitt D. C., and Sheppard S. S. (2001) Low albedos among extinct comet candidates. *Astrophys. J. Lett.*, 553, L197–L200.
- Fernández Y. R., Jewitt D. C., and Sheppard S. S. (2005) Albedos of asteroids in comet-like orbits. *Astron. J.*, 130, 308–318.
- Fevig R. A. and Fink U. (2007) Spectral observations of 19 weathered and 23 fresh NEAs and their correlations with orbital parameters. *Icarus*, 188, 175–188.
- Fornasier S., Belskaya I., and Perna D. (2015) The potentially hazardous asteroid (214869) 2007 PA<sub>8</sub>: An unweathered L chondrite analog surface. *Icarus*, 250, 280–286.
- Gaffey M. J. (1976) Spectral reflectance characteristics of the meteorite classes. *J. Geophys. Res.*, 81, 905–920.
- Gaffey M. J. and Gilbert S. L. (1998) Asteroid 6 Hebe: The probable parent body of the H-type ordinary chondrites and the IIE iron meteorites. *Meteoritics & Planet. Sci.*, 33, 1281–1295.
- Gaffey M. J., Reed K. L., and Kelley M. S. (1992) Relationship of E-type Apollo asteroid 3103 (1982 BB) to the enstatite achondrite meteorites and the Hungaria asteroids. *Icarus*, 100, 95–109.
- Gaffey M. J., Burbine T. H., Piatek J. L., Reed K. L., Chaky D. A., Bell J. F., and Brown R. H. (1993) Mineralogical variations within the S-type asteroid class. *Icarus*, 106, 573.
- Gaffey M. J., Cloutis E.A., Kelley M. S., and Reed K. L. (2002) Mineralogy of asteroids. In *Asteroids III* (W. F. Bottke Jr. et al., eds.), pp. 183–204. Univ. of Arizona, Tucson.
- Galache J. L., Beeson C. L., McLeod K. K., and Elvis M. (2015) The need for speed in near-Earth asteroid characterization. *Planet. Space Sci.*, 111, 155–166.
- Gradie J. and Tedesco E. (1982) Compositional structure of the asteroid belt. *Science*, 216, 1405–1407.
- Granvik M., Vaubaillon J., and Jedicke R. (2012) The population of natural Earth satellites. *Icarus*, 218, 262–277.
- Greenstreet S., Ngo H., and Gladman B. (2012) The orbital distribution of near-Earth objects inside Earth's orbit. *Icarus*, 217, 355–366.
- Hasselmann P. H., Carvano J. M., and Lazzaro D. (2012) *SDSS-Based Asteroid Taxonomy VI.1. EAR-A-I0035-5-SDSSTAX-VI.1*. NASA Planetary Data System.
- Hicks M. D., Lawrence K. J., Somers J., Teague S., Strojca C., Dombroski D., Davtyan T., Barajas T., Truong T., McCormack M., Gerhart C., Garcia K., Rhoades H., Mayes D., Shitanishi J., Foster J., and McAuley A. (2012) A spectroscopic and photometric survey of selected near-earth asteroids: Results from 2008–2012. *AAS/Division for Planetary Sciences Meeting Abstracts*, 44, Abstract #110.13.
- Hiroi T., Zolensky M. E., and Pieters C. M. (2001) The Tagish Lake meteorite: A possible sample from a D-type asteroid. *Science*, 293, 2234–2236.
- Jenniskens P., Vaubaillon J., Binzel R. P., DeMeo F. E., Nesvorný D., Bottke W. F., Fitzsimmons A., Hiroi T., Marchis F., Bishop J. L., Vernazza P., Zolensky M. E., Herrin J. S., Welten K. C., Meier M. M. M., and Shaddad M. H. (2010) Almahata Sitta (=asteroid 2008 TC<sub>3</sub>) and the search for the ureilite parent body. *Meteoritics & Planet. Sci.*, 45, 1590–1617.
- Jenniskens P., Fries M. D., Yin Q., Zolensky M., Krot A. N., Sandford S. A., Sears D., Beauford R., Ebel D. S., Friedrich J. M., Nagashima K., Wimpenny J., Yamakawa A., Nishiizumi K., Hamajima Y., Caffee M. W., Welten K. C., Laubenstein M., Davis A. M., Simon S. B., Heck P. R., Young E. D., Kohl I. E., Thiemens M. H., Nunn M. H., Mikouchi T., Hagiya K., Ohsumi K., Cahill T. A., Lawton J. A., Barnes D., Steele A., Rochette P., Verosub K. L., Gattaccea J., Cooper G., Glavin D. P., Burton A. S., Dworkin J. P., Elsila J. E., Pizzarello S., Ogliore R., Schmitt-Kopplin P., Harir M., Hertkorn N., Verchovsky A., Grady M., Nagao K., Okazaki R., Takechi H., Hiroi T., Smith K., Silber E. A., Brown P. G., Albers J., Klotz D., Hankey M., Matson R., Fries J. A., Walker R. J., Puchtel I., Lee C. A., Erdman M. E., Eppich G. R., Roeske S., Gabelica Z., Lerche M., Nuevo M., Girten B., and Worden S. P. (2012) Radar-enabled recovery of the Sutter's Mill meteorite, a carbonaceous chondrite regolith breccia. *Science*, 338, 1583–1587.
- Kim Y., Ishiguro M., and Usui F. (2014) Physical properties of asteroids in comet-like orbits in infrared asteroid survey catalogs. *Astrophys. J.*, 789, 9.
- Kohout T., Gritsevich M., Grokhovsky V. I., Yakovlev G. A., Haloda J., Halodova P., Michallik R. M., Penttilä A., and Muinonen K. (2014) Mineralogy, reflectance spectra, and physical properties of the Chelyabinsk LL5 chondrite — Insight into shock-induced changes in asteroid regoliths. *Icarus*, 228, 78–85.
- Kuroda D., Ishiguro M., Takato N., Hasegawa S., Abe M., Tsuda Y., Sugita S., Usui F., Hattori T., Iwata I., Imanishi M., Terada H., Choi Y., Watanabe S., and Yoshikawa M. (2014) Visible-wavelength spectroscopy of subkilometer-sized near-Earth asteroids with a low delta-v. *Publ. Astron. Soc. Japan*, 66, 51-1 to 51-10.
- Lauretta D. S., Bartels A. E., Barucci M. A., Bierhaus E. B., Binzel R. P., Bottke W. F., Campins H., Chesley S. R., Clark B. C., Clark B. E., Cloutis E. A., Connolly H. C., Crombie M. K., Delbó M., Dworkin J. P., Emery J. P., Glavin D. P., Hamilton V. E., Hergenrother C. W., Johnson C. L., Keller L. P., Michel P., Nolan M. C., Sandford S. A., Scheeres D. J., Simon A. A., Sutter B. M., Vokrouhlický D., and Walsh K. J. (2015) The OSIRIS-REx target asteroid (101955) Bennu: Constraints on its physical, geological, and dynamical nature from astronomical observations. *Meteoritics & Planet. Sci.*, 50, 834–849.
- Lazzarin M., Magrin S., and Marchi S. (2008) SINEO: Spectroscopic Investigation of Near Earth Objects. *Mem. Soc. Astron. Ital. Suppl.*, 12, 12–19.
- Lazzaro D., Michtchenko T., Carvano J. M., Binzel R. P., Bus S. J., Burbine T. H., Mothé-Diniz T., Florcak M., Angelis C. A., and Harris A. W. (2000) Discovery of a basaltic asteroid in the outer main belt. *Science*, 288, 2033–2035.
- Licandro J., Alvarez-Candal A., de León J., Pinilla-Alonso N., Lazzaro D., and Campins H. (2008) Spectral properties of asteroids in cometary orbits. *Astron. Astrophys.*, 487, 1195–1196.
- Love S. G. and Alton J. H. (2006) Micrometeoroid impact crater statistics at the boundary of Earth's gravitational sphere of influence. *Icarus*, 184, 302–307.
- Love S. G. and Brownlee D. E. (1993) A direct measurement of the terrestrial mass accretion rate of cosmic dust. *Science*, 262, 550–553.
- Lucas M. P. and Emery J. P. (2014) Asteroid-meteorite connections in the Hungaria background population: Correlations with primitive achondrites? (abstract). *Lunar Planet. Sci. XLV*, Abstract #1777. Lunar and Planetary Institute, Houston.
- Luu J. and Jewitt D. (1989) On the relative numbers of C types and S types among near-Earth asteroids. *Astron. J.*, 98, 1905–1911.
- McCord T. B., Adams J. B., and Johnson T. V. (1970) Asteroid Vesta: Spectral reflectivity and compositional implications. *Science*, 168, 1445–1447.
- McFadden L. A., Gaffey M. J., and McCord T. B. (1985) Near-Earth asteroids — Possible sources from reflectance spectroscopy. *Science*, 229, 160–163.
- Morbidelli A., Bottke W. F., Froeschlé Ch., and Michel P. (2002) Origin and evolution of near-Earth objects. In *Asteroids III* (W. F. Bottke Jr. et al., eds.), pp. 409–422. Univ. of Arizona, Tucson.
- Moskovitz N. A., Jedicke R., Gaidos E., Willman M., Nesvorný D., Fevig R., and Ivezic Ž. (2008) The distribution of basaltic asteroids in the main belt. *Icarus*, 198, 77–90.
- Mothé-Diniz T. and Nesvorný D. (2008) Visible spectroscopy of extremely young asteroid families. *Astron. Astrophys.*, 486, L9–L12.
- Nakamura T., Noguchi T., Tanaka M., Zolensky M. E., Kimura M., Tsuchiyama A., Nakato A., Ogami T., Ishida H., Uesugi M., Yada T., Shirai K., Fujimura A., Okazaki R., Sandford S. A., Ishibashi Y., Abe M., Okada T., Ueno M., Mukai T., Yoshikawa M., and Kawaguchi J. (2011) Itokawa dust particles: A direct link between S-type asteroids and ordinary chondrites. *Science*, 333, 1113–1116.
- Nedelcu D. A., Birlan M., Popescu M., Badescu O., and Pricop D. (2014) Evidence for a source of H chondrites in the outer main asteroid belt. *Astron. Astrophys.*, 567, L7.
- Nesvorný D., Bottke W. F., Dones L., and Levison H. F. (2002) The recent breakup of an asteroid in the main-belt region. *Nature*, 417, 720–771.
- Nesvorný D., Jedicke R., Whiteley R. J., and Ivezic Z. (2005) Evidence for asteroid space weathering from the Sloan Digital Sky Survey. *Icarus*, 173, 132–152.
- Nesvorný D., Vokrouhlický D., Morbidelli A., and Bottke W. F. (2009) Asteroidal source of L chondrite meteorites. *Icarus*, 200, 698–701.

- Nesvorný D., Bottke W. F., and Vokrouhlický D., Chapman C. R., and Rafkin S. (2010) Do planetary encounters reset surfaces of near Earth asteroids? *Icarus*, 209, 510–519.
- Noguchi T., Nakamura T., Kimura M., Zolensky M. E., Tanaka M., Hashimoto T., Konno M., Nakato A., Ogami T., Fujimura A., Abe M., Yada T., Mukai T., Ueno M., Okada T., Shirai K., Ishibashi Y., and Okazaki R. (2011) Incipient space weathering observed on the surface of Itokawa dust particles. *Science*, 333, 1121–1125.
- Ostro S. J., Hudson R. S., Benner L. A. M., Giorgini J. D., Magri C., Margot J.-L., and Nolan M. C. (2002) Asteroid radar astronomy. In *Asteroids III* (W. F. Bottke Jr. et al., eds.), pp. 151–168. Univ. of Arizona, Tucson.
- Pieters C. M., Taylor L. A., Noble S. K., Keller L. P., Hapke B., Morris R. V., Allen C. C., McKay D. S., and Wentworth S. (2000) Space weathering on airless bodies: Resolving a mystery with lunar samples. *Meteoritics & Planet. Sci.*, 35, 1101–1107.
- Pravec P. and Harris A. W. (2000) Fast and slow rotation of asteroids. *Icarus*, 148, 12–20.
- Prettyman T. H., Mittlefehldt D. W., Yamashita N., Lawrence D. J., Beck A. W., Feldman W. C., McCoy T. J., McSween H. Y., Toplis M. J., Titus T. N., Tricarico P., Reedy R. C., Hendricks J. S., Forni O., Le Corre L., Li J. Y., Mizzi H., Reddy V., Raymond C. A., and Russell C. T. (2012) Elemental mapping by Dawn reveals exogenic H in Vesta's regolith. *Science*, 338, 242–246.
- Rayner J. T., Toomey D. W., Onaka P. M., Denault A. J., Stahlberger W. E., Vacca W. D., Cushing M. C., and Wang S. (2003) SpeX: A medium-resolution 0.8–5.5 micron spectrograph and imager for the NASA Infrared Telescope Facility. *Publ. Astron. Soc. Pac.*, 115, 362–382.
- Reddy V., Gaffey M. J., Abell P. A., and Hardersen P. S. (2012) Constraining albedo, diameter and composition of near-Earth asteroids via near-infrared spectroscopy. *Icarus*, 219, 382–392.
- Reddy V., Sanchez J. A., Bottke W. F., Cloutis E. A., Izawa M. R. M., O'Brien D. P., Mann P., Cuddy M., Le Corre L., Gaffey M. J., and Fujihara G. (2014) Chelyabinsk meteorite explains unusual spectral properties of Baptistina asteroid family. *Icarus*, 237, 116–130.
- Richardson D. C., Bottke W. F., and Love S. G. (1998) Tidal distortion and disruption of Earth-crossing asteroids. *Icarus*, 134, 47–76.
- Rivkin A. S., Binzel R. P., and Bus S. J. (2005) Constraining near-Earth object albedos using near-infrared spectroscopy. *Icarus*, 175, 175–180.
- Sanchez J. A., Michelsen R., Reddy V., and Nathues A. (2013) Surface composition and taxonomic classification of a group of near-Earth and Mars-crossing asteroids. *Icarus*, 225, 131–140.
- Sanchez J. A., Reddy V., Kelley M. S., Cloutis E. A., Bottke W. F., Nesvorný D., Lucas M. P., Hardersen P. S., Gaffey M. J., Abell P. A., and Corre L. L. (2014) Olivine-dominated asteroids: Mineralogy and origin. *Icarus*, 228, 288–300.
- Sanchez J. A., Reddy V., Dykhuis M., Lindsay S., and Le Corre L. (2015) Composition of potentially hazardous asteroid (214869) 2007 PA<sub>8</sub>: An H chondrite from the outer asteroid belt. *Astrophys. J.*, 808, 93.
- Scheeres D. J., Benner L. A. M., Ostro S. J., Rossi A., Marzari F., and Washabaugh P. (2005) Abrupt alteration of asteroid 2004 MN<sub>4</sub>'s spin state during its 2029 Earth flyby. *Icarus*, 178, 281–283.
- Scott E. R. D., Greenwood R. C., Franchi I. A., and Sanders I. S. (2009) Oxygen isotopic constraints on the origin and parent bodies of eucrites, diogenites and howardites. *Geochim. Cosmochim. Acta*, 73, 5835–5853.
- Sears D. W. G. (1998) The case for rarity of chondrules and calcium-aluminum-rich inclusions in the early solar system and some implications for astrophysical models. *Astrophys. J.*, 498, 773–778.
- Shkuratov Y. G., Kaydash V. G., and Opanasenko N. V. (1999) Iron and titanium abundance and maturity degree distribution on the lunar nearside. *Icarus*, 137, 222–234.
- Shoemaker E. M., Williams J. G., Helin E. F., and Wolf R. F. (1979) Earth-crossing asteroids: Orbital classes, collision rates with Earth, and origin. In *Asteroids* (T. Gehrels, ed.), pp. 253–282. Univ. of Arizona, Tucson.
- Somers J. M., Hicks M., Lawrence K., Rhoades H., Mayes D., Barajas T., McAuley A., Foster J., Shitanishi J., Truong T., Garcia K. (2010) Optical characterization of planetary radar targets, low-ΔV, and potentially hazardous asteroids: Results from 2009–2010. *Bull. Am. Astron. Soc.*, 42, 1055.
- Stuart J. S. and Binzel R. P. (2004) Bias-corrected population, size distribution, and impact hazard for the near-Earth objects. *Icarus*, 170, 295–311.
- Sunshine J. M., Pieters C. M., and Pratt S. F. (1990) Deconvolution of mineral absorption bands — An improved approach. *J. Geophys. Res.*, 95, 6955–6966.
- Taylor S., Lever J. H., and Harvey R. P. (2000) Numbers, types, and compositions of an unbiased collection of cosmic spherules. *Meteoritics & Planet. Sci.*, 35, 651–666.
- Tholen D. J. and Barucci M. A. (1989) Asteroid taxonomy. In *Asteroids II* (R. P. Binzel et al., eds.), pp. 298–315. Univ. of Arizona, Tucson.
- Tholen D. J. and Whiteley R. J. (1998) Results from NEO searches at small solar elongation. *Bull. Am. Astron. Soc.*, 30, 1041.
- Thomas C. A. and Binzel R. P. (2010) Identifying meteorite source regions through near-Earth object spectroscopy. *Icarus*, 205, 419–429.
- Thomas C. A., Trilling D. E., and Rivkin A. S. (2012) Space weathering of small Koronis family asteroids in the SDSS Moving Object Catalog. *Icarus*, 219, 505–507.
- Thomas C. A., Emery J. P., Trilling D. E., Delbó M., Hora J. L., and Mueller M. (2014) Physical characterization of warm Spitzer-observed near-Earth objects. *Icarus*, 228, 217–246.
- Trombka J. I., Squyres S. W., Brückner J., Boynton W. V., Reedy R. C., McCoy T. J., Gorenstein P., Evans L. G., Arnold J. R., Starr R. D., Nittler L. R., Murphy M. E., Mikheeva I., McNutt R. L., McClanahan T. P., McCartney E., Goldsten J. O., Gold R. E., Floyd S. R., Clark P. E., Burbine T. H., Bhangoo J. S., Bailey S. H., and Petaev M. (2000) The elemental composition of asteroid 433 Eros: Results of the NEAR-Shoemaker X-ray spectrometer. *Science*, 289, 2101–2105.
- Vernazza P., Binzel R. P., Thomas C. A., DeMeo F. E., Bus S. J., Rivkin A. S., and Tokunaga A. T. (2008) Compositional differences between meteorites and near-Earth asteroids. *Nature*, 454, 858–860.
- Vernazza P., Binzel R. P., Rossi A., Fulchignoni M., and Birlan M. (2009) Solar wind as the origin of rapid reddening of asteroid surfaces. *Nature*, 458, 993–995.
- Vernazza P., Fulvio D., Brunetto R., Emery J. P., Dukes C. A., Cipriani F., Witasse O., Schaible M. J., Zanda B., Strazzulla G., and Baragiola R. A. (2013) Paucity of Tagish Lake-like parent bodies in the asteroid belt and among Jupiter Trojans. *Icarus*, 225, 517–525.
- Vernazza P., Zanda B., Binzel R. P., Hiroi T., DeMeo F. E., Birlan M., Hewins R., Ricci L., Barge P., and Lockhart M. (2014) Multiple and fast: The accretion of ordinary chondrite parent bodies. *Astrophys. J.*, 791, 22 pp.
- Vererka J., Robinson M., Thomas P., Murchie S., Bell J. F., Izenberg N., Chapman C., Harch A., Bell M., Carcich B., Cheng A., Clark B., Domingue D., Dunham D., Farquhar R., Gaffey M. J., Hawkins E., Joseph J., Kirk R., Li H., Lucey P., Malin M., Martin P., McFadden L., Merline W. J., Miller J. K., Owen W. M., Peterson C., Prockter L., Warren J., Wellnitz D., Williams B. G., and Yeomans D. K. (2000) NEAR at Eros: Imaging and spectral results. *Science*, 289, 2088–2097.
- Walsh K. J., Richardson D. C., and Michel P. (2008) Rotational breakup as the origin of small binary asteroids. *Nature*, 454, 188–191.
- Wetherill G. W. (1988) Where do the Apollo objects come from? *Icarus*, 76, 1–18.
- Wetherill G. W. and Chapman C. R. (1988) Asteroids and meteorites. In *Meteorites and the Early Solar System* (J. F. Kerridge and M. S. Matthews, eds.), pp. 35–67. Univ. of Arizona, Tucson.
- Whiteley R. J. (2001) A compositional and dynamical survey of the near-Earth asteroids. Ph.D. thesis, University of Hawai'i at Manoa.
- Wiegert P. A., Innanen K. A., and Mikkola S. (1997) An asteroidal companion to the Earth. *Nature*, 387, 685–686.
- Ye Q. (2011) BVRI photometry of 53 unusual asteroids. *Astron. J.*, 141, 32.
- Yu Y., Richardson D. C., Michel P., Schwartz S. R., and Ballouz R. (2014) Numerical predictions of surface effects during the 2029 close approach of asteroid 99942 Apophis. *Icarus*, 242, 82–96.

# Small Near-Earth Asteroids as a Source of Meteorites

Jiří Borovička and Pavel Spurný

*Astronomical Institute of the Czech Academy of Sciences*

Peter Brown

*University of Western Ontario*

Small asteroids intersecting Earth's orbit can deliver extraterrestrial rocks to Earth, called meteorites. This process is accompanied by a luminous phenomena in the atmosphere called bolides or fireballs. Observations of bolides provide pre-atmospheric orbits of meteorites, physical and chemical properties of small asteroids, and the flux (i.e., frequency of impacts) of bodies at Earth in the centimeter to decameter size range. In this chapter we explain the processes occurring during the penetration of cosmic bodies through the atmosphere and review the methods of bolide observations. We compile available data on the fireballs associated with 22 instrumentally observed meteorite falls. Among them are the heterogeneous falls Almahata Sitta (2008 TC<sub>3</sub>) and Benešov, which revolutionized our view on the structure and composition of small asteroids; the Příbram-Neuschwanstein orbital pair, carbonaceous chondrite meteorites with orbits on the asteroid-comet boundary; and the Chelyabinsk fall, which produced a damaging blast wave. While most meteoroids disrupt into fragments during atmospheric flight, the Carancas meteoroid remained nearly intact and caused a crater-forming explosion on the ground.

## 1. INTRODUCTION

Well before the first asteroid was discovered, people unknowingly had asteroid samples in their hands. Could stones fall from the sky? For many centuries, the official answer was no. Only at the end of the eighteenth century and the beginning of the nineteenth century did the evidence that rocks did fall from the sky become so overwhelming that this fact was accepted by the scientific community. It was the German scientist Ernst Chladni who first recognized their extraterrestrial origin in 1794. Nevertheless, it took some time before his idea became accepted (see, e.g., Lauretta and McSween, 2006).

The stones that fell from the sky are distinct from all terrestrial rocks. They are called *meteorites*. Meteorites are classified into many different types according to their mineralogical composition. The two basic classes are stony and iron meteorites, although a mixture of these chemistries (stony-iron meteorites) exists as well. Iron meteorites are composed of metallic iron with an admixture of nickel and some traces of other elements. Stony meteorites are mostly composed of silicates such as olivine and pyroxene, with some metallic iron also present in many cases. The elements and most of minerals found in meteorites are known from terrestrial rocks, but their ratios in meteorites are different. The most common type of stony meteorites, called chondrites, contains millimeter-sized spherical structures called chondrules. Such structures are not present in any terrestrial rock. More detailed classification of meteorites is given in the chapter

by Binzel et al. in this volume. The study of meteorites is a well-developed scientific field and rich literature is available (e.g., Dodd, 1981; Papike, 1998; Hutchison, 2004; Lauretta and McSween, 2006).

According to the circumstances of their recovery, meteorites can be divided into *finds* and *falls*. Finds are meteorites found on ground (by chance or by dedicated searches), but the date of their fall is unknown. Falls are meteorites, whose fall was witnessed — either the meteorite was seen (or heard) to hit the ground or the fireball caused by the ablation of the parent meteoroid in the atmosphere was observed and the meteorites were found later. *Meteoroid* is a term for the original body that dropped the meteorite(s). In fact, there is no strictly defined boundary between large meteoroids and small asteroids. For the purpose of this chapter, we will call meteoroids all bodies smaller than 10 m and larger than 50 µm. Bodies smaller than 50 µm are called *dust particles*. A dust particle, when entering the atmosphere, may not give rise to the phenomenon called a meteor, depending on its initial speed. *Meteor* is the radiation, and associated phenomenon (heat, shock, ionization), caused by the entry of a meteoroid in the atmosphere. Dust particles are sufficiently small that they may decelerate before they start to evaporate, so they do not produce meteors. They gradually sediment through the atmosphere and finally reach the ground.

The vast majority of meteoroids are destroyed in the atmosphere and do not produce any macroscopic meteorites. Parts of them may not be evaporated completely and can reach the ground as dust or *micrometeorites* (objects smaller

than  $\sim 1$  mm). To produce a meteorite, the meteoroid must be large enough and mechanically strong enough, and must have a relatively low entry velocity. The initial velocities of meteoroids at entry to the terrestrial atmosphere in bound heliocentric orbits are between 11 and  $71 \text{ km s}^{-1}$ . The chance of surviving the passage through the atmosphere strongly decreases with increasing velocity. As a rough empirical rule (for which there are many exceptions), a meteoroid of stony composition with a low entry velocity ( $\sim 20 \text{ km s}^{-1}$ ) can produce meteorites with a total mass of 5–10% of the initial (pre-atmospheric) mass of the meteoroid (Halliday *et al.*, 1989a; Popova *et al.*, 2011).

A meteor brighter than stellar magnitude –4 (i.e., brighter than the planet Venus) is called a *fireball* or *bolide*. The term *superbolide* is used for meteors brighter than magnitude –17 (Ceplecha *et al.*, 1999). Meteorite falls are always in the bolide or superbolide category. Nevertheless, it is not true that the brighter the bolide, the larger the meteorite. There are fluffy meteoroids of cometary origin, which produce bright bolides but are completely destroyed high in the atmosphere (e.g., Borovička and Spurný, 1996; Madiedo *et al.*, 2014a).

Meteorites, as extraterrestrial samples, have much scientific value. However, to fully exploit the information they contain, it is necessary to know where they come from. Early researchers thought that meteorites came from interstellar space (see, e.g., the discussions of Öpik, 1950; Fessenkov *et al.*, 1954). It was the Příbram meteorite, which fell in the former Czechoslovakia in 1959 and whose trajectory, impact position, and orbit was determined rigorously for the first time from bolide photographs, that placed meteorites in the context of the solar system (Ceplecha, 1961). Since bolides are rare events and occur unexpectedly, it is necessary to systematically monitor large territories to obtain observational data. For that reason, dedicated arrays of cameras, called fireball networks, were put into operation in several countries. One of their goals was to assist with meteorite recovery and, at the same time, provide orbits of the meteorites (Ceplecha, 1986). In more modern times, when various types of still and video cameras became widespread among the public, casual instrumental records of bolides have become common. These records, after careful calibration (Borovička, 2014) and often laborious computation, also provided some meteorite orbits, although with lower precision than dedicated bolide cameras. As of 2014, there are 22 meteorites with reliably (i.e., instrumentally determined) known pre-impact orbit (see section 5). The orbits confirm that most meteorites are fragments of asteroids, although a cometary origin of a small fraction of meteorites cannot be fully excluded. In addition, it was found that some meteorites, according to their composition, must originate from the Moon and some others from Mars, although no orbits for lunar or martian meteorite falls are yet documented.

It is estimated that about 4500 meteorite falls dropping more than 1 kg of total meteorite mass occur annually on Earth (Halliday *et al.*, 1989b). Only in one case has the meteorite fall been predicted in advance: A small interplanetary object designated as 2008 TC<sub>3</sub> was discovered on October 7,

2008, when approaching Earth, and it was predicted to enter the atmosphere the next day over Sudan. Its remnants were later recovered as the Almahata Sitta meteorites (Jenniskens *et al.*, 2009). On January 1, 2014, another object, 2014 AA, was discovered on an Earth-approaching orbit but the impact point was poorly constrained. There are indications that the impact occurred in the Atlantic Ocean (Chesley *et al.*, 2015).

The observations of bolides, with or without an associated meteorite fall, provide information about the orbital distribution, physical properties, and (when accompanied with spectral observation) composition of fragments of asteroids (and comets) intersecting Earth's orbit. They are therefore a complementary tool to the astronomical and *in situ* studies of asteroids. They also provide direct information on the effects of impacts on Earth. Large bodies generate a strong blast wave in the atmosphere, which can have damaging effects on the surface, as was the case for the Tunguska event over Siberia in 1908 (e.g., Vasilyev, 1998) and Chelyabinsk in 2013 (Brown *et al.*, 2013a; Popova *et al.*, 2013). Even small meteoroids can occasionally cause an impact crater, as was the case for the Carancas impact in 2007 (e.g., Tancredi *et al.*, 2009).

This chapter provides an overview of what is known about bolides producing meteorite falls. Special attention is devoted to instrumentally observed meteorite falls. These are the events with the most complete information available (analysis of both the bolide and the corresponding meteorite). We note that these phenomena are not restricted to Earth. Meteorites (Fairén *et al.*, 2011), fresh impact craters, and crater strewn fields (Daubar *et al.*, 2013) were discovered on the surface of Mars and superbolides have now been observed in the atmosphere of Jupiter (Hueso *et al.*, 2013). On the atmosphereless Moon, flashes caused by the direct impact of meteoroids on the surface can be observed (Suggs *et al.*, 2014).

## 2. METEOROIDS IN THE ATMOSPHERE

In this section we describe in more detail the penetration of large ( $>10 \text{ cm}$ ) meteoroids thorough the atmosphere. The understanding of these processes is important for the derivation of meteoroid properties from bolide observations, for assessment of the hazard connected with meteoroid/asteroid entry, and for improving the efficiency of meteorite recoveries.

In the upper layers of the atmosphere, at heights  $>130 \text{ km}$ , individual atoms and molecules directly impact the meteoroid surface. This leads to gradual heating of the meteoroid surface. Under some circumstances, the collision with atmospheric molecules can lead to the release of a meteoric atom from the surface. This process, called *sputtering*, is a form of slow mass loss at low temperatures (Rogers *et al.*, 2005). It is efficient only at meteoroid velocities larger than  $30 \text{ km s}^{-1}$  (Popova *et al.*, 2007). Intense mass loss starts only when the meteoroid surface is heated to its melting temperature of about 2000 K (Ceplecha *et al.*, 1998). The molten surface layer partly evaporates and is partly lost in the form of liquid droplets, which then continue to evaporate in the hot plasma surrounding the meteoroid in a process

called *thermal ablation*. The hot envelope of heated air and meteoric vapors around the meteoroid is the main source of bolide radiation. The plasma temperature and composition can be studied by the methods of meteor spectroscopy. The typical temperatures are 4000–5000 K (e.g., Borovička, 2005). At these temperatures, the main contributors to the bolide radiation in visible light are meteoric metals, in particular Fe, Mg, Na, Ca, Cr, and Mn. They radiate in the form of atomic emission lines. The atmospheric species (N, O) and some meteoric species (notably Si, S, and C) have no bright lines in the visible range. As a result, their abundance is difficult to determine. Moreover, the composition of meteoric vapors usually does not fully reflect the composition of the meteoroid as some refractory elements, notably Al, Ca, and Ti, are not evaporated completely during thermal ablation, particularly at heights above 30 km (Borovička and Spurný, 1996; Borovička, 2005). Nevertheless, bolide spectroscopy can be used to distinguish the main types of meteoritic material (chondrites, achondrites, irons) in the cases where no meteorite is recovered. There is also a component of higher temperature (~10,000 K) observed in bolide spectra (Borovička, 1994a). The strength of this second component (represented mainly by the lines of Ca<sup>+</sup>, Mg<sup>+</sup>, and Si<sup>+</sup>) increases rapidly with bolide velocity and is not seen in slow bolides. The high-temperature region is probably formed in front of the body, where the interaction of the ablated material and the air flux is the strongest.

In the denser atmospheric layers, atmospheric molecules do not directly impact the meteoroid surface. The *free molecular regime* changes into the *continuous flow* (Popova, 2004), which can be treated within the framework of gas hydrodynamics. A shock wave forms at the boundary between the envelope protecting the meteoroid and the incoming flow of the atmosphere. According to models, the temperature of the shock-heated air can reach tens of thousands of degrees (Artemieva and Shuvalov, 2001).

The interaction with the atmosphere leads to loss of mass, deceleration, and, in many cases, fragmentation of the meteoroid. The classical meteor equations describe the deceleration and mass loss (ablation) of a single (non-fragmenting) meteoroid (Bronshcen, 1983; Ceplecha et al., 1998). In this treatment, the meteoroid with mass m, cross-section S, moving with a velocity v, encounters atmosphere of mass Spvdt, where p is the density of atmosphere and dt is the considered time interval. The momentum of the encountered atmosphere is Spv<sup>2</sup>dt and the kinetic energy is  $\frac{1}{2}Spv^3dt$ . From the conservation of momentum, we have the *drag equation* describing deceleration of the meteoroid

$$m \frac{dv}{dt} = -\Gamma Spv^2$$

where  $\Gamma$  (sometimes written as  $C_D/2$ ) is the *drag coefficient*. The energy is consumed in mass loss according to the *ablation equation*

$$\frac{dm}{dt} = -\Lambda Spv^3/2Q$$

where  $\Lambda$  is the *heat transfer coefficient* and Q is the energy necessary to ablate a unit mass of the meteoroid. These equations are usually rewritten by introducing the *shape factor*  $A = Sm^{-2/3}\delta^{2/3}$ , where  $\delta$  is the bulk density of the meteoroid, and the *ablation coefficient* is  $\sigma = \Lambda/2Q\Gamma$ , the latter of which can be directly inferred from observations. More details and the analytical integrals of the above equations (assuming constant coefficients) can be found in Ceplecha et al. (1998). Theoretical models of meteoroid ablation were discussed by, e.g., Baldwin and Schaeffer (1971), Biberman (1980), Svetsov et al. (1995), Golub' et al. (1996), and Nemtchinov et al. (1997).

The single-body approach is rarely applicable for the entirety of the bolide's flight. Meteoroid fragmentation in the atmosphere is a complex process that is not possible to predict exactly but is ubiquitous. It depends on the structural properties of each individual meteoroid and occurs in various forms, i.e., chipping off a small part of the body, disruption into two or more fragments of similar sizes, catastrophic disruption into large numbers of small fragments, etc. Fragmentation is often a multi-stage process, whereby fragments arising from early fragmentation episodes disrupt again later. If this process has some regularity, it is called *progressive fragmentation*. The term *quasicontinuous fragmentation* refers to a process when small fragments (dust) are released from the main body almost continuously. This is the dominant fragmentation mode for a kind of weak millimeter-sized population of meteoroids of cometary origin (Borovička et al., 2007).

For a given bolide velocity, the structurally weaker is the meteoroid, the higher in altitude the fragmentation starts. Some types of fragmentation can be induced thermally; nevertheless, in most cases (especially when large fragments are involved or when catastrophic disruption occurs) the breakup is likely due to aerodynamic loading. In this process, the dynamic pressure acting at the front surface of the meteoroid is  $p = \Gamma p v^2$ , while the pressure at the rear side is zero, and the difference in the pressures causes structural failure of the meteoroid. Fragmentation occurs when p exceeds the strength of the meteoroid [see Holsapple (2009) for various definitions of strength]. In estimating the dynamic pressure at breakup, the factor  $\Gamma$ , on the order of unity, is often neglected and the meteoroid strength is estimated as  $pv^2$ . The velocity, v, is easily measurable from meteor data, but the determination of the fragmentation height (and thus the corresponding atmospheric density, p) is often difficult. This can be done by a number of methods (geometric, photometric, dynamic, acoustic), depending on the type of available data and the type of fragmentation (Ceplecha et al., 1993; Trigo-Rodríguez and Llorca, 2006; Popova et al., 2011).

The radiation of the bolide is assumed to be proportional to the instantaneous loss of kinetic energy, as expressed by the luminosity equation

$$I = -\tau(\frac{1}{2}v^2 \frac{dm}{dt} + mv \frac{dv}{dt})$$

where I is the radiative output and  $\tau$  is the *luminous efficiency* (which may depend on meteoroid velocity, mass, composition,

and height in the atmosphere). For cases including fragmentation, the total output is the sum of contributions of all fragments. When a large number of fragments is released, a sudden increase in brightness, called a *flare*, occurs due to the increase of the meteoroid total cross-section.

Thermal ablation stops when the meteoroid velocity decreases below about  $3 \text{ km s}^{-1}$ . The end of the bolide therefore occurs when either all mass has been ablated and no macroscopic fragments remain or the velocity of all fragments decreases below this ablation limit. In the latter case, the fragments continue to fall during a period called *dark flight*. Their surface gradually cools and no light is emitted (except perhaps a faint infrared glow at the beginning). Typically, the velocity drops below the ablation limit at a height somewhere between 10 km and 30 km, depending mainly on the initial meteoroid mass and its fragmentation in the atmosphere. The deceleration continues during dark flight. The fragments follow a ballistic trajectory that turns into a nearly vertical fall, influenced by atmospheric winds (Ceplecha, 1987). When they reach the ground, the fragments are called *meteorites*. Typical impact speeds are in the range  $10\text{--}100 \text{ m s}^{-1}$  for meteorites of  $0.1\text{--}100 \text{ kg}$ . Fresh meteorites are characterized by a dark fusion crust representing a resolidified layer of molten material acquired during the latter stages of ablation (Genge and Grady, 1999). Sometimes a part of the fusion crust is missing, suggesting that fragmentation continues to occur during the dark flight.

In rare cases of large, strong meteoroids, the deceleration may not be sufficient to convert the flight into free fall. If the body hits the ground with a velocity larger than about  $0.5\text{--}1 \text{ km s}^{-1}$ , it generates a shock wave in the ground resulting in crater formation. An *impact crater* much larger than the impactor is then formed (Holsapple, 1993).

The radiation is not the only demonstration of meteoroid flight through the atmosphere. The supersonic flight generates a cylindrical *blast wave*, which can be heard on the ground and, if the amplitude and the seismic characteristics of the ground are appropriate, seismic waves may be excited (Edwards et al., 2008). Meteoroid fragmentation events can generate spherical blast waves. These waves travel in the atmosphere with the speed of sound ( $\sim 300 \text{ m s}^{-1}$ ), so they reach the ground tens of seconds to minutes after the bolide, depending on the range of the bolide. Non-audible sound waves of low frequency, termed *infrasound*, attenuate particularly slowly in the atmosphere and can be detected with special detectors over large distances, in some cases for tens of thousands of kilometers (Ens et al., 2012).

Eyewitnesses of bolides sometimes report another type of sound (variously described as a hissing, popping, or crackling) heard simultaneously with the bolide. The origin of these *electrophonic sounds* is not well understood but they are believed to be transmitted as very low frequency/extremely low frequency (VLF/ELF) electromagnetic waves and converted into audible sound by the vibration of objects in the vicinity of the observer (Keay, 1992). Recently, radio emissions at frequencies 20–40 MHz were reported from fireball trails (Obenberger et al., 2014).

Bolides, but also quite faint meteors, produce *ionization trails* in the atmosphere. The lifetimes of the trails vary from a fraction of second to many minutes. They reflect electromagnetic radiation, which is used for the detection of meteors by radars (Ceplecha et al., 1998; Jones et al., 2005). High-power, large-aperture (HPLA) radars are able to detect the plasma that forms in the vicinity of tiny meteoroids (Close et al., 2007). For larger bodies, this so-called *head echo* can also be detected by normal meteor radars (Brown et al., 2011).

### 3. FIREBALL OBSERVATIONS

In this section we provide a brief overview of bolide observations and the basic methods of data analysis.

#### 3.1. Observation Methods

Bolides, and particularly superbolides, are conspicuous phenomena on the sky (Fig. 1) and often draw the attention of the public. They can also be detected by various instruments — optical cameras, photoelectric sensors, radars, acoustic and seismic detectors, or satellite-based sensors. Optical imaging cameras provide the most straightforward data about the bolide trajectory, velocity, and luminosity. The bolide must be imaged from at least two widely separated (optimally about 100 km apart) sites to reconstruct the trajectory. Inspired by success with the Příbram bolide, whole networks of cameras have been established to capture similar events and to characterize the population of large meteoroids. The network, which started in Czechoslovakia in 1963 (Ceplecha and Rajchl, 1965) and was joined by Germany in 1968 (Ceplecha et al., 1973; Oberst et al., 1998), formed the European Fireball Network (EN), which remains in operation today. The network originally used low-resolution all-sky mirror cameras recording on photographic film. The Czech portion has been modernized in several stages following the advancement of technology: Mirrors have been replaced by fish-eye lenses providing



**Fig. 1.** Image of a very bright bolide EN 210199 taken by the photographic all-sky camera at Lysá hora, Czech Republic. Stars form circles around the North Pole during a long exposure. Only part of the all-sky image is shown.

higher resolution after 1975 (*Ceplecha*, 1986), manually operated cameras were replaced by Autonomous Fireball Observatories (AFO) beginning in 2001 (*Spurný et al.*, 2007), and film versions are currently being replaced by digital versions (the Digital AFO, or DAFO). The Australian Desert Fireball Network, which has operated since 2005 (*Bland et al.*, 2012), also uses AFO. The Prairie Network operated in the United States (U.S.) from 1963 to 1975 and used batteries of high-resolution photographic cameras (*McCrosky and Boeschenstein*, 1965). This was also the case for the Meteorite Observation and Recovery Project (MORP) in Canada, which was active from 1971 to 1985 (*Halliday et al.*, 1978, 1996). The three early networks were compared by *Halliday* (1973). The Tajikistan Fireball Network operated in 2009–2012 (two stations have been in operation since 2006 until now) and used manually operated fish-eye film cameras together with digital cameras (*Kokhirova et al.*, 2015). There are also networks based on video cameras, either all-sky versions used in the Southern Ontario Meteor Network, operated in Canada since 2004 (*Brown et al.*, 2010); in the NASA fireball network operated in the U.S. since 2008 (*Cooke and Moser*, 2012), and in the Slovak Video Meteor Network, which started with two stations in 2009 (*Tóth et al.*, 2012), or various types of wide field cameras. The latter is the case of the Spanish Meteor Network dating back to 1997 (*Trigo-Rodríguez et al.*, 2001) and the Polish Fireball Network operated since 2004 (*Olech et al.*, 2006). The video-based networks provide lower resolution and thus lower precision of data than photographic networks. Video cameras are usually more sensitive and capture fainter meteors, while bright bolides are saturated and hardly measurable. The quality and reliability of the data critically depends on the quality of the astrometric procedures. Amateur astronomers in many countries now operate video cameras optimized for fainter meteors (e.g., *Molau and Rendtel*, 2009; *SonotaCo*, 2009). The International Meteor Organization (<http://www.imo.net>) plays an important role in coordinating and popularizing these activities. Occasionally, faint-meteor cameras also capture meteorite falls, as was the case for the Slovenian and Croatian Meteor Networks (*Spurný et al.*, 2010; *Šegon et al.*, 2011) and the professional Cameras for Allsky Meteor Surveillance (CAMS) system in California (*Jenniskens et al.*, 2014).

Optical cameras can be used as meteor spectrographs by putting a diffraction element (prism or grating) in front of the lens. Such objective spectrographs do not need any slit, since meteors are line objects and their monochromatic images form the spectrum. Large-format photographic film cameras with rather long focal length have been used to obtain high-resolution spectra of bright bolides (Fig. 2). The description and analysis of such detailed spectra, containing more than 100 emission lines, was published in a number of papers (e.g., *Halliday*, 1961; *Ceplecha*, 1971; *Borovička*, 1993, 1994b). High-resolution photographic spectrographs are still in use at Ondřejov Observatory. A more sensitive charge-coupled-device (CCD) spectrograph (but having a smaller field of view) was used during the Leonid campaign

(*Jenniskens*, 2007). The Spanish Meteor Network uses video cameras to obtain low-resolution spectra of bolides (*Madiedo et al.*, 2013a,b, 2014a).

Detailed light curves of bolides can be studied by radiometers, i.e., photoelectric or semiconductor devices, which do not image the bolide, but measure the total scattered sky light as a function of time (Fig. 3). Radiometers are part of AFOs and DAFOs in central Europe and of AFOs in Australia and

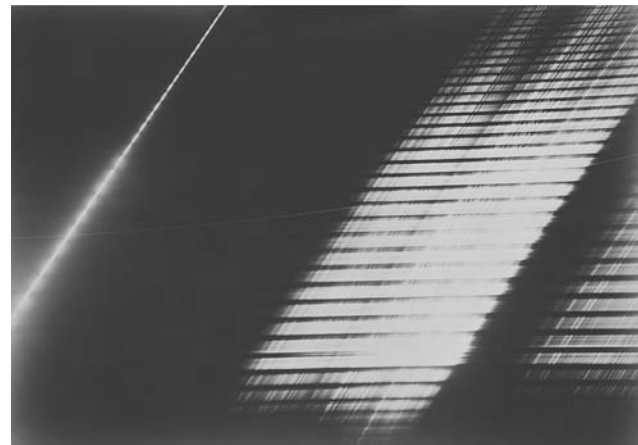


**Fig. 2.** Photographic grating spectrum of a lower part of the Benešov bolide EN 070591. The spectrum was taken from the Ondřejov Observatory, Czech Republic. The zero order (direct image) is on the left, the first order and part of the second order are on the right. The fireball flew from the top to the bottom. The exposure was interrupted by a rotating shutter. See *Borovička and Spurný* (1996) for more detailed description of the spectrum. Benešov is the only bolide with both recovered meteorites and recorded spectrum.

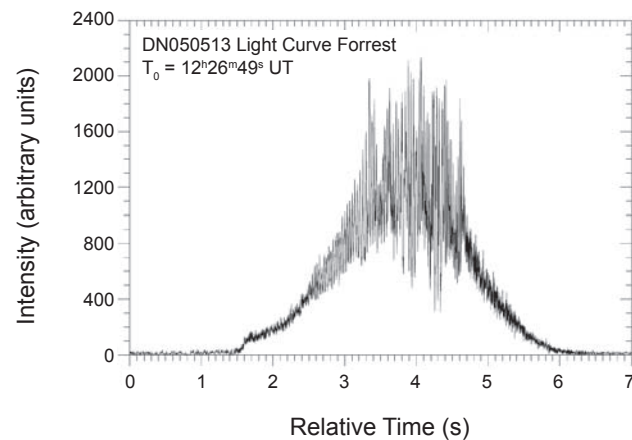


**Fig. 3.** Radiometric light curve of bolide DN 050513 taken by the Autonomous Fireball Observatory at Forrest station in Australia. The sampling rate was 500 Hz. The high amplitude and high frequency variations during the bright phase are real. The amplitude of the noise was much lower, as can be seen at the edges of the curve. DN 050513 was a type I meteorite-dropping bolide (meteorites landed in an inaccessible area and were not recovered).

provide the light curves with either 500 or 5000 samples per second (*Spurný and Ceplecha*, 2008). Radiometric light curves of superbolides are also detected globally as a by-product of satellite-based systems constructed for different purposes. These systems provide global detection of superbolides, with radiometric measurements establishing bolide time and radiant power (*Tagliaferri et al.*, 1994). The total energy of the event may also be estimated under a number of assumptions. A complimentary system provides estimates of the location and in some cases the velocity/altitude or fragmentation height of superbolides. Meteorological and scientific satellites have also detected bolides in flight or their remnant dust/aerosol clouds (*Borovička and Charvát*, 2009; *Klekociuk et al.*, 2005; *Rieger et al.*, 2014).

In addition to systems exploiting the electromagnetic emission of bolides, the atmospheric shock waves produced by fireballs may be detected (*Edwards*, 2010). At large distances from the bolide, these shocks are detectable as infrasound, which is sound below  $\sim$ 20 Hz. Bolide infrasound is detectable by microbarographs, which are instruments able to record coherent pressure amplitudes as low as one part in  $10^8$  of the ambient atmospheric pressure. When three or more such sensors are deployed within a region on the order of 1 km in size, the resulting sensor array can efficiently distinguish coherent sources from noise based on cross-correlation of the pressure signals and measured signal arrival direction and elevation (*Christie and Campus*, 2010). Since approximately 2000, the International Monitoring System (IMS) of the Comprehensive-Test Ban Treaty Organization (CTBTO) has operated infrasound arrays on a global scale. As of 2014, some 47 stations (of a projected network of 60) are operating and provide nearly global detection capability for kiloton-scale superbolides.

In contrast to infrasound observations, which directly detect the very small pressure perturbation from bolides at ranges of thousands of kilometers, seismographs respond to the bolide air waves coupled to the solid Earth. The low efficiency of seismo-acoustic coupling implies that airwaves are normally only directly detectable seismically within a few hundred kilometers of a bolide. For very energetic bolides, surface-coupled waves may also be produced (*Edwards et al.*, 2008). The principle advantage of seismic bolide measurements are the tens of thousands of seismic stations operated globally that provide dense coverage in some areas, sometimes allowing multiple seismo-acoustic detections of a single bolide, which can provide information on trajectory and fragmentation points (e.g., *Borovička and Kalenda*, 2003; *Pujol et al.*, 2006).

Radar may also be used in several modes to characterize bolides. Direct detection of the radar head echo associated with the fireball, whereby radio waves are reflected off electrons in the region of the fireball head, can be used to estimate the velocity of the bolide as well as compute its trajectory (*Brown et al.*, 2011) and, in principle, its mass. The main limitation of this observational mode is the large power aperture (or large radar cross section) needed to detect such head echoes, which effectively limit detectability to small

regions in the atmosphere near the radar (*Kero et al.*, 2011). The ionization trail left behind from a bolide is more easily detected than the corresponding head echo (*Ceplecha et al.*, 1998) — this provides some limited information on the location of the bolide and may be used to place constraints on its ablated mass.

Recently, weather radars (*Fries and Fries*, 2010) have been shown to be effective at detecting the debris plume from a bolide in the form of material in dark flight. These Doppler radars are able to detect macroscopic-sized fragments as well as finer dust drifting to Earth, typically at altitudes  $<$ 20 km (and in some instances at altitudes as low as just a few kilometers) after a bolide. They provide a means to confirm the deposition of meteorites on the ground together with fall location as they probe the terminal stages of dark flight.

### 3.2. Data Analysis

Once analyzed, optical data from fireball networks provides fireball trajectories, velocities, and light curves. The first very important step is astrometric reduction of wide-field or all-sky images (*Borovička et al.*, 1995). In most cases, bolide trajectories can be considered to be straight. The triangulation from two or more stations can be done either with the plane intersection method (*Ceplecha*, 1987) or the straight least-squares method (*Borovička*, 1990; *Gural*, 2012). The trajectories of long-duration, nearly horizontal bolides are nonnegligibly curved by Earth's gravity and special procedures are needed to reconstruct the trajectories of such so-called Earth-grazing fireballs (*Ceplecha*, 1979; *Borovička and Ceplecha*, 1992).

To measure bolide velocities on long-exposure photographic records, the cameras are equipped with a shutter periodically interrupting the exposure (with frequencies on the order of 10 Hz). By measuring the positions of the shutter breaks or individual video images, the fireball position (length along the trajectory or height) as a function of time is obtained. This information forms the basis of dynamic analysis, i.e., determination of bolide velocity and deceleration as a function of time and, consequently, other parameters such as ablation coefficient and *dynamic mass* of the meteoroid. The parameters can be obtained by fitting the integral solution of the drag and mass loss equations first obtained by *Pecina and Ceplecha* (1983). The method assumes a single-body meteoroid, i.e., no fragmentation. The method of *Gritsevich* (2009) is an equivalent treatment. In reality, however, fragmentation is a very common and important process. A more general method allowing the determination of one fragmentation point from bolide dynamics was developed by *Ceplecha et al.* (1993). For a review, see *Ceplecha et al.* (1998).

Another method of estimating the meteoroid mass is derived from the bolide light curve. The mass obtained by the integration of the luminosity equation is called the photometric mass. The crucial parameter is the luminous efficiency, which unfortunately is not well known. It has been discussed in a number of papers (e.g., *Ceplecha and*

*McCrosky, 1976; Pecina and Ceplecha, 1983; Hill et al., 2005; ReVelle and Ceplecha, 2001; Weryk and Brown, 2013*). In general, it appears that luminous efficiency increases with meteoroid velocity and mass. It is also expected on theoretical grounds that the luminous efficiency depends on height of flight and on flow regime. These dependencies are not as important for large meteoroids because they affect mostly the beginning of the bolide. Theoretical estimates of luminous efficiency were published by *Golub' et al.* (1996) and *Nemtchinov et al.* (1997).

In addition to the differential luminous efficiency found in the luminosity equation, an integral luminous efficiency is defined as the ratio of the total energy radiated by the bolide to its initial kinetic energy. The integral luminous efficiency also increases with meteoroid energy (*Brown et al.*, 2002a). To give a rough value, in a typical meteorite fall (velocity  $\sim 15 \text{ km s}^{-1}$ , initial mass  $\sim 100 \text{ kg}$ ), both integral and differential luminous efficiency of large fragments are about 5%.

A major issue that is not explainable by uncertainties in the luminous efficiency is the large difference found between the dynamic and photometric masses of meteoroids. The underlying physical reason for these order-of-magnitude disparities is meteoroid fragmentation, which was not properly taken into account in early treatments. To obtain self-consistent meteoroid mass and other properties of the meteoroid, modeling its atmospheric flight including fragmentation using both dynamic and photometric data (and, if possible, other data as well such as direct observation of fragments) is desirable. One such attempt was done by *Ceplecha and ReVelle* (2005). A somewhat different approach was used by *Borovička et al.* (2013a) when analyzing the Košice meteorite fall.

Besides optical data, the energy of the fireball can also be estimated from acoustic data. The information available for acoustic energy estimation is the pressure amplitude and dominant period of the pressure waveform from infrasound measurements. Due to the complex, changing nature of the atmosphere, it is not generally possible to theoretically determine initial source energy from infrasound measurements alone. Instead, empirical estimates are made using calibrations from explosive sources with known energy. As pressure amplitude is most modified in atmospheric propagation, the signal period tends to be most robust in estimating source energy. Using data derived from simultaneous infrasound and satellite measurements of bolides, *Ens et al.* (2012) found that bolide source energies  $E$  (in tons of TNT equivalent energy) could be related to average infrasound periods (in seconds) via  $E = 3.16\tau^{3.75}$ .

These bolide-specific energy relations are nearly identical to those derived from nuclear weapon tests. These period energy estimates become less certain at small energies (small periods) and more reliable as more stations are used to provide average period estimates. Amplitude-based yields are similarly calibrated from ground explosions and bolides, but are less robust, show wide scatter, and are highly sensitive to stratospheric winds. Amplitude-based yields become increasingly unreliable at large ranges or large source ener-

gies (above  $\sim 1 \text{ kt}$  TNT). Hence at short ranges and small energies, amplitude-based energy estimates are preferred, while for large ranges and large energies periods become more reliable.

The bolide observations can also be used to estimate the terminal mass, i.e., the mass of fragments that survived the flight and landed as meteorites (if any). The mass of an individual well-observed fragment can be computed from the atmospheric density,  $\rho$ , velocity,  $v$ , and deceleration,  $dv/dt$ , at the end of the luminous trajectory using the drag equation

$$m_E = (\Gamma A)^3 \rho^3 v^6 \delta^{-2} (dv/dt)^{-3}$$

where the drag coefficient,  $\Gamma$ , shape factor,  $A$ , and meteorite density,  $\delta$ , must be assumed (for a sphere,  $A = 1.21$ ;  $\Gamma \sim 0.6$  at the relevant heights and velocities). The landing point can be estimated by the numerical integration of the objects motion during dark flight (*Ceplecha, 1987*) without knowing its mass — just the direction of flight, and last observed height, velocity, and deceleration are needed as initial values. The largest uncertainty in this landing point estimate arises from the error in the deceleration (which is not observed directly but must be computed from the observed length as a function of time over some part of the trajectory) and also in the uncertainty in the high-altitude winds, which can shift the meteorite by many kilometers (e.g., *Spurný et al.*, 2012a). Note, however, that in some cases small, not directly observable fragments can form the bulk of the fall mass (e.g., *Borovička et al.*, 2013a; *Spurný et al.*, 2014). Their presence may be revealed when modeling the light curve. Large numbers of meteorites make the recovery more likely, even if they are small ( $\ll 1 \text{ kg}$ ).

Meteorites usually represent only a small part of the initial mass of the meteoroid. In some cases quite a large fraction of the total mass is deposited in the atmosphere in the form of micrometer-sized dust particles that avoid complete vaporization (*Klekociuk et al.*, 2005; *Borovička and Charvát*, 2009). This dust slowly sediments out of the atmosphere over timescales of months and can spread over large geographical areas (*Gorkavyi et al.*, 2013). In addition, part of the vaporized material may recondense, forming nanometer-sized meteoric smoke (*Borovička and Charvát*, 2009) that is distributed globally (*Megner et al.*, 2008).

Early data from fireball networks showed that there are enormous differences in fireball end heights even if the initial conditions (velocity, mass, slope of the trajectory) are similar. This is most readily interpreted as differences in physical strength among meteoroids within the fireball population. On this basis, *Ceplecha and McCrosky* (1976) created the PE criterion (which derives from the symbol  $\rho_E$ , representing the atmospheric mass density at the end point of the fireball) and classified bolides into four types based on physical strength: namely, types I, II, IIIA, and IIIB. A typical meteorite-dropping bolide, which *a priori* is expected to be near the high end of all meteoroid physical strengths, is of type I and was associated by *Ceplecha and McCrosky* (1976) with stony meteoroids of densities  $> 3000 \text{ kg m}^{-3}$ .

Meteoroid densities are not directly measurable from bolide data; nevertheless, statistical arguments led Ceplecha and McCrosky to the conclusion that type II bolides correspond to carbonaceous chondrites of densities  $\sim 2000 \text{ kg m}^{-3}$ , and IIIA and IIIB are two types of cometary material of densities of about  $750 \text{ kg m}^{-3}$  and  $300 \text{ kg m}^{-3}$ , respectively (Ceplecha, 1988). The latter two types disintegrate high in the atmosphere and do not provide meteorites.

The bolide end height is easily measurable and the PE criterion is still used today. A complementary method of classification uses the apparent ablation coefficient of the fireball. It is obtained by fitting the bolide dynamics without considering fragmentation. Typical values are 0.014, 0.042, 0.1, and  $0.21 \text{ s}^2 \text{ km}^{-2}$  (or  $\text{kg MJ}^{-1}$ ) for fireball types I, II, IIIA, and IIIB, respectively (Ceplecha, 1988; Ceplecha *et al.*, 1998). However, as shown by Ceplecha and ReVelle (2005), if fragmentation is taken into account, the obtained *intrinsic ablation coefficient* is nearly the same for all four types and is quite low, about  $0.005 \text{ s}^2 \text{ km}^{-2}$ . This suggests that the composition of the material is similar in all cases (mostly silicates) and the main differences are in the bulk density, porosity, and mechanical strength, which determines the degree of meteoroid fragmentation. Note that iron meteoroids are not considered in this scheme, since they are quite rare and we do not have enough bolide data to characterize them as a population. In fact, iron meteoroids are not easily recognizable without spectral observation or recovered meteorites. They have a higher density than stony meteoroids ( $\sim 7800 \text{ kg m}^{-3}$ ) and probably also have a larger intrinsic ablation coefficient because of lower melting temperature and higher thermal conductivity (ReVelle and Ceplecha, 1994).

Finally, if discrete fragmentation points are identified on the fireball trajectory, the dynamic pressure acting on the meteoroid at that point can be used to classify the meteoroid. The fragile IIIB bodies often disrupt catastrophically at pressures of several to several tens of kilopascals accompanied by conspicuous flares (Borovička and Spurný, 1996; Borovička *et al.*, 2007; Madiedo *et al.*, 2014a). The type I bodies usually fragment into macroscopic pieces, often several times consecutively, at pressures from a few tenths to a few megapascals (Ceplecha *et al.*, 1993; Popova *et al.*, 2011).

The heliocentric orbit of the meteoroid can be computed from the time of entry, direction of flight (radian coordinates), and velocity. The corrections to Earth gravity and Earth rotation must be applied. The corrected radiant and velocity are called *geocentric*. An analytical method of orbit computation was presented by Ceplecha (1987). Clark and Wiegert (2011) presented a computationally more demanding numerical method and showed that Ceplecha's formulation remains valid except in rare particular cases.

#### 4. METEORITE ANALYSES RELEVANT TO FIREBALL STUDIES

Meteorites, when recovered, are subject to detailed mineralogical, chemical, physical, and isotopic analyses in the

laboratory. Some of them are directly relevant to fireball studies because they provide either independent estimates of some parameters or supplementary information.

In interplanetary space, meteoroids are bombarded by energetic particles of solar and galactic cosmic rays. The interaction of cosmic rays with atoms in the meteoroid leads to the formation of atomic nuclei that are otherwise only rare or absent in the meteoric material, namely noble gases and short-lived radionuclides (Verchovsky and Sephton, 2005; Eugster *et al.*, 2006). Cosmic rays penetrate a few meters inside the meteoroid. The measurement of the concentration of selected nuclides, in particular  $^{60}\text{Co}$ ,  $^{10}\text{Be}$ ,  $^{21}\text{Ne}$ , and  $^{22}\text{Ne}$ , can be used to estimate the pre-atmospheric radius of the meteoroid and the depth of the measured sample inside the meteoroid. Note, however, that the calculations are model dependent and rely on derived nuclide production rates (Leya and Masarik, 2009). The correspondence with the fireball-determined pre-atmospheric mass of the meteoroid is not always good (Popova *et al.*, 2011).

The cosmogenic nuclides can be also used to estimate the *cosmic-ray exposure* (CRE) age of the meteoroid. This is the time for which the meteoroid was exposed to cosmic rays, i.e., the time elapsed since the meteoroid was excavated from a deeper depth in its parent body. Lunar meteorites and carbonaceous chondrites have the shortest CRE ages (about 1 m.y. on average), while the CRE ages of iron meteorites are the longest (hundreds of million years) (see Eugster *et al.*, 2006).

The measurement of physical properties of meteorites is also important for modeling the meteoroid flight in the atmosphere. Densities and porosities of meteorites of various types were published in a series of papers (Macke *et al.*, 2011, and references therein). Thermal conductivities (Opeil *et al.*, 2012) and heat capacities (Consolmagno *et al.*, 2013) were also measured. Other measurements of these quantities were obtained by Beech *et al.* (2009) and their application to meteor physics was discussed. The measurements of tensile and compressive strengths of meteorites are still rare because a destructive analysis is needed. Published values were compiled by Popova *et al.* (2011) and Kimberley and Ramesh (2011).

#### 5. INSTRUMENTALLY OBSERVED METEORITE FALLS

Instrumental observations of fireballs that produce meteorite falls and finds are of great scientific interest and importance because meteorites provide us with a surviving physical record of the formation of our solar system, and a direct link to their parent bodies. But most meteorites are also unique — as geological materials — in that they come with virtually no spatial context to aid us in interpreting that record. Reliable orbital information for meteorite falls is known for only 22 cases. This is a tiny fraction of the tens of thousands of meteorites that are known. For this reason, every new fireball with precise orbital data that produces a meteorite gives us invaluable information.

Similarly important is the study of processes accompanying the atmospheric flight of the meteoroid producing a meteorite fall. From every new instrumentally documented fall we learn much to help refine our methods and models. On the other hand, the known properties of the meteorite, such as density, mass, shape, composition, structure, etc., facilitate reverse calibration of other data from fireballs that do not produce meteorites. This provides information on the physical properties of meteoroids not likely contained in our meteorite collections.

Basic data about all instrumentally documented meteorite falls (22 cases so far) are shown in Tables 1–3, where details about their orbital data, atmospheric trajectory data, and meteorite data are collected. When comparing the data, it must be realized that the data were obtained under various circumstances (day/night, different ranges to the bolide) and by widely different techniques. The techniques are listed in the last column of Table 1. Only in a minority of cases (eight) was the fireball trajectory fully determined from professional photographic or video networks aimed at fireball observations. In seven cases, only casual videos and photographs were available. In four cases, a combination of the two or video cameras aimed at fainter meteors were used. Tagish Lake and Almahata Sitta fireballs were not imaged in flight from the ground at all; instead, satellite data and dust cloud images were used. In the case of Almahata Sitta, the orbit was precisely known from pre-impact observation of the meteoroid. To some extent the atmospheric trajectory could be determined from that data as well.

It is difficult to link specific meteorites with individual parent asteroids with some certainty. The orbit measured for any particular meteorite-producing fireball is heavily evolved from the original orbit of the parent asteroid. As a result, linking individual fireballs with specific asteroids is generally not possible. Rather, classes of meteorites and source regions in the main asteroid belt can be statistically associated using the orbit distribution of many meteorites and models of main-belt to near-Earth asteroid (NEA) delivery (*Bottke et al.*, 2002a).

We tried to evaluate the quality of various aspects of fireball data in the thirteenth column of Table 1. The trajectory (direction of flight, geographical coordinates, heights), dynamics (deceleration along trajectory), photometry (absolute brightness, shape of the light curve), and heliocentric orbit (dependent on the precision of the radiant, initial velocity, and time of the fireball) were evaluated on scale of 1–5 (1– means between 1 and 2, etc.). Overall, Tagish Lake, Buzzard Coulee, and Sutter’s Mill have less-reliable data.

The number of digits for orbital elements in Table 1 is given so that the published error is on the last digit. Most orbits are Apollo-type; only one is an Aten-type. The inclinations are mostly low (the median value is about 5°) but go up to 32°. All aphelia lie within the orbit of Jupiter, although the Tisserand parameters ( $T_J$ ) of Maribo and Sutter’s Mill are lower than 3. These two fireballs had the largest entry velocity ( $V_\infty$  in Table 2). The other values given in Table 2

are the observed terminal velocity ( $V_E$ ), the best estimate of the initial mass of the meteoroid ( $m_\infty$ ), the maximal absolute magnitude of the fireball ( $M_{\max}$ ), the slope of the trajectory (the slope is changing along the trajectory due to Earth’s curvature, so only rough values are given), the observed beginning height ( $H_B$ ), the height of maximum brightness ( $H_{\max}$ ), the terminal height ( $H_E$ ), the total length of the trajectory ( $L$ ); the duration of the fireball ( $T$ ), the total energy ( $E$ ) in kilotonnes of TNT (1 kt TNT =  $4.185 \times 10^{12}$  J), and the maximal encountered dynamic pressure ( $P_{\max}$ ). The observed beginnings of the fireballs (and thus also the lengths and durations) strongly depend on the technique and, in the case of casual records, also on pure chance. We therefore also list in some cases values from visual observations. The terminal heights are affected by observation effects to a lesser extent because the drop of brightness at the end is usually steeper.

It can be seen that meteorites were observed to fall from meteoroids of a wide range of masses, causing fireballs that are different by orders of magnitude in terms of energy and brightness. At the lower end, there were meteoroids of initial masses of only a few dozens of kilograms causing fireballs of absolute magnitude of about –10 or slightly more. Some meteorite falls were produced by large (>meter-sized) meteoroids associated with superbolide events, which occur globally every two weeks (*Brown et al.*, 2002a, 2013a). As a result, only a very small number of these events have detailed atmospheric flight observed. Our sample includes several superbolides with good dynamic and photometric data (such as Benešov, Košice, and Chelyabinsk). In these instances we can obtain insight into the internal structure of the pre-atmospheric meteoroid, for comparison with the physical structure of asteroids as determined from other kinds of observations. One of the measurable values is the mechanical strength expressed by the dynamic pressure at fragmentation. The enlarged sample confirms the conclusions of *Popova et al.* (2011) about the low strengths of interplanetary meteoroids and small asteroids. The relatively large value for Chelyabinsk (18 MPa) concerns only a very minor part of the body. The majority of the material was, in fact, destroyed under 1–5 MPa (*Borovička et al.*, 2013b).

Data on types and masses of recovered meteorites are compiled in Table 3. Some of the large meteoroids disrupted heavily in the atmosphere and produced large numbers of small meteorites. This was the case for not only all three carbonaceous chondrite meteorites (which were made of relatively weak rock) and two mineralogically heterogeneous bodies (Almahata Sitta and Benešov), but also for ordinary chondrite bodies like Košice. The opposite example is Carancas, discussed in the next section. But there are bodies also in our sample that did not fragment very heavily (e.g., Morávka, Příbram, and, in particular, Neuschwanstein). Chelyabinsk fragmented extensively; nevertheless, one large (600 kg) piece survived intact to the ground.

In the next section, we discuss in greater detail some particularly notable meteorite falls that were caused by large meteoroids.

TABLE 1. Instrumentally observed meteorite falls — Orbital data.

Name	Geocentric Radiant $\alpha_g$ (deg)	Radiant $\delta_g$ (deg)	$V_g$ (km s <sup>-1</sup> )	a (AU)	e	q (AU)	Q (AU)	$\omega$ (deg)	$\Omega$ (deg)	i (deg)	T <sub>j</sub>	Quality* T/D/P/O	Techniques†
Příbram	192.338	17.467	17.431	2.401	0.6711	0.78951	4.012	241.750	17.7915	10.482	3.16	1, 2-, 3, 1	P
Lost City	315.0	39.1	9.2	1.66	0.417	0.967	2.35	161.0	283.8	12.0	4.14	1, 1, 1-, 2	P
Innisfree	6.66	66.21	9.4	1.872	0.4732	0.986	2.758	177.97	317.52	12.27	3.81	1, 1-, 1, 1	P
Benesov	227.617	39.909	18.081	2.483	0.6274	0.92515	4.040	218.370	47.001	23.981	3.08	1, 1, 1-, 1	P
Peekskill	209.0	-29.3	10.1	1.49	0.41	0.886	2.10	308.0	17.030	4.9	4.47	2-, 3, 3-, 2-	CV, CP
Tagish Lake	90.4	29.6	11.3	1.98	0.55	0.884	3.08	224.4	297.901	2.0	3.66	3-, 4-, 4, 3-	CTP, I, S, Sa
Morávka	250.1	54.96	19.6	1.85	0.47	0.9823	2.71	203.5	46.258	32.2	3.70	2, 2, 3-, 2-	CV, I, S, Sa
Neuschwanstein	192.33	19.54	17.51	2.40	0.670	0.7929	4.01	241.20	16.827	11.41	3.16	1, 1-, 2, 1	P, S, I, PE
Park Forest	171.8	11.2	16.1	2.53	0.680	0.811	4.26	237.5	6.1156	3.2	3.08	2-, 4, 3, 3	CV, I, S, Sa
Villalbeto de la Peña	311.4	-18.0	12.9	2.3	0.63	0.860	3.7	132.3	283.671	0.0	3.30	2, 2-, 3-, 2-	CV, CP, I, S
Bunburra Rockhole	80.73	-14.21	6.743	0.8529	0.2427	0.6459	1.05991	210.04	297.595	8.95	6.88	1, 1, 1, 1	P, PE
Almahata Sitta	348.1	7.6	6.45	1.3082	0.31206	0.89906	1.7164	234.449	194.101	2.542	4.93	3-, 4-, 4-, 1*	I, Sa, T, CTP
Buzzard Coulee	290.1	77.0	14.2	1.25	0.2228	0.9612	1.53	211.3	238.937	25.0	5.04	3-, 4, 5, 3-	CV, I
Maribo	124.7	19.7	25.8	2.48	0.807	0.479	4.5	279.2	297.122	0.11	2.91	2-, 3, 2, 3	P, CV, R, PE
Jesenice	159.9	58.7	8.3	1.75	0.431	0.9965	2.51	190.5	19.196	9.6	4.01	2-, 3, 2-, 2-	P, V, PE, I, S
Grimsby	242.6	54.97	17.9	2.04	0.518	0.9817	3.09	159.9	182.956	28.1	3.50	1, 2, 1-, 1	V, I, R, RD
Košice	114.3	29.0	10.3	2.71	0.647	0.957	4.5	204.2	340.072	2.0	3.02	2-, 2-, 2, 3	CV, PE, I, S
Mason Gully	148.36	9.00	9.322	2.556	0.6158	0.98199	4.130	19.00	203.214	0.895	3.14	1, 1, 1, 1	P, PE
Križevci	131.22	19.53	14.46	1.544	0.521	0.7397	2.35	254.4	315.55	0.640	4.30	1-, 2, 2, 1-	P, PE, V
Sutter's Mill	24.0	12.7	26.0	2.59	0.824	0.456	4.7	77.8	32.77	2.4	2.81	3, 4, 4-, 3	CV, CP, S, RD
Novato	268.1	-48.9	8.21	2.09	0.526	0.9880	3.2	347.37	24.9414	5.5	3.56	2-, 2-, 3, 2	V, I, CP
Chehyabinsk	333.82	0.28	15.14	1.72	0.571	0.738	2.70	107.67	326.459	4.98	3.97	1-, 2, 2, 1-	CV, CP, I, S, Sa

\* Quality coefficient describes the achieved reliability in determination of the atmospheric trajectory (T), dynamics (D), light curve and photometry (P), and heliocentric orbit (O); 1 = best, 5 = worst.  
 † Instrumental techniques used for the data acquisition: P = dedicated photographic network, V = casual video, S = seismics, Sa = seismic, I = infrasound, T = telescope (pre-atmospheric observation of the meteoroid), RD = weather Doppler radar, CP = casual photograph, CTP = causal trail photograph.

\* The most precise orbit thanks to the pre-atmospheric observations; however, very limited precision in the atmospheric trajectory, dynamics, and photometry determination.

All angular orbital values are in J2000.0 equinox.

TABLE 2. Instrumentally observed meteorite falls — Bolide data.

Name	Date (UT) (yyyy/mm/dd)	Time* (UT)	$V_\infty$ (km s <sup>-1</sup> )	$V_E$ (km s <sup>-1</sup> )	$m_\infty$ (kg)	$M_{\max}$	Slope† (deg)	$H_B$ (km)	$H_{\max}$ (km)	$H_E$ (km)	L (km)	T (s)	E (kT)	$P_{\max}$ (MPa)
Příbram	1959/04/07	19:30:20	20.886	—	1300	-19	43	97.8	46	22/13§	111	5	0.07	>0.9
Lost City	1970/01/04	2:14	14.150	3.4	163	-11.6	38	85.9	31.7	107.9	8.9	0.004	2.8	
Innisfree	1977/02/06	2:17:38	14.54	2.7	51	-12.1	68	62.4	36	19.9	45.9	4.09	0.001	3.7
Benesov	1991/05/07	23:03:44	21.256	5.0	3500	-19.5	81	91.675	24.40	19.227	73.41	3.9	0.2	8.4
Peekskill	1992/10/09	23:48	14.72	5	10,000	-16	3	46.80§	—	34/30§	253/800§	20/45§	0.26	1.0
Tagish Lake	2000/01/18	16:43:42	15.8	9	56,000	-22	16	—	34.4	29	—	—	1.7	2.2
Morávka	2000/05/06	11:51:51	22.5	3.8	1500	-20	20	45.7/80§	—	21.2	69.3/168§	3.4	0.09	5
Neuschwanstein	2002/04/06	20:20:13.5	20.95	2.4	300	-17.2	49	84.95	21	16.04	90.6	5.3	0.016	10.9
Park Forest	2003/03/27	5:50:26	19.5	—	11,000	-21.7	61	82	29	<18	73	5	0.5	7.4
Villabeto de la Peña	2004/01/04	16:46:45	16.9	7.8	600	-18	29	47/85§	27.9	22.2	50/130§	9§	0.02	5.1
Bunburra Rockhole	2007/07/20	19:13:53.24	13.365	5.68	22	-9.6	31	62.83	36.3	29.59	64.65	5.68	0.0005	0.9
Almahata Sitta	2008/10/07	2:45:40	12.4	—	40,000	<-19.7	19	—	37	32.7	—	—	0.73	0.9
Buzzard Coulee	2008/11/21	0:26:40	18.0	—	8,000	—	66	81.3	—	17.6	69.6	4	0.31	—
Maribo	2009/01/17	19:08:32.73‡	28.3	—	1500	-19	31	112.4	37.1	30.5	158.0	6.5	0.14	3
Jesenice	2009/04/09	0:59:40.5	13.78	—	170	-15	59	88	26.4	18	82	6.6	0.004	3.9
Grimsby	2009/09/26	1:02:58.40	20.91	3.1	30	-14.8	55	100.5	39	19.6	94	6.04	0.002	3.6
Košice	2010/02/28	22:24:46.6	15.0	4.5	3500	-18	60	68.3	36	17.4	59	4.5	0.1	6
Mason Gully	2010/04/13	10:36:12.68‡	14.648	4.1	14	-10.5	54	83.46	35.78	23.84	73.76	5.97	0.0004	1.5
Križevci	2011/02/04	23:20:39.9	18.21	4.5	50	-13.7	65	98.10	31	21.81	84	5.3	0.002	3.6
Sutter's Mill	2012/04/22	14:51:12	28.6	19	40,000	-18.3	26	90.2	47.6	30.1	135	5	4	—
Novato	2012/10/18	2:44:29.9	13.67	—	80	-13.8	19	94.4	36	22¶	~220	~18	0.002	—
Chelyabinsk	2013/02/15	3:20:21	19.03	3.2	12 × 10 <sup>6</sup>	-28	18	95.1	30	12.6	272	17	500	18

\* Time of the beginning of the fireball unless otherwise noted.

† Angle between the trajectory and horizontal plane.

‡ Time of the fireball given for the maximum brightness of the fireball, which was reached in the short flare near the end of luminous trajectory.

§ Value from visual observations.

¶ Extrapolated value from noncalibrated image not used for the trajectory determination.

TABLE 3. Instrumentally observed meteorite falls—Meteorite data.

Name	Country*	Day/Night Fall†	No. of Meteorites	Meteorite Type(s)	Recovered Mass (kg)	Estimated Terminal Mass (kg)	Meteorite Coordinates‡	First Meteorite Recovery §	References¶
Příbram	CZE	N(E)	4 (5**)	H5	5.6 (~7**)	80	14.242 E 49.658 N	A	1, 13, 15
Lost City	USA	N(E)	4	H5	17.342	25	95.092 W 36.005 N	DS	2, 8, 19
Innisfree	CAN	N(E)	9	L5	4.58	4.9	111.337 W 53.415 N	DS	3, 4, 19
Benešov	CZE	N	4	LL3.5, H5, PA	0.0116	200–300†	14.632 E 49.766 N	DS	46, 7, 10, 5
Peekskill	USA	N(E)	1	H6	12.4	—	73.917 W 41.283 N	I	6, 9
Tagish Lake	CAN	T(M)	~500	C2	~10	1300	134.227 W 59.727 N	I	12, 11, 20, 47
Morávka	CZE	D	6	H5–6	1.40	100	18.538 E 49.592 N	I	14, 15
Neuschwanstein	DEU/AUT	N(E)	3	EL6	6.226	20	10.813 E 47.525 N	DS	13, 16
Park Forest	USA	N	>100	L5	~30	—	87.68 W 41.48 N	I	17
Villalbeto de la Peña	ESP	D(E)	36	L6	5.2	13	4.66 W 42.81 N	I	21, 18, 39
Bunburra Rockhole	AUS	N(M)	3	Euc-anom	0.339	1.1	129.19 E 31.35 S	DS	35, 22
Almahata Sitta (2008 TC <sub>3</sub> )	SDN	N(M)	>650	EL, EH, H, L, LL, CB, R Ure-Anom	~11	39	32.40 E 22.75 N	DS	23, 28, 24, 29, 44
Buzzard Coulee	CAN	N(E)	≥2500	H4	>50	—	109.85 W 53.00 N	TS	25, 27
Maribo	DNK	N(E)	1	CM2	0.026	~10	11.467 E 54.762 N	TS	38, 26, 34
Jesenice	SVN	N	3	L6	3.61	10–30	14.050 E 46.421 N	A	30, 31
Grimsby	CAN	N(E)	13	H4–6	0.215	~5	79.617 W 43.200 N	A	32
Košice	SVK	N	218	H5	11.28	500††	21.16 E 48.76 N	DS	40
Mason Gully	AUS	N(E)	1	H5	0.0245	1	128.215 E 30.275 S	DS	36, 49
Križevci	HRV	N	1	H6	0.291	0.3**	16.590 E 46.039 N	DS	48, 33
Sutter's Mill	USA	D	77	CM2	0.943	—	120.93 W 38.81 N	RD	37
Novato	USA	N(E)	6	L6	0.363	—	122.57 W 38.11 N	A	45
Chelyabinsk	RUS	D(M)	>1000	LL5	>730§§	~10,000§§	61.00 E 54.86 N	I	41, 42, 43

\* ISO 3166-1 alpha-3 code.

† D = day, N = night (dark sky), T = twilight, E = evening, M = morning.

‡ If more than one meteorite was recovered, the approximate middle of the strewn field is given.

§ Circumstances of the recovery of the first meteorite. DS = find from dedicated search based on detailed computation of trajectory and dark flight from instrumental records; TS = find from trial search based on rough analysis of visual and instrumental records; I = casual find independent of bolide observation; A = casual find after an alert was issued regarding a possible meteorite fall in the given area; RD = recovery based on analysis of the Doppler radar data.

¶ References to values in all three tables.

\*\* Including one lost meteorite.

†† Vast majority of terminal mass was in small gram-sized meteorites.

§§ Only one larger piece (~600 kg), otherwise mostly small meteorites.

¶¶ One very large piece (~600 kg), otherwise mostly small meteorites.

References: [1] Cephecha (1961); [2] McCrosky et al. (1971); [3] Halliday et al. (1978); [4] Halliday et al. (1981); [5] Brown et al. (1994); [6] Brown et al. (1994); [7] Borovička and Spurný (1996); [8] Cephecha (1996); [9] Cephecha et al. (1996); [10] Borovička et al. (1998); [11] Brown et al. (2000); [12] Brown et al. (2002b); [13] Spurný et al. (2003); [14] Borovička and Kalenda (2003); [15] Borovička and ReVelle (2005); [16] ReVelle et al. (2004); [17] Brown et al. (2004); [18] Lloreda et al. (2005); [19] Cephecha and ReVelle (2005); [20] Hildebrand et al. (2006); [21] Trigo-Rodríguez et al. (2006); [22] Bland et al. (2009); [23] Jenniskens et al. (2009); [24] Borovička and Cháryá (2009); [25] Hildebrand et al. (2009); [26] Keuer et al. (2009); [27] Milley (2010); [28] Bischoff et al. (2010); [29] Bischoff et al. (2010); [30] Spurný et al. (2010); [31] Bischoff et al. (2011); [32] Brown et al. (2011); [33] Segon et al. (2011); [34] Hauck et al. (2012); [35] Spurný et al. (2012a); [36] Spurný et al. (2012b); [37] Jenniskens et al. (2012); [38] Spurný et al. (2013); [39] Bischoff et al. (2013); [40] Borovička et al. (2013a); [41] Borovička et al. (2013b); [42] Brown et al. (2013); [43] Popova et al. (2013); [44] Horsmann and Bischoff (2014); [45] Jenniskens et al. (2014); [46] Spurný et al. (2014); [47] Cephecha (2007); [48] Borovička et al. (2015); [49] This work.

## 6. NOTABLE METEORITE-PRODUCING FIREBALLS

### 6.1. Almahata Sitta (2008 TC<sub>3</sub>) and Benešov: Heterogeneous Falls

The Almahata Sitta meteorite fall (*Jenniskens et al.*, 2009) is unique in many aspects. It was the first meteorite fall that was predicted in advance — still the only case of this kind. The corresponding meteoroid/asteroid, designed 2008 TC<sub>3</sub>, was discovered 19 hr before it entered the terrestrial atmosphere. During that time interval, numerous astrometric observations were made from various observatories around the world. Thanks to these data, a precise orbit was computed and the impact trajectory was predicted over the Nubian Desert in the Sudan with a precision of better than 1 km. Moreover, photometric and spectroscopic observations of 2008 TC<sub>3</sub> were also made and helped to characterize the body before the atmospheric entry.

There was not enough time to set up any fireball cameras in the region of impact. Consequently, available data for the actual fireball are scarce. Nevertheless, the data clearly showed that the meteoroid was a fragile body and disrupted relatively high in the atmosphere. In accordance with this, a large number (~600) of mostly small (0.2–379 g) meteorites were recovered, but no large meteorite was found. Quite surprisingly, the meteorites were of various mineralogical types. This fact completely changed our paradigm that one meteorite fall produces meteorites of one type and that (undifferentiated) asteroids have a certain mineralogical composition, although polymict meteorite breccias were previously known (*Bischoff et al.*, 2010).

*Shaddad et al.* (2010) described over 600 recovered meteorites. Their total mass was 10.7 kg; the individual masses ranged from 0.2 to 379 g. The locations of all meteorites were carefully documented but only a few of the meteorites were analyzed in detail. Of the classified meteorites, the majority were ureilites, i.e., a relatively rare type of achondrite. However, enstatite chondrites and ordinary chondrites were found as well. *Kohout et al.* (2010) measured magnetic susceptibility of 62 meteorites from that sample. In 25 cases, he found anomalous values suggesting that the meteorites are not ureilites. *Bischoff et al.* (2010) analyzed a different sample of 40 meteorites from undocumented locations within the Almahata Sitta strewn field and found many different types. The mineralogical measurements of 110 meteorites by various authors were summarized by *Horstmann and Bischoff* (2014). Of these, 75 were ureilites or ureilite-related, 28 were enstatite chondrites (both EH and EL), 5 were ordinary chondrites (H, L, LL), one was a carbonaceous chondrite (CB), and one was a previously unknown type of chondrite related to R chondrites. Such a variety of meteorite types within one fall is unprecedented. Naturally, the question arises if all meteorites were really part of 2008 TC<sub>3</sub> and did not come from unrelated meteorite fall(s) with overlapping strewn fields. The main arguments for common origin are as follows: (1) All meteorites are

similarly fresh looking. (2) There is no indication that the non-ureilitic meteorites were located in a specific part of the strewn field (*Shaddad et al.*, 2010). (3) The presence of short-lived radionuclides in two non-ureilitic meteorites is evidence for a recent fall, consistent with the association with 2008 TC<sub>3</sub> (*Bischoff et al.*, 2010). (4) The analysis of noble gases and radionuclides in two other non-ureilitic meteorites provided the same pre-atmospheric radius and the same CRE age (20 m.y.) as for ureilitic meteorites (*Meier et al.*, 2012). So, although not definitely proven, it is very likely that most, if not all, of the various meteorite types really belonged to the same fall and that 2008 TC<sub>3</sub> was therefore a highly heterogeneous body. Although the ureilitic lithology was prevailing, completely different lithologies were present as well. It is worth noting that none of the foreign lithologies was found to be directly embedded within the ureilitic meteorites. It therefore seems that the chondritic material was only loosely bound within the asteroid.

From the foregoing it may seem that asteroid 2008 TC<sub>3</sub> was a rubble pile, i.e., a conglomerate of rocks bound together only by mutual gravity. However, other data do not support that view. *Scheirich et al.* (2010) and *Kozubal et al.* (2011) determined the shape and rotation of 2008 TC<sub>3</sub> from pre-impact photometry. The asteroid was an elongated body with axial ratio of approximately 1:0.54:0.36. It was in an excited rotation state with period of rotation of 99.2 s and period of precession of 97.0 s. The absolute dimensions are uncertain due to uncertainties in albedo. The V-band albedo of selected meteorites was measured as  $0.046 \pm 0.005$  by *Jenniskens et al.* (2009) and as 0.11 by *Hiroi et al.* (2010). The asteroid dimensions can, in principle, be determined from its mass and density as well. The mass can be inferred from bolide energy, since the entry velocity is well known. The bolide energy was estimated as  $(6.7 \pm 2.1) \times 10^{12}$  J from infrasound detection in Kenya (*Jenniskens et al.*, 2009). The radiated energy measured by U.S. government sensors was  $4 \times 10^{11}$  J (*Jenniskens et al.*, 2009), which translates to a total energy  $(2.7\text{--}5.1) \times 10^{12}$  J, depending on the value of luminous efficiency (*Borovička and Charvát*, 2009). The densities of most of the 45 meteorites measured by *Shaddad et al.* (2010) were around  $2800 \text{ kg m}^{-3}$ , but values as high as  $3430 \text{ kg m}^{-3}$  and as low as  $1590 \text{ kg m}^{-3}$  were found. The bulk density of the asteroid could in principle be even lower if significant macroporosity was present. Combining the possible range of all values, *Kozubal et al.* (2011) concluded that the most probable mean size was 4.1 m, mass 50,000 kg, albedo 0.05, and bulk density  $1800 \text{ kg m}^{-3}$ . They did not use the shape model of *Scheirich et al.* (2010). *Kohout et al.* (2011) found a mean density of five Almahata Sitta ureilites of  $3100 \text{ kg m}^{-3}$ . Considering the higher albedo values of *Hiroi et al.* (2010) as more reliable and assuming significant macroporosity, they concluded that the mass of 2008 TC<sub>3</sub> was only between 8000 and 27,000 kg. *Welten et al.* (2010) estimated the radius × density on the basis of radionuclide measurements to  $3000 \pm 300 \text{ kg m}^{-2}$ . We consider the following parameters as the most likely: size  $6.6 \times 3.6 \times 2.4$  m, volume  $22 \text{ m}^3$ , mean radius 1.74 m, mass 40,000 kg, bulk density  $1800 \text{ kg m}^{-3}$ ,

porosity almost 50% [using grain density  $3500 \text{ kg m}^{-3}$  from *Kohout et al.* (2011)], albedo 0.049, bolide energy  $3.1 \times 10^{12} \text{ J}$ , and integral luminous efficiency 13%. This implies that the albedo of *Hiroi et al.* (2010) and the energy derived from infrasound estimates were overestimated. The higher albedo would lead to a smaller mass and thus an even higher conflict with infrasonic energy. On the other hand, if that energy were true, the resulting asteroid density would be too high in comparison with some of the meteorites, and considering the atmospheric behavior of the body or an unrealistically low albedo would be needed.

The fast rotation of 2008 TC<sub>3</sub> means that the centrifugal force at the surface exceeded self-gravity, and therefore 2008 TC<sub>3</sub> was not a classical rubble pile held together only by gravity. Nevertheless, as shown by *Sánchez and Scheeres* (2014), a cohesive strength of only 25 Pa would be sufficient to bind the body together. Such strength could be provided by van der Waals forces between constituent grains (*Sánchez and Scheeres*, 2014). However, such a small mechanical strength would lead to the disintegration of the body just at the beginning of atmospheric entry at heights above 100 km. The bolide observations by U.S. government sensors revealed that the bolide exhibited three flares; that in the middle was the brightest and occurred at a height of 37 km (*Jenniskens et al.*, 2009). The Meteosat satellite data confirmed the maximum at 37 km and revealed two earlier flares at 45 km and 53 km (*Borovička and Charvát*, 2009). Finally, the distribution of meteorites is consistent with their release at a height of 37 km (*Shaddad et al.*, 2010). So the major disruption of 2008 TC<sub>3</sub> occurred at a height of 37 km under the dynamic pressure 0.9 MPa. This pressure is within the lower range as compared to other bodies of similar sizes (see Table 2), confirming the fragile nature of 2008 TC<sub>3</sub>, but it is still much higher than the expected strength of rubble piles. The actual structure of this body remains unclear. In any case, the recovered meteorites of various physical and mineralogical properties represent only a tiny fraction of the original mass, namely the fraction that was the strongest. They were probably embedded within a matrix that mostly disappeared during atmospheric entry. The matrix could be similar to the meteorites with the lowest measured densities, i.e., the porous fine-grained ureilites (*Bischoff et al.*, 2010).

The reflectance spectrum of 2008 TC<sub>3</sub> was taken in the wavelength range 550–1000 nm (*Jenniskens et al.*, 2009). The spectrum was flat and featureless and 2008 TC<sub>3</sub> was classified as F type. *Jenniskens et al.* (2010) searched for asteroids of similar spectra. They were not able to identify an asteroid family as the source of 2008 TC<sub>3</sub>. A similar search was performed by *Gayon-Markt et al.* (2012), who also discussed the origin of 2008 TC<sub>3</sub> and concluded that it is highly improbable that the heterogeneous structure was formed by low-velocity impacts in the current asteroid belt. *Horstmann and Bischoff* (2014) proposed that the material was formed in the early solar system by a four-stage process: (1) heating and partial melting on the ureilite parent body (UPB), including basaltic magmatism; (2) an impact event that resulted in the catastrophic disruption of the UPB;

(3) rapid cooling of the released mantle material; and (4) reaccretion into smaller daughter asteroids, forming ureilitic “second-generation” asteroids. The foreign (chondritic) fragments were more likely incorporated into them at the fourth stage rather than by subsequent impacts. Finally, 2008 TC<sub>3</sub> separated from one of the second-generation ureilitic bodies at 20 Ma. More recently, *Goodrich et al.* (2015) argued that the proportion of foreign clasts in 2008 TC<sub>3</sub> was not larger than in other polymict ureilites and that the same selection of materials as in other polymict ureilites was present. They hypothesized that the immediate parent of 2008 TC<sub>3</sub> was also the immediate parent of all other ureilitic meteorites. In contrast to *Horstmann and Bischoff* (2014), *Goodrich et al.* (2015) considered it more likely that the foreign fragments were accreted by the 2008 TC<sub>3</sub> parent body over long periods of time.

Almahata Sitta is not the only heterogeneous meteorite fall. The second confirmed case is Benešov, a fall instrumentally observed and very well documented in 1991 (*Spurný*, 1994), including a rich bolide spectrum. The search for meteorites was unsuccessful at that time; nevertheless, several papers were devoted to the bolide analysis (e.g., *Borovička and Spurný*, 1996; *Borovička et al.*, 1998). In the spring of 2011, after a complete reanalysis of all available records (*Spurný et al.*, 2014), the meteorite search was resumed with a revised strategy — not looking for big pieces but for small ones produced in large amounts from the disruption at a height of 24 km. The new strategy was successful and four weathered meteorites with masses in the predicted range were found with metal detectors exactly in the predicted area (*Spurný et al.*, 2014). Surprisingly, one meteorite was an H chondrite, one was an LL chondrite, and one was an LL chondrite with an embedded achondritic clast (the fourth meteorite could not be classified because of its small size and weathering stage). The size and location of all four meteorites exactly in the predicted area for corresponding masses, the same degree of weathering and composition consistent with the bolide spectrum, and the extremely low probability of two coincidental falls in the given area means that all the meteorites almost certainly came from the Benešov bolide. The heterogeneous nature of the Benešov meteoroid is supported by its early separation into smaller bodies during atmospheric flight (*Borovička et al.*, 1998).

These findings can shed new light on some old meteorite finds. The Galim meteorite fall contained both LL and EH specimens (*Rubin*, 1997). Other examples of meteorites of different types found close to each other can be found in the Meteoritical Database, e.g., Hajmah (ureilite + L), Gao-Guenie (H + CR), and Markovka (H + L). These meteorites were traditionally classified separately, e.g., as Hajmah (a), Hajmah (b), but may in fact come from the same body. Of course, chance alignment in these non-observed falls is also possible. Studies of the surprisingly rich Franconia strewn field, which contains various meteorite types, concluded that they fell at various times (*Hutson et al.*, 2013). On the other hand, there are some meteorites containing foreign clasts on a microscopic scale. The most prominent example

is the polymict microbreccia Kaidun, which contains materials of many different meteorite types in millimeter-sized clasts (Zolensky and Ivanov, 2003). Other cases have been summarized by Bischoff *et al.* (2010).

## 6.2. Příbram and Neuschwanstein Meteorite Pair

The Příbram meteorite fall has a special status among instrumentally recorded falls. This is not only because of the fact that it was the first such case in history (it fell on April 7, 1959) and that it represents the first time that recovered meteorites were directly linked with asteroids, but also because it was the first time when the so-called dark flight (first use of this term, which was invented by Z. Ceplecha) was rigorously computed for individual meteorite trails seen on the photographs (Ceplecha, 1961). This method was crucial for the future recovery of several subsequent events and it also played a fundamental role in the recovery of the second predicted meteorite fall in Europe, Neuschwanstein. Coincidentally, this other extraordinary case actually increased the original significance of the historic Příbram fall. The spectacular Neuschwanstein bolide was recorded by the all-sky cameras of the EN over Austria and Germany exactly 43 years after the Příbram fall. Based on the analysis of EN photographic records, three meteorites of corresponding masses were found exactly in the predicted area (Spurný *et al.*, 2003). However, the uniqueness of this case is not in the successful recovery of meteorites, but in the fact that the heliocentric orbits of both Příbram and Neuschwanstein meteoroids were almost identical, with  $D_{SH} = 0.025$  (Fig. 4). Such close similarity of orbits for two independent meteorite falls with recovered meteorites is unknown among the other 20 meteorite falls having known orbits. Only in the case of Innisfree and Ridgedale (presumed fall) meteorite falls observed in the MROP Canadian fireball network (Halliday, 1987) has a similarly close orbital pair been observed; unfortunately, meteorites were found only for the Innisfree fall. Nevertheless, this case generated the idea of the existence of meteorite streams (Halliday *et al.*, 1990), a notion strongly supported by the unique orbital similarity of the Příbram–Neuschwanstein pair. On the other hand, Příbram and Neuschwanstein falls differ in meteorite composition (Příbram is H5 while Neuschwanstein is EL6) and in CRE ages (Příbram is 12 m.y. while Neuschwanstein is 48 m.y.). Therefore this case has generated wide discussion as to whether the apparent orbital connection between these two meteoroids is real (e.g., Tóth *et al.*, 2011) or only coincidental (Pauls and Gladman, 2005). This question is not yet reliably solved; it seems from other recent instrumental observed falls such as Almahata Sitta or Benešov that the compositional difference should not be a decisive argument against the Příbram and Neuschwanstein connection.

## 6.3. Carbonaceous Chondrites: The Weakest Meteorites

Three instrumentally recorded fireballs resulted in carbonaceous chondrite meteorite falls. These three falls (Tagish Lake,

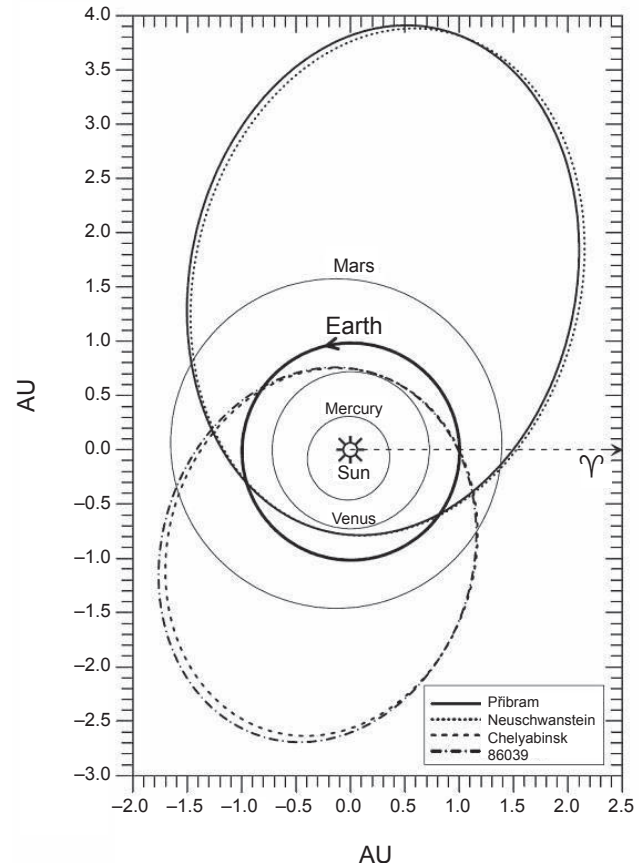


**Fig. 4.** The orbits of Příbram, Neuschwanstein, and Chelyabinsk meteorites and asteroid (86039) 1999 NC<sub>43</sub>, projected into the plane of ecliptic. The arrow with symbol points to vernal equinox. The orbital similarity of Příbram–Neuschwanstein and Chelyabinsk–1999 NC<sub>43</sub> is evident.

Maribo, and Sutter's Mill) have several common characteristics: They were all large (multi-meter-sized) initial objects and they all showed flight characteristics (early fragmentation, high end heights relative to their mass and speed) indicative of a very fragile structure. While the orbit for Tagish Lake (a C2 ungrouped unusual meteorite) is solidly asteroidal (with  $T_J = 3.7$ ), the orbits for Maribo and Sutter's Mill (both CM2 chondrites) are on the borderline between Jupiter-family comets and asteroids. Intriguingly, Maribo and Sutter's Mill have very similar orbits, suggesting both a common and relatively recent origin on the basis of short CRE ages (Jenniskens *et al.*, 2012). Moreover, these two meteorite falls appear to be associated with fireballs having initial speeds in excess of  $28 \text{ km s}^{-1}$ . This is substantially higher than the next fastest recovered fall (Morávka, at  $22.5 \text{ km s}^{-1}$ ). As surviving mass from ablation  $\propto \exp(-v^2)$ , even a small increase in initial speed result in large increases in ablation. This is even more remarkable as these are friable carbonaceous chondrites. The large size of the initial objects and the high altitude of the breakup allowing fragments to decelerate gradually appears to have been critical in survival of a small terminal mass in all three cases. For Tagish Lake, the estimated mass survival

fraction was <2% (*Hildebrand et al.*, 2006), while for Sutter's Mill it is <0.001% (*Jenniskens et al.*, 2012). While the orbits of Maribo and Sutter's Mill suggest a very recent, common origin, the CRE age of Sutter's Mill of 0.082 Ma (*Nishiizumi et al.*, 2014) places it in the 0.1–0.3-Ma CRE age grouplet of predominantly CM2 meteorites (*Caffee and Nishiizumi*, 1997), while the CRE age of Maribo at 0.8–1.4 Ma (*Haack et al.*, 2012) suggests they are not immediately related.

#### 6.4. Carancas: A Rare Monolithic Meteoroid

The Carancas meteorite fall occurred near noon local time on September 15, 2007, in the Andes Altiplano of Peru near the border with Bolivia. Remarkably, this fall produced an impact crater some 14 m in diameter, apparently the result of the hypersonic impact by a stony meteorite (*Tancredi et al.*, 2009). If the impact velocity is low, the size of the formed structure (impact pit/crater) is comparable to the impactor size (e.g., *Petaev*, 1992; *Mukhamednazarov*, 1999), whereas for high-velocity impacts the size of the crater is much larger than the impactor. The prevalence of low-velocity meteorite impacts emphasizes the ubiquity of fragmentation during ablation of stony meteoroids. This is a well-known feature of most meteorite-producing fireballs, which show breakup at altitudes indicating that the mean strength of the parent meteoroid is on the order of 0.1–1 MPa (*Popova et al.*, 2011). No optical recordings of the Carancas fireball were obtained, but airwaves from the fireball were recorded by an infrasound station located less than 100 km from the crater. From analysis of near-field infrasound, *Le Pichon et al.* (2008) and *Brown et al.* (2008) independently derived constraints on the trajectory of the associated fireball suggesting a steep (>45°) entry angle and radiant azimuth located to the east. Using the constraint that the orbit is unlikely to be transjovian and hence placing limits on the entry speed given the infrasonically estimated radiant, *Brown et al.* (2008) and *Borovička and Spurný* (2008) independently estimated that the associated meteoroid experienced >15 MPa ram pressure during flight and was initially most likely a few meters in size. Presuming that the crater formed because the meteoroid did not undergo significant fragmentation during flight (highly unusual for a stony meteoroid), this suggests the initial object was largely devoid of cracks and well described as a monolith. This result emphasizes the fact that meteoroid strengths and physical properties vary significantly, a conclusion well summarized as indicating there is no “average” meteoroid (e.g., *Ceplecha et al.*, 1998). The Carancas impact demonstrates that contrary to entry models, which predict that stony meteoroids require in excess of 10 MT of mass to produce high-velocity impact craters on the ground (*Bland and Artemieva*, 2006), in rare cases much smaller stony objects can impact Earth's surface hypersonically. As Carancas is the only known example of such a small stony meteorite producing a high-velocity impact crater, it is unclear how common strong (>10 MPa) monolithic meter-sized stony meteoroids are among the NEA population. The energy of formation of the crater was

estimated to be 2–3 t of TNT equivalent ( $10^{10}$  J) based on proximal blast effects (*Tancredi et al.*, 2009) as well as interpretation of the infrasonic signals (*Le Pichon et al.*, 2008; *Brown et al.*, 2008). The crater-forming impact generated a surface wave seismically detected some 50 km from the crater. Based on the estimated crater yield and equivalent seismic magnitude of the surface wave the impact coupling was approximately 0.1%, the first direct measure of crater seismic coupling from an impact (*Tancredi et al.*, 2009).

#### 6.5. Chelyabinsk: The Largest Well-Documented Impact

The Chelyabinsk meteorite fall, which occurred in Russia on February 15, 2013, was an event in a fundamentally different category than any other meteorite fall in recent history. It was preceded by an extraordinarily bright superbolide, brighter than the Sun, and accompanied by damaging blast wave. The analysis of the infrasonic, seismic, and satellite data showed that the total energy was ~500 kt TNT, i.e.,  $2 \times 10^{15}$  J (*Brown et al.*, 2013a; *Popova et al.*, 2013). This energy is ~30× larger than the energy of the Hiroshima atomic bomb. Although the explosion of an asteroid near the Tunguska River in Siberia in 1908 had much larger energy, estimated to be 5–20 Mt TNT (*Vasilyev*, 1998; *Boslough and Crawford*, 2008), no meteorites were recovered. Moreover, only limited data exist about the Tunguska event, which occurred over a very remote region. The Chelyabinsk event, on the other hand, was casually recorded by many video cameras and represented a unique opportunity to study the entry of a body larger than 10 m in size into the atmosphere. From the known energy, entry velocity, and density of the meteorites, the effective diameter of the Chelyabinsk was estimated to be 19 m and the mass was 12,000 t.

For such a large initial mass, the mass of material surviving as meteorites was quite small. There was only one large meteorite, which landed in Lake Chebarkul and was later recovered from the lake bottom, having a mass of ~600 kg (*Popova et al.*, 2013). All other meteorites were smaller than 30 kg. Only a few meteorites larger than 1 kg were recovered, although the number of small meteorites was enormous. The total recovered mass is unknown but was probably not larger than 2 t. The percentage of initial mass, which landed as macroscopic (>~1 cm) fragments, was much smaller than in a typical meteorite fall. It was also smaller than theory predicted for an impacting asteroid of such size (*Bland and Artemieva*, 2003, 2006).

The analysis of the atmospheric fragmentation revealed that severe destruction of the asteroid occurred between heights 39–30 km, under dynamic pressures of 1–5 MPa. At this early stage 95% of the mass was ablated and converted into dust and small (<1 kg) fragments. The remaining 5% of the initial mass continued ablating in the form of meter-sized boulders that fragmented again at lower heights, under pressures of 10–18 MPa. The only large piece (mass ~2 t) that emerged withstood a maximum pressure of 15 MPa (*Borovička et al.*, 2013b), comparable in strength to the

Carancas meteoroid, although representing less than 0.01% of the initial mass.

These fragmentation pressures are in the same range as found for smaller meteoroids based on observations of the associated fireballs (Popova et al., 2011). This confirms that there is no clear size-strength correlation among stony NEAs over the size range of centimeters to tens of meters. Since the actual strength and thus atmospheric behavior varies from case to case, we do not expect that Chelyabinsk will be representative of all bodies of similar size. Nevertheless, larger bodies are less decelerated, so they are subject to larger pressures when reaching denser atmospheric layers, which may lead to more destructive fragmentation.

Some asteroids are believed to be rubble piles/gravitational aggregates with a small strength of  $\sim 25$  Pa due to van der Waals forces between constituent grains (Sánchez and Scheeres, 2014). *A priori*, we expect rubble-pile meteoroids to separate into their constitutional parts at the very beginning of their atmospheric entry, under pressures of tens to hundreds of pascals. There is no evidence that such a separation occurred in the Chelyabinsk case. Nevertheless, significant loss of mass in the form of dust, probably from the surface layers, started early in flight at heights of  $>70$  km, as demonstrated by the extent of the dust trail deposited in the atmosphere (Borovička et al., 2013b; Popova et al., 2013).

The Chelyabinsk case also vividly demonstrates the damage potential of small (tens of meters) NEAs. Although no significant damage was caused by the ground impact, the cylindrical blast wave originating at heights of 25–35 km (Brown et al., 2013a) caused structural damage (one collapsed roof, about 10% of windows broken, many large doors of factory halls fallen). The flying glass and other objects injured 1600 people (Popova et al., 2013).

## 7. STATISTICS OF FIREBALLS AND SMALL ASTEROID IMPACTS

The number of meter-sized objects colliding with Earth as a function of energy has been estimated from several independent techniques, as shown in Fig. 5.

Halliday et al. (1996) used data from the MORP fireball network to construct a clear-sky survey, the only controlled flux survey of in-atmosphere fireball detections. The survey provided impact rates for meteoroids between a few tens of grams and a few tens of kilograms with a total area-time product roughly equivalent to one full day of global coverage. Notably, he found that roughly 40% of all fireballs in this size range were associated with meteor showers and that the proportion of asteroidal (as opposed to cometary) meteoroids increased toward the top of the size range in the survey, rising to 70% of all meteoroids having masses of a few kilograms. A pronounced change in the slope also occurs at masses of a few kilograms, and is probably associated with changes in meteoroid population/origin. The primary limitation of this survey is uncertainty in conversion of fireball brightness to meteoroid mass, although most masses are likely accurate to a factor of several.

Independent confirmation of these flux estimates has recently been provided by Suggs et al. (2014), who examined lunar impact flashes. Compared to Halliday et al. (1996), they find absolute flux numbers to be a factor of several lower in the kilogram range and the proportion of shower meteoroids to be  $>60\%$ , although most of their data are in

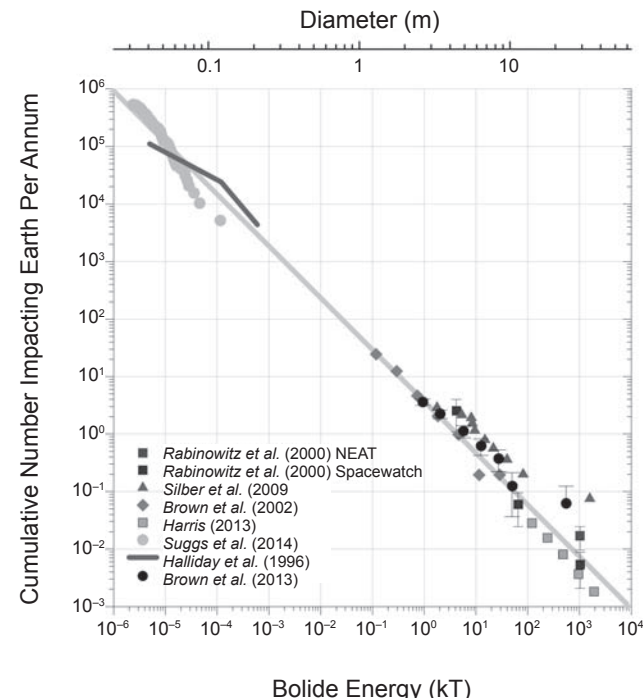


**Fig. 5.** Observational estimates of the terrestrial cumulative impact flux (ordinate) as a function of impact energy (abscissa). The light gray line cutting through the plot represents the power-law fit from Brown et al. (2002a) based on satellite impact flash observations (diamonds) approximately representing the interval 0.1–10 kT where data is most complete. The solid circles are an update to these data as given by Brown et al. (2013a) with better statistics at larger sizes for energies  $>1$  kT. Error bars (where shown) represent counting statistics only. These data consist of debiased estimates of the telescopic near-Earth asteroid population and assumed average impact probabilities as given by Rabinowitz et al. (2000) (dark gray squares) from the NEAT survey and Spacewatch (black squares) surveys, where diameters are determined assuming an albedo of 0.1. The LINEAR values at smaller sizes are normalized to early work that established the absolute population for diameters  $>100$  m (Stuart, 2001). Also shown are the estimated impact rate from infrasonic measurements of bolide airbursts from the Air Force Technical Application Centre (AFTAC) acoustic monitoring network as reanalyzed by Silber et al. (2009) (triangles). More recent telescopic debiased estimates from data compiled from all surveys by Harris (2013) are shown as light gray squares. The circles are the equivalent impact rate for Earth as determined from lunar flashes taking into account gravitational focusing (Suggs et al., 2014). Finally, the dark gray line at the top represents the impact rate from the photographic Meteorite Observation and Recovery Project (MORP) clear sky survey as described by Halliday et al. (1996).

the tens of grams mass range, below the level where the *Halliday et al.* (1996) survey is complete. A larger difference is apparent at the smallest sizes, but the uncertain mass scale in both surveys may be the cause.

Due to the rarity of meter-sized impacts (which occur roughly once every two weeks over the entire Earth), groundbased optical systems are not efficient at recording large enough numbers of such events to estimate fluxes. *Brown et al.* (2002a) used data from spacebased systems to detect impacts on a global scale of multi-meter-sized meteoroids over an eight-year period. Total impact energies were available for 300 events, although individual speeds were not. The resulting cumulative number of impacts per year ( $N$ ) as a function of energy ( $E$ ) — in units of kilotons of TNT =  $4.18 \times 10^{12}$  J — was found to follow a power law of the form  $N = 3.7 E^{-0.9}$ . This fit is appropriate to energies of 0.1–10 kt or diameters ranging from 1–6 m. An extension to this survey by *Brown et al.* (2013a) found similar values at these energies, but evidence for fluxes above the power-law curve at larger sizes. *Silber et al.* (2009) used acoustic records of impacts over a 14-year period to independently estimate fluxes in a similar size range. Their fluxes are systematically higher than the power-law curve from *Brown et al.* (2002a) but in agreement within uncertainty with the revised values at larger sizes (>6 m) from *Brown et al.* (2013a).

At sizes above 10 m diameter, telescopic population estimates are widely used to estimate flux. These estimates generally agree well with the extrapolated *Brown et al.* (2002a) power law, although are somewhat lower than the small-number statistic-limited estimates from bolide impacts at these larger sizes. The telescopic survey impact values have underlying uncertainties due to unknown population-wide collision probabilities at smaller sizes and poorly known albedo distribution of smaller NEAs. Given the widely differing sources of uncertainties across all the surveys shown in Fig. 5, the degree of agreement is good. We note that fluxes may also be derived from counting smaller lunar impact craters, and such estimates (e.g., *Werner et al.*, 2002) agree well with the telescopically determined flux curve (*Harris*, 2013). We chose not to include the estimated flux from small lunar craters due to the controversy surrounding the role and importance of secondary craters at such small sizes (e.g., *McEwan and Bierhaus*, 2006).

Orbital information from telescopic data is only available in quantity for NEAs larger than ~10 m. Unlike the population in the centimeter to tens of centimeter size range, NEA “streams” appear to be non-existent (*Schunová et al.*, 2012), emphasizing both the longer collisional lifetimes of larger NEAs and a probable lack of cometary material among multi-meter-sized bodies. Of the several dozen meter-class impacts recorded in Earth’s atmosphere with orbital and/or physical information about the strength of the impactor, the majority appear to be stony objects, with only a small number of probable, weak cometary bodies. Only 10% of this impacting population had Tisserand values below 3, emphasizing the likely dominance of asteroidal objects

at these larger sizes. Among the 22 meteorite-producing fireballs, eight appear to have been meter-sized or larger prior to impact. None of these had clearly cometary orbits, although Maribo and Sutter’s Mill (both CM2 carbonaceous chondrites) have orbits similar to 2P/Encke.

## 8. OPEN QUESTIONS

We have shown that bolide observations provide information about physical and chemical properties of asteroidal and cometary fragments in the decimeter to decameter size range; about the processes occurring during their interaction with the atmosphere, including potentially hazardous effects; and about the size-frequency distribution of such events. The obtained pre-impact heliocentric orbits enable the study of likely source regions of meteorites. Nevertheless, there are still open questions that need to be answered by further observations and modeling. In this final section of this chapter, we discuss some of these questions.

### 8.1. Meteorites from Comets

The question of whether some meteorites come from comets has been discussed for a long time (e.g., *Öpik*, 1968; *Padevět and Jakeš*, 1993; *Campins and Swindle*, 1998; *Lodders and Osborne*, 1999; *Gounelle et al.*, 2008). Some of the earlier studies were motivated by the apparent difficulty of transferring meteoroids from the asteroid belt to Earth, a problem that has now been solved [by orbital resonances and the Yarkovsky effect (see *Morbidelli et al.*, 2002; *Bottke et al.*, 2002b)]. Nevertheless, it was proposed that cometary nuclei may also contain — in addition to ice and dust — macroscopic boulders similar to carbonaceous asteroidal material, e.g., in the “icy-glue” model of *Gombosi and Houpis* (1986). Although other cometary models seem to be more probable (*Weissman and Lowry*, 2008), the presence of chondrule-like material in the samples of Comet 81P/Wild 2 returned by the Stardust mission (*Nakamura et al.*, 2008) suggests that material that formed meteorites is present in comets as well, at least in small samples.

None of the known meteorite orbits is clearly cometary, although the orbits of Maribo and possibly also Sutter’s Mill are close to the transition between cometary and asteroidal orbits. The carbonaceous chondrites, in particular types CI and CM, would be the primary candidates for cometary origin. These meteorites have been hydrated, while cometary dust is anhydrous, but *Gounelle et al.* (2008) argued that hydration can occur in cometary interiors. *Gounelle et al.* (2006) computed the orbit of the Orgueil CI1 meteorite, which fell in France in 1864, and concluded that the aphelion probably lay beyond the orbit of Jupiter. As determination of the orbit was based on visual observations and there is no direct velocity information available, the assumptions about the orbit cannot be completely trustworthy. *Trigo-Rodríguez et al.* (2009) observed a deeply penetrating fireball (no meteorites were found) and concluded that the orbit was similar to that

of Comet C/1919 Q2 Metcalf. Their paper, however, contains a numerical error in orbit computation. When corrected, the orbit is no more similar to the orbit of Comet Metcalf, although the aphelion still lies beyond Jupiter. However, the orbit is highly sensitive to the value of initial velocity, which was difficult to measure in that particular case. A small change of velocity will make the orbit completely asteroidal. So there remains no clear, unambiguous example of a cometary meteorite fall.

## 8.2. Meteorites from Meteor Showers

Meteor showers are caused by meteoroids of a common origin, in most cases cometary. For many showers, the meteorite survival is hampered by high entry velocity. Until recently,  $30 \text{ km s}^{-1}$  was considered a practical upper velocity limit for the occurrence of a meteorite fall (Ceplecha et al., 1998). The fact that the Maribo meteorite almost reached this limit and was made from a soft material suggests that the actual limit may be higher. Some of the low-velocity meteor showers, like the  $23.5 \text{ km s}^{-1}$  Draconids originating from Comet 21P/Giacobini-Zinner, contain, however, such fragile material that survival is excluded (Borovička et al., 2007). On the other hand, the Taurid meteor shower (entry speeds  $\sim 26\text{--}30 \text{ km s}^{-1}$ ) contains both fragile and strong bodies, some of which seem to be capable of producing meteorites (Brown et al., 2013b). The principal parent body of Taurids is supposed to be Comet 2P/Encke, a comet on a peculiar orbit completely inside Jupiter's orbit. Both Taurids and Comet 2P/Encke may be part of a broader "Taurid complex," which also contains several other showers and possibly several NEAs (see Jenniskens, 2006). Because of this it may be difficult in individual cases to link bolides directly with Comet 2P/Encke.

The Geminid shower, on the other hand, is well defined and is one of the most active annual showers. The entry speed is  $36 \text{ km s}^{-1}$  and the parent body is (3200) Phaethon, which orbits in the inner solar system and closely approaches the Sun ( $q = 0.14 \text{ AU}$ ,  $a = 1.27 \text{ AU}$ ,  $i = 22^\circ$ ). Recently it has been classified as an active asteroid (Jewitt, 2012; Jewitt et al., 2013). Based on the reflectance spectroscopy, asteroid (2) Pallas was identified as the likely parent body of Phaethon (de León et al., 2010). Geminid meteoroids have been known to be relatively dense and strong (e.g., Babadzhanov, 2002; Brown et al., 2013b), but only recently has it been demonstrated that a meteorite-dropping Geminid could occur, although the meteorite was not found (Spurný and Borovička, 2013; Spurný et al., in preparation). Madiedo et al. (2013b) presented similar observations concerning Geminid meteorite survival, but their data were less robust. The recovery of a meteorite originating from Phaethon would undoubtedly be a major milestone.

## 8.3. Meteorite Streams

The very close similarity of orbits of the Příbram and Neuschwanstein meteorites (Spurný et al., 2003) suggested

that they may have a common origin and be part of a meteorite stream. A similar pairing was proposed earlier for the Inisfree meteorite and the Ridgedale bolide (Halliday, 1987). The idea of meteorite streams was also discussed from another perspective by Lipschutz et al. (1997). Meteorite streams are potentially formed by asteroidal collisions. The orbit of Chelyabinsk meteorites was found to be similar to the orbit of asteroid (86039) 1999 NC<sub>43</sub>, suggesting that the Chelyabinsk body could have been ejected from 1999 NC<sub>43</sub> by a collision (Borovička et al., 2013b). In that case, a meteorite stream could exist in Chelyabinsk orbit. However, the typical decoherence time of meteoroid streams in the near-Earth region is only  $10^4\text{--}10^5 \text{ yr}$  (Pauls and Gladman, 2005), while the estimated collisional lifetime of asteroids is much longer (Bottke et al., 2005). Meteorite streams should be therefore rare, although some may be expected to exist (Jones and Williams, 2008). In the Příbram-Neuschwanstein case, the search for a related shower of fainter meteors was negative (Koten et al., 2014), implying that the stream, if it exists, contains only large bodies. For Chelyabinsk, the reflectance spectra of the meteorites and 1999 NC<sub>43</sub> do not match well, so the association seems to be unlikely (Reddy et al., 2015). Direct evidence of a meteorite stream or an association of a meteorite with its immediate parent body is therefore still missing.

Near-Earth asteroids have been also associated with (often unconvincingly) meteor showers or individual fireballs, not necessarily meteorite dropping (e.g., Babadzhanov et al., 2012; Madiedo et al., 2014b, and references therein). If some of these associations are real, they may indicate that the respective NEAs are in fact extinct comets and the stream was formed by cometary activity.

## 8.4. Structure of Meteoroids and Details of Their Interaction with the Atmosphere

The internal structure of meteoroids and their bulk densities are still difficult to infer from bolide observation. Data interpretation is complicated by the fact that the values of luminous efficiencies are not reliably known and the process of meteoroid ablation and fragmentation is not understood in detail. In particular, the structure and frequency of mixed-type meteoroids like Almahata Sitta and Benešov is unknown. There are also unexplained phenomena like periodic variations and high-frequency flickering on fireball light curves (Spurný and Ceplecha, 2008) (see also Fig. 3), large lateral velocities of fragments (Borovička and Kalenda, 2003; Borovička et al., 2013b; Stokan and Campbell-Brown, 2014), and jet-like features on fireball images at high altitudes (Spurný et al., 2000).

**Acknowledgments.** This work was supported by grant no. P209/11/1382 from the Grantová agentura České republiky (GAČR), Praemium Academiae of the Czech Academy of Sciences, the Czech institutional project RVO:67985815, NASA cooperative agreement NNX11AB76A, the Natural Sciences and Engineering Research Council of Canada, and the Canada Research Chairs program.

## REFERENCES

- Artemieva N. A. and Shuvalov V. V. (2001) Motion of a fragmented meteoroid through the planetary atmosphere. *J. Geophys. Res.*, **106**, 3297–3310.
- Babadzhanov P. B. (2002) Fragmentation and densities of meteoroids. *Astron. Astrophys.*, **384**, 317–321.
- Babadzhanov P. B., Williams I. P., and Kokhirova G. I. (2012) Near-Earth object 2004CK39 and its associated meteor showers. *Mon. Not. R. Astron. Soc.*, **420**, 2546–2550.
- Baldwin B. and Sheaffer Y. (1971) Ablation and breakup of large meteoroids during atmospheric entry. *J. Geophys. Res.*, **76**, 4653–4668.
- Beech M., Coulson I. M., Nie W., and McCausland P. (2009) The thermal and physical characteristics of the Gao-Guenie (H5) meteorite. *Planet. Space Sci.*, **57**, 764–770.
- Biberman L. M., Bronin S. Y., and Brykin M. V. (1980) Moving of a blunt body through the dense atmosphere under conditions of severe aerodynamic heating and ablation. *Acta Astronaut.*, **7**, 53–65.
- Bischoff A., Horstmann M., Pack A., Laubenstein M., and Haberer S. (2010) Asteroid 2008 TC3 — Almahata Sitta: A spectacular breccia containing many different ureilitic and chondritic lithologies. *Meteoritics & Planet. Sci.*, **47**, 1638–1656.
- Bischoff A., Jersek M., Grau T., Mirtic B., Ott U., Kučera J., Horstmann M., Laubenstein M., Herrmann S., Řanda Z., Weber M., and Heusser G. (2011) Jesenice — A new meteorite fall from Slovenia. *Meteoritics & Planet. Sci.*, **46**, 793–804.
- Bischoff A., Dyl K. A., Horstmann M., Ziegler K., Wimmer K., and Young E. D. (2013) Reclassification of Villalbeto de la Peña — Occurrence of a winonaite-related fragment in a hydrothermally metamorphosed polymict L-chondritic breccia. *Meteoritics & Planet. Sci.*, **48**, 628–640.
- Bland P. A. and Artiemeva N. A. (2003) Efficient disruption of small asteroids by Earth's atmosphere. *Nature*, **424**, 288–291.
- Bland P. A. and Artiemeva N. (2006) The rate of small impacts on Earth. *Meteoritics & Planet. Sci.*, **41**, 607–631.
- Bland P. A. and 17 colleagues (2009) An anomalous basaltic meteorite from the innermost main belt. *Science*, **325**, 1525–1527.
- Bland P. A., Spurný P., Bevan A. W. R., Howard K. T., Towner M. C., Benedix G. K., Greenwood R. C., Shrbený L., Franchi I. A., Deacon G., Borovička J., Ceplecha Z., Vaughan D., and Hough R. M. (2012) The Australian Desert Fireball Network: A new era for planetary science. *Aust. J. Earth Sci.*, **59**, 177–187.
- Borovička J. (1990) The comparison of two methods of determining meteor trajectories from photographs. *Bull. Astron. Inst. Czech.*, **41**, 391–396.
- Borovička J. (1993) A fireball spectrum analysis. *Astron. Astrophys.*, **279**, 627–645.
- Borovička J. (1994a) Two components in meteor spectra. *Planet. Space Sci.*, **42**, 145–150.
- Borovička J. (1994b) Line identifications in a fireball spectrum. *Astron. Astrophys. Suppl.*, **103**, 83–96.
- Borovička J. (2005) Spectral investigation of two asteroidal fireballs. *Earth Moon Planets*, **97**, 279–293.
- Borovička J. (2014) The analysis of casual video records of fireballs. In *Proceedings of the International Meteor Conference, Poznań, Poland August 22–25, 2013* (M. Gyssens et al., eds.), pp. 101–105. International Meteor Organization, Mechelen, Belgium.
- Borovička J. and Ceplecha Z. (1992) Earth-grazing fireball of October 13, 1990. *Astron. Astrophys.*, **257**, 323–328.
- Borovička J. and Charvát Z. (2009) Meteosat observation of the atmospheric entry of 2008 TC<sub>3</sub> over Sudan and the associated dust cloud. *Astron. Astrophys.*, **507**, 1015–1022.
- Borovička J. and Kalenda P. (2003) The Morávka meteorite fall: 4. Meteoroid dynamics and fragmentation in the atmosphere. *Meteoritics & Planet. Sci.*, **38**, 1023–1043.
- Borovička J. and Spurný P. (1996) Radiation study of two very bright terrestrial bolides and an application to the Comet S-L 9 collision with Jupiter. *Icarus*, **121**, 484–510.
- Borovička J. and Spurný P. (2008) The Carancas meteorite impact — Encounter with a monolithic meteoroid. *Astron. Astrophys.*, **485**, L1–L4.
- Borovička J., Spurný P., and Keclíkova J. (1995) A new positional astrometric method for all-sky cameras. *Astron. Astrophys. Suppl.*, **112**, 173–178.
- Borovička J., Popova O. P., Nemchinov I. V., Spurný P., and Ceplecha Z. (1998) Bolides produced by impacts of large meteoroids into the Earth's atmosphere: Comparison of theory with observations I. Benešov bolide dynamics and fragmentation. *Astron. Astrophys.*, **334**, 713–728.
- Borovička J., Spurný P., Kalenda P., and Tagliaferri E. (2003) The Morávka meteorite fall: 1. Description of the events and determination of the fireball trajectory and orbit from video records. *Meteoritics & Planet. Sci.*, **38**, 975–987.
- Borovička J., Spurný P., and Koten P. (2007) Atmospheric deceleration and light curves of Draconid meteors and implications for the structure of cometary dust. *Astron. Astrophys.*, **473**, 661–672.
- Borovička J., Tóth J., Igaz A., Spurný P., Kalenda P., Haloda J., Svoreň J., Kornoš L., Silber E., Brown P., and Husárik M. (2013a) The Košice meteorite fall: Atmospheric trajectory, fragmentation, and orbit. *Meteoritics & Planet. Sci.*, **48**, 1757–1779.
- Borovička J., Spurný P., Wiegert P., Kalenda P., Clark D., and Shrbený L. (2013b) The trajectory, structure and origin of the Chelyabinsk asteroidal impactor. *Nature*, **503**, 235–237.
- Borovička J., Spurný P., Šegon D., Andreic Ž., Kac J., Korlević K., Atanackov J., Kladnik G., Mucke H., Vida D., and Novoselnik F. (2015) The instrumentally recorded fall of the Križevci meteorite, Croatia, February 4, 2011. *Meteoritics & Planet. Sci.*, **50**, 1244–1259.
- Boslough M. B. E. and Crawford D. A. (2008) Low-altitude airbursts and the impact threat. *Int. J. Impact Eng.*, **35**, 1441–1448.
- Bottke W. F., Morbidelli A., Jedicke R., Petit J.-M., Levison H. F., Michel P., and Metcalfe T. S. (2002a) Debiasing orbital and absolute magnitude distribution of the near-Earth objects. *Icarus*, **156**, 399–433.
- Bottke W. F. Jr., Vokrouhlický D., Rubincam D. P., and Brož M. (2002b) The effect of Yarkovsky thermal forces on the dynamical evolution of asteroids and meteoroids. In *Asteroids III* (W. F. Bottke Jr. et al., eds.), pp. 395–408. Univ. of Arizona, Tucson.
- Bottke W. F., Durda D. D., Nesvorný D., Jedicke R., Morbidelli A., Vokrouhlický D., and Levison H. F. (2005) Linking the collisional history of the main asteroid belt to its dynamical excitation and depletion. *Icarus*, **179**, 63–94. (Erratum: *Icarus*, **183**, 235–236.)
- Bronshten V. A. (1983) *Physics of Meteoric Phenomena*. Reidel, Dordrecht. 356 pp. (Originally published in Russian, 1981, Nauka, Moscow.)
- Brown P. G., Ceplecha Z., Hawkes R. L., Wetherill G. W., Beech M., and Mossman K. (1994) The orbit and atmospheric trajectory of the Peekskill meteorite from video records. *Nature*, **367**, 624–626.
- Brown P. G. and 21 colleagues (2000) The fall, recovery, orbit, and composition of the Tagish Lake meteorite: A new type of carbonaceous chondrite. *Science*, **290**, 320–325.
- Brown P., Spalding R. E., ReVelle D. O., Tagliaferri E., and Worden S. P. (2002a) The flux of small near-Earth objects colliding with the Earth. *Nature*, **420**, 294–296.
- Brown P. G., Revelle D. O., Tagliaferri E., and Hildebrand A. R. (2002b) An entry model for the Tagish Lake fireball using seismic, satellite and infrasound records. *Meteoritics & Planet. Sci.*, **37**, 661–676.
- Brown P. G., Pack D., Edwards W. N., Revelle D. O., Yoo B. B., Spalding R. E., and Tagliaferri E. (2004) The orbit, atmospheric dynamics, and initial mass of the Park Forest meteorite. *Meteoritics & Planet. Sci.*, **39**, 1781–1796.
- Brown P., ReVelle D. O., Silber E. A., Edwards W. N., Arrowsmith S., Jackson L. E., Tancredi G., and Eaton D. (2008) Analysis of a crater-forming meteorite impact in Peru. *J. Geophys. Res.–Planets*, **113**, E09007, DOI: 10.1029/2008JE003105.
- Brown P., Weryk R. J., Kohut S., Edwards W. N., and Krzeminski Z. (2010) Development of an all-sky video meteor network in Southern Ontario, Canada: The ASGARD system. *WGN, J. Intl. Meteor Org.*, **38**, 25–30.
- Brown P., McCausland P. J. A., Fries M., Silber E., Edwards W. N., Wong D. K., Weryk R. J., Fries J., and Krzeminski Z. (2011) The fall of the Grimsby meteorite — I: Fireball dynamics and orbit from radar, video, and infrasound records. *Meteoritics & Planet. Sci.*, **46**, 339–363.
- Brown P. G. and 32 colleagues (2013a) A 500-kiloton airburst over Chelyabinsk and an enhanced hazard from small impactors. *Nature*, **503**, 238–241.
- Brown P., Marchenko V., Moser D. E., Weryk R., and Cooke W. (2013b) Meteorites from meteor showers: A case study of the Taurids. *Meteoritics & Planet. Sci.*, **48**, 270–288.

- Caffee M. and Nishiizumi K. (1997) Exposure ages of carbonaceous chondrites — II. *Meteoritics & Planet. Sci., Suppl.*, 32, A26.
- Campins H. and Swindle T. D. (1998) Expected characteristics of cometary meteorites. *Meteoritics & Planet. Sci.*, 33, 1201–1211.
- Ceplecha Z. (1961) Multiple fall of Příbram meteorites photographed. 1. Double-station photographs of the fireball and their relations to the found meteorites. *Bull. Astron. Inst. Czech.*, 12, 21–47.
- Ceplecha Z. (1971) Spectral data on terminal flare and wake of double-station meteor No. 38421 (Ondřejov, April 21, 1963). *Bull. Astron. Inst. Czech.*, 22, 219–304.
- Ceplecha Z. (1979) Earth-grazing fireballs. The daylight fireball of Aug. 10, 1972. *Bull. Astron. Inst. Czech.*, 30, 349–356.
- Ceplecha Z. (1986) Photographic fireball networks. In *Asteroids, Comets, Meteors II* (C.-I. Lagerkvist et al., eds.), pp. 575–582. Astronomiska Observatoriet Uppsala, Sweden.
- Ceplecha Z. (1987) Geometric, dynamic, orbital and photometric data on meteoroids from photographic fireball networks. *Bull. Astron. Inst. Czech.*, 38, 222–234.
- Ceplecha Z. (1988) Earth's influx of different populations of sporadic meteoroids from photographic and television data. *Bull. Astron. Inst. Czech.*, 39, 221–236.
- Ceplecha Z. (1996) Luminous efficiency based on photographic observations of the Lost City fireball and implications for the influx of interplanetary bodies onto Earth. *Astron. Astrophys.*, 311, 329–332.
- Ceplecha Z. (2007) Fragmentation model analysis of the observed atmospheric trajectory of the Tagish Lake fireball. *Meteoritics & Planet. Sci.*, 42, 185–189.
- Ceplecha Z. and McCrosky R. E. (1976) Fireball end heights — A diagnostic for the structure of meteoric material. *J. Geophys. Res.*, 81, 6257–6275.
- Ceplecha Z. and Rajchl J. (1965) Programme of fireball photography in Czechoslovakia. *Bull. Astron. Inst. Czech.*, 16, 15–22.
- Ceplecha Z. and ReVelle D. O. (2005) Fragmentation model of meteoroid motion, mass loss, and radiation in the atmosphere. *Meteoritics & Planet. Sci.*, 40, 35–50.
- Ceplecha Z., Ježková M., Boček J., Kirsten T., and Kiko J. (1973) Data on three significant fireballs photographed within the European network in 1971. *Bull. Astron. Inst. Czech.*, 24, 13–21.
- Ceplecha Z., Spurný P., Borovička J., and Keclíková J. (1993) Atmospheric fragmentation of meteoroids. *Astron. Astrophys.*, 279, 615–626.
- Ceplecha Z., Brown P. G., Hawkes R. L., Wetherill G. W., Beech M., and Mossman K. (1996) Video observations, atmospheric path, orbit and fragmentation record of the fall of the Peekskill meteorite. *Earth Moon Planets*, 72, 395–404.
- Ceplecha Z., Borovička J., Elford W. G., Revelle D. O., Hawkes R. L., Porubčan V., and Šimek M. (1998) Meteor phenomena and bodies. *Space Sci. Rev.*, 84, 327–471.
- Ceplecha Z., Spalding R. E., Jacobs C. F., ReVelle D. O., Tagliaferri E., and Brown P. G. (1999) Superbolides. In *Meteoroids 1998* (W. J. Baggaley and V. Porubčan, eds.), pp. 37–54. Astronomical Institute of the Slovak Academy of Sciences, Tatranská Lomnica.
- Chesley S. R., Farnocchia D., Brown P. G., and Chodas P. W. (2015) Orbit estimation for late warning asteroid impacts: The case of 2014 AA. In Aerospace Conference, 2015 IEEE , 8 pp., 7–14 March 2015, DOI: 10.1109/AERO.2015.7119148.
- Christie D. R. and Campus P. (2010) The IMS Infrasound Network: Design and establishment of infrasound stations. In *Infrasound Monitoring for Atmospheric Studies* (A. Le Pichon et al., eds.), pp. 29–77. Springer, Berlin.
- Clark D. L. and Wieger P. A. (2011) A numerical comparison with the Ceplecha analytical meteoroid orbit determination method. *Meteoritics & Planet. Sci.*, 46, 1217–1225.
- Close S., Brown P., Campbell-Brown M., Oppenheim M., and Colestock P. (2007) Meteor head echo radar data: Mass-velocity selection effects. *Icarus*, 186, 547–556.
- Consolmagno G. J., Schaefer M. W., Schaefer B. E., Britt D. T., Macke R. J., Nolan M. C., and Howell E. S. (2013) The measurement of meteorite heat capacity at low temperatures using liquid nitrogen vaporization. *Planet. Space Sci.*, 87, 146–156.
- Cooke W. J. and Moser D. E. (2012) The status of the NASA All Sky Fireball Network. In *Proceedings of the International Meteor Conference, Sibiu, Romania, 15–18 Sept., 2011* (M. Gyssens and P. Roggeman, eds.), pp. 9–12. International Meteor Organization, Mechelen, Belgium.
- Daubar I. J., McEwen A. S., Byrne S., Kennedy M. R., and Ivanov B. (2013) The current martian cratering rate. *Icarus*, 225, 506–516.
- de León J., Campins H., Tsiganis K., Morbidelli A., and Licandro J. (2010) Origin of the near-Earth asteroid Phaethon and the Geminids meteor shower. *Astron. Astrophys.*, 513, A26.
- Dodd R. T. (1981) *Meteorites, a Petrologic-Chemical Synthesis*. Cambridge Univ., Cambridge. 368 pp.
- Edwards W. N. (2010) Meteor generated infrasound: Theory and observation. In *Infrasound Monitoring for Atmospheric Studies* (A. Le Pichon et al., eds.), pp. 361–414. Springer, Berlin.
- Edwards W. N., Eaton D. W., and Brown P. G. (2008) Seismic observations of meteors: Coupling theory and observations. *Rev. Geophys.*, 46, Article ID 4007, 1–21.
- Ens T. A., Brown P. G., Edwards W. N., and Silber E. A. (2012) Infrasound production by bolides: A global statistical study. *J. Atmos. Solar Terr. Phys.*, 80, 208–229.
- Eugster O., Herzog G. F., Marti K., and Caffee M. W. (2006) Irradiation records, cosmic-ray exposure ages, and transfer times of meteorites. In *Meteorites and the Early Solar System II* (D. S. Lauretta and H. Y. McSween Jr., eds.), pp. 829–851. Univ. of Arizona, Tucson.
- Fairén A. G. and 15 colleagues (2011) Meteorites at Meridiani Planum provide evidence for significant amounts of surface and near-surface water on early Mars. *Meteoritics & Planet. Sci.*, 46, 1832–1841.
- Fessenkov V. G., Huzarski R. G., and La Paz L. (1954) On the origin of meteorites. *Meteoritics*, 1, 208–227.
- Fries M. and Fries J. (2010) Doppler weather radar as a meteorite recovery tool. *Meteoritics & Planet. Sci.*, 45, 1476–1487.
- Gayon-Markt J., Delbo M., Morbidelli A., and Marchi S. (2012) On the origin of the Almahata Sitta meteorite and 2008 TC3 asteroid. *Mon. Not. R. Astron. Soc.*, 424, 508–518.
- Genge M. J. and Grady M. M. (1999) The fusion crusts of stony meteorites: Implications for the atmospheric reprocessing of extraterrestrial materials. *Meteoritics & Planet. Sci.*, 34, 341–356.
- Golub' A. P., Kosarev I. B., Nemchinov I. V., and Shuvalov V. V. (1996) Emission and ablation of a large meteoroid in the course of its motion through the Earth's atmosphere. *Solar System Res.*, 30, 183–197.
- Gombosi T. I. and Houpis H. L. F. (1986) An icy-glue model of cometary nuclei. *Nature*, 324, 43–44.
- Goodrich C. A., Hartmann W. K., O'Brien D. P., Weidenschilling S. J., Wilson L., Michel P., and Jutzi M. (2015) Origin and history of ureilitic material in the solar system: The view from asteroid 2008 TC<sub>3</sub> and the Almahata Sitta meteorite. *Meteoritics & Planet. Sci.*, 50, 782–809, DOI: 10.1111/maps.12401.
- Gorkavyi N., Rault D. F., Newman P. A., Silva A. M., and Dudorov A. E. (2013) New stratospheric dust belt due to the Chelyabinsk bolide. *Geophys. Res. Lett.*, 40, 4728–4733.
- Gounelle M., Spurný P., and Bland P. A. (2006) The orbit and atmospheric trajectory of the Orgueil meteorite from historical records. *Meteoritics & Planet. Sci.*, 41, 135–150.
- Gounelle M., Morbidelli A., Bland P. A., Spurný P., Young E. D., and Sephton M. (2008) Meteorites from the outer solar system? In *The Solar System Beyond Neptune* (M. A. Barucci et al., eds.), pp. 525–541. Univ. of Arizona, Tucson.
- Gritsevich M. I. (2009) Determination of parameters of meteor bodies based on flight observational data. *Adv. Space Res.*, 44, 323–334.
- Gural P. S. (2012) A new method of meteor trajectory determination applied to multiple unsynchronized video cameras. *Meteoritics & Planet. Sci.*, 47, 1405–1418.
- Haack H., Grau T., Bischoff A., Horstmann M., Wasson J., Sørensen A., Laubenstein M., Ott U., Palme H., Gellissen M., Greenwood R. C., Pearson V. K., Franchi I. A., Gabelica Z., and Schmitt-Kopplin P. (2012) Maribo — A new CM fall from Denmark. *Meteoritics & Planet. Sci.*, 47, 30–50.
- Halliday I. (1961) A study of spectral line identifications in Perseid meteor spectra. *Publ. Dom. Obs. (Ottawa)*, 25, 3–16.
- Halliday I. (1973) Photographic fireball networks. In *Evolutionary and Physical Properties of Meteoroids* (C. L. Hemenway et al., eds.), pp. 1–8. NASA Spec. Publ. 319, Washington, DC.
- Halliday I. (1987) Detection of a meteorite 'stream' — Observations of a second meteorite fall from the orbit of the Innisfree chondrite. *Icarus*, 69, 550–556. (Erratum: *Icarus*, 72, 239.)
- Halliday I., Blackwell A. T., and Griffin A. A. (1978) The Innisfree meteorite and the Canadian camera network. *J. R. Astron. Soc. Can.*, 72, 15–39.
- Halliday I., Griffin A., and Blackwell A. T. (1981) The Innisfree meteorite fall — A photographic analysis of fragmentation, dynamics and luminosity. *Meteoritics*, 16, 153–170.

- Halliday I., Blackwell A. T., and Griffin A. A. (1989a) The typical meteorite event, based on photographic records of 44 fireballs. *Meteoritics*, 24, 65–72.
- Halliday I., Blackwell A. T., and Griffin A. A. (1989b) The flux of meteorites on the Earth's surface. *Meteoritics*, 24, 173–178.
- Halliday I., Blackwell A. T., and Griffin A. A. (1990) Evidence for the existence of groups of meteorite-producing asteroidal fragments. *Meteoritics*, 25, 93–99.
- Halliday I., Griffin A. A., and Blackwell A. T. (1996) Detailed data for 259 fireballs from the Canadian camera network and inferences concerning the influx of large meteoroids. *Meteoritics & Planet. Sci.*, 31, 185–217.
- Harris A. (2013) The value of enhanced NEO surveys. *Planetary Defense Conference*, IAA-PDC13-05-09.
- Hildebrand A. R., McCausland P. J. A., Brown P. G., Longstaffe F. J., Russell S. D. J., Tagliaferri E., Wacker J. F., and Mazur M. J. (2006) The fall and recovery of the Tagish Lake meteorite. *Meteoritics & Planet. Sci.*, 41, 407–431.
- Hildebrand A. R. and 11 colleagues (2009) Characteristics of a bright fireball and meteorite fall at Buzzard Coulee, Saskatchewan, Canada, November 20, 2008. *Lunar Planet. Sci. XL*, Abstract #2505. Lunar and Planetary Institute, Houston.
- Hill K. A., Rogers L. A., and Hawkes R. L. (2005) High geocentric velocity meteor ablation. *Astron. Astrophys.*, 444, 615–624.
- Hiroi T., Jenniskens P., Bishop J. L., Shatir T. S. M., Kudoda A. M., and Shaddad M. H. (2010) Bidirectional visible-NIR and biconical FT-IR reflectance spectra of Almahata Sitta meteorite samples. *Meteoritics & Planet. Sci.*, 45, 1836–1845.
- Holsapple K. (1993) The scaling of impact processes in planetary sciences. *Annu. Rev. Earth Planet. Sci.*, 21, 333–373.
- Holsapple K. (2009) On the strength of the small bodies of the solar system: A review of strength theories and their implementation for analyses of impact disruption. *Planet. Space Sci.*, 57, 127–141.
- Horstmann M. and Bischoff A. (2014) The Almahata Sitta polymict breccia and the late accretion of asteroid 2008 TC<sub>3</sub>. *Chem. Erde-Geochim.*, 74, 149–183.
- Hueso R. and 23 colleagues (2013) Impact flux on Jupiter: From superbolides to large-scale collisions. *Astron. Astrophys.*, 560, A55.
- Hutchison R. (2004) *Meteorites, a Petrologic, Chemical and Isotopic Synthesis*. Cambridge Univ., Cambridge. 511 pp.
- Hutson M., Ruzicka A., Jull A. J., Smaller J. E., and Brown R. (2013) Stones from Mohave County, Arizona: Multiple falls in the “Franconia strewn field.” *Meteoritics & Planet. Sci.*, 48, 365–389.
- Jenniskens P. (2006) *Meteor Showers and Their Parent Comets*. Cambridge Univ., Cambridge. 790 pp.
- Jenniskens P. (2007) Quantitative meteor spectroscopy: Elemental abundances. *Adv. Space Res.*, 39, 491–512.
- Jenniskens P. and 34 colleagues (2009) The impact and recovery of asteroid 2008 TC<sub>3</sub>. *Nature*, 458, 485–488.
- Jenniskens P., Vaubaillon J., Binzel R. P., DeMeo F. E., Nesvorný D., Bottke W. F., Fitzsimmons A., Hiroi T., Marchis F., Bishop J. L., Vernazza P., Zolensky M. E., Herrin J. S., Welten K. C., Meier M. M., and Shaddad M. H. (2010) Almahata Sitta (=asteroid 2008 TC<sub>3</sub>) and the search for the ureilite parent body. *Meteoritics & Planet. Sci.*, 45, 1590–1617.
- Jenniskens P. and 69 colleagues (2012) Radar-enabled recovery of the Sutter’s Mill meteorite, a carbonaceous chondrite regolith breccia. *Science*, 338, 1583–1587.
- Jenniskens P. and 47 colleagues (2014) Fall, recovery and characterization of the Novato L6 chondrite breccia. *Meteoritics & Planet. Sci.*, 49, 1388–1425.
- Jewitt D. (2012) The active asteroids. *Astron. J.*, 143, 66.
- Jewitt D., Li J., and Agarwal J. (2013) The dust tail of asteroid (3200) Phaethon. *Astrophys. J. Lett.*, 771, L36.
- Jones D. C. and Williams I. P. (2008) High inclination meteorite streams can exist. *Earth Moon Planets*, 102, 35–46.
- Jones J., Brown P., Ellis K. J., Webster A. R., Campbell-Brown M., Krzeminski Z., and Weryk R. J. (2005) The Canadian Meteor Orbit Radar: System overview and preliminary results. *Planet. Space Sci.*, 53, 413–421.
- Keay C. S. L. (1992) Electrophonic sounds from large meteor fireballs. *Meteoritics*, 27, 144–148.
- Kero J., Szasz C., Nakamura T., Meisel D. D., Ueda M., Fujiwara Y., Terasawa T., Miyamoto H., and Nishimura K. (2011) First results from the 2009–2010 MU radar head echo observation programme for sporadic and shower meteors: The Orionids 2009. *Mon. Not. R. Astron. Soc.*, 416, 2550–2559.
- Keuer D., Singer W. and Stober G. (2009) Signatures of the ionization trail of a fireball observed in the HF, and VHF range above middle-Europe on Jan 17, 2009. In *Proceedings of the 12th Workshop on Technical and Scientific Aspects of MST Radar* (N. Swarnalingham and W. K. Hocking, eds.), p. 154–158.
- Kimberley J. and Ramesh K. T. (2011) The dynamic strength of an ordinary chondrite. *Meteoritics & Planet. Sci.*, 46, 1653–1669.
- Klekociuk A. R., Brown P. G., Pack D. W., Revelle D. O., Edwards W. N., Spalding R. E., Tagliaferri E., Yoo B. B., and Zagari J. (2005) Meteoritic dust from the atmospheric disintegration of a large meteoroid. *Nature*, 436, 1132–1135.
- Kohout T., Jenniskens P., Shaddad M. H., and Haloda J. (2010) Inhomogeneity of asteroid 2008 TC<sub>3</sub> (Almahata Sitta meteorites) revealed through magnetic susceptibility measurements. *Meteoritics & Planet. Sci.*, 45, 1778–1788.
- Kohout T., Kiuru R., Montonen M., Scheirich P., Britt D., Macke R., and Consolmagno G. (2011) Internal structure and physical properties of the asteroid 2008 TC<sub>3</sub> inferred from a study of the Almahata Sitta meteorites. *Icarus*, 212, 697–700.
- Kokhirova G. I., Babadzhyan P. B., and Khamorev U. Kh. (2015) Tajikistan Fireball Network and results of photographic observations. *Solar System Res.*, 49, 275–283.
- Koten P., Vaubaillon J., Čapek D., Vojáček V., Spurný P., Štork R., and Colas F. (2014) Search for faint meteoroids on the orbits of Příbram and Neuschwanstein meteorites. *Icarus*, 239, 244–252.
- Kozubal M. J., Gasdia F. W., Dantowitz R. F., Scheirich P., and Harris A. W. (2011) Photometric observations of Earth-impacting asteroid 2008 TC<sub>3</sub>. *Meteoritics & Planet. Sci.*, 46, 534–542.
- Lauretta D. S. and McSween H. Y. Jr., eds. (2006) *Meteorites and the Early Solar System II*. Univ. of Arizona, Tucson. 943 pp.
- Le Pichon A., Antier K., Cansi Y., Hernandez B., Minaya E., Burgoa B., Drob D., Evers L. G., and Vaubaillon J. (2008) Evidence for a meteoritic origin of the September 15, 2007, Carancas crater. *Meteoritics & Planet. Sci.*, 43, 1797–1809.
- Leya I. and Masarik J. (2009) Cosmogenic nuclides in stony meteorites revisited. *Meteoritics & Planet. Sci.*, 44, 1061–1086.
- Lipschutz M. E., Wolf S. F., and Dodd R. T. (1997) Meteoroid streams as sources for meteorite falls: A status report. *Planet. Space Sci.*, 45, 517–523.
- Lodders K. and Osborne R. (1999) Perspectives on the comet-asteroid-meteorite link. *Space Sci. Rev.*, 90, 289–297.
- Llorca J., Trigo-Rodríguez J. M., Ortiz J. L., Docobo J. A., García-Guinea J., Castro-Tirado A. J., Rubin A. E., Eugster O., Edwards W., Laubenstein M., and Casanova I. (2005) The Villalbeto de la Peña meteorite fall: I. Fireball energy, meteorite recovery, strewn field, and petrography. *Meteoritics & Planet. Sci.*, 40, 795–804.
- Macke R. J., Consolmagno G. J., and Britt D. T. (2011) Density, porosity, and magnetic susceptibility of carbonaceous chondrites. *Meteoritics & Planet. Sci.*, 46, 1842–1862.
- Madiedo J. M., Trigo-Rodríguez J. M., Ortiz J. L., Castro-Tirado A. J., Pastor S., de los Reyes J. A., and Cabrera-Caño J. (2013a) Spectroscopy and orbital analysis of bright bolides observed over the Iberian Peninsula from 2010 to 2012. *Mon. Not. R. Astron. Soc.*, 435, 2023–2032.
- Madiedo J. M., Trigo-Rodríguez J. M., Castro-Tirado A. J., Ortiz J. L., and Cabrera-Caño J. (2013b) The Geminid meteoroid stream as a potential meteorite dropper: A case study. *Mon. Not. R. Astron. Soc.*, 436, 2818–2823.
- Madiedo J. M., Ortiz J. L., Trigo-Rodríguez J. M., Zamorano J., Konovalova N., Castro-Tirado A. J., Ocaña F., de Miguel A. S., Izquierdo J., and Cabrera-Caño J. (2014a) Analysis of two superbolides with a cometary origin observed over the Iberian Peninsula. *Icarus*, 233, 27–35.
- Madiedo J. M., Trigo-Rodríguez J. M., Ortiz J. L., Castro-Tirado A. J., and Cabrera-Caño J. (2014b) Bright fireballs associated with the potentially hazardous asteroid 2007LQ19. *Mon. Not. R. Astron. Soc.*, 443, 1643–1650.
- McCrosky R. E. and Boeschenstein H. Jr. (1965) *The Prairie Meteorite Network*. SAO Spec. Rept. 173, Smithsonian Astrophysical Observatory, Cambridge. 23 pp.
- McCrosky R. E., Posen A., Schwartz G., and Shao C.-Y. (1971) Lost City meteorites, its recovery and a comparison with other fireballs. *J. Geophys. Res.*, 76, 4090–4108.
- McEwen A. S. and Bierhaus E. B. (2006) The importance of secondary cratering to age constraints on planetary surfaces. *Annu. Rev. Earth Planet. Sci.*, 34, 535–567.

- Megner L., Siskind D. E., Rapp M., and Gumbel J. (2008) Global and temporal distribution of meteoric smoke: A two-dimensional simulation study. *J. Geophys. Res.*, **113**, D03202.
- Meier M. M. M., Welten K. C., Caffee M. W., Friedrich J. M., Jenniskens P., Nishiizumi K., Shaddad M. H., and Wieler R. (2012) A noble gas and cosmogenic radionuclide analysis of two ordinary chondrites from Almahata Sitta. *Meteoritics & Planet. Sci.*, **47**, 1075–1086.
- Milley E. P. (2010) Physical properties of fireball-producing Earth-impacting meteoroids and orbit determination through shadow calibration of the Buzzard Coulee meteorite fall. M.Sc. thesis, Univ. of Calgary, Calgary. 166 pp.
- Molau S. and Rendtel J. (2009) A comprehensive list of meteor showers obtained from 10 years of observations with the IMO Video Meteor Network. *WGN, J. Intl. Meteor Org.*, **37**, 98–121.
- Morbidelli A., Bottke W. F. Jr., Froeschlé C., and Michel P. (2002) Origin and evolution of near-Earth objects. In *Asteroids III* (W. F. Bottke Jr. et al., eds.), pp. 409–422. Univ. of Arizona, Tucson.
- Mukhamednazarov S. (1999) Observation of a fireball and the fall of the first large meteorite in Turkmenistan. *Astron. Lett.*, **25**, 117–118.
- Nakamura T., Noguchi T., Tsuchiya A., Ushikubo T., Kita N. T., Valley J. W., Zolensky M. E., Kakazu Y., Sakamoto K., Mashio E., Uesugi K., and Nakano T. (2008) Chondrule-like objects in short-period Comet 81P/Wild 2. *Science*, **321**, 1664–1667.
- Nemtchinov I. V., Svetsov V. V., Kosarev I. B., Golub' A. P., Popova O. P., Shuvalov V. V., Spalding R. E., Jacobs C., and Tagliaferri E. (1997) Assessment of kinetic energy of meteoroids detected by satellite-based light sensors. *Icarus*, **130**, 259–274.
- Nishiizumi K., Caffee M. W., Hamajima Y., Reedy R. C., and Welten K. C. (2014) Exposure history of the Sutter's Mill carbonaceous chondrite. *Meteoritics & Planet. Sci.*, **49**, 2056–2063.
- Oberberger K. S., Taylor G. B., Hartman J. M., Dowell J., Ellingson S. W., Helmholz J. F., Henning P. A., Kavic M., Schinzel F. K., Simonetti J. H., Stovall K., and Wilson T. L. (2014) Detection of radio emission from fireballs. *Astrophys. J. Lett.*, **788**, L26.
- Oberst J., Molau S., Heinlein D., Gritzner C., Schindler M., Spurný P., Ceplecha Z., Rendtel J., and Betlem H. (1998) The “European Fireball Network”: Current status and future prospects. *Meteoritics & Planet. Sci.*, **33**, 49–56.
- Olech A., Źoładek P., Wiśniewski M., Krasnowski M., Kwinta M., Fajfer T., Fietkiewicz K., Dorosz D., Kowalski L., Olejnik J., Mularczyk K., and Złoczewski K. (2006) Polish Fireball Network. In *Proceedings of the International Meteor Conference, Oostmalle, Belgium, 15–18 Sept.*, 2005 (J. Verbert et al., eds.), pp. 53–62. International Meteor Organization, Mechelen, Belgium.
- Opeil C. P., Consolmagno G. J., Safarik D. J., and Britt D. T. (2012) Stony meteorite thermal properties and their relationship with meteorite chemical and physical states. *Meteoritics & Planet. Sci.*, **47**, 319–329.
- Öpik E. J. (1950) Interstellar meteors and related problems. *Irish Astron. J.*, **1**, 80–96.
- Öpik E. J. (1968) The cometary origin of meteorites. *Irish Astron. J.*, **8**, 185–208.
- Padevět V. and Jakeš P. (1993) Comets and meteorites: Relationship (AGAIN?). *Astron. Astrophys.*, **274**, 944–954.
- Papike J. J., ed. (1998) *Planetary Materials*. Mineralogical Society of America, Washington, DC. 1039 pp.
- Pauls A. and Gladman B. (2005) Decoherence time scales for “meteoroid streams.” *Meteoritics & Planet. Sci.*, **40**, 1241–1256.
- Pecina P. and Ceplecha Z. (1983) New aspects in single-body meteor physics. *Bull. Astron. Inst. Czech.*, **34**, 102–121.
- Petaev M. I. (1992) The Sterlitamak meteorite — A new crater-forming fall. *Solar Sys. Res.*, **26**, 384–398.
- Popova O. (2004) Meteoroid ablation models. *Earth Moon Planets*, **95**, 303–319.
- Popova O. P., Strelkov A. S., and Sidneva S. N. (2007) Sputtering of fast meteoroids’ surface. *Adv. Space Res.*, **39**, 567–573.
- Popova O., Borovička J., Hartmann W. K., Spurný P., Gnos E., Nemtchinov I., and Trigo-Rodríguez J. M. (2011) Very low strengths of interplanetary meteoroids and small asteroids. *Meteoritics & Planet. Sci.*, **46**, 1525–1550.
- Popova O. P. and 59 colleagues (2013) Chelyabinsk airburst, damage assessment, meteorite recovery, and characterization. *Science*, **342**, 1069–1073.
- Pujol J., Rydelek P., and Ishihara Y. (2006) Analytical and graphical determination of the trajectory of a fireball using seismic data. *Planet. Space Sci.*, **54**, 78–86.
- Rabinowitz D., Helin E., Lawrence K., and Pravdo S. (2000) A reduced estimate of the number of kilometre-sized near-Earth asteroids. *Nature*, **403**, 165–166.
- Reddy V. and 17 colleagues (2015) Link between the potentially hazardous Asteroid (86039) 1999 NC<sub>43</sub> and the Chelyabinsk meteoroid tenuous. *Icarus*, **252**, 129–143.
- ReVelle D. O. and Ceplecha Z. (1994) Analysis of identified iron meteoroids: Possible relation with M-type Earth-crossing asteroids? *Astron. Astrophys.*, **292**, 330–336.
- ReVelle D. O. and Ceplecha Z. (2001) Bolide physical theory with application to PN and EN fireballs. In *Proceedings of the Meteoroids 2001 Conference, Kiruna, Sweden* (B. Warmbein, ed.), pp. 507–512. ESA SP-495, Noordwijk, The Netherlands.
- ReVelle D. O., Brown P. G., and Spurný P. (2004) Entry dynamics and acoustics/infrasonic/seismic analysis for the Neuschwanstein meteorite fall. *Meteoritics & Planet. Sci.*, **39**, 1605–1626.
- Rieger L. A., Bourassa A. E., and Degenstein D. A. (2014) Odin — OSIRIS detection of the Chelyabinsk meteor. *Atmos. Meas. Tech.*, **7**, 777–780.
- Rogers L., Hill K. A., and Hawkes R. L. (2005) Mass loss due to sputtering and thermal processes in meteoroid ablation. *Planet. Space Sci.*, **53**, 1341–1354.
- Rubin A. E. (1997) The Galim LL/EH polymict breccia: Evidence for impact-induced exchange between reduced and oxidized meteoritic material. *Meteoritics & Planet. Sci.*, **32**, 489–492.
- Sánchez P. and Scheeres D. J. (2014) The strength of regolith and rubble pile asteroids. *Meteoritics & Planet. Sci.*, **49**, 788–811.
- Scheirich P., Ďurech J., Pravec P., Kozubal M., Dantowitz R., Kaasalainen M., Betzler A. S., Beltrame P., Muler G., Birtwhistle P., and Kugel F. (2010) The shape and rotation of asteroid 2008 TC<sub>3</sub>. *Meteoritics & Planet. Sci.*, **45**, 1804–1811.
- Schunová E., Granvik M., Jedlické R., Gronchi G., Wainscoat R., and Abe S. (2012) Searching for the first near-Earth object family. *Icarus*, **220**, 1050–1063.
- Šegon D., Korlević K., Andreić Ž., Kac J., Atanackov J., and Kladnik G. (2011) Meteorite-dropping bolide over north Croatia on 4th February 2011. *WGN, J. Intl. Meteor Org.*, **39**, 98–99.
- Shaddad M. H. and 19 colleagues (2010) The recovery of asteroid 2008 TC<sub>3</sub>. *Meteoritics & Planet. Sci.*, **45**, 1557–1589.
- Silber E. A., ReVelle D. O., Brown P. G., and Edwards W. N. (2009) An estimate of the terrestrial influx of large meteoroids from infrasonic measurements. *J. Geophys. Res.*, **114**, E08006.
- SonotaCo (2009) A meteor shower catalog based on video observations in 2007–2008. *WGN, J. Intl. Meteor Org.*, **37**, 55–62.
- Spurný P. (1994) Recent fireballs photographed in central Europe. *Planet. Space Sci.*, **42**, 157–162.
- Spurný P. and Borovička J. (2013) Meteorite dropping Geminid recorded. In *Meteoroids 2013*, Abstract #061. Adam Mickiewicz Univ., Poznań, Poland. Available online at [http://www.astro.amu.edu.pl/Meteoroids2013/main\\_content/data/abstracts.pdf](http://www.astro.amu.edu.pl/Meteoroids2013/main_content/data/abstracts.pdf).
- Spurný P. and Ceplecha Z. (2008) Is electric charge separation the main process for kinetic energy transformation into the meteor phenomenon? *Astron. Astrophys.*, **489**, 449–454.
- Spurný P., Betlem H., Jobse K., Koten P., and van't Leven J. (2000) New type of radiation of bright Leonid meteors above 130 km. *Meteoritics & Planet. Sci.*, **35**, 1109–1115.
- Spurný P., Oberst J., and Heinlein D. (2003) Photographic observations of Neuschwanstein, a second meteorite from the orbit of the Příbram chondrite. *Nature*, **423**, 151–153.
- Spurný P., Borovička J., and Shrbený L. (2007) Automation of the Czech part of the European fireball network: Equipment, methods and first results. In *Near Earth Objects, Our Celestial Neighbors: Opportunity and Risk* (A. Milani et al., eds.), pp. 121–130. IAU Symp. 236, Cambridge Univ., Cambridge.
- Spurný P., Borovička J., Kac J., Kalenda P., Atanackov J., Kladnik G., Heinlein D., and Grau T. (2010) Analysis of instrumental observations of the Jesenice meteorite fall on April 9, 2009. *Meteoritics & Planet. Sci.*, **45**, 1392–1407.
- Spurný P., Bland P. A., Shrbený L., Borovička J., Ceplecha Z., Singelton A., Bevan A. W. R., Vaughan D., Towner M. C., McClafferty T. P., Toumi R., and Deacon G. (2012a) The Bunburra Rockhole meteorite fall in SW Australia: Fireball trajectory, luminosity, dynamics, orbit, and impact position from photographic and photoelectric records. *Meteoritics & Planet. Sci.*, **47**, 163–185.

- Spurný P., Bland P. A., Borovička J., Towner M. C., Shrbený L., Bevan A. W. R., and Vaughan D. (2012b) The Mason Gully meteorite fall in SW Australia: Fireball trajectory, luminosity, dynamics, orbit and impact position from photographic records. In *Asteroids, Comets, Meteors 2012*, Abstract #6369. Lunar and Planetary Institute, Houston.
- Spurný P., Borovička J., Haack H., Singer W., Keuer D., and Jobse K. (2013) Trajectory and orbit of the Maribo CM2 meteorite from optical, photoelectric and radar records. Poster presented at the Meteoroids 2013 conference, Poznań, Poland, August 26–30, 2013.
- Spurný P., Haloda J., Borovička J., Shrbený L., and Halodová P. (2014) Reanalysis of the Benešov bolide and recovery of inhomogeneous breccia meteorites — old mystery solved after 20 years. *Astron. Astrophys.*, 570, A39.
- Stokan E. and Campbell-Brown M. D. (2014) Transverse motion of fragmenting faint meteors observed with the Canadian Automated Meteor Observatory. *Icarus*, 232, 1–12.
- Stuart J. S. (2001) A near-Earth asteroid population estimate from the LINEAR survey. *Science*, 294, 1691–1693.
- Suggs R. M., Moser D. E., Cooke W. J., and Suggs R. J. (2014) The flux of kilogram-sized meteoroids from lunar impact monitoring. *Icarus*, 238, 23–36.
- Svetsov V. V., Nemchinov I. V., and Teterov A. V. (1995) Disintegration of large meteoroids in Earth's atmosphere: Theoretical models. *Icarus*, 116, 131–153.
- Tagliaferri E., Spalding R., Jacobs C., Worden S. P., and Erlich A. (1994) Detection of meteoroid impacts by optical sensors in Earth orbit. In *Hazards Due to Comets and Asteroids* (T. Gehrels, ed.), pp. 199–221. Univ. of Arizona, Tucson.
- Tancredi G. and 15 colleagues (2009) A meteorite crater on Earth formed on September 15, 2007: The Carancas hypervelocity impact. *Meteoritics & Planet. Sci.*, 44, 1967–1984.
- Tóth J., Vereš P., and Kornoš L. (2011) Tidal disruption of NEAs — A case of Příbram meteorite. *Mon. Not. R. Astron. Soc.*, 415, 1527–1533.
- Tóth J., Kornoš L., Piffl R., Koukal J., Gajdoš Š., Popek M., Majchrovíč I., Zima M., Világí J., Kalmančok D., Vereš P., and Zigo P. (2012) Slovak Video Meteor Network — Status and results: Lyrids 2009, Geminids 2010, Quadrantids 2011. In *Proceedings of the International Meteor Conference, Sibiu, Romania, 15–18 Sept.*, 2011 (M. Gyssens and P. Roggemans, eds.), pp. 82–84. International Meteor Organization, Mechelen, Belgium.
- Trigo-Rodríguez J. M. and Llorca J. (2006) The strength of cometary meteoroids: Clues to the structure and evolution of comets. *Mon. Not. R. Astron. Soc.*, 372, 655–660. (Erratum: *Mon. Not. R. Astron. Soc.*, 375, 415.)
- Trigo-Rodríguez J. M., Fabregat J., Llorca J., Castro-Tirado A., del Castillo A., de Ugarte A., López A. E., Villares F., and Ruiz-Garrido J. (2001) Spanish Fireball Network: Current status and recent orbit data. *WGN, J. Int. Meteor. Org.*, 29, 139–144.
- Trigo-Rodríguez J. M., Borovička J., Spurný P., Ortiz J. L., Docobo J. A., Castro-Tirado A. J., and Llorca J. (2006) The Villalbeto de la Peña meteorite fall: II. Determination of atmospheric trajectory and orbit. *Meteoritics & Planet. Sci.*, 41, 505–517.
- Trigo-Rodríguez J. M., Madiedo J. M., Williams I. P., Castro-Tirado A. J., Llorca J., Vítek S., and Jelínek M. (2009) Observations of a very bright fireball and its likely link with comet C/1919 Q2 Metcalf. *Mon. Not. R. Astron. Soc.*, 394, 569–576.
- Vasilyev N. V. (1998) The Tunguska meteorite problem today. *Planet. Space Sci.*, 46, 129–150.
- Verchovsky A. B. and Sephton M. A. (2005) Noble gases in meteorites: A noble record. *Astron. Geophys.*, 46, 2.12–2.14.
- Weissman P. R. and Lowry S. C. (2008) Structure and density of cometary nuclei. *Meteoritics & Planet. Sci.*, 43, 1033–1047.
- Welten K. C., Meier M. M. M., Caffee M. W., Nishiizumi K., Wieler R., Jenniskens P., and Shaddad M. H. (2010) Cosmogenic nuclides in Almahata Sitta ureilites: Cosmic-ray exposure age, preatmospheric mass, and bulk density of asteroid 2008 TC<sub>3</sub>. *Meteoritics & Planet. Sci.*, 45, 1728–1742.
- Werner S. C., Harris A. W., Neukum G., and Ivanov B. A. (2002) The near-Earth asteroid size-frequency distribution: A snapshot of the lunar impactor size frequency distribution. *Icarus*, 156, 287–290.
- Weryk R. J. and Brown P. G. (2013) Simultaneous radar and video meteors — II: Photometry and ionisation. *Planet. Space Sci.*, 81, 32–47.
- Zolensky M. and Ivanov A. (2003) The Kaidun microbreccia meteorite: A harvest from the inner and outer asteroid belt. *Chem. Erde—Geochem.*, 63, 185–246.

# Meteoroid Streams and the Zodiacal Cloud

Peter Jenniskens

*SETI Institute and NASA Ames Research Center*

In the last decade, considerable progress has been made in charting meteoroid streams at Earth and in understanding the mechanisms of meteoroid stream formation and evolution that ultimately result in the formation of the zodiacal cloud. This has led to the realization that episodic disruption plays a key role in the decay of comets and primitive asteroids. Several ongoing disruption cascades manifest as multiple meteoroid streams at Earth. Evidence is mounting that the recently released meteoroids also fall apart, on timescales of 100–10,000 yr, into smaller meteoroids that survive for another  $10^5$ – $10^6$  yr to form the zodiacal cloud. The first dynamical models of the zodiacal cloud are being developed to explore the relative importance of the various sources. These show that main-belt asteroids contribute only a small fraction to the cloud. Ironically, the infall to Earth of freshly ejected meteoroids, dominated by the larger meteoroid streams, is currently in significant part from primitive asteroid (3200) Phaethon.

## 1. INTRODUCTION

All asteroids and comets in our solar system are gradually falling apart into meteoroids. These meteoroids move at a high relative speed to other objects in the solar system and are therefore an impact hazard to satellites, a cause of asteroid surface weathering, and create meteors when impacting a planetary atmosphere. Streams of meteoroids provide a history of parent body activity and can warn us about the presence of potentially hazardous objects.

Interplanetary matter falls to Earth at a rate of 10,000–40,000 tons per year, mostly in the form of  $\sim$ 150- $\mu\text{m}$  (10  $\mu\text{m}$ –1 mm)-sized meteoroids (Love and Brownlee, 1993; Ceplecha et al., 1998). They produce the neutral-atom-debris layer (and trails) in our atmosphere, responsible for the sodium airglow (Plane, 2003), and the meteoric smoke particles that condense the ice of noctilucent clouds (Hervig et al., 2012). They are responsible for the interplanetary dust particles (IDP) collected in Earth’s atmosphere, and deliver to Earth’s surface micrometeorites (e.g., Rudraswami et al., 2014), solar wind-implanted  $^3\text{He}$  (e.g., Farley, 2001), platinum-group elements (Peucker-Ehrenbrink, 2001), and the meteoric iron that enables life in the iron-depleted southern oceans (Plane, 2012). In the past, meteoroids may have supplied origin-of-life organics, directly from surviving organics as well as through impact-induced chemistry in the atmosphere (e.g., Chyba et al., 1990; Maurette, 1998; Jenniskens, 2001; see also Chapter 34 in Jenniskens, 2006).

Meteoroids with sizes on the order of the wavelength of light (also called interplanetary dust) scatter light efficiently and cause the visible zodiacal cloud (Leinert et al., 1998).

They are also strong emitters of infrared light when heated (e.g., Levasseur-Regourd and Lasue, 2010; Maris et al., 2011; Krick et al., 2012; Ade et al., 2014). It is these meteoroids that make the presence of minor planets in other solar systems detectable (e.g., Nesvorný et al., 2010; Morlok et al., 2014; Bonsor et al., 2014; Ballering et al., 2014).

Larger >1-mm meteoroids are often only detected when they enter Earth’s atmosphere and cause phenomena collectively called a “meteor.” They cause the ionization trains in radio-detected meteors, the bright lights that are our naked-eye observed meteor showers, as well as the occasional fireballs that produce airbursts and meteorites.

The largest >1-m meteoroids are the topic of the chapter by Borovicka et al. in this volume. The manner in which these larger meteoroids break in the atmosphere probes the physical properties of small near-Earth asteroids (NEAs), while the surviving meteorites sample their material properties.

This chapter is mostly concerned with how active asteroids and the now dormant comets created the meteoroid streams that manifest as meteor showers on Earth and how that matter contributes to the zodiacal cloud and sporadic meteors.

Numerous papers on these topics since the 2002 *Asteroids III* volume and the 2001 review papers on interplanetary dust in Grün et al. (2001a) can be found in conference proceedings of meetings on interplanetary dust by Krueger and Graps (2007); on meteoroids by Trigo-Rodríguez et al. (2008), Cooke et al. (2010), and Jopek et al. (2014); on asteroids, comets, and meteors by Lazzaro et al. (2006); and in abstracts from the Asteroids, Comets, and Meteors (ACM) 2008 meeting in Baltimore, the ACM 2012 meeting in Niigata, and the ACM 2014 meeting in Helsinki, as well

as in the annual Proceedings of the International Meteor Conference. This chapter builds upon, and expands on, an earlier synopsis presented in *Jenniskens* (2006).

## 2. NOMENCLATURE

When discussing the role of asteroids in the production of meteoroids, it is important to understand what is meant by “asteroid.” From an observer’s point of view, that can include both objects from the asteroid main belt and the dormant or mostly inactive comets that originated in the Kuiper belt and Oort cloud (*Levison*, 1996).

It is the instantaneous rate of mass loss and its nature, especially the meteoroid size and size distribution, that determine a telescopic observer’s distinction between an asteroid (star-like) and a comet (fuzzy object). This appearance can change over time. An asteroid can have an associated stream of meteoroids from a period of activity in the past.

A “meteoroid” is defined as “a solid object moving in interplanetary space, of a size considerably smaller than an asteroid and considerably larger than an atom or molecule” (*Millman*, 1963).

At what point an “asteroid” becomes a “meteoroid” is not clear. The definitions approved by the International Astronomical Union in the 1960s are now outdated and efforts are underway to come to terms with this. For example, it is custom these days to also use the term “meteoroid” for the object when it no longer moves through space but through Earth’s atmosphere to cause the meteor. The boundary with asteroids is varyingly put at 1 m or 10 m. However, some researchers protested the use of “asteroid” for the 20-m-sized meteoroid responsible for the Chelyabinsk airburst (*Popova et al.*, 2013), as it had not been seen in space prior to impact, while the small boulders seen in space near Comet 103P/Hartley 2 by the telescopic cameras of NASA’s Deep Impact mission are considered “meteoroids” rather than “asteroids” (*A’Hearn et al.*, 2011).

## 3. INTERPLANETARY DUST PARTICLES

A review of the properties of the IDPs and micrometeorites collected on Earth is given in the chapter on asteroidal dust in the previous *Asteroids III* book (*Dermott et al.*, 2002a). In summary, ~75% of IDPs collected in Earth’s atmosphere are unequilibrated, fine-grained mixtures of thousands to millions of mineral grains and amorphous components with close to chondritic abundances. The compositions of micrometeorites are similar to CM- and CR-type carbonaceous chondrites, but they are 2× richer in carbon. Some hydrous IDPs are extensively altered by liquid water inside a parent body. However, most are anhydrous, with the pyroxene-rich particles that are complex admixtures of 0.1–5-μm-diameter single-mineral grains (most commonly enstatite and Fe-Ni sulfides), amorphous material, carbonaceous material, and submicrometer spheroidal grains of silicate glass with embedded metal and sulfides (GEMS). Some have very large D/H ratios and other isotopic anomalies, and contain presolar grains.

Clearly, interplanetary dust is dominated by relative primitive materials, not by dust from the ordinary chondrites that are recovered from most meteorite falls. Back in 2002, these materials were thought to be the result of prolonged mechanical mixing in the deep regolith of asteroidal rubble piles in the outer main belt (*Dermott et al.*, 2002a).

This view has changed dramatically in recent years with the study of the small cometary dust particles collected from Jupiter-family comet (JFC) 81P/Wild in 2004 during the Stardust mission (e.g., *Zolensky et al.*, 2006; *McKeegan et al.*, 2006; *Hanner and Zolensky*, 2010). This dust proved to consist of the expected fine-grained (submicrometer-sized) loosely bound aggregates with a bulk chondritic composition. However, most aggregates also contained large individual crystals of (most commonly) olivine (33%), low-calcium pyroxene (24%), mixtures of these (10%), and other minerals (33%), mostly Fe-Ni sulfides, formed or altered at temperatures of 1600–2000 K (*Zolensky et al.*, 2012). The cometary dust was even found to have calcium-aluminum-rich inclusions (CAIs) and small chondrule fragments (*Nakamura et al.*, 2008; *Joswiak et al.*, 2014), suggesting that high-temperature inner solar system materials reached the young Kuiper belt. Some magnesium-calcium carbonates and a single occurrence of orthorhombic cubanite even suggested that transient liquid water may have existed within the nucleus or in the inner solar system parent bodies from which this dust originated (*Mikouchi et al.*, 2007; *Berger et al.*, 2011; *Zolensky et al.*, 2012).

These materials are not unlike those found in primitive carbonaceous chondrite meteorites. Indeed, the recent “Grand Tack” planet-formation models suggest that primitive asteroids and Kuiper belt (JFC) comets could both have initially formed beyond the birth region of the giant planets (*Walsh et al.*, 2011; *Morbidelli et al.*, 2011; *Briani et al.*, 2011; *Raymon and Morbidelli*, 2014; see also the chapter by Morbidelli et al. in this volume).

Are meteoroids from primitive asteroids and JFC-type comets different? *Kikwaya et al.* (2011) measured similar densities from meteor lightcurves. CM-type meteorites are likely from a main-belt asteroid source (*Jenniskens et al.*, 2012), although the eccentric orbits of CM-type Maribo and Sutter’s Mill resemble that of JFC 2P/Encke (*Haack et al.*, 2011). The CI-type carbonaceous chondrite Orgueil (also aqueously altered) had an even wider JFC-like pre-atmospheric orbit, but based on the 1864 visual observations of the fireball (*Gounelle et al.*, 2006).

How these materials manifest as IDPs in Earth’s atmosphere and micrometeorites on the ground is determined by changes while in the interplanetary medium and the physical conditions during entry (*Rietmeijer*, 2007). In the interplanetary medium, grains are exposed to solar wind and galactic cosmic rays, causing amorphitization of minerals and polymerization of carbon (e.g., *Rietmeijer*, 2011).

During atmospheric entry, the level and rate of heating is a function of entry speed. This changes the meteoroid density and porosity (*Kohout et al.*, 2014). Because of admixtures of large grains, even the IDPs with nonchondritic

abundances could originate from primitive bodies, with frail aggregate material more easily lost during atmospheric entry (Rietmeijer, 2008).

#### 4. METEOROID STREAMS

Meteoroid streams provide a historic record of dust formation, and still identify their sources. These sources are not necessarily the active comets we can study today, long known to be a source of meteoroid streams and the zodiacal cloud (Shiparelli, 1867; Whipple, 1950, 1967). Instead, the meteoroid input can be dominated by discrete massive disruption events that happened some time ago or, alternatively, by a large population of objects that each contribute small amounts of meteoroids that are hard to measure.

##### 4.1. Formation and Evolution of Meteoroid Streams

Meteoroid streams are observed as meteor showers on Earth and, in some cases, as dust trails in infrared emission (Davies *et al.*, 1984; Sykes *et al.*, 1986). Significant progress was made in recent years in systematically charting meteoroid streams at Earth (e.g., Brown *et al.*, 2008a,b, 2010; Younger *et al.*, 2009; Jenniskens *et al.*, 2011).

Around the time when the *Asteroids III* book came out in 2002, there was a watershed in understanding the mechanisms of meteoroid stream formation and evolution. Many relevant mechanisms were proposed earlier, but only now

were theoretical predictions validated and refined by observations, such as shown in Fig. 1 (see reviews by Jenniskens, 2006; Williams, 2011).

Meteoroid streams are principally first created by small differences in the orbital period of the ejected particles, which cause a comet dust coma to return as a meteoroid stream after one orbit, creating the one-revolution dust trail (Pravec, 1955).

Ejection of meteoroids from parent bodies can occur via gas drag from sublimating ices (Whipple, 1950), parent body disruptions (with collisions, spinup, or other causes), impacts by meteoroids on surfaces, centrifugal forces from Yarkovsky-O'Keefe-Radzievskii-Paddack (YORP) spinup of the parent body, and even from electrostatic levitation (e.g., Walsh *et al.*, 2008).

All common mechanisms tend to result in small relative ejection speeds compared to the heliocentric velocity of the parent body. The hemispherical direction of ejection can either be toward the Sun or be isotropic. Models of ejection from active asteroids follow those for comets (e.g., Whipple, 1950; Crijo and Rodionov, 2000; Vaubaillon *et al.*, 2005; Kelley *et al.*, 2014).

The shorter or longer orbital period resulting from the ejection process will cause the particle to return correspondingly sooner or later in future returns (two-revolution, three-revolution, etc., orbit), spreading the trail along the parent body orbit and creating a meteoroid stream (Fig. 1), but not broadening it (Kondrateva and Reznikov, 1985; McNaught

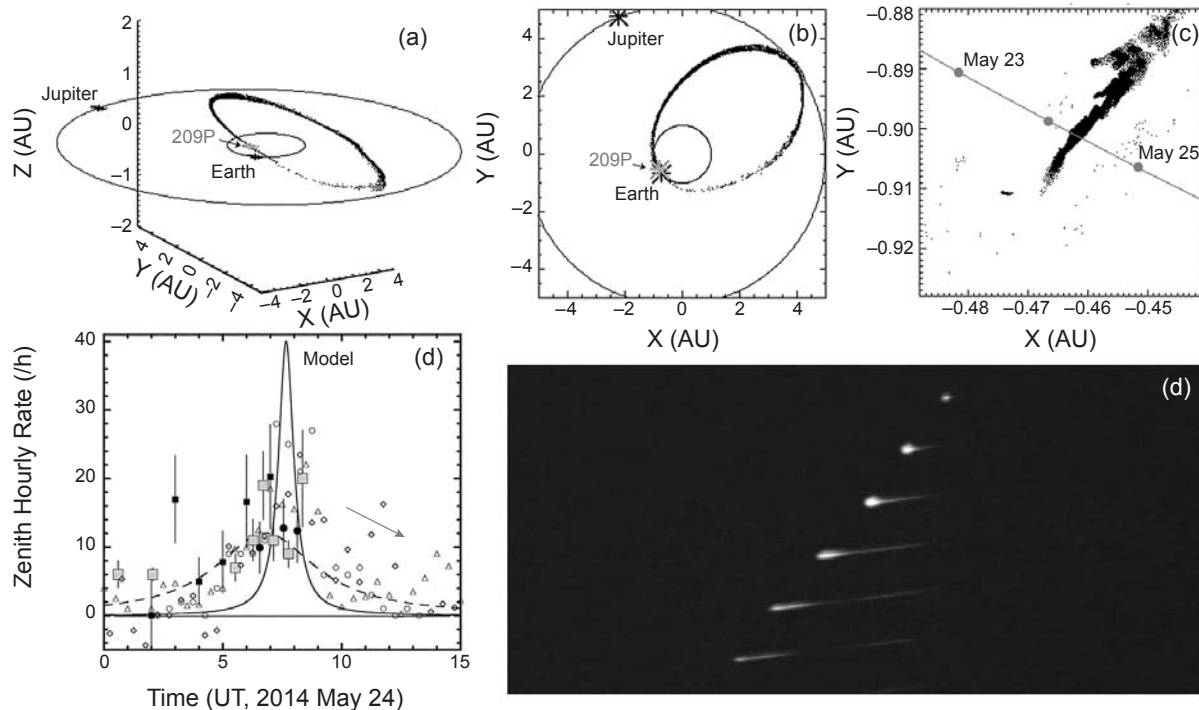


**Fig. 1.** Meteoroid stream model for how the 1903 AD ejecta from weakly active comet 209P/Linear are distributed on May 24, 2014 (top); dust from AD 1803–1924 will be in Earth's path (bottom, left). From Berárd and Vaubaillon (2013). In the bottom left panel, the predicted activity (solid line, scaled down by factor of 10) is compared to the observed activity (dashed line), with different symbols representing different video (right), visual, and radio-MS data. From Jenniskens (2014).

and Asher, 1999; Lyytinen, 1999). Solar radiation pressure tends to increase the orbital period of the meteoroids relative to that of the comet on average, delaying the return of the meteoroids somewhat (Kresak, 1976).

Planetary perturbations act differently on different parts of the trail, with Jupiter and Saturn changing in position relative to the node of the stream from year to year (Jenniskens, 1997; Lyytinen and Jenniskens, 2003). As a result, the dust trails move relative to Earth's orbit, causing meteor outbursts in some years, but not in others (Kondrateva and Reznikov, 1985; Jenniskens, 1997; McNaught and Asher, 1999).

Mean-motion resonances can keep sections of the dust trail stable (e.g., Asher et al., 1999; Jenniskens, 2006). Close encounters with the planets will distort the trails more dramatically, creating gaps, kinks, or a scattering of meteoroids over a wider region around the orbit of the parent body (e.g., Vaubaillon et al., 2005; Jenniskens, 2006).

If close-encounter perturbations by Jupiter and mean-motion resonances are not dominant, then secular perturbations will gradually rotate the nodal line. For parent bodies on orbits that pass inside Earth orbit, this rotation of the nodal line will ultimately result in a stream crossing Earth's orbit (Babadzhanov and Obrubov, 1992; Jenniskens, 2006). When the inclination is higher than 20°, secular perturbations create large oscillations of inclination and perihelion distance, called Kozai cycles (Kozai, 1962).

#### 4.2. Main-Belt Asteroids as a Source of Meteoroid Streams

Main-belt asteroids create meteoroid streams when primitive asteroids have comet-like activity, such as observed for the Geminid shower parent asteroid (3200) Phaethon (see the chapter by Jewitt et al. in this volume), or when rubble-pile asteroids spin up by YORP and fall apart by centrifugal forces (Walsh et al., 2008), if not prevented by cohesion forces (Rozitis et al., 2014).

These events could produce dust trails detectable by the Infrared Astronomical Satellite (IRAS) and Spitzer at mid-infrared (IR) wavelengths for much longer periods of time than the cometary activity. Two such low-inclined and low-eccentricity dust trails may have originated from relatively recent, <100-k.y.-old, collisional breakups of small <10-km-diameter main-belt asteroids (Nesvorný et al., 2006a).

Main-belt asteroids can create meteoroid streams at Earth when such disruptions happen while the asteroid is in a near-Earth orbit. These streams still would have the Tisserand parameter with respect to Jupiter  $T_J \gg 3$  close to that of the parent asteroid (Levison, 1996).

Very few of our meteor showers appear to originate from main-belt asteroids. To illustrate this, Fig. 2 shows  $T_J$  as a function of time in the year for ~1-g (1-cm) meteoroids observed by the Cameras for All-sky Meteor Surveillance (CAMS) project (Jenniskens et al., 2011) between October 2010 and March 2013. The graph covers the range of  $T_J$  for main-belt asteroids and JFCs. Solar longitude is a measure of time throughout the year. Meteoroid streams show up as

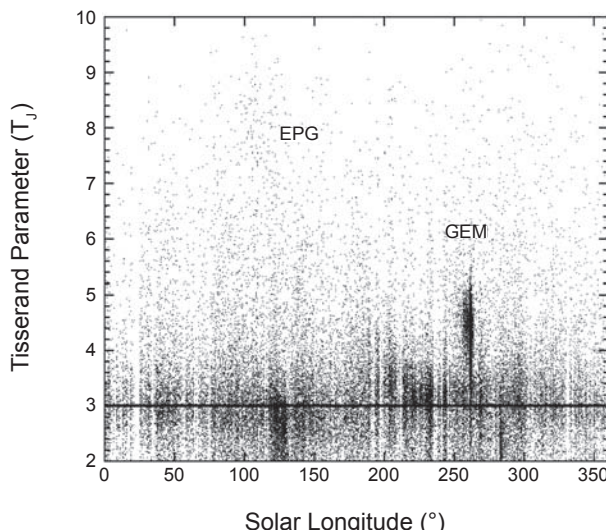


**Fig. 2.** Tisserand parameter of CAMS-observed meteors as a function of solar longitude (time of the year). Note the lack of high  $T_J$  orbits. GEM = Geminids; EPG = ε Pegasiids.

clumps in a narrow range of solar longitude. Measurement errors in meteoroid speed account for some of the diffusion of the  $T_J$  values.

The Geminids (GEM) move in distinctly asteroidal  $T_J \sim 4.4$  orbits (Fig. 2). These meteoroids also have a relatively high meteoroid density, resulting in unusually low meteor beginning heights (Fig. 3). Meteor flares are rarely observed.

The Phaethon parent body is rapidly decaying into streams and remaining fragments. The streams (Geminids and Daytime Sextantids) are still in close proximity to their associated parent bodies (Phaethon and 2005 UD, respectively) in terms of the direction of their nodal line. The Geminids are thought to be only ~1000 yr old (Jones and Hawkes, 1986; Jenniskens, 2006). If (3200) Phaethon originated from the Pallas asteroid family (de Leon et al., 2010), then there must be a more rapid pathway from family to the orbit of Phaethon than proposed, which is possible via the 5:2 resonance with Jupiter.

The Geminids account for 15% of present-day mass influx in the form of meteoroid streams detected by CAMS from the nighttime sky (Jenniskens et al., 2015a). Only 2% of mass is contributed by main-belt asteroidal sources other than the Geminids ( $T_J > 3.2$ ).

This activity will not last. The shower is expected to increase in intensity until about 2050 AD, but then decrease and be gone by 2100 AD (Jenniskens, 2006). Because of this, the dominant role of the Geminids is perhaps not representative for the zodiacal cloud as a whole. On the other hand, individual meteoroid orbits with  $T_J \gg 3$  are commonly measured in CAMS data (Fig. 2) and in photographed meteoroid orbits.

Many asteroidal streams were identified in the past (perhaps unjustified) from only pairs of similar meteoroid orbits from photographed fireballs (Terent'eva, 1990). One example is the pair of similar orbiting Neuschwannstein and Pribram meteorites, which are of EL6 and H6 type, respectively. Such pairings are now mostly thought to be

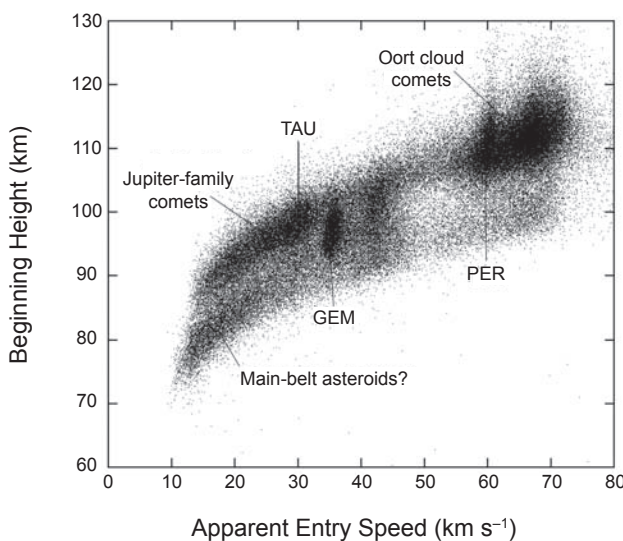


**Fig. 3.** Beginning heights of CAMS-detected meteors. GEM = Geminids; TAU = Taurids; PER = Perseids.

accidental (Koten *et al.*, 2014).

Asteroidal streams are also detected in radar surveys of small meteoroids, such as the Canadian Meteor Orbit Radar (CMOR) (Brown *et al.*, 2008a,b, 2010), in particular pertaining to high-inclination showers (Table 1).

So far, no new meteor showers rich in  $T_J > 4$  meteoroids have been identified from CAMS data. Few of the established CMOR showers with  $T_J > 4$  show a concentration in the CAMS orbital-element diagrams, possibly because they are rich in faint meteors. Table 1 lists only those CMOR-derived streams for which some meteoroids were detected by CAMS ( $N$  being the number of meteoroid orbits). These include the  $\epsilon$  Pegasids (#326, EPG), the  $\beta$  Equuleids (#327, BEQ), and the  $\alpha$  Lacertids (#328, ALA). The  $\epsilon$  Aquilids (#151, EAU) were detected earlier by the Harvard Meteor Radar (Sekanina, 1976). In later work, CMOR also detected a shower called the July  $\beta$  Pegasids (#366, JBP) (Brown *et al.*, 2010). Only the  $\epsilon$  Pegasids stand out well in Fig. 2.

It is possible that these high-inclination short-semimajor-axis showers are not from main-belt asteroids at all. No main-belt asteroid parent bodies have been identified yet, despite the fact that 9.3% of all 11,853 known NEAs have inclinations  $>30^\circ$ , and as much as 25% of the bright  $H \leq 18$  mag NEAs. Instead, old age and Poynting-Robertson (P-R) drag may have decreased the semimajor axis of initial JFC- or Halley-type-comet-derived dust, without fully dispersing the meteoroids.

Many CAMS-detected meteoroids have orbits that straddle the border of asteroids ( $T_J \geq 3$ ) and JFC ( $T_J = 2-3$ ) domains (Fig. 2). The Taurid Complex showers in November, associated with large but weakly active comet 2P/Encke, have  $T_J \sim 3.2$  on average, well into the asteroidal domain, but these meteoroids are fragile, with beginning heights similar to JFCs, higher than those of the Geminids (Fig. 3).

Whipple (1940) first proposed that Comet 2P/Encke is the parent body of the Southern Taurids (#2, STA) and the Northern Taurids (#17, NTA). From the widely dispersed longitude of perihelion, these streams are thought to be at least 20–30,000 yr old. One rotation of the nodal line takes about 5900 yr, explaining the twin showers, as well as the associated daytime  $\beta$  Taurids (#173, BTA) and  $\zeta$  Perseids (#172, ZPE) (Whipple, 1940; Steel and Asher, 1996).

After more asteroids were discovered in Taurid-like orbits, it was proposed that there existed a Taurid complex with a hard-to-understand wide range of semimajor axes ( $a = 1.66-2.57$  AU), proposed to be fragments from a 20-km-sized comet that broke apart 20–30,000 yr ago (Clube and Napier, 1984; Asher *et al.*, 1993; Steel and Asher, 1996).

However, a tally made in 2006 concluded that all proposed members up to that point, with the exception of 2P/Encke, had reflection properties typical of S- or O-class asteroids (Jenniskens, 2006, pp. 462–464). It is now thought that these originally proposed objects are instead asteroids that originated from the inner main belt by ejection from the  $v_6$  resonance, a known source of S-class asteroids.

More recently, the picture is dramatically changing with both more near-Earth objects (NEOs) being discovered in orbits that resemble 2P/Encke in semimajor axis and more

TABLE 1. High  $T_J$  showers.

# IAU	N (AU)	a (AU)	q (°)	i (°)	$\omega$ (°)	Node	$T_J$
<i>Phaethon</i>							
4 GEM	4225	1.32	0.143	23.2	324.4	225.8	4.4
221 DSX	14	1.14	0.147	24.3	214.3	6.4	5.0
<i>Toroidal</i>							
151 EAU	11	0.83	0.405	64.6	322.8	62.5	6.6
326 EPG	33	0.73	0.144	49.0	337.8	109.3	7.4
327 BEQ	35	1.04	0.157	46.5	327.6	84.4	5.3
328 ALA	2	1.07	0.976	77.7	122.2	114.5	5.1

Median orbital elements for  $N$  = number of CAMS-observed meteors:  $a$  = semimajor axis;  $q$  = perihelion distance;  $i$  = inclination;  $\omega$  = argument of perihelion; Node = longitude of the ascending node.

clarity about the Taurid stream being composed of multiple streams (*Porubcan et al.*, 2006).

A recent analysis of CAMS data shows that the Taurid showers are composed of at least 19 individual streams, 7 of which were assigned to parent body asteroids. Importantly, these streams are not twins, having separate values of the longitude of perihelion, but similar to that of their parent bodies. This implies that individual streams fade rapidly, presumably due to meteoroids falling apart, before their node can significantly rotate away from the parent body (*Jenniskens et al.*, 2015b).

Unlike the Taurid complex asteroids proposed in the past, these asteroids all have a narrow range of semimajor axis ( $a = 2.20\text{--}2.35$  AU). Of the 17 known asteroids with semimajor axis in this range and with a Taurid (and related  $\chi$ -Orionid) shower's longitude of perihelion  $\Pi = 130^\circ\text{--}185^\circ$ , 9 can be associated with one of the Taurid and  $\chi$ -Orionid stream components, most in the 0.3–1-km size range. The current completeness of NEO detections in this size range is about 64%, in good agreement (*Jenniskens et al.*, 2015b).

Another example of a complex of comet fragments, each meteoroid stream detected at Earth still having a nodal line similarly oriented to that of the comet fragments, is the complex of comets and meteoroid streams associated with Comet 96P/Machholz (*Sekanina and Chodas*, 2005; *Jenniskens*, 2006; *Jenniskens et al.*, 2015b).

## 5. THE ZODIACAL CLOUD

How important are main-belt asteroids in the formation of the interplanetary dust cloud as a whole? In the *Asteroids III* chapter on asteroidal dust (*Dermott et al.*, 2002a), much focus was given to the zodiacal dust bands at  $2^\circ$  and  $10^\circ$  ecliptic latitude, because these features can be used to estimate the contribution of dust from asteroids to the zodiacal dust cloud.

At the time, the dust bands were thought to be produced in the Eos, Koronis, and Themis families, but a few problems with this interpretation were already noted in *Grogan et al.* (2001). This perception has changed completely in the past decade. Now, the three main bands are believed to sample an ongoing collisional cascade among the smallest fragments in three recently formed families: Karin, Veritas, and Beagle, which represents collisions between asteroids only 6–8 m.y. ago (*Nesvorný et al.*, 2006a,b, 2008; *Kehou et al.*, 2007; *Vokrouhlický et al.*, 2008; *Espy et al.*, 2009).

Based on the earlier proposed source regions, and assuming that all asteroids contribute similar amounts of meteoroids, *Kortenkamp and Dermott* (1998) estimated that >75% of infalling matter on Earth originated from main-belt asteroids, and later increased this estimate to as high as 90% (*Grogan et al.*, 2001; *Dermott et al.*, 2002a,b). With some holdouts, this perception has also completely changed in recent years. Now, dynamical models put this fraction at less than 5% (*Wiegert et al.*, 2009; *Nesvorný et al.*, 2010). That also agrees better with the fact that satellites with dust detectors passing through the asteroid belt have never detected

a significant increase of impact rates of small meteoroids (*Gruen et al.*, 2001b; *Landgraf et al.*, 2002).

Nevertheless, *Ipanov et al.* (2008) still assigned 30–50% to main-belt asteroids, while the “model A” by *Rowan-Robinson and May* (2013) found 22.2% of meteoroids from asteroids originating in the main belt and 7.5% from an isotropic source proposed to be interstellar dust.

### 5.1. DORMANT COMETS AS THE SOURCE OF ZODIACAL DUST

The first dynamical models of the zodiacal cloud were inspired by insight from meteor observations and were made possible by advances in computing techniques, which now make it possible to follow the complex dynamical evolution of clouds of meteoroids. The advance in computing capabilities also has greatly aided the ongoing development of new meteor and meteoroid observing techniques, and has resulted in a better understanding of the observing biases and the astronomical interpretation of meteor observations (e.g., *Taylor and McBride*, 1997; *Galligan and Baggaley*, 2004, 2005; *Campbell-Brown*, 2008; *Close et al.*, 2007).

The new models are calibrated to the optical (peak emission, polarization, and Fraunhofer lines) and infrared observations of the zodiacal cloud (e.g., *Levasseur-Regourd and Lasue*, 2010), but only the meteor observations provide orbital-element distributions of the actual meteoroids.

Before discussing the new models, I will first discuss the latest meteor observations. Meteor observations are capable of probing both the small <1-mm grains that dominate the mass influx from the zodiacal cloud, also probed by dust impact detectors, and the large >1-mm grains that carry most mass loss of their source, but are relatively rare and not easily detected by dust detectors or by remote sensing in astronomical observations.

The small meteoroids are detected by specular meteor radars, which sample underdense echoes from meteors of magnitude +6 and fainter, and by high-power large-aperture (HPLA) radars that can also detect the head-echoes of small meteoroids. The larger meteoroids are observed as visual and video-detectable meteor showers and fireballs (e.g., *Borovička et al.*, 2005; *Jenniskens et al.*, 2011), as head echoes by radar (e.g., *Kero et al.*, 2012; *Piško et al.*, 2013), and as impact flashes on airless bodies such as the Moon (e.g., *Suggs et al.*, 2014). Bright meteors and impact flashes are relatively few, but advances in low-light-level video observations now provide insight into the population of ~1 g–1 kg meteoroids that carry much of a comet's mass loss.

Figure 4 shows the six principal source directions from which sporadic meteors (both small and large) approach Earth (*Hawkins*, 1956; *Taylor*, 1997; *Jones and Brown*, 1993; *Younger et al.*, 2009). Observational and technical biases affect how these sources are sampled.

Most easily detected are the fast 40–72 km s<sup>-1</sup> meteors approaching from the northern and southern apex sources, which originate from Oort cloud comets (long-period comets with orbital period  $P > 250$  yr and retrograde Halley-type comets with  $250 > P > 20$  yr). Of intermediate 30–50 km s<sup>-1</sup>

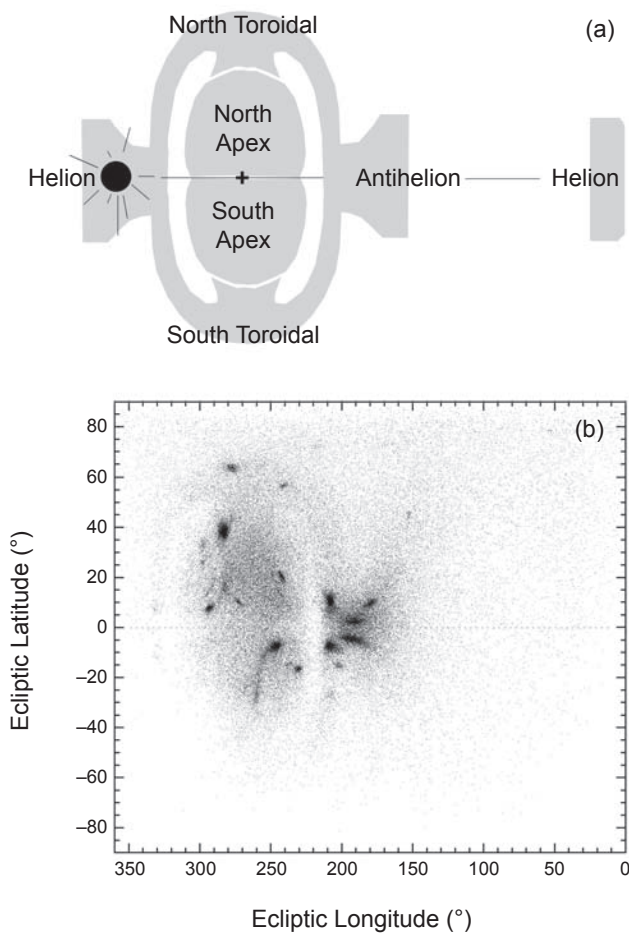


**Fig. 4.** (a) Cartoon showing the sporadic meteoroid source regions identified by Hawkins (1956), Taylor (1997), and Jones and Brown (1993). (b) An example of measured approach directions of meteoroids to Earth; all +1 to +4 magnitude meteors throughout the year observed in CAMS video observations (Jenniskens et al., 2015).

apparent entry speed are the toroidal sources, which mostly are rich in faint meteors and are prominent in radar observations (Campbell-Brown, 2008; Pokorny et al., 2013).

More important for the total mass input in the zodiacal cloud, however, are the slow and therefore hard to see 11–40 km s<sup>-1</sup> meteors in the antihelion and helion sources (Fig. 4), which are meteoroids from JFCs and main-belt asteroids.

Much effort has gone into debiasing the radar-observed populations (e.g., Taylor, 1997; Jones and Brown, 1993; Galligan and Baggaley, 2002; Nesvorný et al., 2011a; Kero et al., 2012, 2013; Píško et al., 2013). Both specular and head-echo radar observations have strong velocity-dependent biases, because ionization has a complex and steep dependence on speed and altitude. After debiasing for these observational effects, most mass from the larger observed particles, and therefore most mass input into the interplanetary dust cloud, arrives from the antihelion and helion sources. The derived orbital data shows that the meteoroid density falls off with heliocentric distance ( $r$ ) according to  $r^{-1}$  inside 1 AU and

according to  $r^{-2}$  outside 1 AU, with a weak excess at 2–4 AU (Galligan and Baggaley, 2002; Dikarev et al., 2004, 2005; Jenniskens, 2006).

Surprisingly, the sensitive AMOR (+14 limiting magnitude) and not-so-sensitive CMOR (+8 limiting magnitude) radar results show a sporadic population with similar orbital-element distributions, with antihelion source orbits on relatively small  $a \sim 1.0$  orbits (Fig. 5).

For CMOR particles to evolve to  $a = 1$  AU orbits by P-R drag requires more time than allowed by the collisional lifetime according to Grün et al. (1985). Nesvorný et al. (2011a) assumed that CMOR-detected particles, about 0.6 mm in size, survived as long as the smaller 0.09-mm-diameter AMOR-detected particles, some  $3 \times 10^5$  yr, about 4–10× as long as calculated by Grün et al. (1985).

The same is measured for the CAMS-detected sporadic meteors (Jenniskens et al., 2015a). The debiased distribution of semimajor axis peaks at 2.1–2.8 AU, but has a P-R-evolved component (Fig. 5). These particles survived collisions for  $1\text{--}3 \times 10^6$  yr, 10× longer than calculated by Grün et al. (1985).

Above 100 µm, the size frequency distribution of meteoroids falling to Earth falls off steeply to larger sizes. The short lifetime required to explain the relative lack of the CAMS-detected 7-mm-sized meteoroids at Earth (Grün et al., 1985) suggests that these meteoroids disappear on a short timescale of 300–10<sup>4</sup> yr, not from collisions, but from other processes that disrupt the meteoroids into smaller grains. A small fraction of large grains remains and goes on to evolve by P-R drag (Jenniskens et al., 2015a).

Large meteoroids deposited by comets disappear over time, before their streams evolve and dynamically merge with the sporadic background. Freshly deposited comet dust fades over timescales as short as 300 yr for the Leonids of Comet 55P/Tempel-Tuttle and 50 yr for the Camelopardalids of 209P/Linear, needing the scaling down of the model activity in Fig. 1 to match the observations, for example (Jenniskens, 2014). Other meteoroids survive longer, but streams linked to weakly active comets or asteroidal parent bodies are rarely older than about 10<sup>4</sup> yr, not old enough to differentially rotate the nodal line and create twin showers at their other node (Jenniskens et al., 2015b).

CMOR samples large enough particles to recognize the meteoroid streams, being most sensitive to showers rich in faint meteors and with intermediate entry speeds of 20–50 km s<sup>-1</sup> (Brown et al., 2008a,b, 2010; Weryk and Brown, 2012).

The meteoroid streams of faster, slower, and larger particles are best detected by optical techniques, but bright meteors are much less frequent. Only in recent years have significant numbers of meteoroid trajectories been measured by scaling up multi-station video observations. These surveys are ongoing, but already show the presence of many additional meteoroid streams.

CAMS is just one of these surveys [for an overview of other projects, see Jenniskens et al. (2011)]. CAMS detects the +1 to +4 meteors (~1-g- and ~1-cm-sized meteoroids)

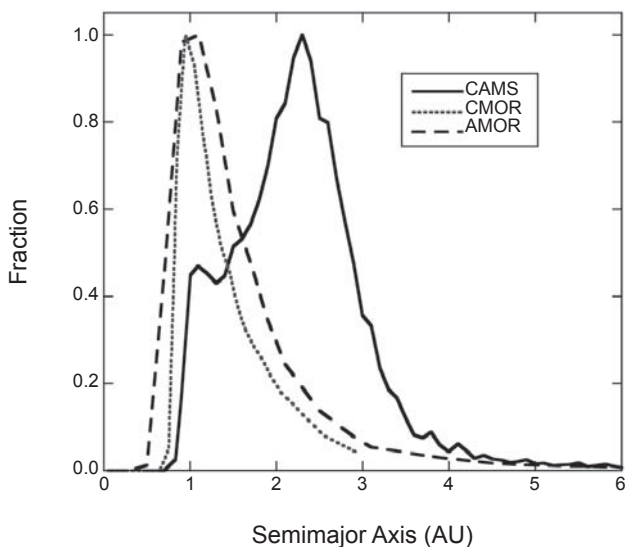


**Fig. 5.** The measured orbital element distribution at Earth for 7-mm-sized (CAMS), 0.6-mm-sized (CMOR), and 0.09-mm-sized (AMOR) meteoroids. The distributions are debiased by correcting for observational effects and mass weighted, but are not corrected for the collisional probability with Earth (Jenniskens et al., 2015a).

approaching from the nightside antihelion source, but not those arriving on the dayside after circling the Sun, called the helion source (Fig. 4). The cameras measure luminosity, with luminous efficiency (= the fraction of kinetic energy converted into the light detected by the cameras) depending in an uncertain manner on entry speed.

Slightly more than a quarter (25.6%) of all CAMS-detected meteors between October 2010 and March 2013 were assigned to 230 meteor showers, of which 86 are newly discovered [listed among the International Astronomical Union (IAU) Meteor Shower Working List numbers 427, 448–502, 506–507, and 623–750]. The IAU keeps a tally of meteor showers and assigns names, numbers, and codes (Jenniskens et al., 2009). So far, only 95 showers are considered “established,” meaning that we can be certain that they exist. Based on the new data, this number is expected to increase.

Only a small fraction of these showers has known parent bodies. It was long thought that the lack of parent bodies for most showers meant they had disappeared. This view has now changed dramatically. With a surge in NEO discoveries, it was realized that many meteor shower parent bodies are hiding as asteroid-looking objects. Most are weakly active or dormant comets and a few are primitive asteroids (Jenniskens, 2008).

Whipple (1983) was the first to point out that asteroid (3200) Phaethon moves in the Geminid stream (#4, GEM), but that association was long dismissed as a possibly coincidental alignment of orbits. However, Phaethon moves in an eccentric asteroid-like orbit with small perihelion distance ( $q$ ), which makes a random association unlikely. As said, the stream has a Tisserand parameter with respect to Jupiter  $T_J = 4.4$ , well into the asteroid regime with  $T_J \geq 3$ . Phaethon now is known to be occasionally weakly active at

perihelion (Jewitt et al., 2013), and there is no longer doubt that Phaethon is the source of the Geminids.

This uncertainty was lifted following the discovery that asteroid 2003 EH<sub>1</sub> moves among the highly inclined 72° Quadrantids (#10, QUA) (Jenniskens, 2004). It was then found that asteroid 2005 UD moved in the Sextantid stream (#221, DSX) (Ohtsuka et al., 2006), which is related to the Geminids (Jewitt and Hsieh, 2006; Jenniskens, 2006), and asteroid 2008 ED<sub>69</sub> moved among the κ Cygnids (#12, KCY) (Jenniskens and Vaubaillon, 2008; Trigo-Rodriguez et al., 2009). Asteroid 2002 EX<sub>12</sub>, now better known as weakly active Comet 169P/NEAT, was proven to be the parent body of the α Capricornids (#1, CAP) (Wiegert and Brown, 2004; Jenniskens and Vaubaillon, 2010), while 2003 WY<sub>25</sub> was identified as a recovered fragment of Comet D/1819 W<sub>1</sub> (Blanpain), the source of the Phoenicids (#254, PHO) (Foglia et al., 2005; Jenniskens, 2006). Work on other proposed associations is ongoing (e.g., Babadzhanov et al., 2008, 2012; Rudawska et al., 2012). The situation should be similar on Mars and Venus (Christou, 2010).

Typically, the mass of meteoroids in each stream is similar to that of the remaining parent body (Jenniskens, 1994, 2006, 2008a,b). The implication is that the main mass-loss mechanism of JFCs is an episodic disruption, during which they lose about half their mass and create meteoroid streams.

Active comets were long known to contribute to the zodiacal cloud (e.g., Whipple, 1967; Zook, 2001), but are insufficient to account for the required steady-state mass input. Active JFCs contribute only about 300 kg s<sup>-1</sup> of large meteoroids that contribute to mid-IR emissions (Reach et al., 2007). The required steady-state averaged mass input in the zodiacal cloud is 10<sup>4</sup>–10<sup>5</sup> kg s<sup>-1</sup> (Nesvorný et al., 2011a).

Based on the new parent body identifications, we now know that the episodic breakup of mostly dormant comets solves this discrepancy (Jenniskens, 2008a,b). With the more prominent JFC streams today measuring about 2 × 10<sup>13</sup> kg (Table 8 in Jenniskens, 2006), there needs to be about 1 such breakup every 30 yr in the inner solar system to maintain the cloud, from a population that is about 2000 dormant comets and 600 active comets (Belton, 2015a).

Jupiter-family comets appear to break apart as often as Oort cloud comets (Levison et al., 2002; Belton, 2015) at a rate of about 5 × 10<sup>-5</sup> disruptions/yr for an active comet and a factor of 3 less for a dormant comet. Recent disruptions include that of meteoroid stream parents D/1819 V1 (Blanpain) in 1819, 3D/Biela in 1843, and 73P/Schwassmann-Wachmann 3 in 1995 (Reach et al., 2009). The latter released meteoroids during the 1995 breakup with a cumulative mass index of 0.85–1.00, dominated by particles >1 mm (Vaubaillon and Reach, 2010), and numerous fragments of which one large object survived. Eleven known short-period comets were observed to split in the last 200 yr, amounting to a rate of 1 in 18 years, but not all may have disrupted to the level required.

Activity from these events can linger, as in the case of weakly active 2P/Encke, the remnant of the Taurid complex (see below). The activity associated with 2P/Encke and the

Taurid complex meteoroid streams is recognized to be a significant contributor to the current helion and antihelion meteor shower sources (Whipple *et al.*, 1967; Wiegert *et al.*, 2009).

Discovering the dominant presence of dormant and weakly active comets among our antihelion source meteoroid streams inspired a revisiting of zodiacal cloud models to investigate whether or not mostly dormant comets can be the main source of our zodiacal meteoroids. Only recently have zodiacal dust cloud models been developed that are based on rigorous dynamical modeling of the meteoroid orbital evolution from their source to their demise in collisions with other meteoroids. All prior zodiacal cloud models were based on artificial constructs of components with presumed orbital dynamics (e.g., Divine, 1993; Dikarev, 2005; Ipatov *et al.*, 2008; Rowan-Robinson and May, 2013).

It was often assumed that main-belt asteroidal dust would evolve by P-R drag into near-circular orbits ( $e \sim 0.3\text{--}0.0$ ), from which they hit Earth at very low entry velocities. However, Doppler radial velocity profiles of Fraunhofer lines in scattered light from the zodiacal cloud show a typical  $e \sim 0.5$  eccentricity of small meteoroids (Ipatov *et al.*, 2008; May, 2008).

The new modeling showed that meteoroids evolving from asteroids would increase their eccentricity as required due to the action of resonances, but would not be pumped up to high enough inclinations to account for the observed latitudinal dispersion of the zodiacal cloud (Nesvorný *et al.*, 2010). In contrast, meteoroids ejected by the population of JFCs naturally created the observed width of the zodiacal cloud (Fig. 6) from an initial higher distribution of inclinations, coupled to an increase of inclinations from interactions with Jupiter when still having an aphelion near this planet. It was calculated that Kuiper belt comets in the form of JFCs

contribute more than 90% of all meteoroids in the inner solar system (Nesvorný *et al.*, 2010). Other derived properties for the zodiacal cloud are summarized in Table 2.

While deposited initially in JFC-like orbits ( $e \sim 0.7$ ), the dust does evolve by P-R and solar-wind drag to lower eccentricities ( $e \sim 0.5$ ) over time, finally hitting Earth with a median speed of  $\sim 14 \text{ km s}^{-1}$ , slow enough to explain these comets as the dominant source of our micrometeorites (Nesvorný *et al.*, 2010). However, if collisional lifetimes are reversed and small 10–100- $\mu\text{m}$  grains collide more frequently than in the Grün *et al.* (1985) model, it is possible that the P-R evolution is interrupted and meteoroids move in  $e \sim 0.3\text{--}0.5$ , as observed.

It was earlier assumed that the relative lack of large grains at Earth was because meteoroids with masses  $>10^{-6} \text{ g}$  ( $>1 \text{ mm}$ ) collided with smaller so-called  $\beta$ -meteoroids (radiation-pressure-driven, on hyperbolic orbits, generated deep inside 1 AU) before they had time to evolve from the asteroid belt to Earth. The observed size distribution slope at Earth was explained through a balance between the collisional loss of particles and the dust supply (Gustafson, 1994; Ishimoto, 1998). Collisional lifetimes at 1 AU were estimated at about 60,000 yr for a 1-mm meteoroid and 200,000 years for centimeter-sized grains (Nikolova and Jones, 2001). Collisional lifetimes may in fact be longer if collisions with larger meteoroids dominate their destruction (e.g., Davis *et al.*, 2012).

In summary, we now understand that the zodiacal cloud results mainly from episodic disruptions of weakly active and mostly dormant JFCs, followed by the formation of meteoroid streams of millimeter- to centimeter-sized particles, which then fade by meteoroid fragmentation to  $\sim 0.15\text{-mm}$  particles, with these smaller particles dynamically evolving to become the zodiacal cloud, until collisions finally shatter

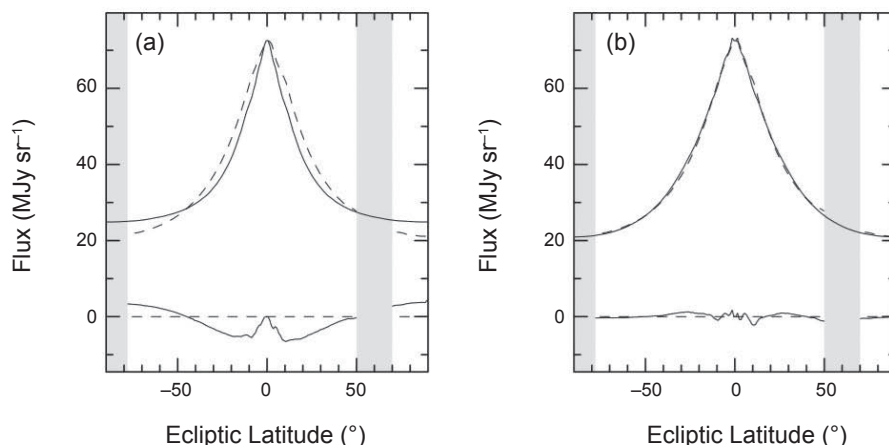


**Fig. 6.** Two models of zodiacal cloud infrared emission (upper solid lines) with 25- $\mu\text{m}$  IRAS flux measurements (upper dashed lines, with gray areas prone to residual galactic plane emissions) and the differential of calculated–observed (bottom). **(a)** The best-fit model with asteroid and Oort cloud comet particles. This model does not fit IRAS observations well. The model profile is too narrow near the ecliptic and too wide overall. **(b)** A model with a dominant contribution of (mostly dormant and weakly active) JFC particles. From Nesvorný *et al.* (2010).

TABLE 2. Zodiacal cloud properties.

Property	Value	Ref.
<i>First stage — sources</i>		
Mass in young comp.	$\sim 5 \times 10^{15}$ kg	[4]
Mean age young comp.	$300\text{--}10^4$ yr	[4]
Steady state mass input	$10^4\text{--}10^5$ kg s $^{-1}$	[1]
Main-belt asteroids	<5% by mass	[1]
Jupiter-family (=Kuiper belt) comets	>90% by mass	[1]
Oort cloud comets	<10% by mass	[1]
Interstellar (at 1 AU)	$\ll 1\%$ by mass	[2]
Dominant size range	1 mm–10 cm	[4]
<i>Second stage — evolved</i>		
Total dust cross section	$1.7\text{--}3.5 \times 10^{17}$ m $^2$	[1]
Total mass	$\sim 4 \times 10^{16}$ kg	[1]
Mean age	$\sim 300,000$ yr	[1]
Dominant size range	150 $\mu$ m	[3]
Mass impacting Earth	$10\text{--}40 \times 10^3$ ton yr $^{-1}$	[1,3]
( $\phi = 1$ $\mu$ m to 5 cm)		

References: [1] Nesvorný *et al.* (2011a); [2] Rowan-Robinson and May (2013); [3] Love and Brownlee (1993), Cepheha *et al.* (1998); [4] Jenniskens *et al.* (2015a).

the grains fine enough to be blown out of the solar system by radiation pressure.

## 5.2. The Contribution from Main-Belt Asteroids

Main-belt asteroids contribute less than 5% to the IR emission of the zodiacal cloud and the population of meteoroids (Wiegert *et al.*, 2009; Nesvorný *et al.*, 2010). The relative contribution of both JFC dust and asteroidal dust to Earth accretion is larger, because gravitational focusing increases the accretion rate of meteoroids that move with a low relative speed to Earth (e.g., Jones and Poole, 2007). If the smallest meteoroids approach Earth as slow as in the model by Nesvorný *et al.* (2010), then the fraction of main-belt asteroidal meteoroids can exceed 10% of the total accreted mass (Nesvorný *et al.*, 2010).

The contribution from main-belt asteroids is not zero. Some objects in the main belt are known to produce dust now (see the chapter by Jewitt *et al.* in this volume). The meteorites that fall from <1-m-sized meteoroids originate from collisions among smaller asteroids, presumably mainly in the asteroid families (e.g., Spurný *et al.*, 2012; Jenniskens *et al.*, 2014; see also the chapter by Borovicka *et al.* in this volume). And a period of increased extraterrestrial influx seen in the  $^3$ He concentration of seafloor sediments, starting  $8.2 \pm 0.1$  m.y. ago, is thought to have been caused by the formation of the Veritas asteroid family  $8.3 \pm 0.5$  m.y. ago (Farley *et al.*, 2006).

Among smaller ~1-g meteoroids, Borovicka *et al.* (2005) found that about 10% of sporadic meteors (out of a sample of 97) in short-period orbits have iron spectra only, lacking magnesium and sodium. Such nonchondritic abundances are possibly related to iron-nickel meteorites. This needs further study.

Another line of evidence for main-belt-asteroid meteoroids points to a group of slow meteoroids that have lower beginning heights compared to those of other JFCs (Fig. 3). All meteoroids impacting Earth with very low speeds (<13 km s $^{-1}$ ) appear to belong to this group. The low beginning heights are thought to be due to different thermal properties of the meteoroids that delay the onset of ablation (Whipple, 1954). It is possible that this group represents main-belt-asteroidal meteoroids (Weryk *et al.*, 2013), but there are some doubts. This group has median orbital-element semimajor axis  $\langle a \rangle = 2.13$  AU, eccentricity  $\langle e \rangle = 0.60$ , and inclination  $\langle i \rangle = 7.2^\circ$  ( $T_J = 3.45$ ), not unlike the meteoroids from Comet 2P/Encke. Their beginning height is also comparatively lower than that of the Geminids, which are thought to derive from a primitive main-belt asteroid. Moreover, CAMS also detected a population of low-beginning heights among the fast Oort cloud comet dust, causing a bimodal distribution of beginning heights (higher speeds in Fig. 3). The retrograde >50 km s $^{-1}$  meteors have  $\langle a \rangle = 4.9$  AU,  $\langle e \rangle = 0.84$ , and  $\langle i \rangle = 149.9^\circ$  ( $T_J = 0.15$ ). The cause of the bimodal behavior is not known. The P-R evolved population dominates the lower group at speeds less than 25 km s $^{-1}$ , which may represent comet dust that has become more sintered over time.

## 5.3. Oort Cloud Comets as a Source of Meteoroids

Oort cloud comets in the form of long-period and Halley-type comets contribute up to 10% of the observed mass of the zodiacal cloud (Nesvorný *et al.*, 2010). To discuss these active comets as a source of zodiacal dust seems outside the scope of this volume, but is relevant to understanding the role of zodiacal dust in meteoroid impacts on asteroid regolith, for example.

Like JFCs, Oort cloud comets produce meteoroids predominantly by disruption, with few surviving to return to the inner solar system on more than a few returns (Levison *et al.*, 2002). These meteoroids strike from retrograde orbits with the highest impact velocities, as a result of which there is little gravitational focusing by Earth.

Again, zodiacal cloud models were revisited using dynamical tools, inspired by the strong detection of the apex source in radar observations (e.g., Campbell-Brown, 2005, 2008), resulting in the work by Wiegert *et al.* (2009) and the discovery that HPLA radar observations of small meteoroids appear to be dominated by apex source meteoroids (e.g., Close *et al.*, 2002; Janches *et al.*, 2005, 2006; Dyrud *et al.*, 2005; Chau *et al.*, 2007; Fenzke *et al.*, 2009; Kero *et al.*, 2013), resulting in the study by Nesvorný *et al.* (2011b). The population is described by Francis (2005) and references therein.

These observations pertain mostly to small meteoroids <0.3 mm, which impact Earth from predominantly 55–65 km s $^{-1}$  orbits [MU radar head echoes (Kero *et al.*, 2013)], only slightly smaller than the 57–70 km s $^{-1}$  orbits detected for larger particles in the CAMS survey. The smaller particles detected by Advanced Research Projects Agency (ARPA) Long-Range Tracking and Instrumentation Radar (ALTAIR) and Arecibo radar observations seem to have lower entry

speeds of 40–65 km s<sup>-1</sup>, as do AMOR and Harvard radar-detected meteoroids (Campbell-Brown, 2005). Some of that is a selection effect, with the radars being most sensitive in this velocity range (Close *et al.*, 2007). Janches *et al.* (2008) have argued, however, that this is not the case for Arecibo. If so, very-small-apex source meteoroids in the inner solar system have also very short semimajor axis  $a \sim 1$  AU and a wide range of eccentricity.

Nesvorný *et al.* (2011b) found that <100-μm-sized particles deposited on long-period orbits are easily blown out of the solar system, while particles larger than 300 μm evolve so slowly that they are scattered by Jupiter before P-R drag lowers the semimajor axis significantly. Only about 1% of ejected particles, mostly particles with sizes in between, reach orbits with semimajor axis  $a \sim 1$  AU by P-R drag, contributing to the radar-observed apex source meteors. If so, the apex source dominates that of the helion/antihelion sources for small (<100 μm) sizes, even if the meteoroids are ejected from JFCs and Oort cloud comets in similar proportions for all sizes. The resulting particle density follows an  $r^{-1.5}$  dependence with heliocentric distance for  $r < 5$  AU and an  $r^{-2}$  dependence for  $r > 10$  AU.

However, the resulting eccentricities tend to still have high  $e \sim 1$ , and the meteoroid radiants peaked at higher ecliptic latitude than observed (Nesvorný *et al.*, 2011b). This needs further study.

#### 5.4. Kuiper Belt and Interstellar Dust

Note that the situation in the outer solar system can be very different, where dust from the Kuiper belt objects and interstellar dust can be important contributors (Landgraf *et al.*, 2002; Moro-Martin and Malhotra, 2002; Sterken *et al.*, 2012; Poppe and Horányi, 2012; Rowan-Robinson and May, 2013). Because this has perhaps less relevance to main-belt asteroids, I refer to these papers for more information.

### 6. FUTURE WORK

The perception that the zodiacal dust bands are caused by ongoing asteroid collisions in the main belt may still change. Precession of the longitude of perihelion can be fast and the rotation of the nodal line can still cause most dust at aphelion to be in the higher inclined orbits. The Taurid complex meteoroid streams, for example, maintain a near constant proper inclination with precessing longitude of perihelion, and spread along 360° in longitude of perihelion over time (Wiegert *et al.*, 2009), even though the meteoroids have relatively high eccentricities ( $e \gg 0.2$ ). The reported fading of meteoroids in the dust bands (Grogan *et al.*, 1997) may not be due to collisions. The relative role of the Taurid complex in the formation of small antihelion source meteoroids needs to be better understood.

We now know that episodic fragmentation of dormant and weakly active comets and active asteroids plays a key role in the evolution from parent body to meteoroids. However, it is unclear what mechanisms will cause a significant fraction of

the comet to fall to dust. The large relative mass in meteoroid streams suggests that whole comet lobes are affected.

Also, what mechanism is responsible for the meteoroids fading over time? This could be the heating and cooling cycles from rotation (day/night) or orbital evolution (perihelion/aphelion). It could also be radial velocity stresses from spinup, or perhaps other effects such as disrupting grain-grain bonds by solar wind or cosmic-ray bombardment. If so, main-belt asteroidal meteoroids in the form of millimeter-sized chondrules, CAIs, and metals and metal sulfide grains may be more resilient against fragmentation and survive longer before falling apart into the smaller zodiacal cloud dust. Are these materials a significant fraction of the millimeter-sized anti-helion source influx at Earth, as hinted at in the study by Borovicka *et al.* (2005)?

The dynamical models for the apex source also need more work, first to better understand the contribution from Halley-type comets. Wiegert *et al.* (2009) pointed to the importance of the three Halley-type comets that currently have strong showers at Earth: 55P/Tempel-Tuttle, 1P/Halley, and 109P/Swift-Tuttle. Tempel-Tuttle and Halley are perhaps responsible for the peak of the north and south apex source being at relatively low ecliptic latitude (Nesvorný *et al.*, 2011b). On the other hand, these comets have been in the inner solar system for only a short period of time: ~1000 yr, <18,000 yr, and <200,000 yr, respectively. It is hard to see how the observed inclination distribution of sporadic meteoroids can be as widely dispersed as observed if only these three sources dominate the input.

The dynamical models for the long-period comet contribution to the apex source need work also. CAMS sees much structure in the apex source of large 2-mm (~0.001 g) meteoroids, which have a high eccentricity  $e \sim 0.95$  (most  $e > 0.8$ ) and semimajor axis  $a \sim 12$  AU, suggesting many intermediate long-period comets have streams of large meteoroids that are not yet dispersed beyond recognition. The question remains how to get from this situation to one of having a broad range of eccentricity  $e = 0.2\text{--}1.0$ , with short semimajor axis ~1 AU for the smaller meteoroids observed by radar.

Meteor shower surveys are ongoing, as are surveys to find NEOs. Together, they are expected to create a more detailed picture of the formation and evolution of the zodiacal cloud in the years to come.

**Acknowledgments.** This review was greatly improved by comments from D. Nesvorný and two anonymous referees, who generously provided their time. J. Vaubaillon contributed three panels of Fig. 1 and D. Nesvorný contributed Fig. 6. I hope that this work will inspire and serve to further the goals of the IAU Commission “Meteors, Meteorites and Interplanetary Dust,” and acknowledge support from NASA’s Near Earth Object Observation program (grant NNX12AM14G).

### REFERENCES

- Ade P. A. R., Aghanim N., and the Planck Collaboration (2014) Planck 2013 results. XIV. Zodiacal emission. *Astron. Astrophys.*, 571, A14.  
A’Hearn M. F., Belton M. J. S., Delamere W. A., et al. (2011) EPOXI at Comet Hartley 2. *Science*, 332, 1396–1400.

- Asher D. J., Clube S. V. M., and Steel D. I. (1993) Asteroids in the Taurid complex. *Mon. Not. R. Astron. Soc.*, **264**, 93–105.
- Asher D. J., Bailey M. E., and Emel'yanenko V. V. (1999) Resonant meteoroids from Comet Tempel-Tuttle in 1933: The cause of the unexpected Leonid outburst in 1998. *Mon. Not. R. Astron. Soc.*, **304**, L53–L56.
- Babadzhanov P. B. and Obrubov Yu. V. (1992) P/Machholz 1986 VIII and Quadrantid meteoroid stream. Orbital evolution and relationship. In *Asteroids, Comets, Meteors 1991*, pp. 27–32. Lunar and Planetary Institute, Houston.
- Babadzhanov P. B., Williams I. P., and Kokhirova G. I. (2008) Near-Earth asteroids among the Piscids meteoroid stream. *Astron. Astrophys.*, **479**, 249–255.
- Babadzhanov P. B., Williams I. P., and Kokhirova G. I. (2012) Near-Earth object 2004 CK<sub>39</sub> and its associated meteor showers. *Mon. Not. R. Astron. Soc.*, **420**, 2546–2550.
- Ballering N. P., Rieke G. H., and Gáspár A. (2014) Probing the terrestrial regions of planetary systems: Warm debris disks with emission features. *Astrophys. J.*, **793**, 57.
- Belton M. J. S. (2015) The mass disruptions of Jupiter family comets. *Icarus*, **245**, 87–93.
- Berárd D. and Vaubaillon J. (2013) The next big meteor shower. Presented at the Meteoroids 2013 conference, held in Poznan, Poland, on August 26–30, 2013, Poster P7.5. Available online at <http://www.imcce.fr/> (last accessed December 5, 2014).
- Berger E. L., Zega T. J., Keller L. P., and Lauretta D. S. (2011) Evidence for aqueous activity on Comet 81P/Wild 2 from sulfide mineral assemblages in Stardust samples and CI chondrites. *Geochim. Cosmochim. Acta*, **75**, 3501–3513.
- Bonsor A., Raymond S. N., Augereau J.-C., and Ormel C. W. (2014) Planetesimal-driven migration as an explanation for observations of high levels of warm, exozodiacal dust. *Mon. Not. R. Astron. Soc.*, **441**, 2380–2391.
- Borovicka J., Koten P., Spurný P., Bocek J., and Stork R. (2005) A survey of meteor spectra and orbits: Evidence for three populations of Na-free meteoroids. *Icarus*, **174**, 15–30.
- Briani G., Morbidelli A., Gounelle M., and Nesvorný D. (2011) Evidence for an asteroid-comet continuum from simulations of carbonaceous micrometeoroid dynamical evolution. *Meteoritics & Planet. Sci.*, **46**, 1863–1877.
- Brown P., Weryk R. J., Wong D. K., and Jones J. (2008a) A meteoroid stream survey using the Canadian Meteor Orbit Radar — I: Methodology and Radiant Catalogue. *Icarus*, **195**, 317–339.
- Brown P., Weryk R. J., Wong D. K., and Jones J. (2008b) The Canadian Meteor Orbit Radar Meteor Stream Catalogue. *Earth Moon Planets*, **102**, 209–219.
- Brown P., Wong D. K., Weryk R. J., and Wieger P. (2010) A meteoroid stream survey using the Canadian Meteor Orbit Radar — II: Identification of minor showers using a 3D wavelet transform. *Icarus*, **207**, 66–81.
- Campbell-Brown M. D. (2005) Radar observations of the Arietids. *Mon. Not. R. Astron. Soc.*, **352**, 1421–1425.
- Campbell-Brown M. D. (2008) High resolution radiant distribution and orbits of sporadic radar meteoroids. *Icarus*, **196**, 144–163.
- Ceplecha Z., Borovicka J., Elford W. G., et al. (1998) Meteor phenomena and bodies. *Space Sci. Rev.*, **84**, 327–471.
- Chau J. L., Woodan R. F., and Galindo F. (2007) Sporadic meteor sources as observed by the Jicamarca high-power large-aperture VHF radar. *Icarus*, **188**, 162–174.
- Christou A. A. (2010) Annual meteor showers at Venus and Mars: Lessons from the Earth. *Mon. Not. R. Astron. Soc.*, **402**, 2759–2770.
- Chyba C. F., Thomas P. J., Brookshaw L., and Sagan C. (1990) Cometary delivery of organic molecules to the early Earth. *Science*, **249**, 366–373.
- Close S., Oppenheim M., Hunt S., and Dyrud L. (2002) Scattering characteristics of high-resolution meteor head echoes detected at multiple frequencies. *J. Geophys. Res.–Space Physics*, **107(A10)**, SIA 9-1.
- Close S., Brown P., Campbell-Brown M., Oppenheim M., and Colestock P. (2007) Meteor head echo radar data: Mass-velocity selection effects. *Icarus*, **186**, 547–556.
- Clube S. V. M. and Napier W. M. (1984) The microstructure of terrestrial catastrophism. *Mon. Not. R. Astron. Soc.*, **211**, 953–968.
- Cooke W. J., Moser D. E., Hardin B. F., and Janches D., eds. (2010) *Meteoroids: The Smallest Solar System Bodies*. Proceedings of the Meteoroids 2010 Conference held in Breckenridge, Colorado, May 24–28, 2010. NASA CP 2011-216469, 366 pp.
- Crifo J. F. and Rodionov A. V. (2000) The dependence of the circumnuclear coma structure on the properties of the nucleus. IV. Structure of the night-side gas coma of a strongly sublimating nucleus. *Icarus*, **148**, 464–478.
- Davies J. K., Green S. F., Stewart B. C., Meadows A. J., and Aumann H. H. (1984) The IRAS fast-moving object search. *Nature*, **309**, 315–319.
- Davis C. J., Davies J. A., St Cyr O. C., et al. (2012) The distribution of interplanetary dust between 0.96 and 1.04 AU as inferred from impacts on the STEREO spacecraft observed by the heliospheric imagers. *Mon. Not. R. Astron. Soc.*, **420**, 1355–1366.
- DeLeón J., Campins H., Tsiganis K., Morbidelli A., and Licandro J. (2010) Origin of the near-Earth asteroid Phaethon and the Geminids meteor shower. *Astron. Astrophys.*, **513**, A26.
- Dermott S. F., Durda D. D., Grogan K., and Kehoe T. J. J. (2002a) Asteroidal dust. In *Asteroids III* (W. F. Bottke Jr. et al., eds.), pp. 423–442. Univ. of Arizona, Tucson.
- Dermott S. F., Fehoe T. J. J., Durda D. D., Grogan K., and Nesvorný D. (2002b) Recent rubble-pile origin of asteroidal solar system dust bands and asteroidal interplanetary dust particles. In *In Proceedings of Asteroids, Comets, Meteors — ACM 2002* (B. Warmbein, ed.), pp. 319–322. ESA SP-500, Noordwijk, The Netherlands.
- Dikarev V., Grün E., Baggaley J., Galligan D., Landgraf M., and Jahn R. (2004) Modeling the sporadic meteoroid background cloud. *Earth Moon Planets*, **95**, 109–122.
- Dikarev V., Grün E., Baggaley J., Galligan D., Landgraf M., and Jahn R. (2005) The new ESA meteoroid model. *Adv. Space Res.*, **35**, 1282–1289.
- Divine N. (1993) Five populations of interplanetary meteoroids. *J. Geophys. Res.*, **98**, 17029–17048.
- Dyrud L. P., Ray L., Oppenheim M., Close S., and Denney K. (2005) Modeling high-power large-aperture radar meteor trails. *J. Atmos. Solar Terr. Phys.*, **67**, 1171–1177.
- Espy A. J., Dermott S. F., Kehoe T. J. J., and Jayaraman S. (2009) Evidence from IRAS for a very young, partially formed dust band. *Planet. Space Sci.*, **57**, 235–242.
- Farley K. A. (2001) Extraterrestrial helium in seafloor sediments: Identification, characteristics, and accretion rate over geologic time. In *Accretion in Extraterrestrial Matter Throughout Earth's History* (B. Peuker-Ehrenbrink and B. Schmitz, eds.), pp. 179–204. Kluwer, New York.
- Farley K. A., Vokrouhlický D., Bottke W. F., and Nesvorný D. (2006) A late Miocene dust shower from the break-up of an asteroid in the main belt. *Nature*, **439**, 295–297.
- Fentzke J. T., Janches D., and Sparks J. J. (2009) Latitudinal and seasonal variability of the micrometeor input function: A study using model predictions and observations from Arecibo and PFISR. *J. Atmos. Solar Terr. Phys.*, **71**, 653–661.
- Foglia S., Micheli M., Jenniskens P., and Marsden B. G. (2005) Comet D/1819 W1 (Blanpain) and 2003 WY<sub>25</sub>. *IAU Circular* 8485.
- Francis P. J. (2005) The demographics of long-period comets. *Astrophys. J.*, **635**, 1348–1361.
- Galligan D. P. and Baggaley W. J. (2002) Determination of the spatial distribution of the solar system meteoroid population using Amor. In *Proceedings of Asteroids, Comets, Meteors — ACM 2002* (B. Warmbein, ed.), pp. 229–232. ESA SP-500, Noordwijk, The Netherlands.
- Galligan D. P. and Baggaley W. J. (2004) The orbital distribution of radar-detected meteoroids of the solar system dust cloud. *Mon. Not. R. Astron. Soc.*, **353**, 422–446.
- Galligan D. P. and Baggaley W. J. (2005) The radiant distribution of AMOR radar meteors. *Mon. Not. R. Astron. Soc.*, **359**, 551–560.
- Gounelle M., Spurný P., and Bland P. A. (2006) The atmospheric trajectory and orbit of the Orgueil meteorite. *Meteoritics & Planet. Sci.*, **41**, 135–150.
- Grogan K., Dermott S. F., Jayaraman S., and Xu Y. L. (1997) Origin of the ten degree solar system dust bands. *Planet. Space Sci.*, **45**, 1657–1665.
- Grogan K., Dermott S. F., and Xu Y. L. (2001) The size-frequency distribution of the zodiacal cloud: evidence from the solar system dust bands. *Icarus*, **152**, 251–267.
- Grün E., Zook H. A., Fechtig H., and Giese R. H. (1985) Collisional balance of the meteoritic complex. *Astron. Astrophys.*, **286**, 915–924.

- Grün E., Gustafson B. Å. S., Dermott S. F., and Fechtig H., eds. (2001a) *Interplanetary Dust*. Springer-Verlag, Berlin. 804 pp.
- Grün E., Baguhl M., Svedhem H., and Zook H. A. (2001b) In situ measurements of cosmic dust. In *Interplanetary Dust* (E. Grün et al., eds.), pp. 295–364. Springer, Berlin.
- Gustafson B. Å. S. (1994) Physics of zodiacal dust. *Annu. Rev. Earth Planet. Sci.*, 22, 553–595.
- Haack H., Michelsen R., Stober G., Keuer D., Singer W., and Williams I. (2011) The Maribo CM fall and its possible relationship to comet Encke and the Taurid meteor complex. *Meteoritics & Planet. Sci. Suppl.*, 74, Abstract #5271.
- Hanner M. and Zolensky M. (2010) The mineralogy of comets. In *Astromineralogy* (T. Henning, ed.), pp. 203–232. Springer, Berlin.
- Hawkins G. S. (1956) A radio echo survey of sporadic meteor radiants. *Mon. Not. R. Astron. Soc.*, 116, 92–104.
- Hervig M. E., Deaver L. E., Bardeen C. G., Russell J. M., Bailey S. M., and Gordley L. L. (2012) The content and composition of meteoric smoke in mesospheric ice particles from SOFIE observations. *J. Atmos. Solar Terr. Phys.*, 84, 1–6.
- Ipatov S. I., Kutyrev A. S., Madsen G. J., Mather J. C., Moseley S. H., and Reynolds R. J. (2008) Dynamical zodiacal cloud models constrained by high resolution spectroscopy of the zodiacal light. *Icarus*, 194, 769–788.
- Ishimoto H. (1998) Collisional evolution and the resulting mass distribution of interplanetary dust. *Earth Planets Space*, 50, 521–529.
- Janches D. and Chau J. L. (2005) Observed diurnal and seasonal behavior of the micrometeor flux using the Arecibo and Jicamarca radars. *J. Atmos. Solar Terr. Phys.*, 67, 1196–1210.
- Janches D., Heinzelman C. J., Chau J. L., Chandran A., and Woodman R. (2006) Modeling the global micrometeor input function in the upper atmosphere observed by high power and large aperture radars. *J. Geophys. Res.—Space Phys.*, 111, 7317–7334.
- Janches D., Close S., and Fenzke J. T. (2008) A comparison of detection sensitivity between ALTAIR and Arecibo meteor observations: Can high power and large aperture radars detect low velocity meteor head-echoes? *Icarus*, 193, 105–111.
- Jenniskens P. (1994) Meteor stream activity I. The annual streams. *Astron. Astrophys.*, 287, 990–1013.
- Jenniskens P. (1997) Meteor stream activity. IV. Meteor outbursts and the reflex motion of the Sun. *Astron. Astrophys.*, 317, 953–961.
- Jenniskens P. (2001) Meteors: A delivery mechanism for organic matter to the early Earth. In *Proceedings of the Meteoroids 2001 Conference* (B. Warmbein, ed.), pp. 247–254. ESA SP 495, Noordwijk, The Netherlands.
- Jenniskens P. (2004) 2003 EH<sub>1</sub> and the Quadrantid shower parent comet. *Astrophys. J.*, 127, 3018–3022.
- Jenniskens P. (2006) *Meteor Showers and Their Parent Comets*. Cambridge Univ., Cambridge. 790 pp.
- Jenniskens P. (2008a) Meteoroid streams that trace to candidate dormant comets. *Icarus*, 194, 13–22.
- Jenniskens P. (2008b) Mostly dormant comets and their disintegration into meteoroid streams: A review. *Earth Moon Planets*, 102, 505–520.
- Jenniskens P. (2014) Camelopardalids (IAU#451) from Comet 209P/LINEAR. *WGN, J. Intl. Meteor. Org.*, 42, 98–105.
- Jenniskens P. and Vaubaillon J. (2008) Minor planet 2008 ED69 and the Kappa Cygnid meteor shower. *Astron. J.*, 136, 725–730.
- Jenniskens P. and Vaubaillon J. (2010) Minor planet 2002 EX<sub>12</sub> (=169P/NEAT) and the Alpha Capricornid Shower. *Astron. J.*, 139, 1822–1830.
- Jenniskens P., Jopek T. J., Rendtel J., Porubcan V., Spurny P., Baggaley J., Abe S., and Hawkes R. (2009) On how to report new meteor showers. *J. Intl. Meteor. Org.*, 37, 19–20.
- Jenniskens P., Gural P. S., Dynneson L., et al. (2011) CAMS: Cameras for allsky meteor surveillance to establish minor meteor showers. *Icarus*, 216, 40–61.
- Jenniskens P., Fries M. D., Yin Q.-Z., et al. (2012) Radar-enabled recovery of the Sutter's Mill meteorite, a carbonaceous chondrite regolith breccia. *Science*, 338, 1583–1587.
- Jenniskens P., Rubin A. E., Yin Q.-Z., et al. (2014) Fall recovery, and characterization of the Novato L6 chondrite breccia. *Meteoritics & Planet. Sci.*, 49, 1388–1425.
- Jenniskens P., Nénon Q., Gural P. S., Albers J., Haberman B., Johnson B., Morales R., Grigsby B. J., Samuels D., and Johannink C. (2015a) CAMS newly detected meteor showers and the sporadic background. *Icarus*, in press.
- Jenniskens P., Nénon Q., Albers J., Gural P. S., Haberman B., Holman D., Morales R., Grigsby B. J., Samuels D., and Johannink C. (2015b) The established meteor showers as observed by CAMS. *Icarus*, in press, DOI: 10.1016/j.icarus.2015.09.013.
- Jewitt D. and Hsieh H. (2006) Physical observations of 2005 UD: A mini-Phaethon. *Astron. J.*, 132, 1624–1629.
- Jewitt D., Li J., and Agarwal J. (2013) The dust tail of asteroid (3200) Phaethon. *Astrophys. J. Lett.*, 711, L36–L41.
- Jones J. and Brown P. (1993) Sporadic meteor radiant distributions — Orbital survey results. *Mon. Not. R. Astron. Soc.*, 265, 524–532.
- Jones J. and Hawkes R. L. (1986) The structure of the Geminid meteor stream. II — The combined action of the ejection process and gravitational perturbations. *Mon. Not. R. Astron. Soc.*, 223, 479–486.
- Jones J. and Poole L. M. G. (2007) Gravitational focusing and shielding of meteoroid streams. *Mon. Not. R. Astron. Soc.*, 375, 925–930.
- Jopek T. J., Rietmeijer F. J. M., Watanabe J., and Williams I. P., eds. (2014) *The Meteoroids 2013*. Proceedings of the Astronomical Conference, Poznan, Poland, Aug. 26–30, 2013. A. M. Univ., Poznan.
- Joswiak D. J., Nakashima D., Brownlee D. E., Matrajt G., Ushikubo T., Kita N. T., Messenger S., and Ito M. (2014) Terminal particle from Stardust track 130: Probable Al-rich chondrule fragment from Comet Wild 2. *Geochim. Cosmochim. Acta*, 144, 277–298.
- Kehoe T. J. J., Dermott S. F., and Mahoney-Hopping L. M. (2007) The effect of inter-particle collisions on the dynamical evolution of asteroidal dust and the structure of the zodiacal cloud. In *Dust in Planetary Systems*, pp. 81–85. ESA SP 643, Noordwijk, The Netherlands.
- Kelley M. S. P., Farnham T. L., Bodewits D., Tricarico P., and Farnocchia D. (2014) A study of dust and gas at Mars from Comet C/2013 A1 (Siding Spring). *Astrophys. J. Lett.*, 792, L16–L22.
- Kero J., Szasz C., Nakamura T., Meisel D. D., Ueda M., Fujiwara Y., Terasawa T., Nishimura K., and Watanabe J. (2012) The 2009–2010 MU radar head echo observation programme for sporadic and shower meteors: Radiant densities and diurnal rates. *Mon. Not. R. Astron. Soc.*, 425, 135–146.
- Kero J., Szasz C., and Nakamura T. (2013) MU head echo observations of the 2010 Geminids: Radiant, orbit and meteor flux observing biases. *Ann. Geophys.*, 31, 439–449.
- Kikwaya J.-B., Campbell-Brown M., and Brown P. G. (2011) Bulk density of small meteoroids. *Astron. Astrophys.*, 530, 113–130.
- Kohout T., Kallonen A., Suuronen J.-P., Rochette P., Hutzler A., Gattaccea J., Badjukov D. D., Skála R., Böhmová V., and Cuda J. (2014) Density, porosity, mineralogy, and internal structure of cosmic dust and alteration of its properties during high-velocity atmospheric entry. *Meteoritics & Planet. Sci.*, 49, 1157–1170.
- Kondrateva E. D. and Reznikov E. A. (1985) Comet Tempel-Tuttle and the Leonid meteor swarm. *Astron. Vestnik*, 19, 144–151 (translated in *Solar System Res.*, 19, 96–101).
- Kortenkamp S. J. and Dermott S. F. (1998) Accretion of interplanetary dust particles by Earth. *Icarus*, 135, 469–495.
- Koten P., Vaubaillon J., Capek D., Vojacek V., Spurny P., Stork R., and Colas F. (2014) Search for faint meteors on the orbits of Pribram and Neuschwanstein meteorites. *Icarus*, 239, 244–252.
- Kozai Y. (1962) Secular perturbations of asteroids with high inclination and eccentricity. *Astron. J.*, 67, 591–598.
- Kresak L. (1976) Orbital evolution of the dust streams released from comets. *Bull. Astron. Inst. Czechosl.*, 27, 35–46.
- Krick J. E., Glaccum W. J., Carey S. J., Lowrance P. J., Surance J. A., Ingalls J. G., Hora J. L., and Reach W. T. (2012) A Spitzer/IRAC measure of the zodiacal light. *Astrophys. J.*, 754, 53.
- Krueger H. and Graps A., eds. (2007) *Workshop on Dust in Planetary Systems*. Kauai, Hawaii. ESA SP 643, Noordwijk, The Netherlands. 264 pp.
- Landgraf M., Liou J.-C., Zook H. A., and Grün E. (2002) Origins of solar system dust beyond Jupiter. *Astron. J.*, 123, 2857–2861.
- Lasue J., Levasseur-Regourd A. C., Fray N., et al. (2007) Inferring the interplanetary dust properties from remote observations and simulations. *Astron. Astrophys.*, 473, 641–649.
- Lasue J., Levasseur-Regourd A. C., Hadamcik E., and Alcouffe G. (2009) Cometary dust properties retrieved from polarization observations: Application to C/1995 O1 Hale Bopp and 1P/Halley. *Icarus*, 199, 129–144.

- Lazzaro D., Ferraz-Mello S., and Fernández J. A., eds. (2006) *Asteroids, Comets, Meteors 2005*. IAU Symp. 229, Cambridge Univ., Cambridge. 480 pp.
- Leinert C., Bowyer S., Haikala L. K., et al. (1998) The 1997 reference of diffuse night sky brightness. *Astron. Astrophys. Suppl. Ser.*, 127, 1–99.
- Levasseur-Regourd A. C. and Lasue J. (2010) Inferring sources in the interplanetary dust cloud, from observations and simulations of zodiacal light and thermal emission. In *Meteoroids: The Smallest Solar System Bodies* (W. J. Cooke et al., eds.), p. 66. NASA CP 2011-216469.
- Levison H. F. (1996) Comet taxonomy. In *Completing the Inventory of the Solar System* (T. W. Rettig and J. M. Hahn, eds.), pp. 173–191. ASP Conf. Proc. 107, Astronomical Society of the Pacific, San Francisco.
- Levison H. F., Morbidelli A., Dones L., Jedicke R., Wiegert P. A., and Bottke W. F. (2002) *Science*, 296, 2212–2215.
- Love S. G. and Brownlee D. E. (1993) *Science*, 262, 550–553.
- Lyytinen E. (1999) Leonid predictions for the years 1999–2007 with the satellite model of comets. *Meta Res. Bull.*, 8, 33–40.
- Lyytinen E. and Jenniskens P. (2003) Meteor outbursts from long period comet dust trails. *Icarus*, 162, 443–452.
- Maris M., Burigana C., Gruppuso A., Finelli F., and Diego J. M. (2011) Large-scale traces of solar system cold dust on cosmic microwave background anisotropies. *Mon. Not. R. Astron. Soc.*, 415, 2546–2552.
- Maurette M. (1998) Carbonaceous micrometeorites and the origin of life. *Origins Life Evol. Biosph.*, 28, 385–412.
- May B. (2008) *A Survey of Radial Velocities in the Zodiacal Dust Cloud*. Ph.D. thesis, Springer, Berlin.
- McKeegan K. D., Aléon J., Bradley J., et al. (2006) Isotopic compositions of cometary matter returned by Stardust. *Science*, 314, 1724–1728.
- McNaught R. H. and Asher D. J. (1999) Leonid dust trails and meteor storms. *J. Intl. Meteor. Org.*, 27, 85–102.
- Mikouchi T., Tachikawa O., Hagiya K., Ohsumi K., Suzuki Y., Uesugi K., Takeuchi A., and Zolensky M. E. (2007) Mineralogy and crystallography of Comet 81P/Wild 2 particles. *Lunar Planet. Sci. XXXVIII*, p. 1946. Lunar and Planetary Institute, Houston.
- Millman P. M. (1963) Terminology in meteoritic astronomy. *Meteoritics*, 2, 7–11.
- Morbidelli A., Walsh K., Raymond S., O'Brien D., and Mandell A. (2011) The Grand Tack scenario: Reconstructing the migration history of Jupiter and Saturn in the disk of gas. *Am. Astron. Soc., ESS Meeting #2*, #8.02.
- Morlok A., Mason A. B., Anand M., Lisse C. M., Bullock E. S., and Grady M. M. (2014) Dust from collisions: A way to probe the composition of exo-planets? *Icarus*, 239, 1–14.
- Moro-Martin A. and Malhotra R. (2002) A study of the dynamics of dust from the Kuiper belt: Spatial distribution and spectral energy distribution. *Astron. J.*, 124, 2305–2321.
- Nakamura T., Noguchi T., Tsuchiyama A., Ushikubo T., Kita N. T., Valley J. W., Zolensky M. E., Kakazu Y., Sakamoto K., Mashio E., Uesugi K., and Nakano T. (2008) Chondrule-like objects in short-period Comet 81P/Wild 2. *Science*, 321, 1664–1667.
- Nesvorný D., Vokrouhlický D., Bottke W. F., and Sykes M. (2006a) Physical properties of asteroidal dust bands and their sources. *Icarus*, 181, 107–144.
- Nesvorný D., Sykes M., Lien D. J., Stansberry J., Reach W. T., Vokrouhlický D., Bottke W. F., Durda D. D., Jayaraman S., and Walker R. G. (2006b) Candidates for asteroid dust trails. *Astron. J.*, 132, 582–595.
- Nesvorný D., Bottke W. F., Vokrouhlický D., Sykes M., Lien D. J., and Stansberry J. (2008) Origin of the near-ecliptic circumsolar dust band. *Astrophys. J. Lett.*, 679, L143–L146.
- Nesvorný D., Jenniskens P., Levison H. F., Bottke W. F., Vokrouhlický D., and Gounelle M. (2010) Cometary origin of the zodiacal cloud and carbonaceous micrometeorites. Implications for hot debris disks. *Astrophys. J.*, 713, 816–836.
- Nesvorný D., Janches D., Vokrouhlický D., Pokorny P., Bottke W. F., and Jenniskens P. (2011a) Dynamical model for the zodiacal cloud and sporadic meteors. *Astrophys. J.*, 743, 129–135.
- Nesvorný D., Vokrouhlický D., Pokorny P., and Janches D. (2011b) Dynamics of dust particles released from Oort cloud comets and their contribution to radar meteors. *Astrophys. J.*, 743, 37–49.
- Nikolova S. and Jones J. (2001) Lifetimes of meteoroids in interplanetary space: The effect of erosive collisions and planetary perturbations. In *Proceedings of the Meteoroids 2001 Conference* (B. Warmbein, ed.), pp. 581–585. ESA SP 495, Noordwijk, The Netherlands.
- Ohtsuka K., Sekiguchi T., Kinoshita D., Watanabe J.-I., Ito T., Arakida H., and Kasuga T. (2006) Apollo asteroid 2005 UD: Split nucleus of (3200) Phaethon? *Astron. Astrophys. Lett.*, 450, L25–L28.
- Peucker-Ehrenbrink B. (2001) Iridium and osmium as tracers of extraterrestrial matter in marine sediments. In *Accretion of Extraterrestrial Matter Throughout Earth's History* (B. Peucker-Ehrenbrink and B. Schmitz, eds.), pp. 163–178. Kluwer, New York.
- Pifko S., Janches D., Close S., Sparks J., Nakamura T., and Nesvorný D. (2013) The meteoroid input function and predictions of mid-latitude meteor observations by the MU radar. *Icarus*, 223, 444–459.
- Plane J. M. C. (2003) Atmospheric chemistry of meteoric metals. *Chem. Rev.*, 103, 4963–4984.
- Plane J. M. C. (2012) Cosmic dust in the Earth's atmosphere. *Chem. Soc. Rev.*, 41, 6507–6518.
- Pokorný P., Vokrouhlický D., Nesvorný D., Campbell-Brown M., and Brown P. (2013) Dynamical model for the Toroidal Sporadic Meteors. *Astrophys. J.*, 789, 25.
- Popova O. P., Jenniskens P., Emelyan'enko V. V., et al. (2013) Chelyabinsk airburst, damage assessment, meteorite recovery, and characterization. *Science*, 342, 1069–1073.
- Poppe A. R. and Horányi M. (2012) On the Edgeworth-Kuiper belt dust flux to Saturn. *Geophys. Res. Lett.*, 39, L15104.
- Porubcan V., Kornos L., and Williams I. P. (2006) The Taurid Complex meteor showers and asteroids. *Contr. Obs. Skalnaté Pleso*, 36, 103–117.
- Pravec M. (1955) Ejection theory of the meteor shower formation I. Orbit of an ejected meteor. *Bull. Astron. Inst. Czechosl.*, 6, 20–26.
- Raymond S. N. and Morbidelli A. (2014) The Grand Tack model: A critical review. In *Proc. IAU*, 9, arXiv:1409.6340, DOI: 10.1017/S1743921314008254.
- Reach W. T., Kelley M. S., and Sykes M. V. (2007) A survey of debris trails from short-period comets. *Icarus*, 191, 298–322.
- Reach W. T., Vaubaillon J., Kelley M. S., Lisse C. M., and Sykes M. V. (2009) Distribution and properties of fragments and debris from the split Comet 73P/Schwassmann-Wachmann 3 as revealed by Spitzer Space Telescope. *Icarus*, 203, 571–588.
- Rietmeijer F. J. M. (2007) Quantitative material properties for meteoroids from interplanetary dust particles. *Adv. Space Res.*, 39, 583–589.
- Rietmeijer F. J. M. (2008) Natural variations in comet-aggregate meteoroid compositions. *Earth Moon Planets*, 102, 461–471.
- Rietmeijer F. J. M. (2011) The irradiation-induced olivine to amorphous pyroxene transformation preserved in an interplanetary dust particle. *Astrophys. J.*, 705, 791–797.
- Rowan-Robinson M. and May B. (2013) An improved model for the infrared emission from the zodiacal dust cloud: Cometary, asteroidal and interstellar dust. *Mon. Not. R. Astron. Soc.*, 429, 2894–2902.
- Rozitis B., MacLennan E., and Emmery J. P. (2014) Cohesive forces prevent the rotational breakup of rubble-pile asteroid (29075) 1950 DA. *Nature*, 512, 174–176.
- Rudawska R., Vaubaillon J., and Atreya P. (2012) Association of individual meteors with their parent bodies. *Astron. Astrophys.*, 541, 50–54.
- Rudraswami N. G., Prasad M. S., Babu E. V. S. S. K., and Kumar T. V. (2014) Chemistry and petrology of Fe-Ni beads from different types of cosmic spherules: Implication for precursors. *Geochim. Cosmochim. Acta*, 145, 139–158.
- Schiaparelli G. V. (1867) *Note e riflessioni intorno alla teoria astronomica delle stelle cadenti*. Stamperia Reale, Rirenze. 132 pp.
- Sekanina Z. (1976) Statistical model of meteor streams. IV — A study of radio streams from the synoptic year. *Icarus*, 27, 265–321.
- Sekanina Z. and Chodas P. (2005) Origin of the Marsden and Kracht groups of sunskirting comets. I. Association with Comet 96P/Machholz and its interplanetary complex. *Astrophys. J. Suppl. Ser.*, 161, 551–586.
- Spurný P., Bland P. A., Shrbený L., Borovicka J., Ceplecha Z., Singelton A., Bevan A. W. R., Vaughan D., Towner M. C., McClafferty T. P., Oumi R., and Deacon G. (2012) The Bunburra Rockhole meteorite fall in SW Australia: Fireball trajectory, luminosity, dynamics, orbit, and impact position from photographic and photoelectric records. *Meteoritics & Planet. Sci.*, 47, 163–185.

- Steel D. and Asher D. (1996) The orbital dispersion of the macroscopic Taurid objects. *Mon. Not. R. Astron. Soc.*, **280**, 860–822.
- Sterken V. J., Altobelli N., Kempf S., Schwehm G., Srama R., and Grün E. (2012) The flow of interstellar dust into the solar system. *Astron. Astrophys.*, **102**, 24–48.
- Suggs R. M., Moser D. E., Cooke W. J., and Suggs R. J. (2014) The flux of kilogram-sized meteoroids from lunar impact monitoring. *Icarus*, **238**, 23–36.
- Sykes M. V., Lebofsky L. A., Hunten D. M., and Low F. (1986) The discovery of dust trails in the orbits of periodic comets. *Science*, **232**, 1115–1117.
- Taylor A. D. (1997) Radiant distribution of meteoroids encountering the Earth. *Adv. Space Res.*, **20**, 1505–1508.
- Taylor A. D. and McBride N. (1997) A radiant resolved meteoroid model. In *Proceedings of the Second European Conference on Space Debris* (B. Kaldeich-Schürmann and B. Harris, eds.), pp. 375–380. ESA SP 393, Noordwijk, The Netherlands.
- Terent'eva A. K. (1990) Fireball streams. In *Asteroids, Comets, Meteors III* (C. I. Lagerkvist et al., eds.), p. 579. Uppsala Univ., Uppsala, Sweden.
- Trigo-Rodriguez J. M., Rietmeijer F. J. M., Llorca J., and Janches D., eds. (2008) *Advances in Meteoroid and Meteor Science*. Springer, Berlin. 443 pp.
- Trigo-Rodriguez J. M., Madiedo J. M., Williams I. P., and Castro-Tirado A. J. (2009) The outburst of the κ Cygnids in 2007: Clues about the catastrophic break up of the comet to produce an Earth-crossing meteoroid stream. *Mon. Not. R. Astron. Soc.*, **392**, 367–375.
- Vaubaillon J. and Reach W. T. (2010) Spitzer Space Telescope observations and the particle size distribution of Comet 73P/Schwassmann-Wachmann 3. *Astron. J.*, **139**, 1491–1498.
- Vaubaillon J., Colas F., and Jorda L. (2005) A new method to predict meteor showers. I. Description of the model. *Astron. Astrophys.*, **439**, 751–760.
- Vokrouhlický D., Nesvorný D., and Bottke W. F. (2008) Evolution of dust trails into bands. *Astrophys. J.*, **672**, 696–712.
- Walsh K. J., Richardson D. C., and Michel P. (2008) Rotational break up as the origin of binary asteroids. *Nature*, **454**, 188–191.
- Walsh K. J., Morbidelli A., Raymond S. N., O'Brien D. P., and Mandell A. M. (2011) A low mass for Mars from Jupiter's early gas-driven migration. *Nature*, **475**, 206–209.
- Weryk R. J. and Brown P. G. (2012) Simultaneous radar and video meteors — I: Metric comparisons. *Planet. Space Sci.*, **62**, 132–152.
- Weryk R. J., Campbell-Brown M. D., Wiegert P. A., Brown P. G., Krzeminski Z., and Musci R. (2013) The Canadian Automated Meteor Observatory (CAMO): System overview. *Icarus*, **225**, 614–622.
- Whipple F. L. (1940) Photographic meteor studies. III. The Taurid shower. *Proc. Am. Philos. Soc.*, **83**, 711–745.
- Whipple F. L. (1950) A comet model. I. The acceleration of Comet Encke. *Astrophys. J.*, **111**, 375–394.
- Whipple F. L. (1954) Photographic meteor orbits and their distribution in space. *Astron. J.*, **59**, 201–217.
- Whipple F. L. (1967) On maintaining the meteoric complex. In *The Zodiacal Light and the Interplanetary Medium* (J. L. Weinberg, ed.), pp. 409–426. NASA SP 150, Washington, DC.
- Whipple F. L. (1983) 1983 TB and the Geminid meteors. *IAU Circular* 3881.
- Whipple F. L., Southworth R. B., and Nilson C. S. (1967) *Studies in Interplanetary Particles*. SAO Spec. Rept. #239, Smithsonian Astrophysical Observatory, Cambridge, Massachusetts. 48 pp.
- Wiegert P. and Brown P. (2004) The problem of linking parent bodies: Initial considerations. *Earth Moon Planets*, **95**, 19–26.
- Wiegert P., Vaubaillon J., and Campbell-Brown M. (2009) A dynamical model of the sporadic meteoroid complex. *Icarus*, **201**, 295–310.
- Williams I. P. (2011) The origin and evolution of meteor showers and meteoroid streams. *Astron. Geophys.*, **52**, 2.20–2.26.
- Younger J. P., Reid I. M., Vincent R. A., Holdsworth D. A., and Murphy D. J. (2009) A southern hemisphere survey of meteor shower radiants and associated stream orbits using single station radar observations. *Mon. Not. R. Astron. Soc.*, **398**, 350–356.
- Zolensky M. (2012) A post Stardust mission view of Jupiter family comets. *Asteroids, Comets, Meteors 2012*, Abstract #6193. Lunar and Planetary Institute, Houston.
- Zolensky M. E., Thomas J., Yano H., et al. (2006) Mineralogy and petrology of Comet 81P/Wild 2 nucleus samples. *Science*, **34**, 1735–1739.
- Zook H. A. (2001) Spacecraft measurements of the cosmic dust flux. In *Accretion of Extraterrestrial Matter Throughout Earth's History* (B. Peucker-Ehrenbrink and B. Schmitz, eds.), pp. 75–92. Kluwer, New York.



# Identification and Dynamical Properties of Asteroid Families

David Nesvorný

*Southwest Research Institute*

Miroslav Brož

*Charles University*

Valerio Carruba

*Universidade Estadual Paulista*

Asteroids formed in a dynamically quiescent disk but their orbits became gravitationally stirred enough by Jupiter to lead to high-speed collisions. As a result, many dozen large asteroids have been disrupted by impacts over the age of the solar system, producing groups of fragments known as asteroid families. Here we explain how the asteroid families are identified, review their current inventory, and discuss how they can be used to get insights into long-term dynamics of main-belt asteroids. Electronic tables of the membership for 122 notable families are reported on the Planetary Data System node. See related chapters in this volume for the significance of asteroid families for studies of physics of large-scale collisions, collisional history of the main belt, source regions of the near-Earth asteroids, meteorites and dust particles, and space weathering.

## 1. INTRODUCTION

As witnessed by the heavily cratered surfaces imaged by spacecrafts, the chief geophysical process affecting asteroids is impacts. On rare occasions, the impact of a large projectile can be so energetic that the target asteroid is violently torn apart, and the pieces are thrown into space. The sites of such cosmic accidents are filled with debris that gravitationally accumulate into larger conglomerates, and drift away at speeds that are roughly commensurate with the escape speed from the original target body ( $V_{\text{esc}}$ ). Initially, all orbits are similar, because  $V_{\text{esc}} \ll V_{\text{orb}}$ , where  $V_{\text{orb}} \approx 15\text{--}20 \text{ km s}^{-1}$  is the orbital speed of main-belt asteroids. On longer timescales, however, the orbits are altered by gravitational perturbations from planets, and the orbital elements of individual bodies start to diverge.

It may therefore seem challenging to identify fragments of a catastrophic collision that happened eons ago. Fortunately, starting with the pioneering work of K. Hirayama (Hirayama, 1918; see also Cimrman, 1917), astronomers have developed various methods to deal with this issue (section 2). Roughly speaking, these methods consist in a transformation that brings the orbital elements at the observed epoch to a standard, called the *proper elements* (Knežević et al., 2002), that is unchanging in time (or, at least, would be unchanging if chaotic dynamics, nongravitational forces, and other perturbations could be ignored). Thus, ideally, daughter fragments produced by breakup of a parent asteroid will appear as a group in space of the proper elements even giga-

years after the original collision. These groups are called asteroid families, or dynamical families, to emphasize that they have been identified from dynamical considerations.

Telescopic surveys such as the Sloan Digital Sky Survey (SDSS), Wide-field Infrared Survey Explorer (WISE), and AKARI All-Sky Survey provide a wealth of data on physical properties of the main-belt asteroids (Ivezic et al., 2001; Mainzer et al., 2011; Usui et al., 2013). They have been used to cross-link the color and albedo measurements with the lists of dynamical families, in much the same way that spectroscopic and taxonomic data have previously been applied to this purpose (for a review, see Cellino et al., 2002). This work is useful to physically characterize the asteroid families (see the chapter by Masiero et al. in this volume), including cases where two or more dynamical families overlap, and identify distant “halo” family members that would otherwise be confused with the local background (e.g., Brož and Morbidelli, 2013). Given that the SDSS and WISE catalogs now contain data for more than 100,000 unique asteroids, it has also become practical to conduct search for families in extended space, where the color and/or albedo data are taken into account simultaneously with the orbital elements (e.g., Parker et al., 2008; Masiero et al., 2013; Carruba et al., 2013a).

The physical data can be used to identify *interlopers*. The problem of interlopers arises because the clustering criterion applied to identify the dynamical families is only a rough expression of the true membership. Unrelated asteroids that just happen to have nearby values of proper elements will

be grouped together with the true members, and will thus appear in the lists of dynamical families obtained from the proper elements (e.g., *Migliorini et al.*, 1995). These interlopers, especially the large ones, introduce ambiguity in the interpretation of impact conditions that produced individual families, and in the implications of these studies for asteroid interiors (cf. *Michel et al.*, 2003; *Nesvorný et al.*, 2006a). Here we discuss how large interlopers and true largest members in families can be found by applying the “V-shape” criterion, which is based on the notion that large fragments are ejected at low speeds, and have less mobility due to the Yarkovsky effect (section 4).

Based on the synthesis of asteroid families extracted from recent publications (*Mothé-Diniz et al.*, 2005; *Nesvorný et al.*, 2005; *Gil-Hutton*, 2006; *Parker et al.*, 2008; *Nesvorný*, 2010, 2012; *Novaković et al.*, 2011; *Brož et al.*, 2013; *Masiero et al.*, 2011, 2013; *Carruba et al.*, 2013a; *Milani et al.*, 2014), we attempt to build a consensus that could serve as a starting point for future studies. We classify the asteroid families into notable cases (those that have a high statistical significance, and are thus real, and/or are notable for other reasons) and candidate families (less interesting cases where the statistical significance is low or cannot currently be established). The distinction between notable and candidate families is somewhat arbitrary, and will intentionally be left strictly undefined, because that is the nature of things. We expect that many candidate families will be confirmed with more data, and that a few notable families may fall into oblivion. The lists of notable families are being made available at the Planetary Data System (PDS) node, and are discussed in section 7.

A new and exciting development in the past decade was the detection of several asteroid families with very young formation ages. For example, the Karin family was shown to have formed only  $5.8 \pm 0.2$  m.y. ago (*Nesvorný et al.*, 2002a). These cases are important, because various collisional and dynamical processes had little time to act on these families to alter their properties. The young families have thus attracted much attention from scientists studying impact physics, space weathering, debris disks, etc. As we explain in section 3, the age of a young family can be determined by numerically integrating the orbits of its members backward in time and demonstrating that they converge to each other at some specific time in the past. This is the time of a breakup, and the family age,  $t_{\text{age}}$ , is the time elapsed from the breakup event.

The method of backward integration of orbits only works for the families with  $t_{\text{age}} \leq 10$  m.y. This is because dynamics of main-belt asteroids on longer timescales is governed by chaos, encounters with (1) Ceres and other large asteroids, and nongravitational forces. A complementary statistical method for the estimation of family age has been developed in *Vokrouhlický et al.* (2006a,b). The method tracks, in detail, how the family structure in semimajor axis changes over time as the family members drift away by the Yarkovsky effect (section 5). The semimajor axis spread of an older family will generally be greater than

that of a younger family. A compilation of formation ages of the asteroid families can be used to constrain how the population of the asteroid belt collisionally evolved over time (e.g., *Bottke et al.*, 2005a,b; *Cibulková et al.*, 2014), and how asteroid surfaces age by space weathering (see the chapter by Brunetto et al. in this volume).

## 2. IDENTIFICATION METHOD

Here we discuss the standard method to identify asteroid families. This method consists of the (1) computation of proper elements, or other elements unchanging with time, for asteroids with well-known orbits; (2) identification of concentrations or groups of asteroids in proper element space; and (3) establishing the statistical significance of identified groups. These steps are discussed in sections 2.1, 2.2, and 2.3. In section 2.4, we examine the “overlap problem,” where two or more families overlap in proper element space and need to be separated. For this it is useful to consider families in *extended* space, with physical data being included in addition to the proper elements. The search in extended space can also lead to the identification of new families (section 2.5). Very young families ( $t_{\text{age}} \leq 1$  m.y.), for which the member orbits have not had time to differentially precess away from each other, can also be identified as groups in space of the *osculating* orbital elements (section 2.6).

### 2.1. Proper Elements

The ejection speeds of sizable fragments produced by collisional breakups of main-belt asteroids are generally much smaller than their orbital speeds. The fragments will therefore initially cluster near the original orbit of their parent body, and will appear as such if the subsequent effects of planetary perturbations are removed by projecting orbits into space of proper elements. The three most useful proper elements are the proper semimajor axis ( $a_p$ ), the proper eccentricity ( $e_p$ ), and the proper inclination ( $i_p$ ). They are close equivalents of their osculating element counterparts in that they define the size, elongation, and tilt of orbits (see Note 1 in section 9).

The definition of proper elements as quasi-integrals of asteroid motion, and the methods used to compute them, were explained in the *Asteroids III* volume (*Knežević et al.*, 2002). As these definitions and methods have not changed much, we do not discuss them here in detail. In brief, the proper elements are obtained from the instantaneous osculating orbital elements by removing periodic oscillations produced by gravitational perturbations of planets. This can be done analytically, using perturbation theory (*Milani and Knežević*, 1990, 1994), or numerically, by integrating the orbits and applying the Fourier analysis (*Knežević and Milani*, 2000; *Knežević et al.*, 2002) (Note 2).

The computation of analytic proper elements is relatively inexpensive in terms of CPU. They are made publicly available by A. Milani for both numbered and unnumbered

multiopposition asteroids at the AstDyS node (Note 3). The analytic proper elements lose precision for highly inclined orbits, because the expansion of the gravitational potential used to calculate them has poor convergence for high inclinations. The more-precise synthetic proper elements (precision generally at least 3× better than that of analytic elements), on the other hand, require a much larger CPU investment, and are only made available at the AstDyS node for the numbered asteroids.

## 2.2. Clustering Algorithm

When these methods are applied to the asteroid belt, things are brought into focus with dozens of obvious clumps — asteroid families — emerging from the background (Fig. 1a). To identify an asteroid family, researchers apply a clustering algorithm to the distribution of asteroids in  $(a_p, e_p, i_p)$  space. The most commonly used algorithm is the Hierarchical Clustering Method (HCM) (Zappalà et al., 1990) (Note 4), which defines a cutoff distance,  $d_{cut}$ , and requires that the length of the link between two neighboring orbits clustered by the algorithm is  $d = d(a_p, e_p, i_p) < d_{cut}$ . A common definition of distance is  $d^2 \equiv (n a_p)^2 (k_a (\delta a_p / a_p)^2 + k_e (\delta e_p)^2 + k_i (\delta i_p)^2)$ , where  $n$  is the orbital frequency,  $(\delta a_p, \delta e_p, \delta \sin i_p)$  is the separation vector between orbits in three-dimensional space of proper elements, and  $(k_a, k_e, k_i)$  are coefficients on the order of unity.

The main advantage of the HCM over other methods is that there is no strong assumption built into the HCM about the shape of an asteroid family in proper element space. This is because the chain created by linking nearby orbits can track down family members even if their orbits dynamically evolved to produce an unusual overall shape. A prime example of this is the case of the Koronis family,

which is split into two parts by the secular resonance  $g + 2g_5 - 3g_6 = 0$  at  $\approx 2.92$  AU, where  $g$  is the apsidal frequency of an asteroid, and  $g_5$  and  $g_6$  are the 5th and 6th apsidal frequencies of the planetary system. The part of the Koronis family with  $a_p > 2.92$  AU has larger eccentricity than the part with  $a_p < 2.92$  AU, because family members drifting by the Yarkovsky effect from  $a_p < 2.92$  AU have their eccentricities increased by interacting with the  $g + 2g_5 - 3g_6 = 0$  resonance (Bottke et al., 2001).

The main disadvantage of the standard HCM, which becomes increasingly difficult to overcome with inclusion of numerous small asteroids in the new catalogs, is the problem of *chaining*. This problem arises because small fragments are typically ejected at higher speeds and have larger mobility due to the Yarkovsky effect. They therefore spread more, tend to be distributed more homogeneously throughout the main belt, and create bridges between different families if a single (large) value of  $d_{cut}$  is used. Clearly,  $d_{cut}$  should be set proportional to the asteroid size, or inversely proportional to the absolute magnitude  $H$ . Expressing this dependence, however, adds additional parameters to the HCM and makes the whole identification procedure more complex. Therefore, in reality, it is preferred to bypass the problem of chaining by artificial means (e.g., cuts in proper element space applied to deal with individual cases), or the proportionality is approximated by a two-step method with different cutoffs for small and large bodies (Milani et al., 2014).

A tricky part of the HCM algorithm is the choice of the cutoff distance. If the value of  $d_{cut}$  is too small, many dispersed but real families will remain unnoticed and large families will artificially be split into parts. If the value is too large, the algorithm will clump different families together, and will identify irrelevant clumps produced by random fluctuations. While many asteroid families can be identified for

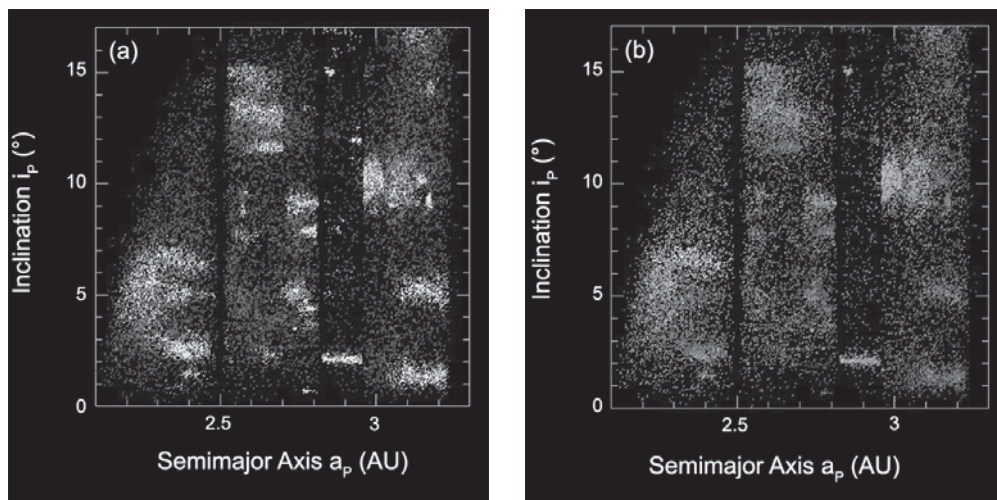


**Fig. 1.** See Plate 5 for color version. **(a)** Clustering algorithm applied to the asteroid belt separates dynamical families from the background. **(b)** Variation in reflectance properties of main-belt asteroids. Here we plot  $\approx 25,000$  asteroids that were observed by both SDSS and WISE. The color code in **(b)** was chosen to highlight the albedo/color contrast of different families.

a wide range of  $d_{\text{cut}}$  values, and are real beyond doubt, some cases require a specific choice of  $d_{\text{cut}}$  and can potentially be confused with random fluctuations. Clearly, the statistical significance of the identified groups, or their insignificance, needs to be established before proceeding further.

### 2.3. Statistical Significance

To make reasonably sure that families identified from the HCM are real, one can opt for a conservative choice of  $d_{\text{cut}}$ . This can be done, for example, by collecting asteroids in a given region of proper element space and redistributing them randomly in that region. The HCM applied to this artificial distribution will reveal that the largest identified group with given  $d_{\text{cut}}$  contains  $N^*(d_{\text{cut}})$  members. Now, this procedure can be repeated, say, 1000 times, recording the largest  $N^*(d_{\text{cut}})$  obtained from these trials. We can then be 99% confident that random fluctuations cannot produce groups with more than  $N^*(d_{\text{cut}})$  members (this conservative estimate includes a 99% confidence interval computed by the Wilson score interval approximation). Any group identified in the real distribution with  $N > N^*(d_{\text{cut}})$  members is therefore reasonably likely to be real. Higher confidence levels can be achieved by increasing the sample size.

This basic concept, and various modifications of it, is known as the Quasi Random Level (QRL) (Zappalà *et al.*, 1994). In the ideal world, the QRL would be the ultimate solution to the family identification problem: Just choose  $d_{\text{cut}}$  and pick up all clumps with more than  $N > N^*(d_{\text{cut}})$ ; those clumps are real. Then there is the real world. First, the number density in proper element space is variable due to the primordial sculpting of the main belt and resonances (e.g., Minton and Malhotra, 2009). Applying a global QRL value in (parts of) the main belt may therefore lead to unsatisfactory results. Second, families do not live in isolation but are frequently close to each other, overlap, and/or are surrounded by empty regions. This introduces an ambiguity in the QRL definition, because it is not clear *a priori* what region in  $(a_p, e_p, i_p)$  space should be considered to define the local QRL in the first place. Results may depend on this choice.

In practice, the first choice made is often the minimum number of group members,  $N_{\min}$ , that is considered to be interesting. Then, the cutoff distance  $d_{\text{cut}}$  in some local region in  $(a_p, e_p, i_p)$  is defined such that groups of  $N > N_{\min}$  members cannot be produced with  $d_{\text{cut}}$  by random fluctuations. All groups with  $N > N_{\min}$  are then treated as meaningful asteroid families. Different researchers made different choices:  $N_{\min} = 5$  in Zappalà *et al.* (1990),  $N_{\min} = 100$  in Parker *et al.* (2008), and  $N_{\min} = 10–20$  in most other publications. The two disadvantages of this method are that (1) meaningful asteroid families with  $N < N_{\min}$  members are explicitly avoided, and (2)  $d_{\text{cut}}(N_{\min})$  depends on the population density in proper element space and must be recomputed when a new classification is attempted from ever-growing catalogs.

Another approach to this problem is to identify all groups, even if they have only a few members, and establish their statistical significance *a posteriori*. Those that are

judged to be insignificant are subsequently discarded and do not appear in the final lists. To determine the statistical significance of a group, one can generate mock distributions and apply the HCM to them. For example, the high statistical significance of the Karin family, which is embedded in the much larger Koronis family, can be demonstrated by generating 1000 orbital distributions corresponding to the Koronis family, and applying the HCM to each one (Nesvorný *et al.*, 2002a). With  $d_{\text{cut}} = 10 \text{ m s}^{-1}$ , no concentrations in this input can be found containing more than a few dozen members, while the Karin family currently has 541 known members. Therefore, the Karin family is significant at a  $<99\%$  level (again including a 99% confidence interval of the estimate). A systematic application of this or similar statistical arguments can be quite laborious if many borderline cases need to be resolved.

### 2.4. Overlap Problem and Interlopers

The overlap between different families has become more of a problem with a progressively larger share being taken in the proper element catalogs by small, kilometer- and subkilometer-sized asteroids. This is because small fragments are generally launched at higher speeds, and are therefore initially spread in a larger volume in  $(a_p, e_p, i_p)$  space. Mainly, however, the problem is caused by the larger mobility of small fragments due to the Yarkovsky effect. For example, the mean drift rate of a diameter  $D = 1 \text{ km}$  main-belt asteroid is estimated to be  $\approx 10^{-4} \text{ AU m.y.}^{-1}$  (Bottke *et al.*, 2006). The kilometer-sized members of a 1-G.y.-old family are therefore expected to be dispersed over  $\approx 0.2 \text{ AU}$  (the additional factor of 2 accounts here for fragments having different spin orientations, and thus  $da/dt < 0$  or  $da/dt > 0$ ), which is roughly one-fifth of the extension of the whole main belt. In addition, drifting asteroids encounter orbital resonances and can be dispersed by them in  $e_p$  and  $i_p$  as well.

A good illustration of this is the case of the Flora and Vesta families in the inner main belt. To separate these families from each other down to their smallest members, the scope of the HCM can be restricted by an artificial cut in proper element space. Alternatively, one can first apply the HCM to the distribution of large members, thus identifying the core of each family, and then proceeding by trying to “attach” the small members to the core. This second step must use a lower  $d_{\text{cut}}$  value than the first step to account for the denser population of smaller asteroids. In practice, this has been done by applying an absolute magnitude cutoff,  $H^*$ , with  $H < H^*$  for the core and  $H > H^*$  for the rest. In the low- $i$  portion of the inner main belt, where the Flora and Vesta families reside, Milani *et al.* (2014) opted to use  $H^* = 15$ , and identified cores of families with  $N_{\min} = 17$  and  $d_{\text{cut}} = 60 \text{ m s}^{-1}$ , and small members with  $N_{\min} = 42$  and  $d_{\text{cut}} = 40 \text{ m s}^{-1}$ .

Another solution to the overlap problem is to consider the *physical* properties of asteroids. Previously, the spectroscopic observations of members of dynamical families have been used to (1) establish the physical homogeneity of asteroid families (the difference between physical prop-

erties of members of the same family tends to be smaller than the differences between physical properties of different families), and (2) identify large interlopers (asteroids classified as family members based on proper elements but having spectroscopic properties distinct from the bulk of the family). With the color and albedo data from SDSS and WISE (Note 5), the physical homogeneity of asteroid families has been demonstrated to hold down to the smallest observable members (Ivezic et al., 2001; Parker et al., 2008) (see Fig. 1b). A straightforward implication of this result is that the interior of each disrupted body was (relatively) homogeneous, at least on a scale comparable to the size of the observed fragments ( $\sim 1\text{--}100$  km) (Note 6).

The physical homogeneity of asteroid families can be used to identify interlopers as those members of a dynamical family that have color and/or albedo significantly distinct from the rest of the family. The number density of apparent color/albedo interlopers in a family can then be compared with the number density of the same color/albedo asteroids in the immediate neighborhood of the family. Similar densities are expected if the identified bodies are actual interlopers in the family. If, on the other hand, the density of color/albedo outliers in the family is found to be substantially higher than in the background, this may help to rule out the interloper premise, and instead indicate that (1) the disrupted parent body may have been heterogeneous, or (2) we are looking at two or more overlapping dynamical families with distinct color/albedo properties. Finally, as for (2), it is useful to verify whether the family members with different color/albedo properties also have different proper element distributions, as expected if breakups happened in two (slightly) different locations in proper element space (e.g., the Nysa-Polana complex; see Fig. 2).

## 2.5. Families in Extended Space

Another useful strategy is to include the color and/or albedo information *directly* in the clustering algorithm. This can be done by first separating the main belt into two (or more) populations according to their color and albedo properties. For example, asteroids in the S-complex can be separated from those in the C/X-complex based on the SDSS colors (Nesvorný et al., 2005), and the high-albedo asteroids can be separated from the low-albedo asteroids based on the albedo measurements of WISE (Masiero et al., 2013). The HCM is then applied to these populations separately. This method is capable of identifying small/dispersed S-complex families in the C/X-type background, and vice versa, or low-albedo families in the high-albedo background, and vice versa. It can also be useful to characterize the so-called family “halos” (section 6.4).

A more general method for including the color/albedo information in the clustering algorithm consists in the application of the HCM in space of increased dimension (e.g., Parker et al., 2008; Carruba et al., 2013a). When considering the proper elements and SDSS colors, the distance in five dimensions can be defined as  $d_2^2 \equiv d^2 + n^2 a_p^2 (k_1(\delta C_1)^2 +$

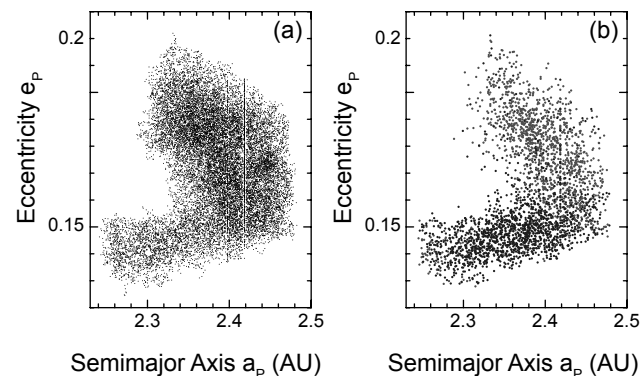


**Fig. 2.** The Nysa-Polana complex. **(a)** The HCM applied to this region of the inner main belt reveals a major concentration of asteroids with  $2.25 < a_p < 2.48$  AU and  $0.13 < e_p < 0.22$ . The shape of the concentration in the  $(a_p, e_p)$  projection is unusual and difficult to interpret. **(b)** The WISE albedos of members of the Nysa-Polana complex: black for  $p_V < 0.15$  and gray for  $p_V > 0.15$ . It becomes clear with the albedo information that the Nysa-Polana complex is two overlapping groups with distinct albedos. Furthermore, based on the V-shape criterion (section 4), the low-albedo group is found to consist of two asteroid families [the Polana and Eulalia families (Walsh et al., 2013)]. The vertical feature at  $a_p \approx 2.42$  AU is the 1:2 mean-motion resonance with Mars.

$k_2(\delta C_2)^2$ ), where  $d$  is the distance in three-dimensional space of proper elements defined in section 2.2,  $C_1$  and  $C_2$  are two diagnostic colors defined from the SDSS (Ivezic et al., 2001; Nesvorný et al., 2005), and  $k_1$  and  $k_2$  are coefficients whose magnitude is set to provide a good balance between the orbital and color dimensions (e.g., Nesvorný et al., 2006b). Similarly, we can define  $d_3^2 \equiv d^2 + n^2 a_p^2 k_p(\delta p_V)^2$  (in four dimensions) and  $d_4^2 \equiv d_2^2 + n^2 a_p^2 k_p(\delta p_V)^2$  (in six dimensions) to include the measurements of albedo  $p_V$  from WISE. The  $d_4$  metric applies the strictest criteria on the family membership, because it requires that the family members have similar proper elements, similar colors, and similar albedos. Note, however, that this metric can only be applied to a reduced set of main-belt asteroids for which the proper elements, colors, and albedos are simultaneously available (presently  $\approx 25,000$ ; Fig. 1b).

## 2.6. Very Young Families in Orbital Element Space

Short after a family’s creation, when the mutual gravity effects among individual fragments cease to be important, the fragments will separate from each other and find themselves moving on heliocentric orbits. Initially, they will have very tightly clustered orbits with nearly the same values of the osculating orbital angles  $\Omega$ ,  $\varpi$ , and  $\lambda$ , where  $\Omega$  is the nodal longitude,  $\varpi$  is the apsidal longitude, and  $\lambda$  is the mean longitude. The debris cloud will be subsequently dispersed by the (1) Keplerian shear (different fragments are ejected with different velocity vectors, have slightly different values of the semimajor axis, and therefore different orbital

periods) and (2) *differential precession* of orbits produced by planetary perturbations.

As for (1), the fragments will become fully dispersed along an orbit on a timescale  $T_n = \pi/(a\partial n/\partial a)(V_{\text{orb}}/\delta V) = (P/3)(V_{\text{orb}}/\delta V)$ , where  $P = 2\text{--}4$  yr is the orbital period and  $\delta V$  is the ejection speed. With  $\delta V = 1\text{--}100$  m s $^{-1}$ , this gives  $T_n = 300\text{--}30,000$  yr. Therefore, the dispersal of fragments along the orbit is relatively fast, and the clustering in  $\lambda$  is *not* expected if a family is older than a few tens of thousand years.

The dispersal of  $\Omega$  and  $\varpi$  occurs on a timescale  $T_f = \pi/(\alpha\partial f/\partial \alpha)(V_{\text{orb}}/\delta V)$ , where the frequency  $f = s$  or  $g$ . For example,  $\partial s/\partial a = -70$  arcsec yr $^{-1}$  AU $^{-1}$  and  $\partial g/\partial a = 94$  arcsec yr $^{-1}$  AU $^{-1}$  for the Karin family ( $a = 2.865$  AU). With  $\delta V = 15$  m s $^{-1}$  (Nesvorný *et al.*, 2006a) and  $V_{\text{orb}} = 17.7$  km s $^{-1}$ , this gives  $T_s = 3.8$  m.y. and  $T_g = 2.8$  m.y. Since  $t_{\text{age}} > T_s$  and  $t_{\text{age}} > T_g$  in this case, the distribution of  $\Omega$  and  $\varpi$  for the Karin family is not expected to be clustered at the present time (Fig. 3). Conversely, the clustering of  $\Omega$  and  $\varpi$  would be expected for families with  $t_{\text{age}} \leq 1$  m.y.

This expectation leads to the possibility that the families with  $t_{\text{age}} \leq 1$  m.y. could be detected in the catalogs of osculating orbital elements (Marsden, 1980; Bowell *et al.*, 1994), where they should show up as clusters in five-dimensional space of  $a$ ,  $e$ ,  $i$ ,  $\varpi$ , and  $\Omega$ . The search in five-dimensional space of the osculating orbital elements can be performed

with the HCM method and metric  $d_5^2 = d^2 + (na)^2(k_\Omega(\delta\Omega)^2 + k_\varpi(\delta\varpi)^2)$ , where  $d = d(a,e,i)$  was defined in section 2.2, and  $k_\Omega$  and  $k_\varpi$  are new coefficients. [Different metric functions were studied by Rožek *et al.* (2011), who also pointed out that using the mean elements, instead of the osculating ones, can lead to more reliable results.]

This method was first successfully used in practice for the identification of the Datura family (Nesvorný *et al.*, 2006c), and soon after for the discovery of the asteroid pairs (Vokrouhlický and Nesvorný, 2008). The Datura family now consists of 15 known members ranging in size from  $\approx 10$ -km-diameter object (1270) Datura to subkilometer fragments. They have  $\Omega$  and  $\varpi$  clustered to within a few degrees near  $98^\circ$  and  $357^\circ$ , respectively. The age of the Datura family is only  $530 \pm 20$  k.y., as estimated from the backward integration of orbits (Vokrouhlický *et al.*, 2009). Table 1 reports other notable cases of families with  $t_{\text{age}} < 1$  m.y.

### 3. DETECTION OF RECENT BREAKUPS

The detection of families with very young formation ages was one of the highlights of asteroid research in the past decade. A poster child of this exciting development is the Karin family, part of the larger Koronis family, that was shown to have formed only  $5.8 \pm 0.2$  m.y. ago (Nesvorný *et al.*, 2002a). The Karin family was identified by the tra-

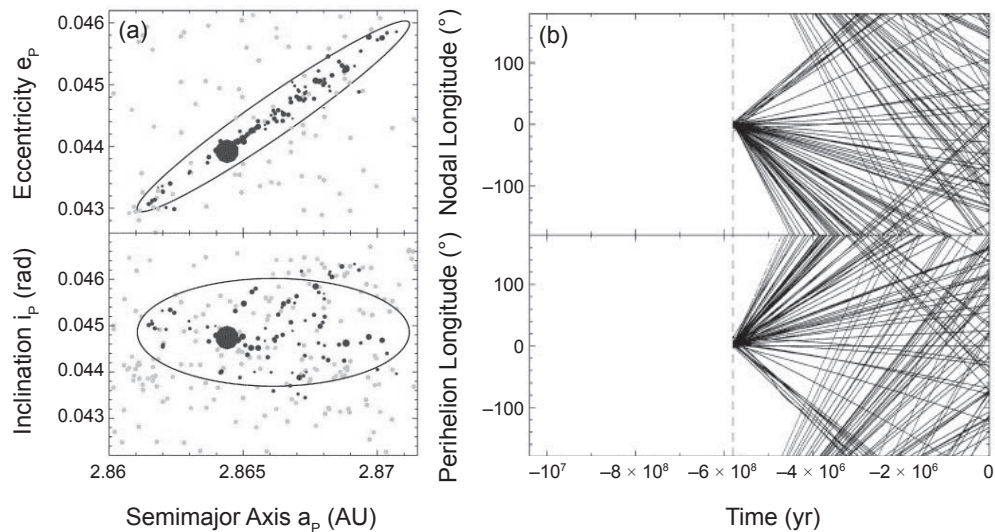


**Fig. 3.** (a) Proper elements of members of the Karin family. The size of each dark symbol is proportional to the diameter of a family member. Light gray dots indicate background bodies near the Koronis family. The black ellipses show the proper orbital elements of test bodies launched at 15 m s $^{-1}$  from  $a_p = 2.8661$  AU,  $e_p = 0.04449$ , and  $i_p = 0.03692$ , assuming that  $f = 30^\circ$  and  $\omega + f = 45^\circ$ , where  $f$  and  $\omega$  are the true anomaly and perihelion argument of the disrupted body at the time of the family-forming collision. (b) The convergence of angles at 5.8 m.y. ago demonstrates that the Karin family was created by a parent asteroid breakup at that time. The plot shows past orbital histories of 90 members of the Karin family: (top) the proper nodal longitude, and (bottom) the proper perihelion longitude. Values of these angles relative to (832) Karin are shown. At  $t = 5.8$  m.y. (broken vertical line), the nodal longitudes and perihelion arguments of all 90 asteroids become nearly the same, as expected if these bodies had initially nearly the same orbits. Adapted from Nesvorný and Bottke (2004).

TABLE 1. Recently formed asteroid families.

Family/Pair	$t_{age}$	References	Notes
(832) Karin	$5.75 \pm 0.05$ m.y.	Ne02,NB04	2.1° dust band
(158) Koronis(2)	10–15 m.y.	MH09	near (832) Karin
(490) Veritas	$8.3 \pm 0.5$ m.y.	Ne03,F06,T07	9.3° band, late Miocene dust shower
(656) Beagle	~10 m.y.	Ne08	1.4° band, member Elst-Pizzaro?
(778) Theobalda	$6.9 \pm 2.3$ m.y.	No10	$t_{age}$ needs to be confirmed
(1270) Datura	$530 \pm 20$ k.y.	Ne06,V09	identified in 5D, E/F dust band?
(2384) Schulhof	$780 \pm 100$ k.y.	VN11	secondary breakup event?
(4652) Iannini	≤5 m.y.	Ne03,W08	chaotic dynamics
(5438) Lorre	$1.9 \pm 0.3$ m.y.	No12a	$i_p \approx 28^\circ$
(14627) Emilkowalski	$220 \pm 30$ k.y.	NV06	only 3 members known
(16598) 1992 YC2	50–250 k.y.	NV06	only 3 members known
(21509) Lucascavin	300–800 k.y.	NV06	only 3 members known
(300163) P/2006 VW139	$7.5 \pm 0.3$ m.y.	No12b	main-belt comet
P/2012 F5 (Gibbs)	$1.5 \pm 0.1$ m.y.	No14	main-belt comet

References: Ne0X = Nesvorný et al. (200X), NoXX = Novaković et al. (20XX), VNXX = Vokrouhlický and Nesvorný (20XX), VXXX = Vokrouhlický et al. (20XX), NB04 = Nesvorný and Bottke (2004), T07 = Tsiganis et al. (2007), F06 = Farley et al. (2006), W08 = Willman et al. (2008), NV06 = Nesvorný and Vokrouhlický (2006), MH09 = Molnar and Haegert (2009).

ditional means, using the HCM on proper elements. The diagonal shape of this family in the  $(a_p, e_p)$  projection is a telltale signature of a recent breakup, because this initial shape is expected if a breakup occurs near the perihelion of the parent body orbit (Fig. 3). In this case, the tilt  $\alpha$  of the family shape in the  $(a_p, e_p)$  projection is expected to be, and indeed is in the case of the Karin family,  $\tan \alpha = \Delta e_p / (\Delta a_p / a_p) = (1 - e_p) = 0.956$ . Thus,  $\alpha \approx 45^\circ$ . All other known families, with an exception of the similarly young Veritas family, have  $\alpha \sim 0$  (i.e., are nearly horizontal features in  $a_p, e_p$ ). This is because these families are old and their original shape was stretched in  $a_p$  by the Yarkovsky effect (e.g., Dell'Oro et al., 2004).

The age of the Karin family has been established by numerically integrating the orbits of identified members back in time in an attempt to identify their past convergence (Fig. 3). The past convergence is expected because the spread of the Karin family in  $a_p, e_p, i_p$  indicates that the ejection speeds of observed fragments were only  $\leq 15$  m s $^{-1}$ . These low speeds imply a very tight *initial* distribution (to within  $\approx 1^\circ$ ) of  $\lambda$ ,  $\varpi$ , and  $\Omega$ . The backward integration showed that the convergence occurred at  $5.8 \pm 0.2$  m.y. ago. In addition, the past convergence improved, with  $\varpi$  and  $\Omega$  of all member orbits converging to within a degree, if the backward integration included the Yarkovsky drift (Nesvorný and Bottke, 2004). This was used to measure the rate of the Yarkovsky drift for individual members of the family, determine their obliquities, and pin down the age of the Karin family to  $t_{age} = 5.75 \pm 0.05$  m.y.

The method of backward integration of orbits was applied to several families (Nesvorný et al., 2002a, 2003, 2008b; Novaković et al., 2010a,b, 2012a,b, 2014) (some of these results will need to be verified; see also Table 1). One of the interesting results that emerged from these studies is a possible relationship between the young families and main-belt comets (MBCs) (see chapter by Jewitt et al. in

this volume). For example, (7968) P/133 Elst-Pizzaro can be linked to the Beagle family [ $t_{age} \sim 10$  m.y. (Nesvorný et al., 2008b)], and (300163) P/2006 VW139 and P/2012 F5 (Gibbs) can be linked to small families that probably formed within the past 10 m.y. (Novaković et al., 2012a, 2014). If this relationship is confirmed by future studies, this can help us to understand how the MBCs are “activated.”

Another notable case of a recent breakup is the Veritas family (Fig. 4). It has previously been hypothesized that the Veritas family is <50 m.y. old (Milani and Farinella, 1994). This claim was based on the argument that the largest member of the dynamical family, (490) Veritas, has chaotic dynamics and would be expected to diffuse away in  $e_p$  from the rest of the family, if the family were older than ~50 m.y. [Note, however, that recent impact modeling may indicate that (490) Veritas is not a true member of the Veritas family (e.g., Michel et al., 2011).] A backward integration of orbits confirmed the young age, and showed that the Veritas family formed only  $8.3 \pm 0.5$  m.y. ago (Nesvorný et al., 2003).

A similarly young age was later obtained by an independent method, known as the “chaotic chronology,” based on tracking the evolution of orbits in one of the diffusive resonances that intersect the Veritas family (Tsiganis et al., 2007; see also Knežević and Pavlović, 2002). Tsiganis et al. (2007) considered the chaotic diffusion of the Veritas family members in the 5J-2S-2 three-body resonance at 3.174 AU (Nesvorný and Morbidelli, 1999). Based on numerical integrations of chaotic orbits, they estimated that the observed spread in the 5J-2S-2 resonance can be obtained for  $t_{age} = 8.7 \pm 1.7$  m.y. Interestingly, the Veritas family is also intersected by the 7J-7S-2 resonance at 3.168 AU. The observed distribution of eccentricities in this resonance is rather wide and cannot be explained by normal diffusion over the estimated age (the 7J-7S-2 resonance is ~100× less diffusive than the 5J-2S-2 resonance). Perhaps the problem is with the HCM chaining, discussed in section 2.2, which

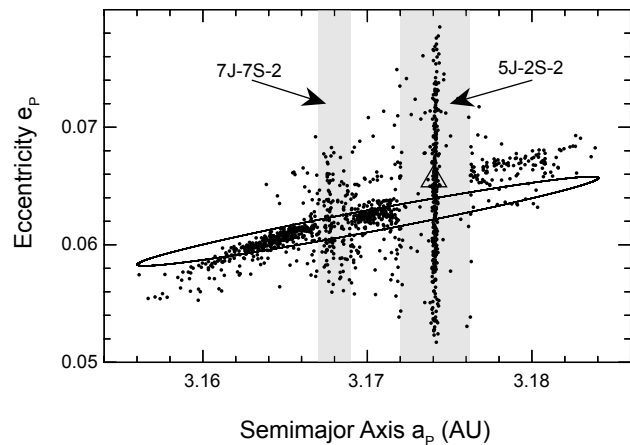


**Fig. 4.** The Veritas family. Here we plot the proper elements of 1294 members of the Veritas family identified from a new catalog (August 2014). (490) Veritas itself is marked by a triangle. The gray vertical strips indicate two three-body resonances that act to diffuse the orbits of family members in  $e_p$ . The black ellipse shows the orbital elements of test bodies launched at  $\delta V = 35 \text{ m s}^{-1}$  from  $a_p = 3.17 \text{ AU}$  and  $e_p = 0.0062$ , assuming that  $f = 30^\circ$ , where  $f$  is the true anomaly of the disrupted body at the time of the family-forming collision.

links unrelated asteroids in the 7J-7S-2 resonance, or the dynamical modeling is missing some important ingredient. Novaković (2010) applied the method of chaotic chronology to the Theobalda family and found that the estimated age is consistent with that obtained from a backward integration of the regular orbits ( $t_{\text{age}} = 6.9 \pm 2.3 \text{ m.y.}$ ).

There is a close relationship between the young asteroid families and the *asteroid dust bands* (see chapter by Jenniskens in this volume), which are strips of infrared emission running roughly parallel to the plane of the solar system (Low *et al.*, 1984). The three most prominent dust bands, known as  $\alpha$ ,  $\beta$ , and  $\gamma$ , have previously been thought to originate in the Themis, Koronis, and Eos families (Dermott *et al.*, 1984). Detailed modeling, however, has shown that the sources of these dust bands are the recently formed Karin, Beagle, and Veritas families (Dermott *et al.*, 2002; Nesvorný *et al.*, 2003, 2006, 2008b), mainly because (1) the Veritas family with  $i_p = 9.3^\circ$  provides a better fit to the latitudinal position of the  $\gamma$  band than the Eos family with  $i_p = 10^\circ$ , and (2) the young families should now be more prolific sources of dust than the old families, because the dust production in a collisional cascade is expected to drop with time. A tracer of the Veritas family breakup has been found in measurements of extraterrestrial  ${}^3\text{He}$  in  $\approx 8.2\text{-m.y.-old}$  deep ocean sediments (Farley *et al.*, 2006).

#### 4. V-SHAPE CRITERION

A correct identification of the brightest/largest members in a family is important for several reasons. For example, the spectroscopic observations are magnitude limited and

can typically only be conducted for bright targets. The interpretation of spectroscopic observations of asteroid families, and implications for the homogeneity/heterogeneity of their parent bodies, therefore depend on whether the bright asteroids are the actual members of a family or not (e.g., Reddy *et al.*, 2011). The large objects in families are also critically important for asteroid impact studies, in which the size frequency distribution (SFD) of family members is used to calibrate the results of impact experiments. Finally, the uncertainty in the membership of the largest family members critically affects our estimates of size of the disrupted parent bodies (e.g., Durda *et al.*, 2007).

While the interloper problem may not have an ideal solution, there exists a straightforward method that can be used to remove obvious bright/large interlopers based on dynamical considerations. This method is inspired by the “V shape” of asteroid families, which becomes apparent when the absolute magnitude  $H$  of family members is plotted against  $a_p$  (Fig. 5). The V shape results from two processes. First, larger (smaller) fragments tend to be ejected at lower (higher) speeds, and thus tend to be located, on average, closer to (further away from) the family center (see the chapter by Michel *et al.* in this volume). The second and typically more dominant “V” is contributed by the Yarkovsky effect.

The Yarkovsky effect (YE) is a recoil force produced by anisotropic emission of thermal photons from an asteroid surface (see the chapter by Vokrouhlický *et al.* in this volume). The diurnal component of the YE, which is more important for asteroid-sized bodies than its seasonal counterpart, can increase the semimajor axis of an asteroid with a prograde rotation and decrease the semimajor axis for a retrograde rotation. The semimajor axis drift is generally given by  $da_p/dt = \text{const.} \cos \theta (a_p^2 D)$ , where  $\theta$  is the asteroid obliquity,  $D$  is the effective diameter, and the constant depends on material properties. The maximum drift occurs for  $\theta = 0^\circ$  or  $\theta = 180^\circ$ . Thus, the envelope of the distribution of family members in  $(a_p, H)$  is expected to follow  $|a_p - a_c| = C_{\text{YE}} 10^{H/5}$ , where  $a_c$  is the family center (often assumed to coincide with the largest fragment), and  $C_{\text{YE}}$  is a constant related to  $t_{\text{age}}$  (section 5). Interestingly, if the ejection speed  $\delta V \propto 1/D$ , as found for the youngest families (e.g., Nesvorný *et al.*, 2006a) and some laboratory experiments (e.g., Fujiwara *et al.*, 1989), then the ejection velocity field will produce the same dependence,  $|a_p - a_c| = C_{\text{EV}} 10^{H/5}$ , where  $C_{\text{EV}}$  is related to the magnitude of the ejection velocities.

These considerations allow us to define the V-shape criterion (e.g., Nesvorný *et al.*, 2003). Consider a family extracted by the HCM as described in section 2.2. Fit an envelope to the distribution of small family members in  $(a_p, H)$  using the functional dependence between  $a_p$  and  $H$  defined above. The envelope is then continued to low  $H$  values, and the bright members of the HCM family that fall outside the envelope boundaries can be rejected. On the other hand, the brightest HCM family members that fall within the envelope boundaries are good candidates for the largest family members. This method is illustrated in Fig. 5.

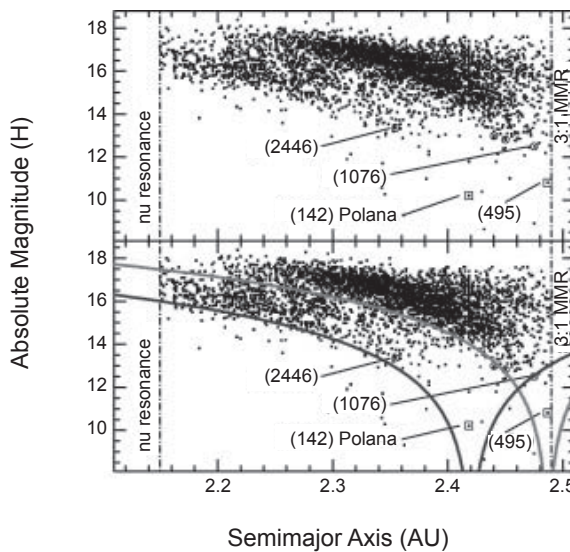


**Fig. 5.** A recent application of the V-shape criterion to define the Polana and Eulalia families, and identify the largest members in these families (Walsh et al., 2013). The plot shows the absolute magnitude  $H$  of dark ( $p_V < 0.1$ ) asteroids with  $0.1 < e_p < 0.2$  and  $i_p < 10^\circ$  as a function of  $a_p$ . The bottom panel illustrates the best-fit V-shape curves to the (left) Polana and (right) Eulalia families. (142) Polana and (495) Eulalia, the largest dark asteroids inside the left and right zones, respectively, are the likely largest members of the two families.

In practice, a number of additional effects can complicate the application of the V-shape criterion described above. For example, strong nearby resonances can remove family members that drifted into them, thus producing cutoffs of the  $a_p - a_c$  distribution beyond which no family members can be identified (e.g., the 3:1 resonance in Fig. 5). Also, family members can be displaced in  $a_p$  by encounters with (1) Ceres and other massive main-belt asteroids (Nesvorný et al., 2002b; Carruba et al., 2003, 2007a, 2012, 2013b; Delisle and Laskar, 2012). In addition, the physics of large-scale collisions is still poorly understood, and the possibility that some large fragments can be accelerated to very high speeds cannot be ruled out. Therefore, while the V-shape criterion defined above is a useful guide, it cannot be rigidly applied.

Possibly the best way to deal with this issue is to define the value of  $C_0 = 10^{-H/5}|a_p - a_c|$  that best fits the V-shaped family envelope and report  $C_j/C_0$ , where  $C_j = 10^{-H_j/5}|a_{p,j} - a_c|$ , for each family member  $j$  identified by the HCM. Asteroids with  $|C_j/C_0| > 1$  can be flagged (but not removed), because they are potential interlopers in a dynamical family according to the V-shape criterion. The results can then be cross-linked with the spectroscopic data (or colors, or albedo measurements) to determine whether there is a good correspondence between the flagged bodies and (suspected) spectroscopic interlopers. An illustration of this procedure can be found in Vokrouhlický et al. (2006a) who examined the Eos family. They found that many large bodies in the

HCM family with  $|C_j/C_0| > 1$  have physical properties that are indeed incompatible (mainly dark C types) with the bulk of the Eos family (mainly brighter K types).

## 5. FAMILY AGE ESTIMATION

The method of backward integrations of orbits described in section 3 cannot be used to determine ages of the families much older than  $\sim 10$  m.y., mainly because the orbital evolution of main-belt asteroids is generally unpredictable on long timescales and sensitively depends on nongravitational effects, which are difficult to model with the needed precision. Instead, the age of an old family can be estimated by a statistical method, which is based on the general notion that the spread of an asteroid family in  $a_p$  increases over time as its members drift away due to the Yarkovsky effect. Expressed in terms of the equations discussed in the previous section, the age can be estimated as

$$t_{\text{age}} \approx 1 \text{ G.y.} \times \left( \frac{C_0}{10^{-4} \text{ AU}} \right) \left( \frac{a}{2.5 \text{ AU}} \right)^2 \times \left( \frac{\rho}{2.5 \text{ g cm}^{-3}} \right) \left( \frac{0.2}{p_V} \right)^{\frac{1}{2}} \quad (1)$$

where  $\rho$  is the asteroid bulk density and  $p_V$  is the visual albedo. While the equation above is scaled to typical values expected for an S-type asteroid, a change to  $\rho = 1.5 \text{ g cm}^{-3}$  and  $p_V = 0.05$ , which would be more appropriate for a dark C-type asteroid, produces two multiplication factors that nearly compensate each other. The biggest uncertainty in the inversion from  $C_0$  to  $t_{\text{age}}$  lies in the unknown density factor. Additional uncertainty, not explicitly apparent from equation (2), stems from the dependence of the drift rate on surface conductivity  $K$ . Together, the conversion from  $C_0$  to  $t_{\text{age}}$  has an uncertainty of about a factor of 2.

More fundamentally, equation (1) neglects complicating factors such as the contribution of the original ejection field and nearby resonances that can remove drifting bodies. If  $C = C_{YE} + C_{EV}$ , under the assumptions on the ejection speeds discussed in section 4, the two effects cannot be decoupled from each other, and  $t_{\text{age}}$  estimated from  $C_0$  will always overshoot the real age of the family. This happens, in essence, because this simple method only fits the family envelope.

Vokrouhlický et al. (2006a,b) have developed a more general statistical method that uses the actual distribution of family members within the V-shape envelope. It works as follows. First, the code generates a newborn family. The distribution of the ejection speeds of fragments is approximated by the Gaussian distribution in each velocity component with the size-dependent standard deviation  $\delta V = V_5(5 \text{ km/D})$ , where  $V_5$  is a free parameter. This functional dependence generally provides a good match to the ejection speeds inferred from the young families and impact simulations (Michel et al., 2001, 2003, 2004; Nesvorný et al., 2002a, 2006a; Durda et al., 2004, 2007). The Yarkovsky-YORP (hereafter YY) code (where YORP is an acronym for

Yarkovsky-O'Keefe-Radzievskii-Paddack) then evolves the orbits of fragments accounting for the semimajor axis drift due to the YE, and the spin evolution from the YORP effect (Rubincam, 2000). To speed up the calculation, planetary perturbations were not taken into account in the original YY code [but see Masiero *et al.* (2012); results based on full N-body integrations are discussed in the following section].

When applied to an asteroid family, the goal is to find a combination of parameters  $V_5$  and  $t_{\text{age}}$  that best fits the observed  $(a_p, H)$  distribution in the family. Since the model does not contain an SFD-related evolution component, this can be conveniently done by simply fitting the observed distribution of  $C_j$ . The results are found to be credible in cases such as the Ergone family (Fig. 6), where the YY model is capable of adequately representing the observed  $C$  distribution, which shows void space near  $C = 0$ , a maximum at intermediate values of  $C$ , and a relatively sharp drop toward the largest  $C$  values seen in the family. This dependence is produced by the YORP effect, which tilts the spin axis away from the orbital plane and therefore, through the  $\cos \theta$  dependence of the YE, tends to maximize the drift rates. This gives some asteroid families the characteristic appearance in  $(a_p, H)$ , which different authors, with noticeably different gifts for subtleties of poetic expression, called “ears,” “wings,” or “petals.”

But not all families have ears, wings, or petals. In fact, most families have more uniform distribution of  $C$  that goes all the way from 0 to  $C_{\text{max}}$ . This is thought to have something to do with how the YE and YORP operate on gigayear-long timescales. It is perhaps related to the variability of the spin-related YORP torque, which sensitively depends on small perturbations of the asteroid surface. As

a result of this dependence, the spin rate of each individual asteroid can undergo a random walk [stochastic YORP (Bottke *et al.*, 2015)] and, when spun down completely, the asteroid spin axis would chaotically tumble for some time, and subsequently reorient. This process could mix up the total drifts suffered by family members and, rather unpoetically, remove the ears, wings, or petals from the old families.

The application of the standard YY code (and also, for that matter, the simple method based on the “V”-shape envelope) is problematic in cases when a family is cut by nearby mean-motion resonances and looks like a box in  $(a_p, H)$ , or when  $C_{\text{EV}}$  is expected to be larger than  $C_{\text{YE}}$ , perhaps because the family's parent was an object with large escape speed [e.g., the Vesta family; (4) Vesta has  $V_{\text{esc}} \approx 360 \text{ m s}^{-1}$ ], or because the family formed recently (e.g., the Datura, Karin, and Veritas families have  $C_{\text{YE}} \approx 0$ ). A complete list of families to which the YY code was successfully applied so far is:

- Agnia ( $t_{\text{age}} = 100 \pm 100 \text{ m.y.}$ ,  $V_5 \approx 15 \text{ m s}^{-1}$ )
- Massalia ( $t_{\text{age}} = 150 \pm 50 \text{ m.y.}$ ,  $V_5 \approx 20 \text{ m s}^{-1}$ )
- Baptista ( $t_{\text{age}} = 160 \pm 50 \text{ m.y.}$ ,  $V_5 \approx 40 \text{ m s}^{-1}$ )
- Merxia ( $t_{\text{age}} = 250 \pm 100 \text{ m.y.}$ ,  $V_5 \approx 25 \text{ m s}^{-1}$ )
- Astrid ( $t_{\text{age}} = 250 \pm 100 \text{ m.y.}$ ,  $V_5 \approx 15 \text{ m s}^{-1}$ )
- Ergone ( $t_{\text{age}} = 300 \pm 100 \text{ m.y.}$ ,  $V_5 \approx 30 \text{ m s}^{-1}$ )
- Eos ( $t_{\text{age}} = 1.3 \pm 0.5 \text{ G.y.}$ ,  $V_5 \approx 70 \text{ m s}^{-1}$ )
- Tina ( $t_{\text{age}} = 170 \pm 50 \text{ m.y.}$ ,  $V_5 \approx 20 \text{ m s}^{-1}$ )

Here we have taken the liberty of updating and rounding off the estimates, and giving more generous errors than in the original publications (Vokrouhlický *et al.*, 2006a,b,c; Bottke *et al.*, 2007; Carruba and Morbidelli, 2011) [for the Padua family, see also Carruba (2009a)]. Note that these errors do not include the uncertainty of about a factor of 2 from the

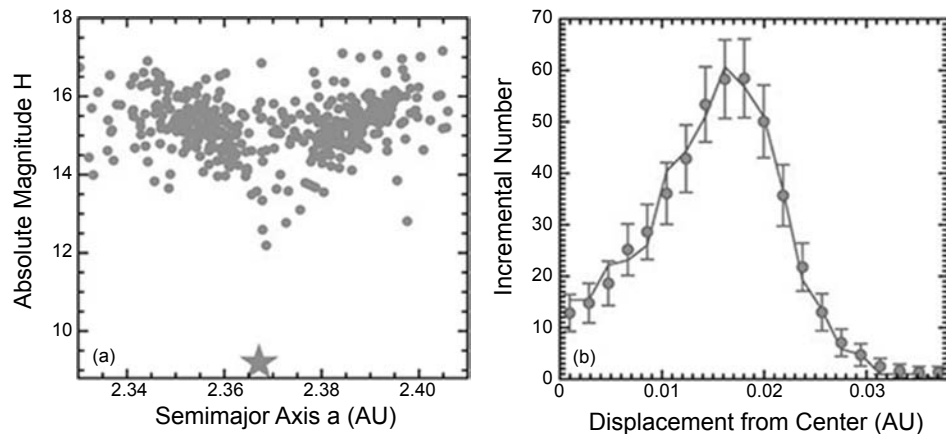


**Fig. 6.** (a) The Ergone family projected onto a plane of proper semimajor axis vs. absolute magnitude  $H$ ; (163) Ergone is the filled star. The family has been separated into two clouds ( $a_p \leq 2.37 \text{ AU}$ ;  $a_p \geq 2.37 \text{ AU}$ ) by the Yarkovsky/YORP evolution. (b) A comparison between model results (solid line) and binned Ergone family [gray dots (see Vokrouhlický *et al.*, 2006b)]. The error bars are the square root of the number of bodies in each bin. The x-axis is the distance of family members from the the family center. Based on this result, Vokrouhlický *et al.* (2006b) estimated that  $t_{\text{age}} = 280^{+30}_{-50} \text{ m.y.}$  and  $V_5 = 26^{+14}_{-11} \text{ m s}^{-1}$ , where the error bars do not include the uncertainty originating from uncertain material properties (e.g., density, surface conductivity).

poorly known bulk density and surface conductivity of the asteroids in question. Including this uncertainty, *Masiero et al.* (2012) found that the best-fitting age of the Baptistina family can be anywhere between 140 and 320 m.y.

The estimated ejection speeds are  $V_5 = 15\text{--}50 \text{ m s}^{-1}$ , except for the Eos family, which formed in a breakup of a very large parent asteroid ( $D_{\text{PB}} \sim 300 \text{ km}$ ). These results are consistent with the ejection speeds inferred from the young Karin family, which has  $V_5 \approx 15 \text{ m s}^{-1}$  for a relatively small parent body [ $D_{\text{PB}} \approx 35 \text{ km}$  (*Nesvorný et al.*, 2006a)]. The ejection speeds contribute by  $\approx 20\%$  (for oldest Eos) to 50% (for youngest Agnia) to the total family spread in the semi-major axis. Ignoring this contribution, as in equation (2), would thus lead to an overestimate of  $t_{\text{age}}$  by  $\approx 20\text{--}50\%$ . While one must therefore be careful in applying equation (2) to the small/young families that did not have enough time to significantly spread by the YE, the effect of the ejection speeds should be less of an issue for old families.

## 6. DYNAMICAL EVOLUTION

### 6.1. Initial State

The dynamical evolution of asteroids in families is similar to the dynamical evolution of main-belt asteroids in general. Studying the dynamical evolution of individual families is useful in this context, because we more or less know how the families should look like initially. Things may thus be learned by comparing these ideal initial states with how different families look now, after having dynamically evolved since their formation. The dynamical studies can also often provide an independent estimate of  $t_{\text{age}}$ .

Assuming that  $\delta V \ll V_{\text{orb}}$ , the initial shape of families in  $(a, e, i)$  can be obtained from the Gauss equations (e.g., *Zappalà et al.*, 2002), which map the initial velocity perturbation  $\delta V = (V_R, V_T, V_Z)$ , where  $V_R$ ,  $V_T$ , and  $V_Z$  are the radial, tangential, and vertical components of the velocity vector, to the change of orbital elements  $\delta E = (\delta a, \delta e, \delta i)$ . If the ejection velocity field is (roughly) isotropic, the Gauss equations imply that initial families should (roughly) be ellipsoids in  $(a, e, i)$  centered at the reference orbit  $(a^*, e^*, i^*)$ . The transformation from  $(a, e, i)$  to  $(a_p, e_p, i_p)$  preserves the shape, but maps  $(a^*, e^*, i^*)$  onto  $(a_p^*, e_p^*, i_p^*)$  such that, in general,  $a_p^* \neq a^*$ ,  $e_p^* \neq e^*$ , and  $i_p^* \neq i^*$ .

The shape of the ellipsoids in  $(a_p, e_p, i_p)$  is controlled by the true anomaly  $f$  and the argument of perihelion  $\omega$  of the parent body at the time of the family-forming breakup. The projected distribution onto the  $(a_p, e_p)$  plane is a tilted ellipse with tightly correlated  $a_p$  and  $e_p$  if the breakup happened near perihelion (see Fig. 3a), or tightly anticorrelated  $a_p$  and  $e_p$  if the breakup happened near aphelion. The two recently formed families for which this shape is clearly discernible, the Karin and Veritas families, have correlated  $a_p$  and  $e_p$ , implying that  $|f| = 30^\circ$  (Figs. 3 and 4).

The projected initial distribution onto the  $(a_p, i_p)$  plane is an ellipse with horizontal long axis and vertical short axis. The short-to-long axis ratio is roughly given by  $\cos(\omega + f)$

$V_Z/V_T$ . Thus, breakups near the ascending ( $\omega + f = 0$ ) and descending ( $\omega + f = \pi$ ) nodes should produce “fat” ellipses while those with  $\omega + f = \pm\pi/2$  should make “squashed” ellipses with  $\delta i_p \approx 0$ . While the Karin family neatly fits in this framework with  $\omega + f \approx \pi/4$  (Fig. 3), the Veritas family shows large  $\delta i_p$  values, indicating that the ejection velocity field should have been anisotropic with  $V_Z$  some  $\approx 2\text{--}4\times$  larger than  $V_T$ .

The reference orbit  $(a_p^*, e_p^*, i_p^*)$  is often taken to coincide with the proper orbit of a largest family member. This should be fine for families produced in cratering or mildly catastrophic events, where the orbital elements of the impacted body presumably did not change much by the impact. For the catastrophic and highly catastrophic breakups, however, the largest surviving remnant is relatively small and can be significantly displaced from the family’s center. For example, (832) Karin, the largest  $\approx 17\text{-km}$ -diameter member of the Karin family produced by a catastrophic breakup of a  $\approx 40\text{-km}$ -diameter parent body [mass ratio  $\approx 0.08$  (*Nesvorný et al.*, 2006a)], is displaced by  $\approx -0.002 \text{ AU}$  from the family center ( $\approx 20\%$  of the whole extension of the Karin family in  $a_p$ ). This shows that, in general, the position of the largest fragment does not need to perfectly coincide with the family center, and has implications for the V-shape criterion discussed in section 4 (where an allowance needs to be given for a possible displacement).

### 6.2. Dynamics on Gigayear Timescales

An overwhelming majority of the observed asteroid families are not simple Gaussian ellipsoids. While this was not fully appreciated at the time of the *Asteroids III* book, today’s perspective on this issue is clear: *The families were stretched in  $a_p$  as their members drifted away from their original orbits by the Yarkovsky effect.* The asteroid families found in the present main belt are therefore nearly horizontal and elongated structures in  $(a_p, e_p)$  and  $(a_p, i_p)$ . This shows that the original ejection velocity field cannot be easily reconstructed by simply mapping back today’s  $(a_p, e_p, i_p)$  to  $(V_R, V_T, V_Z)$  from the Gauss equations (Note 7).

Moreover, many asteroid families have weird shapes that, when taken at face value, would imply funny and clearly implausible ejection velocity fields. A prime example of this, briefly mentioned in section 2.2, is the Koronis family (*Bottke et al.*, 2001). Since the case of the Koronis family was covered in the *Asteroids III* book (*Bottke et al.*, 2002), we do not discuss it here. Instead, we concentrate on the results of new dynamical studies, many of which have been inspired by the Koronis family case. The dynamical effects found in these studies fall into three broad categories:

1. Members drifting in  $a_p$  encounter a mean-motion resonance with one of the planets [mainly Jupiter, Mars, or Earth (see *Nesvorný et al.*, 2002c)]. If the resonance is strong enough (e.g., 3:1, 2:1, or 5:2 with Jupiter), the orbit will chaotically wander near the resonance border, its eccentricity will subsequently increase, and the body will be removed from the main belt and transferred onto a planet-crossing

orbit (*Wisdom*, 1982). If the resonance is weak, or if the asteroid is small and drifts fast in  $a_p$ , the orbit can cross the resonance, perhaps suffering a discontinuity in  $e_p$  during the crossing, and will continue drifting on the other side. If the resonance is weak and the drift rate is not too large, the orbit can be captured in the resonance and will slowly diffuse to larger or smaller eccentricities. It may later be released from the resonance with  $e_p$  that can be substantially different from the original value. The effects of mean-motion resonances on  $i_p$  are generally smaller, because the eccentricity terms tend to be more important in the resonant potential. The inclination terms are important for orbits with  $i_p \geq 10^\circ$ . A good example of this is the Pallas family, with  $i_p = 33^\circ$  (*Carruba et al.*, 2011).

2. Drifting members meet a secular resonance. The secular resonances are located along curved manifolds in  $(a_p, e_p, i_p)$  space (*Knežević et al.*, 1991). Depending on the type and local curvature of the secular resonance, and asteroid's  $da/dt$ , the orbit can be trapped inside the resonance and start sliding along it, or it can cross the resonance with a noticeably large change of  $e_p$  and/or  $i_p$ . A good example of the former case are orbits in the Eos family sliding along the  $z_1 = g - g_6 + s - s_6 = 0$  resonance (*Vokrouhlický et al.*, 2006a). An example of the latter case is the Koronis family, where eccentricities change as a result of crossing of the  $g + 2g_5 - 3g_6 = 0$  resonance (*Bottke et al.*, 2001). If the secular resonance in question only includes the  $g$  (or  $s$ ) frequency, effects on  $e_p$  (or  $i_p$ ) are expected. If the resonance includes both the  $g$  and  $s$  frequencies, both  $e_p$  and  $i_p$  can be affected. If the orbit is captured in a resonance with the  $g$  and  $s$  frequencies, it will slide along the local gradient of the resonant manifold with changes of  $e_p$  and  $i_p$ , depending on the local geometry.

3. Encounters with (1) Ceres and other massive asteroids produce additional changes of  $a_p$ ,  $e_p$ , and  $i_p$  (*Nesvorný et al.*, 2002b; *Carruba et al.*, 2003, 2007a, 2012, 2013b; *Delisle and Laskar*, 2012). These changes are typically smaller than those from the Yarkovsky effect on  $a_p$  and resonances on  $e_p$  and  $i_p$ . They are, however, not negligible. The effect of encounters can be approximated by a random walk (for a discussion, see *Carruba et al.*, 2007a). The mean changes of  $a_p$ ,  $e_p$ , and  $i_p$  increase with time roughly as  $\sqrt{t}$ . The asteroid families become puffed out as a result of encounters, and faster so initially than at later times, because of the nature of the random walk. Also, a small fraction of family members, in some cases perhaps including the largest remnant, can have their orbits substantially affected by a rare, very close encounter. Additional perturbations of asteroid orbits arise from the linear momentum transfer during nondisruptive collisions (*Dell'Oro and Cellino*, 2007).

### 6.3. Discussion of Dynamical Studies

The case of the Koronis family (*Bottke et al.*, 2001) sparked a great deal of interest in studies of the dynamical evolution of asteroid families on very long timescales. Here we review several of these studies roughly in chronologic

order. The goal of this text is to illustrate the dynamical processes discussed in the previous section on specific cases.

*Nesvorný et al.* (2002b) considered the dynamical evolution of the Flora family. The Flora family is located near the inner border of the main belt, where numerous mean-motion resonances with Mars and Earth produce slow diffusion of  $e_p$  and  $i_p$ . The numerical integration of orbits showed how the overall extent of the Flora family in  $e_p$  and  $i_p$  increases with time. The present width of the Flora family in  $e_p$  and  $i_p$  was obtained in this study after  $t = 0.5$  G.y. even if the initial distribution of fragments in  $e_p$  and  $i_p$  was very tight. The Flora family expansion saturates for  $t > 0.5$  G.y., because the Flora family members that diffused to large eccentricities are removed from the main belt by encounters with Mars [the Flora family is an important source of chondritic near-Earth asteroids (NEAs) (*Vernazza et al.*, 2008)]. The present spread of the Flora family in  $a_p$ , mainly contributed by the Yarkovsky effect, indicates  $t_{age} \sim 1$  G.y.

*Carruba et al.* (2005) studied the dynamical evolution of the Vesta family. The main motivation for this study was the fact that several inner main-belt asteroids, such as (956) Elisa and (809) Lundia, have been classified as V-types from previous spectroscopic observations (*Florczak et al.*, 2002), indicating that they may be pieces of the basaltic crust of (4) Vesta. These asteroids, however, have orbits rather distant from that of (4) Vesta and are not members of Vesta's dynamical family even if a very large cutoff distance is used. It was therefore presumed that (1) they have dynamically evolved to their current orbits from the Vesta family, or (2) they are pieces of differentiated asteroids unrelated to (4) Vesta. *Carruba et al.* (2005) found that the interplay of the Yarkovsky drift and the  $z_2 \equiv 2(g - g_6) + s - s_6 = 0$  resonance produces complex dynamical behavior that can indeed explain the orbits of (956) Elisa and (809) Lundia, assuming that the Vesta family is at least  $\approx 1$  G.y. old. This gives support to assumption (1) above.

In a follow-up study, *Nesvorný et al.* (2008a) performed a numerical integration of 6600 Vesta fragments over 2 G.y. They found that most V-type asteroids in the inner main belt can be explained by being ejected from (4) Vesta and dynamically evolving to their current orbits outside the Vesta family. These V-type "fugitives" have been used to constrain the age of the Vesta family, consistent with findings of *Carruba et al.* (2005), to  $t_{age} \geq 1$  G.y. Since previous collisional modeling of the Vesta family suggested  $t_{age} \leq 1$  G.y. (*Marzari et al.*, 1999), the most likely age of the Vesta family that can be inferred from these studies is  $t_{age} \sim 1$  G.y. This agrees well with the age of the  $\approx 500$ -km-diameter Rheasilvia basin on (4) Vesta inferred from crater counts [ $\approx 1$  G.y. (*Marchi et al.*, 2012)] (Note 8).

*Vokrouhlický et al.* (2006a) studied the dynamical evolution of the Eos family. The Eos family has a complicated structure in proper element space, leading some authors to divide it into several distinct families (e.g., *Milani et al.*, 2014). Diagnostically, however, the Eos family, although somewhat physically heterogeneous, has the color, albedo, and spectral properties that contrast with the local, predomi-

nantly C-type background in the outer asteroid belt, which suggests that it is a single family. As we discuss below, the complicated structure of the Eos family arises from the presence of several mean-motion and secular resonances.

To start with, Vokrouhlický et al. (2006a) showed that the Eos family members drifting by the Yarkovsky effect into the 7:3 resonance with Jupiter are removed (see Fig. 7). This cuts the family at 2.957 AU. Members drifting with  $da/dt > 0$ , on the other hand, will encounter the 9:4 resonance at 3.03 AU. This resonance, being of higher order and thus weaker, is not an unpenetrable barrier, especially for smaller members with higher drift rates. The estimated fraction of bodies that can cross the 9:4 resonance is  $<10\%$  for  $H < 12$  but reaches  $\approx 35\%$  for  $H = 16$ . This is consistent with the magnitude distributions of the Eos family members on both sides of the 9:4 resonance. The larger dispersion of the part of the Eos family with  $a_p > 3.03$  AU is attributed to perturbations of  $e_p$  and  $i_p$  during the 9:4 resonance crossing (Fig. 7). Finally, many orbits in the central part of the Eos family are trapped in the secular resonance  $z_1 \equiv g + s - g_6 - s_6 = 0$ , and slide along it while drifting in  $a_p$  (Note 9).

Finally, we discuss additional processes whose significance is shadowed by the Yarkovsky effect and resonances, but which can be important in some cases. Nesvorný et al. (2002b) considered encounters with (1) Ceres and found that the characteristic change of the semimajor axis due to these encounters is  $\Delta a \approx 0.001$  AU over 100 m.y. Assuming that the scattering effect of encounters can be described by a random walk with  $\Delta a \propto \sqrt{t}$ , the expected changes over 1 G.y. and 4 G.y. are  $\approx 0.003$  AU and  $\approx 0.007$  AU, respectively. The orbital changes were found to be larger for orbits

similar to that of (1) Ceres, because the orbital proximity leads to lower encounter speeds and larger gravitational perturbations during the low-speed encounters. Carruba et al. (2003) studied the effect of encounters on the Adeona and Gefion families, both located near (1) Ceres in proper element space. They found that the semimajor axis of members of the Adeona and Gefion families can change by up to  $\sim 0.01$  AU over the estimated age of these families.

With similar motivation, Carruba et al. (2007a) considered the effect of encounters of the Vesta family members with (4) Vesta. They found the characteristic changes  $\Delta a = 0.002$  AU,  $\Delta e = 0.002$ , and  $\Delta i = 0.06^\circ$  over 100 m.y. In a follow-up work, Delisle and Laskar (2012) included the effects of 11 largest asteroids. They showed that encounters of the Vesta family members with (4) Vesta and (1) Ceres are dominant, contributing roughly by 64% and 36% to the total changes, respectively. The functional dependence  $\Delta a = 1.6 \times 10^{-4} \sqrt{t/1 \text{ m.y}} \text{ AU}$  was used in this work to extrapolate the results to longer time intervals. Moreover, Carruba et al. (2013b) studied the influence of these effects on the Pallas, Hygiea, and Euphrosyne families. They showed that the effects of (2) Pallas — the third most massive main-belt asteroid — on the Pallas family are very small, because these asteroids have high orbital inclinations ( $i_p = 33^\circ$ ), lower frequency of encounters, and higher-than-average encounter speeds.

Dell'Oro and Cellino (2007) pointed out that orbits of main-belt asteroids can change as a result of the linear momentum transfer during nondestructive collisions. They found that the expected semimajor axis change from these collisions for a  $D = 50$ -km main-belt asteroid is  $\Delta a \sim$

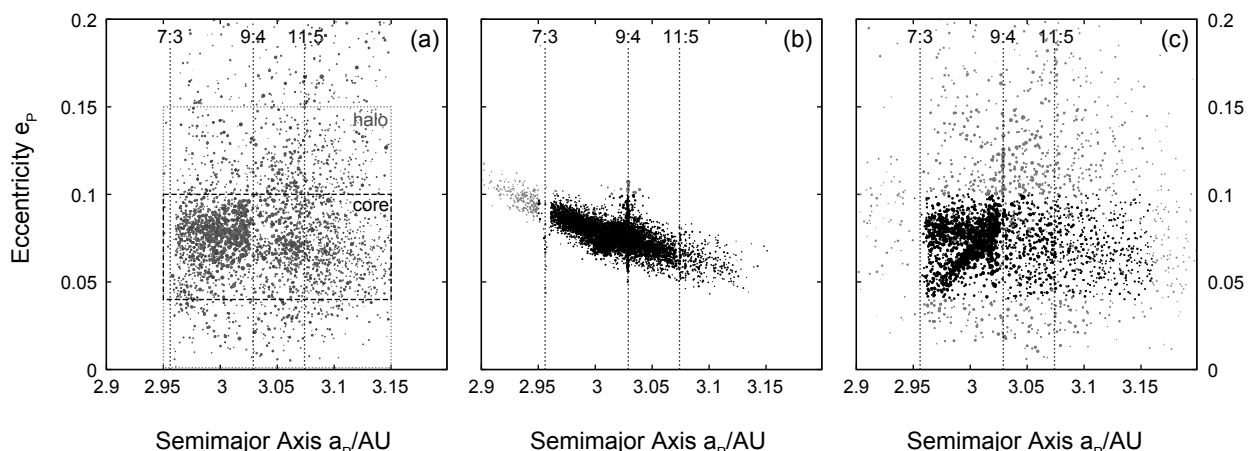


**Fig. 7.** Dynamical evolution of the Eos family. From left to right, the panels show (a) the observed family and its halo in the  $(a_p, e_p)$  projection, (b) the assumed initial shape of the family, and (c) the family's structure after 1.7 G.y. In (a), we plot all asteroids with Eos-family colors [ $0.0 < a^* < 0.1$  mag and  $-0.03 < i-z < 0.08$  mag; see Ivezic et al. (2001) for the definition of color indexes from the SDSS]. The size of a symbol is inversely proportional to absolute magnitude  $H$ . The boxes approximately delimit the extent of the core and halo of the Eos family. In (b), 6545 test particles were distributed with assumed isotropic ejection velocities,  $V_5 = 93 \text{ m s}^{-1}$ ,  $f = 150^\circ$ , and  $\omega = 30^\circ$ . Nearly all initial particles fall within the family core. In (c), an N-body integrator was used to dynamically evolve the orbits of the test particles over 1.7 G.y. The integration included gravitational perturbations from planets, and the Yarkovsky and YORP effects. The vertical lines show the locations of several resonances that contributed to spreading of orbits in  $e_p$  (7:3, 9:4, and 11:5 with Jupiter, also 3J-2S-1) and  $z_1 \equiv g + s - g_6 - s_6 = 0$ . Adapted from Brož and Morbidelli (2013).

$10^{-4}$  AU over 100 m.y. [with the scaling laws from *Benz and Asphaug* (1999)]. This is an order of magnitude lower than the change expected from close encounters with large asteroids and comparable to the sluggish drift rate expected from the Yarkovsky effect for  $D = 50$  km. For  $D < 50$  km, the orbital changes from nondestructive collisions sensitively depend on several unknown parameters, such as the SFD of subkilometer main-belt asteroids, but the general trend is such that  $\Delta a$  drops with decreasing  $D$  [assuming that the cumulative SFD index is  $<4$  (*Dell'Oro and Cellino*, 2007)]. Since  $\Delta a$  is independent of  $D$  for encounters with (1) Ceres, and  $\Delta a \propto 1/D$  for the Yarkovsky force, these two effects outrun the nondestructive collisions for  $D < 50$  km. This limits the significance of nondestructive collisions for the dynamical evolution of asteroid families. Their effect on  $e_p$  and  $i_p$  is also minor.

#### 6.4. Family Halos

When dynamical families are identified and removed from the main belt, they leave behind holes in the distribution of proper elements that are surrounded by regions with increased asteroid density (Fig. 8). These peripheral regions are known as the family halos. The families and family halos surrounding them are clearly related, which can most conveniently be demonstrated by considering their physical properties. For example, the Koronis family and its halo consist of bright asteroids (mean albedo  $p_V = 0.15$ ) that are classified as S in the asteroid taxonomy (moderate spectral slope and shallow absorption band near  $1\text{ }\mu\text{m}$ ). These properties contrast with the local background in the outer main belt, which is mostly dark ( $p_V \approx 0.05$ ) and C-type (featureless neutral spectrum). The Eos family and its halo (K-type,  $p_V = 0.13$ ) also stand out from the dark outer belt background.

The distinction between families and family halos is, in a sense, formal, because it appears as a consequence of the identification method. Indeed, to extract the family halo by applying the HCM in three-dimensional space of proper elements, one would need to increase the value of the  $d_{cut}$  parameter. If it is increased, however, the identification would fail due to the problem of chaining (section 2.2). This is a consequence of the fact that the number density of halo asteroids is comparable to, or only slightly larger than, the number density of background asteroids. A better method for extracting the families jointly with their halos consists in applying the HCM in space of extended dimensions, where physical properties are used in addition to the proper elements (section 2.5) (*Parker et al.*, 2008; *Carruba et al.*, 2013a; *Masiero et al.*, 2013).

The origin of family halos is attributed to at least two processes. In the case of the Eos family, the observed dispersion of halo in  $e_p$  and  $i_p$  is too large ( $0\text{--}0.15$  and  $7^\circ\text{--}14^\circ$ , respectively) to be related to the the ejection speeds. Instead, *Brož and Morbidelli* (2013) showed how the Eos family halo gradually appears as a result of complex orbital dynamics in the Eos family region (Fig. 7). The age of the Eos family inferred from this work,  $1.5\text{ G.y.} < t_{age} < 2.2\text{ G.y.}$ ,

is larger than that obtained from the YY code [ $t_{age} = 1.3 \pm 0.2$  G.y.; *Vokrouhlický et al.* (2006a) and section 5], but the two estimates are consistent at the  $1\sigma$  level.

The Koronis family and its halo, on the other hand, are located in a dynamically quiet region of the main belt ( $2.82 < a_p < 2.95$  AU,  $e_p \approx 0.045$ ,  $i_p = 2^\circ$ ) where no major resonances exist [except for  $g + 2g_5 - 3g_6 = 0$  (*Bottke et al.*, 2001)]. The long-term dynamics of the Koronis family therefore has a relatively small influence on the overall width of the family in  $e_p$  and  $i_p$ . In contrast, the present shift of the Koronis family/halo members from the family's center is relatively large (up to  $\approx 0.015$  in  $e_p$  and  $\approx 0.5^\circ$  in  $i_p$ ). This can plausibly be explained by the ejection speeds.

Assuming an isotropic ejection velocity field and  $\delta V = V_5(5\text{ km/D})$  with  $V_5 = 50\text{ m s}^{-1}$ , we find that  $\delta a_p/a_p \approx 2\delta V/V_{orb} \approx 0.018$  for  $D = 5$  km fragments. This represents a small share of the Koronis family width in  $a_p$  (the population of  $D = 5$  km members stretches from the 5:2 resonance at 2.82 AU to the 7:3 resonance at 2.95 AU), consistent with the idea that the observed spread in  $a_p$  is mainly due to the Yarkovsky effect. With  $D = 1.5$  km, which is roughly the size of the smallest asteroids observed in this part of the main belt, the expected changes are  $\delta e_p = (1\text{--}2) \times \delta V/V_{orb}$ .

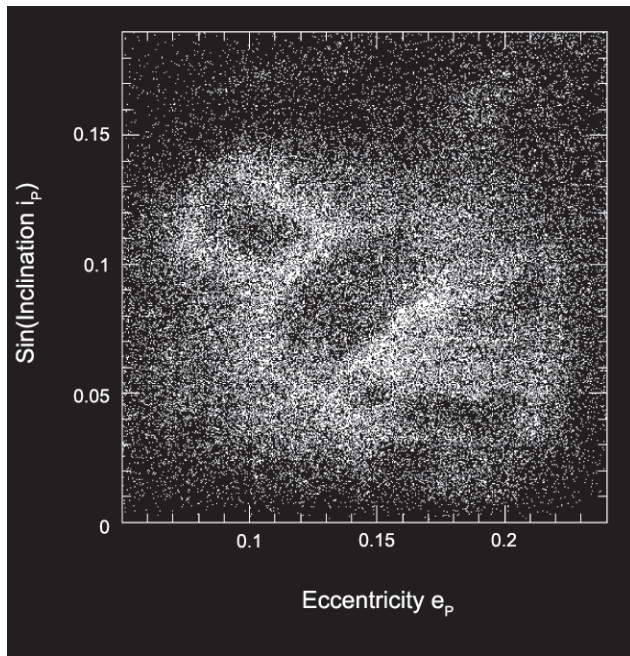


**Fig. 8.** The halos of families in the inner main belt ( $2 < a_p < 2.5$  AU). The dynamical families were identified by the HCM in three dimensions of proper elements and were removed, leaving behind what resembles a fuzzy chalk contour of victim's body removed from a crime scene. The head, body, and bottom leg correspond to the locations of the Vesta, Flora, and Nysa-Polana families. The halos surrounding these families, mainly composed of small asteroids, are rather dramatic in this projection. This figure illustrates a major weakness of the traditional family-identification method based on the HCM in three-dimensional space of proper elements.

$V_{\text{orb}} = 0.015$  and  $\delta i_p \leq \delta V/V_{\text{orb}} \approx 0.6^\circ$ . This is comparable to the present width of the Koronis family/halo in  $e_p$  and  $i_p$ .

Another notable argument in this context is that the Koronis halo is populated by small asteroids with diameters near the minimum detectable size (while the big ones are inside the family core). This suggests a certain size dependency of the process that created the halo, presumably related to the size dependency of the ejection speeds (see the chapter by Michel et al. in this volume). This important trend was pointed out by Cellino et al. (2004), and further discussed in Cellino et al. (2009).

## 7. SYNTHESIS

### 7.1. Method, Family Names, and Family Identification Number

Here we present a synthesis of asteroid families extracted from many past publications (Mothé-Diniz et al., 2005; Nesvorný et al., 2005; Gil-Hutton, 2006; Parker et al., 2008; Nesvorný, 2010, 2012; Novaković et al., 2011; Brož et al., 2013; Masiero et al., 2011, 2013; Carruba et al., 2013a; Milani et al., 2014). The synthesis is based on the numerically computed proper elements [AstDyS catalog from August 2014 with the proper elements for 384,337 numbered asteroids; the proper elements of 4016 Jupiter Trojans were taken from Rozehnal and Brož (2013)] and the latest releases of data from SDSS and WISE.

First, we collected a long list of all (228) families reported in these publications. Second, we checked to see whether the clustering in proper elements of each reported group is meaningful, and whether the group has reasonably homogeneous colors and albedos (see methods in section 2). The families that passed the preliminary tests were scrutinized further to establish the best cutoff value  $d_{\text{cut}}$  (the values of  $d_{\text{cut}}$  were informed from past publications), apply the V-shape criterion to identify large interlopers (section 4), and estimate  $t_{\text{age}}$  from the envelope-based method (section 5).

We made sure that each identified group with  $d_{\text{cut}}$  was complete (i.e., not missing any extension that would make sense dynamically), and not part of a larger structure. In some cases, a cut in proper element space was applied to avoid the problem of chaining. In several cases, following Masiero et al. (2013), we used an albedo cutoff,  $p_V < 0.15$ , to identify dark families in the inner and central belts [the (84) Klio, (313) Chaldaea, and (2262) Mitidika families]. Finally, we removed all identified families and searched for significant groups in the leftover population. This led to the identification of several additional families [e.g., the (589) Croatia, (926) Imhilde, and (1332) Marconia families in the outer belt].

A difficulty we had to deal with is that different authors often listed the same family under different names. For example, Masiero et al. (2013) renamed the families after their largest fragments [e.g., the (158) Koronis family was referred to as the (208) Lacrimosa family]. While it is very useful to identify the largest fragment, this naming conven-

tion creates chaos because some well-established family names disappear (Koronis, Maria, Flora, Gefion, Dora, etc.) and new names are used to refer to the same groups (Lacrimosa, Roma, Augusta, Gudiachvili, Zhongolovich, etc.). It is also not clear in many cases what the true largest member is [(208) Lacrimosa is only slightly larger than (158) Koronis, some large objects have peripheral orbits and can be interlopers, etc.].

A simple solution to this problem is to think of the family names as *labels*, used for historical and other reasons, which do not necessarily reveal what the largest or lowest-numbered asteroid is. Thus, the Koronis family would remain the Koronis family, regardless of whether (158) Koronis, (208) Lacrimosa, or some other large asteroid is an actual family member, largest or not.

Anticipating that some authors will still prefer to rename some families, here we assign each family a unique Family Identifier Number (FIN). The FIN goes from 101 to 399 for families identified from the analytic proper elements: 1XX for the inner belt (2–2.5 AU), 2XX for the middle belt (2.5–2.82 AU), and 3XX for the outer belt (2.82–3.7 AU). The families identified from the synthetic proper elements were assigned FINs from 401 to 999: 4XX and 7XX for the low- and high-inclination families in the inner belt, 5XX and 8XX for the low- and high-inclination families in the middle belt, and 6XX and 9XX for the low- and high-inclination families in the outer belt. The division between low and high inclinations was taken at  $\sin i_p = 0.3$  ( $i_p = 17.5^\circ$ ), which coincides with the highest inclinations for which the analytic proper elements are available. The FINs of the low-inclination families are “aligned” such that 101 and 401, 102 and 402, 201 and 501, etc., are the same families identified from two different datasets. The families among Hungarias with  $a < 2$  AU, Hildas with  $a \approx 3.8$  AU, and Jupiter Trojans with  $a \approx 5.2$  AU are given a FIN between 001 and 099.

The main idea behind this notation is that even if a family is eventually renamed, its FIN will remain the same. Therefore, it should suffice to list the FIN of the renamed family in a new publication to make it clear how the new name relates to the designation(s) used in the past. For example, the Koronis family is given the FIN 605 (synthetic proper elements, outer belt, low  $i$ , 5th notable family), and the *number* will remain “605” even if the *name* “Lacrimosa family” is eventually adopted. Since it will be easy to check and see that the Koronis and Lacrimosa families have the same FIN (assuming that authors list the FIN in their publications), it will be obvious that we are talking about the same family.

A potential difficulty with this scheme would arise if families that were previously assigned a FIN are later found to be nonexistent (e.g., because they are later determined to be statistically insignificant or part of a larger structure that was not evident in the original data). We suggest that such families be deleted and the associated FINs left void (i.e., not assigned to any family), so there is no possibility of confusion. Finally, in order to avoid having numerous

void FINs, and to not run out of the possible FINs with the three-digit scheme described above, FINs should be given only to families that are reasonably secure. Other, less-secure families can be tentatively listed as family candidates and can wait to be assigned a FIN until their existence is verified with the new data. If the number of families in the inner, middle, and/or outer belts exceeds 99, the three-digit FIN scheme described here can be easily modified to a four-digit scheme by adding 0 at the second decimal digit, e.g., FIN 401 (the Vesta family) becomes FIN 4001. This change can be implemented if the need arises.

## 7.2. Family Lists

There are 122 notable asteroid families reported in Table 2 and 19 family candidates listed in Note 10. The vast majority of families listed in Table 2 have been reported in many past publications and are clear beyond doubt (Vesta, Massalia, Eunomia, Gefion, Koronis, Eos, Themis, etc.). Many additional families, reported in only one or two previous publications, are also clear beyond doubt with the new data. Eleven families are reported here for the first time: ((329) Svea and (108138) 2001 GB<sub>11</sub> in the inner belt; (89) Julia, (369) Aeria, (1484) Postrema, (2782) Leonidas, and (3152) Jones in the central belt; and (589) Croatia, (926) Imhilde, (1332) Marconia, and (106302) 2000 UJ<sub>87</sub> in the outer belt. There are 20 notable families in the inner belt (the Nysa-Polana complex is counted as three families here): 47 in the central belt, 46 in the outer belt, 2 among Hildas in the 3:2 resonance with Jupiter, 1 in Hungarias, and 6 among Jupiter Trojans. Of these, 17 have high orbital inclinations ( $i_p > 17.5^\circ$ ). Figure 9 shows the orbital location of the notable families in the main belt.

The lists of members of the notable families can be downloaded from the PDS node (Note 11). Each list contains (1) the asteroid number, (2)  $a_p$ , (3)  $e_p$ , (4)  $\sin i_p$ , and (5) the absolute magnitude  $H$  from the Minor Planet Center. Also, for families that have a well-defined V-shape envelope in ( $a_p, H$ ), we fit  $C_0$  to this shape (section 4, column 7 in Table 2) and report  $C_j/C_0$  for each family member in column 6 of the PDS files. The average albedo of each family was obtained from WISE, and is reported in column 9 of Table 2 ( $p_V$ ). The taxonomic type of families, reported in column 8 of Table 2, was taken from the previous taxonomic classification of families (Cellino et al., 2002) or was deduced from the SDSS colors.

Columns 5 and 6 of Table 2 report the estimated diameter of the largest member,  $D_{LM}$ , and diameter of a sphere with volume equivalent to that of all fragments,  $D_{frag}$ .  $D_{LM}$  was obtained from AKARI, if available, or from WISE, if available, or was estimated from  $H$  and average  $p_V$ . The largest member and suspected interlopers with  $|C_j/C_0| > 2$  were excluded in the estimate of  $D_{frag}$ . The comparison of  $D_{LM}$  and  $D_{frag}$  helps to establish whether a particular breakup event was catastrophic ( $D_{frag} > D_{LM}$ ) or cratering ( $D_{frag} < D_{LM}$ ), but note that this interpretation may depend on sometimes uncertain membership of the largest family objects. Also, the diameter of the parent body of each family can be estimated

as  $D_{PB} = (D_{LM}^3 + D_{frag}^3)^{1/3}$ , but note that this estimate ignores the contribution of small (unobserved) fragments.

## 7.3. Comparison with Previous Datasets

The family synthesis presented here is consistent with the results reported in Nesvorný (2012), Brož et al. (2013), and Carruba et al. (2013a). For example, all families reported in Nesvorný (2012) were found to be real here [except the (46) Hestia family, which was reclassified as a candidate family; see Note 10]. Nesvorný (2012), however, used very conservative criteria for the statistical significance of a family, and reported only 76 families (or 78 if the Nysa-Polana complex is counted, as it should be, as three families). Using the 2014 catalog of proper elements, albedo information from Masiero et al. (2013), and validating several new families from Milani et al. (2014), we now have 44 families that did not appear in Nesvorný (2012). Almost all families reported in Brož et al. (2013) also appear here [a notable exception is a large group surrounding (1044) Teutonia that we do not believe to be a real family; see Note 10], but many new cases were added. The correspondence with Carruba et al. (2013a) is also good.

Parker et al. (2008) used  $N_{min} = 100$  and therefore missed many small families that did not have more than 100 members in the 2008 catalog. Also, given that they used a subset of asteroids with SDSS colors, even relatively large families were unnoticed in this work [e.g., the (752) Sulamitis family in the inner belt now has 303 members]. The high-i families were not reported in Parker et al. (2008) because they only used the analytic proper elements, which are not available for the high-i orbits. The strength of Parker et al.'s identification scheme was its reliability. Indeed, of all the families reported in Parker et al. (2008), only (1044) Teutonia, (1296) Andree, and (2007) McCuskey (part of the Nysa-Polana complex) are not included among the notable families here [Parker et al.'s (110) Lydia family appears here as the (363) Padua family].

Masiero et al. (2013) (hereafter M13) reported 28 new cases and found that 24 old families were lost when compared to the family lists in Nesvorný (2012). Most families not listed in M13 are well-defined families such as Karin, Beagle, Datura, Emilkowalski, Lucascavin, etc. These families were not listed in M13, because they overlap with larger families (and were included in their membership lists in M13) or because they only have a few known members (i.e., fall below  $N_{min}$  used in M13). On the other hand, we verified that many new cases reported in Masiero et al. (2013) are genuine new families that can be conveniently found with the albedo cutoff [e.g., the (84) Klio, (144) Vibilia, (313) Chaldaea — which is the same as (1715) Salli in M13 — (322) Phaeo, (623) Chimarea, (816) Julian, and (1668) Hanna families]. These families were included here. In some cases, we found that M13's new family barely stands out from the background and thus seems uncertain. To stay on the safe side, we therefore report these cases as the candidate families in Note 10. These families may be

TABLE 2. Notable asteroid families.

FIN	Family Name	$d_{\text{cut}}$ (m s <sup>-1</sup> )	No. of Members	$D_{\text{LM}}$ (km)	$D_{\text{frag}}$ (km)	$C_0$ (10 <sup>-4</sup> AU)	Tax. Type	$p_V$	References and Notes
<i>Hungarias, Hildas, and Jupiter Trojans</i>									
001	(153) Hilda	130	409	164	—	—	C	0.04	<i>Brož et al. (2011)</i>
002	(1911) Schubart	60	352	80	91	—	C	0.03	<i>Brož and Vokrouhlický (2008)</i>
003	(434) Hungaria	100	2965	10	24	$0.3 \pm 0.1$	E	0.35	<i>Warner et al. (2009), Milani et al. (2010)</i>
004	(624) Hector	50	12	231	—	—	—	—	<i>satellite, Marchis et al. (2014), Rozehnal and Brož (2013)</i>
005	(3548) Eurybates	50	218	68	87	—	CP	0.06	<i>Roig et al. (2008), Brož and Rozehnal (2011)</i>
006	(9799) 1996 RJ	60	7	72	26	—	—	0.06	<i>Rozehnal and Brož (2013)</i>
007	James Bond	$\infty$	1	(himself)	—	—	ASP	variable	<i>Campbell et al. (1995)</i>
008	(20961) Arkesilaos	50	37	—	—	—	—	—	<i>Rozehnal and Brož (2013)</i>
009	(4709) Ennomos	100	30	(1867,4709)	—	—	—	0.06	<i>Rozehnal and Brož (2013)</i>
010	(247341) 2001 UV <sub>209</sub>	100	13	—	—	—	—	0.09	<i>Rozehnal and Brož (2013)</i>
<i>Inner Main Belt, 2.0 &lt; <math>a</math> &lt; 2.5 AU, <math>i &lt; 17.5^\circ</math></i>									
401	(4) Vesta	50	15252	525	50	$1.5 \pm 0.5$	V	0.35	source of HEDs, two overlapping families?
402	(8) Flora	60	13786	(8,254)	—	$2.5 \pm 0.5$	S	0.30	dispersed, source of LL NEAs, Dykhuis et al. (2014)
403	(298) Baptista	45	2500	21	—	$0.25 \pm 0.05$	X	0.16	related to K/T impact? Bottke et al. (2007)
404	(20) Massalia	55	6424	132	27	$0.25 \pm 0.05$	S	0.22	Vokrouhlický et al. (2006b)
405	(44) Nysa-Polana	50	19073	(135,142,495)	—	$1.0 \pm 0.5$	SFC	0.28/0.06	Walsh et al. (2013), Dykhuis and Greenberg (2015)
406	(163) Erigone	50	1776	72	46	$0.2 \pm 0.05$	CX	0.06	Vokrouhlický et al. (2006b)
407	(302) Clarissa	55	179	34	15	$0.05 \pm 0.01$	X	0.05	compact with ears, cratering
408	(752) Sulamitis	55	303	61	35	$0.3 \pm 0.1$	C	0.04	
409	(1892) Lucienne	100	142	11	11	$0.15 \pm 0.05$	S	0.22	
410	(27) Euterpe	65	474	110	16	$0.50 \pm 0.25$	S	0.26	
411	(1270) Datura	10	6	8	3	—	S	0.21	Nesvorný et al. (2006c)
412	(21509) Lucascavin	10	3	—	—	—	S	—	Nesvorný and Vokrouhlický (2006)
413	(84) Klio	130*	330	78	33	$0.75 \pm 0.25$	C	0.07	interloper 122, Masiero et al. (2013)
414	(623) Chimaera	120	108	43	21	$0.3 \pm 0.1$	CX	0.06	Masiero et al. (2013)
415	(313) Chaldaea	130*	132	(313,1715)	—	$1.0 \pm 0.5$	C	0.07	1715 in Masiero et al. (2013)
416	(329) Svea	150	48	70	21	$0.3 \pm 0.1$	CX	0.06	new, near 3:1
417	(108138) 2001 GB <sub>11</sub>	20	9	—	—	—	—	—	new, compact
701	(25) Phocaea	150	1989	(25,587)	—	$2.0 \pm 1.0$	S	0.22	Carruba (2009b), Carruba et al. (2010)
<i>Central Main Belt, 2.5 &lt; <math>a</math> &lt; 2.82 AU, <math>i &lt; 17.5^\circ</math></i>									
501	(3) Juno	55	1684	231	25	$0.5 \pm 0.2$	S	0.25	cratering, relation to H chondrites?
502	(15) Eunomia	50	5670	256	100	$2.0 \pm 0.7$	S	0.19	continues beyond 5:2?

TABLE 2. (continued)

FIN	Family Name	$d_{\text{cut}}$ (m s <sup>-1</sup> )	No. of Members	$D_{\text{LM}}$ (km)	$D_{\text{frag}}$ (km)	$C_0$ (10 <sup>-4</sup> AU)	Tax. Type	$p_V$	References and Notes
<i>Central Main Belt, <math>2.5 &lt; a &lt; 2.82 \text{ AU}, i &lt; 17.5^\circ</math> (continued)</i>									
503	—	—	—	—	—	—	—	—	—
504	(128) Nemesis	50	1302	178	50	0.25 ± 0.05	C	0.05	46 Hestia moved to candidates
505	(145) Adeona	50	2236	141	78	0.7 ± 0.3	C	0.07	3827 in Milani <i>et al.</i> (2014), 125 in Cellino <i>et al.</i> (2002)
506	(170) Maria	60	2940	(472,170)	—	2.0 ± 1.0	S	0.25	(472) Roma in Masiero <i>et al.</i> (2013)
507	(363) Padua	45	1087	91	48	0.5 ± 0.2	X	0.10	<i>Carruba</i> (2009a), also known as the (110) Lydia family
508	(396) Aeolia	20	296	46	13	0.075 ± 0.025	X	0.17	compact, young?
509	(410) Chloris	80	424	107	56	0.75 ± 0.25	C	0.06	eroded
510	(569) Misa	50	702	65	57	0.5 ± 0.2	C	0.03	V-shaped subfamily inside
511	(606) Brangane	55	195	36	18	0.04 ± 0.01	S	0.10	compact, 606 offset, interloper?
512	(668) Dora	45	1259	(1734,668)	—	—	C	0.05	668 offset, 1734 in Masiero <i>et al.</i> (2013), V-shaped subfamily
513	(808) Merxia	55	1215	34	28	0.3 ± 0.1	S	0.23	<i>Vokrouhlický et al.</i> (2006b)
514	(847) Agnia	30	2125	(847,3395)	—	0.15 ± 0.05	S	0.18	$z_1$ resonance, <i>Vokrouhlický et al.</i> (2006c)
515	(1128) Astrid	60	489	42	29	0.12 ± 0.02	C	0.08	<i>Vokrouhlický et al.</i> (2006b)
516	(1272) Gefion	50	2547	(2595,1272)	—	0.8 ± 0.3	S	0.20	source of L chondrites? Nesvorný <i>et al.</i> (2009), also known as 93 and 2595
517	(3815) Konig	55	354	22	34	0.06 ± 0.03	CX	0.04	compact, young? Nesvorný <i>et al.</i> (2003), 342 and 1639 offset
518	(1644) Rafita	70	1295	(1658,1587)	—	0.5 ± 0.2	S	0.25	1644 probably interloper
519	(1726) Hoffmeister	45	1819	(272,1726)	—	0.20 ± 0.05	CF	0.04	(272) Antonia in Masiero <i>et al.</i> (2013), but 272 offset
520	(4652) Iannini	25	150	5	10	—	S	0.32	1547 offset, compact, Nesvorný <i>et al.</i> (2003)
521	(7353) Kazuya	50	44	11	10	—	S	0.21	small clump
522	(173) Ino	50	463	161	21	0.5 ± 0.2	S	0.24	also known as 18466, large and dark 173 is probably interloper, ears?
523	(14627) Emilkowski	10	4	7	3	—	S	0.20	Nesvorný and Vokrouhlický (2006)
524	(16598) 1992 YC <sub>2</sub>	10	3	—	—	—	S	—	Nesvorný and Vokrouhlický (2006)
525	(2384) Schulhof	10	6	12	4	—	S	0.27	Vokrouhlický and Nesvorný (2011)
526	(53546) 2000 BY <sub>6</sub>	40	58	8	18	—	C	0.06	Milani <i>et al.</i> (2014)
527	(5438) Lorre	10	2	30	—	—	C	0.05	<i>Novaković et al.</i> (2012)
528	(2782) Leonidas	50	135	(4793,2782)	—	—	CX	0.07	new, related to 144?
529	(144) Vibilia	100*	180	142	—	—	C	0.06	Masiero <i>et al.</i> (2013), PDS list identical to 2782
530	(322) Phaeo	100*	146	72	31	0.3 ± 0.1	X	0.06	<i>Cellino et al.</i> (2002), joins (2669) Shostakovich
531	(2262) Mitidika	100*	653	(404,5079)	—	—	C	0.06	dispersed, 404 offset, 2262 has $p_V = 0.21$
532	(2085) Henan	50	1872	18	32	0.75 ± 0.25	L	0.20	2085 offset in $i_p$ , 4 families in Milani <i>et al.</i> (2014)
533	(1668) Hanna	60	280	22	32	0.2 ± 0.1	CX	0.05	Masiero <i>et al.</i> (2013)
534	(3811) Karma	60	124	26	24	0.25 ± 0.05	CX	0.05	Milani <i>et al.</i> (2014)

TABLE 2. (continued)

FIN	Family Name	$d_{\text{cut}}$ (m s <sup>-1</sup> )	No. of Members	D <sub>LM</sub> (km)	D <sub>frag</sub> (km)	C <sub>0</sub> (10 <sup>-4</sup> AU)	Tax. Type	p <sub>V</sub>	References and Notes
<i>Central Main Belt, 2.5 &lt; a &lt; 2.82 AU, i &lt; 17.5° (continued)</i>									
535	(2732) Witt	45	1816	11	25	0.75 ± 0.25	S	0.26	relation to the Charis family beyond 5.2°? 10955 and 19466 in Milani et al.
536	(2344) Xizang	65	275	17	20	0.3 ± 0.1	—	0.12	Milani et al. (2014), includes 396
537	(729) Watsonia	130	99	52	38	—	L	0.13	Cellino et al. (2014)
538	(3152) Jones	40	22	37	11	—	T	0.05	new, compact, diagonal in ( $a_{\text{pe}}$ , $e_{\text{p}}$ )
539	(369) Aeria	90	272	75	17	0.3 ± 0.1	X	0.17	new, part above 2.6778 AU down in $i_{\text{p}}$
540	(89) Julia	70	33	147	6	—	S	0.19	new, compact
541	(1484) Postrema	100	108	47	—	—	CX	0.05	new, large 387,547,599?
<i>Central Main Belt, 2.5 &lt; a &lt; 2.82 AU, i &gt; 17.5°</i>									
801	(2) Pallas	350	128	513	40	—	B	0.16	Carruba et al. (2010, 2012), part beyond 5.2°
802	(148) Gallia	200	182	81	19	0.5 ± 0.1	S	0.17	large interlopers
803	(480) Hansa	200	1094	56	62	—	S	0.26	2 families in Milani et al. (2014)
804	(686) Gersuind	120	415	49	36	—	S	0.15	2 families in Milani et al. (2014)
805	(945) Barcelona	150	306	27	19	0.25 ± 0.05	S	0.25	2 families in Milani et al. (2014)
806	(1222) Tina	200	96	26	10	0.10 ± 0.05	X	0.34	in the g-g <sub>6</sub> = 0 resonance, Carruba and Morbidelli (2011)
807	(4203) Brucato	200	342	18	44	0.5 ± 0.2	CX	0.06	1263 interloper? Carruba (2010), 4 families in Milani et al. (2014)
<i>Outer Main Belt, 2.82 &lt; a &lt; 3.7 AU, i &lt; 17°</i>									
601	(10) Hygiea	60	4854	428	—	—	CB	0.06	Carruba et al. (2014)
602	(24) Themis	60	4782	177	230	2.5 ± 1.0	C	0.07	includes 656 Beagle, Nesvorný et al. (2008b)
603	(87) Sylvia	130	255	263	—	—	X	0.05	Vokrouhlický et al. (2010)
604	(137) Meliboea	85	444	(511,137)	—	—	C	0.05	(511) Davida in Mastiero et al. (2013)
605	(158) Koronis	45	5949	(208,158,462)	—	2.0 ± 1.0	S	0.15	(208) Lacrimosa in Mastiero et al. (2013)
606	(221) Eos	45	9789	(221,579,639)	—	1.5 ± 0.5	K	0.13	Vokrouhlický et al. (2006a), Brož and Morbidelli (2013)
607	(283) Emma	40	76	122	56	0.3 ± 0.1	C	0.05	affected by the z <sub>1</sub> resonance?
608	(293) Brasilia	50	579	(3985)	—	0.20 ± 0.05	X	0.18	293 interloper?, also known as (1521) Sejnajoki, Nesvorný et al. (2003)
609	(490) Veritas	30	1294	113	78	0.2 ± 0.1	CPD	0.07	see Section 3
610	(832) Karin	10	541	17	16	0.03 ± 0.01	S	0.21	see Section 3, Harris et al. (2009)
611	(845) Naema	35	301	61	37	0.20 ± 0.05	C	0.08	8 families in Milani et al. (2014)
612	(1400) Tirela	50	1395	(1040,1400)	—	0.75 ± 0.25	S	0.07	3330 offset, Novaković (2010)
613	(3556) Lixiaohua	45	756	(3330,3556)	—	0.25 ± 0.05	CX	0.04	(179) Klytaemnestra in Mastiero et al. and Milani et al.
614	(9506) Telramund	45	468	(179,9506)	—	—	S	0.22	0.17
615	(18405) 1993 FY <sub>12</sub>	50	104	9	14	0.08 ± 0.03	CX		

TABLE 2. (continued)

FIN	Family Name	$d_{\text{cut}}$ (m s <sup>-1</sup> )	No. of Members	$D_{LM}$ (km)	$D_{\text{frag}}$ (km)	$C_0$ (10 <sup>-4</sup> AU)	Tax. Type	$p_V$	References and Notes
<i>Outer Main Belt, 2.82 &lt; a &lt; 3.7 AU, i &lt; 17.5°</i>									
616	(627) Charis	80	808	50	45	—	C	0.08	16286 in Milani <i>et al.</i> (2014), related to Witt family?
617	(778) Theobalda	60	376	66	50	—	CX	0.06	778 offset, Novaković (2010)
618	(1189) Terentia	60	79	63	18	0.13 ± 0.03	C	0.07	
619	(10811) Lau	120	56	8	6	0.075 ± 0.025	S	0.27	36824 interloper?
620	(656) Beagle	25	148	54	28	0.07 ± 0.03	C	0.09	656 and 90 offset, Nesvorný <i>et al.</i> (2008b)
621	(158) Koronis(2)	8	246	34	13	0.010 ± 0.005	S	0.14	young, Mohnar and Haegert (2009)
622	(81) Terpsichore	120	138	123	27	0.50 ± 0.25	C	0.05	
623	(709) Fringilla	150	134	96	55	—	X	0.05	large 1191
624	(5567) Durisen	100	27	34	23	—	X	0.04	
625	(5614) Yakovlev	120	67	13	23	0.15 ± 0.05	C	0.05	
626	(7481) San Marcello	100	144	(3978,7489)	—	—	X	0.19	also known as 12573
627	(15454) 1998 YB <sub>3</sub>	80	38	(3156,15454)	—	0.10 ± 0.05	CX	0.05	
628	(15477) 1999 CG <sub>1</sub>	95	248	—	—	—	S	0.10	
629	(36256) 1999 XT <sub>17</sub>	70	58	(15610,36256)	—	0.25 ± 0.05	S	0.21	several large bodies
630	(96) Aegle	50	99	165	38	—	CX	0.07	Masiero <i>et al.</i> and Milani <i>et al.</i>
631	(375) Ursula	70	1466	(1306,375)	—	—	CX	0.06	Masiero <i>et al.</i> and Milani <i>et al.</i>
632	(618) Elffriede	40	63	122	26	—	C	0.05	compact, recent?
633	(918) Itha	100	54	21	35	—	S	0.23	dispersed, many sizable members
634	(3438) Inarradas	80	38	25	33	—	CX	0.07	Milani <i>et al.</i> (2014)
635	(7468) Anifimov	60	58	10	14	—	S	0.16	Milani <i>et al.</i> (2014)
636	(1332) Marconia	30	34	50	16	—	CX	0.05	new
637	(106302) 2000 UJ <sub>87</sub>	60	64	7	15	—	CX	0.05	new, large 132999
638	(589) Croatia	45	93	92	31	0.5 ± 0.2	X	0.07	new, 21885 in Milani <i>et al.</i> (2014)
639	(926) Imhilde	70	43	50	18	0.2 ± 0.1	CX	0.05	new
640	P/2012 F5 (Gibbs)	10	8	—	—	—	—	—	Novaković <i>et al.</i> (2014)
641	(816) Juliana	80	76	68	39	—	CX	0.05	Masiero <i>et al.</i> (2013)
<i>Outer Main Belt, 2.82 &lt; a &lt; 3.5 AU, i &gt; 17.5°</i>									
901	(31) Euphrosyne	120	2035	276	130	—	C	0.06	Carruba <i>et al.</i> (2014), 3 families in Milani <i>et al.</i> (2014)
902	(702) Alauda	120	1294	191	—	2.5 ± 1.0	B	0.07	276 and 1901 offset, 4 families in Milani <i>et al.</i> (2014)
903	(909) Ulla	120	26	113	28	—	X	0.05	
904	(1303) Lutheria	50	163	87	56	—	X	0.04	also known as (781) Kartvelia
905	(780) Armenia	50	40	98	22	—	C	0.05	compact

Columns are (1) Family Identification Number (FIN), (2) family name, (3) cutoff distance ( $d_{\text{cut}}$ ) used on a subset of asteroids with  $p_V < 0.15$ , (4) number of family members identified with  $d_{\text{cut}}$ , (5) largest member(s) in the family [either the number designation of the largest member(s), in parenthesis, if different from the asteroid after which the family is named, or the estimated diameter of the largest member,  $D_{LM}$ ], (6) diameter of a sphere with volume equivalent to that of all fragments ( $D_{\text{frag}}$ ), (7)  $C_0$  parameter defined in section 4, (8) taxonomic type, (9) mean geometric albedo from WISE ( $p_V$ ), and (10) various references and notes. We do not report  $t_{\text{age}}$  here but note that  $t_{\text{age}}$  can be estimated from  $C_0$  given in column 7 and equation (2). For additional information on asteroid families, see <http://sirrah.mrao.iap.ac.ru/~mrao/mpfams/> (Brož *et al.*, 2013).

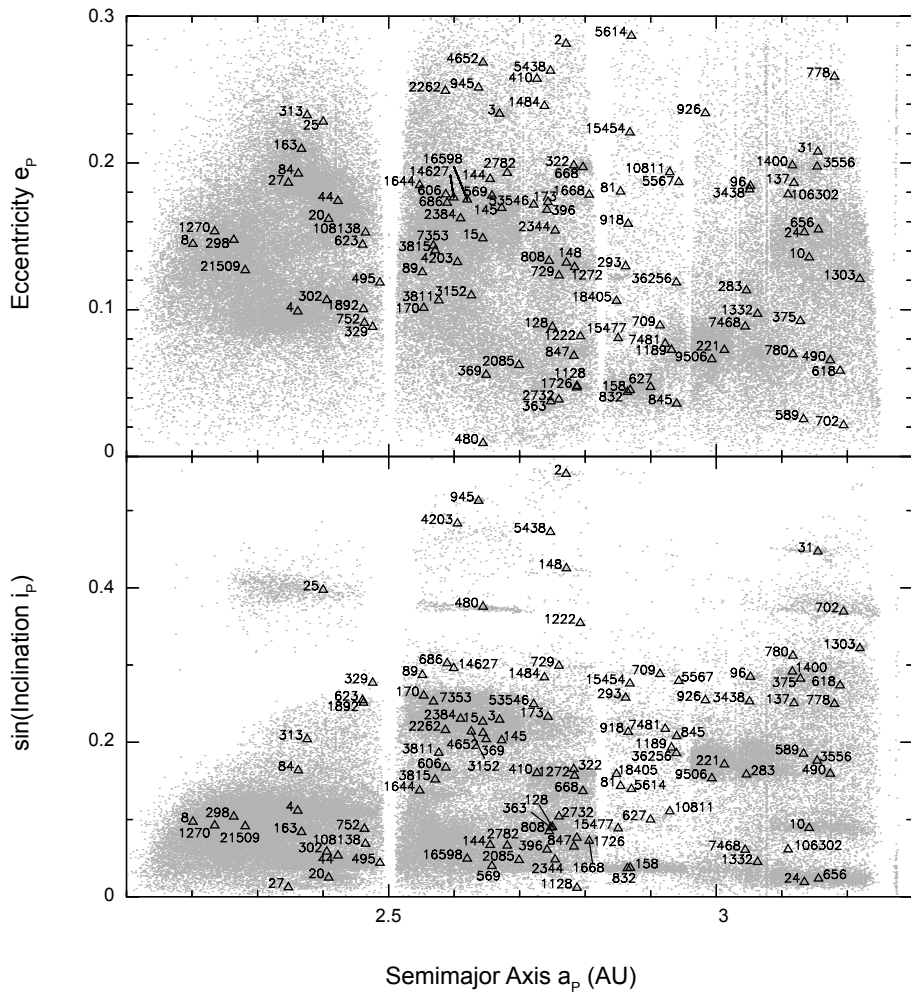


**Fig. 9.** The orbital location of notable families from Table 2. A triangle is placed at the orbit of an asteroid after which the family is named. The label near the triangle shows the designation number of that asteroid.

real, but their statistical significance needs to be carefully tested with the new data.

Finally, we compare the family synthesis with Milani *et al.* (2014) (hereafter M14), who used the newest catalog from all previous works discussed here. They identified many new families that are certain beyond doubt [e.g., (96) Aegle, (618) Elfriede, (2344) Xizang, (3438) Inarradas, (3811) Karma, (7468) Anfimov, and (53546) 2000 BY<sub>6</sub>; the (96) Aegle and (618) Elfriede families were also reported in M13]. These cases highlight the strength of the M14 identification scheme and are included in the family synthesis in Table 2. Some smaller families located inside bigger families [e.g., the (832) Karin family in the (158) Koronis family, (656) Beagle in (24) Themis] were not reported in M14. In addition, several families were not reported, presumably because the QRL was set too low to detect them. This happens, most notably, in the 2.82–2.96-AU region (i.e., between the 5:2 and 7:3 resonances), where the number density of asteroids is relatively low (see Figs. 1 and 9). The notable cases in this region include the (81) Terpsichore, (709) Fringilia,

(5567) Durisen, (5614) Yakovlev, (7481) San Marcello, and (10811) Lau families. A possible solution to this issue, in terms of the M14 identification scheme, would be to use a separate QRL level for the 2.82–2.96-AU region. Also, several families were split in M14 into several parts. This affects (8) Flora (split in four parts), (31) Euphrosyne (three parts), (221) Eos (five parts), (702) Alauda (four parts), (1400) Tirela (eight parts), (2085) Henan (four parts), (4203) Brucato (four parts) (here we only list families that were split to three or more parts in M14).

## 8. CONCLUSIONS

It is clear from several different arguments that the list of known families must be largely incomplete. For example, most families with an estimated parent body size below  $\approx 100$ –200 km are found to have ages  $t_{\text{age}} \leq 1$  G.y. (e.g., Brož *et al.*, 2013). In contrast, the rate of impacts in the main belt, and therefore the rate of family-forming events, should have been roughly unchanging with time over the

past  $\approx 3.5$  G.y. (and probably raised quite a bit toward the earliest epochs). So, there must be many missing families with the formation ages  $t_{\text{age}} > 1$  G.y. (Note 12). These families are difficult to spot today, probably because they have been dispersed by dynamical processes, lost members by collisional grinding, and therefore do not stand out sufficiently well above the dense main-belt background (they are now part of the background).

The significant incompleteness of known families is also indicated by the extrapolation of the number of families detected in the 2.82–2.96-AU zone to the whole main belt. As we hinted on at the end of the last section, the 2.82–2.96-AU zone is sparsely populated such that asteroid families can be more easily detected there. Nearly 20 families with  $i_p < 17.5^\circ$  were identified in this region. In comparison, the 2.96–3.3-AU zone, where  $\approx 20$  families with  $i_p < 17.5^\circ$  can also be found, is about twice as wide as the 2.82–2.96-AU zone and contains about twice as many large asteroids. A straightforward conclusion that can be inferred from this comparison, assuming everything else is equal, is that the families in the 2.96–3.3-AU zone are (at least) a factor of  $\sim 2$  incomplete. A similar argument applies to the inner and central belts.

This is actually good news for future generations of planetary scientists, because this field is open for new discoveries. Figuring out how to find the missing asteroid families with  $t_{\text{age}} > 1$  G.y. will not be easy. One way forward would be to improve our capability to model the dynamical evolution of main-belt asteroids over gigayear timescales, such that we can rewind the clock and track fragments back to their original orbits. The modeling of the Yarkovsky effect could be improved, for example, if we knew the spin states, densities, conductivity, etc., of small main-belt asteroids on an individual basis. Another approach would consist of identifying families based on the physical properties of their members. While this method is already in use, mainly thanks to data from SDSS and WISE, we anticipate that it can be pushed much further, say, with automated spectroscopic surveys, or, in the more distant future, with routine sampling missions.

## 9. NOTES

**Note 1** — Alternatively, one can use the frequencies  $n$ ,  $g$ , and  $s$  (*Carruba and Michtchenko*, 2007, 2009), where  $n$  is the mean orbital frequency and  $g$  and  $s$  are the (constant) precession frequencies of the proper perihelion longitude  $\bar{\omega}_p$  and the proper nodal longitude  $\Omega_p$ , respectively. The use of frequencies, instead of the proper elements, can be helpful for asteroid families near or inside the secular orbital resonances [e.g., the Tina family in the  $v_6$  resonance (*Carruba and Morbidelli*, 2011)].

**Note 2** — Additional methods were developed and/or adapted for specific populations of asteroids such as the ones on the high-inclination and high-eccentricity orbits (*Lemaître and Morbidelli*, 1994) or in orbital resonances (*Morbidelli*, 1993; *Milani*, 1993; *Beaugé and Roig*, 2001; *Brož and Vokrouhlický*, 2008; *Brož and Rozehnal*, 2011).

**Note 3** — <http://hamilton.dm.unipi.it/asstdys/>

**Note 4** — See *Bendjoya and Zappalà* (2002) for a discussion of other clustering algorithms such as the wavelet analysis method (WAM) and D-criterion. The WAM was shown to produce results that are in good agreement with those obtained from the HCM (*Zappalà et al.*, 1994). The D-criterion was originally developed to identify meteorite streams (*Southwork and Hawkins*, 1963). These methods have not been used for the classification of asteroid families in the past decade, and we therefore do not discuss them here.

**Note 5** — The SDSS measured flux densities in five bands with effective wavelengths 354, 476, 628, 769, and 925 nm. The WISE mission measured fluxes in four wavelengths (3.4, 4.6, 12, and 22  $\mu\text{m}$ ), and combined the measurements with a thermal model to calculate albedos ( $p_V$ ) and diameters (D). The latest public releases of these catalogs include color or albedo data for over 100,000 main-belt asteroids with known orbits, of which about 25,000 have both color and albedo measurements. The catalogs are available at [http://www.sdss.org/dr6/products/value\\_added/index.html](http://www.sdss.org/dr6/products/value_added/index.html) and <http://irsa.ipac.caltech.edu/Missions/wise.html>.

**Note 6** — Most but not all asteroid families are physically homogeneous. The Eos family has the highest diversity of taxonomic classes of any known family (e.g., *Mothé-Diniz et al.*, 2008). This diversity has led to the suggestion that the Eos parent body was partially differentiated. It can also be the source of carbonaceous chondrites (*Clark et al.*, 2009). The Eunomia family may be another case of a relatively heterogeneous family (e.g., *Nathues et al.*, 2005). See *Weiss and Elkins-Tanton* (2013) for a review.

**Note 7** — *Dell’Oro et al.* (2004) attempted to model observed family shapes by Gaussian ellipsoids. The distribution of  $|f|$  obtained in this work was strongly peaked near  $\pi/2$ , while a more uniform distribution between 0 and  $\pi$  would be expected if different breakups occurred at random orbital phases. This result was attributed to the Yarkovsky effect.

**Note 8** — *Nesvorný et al.* (2008a) found evidence for a large population of V-type asteroids with slightly lower orbital inclinations ( $i_p = 3^\circ$ – $4^\circ$ ) than the Vesta family ( $i_p \approx 5^\circ$ ). Because these asteroids could not have dynamically evolved from the Vesta family region to their present orbits in  $\approx 1$  G.y., they are presumably fragments excavated from (4) Vesta’s basaltic crust by an earlier impact.

**Note 9** — Other asteroid families whose long-term dynamics have been studied in detail, listed here in alphabetical order, are the Adeona family [affected in  $e_p$  and  $i_p$  by the 8:3 resonance at 2.705 AU (*Carruba et al.*, 2003)], Agnia family [inside the  $z_1$  resonance (*Vokrouhlický et al.*, 2006c)], Astrid family [near the border of the 5:2 resonance (*Vokrouhlický et al.*, 2006b)], Eunomia family (*Carruba et al.*, 2007b), Euphrosyne family [located in a region with many resonances, including  $g-g_6 = 0$ , near the inner border of the 2:1 resonance (*Carruba et al.*, 2014)], Erigone family [cut in the middle by the  $z_2$  resonance (*Vokrouhlický et al.*, 2006b)], Gefion family [affected by various resonances near 2.75 AU (*Carruba et al.*, 2003; *Nesvorný et al.*, 2009)], Hilda and Schubart families in the 3:2 resonance with Jupiter (*Brož and Vokrouhlický*, 2008), Hungaria family [perturbed by  $2g-g_5-g_6 = 0$  and other secular resonances below 1.93 AU (*Warner et al.*, 2009; *Milani et al.*, 2010); see also *Galiazzo et al.* (2013, 2014) for the contribution of Hungarias to the E-type NEAs and *Čuk et al.* (2014) for their suggested relation to the aubrite meteorites], Hygiea family (*Carruba*, 2013; *Carruba et al.*, 2014), Massalia family [the part with

$a_p > 2.42$  AU disturbed by the 1:2 resonance with Mars [Vokrouhlický et al., 2006b)], Merxia family [spread by the 3J-1S-1 three-body resonance at  $a_p = 2.75$  AU (Vokrouhlický et al., 2006b)], Padua family (Carruba, 2009a), Pallas family (Carruba et al., 2011), Phocaea family (Carruba, 2009b), Sylvia family [(87) Sylvia has two satellites, possibly related to the impact that produced the Sylvia family (Vokrouhlický et al., 2010)], and Tina family (Carruba and Morbidelli, 2011).

**Note 10** — The candidate families are (929) Algunde, (1296) Andree, (1646) Rosseland, (1942) Jablunka, (2007) McCuskey, (2409) Chapman, (4689) Donn, (6246) Komurotoru, and (13698) 1998 KF<sub>35</sub> in the inner belt; (46) Hestia, (539) Palmina, (300163) P/2006 VW<sub>139</sub>, (3567) Alvema, and (7744) 1986 QA<sub>1</sub> in the central belt; and (260) Huberta, (928) Hilrun, (2621) Goto, (1113) Katja, and (8737) Takehiro in the outer belt. We tentatively moved the (46) Hestia family, previously known as FIN 503, to the family candidate status, because the existence of this group has not been conclusively proven with present data. The previously reported groups around (5) Astraea, (1044) Teutonia, (3110) Wagman, (4945) Ikenozenni, (7744) 1986 QA<sub>1</sub>, (8905) Bankakuko, (25315) 1999 AZ<sub>8</sub>, and (28804) 2000 HC<sub>81</sub> seem to align with the  $z_1 = g + s - g_6 - s_6 = 0$  resonance and are probably an artifact of the HCM chaining.

**Note 11** — <http://sbn.psi.edu/pds/resource/nesvornymfam.html>

**Note 12** — The list of known families corresponding to parent bodies with  $D > 200$  km, on the other hand, is probably reasonably complete, because the estimated ages of these families appear to be randomly distributed over 4 G.y. (Brož et al., 2013). These largest families can therefore be used to constrain the collisional history of the asteroid belt (see the chapter by Bottke et al. in this volume).

**Acknowledgments.** The work of M.B. was supported by the Czech Grant Agency (grant no. P209-12-01308S). The work of V.C. was supported by the São Paulo State (FAPESP grant no. 2014/06762-2) and Brazilian (CNPq grant no. 305453/2011-4) Grant Agencies.

## REFERENCES

- Beaugé C. and Roig F. (2001) A semi-analytical model for the motion of the Trojan asteroids: Proper elements and families. *Icarus*, 153, 391–415.
- Bendjoya Ph. and Zappalà V. (2002) Asteroid family identification. In *Asteroids III* (W. F. Bottke Jr. et al., eds.), pp. 613–618. Univ. of Arizona, Tucson.
- Benz W. and Asphaug E. (1999) Catastrophic disruptions revisited. *Icarus*, 142, 5–20.
- Bottke W. F., Vokrouhlický D., Brož M., et al. (2001) Dynamical spreading of asteroid families by the Yarkovsky effect. *Science*, 294, 1693–1696.
- Bottke W. F., Vokrouhlický D., Rubincam D. P., and Brož M. (2002) The effect of Yarkovsky thermal forces on the dynamical evolution of asteroids and meteoroids. In *Asteroids III* (W. F. Bottke Jr. et al., eds.), pp. 395–408. Univ. of Arizona, Tucson.
- Bottke W. F., Durda D. D., Nesvorný D., et al. (2005a) The fossilized size distribution of the main asteroid belt. *Icarus*, 175, 111–140.
- Bottke W. F., Durda D. D., Nesvorný D., et al. (2005b) Linking the collisional history of the main asteroid belt to its dynamical excitation and depletion. *Icarus*, 179, 63–94.
- Bottke W. F., Vokrouhlický D., Rubincam D. P., and Nesvorný D. (2006) The Yarkovsky and YORP effects: Implications for asteroid dynamics. *Annu. Rev. Earth Planet. Sci.*, 34, 157–191.
- Bottke W. F., Vokrouhlický D., and Nesvorný D. (2007) An asteroid breakup 160 Myr ago as the probable source of the K/T impactor. *Nature*, 449, 48–53.
- Bottke W. F., Vokrouhlický D., Walsh K. J., Delbo M., Michel P., Lauretta D. S., Campins H., Connolly H. C., Scheeres D. J., and Chesley S. R. (2015) In search of the source of asteroid (101955) Bennu: Applications of the stochastic YORP model. *Icarus*, 247, 191–217.
- Bowell E., Muinonen K., and Wasserman L. H. (1994) A public-domain asteroid orbit data base. *Asteroids Comets Meteors 1993*, 160, 477.
- Brož M. and Morbidelli A. (2013) The Eos family halo. *Icarus*, 223, 844–849.
- Brož M. and Rozehnal J. (2011) Eurybates — the only asteroid family among Trojans? *Mon. Not. R. Astron. Soc.*, 414, 565–574.
- Brož M. and Vokrouhlický D. (2008) Asteroid families in the first-order resonances with Jupiter. *Mon. Not. R. Astron. Soc.*, 390, 715–732.
- Brož M., Vokrouhlický D., Morbidelli A., Nesvorný D., and Bottke W. F. (2011) Did the Hilda collisional family form during the late heavy bombardment? *Mon. Not. R. Astron. Soc.*, 414, 2716–2727.
- Brož M., Morbidelli A., Bottke W. F., et al. (2013) Constraining the cometary flux through the asteroid belt during the late heavy bombardment. *Astron. Astrophys.*, 551, A117.
- Campbell M. (1995) *Golden Eye*. MGM/UA Distribution Company.
- Carruba V. (2009a) The (not so) peculiar case of the Padua family. *Mon. Not. R. Astron. Soc.*, 395, 358–377.
- Carruba V. (2009b) An analysis of the region of the Phocaea dynamical group. *Mon. Not. R. Astron. Soc.*, 398, 1512–1526.
- Carruba V. (2010) The stable archipelago in the region of the Pallas and Hansa families. *Mon. Not. R. Astron. Soc.*, 408, 580–600.
- Carruba V. (2013) An analysis of the Hygiea asteroid family orbital region. *Mon. Not. R. Astron. Soc.*, 431, 3557–3569.
- Carruba V. and Michtchenko T.A. (2007) A frequency approach to identifying asteroid families. *Astron. Astrophys.*, 475, 1145–1158.
- Carruba V. and Michtchenko T. A. (2009) A frequency approach to identifying asteroid families. II. Families interacting with non-linear secular resonances and low-order mean-motion resonances. *Astron. Astrophys.*, 493, 267–282.
- Carruba V. and Morbidelli A. (2011) On the first nu(6) anti-aligned librating asteroid family of Tina. *Mon. Not. R. Astron. Soc.*, 412, 2040–2051.
- Carruba V., Burns J. A., Bottke W. F., and Nesvorný D. (2003) Orbital evolution of the Gefion and Adeona asteroid families: Close encounters with massive asteroids and the Yarkovsky effect. *Icarus*, 162, 308–327.
- Carruba V., Michtchenko T. A., Roig F., Ferraz-Mello S., and Nesvorný D. (2005) On the V-type asteroids outside the Vesta family. I. Interplay of nonlinear secular resonances and the Yarkovsky effect: The cases of 956 Elisa and 809 Lundia. *Astron. Astrophys.*, 441, 819–829.
- Carruba V., Roig F., Michtchenko T. A., Ferraz-Mello S., and Nesvorný D. (2007a) Modeling close encounters with massive asteroids: A Markovian approach. An application to the Vesta family. *Astron. Astrophys.*, 465, 315–330.
- Carruba V., Michtchenko T. A., and Lazzaro D. (2007b) On the V-type asteroids outside the Vesta family. II. Is (21238) 1995 WV7 a fragment of the long-lost basaltic crust of (15) Eunomia? *Astron. Astrophys.*, 473, 967–978.
- Carruba V., Machuca J. F., and Gasparino H. P. (2011) Dynamical erosion of asteroid groups in the region of the Pallas family. *Mon. Not. R. Astron. Soc.*, 412, 2052–2062.
- Carruba V., Huaman M. E., Douwens S., and Domingos R. C. (2012) Chaotic diffusion caused by close encounters with several massive asteroids. *Astron. Astrophys.*, 543, A105.
- Carruba V., Domingos R. C., Nesvorný D., et al. (2013a) A multi-domain approach to asteroid families identification. *Mon. Not. R. Astron. Soc.*, 433, 2075–2096.
- Carruba V., Huaman M. E., Domingos R. C., and Roig F. (2013b) Chaotic diffusion caused by close encounters with several massive asteroids II: The regions of (10) Hygiea, (2) Pallas, and (31) Euphrosyne. *Astron. Astrophys.*, 550, A85.
- Carruba V., Aljbaae S., and Souami D. (2014) Peculiar Euphrosyne. *Astrophys. J.*, 792, 46–61.
- Cellino A., Bus S. J., Doressoundiram A., and Lazzaro D. (2002) Spectroscopic properties of asteroid families. In *Asteroids III* (W. F. Bottke Jr. et al., eds.), pp. 633–643. Univ. of Arizona, Tucson.
- Cellino A., Dell’Oro A., and Zappalà V. (2004) Asteroid families: Open problems. *Planet. Space Sci.*, 52, 1075–1086.
- Cellino A., Dell’Oro A., and Tedesco E. F. (2009) Asteroid families: Current situation. *Planet. Space Sci.*, 57, 173–182.

- Cellino A., Bagnulo S., Tanga P., Novaković B., and Delbó M. (2014) A successful search for hidden Barbarians in the Watsonia asteroid family. *Mon. Not. R. Astron. Soc. Lett.*, **439**, 75–79.
- Cibulková H., Brož M., and Benavidez P. G. (2014) A six-part collisional model of the main asteroid belt. *Icarus*, **241**, 358–372.
- Cimrman J. (1917) On the literal expansion of the perturbation Hamiltonian and its applicability to the curious assemblages of minor planets. *Cimrman Bull.*, **57**, 132–135.
- Clark B. E., Ockert-Bell M. E., Cloutis E. A., Nesvorný D., Mothé-Diniz T., and Bus S. J. (2009) Spectroscopy of K-complex asteroids: Parent bodies of carbonaceous meteorites? *Icarus*, **202**, 119–133.
- Ćuk M., Gladman B. J., and Nesvorný D. (2014) Hungaria asteroid family as the source of aubrite meteorites. *Icarus*, **239**, 154–159.
- Delisle J.-B. and Laskar J. (2012) Chaotic diffusion of the Vesta family induced by close encounters with massive asteroids. *Astron. Astrophys.*, **540**, A118.
- Dell’Oro A. and Cellino A. (2007) The random walk of main belt asteroids: Orbital mobility by non-destructive collisions. *Mon. Not. R. Astron. Soc.*, **380**, 399–416.
- Dell’Oro A., Bigongiari G., Paolicchi P., and Cellino A. (2004) Asteroid families: Evidence of ageing of the proper elements. *Icarus*, **169**, 341–356.
- Dermott S. F., Nicholson P. D., Burns J. A., and Houck J. R. (1984) Origin of the solar system dust bands discovered by IRAS. *Nature*, **312**, 505–509.
- Dermott S. F., Kehoe T. J. J., Durda D. D., Grogan K., and Nesvorný D. (2002) Recent rubble-pile origin of asteroidal solar system dust bands and asteroidal interplanetary dust particles. *Asteroids Comets Meteors*, **500**, 319–322.
- Durda D. D., Bottke W. F., Enke B. L., Merline W. J., Asphaug E., Richardson D. C., and Leinhardt Z. M. (2004) The formation of asteroid satellites in large impacts: Results from numerical simulations. *Icarus*, **170**, 243–257.
- Durda D. D., Bottke W. F., Nesvorný D., et al. (2007) Size-frequency distributions of fragments from SPH/N-body simulations of asteroid impacts: Comparison with observed asteroid families. *Icarus*, **186**, 498–516.
- Dykhuus M. and Greenberg R. (2015) Collisional family structure within the Nysa-Polana complex. *Icarus*, in press, arXiv:1501.04649.
- Dykhuus M. J., Molnar L., Van Kooten S. J., and Greenberg R. (2014) Defining the Flora family: Orbital properties, reflectance properties and age. *Icarus*, **243**, 111–128.
- Farley K. A., Vokrouhlický D., Bottke W. F., and Nesvorný D. (2006) A late Miocene dust shower from the break-up of an asteroid in the main belt. *Nature*, **439**, 295–297.
- Florczak M., Lazzaro D., and Duffard R. (2002) Discovering new V-type asteroids in the vicinity of 4 Vesta. *Icarus*, **159**, 178–182.
- Fujiwara A., Cerroni P., Davis D., Ryan E., and di Martino M. (1989) Experiments and scaling laws for catastrophic collisions. In *Asteroids II* (R. P. Binzel et al., eds.), pp. 240–265. Univ. of Arizona, Tucson.
- Galiazzo M. A., Bazsó Á., and Dvorak R. (2013) Fugitives from the Hungaria region: Close encounters and impacts with terrestrial planets. *Planet. Space Sci.*, **84**, 5–13.
- Galiazzo M. A., Bazsó Á., and Dvorak R. (2014) The Hungaria asteroids: Close encounters and impacts with terrestrial planets. *Mem. Soc. Astron. Ital. Suppl.*, **26**, 38.
- Gil-Hutton R. (2006) Identification of families among highly inclined asteroids. *Icarus*, **183**, 93–100.
- Harris A. W., Mueller M., Lisie C. M., and Cheng A. F. (2009) A survey of Karin cluster asteroids with the Spitzer Space Telescope. *Icarus*, **199**, 86–96.
- Hirayama K. (1918) Groups of asteroids probably of common origin. *Astron. J.*, **31**, 185–188.
- Ivezic Ž., Tabachnik S., Rafikov R., et al. (2001) Solar system objects observed in the Sloan Digital Sky Survey commissioning data. *Astron. J.*, **122**, 2749–2784.
- Knežević Z. and Milani A. (2000) Synthetic proper elements for outer main belt asteroids. *Cel. Mech. Dyn. Astron.*, **78**, 17–46.
- Knežević Z. and Pavlović R. (2002) Young age for the Veritas asteroid family confirmed? *Earth Moon Planets*, **88**, 155–166.
- Knežević Z., Milani A., Farinella P., Froeschle Ch., and Froeschle Cl. (1991) Secular resonances from 2 to 50 AU. *Icarus*, **93**, 316–330.
- Knežević Z., Lemaître A., and Milani A. (2002) The determination of asteroid proper elements. In *Asteroids III* (W. F. Bottke Jr. et al., eds.), pp. 603–612. Univ. of Arizona, Tucson.
- Lemaître A. and Morbidelli A. (1994) Proper elements for highly inclined asteroidal orbits. *Cel. Mech. Dyn. Astron.*, **60**, 29–56.
- Low F. J., Young E., Beintema D. A., Gautier T. N., et al. (1984) Infrared cirrus — New components of the extended infrared emission. *Astrophys. J.*, **278**, 19–22.
- Mainzer A., Grav T., Masiero J., et al. (2011) NEOWISE studies of spectrophotometrically classified asteroids: Preliminary results. *Astrophys. J.*, **741**, 90–115.
- Marchi S., McSween H. Y., O’Brien D. P., et al. (2012) The violent collisional history of asteroid 4 Vesta. *Science*, **336**, 690.
- Marchis F., and 11 colleagues (2014) The puzzling mutual orbit of the binary Trojan asteroid (624) Hektor. *Astrophys. J. Lett.*, **783**, L37.
- Marsden B. G. (1980) The Minor Planet Center. *Cel. Mech. Dyn. Astron.*, **22**, 63–71.
- Masarri F., Farinella P., and Davis D. R. (1999) Origin, aging, and death of asteroid families. *Icarus*, **142**, 63–77.
- Masiero J. R., Mainzer A. K., Grav T., et al. (2011) Main belt asteroids with WISE/NEOWISE. I. Preliminary albedos and diameters. *Astrophys. J.*, **741**, 68–88.
- Masiero J. R., Mainzer A. K., Grav T., Bauer J. M., and Jedicke R. (2012) Revising the age for the Baptistina asteroid family using WISE/NEOWISE data. *Astrophys. J.*, **759**, 14–28.
- Masiero J. R., Mainzer A. K., Bauer J. M., et al. (2013) Asteroid family identification using the hierarchical clustering method and WISE/NEOWISE physical properties. *Astrophys. J.*, **770**, 7–29.
- Michel P., Benz W., Tanga P., and Richardson D. C. (2001) Collisions and gravitational reaccumulation: Forming asteroid families and satellites. *Science*, **294**, 1696–1700.
- Michel P., Benz W., and Richardson D. C. (2003) Disruption of fragmented parent bodies as the origin of asteroid families. *Nature*, **421**, 608–611.
- Michel P., Benz W., and Richardson D. C. (2004) Catastrophic disruption of pre-shattered parent bodies. *Icarus*, **168**, 420–432.
- Michel P., Jutzi M., Richardson D. C., and Benz W. (2011) The asteroid Veritas: An intruder in a family named after it? *Icarus*, **211**, 535–545.
- Migliorini F., Zappalà V., Vio R., and Cellino A. (1995) Interlopers within asteroid families. *Icarus*, **118**, 271–291.
- Milani A. (1993) The Trojan asteroid belt: Proper elements, chaos, stability and families. *Cel. Mech. Dyn. Astron.*, **57**, 59–94.
- Milani A. and Farinella P. (1994) The age of the Veritas asteroid family deduced by chaotic chronology. *Nature*, **370**, 40–42.
- Milani A. and Knežević Z. (1990) Secular perturbation theory and computation of asteroid proper elements. *Cel. Mech.*, **49**, 347–411.
- Milani A. and Knežević Z. (1994) Asteroid proper elements and the dynamical structure of the asteroid main belt. *Icarus*, **107**, 219–254.
- Milani A., Knežević Z., Novaković B., and Cellino A. (2010) Dynamics of the Hungaria asteroids. *Icarus*, **207**, 769–794.
- Milani A., Cellino A., Knežević Z., et al. (2014) Asteroid families classification: Exploiting very large datasets. *Icarus*, **239**, 46–73.
- Minton D. and Malhotra R. (2009) A record of planet migration in the main asteroid belt. *Nature*, **457**, 1109–1111.
- Molnar L. A. and Haegert M. J. (2009) Details of recent collisions of asteroids 832 Karin and 158 Koronis. *AAS/Division for Planetary Sciences Meeting Abstracts*, **41**, #27.05.
- Morbidelli A. (1993) Asteroid secular resonant proper elements. *Icarus*, **105**, 48–66.
- Morbidelli A., Brasser R., Gomes R., Levison H. F., and Tsiganis K. (2010) Evidence from the asteroid belt for a violent past evolution of Jupiter’s orbit. *Astron. J.*, **140**, 1391–1401.
- Mothé-Diniz T., Roig F., and Carvano J. M. (2005) Reanalysis of asteroid families structure through visible spectroscopy. *Icarus*, **174**, 54–80.
- Mothé-Diniz T., Carvano J. M., Bus S. J., et al. (2008) Mineralogical analysis of the Eos family from near-infrared spectra. *Icarus*, **195**, 277–294.
- Nathues A., Mottola S., Kaasalainen M., and Neukum G. (2005) Spectral study of the Eunomia asteroid family. I. Eunomia. *Icarus*, **175**, 452–463.
- Nesvorný D. (2010) *Nesvorný HCM Asteroid Families VI.0*. EAR-A-VARBDT-5-NESVORNYFAM-V1.0, NASA Planetary Data System.

- Nesvorný D. (2012) *Nesvorný HCM Asteroid Families V2.0*. EAR-A-VARGBDAT-5-NESVORNYFAM-V2.0, NASA Planetary Data System.
- Nesvorný D. and Bottke W. F. (2004) Detection of the Yarkovsky effect for main-belt asteroids. *Icarus*, *170*, 324–342.
- Nesvorný D. and Morbidelli A. (1999) An analytic model of three-body mean motion resonances. *Cel. Mech. Dyn. Astron.*, *71*, 243–271.
- Nesvorný D. and Vokrouhlický D. (2006) New candidates for recent asteroid breakups. *Astron. J.*, *132*, 1950–1958.
- Nesvorný D., Bottke W. F., Dones L., and Levison H. F. (2002a) The recent breakup of an asteroid in the main-belt region. *Nature*, *417*, 720–771.
- Nesvorný D., Morbidelli A., Vokrouhlický D., Bottke W. F., and Brož M. (2002b) The Flora family: A case of the dynamically dispersed collisional swarm? *Icarus*, *157*, 155–172.
- Nesvorný D., Ferraz-Mello S., Holman M., and Morbidelli A. (2002c) Regular and chaotic dynamics in the mean-motion resonances: Implications for the structure and evolution of the asteroid belt. In *Asteroids III* (W. F. Bottke Jr. et al., eds.), pp. 379–394. Univ. of Arizona, Tucson.
- Nesvorný D., Bottke W. F., Levison H. F., and Dones L. (2003) Recent origin of the solar system dust bands. *Astrophys. J.*, *591*, 486–497.
- Nesvorný D., Jedicke R., Whiteley R. J., and Ivezić Ž. (2005) Evidence for asteroid space weathering from the Sloan Digital Sky Survey. *Icarus*, *173*, 132–152.
- Nesvorný D., Enke B. L., Bottke W. F., Durda D. D., Asphaug E., and Richardson D. C. (2006a) Karin cluster formation by asteroid impact. *Icarus*, *183*, 296–311.
- Nesvorný D., Bottke W. F., Vokrouhlický D., Morbidelli A., and Jedicke R. (2006b) Asteroid families. *Asteroids Comets Meteors*, *229*, 289–299.
- Nesvorný D., Vokrouhlický D., and Bottke W. F. (2006c) The breakup of a main-belt asteroid 450 thousand years ago. *Science*, *312*, 1490.
- Nesvorný D., Roig F., Gladman B., et al. (2008a) Fugitives from the Vesta family. *Icarus*, *183*, 85–95.
- Nesvorný D., Bottke W. F., Vokrouhlický D., et al. (2008b) Origin of the near-ecliptic circumsolar dust band. *Astrophys. J.*, *679*, 143–146.
- Nesvorný D., Vokrouhlický D., Morbidelli A., and Bottke W. F. (2009) Asteroidal source of L chondrite meteorites. *Icarus*, *200*, 698–701.
- Novaković B. (2010) Portrait of Theobalda as a young asteroid family. *Mon. Not. R. Astron. Soc.*, *407*, 1477–1486.
- Novaković B., Tsiganis K., and Knežević Z. (2010a) Dynamical portrait of the Lixiaohua asteroid family. *Cel. Mech. Dyn. Astron.*, *107*, 35–49.
- Novaković B., Tsiganis K., and Knežević Z. (2010b) Chaotic transport and chronology of complex asteroid families. *Mon. Not. R. Astron. Soc.*, *402*, 1263–1272.
- Novaković B., Cellino A., and Knežević Z. (2011) Families among high-inclination asteroids. *Icarus*, *216*, 69–81.
- Novaković B., Dell’Oro A., Cellino A., and Knežević Z. (2012a) Recent collisional jet from a primitive asteroid. *Mon. Not. R. Astron. Soc.*, *425*, 338–346.
- Novaković B., Hsieh H. H., and Cellino A. (2012b) P/2006 VW139: A main-belt comet born in an asteroid collision? *Mon. Not. R. Astron. Soc.*, *424*, 1432–1441.
- Novaković B., Hsieh H. H., Cellino A., Micheli M., and Pedan M. (2014) Discovery of a young asteroid cluster associated with P/2012 F5 (Gibbs). *Icarus*, *231*, 300–309.
- Parker A., Ivezić Ž., Jurić M., et al. (2008) The size distributions of asteroid families in the SDSS Moving Object Catalog 4. *Icarus*, *198*, 138–155.
- Reddy V., Carvano J. M., Lazzaro D., et al. (2011) Mineralogical characterization of Baptista asteroid family: Implications for K/T impactor source. *Icarus*, *216*, 184–197.
- Rozehnal J. and Brož M. (2013) Jovian Trojans: Orbital structures versus the WISE data. *AAS/Division for Planetary Sciences Meeting Abstracts*, *45*, #112.12.
- Rožek A., Breiter S., and Jopek T. J. (2011) Orbital similarity functions — application to asteroid pairs. *Mon. Not. R. Astron. Soc.*, *412*, 987–994.
- Rubincam D. P. (2000) Radiative spin-up and spin-down of small asteroids. *Icarus*, *148*, 2–11.
- Roig F., Ribeiro A. O., and Gil-Hutton R. (2008) Taxonomy of asteroid families among the Jupiter Trojans: Comparison between spectroscopic data and the Sloan Digital Sky Survey colors. *Astron. Astrophys.*, *483*, 911–931.
- Southworth R. B. and Hawkins G. S. (1963) Statistics of meteor streams. *Smithson. Contrib. Astrophys.*, *7*, 261.
- Tsiganis K., Knežević Z., and Varvoglis H. (2007) Reconstructing the orbital history of the Veritas family. *Icarus*, *186*, 484–497.
- Usui F., Kasuga T., Hasegawa S., et al. (2013) Albedo properties of main belt asteroids based on the all-sky survey of the Infrared Astronomical Satellite AKARI. *Astrophys. J.*, *762*, 56–70.
- Vernazza P., Binzel R. P., Thomas C. A., et al. (2008) Compositional differences between meteorites and near-Earth asteroids. *Nature*, *454*, 858–860.
- Vokrouhlický D. and Nesvorný D. (2008) Pairs of asteroids probably of a common origin. *Astron. J.*, *136*, 280–290.
- Vokrouhlický D. and Nesvorný D. (2009) The common roots of asteroids (6070) Rheinland and (54827) 2001 NQ8. *Astron. J.*, *137*, 111–117.
- Vokrouhlický D. and Nesvorný D. (2011) Half-brothers in the Schulhof family? *Astron. J.*, *142*, 26–34.
- Vokrouhlický D., Brož M., Morbidelli A., et al. (2006a) Yarkovsky footprints in the Eos family. *Icarus*, *182*, 92–117.
- Vokrouhlický D., Brož M., Bottke W. F., Nesvorný D., and Morbidelli A. (2006b) Yarkovsky/YORP chronology of asteroid families. *Icarus*, *182*, 118–142.
- Vokrouhlický D., Brož M., Bottke W. F., Nesvorný D., and Morbidelli A. (2006c) The peculiar case of the Agnia asteroid family. *Icarus*, *183*, 349–361.
- Vokrouhlický D., Durech J., Michałowski T., et al. (2009) Datura family: The 2009 update. *Astron. Astrophys.*, *507*, 495–504.
- Vokrouhlický D., Nesvorný D., Bottke W. F., and Morbidelli A. (2010) Collisionally born family about 87 Sylvia. *Astron. J.*, *139*, 2148–2158.
- Walsh K. J., Delbo M., Bottke W. F., et al. (2013) Introducing the Eulalia and new Polana asteroid families: Re-assessing primitive asteroid families in the inner main belt. *Icarus*, *225*, 283–297.
- Warner B. D., Harris A. W., Vokrouhlický D., et al. (2009) Analysis of the Hungaria asteroid population. *Icarus*, *204*, 172–182.
- Weiss B. P. and Elkins-Tanton L. T. (2013) Differentiated planetesimals and the parent bodies of chondrites. *Annu. Rev. Earth Planet. Sci.*, *41*, 529–560.
- Willman M., Jedicke R., Nesvorný D., Moskovitz N., Ivezić Ž., and Fevig R. (2008) Redetermination of the space weathering rate using spectra of Iannini asteroid family members. *Icarus*, *195*, 663–673.
- Wisdom J. (1982) The origin of the Kirkwood gaps — a mapping for asteroidal motion near the 3/1 commensurability. *Astron. J.*, *87*, 577–593.
- Zappalà V., Cellino A., Farinella P., and Knežević Z. (1990) Asteroid families. I — Identification by hierarchical clustering and reliability assessment. *Astron. J.*, *100*, 2030–2046.
- Zappalà V., Cellino A., Farinella P., and Milani A. (1994) Asteroid families. 2: Extension to unnumbered multiopposition asteroids. *Astron. J.*, *107*, 772–801.
- Zappalà V., Cellino A., dell’Oro A., and Paolicchi P. (2002) Physical and dynamical properties of asteroid families. In *Asteroids III* (W. F. Bottke Jr. et al., eds.), pp. 619–631. Univ. of Arizona, Tucson.



# Asteroid Family Physical Properties

**Joseph R. Masiero**

*NASA Jet Propulsion Laboratory/California Institute of Technology*

**Francesca E. DeMeo**

*Harvard/Smithsonian Center for Astrophysics*

**Toshihiro Kasuga**

*Planetary Exploration Research Center, Chiba Institute of Technology*

**Alex H. Parker**

*Southwest Research Institute*

---

An asteroid family is typically formed when a larger parent body undergoes a catastrophic collisional disruption, and as such, family members are expected to show physical properties that closely trace the composition and mineralogical evolution of the parent. Recently a number of new datasets have been released that probe the physical properties of a large number of asteroids, many of which are members of identified families. We review these datasets and the composite properties of asteroid families derived from this plethora of new data. We also discuss the limitations of the current data, as well as the open questions in the field.

## 1. INTRODUCTION

Asteroid families provide waypoints along the path of dynamical evolution of the solar system, as well as laboratories for studying the massive impacts that were common during terrestrial planet formation. Catastrophic disruptions shattered these asteroids, leaving swarms of bodies behind that evolved dynamically under gravitational perturbations and the Yarkovsky effect to their present-day locations, both in the main belt and beyond. The forces of the family-forming impact and the gravitational reaccumulation of the collisional products also left imprints on the shapes, sizes, spins, and densities of the resultant family members (see the chapter by Michel et al. in this volume). By studying the physical properties of the collisional remnants, we can probe the composition of the parent asteroids, important source regions of transient populations like the near-Earth objects (NEOs), and the physical processes that asteroids are subjected to on million- and billion-year timescales.

In the 13 years since the publication of *Asteroids III*, research programs and sky surveys have produced physical observations for nearly 2 orders of magnitude more asteroids than were previously available. The majority of these characterized asteroids are members of the main belt, and approximately one-third of all known main-belt asteroids (MBAs) with sizes larger than a few kilometers can be associated with asteroid families. As such, these datasets

represent a windfall of family physical property information, enabling new studies of asteroid family formation and evolution. These data also provide a feedback mechanism for dynamical analyses of families, particularly age-dating techniques that rely on simulating the nongravitational forces that depend on an asteroid's albedo, diameter, and density.

In *Asteroids III*, Zappalà et al. (2002) and Cellino et al. (2002) reviewed the physical and spectral properties (respectively) of asteroid families known at that time. Zappalà et al. (2002) primarily dealt with asteroid size distributions inferred from a combination of observed absolute H magnitudes and albedo assumptions based on the subset of the family members with well-measured values. Surveys in the subsequent years have expanded the number of measured diameters and albedos by nearly 2 orders of magnitude, allowing for more accurate analysis of these families. Cellino et al. (2002) discussed the spectroscopic properties of the major asteroid families known at that time. The principal leap forward since *Asteroids III* in the realm of spectroscopy has been the expansion of spectroscopic characterization to near-infrared (NIR) wavelengths. The development of more sensitive instrumentation covering the 1- and 2-m silicate absorption features and new observing campaigns to acquire NIR spectra for a large number of objects have revolutionized studies of asteroid composition and space weathering.

By greatly expanding the number of family members with measured physical properties, new investigations of asteroid

families can be undertaken. Measurements of colors and albedo allow us to identify outliers in our population lists and search for variations in surface properties of family members that might indicate heterogeneity of the parent-body or weathering processes. Diameter measurements let us build a size frequency distribution and estimate the original parent-body size, both of which are critical to probing the physics of giant impacts. Spectra provide detailed mineralogical constraints of family members, allowing for more sensitive tests of space weathering and parent heterogeneity, albeit for a smaller sample size, while also probing the formation environment and allowing for comparisons to meteorite samples.

In this chapter, we highlight the datasets that have been obtained since *Asteroids III*, which have greatly expanded our ability to understand asteroid families. We discuss their implications for specific families, and tabulate average photometric, albedo, and spectroscopic properties for 109 families identified in the chapter by Nesvorný et al. in this volume. We also discuss the key questions that have been answered since *Asteroids III*, those that remain open, and the new puzzles that have appeared over the last decade.

## 2. NEW DATASETS

The field of asteroid research has benefited in the last 13 years from a huge influx of data. Many of these large sets of asteroid characterization data (including photometric and thermophysical data) have been ancillary results of surveys primarily designed to investigate astrophysical sources beyond the solar system. Simultaneously, observing programs designed to acquire more time-intensive data products such as asteroid spectra, photometric light curves, or polarimetric phase curves have also blossomed. We review below the main datasets that have advanced family characterization in recent years.

### 2.1. Optical Colors from the Sloan Digital Sky Survey

The Sloan Digital Sky Survey (SDSS) (York et al., 2000) produced one of the first extremely large, homogeneous datasets that contained information about asteroid surface properties at optical wavelengths. These data are archived in the SDSS Moving Object Catalog (<http://www.astro.washington.edu/users/ivezic/sdssmoc/sdssmoc.html>), which currently contains 471,569 entries of moving objects from survey scans conducted up to March 2007. The catalog entries can be associated with 104,449 unique known moving objects; however, ~250,000 entries do not have corresponding associations in the orbital element catalogs, implying the potential for a significant benefit from future data mining efforts.

While the SDSS five-color photometric system (u, g, r, i, z, with central wavelengths of 0.3543 μm, 0.4770 μm, 0.6231 μm, 0.7625 μm, and 0.9134 μm, respectively) was not designed with asteroid taxonomy in mind [unlike previous surveys such as the Eight Color Asteroid Survey (Zellner et al., 1985a)], the sheer size of the dataset coupled with its

extremely well-characterized performance has made SDSS an immensely valuable asset for defining asteroid families and exploring their properties. The near-simultaneous optical color information obtained during the course of the SDSS survey can be used to infer the spectroscopic properties of tens of thousands of asteroids at optical wavelengths.

The SDSS, primarily designed to measure the redshifts of a very large sample of galaxies, serendipitously observed many asteroids over the course of its several survey iterations. Under standard survey operations with 53.9-s exposures, its five-color camera was sensitive to stationary sources as faint as  $r \sim 22.2$ , with similar performance in u and g and somewhat brighter limits in i and z (21.3 and 20.5, respectively). To enable the accurate determination of photometric redshifts, high-precision internal and absolute calibrations were essential. The care and effort expended on these calibrations carried over into the dataset of moving object photometry, resulting in the largest well-calibrated dataset of multi-band asteroid photometry to date.

As of the latest data release, the Moving Object Catalog 4 (MOC4) (Parker et al., 2008) contains asteroid observations from 519 survey observing runs. The automatic flagging and analysis of moving objects required that they be brighter than magnitude  $r = 21.5$ . The brightest object in the sample is  $r \sim 12.91$ , giving the survey a dynamic range of over 8.5 mag. The large sample size and dynamic range of this survey make it a powerful tool for studying luminosity functions of dynamically — or photometrically — selected subpopulations of the moving objects, of which asteroid families are a natural example.

Because of the much smaller sample size of asteroids with u-band observations having photometric errors  $<0.1$  mag (44,737, compared with 442,743 with a similar precision in r-band), most large-scale asteroid studies using SDSS photometry have considered only the four longer-wavelength bands. These are often further collapsed into two principle components, a\* color [ $a^* = 0.89(g-r) + 0.45(r-i) - 0.57$ ] and the (i-z) color (see Ivezić et al., 2001).

Using the SDSS dataset, Ivezić et al. (2002) showed that asteroid families are easily identified from their optical colors. They found four primary color classes of families, which describe one of four characteristic compositions: Vesta, Koronis, Eos, and Themis. Jedicke et al. (2004) and Nesvorný et al. (2005) expanded upon this to investigate space weathering and find that older asteroid families have steeper spectral slopes from 0.55 to 1 μm than younger asteroid families.

Szabó and Kiss (2008) used SDSS photometry to constrain the shape distributions of eight large asteroid families. By assuming the observed magnitude differences between different epochs of observation were uncorrelated, they showed that both older families and families closer to the Sun tend to have more spherical shape distributions. This effect is what would be expected for a system where small-scale cratering collisions redistributed material into gravitational lows, resulting in a more spherical shape.

Parker et al. (2008) used the family color relationships found by Ivezić et al. (2002) as a springboard to refine the

definition of asteroid families beyond solely dynamical relationships. The ability to spectrophotometrically refine the sample of objects linked to each family meant family membership could be extended further into the background, and allowed the identification of diffuse family “halos” of compositionally distinct objects (Parker et al., 2008; Brož and Morbidelli, 2013; Carruba et al., 2013). Overlapping but compositionally distinct families such as Flora and Baptistina are easily separated with the addition of color information.

Using the wealth of SDSS data, Carvano et al. (2010) modeled established taxonomic classes to define the SDSS color parameters of each class. They then used these constraints to perform photometric taxonomic classifications of SDSS-observed asteroids, including many large asteroid families. This technique was later extended by DeMeo and Carry (2013) to better distinguish the boundaries between taxonomic classes. This taxonomic strategy can be applied to future photometric surveys to rapidly classify asteroids as a tool for improving family associations. While the resulting taxonomic grouping is of lower certainty than spectroscopic classification, spectrophotometric taxonomy offers a fast way to quantify the spectral behavior of large numbers of asteroids and provide high-quality candidates for spectroscopic follow-up.

## 2.2. Visible and Infrared Spectroscopic Surveys

Spectroscopic measurements provide unparalleled sensitivity to the mineralogical features on the surfaces of asteroids. As members of families come from the same progenitor object, surveys of many family members allow us to probe the composition of that parent body and search for mineralogical changes indicative of geological processes during the parent’s formation and early evolution. For families shown to have homogeneous spectral properties, these surveys can also be used to identify outlier objects that are compositionally distinct from the family, especially large objects that can present serious complications to the analysis of family evolution.

A major focus in the study of families has been the characterization of the effects of space weathering on the surfaces of atmosphereless bodies. Recent work using dynamical simulations to determine the ages of asteroid families (see the chapter by Nesvorný et al. in this volume for a discussion of these works) has opened a new avenue into investigating the potential effects of space weathering on asteroid surfaces. Assuming that the family-forming impact completely refreshed the surfaces of family members, we can look for families with similar compositions but different ages to search for spectral changes that would be the hallmark of space weathering. A number of researchers have conducted spectroscopic surveys of families to this end, although the results of these studies have been somewhat conflicting (e.g., Nesvorný et al., 2005; Willman et al., 2008; Vernazza et al., 2009; Thomas et al., 2011, 2012).

Shortly after the publication of *Asteroids III*, large-scale visible-wavelength (0.45–0.9 μm) spectral surveys were

published that were major drivers of asteroid compositional studies. Bus and Binzel (2002) and Lazzaro et al. (2004) published 1341 and 820 asteroid spectra, respectively, providing a wealth of data for asteroid studies. Also around this time NIR spectrometers became widely available, such as SpeX on the NASA Infrared Telescope Facility (IRTF) (Rayner et al., 2003). The NIR provides wavelength coverage that allows better characterization of silicate features (Burbine and Binzel, 2002; Gaffey et al., 1993). While no single large observing campaign has been initiated for main-belt asteroids in the NIR, many small programs have been carried out that targeted specific asteroid families (Sunshine et al., 2004; Mothé-Diniz et al., 2005, 2008; Vernazza et al., 2006; Mothé-Diniz and Nesvorný, 2008a,b; Willman et al., 2008; Harris et al., 2009; Reddy et al., 2009, 2011; de Sanctis et al., 2011; Ziffer et al., 2011; de Leon et al., 2012). A compilation of spectral taxonomic classifications of asteroids is given in the Planetary Data System by Neese (2010) and is periodically updated. We highlight here some of the specific families that were the subject of spectral investigations.

Vernazza et al. (2006) obtained spectra of Karin family members, finding them to be very similar to ordinary chondrite (OC) meteorites. Willman et al. (2008, 2010) extended this survey in an attempt to constrain space-weathering rates for asteroid surfaces, finding that spectral slopes are altered on the billion-year timescale. Harris et al. (2009) surveyed the Karin family using thermal infrared spectroscopy, and found albedos lower than expected for fresh asteroid surfaces, implying space weathering alters albedos on the million-year timescale, in conflict with the Willman et al. (2008, 2010) results.

Nathues (2010) used visible and NIR spectroscopy of the (97) Eunomia family members to study the potential differentiation history of the family parent. They show that the majority of family members have S-type taxonomy and the parent body was likely not fully differentiated, but may have undergone partial differentiation. Fieber-Beyer et al. (2011) obtained NIR spectroscopy of (12) Maria family members. From these data they associate this family with mesosiderite-type meteorites, a type of iron-rich meteorite thought to originate from a differentiated parent body.

Ziffer et al. (2011) obtained NIR spectra of 13 asteroids in the Themis and Veritas families and find distinct differences in the spectral behavior of the two families. They associate both families with CM2 chondrites, but find no evidence for space weathering of C-type objects.

Reddy et al. (2009, 2011) performed a spectroscopic survey of the Baptistina family aimed at constraining the composition of the family members. They found a range of compositions represented, but smaller objects as well as (298) Baptistina itself show clear association with LL-type ordinary chondrites. Ordinary chondrite meteorites show two distinct compositional phases, one at albedos similar to S-complex asteroids and one that is darker with muted silicate absorption bands. This darker material has been associated with former surface regolith that had gases implanted by the solar wind and was later relithified and impact-shocked, resulting in a significantly different reflectivity with only a

nominal difference in composition (Britt and Pieters, 1991). Studies of the recent Chelyabinsk meteorite (Kohout *et al.*, 2014; Reddy *et al.*, 2014) further confirm that shock darkening may play a critical role in the evolution of asteroid family spectra (cf. Cellino *et al.*, 2002).

Licandro *et al.* (2012) used the Spitzer Space Telescope to measure mid-infrared spectra for eight members of the Themis family, and determined their albedos and diameters. They were also able to constrain the surface thermal inertia and set limits on the surface composition, showing that family members must have a very low surface density.

Jasmim *et al.* (2013) performed a spectroscopic survey of objects classified as Qp in the SDSS spectrophotometric system in the Vesta family, but were not able to find any significant differences between these objects and canonical V-type asteroid spectra. This highlights the potential ambiguities in spectrophotometric taxonomic classifications, and the need for further spectroscopic follow-up of interesting asteroids to confirm their spectral behavior.

Recently, Vernazza *et al.* (2014) mineralogically analyzed spectra of six S-complex asteroid families and 83 background S-type objects and compared these results to compositions of various ordinary chondrite meteorites. They found a bimodality in their olivine/pyroxene mineral diagnostic for S-type asteroids that traces the compositional gradients measured for metamorphosed meteorites with a range of iron contents. This bimodality also extended to families, with Koronis, Agnia, Merxia, and Gefion more closely matching high-iron ordinary chondrites and Eunomia and Flora matching either low-iron chondrites from the interiors of bodies or ordinary chondrites from the near-surface regions showing little metamorphism. Mineralogical assessment of NIR spectra thus offers a new method of probing the compositions and metamorphic histories of these S-complex families.

### 2.3. Infrared Space Surveys

Recent improvements in mid-infrared detector technology have spurred renewed interest in their use for astronomical observations. Groundbased thermal infrared detectors can obtain data for a small subset of the brightest targets; however, the thermal background prohibits large-scale surveys of smaller asteroids. The space environment, however, is ideal for thermal infrared surveys of the sky, and two recent satellites have obtained all-sky survey data at mid-infrared wavelengths of a large number of asteroids. A more complete discussion of these surveys is presented in the chapter by Mainzer *et al.* in this volume, and so here we only highlight a few relevant aspects.

The AKARI space telescope was launched on February 21, 2006, and surveyed the sky at two thermal infrared wavelengths from May 6, 2006, until the telescope-cooling liquid helium was exhausted on August 28, 2007, covering over 96% of the sky (Murakami *et al.*, 2007; Ishihara *et al.*, 2010). The Asteroid Catalog Using AKARI (AcuA) (Usui *et al.*, 2011, <http://darts.jaxa.jp/ir/akari/catalogue/>

*AcuA.html*) database summarizes the asteroid survey data. Using the standard thermal model (Lebofsky *et al.*, 1986; Lebofsky and Spencer, 1989), diameters and visible albedos were derived for 5120 asteroids.

During the warm mission phase after the cryogen was exhausted, AKARI also performed spectroscopic observations of 70 asteroids, many of which are the largest members of asteroid families. These observations provide unique spectroscopic data covering the wavelength range from 2 to 5  $\mu\text{m}$  (Usui *et al.*, 2011). Kasuga *et al.* (2012) present physical properties of Cybele family members determined from this dataset, and discuss the taxonomic composition of this family by combining spectrally derived taxonomy with infrared photometry.

The Near-Earth Object Wide-field Infrared Survey Explorer (NEOWISE) mission launched on December 14, 2009, and surveyed the entire sky at four infrared wavelengths over the course of its cryogenic mission. The survey continued during its post-cryogenic and reactivated missions at the two shortest wavelengths. The NEOWISE data catalogs and images are publicly archived at the NASA/IPAC Infrared Science Archive (<http://irsa.ipac.caltech.edu/Missions/wise.html>) and contain thermal infrared measurements of more than 150,000 asteroids (Mainzer *et al.*, 2011, 2014). Many of these were identified as members of asteroid families, allowing for the determination of diameter and albedo distributions for an unprecedented number of families.

Masiero *et al.* (2011) presented albedos and diameters for over 120,000 main-belt asteroids, including over 32,000 members of 46 families from Nesvorný (2012). They showed that the albedo distribution within a family is usually very narrow, but some families have significant contamination from background objects or show a mixing of multiple families that overlap in proper-element space. Masiero *et al.* (2013) split the main belt into distinct orbital and albedo components and showed that overlapping families such as Polana and Hertha (aka Nysa) can be easily distinguished.

Masiero *et al.* (2013) used the NEOWISE diameters to measure the size-frequency distribution (SFD) for 76 asteroid families that they identify in their data. The SFD can be computed as  $N \propto D^\alpha$  where  $N$  is the number of objects with diameter greater than  $D$  and  $\alpha$  is the SFD slope. They found that larger families tended to show cumulative SFD slopes that converge toward the value of  $\alpha = -2.5$ , as expected for a collisionally equilibrated population (Dohnanyi, 1969), while smaller families have a wider dispersion. The family associated with (31) Euphrosyne has an anomalously steep SFD slope, which Carruba *et al.* (2014) explain as the result of a dynamical draining of the largest family fragments by the  $v_6$  resonance, which runs through the center of this family in semimajor axis-inclination space.

Ali-Lagoa *et al.* (2013) used the NEOWISE albedo measurements to show that the Pallas family has visible and infrared albedos that are distinct from the majority of B-type asteroids. Masiero *et al.* (2014) presented the 3.4- $\mu\text{m}$  albedo distributions of 13 asteroid families. They found that

the asteroid families form three distinct groupings of albedos at this wavelength. Additionally, the Eos family has unique NIR reflectance properties, which likely traces a mineralogy not seen elsewhere in the main belt.

#### 2.4. Asteroid Light Curves and Phase Curves

Over the last decade, a number of groups have carried out surveys of asteroid light curves, many focusing on the properties of specific families. Light curve analysis from a single epoch can provide rotation periods and constraints on amplitude, while multi-epoch observations can allow for rotational pole determination, shape model fitting, searches for binarity, and detection of non-principal-axis rotation. The binary fraction is an important test of formation mechanisms, while pole determination for a significant number of family members allows for constraints on Yarkovsky-O'Keefe-Radzievskii-Paddack (YORP) evolution of family spin states.

One of the key results from these lightcurve studies has been the confirmation of the YORP effect on spin poles of objects with similar ages (*Vokrouhlický et al.*, 2003). The YORP mechanism results from asymmetries in the thermal reemission of absorbed light, creating a torque on the asteroid. This can alter the rotation rate of these objects, but is also predicted to rapidly reorient the spin poles of most small objects to be perpendicular to the body's orbital plane. This will result in spin poles clustered near 0° and 180° from the orbital pole, and a spin rate distribution differing from the Maxwellian distribution that is expected for a collisionally equilibrated system. *Slivan et al.* (2003, 2008, 2009) measured light curves for 30 members of the Koronis family, showing a strongly anisotropic distribution of spin poles and a non-Maxwellian rotation rate distribution, both consistent with YORP-induced rotation changes.

Surveys of other families have come to similar conclusions: *Warner et al.* (2009) surveyed the Hungaria family asteroids and determined rotation properties for over 100 of these objects. They find a significant excess of slow rotators, which they attribute to YORP-induced spindown, as well as a binarity fraction of 15%, similar to the near-Earth asteroid (NEA) population. *Kryszczyńska et al.* (2012) surveyed 55 objects in the Flora family to determine their rotation periods and poles. They found that the Flora family rotation rates are non-Maxwellian, as is expected from long-term YORP evolution. *Kim et al.* (2014) determined rotation properties for 57 Maria family members, finding an excess of prograde rotation states consistent with the predictions of YORP and Yarkovsky evolution resulting in retrograde rotators moving into the 3:1 Jupiter resonance and being removed from the family.

*Hanuš et al.* (2011, 2013) used shape models derived from light curve inversion to study the spin pole positions of 10 asteroid families. They found a clear distinction in spin pole direction, where objects at semimajor axes smaller than the largest remnant have retrograde rotations while objects at larger semimajor axes have prograde rotations, as is expected from a system evolving under the Yarkovsky effect.

Using the large amount of photometric data available from the Minor Planet Center and the AstOrb database maintained by Lowell Observatory, *Oszkiewicz et al.* (2011, 2012) rederived the photometric phase functions of all known asteroids, applying the improved H<sub>G1</sub>, G<sub>2</sub> and H<sub>G12</sub> phase equations. They find that asteroid families show statistically similar phase slope parameters and that the major taxonomic complexes can be statistically differentiated. However, these distributions overlap, significantly limiting the use of phase curve parameters for direct family or taxonomy identification. *Bowell et al.* (2014) searched the Lowell data for statistical anisotropies in the ecliptic longitude distribution of rotation poles for asteroid family members. They show that the four largest groups considered (the Flora, Vesta, and Koronis families, and the Nysa-Polana complex) have anisotropic spin longitude distributions showing an excess in the 30°–110° longitude range and a dearth in the 120°–160° longitude range, consistent with the distribution seen for the main belt as a whole. The authors suggest this may be due to pole reorientation by the YORP effect, but that extensive modeling is required as well as consideration of potential selection biases.

#### 2.5. Polarimetric Surveys of Families

Measurement of the polarization of light scattered off the surface of an atmosphereless body as a function of phase angle can be used as an independent constraint on the object's albedo (*Cellino et al.*, 1999). Although the magnitude range accessible to polarimetric observations is comparable to that of NIR spectroscopy, multiple nights are required for each object to constrain the phase behavior and there are fewer available imaging polarimeters that are well-calibrated than NIR spectrometers. As such, there are fewer asteroids with measured polarimetric properties; however, polarimetric studies provide unique data on asteroid surface properties that can be important for disentangling ambiguities in other characterization surveys.

*Cellino et al.* (2010) polarimetrically surveyed the Karin and Koronis families as an independent test of the effect of space weathering on asteroid albedo. They find no significant differences between the albedos of Karin and Koronis, implying that space weathering must act on timescales shorter than the ~6-m.y. age of the Karin family.

*Cellino et al.* (2014) conducted a survey of the linear polarization phase curves of Watsonia asteroid family members, searching for analogs to the unusual polarization of (234) Barbara. Barbara and the related "Barbarian" objects have unusual polarimetric properties indicative of unique surface mineralogy and are taxonomically identified as Ld-type objects from spectra. They found that seven of the nine objects surveyed show indications of a surface rich in spinel, one of the oldest minerals in the solar system (*Burbine et al.*, 1992). This implies that the Watsonia parent object has undergone little to no mineralogical processing since the formation of the first solids in the protosolar disk

(Sunshine *et al.*, 2008), and may have been one of the oldest unprocessed bodies in the solar system.

### 3. COLOR, SPECTRA, ALBEDO, AND SIZE DISTRIBUTIONS OF FAMILIES

With the wealth of asteroid physical observations now available, we can determine the average characteristic properties for families. As the literature contains many different collections of family lists, here we focus on the consolidated list presented in the chapter by Nesvorný *et al.* in this volume. This improves our sensitivity to subtle physical differences between families, especially the biggest families, where the large sample size can greatly reduce the scatter in measured properties among individual members. We can also use these data to reject outlier objects from family lists, particularly when the family of interest is of distinct composition from other nearby families or the majority of background objects. Here we discuss some of the recent applications of the new physical property data that has become available.

#### 3.1. Homogeneity of Families and Use of Physical Properties to Distinguish Outliers

Family-forming collisions are expected to liberate material from a large fraction of the parent body's volume. Many of the resulting family members are likely to be accumulations of smaller ejecta, potentially from a range of lithologies within the parent (see the chapter by Michel *et al.* in this volume). For a heterogeneous parent body, we would expect to see a range of colors, spectra, and albedos among the resultant family members, while a homogeneous parent would instead produce a family with very narrow distributions of these properties. While it is possible that the family formed from an impact on a homogeneous parent by an impactor of a different composition could show heterogeneity, statistically the mass of any probable impactor will only be a small fraction of the mass of either the parent or the ejecta, and so would be unlikely to be a significant contaminant to globally averaged properties obtained from remote sensing. Subfamilies resulting from second-generation impacts could also show subtle property differences compared to the original family due to the reset of any space-weathering processes, but this would be most obvious only for very young families (e.g., Karin).

Early surveys of asteroid family spectra and colors indicated that with the exception of a handful of outliers (e.g., the Nysa-Polana complex), families had narrow distributions of physical properties, indicative of homogeneous parent bodies (see Cellino *et al.*, 2002, and references therein). This enabled the extrapolation of measured physical properties for a handful of family members to the entire family. As many of the largest remnants of family formation had been studied for decades, this became a boon to family research.

However, with the availability of physical property data for large numbers of family members, we can now use this

data to remove interloper objects from family lists when they have a different color, albedo, or spectrum from the bulk of the family. Refining family lists in this way is particularly important for improving the accuracy of age-dating techniques. In the past few years, a number of research groups have been actively using these data to this end, in an effort to better understand the formation and evolution of families and the parent bodies from which they came (e.g., Novaković *et al.*, 2011; Brož *et al.*, 2013; Masiero *et al.*, 2013; Carruba, 2013; Walsh *et al.*, 2013; Carruba *et al.*, 2013; Hanuš *et al.*, 2013; Milani *et al.*, 2014).

#### 3.2. Combined Properties of Individual Families

Using the various datasets presented above, we provide in Table 1 the average SDSS colors, average optical and NIR albedos, majority taxonomic type, and SFD slopes (as well as the diameter range that the SFD was fit to) for the families given in the chapter by Nesvorný *et al.* in this volume. We also present a visualization of the average albedo, SDSS colors, and spectra for families with sufficient data in Fig. 1. While mean values are often useful for extrapolating properties of family members that were not observed, or for comparing families to each other or other ground-truth data, there are important caveats that cannot be ignored. Sample size considerations and the uncertainty about individual measurements are the most critical of these caveats: Average values based on a small number of objects or even a single object should be considered potentially spurious, and treated as such. We include those values here for completeness.

Visible albedo mean values were derived by fitting a Gaussian to the distribution of all measured log  $p_V$  values, following the technique Masiero *et al.* (2011) applied to the NEOWISE data, and the quoted error gives the width of the observed distribution. The uncertainty on the mean value, when comparing mean albedos of various families, will be the measured Gaussian width over the square root of the sample size; thus for large families the mean albedos can be known quite accurately, even if individuals have large uncertainties. Family NIR albedo values are a median of the 3.4- $\mu\text{m}$  albedos given in Masiero *et al.* (2014).

Size-frequency distributions were computed for all families with more than 100 measured diameters from all infrared surveys and were found by fitting a power law to the cumulative size distribution, using only those bins with more than five objects (to reduce the influence of the large remnants) and less than half the total sample (to minimize the effects of incomplete diameter sampling at small sizes). Tabulated SDSS colors were calculated by performing an error-weighted mean of all observations having  $\text{SNR} > 10$  in the g, r, i, and z bands used to calculate  $a^*$  and  $i-z$ . Family taxonomy is given only for cases in which a majority of family members with taxonomic classes had the same class. If no subclass (e.g., Ch, Sq, Ld) had a majority, but a majority of members were in the same complex, that complex is listed (e.g., C, S, L). For each of these parameters we include the number of objects used to compute the listed value.

TABLE 1. Physical properties of asteroid families.

Number	Name	PDS ID	$\langle p_V \rangle$	$n_{p_V}$	$\langle p_{\text{NIR}} \rangle$	$n_{p_{\text{NIR}}}$	$\langle a^* \rangle$	$\langle i-z \rangle$	$n_{\text{SDSS}}$	SFD Slope	SFD Range (km)	Tax	$n_{\text{tax}}$
2	Pallas	801	0.134 ± 0.026	49	0.114 ± 0.047	10	-0.14 ± 0.03	-0.01 ± 0.08	13	... ± ...	...	B	8
3	Juno	501	0.262 ± 0.054	125	0.488 ± 0.000	8	0.08 ± 0.05	-0.03 ± 0.07	87	-2.427 ± 0.108	2.7–7.3	Sq	1
4	Vesta	401	0.363 ± 0.088	1900	0.465 ± 0.156	54	0.12 ± 0.05	-0.26 ± 0.10	2148	-3.417 ± 0.030	2.5–11.9	V	49
8	Flora	402	0.305 ± 0.064	1330	0.440 ± 0.082	142	0.13 ± 0.06	-0.04 ± 0.07	922	-2.692 ± 0.030	2.8–12.2	S	74
10	Hygiea	601	0.070 ± 0.018	1951	0.065 ± 0.028	3	-0.11 ± 0.05	0.01 ± 0.07	606	-3.883 ± 0.040	6.1–19.3	C	1
15	Eunomia	502	0.270 ± 0.059	1448	0.374 ± 0.088	148	0.13 ± 0.05	-0.03 ± 0.06	798	-3.091 ± 0.033	4.4–17.6	S	30
20	Massalia	404	0.247 ± 0.053	214	... ± ...	0	0.07 ± 0.05	-0.04 ± 0.08	386	-3.544 ± 0.140	2.0–4.1	S	1
24	Themis	602	0.068 ± 0.017	2218	0.074 ± 0.030	86	-0.11 ± 0.04	0.01 ± 0.06	640	-2.313 ± 0.017	7.3–55.6	C	7
25	Phocaea	701	0.290 ± 0.066	715	0.355 ± 0.203	119	0.10 ± 0.11	-0.04 ± 0.08	252	-2.663 ± 0.039	3.5–14.6	S	39
27	Euterpe	410	0.270 ± 0.062	45	0.493 ± 0.000	1	0.11 ± 0.05	-0.04 ± 0.08	42	... ± ...	...	S	1
31	Euphrosyne	901	0.059 ± 0.013	742	0.082 ± 0.173	5	-0.08 ± 0.05	0.04 ± 0.06	169	-4.687 ± 0.082	7.3–18.4	Cb	1
44	Nysa (Polana)	405	0.289 ± 0.074	1345	0.356 ± 0.059	22	0.13 ± 0.06	-0.03 ± 0.07	1544	-3.083 ± 0.030	2.5–13.0	...	0
46	Hestia	503	0.267 ± 0.049	28	0.068 ± 0.000	1	0.14 ± 0.04	-0.03 ± 0.04	22	... ± ...	...	Xc	1
81	Terpsichore	622	0.050 ± 0.010	57	0.053 ± 0.000	1	-0.08 ± 0.03	0.08 ± 0.10	15	-4.371 ± 0.508	5.0–7.3	Cb	1
84	Klio	413	0.059 ± 0.014	107	0.089 ± 0.031	3	-0.06 ± 0.04	0.05 ± 0.08	23	-2.478 ± 0.129	3.3–8.0	Ch	1
87	Sylvia	603	0.051 ± 0.012	121	0.082 ± 0.000	1	-0.07 ± 0.05	0.09 ± 0.11	20	-3.339 ± 0.232	7.0–12.4	X	1
89	Julia	540	0.225 ± 0.036	2	0.339 ± 0.000	2	0.05 ± 0.02	0.12 ± 0.07	3	... ± ...	...	Ld	1
96	Aegle	630	0.072 ± 0.013	83	0.102 ± 0.000	1	0.02 ± 0.05	0.10 ± 0.08	23	-3.252 ± 0.305	6.8–11.4	T	1
128	Nemesis	504	0.072 ± 0.019	347	0.071 ± 0.000	1	-0.08 ± 0.06	0.03 ± 0.07	109	-4.320 ± 0.121	3.8–8.4	C	2
137	Meliboea	604	0.060 ± 0.013	163	0.050 ± 0.029	12	-0.10 ± 0.08	0.05 ± 0.07	53	-1.513 ± 0.051	8.0–39.4	Ch	11
142	Polana (Nysa)	n/a	0.056 ± 0.012	1130	0.061 ± 0.006	3	-0.12 ± 0.10	0.00 ± 0.08	375	-3.177 ± 0.041	3.6–12.4	B	3
144	Vibilia	529	0.065 ± 0.011	180	... ± ...	0	-0.10 ± 0.04	0.04 ± 0.07	35	-3.137 ± 0.135	4.5–9.7	Ch	1
145	Adeona	505	0.060 ± 0.011	874	0.068 ± 0.078	19	-0.11 ± 0.08	0.04 ± 0.07	274	-2.854 ± 0.037	5.3–23.2	Ch	12
148	Gallia	802	0.251 ± 0.059	24	... ± ...	0	0.10 ± 0.03	-0.06 ± 0.06	15	... ± ...	...	Sl	1
158	Koronis	605	0.238 ± 0.051	1089	0.325 ± 0.059	67	0.09 ± 0.07	-0.02 ± 0.08	810	-2.451 ± 0.026	5.1–32.0	S	34
163	Erigone	406	0.051 ± 0.010	716	0.061 ± 0.013	17	-0.08 ± 0.10	0.05 ± 0.08	201	-3.215 ± 0.050	3.3–11.9	Ch	1
170	Maria	506	0.255 ± 0.061	1361	0.370 ± 0.068	69	0.12 ± 0.05	-0.02 ± 0.07	809	-2.637 ± 0.025	3.5–24.8	S	23
173	Ino	522	0.244 ± 0.069	90	... ± ...	0	0.09 ± 0.05	-0.06 ± 0.07	93	-3.141 ± 0.268	2.7–4.6	...	0
221	Eos	606	0.163 ± 0.035	3509	0.180 ± 0.053	205	0.05 ± 0.05	0.03 ± 0.07	1692	-2.222 ± 0.013	5.6–47.3	K	30
283	Emma	607	0.047 ± 0.011	260	0.118 ± 0.113	2	-0.07 ± 0.06	0.04 ± 0.08	75	-3.442 ± 0.113	6.7–15.3	C	1
293	Brasilia	608	0.174 ± 0.048	110	0.224 ± 0.017	4	-0.04 ± 0.04	0.05 ± 0.07	78	-3.462 ± 0.243	3.7–6.4	X	2
298	Baptistina	403	0.179 ± 0.056	581	0.390 ± 0.198	25	0.01 ± 0.09	-0.02 ± 0.09	321	-3.254 ± 0.063	2.5–7.2	S	9
302	Clarissa	407	0.048 ± 0.010	44	... ± ...	0	-0.14 ± 0.04	0.00 ± 0.06	10	... ± ...	...	F	1
313	Chaldaea	415	0.063 ± 0.017	169	0.083 ± 0.039	11	-0.10 ± 0.05	0.06 ± 0.07	34	-3.058 ± 0.119	3.7–8.6	C	3
322	Phaeo	530	0.059 ± 0.015	99	0.181 ± 0.000	2	0.00 ± 0.06	0.05 ± 0.08	34	-2.852 ± 0.195	5.1–10.1	D	1
329	Svea	416	0.050 ± 0.009	30	0.134 ± 0.166	2	-0.04 ± 0.06	0.04 ± 0.05	8	... ± ...	...	C	1
363	Padua	507	0.069 ± 0.015	427	0.067 ± 0.022	5	-0.04 ± 0.06	0.05 ± 0.07	135	-2.588 ± 0.053	4.5–16.4	X	10
369	Aeria	539	0.180 ± 0.011	22	0.266 ± 0.000	6	-0.05 ± 0.04	0.03 ± 0.09	18	... ± ...	...	M	1
375	Ursula	631	0.061 ± 0.014	600	0.083 ± 0.047	15	-0.05 ± 0.08	0.06 ± 0.09	194	-2.677 ± 0.046	7.3–27.2	...	0
396	Aeolia	508	0.107 ± 0.022	43	0.115 ± 0.000	1	-0.04 ± 0.05	0.04 ± 0.03	10	... ± ...	...	Xe	1
410	Chloris	509	0.084 ± 0.031	171	0.081 ± 0.095	10	-0.05 ± 0.08	0.06 ± 0.05	59	-2.814 ± 0.103	5.2–14.0	C	8
434	Hungaria	003	0.456 ± 0.217	527	0.727 ± 1.692	9	-0.01 ± 0.08	0.04 ± 0.10	636	... ± ...	...	Xe	14
480	Hansa	803	0.269 ± 0.067	316	0.377 ± 0.068	9	0.10 ± 0.05	-0.06 ± 0.07	134	-3.378 ± 0.104	3.4–7.9	S	2
490	Veritas	609	0.066 ± 0.016	697	0.068 ± 0.011	3	-0.07 ± 0.04	0.05 ± 0.08	207	-2.744 ± 0.043	5.8–22.6	Ch	8
495	Eulalia (Polana)	n/a	0.057 ± 0.012	2008	0.066 ± 0.029	15	-0.12 ± 0.05	0.01 ± 0.07	531	-2.687 ± 0.021	3.0–18.4	C	13
569	Misa	510	0.052 ± 0.013	287	0.064 ± 0.027	3	-0.07 ± 0.07	0.03 ± 0.08	79	-2.508 ± 0.067	4.0–13.3	Ch	1
589	Croatia	638	0.054 ± 0.010	99	0.068 ± 0.000	1	-0.05 ± 0.04	0.02 ± 0.09	22	-3.383 ± 0.224	5.8–11.1	X	1
606	Brangane	511	0.112 ± 0.028	44	0.137 ± 0.000	2	0.07 ± 0.04	0.09 ± 0.06	20	... ± ...	...	L	1
618	Elfriede	632	0.052 ± 0.012	36	0.063 ± 0.000	1	-0.09 ± 0.05	0.06 ± 0.05	8	... ± ...	...	C	1
623	Chimaera	414	0.054 ± 0.012	63	0.049 ± 0.000	3	-0.05 ± 0.03	0.09 ± 0.10	20	-2.586 ± 0.235	3.8–7.2	XC	1
627	Charis	616	0.071 ± 0.010	39	0.264 ± 0.000	2	0.16 ± 0.06	0.04 ± 0.08	59	... ± ...	...	X	1
656	Beagle	620	0.080 ± 0.014	30	0.070 ± 0.006	5	-0.12 ± 0.03	0.01 ± 0.06	16	... ± ...	...	X	1
668	Dora	512	0.056 ± 0.012	667	0.047 ± 0.017	17	-0.12 ± 0.07	0.04 ± 0.07	175	-2.610 ± 0.043	5.7–21.6	Ch	29
686	Gersuind	804	0.145 ± 0.037	106	0.328 ± 0.000	1	0.09 ± 0.07	0.08 ± 0.07	36	-2.653 ± 0.158	3.8–8.0	...	0
702	Alauda	902	0.066 ± 0.015	687	0.071 ± 0.013	26	-0.10 ± 0.06	0.03 ± 0.07	197	-2.707 ± 0.042	9.2–36.7	...	0
709	Fringilla	623	0.050 ± 0.014	51	0.212 ± 0.788	2	-0.03 ± 0.06	0.09 ± 0.08	24	... ± ...	...	X	1
729	Watsonia	537	0.134 ± 0.019	51	0.181 ± 0.000	2	0.08 ± 0.04	0.07 ± 0.02	12	... ± ...	...	L	2
752	Sulamitis	408	0.055 ± 0.011	134	0.048 ± 0.000	1	-0.07 ± 0.07	0.06 ± 0.11	33	-2.417 ± 0.126	3.8–8.8	Ch	1
778	Theobalda	617	0.062 ± 0.016	107	0.070 ± 0.000	1	-0.16 ± 0.03	0.00 ± 0.05	28	-3.097 ± 0.185	6.5–13.3	...	0
780	Armenia	905	0.056 ± 0.013	28	0.060 ± 0.000	2	-0.05 ± 0.01	0.03 ± 0.04	4	... ± ...	...	C	1
808	Merxia	513	0.234 ± 0.054	93	0.347 ± 0.030	3	0.08 ± 0.05	-0.08 ± 0.08	98	-2.662 ± 0.190	3.2–6.7	S	6
832	Karin	610	0.178 ± 0.031	18	0.294 ± 0.000	1	0.03 ± 0.05	-0.01 ± 0.07	33	... ± ...	...	S	47
845	Naema	611	0.064 ± 0.012	155	0.055 ± 0.000	1	-0.10 ± 0.11	0.04 ± 0.06	45	-4.274 ± 0.220	6.0–10.6	C	1
847	Agnia	514	0.238 ± 0.060	110	0.389 ± 0.015	3	0.04 ± 0.05	-0.07 ± 0.08	179	-3.055 ± 0.165	3.8–8.0	S	8
909	Ulla	903	0.048 ± 0.009	19	... ± ...	0	-0.07 ± 0.02	0.02 ± 0.06	3	... ± ...	...	X	1
918	Itha	633	0.239 ± 0.056	28	0.353 ± 0.084	8	0.14 ± 0.04	-0.01 ± 0.05	14	... ± ...	...	Sl	4
945	Barcelona	805	0.290 ± 0.064	52	0.510 ± 0.000	1	0.09 ± 0.05	-0.11 ± 0.09	21	... ± ...	...	Sq	1
1128	Astrid	515	0.045 ± 0.010	213	0.046 ± 0.000	1	-0.07 ± 0.05	0.08 ± 0.08	33	-2.567 ± 0.080	3.5–11.1	C	5
1189	Terentia	618	0.064 ± 0.012	13	0.058 ± 0.000	1	-0.01 ± 0.00	0.09 ± 0.00	1	... ± ...	...	Ch	1
1222	Tina	806	0.128 ± 0.042	26	0.137 ± 0.000	1	0.01 ± 0.00	0.03 ± 0.05	3	... ± ...	...	X	1
1270	Datura	411	0.288 ± 0.000	1	... ± ...	0	0.01 ± 0.00	-0.10 ± 0.00	1	...			

TABLE 1. (continued)

Number	Name	PDS ID	$\langle p_V \rangle$	$n_{p_V}$	$\langle p_{\text{NIR}} \rangle$	$n_{p_{\text{NIR}}}$	$\langle a^* \rangle$	$\langle i-z \rangle$	$n_{\text{SDSS}}$	SFD Slope	SFD Range (km)	Tax	$n_{\text{tax}}$
1272	Gefion	516	0.267 ± 0.058	737	0.350 ± 0.154	25	0.10 ± 0.06	-0.02 ± 0.07	523	-3.262 ± 0.050	4.0–14.3	S	32
1303	Luthera	904	0.050 ± 0.009	125	0.078 ± 0.000	1	0.01 ± 0.04	0.10 ± 0.07	39	-3.955 ± 0.264	7.9–13.0	...	0
1332	Marconia	636	0.042 ± 0.008	6	0.080 ± 0.000	1	... ± ...	... ± ...	0	... ± ...	...	L	1
1400	Tirela	612	0.239 ± 0.057	419	0.073 ± 0.095	7	0.15 ± 0.09	0.08 ± 0.08	225	-3.454 ± 0.073	4.8–14.3	Ld	10
1484	Postrema	541	0.047 ± 0.010	30	0.051 ± 0.006	3	-0.05 ± 0.05	0.02 ± 0.06	5	... ± ...	...	B	1
1658	Innes	518	0.259 ± 0.057	195	0.318 ± 0.149	8	0.09 ± 0.06	-0.04 ± 0.07	163	-3.385 ± 0.128	3.1–7.0	S	2
1668	Hanna	533	0.052 ± 0.011	102	0.048 ± 0.000	1	-0.09 ± 0.03	0.08 ± 0.05	20	-3.502 ± 0.240	3.9–7.2	...	0
1726	Hoffmeister	519	0.047 ± 0.010	609	0.052 ± 0.013	4	-0.10 ± 0.05	0.03 ± 0.08	145	-2.856 ± 0.047	4.5–17.2	C	9
1892	Lucienne	409	0.228 ± 0.029	19	... ± ...	0	0.09 ± 0.03	0.00 ± 0.09	10	... ± ...	...	S	1
2085	Henan	542	0.227 ± 0.065	106	0.165 ± 0.000	3	0.11 ± 0.06	-0.02 ± 0.09	163	-3.667 ± 0.276	3.4–5.8	L	1
2262	Mitidika	531	0.066 ± 0.014	279	0.060 ± 0.013	10	-0.11 ± 0.06	0.01 ± 0.08	71	-2.832 ± 0.091	4.6–11.4	...	0
2344	Xizang	536	0.134 ± 0.044	18	... ± ...	0	0.04 ± 0.05	0.08 ± 0.07	12	... ± ...	...	...	0
2384	Schulhof	525	0.280 ± 0.000	1	0.289 ± 0.000	4	0.08 ± 0.07	-0.05 ± 0.03	2	... ± ...	...	...	0
2732	Witt	535	0.261 ± 0.053	124	0.347 ± 0.018	3	0.15 ± 0.07	0.01 ± 0.08	190	-3.114 ± 0.173	3.8–7.7	...	0
2782	Leonidas	528	0.068 ± 0.013	67	... ± ...	0	-0.10 ± 0.07	0.04 ± 0.07	22	-2.142 ± 0.245	5.1–9.4	...	0
3152	Jones	538	0.054 ± 0.004	14	0.061 ± 0.000	1	-0.02 ± 0.00	0.04 ± 0.01	2	... ± ...	...	T	1
3438	Inarrados	634	0.067 ± 0.015	24	0.069 ± 0.000	1	-0.10 ± 0.03	0.05 ± 0.05	11	... ± ...	...	...	0
3556	Lixiaohua	613	0.044 ± 0.009	367	0.053 ± 0.011	3	-0.06 ± 0.05	0.04 ± 0.09	95	-3.499 ± 0.098	6.8–15.7	...	0
3811	Karma	534	0.054 ± 0.010	78	... ± ...	0	-0.06 ± 0.08	0.03 ± 0.07	20	-2.659 ± 0.241	3.7–6.7	...	0
3815	Konig	517	0.049 ± 0.011	135	... ± ...	0	-0.08 ± 0.02	0.06 ± 0.06	25	-3.032 ± 0.150	4.1–9.2	...	0
4203	Brucato	807	0.064 ± 0.017	233	0.041 ± 0.009	2	-0.11 ± 0.05	0.05 ± 0.07	45	-3.604 ± 0.109	5.3–13.3	...	0
4652	Iannini	520	0.309 ± 0.033	18	... ± ...	0	0.01 ± 0.04	-0.08 ± 0.06	21	... ± ...	...	...	0
5438	Lorre	527	0.054 ± 0.002	2	... ± ...	0	... ± ...	... ± ...	0	... ± ...	...	C	1
5567	Durisen	624	0.043 ± 0.010	16	0.050 ± 0.000	1	-0.02 ± 0.03	0.11 ± 0.05	4	... ± ...	...	...	0
5614	Yakovlev	625	0.046 ± 0.008	25	... ± ...	0	-0.08 ± 0.00	0.07 ± 0.01	2	... ± ...	...	...	0
7353	Kazuia	532	0.214 ± 0.025	13	... ± ...	0	0.06 ± 0.08	-0.03 ± 0.02	3	... ± ...	...	L	1
7468	Anfimov	635	0.166 ± 0.061	10	... ± ...	0	0.23 ± 0.03	-0.14 ± 0.09	13	... ± ...	...	...	0
7481	SanMarcello	626	0.194 ± 0.054	27	... ± ...	0	-0.05 ± 0.04	0.04 ± 0.06	18	... ± ...	...	...	0
9506	Telramund	614	0.237 ± 0.063	46	... ± ...	0	0.09 ± 0.05	-0.02 ± 0.09	33	... ± ...	...	...	0
10811	Lau	619	0.274 ± 0.000	1	... ± ...	0	0.26 ± 0.00	-0.18 ± 0.00	1	... ± ...	...	...	0
14627	Emilkowalski	523	0.149 ± 0.046	4	... ± ...	0	0.06 ± 0.00	0.11 ± 0.00	1	... ± ...	...	...	0
15454	1998 YB <sub>3</sub>	627	0.054 ± 0.006	11	... ± ...	0	-0.11 ± 0.03	0.04 ± 0.03	7	... ± ...	...	...	0
15477	1999 CG <sub>1</sub>	628	0.095 ± 0.030	68	... ± ...	0	0.04 ± 0.04	0.05 ± 0.06	25	-4.768 ± 0.602	4.3–6.0	...	0
16598	1992 YC <sub>2</sub>	524	... ± ...	0	... ± ...	0	0.10 ± 0.00	-0.09 ± 0.00	1	... ± ...	...	Sq	1
18405	1993 FY <sub>12</sub>	615	0.173 ± 0.049	15	... ± ...	0	-0.04 ± 0.03	0.07 ± 0.08	12	... ± ...	...	...	0
36256	1999 XT <sub>17</sub>	629	0.203 ± 0.066	13	... ± ...	0	0.21 ± 0.07	-0.04 ± 0.05	6	... ± ...	...	...	0
53546	2000 BY <sub>6</sub>	526	0.139 ± 0.000	1	... ± ...	0	0.04 ± 0.03	0.06 ± 0.04	9	... ± ...	...	...	0
106302	2000 UJ <sub>87</sub>	637	0.045 ± 0.004	12	... ± ...	0	-0.10 ± 0.04	0.05 ± 0.04	3	... ± ...	...	...	0

Although we implicitly assume that the variation in observed properties is a result of statistical uncertainties and that all family members should have the same physical properties, this is not necessarily true. Outlier objects may be statistical flukes, or background contamination, but they may just as easily be interesting pieces of the parent body warranting further study, a determination that cannot be made or captured here. Additionally, a single mean value ignores any size-dependent effects in the data, either real or imposed by detection or sample-selection biases.

Only a proper debiasing of each survey accounting for observing geometry, detector sensitivity, and detection efficiency can determine the true value for each parameter. This is particularly important for cases of mismatched sensitivities, such as the SDSS r vs. z magnitudes needed for colors or the NEOWISE W3 flux vs. groundbased H<sub>V</sub> magnitude needed for albedo determination; only objects seen in both datasets will have a measured value that strongly biases the outcome as a function of apparent brightness. Thus Table 1 is meant as a overarching guide, but caution is mandated for any interpretation of values or trends.

A number of low-albedo families can only be identified when the low-albedo population of the main belt is considered independently. This is due to the bias toward discovery of high-albedo objects by groundbased visible-light surveys. As the population of high-albedo asteroids is probed to smaller sizes (and thus larger numbers), these families will overwhelm traditional HCM techniques, particularly the calculation of the quasi-random level needed to assess the reality of a given family, making low-albedo families harder to identify. *Masiero et al.* (2013) circumvented this by considering each albedo component separately, and by restricting their sample to objects detected in the thermal infrared, which is albedo-independent (see the chapter by Mainzer et al. in this volume for further discussion). As the sample of known asteroids continues to increase, development of new techniques for the identification of asteroid families from the background population (e.g., *Milani et al.*, 2014) will increase in importance.

Below we discuss individual families that merit specific mention based on recent research. We include the Planetary Data System (PDS) ID number from *Nesvorný et al.* (2012)

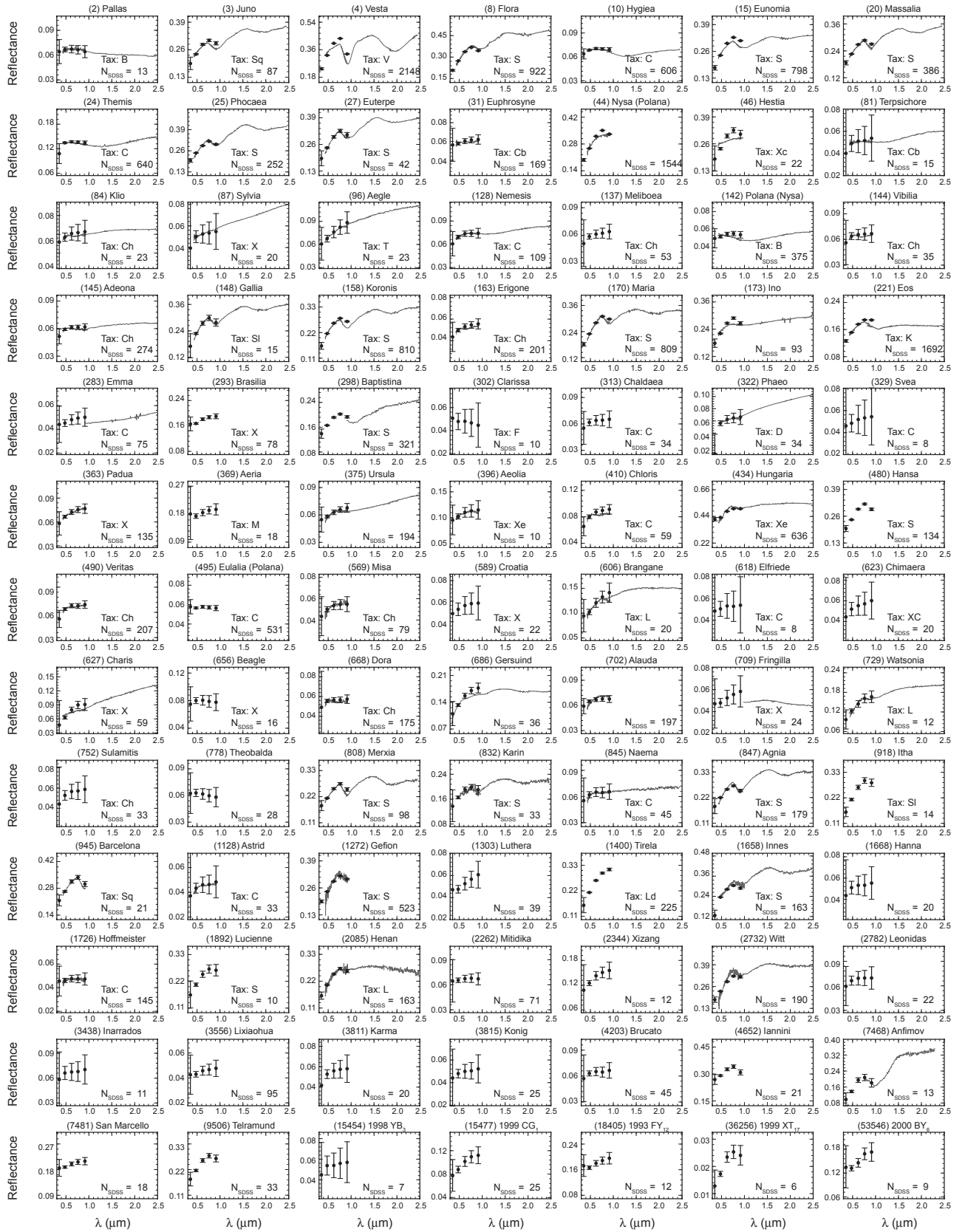


**Fig. 1.** Average solar-corrected SDSS colors (points) and sample optical/NIR spectra (from SMASS) for all asteroid families listed in Table 1 with sufficient data. Plots are scaled such that the interpolated reflectance at 0.55 μm equals the average visible geometric albedo ( $p_V$ ) for the family from all infrared surveys. The “N” in the bottom right of each plot indicates the number of SDSS observations used, and taxonomic class is given when available. Note the reflectance scale in each plot is different.

both below and in Table 1 for easier association with other work and with the family dynamical properties given in the chapter by Nesvorný et al. in this volume.

**3.2.1. Hungaria.** The Hungaria asteroid family (PDS ID 003) occupies a region of space interior to the rest of the main belt and with an orbital inclination above the  $v_6$  secular resonance. This region is an island of stability between the major resonances that dominate this area of the solar system, and likely samples a unique region of the protoplanetary disk (Bottke et al., 2012). Warner et al. (2009) analyzed light curves of 129 Hungaria asteroids, finding a significant excess of very slow rotating bodies. They also showed that the binary fraction of this population is  $\sim 15\%$ , comparable to the fraction seen in the NEO population.

The albedos for Hungaria family members derived from the NEOWISE data by Masiero et al. (2011) have values significantly larger than  $p_V > 0.5$ ; however, this is an artifact of bad absolute magnitude fits for these objects in orbital element databases, which when corrected bring the best-fit albedo values to the range of  $0.4 < p_V < 0.5$  (B. Warner, personal communication). Spectroscopic and SDSS color studies of the Hungaria family show the classification to be X-type, which when combined with the very high albedos translates to an E-type classification (Carvano et al., 2001; Assandri and Gil-Hutton, 2008; Warner et al., 2009). Polarimetric observations by Gil-Hutton et al. (2007) of the overall Hungaria region indicate inconsistencies in the polarimetric behavior of asteroids in and around the Hungaria family.

**3.2.2. Flora.** The Flora family (PDS ID 401) is a large S-type family residing in the inner main belt. The largest remnant, (8) Flora, has an orbit just exterior to the  $v_6$  resonance, and only the half of the family at larger semimajor axes is seen today. The  $v_6$  resonance is particularly good at implanting asteroids into the NEO population (Bottke et al., 2000), meaning that Flora family members are likely well represented in the NEO population and meteorite collections. Recent spectroscopic observations of Flora family members have been combined with analyses of meteorite samples to link the LL chondrite meteorites to the Flora family (Vernazza et al., 2008; de Leon et al., 2010; Dunn et al., 2013). This provides an important ground-truth analog for interpreting physical properties of S-type objects in the main belt and near-Earth populations. We note that in contrast to previous analyses, Milani et al. (2014) did not identify a family associated with Flora, instead finding that candidate member asteroids merged with the Vesta and Massalia families, or are potentially part of their newly identified Levin family. However, the Vesta family has a distinct i-z color that is not shown by Flora family members (see Table 1), making these populations easily distinguished by their photometric properties. While the Flora and Massalia populations overall have properties that are consistent within uncertainties, the difference between the mean albedos of these two populations suggests they in fact are different populations.

**3.2.3. Baptistina.** Over the past decade, the Baptistina family (PDS ID 403) has been the focus of a number of investigations, leading to controversy over the physical char-

acteristics of these asteroids. Initial investigations assumed the family had characteristics similar to C-type asteroids (e.g., low albedo) based on spectra of the largest member, (298) Baptistina (Bottke et al., 2007). This was used in numerical simulations to show that Baptistina was a probable source of the K/T impactor. Further spectral investigations of a 16 large family members found compositions more analogous to LL chondrites, ruling out a C-type association (Reddy et al., 2011). However, a major difficulty in studying this family is the significant overlap in orbital element-space with the much larger Flora family [or with the Levin family, according to Milani et al. (2014)], making it difficult to ensure that the spectral studies were probing Baptistina and not Flora. Using albedos to separate these families finds a mean albedo of  $p_V = 0.16$ , which is not consistent with either C-type or LL-chondrite compositions (Masiero et al., 2013). Recent analysis of the Chelyabinsk meteorite samples showed that shock darkening of chondritic material could produce an albedo consistent with the Baptistina family without altering the composition (Reddy et al., 2014), offering a potential solution to the seemingly contradictory information about this family, but future work will be necessary to confirm this hypothesis.

**3.2.4. "Nysa-Polana."** In the years leading up to *Asteroids III* it had become increasingly clear that Nysa-Polana, interpreted as a single entity, was likely to be a short-lived phenomenon. Cellino et al. (2001) presented a spectroscopic study of 22 asteroids associated with the group, and found that the group was best understood as two compositionally distinct families partly overlapping in orbital-element space, one associated with the F class in the Tholen taxonomy and one with the S class, while (44) Nysa was compositionally distinct and potentially not associated with either family.

Masiero et al. (2011) showed that the albedo distribution of the  $\sim 3000$  asteroids identified as part of the Nysa-Polana complex were strongly bimodal, unlike the majority of families. Although overlapping in semimajor axis-inclination space, the high- and low-albedo components occupy distinct regions of semimajor axis-eccentricity space, supporting the theory that they are two distinct populations coincidentally overlapping as opposed to a single parent body that was composed of two distinct mineralogies.

Using albedo as a discriminant, Masiero et al. (2013) were able to uniquely identify two separate families, a low-albedo one associated with (142) Polana, and a high-albedo one associated with (135) Hertha (PDS ID 405), while (44) Nysa no longer linked to either family. In Table 1 we continue to refer to the high-albedo family as "Nysa" despite the evidence to the contrary, for consistency with other literature. Walsh et al. (2013) expanded on this, and used the family albedos to reject objects with S-type physical properties and focus on the low-albedo component of the Nysa-Polana group. Using dynamical constraints, they were able to further subdivide the low-albedo component of this group into two distinct families, which they identify as the Eulalia family and the "new Polana" family. They estimate ages for each of these families of 0.9–1.5 b.y. and  $> 2$  b.y.,

respectively. Conversely, *Milani et al.* (2014) identify the whole complex as associated with Hertha and split this region into two components by combining dynamics and physical properties, which they identify as the Polana and Burdett families (low and high albedo, respectively).

**3.2.5. Vesta.** The Vesta asteroid family (PDS ID 401) has historically been one of the most well-studied families, due to its clear association with one of the largest known asteroids, the high albedos and locations in the inner main belt making members favorable for groundbased observations, and association with the howardite-eucrite-diogenite (HED) meteorites leading to the interpretation of (4) Vesta as a differentiated parent body (*McCord et al.*, 1970; *Zappala et al.*, 1990; *Binzel and Xu*, 1993; *Consolmagno and Drake*, 1977; *Moskovitz et al.*, 2010; *Mayne et al.*, 2011). With the recent visit of the Dawn spacecraft to (4) Vesta (see the chapter by Russell et al. in this volume), ground-truth data can be compared to remote-sensing observations of family members. Additionally, constraints on the ages of the major impact basins of  $1.0 \pm 0.2$  b.y. for Rheasilvia and  $2.1 \pm 0.2$  b.y. years for Veneneia (*Schenk et al.*, 2012) set strong constraints on the possible age of Vesta family members. *Milani et al.* (2014) find that the Vesta family splits into two subgroups in their analysis, which they attribute to these two events.

The Vesta family has a unique mineralogical composition in the main belt, making it easily distinguishable in color-, albedo-, or spectral-space. In particular, members stand out from all other asteroids in terms of their high albedo, low i-z color, and deep 1- $\mu\text{m}$  and 2- $\mu\text{m}$  absorption bands. This has prompted searches for objects with similar properties at more distant locations in the main belt (e.g., *Moskovitz et al.*, 2008; *Duffard and Roig*, 2009; *Moskovitz et al.*, 2010; *Solontoi et al.*, 2012). These bodies could only have evolved from the Vesta family via a low-probability series of secular resonances (*Carruba et al.*, 2005; *Roig et al.*, 2008a), and may be indicative of other parent bodies that were differentiated. To date only a few candidate objects from these searches have been confirmed to be V-type, indicating that the collisional remnants of the other differentiated objects that must have formed in the early solar system has likely been dynamically erased.

**3.2.6. Eunomia.** The Eunomia family (PDS ID 502) is an old, S-type family located in the middle main belt. Spectral evidence presented by *Lazzaro et al.* (1999) indicates that the Eunomia family may have originated from a partially differentiated parent body. *Natheus et al.* (2005) and *Nathues* (2010) investigated the physical properties of the Eunomia largest remnant and 97 smaller family members as a probe of the composition and differentiation history of the original parent body. They found that the largest remnant shows two hemispheres with slightly different compositions that support an interpretation of the impact causing significant crust loss and some mantle loss on a partially differentiated core. *Milani et al.* (2014) found two subfamilies within Eunomia, which they attribute to separate cratering events.

**3.2.7. Eos.** The Eos family (PDS ID 606) represents the primary reservoir of K-type asteroids in the main belt,

and can easily be identified by their 3.4- $\mu\text{m}$  albedo (*Masiero et al.*, 2014). This spectral class has been proposed as the asteroidal analog of the CO and CV carbonaceous chondrite meteorites (*Bell et al.*, 1988; *Doressoundiram et al.*, 1998; *Clark et al.*, 2009). This would imply that the Eos family is one of the best-sampled collisional families in our meteorite collection, and would mean that many of these samples do not probe the C-complex asteroids as had frequently been assumed.

*Mothé-Diniz and Carvano* (2005) compared spectra of (221) Eos with meteorite samples and inferred that the Eos parent body likely underwent partial differentiation. *Mothé-Diniz et al.* (2008) extended this work to 30 Eos family members and found mineral compositions consistent with forsteritic olivine consistent with a history of differentiation or a composition similar to CK-type meteorites. However, *Masiero et al.* (2014) instead interpret the surface properties as consistent with shock darkening of silicates (cf. *Britt and Pieters*, 1994, *Reddy et al.*, 2014). Future work will enable us to resolve the ambiguity in the composition of these objects. The Eos family represents one of the key fronts of advancing our understanding of family formation that has been opened by our wealth of new data.

**3.2.8. Themis.** The Themis family (PDS ID 602) is one of the largest low-albedo families in the main belt. The majority of Themis family members are classified as C-complex bodies (*Mothé-Diniz et al.*, 2005; *Ziffer et al.*, 2011). Spectral surveys have found variations in the spectral slope among Themis members, ranging from neutral to moderately red (*Ziffer et al.*, 2011; *de Leon et al.*, 2012). As the first asteroid discovered to show cometary activity (133P Elst-Pizarro) is dynamically associated with Themis, *Hsieh and Jewitt* (2006) searched 150 other Themis family members for signs of cometary activity, discovering one additional object: (118401) 1999 RE<sub>70</sub>. The periodic nature of this activity points to volatile sublimation as the probable cause, as opposed to collisions or YORP spinup (see the chapter by Jewitt et al. in this volume), meaning that the Themis family members, and (24) Themis itself, likely harbor subsurface ice. Further, *Rivkin and Emery* (2010) and *Campins et al.* (2010) reported evidence of water ice features on the surface of (24) Themis. If this icy material was primordial to the Themis parent and not implanted by a later impact, this would set constraints on where the Themis parent formed relative to the “snow line” in the protosolar nebula. These objects are also likely to be a new reservoir of water, and may have contributed to the volatile content of the early Earth.

**3.2.9. Sylvia.** The Sylvia family (PDS ID 603) in the Cybele region resides at the outer edge of the main belt [ $3.27 < a \leq 3.70$  AU (*Zellner et al.*, 1985b)], beyond the 2:1 Jupiter mean-motion resonance. These asteroids, along with the objects in the Hilda and Jupiter Trojan populations, likely have limited contamination by materials from the inner solar system, and represent a pristine view of the materials present near Jupiter at the end of planetary migration. The Nice model proposed that these asteroids are transneptunian

objects (TNOs) that were scattered inward during the chaotic phase of planetary evolution (Levison *et al.*, 2009); however, the Cybeles show different spectral characteristics from the Hildas and Trojans, and thus may represent the material native to this region of the solar system.

Kasuga *et al.* (2012) studied the size- and albedo-distributions of the Sylvia asteroid family to better understand the history of these bodies. They found that the largest Cybeles ( $D > 80$  km) are predominantly C- or P-types, and the best-fit power law to the size distribution is consistent with a catastrophic collision. However, the estimated mass and size of the parent body lead to collisional timescales larger than the age of the solar system, assuming an equilibrium collisional cascade. These are comparable to the timescales for the Hildas, although they find that the Trojan population is consistent with collisional origin. Numerical simulations of the collisional formation and dynamical evolution of the Cybeles will allow for a more detailed study of the history of this population.

### 3.3. Relationship Between Albedo and Color

Almost every major taxonomic class of asteroid is represented in the list of asteroid families. Using the physical property data described above, we can investigate relationships between the averaged physical properties for each family. By nature of the large sample sizes, the SDSS colors and optical albedos are the best-determined parameters for the majority of families. Figure 2 shows the composite  $a^*$  and  $i-z$  colors derived for each family from SDSS compared to the composite optical albedo as determined via thermal radiometry. There is a clear linear correlation between the SDSS  $a^*$  color and the log of the albedo, although with significant scatter. The  $i-z$  color is approximately flat for low and moderate albedos, but decreases noticeably for high-albedo families. It is important to again note that these data are subject to

observational selection and completeness biases, and so these relations should be interpreted with caution.

## 4. DISCUSSION

### 4.1. Correlation of Observed Properties with the Primordial Composition of the Main Belt

When considering the distributions of colors and albedos, asteroid families fall into one of only a small number of groupings. The Hungaria, Vesta, and Eos families have unique properties that distinguish them from all other families. Similarly, the Watsonia family shows unique polarimetric properties. While the properties of these families can be used to efficiently identify family members and mineral analogs, it is more difficult to relate the mineralogy and history of these families to that of the currently observed main belt as a whole [although they may be good analogs for now-extinct populations (cf. Bottke *et al.*, 2012)].

Conversely, almost all other families fall into either the S-complex or the C-complex, both of which can be further subdivided by spectral taxonomic properties. Given the number of different parent bodies with these compositions, it has been inferred that these two complexes are probes of the pristine material from the protoplanetary disk in this region of the solar system. However, studies of the evolution of the giant planets in the early solar system call into question the specific locations from which these bodies originated (e.g., Gomes *et al.*, 2005). One possible scenario, known as the “Grand Tack” (Walsh *et al.*, 2012), postulates that the protoplanetary core of Jupiter migrated through the planetesimal disk, evacuating the main-belt region of its primordial material and repopulating it with material from both inward and outward in the disk (see the chapter by Morbidelli *et al.* in this volume). In this case, the two different compositional complexes would represent these implanted objects. Further

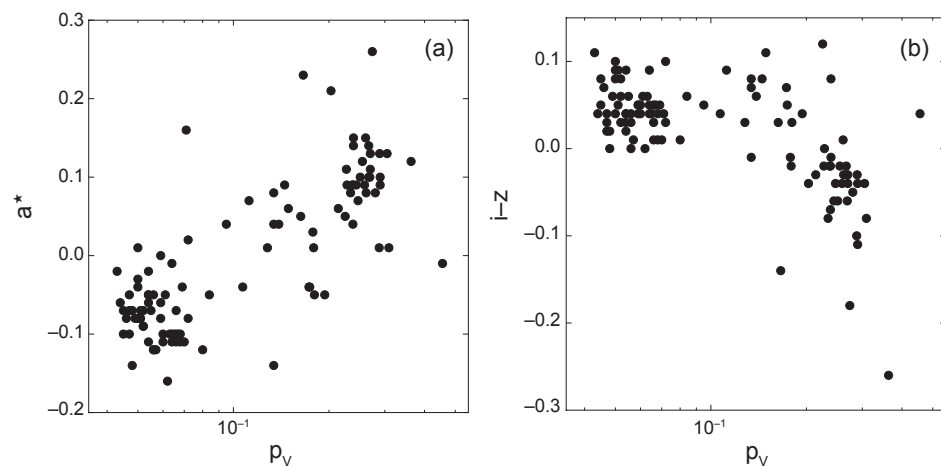


**Fig. 2.** Average SDSS  $a^*$  and  $i-z$  colors compared with optical albedos (logarithmically scaled) for asteroid families, as given in Table 1.

study of the physical properties of asteroid families and the other small-body populations of the solar system will allow us to test this theory.

#### 4.2. Properties of Observed Families Contrasted with the Background Population

Using computed  $a^*$  colors from the SDSS MOC 4, *Parker et al.* (2008) divided asteroid families into blue and red groups, tracing the C and S taxonomic complexes, respectively. For both groups, they found that family membership as a fraction of total population increased with decreasing brightness from  $\sim 20\%$  at  $H_V = 9$  to  $\sim 50\%$  at  $H_V = 11$ . For objects with absolute magnitudes of  $H > 11$  the fractions of blue and red asteroids in families diverge, with blue objects in families making up a smaller fraction of the total population while red objects stay at the levels seen at brighter magnitudes; however, it is unclear what contribution the survey biases have to these observed differences. If this difference in behavior is indeed a physical effect, it may indicate a difference in internal structure or collisional processing rates between the two populations.

When exploring the taxonomic distribution of asteroids as a function of distance from the Sun, families have been problematic because the large number of homogeneous objects concentrated in small regions of orbital-element space can skew the results. Studies of the overall distributions of physical properties therefore typically use only the largest member of the family, removing the smaller members (e.g., *Mothé-Diniz et al.*, 2003). Alternatively, the distribution could be explored by volume or mass, in which case all family members may be included because their individual volumes or masses contribute to the whole (e.g., *DeMeo and Carry*, 2013).

A comprehensive study of the taxonomic contribution of families to the population of small asteroids has not yet been undertaken; however, disentangling families from the background is critical to correctly interpreting an overall picture of the compositional makeup of the asteroid belt and how the asteroid belt and the bodies within it formed. Distinguishing between families and the background becomes increasingly difficult at smaller sizes where orbital parameters have evolved further due to gravitational and nongravitational forces. Even the background itself is likely composed of many small families forming from small parent bodies (*Morbidelli et al.*, 2003).

#### 4.3. Families as Feeders for the Near-Earth Object Population

The Yarkovsky and YORP nongravitational effects play a critical role in repopulating the NEOs with small bodies from the main belt (*Bottke et al.*, 2000). Primordial asteroids with diameters of  $\sim 100$  m should be efficiently mobilized from their formation locations into a gravitational resonance over the age of the solar system, limiting the contribution of these objects to the currently observed NEO population.

However, family-formation events act as an important source of objects in this size regime, injecting many thousands of small asteroids into the main belt with each impact (*Durda et al.*, 2007). The complete census of family physical properties, combined with better estimates for family ages that can now be made, enable us to trace the history of specific NEAs from their formation in the main belt to their present-day orbits. For the same reasons, recently fallen meteorites are also good candidates for comparisons to asteroid families, but the differences between the surface properties we can observe on asteroids and the atmosphere-selected materials surviving to the ground complicate this picture.

#### 4.4. Families Beyond the Main Belt

Although the vast majority of known asteroid families are in the main belt, massive collisions resulting in family-formation events are not unique to this region of the solar system. While the NEA population is dynamically young (*Gladman et al.*, 2000) and thus these objects have a low probability of undergoing collisional breakup, the more-distant reservoirs that date back to the beginning of the solar system are expected to undergo the same collisional processing as the main belt, albeit with lower impact velocities. Searches for young families in both the NEO and Mars Trojan populations have yielded only a single candidate family cluster associated with (5261) Eureka (*Schunová et al.*, 2012; *Christou*, 2013). Dynamical families have been identified in the Hilda, Jupiter Trojan, and TNO populations. The first two populations are trapped in long-term stable resonant orbits with Jupiter, providing a population that has suffered far less dispersion than the majority of main-belt families. Similarly, the TNO population is cross-cut by a range of Neptune resonances, some of which are similarly stable long term. The Yarkovsky and YORP effects are greatly diminished for all three populations compared to the main belt (especially the TNOs) due to the larger distances from the Sun, further reducing the dispersion of collisional fragments.

*Grav et al.* (2012) present visible and infrared albedos for the Hilda and Schubart asteroid families found in the 3:2 Jupiter mean-motion resonance. Using these albedos, they show the Hilda family is associated with D-type taxonomy, while the Schubart family is associated with C- or P-type taxonomy. The Hilda population in general is dominated by C- and P-type objects at the largest sizes, but transitions to primarily D-class at the smallest sizes measured, which may be indicative of the effect of the Hilda family on the overall population (*Grav et al.*, 2012; *DeMeo and Carry*, 2014). However, we note that recent family analysis by *Milani et al.* (2014) showed that the Hilda family was not statistically significant using their methodology, in contrast to previous work.

The Jupiter Trojans comprise the L4 and L5 Lagrange point swarms that lead and trail Jupiter (respectively) on its orbit. Multiple families have been identified in each of the swarms (*Milani*, 1993; *Beaugá and Roig*, 2001), but there is some debate as to the significance of these families

(cf. Brož and Rozehnal, 2011). Fornasier et al. (2007) combined measured spectra from multiple sources (Fornasier et al., 2004; Dotto et al., 2006) to characterize Trojan family members. In the L5 cloud, members of the Aneas, Anchises, Misenus, Phereclos, Sarpedon, and Panthoos families were found to have spectra with moderate-to-high spectral slopes, with most members being classified as D-type. The background population had a wider range of slopes and taxonomies from P- to D-type (Fornasier et al., 2004).

In the L4 cloud members of the Eurybates, 1986 WD and 1986 TS<sub>6</sub> families were studied. The 1986 WD and 1986 TS<sub>6</sub> family members had featureless spectra and high slopes resulting in a classification for most as D-types, while the few with lower slopes were placed in the C- and P-classes. Eurybates members, however, have markedly different spectra with low to moderate slopes splitting the classifications evenly between the C- or P-classes (Fornasier et al., 2007; De Luise et al., 2010). Roig et al. (2008b) used the SDSS data to investigate asteroid families in the Jupiter Trojan population, and found that the families in the Trojan populations account for the differences in the compositional distributions between the L4 and L5 clouds. In particular, the families in the L4 cloud show an abundance of C- and P-type objects not reflected in the L5 families or the background populations in either cloud.

The TNO population covers a much larger volume of space than any of the populations of objects closer to the Sun, but is also estimated to contain over  $1000\times$  the mass of the main belt. Collisions resulting in catastrophic disruptions are believed to have occurred at least twice in the TNO population. Pluto's five [or potentially more (Weaver et al., 2006)] satellites speak to a massive collision, which will be a key area of investigation of the New Horizons flyby of the Pluto system.

The dwarf planet Haumea is highly elongated with a very short rotational period ( $\sim 4$  h), is orbited by two small satellites, has a relatively high density, and has a spectrum that is consistent with nearly pure water ice. These properties are thought to be the result of a mantle-shattering collisional event, although the details of this event remain contentious. A group of TNOs with colors substantially bluer than the typical neutral-to-ultrared surfaces of the Kuiper belt, all sharing high inclinations similar to Haumea, has been identified as a collisional family produced by this event (Brown et al., 2007). Because of the orbital velocity regimes in transneptunian space, collisional families are in general unlikely to be identified there through dynamics alone (as they are in the asteroid belt). It was only through the unique composition of the family members (akin to the extremely distinct photometric properties of the Vesta family members) that the Haumea family could be readily identified. This implies that more collisional families may be hiding in the TNO population, but cannot be spotted by orbits alone.

Although massive collisions dominated the solar system environment during the epoch of planet building, they also played an important role in shaping all the major populations of small bodies during the subsequent  $\sim 4$  b.y. Collisional

evolution, although stochastic in nature, was a major determinant in the structure of the solar system we see today (see the chapter by Bottke et al. in this volume).

## 5. OPEN PROBLEMS AND FUTURE PROSPECTS

The effect of space weathering on asteroidal surfaces still remains an important topic for future exploration (see the chapter by Brunetto et al. in this volume for further discussion). The range of studies carried out so far have found a wide dispersion of results, both in terms of the timescale of weathering and the specific effects on various taxonomic classes. Studies to date have relied on the assumption that all asteroids with similar taxonomic types have identical mineralogical compositions, or have been based on a single pair of families known to be compositionally identical but with different ages (i.e., Karin and Koronis). As deeper surveys and dynamical analysis techniques begin to increase the number of identified cases of family-within-a-family, physical studies of these interesting populations will allow better measurements of the specific effects and timing of space-weathering processes.

Advances in physical measurements of asteroid families have not uniformly addressed the various parameters needed for a robust scientific investigation. In particular, there has been only a nominal advancement in the measurement of asteroid masses and densities, owing to the difficulty in determining these parameters. Carry (2012) compiled known measurements of asteroid densities into a comprehensive list; however, only a handful of families have more than one member represented, and for most the only measurement is of the largest remnant body. A larger survey of densities including many family members over a range of sizes would enable testing of family formation conditions via reaccretion (cf. the chapter by Michel et al. in this volume), as well as improve family ages derived from numerical simulations of gravitational and Yarkovsky orbital evolution (cf. the chapter by Nesvorný et al. in this volume). This could be accomplished by a more comprehensive search for binaries, or through modeling of gravitational perturbations to asteroid orbits detectable in next-generation astrometric catalogs.

One highly anticipated survey will be carried out by the European Space Agency's (ESA) Gaia mission (Hestroffer et al., 2010), which is expected to provide spectral characterization of all objects down to an apparent magnitude of  $V = 20$ , including many asteroid family members (Campins et al., 2012; Delbó et al., 2012; Cellino and Dell'Oro, 2012). This dramatic increase in the number of characterized family members will enable a host of new investigations of the composition and differentiation of family parent bodies. By spectrally probing bodies as small as  $\sim 2$  km, inhomogeneities in asteroid family composition may begin to be revealed. Another key scientific product will be refined astrometry for all asteroids, which can be searched for gravitational perturbations and used to determine the masses of the largest asteroids (Mignard et al., 2007). This wealth

of new data will feed into theoretical models and numerical simulations, allowing us to improve the ages determined from orbital evolution simulations (e.g., *Masiero et al.*, 2012; *Carruba et al.*, 2014).

The collision events that form families are very rare, and the probability of a massive collision in the next 10, 100, or 1000 years is vanishingly small (see the chapter by Bottke et al. in this volume). However, a new class of active main-belt objects has recently been identified that may nonetheless provide a window into the collisional environment of the solar system (see the chapter by Jewitt et al. in this volume for further discussion). While some of these objects show repeated activity indicative of a cometary nature complete with subsurface volatiles, others are best explained by impact events. In particular, the observed outburst events of P/2010 A2 (*Jewitt et al.*, 2010) and (596) Scheila (*Jewitt et al.*, 2011) are consistent with impacts by very small ( $D < 50$  m) asteroids. As current and future sky surveys probe to smaller diameters in the main belt, the frequency at which these events will be observed, or even predicted in advance, will increase. Study of these small-scale disruptions offers an important constraint on impact physics in the low-gravity environment of asteroids, and provides test cases for comparing to the small-scale impact experiments that can be performed in Earth-based laboratories.

Recently, *Reddy et al.* (2014) presented evidence that shock darkening may play a role in altering the spectroscopic properties of chondritic materials in the Baptistina and Flora families. If evidence for this effect is seen in other families across a range of compositions, this technique may provide a method for determining the conditions of family-forming impacts in the main belt, and thus provide better constraints on the ages of families. This may also help explain some of the differences observed in space-weathering studies that find albedo changes happen very quickly while spectral changes have long timescales.

As new datasets have rapidly increased our ability to characterize asteroid family members, and through this the parent body from which they originated, one glaring question remains at the forefront of the field: Where are the families of differentiated parent bodies that were completely disrupted? Vesta and its family members have given us a excellent example of the composition and resultant albedo, color, and spectral properties of the crust of a differentiated body (see the chapter by Russell et al. in this volume for further discussion). However, searches for objects with similar properties in different regions of the main belt have yielded no significant populations of these basaltic crust and mantle fragments that should be left over from these collisions. On the other hand, data from iron meteorites has indicated that differentiation of protoplanets, if not common, at a minimum happened multiple times (see the chapters by Scheinberg et al. and Scott et al. in this volume for further discussion). While it is possible that these collisions happened at the earliest stages of the solar system's formation and the evidence (in the form of families) was erased during the epoch of giant planet migration — the foundation

of the “Nice” model (see the chapter by Morbidelli et al. in this volume) — a dynamical explanation of this problem would need to preserve in the main belt the core material that still falls to Earth today. Conversely, if these impacts happened after the last great breakup of the solar system, a mineralogical explanation for how metallic cores could form without leaving a basaltic “residue” in the main belt is required. The limitations on what *could not* have happened that are being set by current surveys are just as important as our discoveries of what did happen.

The next decade of large surveys, both ground- and spacebased, promises to expand our knowledge of asteroid physical properties by potentially another order of magnitude beyond what is known today. In this data-rich environment, family research will focus not just on individual families and their place in the main belt, but on specific subgroupings within families: on the knots, clumps, and collisional cascade fragments that trace the disruption and evolutionary dynamics that families have undergone. As the sizes of objects probed reach smaller and smaller, we can expect to find more young families like Karin and Iannini that can be directly backward-integrated to a specific time of collision, improving our statistics of collisions in the last 10 m.y. As catalogs increase in size, we can also expect to more frequently have characterization data of objects both before and after they undergo catastrophic disruption. This will enable us to test our impact-physics models on scales not achievable on Earth. Additionally, we will begin to see a time when we routinely use remote sensing data of asteroids to not just associate families but also assess the mineralogy of family members as a probe of the parent body. Asteroid family physical properties, numerical simulations, and evolutionary theory will leapfrog off each other, pushing forward our understanding of the asteroids and of the solar system as a whole.

**Acknowledgments.** J.R.M. was partially supported by a grant from the NASA Planetary Geology and Geophysics Program. F.E.D. was supported by NASA through Hubble Fellowship grant HST-HF-51319.01-A, awarded by the Space Telescope Science Institute, which is operated by the Association of Universities for Research in Astronomy, Inc., for NASA under contract NAS 5-26555. This publication makes use of data products from the Wide-field Infrared Survey Explorer, which is a joint project of the University of California, Los Angeles, and the Jet Propulsion Laboratory/California Institute of Technology, funded by NASA. This publication also makes use of data products from NEOWISE, which is a project of the Jet Propulsion Laboratory/ California Institute of Technology, funded by the Planetary Science Division of NASA. Funding for the creation and distribution of the SDSS archive (<http://www.sdss.org/>) has been provided by the Alfred P. Sloan Foundation, the Participating Institutions, NASA, the National Science Foundation, the U.S. Department of Energy, the Japanese Monbukagakusho, and the Max Planck Society. The SDSS is managed by the Astrophysical Research Consortium (ARC) for the participating institutions. The participating institutions are The University of Chicago, Fermilab, the Institute for Advanced Study, the Japan Participation Group, The Johns Hopkins University, the Korean Scientist Group, Los Alamos National Laboratory, the Max-Planck-Institute for Astronomy

(MPIA), the Max-Planck-Institute for Astrophysics (MPA), New Mexico State University, University of Pittsburgh, University of Portsmouth, Princeton University, the U.S. Naval Observatory, and the University of Washington. This research is based on observations with AKARI, a Japan Aerospace Exploration Agency (JAXA) project with the participation of ESA. The authors wish to thank B. Bus, B. E. Clark, H. Kaluna, and P. Vernazza for providing proprietary spectra to include in Fig. 1. We also thank the referees, A. Cellino and B. Bus, and editor P. Michel for helpful comments that improved this chapter.

## REFERENCES

- Ali-Lagoa V., de León J., Licandro J., et al. (2013) Physical properties of B-type asteroids from WISE data. *Astron. Astrophys.*, **554**, A71.
- Assandri M. C. and Gil-Hutton R. (2008) Surface composition of Hungaria asteroids from the analysis of the Sloan Digital Sky Survey. *Astron. Astrophys.*, **488**, 339.
- Beaugé C. and Roig F. (2001) A semianalytical model for the motion of the Trojan asteroids: Proper elements and families. *Icarus*, **153**, 391.
- Bell J. F. (1988) A probable asteroidal parent body for the CO or CV chondrites. *Meteoritics*, **23**, 256.
- Binzel R. P. and Xu S. (1993) Chips off of asteroid 4 Vesta — Evidence for the parent body of basaltic achondrite meteorites. *Science*, **260**, 186.
- Bottke W. F., Vokrouhlický D., and Nesvorný D. (2007) An asteroid breakup 160 Myr ago as the probable source of the K/T impactor. *Nature*, **449**, 48.
- Bottke W. F., Rubincam D. P., and Burns J. A. (2000) Dynamical evolution of main belt meteoroids: Numerical simulations incorporating planetary perturbations and Yarkovsky thermal forces. *Icarus*, **145**, 301.
- Bottke W. F., Vokrouhlický D., Minton D., et al. (2012) An Archaean heavy bombardment from a destabilized extension of the asteroid belt. *Nature*, **485**, 78.
- Bowell E., Oszkiewicz D. A., Wasserman L. H., Muinonen K., Penttilä A., and Trilling D. E. (2014) Asteroid spin-axis longitudes from the Lowell Observatory database. *Meteoritics & Planet. Sci.*, **49**, 95.
- Britt D. T. and Pieters C. M. (1991) Black ordinary chondrites: An analysis of abundance and fall frequency. *Meteoritics*, **26**, 279.
- Britt D. T. and Pieters C. M. (1994) Darkening in black and gas-rich ordinary chondrites: The spectral effect of opaque morphology and distribution. *Geochim. Cosmochim. Acta*, **58**, 3905.
- Brown M. E., Barkume K. M., Ragazzine D., and Schaller E. L. (2007) A collisional family of icy objects in the Kuiper belt. *Nature*, **446**, 294.
- Brož M. and Morbidelli A. (2013) The Eos family halo. *Icarus*, **223**, 844.
- Brož M. and Rozehnal J. (2011) Eurybates — the only asteroid family among Trojans? *Mon. Not. R. Astron. Soc.*, **414**, 565.
- Brož M., Morbidelli A., Bottke W. F., Rozehnal J., Vokrouhlický D., and Nesvorný D. (2013) Constraining the cometary flux through the asteroid belt during the late heavy bombardment. *Astron. Astrophys.*, **551**, A117.
- Burbine T. and Binzel R. P. (2002) Small Main-Belt Asteroid Spectroscopic Survey in the near-infrared. *Icarus*, **159**, 468.
- Burbine T. H., Gaffey M. J., and Bell J. F. (1992) S-asteroids 387 Aquitania and 980 Anacostia — Possible fragments of the breakup of a spinel-bearing parent body with CO3/CV3 affinities. *Meteoritics*, **27**, 424.
- Bus S. J. and Binzel R. P. (2002) Phase II of the Small Main-Belt Asteroid Spectroscopic Survey: A feature-based taxonomy. *Icarus*, **158**, 146.
- Camps H., Hargrove K., Pinilla-Alonso N., et al. (2010) Water ice and organics on the surface of the asteroid 24 Themis. *Nature*, **464**, 1320.
- Camps H., de León J., Licandro J., et al. (2012) Spectra of asteroid families in support of Gaia. *Planet. Space Sci.*, **73**, 95–97.
- Carruba V. (2013) An analysis of the Hygiea asteroid family orbital region. *Mon. Not. R. Astron. Soc.*, **431**, 3557–3569.
- Carruba V., Michchenko T. A., Roig F., Ferraz-Mello S., and Nesvorný D. (2005) On the V-type asteroids outside the Vesta family.
- I. Interplay of nonlinear secular resonances and the Yarkovsky effect: The cases of 956 Elisa and 809 Lundia. *Astron. Astrophys.*, **441**, 819.
- Carruba V., Domingos R. C., Nesvorný D., Roig F., Huaman M. E., and Souami D. (2013) A multidomain approach to asteroid families' identification. *Mon. Not. R. Astron. Soc.*, **433**, 2075–2096.
- Carruba V., Aljbaae S., and Souami D. (2014) Peculiar Euphrosyne. *Astrophys. J.*, **792**, 46.
- Carry B. (2012) Density of asteroids. *Planet. Space Sci.*, **73**, 98.
- Carvano J. M., Lazzaro D., Mothé-Diniz T., Angeli C. A., and Florcak M. (2001) Spectroscopic survey of the Hungaria and Phocaea dynamical groups. *Icarus*, **149**, 173.
- Carvano J. M., Hasselmann P. H., Lazzaro D., and Mothé-Diniz T. (2010) SDSS-based taxonomic classification and orbital distribution of main belt asteroids. *Astron. Astrophys.*, **510**, A43.
- Clark B. E., Ockert-Bell M. E., Cloutis E. A., Nesvorný D., Mothé-Diniz T., and Bus S. J. (2009) Spectroscopy of K-complex asteroids: Parent bodies of carbonaceous meteorites? *Icarus*, **202**, 119.
- Cellino A. and Dell'Oro A. (2012) The derivation of asteroid physical properties from Gaia observations. *Planet. Space Sci.*, **73**, 52.
- Cellino A., Gil-Hutton R., Tedesco E. F., Di Martino M., and Brunini A. (1999) Polarimetric observations of small observations: Preliminary results. *Icarus*, **138**, 129.
- Cellino A., Zappala V., Doressoundiram A., et al. (2001) The puzzling case of the Nysa-Polana family. *Icarus*, **152**, 225.
- Cellino A., Bus S. J., Doressoundiram A., and Lazzaro D. (2002) Spectroscopic properties of asteroid families. In *Asteroids III* (W. F. Bottke Jr. et al., eds.), p. 633. Univ. of Arizona, Tucson.
- Cellino A., Dell'Oro A., and Tedesco E. F. (2009) Asteroid families: Current situation. *Planet. Space Sci.*, **57**, 173.
- Cellino A., Delbò M., Bendjoya Ph., and Tedesco E. F. (2010) Polarimetric evidence of close similarity between members of the Karin and Koronis dynamical families. *Icarus*, **209**, 556.
- Cellino A., Bagnulo S., Tanga P., Novaković B., and Delbò M. (2014) A successful search for hidden Barbarians in the Watsonia asteroid family. *Mon. Not. R. Astron. Soc.*, **439**, L75–L79.
- Christou A. A. (2013) Orbital clustering of martian Trojans: An asteroid family in the inner solar system? *Icarus*, **224**, 144.
- Consolmagno G. J. and Drake M. J. (1977) Composition and evolution of the eucrite parent body — Evidence from rare earth elements. *Geochim. Cosmochim. Acta*, **41**, 1271.
- Delbò M., Gayon-Markt J., Busso G., et al. (2012) Asteroid spectroscopy with Gaia. *Planet. Space Sci.*, **73**, 86.
- de León J., Licandro J., Serra-Ricart M., Pinilla-Alonso N., and Campins H. (2010) Observations, compositional, and physical characterization of near-Earth and Mars-crosser asteroids from a spectroscopic survey. *Astron. Astrophys.*, **517**, 23.
- de León J., Pinilla-Alonso N., Campins H., Licandro L., and Marzo G. A. (2012) Near-infrared spectroscopic survey of B-type asteroids: Compositional analysis. *Icarus*, **218**, 196.
- De Luise F., Dotto E., Fornasier S., Barucci M. A., Pinilla-Alonso N., Perna D., and Marzari F. (2010) A peculiar family of Jupiter Trojans: The Eurybates. *Icarus*, **209**, 586–590.
- DeMeo F. E. and Carry B. (2013) The taxonomic distribution of asteroids from multi-filter all-sky photometric surveys. *Icarus*, **226**, 723.
- DeMeo F. E. and Carry B. (2014) Solar system evolution from compositional mapping of the asteroid belt. *Nature*, **505**, 629.
- de Sanctis M. C., Migliorini A., Luzia Jasmin F., Lazzaro D., et al. (2011) Spectral and mineralogical characterization of inner main-belt V-type asteroids. *Astron. Astrophys.*, **533**, A77.
- Dohnanyi J. S. (1969) Collisional model of asteroids and their debris. *J. Geophys. Res.*, **74**, 2531.
- Doressoundiram A., Barucci M. A., Fulchignoni M., and Florcak M. (1998) Eos family: A spectroscopic study. *Icarus*, **131**, 15.
- Dotto E., Fornasier S., Barucci M. A., et al. (2006) The surface composition of Jupiter Trojans: Visible and near-infrared survey of dynamical families. *Icarus*, **183**, 420.
- Duffard R. and Roig F. (2009) Two new V-type asteroids in the outer main belt? *Planet. Space Sci.*, **57**, 229.
- Dunn T. L., Burbine T. H., Bottke W. F., and Clark J. P. (2013) Mineralogies and source regions of near-Earth asteroids. *Icarus*, **222**, 273–282.
- Durda D. D., Bottke W. F., Nesvorný D., et al. (2007) Size frequency distribution of fragments from SPH/N-body simulations of asteroid

- impacts: Comparison with observed asteroid families. *Icarus*, 186, 498.
- Fiebel-Beyer S. K., Gaffey M. J., Kelley M. S., Reddy V., Reynolds C. M., and Hicks T. (2011) The Maria asteroid family: Genetic relationships and a plausible source of mesosiderites near the 3:1 Kirkwood gap. *Icarus*, 213, 524.
- Fornasier S., Dotto E., Marzari F., et al. (2004) Visible spectroscopic and photometric survey of L5 Trojans: Investigation of dynamical families. *Icarus*, 172, 221.
- Fornasier S., Dotto E., Hainaut O., et al. (2007) Visible spectroscopic and photometric survey of Jupiter Trojans: Final results on dynamical families. *Icarus*, 190, 622.
- Gaffey M. J., Burbine T. H., Piatek J. L., et al. (1993) Mineralogical variations within the S-type asteroid class. *Icarus*, 106, 573.
- Gil-Hutton R., Lazzaro D., and Benavidez P. (2007) Polarimetric observations of Hungaria asteroids. *Astron. Astrophys.*, 468, 1109.
- Gladman B., Michel P., and Froeschlé C. (2000) The near-Earth object population. *Icarus*, 146, 176.
- Gomes R., Levison H. F., Tsiganis K., and Morbidelli A. (2005) Origin of the cataclysmic late heavy bombardment period of the terrestrial planets. *Nature*, 435, 26.
- Grav T., Mainzer A. K., Bauer J., et al. (2012) WISE/NEOWISE observations of the Hilda population: Preliminary results. *Astrophys. J.*, 744, 197.
- Hanuš J., Durech J., Brož M., et al. (2011) A study of asteroid pole-latitude distribution based on an extended set of shape models derived by the light curve inversion method. *Astron. Astrophys.*, 530, A134.
- Hanuš J., Brož M., Durech J., et al. (2013) An anisotropic distribution of spin vectors in asteroid families. *Astron. Astrophys.*, 559, A134.
- Harris A. W., Muller M., Lisse C. M., and Cheng A. F. (2009) A survey of Karin cluster asteroids with the Spitzer Space Telescope. *Icarus*, 199, 86.
- Hestroffer D., Dell'Oro A., Cellino A., and Tanga P. (2010) The Gaia mission and the asteroids. In *Dynamics of Small Solar System Bodies and Exoplanets* (J. Souchay and R. Dvorak, eds.), pp. 251–340. Lecture Notes in Physics Vol. 790, Springer-Verlag, Berlin.
- Hsieh H. H. and Jewitt D. J. (2006) A population of comets in the main asteroid belt. *Science*, 312, 561.
- Ishihara D., Onaka T., Kataza H., et al. (2010) The AKARI/IRC mid-infrared all-sky survey. *Astron. Astrophys.*, 514, 1.
- Ivezic Ž., Tabachnik S., Rafikov R., et al. (2001) Solar system objects observed in the Solar Digital Sky Survey commissioning data. *Astron. J.*, 122, 2749.
- Ivezic Ž., Lupton R. H., Jurić M., et al. (2002) Color confirmation of asteroid families. *Astron. J.*, 124, 2943.
- Jasmin F. L., Lazzaro D., Carvano J. M. F., Mothé-Diniz T., and Hasselmann P. H. (2013) Mineralogical investigation of several Qp asteroids and their relation to the Vesta family. *Astron. Astrophys.*, 552, A85.
- Jedicke R., Nesvorný D., Whiteley R. J., Ivezic Ž., and Jurić M. (2004) An age-colour relationship for main-belt S-complex asteroids. *Nature*, 429, 275.
- Jewitt D., Weaver H., Agarwal J., Mutchler M., and Drahus M. (2010) A recent disruption of the main-belt asteroid P/2010A2. *Nature*, 467, 817.
- Jewitt D., Weaver H., Mutchler M., Larson S., and Agarwal J. (2011) Hubble Space Telescope observations of main-belt Comet (596) Scheila. *Astrophys. J. Lett.*, 733, 4.
- Kasuga T., Usui F., Hasegawa S., et al. (2012) AKARI/AcuA physical studies of the Cybele asteroid family. *Astron. J.*, 143, 141.
- Kim M.-J., Choi Y.-J., Moon H.-K., et al. (2014) Rotational properties of the Maria asteroid family. *Astron. J.*, 147, 56.
- Kohout T., Gritsevich M., Grokhovsky V. I., et al. (2014) Mineralogy, reflectance spectra, and physical properties of the Chelyabinsk LL5 chondrite — Insight into shock-induced changes in asteroid regoliths. *Icarus*, 228, 78.
- Kryszczyńska A., Colas F., Polińska M., et al. (2012) Do Slivan states exist in the Flora family? I. Photometric survey of the Flora region. *Astron. Astrophys.*, 546, A72.
- Lazzaro D., Mothé-Diniz T., Carvano J. M., et al. (1999) The Eunomia family: A visible spectroscopic survey. *Icarus*, 142, 445.
- Lazzaro D., Angeli C. A., Carvano J. M., Mothé-Diniz T., Duffard R., and Florcak M. (2004) S3OS2: The visible spectroscopic survey of 820 asteroids. *Icarus*, 172, 179.
- Lebofsky L. A. and Spencer J. R. (1989) Radiometry and a thermal modeling of asteroids. In *Asteroids II* (R. P. Binzel et al., eds.), p. 128. Univ. of Arizona, Tucson.
- Lebofsky L. A., Sykes M. V., Tedesco E. F., et al. (1986) A refined ‘standard’ thermal model for asteroids based on observations of 1 Ceres and 2 Pallas. *Icarus*, 68, 239.
- Levison H. F., Bottke W. F., Gounelle M., Morbidelli A., Nesvorný D., and Tsiganis K. (2009) Contamination of the asteroid belt by primordial trans-Neptunian objects. *Nature*, 460, 364–366.
- Licandro J., Hargrove K., Kelley M., et al. (2012) 5–14 μm Spitzer spectra of Themis family asteroids. *Astron. Astrophys.*, 537, A73.
- Mainzer A. K., Bauer J., Grav T., et al. (2011) Preliminary results from NEOWISE: An enhancement to the Wide-field Infrared Survey Explorer for solar system science. *Astrophys. J.*, 731, 53.
- Mainzer A. K., Bauer J., Cutri R. M., et al. (2014) Initial performance of the NEOWISE reactivation mission. *Astrophys. J.*, 792, 30.
- Masiero J. R., Mainzer A. K., Grav T., et al. (2011) Main belt asteroids with WISE/NEOWISE. I. Preliminary albedos and diameters. *Astrophys. J.*, 741, 68.
- Masiero J. R., Mainzer A. K., Grav T., Bauer J. M., and Jedicke R. (2012) Revising the age for the Baptistina asteroid family using WISE/NEOWISE data. *Astrophys. J.*, 759, 14.
- Masiero J. R., Mainzer A. K., Bauer J. M., Grav T., Nugent C. R., and Stevenson R. (2013) Asteroid family identification using the hierarchical clustering method and WISE/NEOWISE physical properties. *Astrophys. J.*, 770, 7.
- Masiero J. R., Grav T., Mainzer A. K., et al. (2014) Main belt asteroids with WISE/NEOWISE: Near-infrared albedos. *Astrophys. J.*, 791, 121.
- Mayne R. G., Sunshine J. M., McSween H. Y., Bus S. J., and McCoy T. J. (2011) The origin of Vesta’s crust: Insights from spectroscopy of the vestoids. *Icarus*, 214, 147.
- McCord T. B., Adams J. B., and Johnson T. V. (1970) Asteroid Vesta: Spectral reflectivity and compositional implications. *Science*, 168, 1445.
- Mignard F., Cellino A., Muinonen K., et al. (2007) The Gaia mission: Expected applications to asteroid science. *Earth Moon Planets*, 101, 97.
- Milani A. (1993) The Trojan asteroid belt: Proper elements, stability, chaos and families. *Cel. Mech. Dyn. Astron.*, 57, 59.
- Milani A., Cellino A., Knežević Z., Novaković B., Spoto F., and Paolicchi P. (2014) Asteroid families classification: Exploiting very large datasets. *Icarus*, 239, 46.
- Morbidelli A., Nesvorný D., Bottke W. F., Michel P., Vokrouhlický D., and Tanga P. (2003) The shallow magnitude distribution of asteroid families. *Icarus*, 162, 328.
- Moskovitz N. A., Jedicke R., Gaidos E., Willman M., Nesvorný D., Feigl R., and Ivezic Ž. (2008) The distribution of basaltic asteroids in the main belt. *Icarus*, 198, 77.
- Moskovitz N. A., Willman M., Burbine T. H., Binzel R. P., and Bus S. J. (2010) A spectroscopic comparison of HED meteorites and V-type asteroids in the inner main belt. *Icarus*, 208, 773.
- Mothé-Diniz T. and Carvano J. M. (2005) 221 Eos: A remnant of a partially differentiated parent body? *Astron. Astrophys.*, 442, 727.
- Mothé-Diniz T. and Nesvorný D. (2008a) Visible spectroscopy of extremely young asteroid families. *Astron. Astrophys. Lett.*, 486, 9.
- Mothé-Diniz T. and Nesvorný D. (2008b) Tirela: An unusual asteroid family in the outer main belt. *Astron. Astrophys.*, 492, 593.
- Mothé-Diniz T., Carvano J. M., and Lazzaro D. (2003) Distribution of taxonomic classes in the main belt asteroids. *Icarus*, 162, 10.
- Mothé-Diniz T., Roig F., and Carvano J. M. (2005) Reanalysis of asteroid families structure through visible spectroscopy. *Icarus*, 174, 54.
- Mothé-Diniz T., Carvano J. M., Bus S. J., Duffard R., and Burbine T. H. (2008) Mineralogical analysis of the Eos family from near-infrared spectra. *Icarus*, 195, 277.
- Murakami H., Baba H., Barthel P., et al. (2007) The infrared astronomical mission AKARI. *Publ. Astron. Soc. Japan*, 59, S369.
- Nathues A. (2010) Spectral study of the Eunomia asteroid family. Part II: The small bodies. *Icarus*, 208, 252.
- Nathues A., Mottola S., Kaasalainen M., and Neukum G. (2005) Spectral study of the Eunomia asteroid family. I. Eunomia. *Icarus*, 175, 452.
- Neese C., ed. (2010) *Asteroid Taxonomy V6.0*. EAR-A-5-DDRTAXONOMY-V6.0, NASA Planetary Data System.

- Nesvorný D. (2012) *Nesvorný HCM Asteroid Families V2.0*. EAR-A-VARGBDAT-5-NESVORNYFAM-V2.0, NASA Planetary Data System.
- Nesvorný D., Jedicke R., Whiteley R. J., and Ivezić Ž. (2005) Evidence for asteroid space weathering from the Sloan Digital Sky Survey. *Icarus*, 173, 132.
- Novaković B., Cellino A., and Knežević Z. (2011) Families among high-inclination asteroids. *Icarus*, 216, 184.
- Oszkiewicz D. A., Muinonen K., Bowell E., et al. (2011) Online multi-parameter phase-curve fitting and application to a large corpus of asteroid photometric data. *J. Quant. Spectrosc. Radiat. Transfer*, 112, 1919.
- Oszkiewicz D. A., Bowell E., Wasserman L. H., Muinonen K., Penttilä A., et al. (2012) Asteroid taxonomic signatures from photometric phase curves. *Icarus*, 219, 283.
- Parker A., Ivezić Ž., Jurić M., Lupton R., Sekora M. D., and Kowalski A. (2008) The size distributions of asteroid families in the SDSS Moving Object Catalog 4. *Icarus*, 198, 138.
- Rayner J. T., Toomey D. W., Onaka P. M., et al. (2003) SpeX: A medium-resolution 0.8–5.5 micron spectrograph and imager for the NASA Infrared Telescope Facility. *Publ. Astron. Soc. Pac.*, 115, 362.
- Reddy V., Emery J. P., Gaffey M. J., Bottke W. F., Cramer A., and Kelley M. S. (2009) Composition of 298 Baptistina: Implications for the K/T impactor link. *Meteoritics & Planet. Sci.*, 44, 1917.
- Reddy V., Carvano J. M., Lazzaro D., et al. (2011) Mineralogical characterization of Baptistina asteroid family: Implications for K/T impactor source. *Icarus*, 216, 184.
- Reddy V., Sanchez J. A., Bottke W. F., et al. (2014) Chelyabinsk meteorite explains unusual spectral properties of Baptistina asteroid family. *Icarus*, 237, 116.
- Rivkin A. S. and Emery J. P. (2010) Detection of ice and organics on an asteroidal surface. *Nature*, 464, 1322.
- Roig F., Nesvorný D., Gil-Hutton R., and Lazzaro D. (2008a) V-type asteroids in the middle main belt. *Icarus*, 194, 125.
- Roig F., Ribeiro A. O., and Gil-Hutton R. (2008b) Taxonomy of asteroid families among the Jupiter Trojans: Comparison between spectroscopic data and the Sloan Digital Sky Survey colors. *Astron. Astrophys.*, 483, 911.
- Schenk P., O'Brien D. P., Marchi S., et al. (2012) The geologically recent giant impact basins at Vesta's south pole. *Science*, 336, 694.
- Schunová E., Granvik M., Jedicke R., Gronchi G., Wainscoat R., and Abe S. (2012) Searching for the first near-Earth object family. *Icarus*, 220, 1050.
- Slivan S. M., Binzel R. P., Crespo da Silva L. D., et al. (2003) Spin vectors in the Koronis family: Comprehensive results from two independent analyses of 213 rotation lightcurves. *Icarus*, 162, 285.
- Slivan S. M., Binzel R. P., Kaasalainen M., et al. (2009) Spin vectors in the Koronis family. II. Additional clustered spins, and one stray. *Icarus*, 200, 514.
- Slivan S. M., Binzel R. P., Boroumand S. C., et al. (2008) Rotation rates in the Koronis family, complete to H11.2. *Icarus*, 195, 226.
- Solontoi M. R., Hammergren M., Gyuk G., and Puckett A. (2012) AVAST survey 0.4–1.0 μm spectroscopy of igneous asteroids in the inner and middle main belt. *Icarus*, 220, 577.
- Sunshine J. M., Bus S. J., McCoy T. J., Burbine T. H., Corrigan C. M., and Binzel R. P. (2004) High-calcium pyroxene as an indicator of igneous differentiation in asteroids and meteorites. *Meteoritics & Planet. Sci.*, 39, 1343.
- Sunshine J. M., Connolly H. C., McCoy T. J., Bus S. J., and La Croix L. M. (2008) Ancient asteroids enriched in refractory inclusions. *Science*, 320, 514.
- Szabó G. M. and Kiss L. L. (2008) The shape distribution of asteroid families: Evidence for evolution driven by small impacts. *Icarus*, 196, 135.
- Thomas C. A., Rivkin A. S., Trilling D. E., Enga M.-T., and Grier J. A. (2011) Space weathering of small Koronis family members. *Icarus*, 212, 158.
- Thomas C. A., Trilling D. E., and Rivkin A. S. (2012) Space weathering of small Koronis family members in the SDSS Moving Object Catalog. *Icarus*, 219, 505.
- Usui F., Kuroda D., Müller T. G., et al. (2011) Asteroid catalog using Akari: AKARI/IRC Mid-infrared asteroid survey. *Publ. Astron. Soc. Japan*, 63, 1117.
- Vernazza P., Burlan M., Rossi A., et al. (2006) Physical characterization of the Karin family. *Astron. Astrophys.*, 460, 945.
- Vernazza P., Binzel R. P., Thomas C. A., et al. (2008) Compositional differences between meteorites and near-Earth asteroids. *Nature*, 454, 858.
- Vernazza P., Binzel R. P., Rossi A., Fulchignoni M., and Burlan M. (2009) Solar wind as the origin of rapid reddening of asteroid surfaces. *Nature*, 458, 993.
- Vernazza P., Zanda B., Binzel R. P., et al. (2014) Multiple and fast: The accretion of ordinary chondrite parent bodies. *Astrophys. J.*, 791, 120.
- Vokrouhlický D., Nesvorný D., and Bottke W. F. (2003) The vector alignments of asteroid spins by thermal torques. *Nature*, 425, 147.
- Walsh K. J., Morbidelli A., Raymond S. N., O'Brien D. P., and Mandell A. M. (2012) Populating the asteroid belt from two parent source regions due to the migration of giant planets — “The Grand Tack.” *Meteoritics & Planet. Sci.*, 47, 1941.
- Walsh K. J., Delbó M., Bottke W. F., Vokrouhlický D., and Lauretta D. S. (2013) Introducing the Eulalia and new Polana asteroid families: Re-assessing primitive asteroid families in the inner main belt. *Icarus*, 225, 283–297.
- Warner B. D., Harris A. W., Vokrouhlický D., Nesvorný D., and Bottke W. F. (2009) Analysis of the Hungaria asteroid population. *Icarus*, 204, 172.
- Weaver H. A., Stern S. A., Mutchler M. J., et al. (2006) Discovery of two new satellites of Pluto. *Nature*, 439, 943.
- Willman M., Jedicke R., Nesvorný D., Moskovitz N., Ivezić Ž., and Fevig R. (2008) Redetermination of the space weathering rate using spectra of Iannini asteroid family members. *Icarus*, 195, 663.
- Willman M., Jedicke R., Moskovitz N., Nesvorný D., Vokrouhlický D., and Mothé-Diniz T. (2010) Using the youngest asteroid clusters to constrain the space weathering and gardening rate on S-complex asteroids. *Icarus*, 208, 758.
- York D. G., Adelman J., Anderson J. E., et al. (2000) The Sloan Digital Sky Survey: Technical summary. *Astron. J.*, 120, 1579.
- Zappala V., Cellino A., Farinella P., and Knezevic Z. (1990) Asteroid families. I — Identification by hierarchical clustering and reliability assessment. *Astron. J.*, 100, 2030.
- Zappala V., Cellino A., Dell'Oro A., and Paolicchi P. (2002) Physical and dynamical properties of asteroid families. In *Asteroids III* (W. F. Bottke Jr. et al., eds.), p. 619. Univ. of Arizona, Tucson.
- Zellner B., Tholen D. J., and Tedesco E. F. (1985a) The eight-color asteroid survey — results for 589 minor planets. *Icarus*, 61, 355.
- Zellner B., Thirunagari A., and Bender D. (1985b) The large-scale structure of the asteroid belt. *Icarus*, 62, 505–511.
- Ziffer J., Campins H., Licandro J., et al. (2011) Near-infrared spectroscopy of primitive asteroid families. *Icarus*, 213, 538.

# Collisional Formation and Modeling of Asteroid Families

**Patrick Michel**

*Lagrange Laboratory, University of Nice-Sophia, CNRS, Côte d'Azur Observatory*

**Derek C. Richardson**

*University of Maryland*

**Daniel D. Durda**

*Southwest Research Institute*

**Martin Jutzi**

*University of Bern*

**Erik Asphaug**

*Arizona State University*

---

In the last decade, thanks to the development of sophisticated numerical codes, major breakthroughs have been achieved in our understanding of the formation of asteroid families by catastrophic disruption of large parent bodies. In this review, we describe numerical simulations of asteroid collisions that reproduced the main properties of families, accounting for both the fragmentation of an asteroid at the time of impact and the subsequent gravitational interactions of the generated fragments. The simulations demonstrate that the catastrophic disruption of bodies larger than a few hundred meters in diameter leads to the formation of large aggregates due to gravitational reaccumulation of smaller fragments, which helps explain the presence of large members within asteroid families. Thus, for the first time, numerical simulations successfully reproduced the sizes and ejection velocities of members of representative families. Moreover, the simulations provide constraints on the family dynamical histories and on the possible internal structure of family members and their parent bodies.

## 1. INTRODUCTION

Observed asteroid families in the main asteroid belt are each composed of bodies that are thought to originate from the catastrophic disruption of larger parent bodies (e.g., Farinella et al., 1996). Cratering collisions can also lead to families, such as the one associated with asteroid Vesta, but we do not address this origin scenario here as few families have been linked to cratering events and their modeling requires a different approach (for more details, see the chapter by Jutzi et al. in this volume). A few tens of asteroid families have been identified, corresponding to groups of small bodies well-concentrated in proper-orbital-element space (see, e.g., Hirayama, 1918; Arnold, 1969; and the chapter by Nesvorný et al. in this volume) and sharing similar spectral properties (see, e.g., Chapman et al., 1989 and the chapter by Masiero et al. in this volume). Large families contain up to several hundred identified members, while small and compact families have on the order of 10 identified members. Interestingly,

the theory of the collisional origin of asteroid families rested for decades entirely on these similarities in dynamical and spectral properties and not on the detailed understanding of the collisional physics itself. Indeed, laboratory experiments on centimeter-scale targets, analytical scaling rules, or even complete numerical simulations of asteroid collisions were unable to reproduce the physical and dynamical properties of asteroid families (e.g., Ryan and Melosh, 1998). The extrapolation of laboratory experiments to asteroidal scales yielded bodies much too weak to account for both the size distribution and the dynamical properties of family members. In other words, there was no solution to match both the sizes and ejection velocities of family members simultaneously. To produce the large (assumed coherent) fragments seen in real families required an impact energy leading to ejection speeds of individual fragments that were much too small for them to overcome their own gravitational attraction. The parent body would then be merely shattered but not dispersed and therefore no family would be created (Davis et al., 1979).

Conversely, matching individual ejection velocities and deriving the necessary fragment distribution resulted in a size distribution in which no big fragment was present, contrary to most real families (e.g., *Davis et al.*, 1985; *Chapman et al.*, 1989). Thus, big sizes implied no fragment dispersion (at the level of the dispersion of family members), and fragment dispersion implied no big fragments (at the level of the sizes of family members).

A big caveat in the extrapolation of laboratory results to large asteroid scales is that the role of gravity (of both the targets and their fragments) is not taken into account in a laboratory-scale disruption involving centimeter-sized targets. Thus, the role of gravity in the catastrophic disruption of a large asteroid at the origin of a family remained to be assessed. Indeed, a possible scenario reconciling the sizes and ejection velocities of family members could be that the parent body (up to several hundred kilometers in size) is disrupted into small pieces by the propagation of cracks resulting from a hypervelocity impact but then the small fragments generated this way would typically escape from the parent and, due to their mutual gravitational attraction, reaccumulate elsewhere in groups in order to build up the most massive family members. This idea had been suggested previously by *Chapman et al.* (1982), and numerical simulations by *Benz and Asphaug* (1999) had already shown that at least the largest remnant of an asteroid disruption had to be a bound aggregate. However, the formation of a full family by reaccumulation of smaller fragments remained to be demonstrated.

In the last decade, the formation of asteroid families was simulated explicitly for the first time accounting for the two phases of a large-scale disruption: the fragmentation phase and the gravitational reaccumulation phase. In these simulations, the two phases are usually computed separately using a hybrid approach. This chapter reviews the major advances achieved since *Asteroids III* thanks to this new modeling work, and the implications for our understanding of asteroid family formation and properties.

## 2. SIMULATING A FAMILY-FORMING EVENT

Families are thought to form from the disruption of a large asteroid, called the parent body, as a result of the impact of a smaller projectile. Simulating such a process requires accounting for both the propagation of cracks in the parent body, leading to its conversion into separate fragments, and the possible gravitational interactions of these fragments. As explained above, the latter gravitational phase turns out to be crucial for reproducing asteroid family properties. In asteroid disruptions resulting from an hypervelocity impact, the fragmentation and the gravitational reaccumulation phases have very different associated dynamical times. In the fragmentation phase, the timescale for the propagation of the shock wave is determined by the target's diameter divided by the sound speed of the material (a few to tens of seconds for an asteroid 100 km in diameter). In the second phase, the timescale for gravitational reaccumulation is proportional

to  $1/\sqrt{G\rho}$ , where G is the gravitational constant and  $\rho$  is the target bulk density, which corresponds to at least hours for  $\rho = 1$  to 3 g cm<sup>-3</sup>. Therefore it is possible to model the collisional event by separating the two phases. A hybrid approach is generally adopted that consists of simulating first the fragmentation phase using an appropriate fragmentation code (called a hydrocode; see the chapter by Jutzi et al. in this volume), and then the gravitational phase, during which the fragments produced by the fragmentation phase can interact under their mutual attraction, using a gravitational N-body code.

### 2.1. The Fragmentation Phase

Several hydrocodes exist and are used in the planetary science community (see the chapters by Asphaug et al. and Jutzi et al. in this volume). In the first studies devoted to direct simulations of asteroid family formation (*Michel et al.*, 2001, 2002, 2003, 2004), a three-dimensional “smoothed-particle hydrodynamics” (SPH) code was used. This code solves in a Lagrangian framework the usual conservation equations (mass, momentum, and energy) in which the stress tensor has a nondiagonal part. The first families modeled in this way (Eunomia, Koronis, and Flora) were of the S taxonomic type. S-type asteroids are expected to be mostly made of ordinary chondrite materials, for which basalt plausibly has similar properties, and therefore the parent bodies of these S-type families were assumed to be nonporous basalt. The Tillotson equation of state for basalt was used (*Tillotson*, 1962), which is computationally expedient while sophisticated enough to allow its application over a wide range of physical conditions. Plasticity was introduced by modifying the stresses beyond the elastic limit with a von Mises yielding relation (*Benz and Asphaug*, 1994, 1995). A yielding relation accounting for the dependence of shear stress on pressure, such as Mohr-Coulomb or Drucker Prager, is generally more appropriate for rock material (see the chapter by Jutzi et al. in this volume). It turns out to be important for cratering events for which part of the process is dominated by shearing or when the impacted body is composed of interacting boulders [a so-called “rubble pile” (*Davis et al.*, 1979) or gravitational aggregate (*Richardson et al.*, 2002); see also *Jutzi* (2015)]. However, it was found that in the case of the disruption of monolithic parent bodies, the details of the strength model (e.g., pressure-dependent vs. pressure-independent yield strength) do not play an important role (*Jutzi*, 2015). For the lower tensile stresses associated with brittle failure, a fracture model was used, based on the nucleation of incipient flaws whose number density is given by a Weibull distribution (*Weibull*, 1939; *Jaeger and Cook*, 1969). *Durda et al.* (2004) and *Nesvorný et al.* (2006) used a similar hydrocode to study the formation of satellites from asteroid disruptions and other family-forming events. *Leinhardt and Stewart* (2009) studied large-scale disruptions and modeled the shock deformation with an Eulerian shock-physics code, CTH (*McGlaun et al.*, 1990), instead of the Lagrangian SPH code used in previous works.

Recently, the SPH impact code used by Michel et al. (2001, 2002, 2003, 2004) was extended to include a model adapted for microporous materials (Jutzi et al., 2008, 2009) (see also the Jutzi et al. chapter in this volume). The formation of asteroid families formed from a microporous parent body, such as for dark- (carbonaceous) type families, could thus also be investigated (Jutzi et al., 2010; Michel et al., 2011). Another study looked at the case of rubble-pile parent bodies [containing macroporous voids (Benavidez et al., 2012)].

## 2.2. The Gravitational Phase

Once the fragmentation phase is over and fractures cease to propagate (within the first simulated tens of seconds), the hydrodynamic simulations are stopped and intact fragments are identified. For impact energies typical of asteroid disruptions and for targets with a diameter typically greater than 1 km, it was found that the bodies are totally shattered into fragments of mass equal to the mass resolution of the simulations. In the first simulations performed in this way, the numerical resolution was limited to a few  $10^5$  particles and corresponded to minimum boulder diameters of about 1 to 4 km, for a parent body of a few hundred kilometers in diameter. Thanks to increased computer performance, it is now possible to perform simulations with up to several million particles. However, the gain in particle size resolution is not dramatic and simulations are still limited to minimum fragment diameters of a few hundred meters for target diameter of a few hundred kilometers. Reaching fragment diameters down to meters or less is beyond the capabilities of current and probably near-future technologies. Only when the target's diameter is in the few hundred meters range can this minimum size be reached, but unfortunately, no asteroid family can be identified involving a parent body of such a small size.

Once identified in the simulation outcome, the fragments and their corresponding velocity distributions are then fed into a gravitational N-body code, which computes the gravitational evolution of the system from the handoff point to subsequent hours or days of simulated time. Because the number of fragments is up to a few  $10^6$ , and their gravitational interaction as well as their potential collisions need to be computed over long periods of time (up to several simulated days), a very efficient N-body code is required to compute the dynamics. The most appropriate code to tackle this problem, which is the only one used so far by various groups to simulate the outcome of the gravitational phase of a collision, is the code called *pkdgrav* [see Richardson et al. (2000) for the first application of this code to solar system problems]. This parallel hierarchical tree code was developed originally for cosmological studies. Essentially, the tree component of the code provides a convenient means of consolidating forces exerted by distant particles, reducing the computational cost, with the tradeoff of introducing a slight force error (on the order of 1%) that does not affect the results appreciably since the dynamics are dominated by dissipative collisions. The parallel component divides the

work evenly among available processors, adjusting the load at each timestep according to the amount of work done in the previous force calculation. The code uses a straightforward second-order leapfrog scheme for the integration and computes gravity moments from tree cells to hexadecapole order.

For the purpose of computing the gravitational phase of an asteroid disruption during which the generated fragments can interact and collide with each other, collisions are identified at each step with a fast neighbor-search algorithm in *pkdgrav*. Once a collision occurs, because the relative speeds are small enough (on the order of meters per second), it is assumed that no further fragmentation takes place between components generated during the fragmentation phase. In fact, the simulations presented by Michel et al. (2001) assumed perfect sticking of colliding fragments and all colliding fragments were forced to merge into a single particle regardless of their relative velocities. This assumption is justified because the initial impact results in an overall expanding cloud of fragments of relatively small individual masses, down to the minimum fragment size imposed by the numerical resolution, and colliding fragments have typical relative speeds that are smaller than their individual escape speeds. Since the fragments in *pkdgrav* are represented by spheres, when two spherical fragments reaccumulate, they are merged into a single spherical particle with the same momentum. The same assumption was used by Durda et al. (2004) and Nesvorný et al. (2006) in their studies of satellite formation and other family-forming events. In a second and subsequent papers, Michel et al. (2002, 2003, 2004) improved their treatment of fragment collisions by using a merging criterion based on relative speed and angular momentum. In this case, fragments are allowed to merge only if their relative speed is smaller than their mutual escape speed and the resulting spin of the merged fragment is smaller than the threshold value for rotational fission (based on a simple prescription of a test particle remaining on the equator of a sphere). Nonmerging collisions are modeled as bounces between hard spheres whose post-collision velocities are determined by the amount of dissipation taking place during the collisions. The latter is computed in these simulations using coefficients of restitution in the normal and tangential directions [see Richardson (1994) for details on this computation]. Note that Durda et al. (2011, 2013) performed bouncing experiments between 1-m granite spheres as well as between centimeter-scale rocky spheres. These experiments gave a value for the normal coefficient of restitution of  $\approx 0.8$ , although much lower values are found with increasing roughness of contact surfaces. These results are particularly interesting because they are performed in an appropriate size regime (meter-sized bodies). However, bouncing in simulations occur at somewhat higher speeds (up to tens of meters per second) than in those experiments, which may result in a decrease in the coefficient of restitution due to the start of cracking and other energy dissipation processes. Moreover, although in our numerical modeling, perfect spheres are used, it is reasonable to account for actual irregularities of fragments formed during the fragmentation phase to set the value of the coefficient of restitution. Since

the values of these coefficients are poorly constrained, we usually arbitrarily set them equal to 0.5, meaning, for example, the rebound speed is set to half the impact speed.

More recently, *Richardson et al.* (2009) enhanced the collision handling in *pkdgrav* to preserve shape and spin information of reaccumulated bodies in high-resolution simulations of asteroid family formation. Instead of merging, fragments are able to stick on contact and optionally bounce or subsequently detach, depending on user-selectable parameters that include for the first time several prescriptions for variable material strength/cohesion. As a result, the reaccumulated fragments can take a wide range of shapes and spin states, which can be compared with those observed. This comes with a cost in terms of computation time as several weeks to months are needed for one simulation using a few tens of current processors. This is the reason why this approach has so far only been used for particular cases, such as modeling the formation of the asteroid Itokawa (*Michel and Richardson*, 2013), and not systematically for family-formation investigations.

And finally, we must note that the Soft-Sphere Discrete Element Method (SSDEM) has been introduced in *pkdgrav* (*Schwartz et al.*, 2012; chapter by Murdoch et al. in this volume), which accounts more realistically for the contact forces between colliding/reaccumulating particles. This method should eventually replace the one developed by *Richardson et al.* (2009) to investigate the shape of reaccumulated fragments as it avoids arbitrary particle sticking and rather lets the reaccumulated particles evolve naturally toward the resulting equilibrium shape of the aggregate. However, solving for all contact forces between particles over the whole timescale of the gravitational phase, and covering a large enough parameter space (accounting for the uncertainty on the various friction coefficients), remains a computational challenge. Nevertheless, some collisional studies started using the SSDEM implementation in *pkdgrav* focusing on low-speed impact events. In effect, no fragmentation code was used for the impact phase, which is needed for impacts during which the sound speed of the material is reached. Thus, *Ballouz et al.* (2014, 2015) used *pkdgrav* and SSDEM to simulate low-speed impacts between rotating aggregates and investigate the influence of the initial rotation of colliding bodies on the impact outcome and the sensitivity of some friction parameters. The number of particles was small enough ( $10^4$  at most) that simulations could be performed within a reasonable computation time. In the case of a family formation, the outcome of hydrocode simulations consists in several hundred thousands to millions of particles. Feeding them into the SSDEM version of *pkdgrav* requires another level of computer performance, although tests are underway.

### 3. MODELING THE FAMILY PARENT BODIES

Different possible internal structures have been considered for the family parent bodies. Monolithic parent bodies composed of one material type with or without microporosity (meaning micropores in the solid rock; for a definition of

microporosity, see the chapter by Jutzi et al. in this volume) have been considered, as well as pre-shattered or rubble-pile parent bodies, with or without microporosity in the solid components. The assumed pre-shattered state could be seen as a natural consequence of the collisional evolution of main-belt asteroids. Indeed, several studies (see, e.g., *Asphaug et al.*, 2002; *Davis et al.*, 2002; *Richardson et al.*, 2002) have indicated that for any asteroid, collisions at high impact energies leading to a disruption occur with a smaller frequency than collisions at lower impact energies leading to shattering effects only. Thus, in general, a typical asteroid gets battered over time until a major collision eventually disrupts it into smaller dispersed pieces. Consequently, since the formation of an asteroid family corresponds to the ultimate disruptive event of a large object, the internal structure of this body before its disruption may be shattered by all the smaller collisional events that it has suffered over its lifetime in the belt, as suggested by *Housen* (2009) based on laboratory experiments and extrapolations using scaling laws. This would result in the presence of internal macroscopic damaged zones and/or voids.

To model a pre-shattered target, *Michel et al.* (2003, 2004) devised an algorithm that distributes a given number of internal fragments of arbitrary shape and size within the volume of the parent body. The reason the internal fragments are given arbitrary shapes is that a network of fractures inside a parent body resulting from many uncorrelated small impacts is unlikely to yield spherical internal fragments whose sizes follow a well-defined power law. Then, void spaces are created by randomly removing a given number of particles from the fractured set. Since there are various ways to define a pre-shattered internal structure, *Michel et al.* (2004) also built a model of a pre-shattered parent body in which large fragments are preferentially distributed near the center and smaller fragments are generated close to the surface.

Another model, closer to the definition of a rubble pile, was also built by *Michel et al.* (2003). In that case, spherical components whose sizes followed a specified power law distribution were distributed at random inside the parent body. Particles not belonging to one of these spherical components were removed to create void space and particles at the interface of two or more spherical components were assigned to fractures. Some simulations were performed using those two additional models and the collisional outcomes did not show any major qualitative difference compared to those obtained from the first pre-shattered model. *Benediz et al.* (2012) constructed arbitrary rubble-pile targets by filling the interior of a 100-km-diameter spherical shell with an uneven distribution of solid basalt spheres having diameters between 8 km and 20 km. However, simulations performed so far using such rubble-pile parent bodies used a version of a SPH hydrocode with a strength model that did not allow the proper modeling of friction between the individual components of the rubble pile. As found by *Jutzi* (2015), the bodies in this case show a fluid-like behavior and are very (somewhat unrealistically) weak. Therefore, in the following, we will only consider the results obtained for

monolithic and pre-shattered bodies (as defined by Michel et al., 2003, 2004) either with or without microporosity.

#### 4. REPRODUCING WELL-KNOWN FAMILIES

For the first time, Michel et al. (2001) simulated entirely and successfully the formation of asteroid families from monolithic basalt-like parent bodies in two extreme regimes of impact energy leading to either a small or a large mass ratio of the largest remnant to the parent body  $M_{lr}/M_{pb}$ . Two well-identified families were used for comparison with simulations: The Eunomia family, with a 284-km-diameter parent body and  $M_{lr}/M_{pb} \approx 0.67$ , was used to represent the barely disruptive regime, whereas the Koronis family, with a 119-km-diameter parent body and  $M_{lr}/M_{pb} \approx 0.04$ , represented the highly catastrophic one. Both families are of the S taxonomic type, for which ordinary chondrites are the best meteorite analog, but basalt material is typically used as an analog material in collisional studies. In these simulations, the collisional process was carried out to late times (typically several days), during which the gravitational interactions between the fragments could eventually lead to the formation of self-gravitating aggregates (as a representation of rubble piles) far from the largest remnant. These first simulations assumed perfect sticking of reaccumulated fragments, regardless of relative speed and mass. This treatment was improved by Michel et al. (2002), allowing for the dissipation of kinetic energy in such collisions and applying an energy-based merging criterion, as described previously. This improved treatment did not change the conclusion obtained with the more simplistic method because typical relative speeds between ejected fragments are most often below their mutual escape speed. Therefore, this new set of simulations confirmed the idea that the reaccumulation process is at the origin of large family members. Durda et al. (2007) and Benavidez et al. (2012) made a systematic study of collisional disruption of monolithic and rubble-pile basalt-like 100-km-diameter parent bodies, assuming perfect sticking during reaccumulation, over a large range of impact conditions, and then rescaled their results to compare with real families, showing again that the reaccumulation process is necessary to find any good solution. However, a caution about extending results from the disruption of 100-km-diameter parent bodies to observed families that originated from parent bodies very different in size from 100 km is in order and was acknowledged by Durda et al. (2007).

##### 4.1. The Size Distribution of Family Members

The role of geometric constraints accounting for the finite volume of the parent body in the production of family members was investigated by Tanga et al. (1999) and Campo Bagatin and Petit (2001). By filling the parent body with spherical (Tanga et al., 1999) or irregular (Campo Bagatin and Petit, 2001) pieces, starting from the largest member, they were able to reproduce the size distribution of some asteroid families to an encouraging level of agreement.

However, these models do not incorporate any physics, nor do they take into account fragment reaccumulation, and therefore they do not provide any explanation for how family members are formed nor any prediction for their internal properties. Moreover, ejection velocities are not addressed by this approach.

The first full numerical simulations of catastrophic disruption and gravitational reaccumulation by Michel et al. (2001) assumed a monolithic structure of the parent body represented by a sphere with material properties of basalt (no internal porosity was considered). These simulations already reproduced qualitatively the main properties of real family member size distributions. However, when looking into more quantitative details, it was found that the cumulative size distribution of simulated fragments was characterized systematically by a lack of intermediate-sized bodies and a very steep slope for the smaller ones (see an example in Fig. 1). Such characteristics are not always observed in the size distributions of real family members. In fact, for some families, the size distribution looks rather continuous. In their systematic study, Durda et al. (2007), using the same internal structures (monolithic, basalt) but considering 100-km-diameter parent bodies only, found a larger variety of size distributions in terms of power-law slopes and discontinuities, depending on the considered impact conditions.

Nevertheless, it is also known that the outcome of a collision is influenced by the initial internal structure of the parent body and that, depending on the initial structure, the fragment size distribution may be more or less continuous. In order to check this, Michel et al. (2003, 2004) modeled parent bodies with an internal structure composed of different zones of voids and fractures, as if they had first been shattered during their collisional history before undergoing a major event leading to their disruption, as explained in section 3. The simulations of the Eunomia and Koronis family formations were redone using pre-shattered parent bodies (Michel et al., 2004), and the results were compared with those obtained using monolithic parent bodies. The best agreement was actually found with pre-shattered parent bodies. In particular, in the case of the Koronis family, an interesting result was obtained from these simulations, which may have important implications concerning the real family history. The size distribution obtained from the disruption of a pre-shattered parent body contains four largest fragments of approximately the same size, as can be seen in Fig. 1. This peculiar characteristic is shared by the real family, and has been a source of debate as it was assumed that a single collisional event cannot produce such a property (see Michel et al., 2004, for a discussion). Moreover, the simulation using a monolithic parent body did not result in such a distribution. It was then demonstrated numerically for the first time, by using a pre-shattered parent body, that these fragments can actually be produced by the original event, and therefore no subsequent mechanism needs to be invoked to form them, which would otherwise require a revision of the entire family history (Marzari et al., 1995). According to these results, which show that even old families

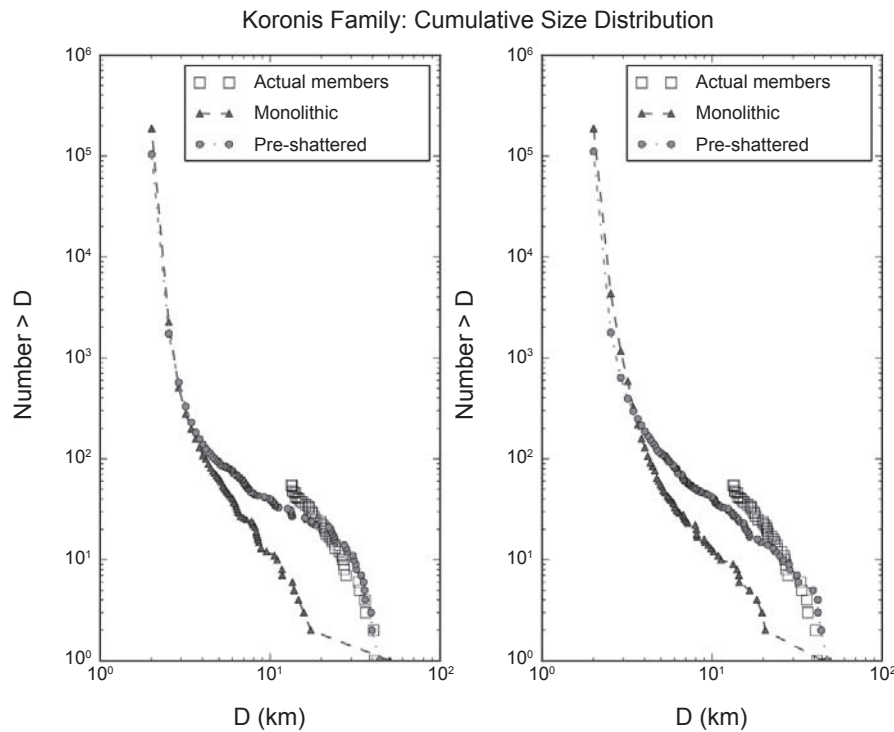


**Fig. 1.** Cumulative diameter distributions in log-log plots for the fragments of the simulated Koronis families. The plot on the left was obtained with a projectile colliding head-on, whereas an impact with an angle of incidence  $\theta$  equal to  $45^\circ$  gave rise to that on the right. Different symbols are used to distinguish between parent-body models. The plots also show the estimated sizes of the actual members down to the completeness limit (Tanga et al., 1999). Note that the simulations using a pre-shattered target reproduce the four nearly identical largest members.

may well have originated from pre-shattered parent bodies, it was concluded that most large objects in the present-day asteroid belt may well be pre-shattered or self-gravitating aggregates/rubble piles.

Constraints provided by the measured size distribution of family members can eliminate formation scenarios in numerical simulations. An interesting example is the Karin cluster, a small asteroid family identified by Nesvorný et al. (2002) that formed  $\sim 5.8$  m.y. ago in the outer main belt. The estimated size distribution for this family, when first identified, was fairly smooth and continuous over all sizes. In particular, there was no big gap between the size of the largest member of the family, (832) Karin, and that of the second-largest member, (4507) 1990 FV. Numerical simulations by Michel et al. (2003) indicated that the best match to the continuous size distribution was provided by the breakup of a pre-shattered or rubble-pile parent body. Simulations starting from a monolithic parent body, on the other hand, produced size distributions showing a large gap between the sizes of the largest and next-largest fragments. The finding that the parent body of the Karin cluster needed to be a rubble pile was actually consistent with its history. Specifically, the parent asteroid of the Karin cluster is thought to have been produced by an early disruptive collision that created the much larger Koronis family some 2–3 G.y. ago. According

to the results of Koronis family-formation simulations, the parent asteroid of the Karin cluster should have been formed as a rubble pile from Koronis family debris.

However, Nesvorný et al. (2006) later revised the definition of the Karin cluster. In particular, they found that the original second-largest identified member of the family, (4507) 1990 FV, is in fact a background asteroid with no relation whatsoever to the recent breakup at the origin of the Karin cluster. Once this body is removed from the cluster membership, a large gap opens between the size of the largest family member and smaller members, a distribution that is now best reproduced in simulation by starting with a monolithic parent body. This change in implication for the internal structure of the parent body shows the importance of having a reliable estimate of the actual size distribution of family members. However, in the case of the Karin cluster, this change is problematic because the parent body of the Karin cluster is expected to be a rubble pile, if it is an original fragment of the Koronis-forming event. A solution proposed by Nesvorný et al. (2006) is that the Karin cluster parent body was really formed by reaccumulation of smaller fragments during the Koronis family formation, as found in numerical simulations, but then was somehow consolidated into a more coherent body by various possible processes (lithification of regolith filling the interior, etc.). Another pos-

sibility is that in simulations, we are missing cases in which large intact fragments are created, so that the Karin cluster parent body could really have been a monolithic body. In fact, this systematic absence of large intact fragments in asteroid disruption simulations is often mentioned as a potential issue when discussing, for example, the internal structure of Eros, imaged by the Near Earth Asteroid Rendezvous (NEAR) Shoemaker spacecraft (see section 5.1).

A model of fragmentation adapted for microporous bodies (for a definition of microporosity, see the chapter by Jutzi et al. in this volume) has recently been implemented into an SPH hydrocode and tested against experiments on pumice targets (Jutzi et al., 2008, 2009). It then became possible to simulate the formation of asteroid families from a microporous parent body. A microporous structure is assumed to be appropriate for parent bodies of dark taxonomic type or primitive asteroid families. In effect, several pieces of evidence point to the presence of a high degree of porosity in asteroids belonging to the C-complex, such as the low bulk density ( $\approx 1.3 \text{ g cm}^{-3}$ ) estimated for some of them, for instance, the asteroid (253) Mathilde encountered by the NEAR Shoemaker spacecraft (Yeomans et al., 1997), and as inferred from meteorite analysis (Britt et al., 2006). This model adapted for microporous bodies was used to reproduce the formation of the Veritas family, which is classified as a dark-type family whose members have spectral characteristics of low-albedo, primitive bodies, from C to D taxonomic types (Di Martino et al., 1997). This family is located in the outer main belt and is named after its apparent largest constituent, the asteroid (490) Veritas. The family age was estimated by two independent studies to be quite young, around 8 m.y. (Nesvorný et al., 2003; Tsiganis et al., 2007). Therefore, current properties of the family may retain signatures of the catastrophic disruption event that formed it. Michel et al. (2011) investigated the formation of the Veritas family by numerical simulations of catastrophic disruption of a 140-km-diameter parent body, which was considered to be the size of the original family parent body, made of either porous or nonporous material. Pumice material properties were used for the porous body, while basalt material properties were used for the nonporous body. Not one of these simulations was able to produce satisfactorily the estimated size distribution of real family members. Previous studies devoted to either the dynamics or the spectral properties of the Veritas family treated (490) Veritas as a special object that may be disconnected from the family. Simulations of the Veritas family formation were then performed representing the family with all members except Veritas itself. For that case, the parent body was smaller (112 km in diameter), and a remarkable match was found between the simulation outcome, using a porous parent body, and the real family. Both the size distribution and the velocity dispersion of the real reduced family were reproduced, while the disruption of a nonporous parent body did not reproduce the observed properties very well (see Fig. 2). This finding was consistent with the C spectral type of family members, which suggests that the parent body was porous and showed the importance

of modeling the effect of porosity in the fragmentation process. It was then concluded that it is very likely that the asteroid (490) Veritas and probably several other small members do not belong to the family as originally defined, and that the definition of this family should be revised. This example shows how numerical modeling can better constrain the definition of (or the belonging to) an asteroid family, provided that (1) the fragmentation model used to simulate its formation is consistent with the possible material properties of the parent body, and (2) the family is young enough that a direct comparison with the modeling is possible.

#### 4.2. The Ejection Velocity Distribution of Family Members

In addition to fragment sizes, numerical simulations also provide the ejection velocities. In general, impact simulations find that smaller fragments tend to have greater ejection speeds than larger ones. However, there is still a wide spread of values for fragments of a given mass, which makes it difficult to define a power-law relationship between fragment masses and speeds, such as the ones often used in collisional evolution models (see, e.g., Davis et al., 2002). Figure 3 shows an example of this relation for a simulation reproducing the Eunomia family as a result of the disruption of a monolithic (basalt-like) parent body impacted at an impact angle of 45°.

In the case of real asteroid families, however, the dispersion of their members is characterized through their orbital proper elements, in particular their proper semimajor axis, eccentricity, and inclination. These elements have long been assumed to be essentially constants of motion that remain practically unchanged over astronomically long timescales (e.g., Milani and Knezević, 1994), although some perturbations have been found to be capable of modifying them, as we will explain below. Thus, we do not have direct access to the ejection velocities of family members. Fortunately, ejection velocities can be converted into a dispersion in orbital elements through Gauss' equations (Zappalà et al., 1996), provided that both the true anomaly and the argument of perihelion of the family parent body at the impact instant are known or assumed. For a given family, the estimated values of the barycenter semimajor axis, eccentricity, and inclination can be used with the Gauss formulae up to first order in eccentricity to compute for each member the distance of its orbital elements  $\delta a$ ,  $\delta e$ , and  $\delta I$  from the barycenter of the family

$$\left\{ \begin{array}{l} \frac{\delta a}{a_b} = \frac{2}{na_b\sqrt{1-e_b^2}} [(1+e_b \cos f_0)V_T + e_b \sin f_0 V_R] \\ \delta e = \frac{\sqrt{1-e_b^2}}{na_b} \left[ \frac{e_b + 2 \cos f_0 + e_b \cos^2 f_0}{1+e_b \cos f_0} V_T + \sin f_0 V_R \right] \\ \delta I = \frac{\sqrt{1-e_b^2}}{na_b} \frac{\cos(\omega + f_0)}{1+e_b \cos f_0} V_W \end{array} \right. \quad (1)$$

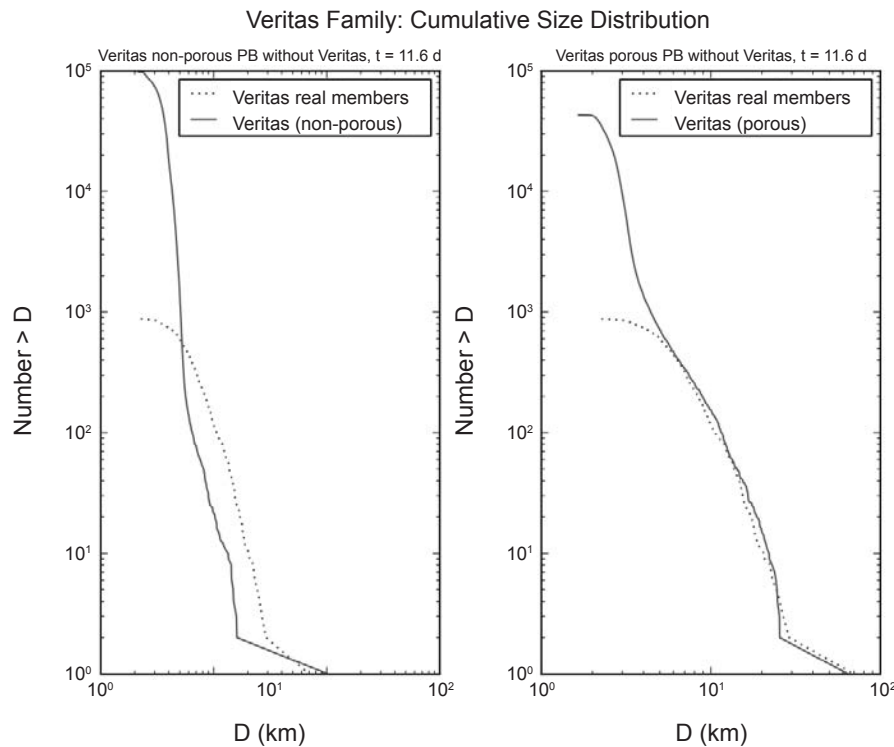


**Fig. 2.** Cumulative size distributions of fragments from the simulations of the disruption of a Veritas monolithic parent body, either nonporous (left) or porous (right). The impact angle is  $0^\circ$  (head-on) and the impact speed is  $5 \text{ km s}^{-1}$ . The distribution of the real family is also shown for comparison. In this case, the family consists of all members except Veritas itself, which reduces the size of the parent body to 112 km. The simulated time is about 11.6 d after the impact.

where  $V_T$ ,  $V_R$ , and  $V_W$  are the components of the ejection velocity in the along-track, radial, and out-of-plane directions, respectively,  $n$  is the mean motion,  $f_0$  is the true anomaly of the parent body at the instant of the breakup, and  $\omega$  is its argument of perihelion. Since these last two angles are not known, their values must be assumed. Zappalà *et al.* (1996) showed that the most sensitive angle is  $f_0$ . Assuming different values of this angle changes the shape of the cluster containing the family members in orbital element space. In other words, it defines whether the breakup generates a family that is spread in semimajor axis, in eccentricity, or in inclination.

Thanks to this conversion, it is thus possible to assess the realism of a numerical simulation of a family formation by comparing the dispersion of family members and simulated fragments in the same space. Unfortunately, other mechanisms exist that, depending on the age of the considered family, can obscure the original dispersion of family members. In fact, once a family is created, its members are subjected to various perturbations. In particular, high-order secular resonances, mean-motion resonances even involving multiple planets (Morbidelli and Nesvorný, 1999), and the Yarkovsky thermal effect (Farinella and Vokrouhlický, 1999) have been shown to be capable of altering the proper elements. Therefore, while proper elements have been assumed conventionally to retain the memory of the disruption

outcome conditions, these later studies demonstrated that this is not necessarily true, even for the proper semimajor axis in the case when the asteroid is small enough that Yarkovsky drift is effective (see Bottke *et al.*, 2002; chapter by Vokrouhlický *et al.* in this volume). Depending on how old the family is, the current proper elements of family members cannot be interpreted as reflecting their starting conditions; rather, they must be seen as a result of such secular processes acting over time, whose effects are to cause a slow diffusion of family members in orbital-element space, starting from a smaller dispersion. The Koronis family is a good example showing these effects. The current distribution of Koronis family members in proper-element space is quite spread and its shape suggests that it has been subjected to the Yarkovsky effect as well as to the effects of nearby secular resonances and mean-motion resonances. Bottke *et al.* (2001) computed the dynamical evolutions of 210 simulated Koronis family members under the influence of the Yarkovsky effect and dynamical diffusion due to several resonances (namely, the 5:2 and 7:3 mean-motion resonances with Jupiter, a secular resonance that involves the precession rate of the small body's longitude of perihelion  $g$  and the fundamental frequencies of Jupiter  $g_5$  and Saturn  $g_6$ ). The test family members were started with a dispersion that is consistent with the ones obtained from impact simulations of Koronis

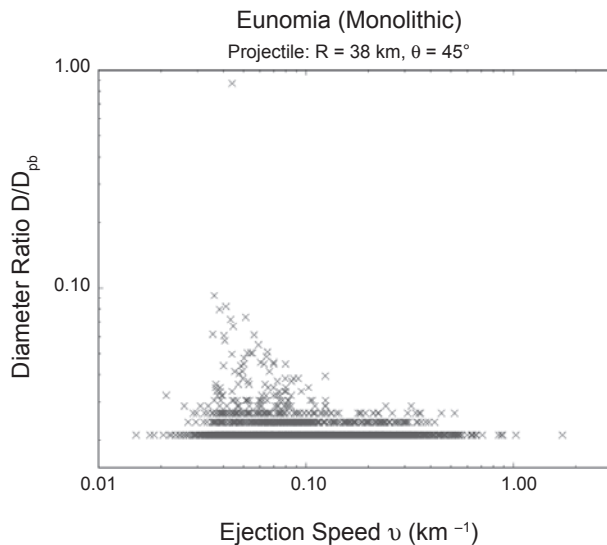


**Fig. 3.** Fragment diameter  $D$  (normalized to that of the parent body  $D_{pb}$ ) vs. ejection speed in a log-log plot obtained from a monolithic Eunomia parent body simulation using a projectile impacting at an angle of incidence  $\theta = 45^\circ$ . Only fragments with size above the resolution limit (i.e., those that underwent at least one reaccumulation event) are shown here. From Michel et al. (2004).

family formation. They were integrated over 700 m.y., which is still shorter than the estimated age of the family ( $>1$  G.y.). However, this evolution showed that the current shape of the family cluster in proper-element space does not represent the original shape from the collisional event but is well explained by its subsequent evolution.

Fortunately, if a family is young enough, its dispersion can still be close to the original one resulting from the parent body breakup, and in that case, the comparison between numerical simulations of family formation and actual family dispersion is straightforward. On the other hand, the degree of spreading observed now, together with the knowledge of the degree of dispersion resulting directly from the breakup by numerical simulations, can better constrain the age of the family, once the efficiency of the diffusion processes is well assessed. Nesvorný et al. (2002, 2003) identified several asteroid families with formation ages smaller than 10 m.y. These families represent nearly the direct outcome of disruptive asteroid collisions, because the observed remnants of such recent breakups have apparently suffered limited dynamical and collisional erosion (Bottke et al., 2005). As already described in the previous section, the Karin cluster and the Veritas family belong to this group of young families.

Figure 4 shows an example in which the dispersion of the actual Veritas family is compared with that of fragments from an impact simulation of Veritas family formation. The simulated dispersion matches the shape of the ellipses representing the real dispersion. This result is consistent with the expectation that the orbital extent of the family is not produced by post-diffusion processes, which gives some cred-

ability to family-formation simulations that reproduce both the size distribution and velocity dispersion of actual members.

## 5. IMPLICATIONS

### 5.1. Internal Structure of Asteroids

According to numerical simulations of family formation, all fragments produced by the catastrophic disruption of a large asteroid (typically larger than 1 km in diameter, e.g., in the gravity regime) consist of self-gravitating aggregates, except the smallest ones. If this is correct, then most asteroids that are at least second generation should be rubble piles. We note that Campo Bagatin et al. (2001) ran a number of simulations of main-belt collisional evolution to assess the size range where reaccumulated bodies should be expected to be abundant in the main asteroid belt. They found that this diameter range goes from about 10 to 100 km, but may extend to smaller or larger bodies, depending on the prevailing collisional response parameters, such as the strength of the material, the strength scaling law, the fraction of kinetic energy of the impact transferred to the fragments, and the reaccumulation model.

The collisional lifetime of bodies larger than a few tens to hundreds of kilometers in diameter is longer than the age of the solar system, suggesting that most bodies in that size range are likely to be primordial, while smaller bodies are probably collisional fragments (see, e.g., Bottke et al., 2005, and the chapter by Bottke et al. in this volume). The exact size above which a body is more likely to be primordial is somewhat model-dependent. Binzel et al. (1989), from a study of light curves, suggested that this transition occurs at a diameter of  $\approx 125$  km. However, as this is a statistical measure, some smaller asteroids may still be primordial and some larger ones may have broken up in the past. In fact, due to the variability in possible interior starting compositions, and variations in the chaotic dynamics of accumulation, the size above which a body is more likely to be primordial is dependent on the specific formation scenario, as well as the compositions, masses, and velocities involved. Thus, some asteroids smaller than 100 km may still be primordial, and some larger ones may have broken up catastrophically in the past. This is especially true if one goes back to the very earliest formation, in the first few million years, when considering hit-and-run collisions (see the chapter by Asphaug et al. in this volume). These may have completely disrupted some of the largest asteroids, as projectiles, when they experienced grazing collisions into larger target embryos. This makes the internal structure of middle-sized asteroids one of the most important aspects of these bodies that can be determined by future space missions and observations, allowing us to test our interpretations based on theoretical collisional studies (see also the chapter by Scheeres et al. in this volume).

During the past 4 b.y., catastrophic disruption has been the result of hypervelocity collisions. Bottke et al. (2005) estimate that about 20 asteroid families have formed from the breakup of parent bodies larger than 100 km diameter over

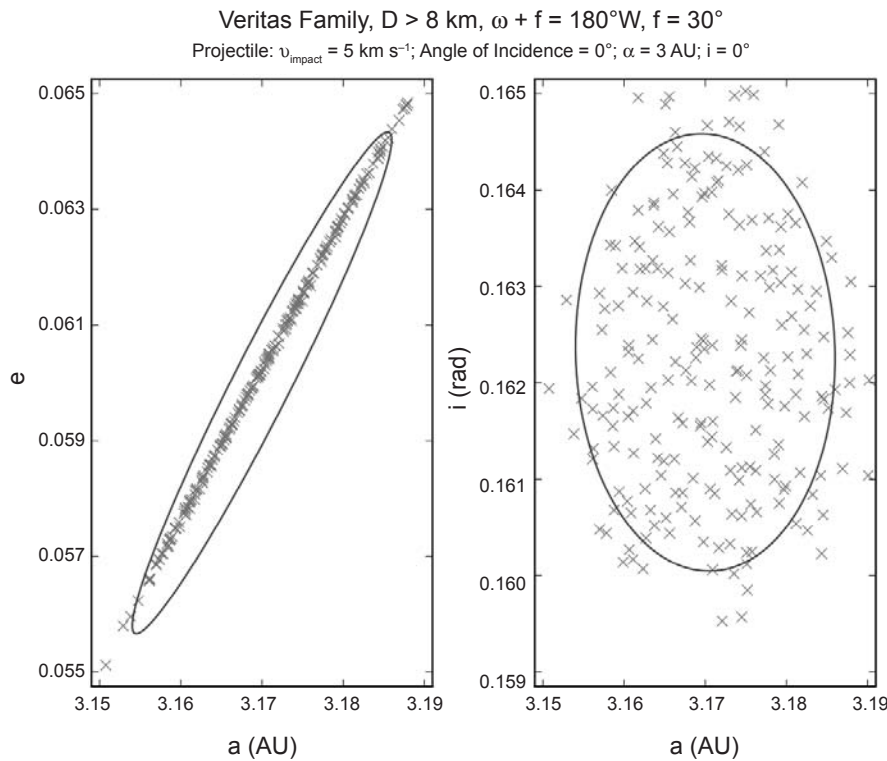


**Fig. 4.** Distribution of fragments larger than 8 km from a simulation of disruption of a porous monolithic Veritas family parent body excluding Veritas itself as a result of a head-on impact of a projectile at  $5 \text{ km s}^{-1}$  with orbital semimajor axis  $a$  of 3 AU and inclination  $i$  of  $0^\circ$ . The outcome is represented in the  $a-e$  plane (left) and  $a-i$  plane (right). The superimposed ellipse is an equipartition curve for speed cutoff of  $40 \text{ m s}^{-1}$ , parent body true anomaly  $f = 30^\circ$  and argument of perihelion  $\omega = 150^\circ$ . This curve was defined by Tsiganis *et al.* (2007) as that closest to representing the dispersion of the real Veritas family in orbital element space. From Michel *et al.* (2011).

the last 4 b.y. But several hundred asteroids currently exist in the 100-km size range, making it likely that most of these are original bodies. In this regard, asteroid (21) Lutetia, approximately 90 km in diameter, is a scientifically important object of which we have obtained a quick glimpse during Rosetta's 2010 flyby (see the chapter by Barucci *et al.* in this volume). The relatively high measured mass (bulk density  $3.1 \text{ g cm}^{-3}$ ) led Weiss *et al.* (2012) to interpret Lutetia as being a partly differentiated, impact-shattered, but largely intact parent body, covered in a predominately chondritic outer component. Other interpretations are of course possible.

Assuming that the transition between primordial and second-generation bodies occurs at diameters  $\sim 100$  km, what about (433) Eros, whose diameter is much below this threshold and therefore should be a fragment of a larger body? There is still a debate about the internal structure of this asteroid, as the images of its surface can be explained by either a fractured (but solid/strength-dominated) structure or a rubble pile (Asphaug, 2009; chapter by Marchi *et al.* in this volume). However, if Eros is not a rubble pile, its formation as a fragment of a large asteroid would need a solution that is not yet found in numerical simulations of catastrophic disruptions.

Another point of view could thus be that it is a monolithic body that has been shattered in place (e.g., Housen, 2009; Buczkowski *et al.*, 2008). In this case, major impacts fracture it in place, introducing only modest increases to its porosity. This requires a very low strain rate of expansion, e.g., a small elastic strain at fracture, which may be consistent with size-dependent relationships for brittle failure. So this is probably feasible to form a shattered monolith when a single monolithic body is impacted, but with relatively low energy compared to disruption. But then one must ask, where did the single monolithic body come from to begin with, and why has it not been subsequently fragmented and jumbled by slightly more energetic collisions? The alternative is that the grooves have nothing to do with brittle failure, but are instead planes of granular failure.

Thus, so far, the formation of a dispersed cloud of sizable fragments (larger than a few hundreds of meters) systematically requires that the parent body is first fragmented into small pieces, down to the resolution limit of simulations (a few hundreds of meters), and then that gravitational reaccumulation takes place to form larger final remnants. This is probably what happened for (25143) Itokawa, which appears

to be a rubble pile (*Fujiwara et al.*, 2006). In fact, if the major blocks on Itokawa were intact monolithic, then they would give us a kind of lower size range of intact fragments produced from large impacts. Using the version of *pckgrav* with enhanced collision handling to preserve shape and spin information of reaccumulated bodies (*Richardson et al.*, 2009), *Michel and Richardson* (2013) showed that the process of catastrophic disruption and gravitational reaccumulation can form fragments with shapes similar to that of Itokawa, and can explain the presence of a large amount of boulders on the surface, as observed. Figure 5 shows the outcome of such a simulation. We note that in this kind of modeling, the shapes of the aggregates formed by the reaccumulation process are parameter dependent. In particular, if we change the assumed strength of the aggregates or the bouncing coefficients (see *Michel and Richardson*, 2013, for a definition of these parameters), the final shape may be different. For instance, a preliminary simulation using a lower strength leads to a final largest aggregate that is more spherical. Because of the lower assumed strength, reaccumulating aggregates break more easily as a result of tidal and rotational forces, and therefore the object produced by this reaccumulation has difficulty keeping its irregular shape and instead becomes more and more rounded. Further studies are required to determine whether this type of outcome has some interesting implications, and to assess the actual sensitivity of the final shapes of reaccumulated objects to the parameters. It may be that we can provide some rough constraints on some of the mechanical properties of asteroids whose shapes are known, based on the parameters required to form them using this model. An extensive set of simulations that will require long runs with current computer power is planned for this purpose.

The production of rubble goes up with size, because it gets harder and harder (with increasing gravity) to liberate mass to escape speed than to beat it into small fragments that eventually can reaccumulate. The implication is that if Itokawa is a rubble pile, then Eros should be even more so. Whether this is in fact reality awaits direct seismic or internal-structure exploration (e.g., by radar tomography)

of objects Eros-sized and larger (see also the chapter by Scheeres et al. in this volume).

## 5.2. Compositions

Originally families were only identified on the basis of dynamical considerations. Then, once spectral observations became available, it was found that the vast majority of those families identified by dynamics showed remarkable homogeneous spectral properties (see the chapter by Masiero et al. in this volume). So, homogeneity in terms of spectral properties seems to be the norm. However, when an object satisfies the distance criterion to be associated with a family, it is often considered as an interloper when its spectral properties do not match. Therefore, the identification of family membership also relies on homogeneous spectral properties and whether the homogeneity in spectral properties is a reality, or an assumption is not yet clear. Such homogeneity can only be explained if the family parent body was homogenous itself, so that when fragments reaccumulate during the reaccumulation phase, there's no mixture of different materials taking place. Alternatively, it may also be that the reaccumulation process does not mix different materials that could be initially present in the parent body or mixes it so well that the outcome still looks homogeneous. Otherwise, if the parent body was heterogeneous in composition and if some mixtures happened, then the resulting family would show a variety of spectral properties within its members. In fact, if reaccumulation is a random process, we expect the particles of a given large fragment to originate from uncorrelated regions within the parent body. In that case, if the parent body was heterogeneous in composition, then the composition of reaccumulated fragments could be a mixture of various material. Conversely, if the initial velocity field imposed by the fragmentation process determines the reaccumulation phase, the particles belonging to the same fragment should originate from well-defined areas inside the parent body. In addition, the position and extent of these regions would provide indications about the mixing occurring as a result of the reaccumulation process.

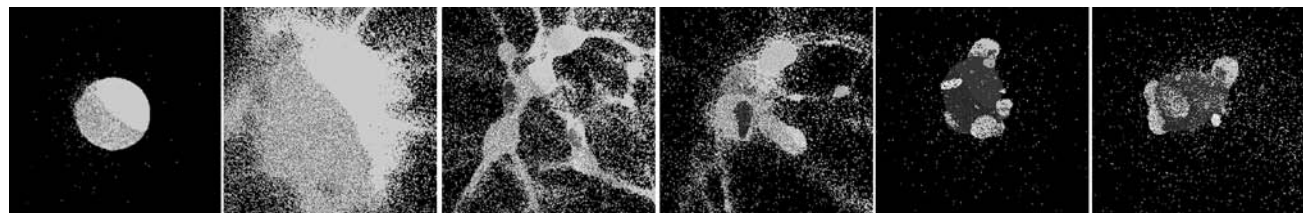


**Fig. 5.** Snapshots of the reaccumulation process following the disruption of a 25-km-diameter asteroid. From left to right: first instant at the end of the fragmentation phase when all fragments (white dots) are about 200 m in diameter; the ejection of those fragments a few seconds later; the first reaccumulations that occur because of the slow relative speed between some fragments, showing the formation of a few aggregates represented by different gray levels; the formation of the largest fragment of this disruption by reaccumulation of several aggregates into a single body; and the final largest fragment shown at two different instants: The boulders on its surface and its overall shape are reminiscent of Itokawa. Credit: Michel and Richardson, A&A, 554, L1, 2013, reproduced with permission ©ESO.

*Michel et al.* (2004) traced back, at least for some of the largest fragments, the original positions within the parent body of the particles that end up forming the aggregates during some family formations. As an example, they traced the particles belonging to the three largest fragments of their simulation of the Koronis family formation back to their original positions inside the parent body. Recall that the Koronis family was formed in a highly catastrophic event, as its largest member is estimated to contain only 4% of the parent body's mass. In such an event, the reaccumulation process lasts up to several days, much longer than for a barely disruptive event, and gives rise to many gravitational encounters. Therefore, this kind of event may well lose the memory of the initial velocity field. Nevertheless, it was found that particles forming a large reaccumulated fragment originate from well-clustered regions within the parent body. This indicates that reaccumulation is definitely not a random process. Interestingly, the position of the original region depends greatly on the internal properties of the parent body. The largest remnant of the pre-shattered model of the Koronis parent body involves particles that were initially located between the core and the region antipodal to the impact point. Conversely, in the monolithic parent body, those particles were initially much more clustered in the core region, with no particles originating from the antipode. This difference also holds true for the next-largest fragments. Nevertheless, these results indicate that the velocity field arising from the fragmentation phase has a major influence on the reaccumulation process. Particles that eventually belong to a given fragment originate from the same region inside the parent body. However, this location (as well as its extent, which determines the degree of mixing of the fragments) depends also on the parent body's internal properties in a complex way. Recently *Michel et al.* (2015) looked at the cases of parent bodies with internal structures that could represent large asteroids formed early in solar system history. Some results are shown in the chapter by Jutzi et al. in this volume. They confirm that most particles in each reaccumulated fragment are sampled from the same original region within the parent body. However, they also found that the extent of the original region varies considerably depending on the internal structure of the parent body and seems to shrink with its solidity.

As a conclusion, the spectral homogeneity within a family may represent the material homogeneity of the initial parent body. It may also be due to the way reaccumulation takes place. But in that case, and if the parent body was heterogeneous, although each family member would still be homogeneous, we may expect different spectral properties from one member to another, depending on which original region of the parent body it samples. The fact that most families do not show strong spectral variations between family members, at least in the data from groundbased observations — except if this is imposed by the membership criterion — is consistent with the theory of homogeneity of the family parent body.

## 6. CONCLUSIONS

Our understanding of the collisional physics and our account for gravity in large asteroid disruptions have allowed numerical simulations to successfully reproduce the formation of asteroid families, in agreement with the idea that these families originate from the disruption of a large parent body. Simulation results indicate that asteroid family members are not just the product of the fragmentation of the parent body, leading to intact fragments, but rather the outcome of the subsequent gravitational phase of the event, which allows some of the intact fragments to reaccumulate and form gravitational aggregates, or rubble piles. For all considered cases so far (family parent bodies of diameter typically larger than tens of kilometers), this outcome is systematic for fragments larger than a few hundred meters. Thus, according to simulations, since it is believed that most bodies smaller than 100 km in diameter originate from the disruption of a larger body, then they should be rubble piles or heavily shattered bodies, which is consistent with the low measured bulk densities for some of them and the finding by *Campo Bagatin et al.* (2001) based on main-belt collisional evolution modeling. Therefore, exploring the origin of asteroid families unexpectedly led to a result that has great implications for the entire asteroid population and its history.

Moreover, it was also found that the outcome of a disruption is very sensitive to the original internal structure of the parent body, in particular the kind and amount of internal porosity. Thus, the comparison between simulation outcomes for various kinds of parent-body structures (monolithic, pre-shattered, microporous, rubble pile) and real family properties can help to constrain the internal properties of the parent body of the considered families and in the family identification itself. For instance, it was found that the Veritas family is very well reproduced if the asteroid Veritas itself is excluded from its family, which was already recognized as a possibility before disruption simulations were performed to model the formation of this family.

Thanks to the improved sensitivity of observations, allowing us to reach smaller asteroid sizes, and to the tools developed to better define asteroid families, new asteroid families keep being identified, especially small and young ones. The latter, which have not yet been affected by dynamical diffusion or post-collisional processes, are a good test for numerical simulations, which must be able to reproduce them as they are. Such an exercise, which has already been done successfully for some young families (e.g., Veritas, Karin), must keep being performed as a check for our numerical models. In particular, new fragmentation models are continuously being developed, accounting for various possible strength models and fragmentation modes. Once they are validated at small laboratory scales by comparison with impact experiments, they can be used at large scale (with an associated N-body code) to reproduce young family properties, allowing us to increase the range of internal

structures and fragmentation modes that can be considered for the parent body. This modeling work, calling for different models, is crucial to better constrain the possible internal structure of family parent bodies, to refine the definition of a family, and to understand whether some families are formed from differentiated/heterogeneous parent bodies, despite their apparent (or assumed) homogeneities. Asteroid families are very important tracers of the entire asteroid belt history and as we have already seen, our understanding of them can have profound implications on determination of the physical properties of asteroids in general.

More work is also required to check in which context large intact fragments can be produced in numerical simulations of large asteroid disruptions. Although there is no firm conclusion about Eros' internal structure, the fact that it may be a shattered object only and not a rubble pile raises the issue of the formation of such large fragments in a collision. It may also be that the reaccumulation process is followed by internal processes that may consolidate boulders. Such processes would eventually transform reaccumulated fragments into a coherent body. If this were the case, then reaccumulation would not necessarily imply a rubble-pile structure. Simulations of the reaccumulation phase now include the possibility of accounting for the final possible shapes of reaccumulated fragments. This modeling needs further improvement to increase its realism, but it will be very difficult, if even possible, to achieve the level of complexity needed to model the internal processes that may consolidate boulders. Asteroid internal processes are poorly understood and depend on too many parameters and unknowns.

Space missions dedicated to direct measurement of internal structures, and possibly to their response to an impact (e.g., by using a kinetic impactor), are thus crucial to improve our understanding of these important internal properties of asteroids and to check our modeling of the collisional and internal processes. Moreover, sample return missions as well as visits/flybys of members of asteroid families would also provide detailed information on their physical properties and would allow us to check whether groundbased measurements wash out some important data regarding their composition and possible variations among members. Asteroid families and the collisional process, which is at the heart of family formation and evolutionary main-belt history, rely on our efforts to combine complex models and space-/groundbased measurements.

**Acknowledgments.** We are grateful to Clark Chapman and an anonymous reviewer for their comments that greatly helped to improve the chapter. P.M. acknowledges support from the French space agency CNES and the French national program of planetology. D.C.R. acknowledges NASA grant NNX08AM39G and NSF grant AST1009579 (and previous NASA/NSF grants). D.D.D. acknowledges support from the National Science Foundation (Planetary Astronomy Program grants AST0098484, AST0407045, and AST0708517). M.J. is supported by the Ambizione program of the Swiss National Science Foundation.

## REFERENCES

- Arnold J. R. (1969) Asteroid families and jet streams. *Astron. J.*, **74**, 1235–1242.
- Asphaug E. (2009) Growth and evolution of asteroids. *Annu. Rev. Earth Planet. Sci.*, **37**, 413–448.
- Asphaug E., Ryan E. V., and Zuber M. T. (2002) Asteroid interiors. In *Asteroids III* (W. F. Bottke Jr. et al., eds.), pp. 463–484. Univ. of Arizona, Tucson.
- Ballouz R.-L., Richardson D. C., Michel P., and Schwartz S. R. (2014) Rotation-dependent catastrophic disruption of gravitational aggregates. *Astrophys. J.*, **789**, 158.
- Ballouz R. L., Richardson D. C., Michel P., Schwartz S. R., and Yu Y. (2015) Numerical simulations of collisional disruption of rotating gravitational aggregates: Dependence on material properties. *Planet. Space Sci.*, **107**, 29–35.
- Benavidez P., Durda D. D., Enke B. L., et al. (2012) A comparison between rubble-pile and monolithic targets in impact simulations: Application to asteroid satellites and family size distributions. *Icarus*, **219**, 57–76.
- Benz W. and Asphaug E. (1994) Impact simulations with fracture. I. Method and tests. *Icarus*, **107**, 98–116.
- Benz W. and Asphaug E. (1995) Simulations of brittle solids using smooth particle hydrodynamics. *Comp. Phys. Commun.*, **87**, 253–265.
- Benz W. and Asphaug E. (1999) Catastrophic disruptions revisited. *Icarus*, **142**, 5–20.
- Binzel R. P., Farinella P., Zappalà V., and Cellino A. (1989) Asteroid rotation rates-distributions and statistics. In *Asteroids II* (R. P. Binzel et al., eds.), pp. 416–441. Univ. of Arizona, Tucson.
- Bottke W. F., Vokrouhlický D., Borz M., Nesvorný D., and Morbidelli A. (2001) Dynamical spreading of asteroid families via the Yarkovsky effect. *Science*, **294**, 1693–1696.
- Bottke W. F., Vokrouhlický D., Rubincam D. P., and Broz M. (2002) The effect of Yarkovsky thermal forces on the dynamical evolution of asteroids and meteoroids. In *Asteroids III* (W. F. Bottke Jr. et al., eds.), pp. 395–408. Univ. of Arizona, Tucson.
- Bottke W. F., Durda D. D., Nesvorný D., Jedicke R., Morbidelli A., Vokrouhlický D., and Levison H. (2005) The fossilized size distribution of the main asteroid belt. *Icarus*, **175**, 111–140.
- Britt D.T., Consolmagno G. J., and Merline W. J. (2006) Small body density and porosity: New data, new insights. *Lunar Planet. Sci. XXXVII*, Abstract #2214. Lunar and Planetary Institute, Houston.
- Buczkowski D. L., Barnouin-Jha O. S., and Prockter L. M. (2008) 433 Eros lineaments: Global mapping and analysis. *Icarus*, **193**, 39–52.
- Campo Bagatin A. and Petit J.-M. (2001) Effects of the geometric constraints on the size distributions of debris in asteroidal fragmentation. *Icarus*, **149**, 210–221.
- Campo Bagatin A., Petit J.-M., and Farinella P. (2001) How many rubble piles are in the asteroid belt? *Icarus*, **149**, 198–209.
- Chapman C. R., Davis D. R., and Greenberg R. (1982) Apollo asteroids: Relationships to main belt asteroids and meteorites. *Meteoritics*, **17**, 193–194.
- Chapman C. R., Paolicchi P., Zappalà V., Binzel R. P., and Bell J. F. (1989) Asteroid families: Physical properties and evolution. In *Asteroids II* (R. P. Binzel et al., eds.), pp. 386–415. Univ. of Arizona, Tucson.
- Davis D. R., Chapman C. R., Greenberg R., Weidenschilling S. J., and Harris A. W. (1979) Collisional evolution of asteroids — Populations, rotations, and velocities. In *Asteroids* (T. Gehrels ed.), pp. 528–557. Univ. of Arizona, Tucson.
- Davis D. R., Chapman C. R., Greenberg R., and Weidenschilling S. J. (1985) Hirayama families: Chips off the old block or collections of rubble piles? *Bull. Am. Astron. Soc.*, **14**, 720.
- Davis D. R., Durda D. D., Marzari F., Campo Bagatin A., and Gil-Hutton R. (2002) Collisional evolutions of small body populations. In *Asteroids III* (W. F. Bottke Jr. et al., eds.), pp. 545–558. Univ. of Arizona, Tucson.
- Di Martino M., Migliorini F., Zappalà V., Manara A., and Barbieri C. (1997) Veritas asteroid family: Remarkable spectral differences inside a primitive parent body. *Icarus*, **127**, 112–120.

- Durda D. D., Bottke W. F., Enke B. L., Merline W. J., Asphaug E., Richardson D. C., and Leinhardt Z. M. (2004) The formation of asteroid satellites in large impacts: Results from numerical simulations. *Icarus*, 170, 243–257.
- Durda D. D., Bottke W. F., Nesvorný D., Enke B. L., Merline W. J., Asphaug E., and Richardson D. C. (2007) Size frequency distributions of fragments from SPH/N-body simulations of asteroid impacts: Comparison with observed asteroid families. *Icarus*, 186, 498–516.
- Durda D. D., Movshovitz N., Richardson D. C., Asphaug E., Morgan A., Rawlings A. R., and Vest C. (2011) Experimental determination of the coefficient of restitution for meter-scale granite spheres. *Icarus*, 211, 849–855.
- Durda D. D., Richardson D. C., Asphaug E., and Movshovitz N. (2013) Size dependence of the coefficient of restitution: Small scale experiments and the effects of rotation. *Lunar Planet. Sci. XLIV*, Abstract #2263. Lunar and Planetary Institute, Houston.
- Farinella P. and Vokrouhlický D. (1999) Semimajor axis mobility of asteroidal fragments. *Science*, 283, 1507–1510.
- Farinella P., Davis D. R., and Marzari F. (1996) Asteroid families, old and young. In *Completing the Inventory of the Solar System* (T. W. Rettig and J. M. Hahn, eds.), pp. 45–55. ASP Conf. Ser. 107, Astronomical Society of the Pacific, San Francisco.
- Fujiwara A., Kawaguchi J., Yeomans D. K., et al. (2006) The rubble-pile asteroid Itokawa as observed by Hayabusa. *Science*, 312, 1330–1334.
- Hirayama K. (1918) Groups of asteroids probably of common origin. *Astron. J.*, 31, 185–188.
- Housen K. (2009) Cumulative damage in strength-dominated collisions of rocky asteroids: Rubble piles and brick piles. *Planet. Space Sci.*, 57, 142–153.
- Jaeger J. C. and Cook N. G. W. (1969) *Fundamentals of Rock Mechanics*. Chapman and Hall, London.
- Jutzi M. (2015) SPH calculations of asteroid disruptions: The role of pressure dependent failure models. *Planet. Space Sci.*, 107, 3–9.
- Jutzi M., Benz W., and Michel P. (2008) Numerical simulations of impacts involving porous bodies. I. Implementing subresolution porosity in a 3D SPH hydrocode. *Icarus*, 198, 242–255.
- Jutzi M., Michel P., Hiraoka K., Nakamura A. M., and Benz W. (2009) Numerical simulations of impacts involving porous bodies. II. Confrontation with laboratory experiments. *Icarus*, 201, 802–813.
- Jutzi M., Michel P., Benz W., and Richardson D. C. (2010) The formation of the Baptistina family by catastrophic disruption: Porous versus non-porous parent body. *Meteoritics & Planet. Sci.*, 44, 1877–1887.
- Leinhardt Z. M. and Stewart S. T. (2009) Full numerical simulations of catastrophic small body collisions. *Icarus*, 199, 542–559.
- Marzari F., Davis D., and Vanzani V. (1995) Collisional evolution of asteroid families. *Icarus*, 113, 168–187.
- McGlaun J. M., Thompson S. L., and Elrick M. G. (1990) CTH: A 3-dimensional shock-wave physics code. *Int. J. Impact Eng.*, 10, 351–360.
- Michel P. and Richardson D. C. (2013) Collision and gravitational reaccumulation: Possible formation mechanism of the asteroid Itokawa. *Astron. Astrophys.*, 554, L1–L4.
- Michel P., Benz W., Tanga P., and Richardson D. C. (2001) Collisions and gravitational reaccumulation: Forming asteroid families and satellites. *Science*, 294, 1696–1700.
- Michel P., Benz W., Tanga P., and Richardson D. C. (2002) Formation of asteroid families by catastrophic disruption: Simulations with fragmentation and gravitational reaccumulation. *Icarus*, 160, 10–23.
- Michel P., Benz W., and Richardson D. C. (2003) Fragmented parent bodies as the origin of asteroid families. *Nature*, 421, 608–611.
- Michel P., Benz W., and Richardson D. C. (2004) Disruption of pre-shattered parent bodies. *Icarus*, 168, 420–432.
- Michel P., Jutzi M., Richardson D. C., and Benz W. (2011) The asteroid Veritas: An intruder in a family named after it? *Icarus*, 211, 535–545.
- Michel P., Jutzi M., Richardson D. C., Goodrich C. A., Hartmann W. K., and O'Brien D. P. (2015) Selective sampling during catastrophic disruption: Mapping the location of reaccumulated fragments in the original parent body. *Planet. Space Sci.*, 107, 24–28.
- Milani A. and Knezević Z. (1994) Asteroid proper elements and the dynamical structure of the asteroid belt. *Icarus*, 107, 219–254.
- Morbidelli A. and Nesvorný D. (1999) Numerous weak resonances drive asteroids toward terrestrial planets orbits. *Icarus*, 139, 295–308.
- Nesvorný D., Bottke W. F., Dones L., and Levison H. F. (2002) The recent breakup of an asteroid in the main-belt region. *Nature*, 417, 720–771.
- Nesvorný D., Bottke W. F., Levison H. F., and Dones L. (2003) Recent origin of the solar system dust bands. *Astrophys. J.*, 591, 486–497.
- Nesvorný D., Enke B. L., Bottke W. F., Durda D. D., Asphaug E., and Richardson D. C. (2006) Karin cluster formation by asteroid impact. *Icarus*, 183, 296–311.
- Richardson D. C. (1994) Tree code simulations of planetary rings. *Mon. Nat. R. Astron. Soc.*, 269, 493–511.
- Richardson D. C., Quinn T., Stadel J., and Lake G. (2000) Direct large-scale N-body simulations of planetesimal dynamics. *Icarus*, 143, 45–59.
- Richardson D. C., Leinhardt Z. M., Melosh H. J., Bottke W. F. Jr., and Asphaug E. (2002) Gravitational aggregates: Evidence and evolution. In *Asteroids III* (W. F. Bottke Jr. et al., eds.), pp. 501–515. Univ. of Arizona, Tucson.
- Richardson D. C., Michel P., Walsh K. J., and Flynn K. W. (2009) Numerical simulations of asteroids modelled as gravitational aggregates with cohesion. *Planet. Space Sci.*, 57, 183–192.
- Ryan E. V. and Melosh H. J. (1998) Impact fragmentation: From the laboratory to asteroids. *Icarus*, 133, 1–24.
- Schwartz S. R., Richardson D. C., and Michel P. (2012) An implementation of the soft-sphere discrete element method in a high-performance parallel gravity tree-code. *Granular Matter*, 14(3), 363–380, DOI: 10.1007/s10035-012-0346-z.
- Tanga P., Cellino A., Michel P., Zappalà V., Paolicchi P., and Dell'Oro A. (1999) On the size distribution of asteroid families: The role of geometry. *Icarus*, 141, 65–78.
- Tillotson J. H. (1962) *Metallic Equations of State for Hypervelocity Impact*. General Atomic Report GA-3216.
- Tsiganis K., Knezević Z., and Varvoglis H. (2007) Reconstructing the orbital history of the Veritas family. *Icarus*, 186, 484–497.
- Weibull W. A. (1939) A statistical theory of the strength of material (transl.). *Ingvetensk. Akad. Handl.*, 151, 5–45.
- Weiss B. P., Elkins-Tanton L. T., Barucci M. A., et al. (2012) Possible evidence for partial differentiation of asteroid Lutetia from Rosetta. *Planet. Space Sci.*, 66, 137–146.
- Yeomans D. K. and 12 colleagues (1997) Estimating the mass of asteroid 253 Mathilde from tracking data during the NEAR flyby. *Science*, 278, 2106–2109.
- Zappalà V., Cellino A., Dell'Oro A., Migliorini F., and Paolicchi P. (1996) Re-constructing the original ejection velocity fields of asteroid families. *Icarus*, 124, 156–180.

# Asteroid Systems: Binaries, Triples, and Pairs

Jean-Luc Margot

*University of California, Los Angeles*

Petr Pravec

*Astronomical Institute of the Czech Republic Academy of Sciences*

Patrick Taylor

*Arecibo Observatory*

Benoît Carry

*Institut de Mécanique Céleste et de Calcul des Éphémérides*

Seth Jacobson

*Côte d'Azur Observatory*

---

In the past decade, the number of known binary near-Earth asteroids has more than quadrupled and the number of known large main-belt asteroids with satellites has doubled. Half a dozen triple asteroids have been discovered, and the previously unrecognized populations of asteroid pairs and small main-belt binaries have been identified. The current observational evidence confirms that small ( $\leq 20$  km) binaries form by rotational fission and establishes that the Yarkovsky-O'Keefe-Radzievskii-Paddack (YORP) effect powers the spin-up process. A unifying paradigm based on rotational fission and post-fission dynamics can explain the formation of small binaries, triples, and pairs. Large ( $\geq 20$  km) binaries with small satellites are most likely created during large collisions.

## 1. INTRODUCTION

### 1.1. Motivation

Multiple-asteroid systems are important because they represent a sizable fraction of the asteroid population and because they enable investigations of a number of properties and processes that are often difficult to probe by other means. The binaries, triples, and pairs inform us about a great variety of asteroid attributes, including physical, mechanical, and thermal properties, composition, interior structure, formation processes, and evolutionary processes.

Observations of binaries and triples provide the most powerful way of deriving reliable masses and densities for a large number of objects. The density measurements help us understand the composition and internal structure of minor planets. Binary systems offer opportunities to measure thermal and mechanical properties, which are generally poorly known.

The binary and triple systems within near-Earth asteroids (NEAs), main-belt asteroids (MBAs), and transneptunian objects (TNOs) exhibit a variety of formation mechanisms

(Merline et al., 2002c; Noll et al., 2008). As such, they provide an invaluable window on accretional, collisional, tidal, and radiative processes that are critical in planet formation. The distribution and configurations of the multiple-asteroid systems also provide a rich array of constraints on their environment, their formation, and their evolutionary pathways.

Observations rely primarily on groundbased telescopes and the Hubble Space Telescope (HST). For an up-to-date list of binaries and triples in the solar system, see Johnston (2014). We describe observational techniques only briefly because this material is available elsewhere (e.g., Merline et al., 2002c). A few emerging techniques will be described in more detail. Likewise, we refer the reader to other texts for an extensive history of the field (e.g., Merline et al., 2002c) and highlight only a few of the developments here.

### 1.2. History

Early search programs for asteroid satellites were unsuccessful, returning negative or dubious results, such that the authors of the *Asteroids II* review chapter chose the prudent title “Do asteroids have satellites?” (Weidenschilling et al.,

1989). The chapter provides an excellent discussion of the physics of several formation mechanisms that were postulated at the time. The perspective changed with the flyby of (243) Ida by the Galileo spacecraft in 1993 and the discovery of its small satellite Dactyl (Chapman *et al.*, 1995; Belton *et al.*, 1995). Groundbased efforts intensified and resulted in the discovery of a satellite around (45) Eugenia by Merline *et al.* (1999). Several other discoveries followed in rapid succession. The relatively small sizes of the MBA satellites suggested formation in subcatastrophic or catastrophic collisions (Durda, 1996; Doressoundiram *et al.*, 1997).

The discovery of MBA satellites, coupled with analysis of terrestrial doublet craters (Bottke and Melosh, 1996a,b) and anomalous lightcurve observations (Pravec and Hahn, 1997), suggested the existence of binary asteroids in the near-Earth population as well. The unambiguous detection of five NEA binaries by radar cemented this finding and indicated that NEA satellites form by a spin-up and rotational fission process (Margot *et al.*, 2002). Lightcurve observers reached the same conclusion independently (Pravec and Harris, 2007). Both radar and lightcurve observations revealed that, far from being rare, binary asteroids are relatively common (Pravec *et al.*, 1999, 2006; Margot *et al.*, 2002). By the time the *Asteroids III* review chapter was written, a more decisive title (“Asteroids do have satellites”) had become appropriate (Merline *et al.*, 2002c). This review focuses on the developments that followed the publication of *Asteroids III*.

### 1.3. Terminology

Two- and three-component asteroids that are gravitationally bound will be referred to as binary asteroids (or binaries) and triple asteroids (or triples), respectively. (Triple is favored over the more directly analogous terms trinary and ternary because of long-established usage in astronomy.) Asteroid pairs denote asteroid components that are genetically related but not gravitationally bound. Paired binaries or paired triples are asteroid pairs where the larger asteroid is itself a binary or triple asteroid. The larger component in binaries, triples, and pairs is referred to as the primary component or primary. The smaller component in binaries is referred to as the secondary component or secondary.

There has been some confusion in the literature about the meaning of the word “asynchronous.” Here, we adopt the terminology proposed by Margot (2010) and later implemented by Jacobson and Scheeres (2011b) and Fang and Margot (2012c). Binaries with an absence of spin-orbit synchronism are called asynchronous binaries. Binaries with a secondary spin period synchronized to the mutual orbit period are called synchronous binaries. Binaries with both primary and secondary spin periods synchronized to the mutual orbit period are called doubly synchronous binaries. If generalization to systems with more than one satellite is needed, we affix the terms synchronous and asynchronous to the satellites being considered.

It is useful to present results for small and large asteroids. We place an approximate dividing line at the size at which

objects are substantially affected by the Yarkovsky-O’Keefe-Radzievskii-Paddack (YORP) effect during their lifetime. For typical NEAs and MBAs, this dividing line corresponds to a diameter of about 20 km (Jacobson *et al.*, 2014a). We define very small asteroids as those with diameters of <200 m. This is the approximate size below which many asteroids are observed to spin faster than the disruption rate of a body with no shear or tensile strength  $\omega_d = \sqrt{4\pi\rho G/3}$ , where  $\rho$  is the density and  $G$  is the gravitational constant.

We use two additional acronyms. The YORP effect is a radiation-powered rotational acceleration mechanism for small asteroids (Rubincam, 2000). The binary YORP (BYORP) effect is a radiation-powered acceleration mechanism that may expand or contract the orbits of some synchronous asteroids (Čuk and Burns, 2005).

## 2. OBSERVATIONS

Several observational techniques are available for discovering, detecting, and studying binaries, triples, and pairs, each with its strengths and weaknesses. This section describes recent results and illustrates the complementarity of the observational techniques that characterize individual asteroid systems and entire populations.

### 2.1. Radar Observations of Near-Earth Asteroid Systems

Radar has proven to be a powerful method of detecting secondaries to NEAs, enabling the discovery (as of September 2014) of the satellites in 71% of the 49 known multiple-component NEA systems, including 33 of 47 binaries and both undisputed triple systems. Of the 14 binary NEAs discovered via optical lightcurve techniques, 6 have been confirmed with follow-up radar observations during later apparitions. Overall, radar detections suggest that about one in six NEAs larger than 200 m in diameter are multiple-asteroid systems (Margot *et al.*, 2002; Taylor *et al.*, 2012a), although 200 m is not a sharp cutoff. Three binary NEA systems identified by radar have primary components with suggested diameters of 120 m to 180 m: 2003 SS<sub>84</sub> (Nolan *et al.*, 2003), (363599) 2004 FG<sub>11</sub> (Taylor *et al.*, 2012c), and 1994 CJ<sub>1</sub> (Taylor *et al.*, 2014). For comparison, the largest primaries of binary NEAs imaged with radar — (5143) Heracles (Taylor *et al.*, 2012b), the possible triple (276049) 2002 CE<sub>26</sub> (Shepard *et al.*, 2006), and (285263) 1998 QE<sub>2</sub> (Springmann *et al.*, 2014) — are more than an order of magnitude larger at >3 km in diameter. It is likely that ~8-km-diameter (1866) Sisyphus has a secondary based on analysis of frequency-only observations obtained on four separate dates in 1985 (S. Ostro, personal communication, 2001).

Radar observations can be used to detect asteroid satellites because of the ability to resolve the components of the system both spatially (along the observer’s line of sight) and in terms of frequency (due to Doppler shifts from the rotational and orbital line-of-sight velocities), resulting in

a measurable separation between the components in two dimensions. Direct detection of a satellite in frequency-only spectra or radar images typically occurs within one observing session and often within minutes of observation. The bandwidth of the echo of a component scales directly with the diameter and rotation rate. Thus, in a frequency-only experiment, the signal of the smaller, relatively slowly rotating satellite is condensed to a smaller bandwidth that is superimposed upon the broadband signal of the larger, often rapidly rotating, primary (Fig. 1a). Not all radar-observed binaries present this characteristic spectrum (e.g., where the secondary spins faster than the synchronous rate), but all are readily detected in radar images when the components are also resolved spatially (Fig. 1b). Because the spatial resolution achieved with radar instruments corresponds to an effective angular resolution of better than  $\sim 1$  milliarcsecond (mas), there is no bias against the detection of satellites orbiting very close to the primary component. Multiple measurements of the range and frequency separations of the components over days of sky motion provide the geometric leverage required to determine the orbit of the secondary around the primary. This can be done for any orbital orientation and yields the total system mass, a property that is difficult to estimate otherwise. Other techniques involve analyzing spacecraft flyby and orbit trajectories (e.g., Yeomans *et al.*, 1999), measuring the Yarkovsky orbital drift in conjunction with thermal properties (e.g., Chesley *et al.*, 2014), or observing the gravitational perturbations resulting from asteroid encounters (e.g., Hilton, 2002).

Most binary NEA systems observed to date have a rapidly rotating primary and a smaller secondary on the order of a few tenths the size of the primary (a secondary-to-primary mass ratio of roughly 0.001 to 0.1), whose rotation is synchronized to the mutual orbit period. The majority of primaries rotate in less than 2.8 h, although they range from 2.2593 h for (65803) Didymos (Pravec *et al.*, 2006) to 4.749 h for 1998 QE<sub>2</sub> (P. Pravec, personal communication, 2013). The known outlier is the nearly equal-mass binary (69230) Hermes, whose components both appear to have 13.894-h periods synchronized to their mutual orbit period (Margot *et al.*, 2006). This doubly synchronous configuration is most likely due to rapid tidal evolution (Taylor and Margot, 2011). While the rotations of satellites in NEA binaries tend to be tidally locked to their orbital mean motions with periods typically within a factor of 2 of 24 h (often resulting in the characteristic appearance shown in Fig. 1), about one in four radar-observed multiple-asteroid systems have an asynchronous satellite (Brozović *et al.*, 2011), all of which rotate faster than their orbital rate. Well-studied examples include (35107) 1991 VH (Naidu *et al.*, 2012), (153958) 2002 AM<sub>31</sub> (Taylor *et al.*, 2013), (311066) 2004 DC (Taylor *et al.*, 2008), and the outer satellites of both undisputed triple systems (153591) 2001 SN<sub>263</sub> (Nolan *et al.*, 2008; Fang *et al.*, 2011; Becker *et al.*, 2015) and (136617) 1994 CC (Brozović *et al.*, 2011; Fang *et al.*, 2011). Of the known asynchronous satellites, all have wide component separations ( $>7$  primary radii), translating to

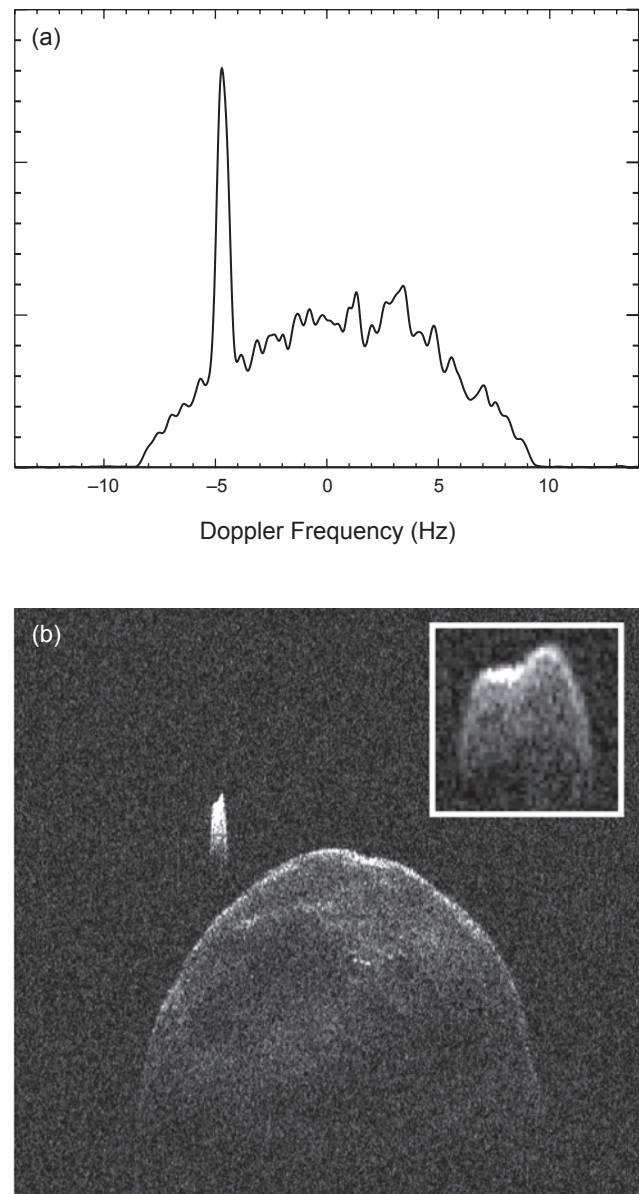


**Fig. 1.** Binary near-Earth asteroid (285263) 1998 QE<sub>2</sub> as detected using the Arecibo planetary radar system. **(a)** In this frequency-only spectrum showing echo power as a function of Doppler frequency, the narrowband echo of the tidally locked secondary stands out against the broadband echo of the larger, faster-rotating primary. **(b)** In this radar image, the components are spatially resolved (7.5 m/pixel). The vertical axis represents distance from the observer increasing downward. The horizontal axis is Doppler frequency due to the orbital and rotational motion of the components. Note that if one summed the pixel values in each column of the image, the intensity as a function of Doppler frequency would approximate the spectrum above. The secondary is roughly one-fourth the size of the primary (measured in the vertical dimension), although the Doppler breadth of the primary gives the illusion of a greater size disparity. The shape of the secondary (inset on **(b)**) is distinctly nonspherical when viewed with finer frequency resolution.

longer-than-typical orbital periods, and/or eccentric orbits ( $>0.05$ ) that are either remnants of their formation mechanism or products of subsequent dynamical evolution (Fang and Margot, 2012c).

The shortest orbital periods detected with radar so far are those of Didymos and 2006 GY<sub>2</sub> with  $P_{\text{orb}} = 11.90^{+0.03}_{-0.02}$  h and  $11.7 \pm 0.2$  h, respectively (Benner et al., 2010; Brooks, 2006). For Didymos, the semimajor axis is  $a = 1.18^{+0.04}_{-0.02}$  km, just outside the classical fluid Roche limit of  $\sim 1$  km for equal-density components. Other systems with satellites orbiting near the Roche limit include 2002 CE<sub>26</sub> and 2001 SN<sub>263</sub>. The significance of this is unclear, as  $\sim 100$ -m secondaries with a cohesion comparable to comet regolith or sand can likely survive on orbits interior to the Roche limit (Taylor and Margot, 2010, and references therein).

Inversion of a series of radar images can provide a three-dimensional shape model and complete spin-state description given sufficient signal, resolution, and orientational coverage (Hudson, 1993; Magri et al., 2007). Shape reconstruction of the larger component of (66391) 1999 KW<sub>4</sub> (Ostro et al., 2006) demonstrated that the canonical shape of an NEA primary has a characteristic circular equatorial bulge, uniformly sloped sides, and polar flattening akin to a spinning top. Such a shape is shared by the primaries of 2004 DC, 1994 CC, 2001 SN<sub>263</sub>, and (185851) 2000 DP<sub>107</sub> (Naidu et al., 2015), although some primaries have less pronounced equatorial belts, e.g., 2002 CE<sub>26</sub> and 1998 QE<sub>2</sub>. Some single asteroids have a similar shape, e.g., (101955) Bennu (Nolan et al., 2013) and (341843) 2008 EV<sub>5</sub> (Busch et al., 2011), but do not have satellites, possibly because one has not yet formed or has been lost in the past. Shape model renditions are shown in the chapter by Benner et al. in this volume. Often the resolution of radar images of the smaller satellites is insufficient for shape inversion, but radar images suggest that the satellites are typically elongated, e.g., 2000 DP<sub>107</sub>, 1999 KW<sub>4</sub>, 2001 SN<sub>263</sub>, 1991 VH, and 1998 QE<sub>2</sub>.

Shapes and volumes obtained from inversion of radar images, combined with the system mass derived from the orbital motion observed in radar images, provide the density of the system (or of the individual components if the mass ratio is measurable from reflex motion). Low densities on the order of  $1 \text{ g cm}^{-3}$  (Shepard et al., 2006; Becker et al., 2015) to  $2 \text{ g cm}^{-3}$  (Ostro et al., 2006; Brozović et al., 2011) suggest significant internal macroporosity on the order of 50%, implying a rubble-pile internal structure for the components. At such low densities, the rapid rotation of the primary places particles along the equatorial belt in a near-weightless environment. The combination of rapid rotation, shape, and implied porosity and rubble-pile structure has implications for the formation mechanism of small multiple-asteroid systems (section 4).

While radar allows for direct, unambiguous detection of asteroid satellites, its range is limited. Because radar requires the transmission and reception of a signal, the strength of the received signal falls as the fourth power of the distance to the target and, thus, is best suited for detecting multiple-component systems passing within  $\sim 0.2$  astronomical units

(AU) of Earth. Satellites in the main asteroid belt simply tend to be too small and too far away to detect with present radar capabilities and require application of different observational techniques.

## 2.2. Lightcurve Observations of Near-Earth-Asteroid and Small-Main-Belt-Asteroid Systems

A photometric lightcurve is a time series of measurements of the total brightness of an asteroid. Detections of binary asteroids by photometric lightcurve observations utilize the fact that the components can obscure or cast a shadow on one another, producing occultations or eclipses, respectively. The attenuations can be used to both reveal and characterize binaries (Fig. 2). The observational, analysis, and modeling techniques were described in Pravec et al. (2006), Scheirich and Pravec (2009), and Scheirich et al. (2015).

Early reports (Tedesco, 1979; Cellino et al., 1985) of asteroids suspected to be binaries on the basis of anomalous lightcurves [including (15) Eunomia, (39) Laetitia, (43) Ariadne, (44) Nysa, (49) Pales, (61) Danae, (63) Ausonia, (82) Alkmene, (171) Ophelia, and (192) Nausikaa] have remained largely unconfirmed despite extensive follow-up searches. The first serious candidate for detection with this technique was NEA (385186) 1994 AW<sub>1</sub> (Pravec and Hahn, 1997), whose binary nature was confirmed by photometric observations in 2008 (Birlan et al., 2010). Since 1997, nearly 100 binaries among NEAs and small MBAs have been detected with the photometric method. The binary asteroid database constructed by Pravec and Harris (2007) (<http://www.asu.cas.cz/~asteroid/binastdata.htm>) includes data for 86 MBA and NEA binaries that were securely detected by photometry and for which basic parameters have been derived, such as the primary spin period, the orbital period, and the primary-to-secondary mean diameter ratio. A few tens of additional MBAs and NEAs are suspected to be binaries and await confirmation with more detailed observations in the future.

Among the main findings obtained from photometric observations is that binary asteroids are ubiquitous. They have been found among NEAs and Mars-crossers (MCs), as well as throughout the main belt, both among asteroids that have been identified as family members and among asteroids that have not. Pravec et al. (2006) derived the fraction of binaries among NEAs larger than 300 m to be  $15 \pm 4\%$ . A binary fraction among MBAs has not been derived precisely due to less-well-characterized observational selection effects, but their photometric discovery rate is similar to the discovery rate of binaries among NEAs. Thus, binaries are suspected to be as frequent among MBAs as they are among NEAs. There appears to be an upper limit on the primary diameter for photometrically detected binaries of about 13 km; the largest detected binary is (939) Isberga with  $D_p = 13.4 \pm 1.3$  km (Carry et al., 2015). A lower size limit on the primary diameter  $D_p$  is less clear. The smallest detected binary is 2000 UG<sub>11</sub> with  $D_p = 0.26 \pm 0.03$  km (Pravec et al., 2006), but smaller binaries are known to exist (section 2.1). Their

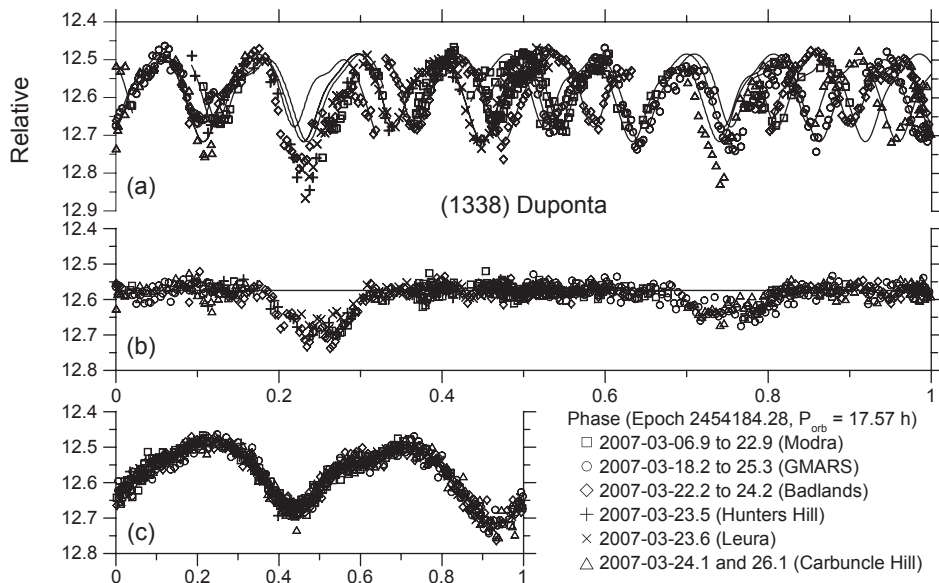


**Fig. 2.** Lightcurve data of (1338) Duponta, which has a secondary-to-primary diameter ratio of about 0.24. (a) The original data showing both lightcurve components, folded with the orbit period. (b) The orbital lightcurve component, derived after subtraction of the primary lightcurve component, showing the mutual events between components of the binary system. (c) The primary lightcurve component. Figure from Pravec et al. (2012).

absence in lightcurve datasets may be due in part to a bias against detecting small binaries in the initial surveys.

Another key finding is that small binary asteroids have, with only two or three exceptions, a near-critical angular momentum content (Fig. 3). As shown by Pravec and Harris (2007), their angular momentum is consistent with formation by fission of critically spinning parent bodies of a cohesionless, rubble pile structure. The exceptions are the semi-wide systems (32039) 2000 JO<sub>23</sub> and (4951) Iwamoto, and possibly also (1717) Arlon, with orbital periods of 117 h to 360 h and supercritical total angular momentum content.

The orbital poles of main-belt binaries were found to have a highly anisotropic distribution, concentrating within 30° of the poles of the ecliptic (Pravec et al., 2012). The preferential orientations of the orbital poles suggest that their parent bodies or the primaries were tilted by the YORP effect toward the asymptotic spin states near obliquities 0° and 180°, consistent with observations of single asteroids (Hanuš et al., 2011).

Another significant finding is that there appears to be a lower limit on the separation between components of binary systems of about  $a/D_p = 1.5$ , corresponding to an orbital period of 11–12 h for typical densities. Lightcurve observations indicate that the orbital period of Didymos is  $P_{\text{orb}} = 11.91 \pm 0.02$  h (Pravec et al., 2006), consistent with the radar estimate. This suggests an orbit close to the Roche limit for strengthless satellites (but see prior remark about orbits interior to the Roche limit).

Photometric observations of a binary system over multiple apparitions can be used to detect a change in the separation

of the components due to the effect on mutual event timing. An extensive set of photometric observations of the synchronous binary (175706) 1996 FG<sub>3</sub> obtained during 1996–2013 places an upper limit on the drift of its semimajor axis that is 1 order of magnitude less than estimated on the basis of the BYORP theory (Scheirich et al., 2015). This system may be in an equilibrium between BYORP and tidal torques, as proposed for synchronous binary asteroids by Jacobson and Scheeres (2011a).

Some datasets strongly suggest the presence of triple asteroids. In these cases, an additional rotational component that does not belong to the primary or the close eclipsing secondary is present in the lightcurve. This additional rotational component does not disappear during mutual events where the eclipsing close secondary is obscured by or in the shadow of the primary. Pravec et al. (2012) identified three such cases: (1830) Pogson, (2006) Polonskaya, and (2577) Litva. The latter has been confirmed by direct imaging observations of the third body (second satellite) on a wide orbit (Merline et al., 2013).

Other datasets reveal the existence of paired binaries/triples. Two such cases have been published: the pair composed of (3749) Balam and 2009 BR<sub>60</sub> (Vokrouhlický, 2009, and references therein) and the pair composed of (8306) Shoko and 2011 SR<sub>158</sub> (Pravec et al., 2013). Balam is a confirmed triple, with a distant satellite detected by direct imaging (Merline et al., 2002a) and a close satellite detected by lightcurve observations (Marchis et al., 2008d). Shoko is a suspected triple as well: Using lightcurve observations, Pravec et al. (2013) detected an eclipsing, synchronous close

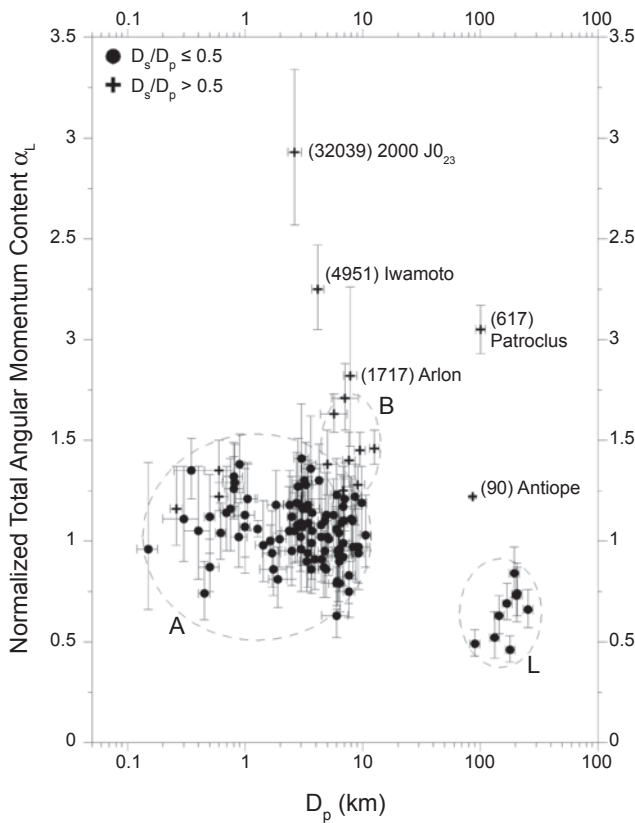


**Fig. 3.** Estimated values of the normalized total angular momentum content of binaries vs. primary diameter. The quantity  $\alpha_L$  is the sum of orbital and spin angular momenta normalized by the angular momentum of an equivalent sphere spinning at the critical disruption spin rate  $\omega_d = \sqrt{4\pi\rho G/3}$  where  $\rho$  is the density and  $G$  is the gravitational constant. In the Darwin notation,  $\alpha_L = 1$  corresponds to  $J/J' = 0.4$ . Group A contains small NEAs, MC, and MBA binaries. Group B consists of doubly synchronous small MBAs with nearly equal-sized components. Group L represents large MBAs with small satellites (section 2.5). Two exceptional cases are the doubly synchronous asteroids (90) Antiope and (617) Patroclus (section 2.5). Figure updated from Pravec and Harris (2007).

satellite with  $P_{\text{orb}} = 36.2$  h and a third rotational component attributed to an outer satellite.

While the population of binary NEAs and small MBAs is composed primarily of synchronous systems, and secondarily of asynchronous systems with low secondary-to-primary size ratios ( $D_s/D_p < 0.5$ ), doubly synchronous binaries with nearly equal-sized components also exist (Fig. 4). Nine such systems with  $D_s/D_p > 0.7$  and orbital periods between 15 h and 118 h have been reliably identified in the main belt (e.g., Behrend *et al.*, 2006; Kryszczyńska *et al.*, 2009) (see also the Pravec and Harris binary database described above).

Another important observation is that, with the exception of doubly synchronous systems, all binaries have unelongated, near-spheroidal primary shapes, as evidenced by their low primary amplitudes not exceeding 0.3 mag (when

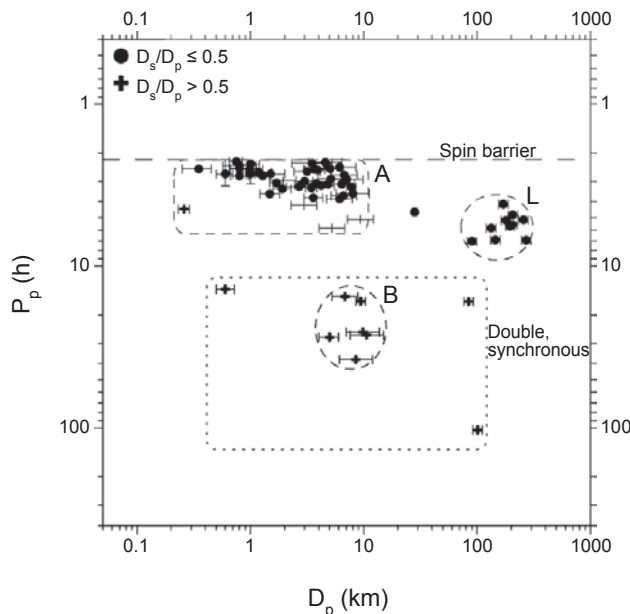


**Fig. 4.** Primary rotation period vs. primary diameter. Groups A, B, and L are defined in the caption of Fig. 3. Three doubly synchronous asteroids with nearly equal-sized components lie isolated in the plot: (69230) Hermes on the left, and (90) Antiope and (617) Patroclus on the right of group B. Note that members of group A cluster near the disruption spin limit for strengthless bodies. Figure from Pravec and Harris (2007).

corrected to zero phase angle). This suggests that their primaries may have shapes similar to the top-like shapes that have been observed for 1999 KW<sub>4</sub> (Ostro *et al.*, 2006) and several other binaries by radar.

All the properties revealed by photometric observations indicate that binary systems among NEAs and small MBAs were formed from critically spinning cohesionless parent bodies, with YORP as the predominant spin-up mechanism. This finding is consistent with the fact that the observed 0.2–13-km size range of binaries corresponds to the size range where the spin barrier against asteroid rotations faster than about 2.2 h has been observed (e.g., Pravec *et al.*, 2007).

Although lightcurve observations provide powerful constraints on binaries, there are limitations. Detection of mutual events requires an edge-on geometry and observations at the time of the events, such that some binaries remain undetected [e.g., (69230) Hermes during its 2003 apparition]. Small satellites also escape detection because their effect on the lightcurve is not measurable (e.g., satellites with  $D_s/D_p \leq 0.17$  remain undetected if the minimum detectable relative brightness attenuation is  $\sim 0.03$  mag). The probability of mutual event detection is larger at smaller semimajor axes (expressed in units of primary radius) and at larger size ratios, resulting in observational biases (e.g., Pravec *et al.*, 2012). Finally, lightcurve observations yield relative, not absolute, measurements of orbital separations. Detection of small or distant secondaries and direct measurement of orbital separation must instead rely on other observational techniques.

### 2.3. Lightcurve Observations of Asteroid Pairs

*Vokrouhlický and Nesvorný* (2008) reported evidence for pairs of MBAs with bodies in each pair having nearly identical heliocentric orbits. Because chance associations can be ruled out, the asteroids in each pair must be genetically related. Quantifying the difference in orbital parameters is accomplished with a metric  $d$  that corresponds roughly to the relative velocity between the bodies at close encounter. *Vokrouhlický and Nesvorný* identified 44 asteroid pairs (excluding family members) with a distance between the orbits of their components amounting to  $d < 10 \text{ m s}^{-1}$ . They showed that, when integrated backward in time, the orbits converge at a certain moment in the past with a physical distance much less than the radius of the Hill sphere and with a low relative velocity on the order of  $1 \text{ m s}^{-1}$ .

*Pravec and Vokrouhlický* (2009) developed a method to identify probable asteroid pairs by selecting candidate pairs with a similar distance criterion, then computing the probability that each candidate pair emerged as a result of a coincidence between two unrelated asteroids. They identified 72 probable asteroid pairs, reproducing most of the 44 previously known pairs. Most of the new candidates were later confirmed to be real pairs using backward integrations of their heliocentric orbits.

*Vokrouhlický and Nesvorný* (2008) proposed a few possible formation mechanisms for the asteroid pairs: collisional disruption, rotational fission, and splitting of unstable asteroid binaries. *Pravec et al.* (2010) conducted a survey of the rotational properties of asteroid pairs, and they found a strong correlation between the primary rotational periods and the secondary-to-primary mass ratio (Fig. 5). They showed that this correlation fits precisely with the predictions of a model by *Scheeres* (2007) in which a parent body with zero tensile strength undergoes rotational fission. The model predicts that primaries of low-mass-ratio pairs ( $q \leq 0.05$ ) have not had their spin substantially slowed down in the separation process and should rotate rapidly with frequencies close to the fission spin rate. The observed periods are between 2.4 and 5 h. Primaries of medium mass ratio pairs ( $q = 0.05$  to  $\sim 0.2$ ) have had their spin slowed down according to the model because a substantial amount of angular momentum was taken away by the escaped secondary. This trend is observed in the data (Fig. 5). Finally, high-mass-ratio pairs with  $q > 0.2$  should not exist, as the free energy in the protobinary system formed by rotational fission would be negative and the components would be unable to separate. Observations mostly corroborate this prediction: All 32 pairs in the sample of *Pravec et al.* (2010) were found to have a mass ratio  $\leq 0.2$ . However, an expanded photometric survey with 64 asteroid pairs observed between 2012 and the date of this writing reveals 3 pairs with high mass ratio ( $q > 0.5$ ). Their formation requires an additional supply of angular momentum. Another important finding by *Pravec et al.* (2010) is that the primaries of asteroid pairs have lightcurve amplitudes that imply shapes with a broad range of elongations; i.e., unlike the primaries of binaries (sec-

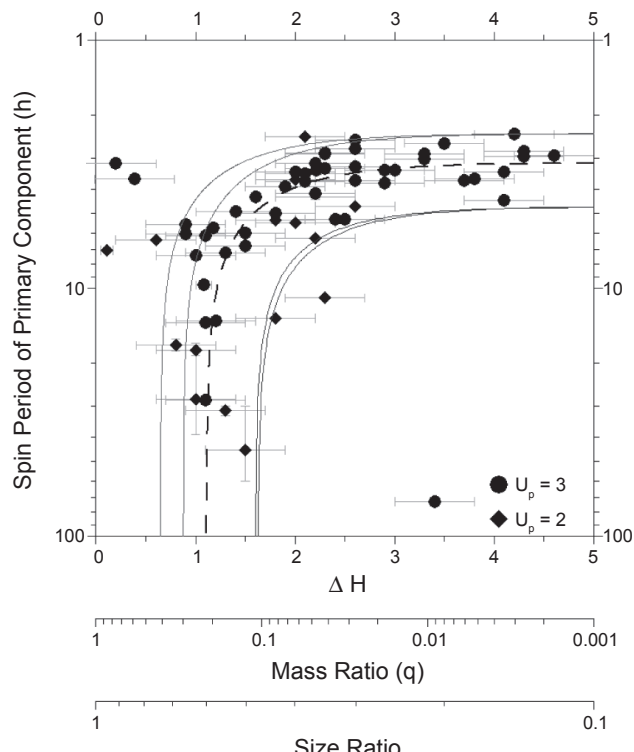


**Fig. 5.** Primary rotation periods vs. mass ratios of asteroid pairs. The mass ratio values were estimated from the differences between the absolute magnitudes of the pair components,  $\Delta H$ . Circles are data points with quality code rating  $U_p = 3$ , meaning a precise period determination. Diamonds are data points with  $U_p = 2$ , which are somewhat less certain estimates. Error bars are one standard deviation. The data match the predictions (curves) of a model of rotational fission with a few adjustable parameters. In the model,  $A_{\text{ini}}$  is the binary system's initial orbit semimajor axis,  $\alpha_L$  is the normalized total angular momentum of the system (Fig. 3), and  $a_p, b_p, c_p$  are the long, intermediate, and short axis of the dynamically equivalent equal mass ellipsoid of the primary. All models shown assume  $b_p/c_p = 1.2$ . The dashed curve shows the best-fit model with  $\alpha_L = 1.0$ ,  $a_p/b_p = 1.4$  and  $A_{\text{ini}}/b_p = 3$ . Solid curves represent upper and lower limiting cases with  $\alpha_L = 0.7$ – $1.2$ . Figure updated from *Pravec et al.* (2010).

tions 2.1 and 2.2), the primaries of asteroid pairs do not tend to be nearly spheroidal.

### 2.4. Spectral Observations of Asteroid Pairs

Colorimetric and spectral observations of about 20 asteroid pairs indicate that members of an asteroid pair generally have similar spectra (*Duddy et al.*, 2012, 2013; *Moskovitz*, 2012; *Polishook et al.*, 2014a; *Wolters et al.*, 2014). In some pairs, the authors observed subtle spectral differences between the components and attributed them to a larger amount of weathered material on the surface of the primary. In two pairs, they observed somewhat more significant spectral differences. For the pair (17198)–(229056), both *Duddy et al.* (2013) and

*Wolters et al.* (2014) found that the primary is redder, i.e., it has a somewhat higher spectral slope than the secondary in the observed spectral range 0.5–0.9  $\mu\text{m}$ . It is unclear why their spectra differ despite a strong dynamical link between the two asteroids. For the pair (19289)–(278067), *Wolters et al.* (2014) observed a spectral difference similar to that seen in (17198)–(229056), but *Duddy et al.* (2013) observed very similar spectra. Cross-validation of the methods or additional observations, perhaps rotationally resolved, are needed to resolve the discrepancy.

## 2.5. Direct Imaging of Main-Belt-Asteroid and Trojan Systems

Direct imaging of asteroids can reveal the presence of satellites and, following the long tradition of orbit determination of binary stars and planetary satellites, lead to estimates of orbital parameters (Fig. 6). This observing mode remains challenging because the satellites are generally much smaller and fainter than their respective primaries and because most satellites known to date orbit at angular separations below 1 arcsec. Satellite discoveries have therefore followed the development of adaptive optics (AO), and recent advances have enabled the detection of asteroid satellites that had remained undetected in prior searches.

Instruments must have sufficient contrast and resolving power to detect asteroid satellites with direct imaging. For a 50–100-km-diameter asteroid in the main belt orbited by a satellite a few kilometers across, the typical angular separation is generally less than an arcsecond with a contrast of 5–10 mag [computed as  $2.5 \log(F_p/F_s)$ , where  $F$  is the flux and  $p$  and  $s$  indicate primary and secondary, respectively].

In some situations, direct images can actually resolve the primary. A 50–100-km-diameter asteroid at 2 AU subtends 34–68 mas while the diffraction limit of a 10-m telescope at a typical imaging wavelength of 1.2  $\mu\text{m}$  is about 30 mas. Although the diffraction limit is not reached, it can be approached with high-performance AO instruments in excellent

conditions. With a sequence of disk-resolved images that provide sufficient orientational coverage, it is possible to estimate the three-dimensional shape of the primary. This enables volume and density determinations.

Instruments capable of meeting the contrast and resolution requirements include HST and large (10-m-class) ground-based telescopes equipped with AO. Spacecraft encounters provide an opportunity to detect small satellites at small separations because of proximity to the target and the absence of the point-spread-function halo that affects groundbased AO instruments.

At the time *Asteroids III* was published, MBA satellite discoveries included one by spacecraft [(243) Ida], one by HST [(107) Camilla], and six by groundbased AO instruments. Since then, groundbased AO instruments have been responsible for almost all large MBA satellite discoveries: (121) Hermione (*Merline et al.*, 2002b), (379) Huenna (*Margot*, 2003), (130) Elektra (*Merline et al.*, 2003c), a second satellite to (87) Sylvia (*Marchis et al.*, 2005b) and to (45) Eugenia (*Marchis et al.*, 2007), (702) Alauda (*Rojo and Margot*, 2007), (41) Daphne (*Conrad et al.*, 2008), two satellites to (216) Kleopatra (*Marchis et al.*, 2008b) and (93) Minerva (*Marchis et al.*, 2009), and (317) Roxane (*Merline et al.*, 2009). The wide binaries (1509) Esclangona (*Merline et al.*, 2003a) and (4674) Pauling (*Merline et al.*, 2004), which are small asteroids in our classification, have also been identified using AO-fed cameras. HST enabled detections of two additional wide binaries: (22899) 1999 TO<sub>14</sub> (*Merline et al.*, 2003b) and (17246) 2000 GL<sub>74</sub> (*Tamblyn et al.*, 2004), both of which are small MBAs. No satellites have been discovered around any of the seven asteroids recently visited by spacecraft: (4) Vesta, (21) Lutetia, (2867) Šteins, (4179) Toutatis, (5535) Annefrank, (25143) Itokawa, and (132524) APL. The number of known large MBAs with satellites is now 16, which includes the only known large doubly synchronous system, (90) Antiope (*Merline et al.*, 2000; *Michałowski et al.*, 2004; *Descamps et al.*, 2007, 2009). The fraction of large MBAs with satellites is difficult

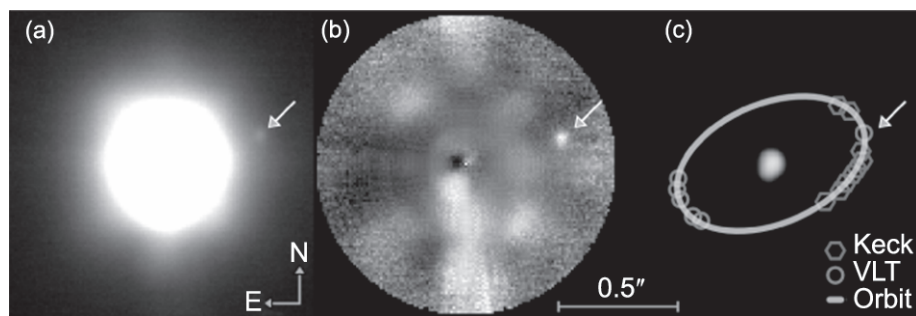


**Fig. 6.** Satellite detection by direct imaging with adaptive optics (AO). **(a)** Image of asteroid (41) Daphne ( $V_{\text{mag}} = 10$ ) obtained with a groundbased AO-fed camera (NACO at ESO VLT, 5 s exposure). **(b)** Same image after subtraction of the flux from the primary, enabling more accurate measurements of the flux and position of the secondary. **(c)** Orbit determination. The relative positions of the satellite from VLT/NACO and Keck/NIRC2 images are indicated. Figure adapted from *Carry* (2009).

to estimate because of a complex dependence of satellite detectability on primary-to-secondary angular separation and primary-to-secondary flux ratio. However, because several independent programs have surveyed more than 300 large MBAs, it is likely that the abundance of binaries in large MBAs is substantially smaller than the ~16% abundance in NEAs and small MBAs.

Properties of large MBA binaries and triples are summarized in Figs. 7 and 8. With the exception of the nearly equal-mass binary (90) Antiope, the known satellites have secondary-to-primary mass ratios between  $10^{-6}$  and  $10^{-2}$ . All have orbital periods between 1 and 5.5 d, except (379) Huen-na, whose orbit has a period of ~88 d and an eccentricity of ~0.2 (Marchis et al., 2008c). Many orbits have near-zero eccentricity (e.g., Marchis et al., 2008a), likely the result of tidal damping, but the inner satellites of triples generally have nonzero eccentricities. These eccentricities may have originated when orbits crossed mean-motion resonances while tidally expanding (e.g., Fang et al., 2012).

At first glance, large MBA densities appear to cluster in two groups, between 1 and 2 g cm<sup>-3</sup> and above 3 g cm<sup>-3</sup>. However, interpretations are limited by the possibility of systematic errors, including overestimates of volumes and underestimates of densities (Pravec and Harris, 2007). Because volume uncertainties almost always dominate the error budget for binary asteroid densities (e.g., Merline et al., 2002c; Carry, 2012), it is important to assess the realism of uncertainties associated with volume determinations. Some published density values should be regarded with caution because overconfidence in the fractional uncertainty of volume estimates has led to underestimates of bulk density uncertainties. The platinum standard of an orbiting spacecraft yields densities with ~1% accuracy. The gold standard of radar observations where tens of images with hundreds or thousands of pixels per image are used to reconstruct a detailed three-dimensional shape model yields volumes (and densities) with ~10% accuracy. In contrast, AO images contain at most a few independent resolution cells of the target asteroid. Shape reconstructions based on AO images and/or lightcurve data may not routinely yield volume accuracies at the 10% level, although one analysis reached that level (Carry et al., 2012). In the absence of precise volume information, one might be tempted to infer bulk densities from the theory of fluid equilibrium shapes, but this approach is problematic (Holsapple, 2007; Harris et al., 2009).

In the Jupiter Trojan population, one satellite to (624) Hektor has been reported (Marchis et al., 2006b) since the discovery of the first Trojan satellite to (617) Patroclus (Merline et al., 2001). These are the only Trojans confirmed to have satellites in spite of several active search programs. The apparent low abundance of binary Trojans is intriguing and, if confirmed, may provide additional support for the idea that Jupiter Trojans originated in the transneptunian region (Morbidelli et al., 2005; Levison et al., 2009) where they experienced a different collisional environment than in the main belt of asteroids. (624) Hektor has a satellite in a ~3-d orbit that is eccentric (~0.3) and inclined (~50°) with respect

to Hektor's equator (Marchis et al., 2014). (617) Patroclus is unusual because it has two components of similar size in a relatively tight (~680 km) orbit, with a normalized total angular momentum exceeding that available from fission of a single parent body (Marchis et al., 2006a).

In the transneptunian region, 14 and 64 binary systems have been discovered with AO and HST, respectively (Johnston, 2014). The apparent larger abundance of binary TNOs in the cold classical belt may be due to a different dynamical environment and formation mechanism (section 5).

Objects in the Trojan and TNO populations are generally too faint for AO observations in natural guide star (NGS) mode, in which the science target is also used to measure the properties of the wavefront and command the deformable mirror. These objects can be observed in appulse when their sky position happens to be within  $\leq 1$  arcmin of a bright star. The advent of laser guide star (LGS) adaptive optics has been an important development that has freed the observer from finding such chance alignments and has opened up a larger fraction of the sky for observation of faint objects. Even with LGS, however, the availability of a tip-tilt star ( $R_{\text{mag}} \leq 18$ ) within  $\leq 1$  arcmin of the target is still required.

High-resolution and high-contrast imaging capabilities are aggressively sought by instrument builders, in part to enable direct imaging of exoplanets. Cameras equipped with high-performance AO are currently being installed or commissioned on large groundbased telescopes: the High-Contrast Coronographic Imager for Adaptive Optics (HiCIAO) on Subaru, Gemini Planet Imager (GPI) on Gemini, and Spectro-Polarimetric High-contrast Exoplanet REsearch (SPHERE) at the European Southern Observatory's (ESO) Very Large Telescope (VLT). These instruments will improve the ability to detect faint satellites orbiting close to their respective primaries. However, in most cases, asteroids fall in the faint-end range of these instrument capabilities. The next generation of large telescopes (~30 m diameter) such as the Thirty Meter Telescope (TMT) and European Extremely Large Telescope (E-ELT) will provide an improvement in sensitivity by a factor of ~10 and in angular resolution by a factor of ~3 compared to current 10-m telescopes. With the anticipated development of AO capabilities at shorter wavelengths, the second generation of instruments at these facilities is expected to provide improvements in angular resolution by a factor of ~5. Such instruments may allow detection of the small MBA binaries that are currently beyond the reach of direct imaging instruments. In many of these systems, the components are separated by only a few milliarcseconds and the size ratios are larger than in large MBA binaries, resulting in flux ratios closer to unity.

## 2.6. Spectral Observations of Main-Belt-Asteroid and Trojan Systems

It is generally difficult to separate the light emitted or reflected from the secondary from that of the brighter primary. Nevertheless, such observations can be attempted when the secondary happens to be at a large angular separation from

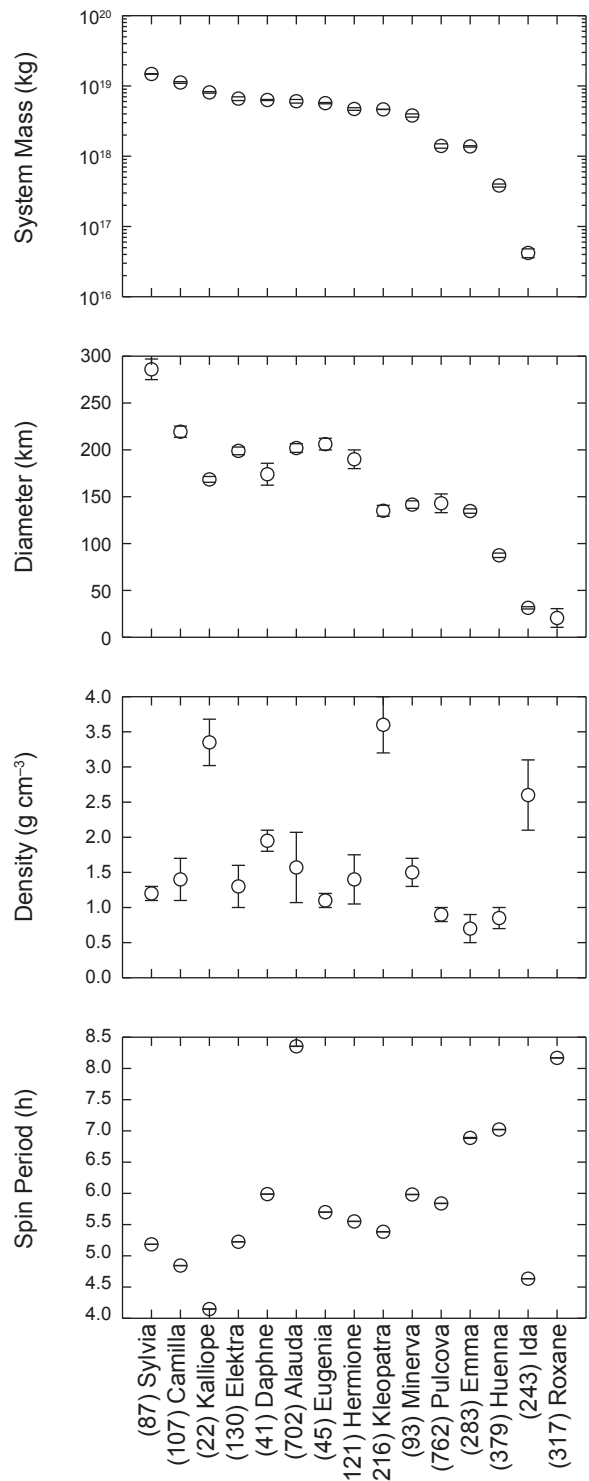


**Fig. 7.** Properties of large MBA binaries and triples, excluding the doubly synchronous (90) Antiope. Error bars or upper limits, when available, are shown. Based on data compiled by Johnston (2014) from references therein.

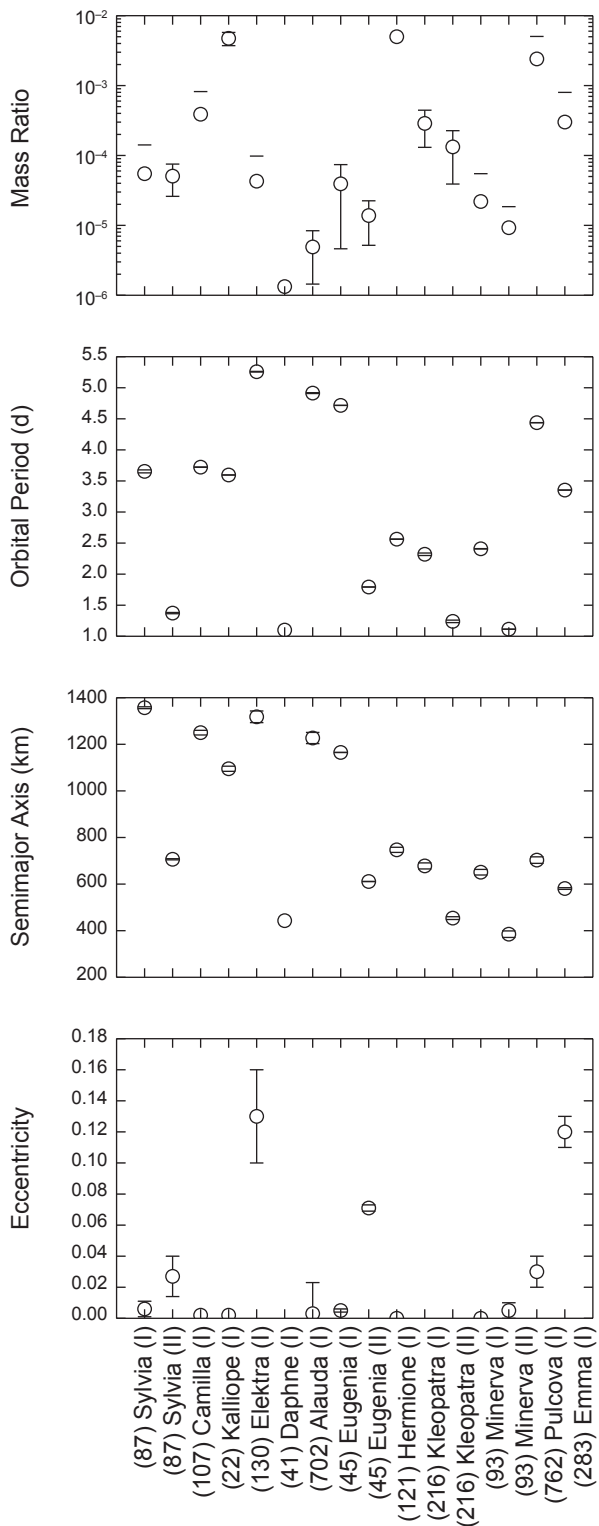


**Fig. 8.** Properties of satellites of large MBAs, excluding outliers (90) Antiope and (379) Huenna (see text). Satellites of (243) Ida and (317) Roxane, whose orbits are not well known, are not shown. Based on data compiled by Johnston (2014) from references therein.

the primary, when the system is undergoing mutual events, or with the help of an integral field spectrograph.

Spectra of (22) Kalliope and its satellite Linus in the 1–2.4- $\mu\text{m}$  region appear to be similar (Laver et al., 2009), which the authors attribute to satellite formation after a major impact on the precursor body. Observations of both components of (90) Antiope in the same spectral region also shows surface reflectances that are similar (Marchis et al., 2011). The spectrum of (379) Huenna is characteristic of C-type asteroids and the secondary does not exhibit a significantly different taxonomic type (DeMeo et al., 2011). Both components of (809) Lundia are consistent with a V-type classification (Birlan et al., 2014).

In the mid-infrared, Spitzer observations of the Trojan (617) Patroclus, including during mutual events, provided size estimates for its components and a thermal inertia of  $20 \pm 15 \text{ J s}^{-1/2} \text{ K}^{-1} \text{ m}^{-2}$  (Mueller et al., 2010). Spitzer observations combined with photometric results in the visible yielded size and albedo estimates for (624) Hektor (Emery et al., 2006). Spitzer observations did not resolve the binaries and results typically cannot be compared to observations that place many resolution elements on individual components. One exception is 2000 DP<sub>107</sub>, where analysis of Spitzer data yields a system density of  $0.9 \pm 0.3 \text{ g cm}^{-3}$  (Marchis et al., 2012) and the radar results indicate  $1.4 \pm 0.2 \text{ g cm}^{-3}$  (Naidu et al., 2015).

## 2.7. Stellar Occultations of Main-Belt-Asteroid and Trojan Systems

Stellar occultations provide a way of detecting components of a multiple-asteroid system, of placing bounds on component sizes, and of obtaining the relative positions of components on the plane of the sky. A recording of star light as a function of time shows a deep extinction when a target body crosses the line of sight between the observer and the star. This can be interpreted in terms of a chord on the apparent disk of the target body projected on the plane of the sky. If several observers are placed across the occultation path on the surface of Earth, multiple chords can be obtained, and the size and shape of the target projected on the sky can be reconstructed (Fig. 9). When two or more components are present, it is also possible to measure their relative position. While the reliability of this technique was disputed a decade ago due to the lack of digital recordings, the availability of low-cost cameras and global positioning systems has enabled a dramatic improvement in the precision of timing reports. Stellar occultations have become an important observational tool for the study of binary asteroids.

Early reports (e.g., Binzel and van Flandern, 1979) of asteroids suspected to be binaries on the basis of occultation data [including (3) Juno, (6) Hebe, (9) Metis, (12) Victoria, (18) Melpomene, (146) Lucina, and (532) Herculina] have remained largely unconfirmed despite extensive follow-up searches. However, it is likely that the outer satellite of (216) Kleopatra was detected during a 1980 occultation (Dunham, 1981; Descamps et al., 2011). The detection of a

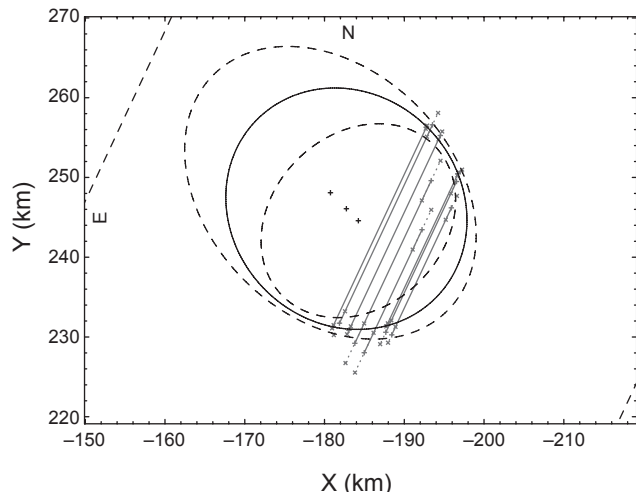


**Fig. 9.** The apparent shape of Linus, a satellite of (22) Kalliope (Margot and Brown, 2003), detected by stellar occultations. In this analysis, the profile of the satellite (solid curve) fitted to the observed chords (straight lines) yields an equivalent diameter of  $30 \pm 6 \text{ km}$ . Dashed curves show the corresponding uncertainty of the fitted profile, and dashed lines show negative detections. Figure adapted from Desamps et al. (2008).

satellite around the Trojan (911) Agamemnon has been suggested (Timerson et al., 2013) but not yet confirmed. The occultation technique has also been used to detect rings around the Centaur (10199) Chariklo (Braga-Ribas et al., 2014).

One strength of the stellar occultation technique lies in the fact that the observability of the event depends mainly on the brightness of the star and not of the asteroid or satellite. Stellar occultations can thus be used to detect small (kilometer-sized) satellites, even those that are close to the primary and that would remain undetected in direct imaging.

Another strength of the technique is the potential for high-precision measurements. Stellar occultations are based on time-series photometry. Given a sufficiently high cadence (e.g., 10–30 images per second), it is possible to obtain a precision of a few milliarcseconds on the relative position of binary components, which is 5–10 times better than with direct imaging with current instrumentation.

Finally, well-sampled stellar occultations allow for recovery of the size and apparent shape of asteroids and their satellites, whereas optical lightcurves and direct imaging observations primarily provide the diameter ratio of the components and more limited shape information. So far, four successful observations of satellite size and shape have been reported: Linus, satellite of (22) Kalliope (Desamps et al., 2008); Romulus, the outer satellite of (87) Sylvia (Berthier et al., 2014); and both components of the equal-sized binaries (90) Antiope (Bartczak et al., 2014) and (617) Patroclus (Buie et al., 2014).

Despite all these strengths, there remains a relatively low number of well-covered stellar occultation events. This is due, in part, to the requirement of successful observations at

many stations. Owing to uncertainties on both the star and asteroid positions, the occultation path can shift by several tens or even hundreds of kilometers on Earth compared to the prediction. Observers must therefore spread geographically to cover an event, but the detection of a satellite by several stations requires a fine grid of observers.

The situation is, however, expected to improve dramatically with the availability of the Gaia stellar catalog and better asteroid orbits (Tanga and Delbo, 2007). Predictions of the occultation paths (for the center of mass) will be accurate to a few kilometers, and the main source of uncertainty will become the prediction of the relative position of the satellite around the primary.

## 2.8. Other Observations

There have been several attempts to use groundbased interferometers to measure the angular separation of binary systems (Delbo et al., 2009; Carry et al., 2015). However, asteroid satellites are too faint for current interferometers operating in the visible and near-infrared and at the edge of detection in the mid-infrared. Future instrumentation may allow such observations. There are also prospects for observations with the Atacama Large Millimeter Array (ALMA) submillimeter array (Busch, 2009).

## 3. DYNAMICS

In parallel with advances in instrumentation and observing capabilities, the field has seen tremendous developments in understanding the dynamical processes that affect asteroid systems. This has been enabled in large part by the availability of detailed shape models and orbital parameters, by the need to model the dynamics of newly discovered triple systems, and by the desire to understand formation and evolution processes.

A non-exhaustive list of some dynamical problems that have been explored since *Asteroids III* includes the stability of asteroid satellite orbits (Scheeres, 2002; Frouard and Compère, 2012); the dynamics around triaxial bodies (Scheeres, 2009a); the fate of asteroid ejecta (Scheeres, 2007); the formation of contact binaries via dynamical evolution (Scheeres, 2009a; Taylor and Margot, 2011, 2014); the genesis of eccentric and mutually inclined orbits (Fang et al., 2011; Fang and Margot, 2012c); the orbital determination of triple systems using point-mass approximations (Marchis et al., 2010) and full N-body calculations (Fang et al., 2012); the influence of Kozai cycles on binaries (Perets and Naoz, 2009; Fang and Margot, 2012b); the effects of close planetary encounters on mutual orbits (Fang and Margot, 2012a) and spin states (Takahashi et al., 2013); the complex spin-orbit interactions with irregular component shapes (Scheeres et al., 2006), including the libration and irregular rotation of secondaries (Naidu and Margot, 2015); the influence of internal structure (Goldreich and Sari, 2009), material properties (Taylor and Margot, 2011), and nonspherical shapes (Taylor and Margot, 2014) on tidal evolution; the possibility of tidal saltation

(Harris et al., 2009; Fahnestock and Scheeres, 2009); the possibility of significant radiative evolution (Ćuk and Burns, 2005; Ćuk, 2007; Ćuk and Nesvorný, 2010; McMahon and Scheeres, 2010a,b); and the possibility of a stable equilibrium between tidal and radiative evolution (Jacobson and Scheeres, 2011a).

Several radar datasets provide exquisite constraints for dynamical studies. Reflex motion has been measured for 2000 DP<sub>107</sub> (Margot et al., 2002; Naidu et al., 2015), 1999 KW<sub>4</sub> (Ostro et al., 2006), and 1991 VH (Naidu et al., 2012), allowing masses of individual components to be determined. Because detailed component shapes are also available, one can fully model the system dynamics and study spin-orbit coupling in detail (Scheeres et al., 2006; Fahnestock and Scheeres, 2008; Naidu and Margot, 2015). One finding from this work is that even moderately elongated secondaries on mildly eccentric orbits are likely to experience chaotic rotation that substantially affects binary evolution timescales (Fig. 10).

## 4. SMALL ASTEROIDS: SYNTHESIS

### 4.1. Rotational Fission Hypothesis

With the exception of the doubly synchronous binary asteroid systems, the primary asteroids of all small binary systems are rapidly rotating (within a factor of only a few of the critical disruption spin limit for bodies with no shear or tensile strength  $\omega_d = \sqrt{4\pi\rho G/3}$ ). Furthermore, almost all

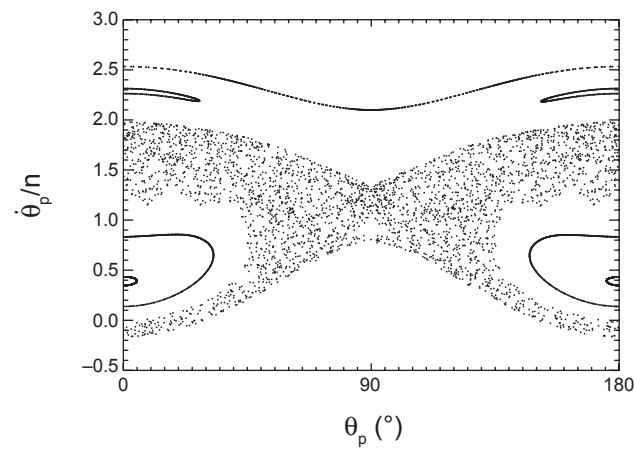


**Fig. 10.** Surface of section plot showing the possible rotational regimes of the ~200 m secondary of 1991 VH (secondary elongation  $a/b = 1.5$  and mutual orbit eccentricity  $e = 0.05$ ). The plot shows the angle between the long axis and the line of apsides of the mutual orbit,  $\theta_p$ , against its time derivative,  $\dot{\theta}_p$ , normalized by the mean motion,  $n$ , at each pericenter passage. Five trajectories are illustrated (from top to bottom: nonresonant quasiperiodic, periodic, chaotic, periodic, periodic). While trapped in the sea of chaos, the secondary experiences torques on its permanent deformation that result in a highly variable spin rate, preventing BYORP-type evolution. Figure from Naidu and Margot (2015).

known small binary asteroids have high angular momentum contents (*Pravec and Harris*, 2007). These characteristics are not consistent with formation following a subcatastrophic impact, capture through a three-body interaction in the near-Earth or main belt, or capture after a catastrophic impact. Instead, they are indicative of formation from a rotational fission event (e.g., *Margot et al.*, 2002; *Pravec and Harris*, 2007). The rotational fission hypothesis posits that a parent asteroid can be torqued to a rotation rate so great that the centrifugal accelerations overpower the gravitational accelerations holding a strengthless asteroid together (*Weidenschilling*, 1980). It is possible that some small asteroids have cohesive or molecular strength in addition to self-gravity (e.g., *Rozitis et al.*, 2014). In these cases, the centrifugal accelerations must overcome these additional forces in order for the asteroid to fission (*Pravec and Harris*, 2000; *Sánchez and Scheeres*, 2014). At rapid rotation rates, loose surface material can flow from high-latitude regions to the equator along potential gradients (*Ostro et al.*, 2006). It has been shown that rotational acceleration could trigger local slope failures and landslides, which can form the canonical top shape and equatorial bulge seen on primary components in small multiple-asteroid systems (*Walsh et al.*, 2008; *Harris et al.*, 2009).

*Bottke et al.* (2002) proposed a YORP-induced rotational fission hypothesis. It has since been shown that the YORP effect controls the rotational acceleration of small asteroids (*Bottke et al.*, 2006; *Marzari et al.*, 2011) and naturally explains the period distribution among small asteroids (*Pravec et al.*, 2008; *Rossi et al.*, 2009; *Polishook and Brosch*, 2009). Furthermore, including the YORP-induced rotational fission hypothesis in size-frequency distribution models improves the agreement with observations (*Jacobson et al.*, 2014a). The observed characteristics of the systems described in sections 2.1–2.3 as well as thermal inertia observations (*Delbo et al.*, 2011) are consistent with a binary formation mechanism that involves spin-up and mass shedding. The YORP-induced rotational fission hypothesis is the leading candidate for explaining the formation of binaries, triples, and pairs among small asteroids.

#### 4.2. Asteroid Pairs

The YORP effect can increase the spin rate of asteroids beyond the critical disruption spin limit, thereby triggering rotational fission. In actuality, there is some uncertainty regarding the spin rate at which disruption occurs — there may be failure and deformation before fission (*Walsh et al.*, 2008; *Sánchez and Scheeres*, 2011; *Cotto-Figueroa et al.*, 2013). The critical disruption spin limit also depends on the detailed shapes, masses, and interlocking nature of the interior components and any cohesive forces (*Scheeres*, 2007, 2009b; *Sánchez and Scheeres*, 2014). Despite ignoring these details, simple calculations provide a rotational fission model that can be compared directly and successfully with observations.

If a spherical approximation of each component is made, then the rotational breakup spin rate  $\omega_q$  necessary for fission

as a function of the secondary-to-primary mass ratio  $q$  is (*Scheeres*, 2007)

$$\omega_q = \omega_d \sqrt{\frac{1+q}{(1+q^{1/3})^3}} \quad (1)$$

This is the exact solution for two spheres resting on each other with a mass ratio of  $q$  and rotating about the axis of maximum moment of inertia.

The spherical component model described above demonstrates the important reality that the larger the mass ratio  $q$  of the two future binary members, the slower the required rotation rate necessary to create the binary system. This slower required rotation rate translates into a small initial free energy for the ensuing binary system. The free energy  $E_f$  is the energy that is accessible to the different energy reservoirs in the system, including the rotation states of each member and the orbit. It does not include the internal binding energy of each object. The free energy is an important quantity because it determines the boundedness of the system. Bound systems have negative free energy, while unbound systems have positive free energy. An unbound binary system implies that the system is capable of disruption but does not imply that the system will disrupt. For the idealized case of two spheres, the free energy can be expressed as (*Scheeres*, 2007)

$$E_f = \frac{2\pi\rho\omega_d^2 R_p^5}{15} f(q) \quad (2)$$

where  $R_p$  is the radius of the primary and  $f(q)$  is an algebraic, monotonically decreasing function for  $0 < q \leq 1$ . For the equation above corresponding to two spheres, the function crosses zero when  $q \approx 0.204$ . Similar equations can be written for any two component shapes, but  $q \sim 0.2$  remains near the binding energy transition point, so the model uses this point as a simple approximation. This crossing point divides bound systems with negative energy and mass ratios  $q > 0.2$  and unbound systems with positive energy and mass ratios  $q < 0.2$ . Because of this fundamental difference, high-mass-ratio  $q > 0.2$  and low-mass-ratio  $q < 0.2$  binary systems evolve differently (*Scheeres*, 2009a; *Jacobson and Scheeres*, 2011b). Primarily, positive-energy low-mass-ratio systems will chaotically explore orbital phase space until the majority find a disruption trajectory creating an asteroid pair; this evolutionary route is unavailable to high-mass-ratio systems.

The asteroid pair population provides a natural laboratory to test this relationship (*Scheeres*, 2007; *Vokrouhlický and Nesvorný*, 2008). *Pravec et al.* (2010) examined many asteroid pair systems and measured the rotation rate of the primary and the absolute magnitude difference between the pair members. These two quantities should follow a simple relationship related to  $\omega_q$ , although many of the ignored details mentioned at the beginning of this section can move asteroids away from this relationship. Indeed, *Pravec et al.* (2010) discovered that asteroid pairs do follow this

relationship (Fig. 5). Furthermore, they found that the large members of asteroid pairs have a broader range of elongations than the primaries of binary systems, consistent with the findings of *Jacobson and Scheeres* (2011b) that prolate primaries are less likely to remain in a bound binary system after rotational fission. Thus, there is strong evidence to support the hypothesis that asteroid pairs are the products of rotational fission.

Asteroid pairs continue to be a fertile observational landscape. Since dynamical integrations can derive the “birthdate” of such systems, observers can test ideas regarding space-weathering timescales and YORP evolution after fission (*Polishook et al.*, 2014a; *Polishook*, 2014). Along with binary systems, the surfaces of asteroid pairs may provide clues in the future regarding the violence of the rotational fission process (*Polishook et al.*, 2014b).

### 4.3. Binary and Triple Systems

*Jacobson and Scheeres* (2011b) showed that after rotational fission there are a number of possible outcomes. Their numerical studies produced the evolutionary flow chart shown in Fig. 11; many of these outcomes were also found by *Fang and Margot* (2012c). The high- and low-mass-ratio distinction for rotational fission emphasized above plays

an important role in distinguishing the two evolutionary pathways. Along the high-mass-ratio pathway, both binary members tidally synchronize and then evolve according to the BYORP effect.

Along the low-mass-ratio pathway, the binary system is unbound. Since these systems are chaotic, many are disrupted and become asteroid pairs. During this chaotic binary state, the secondary can often go through rotational fission itself, although this rotational fission is torqued by spin-orbit coupling (Fig. 10) rather than the YORP effect. Loss of material from the secondary stabilizes the remaining orbiting components. The lost mass may reaccrete onto the primary, perhaps contributing to the observed equatorial ridges, or may escape from the system. In these cases, the system undergoes another chaotic binary episode with three possible outcomes: a reshaped asteroid, an asteroid pair, or a stable binary. These binaries still possess positive free energy such that they may disrupt if disturbed. In other cases, the system retains three components after secondary fission. While the numerical simulations of *Jacobson and Scheeres* (2011b) did not yield this latter outcome, it is possible that this pathway explains the existence of stable triple systems.

After stabilization of the low-mass-ratio binary system, the secondary synchronizes due to tides (e.g., *Goldreich and Sari*, 2009), although some satellites may be trapped in a

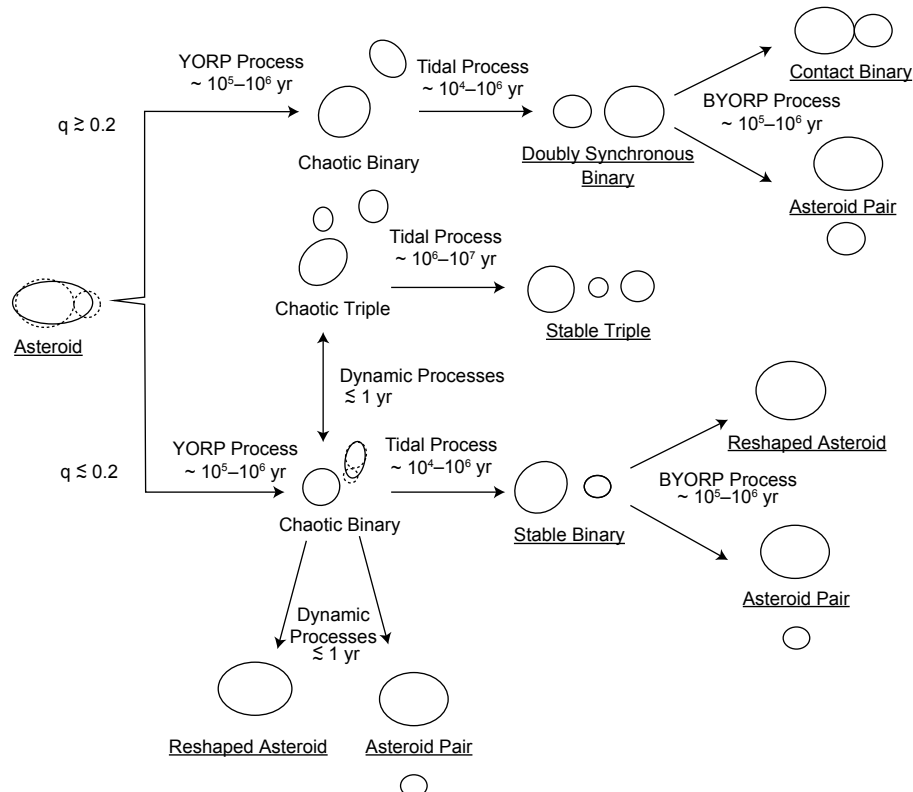


**Fig. 11.** Flowchart showing the possible evolutionary paths for an asteroid after it undergoes rotational fission. Each arrow is labeled with the dominant process and an estimated timescale for this process. Underlined states are nominally stable for a YORP effect timescale. Figure from *Jacobson and Scheeres* (2011b).

chaotic rotation state for durations that exceed the classic spin synchronization timescales (Naidu and Margot, 2015). Then the system evolves according to the BYORP effect and tides. These binary evolutionary processes and their outcomes are discussed in the chapter by Walsh and Jacobson in this volume. As shown in Fig. 11, these evolutionary paths include each of the binary morphologies identified in this chapter and by other teams (Pravec and Harris, 2007; Fang and Margot, 2012c). In particular, the formation of wide asynchronous binaries such as (1509) Esclangonga, (4674) Pauling, (17246) 2000 GL<sub>74</sub>, and (22899) 1999 TO<sub>14</sub> is best explained by a rotational fission mechanism (Polishook et al., 2011) followed by BYORP orbital expansion (Jacobson et al., 2014b).

An alternative formation mechanism for triples such as (153591) 2001 SN<sub>263</sub> and (136617) 1994 CC is that after creating a stable binary system, the primary undergoes rotational fission a second time. As long as the third component is on a distant enough orbit, then this process may result in a stable triple system (Fang et al., 2011; Fang and Margot, 2012c; Jacobson et al., 2014b).

## 5. LARGE ASTEROIDS: SYNTHESIS

The primaries of most known binary and triple asteroids greater than 20 km have spin periods in the range of 4 h to 7 h (Fig. 7). While these spin rates are not near the disruption spin limit, they are typically faster than the mean spin rates for asteroids of similar sizes. The total angular momentum content, however, is well below that required for rotational fission. The secondary-to-primary mass ratios in these systems range from 10<sup>-6</sup> to 10<sup>-2</sup>. These properties are consistent with satellite formation during large collisions (Fig. 12). Durda et al. (2004) have shown in numerical simulations that impacts of 10- to 30-km-diameter projectiles striking at impact velocities between 3 km s<sup>-1</sup> and 7 km s<sup>-1</sup> can produce satellites that match observed properties. Multiple asteroid systems, e.g., (45) Eugenia (Merline et al., 1999; Marchis et al., 2007) and (87) Sylvia (Margot and Brown, 2001; Marchis et al., 2005a), can also plausibly form through collisions.

There is more uncertainty related to the formation of (90) Antiope and (617) Patroclus, which are both too large to be substantially affected by YORP. Hypotheses for the formation of (90) Antiope include primordial fission due to excessive angular momentum (Pravec and Harris, 2007), an improbable low-velocity collision of a large impactor (Weidenschilling et al., 2001), or shrinking of an initially wide binary formed by gravitational collapse (Nesvorný et al., 2010). Gravitational collapse in a gas-rich protoplanetary disk has been invoked to explain the formation of numerous binaries in the transneptunian region. (617) Patroclus may be a primordial TNO that avoided disruption during emplacement in the Trojan region (Nesvorný et al., 2010). Wide TNO binaries would not be expected to survive this process, but encounter calculations (e.g., Fang and Margot, 2012a) show that tight binaries would.

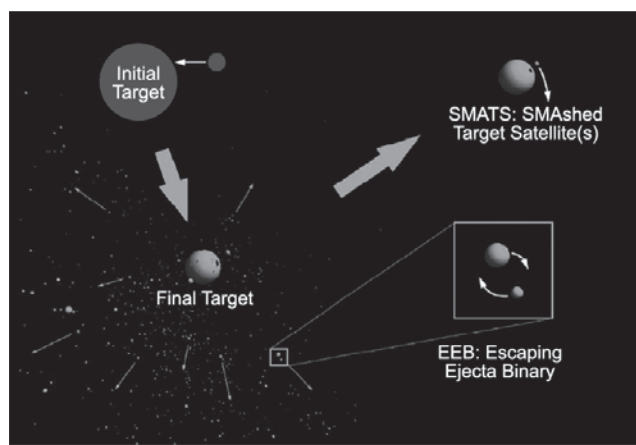


**Fig. 12.** Numerical simulations show that binaries can form as a result of large impacts between asteroids. In some scenarios, impact debris can remain gravitationally bound to the target body, forming a satellite (SMATs). This process likely explains the formation of large MBA binaries. In other scenarios, two fragments from the escaping ejecta have sufficiently similar trajectories, such that they become bound to one another (EEBs). Figure from Durda et al. (2004).

## 6. CONCLUSIONS

Studies of binaries, triples, and pairs remain a fertile ground for observing processes that are important in planet formation and for measuring quantities that are difficult to obtain by other means. These include masses and densities as well as thermal, mechanical, and interior properties. Binaries or triples have been found in ~50 NEAs, ~50 small MBAs, ~20 large MBAs, and 2 Trojans. A unifying paradigm based on rotational fission and post-fission dynamics explains the formation of small binaries, triples, and pairs. Because the Sun-powered rotational fission process is unrelenting, and because the production of pairs is a frequent outcome of this process, a substantial fraction of small bodies likely originated in a rotational disruption event. This origin affects the size distribution of asteroids and may explain the presence of single NEAs with equatorial bulges observed with radar. Small satellites of large MBAs are likely formed during large collisions. Advances in instrumentation, observational programs, and analysis techniques hold the promise of exciting findings in the next decade.

## REFERENCES

- Bartczak P., Michałowski T., Santana-Ros T., and Dudziński G. (2014) A new non-convex model of the binary asteroid 90 Antiope obtained with the SAGE modelling technique. *Mon. Not. R. Astron. Soc.*, 443, 1802–1809.
- Becker T. M., Howell E. S., Nolan M. C., Magri C., Pravec P., Taylor P. A., Oey J., Higgins D., Világi J., Kornoš L., Galád A., Gajdoš Š., Gaftonyuk N. M., Krugly Y. N., Molotov I. E., Hicks M. D., Carbognani A., Warner B. D., Vachier F., Marchis F., and Pollock J. T. (2015) Physical modeling of triple near-Earth asteroid (153591) 2001 SN<sub>263</sub> from radar and optical light curve observations. *Icarus*, 248, 499–515.

- Behrend R., Bernasconi L., Roy R., Klotz A., Colas F., Antonini P., Aoun R., Augustesen K., Barbotin E., Berger N., Berrouachdi H., Brochard E., Cazenave A., Cavadore C., Coloma J., Cotre V., Deconihout S., Demeautis C., Dorseuil J., Dubos G., Durkee R., Frappa E., Hormuth F., Itkonen T., Jacques C., Kurtze L., Laffont A., Lavayssière M., Lecacheux J., Leroy A., Manzini F., Masi G., Matter D., Michelsen R., Nomen J., Oksanen A., Pääkkönen P., Peyrot A., Pimentel E., Pray D., Rinner C., Sanchez S., Sonnenberg K., Sposetti S., Starkey D., Stoss R., Teng J.-P., Vignard M., and Waelchli N. (2006) Four new binary minor planets: (854) Frostia, (1089) Tama, (1313) Berna, (4492) Debussy. *Astron. Astrophys.*, 446, 1177–1184.
- Belton M., Chapman C., Thomas P., Davies M., Greenberg R., Klaasen K., Byrnes D., D'Amario L., Synnott S., Merline W., Petit J.-M., Storrs A., and Zellner B. (1995) The bulk density of asteroid 243 Ida from Dactyl's orbit. *Nature*, 374, 785–788.
- Benner L. A. M., Margot J. L., Nolan M. C., Giorgini J. D., Brozovic M., Scheeres D. J., Magri C., and Ostro S. J. (2010) Radar imaging and a physical model of binary asteroid 65803 Didymos. *Bull. Am. Astron. Soc.*, 42, 1056.
- Berthier J., Vachier F., Marchis F., Ďurech J., and Carry B. (2014) Physical and dynamical properties of the main belt triple asteroid (87) Sylvia. *Icarus*, 239, 118–130.
- Binzel R. P. and van Flandern T. C. (1979) Minor planets — The discovery of minor satellites. *Science*, 203, 903–905.
- Birlan M., Vaduvescu O., Tudorica A., Sonka A., Nedelcu A., Galad A., Colas F., Pozo F. N., Barr A. D., Toma R., Comsa I., Rocher P., Lainey V., Vidican D., Asher D., Opriseanu C., Vancea C., Colque J. P., Soto C. P., Rekola R., and Unda-Sanzana E. (2010) More than 160 near Earth asteroids observed in the EURONEAR network. *Astron. Astrophys.*, 511, A40.
- Birlan M., Nedelcu D. A., Popescu M., Vernazza P., Colas F., and A. Kryszczynska (2014) Spectroscopy and surface properties of (809) Lundia. *Mon. Not. R. Astron. Soc.*, 437, 176–184.
- Bottke W. F. and Melosh H. J. (1996a) The formation of asteroid satellites and doublet craters by planetary tidal forces. *Nature*, 381, 51–53.
- Bottke W. F. and Melosh H. J. (1996b) Binary asteroids and the formation of doublet craters. *Icarus*, 124, 372–391.
- Bottke W. F., Vokrouhlický D., Rubincam D. P., and Brož M. (2002) The effect of Yarkovsky thermal forces on the dynamical evolution of asteroids and meteoroids. In *Asteroids III* (W. F. Bottke Jr. et al., eds.), pp. 395–408. Univ. of Arizona, Tucson.
- Bottke W. F., Vokrouhlický D., Rubincam D. P., and Nesvorný D. (2006) The Yarkovsky and YORP effects: Implications for asteroid dynamics. *Annu. Rev. Earth Planet. Sci.*, 34, 157–191.
- Braga-Ribas F., Sicardi B., Ortiz J. L., Snodgrass C., Roques F., Vieira-Martins R., Camargo J. I. B., Assafin M., Duffard R., Jehin E., Pollock J., Leiva R., Emilio M., Machado D. I., Colazo C., Lellouch E., Skottfelt J., Gillon M., Ligier N., Maquet L., Benedetti-Rossi G., Gomes A. R., Kervella P., Monteiro H., Sfair R., El Moutamid M., Tancredi G., Spagnotto J., Maury A., Morales N., Gil-Hutton R., Roland S., Ceretta A., Gu S.-H., Wang X.-B., Harpsøe K., Rabus M., Manfroid J., Opitom C., Vanzi L., Mehret L., Lorenzini L., Schneiter E. M., Melia R., Lecacheux J., Colas F., Vachier F., Widemann T., Almenares L., Sandness R. G., Char F., Perez V., Lemos P., Martinez N., Jørgensen U. G., Dominik M., Roig F., Reichart D. E., Lacluyze A. P., Haislip J. B., Ivarsen K. M., Moore J. P., Frank N. R., and Lambas D. G. (2014) A ring system detected around the Centaur (10199) Chariklo. *Nature*, 508, 72–75.
- Brooks H. E. (2006) Orbits of binary near-Earth asteroids from radar observations. *Bull. Am. Astron. Soc.*, 38, 934.
- Brozović M., Benner L. A. M., Taylor P. A., Nolan M. C., Howell E. S., Magri C., Scheeres D. J., Giorgini J. D., Pollock J. T., Pravec P., Galád A., Fang J., Margot J. L., Busch M. W., Shepard M. K., Reichart D. E., Ivarsen K. M., Haislip J. B., Lacluyze A. P., Jao J., Slade M. A., Lawrence K. J., and Hicks M. D. (2011) Radar and optical observations and physical modeling of triple near-Earth asteroid (136617) 1994 CC. *Icarus*, 216, 241–256.
- Buie M. W., Olkin C. B., Merline W. J., Timerson B., Herald D., Owen W. M., Abramson H. B., Abramson K. J., Breit D. C., Caton D. B., Conard S. J., Croom M. A., Dunford R. W., Dunford J. A., Dunham D. W., Ellington C. K., Liu Y., Maley P. D., Olsen A. M., Royer R., Scheck A. E., Sherrod C., Sherrod L., Swift T. J., Taylor L. W., and Venable R. (2014) Shape and size of Patroclus and Menoetius from a stellar occultation. *Bull. Am. Astron. Soc.*, 46, #506.09.
- Busch M. W. (2009) ALMA and asteroid science. *Icarus*, 200, 347–349.
- Busch M. W., Ostro S. J., Benner L. A. M., Brozovic M., Giorgini J. D., Jao J. S., Scheeres D. J., Magri C., Nolan M. C., Howell E. S., Taylor P. A., Margot J. L., and Brisken W. (2011) Radar observations and the shape of near-Earth asteroid 2008 EV<sub>5</sub>. *Icarus*, 212, 649–660.
- Carry B. (2009) Asteroids physical properties from high angular-resolution imaging. Ph.D. thesis, Observatoire de Paris.
- Carry B. (2012) Density of asteroids. *Planet. Space Sci.*, 73, 98–118.
- Carry B., Kaasalainen M., Merline W. J., Müller T. G., Jordá L., Drummond J. D., Berthier J., O'Rourke L., Ďurech J., Küppers M., Conrad A., Tamblyn P., Dumas C., Siersk H., and the OSIRIS Team (2012) Shape modeling technique KOALA validated by ESA Rosetta at (21) Lutetia. *Planet. Space Sci.*, 66, 200–212.
- Carry B., Matter A., Scheirich P., Pravec P., Molnar L., Mottola S., Carbognani A., Jehin E., Marciniak A., Binzel R. P., DeMeo F. E., Birlan M., Delbo M., Barbotin E., Behrend R., Bonnaireau M., Colas F., Farissier P., Fauvaud M., Gillier C., Gillon M., Hellmich S., Hirsch R., Leroy A., Manfroid J., Montier J., Morelle E., Richard F., Sobkowiak K., Strajnic J., and Vachier F. (2015) The small binary asteroid (939) Isberga. *Icarus*, 248, 516–525.
- Cellino A., Pannunzio R., Zappala V., Farinella P., and Paolicchi P. (1985) Do we observe light curves of binary asteroids? *Astron. Astrophys.*, 144, 355–362.
- Chapman C. R., Veverka J., Thomas P. C., Klaasen K., Belton M. J. S., Harch A., McEwen A., Johnson T. V., Helfenstein P., Davies M. E., Merline W. J., and Denk T. (1995) Discovery and physical properties of Dactyl a satellite of asteroid 243 Ida. *Nature*, 374, 783.
- Chesley S. R., Farnocchia D., Nolan M. C., Vokrouhlický D., Chodas P. W., Milani A., Spoto F., Rozitis B., Benner L. A. M., Bottke W. F., Busch M. W., Emery J. P., Howell E. S., Lauretta D. S., Margot J.-L., and Taylor P. A. (2014) Orbit and bulk density of the OSIRIS-REx target asteroid (101955) Bennu. *Icarus*, 235, 5–22.
- Conrad A. R., Merline W. J., Drummond J. D., Tamblyn P. M., Dumas C., Carry B. X., Campbell R. D., Goodrich R. W., Owen W. M., and Chapman C. R. (2008) S/2008 (41) I. *IAU Circular* 8930.
- Cotto-Figueredo D., Statler T. S., Richardson D. C., and Tanga P. (2013) Killing the YORP cycle: A stochastic and self-limiting YORP effect. *Bull. Am. Astron. Soc.*, 45, #106.09.
- Ćuk M. (2007) Formation and destruction of small binary asteroids. *Astrophys. J. Lett.*, 659, L57–L60.
- Ćuk M. and Burns J. A. (2005) Effects of thermal radiation on the dynamics of binary NEAs. *Icarus*, 176, 418–431.
- Ćuk M. and Nesvorný D. (2010) Orbital evolution of small binary asteroids. *Icarus*, 207, 732–743.
- Delbo M., Ligori S., Matter A., Cellino A., and Berthier J. (2009) First VLTI-MIDI direct determinations of asteroid sizes. *Astrophys. J.*, 694, 1228–1236.
- Delbo M., Walsh K., Mueller M., Harris A. W., and Howell E. S. (2011) The cool surfaces of binary near-Earth asteroids. *Icarus*, 212, 138–148.
- DeMeo F. E., Carry B., Marchis F., Birlan M., Binzel R. P., Bus S. J., Descamps P., Nedelcu A., Busch M., and Bouy H. (2011) A spectral comparison of (379) Huenna and its satellite. *Icarus*, 212, 677–681.
- Descamps P., Marchis F., Michałowski T., Vachier F., Colas F., Berthier J., Assafin M., Dunckel P. B., Polinska M., Pych W., Hestroffer D., Miller K. P. M., Vieira-Martins R., Birlan M., Teng-Chuen-Yu J.-P., Peyrot A., Payet B., Dorseuil J., Léonie Y., and Dijoux T. (2007) Figure of the double asteroid 90 Antiope from adaptive optics and lightcurve observations. *Icarus*, 187, 482–499.
- Descamps P., Marchis F., Pollock J., Berthier J., Vachier F., Birlan M., Kaasalainen M., Harris A. W., Wong M. H., Romanishin W. J., Cooper E. M., Kettner K. A., Wiggins P., Kryszczynska A., Polinska M., Coliac J.-F., Devyatkin A., Verestchagina I., and Gorshakov D. (2008) New determination of the size and bulk density of the binary asteroid 22 Kalliope from observations of mutual eclipses. *Icarus*, 196, 578–600.
- Descamps P., Marchis F., Michałowski T., Berthier J., Pollock J., Wiggins P., Birlan M., Colas F., Vachier F., Fauvaud S., Fauvaud M., Sareyan J.-P., Pilcher F., and Klinglesmith D. A. (2009) A giant crater on 90 Antiope? *Icarus*, 203, 102–111.
- Descamps P., Marchis F., Berthier J., Emery J. P., Duchêne G., de Pater I., Wong M. H., Lim L., Hammel H. B., Vachier F., Wiggins P., Teng-Chuen-Yu J.-P., Peyrot A., Pollock J., Assafin M., Vieira-Martins R., Camargo J. I. B., Braga-Ribas F., and Macomber B. (2011) Triplicity and physical characteristics of asteroid (216) Kleopatra. *Icarus*, 211, 1022–1033.

- Doresoundiram A., Paolicchi P., Verlicchi A., and Cellino A. (1997) The formation of binary asteroids as outcomes of catastrophic collisions. *Planet. Space Sci.*, *45*, 757–770.
- Duddy S. R., Lowry S. C., Wolters S. D., Christou A., Weissman P. R., Green S. F., and Rozitis B. (2012) Physical and dynamical characterisation of the unbound asteroid pair 7343-154634. *Astron. Astrophys.*, *539*, A36.
- Duddy S. R., Lowry S. C., Christou A., Wolters S. D., Rozitis B., Green S. F., and Weissman P. R. (2013) Spectroscopic observations of unbound asteroid pairs using the WHT. *Mon. Not. R. Astron. Soc.*, *429*, 63–74.
- Dunham D. W. (1981) Recently-observed planetary occultations. *Occultation Newsletter, International Occultation Timing Association (IOTA)*, *2*, 139–143.
- Durda D. D. (1996) The formation of asteroidal satellites in catastrophic collisions. *Icarus*, *120*, 212–219.
- Durda D. D., Bottke W. F., Enke B. L., Merline W. J., Asphaug E., Richardson D. C., and Leinhardt Z. M. (2004) The formation of asteroid satellites in large impacts: Results from numerical simulations. *Icarus*, *170*, 243–257.
- Emery J. P., Cruikshank D. P., and Van Cleve J. (2006) Thermal emission spectroscopy (5.2–38  $\mu\text{m}$ ) of three Trojan asteroids with the Spitzer Space Telescope: Detection of fine-grained silicates. *Icarus*, *182*, 496–512.
- Fahnestock E. G. and Scheeres D. J. (2008) Simulation and analysis of the dynamics of binary near-Earth asteroid (66391) 1999 KW<sub>4</sub>. *Icarus*, *194*, 410–435.
- Fahnestock E. G. and Scheeres D. J. (2009) Binary asteroid orbit expansion due to continued YORP spin-up of the primary and primary surface particle motion. *Icarus*, *201*, 135–152.
- Fang J. and Margot J. L. (2012a) Binary asteroid encounters with terrestrial planets: Timescales and effects. *Astron. J.*, *143*, 25.
- Fang J. and Margot J. L. (2012b) The role of Kozai cycles in near-Earth binary asteroids. *Astron. J.*, *143*, 59.
- Fang J. and Margot J. L. (2012c) Near-Earth binaries and triples: Origin and evolution of spin-orbital properties. *Astron. J.*, *143*, 24.
- Fang J., Margot J. L., Brozovic M., Nolan M. C., Benner L. A. M., and Taylor P. A. (2011) Orbits of near-Earth asteroid triples 2001 SN<sub>263</sub> and 1994 CC: Properties, origin, and evolution. *Astron. J.*, *141*, 154.
- Fang J., Margot J. L., and Rojo P. (2012) Orbits, masses, and evolution of main belt triple (87) Sylvia. *Astron. J.*, *144*, 70.
- Frouard J. and Compère A. (2012) Instability zones for satellites of asteroids: The example of the (87) Sylvia system. *Icarus*, *220*, 149–161.
- Goldreich P. and Sari R. (2009) Tidal evolution of rubble piles. *Astrophys. J.*, *691*, 54–60.
- Hanuš J., Durech J., Brož M., Warner B. D., Pilcher F., Stephens R., Oey J., Bernasconi L., Casulli S., Behrend R., Polishook D., Henych T., Lehký M., Yoshida F., and Ito T. (2011) A study of asteroid pole-latitude distribution based on an extended set of shape models derived by the lightcurve inversion method. *Astron. Astrophys.*, *530*, A134.
- Harris A. W., Fahnestock E. G., and Pravec P. (2009) On the shapes and spins of rubble pile asteroids. *Icarus*, *199*, 310–318.
- Hilton J. L. (2002) Asteroid masses and densities. In *Asteroids III* (W. F. Bottke Jr. et al., eds.), pp. 103–112. Univ. of Arizona, Tucson.
- Holsapple K. A. (2007) Spin limits of solar system bodies: From the small fast-rotators to 2003 EL<sub>61</sub>. *Icarus*, *187*(2), 500–509.
- Hudson R. S. (1993) Three-dimensional reconstruction of asteroids from radar observations. *Remote Sensing Rev.*, *8*, 195–203.
- Jacobson S. A. and Scheeres D. J. (2011a) Long-term stable equilibria for synchronous binary asteroids. *Astrophys. J. Lett.*, *736*, L19.
- Jacobson S. A. and Scheeres D. J. (2011b) Dynamics of rotationally fissioned asteroids: Source of observed small asteroid systems. *Icarus*, *214*(1), 161–178.
- Jacobson S. A., Marzari F., Rossi A., Scheeres D. J., and Davis D. R. (2014a) Effect of rotational disruption on the size-frequency distribution of the main belt asteroid population. *Mon. Not. R. Astron. Soc. Lett.*, *439*, L95–L99.
- Jacobson S. A., Scheeres D. J., and McMahon J. (2014b) Formation of the wide asynchronous binary asteroid population. *Astrophys. J.*, *780*, 60.
- Johnston W. R. (2014) *Binary Minor Planets V7.0*. EAR-A-COMPIL-5-BINMP-V7.0, NASA Planetary Data System.
- Kryszczyńska A., Colas F., Descamps P., Bartczak P., Polińska M., Kwiatkowski T., Lecacheux J., Hirsch R., Fagas M., Kamiński K., Michałowski T., and Marciniak A. (2009) New binary asteroid 809 Lundia. I. Photometry and modelling. *Astron. Astrophys.*, *501*, 769–776.
- Lauer C., de Pater I., Marchis F., Ádámkovics M., and Wong M. H. (2009) Component-resolved near-infrared spectra of the (22) Kalliope system. *Icarus*, *204*, 574–579.
- Levison H. F., Bottke W. F., Gounelle M., Morbidelli A., Nesvorný D., and Tsiganis K. (2009) Contamination of the asteroid belt by primordial trans-neptunian objects. *Nature*, *460*, 364–366.
- Magri C., Ostro S. J., Scheeres D. J., Nolan M. C., Giorgini J. D., Benner L. A. M., and Margot J. L. (2007) Radar observations and a physical model of asteroid 1580 Betulia. *Icarus*, *186*, 152–177.
- Marchis F., Descamps P., Hestroffer D., and Berthier J. (2005a) Discovery of the triple asteroidal system 87 Sylvia. *Nature*, *433*, 822–824.
- Marchis F., Descamps P., Hestroffer D., Berthier J., Brown M. E., and Margot J. L. (2005b) Satellites of (87) Sylvia. *IAU Circular* 8582.
- Marchis F., Hestroffer D., Descamps P., Berthier J., Bouchez A. H., Campbell R. D., Chin J. C. Y., van Dam M. A., Hartman S. K., Johansson E. M., Lafon R. E., Le Mignant D., de Pater I., Stomski P. J., Summers D. M., Vachier F., Wizinowich P. L., and Wong M. H. (2006a) A low density of 0.8 g cm<sup>-3</sup> for the Trojan binary asteroid 617 Patroclus. *Nature*, *439*, 565–567.
- Marchis F., Wong M. H., Berthier J., Descamps P., Hestroffer D., Vachier F., Le Mignant D., and de Pater I. (2006b) S/2006 (624) 1. *IAU Circular* 8732.
- Marchis F., Baek M., Descamps P., Berthier J., Hestroffer D., and Vachier F. (2007) S/2004 (45) 1. *IAU Circular* 8817.
- Marchis F., Descamps P., Baek M., Harris A. W., Kaasalainen M., Berthier J., Hestroffer D., and Vachier F. (2008a) Main belt binary asteroidal systems with circular mutual orbits. *Icarus*, *196*, 97–118.
- Marchis F., Descamps P., Berthier J., and Emery J. P. (2008b) S/2008 (216) 1 and S/2008 (216) 2. *IAU Circular* 8980.
- Marchis F., Descamps P., Berthier J., Hestroffer D., Vachier F., Baek M., Harris A. W., and Nesvorný D. (2008c) Main belt binary asteroidal systems with eccentric mutual orbits. *Icarus*, *195*, 295–316.
- Marchis F., Pollock J., Pravec P., Baek M., Greene J., Hutton L., Descamps P., Reichart D. E., Ivarsen K. M., Crain J. A., Nysewander M. C., LaCluyze A. P., Haislip J. B., and Harvey J. S. (2008d) (3749) Balam. *IAU Circular* 8928.
- Marchis F., Macomber B., Berthier J., Vachier F., and Emery J. P. (2009) S/2009 (93) 1 and S/2009 (93) 2. *IAU Circular* 9069.
- Marchis F., Lainey V., Descamps P., Berthier J., Van Dam M., de Pater I., Macomber B., Baek M., Le Mignant D., Hammel H. B., Showalter M., and Vachier F. (2010) A dynamical solution of the triple asteroid system (45) Eugenia. *Icarus*, *210*, 635–643.
- Marchis F., Enriquez J. E., Emery J. P., Berthier J., Descamps P., and Vachier F. (2011) The origin of (90) Antiope from component-resolved near-infrared spectroscopy. *Icarus*, *213*, 252–264.
- Marchis F., Enriquez J. E., Emery J. P., Mueller M., Baek M., Pollock J., Assafin M., Vieira Martins R., Berthier J., Vachier F., Cruikshank D. P., Lim L. F., Reichart D. E., Ivarsen K. M., Haislip J. B., and LaCluyze A. P. (2012) Multiple asteroid systems: Dimensions and thermal properties from Spitzer Space Telescope and ground-based observations. *Icarus*, *221*, 1130–1161.
- Marchis F., Durech J., Castillo-Rogez J., Vachier F., Cuk M., Berthier J., Wong M. H., Kalas P., Duchene G., van Dam M. A., Hamanowa H., and Viikinkoski M. (2014) The puzzling mutual orbit of the binary Trojan asteroid (624) Hektor. *Astrophys. J. Lett.*, *783*, L37.
- Margot J. L. (2003) S/2003 (379) 1. *IAU Circular* 8182.
- Margot J. L. (2010) Recent observations of binary and multiple systems. In *Second Workshop on Binaries in the Solar System*, Wasowo, Poland.
- Margot J. L. and Brown M. E. (2001) Discovery and characterization of binary asteroids 22 Kalliope and 87 Sylvia. *Bull. Am. Astron. Soc.*, *33*, 1133.
- Margot J. L. and Brown M. E. (2003) A low density M-type asteroid in the main belt. *Science*, *300*(5627), 1939–1942.
- Margot J. L., Nolan M. C., Benner L. A. M., Ostro S. J., Jurgens R. F., Giorgini J. D., Slade M. A., and Campbell D. B. (2002) Binary asteroids in the near-Earth object population. *Science*, *296*, 1445–1448.
- Margot J. L., Pravec P., Nolan M. C., Howell E. S., Benner L. A. M., Giorgini J. D., Jurgens R. F., Ostro S. J., Slade M. A., Magri C., Taylor P. A., Nicholson P. D., and Campbell D. B. (2006) Hermes as an exceptional case among binary near-Earth asteroids. In *IAU General Assembly*.

- Marzari F., Rossi A., and Scheeres D. J. (2011) Combined effect of YORP and collisions on the rotation rate of small main belt asteroids. *Icarus*, 214(2), 622–631.
- McMahon J. and Scheeres D. (2010a) Secular orbit variation due to solar radiation effects: A detailed model for BYORP. *Cel. Mech. Dyn. Astron.*, 106, 261–300.
- McMahon J. and Scheeres D. (2010b) Detailed prediction for the BYORP effect on binary near-Earth asteroid (66391) 1999 KW<sub>4</sub> and implications for the binary population. *Icarus*, 209, 494–509.
- Merline W. J., Close L. M., Dumas C., Chapman C. R., Roddier F., Menard F., Slater D. C., Duvert G., Shelton C., and Morgan T. (1999) Discovery of a moon orbiting the asteroid 45 Eugenia. *Nature*, 401, 565.
- Merline W. J., Close L. M., Shelton J. C., Dumas C., Menard F., Chapman C. R., and Slater D. C. (2000) Satellites of minor planets. *IAU Circular* 7503.
- Merline W. J., Close L. M., Siegler N., Potter D., Chapman C. R., Dumas C., Menard F., Slater D. C., Baker A. C., Edmunds M. G., Mathlin G., Guyon O., and Roth K. (2001) S/2001 (617) 1. *IAU Circular* 7741.
- Merline W. J., Close L. M., Siegler N., Dumas C., Chapman C., Rigaut F., Menard F., Owen W. M., and Slater D. C. (2002a) S/2002 (3749) 1. *IAU Circular* 7827.
- Merline W. J., Tamblyn P. M., Dumas C., Close L. M., Chapman C. R., Menard F., Owen W. M., Slater D. C., and Pepin J. (2002b) S/2002 (121) 1. *IAU Circular* 7980.
- Merline W. J., Weidenschilling S. J., Durda D. D., Margot J. L., Pravec P., and Storrs A. D. (2002c) Asteroids do have satellites. In *Asteroids III* (W. F. Bottke Jr. et al., eds.), pp. 289–312. Univ. of Arizona, Tucson.
- Merline W. J., Close L. M., Tamblyn P. M., Menard F., Chapman C. R., Dumas C., Duvert G., Owen W. M., Slater D. C., and Sterzik M. F. (2003a) S/2003 (1509) 1. *IAU Circular* 8075.
- Merline W. J., Tamblyn P. M., Chapman C. R., Nesvorný D., Durda D. D., Dumas C., Storrs A. D., Close L. M., and Menard F. (2003b) S/2003 (22899) 1. *IAU Circular* 8232.
- Merline W. J., Tamblyn P. M., Dumas C., Close L. M., Chapman C. R., and Menard F. (2003c) S/2003 (130) 1. *IAU Circular* 8183.
- Merline W. J., Tamblyn P. M., Dumas C., Menard F., Close L. M., Chapman C. R., Duvert G., and Ageorges N. (2004) S/2004 (4674) 1. *IAU Circular* 8297.
- Merline W. J., Tamblyn P. M., Drummond J. D., Christou J. C., Conrad A. R., Carry B., Chapman C. R., Dumas C., Durda D. D., Owen W. M., and Enke B. L. (2009) S/2009 (317) 1. *IAU Circular* 9099.
- Merline W. J., Tamblyn P. M., Warner B. D., Pravec P., Tamblyn J. P., Neyman C., Conrad A. R., Owen W. M., Carry B., Drummond J. D., Chapman C. R., Enke B. L., Grundy W. M., Veillet C., Porter S. B., Arcidiacono C., Christou J. C., Durda D. D., Harris A. W., Weaver H. A., Dumas C., Terrell D., and Maley P. (2013) S/2012 (2577) 1. *IAU Circular* 9267.
- Michałowski T., Bartczak P., Velichko F. P., Kryszczyńska A., Kwiatkowski T., Breiter S., Colas F., Fauvaud S., Marciniak A., Michałowski J., Hirsch R., Behrend R., Bernasconi L., Rinner C., and Charbonnel S. (2004) Eclipsing binary asteroid 90 Antiope. *Astron. Astrophys.*, 423, 1159–1168.
- Morbidielli A., Levison H. F., Tsiganis K., and Gomes R. (2005) Chaotic capture of Jupiter's Trojan asteroids in the early solar system. *Nature*, 435, 462–465.
- Moskovitz N. A. (2012) Colors of dynamically associated asteroid pairs. *Icarus*, 221(1), 63–71.
- Mueller M., Marchis F., Emery J. P., Harris A. W., Mottola S., Hestroffer D., Berthier J., and di Martino M. (2010) Eclipsing binary Trojan asteroid Patroclus: Thermal inertia from Spitzer observations. *Icarus*, 205, 505–515.
- Naidu S. P. and Margot J. L. (2015) Near-Earth asteroid satellite spins under spin-orbit coupling. *Astron. J.*, 149, 80.
- Naidu S. P., Margot J. L., Busch M. W., Taylor P. A., Nolan M. C., Howell E. S., Giorgini J. D., Benner L. A. M., Brozovic M., and Magri C. (2012) Dynamics of binary near-Earth asteroid system (35107) 1991 VH. *Bull. Am. Astron. Soc.*, 43, #07.07.
- Naidu S. P., Margot J. L., Taylor P. A., Nolan M. C., Busch M. W., Benner L. A. M., Brozovic M., Giorgini J. D., Jao J. S., and Magri C. (2015) Radar imaging and characterization of binary near-Earth asteroid (185851) 2000 DP<sub>107</sub>. *Astron. J.*, 150, 54.
- Nesvorný D., Youdin A. N., and Richardson D. C. (2010) Formation of Kuiper belt binaries by gravitational collapse. *Astron. J.*, 140, 785–793.
- Nolan M. C., Hine A. A., Howell E. S., Benner L. A. M., and Giorgini J. D. (2003) 2003 SS84. *IAU Circular* 8220.
- Nolan M. C., Howell E. S., Becker T. M., Magri C., Giorgini J. D., and Margot J. L. (2008) Arecibo radar observations of 2001 SN<sub>263</sub>: A near-Earth triple asteroid system. *Bull. Am. Astron. Soc.*, 40, 432.
- Nolan M. C., Magri C., Howell E. S., Benner L. A. M., Giorgini J. D., Hergenrother C. W., Hudson R. S., Lauretta D. S., Margot J. L., Ostro S. J., and Scheeres D. J. (2013) Shape model and surface properties of the OSIRIS-REx target asteroid (101955) Bennu from radar and lightcurve observations. *Icarus*, 226, 629–640.
- Noll K. S., Grundy W. M., Chiang E. I., Margot J. L., and Kern S. D. (2008) Binaries in the Kuiper belt. In *The Solar System Beyond Neptune* (A. Barucci et al., eds.), pp. 345–363. Univ. of Arizona, Tucson.
- Ostro S. J., Margot J. L., Benner L. A. M., Giorgini J. D., Scheeres D. J., Fahnestock E. G., Broschart S. B., Bellerose J., Nolan M. C., Magri C., Pravec P., Scheirich P., Rose R., Jurgens R. F., De Jong E. M., and Suzuki S. (2006) Radar imaging of binary near-Earth asteroid (66391) 1999 KW<sub>4</sub>. *Science*, 314, 1276–1280.
- Perets H. B. and Naoz S. (2009) Kozai cycles, tidal friction, and the dynamical evolution of binary minor planets. *Astrophys. J. Lett.*, 699, L17–L21.
- Polishook D. (2014) Spin axes and shape models of asteroid pairs: Fingerprints of YORP and a path to the density of rubble piles. *Icarus*, 241, 79–96.
- Polishook D. and Brosch N. (2009) Photometry and spin rate distribution of small-sized main belt asteroids. *Icarus*, 199, 319–332.
- Polishook D., Brosch N., and Prialnik D. (2011) Rotation periods of binary asteroids with large separations — Confronting the escaping ejecta model with observations. *Icarus*, 212, 167–174.
- Polishook D., Moskovitz N., Binzel R. P., DeMeo F. E., Vokrouhlický D., Žížka J., and Oszkiewicz D. (2014a) Observations of “fresh” and weathered surfaces on asteroid pairs and their implications on the rotational-fission mechanism. *Icarus*, 233, 9–26.
- Polishook D., Moskovitz N., DeMeo F. E., and Binzel R. P. (2014b) Rotationally resolved spectroscopy of asteroid pairs: No spectral variation suggests fission is followed by settling of dust. *Icarus*, 243, 222–235.
- Pravec P. and Hahn G. (1997) Two-period lightcurve of 1994 AW<sub>1</sub>: Indication of a binary asteroid? *Icarus*, 127, 431–440.
- Pravec P. and Harris A. W. (2000) Fast and slow rotation of asteroids. *Icarus*, 148, 12–20.
- Pravec P. and Harris A. W. (2007) Binary asteroid population. 1. Angular momentum content. *Icarus*, 190, 250–259.
- Pravec P. and Vokrouhlický D. (2009) Significance analysis of asteroid pairs. *Icarus*, 204, 580–588.
- Pravec P., Wolf M., and Šarounová L. (1999) How many binaries are there among the near-Earth asteroids? In *Evolution and Source Regions of Asteroids and Comets* (J. Svoren et al., eds.), p. 159. IAU Colloq. 173.
- Pravec P., Scheirich P., Kušnírák P., Šarounová L., Mottola S., Hahn G., Brown P., Esquerdo G., Kaiser N., Krzeminski Z., Pray D. P., Warner B. D., Harris A. W., Nolan M. C., Howell E. S., Benner L. A. M., Margot J. L., Galád A., Holliday W., Hicks M. D., Krugly Y. N., Tholen D., Whiteley R., Marchis F., Degraff D. R., Grauer A., Larson S., Velichko F. P., Cooney W. R., Stephens R., Zhu J., Kirsch K., Dyvig R., Snyder L., Reddy V., Moore S., Gajdoš Š., Világí J., Masi G., Higgins D., Funkhouser G., Knight B., Slivan S., Behrend R., Grenon M., Burki G., Roy R., Demeautis C., Matter D., Waelchli N., Revaz Y., Klotz A., Rieugné M., Thierry P., Cotrez V., Brunetto L., and Kober G. (2006) Photometric survey of binary near-Earth asteroids. *Icarus*, 181, 63–93.
- Pravec P., Harris A. W., and Warner B. D. (2007) NEA rotations and binaries. In *Near Earth Objects, Our Celestial Neighbors: Opportunity and Risk* (A. Milani et al., eds.), pp. 167–176. IAU Symp. 236, Cambridge Univ., Cambridge.
- Pravec P., Harris A. W., Vokrouhlický D., Warner B. D., Kušnírák P., Hornoch K., Pray D. P., Higgins D., Oey J., Galád A., Gajdoš Š., Kornoš L., Világí J., Husárik M., Krugly Y. N., Shevchenko V.,

- Chiorny V., Gaftonyuk N., Cooney W. R., Gross J., Terrell D., Stephens R. D., Dyvig R., Reddy V., Ries J. G., Colas F., Lecacheux J., Durkee R., Masi G., Koff R. A., and Goncalves R. (2008) Spin rate distribution of small asteroids. *Icarus*, **197**, 497–504.
- Pravec P., Vokrouhlický D., Polishook D., Scheeres D. J., Harris A. W., Galád A., Vaduvescu O., Pozo F., Barr A., Longa P., Vachier F., Colas F., Pray D. P., Pollock J., Reichart D., Ivarsen K., Haislip J., LaCluyze A., Kušnírák P., Henych T., Marchis F., Macomber B., Jacobson S. A., Krugly Y. N., Sergeev A. V., and Leroy A. (2010) Formation of asteroid pairs by rotational fission. *Nature*, **466**, 1085–1088.
- Pravec P., Scheirich P., Vokrouhlický D., Harris A. W., Kušnírák P., Hornoch K., Pray D. P., Higgins D., Galád A., Világí J., Gajdoš Š., Kornoš L., Oey J., Husarik M., Cooney W. R., Gross J., Terrell D., Durkee R., Pollock J., Reichart D. E., Ivarsen K., Haislip J., LaCluyze A., Krugly Y. N., Gaftonyuk N., Stephens R. D., Dyvig R., Reddy V., Chiorny V., Vaduvescu O., Longa-Peña P., Tudorica A., Warner B. D., Masi G., Brinsfield J., Gonçalves R., Brown P., Krzeminski Z., Gerashchenko O., Shevchenko V., Molotov I., and Marchis F. (2012) Binary asteroid population. 2. Anisotropic distribution of orbit poles of small, inner main-belt binaries. *Icarus*, **218**, 125–143.
- Pravec P., Kusnirak P., Hornoch K., Galad A., Krugly Y. N., Chiorny V., Inasaridze R., Kvaratskhelia O., Ayvazian V., Parmonov O., Pollock J., Mottola S., Oey J., Pray D., Zizka J., Vrastil J., Molotov I., Reichart D. E., Ivarsen K. M., Haislip J. B., and LaCluyze A. (2013) (8306) Shoko. *IAU Circular* 9268.
- Rojo P. and Margot J. L. (2007) S/2007 (702) 1. *Central Bureau Electronic Telegram* 1016.
- Rossi A., Marzari F., and Scheeres D. J. (2009) Computing the effects of YORP on the spin rate distribution of the NEO population. *Icarus*, **202**(1), 95–103.
- Rozitis B., MacLennan E., and Emery J. P. (2014) Cohesive forces prevent the rotational breakup of rubble-pile asteroid (29075) 1950 DA. *Nature*, **512**, 174–176.
- Rubincam D. P. (2000) Radiative spin-up and spindown of small asteroids. *Icarus*, **148**(1), 2–11.
- Sánchez D. P. and Scheeres D. J. (2011) Simulating asteroid rubble piles with a self-gravitating soft-sphere distinct element method model. *Astrophys. J.*, **727**(2), 120.
- Sánchez D. P. and Scheeres D. J. (2014) The strength of regolith and rubble pile asteroids. *Meteoritics & Planet. Sci.*, **49**(5), 788–811.
- Scheeres D. J. (2002) Stability of binary asteroids. *Icarus*, **159**, 271–283.
- Scheeres D. J. (2007) Rotational fission of contact binary asteroids. *Icarus*, **189**, 370–385.
- Scheeres D. J. (2009a) Stability of the planar full 2-body problem. *Cel. Mech. Dyn. Astron.*, **104**, 103–128.
- Scheeres D. J. (2009b) Minimum energy asteroid reconfigurations and catastrophic disruptions. *Planet. Space Sci.*, **57**(2), 154–164.
- Scheeres D. J., Fahnestock E. G., Ostro S. J., Margot J. L., Benner L. A. M., Broschart S. B., Bellerose J., Giorgini J. D., Nolan M. C., Magri C., Pravec P., Scheirich P., Rose R., Jurgens R. F., De Jong E. M., and Suzuki S. (2006) Dynamical configuration of binary near-Earth asteroid (66391) 1999 KW<sub>4</sub>. *Science*, **314**, 1280–1283.
- Scheirich P. and Pravec P. (2009) Modeling of lightcurves of binary asteroids. *Icarus*, **200**, 531–547.
- Scheirich P., Pravec P., Jacobson S. A., Šurech J., Kušnírák P., Hornoch K., Mottola S., Mommert M., Hellmich S., Pray D., Polishook D., Krugly Y. N., Inasaridze R. Y., Kvaratskhelia O. I., Ayvazian V., Slyusarev I., Pittichová J., Jehin E., Manfroid J., Gillon M., Galád A., Pollock J., Licandro J., Alí-Lagoa V., Brinsfield J., and Molotov I. E. (2015) The binary near-Earth asteroid (175706) 1996 FG<sub>3</sub> — An observational constraint on its orbital evolution. *Icarus*, **245**, 56–63.
- Shepard M. K., Margot J. L., Magri C., Nolan M. C., Schlieder J., Estes B., Bus S. J., Volquardsen E. L., Rivkin A. S., Benner L. A. M., Giorgini J. D., Ostro S. J., and Busch M. W. (2006) Radar and infrared observations of binary near-Earth asteroid 2002 CE<sub>26</sub>. *Icarus*, **184**, 198–210.
- Springmann A., Taylor P. A., Howell E. S., Nolan M. C., Benner L. A. M., Brozović M., Giorgini J. D., and Margot J. L. (2014) Radar shape model of binary near-Earth asteroid (285263) 1998 QE<sub>2</sub>.
- Lunar Planet. Sci. Conf. XLV*, Abstract #1313. Lunar and Planetary Institute, Houston.
- Takahashi Y., Busch M. W., and Scheeres D. J. (2013) Spin state and moment of inertia characterization of 4179 Toutatis. *Astron. J.*, **146**, 95.
- Tamblyn P. M., Merline W. J., Chapman C. R., Nesvorný D., Durda D. D., Dumas C., Storrs A. D., Close L. M., and Menard F. (2004) S/2004 (17246) 1. *IAU Circular* 8293.
- Tanga P. and Delbo M. (2007) Asteroid occultations today and tomorrow: Toward the GAIA era. *Astron. Astrophys.*, **474**, 1015–1022.
- Taylor P. A. and Margot J. L. (2010) Tidal evolution of close binary asteroid systems. *Cel. Mech. Dyn. Astron.*, **108**, 315–338.
- Taylor P. A. and Margot J. L. (2011) Binary asteroid systems: Tidal end states and estimates of material properties. *Icarus*, **212**, 661–676.
- Taylor P. A. and Margot J. L. (2014) Tidal end states of binary asteroid systems with a nonspherical component. *Icarus*, **229**, 418–422.
- Taylor P. A., Margot J. L., Nolan M. C., Benner L. A. M., Ostro S. J., Giorgini J. D., and Magri C. (2008) The shape, mutual orbit, and tidal evolution of binary near-Earth asteroid 2004 DC. In *Asteroids, Comets, Meteors Conference*, Abstract #8322. Lunar and Planetary Institute, Houston.
- Taylor P. A., Howell E. S., Nolan M. C., and Thane A. A. (2012a) The shape and spin distributions of near-Earth asteroids observed with the Arecibo radar system. *Bull. Am. Astron. Soc.*, **44**, #302.07.
- Taylor P. A., Nolan M. C., and Howell E. S. (2012b) 5143 Heracles. *Central Bureau Electronic Telegram* 3176.
- Taylor P. A., Nolan M. C., Howell E. S., Benner L. A. M., Brozovic M., Giorgini J. D., Margot J. L., Busch M. W., Naidu S. P., Nugent C., Magri C., and Shepard M. K. (2012c) 2004 FG<sub>11</sub>. *Central Bureau Electronic Telegram* 3091.
- Taylor P. A., Howell E. S., Nolan M. C., Springmann A., Brozovic M., Benner L. M., Jao J. S., Giorgini J. D., Margot J., Fang J., Becker T. M., Fernandez Y. R., Vervack R. J., Pravec P., Kusnirak P., Franco L., Ferrero A., Galad A., Pray D. P., Warner B. D., and Hicks M. D. (2013) Physical characterization of binary near-Earth asteroid (153958) 2002 AM<sub>31</sub>. *Bull. Am. Astron. Soc.*, **45**, #208.08.
- Taylor P. A., Warner B. D., Magri C., Springmann A., Nolan M. C., Howell E. S., Miller K. J., Zambrano-Marin L. F., Richardson J. E., Hannan M., and Pravec P. (2014) The smallest binary asteroid? The discovery of equal-mass binary 1994 CJ<sub>1</sub>. *Bull. Am. Astron. Soc.*, **46**, #409.03.
- Tedesco E. F. (1979) Binary asteroids — Evidence for their existence from lightcurves. *Science*, **203**, 905–907.
- Timerson B., Brooks J., Conard S., Dunham D. W., Herald D., Tolea A., and Marchis F. (2013) Occultation evidence for a satellite of the Trojan asteroid (911) Agamemnon. *Planet. Space Sci.*, **87**, 78–84.
- Vokrouhlický D. (2009) (3749) Balam: A very young multiple asteroid system. *Astrophys. J. Lett.*, **706**, L37–L40.
- Vokrouhlický D. and Nesvorný D. (2008) Pairs of asteroids probably of a common origin. *Astron. J.*, **136**, 280–290.
- Walsh K. J., Richardson D. C., and Michel P. (2008) Rotational breakup as the origin of small binary asteroids. *Nature*, **454**, 188–191.
- Weidenschilling S. J. (1980) Hektor — Nature and origin of a binary asteroid. *Icarus*, **44**, 807–809.
- Weidenschilling S. J., Paolicchi P., and V. Zappalà (1989) Do asteroids have satellites? In *Asteroids II* (R. P. Binzel et al., eds.), pp. 643–660. Univ. of Arizona, Tucson.
- Weidenschilling S. J., Marzari F., Davis D. R., and Neese C. (2001) Origin of the double asteroid 90 Antiope: A continuing puzzle. *Lunar Planet. Sci. XXXII*, Abstract #1890. Lunar and Planetary Institute, Houston.
- Wolters S. D., Weissman P. R., Christou A., Duddy S. R., and Lowry S. C. (2014) Spectral similarity of unbound asteroid pairs. *Mon. Not. R. Astron. Soc.*, **439**, 3085–3093.
- Yeomans D. K., Antreasian P. G., Cheng A., Dunham D. W., Farquhar R. W., Gaskell R. W., Giorgini J. D., Helfrich C. E., Konopliv A. S., McAdams J. V., Miller J. K., Owen W. M. Jr., Thomas P. C., Veverka J., and Williams B. G. (1999) Estimating the mass of asteroid 433 Eros during NEAR spacecraft flyby. *Science*, **285**, 560–561.



# Formation and Evolution of Binary Asteroids

Kevin J. Walsh

*Southwest Research Institute*

Seth A. Jacobson

*Observatoire de la Côte d'Azur and University of Bayreuth*

Satellites of asteroids have been discovered in nearly every known small-body population, and a remarkable aspect of the known satellites is the diversity of their properties. They tell a story of vast differences in formation and evolution mechanisms that act as a function of size, distance from the Sun, and the properties of their nebular environment at the beginning of solar system history and their dynamical environment over the next 4.5 G.y. The mere existence of these systems provides a laboratory to study numerous types of physical processes acting on asteroids, and their dynamics provide a valuable probe of their physical properties otherwise possible only with spacecraft. Advances in understanding the formation and evolution of binary systems have been assisted by (1) the growing catalog of known systems, increasing from 33 to ~250 between the Merline *et al.* (2002) chapter in *Asteroids III* and now; (2) the detailed study and long-term monitoring of individual systems such as 1999 KW<sub>4</sub> and 1996 FG<sub>3</sub>, (3) the discovery of new binary system morphologies and triple systems, (4) and the discovery of unbound systems that appear to be end-states of binary dynamical evolutionary paths. Specifically for small bodies (diameter smaller than 10 km), these observations and discoveries have motivated theoretical work finding that thermal forces can efficiently drive the rotational disruption of small asteroids. Long-term monitoring has allowed studies to constrain the system's dynamical evolution by the combination of tides, thermal forces, and rigid-body physics. The outliers and split pairs have pushed the theoretical work to explore a wide range of evolutionary end-states.

## 1. INTRODUCTION

There have been considerable advances in the understanding of the formation and evolution of binary systems since the *Asteroids III* review by Merline *et al.* (2002) and a subsequent comprehensive review by Richardson and Walsh (2006). The current properties of this population are detailed in the chapter in this volume by Margot *et al.*, and this review will rely on their analysis in many places as we review work on the formation and dynamics of these systems. While the inventory of known binary systems in all populations has increased, for some populations the understanding of dynamics and formation have advanced only minimally, while in others areas research has moved rapidly. Therefore this chapter will not be evenly weighted between different populations; rather there will be substantial discussion of small asteroids and the Yarkovsky-O'Keefe-Radzievskii-Paddack (YORP) effect.

The scope of this chapter will be different from that of the *Asteroids III* chapter by Merline *et al.* (2002). Thanks to an excellent review of binary systems in the Kuiper belt by Noll *et al.* (2008) in the *Solar System Beyond Neptune* book, and the apparent physical, dynamical, and evolutionary differences between binary minor planets in the outer

and inner regions of the solar system, we will exclude the Kuiper belt population from our discussion here.

### 1.1 The Known Population of Binary Minor Planets

The known population of asteroid satellites has increased from 33 to ~244 between the time of the Merline *et al.* (2002) *Asteroids III* chapter and now: 49 near-Earth, 19 Mars-crossing, and 93 main-belt asteroids (MBAs) (Pravec and Harris, 2007; Johnston, 2014). As noted in 2002, the binary systems found among near-Earth asteroids (NEAs) have only a subset of the properties of those found among the MBAs. While the orbital and collisional dynamics differ substantially in these two populations, further study has found that the variation and similarities between binary properties is most strongly dependent on size.

The known binary systems among NEAs have primary component diameters exclusively less than 10 km. These small systems typically have moderately sized secondaries between 4% and 58% the size of the primary — corresponding to a mass ratio range of  $6.4 \times 10^{-5}$ – $2.0 \times 10^{-1}$  assuming equal densities, are on tight orbits with typically 2.5–7.2 primary radii separation, and have a fast-spinning primary with rotation period between 2.2 and 4.5 h — all are below

twice the critical disruption spin period of 2.3 h for a sphere with a density of 2 g cm<sup>-3</sup>. The data for these systems is presented in Fig. 1. When lightcurve surveys probed similar-sized asteroids in the main belt, they found systems with the same characteristics existing at roughly the same proportion of the population (Warner and Harris, 2007).

The known binary systems among MBAs have properties that vary with their size. The small population [ $D < 15$  km; (4492) Debussy is the largest] look similar to the various morphologies found among NEAs, including a few that appear similar to (69230) Hermes, while asteroid satellites around large asteroids [ $D > 25$  km; (243) Ida is the smallest of this group] fall into other categories. These larger asteroid systems have by comparison much smaller satellites on much more distant orbits. While a number of the large asteroids with satellites have rotation periods lower than the average asteroids of these sizes [geometric means and 1 $\sigma$  deviations are  $7.6 \pm 0.4$  h vs.  $12.2 \pm 0.5$  h (Warner *et al.*, 2009; Pravec *et al.*, 2012)], their rotation periods are all more than twice the critical disruption spin period of 2.3 h for a sphere with a density of 2 g cm<sup>-3</sup>, with the exception of (22) Kalliope (Pravec *et al.*, 2012; Johnston, 2014).

The techniques used to increase this database of known systems over time are important as they define any biases of our knowledge of each population. Lightcurve techniques, which are important for finding close companions around

small asteroids, are strongly biased against finding distant companions. Meanwhile, radar can discover satellites widely separated from their primaries, but is ineffective for observing distant MBAs (Ostro *et al.*, 2002). Direct high-resolution imaging is best for finding distant companions of large MBAs (Merline *et al.*, 2002). The size of the known population of small binary asteroid systems has increased substantially owing to the ready availability of small telescopes to survey asteroid light curves and the increased frequency of radar observations. Meanwhile, many large MBAs have been surveyed with groundbased telescopes with far fewer recent discoveries — although new adaptive optics (AO) technologies may uncover previously unseen satellites at previously studied asteroids (Marchis and Vega, 2014).

## 1.2. The YORP Effect

The largest shift in the understanding of binary formation and evolution has come from studies of thermal forces that can affect a single body or a binary system. The reflection and reemission of solar radiation can produce a torque that changes the rotation rate and obliquity of a small body. This effect is referred to as the YORP effect, coined by Rubincam (2000), and evolved out of the work of many researchers on similar topics (Radzievskii, 1952; Paddock, 1969; Paddock and Rhee, 1975; O'Keefe, 1976). We only provide a brief summary here [see Bottke *et al.* (2006) and the Vokrouhlický *et al.* chapter in this volume for a detailed discussion of the effect].

The YORP effect has been directly detected for several asteroids through observed rotation-rate changes (Taylor *et al.*, 2007; Lowry *et al.*, 2007; Kaasalainen *et al.*, 2007; Ďurech *et al.*, 2008a,b, 2012). These rotation-rate changes match the predicted magnitude of the effect from theoretical predictions (Rubincam, 2000; Bottke *et al.*, 2002; Vokrouhlický and Čapek, 2002; Čapek and Vokrouhlický, 2004; Rozitis and Green, 2013b). The YORP effect has a straightforward dependence on asteroid size (timescales increase with  $R^2$ ) and distance from the Sun (timescales increase with  $a^2$ ), but a complicated relationship with shape (Nesvorný and Vokrouhlický, 2007; Scheeres, 2007b). This shape dependence is characterized by a YORP coefficient, which measures the asymmetry of the body averaged about a rotation state and a heliocentric orbit. While instantaneous estimates of the YORP coefficient are available from astronomical measurements of the radial accelerations of asteroids, theoretical models of long-term averaged values are stymied by a sensitive dependence on small-scale topography (Statler, 2009; McMahon and Scheeres, 2013a; Cotto-Figueroa *et al.*, 2015) and regolith properties (Rozitis and Green, 2012, 2013a). NEAs and MBAs with diameters below about 20 km are likely to be affected on solar system timescales (Bottke *et al.*, 2006; Jacobson *et al.*, 2014b). Kilometer-sized NEAs can have rotation-rate-doubling timescales shorter than their dynamical lifetime of ~10 m.y. and MBAs shorter than their collision lifetime of ~100 m.y. (Bottke *et al.*, 2006; Jacobson, 2014).

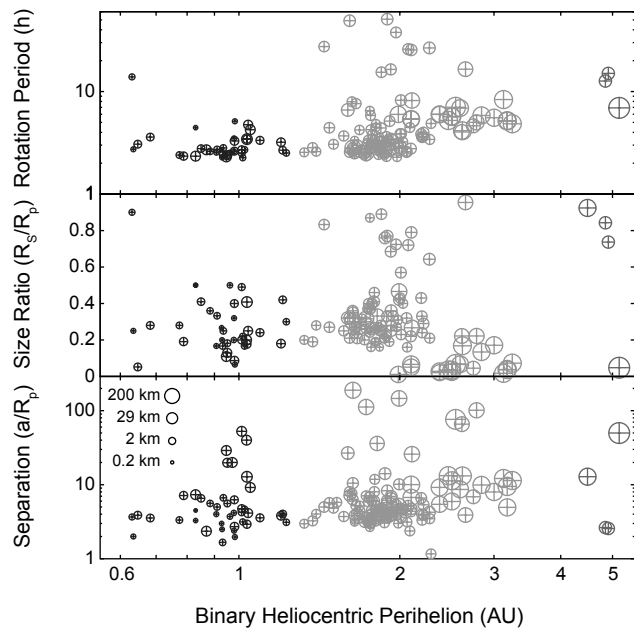


**Fig. 1.** The known population of binary asteroids. The three panels show (bottom) the component separation in terms of the primary radius, (middle) the size ratio of the two components, and (top) the rotation period of the primary, all plotted as a function of the system's heliocentric orbit's pericenter (Johnston, 2014). The size of the symbol indicates the size of the primary body, with the scale being on the left side of the bottom panel.

The distribution of spin rates observed for bodies smaller than 40 km in size show excesses of very fast and slow rotators (Pravec and Harris, 2000; Warner and Harris, 2007), which is matched very well by a spin-distribution model that includes the YORP effect (Pravec *et al.*, 2008; Rossi *et al.*, 2009; Marzari *et al.*, 2011), as suspected in the *Asteroids III* chapter by Pravec *et al.* (2002). Note that the very large asteroid lightcurve survey of Masiero *et al.* (2009) found a more Maxwellian distribution of spin rates among small asteroids, although it is not necessarily incompatible with YORP spin evolution. Among larger bodies, a subset of the Koronis asteroid family was found to have aligned obliquity and clustered spin rates (Slivan, 2002), which is due to the YORP effect driving them into spin-orbit resonances (Vokrouhlický *et al.*, 2003). Among asteroid families, whose spreading is controlled by the Yarkovsky drift of family members, there are clear signatures of the YORP effect changing the obliquity of smaller bodies and in turn changing their Yarkovsky drift rates (Vokrouhlický *et al.*, 2006; Bottke *et al.*, 2006, 2015).

Morning and evening thermal differences across regolith blocks torque the asteroid similarly in magnitude to the “normal” YORP effect. Unlike the effect described above, this “tangential” YORP effect does depend on the rotation rate, material properties of the regolith, and size distribution of the blocks (Golubov and Krugly, 2012; Golubov *et al.*, 2014). Furthermore, the tangential YORP effect has a prograde bias unlike the normal YORP effect, which is unbiased. This additional torque may explain the difference between the predicted rotational deceleration of (25143) Itokawa (Scheeres *et al.*, 2007; Ďurech *et al.*, 2008b; Breiter *et al.*, 2009) and the observed acceleration by the Japanese space mission Hayabusa (Lowry *et al.*, 2014; Golubov *et al.*, 2014). Similarly, a preference for spinning up may be necessary to explain the large fraction of observed binary systems, ~15% of small asteroids, which are presumed to be formed from rotational disruption caused by continued YORP spinup (discussed in detail below).

As mentioned as early as the Vokrouhlický and Čapek (2002) and Bottke *et al.* (2002) works on the YORP effect, this effect was a very good candidate to rotationally disrupt rubble-pile asteroids. As the catalog of known systems has grown, and the subpopulations of binary systems became more defined, rotational disruption by the YORP effect emerged as the primary candidate as the dominant formation mechanism. Much of the recent research, and the discussion below, is focused on the step(s) between when the YORP effect starts increasing the angular momentum of an asteroid and when we observe the diverse catalog of systems today. Some subpopulations may emerge directly from YORP-induced rotational disruption, while others seem to demand further evolutionary forces.

## 2. BINARY SUBPOPULATIONS

With over 100 systems spread between NEAs and MBAs, clear subpopulations of binary systems have emerged.

Pravec and Harris (2007) compiled the parameters for the catalog of known binary systems, including a calculation of the total angular momentum of each system. They used this data to create a classification system of the known inner solar system binary systems that is well suited for the topics in this chapter (most of these populations are clear in Figs. 1 and 2), and we update it below:

**Group L:** Large asteroids (diameter:  $D > 20$  km) with relatively very small satellites (secondary to primary diameter ratio:  $D_2/D_1 \leq 0.2$ ). We identify 11 members.

**Group A:** Small asteroids ( $D < 20$  km) with relatively small satellites ( $0.1 \geq D_2/D_1 \leq 0.6$ ) in tight mutual orbits (semimajor axis,  $a$ , less than 9 primary radii,  $R_p$ ). We identify 88 members.

**Group B:** Small asteroids ( $D < 20$  km) with relatively large satellites ( $0.7 \geq D_2/D_1$ ) in tight mutual orbits ( $a \leq 9 R_p$ ). We identify 9 members.

**Group W:** Small asteroids ( $D < 20$  km) with relatively small satellites ( $0.2 \geq D_2/D_1 \leq 0.7$ ) in wide mutual orbits ( $a \geq 9 R_p$ ). We identify 9 members.

**Three outliers:** Two would-be Group L members [(90) Antiope and (617) Patroclus] have the Group B characteristic of similar-sized components but are much larger than the other Group B members ( $D \sim 87$  and 101 km, respectively), and a would-be Group W member [(4951) Iwamoto] has the Group B characteristic of similar-sized components but a much wider mutual orbit ( $a \sim 17 R_p$ ).

**Split pairs:** These are inferred systems due to dynamical models that very closely link their heliocentric orbits.

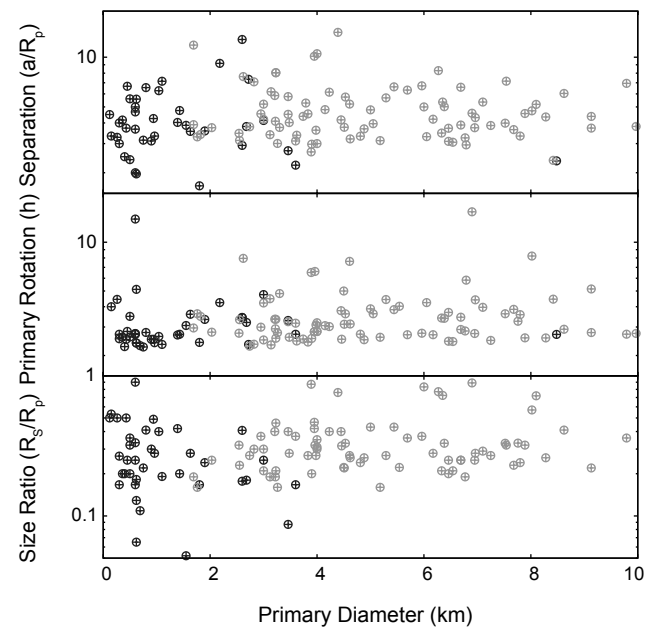


**Fig. 2.** The population of small binary systems, showing their (bottom) size ratio, (middle) primary rotation period, and (top) component separation, all plotted as a function of their primary diameter (Pravec and Harris, 2007; Johnston, 2014). The NEAs are black symbols and MBAs are gray symbols.

Therefore they are not actual binaries, but are rather inferred dynamical end-states. Some pair members are binaries themselves.

The principal change in this classification scheme from *Pravec and Harris* (2007) is the size — splitting “large” and “small” asteroids. Previously, “large” was defined to be asteroids with diameters larger than 90 km, but from more recent binary asteroid observations and YORP theory, a more natural boundary between “large” and “small” is 20 km (*Pravec et al.*, 2012; *Jacobson et al.*, 2014a). The boundaries between the various defining characteristics appear robust in Fig. 1, where adjustments on the order of 10% lead to the creation of no or only a few new outliers. The data in the paragraphs above come from P. Pravec’s binary catalog (*Pravec et al.*, 2012).

## 2.1. Large Systems: Group L

Group L members are distinct in the bottom two panels of Fig. 1, and are defined by having large primaries with  $D > 20$  km (large symbols), and relatively smaller size ratios ( $D_2/D_1 \leq 0.2$ ). These size ratios range from 0.03 to 0.2 with the lowest mean of any group:  $0.08 \pm 0.06$  ( $1\sigma$ ) (*Pravec et al.*, 2012). They are typically discovered with groundbased high-resolution imaging with (243) Ida a notable exception, whose satellite was discovered by the Galileo space mission (*Belton and Carlson*, 1994). There are 11 known systems, with the largest being (87) Sylvia ( $D \sim 256$  km) with its satellites Romulus and Remus (*Brown et al.*, 2001; *Marchis et al.*, 2005) and the smallest being (243) Ida ( $D \sim 32$  km) with its satellite Dactyl (*Belton and Carlson*, 1994). None of the eight asteroids larger than (87) Sylvia have been reported to have satellites, but there are likely many satellites among the asteroids with sizes near that of (243) Ida and up to that of (87) Sylvia since severe biases limit detection in that population.

The rotation periods of these large asteroids range from 4.1 to 7.0 h with a geometric mean:  $5.6 \pm 0.8$  ( $1\sigma$  h) (*Pravec et al.*, 2012). With the exception of (22) Kalliope, all the Group L members rotate at less than half the critical disruption rate for a spherical body with a density of  $2 \text{ g cm}^{-3}$  (2.3-h rotation period). As discussed in *Descamps et al.* (2011), the lower than typical rotation periods [asteroids of similar sizes have  $12.2 \pm 0.5$ -h rotation periods (*Warner et al.*, 2009)] and the elongated shapes of the primaries [e.g., the bean-shape of (87) Sylvia (*Marchis et al.*, 2005)] are suggestive of a violent disruption process, with the reaccumulation of the parent body into high-angular-momentum shape and spin configurations. However, previous numerical models of asteroid disruptions did not retain shape and spin information of the reaccumulated remnants (*Durda et al.*, 2007), except in the case of (25143) Itokawa (*Michel and Richardson*, 2013), so this has not been explicitly tested.

It is important to note that due to an increase of YORP timescales with surface area, YORP cannot play a role for these large systems.

## 2.2. Small Systems: Groups A, B, and W

Systems with small primary bodies ( $D < 20$  km) almost all fit in the subpopulation of Group A, and are found among NEAs, small MBAs and Mars crossers. Members of Group A have diameters between 0.15 and 11 km (*Pravec et al.*, 2012). Their mutual orbits are within 2.7 and 9.0 primary radii (mean statistics:  $4.8 \pm 1.3 R_p$ ), and the satellites are between 0.09 and 0.58 the size of the primary (mean statistics:  $0.3 \pm 0.1$ ).

Group A members have similar amounts of angular momentum relative to their critical values (where critical is enough to break up the combined masses if in a single body). Typically this is due to the rapidly rotating primary with a period between 2.2 and 4.4 h (*Margot et al.*, 2002; *Pravec et al.*, 2006, 2012) — always within a factor of 2 of the critical disruption rate for a spherical body with a density of  $2 \text{ g cm}^{-3}$  (2.3-h rotation period). The geometric mean of their rotation periods is  $2.9 \pm 0.8$  ( $1\sigma$ ) h compared to  $7.4 \pm 0.3$  h for asteroids in the same size range (*Pravec et al.*, 2012; *Warner et al.*, 2009).

While the orbit period is never synchronous with the very fast primary rotation (see Figs. 1 and 2), the synchronicity of the satellite rotation with the orbit period divides Group A into two distinct subgroups. Most belong to the synchronous satellite subgroup [ $\sim 66\%$  (*Pravec et al.*, 2012)], although it is possible that these satellites have chaotic rotation but appear nearly synchronous (*Naidu and Margot*, 2015). The rest of the asteroids have satellites that are asynchronous, and have rotation periods between the primary rotation period and the orbit period (*Pravec et al.*, 2012).

There are very few well-characterized mutual orbits — only seven binary and two triple systems (*Fang and Margot*, 2012b). Among these, there is a trend between their measured orbital eccentricity and the synchronicity of the satellites’ rotation and orbit periods [see Fig. 1 of *Fang and Margot* (2012b)], where synchronous satellites are generally less eccentric. This trend is consistent with limits on the eccentricity determined by lightcurve studies (*Pravec and Harris*, 2007). Some asynchronous satellites on eccentric orbits may be in chaotic rotation as a result of torques on their elongated shapes [e.g., 1991 VH (*Naidu and Margot*, 2015)]. This could explain the high frequency ( $\sim 33\%$ ) of asynchronous satellites in light of possibly rapid theoretical despinning timescales — around  $10^2$ – $10^8$  yr [the tidal parameters are very uncertain (*Goldreich and Sari*, 2009; *Jacobson and Scheeres*, 2011c; *Fang and Margot*, 2012b)], compared to a  $\sim 10^7$ -yr dynamical lifetime in the NEA population or a  $\sim 10^8$ -yr collisional lifetime in the MBA population.

The Group B members have nearly equal-sized components (mean  $D_2/D_1$  is  $0.88 \pm 0.09$ ; they stand out in the middle panel of Fig. 1). There is a break among the small binary population between Group A and Group B, suggesting an alternate evolutionary route (*Scheeres*, 2004; *Jacobson and Scheeres*, 2011a). These systems are in a doubly synchronous state with synchronized rotation and orbital periods (*Pravec*

and Harris, 2007). Orbital periods extend from 13.9 h to 49.1 h, similar to the Group A binaries [11.7 h to 58.6 h (Pravec et al., 2012)]. Nearly all this population is found in the main belt and discovered by lightcurve observations with the exception of the NEA (69230) Hermes. Hermes is decidedly smaller [ $D \sim 0.6$  km (Margot et al., personal communication)] than the next smallest confirmed Group B member [(7369) Gavrilin,  $D \sim 4.6$  km (Pravec and Harris, 2007)], but an unconfirmed member of Group B, 1994 CJ<sub>1</sub>, is even smaller [ $D < 0.15$  km (Taylor et al., 2014)]. The mean size D is  $7 \pm 3$  km, and the largest, (4492) Debussy, is 12.6 km (Pravec et al., 2012). Because these systems are doubly synchronous, there are strong biases against discovery; only mutual events reveal the presence of the satellite. Furthermore, they are not typically separated enough to be detected by high-resolution imaging [the widest is (854) Frostia, with a component separation of only 36.9 km], and too distant and small for radar detection in the main belt. Thus they are possibly significantly underrepresented among known asteroid binaries.

Group W binary members have very large separations (between 9 and 116  $R_p$ ), and are typically detected by the Hubble Space Telescope or AO observations from ground-based telescope observatories. The existence of some of this group in the main belt defies formation only from planetary encounters (Fang and Margot, 2012a). Like Group A and B members, they are small [mean size D is  $4.8 \pm 2.3$  km (Pravec et al., 2012)], so radiative torques like the YORP effect are important. Like Group A members, they are rapidly rotating [geometric mean primary rotation period  $3.3 \pm 0.8$  hr; Polishook et al., 2011] and have moderate size ratios [mean size ratio  $D_2/D_1$  is  $0.4 \pm 0.2$  (Pravec et al., 2012)]. They follow the pattern of the asynchronous subgroup of Group A and all their satellites have rotation periods that are between that of the primary's rotation and the satellite's orbital period. The links between Group A and Group W are strong, and Jacobson et al. (2014b) developed an evolutionary pathway from the former to the latter. Previously, Group W members have been suspected to be debris from catastrophic collisions [dubbed escaping ejecta binary systems (EEBs) in Durda et al. (2004)], but further study consistently finds rapidly rotating primaries (Polishook et al., 2011).

Many of these systems were discovered and characterized by lightcurve observations, which produce rotation periods as well as some information on shape from the amplitude of the light curve (Pravec and Harris, 2007). The lightcurve amplitude principally constrains two of the axes of the body, the long a and intermediate b axis (for principal axis rotation about its shortest c principal axis). It can constrain the other axis ratio if there are multiple observing geometries. The lightcurve amplitude can be converted to determine the a/b relationship, which roughly describes the shape of the body's equatorial cross-section. Group A, B, and W members have a/b from 1.01 to 1.35 with an average value of  $1.13 \pm 0.07$  (Pravec et al., 2012) — nearly circular equatorial cross-

sections. Meanwhile, the satellites of Group A, B, and W members have a/b from 1.06 to 2.5 with an average value of  $1.44 \pm 0.24$  (Pravec et al., 2012). Thus satellites represent a much larger variety of equatorial cross-sections.

Finally, some primary members of Group A and W have a characteristic spheroidal “top” shape due to a pronounced deviation from a sphere along an equatorial ridge. This radar-derived shape was made famous by 1999 KW<sub>4</sub> (Ostro et al., 2006), but has been found for many other binary and single asteroids [(29075) 1950 DA (Busch et al., 2007); 2004 DC (Taylor et al., 2008); 2008 EV<sub>5</sub> (Busch et al., 2011); (101955) Bennu (Nolan et al., 2013); (136617) 1994 CC (Brozović et al., 2011); (153591) 2001 SN<sub>263</sub> (Becker et al., 2015)]. This ridge preserves a low a/b ratio, i.e., a circular equatorial cross-section, but due to the confluence of rotation and shape, this reduces the gravitational binding energy of material on the ridge (Ostro et al., 2006; Busch et al., 2011; Scheeres, 2015). At high rotation rates, the entire mid-latitudes obtain high slopes and therefore disturbed loose material would naturally move toward the potential low at the equator; this material upon reaching the equator may move off the surface entirely and enter into orbit (Ostro et al., 2006; Walsh et al., 2008; Harris et al., 2009). This discovery has driven studies of asteroid reshaping focusing on the granular and cohesive properties of the surface material and possible secondary fragmentation and infall of orbital material (Ostro et al., 2006; Walsh et al., 2008; Harris et al., 2009; Holsapple, 2010; Jacobson and Scheeres, 2011a; Scheeres, 2015).

### 2.3. Triples

The first discovered triple in the main belt was (87) Sylvia, with two small satellites orbiting its beanshaped primary body (Marchis et al., 2005). More triples have since been found, with (45) Eugenia (Marchis et al., 2007), (93) Minerva (Marchis et al., 2009), and (216) Kleopatra joining the list (Marchis et al., 2008). As discussed below, this is believed to be a natural outcome of formation via asteroid collisions.

There are also a few confirmed and suspected small asteroid triple systems: (136617) 1994 CC, (153591) 2001 SN<sub>263</sub>, 2002 CE<sub>26</sub>, (3749) Balam, and (8306) Shoko (Brozović et al., 2009; Nolan et al., 2008; Shepard et al., 2006; Marchis et al., 2008; Pravec et al., 2013). All have rapidly rotating primaries (2001 SN<sub>263</sub> is the lowest at 3.425 h) and low size ratios between the smaller two members and the primary (Balam has the largest measured satellite at 46.6% its size). For the two triple systems with known primary shapes [(136617) 1994 CC, (153591) 2001 SN<sub>263</sub>], both have the typical “top” shape described above (Brozović et al., 2011; Becker et al., 2009).

Both Balam and Shoko are also members of split pairs, and the other members are 2009 BR<sub>60</sub> and 2011 SR<sub>158</sub>, respectively (Vokrouhlický, 2009; Pravec et al., 2013). As explained in the next subsection, split pairs have a dynamical

age that is interpreted as the rotational fission formation age. Since it is unlikely that the split pair member could have formed without significantly affecting the triple system, it is possible that all components were created at the same time from a single rotational fission event (*Jacobson and Scheeres*, 2011b).

#### 2.4. Outliers

Large double asteroids such as the MBA (90) Antiope and Trojan (617) Patroclus appear unique in the inner solar system. These are too large, with diameters greater than 100 km, to have gained angular momentum from thermal effects, and collision simulations do not typically create such systems (*Durda et al.*, 2004). They have very large angular momentum content, owing to the similar-sized components (*Pravec and Harris*, 2007; *Descamps et al.*, 2007; *Michałowski et al.*, 2004). Antiope is notable as it is among the largest fragments in an asteroid family, owing to the exceptional size of Themis and its family. Meanwhile, Patroclus is a Trojan, and solar system formation models suggest that many or all of them may have been implanted from the primordial Kuiper belt region (*Morbidelli et al.*, 2005; *Nesvorný et al.*, 2013). Thus this system may share a common origin with the systems found in the Kuiper belt (see *Noll et al.*, 2008; *Nesvorný et al.*, 2010).

The other outlier, (4951) Iwamoto, has a much wider mutual orbit than other Group B members, but this may be explained by orbit expansion due to the BYORP effect as discussed below (*Ćuk*, 2007; *Jacobson and Scheeres*, 2011b).

#### 2.5. Split Pairs

An important discovery related to the dynamics of binary systems is the existence of individual asteroids that are not bound to each other but instead show convincing signs of being split pairs (*Vokrouhlický and Nesvorný*, 2008, 2009; *Pravec and Vokrouhlický*, 2009; *Pravec et al.*, 2010). These were found using dynamical studies similar to those that search for families of asteroids, but here pairs were found to be closely linked dynamically.

Follow-up observations have found convincing links in both size and rotation of the pairs (*Pravec et al.*, 2010) as well as photometric appearance (*Moskovitz*, 2012; *Duddy et al.*, 2012). Their sizes and rotation make a very strong case that the smaller member of the pair was ejected during a rotational fission event, with the signature of this in the slow rotation of the larger object as a function of the size of the smaller object. The latter work finds similar photometric colors for the pairs, supporting the dynamical links between them. The dynamical models suggest that some of these pairs separated less than just  $\sim$ 17 k.y. ago, and hence the photometric colors have not had time to evolve significantly due to space weathering or other effects (*Vokrouhlický and Nesvorný*, 2009; *Vokrouhlický et al.*, 2011).

### 3. FORMATION

While the community and the literature largely agree on the collisional origin of the satellites of large asteroids (Group L), there is continued work on the details of how the small systems (Groups A, B, W) form and evolve. An important part of understanding the formation of the small systems concerns both the properties and variety of outliers and the possible complicated evolutionary paths for satellites or building blocks of satellites once in orbit around a rubble-pile asteroid.

#### 3.1. Large Systems: Collision

Collisions were proposed as a potentially important formation mechanism even before the discovery of Ida's moon Dactyl in 1993. Most works focused on ejecta from a collision becoming mutually bound, becoming bound around the largest remnant, or rotational fission due to a highly oblique or glancing impact (*Weidenschilling et al.*, 1989; *Merline et al.*, 2002; *Richardson and Walsh*, 2006). Both *Weidenschilling et al.* (1989) and *Merline et al.* (2002) found that complete disruption is a far more likely outcome than collisionally induced rotational fission, and there are no observed systems that can be clearly attributed to this latter process.

The study of the other collisional mechanisms first focused on cratering events on the asteroid Ida, numerically tracking the evolution of ejected debris in order to form its small satellite Dactyl (*Durda*, 1996; *Doressoundiram et al.*, 1997). Studies of asteroid impacts gained a numerical boost by combining smoothed particle hydrodynamics models of asteroid fragmentation with N-body models of their gravitational reaccumulation (*Michel et al.*, 2001, 2002, 2003, 2004; *Durda et al.*, 2004, 2007). These models were more capable of modeling the physics of catastrophic collisions and maintaining high-resolution models of the fragments' long-term gravitational interactions and reaccumulation. They found that the formation of satellites is a natural outcome in an asteroid disruption.

*Durda et al.* (2004) further explored the different types of systems formed during a collision. This large suite of 161 impact simulations studied 100-km basalt targets being impacted by objects of various sizes hitting at a range of velocities and angles. In their suite of collision and reaccumulation simulations they observed, and named, the two previously proposed types of systems: escaping ejecta binary systems (EEBs) and smashed target satellites (SMATS). The SMATS generally featured small satellite(s) orbiting the reaccumulated target body. The known satellites around large ( $D > 10$  km) MBAs share similar properties: extreme size ratio between primary and secondary and large orbital separation (where the orbital separations are too large to be explained by tides; see section 4.2). They predicted a formation rate that should roughly produce the observed number of satellites detected around very large asteroids ( $D > 140$  km), accounting for their production due to colli-

sions, satellites destroyed by collisions, and the very early clearing of the asteroid belt.

Meanwhile, they proposed that some small main-belt systems featuring two small components of roughly similar size on distant orbits are possibly EEBs. Their examples were (3749) Balam and (1509) Esclangona, and while at the time both were interesting candidates, (3749) Balam has been discovered to have a third component and a split pair and (1509) Esclangona has been found to have a very rapid rotation period similar to that found among many of the binary systems formed by the YORP effect (Warner *et al.*, 2010). The best remaining candidates are (317) Roxane because of its slow primary rotation [8.2 h (Harris *et al.*, 1992; Polishook *et al.*, 2011; Jacobson *et al.*, 2014b)] and (1717) Arlon because of its slow primary rotation [5.1 h (Cooney *et al.*, 2006)] and high size ratio [ $>0.22$  (Cooney *et al.*, 2006; Jacobson *et al.*, 2014b)]. The lack of EEBs in the known catalog is curious, as the simulations of Durda *et al.* (2004) formed hundreds of systems immediately after a collision, although the stability of these binaries was not thoroughly examined. This is an important avenue for future work, especially given the importance of spin-orbit coupling for binaries after rotational fission (Jacobson and Scheeres, 2011a). Tens of asteroid families are known (see the chapter by Nesvorný *et al.* in this volume) and there is evidence for even very recent impacts throughout the solar system (Nesvorný *et al.*, 2002; Vokrouhlický and Nesvorný, 2009). However, small and wide binary systems are difficult to find, and small components are more susceptible to collisional grinding (see the chapter by Bottke *et al.* in this volume), which may explain the lack of discoveries of this type of system. Meanwhile, the known systems need substantial characterization (rotation periods, etc.) to try to distinguish between possible EEBs and end-states of YORP/BYORP evolution processes (see below).

All the numerical work to understand formation of satellites during collisions have found triple and multiple systems in their simulations. Durda *et al.* (2004) reported temporary multiple systems, and Leinhardt and Richardson's (2005) reanalysis of a single simulation found 10% triples and 3% quadruple systems that lasted the length of the simulations (days). While triples have now been found among some large systems, longer-term dynamical simulations of their formation and evolution following large impacts would be needed to quantify the match between observations and models.

Catastrophic impact modeling has generally relied on very similar collision scenarios (impact speeds and angles, etc.) to model both the formation of satellites and asteroid families (Michel *et al.*, 2001, 2003; Durda *et al.*, 2004, 2007). While asteroid families are strictly correlated with collisions, it does not mean that the presence of a family demands satellites, as not every collision forms satellites, and small satellites themselves are susceptible to collisional evolution/destruction on timescales shorter than the age of many observed asteroid families (Durda *et al.*, 2004).

### 3.2. Small Systems: Rotational Disruption

Even before the discovery of small binary systems, the doublet craters found on the terrestrial planets (Melosh and Stansberry, 1991; Bottke and Melosh, 1996) and crater chains on the Moon (see Richardson *et al.*, 1998) suggested that there were mechanisms to disrupt small asteroids. The demonstration provided by Comet Shoemaker-Levy 9 and its tidal disruption at Jupiter further instigated models of “rubble-pile” interiors and their tidal disruptions while encountering planetary bodies (Asphaug and Benz, 1996; Richardson *et al.*, 1998).

Bottke and Melosh (1996) suggested that searches for asteroid satellites “place emphasis on kilometer-sized Earth-crossing asteroids with short-rotation periods,” and lightcurve surveys found many interesting targets in this sample. Observations of multi-frequency light curves and possible eclipse/occultation events became common, and gave very strong indications of possible satellites (Pravec and Hahn, 1997; Pravec *et al.*, 1998, 2000; Mottola and Lahulla, 2000). The radar imaging of NEA 2000 DP<sub>107</sub> confirmed that the lightcurve observations were detecting actual satellites (Margot *et al.*, 2002). Combining all possible detections, Margot *et al.* (2002) suggested that up to 16% of the population were binaries and that rotational disruption was a primary culprit (Pravec *et al.*, 1999; Margot *et al.*, 2002; Pravec and Harris, 2007).

Rubble-pile asteroids encountering Earth were studied with a granular dynamics code by Richardson *et al.* (1998) and again by Walsh and Richardson (2006). While both groups found that binaries are at least initially formed following some disruptive tidal event, Walsh and Richardson (2006) found that the primary bodies were typically elongated, the secondaries were on very eccentric orbits, and the primary rotated with a period around 3.5–6 h, rather than the near-critical 2–4-h periods. Walsh and Richardson (2008) took the resulting simulation outcomes and built a Monte Carlo model including the expected time between planetary encounters, expected encounter outcomes, nominal tidal evolution of orbits and primary spin, and observed asteroid shape and spin characteristics. They found that the produced systems are not expected to survive very long, owing to the large semimajor axes and high eccentricities. These works, and the discovery of small binary systems in the main belt (Warner and Harris, 2007) where there is no planetary body to tidally disrupt an asteroid, strongly suggested that tidal disruption is not a primary mechanism. Tidal disruption of NEAs could still account for a small subset of the population, although it is not clear if the elongated primaries and eccentric secondaries could survive long enough to be observed (Walsh and Richardson, 2008).

A more ubiquitous method for rotational disruption of small asteroids is the YORP effect. Rubincam (2000) proposed that the YORP effect could spin centimeter-sized objects so fast that they would eventually burst. Vokrouhlický and Čapek (2002) pointed out that this effect will likely drive asteroids to  $0^\circ/180^\circ$  obliquity end-states and then in many cases of

continued spinup could drive them to “rotational fission.” YORP was connected directly with binary formation in *Asteroids III* (Bottke et al., 2002), where it was proposed as a possible means for forming small binary asteroids and inducing reshaping.

*Ostro et al.* (2006) observed NEA 1999 KW<sub>4</sub> with radar and produced an incredibly detailed shape model of the primary, while *Scheeres et al.* (2006) analyzed the dynamics of the system (see *Fahnestock and Scheeres*, 2008). This system was similar to previously discovered NEA systems — it featured a rapidly rotating primary (essentially at critical rotation rate) and a small secondary on a close orbit just beyond its Roche limit. However, owing to the exceptional resolution of these radar observations, the derived shape model was found to have a bulging equatorial ridge (see Fig. 3).

As part of the dynamical analysis of the system, *Scheeres et al.* (2006) hypothesized that the system disrupted and shed mass due to tidal torques from a planetary flyby or the YORP effect. The primary would have evolved to build the ridge and reach the very rapid rotation rate due to the infall of material that was not accreted/incorporated in the satellite.

Starting with the *Scheeres et al.* (2006) work on the state of the 1999 KW<sub>4</sub> system, and their suggestion that the equatorial ridge could have been formed by the infall of material, this started one of two tracks of thought about the ridge and its formation that were followed up in a number of works (*Scheeres*, 2007b; *Jacobson and Scheeres*, 2011a). These works posited that the mass loss was a more singular catastrophic event — a fission event — and that later processing of this lost mass accounts for the equatorial ridge and other widely observed system properties. At the other end of the discussion, *Walsh et al.* (2008) modeled YORP-spinup of rubble piles made of thousands of constituent particles and

proposed that the equatorial ridge was caused by reshaping of the primary rubble-pile asteroid as a result of spinup and consequent mass loss. In this model the satellite was slowly built in orbit by repeated mass-shedding events.

These models in some ways were working from opposite ends of a spectrum of model resolution and techniques. The *Scheeres* (2007b) work focused on the rigid body dynamics of separated contact binaries, and *Jacobson and Scheeres* (2011a) extended this to consider what might happen if the ejected fragment itself was allowed to fragment once in orbit, which is critical to prevent rapid ejection of the fragment, and also whether the infall of some of the material could explain the ubiquitous top-shape primaries. Meanwhile, *Walsh et al.* (2008, 2012) started with model asteroids constructed of thousands of individual solid spherical particles interacting through their gravity and through mutual collisions. While the gravity and collisions of the particles are efficiently modeled throughout the simulations, the timescales for spinup were necessarily shortened for computational reasons and the structure of the body consisted of different, but very simple, size distributions of spherical particles. A valuable test of these different ideas may occur when NASA’s Origins Spectral Interpretation Resource Identification and Security-Regolith Explorer (OSIRIS-REx) space mission reaches asteroid (101955) Bennu, which shows signs of having an equatorial ridge (*Nolan et al.*, 2013; *Lauretta et al.*, 2014).

All scenarios suffer confusion from new studies of the sensitivity of the YORP effect to very small changes in an asteroid’s shape. Model asteroids were generated, inclusive of small features such as boulders and small craters, and when YORP evolutions were calculated it was found that very small changes on the surface of a small body can dramatically change its YORP behavior (*Statler*, 2009; *Cotto-Figueroa et al.*, 2015). The changes could be so dramatic that nearly any reshaping of a body during its YORP spinup could essentially result in a completely different YORP state. Essentially each shape change, no matter the scale, results in a coin-flip outcome to determine if the body continues spinning up or reverses and spins down.

The population of asteroids with secondaries is ~15% (*Pravec and Harris*, 2007), and so the rotational disruption mechanism appears to be quite efficient. If each movement on the surface of an asteroid results in a coin-flip to determine spinup or spindown, then seemingly bodies would never spin up enough to rotationally disrupt. This perplexing issue may demand some underlying tendency for small bodies to “spin up” by the YORP effect. It is possible that the YORP effect could actually induce preferential spinup for even a symmetrically shaped asteroid, following the “tangential YORP effect,” which may play a big role in understanding these issues (*Golubov and Krugly*, 2012; *Golubov et al.*, 2014).

### 3.3. Split Pairs

The rotational fission hypothesis states that at a critical spin rate an asteroid’s components enter into orbit about

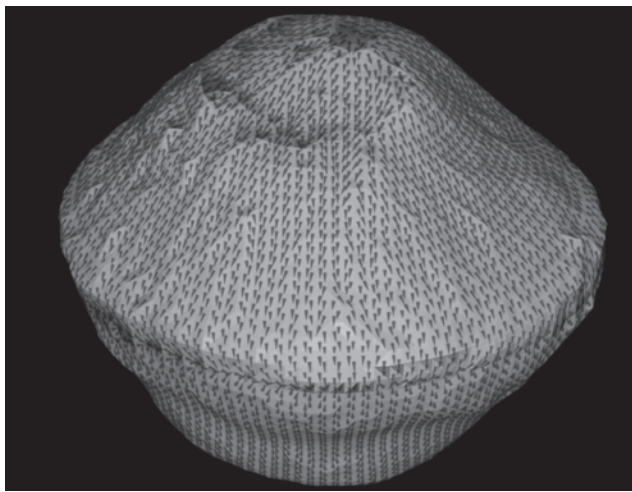


**Fig. 3.** The radar-derived shape model of 1999 KW<sub>4</sub>. The shading indicates local gravitational slopes, with the majority being near 30–40 and the lighter and darker shades at the equator and poles near zero (*Ostro et al.*, 2006; *Scheeres et al.*, 2006).

each other from a state of resting on each other (*Jacobson and Scheeres*, 2011a). The spin energy of the asteroid at this critical spin and any released binding energy is the free energy available to disrupt the asteroid system. Therefore, there is a direct energy and angular momentum relationship between the spin states of the newly formed components and the mutual orbit. From these considerations and some simple assumptions, this theory predicts a relationship between the sizes of the two components and the rotation rate of the larger component. Observations of split pairs directly confirm this theoretical prediction (*Pravec et al.*, 2010). This is powerful evidence that the rotational fission hypothesis is correct for split pairs.

Further observations of split pairs confirm that each member is a good spectroscopic match to the other (*Moskovitz*, 2012; *Duddy et al.*, 2012; *Polishook et al.*, 2014a). Interesting observations that there is no significant longitudinal spectroscopic variations and that the spin axes between members are identical are interesting twists that future theory must account for (*Polishook et al.*, 2014a,b).

#### 4. EVOLUTION OF BINARY SYSTEMS

There are a number of different binary evolution mechanisms. Classical solid body tides are long studied and binary asteroids provide useful test cases. Meanwhile, thermal effects can affect a single body in the system or the pair of bodies. A single body having its spin state changed by a thermal effect can possibly reshape due to its angular momentum increase. Binaries on near-Earth orbits can encounter the terrestrial planets, which can destabilize or otherwise alter a system's mutual orbit, while also distorting or disrupting either component. Finally, an impact can destroy a satellite, remove it from a system, or simply perturb its orbit.

The small number of known large systems are unaffected by many of these evolutionary mechanisms: Their satellites are typically too distant for tides and their sizes too large for thermal effects, and there are no planets in the main belt to perturb them. Meanwhile, the known small systems may be affected by multiple effects simultaneously in ways that are difficult to disentangle. Therefore, the primary set of data used to understand evolutionary effects are the large number of small systems — Groups A, B, and W. The majority of all systems (Group A) look quite similar — they have rapidly rotating primaries, their secondaries just beyond the nominal Roche limit at  $\sim 2.5$   $a/R_p$  (where  $a$  is the semimajor axis and  $R_p$  is the primary radius), and they are between 9% and 58% the size of the primary (typically less than 2–3% of the primary mass). The outliers are a minority, but they and the split pairs point to important evolutionary end-states of the small systems.

##### 4.1. Binary YORP

The theory of binary YORP (BYORP) is a direct extension of the Yarkovsky and YORP effects; instead of modifying the spin state of an asteroid, the BYORP effect modifies the mutual orbit of a double asteroid system in a spin-orbit

resonance, typically the synchronous 1:1 spin-orbit resonance (*Ćuk and Burns*, 2005). Similar to YORP, the back-reaction force from the photon causes a torque, but here the lever arm connects the center of mass of the binary system to the emitting surface element. The back-reaction torques the satellite about this mass center, changing the mutual orbit. Unlike the YORP effect, the relative position and orientation of the emitting surface element can change the mutual orbit's semimajor axis  $a$  with respect to the center of mass of the binary system (unlike a rigidly rotating asteroid in the case of the YORP effect), so only binary members that occupy a spin-orbit resonance have nonzero cumulative BYORP effects; the torques on all binary members outside of spin-orbit resonances cancel out over time.

*Ćuk and Burns* (2005) recognized that this effect could be significant for small asteroids found throughout the binary asteroid population. Most discovered binaries in the near-Earth and main-belt populations have small (radius  $< 10$  km) secondaries, which are tidally locked in a synchronous spin-orbit resonance (*Richardson and Walsh*, 2006; *Pravec et al.*, 2006). From these characteristics and shape estimates, simple estimates scaled from the YORP effect concluded that the BYORP effect is able to significantly modify an orbit in as little as  $\sim 10^5$  yr (*Ćuk and Burns*, 2005; *Ćuk*, 2007; *Goldreich and Sari*, 2009). Secular averaging theory has agreed with these short timescale estimates (*McMahon and Scheeres*, 2010b,a; *Steinberg and Sari*, 2011).

Assuming the smaller secondary is synchronously rotating and expanding the solution to only first order in eccentricity, the secular evolution of the mutual orbit's semimajor axis  $a$ , measured in primary radii  $R_p$ , and eccentricity  $e$  are (equations (93) and (94) from *McMahon and Scheeres*, 2010a, with redefined variables)

$$\frac{da}{dt} = \frac{3H_{\odot}B_s a^{3/2} \sqrt{1+q}}{2\pi\rho\omega_d R_p^2 q^{1/3}} \quad (1a)$$

$$\frac{de}{dt} = -\frac{3H_{\odot}B_s a^{1/2} e \sqrt{1+q}}{8\pi\rho\omega_d R_p^2 q^{1/3}} = -\frac{e}{4a} \frac{da}{dt} \quad (1b)$$

where  $q$  is the mass ratio between the secondary and the primary,  $\rho$  is the density of both asteroids assumed to be the same since they are likely to be of common origin,  $\omega_d = \sqrt{4\pi\rho G/3}$  is the critical rotational disruption rate for a sphere of density  $\rho$ ,  $G$  is the gravitational constant,  $H_{\odot} = F_{\odot}/(a_{\odot}^2 \sqrt{1-e_{\odot}^2})$  is a heliocentric orbit factor,  $F_{\odot}$  is the solar radiation constant, and  $a_{\odot}$  and  $e_{\odot}$  are the heliocentric semimajor axis and eccentricity of the binary asteroid system. Finally,  $B_s$  is the BYORP coefficient of the secondary.

As defined here,  $B_s$  does not depend on the size of the secondary, only its shape relative to its orientation (see *McMahon and Scheeres*, 2010a). The BYORP coefficient can be positive corresponding to outward expansion of the mutual orbit or negative corresponding to inward shrinking. (66391) 1999 KW<sub>4</sub> has the only existing detailed secondary shape model (*Ostro et al.*, 2006), and it has an

estimated magnitude of  $|B_s| \sim 0.04$  (*McMahon and Scheeres*, 2010a, 2012b). Estimates of  $B_s$  from other asteroid shape models and Gaussian ellipsoids suggest that the BYORP coefficients are typically  $|B_s| < 0.05$  (*McMahon and Scheeres*, 2012a). Scaling the (66391) 1999 KW<sub>4</sub> estimate to other binary asteroid systems, *Pravec and Scheirich* (2010) calculated mutual orbit evolution predictions for seven observable binaries: (7088) Ishtar, (65803) Didymos, (66063) 1998 RO<sub>1</sub>, (88710) 2001 SL<sub>9</sub>, (137170) 1999 HF<sub>1</sub>, (175706) 1996 FG<sub>3</sub>, and (185851) 2000 DP<sub>107</sub>. First results regarding (175706) 1996 FG<sub>3</sub> have been reported in *Scheirich et al.* (2015) and are discussed below. Close observations of these candidates over the next few years will test the nascent BYORP theories.

As noticed initially by *Ćuk and Burns* (2005), outward BYORP expansion of the mutual orbit damps the eccentricity. This potentially provides a disruption pathway for binary asteroids. Their orbit can expand until the semimajor axis reaches their Hill radii since outward expansion is a runaway process. If so, then these binaries would become unbound by three-body interactions with the Sun and create asteroid pairs. Unlike most observed asteroid pairs, these would not follow the rotation-size ratio relationship set by immediate disruption after rotational fission (*Scheeres*, 2004; *Pravec et al.*, 2010). No such pairs have yet been identified; however, the expected ratio between pairs formed from fission to those formed from BYORP expansion is high (*Jacobson and Scheeres*, 2011a).

BYORP expansion of the orbit of the secondary will only continue if the rotation of the secondary remains synchronous with its orbital period. However, a numerical experiment by *Ćuk and Nesvorný* (2010) found that the eccentricity may actually increase. Eccentricity growth induces chaotic rotation that is then halted by the BYORP effect, and if the orientation of the secondary is reversed, then the mutual orbit will contract. *Ćuk and Nesvorný* (2010) rule out the role of the evection resonance for responsibility of this eccentricity increase and attributes it to spin-orbit coupling. This disagrees with evolution resulting from the force decomposition and averaged equations (*Ćuk and Burns*, 2005; *Goldreich and Sari*, 2009; *McMahon and Scheeres*, 2010b; *Steinberg and Sari*, 2011). Future work directly comparing long-term evolution of a *Ćuk and Nesvorný* (2010)-type model and the secular evolution equations is needed to determine resolutely the consequences of outward BYORP evolution on eccentricity.

Using the secular evolution equations and including mutual tides, *Jacobson et al.* (2014b) found that outward expansion can be interrupted by an adiabatic invariance between the mutual semimajor axis and libration state of the secondary. As the mutual orbit expands, a small libration can grow until the rotation of the secondary desynchronizes and begins to circulate. This has been proposed as the mechanism by which to explain the small known population of wide binary asteroid systems that are found among NEAs and in the main belt, as this process can leave secondaries stranded so far from the primary to make tidal synchronization timescales very long (*Jacobson et al.*, 2014b). As observations continue

to be made of wide and possibly expanding binaries such as (185851) 2000 DP<sub>107</sub>, the theories regarding expansion due to the BYORP effect will continue to be tested.

The BYORP effect can also shrink orbits and simultaneously increase eccentricity (*Ćuk and Burns*, 2005; *Goldreich and Sari*, 2009; *McMahon and Scheeres*, 2010b; *Steinberg and Sari*, 2011). This will be discussed after describing tides, which are important when considering very tight binary asteroid systems.

## 4.2. Tides

The evolutionary consequences of mutual body tides have been considered for the evolution of asteroids since the discovery of the first asteroid satellite, Dactyl, about (243) Ida (*Petit et al.*, 1997; *Hurford and Greenberg*, 2000). These body tides are the result of the asteroid's mass distribution chasing an ever-changing equilibrium figure determined by the asteroid's spin state and the gravitational potentials of both binary members. Since the relaxation toward this figure is dissipative, energy is lost in the form of heat and removed from the rotation state of the asteroid. The difference in potential between the delayed figure and the theoretical equilibrium figure is referred to as the tidal bulge. This tidal bulge torques the mutual orbit, ensuring conservation of angular momentum within the asteroid system. Unlike lunar tides on Earth, where most of the energy is dissipated at the ocean-seabed interface and in the deep ocean itself (*Taylor*, 1920; *Jeffreys*, 1921; *Egbert and Ray*, 2000), the mutual tides between asteroids do not dissipate energy along an interface or in a fluid layer but rather throughout the solid body. However, new results indicate that tidal dissipation in rubble piles may be much higher (*Scheirich et al.*, 2015) than previously expected (*Goldreich and Sari*, 2009), so where and how tidal energy is dissipated must be examined much more thoroughly in the future.

Under most proposed formation circumstances and observed in nearly all small systems, except for those with synchronous rotations, asteroids rotate at rates greater than their mutual orbit mean motion (*Pravec et al.*, 2006). In this case, the tidal bulge lags behind the line connecting the mass centers of the binary members, and the binary's primary is rotationally decelerated. In this case, the mutual orbit expands, similar to the Earth-Moon system. Alternatively, the tidal bulge precedes the line connecting the two asteroids, and the binary's primary is rotationally accelerated. In this case, the mutual orbit shrinks, similar to the Mars-Phobos system. No observed binary asteroids currently occupy this state. A third tidal state also exists: Librational tides can oscillate through tidally locked binary members. This tide is responsible for removing libration from synchronous satellites. The tidal bulge oscillates from the trailing to leading hemisphere as the secondary librates, so the torque on the orbit cancels out and the orbit does not evolve.

Formally deriving an explicit set of equations to describe these torques has been a focus of research for over a century (*Darwin*, 1879). Historically, most theoretical descriptions

of tides have fallen into two camps, split by their assumptions regarding the relationship between the tidal bulge and the line connecting the mass centers of the two asteroids: (1) Some assume a constant lag angle (*Goldreich*, 1963; *Kaula*, 1964; *MacDonald*, 1964; *Goldreich and Soter*, 1966; *Taylor and Margot*, 2010), and (2) some assume a constant lag time (*Singer*, 1968; *Mignard*, 1979, 1980; *Hut*, 1980, 1981). Neither relationship is expected to accurately reflect potential asteroid rheology (*Efroimsky and Williams*, 2009; *Greenberg*, 2009; *Goldreich and Sari*, 2009; *Jacobson and Scheeres*, 2011c; *Ferraz-Mello*, 2013). Although the constant lag angle is believed to better represent circulating tides through solid bodies, *Greenberg* (2009) describes its shortcomings in vivid starkness. For the sake of this review, we will consider using the theory only for nearly circular orbits and will be careful to state when we feel that this theory may not be adequate. If systems have a nonnegligible eccentricity, the tidal despinning calculated by the first-order theory will be a lower bound, but the effects on the orbital evolution, particularly the eccentricity, are more difficult to determine. For instance, the theories in *Goldreich* (1963) and *Hut* (1981) give different predictions regarding the orbital evolution of asynchronous asteroids depending on orbital parameters.

Constant lag angle tidal theory assumes that the tidal bulge raised by an orbiting companion lags the line connecting the bodies' centers by a constant angle  $\epsilon$ , which is related to a tidal dissipation number  $Q$  via  $Q = 1/2\epsilon$ . The tidal dissipation number quantifies the amount of energy dissipated each tidal frequency cycle over the maximum energy stored in the tidal distortion [for further discussion, see *Goldreich and Soter* (1966), *Greenberg* (2009), and *Efroimsky and Williams* (2009)]. This theory is appropriate for determining the tidal torque on a circulating body, but as the body approaches synchronization and when the body is librating, this theory likely overestimates the actual tidal torque. The circulating tidal torque on a spherical asteroid with radius  $R$  from a perturbing binary member with a mass ratio of  $q$  is

$$\Gamma_C = \frac{2\pi k_2 \omega_d^2 \rho R^5 q^2}{Q a^6} \left( \frac{\omega - n}{|\omega - n|} \right) \quad (2)$$

where the semimajor axis  $a$  is measured in asteroid radii  $R$ ,  $(\omega - n)/|\omega - n|$  indicates the direction of the torque given the spin rate of the asteroid  $\omega$  and the mean motion of the mutual orbit  $n$ , and  $k_2$  is the second-order Love number of the asteroid. The potential Love number  $k$  quantifies the additional gravitational potential produced by the tidal bulge over the perturbing potential. In other words, it captures how much the tidal bulge responds to the deforming potential. We are currently considering only the lowest-order relevant surface harmonic, namely the second [for further discussion of the perturbing potential and its expansion, see *Ferraz-Mello et al.* (2008)]. A perfectly rigid asteroid would have a tidal Love number of 0, whereas a inviscid fluid would have a Love number of 3/2 according to its definition (*Goldreich and Sari*, 2009).

This tidal torque is most applicable to the primary, which is often rapidly rotating compared to the mean motion of the mutual orbit (*Pravec et al.*, 2006; *Richardson and Walsh*, 2006). In the most common case, the secondary is tidally locked and so does not contribute to the evolution of the semimajor axis of the mutual orbit. Given the torque above, the semimajor axis  $a$ , measured in primary radii  $R_p$ , and the primary spin rate  $\omega_p$  evolution are (*Goldreich and Sari*, 2009)

$$\frac{da}{dt} = \frac{3k_{2,p}\omega_d q \sqrt{1+q}}{Q_p a^{11/2}} \quad (3a)$$

$$\frac{d\omega_p}{dt} = -\frac{15k_{2,p}\omega_d^2 q^2}{4Q_p a^6} \quad (3b)$$

where  $k_{2,p}$  and  $Q_p$  are the tidal Love and dissipation numbers for the primary [for higher-order expansions, see *Taylor and Margot* (2010)].

The ratio of tidal despinning timescales for the primary and secondary are

$$\frac{\tau_s}{\tau_p} = \frac{k_{2,p} Q_s}{k_{2,s} Q_p} q^2 \quad (4)$$

where  $k_{2,s}$  and  $Q_s$  are the tidal Love and dissipation numbers for the secondary. Since the mass ratio is often on the order of  $q \sim 0.01\text{--}0.1$ , it is immediately clear that the secondary tidally locks first. It is possible that the ratio of tidal parameters could counteract this; however, both the tidal parameters derived from a modified continuum tidal theory (*Goldreich and Sari*, 2009) and the observed parameters from a hypothetical tidal-BYORP equilibrium (*Jacobson and Scheeres*, 2011c) are consistent with faster tidal synchronization of the secondary,  $\tau_s/\tau_p \propto q^{3/2}$  and  $\tau_s/\tau_p \propto q^{5/2}$ , respectively.

When the mass ratio is nearly equal, tides drive both bodies to synchronization in nearly the same timescale (*Jacobson and Scheeres*, 2011a). From this configuration, where both members are tidally locked, the BYORP effect can expand or shrink the mutual orbit to great affect. Acting independently on each body, in addition to the YORP effect acting on each component, BYORP can effectively transfer angular momentum to the orbit (*Taylor and Margot*, 2014). This could lead to rapid separation (*Jacobson and Scheeres*, 2011a), inward drift leading to unstable configurations (*Bellerose and Scheeres*, 2008; *Scheeres*, 2009; *Taylor and Margot*, 2014), or gentle collisions and contact binaries (*Scheeres*, 2007a; *Jacobson and Scheeres*, 2011a).

Although circulating tides drive the secondary to synchronous rotation, the secondary still has significant tidal dissipation occurring within it due to librational tides. The circulating theory is inappropriate for libration since according to this theory the tidal bulge instantaneously moves across the body. *Mignard* (1979) developed an alternative approach that assumes that the phase lag is proportional to the frequency of the tidal forcing. Here  $\lambda_0$  is the characteristic spin rate at which the body transitions from a circulation torque to the

libration torque or vice versa [where  $\lambda_0$  is related to tidal lag time  $\Delta t$  by  $2Q|\lambda_0|\Delta t = 1$  (*Mignard*, 1979)]. In the tidal torque,  $\lambda_0$  takes the place of  $|\omega - n|$  in the denominator of equation (2). The libration torque is not only appropriate when the system is librating, but also when the system is circulating slowly compared to  $\lambda_0$ . However, this torque becomes inappropriate as the body begins to circulate quickly since the tidal bulge could wrap about the body.

These two theories are actually one and the same if  $\lambda = \omega - n$  when  $\omega - n > \lambda_0$  and if  $\lambda = \lambda_0$  when  $\omega - n \leq \lambda_0$ , in which case  $\lambda$  replaces  $\lambda_0$  in equation (2). This approximate tidal torque can handle both libration and circulation for nearly circular and non-inclined systems (*Jacobson and Scheeres*, 2011a).

### 4.3. BYORP Effect and Tides

The leading hypothesized formation mechanism for Group A binary asteroids is by rotational disruption, which is observed to produce a rapidly rotating primary and a secondary that is quickly tidally locked — the secondary is even predicted to begin rotating more slowly (*Scheeres*, 2007a; *Walsh et al.*, 2008; *Jacobson and Scheeres*, 2011a). When considering this configuration for nearly circular orbits, circulating tides on the primary and librational tides on the secondary contribute to the change in eccentricity of the mutual orbit. Since the libration of the secondary and the mutual eccentricity are coupled (*McMahon and Scheeres*, 2013b), the librational tides on the secondary are often broken into direct librational and radial components (*Murray and Dermott*, 2000). The sum effect of all these tides on the mutual eccentricity is that the eccentricity is always being damped due to the dominance of the librational tides on the secondary, for a wide range of tidal parameters considered (*Goldreich and Sari*, 2009; *Jacobson and Scheeres*, 2011c).

In the singly synchronous configuration — rapidly rotating primary and tidally locked secondary — the mutual orbit of a small binary asteroid can evolve according to both the BYORP effect and tides. While tides in synchronous binary asteroids systems act only to expand the semimajor axis and decrease eccentricity, the BYORP effect can expand or shrink the semimajor axis depending on the shape and orientation of the secondary. In the case of BYORP effect driven expansion, both processes are growing the semimajor axis and both are reducing the eccentricity. As discussed above, this process can lead to disruption at the Hill radius or desynchronization of the secondary, which can strand the mutual orbit at a wide semimajor axis. Alternatively, the BYORP effect and tides can act in opposite directions. These effects drive the semimajor axis to an equilibrium location

$$a^* = \left( \frac{2\pi k_{2,p} \omega_d^2 \rho R_p^2 q^{4/3}}{B_s H_\odot Q_p} \right)^{1/7} \quad (5)$$

This semimajor axis location depends directly on the tidal parameters and the BYORP coefficient. If this location is dis-

tant, then secondaries could be rapidly lost (*Cuk and Burns*, 2005; *Cuk*, 2007; *Goldreich and Sari*, 2009; *McMahon and Scheeres*, 2010a), and the binary formation rate would have to be significant to account for the observed ~15% fraction (*Cuk*, 2007). Alternatively, the proposed equilibrium of tides and BYORP prevents this rapid destruction of systems and no longer requires binary formation rates to match potentially very fast BYORP disruption rates (*Jacobson et al.*, 2014c).

A prediction for occupying this equilibrium is that the semimajor axis should not be changing significantly. While measured changes in the semimajor axis or orbital period require precision that is currently unobtainable, a change in the semimajor axis does lead to a quadratic drift in the mean anomaly (*McMahon and Scheeres*, 2010a), which can be measured very precisely through the timing of mutual events in photometric light curves. A large survey has been undertaken to examine whether these drifts occur (*Scheirich and Pravec*, 2009). The first results from this survey find no drift in mean anomaly for NEA binary (175706) 1996 FG<sub>3</sub> (*Scheirich et al.*, 2015), which may point to this equilibrium.

If the singly synchronous binary population occupies this equilibrium, then we are able to learn about the internal properties of asteroids only from remote sensing measurements (*Jacobson and Scheeres*, 2011c); however, the tidal and BYORP coefficients are degenerate

$$\frac{B_s Q_p}{k_{2,p}} = \frac{2\pi \omega_d^2 \rho R_p^2 q^{4/3}}{H_\odot a^7} \quad (6)$$

This parameter relationship is shown in Fig. 4 along with a fit to the data:  $B_s Q_p / k_{2,p} = 6 \times 10^3$  (R<sub>p</sub>/1 km). As discussed above, estimates for the BYORP coefficient are around  $B_s \sim 0.01$  (*Cuk and Burns*, 2005; *Goldreich and Sari*, 2009; *McMahon and Scheeres*, 2010a, 2012a). From the data, the tidal parameters then follow:  $Q/k_2 = 6 \times 10^5$  (R<sub>p</sub>/1 km), very different than the  $Q/k_2 \gtrsim 10^7$  (1 km/R<sub>p</sub>) predicted from a modification of the continuum theory for rubble-pile asteroids (*Goldreich and Sari*, 2009).

*Taylor and Margot* (2011) predict tidal properties by assuming a tidal evolutionary path from twice the primary radius to the current orbital separation in under a certain timescale. For (175706) 1996 FG<sub>3</sub>, they estimate that  $Q/k_2 \approx 2.7 \times 10^7$  in order to migrate from 2 to 3.6 primary radii in 10 m.y. Using the new estimate of the tidal parameters from *Scheirich et al.* (2015),  $Q/k \approx 2.4 \times 10^5$  and this same tidal migration (assuming no influence from the BYORP effect) could take place in  $5.6 \times 10^4$  yr. This much higher rate of tidal dissipation or much larger tidal Love number can only be consistent with a tidal rheology very different than that for terrestrial planets and moons. Furthermore, the equations that convert the tidal Love number to a rigidity or elastic modulus, often denoted  $\mu$ , assume a continuum model that may not apply for this rubble-pile tidal rheology.

So far, the discussed tidal theory assumes that all the rotation axes are aligned and that the mutual orbit is nearly circular. If this is not the case, then the tidal bulge can have a

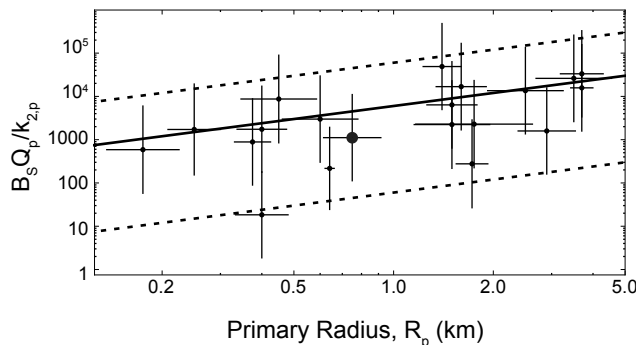


**Fig. 4.**  $B_s Q_p / k_{2,p}$  were calculated directly from observed quantities according to equation (6) for each known synchronous binary, and plotted as a function of primary radius  $R_p$  along with  $1\sigma$  uncertainties. The large circle in the center highlights the binary (175706) 1996 FG<sub>3</sub>. All the data is from <http://www.asu.cas.cz/asteroid/binastdata.htm>, maintained by P. Pravec according to Pravec et al. (2006). The solid line is a fitted model to the data:  $B_s Q_p / k_{2,p} = 6 \times 10^3 R_p$ . The dashed lines indicate the range of predicted scatter in the model due to the BYORP coefficient (possibly 10x stronger or 100x weaker). Reproduced with some updated binary parameters from Jacobson and Scheeres (2011c).

significant effect on the mutual orbit and rotation state of the asteroid. The differences between the different tidal theories become more extreme, and they differ by more than a matter of magnitudes, but also of direction. This is an ongoing area of active research, with new tidal theories being developed to eventually accurately describe asteroid lithologies (Goldreich and Sari, 2009; Efroimsky and Williams, 2009).

A separate tidal effect relies on “tidal saltation,” or the physical lofting of material off the surface of the primary. The very rapid, near critical, rotation of the primary permits the very small perturbations of the secondary to loft debris off the primary’s equator (Fahnestock and Scheeres, 2009; Harris et al., 2009), and during flight angular momentum is transferred from the debris to the orbit of the secondary. This expands the orbit of the secondary at rates that could potentially compete with tidal forces. Given the direct physical alteration of the primary by the repeated lofting and landing of particles on the equator, this theory provides an interesting observational test for future observations of equatorial ridges on NEAs.

#### 4.4. Asteroid Reshaping

If the asteroids were simply fluids, then they would follow permissible shape and spin configurations that have been studied by many, including Newton, Maclaurin, Jacobi, Poincaré, Roche, and Chandrasekhar. Observations of asteroids clearly show that they are not fluids, and their distribution of shape and spin configurations agree (Pravec et al., 2002). Observations also suggest that they are not simply monolithic rocks.

Rather, the population of small asteroids ( $D < 10$  km) are thought to be primarily gravitational aggregates consisting

of small bodies held together almost strictly by their self-gravity. Numerous observations and models contribute to this line of thought, including not only their spin and shape distributions, but also observations of crater chains on the Moon, the breakup of Comet Shoemaker-Levy 9, the very large observed impact crater on the large primitive asteroid (253) Mathilde, and, of course, the striking images of the small asteroid (25143) Itokawa. These arguments were last summarized in *Asteroids III* by Richardson et al. (2002), and the chapter by Scheeres et al. in this volume reviews our general knowledge of asteroid interiors.

Efforts to understand asteroid shape and spin configurations borrow cohesionless elastic-plastic yield criteria from soil mechanics (Holsapple, 2001, 2004; Sharma, 2009). These formulations calculate envelopes of allowable spin and shape configurations as a function of the material properties — typically relying on an angle of friction as the critical parameter. Neither cohesion nor tensile strength is required to explain the shapes and spins of nearly all large ( $D > 200$  m) observed asteroids (Holsapple, 2001, 2004), although the spins and shapes do not rule out any material strength either.

What about cohesion? Multiple recalculations of allowable spin rates as a function of cohesive forces find that even very small amounts of cohesion can dramatically change the allowable spin rates for a body. Even amounts as low as 100 Pa allow for kilometer-sized asteroids to rotate much faster than the observed 2.3–4-h limit (Holsapple, 2007; Sánchez and Scheeres, 2014). Only a single body is observed to be larger than 200 m and rotate faster than 2.3–4 h (Warner et al., 2009).

Rozitis et al. (2014) combined measurements of Yarkovsky drift and thermal properties to estimate the density of a kilometer-sized NEA, 1950 DA. Measurements of this asteroid’s spin rate find that it is rotating faster than what simply gravity and friction would allow, and thus it must have nonzero cohesive strength to prevent disruption. As pointed out by Holsapple (2007), very small amounts of cohesive strength are needed to allow bodies to rotate faster than the classical spin limits. Hirabayashi et al. (2014) estimated between 40 and 210 Pa for the cohesive strength of main-belt comet P/2013 R3, and Rozitis et al. (2014) estimated only  $64^{+12}_{-20}$  Pa of cohesive strength of (29075) 1950 DA. This amount of cohesion is in line with the predictions for cohesion produced by fine grain “bonding” larger constituent pieces of an asteroid (Scheeres et al., 2010; Sánchez and Scheeres, 2014), and would be similar to what is found in weak lunar regolith (see the chapter by Scheeres et al. in this volume).

The exciting radar-produced shape model of 1999 KW<sub>4</sub> showed that the asteroid shape held more information than could be contained in a simple triaxial ellipsoid model (Ostro et al., 2006). The equatorial bulge seen in those radar shape models became ubiquitous among primaries of other rapidly rotating asteroids (see the chapter by Margot et al. in this volume). A simple rigid ellipsoid that increases its angular momentum will drive surface material toward its equator, and this happens before the material would simply become

unbound (*Guibout and Scheeres*, 2003). This suggests that shape change would precede mass loss if there is loose material available.

Basic granular flow models can estimate what shapes the body might actually take. As the spin rate increases, the effective slope angle on the surface changes owing to the increased centrifugal force, and as slopes become higher on certain regions of the surface they can surpass critical values (angle of repose or angle of friction) and fail. After failing, material will flow “down” to the potential lows near the equator, settling in at lower slopes. This model found a surprisingly good match for the equatorial ridge shape of 1999 KW<sub>4</sub>, using an angle of failure of 37° (*Harris et al.*, 2009). The failure causes very regular slopes through mid-latitudes on nearly circular bodies, a trait clearly observed in the shape of 1999 KW<sub>4</sub> (*Harris et al.*, 2009; *Sánchez and Scheeres*, 2014; *Scheeres*, 2015).

Discrete particle approaches to modeling rubble-pile interior structure and evolution rely on N-body billiard-ball-style granular mechanics. Many of the first models of rubble-pile dynamics, tidal disruption, and spin/shape configurations relied on hard spherical particles that never overlap or interpenetrate (*Richardson et al.*, 1998, 2005). While these “hard-sphere” incarnations of the models did not directly account for friction forces, *Richardson et al.* (2005) showed that standard hexagonal closest packing configurations of the spheres produce enough shear strength so that modeled bodies can maintain spin and shape configurations within ~40° angle-of-friction-allowable envelopes produced by *Holsapple* (2001). While different and more simplistic than the “soft-sphere” representations used to model rubble-pile asteroids (*Sánchez and Scheeres*, 2011, 2012; *Schwartz et al.*, 2012), the modeled aggregates can hold shape and spin configurations similar to those observed on actual asteroids (see Fig. 10 of *Walsh et al.*, 2012). Further detail can be found in the chapter by Murdoch et al. in this volume.

When a rubble-pile asteroid is slowly spun up by the YORP effect, it can eventually be pushed to mass loss (*Rubincam*, 2000; *Vokrouhlický and Čapek*, 2002; *Bottke et al.*, 2002). If the asteroid is made of only a very few constituent pieces than they will reconfigure and eventually separate (*Scheeres*, 2007b). What happens to those two components is a complicated dynamical dance that involves angular momentum transfer due to nonspherical shapes (*Scheeres*, 2007b; *Jacobson and Scheeres*, 2011a).

When the asteroid is made of thousands of particles, different evolutions are found for different particle surface interactions. The “hard-sphere” models include dissipation of energy during collisions, but have to rely on structural packing (crystalline) to provide shear strength rather than surface friction (*Walsh et al.*, 2008, 2012). These models found that model asteroids can maintain oblate shapes at critical rotation rates, which leads to equatorial mass-shedding. While it was hypothesized that this could lead to in-orbit growth of the satellite (*Čuk*, 2007; *Walsh et al.*, 2008), it is clear from the dynamics of such close orbits (*Scheeres*, 2009; *Jacobson and Scheeres*, 2011a) that to avoid almost immediate ejection

from the system, many particles would have to be shed at the same time in order to collide, circularize, and stabilize their orbits beyond the Roche limit.

*Sánchez and Scheeres* (2011, 2012) utilized “soft-sphere” granular models, which allow for more complex surface interactions, including various friction forces and inter-particle cohesion. These works explore a wider range of parameters and find a large variety of outcomes, including “fission” events of bodies splitting into nearly equal parts. There is still a strong dependence on the angle of friction for the outcome, with some of the observed oblate-shaped and critically rotating outcomes observed.

Observed mass-loss events have been associated with YORP-induced rotational fission (*Jewitt et al.*, 2013, 2014, 2015; *Sheppard and Trujillo*, 2015). The rotation period of (62412) 2000 SY<sub>178</sub> is only 3.33 h (*Sheppard and Trujillo*, 2015). Minor components outside of the dust are difficult to observe, and the shape of the primary is impossible to deduce. Future observations are necessary to determine whether the dust is associated only with surface failure or satellite formation in these cases.

#### 4.5. Kozai and Planetary Encounters

Most secondaries in NEA systems are too close to their primary to experience excursions in eccentricity or inclination due to the Kozai effect (*Fang and Margot*, 2012c). For more distant NEA systems, such 1998 ST<sub>27</sub> at a ~16 R<sub>pri</sub>, the Kozai effect could play a role of disrupting systems or driving them to collision and possibly creating contact binaries (*Fang and Margot*, 2012c).

Binary systems in the main belt do not encounter planets, but those on near-Earth orbits can have encounters with terrestrial planets close enough to alter or disrupt their systems (*Farinella*, 1992; *Farinella and Chauvineau*, 1993; *Walsh and Richardson*, 2008; *Fang and Margot*, 2012a). The timescales for encounters close enough to disrupt or disturb a system depend on its heliocentric orbit (how frequently it approaches a planet), and also depend strongly on the system’s properties — primarily the separation of the primary and secondary. Disruption of a typical system with  $a = 4 R_{\text{pri}}$ , where  $a$  is semimajor axis and  $R_{\text{pri}}$  is the primary’s radius, becomes significant (50% of encounters randomized over phasings) at encounters of 3 R<sub>⊕</sub>, which occur on average every 2 m.y. for NEAs (*Walsh and Richardson*, 2008). Planetary flybys may also stymie other evolutionary effects, such as BYORP, by either torquing the secondary and breaking its synchronous rotation, or by exciting its orbital eccentricity (*Fang and Margot*, 2012a). Eccentricity of 0.2 can be excited for a similar  $a = 4 R_{\text{pri}}$  system at only 8 R<sub>⊕</sub>, which happen every ~1 m.y. on average for NEAs (*Walsh and Richardson*, 2008; *Fang and Margot*, 2012a).

### 5. THE FUTURE

The advances made in the last decades have been driven by the increased database of known binary systems and the

mounting evidence and measurements of thermal effects acting widely in the solar system. Naturally, many questions remain, and we are optimistic that the trajectory of current studies is well aligned to answer many of the outstanding questions. We roughly outline the expected progress, discoveries, and events that we think will be the focus of an *Asteroids V* chapter on this topic in a decade.

1. More observations from a variety of sources will help to expand the catalog of rare and outlier populations. Large-scale surveys should provide a flood of data and continue to increase the size of our catalog [e.g., Gaia and the Large Synoptic Survey Telescope (LSST)]. While observations from small telescopes, including significant contributions from amateurs, have been the basis of many lightcurve discoveries of small systems, some of the high-cadence all-sky-survey telescopes may begin to eclipse the production of the network of small telescopes.

2. The nondetection of BYORP at 1996 FG<sub>3</sub> is curious and possibly revealing (Scheirich *et al.*, 2015). While there is a proposed theory to explain why and how the effect may be balanced by tides (Jacobson and Scheeres, 2011a), and other nontidal effects may be similarly important (Fahnestock and Scheeres, 2009; Harris *et al.*, 2009), a nondetection is not a detection, and the community awaits a measurement of this interesting thermal effect. A system with a more distant companion, or perhaps one of the triple systems, may allow for a detection in an environment where tides are small and BYORP is strong (Pravec and Scheirich, 2010). The BYORP effect may be a fundamental and dominating mechanism that is widely shaping the observed population of small binary asteroids — so observing it in action will be a great step forward.

3. There are spacecraft visits planned to asteroids with “top shapes.” The KW<sub>4</sub> shape (or top shape) that is becoming ubiquitous in shape models of the primaries of binary systems was a revealing discovery in this field. Hopefully careful mapping and geologic studies of these systems will reveal how small asteroids become that particular shape. In turn, knowing how the ridge formed might help researchers answer the many remaining questions about the formation and evolution of the satellites that are so often found around these top-shaped bodies. The currently planned space missions from NASA and the Japan Aerospace Exploration Agency (JAXA), OSIRIS-REx and Hayabusa-2 respectively, are each currently seeking to visit primitive NEAs, and each target appears to show some signs of an equatorial ridge (Nolan *et al.*, 2013; Lauretta *et al.*, 2014). It is hoped that the mission surveys of the asteroid surface will elucidate the reshaping histories of these bodies by showing signs of material flow patterns, variations in ages of different surface features, and material differences in different geologic units.

**Acknowledgments.** K.J.W. was partially supported by the NASA Planetary Geology and Geophysics Program under grant NNX13AM82G. S.A.J. was supported by the European Research Council Advanced Grant ACCRETE (contract number 290568).

## REFERENCES

- Asphaug E. and Benz W. (1996) Size, density, and structure of Comet Shoemaker-Levy 9 inferred from the physics of tidal breakup. *Icarus*, 121(2), 225–248.
- Becker T. M., Nolan M., Howell E. S., and Magri C. (2009) Physical modeling of triple near-Earth asteroid (153591) 2001 SN263. *Bull. Am. Astron. Soc.*, 41, 190.
- Becker T. M., Howell E. S., Nolan M. C., Magri C., Pravec P., Taylor P. A., Oey J., Higgins D., Vilagi J., Kornos L., Galad A., Gajdos S., Gaftonyuk N. M., Krugly Y. N., Molotov I. E., Hicks M. D., Carbognani A., Warner B. D., Vachier F., Marchis F., and Pollock J. (2015) Physical modeling of triple near-Earth asteroid (153591) 2001 SN263 from radar and optical light curve observations. *Icarus*, 248, 499–515.
- Bellerose J. and Scheeres D. J. (2008) Energy and stability in the full two body problem. *Cel. Mech. Dyn. Astron.*, 100(1), 63–91.
- Belton M. and Carlson R. (1994) 1993 (243) 1. *IAU Circular* 5948, 2.
- Bottke W. F. and Melosh H. J. (1996) Formation of asteroid satellites and doublet craters by planetary tidal forces. *Nature*, 381(6), 51–53.
- Bottke W. F., Vokrouhlický D., Rubincam D. P., and Brož M. (2002) The effect of Yarkovsky thermal forces on the dynamical evolution of asteroids and meteoroids. In *Asteroids III* (W. F. Bottke Jr. *et al.*, eds.), pp. 395–408. Univ. of Arizona, Tucson.
- Bottke W. F., Vokrouhlický D., Rubincam D. P., and Nesvorný D. (2006) The Yarkovsky and YORP effects: Implications for asteroid dynamics. *Annu. Rev. Earth Planet. Sci.*, 34, 157–191.
- Bottke W. F., Vokrouhlický D., Walsh K. J., Delbo M., Michel P., Lauretta D. S., Campins H., Connolly H. C., Scheeres D. J., and Chelsey S. R. (2015) In search of the source of asteroid (101955) Bennu: Applications of the stochastic YORP model. *Icarus*, 247, 191–217.
- Breiter S., Bartczak P., Czekaj M., Oczujska B., and Vokrouhlický D. (2009) The YORP effect on 25143 Itokawa. *Astron. Astrophys.*, 507(2), 1073–1081.
- Brown M. E., Margot J.-L., Keck W. M. I., de Pater I., and Roe H. (2001) S/2001 (87) 1. *IAU Circular* 7588, 1.
- Brozović M., Benner L. A. M., Nolan M. C., Howell E. S., Magri C., Giorgini J. D., Taylor P. A., Margot J.-L., Busch M. W., Shepard M. K., Carter L. M., Jao J. S., Van Brimmer J., Franck C. R., Silva M. A., Kodis M. A., Kelley D. T., Slade M. A., Bramson A., Lawrence K. J., Pollock J. T., Pravec P., Reichart D. E., Ivarsen K. M., Haislip J. B., Nysewander M. C., and LaCluyze A. P. (2009) (136617) 1994 CC. *IAU Circular* 9053, 2.
- Brozović M., Benner L. A. M., Taylor P. A., Nolan M. C., Howell E. S., Magri C., Scheeres D. J., Giorgini J. D., Pollock J., Pravec P., Galad A., Fang J., Margot J.-L., Busch M. W., Shepard M. K., Reichart D. E., Ivarsen K. M., Haislip J. B., LaCluyze A. P., Jao J. S., Slade M. A., Lawrence K. J., and Hicks M. D. (2011) Radar and optical observations and physical modeling of triple near-Earth asteroid (136617) 1994 CC. *Icarus*, 216(1), 241–256.
- Busch M. W., Giorgini J. D., Ostro S. J., Benner L. A. M., Jurgens R. F., Rose R., Hicks M. D., Pravec P., Kusnirák P., Ireland M. J., Scheeres D. J., Broschart S. B., Magri C., Nolan M. C., Hine A. A., and Margot J.-L. (2007) Physical modeling of near-Earth asteroid (29075) 1950 DA. *Icarus*, 190(2), 608–621.
- Busch M. W., Ostro S. J., Benner L. A. M., Brozović M., Giorgini J. D., Jao J. S., Scheeres D. J., Magri C., Nolan M. C., Howell E. S., Taylor P. A., Margot J.-L., and Briskin W. (2011) Radar observations and the shape of near-Earth asteroid 2008 EV5. *Icarus*, 212(2), 649–660.
- Capek D. and Vokrouhlický D. (2004) The YORP effect with finite thermal conductivity. *Icarus*, 172(2), 526–536.
- Cooney W. R. Jr., Gross J., Terrell D., Stephens R. D., Pravec P., Kusnirák P., Durkee R., and Galad A. (2006) (1717) Arlon. *Central Bureau Electronic Telegram*, 369, 1.
- Cotto-Figueroa D., Statler T. S., Richardson D. C., and Tanga P. (2015) Coupled spin and shape evolution of small rubble-pile asteroids: Self-limitation of the YORP effect. *Astrophys. J.*, 803(1), 25.
- Ćuk M. (2007) Formation and destruction of small binary asteroids. *Astrophys. J. Lett.*, 659(1), L57–L60.
- Ćuk M. and Burns J. A. (2005) Effects of thermal radiation on the dynamics of binary NEAs. *Icarus*, 176(2), 418–431.
- Ćuk M. and Nesvorný D. (2010) Orbital evolution of small binary asteroids. *Icarus*, 207(2), 732–743.

- Darwin G. H. (1879) A tidal theory of the evolution of satellites. *The Observatory*, 3, 79–84.
- Descamps P., Marchis F., Michalowski T., Vachier F., Colas F., Berthier J., Assafin M., Dunckel P. B., Polinska M., Pych W., Hestroffer D., Miller K. P. M., Vieira Martins R., Birlan M., Teng-Chuen-Yu J. P., Peyrot A., Payet B., Dorseuil J., Léonie Y., and Dijoux T. (2007) Figure of the double asteroid 90 Antiope from adaptive optics and lightcurve observations. *Icarus*, 187(2), 482–499.
- Descamps P., Marchis F., Berthier J., Emery J. P., Duchêne G., de Pater I., Wong M. H., Lim L., Hammel H. B., Vachier F., Wiggins P., Teng-Chuen-Yu J.-P., Peyrot A., Pollock J., Assafin M., Vieira-Martins R., Camargo J. I. B., Braga-Ribas F., and Macomber B. (2011) Triplicity and physical characteristics of asteroid (216) Kleopatra. *Icarus*, 211, 1022–1033.
- Doressoundiram A., Paolicchi P., Verlicchi A., and Cellino A. (1997) The formation of binary asteroids as outcomes of catastrophic collisions. *Planet. Space Sci.*, 45, 757–770.
- Duddy S. R., Lowry S. C., Wolters S. D., Christou A., Weissman P. R., Green S. F., and Rozitis B. (2012) Physical and dynamical characterisation of the unbound asteroid pair 7343–154634. *Astron. Astrophys.*, 539, A36.
- Durda D. D. (1996) The formation of asteroidal satellites in catastrophic collisions. *Icarus*, 120(1), 212–219.
- Durda D. D., Bottke W. F., Enke B. L., Merline W. J., Asphaug E., Richardson D. C., and Leinhardt Z. M. (2004) The formation of asteroid satellites in large impacts: Results from numerical simulations. *Icarus*, 170(1), 243–257.
- Durda D. D., Bottke W. F., Nesvorný D., Enke B. L., Merline W. J., Asphaug E., and Richardson D. C. (2007) Size-frequency distributions of fragments from SPH/N-body simulations of asteroid impacts: Comparison with observed asteroid families. *Icarus*, 186(2), 498–516.
- Ďurech J., Vokrouhlický D., Kaasalainen M., Higgins D., Krugly Y. N., Gaftonyuk N. M., Shevchenko V. S., Chiorny V. G., Hamanowa H., Hamanowa H., Reddy V., and Dyvig R. R. (2008a) Detection of the YORP effect in asteroid (1620) Geographos. *Astron. Astrophys.*, 489(2), L25–L28.
- Ďurech J., Vokrouhlický D., Kaasalainen M., Weissman P. R., Lowry S. C., Beshore E., Higgins D., Krugly Y. N., Shevchenko V. S., Gaftonyuk N. M., Choi Y.-J., Kowalski R. A., Larson S., Warner B. D., Marshalkina A. L., Ibrahimov M. A., Molotov I. E., Michałowski T., and Kitazato K. (2008b) New photometric observations of asteroids (1862) Apollo and (25143) Itokawa — an analysis of YORP effect. *Astron. Astrophys.*, 488(1), 345–350.
- Ďurech J., Vokrouhlický D., Baransky A. R., Breiter S., Burkhanov O. A., Cooney W. R. Jr., Fuller V., Gaftonyuk N. M., Gross J., Inasaridze R. Y., Kaasalainen M., Krugly Y. N., Kvaratskhelia O. I., Litvinenko E. A., Macomber B., Marchis F., Molotov I. E., Oey J., Polishook D., Pollock J., Pravec P., Sárneczky K., Shevchenko V. S., Slyusarev I., Stephens R. D., Szabó G., Terrell D., Vachier F., Vanderplate Z., Viikinkoski M., and Warner B. D. (2012) Analysis of the rotation period of asteroids (1865) Cerberus, (2100) Ra-Shalom, and (3103) Eger — search for the YORP effect. *Astron. Astrophys.*, 547, 10.
- Efroimsky M. and Williams J. G. (2009) Tidal torques: A critical review of some techniques. *Cel. Mech. Dyn. Astron.*, 104(3), 257–289.
- Egbert G. D. and Ray R. D. (2000) Significant dissipation of tidal energy in the deep ocean inferred from satellite altimeter data. *Nature*, 405(6), 775–778.
- Fahnestock E. G. and Scheeres D. J. (2008) Simulation and analysis of the dynamics of binary near-Earth asteroid (66391) 1999 KW4. *Icarus*, 194, 410.
- Fahnestock E. G. and Scheeres D. J. (2009) Binary asteroid orbit expansion due to continued YORP spin-up of the primary and primary surface particle motion. *Icarus*, 201(1), 135–152.
- Fang J. and Margot J.-L. (2012a) Binary asteroid encounters with terrestrial planets: Timescales and effects. *Astron. J.*, 143(1), 25.
- Fang J. and Margot J.-L. (2012b) Near-Earth binaries and triples: Origin and evolution of spin-orbital properties. *Astron. J.*, 143(1), 24.
- Fang J. and Margot J.-L. (2012c) The role of Kozai cycles in near-Earth binary asteroids. *Astron. J.*, 143(3), 59.
- Farinella P. (1992) Evolution of Earth-crossing binary asteroids due to gravitational encounters with the Earth. *Icarus*, 96, 284.
- Farinella P. and Chauvineau B. (1993) On the evolution of binary Earth-approaching asteroids. *Astron. Astrophys.*, 279, 251–259.
- Ferraz-Mello S. (2013) Tidal synchronization of close-in satellites and exoplanets. A rheophysical approach. *Cel. Mech. Dyn. Astron.*, 116(2), 109–140.
- Ferraz-Mello S., Rodríguez A., and Hussmann H. (2008) Tidal friction in close-in satellites and exoplanets: The Darwin theory re-visited. *Cel. Mech. Dyn. Astron.*, 101(1), 171–201.
- Goldreich P. (1963) On the eccentricity of satellite orbits in the solar system. *Mon. Not. R. Astron. Soc.*, 126, 257.
- Goldreich P. and Sari R. (2009) Tidal evolution of rubble piles. *Astrophys. J.*, 691(1), 54–60.
- Goldreich P. and Soter S. (1966) Q in the solar system. *Icarus*, 5, 375–389.
- Golubov O. and Krugly Y. N. (2012) Tangential component of the YORP effect. *Astrophys. J. Lett.*, 752(1), L11.
- Golubov O., Scheeres D. J., and Krugly Y. N. (2014) A three-dimensional model of tangential YORP. *Astrophys. J.*, 794(1), 22.
- Greenberg R. (2009) Frequency dependence of tidal q. *Astrophys. J. Lett.*, 698(1), L42–L45.
- Guibout V. and Scheeres D. J. (2003) Stability of surface motion on a rotating ellipsoid. *Cel. Mech. Dyn. Astron.*, 87(3), 263–290.
- Harris A. W., Young J. W., Dockweiler T., Gibson J., Poutanen M., and Bowell E. (1992) Asteroid lightcurve observations from 1981. *Icarus*, 95(1), 115–147.
- Harris A. W., Fahnestock E. G., and Pravec P. (2009) On the shapes and spins of “rubble pile” asteroids. *Icarus*, 199(2), 310–318.
- Hirabayashi M., Scheeres D. J., Sánchez D. P., and Gabriel T. (2014) Constraints on the physical properties of main belt comet P/2013 R3 from its breakup event. *Astrophys. J. Lett.*, 789(1), L12.
- Holsapple K. A. (2001) Equilibrium configurations of solid cohesionless bodies. *Icarus*, 154(2), 432–448.
- Holsapple K. A. (2004) Equilibrium figures of spinning bodies with self-gravity. *Icarus*, 172(1), 272–303.
- Holsapple K. A. (2007) Spin limits of solar system bodies: From the small fast-rotators to 2003 EL61. *Icarus*, 187(2), 500–509.
- Holsapple K. A. (2010) On YORP-induced spin deformations of asteroids. *Icarus*, 205(2), 430–442.
- Hurford T. A. and Greenberg R. (2000) Tidal evolution by elongated primaries: Implications for the Ida/Dactyl system. *Geophys. Res. Lett.*, 27(1), 1595–1598.
- Hut P. (1980) Stability of tidal equilibrium. *Astron. Astrophys.*, 92, 167–170.
- Hut P. (1981) Tidal evolution in close binary systems. *Astron. Astrophys.*, 99, 126–140.
- Jacobson S. A. (2014) Small asteroid system evolution. In *Complex Planetary Systems* (Z. Knežević and A. Lemaître, eds.), pp. 108–117. Proc. IAU Vol. 9, Symposium S310.
- Jacobson S. A. and Scheeres D. J. (2011a) Dynamics of rotationally fissioned asteroids: Source of observed small asteroid systems. *Icarus*, 214(1), 161–178.
- Jacobson S. A. and Scheeres D. J. (2011b) Evolution of small near-Earth asteroid binaries. *EPSC-DPS Joint Meeting 2011*, 647.
- Jacobson S. A. and Scheeres D. J. (2011c) Long-term stable equilibria for synchronous binary asteroids. *Astrophys. J. Lett.*, 736(1), L19.
- Jacobson S. A., Marzari F., Rossi A., Scheeres D. J., and Davis D. R. (2014a) Effect of rotational disruption on the size-frequency distribution of the main belt asteroid population. *Mon. Not. R. Astron. Soc. Lett.*, 439, L95–L99.
- Jacobson S. A., Scheeres D. J., and McMahon J. W. (2014b) Formation of the wide asynchronous binary asteroid population. *Astrophys. J.*, 780(1), 60.
- Jacobson S. A., Scheeres D. J., Rossi A., and Marzari F. (2014c) The effects of rotational fission on the main belt asteroid population. *Lunar Planet. Sci. XLV*, Abstract #2363. Lunar and Planetary Institute, Houston.
- Jeffreys H. (1921) Tidal friction in shallow seas. *Philos. Trans. R. Soc. Ser. A*, 221, 239–264.
- Jewitt D., Ishiguro M., and Agarwal J. (2013) Large particles in active asteroid P/2010 A2. *Astrophys. J. Lett.*, 764(1), L5.
- Jewitt D., Agarwal J., Li J.-Y., Weaver H., Mutchler M., and Larson S. (2014) Disintegrating asteroid P/2013 R3. *Astrophys. J. Lett.*, 784(1), L8.
- Jewitt D., Agarwal J., Peixinho N., Weaver H., Mutchler M., Hui M.-T., Li J.-Y., and Larson S. (2015) A new active asteroid 313P/Gibbs. *Astron. J.*, 149(2), 81.

- Johnston W. R. (2014) *Binary Minor Planets V7.0*. EAR-A-COMPIL-5-BINMP-V7.0, NASA Planetary Data System.
- Kaasalainen M., Durech J., Warner B. D., Krugly Y. N., and Gaftonyuk N. M. (2007) Acceleration of the rotation of asteroid 1862 Apollo by radiation torques. *Nature*, 446(7), 420–422.
- Kaula W. M. (1964) Tidal dissipation by solid friction and the resulting orbital evolution. *Rev. Geophys. Space Phys.*, 2, 661–685.
- Lauretta D. S., Bartels A. E., Barucci M. A., Bierhaus E. B., Binzel R. P., Bottke W. F., Campins H., Chesley S. R., Clark B. C., Clark B. E., Cloutis E. A., Connolly H. C., Crombie M. K., Delbo M., Dworkin J. P., Emery J. P., Gladin D. P., Hamilton V. E., Hergenrother C. W., Johnson C. L., Keller L. P., Michel P., Nolan M. C., Sandford S. A., Scheeres D. J., Simon A. A., Sutter B. M., Vokrouhlický D., and Walsh K. J. (2014) The OSIRIS-REx target asteroid (101955) Bennu: Constraints on its physical, geological, and dynamical nature from astronomical observations. *Meteoritics & Planet. Sci.*, 50(4), 834–849.
- Leinhardt Z. M. and Richardson D. C. (2005) A fast method for finding bound systems in numerical simulations: Results from the formation of asteroid binaries. *Icarus*, 176(2), 432–439.
- Lowry S. C., Fitzsimmons A., Pravec P., Vokrouhlický D., Boehnhardt H., Taylor P. A., Margot J.-L., Galad A., Irwin M., Irwin J., and Kusnirák P. (2007) Direct detection of the asteroidal YORP effect. *Science*, 316(5), 272–274.
- Lowry S. C., Weissman P. R., Duddy S. R., Rozitis B., Fitzsimmons A., Green S. F., Hicks M. D., Snodgrass C., Wolters S. D., Chesley S. R., Pittichová J., and van Oers P. (2014) The internal structure of asteroid (25143) Itokawa as revealed by detection of YORP spin-up. *Astron. Astrophys.*, 562, A48.
- MacDonald G. J. F. (1964) Tidal friction. *Rev. Geophys. Space Phys.*, 2, 467–541.
- Marchis F. and Vega D. (2014) The potential of GPI extreme AO system to image and characterize exoplanets and asteroids. In *AAS/Division for Planetary Sciences Meeting Abstracts*, 46, #201.07.
- Marchis F., Descamps P., Hestroffer D., and Berthier J. (2005) Discovery of the triple asteroidal system 87 Sylvia. *Nature*, 436(7), 822–824.
- Marchis F., Baek M., Descamps P., Berthier J., Hestroffer D., and Vachier F. (2007) S/2004 (45) 1. *IAU Circular* 8817, 1.
- Marchis F., Pollock J., Pravec P., Baek M., Greene J., Hutton L., Descamps P., Reichart D. E., Ivarsen K. M., Crain J. A., Nysewander M. C., Lacluyze A. P., Haislip J. B., and Harvey J. S. (2008) (3749) Balam. *Central Bureau Electronic Telegram*, 1297, 1.
- Marchis F., Descamps P., Berthier J., Colas F., Melbourne J., Stockton A. N., Fassnacht C. D., and Dupuy T. J. (2009) Occultations of the (93) Minerva system. *Central Bureau Electronic Telegram*, 1986, 1.
- Margot J.-L., Nolan M. C., Benner L. A. M., Ostro S. J., Jurgens R. F., Giorgini J. D., Slade M. A., and Campbell D. B. (2002) Binary asteroids in the near-Earth object population. *Science*, 296(5), 1445–1448.
- Marzari F., Rossi A., and Scheeres D. J. (2011) Combined effect of YORP and collisions on the rotation rate of small main belt asteroids. *Icarus*, 214(2), 622–631.
- Masiero J. R., Jedicek R., Durech J., Gwyn S., Denneau L., and Larsen J. (2009) The Thousand Asteroid Light Curve Survey. *Icarus*, 204(1), 145–171.
- McMahon J. W. and Scheeres D. J. (2010a) Detailed prediction for the BYORP effect on binary near-Earth asteroid (66391) 1999 KW4 and implications for the binary population. *Icarus*, 209(2), 494–509.
- McMahon J. W. and Scheeres D. J. (2010b) Secular orbit variation due to solar radiation effects: A detailed model for BYORP. *Cel. Mech. Dyn. Astron.*, 106(3), 261–300.
- McMahon J. W. and Scheeres D. J. (2012a) Binary-YORP coefficients for known asteroid shapes. *AAS/Division for Planetary Sciences Meeting Abstracts*, 44, #105.08.
- McMahon J. W. and Scheeres D. J. (2012b) Effect of small scale surface topology on near-Earth asteroid YORP and bYORP coefficients. *AAS/Division of Dynamical Astronomy Meeting*, 43, #7.04.
- McMahon J. W. and Scheeres D. J. (2013a) A statistical analysis of YORP coefficients. *AAS/Division for Planetary Sciences Meeting Abstracts*, 45, #112.17.
- McMahon J. W. and Scheeres D. J. (2013b) Dynamic limits on planar libration-orbit coupling around an oblate primary. *Cel. Mech. Dyn. Astron.*, 115, 365–396.
- Melosh H. J. and Stansberry J. A. (1991) Doublet craters and the tidal disruption of binary asteroids. *Icarus*, 94, 171–179.
- Merline W. J., Weidenschilling S. J., Durda D. D., Margot J.-L., Pravec P., and Storrs A. D. (2002) Asteroids do have satellites. In *Asteroids III* (W. F. Bottke Jr. et al., eds.), pp. 289–312. Univ. of Arizona, Tucson.
- Michałowski T., Bartczak P., Velichko F. P., Kryszczynska A., Kwiatkowski T., Breiter S., Colas F., Fauvaud S., Marciniak A., Michałowski J., Hirsch R., Behrend R., Bernasconi L., Rinner C., and Charbonnel S. (2004) Eclipsing binary asteroid 90 Antiope. *Astron. Astrophys.*, 423, 1159–1168.
- Michel P. and Richardson D. C. (2013) Collision and gravitational reaccumulation: Possible formation mechanism of the asteroid Itokawa. *Astron. Astrophys.*, 554, L1.
- Michel P., Benz W., Tanga P., and Richardson D. C. (2001) Collisions and gravitational reaccumulation: Forming asteroid families and satellites. *Science*, 294(5), 1696–1700.
- Michel P., Tanga P., Benz W., and Richardson D. C. (2002) Formation of asteroid families by catastrophic disruption: Simulations with fragmentation and gravitational reaccumulation. *Icarus*, 160(1), 10–23.
- Michel P., Benz W., and Richardson D. C. (2003) Disruption of fragmented parent bodies as the origin of asteroid families. *Nature*, 421(6923), 608–611.
- Michel P., Benz W., and Richardson D. C. (2004) Catastrophic disruption of pre-shattered parent bodies. *Icarus*, 168(2), 420–432.
- Mignard F. (1979) The evolution of the lunar orbit revisited. I. *Moon Planets*, 20, 301–315.
- Mignard F. (1980) The evolution of the lunar orbit revisited. II. *Moon Planets*, 23, 185–201.
- Morbidelli A., Levison H. F., Tsiganis K., and Gomes R. S. (2005) Chaotic capture of Jupiter's Trojan asteroids in the early solar system. *Nature*, 435(7041), 462–465.
- Moskovitz N. A. (2012) Colors of dynamically associated asteroid pairs. *Icarus*, 221(1), 63–71.
- Mottola S. and Lahulla F. (2000) Mutual eclipse events in asteroidal binary system 1996 FG3: Observations and a numerical model. *Icarus*, 146(2), 556–567.
- Murray C. D. and Dermott S. F. (2000) *Solar System Dynamics*. Cambridge Univ., Cambridge.
- Naidu S. P. and Margot J.-L. (2015) Near-Earth asteroid satellite spins under spin-orbit coupling. *Astron. J.*, 149(2), 80.
- Nesvorný D. and Vokrouhlický D. (2007) Analytic theory of the YORP effect for near-spherical objects. *Astron. J.*, 134(5), 1750.
- Nesvorný D., Bottke W. F., Dones L., and Levison H. F. (2002) The recent breakup of an asteroid in the main-belt region. *Nature*, 417(6), 720–771.
- Nesvorný D., Youdin A. N., and Richardson D. C. (2010) Formation of Kuiper belt binaries by gravitational collapse. *Astron. J.*, 140(3), 785–793.
- Nesvorný D., Vokrouhlický D., and Morbidelli A. (2013) Capture of Trojans by jumping Jupiter. *Astrophys. J.*, 768(1), 45.
- Nolan M. C., Howell E. S., Benner L. A. M., Ostro S. J., Giorgini J. D., Busch M. W., Carter L. M., Anderson R. F., Magri C., Campbell D. B., Margot J.-L., Vervack R. J. Jr., and Shepard M. K. (2008) (153591) 2001 SN26. *IAU Circular* 8921.
- Nolan M. C., Magri C., Howell E. S., Benner L. A. M., Giorgini J. D., Hergenrother C. W., Hudson R. S., Lauretta D. S., Margot J.-L., Ostro S. J., and Scheeres D. J. (2013) Shape model and surface properties of the OSIRIS-REx target asteroid (101955) Bennu from radar and lightcurve observations. *Icarus*, 226(1), 629–640.
- Noll K. S., Grundy W. M., Chiang E. I., Margot J.-L., and Kern S. D. (2008) Binaries in the Kuiper belt. In *The Solar System Beyond Neptune* (M. A. Barucci et al., eds.), pp. 345–363. Univ. of Arizona, Tucson.
- O'Keefe J. A. (1976) *Tektites and Their Origin*. Elsevier, Amsterdam.
- Ostro S. J., Hudson R. S., Benner L. A. M., Giorgini J. D., Magri C., Margot J.-L., and Nolan M. C. (2002) Asteroid radar astronomy. In *Asteroids III* (W. F. Bottke Jr. et al., eds.), pp. 151–168. Univ. of Arizona, Tucson.
- Ostro S. J., Margot J.-L., Benner L. A. M., Giorgini J. D., Scheeres D. J., Fahnestock E. G., Broschart S. B., Bellerose J., Nolan M. C., Magri C., Pravec P., Scheirich P., Rose R., Jurgens R. F., De Jong E. M., and Suzuki S. (2006) Radar imaging of binary near-Earth asteroid (66391) 1999 KW4. *Science*, 314(5), 1276–1280.
- Paddack S. J. (1969) Rotational bursting of small celestial bodies: Effects of radiation pressure. *J. Geophys. Res.*, 74, 4379–4381.

- Paddack S. J. and Rhee J. W. (1975) Rotational bursting of interplanetary dust particles. *Geophys. Res. Lett.*, 2, 365–367.
- Petit J.-M., Durda D. D., Greenberg R., Hurlford T. A., and Geissler P. E. (1997) The long-term dynamics of Dactyl's orbit. *Icarus*, 130(1), 177–197.
- Polishook D., Brosch N., and Prialnik D. (2011) Rotation periods of binary asteroids with large separations — Confronting the escaping ejecta binaries model with observations. *Icarus*, 212(1), 167–174.
- Polishook D., Moskovitz N. A., Binzel R. P., Demeo F. E., Vokrouhlický D., Žížka J., and Oszkiewicz D. A. (2014a) Observations of “fresh” and weathered surfaces on asteroid pairs and their implications on the rotational-fission mechanism. *Icarus*, 233, 9–26.
- Polishook D., Moskovitz N. A., DeMeo F., and Binzel R. P. (2014b) Rotationally resolved spectroscopy of asteroid pairs: No spectral variation suggests fission is followed by settling of dust. *Icarus*, 243, 222–235.
- Pravec P. and Hahn G. (1997) Two-period lightcurve of 1994 AW1: Indication of a binary asteroid? *Icarus*, 127(2), 431–440.
- Pravec P. and Harris A. W. (2000) Fast and slow rotation of asteroids. *Icarus*, 148(1), 12–20.
- Pravec P. and Harris A. W. (2007) Binary asteroid population. 1. Angular momentum content. *Icarus*, 190(1), 250–259.
- Pravec P. and Scheirich P. (2010) Binary system candidates for detection of BYORP. *Bull. Am. Astron. Soc.*, 42, 1055.
- Pravec P. and Vokrouhlický D. (2009) Significance analysis of asteroid pairs. *Icarus*, 204(2), 580–588.
- Pravec P., Wolf M., and Šarounová L. (1998) Occultation/eclipse events in binary asteroid 1991 VH. *Icarus*, 133(1), 79–88.
- Pravec P., Wolf M., and Šarounová L. (1999) How many binaries are there among the near-Earth asteroids? In *Evolution and Source Regions of Asteroids and Comets* (J. Svoren et al., eds.), p. 159. IAU Colloq. 173, Univ. of Rochester.
- Pravec P., Šarounová L., Rabinowitz D. L., Hicks M. D., Wolf M., Krugly Y. N., Velichko F. P., Shevchenko V. G., Chiorny V. G., Gaftonyuk N. M., and Genevier G. (2000) Two-period lightcurves of 1996 FG3, 1998 PG, and (5407) 1992 AX: One probable and two possible binary asteroids. *Icarus*, 146(1), 190–203.
- Pravec P., Harris A. W., and Michalowski T. (2002) Asteroid rotations. In *Asteroids III* (W. F. Bottke Jr. et al., eds.), pp. 113–122. Univ. of Arizona, Tucson.
- Pravec P., Scheirich P., Kusnirák P., Šarounová L., Mottola S., Hahn G., Brown P., Esquerdo G., Kaiser N., Krzeminski Z., Pray D. P., Warner B. D., Harris A. W., Nolan M. C., Howell E. S., Benner L. A. M., Margot J.-L., Galad A., Holliday W., Hicks M. D., Krugly Y. N., Tholen D. J., Whiteley R. J., Marchis F., Degraff D. R., Grauer A., Larson S., Velichko F. P., Cooney W. R. Jr., Stephens R. D., Zhu J., Kirsch K., Dyvig R., Snyder L., Reddy V., Moore S., Gajdos S., Vilagi J., Masi G., Higgins D., Funkhouser G., Knight B., Slivan S. M., Behrend R., Grenon M., Burki G., Roy R., Demeautis C., Matter D., Waelchli N., Revaz Y., Klotz A., Rieugné M., Thierry P., Cotrez V., Brunetto L., and Kober G. (2006) Photometric survey of binary near-Earth asteroids. *Icarus*, 181(1), 63–93.
- Pravec P., Harris A. W., Vokrouhlický D., Warner B. D., Kusnirák P., Hornoch K., Pray D. P., Higgins D., Oey J., Galad A., Gajdos S., Kornoš L., Vilagi J., Husarik M., Krugly Y. N., Shevchenko V. S., Chiorny V., Gaftonyuk N. M., Cooney W. R. Jr., Gross J., Terrell D., Stephens R. D., Dyvig R., Reddy V., Ries J. G., Colas F., Lecacheux J., Durkee R., Masi G., Koff R. A., and Goncalves R. (2008) Spin rate distribution of small asteroids. *Icarus*, 197(2), 497–504.
- Pravec P., Vokrouhlický D., Polishook D., Scheeres D. J., Harris A. W., Galad A., Vaduvescu O., Pozo F., Barr A., Longa P., Vachier F., Colas F., Pray D. P., Pollock J., Reichtart D. E., Ivarsen K. M., Haislip J. B., Lacluyze A. P., Kusnirák P., Henych T., Marchis F., Macomber B., Jacobson S. A., Krugly Y. N., Sergeev A. V., and Leroy A. (2010) Formation of asteroid pairs by rotational fission. *Nature*, 466(7), 1085–1088.
- Pravec P., Scheirich P., Vokrouhlický D., Harris A. W., Kusnirák P., Hornoch K., Pray D. P., Higgins D., Galad A., Vilagi J., Gajdos S., Kornoš L., Oey J., Husarik M., Cooney W. R. Jr., Gross J., Terrell D., Durkee R., Pollock J., Reichtart D. E., Ivarsen K. M., Haislip J. B., Lacluyze A. P., Krugly Y. N., Gaftonyuk N. M., Stephens R. D., Dyvig R., Reddy V., Chiorny V., Vaduvescu O., Longa-Peña P., Tudorica A., Warner B. D., Masi G., Brinsfield J., Goncalves R., Brown P., Krzeminski Z., Gerashchenko O., Shevchenko V. S., Molotov I. E., and Marchis F. (2012) Binary asteroid population. 2. Anisotropic distribution of orbit poles of small, inner main-belt binaries. *Icarus*, 218(1), 125–143.
- Pravec P., Kusnirák P., Hornoch K., Galad A., Krugly Y. N., Chiorny V., Inasaridze R. Y., Kvaratskhelia O. A., Ayvazian V., Parmonov O., Pollock J., Mottola S., Oey J., Pray D., Zizka J., Vraštil J., Molotov I. E., Reichtart D. E., Ivarsen K. M., Haislip J. B., and Lacluyze A. P. (2013) (8306) Shoko. *IAU Circular* 9268, 1.
- Radzievskii V. V. (1952) A mechanism for the disintegration of asteroids and meteorites. *Astron. Zh.*, 29, 162–170.
- Richardson D. C. and Walsh K. J. (2006) Binary minor planets. *Annu. Rev. Earth Planet. Sci.*, 34, 47–81.
- Richardson D. C., Bottke W. F., and Love S. G. (1998) Tidal distortion and disruption of Earth-crossing asteroids. *Icarus*, 134(1), 47–76.
- Richardson D. C., Leinhardt Z. M., Melosh H. J., Bottke W. F., and Asphaug E. (2002) Gravitational aggregates: Evidence and evolution. In *Asteroids III* (W. F. Bottke Jr. et al., eds.), pp. 501–515. Univ. of Arizona, Tucson.
- Richardson D. C., Elankumaran P., and Sanderson R. E. (2005) Numerical experiments with rubble piles: Equilibrium shapes and spins. *Icarus*, 173(2), 349–361.
- Rossi A., Marzari F., and Scheeres D. J. (2009) Computing the effects of YORP on the spin rate distribution of the NEO population. *Icarus*, 202(1), 95–103.
- Rozitis B. and Green S. F. (2012) The influence of rough surface thermal-infrared beaming on the Yarkovsky and YORP effects. *Mon. Not. R. Astron. Soc.*, 423(1), 367–388.
- Rozitis B. and Green S. F. (2013a) The influence of global self-heating on the Yarkovsky and YORP effects. *Mon. Not. R. Astron. Soc.*, 433(1), 603–621.
- Rozitis B. and Green S. F. (2013b) The strength and detectability of the YORP effect in near-Earth asteroids: A statistical approach. *Mon. Not. R. Astron. Soc.*, 430(2), 1376–1389.
- Rozitis B., MacLennan E., and Emery J. P. (2014) Cohesive forces prevent the rotational breakup of rubble-pile asteroid (29075) 1950 DA. *Nature*, 512(7), 174–176.
- Rubincam D. P. (2000) Radiative spin-up and spin-down of small asteroids. *Icarus*, 148(1), 2–11.
- Sánchez D. P. and Scheeres D. J. (2011) Simulating asteroid rubble piles with a self-gravitating soft-sphere distinct element method model. *Astrophys. J.*, 727(2), 120.
- Sánchez D. P. and Scheeres D. J. (2012) DEM simulation of rotation-induced reshaping and disruption of rubble-pile asteroids. *Icarus*, 218(2), 876–894.
- Sánchez D. P. and Scheeres D. J. (2014) The strength of regolith and rubble pile asteroids. *Meteoritics & Planet. Sci.*, 49(5), 788–811.
- Scheeres D. J. (2004) Bounds on rotation periods of disrupted binaries in the full 2-body problem. *Cel. Mech. Dyn. Astron.*, 89(2), 127–140.
- Scheeres D. J. (2007a) Rotational fission of contact binary asteroids. *Icarus*, 189, 370.
- Scheeres D. J. (2007b) The dynamical evolution of uniformly rotating asteroids subject to YORP. *Icarus*, 188(2), 430–450.
- Scheeres D. J. (2009) Stability of the planar full 2-body problem. *Cel. Mech. Dyn. Astron.*, 104(1), 103–128.
- Scheeres D. J. (2015) Landslides and mass shedding on spinning spheroidal asteroids. *Icarus*, 247, 1–17.
- Scheeres D. J., Fahnestock E. G., Ostro S. J., Margot J.-L., Benner L. A. M., Broschart S. B., Bellerose J., Giorgini J. D., Nolan M. C., Magri C., Pravec P., Scheirich P., Rose R., Jurgens R. F., De Jong E. M., and Suzuki S. (2006) Dynamical configuration of binary near-Earth asteroid (66391) 1999 KW4. *Science*, 314(5), 1280–1283.
- Scheeres D. J., Abe M., Yoshikawa M., Nakamura R., Gaskell R. W., and Abell P. A. (2007) The effect of YORP on Itokawa. *Icarus*, 188, 425.
- Scheeres D. J., Hartzell C. M., Sánchez D. P., and Swift M. (2010) Scaling forces to asteroid surfaces: The role of cohesion. *Icarus*, 210(2), 968–984.
- Scheirich P. and Pravec P. (2009) Modeling of lightcurves of binary asteroids. *Icarus*, 200(2), 531–547.
- Scheirich P., Pravec P., Jacobson S. A., Ďurech J., Kusnirák P., Hornoch K., Mottola S., Mommert M., Hellmich S., Pray D., Polishook D., Krugly Y. N., Inasaridze R. Y., Kvaratskhelia O. I., Ayvazian V., Slyusarev I., Pittichová J., Jehin E., Manfroid J., Gillon M., Galad A., Pollock J., Licandro J., Ali-Lagoa V., Brinsfield J., and Molotov I. E. (2015) The binary near-Earth asteroid (175706) 1996 FG3 — An observational constraint on its orbital evolution. *Icarus*, 245, 56–63.

- Schwartz S. R., Richardson D. C., and Michel P. (2012) An implementation of the soft-sphere discrete element method in a high-performance parallel gravity tree-code. *Granular Matter*, 14(3), 363–380.
- Sharma I. (2009) The equilibrium of rubble-pile satellites: The Darwin and Roche ellipsoids for gravitationally held granular aggregates. *Icarus*, 200(2), 636–654.
- Shepard M. K., Margot J.-L., Magri C., Nolan M. C., Schlieder J., Estes B., Bus S. J., Volquardsen E. L., Rivkin A. S., Benner L. A. M., Giorgini J. D., Ostro S. J., and Busch M. W. (2006) Radar and infrared observations of binary near-Earth asteroid 2002 CE26. *Icarus*, 184(1), 198–210.
- Sheppard S. S. and Trujillo C. (2015) Discovery and characteristics of the rapidly rotating active asteroid (62412) 2000 SY178 in the main belt. *Astron. J.*, 149(2), 44.
- Singer S. F. (1968) The origin of the Moon and geophysical consequences. *Geophys. J. R. Astron. Soc.*, 15(1–2), 205–226.
- Slivan S. M. (2002) Spin vector alignment of Koronis family asteroids. *Nature*, 419(6), 49–51.
- Statler T. S. (2009) Extreme sensitivity of the YORP effect to small-scale topography. *Icarus*, 202(2), 502–513.
- Steinberg E. and Sari R. (2011) Binary YORP effect and evolution of binary asteroids. *Astron. J.*, 141(2), 55.
- Taylor G. I. (1920) Tidal friction in the Irish Sea. *Philos. Trans. R. Soc. Ser. A*, 220, 1–33.
- Taylor P. A. and Margot J.-L. (2010) Tidal evolution of close binary asteroid systems. *Cel. Mech. Dyn. Astron.*, 108(4), 315–338.
- Taylor P. A. and Margot J.-L. (2011) Binary asteroid systems: Tidal end states and estimates of material properties. *Icarus*, 212(2), 661–676.
- Taylor P. A. and Margot J.-L. (2014) Tidal end states of binary asteroid systems with a nonspherical component. *Icarus*, 229, 418–422.
- Taylor P. A., Margot J.-L., Vokrouhlický D., Scheeres D. J., Pravec P., Lowry S. C., Fitzsimmons A., Nolan M. C., Ostro S. J., Benner L. A. M., Giorgini J. D., and Magri C. (2007) Spin rate of asteroid (54509) 2000 PH5 increasing due to the YORP effect. *Science*, 316(5), 274–277.
- Taylor P. A., Margot J.-L., Nolan M. C., Benner L. A. M., Ostro S. J., Giorgini J. D., and Magri C. (2008) The shape, mutual orbit, and tidal evolution of binary near-Earth asteroid 2004 DC. In *Asteroids, Comets, Meteors 2008*, Abstract #8322. Lunar and Planetary Institute, Houston.
- Taylor P. A., Warner B. D., Magri C., Springmann A., Nolan M. C., Howell E. S., Miller K. J., Zambrano-Marin L. F., Richardson J. E., Hannan M., and Pravec P. (2014) The smallest binary asteroid? The discovery of equal-mass binary 1994 CJ1. *AAS/Division for Planetary Sciences Meeting Abstracts*, 46, #409.03.
- Vokrouhlický D. (2009) (3749) Balam: A very young multiple asteroid system. *Astrophys. J. Lett.*, 706(1), L37–L40.
- Vokrouhlický D. and Čapek D. (2002) YORP-induced long-term evolution of the spin state of small asteroids and meteoroids: Rubincam's approximation. *Icarus*, 159(2), 449–467.
- Vokrouhlický D. and Nesvorný D. (2008) Pairs of asteroids probably of a common origin. *Astron. J.*, 136(1), 280–290.
- Vokrouhlický D. and Nesvorný D. (2009) The common roots of asteroids (6070) Rheinland and (54827) 2001 NQ8. *Astron. J.*, 137(1), 111–117.
- Vokrouhlický D., Nesvorný D., and Bottke W. F. (2003) The vector alignments of asteroid spins by thermal torques. *Nature*, 425(6), 147–151.
- Vokrouhlický D., Brož M., Bottke W. F., Nesvorný D., and Morbidelli A. (2006) Yarkovsky/YORP chronology of asteroid families. *Icarus*, 182(1), 118–142.
- Vokrouhlický D., Ďurech J., Polishook D., Krugly Y. N., Gaftonyuk N. N., Burkhanov O. A., Ehgamberdiev S. A., Karimov R., Molotov I. E., Pravec P., Horoch K., Kusnirák P., Oey J., Galad A., and Žížka J. (2011) Spin vector and shape of (6070) Rheinland and their implications. *Astron. J.*, 142(5), 159.
- Walsh K. J. and Richardson D. C. (2006) Binary near-Earth asteroid formation: Rubble pile model of tidal disruptions. *Icarus*, 180, 201.
- Walsh K. J. and Richardson D. C. (2008) A steady-state model of NEA binaries formed by tidal disruption of gravitational aggregates. *Icarus*, 193, 553.
- Walsh K. J., Richardson D. C., and Michel P. (2008) Rotational breakup as the origin of small binary asteroids. *Nature*, 454(7), 188–191.
- Walsh K. J., Richardson D. C., and Michel P. (2012) Spin-up of rubble-pile asteroids: Disruption, satellite formation, and equilibrium shapes. *Icarus*, 220(2), 514–529.
- Warner B. D. and Harris A. W. (2007) Lightcurve studies of small asteroids. *Bull. Am. Astron. Soc.*, 39, 432.
- Warner B. D., Harris A. W., and Pravec P. (2009) The asteroid lightcurve database. *Icarus*, 202(1), 134–146.
- Warner B. D., Pravec P., Kusnirák P., Horoch K., Harris A. W., Stephens R. D., Casulli S., Cooney, W. R. Jr., Gross J., Terrell D., Durkee R., Gajdos S., Galad A., Kornos L., Toth J., Vilagi J., Husarik M., Marchis F., Reiss A. E., Polishook D., Roy R., Behrend R., Pollock J., Reichart D., Ivarsen K. M., Haislip J., Lacluyze A. P., Nysewander M. C., Pray D. P., and Vachier F. (2010) A trio of Hungaria binary asteroids. *Minor Planet Bull.*, 37, 70–73.
- Weidenschilling S. J., Paolicchi P., and Zappalá V. (1989) Do asteroids have satellites? In *Asteroids II* (R. P. Binzel et al., eds.), pp. 643–658. Univ. of Arizona, Tucson.



*Part 3:*

*Space Missions*



# Hayabusa Sample Return Mission

**Makoto Yoshikawa, Junichiro Kawaguchi, and Akira Fujiwara**  
*Japan Aerospace Exploration Agency*

**Akira Tsuchiyama**  
*Kyoto University*

---

Hayabusa was the first asteroid sample return mission. It was launched in May 2003, and arrived at the target asteroid (25143) Itokawa in September 2005. The mission enabled us to see close up a very tiny asteroid in detail for the first time. Hayabusa observed Itokawa with its scientific instruments, and attempted to collect surface material. The mission experienced several serious problems, but successfully returned to Earth in June 2010. After retrieving the capsule, we found thousands of small grains that had been captured from the asteroid. We studied Itokawa in detail with both the remote sensing data and the returned samples, which revealed a great deal of new information to shed light on its origin. In this chapter, we review the Hayabusa mission and summarize the scientific results.

## 1. INTRODUCTION

Hayabusa, the world's first asteroid sample return mission, was built and launched by the Institute of Space and Astronautical Science (ISAS), which was later merged with the Japan Aerospace Exploration Agency (JAXA). The project code name was MUSES-C, and after launch in May 2003 was given the name "Hayabusa," which literally translates to "falcon." Hayabusa arrived at its target asteroid in September 2005, and returned to Earth in June 2010. The main purpose of the mission was to demonstrate the key technologies required for future planetary missions. Hayabusa made a roundtrip flight to a celestial object outside of Earth's gravity sphere. The voyage, however, entailed many hardships, most of which were not anticipated before launch, but Hayabusa successfully returned surface material from the asteroid.

Hayabusa was also the first spacecraft to explore a sub-kilometer-sized asteroid. The target asteroid was the S-type near-Earth asteroid (25143) Itokawa, about 500 m in length. Hayabusa revealed the strange nature of Itokawa by observing it with its remote sensing instruments in 2005. Although the amount of sample from Itokawa was quite small, the analyses of the returned samples have been continued worldwide after the capsule returned to Earth in 2010, and much new information has been gained from this sample analysis.

In this chapter, we first explain the mission description as originally conceived and provide a flight summary, including what anomalies occurred and how the project team coped with those anomalies during the flight. The science results are then summarized in section 3 for remote sensing observations and in section 4 for sample analyses.

## 2. HAYABUSA MISSION DESCRIPTION AND FLIGHT RESULTS

### 2.1. Mission Objectives

The Hayabusa project was primarily a technology demonstration for future sample-return attempts from primitive bodies such as comets and asteroids (Kawaguchi, 1986, 2003; Kawaguchi et al., 2002).

The spacecraft lifted off on May 9, 2003, onboard an M-V vehicle from Uchinoura, Japan. It performed an Earth swing-by the following May. The mission plan adopted by Hayabusa was a little different from that taken by such missions as Rosetta, whose efforts were concentrated on the *in situ* analysis of the surface material of a comet. Instead of delivering the analysis equipment, the Hayabusa project intended to return a small amount of the surface sample to Earth, where large state-of-the-art facilities are available for detailed analysis. According to the original scenario, the spacecraft was to jettison a small reentry capsule in June 2007, when it would have returned back to Earth. The flight period scheduled was approximately four years. However, as this chapter describes later, due to unexpected incidents, the flight was extended and it actually returned home on June 13, 2010, resulting in a flight duration of seven years.

Hayabusa carried five key technology objectives to be demonstrated: (1) interplanetary cruise via ion engines as primary propulsion, (2) autonomous navigation and guidance using optical measurements, (3) sample collection from the asteroid surface under microgravity, (4) direct reentry for sample recovery from interplanetary orbit, and (5) combination of

low thrust and gravity assist. In addition to these, Hayabusa also carried other new technologies, such as a bi-propellant small thrust reaction control system (20N), X-band up/down communication, complete Consultative Committee for Space Data Systems (CCSDS) packet telemetry, duty guaranteed heater control electronics, wheel unloading via ion engines, pseudo-noise (PN) code ranging, lithium ion rechargeable battery, multi-junction solar cell, etc.

The development of Hayabusa was proposed to the government in 1995, and the project began in 1996. The original target asteroid was the near-Earth asteroid (4660) Nereus and the backup target was another near-Earth asteroid, (10302) 1989 ML. However, when the spacecraft development started, the project faced mass capability issues and Nereus was replaced by 1989 ML as the primary target body. In 2000, a launch mishap occurred as the result of a launcher propulsion element flaw. As a result, the launch of MUSES-C was shifted half a year and the target asteroid was again switched to a different object, the near-Earth asteroid (25143) 1998 SF<sub>36</sub>, which was renamed Itokawa after Hayabusa's launch. It should be noted that there were only a very few objects for which sampling and return opportunities were possible. While there were a great number of known asteroids, the number of those for which a low-energy mission scenario could be employed was approximately 10 to 20.

In contrast to Nereus and 1989 ML, the new mission target was found to be accessible only via an Earth gravity assist due to the low thrust propulsion of the spacecraft. This technique is what is known as the Electric Delta-V Earth Gravity Assist (EDVEGA) strategy, and was first devised by the ISAS of JAXA. It is the most efficient way of accelerating a spacecraft from Earth when electric or low-thrust propulsion is used. The Hayabusa spacecraft was the first demonstration of the EDVEGA technology (Kawaguchi *et al.*, 2004). The first year after launch was devoted to acceleration in the vicinity of Earth. The EDVEGA phase was followed by the transfer phase, which took approximately one year, and the spacecraft arrived at asteroid Itokawa in the summer of 2005 (Fig. 1). The spacecraft's return was originally planned to occur in June 2007, and the mission should have been completed in four years. However, as a result of numerous difficulties, the flight was extended to seven years and it finally returned in June 2010.

## 2.2. The Hayabusa Spacecraft System

**2.2.1. Configuration.** Hayabusa was a small probe whose dimensions were 1.0 m × 1.6 m × 1.1 m, with a total weight (wet mass) of 510 kg, including 70 kg of chemical fuel for the reaction control system (RCS) and 60 kg of Xe propellant for the ion engines. The relatively large solar array generated 2.6 kW of electric power at Earth. The top and bottom views of the Hayabusa spacecraft are shown in Fig. 2. It was a three-axis stabilized spacecraft with a fixed high-gain antenna (HGA) and solar array panel (SAP). Most of the instruments were on the bottom of the spacecraft so they could be pointed to the asteroid surface when the spacecraft descended and

touched down on the surface. The ion engine thruster apertures were located on a side panel (+X panel), while the reentry capsule and star tracker were on the -X panel.

The ion engine system adopted consisted of four thruster heads located on a two-axis gimbal plate so that the thrust could always penetrate the center of gravity and the attitude could eliminate the disturbance torque. On both ±X panels there were medium-gain antennas (MGA) that enabled the spacecraft to communicate with ground stations while the ion engines were turned on, and the HGA was not pointed to Earth. There was a sample collection horn that extended down from the -Z panel. The -X panel was the surface that was not supposed to be illuminated by the Sun, while the +X panel could be exposed to the Sun to a certain extent. The HGA was basically the same as that on the ISAS Mars Exploration spacecraft Nozomi, and its diameter was 1.6 m. The communication system adopted X-band for both up and down links. During the EDVEGA phase, since the distance from the Sun decreased below 1 AU, the HGA was painted white for thermal control. There was a Sun angle sensor and a low-gain antenna (LGA) at the top of the HGA.

**2.2.2. Special ion engines adopted.** The special characteristics of the ion engines onboard Hayabusa were (1) the use of microwave discharge to generate plasma and (2) the use of a carbon-carbon (CC) composite for the grids. Since there were no electrodes in the system, the life of the thruster was greatly extended to 18,000 hours.

**2.2.3. Autonomous descent and touchdown.** When the spacecraft made its initial approach to the surface of Itokawa, it jettisoned a target marker that served as an artificial landmark, illuminated by a flash lamp onboard the spacecraft once every second so that the optical navigation camera (ONC) could detect the marker by subtracting two images,

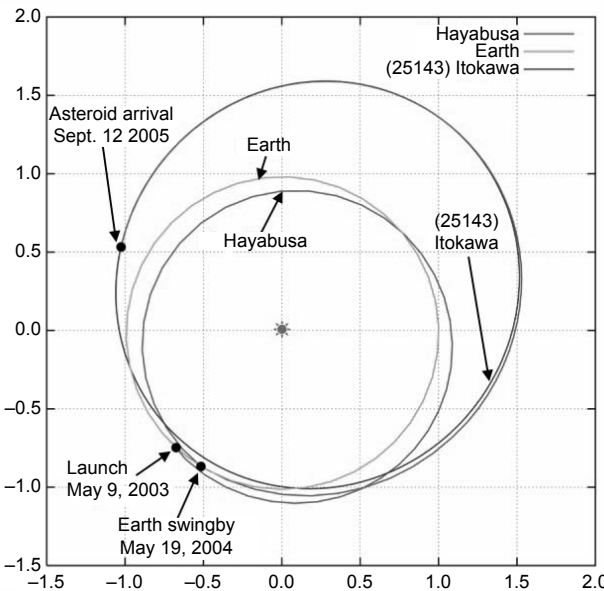


**Fig. 1.** Orbit of Hayabusa from launch to asteroid arrival. The EDVEGA phase was from launch to Earth swingby, and the transfer phase was from Earth swingby to asteroid arrival.

one that was illuminated by a lamp and the other that was not illuminated. The primary purpose of the target marker was to enable the spacecraft to autonomously identify lateral velocity. As is often the case with soft landing, the horizontal velocity detection and control is always key, while the vertical navigation and control is less difficult. The spacecraft then stopped RCS firings and touchdown was performed in a free-fall manner in order to avoid surface contamination.

**2.2.4. Sample collection device.** The sample collection was designed to be performed in a very unique manner, and depended upon the motion of fragments when a projectile impacts a surface in a vacuum in microgravity. The mission designers decided to avoid the problems of anchoring and drilling. Instead, the Hayabusa mission adopted ejecta collection via a projectile shot, which can cope with a variety of surface conditions, even sand, and collect sufficient samples for detailed analysis in a rapid manner.

In the adopted sampling technique, the ejected fragments are guided through a funnel-like device, the sampler horn. The device was deployed immediately after the spacecraft was in orbit. The length of the horn was  $\sim 1$  m, sufficient to prevent the tip of the SAP from hitting the asteroid's surface. The design called for the ejected sample to reach the canister, which would be pushed into the reentry capsule for recovery. The expected collected sample amount was approximately less than 1 g. The main advantage of sample return is that a very small sample is adequate.

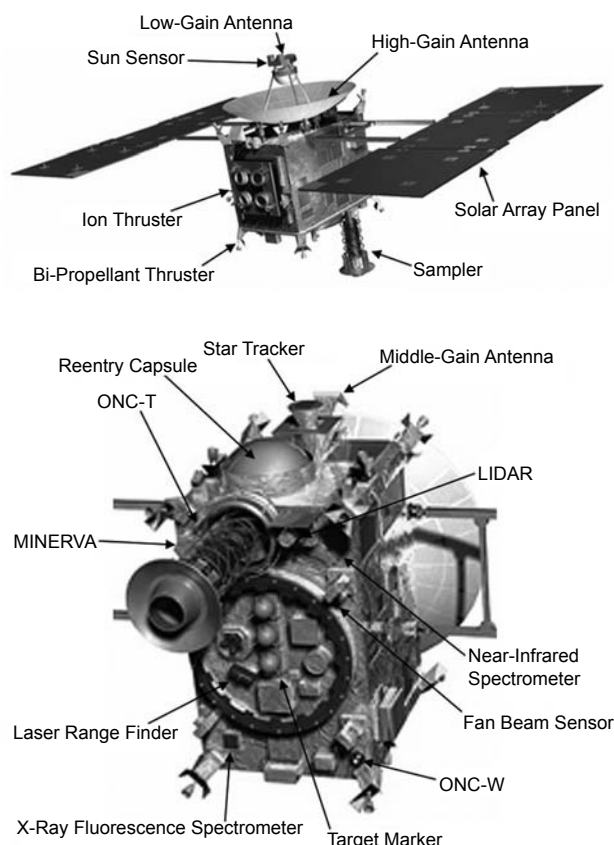


**Fig. 2.** Diagram of the Hayabusa spacecraft and its instruments.

**2.2.5. Sample recovery capsule and its operation.** When the spacecraft returned to Earth, since the trajectory's incoming asymptote would point to the southern hemisphere so that the reentry flight path angle remained shallow, the reentry point needed to be in the southern hemisphere. Otherwise, the reentry would become steep and the heat flux experienced would become too high for successful recovery. As a result, the recovery location was situated in the Woomera Prohibited Area in Southern Australia.

The diameter of the capsule was 400 mm and weighed about 20 kg. The reentry capsule consisted of the thermal protection shield, structure, sample container, and sequencer, including the beacon transmitter. The heat shield shells consisted of forward and aft shells that were designed to be separated from the instrument section when the parachute deployed. The development of the heat shield was one of the most critical issues in the Hayabusa project. ISAS built an arc-heating test facility and also performed heating experiments at the NASA Ames Research Center in collaboration with NASA.

### 2.3. Summary of Incidents and Difficulties

The spacecraft was launched in May 2003. From the beginning, the flight was not easy and experienced many unfortunate events. The spacecraft experienced the largest solar flare that had ever happened, consequently resulting in degradation of a solar cell, eventual loss of two out of the three reaction wheels, a fuel gas eruption and consequent loss of attitude, loss of communication with the ground for seven weeks, loss of the lithium ion battery during loss of attitude, loss of the onboard chemical engines, the gradual loss of ion engines and loss of three out of the four neutralizers, and failure of the sample collector. The most significant critical events occurred when the spacecraft got lost after the completion of the second touchdown to the surface of asteroid Itokawa at the end of 2005, and when the spacecraft's ion engine shut down due to the end of life associated with the neutralizer six months prior to the return to Earth.

**2.3.1. Proximity operation and descent and touchdown sampling.** After the spacecraft arrived at the home position located 20 km above the asteroid's surface, the spacecraft conducted a mapping and imaging operation for more than a month. The spacecraft utilized asteroid gravity along with RCS firings to move up and down and side to side. Shape modeling of the asteroid was done during this period.

The spacecraft then performed practice descent maneuvers to practice and confirm the touchdown scenario. During this period the spacecraft released a surface robot, the Micro/Nano Experimental Robot Vehicle Asteroid (MINERVA), aiming it at the asteroid's surface. However, due to the very subtle but inaccurate ground-control operation, MINERVA was not accurately released, and it was traveling away from the asteroid. Thus the MINERVA operation largely failed, but the relay capability was successful and a photo of the solar paddle of Hayabusa taken by MINERVA was relayed back to the ground.

A sophisticated autonomous maneuver was successfully performed when Hayabusa performed its first touchdown attempt on November 20, 2005. At the first touchdown, after releasing a target marker, the spacecraft detected the marker and everything seemed ready for shooting a projectile. However, the spacecraft-carried obstruction detection sensor detected a reflection from some small particles, probably aloft above the surface, and the sample collection shot was not directed. The spacecraft bounced a few times and it settled down on the surface near the polar region waiting for commands from the ground for almost 30 minutes. The spacecraft lifted off when the emergency lift command was sent from the ground.

The second touchdown was attempted on November 25, 2005. During this attempt, a new target marker was not deployed because of the possibility that the spacecraft could detect two target markers at the same time, resulting in confusion. The guidance accuracy was well developed and the expected landing accuracy was sufficiently high. The spacecraft clearly photographed the target marker placed one week before when the spacecraft made its first touchdown (Fig. 3). The spacecraft touched down as planned and the projectile shot was directed from the inboard computer, and the sampling was thought at first to have been performed perfectly. However, it was revealed later that the shooting pyro control circuit was turned to safe mode and the projectile was not fired. Fortunately, the recovered capsule carried back many particles that must have been caught by static electricity when the spacecraft descended to the surface two times.

**2.3.2. Leak of reaction control system fuel.** When the spacecraft made a successful landing on the surface and lifted off from there on November 25, 2005, firing RCS thrusters on the top panel to decelerate the ascent speed, one of the thrusters began leaking fuel. This caused the

spacecraft to be placed in safe-hold mode. All the hydrazine leaked out, and the RCS became unusable for the remainder of the mission. Another large gas eruption made the spacecraft tumble, and beginning in December 2005, radio communication was lost for seven weeks.

### 2.3.3. Resumption of communication and restoration.

The tumbling precluded solar power and the spacecraft power was turned completely off. The onboard battery probably maintained the system for approximately 40 minutes, but it was probably dead after that. The project team developed a rescue operation plan to wake up the spacecraft. Fortunately, the spacecraft was designed to settle into a single spin motion around the maximum moment of inertia, the Z-axis. Once the gas eruption stopped, the attitude settled into a single spin whose rotation axis was fixed to a particular direction with respect to the background sky. There was a chance for the spacecraft to acquire solar power together with the omni-antenna aperture open toward Earth. The probability of this was calculated to be up to 60–70% during the following year. The project team devised the operation so that the command could be heard at any high spin rate, at any attitude, regardless of any antenna profile gaps. The ground team continued to monitor the spacecraft, hoping to receive any signal. The miracle occurred at the end of January 2006, when a carrier signal was finally received by JAXA's deep space antenna. The spacecraft was rotating in the opposite spin direction because of the gas eruption torque. The spin rate was high, and the radio signal was intermittent.

**2.3.4. Recovery operation.** The project team began recovery operations immediately. The biggest challenge was how to reorient the spacecraft attitude to Earth with the lowered spin motion. The operation started by initial Sun acquisition using the coarse Sun sensor. Ion engines were used to decelerate the spin motion by exhausting Xe gas with no electric acceleration. It took five months to properly correct the spacecraft attitude. There was the constant threat of loss of solar power, since the spacecraft spin direction was frozen in the inertial frame and the Sun direction shifts 90° over three months. The operation also had severe time constraints, and thus the project team gave up on the goal of the spacecraft returning in 2007. Instead, the project team amended the flight sequence, and decided to have it return in 2010.

**2.3.5. Auto-Sun tracking with no fuel.** While the spacecraft was restored and telemetry was again being received, the biggest anticipated obstacle was how to perform the attitude control to make sure the spacecraft was appropriately pointed toward the Sun while at the same time making sure that the apertures of its ion engines are properly pointed to the intended direction with no fuel. Hayabusa was equipped with ion engines independent of RCS and carried an additional propulsion system, even though the thrust was very weak and was never really intended for impulsive maneuvers. With the gimballed table on which ion engines were mounted, the angular momentum of the spacecraft was managed in the Y- and Z-axes. Since the ion engine thrust was along the X-axis, no propulsion torque was available



**Fig. 3.** Hayabusa's shadow on the surface during the second touchdown. The white dot in the circle is the target marker released during the first touchdown.

around that axis, and therefore the project team came up with another new strategy. It used solar radiation torque to maintain the spacecraft spin direction, keeping it automatically pointed toward the Sun like an arrow in the wind.

**2.3.6. Ion engine end of life and cross-connection of engines.** The spacecraft's ion engine drive performed successfully from 2007 to till 2009. However, the engines reached the end of their life in November 2009, when all four engines became inoperable due to the death of the neutralizers. Among the four engines, three neutralizers were broken and it was therefore not possible to extract electrons from them. However, there was a single intact neutralizer left, Neutralizer A. Engine A had remained undriven since launch, since a problem was discovered in its radio frequency cable, and the ion source A did not work well and had been left unused. Engine A was still not usable, but the decision was made to use its neutralizer combined with ion sources B, C, and D, even though the engines were not designed to function in such a cross-connection configuration. Thus the project team found that they could successfully drive engine B with neutralizer A, which allowed was a miraculous restoration of the propulsion system.

**2.3.7. Guidance via ion engines.** The consecutive ion engine cruise lasted until the end of March 2010. The reentry required accurate trajectory corrections. These were applied in five segments, from April to June 2010, with the goal of reentry on June 13, 2010. The trajectory correction maneuvers (TCMs) actually took 250 h 46 min 40 s just for  $13.54 \text{ m s}^{-1} \Delta V$ . There was a stringent attitude constraint in Hayabusa. The ion engine heads were aligned to the X-axis only, while the power source solar array panels were fixed to the Z-axis. Orbital control via ion engines only was a big challenge.

**2.3.8. Capsule reentry and recovery.** The project team had performed the successive TCMs via ion engine operation. The final maneuver, TCM 4, was performed to accurately target the touchdown point within the recovery area where the ground staff was deployed to locate the capsule landing point via radio signal. The anticipated accuracy was within several kilometers.

On June 13, 2010, Hayabusa returned to Earth, and a small reentry capsule containing the asteroid sample separated from the spacecraft three hours prior to its own reentry. Hayabusa plunged into the atmosphere over the Australian desert (Fig. 4). The deployment of the parachute was designed to be triggered by not only a given time, but also by the peak acceleration detected onboard, whichever occurred first.

The primary capsule detection system consisted of three sets of double UHF antenna arrays that precisely identified the signal direction. The combination of the signal confirmed the possible landing area within 5–10 km, and a helicopter was used to find the sample return container. The capsule was discovered within 30 minutes of reentry, about 500 m from the presumed location. The recovered capsule was placed inside a special container filled with nitrogen and shipped to Japan for sample removal (Kawaguchi, 2010a,b; Kawaguchi et al., 2011).



**Fig. 4.** Hayabusa's reentry into Earth's atmosphere.

**2.3.9. Remarks.** The Hayabusa mission presented a huge challenge that had never before been achieved. For seven years the Hayabusa mission was plagued with incidents and mishaps, but the mission team and engineers maintained their spirit and commitment to bringing the spacecraft safely home.

### 3. RESULTS OBTAINED BY IN SITU OBSERVATION

#### 3.1. Global Properties of (25143) Itokawa

Itokawa measures  $535 \times 294 \times 209$  m, and has a mean diameter of 320 m, a spin period of 12.1 h, a density of  $1.9 \text{ g cm}^{-3}$ , and revolves with retrograde rotation. More detailed information is given by Fujiwara et al. (2006). The mean diameter is in good agreement with the value obtained by groundbased mid-infrared (Sekiguchi et al., 2003) and radar observations (Ostro et al., 2004, 2005; see the chapter by Benner et al. in this volume). The pre-arrival results from groundbased observations of the rotation period and spin direction (retrograde rotation, perpendicularity of the spin axis to the ecliptic), along with its spectral type (Binzel et al., 2001; Dermawan et al., 2002; Kaasalainen et al., 2003; Ohba et al., 2003; Ostro et al., 2004, 2005; Lowry et al., 2005; see the chapter by Li et al. in this volume), were confirmed by the more detailed data obtained by Hayabusa. There is no apparent short-term precession of the spin pole, which shows that enough time has passed for the asteroid to be dynamically relaxed after the last large impact event.

No satellites were found by the Asteroid Multi-band Imaging Camera (AMICA) (also called ONC-T, one of the optical navigation cameras) images (Fuse et al., 2008), which is consistent with past optical and radar observations and not inconsistent with the suggestion of the existence of meteoroids related with Itokawa from groundbased observations (Otsuka et al., 2011), although none were directly observed by the spacecraft.

The mass of the asteroid was estimated from Hayabusa tracking and navigation. Using lidar (light radar) data (Abe et al., 2006b; Mukai et al., 2007), as well as navigation data, and considering the effects of attitude maneuvers, the mass was determined to be  $3.51 \times 10^{10} \text{ kg}$ . Coupled with the volume of Itokawa, estimated from the three-dimensional

shape models (*Demura et al.*, 2006), the bulk density of Itokawa is estimated to be  $1.9 \text{ g cm}^{-3}$ .

Itokawa has a bifurcated shape like a floating sea otter (Figs. 5, 6, and 7). The smaller part is called the “head” and the larger part is called the “body.” In the attitude of Fig. 6, south is up and north is down due to retrograde rotation. The overall shape of both parts is not angular like the asteroid (951) Gaspra (*Everka et al.*, 1994), but rather rounded and there is no global lineament as seen on (433) Eros (*Cheng et al.*, 2007). The size of the ellipsoid fitted to the body is  $490 \times 310 \times 260 \text{ m}$ , and that to the head is  $230 \times 200 \times 180 \text{ m}$ , respectively (*Demura et al.*, 2006). The appearance of the surface is different from any other asteroids so far observed by spacecraft, including (243) Ida, (253) Mathilde, and Eros, whose surfaces are globally covered with a thick regolith layer and many craters (*Chapman*, 2002), as seen even in images of Eros taken with scales comparable with Itokawa.

The surface of Itokawa is divided into two distinct types of terrain: *rough terrain*, consisting of numerous boulders, and *smooth terrain*, which shows the existence of a smoother regolith layer (see the chapter by Murdoch et al. in this volume). Rough terrain (see close-up view in Fig. 8) makes up ~80% of the surface (*Saito et al.*, 2006). The smooth terrain is distributed into two distinct regions: “MUSES-C,”

named for the wide region extending around the “breast” on the “body,” where the spacecraft landed for sampling, and “Sagamihara,” around the north-polar region near the “back” of the body. Close-up viewing of the MUSES-C Regio (Fig. 9) shows that the smooth terrain is composed of centimeter- to millimeter-scale fragmental debris and pebbles (*Yano et al.*, 2006). Most grains in the MUSES-C Regio are larger than those observed in the close-up view of Eros’ surface, and there is a strong depletion of fine grains on Itokawa compared with Eros. The boundaries between the rough and smooth terrains are relatively sharp, but a gradient of boulder number density and some evidence of movement of the surface material are evident (*Miyamoto et al.*, 2007).

### 3.2. Boulders

Most boulders are found in the rough terrain, while in the smooth terrain boulders appear buried by regolith. The average number density of boulders larger than  $5 \text{ m}$  is  $10^3 \text{ km}^{-2}$  (*Michikami et al.*, 2008), which is slightly larger than that on the surface of Eros (*Thomas et al.*, 2001). A black boulder is found at the top of the head, where the gravitational potential is the highest (Fig. 7), and which was assigned as the prime meridian (longitude  $0^\circ$ ) (*Fujiwara et al.*, 2006). This boulder measures ~6 m and has unusually low brightness, resulting in a striking contrast with its surroundings. Three other smaller similar boulders were also found (*Hirata and Ishiguro*, 2011).

The largest boulder, named Yoshinodai, is about  $50 \times 30 \times 20 \text{ m}$  in size (*Saito et al.*, 2006) and is located near the “right foot” of the “body” (Fig. 6). There are several boulders with sizes larger than a few tens of meters on the western side (longitude  $0^\circ$ – $180^\circ\text{W}$ ) while large boulders are less abun-

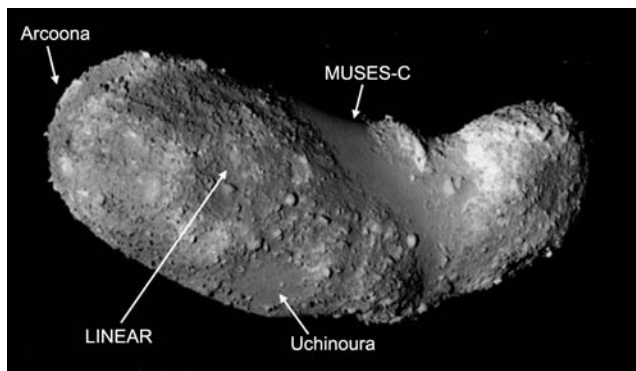


**Fig. 5.** Eastern side of Itokawa. The bottom is north. The spacecraft landed on the smooth terrain near MUSES-C.

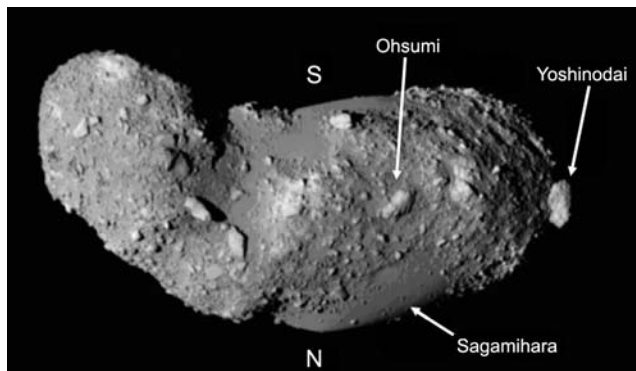


**Fig. 6.** Western side of Itokawa. On this side, large boulders are more abundant than on the eastern side. Yoshinodai is the largest boulder.

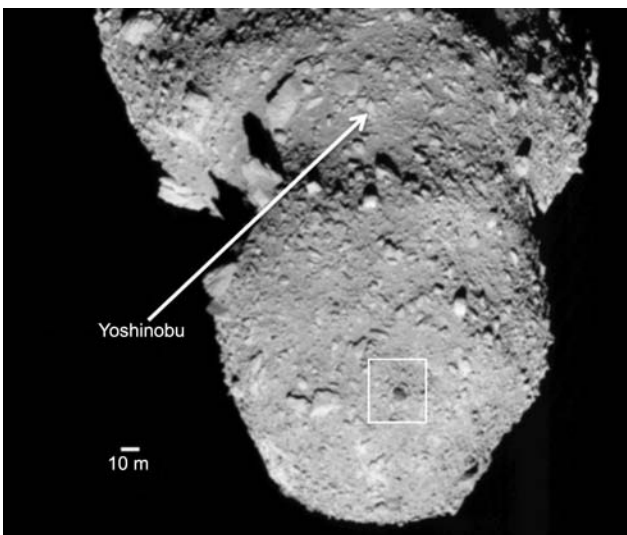


**Fig. 7.** “Back head” of Itokawa viewed from top. A large depression at the “neck” is Yoshinobu. On the top of the “head” a black boulder is evident (inside the square). Scale bar is 10 m.

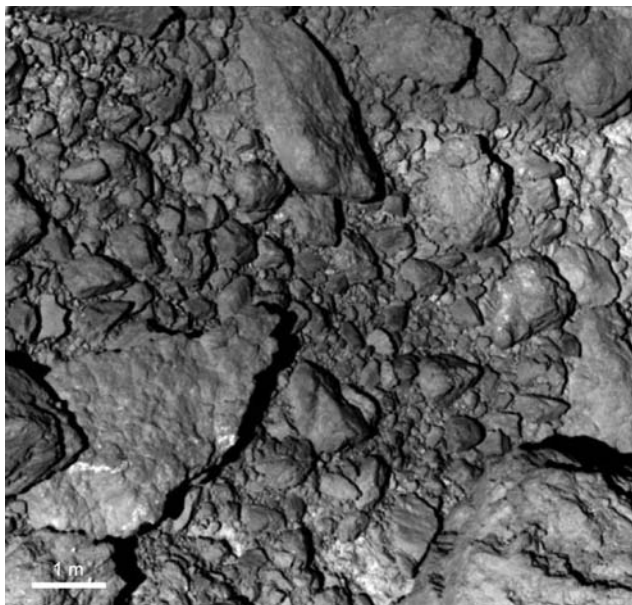


**Fig. 8.** Close-up view of rough terrain on Itokawa. Irregular plate-like fragments are characteristic of impact spalls.

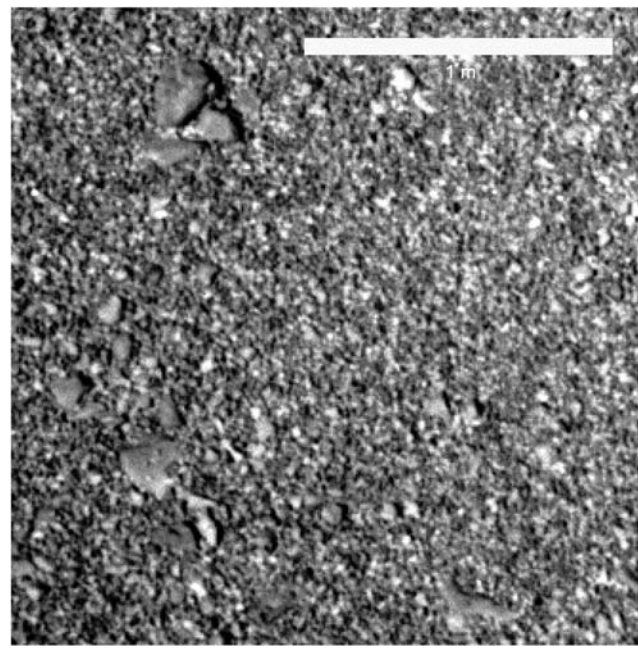


**Fig. 9.** Close-up view of MUSES-C Regio.

dant on the eastern side. There are several large pinnacles at the neck region on the western side (Fig. 6), believed to have resulted from landside from the higher gravitational potential of the “head” to the lower potential region of the “neck” to “breast” region.

An experimental relationship exists between the size of a crater and the maximum size of the excavated fragment (Gault *et al.*, 1963), which was confirmed observationally for the main-belt asteroid Ida and other asteroids (Lee *et al.*, 1996). These are also consistent with boulders around the Shoemaker crater on Eros (Thomas *et al.*, 2001). Following these empirical relationships, the size of the crater that would have produced the largest boulder, Yoshinodai, and some others actually exceeds the size of the largest crater candidates found on Itokawa. Hence these boulders are the likely relics formed in some cataclysmic event related to the formation of Itokawa’s current configuration.

The cumulative size distribution of boulders obtained by Michikami *et al.* (2008) is shown in Fig. 10. The slope index of the distribution is  $-3.1 \pm 0.1$ , which is comparable with the value of  $-3.2$  for the 15–80-m boulder size range on Eros (Thomas *et al.*, 2001). It should be noted that the index changes slightly depending on the measurement method, and in Michikami *et al.*’s (2008) work the size is defined as that measured horizontally. If the largest size is measured instead of horizontal size, the index is  $-2.8$  (Saito *et al.*, 2006). This is because larger boulders have longer or spall-like shapes, which suggests that those fragments are produced by impacts. Actually, this is consistent with the shape of many fragments observed on Itokawa’s surface (as shown in Fig. 8), which are very similar to those observed in some laboratory impact experiments (Nakamura *et al.*, 2008a; Michikami *et al.*, 2008). Morphological features

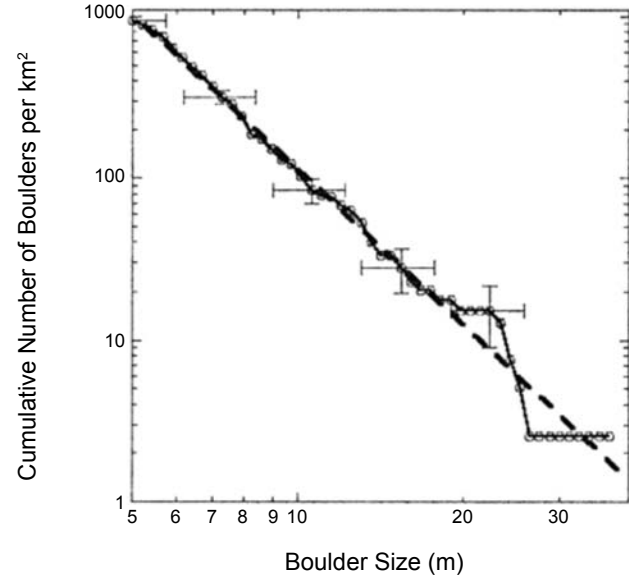


**Fig. 10.** Boulder size distribution on Itokawa (Michikami *et al.*, 2008). Size is defined as the mean horizontal dimension of a boulder. The broken line is a fitted regression line. The power-law index is  $-3.1 \pm 0.1$ .

of Itokawa boulders are also discussed by Noguchi *et al.* (2010). Mazrouei *et al.* (2014) performed a more detailed study of the size distribution of boulders greater than 6 m and showed that the slope index is  $-3.5$ , which is significantly steeper than the slope obtained by Michikami *et al.* (2008). A latitudinal variation of the block population also exists on the body, which may suggest that the asteroid is a composite of two different bodies (i.e., a binary asteroid).

The boulder density does not show a correlation with the crater density. The boulders exist regardless of the position of the craters. The total estimated volume of boulders is  $8.2 \times 10^4 \text{ m}^{-3}$ , and the ratio of boulder volume to crater volume is  $\sim 25\%$  (Michikami *et al.*, 2008). This value is higher than that obtained so far for other small bodies. For example, on Eros the ratio is less than 1% (Thomas *et al.*, 2001), and on the Moon it is  $\sim 5\%$  (Cintala *et al.*, 1982). Considering that Itokawa is very small and has a very low escape velocity (on the order of  $10 \text{ cm s}^{-1}$ ), boulders currently observed on Itokawa could not have been produced from the recent craters.

### 3.3. Craters

Many crater-like depressions are found on Itokawa, but most of them have a shape that does not make them as easily identified as craters as those found on the surface of other asteroids. Hirata *et al.* (2009) listed 38 crater candidates on Itokawa's surface (see the chapter by Marchi *et al.* in this volume): five candidates — Yoshinobu (Fig. 7), Arcoona, LINEAR, Uchinoura (Fig. 5), and Ohsumi (Fig. 6) — have diameters larger than 100 m, and the others are smaller than 100 m. Generally, most of the crater-like depressions are shallower than craters observed on the surface of other planetary bodies and asteroids. Large craters have flat or convex floors affected by the pre-impact local surface curvature as shown in laboratory impact experiments (Fujiwara, *et al.*, 1993), and a typical example of this type is Arcoona, which has a circular structure about 150 m in diameter extending around the bottom of the “body” (longitude of  $\sim 180^\circ$ ). Many small craters are found on the smooth terrains on Itokawa, and those are also shallow. The depth/diameter ratio for the crater candidates is around 0.1 for diameters larger than 50 m, and has lower values for diameters less than 50 m (Hirata *et al.*, 2009). For comparison, the same ratio is 0.14 for fresh craters on Gaspra (Carr *et al.*, 1994), 0.15 for fresh craters on Ida (Sullivan *et al.*, 1996), and 0.13 for Eros (Barnouin-Jha *et al.*, 2001; Robinson *et al.*, 2002). The low value of the ratio for small craters on Itokawa could be due to some granular processes, such as seismic shaking and granular convection (Güttler *et al.*, 2014; Yamada and Katsuragi, 2014; Matsuura *et al.*, 2014).

The observed density of the crater candidates on Itokawa is close to the empirical saturation level at the largest diameter, and declines with decreasing diameter (Fig. 11). This decreasing trend is also seen for crater diameters less than 100 m for Eros (Chapman *et al.*, 2002). The lack of small craters on Itokawa may be attributed in part to elimination of craters due to seismic shaking and as well as the inefficiency of creating craters due to the effect of armoring by boulders (Miyamoto *et al.*, 2007; Barnouin-Jha *et al.*, 2008), as demonstrated by laboratory experiments (Güttler *et al.*, 2012). Michel *et al.* (2009) studied cratering and crater erasure processes and provided an age estimate for Itokawa. They find that the time necessary to accumulate Itokawa's craters was at least  $\sim 75$  m.y., and perhaps as long as 1 G.y.,

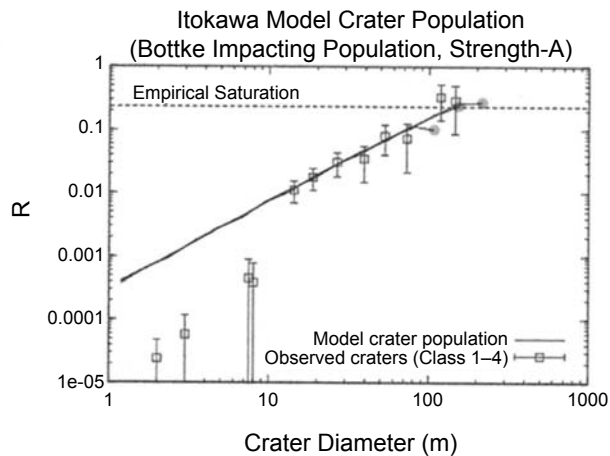


**Fig. 11.** R-plot diagram (differential crater size-frequency distribution divided by  $D^{-3}$ , where D is the crater's diameter) of Itokawa's crater population (Michel *et al.*, 2009). The observed data [including all crater candidates classified as class 1–4 by Hirata *et al.* (2009)] and one of the model fits (solid line) by Michel *et al.* (2009) are shown. The impacting population of Bottke *et al.* (2005) is assumed in the model to accumulate craters on Itokawa's surface over time and impact scaling laws (labeled Strength A) by Nolan *et al.* (1996) are used in this example to convert projectile size to crater size. The exposure times represented are 25, 75, and 150 m.y. (gray dots are placed to help discriminate between the different curves). The best fit occurs after about 75 m.y. However, given the small number statistics for the few largest craters, any exposure time in the range 25–150 m.y. is actually plausible. Note that the model predicts significantly more craters smaller than 10 m in diameter than are actually observed, which suggests that some processes may be efficient at erasing craters smaller than this size (see Michel *et al.*, 2009, for details).

and suggest that the pronounced deficiency of small craters ( $< 10$  m in diameter) may require another specific event (such as a low-velocity impact causing surface motion and crater erasure) in addition to the above-mentioned mechanisms.

The origin of the largest depression seen on the narrow “neck” region, Yoshinobu (Fig. 7), is enigmatic. If a crater of this size were formed by an impact on such a narrow “neck” made of competent material, the neck itself should have been altered. Instead, if the neck was composed of loosely coupled granular material, shock waves would quickly attenuate and the neck could be preserved. It is thus plausible that the neck region is made of granular material.

Careful observation of the “head” and “body” shows that these are multi-faceted surfaces (Saito *et al.*, 2006, Demura *et al.*, 2006). There is a possibility that some facets could be the exposed surfaces of large fragments embedded near the asteroid's surface.

### 3.4. Spectra and Space Weathering

Visible and near-infrared reflectance spectra of Itokawa collected by the Hayabusa spacecraft show typical S-type

characteristics with a broad absorption band near 1  $\mu\text{m}$  (*Abe et al.*, 2006a; *Saito et al.*, 2006) as observed by groundbased observations (*Binzel et al.*, 2001; *Lederer, et al.*, 2005). There is a slight difference between optical albedo and near-infrared spectra depending on the location (*Saito et al.*, 2006; *Abe et al.*, 2006a), which was also recognized from groundbased observations (*Abell et al.*, 2007). This difference was interpreted as being due to space weathering (*Hiroi et al.*, 2006). In lunar samples, space weathering makes the visible and near-infrared reflectance spectrum of a body darker and redder by increasing nanophase metallic iron particles in the space-exposed surface layer, as simulated experimentally (*Sasaki et al.*, 2001). Continuum-removed spectra of the dark regions were compared with meteorites mixed with a small amount of metallic iron nanoparticles and concluded that Itokawa's material is LL5–6 chondrite and the slight difference in spectra was interpreted as being due to differing degrees of space weathering (see the chapter by Brunetto et al. in this volume).

Albedo and color maps were made over Itokawa's surface in the visible and near-infrared (*Saito et al.*, 2006; *Ishiguro et al.*, 2007). Darker regions on Itokawa are interpreted as being more space-weathered, since brighter regions probably indicate areas newly exposed by impacts or shaking.

### 3.5. Shape/Potential Model and YORP Effect

Three-dimensional numerical shape models of Itokawa were developed using different methods, and based on these, potential and slope maps were constructed (*Fujiwara et al.*, 2006; *Demura et al.*, 2006; *Gaskell et al.*, 2006) [for a discussion that also includes the dynamical environment in Itokawa's near-space, see *Scheeres et al.* (2006)]. Toward the head and body the potential increases, while low potential regions exist near the neck and northern areas on the body. There are two areas where the surface consistently has slopes less than  $8^\circ$ : an isolated region around the north pole, and the MUSES-C Regio. In these regions, regolith is observed that maintains its smoothness down to at least centimeter to millimeter grain sizes (Fig. 9). A surface region with zero slopes is considered to be an energetically relaxed shape to the surface normal. This would be consistent with the existence of a loose regolith layer in these regions of minimum energy. Hence the accumulation of small grains could be explained by transport of these grains across the surface through seismic shaking induced by impacts (*Cheng et al.*, 2002; *Miyamoto et al.*, 2007), or by tidal disturbance from close planetary encounters or electrostatic levitation (*Lee*, 1996).

The YORP effect (radiative spin-up/spin-down effect) was proposed for Itokawa based on groundbased observation (*Vokrouhlický et al.*, 2004; *Scheeres et al.*, 2007; see also the chapter by Vokrouhlický et al. in this volume). *Scheeres et al.* (2007) reported that Itokawa was spinning with a period of 6.5 h 100,000 to 180,000 years ago and has slowed to the current spin state in the absence of a disturbing event. This rotation rate is fast enough for the head and body to have gone into mutual orbit.

However, the theoretical YORP value (spin-up or spin-down rate) is sensitive to the resolution of the shape model (*Scheeres and Gaskell*, 2008; *Ďurech et al.*, 2008; *Breiter et al.*, 2009) and lies in the range from  $-2$  to  $-3 \times 10^{-7}$  rad d $^{-2}$  (*Ďurech et al.*, 2008). The observed change of rotation rate  $-9.0 \times 10^{-8}$  rad d $^{-2}$  (*Kitazato et al.*, 2007) and upper limit  $\sim 1.5 \times 10^{-7}$  rad d $^{-2}$  (*Ďurech et al.*, 2008) are slightly lower than the expected value. To solve this inconsistency, the possibility of density inhomogeneity for Itokawa was suggested (*Scheeres and Gaskell*, 2008). Recently, *Lowry et al.* (2014) measured an acceleration of rotation  $3.54 \times 10^{-8}$  rad d $^{-2}$  (equivalent to a decrease of the rotation period of  $\sim 45$  ms yr $^{-1}$ ). From thermophysical analysis they found that the center of mass must be shifted by  $\sim 21$  m along the long axis of the asteroid to reconcile the observed YORP strength with theory. From these results they proposed that Itokawa is composed of two bodies of very different bulk densities,  $1750 \pm 110$  kg m $^{-3}$  and  $2850 \pm 500$  kg m $^{-3}$ , and was formed by their merging via either reaccumulation following a catastrophic disruption of a larger, partially differentiated body, or the collapse of a binary system.

### 3.6. Regolith

Past impacts by interplanetary projectiles would have repeatedly fragmented and released Itokawa's surface material since most of the excavated finer particles would have velocities much higher than Itokawa's escape velocity. In impact experiments, fragments having velocities less than this escape velocity are limited to a very small number of the largest fragments (*Nakamura and Fujiwara*, 1991; *Onose and Fujiwara*, 2004; *Michikami et al.*, 2007). Hence one could suppose that fine-grained regolith is gradually lost and the surface becomes covered with large boulders.

In spite of this expectation, a significant amount of regolith with millimeter- to centimeter-sized grains is present on Itokawa, although the constituent particle size may be larger than that on larger asteroids. This is a remarkable result given that Itokawa is very small. One probable scenario is that the regolith existed from the time of the initial formation of the head and body and has been gradually depleted through cratering. If the strength of Itokawa is weak, the excavated materials have lower speeds as suggested by experiments (*Onose and Fujiwara*, 2004) and will be able to accumulate on the surface. *Barnouin-Jha et al.* (2008) estimated the strength from this point of view and it should be less than 100 Pa. This value is small compared with loosely consolidated breccia ( $\sim 1$  kPa) and is higher than typical values for lunar regolith (approximately a few Pascals). Another probable scenario for creating small particles is that larger blocks cracked as the result of fatigue by thermal cycling (*Dombard et al.*, 2010; *Delbo et al.*, 2014).

Moreover, it is probable that regolith grains may be continuously produced if Itokawa is composed of boulder aggregates of various sizes and has considerable macroporosity — at least near the surface. Such a structure would not only reduce the shock effect during impacts, but could also

help produce fine fragments in the shallow interior near the aggregated body's surface, if the characteristic sizes of the aggregate boulders are roughly comparable with the projectile sizes. This is also the armoring process that appears to create the shallow crater-like deposits. Thus a considerable amount of grains will be retained within the interior of the asteroid, and the fine particles can easily migrate through spacing between larger boulders toward low potential regions like MUSES-C, triggered by seismic shaking.

No small amount of fine particles such as found inside the returned sampler capsule seems to exist on Itokawa's surface. These may be continuously produced by thermal cycling and migrate on the surface through levitation by their electrical charge (Lee, 1996; Kimura *et al.*, 2014).

### 3.7. Rubble-Pile Structure

Itokawa's bulk density was found to be  $1.9 \text{ g cm}^{-3}$ , which is considerably lower than the  $\sim 2.6 \text{ g cm}^{-3}$  determined for other S-type asteroids with well-determined bulk densities (Thomas *et al.*, 2001). Assuming Itokawa's composition is like LL chondrites, and that Itokawa's grain density is similar to the bulk density of LL chondrites,  $3.2 \text{ g cm}^{-3}$  (Britt *et al.*, 2002), the macroporosity of Itokawa is estimated to be 41% (Fujiwara *et al.*, 2006; Abe *et al.*, 2006b). Although it is not clear what the relative micro- and macroporosity values are, it is clear that Itokawa contains considerable void spaces in its interior, and it is likely that Itokawa has a rubble-pile structure (Fujiwara *et al.*, 2006). It is also noted that near-surface bulk density was estimated to be within 20% of  $2.5 \text{ g cm}^{-3}$  based on radar observations from the ground (Ostro *et al.*, 2004).

The ellipsoidal shapes of the head and body are also suggestive of a rubble-pile structure, because an ellipsoid is the configuration that an aggregated body takes under self-gravitation and centrifugal force. However, the fact that the current shape of Itokawa is not gravitationally relaxed to a single ellipsoid means that the head and body acquired some strength before the contact of these bodies. Shrama's (2010) theoretical study on the shape of rubble-pile binaries shows that Itokawa material has a high global friction angle, suggestive of internal cohesion. There are no conspicuous long linear structures on Itokawa (Fujiwara *et al.*, 2006; Hirata *et al.*, 2009), which is consistent with Itokawa being an aggregate of rubbles  $<50 \text{ m}$  in size. In fact, numerical simulations of catastrophic disruptions of asteroids and fragment reaccumulations were able to produce aggregate objects whose shape resemble that of Itokawa (Michel and Richardson, 2013; see the chapter by Michel *et al.* in this volume), suggesting that Itokawa is the product of the reaccumulation of small fragments generated by the disruption of a larger parent body.

Large-scale, landslide-like deposits are observed at the base of the head (Fujiwara *et al.*, 2006; Demura *et al.*, 2006), and this region has slopes in excess of  $35^\circ$  while most angular grain materials have an angle of repose on the order of  $32^\circ\text{--}35^\circ$ . The observation of the candidate landslides, along

with the fact that the steep slopes on the head measure up to  $50^\circ$ , suggests the possibility that this region at the base of the head resulted from an angular rubble pile that collapsed.

The existence of a thermally insulating layer consisting of gravel on the smooth terrain (Yano *et al.*, 2006) and many boulders in the rough terrain is also suggestive of rubble-pile structure, and this is consistent with groundbased thermal inertia measurements (Mueller *et al.*, 2005) — Itokawa's thermal inertia of  $350 \text{ J m}^{-2} \text{ s}^{-0.5} \text{ K}^{-1}$  is at least an order of magnitude higher than large main-belt asteroids ( $5\text{--}25 \text{ J m}^{-2} \text{ s}^{-0.5} \text{ K}^{-1}$ ) and the Moon ( $50 \text{ J m}^{-2} \text{ s}^{-0.5} \text{ K}^{-1}$ ).

Thus Itokawa is the first observationally verified rubble-pile body, although the existence of rubble piles was predicted long ago (Davis *et al.*, 1979; Hartmann, 1979; Fujiwara and Tsukamoto, 1980) and more recently through numerical simulations of asteroid disruptions (Michel *et al.*, 2001; see the chapter by Michel *et al.* in this volume). According to recent groundbased studies of rotation rates and amplitudes, most small asteroids may well be rubble piles or have shattered interior structures (Pravec *et al.*, 2002). The rubble-pile structure of Itokawa supports speculation that most asteroids larger than about 150 m may be rubble piles (Benz and Asphaug, 1999; Whitely *et al.*, 2002).

## 4. THE SCIENTIFIC RESULTS OF SAMPLE ANALYSIS

### 4.1. Sample Collection and Curation

The Hayabusa spacecraft made two touchdowns on Itokawa's regolith area, named MUSES-C Regio (Fig. 5). In the original sampling plan, a bullet was to have been shot from the spacecraft at the touchdown, and up to  $\sim 1 \text{ g}$  of small particles should have been collected (Yano *et al.*, 2006). Unfortunately, no bullets were shot during the two touchdowns, but thousands of very small particles were recovered in the two sample catcher rooms in the sample container, A (samples from the second touchdown) and B (samples from the first touchdown) (Nakamura *et al.*, 2011).

The sample container was opened in the clean chamber at the Planetary Material Sample Curation Facility (PMSCF) of JAXA (Yada *et al.*, 2014a). All the processes for sample transfer and storage were performed in a high-purity nitrogen atmosphere. Four methods were used to remove particles from the sample containers (Nakamura *et al.*, 2011; Yada *et al.*, 2014a). The first attempt was made using an electrostatic needle to try to remove apparent grains clinging to the walls of Catcher A, but this was unsuccessful. The second method involved sweeping the inner wall of catcher Catcher A with a Teflon spatula. However, most of the particles collected on the spatula were too small (smaller than  $10 \mu\text{m}$ ) to be safely handled without losing them. The third method was to collect particles that fell from Catchers A and B onto a quartz (silica glass) disk after physically tapping the container with a very clean screwdriver. Relatively larger particles (with a maximum size about  $300 \mu\text{m}$ ) were safely collected from the quartz plates (Fig. 12). Most recently, particles sticking on the

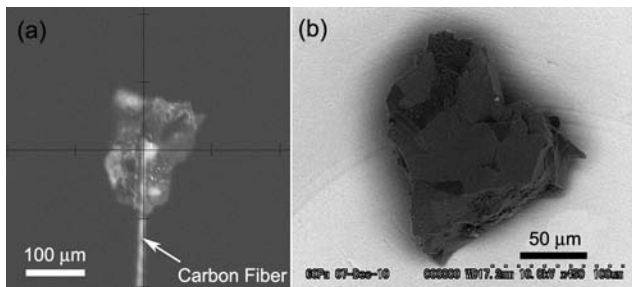


**Fig. 12.** (a) Optical microscope image and (b) SEM image of particle RA-QD02-0010 collected by the Hayabusa spacecraft. This particle is mainly composed of olivine.

cover lid of sample Catcher B were also removed (Yada et al., 2014b). Gas in the sample container, which might have been released from Itokawa particles during the return to Earth or entry into Earth's atmosphere due to temperature increase, was also sampled during the opening procedure. The noble gas elemental ratios of the gas, however, are essentially identical to those of the terrestrial atmosphere, probably due to atmospheric contamination across the O-ring seal (Okazaki et al., 2011).

Initial descriptions of harvested particles were performed using a scanning electron microscope equipped with an energy dispersive X-ray spectrometer (SEM/EDX) at the PMSCF (Yada et al., 2014a). Analyses were made using a low-vacuum, low-beam current mode without a conductive coating. The particles were grouped into four categories: Category 1 particles are composed mainly of olivine, pyroxene, and feldspar; Category 2 particles consist of additional minerals, i.e., troilite, pentlandite, Fe-Ni metal, phosphates, and chromite; Category 3 particles are composed mainly of carbon-bearing phases; and Category 4 particles are contaminants such as aluminum, quartz glass, and stainless steel. The particles are given unique names such as RA-QD02-XXXX, RB-QD04-XXXX or RB-CV-XXXX (XXXX: four-digit sequential numbers), where RA and RB mean Catcher A or B respectively, QD means quartz disk, and CV means cover lid. The harvested samples are stored in a clean chamber at PMSCF with a clean nitrogen atmosphere. By agreement, one-tenth of the harvested samples were transferred to NASA's curation facility at the Johnson Space Center in Houston (<http://curator.jsc.nasa.gov/hayabusa/index.cfm>).

#### 4.2. The Purpose of Sample Analysis

The particles from Itokawa were the first samples recovered by spacecraft from a known asteroid with an observed geological context and returned to Earth. It has long been accepted that most meteorites originate from asteroids, as demonstrated by orbital determinations from observed meteorite falls (e.g., Cloutis et al., 2014). Groundbased observations indicate that the materials on S-type asteroid Itokawa are similar to thermally metamorphosed LL chondrites belonging to petrologic type 5–6 (i.e., LL5–6), which suffered limited space weathering (see the chapter by

Brunetto et al. in this volume) (Binzel et al., 2001; Abe et al., 2006a). Itokawa samples thus provide a direct validation of the relation between S-class asteroids and ordinary chondrites. They can also be compared with the other extraterrestrial regoliths, particularly lunar regolith materials sampled by the Apollo and Luna mission (Heiken et al., 1991), and studied to understand surface processes on an asteroid, such as regolith formation and space weathering. Exotic materials, including organic-rich matter brought by impacts on the asteroid's surface, might also be included in the samples. The returned samples from Itokawa are ideal for such examination because they come from a known source, they have experienced minimal contamination from Earth's atmosphere and organic materials, and the surface of the samples was not chemically or physically processed during Earth entry, i.e., the surface structure of the samples has been preserved.

#### 4.3. Sample Analysis

Sixty-five particles 30–180 μm in size removed from the quartz disks (61 and 4 particles from Catcher A and B respectively) were examined by the Hayabusa preliminary analysis team (HASPET) in the year following recovery on Earth (Nakamura et al., 2011, 2012; Tsuchiyama, 2014). The total volume of 48 particles examined by X-ray microtomography was approximately  $4 \times 10^6 \mu\text{m}^3$ , corresponding to a sphere of about 100 μm in radius or 15 μg in mass (Tsuchiyama et al., 2014). This may suggest that the total mass of samples collected by the spacecraft is roughly 100 μg, although the exact amount is not known. It was critical to make the initial analysis according to a systematic sample-analysis program, where different analyses were made grain by grain, to obtain as much information as possible from the limited number of tiny particles. Sixty particles were divided among the two HASPET groups: one for sequential analysis from nondestructive to progressively more destructive methods (mainstream group), and the other for the characterization of space weathering, noble gases, and carbonaceous and organic materials, while minimizing contamination (Fig. 13).

Forty-eight particles were examined as the mainstream group (Nakamura et al., 2011). First, X-ray microtomography (XCT) and X-ray diffraction (XRD) using synchrotron radiation were applied to obtain three-dimensional structures (Tsuchiyama et al., 2011, 2013a, 2014) and mineral phases together with their specific crystallographic structures (Nakamura et al., 2011, 2014; Tanaka et al., 2014), respectively. The use of these nondestructive analyses, which were previously applied to comet coma dust samples returned from Comet 81P/Wild 2 by the Stardust mission (Nakamura et al., 2007, 2008b; Tsuchiyama et al., 2009), is one of the key features of the Hayabusa initial analysis strategy involving sequential studies. The three-dimensional distribution of minerals using analytical dual-energy microtomography (Tsuchiyama et al., 2011, 2013a) provided critical information concerning where a particle should be cut to ensure that the subsequent destructive analyses examined the optimal

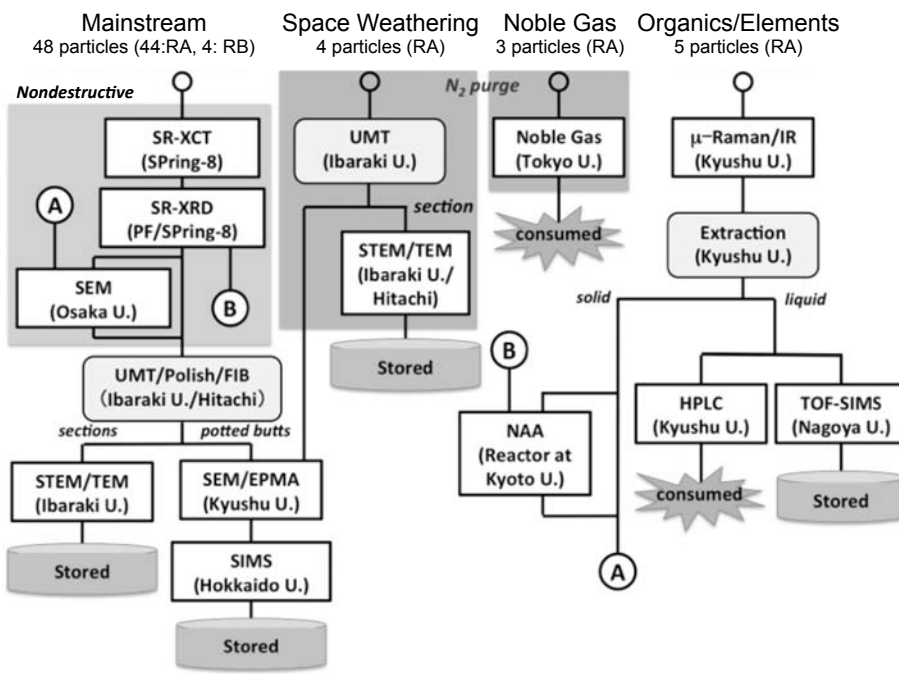


**Fig. 13.** Flowchart of the Hayabusa preliminary sample analysis. RA and RB mean Catcher A and B, respectively. SR-XCT: synchrotron radiation (SR)-based X-ray computed tomography, SR-XRD: SR-based X-ray diffraction, SEM: scanning electron microscopy, UMT: ultramicrotome, FIB: focused ion beam micro-sampling, Hitachi: Hitachi High-Technologies Co., (S)TEM: (scanning) transmission electron microscopy, EPMA: electron-probe microanalysis, SIMS: secondary ion mass spectroscopy,  $\mu$ -Raman/IR: micro-Raman and infrared spectroscopy, Extraction: extraction by dichloromethane/methanol solution, NAA: neutron activation analysis, HPLC: high-precision liquid chromatography, TOF-SIMS: time-of-flight secondary ion mass spectroscopy. "A" and "B" show connections of the analytical flows, respectively.

areas of the minerals exposed in the cross sections. Then, the particles were polished or sectioned using an ultramicrotome (UMT) or focused ion beam (FIB) and analyzed by transmission electron microscopy (TEM) to examine the nanostructures (Nakamura *et al.*, 2011; Noguchi *et al.*, 2011, 2014a). Some sections were examined using an optical microscope and a field-emission scanning electron microscope (FE-SEM) coupled with electron backscattered diffraction (EBSD) (Zolensky *et al.*, 2012), and the chemical compositions of minerals were measured by an electron probe microanalyzer (EPMA) (Nakamura *et al.*, 2011, 2014). Subsequently, oxygen and magnesium isotope compositions of minerals together with some minor-element compositions were determined using secondary ion mass spectroscopy (SIMS) (Yurimoto *et al.*, 2011a,b). The surface nanomorphologies of eight particles were also observed by FE-SEM before sectioning (Matsumoto *et al.*, 2012, 2014, 2015; Tsuchiyama *et al.*, 2012, 2013b).

For the analysis of space weathering, TEM observation was made of ultrathin sections from 12 particles (Noguchi *et al.*, 2011, 2014a). Some of these were prepared by a UMT in a purged nitrogen atmosphere to avoid oxidation of Fe nanoparticles. The isotopic compositions of noble gases in

three different particles were measured by laser ablation mass spectrometry (Nagao *et al.*, 2011). The surfaces of five different particles were examined nondestructively by micro-Raman and micro-infrared spectroscopy to seek carbonaceous materials (Kitajima *et al.*, 2011). These particles were then rinsed with a small amount of dichloromethane/methanol solution, and the extracts were examined using high-precision liquid chromatography (HPLC) to seek amino acids or using time-of-flight secondary ion mass spectrometry (TOF-SIMS) to analyze other organic compounds, including a search for polycyclic aromatic hydrocarbons (Naraoka *et al.*, 2012). Neutron activation analysis (NAA) was made of one particle after rinsing (Ebihara *et al.*, 2011). Two additional samples have recently been examined by NAA (Ebihara *et al.*, 2015). Unconsumed samples were returned to the PMSCF after initial analysis.

Five different particles were independently studied by Nakamura *et al.* (2012). The surface micronano morphologies of these particles were first observed by FE-SEM, and then FIB sections of them were observed using an optical microscope and FE-SEM; the elemental and oxygen isotope compositions of minerals were measured by EPMA and SIMS, respectively.

#### 4.4. Results from Sample Analysis

**4.4.1. Materials on Itokawa's surface.** The Hayabusa samples mainly consist of olivine, Ca-poor and Ca-rich pyroxenes, plagioclase, and troilite with small amounts of kamacite, taenite, chromite, K-feldspar (sanidine), apatite, and merrillite. The chemical compositions, oxygen isotope compositions, and modal abundances of these minerals are shown in Table 1. The chemical compositions of minerals fall within the compositional range of LL chondrites (Fig. 14) (Nakamura et al., 2011, 2012, 2014; Mikouchi et al., 2014; Noguchi et al., 2014b; Ebihara et al., 2015; see the chapter by Vernazza et al. in this volume). The oxygen isotope compositions of the minerals are consistent with equilibrated LL chondrites (Fig. 15) (Yurimoto et al., 2011a; Nakashima et al., 2013). The modal abundances are also consistent with LL chondrites (Table 1) (Tsuchiyama et al., 2011, 2014). The  $\text{Fe}^{3+}/(\text{Fe}^{2+} + \text{Fe}^{3+})$  ratio of plagioclase, determined by synchrotron radiation-based X-ray absorption near-edge structure (SR-XANES), is approximately 0.5, indicating formation under a relatively oxidizing environment, which also is consistent with LL chondrites (Mikouchi et al., 2014). Based on the abundances and the chemical compositions of minerals, the bulk chemical composition (Table 2) (Nakamura et al., 2011, 2014) and the bulk density of the samples ( $3.4 \text{ g cm}^{-3}$ ) (Tsuchiyama et al., 2011, 2014) were calculated and these values also correspond to LL chondrites. The Fe/Sc and Ni/Co ratios by NAA are consistent with those of ordinary chondrites. Depletion of Ir, which may be the result of condensation in the early solar nebula before chondrite formation, was also reported (Ebihara et al., 2011).

The textures of the samples were examined by X-ray tomography (Tsuchiyama et al., 2011, 2014) and FE-SEM (Nakamura et al., 2011, 2012, 2014). About 90% of the Itokawa particles examined exhibit triple junctions at the boundaries between coarse silicates (Fig. 16a) or almost monomineralic features (Figs. 16c, d). Minerals have almost homogeneous chemical compositions, indicating that they have been thermally annealed, and thus they are similar to LL5 and/or LL6 chondrites (Nakamura et al., 2011, 2014). Their microtextures, including porosity (1.5% average), grain size, voids, and cracks, are also similar to LL5/LL6 chondrites (Tsuchiyama et al., 2011, 2014). Most of the remaining Itokawa particles (~10%), which are made of fine silicate grains and/or have more heterogeneous chemical compositions (Fig. 16b), are similar to LL4 chondrites (Nakamura et al., 2011, 2014; Tsuchiyama et al., 2011). No differences were found between particles from Catchers A and B (Nakamura et al., 2014; Noguchi et al., 2014b; Tsuchiyama et al., 2014). The above results clearly show that the materials making up Itokawa's surface correspond to equilibrated LL chondrites. This provides the first direct link between one class of asteroids and one group of meteorites.

**4.4.2. Itokawa's parent body.** The maximum temperature estimated from the chemical compositions of an equilibrated mineral pair of Ca-poor and Ca-rich pyroxenes is about  $800^\circ\text{C}$  (Nakamura et al., 2011). Crystallization temperatures

of plagioclase based on crystal structure range from  $\sim 800^\circ\text{C}$  (Nakamura et al., 2011; Mikouchi et al., 2014) to  $655^\circ\text{--}660^\circ\text{C}$  (Tanaka et al., 2014). The latter indicates the temperature during prograde metamorphism. If a small body like Itokawa were heated to  $800^\circ\text{C}$ , even its interior would have cooled very fast. Based on a heating model calculation using the extinct nuclide  $^{26}\text{Al}$  as a heat source, the original Itokawa parent body radius should have been larger than 20 km (Nakamura et al., 2011), and accreted between 1.9 and 2.2 m.y. after CAI formation (Fig. 17) (Wakita et al., 2014), which is consistent with the  $^{26}\text{Al}$ - $^{26}\text{Mg}$  isotope evidence (Yurimoto et al., 2011b). The LL4 Itokawa particles probably formed near the original parent-body surface.

Some of the Itokawa particles have minerals with impact shock features. Optical microscope observations suggest moderate impact at the meteorite shock stage of S3–4 (Zolensky et al., 2012, 2014; Mikouchi et al., 2014), which corresponds to a shock pressure of 30–35 GPa. These features might be due to moderate impacts on Itokawa's parent body, although we cannot exclude the possibility that the impact was responsible for destroying the Itokawa's precursor asteroid if the investigated particles were located at some distance from the impact point.

Some features on Itokawa particles might be related to annealing after shock events, such as the presence of healed cracks [negative crystals aligned on a plane; see Fig. 4 in Tsuchiyama et al. (2014)] and euhedral mineral grains with condensation steps on the surfaces of porous particles, probably due to annealing of fine regolith breccia (Figs. 18c,d) (Tsuchiyama et al., 2014). Shock-induced disturbance of the Na-K distribution in plagioclase was also reported (Nakamura et al., 2014).

We can draw up the following scenario for the Itokawa parent body: (1) Formation of the Itokawa parent body  $>20$  km in radius as a planetesimal composed of LL-chondrite material. According to one heating model, this occurred at  $\sim 2$  m.y. after CAI formation ( $\sim 4.565$  G.y. ago). (2) Thermal metamorphism with a peak temperature of  $\sim 800^\circ\text{C}$  (probably  $\sim 4$  m.y. later) followed by slow cooling. (3) Post-metamorphic impact heating. (4) A catastrophic impact should occur to form Itokawa as a rubble-pile asteroid (Fujiwara et al., 2006; Michel and Richardson, 2013), although direct evidence of this has not been obtained by the sample analyses. It should be noted that neither the absolute ages of metamorphism nor the age of the catastrophic impact have been yet measured.

**4.4.3. Surface processes on Itokawa.** Regolith particles can be regarded as the interface with the space environment, where the impacts of small objects and irradiation by the solar wind and galactic cosmic rays can be recorded.

Examination of regolith particle size and shape provides important information on surface processes that cannot be obtained from existing meteorites. The particle size distribution determined both by SEM and microtomography has a slope index of about  $-2$ , which is more gradual than that of the Itokawa boulders (Fig. 10) [about  $-3$  (Saito et al., 2006; Michikami et al., 2008)], indicating a lower abundance of  $10\text{--}100\text{-}\mu\text{m}$  particles than of millimeter- to centimeter-sized

TABLE 1. Chemical compositions, oxygen isotope ratios, and bulk modal abundances of minerals in Itokawa particles in comparison with modal abundances in ordinary chondrites.

	Olivine wt.%	Low-Ca Pyroxene std wt.%	High-Ca Pyroxene std wt.%	Plagioclase std wt.%	K Feldspar std wt.%	Chromite wt.%	Apatite wt.%	Merrillite wt.%	Kamacite wt.%	Taenite wt.%	Troilite wt.%		
SiO <sub>2</sub>	37.84	0.73	55.10	0.85	53.82	1.18	65.38	1.29	64.64	0.29	0.15	0.2	0.23
TiO <sub>2</sub>			0.17	0.06	0.37	0.05	0.05	0.02	0.06	0.08	1.97	b.d.	b.d.
Al <sub>2</sub> O <sub>3</sub>	0.02	0.03	0.19	0.09	0.66	0.49	20.12	0.58	19.2	0.19	6.35	b.d.	0.04
FeO	25.75	0.94	15.10	1.32	5.52	0.98	0.42	0.39	0.4	0.07	33.62	0.17	0.63
MnO	0.47	0.02	0.46	0.03	0.24	0.03	0.03	0.02	0.02	0.43	b.d.	b.d.	b.d.
MgO	36.33	0.82	27.72	1.01	16.57	1.23	0.31	0.71	0.02	0.02	1.38	b.d.	3.64
CaO	b.d.	b.d.	0.86	0.77	20.79	2.13	2.15	0.14	1.46	0.17	b.d.	56.56	47.14
Na <sub>2</sub> O	0.02	0.02	0.03	0.03	0.57	0.18	9.58	0.51	1.6	0.14	b.d.	0.3	2.69
K <sub>2</sub> O	b.d.	b.d.	b.d.	b.d.	0.02	0.04	0.92	0.22	13.8	0.3	0.02	b.d.	0.06
Cr <sub>2</sub> O <sub>3</sub>	b.d.	b.d.	0.13	0.10	0.72	0.20	b.d.	0.03	0.03	54.21	b.d.	b.d.	0.06
NiO	b.d.	b.d.	b.d.	b.d.	0.03	0.03	0.05	0.05	0.03	0.04	b.d.	b.d.	b.d.
P <sub>2</sub> O <sub>5</sub>	0.04	0.03	b.d.	b.d.	b.d.	0.07	0.10	0.10	b.d.	b.d.	43.89	46.05	
SO <sub>3</sub>	b.d.	b.d.	n.a.	n.a.	n.a.	n.a.	n.a.	n.a.	b.d.	b.d.	b.d.	b.d.	
ZnO	n.a.	n.a.	n.a.	n.a.	n.a.	n.a.	n.a.	n.a.	n.a.	n.a.	n.a.	n.a.	
V <sub>2</sub> O <sub>3</sub>	n.a.	n.a.	n.a.	n.a.	n.a.	n.a.	n.a.	n.a.	n.a.	0.38	n.a.	n.a.	
F	n.a.	n.a.	n.a.	n.a.	n.a.	n.a.	n.a.	n.a.	n.a.	0.57	n.a.	n.a.	
Cl	n.a.	n.a.	n.a.	n.a.	n.a.	n.a.	n.a.	n.a.	b.d.	0.74	n.a.	n.a.	
Ni									2.47	0.11	3.9	47.7	0.1
Fe											86.2	48.1	63.4
Mn											0.0	b.d.	0.0
Co											9.9	2.5	0.1
Cr											b.d.	b.d.	b.d.
S											b.d.	b.d.	35.6
P											b.d.	b.d.	b.d.
Cu	Total	100.47	0.89	99.76	0.89	99.31	0.91	99.06	1.29	101.27	0.64	99.06	103.02*
Fa#	Fa#	28.4	1.2	23.0	2.0	9.0	1.5					100.00†	101.05*
Fs#	Fs#			1.7	1.5	43.2	4.3						
Wof#	Wof#			75.3	2.3	47.9	2.9						
En#	En#												
O#	O#												
An#	An#												
Ab#	Ab#												
Oxygen isotope (‰)													
$\delta^{18}\text{O}$	4.57	0.74	5.07	0.28	2s						79.07	1.59	
$\delta^{17}\text{O}$	3.77	0.46	3.82	0.49	4.30	0.36	2s				70.3	0.74	
$\Delta^{17}\text{O}$	1.39	0.31	1.18	0.49	3.44	0.38	4.23				13.9	1.13	
Mode (vol.%)											2s		
Itokawa													
LL4-6													
L4-6													
H4-6													

\* The total was recalculated by subtracting O that is substituted by F and Cl.

† The total was normalized by 100%.

b.d.: below the detection limit. n.a.: not analyzed. Data for the chemical compositions of olivine, pyroxenes, and plagioclase are from Nakamura *et al.* (2014) and those of other minerals are from Nakamura *et al.* (2011). Data for oxygen isotope ratios are from Nakashima *et al.* (2013). Data for the modal abundances are from Tsuchiyama *et al.* (2014).

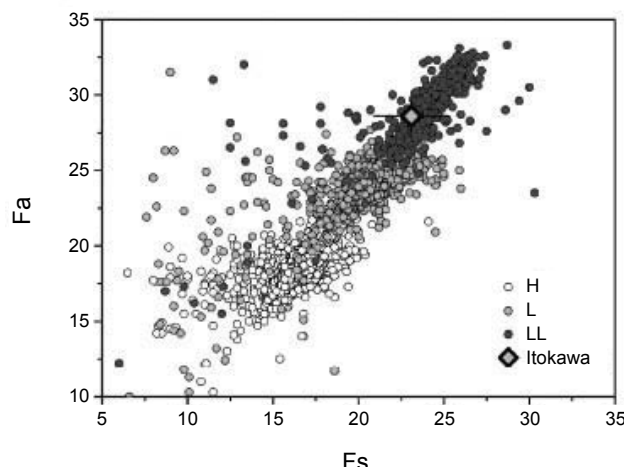


**Fig. 14.** Mean Fa contents in olivine and Fs contents in Ca-poor pyroxene of Itokawa particles in comparison with those of H, L, and LL chondrites (from Nakamura et al., 2011).

regolith (Tsuchiyama et al., 2011, 2014). This is consistent with the close-up images of regolith taken by the Hayabusa spacecraft (Fig. 9) (Yano et al., 2006). This size distribution may be explained by smaller particles having higher ejection velocities and thus higher loss rates. In contrast, abundant submillimeter-sized fragments in regolith are observed on much larger bodies such as the Moon (Heiken et al., 1991).

The shape distribution of Itokawa particles with respect to their three axial ratios is not statistically different from that of fragments formed by high-speed impact in laboratory experiments (Fig. 19), indicating that Itokawa's particles resulted from mechanical disaggregation, primarily as a response to impacts (Tsuchiyama et al., 2011, 2014). The shape distribution of lunar regolith particles (Tsuchiyama et al., 2013c; Katagiri et al., 2014) indicates that the lunar particles are more spherical than the Itokawa particles, indicating that the shape of the lunar particles may have evolved, probably by gardening in the regolith. Thermal fatigue is another possibility for regolith formation on asteroids (Delbo et al., 2014). Fragments produced by thermal fatigue experiments should be compared with Itokawa particles.

Submicrometer-sized impact craters were observed on the surfaces of only a limited number of Itokawa particles (Fig. 18e) (Nakamura et al., 2012); they may have been created by the impact of high-speed secondary nanoparticles produced by impact into Itokawa's regolith. Tiny, flattened glass objects, which seem to be melt splashes (Fig. 18f) (Nakamura et al., 2012; Matsumoto et al., 2012), also formed as a result of small-scale impacts. Similar melt droplets were also observed on Itokawa particle surfaces by TEM (Keller and Berger, 2014; Thompson et al., 2014). Large-scale melting features, such as agglutinates found in lunar regolith, have not been observed among the Itokawa samples (Tsuchiyama et al., 2011). This can be explained by the differences between the mass and impact velocities for asteroids and the Moon (representative velocity of about  $5 \text{ km s}^{-1}$  and over  $10 \text{ km s}^{-1}$ ,

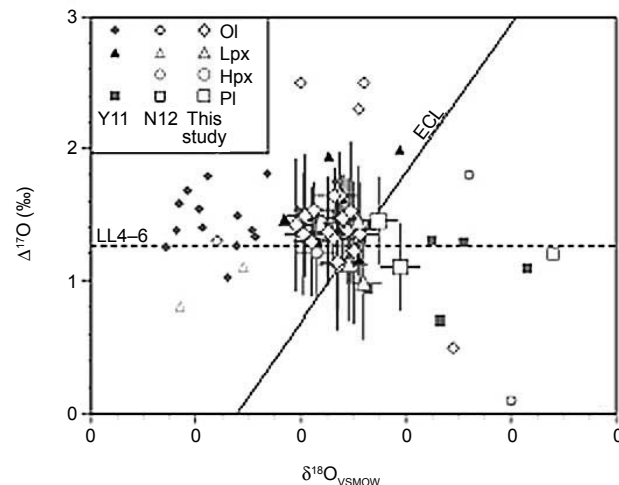


**Fig. 15.** Oxygen three-isotope ratios of Itokawa particles (from Nakashima et al., 2013). ECL represents the equilibrated chondrite line. The dashed line labeled LL4–6 is defined by average  $\Delta^{17}\text{O}$  values of equilibrated LL-chondrite data. The line at  $\Delta^{17}\text{O} = 0\text{‰}$  corresponds to the terrestrial fractionation line.

respectively). Shock defects in olivine and tetrataenite were observed by TEM only below local particle surfaces, indicating small-scale impact and collisional fragmentation during regolith formation (Langenhorst et al., 2014).

Two kinds of surface modifications, formation of space-weathering rims and surface abrasion, have been recognized on Itokawa's particles. Space-weathering rims were observed by TEM and scanning transmission electron microscopy (STEM) (Noguchi et al., 2011, 2014a,b; Matsumoto et al., 2015; Keller and Berger, 2014; Thompson et al., 2014). They are classified into three types (Noguchi et al., 2014a): (1) redeposition rim composed of only a very thin (2–3 nm) amorphous zone with

TABLE 2. Bulk chemical compositions of Itokawa particles and ordinary chondrite falls (data from Nakamura et al., 2014).

wt.%	Itokawa	LL	L	H
SiO <sub>2</sub>	42.4	40.6	39.7	36.6
TiO <sub>2</sub>	0.1	0.1	0.1	0.1
Al <sub>2</sub> O <sub>3</sub>	1.8	2.2	2.3	2.1
FeO	20.7	17.4	14.5	10.3
MnO	0.4	0.4	0.3	0.3
MgO	29.6	25.2	24.7	23.3
CaO	0.9	1.9	1.9	1.7
Na <sub>2</sub> O	0.8	1.0	1.0	0.9
K <sub>2</sub> O	0.1	0.1	0.1	0.1
Cr <sub>2</sub> O <sub>3</sub>	0.1	0.5	0.5	0.5
P <sub>2</sub> O <sub>5</sub>	0.1	0.2	0.2	0.3
Oxide total	96.9	89.7	85.3	76.2
Fe	0.3	2.4	7.0	16.0
Ni	0.3	1.1	1.2	1.7
FeS	2.8	5.8	5.8	5.4
Total	100.2	99.0	99.3	99.4

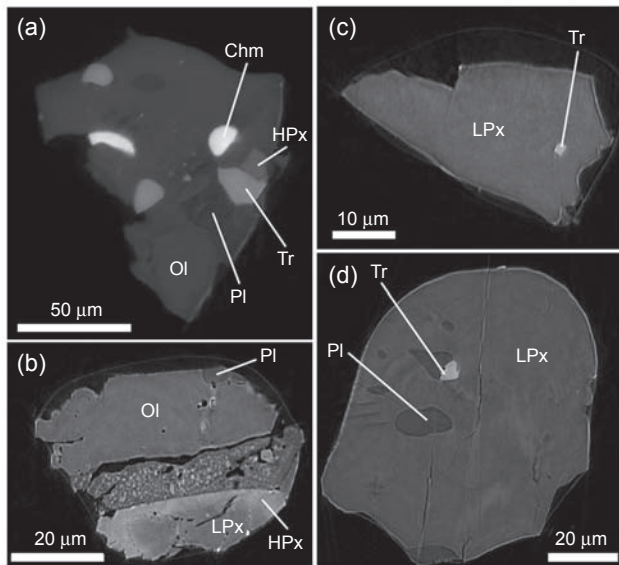


**Fig. 16.** Slice images of Itokawa particles obtained by microtomography for samples (a) RA-QD02-0031, (b) RA-QD02-0048, (c) RA-QD02-0038, and (d) RA-QD02-0042. OI: olivine, LPx: low-Ca pyroxene, HPx: high-Ca pyroxene, PI: plagioclase, Chm: chromite, Tr: troilite. The image contrast corresponds to the X-ray linear attenuation coefficient of the minerals. The bright edges of the objects are artifacts resulting from X-ray refraction contrast. From Tsuchiyama (2014).

different compositions from the substrate mineral (Zone I), indicating vapor deposition from micrometeorite impacts or radiation-induced sputter deposition (Figs. 20a,b); (2) composite rim composed of Zone I and a partially amorphized zone (30–60 nm) containing nanophase Fe ± S (Zone II) (Figs. 20c,d); and (3) composite vesicular rim composed of Zone I and a thicker Zone II (60–80 nm) with vesicles about 100 nm across (Figs. 20e,f). The rim structures of the latter two types can be explained by amorphization, *in situ* reduction of iron, and blistering due to the implantation of solar wind particles, particularly He, as deduced from the mean penetration depth (about 40 nm for 4 keV  ${}^4\text{He}^+$ ).

Blisters were also recognized on the particle surfaces by FE-SEM (Fig. 18d) (Matsumoto *et al.*, 2015). The presence of blisters on both sides of one particle shows that the particle rotated on the surface of Itokawa. Solar flare tracks were observed on particles with well-developed space-weathered rims, and their densities give an exposure age on the order of  $10^3$ – $10^4$  yr (Noguchi *et al.*, 2014a,b; Keller *et al.*, 2014). Noguchi *et al.* (2014b) reported that space-weathered rims are less developed and solar flare tracks are rarely observed on particles from the first touchdown site (Catcher B) as compared to the second (Catcher A).

The presence of nanophase Fe below particle surfaces (Fig. 20) is the cause of the reddening and darkening of the reflectance spectra. The cause of the space-weathered rim formation is significantly different from that on the Moon, where the process primarily involves vapor deposition of

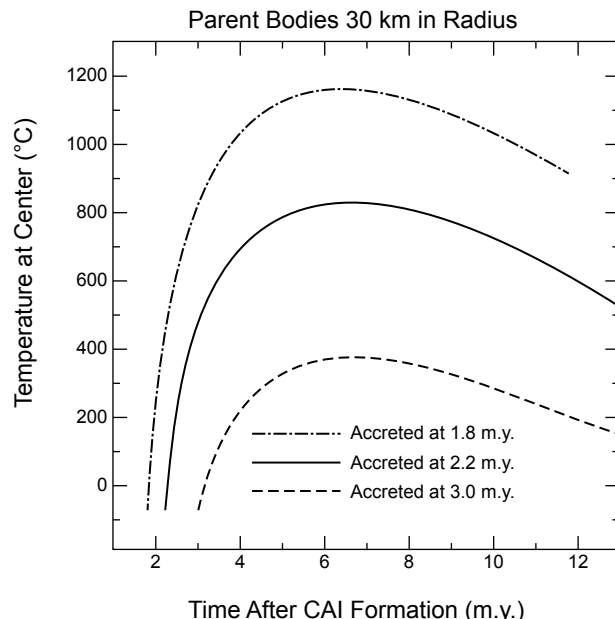


**Fig. 17.** Temperature at the center of parent bodies 30 km in radius plotted against the time after CAI formation as a function of accretion period (1.8, 2.2, and 3.0 m.y. after CAI formation). From Wakita *et al.* (2014).

amorphous materials containing nanophase Fe caused by bombardment of micrometeoroids (e.g., Pieters *et al.*, 2000). This difference might be due to the much larger residence timescales for regolith on the Moon (typically over 400 m.y.) than on Itokawa (roughly 1 m.y. as described below).

The other observed surface modification that has taken place on Itokawa's particles is grain abrasion (Tsuchiyama *et al.*, 2011, 2013b, 2014). The particle surfaces observed by microtomography are usually angular (Figs. 16a,c), but some are rounded (Figs. 16b,d). Both types of surfaces can be present on a single particle. Similar features were also observed at higher resolution by FE-SEM: sharp steps formed by fracturing on angular surfaces (Fig. 18a), faint or no steps on rounded surfaces (Fig. 18b) (Tsuchiyama *et al.*, 2013b; Matsumoto *et al.*, 2014). These results indicate that mechanically crushed fragments were abraded later. The degree of space-weathered rim development is apparently not related to the abrasion (Tsuchiyama *et al.*, 2013b). Thus, the abrasion process can be regarded as a different type of space weathering with a longer timescale, and has been called “space microerosion.” Tsuchiyama *et al.* (2011) proposed that the abrasion is probably the result of grain migration, which is caused by impact-driven seismic waves repeatedly reflecting off the surface of Itokawa (e.g., Miyamoto *et al.*, 2007). Alternatively, Connolly *et al.* (2014) proposed tidal disruption and YORP effects as possible causes of the physical weathering.

Solar-wind-implanted noble gases (He, Ne, and Ar) have been detected in Itokawa particles (Nagao *et al.*, 2011, 2013). This clearly shows that the particles were for some period of time located on the uppermost regolith layer. The residence

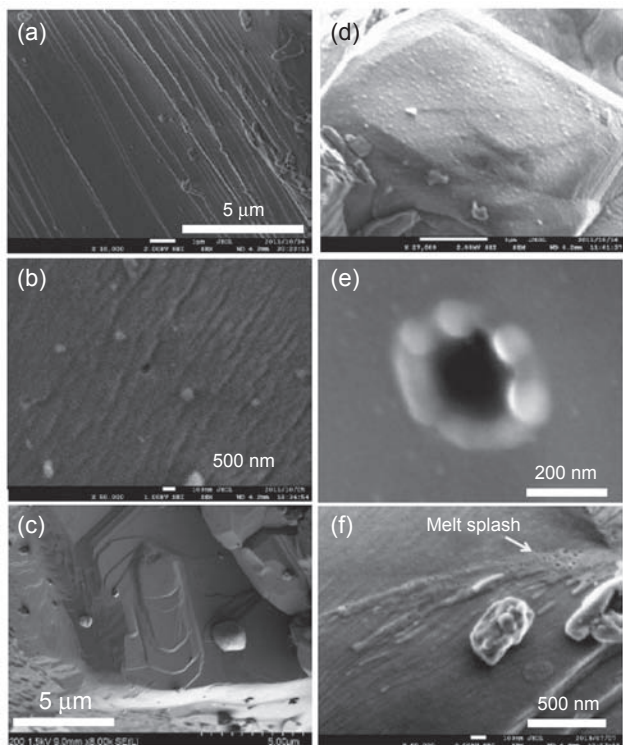


**Fig. 18.** Surface micronanomorphologies of Itokawa particles observed using a field-emission scanning microscope (FE-SEM). (a) Sharp steps on a fractured surface (sample RB-QD04-0049), (b) faint steps on a rounded surface (RB-QD04-0023), (c) growth steps on an olivine surface with facets (RB-QD04-0102), (d) blister structure on a surface with an euhedral grain (RA-QD02-0033), (e) pit with ornaments resembling a crater (sample RA-QD02-0093), (f) flattened glass like melt splash with bubble (sample RB-QD04-0043). Substrates of all the images are olivine (Ol). (a),(b),(f) are from Tsuchiyama (2014); (e) from Nakamura et al. (2012). Ca-zoning in pyroxene and mesostasis are seen in (b), which corresponds to a less-equilibrated sample (LL4-like).

time spans were estimated to be 150–550 yr from the Ne concentrations (Nagao et al., 2011). Release profiles of the solar noble gases are consistent with grain motion in the regolith layer, and observed He losses suggest preferential abrasion of the space-weathered rims from the particle surfaces (Nagao et al., 2011). Galactic cosmic rays (GCR) can reach much deeper levels (several tens of centimeters to 1 m below the surface) in an asteroid. Nagao et al. (2011, 2013) detected no measurable GCR-produced Ne, which permits estimation of the upper limit of the residence timescale of grains in the regolith layer, namely, about 8 m.y. Meier et al. (2014) detected GCR-produced Ne, giving a residence timescale of ~1.5 m.y., which is much smaller than the crater age of Itokawa [60–75 m.y. (Michel et al., 2009)] but comparable with the period that Itokawa spent in near-Earth object (NEO) orbit [on the order of millions of years (Michel and Yoshikawa, 2005)]. This is much shorter than the nominal exposure ages of >400 m.y. for mature lunar regolith (Wieler, 2002).

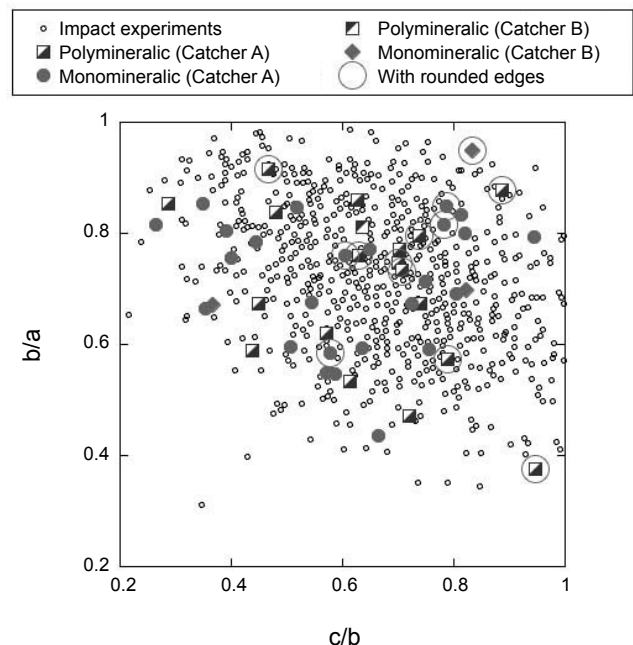


**Fig. 19.** Three-dimensional shape distributions of Itokawa particles in comparison with fragments of impact experiments (from Tsuchiyama et al., 2014). a, b, and c are the longest, intermediate, and shortest axis lengths, respectively.

We can construct the following scenario for Itokawa's surface: (1) Formation of regolith by impacts of small objects, with selective escape of the finest-scale particles. Thermal fatigue might also play an important role in regolith formation. (2) Implantation of solar wind into the uppermost particle surfaces and formation of space-weathered rims with a timescale of ~10<sup>3</sup>–10<sup>4</sup> yr. (3) Grain abrasion, probably due to seismic-induced particle motion, with time periods significantly longer than 10<sup>4</sup> yr. Processes (2) and (3) and impact fragmentation occurred repeatedly. (4) Final escape of some particles from the asteroid by impact(s) within the final 1 m.y. Vernazza et al. (2009) proposed two-stage space-weathering models for asteroids based on the reflectance spectrum of S-type asteroid families and their ages: rapid spectral change mainly by solar wind implantation within 1 m.y. followed by slow change due to micrometeorite impact effects (~1 m.y. to ~30 b.y.). The timescale for the space-weathered rim formation (10<sup>3</sup>–10<sup>4</sup> yr) is much shorter than that for the observed reflectance spectral change (1 m.y.). The spectral change should proceed more slowly than simple space-weathered rim formation because of grain migration, removal of space-weathered rims by grain abrasion, and the refreshment of particle surfaces by impact fragmentation.

**4.4.4. Exotic materials that fell on Itokawa.** It is expected that exotic materials that originated from other celestial bodies fell on Itokawa and should be included among the Hayabusa samples. Carbonaceous materials, especially organic materials, are being actively sought but have not been detected for Category 1 and 2 particles thus far (Naraoka et al., 2012; Kitajima et al., 2011). Category 3

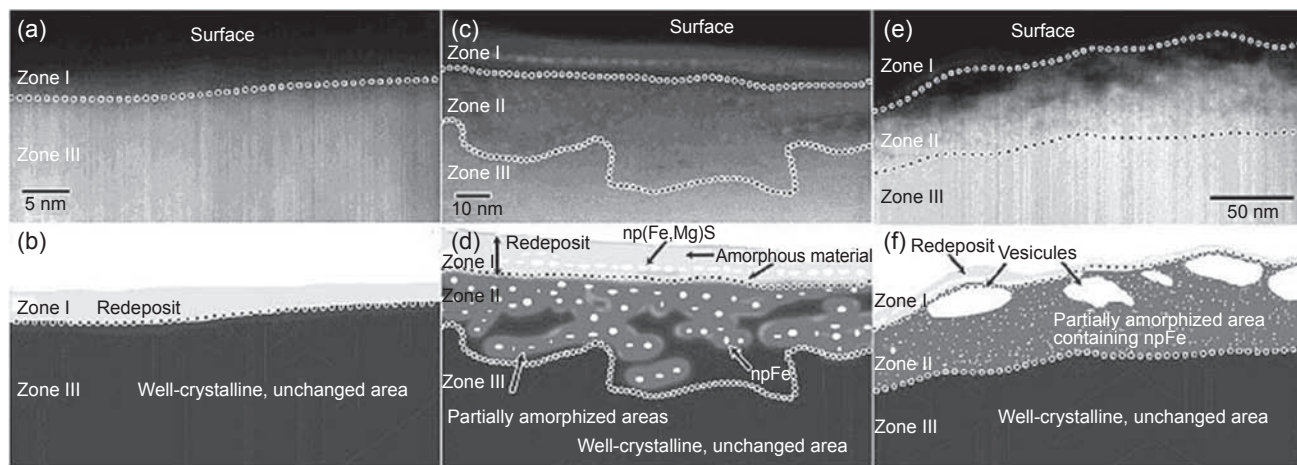


**Fig. 20.** Three typical surface features observed by HAADF-STEM on surficial olivine and pyroxene in Itokawa particles and corresponding schematic diagrams with interpretation of their textures (from Noguchi *et al.*, 2014a). np(Fe,Mg)S: nanophase (Fe,Mg)S; npFe: nanophase Fe.

carbonaceous particles were also examined. Differences in their microstructures and elemental distributions suggest multiple origins (Uesugi *et al.*, 2014), but measured H, C, and N isotopic compositions suggest (but do not prove) that they are of terrestrial origin (Ito *et al.*, 2014).

Micrometer- to submicrometer-sized alkali halides (NaCl and KCl) were identified on the surfaces of two Itokawa particles (Noguchi *et al.*, 2014c). These phases were clearly present on the particles' surfaces before allocation from JAXA, but there is not at this time direct evidence for their extraterrestrial origin. Handling of these very tiny grains (less than 10  $\mu\text{m}$  across) is difficult at present, but their examination is proceeding. Halides are occasionally found in ordinary chondrite regolith breccias (Zolensky *et al.*, 1999), and are of considerable interest.

## 5. SUMMARY

Although the origin and evolution of Itokawa are still speculative, from the results of the Hayabusa mission we can construct the following scenario: Originally, a parent body  $\sim$ 20 km in diameter was catastrophically disrupted by a smaller projectile. Among the dispersing fragments, some aggregated bodies were formed through gravitational interaction, as numerically demonstrated by Michel and Richardson (2013). The rubble-piled “head” and “body” were two of these aggregates, and they formed a co-rotating binary that eventually came into contact by collision at relatively low velocity, forming Itokawa as a result. The different orientations of the principal axes of the head and body (Saito *et al.*, 2006) also imply that these bodies were originally separate bodies. As suggested by Scheeres *et al.* (2007), the mutual configuration of the “head” and “body” might have changed from the initial contact of both bodies, due to various disturbances such as planetary encounters, impacts, and the YORP effect. This is the scenario that we derived from the Hayabusa data.

Itokawa was brought into a typical NEO orbit through  $v_6$  secular resonance in the main belt, as suggested by the numerical backtrack study of Itokawa's current orbit (Michel and Yoshikawa, 2006). Major craters had been formed on the surface of the asteroid before injection into NEO orbit, and the exposure time of the surface for cratering is estimated to be at least 60–75 m.y. (Michel *et al.*, 2009). The length of time that Itokawa spent in NEO orbit may have been on the order of millions of years, which is equivalent to its expected lifetime against an impact with Earth (Michel and Yoshikawa, 2005).

Hayabusa was a technological demonstration. We have learned a lot about the technology of sample return missions, and experienced the reality that sample return is very difficult, to say the least. However, this first experience demonstrated that the results are worth the challenge. We revealed the nature of a very small asteroid for the first time, and this will lead to an improved understanding of the origin of the solar system.

Thanks to the splendid results from Hayabusa, the next asteroid sample return mission, Hayabusa2 (Fig. 21), was planned (Tsuda *et al.*, 2013; Yoshikawa *et al.*, 2014) and then successfully launched on December 3, 2014. Hayabusa2 is similar to Hayabusa, but the target asteroid is a C-type asteroid, (162173) Ryugu (1999 JU<sub>3</sub>), which is expected to be more primitive and to contain organic material. Hayabusa2 will arrive at 1999 JU<sub>3</sub> in 2018, and return to Earth in 2020. The result of Hayabusa2 will be yet another breakthrough in the study of asteroids and of the solar system as a whole.

**Acknowledgments.** The Hayabusa mission was accomplished through the tremendous effort of many people. We appreciate all the engineers, scientists, researchers, administrative staff, and others who supported the Hayabusa mission so well. We are grateful to M. Zolensky, P. Michel, and an anonymous reviewer for their useful comments that helped to improve the manuscript greatly.



**Fig. 21.** Artist's concept of the Hayabusa2 spacecraft touching down on a small, artificially created crater. Illustration by A. Ikeshita.

## REFERENCES

- Abe M., Takagi Y., Abe S., Hiroi T., Clark B., Abell P. A., Lederer S. M., Jarvis K. S., Nimura T., Ueda Y., and Fujiwara A. (2006a) Near-infrared spectral results of asteroid Itokawa from the Hayabusa spacecraft. *Science*, **312**, 1334–1338.
- Abe S., Mukai T., Hirata N., Barnouin-Jha O. S., Cheng A. F., Demura H., Gaskell R. W., Hashimoto T., Hiraoka K., Honda T., Kubota T., Matsuoka M., Mizuno T., Nakamura R., Scheeres D. J., and Yoshikawa M. (2006b) Mass and local topography measurements of Itokawa by Hayabusa. *Science*, **312**, 1344–1347.
- Abell P. A., Vilas F., Jarvis K. S., Gaffey M., and Kelley M. S. (2007) Mineralogical composition of (25143) Itokawa 1998 SF<sub>36</sub> from visible and near-infrared reflectance spectroscopy: Evidence or partial melting. *Meteoritics & Planet. Sci.*, **42**, 2185–2177.
- Barnouin-Jha O. S., Garvin J. B., Cheng A. F., Zuber M., Smith D., Neumann G., Murchie S., Robinson M., and Veverka J. (2001) Preliminary impact crater dimensions on 433 Eros from the NEAR laser range finder and imager. *Lunar Planet. Sci. XXXII*, Abstract #1786. Lunar and Planetary Institute, Houston.
- Barnouin-Jha O. S., Cheng A. F., Mukai T., Abe S., Hirata N., Nakamura R., Gaskell R., Saito J., and Clark B. E. (2008) Small-scale topography of 25143 Itokawa from the Hayabusa laser altimeter. *Icarus*, **198**, 108–124.
- Benz W. and Asphaug E. (1999) Catastrophic disruption revisited. *Icarus*, **142**, 5–20.
- Binzel R. P., Rivkin A. S., Bus S., Sunshine J. M., and Burbine T. H. (2001) MUSES-C target asteroid 1998 SF<sub>36</sub>: A reddened ordinary chondrite. *Meteoritics & Planet. Sci.*, **36**, 1167–1172.
- Bottke W. F., Durda D. D., Nesvorný D., Jedicke R., Moidelli A., Vokrouhlický D., and Levison H. (2005) The fossilized size distribution of the main asteroid belt. *Icarus*, **175**, 111–140.
- Breiter S., Bartczak P., Czajk M., Oczujda B., and Vokrouhlický D. (2009) The YORP effect on 25143 Itokawa. *Astron. Astrophys.*, **507**, 1073–1081.
- Britt D. T., Yeomans D., Housen K., and Consolmagno G. (2002) Asteroid density, porosity, and structure. In *Asteroids III* (W. F. Bottke Jr. et al., eds.), pp. 485–500. Univ. of Arizona, Tucson.
- Carr M. H., Kirk R. L., McEwen A., Veverka J., Thomas P., Head J. W., and Murchie S. (1994) The geology of Gaspra. *Icarus*, **107**, 61–71.
- Chapman C. R. (2002) Cratering on asteroids from Galileo and NEAR Shoemaker. In *Asteroids III* (W. F. Bottke Jr. et al., eds.), pp. 315–330. Univ. of Arizona, Tucson.
- Chapman C. R., Merline W. J., Thomas P. C., Joseph J., Cheng A. F., and Izenberg N. (2002) Impact history of Eros. *Icarus*, **155**, 104–118.
- Cheng A. F., Izenberg N., Chapman C. R., and Zuber M. T. (2002) Ponded deposits on asteroid 433 Eros. *Meteoritics & Planet. Sci.*, **37**, 1095–1105.
- Cheng A. F., Barnouin-Jha Hirata N., Miyamoto H., Miyamoto H., Nakamura R., and Yano H. (2007) Fundamentally distinct outcomes of asteroid collisional evolution: Itokawa and Eros. *Geophys. Res. Lett.*, **34**, DOI: 10.1029/2007GL029559.
- Cintala M. J., Garvin J. B., and Wetzel S. J. (1982) The distribution of blocks around a flesh lunar mare crater. *Proc. Lunar Planet. Sci. Conf. 13th*, in *J. Geophys. Res.*, **XX**, A100–A101.
- Cloutis E. A., Binzel R. P., and Gaffey M. J. (2014) Establishing asteroid-meteorite links. *Elements*, **10**, 25–30.
- Connolly H. C. Jr., Lauretta D. S., Walsh K. J., Tachibana S., and Bottke W. F. (2014) The dynamical evolution of asteroid 25143 Itokawa: Constraints from sample analysis. *Meteoritics & Planet. Sci. Suppl.*, **49**, A78.
- Davis D., Chapman C. R., Greenberg R., and Weidenschilling S. J. (1979) Collisional evolution of asteroids: Populations, rotations, and velocities. In *Asteroids* (T. Gehrels, ed.), pp. 528–557. Univ. of Arizona, Tucson.
- Delbo M. and 8 colleagues (2014) Thermal fatigue as the origin of regolith on small asteroids. *Nature*, **508**, 233–236.
- Demura H., Kobayashi S., Nemoto E., Matsumoto N., Furuya M., Yukishita A., Muranaka N., Morita H., Shirakawa K., Maruya M., Ohyama H., Uo M., Kubota T., Hashimoto T., Kawaguchi J., Fujiwara A., Saito J., Sasaki S., Miyamoto H., and Hirata N. (2006) Pole and global shape of 25143 Itokawa. *Science*, **312**, 1347–1349.
- Dermawan B., Nakamura T., Fukushima H., Sato H., Yoshida F., and Sato Y. (2002) CCD photometry of the MUSES-C mission target: Asteroid (25143) 1998 SF<sub>36</sub>. *Publ. Astron. Soc. Japan*, **54**, 635–640.
- Dombard A. J., Barnouin O. S., Prockter L. M., and Thomas P. C. (2010) Boulders and ponds on the asteroid 433 Eros. *Icarus*, **210**, 713–721.
- Durech J., Vokrouhlický D., Kaasalainen M., Weissman P., Lowry S. C., Beshore E., Higgins D., Krugly Y. N., Shevchenko V. G., Gaftonyuk N. M., Choi Y.-J., Kowalski R. A., Larson S., Warner B. D., Marshalkina A. L., Ibrahimov M. A., Molotov I. E., Michłowski T., and Kitazato K. (2008) New photometric observations of asteroids (1862) Apollo and (25143) Itokawa — an analysis of YORP effect. *Astron. Astrophys.*, **488**, 345–350.
- Ebihara M. and 21 colleagues (2011) Neutron activation analysis of a particle returned from asteroid Itokawa. *Science*, **333**, 1119–1121.
- Ebihara M. and 15 colleagues (2015) Chemical and mineralogical compositions of two grains recovered from an asteroid Itokawa. *Meteoritics & Planet. Sci.*, **50**, 243–254.
- Fujiwara A. and Tsukamoto A. (1980) Experimental study on the velocity of fragments in collisional breakup. *Icarus*, **44**, 142–153.
- Fujiwara A., Kadono T., and Nakamura A. (1993) Cratering experiments into curved surfaces and their implication for craters on small satellites. *Icarus*, **105**, 345–350.
- Fujiwara A., Kawaguchi J., Yeomans D. K., Abe M., Mukai T., Okada T., Saito J., Yano H., Yoshikawa M., Scheeres D. J., Barnouin-Jha O., Cheng A. F., Demura H., Gaskell R. W., Hirata N., Ikeda H., Kominato T., Miyamoto H., Nakamura A. M., Nakamura R., Sasaki S., and Uesugi K. (2006) The rubble-pile asteroid Itokawa as observed by Hayabusa. *Science*, **312**, 1330–1334.
- Fuse T., Yoshida F., Tholen D., Ishiguro M., and Saito J. (2008) Searching satellites of asteroid Itokawa by imaging observation with Hayabusa spacecraft. *Earth Planets Space*, **60**, 33–37.
- Gaskell R., Barnouin-Jha O. S., Scheeres D. J., Mukai T., Hirata N., Abe S., Saito J., Ishiguro M., Kubota T., Hashimoto T., Kawaguchi J., Yoshikawa M., and Kominato T. (2006) Landmark navigation studies and target characterization in the Hayabusa encounter with Itokawa. In *AIAA/AAS Astrodynamics Specialist Conference and Exhibit*, AIAA Paper 2006-6660.
- Gault D. E., Shoemaker E. M., and Moore H. J. (1963) *Spray Ejected from the Lunar Surface by Meteoroid Impact*. NASA TN D-1767, Washington, DC. 40 pp.
- Güttler C., Hirata N., and Nakamura A. M. (2012) Cratering experiments on the self-armoring of coarse grained granular targets. *Icarus*, **220**, 1040–1049.
- Güttler C., von Bostel I., Schräpler R., and Blum J. (2014) Granular convection and the Brazil nut effect in reduced gravity. *Phys. Rev. E*, **87**, 4, Article ID 044201.
- Hartmann W. K. (1979) Diverse puzzling asteroids and a possible unified explanation. In *Asteroids* (T. Gehrels, ed.), pp. 466–479. Univ. of Arizona, Tucson.

- Heiken G. H., Vaniman D. T., and French B. M., eds. (1991) *Lunar Sourcebook: A User's Guide to the Moon*. Cambridge Univ., Cambridge. 756 pp.
- Hirata N. and Ishiguro M. (2011) Properties and possible origin of black boulders on the asteroid Itokawa. *Lunar Planet. Sci. XLII*, Abstract #1821. Lunar and Planetary Institute, Houston.
- Hirata N., Barnouin-Jha O. S., Honda C., Nakamura R., Miyamoto H., Sasaki S., Demura H., Nakamura A. M., Michikami T., Gaskell R. W., and Saito J. (2009) Survey of possible impact structured on 25143 Itokawa. *Icarus*, 200, 486–502.
- Hiroi T., Abe M., Kitazato K., Abe S., Clark B. E., Sasaki S., Ishiguro M., and Barnouin-Jha O. S. (2006) Developing space weathering on the asteroid 25143 Itokawa. *Nature*, 443, 56–58.
- Ishiguro M., Hiroi T., Tholen D. J., Sasaki S., Ueda Y., Nimura T., Abe M., Clark R. E., Yamamoto A., Yoshida F., Nakamura R., Hirata N., Miyamoto H., Yokota Y., Hashimoto T., Kubota T., Nakamura A. M., Gaskell R. W., and Saito J. (2007) Global mapping of the degree of space weathering on asteroid 25143 Itokawa by Hayabusa/AMICA observations. *Meteoritics & Planet. Sci.*, 42, 1791–1800.
- Ito M. and 11 colleagues (2014) H, C, and N isotopic compositions of Hayabusa category 3 organic samples. *Earth Planets Space*, 66, 91.
- Kaasalainen M., Kwiatkowski M., Abe M., Pirone J., Nakamura T., Ohba Y., Dermawan B., Farnham T., Colas F., Lowry S., Weissman P., Whitley R. J., Tholen D. J., Larson S. M., Yoshikawa M., Toth I., and Velichko F. P. (2003) *Astron. Astrophys.*, 405, L29–L32.
- Katagiri J. and 7 colleagues (2014) Investigation of 3D grain shape characteristics of lunar soil retrieved in Apollo 16 using image-based discrete-element modeling. *J. Aerosp. Eng.*, 10, 1061.
- Kawaguchi J. (1986) *Scientific Satellites Prospect*. ISAS Report No. 43, ISSN 0285-2853.
- Kawaguchi J. (2003) MUSES-C launch and early operations report. In *AAS/AIAA Astrodynamics Specialists Conference*, AAS-03-662.
- Kawaguchi J. (2010a) Hayabusa reentry and recovery of its capsule. *COSPAR 2010*, B04-0027-10.
- Kawaguchi J. (2010b) Hayabusa's reentry and recovery of its capsule. *International Astronautical Congress IAC-2010*, IAC-10.A3.5.1.
- Kawaguchi J., et al. (2002) Launch readiness of the MUSES-C, a sample and return from an asteroid. *53rd International Astronautical Congress/World Space Congress 2002*, IAC-02-Q.5.2.0.4.
- Kawaguchi J. et al. (2004) The ion engines cruise operation and the Earth swingby of 'Hayabusa' (MUSES-C). *55th International Astronautical Congress of the International Astronautical Federation, the International Academy of Astronautics, and the International Institute of Space Law*, IAC-04-Q\_5\_02.
- Kawaguchi J., Kuninaka H., and Yoshikawa M. (2011) Return of Hayabusa spacecraft and reentry of its capsule. *33rd Annual AAS Guidance and Control Conference*, AAS 11-058.
- Keller L. P. and Berger E. L. (2014) A transmission electron microscope study of Itokawa regolith grains. *Earth Planets Space*, 66, 71.
- Kimura H., Senshu H., and Wada K. (2014) Electrostatic lofting of dust aggregates near the terminator of airless bodies and its implication for the formation of exozodiacal disks. *Planet. Space Sci.*, 100, 64–72.
- Kitajima F. and 19 colleagues (2011) A micro-spectroscopic approach to the carbonaceous matter in the particles recovered by the Hayabusa mission. *Lunar Planet. Sci. XLII*, Abstract #1855. Lunar and Planetary Institute, Houston.
- Kitazato K., Abe M., Ishiguro M., and Ip W.-H. (2007) 25143 Itokawa: Direct detection of the current decelerating spin state due to YORP effect. *Astron. Astrophys.*, 472, L5–L8.
- Langenhorst F., Harries D., Pollock K., and van Aken P. A. (2014) Mineralogy and defect microstructure of an olivine-dominated Itokawa dust particle: Evidence for shock metamorphism, collisional fragmentation, and LL chondrite origin. *Earth Planets Space*, 66, 118.
- Lederer S. M., Domingue D. L., Vilas F., Abe M., Farnham T. L., Jarvis K. S., Lowry S. C., Ohba Y., Weissman P. R., French L. M., Fukai H., Hasagawa S., Ishiguro M., Larson S. M., and Takagi Y. (2005) Physical characteristics of Hayabusa target asteroid 25143 Itokawa. *Icarus*, 173, 153–165.
- Lee P. (1996) Dust levitation on asteroids. *Icarus*, 124, 181–194.
- Lee P., Veverka J., Thomas P. C., Helfenstein P., Belton M. J. S., Chapman C. R., Greeley R., Pappalardo R. T., Sullivan R., Head J. W. III (1996) Ejecta blocks on 243 Ida on other asteroids. *Icarus*, 120, 87–105.
- Lowry S. C., Weissman P. R., Hicks M. D., Whitely R. J., and Larson S. (2005) Physical properties of asteroid (25143) Itokawa — target of the Hayabusa sample return mission. *Icarus*, 176, 408–417.
- Lowry S. C., Weissman P. R., Duddy S. R., Rozitis B., Fitzsimmons A., Green S. F., Hicks M. D., Snodgrass C., Wolters S. D., Chesley S. R., Pittichová J., and van Oers P. (2014) The internal structure of asteroid (25143) Itokawa as revealed by detection of YORP spin-up. *Astron. Astrophys.*, 562, A48, DOI: 10.1051/0004-6361/201322602.
- Matsumoto T. and 18 colleagues (2012) Micro-structures of particle surfaces of Itokawa regolith and LL chondrite fragments. *Lunar Planet. Sci. XLIII*, Abstract #1969. Lunar and Planetary Institute, Houston.
- Matsumoto T. and 9 colleagues (2014) Surface micromorphologies of regolith particles from asteroid Itokawa and its implication to space weathering. *Meteoritics & Planet. Sci., Suppl.*, 49, A266.
- Matsumoto T., Tsuchiya A., Miyake A., Noguchi T., Nakamura M., Uesugi K., Takeuchi A., Suzuki Y., and Nakano T. (2015) Surface and internal structures of a space-weathered rim of an Itokawa regolith particle. *Icarus*, in press.
- Matsuura S., Richardson D. C., Michel P., Schwarz S., and Ballouz R. (2014) The Brazil nut effect and its application to asteroids. *Mon. Not. R. Astron. Soc.*, 443, 3368–3380.
- Mazrouei S., Daly M., Barnouin O., Ernst C. M., and DeSouza I. (2014) Block distribution on Itokawa. *Icarus*, 229, 181–189.
- Meier M. M. M. and 16 colleagues (2014) A precise cosmic-ray age for an olivine grain from the surface of near-Earth asteroid (25143) Itokawa. *Lunar Planet. Sci. XLIV*, Abstract #1247. Lunar and Planetary Institute, Houston.
- Michel P. and Richardson D. C. (2013) Collision and gravitational reaccumulation: Possible formation mechanism of the asteroid Itokawa. *Astron. Astrophys.*, 554, L1–L4.
- Michel P. and Yoshikawa M. (2005) Earth impact probability of the asteroid (25143) Itokawa to be sampled by the spacecraft Hayabusa. *Icarus*, 179, 291–296.
- Michel P. and Yoshikawa M. (2006) Dynamical origin of asteroid (25143) Itokawa: The target of the sample return mission Hayabusa. *Astron. Astrophys.*, 449, 817–820.
- Michel P., Benz W., Tanga P., and Richardson D. C. (2001) Collisions and gravitational reaccumulation: Forming asteroid families and satellites. *Science*, 294, 1696–1700.
- Michel P., O'Brien D. P., Abe A., and Hirata N. (2009) Itokawa's cratering record as observed by Hayabusa: Implications for its age and collisional history. *Icarus*, 200, 503–513.
- Michikami T., Moriguchi K., Hasegawa S., and Fujiwara A. (2007) Ejecta velocity distribution for impact cratering experiments on porous and low strength targets. *Planet. Space Sci.*, 55, 70–88.
- Michikami T., Nakamura A. M., Hirata N., Gaskell R., Nakamura R., Honda C., Hiraoka K., Saito J., Demura H., Ishigura M., and Miyamoto H. (2008) Size-frequency statistics of boulders on global surface on asteroid 25143 Itokawa. *Earth Planets Space*, 60, 13–20.
- Mikouchi T. and 17 colleagues (2014) Mineralogy and crystallography of some Itokawa particles returned by the Hayabusa asteroidal sample return mission. *Earth Planets Space*, 66, 82.
- Miyamoto H., Yano H., Scheeres D., Abe S., Barnouin-Jha O. S., Cheng A. F., Demura H., Gaskell R. W., Hirata N., Ishiguro M., Michikami T., Nakamura A. M., Nakamura R., Saito J., and Sasaki S. (2007) Regolith migration and sorting on asteroid Itokawa. *Science*, 316, 1011–1014.
- Mueller T. G., Sekiguchi T., Kaasalainen M., Abe M., and Hasegawa S. (2005) Thermal infrared observations of the Hayabusa spacecraft target asteroid 25143 Itokawa. *Astron. Astrophys.*, 443, 347–355.
- Mukai T., Abe S., Hirata N., Nakamura R., Barnouin-Jha O. S., Cheng A. F., Mizuno T., Matsuoka M., Scheeres D. J., and Yoshikawa M. (2007) An overview of the LIDAR observations of asteroid 25143 Itokawa. *Adv. Space Res.*, 40, 187–192.
- Nagao K. and 25 colleagues (2011) Irradiation history of Itokawa regolith material deduced from noble gases in the Hayabusa samples. *Science*, 333, 1128–1131.
- Nagao K., Okazaki R., Miura Y. N., Osawa T., Gilmour J., and Nishimura Y. (2013) Noble gas analysis of two Hayabusa samples as the first international A/O investigation: A progress report. *Lunar Planet. Sci. XLIV*, Abstract #1976. Lunar and Planetary Institute, Houston.
- Nakamura A. and Fujiwara A. (1991) Velocity distribution of fragment formed in a simulated collisional disruption. *Icarus*, 92, 132–146.

- Nakamura T. and 11 colleagues (2007) Chondrule-like objects in short-period Comet 81P/Wild 2. *Science*, **321**, 1664–1667.
- Nakamura A. M., Michikami T., Hirata N., Fujiwara A., Nakamura R., Ishiguro M., Demura H., Miyamoto H., Hiraoka T., Honda C., Saito J., Hashimoto T., and Kubota T. (2008a) Impact process of boulders on the surface of asteroid 25143 Itokawa — Fragments from collisional disruption. *Earth Planets Space*, **60**, 7–12.
- Nakamura T. and 7 colleagues (2008b) Bulk mineralogy and three-dimensional structures of individual Stardust particles deduced from synchrotron X-ray diffraction and microtomography analysis. *Meteoritics & Planet. Sci.*, **43**, 247–259.
- Nakamura T. and 21 colleagues (2011) Itokawa dust particles: A direct link between S-type asteroids and ordinary chondrites. *Science*, **333**, 1113–1116.
- Nakamura E. and 17 colleagues (2012) Space environment of an asteroid preserved on micrograins returned by the Hayabusa spacecraft. *Proc. Natl. Acad. Sci.*, **109**, E624–E629.
- Nakamura T. and 22 colleagues (2014) Mineral chemistry of MUSES-C Regio inferred from analysis of dust particles collected from the first- and second-touchdown sites on asteroid Itokawa. *Meteoritics & Planet. Sci.*, **49**, 215–227.
- Nakashima D., Kita N. T., Ushikubo T., Noguchi T., Nakamura T., and Valley J. W. (2013) Oxygen three-isotope ratios of silicates particles returned from asteroid Itokawa by the Hayabusa spacecraft: A strong link with equilibrated LL chondrites. *Earth Planets Sci. Lett.*, **379**, 127–136.
- Naraoka H. and 25 colleagues (2012) Preliminary organic compound analysis of microparticles returned from asteroid 25143 Itokawa by the Hayabusa mission. *Geochem. J.*, **46**, 61–72.
- Noguchi T., Tsuchiyama A., Hirata N., Demura H., Nakamura R., Miyamoto H., Yano H., Nakamura T., Saito J., Sasaki S., Hashimoto T., Kubota T., Ishiguro M., and Zolensky M. E. (2010) Surface morphological features on asteroid 25143 Itokawa. *Icarus*, **206**, 319–328.
- Noguchi T. and 17 colleagues (2011) Incipient space weathering observed on the surface of Itokawa dust particles. *Science*, **333**, 1121–1125.
- Noguchi T. and 23 colleagues (2014a) Space weathered rims found on the surfaces of the Itokawa dust particles. *Meteoritics & Planet. Sci.*, **49**, 188–214.
- Noguchi T. and 16 colleagues (2014b) Mineralogy of four Itokawa particles collected from the first touchdown site. *Earth Planets Space*, **66**, 124.
- Noguchi T. and 16 colleagues (2014c) Sylvite and halite on particles recovered from 25143 Itokawa: A preliminary report. *Meteoritics & Planet. Sci.*, **49**, 1305–1314.
- Nolan M. C., Asphaug E., Melosh H. J., and Greenberg R. (1996) Impact craters on asteroids: Does gravity or strength control their size? *Icarus*, **124**, 359–212.
- Ohba Y., Abe M., Hasagawa S., Ishiguro M., Kwiatkowski T., Colas F., Dermawan B., and Fujiwara A. (2003) Pole orientation and triaxial ellipsoid shape of (25143) 1998 SF<sub>36</sub>, a target asteroid of the MUSES-C mission. *Earth Planets Space*, **55**, 341–347.
- Ohtsuka K., Abe S., Ito T., Nakamura T., Abe M., Yano H., and Watanabe J. (2011) Do meteoroids originating from near-Earth asteroid (25143) Itokawa exist? *Publ. Astron. Soc. Japan*, **63**, L73–L77.
- Okazaki R. and 9 colleagues (2011) Noble gas recovered from the Hayabusa sample container. *Lunar Planet. Sci. XLII*, Abstract #1653. Lunar and Planetary Institute, Houston.
- Onose N. and Fujiwara A. (2004) Mass-velocity distribution of fragments in oblique impact on gypsum. *Meteoritics & Planet. Sci.*, **39**, 321–331.
- Ostro S. J., Benner L. A. M., Nolan M. C., Magri C., Giorgini J. D., Scheeres D. J., Broschart S. B., Kaasalainen D. J., Vokrouhlický D., Chesley S. R., Margot J., Jurgens R. F., Rose R., Yeomans D. K., Suzuki S., and DeJong E. M. (2004) Radar observations of asteroid 25143 Itokawa (1998 SF<sub>36</sub>). *Meteoritics & Planet. Sci.*, **39**, 407–424.
- Ostro S. J., Benner L. A. M., Magri C., Giorgini J. D., Rose R., Jurgens R. F., Yeomans D. K., Hine A. A., Nolan M. C., Scheeres D. J., Broschart S. B., Kaasalainen M., and Margot J. (2005) Radar observations of Itokawa in 2004 and improved shape estimation. *Meteoritics & Planet. Sci.*, **40**, 1563–1574.
- Pieters C. M. and 8 colleagues (2000) Space weathering on airless bodies: Resolving a mystery with lunar samples. *Meteoritics & Planet. Sci.*, **35**, 1101–1107.
- Pravec P., Harris A. W., and Michalowski T. (2002) Asteroid rotaion. In *Asteroids III* (W. F. Bottke Jr. et al., eds.), pp. 113–122. Univ. of Arizona, Tucson.
- Robinson M. S., Thomas P. C., Veverka J., Murchie S. L., and Wilcox B. B. (2002) The geology of 433 Eros. *Meteoritics & Planet. Sci.*, **37**, 1651–1684.
- Saito J., Miyamoto H., Nakamura R., Ishiguro M., Michikami T., Nakamura A. M., Demura H., Sasaki S., Hirata N., Honda C., Yamamoto A., Yokota Y., Fuse T., Yoshida F., Tholen D. J., Gaskell R. W., Hashimoto T., Kubota T., Higuchi Y., Nakamura T., Smith P., Hiraoka K., Honda T., Kobayashi S., Furuya M., Matsumoto N., Nemoto E., Yukishita A., Kitazato K., Dermawan B., Sogame A., Terazono J., Shinohara C., and Akiyama H. (2006) Detailed images of asteroid 25143 Itokawa from Hayabusa. *Science*, **312**, 1341–1344.
- Sasaki S., Nakamura K., Hamabe Y., Kurahashi E., and Hiroi T. (2001) Production of iron nanoparticles by laser irradiation in a simulation of lunar-like space weathering. *Nature*, **410**, 555–557.
- Seikuchi T., Abe M., Boehnhardt H., Dermawan B., Hainaut O. R., and Hasegawa S. (2003) Thermal observations of MUSES-C mission target (25143) 1998 SF<sub>36</sub>. *Astron. Astrophys.*, **397**, 325–328.
- Scheeres D. J. and Gaskell R. W. (2008) Effect of density inhomogeneity on YORP: The case of Itokawa. *Icarus*, **198**, 125–129.
- Scheeres D. J., Gaskell R., Abe S., Barnouin-Jha O., Hashimoto T., Kawaguchi J., Kubota T., Saito J., Yoshikawa M., Hirata N., Mukai T., Ishiguro M., Kominato T., Shirakawa K., and Uo M. (2006) The actual dynamical environment about Itokawa. *AIAA/AAS Astrodynamics Specialist Conference and Exhibit*, AIAA 2006-6661.
- Scheeres D. J., Abe M., Yoshikawa M., Nakamura R., Gaskell R. W., and Abell P. A. (2007) The effect of YORP on Itokawa. *Icarus*, **188**, 425–429.
- Sharma I. (2010) Equilibrium shapes of rubble-pile binaries: The Darwin ellipsoids for gravitationally held granular aggregates. *Icarus*, **205**, 638–657.
- Sullivan R., Greely R., Pappalardo R., Asphaug E., Moore J. M., Morrison D., Belton M. J. S., Carr M., Geissler P., Greenberg R., Granahan J., Head J. W., Kirk R., McEwen A., Lee P., Thomas P. C., and Veverka J. (1996) Geology of 243 Ida. *Icarus*, **120**, 119–139.
- Tanaka M. and 12 colleagues (2014) Crystallization temperature determination of Itokawa particles by plagioclase thermometry with X-ray diffraction data obtained by a high-resolution synchrotron Gandolfi camera. *Meteoritics & Planet. Sci.*, **49**, 237–244.
- Thomas P. C., Veverka J., Robinson M. S., and Murchie S. (2001) Shoemaker crater as the source of most ejecta blocks on the asteroid 433 Eros. *Nature*, **413**, 394–396.
- Thompson M. S., Christoffersen R., Zega T. Z., and Keller L. P. (2014) Microchemical and structural evidence for space weathering in soils from asteroid Itokawa. *Earth Planets Space*, **66**, 89.
- Tsuchiyama A. (2014) Asteroid Itokawa: A source of ordinary chondrites and a laboratory for surface processes. *Elements*, **10**, 45–50.
- Tsuchiyama A. and 12 colleagues (2009) Three-dimensional structures and elemental distributions of Stardust impact tracks using synchrotron microtomography and X-ray fluorescence analysis. *Meteoritics & Planet. Sci.*, **44**, 1203–1224.
- Tsuchiyama A. and 32 colleagues (2011) Three-dimensional structure of Hayabusa samples: Origin and evolution of Itokawa regolith. *Science*, **333**, 1125–1128.
- Tsuchiyama A., Matsumoto T., Nagano T., and Matsuno J. (2012) Microstructures of voids in Itokawa particles collected by Hayabusa. *Meteoritics & Planet. Sci.*, **47**, A386.
- Tsuchiyama A. and 12 colleagues (2013a) Analytical dual-energy microtomography: A new method for obtaining three-dimensional mineral phase images and its application to Hayabusa samples. *Geochim. Cosmochim. Acta*, **116**, 5–16.
- Tsuchiyama A., Matsumoto T., and Noguchi T. (2013b) “Space erosion”: A new type of space weathering process on the surface of asteroid Itokawa. *Lunar Planet. Sci. XLIV*, Abstract #2169. Lunar and Planetary Institute, Houston.
- Tsuchiyama A. and 11 colleagues (2013c) 3D shapes of regolith particles: Comparison between Itokawa and Moon. *Goldschmidt 2013 Conference*, Abstract #2361.
- Tsuchiyama A. and 16 colleagues (2014) Three-dimensional microstructure of samples recovered from asteroid 25143 Itokawa: Comparison with LL5 and LL6 chondrite particles. *Meteoritics & Planet. Sci.*, **49**, 172–187.

- Tsuda Y., Yoshikawa M., Abe M., Minamino H., and Nakazawa S. (2013) System design of the Hayabusa 2 — Asteroid sample return mission to 1999 JU<sub>3</sub>. *Acta Astronautica*, **91**, 356–362.
- Uesugi U. and 14 colleagues (2014) Sequential analysis of carbonaceous materials in Hayabusa — returned samples for the determination of their origin. *Earth Planets Space*, **66**, 102.
- Yamada T. and Katsuragi H. (2014) Scaling of convective velocity in a vertically vibrated granular bed. *Planet. Space Sci.*, **100**, 79–86.
- Vernazza P., Binzel R. P., Rossi A., Fulchignoni M., and Birlan M. (2009) Solar wind as the origin of rapid reddening of asteroid surfaces. *Nature*, **458**, 993–995.
- Everka J., Belton M., Klaasen K., and Chapman C. (1994) Galileo's encounter with 951 Gaspra: Overview. *Icarus*, **107**, 2–17.
- Vokrouhlický D., Čapek D., Kaasalainen M., and Ostro S. J. (2004) Detectability of YORP rotational slowing of asteroid 25143 Itokawa. *Astron. Astrophys.*, **414**, L21–L24.
- Wakita S., Nakamura T., Ikeda T., and Yurimoto H. (2014) Thermal modeling for a parent body of Itokawa. *Meteoritics & Planet. Sci.*, **49**, 228–236.
- Whitely R. J., Tholen D., and Hergueroth C. W. (2002) Lightcurve analysis of four new monolithic fast-rotation asteroids. *Icarus*, **157**, 139–154.
- Wieler R. (2002) Noble gases in the solar system. *Rev. Mineral. Geochem.*, **47**, 21–70.
- Yada T. and 19 colleagues (2014a) HayabusaReturned sample curation in the Planetary Material Sample Curation Facility of JAXA. *Meteoritics & Planet. Sci.*, **49**, 135–153.
- Yada T. and 8 colleagues (2014b) A nature of particles in the Hayabusa sample catcher and contamination controls for Hayabusa2 sample containers. *Meteoritics & Planet. Sci., Suppl.*, **49**, A444.
- Yano H., Kubota T., Miyamoto H., Okada T., Scheeres D., Takagi Y., Yoshida K., Abe M., Abe S., Barnouin-Jha O., Fujiwara A., Hasegawa S., Hashimoto T., Ishiguro M., Kato M., Kawaguchi J., Mukai T., Sasaki S., and Yoshikawa M. (2006) Touchdown of the Hayabusa spacecraft at Muse Sea on Itokawa. *Science*, **312**, 1350–1353.
- Yoshikawa M., Watanabe S., Tsuda Y., and Kuninaka H. (2014) Hayabusa2 — The next asteroid sample return mission of Japan. *Trans. JSASS Aerospace Tech. Japan*, **12**(29), Tk\_29 to Tk\_33.
- Yurimoto H. and 32 colleagues (2011a) Oxygen isotopic compositions of asteroidal materials returned from Itokawa by the Hayabusa mission. *Science*, **333**, 1116–1119.
- Yurimoto H. and 32 colleagues (2011b) Oxygen and magnesium isotopic compositions of asteroid 25143 Itokawa returned by the Hayabusa mission. *Meteoritics & Planet. Sci., Suppl.*, **46**, A260.
- Zolensky M. E., Bodnar R. J., Gibson E. K., Gounelle M., Nyquist L. E., Reese Y., Shih C.-Y., and Wiesmann H. (1999) Asteroidal water within fluid inclusion-bearing halite in an H5 chondrite. *Science*, **285**, 1377–1379.
- Zolensky M. E. and 23 colleagues (2012) The shock state of Itokawa samples. *Lunar Planet. Sci. XLIII*, Abstract #1477. Lunar and Planetary Institute, Houston.
- Zolensky M., Nishizumi K., Mikouchi T., Chan Q. H. S., Martinez J., and Caffee M. (2014) Shock state of Itokawa regolith grains. *Hayabusa 2014: 2nd Symposium of Solar System Materials Abstracts*.

# The Dawn Mission to Vesta and Ceres

C. T. Russell

*University of California*

H. Y. McSween

*University of Tennessee*

R. Jaumann

*German Aerospace Center*

C. A. Raymond

*Jet Propulsion Laboratory*

---

The objective of the Dawn mission is to travel back in time by interviewing two intact survivors of the earliest days of the solar system in the heart of the asteroid belt. The means of transport is a solar-powered spacecraft using electrostatically accelerated xenon ions to propel the flight system outward in the solar gravitational well to the points where it can orbit Vesta and later Ceres. While in orbit, it completely maps the surface topography, composition, and gravitational fields of the target bodies. At this writing, the Vesta phase of the mission is complete, and the spacecraft is nearing Ceres. Vesta's structure and composition are consistent with it being the parent body of the howardite, eucrite, and diogenite meteorites (HEDs). Although heavily bombarded and sheathed in a thick regolith, Vesta is largely intact and shows signs of possible endogenic processes, suggesting that Vesta is neither completely dry nor dormant. Resurfacing due to impacts and associated gravitational forces and seismic activity dominate the complex geologic history. While early understanding of Vesta's differentiation was modeled using very simple magma ocean models, Dawn's observations coupled with geochemical analyses of HEDs suggest a more complex evolutionary path. Since Ceres has provided no recognizable meteorites to our terrestrial collections, our pre-encounter understanding of Ceres is much less informed than it was at Vesta. Remote sensing has prepared us for a darker, water-rich environment.

## 1. INTRODUCTION

Geochemical investigations of meteorites pinpoint the beginning of the solar system to be 4.567 Ga, when the calcium-aluminum-rich inclusions (CAIs) were formed. At that time, the solar system was seeded with short-lived radioactive elements such as  $^{26}\text{Al}$  and bodies that accreted then trapped these radionuclides and their heat. If sufficiently large, the earliest-formed bodies melted and differentiated. The differentiation led to metallic cores, ultramafic mantles, and mafic crusts. Bodies that accreted later did not incorporate as much radiogenic heat of short-lived nuclides, and hence did not differentiate, so they did not devolatilize as completely as those formed earlier. The period of accretion in the region of the asteroid belt is thought to have continued until the formation of Jupiter, whose gravitational stirring perturbed the more regular orbits present in the earlier days of the solar system. Eventually the outer solar system became

fully developed, and interactions between the giant planets led to their migration, possibly into the asteroid belt, causing havoc and much scattering among the original members of the belt (Tsiganis *et al.*, 2005; Walsh, 2012).

While early civilizations realized that Venus, Mars, Jupiter, and Saturn existed, the only hint of the asteroid belt's existence was a gap where a planet should have existed, if the solar system followed a regular sequence. In the eighteenth century, this led astronomers to postulate such a body; and in the beginning of the nineteenth century, astronomers were rewarded by the discovery of (1) Ceres in 1801 and (4) Vesta in 1807. Remote sensing data eventually linked Vesta to the howardite-eucrite-diogenite (HED) meteorites (McCord *et al.*, 1970), but no link to Ceres has been found in the meteorite collection. Geochemical analysis of these meteorites provided a glimpse of the composition and structure of its parent body, but these studies took us only so far. We needed to obtain a closer look than remote sensing and

geochemistry could provide. Even the resolved imagery of the Hubble Space Telescope did little but increase the desire to visit the major asteroids.

In the early days of space exploration, flagship missions were sent to the major planets while the minor planets were ignored. It took the advent of NASA's Discovery program in 1992, which allows a principal investigator to lead a focused investigation to a particular target, for attention to turn to the minor planets. The Near Earth Asteroid Rendezvous (NEAR) mission (Russell, 1997) was one of the first two Discovery class missions and was sent to the near-Earth asteroid (433) Eros. In order to study larger asteroids, farther away, a much greater change in spacecraft velocity was required. Fortunately, xenon ion thrusters had become available that could accomplish the significant change in velocity required by such missions. By the time of the celestial alignment of Vesta and Ceres that enabled a visit to both on a single mission, these thrusters had been tested by the Deep Space 1 (DS-1) spacecraft and were ready for use on Discovery missions. The Dawn team's proposal to NASA was selected for implementation in 2001, launched in 2007, reaching Vesta in July 2011, leaving in September 2012, and currently destined to arrive at Ceres in March 2015.

## 2. THE DAWN MISSION

The Dawn spacecraft (Fig. 1) is powered by a large solar array that can rotate to allow the panels to remain orthogonal to the solar direction while the spacecraft points its instruments either at the body around which it orbits or to its telemetry antenna at Earth. It has two means of orienting itself in space: reaction wheels and thrusters. The reaction wheels were available for Vesta mapping, but most of the Ceres mission will be performed using the thrusters. The spacecraft carries a framing camera (FC) (Sierks *et al.*, 2011) that returns either clear filter images or images in one of seven color bands in the visible and near-infrared (IR). A visible and IR mapping spectrometer (VIR) (De Sanctis *et al.*, 2011) also covers the visible range and extends further into the near-IR. Here the silicate pyroxene has several absorption bands that allow the separation of diogenite and eucrite as well as the

identification of olivine. The VIR instrument has greater sensitivities for mineral identifications, but the FC provides greater spatial resolution and hence these two instruments are complementary. A gamma-ray and neutron detector (GRaND) (Prettyman *et al.*, 2011) provides elemental abundances of the major rock-forming elements (including H, Fe, Si, K, and O and other elements) included in a determination of mean atomic mass. The mineralogical and chemical data from Dawn's instruments have solidified the link between Vesta and the HEDs (McSween *et al.*, 2013a), allowing the meteorites to be used in instrument calibration and data interpretation. The camera is used to obtain topographic information by acquiring images from different vantage points (Raymond *et al.*, 2011), and radiometric tracking allows the gravity field to be determined (Konopliv *et al.*, 2011).

The science data are acquired in three separate orbits called the survey orbit, high-altitude mapping orbit (HAMO), and low-altitude mapping orbit (LAMO), as shown in Fig. 2. The HAMO observations were repeated as Dawn was leaving Vesta to obtain more complete stereo coverage and to see closer to the pole. The initial gravity field is determined in the survey orbit as is the VIR's global, but low-resolution, mineralogy map. In HAMO, the FC is the prime instrument obtaining full coverage and multiple views for topography. In LAMO, both the gravity survey and the GRaND measurements are prime, but there are ride-along measurements



**Fig. 1.** See Plate 6 for color version. The Dawn spacecraft depicted as it left Earth on September 27, 2007.

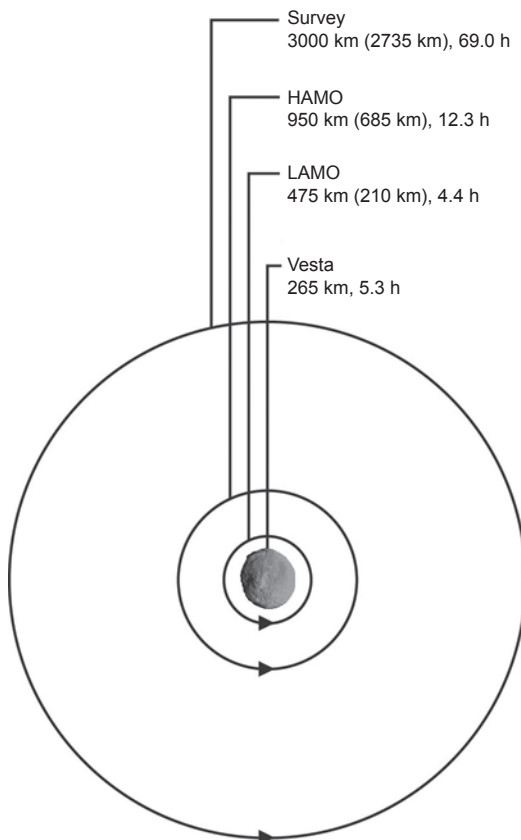


**Fig. 2.** Dawn's orbits at Vesta giving the orbital radii, altitudes, and periods. Vesta's rotational period is 5.3 h.

that provide high-resolution near-global imaging by the FC and targeted coverage with VIR. The observation plans for Ceres are similar to those used at Vesta, adjusted for Ceres' larger size. A summary of the mission can be found in the overview and accompanying articles of a special issue of the journal *Space Science Reviews* (Russell and Raymond, 2011).

One of the objectives of the Dawn mission is to produce geologic maps of the surfaces at Vesta and Ceres. To accomplish this, Vesta was divided into 15 quadrangles (Roatsch, 2012, 2013). A band of five quadrangles is identified around the equator going from  $0^{\circ}$  to  $360^{\circ}$  in  $72^{\circ}$  steps with a north-south extent of  $\pm 22.5^{\circ}$ . Above and below this are two bands of four quadrangles, each  $90^{\circ}$  in extent, also beginning at  $0^{\circ}$  and  $45^{\circ}$  wide in latitude. The north and south polar cap quadrangles had radii of  $22.5^{\circ}$ . Since Dawn found a significantly different rotation axis than had been derived from groundbased data, and since the earlier longitude reference was a broad feature whose source was not obvious in Dawn's images, a new coordinate system was drawn that was anchored in the small crater Claudia whose position could be well measured; this system used a prime meridian that was different than that derived previously. The Dawn project felt there were advantages to defining a new system to clearly distinguish it from the older system based on the incorrect pole. Subsequently, the International Astronomical Union (IAU) approved a system using the new rotational elements but with a prime meridian defined to align with that of the pre-Dawn system. To date, all papers in the literature use the Claudia-anchored Dawn coordinate system. Data in this coordinate system are available from the Dawn project (<http://dawndata.igpp.ucla.edu>). For Ceres, close collaboration with the IAU has been established to define the Ceres coordinate system.

The names selected for Vesta's craters were drawn from an IAU-approved database based on the written history of the Vestals, who devoted themselves to the service of

the goddess Vesta. This was supplemented with a list of historical Roman women. Other feature names were associated with festivals related to Vesta and Roman towns. Naming has gone smoothly and an analogous process with a different theme is in progress for Ceres. Figure 3 shows a mosaic of the surface of Vesta in Dawn Claudia coordinates with the names approved to date. Figure 4 shows the same projection of the FC color data, using Clementine color ratio composites, as derived for the Clementine mission data analysis (*Pieters et al.*, 2011). These ratios demonstrate the broad chemical diversity of the vestan surface, indicating that our simplistic models of Vesta's formation and evolution needed revision.

As had been proposed originally for both Vesta and Ceres, participating scientists were added to the science team in the year before arrival at Vesta. Many of these new participants had experience developing geologic maps of planetary surfaces. When the images were returned to Earth, these geologic mappers selected quadrangles and mapped their geology. These maps were then combined into a planet-wide geologic map as shown in Fig. 5. In addition to the geologic characterization of the surface, Dawn determined Vesta's physical properties. Vesta has a mass of  $2.591 \times 10^{20}$  kg, with a volume of  $74.97 \times 10^6$  km $^3$ , resulting in an average density of 3456 kg m $^{-3}$  (*Russell et al.*, 2012). Its shape is described by a triaxial ellipsoid of radii 286.3/278.6/223.2 km.

### 3. EVOLUTION OF CRUST

The Dawn spacecraft extensively imaged Vesta's surface, revealing a collision-dominated history. Vesta's cratering record has a strong north-south dichotomy (Figs. 3, 4, and 5). The northern heavily cratered terrains retain much of their earliest history, while the southern hemisphere was reset by two major collisions in more recent times (Fig. 6). The younger, larger Rheasilvia basin, centered at 300°E and 78°S,

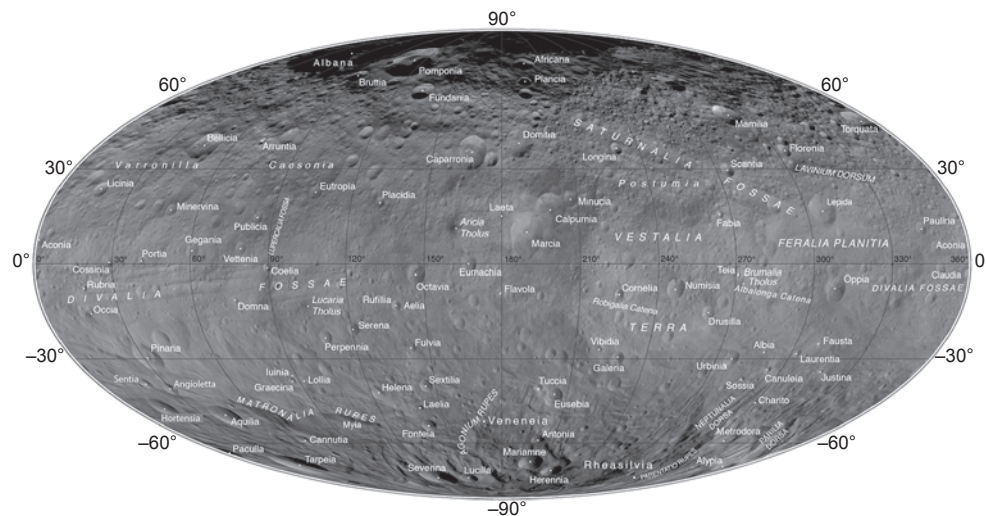


**Fig. 3.** Mosaic of Vesta's surface using Mollweide projection. Names of surface features are those approved by the International Astronomical Union (IAU) at the time of this writing. From Roatsch *et al.* (2014).



**Fig. 4.** See Plate 7 for color version. Mollweide projection of FC color mosaic using Clementine ratios (A. Nathues, personal communication, 2014).

has a diameter of  $500 \pm 25$  km and a central mound 180 km wide and about 20 km high, and the older, more degraded Veneneia basin, centered at  $173^{\circ}\text{E}$ ,  $51^{\circ}\text{S}$ ,  $400 \pm 25$  km wide, is partly overlapped by the Rheasilvia structure (Russell *et al.*, 2012; Jaumann *et al.*, 2012; Schenk *et al.*, 2012). The Rheasilvia event occurred at about 1 Ga (Schenk *et al.*, 2012; Marchi *et al.*, 2012) according to an asteroid flux-derived chronology (e.g., O'Brien *et al.*, 2014) or 3.5 Ga, according to a lunar-derived chronology (e.g., Schmedemann *et al.*, 2014). The material excavated by this collision formed asymmetric mega-ejecta deposits close to Vesta's equator as can be seen in the global topography shown in Fig. 7. Because Vesta was subject to intense cratering, impact-related processes played a major role in (re)shaping the surface. With respect to their erosional appearance, impact craters on Vesta range from fresh craters, showing sharp, uneroded crater rims and ejecta deposits, to craters with heavily degraded, even ruined, crater rims (Jaumann *et al.*, 2012).

Large-scale structural features, including sets of graben, occur in the equatorial and northern regions of Vesta, as

shown well in Fig. 7. The equatorial troughs (Divalia formation) are wide, flat-floored, and bounded by steep scarps circling about two-thirds of the asteroid, as illustrated in the FC image shown in Fig. 8. Their lengths vary from 19 to 380 km and can be as wide as 15 km (Jaumann *et al.*, 2012). Muted troughs, grooves, and pit crater chains are evident in the remaining part of the asteroid (Jaumann *et al.*, 2012; Buczkowski *et al.*, 2012). The other set of large-scale linear trough structures extend to the northwest at an angle of about  $30^{\circ}$  from the equatorial troughs (Saturnalia formation). The primary structure in this group is 390 km long and 38 km wide. Although larger than the equatorial troughs, their walls display gentler slopes and rounded edges. They show considerable infilling and heavy cratering, suggesting an older age (Jaumann *et al.*, 2012; Buczkowski *et al.*, 2012). Most of the large-scale graben are co-planar (Buczkowski *et al.*, 2012). The poles of the global equatorial and northern troughs agree within the errors with the coordinates of the basin centers of Rheasilvia ( $318^{\circ}\text{E}$ ,  $70^{\circ}\text{S}$ ) and Veneneia ( $173^{\circ}\text{E}$ ,  $51^{\circ}\text{S}$ ) at the south pole (Jaumann *et al.*, 2012; Buczkowski *et al.*, 2012), respectively. This strongly suggests that the formation of the troughs is related to the formation of the basins as extensional graben. The older sets of graben are exposed only in the northern hemisphere; they were obliterated in the southern hemisphere by the Rheasilvia impact. This is consistent with the younger age of Rheasilvia, and also indicates that all structures in the southern hemisphere were destroyed or at least affected by the Rheasilvia impact and its ejecta (Jaumann *et al.*, 2012).

Vesta can be divided geologically into three terrain types: heavily cratered terrain; ridge-and-trough terrain (equatorial and northern); and terrain associated with the Rheasilvia basin (Fig. 5) (Jaumann *et al.*, 2012; Yingst *et al.*, 2014; Williams *et al.*, 2014c). Localized features include bright and dark material and ejecta (some defined specifically by color), lobate deposits, and mass-wasting materials (Otto *et*

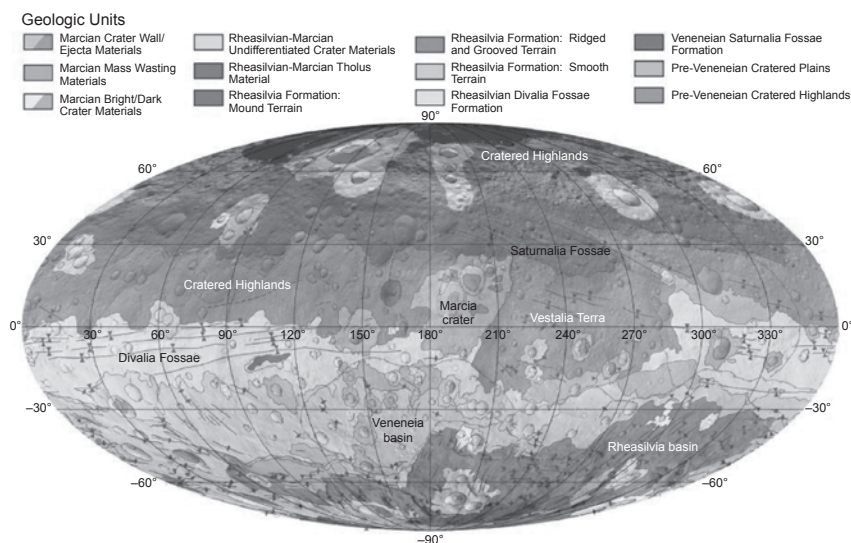


**Fig. 5.** See Plate 8 for color version. Geologic map of Vesta using Mollweide projection. Major terrains are identified here. From Jaumann *et al.* (2012) and Williams *et al.* (2014a).

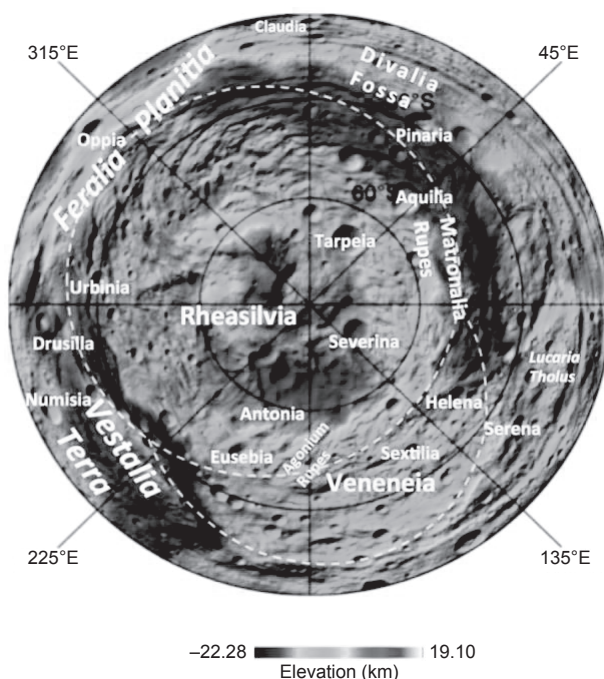


**Fig. 6.** See Plate 9 for color version. The Veneneia and Rheasilvia south polar basins and their geological environment. From Jaumann et al. (2012).

al., 2013; Krohn et al., 2014a). The ages of these deposits range from 3.4 Ga for ancient cratered highlands and the Saturnalia Fossa formation, to 100 Ma or less for more recent deposits associated with Marcia crater (Fig. 5). The units associated with the Rheasilvia impact structure range from 1.5 to 1.8 Ga (Marchi et al., 2012; Schmedemann et al., 2014; Williams et al., 2014c). Stratigraphy of Vesta's geologic units suggests a history in which magmatic differentiation and crystallization of a primary crust were followed by the formation of impact basins and craters, including Veneneia and the associated Saturnalia formation. Formation of Rheasilvia followed, along with associated structural deformation that formed the Divalia ridge-and-trough formation at the equator (Figs. 7 and 8). Subsequent impacts and mass wasting events subdued impact craters, basin rims, and portions of ridge-and-trough sets, and formed slumps and landslides, especially within crater floors and along basin rims and scarps (Jaumann et al., 2012). Subsequent to the Rheasilvia formation, discontinuous low-albedo deposits were emplaced stratigraphically above the equatorial ridges that likely were triggered by the Rheasilvia event. The latest features to be formed were craters with bright rays and other surface mantling deposits.

The geologic maps also enabled the development of a time stratigraphic sequence for Vesta (Fig. 9). We identified four geologic time periods: pre-Veneneian, Veneneian, Rheasilvian, and Marcian (Williams et al., 2014a). The Pre-Veneneian period covers the time from the formation of Vesta (1–2 m.y. after the formation of the first solids in the protosolar disk) up to the Veneneia impact event. The

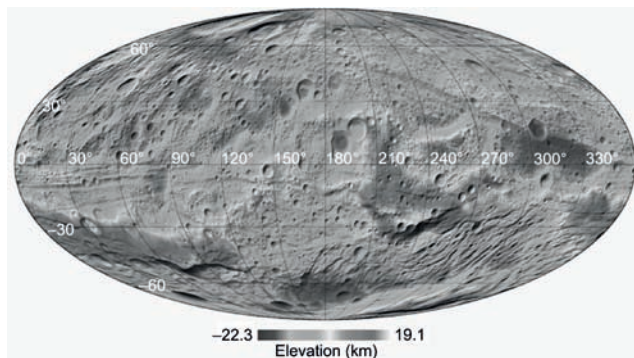


**Fig. 7.** See Plate 10 for color version. Mollweide projection of Dawn topography data.



**Fig. 8.** Divalia Fossae, large-scale grabens on Vesta circling around the equator. The tectonic graben structures are related to the Rheasilvia and Veneneia impacts.

Veneneian period encompasses the time between the Veneneia and Rheasilvia impact events. The Rheasilvian period is defined as the time between the formation of Rheasilvia and Marcia craters, and the Marcian period covers the time between the formation of Marcia crater until the present. Absolute ages for the boundaries of these periods have been derived by applying two crater chronologies: One is based on the current understanding on asteroidal impact rate at Vesta and its evolution over time (Marchi et al., 2014), and the other is based on an extrapolated version of the lunar crater chronology (Schmedemann et al., 2014). While the ages and durations of the various periods change considerably depending on which chronology is applied, the relative age of the Veneneia and Rheasilvia impact is unambiguously determined by superposition relationships, while the formation of Marcia crater clearly represents the youngest major geologic event on Vesta. This system is consistent with those developed for the Moon, Earth, Mars, and Mercury.

### 3.1. Particular Geologic Features (Asymmetric Craters, Spirals, Pits, Gullies, etc.)

Topography plays a significant role in crater formation and modification processes on Vesta. Compared to its radius,

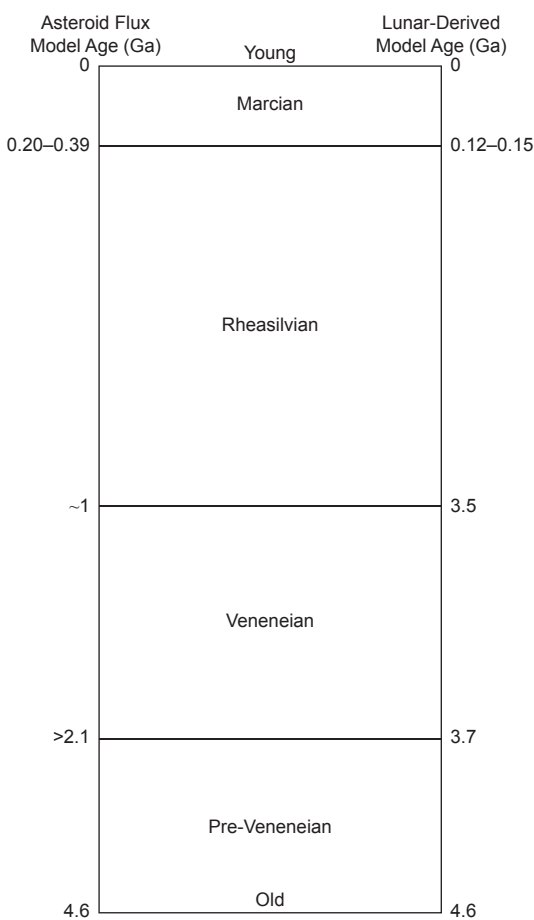


**Fig. 9.** Chronostratigraphy of Vesta. From Williams *et al.* (2014a).

Vesta has a very intense relief resulting in relatively steep slopes (reaching up to 55°) (Jaumann *et al.*, 2012). Impacts onto such steep surfaces, followed by slope failure, makes resurfacing due to impacts and their associated gravitational and seismic activity an important geologic process on Vesta that significantly alters the morphology of geologic features and adds to the complexity of Vesta's surface evolution. There are numerous cases of craters formed on slopes where pronounced collapse and slumping occurred on upslope sides of the craters, resulting in an extreme asymmetric morphology with a wider upslope crater wall and a narrower downslope wall. In extreme cases, the upslope material has fallen back into the crater, overrun the downslope rims, and flowed out of the craters (Jaumann *et al.*, 2012). Slopes >20° prevent the deposition of ejected material in the uphill direction, and slumping material superimposes the ejecta deposit on the downhill side. Crater-sized frequency measurements for ejecta deposits, crater interiors, and surrounding surfaces reveal similar ages, within measurement and cratering chronology model uncertainties, indicating that the deposits most likely formed during impact and no major post-impact processes modified the crater (Krohn *et al.*, 2014b). These asymmetries are the result of the local slope, which prevents deposition of ejected material in the

uphill direction and results in a larger accumulation of ejecta within the crater and on the downhill crater rim (Fig. 10).

Smooth, flat regions occur in the interiors of some craters and in small depressions as pond-like accumulations with well-defined geological contacts, which indicate that they are younger than their surroundings (Jaumann *et al.*, 2012). Several scenarios of the origin of these deposits seem plausible, including impact deposition, impact melt, dust levitation and transport, seismic shaking, or slumping of fine material. Another observation is pitted terrain on the floor of some impact craters like Marcia (Fig. 11) and Cornelia (Fig. 12). Pitted terrain is characterized by irregular rimless depressions, a distinct morphology not observed on other airless bodies (Denevi *et al.*, 2012). Similar terrain is associated with numerous martian craters, where pits are thought to form through degassing of volatile-bearing material heated by the impact. Pitted terrain on Vesta may have formed by a similar process, indicating the surface contains a relatively large volatile component (Denevi *et al.*, 2012).

Some of Vesta's craters, notably Marcia and Cornelia, exhibit gullies eroding the crater walls as linear systems or curvilinear systems (Fig. 11) (Scully *et al.*, 2014). Linear systems consist of straight and non-intersecting gullies that are parallel to one another, similar to lunar gullies, suggesting an origin by dry granular flow. Complete curvilinear systems, however, consist of interconnected, partly dendritic to subparallel nonlinear gullies. They originate from the upper and middle sections of crater walls out of alcove-like features and terminate in lobate deposits near the base of the walls. In places, lobate deposits partially lie on top of one another, indicating multiple phases of accumulation. The shapes of the

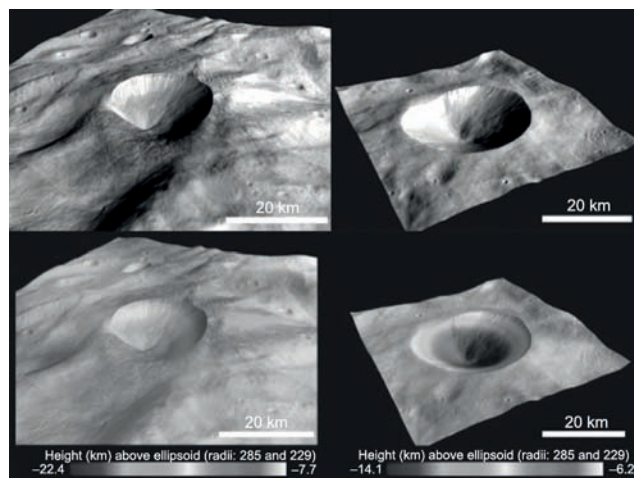


**Fig. 10.** See Plate 11 for color version. Typical impact crater on Vesta: Antonia (200.8°E, 58.7°S; diameter 16.75 km) is an impact on a slope of asymmetric shape with the ejecta mainly concentrated downhill also covering the downslope crater rim; Sextilia (145.9°E, 39°S; diameter 19.48 km) is of approximately the same size, located on a more gentle slope, and circular in shape but exposing significant mass wasting inside the crater on the uphill rim (Jaumann *et al.*, 2012; Krohn *et al.*, 2014b).

lobate deposits resemble terrestrial alluvial fans formed by debris flows. The morphological preservation of curvilinear systems is age-dependent: Well-preserved systems occur in the walls of young (less than hundreds of million years old) craters such as Marcia, whereas less well-preserved systems, characterized by strong modification of original morphology by later geologic processes, occur in the older Calpurnia crater. Curvilinear gullies differ markedly from linear gullies (Scully et al., 2014). Recent studies suggest the presence of hydrated minerals (De Sanctis et al., 2012b; McCord et al., 2012; Prettyman et al., 2012; Reddy et al., 2012; Jaumann et al., 2014) and past subsurface water on Vesta (Sarafian et al., 2013; Warren et al., 2013), and the gullies are direct geologic evidence of water activity on Vesta's surface. The morphology of the curvilinear systems suggests that they formed by flow of transient water that was released from buried ice-bearing deposits by impact-induced heating and melting. This interpretation is also in accordance with the occurrence of pitted terrain on Vesta, resulting from degassing of volatiles. The buried ice-bearing deposits are likely localized in extent and may still be present in Vesta's subsurface (Scully et al., 2014).

### 3.2. Regolith (Formation, Structure, Thickness, Mixing Models, Dark Material, and Space Weathering)

Vesta is quite different from other airless bodies. Although freshly exposed material on the surface of Vesta is mixed into surrounding background regolith with time (a form of mechanical space weathering), Vesta's surface does not involve significant accumulation of nanophase opaque particles on rims of regolith grains (Pieters et al., 2012). Instead, physical regolith processes on Vesta appear to be sufficiently robust to produce a locally well-mixed regolith derived from host lithologies containing variable amounts of bright and darker components (McCord et al., 2012). The

dominant processes involved with regolith mixing at Vesta must include large- and small-scale impact events that not only produce particulate material and distribute absorbing components at a fine scale, but also continually garden the local regolith vertically and laterally. The low average impact velocity ( $\sim 5 \text{ km s}^{-1}$ ) (Bottke et al., 1994) expected for Vesta's location in the main asteroid belt suggests that mechanical brecciation dominates over melting and vaporization (Pieters et al., 2012). Vesta's basaltic composition, coupled with relatively steep topography (Jaumann et al., 2012) and weak gravity (Konopliv et al., 2013) compared to planets and large moons, certainly contributes to the mobility of its regolith. The regolith of Vesta indicates space weathering focuses on solar wind and micrometeorite interactions accompanied by regolith mobility and fine-scale mixing as part of the complex assortment of processes acting on the planetary surface with time (Pieters et al., 2012). The cratering record of Vesta comprises crater sizes of up to tens of kilometers in diameter that are partly covered by ejecta. Scaling to the depth/diameter ratio to these sizes suggest regolith thicknesses of up to a few thousand meters (Jaumann et al., 2012). However, the ejecta of the youngest basin Rheasilvia presumably exceed this number significantly and dominate the surface of the southern hemisphere.

Deposits of dark material appear on Vesta's surface as features of relatively low-albedo in the visible wavelength range of Dawn's camera and spectrometer (Jaumann et al., 2012, 2014; McCord et al., 2012; Reddy et al., 2012). Mixed with the regolith and partially excavated by younger impacts, the material is exposed as individual layered outcrops in crater walls (Fig. 11) or ejecta patches, having been uncovered and broken up by the impact. Dark fans on crater walls and dark deposits on crater floors are the result of gravity-driven mass wasting triggered by steep slopes and impact seismicity. The fact that dark material is mixed with impact ejecta indicates that it has been deposited together with the ejected material. Some small craters display continuous dark ejecta, indicating that the impact excavated the material from beneath (Jaumann et al., 2014). The asymmetric distribution of dark

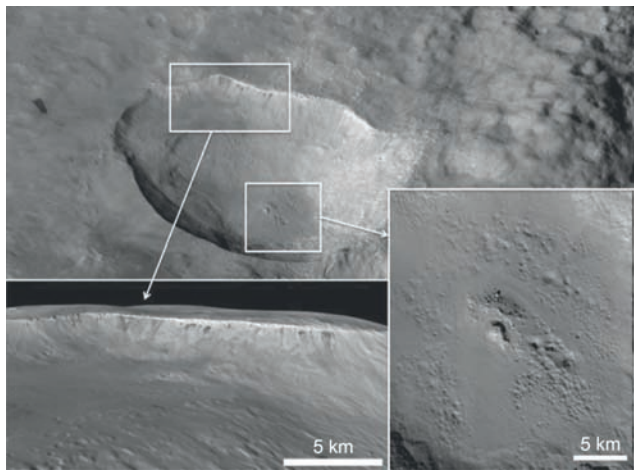


**Fig. 11.** This true-color composite of Marcia crater ( $189.5^\circ\text{E}$ ,  $9^\circ\text{N}$ ; diameter  $67.6 \text{ km}$ ) shows pitted terrain on its crater floor (lower right), gullies on its crater walls, and dark material cropping out from the crater wall (lower left). From Denevi et al. (2012) and Jaumann et al. (2014).

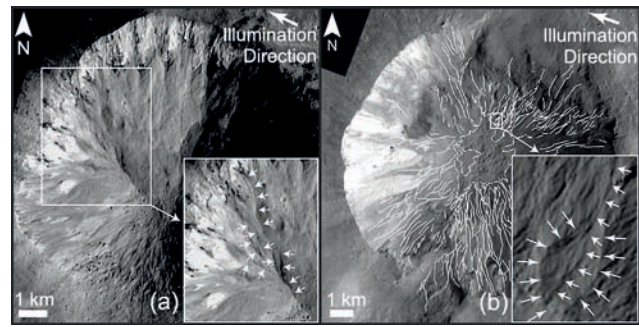


**Fig. 12.** (a) Rubria crater ( $18.3^\circ\text{E}$ ,  $7.3^\circ\text{S}$ ; diameter  $10.27 \text{ km}$ ) with gullies originating from alcoves, cutting the crater wall in subdendritic and subparallel pattern ending in an apron; (b) Cornelia crater ( $225.6^\circ\text{E}$ ,  $9.4^\circ\text{S}$ ; diameter  $14.9 \text{ km}$ ) showing a dense dendritic pattern of gullies and pitted terrain in the center of the crater floor. From Scully et al. (2014).

material in impact craters and ejecta suggests noncontinuous distribution in the local subsurface (Jaumann *et al.*, 2014). Some positive-relief dark edifices appear to be impact-sculpted hills with dark material distributed over the hill slopes (Jaumann *et al.*, 2012; Williams *et al.*, 2014b). Dark features inside and outside of craters are in some places arranged as linear outcrops along scarps or as dark streaks perpendicular to the local topography. The spectral characteristics of the dark material resemble that of Vesta's regolith (De Sanctis *et al.*, 2012b; Stephan *et al.*, 2013). Dark material is distributed unevenly across Vesta's surface with clusters of all types of dark material exposures. On a local scale, some craters expose or are associated with dark material, while others in the immediate vicinity do not show evidence of dark material. The variety of surface exposures of dark material and their variable geological correlations with surface features, as well as their uneven distribution, indicate a globally inhomogeneous distribution in the subsurface. However, the dark material seems to be concentrated near the rim and ejecta of the older Veneneia south polar basin structure (Jaumann *et al.*, 2014). The origin of the dark material is still being debated; however, the geological analysis suggests that it is exogenic, from carbon-rich low-velocity impactors, rather than endogenic, from freshly exposed mafic material or melt, exposed or created by impacts (McCord *et al.*, 2012; Reddy *et al.*, 2012; Jaumann *et al.*, 2014). Among the three types of dark components found in HED meteorites (Russell *et al.*, 2012), which include clasts of carbonaceous chondritic material, impact melt, and impact-shock-blackened material (McSween *et al.*, 2011, 2013a), the carbonaceous component provides the best match with the spectral properties (McCord *et al.*, 2012) and in almost all cases with the geological setting and the subsurface structure of the dark material.

#### 4. VESTA'S SURFACE AND INTERIOR COMPOSITIONS

##### 4.1. Accretion and Bulk Composition

Vesta formed early and differentiated rapidly. Thermal evolution models based on heating by decay of short-lived radionuclides require Vesta to have accreted within  $\sim 1.4$  m.y. of solar system formation (Formisano *et al.*, 2013; Neumann *et al.*, 2014). The measured  $^{53}\text{Mn}$ - $^{53}\text{Cr}$  and  $^{26}\text{Al}$ - $^{26}\text{Mg}$  isochrons for HEDs indicate crust-mantle differentiation at 1–3 m.y. after the formation of the earliest solar system solids (CAIs) (Trinquier *et al.*, 2008; Schiller *et al.*, 2011), consistent with the  $\sim 3$ -Ma age of core formation determined from the  $^{182}\text{Hf}$ - $^{182}\text{W}$  chronometer (Kleine *et al.*, 2009).

The geochemistry of HED meteorites together with the gravity field constrains Vesta's bulk composition. The most successful model (Toplis *et al.*, 2013) combines 75% Na-depleted H chondrite and 25% CM chondrite. This composition has an ultramafic mantle rich enough in orthopyroxene to produce abundant diogenite cumulates that can also yield basaltic (eucrite) melts, a Fe/Mn ratio, oxygen-isotopic composition, and oxidation state consistent with HEDs,

and a bulk silicate density and inferred core mass like those estimated from Dawn gravity data.

#### 4.2. Surface Distribution of Howardite-Eucrite-Diogenite Compositions

Dawn compositional data have significantly reinforced the pre-Dawn (Gaffey, 1997) identification of Vesta as the HED parent body (McSween *et al.*, 2013b). Using HED calibrations, Dawn instruments have mapped the distributions of the various lithologies on Vesta's surface. These match basalts or gabbros (eucrites), ultramafic rocks composed of orthopyroxene and olivine (diogenites), and brecciated mixtures of eucrites and diogenites (howardites). The identification of eucrites, diogenites, and howardites is based on the positions of 1- $\mu\text{m}$  and 2- $\mu\text{m}$  band centers (called BI and BII) from VIR reflectance spectra (De Sanctis *et al.*, 2013). This relationship (Fig. 13) was used to construct a global lithologic map (Fig. 14) (De Sanctis *et al.*, 2012b), which documents that howardites and/or eucrites (many pixels plot in the overlapping fields) comprise most of Vesta's surface. The VIR map is fully consistent with a higher-spatial-resolution FC map of color parameters (Thangjam *et al.*, 2013), as shown in Fig. 4.

The distribution of HED lithologies has also been mapped using GRaND's neutron-absorption properties (Prettyman *et al.*, 2013). A GRaND map, cast in terms of percentage of eucrites in the regolith, shows very similar abundances and distributions as the VIR map (Fig. 14). Other GRaND map products, including global maps of iron abundance (Yamashita *et al.*, 2013) and high-energy gamma rays (Peplowski *et al.*, 2013), give similar distribution patterns.

All these maps show a regolith surface composed mostly of howardites, except for an equatorial region dominated by basaltic eucrites and a concentration of diogenites within the Rheasilvia basin and its ejecta blanket. The regional diversity in proportions of eucrites and diogenites in Vesta's regolith, as seen Fig. 14, is similar to the diverse mixing ratios in

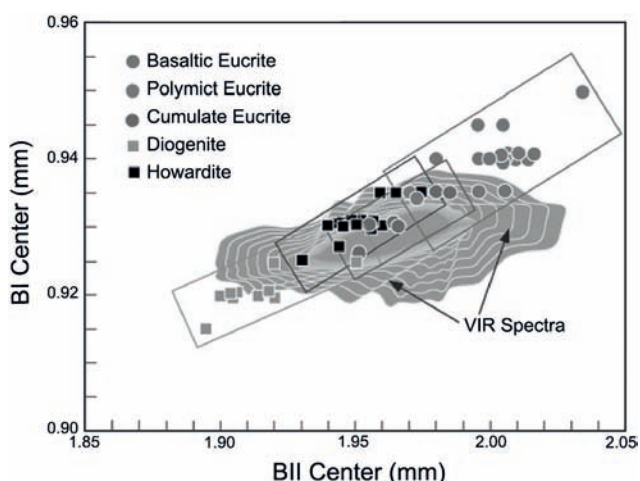


**Fig. 13.** See Plate 12 for color version. BI vs. BII for VIR data and HEDs (De Sanctis *et al.*, 2012a, 2013).

howardites (Warren et al., 2009). A swath of diogenite-rich material extends northward from Rheasilvia. The iron map also shows a distinctive low-Fe region in the western hemisphere that is not evident in other maps and may indicate cumulate eucrites (Yamashita et al., 2013), which are otherwise difficult to distinguish spectrally from basaltic eucrites. The mapped distributions are plausible based on geologic reasoning—slowly cooled diogenite cumulates should have been excavated from the largest impact basin, and basaltic eucrites are expected to dominate regions having the oldest surfaces, as determined from crater densities. Basin ejecta are howardites rich in the diogenite component, and howardites elsewhere have a higher proportion of crustal eucrites. However, none of these regions should necessarily be considered launch sites for HEDs; nearly all these meteorites were probably carved out of, and ejected from, the Rheasilvia cavity, forming the vestoids (Binzel and Xu, 1993).

GRaND analyses showed regions of dark material (described in section 3.2) to have higher H abundances ( $>400 \mu\text{g g}^{-1}$ ) (Prettyman et al., 2012), and VIR spectra identified an OH absorption feature in the same areas (De Sanctis et al., 2012b). This compositional anomaly is attributed to exogenic carbonaceous chondrites incorporated into the regolith. Some howardites contain clasts of carbonaceous chondrites, and comparison of the VIR spectra with those

of eucrite-CM chondrite mixtures suggests 1–6% chondrites (Reddy et al., 2012). This amount is consistent with the H abundance measured by GRaND (Prettyman et al., 2012).

### 4.3. Vesta's Excavated Interior

Models for formation of the overlapping Rheasilvia and Veneneia basins estimate excavation depths of as much as 60–100 km (Jutzi et al., 2013). Given Vesta's nominal basaltic crustal thickness of ~15–20 km (McSween et al., 2013b; Toplis et al., 2013), these impacts should have exposed mantle rocks, thought to contain significant amounts of olivine.

Some diogenite breccias contain harzburgite (olivine + orthopyroxene) or dunite (>90% olivine) clasts (Beck and McSween, 2010), so exposure of mantle olivine in the Rheasilvia and Veneneia basins was expected. However, spectrally identifying <25% olivine in the presence of orthopyroxene is challenging (Beck et al., 2013), and no olivine has been detected in Rheasilvia by VIR (McSween et al., 2013b). However, a few higher concentrations of olivine (>50%) in other areas have been identified in VIR spectra. Ammannito et al. (2013) found olivine in the Bellicia and Arruntia craters in the northern hemisphere, and other isolated occurrences have been noted in the diogenite “lane” in Vesta's eastern hemisphere (Fig. 14a) (Ruesch et al., 2014). These exposures

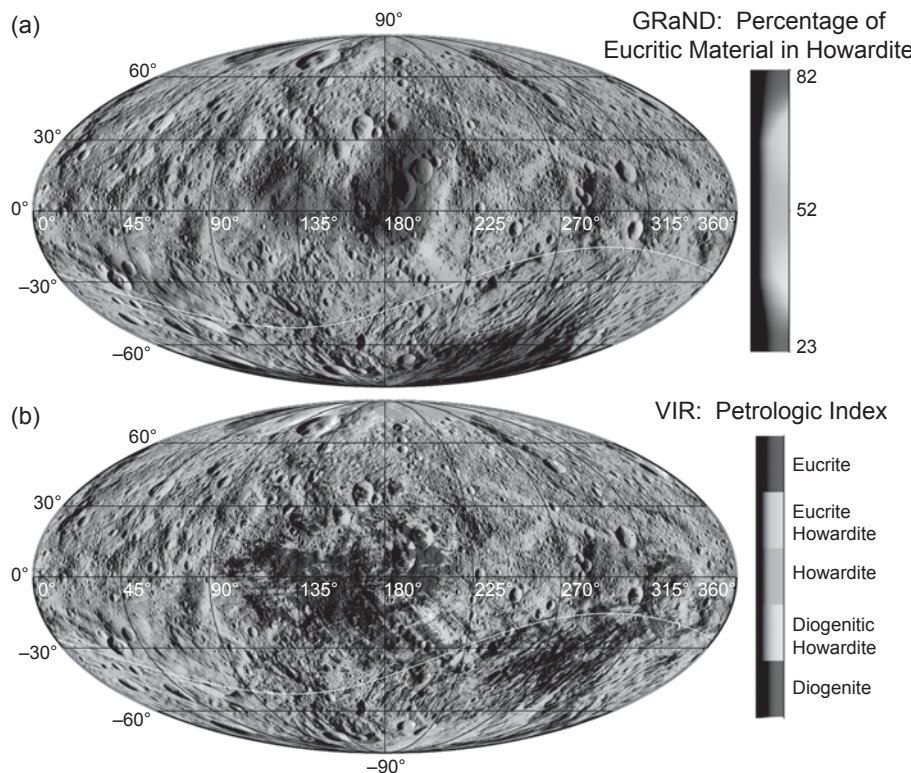


**Fig. 14.** See Plate 13 for color version. Lithologic maps of Vesta remapped in Mollweide projection. (a) Map of HED distribution mapped by VIR (Ammannito et al., 2013). (b) Map of the percentage of eucritic material from GRaND data (Prettyman et al., 2013). Eucritic regions appear as blue in the color version, whereas regions that are more diogenitic appear as red.

occur in association with howardite rather than diogenite in regions of thin crust, as determined from gravity models. Highly magnesian olivines discovered in a few howardites have been interpreted as mantle grains (Lunning *et al.*, 2014), but they comprise only a tiny fraction of the meteorites.

Noting the lack of detection of olivine in Rheasilvia, Clenet *et al.* (2014) suggested that the crust of Vesta must be >80 km thick. Their notion of “mantle” is olivine-rich rock, and they apparently define other ultramafic rocks, such as orthopyroxene-rich diogenites, as “crust.” In arguing that Rheasilvia sampled the mantle, McSween *et al.* (2013b) defined the crust as mafic rocks (eucrites) and upper mantle rocks (diogenites). This distinction is not trivial; a bulk-chondritic Vesta, if fully differentiated, could only produce a ~20-km thickness of basalt. Earth’s crust-mantle boundary (“moho”) separates mafic and ultramafic rocks, and Vesta’s moho should be defined similarly. The missing olivine in the diogenitic upper mantle is likely to be sequestered in the lower mantle, as a solid residue from incomplete but widespread partial melting (Neumann *et al.*, 2014).

#### 4.4. Differentiation from a Magma Ocean or Serial Magmatism?

Pervasive melting to form an early magma ocean is consistent with Vesta’s rapid differentiation and the HED’s homogenized oxygen isotopes (Greenwood *et al.*, 2005), and numerous magma ocean models have been proffered (e.g., Righter and Drake, 1997). Fractional crystallization in a Vestan magma ocean would be difficult because crystal setting is impeded by high effective viscosity resulting from a large fraction of crystals at all depths. The magma ocean model of Mandler and Elkins-Tanton (2013) thus involves equilibrium crystallization of olivine and orthopyroxene, at least until 60–70% solidification.

The model of Wilson and Keil (2012) predicts very efficient removal of melts from the mantles of asteroid-sized bodies, so that only a small amount of melt is present at any one time, precluding a magma ocean. Mandler and Elkins-Tanton (2013) recognize the need for crystal fractionation to make orthopyroxene cumulates (diogenites), so their model incorporates continuous extraction of residual melts from the mostly crystallized magma ocean into shallow magma chambers. Crystal accumulation in these chambers, accompanied by magma recharge, can explain the perplexing geochemical variations in eucrites and diogenites (McSween *et al.*, 2011). These magma bodies might stagnate at the crust-mantle boundary or intrude higher in the crust, in either case forming plutons that would make the crust appear thicker and shield the lower mantle from excavation by impacts consistent with Dawn observations.

#### 4.5. Gravity Constraints on Interior Structure

High-accuracy radiometric tracking data, in combination with optical landmark tracking, was used to produce a spherical harmonic gravity field of Vesta accurate to degree

and order 18 (Konopliv *et al.*, 2013). The radial gravity field, shown in Fig. 15, is dominated by the shape of Vesta. The gravity data are consistent with a ~110-km-radius iron-nickel core (Russell *et al.*, 2012); a range for the core radius of 126–105 km is obtained for a geochemically plausible core density range of 6000–8000 kg m<sup>-3</sup> (Toplis *et al.*, 2013). Average crustal and mantle densities, found by minimizing the residuals between the observed gravity and the field calculated for a three-layer model that uses the derived average core size and density (7400 kg m<sup>-3</sup> and 110-km radius) and a crustal layer whose outer surface follows the shape of Vesta and whose thickness is defined by a mantle ellipsoid that touches the surface at the deepest point on Vesta, are 2970 kg m<sup>-3</sup> and 3160 kg m<sup>-3</sup>, respectively (Park *et al.*, 2013). The derived crustal density is lower than the 3260 kg m<sup>-3</sup> grain density of the expected 2:1 eucrite-diogenite mixture (Consolmagno *et al.*, 2008), and the mantle density is lower than expected for a harzburgitic composition, indicating significant macro-porosity in the silicate fraction and a more complex interior structure than predicted by fractional crystallization.

Crustal density variations obtained for the three-layer model reveal the underlying structure as well as porosity variations in the megaregolith. As shown in Fig. 15 from Konopliv *et al.* (2013), density variations of 2310–3440 kg m<sup>-3</sup> in the crustal layer are required to account for the gravity variations. This crustal layer has an average thickness of 22.4 km, consistent with estimates from geochemical differentiation models (e.g., Righter and Drake, 1997; Toplis *et al.*, 2013). However, these derived density variations indicate significant heterogeneity in the layer, and likely reflect significant variations in magmatic architecture, indicating that Vesta’s crust is not sharply defined, in agreement with recent modeling (Mandler and Elkins-Tanton, 2013). The density and thickness of the megaregolith also contribute to the bulk crustal density variations, but to a lesser degree than the compositional variations.

The crustal density distribution in Fig. 16 shows a preponderance of isolated, high-density anomalies and broader low-density regions. Higher density is found in a broad region of the eastern hemisphere, northward of the rim of the Rheasilvia basin. The highest density of 3440 kg m<sup>-3</sup> occurs in the region of the eastern equatorial troughs (Divalia Fossae formation), while the deepest density deficit is associated with the older troughs of the Saturnalia Fossae formation in the northern hemisphere. Low density within the Rheasilvia and Veneneia basins is consistent with thick ejecta fill, and a high occurs over the central mound, as expected for uplifted mantle; however, isolated, high-density anomalies are also present whose origin is difficult to explain within the construct of excavation of a layered body. One such high-density anomaly occurs over the southern portion of Vestalia Terra, at the western intersection of the two giant basins. Vestalia Terra is an ancient highland that appears to be resistant to shattering, as evidenced by the lack of well-defined troughs crossing this structure (Buczkowski *et al.*, 2012). The age, strength, and high density (3200 kg m<sup>-3</sup>) of southern Vestalia Terra argue for a primordial plutonic origin

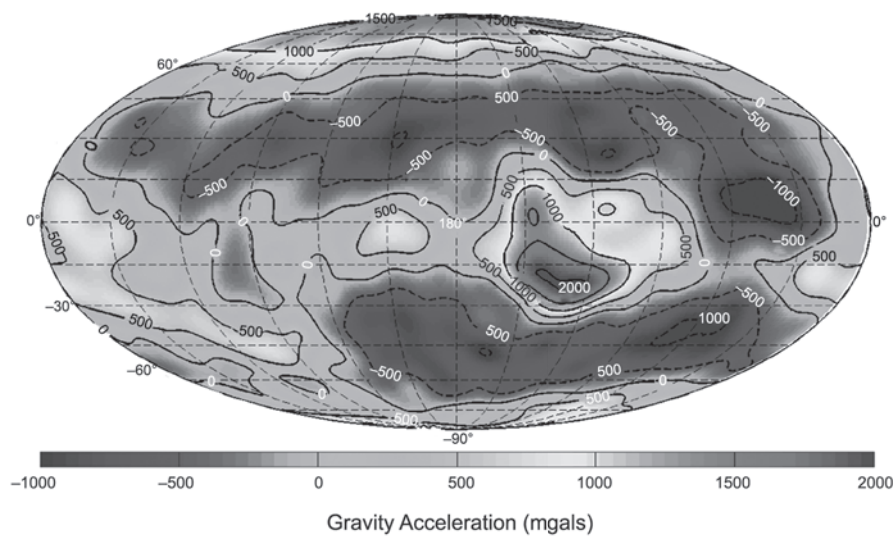


**Fig. 15.** See Plate 14 for color version. The Vesta radial gravity solution mapped to a  $290 \times 265$ -km ellipsoid surface through degree 20. The  $J_2$  coefficient has been removed. The maximum and minimum range is given by 2100 mgal at the large equatorial high near  $126^\circ\text{W}$  longitude and  $-1270$  mgal, also near the equator at  $44^\circ\text{W}$ . From Konopliv et al. (2013).

(Raymond et al., 2014). The isolated high-density anomalies within Rheasilvia may have a similar origin. Of note is the high density associated with the Rheasilvia rim near the center of the older Veneneia basin, which likely represents the uplifted central mound of Veneneia that was disrupted by the Rheasilvia impact.

The broad swath of high density in the eastern hemisphere is bounded on the west by the cratered highlands of eucritic composition, and on the east by the northern troughs and Ferialia Planitia. This large region shows generally higher density but also includes isolated highs and lows of similar size to those in the southern hemisphere. The region is associated with the “lane” of diogenite and diogenite-rich howardite that extends from Rheasilvia to the north polar region. The association of the high density with the presence of diogenitic terrains argues for a variation in crustal properties in this region, rather than Rheasilvia ejecta deposited on the surface, as the cause of the compositional variation. The high density is consistent with the presence of diogenite and olivine-bearing rocks in the near surface, which provide a source for the diogenite present in the regolith and are consistent with magma chambers at the base of the eucritic crust predicted by serial magmatism models discussed previously. Furthermore, olivine has been detected by VIR at the edge of one of two isolated lows at the center of this broad region of high density, indicating that olivine-dominated rocks have been exhumed from depth in this region. The presence of olivine near the density low is consistent with excavation of the high density material to the surface by impact, where it was later exposed by subsequent impact. As discussed in Raymond et al. (2014), the preponderance of the high-density anomalies in the eastern hemisphere, and their association with olivine and

diogenitic-rich ejecta, points toward a plutonic or plume-dominated crustal architecture in this region.

## 5. SUMMARY AND CONCLUSIONS

The Dawn spacecraft arrived at Vesta in July 2011, mapping the body in three separate orbits: survey orbit, high-altitude mapping orbit, and low-altitude mapping orbit. It remained in orbit until September 2012, at which time solar illumination reached the north pole. Dawn found Vesta’s surface to be characterized by impact craters of all sizes, a variety of ejecta blankets, large troughs extending around the equatorial region, enigmatic dark material, and considerable evidence for mass wasting (e.g., Jaumann et al., 2012). Dawn confirms the large impact basin covering Vesta’s south pole (Rheasilvia), inferred from the Hubble Space Telescope images (Thomas et al., 1997), and reveals evidence for an earlier, underlying large basin. Vesta’s global tectonic patterns (two distinct sets of large troughs) strongly correlate with the locations of the two south polar impact basins, and were likely created by the formation of the basins. Impact craters on Vesta range from fresh to highly degraded, comparable to the Moon, indicating an intensive cratering history over the age of the solar system. The primary crust is covered by a thick (100 m to a few kilometers), multi-layered sheet of debris (regolith) formed by the accumulation of ejecta from the numerous impacts that have resurfaced Vesta over time. The surface of Vesta exhibits very steep topographic slopes that are near to the angle of repose. Impacts onto these steep surfaces, followed by slope failure, makes resurfacing due to impacts and their associated gravitational forces and seismic activity an important geologic process on Vesta that significantly alters the

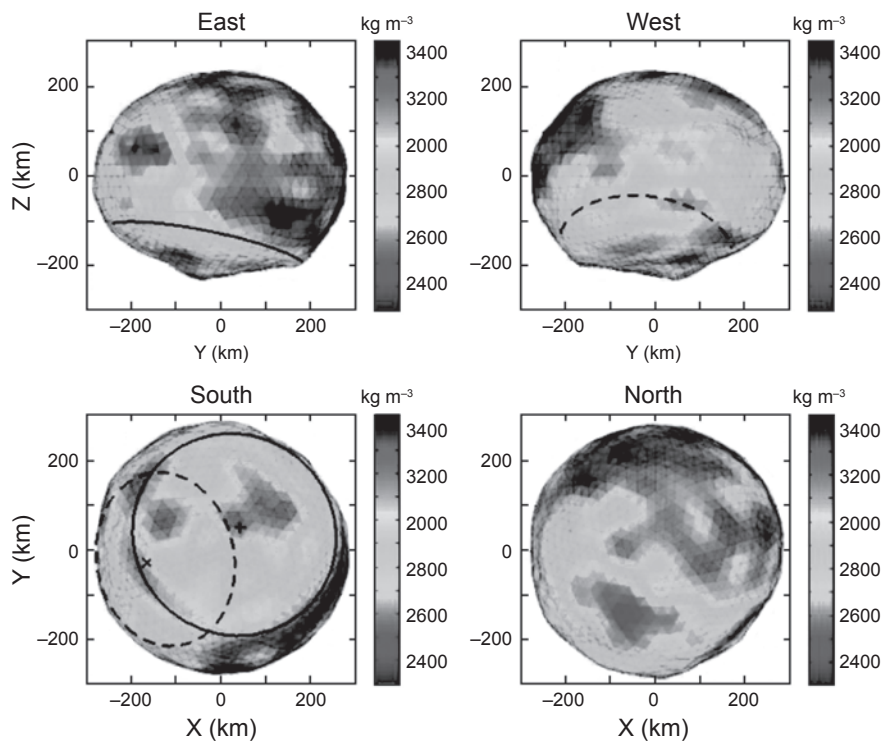


**Fig. 16.** See Plate 15 for color version. The lateral crustal density estimation of the three-layer Vesta (257 × 207-km mantle and 117 × 105-km core). Solid black and dashed black circles represent Rheasilia and Veneneia impact basins, respectively. The lateral crustal density variation ranges from 2310 to 3440  $\text{kg m}^{-3}$ , which is required to remove the gravity anomaly. From R. S. Park (personal communication, 2014).

morphology of geologic features and adds to the complexity of its geologic history. Linear gullies are interpreted to form by flow of dry granular material and curvilinear gullies are possibly formed by transient flow of water. Deposits of dark material intermixed into the regolith and partially excavated by younger impacts are exposed as blocks or layers outcropping in crater walls and rims. The mixing of dark material with impact ejecta indicates that this material is processed together with the ejected material. Small craters possess continuous dark ejecta similar to lunar dark-halo impact craters, indicating that the impact excavated the material from beneath the surface. Asymmetric distribution of dark material in impact craters and ejecta suggests noncontinuous distribution in the local subsurface. The composition of the dark material resembles that of the Vesta regolith. Dark material is distributed unevenly across Vesta's surface. On a global scale the dark material seems to be correlated with the rim and ejecta of the older Veneneia south polar basin structure. The origin of the dark material is still debated and it is tentatively suggested that dark material is exogenic, from carbon-rich low velocity impactors. This is supported by the broad correlation between dark material and the OH hydration band, suggesting carbonaceous chondrites as a darkening agent. Besides Vestalia Terra, direct surface evidence for volcanic or plutonic activity is lacking so far. This may be due to a dearth of large-scale volcanic features

on Vesta and/or to volcanism ending early in Vesta's evolution so that the evidence has been destroyed and covered up by extensive subsequent cratering, regolith formation, and resurfacing. However, the pattern of the high-density anomalies and their association with olivine and diogenite-rich ejecta points toward a plutonic or plume-dominated crustal architecture that is consistent with the geochemical considerations that magma bodies might stagnate at the crust-mantle boundary or intrude higher in the crust, in either case forming plutons.

The time stratigraphic sequence for Vesta comprises four major periods: pre-Veneneian, Veneneian, Rheasilvian, and Marcian. The pre-Veneneian period covers the time from the formation of Vesta (1–2 m.y. after the formation of the first solids in the protosolar disk) up to the Veneneia impact event. The Veneneian period encompasses the time between the Veneneia and Rheasilvia impact events. The Rheasilvian period is defined as the time between the formation of Rheasilvia and Marcia craters, and the Marcian period covers the time between the formation of Marcia crater until the present.

The composition of Vesta's regolith is consistent with mixtures of HEDs in various proportions, as mapped by VIR spectra, GRaND neutron absorption and high-energy gamma rays, and FC band ratios. Euclidean-rich regions occur near the equator, corresponding to older terrains. Diogenite-rich areas

are associated with the Rheasilvia basin and its ejecta, or with relatively thin crust. Olivine is uncommon, but when mixed with orthopyroxene, amounts <25% are difficult to detect spectrally. Diogenite is interpreted as mantle material, likely occurring in plutons underplating the basaltic crust. The missing olivine may be sequestered in the lower mantle, as a residue from incomplete melting. The lithologic distributions represent reflect differentiation by pervasive, early magmatism, although not necessarily whole-body melting. Redistribution of these lithologies by large impacts is illustrated by dark, hydrogen-rich regions with OH absorption features, interpreted as admixed carbonaceous chondrite, possibly introduced during the Veneneia impact.

The instrumentation carried by Dawn has enabled the geology, structure, and chemistry of the vestan surface to be extensively characterized, and has proven it to be consistent with the HED meteorites, which have been even more extensively studied on Earth. These analyses have allowed Vesta to join the Moon and Mars as the best characterized solar system bodies.

**Acknowledgments.** We thank the many people who made this mission possible: the teams at Orbital Sciences Corporation and the Jet Propulsion Laboratory/California Institute of Technology who built the spacecraft; the teams at the Max Planck Institute for Solar System Research, Galileo-SeleX, and Los Alamos National Laboratory who built the instruments; the women and men at the Jet Propulsion Laboratory who operate and navigate the spacecraft; and the Max Planck Society, the German Space Agency, the Italian Space Agency, the National Institute for Astrophysics (INAF), and NASA for their support, as well as the many team members who analyzed the data.

## REFERENCES

- Ammannito E., De Sanctis M. C., Palomba E., et al. (2013) Olivine in an unexpected location on Vesta's surface. *Nature*, **504**, 122–125.
- Beck A. W. and McSween H. Y. (2010) Diogenites as polymict breccias composed of orthopyroxenite and harzburgite. *Meteoritics & Planet. Sci.*, **45**, 850–872.
- Beck A. W., McCoy T. J., Sunshine J. M., Viviano C. E., Corrigan C. M., Hiroi T., and Mayne R. G. (2013) Challenges in detecting olivine on the surface of 4 Vesta. *Meteoritics & Planet. Sci.*, **48**, 2155–2165.
- Binzel R. P. and Xu S. (1993) Chips off asteroid 4 Vesta: Evidence for the parent body of basaltic achondrite meteorites. *Science*, **260**, 186–191.
- Bottke W. F. Jr., Nolan M. C., Greenberg R., and Kavelaars J. (1994) Velocity distributions among colliding asteroids. *Icarus*, **107**, 255–268.
- Buczkowski D. L., Wyryck D. Y., Iyer K. A., et al. (2012) Large-scale troughs on Vesta: A signature of planetary tectonics. *Geophys. Res. Lett.*, **39**, 18205–18210.
- Clenet H., Jutzi M., Barrat J.-A., Asphaug E. I., Benz W., and Gillet P. (2014) A deep crust–mantle boundary in the asteroid 4 Vesta. *Nature*, **511**, 303–306.
- Consolmagno G. J., Britt D. T., and Macke R. J. (2008) The significance of meteorite density and porosity. *Chem. Erde–Geochem.*, **68**, 1–29.
- Denevi B. W., Blewett D. T., Buczkowski D. L., et al. (2012) Pitted terrain on Vesta and implications for the presence of volatiles. *Science*, **338**, 246–249.
- De Sanctis M. C., Coradini A., Ammannito E., et al. (2011) The VIR spectrometer. *Space Sci. Rev.*, **163**, 329–369.
- De Sanctis M. C., Ammannito E., Capria M. T., et al. (2012a) Spectroscopic characterization of mineralogy and its diversity across Vesta. *Science*, **336**, 697–700.
- De Sanctis M. C., Combe J.-P., Ammannito E., et al. (2012b) Detection of widespread hydrated materials on Vesta by VIR imaging spectrometer on board the Dawn mission. *Astrophys. J. Lett.*, **758**, L36.
- De Sanctis M. C., Ammannito E., Capria M. T., et al. (2013) Vesta's mineralogical composition as revealed by the visible and infrared spectrometer on Dawn. *Meteoritics & Planet. Sci.*, **48**, 2166–2184.
- Formisano M., Federico C., Turrini D., Coradini A., Capaccioni F., De Sanctis M. C., and Pauselli C. (2013) The heating history of Vesta and the onset of differentiation. *Meteoritics & Planet. Sci.*, **48**, 2316–2332.
- Gaffey M. J. (1997) Surface lithologic heterogeneity of asteroid 4 Vesta. *Icarus*, **127**, 130–157.
- Greenwood R. C., Franchi I. A., Jambon A., and Buchanan P. C. (2005) Widespread magma oceans on asteroidal bodies in the early solar system. *Nature*, **435**, 916–918.
- Jaumann R., Williams D. A., Buczkowski D. L., et al. (2012) Vesta's shape and morphology. *Science*, **336**, 687–690.
- Jaumann R., Nass A., Otto K., et al. (2014) The geological nature of dark material on Vesta and implications for the subsurface structure. *Icarus*, **240**, 3–19.
- Jutzi M., Asphaug E., Gillet P., Barrat J.-A., and Benz W. (2013) The structure of asteroid 4 Vesta as revealed by models of planet-scale collisions. *Nature*, **494**, 207–210.
- Kleine T., Touboul M., Bourdon B., Minno F., Mezger K., Palme H., Jacobsen S. B., Yin Q.-Z., and Halliday A. N. (2009) Hf–W chronology of the accretion and early evolution of asteroids and terrestrial planets. *Geochim. Cosmochim. Acta*, **73**, 5150–5188.
- Konopliv A. S., Asmar S. W., Bills B. G., Mastodemos N., Park R. S., Raymond C. A., Smith D. E., and Zuber M. T. (2011) The Dawn gravity investigation at Vesta and Ceres. *Space Sci. Rev.*, **163**, 461–486.
- Konopliv A. S., Asmar S. W., Park R. S., et al. (2013) The Vesta gravity field, spin pole and rotation, landmark positions and ephemeris from the Dawn tracking and optical data. *Icarus*, **240**, 103–117.
- Krohn K., Jaumann R., Otto K., et al. (2014a) Mass movement on Vesta at steep scarps and crater rims. *Icarus*, **244**, 120–132.
- Krohn K., Jaumann R., Elbeshausen D., et al. (2014b) Bimodal craters: Impacts on slopes. *Planet. Space Sci.*, **103**, 36–56.
- Lunning N., McSween H. Y., Tenner T. J., and Kite N. T. (2014) Olivine from the mantle of 4 Vesta identified in howardites. In *Lunar Planet. Sci. XLV*, Abstract #1921. Lunar and Planetary Institute, Houston.
- Mandler B. E. and Elkins-Tanton L. T. (2013) The origin of eucrites, diogenites, and olivine diogenites: Magma ocean crystallization and shallow magma chamber processes on Vesta. *Meteoritics & Planet. Sci.*, **48**, 2333–2349.
- Marchi S., McSween H. Y., O'Brien D. P., et al. (2012) The violent collisional history of asteroid 4 Vesta. *Science*, **336**, 690–694.
- Marchi S., Bottke W. F., O'Brien D. P., et al. (2014) Small crater populations on Vesta. *Planet. Space Sci.*, **103**, 96–103.
- McCord T. B., Adams J. B., and Johnson T. V. (1970) Asteroid Vesta: Spectral reflectivity and compositional implications. *Science*, **168**, 1445–1447.
- McCord T. B., Li J.-Y., Combe J.-P., et al. (2012) Dark material on Vesta from the infall of carbonaceous volatile-rich material. *Nature*, **491**, 83–86.
- McSween H. Y., Mittlefehldt D. W., Beck A. W., Mayne R. G., and McCoy T. J. (2011) HED meteorites and their relationship to the geology of Vesta and the Dawn mission. *Space Sci. Rev.*, **163**, 141–174.
- McSween H. Y. Jr., Binzel R. P., De Sanctis M. C., et al. (2013a) Dawn; the Vesta–HED connection; and the geologic context for eucrites, diogenites, and howardites. *Meteoritics & Planet. Sci.*, **48**, 2090–2014.
- McSween H. Y., Ammannito E., Reddy V., et al. (2013b) Composition of the Rheasilvia basin, a window into Vesta's interior. *J. Geophys. Res.*, **118**, 335–346.
- Neumann W., Breuer D., and Spohn T. (2014) Differentiation of Vesta: Implications for a shallow magma ocean. *Earth Planet. Sci. Lett.*, **395**, 267–280.
- O'Brien D. P. et al. (2014). Constraining the cratering chronology of Vesta. *Planet. Space Sci.*, **103**, 131–142.
- Otto K. A., Jaumann R., Krohn K., et al. (2013) Mass-wasting features and processes in Vesta's south polar basin Rheasilvia. *J. Geophys. Res.*, **118**, 2279–2294.

- Park R. S., Konopliv A. S., Asmar S. W., Bills B. G., Gaskell R., Raymond C. A., Smith D. E., Toplis M. J., and Zuber M. T. (2013) Gravity field expansion in ellipsoidal harmonic and polyhedral internal representations applied to Vesta. *Icarus*, 240, 118–132.
- Peplowski P. N., Lawrence D. J., Prettyman T. H., et al. (2013) Compositional variability on the surface of 4 Vesta revealed through GRAND measurements of high-energy gamma rays. *Meteoritics & Planet. Sci.*, 48, 2252–2270.
- Pieters C. A., McFadden L. A., Prettyman T., De Sanctis M. C., McCord T. B., Hiroi T., Klima R., Li J.-Y., and Jaumann R. (2011) Surface composition of Vesta: Issues and integrated approach. *Space Sci. Rev.*, 163, 117–139.
- Pieters C. M., Ammannito E., Blewett D. T., et al. (2012) Distinctive space weathering on Vesta from regolith mixing processes. *Nature*, 491, 79–82.
- Prettyman T. H., Feldman W. C., McSween H. Y. Jr., et al. (2011) Dawn's gamma ray and neutron detector. *Space Sci. Rev.*, 163, 371–459.
- Prettyman T. H., Mittlefehldt D. W., Yamashita N., et al. (2012) Elemental mapping by Dawn reveals exogenic H in Vesta's regolith. *Science*, 338, 242–246.
- Prettyman T. H., Mittlefehldt D. W., Yamashita N., et al. (2013) Neutron absorption constraints on the composition of 4 Vesta. *Meteoritics & Planet. Sci.*, 48, 2211–2236.
- Raymond C. A., Jaumann R., and Nathues A. (2011) The Dawn topography investigation. *Space Sci. Rev.*, 163, 487–510.
- Raymond C. A., Park R. S., Konopliv A. S., et al. (2014) Geophysical constraints on the structure and evolution of Vesta's crust and mantle. In *Lunar Planet. Sci. XLV*, Abstract #1777. Lunar and Planetary Institute, Houston.
- Reddy V., Le Corre L., O'Brien D. P., et al. (2012) Delivery of dark material to Vesta via carbonaceous chondritic impacts. *Icarus*, 221, 544–559.
- Righter K. and Drake M. J. (1997) A magma ocean on Vesta: Core formation and petrogenesis of eucrites and diogenites. *Meteoritics & Planet. Sci.*, 32(6), 929–944.
- Roatsch T., Kersten E., Matz K.-M., Preusker F., Scholten F., Jaumann R., Raymond C. A., and Russell C. T. (2012) High resolution Vesta high altitude mapping orbit (HAMO) atlas derived from Dawn framing camera images. *Planet. Space Sci.*, 73, 283–286.
- Roatsch T., Kersten E., Matz K.-D., Preusker F., Scholten F., Elgner S., Jaumann R., Raymond C. A., and Russell C. T. (2013) High-resolution Vesta low altitude mapping orbit atlas derived from Dawn framing camera images. *Planet. Space Sci.*, 85, 293–298.
- Roatsch T., Kersten, E., Matz K.-D., et al. (2014) The atlases of Vesta. In *Vesta in the Light of Dawn: First Exploration of a Protoplanet in the Asteroid Belt*, Abstract #2007, Lunar and Planetary Institute, Houston.
- Ruesch O., Hiesinger H., DeSanctis M. C., et al. (2014) Detections of the near-IR spectral signature of olivine on Vesta with VIR/Dawn data: Insights into Vesta olivine-bearing lithologies. *J. Geophys. Res.*, in press.
- Russell C. T., ed. (1997) *The Near Earth Asteroid Rendezvous Mission*. Kluwer, Dordrecht. 308 pp.
- Russell C. T. and Raymond C. A. (2011) The Dawn Mission to minor planets 4 Vesta and 1 Ceres: Foreword. *Space Sci. Rev.*, 164, 1–2.
- Russell C. T., Raymond C. A., Coradini A., et al. (2012) Dawn at Vesta: Testing the protoplanetary paradigm. *Science*, 336, 684–686.
- Sarafian A. R., Roden M. F., and Patiño-Douce A. E. (2013) The volatile content of Vesta: Clues from apatite in eucrites. *Meteoritics & Planet. Sci.*, 48, 2135–2154.
- Schenk P., O'Brien D. P., Marchi S., et al. (2012) The geologically recent giant impact basins at Vesta's south pole. *Science*, 336, 694–697.
- Schiller M., Baker J., Creech J., Paton C., Millet M.-A., Irving A., and Bizzarro M. (2011) Rapid timescales for magma ocean crystallization on the howardite-eucrite-diogenite parent body. *Astrophys. J. Lett.*, 740, L22.
- Schmedemann N., Kneissl T., Ivanov B. A., et al. (2014) The cratering record, chronology and surface ages of (4) Vesta in comparison to smaller asteroids and ages of HED meteorites. *Planet. Space Sci.*, 103, 104–130.
- Scully J. E. C., Russell C. T., Yin A., et al. (2014) Sub-curvilinear gullies interpreted as evidence for transient water flow on Vesta. In *Lunar Planet. Sci. XLV*, Abstract #1796. Lunar and Planetary Institute, Houston.
- Siers H., Keller H. U., Jaumann R., et al. (2011) The Dawn framing camera. *Space Sci. Rev.*, 163, 263–327.
- Stephan K., Jaumann R., De Sanctis, M. C. et al. (2013) A compositional and geological view of fresh ejecta of small impact craters on asteroid 4 Vesta. *J. Geophys. Res.*, 119, 771–797.
- Thangjam G., Reddy V., Le Corre L., Nathues A., Sierks H., Hiesinger H., Li J.-Y., Sanchez J. A., Russell C. T., Gaskell R., and Raymond C. A. (2013) Lithologic mapping of HED terrains on Vesta using Dawn framing camera color data. *Meteoritics & Planet. Sci.*, 48, 2199–2210.
- Thomas P. C., Binzel R. P., Gaffey M. J., Storrs A. D., Wells E. N., and Zellner B. H. (1997) Impact excavation on asteroid 4 Vesta: Hubble Space Telescope results. *Science*, 277, 1492–1495.
- Toplis M. J., Mizzi H., Monnereau M., Forni O., McSween H. Y., Mittlefehldt D. W., McCoy T. J., Prettyman T. H., De Sanctis M. C., Raymond C. A., and Russell C. T. (2013) Chondritic models of 4 Vesta: Implications for geochemical and geophysical properties. *Meteoritics & Planet. Sci.*, 48, 2300–2315.
- Trinquier A., Birck J. L., Allegre C. J., Gopel C., and Ulfbeck D. (2008)  $^{53}\text{Mn}$ - $^{53}\text{Cr}$  systematics of the early solar system revisited. *Geochim. Cosmochim. Acta*, 72, 5146–5163.
- Tsiganis K., Gomes R., Morbidelli K., and Levinson H. F. (2005) Origin of the orbital architecture of giant planets of the solar system. *Nature*, 435, 459–461.
- Walsh K. J., Morbidelli A., Raymond S. N., O'Brien D. P., Mandell A. M. (2012) Populating the asteroid belt from two parent source regions due to the migration of giant planets — “The Grand Tack.” *Meteoritics & Planet. Sci.*, 47, 1941–1947.
- Warren P. H., Kalleymen G. W., Huber H., et al. (2009) Siderophile and other geochemical constraints on mixing relationships among HED-meteorite breccias. *Geochim. Cosmochim. Acta*, 73, 5818–5943.
- Warren P. H., Isa J., and Gessler N. (2013) Petrology of secondary mineral development, probably fluid-driven, within the uniquely evolved eucrite northwest Africa. In *Lunar Planet. Sci. XLIV*, Abstract #2875. Lunar and Planetary Institute, Houston.
- Williams D. A., Jaumann R., McSween H. Y., et al. (2014a) The chronostratigraphy of protoplanet Vesta. *Icarus*, 244, 158–165.
- Williams D. A., Denewi B. W., Mittlefehldt D. W., et al. (2014b) The geology of the Marcia Quadrangle of asteroid Vesta: Assessing the effects of large, young craters. *Icarus*, 244, 74–88.
- Williams D. A., Yingst R. A., and Garry W. B. (2014c) Introduction: The geologic mapping of Vesta. *Icarus*, 244, 1–12.
- Wilson L. and Keil K. (2012) Volcanic activity on differentiated asteroids: A review and analysis. *Chem. Erde–Geochem.*, 72, 289–321.
- Yamashita N., Prettyman T. H., Mittlefehldt D. W., et al. (2013) Distribution of iron on Vesta. *Meteoritics & Planet. Sci.*, 48, 2237–2215.
- Yingst A., Mest S., Berman D., et al. (2014) Geologic mapping of Vesta. *Planet. Space Sci.*, 103, 2–23.

# The Flybys of Asteroids (2867) Šteins, (21) Lutetia, and (4179) Toutatis

M. Antonietta Barucci

*LESIA-Paris Observatory*

Marcello Fulchignoni

*Université de Paris 7*

Jianghui Ji

*Purple Mountain Observatory, Chinese Academy of Sciences*

Simone Marchi

*Southwest Research Institute*

Nicolas Thomas

*University of Bern*

---

Three flybys of asteroids have occurred in the period between 2008 and 2012. (2867) Šteins and (21) Lutetia have been observed by the European Space Agency's Rosetta spacecraft, and (4179) Toutatis was observed by the Chinese National Space Agency's Chang'e-2. The properties of these three bodies are very different from other asteroids visited to date. Šteins seems to have been subject to a combination of various processes, including collisions and significant reshaping as a result of rotational forces (the YORP effect). Lutetia has a high density, which has led to speculation that it is a partially differentiated body. Images display a surface with complex morphology exhibiting different structures: pits, craters, crater chains, scarps, and vast younger terrains have been observed. The shape of Toutatis shows two major lobes, suggesting a contact binary object. A comparison with data obtained by previous asteroid flybys is presented. Limitations of flyby results, in particular interpretation of the composition, are also discussed.

## 1. INTRODUCTION

In the last few years three successful asteroid flybys have been completed by two spacecraft. Two main-belt asteroids, (2867) Šteins and (21) Lutetia, were visited in September 2008 and July 2010 respectively by the European Space Agency's (ESA) Rosetta spacecraft on its journey toward Comet 67P/Churyumov-Gerasimenko (Schulz et al., 2009). The near-Earth asteroid (4179) Toutatis was flown by on December 2012 by the China National Space Administration (CNSA) lunar exploration probe, Chang'e-2.

### 1.1. Rosetta Mission

Rosetta is an ESA cornerstone mission and is expected to make a major contribution to the study of the small bodies of the solar system. The mission, named after the Rosetta Stone, housed in the British Museum in London, has the objective of deciphering the mysteries of the building blocks of our solar system. The mission, launched on March 2, 2004, is composed of two elements: the orbiter and the lander, Philae.

The combined scientific payload consists of 25 remote sensing and *in situ* experiments with an unprecedented capability to characterize the nature of comets and asteroids (Schulz et al., 2009). To reach the target comet, the Rosetta spacecraft needed to acquire the necessary orbit characteristics. The journey was to take more than 10 years and included two swingbys of Earth and one of Mars before the first asteroid flyby with Šteins. Another Earth gravity assist followed before the flyby of Lutetia. On June 8, 2011, the spacecraft was placed in deep-space hibernation mode for 31 months. The spacecraft was successfully woken up on January 20, 2014. It reached Comet 67P/Churyumov-Gerasimenko when it was still far away from the Sun (heliocentric distance of about 4 AU) in order to start the characterization of the comet nucleus prior to the delivery of the Philae lander (at a time when the nucleus was still at a low state of activity) and to start the comet escort phase until its perihelion passage in August 2015, with the end of the nominal mission on December 31, 2015. Rosetta performed a complex series of maneuvers to reduce the separation between the spacecraft and comet up to a distance of 10 km in order to map the

comet and choose a landing site for Philae. On November 12, 2014, when the comet was at a heliocentric distance of 3 AU, Philae landed successfully on the comet nucleus.

For the Rosetta mission, the final choice of the asteroid flyby targets was made only after the launch and the first orbital correction maneuver. In this way, an accurate value for the available  $\Delta V$  could be used to identify potential targets for the asteroid flybys. Barucci *et al.* (2005) analyzed all the possible candidates proposed before the launch and recommended the selection of (21) Lutetia and (2867) Šteins to the Rosetta Project because of their high potential scientific return. Lutetia was selected mostly because of its large size (it would be the largest asteroid to be visited by a spacecraft at the time of selection), which was expected to lead to accurate mass and density determinations. Šteins was known to have an unusual surface composition, similar to the rare E-type class, which had never been observed by space missions before.

The flyby with Šteins took place on September 5, 2008, at a relative velocity of  $8.6 \text{ km s}^{-1}$  and a closest approach distance of 803 km. Fourteen instruments were switched on, providing spatially resolved multi-wavelength observations and *in situ* measurements of its dust, plasma, magnetic, and radiation environment. Four instruments performed imaging and spectrometric observations from the ultraviolet (70 nm) through the visible and infrared to the millimeter range (1.3 mm). The flyby of Lutetia was performed on June 10, 2010, at a closest distance of 3168.2 km and a velocity of  $15.0 \text{ km s}^{-1}$ . The same suite of instruments was switched on. The main scientific results for both asteroids have been obtained by the Optical, Spectroscopic, and Infrared Remote Imaging System (OSIRIS) imaging system, the Visible and Infrared Thermal Imaging Spectrometer (VIRTIS), the Alice ultraviolet spectrometer, the Microwave Instrument for Rosetta Orbiter (MIRO), and the radio science investigation (RSI) [see Shulz *et al.* (2009) for details of all the Rosetta instruments]. Both asteroids were also observed by the Spitzer Space Telescope to support preparation and optimization of the operations of the spacecraft in order to maximize the scientific return from the flybys (Barucci *et al.*, 2008). Lutetia was also observed by the Herschel infrared space telescope prior to and around the time of the Rosetta flyby (O'Rourke *et al.*, 2012).

## 1.2. Chang'e-2 Mission

Chang'e-2 was the second Chinese mission dedicated to the investigation of the Moon. The spacecraft was launched on October 1, 2010, and was in orbit around the Moon for six months, obtaining high-resolution maps of the lunar surface. After completing its prime mission, Chang'e-2 still had significant amounts of propellant onboard. The spacecraft was capable of escaping lunar orbit and traveling into interplanetary space.

On June 9, 2011, Chang'e-2 departed its lunar orbit and was commanded to perform a slow transfer to the Sun-Earth Lagrangian point (L2). L2 has technical interest as a

potential parking position for spacecraft, allowing assembly, refueling, and efficient dispatch toward solar system objects. Chang'e-2 arrived at L2 on August 25, 2011, and started to explore the space environment. The selection of a potential flyby asteroid was proposed prior to the launch of Chang'e-2. After Chang'e-2 reached L2, asteroid (4179) Toutatis was finally selected for the flyby, taking into account its closest approach to Earth (to occur on December 12, 2012), the residual fuel of the spacecraft, and the capability of the tracking and control network. Chang'e-2 had been intentionally controlled to move near L2 for more than 230 days to favor the Toutatis-flyby injection maneuvers until April 15, 2012, when Chang'e-2 left L2.

A groundbased observation campaign for Toutatis was organized by the Chinese Academy of Sciences from May to November 2012, to improve the orbit of Toutatis, which was refined with uncertainties on the order of a few kilometers. Chang'e-2 completed its flyby of Toutatis on December 13, 2012, passing at a closest distance of  $770 \pm 120 \text{ m}$  (Huang *et al.*, 2013) from the asteroid's surface at a relative velocity of  $10.73 \text{ km s}^{-1}$ . At the time of writing, Chang'e-2 remains alive and is more than 100 million kilometers away from Earth in a heliocentric orbit.

## 2. (2867) ŠTEINS

Images of Šteins were acquired by the OSIRIS imaging system, a two-camera system comprising a narrow-angle camera (NAC) and a wide-angle camera (WAC) (Keller *et al.*, 2007). Resolved images were obtained starting 4 h before closest approach at a distance of  $\sim 60,000 \text{ km}$  when the phase angle was  $38^\circ$ . The spacecraft was targeted to pass close to opposition geometry and actually reached a minimum phase angle of  $0.27^\circ$  before reaching  $51^\circ$  at the closest distance of 803 km and finally  $141^\circ$  at the end of observations at a distance of 60,000 km post-encounter. The high-resolution camera (NAC) unfortunately stopped 10 min before the closest approach (putting itself in safe mode) when the spacecraft was 5200 km from the asteroid. Consequently, the highest-resolution images were acquired by the WAC. The numerous images taken up to a best resolution of about 80 m/pixel (Keller *et al.*, 2010) covered 60% of the surface and showed a diamond-shaped object (Fig. 1) with a surface dominated by depressions of possible impact origin (Marchi *et al.*, 2010; Besse *et al.*, 2012). The complete shape with dimensions of  $6.8 \times 5.7 \times 4.4 (\pm 0.1) \text{ km}^3$  was derived using these images and the inversion of lightcurves taken from ground and by OSIRIS during approach (Jorda *et al.*, 2012). The pole was found to be almost perpendicular to the ecliptic plane with ecliptical coordinates of  $99^\circ \pm 5^\circ$ ,  $59^\circ \pm 5^\circ$  and retrograde rotation. The siderial rotational period of  $6.04681 \pm 0.00002 \text{ h}$  had already been computed by Lamy *et al.* (2008) and confirmed by OSIRIS data. The phase function obtained with more than 100 images covering  $0^\circ$  to  $132^\circ$  in phase allowed a determination of the geometric albedo of  $0.410 \pm 0.016$  with an absolute magnitude of  $H = 12.90$  and a slope parameter  $G = 0.45$ .

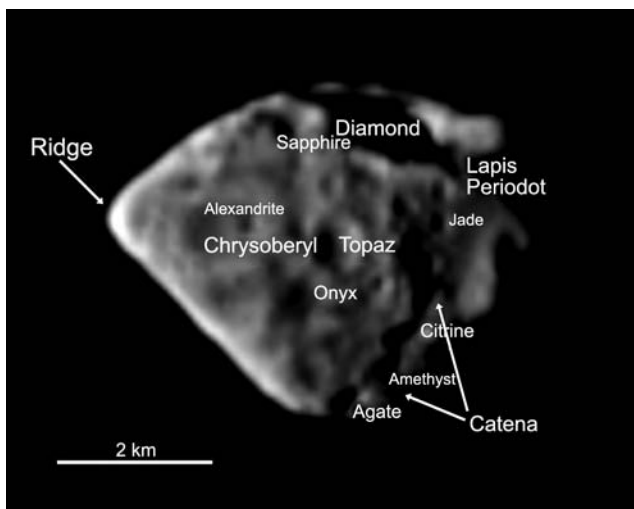


**Fig. 1.** Image of asteroid (2867) Šteins acquired with the Rosetta/OSIRIS wide-angle camera on September 5, 2008, at 18:38:06 from a distance of 803 km. The principal regions and craters have the name reported. The south pole is up. (For feature names, see <http://planetarynames.wr.usgs.gov/Page/Steins/target>.) Credit: ESA/Rosetta/MPS for OSIRIS Team MPS/UPD/LAM/IAA/SSO/INTA/UPM/DASP/IDA.

## 2.1. Surface Structures and Age

Most notably, Šteins shows an equatorial ridge (Keller et al., 2010; Jorda et al., 2012), which has been suggested to have formed by centrifugal acceleration as the asteroid was spun up by the Yarkovsky-O’Keefe-Radzievskii-Paddack (YORP) effect (see the chapter by Vokrouhlický et al. in this volume). The YORP effect can cause the migration of the regolith from the polar regions toward the equator, thereby forming the ridge (see the chapter by Walsh and Jacobson in this volume).

At higher resolution, the surface of Šteins is covered by shallow craters, pits, ejecta and regolith. The asteroid exhibits a large crater (2.1 km in diameter, dubbed Diamond) near the south pole, and a series of circular features (catena) 250–600 m in diameter extends from this crater to the north side. This catena may be linked to the impact that caused the larger crater, and another groove, surrounded by small craters, is visible on the opposite side of the asteroid as a possible continuation of the catena. This is somewhat remarkable given that such chains are normally associated with breakup of a body, such as a comet, in a gravitational field immediately prior to impact [see similar structures on Callisto, e.g., Schenk et al. (2004)]. Alternative mechanisms, possibly of endogenic origin such as the formation of drainage pits, should also be considered as a potential formation mechanism (see, e.g., Basilevsky et al., 2014).

Based on analysis of the images, Šteins can be considered a rubble-pile body. Around 42 craters-like depressions were identified on the surface and the crater population seems to exhibit a dichotomy between the two sides of Šteins (Besse

et al., 2012). For the analysis of Šteins’ age, we limited our study to the portion of the surface better imaged and retained a total of 18 craters in the assessment (Marchi et al., 2010). Their cumulative crater size-frequency distribution (SFD) is remarkably shallow (Fig. 2a), if compared to that of larger siblings (see the chapter by Marchi et al. in this volume). The slope of the cumulative crater SFD is, however, comparable to that of (25143) Itokawa and (433) Eros for crater sizes smaller than 0.1 km. A possible interpretation for the shallow slope is that it is the result of erasure of small craters. Given the small size of Šteins, there are a number of processes that may be responsible for this erasure; in particular, seismic shaking may be relevant (Richardson et al., 2004). On the basis of this, Marchi et al. (2010) concluded that small craters could have been erased by cumulative seismic shaking of small impacts or by an impulse of erasure caused by the formation of the Diamond impact crater (see Fig. 1 and the chapter by Marchi et al. in this volume).

An alternative view is that many of the observed crater-like features are not impact craters at all, but rather drainage pits caused by regolith sinking into subsurface fractures and voids. Support for this hypothesis comes for numerical simulations. Jutzi et al. (2010) simulated the impact resulting in Diamond crater and concluded that the impact would have damaged a monolithic parent body and transformed Šteins into a rubble pile structure, allowing it to be reshaped in its current form by the YORP spinup thermal effect.

Following the interpretation of Šteins’ shape as being the result of YORP evolution, mass wasting of loose regolith may also have contributed to the degraded and shallow depression of almost all the craters (except Diamond).

The determination of the absolute cratering retention age of Šteins is challenging in light of the above-mentioned processes that may have resulted in significant changes to the observed crater SFD. On the other hand, if most of the crater-like features are indeed drainage pits, then their number provides no constraint on the surface age. In the assumption that all bona fide craters are impact craters, we have estimated the surface cratering retention age following the methodology presented in Marchi et al. (this volume). Given the likely highly fractured nature of Šteins, an improved rubbly material crater-scaling law has been implemented (see Marchi et al. this volume) and an estimate of the current impact rate for Šteins (Marchi et al., 2010) has been used. The propagation back in time of the impact flux follows the recent model of O’Brien et al. (2014). The main conclusion of this analysis is that our model represents a poor fit of Šteins’ crater SFD (Fig. 3a), thus making the age estimate highly uncertain. If we attempt to fit the largest craters ( $>0.6$  km), the resulting surface age is  $\sim 1.3$  Ga (for an assumed material strength of  $2 \times 10^5$  Pa; for comparison, lunar regolith has a strength of  $\sim 10^3$  Pa, while terrestrial near-surface alluvium has  $\sim 6 \times 10^4$  Pa). If the formation of the largest crater occurred during this time, it may have triggered an impulse of erasure, responsible for the mismatch at small crater sizes (0.1–0.5 km). In this case, for our estimate to be reliable, Šteins should have been already

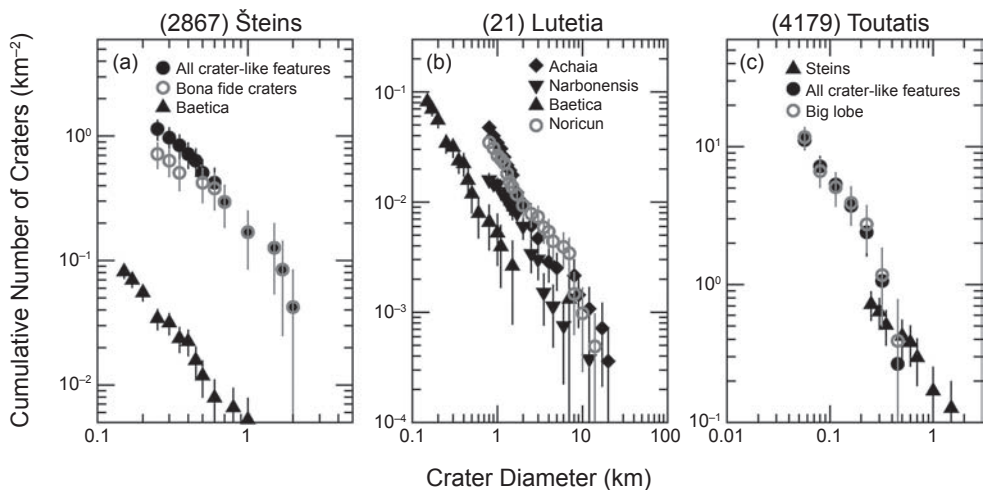


**Fig. 2.** A comparative view of cratering on recent flyby asteroids. (a) (2867) Šteins crater size-frequency distributions. (b) (21) Lutetia crater size-frequency distributions. The most representative units are shown here (Achaia, Noricum, Narbonensis, Baetica). (c) (4179) Toutatis crater size-frequency distributions. Data from Marchi *et al.* (2010, 2012), Besse *et al.* (2012), and Huang *et al.* (2013).

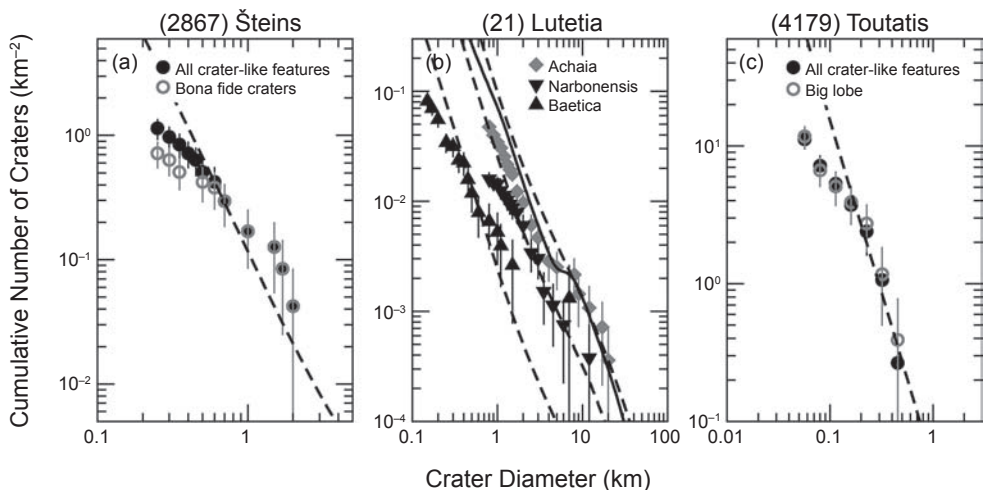


**Fig. 3.** Best fits (solid and dashed thick black curves) of some of the crater SFDs presented in Fig. 2.

highly fractured. However, we caution that it is likely that most of the observed crater-like depressions are not impact craters, therefore the age of  $\sim 1.3$  Ga should be considered as an upper, highly uncertain limit.

## 2.2. Composition

The spectra obtained by Visible and Infrared Thermal Imaging Spectrometer (VIRTIS)-M, observing from 200 to 5000 nm, and by the NAC and WAC cameras observing with 11 filters from 220 to 960 nm are very similar to those from the ground, showing a reddening at wavelengths  $< 1000$  nm with strong signature at 490 nm, a steep drop below 400 nm, and almost flat and featureless for wavelengths  $> 1000$  nm.

They confirm the surface taxonomy of an E-type asteroid. This rare taxonomic class is dominated by iron-free or iron-poor silicates (Gaffey *et al.*, 1993). The characteristic absorption feature at 490 nm is tentatively attributed to sulfides. In particular, Šteins' spectra are similar to the "Angelina-like" asteroid E(II) subtype (Gaffey and Kelley, 2004), for which the main mineralogical components are enstatite and oldhamite with small amounts of low-iron silicate mineral. Generally, the E-type class is associated with aubrites, but this meteorite does not fit the prominent 490-nm absorption band. Aubrites are achondrite meteorites mainly composed of Fe-poor, Mg-rich orthopyroxene, or enstatite containing a variable amount of olivine, nickel-iron metal, sulfides such as oldhamite and troilite, and rare minerals. To reproduce

the spectra, an additional significant percentage of oldhamite seems necessary to be present on the surface of Šteins (*Fornasier et al.*, 2008). None of the known meteorites alone fit the spectral properties of this rare asteroid. The igneous composition argues for an origin as part of the interior of a larger differentiated parent body. *Leyrat et al.* (2010) searched for surface inhomogeneity over almost 30% of the surface using OSIRIS images with multiple filters and using the G-mode multivariate statistical method (*Barucci et al.*, 1987). The analyzed data, adopting a polyhedron shape model of 58,000 facets with photometric corrections using Hapke's model, suggested no surface inhomogeneity greater than 4% at the 95% confidence level. *Schroder et al.* (2010) found a small variation (5–10%) around Diamond crater, which is spectrally slightly bluer than the rest of the object, although an influence of illumination cannot be ruled out.

### 2.3. Thermal Inertia

The surface temperature of Šteins was measured by inversion of the infrared spectra acquired by the VIRTIS-M imaging spectrometer (*Leyrat et al.*, 2011). Minimum and maximum temperatures of 185 K and 225 K were measured, leading to a thermal inertia of  $110 \text{ J m}^{-2} \text{ K}^{-1} \text{ s}^{-1/2}$  assuming a smooth surface. This value is in good agreement with the previous results obtained using the Spitzer Space Telescope (*Barucci et al.*, 2008; *Groussin et al.*, 2011) and implies a thick layer of regolith. The conclusion by *Leyrat et al.* (2011) was that the thermal inertia is not uniform over the surface, with some surfaces having a higher thermal inertia, implying that roughness may be different in some areas. The MIRO instrument also observed Šteins during closest approach observing at millimeter wavelengths at 190 GHz (1.6 mm) and submillimeter at 562 GHz (0.53 mm). Unfortunately, due to pointing uncertainties, the MIRO main beams were never filled by the nightside of Šteins, limiting the ability to measure the day-night temperature contrast and consequently the measurements were difficult to interpret (*Gulkis et al.*, 2010). A higher value for the thermal inertia was nonetheless deduced.

## 3. (21) LUTETIA

The Rosetta spacecraft flew by asteroid (21) Lutetia, obtaining resolved images for about 10 h around closest approach and revealing an object with a highly complex history. The camera systems observed the asteroid in 21 broad and narrow-band filters covering more than 50% of the surface with spatial scales of  $\geq 60 \text{ m/pixel}$  (*Sierks et al.*, 2011). The global shape with principal axis dimensions of  $121 \pm 1 \times 101 \pm 1 \times 75 \pm 13 \text{ km}^3$  was modeled using OSIRIS data. In combination with the inversion of photometric lightcurves and contours of adaptative optics images, a north pole directed toward ecliptical coordinates  $51.8^\circ \pm 0.4^\circ$  and  $+10.8^\circ \pm 0.4^\circ$  was found (*Sierks et al.*, 2011). The rotational period of  $8.168271 \pm 0.000002 \text{ h}$  had already been computed from OSIRIS data acquired in 2007 when

the spacecraft was 1.64 AU from the asteroid (*Lamy et al.*, 2010). From the shape model, a volume of  $(5.0 \pm 0.4) \times 10^5 \text{ km}^3$  has been derived. The northern hemisphere was well imaged with a good three-dimensional reconstruction (*Preusker et al.*, 2012). However, a large fraction of the asteroid's southern hemisphere was not visible during the flyby and consequently the shortest semimajor dimension is not well constrained (*Carry et al.*, 2012), giving uncertainty in the volume estimation. Combining the estimated volume and the mass obtained by the RSI ( $1.7 \times 10^{18} \text{ kg} \pm 1\%$ ), a bulk density of  $3.4 \pm 0.3 \text{ g cm}^{-3}$  has been computed (*Pätzold et al.*, 2011). The north pole is located near a depression that has been produced by multiple impacts: the north polar crater cluster (NPCC). The north rotational pole was roughly pointed toward the Sun at the time of the Rosetta encounter and hence high-resolution imaging was restricted by the illumination to one hemisphere despite the relatively rapid rotation rate (*Carry et al.*, 2010). Some parts of the northern hemisphere were not well imaged because of the low phase angle of the approach ( $\sim 7.7^\circ$ ) and hence interpretation must account for possible observational biases. The measured visible albedo is  $0.19 \pm 0.02$ . Variations on the surface up to 30% in reflectivity correlated with geographic morphologies have been detected (*Sierks et al.*, 2011).

### 3.1. Surface Structures

Impact craters dominate the overall structure. The largest depression is the Massilia structure (see Fig. 4), which is a highly degraded 57-km-diameter crater-like structure. Its rim appears to have been modified by subsequent impacts to such an extent that its origin as an impact structure has been questioned (*Thomas et al.*, 2012), although alternative formation mechanisms have not been identified. The other dominant feature in the images is the NPCC itself, which forms the most striking construct within the Baetica region. This appears to be one of the youngest surfaces on the object and is made up of four principal impacts of varying size that have overlapped each other. Other smaller impacts have also influenced the structure. The largest crater (Corduba) is  $\sim 34 \text{ km}$  in diameter and slightly elliptical. Subsequently the Gades crater, roughly into the center of Corduba, has produced a remarkable structure with boulders and landslides evident within it. The relatively low density of smaller impact craters within the NPCC contrasts sharply with the high crater density seen in the Noricum region. Other surfaces (notably Narbonensis) have intermediate crater densities.

**3.1.1. Ejecta deposition.** The impacts producing the NPCC appear to have erased craters in a non-uniform manner about the impact site. The transition between low and high crater density regions across the Noricum boundary is remarkably abrupt ( $< 150 \text{ m}$  in width) with no evidence of ejecta falling onto the Noricum region (*Thomas et al.*, 2012). Significant amounts of ejecta were observed on the opposite side of the impact crater, which has draped and partially covered the Achaia region. This has been taken as evidence that the largest impact of the NPCC was a relatively oblique one

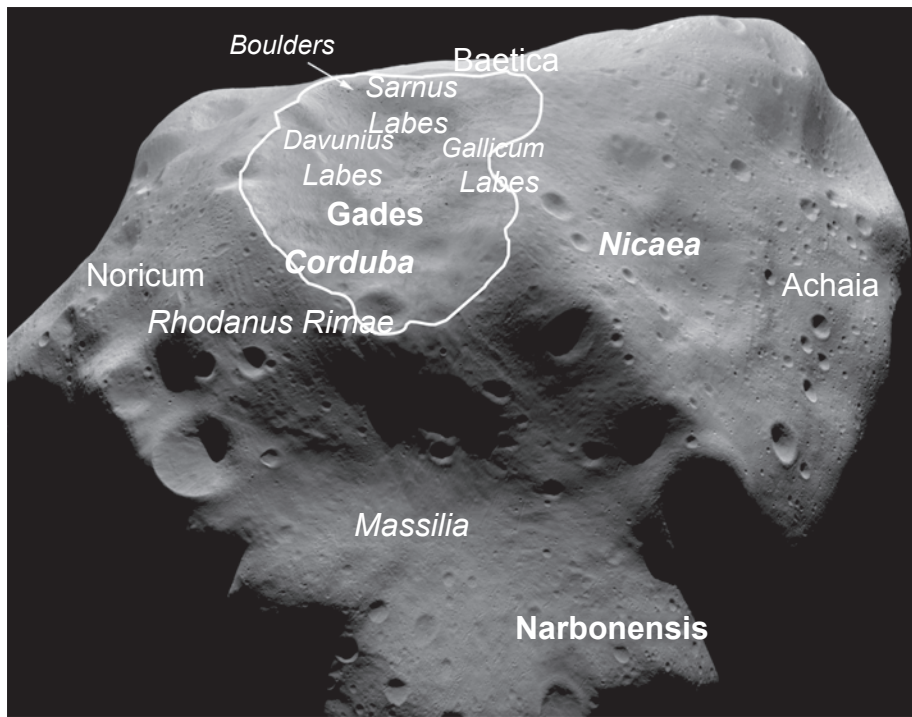


**Fig. 4.** (21) Lutetia as seen using the OSIRIS imaging system on Rosetta. Some regions mentioned in the text are noted in large font. Craters mentioned are identified in bold italic. Other surface features are in regular italic. The NPCC area is reported by white line. See <http://planetarynames.wr.usgs.gov/Page/LUTETIA/target> for more information. Credit: ESA/Rosetta/MPS for OSIRIS Team MPS/UPD/LAM/IAA/SSO/INTA/UPM/DASP/IDA.

with respect to the local surface (*Jutzi et al.*, 2013). *Krohn et al.* (2014) studied oblique impacts into slopes on the more rounded asteroid (4) Vesta, and concluded that slopes  $>20^\circ$  prevent deposition of ejected material in the uphill direction. Given the limited knowledge of the surface topography of (21) Lutetia prior to the largest NPCC impact and the lower gravity, this conclusion is somewhat difficult to apply in this case. The modeling work of *Jutzi et al.* (2013), using the smooth particle hydrodynamics (SPH) technique, has shown that collection of ejecta in potential wells (e.g., in craters) is surprisingly effective, providing an explanation for younger surface ages in some depressions within older units. In particular, ejecta from the NPCC impact(s) can be deposited in the interior of Massilia, potentially explaining its younger age (see section 3.2), while a relatively limited amount of material ends up on the older units of Noricum. Furthermore, the apparent youth of surfaces in depressions in Achaia such as Nicaea can be explained by the same mechanism. The irregular gravitational field is clearly something that must be taken into account in ejecta calculations on intermediate-sized asteroids and, in ideal cases, may provide constraints on internal mass distributions. The maximum extent of the ejecta toward the subsolar point at the time of the Rosetta flyby is unclear. The low phase angle of the approach led to low contrast in the data acquired (comprising the Etruria and Raetia regions), but qualitatively lower densities of

intermediate-sized craters were reported in the Etruria region (*Thomas et al.*, 2012).

**3.1.2. Lineaments.** Lutetia possesses a remarkable set of lineaments. The prevalence and diversity of lineaments on the surface is striking. Some of the observed lineament sets are  $>80$  km long, although their depths are mostly below the resolution limit of the best digital terrain model ( $\sim 100$  m). An example of the prevalence of lineaments is shown in Fig. 5.

*Thomas et al.* (2012) attempted to categorize the various types of linear structures (Table 1). The table illustrates that there are different types of linear and quasi-linear troughs and linear reflectance discontinuities all over the surface except in the Baetica region. The lineaments show alignment (preferred orientation) in several regions. The preferred orientation is not uniformly circumferential about any one crater. Three possibilities to reconcile this observation are being studied independently: (1) *Jutzi et al.* (2013) used the SPH code discussed above with respect to ejecta to compute the surface velocity field caused by the 34-km impact into the Baetica region. They showed that the velocity vector orientations were strongly affected by the irregular shape of the body and some qualitative agreement with observed orientations of lineaments was noted. (2) *Besse et al.* (2014) have suggested that impacts produce circumferential lineaments and have then further suggested that the lineaments

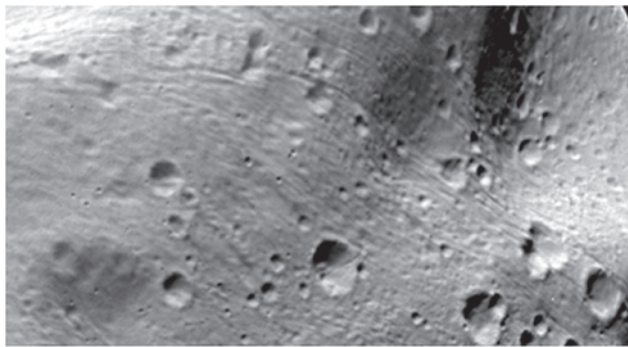


**Fig. 5.** Lineament set in the Etruria-Achaia region. Note the craters that have been cut and distorted by lineaments. Credit: ESA/Rosetta/MPS for OSIRIS Team MPS/UPD/LAM/IAA/SSO/INTA/UPM/ DASP/ IDA.

on Lutetia require production via three separate impacts, one of which is on the hemisphere unseen by OSIRIS. (3) *Giacomini et al.* (2014) suggested that the lineaments reflect previously defined fault planes within a parent body from which Lutetia was formed and that the lineaments pre-date all the major cratering events.

These three competing models have advantages and disadvantages. The *Jutzi et al.* (2013) model does not clearly identify, as the authors note themselves, why the lineaments should be generated parallel to the local surface velocity field. However, the model is physical and explains the observed ejecta deposition. There is also no doubt that reflections from

interfaces should play a role in modifying the disturbance as it passes through the body, and this is most accurately computed using the SPH approach. The *Besse et al.* (2014) model follows approaches used at other asteroids (e.g., *Buzkowski et al.*, 2008). However, the approach is empirical and requires that lineaments produced by previous impacts are not erased by the newer ones on Lutetia [which would place significant constraints on the transmission of seismic waves; e.g., see *Asphaug et al.* (1996)]. It should be noted that depth-diameter plots of impact craters show depth dropping more steeply with decreasing diameter (*Vincent et al.*, 2012) — an effect noted on, e.g., (951) Gaspra (*Carr et al.*, 1994) and an indication of degradation by either impact erosion, filling by ejecta from younger craters, or seismic-induced downslope motion (*Carr et al.*, 1994), all of which must influence lineaments as well. The *Giacomini et al.* (2014) model requires that the internal and external structure has retained its properties since its formation as a fragment of a bigger body and that, again, disturbance of the lineaments via mechanisms such as seismic jolt are ineffective. *Jaumann et al.* (2012) note that troughs on Vesta, when mapped onto the shape model, can be modeled as planes that cut through the asteroid. However, *Buczkowski et al.* (2012) suggest an impact origin for the troughs, which would be dissimilar to the *Giacomini et al.* (2014) concept. On the other hand, as *Buczkowski et al.* (2012) note, the Vesta troughs are morphologically and structurally different from the lineaments seen on Lutetia.

Three other observations may be significant in assessing these models. First, crossing of lineaments is evident in several places (notably in the Achaia and Etruria regions;

TABLE 1. Lineament categories on (21) Lutetia (after *Thomas et al.*, 2012).

Lineament Type	Description	Where Best Seen
Irregular troughs	Older, 1-km-wide depression, often curved, possibly result of extension due to tensile stress; often cut by craters; some examples on ridge apexes	Everywhere outside NPCC
Larger faults	Linear, narrow faults; possibly tectonic in origin; unknown depth; observed to cut craters	Narbonensis/Noricum
Organized linear reflectance variations (OLRV)	Quasi-regular reflectance variations produced by subtle topographic changes	Noricum/Achaia
Pit-chains	Lineaments with alternating bright/dark pattern along their length	Narbonensis, possibly Achaia
Intracrater trenches	Irregular depressions or faults within craters	All except NPCC
Intracrater layers	Horizontal lineaments in crater wall	NPCC
Ejecta layers	Curved discontinuities in layers of ejecta	Baetica-Etruria border
Ridges	Major structural element as a topographic high	Possibly all areas
Scars	Isolated steep scarps often separating different surface textures	All except NPCC

see Fig. 5). Crossing of lineaments at angles  $>60^\circ$  in, e.g., Achaia suggests noncoeval production under the assumption that Anderson faulting is applicable. Hence multiple impacts may have been necessary to produce the observed lineaments. Second, like Eros (*Veverka et al.*, 2001), the presence of lineament sets over distances greater than the radius of the asteroid implies that Lutetia may have some structural coherence over such distance scales. Conversely, the age and substantial numbers of large craters should have provoked considerable fracturing. Being able to reconcile these two points would provide a step forward. Finally, the major ridge on Lutetia (*Sèquana*) has topographic relief of more than 10 km. The base of the ridge shows evidence of old slides that have produced relatively sharp discontinuities in the surface reflectance arising from abrupt changes in slope. Although gravity is weak, some deformation of this feature under its own weight may occur, particularly if the structural strength is as low as that of lunar regolith (e.g., *Arslan et al.*, 2010). A quantitative analysis may provide knowledge of the strength of the surface material.

**3.1.3. Boulders.** Inside and around the NPCC, there are large numbers of boulders (*Küppers et al.*, 2012). The boulders are up to 250 m in size and are mostly draped over the rim of Gades and extending off in the direction of Etruria (see Fig. 6). On larger objects, boulders are mostly found outside the crater rim of an impact structure. However, the low surface gravity may have played a role in producing a more complex spatial distribution of boulders with respect to the Gades impact. The history of the impact site may complicate this issue. Following the larger Corduba-forming impact, the asteroid, particularly near the NPCC, should have been highly fractured. The Gades impactor struck this fractured material and hence the boulders we see on the surface have probably been shocked and modified by impact at least twice.

Assuming that boulders are broken down with time by micrometeorite impacts [other processes such as thermal fatigue may also contribute (*Delbo et al.*, 2014)], together

with assumptions about the impact rates, this can be used to constrain the surface age of the NPCC with values of  $\sim 300$  m.y. being suggested (*Küppers et al.*, 2012). From the relative positioning of the boulders and the landslides inside Gades (see Fig. 6), some boulders may have been buried by the landslides, suggesting that the landslides occurred later. The landslides do not appear to have carried boulders to the lowest part of Gades, suggesting a rather weak flow.

**3.1.4. Landslides and local material motion.** The interior of Gades in the NPCC of Lutetia shows evidence of three landslides (named Danuvius, Gallicum, and Sarnus Labes). Davunius Labes seems to be a debris slide or avalanche about 10 km wide with several lobes of 200-m scale relief at its base (see Fig. 6). The surface appearance of the debris is mottled, possibly indicating a poorly sorted mixture of particle sizes and not a uniform regolith. However, the strong forward scattering of the surfaces of Danuvius and especially Gallicum, noted in *Thomas et al.* (2012), indicates low macroscopic roughness at subpixel scales ( $\sim 100$  m). This, together with the absence of boulders on the surfaces of the landslides, indicates that the landslides are some of the most recently produced surfaces on Lutetia.

The major ridge on Lutetia (*Sèquana*) has topographic relief of more than 10 km. It would form part of the rim of Massilia crater, although we note that it is linear rather than curved. The base of the ridge shows evidence of old slides that have produced relatively sharp discontinuities in the surface reflectance arising from abrupt changes in slope. Although gravity is weak, some deformation of *Sèquana* under its own weight may also have occurred, particularly if the structural strength is as low as that of lunar regolith (e.g., *Arslan et al.*, 2010). Finally, *Vincent et al.* (2012) have investigated asymmetric craters with flow-like features on Lutetia and concluded that flow of fine material is widespread, including within the Narbonensis region, where flow is primarily directed toward the center of a local gravitational well. This forms a plausible explanation for the lower apparent age of the surface within the Massilia structure.

## 3.2. Crater Populations and Surface Ages

The surface of Lutetia shows abundant impact craters, the spatial distribution of which appear highly variable across the surface. The geometry of the flyby resulted in variable spatial resolution and illumination conditions that did not allow a uniform detection of craters across the imaged surface. The best conditions were achieved for the Achaia, Baetica, Narbonensis, and (partially) Noricum regions, and for these areas estimates of the ages have been computed.

Achaia exhibits the highest crater density (Fig. 2b). The overall distribution of craters revealed 157 craters larger than  $\sim 0.6$  km. The largest crater is called Nicaea and measures about 22 km across. A remarkable feature is the presence of a sharp kink in the cumulative crater SFD at crater sizes between 4 and 7 km. The presence of the kink can have several explanations, such as a similar inflection in the impactor SFD. Although the impactor SFD is not well constrained at

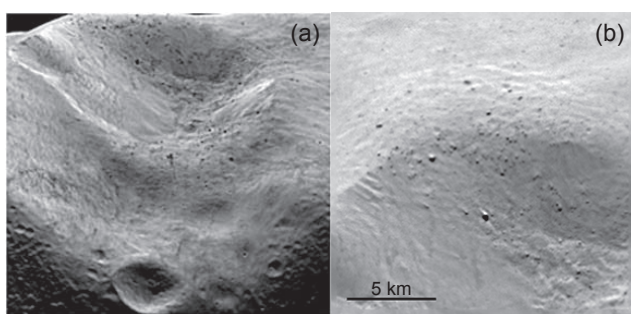


**Fig. 6.** (a) Nonlinear enhanced (unsharp masking) version of the central portion of image taken by NAC showing the NPCC. The Gades impact crater is toward the top. The lobate smooth material in the crater center comes from the Davunius Labes landslide. (b) Boulders distributed over the rim of Gades in the NPCC. The largest visible is about 250 m in width. Credit: ESA/Rosetta/MPS for OSIRIS Team MPS/UPD/LAM/IAA/SSO/INTA/UPM/DASP/IDA.

the corresponding impactor sizes (~0.5 km), comparison with crater SFDs from other asteroids (e.g., Vesta, Gaspra) make this interpretation unlikely (see the chapter by Marchi et al. in this volume). Other processes seem more likely. Examples would include preferential erasure of craters smaller than ~7 km, or a change of the target mechanical properties with depth (Marchi et al., 2012).

Noricum exhibits a similarly high crater density; however, at closest approach the region was seen under a grazing angle; which may affect the detection of craters. A total of 76 craters larger than 0.6 km were mapped (Marchi et al., 2012). Noricum is also characterized by significant topography variations (Thomas et al., 2012), possibly due to impact sculpting, but these large concavities were not included in the crater SFD due to inconclusive evidence. These factors may explain why the Noricum crater SFD appears distorted if compared with that of Achaia.

Narbonensis corresponds to the floor of the largest impact structure on Lutetia, Massilia crater. Most of this region has a high slope with respect to the local gravity and many craters show clear evidence of rim slumping (Vincent et al., 2012). A total of 47 craters larger than 0.6 km were mapped, and the overall crater density is somewhat lower than that of Achaia/Noricum, implying a lower crater retention age (Marchi et al., 2012). It is a matter of debate whether the Narbonensis crater SFD is representative of the formation age of Massilia, or rather indicates a younger age due to internal resurfacing (e.g., because of mass wasting). A related important issue is the degree of crater erasure that the formation of Massilia may have triggered on surrounding terrains. A possibility is that the formation of Massilia was so intense that it caused significant erasure of craters in the Achaia and Noricum regions, both via seismic shaking and ejecta burial. In this case, given that regions appear roughly spatially uniform, the erasing must have been on a global scale, and therefore the age of Achaia/Noricum would indicate the formation age of Massilia, while Massilia's floor appears younger. This would imply post-formation resurfacing. Support for this interpretation may come from the degraded and shallow appearance of Nicaea and other large craters in Achaia, which require significant infilling with loose material to explain their shallow depths. If one assumes that all the craters larger than 7 km pre-date Massilia and survived its formation, then smaller craters may post-date Massilia. Alternatively, Massilia may not have significantly affected the Achaia/Noricum crater populations and their crater retention ages would pre-date Massilia. In this case, the kink in the crater SFD (Fig. 2b) could be the result of a layered structure, with increasing target strength with depth (Sierks et al., 2011; Marchi et al., 2012).

Baetica is the youngest region and shows very few small impact craters. The region appears to have been produced by the formation of three superposed large impact structures with a subsequent smaller impact. The stratigraphically oldest of them is a 34-km crater called Corduba. Crater measurements were performed only on a subregion using the highest spatial resolution. A total of 62 craters in the range 0.2–1 km were mapped (Marchi et al., 2012). The resulting crater SFD

shows a remarkably flat slope when compared with Achaia (and its extrapolation to smaller sizes), or other asteroids such as Vesta (see the chapter by Marchi et al. in this volume). A possible explanation for such behavior includes a shallower slope of the impactor SFD or erasure of small craters caused by mass wasting given the high gravitational slope of this terrain.

The formation of Corduba was investigated in detail using SPH simulations (Jutzi et al., 2013). It was found that ejecta accumulation may have triggered some crater erasure in nearby regions, including Achaia and Narbonensis, because of ejecta accumulation. The predicted size of buried craters on Achaia depends on the impact geometry, but is generally below or comparable to the range of crater sizes studied here (<0.6 km), and could potentially explain the shallow slope of Achaia crater SFD below 4 km if compared with the production function. A more significant accumulation of ejecta is predicted within Narbonensis, which along with rim slumping may have resulted in significant crater erasures.

As briefly discussed for Šteins, the absolute age determination requires some assumptions on the crater-scaling law and mechanical properties of the target. The latter has an important role given that all the craters analyzed formed in the so-called strength regime, and therefore the final crater size is sensitive to the target strength. Furthermore, the crater density on the oldest regions is such that crater obliteration processes may play a role. Here we revise the age estimates published by Marchi et al. (2012). In particular, we have implemented an improved model for the time-dependence of the impact flux in the past following O'Brien et al. (2014) and improved crater-scaling laws. Concerning the latter, we implemented two cases: a hard rock case and a rubbly material case. Both crater-scaling laws are from Holsapple and Housen (2007). In the case of hard rock, we assumed a typical strength of  $2 \times 10^7$  Pa (Asphaug et al., 1996), while for the rubbly material case, we adopted  $2 \times 10^6$  Pa, i.e., one-tenth that of the assumed competent rocks (note that this is higher than what assumed for Šteins, but lower values are also plausible). The first set of fits was performed assuming a uniform target, and only considering craters larger than 8 km. The resulting age is ~3.7 Ga for both scaling laws. We also implemented a case of a two-layered target, as discussed in Marchi et al. (2011, 2012). We considered cases both with and without crater obliteration. The resulting ages are ~2.6 and 3.3 Ga, respectively. The best fits (Fig. 3b) are achieved for an assumed thickness of the top layer of ~2.5 km. Despite the improved quality of the fit resulting from the two-layer model, there is still a mismatch for craters smaller than ~3 km. It is important to realize that the slope of the model curve depends on the assumed strength and density profiles with depth, which are assumed to be linearly increasing from the surface to the bottom of the top layer (2.5 km). It is therefore conceivable that a different choice of profile may improve the quality of the fit. A similar age estimate applies to Noricum, given the similar crater density. Under the same assumptions of uniform target structure, Narbonensis has an age of ~1 Ga. The age of Baetica is highly uncertain given the very shallow

slope, which does not match the assumed production function for the crater SFD. Also, it seems plausible that this region is constituted by a thick layer of regolith (with no layering), for which rubbly material models with low strength values could be more appropriate. Possible values range from tens of millions of years to 100 m.y., depending on which size range is used for the best fit as well as on the assumed tensile strength of the regolith. The given age limits correspond to  $2 \times 10^5$  and  $2 \times 10^6$  Pa, respectively.

### 3.3. Composition

The VIRTIS observations of Lutetia showed flat featureless spectra in the visible and near-infrared (*Coradini et al.*, 2011). VIRTIS has two channels: VIRTIS-M for hyperspectral images in the wavelength 250–5100 nm with a spatial resolution of 250 mrad and VIRTIS-H, a higher-resolution spectrometer from 2000 to 5000 nm with a spectral resolution of 3000 ( $\lambda/\Delta\lambda$ ) and a spatial resolution of  $1.74 \times 0.58$  mrad. VIRTIS-M obtained hyperspectral images of the surface with a spatial resolution varying from 12 km to about 1 km. VIRTIS-M and VIRTIS-H did not identify any spectral features associated with OH at 3000 nm or any feature associated with organic material at 3300–3600 nm (*Coradini et al.*, 2011). The flat and featureless visible and near-infrared spectra obtained during the flyby do not allow discrimination between a carbonaceous and/or enstatite nature, although mid-infrared observations by the Spitzer Space Telescope obtained a few years before with different viewing geometry are more in favor of carbonaceous chondrites (*Barucci et al.*, 2008). The 3000-nm band was not observable by the VIRTIS instrument on the visible 50% of the Lutetia's surface (*Coradini et al.*, 2011), although the other surface of the asteroid, not visible to Rosetta, shows the hydration feature (*Rivkin et al.*, 2011). *Barucci et al.* (2012) assembled all the available data that are diagnostic of composition, with the aim of gathering all the pieces of the Lutetia composition puzzle. From analysis of all the data from ultraviolet to mid-infrared and including polarimetric data, it is evident that Lutetia has a complex composition that can be explained with local variations connected to different composition and different surface textures (structure and regolith). Analogies with existing meteorites remain inconclusive. The surface is probably composed of different chondritic-like materials. Some regions in the southern hemisphere seem to be dominated by carbonaceous chondrites with the presence of aqueous altered materials, while the northern hemisphere could be similar to a mixture of enstatite and carbonaceous chondrites (*Barucci et al.*, 2012). The complicated surface composition associated with the complex structures and history may be explained by collisions of objects with different composition.

The Alice ultraviolet spectrometer observed Lutetia from 70 to 205 nm (*Stern et al.*, 2011). No gas emission was observed around the object and the spectra show a precipitous drop between 180 and 160 nm, which is the strongest feature detected in the spectra. No similar feature has been observed in any asteroid so far, and its interpretation is particularly

difficult because of the lack of laboratory data at these wavelengths. A tentative model with 77% EH5 chondrite and 7.7% each of anorthite, H<sub>2</sub>O frost, and SO<sub>2</sub> frost has been proposed by *Stern et al.* (2011), although the authors were cautious, as other materials could be also consistent with the ultraviolet feature.

Seven other instruments [Rosetta Orbiter Spectrometer for Ion and Neutral Analysis (ROSINA), Cometary Sampling and Composition experiment (COSAC)/Philae, Ptolemy/Philae, Alice, MIRO, OSIRIS, Rosetta Plasma Consortium (RPC)] were switched on during the flyby to search for an exosphere, and, even if none of the attempts gave a detection, stringent upper limits have been found by *Altweiss et al.* (2012) for CO ( $<1.7 \times 10^{25}$  molecules s<sup>-1</sup>) and by *Gulkis et al.* (2012) for H<sub>2</sub>O ( $<4.3 \times 10^{23}$  molecules s<sup>-1</sup>), providing the limit of the possible presence of volatiles on Lutetia's surface. MIRO was used to search for H<sub>2</sub>O, CO, CH<sub>3</sub>OH, and NH<sub>3</sub>, but none of the molecules were detected. The MIRO team estimated an upper limit for the column density of water of  $<5 \times 10^{11}$  molecules cm<sup>-2</sup> and concluded that a layer of ice could not exist at depths less than 4 m.

### 3.4. Thermal Inertia

The spectral emission beyond 3500 nm can be used to estimate the surface temperature. Variations between 170 and 245 K with some correlation with topographic features were found. A thermal inertia of  $20\text{--}30 \text{ J m}^{-2} \text{ K}^{-1} \text{ s}^{-1/2}$  has been computed using VIRTIS observations (*Coradini et al.*, 2011). MIRO (*Gulkis et al.*, 2012) estimated a value of  $<20 \text{ J m}^{-2} \text{ K}^{-1} \text{ s}^{-1/2}$  in the upper surface layer (a few centimeters). The combination of VIRTIS and MIRO data allowed *Keihm et al.* (2012) to model the surface roughness, adding 50% fractional coverage of hemispherical mini-craters. An extremely low thermal inertia value was also computed on the basis of Spitzer Space Telescope (*Barucci et al.*, 2008) and Herschel Space Observatory (*O'Rourke et al.*, 2012) observations. The interpretation of the ensemble (combination) of the thermal observations confirm the existence on the surface of a significant amount of small-scale roughness with a surface layer of high porosity.

### 3.5. Internal Structure

The relatively high density of Lutetia [ $3.4 \pm 0.3 \text{ g cm}^{-3}$  (*Pätzold et al.*, 2011)] has led to speculation that Lutetia may be partially differentiated (*Weiss et al.*, 2012). The OSIRIS observations provide no meaningful constraints on this hypothesis. In the model of the NPCC impact in *Jutzi et al.* (2013), the asteroid was modeled with an internal core to establish whether this would influence the model results. The depth of the “mantle” and the magnitude of the inferred damage (fracturing) of this layer was sufficient to damp waves passing through the mantle so that reflections from the modeled core were of little account. Hence, it appears that any further constraints on the putative core will require a follow-up mission with an orbiter and/or lander.

The density of Lutetia is the highest of any measured asteroid density (Britt *et al.*, 2002) and it is similar to that of the differentiated asteroid (4) Vesta. Considering the possibility of a surface layer of significant porosity (as can be deduced from the thermal inertia properties), the bulk density of Lutetia's materials would exceed the mean value of known chondritic meteorites. Weiss *et al.* (2012) analyzed the porosity constraints and suggested that Lutetia could have experienced an early thermal metamorphism and that it could have a partially differentiated metallic core overlain by a primitive chondrite crust. No magnetic field signature associated to Lutetia was detected, which allowed Richter *et al.* (2012) to derive a global upper limit of the magnetic field strength to be <1 nT. This is not in contradiction with the Weiss *et al.* (2012) conclusions, as this measurement does not establish whether Lutetia has remnant magnetization.

#### 4. (4179) TOUTATIS

The approach and observations of Toutatis were relatively short because of the high relative velocity of the spacecraft. Furthermore, the geometry of the asteroid encounter was not optimal. Imaging during the inbound trajectory was not prioritized because the Sun-Toutatis-Chang'e-2 phase angle of 143.6° was considered to be too large. The side of the asteroid facing the probe was mostly shadowed as Chang'e-2 approached, and the best views were expected only after the probe passed by the asteroid. Therefore, Chang'e-2 completed an attitude adjustment approximately 1 h ahead of the flyby to prepare for outbound imaging. Thus, Chang'e-2 adjusted the camera's optical axis to lie antiparallel to the direction of the relative velocity vector between the probe and Toutatis.

Rather than use its high-resolution lunar-mapping camera, which was designed to operate in "push-broom" mode, scanning a wide swath of the lunar surface as it passed directly below, a small engineering CMOS camera was utilized for imaging. This was originally designed to monitor the deployment of solar panels on the spacecraft and to image other objects. The color imaging camera has a  $1024 \times 1024$ -pixel detector, and a field of view of  $7.2^\circ \times 7.2^\circ$ . The asteroid came into the field of view several seconds after closest approach. At first, Toutatis was mostly blocked from view by the solar array, but seconds later, the asteroid moved out from behind the array. The entire imaging procedure lasted approximately 25 min. Five snapshots per second were captured. Figure 7 shows several outbound images of Toutatis. Figure 7e, which was the first panoramic image, was taken at a distance of 67.7 km at a resolution of 8.30 m, whereas Fig. 7a, which was the third in a sequence of images, was shot at an imaging distance of 18.3 km at a local resolution of 2.25 m (Huang *et al.*, 2013).

Three-dimensional models based on delay-Doppler radar measurements (Hudson *et al.*, 2003; Busch *et al.*, 2012; Takahashi *et al.*, 2013) were adopted to determine the attitude of Toutatis during the approach phase. Based on the attitude of the probe and its camera, the relative position between the asteroid and the probe, and optical images, in combination with previous models (Hudson *et al.*, 2003; Busch *et al.*, 2012; Takahashi *et al.*, 2013), the direction of the principal axis was found to be directed toward ecliptic coordinates  $250^\circ \pm 5^\circ$ ,  $63^\circ \pm 5^\circ$ . The size of Toutatis was derived from the visible cross-sectional area. Its maximum length and width of  $(4.75 \times 1.95 \text{ km}) \pm 10\%$ , respectively, have been measured (Huang *et al.*, 2013).

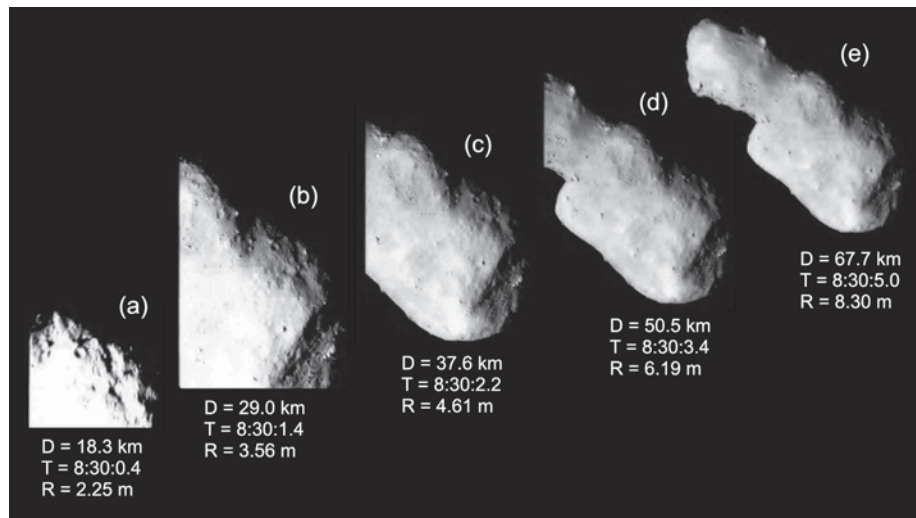


**Fig. 7.** Outbound images of (4179) Toutatis acquired on December 13, 2012, during the Chang'e-2 flyby, indicative of the spacecraft being away from the asteroid [from (a) to (e)]. The left side of Toutatis is blocked by the solar panel in (a) through (d). The imaging distance (D), epoch of flyby (T, UTC), and resolution of each image (R) are shown for each snapshot. Adapted from Huang *et al.* (2013).

#### 4.1. Surface Structures

The spacecraft collected over 400 optical images. The highest-resolution optical image has a resolution that is significantly better than the resolution of the known radar model (Busch *et al.*, 2012; Takahashi *et al.*, 2013), and many detailed features have been newly observed on its surface.

Images from Chang'e-2 show that Toutatis is shaped like a ginger root and consists mainly of a head (small lobe) and a body (large lobe), in agreement with previous radar observations. The detailed similarities and differences between the radar model and Chang'e-2's images are discussed in Zou *et al.* (2014). The observations during Chang'e-2's flyby have revealed several interesting discoveries (Huang *et al.*, 2013): the existence of a large crater-like depression in the body (800 m), the sharply perpendicular silhouette in the neck region that connects the head and body, boulders, and surface regolith.

From the large crater and the ridge around it, Toutatis may have suffered from one or more large impacts. The interior of Toutatis could be therefore very likely be fractured — a rubble-pile structure. The highly porous internal structure could prevent the asteroid from catastrophically disintegrating owing to its high attenuation of shock wave. In this sense, Toutatis may reassemble itself into a weak aggregate of large fragments through a heavy impact or successive smaller impacts. Large interior voids could help damp the collisional energy and further resist larger collisions in the formation scenario.

More than 200 boulders scattered across its surface have been counted (Fig. 7), a large portion of which are identified on the large lobe. They have dimensions ranging from 7 to 64 m, with an average of ~18 m. Approximately 90% of the boulders are less than 30 m in diameter. The largest boulder, along with other large boulders, are mainly distributed near the neck region. The boulders are usually suggested to be non-escaping ejecta that have reimpacted the asteroid's surface (Scheeres *et al.*, 1998).

Evidence suggests that Toutatis is likely to be covered with a regolith layer (Huang *et al.*, 2013). Redistribution of surface regolith was observed in two craters at the neck area. The upper regolith approximate to the craters is fine grained, whereas the lower appears to be relatively coarse, and many fragments are present (see Fig. 7). Such properties of the regolith may arise from the inclined terrain and the orientation of gravity (Scheeres *et al.*, 1998). The average terrain looks a bit smoother than that of Itokawa.

#### 4.2. Surface Age

Toutatis was partially imaged at varying scale (from ~2 m/pixel to ~8 m/pixel), significantly higher than Šteins and Lutetia. However, the overall quality of the pictures is somewhat degraded because they were captured with the monitoring camera. In addition, the low solar phase angle was not favorable for topographic studies. As result, only a few impact craters can be discerned with high fidelity.

However, a number of shallow depressions have been identified and catalogued as impact craters (Huang *et al.*, 2013; Zou *et al.*, 2014). These features appear almost rimless and very shallow, possibly indicating significant regolith movement. A total of 50–70 crater-like features have been mapped (Huang *et al.*, 2013; Zou *et al.*, 2014) on the large lobe, the largest of which is about 0.4–0.5 km across. A few larger craters have been proposed, but their existence appears inconclusive with current imaging. To compute the cumulative crater SFDs (Fig. 2c) we used the improved list of craters presented by Huang *et al.* (2013), for the whole body and the large lobe. Interestingly, the crater SFDs have shallow slopes, resembling that of Šteins, indicating that crater erasure may also be at work on Toutatis.

Here we apply target properties similar to those used for Šteins (a valid assumption given that both objects have a similar size and appear to be covered by loose material). As for the impact rate, we considered the average impact condition for main-belt asteroids. The reason for this choice is that the time spent by Toutatis on near-Earth orbits is typically several orders of magnitude smaller than the time spent in the main belt, hence most — if not all — of the observed craters were formed via collisions within the main belt. The resulting cratering age, for rubbly material and a strength of  $2 \times 10^6$  Pa, is ~1.6 Ga, supporting the validity of our assumption.

#### 4.3. Possible Formation Scenarios

Asteroid (25143) Itokawa is considered to be a contact binary formed by two or more smaller asteroids that have stuck together. Its surface shows few impact craters but is studded with boulders, which, along with its low density, implies that Itokawa may have formed from fragments that have coalesced over time (Michel and Richardson, 2013). Compared with Itokawa (see the chapter by Yoshikawa *et al.* in this volume), Toutatis is composed of two major lobes, suggesting a contact binary and possibly a rubble-pile structure. Several formation mechanisms have been proposed to produce these bifurcated bodies. One model assumes that the two major lobes were previously two separate objects moving at a very low relative speed, and that collision produces the contact binary (Fujiwara *et al.*, 2006). Another scenario assumes that the two components of a binary asteroid system could recombine through the binary YORP effects (Steinberg and Sari, 2011).

### 5. COMPARISON WITH PREVIOUS FLYBY TARGET ASTEROIDS

At the time of writing, seven other asteroids have been visited by spacecraft with fast flybys: (951) Gaspra, (243) Ida (with its satellite Dactyl), (253) Mathilde, (9969) Braille, (2486) Masursky, and (5535) Annefrank. In this discussion, we do not make comparisons with the three asteroids visited by orbital or sample return missions, namely (433) Eros [see detailed description by Cheng (2002)], (4) Vesta (see the

chapter by Russell et al. in this volume) and (25143) Itokawa (see the chapter by Yoshikawa et al. in this volume).

The asteroids in our chosen subset are different from each other in their physical properties (see Table 2). All have been targets of opportunity on missions devoted to other technological or other scientific objectives. It is clear that most of the information collected during a fast flyby is deduced by the analysis of images: the object's shape (usually partial), its rotational properties, its global and regional surface morphology, its age, and some assessment of the geological history. If the flyby geometry is favorable and more data are available (e.g., a very good estimate of the volume), then mass, density, and porosity can be estimated. These results, with possible analogies with meteoritic material, may provide some hints on asteroid internal structure. Visible and near-infrared spectroscopy provide information on surface composition and mineralogy. When adequate spectral coverage is obtained around closest approach, it is also possible to look for compositional heterogeneity of the asteroid.

In this section we compare the information obtained from all the performed asteroid flybys, underlying their importance in unraveling the nature of each individual object, their similarities and dissimilarities, and analyzing how these data can contribute to the understanding of the evolution of the asteroid population.

Spacecraft observations, even at large distances, allow investigation of the rotational properties of an asteroid, including rotation period, pole orientation, and bulk shape. The rotation periods of the flownby asteroids show a large excess of slow rotators with respect to the typical rotation period distribution of intermediate-sized asteroids ( $10 < D < 40$  km) (Fulchignoni et al., 1995). They do not reproduce a Maxwellian distribution, as is seen with larger asteroids, which would indicate that the population has reached a collisional equilibrium (Fulchignoni et al., 1995). Seven of these asteroids (out of ten) have a rotational period ranging from 4 h to 15 h and three of them (30% of the sample) are slow and/or complex rotators: Mathilde, with a period of 17.4 d (Mottola et al., 1995); Braille, with a period of 9.43 d (Oberst et al., 2001); and Toutatis, with a rotation period of 5.4 d and a precession period of 7.4 d (Takahashi et al., 2013). Pravec et al. (2002) discussed the possible causes of the excess of slow rotators in the size range of these bodies, but no definitive solution to this problem has been given. Their bulk shapes, obtained by various lightcurve inversion methods (Kaasalainen et al., 2002; Carry et al., 2012), are good approximations of the real shape as obtained by direct images, thereby validating the technique. The rotational properties of these asteroids deduced from Earth-based observations have a precision comparable to that obtained during the flyby. It indicates that the inversion of asteroid photometric lightcurves obtained by groundbased observations is a powerful tool for the characterization of the asteroid nature, giving precise information on its dynamical behavior and hints regarding its size and coarse shape (if it is convex).

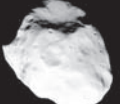
The 10 asteroid flybys covered objects varying in size by more than 2 orders of magnitude, from a little bit more than

1 km (Dactyl, Braille) to more than 100 km (Lutetia), and their shapes are quite irregular. The larger bodies (Mathilde and Lutetia) exhibit more spherical bulk profiles, although large craters modify strongly their surface and limb profiles (see the chapter by Marchi et al. in this book). The mid-sized asteroids, Gaspra and Ida (and possibly also Masursky), have elongated shapes, which can be described by a triaxial ellipsoid. Annefrank, Braille, and Toutatis have very elongated shapes and seem to have a rubble-pile structure, which is probably the result of their collisional origin and subsequent history. The diamond shape of Šteins could have been the consequence of its rotational behavior, dominated by the YORP effect, which forces the migration of the regolith from the polar regions toward the equator. This shape is similar to that of several other small asteroids, particularly among the primaries of small asteroid binaries. Dactyl is very small and quite spherical, as are most of the secondary bodies in asteroid binary/multiple systems.

Mass, volume, and consequently bulk densities are known with good precision only for Ida (thanks to the presence of its satellite Dactyl); Mathilde (Yeomans et al., 1997) and Lutetia were large enough to produce a detectable velocity change observable via the Doppler effect on the radio signal during the flyby. Consequently it has been possible to have an estimate of their micro- and/or macroporosities by comparison of their densities with densities of assumed meteorite analogs and some hints on their internal state. For the other asteroids, it is only possible to estimate some of those parameters based on (1) comparison of their surface composition (obtained by spectroscopy) with the composition of possible meteorite analogs, (2) their reconstructed shapes, and (3) hints on their porosity obtained by the surface morphology (presence of regolith, crater sizes, and depths) and possible analogies with known small bodies [e.g., Itokawa (see Abe et al., 2006)].

Some hints on global geology have been given only for Gaspra (Carr et al., 1994), the Ida-Dactyl system (Sullivan et al., 1996; Veverka et al., 1996b), and Mathilde (Thomas et al., 1999), as the other three flownby asteroids have only obtained images at poor resolution. The surface of Gaspra shows several facets separated by ridges. The effects of impacts dominate the surface of Ida. Very large craters are the dominating character of Mathilde (Chapman et al., 1999); their diameters are equal or greater than the average radius of the asteroid itself. These observations were the first to suggest that asteroids containing a large fraction of porosity may be stronger against impacts than nonporous ones, so that they can survive the energy required to form such big craters (for an explanation on the influence of porosity in impact events, see the chapter by Jutzi et al. in this volume). Grooves and lineaments that have topographic expressions of troughs or aligned rows of pits have been recognized on Gaspra and Ida. The grooves could mark in surface debris the presence, in the deeper interior, of fractures reactivated by subsequent impacts. There are suggestions of structures such as faults or layers on Mathilde but only two features have been clearly recognized: (1) one definite linear feature, a 20-km-long

TABLE 2. Characteristics of asteroids visited by flybys.

Asteroid Flyby Date (mm-dd-yyyy)	Space Mission	Flyby Distance (km)	D (km)	Rotation	Albedo	Spectral Type	Density (g cm <sup>-3</sup> )	Oldest Surface Age (G.y.)	Shape
(951) Gaspra 10-29-1991	Galileo	1600 <sup>[1]</sup>	$18.2 \times 10.5 \times 8.9$ <sup>[1]</sup>	7.042 h <sup>[1]</sup>	$0.23 \pm 0.06$ <sup>[1]</sup>	S <sup>[1]</sup>	—	1.8 <sup>[11]</sup>	
(243) Ida 08-28-1993	Galileo	2391.6 <sup>[2]</sup>	$59.9 \times 25.4 \times 18.6$ <sup>[2]</sup>	4.63 h <sup>[2]</sup>	$0.21 \pm 0.04$ <sup>[2]</sup>	S <sup>[2]</sup>	$2.6 \pm 0.5$ <sup>[2]</sup>	3.5 <sup>[11]</sup>	
(243) Ida I Dactyl 08-28-1993	Galileo	2391.6 <sup>[2]</sup>	$1.6 \times 1.4 \times 1.2$ <sup>[2]</sup>	>8 h <sup>[2]</sup>	0.20 <sup>[2]</sup>	S <sup>[2]</sup>	—	1?	
(253) Mathilde 06-27-1997	NEAR	1212 <sup>[3]</sup>	$66 \times 48 \times 46$ <sup>[3]</sup>	17.4 d <sup>[3]</sup>	$0.047 \pm 0.005$ <sup>[3]</sup>	C <sup>[3]</sup>	$1.3 \pm 0.2$ <sup>[3]</sup>	~4 <sup>[11]</sup>	
(9969) Braille 07-29-1999	Deep Space 1	26 <sup>[4]</sup>	$2.1 \times 1 \times 1$ <sup>[4]</sup>	226.4 h <sup>[4]</sup>	0.34 <sup>[5]</sup>	Q <sup>[5]</sup>	—	—	
(2685) Masursky 01-23-2000	Cassini	$1.6 \times 10^6$ <sup>[5]</sup>	15/20 <sup>[6]</sup>	—	—	S <sup>[7]</sup>	—	—	
(5535) Annefrank 11-02-2002	Stardust	2078.5 <sup>[8]</sup>	$6.6 \times 5.0 \times 3.4$ <sup>[9]</sup>	—	0.24 <sup>[8]</sup>	S <sup>[8]</sup>	—	—	
(2867) Šteins 09-05-2008	Rosetta	800 <sup>[10]</sup>	$6.7 \times 5.9 \times 4.3$ <sup>[10]</sup>	6.047 h <sup>[10]</sup>	$0.41 \pm 0.02$ <sup>[10]</sup>	E <sup>[10]</sup>	—	1.3 <sup>[10]</sup>	
(21) Lutetia 07-10-2010	Rosetta	2162 <sup>[10]</sup>	$121 \times 112 \times 87$ <sup>[10]</sup>	8.168 h <sup>[10]</sup>	$0.19 \pm 0.02$ <sup>[10]</sup>	C? <sup>[10]</sup>	$3.40 \pm 0.21$ <sup>[10]</sup>	3.7 <sup>[10]</sup>	
(4179) Toutatis 12-13-2012	Change'e-2	1.3 <sup>[10]</sup>	$4.75 \times 1.95$ <sup>[10]</sup>	$5.4 + 7.4$ d <sup>[10]</sup>	0.24 <sup>[10]</sup>	S <sup>[10]</sup>	—	1.6 <sup>[9]</sup>	

References: [1] Veverka et al. (1994); [2] Belton et al. (1996); [3] Veverka et al. (1999); [4] Oberst et al. (2001); [5] Buratti et al. (2004); [6] <http://photojournal.jpl.nasa.gov/catalog/PLA02449>; [7] Lazzaro et al. (2004); [8] Newburn et al. (2003); [9] Davies et al. (1999); [10] Duxbury et al. (2004); [11] this chapter.

marking (west from the large Karoo crater), that has a step-like topography on the order of 200 m, and (2) a curving slightly brighter, marking runs over 20 km wide (south from near the crater Otago) and 1.3–2 km across, suggesting either the direct exposure of a layer or the indirect effects of cratering exposing different materials. Neither feature appears to be the same type of feature as the more subtle grooves on Gaspra and Ida (for additional comments, see the chapter by Marchi et al. in this volume).

Isolated positive relief features as large as 150 m are probably ejecta blocks related to large impacts, such as those found on Eros, Lutetia, Vesta, and Toutatis. Extrapolation

of successful ejecta scaling laws to other asteroids suggests that blocks ~15 and 70 m across could be present on Dactyl and Gaspra (Lee et al., 1996) respectively. Evidence for the presence of debris on the surface (e.g., chute depths, grooves, swallowing of the largest degraded craters, and the rounded form of ridges) are present in all these asteroids. Estimates of the average depth of mobile materials suggest that Gaspra is covered with a regolith a few tens to several tens of meters thick, while the thickness of mobile materials on Ida would be 50 m, with a typical thickness for the debris layer ranging from 50 to 100 m (Sullivan et al., 1996). All these geological features have been found, to a greater or lesser extent, on all

asteroids visited by space missions. But the larger the body, the wider the observed effects of its geological evolution.

Looking at surface composition, five out of the ten asteroids considered here belong to the S taxonomic class. The spectral signature of iron-bearing minerals on S-type asteroid (951) Gaspra has been detected by *Carlson et al.* (1992) and *Granahan et al.* (1994) with the Galileo Near Infrared Mapping Spectrometer (NIMS); two spectral units were identified by *Granahan* (2011), both containing a higher relative abundance of olivine than those found in ordinary chondrites, indicating that Gaspra's surface composition could imply bulk materials that have undergone igneous differentiation processes. Recently 2.8- and 3.4- $\mu\text{m}$  spectral features have also been detected on the surface of Gaspra with the reanalysis of the NIMS spectra (*Granahan*, 2014) and interpreted as possibly being due to the presence of structural OH. (243) Ida was identified on the basis of groundbased observations (*Tholen and Barucci*, 1989; *DeMeo et al.*, 2009) as an S-type and Dactyl (*Chapman et al.*, 1995) with a similar but distinct spectrum. *Carlson et al.* (1994), using NIMS, and *Veverka et al.* (1996a), analyzing Galileo Solid State Imager (SSI) color data, observed small color variations both in the blue part of the spectrum and in the depth of the 1- $\mu\text{m}$  pyroxene-olivine band. Two terrains different in color, interpreted as "more processed," or "more weathered," have been recognized on Ida's surface. *Granahan* (2012) revisited the NIMS data of (243) Ida and Dactyl and measured the olivine and pyroxene spectral bands to compare the asteroid spectra with those of meteorites (*Dunn et al.*, 2010), and found that Ida's spectra correspond to measurements of LL chondrites and that of Dactyl correlates to L chondrites. Analyzing 44 images of (5535) Annefrank, *Newburn et al.* (2003) built a phase curve extending to 134°. Flux fell by more than six magnitudes between the extrapolated 0° and 134°. A broadband (470–940 nm) geometric albedo of 0.24 was derived for Annefrank, indicating its appurtenance with the S class. (4179) Toutatis has been extensively observed during its 1992–1993 close encounter with Earth. *Lazzarin et al.* (1994) obtained low-resolution spectra of the asteroid showing a typical behavior of an S-type object with no evidence of surface composition variations. *Reddy et al.* (2012) found that the Toutatis spectrum is consistent with an undifferentiated L-chondrite composition. The only available spectrum of (2486) Masursky obtained in the visible by *Lazzaro et al.* (2004) allowed them to classify it as an S type. *Buratti et al.* (2004) published some spectra of (9969) Braille in the 1.25–2.6- $\mu\text{m}$  region taken during the asteroid flyby. The 0.4–2.5- $\mu\text{m}$  spectrum obtained adding some groundbased observations (*Lazzarin et al.*, 2001; *Binzel et al.*, 2001) to the spacebased ones matches that of the ordinary chondrites and indicates (together with the high albedo,  $p_v = 0.34$ ) the appurtenance of the asteroid to the Q taxonomic type. The main features in the infrared are a 10% absorption band centered at 2  $\mu\text{m}$ , and a reflectance peak at 1.6  $\mu\text{m}$ , suggesting that the asteroid is composed by pyroxene and olivine in a ratio 1:1. The analysis of these spectra suggests also that Braille has a relatively fresh surface, scarcely affected by weathering

processes. In the case of the flyby of (253) Mathilde, only the Multi-Spectral Imager (MSI) and the Radio Science (RSS) instruments acquired data. *Binzel et al.* (1996) have obtained the first spectrum of Mathilde in the visible range by ground observations. *Rivkin et al.* (1997) found Mathilde to have a spectrum consistent with C-class asteroids in the near-infrared, although without the 3- $\mu\text{m}$  water-of-hydration feature commonly (but not always) seen on asteroids of this class. They compare Mathilde with plausible meteorite analogs, and find that the surface of this asteroid is not consistent with a surface composition of common carbonaceous chondritic material. To search for any variation on the asteroid surface, *Doressoundiram et al.* (1997) performed several observations in the visible range showing that Mathilde's surface is homogeneous over almost half of its rotational period. In these last cases of asteroid flybys, the on board instruments did not improve our knowledge of the surface composition.

## 6. CONCLUSIONS

The successful flybys by Rosetta and Chang'e-2 provided precious information on the visited asteroids revealing markedly different bodies. (21) Lutetia, (2867) Šteins, and (4179) Toutatis are different in size, shape, surface morphology, albedo, composition, and history. The three asteroids represent three new complex worlds completely different from previously visited asteroids. The analyzed surfaces have given important constraints on surface evolution and history of the visited bodies. The crater analysis revealed relative ages and provided constraints on their absolute ages and collisional histories, even if at different levels of incertitude. The major limit of flybys is in fact connected with the geometry of the trajectory, which can imply only partial vision of the body, but the velocity of the encounter can also influence and limit the data collection, rapidly changing the viewing geometry. The large size of Lutetia allowed measurement of its density. The images obtained during the Lutetia flyby form an excellent dataset to investigate a wide range of processes on intermediate-sized, irregular-shaped, main-belt asteroids. The production mechanism(s) for lineaments and other surface structures remains a subject for debate. However, recent papers (e.g., *Jutzi et al.*, 2013; *Cremonese et al.*, 2012) suggest that impact modeling has reached a sufficient level of sophistication that processes and mechanisms can be quantitatively assessed rather than speculated about.

In conclusion, Šteins must have suffered a combination of various processes to explain its present physical characteristics, including impacts, seismic shaking, and the YORP effect. Lutetia, with its geological complex surface and high density, seems to be a primordial object, which could have retained a record of early metamorphic and melting processes. Surface material motion appears to be common on Lutetia and could be expected on other intermediate-sized asteroids. All the detailed analyses do not allow us to unveil the real composition of Lutetia, and only a sample return mission will resolve the compositional puzzle of this intriguing object. As for the case of Toutatis, its contact binary shape

allows comparison with Itokawa even though the two bodies have different surface and rotational properties, but the formation mechanisms are still debated. Information about cratering of the surfaces are important contributions from asteroid flybys. Even if the crater analysis was challenging on small objects (like Šteins and Toutatis), crater SFDs can be used to investigate the processes of mass-wasting (some due to cratering itself, such as seismic shaking). Of course the low-quality data imply that the evidence for a rubble-pile nature of these asteroids cannot be conclusive. The generally limited low numbers statistic does not allow for a robust age assessment, but comparative analyses can nevertheless reveal additional details of the evolution of the bodies. On large asteroids (like Lutetia), crater SFDs allow for detailed stratigraphic studies (relative ages of various units) as well as absolute ages, provided the imaging resolution is good enough to obtain robust crater statistics.

Spectral observations give in general appropriate information, but might not allow interpretation of the real composition of the body (in particular, if the targets lack clear, recognizable absorption bands). In fact, from the discussion reported in section 5, it is evident that the information obtained by spectroscopy during a flyby of an asteroid represents a step forward in understanding the degree of homogeneity of the asteroid surface, thanks to the better resolution (e.g., the cases of Gaspra and Ida). However, concerning the asteroid composition, flybys do not seem to allow us to infer composition more accurately than using groundbased observations. Too many microscopic (e.g., space weathering, regolith depth, and size distribution) and macroscopic (e.g., collisions, aging, landslides) effects may affect the behavior of a spectrum, by changing the slope or masking features that reveal the presence of the minerals or processes characterizing an asteroid's composition. Even the search for meteoritic analogs by comparison of the spectra does not guarantee certain answers but only useful indications. Asteroid spectra taken from a distance refer to an average of unknown materials covering a given surface, while the meteorite spectra taken in a laboratory concern small amounts of very well-known, well-characterized materials. The only way to determine the real composition of an asteroid is to analyze the samples collected on its surface by sample return missions, and this is one of the main justifications for sample return missions. Even a very small amount of material analyzed in a laboratory provides fundamental information about the composition and history of the visited objects, as demonstrated by the results of the analysis of the few micrograms returned from the asteroid Itokawa by the Hayabusa mission [see the collection of papers in the *Science*, 333(6046)]. In the next decade, Hayabusa-2 (Japan Aerospace Exploration Agency) and the Origins Spectral Interpretation Resource Identification and Security-Regolith Explorer (OSIRIS-REx) (NASA) will take samples from the C-type asteroid (162173) 1999 JU<sub>3</sub> and the B-type asteroid (101955) Bennu, respectively, unveiling their chemical and mineralogical nature.

The 3 recent asteroid flyby missions together with the others (for a total of 10 flyby missions), the 2 orbiting ones

[Near Earth Asteroid Rendezvous (NEAR) at Eros and Dawn at Vesta], and the only sample return mission (Hayabusa at Itokawa), represent more than 20 years of “*in situ*” exploration of asteroids. The data collected are precious and of high scientific value, but perhaps the major benefit obtained from these efforts is that they provided us with a ground truth for checking the methods to interpret the groundbased observations, which will allow us to characterize a larger and larger number of asteroids knowing the limit of the possible interpretations at a much lower cost.

**Acknowledgments.** M.A.B. and M.F. acknowledge the funding of the French national space agency Centre National d'Etudes Spatiales. The participation of S.M. participation was supported by NASA's Solar System Evolution Research Virtual Institute (SSERVI) program through a grant to the Institute for the Science of Exploration Targets at the Southwest Research Institute in Boulder, Colorado. N.T. is supported through the Swiss National Science Foundation under grant 200020\_152560. J.J.H. is supported by the National Natural Science Foundation of China (Grants No. 11273068, 11473073), the Natural Science Foundation of Jiangsu Province (Grant No. BK20141509), the Strategic Priority Research Program—The Emergence of Cosmological Structures of the Chinese Academy of Sciences (Grant No. XDB09000000), and the innovative and interdisciplinary program by the Chinese Academy of Sciences (CAS) (Grant No. KJZD-EW-Z001). We would also like to thank L. Tian, Y. Jiang, and Y. Li for their contributions. We are grateful to the entire Chang'e-2 and Rosetta teams.

## REFERENCES

- Abe S., Mukai T., Hirata N., et al. (2006) Mass and local topography measurements of Itokawa by Hayabusa. *Science*, 312, 1344–1349.
- Altweig K., Balsiger H., Calmonte U., et al. (2012) In situ mass spectrometry during the Lutetia fly-by. *Planet. Space Sci.*, 66, 173–178.
- Arslan H., Batiste S., and Sture S. (2010) Engineering properties of lunar soil simulant JSC-1A. *J. Aerosp. Eng.*, 23, 70, DOI: 10.1061/(ASCE)0893-1321(2010)23:1(70).
- Asphaug E., Moore J., Morrison D., et al. (1996) Mechanical and geological effects of impact cratering on Ida. *Icarus*, 120, 158–184.
- Barucci M. A., Capria M. T., Coradini A., and Fulchignoni M. (1987) Classification of asteroids using G-mode analysis. *Icarus*, 72, 304.
- Barucci M. A., Fulchignoni M., Fornasier S., et al. (2005) Asteroid target selection for the new Rosetta mission baseline 21 Lutetia and 2867 Steins. *Astron. Astrophys.*, 430, 313–317.
- Barucci M. A., Fornasier F., Dotto E., et al. (2008) Asteroids 2867 Steins and Lutetia: Surface composition from far infrared observations with the Spitzer space telescope. *Astron. Astrophys.*, 477, 665–670.
- Barucci M. A. and 12 colleagues (2012) Overview of Lutetia's surface composition. *Planet. Space Sci.*, 66, 23–30.
- Basilevsky A. T., Lorenz C. A., Shingareva T. V., et al. (2014) The surface geology and geomorphology of Phobos. *Planet. Space Sci.*, 102, 95–118.
- Belton M. J. S., Chapman C. R., and Klaasen K. P. (1996) Galileo's encounter with 243 Ida: An overview of the imaging experiment. *Icarus*, 120, 1–19.
- Besse S., Lamy P., Jorda P., et al. (2012) Identification and physical properties of craters on asteroid (2867) Steins. *Icarus*, 221, 1119–1129.
- Besse S., Kueppers M., Barnouin O. S., et al. (2014) Lutetia's lineaments. *Planet. Space Sci.*, 101, 186–195.
- Binzel R. P., Burbine T. H., and Bus S. J. (1996) Groundbased reconnaissance of asteroid 253 Mathilde: Visible wavelength spectrum and meteorite comparison. *Icarus*, 119, 447–449.
- Binzel R. P., Harris A. W., Bus S. J., and Burbine T. H. (2001) Spectral properties of near Earth objects: Palomar and IRTF

- results for 48 objects including spacecraft targets 9969 Braille and (10302) 1989 ML. *Icarus*, 151, 139–149.
- Britt D. T., Yeomans D., Housen K., and Consolomagno G. (2002) Asteroid density, porosity and structure. In *Asteroids III* (W. F. Bottke Jr. et al., eds.), pp. 485–500. Univ. of Arizona, Tucson.
- Buczkowski D. L., Barnouin-Jha O. S., and Prockter L. M. (2008) 433 Eros lineaments: Global mapping and analysis. *Icarus*, 193, 39–52.
- Buczkowski D. L. and 19 colleagues (2012) Large-scale troughs on Vesta: A signature of planetary tectonics. *Geophys. Res. Lett.*, 39, L18205–L18011.
- Buratti B. J., Britt D. T., Soderblom L. A., et al. (2004) 9969 Braille: Deep Space 1 infrared spectroscopy, geometric albedo, and classification. *Icarus*, 167, 129–135.
- Busch M. W., Takahashi Y., Scheeres D. J., et al. (2012) Internal structure of 4179 Toutatis. *AGU Fall Meeting*, P31A-1873.
- Carlson R. W., Weissman P. R., Smythe W. D., et al. (1992) Gaspra: Spatially resolved infrared spectra from Galileo. *Bull. Am. Astron. Soc.*, 24, 932.
- Carlson R. W., Weissman P. R., Segura M., et al. (1994) Infrared imaging spectroscopy of asteroid 243 Ida and discovery spectra of satellite 1993 (243) I. *Bull. Am. Astron. Soc.*, 26, 1156.
- Carr M. H., Kirk R. L., McEwen A., et al. (1994) The geology of Gaspra. *Icarus*, 107, 61–71.
- Carry B., Kaasalainen M., Leyrat C., et al. (2010) Physical properties of the ESA Rosetta target asteroid (21) Lutetia. II. Shape and flyby geometry. *Astron. Astrophys.*, 523, A94.
- Carry B., Kaasalainen M., Merline W. J., et al. (2012) Shape modeling technique KOALA validated by ESA Rosetta at (21) Lutetia. *Planet. Space Sci.*, 66, 200–212.
- Chapman C. R., Veveka J., Thomas P. C., et al. (1995) Discovery and physical properties of Dactyl, a satellite of asteroid 243 Ida. *Nature*, 374, 783–785.
- Chapman C. R., Merline W. I., and Thomas P. C. (1999) Cratering on Mathilde. *Icarus*, 140, 28–33.
- Cheng A. F. (2002) Near Earth Asteroid Rendezvous: Mission summary. In *Asteroids III* (W. F. Bottke Jr. et al., eds.), pp. 351–366. Univ. of Arizona, Tucson.
- Coradini A. and 48 colleagues (2011) The surface composition and temperature of asteroid 21 Lutetia as observed by Rosetta/VIRTIS. *Science*, 334, 492–494.
- Cremonese G., Martellato E., Marzari F., et al. (2012) Hydrocode simulations of the largest crater on asteroid Lutetia. *Planet. Space Sci.*, 66, 147–154.
- Davies D. R. (1999) The collisional history of asteroid 253 Mathilde. *Icarus*, 140, 49–52.
- Delbo M., Libourel G., Wilkerson J., et al. (2014) Thermal fatigue as the origin of regolith on small asteroids. *Nature*, 508, 233–236.
- DeMeo F. E., Binzel R. P., Slivan S. M., et al. (2009) An extension of the Bus asteroid taxonomy into the near-infrared. *Icarus*, 202, 160–180.
- Doressoundiram A., Barucci M. A., and Fulchignoni M. (1997) Search for rotational variation in the spectra of 253 Mathilde. *Astron. Astrophys.*, 325, L9–L11.
- Dunn T. L., McCoy T. J., Sunshine J. M., et al. (2010) A coordinated spectral, mineralogical, and compositional study of ordinary condrites. *Icarus*, 208, 789–797.
- Duxbury T. C., Newburn R. L., Acton C. H., et al. (2004) Asteroid 5535 Annefrank size, shape, and orientation: Stardust first results. *J. Geophys. Res.*, 109, E02002.
- Fornasier S., Migliorini A., Dotto E., and Barucci M. A. (2008) Visible and near infrared spectroscopic investigation of E-type asteroids, including Steins, a target of the Rosetta mission. *Icarus*, 196, 119–134.
- Fujiwara A., Kawaguchi J., Yeomans D. K., et al. (2006) The rubble-pile asteroid Itokawa as observed by Hayabusa. *Science*, 312, 1330–1334.
- Fulchignoni M., Barucci M. A., Di Martino M., and Dotto E. (1995) On the evolution of the asteroid spin. *Astron. Astrophys.*, 299, 929–932.
- Gaffey M. J. and Kelley M. S. (2004) Mineralogical variations among high albedo E-type asteroids: Implications for asteroid igneous processes. *Lunar Planet. Sci. XXXV*, Abstract #1812. Lunar and Planetary Institute, Houston.
- Gaffey M. J., Burbine T. H., and Binzel R. P. (1993) Asteroid spectroscopy: Progress and perspectives. *Meteoritics*, 28, 161–187.
- Giacomini L., Massironi M., Aboudan A., et al. (2014) 3D Study of Lutetia lineaments: New clues to understand the asteroid origin. *Lunar Planet. Sci. XLV*, Abstract #2157. Lunar and Planetary Institute, Houston.
- Granahan J. C. (2011) Spatially resolved spectral observations of asteroid 951 Gaspra. *Icarus*, 213, 265–272.
- Granahan J. C. (2012) Ordinary chondrite spectral signatures in the 243 Ida asteroid system. *AGU Fall Meeting*, P31A-1876.
- Granahan J. C. (2014) Asteroid 951 Gaspra's three micrometer region spectral features. *Lunar Planet. Sci. XLV*, Abstract #1092. Lunar and Planetary Institute, Houston.
- Granahan J. C., Fanale F. P., Robinson M. S., et al. (1994) A Galileo multi-instrument spectral analysis of 951 Gaspra. *Lunar Planet. Sci. XXV*, p. 453. Lunar and Planetary Institute, Houston.
- Groussin O., Lamy P., Fornasier S., and Jorda L. (2011) The properties of asteroid (2967) Steins from Spitzer Space telescope observations and OSIRIS shape reconstruction. *Astron. Astrophys.*, 529, A73.
- Gulkis S., Keihm S., Kamps L., et al. (2010) Millimeter and submillimeter measurements of asteroid (2867) Steins during the Rosetta fly-by. *Planet. Space Sci.*, 58, 1077–1087.
- Gulkis S., Keihm S., Kamp L., et al. (2012) Continuum and spectroscopic observations of asteroid (21) Lutetia at millimetre and submillimeter wavelengths with the MIRO instruments on the Rosetta spacecraft. *Planet. Space Sci.*, 66, 31–42.
- Holsapple K. A. and Housen K. R. (2007) A crater and its ejecta: An interpretation of Deep Impact. *Icarus*, 187, 345–356.
- Huang J. C., Ji J. H., Ye P. J., et al. (2013) The ginger-shaped asteroid 4179 Toutatis: New observations from a successful flyby of Chang'e-2. *Sci. Rept.*, 3, 3411–3416.
- Hudson R. S., Ostro S. J., and Scheeres D. J. (2003) High-resolution model of asteroid 4179 Toutatis. *Icarus*, 161, 346–355.
- Jaumann R. and 42 colleagues (2012) Vesta's shape and morphology. *Science*, 336, 687–690.
- Jorda L., Lamy P. L., Gaskell R. W., et al. (2012) Asteroid (2867) Steins: Shape, topography and global physical properties from OSIRIS observations. *Icarus*, 221, 1089–1100.
- Jutzi M., Michel P., and Benz W. (2010) A large crater as a probe of the internal structure of the E-type asteroid Steins. *Astron. Astrophys.*, 509, L2–L5.
- Jutzi M., Thomas N., Benz W., et al. (2013) The influence of recent major crater impacts on the surrounding surfaces of (21) Lutetia. *Icarus*, 226, 89–100.
- Kaasalainen M., Mottola S., and Fulchignoni M. (2002) Asteroid models from disk-integrated data. In *Asteroids III* (W. F. Bottke Jr. et al., eds.), pp. 139–150. Univ. of Arizona, Tucson.
- Keihm S., Tosi F., Kamp L., et al. (2012) Interpretation of combined infrared, submillimeter, and millimeter flux data obtained during the Rosetta fly-by of asteroid (21) Lutetia. *Icarus*, 221, 395–404.
- Keller H. U., Barbieri C., Lamy P., et al. (2007) OSIRIS the scientific camera system onboard Rosetta. *Space Sci. Rev.*, 128, 433–506.
- Keller H. U., Barbieri C., Koschny D., et al. (2010) E-type asteroid (2867) Steins as imaged by OSIRIS on board Rosetta. *Science*, 327, 190.
- Krohn K., Jaumann R., Elbeshausen D., et al. (2014) Asymmetric craters on Vesta: Impact on sloping surfaces. *Planet. Space Sci.*, 244, 120–132.
- Küppers M., Moissl R., Vincent J.-B., et al. (2012) Boulders on Lutetia. *Planet. Space Sci.*, 66, 71–78.
- Lamy P. L., Kaasalainen M., Lowry S., et al. (2008) Asteroid 2867 Steins. II. Multi-telescope visible observations, shape reconstruction, and rotational state. *Astron. Astrophys.*, 487, 1179–1185.
- Lamy P. L., Faury G., Jorda L., et al. (2010) Multicolor, rotationally resolved photometry of asteroid 21 Lutetia from OSIRIS/Rosetta observations. *Astron. Astrophys.*, 521, A19.
- Lazzarin M., Barbieri C., and Marzari F. (1994) CCD reflectance spectra of Apollo asteroid 4179 Toutatis. *Planet. Space Sci.*, 42(4), 327–338.
- Lazzarin M., Fornasier S., Barucci M. A., et al. (2001) Groundbased investigation of asteroid 9969 Braille, target of the spacecraft mission Deep Space 1. *Astron. Astrophys.*, 375, 281–284.
- Lazzaro D., Angeli C. A., Carvano J. M., et al. (2004) S<sup>2</sup>O<sup>3</sup>: The visible spectroscopic survey of 820 asteroids. *Icarus*, 172(1), 179–220.
- Lee P., Veveka J., Thomas P. C., et al. (1996) Ejecta blocks on 243 Ida and on other asteroids. *Icarus*, 120, 85–105.
- Leyrat C., Fornasier S., Barucci M. A., et al. (2010) Search for Steins' surface inhomogeneities from OSIRIS Rosetta images. *Planet. Space Sci.*, 58, 1097–1106.

- Leyrat C., Coradini A., Erard S., et al. (2011) Thermal properties of the asteroid (2867) Steins as observed by VIRTIS/Rosetta. *Astron. Astrophys.*, 531, A168.
- Marchi S., Barbieri C., and Küppers M. (2010) The cratering history of asteroid (2867) Steins. *Planet. Space Sci.*, 58, 1116–1123.
- Marchi S., Massironi M., and Cremonese G. (2011) The effects of the target material properties and layering on the crater chronology: The case of Raditladi and Rachmaninoff basins on Mercury. *Planet. Space Sci.*, 59, 1968–1980.
- Marchi S., Massironi M., Vincent J. B., et al. (2012) The cratering history of asteroid (21) Lutetia. *Planet. Space Sci.*, 66, 87–95.
- Michel P. and Richardson D. C. (2013) Collision and gravitational reaccumulation: Possible formation mechanism of the asteroid Itokawa. *Astron. Astrophys.*, 554, L1–L4.
- Mottola S., Sears W. D., Erikson A., et al. (1995) The slow rotation of 253 Mathilde. *Planet. Space Sci.*, 43, 1609–1613.
- Newburn R. L., Duxbury T. C., Hanner M., et al. (2003) Phase curve and albedo of asteroid 5535 Annefrank. *J. Geophys. Res.*, 108, E11.
- Oberst J., Mottola S., Di Martino M., et al. (2001) A model for rotation and shape of asteroid 9969 Braille from ground-based observations and images obtained during the Deep Space 1 (DS1) flyby. *Icarus*, 153, 16–23.
- O'Brien D. P., Marchi S., Morbidelli A., et al. (2014) Constraining the cratering chronology of Vesta. *Planet. Space Sci.*, 103, 131–142.
- O'Rourke L., Müller T., Valtchanov I., et al. (2012) Thermal and shape properties of asteroid (21) Lutetia from Herschel observations around the Rosetta flyby. *Planet. Space Sci.*, 66, 192–199.
- Pätzold M., Andert T. P., Asmar S. W., et al. (2011) Asteroid 21 Lutetia: Low mass, high density. *Science*, 334, 491–492.
- Pravec P., Harris A. W., and Michalowski T. (2002) Asteroid rotations. In *Asteroids III* (W. F. Bottke Jr. et al., eds.), pp. 113–122. Univ. of Arizona, Tucson.
- Preusker F., Scholten F., Krolleberg J., et al. (2012) The northern hemisphere of asteroid (21) Lutetia — topography and orthoimages from Rosetta OSIRIS NAC image data. *Planet. Space Sci.*, 66, 54–63.
- Reddy V., Corre L. L., Hicks M., et al. (2012) Composition of near-Earth asteroid 2008 EV5: Potential target for robotic and human exploration. *Icarus*, 221(2), 678–681.
- Richardson J. E., Melosh H. J., and Greenberg R. (2004) Impact-induced seismic activity on asteroid 433 Eros: A surface modification process. *Science*, 306, 1526–1529.
- Richter I., Auster H. U., Glassmeier K. H., et al. (2012) Magnetic field measurements during the Rosetta flyby at asteroid (21) Lutetia. *Planet. Space Sci.*, 66, 155–164.
- Rivkin A. S., Clark B. E., Britt D. T., et al. (1997) Infrared spectrophotometry of the NEAR flyby target 253 Mathilde. *Icarus*, 127(I), 255–257.
- Rivkin A. S., Clark B. E., Ockert-Bell M., et al. (2011) Observations of 21 Lutetia in the 2–4 μm region with the NASA IRTF. *Icarus*, 216, 62–68.
- Scheeres D. J., Ostro S. J., Hudson R. S., et al. (1998) Dynamics of orbits close to asteroid 4179 Toutatis. *Icarus*, 132, 53–79.
- Schenk P. M., Chapman C. R., Zahnle K., and Moore J. M. (2004) Ages and interiors: The cratering record of the Galilean satellites. In *Jupiter: The Planet, Satellites and Magnetosphere* (F. Bagenal et al., eds.), pp. 427–456. Cambridge Univ., Cambridge.
- Schröder S. E., Keller H. U., Gutierrez P., et al. (2010) Evidence for surface variegation in Rosetta OSIRIS images of asteroid 2867 Steins. *Planet. Space Sci.*, 58, 1107–1115.
- Schulz R., Alexander C., Boehnhardt H., and Glassmeier K.-H., eds. (2009) *Rosetta ESA's Mission to the Origin of the Solar System*. Springer-Verlag, Berlin.
- Sierks H. and 57 colleagues (2011) Images of asteroid 21 Lutetia: A remnant planetesimal from the early solar system. *Science*, 334, 487–490.
- Steinberg E. and Sari R. (2011) Binary YORP effect and evolution of binary asteroids. *Astron. J.*, 141, 55.
- Stern S. A., Parker J. W., Feldman P. D., et al. (2011) Ultraviolet discoveries at asteroid (21) Lutetia by the Rosetta Alice ultraviolet spectrometer. *Astron. J.*, 141, 199–202.
- Sullivan R., Greeley R., Pappalardo R., et al. (1996) Geology of 243 Ida. *Icarus*, 120, 119–139.
- Takahashi Y., Busch M. W., and Scheeres D. J. (2013) Spin state and moment of inertia characterization of 4179 Toutatis. *Astron. J.*, 146, 95–104.
- Tholen D. J. and Barucci M. A. (1989) Asteroid taxonomy. In *Asteroids II* (R. P. Binzel et al., eds.), pp. 1139–1150. Univ. of Arizona, Tucson.
- Thomas N., Barbieri C., Keller H. U., et al. (2012) The geomorphology of (21) Lutetia: Results from the OSIRIS imaging system onboard ESA's Rosetta spacecraft. *Planet. Space Sci.*, 66, 96–124.
- Thomas P. C., Everka J., and Bell J. F. (1999) Mathilde: Size, shape and geology. *Icarus*, 140, 17–27.
- Everka J., Belton M., Klaasen K., et al. (1994) Galileo's encounter with 951 Gaspra: Overview. *Icarus*, 107, 2–17.
- Everka J., Helfenstein P., Lee P., et al. (1996a) Ida and Dactyl: Spectral reflectance and color variations. *Icarus*, 120, 66–76.
- Everka J., Thomas P. C., Helfenstein P., et al. (1996b) Dactyl: Galileo observations of Ida's satellite. *Icarus*, 120, 200–211.
- Everka J., Thomas P., Harch A., et al. (1999) NEAR encounter with asteroid 253 Mathilde: Overview. *Icarus*, 140, 3–16.
- Everka J., Farquhar B., Robinson M., et al. (2001) The landing of the NEAR-Shoemaker spacecraft on asteroid 433 Eros. *Nature*, 413, 390–393.
- Vincent J. B., Besse S., Marchi S., et al. (2012) Physical properties of craters on asteroid (21) Lutetia. *Planet. Space Sci.*, 66, 79–86.
- Weiss B. P., Elkins-Tanton L. T., Barucci M. A., et al. (2012) Possible evidence for partial differentiation of asteroid Lutetia from Rosetta. *Planet. Space Sci.*, 66, 137–146.
- Yeomans D. K., Barriot J.-P., Dunham D. W., et al. (1997) Estimating the mass of asteroid 253 Mathilde from tracking data during the NEAR flyby. *Science*, 278, 2106–2109.
- Zou X. D., Li C., Liu J., et al. (2014) The preliminary analysis of the 4179 Toutatis snapshots of the Chang'e-2 flyby. *Icarus*, 229, 348–354.

# Phobos and Deimos

Scott L. Murchie

*The Johns Hopkins University Applied Physics Laboratory*

Peter C. Thomas

*Cornell University*

Andrew S. Rivkin and Nancy L. Chabot

*The Johns Hopkins University Applied Physics Laboratory*

Phobos and Deimos, the satellites of Mars, occupy a unique place in the solar system. They are the only terrestrial planet satellites besides the Moon, yet have traits in common with low-reflectance bodies more typical of the outer solar system. Understanding their composition, origin, and geologic evolution will provide insights into the earliest stages of terrestrial planet formation. Early exploration by the Viking and Mariner 9 missions, decades before the first “proper” asteroid encounters, hinted at several asteroidal properties yet to be discovered: lower than expected densities, abundant regolith even on relatively small bodies, and complicated geology. The first book in this series, *Asteroids* (1979), had an entire chapter on Phobos and Deimos. We have learned much about these objects in the last 35 years from telescopic and spacecraft observations.

## 1. DISCOVERY AND EXPLORATION

### 1.1. Discovery and Early Groundbased Observations

Once the Galilean satellites of Jupiter were discovered and the Copernican model of the solar system became widely accepted, Mars’ apparent lack of a moon was notable. By the end of the seventeenth century, Saturn was known to have at least five satellites, a number that swelled to seven by the end of the eighteenth century. By 1800 a new planet, Uranus, was discovered and found to have at least two satellites. By 1870, two more uranusian satellites and another saturnian satellite were detected, along with another new planet (Neptune) with its own satellite. Yet Mars remained moonless. Based on numerology, Kepler predicted that Mars should have two satellites, as two made the most sense when interpolating between Earth’s single moon and Jupiter’s four. Jonathan Swift and Voltaire both “predicted” that Mars would have two moons, but their predictions were based on satire (*Hall*, 1878).

Both William Herschel and Heinrich Louis d’Arrest performed unsuccessful searches for martian moons before Asaph Hall, using the U.S. Naval Observatory 26-inch (66-cm) refractor, found first Deimos then Phobos during the excellent Mars apparition of 1877. Because of the primitive state of astrophotography, only visual observations using eyepieces were possible at the time. The satellites were

named for characters in the Iliad, Phobos (Fear) and Deimos (Terror), who are the attendants of the god Ares, the Greek equivalent of the Roman god Mars. Despite searches for additional satellites, using both ground- and spacecraft-based observations, no additional satellites of Mars have been found within its Hill sphere to a diameter of 180 m assuming an albedo of 0.07 (*Sheppard et al.*, 2004).

Given the close proximity of Phobos and Deimos to Mars, positional measurements were typically the only ones undertaken. *Pascu et al.* (2013) compiled and reviewed these measurements as well as other early observations. A focus of early observations was the secular acceleration of Phobos in its orbit (e.g., *Sharpless*, 1945), now known to originate from tidal effects that cause the moon to spiral in toward Mars, which eventually will result in Phobos’ impact (*Burns*, 1978). The first photometric study to estimate the moons’ diameters from their brightnesses, by Edward Charles Pickering of the Harvard College Observatory and reported by *Hall* (1878), suggested diameters of 9 km for Deimos and 11 km for Phobos. These assumed a Mars-like albedo and hence resulted in diameters smaller than the actual values. Just prior to the first spacecraft encounters with the moons, a combination of photoelectric photometry (*Harris*, 1961) and albedo estimates from polarimetry (*Zellner*, 1972) resulted in diameter estimates within 10% of current values (*Zellner and Capen*, 1974).

## 1.2. 1969–1980: Exploration by the Mariner and Viking Spacecraft

It was not until the visit of spacecraft to Mars that bulk properties and the physical geology of the moons would become known (Table 1, Figs. 1 and 2). The first image of Phobos, by Mariner 7, was made in silhouette against the martian surface. Smith (1970) found an albedo of 0.065 from those data, at that time the lowest-known albedo in the solar system. The first images resolving surface features, from Mariner 9, established approximate dimensions of the two moons, their heavily cratered surfaces, low albedos, and coverage by regolith (Pollack *et al.*, 1972, 1973). Polarimetric measurements indicated a finely granular regolith (Noland *et al.*, 1973).

Higher-resolution imaging from close flybys of the moons by the Viking 1 and Viking 2 orbiters revolutionized understanding of both moons (Duxbury and Veverka, 1977), and still provides most of the current knowledge about the physical geology of Deimos. Results through Viking were

thoroughly reviewed by Thomas *et al.* (1992) and Burns (1992). Phobos' surface exhibits rough topography, including craters in a variety of degradation states. One moderately well preserved large crater, Stickney, is about 9.4 km in diameter. Reflectance varies spatially, with brighter materials apparently less affected by “space weathering” being exposed on crater rims (Thomas, 1979). [Space weathering refers to processes that alter the optical properties of regolith over geologic time. On the Moon, this includes darkening accompanied by reddening of the spectrum and weakening of mineral absorptions. It is understood to occur by formation of nanophase metallic iron by redeposition of vapor from micrometeoroid impacts (Hapke, 2001).] Topographic grooves 100–200 m wide, tens of meters deep, and kilometers in length form several subparallel sets, most of which define planes that are nearly parallel to Phobos' intermediate axis (i.e., to the direction of orbital motion) (Thomas *et al.*, 1979). In contrast, Deimos has a markedly smoother surface (Fig. 3) with craters that are more degraded and infilled by regolith (Thomas, 1979). Migration of regolith down slopes has formed elongate streamers (Thomas and Veverka, 1980; Thomas *et al.*, 1996). Grooves have not been recognized on Deimos.

Several spectra of Phobos were acquired at ultraviolet through near-infrared wavelengths by Mariner 9 and Viking, and assembled into a single, composite spectrum

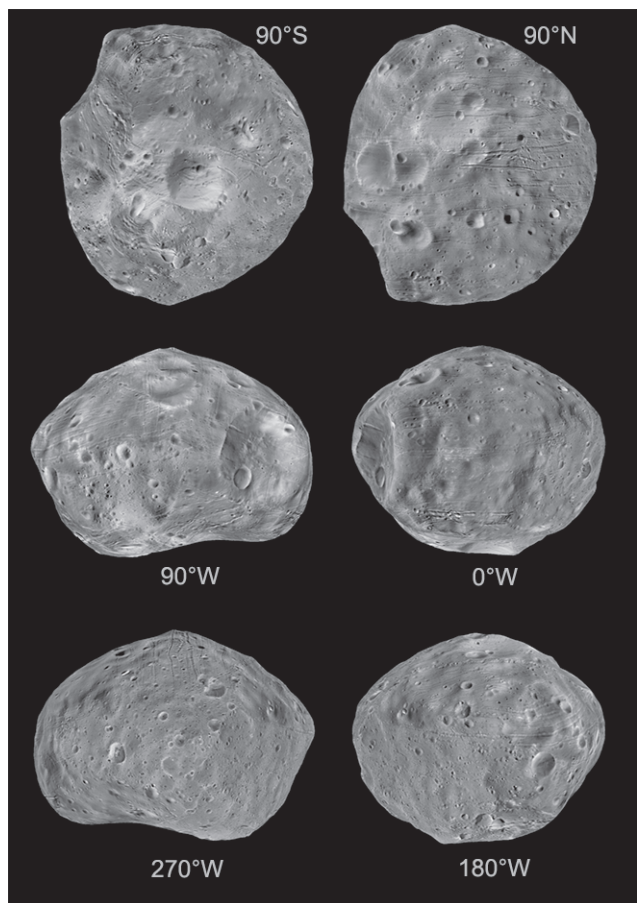


**Fig. 1.** Phobos image mosaic (Stooke, 2011) projected on a shape model from Gaskell (2011). *Upper left:* Southern hemisphere. *Upper right:* Northern hemisphere. *Center left:* Leading hemisphere. *Center right:* Sub-Mars hemisphere. *Lower left:* Trailing hemisphere. *Lower right:* Anti-Mars hemisphere.

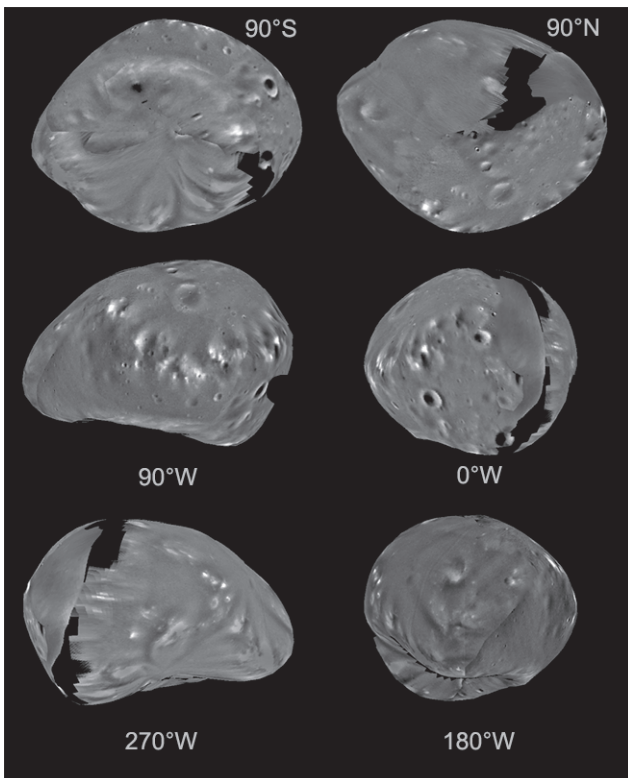


**Fig. 2.** Deimos image mosaic projected on shape model, both from Thomas (1993). *Upper left:* Southern hemisphere. *Upper right:* Northern hemisphere. *Center left:* Leading hemisphere. *Center right:* Sub-Mars hemisphere. *Lower left:* Trailing hemisphere. *Lower right:* Anti-Mars hemisphere.

TABLE 1. Current best estimates of global properties of Phobos and Deimos.

	Phobos	Deimos
Orbital semimajor axis	9377 km (2.8 R <sub>Mars</sub> )	23,460 km (7 R <sub>Mars</sub> )
Orbital period	7.66 h	30.3 h
Orbital eccentricity	0.0151	0.0003
Orbital inclination, to Mars' equator	1.093°	0.93°
Rotational period	Synchronous	Synchronous
Size	26.06 × 22.80 × 18.28 km *	15.0 × 12.2 × 10.4 km †
Density	1860 ± 13 kg m <sup>-3</sup> *	1490 ± 190 kg m <sup>-3</sup> ‡
Gravity	3–8 × 10 <sup>-3</sup> m s <sup>-2</sup>	2 × 10 <sup>-3</sup> m s <sup>-2</sup>
Normal reflectance, 0.55 μm	0.071 ± 0.012 §	0.068 ± 0.007 ¶

\* Willner et al. (2014).

† Thomas (1993).

‡ Mass from Jacobson (2010), volume from Thomas (1993).

§ Simonelli et al. (1998).

¶ Thomas et al. (1996).

by Pang et al. (1978). That composite spectrum is flat at wavelengths longer than 0.4 μm but falls off steeply into the ultraviolet. Similarity to the reflectance spectrum of carbonaceous chondrite meteorites drove a long-standing hypothesis that the moons are primitive, carbonaceous bodies captured into orbit around Mars (Pang et al., 1978; Pollack et al., 1978). Alternatively, it has been proposed that the moons accreted in Mars orbit from material like that forming bulk Mars (Burns, 1992), or from ejecta from a large impact with Mars (Singer, 1966; Craddock, 2011), and that they are dark because of extreme space weathering (Britt and Pieters, 1988).

Measurement of the moons' masses, made by tracking perturbations of the Viking Orbiters' trajectories during close flybys, combined with volume estimates from imaging, yielded the first density estimates of 2000 ± 500 kg m<sup>-3</sup> for Phobos and 1900 ± 700 kg m<sup>-3</sup> for Deimos (Veverka and Burns, 1980). Although subsequent data and new analyses improved these values (Table 1), the Viking results clearly showed that Mars' moons are much less dense than the bulk rock making up Mars, requiring that they must be either highly porous, composed of lower-density material, or both.

### 1.3. 1980–2004: Incremental New Understanding

The next phase of exploration included groundbased observations that refined earlier understanding of the moons' properties, a partially failed close rendezvous, and distant observations by other Mars-orbiting or landed spacecraft. Earth-based spectra revealed that the 3-μm H<sub>2</sub>O absorption expected for a hydrated-mineral-bearing carbonaceous composition was undetectable (Bell et al., 1989; Rivkin et al.,

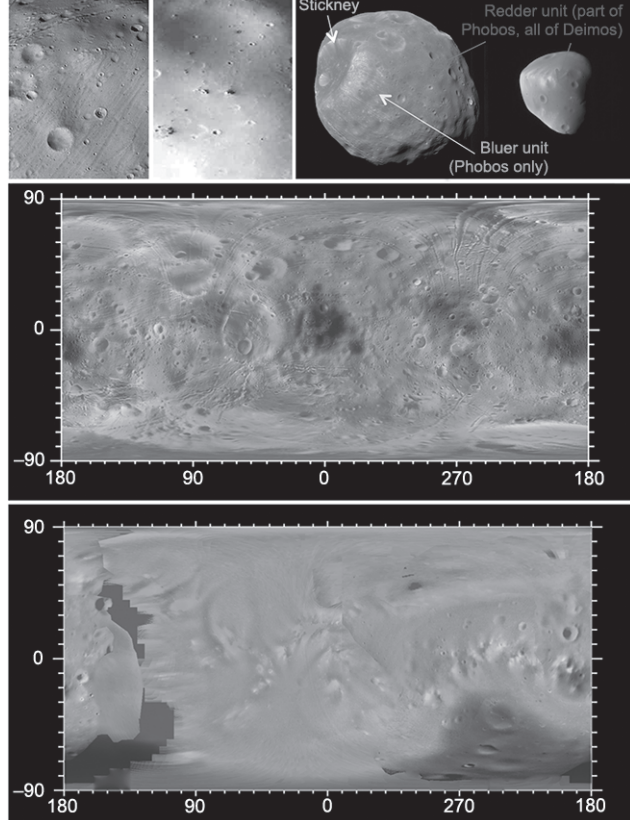


**Fig. 3.** See Plate 16 for color version. Spacecraft exploration reveals global properties of Phobos and Deimos, and basic differences between them. *Top left:* Viking images revealed that Phobos' surface is relatively rough, with well-preserved craters, and parallel topographic grooves. *Top center:* Deimos' surface is smooth with craters infilled by regolith. *Top right:* Multispectral and hyperspectral imaging from Phobos 2, Mars Express, and the Mars Reconnaissance Orbiter (shown, centered on the sub-Mars hemispheres) reveal spatial variations in Phobos' spectral properties, especially associated with Stickney. Deimos' brightness variations are accompanied by less color variation. *Middle:* Phobos simple cylindrical image map and dynamical height, using shape model from Gaskell (2011) and image mosaic from Stooke (2011). Red is high, blue low, with a range of heights of 1.8 km. *Bottom:* Deimos simple cylindrical image map and dynamical heights, using shape model and image mosaic updated from Thomas (1993). Red is high, blue low, with a range of heights of 1.9 km.

2002), and that disk-integrated spectra of Deimos (*Grundy and Fink*, 1992) and Phobos (*Murchie and Zellner*, 1994) were featureless and much redder than previously thought. In hindsight, the shape of the composite spectrum of *Pang et al.* (1978) was a result of mixing shorter wavelengths that covered a more red-sloped part of Phobos and longer wavelengths covering a much less red part of Phobos (*Murchie and Erard*, 1996).

The Phobos 2 mission (*Sagdeev and Zakharov*, 1989) was to have conducted proximity measurements of Phobos' chemical composition, but the spacecraft was lost after its first month of distant observations, before closest approach to the moon. Three medium-distance encounters with Phobos that did occur provided the most precise estimate of density to date (*Avanesov et al.*, 1991). During those encounters, color imaging returned by the Videospectrometric Camera (VSK) (*Avanesov et al.*, 1991) and ultraviolet through near-infrared spectra by the Combined Radiometer and Photometer for Mars (KRFM) (*Ksanfomality et al.*, 1990) and Imaging Spectrometer for Mars (ISM) (*Bibring et al.*, 1989) provided the first spatially resolved measurements of spectral properties of a low-reflectance body. Phobos' surface was revealed to be heterogeneous, with a "redder unit" occupying most of the surface, and a "bluer unit" associated with Stickney (Fig. 3). The two units differ mainly in spectral slope, and any mineral absorptions are weak. The 3- $\mu\text{m}$  absorption remained undetected even with improved spatial resolution (*Murchie et al.*, 1991; *Murchie and Erard*, 1996). The red spectral slopes of the two bodies, plus weak to absent 3- $\mu\text{m}$  absorptions, are more consistent with D-type asteroids than with carbonaceous chondrites (*Rivkin et al.*, 2002).

Measurements by Mars Global Surveyor and Mars Pathfinder added to the growing understanding of the moons. Images from the Mars Orbiter Camera, comparable to the best from Viking, revealed a high spatial density of blocks just east of Stickney, where ejecta from that crater are predicted to be thickest (*Thomas et al.*, 2000). Thermal emission spectrometer (TES) measurements revealed a nearly blackbody spectrum from 10 to 30  $\mu\text{m}$ , possibly with weak superimposed silicate features (*Roush and Hogan*, 2000, 2001; *Glotch et al.*, 2015). Whole-disk spectra of both moons from the Imager for Mars Pathfinder (*Murchie et al.*, 1999) confirmed the red-sloped spectra of both moons, and identified a 0.7- $\mu\text{m}$  absorption that they suggested could be due to Fe-bearing minerals.

#### 1.4. Beginning in 2004: Exploration by Mars Express and Mars Reconnaissance Orbiter

Knowledge of Phobos and Deimos was revolutionized again by the Mars Express and Mars Reconnaissance Orbiter (MRO) missions. During multiple close flybys of Phobos, Mars Express (*Witasse et al.*, 2013) acquired nearly global coverage with the High Resolution Stereo Camera (HRSC) (*Neukum et al.*, 2004; *Jaumann et al.*, 2007) and the Observatoire pour la Mineralogie, l'Eau, les Glaces et l'Activité (OMEGA) (*Bibring et al.*, 2004) imaging spectrometer, at

multiple viewing geometries that support derivation of the photometric properties of the surface over a broad wavelength range (*Fraeman et al.*, 2012). Additional spectral information came from the thermal infrared Point Fourier Spectrometer (PFS) (*Giuranna et al.*, 2011). The MaRS radio science experiment further improved the accuracy of mass determination, which, combined with a refined global volume estimate from HRSC, yields a density estimate for Phobos with a precision of <1% (Table 1). From low Mars orbit, MRO conducted several observing sessions dedicated to the moons. By virtue of its very high spatial resolution, the High-Resolution Imaging Science Experiment (HiRISE) (*McEwen et al.*, 2007) obtained the highest-resolution color imaging of the moons to date in three broad bands from 0.4 to 1.0  $\mu\text{m}$ . The Compact Reconnaissance Imaging Spectrometer for Mars (CRISM) (*Murchie et al.*, 2007) collected hyperspectral imaging of Phobos complementary to the OMEGA data, and the first spatially resolved hyperspectral measurements of Deimos.

Results from Mars Express and MRO frame the current debates about the composition, geological processes, and origin of the moons, as described in the following sections. In particular, the complexity of the grooves on Phobos frustrates simple explanation of their origins (*Ramsley and Head*, 2013b; *Murray and Heggie*, 2014). Similarly, spectral features are weak and have been interpreted as resulting from dissimilar compositions corresponding to the range of hypotheses for the moons' origins (*Giuranna et al.*, 2011; *Fraeman et al.*, 2012, 2014).

#### 1.5. Relationship to Themes of Solar System Exploration

The origin and evolution of the martian moons provides insight into fundamental questions regarding formation of the terrestrial planets and the geology of asteroidal bodies. For example, questions from Planetary Science Decadal Survey (*Squyres et al.*, 2011) include: (1) What were the initial stages, conditions, and processes of solar system formation? (2) What governed the supply of water to the terrestrial planets? (3) What were their primordial sources of organic matter? (4) What processes have controlled the surface evolution of small bodies?

Table 2 lists five possible origins for Phobos and Deimos, resulting from capture (*Pollack et al.*, 1978) or *in situ* formation hypotheses (*Burns*, 1992; *Craddock*, 2011). Each origin corresponds to a distinct range of compositions, some of which are in the meteorite collection and some of which have only been modeled. If either Phobos or Deimos is a captured carbon- or water-rich body, then that moon may be a sample of the population of bodies that provided carbon and volatiles to the accreting terrestrial planets; such a result would address the second and third Decadal Survey questions. However, capture does not necessarily imply a carbon-rich composition, or even the same origin for Phobos and Deimos. Alternatively, if Phobos or Deimos originated by capture of an ordinary chondrite, that finding would provide new

TABLE 2. Proposed origins for Phobos and Deimos and predicted compositions.

Hypothesis	Corresponding Composition	Elemental Abundances	Mineral Abundances
Capture of organic- and water-rich outer main belt or outer solar system body	Ultraprimitive; Tagish Lake is best-known analog *	High C, S, H, Zn/Mn; composition possibly distinct from known meteorites	Abundant phyllosilicates; carbonates and organic phases; anhydrous silicate phases rare
	Primitive; like CI or CM †	Medium C, S, H; may grade into other carbonaceous chondrite types — if so, distinguishable with Al/Mn, Zn/Mn	Abundant phyllosilicates; low carbonates; medium organics; olivine and Al-rich grains
Capture of organic-, water-poor outer solar system body	Anhydrous silicates plus elemental C ‡	High C, low H; Mg/Fe ratio ~2–4; bulk composition unlike any meteorite analogs	Anhydrous, medium Fe (20–40%) pyroxene; possibly abundant amorphous C or graphite
Capture of inner solar system body	Ordinary chondrites †	Very low C, H; Mg/Si ~0.8–1, Al/Si ~0.05–0.1; low Zn/Mn, Al/Mn; common composition in meteorite collections	Low carbonates, phyllosilicates; pyroxene, olivine in range of known meteorites
Coaccretion with Mars	Bulk Mars; like ordinary chondrites, but an SNC-derived composition §	Very low C, H; Mg/Si, Al/Si, Fe/Si indicative of bulk Mars; Zn/Mn, Al/Mn like ordinary chondrites	Anhydrous silicates with Fe, Mg expected for bulk Mars; low abundance of C-bearing phases
Accretion disk from giant impact on Mars	Impactor material; mixed with martian crust or mantle, like SNC meteorites ¶	Extremely low H; volatile depletions such as in C, S, K/Th; other elements depend on mix of Mars and impactor material; high Al/Si, Ca/Si indicate evolved igneous materials	Anhydrous phases; a primitive impactor would suggest abundant olivine, possibly C phases; any surviving Mars material is basaltic consistent with many datasets for Mars

\* Brown et al. (2000).

† Brearley and Jones (1998).

‡ Emery and Brown (2004).

§ Wanke and Dreibus (1988).

¶ McSween et al. (2009).

insight into how space weathering affects the link between common meteorites and D-type bodies. Formation by coaccretion with Mars would provide access to a building block of Mars, whereas formation from a large impact would sample Mars' earliest crust plus the impactor material. Whatever the moons' origins, addressing this question also addresses the first Decadal Survey question, and characterizing geological processes on Phobos and Deimos addresses the last.

## 2. PHYSICAL GEOLOGY

The two martian moons differ from one another in appearance, and each has fundamental surface characteristics that remain poorly understood. There was an early expectation that the moons were exemplary of the geology of small bodies in general (Veverka and Burns, 1980), but that expectation has been only partially met, due in part to the moons' distinct features compared with features observed on asteroids (see the chapters by Yoshikawa et al., Russell et al., and Barucci et al. in this volume). Yet the fundamental influences on all the bodies are similar: impact cratering,

orbital mechanics and evolution, low gravity, rotational accelerations, thermal cycling, and solid-body mechanical properties. One of the fundamental questions about Phobos' and Deimos' history is, given their similar environments, why does geology of their surfaces appear so different?

### 2.1. Basic Appearance

Phobos is modestly elongated (Table 1), heavily cratered, and distinctively marked with patterns of elongated depressions, termed grooves (Fig. 1). The largest crater, Stickney, is ~9.4 km in diameter, ~0.85× the satellite's mean radius. This size is within the normal range for the largest craters on small objects (Thomas, 1999; Morrison et al., 2009). The depth of the crater at present is about 1 km, but a large debris accumulation in the center is probably over 400 m thick (Thomas, 1998). Depth-to-diameter ratios of Phobos' craters appear to be generally 0.2 or less (Thomas et al., 1979; Basilevsky et al., 2014; Kokhanov et al., 2014). The differences between crater morphologies on small objects and the Moon are still not well established (Morrison et al.,

2009; Basilevsky *et al.*, 2014), in part because evaluation of crater degradation states on small objects is not well defined.

Deimos presents a surface whose smoothness contrasts greatly with the cratered and grooved roughness of Phobos (Fig. 2). Albedo features are conspicuous on ridges and some crater rims, further distinguishing its appearance from that of Phobos. It is even more irregularly shaped than Phobos, with a large concavity centered on the south pole (Thomas, 1998).

## 2.2. Shape, Density, and Internal Porosity

The dimensions of Phobos are well known, but Deimos' are less so. Willner *et al.* (2014) used a set of 665 surface control points on Phobos from HRSC and Viking Orbiter images to generate a spherical harmonic function up to degree and order 17 to describe Phobos' shape. Their best-fit triaxial ellipsoid dimensions (diameters) are  $a = 26.06$  km,  $b = 22.80$  km,  $c = 18.28$  km; the full shape model has a volume of  $5742 \pm 35$  km<sup>3</sup>. These numbers compare closely to the previous dimensions and volume obtained by Duxbury (1989, 1991) and Thomas (1989). Uncertainty in Deimos' volume and shape result from limited coverage and poor resolution of the trailing hemisphere and southern latitudes (Fig. 2). Its ellipsoidal fit dimensions are reported by Thomas (1993) as  $a = 15.6$  km,  $b = 12.0$  km, and  $c = 10.2$  km with a volume of  $1017 \pm 130$  km<sup>3</sup>, the latter obtained directly from the shape model.

Phobos' overall shape is elongated, with the long axis aligned with Mars. Stickney creates a large concavity in the leading part of the sub-Mars hemisphere (Fig. 1). Due to the eccentricity of Phobos' orbit, the moon librates about its mean position by  $\sim 1^\circ$ ; the exact magnitude of that libration is affected by internal density structure. If Phobos' interior is homogeneous, then a libration in longitude of  $1.10^\circ$  is predicted; however, increased porosity beneath Stickney due to impact fracturing could result in a libration up to  $1.24^\circ$  (Rambaux *et al.*, 2012). Previous determinations each have uncertainties of  $0.1^\circ$ – $0.2^\circ$ , and differ from each other by a larger amount than the difference between the two predictions (Duxbury, 1991; Willner *et al.*, 2014; Oberst *et al.*, 2014). Even the most recent and presumably accurate determination,  $1.09^\circ + 0.10^\circ$  (Oberst *et al.*, 2014), is insufficient to distinguish models of interior porosity. In the future, more accurate measurement of libration in longitude may provide a window into heterogeneity in Phobos's interior structure.

Deimos' shape can be described as having several rounded facets (Fig. 2). Ridges at the edges of the facets form gravitational highs, and the centers of the facets are gravitationally low (Fig. 3), creating regional slopes (Thomas, 1993; Thomas *et al.*, 1996). High southern latitudes lie in a major concavity, possibly a highly degraded crater whose ejecta reaccreted onto the moon and created the smooth surface (Thomas *et al.*, 1996; Thomas, 1998).

Although Phobos is low in density compared to mafic mineral assemblages and the bulk terrestrial planets, it is significantly denser than Deimos. Pätzold *et al.* (2013) used

mass determined from Mars Express' flyby of Phobos on March 3, 2010, at 77 km distance, and the global volume from Willner *et al.* (2010), to derive a bulk density of  $1862 \pm 20$  kg m<sup>-3</sup>. They were unable to solve for the second-degree gravity field to constrain internal heterogeneity. The best current mass for Deimos (Jacobson, 2010), divided by the best Viking-era volume estimate (Thomas, 1993), yields a bulk density of  $1490 \pm 190$  kg m<sup>-3</sup>,  $2\sigma$  below Phobos's density. In section 3.4 potential implications for the moons' density difference are discussed. Both densities are lower than those of nearly all analog materials, and substantial internal porosity is probably present at least within Deimos (Rosenblatt, 2011; Murchie *et al.*, 2013).

## 2.3. Gravitational Environment

Small asteroids and small bodies commonly have non-intuitive vectors for surface acceleration. These result from their irregular shapes; rapid spin, which enhances centripetal force; low mass, which decreases gravity; and especially in the case of Phobos, tidal effects. Determining what is "upslope" or "downslope" is best accomplished by calculating potential energies over the surface (Vanicek and Kakiwsky, 1986; Thomas, 1993). One measure of relative height, dynamical height, is obtained by dividing potential energy by acceleration. In the case of Phobos, as it spirals toward Mars, the longer ends (pointing toward and away from Mars,  $0^\circ$  and  $180^\circ$  longitude) become conspicuous gravitational lows due to tides and rotational accelerations (Fig. 3) (Thomas, 1993; Shi *et al.*, 2012). Escape velocities near those locations are also highly directionally dependent, less than  $3$  m s<sup>-1</sup> toward the east, but over  $9$  m s<sup>-1</sup> to the west (Thomas, 1993). Deimos, orbiting much farther from Mars, experiences less effect from tides and rotational accelerations.

## 2.4. Regolith Properties

Having formed on small objects without atmospheres or internal activity, the regoliths of the two moons are expected to be the product of impacts and redistribution of their ejecta over geologic time. Nearly all ejecta from craters on Phobos and Deimos either reimpact the satellites directly [that fraction being a function of strength, which affects ejecta velocity (Asphaug and Melosh, 1993)], or escape to Mars orbit and reaccumulate over time (Soter, 1971; Ramsley and Head, 2014). An important question has been the abundance of Mars ejecta in Phobos' regolith (Chappaz *et al.*, 2013; Ramsley and Head, 2013a, 2014). Chappaz *et al.* (2013) and Ramsley and Head (2013a) calculated that Mars ejecta may constitute a few parts per million to a few hundred parts per million of Phobos' regolith, most having accreted later in Phobos' evolution as it has spiraled to lower altitudes. The presence of at least a few centimeters of low thermal inertia material, indicated by surface temperatures determined from Viking Orbiter thermal infrared measurements (Lunine *et al.*, 1982), is consistent with fine-grained, unconsolidated regolith.

Crater morphology reveals evidence for layering in Phobos' regolith. Layering is directly exposed in one crater wall (Thomas, 1979). Crater floor morphologies [e.g., flat floors, concentric craters (Quaide and Oberbeck, 1968)] suggest depths to discontinuities of a few to several tens of meters in some areas of Phobos (Thomas et al., 2000). Basilevsky et al. (2014) used similar criteria to map crater morphology with Mars Express images, and found that the depth to discontinuities varies greatly over short distances. These and MARSIS radar sounder data (Heggy et al., 2014) suggest that Phobos' regolith varies in modest ways horizontally and that it gradationally merges at greater depths with a more solid, but likely still porous object.

Large ejecta blocks are found on both moons. The largest on Phobos may be an ~85-m boulder near the crater Stickney; Deimos has a poorly resolved block ~150 m across. Basilevsky et al. (2014) noted that the surface density of large blocks (from a variety of source data) approximates that on some lunar terrains, and that mapping of both obvious blocks and mounds interpreted as blocks reveals an association with specific craters. Lee et al. (1986) found that large blocks are more widespread on Deimos than on Phobos, and typify the surface seen in the highest-resolution images (Fig. 3). The sizes of the large blocks are within ranges expected for the possible source craters, and likely were formed by similar excavation and fragmentation phenomena as lunar ejecta blocks. The abundance of smaller blocks on Phobos is known only for the region near Stickney imaged at high resolution, and it is comparable to the number density and size-frequency distributions of blocks on Eros and Itokawa (Ernst et al., 2015).

Phobos' regolith exhibits color as well as albedo variations, whereas Deimos' regolith has albedo variations but little color variation (Murchie et al., 1991; Thomas et al., 2011); both bodies are a factor of 2 lower in reflectance than even the most space-weathered lunar mare materials (sections 3.1, 3.2). Phobos' greatest color variation is associated with the crater Stickney (Fig. 3), a "bluer" region that includes most of the crater, the ejecta to the east, and less distinct lobes to the northwest and southwest (Patsyn et al., 2012; Pieters et al., 2014). These locations correspond to predicted locations of the thickest ejecta from Stickney (Thomas, 1998). The rest of the surface is a "redder unit," and close to the color exhibited by Deimos. Phobos has some brighter crater rims, and accumulations of relatively dark material on the floors of some craters. Deimos' albedo features are mostly streamers that taper downslope from crater rims and blocks on the regional gravitational highs at ridge crests (Fig. 3) (Thomas et al., 1996). These albedo features exhibit little color contrast from the darker surroundings, but are up to 30% brighter than the rest of Deimos' surface. It is likely that some of the elevated reflectances are related to lesser space weathering of more freshly exposed regolith, particularly on Phobos' bright crater rims and in Deimos' streamers. The detailed processes by which space weathering operates on Mars' moons depends on the composition of the starting material, which is debated

(section 3.2). However, it is unlikely that Phobos' redder material results from space weathering of the bluer material: Space weathering is understood to weaken mineral absorptions (Hapke, 2001), and absorptions present at 0.65 and 2.8  $\mu\text{m}$  in the redder material are weaker or absent in the bluer material (section 3.2).

Deimos exhibits clear evidence for widespread motion of material down regional slopes: brighter streamers trending down gravitational slopes, asymmetric ponded material within craters concentrated on their downslope sides, and more blocks and small craters on higher terrain (those at lower elevations having been buried). Deimos has perhaps the largest recognized crater of any small body relative to body size, the south polar concavity with a diameter of ~10 km (Thomas, 1989; Morrison et al., 2009). The estimated volume of this crater is  $43 \pm 20 \text{ km}^3$  on an object with a surface area  $520 \text{ km}^2$ . In comparison, Stickney's initial volume was  $50 \pm 15 \text{ km}^3$  on an object with a surface area of  $1600 \text{ km}^2$  (Thomas, 1998). Nearly all crater ejecta should have eventually reaccreted on Deimos. At present, an uneven distribution of craters larger than 350 m indicates uneven blanketing or other degradation of craters. The simplest explanation, consistent with the topographic slopes, is concentration of reaccreted ejecta into lower areas by mass wasting, yielding thicknesses up to 200–400 m in gravitational lows (Fig. 14 of Thomas, 1998). Deimos' globally uniform appearance suggests that the south polar cratering event does not date to Deimos' earliest history: If the cratering event was that old, then downslope movement of regolith might have exposed substrate in topographically higher regions, which would then have accumulated a high density of small impact craters.

Whereas Deimos exhibits mass wasting on slopes as low as  $2^\circ$ , Phobos' rougher surface has only localized examples of mass wasting. The most obvious are on the western interior slope of Stickney (Thomas et al., 2000; Basilevsky et al., 2014), which is at the angle of repose and has few superposed small craters and numerous downslope albedo streamers. On the floor of Stickney is a hummocky mound several hundred meters in thickness that is probably a debris slide formed substantially after Stickney's formation, judging from its well-preserved hummocks and few superposed craters. As noted in section 2.3, the gravitational slopes on Phobos are changing as it approaches Mars; Stickney's western slope has probably increased with time, encouraging further and future mass movement. Other mass movement on Phobos is observed in smaller craters (Basilevsky et al., 2014) and in some grooves.

Both martian moons have been observed by Earth-based radar. Busch et al. (2007), using Arecibo observations at 13-cm wavelength, measured radar albedos of  $0.056 \pm 0.014$  for Phobos, consistent with a recalibrated value of  $0.049 \pm 0.01$  for Phobos found by Ostro et al. (1989), and  $0.021 \pm 0.006$  for Deimos. Both radar albedos are low: Phobos is near the low end of asteroid radar albedos and Deimos has the lowest detected radar albedo in the solar system to date. Given the radar albedos, a near-surface density and porosity can be calculated if a composition is assumed;

*Busch et al.* (2007) considered lunar soils and dehydrated low-grade carbonaceous chondrites, and for each used grain densities of  $2700 \text{ kg m}^{-3}$ . Phobos' near-surface bulk density was estimated to be  $1600 \pm 300 \text{ kg m}^{-3}$ , indicating a near-surface total porosity of  $40 \pm 10\%$ , while for Deimos the values are  $1100 \pm 300 \text{ kg m}^{-3}$  and  $60 \pm 10\%$ .

## 2.5. Crater Densities and Surface Ages of the Moons

Crater densities on Phobos have been studied by *Thomas and Veverka* (1980), *Thomas* (1998), and *Schmedemann et al.* (2013, 2014). Studies of crater density on irregular objects must deal with geographic variations in image quality and lighting, effects of differing slopes, and relief of the substrate that can affect crater shape and size. Crater degradation on small objects may involve seismic shaking induced by impacts (*Richardson et al.*, 2005). *Schmedemann et al.* (2014) found spatial variations in crater density on Phobos, and possibly discontinuities in the cratering record (kinks in the cumulative crater density curves), which they hypothesized to be created by seismic shaking or ejecta emplacement events. Absolute ages are model-dependent: If Phobos has experienced the expected crater flux at Mars' orbit since its earliest history, then the oldest surface may approach 4.3 Ga and Stickney may be as old as 4.2 Ga. Model ages for grooves are younger than Stickney, consistent with the observation that grooves cross-cut Stickney and its ejecta, but their absolute age probably exceeds 3 Ga. The role of secondaries is unclear: *Ramsley and Head* (2014) interpreted it to be significant, whereas *Schmedemann et al.* (2014) did not. The antapex (around  $270^\circ\text{W}$  longitude) lacks significant grooves and has been suggested to have less regolith than other areas (*Thomas*, 1998), perhaps relating both to deposition of ejecta near Stickney, and to disturbance near Stickney's antipode. A global crater catalog of Phobos has been compiled, and is likely close to complete for craters  $>50 \text{ m}$  in diameter (*Bandeira et al.*, 2014).

Deimos' distinct morphology indicates a different history of crater modification from that on Phobos. Despite smoothing of the surface by deposition or reaccumulation of a large amount of ejecta (section 2.4), there remains a high density of large craters (*Thomas*, 1998) not very different from that on Phobos. However, although rims of larger craters are visible for counting, crater interiors have been largely filled by debris (*Thomas*, 1998). The uneven geographic distribution of smaller craters on Deimos, with fewer small craters near the center of the topographic facets, indicates greater burial by debris in gravitational lows (Fig. 16 of *Thomas*, 1998).

## 2.6. Grooves on Phobos

Viking Orbiter views of Phobos revealed linear, often parallel depressions 100–200 m wide, extending up to several kilometers (*Veverka and Burns*, 1980). Several spacecraft missions later, these features remain without consensus explanations. Similar but not identical features have been found on small icy satellites (*Morrison et al.*, 2009), and on

small asteroids including (951) Gaspra (*Veverka et al.*, 1994), (243) Ida (*Sullivan et al.*, 1996), (433) Eros (*Buczkowski et al.*, 2008), and (21) Lutetia (*Thomas et al.*, 2012). A large fraction of Phobos' grooves fall into at least four parallel sets, whose normals are close to the plane defined by the long and short axes of Phobos (*Thomas et al.*, 1979; *Murray et al.*, 1994). Some grooves cut other grooves, and many cut crater rims, including Stickney's. They traverse a wide range of angles with respect to local slope directions. Many have a pitted appearance, although some have straight rims with no apparent pitting. Many are "shoulder-to-shoulder." Raised rims appear to bound some grooves, although the shoulder-to-shoulder groove spacing in some places and subtle reflectance variations make rim topography difficult to characterize. Interior slopes are typically well below angles of repose. A few wide, shallow grooves are the clearest examples of linear arrays of discrete pits (D grooves of *Thomas et al.*, 1979).

Hypotheses for the origin of the grooves include secondary cratering from Phobos impacts (*Veverka and Duxbury*, 1977; *Head and Cintala*, 1979), secondary cratering from Mars impacts (*Murray et al.*, 1994, 2014), cratering from debris in Mars orbit (*Schultz and Crawford*, 1989; *Kikuchi and Miyamoto*, 2014), tracks formed by rolling ejecta blocks (*Wilson and Head*, 2005; *Duxbury*, 2011; *Hamelin*, 2011; *Ramsley and Head*, 2013b), and fractures of the body of Phobos into which regolith has drained or from which regolith has been ejected by degassing of water from the interior (*Thomas et al.*, 1979; *Weidenschilling*, 1979; *Horstman and Melosh*, 1989). The grooves show a variety of morphologies, which could be evidence that their formation involved more than a single mechanism. The range of groove morphologies observed in different materials and dynamical environments of asteroids and icy satellites (*Buczkowski et al.*, 2008; *Morrison et al.*, 2009; *Thomas et al.*, 2012) suggests that multiple formation mechanisms act throughout the solar system. One common feature in all models of groove formation, however, is a requirement for loose regolith, to tens of meters in depth, where grooves occur.

None of the hypotheses for groove formation is overwhelmingly supported for all of Phobos' grooves by existing observations. Secondary cratering from Mars theoretically could explain some grooves' alignments (*Murray et al.*, 1994), but the close spacing of the grooves, the even spacing of similarly sized pits along the grooves, and the large area of coverage by grooves cannot obviously be explained by secondary cratering from impacts many thousands of kilometers away (*Ramsley and Head*, 2013b). A few distinct, wide grooves do have morphologies consistent with secondary crater chains, and have orientations that match predicted ejecta patterns from Stickney (*Thomas*, 1998), but most grooves do not. Impacts from debris in orbit about Mars might be consistent with some patterns (*Schultz and Crawford*, 1989; *Kikuchi and Miyamoto*, 2014), but this hypothesis is not well developed theoretically. Rolling ejecta blocks can form somewhat similar aligned markings, but there is no explanation for the consistent parallel patterns of grooves instead of meandering paths deflected

by topography that are typical of lunar boulder tracks, or for the paths traversing all slope angles [especially apparent east of Stickney; see Fig. 10 of Thomas (1998)]. Some grooves, especially those crossing the northern polar region, have morphologies (straight walls, nearly constant widths) suggestive of graben, as do some grooves on saturnian satellites with similar body-related patterns (Morrison et al., 2009). Other grooves consist of regularly spaced chains of similarly-sized pits consistent with drainage of loose regolith into underlying fractures (Horstman and Melosh, 1989). Tidal stretching has been a favored source of stress to generate fractures underlying grooves (Soter and Harris, 1977; Weidenschilling, 1979; Morrison et al., 2009). Mechanical modeling based on the real shape of Phobos and on a layered or gradational regolith is needed to test a possible origin by fracturing.

## 2.7. Surface and Orbital Environment

The surface environments of Phobos and Deimos are strongly affected by their location in Mars orbit. At the surface, at noon near the subsolar point, surface temperature may exceed 350 K at perihelion, but only reach 270 K when Mars is at aphelion (Giuranna et al., 2011). Modeling predicts that nighttime surface temperature depends on latitude and season, typically cooling to 100 K before dawn, although temperatures during polar night may reach 60 K. The diurnal thermal wave penetrates to less than 1 cm, and at depth the average temperature is near 230 K (Kuhrt and Giese, 1989). Unlike the Moon and Mercury, Phobos and Deimos do not have polar craters that are permanently shadowed and  $\leq 100$  K in temperature over geologic time. On geologic timescales, Mars' obliquity is chaotic, ranging between  $0^\circ$  and  $60^\circ$  (Laskar and Robutel, 1993). For the moons' low orbital inclinations to Mars' equator, orbit inclination reckoned from Mars' equator of date is subject only to small variations — in other words, as Mars' obliquity varies, the moons' orbits track the equator (Gurfil et al., 2007). Thus, presently cold polar regions were subjected to prolonged heating by insolation in the past (Laskar et al., 2004). This history also affects the moons' ability to have retained internal ice that has been hypothesized to have been present at the moons' formation (e.g., Rosenblatt, 2011): At all latitudes, any initial pore-filling ice will have ablated to a depth of between hundreds of meters to over 3 km, depending on typical pore size (Fanale and Salvail, 1989).

The regolith environment may be even more exotic, with the moons predicted by theory to reside in a "dust belt" (Soter, 1971). No direct measurement provides confirmation that such a belt exists, so the details of dust belt density and morphology are based on models. Observations by the Hubble Space Telescope place upper limits on the optical depths (Showalter et al., 2006). Modeling predicts that much of the ejecta from small impacts on the moons will exceed the escape velocity of either moon and remain in Mars orbit. Larger particles will follow Keplerian trajectories and eventually reimpact the parent moon, whereas the orbits of

smaller particles will be perturbed by solar radiation pressure, and become asymmetric about Mars. Small particles originating from Phobos are perturbed toward the Sun, and those originating from Deimos are perturbed away from the Sun. In addition, grains from Deimos will oscillate about size-dependent Laplace planes, creating a vertically asymmetric ring. For the Deimos ring, interaction between the two asymmetries gives rise to a time-dependent structure that varies with martian season. The smaller particles eventually either impact Mars or are lost from the Mars system (Horanyi et al., 1990, 1991; Kholshevnikov et al., 1993; Juhasz and Horanyi, 1995; Sasaki, 1996; Hamilton, 1996; Krivov and Hamilton, 1997; Makuch et al., 2005; Krivov et al., 2006; Zakharov et al., 2014).

## 3. COMPOSITION, ORIGIN, AND ORBITAL EVOLUTION

The compositions of Phobos and Deimos are interesting in themselves, but more importantly, they help to constrain the moons' origins. At the present time, remote measurements can provide two major constraints on the moons' composition, their overall reflectance and spectral continuum, and the presence of absorption or emission features diagnostic of particular minerals.

### 3.1. Constraints from Reflectance

Comparisons of the visible to near-infrared reflectances of Phobos and Deimos with analog materials have been hampered over the years by comparison of dissimilar quantities, e.g., geometric albedo and bidirectional reflectance measured in the laboratory, or single-wavelength measures of reflectance that do not include an assessment of the spectral continuum. Mars Express/OMEGA and MRO/CRISM observations have overcome these challenges because they cover hundreds of wavelengths, and the OMEGA data cover a range of geometries that allows derivation of an accurate photometric correction to the geometry at which analog materials are commonly observed in the laboratory, i.e., incidence angle  $i = 30^\circ$ , emergence angle  $e = 0^\circ$ , and phase angle  $\alpha = 30^\circ$  (Framan et al., 2012). Figures 4a,b compare corrected spectral reflectance of Phobos to examples of the two broad classes of proposed composition, carbon-rich materials exemplified by low-grade carbonaceous chondrites, and space-weathered mafic assemblages exemplified by mature lunar mare soils. Reflectance and spectral slope are closely comparable to low-grade, carbon-rich CI and CM carbonaceous chondrites, and are particularly well matched by samples of the CM chondrite Murchison that have been heated by laser pulses to simulate the effects of space weathering (Hiroi et al., 2003). Pajola et al. (2013) were able to model the spectrum of the redder unit by adding a component of Mg-rich glass to the Tagish Lake ungrouped, phyllosilicate-rich carbonaceous chondrite. In contrast with the close match in reflectance and spectral slope with primitive carbonaceous materials, Phobos and Deimos are a factor of 2 darker than even the most space-weathered

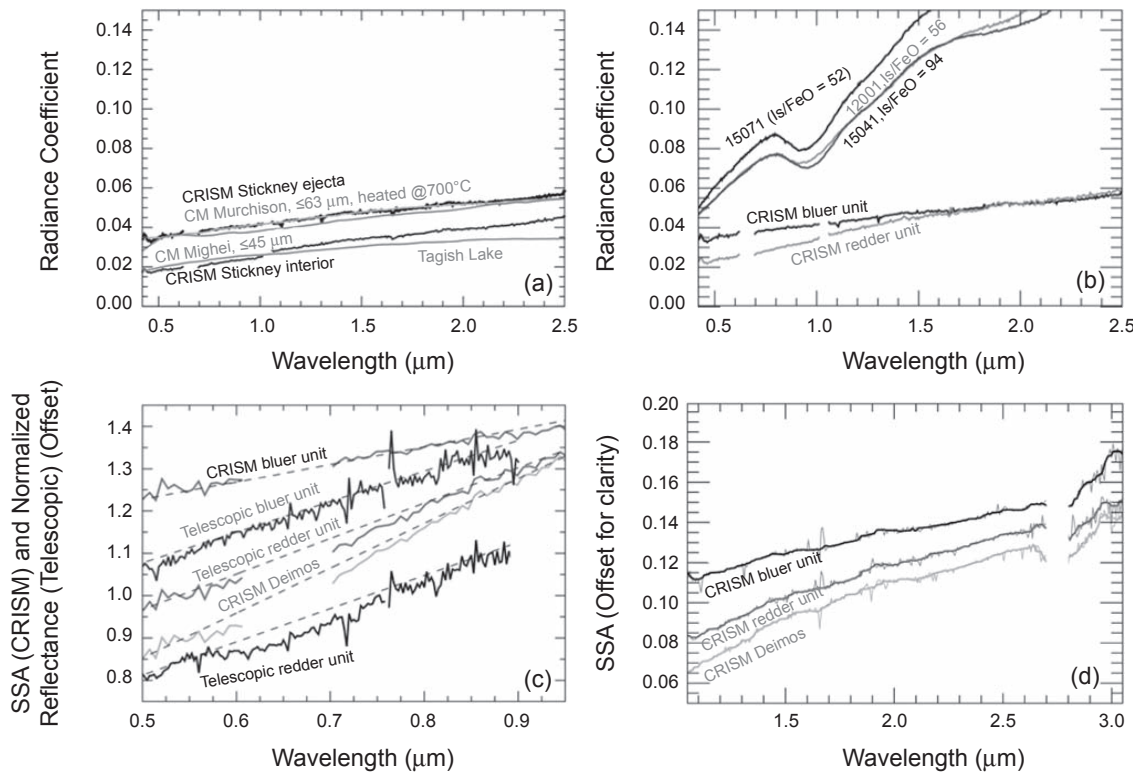


**Fig. 4.** CRISM spectral reflectance measurements of Phobos and Deimos. Uncertainty in the data is typically  $\pm 1\%$  near  $0.7\text{ }\mu\text{m}$  and  $\pm 3\%$  near  $3\text{ }\mu\text{m}$  (Fraeman et al., 2014). (a) Reflectance of bluer unit corrected to  $i = 30^\circ$ ,  $e = 0^\circ$ ,  $\alpha = 30^\circ$  compared with meteorite analogs measured at the same geometry. Stickney ejecta and heated Murchison overplot each other. Adapted from Fraeman et al. (2012). (b) Redder and bluer units compared with mature lunar mare soils. Is/FeO is magnetic susceptibility divided by Fe content expressed as FeO, and is proportional to the extent of space weathering. Adapted from Fraeman et al. (2012). (c) CRISM spectra of redder and bluer units covering the  $0.65\text{-}\mu\text{m}$  feature, compared with telescopic spectra that reproduce the absorption. Adapted from Fraeman et al. (2014). (d) Spectra corrected for thermal emission extending to  $3.1\text{ }\mu\text{m}$ , showing the  $2.8\text{-}\mu\text{m}$  OH absorption. Adapted from Fraeman et al. (2014).

lunar mare soils, making space-weathered Mars crustal material unsuitable as a spectral analog despite the similarity in spectral continuum slope. Phobos and Deimos are also much darker, and much redder, than shock-darkened ordinary chondrites, which have been suggested as compositional analogs to several low-reflectance planetary surfaces (Britt and Pieters, 1988; Gillis-Davis et al., 2013).

### 3.2. Constraints from Spectral Features

Constraining the compositions of Phobos and Deimos from weak mineral spectral signatures requires accurate calibration of remote spectral measurements, confirmation of the mineral signatures in multiple datasets, and determining the diagnostic character of the signatures. In ISM spectra taken from Phobos 2, upward curvature in the  $1\text{-}\mu\text{m}$  region in a ratio spectrum of bluer to redder material resembles an absorption due to olivine or possibly pyroxene. Such a feature would be consistent with less-red material having experienced less lunar-like space weathering and having a stronger mineral signature (Murchie and Erard,

1996; Gendrin et al., 2005). Disk-integrated observations of the moons acquired from Mars' surface by the Imager for Mars Pathfinder showed no evidence for the  $1\text{-}\mu\text{m}$  feature, and indicated instead a broad, shallow feature near  $0.7\text{ }\mu\text{m}$  (Murchie et al., 1999) comparable to that seen in some low-albedo asteroid spectra (Vilas et al., 1994). Subsequent OMEGA and CRISM data do not reproduce detection of a  $1\text{-}\mu\text{m}$  absorption due to olivine or pyroxene (Fraeman et al., 2012, 2014) or detect a feature due to  $\text{H}_2\text{O}$  at  $3\text{ }\mu\text{m}$  (Fraeman et al., 2012).

However, CRISM data do reveal spectral features in both units (Fraeman et al., 2014). Deimos and the redder unit on Phobos both exhibit a broad, shallow absorption centered near  $0.65\text{ }\mu\text{m}$  — the feature detected earlier in Mars Pathfinder data — but the feature is absent from Phobos' bluer unit. The strength of this feature is highly correlated with visible color observed by HiRISE and CRISM. The  $0.65\text{-}\mu\text{m}$  absorption is reproduced in telescopic spectra dominated by the redder unit, but absent in telescopic spectra dominated by the bluer unit (Fig. 4c). Both units also exhibit a sharp absorption near  $2.8\text{ }\mu\text{m}$  (Fig. 4d) attributable to OH (Clark

*et al.*, 1990); the feature is strongest on Deimos and weakest in Phobos' bluer unit. Spectrally, Phobos and Deimos belong to the “Pallas group” described in the chapter by Rivkin et al. in this volume. With more complete wavelength coverage, the false detection of olivine from ISM spectra is now recognizable as the artifact of ratioing a bland bluer unit spectrum to a redder unit spectrum with a 0.65- $\mu\text{m}$  absorption having a longer-wavelength shoulder near 1  $\mu\text{m}$ .

One interpretation of these absorptions, consistent with the reflectance and spectral slope characteristics described in section 3.1, is a composition rich in phyllosilicate that has been desiccated of molecular  $\text{H}_2\text{O}$ . In particular, phyllosilicate-rich CM carbonaceous chondrites exhibit an OH feature like that observed at 2.8  $\mu\text{m}$  as well as an absorption due to Fe in phyllosilicate near 0.7  $\mu\text{m}$  (*Cloutis et al.*, 2011; *Takir et al.*, 2013; see also the chapter by Rivkin et al. in this volume). Phobos' and Deimos' Fe feature is centered closer to 0.65  $\mu\text{m}$ , possibly suggesting a different desiccated phyllosilicate, such as Fe-bearing nontronite (*Fraeman et al.*, 2014). That interpretation would be consistent with an origin of the moons that includes primitive material. However, alternate interpretations involving anhydrous minerals consistent with other proposed origins cannot be entirely excluded. Curvature in the spectrum near 0.65  $\mu\text{m}$  might result from Rayleigh scattering by a mixture of microphase and nanophase Fe in the right proportion that is formed by space-weathering processes (*Clark et al.*, 2012). The OH feature near 2.8  $\mu\text{m}$  is similar in its reflectance minimum to an OH feature observed on the Moon (*Clark*, 2009; *Peters et al.*, 2009; *Sunshine et al.*, 2009) and attributed to anhydrous reaction of implanted solar wind protons with oxygen in silicate minerals (*McCord et al.*, 2011), although the lunar feature is considerably broader than that observed on Phobos, Pallas, or CM meteorites.

Thermal infrared spectra complement the mineral detection capabilities of visible to near-infrared spectra. However, their analysis is complicated by the need to ratio to a blackbody spectrum, and the fact that Phobos' and Deimos' thermal emissions are not well fit by an ideal blackbody (*Lynch et al.*, 2007). *Giuranna et al.* (2011) calculated emissivity spectra from TES and PFS data whose footprints cover large segments of Phobos, assuming an areal mixture of blackbody spectra representing three different surface temperatures (shaded surfaces, low and high thermal inertia solar-illuminated surfaces). Selected regions exhibit apparent emissivity features consistent with phyllosilicate, although features in other spectra resemble those due to feldspathoid minerals. *Giuranna et al.* favored the feldspathoid interpretation, and a composition of highly evolved Mars crustal material. Difficulties in this interpretation include the lack of feldspathoid-rich meteorite analogs, the dominance of basaltic compositions in Mars' crust (*McSween et al.*, 2009), the lack of detection of feldspathoids on Mars despite detection of over 30 other minerals (*Viviano-Beck et al.*, 2014), and the possibility of artifacts from assuming a mixture of surfaces with discrete temperatures. More recently, using TES data, *Glotch et al.* (2015) modeled thermal emissivity

from TES data covering the redder unit using a surface with many different temperatures. They find evidence for bound molecular water and carbonate, which if correct would be diagnostic of primitive carbonaceous compositions, and for silicate consistent with the desiccated phyllosilicate inferred from visible to near-infrared reflectance.

Regardless of precise compositions, the contrast in spectral properties between the bluer and redder units provides information on three-dimensional structure within Phobos. Inside Stickney, either redder or bluer material is exposed in different locations (*Thomas et al.*, 2011). The heterogeneity inside Stickney led *Basilevsky et al.* (2014) to suggest that at depth Phobos consists of a rubble of discrete bluer and redder blocks as proposed by *Murchie et al.* (1991). Alternatively, the interior may be relatively coherent as suggested by average density if a CM-chondrite-like composition is assumed (section 3.4), with the bluer material that is relatively “pristine” chemically having zones and pockets of hydration into redder material richer in phyllosilicates, which exhibit 0.65- $\mu\text{m}$  and 2.8- $\mu\text{m}$  absorptions.

### 3.3. Comparison with D-Type and Related Asteroids

The spectra of martian satellites are consistent with low-reflectance, outer-belt D-class asteroids, which also dominate the Trojan asteroid region. This similarity was first noted for Deimos by *Grundy and Fink* (1992), and for Phobos by *Murchie and Erard* (1996), who found that most of Phobos' surface has a spectrum similar to that of Deimos, although the area near Stickney has a flatter spectral slope. *Rivkin et al.* (2002) combined 1.65–3.5- $\mu\text{m}$  spectra from the Infrared Telescope Facility (IRTF) with shorter-wavelength Phobos 2 data, and interpreted D-class asteroids to best match Deimos and Phobos' redder unit, whereas Phobos' bluer unit is more similar to P- or T-class asteroids.

The weak absorptions observed on Phobos and Deimos are also consistent with those observed on low-reflectance asteroids. Absorptions near 0.7  $\mu\text{m}$  on low-reflectance asteroids have been attributed to Fe-bearing phyllosilicates, which are usually accompanied by absorptions due to OH or  $\text{H}_2\text{O}$  near 3  $\mu\text{m}$  (*Vilas and Gaffey*, 1989; *Vilas et al.*, 1993; *Vilas*, 1994; *Rivkin et al.*, 2002). Mineralogical interpretations for the asteroids most similar to Phobos and Deimos having absorptions near 0.65  $\mu\text{m}$  without an accompanying feature near 0.9  $\mu\text{m}$  remain uncertain (*Jarvis et al.*, 1993; *Vilas et al.*, 1994). Many low-reflectance asteroids also display an absorption centered near 2.8  $\mu\text{m}$ , and these features can be grouped qualitatively into three classes (see the chapter by Rivkin et al. in this volume): (1) Ceres-type, with symmetric absorption minima near 3.0 and 3.3  $\mu\text{m}$ , possibly attributable to brucite (*Milliken and Rivkin*, 2009); (2) Themis-type, with an absorption minimum near 3.1  $\mu\text{m}$  attributable to water frost (*Rivkin and Emery*, 2010; *Campins et al.*, 2010); and (2) Pallas-type, having a checkmark-shaped absorption with a minimum near 2.8  $\mu\text{m}$  attributable to OH-bearing phases (*Rivkin et al.*, 2011). Phobos' and Deimos' features group with those of the (2) Pallas class.

### 3.4. Implications for Internal Structure

Given a compositional determination for either Phobos or Deimos, and a measurement of the moon's average density, the approximate internal structure of the moon can be inferred. As the extent of fracturing of an asteroidal body increases and its mechanical coherence decreases, internal structure transitions through four classes described by *Wilkison et al.* (2002) and *Britt et al.* (2002): coherent, with minimal macroporosity; fractured but mechanically coherent, with up to 20% macroporosity; heavily fractured, with 20–30% macroporosity; and loosely consolidated or rubble pile, with  $\geq 30\%$  macroporosity. For small bodies whose internal pressures are smaller than the mechanical strength of the constituent materials, additional porosity (microporosity) occurs as pores or microfractures between individual mineral grains within mechanically coherent chunks. The macroporosity is needed to infer interior structure. [Definitions of density and porosity of meteorites and asteroids used here follow those of *Britt and Consolmagno* (2003) and *Consolmagno et al.* (2008). Grain density is defined as the density of the solid phase of a meteoritic or asteroidal material, excluding voids. Bulk density is the density of a porous meteoritic material, and differs from grain density due to the presence of pores and microfractures between grains. Macroporosity is the volume percent of an asteroidal body occupied by fractures between mechanically coherent chunks, not including pores between grains within those chunks (microporosity). Total porosity of an asteroidal body is the sum of macroporosity and microporosity.]

Inferred internal structures inferred for Phobos and Deimos depend strongly on the composition assumed. CM meteorites, arguably the closest spectral analog to the moons, have a bulk density (including pores and microfractures) of  $2250 \pm 80 \text{ kg m}^{-3}$ , and a grain density (for the solid phase only) of  $2900 \pm 80 \text{ kg m}^{-3}$  (*Consolmagno et al.*, 2008). Using this CM bulk density, *Murchie et al.* (2013) calculated a macroporosity for Phobos of  $17 \pm 4\%$ , placing it in the fractured but coherent category, and a macroporosity for Deimos of  $34 \pm 11\%$ , consistent with a rubble pile. A more porous structure for Deimos would be consistent with its south polar concavity having originated from an impact that partially shattered the moon, followed by reaccretion of the fragments to explain the smooth surface (*Thomas*, 1996). The derived macroporosity for Deimos is comparable with typical values for fragmental lunar mare regolith at tens of centimeters to meter depth, 35–38% (*Mitchell et al.*, 1972), where overburden pressure is comparable to that in the martian moon interiors. *Andert et al.* (2010) used a slightly lower grain density to estimate a total porosity for Phobos of  $30 \pm 5\%$ . Andert et al. equated this result with a loosely consolidated interior, but that interpretation did not allow for partitioning of total porosity into microporosity and macroporosity, only the latter of which is relevant for internal structure.

*Rosenblatt* (2011) considered what macroporosities would correspond with differing compositional interpretations of

existing spectral measurements. For example, if the moons are dominated by Mars crustal material (*Craddock*, 2011; *Giuranna et al.*, 2011) or shock-darkened ordinary chondrite (*Britt and Pieters*, 1988), macroporosity for Phobos could be in the range of 25–47% and for Deimos in the range 41–58%. Rosenblatt speculated that the higher porosities would be unrealistic and require portions of the void spaces to be filled by water ice. However, an explanation for the geochemically unexpected combination of anhydrous silicates with a large fraction of ice — two components expected to have condensed in different parts of the solar system — was not proposed.

Interpretation of geologic surface features on the martian moons, and in particular the grooves on Phobos, also has the potential to provide insights into internal structure. The formation mechanisms for Phobos' grooves are actively debated, as discussed in section 2.6. Models that invoke extensive fracturing, if correct, would indicate mechanical coherence consistent with that implied by a CM-chondrite-like composition. In contrast, continuous fracturing over kilometers would be inconsistent with the rubble-pile structure required by mafic or ordinary chondritic compositions.

### 3.5. Orbital Evolution and Formation Mechanisms

Any hypothesis for the origin of Phobos and Deimos must be consistent with the dynamics of the moons' orbital evolution. Reconciling empirical observations of the moons' properties with predictions of orbital dynamical models has proven challenging. A primitive carbonaceous composition, if that interpretation is correct, could have resulted from formation in the solar nebula at heliocentric distances beyond Mars' orbit (*Pollack et al.*, 1978), migration toward the inner solar system as proposed by some dynamical models [namely the Nice model (*Tsiganis et al.*, 2005; *Gomes et al.*, 2005)], and capture into Mars orbit. Capture requires special circumstances such as drag from an extended protoatmosphere (*Hunten*, 1979; *Pollack et al.*, 1979; *Sasaki*, 1990).

Circularizing an initially eccentric orbit after capture, and reducing orbital inclination to the present near-equatorial orbit, can be achieved by tidal processes in the case of Phobos over the last 4.6 G.y. However, this requires a high tidal dissipation rate that is difficult to reconcile with a largely coherent Phobos. Instead, the interior would need to be highly fragmented, or have a substantial fraction of ice to increase the tidal dissipation rate (*Lambeck*, 1979; *Mignard*, 1981; *Rosenblatt*, 2011; *McCarthy and Castillo-Rogez*, 2011). In the case of Deimos, tidally induced orbital changes are probably too slow to account for evolution of an eccentric, inclined orbit over the last 4.6 G.y. (*Lambeck*, 1979; *Szeto*, 1983), unless there was enhanced tidal dissipation due to internal ice (*Rosenblatt*, 2011). Alternatively, drag in the protoatmosphere, particularly efficient in circularizing an orbit, may have played a role. This scenario requires a very early capture, a suitable density of the protoatmosphere to prevent the captured asteroid from impacting Mars (*Sasaki*, 1990), and an extent of the protoatmosphere beyond the current orbit of Deimos.

The moons' present orbits are thought to have evolved considerably once in the equatorial plane. Because Phobos orbits inside a synchronous orbit, it exhibits acceleration along its orbit resulting from the solid body tides raised by Phobos in Mars (e.g., Burns, 1992), by about  $1.27 \times 10^{-3}$  deg yr $^{-2}$  (Lainey et al., 2007; Jacobson, 2010). Phobos' orbit thus decays by about 20 cm yr $^{-1}$ . Former moons orbiting well inside Phobos already will have impacted Mars. The interpretation of elongated martian impact craters being formed by obliquely impacting former moons is debated (Schultz and Luz-Garihan, 1982; Bottke et al., 2000; Chappelow and Herrick, 2008). The same mechanism is expected to cause Deimos' orbit to recede away from Mars, because Deimos orbits beyond a synchronous orbit. When Phobos' and Deimos' orbits are integrated backward in time, inevitably the moons must once have been in close proximity, raising the possibility that they both formed near a synchronous orbit (Rosenblatt and Charnoz, 2012), or even are fragments of a single captured object (Singer, 2007; Rosenblatt, 2011).

Formation of Phobos and Deimos in orbit around Mars avoids the challenges of explaining the orbital evolution of captured objects. Phobos and Deimos could have coaccreted with Mars (Safronov et al., 1986), which would account for the current near-equatorial and near-circular orbits of both moons. However, this hypothesis implies that Phobos and Deimos would have ordinary-chondrite-like or bulk-Mars-like compositions, which is hard to reconcile with their low densities and spectral properties. One hypothesis that may be reconcilable with many observed properties of the moons is that they formed from a hot, circumplanetary accretion disk formed by the impact of a large carbonaceous body on Mars (Craddock, 2011; Rosenblatt and Charnoz, 2012; Canup and Salmon, 2014). Crater scaling relations identify the Daedalia, Chryse, and newly recognized Borealis (Andrews-Hanna et al., 2008) basins on Mars as the most plausible records of that impact (Craddock, 2011). The 4.3-Ga estimated crater age of the Borealis basin (Frey, 2010) agrees with the observed crater density on Phobos (Sche medemann et al., 2014). Material from the impactor could have dominated the accretion disk. Even if a carbonaceous impactor caused the moons' low reflectances, heating of the material should have driven off molecular water, explaining the lack of a strong 3-μm absorption at present (Craddock, 2011). Rosenblatt and Charnoz (2012) examined several different scenarios for satellite formation from such an accretion disk, in a strong-tide regime close to the Roche limit and in a weak-tide regime further out. They concluded that formation in a strong-tide regime would have formed bodies whose dynamic lifetime against reimpact on Mars is much less than the moons' age, so that such a mechanism cannot have formed the moons. In contrast, formation in a weak-tide regime between the Roche limit and synchronous orbit may have been capable of forming the satellites. They suggested that Phobos and Deimos may be the last two remnants of such bodies formed near the synchronous distance to Mars, other now extinct moons having since impacted Mars.

#### 4. OUTSTANDING QUESTIONS FOR FUTURE STUDY

After Mars Express, four key uncertainties remain about Phobos and Deimos for which resolution is required to answer high-level science questions. First, what are the moons' compositions, and how does that constrain the moons' origins? Some remote measurements are highly suggestive of a CM-carbonaceous-chondrite-like composition, but alternative interpretations of the moons' low reflectance and weak spectral features cannot be ruled out based on existing data. Sample return answers this question definitively using major and minor elements and isotopes to link the moons to particular reservoirs. Short of sample return, future remote or *in situ* spacecraft measurements could also provide key compositional information to address the fundamental question of the moons' origins. As shown in Table 2, a diagnostic set of measurements would be elemental abundances, particularly measurements that would constrain abundances of H, C, S, and major and minor elements exhibiting a range of volatilities (e.g., Zn, Mn, and Al). Another diagnostic measurement set would be of mineralogy with a focus on phases whose abundances differ greatly between proposed compositions, particularly olivine, pyroxene, phyllosilicate, and carbonate. The ambiguity of detection of these phases in existing measurements suggests that new measurements should include fresh, non-space-weathered surfaces, or should resolve single mineral grains to enhance spectral signatures of minor phases. The presence of molecular water, hydroxylated minerals, or subsurface ice is a critical test of models of the moons' formation: A high content of water or hydroxyl in minerals (or water-equivalent H) is consistent with capture of a primitive body, but is probably inconsistent with formation *in situ*. For *in situ* formation, either the source material was low-water (ordinary chondrite, martian crust) or it accreted from a circumplanetary disk from which water was baked out.

Second, what is the relationship of Phobos to Deimos? In part this depends on their origins — if formed in Mars orbit, they are related, but if captured, they could be either unrelated or fragments of a single body that was disrupted during capture (Singer, 2007; Rosenblatt, 2011). In addition, the moons' closer proximity earlier in their history and regolith exchange between the moons via the hypothesized dust belts raises the possibility that Phobos' redder unit could be derived from Deimos. Testing these hypotheses requires modeling as well as compositional measurements of both moons.

Third, what is the moons' deep structure and could there be deep water ice? The two most important new groups of measurements would be composition of both moons to estimate internal macroporosity, and volume of Deimos to reduce the uncertainty in its average density. Higher-degree gravity coefficients for both moons would also be useful. Given the likelihood that any internal ice has ablated to a depth of 1 km or greater, near-surface detection of it by shallow radar sounding may not be feasible. Alternatively, heterogeneity in the filling of deep pores by water ice may be detectable by measuring the amplitude of Phobos' forced

libration and the second-order coefficients of the nonspherical part of the gravity field (Rosenblatt, 2011). Measurement of the forced libration can also be used to test for enhanced macroporosity beneath Stickney due to impact fracturing (Rambaux et al., 2012; LeMaistre et al., 2013).

Fourth, what is the origin of the grooves on Phobos? The global distribution, orientation, and stratigraphic relations of grooves is now relatively well known, but implications of these observables for models of groove origin remain debatable (Ramsley and Head, 2013b; Murray and Heggie, 2014). Given the widespread occurrence of somewhat similar, but varied features on asteroids and on small icy bodies, understanding the way or ways in which grooves form is important for interpreting the evolution of small bodies across the solar system. New tests for models of groove origin may be obtained using high-resolution, meter-scale measurements of groove topography and color. Various models make different predictions about topography of groove rims and floors, and about stratigraphic relations of groove floor and rim materials. Seismic measurements across grooves could determine whether they are surface expressions of fractures at depth.

Many key outstanding scientific questions about the martian moons may be solved by future robotic missions, even before ultimate human exploration of these destinations.

## REFERENCES

- Andert T. P., Rosenblatt P., Pätzold M., Häusler B., Dehant V., Tyler G. L., and Marty J. C. (2010) Precise mass determination and the nature of Phobos. *Geophys. Res. Lett.*, 37, 1–4, DOI: 10.1029/2009GL041829.
- Andrews-Hanna J. C., Zuber M. T., and Banerdt W. B. (2008) The Borealis Basin and the origin of the martian crustal dichotomy. *Nature*, 453, 1212–1215.
- Asphaug E. and Melosh H. J. (1993) The Stickney impact of Phobos — A dynamical model. *Icarus*, 101, 144–164.
- Avanesov G., Zhukov B., Ziman Y., Kostenko V., Kuzmin A., Muravev V., Fedotov V., Bonev B., Mishev D., Petkov D., Krumov A., Simeonov S., Boycheva V., Uzunov Y., Weide G. G., Halmann D., Posse W., Head J., Murchie S., Shkuratov Y. G., Berghelan R., Danz M., Mangoldt T., Pihau U., Weidlich U., Lumme K., Muinonen K., Peltoniemi J., Duxbury T., Murray B., Herkenhoff K., Fanale F., Irvine W., and Smith B. (1991) Results of TV imaging of Phobos — experiment VSK-Fregat. *Planet. Space Sci.*, 39, 281–295.
- Bandeira L., Salamunicar G., and Hare T. M. (2014) Global crater catalogues of the Moon, Mars and Phobos. *Lunar Planet. Sci. XLV*, Abstract #2088. Lunar and Planetary Institute, Houston.
- Basilevsky A. T., Lorenz C. A., Shingareva T. V., Head J. W., Ramsley K. R., and Zubarev A. E. (2014) The surface geology and geomorphology of Phobos. *Planet. Space. Sci.*, 102, 95–118.
- Bell J., Piscitelli J., and Lebofsky L. (1989) Deimos: Hydration state from infrared spectroscopy. *Lunar Planet. Sci. XX*, pp. 58–59. Lunar and Planetary Institute, Houston.
- Bibring J.-P., Combes M., Langevin Y., Soufflot A., Cara C., Drossart P., Encrenaz T., Erard S., Forni O., Gondet B., Ksanfonality L., Lellouch E., Masson P., Moroz V., Rocard F., Rosenqvist J., and Sotin C. (1989) Results from the ISM experiment. *Nature*, 341, 591–593.
- Bibring J.-P. et al. (2004) OMEGA: Observatoire pour la Minéralogie, l'Eau, les Glaces et l'Activité. In *Mars Express: The Scientific Payload* (A. Wilson, ed.), pp. 37–49. ESA SP-1240, Noordwijk, The Netherlands.
- Bottke W. F., Love S. G., Tytell D., and Glotch T. (2000) Interpreting the elliptical crater populations on Mars, Venus, and the Moon. *Icarus*, 145, 108–121.
- Brearley A. and Jones R. (1998) Chondritic meteorites. In *Planetary Materials* (J. Papike, ed.), pp. 3–1 to 3–398. Reviews in Mineralogy, Vol. 36, Mineralogical Society of America, Washington.
- Britt D. T. and Consolmagno G. J. (2003) Stony meteorite porosities and densities: A review of the data through 2001. *Meteoritics & Planet. Sci.*, 38, 1161–1180.
- Britt D. and Pieters C. (1988) The origin of Phobos: Implications of compositional properties. *Astron. Vestnik*, 22, 229–239.
- Britt D. T., Yeomans D., Housen K., and Consolmagno G. (2002) Asteroid density, porosity, and structure. In *Asteroids III* (W. F. Bottke Jr. et al., eds.), pp. 485–500. Univ. of Arizona, Tucson.
- Brown P. et al. (2000) The fall, recovery, orbit, and composition of Tagish Lake meteorite: A new type of carbonaceous chondrite. *Science*, 290, 320.
- Buczkowski D. L., Barnouin-Jha O. S., and Pockter L. M. (2008) 433 Eros lineaments: Global mapping and analysis. *Icarus*, 193, 39–52.
- Burns J. A. (1978) The dynamical evolution and origin of the martian moons. *Vistas Astron.*, 22, 193–210.
- Burns J. A. (1992) Contradictory clues as to the origin of the martian moons. In *Mars* (H. H. Kieffer et al., eds.), pp. 1283–1302. Univ. of Arizona, Tucson.
- Busch M. W. et al. (2007) Arecibo radar observations of Phobos and Deimos. *Icarus*, 186, 581–584.
- Campins H. et al. (2010) Water ice and organics on the surface of the asteroid 24 Themis. *Nature*, 464, 1320–1321.
- Canup R. M. and Salmon J. (2014) On an impact origin of Phobos–Deimos. *AAS/Division for Planetary Sciences Meeting Abstracts*, 46, #501.09.
- Chappaz L., Melosh H. J., Vaquero M., and Howell K. C. (2013) Transfer of impact ejecta material from the surface of Mars to Phobos and Deimos. *Astrobiology*, 13, 963–980.
- Chappelow J. E. and Herrick R. R. (2008) On the origin of a double, oblique impact on Mars. *Icarus*, 197, 452–457.
- Clark R. N. (2009) Detection of adsorbed water and hydroxyl on the Moon. *Science*, 326, 562–564, DOI: 10.1126/science.1178105.
- Clark R. N., King T. V. V., Klejwa M., Swayze G.A., and Vergo N. (1990) High spectral resolution reflectance spectroscopy of minerals. *J. Geophys. Res.*, 95, 12653–12680, DOI: 10.1029/JB095iB08p12653.
- Clark R. N., Cruikshank D. P., Jaumann R., Brown R. H., Stephan K., Dalle Ore C. M., Eric Livo K., Pearson N., Curchin J. M., Hoefer T. M., Buratti B. J., Filacchione G., Baines K. H., and Nicholson P. D. (2012) The surface composition of Iapetus: Mapping results from Cassini VIMS. *Icarus*, 218, 831–860, DOI: 10.1016/j.icarus.2012.01.008.
- Cloutis E. A., Hudon P., Hiroi T., Gaffey M. J., and Mann P. (2011) Spectral reflectance properties of carbonaceous chondrites: 2. CM chondrites. *Icarus*, 216, 309–346, DOI: 10.1016/j.icarus.2011.09.009.
- Craddock R. A. (2011) Are Phobos and Deimos the result of a giant impact? *Icarus*, 211, 1150–1161.
- Consolmagno G. J., Britt D. T., and Macke R. J. (2008) The significance of meteorite density and porosity. *Chem. Erde*, 68, 1–29.
- Duxbury T. C. (1989) The figure of Phobos. *Icarus*, 78, 169–180.
- Duxbury T. C. (1991) An analytic model for the Phobos surface. *Planet. Space Sci.*, 39, 355–376.
- Duxbury T. (2011) Possible lunar analogy to the Phobos grooves. In *EPSC-DPS Joint Meeting 2011*, p. 243.
- Duxbury T. C. and Everka J. (1977) Viking imaging of Phobos and Deimos: An overview of the primary mission. *J. Geophys. Res.*, 82, 4203–4211.
- Emery J. and Brown R. (2004) The surface composition of Trojan asteroids: Constraints set by scattering theory. *Icarus*, 170, 131.
- Ernst C. M., Rodgers D. J., Barnouin O. S., Murchie S. L., and Chabot N. L. (2015) Evaluating small body landing hazards due to blocks. *Lunar Planet. Sci. XLVI*, Abstract #2625. Lunar and Planetary Institute, Houston.
- Fanale F. P. and Salvail J. R. (1989) Loss of water from Phobos. *Geophys. Res. Lett.*, 16, 287–290.
- Fraeman A. A., Arvidson R. E., Murchie S. L., Rivkin A., Choo T., Bibring J.-P., Gondet B., Humm D., Kuzmin R. O., Manaud N., and Zabalueva E. V. (2012) Analysis of disk-resolved OMEGA and CRISM spectral observations of Phobos and Deimos. *J. Geophys. Res.*, 117, DOI: 10.1029/2012JE004137.

- Fraeman A. A., Murchie S. L., Arvidson R. E., Clark R. N., Morris R. V., Rivkin A. S., and Vilas F. (2014) Spectral absorptions on Phobos and Deimos in the visible/near infrared wavelengths and their compositional constraints. *Icarus*, 229, 196–205.
- Frey H. V. (2010) A minimum crater retention age for the proposed “Borealis Basin” on Mars. *Lunar Planet. Sci. XLI*, Abstract #1136. Lunar and Planetary Institute, Houston.
- Gaskell R. W. (2011) *Phobos Shape Model V1.0*. NASA Planetary Data System.
- Gendrin A., Langevin Y., and Erard S. (2005) ISM observation of Phobos reinvestigated: Identification of a mixture of olivine and low-calcium pyroxene. *J. Geophys. Res.*, 110, DOI: 10.1029/2004 JE002245.
- Gillis-Davis J., van Niekerk D., Scott E., McCubbin F. M., and Blewett D. T. (2013) Impact darkening: A possible mechanism to explain why Mercury is spectrally dark and featureless. Abstract P11A-07 presented at 2013 Fall Meeting, AGU, San Francisco, Calif., 9–13 Dec.
- Giuranna M. et al. (2011) Compositional interpretation of PFS/MEx and TES/MGS thermal infrared spectra of Phobos. *Planet. Space Sci.*, 59, 1308–1325, DOI: 10.1016/j.pss.2011.01.019.
- Glotch T., Edwards C., and Ebel D. (2015) Spectral properties of Phobos from the Mars Global Surveyor Thermal Emission Spectrometer: Evidence for water and carbonate. *Lunar Planet. Sci. XLVI*, Abstract #2587. Lunar and Planetary Institute, Houston.
- Gomes R., Levison H. F., Tsiganis K., and Morbidelli A. (2005) Origin of the cataclysmic late heavy bombardment period of the terrestrial planets. *Nature*, 435, 466.
- Grundy W. M. and Fink U. (1992) Deimos: A reddish, D-type asteroid spectrum. In *Asteroids, Comets, Meteors 1991*, pp. 215–218. Lunar and Planetary Institute, Houston.
- Gurfil P., Valéry Lainey V., and Efroimsky M. (2007) Long-term evolution of orbits about a precessing oblate planet: 3. A semi-analytical and a purely numerical approach. *Cel. Mech. Dyn. Astron.*, 99, 261–292.
- Hall A. (1878) *Observations and Orbits of the Satellites of Mars with Data for Ephemerides in 1879*. U.S. Government Printing Office, Washington, DC.
- Hamelin M. (2011) Motion of blocks on the surface of Phobos: New constraints for the formation of grooves. *Planet. Space Sci.*, 59, 1293–1307.
- Hamilton D. P. (1996) The asymmetric time-variable rings of Mars. *Icarus*, 119, 153–172.
- Hapke B. (2001) Space weathering from Mercury to the asteroid belt. *J. Geophys. Res.*, 106, 10039–10073.
- Harris D. L. (1961) Photometry and colorimetry of planets and satellites. In *Planets and Satellites* (G. P. M. Kuiper and B. M. Middlehurst, eds.), pp. 272–342. Univ. of Chicago, Chicago.
- Head J. W. and Cintala M. J. (1979) Grooves on Phobos: Evidence for possible secondary cratering origin. In *Reports of Planetary Geology Program 1978–1979*, pp. 19–21. National Aeronautics and Space Administration, Washington, DC.
- Heggy E., Herique A., Cichetti A., and Gim Y. (2014) Understanding Phobos shallow subsurface geophysical properties from MARSIS radar observations. In *Eighth International Mars Conference*, Abstract #1453. Lunar and Planetary Institute, Houston.
- Hiroi T., Moroz L. V., Shingareva T. V., Basilevsky A. T., and Pieters C. M. (2003) Effects of microsecond pulse laser irradiation on Vis-NIR reflectance spectrum of carbonaceous chondrite simulant: Implications for martian moons and primitive asteroids. *Lunar Planet. Sci. XXXIV*, Abstract #1324. Lunar and Planetary Institute, Houston.
- Horanyi M., Burns J. A., Tatrallyay M., and Luhmann J. G. (1990) Toward understanding the fate of dust lost from the martian satellites. *Geophys. Res. Lett.*, 17, 853–856.
- Horanyi M., Tatrallyay M., Juhasz A., and Luhmann J. G. (1991) The dynamics of submicron-sized dust particles lost from Phobos. *J. Geophys. Res.*, 96, 11283–11290.
- Horstman K. C. and Melosh H. J. (1989) Drainage pits in cohesionless materials—Implications for the surface of Phobos. *J. Geophys. Res.*, 94, 12433–12441.
- Hunten D. (1979) Capture of Phobos and Deimos by protoatmospheric drag. *Icarus*, 37, 113–123.
- Jacobson R. A. (2010) The orbits and masses of the martian satellites and the libration of Phobos. *Astron. J.*, 139, 668–679.
- Jarvis K. S., Vilas F., and Gaffey M. J. (1993) Iron oxide bands in the visible and near-infrared reflectance spectra of primitive asteroids. *Lunar Planet. Sci. XXIV*, pp. 715–716. Lunar and Planetary Institute, Houston.
- Jaumann R., Neukum G., Behnke T., Duxbury T., Eichendorf K., Flohrer J. v., Gasselt S., Giese B., Gwinner K., Hauber E., Hoffmann H., Hoffmeister A., Koehler U., Matz K.-D., McCord T. B., Mertens V., Oberst J., Pischel R., Reiss D., Ress E., Roatsch T., Saiger P., Scholten F., Schwarz G., Stephan K., Waehlisch M., et al. (2007) The high resolution stereo camera (HRSC) experiment on Mars Express: Instrument aspects and experiment conduct from interplanetary cruise through the nominal mission. *Planet. Space Sci.*, 55, 928–952.
- Juhasz A. and Horanyi M. (1995) Dust torus around Mars. *J. Geophys. Res.*, 100, 3277–3284.
- Kikuchi H. and Miyamoto H. (2014) Tidally disrupted small bodies may form grooves on Phobos. *Lunar Planet. Sci. XLV*, Abstract #2007. Lunar and Planetary Institute, Houston.
- Kokhanov A. A., Kreslavsky M. A., Basilevsky A. T., Karachevtseva I. P., and Zubarev A. E. (2014) Morphometry of large craters on Phobos and comparison with other bodies. *Lunar Planet. Sci. XLV*, Abstract #1084. Lunar and Planetary Institute, Houston.
- Kholshevnikov K. V., Krivov A. V., Sokolov L. L., and Titov V. B. (1993) The dust torus around Phobos orbit. *Icarus*, 105, 351–362.
- Krivov A. V. and Hamilton D. P. (1997) Martian dust belts: Waiting for discovery. *Icarus*, 128, 335–353.
- Krivov A. V., Feofilov A. G., and Dikarev V. V. (2006) Search for the putative dust belts of Mars: The late 2007 opportunity. *Planet. Space Sci.*, 54, 871–878.
- Ksanfonality L., Murchie S., Britt D., Duxbury T., Fisher P., Goroshkova N., Head J., Kuhrt E., Moroz V., Murray B., Nikitin G., and Petrova E. (1990) Phobos: Spectrophotometry between 0.3 and 0.6 μm and IR radiometry. *Planet. Space Sci.*, 39, 311–326.
- Kuhrt E. and Giese B. (1989) A thermal model of the martian satellites. *Icarus*, 81, 102–111.
- Lainey V., Dehant V., and Pätzold M. (2007) First numerical ephemerides of the martian moons. *Astron. Astrophys.*, 465, DOI: 10.1051/0004-6361:20065466.
- Lambeck K. (1979) On the orbital evolution of the martian satellites. *J. Geophys. Res. B*, 84, 5651–5658.
- Laskar J. and Robutel P. (1993) The chaotic obliquity of the planets. *Nature*, 361, 608–612.
- Laskar J., Correia A. C. M., Gastineau M., Joutel F., Levrard B., and Robutel P. (2004) Long term evolution and chaotic diffusion of the insolation quantities of Mars. *Icarus*, 170, 343–364.
- Lee S. W., Thomas P., and Ververka J. (1986) Phobos, Deimos, and the moon—Size and distribution of crater ejecta blocks. *Icarus*, 68, 77–86.
- LeMaistre S., Rosenblatt P., Rambaux N., Castillo-Rogez J. C., Dehant V., and Marty J. C. (2013) Phobos interior from librations determination using Doppler and star tracker measurements. *Planet. Space Sci.*, 85, 106–122, DOI: 10.1016/j.pss.2013.06.015.
- Lunine J. I., Negebeau G., and Jakosky B. (1982) Infrared observations of Phobos and Deimos from Viking. *J. Geophys. Res.*, 87, 10297.
- Lynch D. K. et al. (2007) Infrared spectra of Deimos (1–13 μm) and Phobos (3–13 μm). *Astron. J.*, 134, 1459–1463.
- Makuch M., Krivov A. V., and Spahn F. (2005) Long-term dynamical evolution of dusty ejecta from Deimos. *Planet. Space Sci.*, 53, 357–369.
- McCarthy M. C. and Castillo-Rogez J. C. (2011) Planetary ice attenuation properties. In *The Science of Solar System Ices* (M. Gudipati and J. C. Castillo-Rogez, eds.), pp. 183–226. Springer, Berlin.
- McCord T. B., Taylor L. A., Combe J.-P., Kramer G., Pieters C. M., Sunshine J. M., and Clark R. N. (2011) Sources and physical processes responsible for OH/H<sub>2</sub>O in the lunar soil as revealed by the Moon Mineralogy Mapper (M<sup>3</sup>). *J. Geophys. Res.–Planets*, 116, E00G05, DOI: 10.1029/2010JE003711.
- McEwen A. S. et al. (2007) Mars Reconnaissance Orbiter’s High Resolution Imaging Science Experiment (HiRISE). *J. Geophys. Res.*, 112, E05S02, DOI: 10.1029/2005JE002605.
- McSween H. Y., Taylor G. J., and Wyatt M. B. (2009) Elemental composition of the martian crust. *Science*, 324, 736.
- Mignard F. (1981) Evolution of the martian satellites. *Mon. Not. R. Astron. Soc.*, 194, 365–379.
- Milliken R. E. and Rivkin A. S. (2009) Brucite and carbonate assemblages from altered olivine-rich materials on Ceres. *Nature Geosci.*, 2, 258–261, DOI: 10.1038/ngeo478.

- Mitchell K. K., Houston W. N., Scott R. F., Costes N. C., Carrier W. D. III, and Bromwell L. G. (1972) Mechanical properties of lunar soil: Density, porosity, cohesion, and angle of internal friction. *Proc. Lunar Planet. Sci. Conf. 3rd*, pp. 3235–3253.
- Morrison S. J., Thomas P. C., Tiscareno M. S., Burns J. A., and Veverka J. (2009) Grooves on small saturnian satellites and other objects: Characteristics and significance. *Icarus*, 204, 262–270.
- Murchie S. and Erard S. (1996) The spectral properties and composition of Phobos from measurements by Phobos 2. *Icarus*, 123, 63–86.
- Murchie S. and Zellner B. (1994) The HST spectrum of Phobos: Comparison with Mariner 9, Viking, and Phobos-2 results and with meteorite analogs. *Lunar Planet. Sci. XXV*, pp. 957–958. Lunar and Planetary Institute, Houston.
- Murchie S., Britt D., Head J., Pratt S., Fisher P., Zhukov B., Kuzmin A., Ksanfomality L., Zharkov A., Nikitin G., Fanale F., Blaney D., Robinson M., and Bell J. (1991) Color heterogeneity of the surface of Phobos: Relationships of geologic features and comparison to meteorite analogs. *J. Geophys. Res.*, 96, 5925–5945.
- Murchie S., Thomas N., Britt D., Herkenhoff K., and Bell J. F. III (1999) Mars Pathfinder spectral measurements of Phobos and Deimos: Comparison with previous data. *J. Geophys. Res.*, 104, 9069–9080.
- Murchie S. et al. (2007) Compact Reconnaissance Imaging Spectrometer for Mars (CRISM) on Mars Reconnaissance Orbiter (MRO). *J. Geophys. Res.*, 112, E05S03, DOI: 10.1029/2006JE002682.
- Murchie S. L., Fraeman A. A., Arvidson R. E., Rivkin A. S., and Morris R. V. (2013) Internal characteristics of Phobos and Deimos from spectral properties and density: Relationship to landforms and comparison with asteroids. *Lunar Planet. Sci. XLIV*, Abstract #1604. Lunar and Planetary Institute, Houston.
- Murray J. B. and Heggie D. C. (2014) Character and origin of Phobos' grooves. *Planet. Space. Sci.*, 102, 119–143, DOI: 10.1016/j.pss.2014.03.001.
- Murray J. B., Rothery D. A., Thornhill G. D., Muller J.-P., Iliffe J. C., Day T., and Cook A. C. (1994) The origin of Phobos' grooves and crater chains. *Planet. Space. Sci.*, 42, 519–526.
- Neukum G., Jaumann R., and HRSC Co-Investigator and Experiment Team (2004) HRSC: the High Resolution Stereo Camera of Mars Express. In *Mars Express: The Scientific Payload* (A. Wilson, ed.), ESA SP-1240, Noordwijk, The Netherlands.
- Noland M., Veverka J., and Pollack J. B. (1973) Mariner 9 polarimetry of Phobos and Deimos. *Icarus*, 20, 490–499.
- Oberst J., Zubarev A., Nadezhina I., Shishkina L., and Rambaux N. (2014) The Phobos geodetic control point network and rotation model. *Planet. Space. Sci.*, 102, 45–50.
- Ostro S. J., Jurgens R. F., Yeomans D. K., Standish E. M., and Greiner W. (1989) Radar detection of Phobos. *Science*, 243, 1584–1586.
- Pajola M., Lazzarin M., Dalle Ore C. M., Cruikshank D. P., Roush T. L., Magrin S., Bertini I., La Forgia F., and Barbieri C. (2013) Phobos as a D-type captured asteroid, spectral modeling from 0.25 to 4.0  $\mu\text{m}$ . *Astrophys. J.*, 777, 127.
- Pang K., Pollack J., Veverka J., Lane A., and Ajello J. (1978) The composition of Phobos: Evidence for carbonaceous chondrite surface from spectral analysis. *Science*, 199, 64–66.
- Pascu D., Erard S., Thuillot W., and Lainey V. (2013) History of telescopic observations of the martian satellites. *Planet. Space Sci.*, 102, 2–8, DOI: 10.1016/j.pss.2013.07.006.
- Patsyn V., Andreev M., Malinnikov V., Grechishchev A., Pasewaldt A., and Oberst J. (2012) Spectrometric characteristics of the surface of Phobos from data obtained by HRSC on Mars Express. In *European Planet. Sci. Congr. 2012*, Madrid, Spain.
- Pätzold M., Andert T. P., Tyler G. L., Asmar S. W., Hausler B., and Tellmann S. (2013) Phobos mass determination from the very close flyby of Mars Express in 2010. *Icarus*, 229, 92–98, DOI: 10.1016/j.icarus.2013.10.021.
- Pieters C. M. et al. (2009) Character and spatial distribution of OH/H<sub>2</sub>O on the surface of the Moon seen by M<sup>3</sup> on Chandrayaan-1. *Science*, 326, 568–572, DOI: 10.1126/science.1178658.
- Pieters C. M., Murchie S., Thomas N., and Britt D. (2014) Composition of surface materials on the moons of Mars. *Planet. Space Sci.*, 102, 144–151, DOI: 10.1016/j.pss.2014.02.008.
- Pollack J. B., Veverka J., Noland M., Sagan C., Hartmann W. K., Duxbury T. C., Born G. H., Milton D. J., and Smith B. A. (1972) Mariner 9 television observations of Phobos and Deimos. *Icarus*, 17, 394–407.
- Pollack J. B., Veverka J., and Noland M. (1973) Mariner 9 television observations of Phobos and Deimos. *J. Geophys. Res.*, 78, 4313–4326.
- Pollack J. B., Veverka J., Pang K. D., Colburn D. S., Lane A. L., and Ajello J. M. (1978) Multicolor observations of Phobos with the Viking lander cameras — evidence for a carbonaceous chondritic composition. *Science*, 199, 66–69.
- Pollack J. B., Burns J. A., and Tauber M. E. (1979) Gas drag in primordial circumplanetary envelopes: A mechanism for satellite capture. *Icarus*, 37, 587–611.
- Quaide W. L. and Oberbeck V. R. (1968) Thickness determinations of the lunar surface layer from lunar impact craters. *J. Geophys. Res.*, 73, 5247.
- Rambaux N., Castillo-Rogez J. C., Le Maistre S., and Rosenblatt P. (2012) Rotational motion of Phobos. *Astron. Astrophys.*, 548, A14, DOI: 10.1051/0004-6361/201219710.
- Ramsley K. R. and Head J. W. (2013a) Mars impact ejecta in the regolith of Phobos: Bulk concentration and distribution. *Planet. Space Sci.*, 87, 115–129.
- Ramsley K. R. and Head J. W. (2013b) The origin of Phobos grooves from ejecta launched from impact craters on Mars: Tests of the hypothesis. *Planet. Space Sci.*, 75, 69–95.
- Ramsley K. R. and Head J. W. (2014) Constraints on the age of Stickney crater and associated features on Phobos. *Lunar Planet. Sci. XLV*, Abstract #1414. Lunar and Planetary Institute, Houston.
- Richardson J. E., Melosh H. J., Greenberg R. J., and O'Brien D.P. (2005) The global effects of impact-induced seismic activity on fractured asteroid surface morphology. *Icarus*, 179, 325–349.
- Rivkin A. S. and Emery J. P. (2010) Detection of ice and organics on an asteroidal surface. *Nature*, 464, 1322–1323.
- Rivkin A. S., Brown R. H., Trilling D. E., Bell J. F. III, and Plassmann J. H. (2002) Near-infrared spectrophotometry of Phobos and Deimos. *Icarus*, 156, 64–75, DOI: 10.1006/icar.2001.6767.
- Rivkin A. S., Milliken R. E., Emery J. P., Takir D., and Schmidt B. E. (2011) 2 Pallas and 10 Hygiea in the 3- $\mu\text{m}$  spectral region. In *EPSC-DPS Joint Meeting 2011*, p. 1271.
- Rosenblatt P. (2011) The origin of the martian moons revisited. *Astron. Astrophys. Rev.*, 19, 19–44.
- Rosenblatt P. and Charnoz S. (2012) On the formation of the martian moons from a circum-martian accretion disk. *Icarus*, 221, 806–815, DOI: 10.1016/j.icarus.2012.09.009.
- Roush T. L. and Hogan R. C. (2000) Mars Global Surveyor Thermal Emission Spectrometer observations of Phobos. *Lunar Planet. Sci. XXI*, Abstract #1598. Lunar and Planetary Institute, Houston.
- Roush T. L. and Hogan R. C. (2001) Compositional variability associated with Stickney Crater on Phobos. *Lunar Planet. Sci. XXII*, Abstract #1915. Lunar Planetary Institute, Houston.
- Safronov V. S., Pechernikova G. V., Ruskol E. L., and Vitjazev A. V. (1986) Protosatellite swarms. In *Satellites* (J. A. Burns and M. S. Matthews, eds.), pp. 89–116. Univ. of Arizona, Tucson.
- Sagdeev R. Z. and Zakharov A. V. (1989) Brief history of the Phobos mission. *Nature*, 341, 581–585.
- Sasaki S. (1990) Origin of Phobos — aerodynamic drag capture by the primary atmosphere of Mars. *Lunar Planet. Sci. XXI*, pp. 1069–1070. Lunar and Planetary Institute, Houston.
- Sasaki S. (1996) Phobos and Deimos as sources of martian dust ring/torus. *Lunar Planet. Sci. XXVII*, pp. 1127–1128. Lunar and Planetary Institute, Houston.
- Schmedemann N., Michael G. G., Ivanov B. A., Murray J., and Neukum G. (2013) Crater retention ages of Phobos based on a lunar-like chronology. *Lunar Planet. Sci. XLIV*, Abstract #2193. Lunar and Planetary Institute, Houston.
- Schmedemann N., Michael G. G., Ivanov B. A., Murray J., and Neukum G. (2014) The age of Phobos and its largest crater Stickney. *Planet. Space Sci.*, 102, 152–163.
- Schultz P. H. and Crawford D. A. (1989) Grooves on Phobos: Evidence for an ancient ring around Mars. *Bull. Am. Astron. Soc.*, 21, 932.
- Schultz P. H. and Lutz-Garihan A. B. (1982) Grazing impacts on Mars: A record of lost satellites. *Proc. Lunar Sci. Conf. 13th*, in *J. Geophys. Res.*, 87, A84–A96.
- Sharpless B. (1945) Secular accelerations in the longitudes of the satellites of Mars. *Astron. J.*, 51, 185–186.
- Sheppard S. S., Jewitt D., and Kleyna J. (2004) A survey for outer satellites of Mars: Limits to completeness. *Astrophys. J.*, 128, 2542–2546.

- Shi X., Willner K., Oberst J., Ping J. S., and Ye S. H. (2012) Working models for the gravitational field of Phobos. *Sci. China Phys. Mech. Astron.*, 55, 358–364.
- Showalter M. R., Hamilton D. P., and Nicholson P. D. (2006) A deep search for martian-dust rings and inner moons using the Hubble Space Telescope. *Planet. Space Sci.*, 54, 844–854.
- Simonelli D. P., Wisz M., Switala A., Adinolfi D., Veverka J., Thomas P. C., and Helfenstein P. (1998) Photometric properties of Phobos surface materials from Viking images. *Icarus*, 131, 52–77.
- Singer S. F. (1966) On the origin of the martian satellites Phobos and Deimos. In *Moon and Planets* (A. Dollfus, ed.), pp. 317–321. COSPAR Seventh Intl. Space Sci. Symp., Vienna.
- Singer S. F. (2007) Origin of the martian satellites Phobos and Deimos. In *First International Conference on the Exploration of Phobos and Deimos*, Abstract #7020. Lunar and Planetary Institute, Houston.
- Smith B. A. (1970) Phobos: Preliminary results from Mariner 7. *Science*, 168, 828–830.
- Soter S. L. (1971) *The Dust Belts of Mars*. Report 462, Center for Radiophysics and Space Research, Cornell Univ., Ithaca, New York.
- Soter S. and Harris A. (1977) Are striations on Phobos evidence for tidal stress? *Nature*, 268, 421–422.
- Squyres S. et al. (2011) *Vision and Voyages for Planetary Science in the Decade 2013–2022*. National Academies, Washington, DC.
- Stooke P. J. (2011) New photomaps of Phobos, Deimos, Itokawa, Steins, Wild 2 and Tempel 1. *Lunar Planet. Sci. XLII*, Abstract #1312. Lunar and Planetary Institute, Houston.
- Sullivan R. et al. (1996) Geology of 243 Ida. *Icarus*, 120, 119–139.
- Sunshine J. M. et al. (2009) Temporal and spatial variability of lunar hydration as observed by the Deep Impact spacecraft. *Science*, 326, 565–568, DOI: 10.1126/science.1179788.
- Szeto A. M. K. (1983) Orbital evolution and origin of the martian satellites. *Icarus*, 55, 133–168.
- Takir D., Emery J. P., McSween H. Y., Hibbitts C. A., Clark R. N., Pearson N., and Wang A. (2013) Nature and degree of aqueous alteration in CM and CI carbonaceous chondrites. *Meteoritics & Planet. Sci.*, 48, 1618–1637, DOI: 10.1111/maps.12171.
- Thomas N., Stelter R., Ivanov A., Bridges N. T., Herkenhoff K. E., and McEwen A. S. (2011) Spectral heterogeneity on Phobos and Deimos: HiRISE observations and comparisons to Mars Pathfinder results. *Planet. Space Sci.*, 59, 1281–1292, DOI: 10.1016/j.pss.2010.04.018.
- Thomas N. et al. (2012) The geomorphology of 21 Lutetia: Results from the OSIRIS imaging system onboard ESA's Rosetta spacecraft. *Planet. Space Sci.*, 66, 96–124.
- Thomas P. (1979) Surface features of Phobos and Deimos. *Icarus*, 40, 223–243.
- Thomas P. C. (1989) The shapes of small satellites. *Icarus*, 77, 248–274.
- Thomas P. C. (1993) Gravity, tides, and topography on small satellites and asteroids — Application to surface features of the martian satellites. *Icarus*, 105, 326.
- Thomas P. C. (1998) Ejecta emplacement on the martian satellites. *Icarus*, 131, 78–106.
- Thomas P. C. (1999) Large craters on small objects: Occurrence, morphology, and effects. *Icarus*, 142, 89–96.
- Thomas P. and Veverka J. (1980) Downslope movement of material on Deimos. *Icarus*, 42, 234–250.
- Thomas P., Veverka J., Bloom A., and Duxbury T. (1979) Grooves on Phobos — Their distribution, morphology and possible origin. *J. Geophys. Res.*, 84, 8457–8477.
- Thomas P., Veverka J., Bell J., Lunine J., and Cruikshank D. (1992) Satellites of Mars — Geologic history. In *Mars* (H. H. Kieffer et al., eds.), pp. 1257–1282. Univ. of Arizona, Tucson.
- Thomas P. C., Adinolfi D., Helfenstein P., Simonelli D., and Veverka J. (1996) The surface of Deimos: Contribution of materials and processes to its unique appearance. *Icarus*, 123, 536–556.
- Thomas P. C., Veverka J., Sullivan R., Simonelli D. P., Malin M. C., Caplinger M., Hartmann W. K., and James P. B. (2000) Phobos: Regolith and ejecta blocks investigated with Mars Orbiter Camera images. *J. Geophys. Res.*, 105, 15091–15106.
- Tsiganis K., Gomes R., Morbidelli A., and Levison H. F. (2005) Origin of the orbital architecture of the giant planets of the solar system. *Nature*, 435, 459–461.
- Vanicek P. and Krakiwsky E. J. (1986) *Geodesy: The Concepts*, 2nd edition. Elsevier, New York.
- Veverka J. and Burns J. A. (1980) The moons of Mars. *Annu. Rev. Earth Planet. Sci.*, 8, 527–558.
- Veverka J. and Duxbury T. C. (1977) Viking observations of Phobos and Deimos — Preliminary results. *J. Geophys. Res.*, 82, 4213–4223.
- Veverka J., Thomas P., Simonelli D., Belton M. J. S., Carr M., Chapman C., Davis M. E., Greeley R., Greenberg R., and Head J. (1994) The discovery of grooves on Gaspra. *Icarus*, 107, 72–83.
- Vilas F. (1994) A cheaper, faster, better way to detect water of hydration on solar system bodies. *Icarus*, 111, 456–467, DOI: 10.1006/icar.1994.1156.
- Vilas F. and Gaffey M. (1989) Phyllosilicate absorption features in main-belt and outer-belt asteroid reflectance spectra. *Science*, 246, 790–792, DOI: 10.1126/science.246.4931.790.
- Vilas F., Larson S. M., Hatch E. C., and Jarvis K. S. (1993) CCD reflectance spectra of selected asteroids. II. Low-albedo asteroid spectra and data extraction techniques. *Icarus*, 105, 67–78, DOI: 10.1006/icar.1993.1111.
- Vilas F., Jarvis K. S., and Gaffey M. J. (1994) Iron alteration minerals in the visible and near-infrared spectra of low-albedo asteroids. *Icarus*, 109, 274–283, DOI: 10.1006/icar.1994.1093.
- Viviano-Beck C. E., Seelos F. P., Murchie S. L., Kahn E. G., Seelos K. D., Taylor H. W., Taylor K., Ehlmann B. L., Wiseman S. M., Mustard J. F., and Morgan M. F. (2014) Revised CRISM spectral parameters and summary products based on the currently detected mineral diversity on Mars. *J. Geophys. Res.—Planets*, 119, 1403–1431, DOI: 10.1002/2014JE004627.
- Wanke H. and Dreibus G. (1988) Chemical composition and accretion history of terrestrial planets. *Philos. Trans. R. Soc. London Ser. A*, 325, 545.
- Weidenschilling S. J. (1979) A possible origin for the grooves on Phobos. *Nature*, 282, 697–698.
- Willkison S., Robinson M., Thomas P., Veverka J., McCoy T., Murchie S., Prockter L., and Yeomans D. (2002) An estimate of Eros's porosity and implications for internal structure. *Icarus*, 155, 94–103.
- Willner K., Oberst J., Hussmann H., Giese B., Hoffmann H., Matz K.-D., Roatsch T., and Duxbury T. (2010) Phobos control point network, rotation, and shape. *Earth Planet. Sci. Lett.*, 294, 541–546.
- Willner K., Shi X., and Oberst J. (2014) Phobos' shape and topography models. *Planet. Space Sci.*, 102, 52–59, DOI: 10.1016/j.epsl.2009.07.033.
- Wilson L. and Head J. W. III (2005) Dynamics of groove formation on Phobos by ejecta from Stickney crater: Predictions and tests. *Lunar Planet. Sci. XXXVI*, Abstract #1186. Lunar and Planetary Institute, Houston.
- Witasse O., Duxbury T., Chicarro A., Altobelli N., Andert T., Aronica A., Barabash S., Bertaux J.-L., Bibring J.-P., Cardesin-Moinelo A., Cicchetti A., Companys V., Dehant V., Denis M., Formisano V., Futaana Y., Giuranna M., Gondet B., Heather D., Hoffmann H., Holmstrom M., Manaud N., Martin P., Matz K.-D., Montmessin F., Morley T., Muelle M., Neukum G., Oberst J., Orosei R., Pätzold M., Picardi G., Pischel R., Plaut J. J., Reberac A., Pardo Voss P., Roatsch T., Rosenblatt P., Remus S., Schmedemann N., Willner K., and Zegers T. (2013) Mars Express investigations of Phobos and Deimos. *Planet. Space Sci.*, 102, 9–17.
- Zakharov A., Horanyi M., Lee P., Witasse O., and Cipriani F. (2014) Dust at the martian moons and in the circummartian space. *Planet. Space Sci.*, 102, 171–175.
- Zellner B. (1972) Minor planets and related objects. VIII. Deimos. *Astron. J.*, 77, 183–185.
- Zellner B. H. and Capen R. C. (1974) Photometric properties of the martian satellites. *Icarus*, 23, 437–444.



*Part 4:*

*Evolutionary Processes*



# New Paradigms for Asteroid Formation

**Anders Johansen**

*Lund University*

**Emmanuel Jacquet**

*Canadian Institute for Theoretical Astrophysics, University of Toronto*

**Jeffrey N. Cuzzi**

*NASA Ames Research Center*

**Alessandro Morbidelli**

*Lagrange Laboratory, Université Côte d'Azur, Observatoire de la Côte d'Azur, CNRS*

**Matthieu Gounelle**

*Muséum National d'Histoire Naturelle, Institut Universitaire de France*

---

Asteroids and meteorites provide key evidence on the formation of planetesimals in the solar system. Asteroids are traditionally thought to form in a bottom-up process by coagulation within a population of initially kilometer-scale planetesimals. However, new models challenge this idea by demonstrating that asteroids of sizes from 100 to 1000 km can form directly from the gravitational collapse of small particles that have organized themselves in dense filaments and clusters in the turbulent gas. Particles concentrate passively between eddies down to the smallest scales of the turbulent gas flow and inside large-scale pressure bumps and vortices. The streaming instability causes particles to take an active role in the concentration, by piling up in dense filaments whose friction on the gas reduces the radial drift compared to that of isolated particles. In this chapter we review new paradigms for asteroid formation and critically compare them against the observed properties of asteroids as well as constraints from meteorites. Chondrules of typical sizes from 0.1 to 1 mm are ubiquitous in primitive meteorites and likely represent the primary building blocks of asteroids. Chondrule-sized particles are nevertheless tightly coupled to the gas via friction and are therefore hard to concentrate in large amounts in the turbulent gas. We review recent progress on understanding the incorporation of chondrules into the asteroids, including layered accretion models where chondrules are accreted onto asteroids over millions of years. We highlight in the end 10 unsolved questions in asteroid formation where we expect that progress will be made over the next decade.

## 1. INTRODUCTION

The solar system contains large populations of pristine planetesimals that have remained relatively unchanged since their formation. Our proximity to the asteroid belt provides astronomers, planetary scientists, and cosmochemists access to extremely detailed data about asteroid compositions, sizes, and dynamics. Planetesimals are the building blocks of both terrestrial planets and the cores of the giant planets, as well as the super-Earths (with various degrees of gaseous envelopes) that are now known to orbit around a high fraction of solar-type stars (Fressin *et al.*, 2013). The formation of planetesimals is thus a key step toward the assembly of planetary systems, but many aspects of the planetesimal formation process remain obscure.

Recent progress in understanding planetesimal formation was triggered by two important realizations. The first is that macroscopic dust particles (millimeter or larger) have poor sticking properties. Laboratory experiments and coagulation models show that it is difficult to form planetesimals by direct sticking of silicate particles, most importantly because particle growth stalls at millimeter sizes where the particles bounce off each other rather than stick (Güttler *et al.*, 2010). While some particle growth is still possible at relatively high collision speeds, due to the net transfer of mass from small impactors onto large targets (Wurm *et al.*, 2005; Windmark *et al.*, 2012a), the resulting growth rate is too low to compete with the radial drift of the particles.

The second important realization is that particles are concentrated to very high densities in the turbulent gas flow.

This idea is not new — *Whipple* (1972) already proposed that large-scale pressure bumps can trap particles, as their radial drift speed vanishes in the pressure bump where the radial pressure gradient is zero. However, the advent of supercomputing led to the discovery and exploration of a large number of particle concentration mechanisms. Large-scale axisymmetric pressure bumps, akin to those envisioned by *Whipple* (1972), have been shown to arise spontaneously in simulations of protoplanetary disk turbulence driven by the magnetorotational instability (*Johansen et al.*, 2009a; *Simon et al.*, 2012). Particle densities reach high enough values inside these pressure bumps to trigger gravitational collapse to form planetesimals with sizes up to several 1000 km (*Johansen et al.*, 2007, 2011; *Kato et al.*, 2012). The baroclinic instability, which operates in the absence of coupling between gas and magnetic field, leads to the formation of slowly overturning large-scale vortices (*Klahr and Bodenheimer*, 2003), which can act as dust traps in a similar way as pressure bumps (*Barge and Sommeria*, 1995).

In the streaming instability scenario the particles play an active role in the concentration (*Youdin and Goodman*, 2005). The relative motion between gas and particles is subject to a linear instability whereby axisymmetric filaments of a slightly increased particle density accelerate the gas toward the Keplerian speed and hence experience reduced radial drift. This leads to a runaway pileup of fast-drifting, isolated particles in these filaments (*Johansen and Youdin*, 2007). The densities achieved can be as high as 10,000× the local gas density (*Bai and Stone*, 2010; *Johansen et al.*, 2012), leading to the formation of planetesimals with characteristic diameters of 100–200 km for particle column densities relevant for the asteroid belt, on a timescale of just a few local orbital periods.

A concern about large-scale particle concentration models is that typically very large particles are needed for optimal concentration (at least decimeter in size when the models are applied to the asteroid belt). Chondrules of typical sizes from 0.1 to 1 mm are ubiquitous in primitive meteorites, but such small particles are very hard to concentrate in vortices and pressure bumps or through the streaming instability. One line of particle concentration models has nevertheless been successful in concentrating chondrules. Swiftly rotating low-pressure vortex tubes expel particles with short friction times (*Squires and Eaton*, 1990, 1991; *Wang and Maxey*, 1993). This was proposed to explain the characteristic sizes and narrow size ranges of chondrules observed in different chondrites (*Cuzzi et al.*, 2001) and leads to the formation of 100-km-scale asteroids from rare high-density concentrations (*Cuzzi et al.*, 2008, 2010). However, the evaluation of the probability for such high-density concentrations to occur over sufficiently large scales depends on scaling computer simulations to the very large separations between the energy injection scale and the dissipation scale relevant for protoplanetary disks; *Pan et al.* (2011) found that the particle clustering gets less contribution from the addition of consecutively larger scales than originally thought in the model of *Cuzzi et al.* (2008, 2010).

Therefore the incorporation of chondrules into the asteroids is still an unsolved problem in asteroid formation. This is one of the main motivations for this review. We refer the readers to several other recent reviews on the formation of planetesimals that provide a broader scope of the topic beyond asteroid formation (e.g., *Cuzzi and Weidenschilling*, 2006; *Chiang and Youdin*, 2010; *Johansen et al.*, 2014).

The review is organized as follows. The first two sections discuss the constraints on asteroid formation from the study of meteorites (section 2) and asteroids (section 3). In section 4 we review laboratory experiments and computer simulations of dust coagulation to illustrate the formidable barriers that exist to planetesimal formation by direct sticking. The turbulent concentration model, in which chondrule-sized particles are concentrated at the smallest scales of the turbulent gas flow, is discussed in section 5. Section 6 is devoted to particle concentration in large-scale pressure bumps and through streaming instabilities. In section 7 we discuss layered accretion models where the chondrules are accreted onto planetesimals over millions of years. Finally, in section 8 we pose 10 open questions regarding the formation of asteroids on which we expect major progress in the next decade.

## 2. CONSTRAINTS FROM METEORITES

Meteorites provide a direct view of the solid material from which the asteroids accumulated, while the crystallization ages of the component particles and the degree of heating and differentiation of the parent bodies give important information about the timescales for planetesimal formation in the solar system.

Meteorites may be broadly classified in two categories (*Weisberg et al.*, 2006): primitive meteorites (also known as chondrites) and differentiated meteorites. Chondrites, which make up 85% of the observed falls, are basically collections of millimeter- and submillimeter-sized solids, little modified since agglomeration and lithification (compression) in their parent bodies. They exhibit nonvolatile element abundances comparable to the solar photosphere's (*Palme and Jones*, 2005). Differentiated meteorites derive from parent bodies that underwent significant chemical fractionations on the scale of the parent body, resulting in the asteroid-wide segregation of an iron core and silicate mantle and crust. In the process, differentiated meteorites have lost not only their accretionary (presumably chondritic) texture, but also their primitive chemical composition; depending on which part of the parent body they sample, some may be essentially pure metal (the iron meteorites) while others are essentially metal-free (the achondrites).

It is among the components of chondrites that the oldest solids of the solar system, the refractory inclusions (*Krot et al.*, 2004; *MacPherson*, 2005), in particular calcium-aluminium-rich inclusions (CAIs), have been identified. Their age of  $4567.3 \pm 0.16$  m.y. (*Connelly et al.*, 2012) marks the commonly accepted “time zero” of the solar system. But the ubiquitous components of chondrites are the eponymous

chondrules (*Hewins et al.*, 2005; *Connolly and Desch*, 2004), which are millimeter-sized silicate spherules presumably resulting from transient (and repeated) high-temperature episodes in the disk, but whose very nature remains a longstanding cosmochemical and astrophysical enigma (*Boss*, 1996; *Desch et al.*, 2012). All these components are set in a fine-grained matrix consisting of amorphous and crystalline grains native to the disk as well as rare presolar grains (*Brearley*, 1996). While compositionally primitive, chondrites may have undergone some degree of thermal metamorphism, aqueous alteration, and shock processing on their parent body.

Despite their general petrographic similarity and roughly solar composition, chondrites are actually quite variable, and 14 distinct chemical groups have been recognized so far, each of which is believed to represent a single parent body — sometimes with supporting evidence from cosmic-ray exposure ages (*Eugster et al.*, 2006) — or at least a family of parent bodies formed in the same nebular reservoir (i.e., a compositionally distinctive space-time section of the disk). There are various levels of affinities between these groups (e.g., clans, classes) but we will be content here to distinguish carbonaceous chondrites (henceforth “CCs,” comprising the CI, CM, CO, CV, CK, CR, CH, and CB groups) from noncarbonaceous chondrites [henceforth “EORs,” as they include the enstatite (EH, EL), ordinary (H, L, LL), and Rumuruti (R) chondrite groups]. Carbonaceous chondrites are more primitive in the sense that they have a solar Mg/Si ratio and a  $^{16}\text{O}$ -rich oxygen isotopic composition closer to that of the Sun (e.g., *Scott and Krot*, 2003). Noncarbonaceous chondrites, although poorer in refractory elements, are more depleted in volatile elements, have sub-solar Mg/Si ratios and a more terrestrial isotopic composition for many elements (*Trinquier et al.*, 2009). EORs have generally undergone thermal metamorphism (see Fig. 1), while aqueous alteration has been prevalent in CCs (*Huss et al.*, 2006; *Brearley*, 2003), but again there are exceptions.

## 2.1. Primary Texture and Aerodynamic Sorting

The texture of most chondrites has been reworked by impact fragmentation and erosion on their parent body. However, rare pieces of CM and CO chondrites have been found, referred to as “primary texture” (*Metzler et al.*, 1992; *Brearley*, 1993), which seem to retain the nature of a prebrecciated body. Primary texture appears to consist of nothing but dust-rimmed chondrules of very similar properties, loosely pressed together.

The constituents of most chondrites appear well-sorted by size, with strong mean size differences from one group to another (*Brearley and Jones*, 1998). Whether these differences arise from some regionally or temporally variable bouncing-barrier (*Jacquet*, 2014a), some aerodynamic sorting process (sections 5 and 7), or some aspect of the mysterious chondrule-formation process itself, they provide an important clue to primary accretion. *Hezel et al.* (2008) have emphasized the need for better particle counting statistics, and indeed one recent chondrule size distribution measurement

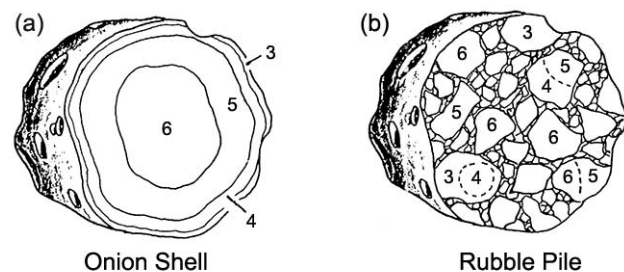


**Fig. 1.** (a) Initial state of a parent body with a radius of 100 km, which was initially homogeneous throughout, after heating by  $^{26}\text{Al}$ . The proportions of the least (3) to most (6) altered material are constrained by meteorite statistics. (b) The same body after catastrophic fragmentation and reassembly as a rubble pile with some highly altered material now near the surface. This body is then cratered by subsequent impacts, releasing samples of all metamorphic grades (adapted from *Scott and Rajan*, 1981).

taken from Allende, of a far larger sample than analyzed previously (*Fisher et al.*, 2014), points to a distribution substantially broader for that chondrite than previously reported.

Aerodynamic sorting has been suggested often as an important factor in selecting for the contents of primary texture (see *Cuzzi and Weidenschilling*, 2006, for a review). Comparing the aerodynamical friction time of objects of greatly different density, such as silicate and metal grains, shows that their friction times are quite similar in the least-altered meteorites (*Dodd*, 1976; *Kuebler et al.*, 1999), suggesting that asteroids selectively incorporated components with specific aerodynamical properties (we discuss this further in section 3.3).

## 2.2. The Abundance and Distribution of Aluminum-26 and Iron-60

The melting of the parent bodies of differentiated meteorites puts important constraints on the timescale for planetesimal formation in the asteroid belt. While electromagnetic heating (*Sonett and Colburn*, 1968) or impact heating (*Keil et al.*, 1997) have been considered in the literature, the most likely source of planetesimal heating is the decay of the short-lived radionuclides (SLRs)  $^{26}\text{Al}$  (with mean lifetime  $\tau = 1.0$  m.y.) and  $^{60}\text{Fe}$  ( $\tau = 3.7$  m.y.) (*Urey*, 1955). Depending on their respective initial abundance, and on the time of planetesimal accretion, both could have significantly contributed to planetesimal heating. Additionally, short-lived nuclides provide crystallization ages that can be calibrated using a long-lived radionuclide decay system such as Pb-Pb, under the assumption that the short-lived radionuclide was homogeneously distributed in the solar protoplanetary disk.

The content of SLRs in CAIs is usually identified with that of the nascent solar system (*Dauphas and Chaussidon*, 2011). Excesses of  $^{26}\text{Mg}$  linearly correlating with  $^{27}\text{Al}$  content were first observed in an Allende CAI in 1976 (*Lee et al.*,

1976). This isochron diagram demonstrated the presence of  $^{26}\text{Al}$  in the nascent solar system. The CAIs from a diversity of chondrite groups formed with an initial  $(^{26}\text{Al}/^{27}\text{Al})_0$  of roughly  $5 \times 10^{-5}$  (MacPherson *et al.*, 2014). A remarkably tight isochron for CAIs in the CV chondrites was obtained by Jacobsen *et al.* (2008). The deduced  $(^{26}\text{Al}/^{27}\text{Al})_0$  ratio of  $(5.23 \pm 0.13) \times 10^{-5}$  is often considered as the initial value for the solar system and the small dispersion as indicative of a narrow formation interval ( $\leq 40,000$  yr). However, this interpretation should be limited to the region where the unusually large CV CAIs have formed (Krot *et al.*, 2009). This is especially true since many CAIs are known to have formed without any  $^{26}\text{Al}$  (Liu *et al.*, 2012; Makide *et al.*, 2013). This indicates some level of heterogeneity in the  $^{26}\text{Al}$  distribution within the region where CAIs formed (assuming that region was unique, which is supported by the ubiquitous  $^{16}\text{O}$  enrichment of CAIs compared to, e.g., chondrules). Larsen *et al.* (2011) used bulk magnesium isotopic measurements to suggest that the heterogeneity of  $^{26}\text{Al}$  distribution might have reached 80% of the canonical value in the solar protoplanetary disk. However, Kita *et al.* (2013) and Wasserburg *et al.* (2012) argue that the observed variations can be better ascribed to small heterogeneities in the stable isotope  $^{26}\text{Mg}$ .

Although the presence of live  $^{60}\text{Fe}$  in the early solar system was demonstrated almost 20 years ago (Shukolyukov and Lugmair, 1993), the determination of the solar system initial abundance is complicated by the difficulty of obtaining good isochrons for CAIs (Quitté *et al.*, 2007), given their low abundance in Ni. To bypass that difficulty, most measurements were performed on chondrules that are believed to have formed from around the same time as CAIs up to 3 m.y. later (Connelly *et al.*, 2012). High initial  $(^{60}\text{Fe}/^{56}\text{Fe})_0$  ratios were originally reported in chondrules from unequilibrated ordinary chondrites (UOC), which experienced very little heating or aqueous alteration (e.g., Tachibana and Huss, 2003; Mostefaoui *et al.*, 2005; Tachibana *et al.*, 2006). Telus *et al.* (2012) showed that most of these previous data were statistically biased and that most chondrules do not show any Ni excesses indicative of the decay of  $^{60}\text{Fe}$ . The high values obtained in older publications could be due to statistical biases related to low counts (Telus *et al.*, 2012) or to thermal metamorphism, which would have led to the redistribution of Ni isotopes (Chaussidon and Barat, 2009). Recently, improved techniques for measuring bulk chondrules in unequilibrated ordinary chondrites have yielded initial solar system values for  $(^{60}\text{Fe}/^{56}\text{Fe})_0$  of  $\approx 1 \times 10^{-8}$  (Tang and Dauphas, 2012; Chen *et al.*, 2013). This value is consistent with that inferred from Fe-Ni isotope measurements of a diversity of differentiated meteorites (Quitté *et al.*, 2011; Tang and Dauphas, 2012).

In conclusion, it seems that most CAIs formed with an initial ratio  $(^{26}\text{Al}/^{27}\text{Al})_0$  of roughly  $5 \times 10^{-5}$ , which can be considered in a first approximation as the solar system average or typical initial value. Some heterogeneity was undoubtedly present, but its exact level is still unknown. On the other hand, it is likely that the initial  $(^{60}\text{Fe}/^{56}\text{Fe})_0$  of the solar system was lower than  $1 \times 10^{-8}$ , although high levels of  $^{60}\text{Fe}$  (up to  $10^{-6}$ )

have been detected in some components of chondrites. At the time of writing this review, there was no evidence of  $^{60}\text{Fe}$  heterogeneity within the solar protoplanetary disk.

### 2.3. The Origin of Aluminum-26 and Iron-60

The initial solar system ratio  $(^{26}\text{Al}/^{27}\text{Al})_0$  of roughly  $5 \times 10^{-5}$  is well above the calculated average galactic abundance (Huss *et al.*, 2009). This elevated abundance indicates a last-minute origin for  $^{26}\text{Al}$ . Production of  $^{26}\text{Al}$  by irradiation has been envisioned in different contexts (e.g., Lee, 1978; Gounelle *et al.*, 2006), but fails to produce enough  $^{26}\text{Al}$  relative to  $^{10}\text{Be}$  ( $\tau = 2.0$  m.y.), another SLR whose origin by irradiation is strongly supported by experimental data (Gounelle *et al.*, 2013). This leaves stellar delivery as the only possibility for  $^{26}\text{Al}$  introduction in the solar system. Although asymptotic giant branch stars produce elevated amounts of  $^{26}\text{Al}$  (Lugardo *et al.*, 2012), it is extremely unlikely that stars at this evolutionary stage are present in a star-forming region (Kastner and Myers, 1994). Thus massive stars are the best (unique) candidates for the origin of the solar system's  $^{26}\text{Al}$ .

The recently obtained lower estimates for the abundance of  $^{60}\text{Fe}$  (see section 2.2) are compatible with a galactic background origin, independently of whether this is calculated crudely using a box model (Huss *et al.*, 2009), or taking into account the stochastic nature of star formation in molecular clouds (Gounelle *et al.*, 2009). However, if the initial  $^{60}\text{Fe}$  abundance corresponds instead to a much higher  $(^{60}\text{Fe}/^{56}\text{Fe})_0$  ratio of  $\approx 10^{-6}$ , a last-minute origin is needed. Irradiation processes cannot account for  $^{60}\text{Fe}$  production because of its richness in neutrons (Lee *et al.*, 1998). The winds of massive stars can also be excluded, given their low abundance in  $^{60}\text{Fe}$ . In contrast, supernovae are copious producers of  $^{60}\text{Fe}$ , essentially because this SLR is synthesized in abundance during the hydrostatic and explosive phases of such massive stars (Woosley and Heger, 2007). Two astrophysical settings have been envisioned so far. In the first (classical) model (Cameron and Truran, 1977), the supernova ejecta hits a molecular cloud core and provokes its gravitational collapse (Boss and Keiser, 2013) as well as injecting  $^{60}\text{Fe}$  and other SLRs. A newer model injects  $^{60}\text{Fe}$  in an already formed protoplanetary disk (Hester *et al.*, 2004; Ouellette *et al.*, 2007). In either cases, the supernova progenitor mass is in the range  $20\text{--}60 M_{\odot}$ , because too-massive supernovae are extremely rare and very disruptive to their environment (Chevalier, 2000). Alternatively, generations of supernovae could have enriched the gas of the giant molecular cloud, so that the solar protoplanetary disk simply inherited the elevated abundances of the birth cloud (Vasiliadis *et al.*, 2013).

All these models suffer from an important difficulty, namely the overabundance of  $^{60}\text{Fe}$  in supernova ejecta relative to  $^{26}\text{Al}$ . The solar system  $^{60}\text{Fe}/^{26}\text{Al}$  mass ratio was either  $4 \times 10^{-3}$  or 0.4 depending on the adopted initial  $^{60}\text{Fe}$  abundance. In any case, this is well below the  $^{60}\text{Fe}/^{26}\text{Al}$  mass ratio predicted by supernovae nucleosynthetic models whose variation domain extends from 1.5 to 5.5 for a progenitor mass varying between 20 and  $60 M_{\odot}$ . Heterogeneity in

the composition of supernova ejecta has been proposed as a possible solution to that discrepancy (*Pan et al.*, 2012). However, that variability is limited to a factor of 4, which would help resolve the discrepancy only marginally in the case of the (unlikely) high  $^{60}\text{Fe}$  value. Finally, the astrophysical context of any supernova model is difficult to reconcile with observations of star-forming regions (*Williams and Gaidos*, 2007; *Gounelle and Meibom*, 2008). The commonly proposed setting for supernova contamination of a protoplanetary disk or a dense core is similar to that of the Orion Nebula, where disks are seen within a few tenths of parsec of the massive star  $\theta^1\text{ C Ori}$ . The problem with that setting is that, when  $\theta^1\text{ C Ori}$  will explode in 4 m.y. from now, these disks will have long evaporated or formed planets. New disks or cores will have obviously formed by then, but they will be at the outskirts of the 10-pc-wide H $\alpha$  region created by  $\theta^1\text{ C Ori}$  (*Chevalier*, 1999). At such a distance, the quantity of  $^{26}\text{Al}$  delivered into these disks or cores is orders of magnitude lower than the quantity present in the solar system (*Looney et al.*, 2006). In other words, supernova remnants nearby dense phases are extremely rare (*Tang and Chevalier*, 2014). In conclusion, it seems very unlikely that a nearby supernova was close enough to the solar system to provide the known inventory of  $^{26}\text{Al}$ .

If the low value of  $^{60}\text{Fe}$  inferred from chondrites is correct, then the presence of  $^{26}\text{Al}$  remains to be explained. Supernovae can be excluded as they would vastly overproduce  $^{60}\text{Fe}$  (see above). The winds of massive stars have long been known to be  $^{26}\text{Al}$  and  $^{60}\text{Fe}$ -poor (*Arnould et al.*, 1997). In the models of *Gaidos et al.* (2009) and *Young* (2014),  $^{26}\text{Al}$  is injected at the molecular cloud phase by the winds from a large number of Wolf-Rayet stars. The problem with these models is that the Wolf-Rayet phase is followed by the supernova explosion, and therefore they produce a large excess of  $^{60}\text{Fe}$  relative to  $^{26}\text{Al}$  and their respective solar system values. To escape that caveat, *Young* (2014) has argued that Wolf-Rayet stars do not explode as supernovae but directly collapse into black holes. Although this possibility has been theoretically envisioned, the recent observation of a Wolf-Rayet star going supernova shows this is far from being the rule (*Gal-Yam et al.*, 2014). In addition, models considering injection at the global molecular cloud phase cannot account for the observed heterogeneity of  $^{26}\text{Al}$  (see section 2.2).

The last class of models considered injection at the scale of single massive stars. *Tatischeff et al.* (2010) have envisioned a single star that escaped from its parent cluster and interacted with a neighboring molecular cloud, injecting  $^{26}\text{Al}$  through its dense wind. It is compromised again by the proximity of the Wolf-Rayet phase with the supernova phase. In addition, Wolf-Rayet stars are rare. In contrast, *Gounelle and Meynet* (2012) proposed that  $^{26}\text{Al}$  has been injected in a dense shell of mass  $\sim 1000\text{ M}_\odot$  collected by the wind of a massive star. Evolutionary models of rotating stars are used, so the injection in the shell starts as early as the entry of the star onto the main sequence, lasts for some million years, and ends well before the supernova explosion. When the collected shell has become dense enough and gravitationally

unstable, it collapses and a second generation of stars form that contain  $^{26}\text{Al}$ . Detailed calculations have shown that as long as the parent star, called “Coatlicue,” is more massive than  $M_{\min} = 32\text{ M}_\odot$ , the abundance of  $^{26}\text{Al}$  in the shell is equal to or larger than that of the solar system, depending on the mixing efficiency of the wind material with the shell. Because the mixing timescale of the dense shell is comparable to its collapse timescale, a certain level of  $^{26}\text{Al}$  heterogeneity is expected (*Gounelle and Meynet*, 2012), in agreement with observations. This model is in line with observations of induced star formation within dense shells around massive stars (*Deharveng et al.*, 2010). Because it corresponds to a common — although not universal — mode of star formation, it implies that the solar system is not the only of its kind to have formed with  $^{26}\text{Al}$ , and that early differentiation of planetesimals might have been common in exoplanetary systems. *Gounelle* (2014) has estimated that the occurrence of planetary systems that are rich in  $^{26}\text{Al}$  and poor in  $^{60}\text{Fe}$  is on the order of 1%.

#### 2.4. Timing of Planetesimal Accretion

Planetesimal accretion itself cannot be dated directly with radioisotopic systems, since the mere agglomeration of different solids incurs no isotopic rehomogenization between different mineral phases. Thus one can only obtain upper limits with the age-dating of preaccretionary components (for chondrites) and lower limits from that of secondary (parent body) processes.

Important and ever-improving constraints have emerged since the publication of *Asteroids III*. In particular, Hf-W systematics of achondrites and irons have evidenced early differentiation, sometimes contemporaneous (within errors) with refractory inclusion formation (*Kruijer et al.*, 2012). This indicates that planetesimal formation started very early in the evolution of the solar system. Intriguingly, *Libourel and Krot* (2007) ascribed some olivine aggregates in chondrites to this first generation of planetesimals [but see *Whattam et al.* (2008) and *Jacquet et al.* (2012a) for the alternative view that these formed in the protoplanetary disk]. The above evidence for early differentiation is consistent with thermal modeling expectations, as the initial abundance of  $^{26}\text{Al}$  was sufficient to melt planetesimals, so that chondrites had to be accreted later to be preserved to the present day.

Lower limits on chondrite accretion ages may be obtained from phases precipitated during aqueous alteration (see the chapter by Krot et al. in this volume). *Fujiya et al.* (2013) obtained ages of 4562.5–4563.8 m.y. in CI and CM chondrites [recall the accepted age of CAI formation of  $4567.3 \pm 0.16$  m.y. (*Connelly et al.*, 2012)]. As for non-carbonaceous chondrites, recent Mn-Cr dating of fayalite formed during incipient fluid-assisted metamorphism in the least-metamorphosed LL ordinary chondrites yields an age of  $4564.9^{+1.3}_{-1.8}$  m.y. (*Doyle et al.*, 2014). Al-Mg systematics in the mildly metamorphosed H chondrite Sainte Marguerite indicate an age of  $4563.1 \pm 0.2$  m.y. (*Zinner and Göpel*, 2002). Thermal modeling based on  $^{26}\text{Al}$  heating of

the H-chondrite parent body (one of the ordinary chondrite groups) constrained by dating of chondrites of different metamorphic degrees indicate accretion ages ranging from 1.8 to 2.7 m.y. after refractory inclusions (see *Gail et al.*, 2014, and references therein), while *Fujiya et al.* (2013) advocate accretion of CI and CM chondrites 3–4 m.y. after “time zero” based on similar calculations. If  $^{26}\text{Al}$  really is the heat source behind chondrite alteration, then it would indeed make sense that carbonaceous chondrites, little affected by thermal metamorphism, accreted later than their noncarbonaceous counterparts (*Grimm and McSween*, 1993).

Upper limits are provided by the ages of chondrules. In both carbonaceous and noncarbonaceous chondrites, chondrule Pb-Pb ages in individual meteorites span a range of ~4564–4567 m.y. (*Connelly et al.*, 2012), i.e., 0–3 m.y. after refractory inclusions, with younger ages reported by Al-Mg dating for CR (*Kita and Ushikubo*, 2012) and enstatite chondrite (*Guan et al.*, 2006) chondrules. Little correlation is seen between the age of chondrules and their composition (*Villeneuve et al.*, 2012). The significance of Al-Mg ages for chondrules, in particular in relationship with apparently somewhat older Pb-Pb ages (e.g., *Connelly et al.*, 2012), nevertheless remains uncertain.

To summarize, it seems clear that differentiated planetesimals accreted from the outset of the disk evolution while the known chondrites accreted later in the evolution of the disk (~2–4 m.y. after refractory inclusions), as presumably required to escape differentiation, but the exact chronology of chondrite formation and alteration is still in the process of being firmly established.

## 2.5. Accretion of Chondrules Directly After Formation?

*Alexander et al.* (2008) proposed that the retention of sodium, a volatile element, in chondrules during their formation indicated high solid densities in the chondrule-forming regions, up to 7 orders of magnitude above expectations for the solar protoplanetary disk and possibly gravitationally bound (see also *Cuzzi and Alexander*, 2006), although quite in excess of what the proportion of compound chondrules suggest (*Ciesla et al.*, 2004). This raises the possibility that the formation of chondrules and chondrites, respectively, may have been contemporaneous, as also advocated by *Metzler* (2012) based on the existence of “cluster chondrites” comprised of mutually indented chondrules [but see *Rubin and Brearley* (1996) for a criticism of such hot accretion models].

A further argument put forward by *Alexander and Ebel* (2012) is that chondrule populations in different chondrite groups are quite distinct (*Jones*, 2012). Indeed, *Cuzzi et al.* (2010) noted that two populations of particles formed simultaneously at 2 and 4 AU would be well-mixed within 1 m.y. for  $\alpha = 10^{-4}$ . Here  $\alpha$  is the nondimensional measure of the turbulent viscosity and diffusion. Relevant values for protoplanetary disks are discussed further in section 6, but we note here that a value of  $10^{-4}$  corresponds to the conditions that are expected if the mid-plane in the asteroid formation

region is stirred by turbulent surface layers (*Oishi et al.*, 2007). This would suggest that chondrules had to accrete rapidly to avoid homogenization. However, we do not know exactly the turbulence level or original space time separations between chondrule-/chondrite-forming locations, as the asteroid belt may have undergone significant reshuffling (*Walsh et al.*, 2011). Chondrite groups vary significantly in bulk composition. This indicates that there has been no thorough mixing of chondrite components, whatever their individual transformations in the intervening time were, over the whole chondrite-formation timescale. So whatever fraction of that time the period between chondrule formation and chondrite accretion actually represents, it is not to be expected that chondrules should have been well-mixed over the different chondrite-forming reservoirs (*Jacquet*, 2014b).

A link between chondrules and matrix is suggested, in the case of carbonaceous chondrites, by complementarity: The bulk meteorite is solar in some respect (e.g., the Mg/Si ratio), but its separate components (chondrules/matrix/refractory inclusions) are not [chondrules have a typically higher Mg/Si than solar while the converse is true for the matrix (*Hezel and Palme*, 2010)]. Complementarity—if verified, as for at least some elements it may reflect analytical biases or parent-body processes (*Zanda et al.*, 2012)—would indicate a genetic relationship between chondrules and matrix, which would have exchanged chemical elements upon formation, a relationship that would not be predicted, e.g., in an X-wind scenario for chondrule formation (*Hezel and Palme*, 2010) in which chondrules and matrix would have formed in different locations. But it does not require immediate accretion of chondrule and matrix. It only requires chondrules and dust grains to have been transported in a statistically similar way, as was likely the case for a large portion of the disk evolution until accretion. Several batches of chondrule + dust may have contributed to a given chondrite-forming reservoir, again provided they suffered no loss of chondrules relative to dust or vice versa (*Cuzzi et al.*, 2005; *Jacquet et al.*, 2012b). This nonetheless does assume that at the stage of chondrule/matrix agglomeration, there was no bias for or against the incorporation of any component (*Jacquet*, 2014a), which may be an important constraint on the accretion process. The problem is that small dust grains are much harder to incorporate into asteroidal bodies than the macroscopic chondrules, due to their strong frictional coupling with the gas. One could nevertheless envision that chondrules and matrix aggregated together as compound objects (see section 4.2.5) prior to incorporation in asteroidal bodies and/or that matrix-sized dust coagulated with ice into lumps with aerodynamical properties equivalent to chondrules.

So the jury is still out on whether chondrule formation immediately preceded incorporation in a chondrite or not. Given the chondrule age spread of 3 m.y. within individual chondrites (*Connelly et al.*, 2012), as well as the presence of refractory inclusions and presolar grains that would not have survived chondrule-forming events, it is possible that chondrite components did spend up to a few million years as free-floating particles in the gaseous disk prior to accretion.

### 3. CONSTRAINTS FROM THE ASTEROID BELT

The modern asteroid belt contains only a fraction of its original planetesimal population. However, the shape of the size distribution of the largest asteroids is primordial and gives important insights into the birth sizes of the planetesimals. Asteroid families provide a way to probe whether the asteroids are internally homogeneous or heterogeneous on large scales.

#### 3.1. Asteroid Size Distribution

The observed size distribution of asteroids in the main belt shows a quite steep slope for bodies with diameter  $D > 100$  km and a much shallower slope for smaller bodies (Bottke et al., 2005). A similar change of slope with an elbow at  $D \sim 130$  km is observed in the Kuiper belt population (Fraser et al., 2014).

It was expected that the transition from a steep to a shallower slope is the consequence of the collisional disruption of smaller bodies. However, Bottke et al. (2005) reached the opposite conclusion by examining the collisional evolution of the asteroid belt in detail. They used a number of constraints (the total number of catastrophic asteroid families, the survival of the basaltic crust on Vesta, the existence of only 1–2 major basins on that body, etc.) to conclude that the integrated collisional activity of the asteroid belt had to be less than that of the current main-belt population in a putative timespan of 10 G.y. If one supposes that initially the asteroid belt size distribution had a unique slope (the slope now observed for  $D > 100$  km), such a limited collisional evolution is not sufficient to reduce the slope of the size distribution of objects smaller than 100 km down to the observed value, i.e., to create the observed elbow. Therefore, Bottke et al. (2005) concluded that the elbow at  $D \sim 100$  km is a fossil feature of the primordial size distribution. For the Kuiper belt, the constraints on the integrated collisional activity are not as tight as for the asteroid belt. Nevertheless, models seem to suggest that collisional evolution alone could not create an elbow at diameters larger than 8 km (Pan and Sari, 2005), which is significantly smaller than the observed value.

Morbidelli et al. (2009) failed to produce the elbow at  $D \sim 100$  km in the asteroid belt in collisional coagulation simulations starting from a population of small planetesimals (see Fig. 2). So, having in mind the new models of formation of large planetesimals from self-gravitating clumps of chondrules or larger pebbles and boulders (Johansen et al., 2007; Cuzzi et al., 2008), they proposed that 100 km was the minimal diameter of the original planetesimals. Moreover, not being able to reproduce the current slope of  $D > 100$  km asteroids by mutual collisions between bodies 100 km in size, Morbidelli et al. (2009) argued that these large planetesimals were born with a similar slope. However, as we will see in section 7, the current slope can be reproduced by considering the accretion of chondrule-sized particles by 100-km-scale planetesimals during the gaseous disk phase, a process not considered by Morbidelli et al. (2009).

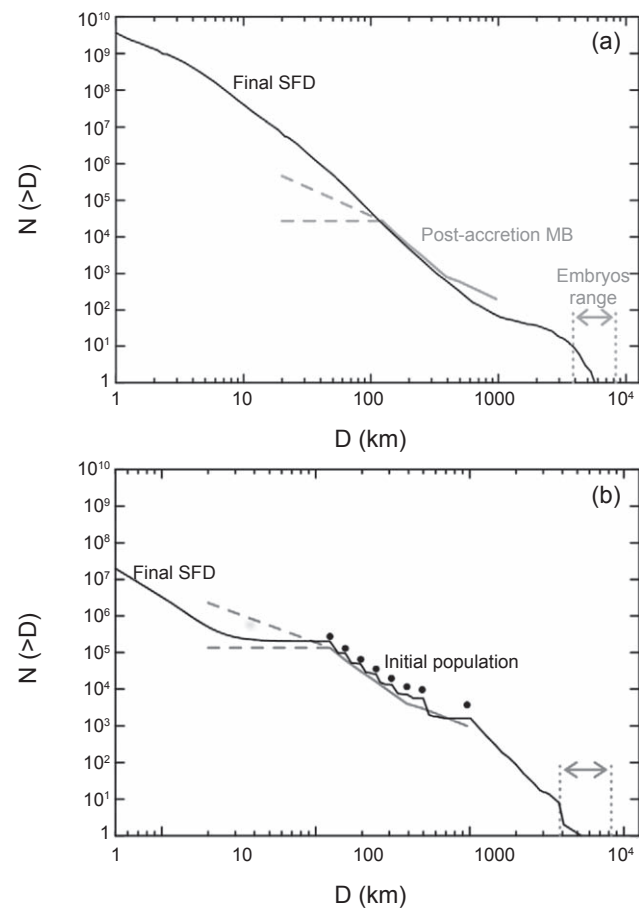


**Fig. 2.** The cumulative size distribution of asteroids  $N(>D)$ , as a function of asteroid diameter  $D$ , from Morbidelli et al. (2009). These coagulation models started with either (a) kilometer-sized planetesimals or (b) an initial size distribution following the current, observed size distribution of asteroids between 100 and 1000 km in diameter. The gray line shows the current size distribution of asteroids larger than 100 km in diameter. The model with small planetesimals overproduces asteroids smaller than 100 km in diameter (the upper dashed line represents the current size distribution of small asteroids while the lower dashed lines indicates a tighter constraint on the size distribution directly after accretion of the main belt). Starting with large asteroids gives a natural bump in the size distribution at 100 km in diameter, as the smaller asteroids are created in impacts between the larger primordial counterparts.

Weidenschilling (2011) managed to reproduce the elbow at  $D \sim 100$  km in the asteroid belt from collisional coagulation simulations starting from objects 50–200 m in radius. Because of the small size of these objects, collisional damping and gas drag keep the disk very dynamically cold (i.e., with a small velocity dispersion among the objects). Hence, in the simulations of Weidenschilling (2011), the elbow at  $D \sim 100$  km is produced by a transition from dispersion-dominated runaway growth to a regime dominated by Keplerian shear, before the formation of large planetary embryos. However, any external dynamical stirring of the population,

for instance due to gas turbulence in the disk, would break this process. Moreover, these simulations are based on the assumption that any collision that does not lead to fragmentation results in a merger, but 100-m-scale objects have very weak gravity and the actual capability of bodies so small to remain bound to each other is questionable. Finally, we stress that the formation of 100-m-scale bodies is an open issue, in view of the bouncing barrier and meter-sized barrier discussed in section 4.

### 3.2. Snowline Problems

Among the various meteorite types that we know, carbonaceous meteorites (or at least some of them like CI and CM) contain today a considerable amount (5–10%) of water by mass. Evidence for water alteration is widespread, and it is possible that the original ice content of these bodies was higher, close to the 50% value expected from unfractionated solar abundances. Instead, ordinary chondrites contain <2% water by weight (e.g., Jarosewich, 1990; Krot *et al.*, 2009); while ordinary chondrites do show signs of water alteration, it is unlikely that they ever contained 50% water ice by mass. This suggests that the parent bodies of these meteorites (CI and CM vs. ordinary) formed on either side of the condensation line for water, also called the snowline. In other words, the snowline was located in the middle of the asteroid belt at the time when the asteroids formed. Earth is also very water poor (some 0.1% by mass, although uncertain by a factor of ~5), suggesting that the planetesimals in its neighborhood were mostly dry and that water was delivered only by the small amount of planetesimals accreted from farther out (Morbidelli *et al.*, 2000; Raymond *et al.*, 2004; O'Brien *et al.*, 2014). The very dry enstatite chondrites have been proposed to arise from an extinct portion of the asteroid belt located between 1.6 and 2.1 AU from the Sun (Bottke *et al.*, 2012).

The problem with this picture is that chondritic bodies accreted late (2–4 m.y. after CAIs) and that the snowline is expected to migrate toward the Sun with time. The temperature of the disk is set by the equilibrium between heating and cooling. In the inner part of the disk, the heating is predominantly due to the viscous friction of the gas in differential rotation around the Sun, so it is related to the gas accretion rate of the star. The cooling rate is governed by how much mass is in the disk in the form of micrometer-sized grains. In Bitsch *et al.* (2015), the snowline is at 2–3 AU only in the earliest phases of disk evolution when the accretion rate is  $\dot{M} = 10^{-7} M_{\odot} \text{ yr}^{-1}$ , but the snowline migrates to 1–2 AU already after 500,000 yr when the accretion rate drops below  $\dot{M} = 10^{-8} M_{\odot} \text{ yr}^{-1}$ . These models are probably optimistically warm, because it is assumed that the ratio between the mass in micrometer-sized dust and the mass in gas is 1% (this reflects the solar metallicity but planetesimal accretion should eventually decrease the dust content) and account for the heating produced by stellar irradiation by a star more luminous than our early Sun. According to the observation of the accretion rate of stars as a function of age (Hartmann *et al.*, 1998) and photoevaporation models (Alexander and

Armitage, 2006), the accretion rate of the star should drop to  $\dot{M} = 10^{-9} M_{\odot} \text{ yr}^{-1}$  at 2–3 m.y., i.e., at the time of chondrite formation. The fact that there is no sign of primary accretion in the solar system after ~3 m.y. also suggests that the disk disappeared at that time (or that all the solids could have been incorporated into parent bodies at that time — however, accretion of solids is unlikely to reach 100% efficiency). Thus, at the time of chondrite formation, the snowline should have been well inside the inner edge of the asteroid belt, possibly even inside 1 AU. This is at odds with the paucity of water in the ordinary chondrites and in Earth.

A way to keep the disk warm has been proposed recently by Martin and Livio (2012, 2013). In their model, a dead zone in the disk, with low turbulent viscosity, becomes very massive and develops gravitational instabilities that heat the gas. The unlimited pileup of gas in the dead zone, however, could be a consequence of a simplified disk transport model, and is not observed in more complex three-dimensional hydrodynamical calculations (Bitsch *et al.*, 2014). Also, the model of Martin and Livio (2012) predicts a cold region where ice could condense inside the orbit of Earth, which seems inconsistent with the compositions of Venus and Mercury.

A possible way to keep the asteroid belt ice poor, despite freezing conditions, is to stop the inward flow of icy pebbles in a pressure bump. The inward drift of pebbles is caused by friction with the slower-moving gas (this effect is discussed more in section 6.1). Then, when the nebula cooled locally below the ice condensation temperature, there was no water vapor present to condense, and the planetesimals formed there would have a volatile depletion similar to that achieved in a warm disk. Bitsch *et al.* (2014) explored the effects of viscosity transitions at the snowline (as suggested by Kretke and Lin, 2007), but found that only very steep radial gradients in the  $\alpha$  parameter allow the formation of a pressure bump. Lambrechts *et al.* (2014) showed that the formation of a proto-Jupiter of about  $20 M_{\oplus}$  can produce a strong pressure bump just exterior to its orbit. If proto-Jupiter formed at the snowline when the snowline was at the outer edge of the asteroid belt, then its presence would have shielded the asteroid belt and the terrestrial planet region from the flow of icy pebbles, while small silicate dust and chondrules would remain for longer times in the asteroid belt due to their slow radial drift.

### 3.3. Are Asteroids Internally Homogeneous?

The possibility that the asteroids grew incrementally by layered accretion of chondrules (section 7) implies that asteroids are internally heterogeneous, in the most extreme case with a chondritic surface layer residing on a differentiated interior. We discuss here briefly whether such internal heterogeneity is supported by observations of the asteroid belt. Burbine *et al.* (2002) note that 100–150 distinct meteorite parent bodies, three-fourths of them differentiated, are represented in the meteorite collection. However, this sample is biased toward the sturdy irons and against the weaker, never-melted primitive chondrites.

Differentiation is a constraint on formation age. Most studies have suggested that sizeable asteroids forming  $<10^6$  yr after CAIs are almost certain to have thoroughly melted, but those that formed more than 2 m.y. after CAIs may have escaped melting except near their centers. More recent work paints a more complicated picture (see the chapter by Scheinberg et al. in this volume). Specifically, the Allende parent body, source of primitive CV3 chondrites, is thought to have melted near its center, as evidenced by the paleomagnetism detected in these meteorites (*Elkins-Tanton et al.*, 2011); other CV chondrites may show a similar signal (*Weiss et al.*, 2010). This suggests that the CV parent body was differentiated in its interior, but preserved an undifferentiated chondritic layer. Other authors have ascribed the magnetic field in the CV chondrites to impacts (e.g., *Wasson et al.*, 2013).

Modeling of the buoyancy of silicate melts of different composition suggests that, for C-type composition, melt might be dense and remain stable at depth, but for S-type (OC) compositions, and certainly for enstatite compositions, melt is less dense than surrounding material and will rise to manifest on the surface (*Fu and Elkins-Tanton*, 2014). Thus there might be old, centrally melted C-type asteroids such as the Allende parent body, where the evidence for differentiation remains buried, but the lack of evidence for significant surface melting on most S-type asteroids may argue that most of them remain unmelted and undifferentiated throughout (see the chapter by Scheinberg et al. in this volume) (*Weiss and Elkins-Tanton*, 2013).

We can sample the internal properties of asteroids in two ways: from the observed color and albedo distributions of collisionally disrupted asteroids in families (see also the chapters by Nesvorný et al. and Michel et al. in this volume) and from the meteorites that derive from them (see next paragraph). The Near-Earth Object Wide-field Infrared Survey Explorer (NEOWISE) mission has measured the albedos of a large number of asteroids and families, finding a dichotomy in albedo, roughly corresponding to the classical S- and C-types, that is most evident in the outer main belt. Collisional families cover the entire belt, so they avoid the sampling bias that affects meteorites. Many families have internal albedo distributions that are narrower than the global spread of albedos across families. A similar story is told by observations at visual and near-infrared wavelengths (*Mothé-Diniz and Nesvorný*, 2008). This conclusion is nevertheless complicated by the identification of interlopers in (and exclusion from) the asteroid families. Hence there is an inherent tendency to observe low-albedo variations within asteroid families. In contrast, the Eos family and the Eunomia family have unusually large internal variance (*Mothé-Diniz et al.*, 2005, 2008) and the Eunomia family looks like what an internally differentiated S-type might produce (see discussion in *Weiss and Elkins-Tanton*, 2013).

The three ordinary chondrite groups (H, L, and LL) are each thought to derive from a single parent body, based on a clustering of cosmic-ray-exposure ages of chondrites in each group, as if they were excavated by the same few large impacts (*Eugster et al.*, 2006). The thermal history of the

H-chondrite parent body under internal heating by  $^{26}\text{Al}$  was modeled by *Tieloff et al.* (2003), *Monnereau et al.* (2013), and *Henke et al.* (2013), who all concluded it was a roughly 100-km-radius body. Chondrites from all three OC groups show different amounts of thermal alteration from this process, designated as metamorphic grades 3–6. Models imply that the H-chondrite parent, at least, first incurred thermal alteration in an “onion-shell” fashion, with the most strongly heated H5/H6 material heated deep in the interior, and then was catastrophically disrupted and reassembled as a rubble pile (see Fig. 1) (*Taylor et al.*, 1987; *Scott et al.*, 2014). The small fractional abundance of minimally altered chondrites (H3/H4; Fig. 1) constrains the accretion of the H-chondrite parent body to have happened quickly — probably faster than  $3 \times 10^5$  yr (*Henke et al.*, 2013; *Vernazza et al.*, 2014). The constant mass growth rate adopted in *Henke et al.* (2013) is nevertheless not applicable to layered accretion, which results in runaway accretion and deposition of most of the mass toward the end of the growth phase (see further discussion in section 7).

While the major-element chemical compositions, and the oxygen isotopic compositions, of the OC groups differ significantly, there is little or no discernible variation of either chemical or isotopic composition across metamorphic grades in any of the three groups (*Jarosewich*, 1990; *Wood*, 2005; see also Tables 1 and 2 of *Clayton et al.*, 1991). The variation of chondrule size across metamorphic grade is less well studied (A. Rubin, personal communication, 2014).

*Dodd* (1976) demonstrated that the difference in the aerodynamical friction time between metal grains and silicate chondrules can explain silicate-metal fractionation in the ordinary chondrites. In this picture the LL chondrites are underabundant in metal because the parent body was successfully able to accrete large silicate-rich chondrules [the chondrules in the LL chondrites are larger than those in both H and L chondrites (see, e.g., *Nelson and Rubin*, 2002)]. The oxidation of metallic Fe could have happened as the LL-chondrite parent body accreted water-bearing phyllosilicates (*Rubin*, 2005). In the layered accretion model presented in section 7, asteroids will accrete larger and larger particles as they grow. Metal grains had a more restricted size range and hence a relatively small parent body of the H chondrites would accrete mainly small chondrules together with metal grains. A small size of the H-chondrite parent body is further supported by the low fraction of strongly metamorphosed samples that we have from that group (*Dodd*, 1976). A similar story is told for the enstatite chondrites (*Schneider et al.*, 1998): The EH group has more metal and smaller chondrules than the EL group. This aerodynamical size sorting may be evidence of asteroid growth by layered accretion (section 7) or asteroid formation by turbulent concentration (section 5).

#### 4. DUST GROWTH BY STICKING

Now that we have given an overview of some of the constraints from meteorites and asteroids, we can turn to the theoretical models of planetesimal formation. In this section

we discuss the growth of dust by direct sticking; subsequent chapters discuss gravitational instability models.

#### 4.1. Particle-Gas Interaction

The dynamical behavior of a particle in gas depends on both its size and density, as determined by its friction time  $\tau_f$  in the nebula gas (Whipple, 1972; Weidenschilling, 1977a). For particles smaller than the gas molecule mean free path (approximately 10–100 cm in the asteroid-belt region, depending on the uncertain value of the gas density), the friction time is

$$\tau_f = \frac{a\rho_*}{v_{\text{th}}\rho_g} \quad (1)$$

where  $a$  and  $\rho_*$  are the particle radius and density, and  $v_{\text{th}}$  and  $\rho_g$  are the gas thermal speed and mid-plane density. The thermal speed of the gas molecules is in turn connected to the isothermal sound speed through  $v_{\text{th}} = \sqrt{8/\pi c_s}$ . The Stokes number  $St$  is defined as  $St = \Omega\tau_f$ , where  $\Omega$  is the (local) orbital frequency of the protoplanetary disk. The translation from Stokes number to particle size follows

$$a = \frac{(2/\pi)\Sigma_g St}{\rho_*} \approx 80 St f_g(r) \left( \frac{r}{2.5 \text{ AU}} \right)^{-1.5} \text{ cm} \quad (2)$$

Here  $\Sigma_g = \sqrt{2\pi}\rho_g H_g$  is the gas column density and  $f_g(r)$  a parameter that sets gas depletion relative to the minimum mass solar nebula (MMSN) as a function of semimajor axis  $r$ . We set in the second equality  $\rho_* = 3.5 \text{ g cm}^{-3}$ , relevant for chondrules. The Stokes number controls many aspects of dust dynamics. Particles of larger Stokes numbers couple increasingly to larger, longer-lived, and higher-velocity eddies in nebula turbulence, thus acquiring larger relative velocities. Solutions for particle velocities have been developed by Voelk *et al.* (1980) and Mizuno *et al.* (1988), including closed-form analytical expressions by Cuzzi and Hogan (2003) and Ormel and Cuzzi (2007). Importantly, the Stokes number also controls the degree of sedimentation, with the scale height of the sedimented mid-plane layer,  $H_p$ , given by

$$H_p = H_g \sqrt{\frac{\alpha}{St + \alpha}} \quad (3)$$

Here  $H_g$  is the gas scale-height and  $\alpha$  is a measure of the turbulent diffusion coefficient  $D$  normalized as  $D = \alpha c_s H_g$  (see Johansen *et al.*, 2014, for references). Significant sedimentation can occur when  $St \geq \alpha$ . Chondrules of millimeter sizes have a Stokes number of  $St \sim 10^{-3}$ ; hence chondrules will only settle out of the gas if  $\alpha \ll 10^{-3}$ .

#### 4.2. Dust Growth

The study of dust growth has been an extremely active field, both experimentally and numerically, since *Asteroids III*. Subsequent reviews were presented by Dominik *et al.* (2007), Blum and Wurm (2008), and Chiang and

Youdin (2010); the older review by Beckwith *et al.* (2000) is also valuable for basics. Two very recent overview chapters presenting both the basic physics and selected recent highlights are Johansen *et al.* (2014) and Testi *et al.* (2014); for efficiency we build on those chapters and here emphasize specifics relevant to asteroid formation.

**4.2.1. Sticking.** Particles can stick if their relative kinetic energy exceeds certain functions of the surface energy of the material, which depends on composition. At the low relative velocities for small monomers (0.1–10  $\mu\text{m}$ ) under nebula conditions, both ice and silicate particles stick easily and form loose, porous aggregates. The process continues until the aggregates are at least 100  $\mu\text{m}$  in radius. Aggregates can continue to grow and stick at larger velocities, if their open structure is able to deform and dissipate energy (Wada *et al.*, 2009). The entire process of growth beyond roughly 100  $\mu\text{m}$  fluffy aggregates depends on just how much these aggregates can be compacted by their mutual collisions. Recent studies that concentrate on icy particles outside the snowline have argued that the high surface energy of ice prevents significant compaction from occurring (and keeps relative velocities small) until particles have grown to extremely large size — hundreds of meters — with extremely low density (Okuzumi *et al.*, 2012).

**4.2.2. Bouncing.** The surface energies of silicates are much smaller than those of ice, so it is easy for even millimeter-sized silicate particles to compact each other in mutual collisions. Relative velocities large enough to cause compaction and bouncing are acquired by roughly millimeter-sized silicate particles in nebula turbulence. Coagulation modeling by Zsom *et al.* (2010), consistent with experiments (Güttler *et al.*, 2010; Weidling *et al.*, 2012), revealed a bouncing barrier in this size range where growth of silicate aggregates by sticking ceased. This new barrier joins the long-known fragmentation barrier and radial drift barrier, which, even if the bouncing barrier can be breached, tend to frustrate growth in the asteroid-belt region beyond decimeter to meter size (Brauer *et al.*, 2008; Birnstiel *et al.*, 2010, 2011).

**4.2.3. Fragmentation.** A simple critical velocity  $v_{\text{frag}}$  can be used to refer to fragmentation of two comparable masses. This approach has been modified in some treatments to include some mass transfer by a smaller projectile hitting a larger target at high velocity, even if the projectile is destroyed and some mass is ejected from the target (Wurm *et al.*, 2005). An alternate approach is to treat the fragmentation threshold as a critical kinetic energy per unit mass  $Q^*$ , which can be thought of as a critical velocity squared for same-sized particles (Stewart and Leinhardt, 2009). The latter treatment automatically accounts for particle size differences and thus allows accretion of small particles to proceed at collision velocities much higher than the nominal  $v_{\text{frag}} \sim \sqrt{Q^*}$ . Stewart and Leinhardt (2009) treated solids as weak rubble piles, all calibrated using experimental work by Setor *et al.* (2007). These expressions allow for the higher efficiency of low-velocity collisions in fragmentation than for hypervelocity impacts. For particles made of small silicate grains, a value of  $Q^*$  on the order of  $10^4 \text{ cm}^2 \text{ s}^{-2}$  is suggested, with an

associated  $v_{\text{frag}} \sim 1$  to several meters per second, for weak centimeter- to meter-sized aggregates (Schräpler et al., 2012; Stewart and Leinhardt, 2009; Wada et al., 2009, 2013) or even less (Beitz et al., 2011).

**4.2.4. Lucky particles.** The bouncing barrier, in preserving most of the available solids at small sizes, may provide a target-rich environment for growth of much larger “lucky” particles, which experience few, or low-velocity, collisions and avoid destruction while steadily growing from much smaller particles to large sizes (Windmark et al., 2012a,b; Garaud et al., 2013; Drążkowska et al., 2013). However, Windmark et al. (2012a,b) and Garaud et al. (2013) did not include radial drift, which is important because the growth time for these lucky particles greatly exceeds the drift time to the Sun. Drążkowska et al. (2013) removed the radial drift problem with a pressure bump at the edge of a dead zone, and still found that the total number of meter-sized particles they could produce in  $3 \times 10^4$  yr was in the single digits. An isolated particle cannot trigger collective effects such as the streaming instability (section 6), but can only keep growing by sweep-up. Johansen et al. (2008) and Xie et al. (2010) have modeled this “snowball” stage and find that growth in this fashion is extremely slow unless the nebula turbulent  $\alpha$  is very low, because the small feedstock particles are vertically diffused to a low spatial density otherwise.

**4.2.5. Chondrule rims and chondrule aggregates.** The fine-grained component of chondrites is not only found in a featureless background matrix, it is also found rimming individual chondrules and other coarse particles, often filling cavities (Metzler et al., 1992; Brearley, 1993; Cuzzi et al., 2005). The origin of these fine-grained rims has been debated (Lauretta et al., 2006). One school of thought regards them as accretionary rims, swept up as a cooled chondrule moves relative to the gas and entrained dust or small aggregates (MacPherson et al., 1985; Metzler et al., 1992; Bland et al., 2011). Matrix and rims were reviewed in depth by Scott et al. (1984); among many interesting results, they found evidence that rims were accreted as numerous aggregates of variable mean composition, rather than as monomers. Rubin (2011) suggested that carbonaceous chondrites formed in dusty regions of the solar protoplanetary disk and that matrix accumulated into millimeter- to centimeter-sized highly porous dust balls. In this picture, chondrules acquired matrix rims by collisions with these dust balls rather than in collisions with smaller particles.

The accretion of fine-grained rims was modeled by Morfill et al. (1998), Cuzzi (2004), and Ormel et al. (2008). In these models, relative velocities predicted for the nebula environment have been shown to be compatible with sticking and compaction under the theory of Dominik and Tielens (1997); Ormel et al. (2008) added the effects of interchondrule collisions on further compacting the rims. Ormel et al. found that chondrules that had accreted porous rims of dust between collisions could stick more easily because the porous rims acted as shock absorbers, resulting in composite, centimeter- to decimeter-sized objects, depending on the value of  $\alpha$ , formed of rimmed chondrules.

**4.2.6. Gravitational scattering barrier.** There is one further barrier for particles trying to grow incrementally, by sticking, to kilometer-sized and larger. This gravitational scattering barrier arises because, in turbulence, nebula gas has small density fluctuations associated with pressure and vorticity. These density fluctuations, primarily on large scales, scatter growing planetesimals to achieve high relative speeds (Laughlin et al., 2004; Nelson and Papaloizou, 2004; Nelson and Gressel, 2010; Yang et al., 2012). The random velocities acquired by 1–10-km-scale planetesimals in this way are sufficient to put them into an erosive, rather than accretionary, regime throughout most of the solar system for a range of the most plausible  $\alpha$  values (Ida et al., 2008; Stewart and Leinhardt, 2009). Ormel and Okuzumi (2013) found that planetesimals need to have radii of 100 km or more to be able to undergo runaway accretion.

Overall, the barriers to formation of 100-km-scale asteroids by incremental growth by sticking appear formidable. For these reasons, a number of models have arisen that avoid these problems with a leapfrog process in which 10–1000-km-scale asteroids form directly from smaller particles stuck at one of these barriers.

## 5. TURBULENT CONCENTRATION

The leapfrog model, sometimes referred to as turbulent concentration (TC) or turbulent clustering, can in principle make 10–100-km-radius planetesimals directly from chondrule-sized particles. The turbulent concentration model was motivated originally by laboratory and numerical experiments that showed dense particle clusters forming spontaneously in isotropic turbulence, in which the most intense clustering was seen for particles with friction time  $\tau_f$  equal to the Kolmogorov (or smallest eddy) timescale (Squires and Eaton, 1990, 1991; Wang and Maxey, 1993; Eaton and Fessler, 1994). It was realized that this condition was very closely satisfied under canonical nebula conditions by the very chondrule-sized particles that make up the bulk of primitive chondrites (Cuzzi et al., 1996, 2001).

### 5.1. A Brief History of Turbulent Concentration Models

What remains uncertain and a subject of current study, as with many properties of turbulence, is just how the laboratory experiments and numerical simulations translate into actual nebula conditions. The flow regime is described by its turbulence Reynolds number  $Re = UL/v = \alpha c_s H_g/v$ , where  $U$  and  $L$  are some typical velocity and length scale of the flow, and  $v$  is the molecular viscosity. All current experiments and simulations are run at  $Re$  far smaller than likely nebula values. Cuzzi et al. (2001) noticed that the volume fraction of dense clumps increased with increasing  $Re$  and suggested a scaling that would map the behavior to the much higher values of  $Re$  relevant for turbulence in protoplanetary disks.

Hogan and Cuzzi (2007) showed that mass-loading feedback of the particle burden on gas turbulence caused

the concentration process to saturate at a mass loading  $\Phi = \rho_p/\rho_g \sim 100$ , precluding the small, dense clumps advocated by Cuzzi *et al.* (2001). Based on this, Cuzzi *et al.* (2008) advocated gravitational binding and ultimate sedimentation of much larger clumps, on the order of  $10^3$ – $10^4$  km, with  $\Phi \sim 10$ – $100$ . They showed that a long-neglected discovery by Sekiya (1983) precludes genuine, dynamical timescale collapse for dense clumps of chondrule-sized particles under plausible conditions. Particles of these sizes and friction times can only sediment slowly toward the center of their bound clump, on a much longer timescale ( $10^2$ – $10^3$  orbits). Cuzzi *et al.* (2008) suggested a criterion for stability of these bound, yet only slowly shrinking, clumps that led directly to the conclusion that they would preferentially form large planetesimals comparable in size with the mass-dominant 100-km-radius mode advocated for the early asteroid belt by Bottke *et al.* (2005)—thus leaping over the long-troublesome millimeter- to meter- to kilometer-sized barriers. Objects formed in this way are compatible with the primary texture seen in the most primitive unbreciated CM and CO chondrites (Metzler *et al.*, 1992; Brearley, 1993), and would display deep homogeneity of bulk chemical and isotopic properties.

Cuzzi *et al.* (2010) and Chambers (2010) went on to describe an end-to-end primary accretion scenario, combining stability thresholds with calculated probability distributions of clump density, finding that a range of nebula conditions (all implying  $>10\times$  local enhancement of the usually assumed 1% cosmic solids-to-gas ratio within some few  $10^4$  km of the mid-plane) could match the required rate of planetesimal formation and the characteristic mass mode around 100–200-km diameter. Cuzzi *et al.* (2010) gave a number of caveats regarding the built-in assumptions of this model; one caveat regarding scale-dependence of the concentration process has been found to be important enough to change the predictions of the scenario quantitatively (see below). Subsequently, Cuzzi and Hogan (2012) resolved a discrepancy in a key timescale between Cuzzi *et al.* (2010) and Chambers (2010), which makes planetesimal formation  $1000\times$  faster than in Cuzzi *et al.* (2010) [and correspondingly slower than in Chambers (2010)].

## 5.2. New Insights into Turbulent Concentration

The primary issues are whether it is *always* Kolmogorov friction time particles that are most effectively concentrated, and whether the physics of their concentration are scale-invariant. Hogan and Cuzzi (2007) argued by analogy with the observed scale-invariance of turbulent dissipation, which is dominated by Kolmogorov-time vortex tubes (little tornados in turbulence) that the concentration of Kolmogorov-friction-time particles would also be scale-invariant (see also Cuzzi and Hogan, 2012). They developed a so-called cascade model by which to extend the low-Re results to nebula conditions.

The primary accretion scenarios of Cuzzi *et al.* (2010) and Chambers (2010) used this cascade model to generate density-vorticity probability density functions (PDFs) as

a function of nebula scale. Pan *et al.* (2011) ran simulations at higher Re than Hogan and Cuzzi (2007) and found that the clump density PDFs dropped faster than would be predicted by the scale-invariant cascade. They suggested that the physics of particle concentration might indeed be scale-dependent, and that planetesimal formation rates obtained using the Hogan and Cuzzi (2007) cascade might be significantly overestimated.

Ongoing work supports this concern about scale dependence. Cuzzi *et al.* (2014) have analyzed much higher Re simulations (Bec *et al.*, 2010) and found that the cascade measures, called “multiplier distributions,” that determine how strongly particles get clustered at each spatial scale *do* depend on scale at least over the largest decade or so of length scale; i.e., the scale-invariant inertial range for particle concentration and dissipation does not become established at the largest scale, causing little concentration to occur until roughly an order of magnitude smaller scale. Because the cascade process is multiplicative, this slow start means that fewer dense zones are to be found at any given scale size than previously thought.

New, scale-dependent cascades can now be implemented to predict planetesimal IMFs using the approach of Cuzzi *et al.* (2010, 2014). The quantitative implications are not clear as yet, but particles with friction times significantly longer than those of single chondrules are most strongly clustered at length scales most relevant to direct planetesimal formation (see also Bec *et al.*, 2007). Meanwhile, turbulent concentration of small particles may play a critical and as yet unmodeled (in astrophysics) role in formation of aggregates by collisions and sticking (see, e.g., Shaw, 2003; Pan *et al.*, 2011) (section 4). Some combination of these effects probably contributes to observed chondrule size distributions, some (but not all) of which appear broader than previously thought (Fisher *et al.*, 2014; Friedrich *et al.*, 2015; Ebel *et al.*, 2015).

## 6. PRESSURE BUMPS AND STREAMING INSTABILITY

The turbulent concentration mechanism described in the previous section operates on the smallest scales of the turbulent flow (although the vortical structures that expel particles can be very elongated). The dynamical timescales on such small-length scales are much shorter than the local orbital timescale of the protoplanetary disk. In contrast, the largest scales of the turbulent flow are dominated by the Coriolis force, and this allows for the emergence of large-scale geostrophic structures (high-pressure regions in perfect balance between the outward-directed pressure gradient force and the inward-directed Coriolis force).

Whipple (1972) found that particles are trapped by the zonal flow surrounding large-scale pressure bumps. Pressure bumps [in a way azimuthally extended analogs to the vortices envisioned in Barge and Sommeria (1995)] can arise through an inverse cascade of magnetic energy (Johansen *et al.*, 2009a; Simon *et al.*, 2012; Dittrich *et al.*, 2013) in tur-

bulence driven by the magnetorotational instability (*Balbus and Hawley*, 1991). Pressure bumps concentrate primarily large (0.1–10 m) particles that couple to the gas on an orbital timescale (*Johansen et al.*, 2006), reaching densities at least 100× the gas density, which leads to the formation of 1000-km-scale planetesimals (*Johansen et al.*, 2007, 2011). The magnetorotational instability is nevertheless no longer favored as the main driver of angular momentum transport in the asteroid-formation region of the solar protoplanetary disk, since the ionization degree is believed to be too low for coupling the gas to the magnetic field (see review by *Turner et al.*, 2014).

The magnetorotational instability can still drive turbulence (with  $\alpha$  in the interval from  $10^{-3}$  to  $10^{-2}$ ) in the mid-plane close to the star (within approximately 1 AU where the ionization is thermal) and far away from the star (beyond 20 AU where ionizing cosmic rays and X-rays penetrate to the mid-plane). Accretion through the “dead zone,” situated between these regions of active turbulence, can occur in ionized surface layers far above the mid-plane (*Oishi et al.*, 2007), from disk winds (*Bai and Stone*, 2013) and by purely hydrodynamical instabilities in the vertical shear of the gas (*Nelson et al.*, 2013) or radial convection arising from the subcritical baroclinic instability (*Klahr and Bodenheimer*, 2003; *Lesur and Papaloizou*, 2010). The mid-plane is believed to be stirred to a mild degree by these hydrodynamical instabilities or by perturbations from the active layers several scale-heights above the mid-plane, driving effective turbulent diffusivities in the interval from  $10^{-5}$  to  $10^{-3}$  in the mid-plane. The inner and outer edges of this “dead zone,” where the turbulent viscosity transitions abruptly, are also possible sites of pressure bumps and large-scale Rossby vortices that feed off the pressure bumps (*Lyra et al.*, 2008, 2009).

## 6.1. Streaming Instability

The low degree of turbulent stirring in the asteroid-formation region also facilitates the action of the streaming instability, a mechanism where particles take an active role in the concentration process (*Youdin and Goodman*, 2005; *Youdin and Johansen*, 2007; *Johansen and Youdin*, 2007). The instability arises from the speed difference between gas and solid particles. The gas is slightly pressure-supported in the direction pointing away from the star, due to the higher temperature and density close to the star, which mimics a reduced gravity on the gas. The result is that the gas orbital speed is approximately 50 m s<sup>-1</sup> slower than the Keplerian speed at any given distance from the star. Solid particles are not affected by the global pressure gradient — they would move at the Keplerian speed in the absence of drag forces, but drift radially due to the friction from the slower-moving gas. The friction exerted from the particles back onto the gas leads to an instability whereby a small overdensity of particles accelerates the gas and diminishes the difference from the Keplerian speed. The speed increase in turn reduces the local headwind on the dust. This slows down the radial drift of particles locally, which leads to a runaway process

where isolated particles drift into the convergence zone and the density increases exponentially with time. This picture is a bit simplified, as *Youdin and Goodman* (2005) and *Jacquet et al.* (2011) showed that the streaming instability operates only in the presence of rotation, i.e., the instability relies on the presence of Coriolis forces. This explains why the instability occurs on relatively large scales of the protoplanetary disk where Coriolis forces are important, typically a fraction of an astronomical unit, and operates most efficiently on large particles with frictional coupling times around one-tenth of the orbital timescale (typically decimeter sizes at the location of the asteroid belt).

## 6.2 Computer Simulations of the Streaming Instability

Computer simulations that follow the evolution of the streaming instability into its nonlinear regime show the emergence of axisymmetric filaments with typical separations of  $0.2 \times$  the gas scale-height (*Yang and Johansen*, 2014) and local particle densities reaching several thousand times the gas density (*Bai and Stone*, 2010; *Johansen et al.*, 2012). These high densities trigger the formation of large planetesimals (100–1000 km in diameter) by gravitational fragmentation of the filaments (*Johansen et al.*, 2007), although planetesimal sizes decrease to approximately 100 km for a particle column density comparable to that of the solar protoplanetary disk (*Johansen et al.*, 2012).

An important question concerning planetesimal formation through the streaming instability is whether the process can operate for particles as small as chondrules in the asteroid belt. In Fig. 3, we show numerical experiments from *Carrera et al.* (2015) on the streaming instability in particles with sizes down to a fraction of a millimeter. The streaming instability requires a threshold particle mass loading  $Z = \Sigma_p/\Sigma_g$ , where  $\Sigma_p$  and  $\Sigma_g$  are the particle and gas column densities, to trigger the formation of overdense filaments (*Johansen et al.*, 2009b; *Bai and Stone*, 2010). The simulations in Fig. 3 start at  $Z = Z_0 = 0.01$ , but the particle mass-loading is continuously increased by removing the gas on a timescale of 30 orbital periods. This was done to identify how the critical value of  $Z$  depends on the particle size. The result is that overdense filaments form already at  $Z = 0.015$  for centimeter-sized particles, while large chondrules of millimeter sizes require  $Z = 0.04$  to trigger filament formation. Chondrules smaller than millimeters do not form filaments even at  $Z = 0.08$ .

A lowered gas column density may thus be required to trigger concentration of chondrule-sized particles by the streaming instability. It is possible that the solar protoplanetary disk had a lower gas density than what is inferred from the current mass of rock and ice in the planets (which multiplied by 100 gives the MMSN), if the planet-forming regions of the nebula were fed by pebbles drifting in from larger orbital distances (*Birnstiel et al.*, 2012). In this picture the growing planetesimals and planets are fed by drifting pebbles, so that the current mass of the planets was achieved by the integrated capture efficiency of the drifting solids; this

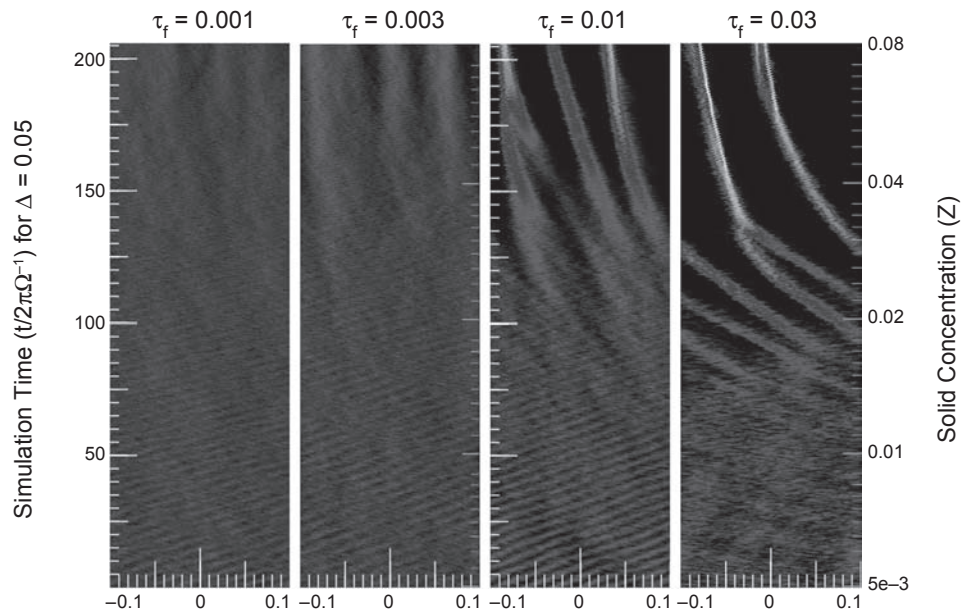


**Fig. 3.** Space-time plots of particle concentration by streaming instabilities, from Carrera et al. (2015), with the x-axis indicating the radial distance from the center of the simulation box and the y-axis the time (on the left) and the dust-to-gas ratio (on the right). The four columns show particle sizes 0.8 mm ( $\tau_f = 0.001\Omega^{-1}$ ), 2.4 mm ( $\tau_f = 0.003\Omega^{-1}$ ), 8 mm ( $\tau_f = 0.01\Omega^{-1}$ ), and 2.4 cm ( $\tau_f = 0.03\Omega^{-1}$ ). Simulations start with a mean dust-to-gas ratio of  $Z = 0.01$ , but gas is removed on a timescale of 30 orbits (1 orbit =  $2\pi\Omega^{-1}$ ), increasing the dust-to-gas ratio accordingly. While centimeter-sized particles concentrate in overdense filaments already at a modest increase in dust-to-gas ratio to  $Z = 0.015$ , smaller particles require consecutively increasing gas removal to trigger clumping.

allows for gas column densities lower than in the MMSN to be consistent with the current masses of planets in the solar system. The gas will also be removed by accretion and photoevaporation (Alexander and Armitage, 2006). The high mass-loading in the gas could be obtained through pileup by radial drift and release of refractory grains near the iceline (Sirono, 2011).

Turbulence as weak as  $\alpha \sim 10^{-7}$  is necessary to allow the sedimentation of chondrules (with  $St \sim 10^{-3}$ ) into a thin mid-plane layer with scale-height  $H_p = 0.01H_g$  and  $\rho_p \approx \rho_g$  (see equation (2)), the latter being a necessary density criterion for activating particle pileup by streaming instabilities. Very low levels of  $\alpha$  are consistent with protoplanetary disk models where angular momentum is transported by disk winds and the mid-plane remains laminar (Bai and Stone, 2013), except for mild stirring by Kelvin-Helmholtz (Youdin and Shu, 2002) and streaming instabilities (Bai and Stone, 2010).

Weak turbulence also facilitates the formation of decimeter-sized chondrule aggregates (Ormel et al., 2008), which would concentrate much more readily in the gas. Stirring by hydrodynamical instabilities in the mid-plane, such as the vertical shear instability (Nelson et al., 2013), would preclude significant sedimentation of chondrule-sized particles and affect the streaming instability, as well as the formation of chondrule aggregates, negatively. An alternative possibility is that the first asteroid seeds in fact did not form from

chondrules (or chondrule aggregates), but rather from larger icy particles that would have been present in the asteroid-formation region in stages of the protoplanetary disk where the iceline was much closer to the star (Martin and Livio, 2012; Ros and Johansen, 2013). Chondrules could have been incorporated by later chondrule accretion (see section 7).

## 7. LAYERED ACCRETION

The turbulent concentration model and the streaming instability, reviewed in the previous sections, are the leading contenders for primary accretion of chondrules into chondrites. However, neither of the two are completely successful in explaining the dominance of chondrules in chondrites: The turbulent concentration models may not be able to concentrate sufficient amounts for gravitational collapse, while the streaming instability relies on the formation of chondrule aggregates and/or gas depletion and pileup of solid material from the outer parts of the protoplanetary disk. In the layered accretion model the chondrules are instead accreted onto the growing asteroids over millions of years after the formation of the first asteroid seeds — those first seeds forming by direct coagulation from a population of 100-m-sized planetesimals as envisioned in Weidenschilling (2011) or by one or more of the particle concentration mechanisms described in the previous sections.

## 7.1. Chondrule Accretion

Chondrules are perfectly sized for drag-force-assisted accretion onto young asteroids. The ubiquity of chondrules inside chondrites, and their large age spread (Connelly et al., 2012), indicates that planetesimals formed and orbited within a sea of chondrules. Chondrules would have been swept past these young asteroids with the sub-Keplerian gas. The gas is slightly pressure-supported in the radial direction and hence moves slower than the Keplerian speed by the positive amount  $\Delta v$  (Weidenschilling, 1977b; Nakagawa et al., 1986). The Bondi radius  $R_B = GM/(\Delta v)^2$  marks the impact parameter for gravitational scattering of a chondrule by an asteroid of mass  $M$ , with

$$\frac{R_B}{R} = 0.87 \left( \frac{R}{50 \text{ km}} \right)^2 \left( \frac{\Delta v}{53 \text{ m s}^{-1}} \right)^{-2} \left( \frac{\rho_*}{3.5 \text{ g cm}^{-3}} \right) \quad (4)$$

Here we have normalized by  $\Delta v = 53 \text{ m s}^{-1}$ , the nominal value in the MMSN model of Hayashi (1981), and used the chondrule density  $\rho_* = 3.5 \text{ g cm}^{-3}$  as a reference value. Chondrules with friction time comparable to the Bondi timescale  $t_B = R_B/\Delta v$  are accreted by the asteroid (Johansen and Lacerda, 2010; Ormel and Klahr, 2010; Lambrechts and Johansen, 2012). The accretion radius  $R_{\text{acc}}$  can be calculated numerically as a function of asteroid size and chondrule size by integrating the trajectory of a chondrule moving with the sub-Keplerian gas flow past the asteroid. The accretion radius peaks at  $R_{\text{acc}} \approx R_B$  for  $t_f/t_B$  in the range from 0.5 to 10 (Lambrechts and Johansen, 2012). Accretion at the full Bondi radius happens for particle sizes

$$a = [0.008, 0.16] \text{ mm} \left( \frac{R}{50 \text{ km}} \right)^3 \left( \frac{\Delta v}{53 \text{ m s}^{-1}} \right)^{-3} \times \left( \frac{r}{2.5 \text{ AU}} \right)^{-3} \left( \frac{\Sigma_g}{\Sigma_{\text{MMSN}}} \right) \quad (5)$$

An asteroid of radius 50 km thus “prefers” to accrete chondrules of sizes smaller than 0.1 mm, corresponding to the smallest chondrules found in chondrites. At 100 km in radius, the preferred chondrule size is closer to 0.2 mm, a 200-km-radius body prefers millimeter-sized chondrules, and larger bodies can only grow efficiently if they can accrete chondrules of several millimeters or centimeters in diameter. Carbonaceous chondrites accreted significant amounts of CAIs and matrix together with their chondrules; Rubin (2011) suggested that matrix was accreted in the form of centimeter-sized porous aggregates with aerodynamical friction time comparable to chondrules and CAIs.

Aerodynamical accretion of chondrules could explain the narrow range of chondrule sizes found in the various classes of meteorites. The model predicts that asteroids accrete increasingly larger chondrules as they grow. This prediction

may be at odds with the little variation in chondrule sizes found within chondrite classes [70% of EH3 and CO3 chondrules have apparent diameters within a factor of 2 of the mean apparent diameters in the group, according to Rubin (2000)]. The least-metamorphosed LL chondrites nevertheless do seem to host on the average larger chondrules (Nelson and Rubin, 2002). More metamorphosed LL chondrites actually show a lack of small chondrules; this could be due to the fact that the smallest chondrules disappeared from the strongly heated central regions of the parent body.

## 7.2 Chondrule Accretion Rates

The accretion rate of chondrules (and other macroscopic particles) is

$$\dot{M} = \pi f_B^2 R_B^2 \rho_p \Delta v \quad (6)$$

Here  $f_B$  parameterizes the actual accretion radius relative to the Bondi radius and  $\rho_p$  is the chondrule density. Accretion of chondrules is a runaway process, since  $\dot{M} \propto R_B^2 \propto M^2$  if the optimal chondrule size is present (so that  $f_B = 1$  in equation (6)). The characteristic growth timescale is

$$t_{\text{exp}} = \frac{M}{\dot{M}} = 1.66 \text{ m.y.} \left( \frac{R}{50 \text{ km}} \right)^{-3} \left( \frac{\Delta v}{53 \text{ m s}^{-1}} \right)^3 \times \left( \frac{r}{2.5 \text{ AU}} \right)^{2.75} \left( \frac{\Sigma_g}{\Sigma_{\text{MMSN}}} \right)^{-1} \left( \frac{\rho_*}{3.5 \text{ g cm}^{-3}} \right)^{-1} \quad (7)$$

We assumed here that the chondrules have sedimented to a thin mid-plane layer of thickness 1% relative to the gas scale-height. The strong dependence of the accretion rate on the planetesimal mass will drive a steep differential size distribution of a population of planetesimals accreting chondrules. This is illustrated in Fig. 4, where asteroid seeds with initial sizes from 10 to 50 km in radius have been exposed to chondrule accretion over 5 m.y. The value of the turbulent viscosity is  $\alpha = 2 \times 10^{-6}$ . The resulting differential size distribution (which manifests itself after around 3 m.y. of chondrule accretion) shows a bump at 70 km in radius, a steep decline toward 200 km in radius, and finally a slower decline toward larger asteroids. The shallower decline is caused by the lack of centimeter-sized particles needed to drive the continued runaway accretion of large asteroids (this can be seen as a drop in  $f_B$  in equation (6)). All the features in the size distribution in Fig. 4 are in good agreement with features of the observed size distribution of asteroids that are not explained well in coagulation models (Morbidelli et al., 2009).

Layered accretion of chondrules can readily explain the large age spread of individual chondrules inside chondrites (Connelly et al., 2012), as well as the remnant magnetization of the Allende meteorite (Elkins-Tanton et al., 2011), imposed on the accreted chondrules from the internal dynamo in the

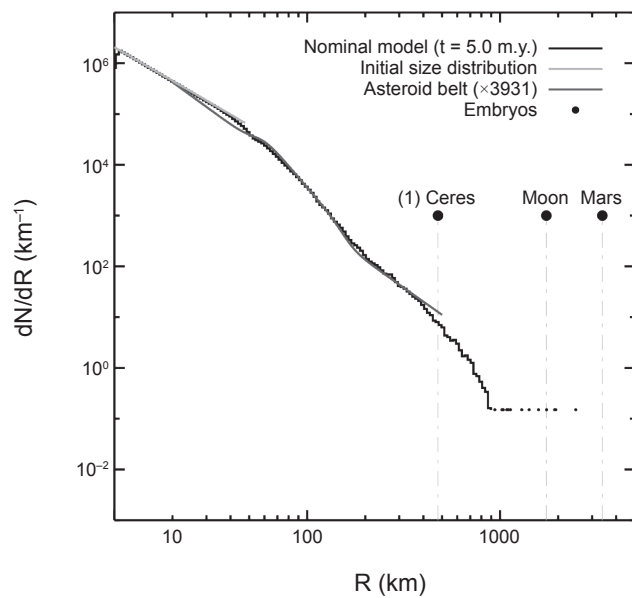


**Fig. 4.** The size distribution of asteroids and planetary embryos after accreting chondrules with sizes from 0.1 to 1.6 mm in diameter for 5 m.y. The original asteroid sizes had sizes between 10 and 50 km in radius (light gray line), here envisioned to form by the streaming instability in a population of decimeter-sized icy particles. The resulting size distribution of asteroids is in good agreement with the bump at 70 km in radius, the steep size distribution from 70 km to 200 km, and the shallower size distribution of larger asteroids whose chondrule accretion is slowed down by friction within their very large Bondi radius. Figure based on Johansen *et al.* (2015).

parent body's molten core. Efficient chondrule accretion requires, as does the streaming instability discussed in the previous section, sedimentation of chondrules to a thin mid-plane layer. The turbulent viscosity of  $\alpha = 2 \times 10^{-6}$  in Fig. 4 is nevertheless significantly larger than the  $\alpha \sim 10^{-7}$  needed to sediment chondrules to a thin mid-plane layer of thickness 1% of the gas scale height; indeed the timescale to grow to the current asteroid population is 3 m.y. in the simulation shown in Fig. 4, about twice as long as in equation (7), but in good agreement with the ages of the youngest chondrules.

## 8. OPEN QUESTIONS

The formation of asteroids is a complex problem that will only be solved through a collective effort from astronomers, planetary scientists, and cosmochemists. Although many details of asteroid formation are still not understood, we hope to have convinced the reader that new insights have been achieved in many areas in the past years. Here we highlight 10 areas of open questions in which we believe that major progress will be made in the next decade:

1. *Short-lived radionuclides.* What is the origin of the short-lived radioactive elements that melted the differentiated parent bodies? Was  $^{26}\text{Al}$  heterogeneous in the solar protoplanetary disk? How did the young solar system

become polluted in  $^{26}\text{Al}$  without receiving large amounts of  $^{60}\text{Fe}$ , an element that is copiously produced in supernovae?

2. *Maintaining free-floating chondrules and CAIs.* How is it possible to preserve chondrules and CAIs for millions of years in the disk before storing them in a chondritic body, without mixing them too much to erase chondrule classes and chondrule-matrix complementarity? What are we missing that makes this issue so paradoxical?

3. *Chondrules vs. matrix.* Why do carbonaceous chondrites contain large amounts of matrix while ordinary chondrites contain very little matrix? Did the matrix enter the chondrites as (potentially icy) "matrix lumps" or on fine-grained rims attached to chondrules and other macroscopic particles?

4. *Initial asteroid sizes.* What is the origin of the steep differential size distribution of asteroids beyond the knee at 100 km? Did asteroids form small as in the coagulation picture, medium-sized as in the layered accretion model, or large as in some turbulent concentration models? Why do Kuiper belt objects, which formed under very different conditions in temperature and density, display a similar size distribution as asteroids?

5. *The origin of asteroid classes.* How is the radial gradient of asteroid composition produced and retained in the presence of considerable preaccretionary turbulent mixing and postaccretionary dynamical mixing? Is asteroid formation a continuous process that happens throughout the lifetime of the protoplanetary disk? What do the different chondrite groups mean in terms of formation location and time?

6. *Dry and wet chondrites.* Why do we have dry chondrites (enstatite, ordinary)? If chondrites form at 2–4 m.y. after CAIs, then the snowline should have been well inside the inner edge of the asteroid belt. Are there overlooked heating sources that could keep the iceline at 3 AU throughout the lifetime of the protoplanetary disk? Or did the asteroid classes form at totally different places only to be transported to their current orbits later?

7. *Internal structure of asteroids.* Does the chondrite and asteroid family evidence suggest that the primary asteroids — before internal heating — are homogeneous, roughly 100-km-diameter bodies composed of a physically, chemically, and isotopically homogeneous mix of chondrule-sized components? Or is internal heterogeneity, as may be the case for the Allende parent body, prevalent?

8. *Turbulent concentration of chondrules.* Under what nebula conditions can vortex tubes over a range of nebula scales concentrate enough chondrules into volumes that are gravitationally bound, at a high enough rate to produce the primordial asteroids and meteorite parent bodies directly? What other roles could turbulent concentration play in planetesimal formation given that the optimally concentrated particle is chondrule-sized under nominal values of the turbulent viscosity?

9. *Streaming instability with chondrules.* Will the conditions for streaming instabilities to concentrate chondrule-sized particles, i.e., gas depletion and/or particle pileup, be fulfilled in the protoplanetary disk? How does an overdense

filament of chondrule-sized particles collapse under self-gravity given the strong support by gas pressure?

10. *Layered accretion.* What is the origin of the apparent scarcity of heterogeneous asteroid families, given that asteroids orbiting within an ocean of chondrules should accrete these prodigiously? What is the thermal evolution of early-formed asteroid seeds that continue to accrete chondrules over millions of years?

**Acknowledgments.** A.J. was supported by the Swedish Research Council (grant 2010-3710), the European Research Council under ERC Starting Grant agreement 278675-PEBBLE2PLANET, and the Knut and Alice Wallenberg Foundation. He would like to thank B. Weiss for stimulating discussions on layered accretion. E.J. wishes to remember his colleague and friend G. Barlet (1985–2014), who as a short-lived radionuclide theorist and chondrule/refractory inclusion specialist would certainly have contributed to the new paradigms discussed herein, true to his attachment to interdisciplinary interactions, but left us far too early. J.C. thanks C. Ormel for a careful reading, and E. Scott, A. Rubin, N. Kita, and G. Wasserburg for helpful comments and references. We would like to thank A. Rubin and an additional anonymous referee for insightful referee reports.

## REFERENCES

- Alexander C. M. O. and Ebel D. S. (2012) Questions, questions: Can the contradictions between the petrologic, isotopic, thermodynamic, and astrophysical constraints on chondrule formation be resolved? *Meteoritics & Planet. Sci.*, **47**, 1157.
- Alexander C. M. O., Grossman J. N., Ebel D. S., et al. (2008) The formation conditions of chondrules and chondrites. *Science*, **320**, 1617.
- Alexander R. D. and Armitage P. J. (2006) The stellar mass-accretion rate relation in T Tauri stars and brown dwarfs. *Astrophys. J. Lett.*, **639**, L83.
- Arnould M., Paulus G., and Meynet G. (1997) Short-lived radionuclide production by non-exploding Wolf-Rayet stars. *Astron. Astrophys.*, **321**, 452.
- Bai X.-N. and Stone J. M. (2010) Dynamics of solids in the midplane of protoplanetary disks: Implications for planetesimal formation. *Astrophys. J.*, **722**, 1437.
- Bai X.-N. and Stone J. M. (2013) Wind-driven accretion in protoplanetary disks. I. Suppression of the magnetorotational instability and launching of the magnetocentrifugal wind. *Astrophys. J.*, **769**, 76.
- Balbus S. A. and Hawley J. F. (1991) A powerful local shear instability in weakly magnetized disks. I — Linear analysis. II — Nonlinear evolution. *Astrophys. J.*, **376**, 214.
- Barge P. and Sommeria J. (1995) Did planet formation begin inside persistent gaseous vortices? *Astron. Astrophys.*, **295**, L1.
- Bec J., Biferale L., Cencini M., et al. (2007) Heavy particle concentration in turbulence at dissipative and inertial scales. *Phys. Rev. Lett.*, **98**(8), Article ID 084502.
- Bec J., Biferale L., Cencini M., et al. (2010) Intermittency in the velocity distribution of heavy particles in turbulence. *J. Fluid Mech.*, **646**, 527.
- Beckwith S. W., Henning T., and Nakagawa Y. (2000) Dust properties and assembly of large particles in protoplanetary disks. In *Protostars and Planets IV* (V. Mannings et al., eds.), p. 533. Univ. of Arizona, Tucson.
- Beitz E., Güttler C., Blum J., et al. (2011) Low-velocity collisions of centimeter-sized dust aggregates. *Astrophys. J.*, **736**, 34.
- Birnstiel T., Dullemond C. P., and Brauer F. (2010) Gas- and dust evolution in protoplanetary disks. *Astron. Astrophys.*, **513**, A79.
- Birnstiel T., Ormel C. W., and Dullemond C. P. (2011) Dust size distributions in coagulation/fragmentation equilibrium: Numerical solutions and analytical fits. *Astron. Astrophys.*, **525**, A11.
- Birnstiel T., Klahr H., and Ercolano B. (2012) A simple model for the evolution of the dust population in protoplanetary disks. *Astron. Astrophys.*, **539**, A148.
- Bitsch B., Morbidelli A., Lega E., et al. (2014) Stellar irradiated discs and implications on migration of embedded planets. III. Viscosity transitions. *Astron. Astrophys.*, **570**, A75.
- Bitsch B., Johansen A., Lambrechts L., and Morbidelli A. (2015) The structure of protoplanetary discs around evolving young stars. *Astron. Astrophys.*, **575**, A28.
- Bland P. A., Howard L. E., Prior D. J., et al. (2011) Earliest rock fabric formed in the solar system preserved in a chondrule rim. *Nature Geosci.*, **4**, 244.
- Blum J. and Wurm G. (2008) The growth mechanisms of macroscopic bodies in protoplanetary disks. *Annu. Rev. Astron. Astrophys.*, **46**, 21.
- Boss A. P. (1996) A concise guide to chondrule formation models. In *Chondrules and the Protoplanetary Disk* (R. H. Hewins et al., eds.) pp. 257–263. Cambridge Univ., Cambridge.
- Boss A. P. and Keiser S. A. (2013) Triggering collapse of the presolar dense cloud core and injecting short-lived radioisotopes with a shock wave. II. Varied shock wave and cloud core parameters. *Astrophys. J.*, **770**, 51.
- Bottke W. F., Durda D. D., Nesvorný D., et al. (2005) The fossilized size distribution of the main asteroid belt. *Icarus*, **175**, 111.
- Bottke W. F., Vokrouhlický D., Minton D., et al. (2012) An Archaean heavy bombardment from a destabilized extension of the asteroid belt. *Nature*, **485**, 78.
- Brauer F., Dullemond C. P., and Henning T. (2008) Coagulation, fragmentation and radial motion of solid particles in protoplanetary disks. *Astron. Astrophys.*, **480**, 859.
- Brearley A. J. (1993) Matrix and fine-grained rims in the unequilibrated CO<sub>3</sub> chondrite, ALHA77307 — Origins and evidence for diverse, primitive nebular dust components. *Geochim. Cosmochim. Acta*, **57**, 1521.
- Brearley A. J. (1996) Nature of matrix in unequilibrated chondrites and its possible relationship to chondrules. In *Chondrules and the Protoplanetary Disk* (by R. H. Hewins et al., eds.), pp. 137–151. Cambridge Univ., Cambridge.
- Brearley A. J. (2003) Nebular versus parent-body processing. In *Treatise on Geochemistry, Vol. 1: Meteorites, Comets and Planets* (A. M. Davis, ed.), p. 247. Elsevier, Amsterdam.
- Brearley A. and Jones A. (1998) Chondritic meteorites. In *Planetary Materials* (J. J. Papike, ed.), pp. 3-1 to 3-398. Mineralogical Society of America, Chantilly, Virginia.
- Burbine T. H., McCoy T. J., Meibom A., et al. (2002) Meteoritic parent bodies: Their number and identification. In *Asteroids III* (W. F. Bottke Jr. et al., eds.), pp. 653–667. Univ. of Arizona, Tucson.
- Cameron A. G. W. and Truran J. W. (1977) The supernova trigger for formation of the solar system. *Icarus*, **30**, 447.
- Carrera D., Johansen A., and Davies M. B. (2015) Formation of asteroids from mm-sized chondrules. *Astron. Astrophys.*, **579**, A43.
- Chambers J. E. (2010) Planetesimal formation by turbulent concentration. *Icarus*, **208**, 505.
- Chaussidon M. and Barrat J.-A. (2009) <sup>60</sup>Fe in eucrite NWA 4523: Evidences for secondary redistribution of Ni and for secondary apparent high <sup>60</sup>Fe/<sup>56</sup>Fe ratios in troilite. *Lunar Planet. Sci. XL*, Abstract #1752. Lunar and Planetary Institute, Houston.
- Chen J. H., Papanastassiou D. A., Telus M., et al. (2013) Fe-Ni isotopic systematics in UOC QUE 97008 and Semarkona chondrules. *Lunar Planet. Sci. XLIV*, Abstract #2649. Lunar and Planetary Institute, Houston.
- Chevalier R. A. (1999) Supernova remnants in molecular clouds. *Astrophys. J.*, **511**, 798.
- Chevalier R. A. (2000) Young circumstellar disks near evolved massive stars and supernovae. *Astrophys. J. Lett.*, **538**, L151.
- Chiang E. and Youdin A. N. (2010) Forming planetesimals in solar and extrasolar nebulae. *Annu. Rev. Earth Planet. Sci.*, **38**, 493.
- Ciesla F. J., Lauretta D. S., and Hood L. L. (2004) The frequency of compound chondrules and implications for chondrule formation. *Meteoritics & Planet. Sci.*, **39**, 531.
- Clayton R. N., Mayeda T. K., Olsen E. J., et al. (1991) Oxygen isotope studies of ordinary chondrites. *Geochim. Cosmochim. Acta*, **55**, 2317.
- Connolly H. C. Jr. and Desch S. J. (2004) On the origin of the ‘kleine Kugelchen’ called chondrules. *Chem. Erde—Geochem.*, **64**, 95.
- Connelly J. N., Bizzarro M., Krot A. N., et al. (2012) The absolute chronology and thermal processing of solids in the solar protoplanetary disk. *Science*, **338**, 651.
- Cuzzi J. N. (2004) Blowing in the wind: III. Accretion of dust rims by chondrule-sized particles in a turbulent protoplanetary nebula. *Icarus*, **168**, 484.

- Cuzzi J. N. and Alexander C. M. O. (2006) Chondrule formation in particle-rich nebular regions at least hundreds of kilometers across. *Nature*, 441, 483.
- Cuzzi J. N. and Hogan R. C. (2003) Blowing in the wind. I. Velocities of chondrule-sized particles in a turbulent protoplanetary nebula. *Icarus*, 164, 127.
- Cuzzi J. N. and Hogan R. C. (2012) Primary accretion by turbulent concentration: The rate of planetesimal formation and the role of vortex tubes. *Lunar Planet. Sci. XLIII*, Abstract #2536. Lunar and Planetary Institute, Houston.
- Cuzzi J. N. and Weidenschilling S. J. (2006) Particle-gas dynamics and primary accretion. In *Meteorites and the Early Solar System II* (D. S. Lauretta and H. Y. McSween Jr., eds.), pp. 353–381. Univ. of Arizona, Tucson.
- Cuzzi J. N., Dobrovolskis A. R., and Hogan R. C. (1996) Turbulence, chondrules, and planetesimals. In *Chondrules and the Protoplanetary Disk* (R. H. Hewins et al., eds.), pp. 35–43. Cambridge Univ., Cambridge.
- Cuzzi J. N., Hogan R. C., Paque J. M., et al. (2001) Size-selective concentration of chondrules and other small particles in protoplanetary nebula turbulence. *Astrophys. J.*, 546, 496.
- Cuzzi J. N., Ciesla F. J., Petaev M. I., et al. (2005) Nebula evolution of thermally processed solids: Reconciling models and meteorites. In *Chondrites and the Protoplanetary Disk* (A. N. Krot et al., eds.), p. 732. ASP Conf. Series 341, Astronomical Society of the Pacific, San Francisco.
- Cuzzi J. N., Hogan R. C., and Shariff K. (2008) Toward planetesimals: Dense chondrule clumps in the protoplanetary nebula. *Astrophys. J.*, 687, 1432.
- Cuzzi J. N., Hogan R. C., and Bottke W. F. (2010) Towards initial mass functions for asteroids and Kuiper Belt Objects. *Icarus*, 208, 518.
- Cuzzi J. N., Hartlep T., Weston B., et al. (2014) Turbulent concentration of mm-size particles in the protoplanetary nebula: Scale-dependent multiplier functions. *Lunar Planet. Sci. XLIV*, Abstract #2764. Lunar and Planetary Institute, Houston.
- Dauphas N. and Chaussidon M. (2011) A perspective from extinct radionuclides on a young stellar object: The Sun and its accretion disk. *Annu. Rev. Earth Planet. Sci.*, 39, 351.
- Deharveng L., Schuller F., Anderson L. D., et al. (2010) A gallery of bubbles. The nature of the bubbles observed by Spitzer and what ATLASGAL tells us about the surrounding neutral material. *Astron. Astrophys.*, 523, A6.
- Desch S. J., Morris M. A., Connolly H. C., et al. (2012) The importance of experiments: Constraints on chondrule formation models. *Meteoritics & Planet. Sci.*, 47, 1139.
- Dittrich K., Klahr H., and Johansen A. (2013) Graviturbulent planetesimal formation: The positive effect of long-lived zonal flows. *Astrophys. J.*, 763, 117.
- Dodd R. T. (1976) Accretion of the ordinary chondrites. *Earth Planet. Sci. Lett.*, 30, 281.
- Dominik C. and Tielens A. G. G. M. (1997) The physics of dust coagulation and the structure of dust aggregates in space. *Astrophys. J.*, 480, 647.
- Dominik C., Blum J., Cuzzi J. N., et al. (2007) Growth of dust as the initial step toward planet formation. In *Protostars and Planets V* (B. Reipurth et al., eds.), pp. 783–800. Univ. of Arizona, Tucson.
- Doyle P. M., Krot A. N., Nagashima K., et al. (2014) Manganese-chromium ages of aqueous alteration of unequilibrated ordinary chondrites. *Lunar Planet. Sci. XLIV*, Abstract #1726. Lunar and Planetary Institute, Houston.
- Drażkowska J., Windmark F., and Dullemond C. P. (2013) Planetesimal formation via sweep-up growth at the inner edge of dead zones. *Astron. Astrophys.*, 556, A37.
- Eaton J. K. and Fessler J. R. (1994) Preferential concentration of particles by turbulence. *Int. J. Multiphase Flow, Suppl.*, 20, 169–209.
- Ebel D., Brunner C., Leftwich K., Erb I., Lu M., Konrad K., Rodriguez H., Friedrich J., and Weisberg M. (2015) Abundance, composition and size of inclusions and matrix in CV and CO chondrites. *Geochim. Cosmochim. Acta*, in press.
- Elkins-Tanton L. T., Weiss B. P., and Zuber M. T. (2011) Chondrites as samples of differentiated planetesimals. *Earth Planet. Sci. Lett.*, 305, 1.
- Eugster O., Herzog G. F., Marti K., et al. (2006) Irradiation records, cosmic-ray exposure ages, and transfer times of meteorites. In *Meteorites and the Early Solar System II* (D. S. Lauretta and H. Y. McSween Jr., eds.), pp. 829–851. Univ. of Arizona, Tucson.
- Fisher K. R., Tait A. W., Simon J. I., et al. (2014) Contrasting size distributions of chondrules and inclusions in Allende CV3. *Lunar Planet. Sci. XLIV*, Abstract #2711. Lunar and Planetary Institute, Houston.
- Fraser W. C., Brown M. E., Morbidelli A., et al. (2014) The absolute magnitude distribution of Kuiper belt objects. *Astrophys. J.*, 782, 100.
- Fressin F., Torres G., Charbonneau D., et al. (2013) The false positive rate of Kepler and the occurrence of planets. *Astrophys. J.*, 766, 81.
- Friedrich J. M., Weisberg M. K., Ebel D. S., Biltz A. E., Corbett B. M., Iotov I. V., Khan W. S., and Wolman M. D. (2015) Chondrule size and related physical properties: A compilation and evaluation of current data across all meteorite groups. *Chem. Erde*, in press, DOI: 10.1016/j.chemer.2014.08.003.
- Fu R. R. and Elkins-Tanton L. T. (2014) The fate of magmas in planetesimals and the retention of primitive chondritic crusts. *Earth Planet. Sci. Lett.*, 390, 128.
- Fujiya W., Sugiyama N., Sano Y., et al. (2013) Mn-Cr ages of dolomites in CI chondrites and the Tagish Lake ungrouped carbonaceous chondrite. *Earth Planet. Sci. Lett.*, 362, 130.
- Gaidos E., Krot A. N., Williams J. P., et al. (2009)  $^{26}\text{Al}$  and the formation of the solar system from a molecular cloud contaminated by Wolf-Rayet winds. *Astrophys. J.*, 696, 1854.
- Gail H.-P., Trieloff M., Breuer D., et al. (2014) Early thermal evolution of planetesimals and its impact on processing and dating of meteoritic material. In *Protostars and Planets VI* (H. Beuther et al., eds.), pp. 571–593. Univ. of Arizona, Tucson.
- Gal-Yam A., Arcavi I., Ofek E. O., et al. (2014) A Wolf-Rayet-like progenitor of SN 2013cu from spectral observations of a stellar wind. *Nature*, 509, 471.
- Garaud P., Meru F., Galvagni M., et al. (2013) From dust to planetesimals: An improved model for collisional growth in protoplanetary disks. *Astrophys. J.*, 764, 146.
- Gounelle M. (2014) Aluminium-26 in the early solar system: A probability estimate. *Lunar Planet. Sci. XLIV*, Abstract #2113. Lunar and Planetary Institute, Houston.
- Gounelle M. and Meibom A. (2008) The origin of short-lived radionuclides and the astrophysical environment of solar system formation. *Astrophys. J.*, 680, 781.
- Gounelle M. and Meynet G. (2012) Solar system genealogy revealed by extinct short-lived radionuclides in meteorites. *Astron. Astrophys.*, 545, A4.
- Gounelle M., Shu F. H., Shang H., et al. (2006) The irradiation origin of beryllium radioisotopes and other short-lived radionuclides. *Astrophys. J.*, 640, 1163.
- Gounelle M., Meibom A., Hennebelle P., et al. (2009) Supernova propagation and cloud enrichment: A new model for the origin of  $^{60}\text{Fe}$  in the early solar system. *Astrophys. J. Lett.*, 694, L1.
- Gounelle M., Chaussidon M., and Rollion-Bard C. (2013) Variable and extreme irradiation conditions in the early solar system inferred from the initial abundance of  $^{10}\text{Be}$  in Isheyev CAIs. *Astrophys. J. Lett.*, 763, L33.
- Grimm R. E. and McSween H. Y. (1993) Heliocentric zoning of the asteroid belt by aluminum-26 heating. *Science*, 259, 653.
- Guan Y., Huss G. R., Leshin L. A., et al. (2006) Oxygen isotope and  $^{26}\text{Al}$ - $^{26}\text{Mg}$  systematics of aluminum-rich chondrules from unequilibrated enstatite chondrites. *Meteoritics & Planet. Sci.*, 41, 33.
- Güttler C., Blum J., Zsom A., et al. (2010) The outcome of protoplanetary dust growth: Pebbles, boulders, or planetesimals? I. Mapping the zoo of laboratory collision experiments. *Astron. Astrophys.*, 513, A56.
- Hartmann L., Calvet N., Gullbring E., et al. (1998) Accretion and the evolution of T Tauri disks. *Astrophys. J.*, 495, 385.
- Hayashi C. (1981) Structure of the solar nebula, growth and decay of magnetic fields and effects of magnetic and turbulent viscosities on the nebula. *Progr. Theor. Phys. Suppl.*, 70, 35.
- Henke S., Gail H.-P., Trieloff M., et al. (2013) Thermal evolution model for the H chondrite asteroid-instantaneous formation versus protracted accretion. *Icarus*, 226, 212.
- Hester J. J., Desch S. J., Healy K. R., et al. (2004) The cradle of the solar system. *Science*, 304, 1116.
- Hewins R. H., Connolly H. C., Lofgren G. E., et al. (2005) Experimental constraints on chondrule formation. In *Chondrites and the Protoplanetary Disk* (A. N. Krot et al., eds.), pp. 286–316. ASP Conf. Series 341, Astronomical Society of the Pacific, San Francisco.

- Hezel D. C. and Palme H. (2010) The chemical relationship between chondrules and matrix and the chondrule matrix complementarity. *Earth Planet. Sci. Lett.*, 294, 85.
- Hezel D. C., Russell S. S., Ross A. J., et al. (2008) Modal abundances of CAIs: Implications for bulk chondrite element abundances and fractionations. *Meteoritics & Planet. Sci.*, 43, 1879.
- Hogan R. C. and Cuzzi J. N. (2007) Cascade model for particle concentration and enstrophy in fully developed turbulence with mass-loading feedback. *Phys. Rev. E*, 75(5), Article ID 056305.
- Huss G. R., Rubin A. E., and Grossman J. N. (2006) Thermal metamorphism in chondrites. In *Meteorites and the Early Solar System II* (D. S. Lauretta and H. Y. McSween Jr., eds.), pp. 567–586. Univ. of Arizona, Tucson.
- Huss G. R., Meyer B. S., Srinivasan G., et al. (2009) Stellar sources of the short-lived radionuclides in the early solar system. *Geochim. Cosmochim. Acta*, 73, 4922.
- Ida S., Guillot T., and Morbidelli A. (2008) Accretion and destruction of planetesimals in turbulent disks. *Astrophys. J.*, 686, 1292.
- Jacobsen B., Yin Q.-Z., Moynier F., et al. (2008)  $^{26}\text{Al}$ - $^{26}\text{Mg}$  and  $^{207}\text{Pb}$ - $^{206}\text{Pb}$  systematics of Allende CAIs: Canonical solar initial  $^{26}\text{Al}$ / $^{27}\text{Al}$  ratio reinstated. *Earth Planet. Sci. Lett.*, 272, 353.
- Jacquet E. (2014a) The quasi-universality of chondrule size as a constraint for chondrule formation models. *Icarus*, 232, 176.
- Jacquet E. (2014b) Transport of solids in protoplanetary disks: Comparing meteorites and astrophysical models. *Compt. Rend. Geosci.*, 346, 3.
- Jacquet E., Balbus S., and Latter H. (2011) On linear dust-gas streaming instabilities in protoplanetary discs. *Mon. Not. R. Astron. Soc.*, 415, 3591.
- Jacquet E., Alard O., and Gounelle M. (2012a) Chondrule trace element geochemistry at the mineral scale. *Meteoritics & Planet. Sci.*, 47, 1695.
- Jacquet E., Gounelle M., and Fromang S. (2012b) On the aerodynamic redistribution of chondrite components in protoplanetary disks. *Icarus*, 220, 162.
- Jarosewich E. (1990) Chemical analyses of meteorites — A compilation of stony and iron meteorite analyses. *Meteoritics*, 25, 323.
- Johansen A. and Lacerda P. (2010) Prograde rotation of protoplanets by accretion of pebbles in a gaseous environment. *Mon. Not. R. Astron. Soc.*, 404, 475.
- Johansen A. and Youdin A. (2007) Protoplanetary disk turbulence driven by the streaming instability: Nonlinear saturation and particle concentration. *Astrophys. J.*, 662, 627.
- Johansen A., Klahr H., and Henning T. (2006) Graviturbulent formation of planetesimals. *Astrophys. J.*, 636, 1121.
- Johansen A., Oishi J. S., Mac Low M.-M., et al. (2007) Rapid planetesimal formation in turbulent circumstellar disks. *Nature*, 448, 1022.
- Johansen A., Brauer F., Dullemond C., et al. (2008) A coagulation fragmentation model for the turbulent growth and destruction of preplanetesimals. *Astron. Astrophys.*, 486, 597.
- Johansen A., Youdin A., and Klahr H. (2009a) Zonal flows and long-lived axisymmetric pressure bumps in magnetorotational turbulence. *Astrophys. J.*, 697, 1269.
- Johansen A., Youdin A., and Mac Low M.-M. (2009b) Particle clumping and planetesimal formation depend strongly on metallicity. *Astrophys. J. Lett.*, 704, L75.
- Johansen A., Klahr H., and Henning T. (2011) High-resolution simulations of planetesimal formation in turbulent protoplanetary discs. *Astron. Astrophys.*, 529, A62.
- Johansen A., Youdin A. N., and Lithwick Y. (2012) Adding particle collisions to the formation of asteroids and Kuiper belt objects via streaming instabilities. *Astron. Astrophys.*, 537, A125.
- Johansen A., Blum J., Tanaka H., et al. (2014) The multifaceted planetesimal formation process. In *Protostars and Planets V* (B. Reipurth et al., eds.), pp. 547–570. Univ. of Arizona, Tucson.
- Johansen A., Mac Low M.-M., Lacerda P., and Bizzarro M. (2015) Growth of asteroids, planetary embryos, and Kuiper belt objects by chondrule accretion. *Sci. Adv.*, 1(3), 1500109.
- Jones R. H. (2012) Petrographic constraints on the diversity of chondrule reservoirs in the protoplanetary disk. *Meteoritics & Planet. Sci.*, 47, 1176.
- Kastner J. H. and Myers P. C. (1994) An observational estimate of the probability of encounters between mass-losing evolved stars and molecular clouds. *Astrophys. J.*, 421, 605.
- Kato M. T., Fujimoto M., and Ida S. (2012) Planetesimal formation at the boundary between steady super/sub-Keplerian flow created by inhomogeneous growth of magnetorotational instability. *Astrophys. J.*, 747, 11.
- Keil K., Stoeffler D., Love S. G., et al. (1997) Constraints on the role of impact heating and melting in asteroids. *Meteoritics & Planet. Sci.*, 32, 349.
- Kita N. T. and Ushikubo T. (2012) Evolution of protoplanetary disk inferred from  $^{26}\text{Al}$  chronology of individual chondrules. *Meteoritics & Planet. Sci.*, 47, 1108.
- Kita N. T., Yin Q.-Z., MacPherson G. J., et al. (2013)  $^{26}\text{Al}$ - $^{26}\text{Mg}$  isotope systematics of the first solids in the early solar system. *Meteoritics & Planet. Sci.*, 48, 1383.
- Klahr H. H. and Bodenheimer P. (2003) Turbulence in accretion disks: Vorticity generation and angular momentum transport via the global baroclinic instability. *Astrophys. J.*, 582, 869.
- Kretke K. A. and Lin D. N. C. (2007) Grain retention and formation of planetesimals near the snow line in MRI-driven turbulent protoplanetary disks. *Astrophys. J. Lett.*, 664, L55.
- Krot A., Petaev M., Russell S. S., et al. (2004) Amoeboid olivine aggregates and related objects in carbonaceous chondrites: Records of nebular and asteroid processes. *Chem. Erde—Geochem.*, 64, 185.
- Krot A. N., Amelin Y., Bland P., et al. (2009) Origin and chronology of chondritic components: A review. *Geochim. Cosmochim. Acta*, 73, 4963.
- Kruijer T. S., Sprung P., Kleine T., et al. (2012) Hf-W chronometry of core formation in planetesimals inferred from weakly irradiated iron meteorites. *Geochim. Cosmochim. Acta*, 99, 287.
- Kuebler K. E., McSween H. Y., Carlson W. D., et al. (1999) Sizes and masses of chondrules and metal-troilite grains in ordinary chondrites: Possible implications for nebular sorting. *Icarus*, 141, 96.
- Lambrechts M. and Johansen A. (2012) Rapid growth of gas-giant cores by pebble accretion. *Astron. Astrophys.*, 544, A32.
- Lambrechts M., Johansen A., and Morbidelli A. (2014) Separating gas-giant and ice-giant planets by halting pebble accretion. *Astron. Astrophys.*, 572, A35.
- Larsen K. K., Trinquier A., Paton C., et al. (2011) Evidence for magnesium isotope heterogeneity in the solar protoplanetary disk. *Astrophys. J. Lett.*, 735, L37.
- Laughlin G., Steinacker A., and Adams F. C. (2004) Type I planetary migration with MHD turbulence. *Astrophys. J.*, 608, 489.
- Lauretta D. S., Nagahara H., and Alexander C. M. O. (2006) Petrology and origin of ferromagnesian silicate chondrules. In *Meteorites and the Early Solar System II* (D. S. Lauretta and H. Y. McSween, Jr., eds.), pp. 431–459. Univ. of Arizona, Tucson.
- Lee T. (1978) A local proton irradiation model for isotopic anomalies in the solar system. *Astrophys. J.*, 224, 217.
- Lee T., Papanastassiou D. A., and Wasserburg G. J. (1976) Demonstration of Mg-26 excess in Allende and evidence for Al-26. *Geophys. Res. Lett.*, 3, 41.
- Lee T., Shu F. H., Shang H., et al. (1998) Protostellar cosmic rays and extinct radioactivities in meteorites. *Astrophys. J.*, 506, 898.
- Lesur G. and Papaloizou J. C. B. (2010) The subcritical baroclinic instability in local accretion disc models. *Astron. Astrophys.*, 513, A60.
- Libourel G. and Krot A. N. (2007) Evidence for the presence of planetesimal material among the precursors of magnesian chondrules of nebular origin. *Earth Planet. Sci. Lett.*, 254, 1.
- Liu M.-C., Chaussidon M., Göpel C., et al. (2012) A heterogeneous solar nebula as sampled by CM hibonite grains. *Earth Planet. Sci. Lett.*, 327, 75.
- Looney L. W., Tobin J. J., and Fields B. D. (2006) Radioactive probes of the supernova-contaminated solar nebula: Evidence that the Sun was born in a cluster. *Astrophys. J.*, 652, 1755.
- Lugardo M., Doherty C. L., Karakas A. I., et al. (2012) Short-lived radioactivity in the early solar system: The super-AGB star hypothesis. *Meteoritics & Planet. Sci.*, 47, 1998.
- Lyra W., Johansen A., Klahr H., et al. (2008) Embryos grown in the dead zone. Assembling the first protoplanetary cores in low mass self-gravitating circumstellar disks of gas and solids. *Astron. Astrophys.*, 491, L41.
- Lyra W., Johansen A., Zsom A., et al. (2009) Planet formation bursts at the borders of the dead zone in 2D numerical simulations of circumstellar disks. *Astron. Astrophys.*, 497, 869.
- MacPherson G. J. (2005) Calcium-aluminum-rich inclusions in chondritic meteorites. In *Treatise on Geochemistry, Vol. 1: Meteorites, Comets and Planets* (A. M. Davis, ed.), pp. 201–246. Elsevier, Amsterdam.

- MacPherson G. J., Hashimoto A., and Grossman L. (1985) Accretionary rims on inclusions in the Allende meteorite. *Geochim. Cosmochim. Acta*, **49**, 2267.
- MacPherson G. J., Davis A. M., and Zinner E. K. (2014) Distribution of  $^{26}\text{Al}$  in the early solar system: A 2014 reappraisal. *Lunar Planet. Sci. XLIV*, Abstract #2134. Lunar and Planetary Institute, Houston.
- Makide K., Nagashima K., Krot A. N., et al. (2013) Heterogeneous distribution of  $^{26}\text{Al}$  at the birth of the solar system: Evidence from corundum-bearing refractory inclusions in carbonaceous chondrites. *Geochim. Cosmochim. Acta*, **110**, 190.
- Martin R. G. and Livio M. (2012) On the evolution of the snow line in protoplanetary discs. *Mon. Not. R. Astron. Soc.*, **425**, L6.
- Martin R. G. and Livio M. (2013) On the evolution of the snow line in protoplanetary discs — II. Analytic approximations. *Mon. Not. R. Astron. Soc.*, **434**, 633.
- Metzler K. (2012) Ultrarapid chondrite formation by hot chondrule accretion? Evidence from unequilibrated ordinary chondrites. *Meteoritics & Planet. Sci.*, **47**, 2193.
- Metzler K., Bischoff A., and Stoeffler D. (1992) Accretionary dust mantles in CM chondrites — Evidence for solar nebula processes. *Geochim. Cosmochim. Acta*, **56**, 2873.
- Mizuno H., Markiewicz W. J., and Voelk H. J. (1988) Grain growth in turbulent protoplanetary accretion disks. *Astron. Astrophys.*, **195**, 183.
- Monnereau M., Toplis M. J., Baratoux D., et al. (2013) Thermal history of the H-chondrite parent body: Implications for metamorphic grade and accretionary time-scales. *Geochim. Cosmochim. Acta*, **119**, 302.
- Morbidelli A., Chambers J., Lunine J. I., et al. (2000) Source regions and time scales for the delivery of water to Earth. *Meteoritics & Planet. Sci.*, **35**, 1309.
- Morbidelli A., Bottke W. F., Nesvorný D., et al. (2009) Asteroids were born big. *Icarus*, **204**, 558.
- Morfill G. E., Durisen R. H., and Turner G. W. (1998) NOTE: An accretion rim constraint on chondrule formation theories. *Icarus*, **134**, 180.
- Mostefaiou S., Lugmair G. W., and Hoppe P. (2005)  $^{60}\text{Fe}$ : A heat source for planetary differentiation from a nearby supernova explosion. *Astrophys. J.*, **625**, 271.
- Mothé-Diniz T. and Nesvorný D. (2008) Visible spectroscopy of extremely young asteroid families. *Astron. Astrophys.*, **486**, L9.
- Mothé-Diniz T., Roig F., and Carvano J. M. (2005) Reanalysis of asteroid families structure through visible spectroscopy. *Icarus*, **174**, 54.
- Mothé-Diniz T., Carvano J. M., Bus S. J., et al. (2008) Mineralogical analysis of the Eos family from near-infrared spectra. *Icarus*, **195**, 277.
- Nakagawa Y., Sekiya M., and Hayashi C. (1986) Settling and growth of dust particles in a laminar phase of a low-mass solar nebula. *Icarus*, **67**, 375.
- Nelson R. P. and Gressel O. (2010) On the dynamics of planetesimals embedded in turbulent protoplanetary discs. *Mon. Not. R. Astron. Soc.*, **409**, 639.
- Nelson R. P. and Papaloizou J. C. B. (2004) The interaction of giant planets with a disc with MHD turbulence — IV. Migration rates of embedded protoplanets. *Mon. Not. R. Astron. Soc.*, **350**, 849.
- Nelson V. E. and Rubin A. E. (2002) Size-frequency distributions of chondrules and chondrule fragments in LL3 chondrites: Implications for parent-body fragmentation of chondrules. *Meteoritics & Planet. Sci.*, **37**, 1361.
- Nelson R. P., Gressel O., and Umurhan O. M. (2013) Linear and non-linear evolution of the vertical shear instability in accretion discs. *Mon. Not. R. Astron. Soc.*, **435**, 2610.
- O'Brien D. P., Walsh K. J., Morbidelli A., et al. (2014) Water delivery and giant impacts in the “Grand Tack” scenario. *Icarus*, **239**, 74.
- Oishi J. S., Mac Low M.-M., and Menou K. (2007) Turbulent torques on protoplanets in a dead zone. *Astrophys. J.*, **670**, 805.
- Okuzumi S., Tanaka H., Kobayashi H., et al. (2012) Rapid coagulation of porous dust aggregates outside the snow line: A pathway to successful icy planetesimal formation. *Astrophys. J.*, **752**, 106.
- Ormel C. W. and Cuzzi J. N. (2007) Closed-form expressions for particle relative velocities induced by turbulence. *Astron. Astrophys.*, **466**, 413.
- Ormel C. W. and Klahr H. H. (2010) The effect of gas drag on the growth of protoplanets. Analytical expressions for the accretion of small bodies in laminar disks. *Astron. Astrophys.*, **520**, A43.
- Ormel C. W. and Okuzumi S. (2013) The fate of planetesimals in turbulent disks with dead zones. II. Limits on the viability of runaway accretion. *Astrophys. J.*, **771**, 44.
- Ormel C. W., Cuzzi J. N., and Tielens A. G. G. M. (2008) Co-accretion of chondrules and dust in the solar nebula. *Astrophys. J.*, **679**, 1588.
- Ouellette N., Desch S. J., and Hester J. J. (2007) Interaction of supernova ejecta with nearby protoplanetary disks. *Astrophys. J.*, **662**, 1268.
- Palme H. and Jones A. (2005) Solar system abundances of the elements. In *Treatise on Geochemistry, Vol. 1: Meteorites, Comets and Planets* (A. M. Davis, ed.), pp. 41–60. Elsevier, Amsterdam.
- Pan M. and Sari R. (2005) Shaping the Kuiper belt size distribution by shattering large but strengthless bodies. *Icarus*, **173**, 342.
- Pan L., Padoa P., Scalo J., et al. (2011) Turbulent clustering of protoplanetary dust and planetesimal formation. *Astrophys. J.*, **740**, 6.
- Pan L., Desch S. J., Scannapieco E., et al. (2012) Mixing of clumpy supernova ejecta into molecular clouds. *Astrophys. J.*, **756**, 102.
- Quitté G., Halliday A. N., Meyer B. S., et al. (2007) Correlated iron 60, nickel 62, and zirconium 96 in refractory inclusions and the origin of the solar system. *Astrophys. J.*, **655**, 678.
- Quitté G., Latkoczy C., Schönbachler M., et al. (2011)  $^{60}\text{Fe}$ - $^{60}\text{Ni}$  systematics in the eucrite parent body: A case study of Bouvante and Juvinas. *Geochim. Cosmochim. Acta*, **75**, 7698.
- Raymond S. N., Quinn T., and Lunine J. I. (2004) Making other Earths: Dynamical simulations of terrestrial planet formation and water delivery. *Icarus*, **168**, 1.
- Ros K. and Johansen A. (2013) Ice condensation as a planet formation mechanism. *Astron. Astrophys.*, **552**, A137.
- Rubin A. E. (2000) Petrologic, geochemical and experimental constraints on models of chondrule formation. *Earth Sci. Rev.*, **50**, 3.
- Rubin A. E. (2005) Relationships among intrinsic properties of ordinary chondrites: Oxidation state, bulk chemistry, oxygen isotopic composition, petrologic type, and chondrule size. *Geochim. Cosmochim. Acta*, **69**, 4907.
- Rubin A. E. (2011) Origin of the differences in refractory lithophile-element abundances among chondrite groups. *Icarus*, **213**, 547.
- Rubin A. E. and Brearley A. J. (1996) A critical evaluation of the evidence for hot accretion. *Icarus*, **124**, 86.
- Schneider D. M., Akridge D. G., and Sears D. W. G. (1998) Size distribution of metal grains and chondrules in enstatite chondrites. *Meteoritics & Planet. Sci., Suppl.*, **33**, 136.
- Schräpler R., Blum J., Seizinger A., et al. (2012) The physics of protoplanetesimal dust agglomerates. VII. The low-velocity collision behavior of large dust agglomerates. *Astrophys. J.*, **758**, 35.
- Scott E. R. D. and Krot A. N. (2003) Chondrites and their components. In *Treatise on Geochemistry, Vol. 1: Meteorites, Comets and Planets* (A. M. Davis, ed.), p. 143. Elsevier, Amsterdam.
- Scott E. R. D. and Rajan R. S. (1981) Metallic minerals, thermal histories and parent bodies of some xenolithic, ordinary chondrite meteorites. *Geochim. Cosmochim. Acta*, **45**, 53.
- Scott E. R. D., Rubin A. E., Taylor G. J., et al. (1984) Matrix material in type 3 chondrites — Occurrence, heterogeneity and relationship with chondrules. *Geochim. Cosmochim. Acta*, **48**, 1741.
- Scott E. R. D., Krot T. V., Goldstein J. I., et al. (2014) Thermal and impact history of the H chondrite parent asteroid during metamorphism: Constraints from metallic Fe-Ni. *Geochim. Cosmochim. Acta*, **136**, 13.
- Sekiya M. (1983) Gravitational instabilities in a dust-gas layer and formation of planetesimals in the solar nebula. *Progr. Theor. Phys. Suppl.*, **69**, 1116.
- Setoh M., Hiraoka K., Nakamura A. M., et al. (2007) Collisional disruption of porous sintered glass beads at low impact velocities. *Adv. Space Res.*, **40**, 252.
- Shaw R. (2003) Particle-turbulence interactions in atmospheric clouds. *Annu. Rev. Fluid Mech.*, **35**, 183–227.
- Shukolyukov A. and Lugmair G. W. (1993) Live iron-60 in the early solar system. *Science*, **259**, 1138.
- Simon J. B., Beckwith K., and Armitage P. J. (2012) Emergent mesoscale phenomena in magnetized accretion disc turbulence. *Mon. Not. R. Astron. Soc.*, **422**, 2685.
- Sirono S.-i. (2011) Planetesimal formation induced by sintering. *Astrophys. J. Lett.*, **733**, L41.
- Sonett C. P. and Colburn D. S. (1968) Electrical heating of meteorite parent bodies and planets by dynamo induction from a pre-main sequence T Tauri “solar wind.” *Nature*, **219**, 924.
- Squires K. D. and Eaton J. K. (1990) Particle response and turbulence modification in isotropic turbulence. *Phys. Fluids*, **2**, 1191.
- Squires K. D. and Eaton J. K. (1991) Preferential concentration of particles by turbulence. *Phys. Fluids*, **3**, 1169.

- Stewart S. T. and Leinhardt Z. M. (2009) Velocity-dependent catastrophic disruption criteria for planetesimals. *Astrophys. J. Lett.*, **691**, L133.
- Tachibana S. and Huss G. R. (2003) The initial abundance of  $^{60}\text{Fe}$  in the solar system. *Astrophys. J. Lett.*, **588**, L41.
- Tachibana S., Huss G. R., Kita N. T., et al. (2006)  $^{60}\text{Fe}$  in chondrites: Debris from a nearby supernova in the early solar system? *Astrophys. J. Lett.*, **639**, L87.
- Tang H. and Dauphas N. (2012) Abundance, distribution, and origin of  $^{60}\text{Fe}$  in the solar protoplanetary disk. *Earth Planet. Sci. Lett.*, **359**, 248.
- Tang X. and Chevalier R. A. (2014) Gamma-ray emission from supernova remnant interactions with molecular clumps. *Astrophys. J. Lett.*, **784**, L35.
- Tatischeff V., Duprat J., and de Séreille N. (2010) A runaway Wolf-Rayet star as the origin of  $^{26}\text{Al}$  in the early solar system. *Astrophys. J. Lett.*, **714**, L26.
- Taylor G. J., Maggiore P., Scott E. R. D., et al. (1987) Original structures, and fragmentation and reassembly histories of asteroids - Evidence from meteorites. *Icarus*, **69**, 1.
- Telus M., Huss G. R., Ogliore R. C., et al. (2012) Recalculation of data for short-lived radionuclide systems using less-biased ratio estimation. *Meteoritics & Planet. Sci.*, **47**, 2013.
- Testi L., Birnstiel T., Ricci L., et al. (2014) Dust evolution in protoplanetary disks. In *Protostars and Planets VI* (H. Beuther et al., eds.), pp. 339–362. Univ. of Arizona, Tucson.
- Trieloff M., Jessberger E. K., Herrwerth I., et al. (2003) Structure and thermal history of the H-chondrite parent asteroid revealed by thermochronometry. *Nature*, **422**, 502.
- Trinquier A., Elliott T., Ulfbeck D., et al. (2009) Origin of nucleosynthetic isotope heterogeneity in the solar protoplanetary disk. *Science*, **324**, 374.
- Turner N. J., Fromang S., Gammie C., et al. (2014) Transport and accretion in planet-forming disks. In *Protostars and Planets VI* (H. Beuther et al., eds.), pp. 411–432. Univ. of Arizona, Tucson.
- Urey H. C. (1955) The cosmic abundances of potassium, uranium, and thorium and the heat balances of the Earth, the Moon, and Mars. *Proc. Natl. Acad. Sci.*, **41**, 127.
- Vasileiadis A., Nordlund Å., and Bizzarro M. (2013) Abundance of  $^{26}\text{Al}$  and  $^{60}\text{Fe}$  in evolving giant molecular clouds. *Astrophys. J. Lett.*, **769**, L8.
- Vernazza P., Zanda B., Binzel R. P., et al. (2014) Multiple and fast: The accretion of ordinary chondrite parent bodies. *Astrophys. J.*, **791**, 120.
- Villeneuve J., Chaussidon M., and Libourel G. (2012) Lack of relationship between aluminum-26 ages of chondrules and their mineralogical and chemical compositions. *Compt. Rend. Geosci.*, **344**, 423.
- Voelk H. J., Jones F. C., Morfill G. E., et al. (1980) Collisions between grains in a turbulent gas. *Astron. Astrophys.*, **85**, 316.
- Wada K., Tanaka H., Suyama T., et al. (2009) Collisional growth conditions for dust aggregates. *Astrophys. J.*, **702**, 1490.
- Wada K., Tanaka H., Okuzumi S., et al. (2013) Growth efficiency of dust aggregates through collisions with high mass ratios. *Astron. Astrophys.*, **559**, A62.
- Walsh K. J., Morbidelli A., Raymond S. N., et al. (2011) A low mass for Mars from Jupiter's early gas-driven migration. *Nature*, **475**, 206.
- Wang L.-P. and Maxey M. R. (1993) Settling velocity and concentration distribution of heavy particles in homogeneous isotropic turbulence. *J. Fluid Mech.*, **256**, 27.
- Wasserburg G. J., Wimpenny J., and Yin Q.-Z. (2012) Mg isotopic heterogeneity, Al-Mg isochrons, and canonical  $^{26}\text{Al}/^{27}\text{Al}$  in the early solar system. *Meteoritics & Planet. Sci.*, **47**, 1980.
- Wasson J. T., Isa J., and Rubin A. E. (2013) Compositional and petrographic similarities of CV and CK chondrites: A single group with variations in textures and volatile concentrations attributable to impact heating, crushing and oxidation. *Geochim. Cosmochim. Acta*, **108**, 45.
- Weidenschilling S. J. (1977a) Aerodynamics of solid bodies in the solar nebula. *Mon. Not. R. Astron. Soc.*, **180**, 57.
- Weidenschilling S. J. (1977b) Aerodynamics of solid bodies in the solar nebula. *Mon. Not. R. Astron. Soc.*, **180**, 57.
- Weidenschilling S. J. (2011) Initial sizes of planetesimals and accretion of the asteroids. *Icarus*, **214**, 671.
- Weidling R., Gütter C., and Blum J. (2012) Free collisions in a microgravity many-particle experiment. I. Dust aggregate sticking at low velocities. *Icarus*, **218**, 688.
- Weisberg M. K., McCoy T. J., and Krot A. N. (2006) Systematics and evaluation of meteorite classification. In *Meteorites and the Early Solar System II* (D. S. Lauretta and H. Y. McSween, Jr., eds.), pp. 19–52. Univ. of Arizona, Tucson.
- Weiss B. P. and Elkins-Tanton L. T. (2013) Differentiated planetesimals and the parent bodies of chondrites. *Annu. Rev. Earth Planet. Sci.*, **41**, 529.
- Weiss B. P., Gattaccea J., and Stanley S. et al. (2010) Paleomagnetic records of meteorites and early planetesimal differentiation. *Space Sci. Rev.*, **152**, 341.
- Whattam S. A., Hewins R. H., Cohen B. A., et al. (2008) Granoblastic olivine aggregates in magnesian chondrules: Planetesimal fragments or thermally annealed solar nebula condensates? *Earth Planet. Sci. Lett.*, **269**, 200.
- Whipple F. L. (1972) On certain aerodynamic processes for asteroids and comets. In *From Plasma to Planet* (A. Elvius, ed.), p. 211. Wiley, New York.
- Williams J. P. and Gaidos E. (2007) On the likelihood of supernova enrichment of protoplanetary disks. *Astrophys. J. Lett.*, **663**, L33.
- Windmark F., Birnstiel T., Gütter C., et al. (2012a) Planetesimal formation by sweep-up: How the bouncing barrier can be beneficial to growth. *Astron. Astrophys.*, **540**, A73.
- Windmark F., Birnstiel T., Ormel C. W., et al. (2012b) Breaking through: The effects of a velocity distribution on barriers to dust growth. *Astron. Astrophys.*, **544**, L16.
- Wood J. A. (2005) The chondrite types and their origins. In *Chondrites and the Protoplanetary Disk* (A. N. Krot et al., eds.), p. 953. ASP Conf. Series 341, Astronomical Society of the Pacific, San Francisco.
- Woosley S. E. and Heger A. (2007) Nucleosynthesis and remnants in massive stars of solar metallicity. *Phys. Rept.*, **442**, 269.
- Wurm G., Paraskov G., and Krauss O. (2005) Growth of planetesimals by impacts at  $\sim 25 \text{ m/s}$ . *Icarus*, **178**, 253.
- Xie J.-W., Payne M. J., Thébault P., et al. (2010) From dust to planetesimal: The snowball phase? *Astrophys. J.*, **724**, 1153.
- Yang C.-C. and Johansen A. (2014) On the feeding zone of planetesimal formation by the streaming instability. *Astrophys. J.*, **792**, 86.
- Yang C.-C., Mac Low M.-M., and Menou K. (2012) Planetesimal and protoplanet dynamics in a turbulent protoplanetary disk: Ideal stratified disks. *Astrophys. J.*, **748**, 79.
- Youdin A. N. and Goodman J. (2005) Streaming instabilities in protoplanetary disks. *Astrophys. J.*, **620**, 459.
- Youdin A. and Johansen A. (2007) Protoplanetary disk turbulence driven by the streaming instability: Linear evolution and numerical methods. *Astrophys. J.*, **662**, 613.
- Youdin A. N. and Shu F. H. (2002) Planetesimal formation by gravitational instability. *Astrophys. J.*, **580**, 494.
- Young E. D. (2014) Inheritance of solar short- and long-lived radionuclides from molecular clouds and the unexceptional nature of the solar system. *Earth Planet. Sci. Lett.*, **392**, 16.
- Zanda B., Humayun M., and Hewins R. H. (2012) Chemical composition of matrix and chondrules in carbonaceous chondrites: Implications for disk transport. *Lunar Planet. Sci. XLIII*, Abstract #2413. Lunar and Planetary Institute, Houston.
- Zinner E. and Göpel C. (2002) Aluminum-26 in H4 chondrites: Implications for its production and its usefulness as a fine-scale chronometer for early solar system events. *Meteoritics & Planet. Sci.*, **37**, 1001.
- Zsom A., Ormel C. W., Gütter C., et al. (2010) The outcome of protoplanetary dust growth: Pebbles, boulders, or planetesimals? II. Introducing the bouncing barrier. *Astron. Astrophys.*, **513**, A57.



# The Dynamical Evolution of the Asteroid Belt

**Alessandro Morbidelli**

*Lagrange Laboratory, Université Côte d'Azur, Observatoire de la Côte d'Azur, CNRS*

**Kevin J. Walsh**

*Southwest Research Institute*

**David P. O'Brien**

*Planetary Science Institute*

**David A. Minton**

*Purdue University*

**William F. Bottke**

*Southwest Research Institute*

---

The asteroid belt is the remnant of the original planetesimal population in the inner solar system. However, the asteroids currently have orbits with all possible values of eccentricities and inclinations compatible with long-term dynamical stability, whereas the initial planetesimal orbits should have been quasicircular and almost coplanar. The total mass now contained in the asteroid population is a small fraction of that existing primordially. Also, asteroids with different chemical/mineralogical properties are not ranked in an orderly manner with mean heliocentric distance (orbital semimajor axis) as one might expect from the existence of a radial gradient of the temperature in the protoplanetary disk, but they are partially mixed. These properties show that the asteroid belt has been severely sculpted by one or a series of processes during its lifetime. This paper reviews the processes that have been proposed so far, discussing the properties that they explain and the problems with which they are confronted. Emphasis is paid to the interplay between the dynamical and the collisional evolution of the asteroid population, which allows the use of the size distribution or crater densities observed in the asteroid belt to constrain the dynamical models. We divide the asteroid belt evolution into three phases. The first phase started during the lifetime of the gaseous protoplanetary disk, when the giant planets formed and presumably experienced large-scale migrations, and continued after the removal of the gas, during the buildup of the terrestrial planets. The second phase occurred after the removal of the gaseous protoplanetary disk, and it became particularly lively for the asteroid belt when the giant planets suddenly changed their orbits as a result of a mutual dynamical instability and the interaction with the transneptunian planetesimal disk. The third phase covers the aftermath of the giant-planet instability through the present day.

## 1. INTRODUCTION

The asteroid belt helps us in reconstructing the origin and the evolution of the solar system, probably better than the planets themselves. This is because the asteroid belt provides several key constraints that can be used to effectively guide the development, calibration, and validation of evolutionary models. Compared to other small-body populations, such as the Kuiper belt or Oort cloud, the constraints provided by the asteroid belt are probably more stringent, due to the fact that the number and the properties of the asteroids are better known, thanks to groundbased observations, space missions, and meteorite analysis.

The structure of this review chapter is therefore as follows. We start by reviewing in section 2 what the most important observational constraints on the asteroid belt are and what they suggest. Then, in section 3, we will review the main models proposed, from the oldest to the most recent, and from the earliest to the latest evolutionary phases they address. In section 4, we will discuss several implications for asteroid science from our current preferred view of the dynamical evolution of the asteroid belt.

The dynamical evolution of the asteroid belt has already been the object of a review chapter by Petit *et al.* (2002) in the *Asteroids III* book. This review therefore has an important overlap with that chapter. Nevertheless, both our

observational knowledge of the asteroid belt and our theoretical understanding of solar system evolution have improved significantly since the early 2000s, providing an emerging view of a very dynamic early solar system, in which various episodes of planet migration played a fundamental role in sculpting the small-body reservoirs and displacing planetesimals far from their original birthplaces. Thus this chapter will present in greater details models proposed after 2002, focusing on their implications for asteroid science. Moreover, when reviewing models already presented in Petit et al., we will refer to numerical simulations of these models made after the publication of the Petit et al. chapter.

## 2. OBSERVATIONAL CONSTRAINTS ON THE PRIMORDIAL EVOLUTION OF THE ASTEROID BELT

The observational constraints most useful for reconstructing the formation and evolution of the asteroid belt are those related to large asteroids (larger than  $\sim 50$ – $100$  km in diameter). In fact, it has been argued that these asteroids are the most likely to be “pristine” in the sense that they were not generated in large numbers in collisional breakup events of larger parent bodies (Bottke et al., 2005a; see also the chapter by Bottke et al. in this volume), nor have they been affected by gas drag and other nongravitational forces (e.g., the Yarkovsky effect; see the chapter by Vokrouhlický et al. in this volume). Moreover, there is an emerging view that the first planetesimals were big, with a preferred diameter in the range mentioned above (Morbidelli et al., 2009; see also the chapter by Johansen et al. in this volume). Thus, throughout this chapter we will limit our discussion to the properties of large asteroids and refer to smaller asteroids only when explicitly mentioned.

A key major characteristic of the asteroid belt population is the orbital excitation, i.e., the fact that the eccentricities and inclinations of many asteroidal orbits are quite large (e.g., Petit et al., 2002). The median proper inclination of  $D > 100$  km asteroids is  $11^\circ$  and the median proper eccentricity is 0.145. More importantly, the values of eccentricities and inclinations of the largest asteroids are considerably dispersed, with the former ranging between 0 and 0.30, while the latter ranges between  $0^\circ$  and  $33^\circ$  (see Fig. 1). It has been shown that asteroids of modest inclinations ( $i < 20^\circ$ ) fill the entire orbital space available for long-term dynamical stability, although some stable regions are more densely populated than others (Minton and Malhotra, 2009, 2011). The reader should be aware that, whatever the preferred formation mechanism (see the chapter by Johansen et al. in this volume), planetesimals are expected to have formed on circular and coplanar orbits. Thus, one or more dynamical excitation mechanism(s) within the primordial asteroid belt were needed to stir up eccentricities and inclinations to randomly dispersed values. Asteroid eccentricities and inclinations do not show a strong dependence on semimajor axis (Fig. 1).

A second fundamental characteristic of the asteroid belt is the partial mixing of taxonomic classes. Asteroids can be

grouped into many taxonomic classes on the basis of their visual and infrared spectroscopic signatures (Tholen, 1984; Bus and Binzel, 2002; DeMeo et al., 2009). As shown first by Gradie and Tedesco (1982) for the largest asteroids, the inner belt is dominated by S-complex asteroids, many of which are probably related to the meteorites known as ordinary chondrites (Binzel et al., 1996; see also the chapter by Vernazza et al. in this volume). The central belt (2.5–3.2 AU) is dominated by C-complex asteroids, probably related to carbonaceous chondrites (Burbine et al., 2002; see also the chapters by DeMeo et al. and Rivkin et al. in this volume). The Cybeles asteroids (3.2–3.7 AU), the Hilda asteroids (in the 3:2 mean-motion resonance with Jupiter), and the Jupiter Trojan asteroids (in the 1:1 resonance with Jupiter) are dominated by P- and D-type asteroids (see the chapter by Emery et al. in this volume). The C2 ungrouped meteorite “Tagish Lake” has been proposed to be a fragment of a D-type asteroid (Hiroi et al., 2001).

This stratification of the main belt makes intuitive sense in terms of a general view that protoplanetary disks should have temperatures decreasing with increasing distance from the central star. In fact, ordinary chondrites are less abundant in organics and water than carbonaceous chondrites and therefore are more likely to have formed in a warmer part of the disk. The small water content in ordinary chondrites, well below the solar proportion, suggests that these bodies accreted closer to the Sun than the snowline. The fact that some water is nevertheless present is not in contradiction with this statement. A small amount of water could have been accreted by collisions with primitive bodies scattered or drifting into the inner part of the disk. At the opposite extreme, the CI meteorites show no chemical fractionation relative to the solar composition, except H, C, N, O, and all noble gases, suggesting that they formed in a region of

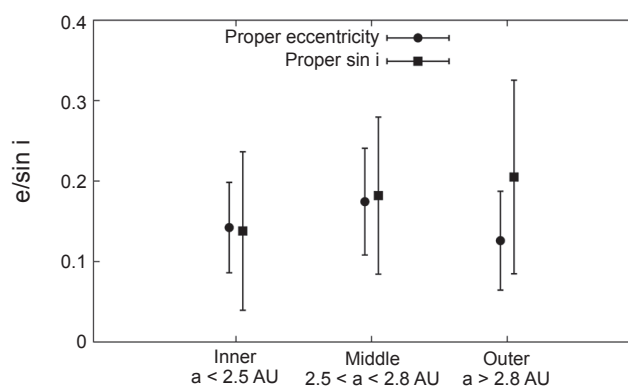


**Fig. 1.** The points show mean proper eccentricity (circles) and mean proper inclination (squares) for the  $D > 100$  km asteroids, divided into three bins of semimajor axis. The error bars show the  $1\sigma$  standard deviation. There is little systematic difference in excitation across the main belt. The slightly increase of inclination from the inner to the outer belt is due to the effect of the  $g = g_6$  secular resonance (see section 3), which most strongly affects high-inclination asteroids in the inner belt.

the disk where the temperature was low enough to allow the condensation of most elements.

As shown in Fig. 2, however, asteroids of different taxonomic types are partially mixed in orbital semimajor axis, which smears the trend relating physical properties to heliocentric distance. The mixing of taxonomic type should not be interpreted as the existence of asteroids of intermediate physical properties between those of adjacent types; instead, it is due to the coexistence of asteroids of different types with various relative proportions at each value of semimajor axis. Some mixing could come from the fact that the thermal and chemical compositional properties of the disk probably changed over time. However, given that no systematic differences in accretion ages is observed among the main group of chondrites (Villeneuve et al., 2009), it is more likely that some mechanism, possibly the same that excited the orbital eccentricities and inclinations, also changed somewhat in a random fashion the original semimajor axes of the bodies, causing the observed partial mixing.

The asteroid belt contains overall very little mass. From the direct determination of the masses of the largest asteroids and an estimate of the total mass of the ring of bodies, which cannot be individually “weighted,” based on the collective gravitational perturbations exerted on Mars, Krasinsky et al. (2002), Kuchynka and Folkner (2013), and Somenzi et al. (2010) concluded that the total mass contained in the asteroid belt is  $\sim 4.5 \times 10^{-4}$  Earth masses ( $M_{\oplus}$ ). This value is very low compared to that estimated to have originally existed in the primordial asteroid belt region by interpolating the mass densities required to form the terrestrial planets and the core of Jupiter at both ends of the belt (Weidenschilling, 1977), which is on the order of  $1 M_{\oplus}$  (within a factor of a few). Thus, the mass in the asteroid belt has potentially been depleted by 3 orders of magnitude compared to these expectations.

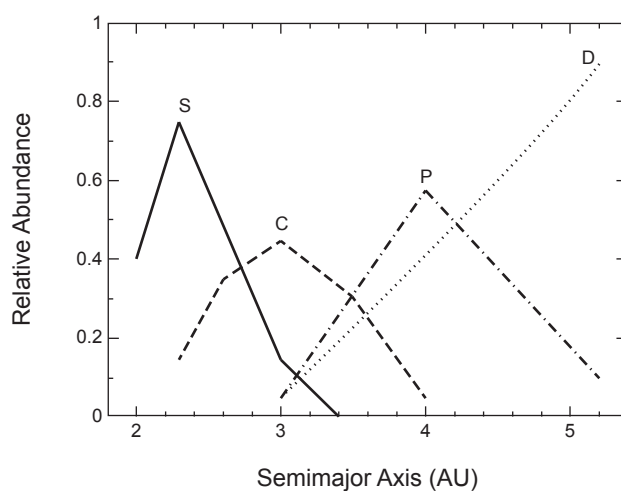


**Fig. 2.** The relative distribution of large asteroids ( $D > 50$  km) of different taxonomic types as originally observed by Gradie and Tedesco (1982). Further works by Mothé-Diniz et al. (2003), Carvano et al. (2010), and DeMeo and Carry (2014) demonstrate that the level of mixing increases for smaller asteroid sizes.

We can glean insights into how the primordial belt lost its mass by investigating what we know about its collisional evolution. The collisional history of asteroids is the subject of the chapter by Bottke et al. in this volume, but we report the highlights here that are needed for this discussion. In brief, using a number of constraints, Bottke et al. (2005a) concluded that the integrated collisional activity of the asteroid belt is equivalent to the one that would be produced at the current collisional rate over 8–10 G.y.

This result has several implications. First, it strongly suggests that the 3-orders-of-magnitude mass depletion could not come purely from collisional erosion; such intense comminution would violate numerous constraints. Second, it argues that the mass depletion of the asteroid belt occurred very early. This is because once the eccentricities and inclinations are excited to values comparable to the current ones, for a given body every million years spent in an asteroid belt 1000× more populated brings a number of collisions equivalent to that suffered in 1 G.y. within the current population. For this reason, the third implication is that the dynamical excitation and the mass-depletion event almost certainly coincided. This argues that the real dynamical excitation event was stronger than suggested by the current distribution of asteroid eccentricities. One way to reconcile a massive asteroid belt with this scenario is to assume that more than 99% of the asteroids had their orbits so excited that they left the asteroid belt forever (hence the mass depletion). This would make the eccentricities (and to a lesser extent the inclinations) we see today to be those defined by the lucky survivors, namely the bodies whose orbits were excited the least.

Using these constraints, we discuss in the next section the various models that have been proposed for the primordial sculpting of the asteroid belt.

### 3. MODELS OF PRIMORDIAL EVOLUTION OF THE ASTEROID BELT

#### 3.1. Early Models

The first attempts to explain the primordial dynamical excitation of the asteroid belt were made by Heppenheimer (1980) and Ward (1981), who proposed that secular resonances swept through the asteroid belt region during the dissipation of gas in the protoplanetary disk. Secular resonances occur when the precession rate of the orbit of an asteroid is equal to one of the fundamental frequencies of precession of the orbits of the planets. There are two angles that characterize the orientation of an orbit in space, the longitude of perihelion ( $\omega$ ) and the longitude of the ascending node ( $\Omega$ ), each of which can precess at different rates depending on the gravitational effects of the other planets and nebular gas (if present). The resonances that occur when the precession rates of the longitudes of perihelion of an asteroid (denoted by  $g$ ) and of a planet are equal to each other excite the asteroid’s eccentricity. Similarly, the resonances occurring when the precession rates of the longitudes of node of an asteroid (denoted by  $s$ ) and of a planet are equal to each other

excite the asteroid's inclination. In the case of asteroids in the main belt, the planets' precession frequencies that most influence their dynamics are those associated with the orbits of Jupiter and Saturn. These are called  $g_5$  and  $g_6$  for the longitude of perihelion precession (the former dominating in the precession of the perihelion of Jupiter, the latter in that of Saturn), and  $s_6$  for the longitude of the node precession (both the nodes of Jupiter and Saturn precess at the same rate, if measured relative to the *invariable plane*, defined as the plane orthogonal to their total angular momentum vector).

The dissipation of gas from the protoplanetary disk changes the gravitational potentials that the asteroids and planets feel, and hence changes the precession rates of their orbits. Given that the planets and asteroids are at different locations, they will be affected somewhat differently by this change of gravitational potential and consequently their precession rates will not change proportionally. It is therefore possible that secular resonances sweep through the asteroid belt as the gas dissipates. This means that every asteroid, whatever its location in the belt, first has orbital precession rates slower than the  $g_5$ ,  $g_6$  frequencies of Jupiter and Saturn when there is a lot of gas in the disk, then enters resonance ( $g = g_5$  or  $g = g_6$ ) when some appropriate fraction of the gas has been removed, and eventually is no longer in resonance (its orbital precession frequency being faster than those of the giant planets, i.e.,  $g > g_6$ ) after all the gas has disappeared. The same occurs for the asteroid's nodal frequency  $s$  relative to the planetary frequency  $s_6$ . This sweeping of perihelion and nodal secular resonances has the potential to excite the orbital eccentricities and inclinations of all asteroids.

This mechanism of asteroid excitation due to disk dissipation has been revisited with numerical simulations in *Lemaître and Dubru* (1991), *Lecar and Franklin* (1997), *Nagasawa et al.* (2000, 2001, 2002), *Petit et al.* (2002), and finally by *O'Brien et al.* (2007). *Nagasawa et al.* (2000) found that of all the scenarios for gas depletion they studied (uniform depletion, inside-out, and outside-in), inside-out depletion of the nebula was most effective at exciting eccentricities and inclinations of asteroids throughout the main belt. However, they (unrealistically) assumed that the nebula coincided with the ecliptic plane. Protoplanetary disks can be warped, but they are typically aligned with the orbit of the locally dominant planet (*Mouillet et al.*, 1997). Thus, there is no reason that the gaseous disk in the asteroid belt region was aligned with the current orbital plane of Earth (which was not yet formed). Almost certainly it was aligned with the orbits of the giant planets. Taking the invariable plane (the plane orthogonal to the total angular momentum of the solar system) as a proxy of the original orbital plane of Jupiter and Saturn, *Nagasawa et al.* (2001, 2002) found that the excitation of inclinations would be greatly diminished. Furthermore, since nebular gas in the inside-out depletion scenario would be removed from the asteroid belt region before the resonances swept through it, there would be no gas drag effect to help deplete material from the main-belt region.

The work of *O'Brien et al.* (2007) accounted for the fact that the giant planets should have had orbits significantly

less inclined and eccentric than their current values when they were still embedded in the disk of gas, because of the strong damping that gas exerts on planets (*Cresswell et al.*, 2008; *Kley and Nelson*, 2012). They concluded that secular resonance sweeping is effective at exciting eccentricities and inclinations to their current values only if gas is removed from the inside-out and very slowly, on a timescale of  $\sim 20$  m.y. This gas-removal mode is very different from our current understanding of the photoevaporation process (*Alexander et al.*, 2014), and inconsistent with observations suggesting that disks around solar-type stars have lifetimes of only 1–10 m.y., with an average of  $\sim 3$  m.y. (e.g., *Strom et al.*, 1993; *Zuckerman et al.*, 1995; *Kenyon and Hartmann*, 1995; *Haisch et al.*, 2001).

Earlier studies found that the final eccentricities of the asteroids are quite randomized because two perihelion secular resonances sweep the entire asteroid belt in sequence: first the resonance  $g = g_5$ , then the resonance  $g = g_6$ . The first resonance excites the eccentricities of the asteroids from zero to approximately the same value, but the second resonance, sweeping an already excited belt, can increase or decrease the eccentricity depending on the position of the perihelion of each asteroid at the time of the encounter with the resonance (*Ward et al.*, 1976; *Minton and Malhotra*, 2011). *O'Brien et al.* (2007) found that when Jupiter and Saturn were on orbits initially closer together, as predicted by the Nice model (e.g., *Tsiganis et al.*, 2005), the resonance with frequency  $g_6$  would only sweep part of the outer belt, leading to less randomization of eccentricities in the inner belt. All studies in which the mid-plane of the protoplanetary disk of gas coincides with the invariable plane of the solar system find that the final inclinations tend to have comparable values. This is because there is only one dominant frequency ( $s_6$ ) in the precession of the nodes of Jupiter and Saturn and hence there is only one nodal secular resonance and no randomization of the final inclinations of the asteroids. Clearly, this is in contrast with the observations. For all these problems, the model of secular resonance sweeping during gas removal is no longer considered to be able to alone explain the excitation and depletion of the primordial asteroid belt.

An alternative model for the dynamical excitation of the asteroid belt was proposed by *Ip* (1987). In this model, putative planetary embryos are scattered out of the Jupiter region and cross the asteroid belt for some timescale before being ultimately dynamically ejected from the solar system. If the embryos are massive enough, their repeated crossing of the asteroid belt can excite and randomize the eccentricities and inclinations of the asteroids, through close encounters and secular effects. That scenario has been revisited by *Petit et al.* (1999), who found that, whatever the mass of the putative embryos, the resulting excitation in the asteroid belt ought to be very unbalanced. Excitation would be much stronger in the outer belt than in the inner belt (because the embryos come from Jupiter's region) and it would be much stronger in eccentricity than in inclination. By contrast, the main asteroid belt shows no such trend (see Fig. 1). So, again, this model has since been abandoned. If massive embryos have been

scattered from Jupiter's zone, they must have crossed the asteroid belt very briefly so that their limited effects could be completely overprinted by other processes, such as those discussed below.

### 3.2. Wetherill's Model

The first comprehensive model of asteroid belt sculpting, which linked the evolution of the asteroid belt with the process of terrestrial planet formation, was that proposed by Wetherill (1992) and later simulated in a number of subsequent papers (e.g., Chambers and Wetherill, 1998; Petit et al., 2001, 2002; O'Brien et al., 2006, 2007). In this model, at the time gas was removed from the system, the protoplanetary disk interior to Jupiter consisted of a bimodal population of planetesimals and planetary embryos, the latter with masses comparable to those of the Moon or Mars. Numerical simulations show that, under the effect of the mutual perturbations among the embryos and the resonant perturbations from Jupiter, embryos are generally cleared from the asteroid belt region, whereas embryos collide with each other and build terrestrial planets inside 2 AU. While they are still crossing the asteroid belt, the embryos also excite and eject most of the original resident planetesimals. Only a minority of the planetesimals (and often no embryos) remain in the belt at the end of the terrestrial planet formation process, which explains the mass depletion of the current asteroid population. The eccentricities and inclinations of the surviving asteroids are excited and randomized, and the remaining asteroids have generally been scattered somewhat relative to their original semimajor axes. A series of simulation snapshots demonstrating this process is shown in Fig. 3.

Whereas earlier simulations assumed that Jupiter and Saturn were originally on their current orbits, O'Brien et al. (2006, 2007) performed simulations with Jupiter and Saturn on the low-inclination, nearly circular orbits predicted in the Nice model. The resulting asteroids from a set of simulations with these initial conditions are shown in Fig. 4. Overall, the range of values compare well with those observed for the real asteroids, although the final inclination distribution is skewed toward large inclinations. The reason for this is that it is easier to excite a low-inclination asteroid to large eccentricity and remove it from the belt than it is for a high-inclination asteroid, because the encounter velocities with the embryos are slower and more effective in deflecting the low-inclination asteroid's orbit. Also, with the giant planets on nearly circular orbits, it takes longer to clear embryos from the asteroid belt, allowing more time to excite asteroids to large inclinations.

As noted earlier, the surviving asteroids have their orbital semimajor axes displaced from their original values, as a result of the embryos' gravitational scattering. O'Brien et al. (2007) found that the typical change in semimajor axis is on the order of 0.5 AU (comparable to earlier simulations), with a tail extending to 1–2 AU, and the semimajor axis can be either decreased or increased. This process can explain the partial mixing of taxonomic types. As shown in Fig. 2, the distribution of the S-type and C-type asteroids

has a Gaussian-like shape, with a characteristic width of ~0.5 AU. Thus, if one postulates that all S-type asteroids originated from the vicinity of 2 AU and all C-type asteroids originated in the vicinity of 3 AU, Wetherill's model explains the current distribution.

### 3.3. The Grand Tack Model

A more recent, alternative model to Wetherill's is the so-called Grand Tack scenario, proposed in Walsh et al. (2011). Initially the Grand Tack scenario had not been developed to explain the asteroid belt, but to answer two questions left open by Wetherill's model: Why is Mars so small relative to Earth? Why is Jupiter so far from the Sun despite planets having a tendency to migrate inward in protoplanetary disks? Nevertheless, this scenario has profound implications for the asteroid belt, as we discuss below.

The Grand Tack scenario is built on results from hydrodynamics simulations finding that Jupiter migrates toward the Sun if it is alone in the gas disk, while it migrates outward if paired with Saturn (Masset and Snellgrove, 2001; Morbidelli and Crida, 2007; Pierens and Nelson, 2008; Pierens and Raymond, 2011; D'Angelo and Marzari, 2012). Thus, the scenario postulates that Jupiter formed first. As long as the planet was basically alone, Saturn being too small to influence its dynamics, Jupiter migrated inward from its initial position (poorly constrained but estimated at ~3.5 AU) down to 1.5 AU. Then, when Saturn reached a mass close to its current one and an orbit close to that of Jupiter, Jupiter reversed migration direction (i.e., it "tacked," hence the name of the model) and the pair of planets started to move outward. This outward migration continued until the final removal of gas in the disk, which the model assumes happened when Jupiter reached a distance of ~5.5 AU. The migration of the cores of giant planets is still not fully understood (see Kley and Nelson, 2012, for a review). Thus, the Grand Tack model comes in two "flavors." In one, Saturn, while growing, migrates inward with Jupiter. In another, Saturn is stranded at a no-migration orbital radius until its mass exceeds  $50 M_{\oplus}$  (Bitsch et al., 2014), then it starts migrating inward and it catches Jupiter in resonance because it migrates faster. Both versions exist with and without Uranus and Neptune. All these variants are described in Walsh et al. (2011); the results are very similar in all these cases, which shows the robustness of the model, at least within the range of tested possibilities. The scheme presented in Fig. 5 has been developed in the framework of the first "flavor."

Assuming that Jupiter formed at the snowline (a usual assumption to justify the large mass of its core and its fast formation), the planetesimals that formed inside its initial orbit should have been mostly dry. It is therefore reasonable to associate these planetesimals (whose distribution is sketched as a dashed area in Fig. 5) with the S-type asteroids and other even dryer bodies (enstatite-type, Earth precursors, etc.). During its inward migration, Jupiter penetrates into the disk of these planetesimals. In doing so, most planetesimals (and planetary embryos) are captured in mean-motion resonances

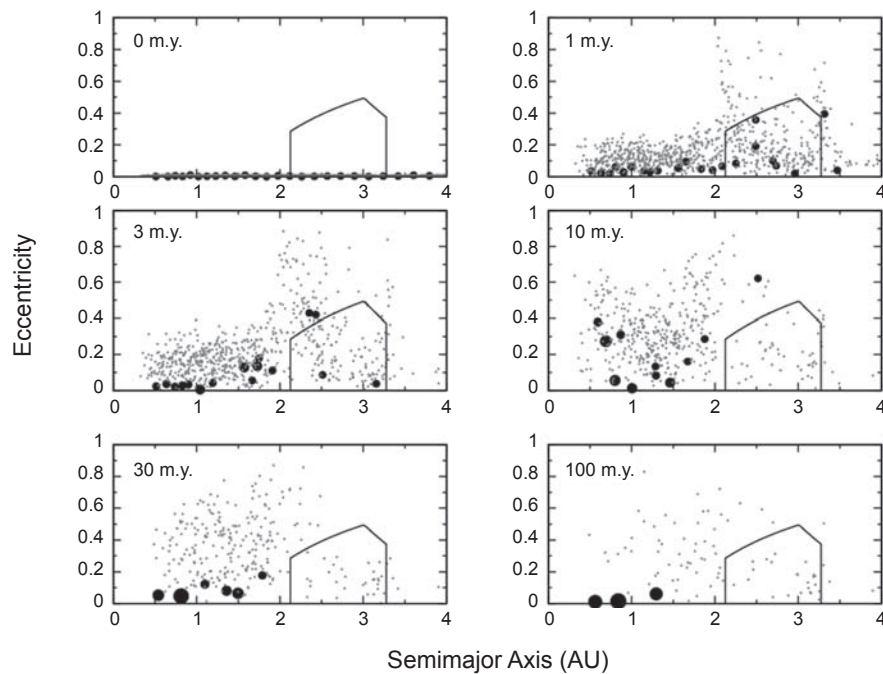


**Fig. 3.** Snapshots of the evolution of the solar system and of the asteroid belt in a simulation of Wetherill's model performed in O'Brien *et al.* (2006) and assuming Jupiter and Saturn on initial quasicircular orbits. Each panel depicts the eccentricity vs. semimajor axis distribution of the particles in the system at different times, labeled on top. Planetesimals are represented with gray dots and planetary embryos by black circles, whose size is proportional to the cubic root of their mass. The solid lines show the approximate boundaries of the current main belt.

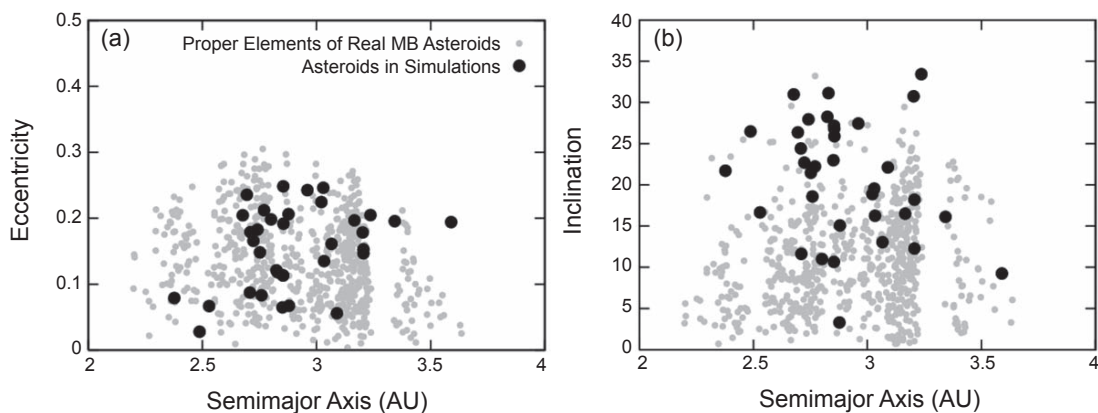


**Fig. 4.** The final eccentricities and inclinations of asteroids in Wetherill's (1992) model (black dots), according to the simulations presented in O'Brien *et al.* (2007). For comparison, the observed distribution of large asteroids is depicted with gray dots.

with Jupiter and are pushed inward, increasing the mass density of the inner part of the disk. However, some 10% of the planetesimals are kicked outward by an encounter with Jupiter, reaching orbits located beyond Saturn that collectively have an orbital ( $a, e$ ) distribution typical of a scattered disk (i.e., with mean eccentricity increasing with semimajor axis). In semimajor axis range, this scattered disk overlaps with the inner part of the disk of primitive bodies (whose distribution is sketched as a dotted area in Fig. 5) that are initially on circular orbits beyond the orbit of Saturn. These bodies, being formed beyond the snowline, should be rich

in water ice and other volatile elements, and therefore it is again reasonable to associate them with C-type asteroids.

After reaching  $\sim 1.5$  AU [this value is constrained by the requirement to form a small Mars and a big Earth (Walsh *et al.*, 2011; Jacobson *et al.*, 2014; Jacobson and Morbidelli, 2014)], Jupiter reverses its migration direction and begins its outward migration phase, during which the giant planets encounter the scattered S-type disk, and then also the primitive C-type disk. Some of the bodies in both populations are scattered inward, reach the asteroid-belt region, and are implanted there as Jupiter moves out of it.

The final orbits of the planetesimals, at the end of the outward migration phase, are shown in Fig. 6. A larger dot size is used to highlight the planetesimals trapped in the asteroid belt region and distinguish them from those in the inner solar system or at eccentricities too large to be in the asteroid belt. Notice that the asteroid belt is not empty, although it has been strongly depleted (by a factor of several hundred relative to its initial population). This result is not trivial. One could have expected that Jupiter migrating through the asteroid belt twice (first inward then outward) would have completely removed the asteroid population, invalidating the Grand Tack scenario. The eccentricities and the inclinations of the particles in the asteroid belt are excited and randomized. The S-type particles (black) are found predominantly in the inner part of the belt and the C-type particles (gray) in the outer part, but there is a wide overlapping region where both are present. This is qualitatively consistent with what is observed.

As discussed above, the Grand Tack scenario solves open problems in Wetherill's model. The small mass of Mars is explained as a result of the disk of the remaining solid material being truncated at  $\sim 1$  AU (Hansen, 2009; Walsh et al., 2011). Fischer and Ciesla (2014) reported that they could obtain a small-mass Mars in a few percent of simulations conducted in the framework of Wetherill's model. However, the rest of the planetary system in these simulations does not resemble

the real terrestrial planet system (Jacobson and Walsh, 2015). For instance, another massive planet is formed in the Mars region or beyond. The outward migration of Jupiter explains why the giant planets in our solar system are so far from the Sun, whereas most giant planets found so far around other stars are located at 1–2 AU. For all these reasons, one can consider the Grand Tack model more as an improvement of Wetherill's model than an alternative, because it is built in the same spirit of linking the asteroid belt sculpting to the evolution of the rest of the solar system (terrestrial planet formation and giant-planet migration, the latter of which was still unknown during Wetherill's time).

It is nevertheless interesting to compare the Grand Tack model and Wetherill's model on the basis of the final asteroid belts that they produce. Comparing Fig. 6 with Fig. 4, it is apparent that the Grand Tack model provides a better inclination distribution, more uniform than Wetherill's, but it produces a worse eccentricity distribution, which is now more skewed toward the upper eccentricity boundary of the asteroid belt.

As we will see in section 3.5, however, the eccentricity distribution can be remodeled somewhat during a later evolutionary phase of the solar system. This is also partially true for the inclination distribution. So, for what concerns the eccentricity and inclination distributions, one might declare a tie in the competition between the two models.

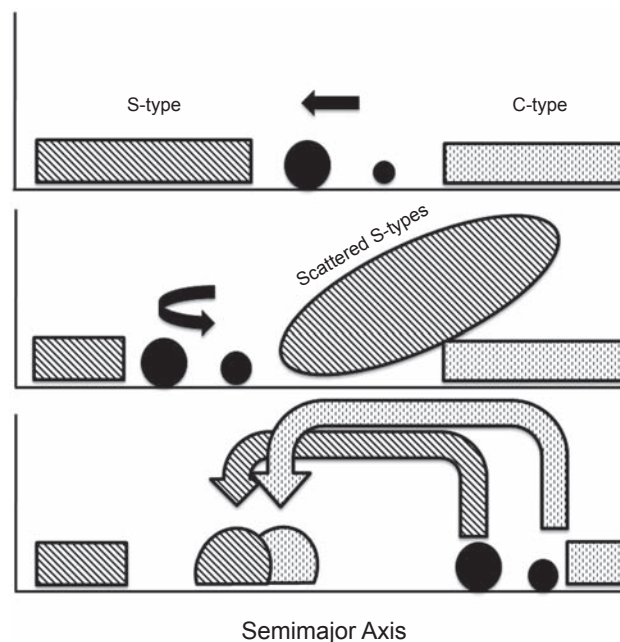


**Fig. 5.** A scheme showing the Grand Tack evolution of Jupiter and Saturn and its effects on the asteroid belt. The three panels show three evolutionary states in temporal sequence. First, the planets migrate inward, then, when Saturn reaches its current mass, they move outward. The dashed and dotted areas schematize the (a,e) distributions of S-type and C-type asteroids respectively. The dashed and dotted arrows in the lower panel illustrate the injection of scattered S-type and C-type asteroids into the asteroid belt during the final phase of outward migration of the planets.

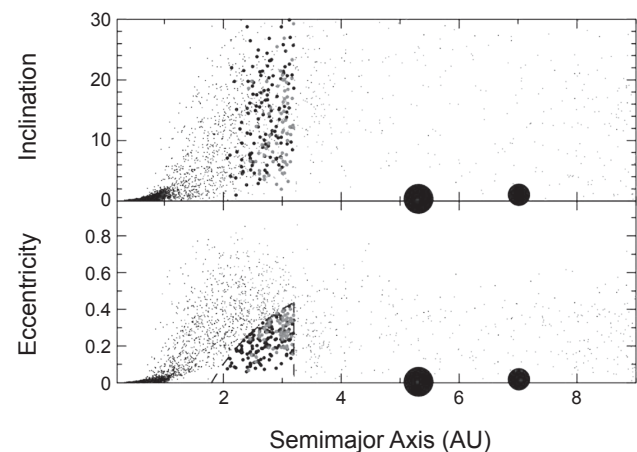


**Fig. 6.** Final semimajor axis, eccentricity, and inclination distribution of bodies surviving the inward and outward migration of Jupiter and Saturn. The black particles were originally placed inside the initial orbit of Jupiter and the gray particles outside the initial orbit of Saturn. The particles finally trapped in the asteroid belt are depicted with larger symbols than the others. The dashed curve in the lower panel shows the approximate boundaries of the asteroid belt inward of the 2:1 resonance with Jupiter. This final distribution was achieved in the simulations of Walsh et al. (2011) accounting only for Jupiter and Saturn (i.e., not including Uranus and Neptune) moving together in the 2:3 resonance, as shown in Fig. 5.

The Grand Tack model makes it conceptually easier to understand the significant differences between S-type and C-type asteroids and their respective presumed daughter populations: the ordinary and carbonaceous chondrites. In fact, in the Grand Tack model these two populations are sourced from clearly distinct reservoirs on either side of the snowline. Instead, in Wetherill's model these bodies would have formed just at the two ends of the asteroid belt, so less than 1 AU apart. Despite such a vast difference in predicted formation locations for these two populations, the debate is open. Some authors (e.g., Alexander *et al.*, 2012) think that bodies formed in the giant-planet region would be much more similar to comets than to asteroids, while others (Gounelle *et al.*, 2008) argue that there is a continuum between C-type asteroids and comets and a clear cleavage of physical properties between ordinary and carbonaceous chondrites. We review the available cosmochemical constraints and their uncertain compatibility with the model in section 3.4.

A clear distinction between the Grand Tack model and Wetherill's model is that the former provides a faster and more drastic depletion of the asteroid belt. This point is illustrated in Fig. 7, which shows the fraction of the initial asteroid population that is in the main-belt region at any time.

The Grand Tack scenario depletes the asteroid belt down to 0.3%, and does so basically in 0.1 m.y. Assuming that the final asteroid belt consisted of one current asteroid belt mass in S-type asteroids and three current asteroid belt masses in C-type asteroids (the reason for 4 $\times$  more total mass in the asteroid belt will be clarified in section 3.6), this implies that the asteroid belt at  $t = 0$  should have contained  $0.6 M_{\oplus}$  in planetesimals (the rest in embryos). Also, a calculation of

the collision probability of the asteroids as a function of time (both among each other and with the planetesimals outside the asteroid belt) shows that the integrated collisional activity suffered by the surviving asteroids during the first 200 m.y. would not exceed the equivalent of 4 G.y. in the current population. Thus, assuming that the exceeding factor of 4 in the asteroid population is lost within the next 500 m.y. (see sections 3.5 and 3.6), the integrated collisional activity of asteroids throughout the entire solar system age would probably remain within the 10-G.y. constraint described in section 2. In contrast, Wetherill's model depletes the asteroid belt on a timescale of 100 m.y. Also, about 2–3% of the initial population remains in the belt at the end. Thus, to be consistent with constraints on the current population and its integrated collisional activity, the initial mass in planetesimals in the asteroid-belt region should have been no larger than 200 $\times$  the current asteroid-belt mass, or less than one Mars mass (Bottke *et al.*, 2005b).

### 3.4. Are Cosmochemical Constraints Consistent with the Grand Tack Model?

The Grand Tack model predicts that C-type asteroids have been implanted into the asteroid belt from the giant-planet region. Is this supported or refuted by cosmochemical evidence?

Although there is a spread in values, the D/H ratios of carbonaceous chondrites (with the exception of CR chondrites) are a good match to Earth's water (Alexander *et al.*, 2012). Oort cloud comets are usually considered to have formed in the giant-planet region (e.g., Dones *et al.*, 2004). The D/H ratio was measured for the water from seven Oort cloud comets (see Bockelée-Morvan *et al.*, 2012, and references within). All but one [Comet 153P/Ikeya-Zhang (Biver *et al.*, 2006)] have water D/H ratios about twice as high as chondritic. This prompted Yang *et al.* (2013) to develop a model where the D/H ratio of ice in the giant-planet region is high. However, Brasser *et al.* (2007) showed that comet-sized bodies could not be scattered from the giant-planet region into the Oort cloud in the presence of gas drag (i.e., when the giant planets formed), and Brasser and Morbidelli (2013) demonstrated that the Oort cloud population is consistent with an origin from the primordial transneptunian disk at a later time. The recent measurement (Altweig *et al.*, 2014) of a high D/H ratio for the ice of Comet 67P/Churyumov-Gerasimenko, which comes from the Kuiper belt, supports this conclusion by showing that there is no systematic difference between Oort cloud comets and Kuiper belt comets. Care should therefore be taken in using Oort cloud comets as indicators of the D/H ratio in the giant-planet region. Conflicting indications on the local D/H ratio come from the analysis of Saturn's moons. Enceladus' D/H ratio is roughly twice Earth's (Waite *et al.*, 2009), but Titan's D/H ratio is Earth-like (Cousenit *et al.*, 2008; Abbas *et al.*, 2010; Nixon *et al.*, 2012).

Alexander *et al.* (2012) also noticed a correlation between D/H and C/H in meteorites and interpreted it as evidence

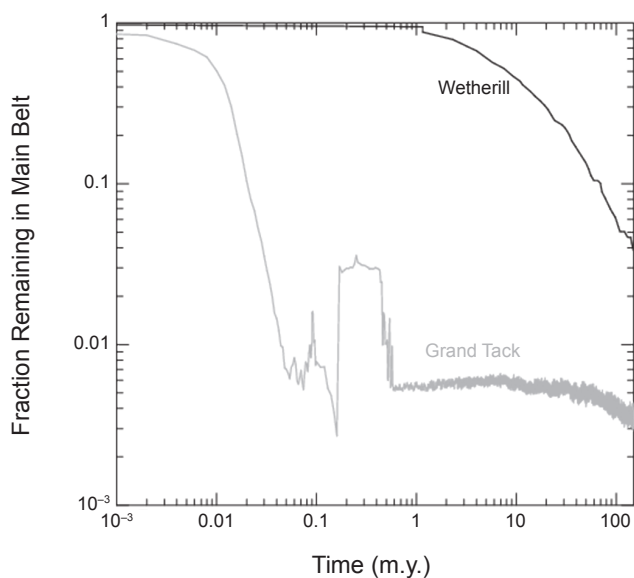


**Fig. 7.** The depletion of the asteroid belt in Wetherill's model (black) and Grand Tack model (gray). In the Grand Tack model notice the bump between 0.1 and 0.6 m.y. due to the implantation of primitive objects into the main belt. Overall, the depletion of the asteroid belt is faster and stronger in the Grand Tack model.

for an isotopic exchange between pristine ice and organic matter within the parent bodies of carbonaceous chondrites. From this consideration, they argued that the original water reservoir of carbonaceous asteroids had a D/H ratio lower than Titan, Enceladus, or any comet, again making asteroids distinct from bodies formed in the giant-planet region and beyond. However, a reservoir of pristine ice has never been observed; the fact that Earth's water and other volatiles are in chondritic proportion (Marty, 2012; however, see Halliday, 2013) means that carbonaceous chondrites — wherever they formed — reached their current D/H ratios very quickly, before delivering volatiles to Earth. It is also possible that the D/H ratio measured for comets and satellites might have been the result of a similar rapid exchange between a pristine ice and the organic matter.

Another isotopic constraint comes from the nitrogen isotope ratio. Comets seem to have a rather uniform  $^{15}\text{N}/^{14}\text{N}$  ratio (Rousselot et al., 2014). Even the comets with a chondritic D/H ratio [e.g., Comet Hartley 2 (Hartogh et al., 2011)] have a nonchondritic  $^{15}\text{N}/^{14}\text{N}$  ratio (Meech et al., 2011). The  $^{15}\text{N}/^{14}\text{N}$  ratio, however, is only measured in HCN or  $\text{NH}_2$ , never in molecular nitrogen ( $\text{N}_2$ ). Titan has a cometary  $^{15}\text{N}/^{14}\text{N}$  ratio as well [in this case measured in  $\text{N}_2$  (Niemann et al., 2010)]. Here, again, a few caveats are in order. First, it is difficult to relate the composition of a satellite, born from a circumplanetary disk with its own thermal and chemical evolution, to the composition of bodies born at the same solar distance but on heliocentric orbits. Second, it is unclear whether any comets for which isotope ratios have been measured originate from the giant-planet region, as opposed to the transneptunian disk (Brasser and Morbidelli, 2013). We also point out that hot spots with large  $^{15}\text{N}/^{14}\text{N}$  ratios are found in primitive meteorites (Busemann et al., 2006).

Arguments in favor of an isotopic similarity between carbonaceous chondrites and comets come from the analysis of micrometeorites. Most micrometeorites (particles of  $\sim 100 \mu\text{m}$  collected in the Antarctic ice) have chondritic isotopic ratios for H, C, N, and O [with the exception of ultracarbonaceous micrometeorites, which have a large D/H ratio, comparable to that in the organics of some chondrites, but which constitute only a minority of the micrometeorite population (Duprat et al., 2010)]. Yet according to the best available model of the dust distribution in the inner solar system (Nesvorný et al., 2010), which is compelling given that it fits the zodiacal light observations almost perfectly, most of the dust accreted by Earth should be cometary, even when the entry velocity bias is taken into account. Similarly, from orbital considerations, Gounelle et al. (2006) concluded that the CI meteorite Orgueil is a piece of a comet. Compelling evidence for a continuum between chondrites and comets also comes from the examination of Comet Wild 2 particles returned to Earth by the Stardust mission (e.g., Zolensky et al., 2006, 2008; Ishii et al., 2008; Nakamura et al., 2008).

These considerations suggest that if one looks at their rocky components, comets and carbonaceous asteroids are very similar from a compositional and isotopic point of view, if not in fact indistinguishable.

Finally, it has been argued that if the parent bodies of carbonaceous chondrites had accreted among the giant planets, they would have contained  $\sim 50\%$  water by mass. Instead, the limited hydrous alteration in carbonaceous meteorites suggests that only about 10% of the original mass was in water (A. N. Krot, personal communication, 2014; but see Alexander et al., 2010). However, a body's original water content cannot easily be estimated from its aqueous alteration. Even if alteration is complete, there is a finite amount of water that the clays can hold in their structures. Thus, the carbonaceous parent bodies may have been more water-rich than their alteration seems to imply. In fact, the discoveries of main-belt comets releasing dust at each perihelion passage (Hsieh and Jewitt, 2006), of water ice on asteroids Themis (Campins et al., 2010; Rivkin and Emery, 2010) and Cybele (Licandro et al., 2011; Hargrove et al., 2012), and of vapor plumes on Ceres (Kuppers et al., 2014) show that C-type asteroids are more rich in water than their meteorite counterpart seems to suggest, supporting the idea that they might have formed near or beyond the snowline. Meteorites may simply represent rocky fragments of bodies that were far wetter/icier.

Clearly, the debate on whether carbonaceous asteroids really come from the giant-planet region as predicted by the Grand Tack model is wide open. More data are needed from a broader population of comets. The investigation of main-belt comets, both remote and *in situ*, and the Dawn mission at Ceres will be key to elucidating the real ice content of carbonaceous asteroids and their relationship with classic "comets."

### 3.5. The Nice Model: A Second Phase of Excitation and Depletion for the Asteroid Belt

Figure 7 seems to suggest that after  $\sim 100$  m.y. the asteroid belt had basically reached its final state. However, at this time the orbits of the giant planets were probably still not the current ones. In fact, the giant planets are expected to have emerged from the gas-disk phase in a compact and resonant configuration as a result of their migration in the gas-dominated disk. This is true not only in the Grand Tack model, but in any model where Jupiter is refrained from migrating inside  $\sim 5$  AU by whatever mechanism (Morbidelli et al., 2007).

The transition of the giant planets from this early configuration to the current configuration is expected to have happened via an orbital instability, driven by the interaction of the planets with a massive disk of planetesimals located from a few astronomical units beyond the original orbit of Neptune to about 30 AU (Morbidelli et al., 2007; Batygin and Brown, 2010; Levison et al., 2011; Nesvorný, 2011; Batygin et al., 2012; Nesvorný and Morbidelli, 2012; see also a precursor work by Thommes et al., 1999). In essence, the planetesimals disturbed the orbits of the giant planets and, as soon as two planets fell off resonance, the entire system became unstable. In the simulations, the instability can occur early (e.g., Morbidelli et al., 2007) or late (Levison et al., 2011), depending on the location of the inner edge of the transneptunian disk.

Constraints suggest that in the real solar system the instability occurred relatively late, probably around 4.1 G.y. ago (namely 450 m.y. after gas removal). These constraints come primarily from the Moon. Dating lunar impact basins is difficult, because it is not clear which samples are related to which basin (e.g., *Norman and Nemchin*, 2014). Nevertheless, it is clear that several impact basins, probably a dozen, formed in the 4.1–3.8-Ga period (see *Fassett and Minton*, 2013, for a review). Numerical tests demonstrate that these late basins (even just Imbrium and Orientale, whose young ages are undisputed) are unlikely to have been produced by a declining population of planetesimals, left over from the terrestrial planet accretion process, because of their short dynamical and collisional lifetimes (*Bottke et al.*, 2007). There is also a surge in lunar rock impact ages ~4 G.y. ago, which contrasts with a paucity of impact ages between 4.4 and 4.2 Ga (*Cohen et al.*, 2005). This is difficult to explain if the bombardment had been caused by a population of leftover planetesimals slowly declining over time. The situation is very similar for the bombardment of asteroids, with meteorites showing a surge in impact ages at 4.1 Ga and a paucity of ages between 4.2 and 4.4 Ga (*Marchi et al.*, 2013). Meteorites also show many impact ages near 4.5 Ga, demonstrating that the apparent lack of events in the 4.2–4.4-Ga interval is not due to clock resetting processes. All these constraints strongly suggest the appearance of a new generation of projectiles in the inner solar system about 4.1 G.y. ago, which argues that either a very big asteroid broke up at that time (*Cuk*, 2012) (but such a breakup is very unlikely from collision probability arguments and we do not see any remnant asteroid family supporting this hypothesis), or that the dynamical instability of the giant planets occurred at that time, partially destabilizing small-body reservoirs that had remained stable until then.

Other constraints pointing to the late instability of the giant planets come from the outer solar system. If the planets had become unstable at the disappearance of the gas in the disk, presumably the Sun would still have been in a stellar cluster and consequently the Oort cloud would have formed more tightly bound to the Sun than it is thought to be from the orbital distribution of long-period comets (*Brasser et al.*, 2008, 2012). Also, the impact basins on Iapetus (a satellite of Saturn) have topographies that have relaxed by 25% or less, which argues that they formed in a very viscous lithosphere; according to models of the thermal evolution of the satellite, these basins can not have formed earlier than 200 m.y. after the beginning of the solar system (*Robuchon et al.*, 2011).

For all these reasons, it is appropriate to discuss the consequences of the giant-planet instability on the asteroid belt, after the events described by the Grand Tack or Wetherill's models. In fact, it is important to realize that the model of giant-planet instability (often called the Nice model) is not an alternative to the models described before on the early evolution of the asteroid belt; instead it is a model of the subsequent evolution.

The phase of giant-planet instability is very chaotic and therefore a variety of orbital evolutions are possible. Neverthe-

less, the planetary evolutions can be grouped in two categories. In the first category, Saturn, Uranus, and Neptune have close encounters with each other, but none of them have encounters with Jupiter. Saturn typically scatters either Uranus or Neptune outward and thus it recoils inward. As a result, Uranus and Neptune acquire large eccentricity orbits that cross the transneptunian disk. The dispersal of the planetesimal disk damps the eccentricities of the planets by dynamical friction and drives the planets' divergent migration in semimajor axis (*Tsiganis et al.*, 2005). Thus, the planets achieve stable orbits that are well separated from each other. The orbital separation between Jupiter and Saturn first decreases, when Saturn recoils, and then increases due to planetesimal-driven migration. The timescale for the latter is typically ~10 m.y. The slow separation between the two major planets of the solar system drives a slow migration of secular resonances across the asteroid belt (*Minton and Malhotra*, 2009, 2011) and the terrestrial planet region (*Brasser et al.*, 2009). The problem is that the resulting orbital distribution in the asteroid belt is very uneven, as shown in Fig. 8a, with most asteroids surviving at large inclination (*Morbidelli et al.*, 2010), and the orbits of the terrestrial planets become too excited (*Brasser et al.*, 2009; *Agnor and Lin*, 2012).

In the second category of evolutions, Saturn scatters an ice giant planet (Uranus, Neptune, or a putative fifth planet) inward, thus recoiling outward, and then Jupiter scatters the ice giant outward, thus recoiling inward. The interaction with the planetesimals eventually damps and stabilizes the orbits of the planets. In this evolution, dubbed “jumping-Jupiter,” the orbital separation between Jupiter and Saturn initially jumps, when Saturn recoils outward and Jupiter inward; then there is a final smooth phase of separation, due to planetesimal-driven migration. In the jump, the secular resonances can jump across the asteroid belt (*Morbidelli et al.*, 2010) and across the terrestrial planet region (*Brasser et al.*, 2009) without disrupting their orbital structure (see Fig. 8b).

The jumping-Jupiter evolution also explains the capture of the irregular satellites of Jupiter with an orbital distribution similar to those of the irregular satellites of the other giant planets (*Nesvorný et al.*, 2007, 2014). It can also explain the capture of Jupiter's Trojans in uneven proportions around the L4 and L5 Lagrangian points (*Nesvorný et al.*, 2013; see also the chapter by Emery et al. in this volume). So far, no other model is capable of achieving these results. For all these reasons, simulated solar system evolutions these days are required to show a jumping-Jupiter evolution to be declared successful (*Nesvorný and Morbidelli*, 2012).

Although it avoids secular resonances sweeping across the asteroid belt, a jumping-Jupiter evolution is not without consequences for the asteroids. The sudden change in the eccentricity of Jupiter (from an initial basically circular orbit, like that observed in hydrodynamical simulations of the four giant planets evolving in the gaseous protoplanetary disk, to one with current eccentricity) changes the forced eccentricity felt by the asteroids in their secular evolution. Consequently, the proper eccentricities of the asteroids are changed. Depending on the value of the longitude of

perihelion when the forced eccentricity changes, the proper eccentricity of an asteroid can decrease or increase. Roughly, 50% of the asteroids are kicked to larger eccentricities and therefore are removed from the asteroid belt. The remaining 50% of the asteroids have their eccentricities reduced. This can potentially reconcile the eccentricity distribution of asteroids at the end of the Grand Tack evolution (see Fig. 6) with the current distribution. Indeed, Minton and Malhotra (2011) showed that the current eccentricity distribution can be achieved starting from a primordial distribution peaked at  $e \sim 0.3$ , similar to that produced by the Grand Tack evolution of Jupiter (Fig. 6). They obtained this result using secular resonance sweeping, but the basic result should hold also for a sudden enhancement of Jupiter's eccentricity. Nevertheless, specific numerical simulations have never been done to demonstrate that the eccentricity distribution of asteroids at the end of the Grand Tack model can be transformed into the current distribution via the jumping-Jupiter evolution [at

the time of this writing, this work is ongoing and seems to give positive results (Deienno and Gomes, personal communication)]. The jump in Jupiter's inclination due to its encounter(s) with another planet should also have partially reshuffled the asteroid inclination distribution, possibly reconciling the final distribution in Wetherill's model (see Fig. 4) with the current one. However, the effects on the inclination during Jupiter's jump seem less pronounced than those on the eccentricity (Morbidelli et al., 2010).

The current inner edge of the asteroid belt is marked by the presence of the secular resonance between the precession frequency of the perihelion of an asteroid and the  $g_6$  planetary frequency. The resonance makes unstable all objects inside 2.1 AU at low to moderate inclinations, which truncates the belt at its current edge. But before the impulsive separation between the inner orbits of Jupiter and Saturn, this resonance was much weaker (because the  $g_6$  mode was less excited in the planetary system, the giant-planet orbits being more circular) and located away from the asteroid belt. Thus, in principle the asteroid belt might have extended closer to Mars before the giant-planet-instability event. Bottke et al. (2012) showed that the destabilization of this extended belt — or “E belt” — could have dominated the formation of impact basins on the Moon, producing 12–15 basins over a 400-m.y. interval. Given the age of the Orientale basin (usually estimated at 3.7–3.8 Ga), this implies that the giant-planet instability and the destabilization of the E belt happened 4.1–4.2 G.y. ago and was responsible for the production of the last dozen lunar basins, known as the Nectarian and post-Nectarian basins. Earlier basins and craters would have to have come from other sources, such as the planetesimals leftover from the terrestrial planet-formation process. The existence of two populations of projectiles, namely the leftover planetesimals dominating the bombardment at early times and the E-belt asteroids dominating the impact rate at a later epoch, should have produced a sawtooth-shaped bombardment history of the Moon (Morbidelli et al., 2012). The E belt should also have caused a long, slowly decaying tail of Chicxulub-sized impacts on Earth, possibly continuing until  $\sim 2$  G.y. ago. Evidence for this long tail in the time-distribution of impacts is provided by the existence of terrestrial impact spherule beds, which are globally distributed ejecta layers created by the formation of Chicxulub-sized or larger craters (Johnson and Melosh, 2012): 10, 4, and 1 of these beds have been found on well-preserved, non-metamorphosed terrains between 3.23 and 3.47 Ga, 2.49 and 2.63 Ga, and 1.7 and 2.1 Ga, respectively (Simonson and Glass, 2004; Bottke et al., 2012).

Moreover, the escape to high-eccentricity orbits of bodies from the main-belt and E-belt regions produced a spike in the impact velocities on main-belt asteroids at the time of the giant-planet instability. Thus, although the impact frequency on asteroids decreased with the depletion of 50% of the main-belt population and 100% of the E-belt population, the production of impact melt on asteroids increased during this event because melt production is very sensitive to impact velocities (Marchi et al., 2013). For this reason, the impact ages of meteorites show a spike at 4.1 Ga like

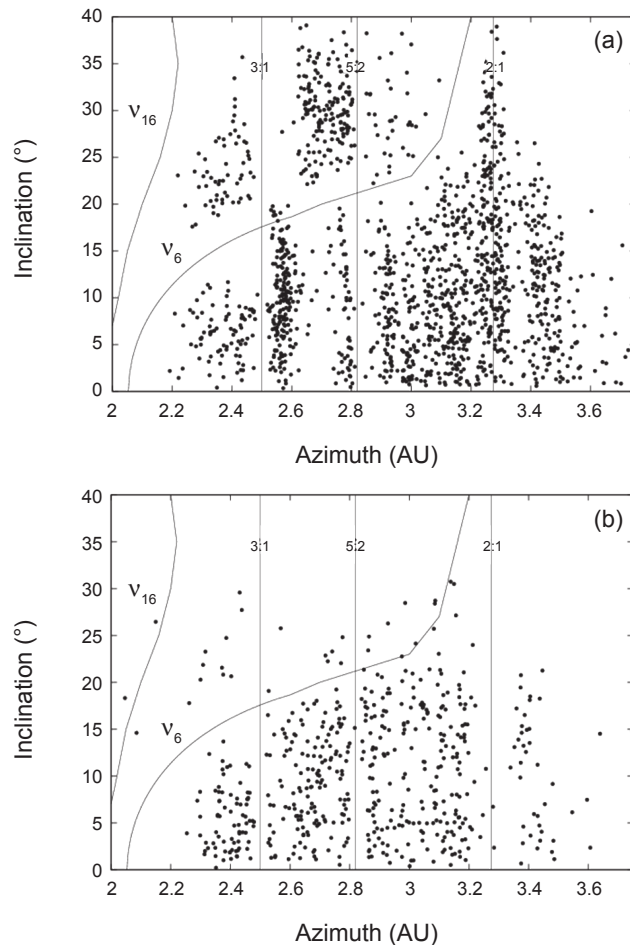


**Fig. 8.** A comparison between the final (a,i) distribution of asteroids if (a) Jupiter and Saturn migrate slowly away from each other or (b) jump due to them scattering an ice giant planet. In the first case the orbital distribution is inconsistent with that observed, while in the second case it is. From Morbidelli et al. (2010).

the lunar rocks, although for the latter this is due to a surge in the impact rate.

A final consequence of the giant-planet instability on the asteroid belt is the capture into its outer region of planetesimals from the transneptunian disk (Levison *et al.*, 2009). Because Jupiter Trojans are captured in the same event, these last captured asteroids should have had the same source as the Trojans and therefore they should be mostly taxonomic D- and P-types. The probability of capture in the asteroid belt is nevertheless small, so it is unlikely that an object as big as Ceres was trapped from the transneptunian region in this event.

### 3.6. After the Giant-Planet Instability

After the giant-planet instability the orbits of all planets, giants and terrestrial, are similar to the current ones (within the range of semimajor axis, eccentricity, and inclination oscillation provided by the current dynamical evolution). Thus, the asteroid belt has finished evolving substantially under the effect of external events such as giant-planet migration or instability.

The asteroid belt thus entered into the current era of evolution. Asteroids became depleted at the locations of unstable resonances (mean-motion and secular) on time-scales that varied from resonance to resonance. In this way, the asteroid belt acquired its current final orbital structure. In this process, it is likely that another ~50% of the asteroids were removed from the belt, most of them during the first 100 m.y. after the giant-planet instability (Minton and Malhotra, 2010). Combining this 50% with the 50% loss during the instability itself is the reason that we require that the primordial depletion event (Wetherill's model or Grand Tack) left a population of asteroids in the belt that was about 4× the current one.

With the depletion of unstable resonances, the asteroid belt would have become an extraordinarily boring place from a dynamical point of view. Fortunately, collisional breakup events keep refreshing the asteroid population, generating dynamical families very rich in small objects, while non-gravitational forces, mostly the Yarkovsky effect (Bottke *et al.*, 2006), cause small asteroids to drift in semimajor axis, eventually supplying new bodies to the unstable resonances. This combination of collisional activity and nongravitational forces allow the main asteroid belt to resupply and sustain in a quasi-steady state the intrinsically unstable population of near Earth objects. But this is the subject of another chapter.

## 4. CONCLUSIONS AND IMPLICATIONS

In this chapter, we have reviewed our current understanding of the evolution of the asteroid belt, from a massive and dynamically quiet disk of planetesimals to its current state, which is so complex and rich from the points of view of both its dynamical and physical structures.

According to this understanding, the asteroid population mainly evolved in two steps. There was an early event of strong dynamical excitation and asteroid removal, which left about 4× the current asteroid population on orbits with a wide range of eccentricities and inclinations. This event may have been due to the self-stirring of a population of planetary embryos resident in the asteroid belt (Wetherill, 1992), or to the migration of Jupiter through the asteroid belt [the Grand Tack scenario (Walsh *et al.*, 2011)]. The second step occurred later, possibly as late as 4.1 G.y. ago or ~400 m.y. after the removal of gas from the protoplanetary disk. At that time, the asteroid belt underwent a second dynamical excitation and depletion when the giant planets became temporarily unstable and their orbits evolved from an initial resonant and compact configuration to the current configuration. During this second event, the asteroid belt lost about 50% of its members. After this second event, the asteroid belt structure settled down with the progressive depletion at unstable resonances with the giant and terrestrial planets. Another 50% of the asteroid population was lost in this process, mostly during the subsequent 100 m.y.

If the first evolutionary step was due to the Grand Tack migration of Jupiter, we expect that S-type asteroids formed more or less *in situ* (2–3 AU region); the C-type asteroids formed in the giant-planet region (roughly 3–15 AU), and the P- and D-type asteroids formed beyond the initial location of Neptune (roughly 15–30 AU). The hot population of the Kuiper belt, the scattered disk, and the Oort cloud would also derive from the same transneptunian disk (Levison *et al.*, 2008; Brasser and Morbidelli, 2013). There is a growing consensus that the cold Kuiper belt (42–45 AU) is primordial and born *in situ* (Petit *et al.*, 2011; Parker *et al.*, 2011; Batygin *et al.*, 2011; Fraser *et al.*, 2014). Thus, the cold Kuiper belt objects should not have any correspondent in the asteroid belt.

If instead the first step was due to the self-stirring of resident embryos as in Wetherill's model, we expect that S-type asteroids formed in the inner part of the belt, C-type asteroids in the outer part, and no asteroids sample the planetesimal population in the giant-planet region. The origin of P- and D-type asteroids would be the same as above. Thus, deciding which of these two models is preferable requires a better understanding of the nature of C-type asteroids and their water content, the similarities and differences between them and comets, and among comets themselves. This may not be an easy task. The population of main-belt comets (asteroids showing cometary activity such as 133P/Elst-Pizarro or 238P/Read) and their relationship with the parent bodies of carbonaceous chondrites is key in this respect. If it turns out that main-belt comets are consistent with carbonaceous chondrites in terms of isotope composition (mostly for H, N, and O), then this will argue that carbonaceous chondrites are just the rocky counterpart of bodies much richer in water/ice than meteorites themselves. This would imply that C-type asteroids formed beyond the snowline, thus presumably in the vicinity of the giant planets. If instead the main-belt comets

are not related to carbonaceous chondrites, but are more similar to comets from their isotope composition (it should be noted that even though Comet Hartley 2 has a chondritic water D/H ratio, it has a nonchondritic  $^{14}\text{N}/^{15}\text{N}$  ratio), then this would argue for their injection in the belt from the cometary disk and would suggest that the parent bodies of carbonaceous chondrites are not so water-rich, and therefore formed somewhat closer to the Sun than the snowline.

Whatever the preferred scenario for the first depletion and excitation of the asteroid belt, it is clear that the asteroid population must have suffered in the first hundreds of millions of years as much collisional evolution as over the last 4 G.y. However, all asteroid families formed during the early times are not identifiable today because the dynamical excitation events dispersed them (and possibly depleted them) too severely. The presence of metallic asteroids not associated with a family of objects of basaltic or dunitic nature, as well as the existence of rogue basaltic asteroids such as 1459 Magnya, should therefore not come as a surprise. The only families that are preserved are those that formed after the last giant-planet-instability event and have not been made unrecognizable by subsequent collisional evolution and Yarkovsky drift; thus they are either relatively young or large.

In this chapter, we have also examined several other asteroid excitation and depletion scenarios, most of which have serious difficulties in reconciling their predicted outcomes with observations. We have done this not just for historical completeness, but also to illustrate the critical constraints on putative alternative scenarios of solar system evolution. For instance, numerous studies on the possible *in situ* formation of extrasolar super-Earths close to their host stars assume a large pileup of drifting material of various sizes, from grains to small-mass embryos, in the inner part of the protoplanetary disks (Hansen, 2014; Chatterjee and Tan, 2014; Boley et al., 2014). By analogy, these models could be used to suggest that the outer edge of the planetesimal disk at 1 AU, required to form a small Mars, was due to the same phenomenon rather than to the Grand Tack migration of Jupiter. However, from what we reported in this chapter, we think that the asteroid belt rules out this possibility. In fact, the inward migration of small planetesimals (due to gas drag) and large embryos (due to disk tides) could explain the pileup of solid mass inside 1 AU and the mass deficit of the asteroid belt, but not the asteroids' orbital distribution (Izidoro et al., 2015). In the absence of the Grand Tack migration of Jupiter, we showed in section 3 that the only mechanism that could give the belt an orbital structure similar to that observed is Wetherill's model of mutual scattering of resident embryos. But if this was the case, then the mass distribution could not be concentrated within 1 AU because a massive population of embryos is required in the main-belt region. Thus, at the current state of knowledge (which may change in the future), only the Grand Tack scenario seems able to explain the required mass concentration to make a small Mars.

In summary, the asteroid belt remains the population of choice to test old, current, and future models of solar system evolution.

**Acknowledgments.** A.M. was supported by the European Research Council (ERC) Advanced Grant ACCRETE (contract number 290568).

## REFERENCES

- Abbas M. M. and 11 colleagues (2010) D/H ratio of Titan from observations of the Cassini/Composite Infrared Spectrometer. *Astrophys. J.*, **708**, 342–353.
- Agnor C. B. and Lin D. N. C. (2012) On the migration of Jupiter and Saturn: Constraints from linear models of secular resonant coupling with the terrestrial planets. *Astrophys. J.*, **745**, 143.
- Alexander C. M. O'D., Newsome S. D., Fogel M. L., Nittler L. R., Busemann H., and Cody G. D. (2010) Deuterium enrichments in chondritic macromolecular material — Implications for the origin and evolution of organics, water and asteroids. *Geochim. Cosmochim. Acta*, **74**, 4417–4437.
- Alexander, C. M. O'D., Bowden R., Fogel M. L., Howard K. T., Herd C. D. K., and Nittler L. R. (2012) The provenances of asteroids, and their contributions to the volatile inventories of the terrestrial planets. *Science*, **337**, 721–723.
- Alexander R., Pascucci I., Andrews S., Armitage P., and Cieza L. (2014) The dispersal of protoplanetary disks. In *Protoplanets and Planets VI* (H. Beuther et al., eds.), pp. 475–496. Univ. of Arizona, Tucson.
- Altweig K. and 32 colleagues (2014) 67P/Churyumov-Gerasimenko, a Jupiter family comet with a high D/H ratio. *Science*, **347**(6220), DOI: 10.1126/science.1261952.
- Batygin K. and Brown M. E. (2010) Early dynamical evolution of the solar system: Pinning down the initial conditions of the Nice model. *Astrophys. J.*, **716**, 1323–1331.
- Batygin K., Brown M. E., and Fraser W. C. (2011) Retention of a primordial cold classical Kuiper belt in an instability-driven model of solar system formation. *Astrophys. J.*, **738**, 13.
- Batygin K., Brown M. E., and Betts H. (2012) Instability-driven dynamical evolution model of a primordially five-planet outer solar system. *Astrophys. J. Lett.*, **744**, L3.
- Binzel R. P., Bus S. J., Burbine T. H., and Sunshine J. M. (1996) Spectral properties of near-Earth asteroids: Evidence for sources of ordinary chondrite meteorites. *Science*, **273**, 946–948.
- Bitsch B., Morbidelli A., Lega E., and Crida A. (2014) Stellar irradiated discs and implications on migration of embedded planets. II. Accreting-discs. *Astron. Astrophys.*, **564**, AA135.
- Biver N., Bockelée-Morvan D., Crovisier J., Lis D. C., Moreno R., Colom P., Henry F., Herpin F., Paubert G., and Womack M. (2006) Radio wavelength molecular observations of comets C/1999 T1 (McNaught-Hartley), C/2001 A2 (LINEAR), C/2000 WM1 (LINEAR) and 153P/Ikeya-Zhang. *Astron. Astrophys.*, **449**, 1255–1270.
- Bockelée-Morvan D. and 21 colleagues (2012) Herschel measurements of the D/H and  $^{16}\text{O}/^{18}\text{O}$  ratios in water in the Oort-cloud comet C/2009 P1 (Garradd). *Astron. Astrophys.*, **544**, LL15.
- Boley A. C., Morris M. A., and Ford E. B. (2014) Overcoming the meter barrier and the formation of systems with tightly packed inner planets (STIPs). *Astrophys. J. Lett.*, **792**, L27.
- Bottke W. F., Durda D. D., Nesvorný D., Jedicke R., Morbidelli A., Vokrouhlický D., and Levison H. (2005a) The fossilized size distribution of the main asteroid belt. *Icarus*, **175**, 111–140.
- Bottke W. F., Durda D. D., Nesvorný D., Jedicke R., Morbidelli A., Vokrouhlický D., and Levison H. F. (2005b) Linking the collisional history of the main asteroid belt to its dynamical excitation and depletion. *Icarus*, **179**, 63–94.
- Bottke W. F. Jr., Vokrouhlický D., Rubincam D. P., and Nesvorný D. (2006) The Yarkovsky and YORP effects: Implications for asteroid dynamics. *Annu. Rev. Earth Planet. Sci.*, **34**, 157–191.
- Bottke W. F., Levison H. F., Nesvorný D., and Dones L. (2007) Can planetesimals left over from terrestrial planet formation produce the lunar late heavy bombardment? *Icarus*, **190**, 203–223.

- Bottke W. F., Vokrouhlický D., Minton D., Nesvorný D., Morbidelli A., Brasser R., Simonson B., and Levison H. F. (2012) An Archaean heavy bombardment from a destabilized extension of the asteroid belt. *Nature*, **485**, 78–81.
- Brasser R. and Morbidelli A. (2013) Oort cloud and Scattered Disc formation during a late dynamical instability in the Solar System. *Icarus*, **225**, 40–49.
- Brasser R., Duncan M. J., and Levison H. F. (2007) Embedded star clusters and the formation of the Oort cloud. II. The effect of the primordial solar nebula. *Icarus*, **191**, 413–433.
- Brasser R., Duncan M. J., and Levison H. F. (2008) Embedded star clusters and the formation of the Oort cloud. III. Evolution of the inner cloud during the galactic phase. *Icarus*, **196**, 274–284.
- Brasser R., Morbidelli A., Gomes R., Tsiganis K., and Levison H. F. (2009) Constructing the secular architecture of the solar system II: The terrestrial planets. *Astron. Astrophys.*, **507**, 1053–1065.
- Brasser R., Duncan M. J., Levison H. F., Schwamb M. E., and Brown M. E. (2012) Reassessing the formation of the inner Oort cloud in an embedded star cluster. *Icarus*, **217**, 1–19.
- Burbine T. H., McCoy T. J., Meibom A., Gladman B., and Keil K. (2002) Meteoritic parent bodies: Their number and identification. In *Asteroids III* (W. F. Bottke Jr. et al., eds.), pp. 653–667. Univ. of Arizona, Tucson.
- Bus S. J. and Binzel R. P. (2002) Phase II of the Small Main-Belt Asteroid Spectroscopic Survey. A feature-based taxonomy. *Icarus*, **158**, 146–177.
- Busemann H., Young A. F., Alexander C. M. O'D., Hoppe P., Mukhopadhyay S., and Nittler L. R. (2006) Interstellar chemistry recorded in organic matter from primitive meteorites. *Science*, **312**, 727–730.
- Campins H., Hargrove K., Pinilla-Alonso N., Howell E. S., Kelley M. S., Licandro J., Mothé-Diniz T., Fernández Y., and Ziffer J. (2010) Water ice and organics on the surface of the asteroid 24 Themis. *Nature*, **464**, 1320–1321.
- Carvano J. M., Hasselmann P. H., Lazzaro D., and Mothé-Diniz T. (2010) SDSS-based taxonomic classification and orbital distribution of main belt asteroids. *Astron. Astrophys.*, **510**, A43.
- Chambers J. E. and Wetherill G. W. (1998) Making the terrestrial planets: N-body integrations of planetary embryos in three dimensions. *Icarus*, **136**, 304–327.
- Chatterjee S. and Tan J. C. (2014) Inside-out planet formation. *Astrophys. J.*, **780**, 53.
- Cohen B. A., Swindle T. D., and Kring D. A. (2005) Geochemistry and  $^{40}\text{Ar}$ - $^{39}\text{Ar}$  geochronology of impact-melt clasts in feldspathic lunar meteorites: Implications for lunar bombardment history. *Meteoritics & Planet. Sci.*, **40**, 755.
- Coustenis A. and 10 colleagues (2008) Detection of C<sub>2</sub>HD and the D/H ratio on Titan. *Icarus*, **197**, 539–548.
- Cresswell P. and Nelson R. P. (2008) Three-dimensional simulations of multiple protoplanets embedded in a protostellar disc. *Astron. Astrophys.*, **482**, 677–690.
- Ćuk M. (2012) Chronology and sources of lunar impact bombardment. *Icarus*, **218**, 69–79.
- D'Angelo G. and Marzari F. (2012) Outward migration of Jupiter and Saturn in evolved gaseous disks. *Astrophys. J.*, **757**, 50.
- DeMeo F. E. and Carry B. (2014) Solar system evolution from compositional mapping of the asteroid belt. *Nature*, **505**, 629–634.
- DeMeo F. E., Binzel R. P., Slivan S. M., and Bus S. J. (2009) An extension of the Bus asteroid taxonomy into the near-infrared. *Icarus*, **202**, 160–180.
- Dones L., Weissman P. R., Levison H. F., and Duncan M. J. (2004) Oort cloud formation and dynamics. In *Comets II* (M. C. Festou et al., eds.) pp. 153–174. Univ. of Arizona, Tucson.
- Duprat J., Dobrica E., Engrand C., Aleon J., Marrocchi Y., Mostefaioui S., Meibom A., Leroux H., Rouzaud J. N., Gounelle M., and Robert F. (2010) Extreme deuterium excesses in ultracarbonaceous micrometeorites from central Antarctic snow. *Science*, **1126**, 742–745.
- Fassett C. I. and Minton D. A. (2013) Impact bombardment of the terrestrial planets and the early history of the solar system. *Nature Geosci.*, **6**, 520–524.
- Fischer R. A. and Ciesla F. J. (2014) Dynamics of the terrestrial planets from a large number of N-body simulations. *Earth Planet. Sci. Lett.*, **392**, 28–38.
- Fraser W. C., Brown M. E., Morbidelli A., Parker A., and Batygin K. (2014) The absolute magnitude distribution of Kuiper belt objects. *Astrophys. J.*, **782**, 100.
- Gounelle M., Spurný P., and Bland P. A. (2006) The orbit and atmospheric trajectory of the Orgueil meteorite from historical records. *Meteoritics & Planet. Sci.*, **41**, 135–150.
- Gounelle M., Morbidelli A., Bland P. A., Spurný P., Young E. D., and Sephton M. (2008) Meteorites from the outer solar system? In *The Solar System Beyond Neptune* (M. A. Barucci et al., eds.), pp. 525–541. Univ. of Arizona, Tucson.
- Gradie J. and Tedesco E. (1982) Compositional structure of the asteroid belt. *Science*, **216**, 1405–1407.
- Haisch K. E. Jr., Lada E. A., and Lada C. J. (2001) Disk frequencies and lifetimes in young clusters. *Astrophys. J. Lett.*, **553**, L153–L156.
- Halliday A. N. (2013) The origins of volatiles in the terrestrial planets. *Geochim. Cosmochim. Acta*, **105**, 146–171.
- Hansen B. M. S. (2009) Formation of the terrestrial planets from a narrow annulus. *Astrophys. J.*, **703**, 1131–1140.
- Hansen B. M. S. (2014) The circulation of dust in protoplanetary discs and the initial conditions of planet formation. *Mon. Not. R. Astron. Soc.*, **440**, 3545–3556.
- Hargrove K. D., Kelley M. S., Campins H., Licandro J., and Emery J. (2012) Asteroids (65) Cybele, (107) Camilla and (121) Hermione: Infrared spectral diversity among the Cybeles. *Icarus*, **221**, 453–455.
- Hartogh P. and 12 colleagues (2011) Ocean-like water in the Jupiter-family comet 103P/Hartley 2. *Nature*, **478**, 218–220.
- Heppenheimer T. A. (1980) Secular resonances and the origin of eccentricities of Mars and the asteroids. *Icarus*, **41**, 76–88.
- Hiroi T., Zolensky M. E., and Pieters C. M. (2001) The Tagish Lake meteorite: A possible sample from a D-type asteroid. *Science*, **293**, 2234–2236.
- Hsieh H. H. and Jewitt D. (2006) A population of comets in the main asteroid belt. *Science*, **312**, 561–563.
- Ip W.-H. (1987) Gravitational stirring of the asteroid belt by Jupiter zone bodies. *Beitr. Geophys.*, **96**, 44–51.
- Ishii H. A., Bradley J. P., Dai Z. R., Chi M., Kearsley A. T., Burchell M. J., Browning N. D., and Molster F. (2008) Comparison of Comet 81P/Wild 2 dust with interplanetary dust from comets. *Science*, **319**, 447.
- Izidoro A., Raymond S. N., Morbidelli A., and Winter D. C. (2015) Terrestrial planet formation constrained by Mars and the structure of the asteroid belt. *Mon. Nat. R. Astron. Soc.*, in press.
- Jacobson S. A. and Morbidelli A. (2014) Lunar and terrestrial planet formation in the Grand Tack scenario. *Philos. Trans. R. Soc. London Ser. A*, **372**, 174.
- Jacobson S. A. and Walsh K. J. (2015) The Earth and terrestrial planet formation. In *The Early Earth* (J. Badro and M. Walter, eds.), in press. Wiley, New York.
- Jacobson S. A., Morbidelli A., Raymond S. N., O'Brien D. P., Walsh K. J., and Rubie D. C. (2014) Highly siderophile elements in Earth's mantle as a clock for the Moon-forming impact. *Nature*, **508**, 84–87.
- Johnson B. C. and Melosh H. J. (2012) Impact spherules as a record of an ancient heavy bombardment of Earth. *Nature*, **485**, 75–77.
- Kenyon S. J. and Hartmann L. (1995) Pre-main-sequence evolution in the Taurus-Auriga molecular cloud. *Astrophys. J. Suppl.*, **101**, 11.
- Kley W. and Nelson R. P. (2012) Planet-disk interaction and orbital evolution. *Annu. Rev. Astron. Astrophys.*, **50**, 211–249.
- Krasinsky G. A., Pitjeva E. V., Vasilyev M. V., and Yagudina E. I. (2002) Hidden mass in the asteroid belt. *Icarus*, **158**, 98–105.
- Kuchynka P. and Folkner W. M. (2013) A new approach to determining asteroid masses from planetary range measurements. *Icarus*, **222**, 243–253.
- Küppers M., and 12 colleagues (2014) Localized sources of water vapour on the dwarf planet (1) Ceres. *Nature*, **505**, 525–527.
- Lecar M. and Franklin F. (1997) The solar nebula, secular resonances, gas drag, and the asteroid belt. *Icarus*, **129**, 134–146.
- Lemaitre A. and Dubro P. (1991) Secular resonances in the primitive solar nebula. *Cel. Mech. Dyn. Astron.*, **52**, 57–78.
- Levison H. F., Morbidelli A., Van Laerhoven C., Gomes R., and Tsiganis K. (2008) Origin of the structure of the Kuiper belt during a dynamical instability in the orbits of Uranus and Neptune. *Icarus*, **196**, 258–273.
- Levison H. F., Bottke W. F., Gounelle M., Morbidelli A., Nesvorný D., and Tsiganis K. (2009) Contamination of the asteroid belt by primordial trans-neptunian objects. *Nature*, **460**, 364–366.
- Levison H. F., Morbidelli A., Tsiganis K., Nesvorný D., and Gomes R. (2011) Late orbital instabilities in the outer planets induced by interaction with a self-gravitating planetesimal disk. *Astron. J.*, **142**, 152.
- Licandro J., Campins H., Kelley M., Hargrove K., Pinilla-Alonso N., Cruikshank D., Rivkin A. S., and Emery J. (2011) (65) Cybele:

- Detection of small silicate grains, water-ice, and organics. *Astron. Astrophys.*, 525, A34.
- Marchi S. and 10 colleagues (2013) High-velocity collisions from the lunar cataclysm recorded in asteroidal meteorites. *Nature Geosci.*, 6, 303–307.
- Marty B. (2012) The origins and concentrations of water, carbon, nitrogen and noble gases on Earth. *Earth Planet. Sci. Lett.*, 313, 56–66.
- Masset F. and Snellgrove M. (2001) Reversing type II migration: Resonance trapping of a lighter giant protoplanet. *Mon. Not. R. Astron. Soc.*, 320, L55–L59.
- Meech K. J. and 196 colleagues (2011) EPOXI: Comet 103P/Hartley 2 observations from a worldwide campaign. *Astrophys. J. Lett.*, 734, L1.
- Minton D. A. and Malhotra R. (2009) A record of planet migration in the main asteroid belt. *Nature*, 457, 1109–1111.
- Minton D. A. and Malhotra R. (2010) Dynamical erosion of the asteroid belt and implications for large impacts in the inner solar system. *Icarus*, 207, 744–757.
- Minton D. A. and Malhotra R. (2011) Secular resonance sweeping of the main asteroid belt during planet migration. *Astrophys. J.*, 732, 53.
- Morbidelli A. and Crida A. (2007) The dynamics of Jupiter and Saturn in the gaseous protoplanetary disk. *Icarus*, 191, 158–171.
- Morbidelli A., Tsiganis K., Crida A., Levison H. F., and Gomes R. (2007) Dynamics of the giant planets of the solar system in the gaseous protoplanetary disk and their relationship to the current orbital architecture. *Astron. J.*, 134, 1790–1798.
- Morbidelli A., Bottke W. F., Nesvorný D., and Levison H. F. (2009) Asteroids were born big. *Icarus*, 204, 558–573.
- Morbidelli A., Brasser R., Gomes R., Levison H. F., and Tsiganis K. (2010) Evidence from the asteroid belt for a violent past evolution of Jupiter's orbit. *Astron. J.*, 140, 1391–1401.
- Morbidelli A., Marchi S., Bottke W. F., and Kring D. A. (2012) A sawtooth-like timeline for the first billion years of lunar bombardment. *Earth Planet. Sci. Lett.*, 355, 144–151.
- Mothé-Diniz T., Carvano J. M. á., and Lazzaro D. (2003) Distribution of taxonomic classes in the main belt of asteroids. *Icarus*, 162, 10–21.
- Mouillet D., Larwood J. D., Papaloizou J. C. B., and Lagrange A. M. (1997) A planet on an inclined orbit as an explanation of the warp in the Beta Pictoris disc. *Mon. Not. R. Astron. Soc.*, 292, 896.
- Nagasawa M., Tanaka H., and Ida S. (2000) Orbital evolution of asteroids during depletion of the solar nebula. *Astron. J.*, 119, 1480–1497.
- Nagasawa M., Ida S., and Tanaka H. (2001) Origin of high orbital eccentricity and inclination of asteroids. *Earth Planets Space*, 53, 1085–1091.
- Nagasawa M., Ida S., and Tanaka H. (2002) Excitation of orbital inclinations of asteroids during depletion of a protoplanetary disk: Dependence on the disk configuration. *Icarus*, 159, 322–327.
- Nakamura T. and 11 colleagues (2008) Chondrule-like objects in short-period Comet 81P/Wild 2. *Science*, 321, 1664.
- Nesvorný D. (2011) Young solar system's fifth giant planet? *Astrophys. J. Lett.*, 742, L22.
- Nesvorný D. and Morbidelli A. (2012) Statistical study of the early solar system's instability with four, five, and six giant planets. *Astron. J.*, 144, 117.
- Nesvorný D., Vokrouhlický D., and Morbidelli A. (2007) Capture of irregular satellites during planetary encounters. *Astron. J.*, 133, 1962–1976.
- Nesvorný D., Jenniskens P., Levison H. F., Bottke W. F., Vokrouhlický D., and Gounelle M. (2010) Cometary origin of the zodiacal cloud and carbonaceous micrometeorites. Implications for hot debris disks. *Astrophys. J.*, 713, 816–836.
- Nesvorný D., Vokrouhlický D., and Morbidelli A. (2013) Capture of Trojans by jumping Jupiter. *Astrophys. J.*, 768, 45.
- Nesvorný D., Vokrouhlický D., and Deienno R. (2014) Capture of irregular satellites at Jupiter. *Astrophys. J.*, 784, 22.
- Niemann H. B., Atreya S. K., Demick J. E., Gautier D., Haberman J. A., Harpold D. N., Kasprzak W. T., Lunine J. I., Owen T. C., and Raulin F. (2010) Composition of Titan's lower atmosphere and simple surface volatiles as measured by the Cassini-Huygens probe gas chromatograph mass spectrometer experiment. *J. Geophys. Res.–Planets*, 115, E1(2006).
- Nixon C. A. and 12 colleagues (2012) Isotopic ratios in titan's methane: Measurements and modeling. *Astrophys. J.*, 749, 159.
- Norman M. D. and Nemchin A. A. (2014) A 4.2 billion year old impact basin on the Moon: U-Pb dating of zirconolite and apatite in lunar melt rock 67955. *Earth Planet. Sci. Lett.*, 388, 398–398.
- O'Brien D. P., Morbidelli A., and Levison H. F. (2006) Terrestrial planet formation with strong dynamical friction. *Icarus*, 184, 39–58.
- O'Brien D. P., Morbidelli A., and Bottke W. F. (2007) The primordial excitation and clearing of the asteroid belt — Revisited. *Icarus*, 191, 434–452.
- Parker A. H., Kavelaars J. J., Petit J.-M., Jones L., Gladman B., and Parker J. (2011) Characterization of seven ultra-wide trans-neptunian binaries. *Astrophys. J.*, 743, 1.
- Petit J., Morbidelli A., and Valsecchi G. B. (1999) Large scattered planetesimals and the excitation of the small body belts. *Icarus*, 141, 367–387.
- Petit J., Morbidelli A., and Chambers J. (2001) The primordial excitation and clearing of the asteroid belt. *Icarus*, 153, 338–347.
- Petit J., Chambers J., Franklin F., and Nagasawa M. (2002) Primordial excitation and depletion of the main belt. In *Asteroids III* (W. F. Bottke Jr. et al., eds.), pp. 711–738. Univ. of Arizona, Tucson.
- Petit J.-M. and 16 colleagues (2011) The Canada-France Ecliptic Plane Survey — Full data release: The orbital structure of the Kuiper belt. *Astron. J.*, 142, 131.
- Pierens A. and Nelson R. P. (2008) Constraints on resonant-trapping for two planets embedded in a protoplanetary disc. *Astron. Astrophys.*, 482, 333–340.
- Pierens A. and Raymond S. N. (2011) Two phase, inward-then-outward migration of Jupiter and Saturn in the gaseous solar nebula. *Astron. Astrophys.*, 533, A131.
- Rivkin A. S. and Emery J. P. (2010) Detection of ice and organics on an asteroidal surface. *Nature*, 464, 1322–1323.
- Robuchon G., Nimmo F., Roberts J., and Kirchoff M. (2011) Impact basin relaxation at Iapetus. *Icarus*, 214, 82–90.
- Rousselot P. and 11 colleagues (2014) Toward a unique nitrogen isotopic ratio in cometary ices. *Astrophys. J. Lett.*, 780, L17.
- Simonson B. M. and Glass B. B. (2004) Spherule layers — records of Ancient Impacts. *Annu. Rev. Earth Planet. Sci.*, 32, 329–361.
- Somenzi L., Fienga A., Laskar J., and Kuchynka P. (2010) Determination of asteroid masses from their close encounters with Mars. *Planet. Space Sci.*, 58, 858–863.
- Strom S. E., Edwards S., and Skrutskie M. F. (1993) Evolutionary time scales for circumstellar disks associated with intermediate- and solar-type stars. In *Protoplanets III* (E. H. Levy and J. I. Lunine, eds.), pp. 837–866. Univ. of Arizona, Tucson.
- Tholen D. J. (1984) Asteroid taxonomy from cluster analysis of photometry. Ph.D. thesis, Univ. of Arizona, Tucson.
- Thommes E. W., Duncan M. J., and Levison H. F. (1999) The formation of Uranus and Neptune in the Jupiter-Saturn region of the solar system. *Nature*, 402, 635–638.
- Tsiganis K., Gomes R., Morbidelli A., and Levison H. F. (2005) Origin of the orbital architecture of the giant planets of the solar system. *Nature*, 435, 459–461.
- Villeneuve J., Chaussidon M., and Libourel G. (2009) Homogeneous distribution of  $^{26}\text{Al}$  in the solar system from the Mg isotopic composition of chondrules. *Science*, 325, 985.
- Waite J. H. Jr. and 15 colleagues (2009) Liquid water on Enceladus from observations of ammonia and  $^{40}\text{Ar}$  in the plume. *Nature*, 460, 487–490.
- Walsh K. J., Morbidelli A., Raymond S. N., O'Brien D. P., and Mandell A. M. (2011) A low mass for Mars from Jupiter's early gas-driven migration. *Nature*, 475, 206–209.
- Ward W. R. (1981) Solar nebula dispersal and the stability of the planetary system. I — Scanning secular resonance theory. *Icarus*, 47, 234–264.
- Ward W. R., Colombo G., and Franklin F. A. (1976) Secular resonance, solar spin down, and the orbit of Mercury. *Icarus*, 28, 441–452.
- Weidenschilling S. J. (1977) The distribution of mass in the planetary system and solar nebula. *Astrophys. Space Sci.*, 51, 153–158.
- Wetherill G. W. (1992) An alternative model for the formation of the asteroids. *Icarus*, 100, 307–325.
- Yang L., Ciesla F. J., and Alexander C. M. O'D. (2013) The D/H ratio of water in the solar nebula during its formation and evolution. *Icarus*, 226, 256–267.
- Zolensky M. E. and 74 colleagues (2006) Mineralogy and petrology of Comet 81P/Wild 2 nucleus samples. *Science*, 314, 1735.
- Zolensky M. and 30 colleagues (2008) Comparing Wild 2 particles to chondrites and IDPs. *Meteoritics & Planet. Sci.*, 43, 261–272.
- Zuckerman B., Forveille T., and Kastner J. H. (1995) Inhibition of giant-planet formation by rapid gas depletion around young stars. *Nature*, 373, 494–496.



# The Yarkovsky and YORP Effects

**David Vokrouhlický**  
*Charles University, Prague*

**William F. Bottke**  
*Southwest Research Institute*

**Steven R. Chesley**  
*Jet Propulsion Laboratory/California Institute of Technology*

**Daniel J. Scheeres**  
*University of Colorado*

**Thomas S. Statler**  
*Ohio University and University of Maryland*

---

The Yarkovsky effect describes a small but significant force that affects the orbital motion of meteoroids and asteroids smaller than 30–40 km in diameter. It is caused by sunlight; when these bodies heat up in the Sun, they eventually reradiate the energy away in the thermal waveband, which in turn creates a tiny thrust. This recoil acceleration is much weaker than solar and planetary gravitational forces, but it can produce measurable orbital changes over decades and substantial orbital effects over millions to billions of years. The same physical phenomenon also creates a thermal torque that, complemented by a torque produced by scattered sunlight, can modify the rotation rates and obliquities of small bodies as well. This rotational variant has been coined the Yarkovsky-O’Keefe-Radzievskii-Paddack (YORP) effect. During the past decade or so, the Yarkovsky and YORP effects have been used to explore and potentially resolve a number of unsolved mysteries in planetary science dealing with small bodies. Here we review the main results to date, and preview the goals for future work.

## 1. INTRODUCTION

Interesting problems in science usually have a long and complex history. It is rare, though, that they have a prehistory or perhaps even mythology. Yet, until recently this was the case for the Yarkovsky effect. Ivan O. Yarkovsky, a Russian civil engineer born in a family of Polish descent, noted in a privately published pamphlet (Yarkovsky, 1901; Beekman, 2006) that heating a prograde-rotating planet should produce a transverse acceleration in its motion and thus help to counterbalance the assumed drag from the then-popular ether hypothesis. While this context of Yarkovsky’s work was mistaken and he was only roughly able to estimate the magnitude of the effect, he succeeded in planting the seed of an idea that a century later blossomed into a full-fledged theory of how the orbits of small objects revolving about the Sun are modified by the absorption and reemission of solar energy.

It is mainly Ernst J. Öpik who is to be credited for keeping Yarkovsky’s work alive and introducing it to western literature, long after the original pamphlet had been lost

(Öpik, 1951). Curiously, at about the same time, similar ideas also started to appear in Russian regular scientific literature through the works of Vladimir V. Radzievskii and his collaborators (Radzievskii, 1952). While Radzievskii was also the first to consider the effects of systematic photon thrust on a body’s rotation, his concept was based on a variable albedo coefficient across the surface (Radzievskii, 1954). However, there is no strong evidence of large enough albedo variations over surfaces of asteroids or meteoroids. Stephen J. Paddack and John O’Keefe pushed the idea forward by realizing that irregular shape, and thermal radiation rather than just reflected sunlight, will more efficiently change the meteoroid’s spin rate. Thence, the Yarkovsky-O’Keefe-Radzievskii-Paddack (YORP) effect was born as an alter ego of the Yarkovsky effect little more than half a century after Yarkovsky’s work (see Paddack (1969), Paddack and Rhee (1975), and Rubincam (2000) for a summation of the history and coining of the terminology). Radzievskii’s school also briefly touched upon a concept of a radiation-induced acceleration of synchronous planetary satellites (Vinogradova

and Radzievskii, 1965), an idea that reappeared much later in a slightly different form as a binary YORP (BYORP) effect (Ćuk and Burns, 2005).

The three decades from the 1950s to the 1970s resulted in today's understanding of Yarkovsky and YORP effects. The works that led to a major resurgence in these studies, however, occurred in the second half of the 1990s through the work of David P. Rubincam and Paolo Farinella. Interestingly, both were studying thermal perturbations of artificial satellite motion. With that expertise, they realized a direct link between the orbital effects acting on the artificial satellites such as the Laser Geodynamics Satellites (LAGEOS) and the orbital effects on small meteoroids (e.g., Afonso *et al.*, 1995; Rubincam, 1995, 1998; Farinella *et al.*, 1998).

From there, a momentum was gained and a wealth of new results appeared, with applications extending to dynamics of small asteroids and their populations (e.g., Bottke *et al.*, 2002a, 2006). Studies of the Yarkovsky effect were soon followed by those of the YORP effect (Rubincam, 2000). Today, both effects belong to a core culture in planetary sciences, as well as beyond (e.g., <http://www.youtube.com/watch?v=kzlgxqTtxYs>), and have become an important part of the agenda of space missions (e.g., Lauretta *et al.*, 2015). Especially after the spectacular discovery of the “once lost” Yarkovsky pamphlet in Russian archives by Dutch amateur astronomer George Beekman (see Beekman, 2006), it seems timely to review the current knowledge of the Yarkovsky and YORP effects. This effort could start with a translation, and perhaps a commented edition, of the Yarkovsky work (presently available in its original form as an Appendix to Miroslav Brož's thesis, <http://sirrah.troja.mff.cuni.cz/mira/mp/phdth>). We look forward to future historians editing the more than a century long story of the Yarkovsky and YORP effects, with all the known and possibly hidden roots, into a consolidated picture.

Leaving historical issues to their own time, we now turn to current scientific issues related to the Yarkovsky and YORP effects. There are several good technical reviews already existing in the literature (e.g., Bottke *et al.*, 2002a, 2006). While not always possible, we try to avoid discussing the same topics as presented in these previous texts. For instance, we do not review the elementary concepts of the Yarkovsky and YORP effects, assuming the reader is familiar with them. Rather, we try to focus on new results and ideas that emerged during the past decade and that will lead to research efforts in the next several years.

## 2. THEORY OF THE YARKOVSKY AND YORP EFFECTS

We start with the simplest analytical models of the Yarkovsky and YORP effects (section 2.1). This is because they provide useful insights, such as scalings with several key parameters, and their results are correct to leading order. They also allow us to understand why modeling of the YORP effect is inevitably more complicated than modeling of the Yarkovsky effect. And yet, the quality of the Yarkovsky

and YORP effects detections, as well as other applications, have reached a level that requires more accurate models to be used. The first steps toward these new models have been taken recently and these are briefly reviewed in section 2.2.

### 2.1. Classical Models

**2.1.1. The Yarkovsky effect.** Absorbed and directly reflected sunlight does not tend to produce long-term dynamical effects as far as orbital motion is concerned (e.g., Vokrouhlický and Milani, 2000; Žížka and Vokrouhlický, 2011). The Yarkovsky effect thus fundamentally depends on emitted thermal radiation and requires a body to have a nonzero thermal inertia. Any meaningful evaluation of the Yarkovsky effect, therefore, requires a thermophysical model of that body. Fortunately, an evaluation of the Yarkovsky effect imposes a minimum of requirements on the shape of the body; even a simple spherical model provides us with a fair approximation of how the body will orbitally evolve.

While the Yarkovsky effect results in variations to all the orbital elements, what is distinct from most other perturbations is the secular effect in the semimajor axis  $a$ , and therefore we only discuss this contribution. Assuming (1) a linearization of the surface boundary condition, (2) a rotation about a spin axis fixed in the inertial space (at least on a timescale comparable with the revolution about the Sun), and (3) a circular orbit about the Sun, one easily finds that the total, orbit-averaged change in  $a$  is composed of two contributions (e.g., Rubincam, 1995, 1998; Farinella *et al.*, 1998; Vokrouhlický, 1998a, 1999), the diurnal effect

$$\left( \frac{da}{dt} \right)_{\text{diurnal}} = -\frac{8}{9} \frac{\alpha \Phi}{n} W(R_\omega, \Theta_\omega) \cos \gamma \quad (1)$$

and the seasonal effect

$$\left( \frac{da}{dt} \right)_{\text{seasonal}} = \frac{4}{9} \frac{\alpha \Phi}{n} W(R_n, \Theta_n) \sin^2 \gamma \quad (2)$$

Here,  $\Phi = \pi R^2 F / (mc)$ , where  $R$  is the radius of the body,  $F$  the solar radiation flux at the orbital distance  $a$  from the Sun,  $m$  the mass of the body,  $c$  the light velocity,  $n$  the orbital mean motion, and  $\alpha = 1-A$ , with  $A$  denoting the Bond albedo (e.g., Vokrouhlický and Bottke, 2001). The  $\Phi$  factor is characteristic to any physical effect related to sunlight absorbed or scattered by the surface of the body. Since  $m \propto R^3$ , one obtains a typical scaling  $\Phi \propto 1/R$ .

More importantly, the diurnal and seasonal components of the Yarkovsky effect have a different dependence on the spin axis obliquity  $\gamma$ : (1) the diurnal part is  $\propto \cos \gamma$ , and consequently can make a positive or negative change in the semimajor axis, being maximum at  $0^\circ$  and  $180^\circ$  obliquity values; and (2) the seasonal part is  $\propto \sin^2 \gamma$ , and consequently always results in a decrease in semimajor axis, being

maximum at 90° obliquity. Their magnitude is proportional to the function

$$W(R_v, \Theta_v) = -\frac{\kappa_1(R_v)\Theta_v}{1 + 2\kappa_2(R_v)\Theta_v + \kappa_3(R_v)\Theta_v^2} \quad (3)$$

determined by the thermal parameters of the body and a frequency  $v$ . The latter is equal either to the rotation frequency  $\omega$  for the diurnal component, or the orbital mean motion  $n$  for the seasonal component. The thermal parameters required by the model are (1) the surface thermal conductivity  $K$ , (2) the surface heat capacity  $C$ , and (3) the surface density  $\rho$ . These parameters, together with the frequency  $v$ , do not appear in equation (3) individually. Rather, in the process of solving the heat diffusion problem and determination of the orbital perturbations, they combine in two relevant parameters. First, they provide a scale length  $\ell_v = \sqrt{K/(\rho Cv)}$ , which indicates a characteristic penetration depth of temperature changes assuming the surface irradiation is periodic with the frequency  $v$ . The nondimensional radius of the body  $R_v$  in equation (3) is defined by  $R_v = R/\ell_v$ . Second, the surface thermal inertia  $\Gamma = \sqrt{K\rho C}$  enters the nondimensional thermal parameter  $\Theta_v$  in equation (3) using a definition  $\Theta_v = \Gamma\sqrt{v}/(\epsilon\sigma T_\star^3)$ , with  $\epsilon$  the thermal emissivity of the surface,  $\sigma$  the Stefan-Boltzmann constant, and  $T_\star$  the subsolar temperature ( $\epsilon\sigma T_\star^4 = \alpha F$ ). When the characteristic size  $R$  of the body is much larger than  $\ell_v$  (a large-body limit), a situation met in the typical applications so far, the three  $\kappa$  coefficients in equation (3) are simply equal to  $\frac{1}{2}$  [Rubincam (1995); see Vokrouhlický (1998a) for their behavior for an arbitrary value of  $R_v$ ]. Hence, for large bodies the  $W$  factors do not depend on the size  $R$  and read  $W \approx W(\Theta_v) = -0.5 \Theta_v / (1 + \Theta_v + 0.5 \Theta_v^2)$ . Consequently, the Yarkovsky effect is maximum when  $\Theta_v \approx 1$ ; for small or large values of  $\Theta_v$  the effect vanishes. In this case, the semimajor axis secular change  $da/dt$  due to the Yarkovsky effect scales as  $\propto 1/R$  with the characteristic radius  $R$ . For small asteroids, either in near-Earth space or in the main belt,  $\Theta_\omega$  is typically on the order of unity (see also the chapter by Delbò et al. in this volume), while  $\Theta_n$  is much smaller, which implies that the diurnal Yarkovsky component usually dominates the seasonal component.

A handful of models were subsequently developed to probe the role of each of the simplifying assumptions mentioned above using analytical, semianalytical, or fully numerical methods. These include (1) an inhomogeneity of the thermal parameters (e.g., Vokrouhlický and Brož, 1999), (2) a coupling of the diurnal and seasonal components of the Yarkovsky effect (e.g., Vokrouhlický, 1999; Sekiya and Shimoda, 2013, 2014), (3) effects of a nonspherical shape for simple (e.g., Vokrouhlický, 1998b) or general geometries (including nonconvex shapes and the role of small-scale surface features; section 2.2), (4) a nonlinearity of the surface boundary condition of the thermal model (e.g., Sekiya and Shimoda, 2013, 2014), (5) the role of very high orbital eccentricity (e.g., Spitale and Greenberg, 2001, 2002; Sekiya

and Shimoda, 2014); (6) a nonprincipal-axis rotation state (e.g., Vokrouhlický et al., 2005a), or (7) the Yarkovsky effect for binary asteroids (e.g., Vokrouhlický et al., 2005b). Each of them was found to modify results from the zero approximation model by as much as several tens of percent without modifying the fundamental dependence of the Yarkovsky effect on obliquity, size, or thermal parameters [except perhaps for the special case of very high eccentricity orbits, where the sign of the Yarkovsky effect may be changed (see Spitale and Greenberg, 2001)].

**2.1.2. The YORP effect.** The YORP effect, the rotational counterpart of the Yarkovsky effect, broadly denotes the torque arising from interaction with the impinging solar radiation. As in the orbital effect, the absorbed sunlight does not result in secular effects (e.g. Breiter et al., 2007; Nesvorný and Vokrouhlický, 2008b; Rubincam and Paddack, 2010). Both directly scattered sunlight in the optical band and the recoil due to thermally reprocessed radiation, however, produce dynamical effects that accumulate over long timescales. In principle, one would need to treat the two components of the YORP effect independently, since the bidirectional characteristics of the scattered and thermally emitted radiation are not the same and would produce different torques. Additionally, the thermal component has a time lag due to the finite value of the surface thermal inertia and its bidirectional function should formally depend on the time history of the particular surface element.

While these issues are at the forefront of current research (section 2.2), we start with a zero-order approximation initially introduced by Rubincam (2000): (1) the surface thermal inertia is neglected, such that thermal radiation is reemitted with no time lag; and (2) the reflected and thermally radiated components are simply assumed to be Lambertian (isotropic). This approximation avoids precise thermal modeling and the results are relatively insensitive to the body's surface albedo value. At face value, this looks simple, but layers of complexity unfold with the geometrical description of the surface. This is because the YORP effect vanishes for simple shape models [such as ellipsoids of rotation (Breiter et al., 2007)] and stems from the irregular shape of the body (see Paddack, 1969). Obviously, its quantitative description involves a near infinity of degrees of freedom if middle- to small-scale irregularities are included. This may actually be the case for real asteroids because these irregularities may present a large collective cross-section and thus could dominate the overall strength of the YORP effect. This is now recognized as a major obstacle to our ability to model the YORP effect (section 2.2).

The importance of fine details of geometry, somewhat unnoticed earlier, were unraveled by the first analytical and semianalytical models of the YORP effect. There were two approaches developed in parallel. Scheeres (2007) and Scheeres and Mirrahimi (2008) used the polyhedral shape description as a starting point for their study, while Nesvorný and Vokrouhlický (2007, 2008a) and Breiter and Michalska (2008) used shape modeling described by a series expansion in spherical harmonics. To keep things simple,

these initial models assumed principal axis rotation and disregarded mutual shadowing of the surface facets. Both models predicted, after averaging the results over the rotation and revolution cycles, a long-term change of the rotational rate  $\omega$  and obliquity  $\gamma$  (the precession rate effect is usually much smaller than the corresponding gravitational effect due to the Sun), which could be expressed as

$$\frac{d\omega}{dt} = \frac{\Lambda}{C} \sum_{n \geq 1} A_n P_{2n}(\cos \gamma) \quad (4)$$

and

$$\frac{d\gamma}{dt} = \frac{\Lambda}{C\omega} \sum_{n \geq 1} B_n P_{2n}^1(\cos \gamma) \quad (5)$$

Here,  $\Lambda = 2 FR^3/(3c)$  with  $C$  being the moment of inertia corresponding to the rotation axis (shortest axis of the inertia tensor),  $P_{2n}(\cos \gamma)$  are the Legendre polynomials of even degrees, and  $P_{2n}^1(\cos \gamma)$  are the corresponding associated Legendre functions. The particular characteristics of the even-degree Legendre polynomials and Legendre functions on the order of 1 in equations (4) and (5) under prograde to retrograde reflection  $\gamma \leftrightarrow \pi - \gamma$  indicate the behavior of  $d\omega/dt$  and  $d\gamma/dt$ : (1) the rotation-rate change is symmetric, while (2) the obliquity change is antisymmetric under this transformation. Earlier numerical studies (e.g., Rubincam, 2000; Vokrouhlický and Čapek, 2002; Čapek and Vokrouhlický, 2004) had suggested that the net effect of YORP on rotation-rate often vanishes near  $\gamma \sim 55^\circ$  and  $\gamma \sim 125^\circ$ . This feature was finally understood using equation (4) because these obliquity values correspond to the roots of the second-degree Legendre polynomial. The previous works that numerically treated smoothed surfaces thus mostly described situations when the first term in the series played a dominant role. When the effects of the surface finite thermal inertia are heuristically added to these models, one finds that only the coefficients  $B_n$  change (e.g., Nesvorný and Vokrouhlický, 2007, 2008a; Breiter and Michalska, 2008). This confirms an earlier numerical evidence of Čapek and Vokrouhlický (2004).

Since  $C \propto R^5$ , equations (4) and (5) imply that both rotation rate and obliquity effects scale with the characteristic radius as  $\propto 1/R^2$ . This is an important difference with respect to the “more shallow” size dependence of the Yarkovsky effect, and it implies that YORP’s ability to change the rotation state increases very rapidly moving to smaller objects. Additionally, we understand well that for very small bodies the Yarkovsky effect becomes eventually nil. When the characteristic radius  $R$  becomes comparable to the penetration depth  $\ell_\omega$  of the diurnal thermal wave the efficient heat conduction across the volume of the body makes temperature differences on the surface very small. However, Breiter et al. (2010a) suggested that in the same limit the YORP strength becomes  $\propto 1/R$ , still increasing for small objects. Additionally, their result was only concerned with the thermal component of the YORP effect, while the part

related to the direct sunlight scattering in optical waveband continues to scale with  $\propto 1/R^2$ . Thus, the fate of the rotation of small meteoroids is still unknown at present.

The principal difference in complexity of the YORP effect results in equations (4) and (5), as compared to simple estimates in equations (1) and (2) for the Yarkovsky effect, is their infinite series nature. The nondimensional coefficients  $A_n$  and  $B_n$  in equations (4) and (5) are determined by the shape of the body, either analytically or semianalytically (e.g., Nesvorný and Vokrouhlický, 2007, 2008a; Scheeres and Mirrahimi, 2008; Breiter and Michalska, 2008; Kaasalainen and Nortunen, 2013). Interestingly, analytical methods help us to understand the torque component that changes the spin rate and the components that change the axis orientation couple, at leading order, to different attributes of the surface. The spin torque couples to chirality — the difference between eastward and westward facing slopes — while the other components couple merely to asphericity. Mathematically, this concerns the symmetric and antisymmetric terms in the Fourier expansion of the topography. If mutual shadowing of the surface facets is to be taken into account, one may use the semianalytic approach mentioned by Breiter et al. (2011) (see also Scheeres and Mirrahimi, 2008). Depending on details of the shape, the series in equations (4) and (5) may either converge quickly, with the first few terms dominating the overall behavior, or may slowly converge, with high-degree terms continuing to contribute (e.g., Nesvorný and Vokrouhlický, 2007, 2008a; Kaasalainen and Nortunen, 2013).

While this behavior had been noticed in analytical modeling, a detailed numerical study of YORP sensitivity on astronomically motivated, small-scale surface features such as craters and/or boulders was performed by Statler (2009). This also allowed Statler to suggest a new direction to YORP studies. He noted that the sensitivity of YORP on such small-scale features may affect its variability on short enough timescales to significantly modify the long-term evolution of the rotation rate, with the evolution changing from a smooth flow toward asymptotic state to a random walk (section 2.2).

The quadrupole ( $2n = 2$ ), being the highest multipole participating in the series expansion in equations (4) and (5), is related to the assumption of coincidence between the reference frame origin and the geometric center of the body (i.e., its center of mass for homogeneous density distribution). If instead the rotation axis is displaced from this point, additional terms in the series become activated and the coefficients ( $A_n, B_n$ ) become modified, and thus the predicted YORP torque will change (e.g., Nesvorný and Vokrouhlický, 2007, 2008a). This theoretical possibility has found an interesting geophysics interpretation for (25143) Itokawa’s anomalously small YORP value by Scheeres and Gaskell (2008) [see section 3.2, Breiter et al. (2009), and eventually Lowry et al. (2014)].

## 2.2. Frontiers in Modeling Efforts

### 2.2.1. Resolved and unresolved surface irregularities.

While the models discussed above suffice to describe broad-

scale features of the Yarkovsky and YORP effects, there are important aspects that are intrinsically *nonlinear*. Current models need to explicitly treat these nonlinearities in order to capture the physical essence of radiation recoil mechanisms and to provide precise predictions. Here we discuss some recent efforts along these lines.

The simplest of such nonlinear effects is shadowing of some parts of the surface by other parts, which can occur on surfaces that are not convex. By blocking the Sun, shadowing lowers the incident flux, and increases the temperature contrast, compared to the clear-horizon case. Computationally, shadowing requires testing whether the sunward-pointing ray from each surface element intersects another surface element (e.g., Vokrouhlický and Čapek, 2002). This “who blocks whom” problem is of  $O(N^2)$  complexity (where  $N$  is the number of surface elements); but there are strategies for storing an initial  $O(N^2)$  calculation so that all subsequent calculations are only  $O(N)$  (e.g., Statler, 2009).

Closely related to shadowing are the processes of *self-heating* (e.g., Rozitis and Green, 2013); these can be split conceptually into *self-illumination*, in which a surface element absorbs reflected solar flux from other parts of the surface, and *self-irradiation*, where it absorbs reradiated thermal infrared. Self-heating has the tendency to reduce the temperature contrast, by illuminating regions in shadow. Computing these effects requires prescriptions for the angular distribution of reflected and reradiated power from an arbitrary surface element, as well as the solution to the “who sees whom” problem — similar to the “who blocks whom” problem from shadowing. But since energy is traded between pairs of surface elements, self-heating, unlike shadowing, is unavoidably  $O(N^2)$  if full accuracy is required.

As mentioned in section 2.1, a periodic driving at a frequency  $v$  introduces a length scale, the thermal skin depth  $\ell_v$ . Asteroid surfaces are driven quasiperiodically, with the fundamental modes at the diurnal and seasonal frequencies. For typical materials,  $\ell_v$  is on the order of meters for the seasonal cycle and millimeters to centimeters for the diurnal cycle. If the surface’s radius of curvature  $s$  satisfies the condition  $s \gg \ell_v$ , one can consider surface elements to be independent (facilitating parallelization) and solve the heat conduction problem as a function of the depth only. The radiated flux then depends on the material parameters only through the thermal inertia  $\Gamma$ . Most models that treat conduction explicitly do so in such one-dimensional approximation. Standard finite-difference methods are typically used to find a solution over a rotation or around a full orbit; but numerical convergence can be slow [although acceleration schemes were also considered (Breiter et al., 2010b)]. Whether the condition  $s \gg \ell_v$  is truly satisfied depends on the scale on which topography is resolved. A surface boulder can give an object a locally small radius of curvature and three-dimensional effects may become important. Full three-dimensional conduction is computationally expensive (e.g., Golubov et al., 2014; Ševeček et al., 2015), but the potential consequences are significant. In this case, a general finite-element method is used to solve the heat diffusion problem.

Surface roughness concerns the effects of unresolved texture on reflection, absorption, and reradiation. Parametric models for a rough-surface reflectance are well developed [e.g., see Hapke (1993), and references therein; and see Breiter and Vokrouhlický (2011) for an application to the YORP effect], although the functional forms and parameter values are matters of current research. Models for the thermal emission are at present purely numerical. In the most complete implementation (Rozitis and Green, 2012, 2013), a high-resolution model of a crater field is embedded inside a coarse-resolution model of a full object. The primary effects of roughness in this model are to enhance the directionality (“beaming”) of the radiated intensity (relative to Lambertian emission), and to direct the radiated momentum slightly away from the surface normal, toward the Sun. Roughness models for emission and for reflection are not automatically mutually consistent, and the emission models employ the one-dimensional approximation for heat conduction despite the likelihood that  $s$  may not be much larger than  $\ell_\omega$  at the roughness scale.

Finally, nonlinear *dynamical coupling* affects both spin evolution and the orbital drift modulated by the spin state. Yarkovsky evolution models have generally incorporated heuristic prescriptions based on the YORP cycle (e.g., Rubincam, 2000; Vokrouhlický and Čapek, 2002), with possibly important effects of spin-induced material motion or reshaping included only in rudimentary ways. These processes may be modeled with particle-based discrete-element numerical codes (e.g., Richardson et al., 2005; Schwartz et al., 2012) and seminumerical granular dynamics in predefined potential fields (e.g., Scheeres, 2015). Simulated rubble piles artificially fed with angular momentum are seen to reshape and shed mass (e.g., Walsh et al., 2008; Scheeres, 2015). Linking a particle code with a thermophysical YORP model would then allow the coupled spin and shape evolution to be followed self-consistently.

Statler (2009) argued that topographic sensitivity would make rubble piles, or any objects with loose regolith, susceptible to possibly large changes in torque triggered by small, centrifugally driven changes in shape. Repeated interruptions of the YORP cycle might then render the overall spin evolution stochastic and significantly extend the timescale of the YORP cycles (self-limitation property of YORP). Cotto-Figueroa et al. (2015) have tested this prediction by simulating self-consistently the coupled spin and shape evolution (toggling between configurations in a limit cycle), and stagnating behaviors that result in YORP *self-limitation*. Bottke et al. (2015) implemented a heuristic form of such stochastic YORP in a Yarkovsky drift model to find an agreement with the structure of the Eulalia asteroid family.

Accurate Yarkovsky measurements allow constraining mass and bulk density (section 4.1), but rely on precise models, with an important component due to the surface features discussed above. Rozitis and Green (2012) show that surface roughness can increase the Yarkovsky force by tens of percent, owing mainly to the beaming. Including the seasonal effect caused by the deeper-penetrating thermal wave can

have a comparable influence. Self-heating, in contrast, has a minimal influence on Yarkovsky forces (e.g., *Rozitis and Green*, 2013). On the other hand, the same works indicate that the YORP effect is in general damped by beaming because it equalizes torques on opposite sides of the body.

*Golubov and Krugly* (2012) highlight another small-scale aspect of the YORP effect: an asymmetric heat conduction across surface features for which  $s \leq \ell_\omega$ . A rock conducts heat from its sunlit east side to its shadowed west side in the morning, and from its west side back to its east side in the afternoon. Owing to nighttime cooling, the morning temperature gradient is steeper, and hence more heat is conducted to, and radiated from, the west side, resulting in an eastward recoil. Clearly, if the collective cross section of such surface features is large, details of conduction across them may have significant consequences. Ideally, the situation calls for a complete three-dimensional heat transfer model (e.g., *Golubov et al.*, 2014; *Ševeček et al.*, 2015). Importantly, these studies indicate an overall tendency for YORP to spin objects up. However, a better understanding of small-scale surface effects is essential to understand YORP's long-term dynamics.

**2.2.2. Time domain issues (tumbling).** A particular problem in the modeling of the thermal effects occurs for tumbling bodies. This is because solving the heat diffusion in the body also involves the time domain. While the spatial dimensions are naturally bound, the time coordinate in general is not. However, both analytical and numerical methods involve finite time domains: The analytical approaches use a development in the Fourier series, while the effective numerical methods use iterations that require one to identify configurations at some moments in time. For bodies rotating about the principal axis of the inertia tensor, thus having a fixed direction in the inertial space, it is usually easy to modify the rotation period within its uncertainty limits such that it represents an integer fraction of the orbital period. The orbital period is then the fundamental time interval for the solution. This picture becomes more complicated for tumbling objects whose rotation is not characterized by a single time period. Rather, it is fully described with two periods, the proper rotation period and precession period, which may not be commensurable.

This situation has been numerically studied by *Vokrouhlický et al.* (2005a) in the case of (4179) Toutatis, and more recently in the case of (99942) Apophis by *Vokrouhlický et al.* (2015). Both studies suggest the tumbling may not necessarily “shut down the Yarkovsky effect,” at least in the large-bodies regime. Rather, it has been found that the Yarkovsky acceleration for these tumbling objects is well represented by a simple estimate valid for bodies rotating about the shortest axis of the inertia tensor in a direction of the rotational angular momentum and with the fundamental period of tumbling, generally the precession period.

**2.2.3. More than one body (binarity).** Another particular case is the Yarkovsky effect for binaries (see *Vokrouhlický et al.*, 2005b). Unless the satellite has nearly the same size as the primary component, the rule of thumb is that the heliocentric

motion of the system's center of mass is affected primarily by the Yarkovsky acceleration of the primary component, while the motion of the satellite feels the Yarkovsky acceleration of the satellite itself. Nevertheless, a secular change in the orbit of the satellite is actually caused by an interplay of the thermal effects and the shadow geometry in the system dubbed the Yarkovsky-Schach effect [and introduced years ago in space geodesy (*Rubincam*, 1982)]. However, it turns out that the BYORP effect, discussed in section 2.3, is more important and dominates the orbital evolution of the satellite.

### 2.3. Binary YORP

The binary YORP (BYORP) effect was first proposed in a paper by *Ćuk and Burns* (2005). They noted that an asymmetrically shaped synchronous secondary asteroid in a binary system should be subject to a net force differential that acts on average in a direction tangent to the orbit. Thus, as the secondary orbits about the primary body and maintains synchronicity, this would lead to either an acceleration or deceleration of the secondary, which would cause the mutual orbit of the system to spiral out or in, respectively. This seminal paper presented a basic conceptual model for the BYORP effect and provided a broad survey of many of the possible implications and observable outcomes of this effect. It also numerically studied the evolution of randomly shaped secondary bodies over a year to establish the physical validity of their model. It is key to note that a necessary condition for the BYORP effect is that at least one of the bodies be synchronous with the orbit, and it can be shut off if both bodies are nonsynchronous. *Ćuk and Burns* concluded that the BYORP effect should be quite strong and lead binary asteroids to either spiral in toward each other or cause them to escape in relatively short periods of time. This was further expanded in a second paper by *Ćuk* (2007) that outlined significant implications for the rate of creation and destruction of binary asteroid systems in both the near-Earth asteroid (NEA) and main-belt population, leading to the initial estimate of binary asteroid lifetimes due to BYORP on the order of only 100 k.y.

*McMahon and Scheeres* (2010a,b) then developed a detailed analytical model of the BYORP effect that utilized the existing shape model of the (66391) 1999 KW<sub>4</sub> binary asteroid satellite (*Ostro et al.*, 2006). In their approach the solar radiation force was mapped into the secondary-fixed frame and expanded as a Fourier series, following a similar approach to the YORP model development of *Scheeres* (2007). This enables any given shape model to be expressed with a series of coefficients that can be directly computed, and allows for time averaging. Using this approach they showed that the primary outcome of the BYORP effect could be reduced to a single parameter — the so-called “BYORP coefficient,”  $B$  — uniquely computed from a given shape model. Henceforth, if the secondary is in a near-circular orbit, the entire BYORP effect results in simple evolutionary equations for semimajor axis  $a$  and eccentricity  $e$  ( $\ll 1$ ) of the binary orbit

$$\frac{da}{dt} = \frac{FB}{c\eta'} \frac{a^{3/2}}{m_2 \sqrt{\mu}} \quad (6)$$

$$\frac{de}{dt} = -\frac{FB}{4c\eta'} \frac{ea^{3/2}}{m_2 \sqrt{\mu}} \quad (7)$$

where again  $F$  is the solar radiation flux at the heliocentric distance  $a'$  (equal to the semimajor axis of the heliocentric orbit),  $\eta' = \sqrt{1 - e'^2}$  with  $e'$  being the eccentricity of the heliocentric orbit,  $c$  the light velocity,  $m_2$  the mass of the secondary, and  $\mu = G(m_1 + m_2)$  the gravitational parameter of the binary system. If the orbit is expansive ( $B > 0$ ), the eccentricity will be stabilized, and vice-versa (see Čuk and Burns, 2005). In the case where the binary orbit is highly elliptic, the evolutionary equations become much more complex, and require additional Fourier coefficients to be included into the secular equations, as discussed in detail in McMahon and Scheeres (2010a).

The BYORP coefficient  $B$  is computed as a function of the shape of the body and the obliquity of the binary's orbit relative to the heliocentric orbit of the system. Assume a model for the instantaneous solar radiation force acting on the secondary has been formulated by some means, denoted as  $\mathbf{F}_{SRP}(M, M')$ , where  $M$  and  $M'$  are the mean anomalies of the binary mutual orbit and heliocentric orbit, respectively. Then the computation of the BYORP coefficient requires double averaging of the radiation force over the binary and heliocentric revolution cycles, and projection in the direction of binary orbital motion (denoted here in abstract as  $\hat{\mathbf{t}}$ )

$$B = \hat{\mathbf{t}} \cdot \frac{1}{(2\pi)^2} \int_0^{2\pi} \int_0^{2\pi} \frac{\mathbf{F}_{SRP}}{P(r_s)} dM dM' \quad (8)$$

where  $P(r_s) = (F/c)(a'/r_s)^2$  is the solar radiation pressure acting on the unit surface area of the body at the heliocentric distance  $r_s$ . The normalization by  $P$  implies that units of the BYORP coefficient are measured in area; thus  $B$  can be further normalized by dividing it by the effective radius squared of the secondary body. The BYORP coefficient is a function of several physical quantities such as albedo, surface topography, and potentially thermophysical effects. However, the strongest variation of the BYORP coefficient is seen to vary with the binary obliquity with respect to the heliocentric orbit (Fig. 1). If the synchronous body is rotated by  $180^\circ$  relative to the orbit, then the sign of the BYORP coefficient will be uniformly reversed. Due to this, when a body initially enters into a synchronous state it is supposed that the probability of it being either positive or negative is 50%.

A more recent analysis of the BYORP effect was published by Steinberg and Sari (2011), who found a positive correlation between the strength of the BYORP and YORP effects for bodies, and provided predictions related to the BYORP-driven evolution of the obliquity of a binary asteroid. In addition, they probed the possible effects of thermophysical models on the evolution of a binary system.

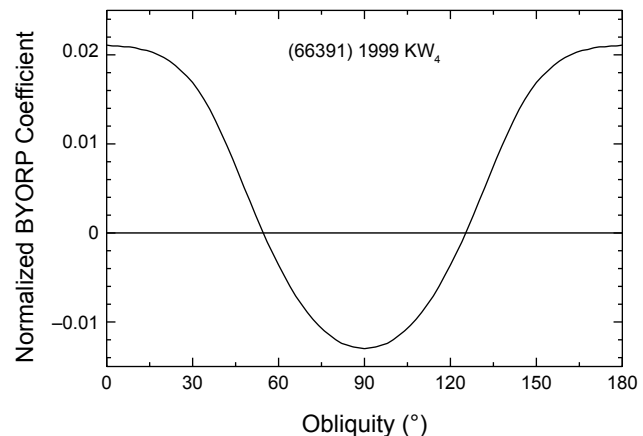


**Fig. 1.** BYORP coefficient  $B$ , normalized by the square of the effective radius, computed for the secondary of the (66391) 1999 KW<sub>4</sub> binary asteroid system, as a function of the binary orbital obliquity (abscissa).

The above discussions focus on the effect of BYORP in isolation, and not in conjunction with other evolutionary effects. However, recent work has found that the BYORP effect can mix with other evolutionary effects in surprising ways that require additional verification and study. These are primarily discussed later in section 5.3, where the long-term evolution of binary systems subject to BYORP is briefly considered. However, one of these combined effects has significant implications and is discussed here.

In particular, Jacobson and Scheeres (2011b) proposed the existence of an equilibrium between the BYORP effect and tides. For this equilibrium to exist, the BYORP coefficient must be negative, leading to a contractive system, and the primary asteroid must be spinning faster than the orbit rate. This creates a tidal dissipation torque that acts to expand the secondary orbit. Based on current theories of energy dissipation within rubble-pile asteroids (e.g., Goldreich and Sari, 2009), Jacobson and Scheeres (2011b) noted that all singly-synchronous rubble-pile binary asteroids with a negative BYORP coefficient for the secondary should approach a stable equilibrium that balances these two effects. This is significant, as it provides a mechanism for the persistent effect of BYORP to become stalled, leaving binary asteroids that should remain stable over long time spans. This, in turn, means that rapid formation of binary asteroids is not needed to explain the current population.

### 3. DIRECT DETECTIONS

Accurate observations have now allowed direct detections of both the Yarkovsky and YORP effects. This is an important validation of their underlying concepts, but also it motivates further development of the theory. These direct detections have two aspects of usefulness or application. First, the Yarkovsky effect is being currently implemented as a routine part of the orbit determination of small NEAs whose orbits are accurately constrained in the forefront software packages.

Additionally, the Yarkovsky effect is already known to be an essential part of the Earth impact hazard computations in selected cases (section 4.2 and the chapter by Farnocchia et al. in this volume). Second, many applications of the Yarkovsky and YORP effects involve statistical studies of small-body populations in the solar system rather than a detailed description of the dynamics of individual objects. Aside from a general validation, the known detections help in setting parameter intervals that could be used in these statistical studies.

### 3.1. Yarkovsky Effect

The possibility of detecting the Yarkovsky effect as a measurable orbital deviation was first proposed by Vokrouhlický et al. (2000). The idea is at first astounding given that the transverse thermal recoil force on a half-kilometer NEA should be at most 0.1 N, causing an acceleration of only  $\sim 1 \text{ pm s}^{-2}$ . And yet such small perturbations can lead to tens of kilometers of orbital deviation for 0.5-km NEAs after only a decade. In principle, such a deviation is readily detectable during an Earth close approach, either by optical or radar observations, but the key challenge is that the precision of the position prediction must be significantly smaller than the Yarkovsky deviation that is to be measured. In practical terms, this means that detection of the Yarkovsky effect acting on a typical 0.5-km NEA requires at least three radar ranging apparitions spread over a decade, or several decades of optical astrometry in the absence of radar ranging. Of course, smaller objects could in principle reveal the Yarkovsky effect much more quickly, but the problem for small objects is that it is more difficult to build up suitable astrometric datasets. Because of this, only a few objects with diameters  $D < 100 \text{ m}$  have direct detections of the Yarkovsky effect.

It should be pointed out that observations do not allow measurement of the secular change in the orbital semimajor axis directly. Rather, they reveal an associated displacement in the asteroid position along the orbit, an effect that progresses  $\propto t^2$  in a given time  $t$  (see Vokrouhlický et al., 2000). This is similar to the way the YORP effect is observed as discussed in section 3.2.

As predicted by Vokrouhlický et al. (2000), (6489) Golevka was the first asteroid with an unambiguous detection of the signature of the Yarkovsky effect in its orbit (Chesley et al., 2003). In this case the detection was possible only due to the availability of three well-separated radar ranging apparitions, in 1991, 1995, and 2003. The first two radar apparitions constrain the semimajor axis, affording a precise position prediction in 2003, while the 2003 radar ranging revealed a deviation from a ballistic trajectory. Figure 2 depicts the predicted 2003 delay-Doppler observations with their uncertainty along with the associated uncertainties. The predictions were well separated with  $>90\%$  confidence, and the actual asteroid position fell close to the Yarkovsky prediction.

The second reported detection of the Yarkovsky effect was for (152563) 1992 BF, which was also the first detection that did not rely on radar astrometry (Vokrouhlický et

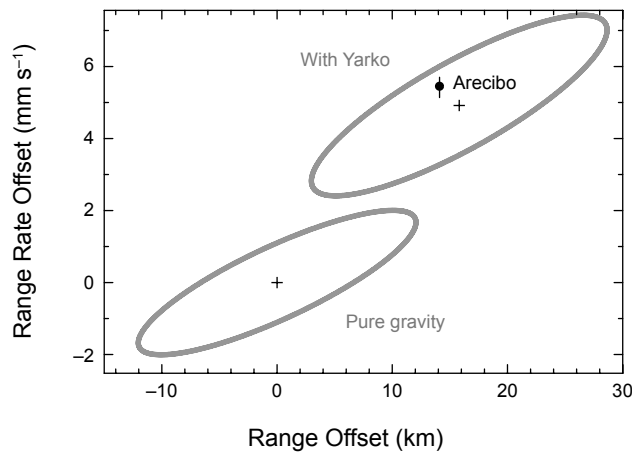


**Fig. 2.** Orbital solution of near-Earth asteroid (6489) Golevka from astrometric data before May 2003 projected into the plane of radar observables: (1) range at the abscissa, and (2) range-rate on the ordinate. The origin referred to the center of the nominal solution that only includes gravitational perturbations. The gray ellipse labeled “pure gravity” represents a 90% confidence level in the orbital solution due to uncertainties in astrometric observations as well as small body and planetary masses. The center of the gray ellipse labeled “with Yarko” is the predicted solution with the nominal Yarkovsky forces included (taken from Vokrouhlický et al., 2000); note the range offset of  $\sim 15 \text{ km}$  and the range rate offset of  $\sim 5 \text{ mm s}^{-1}$ . The actual Arecibo observations from May 24, 26, and 27, 2003, are shown by the black symbol (the measurement uncertainty in range is too small to be noted in this scale). The observations fall perfectly in the uncertainty region of the orbital solution containing the Yarkovsky forces. Adapted from Chesley et al. (2003).

al., 2008). This 0.5-km asteroid had a 13-yr optical arc (1992–2005) and four archival positions over two nights dating to 1953. These so-called precovery observations could not be fit to a purely gravitational orbit, but including the Yarkovsky effect in the orbit fitting enabled the observations to fit well and allowed a  $da/dt$  estimate with the signal-to-noise ratio  $\text{SNR} \simeq 15$  (Fig. 3). In these cases, where the detection relies heavily on isolated and archival data, caution is warranted to avoid the possibility that mismeasurement or astrometric time tag errors are corrupting the result. As depicted in Fig. 3, the 1953 position offsets could not be attributed to timing errors, and the trail positions were re-measured with modern catalogs.

In subsequent studies a progressively increasing number of Yarkovsky detections have been announced (Chesley et al., 2008; Nugent et al., 2012a; Farnocchia et al., 2013b). The most precise Yarkovsky measurement is that of (101955) Bennu, the target of the OSIRIS-REx asteroid sample return mission, which has a 0.5% precision Yarkovsky detection, by far the finest precision reported to date. At the extremes, asteroid 2009 BD is the smallest object ( $D \sim 4 \text{ m}$ ) with a verified Yarkovsky detection, which was achieved

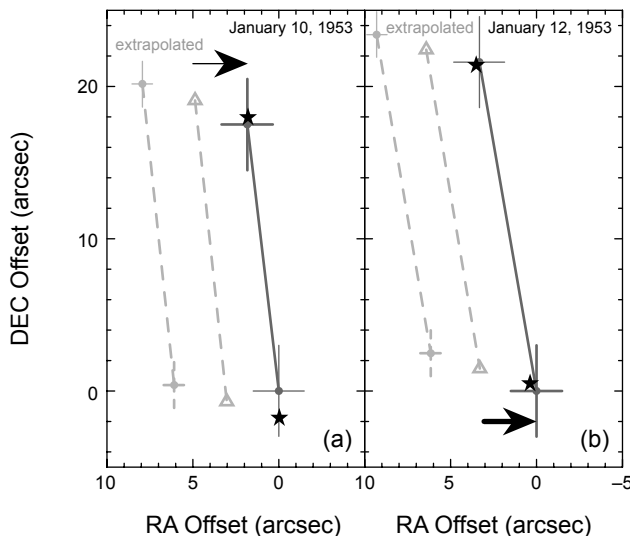


**Fig. 3.** Measured and predicted positions of (152563) 1992 BF on (a) January 10 and (b) January 12, 1953. The dark gray solid line is the asteroid trail appearing on Palomar plates on the two nights. Coordinate origin, right ascension at the abscissa, and declination at the ordinate are arbitrarily set to the end of the respective trail. The leftmost dashed trail labeled “extrapolated” represent pure extrapolation of the modern orbit without the thermal forces included. The mismatch in right ascension slightly improves if the 1953 data are included in the orbital solution as shown by the middle dashed trail. Still, the solution is more than  $3\sigma$  away from the measured trail. Only when the thermal accelerations are included in the orbital solution do the predicted orbital positions match the observations: Stars show fitted position at the beginning and the end of the trail. Adapted from Vokrouhlický et al. (2008).

because of its Earth-like orbit and the 2-yr arc of observations that the orbit enabled (Mommert et al., 2014). On the large end, there are two detections of 2- to 3-km-diameter asteroids, namely (2100) Ra-Shalom and (4179) Toutatis (Nugent et al., 2012a; Farnocchia et al., 2013b), which are both exceptionally well observed, having four and five radar apparitions, respectively.

To initially test for a signal from the Yarkovsky effect in the astrometric data of a given object, one can fit the orbit with a transverse nongravitational acceleration  $a_T = A_2/r^2$ , with  $A_2$  being an estimated parameter, in addition to the orbital elements. This simple model yields a mean semimajor axis drift rate proportional to  $A_2$ , thus capturing the salient orbital deviation due to the Yarkovsky effect. The approach of using a one-parameter ( $A_2$ ) Yarkovsky model is particularly convenient because it completely bypasses the thermophysical processes that are otherwise fundamental to the Yarkovsky effect. Instead, by focusing only on the level of perturbation visible in the orbit, one is able to discern the Yarkovsky effect in the absence of any knowledge of physical properties. And yet, as we shall see in section 4.1,

the detection of a Yarkovsky drift can be used to estimate or infer a number of the physical and dynamical characteristics of the body. Obviously, in the case of bodies with particular interest, one can use a detailed thermophysical model of the Yarkovsky acceleration for the orbit determination in a subsequent analysis.

A population-wise, head-on approach to Yarkovsky detection thus starts with the list of asteroids with relatively secure orbits, e.g., at least 100 d of observational arc, among the NEAs. For each considered object the statistical significance of the Yarkovsky effect is obtained from the estimated value of  $A_2$  and its *a posteriori* uncertainty  $\sigma_{A_2}$  according to  $\text{SNR} = |A_2|/\sigma_{A_2}$ , where  $\text{SNR} > 3$  is generally considered to be a significant detection. Another parameter that is helpful in interpreting the results for a given object is the ratio between the estimated value of  $A_2$  and the expected value for extreme obliquity and the known or inferred asteroid size, which we call  $A_{2\max}$ . The value of  $A_{2\max}$  can be obtained by, for instance, a simple diameter scaling from the Bennu result (Farnocchia et al., 2013b; Chesley et al., 2014). The ratio  $S = A_2/A_{2\max} = \text{SNR}/\text{SNR}_{\max}$  provides an indication of how the estimated value of  $A_2$  compares to what could be theoretically expected. A value of  $S \gg 1$  indicates that the transverse nongravitational acceleration may be too strong to be related to the Yarkovsky effect. This could imply that the body has a far smaller density or size than assumed, or that nongravitational accelerations other than Yarkovsky are at play. A large value of  $S$  could also imply a spurious  $A_2$  estimate due to corrupt astrometry in the orbital fit. On the other hand,  $S \ll 1$  would suggest the possibility of higher density, size, or surface thermal inertia than assumed, but is often more readily explained by mid-range obliquity, which tends to null the diurnal component of the Yarkovsky drift.

Figure 4 depicts the distribution of NEAs in the  $\text{SNR}$  and  $\text{SNR}_{\max}$  space that we divide into four regions:

- We consider cases with  $\text{SNR} > 3$  and  $S < 1.5$  to be *valid detections* because the estimated value is no more than 50% larger than expected, perhaps as a result of unusually low density or a size far smaller than assumed. Table 1 lists the 36 objects with valid Yarkovsky detections given currently available astrometry.
- *Spurious detections* are those with  $\text{SNR} > 3$  and  $S > 1.5$ . Many of these are due to astrometric errors in isolated observation sets, such as precoveries, and can be moved to the left in Fig. 4 by deweighting the questionable data. We find 56 cases in this category, but only 12 with  $\text{SNR} > 4$ . There are two spurious cases with  $\text{SNR} > 10$  and  $S \gtrsim 10$  that cannot be due to astrometric errors and are yet unlikely to be attributed to the Yarkovsky effect.
- There are a number of objects with relatively low values for  $\sigma_{A_2}$  and yet the orbit does not reveal an  $\text{SNR} > 3$  detection (denoted as *weak signal* zone on Fig. 4). Specifically, these cases have  $\text{SNR}_{\max} > 3$  and  $\text{SNR} < 3$ , with  $S < 2/3$ . These cases are potentially interesting because they generally

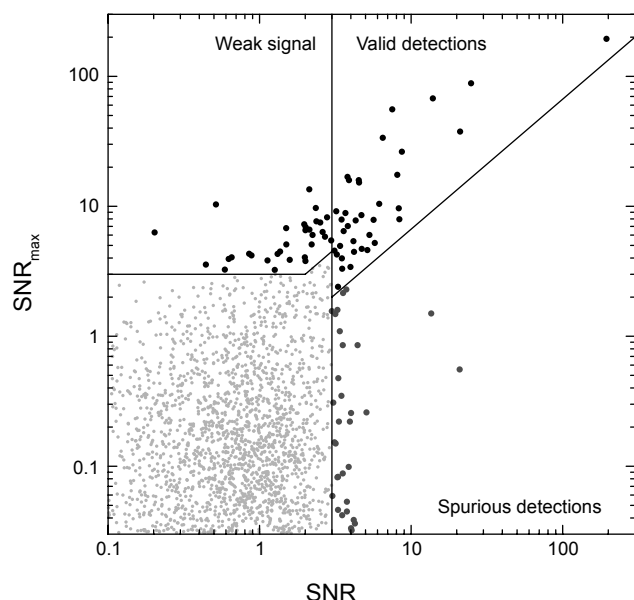


**Fig. 4.**  $\text{SNR} = A_2/\sigma_{A_2}$ , with  $A_2$  being the parameter of an empirical transverse acceleration and  $\sigma_{A_2}$  its formal uncertainty, for reliable orbits of NEAs at the abscissa. The ordinate shows  $\text{SNR}_{\max}$ , the maximum expected value of SNR for the body (from an estimate of its size and given an extremal obliquity, optimizing the Yarkovsky effect). Various classes of solutions, organized into four sectors by the straight lines, are discussed in the text. Situation as of December 2014.

indicate a mid-range obliquity and, despite the lack of significance in the  $A_2$  estimate, useful bounds can be still placed on the Yarkovsky mobility of the object. We find 35 such cases in the current NEA catalog, six of which have  $S < 0.05$  (Table 2). In fact, this class warrants further dedicated analysis, similar to the search of new detections.

- The vast majority of NEAs are currently uninteresting due to  $\text{SNR} < 3$  and  $\text{SNR}_{\max} < 3$ , meaning that no detection was found nor was one reasonably expected.

It is worth noting that objects with nonprincipal-axis rotation states can reveal the Yarkovsky effect (e.g., Vokrouhlický *et al.*, 2005a); (4179) Toutatis is a large, slowly tumbling asteroid (e.g., Hudson and Ostro, 1995) with Yarkovsky SNR  $\approx 8$  (and  $S \approx 1$ ) due to an extensive set of radar ranging data. Also, the much smaller asteroid (99942) Apophis, which has been reported to have a measurable polar precession (Pravec *et al.*, 2014), presently has a solid Yarkovsky signal with  $\text{SNR} \approx 1.8$  (and  $S < 1$ ), although not high enough to be listed in Table 1, but still significant in light of the abundant radar astrometry available for Apophis (Vokrouhlický *et al.*, 2015). Similarly, binary asteroid systems may also reveal Yarkovsky drift in their heliocentric orbits (e.g., Vokrouhlický *et al.*, 2005b), although none presently appears in Table 1. We note that (363599) 2004 FG<sub>11</sub> has a satellite (Taylor *et al.*, 2012) and currently has a Yarkovsky SNR  $\approx 2.8$  (and  $S \approx 1$ ).

### 3.2. YORP Effect

Analyses of small-asteroid populations indicate clear traits of their evolution due to the YORP effect, both in rotation rate and obliquity (sections 4.5, 5.1, and 5.2). Accurate observations of individual objects, however, do not presently permit detection of the secular change in obliquity and reveal only the secular effect in rotation rate. Even that is a challenging task, because the YORP torque has a weak effect on kilometer-sized asteroids at roughly 1 AU heliocentric distance. Similar to the case of the Yarkovsky effect, the YORP detection is enabled via accurate measurement of a phase  $\phi$  associated with the rotation rate. This is because when the rotation frequency  $\omega$  changes linearly with time,  $\omega(t) = \omega_0 + (d\omega/dt)t$  (adopting the simplest possible assumption, since  $d\omega/dt$  may have its own time variability), the related phase  $\phi$  grows quadratically in time,  $\phi(t) = \phi_0 + \omega_0 t + \frac{1}{2}(d\omega/dt)t^2$ . Additionally, other perturbations (such as an unresolved weak tumbling) do not produce an aliasing signal that would disqualify YORP detection. So the determination of the YORP-induced change in the rotation rate  $d\omega/dt$  may basically alias with the rotation rate frequency  $\omega_0$  itself in the  $d\omega/dt = 0$  model. This is because small variations in  $\omega_0$  propagate linearly in time in the rotation phase. The YORP detection stems from the ability to discern this linear trend due to the  $\omega_0$  optimization and the quadratic signal due to a nonzero  $d\omega/dt$  value. In an ideal situation of observations sufficiently densely and evenly distributed over a given time interval  $T$ , one avoids the  $\omega_0$  and  $d\omega/dt$  correlation setting time origin at the center of the interval. At the interval limits the YORP effect manifests via phase change  $\approx \frac{1}{8}(d\omega/dt)T^2$ . Therefore, a useful approximate rule is that the YORP effect is detected when this value is larger than the phase uncertainty  $\delta\phi$  in the observations. Assuming optimistically  $\delta\phi \approx 5^\circ$  and  $T$  about a decade, the limiting detectable  $d\omega/dt$  value is  $\approx 5 \times 10^{-8}$  rad d<sup>-2</sup>. Obviously, detection favors a longer time-base  $T$  if accuracy of the early observations permits. In practice, the late 1960s or early 1970s was the time during which photoelectric photometry was introduced and allowed sufficiently reliable light curve observations. This sets a maximum  $T$  of about 40 yr today for bright-enough objects [e.g., (1620) Geographos (Durech *et al.*, 2008a); see, for completeness, an interesting YORP study for asteroid (433) Eros by Durech (2005)]. We should also mention that  $\omega$  and  $\phi$  above denote sidereal rotation rate and phase, respectively. Hence to convert asteroid photometry to  $\phi$  one needs to know the orientation of its spin axis in the inertial space and the shape model. Their solution may increase the realistic uncertainty in  $d\omega/dt$  if compared to the simple estimate discussed above.

Figure 5 shows an example of detected quadratic advance in sidereal rotation phase  $\phi$  in the case of the small coorbital asteroid (54509) YORP (see Lowry *et al.*, 2007; Taylor *et al.*, 2007). The expected YORP value of rotation-rate change matched the observed value, thus allowing interpretation of the signal as a YORP effect detection, although an accurate comparison is prohibited by lack of knowledge of

TABLE 1. List of the Yarkovsky effect detections as of December 2014.

Object	$\bar{r}$ (AU)	H (mag)	D (m)	da/dt ( $\times 10^{-4}$ AU m.y. $^{-1}$ )	SNR	S	Data Arc	N <sub>rad</sub>
(101955) Bennu	1.10	20.6	493	-18.95 ± 0.10	194.6	1.0	1999–2013	3
(2340) Hathor	0.75	20.2	210	-17.38 ± 0.70	24.9	0.3	1976–2014	1
(152563) 1992 BF	0.87	19.7	510	-11.82 ± 0.56	21.0	0.6	1953–2011	0
2009 BD	1.01	28.2	4	-489 ± 35	13.9	0.2	2009–2011	0
2005 ES <sub>70</sub>	0.70	23.7	61	-68.9 ± 7.9	8.7	0.3	2005–2013	0
(4179) Toutatis	1.96	15.1	2800	-3.75 ± 0.45	8.4	1.1	1934–2014	5
(2062) Aten	0.95	17.1	1300	-6.60 ± 0.80	8.3	0.9	1955–2014	4
1999 MN	0.50	21.4	175	54.6 ± 6.8	8.1	0.5	1999–2014	0
(6489) Golevka	2.01	19.1	280	-4.52 ± 0.60	7.5	0.1	1991–2011	3
(1862) Apollo	1.22	16.3	1400	-1.58 ± 0.24	6.5	0.2	1930–2014	2
2006 CT	1.07	22.3	119	-47.6 ± 7.7	6.2	0.6	1991–2014	1
(3908) Nyx	1.71	17.3	1000	9.6 ± 1.7	5.8	1.1	1980–2014	2
2000 PN <sub>8</sub>	1.22	22.1	130	49.3 ± 8.7	5.7	0.7	2000–2014	0
(162004) 1991 VE	0.67	18.1	827	19.2 ± 3.6	5.3	0.9	1954–2014	0
(10302) 1989 ML	1.26	19.4	248	38.7 ± 7.5	5.2	1.1	1989–2012	0
(2100) Ra-Shalom	0.75	16.1	2240	-5.8 ± 1.2	4.7	1.0	1975–2013	4
(29075) 1950 DA	1.46	17.1	1300	-2.70 ± 0.57	4.7	0.6	1950–2014	2
(85953) 1999 FK <sub>21</sub>	0.53	18.0	590	-11.0 ± 2.4	4.5	0.3	1971–2014	0
(363505) 2003 UC <sub>20</sub>	0.74	18.2	765	-4.5 ± 1.0	4.5	0.3	1954–2014	1
2004 KH <sub>17</sub>	0.62	21.9	197	-42.0 ± 9.8	4.3	0.6	2004–2013	1
(66400) 1999 LT <sub>7</sub>	0.70	19.4	411	-35.0 ± 8.3	4.2	0.9	1987–2014	0
1995 CR	0.45	21.7	100	-314 ± 76	4.2	0.8	1995–2014	0
(4034) Vishnu	0.95	18.3	420	-31.8 ± 8.0	4.0	1.2	1986–2014	1
(85774) 1998 UT <sub>18</sub>	1.33	19.1	900	-2.45 ± 0.63	3.9	0.2	1989–2014	3
1994 XL <sub>1</sub>	0.57	20.8	231	-37.6 ± 9.8	3.8	0.5	1994–2011	0
(3361) Orpheus	1.14	19.0	348	6.2 ± 1.7	3.8	0.2	1982–2014	0
(377097) 2002 WQ <sub>4</sub>	1.63	19.5	422	-9.6 ± 2.6	3.7	0.4	1950–2014	0
(138852) 2000 WN <sub>10</sub>	0.97	20.1	328	17.7 ± 4.9	3.6	0.6	2000–2014	0
(399308) 1999 GD	1.07	20.8	180	47 ± 13	3.5	0.9	1993–2014	0
(4581) Asclepius	0.96	20.7	242	-19.7 ± 5.7	3.5	0.4	1989–2014	1
2007 TF <sub>68</sub>	1.36	22.7	100	-60 ± 18	3.4	0.7	2002–2012	0
1999 FA	1.07	20.6	300	-43 ± 13	3.3	1.4	1978–2008	0
(2063) Bacchus	1.01	17.2	1200	-6.6 ± 2.0	3.2	0.8	1977–2014	2
(350462) 1998 KG <sub>3</sub>	1.15	22.2	125	-25.2 ± 7.9	3.2	0.4	1998–2013	0
(256004) 2006 UP	1.51	23.0	85	-67 ± 21	3.1	0.7	2002–2014	0
(37655) Illapa	0.97	17.8	950	-10.3 ± 3.5	3.0	0.5	1994–2013	2

Reliable detections with SNR larger than 3 are listed:  $\bar{r} = a\sqrt{1 - e^2}$  is the solar flux-weighted mean heliocentric distance, H is the absolute magnitude, D is the diameter derived from the literature when available [and obtained here from the European Asteroid Research Node (EARN) Near-Earth Asteroids Database, <http://earn.dlr.de/nea>] or from absolute magnitude with 15.4% albedo, the da/dt and formal uncertainty  $\sigma_{da/dt}$  are derived from the orbital fit (via  $A_2$  and  $\sigma_{A_2}$  values as described in Farnocchia et al., 2013b). SNR = (da/dt)/ $\sigma_{da/dt}$  is the quality of the semimajor axis drift determination, and S = SNR/SNR<sub>max</sub>, where SNR<sub>max</sub> is the maximum estimated SNR for the Yarkovsky effect. Data arc indicates the time interval over which the astrometric information is available, and N<sub>rad</sub> denotes the number of radar apparitions in the fit.

TABLE 2. List of the most notable Yarkovsky effect nondetections as of December 2014.

Object	$\bar{r}$ (AU)	H (mag)	D (m)	1/S	Data Arc	N <sub>rad</sub>
(3757) Anagolay	1.65	19.1	390	86.8	1982–2014	1
(247517) 2002 QY <sub>6</sub>	0.62	19.6	270	56.9	2002–2014	0
(5797) Bivoj	1.71	18.8	500	53.6	1953–2014	0
(152742) 1998 XE <sub>12</sub>	0.62	18.9	413	39.7	1995–2014	0
(1221) Amor	1.74	17.4	1100	31.0	1932–2012	0
(225312) 1996 XB <sub>27</sub>	1.19	21.7	85	20.1	1996–2014	0

Notable nondetections of the Yarkovsky effect with 1/S > 10 are listed. Columns as in Table 1.

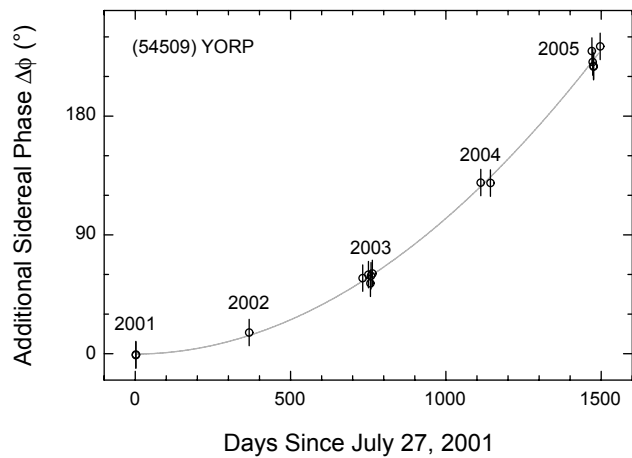


**Fig. 5.** Advance of the sidereal rotation phase  $\Delta\phi$  (ordinate in degrees) vs. time (in days) for the small Earth-coorbital asteroid (54509) YORP. Symbols are measurements with their estimated uncertainty, as follow from assembling the radar observations at different apparitions. The gray line is a quadratic progression  $\Delta\phi = \frac{1}{2}(\mathrm{d}\omega/\mathrm{d}t)t^2$ , with  $\mathrm{d}\omega/\mathrm{d}t = 350 \times 10^{-8} \text{ rad d}^{-2}$ . Time origin set arbitrarily to July 27, 2001, corresponding to the first measurement. Adapted from *Taylor et al.* (2007).

the full shape of this body (due to repeated similar viewing geometry from Earth). A complete list of the YORP detections, as of September 2014, is given in Table 3. To appreciate their accuracy, we note that they correspond to a tiny change in sidereal rotation period by a few milliseconds per year: 1.25 ms  $\text{y}^{-1}$  for (54509) YORP to a maximum value of 45 ms  $\text{y}^{-1}$  for (25143) Itokawa. While not numerous at the moment, we expect the list will more than double during the next decade. There are presently two asteroids, (1620) Geographos and (1862) Apollo, for which both Yarkovsky and YORP effects have been detected. These cases are of special value, provided a sufficiently accurate physical model of the body is available (see *Rozitis et al.*, 2013; *Rozitis and Green*, 2014).

(25143) Itokawa holds a special place among the asteroids for which the YORP effect has been detected. Not

only was this the first asteroid for which YORP detection was predicted (*Vokrouhlický et al.*, 2004), but the shape of this body is known very accurately thanks to the visit of the Hayabusa spacecraft. This has led researchers to push the attempts for an accurate YORP prediction to an extreme level (e.g., *Scheeres et al.*, 2007; *Breiter et al.*, 2009; *Lowry et al.*, 2014), realizing that the results depend in this case very sensitively on the small-scale irregularities of the shape (see *Statler*, 2009, for a general concept). However, in spite of an uncertainty in the YORP prediction, the most detailed computation consistently predicted deceleration of the rotation rate by YORP, as opposed to the detected value (Table 3). A solution to this conundrum has been suggested by *Scheeres et al.* (2007), who proposed that the difference in density between the “head” and “body” of this asteroid may significantly shift the center of mass. This effect introduces an extra torque component that could overrun the YORP torque, canonically computed for homogeneous bodies, and make the predicted deceleration become acceleration of the rotation rate. *Lowry et al.* (2014) adopted this solution, predicting that the two parts of Itokawa have a very different densities of  $\approx 1.75 \text{ g cm}^{-3}$  and  $\approx 2.85 \text{ g cm}^{-3}$ . Nevertheless, the situation may be even more complicated: *Golubov and Krugly* (2012) have shown that transverse heat communication across boulder-scale features on the surface of asteroids may cause a systematic trend toward acceleration of the rotation rate. Indeed, in the most complete works so far, *Golubov et al.* (2014) and *Ševeček et al.* (2015) show that the detected acceleration of Itokawa’s rotation rate may be in large part due to detailed modeling of the effects described by *Golubov and Krugly* (2012) without invoking a large density difference in the asteroid. The complicated case of Itokawa thus keeps motivating detailed modeling efforts of the YORP effect. Luckily, not all asteroidal shapes show such an extreme sensitivity on the small-scale surface features (e.g., *Kaasalainen and Nortunen*, 2013), thus allowing an easier comparison between the detected and predicted YORP signals.

On a more general level, we note that in spite of rotation periods ranging from a fraction of an hour to more than 12 h, all five asteroids for which the YORP effect was detected reveal acceleration of the rotation rate. It is not yet known

TABLE 3. List of the YORP effect detections as of September 2014.

Object	$\mathrm{d}\omega/\mathrm{d}t$ ( $\times 10^{-8} \text{ rad/d}^2$ )	H (mag)	P (h)	$\gamma$ (deg)	$\bar{r}$ (AU)	Reference
(54509) YORP	$350 \pm 35$	22.6	0.203	173	0.98	<i>Lowry et al.</i> (2007); <i>Taylor et al.</i> (2007)
(25143) Itokawa	$3.5 \pm 0.4$	18.9	12.132	178	1.27	<i>Lowry et al.</i> (2014)
(1620) Geographos	$1.2 \pm 0.2$	15.6	5.223	152	1.18	<i>Ďurech et al.</i> (2008a)
(1862) Apollo	$5.5 \pm 1.2$	16.3	3.065	162	1.22	<i>Kaasalainen et al.</i> (2007); <i>Ďurech et al.</i> (2008b)
(3103) Eger	$1.4 \pm 0.6$	15.3	5.710	176	1.32	<i>Ďurech et al.</i> (2012)
(1865) Cerberus	$<0.8$	16.8	6.803	178	0.96	<i>Ďurech et al.</i> (2012)

For each of the asteroids with the YORP effect detected we give (1) rotation rate change  $\mathrm{d}\omega/\mathrm{d}t$  derived from the photometric data, (2) absolute magnitude H, (3) rotation period P, (4) obliquity  $\gamma$ , and (5) the solar flux weighted mean heliocentric distance  $\bar{r} = a\sqrt{1 - e^2}$ , with semimajor axis a and eccentricity e. In the case of (1865) Cerberus, the observational limit  $|\mathrm{d}\omega/\mathrm{d}t| < 0.8 \times 10^{-8} \text{ rad/d}^2$  is nontrivial for a body of its size, orbit, and rotation state. Less severe limits on  $|\mathrm{d}\omega/\mathrm{d}t|$  were also derived for (2100) Ra-Shalom (*Ďurech et al.*, 2012) and (433) Eros (*Ďurech*, 2005).

whether this expresses observational bias against detection of the YORP-induced deceleration of the rotation rate, or whether it points toward the true asymmetry in YORP's ability to accelerate vs. decelerate rotation rate. Note that one would statistically expect to detect YORP deceleration of the rotation rate principally among asteroids rotating slowly, but this is exactly where accurate photometric observations are especially difficult. Efforts with the goal of detecting the YORP effect for asteroids with rotation periods in the 20–40-h range are underway, with the results expected in the next couple of years. Hopefully, they will help in settling the issue of possible asymmetry in the YORP effect on  $\omega$ .

### 3.3. Binary YORP Effect

The BYORP effect has not been directly observed as of yet, although some predictions stemming from this effect have been confirmed. There are currently significant campaigns observing binary asteroids to search for predicted outcomes of the BYORP effect, both in isolation or mixing with other evolutionary effects. The basic technique for detecting the BYORP effect as it acts in solitude was proposed by *McMahon and Scheeres* (2010b) and suggests that computing the drift in a binary system's mean anomaly due to changes in the semimajor axis is the most effective approach, as this drift will increase quadratically in time as compared to purely Keplerian motion. The relative change  $\Delta M$  in the mean anomaly  $M$  of a binary asteroid due to the BYORP effect in time  $t$  is  $a\Delta M = -\frac{3}{4}n(da/dt)t^2$ , where  $n$  is the binary mean motion and  $(da/dt)$  should be substituted from equation (6). The corresponding delay, or advance, in occultation timing of the binary is  $\approx -\frac{3}{4}[(da/dt)/a]t^2$ .

*McMahon and Scheeres* (2010b) provide a table of known and possibly synchronous binary asteroids along with an estimate of mean anomaly drift, based on scaling the computed (66391) 1999 KW<sub>4</sub> BYORP coefficient to the different asteroid systems, accounting for secondary size, system mass, and heliocentric orbit. As these stated drifts make a strong assumption in applying the KW<sub>4</sub> BYORP coefficient, they are not true predictions, but rather provide a prediction of relative strength of the BYORP effect for different bodies. Petr Pravec has expanded this list of predicted drift rates, making them accessible in the Binary Asteroid Database (<http://www.asu.cas.cz/~asteroid/binasdata.htm>) and indicating which should have the largest, and hence easiest to detect, drifts along with other information of use to observers.

This list represents an active longer-term campaign by Pravec and colleagues to observe binary asteroid systems during predicted occultation events. The most significant result of this effort to date has been focused on the binary asteroid (175706) 1996 FG<sub>3</sub> (*Scheirich et al.*, 2015). For this body, observations over a 17-yr time span provided a strong “zero” constraint on the BYORP drift rate. While not a direct detection of the BYORP effect, this is fully consistent with a current prediction that involves the BYORP-tide equilibrium state. The confirmation of a binary system in this state has scientific implications as it means that the tidal dissipation

that occurs within a rapidly spinning primary body can be determined once the BYORP coefficient for a secondary asteroid is determined. Although it cannot be directly measured when this will occur in such an equilibrium, it is possible to estimate the BYORP coefficient based on detailed models of the secondary and its albedo, such as could be obtained by an *in situ* spacecraft. Thus, a space mission to a binary in such a state could provide an unprecedented view into the internal geophysics of a rubble pile.

Other bodies of current interest include any binary systems with a synchronous secondary. A direct detection of BYORP is feasible if the body is in an expansive state, although the relatively short lifetime predicted for such binaries would imply that finding such a binary may be difficult. Similarly, this is also true of a contractive state, as this should be heading toward a BYORP-tide equilibrium. Additional measurements are important, however, as the number of binaries found to be in the equilibrium state relative to the number found in expansive or contractive states will be an important measurement with implications beyond the BYORP effect in isolation. Specifically, such observations could provide insights into the internal tidal dissipation of energy that occurs for rubble-pile binary asteroid primaries (e.g., *Jacobson and Scheeres*, 2011b).

## 4. APPLICATIONS OF THE YARKOVSKY EFFECT

### 4.1. Physical Properties of Asteroids

The Yarkovsky effect can be used as a tool to probe the nature of individual asteroids. This is possible because an asteroid's Yarkovsky drift is a manifestation of several of its physical properties, and so a direct measurement of  $da/dt$  allows insight into the characteristics of the body. Of primary importance are the obliquity, size, and mass of the asteroid, although the thermal and reflective properties and the rotation rate are also important.

Not surprisingly, the more that is known about the asteroid, the more that can be divined from a Yarkovsky detection. In the weakest situation, which is not so unusual, we have only  $da/dt$  and the absolute magnitude  $H$ . Even in this case we can already put meaningful constraints on the obliquity of the body through the  $\cos \gamma$  dependence. For instance, the sign of  $da/dt$  reveals immediately whether the rotation is retrograde or direct. Moreover, the value of  $S$  from Table 1 can serve as a proxy for  $|\cos \gamma|$ , while variations in  $pD$  and  $\Theta_\omega$  add uncertainty to this estimate. *Vokrouhlický et al.* (2008) used this principle to infer that (152563) 1992 BF must have obliquity  $\gamma > 120^\circ$ , after accounting for reasonable variations in other unknowns.

If the spin state of the body is known, generally from some combination of radar imaging and optical light curves, we have a much clearer insight into the nature of the body because  $\cos \gamma$  is removed as an unknown and the thermal parameter  $\Theta_\omega$  is better constrained. Indeed, in such cases we are left with a simple relationship between  $pD$  and the

thermal inertia  $\Gamma$ . But the diameter  $D$  can be measured directly by radar, or inferred from taxonomic type or measured albedo, or can just be derived from an assumed distribution of asteroid albedo, allowing the constraint to be cast in terms of the bulk density  $\rho$  and thermal inertia  $\Gamma$ . The gray region of Fig. 6 depicts this type of constraint for the case of (101955) Bennu. The peak in  $\rho$  seen in Fig. 6 is associated with  $\Theta_{\omega} \approx 1$ , where the Yarkovsky effect obtains its maximum effectiveness. This characteristic peak in the  $\rho$  vs.  $\Gamma$  relationship often allows strict upper bounds on  $\rho$  (e.g., Chesley et al., 2003).

We note that the degeneracy between  $\rho$  and  $\Gamma$  could in principle be broken by an independent estimate of  $\rho$  that would allow a direct estimate of  $\Gamma$ , albeit with the possibility of two solutions. While this approach has so far not been possible, we anticipate it here as a natural outcome of the first detection of the Yarkovsky effect on a well-observed binary system.

Another approach to breaking the correlation between  $\rho$  and  $\Gamma$  makes use of measurable solar radiation pressure deviations on the orbit, which yields an area-to-mass ratio. With a size estimate, an independent mass estimate can lead to a double solution for the thermal inertia of the body (e.g., Mommert et al., 2014).

The alternative approach has been applied successfully in a few special cases to date. Specifically, observations of an asteroid's thermal emissions can afford independent constraints on the thermal inertia, breaking the degeneracy between  $\rho$  and  $\Gamma$ , allowing a direct estimate of the asteroid's bulk density. Perhaps the most striking example here is the

case of (101955) Bennu, which has a well-constrained shape, spin state, and thermal inertia. When these are linked with the high precision  $da/dt$  estimate (Table 1), the result is a bulk density of  $1260 \pm 70 \text{ kg m}^{-3}$  (Fig. 6), where the formal precision is better than 6% (Chesley et al., 2014). Other similar cases include (1862) Apollo, (1620) Geographos, and (29075) 1950 DA (respectively, Rozitis et al., 2013, 2014; Rozitis and Green, 2014). In each of these cases the authors combine  $da/dt$ , radar imaging, and thermal measurements to derive the bulk density of the asteroid.

In the best cases of Yarkovsky detection, where we also have a shape model, spin state, and thermophysical characterization, one can infer the local gravity of the body. This can be of profound engineering interest for the asteroid targets of space missions, e.g., (101955) Bennu. The mission design challenges for the OSIRIS-REx mission are significantly eased due to the Yarkovsky constraint on Bennu's mass and bulk density. Another such case is (29075) 1950 DA, which is not a space mission target, and yet the estimates of local surface gravity derived from Yarkovsky have profound implications. Rozitis et al. (2014) found that their thermal measurements, when combined with the Yarkovsky drift reported for 1950 DA by Farnocchia and Chesley (2014), required a low asteroid mass. The estimated mass was so low, in fact, that it implied that the equatorial surface material on 1950 DA is in tension due to centrifugal forces. And yet the estimated thermal inertia was low enough that it required a loose, fine-grained regolith on the surface. This seeming contradiction is most readily resolved by the action of cohesive forces due to van der Waals attraction between regolith grains, and represents the first confirmation of such forces acting on an asteroid, which had already been anticipated by Scheeres et al. (2010). And so, through a curious interdisciplinary pathway, the measurement of the Yarkovsky drift on 1950 DA reveals the nature of minute attractive forces at work in the asteroid's regolith.

**Population implications** — The discussion above treats Yarkovsky detections in a case-by-case manner, deriving additional information for the specific asteroid at hand. However, the wealth of Yarkovsky detections listed in Table 1 allows an insight into the NEA population as a whole. Of particular interest is the distribution of obliquities implied by the tabulated detections, of which 28 out of 36 detections reveal  $da/dt < 0$  and thus about 78% of the sample requires retrograde rotation (see also Fig. 9).

This excess of retrograde rotators represents an independent confirmation of a result first reported by La Spina et al. (2004). The mechanism for an excess of retrograde rotators in the NEA population is a result of the Yarkovsky driven transport mechanism (e.g., Morbidelli and Vokrouhlický, 2003). The location of the  $v_6$  resonance at the inner edge of the main belt implies that main-belt asteroids entering the inner solar system through this pathway must have  $da/dt < 0$  and thus retrograde rotation. Direct rotators will tend to drift away from the resonance. Asteroids entering the inner solar system through other resonance pathways, principally the 3:1 mean-motion resonance with Jupiter, may drift either in or out into the resonance, and so will have parity between retrograde

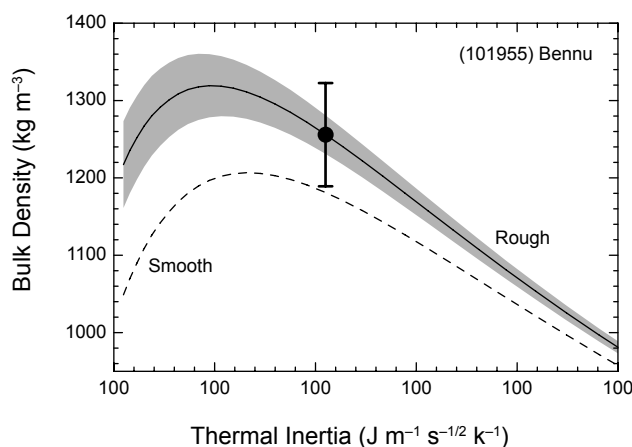


**Fig. 6.** Bulk density  $\rho$  solution for (101955) Bennu from detected value of the Yarkovsky orbital effect as a function of the surface thermal inertia  $\Gamma$ . The dashed line corresponds to the  $da/dt = \text{const.}$  solution for a smooth-surface model, taking into account a detailed shape model and a nonlinear boundary condition. The solid line accounts for 50% small-scale roughness in each of the surface facets of the shape model, while the gray zone takes into account the estimated ~17% uncertainty in the roughness value. The nonlinearity of the  $da/dt$  isoline in the  $\rho$  vs.  $\Gamma$  plane follows from equations (1) and (3). Adapted from Chesley et al. (2014).

and direct rotators. *Farnocchia et al.* (2013b) analyze this retrograde prevalence, including selection effects among the Yarkovsky detections, and find that it is fully consistent with the Yarkovsky-driven transport, and point out that this can be used to derive a distribution of the obliquities of NEAs.

#### 4.2. Impact Hazard Assessment

Most reported potential impacts are associated with newly discovered objects for which the uncertainty at the threatening Earth encounter is dominated by the uncertainties in the available astrometric observations. However, as the astrometric dataset grows, the fidelity of the force model used to propagate the asteroid from discovery to potential impact becomes more and more important. For a few asteroids with extraordinarily precise orbits, the Yarkovsky effect is a crucial aspect of an analysis of the risk posed by potential impacts on Earth. When the Yarkovsky effect is directly revealed by the astrometric data, the analysis approach is straightforward, as is the case for (101955) Bennu and (29075) 1950 DA (e.g., *Milani et al.*, 2009; *Chesley et al.*, 2014; *Farnocchia and Chesley*, 2014).

However, there are some cases in which the astrometry provides little or no constraint on the Yarkovsky effect, and yet Yarkovsky drift is a major contributor to uncertainties at a potentially threatening Earth encounter. In these situations we are forced to assume distributions on albedo, obliquity, thermal inertia, etc., and from these we can derive a distribution of  $A_2$  or  $da/dt$ . A Monte Carlo approach with these distributions allows us to better represent uncertainties at the threatening Earth encounter, and thereby compute more realistic impact probabilities. This technique has been necessary for (99942) Apophis and has been applied by *Farnocchia et al.* (2013a) before *Vokrouhlický et al.* (2015) made use of rotation-state determination of this asteroid. See the chapter by Farnocchia et al. in this volume) for a more complete discussion of Yarkovsky-driven impact hazard analyses.

#### 4.3. Meteorite Transport Issues

The Yarkovsky effect, with its ability to secularly change the semimajor axes of meteoroids (precursors of meteorites, which are believed to be fragments of larger asteroids located in the main belt between the orbits of Mars and Jupiter), was originally proposed to be the main element driving meteorites to Earth (see *Öpik*, 1951; *Peterson*, 1976). However, direct transport from the main belt, say as a small body slowly spiraling inward toward the Sun by the Yarkovsky effect, required very long timescales and unrealistic values of the thermal parameters and/or rotation rates for meter-sized bodies. Moreover, a.m./p.m. fall statistics and measured preatmospheric trajectories in rare cases (like the Příbram meteorite) indicated many meteorites had orbits with the semimajor axis still close to the main-belt values.

The problem was overcome in the late 1970s and early 1980s by advances in our understanding of asteroid dynamics. Numerous works have shown that the transport routes

that connect main-belt objects to planet-crossing orbits are in fact secular and mean-motion resonances with giant planets, such as the  $v_6$  secular resonance at the lower border of the main asteroid belt and/or the 3:1 mean-motion resonance with Jupiter. Putting this information together with the Yarkovsky effect, *Vokrouhlický and Farinella* (2000) were able to construct a model in which meteoroids or their immediate precursor objects are collisionally born in the inner and/or central parts of the main belt, from where they are transported to the resonances by the Yarkovsky effect. En route, some of the precursors may fragment, which can produce new swarms of daughter meteoroids that eventually reach the escape routes to planet-crossing orbits. With this model, Vokrouhlický and Farinella could explain the distribution of the cosmic-ray exposure ages of stony meteorites as a combination of several timescales: (1) the time it takes for a meteoroid to collisionally break, (2) the time it takes a meteoroid to travel to a resonance, (3) the time it takes for that resonance to deliver the meteoroid to an Earth-crossing orbit, and (4) the time it takes the meteoroid on a planet-crossing orbit to hit Earth.

While successful to the first order, this model certainly contains a number of assumptions and potentially weak elements, especially in the light of subsequent rapid development of the YORP effect theory, that warrant further work. For instance, one of the difficulties in refining the meteorite delivery models is the uncertainty in identification of the ultimate parent asteroid (or asteroids) for a given meteorite class (e.g., see the chapter by Vernazza et al. in this volume). Thus, among the ordinary chondrites we have a reasonable guess that LL-chondrites originate from the Flora region [or the asteroid (8) Flora itself] and the L-chondrites originate from disruption of the Gefion family. There were numerous guesses for the H-chondrite source region [such as the asteroid (6) Hebe], but none of them has been unambiguously confirmed. The model presented by *Nesvorný et al.* (2009), while more educated in the choice of the L-chondrite source region than the previous work of *Vokrouhlický and Farinella* (2000), requires immediate parent bodies of these meteorites, 5–50 m in size, to reach the powerful 3:1 mean-motion resonance with Jupiter. This means they should have migrated by the Yarkovsky effect some 0.25–0.3 AU from their source location in less than 0.5 b.y. While this is not a problem in a scenario where the bodies rotate about the body-fixed axis whose direction is preserved in the inertial space, it is not clear if this holds when the bodies would start to tumble or their axes started to evolve rapidly due to the YORP effect. Clearly, more work is needed to understand the Yarkovsky effect in the small-size limit for bodies whose spin axis may undergo fast evolution.

#### 4.4. Orbital Convergence in Asteroid Families and Pairs

Over the past decade the Yarkovsky and YORP effects have helped to significantly boost our knowledge of the asteroid families (e.g., see the chapter by Nesvorný et al. in

this volume). This is because they represent a unique time-dependent process in modeling their structure, thus allowing us to constrain their ages for the first time.

The most accurate results are obtained for young-enough families (ages  $< 10$  m.y., say), for which effects of the deterministic chaos are weak. As shown in the pioneering works of Nesvorný *et al.* (2002, 2003), the basic tool to determine the origin of the family is provided by the convergence of orbital secular angles (the nodal and pericenter longitudes  $\Omega$  and  $\varpi$ ) at some moment in the past. Because the rate at which these angles precess in space depends sensitively on the semimajor axis value, the past values of  $\Omega$  and  $\varpi$  of the family members depend on their Yarkovsky drift-rates  $da/dt$ . This contribution may not be negligible, because the changes in precession rates produce effects that grow quadratically in time (the same way as described in sections 3.1 and 3.2 for longitude in orbit or sidereal rotation phase). Thus Nesvorný and Bottke (2004) were able to significantly improve the uncertainty in the age of the Karin family by including the Yarkovsky effect in their model. At the same time, this work provided an effective detection of the Yarkovsky effect for the main-belt asteroids. This technique has been later used for age constraints of several other young families (e.g., Novaković, 2010; Novaković *et al.*, 2012, 2014), including sub-million-year-old clusters (e.g., Nesvorný *et al.*, 2006, 2008; Nesvorný and Vokrouhlický, 2006; Vokrouhlický *et al.*, 2009).

While the methods of dating young asteroid families involve convergence of the orbital angles only, the determination of ages of the asteroid pairs (e.g., Vokrouhlický and Nesvorný, 2008; Pravec *et al.*, 2010) represents an even more ambitious task. In this case, one seeks to achieve a full convergence of two asteroidal orbits into a single location in the Cartesian space (within the distance of about a radius of the Hill sphere of the parent body) and with a small relative velocity (comparable to the escape velocity from the parent body). It is not surprising that the Yarkovsky effect again plays important role in this effort. The best cases, such as the pair (6070) Rheinland and (54827) 2001 NQ<sub>8</sub>, allow one to also infer constraints on the obliquities of the individual components, consequently providing predictions directly testable by further observations (e.g., Vokrouhlický and Nesvorný, 2009; Vokrouhlický *et al.*, 2011).

#### 4.5. Spreading of Asteroid Families

Older asteroid families (ages  $> 10$  m.y., say) do not permit application of the fine age-determination methods described in section 4.4. This is because orbits in the main asteroid belt are affected by deterministic chaos over long timescales. Hence it is not possible to reliably reconstruct past values of the orbital secular angles, with the proper values of semimajor axis  $a_p$ , eccentricity  $e_p$ , and inclination  $i_p$  being the only well-defined parameters at hand. Still, these proper elements are constructed using approximate dynamical models, spanning time intervals quite shorter than the typical ages of large asteroid families. While the deterministic chaos is still in action over long timescales and produces a

slow diffusion of the proper  $e_p$  and  $i_p$  values, the Yarkovsky effect is the principal phenomenon that changes the proper  $a_p$  values of multi-kilometer-sized asteroids. Bottke *et al.* (2001), studying an anomalous structure of the Koronis family, presented the first clear example of the Yarkovsky effect sculpting a large-scale shape of an asteroid family in  $a_p$  and  $e_p$ . It also approximately constrained its age to  $\sim 2.5\text{--}3$  b.y. [see also Vokrouhlický *et al.* (2010) for a similar study of the Sylvia family].

A novel method suitable for age determination of families a few hundred million years old has been presented by Vokrouhlický *et al.* (2006a). It stems from the observation that small asteroids in some families are pushed toward extreme values of the semimajor axis and, if plotted in the  $a_p$  vs.  $H$  (absolute magnitude) diagram, they acquire an “eared” structure (Fig. 7). Since this peculiar structure is not compatible with a direct emplacement by any reasonable ejection field, Vokrouhlický *et al.* (2006a) argued it must result from a long-term dynamical evolution of the family. In particular, postulating that the initial dispersal in  $a_p$  of the family members was actually small, they showed that Yarkovsky drift itself accounted for most of the family’s extension in semimajor axis. Assisted by the YORP effect, which over a YORP-cycle timescale tilts obliquities toward extreme values, the Yarkovsky effect (dominated by its diurnal component) is maximized, and pushes small family members toward the extreme values in  $a_p$ . If properly modeled, this method allows us to approximately constrain the interval of time needed since the family-forming event to reach the observed extension (Fig. 7). Several applications of this method can be found in Vokrouhlický *et al.* (2006a,b,c), Bottke *et al.* (2007), Carruba (2009), or Carruba and Morbidelli (2011). Recently Bottke *et al.* (2015) noticed that the classical setting of this method does not permit a satisfactory solution for the low-albedo, inner-belt Eulalia family. Their proposed modification requires an extended time spent by small asteroids in the extreme obliquity state, which in turn requires a simultaneous slowdown in the evolution of their rotation rates by the YORP effect. In fact, this may be readily obtained by postulating that the YORP strength changes on a timescale shorter than the YORP cycle, an assumption that may follow from the extreme sensitivity of the YORP effect to asteroid shape [the self-limitation effect discussed in section 2.1; see also Cotto-Figueroa *et al.* (2015)]. It is not clear, however, why this phenomenon should manifest itself primarily in this particular family, or whether it generally concerns all families  $\sim 1$  b.y. old.

The model of Vokrouhlický *et al.* inherently contains a prediction that the small members in the “eared” families have preferred obliquity values (such that prograde-rotating objects occupy regions in the family with largest  $a$  values, and vice versa). Interestingly, recent works of Hanuš *et al.* (2013b) and Kryszczyńska (2013) confirm this trend in the cases of several families, and more detailed studies are underway.

A peculiar situation arises for families embedded in the first-order mean-motion resonances with Jupiter. In these cases, the resonant lock prohibits large changes in the

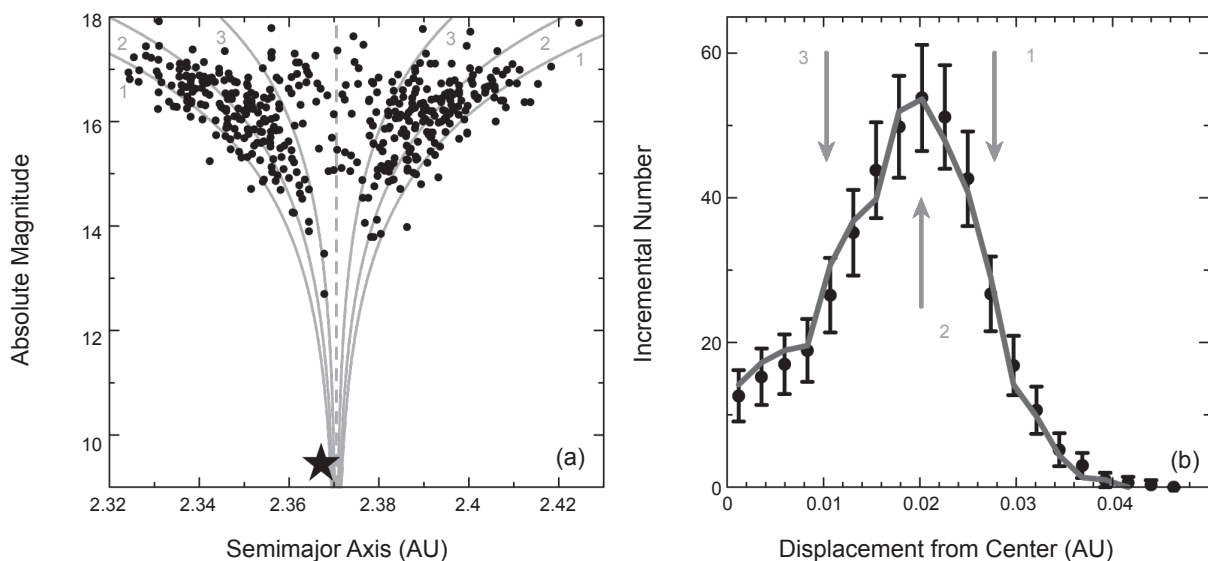


**Fig. 7.** (a) The Ergone family members projected on the plane of the proper semimajor axis  $a_p$  and the absolute magnitude  $H$ ; 432 numbered family members, including (163) Ergone (star), are shown as black symbols. The gray lines show  $0.2 H = \log(|a_p - a_0|/C)$ , with  $a_0 = 2.3705$  AU and three different values of the  $C$  parameter labeled 1, 2, and 3. (b) Fixing the  $H$  level (16 mag in our case) results in a one-to-one link between the  $C$  value and a displacement from the center  $a_0$ , shown here at the abscissa. The symbols represent the Ergone family using a statistical distribution in the  $C$ -bins (assuming a symmetry  $C \rightarrow -C$  in this case); uncertainty is simply  $\sqrt{N}$ , where  $N$  is the number of asteroids in the bin. A numerical model (dark gray line) seeks to match the distribution by adjusting several free parameters such as the family age and initial dispersal of fragments from the largest fragment. The gray arrows point to the corresponding  $C = \text{const.}$  lines on (a). Adapted from Vokrouhlický et al. (2006a), with the family update as of April 2014.

semimajor axis, but the Yarkovsky effect manifests itself by a secular increase or decrease of the eccentricity. Modeling of this evolution allowed Brož and Vokrouhlický (2008) and Brož et al. (2011) to estimate the age of the Schubart and Hilda families located in the 3:2 mean-motion resonance with Jupiter.

## 5. APPLICATIONS OF THE YORP AND BINARY YORP EFFECTS

### 5.1. Distribution of Rotation Rate and Obliquity for Small Asteroids

As explained in section 2.1, a secular change in rotation rate and obliquity are the two main dynamical implications of the YORP effect. Therefore, it is has been natural to seek traits of these trends among the populations of small asteroids. Luckily, the amount of data and their quality have significantly increased over the last decade and allowed such analyses.

**5.1.1. Rotation-rate distribution.** The distribution of rotation frequencies of large asteroids in the main belt matches a Maxwellian function quite well with a mean rotation period of  $\sim 8\text{--}12$  h, depending on the size of the bin used. However, data for asteroids smaller than  $\sim 20$  km show significant deviations from this law, with many asteroids either having very slow or very fast rotation rates. Note that similar data are also available for NEAs, but the main-belt sample is more

suitable because its interpretation is not complicated by possible effects of planetary close approaches. After eliminating known or suspected binary systems, solitary kilometer-sized asteroids in the main asteroid belt were shown to have a roughly uniform distribution of rotation frequencies (Pravec et al., 2008) (Fig. 8). The only statistically significant deviation was an excess of slow rotators (periods less than a day or so). Note that the sample described by Pravec et al. (2008) is superior to other existing datasets so far in elimination of all possible survey biases [which may prevent recognition of slow rotators (P. Pravec, personal communication)].

These results are well explained with a simple model of a relaxed YORP evolution. In this view asteroid spin rates are driven by the YORP effect toward extreme (large or small) values on a characteristic (YORP) timescale dependent on the size. Asteroids evolving toward a state of rapid rotation shed mass and thus put a brake on their rotation rate, while those who slow their rotation too much enter into a tumbling phase. They may later emerge from this state naturally, with a new spin vector, or may gain rotation angular momentum by subcatastrophic impacts. After a few cycles the spin rates settle to an approximately uniform distribution and the memory of its initial value is erased. In fact, the observations similar to those shown in Fig. 8 may help to quantitatively calibrate the processes that allow bodies to reemerge from the slow-rotating state.

Statler et al. (2013) presented a first attempt to obtain unbiased rotation properties of very small NEAs. They found

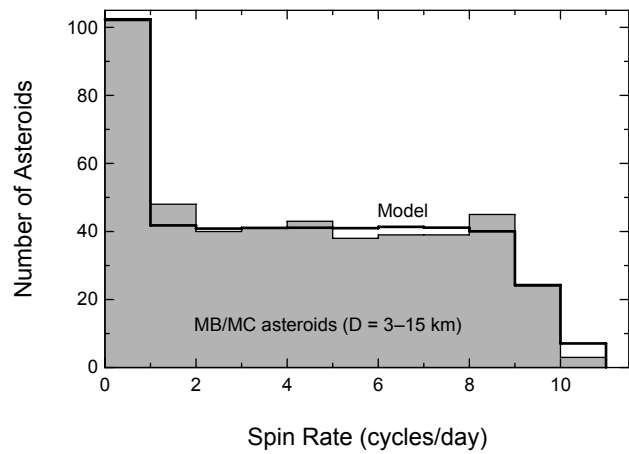


**Fig. 8.** Spin rate distribution of 462 small main-belt and Mars-crossing asteroids (sizes in the 3–15-km range, with a median value of 6.5 km). The distribution is flat with only two features: (1) an excess of slow rotators with periods longer than 1 d (the first bin), and (2) a linear decrease on the 8–10 cycles d<sup>-1</sup> interval. The latter is simply due to rotational fission limit dependence on the actual shape of the body, while the former holds information how the spin reemerges from the slow-rotation limit. Results from a simple model of a YORP-relaxed population of objects is shown in black (model). Adapted from Pravec *et al.* (2008), with an update from P. Pravec as of April 2014.

an anomalously large fraction of very fast rotating bodies in the <60-m group, which may witness a preferential ability of YORP to accelerate the rotation rate of small asteroids. A larger sample, less vulnerable to potential errors and biases, will be needed to verify this potentially important result.

**5.1.2. Obliquity distribution.** Similarly, the distribution of pole orientation of large asteroids in the main belt is roughly isotropic, with only a moderate excess of prograde rotating bodies. On the other hand, rotation poles of small asteroids (sizes  $\leq$ 30 km) are strongly concentrated toward ecliptic south and north poles (Hanuš *et al.*, 2013a) (Fig. 9). Note that this trend is better exhibited in the retrograde-rotating group (obliquities  $>90^\circ$ ), because the prograde-rotating asteroids are perturbed by secular spin-orbit resonances (e.g., Vokrouhlický *et al.*, 2006d). As a result, there is more mixing among the obliquities  $<90^\circ$ , which causes their flatter distribution in Fig. 9. Overall, this result can again be matched with the above-mentioned simple model of YORP evolution, because YORP torques drive obliquity toward its extreme values (e.g., Čapek and Vokrouhlický, 2004).

The pole distribution of NEAs, in spite of a still limited sample, indicates a strong preference of directions near the south ecliptic pole (La Spina *et al.*, 2004) (Fig. 9). The ratio between the number of retrograde- vs. prograde-rotating bodies is nearly 3:1. This is in a very good agreement with prediction from a model, where most NEAs are delivered from the main belt via principal resonant routes, secular v<sub>6</sub> resonance, and 3:1 mean-motion resonance with Jupiter

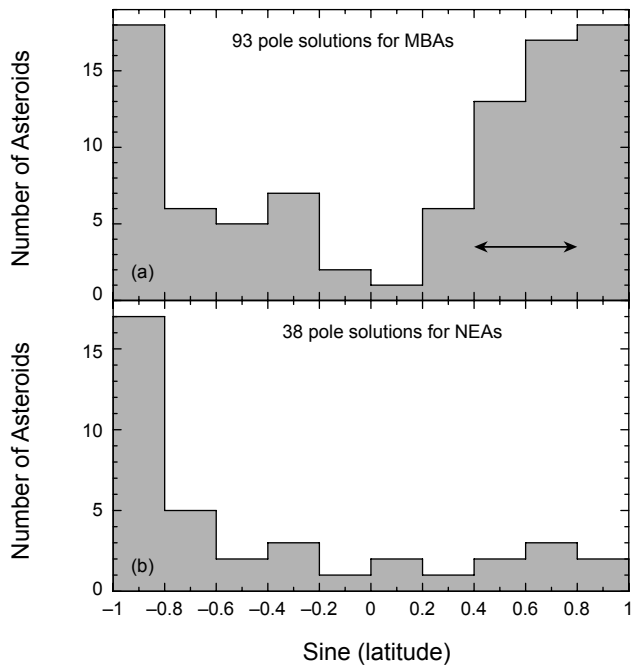


**Fig. 9.** (a) Distribution of ecliptic pole latitude for 93 small main-belt asteroids (MBAs; sizes less than 30 km). The arrow indicates the zone of prograde-rotating objects potentially affected by the spin-orbit resonances (e.g., Vokrouhlický *et al.*, 2006d). This effect is nonexistent for retrograde-rotating objects and the poles are let to drift closer to the extreme value. (b) Distribution of ecliptic pole latitude for 38 near-Earth asteroids (NEAs). This is dominated by retrograde-rotating objects ( $\approx$ 73% cases), because this sense of rotation offers a better chance to migrate to the planet-crossing space. In both cases, the tendency to extreme latitude values is due to the YORP effect. MBA data adapted from Hanuš *et al.* (2013a), NEA data from the Asteroid Lightcurve Database (LCDB) compilation as of February 2014.

(Bottke *et al.*, 2002b), resupplied by the Yarkovsky effect (Morbidelli and Vokrouhlický, 2003). This is because while the 3:1 resonance may be reached from heliocentric orbits with both larger and smaller value of the semimajor axis, asteroids can enter the v<sub>6</sub> resonance only by decreasing their semimajor axis. Taking into account the proportion by which these resonances contribute to the NEA population (Bottke *et al.*, 2002b), one obtains the observed 3:1 ratio between spin retrograde vs. prograde rotators. This obviously assumes that the rotation pole directions do not become significantly modified after the asteroids enter the planet-crossing zone.

Another interesting piece of information comes from a study of orbital pole distribution of small binary systems in the main belt. Pravec *et al.* (2012) show that poles of these systems are non-isotropic with strong concentration toward the ecliptic poles, thus mimicking the spin distribution of solitary asteroids in the same class. This picture is consistent with a model in which these small binaries are formed by fission of the parent body, whose rotation has been brought to the rotational limit by the YORP effect.

## 5.2. Asteroids with Rotation Axes Caught in Spin-Orbit Resonances

In an attempt to generalize Cassini's second and third laws, Giuseppe Colombo developed a mathematical model in the 1960s that describes the evolution of a body's spin axis rotating about a principal axis of its inertia tensor (Colombo, 1966). Colombo included two fundamental elements in his approach: (1) gravitational torques due to a massive center (e.g., the Sun), and (2) regular precession of the orbital plane of the body by exterior perturbers (e.g., planets). Because approach (1) produces a regular precession of the spin axis, a secular spin-orbit resonance (with a stable fixed point called Cassini state 2) may occur between its frequency and the frequency by which the orbital plane precesses in the inertial space. Such a resonance may occur only for a certain range of obliquity and rotation period values, and thus there is only a small probability that the spin state of any given asteroid is located in the Cassini state 2 associated with one of the frequencies by which its orbital plane precesses in space.

With this as background, the discovery of five prograde-rotating Koronis member asteroids with similar spin vectors (i.e., spin axes nearly parallel in inertial space and similar rotation periods) was a surprise. Additionally, the sample of retrograde-rotating asteroids in the same observation campaign showed obliquities anomalously large ( $\geq 154^\circ$ ) and either short or long rotation periods (Slivan, 2002; Slivan et al., 2009). This puzzling situation, however, was solved with a model where the gravitational spin dynamics were complemented with the long-term effects of YORP torques (Vokrouhlický et al., 2003). The YORP effect was shown to bring, on a  $\sim 2\text{--}3\text{-G.y.}$  timescale, prograde states close to Cassini state 2 associated with the prominent  $s_6$  frequency in the orbital precession, thus providing a natural explanation for the alignment in inertial space. Note that while the capture is fundamentally unstable, the evolution becomes slowed down near the observed obliquities where the YORP effect changes rotation period only slowly (section 2.1). No resonant trapping zone exists for retrograde-rotating bodies, whose evolution is thus simpler and, driven solely by the YORP effect, evolve toward extreme values in both their obliquities and rotation periods.

The possibility exists for asteroid spin states to be trapped in similar spin-orbit resonant states, dubbed "Slivan states," for bodies residing on low-inclination orbits, especially in the central and outer parts of the main asteroid belt. Recently reported Slivan states in the inner part of the belt, namely in the Flora region (Kryszczyńska, 2013), are questionable because of their instability. Yet model refinement would be clearly needed if more bodies are observed near these states in the Flora region (Vraštil and Vokrouhlický, 2015).

## 5.3. Formation and Long-Term Evolution of Binary Systems

The BYORP effect is predicted to play a fundamental role in the evolution of asteroid binaries. As noted earlier, it has

been hypothesized that nearly all observed small, rubble-pile binary asteroid systems lie in an equilibrium state where BYORP and tidal torques are balanced.

The BYORP effect plays many other roles in controlling the evolution of a binary asteroid. Jacobson and Scheeres (2011a) studied the evolution of asteroid systems arising from the rotational fission of a primary body (due to YORP torques). While the initial creation of a stable binary system is a complex process (see the chapter by Walsh and Jacobson in this volume), once a stable binary forms with at least one of the bodies being synchronous, the BYORP effect can take control of its subsequent evolution. There are several different pathways, which we briefly review here.

First, if the ratio between the secondary and primary is greater than  $\sim 0.2$ , the system is expected to eventually settle into a double-synchronous binary asteroid such as (69230) Hermes. In this configuration both of the synchronous bodies can contribute to the BYORP effect, either working together to contract or expand the system, or working against each other. In none of these cases is it expected that the system will settle into a stable equilibrium, as migration would only stop if the two BYORP effects counteract each other exactly. Similarly, there are no significant tidal dissipation effects once a system is doubly synchronous, and thus the case of contraction will lead directly to collapse (e.g., Taylor and Margot, 2014). The expansion phase of a doubly synchronous binary asteroid has not been investigated in detail as of yet in terms of physical evolution. However, as the system becomes larger, it should be more susceptible to other exogenous perturbations (e.g., Fang and Margot, 2012).

For stable binaries that have a mass ratio  $< 0.2$  between the secondary and primary, the evolutionary path is seen to be quite different (see also the chapter by Walsh and Jacobson in this volume). If a stable binary is formed, it is generally a singly synchronous system with the secondary in a synchronous state and the primary rotating faster than the spin rate. If the secondary's BYORP coefficient is negative and the system contracts, then it should migrate into a BYORP-tide equilibrium. Once in this state it may persist for long periods of time, as the system has been hardened against exogenous perturbations due to its more compact state (e.g., Fang and Margot, 2012). A noticeable outcome is that the primary body should lose spin rate, due to the tidal transfer of torque. However, the primary may still be subject to the YORP effect and thus may not exhibit a clear slowing of its spin rate.

If the secondary's BYORP coefficient is positive, the system expands, with tides now working in the same direction. In this case there is also an interesting interplay between the libration of the secondary about its synchronous state and tidal dissipation that acts to damp out such librations. In the expansive case without librational damping, the amplitude of libration is expected to increase as the orbit increases, due to an adiabatic integral involving the libration state (e.g., Jacobson et al., 2014). How these two effects combine can control when the secondary can lose synchronous lock, causing the BYORP effect to shut down. The model and

simulations developed in *Jacobson et al.* (2014) indicate that synchronicity is lost at a far enough distance so that further tidal evolution of the system does not occur, and the system can be described as a wide-asynchronous binary. This paper makes favorable comparisons between predictions of the theory and such observed binary systems. An alternate, earlier theory was proposed by *Ćuk and Nesvorný* (2010) in which the expanding system can become trapped in a resonance with the eccentricity of the orbit growing secularly. They hypothesized that such a system would then lose synchronicity, but subsequently relax back into synchronous rotation several times until the system enters a contractive phase. The very different predictions from these models indicate that the full interaction of such expanding binary systems is not yet fully understood.

In addition to expansion and contraction effects, there may also be out-of-plane BYORP effects that cause migration of the binary system's orbit pole, similar to the YORP effect (see *Ćuk and Burns*, 2005). *Steinberg and Sari* (2011) further studied these situations and proposed that, similar to YORP, the obliquity states should preferentially migrate toward some asymptotic values (either 0°, 90°, or 180° in their model). *Ćuk* (2007) noted that this effect, when combined with the characteristic zero-crossing of the BYORP coefficient as a function of obliquity, could create an accumulation of binaries at obliquities between these limits. It should also be mentioned that *McMahon and Scheeres* (2010b) did not predict an inclination evolution due to the BYORP effect, owing to the effects of the primary oblateness. Thus, it is apparent that the obliquity migration of a binary orbit due to BYORP is not fully understood or settled, and remains a ripe topic for further investigation.

## 6. CONCLUSION AND FUTURE WORK

As with many mature disciplines in science, studies of the Yarkovsky and YORP effects have their own agenda of development in the future years. What makes them even more appealing is that some of these future results have interesting implications for other domains in planetary astronomy. Here we try to summarize at least a few examples.

While it seems nearly certain that numerous detections of the Yarkovsky effect will emerge from current and upcoming astrometric surveys in the next decade (e.g., *Delbò et al.*, 2008; *Mouret and Mignard*, 2011; *Nugent et al.*, 2012b; *Desmars*, 2015), more work is needed to secure YORP detections, especially across the whole range of possible rotation periods. This should help us understand in what proportion the YORP effect results in acceleration or deceleration of the rotation rate.

The binary YORP detections are in their infancy but will become an important topic of future research. This is because the BYORP effect is an essential element, as far as we understand it today, in orbital evolution of binary asteroids. Detections, or continuing nondetections, of the expected BYORP signal will have implications not only for the orbital

evolution pathways of binaries and their physical parameters, but also for estimates of their lifetime and formation rate.

As the rotations of asteroids become slower by the YORP effect, they naturally enter the tumbling state. The available models so far, whether analytical or numerical in nature (*Vokrouhlický et al.*, 2007; *Cicalò and Scheeres*, 2010; *Breiter et al.*, 2011), indicate that the YORP effect keeps navigating the rotation through the tumbling phase space without an easy return to the rotation about the shortest axis of the inertia tensor. Yet, more than 90% of asteroids do rotate in the shortest-axis mode. A solution for this conundrum is not yet clear and warrants further work. The above-mentioned models of the YORP effect in the tumbling regime neglect thermal inertia, which may be an important factor. Additionally, no detailed model combining the YORP effect and the effects of inelastic energy dissipation inside the body has been presented [although the initial work does not seem to remedy the problem (*Breiter and Murawiecka*, 2015)].

While it is generally accepted that the YORP effect is the driving dynamical process that brings small asteroids to their fission, more work is needed to understand how the fission mechanics really work. Along the path to the fission limit, the body may undergo structural and shape changes that could either help the fission process, or potentially invert the YORP acceleration to effectively prevent fission. It is not known which of these alternatives typically dominates and in what proportion. This, again, could have important implications for the formation rate of both small binaries and asteroid pairs. Additionally, this would help us to better understand the YORP self-limitation processes and the way in which they potentially modify classical YORP results.

**Acknowledgments.** The authors are grateful to D. Farnocchia for assistance in the compilation of Table 1 and P. Pravec for providing data shown in Fig. 8. We also thank reviewers D. P. Rubincam and B. Rozitis for their suggestions, which helped to improve the original form of the chapter. The work of D.V. was partially supported by the Czech Grant Agency (grant P209-13-01308S). The participation of W.F.B. was supported by NASA's Solar System Evolution Research Virtual Institute (SSERVI) program through a grant to the Institute for the Science of Exploration Targets at the Southwest Research Institute in Boulder, Colorado. The work of S.R.C. was conducted at the Jet Propulsion Laboratory, California Institute of Technology, under a contract with NASA. T.S.S. acknowledges support from NASA Planetary Geology and Geophysics grant NNX11AP15G.

## REFERENCES

- Afonso G. B., Gomes R. S., and Florcza M. A. (1995) Asteroid fragments in Earth-crossing orbits. *Planet. Space Sci.*, 43, 787–795.
- Beekman G. (2006) I. O. Yarkovsky and the discovery of ‘his’ effect. *J. Hist. Astron.*, 37, 71–86.
- Bottke W. F., Vokrouhlický D., Brož M., Nesvorný D., and Morbidelli A. (2001) Dynamical spreading of asteroid families via the Yarkovsky effect: The Koronis family and beyond. *Science*, 294, 1693–1696.
- Bottke W. F., Vokrouhlický D., Rubincam D. P., and Brož M. (2002a) Dynamical evolution of asteroids and meteoroids using the Yarkovsky effect. In *Asteroids III* (W. F. Bottke Jr. et al., eds.), pp. 395–408. Univ. of Arizona, Tucson.

- Bottke W. F., Morbidelli A., Jedicke R., et al. (2002b) Debiased orbital and absolute magnitude distribution of the near-Earth objects. *Icarus*, **156**, 399–433.
- Bottke W. F., Vokrouhlický D., Rubincam D. P., and Nesvorný D. (2006) The Yarkovsky and YORP effects: Implications for asteroid dynamics. *Annu. Rev. Earth Planet. Sci.*, **34**, 157–191.
- Bottke W. F., Vokrouhlický D., and Nesvorný D. (2007) An asteroid breakup 160 My ago as a probable source of the K-T impactor. *Nature*, **449**, 48–53.
- Bottke W. F., Vokrouhlický D., Walsh K., et al. (2015) In search of the source of asteroid (101955) Bennu: Application of the stochastic YORP model. *Icarus*, **247**, 191–217.
- Breiter S. and Michałska H. (2008) YORP torque as the function of shape harmonics. *Mon. Not. R. Astron. Soc.*, **388**, 927–944.
- Breiter S. and Murawiecka M. (2015) Tumbling asteroid rotation with the YORP torque and inelastic energy dissipation. *Mon. Not. R. Astron. Soc.*, **449**, 2489–2497.
- Breiter S. and Vokrouhlický D. (2011) YORP effect with anisotropic radiation. *Mon. Not. R. Astron. Soc.*, **410**, 2807–2816.
- Breiter S., Michałska H., Vokrouhlický D., and Borczyk W. (2007) Radiation induced torques on spheroids. *Astron. Astrophys.*, **471**, 345–353.
- Breiter S., Bartczak P., Czekaj M., Oczujska B., and Vokrouhlický D. (2009) The YORP effect on 25143 Itokawa. *Astron. Astrophys.*, **507**, 1073–1081.
- Breiter S., Vokrouhlický D., and Nesvorný D. (2010a) Analytical YORP torques model with an improved temperature distribution function. *Mon. Not. R. Astron. Soc.*, **401**, 1933–1949.
- Breiter S., Bartczak P., and Czekaj M. (2010b) YORP torques with 1D thermal model. *Mon. Not. R. Astron. Soc.*, **408**, 1576–1589.
- Breiter S., Rożek A., and Vokrouhlický D. (2011) YORP effect on tumbling objects. *Mon. Not. R. Astron. Soc.*, **417**, 2478–2499.
- Brož M. and Vokrouhlický D. (2008) Asteroids in the first order resonances with Jupiter. *Mon. Not. R. Astron. Soc.*, **390**, 715–732.
- Brož M., Vokrouhlický D., Morbidelli A., Nesvorný D., and Bottke W. F. (2011) Did the Hilda collisional family form during the late heavy bombardment? *Mon. Not. R. Astron. Soc.*, **414**, 2716–2727.
- Čapek D. and Vokrouhlický D. (2004) The YORP effect with finite thermal conductivity. *Icarus*, **172**, 526–536.
- Carruba V. (2009) The (not so) peculiar case of the Padua family. *Mon. Not. R. Astron. Soc.*, **395**, 358–377.
- Carruba V. and Morbidelli A. (2011) On the first  $v_6$  anti-aligned librating asteroid family of Tina. *Mon. Not. R. Astron. Soc.*, **412**, 2040–2051.
- Chesley S. R., Ostro S. J., Vokrouhlický D., et al. (2003) Direct detection of the Yarkovsky effect via radar ranging to the near-Earth asteroid 6489 Golevka. *Science*, **302**, 1739–1742.
- Chesley S. R., Vokrouhlický D., Ostro S. J., et al. (2008) Direct estimation of Yarkovsky accelerations on near-Earth asteroids. In *Asteroids, Comets, Meteors*, Abstract #8330. Lunar and Planetary Institute, Houston.
- Chesley S. R., Farnocchia D., Nolan M. C., et al. (2014) Orbit and bulk density of the OSIRIS-REx target asteroid (101955) Bennu. *Icarus*, **235**, 5–22.
- Cicalò S. and Scheeres D. J. (2010) Averaged rotational dynamics of an asteroid in tumbling rotation under the YORP torque. *Cel. Mech. Dyn. Astron.*, **106**, 301–337.
- Colombo G. (1966) Cassini's second and third laws. *Astron. J.*, **71**, 891–896.
- Cotto-Figueroa D., Statler T. S., Richardson D. C., and Tanga P. (2015) Coupled spin and shape evolution of small rubble-pile asteroids: Self-limitation of the YORP effect. *Astrophys. J.*, **803**, 25.
- Ćuk M. (2007) Formation and destruction of small binary asteroids. *Astrophys. J. Lett.*, **659**, L57–L60.
- Ćuk M. and Burns J. A. (2005) Effects of thermal radiation on the dynamics of binary NEAs. *Icarus*, **176**, 418–431.
- Ćuk M. and Nesvorný D. (2010) Orbital evolution of small binary asteroids. *Icarus*, **207**, 732–743.
- Delbò M., Tanga P., and Mignard F. (2008) On the detection of the Yarkovsky effect on near-Earth asteroids by means of Gaia. *Planet. Space Sci.*, **56**, 1823–1827.
- Desmars J. (2015) Detection of Yarkovsky acceleration in the context of precovery observations and the future Gaia catalogue. *Astron. Astrophys.*, **575**, A53.
- Durech J. (2005) 433 Eros — comparison of lightcurve extrema from 1901–1931 with the present rotation state. *Astron. Astrophys.*, **431**, 381–383.
- Durech J., Vokrouhlický D., Kaasalainen M., et al. (2008a) Detection of the YORP effect for asteroid (1620) Geographos. *Astron. Astrophys.*, **489**, L25–L28.
- Durech J., Vokrouhlický D., Kaasalainen M., et al. (2008b) New photometric observations of asteroids (1862) Apollo and (25143) Itokawa — analysis of YORP effect. *Astron. Astrophys.*, **488**, 345–350.
- Durech J., Vokrouhlický D., Baransky A. R., et al. (2012) Analysis of the rotation period of asteroids (1865) Cerberus, (2100) Ra-Shalom and (3103) Eger — search for the YORP effect. *Astron. Astrophys.*, **547**, A10.
- Fang J. and Margot J.-L. (2012) Near-Earth binaries and triples: Origin and evolution of spin-orbital properties. *Astron. J.*, **143**, 24.
- Farinella P., Vokrouhlický D., and Hartmann W. K. (1998) Meteorite delivery via Yarkovsky orbital drift. *Icarus*, **132**, 378–387.
- Farnocchia D., and Chesley S. R. (2014) Assessment of the 2880 impact threat from asteroid (29075) 1950 DA. *Icarus*, **229**, 321–327.
- Farnocchia D., Chesley S. R., Chodas P. W., Micheli M., Tholen D. J., Milani A., Elliott G. T., and Bernardi F. (2013a) Yarkovsky-driven impact risk analysis for asteroid (99942) Apophis. *Icarus*, **224**, 192–200.
- Farnocchia D., Chesley S. R., Vokrouhlický D., Milani A., Spoto F., and Bottke W. F. (2013b) Near Earth asteroids with measurable Yarkovsky effect. *Icarus*, **224**, 1–13.
- Goldreich P. and Sari R. (2009) Tidal evolution of rubble piles. *Astrophys. J.*, **691**, 54–60.
- Golubov O. and Krugly Y. N. (2012) Tangential component of the YORP effect. *Astrophys. J. Lett.*, **752**, L11.
- Golubov O., Scheeres D. J., and Krugly Y. N. (2014) A three-dimensional model of tangential YORP. *Astrophys. J.*, **794**, 22.
- Hanuš J., Ďurech J., Brož M., et al. (2013a) Asteroids' physical models from combined dense and sparse photometry and scaling of the YORP effect by the observed obliquity distribution. *Astron. Astrophys.*, **551**, A67.
- Hanuš J., Brož M., Ďurech J., et al. (2013b) An anisotropic distribution of spin vectors in asteroid families. *Astron. Astrophys.*, **559**, A134.
- Hapke B. (1993) *Theory of Reflectance and Emittance Spectroscopy*. Cambridge Univ., Cambridge.
- Hudson R. S., and Ostro S. J. (1995) Shape and non-principal axis spin state of asteroid 4179 Toutatis. *Science*, **270**, 84–86.
- Jacobson S. A. and Scheeres D. J. (2011a) Dynamics of rotationally fissioned asteroids: Source of observed small asteroid systems. *Icarus*, **214**, 161–178.
- Jacobson S. A. and Scheeres D. J. (2011b) Long-term stable equilibria for synchronous binary asteroids. *Astrophys. J. Lett.*, **736**, L19.
- Jacobson S. A., Scheeres D. J., and McMahon J. (2014) Formation of the wide asynchronous binary asteroid population. *Astrophys. J.*, **780**, 60.
- Kaasalainen M. and Nurturen H. (2013) Compact YORP formulation and stability analysis. *Astron. Astrophys.*, **558**, A104.
- Kaasalainen M., Ďurech J., Warner B. D., Krugly Y. N., and Gaftonyuk N. M. (2007) Acceleration of the rotation of asteroid 1862 Apollo by radiation torques. *Nature*, **446**, 420–422.
- Kryszczyńska A. (2013) Do Slivan states exist in the Flora family? II. Fingerprints of the Yarkovsky and YORP effects. *Astron. Astrophys.*, **551**, A102.
- La Spina A., Paolicchi P., Kryszczyńska A., and Pravec P. (2004) Retrograde spins of near-Earth asteroids from the Yarkovsky effect. *Nature*, **428**, 400–401.
- Lauretta D. S., Barucci M. A., Binzel R. P., et al. (2015) The OSIRIS-REx target asteroid (101955) Bennu: Constraints on its physical, chemical, and dynamical nature from astronomical observations. *Meteoritics & Planet. Sci.*, **50**, 834–849.
- Lowry S. C., Fitzsimmons A., Pravec P., et al. (2007) Direct detection of the asteroidal YORP effect. *Science*, **316**, 272–274.
- Lowry S. C., Weissman P. R., Duddy S. R., et al. (2014) The internal structure of asteroid (25143) Itokawa as revealed by detection of YORP spin-up. *Astron. Astrophys.*, **562**, A48.
- McMahon J. and Scheeres D. J. (2010a) Secular orbit variation due to solar radiation effects: A detailed model for BYORP. *Cel. Mech. Dyn. Astron.*, **106**, 261–300.

- McMahon J. and Scheeres D. J. (2010b) Detailed prediction for the BYORP effect on binary near-Earth asteroid (66391) 1999 KW<sub>4</sub> and implications for the binary population. *Icarus*, 209, 494–509.
- Milani A., Chesley S. R., Sansaturo M. E., Bernardi F., Valsecchi G. B., and Arratia O. (2009) Long term impact risk for (101955) 1999 RQ<sub>36</sub>. *Icarus*, 203, 460–471.
- Mommert M., Hora J. L., Farnocchia D., et al. (2014) Constraining the physical properties of near-Earth object 2009 BD. *Astrophys. J.*, 786, 148.
- Morbidelli A. and Vokrouhlický D. (2003) The Yarkovsky driven origin of near-Earth asteroids. *Icarus*, 163, 120–134.
- Mouret S. and Mignard F. (2011) Detecting the Yarkovsky effect with the Gaia mission: List of the most promising candidates. *Mon. Not. R. Astron. Soc.*, 413, 741–748.
- Nesvorný D. and Bottke W. F. (2004) Detection of the Yarkovsky effect for main-belt asteroids. *Icarus*, 170, 324–342.
- Nesvorný D. and Vokrouhlický D. (2006) New candidates for recent asteroid breakups. *Astron. J.*, 132, 1950–1958.
- Nesvorný D. and Vokrouhlický D. (2007) Analytic theory of the YORP effect for near-spherical objects. *Astron. J.*, 134, 1750–1768.
- Nesvorný D. and Vokrouhlický D. (2008a) Analytic theory for the YORP effect on obliquity. *Astron. J.*, 136, 291–299.
- Nesvorný D. and Vokrouhlický D. (2008b) Vanishing torque from radiation pressure. *Astron. Astrophys.*, 480, 1–3.
- Nesvorný D., Bottke W. F., Dones L., and Levison H. F. (2002) The recent breakup of an asteroid in the main-belt region. *Nature*, 417, 720–722.
- Nesvorný D., Bottke W. F., Levison H. F., and Dones L. (2003) Recent origin of the zodiacal dust bands. *Astrophys. J.*, 591, 486–497.
- Nesvorný D., Vokrouhlický D., and Bottke W. F. (2006) A main belt asteroid break-up 450 ky ago. *Science*, 312, 1490.
- Nesvorný D., Bottke W. F., Vokrouhlický D., Sykes M., Lien D. J., and Stansberry J. (2008) Origin of the near-ecliptic zodiacal dust band. *Astrophys. J. Lett.*, 679, L143–L146.
- Nesvorný D., Vokrouhlický D., Morbidelli A., and Bottke W. F. (2009) Asteroidal source of L chondrite meteorites. *Icarus*, 200, 698–701.
- Novaković B. (2010) Portrait of Theobalda as a young asteroid family. *Mon. Not. R. Astron. Soc.*, 407, 1477–1486.
- Novaković B., Dell’Oro A., Cellino A., and Knežević Z. (2012) Recent collisional jet from a primitive asteroid. *Mon. Not. R. Astron. Soc.*, 425, 338–346.
- Novaković B., Hsieh H. H., Cellino A., Micheli M., and Pedani M. (2014) Discovery of a young asteroid cluster associated with P/2012 F5 (Gibbs). *Icarus*, 231, 300–309.
- Nugent C. R., Margot J. L., Chesley S. R., and Vokrouhlický D. (2012a) Detection of semi-major axis drifts in 54 near-Earth asteroids. *Astron. J.*, 144, 60.
- Nugent C. R., Mainzer A., Masiero J., Grav T., and Bauer J. (2012b) The Yarkovsky drift’s influence on NEAs: Trends and predictions with NEOWISE measurements. *Astron. J.*, 144, 75.
- Öpik E. J. (1951) Collision probabilities with the planets and the distribution of interplanetary matter. *Proc. R. Irish Acad.*, A54, 165–199.
- Ostro S. J., Margot J.-L., Benner L. A. M., et al. (2006) Radar imaging of binary near-Earth asteroid (66391) 1999 KW<sub>4</sub>. *Science*, 314, 1276–1280.
- Paddack S. J. (1969) Rotational bursting of small celestial bodies: Effects of radiation pressure. *J. Geophys. Res.*, 74, 4379–4381.
- Paddack S. J. and Rhee J. W. (1975) Rotational bursting of interplanetary dust particles. *Geophys. Res. Lett.*, 2, 365–367.
- Peterson C. (1976) A source mechanism for meteorites controlled by the Yarkovsky effect. *Icarus*, 29, 91–111.
- Pravec P., Harris A. W., Vokrouhlický D., et al. (2008) Spin rate distribution of small asteroids. *Icarus*, 197, 497–504.
- Pravec P., Vokrouhlický D., Polishook D., et al. (2010) Asteroid pairs formed by rotational fission. *Nature*, 466, 1085–1088.
- Pravec P., Scheirich P., Vokrouhlický D., et al. (2012) Binary asteroid population. II. Anisotropic distribution of orbit poles. *Icarus*, 218, 125–143.
- Pravec P., Scheirich P., Ďurech J., et al. (2014) The tumbling spin state of (99942) Apophis. *Icarus*, 233, 48–60.
- Radzievskii V. V. (1952) The influence of anisotropy of reemitted sunlight on the orbital motion of asteroids and meteoroids. *Astron. Zh.*, 29, 162–170.
- Radzievskii V. V. (1954) A mechanism for the disintegration of asteroids and meteorites. *Dokl. Akad. Nauk SSSR*, 97, 49–52.
- Richardson D. C., Elankumaran P., and Sanderson R. E. (2005) Numerical experiments with rubble piles: Equilibrium shapes and spins. *Icarus*, 173, 349–361.
- Rozitis B. and Green S. F. (2012) The influence of rough surface thermal-infrared beaming on the Yarkovsky and YORP effects. *Mon. Not. R. Astron. Soc.*, 423, 367–388.
- Rozitis B. and Green S. F. (2013) The influence of global self-heating on the Yarkovsky and YORP effects. *Mon. Not. R. Astron. Soc.*, 433, 603–621.
- Rozitis B. and Green S. F. (2014) Physical characterization of near-Earth asteroid (1620) Geographos. Reconciling radar and thermal-infrared observations. *Astron. Astrophys.*, 568, A43.
- Rozitis B., Duddy S. R., Green S. F., and Lowry S. C. (2013) A thermophysical analysis of the (1862) Apollo Yarkovsky and YORP effects. *Astron. Astrophys.*, 555, A20.
- Rozitis B., MacLennan E., and Emery J. P. (2014) Cohesive forces prevent the rotational breakup of rubble-pile asteroid (29075) 1950 DA. *Nature*, 512, 174–176.
- Rubincam D. P. (1982) On the secular decrease in the semimajor axis of LAGEOS’s orbit. *Cel. Mech.*, 26, 361–382.
- Rubincam D. P. (1995) Asteroid orbit evolution due to thermal drag. *J. Geophys. Res.*, 100, 1585–1594.
- Rubincam D. P. (1998) Yarkovsky thermal drag on small asteroids and Mars-Earth delivery. *J. Geophys. Res.*, 103, 1725–1732.
- Rubincam D. P. (2000) Radiative spin-up and spin-down of small asteroids. *Icarus*, 148, 2–11.
- Rubincam D. P. and Paddock S. J. (2010) Zero secular torque on asteroids from impinging solar photons in the YORP effect: A simple proof. *Icarus*, 209, 863–865.
- Scheeres D. J. (2007) The dynamical evolution of uniformly rotating asteroids subject to YORP. *Icarus*, 188, 430–450.
- Scheeres D. J. (2015) Landslides and mass shedding on spinning spheroidal asteroids. *Icarus*, 247, 1–17.
- Scheeres D. J. and Gaskell R. W. (2008) Effect of density inhomogeneity on YORP: The case of Itokawa. *Icarus*, 198, 125–129.
- Scheeres D. J. and Mirrahimi S. (2008) Rotational dynamics of a solar system body under solar radiation torques. *Cel. Mech. Dyn. Astron.*, 100, 69–103.
- Scheeres D. J., Abe M., Yoshikawa M., Nakamura R., Gaskell R. W., and Abell P. A. (2007) The effect of YORP on Itokawa. *Icarus*, 188, 425–429.
- Scheeres D. J., Hartzell C. M., Sánchez P., and Swift M. (2010) Scaling forces to asteroid surfaces: The role of cohesion. *Icarus*, 210, 968–984.
- Scheirich P., Pravec P., Jacobson S. A., et al. (2015) The binary near-Earth asteroid (175706) 1996 FG<sub>3</sub> — An observational constraint on its orbital stability. *Icarus*, 245, 56–63.
- Schwartz S. R., Richardson D. C., and Michel P. (2012) An implementation of the soft-sphere discrete element method in a high-performance parallel gravity tree-code. *Granular Matter*, 14, 363–380.
- Ševeček P., Brož M., Čapek D., and Ďurech J. (2015) The thermal emission from boulders on (25143) Itokawa and general implications for the YORP effect. *Mon. Not. R. Astron. Soc.*, 450, 2104–2115.
- Sekiya M. and Shimoda A. A. (2013) An iterative method for obtaining a nonlinear solution for the temperature distribution of a rotating spherical body revolving in a circular orbit around a star. *Planet. Space Sci.*, 84, 112–121.
- Sekiya M. and Shimoda A. A. (2014) An iterative method for obtaining a nonlinear solution for the temperature distribution of a rotating spherical body revolving in an eccentric orbit. *Planet. Space Sci.*, 97, 23–33.
- Slivan S. M. (2002) Spin vector alignment of Koronis family asteroids. *Nature*, 419, 49–51.
- Slivan S. M., Binzel R. P., Kaasalainen M., et al. (2009) Spin vectors in the Koronis family. II. Additional clustered spins, and one stray. *Icarus*, 200, 514–530.
- Spitale J. and Greenberg R. (2001) Numerical evaluation of the general Yarkovsky effect: Effects on semimajor axis. *Icarus*, 149, 222–234.
- Spitale J. and Greenberg R. (2002) Numerical evaluation of the general Yarkovsky effect: Effects on eccentricity and longitude of perapse. *Icarus*, 156, 211–222.

- Statler T. S. (2009) Extreme sensitivity of the YORP effect to small-scale topography. *Icarus*, *202*, 502–513.
- Statler T. S., Cotto-Figueroa D., Riethmiller D. A., and Sweeney K. M. (2013) Size matters: The rotation rates of small near-Earth asteroids. *Icarus*, *225*, 141–155.
- Steinberg E. and Sari R. (2011) Binary YORP effect and evolution of binary asteroids. *Astron. J.*, *141*, 55.
- Taylor P. A. and Margot J. L. (2014) Tidal end states of binary asteroid systems with a nonspherical component. *Icarus*, *229*, 418–422.
- Taylor P. A., Margot J. L., Vokrouhlický D., et al. (2007) Spin rate of asteroid (54509) 2000 PH<sub>5</sub> increasing due to the YORP effect. *Science*, *316*, 274–277.
- Taylor P. A., Nolan M. C., Howell E. S., et al. (2012) 2004 FG<sub>11</sub>. *Central Bureau Electronic Telegram (CBET)*, *3091*, 1.
- Vinogradova V. P. and Radzievskii V. V. (1965) The acceleration of the martian satellites and the stabilization of orbits of artificial satellites. *Astron. Zh.*, *42*, 424–432.
- Vokrouhlický D. (1998a) Diurnal Yarkovsky effect for metersized asteroidal fragments' mobility I. Linear theory. *Astron. Astrophys.*, *335*, 1093–1100.
- Vokrouhlický D. (1998b) Diurnal Yarkovsky effect for metersized asteroidal fragments' mobility II. Non-sphericity effects. *Astron. Astrophys.*, *338*, 353–363.
- Vokrouhlický D. (1999) A complete linear model for the Yarkovsky thermal force on spherical asteroid fragments. *Astron. Astrophys.*, *344*, 362–366.
- Vokrouhlický D. and Bottke W. F. (2001) The Yarkovsky thermal force on small asteroids and their fragments: Choosing the right albedo. *Astron. Astrophys.*, *371*, 350–353.
- Vokrouhlický D. and Brož M. (1999) An improved model of the seasonal Yarkovsky force for the regolith-covered asteroid fragments. *Astron. Astrophys.*, *350*, 1079–1084.
- Vokrouhlický D. and Čapek D. (2002) YORP-induced long-term evolution of the spin state of small asteroids and meteoroids. I. Rubincam's approximation. *Icarus*, *159*, 449–467.
- Vokrouhlický D. and Farinella P. (2000) Efficient delivery of meteorites to the Earth from a wide range of asteroid parent bodies. *Nature*, *407*, 606–608.
- Vokrouhlický D. and Milani A. (2000) Direct solar radiation pressure on the orbits of small near-Earth asteroids: Observable effects? *Astron. Astrophys.*, *362*, 746–755.
- Vokrouhlický D. and Nesvorný D. (2008) Pairs of asteroids probably of common origin. *Astron. J.*, *136*, 280–290.
- Vokrouhlický D. and Nesvorný D. (2009) The common roots of asteroids (6070) Rheinland and (54827) 2001 NQ<sub>8</sub>. *Astron. J.*, *137*, 111–117.
- Vokrouhlický D., Milani A., and Chesley S. R. (2000) Yarkovsky effect on near-Earth asteroids: Mathematical formulation and examples. *Icarus*, *148*, 118–138.
- Vokrouhlický D., Nesvorný D., and Bottke W. F. (2003) The vector alignments of asteroid spins by thermal torques. *Nature*, *425*, 147–151.
- Vokrouhlický D., Čapek D., Kaasalainen M., and Ostro S. J. (2004) Detectability of YORP rotational slowing of asteroid 25143 Itokawa. *Astron. Astrophys.*, *414*, L21–L24.
- Vokrouhlický D., Čapek D., Chesley S. R., and Ostro S. J. (2005a) Yarkovsky detection opportunities. I. Solitary asteroids. *Icarus*, *173*, 166–184.
- Vokrouhlický D., Čapek D., Chesley S. R., and Ostro S. J. (2005b) Yarkovsky detection opportunities. II. Binary asteroids. *Icarus*, *179*, 128–138.
- Vokrouhlický D., Brož M., Bottke W. F., Nesvorný D., and Morbidelli A. (2006a) Yarkovsky/YORP chronology of asteroid families. *Icarus*, *182*, 118–142.
- Vokrouhlický D., Brož M., Bottke W. F., Nesvorný D., and Morbidelli A. (2006b) The peculiar case of the Agnia asteroid family. *Icarus*, *183*, 349–361.
- Vokrouhlický D., Brož M., Morbidelli A., Bottke W. F., Nesvorný D., Lazzaro D., and Rivkin A. S. (2006c) Yarkovsky footprints in the Eos family. *Icarus*, *182*, 92–117.
- Vokrouhlický D., Nesvorný D., and Bottke W. F. (2006d) Secular spin dynamics of inner main-belt asteroids. *Icarus*, *184*, 1–28.
- Vokrouhlický D., Breiter S., Nesvorný D., and Bottke W. F. (2007) Generalized YORP evolution: Onset of tumbling and new asymptotic states. *Icarus*, *191*, 636–650.
- Vokrouhlický D., Chesley S. R., and Matson R. D. (2008) Orbital identification for asteroid 152563 (1992 BF) through the Yarkovsky effect. *Astron. J.*, *135*, 2336–2340.
- Vokrouhlický D., Ďurech J., Michalowski T., et al. (2009) Datura family: The 2009 update. *Astron. Astrophys.*, *507*, 495–504.
- Vokrouhlický D., Nesvorný D., Bottke W. F., and Morbidelli A. (2010) Collisionally born family about 87 Sylvia. *Astron. J.*, *139*, 2148–2158.
- Vokrouhlický D., Ďurech J., Polishook D., et al. (2011) Spin vector and shape of (6070) Rheinland and their implications. *Astron. J.*, *142*, 159.
- Vokrouhlický D., Farnocchia D., Čapek D., et al. (2015) The Yarkovsky effect for 99942 Apophis. *Icarus*, *252*, 277–283.
- Vraštil J. and Vokrouhlický D. (2015) Slivan states in the Flora region? *Astron. Astrophys.*, *579*, A14.
- Walsh K. J., Richardson D. C., and Michel P. (2008) Rotational breakup as the origin of small binary asteroids. *Nature*, *454*, 188–191.
- Yarkovsky I. O. (1901) The density of luminiferous ether and the resistance it offers to motion (in Russian). Bryansk, published privately by the author.
- Žižka J. and Vokrouhlický D. (2011) Solar radiation pressure on (99942) Apophis. *Icarus*, *211*, 511–518.



# Asteroid Differentiation: Melting and Large-Scale Structure

**A. Scheinberg and R. R. Fu**  
*Massachusetts Institute of Technology*

**L. T. Elkins-Tanton**  
*Arizona State University*

**B. P. Weiss**  
*Massachusetts Institute of Technology*

The diversity of mineralogies and textures in the asteroidal meteorite collection promises a similarly diverse array of parent bodies and relatives as we continue exploring the asteroid belt. The presence of metamorphosed and igneous meteorites demonstrates that even some small bodies were heated significantly, permitting a variety of complexly interacting processes and heterogeneities within an individual planetesimal. In particular, chondritic meteorites could even originate from the same parent body as some highly differentiated meteorites. The histories and present-day features of the asteroids depend on their initial composition and the timing and duration of the accretion process. We first discuss the energy sources driving thermal modification of planetesimals and summarize the processes involved in differentiation as hydrous, metal, and silicate melting occurs. Then we outline the aftermath of differentiation as the body cools, and close with a discussion of magnetic, geophysical, and meteoritic evidence for differentiation in planetesimals.

## 1. ENERGY SOURCES FOR METAMORPHISM AND MELTING

Chondrites consist of material that never heated sufficiently to melt, while primitive achondrites only underwent partial melting. Such samples can be explained as fragments of relatively homogeneous small bodies without invoking differentiation processes. However, iron meteorites analogous to planetary cores and stony achondrites analogous to differentiated planetary crusts demonstrate that metal-silicate differentiation occurred in planetesimals during the first few million years after the formation of calcium-aluminum-rich inclusions (CAIs) (e.g., Kleine et al., 2012; Markowski et al., 2006; Baker et al., 2005).

Differentiation requires heating above the melting temperature of iron-nickel alloys, and may require melting beyond the silicate solidus as well. First melting of bulk chondritic meteoritic material occurs at the Fe,Ni-FeS eutectic at 950°C (Kullerud, 1963). Even higher temperatures are probably necessary to facilitate large-scale differentiation (see further discussion in section 2.2).

Two potential heat sources contributed largely to melting in a planetesimal: radiogenic heating from short-lived radioisotopes  $^{26}\text{Al}$  and  $^{60}\text{Fe}$  (Fish et al., 1960; Huss et al., 2006; LaTourette and Wasserburg, 1998; Lee et al., 1976; Urey, 1955) and the gravitational energy of accretion. A

third potential source, electromagnetic induction heating (Sonnett and Colburn, 1968; Sonnett et al., 1968; Herbert et al., 1991), has received little attention recently, and relies on relatively unconstrained parameters. A better understanding of T Tauri star mass loss has rendered it less plausible as a dominant heat source (Ghosh et al., 2006) and it has not been included in recent thermal models.

### 1.1. Distribution and Effects of Initial Solar System Aluminum-26

Radioactive decay of the aluminum isotope  $^{26}\text{Al}$  into  $^{26}\text{Mg}$  is thought to be the primary heat source for planetesimals in the early history of the solar system. The idea was first postulated by Urey (1955), who suggested that short-lived radionuclides (SLRs) such as  $^{26}\text{Al}$  could have contributed more energy than the primary modern-day contributors to radiogenic heating,  $^{238}\text{U}$ ,  $^{232}\text{Th}$ , and  $^{40}\text{K}$ . Heating of a parent body is significantly affected by the initial isotopic abundance of  $^{26}\text{Al}$ . Much effort has therefore been expended in measuring meteoritic materials in an attempt to determine the distribution of  $^{26}\text{Al}$  in the planetary nebula and in planetesimals.

Most CAIs contained an initial  $^{26}\text{Al}/^{27}\text{Al}$  ratio near what has been called the “canonical” value,  $5.23 \pm 0.13 \times 10^{-5}$  (Jacobsen et al., 2008), derived from bulk CAI measurements in CV chondrites. However, the initial ratio of  $^{26}\text{Al}/^{27}\text{Al}$  in

individual CAIs is known to have varied from  $<2 \times 10^{-6}$  to  $5 \times 10^{-5}$  (Krot et al., 2012). For example, CH chondrites, which are among the most primitive identified, had an initial  $^{26}\text{Al}/^{27}\text{Al} < 5 \times 10^{-6}$  (Makide et al., 2009; Sahijpal and Goswami, 1998; Liu et al., 2009; Krot et al., 2008). Krot et al. (2012) comprehensively summarized variations in initial  $^{26}\text{Al}$  concentrations of CAIs between and within chondrite groups. Rather than a homogenous distribution of initial  $^{26}\text{Al}$  at the canonical ratio, meteoritic evidence implies that  $^{26}\text{Al}$  was unevenly distributed through the planetary disk.

Primitive materials with very low radiogenic content may have formed before injection of  $^{26}\text{Al}$  into the solar system (e.g., Makide et al., 2009; Liu et al., 2009; Krot et al., 2008), or they may have formed after  $^{26}\text{Al}$  mostly decayed (Krot et al., 2005; MacPherson et al., 1995). The isotopic ratio is too high to be explained by solar irradiation (Duprat and Tatischeff, 2007) and thus must have been exogenous to the solar system. The nature of the stellar source of SLRs is still unsettled, although massive star wind is a good candidate (Gounelle and Meynet, 2012). See further discussion in the chapter by Johansen et al. in this volume.

The radiogenic component may have been mixed into the nebula before the formation of a planetary disk, and the planetary disk may have partially homogenized the aluminum composition (Krot et al., 2012). Further homogenization of  $^{26}\text{Al}$  distribution may have occurred with radial mixing and accretion, effectively damping the range of compositions from the CAIs samples as they accreted into larger bodies. If this homogenization was not complete, then planetesimals would not be expected to have had identical  $^{26}\text{Al}$  compositions. Instead, the  $^{26}\text{Al}$  content of a given planetesimal would have depended upon both time and radial domain within the planetary disk of its accretion.

The range of  $^{26}\text{Al}$  content within CAIs is large enough to influence whether significant melting will occur. Kunihiro et al. (2004) found that there is insufficient radiogenic aluminum in CO and CV chondrites to cause more than minimal melting even with the help of radiogenic  $^{60}\text{Fe}$ . However, they assumed that these bodies accreted instantaneously after the age of the youngest chondrules (estimated to be  $\sim 2\text{--}3$  m.y. after CAI formation). In contrast, Elkins-Tanton et al. (2011) and Weiss and Elkins-Tanton (2013) found that the potentially older age of CV chondrules (the oldest being essentially as old as CAIs) means the CV body could have melted if it started to accrete before the age of the youngest chondrules (i.e., before  $\sim 1.5$  m.y. after CAI formation).

The canonical  $^{26}\text{Al}$  concentration yields an integrated energy output of around  $\epsilon_i = 6.7 \times 10^6 \text{ J kg}^{-1}$  (Moskovitz and Gaidos, 2011). If this energy were converted to heat all at once, it would suffice to raise temperatures by several thousand degrees and completely melt the host material. The energy output is derived by integrating over time the power from radiogenic decay

$$\epsilon_i = \int_0^\infty W \frac{m_{\text{Al}}}{m} \frac{^{26}\text{Al}}{^{27}\text{Al}} e^{-\lambda t} dt \quad (1)$$

where  $w$  is heat production for pure  $^{26}\text{Al}$  [ $\text{W kg}^{-1}$ ], given by  $w = \lambda E_0/m_0$ , where  $\lambda$  is the decay constant of  $^{26}\text{Al}$ ,  $m_0$  is the mass of a single isotope, and  $E_0$  is the energy produced by its decay;  $(m_{\text{Al}}/m)$  is the bulk elemental mass fraction of Al (approximately the same as solely for the isotope  $^{27}\text{Al}$ ); and  $(^{26}\text{Al}/^{27}\text{Al})$  is the isotopic ratio at CAI formation ( $t = 0$ ).

To obtain the energy output available for heating for accretion times after the time of first formation of solids in the solar system, the initial power is multiplied by  $e^{-\lambda t}$ , where  $t$  is the time from CAI formation to instantaneous accretion. By definition, half the integrated energy output is produced within the first half-life. Therefore, due to its short half-life [0.71 m.y. (Norris et al., 1983)], the effect of  $^{26}\text{Al}$  on planetary bodies strongly depends on the timeline of accretion. Radiogenic heating depends on the quantity of material, and therefore is proportional to the radius cubed of a body, while radiative heat loss depends on area, which grows as radius squared. Thus if the bulk of accretion occurred within a million years, the majority of radiogenic heat would have remained in the body; otherwise, it would have readily dissipated.

Given the chondritic abundance of  $^{26}\text{Al}$  shown in Table 1,  $^{26}\text{Al}$  decay provides sufficiently large amounts of heating that models agree that bodies that accreted to more than  $\sim 7\text{--}10$  km radius before  $\sim 1.5$  m.y. after the formation of CAIs likely contained sufficient  $^{26}\text{Al}$  to melt internally from radiogenic heating (Hevey and Sanders, 2006; Merk et al., 2002; Sahijpal et al., 2007; Urey, 1955). A summary of papers modeling the internal heating, melting, and differentiation of planetesimals is given in Table 2.

Another potentially important radiogenic element is  $^{60}\text{Fe}$ , but it has been difficult to constrain the initial  $^{60}\text{Fe}/^{56}\text{Fe}$  ratio because of the isotope's low abundance in CAIs. Until recently, it was estimated at initial  $^{60}\text{Fe}/^{56}\text{Fe} \sim 1 \times 10^{-6}$  (Tachibana et al., 2006; Dauphas et al., 2008; Mishra et al., 2010). However, recent studies have revised the value downward to  $\sim 1 \times 10^{-8}$  (Tang and Dauphas, 2012; Chen et al., 2013). With this reduced value, the integrated energy output from  $^{60}\text{Fe}$  would have been only  $1.2 \times 10^4 \text{ J kg}^{-1}$ , insignificant in comparison with  $^{26}\text{Al}$  output, although its half-life [2.4 m.y. (Rugel et al., 2009)] is several times longer.

Aluminum-26 and  $^{60}\text{Fe}$  behave differently in differentiating bodies. Because aluminum is lithophilic, the formation of a core results in an increased concentration of  $^{26}\text{Al}$  in the remainder of a planetesimal. While this does subject the mantle to slightly more heating and higher temperatures than would occur in an undifferentiated body, the concentration of radiogenic heating nearer the surface means that that energy reaches the surface more easily, cooling the planetesimal faster. Moskovitz and Gaidos (2011) also point out that silicate melt could form a crust that would be especially enriched in  $^{26}\text{Al}$ , further enhancing heat flow (see section 2.3 for further discussion). On the other hand, most  $^{60}\text{Fe}$  would proceed to the core and would be the only potentially significant radiogenic heat source of a metal planetesimal shard or stripped core (Moskovitz and Walker, 2011).

In summary,  $^{26}\text{Al}$ , with its relatively high concentration and short half life, would have been the main driving heat

TABLE 1. Primary short-lived radionuclides and their properties.

Variable	Isotope/Element	Value(s)	Units	Reference
Heat production from decay	$^{26}\text{Al}$	0.355	$\text{W kg}^{26}\text{Al}^{-1}$	<i>Castillo-Rogez et al. (2009)</i>
	$^{60}\text{Fe}$	0.044*		
Bulk content of CV chondrites	Al	1.8	wt. %	<i>Lodders and Fegley (1998)</i>
	Fe	24		
Initial isotopic ratio	$^{26}\text{Al}/^{27}\text{Al}$	$5.23 \times 10^{-5}$	—	<i>Jacobsen et al. (2008)</i> <i>Chen et al. (2013); Dauphas et al. (2008)</i>
	$^{60}\text{Fe}/^{50}\text{Fe}$	$1 \times 10^{-8}-1 \times 10^{-6}$		
Decay constant	$^{26}\text{Al}$	$3.0124 \times 10^{-14}$	$\text{s}^{-1}$	<i>Castillo-Rogez et al. (2009)</i> <i>Rugel et al. (2009)</i>
	$^{60}\text{Fe}$	$9.08 \times 10^{-15}$		

\*Derived given  $w = \lambda E/m$ , where  $w$  is heat production from decay,  $\lambda$  is the decay constant,  $m$  is the mass of a single isotope, and  $E$  is the energy produced by its decay.

TABLE 2. Chronological summary of selected published asteroid thermal evolution models.

Reference	Model
<i>Urey (1955)</i>	First feasibility calculation of $^{26}\text{Al}$ as an asteroid heat source
<i>Grimm (1985)</i>	Model of asteroid metamorphism with fragmentation and reassembly
<i>Grimm and McSween (1989)</i>	$^{26}\text{Al}$ heating model of ice-bearing planetesimals, to account for aqueous alteration in CC
<i>Haack et al. (1990)</i>	Thermal model of a differentiated asteroid based on decay of long-lived radionuclides
<i>Miyamoto (1991)</i>	$^{26}\text{Al}$ heating model to account for aqueous alteration in CC asteroids
<i>Grimm and McSween (1993)</i>	Explanation of inferred thermal stratification of the asteroid belt based on heliocentric accretion and $^{26}\text{Al}$ heating
<i>Bennett and McSween (1996)</i>	Updated $^{26}\text{Al}$ heating model for OC asteroids, using revised chronology and thermophysical properties
<i>Akridge et al. (1998)</i>	Model for $^{26}\text{Al}$ heating of OC asteroid [(6) Hebe] with a megaregolith
<i>Ghosh and McSween (1998)</i>	$^{26}\text{Al}$ heating model of HED parent body (4) Vesta
<i>Wilson et al. (1999)</i>	Overpressure and explosion resulting from heating CC asteroids
<i>Young et al. (1999)</i>	$^{26}\text{Al}$ heating model of CC asteroids with fluid flow, to explain O-isotopic fractionations
<i>Wilson and Keil (2000)</i>	Thermal effects of magma migration in (4) Vesta
<i>Ghosh et al. (2001)</i>	Effect of incremental accretion on inferred thermal distribution of asteroids in the main belt
<i>Merk et al. (2002)</i>	Effect of incremental accretion on internal melting
<i>Hevey and Sanders (2006)</i>	Incorporate silicate melt convection for 64-km body
<i>Sahijpal et al. (2007)</i>	Included $^{60}\text{Fe}$ heating and partitioning during differentiation
<i>Davison et al. (2010)</i>	Heating due to impacts of porous planetesimals
<i>Moskovitz and Gaidos (2011)</i>	Included removal of $^{26}\text{Al}$ in interior due to melt migration
<i>Šrámek et al. (2012)</i>	Compaction and differentiation in bodies 500 km with radius-dependent accretion rates
<i>Neumann et al. (2012)</i>	Compaction and differentiation in initially porous bodies 120 km
<i>Henke et al. (2012)</i>	Sintering in initially porous planetesimals
<i>Golabek et al. (2014)</i>	Three-dimensional finite-element model including parameterized melt convection for the acapulcoite-lodranite parent body

Extended from *McSween et al. (2002)*.

source for melting prior to  $\sim 2$  m.y. after CAIs (e.g., *Merk et al., 2002*), while  $^{60}\text{Fe}$ , with a longer half-life, might have supplied some critical late heating within the core if the first concentration estimates are accurate.

## 1.2. Effects of Accretion Characteristics and Body Size

Accretionary energy is the potential gravitational energy input released by assembling a body from materials initially at infinite distance

$$E = \int_0^R \frac{G M(r) dm}{r} \quad (2)$$

where  $E$  is accretionary gravitational potential energy [J],  $G$  is the gravitational constant,  $M(r)$  is the mass of the planet as a function of radius  $r$ , expressed as  $4/3\pi r^3 \rho$  [kg] where  $\rho$  is density, and  $dm$  can be expressed as  $4\pi r^2 \rho dr$ . This integration yields  $E = 16/15\pi^2 \rho^2 G R^5$ . For a planetesimal with a 10-km radius, total accretionary gravitational potential energy  $E$  is  $\sim 10^{17}$  J, and for a 300-km-radius body,  $\sim 10^{25}$  J (in comparison, for Earth  $E$  is  $\sim 2 \times 10^{32}$  J; for Mars,  $\sim 5 \times 10^{30}$  J; and for Mercury,  $\sim 2 \times 10^{30}$  J).

The addition of energy can be roughly translated to temperature increase using the expression  $\Delta T = E/MC_p$ , where  $C_p$ , the heat capacity, is  $\sim 800 \text{ J kg}^{-1} \text{ K}^{-1}$  for silicates (*Fabrichnaya, 1999*) and is only slightly higher for metallic core material (*Bartels and Grove, 1991*). The hypothetical

10-km-radius planetesimal would have been heated only a fraction of a degree if all accretionary energy were instantaneously applied homogeneously to the whole body, and the hypothetical body with 300-km radius would have been heated by only 10° to 20°C.

Due to radiogenic heating, these early accreting bodies would have melted from the interior outward, resulting in an interior magma ocean under a solid, conductive, undifferentiated shell (Ghosh and McSween, 1998; Hevey and Sanders, 2006; McCoy et al., 2006; Merk et al., 2002; Sahijpal et al., 2007; Schölling and Breuer, 2009). The size of the body therefore strongly impacted thermal evolution, since heat was being produced in the bulk interior and being radiated from the surface. Other critical controlling parameters are the rate of accretion, the initial  $^{26}\text{Al}$  ratio, the initial Al bulk composition, the material density and composition (which control both radiogenic content and heat transfer), and the rate of accretion.

The rate and timing of accretion are highly dependent on the assumed model of planetesimal accretion. In one scenario, sticking collisions between solid particles in the nebula may lead to steady incremental growth of the first planetesimals (Windmark et al., 2012). Alternatively, centimeter- to meter-sized objects may be concentrated by streaming instabilities or by turbulent eddies into 10- to >100-km-sized solid bodies on timescales of just tens to hundreds of years in the asteroid belt region (Cuzzi et al., 2008; Johansen et al., 2007; Morbidelli et al., 2009). For many bodies, this early collapse phase may have been followed by a subsequent period of incremental growth. Turbulent concentration is an inefficient process, owing to disruption of clumps by rotational breakup and ram pressure from the surrounding gas, such that bodies were likely produced sporadically over millions of years (Chambers, 2010). Each body would have collapsed quickly, but may have had further coatings added to their surfaces over the tail of accretion as the disk cleared out.

Despite this complexity, most models consider instantaneous accretion over a range of times starting with the age of CAIs. Recent numerical modeling incorporating the effects of prolonged accretion suggests that molten planetesimals can build up substantial (kilometers to tens of kilometers thick) crusts if they accrete to radii of at least a few tens of kilometers by 1.5 m.y. after CAI formation and continue to accrete over a minimum period of perhaps one to several million years (Sahijpal and Gupta, 2011; Elkins-Tanton et al., 2011; Šrámek et al., 2012; Neumann et al., 2012; Weiss and Elkins-Tanton, 2013).

### 1.3. Impact-Induced Metamorphism and Melting

Aside from their bulk contribution of accretionary energy, impacts also played a more direct role in metamorphism and melting on planetesimals, although current consensus assigns an uncertain but likely volumetrically minor effect (Keil et al., 1997; Šrámek et al., 2012).

The abundance of metamorphosed ordinary chondrites suggests global-scale metamorphism (e.g., Wood, 1962;

Van Schmus and Wood, 1967; Dodd, 1969). Wasson et al. (1987), Cameron et al. (1990), and Rubin (1995) argued for impact-induced heating as the most likely heat source. Keil et al. (1997) disfavored this hypothesis after determining, based on laboratory shock wave and cratering experiments and numerical models, that the cumulative global temperature increase due to impacts would be at most a few tens of degrees. However, Rubin and Jones (2003) and Rubin (2004) presented further evidence of impact heating in meteorites and argued for a major effect of porosity, which although mentioned, was not accounted for in numerical heating models. Most asteroids are believed to have porosities near 30%, although estimates for some range up to 70% (Britt et al., 2002); this would have been even higher in the early solar system before compaction processes (impacts included). Davison et al. (2010) accounted for porosity and found that collision of highly porous bodies could in some cases result in nearly global melting. However, they conclude that the cumulative effects of nondisruptive impacts for a typical planetesimal would be minor, with no more than 3% heated by more than 100°C. A final disruptive impact, on the other hand, would melt one-tenth of the parent body.

Ciesla et al. (2013) numerically modeled impacts on porous bodies that were already being heated by  $^{26}\text{Al}$ . They concluded that while local heating and metamorphism would occur near the site of the impact, impacts would actually accelerate global cooling of the planetesimal in two ways. First, hot material (primarily heated by  $^{26}\text{Al}$ ) from deep in the body would be drawn up toward the surface by the impact, leading to a faster cooling rate for this hot material and thus a larger net heat flow rate out of the body. Second, newly compacted material would have a higher thermal conductivity, further enabling heat flow from the body.

Evidence of shock events in meteorites (e.g., Scott et al., 1992; Sharp and de Carli, 2006) probably records impact events in the early solar system. However, the contribution of impacts to metamorphism and melting was probably low on a global scale. Subcatastrophic impacts may have even reduced the likelihood of melting by allowing internally heated material to cool more quickly.

## 2. PLANETESIMAL DIFFERENTIATION PROCESSES DURING HEATING

Based on our current knowledge of their physics and chemistry, planetesimals may have a range of internal structures and material states following peak heating, including an unmelted onion-skin structure, a partially differentiated body with some magma within and a primitive crust, a partially differentiated body with magma that erupted and flooded a primitive crust, and a body that melted entirely (Fig. 1).

Internal radiogenic heating coupled with radiation from the planetary surface means that a planetesimal would initially form an “onion shell” structure, with the highest temperatures reached in its center, surrounded by concentric zones of materials exposed to progressively lower peak temperatures (see McSween et al., 2002, and references therein).

Such a body, should it never reach a melting temperature, is considered primitive, but still could be highly altered from its original, unheated material. Its interior may be variably heated and metasomatized by mobile fluids, and these fluids may be unevenly redistributed within the body, or lost to space, or both. Furthermore, the bulk density of the body may change due to sintering and fluid migration.

Should the interior be heated to the point of melting, a further spectrum of potential planetesimal structures is possible. As temperature rises in a young planetesimal interior, the silicates will pass through the stability zones for several possible hydrated silicate minerals, but then a free hydrous fluid will be released. The first melting to occur will be eutectic melting of iron-nickel sulfide. This metal liquid may or may not be able to migrate downward and form a core without silicate melting.

If accretion is rapid and aluminum remains in the matrix [i.e., it is not all pulled away through buoyant melt migration, as in Moskovitz and Gaidos (2011)], then the planetesimal may be rapidly and completely melted and differentiated (e.g., Hevey and Sanders, 2006). Vesta itself may be such a body.

Other planetesimals may only undergo *partial differentiation*. In this scenario, the body differentiates internally

into a primarily metallic core and a bulk silicate mantle. A chondritic lid would either be retained from original material that never melted, or accreted onto the surface during and after the primary melting phase. Models indicate that in some cases this chondritic lid would be flooded with magma from the interior, while in other cases it would remain at the surface (Fu and Elkins-Tanton, 2014; Wilson and Keil, 2012). In either case, a partially differentiated planetesimal would be differentiated internally but retain chondritic material at or near the surface. Multiple meteorite types could therefore be sourced from the same parent body (Elkins-Tanton et al., 2011; Weiss and Elkins-Tanton, 2013; Golabek et al., 2014).

In the next three sections, we consider the behavior of volatile, metal, and silicate material, respectively, as they successively melt during the progressive heating of a planetesimal.

## 2.1. Flow and Escape of Volatile Compounds

For planetesimals accreting with a water ice component, progressive internal heating due to radiogenic decay results in ice melting once temperature surpasses approximately 0°C (Fig. 2). In such a scenario, the formation of liquid water may lead to mineralogical changes that are reflected in the observed

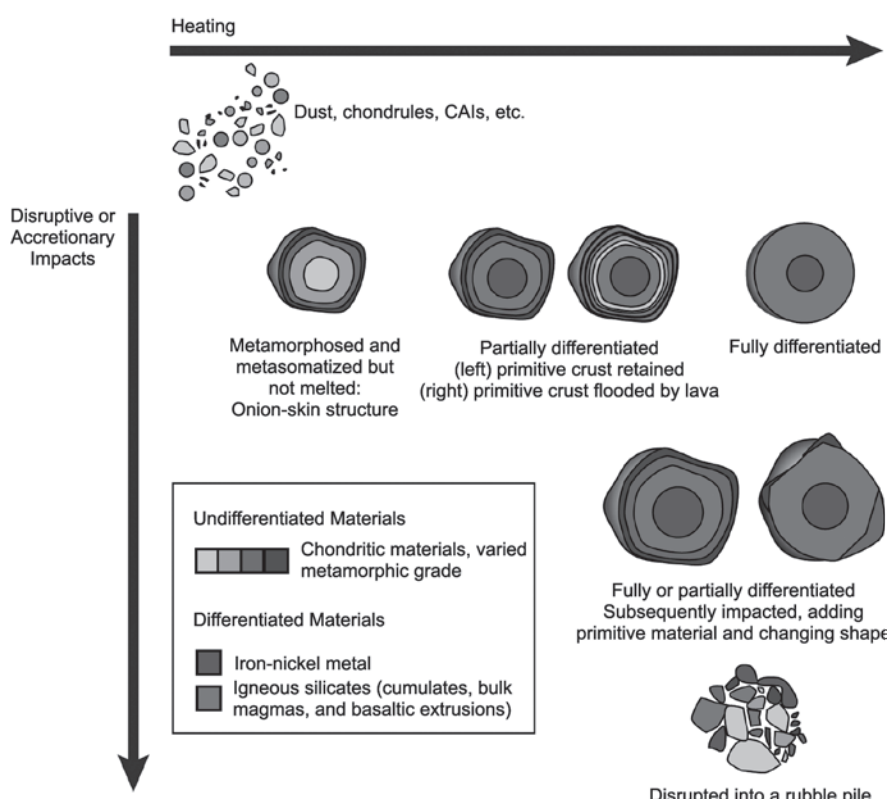


**Fig. 1.** See Plate 17 for color version. Three possible end-states of asteroid differentiation. *Left:* Unmelted but variably metamorphosed and aqueously altered body composed of chondritic materials. *Middle:* Partially differentiated body with melted interior and unmelted surface layer. *Right:* Fully differentiated body with metallic core and igneous silicate mantle. *Bottom:* Partially or fully differentiated bodies disrupted and coated by later impacts, disrupted even to the point of internal disorganization into a rubble pile.

elemental, isotopic, and modal compositions of meteorites and asteroids. Flow of interstitial water, if it occurred, may have also resulted in the transport of labile elements, altering the local bulk composition in affected regions of the planetesimal. Finally, the presence of water and other volatiles during the melting of the metallic and silicate components of the planetesimal may alter the migration patterns of the resulting melt.

Meteoritic observations indicate that most chondritic parent bodies indeed accreted with significant quantities of water (Brearley, 2006). Carbonaceous chondrites include abundant hydrated minerals in addition to free water. The total mass fraction of  $H_2O$  measured in highly altered CM and CI chondrites ranges between 0.09 and 0.17 (Jarosewich, 1990). Ordinary chondrites typically display lower  $H_2O$  abundances of <0.02. However, metamorphism above 200°–300°C leads to the dehydration of silicate phases and removal of  $H_2O$  in chondritic material (Akai, 1992; Meunow *et al.*, 1995). The high metamorphic grade of most ordinary chondrites, coupled with observations that mildly metamorphosed ordinary chondrites contain hydrated phases (Alexander *et al.*, 1989; Hutchison *et al.*, 1987), suggests that ordinary chondrite parent bodies accreted with significantly higher water content than presently observed, likely greater than 0.02 mass fraction. Metamorphism may also be responsible for the low water contents of dry carbonaceous chondrites. In a well-studied case, the Allende CV chondrite contains no water at the present time while displaying mineral assemblages that strongly imply the past presence of hydrated minerals during a period of fluid-assisted metamorphism (Brearley and Krot, 2012; Krot *et al.*, 1997, 1998). Spectroscopic observations of main-belt asteroids confirm the prevalence of hydrated mineralogies (Jones *et al.*, 1990; Rivkin *et al.*, 2002).

The hydration of originally anhydrous phases in chondritic planetesimals commenced shortly after internal heat-

ing led to the formation of liquid water. The oxygen and carbon isotopic composition of material from several CM chondrites shows that aqueous alteration occurred between 0° and 70°C (Clayton and Mayeda, 1984; Guo and Eiler, 2007; Lerner, 1995). Meanwhile, altered minerals in CR and CI chondrites likely formed in conditions of <130°C and 50°–150°C, respectively (Lee *et al.*, 1992; Zolensky *et al.*, 1989). Continued heating leads to the decomposition of alteration phases between 200° and 900°C (Akai, 1992; Meunow *et al.*, 1992, 1995). Even in the largest, Vesta-sized planetesimals, pressures in the deep interior are unable to stabilize hydrated minerals above ~950°C (Niida and Green, 1999). Therefore, progressive interior heating of differentiating planetesimals implies both a hydration and a dehydration phase — free water becomes bonded to secondary, hydrous silicates in the 0°–200°C range and are released again as a free fluid between 200° and 900°C.

The presence of free fluids inside internally heated planetesimals over a wide range of temperatures permits the redistribution of labile elements during fluid flow. For differentiating bodies undergoing progressive heating due to  $^{26}Al$ , the rapid rise in temperature implies that free fluids in most of the interior persist for a timescale of only 0.1–1 m.y. before the onset of metallic and silicate melting (Fu and Elkins-Tanton, 2014). The length scale of elemental redistribution during this time period depends on the velocity of fluid advection.

Fluid flow velocities in planetesimals may be modeled by balancing driving forces arising from gravitational and thermal sources with resistive forces arising from the low permeability of chondritic material. The density of liquid and supercritical water at the relevant pressures ranges between 900 kg m<sup>-3</sup> at 200°C and only 4.5 kg m<sup>-3</sup> at 900°C (Smits *et al.*, 1994). The large difference between these

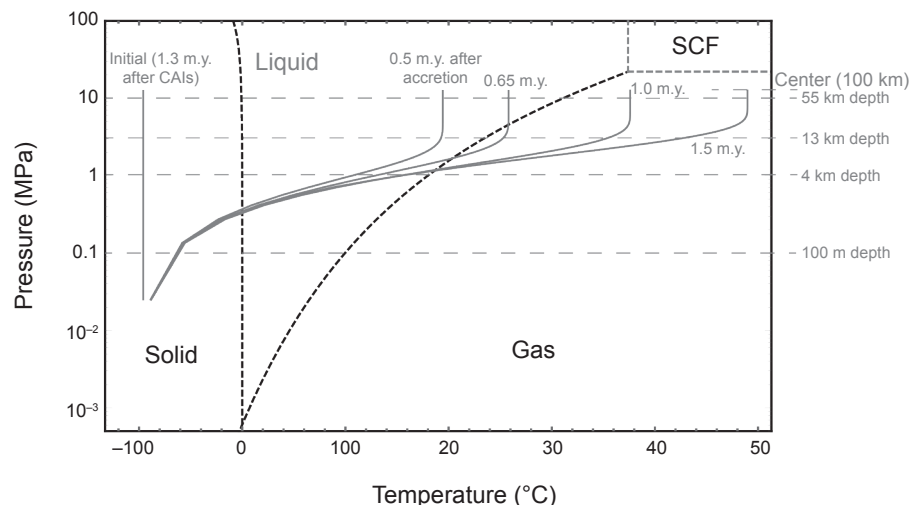


**Fig. 2.** The evolving temperature profile of an early forming, 200-km-diameter planetesimal internally heated by the decay of  $^{26}Al$ . Temperatures in the body interior are compared to the phase diagram of pure  $H_2O$ . Note the formation of gas phase at ~10 km depth during progressive heating. SCF = supercritical fluid.

densities and those of the surrounding chondrite matrix [2100–3700 kg m<sup>-3</sup> (*Britt and Consolmagno*, 2003)] is one potentially significant driving force, especially after heating above the 374°C critical point of water. The velocity ( $v_D$ ) of such density-induced Darcy flow is given by (*Bear*, 1972)

$$v_D = \frac{kg\Delta\rho}{\eta\phi} \quad (3)$$

where  $k$  is the rock permeability,  $g$  is the gravitational acceleration,  $\Delta\rho$  is the difference in density between the fluid and rock,  $\eta$  is the dynamic viscosity, and  $\phi$  is the dimensionless volumetric porosity. For a permeability of 10<sup>-15</sup> m<sup>2</sup> corresponding to permeable carbonaceous and ordinary chondrites [see discussion below and *Corrigan et al.* (1997) and *Sugiura et al.* (1984)], a dynamic viscosity of 5 × 10<sup>-5</sup> Pa s (*Sengers and Kamgar-Parsi*, 1984), and a dimensionless porosity of 0.1, fluid is expected to migrate at rates of ~1 m yr<sup>-1</sup> (*Fu and Elkins-Tanton*, 2014), implying that whole-body fluid flow can occur within the time span of radiogenic heating. Assuming a body radius on the order of 100 km, permeabilities as low as 10<sup>-16</sup> m<sup>2</sup> would permit the migration of fluids from the deep interior to the surface on 1-m.y. timescales. Migration driven by this mechanism is expected to result in a single pass of fluids from the deep interior to the surface, which has been termed *exhalation flow*. The buoyant fluid may freeze in any conductive lid, after metasomatizing some regions, or it may be lost to space (*Young et al.*, 2003).

In contrast, multiple pass flow of pore fluid due to thermal convection may result from the large vertical temperature gradient in early forming planetesimals. After deriving the convective stability criterion for fluids in an internally heated, radially symmetric body with an equilibrium conductive temperature gradient, *Young et al.* (2003) concluded that, assuming permeabilities of 10<sup>-13</sup> m<sup>2</sup> (*Grimm and McSween*, 1989), fluids in bodies larger than 120 km diameter would undergo convection.

A major uncertainty in the above fluid transport models is the permeability of chondritic material. Direct measurements on unfractured chondrites have yielded a wide range of permeabilities between 10<sup>-15</sup> and <10<sup>-21</sup> m<sup>2</sup>, with most measured carbonaceous and ordinary chondrites falling in a range between 0.01 and 2 × 10<sup>-15</sup> (*Corrigan et al.*, 1997; *Sugiura et al.*, 1984). The extreme value of <10<sup>-21</sup> m<sup>2</sup> was obtained from an enstatite chondrite, suggesting that systematic variations in permeability exist between chondrite groups. Models and arguments based on terrestrial analogs have estimated chondritic permeabilities between 10<sup>-11</sup> m<sup>2</sup> (*Grimm and McSween*, 1989) and 10<sup>-19</sup> m<sup>2</sup> (*Bland et al.*, 2009). These estimates represent lower bounds on the permeability of bulk material, as fractures may increase the effective permeability by 2 to 9 orders of magnitude (*Brace*, 1980; *Trimmer et al.*, 1980). Furthermore, increasing the relevant length scale from hand sample to kilometers may augment permeability by another factor of 10<sup>3</sup> (*Clauser*, 1992). Observations of chondrite samples reveal a high degree of fracturing and brecciation while the production of gas and supercritical

fluids can overcome the tensile strength of chondritic material and lead to fracturing in the deep interior (Fig. 2) (*Grimm and McSween*, 1989; *Young et al.*, 2003). Fractures therefore likely had a significant effect on the permeability of strongly heated planetesimals. Integrating these constraints, for fractured carbonaceous and ordinary chondrite material at the global scale, most permeabilities were likely greater than 10<sup>-14</sup> m<sup>2</sup>, while enstatite chondrite materials may have had permeabilities <10<sup>-16</sup> m<sup>2</sup>, depending on the effect of fractures. The permeabilities for carbonaceous and ordinary chondrites were likely sufficient to permit the planetesimal-scale ascent of fluids (*Fu and Elkins-Tanton*, 2014). In contrast, in the case of parent bodies with low permeabilities of <10<sup>-16</sup> m<sup>2</sup>, fluid-facilitated elemental redistribution may have occurred on only the <100-μm scale (*Bland et al.*, 2009).

The large observed spread in oxygen isotopic composition in the altered components of carbonaceous chondrites provide meteoritic evidence in favor of large-scale fluid migration (*Young*, 2001; *Young et al.*, 1999). The expected heterogeneity in a small volume of water trapped in pore space appears insufficient to explain the isotopic variation, while open-system fluid flow down a temperature gradient is capable of reproducing the measured oxygen isotopes. On the other hand, the essentially solar abundance of elements in CI chondrites (*Lodders*, 2003) and the depletions of volatile elements in other chondrites (*Kallemeyn and Wasson*, 1981) have been cited as evidence against open-system behavior of planetesimal fluids (*Bland et al.*, 2009). However, because most volatile elements are also the most labile, the depletion patterns in carbonaceous chondrites have also been interpreted to be a consequence of open-system fluid flow (*Matza and Lipschutz*, 1977; *Young et al.*, 2003).

To summarize, abundant meteoritic and spectroscopic evidence shows that early forming planetesimals accreted with a significant budget of H<sub>2</sub>O and other volatiles. Progressive heating of differentiating planetesimals above ~200°C generated free fluids in the liquid, gas, and supercritical phases. For probable values of permeability in fractured carbonaceous and ordinary chondrite parent bodies, heated fluids were likely able to participate in single-pass exhalation flow and multiple-pass thermal convection in regions with a high temperature gradient. Depending on the degree of fracturing, enstatite chondrite parent bodies may have insufficient permeability to permit large-scale fluid flow.

## 2.2. Metal Fluid Flow and Core Formation

In order to form a core, the dense melted metal must be able to drain to the body's center and displace the lighter silicate material present there. Although melting of core-forming material likely began when temperatures reached the Fe,Ni-FeS eutectic at 950°C (*Kullerud*, 1963), the core-formation process was complicated by the necessity of pore connectivity, slow adjustment of the silicate matrix, and the presence of volatiles.

The threshold for connectivity of molten Fe-S in an olivine matrix has been estimated as low as 3–6% melt (*Yoshino*

*et al.*, 2003, 2004) but as high as 17.5% (*Bagdassarov et al.*, 2009). An even smaller percent melt is needed when the dihedral angle between the molten metal and solid silicate is less than a critical value of 60°. *Terasaki et al.* (2008) found dihedral angles below 60° for pressures of 2–3 GPa, depending on the liquid's oxygen content. The volume fraction of metal in primitive chondrites typically varies from a few percent to <20% (*Scott et al.*, 1996a), while Earth's metal core is about 15% of its volume. Silicate melting was thus probably unnecessary to reach the connectivity threshold for most planetesimals.

Additionally, the silicate material must have a sufficiently low viscosity that it can be deformed and displaced. If this process is inefficient, then significant differentiation could occur only after partial or complete melting of the silicate, which would occur between the solidus and liquidus temperatures, around 1100°C and 1500°C respectively for planetary silicates (*McKenzie and Bickle*, 1988; *Agee*, 1997). An experimental study by *McCoy et al.* (1999) concluded that significant (~50%) silicate melting, reached at ~1450°C, is necessary to initiate migration of metallic melt in an enstatite chondrite.

However, *Šrámek et al.* (2012) noted that percolation through a solid silicate matrix would proceed on a timescale inversely proportional to length scale and thus would not be observable in a laboratory setting, where length scale is on the order of 1 cm rather than 100 km. The timescale is also inversely proportional to gravity, which scales with radius in a homogenous body. The larger the body, the more quickly this process could occur. This would only be one factor that makes a larger body differentiate faster; more directly, a larger body would reach higher interior temperatures and thus partially melt more readily.

Finally, as discussed in the previous section, volatile elements were likely still present at this stage of heating either as free fluids or as hydrous silicate phases (*Fu and Elkins-Tanton*, 2014). The resulting oxygen fugacity may result in oxidized iron, which could then only be reduced to a metal and flow to form a core after further heating and removal of oxidizing agents through fluid migration. Thus the presence of volatiles may delay metal melting and lead to an overall reduction in melt available for core formation.

*Ghosh and McSween* (1998) modeled differentiation of the asteroid (4) Vesta (mean radius 263 km) and determined core formation was not possible if accretion (assumed instantaneous) occurred later than 3 m.y. after CAI formation, and that core formation would occur effectively instantaneously at around 4.6 m.y.

*Šrámek et al.* (2012) modeled the liquid percolation and silicate compaction process for a body heated by  $^{26}\text{Al}$  decay and impacts and assumed accretion occurred gradually rather than instantaneously. They considered a multi-phase model tracking metal and silicate material in both solid and liquid form and found that partial melting of silicate is necessary for compaction of the remaining silicate to occur on the planetesimal timescale. They conclude that due to the similar timescales of accretion and radiogenic heating, diverse outcomes are possible depending on size and accretion rate.

Bodies with radii of 500–1000 km, if accreted steadily over the first 3 m.y. of solar system history, could have retained enough heat to segregate about half of its metal component, although only half of that (about a quarter of the total metal content) would have formed a core. On the other hand, accretion within 1 m.y. of a 1500-km body would have easily produced a large core. Even a body of this size would not have been able to form a core if accretion were extended over 5 m.y. (about seven  $^{26}\text{Al}$  half-lives).

*Neumann et al.* (2012) considered differentiation of planetesimals with radii smaller than 120 km. Their model included heat loss due to transport toward the surface by silicate melt and found this process would diminish planetesimal heating by tens to 100 K. They found that the core-formation process would have lasted for 2–10 m.y., but that core formation would only be likely if the bulk of accretion occurred within 3.5 m.y. of CAI formation. Porosity played a large role, with the maximum reachable temperature much higher for porous bodies than for comparable consolidated ones. This was especially true for small bodies.

Another scenario for core formation involves the accretion of already differentiated iron-nickel. This would occur when a separate differentiated body or a fragment of one impacted the planetesimal. In this case, the metal could descend as a diapir due to its gravitational instability (e.g., *Stevenson*, 1981; *King and Olson*, 2011). Of course, this can only occur if diffusion through silicate melting or metal melt percolation, as described as above, occurred to differentiate the earlier body. Since the magnitude of the gravitational instability is proportional to gravity and thus radius, it is more likely to occur on larger, planet-sized bodies than on small, early bodies.

### 2.3. Silicate Transport Effects on Core Formation

An important recent direction in planetesimal modeling involves the role of silicate melt transport in the time evolution of a planetesimal's thermal profile. As the silicate portion begins to melt, this melt may rise buoyantly and depart its source region. *Moskovitz and Gaidos* (2011) argue that because aluminum is preferentially partitioned into the melt phase, the melting source will immediately be depleted in the  $^{26}\text{Al}$  heat source, and melting will cease. The rising, ponding melt, however, will heat up even more vigorously due to its concentrated aluminum content. Migration and concentration of  $^{26}\text{Al}$  into a crust results in remelting of that crust for accretion times less than 2 m.y. and for bodies >100 km in size.

They also find that subsequent heating from the decay of  $^{60}\text{Fe}$  generates melt fractions in excess of 50%, thus completing differentiation for bodies that accreted within 2 m.y. of CAI formation. However, as discussed in section 1.1, these results are based on the larger  $^{60}\text{Fe}$  abundance estimates available in the literature at that time but later revised downward by nearly 2 orders of magnitude: This component of heating is probably overestimated.

The *Moskovitz and Gaidos* (2011) result differs slightly from one-dimensional models, in that they find differentiation would be most likely for planetesimals with radii larger

than 10 km that accreted within approximately 2.7 m.y. of CAI formation; the inclusion of  $^{60}\text{Fe}$  lengthens the possible time of differentiation from its former  $\sim 1.7\text{--}2$  m.y. after CAIs (Hevey and Sanders, 2006; Elkins-Tanton et al., 2011). Neumann et al. (2014) pursued a similar scheme in which  $^{26}\text{Al}$  is partitioned heavily into the melt phase. In a model for Vesta, a magma ocean 1 km to a few tens of kilometers in thickness forms in the near subsurface, as long as accretion occurred before 1.5 m.y. after CAIs. The magma ocean lasts 10,000–1,000,000 yr, and a basaltic crust is extruded onto the surface. Core formation is complete within  $\sim 0.3$  m.y., and silicate melt is present in the mantle for up to 150 m.y.

Both aluminum sequestration, as investigated by Moskovitz and Gaidos (2011) and Neumann et al. (2014), and the formation of an early basaltic crust rely on relatively efficient melt migration within these small bodies. Moskovitz and Gaidos (2011) point out that melt-migration rates are independent of planetesimal size, since the lower gravity of smaller planetesimals is offset by the shorter distances the melt needs to migrate. Migration on any planetesimal, however, requires that the melt be buoyant with respect to its country rock. In the following section we discuss the buoyancy of melt in putative parent bodies.

#### 2.4. Silicate Melting and Magma Migration

As temperatures continue to climb after the first eutectic melting of Fe,Ni-FeS-rich fluids at 950°C, the first silicate melts appear at 1050°–1150°C while complete melting occurs by 1500°C (Agee, 1997; Agee et al., 1995; McCoy et al., 2006). The potential upward migration of these silicate melts may strongly influence the observable surface composition of the body, the style and rate of heat loss (Neumann et al., 2012), the distribution of heat-producing isotopes (Moskovitz and Gaidos, 2011; Neumann et al., 2014), the loss of silicate material to space, and the preservation of the primitive chondritic crust.

The direction and rate of silicate melt migration depends on the buoyancy of the magma relative to the overlying unmolten chondritic lid. The abundance of volatiles is an important control on buoyancy as their presence during silicate melting may lead to exsolution, which would dramatically lower the bulk density of the resulting magma. As discussed in section 2.1, high-temperature fluids on both carbonaceous and ordinary chondrite parent bodies were likely able to ascend efficiently from the deep interior before the onset of silicate melting.

In addition to water, other volatiles, principally CO, CO<sub>2</sub>, N<sub>2</sub>, and Cl, may have been present in sufficient quantities in chondritic protoliths to potentially affect the density of silicate melts. However, among these volatiles, only CO and Cl are retained in the protolith up to  $\sim 1250^\circ\text{C}$ , which is the temperature necessary for efficient silicate melt migration (McCoy et al., 1997; Meunow et al., 1992, 1995). Carbon monoxide is likely present in insufficient quantities (<100 ppm) during silicate melt migration to affect melt densities, except in cases where it is produced by the C-FeO smelting reaction (McCoy et al., 1997; Wilson et al., 2008).

Meanwhile, the residual Cl content of chondrites at 1250°C is likely soluble in silicate magmas at low pressures and would therefore not strongly decrease the magma density via exsolution (Fu and Elkins-Tanton, 2014; Webster, 1997).

Volatile-depleted (dry) melts of ordinary chondrites have model densities similar to those of an overlying fractured lid built from ordinary chondrites. Dry partial melts of carbonaceous and enstatite chondrites are likely denser and lighter, respectively, than a fractured lid with the corresponding composition (Fig. 3) (Fu and Elkins-Tanton, 2014; Jurewicz et al., 1993, 1995; McCoy et al., 1999). For parent bodies of CV chondrite composition, which are relevant to the paleomagnetic constraints discussed later in section 4.2, an unsintered, fractured crust would have a density between  $\sim 2600$  and  $2900 \text{ kg m}^{-3}$ , whereas the density of molten CV chondrite over a range of temperatures and pressures is between  $\sim 2800$  and  $2900 \text{ kg m}^{-3}$ . Therefore, if melts remain volatile poor, silicate magma produced at depth in planetesimals with carbonaceous chondrite compositions are expected to remain in the interior while similar melts on enstatite chondrite parent bodies likely ascend to the surface. Ordinary chondrite parent bodies represent an intermediate case where the fate of silicate magmas depends on the macroporosity of the overlying lid.

Some chondritic parent bodies may retain sufficient volatiles to result in exsolution-driven melt ascent. In the case of enstatite chondrite parent bodies, low bulk permeability may lead to the retention of H<sub>2</sub>O at depth (see section 2.1).

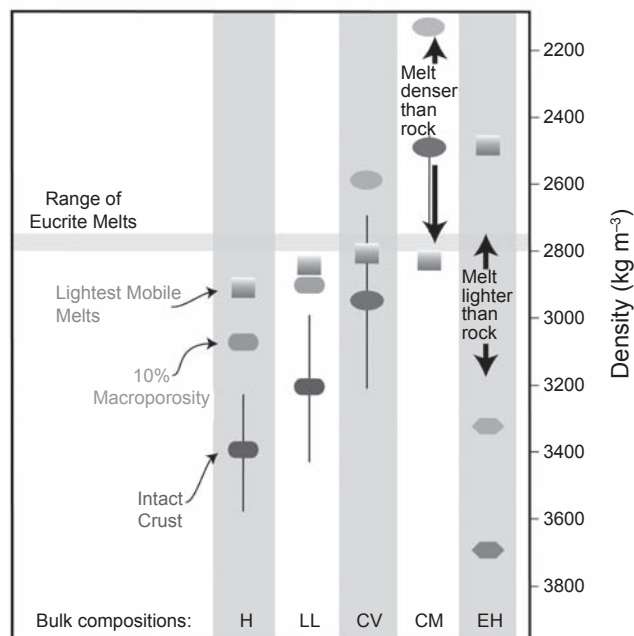


**Fig. 3.** Comparison of the densities of mobile silicate melts and unmolten chondritic material for five meteorite groups. Intact crust densities and uncertainties represent the measured densities of chondrite hand samples, while the values with 10% macroporosity approximate the bulk densities of fractured chondritic lids. Reproduced from Fu and Elkins-Tanton (2014, *EPSL*) with permission of Elsevier.

Likewise, carbonaceous and ordinary chondrite parent bodies with low intrinsic permeability, low degree of fracturing, or high initial volatile contents may have generated sufficiently volatile-rich melts to undergo buoyant ascent.

In such scenarios, magmas forming inside planetesimals may be expected to erupt with force, driven by expanding volatiles (Muenow *et al.*, 1992, 1995; Wilson and Keil, 2012). Melt extraction from the partially molten interior likely occurred in two stages (Wilson *et al.*, 2008; Wilson and Keil, 2012). First, magma would have ascended in dikes, but flow rates were likely insufficient to sustain continuous eruption from the melting region directly to the surface. This was especially the case for parent bodies smaller than ~400 km in diameter. The ascending melt therefore collected in sills within the chondritic lid. Second, the melt in these magma chambers, especially if it was volatile rich, would have explosively erupted onto the surface, propelling silicate fragments up to 1 m in size beyond the escape velocity of small (<100-km-diameter) asteroids (Wilson and Keil, 1991; Wilson *et al.*, 2010). On larger bodies with stronger gravity, most erupting melt may have been retained on the surface in melt ponds that, with sufficient accumulation, led to the subsidence and destruction of the primitive chondritic lid (Wilson and Keil, 1997, 2012).

Ghosh and McSween (1998) describe an end-member model for Vesta in which all melt from the interior erupts onto the surface and another end-member model in which no melt extrudes; their efforts demonstrate the difficulty of arguing completely for one or another eruptive scenario.

In summary, the potential of silicate melts to ascend from the melting region depends critically on the persistence of volatiles at supersolidus temperatures and on the parent body's bulk composition. Volatile-rich melts, which may have formed on bodies with very low fluid permeabilities such as enstatite chondrite parent bodies, are expected to rise efficiently to the surface, potentially resulting in the inundation of the chondritic lid and ejection of mass from the parent body. The discovery of possible pyroclasts of aubritic composition such as Larkman Nunatak (LAR) 04316, which may be sourced from an enstatite-chondrite-like protolith, supports the hypothesis that enstatite chondrite parent bodies retained sufficient volatiles to drive magma ascent (Keil, 2010; Keil *et al.*, 2011). For differentiated planetesimals with carbonaceous and ordinary chondrite compositions, efficient release and upward transport of volatiles before the onset of silicate melt migration likely resulted in negatively buoyant melts that permitted the preservation of the primitive chondritic lid on these bodies.

### 3. COOLING AND SOLIDIFICATION OF PLANETESIMALS

#### 3.1. Solidification of a Partially Molten Silicate Mantle

The physical process of magma solidification influences the range of both composition and texture that will occur in

the mantle and possible crust of a planetesimal. The compositional process of solidification can be viewed as having two end members: fractional solidification and batch solidification (e.g., Solomatov, 2000). For fractional solidification to occur, mineral grains must settle from flow and be effectively removed from communication with the remaining magma ocean liquids. The residual liquid composition thus evolves with the progressive removal of solidified material. In batch solidification, liquid contact and equilibrium are maintained throughout solidification. A fractional solidification model of a magma ocean therefore predicts mineral assemblages, cumulate bulk composition, and cumulate trace-element compositions that are completely different from those occurring in equilibrium solidification.

Due to their relatively small masses, planetesimals have internal pressures so low that, once melted, the bottom of a planetesimal's magma ocean has effectively the same pressure as the top. The high-pressure gradient in planets the size of Earth likely encourages fractional solidification as cool downwellings from the surface develop crystallinity with depth and deposit crystals at the bottom boundary. Without significant pressure or gravity, magma oceans on planetesimals may not fractionally solidify. Over the ~0.5-kbar mantle pressure range of a planetesimal ~200 km in radius, the solidus will change by only about 10°C, and the adiabat by only ~2°C. As it cools, therefore, the entire depth of the magma ocean will contain some crystal fraction. The magma ocean will have a high effective viscosity, perhaps in the range of hundreds to thousands of Pascal seconds. Combined with the high heat flux of a small body cooling without an atmosphere, mineral grains would have to be large, perhaps several to 10 cm, to settle from the magma ocean. Thus, in the time before crystallinity rises, only the earliest-forming crystals will settle (Suckale *et al.*, 2012). Given almost any of the candidates for bulk-chondritic silicate compositions and the low pressures in planetesimals, olivine alone would be the first material to crystallize. The rest of the planetesimal's mantle will solidify in bulk and never produce an olivine cumulate. This may be why we have no such samples in our collections.

Despite the lack of meteoritic olivine cumulate samples, olivine is by far the predominant silicate represented in the stony-iron meteorite group known as pallasites. Apart from olivine and metal, main-group pallasites contain <1 vol.% each of chromite, pyroxene, and phosphates (Buseck, 1977; Ulff-Møller *et al.*, 1998). Pallasites are usually thought to be samples of a core-mantle boundary (e.g., Mittlefehldt *et al.*, 1998; Benedix *et al.*, 2014), although Tarduno *et al.* (2012) argue instead that pallasites are the result of an impact that injected iron from the impactor's core into a planetesimal mantle. Assuming they are samples of a core-mantle boundary, the simplicity of the mineral assemblages in pallasites and iron meteorites strongly supports successful crystal settling of olivine alone at the beginning of magma ocean solidification in an internally differentiated planetesimal. Later solidification would occur in bulk, and thus planetesimal magma oceans will not produce olivine + pyroxene cumulate,

as predicted for the Moon, but would produce melt extraction from mushes consistent with observations from Vesta.

The slowness of magma movement and the inefficiency of mixing on planetesimals not only makes the formation of olivine cumulates unlikely, it predicts that planetesimals' mantles and crusts may well be inhomogeneous. The accreting material is not likely to be compositionally homogeneous, and it may not efficiently melt and mix. This prediction is supported by the findings of Kleine et al. (2012), who find that four texturally and temporally resolved groups of angrites can be identified that were derived from at least two distinct mantle sources. These mantle sources are the result of separate events of core formation, both of which took place within ~2 m.y. of CAI formation. Thus, core formation in the angrite parent body did not occur as a single event of metal segregation from a global magma ocean, but rather took place under varying conditions by several more local events. The disparate Hf-W systematics of the two distinct angrite source regions indicate that convection in the magma ocean was inefficient in homogenizing the composition of the mantle, possibly as a result of a continuous bombardment with small planetesimals during ongoing core formation. Furthermore, they find that mantle differentiation occurred at ~3.6 m.y. after CAI formation, in line with cooling models following early  $^{26}\text{Al}$  melting in the parent body.

In summary, the taxonomy of possible internal structures is not limited to the processes of melting. Mantle heterogeneities caused by a small extent of olivine settling followed by batch solidification, as well as complications from melt percolation and mixing caused by continued accretion, probably also influenced planetesimal structure. The surface of the body may experience ongoing accretion of primitive material while the partially or wholly molten interior continues to cool and differentiate. Finally, later impacts may partially strip the body and then allow blocks of material to fall back onto the surface, or may even break the body into pieces and produce a rubble pile.

### 3.2. Solidification of a Planetesimal Core

Metallic cores would have initially been entirely molten. The temperature at which core crystallization began depends on its composition, in particular, its sulfur content. The liquidus in an Fe-FeS system decreases from 1538°C for pure Fe to 988°C at its eutectic composition (~31 wt.% S), at which point FeS begins to crystallize as well (Kullerud and Yoder, 1959). In some parent cores, sulfur content as high as 17 wt. % has been inferred (Chabot, 2004). Iron sulfide is far less abundant in the meteorite collection than predicted by models, although this may be explained by the mineral's low strength (Kracher and Wasson, 1982; Chabot and Drake, 2000).

Although batch solidification might be expected given the shallow pressure gradient and low gravity, concentration trends of various minor and trace elements (e.g., Ni, Au, Ga, Ge, O, P, Ir) in iron meteorite groups demonstrate that their initially molten parent cores underwent fractional crystal-

lization. However, scatter in these element trends indicate that at some point the assumption of a well-mixed liquid broke down (Haack and Scott, 1992, 1993; Pernicka and Wasson, 1987; Scott et al., 1996b; Wasson, 1999; Wasson and Richardson, 2001; Benedix et al., 2014).

On large planets, high-pressure gradients result in the adiabatic gradient intersecting the solidus at the body's center, causing solidification to first occur at the body's center and produce a solid, growing inner core. For pressures lower than ~4 GPa, the core-mantle boundary would be the first location to reach the liquidus during cooling (Williams, 2009). However, due to the low-pressure gradient in a planetesimal, both the adiabatic gradient and the pressure-induced solidus change in a well-mixed core were very small, with perhaps a ~1°C increase from the core-mantle boundary to the center for an asteroid with a 100-km radius. Because this variation in liquidus is so small, particularly compared to sulfur effects, it is difficult to predict how solidification would have proceeded. Chabot and Haack (2006) and Goldstein et al. (2009) provide recent reviews of the scenarios and supporting evidence.

Four possible core solidification scenarios are (1) outward concentric crystallization (similar to Earth), (2) inward concentric crystallization, (3) inward dendritic growth, and (4) cumulate solid inner-core formation (Fig. 4). None of these scenarios can be decisively confirmed or rejected on the basis of current observation and evidence.

Sulfur is almost fully excluded from crystallizing iron (Willis and Goldstein, 1982). Since increasing sulfur content lowers the melting temperature, a solidification front is inhibited as local sulfur content becomes too high to efficiently diffuse. This likely results in dendritic growth inward from the core-mantle boundary as cooling and solidification continue (Haack and Scott, 1992). Although kilometer-sized dendrites have been proposed (Narayan and Goldstein, 1982), the dendrites could be gravitationally unstable and descend to form a cumulate inner core. On the other hand, if sulfur accumulates near the core-mantle boundary due to its low density and effectively inhibits crystal growth there, solidification would then occur throughout the core in the form of iron snow. While this has not been discussed in a planetesimal context, iron snow has recently been discussed in the context of the small lunar (e.g., Laneuville et al., 2014) and Ganymede (e.g., Christensen, 2015) cores.

These different core scenarios would result in different configurations in modern-day asteroid cores (Fig. 4). An inward-crystallizing concentric solidification front would have the bulk of its late-stage solids (e.g., troilite), which would have formed upon eventually reaching a eutectic Fe-S composition, sequestered in the body's inner core. A dendritic inward-crystallization scenario would show a complicated network of dendrite growth interspersed with light-element-rich pockets. A core that crystallized from the inside out would have an outer core rich in late stage solids. Outward growth through snow or dendritic collapse would have a similar configuration, although inefficient compaction could result in pockets similar to the inward-dendritic-growth scenario.

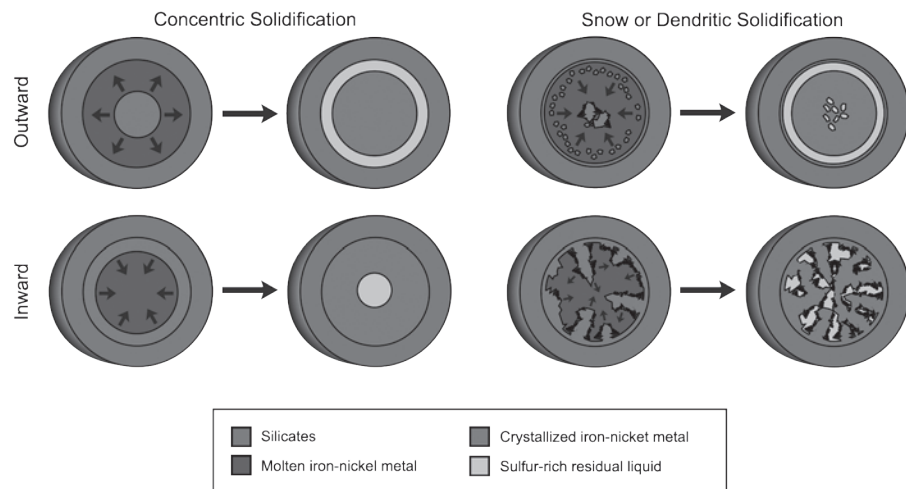


**Fig. 4.** See Plate 18 for color version. Four possible core solidification scenarios and potentially resulting end-states. *Top left:* Outward (Earth-like) solidification. *Bottom left:* Concentric inward solidification. *Top right:* Outward solid core growth due to accumulated iron “snow” and/or destabilized dendrites. *Bottom right:* Dendritic inward solidification.

#### 4. ASTEROID AND METEORITE RECORDS OF THE DIFFERENTIATION PROCESSES

We have a diversity of geochemical and geophysical constraints on the compositions of asteroid surfaces and interiors. Collectively, these datasets provide evidence for surface compositions ranging from apparently chondritic bodies to fully differentiated bodies and possibly also including partially differentiated bodies. Here we review evidence for asteroidal cores from asteroidal shapes, and then discuss two relatively recently acquired datasets that constrain asteroidal differentiation and large-scale interior structures: studies of the remanent magnetization of meteorites, and *in situ* magnetic field observations of asteroids. These observations detect asteroid remanent magnetization, which in turn likely point to a convecting metal core capable of dynamo action in early solar system history.

##### 4.1. Asteroidal Shape and Core Detection

Absorption and emission spectra acquired in wavelengths from the ultraviolet to the far-infrared constrain the mineralogical and elemental composition of the surface layers of asteroids (see the chapters by DeMeo et al., Masiero et al., Reddy et al., and Vernazza et al. in this volume). Albedo and polarimetry data also provide indirect constraints on surface-layer mineralogy. Radar data constrain the bulk density of the surface layer (see the chapters by Benner et al., Delbo et al., Margot et al., and Scheeres et al. in this volume). Gravity data acquired either from spacecraft encounters, binary asteroid orbits, or perturbations to the orbits of more distant bodies constrain asteroid masses (see the chapter by

Scheeres et al. in this volume). When combined with shape data obtained from resolved images and/or joint infrared and optical photometry, the bulk asteroid density and sometimes the interior mass distribution can be constrained (see the chapter by Russell et al. in this volume). For example, the high surface density (ranging up to  $\sim 6 \text{ kg m}^{-3}$ ) of several M-type asteroids strongly suggests they are largely metallic bodies (Shepard et al., 2010), probably derived from early differentiated planetesimals whose silicate mantles were catastrophically removed by a collision (Asphaug, 2010).

Spacecraft-based geophysical observations of main-belt asteroids provides evidence for differentiated internal structure. One such example is the asteroid (21) Lutetia, whose high density strongly suggests that its deep interior underwent substantial heating and sintering. Because its surface spectral properties are most similar to those of carbonaceous or enstatite chondrites (Coradini et al., 2011; Vernazza et al., 2011), Lutetia may represent the first known partially differentiated asteroid (Weiss et al., 2012). Formisano et al. (2013) find that partial differentiation is likely in scenarios in which Lutetia completed its accretion in less than 0.7 m.y. from the injection of  $^{26}\text{Al}$  in the solar nebula and for post-sintering values of macroporosity not exceeding 30 vol.%.

There is indirect evidence for a metallic core in asteroid (4) Vesta from the oblateness of its gravity field and its bulk density (Russell et al., 2012). At the same time, observation of asteroid shape can offer further constraints on the degree of interior melting during the body’s early history. Finite-element models of Vesta indicate that, even in the low-gravity regime of such bodies, strong internal heating resulted in a thin early lithosphere that experienced pervasive fracturing, permitting efficient relaxation of the body to a

closely hydrostatic figure (*Fu et al.*, 2014a). Topography data provided by the Dawn spacecraft, combined with derived crustal thickness maps (*Ermakov et al.*, 2014), suggest that a large region in the northern hemisphere of Vesta has escaped significant reshaping due to late giant impacts and preserved an ancient figure closely consistent with an oblate ellipsoid of rotation, which is the shape expected for a body that nearly reached hydrostatic equilibrium. The presence of such a hydrostatic terrain confirms that the entire vestan interior, with the exception of a lithosphere of up to several tens of kilometers in thickness, underwent intense heating above approximately 800°C, which is necessary to permit viscous relaxation on the relevant timescale of asteroid thermal evolution. Future high-resolution observations of other large asteroids, including (2) Pallas, may reveal the presence of analogous hydrostatic terrain and thereby constrain the degree of early interior heating.

#### 4.2. Paleomagnetism of Meteorites

Remanent magnetization is the semipermanent alignments of electron spins in ferromagnetic minerals and provides a record of the intensity of past magnetic fields. It can be acquired by asteroid materials in the form of thermoremanent magnetization (produced during cooling) or as crystallization-remanent magnetization (produced during crystallization) when these processes occur in the presence of a magnetic field. Asteroidal materials could be remagnetized either on their parent body or, for chondrules and refractory inclusions, when they formed as free-floating objects in the nebula (*Weiss and Elkins-Tanton*, 2013). It is also possible that previously magnetized materials could be aligned by a background field as they accreted onto a planetesimal to produce accretional detrital-remanent magnetization (*Fu and Weiss*, 2012).

By constraining the existence and intensity of ancient magnetizing fields, remanent magnetization can be used to infer the existence and nature of putative magnetic field sources in the early solar system. Proposed field sources are magnetism in the solar nebula (dragged in from the parent molecular cloud and/or generated by *in situ* fluid motions), induction currents generated in advecting planetesimal metallic cores (dynamos), and currents transiently generated by impact-produced plasmas (*Weiss et al.*, 2010a). Of these three field sources, only dynamo fields are generated by internal geophysical processes and would therefore place direct constraints on planetesimal differentiation and thermal evolution.

Paleomagnetic studies over the last five decades have found that many chondrites and achondrites contain remanent magnetization. However, until recently, the origin of this magnetization has been unclear. Over the last decade, a burst of measurements (Fig. 5) combined with a deepening understanding of meteoritics and the fundamentals of rock magnetism and dynamo theory has led to major advances in our understanding of meteorite magnetism. Paleomagnetic analyses have identified remanent magnetization in angrites and howardite-eucrite-diogenite (HED) meteorites, two groups of basaltic achondrites (*Fu et al.*, 2012; *Tarduno and*

*Cottrell*, 2012; *Weiss et al.*, 2008), and main-group pallasites (*Tarduno et al.*, 2012). The slow cooling rates experienced by these meteorites through the Curie points of their ferromagnetic minerals on their parent bodies [e.g., at least thousands of years for the angrite Angra dos Reis and the eucrite Allan Hills (ALH) A81001] are inconsistent with impact-generated plasmas as the field source, which are only thought to persist at most for ~1000 s on asteroidal bodies (*Fu et al.*, 2012). The relatively young age of magnetization in these bodies (i.e., <4.557 Ga for Angra dos Reis and 3.69 Ga for ALH A81001) likely excludes magnetic fields in the solar nebula. By comparison, consideration of the physics of dynamo action on planetesimals suggests that magnetic fields could persist on these bodies on timescales ranging from several million years (*Sterenborg and Crowley*, 2013) up to ~200 m.y. after the formation of CAIs (*Elkins-Tanton et al.*, 2011; *Tarduno et al.*, 2012; *Weiss et al.*, 2008). Therefore, it was concluded that all three parent bodies generate dynamo magnetic fields.

Paleomagnetic analyses of the Allende CV carbonaceous chondrite have identified a unidirectional magnetization blocked up to 290°C in bulk samples (*Butler*, 1972; *Carporzen et al.*, 2011; *Nagata and Funaki*, 1983) and some chondrules (*Fu et al.*, 2014b; *Sugiura and Strangway*, 1985). The unidirectional orientation of this component requires that it was acquired after accretion on the CV parent planetesimal in a field of ~60 µT (see Fig. 7 of *Weiss and Elkins-Tanton*, 2013). This is consistent with the fact that the ferromagnetic minerals in Allende (pyrrhotite, magnetite, and awaruite) are secondary alteration products widely interpreted to have formed as a result of fluid-assisted metasomatism on the CV planetesimal (*Brearley and Krot*, 2012). Furthermore, the formation of these minerals was accompanied by or followed by thermal metamorphism to temperatures of 300°–500°C. These processes should have imprinted a thermoremanent or crystallization-remanent magnetization on the meteorite if a field was present. Although the actual age of the ferromagnetic minerals is uncertain, I/Xe thermochronometry suggests that the thermal event occurred at least 9–10 m.y. after the formation of CAIs. Because the solar nebula is only thought to have persisted for 3–6 m.y. after CAI formation, this likely postdates the existence of putative nebular magnetic fields. Therefore it was concluded that the most likely magnetic field source was an interior core dynamo, such that the CV parent body was partially differentiated with a molten metallic core and an unmelted (but variably metasomatized) relic chondritic crust (*Carporzen et al.*, 2011; *Elkins-Tanton et al.*, 2011). Dynamo generation by flow of briny fluids is extremely unlikely because of their extremely low conductivities (see *Schubert et al.*, 1996).

This proposal, which has roots in the early modern era of meteoritics, challenges the dominant view that individual planetesimals have homogenous structures that are either unmelted, partially melted throughout, or fully melted (*Weiss and Elkins-Tanton*, 2013). It proposes that planetesimals could have reached a continuum of differentiation end states that individual bodies could have restricted regions that varied in their degrees of differentiation. It therefore implies

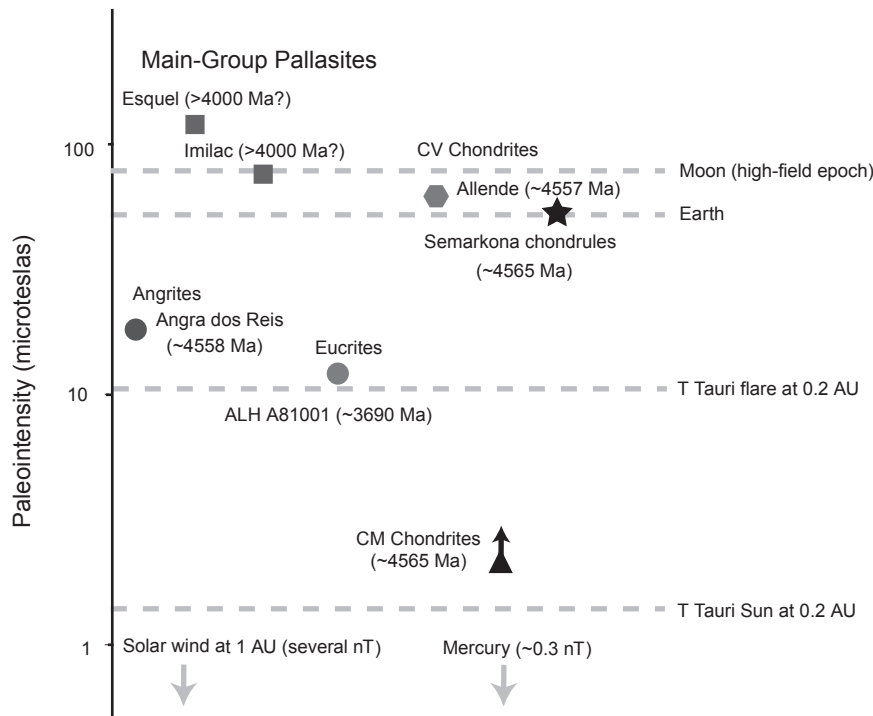


**Fig. 5.** Modern magnetic field paleointensity measurements from meteorites. Shown are paleointensities measured for individual meteorites from the angrite parent body, the main group pallasite parent body, the eucrite parent body, the CV chondrite parent body, and the CM chondrite parent body, all of which have been interpreted as possible records of planetesimal dynamo magnetic fields (Weiss *et al.*, 2008; Tarduno *et al.*, 2012; Fu *et al.*, 2012; Carporzen *et al.*, 2011; Cournède *et al.*, 2015). Paleointensity records of the nebular magnetic field from chondrules from the Semarkona LL ordinary chondrite (Fu *et al.*, 2014b) are shown for comparison. Also shown are the surface magnetic field on the Earth, the inferred lunar surface field from 3.56 to 3.9 Ga (Weiss and Tikoo, 2014), fields from the T Tauri Sun and transient flares at 0.2 AU (Weiss *et al.*, 2010a; Vallee, 2003), and the present-day solar wind field and surface field of Mercury (Anderson *et al.*, 2010).

that some chondrite and achondrites could have originated from a single parent body (Fig. 1). The recent identification of unidirectional magnetization in CM chondrites (Cournède *et al.*, 2015) may provide evidence for another partially differentiated chondrite parent body, although the old age of this magnetization makes it difficult to exclude an external nebular magnetic field source.

Recently, it has been proposed that the unidirectional magnetization in CV chondrites could be the product of impact-generated magnetic fields rather than a core dynamo (Bland *et al.*, 2014). In this scenario, the precursor lithologies of chondrites were heated by an impact-induced compaction event that simultaneously generated an impact plasma field, leading to the acquisition of a unidirectional thermoremanence without requiring partial differentiation. However, it is unclear whether impacts are likely to generate strong magnetic fields with sufficient duration and occurring in the appropriate location to magnetize rocks. For

example, paleomagnetic studies of terrestrial craters have identified no evidence of impact-generated fields (Weiss *et al.*, 2010b). Furthermore, the peak temperatures predicted for carbonaceous meteorites by the impact-compaction hypothesis exceed the Curie temperatures of their constituent ferromagnetic minerals (pyrrhotite and magnetite, 320° and 580°C, respectively), such that the millimeter–centimeter samples studied by Carporzen *et al.* (2011) would be predicted to have magnetization blocked up to 580°C rather than the observed 290°C temperature. Finally, the ferromagnetic minerals in Allende and other CV chondrites are thought to have been produced mostly by secondary metasomatic and aqueous processes on their parent body. In particular, the presence of sulfide veins crosscutting chondrules and into the surrounding matrix (Krot *et al.*, 1998) requires that much of the ferromagnetic minerals postdate any putative compaction event and therefore could not have been magnetized in an associated impact-generated field.

### 4.3. Asteroidal Magnetism

Paleomagnetic studies of meteorites indicate that some asteroids could be magnetized by an internally generated dynamo (for bodies that formed advecting cores) or could acquire large-scale magnetization during accretion by torques associated with a background field in the nebula. These conclusions could be directly tested by direct measurements of remanent magnetic fields around asteroids. Because of the inverse-cube dependence of dipolar fields with distance from the field source, direct detection of asteroidal magnetic fields requires *in situ* magnetometry measurements from spacecraft. Spacecraft have attempted this thus far near six asteroids — (21) Lutetia, (243) Ida, (433) Eros, (951) Gaspra, (2867) Šteins, and (9969) Braille — but none have unambiguously detected a remanent field from these bodies (Kivelson et al., 1995; Richter et al., 2012). One possible exception is Deep Space 1's flyby of the 0.78-km-radius Q-/S-type asteroid (9969) Braille, which observed a weak ( $\sim$ 1–2 nT) change in the ambient magnetic field upon closest approach (28 km) (Richter et al., 2001). However, this field change is near the sensitivity limit of the investigation, as demonstrated by a mismatch between the measured x-component of the field and the best-fit dipole model for the asteroidal field. Another possible exception is Galileo's flyby of the 8-km-radius S-type asteroid (951) Gaspra, during which it was thought to have detected magnetic field rotations produced by interaction of the solar wind with an intrinsic asteroidal magnetic field (Kivelson et al., 1993, 1995). However, it has been subsequently proposed that the observed plasma waves do not require the presence of a significant asteroidal magnetic field but could rather be explained purely by variability of the background solar wind (Blanco-Cano et al., 2003).

The lack of magnetic field detections near some of these asteroids places stringent constraints on the total magnetic moments of these asteroids. In particular, if it is assumed that the asteroids are uniformly magnetized, then the inferred upper limit on the magnetizations of asteroids (21) Lutetia (Richter et al., 2012) and (433) Eros (Acuña et al., 2002) are below that measured for virtually all known meteorites. This means that either these asteroids are made of materials not yet recognized as meteoritic materials on Earth or, more likely, they are made of materials resembling known meteorites but that are nonunidirectionally magnetized at spatial scales exceeding that of meteorite hand samples ( $>10$  cm) (Wasilewski et al., 2002). Therefore, magnetic field measurements of asteroids do not presently support or refute the inference made from meteorite paleomagnetic studies that many asteroids, including fully melted objects and possibly also partially differentiated bodies, likely generated dynamo magnetic fields.

### 4.4. Meteorite Evidence for Partial Differentiation

The existence of chondrites, primitive achondrites, and achondrites indicates that at least localized regions of planetesimals either did not melt, underwent partial melting, or

completely melted. These topics are extensively reviewed elsewhere in this volume (see the chapters by Wilson et al. and Scott et al.). Here we focus on meteorite evidence for partial differentiation.

As discussed in sections 2.3 and 4.3, thermal models of asteroid differentiation and paleomagnetic studies of chondrites indicate that some bodies may have partially differentiated, such that more than one of these meteorite lithologies could have formed on the same body. In fact, the recent discovery of primitive achondrites, thought to be the residues of partial melting of chondritic precursors, as a third major category of meteorite lithologies intermediate between chondrites and achondrites provides *prima facie* evidence for the existence of partially differentiated bodies. Moreover, there is broad consensus that the primitive achondrite group winonaites are derived from the same parent body as IAB iron meteorites (Benedix et al., 2000), which demonstrates that partially differentiated bodies contained regions that experienced a large degree of melting. Three key questions that remain are how common the formation of such bodies was in the early solar system, whether they preserved chondritic crusts, and whether they formed large-scale regions of silicate and iron metallic magmas.

As reviewed extensively by Weiss and Elkins-Tanton (2013), affiliated chondrites and achondrites could be recognized by their isotopic compositions, cosmic-ray exposure age distributions, and/or radioisotopic impact age distribution. The chemical compositions of the achondrites should also be consistent with fractionations expected from igneous differentiation of their chondrite protoliths. Particularly strong evidence would come from the identification of chondritic and achondritic materials that share these properties and are co-located within a single polymict meteorite.

Possible examples of affiliated chondrite and achondrite groups include the H chondrites and the silicate-bearing IIE iron meteorites. The silicates in these rocks share a common oxygen isotopic composition and bulk elemental composition, while the IIE iron meteorites also contain a diversity of silicate lithologies ranging from relic chondritic fragments, to achondritic unmelted chondrites with relic chondrules, to metamorphosed chondrites, to partial melts (Ruzicka, 2014). A connection between enstatite chondrites, aubrites, and recently discovered primitive achondrites of enstatite chondritic parentage has long been considered (Keil, 2010; Watters and Prinz, 1979). The paleomagnetism of at least CV chondrites has been interpreted as evidence for a core dynamo (Carporzen et al., 2011; Elkins-Tanton et al., 2011). Oxygen and Cr isotopic data indicate strong affiliations between CV chondrites and the ungrouped basaltic achondrite Northwest Africa (NWA) 8186 (Agee et al., 2014). There are also numerous “type 7” chondrites, which appear to have been heated to temperatures at or just below metal-sulfide melting (Irving et al., 2005), including metamorphosed clasts within the CV breccias Mokoia and Yamato 86009 (Jogo et al., 2013). Furthermore, oxygen isotopic data link the very primitive CR chondrite group to several highly metamorphosed (type 6) chondrites such as NWA 2994 as well

as to achondrites such as NWA 5131 (*Bunch et al.*, 2008; *Wittke et al.*, 2011). It would be surprising if chondrite parent bodies were heated to temperatures either just below the solidus or else above the silicate liquidus throughout their entire volumes such that virtually no intermediate partially differentiated bodies formed in between these end members.

## 5. CONCLUSION

There were many competing and interacting processes occurring in small bodies in early solar system history, and differences in bulk composition and accretionary history would have led to highly diverse outcomes, only a few of which may be represented in extant meteoritic and asteroidal material.

Aluminum-26 was probably the primary energy source for the heat needed to cause large-scale differentiation, while impacts caused only local melting. Progressive heating above  $\sim 200^{\circ}\text{C}$  generated free fluids that could have been exhaled or have participated in thermal convection, although the enstatite chondrite parent bodies may have had insufficient permeability for large-scale fluid flow. Beyond  $950^{\circ}\text{C}$ , molten metal may have begun to percolate downward and form a core, although this may require even higher temperatures. The formation of a core and the fraction of the planetesimal's total metal content that would migrate there depends on the peak temperature reached and duration of heating. These factors in turn strongly depend on body size and accretion rate.

Silicate melting will commence around  $1100^{\circ}\text{C}$ . If volatiles were not already sufficiently depleted, then volatile-rich silicate melt could rise to eject or form a crust. It could also transport  $^{26}\text{Al}$  away from the interior, cooling the body more quickly and slowing core growth. Alternatively, volatile-depleted melt would be negatively buoyant, thereby permitting the preservation of a chondritic or primitive achondritic crust over a differentiated interior.

On bodies heated sufficiently to form a magma ocean, initial fractional solidification as the magma ocean cools would produce only olivine before a high crystal fraction suppressed fractional solidification and caused bulk solidification. This explains the presence of olivine found in pallasites and its absence from the rest of the meteorite collection. It is difficult to predict how core solidification would have proceeded since the adiabat is shallow and sulfur content is the main factor determining the solidus. However, the different solidification regimes predict different locations of sulfur-rich late-crystallizing material.

Post-accretional remanent magnetization has been found in both chondrites and achondrites, and an internal dynamo is considered the likely magnetic field source. Magnetic fields have not been decisively detected on asteroids, probably because they are non-uniformly magnetized such that they have weak total magnetic moments.

Aspects of differentiation models can be further refined to make better predictions and inferences as solar system exploration continues. For example, the hypothetical process and effects of oxidation of iron in the presence of volatiles, followed by reduction as temperature rises, should be a

topic of further research. Further work permitting thermal modeling of bodies rich in ice and other volatile compounds, which are particularly likely to be present in the outer solar system, would also permit greater understanding of early solar system processes.

**Acknowledgments.** We thank E. D. Young and B. Z. Klein for discussions that improved the manuscript.

## REFERENCES

- Acuña M. H., Anderson B. J., Russell C. T., Wasilewski P., Kletetschka G., Zanetti L., and Omidi N. (2002) NEAR magnetic field observations at 433 Eros: First measurements from the surface of an asteroid. *Icarus*, *155*, 220–228.
- Agee C. B. (1997) Melting temperatures of the Allende meteorite: Implications for a Hadean magma ocean. *Phys. Earth Planet. Inter.*, *100*, 41–47.
- Agee C. B., Li J., Shamon M. C., and Circone S. (1995) Pressure-temperature phase diagram for the Allende meteorite. *J. Geophys. Res.*, *100*, 17725–17740.
- Agee C. B., Muttik N., Ziegler K., McCubbin F. M., Sanborn M. E., and Yin Q.-Z. (2014) NWA 8186: An ungrouped achondrite from the CK/CV chondrite parent body. In *73rd Meteoritical Society Meeting*, Abstract #5385.
- Akai J. (1992) T-T-T diagram of serpentine and saponite, and estimation of metamorphic heating degree of Antarctic carbonaceous chondrites. *Proc. NIPR Symp. Antarct. Meteorites 5th*, pp. 120–135.
- Akrige G., Benoit P. H., and Sears D. W. G. (1998) Regolith and megaregolith formation of H-chondrites: Thermal constraints on the parent body. *Icarus*, *132*, 185–195.
- Alexander C. M. O'D., Barber D. J., and Hutchison R. (1989) The microstructure of Semarkona and Bishunpur. *Geochim. Cosmochim. Acta*, *53*, 3045–3057.
- Anderson B. J. et al. (2010) The magnetic field of Mercury. *Space Sci. Rev.*, *152*, 307–339.
- Asphaug E. (2010) Similar-sized collisions and the diversity of planets. *Chem. Erde*, *70*, 199–219.
- Bagdassarov N., Golabek G. J., Solferino G., and Schmidt M. W. (2009) Constraints on the Fe-S melt connectivity in mantle silicates from electrical impedance measurements. *Phys. Earth Planet. Inter.*, *177*, 139–146.
- Baker J. A., Bizzarro M., Wittig N., Connelly J. N., and Haack H. (2005) Early planetesimal melting from an age of 4.5662 Gyr for differentiated meteorites. *Nature*, *436*, 1127–1131.
- Bartels K. S. and Grove T. L. (1991) High-pressure experiments on magnesian eucrite compositions — constraints on magmatic processes in the eucrite parent body. *Proc. Lunar Planet. Sci. Conf.*, Vol. 21, pp. 351–365.
- Bear J. (1972) *Dynamics of Fluids in Porous Media*. Dover, New York.
- Benedix G. K., McCoy T. J., Keil K., and Love S. G. (2000) A petrologic study of the IAB iron meteorites: Constraints on the formation of the IAB-winonaite parent body. *Meteoritics & Planet. Sci.*, *35*, 1127–1141.
- Benedix G. K., Haack H., and McCoy T. J. (2014) Iron and stony-iron meteorites. In *Treatise on Geochemistry, Vol. 1: Meteorites, Comets, and Planets, 2nd edition* (A. M. Davis, ed.), pp. 325–345. Elsevier, Amsterdam.
- Bennett M. E. and McSween H. Y. Jr. (1996) Revised model calculations for the thermal histories of ordinary chondrite parent bodies. *Meteoritics & Planet. Sci.*, *31*, 783–792.
- Blanco-Cano X., Omidi N., and Russell C. T. (2003) Hybrid simulations of solar wind interaction with magnetized asteroids: Comparison with Galileo observations near Gaspra and Ida. *J. Geophys. Res.*, *108*, 1216.
- Bland P. A., Jackson M. D., Coker R. F., et al. (2009) Why aqueous alteration in asteroids was isochemical: High porosity != high permeability. *Earth Planet. Sci. Lett.*, *287*, 559–568.
- Bland P. A., Collins G. S., Davison T. M., Abreu N. M., Ciesla F. J., Muxowrthy A. R., and Moore J. (2014) Pressure-temperature evolution of primordial solar system solids during impact-induced compaction. *Nature Commun.*, *5*, 5451.
- Brace W. F. (1980) Permeability of crystalline and argillaceous rocks. *Intl. J. Rock Mech. Min. Sci. Geomech.*, *17*, 241–251.

- Brearley A. J. (2006) The action of water. In *Meteorites and the Early Solar System II* (D. S. Lauretta D. S. and H. Y. McSween Jr., eds.), pp. 587–624. Univ. of Arizona, Tucson.
- Brearley A. J. and Krot A. N. (2012) Metasomatism in the early solar system: The record from chondritic meteorites. In *Metasomatism and the Chemical Transformation of Rock* (D. E. Harlov and H. Austrheim, eds.), pp. 659–789. Springer-Verlag, Berlin.
- Britt D. and Consolmagno G. J. (2003) Stony meteorite porosities and densities: A review of the data through 2001. *Meteoritics & Planet. Sci.*, 38, 1161–1180.
- Britt D. T., Yeomans D., Housen K., and Consolmagno C. (2002) Asteroid density, porosity, and structure. In *Asteroids III* (W. F. Bottke Jr. et al., eds.), pp. 485–499. Univ. of Arizona, Tucson.
- Bunch T. et al. (2008) Evidence for pervasive metamorphism on the CR chondrite parent body from highly equilibrated CR6 chondrites Northwest Africa 2994 and Northwest Africa 3100. *Lunar Planet. Sci. XXXIX*, Abstract #1991. Lunar and Planetary Institute, Houston.
- Buseck P. R. (1977) Pallasite meteorites — mineralogy, petrology, and geochemistry. *Geochim. Cosmochim. Acta*, 41, 711–740.
- Butler R. F. (1972) Natural remanent magnetization and thermomagnetic properties of Allende meteorite. *Earth Planet. Sci. Lett.*, 17, 120–128.
- Cameron A. G. W., Benz W., and Wasson J. T. (1990) Heating during asteroidal collisions. *Lunar Planet. Sci. XXI*, pp. 155–156. Lunar and Planetary Institute, Houston.
- Carporzen L., Weiss B. P., Elkins-Tanton L. T., Shuster D. L., Ebel D. S., and Gattacceca J. (2011) Magnetic evidence for a partially differentiated carbonaceous chondrite parent body. *Proc. Natl. Acad. Sci.*, 108, 6386–6389.
- Castillo-Rogez J., Johnson T. V., Lee M. H., Turner N. J., Matson D. L., and Lunine J. (2009)  $^{26}\text{Al}$  decay: Heat production and a revised age for Iapetus. *Icarus*, 204, 658–662.
- Chabot N. L. (2004) Sulfur contents of the parental metallic cores of magmatic iron meteorites. *Geochim. Cosmochim. Acta*, 68, 3607–3618.
- Chabot N. L. and Drake M. J. (2000) Crystallization of magmatic iron meteorites: The effects of phosphorus and liquid immiscibility. *Meteoritics & Planet. Sci.*, 35, 807–816.
- Chabot N. L. and Haack H. (2006) Evolution of asteroidal cores. In *Meteorites and the Early Solar System II* (D. S. Lauretta D. S. and H. Y. McSween Jr., eds.), pp. 747–771. Univ. of Arizona, Tucson.
- Chambers J. E. (2010) Planetesimal formation by turbulent concentration. *Icarus*, 180, 496–513.
- Chen J. H., Papanastassiou D. A., Teus M., and Huss G. R. (2013) Fe-Ni isotopic systematics in UOC QUE 97008 and Semarkona chondrules. *Lunar Planet. Sci. XLIV*, Abstract #2649. Lunar and Planetary Institute, Houston.
- Christensen U. R. (2015) Iron snow dynamo models for Ganymede. *Icarus*, 247, 248–259. DOI: 10.1016/j.icarus.2014.10.024.
- Ciesla F. J., Davison T. M., Collins G. S., and O'Brien D. P. (2013) Thermal consequences of impacts in the early solar system. *Meteoritics & Planet. Sci.*, 48, 2559–2576.
- Clayton R. N. and Mayeda T. K. (1984) The oxygen isotope record in Murchison and other carbonaceous chondrites. *Earth Planet. Sci. Lett.*, 67, 151–161.
- Clauser C. (1992) Permeability of crystalline rocks. *Eos Trans. AGU*, 73, 233–238.
- Coradini A., Capaccioni F., Erard S., et al. (2011) The surface composition and temperature of asteroid 21 Lutetia as observed by Rosetta/VIRTIS. *Science*, 334, 492–494.
- Corrigan C. M., Zolensky M. E., Dahl J., Long M., Weir J., Sapp C., and Burkett P. J. (1997) The porosity and permeability of chondritic meteorites and interplanetary dust particles. *Meteoritics & Planet. Sci.*, 32, 509–515.
- Cournède C., Gattacceca J., Gounelle M., Rochette P., and Weiss B. P. (2015) An early solar system magnetic field recorded in CM chondrites. *Earth Planet. Sci. Lett.*, 410, 62–74.
- Cuzzi J. N., Hogan R. C., and Shariff K. (2008) Towards planetesimals: Dense chondrule clumps in the protoplanetary nebula. *Astrophys. J.*, 687, 1432–1447.
- Davison T. M., Collins G. S., and Ciesla F. J. (2010) Numerical modeling of heating in porous planetesimal collisions. *Icarus*, 208, 468–481.
- Dauphas N., Cook D. L., Sacarabany A., Frohlich C., Davis A. M., Wadhwa M., Pourmand A., Rauscher T., and Gallino R. (2008) Iron-60 evidence for early injection and efficient mixing of stellar debris in the protosolar nebula. *Astrophys. J.*, 686, 560–569.
- Dodd R. T. Jr. (1969) Metamorphism of the ordinary chondrites: A review. *Geochim. Cosmochim. Acta*, 33, 161–203.
- Duprat J. and Tatischeff V. (2007) Energetic constraints on *in situ* production of short-lived radionuclides in the early solar system. *Astrophys. J. Lett.*, 617, L69–L72.
- Elkins Tanton L. T., Weiss B. P., and Zuber M. T. (2011) Chondrites as samples of differentiated planetesimals. *Earth Planet. Sci. Lett.*, 305, 1–10.
- Ermakov A. I., Zuber M. T., Smith D. E., Raymond C. A., Balmino G., Fu R. R., and Ivanov B. A. (2014) Constraints on Vesta's interior structure using gravity and shape models from the Dawn mission. *Icarus*, 240, 146–160.
- Fabrichnaya O. B. (1999) The phase relations in the  $\text{FeO}-\text{MgO}-\text{Al}_2\text{O}_3-\text{SiO}_2$  system: An assessment of thermodynamic properties and phase equilibria at pressures up to 30 GPa. *Calphad*, 23, 19–67.
- Fish R. A., Goles G. G., and Anders E. (1960) The record in meteorites III. On the development of meteorites in asteroidal bodies. *Astrophys. J.*, 132, 243–258.
- Formisano M., Turri D., Federico C., Capaccioni F., and De Sanctis M. C. (2013) The onset of differentiation and internal evolution: The case of 21 Lutetia. *Astrophys. J.*, 770, 9.
- Fu R. R. and Elkins-Tanton L. T. (2014) The fate of magmas in planetesimals and the retention of primitive chondritic crusts. *Earth Planet. Sci. Lett.*, 390, 128–137.
- Fu R. R. and Weiss B. P. (2012) Detrital remanent magnetization in the solar nebula. *J. Geophys. Res.*, 117, E02003.
- Fu R. R., Weiss B. P., Shuster D. L., Gattacceca J., Grove T. L., Suavet C., Lima E. A., Li L., and Kuan A. T. (2012) An ancient core dynamo in asteroid Vesta. *Science*, 338, 238–241.
- Fu R. R., Hager B. H., Ermakov A. I., and Zuber M. T. (2014a) Efficient early global relaxation of asteroid Vesta. *Icarus*, 240, 133–145.
- Fu R. R., Lima E. A., and Weiss B. P. (2014b) No nebular magnetization in the Allende CV carbonaceous chondrite. *Earth Planet. Sci. Lett.*, 404, 54–66.
- Ghosh A. and McSween H. Y. Jr. (1998) A thermal model for the differentiation of asteroid 4 Vesta, based on radiogenic heating. *Icarus*, 134, 187–206.
- Ghosh A., Weidenschilling S. J., and McSween H. Y. Jr. (2001) Thermal consequences of the multizone accretion code on the structure of the asteroid belt. *Lunar Planet. Sci. XXXII*, Abstract #1760. Lunar and Planetary Institute, Houston.
- Ghosh A., Weidenschilling S. J., McSween H. Y. Jr., and Rubin A. (2006) Asteroidal heating and thermal stratification of the asteroidal belt. In *Meteorites and the Early Solar System II* (D. S. Lauretta and H. Y. McSween Jr., eds.), pp. 555–566. Univ. of Arizona, Tucson.
- Golabek G. J., Bourdon B., and Gerya T. V. (2014) Numerical models of the thermomechanical evolution of planetesimals: Application to the acapulcoite-lodranite parent body. *Meteoritics & Planet. Sci.*, 49, 1083–1099.
- Goldstein J. I., Scott E. R. D., and Chabot N. L. (2009) Iron meteorites: Crystallization, thermal history, parent bodies, and origin. *Chem. Erde*, 69, 293–325.
- Gounelle M. and Meynet G. (2012) Solar system genealogy revealed by extinct short-lived radionuclides in meteorites. *Astron. Astrophys.*, 545, A4.
- Grimm R. E. (1985) Peneccontemporaneous metamorphism, fragmentation, and reassembly of ordinary chondrite parent bodies. *J. Geophys. Res.*, 90, 2022–2028.
- Grimm R. E. and McSween H. Y. Jr. (1989) Water and the thermal evolution of carbonaceous chondrite parent bodies. *Icarus*, 82, 244–280.
- Grimm R. E. and McSween H. Y. Jr. (1993) Heliocentric zoning of the asteroid belt by aluminum-26 heating. *Science*, 259, 653–655.
- Guo W. and Eiler J. M. (2007) Temperatures of aqueous alteration and evidence for methane generation on the parent bodies of the CM chondrites. *Geochim. Cosmochim. Acta*, 71, 5565–5575.
- Haack H. and Scott E. R. D. (1992) Asteroid core crystallization by inward dendritic growth. *J. Geophys. Res.*, 97, 14727–14734.
- Haack H. and Scott E. R. D. (1993) Chemical fractionations in group IIIAB iron meteorites — origin by dendritic crystallization of an asteroidal core. *Geochim. Cosmochim. Acta*, 57, 3457–3472.
- Haack H., Rasmussen K. L., and Warren P. H. (1990) Effects of regolith/megaregolith insulation on the cooling histories of differentiated asteroids. *J. Geophys. Res.*, 95, 5111–5124.

- Henke S., Gail H.-P., Trieloff M., Schwarz W. H., and Kleine T. (2012) Thermal evolution and sintering of chondritic planetesimals. *Astron. Astrophys.*, 537, A45.
- Herbert F., Sonnett C. P., and Gaffey M. (1991) Protoplanetary thermal metamorphism: The hypothesis of electromagnetic induction in the protosolar wind. In *The Sun in Time* (C. P. Sonnett et al., eds.), pp. 710–739. Univ. of Arizona, Tucson.
- Hevey P. and Sanders I. (2006) A model for planetesimal meltdown by  $^{26}\text{Al}$  and its implications for meteorite parent bodies. *Meteoritics & Planet. Sci.*, 41, 95–106.
- Huss G. R., Rubin A. E., and Grossman J. N. (2006) Thermal metamorphism in chondrites. In *Meteorites and the Early Solar System II* (D. S. Lauretta and H. Y. McSween Jr., eds.), pp. 567–586. Univ. of Arizona, Tucson.
- Hutchison R., Alexander C. M. O'D., and Barber D. J. (1987) The Semarkona meteorite: First recorded occurrence of smectite in an ordinary chondrite, and its implications. *Geochim. Cosmochim. Acta*, 51, 1875–1882.
- Irving A. J., Bunch T. E., Rumble D., and Larson T. E. (2005) Metachondrites: Recrystallized and/or residual mantle rocks from multiple, large chondritic parent bodies. *68th Meteoritical Society Meeting*, Abstract #5218.
- Jacobsen S., Yin Q.-Z., Moyniera F., Amelin Y., Krot A. N., Nagashima K., Hutcheon I. D., and Palme H. (2008)  $^{26}\text{Al}$ - $^{26}\text{Mg}$  and  $^{207}\text{Pb}$ - $^{206}\text{Pb}$  systematics of Allende CAIs: Canonical solar initial  $^{26}\text{Al}$ / $^{27}\text{Al}$  ratio. *Earth Planet. Sci. Lett.*, 272, 353–364.
- Jarosewich E. (1990) Chemical analyses of meteorites: A compilation of stony and iron meteorite analyses. *Meteoritics*, 25, 323–337.
- Jogo K., Nagashima K., Hutcheon I. D., Krot A. N., and Nakamura T. (2013) Heavily metamorphosed clasts from the CV carbonaceous chondrite breccias Mokoia and Yamato 86009. *Meteoritics & Planet. Sci.*, 47, 2251–2268.
- Johansen A., Oishi J. S., Mac Low M.-M., Klahr H., Henning T., and Youdin A. (2007) Rapid planetesimal formation in turbulent circumstellar disks. *Nature*, 448, 1022–1025.
- Jones T. D., Lebofsky L. A., Lewis J. S., and Marley M. S. (1990) The composition and origin of the C, P, and D asteroids: Water as a tracer of thermal evolution in the outer belt. *Icarus*, 88, 172–192.
- Jurewicz A. J. G., Mittlefehldt D. W., and Jones J. H. (1993) Experimental partial melting of the Allende (CV) and Murchison (CM) chondrites and the origin of asteroidal basalts. *Geochim. Cosmochim. Acta*, 57, 2123–2139.
- Jurewicz A. J. G., Mittlefehldt D. W., and Jones J. H. (1995) Experimental partial melting of the St. Severin (LL) and Lost City (H) chondrites. *Geochim. Cosmochim. Acta*, 59, 391–408.
- Kallemeyn G. W. and Wasson J. T. (1981) The compositional classification of chondrites — I. The carbonaceous chondrite groups. *Geochim. Cosmochim. Acta*, 45, 1217–1230.
- Keil K. (2010) Enstatite achondrite meteorites (aubrites) and the histories of their asteroidal parent bodies. *Chem. Erde*, 70, 295–317.
- Keil K., Stöffler D., Love S. G., and Scott E. R. D. (1997) Constraints on the role of impact heating and melting in asteroids. *Meteoritics & Planet. Sci.*, 32, 349–363.
- Keil K., McCoy T. J., Wilson L., Barrat J. A., Rumble D., Meier M. M. M., Wieler R., and Huss G. R. (2011) A composite Fe,Ni-FeS and enstatite-forsterite-diopside-glass vitrophyre clast in the Larkman Nunatak 04316 aubrite: Origin by pyroclastic volcanism. *Meteoritics & Planet. Sci.*, 46, 1719–1741.
- King C. and Olson P. (2011) Heat partitioning in metal-silicate plumes during Earth differentiation. *Earth Planet. Sci. Lett.*, 304, 577–586.
- Kivelson M. G., Bargatze L. F., Khurana K. K., Southwood D. J., Walker R. J., and Coleman P. J. (1993) Magnetic field signatures near Galileo's closest approach to Gaspra. *Science*, 261, 331–334.
- Kivelson M. G., Wang Z., Joy S., Khurana K. K., Polanskey C., Southwood D. J., and Walker R. J. (1995) Solar wind interaction with small bodies. 2. What can Galileo's detection of magnetic rotations tell us about Gaspra and Ida. *Adv. Space Res.*, 16, 47–57.
- Kleine T., Hans U., Irving A. J., and Bourdon B. (2012) Chronology of the angite parent body and implications for core formation in protoplanets. *Geochim. Cosmochim. Acta*, 84, 186–203.
- Kracher A. and Wasson J. T. (1982) The role of S in the evolution of the parental cores of the iron meteorites. *Geochim. Cosmochim. Acta*, 46, 2419–2426.
- Krot A. N., Scott E. R. D., and Zolensky M. E. (1997) Origin of fayalitic olivine rims and lath-shaped matrix olivine in the CV3 chondrite Allende and its dark inclusions. *Meteoritics & Planet. Sci.*, 32, 31–49.
- Krot A. N., Petaev M. I., Scott E. R. D., Choi B.-G., Zolensky M. E., and Keil K. (1998) Progressive alteration in CV3 chondrites: More evidence for asteroidal alteration. *Meteoritics & Planet. Sci.*, 33, 1065–1085.
- Krot A. N., Amelin Y., Cassen P., and Meibom A. (2005) Young chondrules in CB chondrites from a giant impact in the early solar system. *Nature*, 436, 989–992.
- Krot A. N., Nagashima K., Bizzarro M., Huss G. R., Davis A. M., McKeegan K. D., Meyer B. S., and Ulyanov A. A. (2008) Multiple generations of refractory inclusions in the metal-rich carbonaceous chondrites Acfer 182/214 and Isheyev. *Astrophys. J.*, 672, 713–721.
- Krot A. N., Makide K., Nagashima K., Huss G. R., Ogliore R. C., Ciesla F. J., Yang L., Hellebrand E., and Gaidos E. (2012) Heterogeneous distribution of  $^{26}\text{Al}$  at the birth of the solar system: Evidence from refractory grains and inclusions. *Meteoritics & Planet. Sci.*, 47, 1948–1979.
- Kullerud G. (1963) The Fe-Ni-S system. *Annu. Rept. Geophys. Lab.*, 1412, 175–189.
- Kullerud G. and Yoder H. S. (1959) Pyrite stability relations in the Fe-S system. *Econ. Geol.*, 54, 533–572.
- Kunihiro T., Rubin A. E., McKeegan K. D., and Wasson J. T. (2004) Initial  $^{26}\text{Al}$ / $^{27}\text{Al}$  in carbonaceous-chondrite chondrules: Too little  $^{26}\text{Al}$  to melt asteroids. *Geochim. Cosmochim. Acta*, 68, 2947–2957.
- Laneuville M., Wieczorek M. A., Breuer D., Aubert J., Morard G., and Ruckriem T. (2014) A long-lived lunar dynamo powered by core crystallization. *Earth Planet. Sci. Lett.*, 401, 251–260.
- LaTourette T. and Wasserburg G. J. (1998) Mg diffusion in anorthite: Implications for the formation of early solar system planetesimals. *Earth Planet. Sci. Lett.*, 158, 91–108.
- Lee M. S., Rubin A. E., and Wasson J. T. (1992) Origin of metallic Fe-Ni in Renazzo and related chondrites. *Geochim. Cosmochim. Acta*, 56, 2521–2533.
- Lee T., Papanastassiou D. A., and Wasserburg G. J. (1976) Demonstration of  $^{26}\text{Mg}$  excess in Allende and evidence for  $^{26}\text{Al}$ . *Geophys. Res. Lett.*, 3, 41–44.
- Lerner N. R. (1995) Influence of Murchison or Allende minerals on hydrogen-deuterium exchange of amino acids. *Geochim. Cosmochim. Acta*, 59, 1623–1631.
- Liu M.-C., McKeegan K. D., Goswami J. N., Marhas K. K., Sahijpal S., Ireland T. R., and Davis A. M. (2009) Isotopic records in CM hibonites: Implications for timescales of mixing of isotope reservoirs in the solar nebula. *Geochim. Cosmochim. Acta*, 73, 5051–5079.
- Lodders K. (2003) Solar system abundances and condensation temperatures of the elements. *Astrophys. J.*, 591, 1220–1247.
- Lodders K. and Fegley B. (1998) *The Planetary Scientist's Companion*. Oxford Univ., New York.
- MacPherson G. J., Davis A. M., and Zinner E. K. (1995) The distribution of  $^{26}\text{Al}$  in the early solar system: A reappraisal. *Meteoritics & Planet. Sci.*, 30, 365–386.
- Makide K., Nagashima K., Krot A. N., Huss G. R., Hutcheon I. D., and Bischoff A. (2009) Oxygen- and magnesium-isotope compositions of calcium-aluminum rich inclusions from CR2 carbonaceous chondrites. *Geochim. Cosmochim. Acta*, 73, 5018–5051.
- Markowski A., Quitté G., Halliday A. N., and Kleine T. (2006) Tungsten isotopic compositions of iron meteorites: Chronological constraints vs. cosmogenic effects. *Earth Planet. Sci. Lett.*, 242, 1–15.
- Matza S. D. and Lipschutz M. E. (1977) Volatile/mobile trace elements in Karoonda (C4) chondrite. *Geochim. Cosmochim. Acta*, 41, 1398–1401.
- McCoy T. J., Keil K., Muenow D. W., and Wilson L. (1997) Partial melting and melt migration in the acapulcoite-lodranite parent body. *Geochim. Cosmochim. Acta*, 61, 639–650.
- McCoy T. J., Dickinson T. L., and Lofgren G. E. (1999) Partial melting of the Indarch (EH4) meteorite: A textural, chemical, and phase relations view of melting and melt migration. *Meteoritics & Planet. Sci.*, 34, 735–746.
- McCoy T. J., Mittlefehldt D. W., and Wilson L. (2006) Asteroid differentiation. In *Meteorites and the Early Solar System II* (D. S. Lauretta and H. Y. McSween Jr., eds.), pp. 733–745. Univ. of Arizona, Tucson.

- McKenzie D. and Bickle M. J. (1988) The volume and composition of melt generated by extension of the lithosphere. *J. Petrol.*, **29**, 625–697.
- McSween H. Y. Jr., Ghosh A., Grimm R. E., Wilson L., and Young E. D. (2002) Thermal evolution models of planetesimals. In *Asteroids III* (W. F. Bottke Jr. et al., eds.), pp. 559–571. Univ. of Arizona, Tucson.
- Merk R., Breuer D., and Spohn T. (2002) Numerical modeling of  $^{26}\text{Al}$ -induced radioactive melting of asteroids considering accretion. *Icarus*, **159**, 183–191.
- Mishra R. K., Goswami J. N., Tachibana S., Huss G. R., and Rudraswami N. G. (2010)  $^{60}\text{Fe}$  and  $^{26}\text{Al}$  in chondrules from unequilibrated chondrites: Implications for early solar system processes. *Astrophys. J. Lett.*, **714**, L217–L221.
- Mittlefehldt D. W., McCoy T. J., Goodrich C. A., and Kracher A. (1998) Non-chondritic meteorites from asteroidal bodies. *Rev. Mineral.*, **36**, D1–D195.
- Miyamoto M. (1991) Thermal metamorphism of CI and CM carbonaceous chondrites: An internal heating model. *Meteoritics*, **26**, 111–115.
- Morbidelli A., Nesvorný D., Bottke W. F., and Levison H. F. (2009) Asteroids were born big. *Icarus*, **204**, 558–573.
- Moskovitz N. and Gaidos E. (2011) Differentiation of planetesimals and the thermal consequences of melt migration. *Meteoritics & Planet. Sci.*, **46**, 903–918.
- Moskovitz N. and Walker R. J. (2011) Size of the group IVA iron meteorite core: Constraints from the age and composition of Muonionalusta. *Earth Planet. Sci. Lett.*, **308**, 410–416.
- Muenow D. W., Keil K., and Wilson L. (1992) High-temperature mass spectrometric degassing of enstatite chondrites: Implications for pyroclastic volcanism on the aubrite parent body. *Geochim. Cosmochim. Acta*, **56**, 4267–4280.
- Muenow D. W., Keil K., and McCoy T. J. (1995) Volatiles in unequilibrated ordinary chondrites: Abundances, sources and implications for explosive volcanism on differentiated asteroids. *Meteoritics & Planet. Sci.*, **30**, 639–645.
- Nagata T. and Funaki M. (1983) Paleointensity of the Allende carbonaceous chondrite. *Mem. Natl. Inst. Polar Res., Spec. Issue* **30**, 403–434.
- Narayan C. and Goldstein J. I. (1982) A dendritic solidification model to explain Ge-Ni variations in iron meteorite chemical groups. *Geochim. Cosmochim. Acta*, **46**, 259–268.
- Neumann W., Breuer D., and Spohn T. (2012) Differentiation and core formation in accreting planetesimals. *Astron. Astrophys.*, **543**, A141.
- Neumann W., Breuer D., and Spohn T. (2014) Differentiation of Vesta: Implications for a shallow magma ocean. *Earth Planet. Sci. Lett.*, **395**, 267–280.
- Niida K. and Green D. H. (1999) Stability and chemical composition of pargasitic amphibole in MORB pyrolite under upper mantle conditions. *Contrib. Mineral. Petro.*, **135**, 18–40.
- Norris T. L., Gancharz A. J., Rokop D. J., and Thomas K. W. (1983) Half-life of  $^{26}\text{Al}$ . *Proc. Lunar Planet. Sci. Conf. 14th*, in *J. Geophys. Res.*, **88**, B331–B333.
- Pernicka E. and Wasson J. T. (1987) Ru, Re, Os, Pt and Au in iron meteorites. *Geochim. Cosmochim. Acta*, **51**, 1717–1726.
- Richter I., Brinza D. E., Cassel M., Glassmeier K.-H., Kuhnke F., Musmann G., Othmer C., Schwingenschuh K., and Tsurutani B. T. (2001) First direct magnetic field measurements of an asteroidal magnetic field: DS1 at Braille. *Geophys. Res. Lett.*, **28**, 1913–1916.
- Richter I., Auster H. U., Glassmeier K.-H., Koenders C., Carr C. M., Motschmann U., Müller J., and McKenna-Lawlor S. (2012) Magnetic field measurements during the Rosetta flyby at asteroid (21) Lutetia. *Planet. Space Sci.*, **66**, 155–164.
- Rivkin A. S., Howell E. S., Vilas F., and Lebofsky L. A. (2002) Hydrated minerals on asteroids: The astronomical record. In *Asteroids III* (W. F. Bottke Jr. et al., eds.), pp. 235–254. Univ. of Arizona, Tucson.
- Rubin A. E. (1995) Petrologic evidence for collisional heating of chondritic asteroids. *Icarus*, **113**, 156–167.
- Rubin A. E. (2004) Postshock annealing and postannealing shock in equilibrated ordinary chondrites: Implications for the thermal and shock histories of chondritic asteroids. *Geochim. Cosmochim. Acta*, **68**, 673–689.
- Rubin A. E. and Jones R. H. (2003) Spade: An H chondrite impact-melt breccia that experienced post-shock annealing. *Meteoritics & Planet. Sci.*, **38**, 1507–1520.
- Rugel G., Faestermann T., Knie K., Korschinek G., Poutivtsev M., Schumann D., Kivel N., Gunther-Leopold I., Weinreich R., and Wholmuth M. (2009) New measurement of the  $^{60}\text{Fe}$  half-life. *Phys. Rev. Lett.*, **103**, 1–4.
- Russell C. T., Raymond C. A., Coradini A., et al. (2012) Dawn at Vesta: Testing the protoplanetary paradigm. *Science*, **336**, 684–686.
- Ruzicka A. (2014) Silicate-bearing iron meteorites and their implications for the evolution of asteroidal parent bodies. *Chem. Erde*, **74**, 3–48.
- Sahijpal S. and Goswami J. N. (1998) Refractory phases in primitive meteorites devoid of  $^{26}\text{Al}$  and  $^{41}\text{Ca}$ : Representative samples of first solar system solids? *Astrophys. J. Lett.*, **509**, L137–L140.
- Sahijpal S. and Gupta G. (2011) Did the carbonaceous chondrites evolve in the crustal regions of partially differentiated asteroids? *J. Geophys. Res.*, **116**, E06004.
- Sahijpal S., Soni P., and Gupta G. (2007) Numerical simulations of the differentiation of accreting planetesimals with  $^{26}\text{Al}$  and  $^{60}\text{Fe}$  as the heat sources. *Meteoritics & Planet. Sci.*, **42**, 1529–1548.
- Schölling M. and Breuer D. (2009) Numerical simulation of convection in a partially molten planetesimal. *Proc. European Planet. Sci. Congress 4th*, p. 523.
- Scott E. R. D., Keil K., and Stöffler D. (1992) Shock metamorphism of carbonaceous chondrites. *Geochim. Cosmochim. Acta*, **56**, 4281–4293.
- Scott E. R. D., Love S. G., and Krot A. N. (1996a) Formation of chondrules and chondrites in the protoplanetary nebula. In *Chondrules and the Protoplanetary Disk* (R. H. Hewins et al., eds.), pp. 87–96. Cambridge Univ., Cambridge.
- Scott E. R. D., Haack H., and McCoy T. J. (1996b) Core crystallization and silicate-metal mixing in the parent body of the IVA iron and stony-iron meteorites. *Geochim. Cosmochim. Acta*, **60**, 1615–1631.
- Schubert G., Zhang K., Kivelson M. G., and Anderson J. D. (1996) The magnetic field and internal structure of Ganymede. *Nature*, **384**, 544–545.
- Sengers J. V. and Kamgar-Parsi B. (1984) Representative equations for the viscosity of water substance. *J. Phys. Chem. Ref. Data*, **13**, 185–205.
- Sharp T. G. and De Carli P. G. (2006) Shock effects in meteorites. In *Meteorites and the Early Solar System II* (D. S. Lauretta and H. Y. McSween Jr., eds.), pp. 653–677. Univ. of Arizona, Tucson.
- Shepard M. K., Clark B. E., Ockert-Bell M., Nolan M. C., Howell E. S., Magri C., Giorgini J. D., Benner L. A. M., Ostro S. J., Harris A. W., Warner J. L., Stephens R. D., and Mueller M. (2010) A radar survey of M- and X-class asteroids II. Summary and synthesis. *Icarus*, **208**, 221–237.
- Smits P. J., Economou I. G., Peters C. J., and Arons J. S. (1994) Equation of state description of thermodynamics properties of near-critical and supercritical water. *J. Phys. Chem.*, **98**, 12080–12085.
- Solomatov V. S. (2000) Fluid dynamics of a terrestrial magma ocean. In *Origin of the Earth and Moon* (R. M. Canup and K. Righter, eds.), pp. 323–338. Univ. of Arizona, Tucson.
- Sonnett C. P. and Colburn D. S. (1968) The principle of solar wind induced planetary dynamos. *Phys. Earth Planet. Inter.*, **1**, 326–346.
- Sonnett C. P., Colburn D. S., and Schwartz K. (1968) Electrical heating of meteorite parent bodies and planets by dynamo induction from a pre-main sequence T Tauri “solar wind”. *Nature*, **219**, 924–926.
- Šrámek O., Milelli L., Ricard Y., and Labrosse S. (2012) Thermal evolution and differentiation of planetesimals and planetary embryos. *Icarus*, **217**, 339–354.
- Stenberg M. G. and Crowley J. W. (2013) Thermal evolution of early solar system planetesimals and the possibility of sustained dynamos. *Phys. Earth Planet. Inter.*, **214**, 53–73.
- Stevenson D. J. (1981) Models of the Earth's core. *Science*, **214**, 611–619.
- Suckale J., Elkins-Tanton L. T., and Sethian J. A. (2012) Crystals stirred up: 2. Numerical insights into the formation of the earliest crust on the Moon. *J. Geophys. Res.*, **117**, E08005.
- Sugiura N. and Strangway D. W. (1985) NRM directions around a centimeter-sized dark inclusion in Allende. *Proc. Lunar Planet. Sci. Conf. 15th*, in *J. Geophys. Res.*, **90**, C729–C738.
- Sugiura N., Brar N. S., and Strangway D. W. (1984) Degassing of meteorite parent bodies. *Proc. Lunar Planet. Sci. Conf. 14th*, in *J. Geophys. Res.*, **89**, B641–B644.
- Tachibana S., Huss G. R., Kita N. T., Shimoda G., and Morishita Y. (2006)  $^{60}\text{Fe}$  in chondrites: Debris from a nearby supernova in the early solar system? *Astrophys. J. Lett.*, **639**, L87–L90.

- Tang H. and Dauphas N. (2012) Abundance, distribution, and origin of  $^{60}\text{Fe}$  in the solar protoplanetary disk. *Earth Planet. Sci. Lett.*, 359, 248.
- Tarduno J. A. and Cottrell R. D. (2012) Single crystal paleointensity analyses of olivine-diogenites: Implications for a past Vestan dynamo. *Lunar Planet. Sci. XLIII*, Abstract #2663. Lunar and Planetary Institute, Houston.
- Tarduno J. A., Cottrell R. D., Nimmo F., Hopkins J., Voronov J., Erickson A., Blackman E., Scott E. R. D., and McKinley R. (2012) Evidence for a dynamo in the main group pallasite parent body. *Science*, 338, 939–942.
- Terasaki H., Frost D. J., Rubie D. C., and Langenhorst F. (2008) Percolative core formation in planetesimals. *Earth Planet. Sci. Lett.*, 273, 132–137.
- Trimmer D., Bonner B., Heard H. C., and Duba A. (1980) Effect of pressure and stress on water transport in intact and fractured gabbro and granite. *J. Geophys. Res.*, 85, 7059–7071.
- Ulff-Møller F., Choi B. G., Rubin A. E., Tran J., and Wasson J. T. (1998) Paucity of sulfide in a large slab of Esquel: New perspectives on pallasite formation. *Meteoritics & Planet. Sci.*, 33, 221–227.
- Urey H. C. (1955) The cosmic abundances of potassium, uranium, and thorium and the heat balance of the Earth, the Moon, and Mars. *Proc. Natl. Acad. Sci.*, 41, 127–144.
- Vallée J. P. (2003) Astral magnetic fields as observed in star-forming nurseries, in stars, and in the solar system. *New Astron. Rev.*, 47, 85–168.
- Van Schmus W. R. and Wood J. A. (1967) A chemical-petrologic classification for the chondritic meteorites. *Geochim Cosmochim. Acta*, 31, 747–765.
- Vernazza P., Lamy P., Groussin O., Hiroi T., Jorda L., King P. L., Izawa M. R. M., Marchis F., Birlan M., and Brunetto R. (2011) Asteroid (21) Lutetia as a remnant of Earth's precursor planetesimals. *Icarus*, 216, 650–659.
- Wasilewski P., Acuña M. H., and Kletetschka G. (2002) 433 Eros: Problems with the meteorite magnetism record in attempting an asteroid match. *Meteoritics & Planet. Sci.*, 37, 937–950.
- Wasson J. T. (1999) Trapped melt in IIIAB irons: Solid/liquid elemental partitioning during the fractionation of the IIIAB magma. *Geochim. Cosmochim. Acta*, 63, 2875–2889.
- Wasson J. T. and Richardson J. W. (2001) Fractionation trends among IVA iron meteorites: Contrasts with IIIAB trends. *Geochim. Cosmochim. Acta*, 65, 951–970.
- Wasson J. T., Rubin A. E., and Benz W. (1987) Heating of primitive, asteroid-size bodies by large impacts. *Meteoritics*, 22, 525–526.
- Watters T. R. and Prinz M. (1979) Aubrites: Their origin and relationship to enstatite chondrites. *Proc. Lunar Planet. Sci. Conf. 10th*, pp. 1073–1093.
- Webster J. D. (1997) Chloride solubility in felsic melts and the role of chloride in magmatic degassing. *J. Petrol.*, 38, 1793–1807.
- Weiss B. P. and Elkins-Tanton L. T. (2013) Differentiated planetesimals and the parent bodies of chondrites. *Annu. Rev. Earth Planet. Sci.*, 41, 529–560.
- Weiss B. P. and Tikoo S. M. (2014) The lunar dynamo. *Science*, 346, 1246753.
- Weiss B. P., Berdahl S., Elkins-Tanton L. T., Stanley S., Lima E. A., and Carporzen L. (2008) Magnetism on the angrite parent body and the early differentiation of planetesimals. *Science*, 322, 713–716.
- Weiss B. P., Gattaccea J., Stanley S., Rochette P., and Christensen U. R. (2010a) Paleomagnetic records of meteorites and early planetesimal differentiation. *Space Sci. Rev.*, 152, 341–390.
- Weiss B. P., Pedersen S., Garrick-Bethell I., Stewart S. T., Louzada K. L., Maloof A. C., and Swanson-Hysell N. L. (2010b) Paleomagnetism of impact spherules from Lonar crater, India and a test for impact-generated fields. *Earth Planet. Sci. Lett.*, 298, 66–76.
- Weiss B. P., Elkins-Tanton L. T., Barucci M. A., et al. (2012) Possible evidence for partial differentiation of asteroid Lutetia from Rosetta. *Planet. Space Sci.*, 66, 137–146.
- Williams Q. (2009) Bottom-up versus top-down solidification of the cores of small solar system bodies: Constraints on paradoxical cores. *Earth Planet. Sci. Lett.*, 284, 564–569.
- Willis J. and Goldstein J. I. (1982) The effects of C, P, and S on trace-element partitioning during solidification in Fe-Ni alloys. *Proc. Lunar Planet. Sci. Conf. 13th*, in *J. Geophys. Res.*, 87, A435–A445.
- Wilson L. and Keil K. (1991) Consequences of explosive eruptions on small solar system bodies: The case of the missing basalts on the aubrite parent body. *Earth Planet. Sci. Lett.*, 104, 505–512.
- Wilson L. and Keil K. (1997) The fate of pyroclasts produced in explosive eruptions on the asteroid 4 Vesta. *Meteoritics & Planet. Sci.*, 32, 813–823.
- Wilson L. and Keil K. (2000) Crust development on differentiated asteroids. *Lunar Planet. Sci. XXXI*, Abstract #1576. Lunar and Planetary Institute, Houston.
- Wilson L. and Keil K. (2012) Volcanic activity on differentiated asteroids: A review and analysis. *Chem. Erde*, 72, 289–321.
- Wilson L., Keil K., Browning L. B., Krot A. N., and Bourcher W. (1999) Early aqueous alteration, explosive disruption, and reprocessing of asteroids.. *Meteoritics & Planet. Sci.*, 34, 541–557.
- Wilson L., Goodrich C. A., and Van Orman J. A. (2008) Thermal evolution and physics of melt extraction on the ureilite parent body. *Geochim. Cosmochim. Acta*, 72, 6154–6176.
- Wilson L., Keil K., and McCoy T. J. (2010) Pyroclast loss or retention during explosive volcanism on asteroids: Influence of asteroid size and gas content of melt. *Meteoritics & Planet. Sci.*, 45, 1284–1301.
- Windmark F., Birnstiel T., Ormel C. W., and Dullemond C. P. (2012) Breaking through: The effects of a velocity distribution on barriers to dust growth. *Astron. Astrophys.*, 544, L16.
- Wittke J. H., Bunch T. E., Irving A. J., Rumble D., and Sipiera P. P. (2011) Northwest Africa 5131: Another Tafassasset-like metachondrite related to the CR chondrite parent body. *74th Meteoritical Society Meeting*, Abstract #5222.
- Wood J. A. (1962) Metamorphism in chondrites. *Geochim. Cosmochim. Acta*, 26, 739–749.
- Yoshino T., Walter M. J., and Katsura T. (2003) Core formation in planetesimals triggered by permeable flow. *Nature*, 422, 154–157.
- Yoshino T., Walter M. J., and Katsura T. (2004) Connectivity of molten Fe alloy in peridotite based on *in situ* electrical conductivity measurements: Implications for core formation in terrestrial planets. *Earth Planet. Sci. Lett.*, 222, 501–516.
- Young E. D. (2001) The hydrology of carbonaceous chondrite parent bodies and the evolution of planet progenitors. *Philos. Trans. R. Soc. London Ser. A*, 359, 2095–2110.
- Young E. D., Ash R. D., England P., and Rumble D. III (1999) Fluid flow in chondrite parent bodies: Deciphering the compositions of planetesimals. *Science*, 286, 1331–1335.
- Young E. D., Zhang K., and Schubert G. (2003) Conditions for pore water convection within carbonaceous chondrite parent bodies: Implications for planetesimal size and heat production. *Earth Planet. Sci. Lett.*, 213, 249–259.
- Zolensky M. E., Bourcier W. L., and Gooding J. L. (1989) Aqueous alteration on the hydrous asteroids: Results of EQ3/6 computer simulations. *Icarus*, 78, 411–425.

# Hydrothermal and Magmatic Fluid Flow in Asteroids

**Lionel Wilson**  
*Lancaster University*

**Phil A. Bland**  
*Curtin University*

**Debra Buczkowski**  
*The Johns Hopkins University Applied Physics Laboratory*

**Klaus Keil and Alexander N. Krot**  
*University of Hawai'i*

---

Early forming asteroids greater than ~50 km in diameter underwent extensive thermally driven differentiation, causing heating to a range of maximum temperatures. Some reached the stage of melting of initially incorporated water ice and experienced a range of temperature-dependent aqueous alteration processes; others underwent thermal metamorphism; yet others segregated metal cores; and some were heated to the point of extensive silicate melting, leading to volcanic intrusions or eruptions, controlled in part by the stresses induced in the crust by the prior internal evolution. We review advances in both the theoretical modeling of the migration of the various fluids involved in these processes and the experimental analyses of meteorites that provide constraints on the theoretical models. There is still uncertainty about many issues. Evidence from chondrite chemistry, petrography, and material properties is consistent with limited migration of aqueous fluids (essentially a closed system), although the oxygen isotope record has been used to support both open- and closed-system models, and remains a subject of debate. Opinions seem to be converging on the need for between 5% and 10% silicate melting to allow dense metallic melts to segregate to form cores. However, the locations of large bodies of silicate melt remain controversial, ideas being polarized between retention in asteroid mantles as magma oceans and rapid transfer to the base of the crust to pond as massive intrusions. Direct observations of (4) Vesta by the Dawn spacecraft have at least partially clarified our understanding of the chemical and tectonic states of differentiated asteroid crusts, but much remains to be understood about large-scale geodynamic processes.

## 1. INTRODUCTION

Largely due to the recovery of huge numbers of meteorites from cold and hot deserts, the number of asteroidal meteorites in captivity has increased tremendously in recent years to about 50,000 (*Meteoritical Bulletin Database*, 2014). Study of these meteorites indicates that all asteroids have experienced some degree of parent-body thermal alteration due to internally produced heat. *Keil* (2000) estimated that the world's meteorite collections sample at least ~27 primitive, chondritic and ~108 partially and totally melted asteroids, and *Burbine et al.* (2002) similarly estimate this number to be ~100–150 distinct asteroids. The thermal alteration effects range from aqueous and hydrothermal alteration, notably in various classes of carbonaceous chondrites (CCs), to thermal

metamorphism and recrystallization, notably in ordinary and enstatite chondrites of high petrologic types (4–6), to partial and possibly complete melting, including core formation in various classes of achondrites. We summarize in Table 1 the meteorite classes that have experienced aqueous and hydrothermal alteration. In Table 2 we list those meteorite classes that have experienced heating to metamorphic temperatures that caused solid-state recrystallization. We also list those that experienced partial and complete melting, beginning with partial melting of the Fe,Ni-FeS cotectic, including partial melt removal and core formation, and those that experienced silicate partial to total melting.

Many meteorites have had complex histories. Some are breccias from the impact-shattered and reworked regoliths and megaregoliths of the above types of asteroid. Yet others

appear to be aggregates of fragments from multiple source bodies that individually encountered the above range of histories. Any attempt to disentangle the origins and histories of these most complex meteorites requires that we begin by understanding in detail the thermal histories controlling fluid migration in the first generation of asteroids.

TABLE 1. Classification of chondritic meteorites.

Class/Group	Petrologic Types	Peak Metamorphic Temperature (°C)	Water/Rock Mass Ratio
<i>Carbonaceous</i>			
CI	1	<150	>0.6
CR	2.0–3	<150	0.1–0.6
CM	2.0–2.9	<80	0.1–0.6
CO	3.0–3.8	~600	<0.2
CV	3.0–3.6	~600	<0.2
CK	3–6	~800	<0.2
CB	3.0	unmetamorphosed	unaltered
CH	3.0	unmetamorphosed	unaltered
<i>Ordinary</i>			
H	3–6	~950	<0.2
L	3–6	~950	<0.2
LL	3–6	~950	<0.2
R	3–6	~950	<0.2
<i>Enstatite</i>			
EH	3–6	~950	unaltered
EL	3–6	~950	unaltered

## 2. ASTEROID FORMATION, HEAT SOURCES, AND THERMAL HISTORIES

The ways in which the earliest planetesimals accreted and evolved to form the present asteroid population is still debated (Weidenschilling, 2011; Johansen *et al.*, 2014). Much work is concerned with the rates at which body sizes grew and orbits evolved with time in order to understand the present small-body size population in the solar system. Major redistributions of the semimajor axes of the earliest-forming planetesimals may have been caused by the significant inward and subsequent outward migration of the giant planets (Walsh *et al.*, 2011) during the first 3–4 m.y. after the formation of calcium-aluminum-rich inclusions (CAIs), the oldest solar system solids dated in meteorites, commonly regarded as marking “zero time” in the history of the solar system (Amelin *et al.*, 2002; Connelly *et al.*, 2012). Coupled with the possibilities of subsequent gravitational interactions with the accreting planetary embryos, this suggests that the present locations of asteroids may not necessarily be a good indicator of their distances from the Sun during the first few million years after CAI time (DeMeo and Carry, 2014), the critical period for asteroid differentiation. This is a strong argument for modeling the thermal histories of asteroids using a wide range of initial temperatures and volatile, especially water ice, contents.

However, understanding the evolution of differentiated asteroids within which fluid migration took place also requires knowledge of initial porosity and strength as well as composition and temperature (Binzel *et al.*, 2003; Binzel and

TABLE 2. Meteorites undergoing high-temperature modification.

Meteorite Group	Composition	Melting Amount	Observed Melt Fate *	Predicted Melt Fate †
Ordinary chondrites	Ordinary chondrite	Limited silicate	Limited migration	Limited migration
Enstatite chondrite-like	Enstatite chondrite?	~20% silicate	Extensive migration	Extensive migration
Acapulcoite-lodranite parent	Between ordinary and enstatite chondrite	1–4% Fe,Ni-FeS in acapulcoites; 5–20% Fe,Ni-FeS and silicate in lodranites	Limited migration	Limited to extensive
Brachinites	Primitive (R?) chondrite (volatile-rich)	13–30 % silicate	Extensive migration, loss by explosive volcanism	
Winonaite-IAB irons	Approx. H to E chondrite (relict chondrules)	Substantial	Not clear; impacted and reassembled	Not clear
Ureilites	Akin to CV chondrite	~30% silicate	Extensive migration, loss by explosive volcanism	No migration expected
Angrites	Akin to CV or CM chondrite	Extensive silicate	Extensive migration	No migration expected
Aubrites	Enstatite chondrite-like	Extensive silicate	Melts removed by explosive volcanism	Extensive migration
HED [(4) Vesta]	Akin to ordinary chondrite	4–15–60% silicate	Extensive eucrite migration	Limited migration
11 iron meteorite groups	Unknown	Extensive Fe,Ni-FeS	Formed core	

\* As inferred from meteorites.

† From Fu and Elkins-Tanton (2014).

(*Kofman*, 2005). Key factors are the mechanisms by which small grains formed and later adhered to one another in low-velocity collisions to form larger objects, and the history of the coalescence or breakup of larger objects as they experienced higher-velocity collisions. For the latter reason, much attention has been paid to the apparent strength of asteroids undergoing impacts (*Holsapple*, 2009). However, in addition to local stresses produced by impacts, progressive gravitational loading was important in large asteroids as they accreted and can be modeled theoretically if impacts are ignored (*Kadish et al.*, 2008). No direct estimate of the internal strength of an asteroid exists and so meteorites are used as proxies. Unfortunately, meteorites are inevitably the strongest parts of meteoroids that survive atmospheric passage, and therefore measurements on them (*Kimberley and Ramesh*, 2011) almost certainly overestimate the bulk strength of asteroids. Inferences from the dynamic behavior of meteoroids as they enter the upper atmosphere (*Popova et al.*, 2011) suggest that many are very weak, but there is no guarantee that these are samples of the interiors of large asteroids. Even if they are, the impact event that removed them from their parent body will have induced mechanical damage reducing their strength. One indirect estimate of the internal strength of an asteroid exists: A fault observed on (433) Eros implies a shear strength of ~1–6 MPa on a 100-m length scale (*Watters et al.*, 2011). Asteroid porosity generally decreases with increasing size (*Britt et al.*, 2002). Some asteroids in the 30–300-km range have porosities between 15% and 25%, whereas another group in the 50–250-km size range have porosities greater than 30%. The latter objects are probably true “rubble piles” and the former are heavily fractured but not totally disrupted bodies.

Various heat sources have been suggested for driving the thermal evolution of asteroids. Mutual impacts between accreting cold bodies can cause intense local heating but not a body-wide temperature rise (*Keil et al.*, 1997; *Davison et al.*, 2010), even allowing for the fact that a greater fraction of the kinetic energy of impact is converted to heat if the colliding bodies are rubble piles rather than coherent masses (*Davison et al.*, 2012). Although most modeling assumes a uniform initial temperature for asteroids, the timescale and dynamics of the accretion process may induce a non-uniform temperature distribution within a body immediately post-formation (*Merk et al.*, 2002; *Šrámek et al.*, 2012). Inductive electrical heating in the early strong solar magnetic field, first proposed by *Sonett et al.* (1970) but subsequently largely discounted (*Wood and Pellas*, 1991), may nevertheless have contributed a minor component to asteroid heating within a few astronomical units of the Sun in some circumstances (*Menzel and Roberge*, 2013).

However, the dominant heat source in early-forming asteroids was clearly the decay of short-lived radionuclides (*McCoy et al.*, 2006a), the presence of which is confirmed by technological advances (e.g., *Wadhwa et al.*, 2006) allowing detection of excess amounts of their daughter products. The most important radiogenic heat source was  $^{26}\text{Al}$  (*Schiller et al.*, 2010a), which has a half-life of ~0.72 m.y.

(*Castillo-Rogez et al.*, 2009) and decays to  $^{26}\text{Mg}$ . Thus whenever excess  $^{26}\text{Mg}$  is detected in the meteorites from an asteroid that has undergone large-scale melting, that asteroid must have formed within a very few million years of CAI time. Although  $^{60}\text{Fe}$  that decays to  $^{60}\text{Ni}$  with a half-life of ~1.5 m.y. was considered to be the second most important radiogenic heating source (*Cohen and Coker*, 2000), recent high-precision Fe-Ni isotope measurements of bulk meteorites and their components (*Tang and Dauphas*, 2012, 2014) showed very low initial abundance of  $^{60}\text{Fe}$  in the solar system ( $^{60}\text{Fe}/^{56}\text{Fe}$ )  $< \sim 1.5 \times 10^{-8}$ ). Even if initially uniformly distributed in accreting asteroids, radiogenic isotopes would not remain so. Core segregation increases the residual mantle’s  $^{26}\text{Al}$  content. Also, aluminum partitions preferentially into basaltic melts, so migration of basalts from the mantle to form a crust depletes the mantle and enriches the crust in  $^{26}\text{Al}$ . Thus both core formation and mantle melting dramatically influence the subsequent thermal history of an asteroid (*Zhou et al.*, 2013). Finally, downward settling of dense compounds to form a core is itself a heat source as potential energy is converted to heat, although this heat is not available until an asteroid’s interior temperature has already reached the point where  $\text{Fe},\text{Ni}-\text{FeS}$  melting and separation begin. In contrast to Earth-sized planets, the core formation heat source for asteroids is small: The maximum theoretical temperature rise (which neglects heat loss while the core is forming and therefore is an overestimate) scales as the square of the diameter for a fixed density (*Rubie et al.*, 2007). For differentiated bodies with diameters 1000 and 500 km, the temperature increase would be ~200 K and 50 K, respectively, but would be only ~2 K for a 100-km-diameter asteroid.

Whatever the heat source(s), an asteroid’s thermal structure is always strongly influenced by a thermal boundary layer extending inward from the surface, within which conduction of heat from the interior controls the temperature profile (*Wilson et al.*, 2008). This layer can be defined as the lithosphere on the basis of its rheology determined by the temperature profile. On the lifetime,  $\tau$ , of the  $^{26}\text{Al}$  heat source, a few million years, the boundary layer thickness  $\lambda$  [=  $(\kappa\tau)^{1/2}$ , where  $\kappa = \sim 10^{-6} \text{ m}^2 \text{ s}^{-1}$  is the thermal diffusivity of silicates (*Whittington et al.*, 2009)], is ~10 km, with small uncertainties depending on the extent of any regolith or megaregolith that exists (*Warren*, 2011a). The mean surface temperature is determined by a dynamic equilibrium between incoming heat from the Sun and outgoing radiation from the surface.

The above considerations show that the critical parameters needed in modeling the internal evolution of an asteroid are the formation time after CAIs, including the duration of accretion if this is not a short period; the bulk composition, insofar as this determines the  $^{26}\text{Al}$  content; the mean orbital distance from the early Sun, which controls the initial temperature, the surface temperature, and the ice content; and the size and bulk density of the body at the end of accretion. The most general thermal history of an asteroid includes heating to the onset of ice melting, silicate hydration by aqueous fluids, dehydration of silicates, thermal metamorphism, formation of an  $\text{Fe},\text{Ni}-\text{FeS}$  fluid potentially leading

to core formation, silicate melting, and, in the most extreme cases, melting of Fe,Ni metal before conductive cooling eventually overtakes radiogenic heating. Clearly, some of these stages are bypassed if ice is not initially present, and the sequence may be truncated at any point for asteroids that accrete too late or with too little radiogenic heat source.

### 3. ASTEROIDS THAT EXPERIENCED AQUEOUS/HYDROTHERMAL ALTERATION

#### 3.1. Classes of Altered Bodies

Carbonaceous chondrites are among the most primitive materials available to us. However, the mineralogy, petrography, oxygen-isotope compositions, and short-lived isotope chronology of aqueously/hydrothermally formed minerals clearly indicate that extensive alteration occurred within CC parent bodies (e.g., Zolensky and McSween, 1988; Brearley, 1988; Krot et al., 2006; Zolensky et al., 2008; Brearley and Krot, 2012). Based on bulk chemical and oxygen-isotopic compositions, mineralogy, and petrography, 14 chondrite groups, comprising three major classes — carbonaceous [CI (Ivuna type), CR (Renazzo type), CM (Mighei type), CO (Ornans type), CV (Vigarano type), CK (Karoonda type), CB (Bencubbin type), and CH (metal-rich)], ordinary (H, L, LL) + Rumuruti type (R), and enstatite (EH, EL) — are currently recognized (Krot et al., 2014a). Chondrites that cannot be classified into the existing groups are called ungrouped [e.g., Tagish Lake (Brown et al., 2000)]. It is assumed that each chondrite group originated on a separate parent body. However, it has recently been suggested that CV and CK chondrites may have formed on the same parent body (Greenwood et al., 2010).

Most chondrites experienced different levels of aqueous alteration and/or thermal metamorphism on their parent bodies. To provide a guide to the degree of thermal and aqueous alteration experienced by chondrites, they are divided into petrologic types from 1 to 6. The sequence type 3 to type 6 represents an increasing degree of chemical equilibrium and textural recrystallization due to thermal metamorphism. Type 3 chondrites, commonly called unequilibrated, are widely considered the least modified by thermal metamorphism and aqueous alteration. The type 3 ordinary, CO, and CV chondrites are subdivided into 10 subtypes (3.0–3.9), of which 3.0 is the least metamorphosed (e.g., Grossman and Brearley, 2005). Type 2 represents a higher degree of aqueous alteration compared with type 3. The CM and CR chondrites have been subdivided into 10 subtypes (2.9–2.0), of which 2.0 is the most aqueously altered (Rubin et al., 2007; Harju et al., 2014). In this classification scheme, type 1 is reserved for CI chondrites that consist almost entirely of aqueously formed minerals and probably never contained abundant chondrules. We note that this classification scheme of aqueously altered chondrites is not universally accepted (e.g., Alexander et al., 2013; Beck et al., 2014), and completely aqueously altered CM and CR chondrites are often referred to as CM1 and CR1, respectively.

Based on thermodynamic modeling (e.g., Zolensky et al., 1989; Zolotov and Mironenko, 2008; Zolotov, 2012) and oxygen-isotopic compositions of aqueously formed minerals (e.g., Leshin et al., 1997; Clayton and Mayeda, 1999; Benedix et al., 2003; Guo and Eiler, 2007; Schrader et al., 2011), it is inferred that the CI, CM, and CR chondrites experienced low-temperature aqueous alteration (<150°C) under variable, but relatively high, water/rock (W/R) mass ratios (0.1–0.6 or even higher). The CV, CO, and ordinary chondrites of petrologic type 3 appear to have experienced aqueous alteration at higher temperatures (100°–300°C) and lower W/R mass ratios (<0.2) than the CI, CM, and CR chondrites (e.g., Zolotov et al., 2006; Doyle et al., 2015).

#### 3.2. Chondrule Ages, Ages of Aqueous Alteration, and Chondrite Accretion Ages

In exploring the hydrothermal history of primitive planetesimals, we must first place a constraint on the timing of their accretion because it largely defines the abundance of  $^{26}\text{Al}$  that is generally accepted to be the major internal heating source of planetesimals. Planetesimals that accreted “early” in solar system history would have incorporated enough  $^{26}\text{Al}$  to drive melting and differentiation; bodies that accreted “late” close to the snow line (the distance from the Sun where water ice was stable) could have retained unmelted ices. Most chondrites appear to have been derived from objects somewhere between these extremes — incorporating sufficient  $^{26}\text{Al}$  to drive melting of ice, aqueous alteration, and low-level thermal metamorphism, but not enough to cause silicate melting and differentiation (Tables 1 and 2). However, some recent models have questioned this simple interpretation, postulating early accretion of an object that experienced differentiation at <1.5 m.y. after the beginning of the solar system formation into a convecting magma ocean and Fe,Ni-metal core (notably with a core dynamo), followed by continual accretion of primitive material onto this object, building an undifferentiated crust (Elkins-Tanton et al., 2011; Cournède et al., 2014). Meteorite chronology data may potentially allow us to test and develop some of these ideas.

Most chondrite groups consist of three major components: chondrules, refractory inclusions [CAIs and amoeboid olivine aggregates (AOAs)], and fine-grained matrices. The only exceptions are CI chondrites, which consist almost entirely of hydrated matrix and are virtually devoid of chondrules and refractory inclusions. Since chondrites could not have accreted prior to the formation of chondrules they enclose, the  $^{207}\text{Pb}$ - $^{206}\text{Pb}$  absolute ages and  $^{26}\text{Al}$ - $^{26}\text{Mg}$  relative ages of chondrules define an upper limit on the host chondrite accretion time. Note, however, that because (1) chondrule ages could be easily disturbed or even reset during even mild thermal metamorphism (e.g., Kita and Ushikubo, 2012) and (2) some chondrules may have formed by collisions between chondritic planetesimals (e.g., Krot et al., 2005; Johnson et al., 2014), some caution must be exercised when using the youngest chondrule age to constrain the host chondrite accretion age.

It is generally accepted that aqueous alteration of chondritic meteorites occurred exclusively on their parent bodies that accreted water ices together with anhydrous minerals and subsequently experienced aqueous alteration, which resulted in formation of diverse secondary minerals including phyllosilicates, carbonates, magnetite, and fayalite. As a result, dating of aqueously formed minerals provides an upper limit of the accretion ages of chondrite parent bodies. The chapter by Krot et al. in this volume summarizes recently published  $^{53}\text{Mn}$ - $^{53}\text{Cr}$  ages ( $^{53}\text{Mn}$  decays to  $^{53}\text{Cr}$  with a half-life of 3.7 m.y.) of carbonates and fayalite in several groups of carbonaceous (CI, CM, CR, CO, CV) and ordinary (L, LL) chondrites (see their Fig. 9). The  $^{53}\text{Mn}$ - $^{53}\text{Cr}$  chronology of carbonates and fayalite indicates that aqueous activity on the carbonaceous chondrite parent bodies started almost contemporaneously, ~3.5–5 m.y. after CV CAIs, consistent with  $^{26}\text{Al}$  being the major heat source of these bodies. The  $^{53}\text{Mn}$ - $^{53}\text{Cr}$  ages of aqueous alteration,  $^{26}\text{Al}$ - $^{26}\text{Mg}$  ages of chondrule formation, and peak metamorphic temperatures reached by the carbonaceous chondrite parent bodies suggest that they accreted ~2.5–4 m.y. after CV CAIs; the accretion of ordinary chondrites appears to have predated accretion of CCs by ~0.5 m.y. Below we summarize the recently published chondrule ages of the least-metamorphosed ordinary and CCs.

Variations in  $^{238}\text{U}/^{235}\text{U}$  ratio have been recently reported in CV CAIs (Brennecka et al., 2010). The U-corrected  $^{207}\text{Pb}$ - $^{206}\text{Pb}$  ages for CV CAIs are  $4567.18 \pm 0.50$  m.y. (Amelin et al., 2010) and  $4567.30 \pm 0.16$  m.y. (Connelly et al., 2012). Because of the observed variations of  $^{238}\text{U}/^{235}\text{U}$  ratio in CAIs (Brennecka et al., 2010), the  $^{207}\text{Pb}$ - $^{206}\text{Pb}$  absolute

age dating of individual chondrules requires measurements of their  $^{238}\text{U}/^{235}\text{U}$  ratios, which may be also variable. Due to generally small chondrule size (<1 mm), the U-isotope measurements of individual chondrules are technically a very challenging task, and as a result, the U-corrected  $^{207}\text{Pb}$ - $^{206}\text{Pb}$  absolute ages of chondrules are very limited and so far have been reported only for ~10 individual chondrules from the CV3.6 carbonaceous chondrite Allende, the CR2 carbonaceous chondrite Northwest Africa (NWA) 6043, the L3.1 ordinary chondrite NWA 5697 (Connelly et al., 2012; Bollard et al., 2014), and the CB carbonaceous chondrite Gujba (Bollard et al., 2013) (Fig. 1). Note that Connelly et al. (2012) observed no variations in  $^{238}\text{U}/^{235}\text{U}$  ratios in bulk chondrites, achondrites, and individual chondrules. These authors concluded that  $^{238}\text{U}/^{235}\text{U}$  ratio is uniform in the solar system, except in the region(s) where CAIs formed, and suggested using the measured value  $137.786 \pm 0.013$  as the representative solar system value. If confirmed, measurements of  $^{238}\text{U}/^{235}\text{U}$  ratio in chondrules will not be required. Analysis of two individual Allende chondrules found ages of  $4567.32 \pm 0.42$  Ma and  $4566.24 \pm 0.63$  Ma (Connelly et al., 2012). Bollard et al. (2014) reported ages of  $4567.3 \pm 1.0$  Ma,  $4565.22 \pm 0.53$  Ma, and  $4563.66 \pm 0.91$  Ma in the CR2 chondrite NWA 6043. Four chondrules from the L3.1 chondrite NWA 5697 have ages of  $4566.67 \pm 0.43$  Ma and  $4564.71 \pm 0.30$  Ma (Connelly et al., 2012), and  $4566.1 \pm 1.0$  Ma and  $4563.87 \pm 0.60$  Ma (Bollard et al., 2014). Three Gujba chondrules dated have ages ranging from  $4562.61 \pm 0.28$  to  $4562.32 \pm 0.48$  Ma, with a weighted average of  $4562.52 \pm 0.44$  Ma (Bollard et al., 2013).

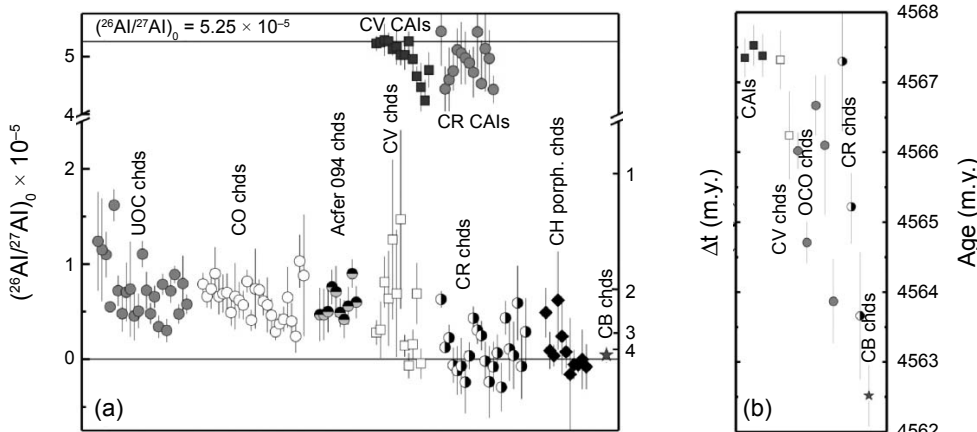


**Fig. 1.** (a) Inferred initial  $^{26}\text{Al}/^{27}\text{Al}$  ratios and relative ages of CAIs from CV and CR carbonaceous chondrites and porphyritic chondrules from unequilibrated ordinary (UOC), CO, Acfer 094 (ungrouped), CR, CH, and CV chondrites. Data from Hutcheon and Hutchison (1989), Kita et al. (2000), Mostefaoui et al. (2002), Kunihiro et al. (2004), Kurahashi et al. (2008), Makide et al. (2009), Villeneuve et al. (2009), Hutcheon et al. (2009), Kita and Ushikubo (2012), Ushikubo et al. (2013), Nagashima et al. (2014), Schrader et al. (2014), and Krot et al. (2014a). The inferred initial  $^{26}\text{Al}/^{27}\text{Al}$  ratio in CV CAIs is from Jacobsen et al. (2008). (b) Absolute U-corrected  $^{207}\text{Pb}$ - $^{206}\text{Pb}$  ages of individual CAIs and chondrules. Data from Amelin et al. (2010), Connelly et al. (2012), and Bollard et al. (2013, 2014).

It appears that after an epoch of CAI formation characterized by heterogeneous distribution of  $^{26}\text{Al}$  (Krot *et al.*, 2012),  $^{26}\text{Al}$  was relatively uniformly distributed in the inner part of the protoplanetary disk at the level of  $^{26}\text{Al}/^{27}\text{Al} \sim 5 \times 10^{-5}$ , called the “canonical” value (Jacobsen *et al.*, 2008; Kruijer *et al.*, 2014); for an alternative view see Larsen *et al.* (2011) and Bizzarro *et al.* (2014). The canonical ratio was defined on the basis of high-precision Al-Mg isotope measurements of CAIs from CV chondrites (Jacobsen *et al.*, 2008; Larsen *et al.*, 2011; MacPherson *et al.*, 2011), and the  $^{26}\text{Al}$ - $^{26}\text{Mg}$  ages of chondrules are calculated relative to the CV CAIs having the canonical  $^{26}\text{Al}/^{27}\text{Al}$  ratio. Relative  $^{26}\text{Al}/^{27}\text{Al}$  ages of chondrules have been measured in several weakly metamorphosed chondrites: Semarkona (LL3.0), Yamato 81020 (CO3.0), Acfer 094 (C3.0 ungrouped), CR2, CH3, and CV3.2–3.6 chondrites (Mostefaoui *et al.*, 2002; Kunihiro *et al.*, 2004; Kurahashi *et al.*, 2008; Hutcheon *et al.*, 2009; Kita *et al.*, 2013; Ushikubo *et al.*, 2013; Nagashima *et al.*, 2014; Schrader *et al.*, 2014; Krot *et al.*, 2014b). The results of these measurements are summarized in Fig. 1. Note that the  $^{26}\text{Al}$ - $^{26}\text{Mg}$  system in chondrules from CV3.2–3.6 chondrites may be disturbed by thermal metamorphism experienced by the CV chondrite parent body (LaTourrette and Wasserburg, 1998; Bonal *et al.*, 2006). The mean values (and one standard deviation) of  $(^{26}\text{Al}/^{27}\text{Al})_0$  in chondrules from Semarkona, CO, and Acfer 094 chondrites are  $(0.78 \pm 0.3) \times 10^{-5}$ ,  $(0.62 \pm 0.19) \times 10^{-5}$ , and  $(0.57 \pm 0.15) \times 10^{-5}$ , respectively, which correspond to  $1.9 \pm 0.4$ ,  $2.2 \pm 0.3$ , and  $2.3 \pm 0.3$  m.y. after CV CAIs. We note that these age uncertainties cannot be considered as estimates for the duration of chondrule formation recorded by these chondrite groups, because they all contain multiple generations (contemporaneously formed objects) of chondrules, as indicated by a wide range of U-Pb ages of chondrules within a chondrite group (Connelly *et al.*, 2012; Bolland *et al.*, 2014). Instead, they may provide upper limits on the formation of the dominant generation of chondrules within a chondrite group, and possibly the average abundance of  $^{26}\text{Al}$  in their host parent body (if the body accreted rapidly after formation of the dominant generation of chondrules).

Relative  $^{26}\text{Al}/^{27}\text{Al}$  chondrule ages broadly agree with their  $^{207}\text{Pb}$ - $^{206}\text{Pb}$  absolute ages, indicating that ordinary and carbonaceous chondrite chondrules were still forming at 3.5–5 m.y. after CV CAIs. These data show that there is no age gap between CAI formation and chondrule formation (Connelly *et al.*, 2012; Bolland *et al.*, 2014). It appears that accretion of ordinary, CO, CR, and CV carbonaceous chondrites was not finished at least 3.5 m.y. after CV CAIs.

In constraining accretion time, the chronometry data provide a valuable guide to the effectiveness of  $^{26}\text{Al}$  as a heat source [assuming that  $^{26}\text{Al}$  was uniformly distributed in the protoplanetary disk with an initial  $^{26}\text{Al}/^{27}\text{Al}$  ratio of  $\sim 5.2 \times 10^{-5}$  as observed in many CAIs (e.g., Jacobsen *et al.*, 2008)]. Taken together, they also allow us to discriminate between models of primordial planetesimals. The observation that chondrules in an individual meteorite formed throughout the lifetime of the protoplanetary disk (e.g., Connelly *et*

*al.*, 2012) does not appear to be consistent with first-order predictions of a model that posits continual accretion of primordial material onto an early formed differentiated object (e.g., Johansen *et al.*, 2014). Instead, the fact that the majority of chondrules in a primitive chondrite [e.g., Semarkona (LL3.0), Acfer 094 (ungrouped carbonaceous 3.0), Yamato 81020 (CO3.0), and CRs] have a relatively narrow range of initial  $^{26}\text{Al}/^{27}\text{Al}$  ratios (Fig. 1a) implies that most chondrules in the chondrite formed during the narrow time period, rapidly accreted after formation into the host meteorite parent body, and defined an average abundance of  $^{26}\text{Al}$  in this body.

### 3.3. Alteration Modeling

Numerous studies have modeled asteroidal aqueous alteration and thermal metamorphism (Grimm and McSween, 1989; Cohen and Coker, 2000; Coker and Cohen, 2001; Young *et al.*, 1999; McSween *et al.*, 2002; Young *et al.*, 2003; Travis and Schubert, 2005). In each case, large-scale fluid flow was predicted, frequently over tens of kilometers. But whether flow took place as a single-pass “exhalation” (Young *et al.*, 1999), or in convecting cells (e.g., Grimm and McSween, 1989; Travis and Schubert, 2005), the movement of liquid water through rock is expected to have fractionated soluble elements. However, CI chondrites (the most aqueously altered chondrite group) have approximately solar element abundances: Of 56 rock-forming elements analyzed in CI chondrites, 41 have abundances within 15% of the solar photosphere (Palme *et al.*, 2014). Recent estimates of solar chemical composition not only confirm the excellent agreement between photospheric and CI chondrite abundances (Grevesse *et al.*, 2007; Palme *et al.*, 2014), they also show no evidence for fractionation of soluble elements: For example, there is no difference, within error, between photosphere and meteorite compositions in the subset of elements that are considered more soluble (~25% of the total) and the larger dataset. Because fractionation of the soluble elements has not occurred, aqueous alteration (by definition) must have been isochemical. Other chondrite groups show monotonic depletions from solar composition in volatile and moderately volatile elements (e.g., Krot *et al.*, 2014b, and references therein); elements with very different chemical affinity, related only by similarity in equilibrium condensation temperature. It should also be noted that there are no differences in bulk chemical compositions of meteorites aqueously altered to various degrees within a chondrite group (e.g., CM1, CM2.0–2.6 or CR1, CR2.0–3.0). The difficulty in establishing these depletions by any geological process has prompted generations of cosmochemists to interpret volatile depletion in chondrites as a nebular process. However, as a counterpoint, Young *et al.* (2003) (also personal communication) have suggested that solubility essentially mimics volatility (as defined by condensation temperature). In this formulation, differences in bulk chemistry between the chondrite groups are a result of aqueous alteration. If this were the case, the observation that CCs show solar abundances or monotonic depletions

from solar, rather than being evidence *against* fluid flow, may in fact be evidence *for* fluid flow. There are a number of arguments that can be made against this. For instance, one of the most soluble elements that is demonstrably highly mobile during aqueous alteration is Ca (carbonates, hedenbergite, andradite, kirschsteinite). Calcium is highly refractory. Large fractionation of Ca from Al, which has a similar condensation temperature, is one of the key arguments in favor of low-temperature aqueous alteration resulting in formation of Al-free Ca-rich secondary phases. The same is true for Mn and Cr. This is the basis for  $^{53}\text{Mn}$ - $^{53}\text{Cr}$  dating of aqueously formed carbonates, fayalite, and kirschsteinite. In addition, elements with very different volatility are highly mobile during aqueous alteration (e.g., Sr and Zn).

Although it is the consensus view that isochemical alteration requires the flow of liquid water to be minimal (*Brearley*, 2003), i.e., a closed system over length scales greater than hundreds of micrometers, this conclusion is not inconsistent with the presence of short (less than hundreds of micrometers) veins in some aqueously altered meteorites, or diffusion over similar distances. Closed system  $\neq$  zero flow. Rather, it means that over the timescale that aqueous alteration is occurring, flow was restricted to relatively short length scales. The presence of these features indicates that redistribution of elements occurred largely between chemically distinct chondrite components — refractory inclusions, chondrules, and matrices (e.g., *Brearley and Krot*, 2012). Finally, chemical analyses of small (10–100 mg) bulk chondrite aliquots support this conclusion, showing remarkable reproducibility between samples and no evidence for element mobility (*Wulf et al.*, 1995). Similarly, analyses of the trace-element composition of fine-grained materials in CCs indicate minimal aqueous mobility (*Bland et al.*, 2005). Although sulfate veins in CIs were initially thought to be a result of extensive fluid flow, there is now ample evidence that remobilization of sulfates occurred in the terrestrial environment (*Gounelle and Zolensky*, 2001). The fact that no chondrite contains large veins, or an interconnected vein network with diffusion/alteration gradients away from veins (as observed in terrestrial hydrothermal systems), can be taken as petrographic evidence against large-scale flow through a vein/fracture network.

Oxygen-isotopic data from CCs have been interpreted as consistent with both a closed-system two-reservoir model (*Clayton and Mayeda*, 1999) and an open-system model (*Young et al.*, 1999). In the former, water/rock is fixed and CC parent bodies are compositionally and mineralogically distinct; in the latter, down-temperature flow produces zones that resemble CV, CM, and CI meteorites. In particular, carbonate grains in a number of CMs exhibit a large range in  $\delta^{18}\text{O}$ , interpreted as suggesting open-system water-rock interaction [varying water/rock ratio with varying temperature (*Young et al.*, 1999)]. Earlier CM calcite oxygen-isotope data have been interpreted as consistent with both closed-system, two-reservoir models (but with a larger matrix-water fractionation factor), and also with fluid-flow in a restricted region of a CC parent body (*Benedix et al.*, 2003). More recent

carbonate oxygen data have been interpreted as requiring water/rock reactions involving flowing water as a result of a temperature gradient. But it should be noted that achieving this oxygen-isotope heterogeneity at the thin-section scale would require a dense network of channels — a feature that is not observed petrographically. With regard to different interpretations of oxygen-isotope data (*Clayton and Mayeda*, 1999; *Young et al.*, 1999; *Benedix et al.*, 2003), given that the arguments center around fixed vs. varying water/rock ratios, it would be interesting to explore the possibility that material properties might have changed during alteration [e.g., by compaction of highly porous primordial materials by impact (*Bland et al.*, 2014), porosity change related to growth of alteration minerals, or flow of the matrix itself as an unconsolidated mud (*Bland et al.*, 2013)].

The numerical modeling results appear to contradict much of the meteorite data — all the modeling studies (*Grimm and McSween*, 1989; *Cohen and Coker*, 2000; *Coker and Cohen*, 2001; *Young et al.*, 1999, 2003; *McSween et al.*, 2002; *Travis and Schubert*, 2005) suggest that alteration occurred in an open system with asteroid-scale fluid flow, whereas meteorite chemistry and petrography suggest that alteration was isochemical, with minimal flow (the debate continues regarding oxygen). Fundamental to fluid flow is rock permeability. Initial permeability estimates of  $10^{-13}$ – $10^{-11}$  m<sup>2</sup> for chondritic asteroids (*Grimm and McSween*, 1989) were based on what were felt to be appropriate terrestrial analog materials: a consolidated tuff from the Waiora formation in New Zealand with 39% porosity and grain size of 50–100  $\mu\text{m}$ ; and an unconsolidated lunar soil with 50% porosity and 60–100- $\mu\text{m}$  grain size (*Mercer et al.*, 1975; *Lambe and Whitman*, 1969; *Costes and Mitchell*, 1970). The permeability values used by *Grimm and McSween* (1989) were adopted in all subsequent studies (*Cohen and Coker*, 2000; *Coker and Cohen*, 2001; *Young et al.*, 1999, 2003; *McSween et al.*, 2002; *Travis and Schubert*, 2005). But are these terrestrial and lunar analogs appropriate for CC precursors? *Bland et al.* (2009) explored this question in some detail. Matrix grain size in CCs that have experienced minimal alteration is ~100 nm (*Greshake*, 1997; *Nuth et al.*, 2005), far smaller than in the analog materials. The petroleum industry is understandably interested in constraining flow in porous media. The familiar Blake-Kozeny-Carman equation (*Dullien*, 1992) is used throughout the industry to predict permeability based on grain sizes and porosities in the range of interest for us (given reasonable estimates of the hydraulic tortuosity coefficient). The value of the Blake-Kozeny-Carman equation is illustrated by the fact that predicted values for the Waiora tuff and lunar soil are identical to measured values. For grain sizes appropriate for primitive CC matrices (tens to hundreds of nanometers), the Blake-Kozeny-Carman equation yields values ranging from  $10^{-17}$ – $10^{-19}$  m<sup>2</sup>, even in a high-porosity matrix (~40%). Matrix grain size dictates mean pore-throat diameter, and therefore is a key control on permeability (which scales with the inverse of grain size squared). But independent measurements of mean pore size have also been made (*Bland et al.*, 2009). Nuclear magnetic resonance cryoporometry shows

a pore-volume distribution for Acfer 094 at extremely low pore diameters. From 200 nm down to the smallest pore diameter currently measurable by this technique in these meteorites ( $\sim 20$  nm), the pore volume distribution averages  $3 \pm 1 \text{ } \mu\text{l nm}^{-1} \text{ g}^{-1}$ , with no sign of a drop-off at low pore diameters. Estimating the mean pore size is difficult, as the smallest pores in Acfer 094 are below the resolution of these measurements. However, a geometric mean pore size in the range 10–100 nm is reasonable based on the available data. Although permeability measurements on meteorites that have experienced geological processing must be treated with some care, these estimates are in line with permeability measurements on chondritic meteorites. Corrigan *et al.* (1997) significantly expanded the gas permeability dataset for chondrites. The average permeability for all the meteorites analyzed was  $8.3 \times 10^{-17} \text{ m}^2$ . CM chondrites — included in this average — proved to be an analytical challenge due to the presence of cracks caused by desiccation while on Earth (Corrigan *et al.*, 1997, and personal communication), occasionally resulting in relatively high permeabilities. For the most mineralogically primitive meteorites in their suite (samples of Vigarano, Efremovka, Leoville — all reduced CV3s), Corrigan *et al.* (1997) found an average permeability of  $2.5 \times 10^{-18} \text{ m}^2$ . To summarize, if this suite of permeability data had been available at the time, it is likely that Grimm and McSween (1989) would have made use of it in their seminal paper, rather than data from coarse-grained analog materials. As noted above, all subsequent numerical modeling studies incorporated Grimm and McSween (1989) permeabilities as inputs. Given much smaller permeability “default” values, we can expect that those studies would have predicted much lower flow in chondritic asteroids as a model output. Although debate continues with respect to the interpretation of chondrite oxygen-isotope data (particularly varying carbonate compositions), an amended “default” permeability value would appear to reconcile the numerical modeling with meteorite compositional data showing isochemical alteration, and petrographic observations suggesting restricted flow. It should be noted that higher permeabilities have been proposed for early accreting chondrite parent bodies resulting from large fracture networks (Fu *et al.*, 2015). Certainly, fracture networks could result in arbitrarily high permeabilities, allowing for asteroid-scale flow. However, as noted previously, alteration in chondrites does not appear to have been controlled by fluid-filled fractures: The petrography of primitive meteorites is not defined by altered zones around fractures; rather, the entire sample (on the scale of thin sections to a large mass such as Murchison) is homogeneously altered.

Various physical consequences of aqueous alteration are predictable. Melting of ice to liquid water involves a volume decrease providing space, in addition to any initial void space, for water vapor and for the gases such as H<sub>2</sub> and CO<sub>2</sub> produced in the alteration reactions (Grimm and McSween, 1989; Browning and Bourcier, 1996; Wilson *et al.*, 1999). However, the alteration process results in an increase in the volume of silicates largely compensating for this (Grimm

and McSween, 1989). Thermal models show that, depending on the nature of pathways for gas to escape to the surface, gas production rates are high enough for significant pressures to build up in asteroid interiors (Wilson *et al.*, 1999). These can exert extensional stress on the primitive crust to the point where the likely tensile strength of a few megapascals could be exceeded on asteroids with radii greater than several tens of kilometers, leading to normal faulting of the crust. Gas escape through fractures could elutriate fine-grained material from asteroid interiors. Wilson *et al.* (1999) suggested that it was possible, in extreme cases, for asteroids with radii between  $\sim 20$  and  $\sim 40$  km to be explosively disrupted by the gas escape, especially if they had unusually well-ice-cemented crusts. In many cases the resulting fragments would reaccrete into heterogeneous mixtures of variably altered components of the original body. Although debate continues regarding the degree to which chondrites were closed systems with respect to aqueous fluids, it is extremely unlikely that they were closed systems with respect to gases.

#### 4. ASTEROIDS THAT EXPERIENCED CORE FORMATION

The first non-aqueous melt to be produced during the heating of any asteroid with at least approximately chondritic bulk chemistry is an Fe,Ni-FeS cotectic liquid forming at  $\sim 1250$  K (e.g., Kubaschewski, 1982; Keil and Wilson, 1993; Benedix *et al.*, 1998). There is still conflicting evidence as to the control of the contact angle between liquid and solid silicate grains on the critical amount of this liquid that must form to allow core formation by percolation along grain boundaries in silicate bodies of asteroidal composition and size. The dihedral angle is a function of both total pressure and oxygen partial pressure: High values reduce the likelihood of percolation without silicate melting. Terasaki *et al.* (2008) inferred that pressures in the interiors of asteroids smaller than  $\sim 2500$  km in diameter were low enough that Fe,Ni-FeS liquid could segregate without silicate melting, but many other studies suggest that several percent (Yoshino *et al.*, 2003, 2004; Roberts *et al.*, 2007; Mann *et al.*, 2008) or even more than 10% (Terasaki *et al.*, 2005; Walte *et al.*, 2007; Bagdassarov *et al.*, 2009; Holzheid, 2013) silicate melting is needed. Matrix deformation may aid interconnection of melt pockets in a partially molten system (Bruhn *et al.*, 2000; Walter, 2000; Rushmer *et al.*, 2000). Rushmer *et al.* (2005) suggested that impacts onto the surfaces of asteroids may have generated transient stress perturbations inducing dilation and local pressure gradients (Petford and Koenders, 2003), driving interconnection of melt pockets, although Walte *et al.* (2011) doubt the efficiency of this process. Direct evidence of some Fe,Ni-FeS liquid migration with limited silicate melting is found in two meteorites, Graves Nunataks (GRA) 95209 and Elephant Moraine (EET) 84302, intermediate in properties between acapulcoites and lodranites (McCoy *et al.*, 2006b).

The total melt fraction in a partially molten system controls the permeability of the remaining solid silicate matrix allowing Darcy flow, but Šrámek *et al.* (2012) point out that

this is not the only factor limiting core formation. Segregation of any liquid requires viscous deformation and compaction of the residual matrix, limited by its bulk viscosity. An order of magnitude estimate of the timescale for core formation can be obtained (Šrámek *et al.*, 2012) by balancing the gravitational deviatoric stress  $\Delta\text{pgd}$  against the viscous resistance of the matrix,  $\eta(v/d) = \eta/\tau$ , where  $\Delta p = \sim 5000 \text{ kg m}^{-3}$  is the density difference between Fe,Ni-FeS and silicate solid,  $g$  is the acceleration due to gravity,  $d$  is the length scale at which the process must occur,  $\eta = \sim 10^{18} \text{ Pa s}$  is a plausible matrix viscosity,  $v$  is the typical deformation velocity, and  $\tau$  is the timescale. For a laboratory experiment  $d$  is  $\sim 10 \text{ mm}$  and  $g = \sim 10 \text{ m s}^{-2}$  so  $\tau = \eta/(\Delta\text{pgd})$  is on the order of 100 m.y., ensuring that no separation is seen. For differentiating asteroids,  $d$  ranges from  $\sim 30 \text{ km}$  (the smallest bodies undergoing significant heating) to  $\sim 100 \text{ km}$  [the mantle of (4) Vesta] and the corresponding values of  $g$  at mid-mantle depths range from  $\sim 0.01$  to  $\sim 0.1 \text{ m s}^{-2}$ . Thus  $\tau$  takes the values  $\sim 20,000$  and  $\sim 600 \text{ yr}$ , respectively. Even the longest of these timescales is much less than the half-life of  $^{26}\text{Al}$ , implying that mantle matrix deformation and Darcy flow in asteroids could allow core formation even though liquid separation is not seen in laboratory experiments.

The above arguments assume that only solids and liquids are present during core formation. However, Keil and Wilson (1993) suggested that any volatiles present at this stage in an asteroid's evolution could have been trapped as gas bubbles in the Fe,Ni-FeS liquid, greatly changing the density contrast between liquid and solid, and possibly even driving the first-forming cotectic liquids upward rather than downward, to be lost to space in explosive activity at the surface. This mechanism could explain the apparent S-depletion of IVA- and IVB-group iron meteorites.

## 5. ASTEROIDS THAT EXPERIENCED SILICATE MELTING

### 5.1. Evidence for Silicate Melting

Numerous types of meteorites are samples of asteroid mantle rocks from which partial silicate melts formed and were removed. Table 2 shows that the maximum degree of partial silicate melting that is inferred to have occurred in the interiors of these differentiated asteroids varies widely, from only a few percent to at least 50% and possibly  $\sim 100\%$ . In some cases, the melts were emplaced on and intruded beneath the surface to form a basaltic crust. This is true of (4) Vesta (McSween *et al.*, 2013) and also of (1459) Magnya (Lazzaro *et al.*, 2000), (1904) Massevitch (DeMeo *et al.*, 2009), and possibly several other small bodies (Moscovitz *et al.*, 2008). In the other cases, the corresponding basalts are not found as discrete meteorites or, except very rarely (Keil *et al.*, 2011), as clasts within breccias, implying that the melts migrated to the surface and, especially for small asteroids, were lost into space as small pyroclasts ejected at greater than escape velocity in explosive volcanic eruptions (Wilson and Keil, 1991).

### 5.2. Modeling Approaches

Various models of the physics and chemistry of silicate melt formation and migration in asteroids have been proposed. Some papers focus on the geochemistry of the processes involved and the consequences for the petrology of meteorites, especially the howardite-eucrite-diogenite (HED) meteorites from (4) Vesta (Righter and Drake, 1997; Nyquist *et al.*, 2003; Weichert *et al.*, 2004; Greenwood *et al.*, 2005; Yamaguchi *et al.*, 2011; Mandler and Elkins-Tanton, 2013; Barrat and Yamaguchi, 2014). Papers focusing on the physics alone include those of Ghosh and McSween (1998), Hevey and Sanders (2006), Sahijpal *et al.* (2007), Goodrich *et al.* (2007), Wilson *et al.* (2008), Gupta and Sahijpal (2010), Moscovitz and Gaidos (2011), Elkins-Tanton *et al.* (2011), Neumann *et al.* (2012), Wilson and Keil (2012), Formisano *et al.* (2013), and Neumann *et al.* (2014). None of these treatments attempts to model all the physical processes taking place. Thus Ghosh and McSween (1998), Sahijpal *et al.* (2007), and Gupta and Sahijpal (2010) segregate a core downward and silicate melt upward when specific temperature or melt fractions are reached without specifying a detailed process. Hevey and Sanders (2006) ignore core formation and transfer heat by conduction until 50% mantle melting occurs, after which heat moves by convection beneath the cool boundary layer. Elkins-Tanton *et al.* (2011) form a core after 10% mantle melting and then postulate heat transfer by convection until late-stage cooling intervenes. Moscovitz and Gaidos (2011), Neumann *et al.* (2012), Formisano *et al.* (2013), and Neumann *et al.* (2014) all move melt by percolation through the unmelted matrix; Neumann *et al.* (2014) also add convection after 50% melting. Finally, Goodrich *et al.* (2007), Wilson *et al.* (2008), and Wilson and Keil (2012) do not treat core formation but assert that the formation of vein and dike networks, on length scales much greater than the sizes of the mantle mineral grains, very greatly increases the efficiency of silicate melt transfer to shallow levels. As a result the mantle melt fraction never exceeds a few percent in these models, and conditions never favor convection.

### 5.3. Magma Oceans

The understanding that, if no other mechanism intervened, percolation along grain boundaries was a slow process in asteroids gave rise to the assumption that melt would be largely retained in mantles until the volume fraction was sufficiently great,  $\sim 40\text{--}50\%$ , for convection to begin. This logically gave rise to the concept of asteroid magma oceans (Righter and Drake, 1997; Greenwood *et al.*, 2005, 2014; Gupta and Sahijpal, 2010; Schiller *et al.*, 2010b; Elkins-Tanton *et al.*, 2011; Yamaguchi *et al.*, 2011; Mandler and Elkins-Tanton, 2013). This use of the term differs from its use in respect to the Moon (and other large planetary bodies), where only the outer layers became molten as a result of the extremely rapid accretion of the body while the inner parts initially remained solid, eventually warming to the point

where partial melting began long after the magma ocean had cooled. In the case of asteroids, the accretion process itself did not result in extreme heating (*Merk et al.*, 2002; *Šrámek et al.*, 2012), but subsequent accumulation of heat from the decay of  $^{26}\text{Al}$  in asteroids that accreted sufficiently soon after CAIs caused all their interiors beneath the conductively controlled outer ~10-km boundary layer to reach temperatures potentially well in excess of the silicate solidus. This implies that extensive melting should have taken place and there is much geochemical (*Greenwood et al.*, 2005, 2014; *Schiller et al.*, 2010b) and petrological (*Yamaguchi et al.*, 2011; *Mandler and Elkins-Tanton*, 2013) evidence for this. However, it does not follow that extensive degrees of melting led to the entire mantles of asteroids becoming largely molten magma oceans. This is because, as argued by *Goodrich et al.* (2007), *Wilson et al.* (2008), and *Wilson and Keil* (2012), and supported by measurements on acapulcoite and lodranite meteorites (*McCoy et al.*, 1997), silicate melts may be able to migrate readily from asteroid interiors after small (~5%) degrees of silicate partial melting have established complex interconnected melt pathways within the mantle, and either erupt at the surface or accumulate in shallow intrusions at the base of, or within, the lithosphere. These shallow accumulations of melt may be very extensive and could themselves qualify as magma oceans.

#### 5.4. Physical Considerations

Melt migration requires a driving force. Local forces, such as the pressurization of a liquid film formed at the contact between two mineral grains when the liquid has a lower density than the material from which it forms, and therefore occupies a larger volume, can drive melt movement in any direction and encourage linking of liquid films along grain boundaries (*Muenow et al.*, 1992). *Sleep* (1988) showed how differential stresses can cause melt to migrate from smaller veins into larger ones, expanding small numbers of large veins at the expense of large numbers of small ones. However, large-scale upward silicate melt separation from a partially molten mantle can only realistically be driven by buoyancy. This can be due to the melt having a lower density than the residual unmelted matrix or due to the melt containing gas bubbles, or both. The upward melt segregation by percolation along grain boundaries (*Maaloe and Schie*, 1982; *Kelemen et al.*, 1997) requires deformation of the unmelted matrix (*McKenzie*, 1984, 1985; *Richter and McKenzie*, 1984; *Scott and Stevenson*, 1984, 1986; *Ribe*, 1985; *Spiegelman and McKenzie*, 1987) and melt networks may develop on scales larger than the mineral grain size (*Maaloe*, 2003; *Spence et al.*, 1987; *Sleep*, 1988; *Hart*, 1993). Partial melt zones in Earth's mantle develop networks of veins and dikes on millimeter to meter scales (*Nicolas and Jackson*, 1982; *Sleep*, 1984, 1988; *Fowler*, 1985; *Nicolas*, 1986; *Petford and Koenders*, 1998; *Bons and van Milligen*, 2001; *Brown*, 2004), allowing very efficient transfer of melt (*Valentini et al.*, 2007).

*Wilson et al.* (2008) used the above concepts to derive a mathematical model of melt extraction from asteroid interi-

ors. They applied the model to the ureilite parent body and found that melt transfer times from deep interior to shallow depth could be as small as a few months, with only ~2% of the asteroid interior being occupied by melt at any one time. This rapid transit time is consistent with geochemical evidence (*Goodrich et al.*, 2007) that negligible chemical interactions had taken place between ascending melts and unmelted host rocks. Care is needed in generalizing this result because it was derived for the ureilite parent body, which was inferred by *Goodrich et al.* (2007) to have been ~100 km in radius and to have produced melts containing copious CO gas generated by smelting, the reaction between graphite and various metal oxides. However, *Wilson and Goodrich* (2012) revisited the model assuming that no gas was present to enhance the buoyancy of the melts and found that transfer timescales were still only on the order of one year provided that volatile-free melts were ~10% less dense than their host rocks. Furthermore, the transit time is inversely proportional to the asteroid radius, so even the smallest (~30 km radius) differentiated asteroids should have required no more than three years to transfer melts from the interior to shallow levels.

The issue of melt buoyancy was raised by *Fu and Elkins-Tanton* (2014), who pointed out that it is not guaranteed that the silicate melts formed in asteroids will be less dense than the residual mantle. Also, they reasoned that volatile species were probably driven from the interiors of asteroids as temperatures rose toward the silicate solidus and therefore argued that it was not safe to rely on entrained gas bubbles to provide positive buoyancy. They therefore calculated the densities of volatile-free melts using experimentally determined partial melt compositions from starting materials having bulk mineralogies equivalent to those of the H, LL, CV, CM, and EH chondrite groups. They found that silicate melts from the CV and CM compositions were likely to be negatively, rather than positively, buoyant, and argued that as a result the melts would be retained in magma oceans and never erupted or intruded to shallow levels. The absence of surface volcanism would allow the retention of primitive chondritic crusts on bodies with these compositions. Table 2 attempts to link the theoretical model of *Fu and Elkins-Tanton* (2014) with the empirical implications of deductions about melt migration on various meteorite parent bodies. In some cases (ordinary chondrites, enstatite chondrites, aubrites) the result is good agreement; however, in other cases it is marginal disagreement (acapulcoite-lodranites, HEDs) to an extreme mismatch (ureilites, angrites).

Two possible reasons for the discrepancies suggest themselves. The first is that the compositions assumed for the calculations are inappropriate. For example, most differentiated asteroids may have completed their accretion before the main period of chondrule formation and, therefore, chondrule accretion (*Kleine et al.*, 2005; *Amelin and Krot*, 2007; *Rudraswami et al.*, 2008; *Kleine et al.*, 2009; *Nyquist et al.*, 2009), and so it may be unsafe to assume that each differentiated body had an initial composition identical to that of one or other of the classes of chondrite meteorites. The observed

differences in Cr- and Ti-isotopic compositions of differentiated meteorites and known groups of chondritic meteorites (Warren, 2011b) support this conclusion. The second possible reason is that the degassing of asteroids during heating is not as efficient as *Fu and Elkins-Tanton* (2014) propose. Although these authors make a good case for the complete loss of H<sub>2</sub>O and any trapped CO, the laboratory experiments of *Muenow et al.* (1992, 1995) suggest that ~400 ppm of S or Cl (or both) may be present in at least the early stages of silicate melting in chondrites. The effectiveness of small quantities of gas in reducing the density of silicate melts depends strongly on the pressure — the higher pressures in larger asteroids increase the gas density and reduce the buoyancy contribution. Using the formulae for internal pressures in asteroids given by *Wilson et al.* (2008), it is easy to find the bulk density of melts containing 400 ppm of molecular weight ~64 kg kmol<sup>-1</sup> (S<sub>2</sub> or SO<sub>2</sub>; Cl<sub>2</sub> would be similar at ~71 kg kmol<sup>-1</sup>) at the pressures corresponding to the middle and top of the mantle of asteroids of a given radius. For radii 30, 50, 100, and 200 km, the amounts by which the bulk melt density is less than the matrix density are 580, 265, 80, and 24 kg m<sup>-3</sup>, respectively, at mid-mantle depths and 660, 410, 210, and 105 kg m<sup>-3</sup>, respectively, at lithosphere-base depths. These positive buoyancy values are to be compared with the negative buoyancies of ~500 and ~200 kg m<sup>-3</sup>, respectively, calculated by *Fu and Elkins-Tanton* (2014) for CM and CV compositions. It is clear that small amounts of retained gases may overcome the buoyancy problem for small asteroids but there would still be an issue for larger bodies. However, if volatile amounts were larger, e.g., on the order of 4000 ppm as measured by *Muenow et al.* (1992, 1995), the density reductions given above would increase to 2115, 1485, 650, and 225 kg m<sup>-3</sup>, for mid-mantle depths and 2210, 1830, 1280, and 800 kg m<sup>-3</sup>, respectively, for lithosphere-base depths, almost completely eliminating all buoyancy problems.

## 5.5. Magma Transport to Shallow Levels

If, as proposed by *Wilson et al.* (2008), networks of veins and dikes develop to allow efficient transport of silicate magma out of asteroid mantles to form intrusions or feed eruptions, buoyancy is not the only parameter controlling the process. The melt production rate is also critical. This is because the final stage of the melt transport to shallow levels must be via a dike that is wide enough to allow a fast enough magma flow rate to avoid excessive cooling as the melt passes through cooler rocks in the outer thermal boundary layer of the asteroid. Furthermore, for surface eruptions, the stress regime produced by the combination of magma pressure and country rock load must be such as to allow a stable dike to exist that has a great enough vertical length to penetrate completely through the thermal boundary layer, i.e., the lithosphere. *Wilson and Keil* (2012) summarized maximum melt-production rates from the asteroid differentiation models of *Hevey and Sanders* (2006), *Wilson et al.* (2008), and *Moskovitz and Gaidos* (2011) to show that, for early forming asteroids with radii in the range 25–250 km, total magma

generation rates should be in the range 3–3000 m<sup>3</sup> s<sup>-1</sup>. *Wilson et al.* (2008) pointed out that not all the melt produced in an asteroid interior will be channeled to the surface through a single dike. Rather, geometry dictates that ~5 roughly equant volumes of the interior will each feed a separate dike, with each zone producing ~0.6–600 m<sup>3</sup> s<sup>-1</sup> of melt. These are maximum rates soon after silicate melting begins; melt production rates inevitably decrease as <sup>26</sup>Al decays.

Using these values, *Wilson and Keil* (2012) modeled the formation of dikes that evolved in size and shape until the dike geometry allowed the volume flow rate of magma to match the volume flux from the source zone. They found that, for all asteroids smaller than ~200 km in radius, direct eruptions to the surface are forbidden because of excessive magma cooling as dikes pass through the crust, implying that at least the earliest melts moving upward from an asteroid mantle will form intrusions in the form of sills or magma reservoirs at, or not far above, the base of the lithosphere. Any surface eruptions would be fed by magmas derived from these reservoirs as a result of their subsequent physicochemical development. A similar conclusion was reached for the ureilite parent body by *Wilson et al.* (2008), who argued that the unmodified primitive crust of an asteroid would probably be fractured by impacts and would be of lower density than at least some of the melts approaching from below, so that a density trap, and to some extent a mechanical/rheological trap, would exist. Melts would intrude the base of the less-competent material in much the same way as magmas appear to have invaded the brecciated zones beneath the floors of floor-fractured craters on the Moon (*Jozwiak et al.*, 2012). The extent of the intrusions would be very much greater on asteroids, however, because of the magma volumes involved. Models that infer efficient removal of melt from asteroid mantles in the early stages of partial melting (*Wilson et al.*, 2008; *Moskovitz and Gaidos*, 2011) have difficulty achieving more than ~30% partial melting of the mantle because aluminum, including the <sup>26</sup>Al heat source, preferentially partitions into the basaltic melt. Using 30% melting as an upper limit, and making due allowance for the volume of the outer thermal boundary layer of the asteroid that never reaches melting temperatures, *Wilson and Keil* (2012) investigated the consequences of erupting and intruding the implied volumes of melt at shallow levels in asteroids of a wide range of sizes. The total melt volume exceeds the volume of the lithosphere for asteroids with radii greater than ~100 km.

If all this melt were to erupt from the mantle directly onto the surface, it would not modify the original primitive crustal material significantly by heating it from above — each lava flow or pyroclast layer would cool so quickly that little of its heat would be transported downward to any significant depth. However, the erupted materials would progressively bury the original crust on asteroids with radii > 100 km to the extent that the geotherm would migrate up into the crust and cause it to become part of the melting mantle; all primitive material would be eliminated. It is not surprising, therefore, that no sign of primitive crustal material is seen in any of the HED meteorites from (4) Vesta. However, *Wilson*

and Keil (2012) point out that it is surprising that primitive clasts are not reported in breccias from smaller differentiated bodies such as the ureilite or aubrite parent asteroids.

### 5.6. Lithospheric Magma Reservoirs

Mantle melts intruded beneath or within the lithosphere could form discrete magma reservoirs or a global sill. A single global sill on a ~250-km-radius body [i.e., (4) Vesta] would have an average thickness of ~22 km; its thickness on asteroids with radii 200, 150, 100, and 50 km would be about 16, 11, 6, and 2 km, respectively (Wilson and Keil, 2012). Depending on the configuration (basal global sill or more equant magma bodies), the extent of thermal metamorphism of the primitive crust could be extensive. The fact that basaltic melts bring with them the  $^{26}\text{Al}$  heat source means that, if they initially accumulate to form a large reservoir quickly enough to offset losses by conduction from the reservoir margins, a very considerable temperature increase can occur before enough  $^{26}\text{Al}$  has decayed that cooling dominates. The concept of a global sill is attractive in that it is, in effect, a magma ocean with 100% melt. The main difference between this shallow version of a magma ocean and the deeper mantle version previously assumed by many authors is that the subsequent cooling and geochemical evolution takes place at lower pressures and more quickly. Among the deep magma ocean models applied to (4) Vesta, that of Neumann *et al.* (2014) comes closest to combining both concepts. These authors extract melt efficiently from a deep ~45% molten ocean (as a result of convection rather than by enhanced porous flow in a vein-dike network) and accumulate it into a shallow magma ocean, i.e., a global sill, for subsequent evolution. Such a picture is probably compatible with the geochemical arguments of Mandler and Elkins-Tanton (2013) and Greenwood *et al.* (2014), who infer a homogeneous source for melts with heterogeneous subsequent evolution. The presence of multiple discrete magma reservoirs at various depths in the outer parts of (4) Vesta is implied by spectral observations of 15 vestoid asteroids (Mayne *et al.*, 2011). Both monomineralic (eucrite or diogenite alone) and mixed (eucrite and diogenite together) compositions are indicated, implying that homogeneous units >5 km in size and smaller-scale heterogeneities at the <1-km scale both exist in the outer 10–20 km of (4) Vesta excavated by impacts to form the vestoids. Additional evidence for this may be implied by the heterogeneous distribution of trace elements in diogenites (Mittlefehldt *et al.*, 2012).

Little attention has been paid to the physical evolution of magma reservoirs, whatever their geometry, in the lithospheres of differentiated asteroids. Wilson *et al.* (2008) considered the growth and stability of discrete magma reservoirs against heat loss, and modeled cyclic eruptions triggered by the buildup of pressure in a reservoir as new magma was injected from below. However, their treatment was specifically directed at the ureilite parent body, where the magmas were inferred to be very positively buoyant due to their extremely large amounts (~20%, i.e., 200,000 ppm)

of CO gas generated by smelting [reaction between graphite and metal, mainly Fe, oxides (Goodrich *et al.*, 2007)]. Wilson and Keil (2012) modeled the development and intermittent eruptive activity of lithospheric magma reservoirs assuming more moderate amounts (~3000 ppm) of CO or similar molecular mass gas in line with the measurements of Muenow *et al.* (1992, 1995). However, none of these treatments considered in detail the likely changes in the density and rheology of reservoir magma as a result of its chemical evolution. Much more work is needed on this topic, taking into account the evolution with time of the magma supply rate from the mantle, the evolving magma composition, and the likely evolution of the density and porosity structure of the lithosphere. Conditions will differ significantly between smaller, more volatile-rich asteroids that lose most of their basalts to space in energetic explosive eruptions and larger, volatile-poor bodies that accumulate lavas on their surfaces. In the latter case, the progressive burial of the first-forming reservoirs will change both the internal pressure and the external lithostatic stress conditions that control their eruptive behavior. Burial of erupted materials will produce compressive stresses, as occurs on Io (Leone *et al.*, 2011), possibly large enough to produce reverse (i.e., thrust) faults (Jaeger *et al.*, 2003). In contrast, intrusions in the lower lithosphere will induce extensional forces leading to normal faulting. For dikes to be able to propagate up to the surface to feed eruptions, extension must exceed compression, at least locally.

### 5.7. Surface Eruptions

Explosive activity is almost inevitable when magmas erupt onto the surface of bodies without atmospheres as free volatiles attempt to decompress to the essentially zero pressure. Volatile expansion will tend to tear apart the host liquid into droplets with sizes in the range 30  $\mu\text{m}$  to 4 mm (Wilson and Keil, 1996b), consistent with the sizes expected for pyroclasts on the Moon (Wilson and Head, 1981) and sampled in the lunar regolith by Apollo astronauts (Taylor, 1982). The concept of explosive volcanic activity ejecting melts at greater than escape velocity has been widely adopted to explain the absence of meteoritic samples of the basalts that should have been erupted onto asteroid surfaces (Wilson and Keil, 1991, 1996b, 1997; Keil and Wilson, 1993; Warren, 2008; Wilson *et al.*, 2008, 2010; Keil, 2010; Keil *et al.*, 2011). The critical requirement is that a sufficiently large mass fraction of free gas should be present to guarantee disruption of the magma reaching the surface into pyroclastic droplets and to provide the energy needed to accelerate the erupting gas-droplet mixture to escape velocity. Fu and Elkins-Tanton (2014) have questioned the retention of sufficient volatiles during the heating processes that preceded silicate melting to allow this mechanism to operate, but no other explanation for the missing basalts has yet been put forward.

The escape speed from an asteroid is a function of its size and mass, and the mean velocity of ejecta in an explosive eruption is a function of the square root of the mass fraction of gas available to expand and accelerate gas and entrained

pyroclasts (Wilson, 1980). Wilson and Keil (1991) combined these ideas to show that pyroclasts could readily escape, especially from small, volatile-rich asteroids. The required critical gas mass fraction is proportional to the square of the asteroid radius, e.g., 50 ppm, 5000 ppm, and 5% gas for radii 30, 100, and 300 km, respectively. In more detail, however, it is necessary to take into account the fact that only the smallest pyroclastic droplets will have essentially the same speed as the gas. Larger clasts will lag behind the gas by a speed equal to their terminal velocity through the gas, and the largest clasts may fall back onto the asteroid surface while all smaller clasts are lost (Wilson and Keil, 1996b). These issues were treated in detail by Wilson et al. (2010) and applied by Keil et al. (2011) to the interpretation of a composite clast, part Fe,Ni-FeS and part basaltic glass, found in an aubrite meteorite.

When the asteroid size is too large or the magma volatile content is too small to allow escape of pyroclasts, fire fountains must form over explosive vents (Wilson and Keil, 1997), and the physics controlling these features will be analogous to that of the umbrella-shaped “plumes” seen on Io (Kieffer, 1982) but with important differences. When the volume discharge rate of magma is relatively high and the volatile content of the magma is relatively low, the small size of pyroclasts in fire fountains on airless bodies can cause the fountains to be optically dense (Wilson and Head, 1981, 2001; Wilson and Keil, 1997, 2012). Only in the outermost shell of the fountain can clasts radiate heat into space. Clasts in the interior of the fountain fall back to the surface still at magmatic temperatures and coalesce into a hot lava pond that feeds surface flows. This process explains the sizes of the thermally eroded ponds around the sources of sinuous rilles on the Moon (Wilson and Head, 1981) and Mars (Wilson and Mouginis-Mark, 2001). It is generally argued that (4) Vesta was very volatile poor, although Sarafian et al. (2013) have described evidence for small amounts of fluorine, chlorine, and some H<sub>2</sub>O in apatite grains in eucrite meteorites. The fire-fountain models imply that explosive activity driven by low-volatile-content magmas would not have broadcast cool pyroclasts over wide areas of (4) Vesta’s surface, a prediction consistent with the findings of Singerling et al. (2013), who specifically looked for frozen pyroclastic droplets as glasses in howardites and failed to identify any. Instead, weakly explosive eruptions on bodies more than ~100 km in radius would have commonly generated hot lava ponds feeding lava flows.

Lava flows on asteroids will have had very different morphologies from flows on larger bodies. Early attempts to predict flow morphology (Wilson and Keil, 1996a) assumed that magma reached the surface directly from the mantle, but the finding that most eruptions took place from shallow magma reservoirs (Wilson and Keil, 2012) increases the implied eruption rates. Maximum rates in the early stages of volcanism on large asteroids may have exceeded those common now on Earth by an order of magnitude. The low acceleration due to gravity on asteroids less than ~100 km in radius would have caused basaltic flows on such bodies to

be much thicker than those on the larger terrestrial planets, possibly forming features more akin to silicic lava domes on Earth than to long, narrow, channelized flows (Wilson and Keil, 2012).

The various silicate melt transfer and eruption processes discussed above are summarized in Fig. 2. Sadly, the only largely intact differentiated asteroid on which we might have hoped to look for examples of the surface features implied, (4) Vesta, has been modified so extensively by post-volcanism impacts that no trace of surface flow morphology remains (McSween et al., 2013).

## 6. TECTONIC PROCESSES ON ASTEROIDS: INSIGHT INTO INTERNAL STRUCTURE AND DENSITY

Various types of linear structural features have been observed on a number of asteroids (e.g., Ververka et al., 1994; Sullivan et al., 1996; Prockter et al., 2002), including (951) Gaspra, (243) Ida, (253) Mathilde, (433) Eros, (25143) Itokawa, (2867) Steins, (21) Lutetia, and (4) Vesta. These lineaments include grooves, troughs, pit crater chains, ridges, and elongate hills (Fig. 3) (Buczkowski and Wyrick, 2014). Grooves have been characterized as shallow, v-shaped gashes and are most likely the result of simple fracturing of the surface, although they may also be the surface representations of larger fractures whose distinct edges have been muted by burial under regolith and crater ejecta. Troughs are wider than grooves and have distinct walls and floors; they may be the result of reactivation of preexisting grooves or fractures, perhaps by later impacts causing further widening of existing cracks. Pit crater chains are linear assemblages of small depressions, theorized to be grooves or troughs that were covered by regolith that may now be draining into the underlying structure (e.g., Thomas et al.,

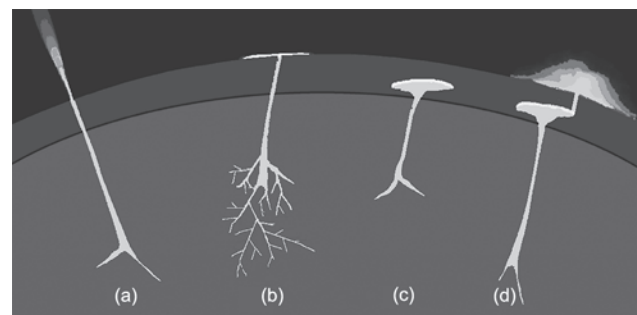


**Fig. 2.** Scenarios of silicate melt transfer from mantle to surface. **(a)** Direct transfer from mantle to surface with loss of gas and pyroclasts into space by explosive volcanism. **(b)** Direct transfer from mantle to surface to form lava flow. **(c)** Transfer from mantle to shallow intrusion. **(d)** Shallow intrusion feeds explosive fire-fountain from which pyroclasts accumulate into lava pond. In **(b)** an impression of the complex vein/dike network facilitating melt flow is given. Scenarios **(c)** and **(d)** are most likely on large differentiated asteroids.

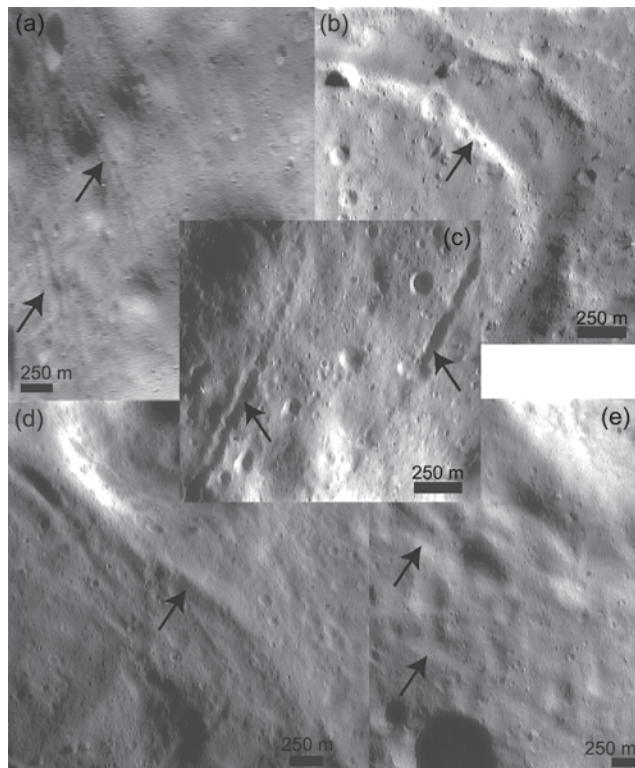


**Fig. 3.** Examples of various asteroid lineation morphologies. Arrows point to features on NEAR-Shoemaker images: (a) Grooves (image 143673751, resolution 9.48 m/pixel). (b) Flat-floored trough (image 134011958, resolution 4.76 m/pixel). (c) Pit chains (image 135344864, resolution 4.91 m/pixel). (d) Ridge (image 131011232, resolution 9.91 m/pixel). (e) Shallow troughs (image 131034292, resolution 9.18 m/pixel).

1979; Horstman and Melosh, 1989; Wyrick *et al.*, 2004). Ridges and elongate hills are linear topographic highs, as determined by image illumination and/or topographic data. While ridges are probably the surface representation of thrust faulting under a compressive state of stress (Prockter *et al.*, 2002), elongate hills have been proposed to be representative of structurally controlled magmatism (Buczkowski *et al.*, 2014; Buczkowski and Wyrick, 2014).

Since small solar system bodies (<200 km radius) do not have sufficient internal heat energy to drive terrestrial-style tectonics (Thomas and Prockter, 2010), determining how these structural features formed yields important information about the nature and geological history of such lineated asteroids. Proposed formation mechanisms for the various lineaments include (1) formation by impact (Thomas and Veverka, 1979), (2) fabric inherited from a parent body (e.g., Veverka *et al.*, 1994; Thomas *et al.*, 2002), (3) downslope scouring (e.g., Head and Cintala, 1979; Wilson and Head, 1989), and (4) thermal stresses (Dombard and Freed, 2002). Each stage in the thermal evolution of the interior of a differentiated asteroid will in principle have involved volume changes that exerted stresses on the cold outer layers of the lithosphere. As shown in earlier sections, these will most

likely have been extensional in bodies that underwent only aqueous alteration, leading to normal faulting, and could be either compressional or extensional in bodies experiencing silicate volcanism, so that both normal and reverse faults might be found.

Most of the lineaments identified on imaged asteroids have been attributed to impact, including Gaspra, Ida, Mathilde, Eros, Lutetia, and Vesta (Buczkowski and Wyrick, 2014). In addition, some features on both Gaspra (Veverka *et al.*, 1994) and Eros (Thomas *et al.*, 2002) suggest that they formed on a parent body. Both of these formation mechanisms suggest a strong and coherent asteroid. However, the few lineaments on Itokawa have been attributed to boulder movement on its surface (Sasaki *et al.*, 2006). As such, their presence does not require a coherent interior.

Vesta is both larger than the other lineated asteroids (525 km diameter) and is differentiated, meaning that internally driven tectonics and magmatism are both theoretically possible (Buczkowski and Wyrick, 2014), and various indications of magmatic processes have been identified. Raymond *et al.* (2013) identified a high Bouger gravity anomaly associated with the topographically elevated region Vestalia Terra, indicating that the plateau is comprised of a denser material than the rest of Vesta's near-surface material. Supporting this conclusion, Vestalia Terra is not cut by the equatorial flat-floored troughs that dominate the rest of the equatorial region of Vesta (Buczkowski *et al.*, 2012), suggesting that the plateau is composed of stronger and denser material than the surrounding region. Raymond *et al.* (2013) suggested that the density difference is due to an ancient mantle plume underlying the plateau. Another possibility is that Vestalia Terra is the location of one of the sill-like intrusions theorized to be at the base of Vesta's lithosphere (Wilson and Keil, 2012).

While the equatorial troughs do not disrupt Vestalia Terra, three long pit-crater chains are observed on the surface of the plateau (Buczkowski *et al.*, 2012, 2014). Pit-crater chains are hypothesized to form when dilatational motion on buried normal faults causes overlying material to collapse into the opening portions of the buried fault (Wyrick *et al.*, 2004), and it has thus been suggested that the pit-crater chains on Vestalia Terra are representative of subsurface faulting of the plateau (Buczkowski *et al.*, 2012). Interestingly, the pit-crater chain Albalonga Catena changes along its length from a topographically low string of merged pits into a topographically high elongate hill (Buczkowski *et al.*, 2014). Named Brumalia Tholus, this hill is 36 km wide and 68 km long, and topographic profiles indicate that it is dome-shaped along both its long and short axes (Buczkowski *et al.*, 2014). Buczkowski *et al.* (2014) suggested that Albalonga Catena does represent a buried normal fault, while Brumalia Tholus formed as a magmatic intrusion (perhaps a laccolith) that utilized the preexisting subsurface fault as a conduit. Molten material traveled toward the surface, intruding into and deforming the rock above it.

This hypothesis was tested by spectroscopic investigation of the core material of Brumalia Tholus. Teia crater impacts the northern face of Brumalia Tholus, and thus its ejecta

likely samples Brumalia's core material (Buczkowski et al., 2014). The Teia ejecta spectra show that they are comprised of a more plutonic material (diogenite) than the background rocks (eucrites and howardites) (De Sanctis et al., 2014). This is consistent with Brumalia Tholus being the surface representation of a magmatic intrusion that cooled slowly at depth, allowing larger crystals to form.

The source of the molten material that putatively formed Brumalia Tholus requires further consideration. The fact that Brumalia Tholus appears to be diogenitic rather than eucritic (or cumulate eucrite) indicates that the magma that formed this potential intrusion was magnesium rich, and less evolved than typical eucrite. One possibility is that the material might be diogenitic impact melt associated with the formation of the Rheasilvia basin (Buczkowski et al., 2014), similar to impact melt dikes identified around the Sudbury (Riller, 2005) and Vredfort (Reimold and Gibson, 2006) impact basins on Earth. In this hypothesis, Rheasilvia impact melt drained through fractures in the basin's floor and invaded the Albalonga fault, forming Brumalia Tholus (Buczkowski et al., 2014). However, modeling indicates that impact melt production on asteroids should be limited, due to the lower impact velocities of main-belt impactors (Keil et al., 1997), and to date only a small amount of impact melt associated with Rheasilvia has been tentatively identified (Schenk et al., 2012; McSween et al., 2013; Williams et al., 2014), suggesting that an igneous rather than impact origin is more likely (Buczkowski et al., 2014). Simple models of the thermal evolution of asteroidal bodies suggest that volcanism on Vesta would have ceased by 10–100 m.y. after formation, i.e., >4.4 Ga (e.g., Schiller et al., 2010b; McSween et al., 2011). However, there is no reason that the Albalonga fault could not pre-date the end of vestan volcanism, as superposition principles suggest that of Vestalia Terra, on which Albalonga Catena outcrops, is one of the oldest intact features on Vesta (Buczkowski et al., 2014). The magmatic material injected into an ancient Albalonga fault could have been sourced by (1) the magma plume theorized by Raymond et al. (2013), (2) the sill-like intrusions hypothesized by Wilson et al. (2008), and Wilson and Keil (2012) or (3) one of the diogenitic intrusions into the eucritic crust predicted by Barrat et al. (2010).

## 7. SUMMARY

While many advances in technology used for the analysis of meteorites and in theoretical modeling of physical and geochemical processes relevant to asteroids have been made in the last decade, there are still numerous unresolved issues. Further laboratory experiments may help, but decisive evidence must come from meteorites. Unfortunately, the stresses to which meteoroids are subjected while passing through Earth's atmosphere tend to cause disassembly along planes of weakness. Thus, while representative bulk chemistry and mineralogy may be preserved, the internal physical structures of asteroids on scales greater than ~1 m are poorly sampled in the meteorite collection.

Most chondrite parent bodies accreted water ices together with anhydrous silicates and subsequently experienced aqueous alteration and fluid-assisted thermal metamorphism. The  $^{53}\text{Mn}$ - $^{53}\text{Cr}$  ages of aqueous alteration, the  $^{207}\text{Pb}$ - $^{206}\text{Pb}$  and  $^{26}\text{Al}$ - $^{26}\text{Mg}$  ages of chondrule formation, and the peak metamorphic temperatures reached by the chondrite parent bodies all suggest they accreted ~2.5–4 m.y. after CAIs, too late to become melted by decay of  $^{26}\text{Al}$ . Although there are significant variations in the degree of aqueous alteration within and among different chondrite groups, the mineralogy, petrography, and bulk chemical compositions of aqueously altered meteorites suggest that they experienced nearly isochemical alteration with a limited fluid flow.

In contrast, the asteroids that experienced silicate melting and core formation must have accreted within ~1–1.5 m.y. of CAI formation. The specific conditions that allowed migration of Fe,Ni-FeS melts downward to form cores and silicate upward to form crusts under the relatively low pressure conditions in asteroid interiors are still unclear. The current consensus is that between 5% and 10% silicate melting is needed to allow dense metallic melts to begin to sink to form cores. Ideas on the maximum amount of silicate melt present at any one time in asteroid mantles are polarized between up to at least 50% melting with retention of melt in mantles as magma oceans and no more than ~30% melting with rapid transfer of melt to the base of the crust to pond as massive intrusions. In the latter case, only a few percent melt would be present in the mantle at any one time, but the intrusions would contain 100% melt.

The Dawn encounter with (4) Vesta has helped enormously to provide data and clarify thinking about the outer layers of a differentiated asteroid. It has also provided guidance on how remote sensing observations of other asteroids are to be interpreted. However, sample return from asteroids must be an important goal for the future. Perhaps a good target for a future spacecraft mission would be a body such as (15) Eunomia, which may be a cross-section from crust to core of its parent asteroid (Gaffey et al., 2002).

## REFERENCES

- Alexander C. M. O.'D., Howard K. T., Bowden R., and Fogel M. L. (2013) The classification of CM and CR chondrites using bulk H, C and N abundances and isotopic compositions. *Geochim. Cosmochim. Acta*, 123, 244–260.
- Amelin Y. and Krot A. (2007) Pb isotopic age of the Allende chondrules. *Meteoritics & Planet. Sci.*, 42, 1321–1335.
- Amelin Y., Krot A. N., Hutcheon I. D., and Ulyanov A. A. (2002) Lead isotopic ages of chondrules and calcium-aluminum-rich inclusions. *Science*, 297, 1678–1683.
- Amelin Y., Kaltenbach A., Izuka T., Stirling C. H., Ireland T. R., Petaev M., and Jacobsen S. B. (2010) U-Pb chronology of the solar system's oldest solids with variable  $^{238}\text{U}$ / $^{235}\text{U}$ . *Earth Planet. Sci. Lett.*, 300, 343–350.
- Bagdassarov N., Golabek G. J., Solferino G., and Schmidt M. W. (2009) Constraints on the Fe-S melt connectivity in mantle silicates from electrical impedance measurements. *Phys. Earth Planet. Inter.*, 177, 139–146.
- Barrat J.-A. and Yamaguchi A. (2014) Comment on “The origin of eucrites, diogenites, and olivine diogenites: Magma ocean crystallization and shallow magma processes on Vesta” by B. E. Mandler and L. T. Elkins-Tanton. *Meteoritics & Planet. Sci.*, 49, 468–472.

- Barrat J.-A., Yamaguchi A., Zanda B., Bollinger C., and Bohn M. (2010) Relative chronology of crust formation on asteroid Vesta: Insights from the geochemistry of diogenites. *Geochim. Cosmochim. Acta*, 74, 6218–6231.
- Beck P., Garenne A., Quirico E., Bonal L., Montes-Hernandez G., Moynier F., and Schmitt B. (2014) Transmission infrared spectra (2–25  $\mu\text{m}$ ) of carbonaceous chondrites (CI, CM, CV-CK, CR, C2 ungrouped): Mineralogy, water, and asteroidal processes. *Icarus*, 229, 263–277.
- Benedix G. K., McCoy T. J., Keil K., Bogard D. D., and Garrison D. H. (1998) A petrologic and isotopic study of winonaites: Evidence for early partial melting, brecciation, and metamorphism. *Geochim. Cosmochim. Acta*, 62, 2535–2553.
- Benedix G. K., Leshin L. A., Jackson T., and Thiemens M. H. (2003) Carbonates in CM2 chondrites: Constraints on alteration conditions from oxygen isotopic compositions and petrographic observations. *Geochim. Cosmochim. Acta*, 67, 1577–1588.
- Binzel R. P. and Kofman W. (2005) Internal structure of near-Earth objects. *Compt. Rend. Phys.*, 6, 321–326.
- Binzel R. P., A'Hearn M., Asphaug E., Barucci M. A., Belton M., Benz W., Cellino A., Festou M. C., Fulchignoni M., Harris A. W., Rossi A., and Zuber M. T. (2003) Interiors of small bodies: Foundations and perspectives. *Planet. Space Sci.*, 51, 443–454.
- Bizzarro M., Olsen M., Itoh S., Kawasaki N., Schiller M., Bonal L., and Yurimoto H. (2014) Evidence for a reduced initial abundance of  $^{26}\text{Al}$  in chondrule forming regions and implications for the accretion timescales of protoplanets. *Meteoritics & Planet. Sci., Suppl.*, 49, Abstract #5125.
- Bland P. A., Alard O., Benedix G. K., Kearsley A. T., Menzies O. N., Watt L. E., and Rogers N. W. (2005) Volatile fractionation in the early solar system and chondrule/matrix complementarity. *Proc. Natl. Acad. Sci.*, 102, 13755–13760.
- Bland P. A., Jackson M. D., Coker R. F., Cohen B. A., Webber J. B. W., Lee M. R., Duffy C. M., Chater R. J., Ardkani M. G., McPhail D. S., McComb D. W., and Benedix G. K. (2009) Why aqueous alteration in asteroids was isochemical: High porosity ≠ high permeability. *Earth Planet. Sci. Lett.*, 287, 559–568.
- Bland P. A., Travis B. J., Dyl K. A., and Schubert G. (2013) Giant convecting mudballs of the early solar system. *Lunar Planet. Sci. XLIV*, Abstract #1447. Lunar and Planetary Institute, Houston.
- Bland P. A., Collins G. S., Davison T. M., Abreu N. M., Ciesla F. J., Muxworry A. R., and Moore J. (2014) Pressure-temperature evolution of primordial solar system solids during impact-induced compaction. *Nature Commun.*, 5, 5451.
- Bolland J., Connelly J. N., and Bizzarro M. (2013) Gujba age formation revisited: A possible use as time anchor. *Goldschmidt Conference*, Abstract #732.
- Bolland J., Connelly J. N., and Bizzarro M. (2014) The absolute chronology of the early solar system revisited. *Meteoritics & Planet. Sci., Suppl.*, 49, Abstract #5234.
- Bonal L., Quirico E., Bourou-Denise M., and Montagnac G. (2006) Determination of the petrologic type of CV3 chondrites by Raman spectroscopy of included organic matter. *Geochim. Cosmochim. Acta*, 70, 1849–1863.
- Bons P. D. and van Milligen B. P. (2001) A new experiment to model self-organized critical transport and accumulation of melt and hydrocarbons from their source rocks. *Geology*, 29, 919–922.
- Brearley A. J. (1988) Nature and origin of matrix in the unique chondrite, Kakangari: A TEM investigation. *Lunar Planet. Sci. XIX*, p. 130. Lunar and Planetary Institute, Houston.
- Brearley A. J. (2003) Nebular versus parent-body processing. In *Treatise on Geochemistry, Vol. 1: Meteorites and Cosmochemical Processes* (A. M. Davis, ed.), pp. 247–268. Elsevier, Oxford.
- Brearley A. J. and Krot A. N. (2012) Metasomatism in the early solar system: The record from chondritic meteorites. In *Metasomatism and the Chemical Transformation of Rock — Lecture Notes in Earth System Sciences*, pp. 659–789. Springer, Berlin.
- Brennecke G. A., Weyer S., Wadhwa M., Janney P. E., Zipfel J., and Anbar A. D. (2010)  $^{238}\text{U}/^{235}\text{U}$  variations in meteorites: Extant  $^{247}\text{Cm}$  and implications for Pb-Pb dating. *Science*, 327, 449–451.
- Britt D. T., Yeomans D., Housen K., and Consolmagno G. (2002) Asteroid density, porosity, and structure. In *Asteroids III* (W. F. Bottke Jr. et al., eds.), pp. 485–500. Univ. of Arizona, Tucson.
- Brown M. (2004) The mechanisms of melt extraction from lower continental crust of orogens: Is it a self-organized critical phenomenon? *Trans. R. Soc. Edinburgh, Earth Sci.*, 95, 35–48.
- Brown P. G., Hildebrand A. R., Zolensky M. E., Grady M., Clayton R. N., et al. (2000) The fall, recovery, orbit, and composition of the Tagish Lake meteorite: A new type of carbonaceous chondrite. *Science*, 290, 320–325.
- Browning L. and Bourcier W. (1996) Fluid conditions during the alteration of CM chondrites. *Meteoritics & Planet. Sci.*, 31, 22–23.
- Bruhn D., Groebner N., and Kohlstedt D. L. (2000) An interconnected network of core-forming melts produced by shear deformation. *Nature*, 403, 883–886.
- Buczkowski D. L. and Wyrick D. Y. (2014) Tectonism and volcanism identified on asteroids. In *Volcanism and Tectonism Across the Inner Solar System* (T. Platz et al., eds.), Geological Society of London Spec. Publ. 401.
- Buczkowski D. L., Wyrick D. Y., Iyer K. A., Kahn E. G., Scully J. E. C., Nathues A., Gaskell R. W., Roatsch T., Preusker F., Schenk P. M., Le Corre L., Reddy V., Yingst R. A., Mest S., Williams D. A., Garry W. B., Barnouin O. S., Jaumann R., Raymond C. A., and Russell C. T. (2012) Large-scale troughs on Vesta: A signature of planetary tectonics. *Geophys. Res. Lett.*, 39, L18205.
- Buczkowski D. L., Wyrick D. Y., Toplis M., Yingst R. A., Williams D. A., Garry W. B., Mest S., Kniessl T., Scully J. E. C., Nathues A., De Sanctis M. C., LeCorre L., Reddy V., Hoffmann M., Ammannito E., Frigeri A., Tosi F., Preusker F., Roatsch T., Raymond C. A., Jaumann R., Pieters C. M., and Russell C. T. (2014) The unique geomorphology and physical properties of the Vestalia Terra plateau. *Icarus*, 244, 89–103.
- Burbine T. H., McCoy T. J., Meibom A., Gladman B., and Keil K. (2002) Meteorite parent bodies: Their number and identification. In *Asteroids III* (W. F. Bottke Jr. et al., eds.), pp. 653–667. Univ. of Arizona, Tucson.
- Castillo-Rogez J., Johnson T. V., Lee M. H., Turner M. J., Matson D. L., and Lunine J. (2009)  $^{26}\text{Al}$  decay: Heat production and a revised age for Iapetus. *Icarus*, 204, 658–662.
- Clayton R. N. and Mayeda T. K. (1999) Oxygen isotope studies of carbonaceous chondrites. *Geochim. Cosmochim. Acta*, 63, 2089–2104.
- Cohen B. A. and Coker R. F. (2000) Modeling of liquid water on CM meteorite parent bodies and implications for amino acid racemization. *Icarus*, 145, 369–381.
- Coker R. F. and Cohen B. A. (2001) The effect of liquid transport on the modeling of CM parent bodies. *Meteoritics & Planet. Sci., Suppl.*, 36, A43.
- Connelly J. N., Bizzarro M., Krot A. N., Nordlund Å., Wielandt D., and Ivanova M. A. (2012) The absolute chronology and thermal processing of solids in the solar protoplanetary disk. *Science*, 338, 651–655.
- Corrigan C. M., Zolensky M. E., Dahl J., Long M., Weir J., Sapp C., and Burkett P. J. (1997) The porosity and permeability of chondritic meteorites and interplanetary dust particles. *Meteoritics & Planet. Sci.*, 32, 509–515.
- Costes N. C. and Mitchell J. K. (1970) Apollo 11 soil mechanics investigation. *Proc. Apollo 11 Lunar Sci. Conf.*, pp. 2025–2044.
- Cournède C., Gattaccea J., Rochette P., and Weiss B. P. (2014) Insights on asteroid partial differentiation and early solar system magnetic fields revealed by paleomagnetism of carbonaceous chondrites. *Meteoritics & Planet. Sci., Suppl.*, 49, Abstract #5292.
- Davison T. M., Collins G. S., and Ciesla F. J. (2010) Numerical modelling of heating in porous planetesimal collisions. *Icarus*, 208, 468–481.
- Davison T. M., Ciesla F. J., and Collins G. S. (2012) Post-impact thermal evolution of porous planetesimals. *Geochim. Cosmochim. Acta*, 95, 252–269.
- DeMeo F. E. and Carry B. (2014) Solar system evolution from compositional mapping of the asteroid belt. *Nature*, 505, 629–634.
- DeMeo F. E., Binzel R. P., Slivan S. M., and Bus S. J. (2009) An extension of the Bus asteroid taxonomy into the near-infrared. *Icarus*, 202, 160–168.
- De Sanctis M. C. et al. (2014) Compositional evidence of magmatic activity on Vesta. *Geophys. Res. Lett.*, 41, 3038–3044.
- Dombard A. J. and Freed A. M. (2002) Thermally induced lineaments on the asteroid Eros: Evidence of orbit transfer. *Geophys. Res. Lett.*, 29, 1818, 65–1–65–4.
- Doyle P. M., Jogo K., Nagashima K., Krot A. N., Wakita S., Ciesla F. J., and Hutcheon I. D. (2015) Early aqueous activity on the ordinary and carbonaceous chondrite parent bodies recorded by fayalite. *Nature Commun.*, 6, 7444.
- Dullien F. A. L. (1992) *Porous Media — Fluid Transport and Pore Structure*. Academic, New York. 575 pp.

- Elkins-Tanton L. T., Weiss B. P., and Zuber M. T. (2011) Chondrites as samples of differentiated planetesimals. *Earth Planet. Sci. Lett.*, **305**, 1–10.
- Formisano M., Federico C., Turrini D., Coradini A., Capaccioni F., De Sanctis M. C., and Pauselli C. (2013) The heating history of Vesta and the onset of differentiation. *Meteoritics & Planet. Sci.*, **48**, 2316–2332.
- Fowler A. C. (1985) A mathematical model of melt transport in the asthenosphere. *Geophys. Astrophys. Fluid Dyn.*, **33**, 63–96.
- Fu R. R. and Elkins-Tanton L. T. (2014) The fate of magmas in pleteisimals and the retention of primitive chondritic crusts. *Earth Planet. Sci. Lett.*, **390**, 128–137.
- Fu R. R., Young E. D., Greenwood R. C., and Elkins-Tanton L. T. (2015) Fluid migration in early-accreting planetesimals. *Lunar Planet. Sci. XLVI*, Abstract #1591. Lunar and Planetary Institute, Houston.
- Gaffey M. J., Cloutis E. A., Kelley M. S., and Reed K. L. (2002) Mineralogy of asteroids. In *Asteroids III* (W. F. Bottke Jr. et al., eds.), pp. 183–204. Univ. of Arizona, Tucson.
- Ghosh A. and McSween H. Y. Jr. (1998) A thermal model for the differentiation of asteroid 4 Vesta, based on radiogenic heating. *Icarus*, **134**, 187–206.
- Goodrich C. A., Van Orman J., and Wilson L. (2007) Fractional melting and smelting on the ureilite parent body. *Geochim. Cosmochim. Acta*, **71**, 2876–2895.
- Gounelle M. and Zolensky M. E. (2011) A terrestrial origin for sulfate veins in CI1 chondrite. *Meteoritics & Planet. Sci.*, **36**, 1321–1329.
- Greenwood R. C., Franchi I. A., Jambon A., and Buchanan P. C. (2005) Widespread magma oceans on asteroidal bodies in the early solar system. *Nature*, **435**, 916–918.
- Greenwood R. C., Franchi I. A., Kearsley A. T., and Alard O. (2010) The relationship between CK and CV chondrites. *Geochim. Cosmochim. Acta*, **74**, 1684–1705.
- Greenwood R. C., Barrat J.-A., Yamaguchi A., Franchi I. A., Scott E. R. D., Bottke W. F., and Gibson J. M. (2014) The oxygen isotope composition of diogenites: Evidence for early global melting on a single, compositionally diverse, HED parent body. *Earth Planet. Sci. Lett.*, **390**, 165–174.
- Greshake A. (1997) The primitive matrix components of the unique carbonaceous chondrite Acfer 094: A TEM study. *Geochim. Cosmochim. Acta*, **61**, 437–452.
- Grevesse N., Asplund M., and Sauval A. J. (2007) The solar chemical composition. *Space Sci. Rev.*, **130**, 105–114.
- Grimm R. E. and McSween H. Y. Jr. (1989) Water and the thermal evolution of carbonaceous chondrite parent bodies. *Icarus*, **82**, 244–280.
- Grossman J. N. and Brearley A. J. (2005) The onset of metamorphism in ordinary and carbonaceous chondrites. *Meteoritics & Planet. Sci.*, **61**, 437–452.
- Guo W. and Eiler J. M. (2007) Temperatures of aqueous alteration and evidence for methane generation on the parent bodies of the CM chondrites. *Geochim. Cosmochim. Acta*, **71**, 5565–5575.
- Gupta G. and Sahijpal S. (2010) Differentiation of Vesta and the parent bodies of other achondrites. *J. Geophys. Res.–Planets*, **115**, E08001.
- Harju E. R., Rubin A. E., Ahn I., Choi B.-G., Ziegler K., and Wasson J. T. (2014) Progressive aqueous alteration of CR carbonaceous chondrites. *Geochim. Cosmochim. Acta*, **71**, 5565–5575.
- Hart S. R. (1993) Equilibration during mantle melting: A fractal tree model. *Proc. Natl. Acad. Sci.*, **90**, 11914–11918.
- Head J. W. and Cintala M. J. (1979) Grooves on Phobos: Evidence for possible secondary cratering origin. In *Reports of the Planetary Geology Program, 1978–1979*, pp. 19–21. NASA Tech. Mem. 80339, Washington, DC.
- Hevey P. J. and Sanders I. S. (2006) A model for planetesimal meltdown by  $^{26}\text{Al}$  and its implications for meteorite parent bodies. *Meteoritics & Planet. Sci.*, **41**, 95–106.
- Holsapple K. A. (2009) On the “strength” of the small bodies of the solar system: A review of strength theories and their implementation for analyses of impact disruptions. *Planet. Space Sci.*, **57**, 127–141.
- Holzheid H. (2013) Sulphide melt distribution in partially molten silicate aggregates: Implications to core formation scenarios in terrestrial planets. *Eur. J. Mineral.*, **25**, 267–277.
- Horstman K. C. and Melosh H. J. (1989) Drainage pits in cohesionless materials: Implications for the surface of Phobos. *J. Geophys. Res.*, **94**, 12433–12441.
- Hutcheon I. D. and Hutchison R. (1989) Evidence from the Semarkona ordinary chondrite for  $^{26}\text{Al}$  heating of small planets. *Nature*, **337**, 238–241.
- Hutcheon I. D., Marhas K., Krot A. N., Goswami J. N., and Jones R. H. (2009)  $^{26}\text{Al}$  in plagioclase-rich chondrules in carbonaceous chondrites: Evidence for an extended duration of chondrule formation. *Geochim. Cosmochim. Acta*, **73**, 5080–5100.
- Jacobsen B., Yin Q.-Z., Moynier F., Amelin Y., Krot A. N., Nagashima K., Hutcheon I. D., and Palme H. (2008)  $^{26}\text{Al}$ - $^{26}\text{Mg}$  and  $^{207}\text{Pb}$ - $^{206}\text{Pb}$  systematics of Allende CAIs: Canonical solar initial  $^{26}\text{Al}/^{27}\text{Al}$  ratio reinstated. *Earth Planet. Sci. Lett.*, **272**, 353–364.
- Jaeger W. L., Turtle E. P., Keszthelyi L. P., Radebaugh J., McEwen A. S., and Pappalardo R. T. (2003) Orogenic tectonism on Io. *J. Geophys. Res.*, **108**, 5093.
- Johansen A., Blum J., Tanaka H., Ormel C., Bizzarro M., and Rickman H. (2014) The multifaceted planetesimal formation process. In *Protostars and Planets VI* (H. Beuther et al., eds.), pp. 547–570. Univ. of Arizona, Tucson.
- Johnson B. C., Minton D. A., and Melosh H. J. (2014) The impact origin of chondrules. *Lunar Planet. Sci. XLV*, Abstract #1471. Lunar and Planetary Institute, Houston.
- Jozwiak L. M., Head J. W., Zuber M. T., Smith D. E., and Neuman G. A. (2012) Lunar floor-fractured craters: Classification, distribution, origin and implications for magmatism and shallow crustal structure. *J. Geophys. Res.*, **117**, E11.
- Kadish J., Barber J. R., Washabaugh P. D., and Scheeres D. J. (2008) Stresses in accreted planetary bodies. *Int. J. Solids Structures*, **45**, 540–550.
- Keil K. (2000) Thermal alteration of asteroids: Evidence from meteorites. *Planet. Space Sci.*, **49**, 887–903.
- Keil K. (2010) Enstatite achondrite meteorites (aubrites) and the histories of their asteroidal parent bodies. *Chem. Erde–Geochem.*, **70**, 295–317.
- Keil K. and Wilson L. (1993) Explosive volcanism and the compositions of cores of differentiated asteroids. *Earth Planet. Sci. Lett.*, **117**, 111–124.
- Keil K., Stöffler D., Love S. G., and Scott E. R. D. (1997) Constraints on the role of impact heating and melting in asteroids. *Meteoritics & Planet. Sci.*, **32**, 349–363.
- Keil K., McCoy T. J., Wilson L., Barrat J.-A., Rumble D., Meier M. M. M., Wieler R., and Huss G. R. (2011) A composite Fe,Ni-FeS and enstatite-forsterite-diopside-glass vitrophyre clast in the Larkman Nunatak 04316 aubrite: Origin by pyroclastic volcanism. *Meteoritics & Planet. Sci.*, **46**, 1719–1741.
- Kelemen P. B., Hirth G., Shimizu N., Spiegelman N., and Dick H. J. B. (1997) A review of melt migration processes in the adiabatically upwelling mantle beneath oceanic spreading ridges. *Philos. Trans. R. Soc. Ser. A*, **355**, 1–35.
- Kieffer S. W. (1982) Dynamics and thermodynamics of volcanic eruptions: Implications for the plumes on Io. In *Satellites of Jupiter* (D. Morrison, ed.), pp. 647–723. Univ. of Arizona, Tucson.
- Kimberley J. and Ramesh K. T. (2011) The dynamic strength of an ordinary chondrite. *Meteoritics & Planet. Sci.*, **46**, 1653–1669.
- Kita N. and Ushikubo T. (2012) Evolution of protoplanetary disk inferred from  $^{26}\text{Al}$  chronology of individual chondrules. *Meteoritics & Planet. Sci.*, **43**, 1108–1119.
- Kita N., Nagahara H., Togashi S., and Morishita Y. (2000) A short duration of chondrule formation in the solar nebula: evidence from  $^{26}\text{Al}$  in Semarkona ferromagnesian chondrules. *Geochim. Cosmochim. Acta*, **64**, 3913–3922.
- Kita N. T., Yin Q.-Z., MacPherson G. J., Ushikubo T., Jacobsen B., Nagashima K., Kurahashi E., Krot A. N., and Jacobsen S. B. (2013)  $^{26}\text{Al}$ - $^{26}\text{Mg}$  isotope systematics of the first solids in the early solar system. *Meteoritics & Planet. Sci.*, **48**, 1383–1400.
- Kleine T., Mezger K., Palme H., Scherer E., and Munker C. (2005) Early core formation in asteroids and late accretion of chondrite parent bodies: Evidence from Hf-182–W-182 in CAIs, metal-rich chondrites, and iron meteorites. *Geochim. Cosmochim. Acta*, **69**, 5805–5818.
- Kleine T., Toublou M., Bourdon B., Nimmo F., Mezger K., Palme H., Jacobsen S. B., Yin Q. Z., and Halliday A. N. (2009) Hf-W chronology of the accretion and early evolution of asteroids and terrestrial planets. *Geochim. Cosmochim. Acta*, **73**, 5150–5188.
- Krot A. N., Amelin Y., Cassen P., and Meibom A. (2005) Young chondrules in CB chondrites from a giant impact in the early solar system. *Nature*, **436**, 989–992.

- Krot A. N., Hutcheon I. D., Brearley A. J., Pravdivtseva O. V., Petaev M. I., and Hohenberg C. M. (2006) Timescales for secondary alteration of chondritic meteorites. In *Meteorites and the Early Solar System II* (D. S. Lauretta and H. Y. McSween Jr., eds.), pp. 525–555. Univ. of Arizona, Tucson.
- Krot A. N., Makide K., Nagashima K., Huss G. R., Ogliore R. C., Ciesla F. J., Yang L., Hellebrand E., and Gaidos E. (2012) Heterogeneous distribution of  $^{26}\text{Al}$  at the birth of the solar system: Evidence from refractory grains and inclusions. *Meteoritics & Planet. Sci.*, 47, 1948–1979.
- Krot A. N., Keil K., Goodrich C., Weisberg M. K., and Scott E. R. D. (2014a) Classification of meteorites. In *Treatise on Geochemistry, Vol. 1: Meteorites and Cosmochemical Processes* (A. M. Davis, ed.), pp. 1–63. Elsevier, Oxford.
- Krot A. N., Nagashima K., and Bizzarro M. (2014b) Aluminum-magnesium isotope systematics of porphyritic chondrules and plagioclase fragments in CH carbonaceous chondrites. *Lunar Planet. Sci. XLV*, Abstract #2142. Lunar and Planetary Institute, Houston.
- Kruijer T. S., Kleine T., Fischer-Gödde M., Burkhardt C., and Wieler R. (2014) Hf-W isochron for bulk CAI: Evidence for homogeneity of  $^{26}\text{Al}$  and  $^{182}\text{Hf}$ . *Lunar Planet. Sci. XLV*, Abstract #1786. Lunar and Planetary Institute, Houston.
- Kubaschewski O. (1982) *Iron-Binary Phase Diagrams*. Springer, New York. 185 pp.
- Kunihiro T., Rubin A. E., McKeegan K. D., and Wasson J. T. (2004) Initial  $^{26}\text{Al}/^{27}\text{Al}$  in carbonaceous chondrite chondrules: Too little  $^{26}\text{Al}$  to melt asteroids. *Geochim. Cosmochim. Acta*, 68, 2947–2957.
- Kurahashi E., Kita N. T., Nagahara H., and Morishita Y. (2008)  $^{26}\text{Al}-^{26}\text{Mg}$  systematics of chondrules in a primitive CO chondrite. *Geochim. Cosmochim. Acta*, 72, 3865–3883.
- Lazzaro D., Michtchenko T., Carvano J. M., Binzel R. P., Bus S. J., Burbine T. H., Mothé-Diniz T., Florcak M., Angeli C. A., and Harris A. W. (2000) Discovery of a basaltic asteroid in the outer main belt. *Science*, 288, 2033–2025.
- Lambe T. W. and Whitman R. V. (1969) *Soil Mechanics*. Wiley, New York. 553 pp.
- Larsen K. K., Trinquier A., Paton C., Schiller M., Wielandt D., Ivanova M. A., Connally J. N., Nordlund A., Krot A. N., and Bizzarro M. (2011) Evidence for magnesium-isotope heterogeneity in the solar protoplanetary disk. *Astrophys. J. Lett.*, 735, L37–L40.
- LaTourrette T. and Wasserburg G. J. (1998) Mg diffusion in anorthite: Implications for the formation of early solar system planetesimals. *Earth. Planet. Sci. Lett.*, 158, 91–108.
- Leone G., Wilson L., and Davies A. G. (2011) The geothermal gradient of Io: Consequences for lithospheric structure and volcanic eruptive activity. *Icarus*, 211, 623–635.
- Leshin L. A., Rubin A. E., and McKeegan K. D. (1997) The oxygen isotopic composition of olivine and pyroxene from CI chondrites. *Geochim. Cosmochim. Acta*, 61, 835–845.
- Maaloe S. (2003) Melt dynamics of a partially molten mantle with randomly oriented veins. *J. Petrol.*, 44, 1193–1210.
- Maaloe S. and Schie A. (1982) The permeability controlled accumulation of primary magma. *Contrib. Mineral. Petro.*, 81, 350–357.
- MacPherson G. J., Bullock E. S., Janney P. E., Kita N. T., Ushikubo T., Davis A. M., Wadhwa M., and Krot A. N. (2011) Early solar nebula condensates with canonical, not supracanonical, initial  $^{26}\text{Al}/^{27}\text{Al}$  ratios. *Astrophys. J. Lett.*, 711, L117–L121.
- Makide K., Nagashima K., Krot A. N., Huss G. R., Hutcheon I. D., and Bischoff A. (2009) Oxygen- and magnesium-isotope compositions of calcium-aluminum-rich inclusions from CR2 carbonaceous chondrites. *Geochim. Cosmochim. Acta*, 73, 5018–5051.
- Mandler B. E. and Elkins-Tanton L. T. (2013) The origin of eucrites, diogenites, and olivine diogenites: Magma ocean crystallization and shallow magma chamber processes on Vesta. *Meteoritics & Planet. Sci.*, 48, 2333–2349.
- Mann U., Frost D. J., and Rubie D. C. (2008) The wetting ability of Si-bearing liquid Fe-alloys in a solid silicate matrix — percolation during core formation under reducing conditions? *Phys. Earth Planet. Inter.*, 167, 1–7.
- Mayne R. G., Sunshine J. M., McSween H. Y., Bus S. J., and McCoy T. J. (2011) The origin of Vesta's crust: Insights from spectroscopy of the vestoids. *Icarus*, 214, 147–160.
- McCoy T. J., Keil K., Muenow D. W., and Wilson L. (1997) Partial melting and melt migration in the acapulcoite-lodranite parent body. *Geochim. Cosmochim. Acta*, 61, 639–650.
- McCoy T. J., Mittlefehldt D. W., and Wilson L. (2006a) Asteroid differentiation. In *Meteorites and the Early Solar System II* (D. S. Lauretta and H. Y. McSween Jr., eds.), pp. 733–745. Univ. of Arizona, Tucson.
- McCoy T. J., Carlson W. D., Nittler L. R., Stroud R. M., Bogard D. D., and Garrison D. H. (2006b) Graves Nunataks 95209: A snapshot of metal segregation and core formation. *Geochim. Cosmochim. Acta*, 70, 516–531.
- McKenzie D. P. (1984) The generation and compaction of partial molten rock. *J. Petrol.*, 25, 713–765.
- McKenzie D. P. (1985) The extraction of magma from the crust and mantle. *Earth Planet. Sci. Lett.*, 74, 81–91.
- McSween H. Y. Jr., Ghosh A., Grimm R. E., Wilson L., and Young E. D. (2002) Thermal evolution models of asteroids. In *Asteroids III* (W. F. Bottke Jr. et al., eds.), pp. 559–571. Univ. of Arizona, Tucson.
- McSween H. Y. Jr., Mittlefehldt D. W., Beck A. W., Mayne R. G., and McCoy T. J. (2011) HED meteorites and their relationship to the geology of Vesta and the Dawn mission. *Space Sci. Rev.*, 163, 141–174.
- McSween H. Y., Ammannito E., Reddy V., et al. (2013) Composition of the Rheasilvia basin, a window into Vesta's interior. *J. Geophys. Res.-Planets*, 118, 335–346.
- Menzel R. L. and Roberge W. G. (2013) Reexamination of induction heating of primitive bodies in protoplanetary disks. *Astrophys. J.*, 776, 89.
- Mercer J. W., Pinder G. F., and Donaldson I. G. (1975) A Galerkin-finite element analysis of the hydrothermal system at Wairakei, New Zealand. *J. Geophys. Res.*, 80, 2608–2621.
- Merk R., Breuer D., and Spohn T. (2002) Numerical modeling of  $^{26}\text{Al}$ -induced radioactive melting of asteroids considering accretion. *Icarus*, 159, 183–191.
- Meteoritical Bulletin Database (2014) <http://www.lpi.usra.edu/meteor/metbull.php>, accessed on 29 June 2014.
- Mittlefehldt D. W., Beck A. W., Lee C.-T. A., McSween H. Y., and Buchanan P. C. (2012) Compositional constraints on the genesis of diogenites. *Meteoritics & Planet. Sci.*, 47, 72–98.
- Moskovitz N. and Gaidos E. (2011) Differentiation of planetesimals and the thermal consequences of melt migration. *Meteoritics & Planet. Sci.*, 46, 903–918.
- Moskovitz N. A., Jedicke R., Gaidos E., Willman M., Nesvorný D., Fevig R., and Ivezic Ž. (2008) The distribution of basaltic asteroids in the main belt. *Icarus*, 198, 77–90.
- Mostefaoui S., Kita N. T., Togashi S., Tachibana S., Nagahara H., and Morishita Y. (2002) The relative formation ages of ferromagnesian chondrules inferred from their initial  $^{26}\text{Al}/^{27}\text{Al}$  ratios. *Meteoritics & Planet. Sci.*, 37, 421–438.
- Muenow D. M., Keil K., and Wilson L. (1992) High-temperature mass spectrometric degassing of enstatite chondrites: Implications for pyroclastic volcanism on the aubrite parent body. *Geochim. Cosmochim. Acta*, 56, 4267–4280.
- Muenow D. W., Keil K., and McCoy T. J. (1995) Volatiles in unequilibrated ordinary chondrites — abundances, sources and implications for explosive volcanism on differentiated asteroids. *Meteoritics*, 30, 639–645.
- Nagashima K., Krot A. N., and Huss G. R. (2014)  $^{26}\text{Al}$  in chondrules from CR2 chondrites. *Geochim. J.*, 48, 561–570.
- Neumann W., Breuer D., and Spohn T. (2012) Differentiation and core formation in accreting planetesimals. *Astron. Astrophys.*, 543, A141.
- Neumann W., Breuer D., and Spohn T. (2014) Differentiation of Vesta: Implications for a shallow magma ocean. *Earth Planet. Sci. Lett.*, 395, 267–280.
- Nicolas A. (1986) A melt extraction model based on structural studies in mantle peridotites. *J. Petrol.*, 27, 999–1022.
- Nicolas A. and Jackson M. (1982) High temperature dikes in peridotites: Origin by hydraulic fracturing. *J. Petrol.*, 23, 568–582.
- Nuth J. A. III, Brearley A. J., and Scott E. R. D. (2005) Microcrystals and amorphous material in comets and primitive meteorites: Keys to understanding processes in the early solar system. In *Chondrites and the Protoplanetary Disk* (A. N. Krot et al., eds.), pp. 675–700. ASP Conf. Ser. 341, Astronomical Society of the Pacific, San Francisco.
- Nyquist L. E., Reese Y., Wiesmann H., Shih C. Y., and Takeda H. (2003) Fossil Al-26 and Mn-53 in the Asuka 881394 eucrite: Evidence of the earliest crust on asteroid 4 Vesta. *Earth Planet. Sci. Lett.*, 214, 11–25.
- Nyquist L. E., Kleine T., Shih C. Y., and Reese Y. D. (2009) The distribution of short-lived radioisotopes in the early solar system and the chronology of asteroid accretion, differentiation, and secondary mineralization. *Geochim. Cosmochim. Acta*, 73, 5115–5136.

- Palme H., Lodders K., and Jones A. (2014) Solar system abundances of the elements. In *Treatise on Geochemistry, Vol. I: Meteorites, Comets and Planets* (A. M. Davis, ed.), pp. 15–36. Elsevier, Oxford.
- Petford N. and Koenders M. A. (1998) Self-organization and fracture connectivity in rapidly heated continental crust. *J. Structural Geol.*, 20, 1425–1434.
- Petford N. and Koenders M. A. (2003) Shear-induced pressure changes and seepage phenomena in a deforming porous layer — I. *Geophys. J. Int'l.*, 155, 857–869.
- Popova O., Borovicka J., Hartmann W. K., Spurny P., Gnos E., Nemtchinov I., and Trigo-Rodriguez J. M. (2011) Very low strengths of interplanetary meteoroids and small asteroids. *Meteoritics & Planet. Sci.*, 46, 1525–1550.
- Prockter L., Thomas P., Robinson M., Joseph J., Milne A., Bussey B., Veverka J., and Cheng A. (2002) Surface expressions of structural features on Eros. *Icarus*, 155, 75–93.
- Raymond C. A. et al. (2013) Vestalia Terra: An ancient mascon in the southern hemisphere of Vesta. *Lunar Planet. Sci. XLIV*, Abstract #2882. Lunar and Planetary Institute, Houston.
- Reimold W. U. and Gibson R. L. (2006) The melt rocks of the Vredefort impact structure — Vredefort granophyre and pseudotachylitic breccias: Implications for impact cratering and the evolution of the Witwatersrand Basin. *Chem. Erde*, 66, 1–35.
- Ribe N. M. (1985) The deformation and compaction of partially molten zones. *Geophys. J. R. Astron. Soc.*, 83, 487–501.
- Richter F. M. and McKenzie D. (1984) Dynamical models for melt extraction from a deformable matrix. *J. Geol.*, 92, 729–740.
- Righter K. and Drake M. J. (1997) A magma ocean on Vesta: Core formation and petrogenesis of eucrites and diogenites. *Meteoritics & Planet. Sci.*, 32, 929–944.
- Riller U. (2005) Structural characteristics of the Sudbury impact structure, Canada: Impact-induced versus orogenic deformation — A review. *Meteoritics & Planet. Sci.*, 40, 1723–1740.
- Roberts J. J., Kinney J. H., Siebert J., and Ryerson F. J. (2007) Fe-Ni-S melt permeability in olivine: Implications for planetary core formation. *Geophys. Res. Lett.*, 34, L14306.
- Rubie D. C., Nimmo F., and Melosh H. J. (2007) Formation of Earth's core. In *Treatise on Geophysics, Vol. 9: Evolution of the Earth* (D. J. Stevenson, ed.), pp. 51–90. Elsevier, Amsterdam.
- Rubin A. E., Trigo-Rodriguez J. M., Huber H., and Wasson J. T. (2007) Progressive aqueous alteration of CM carbonaceous chondrites. *Geochim. Cosmochim. Acta*, 71, 2761–2782.
- Rudraswami N. G., Goswami J. N., Chattopadhyay B., Sengupta S. K., and Thapliyal A. P. (2008) Al-26 records in chondrules from unequilibrated ordinary chondrites: II. Duration of chondrule formation and parent body thermal metamorphism. *Earth Planet. Sci. Lett.*, 274, 93–102.
- Rushmer T., Minarik W. G., and Taylor G. J. (2000) Physical processes of core formation. In *Origin of the Earth and Moon* (R. M. Canup and K. Righter, eds.), pp. 227–245. Univ. of Arizona, Tucson.
- Rushmer T., Petford N., Humayun M., and Campbell A. J. (2005) Fe-liquid segregation in deforming planetesimals: Coupling core-forming compositions with transport phenomena. *Earth Planet. Sci. Lett.*, 239, 185–202.
- Sahijpal S., Soni P., and Gupta G. (2007) Numerical simulations of the differentiation of accreting planetesimals with Al-26 and Fe-60 as the heat sources. *Meteoritics & Planet. Sci.*, 42, 1529–1548.
- Sarafian A. R., Roden M. F., and Patino-Douce A. E. (2013) The volatile content of Vesta: Clues from apatite in eucrites. *Meteoritics & Planet. Sci.*, 48, 2135–2154.
- Sasaki S. et al. (2006) Observations of 25143 Itokawa by the Asteroid Multiband Imaging Camera (AMICA) of Hayabusa: Morphology of brighter and darker areas. *Lunar Planet. Sci. XXXVII*, Abstract #1671. Lunar and Planetary Institute, Houston.
- Schenk P., O'Brien D. P., et al. (2012) The geologically recent giant impact basins at Vesta's south pole. *Science*, 336, 694–697.
- Schiller M., Baker J. A., and Bizzarro M. (2010a)  $^{26}\text{Al}$ - $^{26}\text{Mg}$  dating of asteroidal magmatism in the young solar system. *Geochim. Cosmochim. Acta*, 74, 4844–4864.
- Schiller M., Baker J. A., Bizzarro M., Creech J., and Irving A. J. (2010b) Timing and mechanisms of the evolution of the magma ocean on the HED parent body. *73rd Annual Meeting of the Meteoritical Society*, Abstract #5042, Lunar and Planetary Institute, Houston.
- Schrader D. L., Franchi I. A., Connolly H. C. Jr., Greenwood R. C., Lauretta D. S., and Gibson J. M. (2011) The formation and alteration of the Renazzo-like carbonaceous chondrites I: Implications of bulk-oxygen isotopic composition. *Geochim. Cosmochim. Acta*, 75, 308–325.
- Schrader D. L., Nagashima K., Krot A. N., Ogliore R. C., Yin Q.-Z., and Amelin Y. (2013) Testing the distribution of  $^{26}\text{Al}$  in the protoplanetary disk using CR chondrules. *Meteoritics & Planet. Sci.*, 48, A309.
- Scott D. R. and Stevenson D. J. (1984) Magma solitons. *Geophys. Res. Lett.*, 11, 1161–1164.
- Scott D. R. and Stevenson D. J. (1986) Magma ascent by porous flow. *J. Geophys. Res.*, 91, 9283–9296.
- Singerling S. A., McSween H. Y., and Taylor L. A. (2013) Glasses in howardites: Impact melts or pyroclasts? *Meteoritics & Planet. Sci.*, 48, 715–729.
- Sleep N. H. (1984) Tapping of magma from ubiquitous mantle heterogeneities: An alternative to mantle plumes? *J. Geophys. Res.*, 89, 10029–10041.
- Sleep N. H. (1988) Tapping of melt by veins and dikes. *J. Geophys. Res.*, 93, 10255–10272.
- Sonett C. P., Colburn D. S., Schwartz K., and Keil K. (1970) The melting of asteroidal sized parent bodies by unipolar dynamo induction from a primordial T Tauri sun. *Astrophys. Space Sci.*, 7, 446–488.
- Spence D. A., Sharp P. W., and Turcotte D. L. (1987) Buoyancy-driven crack propagation: A mechanism for magma migration. *J. Fluid Mech.*, 184, 135–153.
- Spiegelman M. and McKenzie D. (1987) Simple 2-D models for melt extraction at mid-ocean ridges and island arcs. *Earth Planet. Sci. Lett.*, 83, 137–152.
- Šrámek O., Milelli L., Ricard Y., and Labrosse S. (2012) Thermal evolution and differentiation of planetesimals and planetary embryos. *Icarus*, 217, 339–354.
- Sullivan R., Greeley R., Pappalardo R., Asphaug E., Moore J. M., Morrison D., Belton M. J. S., Carr M., Chapman C. R., Geissler P., Greenberg R., Granahan J., Head J. W., Kirk R., McEwen A., Lee P., Thomas P. C., and Veverka J. (1996) Geology of 243 Ida. *Icarus*, 120, 119–139.
- Tang H. and Dauphas N. (2012) Abundance, distribution, and origin of  $^{60}\text{Fe}$  in the solar protoplanetary disk. *Earth Planet. Sci. Lett.*, 359–360, 248–263.
- Tang H. and Dauphas N. (2014)  $^{60}\text{Fe}$ - $^{60}\text{Ni}$  systematics in Semarkona chondrules and Sahara 99555: New constraint on  $^{60}\text{Fe}$  in the early solar system. *Lunar Planet. Sci. XLV*, Abstract #1529. Lunar and Planetary Institute, Houston.
- Taylor S. R. (1982) *Planetary Science: A Lunar Perspective*. Lunar and Planetary Institute, Houston. 481 pp.
- Terasaki H., Frost D. J., Rubie D. C., and Langenhorst F. (2005) The effect of oxygen and sulphur on the dihedral angle between Fe-O-S melt and silicate minerals at high pressure: Implications for martian core formation. *Earth Planet. Sci. Lett.*, 232, 379–393.
- Terasaki H., Frost D. J., Rubie D. C., and Langenhorst F. (2008) Peccolative core formation in planetesimals. *Earth Planet. Sci. Lett.*, 273, 132–137.
- Thomas P. C. and Pockert L. M. (2010) Tectonics of small bodies. In *Planetary Tectonics* (T. R. Watters and R. A. Schultz, eds.), pp. 233–263. Cambridge Univ., Cambridge.
- Thomas P. and Veverka J. (1979) Grooves on asteroids: A prediction. *Icarus*, 40, 394–405.
- Thomas P. C., Veverka J., Bloom A., and Duxbury T. (1979) Grooves on Phobos: Their distribution, morphology and possible origin. *J. Geophys. Res.*, 84, 8457–8477.
- Thomas P. C., Pockert L., Robinson M., Joseph J., and Veverka J. (2002) Global structure of asteroid 433 Eros. *Geophys. Res. Lett.*, 29, 46–1–46–4.
- Travis B. J. and Schubert G. (2005) Hydrothermal convection in carbonaceous chondrite parent bodies. *Earth Planet. Sci. Lett.*, 240, 234–250.
- Ushikubo T., Nakashima D., Kimura M., Tenner T. J., and Kita N. T. (2013) Contemporaneous formation of chondrules in distinct oxygen isotope reservoirs. *Geochim. Cosmochim. Acta*, 109, 280–295.
- Valentini L., Perugini D., and Poli G. (2007) The ‘small-world’ nature of fracture/conduit networks: Possible implications for disequilibrium transport of magmas beneath mid-ocean ridges. *J. Volcanol. Geotherm. Res.*, 159, 355–365.
- Veverka J., Thomas P., Simonelli D., Belton M. J. S., Carr M., Chapman C., Davies M. E., Greeley R., Greenberg R., Head J., Klaasen K., Johnson T. V., Morrison D., and Neukum G. (1994) Discovery of grooves on Gaspra. *Icarus*, 107, 399–411.

- Villeneuve J., Chaussidon M., and Libourel G. (2009) Homogeneous distribution of  $^{26}\text{Al}$  in the solar system from the Mg isotopic composition of chondrules. *Science*, 325, 985–988.
- Wadhwa M., Srinivasan G., and Carlson R. W. (2006) Timescales of planetesimal differentiation in the early solar system. In *Meteorites and the Early Solar System II* (D. S. Lauretta and H. Y. McSween Jr., eds.), pp. 715–731. Univ. of Arizona, Tucson.
- Walsh K. J., Morbidelli A., Raymond S. N., O'Brien D. P., and Mandell A. M. (2011) A low mass for Mars from Jupiter's early gas-driven migration. *Nature*, 475, 206–209.
- Walte N. P., Becker J. K., Bons P. D., Rubie D. C., and Frost D. J. (2007) Liquid-distribution and attainment of textural equilibrium in a partially-molten crystalline system with a high-dihedral-angle liquid phase. *Earth Planet. Sci. Lett.*, 262, 517–532.
- Walte N. P., Rubie D. C., Bons P. D., and Frost D. J. (2011) Deformation of a crystalline aggregate with a small percentage of high-dihedral-angle liquid: Implications for core-mantle differentiation during planetary formation. *Earth Planet. Sci. Lett.*, 305, 124–134.
- Walter M. J. (2000) A shear pathway to the core. *Nature*, 403, 839–840.
- Warren P. H. (2008) A depleted, not ideally chondritic bulk Earth: The explosive-volcanic basalt loss hypothesis. *Geochim. Cosmochim. Acta*, 72, 2217–2235.
- Warren P. H. (2011a) Ejecta-megaregolith accumulation on planetesimals and large asteroids. *Meteoritics & Planet. Sci.*, 46, 53–78.
- Warren P. H. (2011b) Stable-isotopic anomalies and the accretionary assemblage of the Earth and Mars: A subordinate role for carbonaceous chondrites. *Earth Planet. Sci. Lett.*, 311, 93–100.
- Watters T. R., Thomas P. C., and Robinson M. S. (2011) Thrust faults and the near-surface strength of asteroid 433 Eros. *Geophys. Res. Lett.*, 38, L02202.
- Weichert U. H., Halliday A. N., Palme H., and Rumble D. (2004) Oxygen isotope evidence for rapid mixing of the HED meteorite parent body. *Earth Planet. Sci. Lett.*, 221, 373–382.
- Weidenschilling S. J. (2011) Initial sizes of planetesimals and accretion of the asteroids. *Icarus*, 214, 671–684.
- Whittington A. G., Hofmeister A. M., and Nabelek P. I. (2009) Temperature-dependent thermal diffusivity of the Earth's crust and implications for magmatism. *Nature*, 458, 319–321.
- Williams D. A. et al. (2014) Lobate and flow-like features on asteroid Vesta. *Planet. Space Sci.*, 103, 24–35.
- Wilson L. (1980) Relationships between pressure, volatile content and ejecta velocity in three types of volcanic explosion. *J. Volcanol. Geotherm. Res.*, 8, 297–313.
- Wilson L. and Goodrich C. A. (2012) Melt formation, migration and rapid extraction from differentiated asteroid interiors: Lessons from ureilites extended to all asteroids. *Lunar Planet. Sci. XLIII, Abstract #1128*. Lunar and Planetary Institute, Houston.
- Wilson L. and Head J. W. (1981) Ascent and eruption of basaltic magma on the Earth and Moon. *J. Geophys. Res.*, 86, 2971–3001.
- Wilson L. and Head J. W. (1989) Dynamics of groove formation on Phobos by ejecta from Stickney. *Lunar Planet. Sci. XX*, pp. 1211–1212. Lunar and Planetary Institute, Houston.
- Wilson L. and Head J. W. (2001) Lava fountains from the 1999 Tvashtar Catena fissure eruption on Io: Implications for dike emplacement mechanisms, eruption rates and crustal structure. *J. Geophys. Res.–Planets*, 106, 32997–33004.
- Wilson L. and Keil K. (1991) Consequences of explosive eruptions on small solar system bodies: The case of the missing basalts on the aubrite parent body. *Earth Planet. Sci. Lett.*, 104, 505–512.
- Wilson L. and Keil K. (1996a) Volcanic eruptions and intrusions on the asteroid 4 Vesta. *J. Geophys. Res.–Planets*, 101, 18927–18940.
- Wilson L. and Keil K. (1996b) Clast sizes of ejecta from explosive eruptions on asteroids: Implications for the fate of the basaltic products of differentiation. *Earth Planet. Sci. Lett.*, 140, 191–200.
- Wilson L. and Keil K. (1997) The fate of pyroclasts produced in explosive eruptions on the asteroid 4 Vesta. *Meteoritics & Planet. Sci.*, 32, 813–823.
- Wilson L. and Keil K. (2012) Volcanic activity on differentiated asteroids: A review and analysis. *Chem. Erde–Geochem.*, 72, 289–322.
- Wilson L. and Mouginis-Mark P. J. (2001) Estimation of volcanic eruption conditions for a large flank event on Elysium Mons, Mars. *J. Geophys. Res.–Planets*, 106, 20621–20628.
- Wilson L., Keil K., Browning L. B., Krot A. N., and Bourcier W. (1999) Early aqueous alteration, disruption and re-processing of asteroids. *Meteoritics & Planet. Sci.*, 34, 541–557.
- Wilson L., Goodrich C. A., and Van Orman J. A. (2008) Thermal evolution and physics of melt extraction on the ureilite parent body. *Geochim. Cosmochim. Acta*, 72, 6154–6176.
- Wilson L., Keil K., and McCoy T. J. (2010) Pyroclast loss or retention during explosive volcanism on asteroids: Influence of asteroid size and gas content of melt. *Meteoritics & Planet. Sci.*, 45, 1284–1301.
- Wood J. A. and Pellas P. (1991) What heated the meteorite parent planets. In *The Sun in Time* (C. P. Sonett et al., eds.), pp. 740–760. Univ. of Arizona, Tucson.
- Wulf A. V., Palme H., and Jochum K. R. (1995) Fractionation of volatile elements in the early solar system: Evidence from heating experiments on primitive meteorites. *Planet. Space Sci.*, 43, 451–468.
- Wyrrick D., Ferrill D. A., Morris A. P., Colton S. L., and Sims D. W. (2004) Distribution, morphology and origins of martian pit crater chains. *J. Geophys. Res.*, 109, E06005.
- Yamaguchi A., Barrat J.-A., Ito M., and Bohn M. (2011) Posteucritic magmatism on Vesta: Evidence from the petrology and thermal history of diogenites. *J. Geophys. Res.–Planets*, 116, E08009.
- Yoshino T., Walter M. J., and Katsura T. (2003) Core formation in planetesimals triggered by permeable flow. *Nature*, 422, 154–157.
- Yoshino T., Walter M. J., and Katsura T. (2004) Connectivity of molten Fe alloy in peridotite based on in situ electrical conductivity measurements: Implications for core formation in terrestrial planets. *Earth Planet. Sci. Lett.*, 222, 501–516.
- Young E. D., Ash R. D., England P., and Rumble D. III (1999) Fluid flow in chondritic parent bodies: Deciphering the compositions of planetesimals. *Science*, 286, 1331–1335.
- Young E. D., Zhang K. K., and Schubert G. (2003) Conditions for pore water convection within carbonaceous chondrite parent bodies — implications for planetesimal size and heat production. *Earth. Planet. Sci. Lett.*, 213, 249–259.
- Zolensky M. E. and McSween H. Y. Jr. (1988) Aqueous alteration. In *Meteorites and the Early Solar System* (J. F. Kerridge and M. S. Matthews, eds.), pp. 114–143. Univ. of Arizona, Tucson.
- Zolensky M. E., Bourcier W. L., and Gooding J. L. (1989) Aqueous alteration on the hydrous asteroids — Results of EQ3/6 computer simulations. *Icarus*, 78, 411–425.
- Zolensky M., Krot A. N., and Benedix G. (2008) Record of low-temperature alteration in asteroids. In *Oxygen in the Solar System* (G. J. MacPherson, ed.), pp. 429–463. Reviews in Mineralogy, Vol. 68, Mineralogical Society of America, Washington.
- Zolotov M. Y. (2012) Aqueous fluid composition in CI chondritic materials: Chemical equilibrium assessments in closed systems. *Icarus*, 220, 713–729.
- Zolotov M. Y. and Mironenko M. V. (2008) Aqueous alteration of CM2 chondrites evaluated with kinetic models. *Meteoritics & Planet. Sci. 33, Suppl.*, A177.
- Zolotov M. Y., Mironenko M. V., and Shock E. L. (2006) Thermodynamic constraints on fayalite formation on parent bodies of chondrites. *Meteoritics & Planet. Sci.*, 41, 1775–1796.
- Zhou Q., Yin Q.-Z., Young E. D., Li X.-H., Wu F.-Y., Li Q.-L., Liu Y., and Tang G.-Q. (2013) SIMS Pb-Pb and U-Pb age determination of eucrite zircons at  $<5\ \mu\text{m}$  scale and the first 50 Ma of the thermal history of Vesta. *Geochim. Cosmochim. Acta*, 110, 152–175.

# Early Impact History and Dynamical Origin of Differentiated Meteorites and Asteroids

**Edward R. D. Scott and Klaus Keil**

*University of Hawai'i at Mānoa*

**Joseph I. Goldstein**

*University of Massachusetts (now deceased)*

**Erik Asphaug**

*Arizona State University*

**William F. Bottke**

*Southwest Research Institute*

**Nicholas A. Moskovitz**

*Lowell Observatory*

---

Differentiated asteroids and igneous meteorites present numerous challenges to our understanding of the impact and dynamical evolution of asteroids and meteorite parent bodies. Igneous meteorites, including irons, achondrites, and stony-iron meteorites, testify to the prior existence of ~100 differentiated bodies. Destruction of these bodies by hypervelocity impact over 4 G.y. would have required numerous giant impacts, although this is inconsistent with the preservation of Vesta's basaltic crust and the lack of differentiated asteroid families. We review recent advances in elucidating the early chronology of meteorites, spectroscopic observations of likely differentiated asteroids, petrological studies of differentiated meteorites, impact disruption of differentiated planetesimals during accretion, and dynamical scenarios for capturing material into the asteroid belt. Together, these advances suggest a new paradigm in which planetesimals accreted rapidly in the inner solar system and were melted by  $^{26}\text{Al}$  less than 2 m.y. after the formation of calcium-aluminum-rich inclusions (CAIs). While molten they were disrupted by grazing hit-and-run impacts during the accretion of planetesimals. Later, when still hot, the survivors were disrupted by hypervelocity impacts. Impact debris from the differentiated bodies was transferred from the newly formed terrestrial planet region to stable orbits in the asteroid belt. This evolutionary history leaves many questions unanswered but suggests new paths for future exploration of the asteroid belt and petrological and isotopic studies of meteorites.

## 1. INTRODUCTION

Laboratory studies of igneously formed meteorites suggest that numerous meteorite parent bodies were melted to form metallic cores and silicate mantles. Studies by the Dawn spacecraft confirm that (4) Vesta melted in this way (*McSween et al.*, 2013; see the chapter by Russell et al. in this volume). In principle, one would think the origin of iron and stony-iron meteorites and achondrites would be straightforward to investigate, but this is not the case. If disrupted Vesta-like differentiated bodies were once common in the main belt and

they were the ultimate source of the differentiated meteorites, one might expect collisions to have created enormous numbers of V-type asteroids that were not derived from Vesta, as well as ample numbers of mantle and core fragments compared to the rest of the main-belt population. This is not observed. Instead, only limited examples of asteroids composed predominantly of core metallic Fe-Ni (possibly some M-type asteroids) or mantle olivine (some A-type asteroids) have been identified. Very few of these bodies are members of asteroid families, with those in families having orbits and sizes most consistent with being interlopers.

Differentiated asteroids and meteorites provide many other challenges to our understanding of the formation and evolution of the asteroid belt. How could core samples have been extracted from numerous large differentiated bodies when Vesta's basaltic crust was preserved (*Davis et al.*, 1985)? Where are the meteorites from the olivine-rich mantles of the parent bodies of the 12 groups of iron meteorites and the ~50–70 parent bodies of the ungrouped irons, the two groups of pallasites, and the type 4–6 ungrouped pallasites — “the great dunite shortage” (*Bell et al.*, 1989)? We also lack mantle and core samples from the parent asteroids of the angrites and the ungrouped eucrites like Northwest Africa (NWA) 011 and Ibitira (*Krot et al.*, 2014). Where is the missing Psyche family of silicate-rich asteroids (*Davis et al.*, 1999)? Why are meteorites derived from far more differentiated parent bodies than chondritic parent bodies even though the asteroid belt is dominated by C and S complex chondritic asteroids (*Bottke et al.*, 2006)?

We reassess ideas about the dynamical origin and early impact histories of differentiated asteroids and meteorites in the light of major advances since *Asteroids III*. These include advances in our understanding of the chronology of the early solar system, the distribution of short-lived isotopes including  $^{26}\text{Al}$ , the identification of pristine chondrites and differentiated meteorites that escaped prolonged alteration or metamorphism, the thermal histories of differentiated meteorites, the nature of S asteroids, impact modeling during accretion, and dynamical studies of planetesimal accretion. Together, these advances suggest a new paradigm (*Bottke et al.*, 2006; *Goldstein et al.*, 2009) in which planetesimals accreted rapidly in the inner solar system and were rapidly melted by  $^{26}\text{Al}$  less than 2 m.y. after CAI formation. While they were still molten or semimolten, planetesimals were disrupted — first by grazing impacts during the accretion that harvested the objects making slow, direct hits (*Asphaug et al.*, 2006), and later by hypervelocity impacts when larger bodies excited their orbits. Impact debris from the differentiated bodies was tossed into the asteroid belt. Most iron meteorites did not cool slowly inside insulating silicate mantles, like Vesta's core, but rapidly with little or no silicate insulation less than 5 m.y. after CAI formation. In this scenario, Vesta — the dominant single source of differentiated meteorites, viz., the howardites, eucrites, and diogenites (HEDs) — is not a typical differentiated asteroid.

In this chapter, we first describe the isotopic evidence that has been used to establish a new chronology for melting and solidification of igneous meteorites and to identify the heat source. Then we review the types, properties, and abundances of differentiated asteroids and asteroid families. Next, we describe the various types of igneous meteorites, focusing on evidence that their parent bodies were disrupted by impacts while they were still partly or wholly molten. Finally, we discuss numerical simulations of grazing impacts between differentiated planetesimals during accretion (“hit-and-run” impacts), and dynamical studies that suggest how planetesimals could have been scattered into the asteroid belt from 1 to 2 AU.

## 2. MELTING AND SOLIDIFICATION OF ASTEROIDS

### 2.1. When Were Meteoritic Bodies Melted and Solidified?

Advances in the use of short-lived and long-lived radioisotopes for dating meteorites since *Asteroids III* have revolutionized our understanding of the timescales for early solar system processes (*Davis and McKeegan*, 2014). The U-Pb system provides two isotopic clocks with different half-lives:  $^{238}\text{U}$  decays to  $^{206}\text{Pb}$  with a half-life of 4469 m.y., and  $^{235}\text{U}$  decays to  $^{207}\text{Pb}$  with a half-life of 704 m.y. Measurements of  $^{207}\text{Pb}/^{204}\text{Pb}$  and  $^{206}\text{Pb}/^{204}\text{Pb}$  can provide ages with precisions of 0.1–1 m.y. in favorable cases. After allowance for small variations in the  $^{238}\text{U}/^{235}\text{U}$  ratio (*Wadhwa*, 2014), the Pb-Pb technique gives ages of 4567.2 to 4568.2 Ma for CAIs from CV3 chondrites, which provide our best estimate of the formation age ( $t_0$ ) of the first solid materials in the solar system. Figure 1, which shows ages of early solar system materials, was constructed using a mean value of 4567.5 Ma for  $t_0$ . [The small difference between this value and that preferred by *Davis and McKeegan* (2014) of  $4567.3 \pm 0.2$  Ma from *Connelly et al.* (2012) is of no consequence in this discussion.]

Short-lived chronometers like  $^{26}\text{Al}$ , which decays to  $^{26}\text{Mg}$  with a half-life of 0.71 m.y., and  $^{182}\text{Hf}$ , which decays to  $^{182}\text{W}$  with a half-life of 8.90 m.y., provide relative ages. For example, CAIs have inferred initial ratios of  $^{26}\text{Al}/^{27}\text{Al}$  that are roughly 8 ( $= 2^3 \times$ ) higher than most chondrules, and so formed about 2 ( $3 \times 0.71$ ) m.y. before chondrules. Manganese-53, which decays to  $^{53}\text{Cr}$  with a half life of 3.7 m.y., also provides valuable relative ages but cannot be used to date CAIs because Mn is depleted in CAIs and Cr shows mass-independent isotopic anomalies. The short-lived and long-lived chronometers are cross-calibrated using angrites — achondrites that crystallized 4–11 m.y. after CAIs and escaped extensive metamorphism and shock heating (*Brennecke and Wadhwa*, 2012; *Kleine et al.*, 2012). The oldest, fine-grained angrites such as D'Orbigny are especially important anchors for the short-lived chronometers as they crystallized and cooled very rapidly (in days).

Radioactive isotopic systems record the time at which diffusion of the parent and daughter isotopes between minerals effectively ceased. Thus ages of slowly cooled rocks depend on cooling rates (*Ganguly and Tirone*, 2001). Many igneous and metamorphosed meteorites cooled slowly at around  $10\text{--}10^3\text{ }^\circ\text{C m.y.}^{-1}$ , so that radiometric ages based on isotopic systems in various minerals with closure temperatures that range from  $\sim 300^\circ$  to  $1100^\circ\text{C}$  could differ by  $\sim 50$  m.y. or more for slowly cooled meteorites, but only  $\sim 1$  m.y. for quickly cooled meteorites. For example, Hf-W closure temperatures for pyroxene are  $\sim 750\text{--}900^\circ\text{C}$ , depending on grain size and cooling rate (*Kleine et al.*, 2008). However, zircons may crystallize from melts above their Hf-W closure temperatures and so record the time of crystallization. Closure temperatures for Pb-Pb ages of phosphates in or-

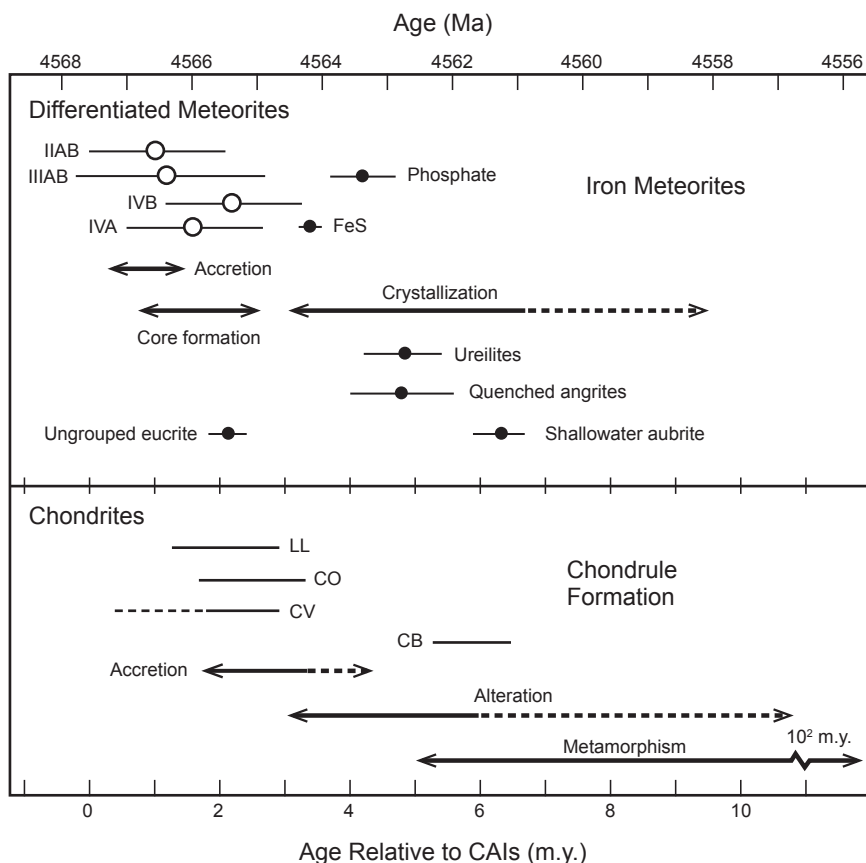


**Fig. 1.** Chronology of differentiated meteorites and chondrites inferred from their radiometric ages. Core formation ages of the IIAB, IIIAB, IVA, and IVB iron meteorite parent bodies are 1–2 m.y. after the CAI formation age, which is 4567.5 Ma. Their parent bodies probably accreted 0.5 to 1.5 m.y. after CAIs. Ages of phosphate and troilite in iron meteorites, ureilites, quenched angrites, the ungrouped eucrite, Asuka 881394, and the Shallowwater aubrite indicate crystallization and cooling within 2–7 m.y. of CAIs. Ages of chondrules in the least-metamorphosed LL, CO, and CV chondrites, which are shown by horizontal lines, suggest that the parent bodies of most chondrites accreted later than the differentiated asteroids — around 2–3 m.y. after CAI formation. The metal-rich CB chondrites accreted much later, at around 5 m.y. after CAIs. Alteration and metamorphic minerals in chondrites formed 5–100 m.y. after CAIs. Dashed lines indicate less common features. (See text for sources of data.)

dinary chondrites range from ~500° to ~750°C depending on the cooling rate (Ganguly *et al.*, 2013), whereas closure temperatures for Pb-Pb ages of pyroxene are ~700–900°C (Amelin *et al.*, 2005).

Radiometric ages based on the  $^{182}\text{Hf}$ - $^{182}\text{W}$ ,  $^{26}\text{Al}$ - $^{26}\text{Mg}$ , and  $^{53}\text{Mn}$ - $^{53}\text{Cr}$  isotopic records for angrites and CAIs are reasonably concordant with the Pb-Pb ages showing that all three short-lived isotopic systems are robust chronometers (Kleine *et al.*, 2013; Kruijer *et al.*, 2014). However, small but significant discrepancies between isotopic chronometers require further study (Davis and McKeegan, 2014). Because of the major advances in the four radiometric dating systems described above and the discovery of pristine chondrites and achondrites that largely escaped alteration, metamorphism, or impact processing after their formation, we now have a

radically new chronology for the inner solar system. Figure 1 summarizes various ages of differentiated meteorites and chondrites and their components based on these four chronometers.

Key evidence that differentiated planetesimals formed soon after CAIs and before the chondrite parent bodies comes from Hf-W isotopic measurements of chondrites, CAIs, and differentiated meteorites (Kleine *et al.*, 2005). Deviations in the  $^{182}\text{W}/^{184}\text{W}$  ratio in parts per 10<sup>4</sup>, which are called  $\varepsilon^{182}\text{W}$  values, can be attributed to separation of metal and silicate when  $^{182}\text{Hf}$  was still decaying to  $^{182}\text{W}$  because tungsten is siderophile (metal-loving) whereas hafnium is lithophile (silicate-loving). The  $\varepsilon^{182}\text{W}$  values of most iron meteorites were fixed when molten metal segregated into metallic cores as the radioactive  $^{182}\text{Hf}$  was retained in the silicate and are

very close to the inferred initial  $\epsilon^{182}\text{W}$  value in CAIs. Figure 1 shows that core formation ages inferred from  $\epsilon^{182}\text{W}$  values for four groups of iron meteorites, IIAB, IIIAB, IVA, and IVB, range from 1.0 to 2.2 m.y. after CAIs (Kruijer *et al.*, 2012, 2013).

Additional isotopic evidence for the early accretion of differentiated planetesimals comes from high-precision Mg isotopic measurements of achondrites (Bizzarro *et al.*, 2005; Davis and McKeegan, 2014). For example, Baker *et al.* (2012) used this technique to infer that the parent body of the main-group pallasites differentiated  $1.2 \pm 0.3$  m.y. after CAIs. The oldest achondrite, Asuka 881394, which is an ungrouped eucrite, crystallized 2 m.y. after CAIs according to Pb-Pb, Al-Mg, and Mn-Cr isotopic constraints (Fig. 1) (Wadhwa *et al.*, 2009). Virtually all vestan eucrites cannot be dated using these techniques, probably because of extensive thermal processing after they crystallized.

Contrary to the expectations of many workers, the new chronology shows that chondrites are not derived from the first generation of planetesimals. Ages of most chondrules based on  $^{26}\text{Al}$ - $^{26}\text{Mg}$  and Pb-Pb isotopic systems are 1.5–2.5 m.y. after CAIs (Fig. 1) (Kita and Ushikubo, 2012; Wadhwa, 2014). These ages are consistent with formation of chondrules by splashing when largely molten planetesimals collided at low speed during accretion (Asphaug *et al.*, 2011; Sanders and Scott, 2012). Since chondrite accretion postdates the formation of the constituent chondrules, most chondrites accreted 2–3 m.y. after CAIs. Although the origin of most chondrules remains uncertain, chondrules in the metal-rich CB chondrites have unique isotopic and chemical signatures indicating that they probably formed in a giant impact that created melt droplets and vapor condensates  $\sim 5\text{--}6$  m.y. after CAIs (Krot *et al.*, 2005, 2010).

## 2.2. Heat Source for Melting

Isotopic data from meteorites provide strong evidence that  $^{26}\text{Al}$  was the most potent heat source for melting planetesimals in the early solar system. Two other short-lived nuclides,  $^{10}\text{Be}$  and  $^{36}\text{Cl}$ , which were not uniformly distributed in the solar system, formed in a late-stage irradiation, but this was insufficient to account for the abundance of  $^{26}\text{Al}$ . An external source is therefore required for this nuclide — probably the winds from a massive star prior to its explosion (Davis and McKeegan, 2014). Some rare CAIs with large isotopic anomalies of nucleogenetic origin appear to have formed before  $^{26}\text{Al}$  was homogenized in the disk by radial mixing (Krot *et al.*, 2012). However, the concordance between isotopic chronometers described above suggests that  $^{26}\text{Al}$  was quickly homogenized. The initial  $^{26}\text{Al}/^{27}\text{Al}$  ratio of  $5.2 \times 10^{-5}$  in CAIs can therefore be used to estimate the heating energy available in dry chondritic material due to the decay of  $^{26}\text{Al}$  (Fig. 2) (Sanders and Scott, 2012). At the time that most CAIs were formed ( $t_0$ ), 6.6 kJ g $^{-1}$  of heat was available from  $^{26}\text{Al}$  decay, which is about four times larger than the 1.6 kJ g $^{-1}$  needed to melt dry chondritic dust in the insulated interior of a planetesimal (Sanders and

Scott, 2012). Thus well-insulated planetesimals with radii of more than 20 km that accreted less than 1.5 m.y. after CAIs (about two half-lives of  $^{26}\text{Al}$ ) were melted. Bodies that accreted soon afterward were heated but not melted. It is likely that  $^{26}\text{Al}$  was also the dominant heat source for alteration on wet asteroids, as most well-dated alteration minerals in carbonaceous chondrites formed 3–6 m.y. after CAIs (Sugiura and Fujiya, 2014; see also the chapter by Krot *et al.* in this volume). For further details on the thermal modeling of melted planetesimals, see Hevey and Sanders (2006), Moskovitz and Gaidos (2009), Sanders and Scott (2012), and Neumann *et al.* (2012).

Although  $^{60}\text{Fe}$  has been considered as a second possible source of radioactive heat, the current best estimate for the solar system initial  $^{60}\text{Fe}/^{56}\text{Fe}$  ratio of  $(1.0 \pm 0.3) \times 10^{-8}$  indicates that heating from  $^{60}\text{Fe}$  decay would have been negligible ( $<20$  K increase in temperature) (Tang and Dauphas, 2012). Alternative heating mechanisms such as electromagnetic induction do not appear to have played a major role in heating asteroids (e.g., Marsh *et al.*, 2006). Impacts cannot cause global heating and melting of asteroids, even very porous ones (Keil *et al.*, 1997). Nevertheless, impacts into highly porous targets can cause localized heating, which may have played a role in the formation of certain igneous meteorites like IAB and IIE irons (Davison *et al.*, 2012, 2013; Ciesla *et al.*, 2013; Wasson and Klemme, 2002). In addition, the Portales Valley H chondrite, which contains centimeter- to millimeter-wide metallic veins with a Widmanstätten pattern like iron meteorites, probably formed by impact heating or impact-induced frictional heating of a hot target (Kring *et al.*, 1999; Rubin *et al.*, 2001).

## 3. DIFFERENTIATED ASTEROIDS

Asteroid compositions have traditionally been established via spectroscopic observations at visible and near-infrared wavelengths (Burbine, 2014). Feature-based taxonomic systems (e.g., DeMeo *et al.*, 2009) allow mapping of spectral classes to broadly defined compositional groups, while detailed modeling of mineral absorption features can yield specific compositional information (see the chapter by Reddy *et al.* in this volume). Asteroids derived from igneously differentiated parent bodies range from those with prominent absorption features and reasonably constrained compositions (e.g., V-types), to those that are challenging to characterize due to muted or absent absorption features (e.g., M-types). Here we focus on asteroids that may have been heated to high enough temperatures to melt or partially melt silicate or metal-sulfide ( $>950^\circ\text{C}$  and  $>1050^\circ\text{C}$  respectively) and to mobilize these melts. We exclude asteroids like (1) Ceres that may have experienced silicate-water differentiation (see the chapter by Rivkin *et al.* in this volume).

### 3.1. Basaltic Crust: V-Types

Named after their archetype, the 530-km-diameter (4) Vesta, V-type asteroids have long been spectroscopically

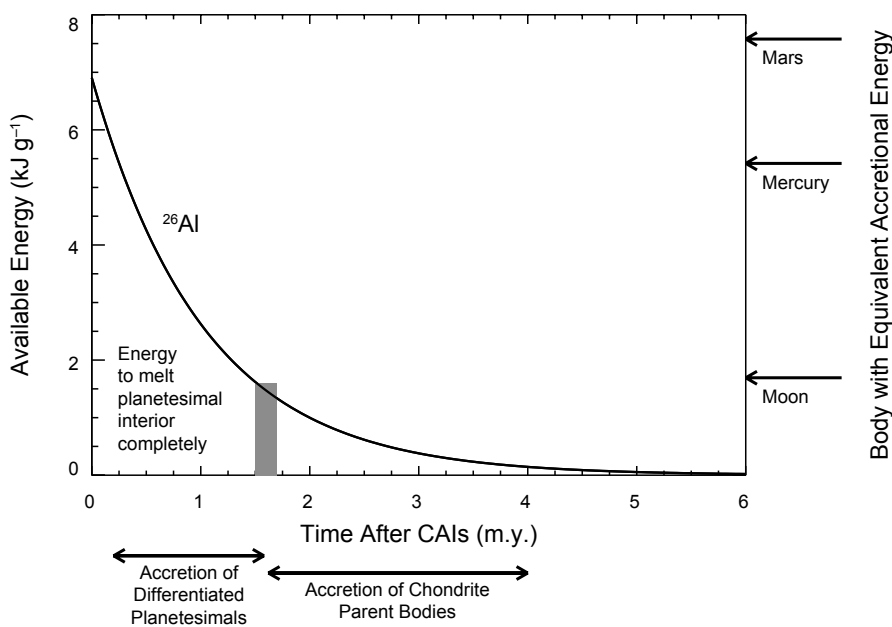


**Fig. 2.** Available thermal energy from  $^{26}\text{Al}$  decay in dry chondrites as a function of time since CAI formation (after Sanders and Scott, 2012). Differentiated planetesimals accreted within 1.6 m.y. of CAI formation when the available energy from  $^{26}\text{Al}$  exceeded  $1.6 \text{ kJ g}^{-1}$ , which is the energy needed to melt a chondrite completely. The parent bodies of nearly all chondrites accreted 1.6–4 m.y. after CAIs formed (see Fig. 1). The righthand axis shows the equivalent accretional energy (or gravitational binding energy) of the Moon, Mercury, and Mars.

linked to the basaltic HED meteorites (McCord *et al.*, 1970; Consolmagno and Drake, 1977; Cruikshank *et al.*, 1991; Binzel and Xu, 1993; Burbine *et al.*, 2001; McSween *et al.*, 2013). Compositional analyses support this link (Duffard *et al.*, 2004; Mayne *et al.*, 2011; De Sanctis *et al.*, 2011). V-type asteroids, apart from Vesta, are small,  $<10$  km in diameter, and the vast majority of V-types are part of the Vesta asteroid family, which spans the inner main belt between the  $v_6$  secular resonance along the inner main belt's periphery at 2.1–2.3 AU (depending on inclination) and the 3:1 mean-motion resonance with Jupiter near 2.5 AU (Carruba *et al.*, 2005; Nesvorný *et al.*, 2008; Moskovitz *et al.*, 2010; see also the chapter by Nesvorný *et al.* in this volume). Most of the Vesta family probably stems from the impact events that made the 500-km basin Rheasilvia, with a crater retention age of  $\sim 1$  Ga, and the 400-km basin Veneneia, with a crater retention age of  $>2$  Ga (Marchi *et al.*, 2012; see also the chapter by Marchi *et al.* in this volume).

Several examples of non-Vesta V-type asteroids have been discovered in the middle and outer main belt beyond 2.5 AU (Lazzaro *et al.*, 2000; Roig *et al.*, 2008; Moskovitz *et al.*, 2008; Duffard and Roig, 2009; Solontoi *et al.*, 2012). These V-types are dynamically separated from Vesta by one or more of the Kirkwood gaps and show a wide range in semimajor axis, eccentricity, and inclination. They are therefore unlikely to have been dynamically transported from the Vesta family to their current locations and are probably

composed of fragments from other Vesta-like bodies (e.g., Nesvorný *et al.*, 2008). In a few cases, compositional analyses suggest that these outer-belt V-types are compositionally distinct from Vesta and the vestoids (Harden *et al.*, 2004; Burbine, 2014).

### 3.2. Olivine-Rich Mantle: A-Types

The spectra of A-type asteroids closely resemble those of olivine-dominated compositions, with slope differences potentially due to the effects of space weathering (e.g., Hiroi and Sasaki, 2001). Some A-types have magnesian olivine compositions consistent with differentiation of ordinary chondrites; others contain ferroan olivine like that found in R-chondrites or igneous differentiates from R-chondrite-like parent bodies (Sunshine *et al.*, 2007; Burbine, 2014). A-types with magnesian compositions tend to be olivine-rich ( $\sim 70$ –90% abundance) with small amounts of pyroxene that produce subtle 2- $\mu\text{m}$  absorption features, whereas the ferroan A-types have spectra consistent with a monomineralic interpretation, i.e., no 2- $\mu\text{m}$  band (Sanchez *et al.*, 2014). A-type asteroids and their meteoritic counterparts (e.g., pallasites, brachinites, R-chondrites) are rare.

If the asteroid belt had been composed largely of highly reduced meteorites like enstatite chondrites and achondrites, which have virtually no  $\text{Fe}^{2+}$ , the apparent lack of meteorites and asteroids composed mainly of olivine would be

understandable, as chondrites have atomic Mg/Si ratios of around 1, like enstatite ( $\text{MgSiO}_3$ ). However, most meteorites and asteroids are much more oxidized with significant concentrations of  $\text{Fe}^{2+}$ , so we should expect differentiated bodies to contain major amounts of olivine ( $(\text{Mg}, \text{Fe})_2 \text{SiO}_4$ ). We discuss the dearth of dunite in section 7.

### 3.3. Metal-Rich: Some M-Types

M-types have traditionally been linked to iron meteorites. An M-type classification is not exclusively a spectroscopic designation, but instead requires knowledge of albedo (10–30%) to distinguish their largely featureless spectra from others within the broad X-complex (Tholen, 1984). Focused studies have suggested that additional information like high radar albedo (Shepard et al., 2010), spectral observations around 3  $\mu\text{m}$  to look for signatures of hydrated minerals (Rivkin et al., 2000; see also the chapter by Rivkin et al. in this volume), and near-infrared continuum curvature (Clark et al., 2004) can be used to further distinguish metal-rich M-types from other spectrally degenerate asteroids. However, it is unclear what fraction of taxonomic M-types are truly metal-rich. Most of the M-types that are inferred to be metal-rich from radar studies also show 1- and 2- $\mu\text{m}$  silicate spectral features (Ockert-Bell et al., 2010). Neeley et al. (2014) found that for one-third of the Xc and Xk objects, the best spectral match was an iron meteorite; one-fifth were matched best by E chondrites. Xk-type asteroids have also been linked with mesosiderites (Vernazza et al., 2009).

The largest of the iron-rich M-types, which is (16) Psyche, with dimensions of  $240 \times 185 \times 145$  km, possibly came from a Vesta-sized differentiated body that completely lost its crust/mantle silicates via one or more hit-and-run collisions (see section 5). (216) Kleopatra is another canonical M-type but has a relatively low density of  $3600 \pm 400 \text{ kg m}^{-3}$  (Descamps et al., 2011), suggesting it may be a highly porous collection of collisionally evolved core fragments.

### 3.4. Chemically Reduced Crust: E-Types

The E-type asteroids are also a part of the X-complex and are distinguished by a high albedo, >30%. These properties are consistent with a link to aubrites, igneous enstatite-rich meteorites that formed in chemically reducing conditions. This link to aubrites is consistent with compositional interpretations of the Rosetta mission target asteroid (2867) Šteins (e.g., Barucci et al., 2008). E-types are scattered within the inner main belt, but they dominate the Hungaria region ( $1.78 < a < 2.0 \text{ AU}$ ,  $e < 0.18$ ,  $16^\circ < i < 34^\circ$ ) and are associated specifically with the Hungaria family (Warner et al., 2009; Milani et al., 2010). These asteroids may represent the best available analogs to the precursor material from which the terrestrial planets formed. It is also possible that they were an important source of impactors on Earth during the late heavy bombardment (Bottke et al., 2012; see also the chapter by Morbidelli et al. in this volume).

### 3.5. Melt Byproducts: S-Complex

Most S-type asteroids are probably composed of ordinary chondrite material (Vernazza et al., 2014; see also the chapter by Vernazza et al. in this volume) rather than differentiated material (e.g., Bell et al., 1989). However, several subclasses within the S-complex (e.g., Sv, Sa, Sr) may be linked to fully or partially differentiated parent bodies (Burbine, 2014). Compositional analysis of several of the largest members in the Merxia and Agnia S-type families, as well as asteroid (17) Thetis, suggest that their ratio of high-calcium pyroxene to total pyroxene is greater than ~40% (Sunshine et al., 2004). Among meteorites, only the eucrites have such high values, suggesting that these S-types may have experienced a history consistent with igneous activity. However, Vernazza et al. (2014; see also the chapter by Vernazza et al. in this volume) find that the Merxia and Agnia asteroid families are likely parent asteroids of H chondrites.

Compositional analyses of the S-type near-Earth object (1036) Ganymed and the main-belt family associated with (170) Maria suggest that these objects may be collisional agglomerations of basalt and metal analogous to mesosiderites (Fieber-Beyer et al., 2011a,b). This raises the interesting possibility that highly collisionally evolved differentiated asteroids could be masquerading as S-type asteroids (see the chapter by Vernazza et al. in this volume).

### 3.6. Spectral End Members and Partial Differentiation

Two objects stand out as the only known members of their respective taxonomic classes: the O-type asteroid (3628) Božněmcová and the R-type asteroid (349) Dembowska. Compositional interpretations of these unusual objects have been varied and include putative links to the angrites in the case of Božněmcová (Cloutis et al., 2006) and some form of pyroxene-olivine melt or melt residual in the case of Dembowska (Burbine, 2014). Neither of these objects have good spectral analogs among meteorites or terrestrial samples.

The K-type taxonomic class has also seen varied compositional interpretations. Both the Eos family (Mothe-Diniz and Carvano, 2005; Mothe-Diniz et al., 2008) and the Eunomia family (Nathues et al., 2005; Nathues, 2010) have been linked to partially differentiated parent bodies.

However, alternative interpretations suggest a link to nondifferentiated CO and CK carbonaceous chondrites (e.g., Clark et al., 2009). The asteroid (21) Lutetia may be a partially differentiated asteroid with a metallic core and a chondritic crust (Weiss et al., 2012; Weiss and Elkins-Tanton, 2013), although this is a point of some debate (Barucci et al. 2012; see also the chapter by Barucci et al. in this volume).

### 3.7. Abundance of Differentiated Asteroids

Figure 3 shows the orbital distribution of the differentiated V-, A-, and E-type taxonomic classes relative to the

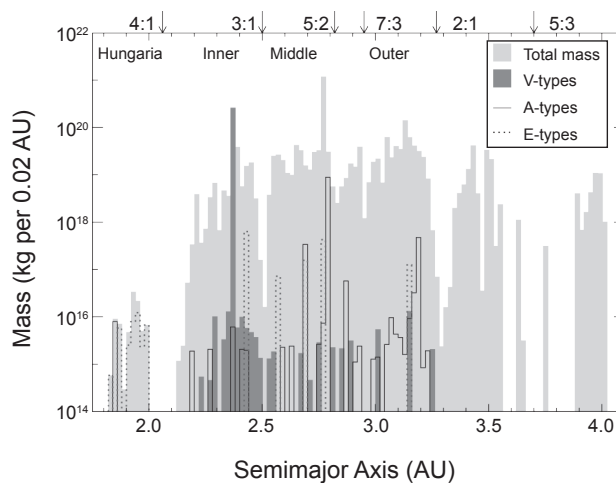


**Fig. 3.** Distribution by mass of differentiated asteroids as a function of their semimajor axis (data from DeMeo and Carry, 2013). M-types are omitted due to uncertainty in the identification of metallic varieties. Differentiated asteroids are relatively small, aside from Vesta, and have semimajor axes from 1.8 to 3.3 AU.

total mass in the asteroid belt (from DeMeo and Carry, 2013, 2014). Accounting for all the previously discussed taxonomic types and asteroid families that are associated with igneous histories, the mass of differentiated material among observed bodies is only  $\sim$ 15–20% of the total mass in the main belt, with Vesta alone accounting for  $\sim$ 10%. Table 1 summarizes some of the largest examples of fully differentiated asteroids, including (1459) Magnya, which is the largest V-type asteroid not related to Vesta. The masses in this table are either referenced or were computed assuming mean densities for the respective taxonomic classes (DeMeo and Carry, 2013) and diameters as given.

Differentiated asteroid families are surprisingly scarce. Only four (Hungaria, Vesta, Merxia, and Agnia) of the currently known 76 asteroid families (Masiero et al., 2013) have been linked (or tentatively linked) to fully differentiated parent bodies. Another two (Eos, Eunomia) have been connected to partially differentiated precursors. However, no known asteroid family contains the crust, mantle, and core fragments expected from a differentiated parent body. The majority of other differentiated asteroids are isolated objects

with no associated collisional families, likely representing relic fragments of now fully eroded parent bodies.

Since family members are composed of fragmental debris, it might be argued that they are “camouflaged,” namely covered with small debris that reaccreted immediately after the family-forming event (e.g., see Michel et al., 2004). However, spacecraft flybys of (951) Gaspra, part of the Flora family, and (243) Ida, part of the Koronis family, provide no compelling evidence that their subsurface materials, revealed via numerous impact craters, are different from the surface material (Farquhar et al., 2002).

The lack of differentiated asteroids and families is surprising in light of the large number ( $\sim$ 50–100) of distinct differentiated parent bodies represented by the iron meteorites (section 4). If differentiation was so common, where are the asteroidal relics of this process? This long-standing paradox is most pronounced for differentiated mantle material, which is quite rare among both asteroids and meteorites (Chapman, 1986; Bell et al., 1989; Burbine et al., 1996).

#### 4. DIFFERENTIATED METEORITES

##### 4.1. Types of Differentiated Meteorites

Differentiated meteorites formed by melting and crystallization in planetesimals with bulk compositions that were near solar, or chondritic, except for their volatile contents. For bodies that experienced low degrees of melting, the products resemble ultrametamorphosed chondrites or residues from low degrees of partial melting and have been called “primitive achondrites” (e.g., Krot et al., 2014). For bodies that were largely molten, the igneous products are grossly different from chondrites in their mineralogy and chemical composition. Metallic Fe-Ni and troilite (FeS) formed molten cores from which most iron meteorites appear to have been derived. Silicates formed basaltic crusts and olivine-rich and pyroxene-rich mantles that supply us with achondrites. Impacts created a third type of differentiated meteorite — stony irons — by mixing metal and silicate in roughly equal proportions. Two major types of stony-irons are known. Pallasites are made of Fe-Ni from molten cores that were mixed with fragments of olivine mantles. Mesosiderites are mixtures of molten metal, basalts, and gabbros, and impact melted silicates, with little olivine. The properties of the major types of differentiated meteorites and their fall

TABLE 1. Examples of the largest asteroids within differentiated asteroid classes.

Object	Type	Mass (kg)	Diameter (km)	Inferred composition	References
(4) Vesta	V-type	2.59e20	525.4	Basaltic surface, fully differentiated	McSween et al. (2013)
(434) Hungaria	E-type	2.6e15	11	Enstatite-rich, aubrite	Shepard et al. (2008)
(354) Eleonora	A-type	8.8e18	165	Olivine mantle	Masiero et al. (2011)
(1459) Magnya	Non-Vesta V-type	4.9e15	17	Basaltic crust	Delbo et al. (2006)
(16) Psyche	M-type	2.7e19	248	Metallic core material	Carry (2012)
(216) Kleopatra	M-type	4.64e18	127	Metallic core material	Descamps et al. (2011)

frequencies are summarized in Table 2. Chemical and isotopic data suggest that each type of differentiated meteorite probably comes from a separate body. Winonaites and IAB irons are exceptions as they are genetically related and probably come from the same body.

Below we review the evidence that early impacts were involved in the formation of differentiated meteorites and the constraints on the timing, nature, and speed of the impacts.

## 4.2. Iron Meteorites

Iron meteorites are composed very largely of Fe with 5–60% Ni (mostly 5–10% Ni) with a few volume percent of troilite (FeS), phosphide (Fe,Ni<sub>3</sub>P), and smaller amounts of chromite, carbides, phosphates, and other minerals (Goldstein *et al.*, 2009; Benedix *et al.*, 2014; Krot *et al.*, 2014). Minor and trace amounts of siderophile elements such as Ni, Co, P, Ga, Ge, Ir, Au, As, and W provide important clues to their origin. Moderately volatile elements like Ga and Ge vary enormously in their abundance: Ge/Ni ratios, for example,

range from chondritic proportions (0.1–1× CI chondrites) to 10<sup>-4</sup> of chondritic values. Depletion of volatiles reflects either early accretion in a hot solar nebula or volatile loss during impacts. Germanium concentrations in irons cluster into 14 groups, each of which contains between 5 and ~250 iron meteorites. Other elements like Au (Fig. 4b) and Ir show wide ranges within most groups, which approach the total range shown by all iron meteorites. Since concentrations of the nine major siderophile elements vary systematically within each group, there is little ambiguity in classifying meteorites into groups and locating each meteorite within its group. Mineralogical and isotopic data confirm that group members are closely related and probably formed in a single body. About 15% of irons have compositions that lie outside those of the groups and are called ungrouped irons. A few small, rapidly cooled and S-rich ungrouped irons probably formed by impact melting in ordinary chondrite bodies, e.g., Sahara 03505 (D’Orazio *et al.*, 2009). However, the remaining ungrouped irons appear to be derived from ~50 to 60 separate bodies (Goldstein *et al.*, 2009).

TABLE 2. Classification of differentiated meteorites.

Name	Fall freq.* (%)	Minerals <sup>†</sup>	Origin	References
<i>Iron meteorites</i>				
Groups IIAB, IIIAB, IVA, IVB, etc.	4.3	Metallic Fe-Ni, troilite (FeS)	Fractionally crystallized cores	Goldstein <i>et al.</i> (2009)
Groups IAB and IIE	3.2	Fe-Ni with silicate inclusions	Metallic pools in partly melted bodies	Ruzicka (2014)
	1.1			
<i>Stony irons</i>				
Pallasites	0.27	Fe-Ni, olivine (Fa <sub>10–20</sub> )	Breccias of core and mantle formed in several bodies	Yang <i>et al.</i> (2010a), Benedix <i>et al.</i> (2014)
Mesosiderites	0.6	Fe-Ni, pyroxene (Fs <sub>10–20</sub> ), plagioclase (An <sub>50–80</sub> )	Impact mixtures of basalt, gabbro, and Fe-Ni-S from a Vesta-like body	Benedix <i>et al.</i> (2014)
<i>Achondrites</i>				
Howardites, eucrites, diogenites	5.5	Pyroxene (En <sub>14–79</sub> Wo <sub>2–5</sub> ), plagioclase (An <sub>73–93</sub> ), silica	Breccias of basalts, gabbros, and pyroxenites from Vesta	McSween <i>et al.</i> (2013)
Angrites	0.09	Al-Ti-diopside (Fs <sub>12–50</sub> ), Ca-olivine, anorthite (An <sub>86–100</sub> )	Oldest basaltic meteorites from a fully differentiated asteroid	Keil (2011)
Aubrites	0.8	Enstatite (Fs <sub>0.1</sub> ), minor plag, ol	Igneous rocks: mostly breccias	Keil (2010)
Ureilites	0.5	OI (Fo <sub>74–95</sub> ), pyx (mostly En <sub>68–87</sub> Wo <sub>2–16</sub> ), graphite	Partial melt residues from which basalts were removed	Goodrich <i>et al.</i> (2004)
<i>Primitive achondrites</i>				
Brachinites	<0.1	OI (Fo <sub>64–73</sub> ), pyx (En <sub>40–63</sub> Wo <sub>36–48</sub> ), plag (An <sub>15–33</sub> )	Partial melt residues from FeO-rich body	Keil (2014)
Acapulcoites and lodranites	0.09	OI (Fo <sub>87–97</sub> ), pyx (En <sub>88–93</sub> Wo <sub>2–3</sub> and En <sub>50–54</sub> Wo <sub>43–46</sub> ), Fe-Ni-S, plag (An <sub>12–31</sub> )	Low-degree partial melting residues in one body	Krot <i>et al.</i> (2014)
Winonaites	0.09	OI (Fa <sub>1–4</sub> ), pyx (Fs <sub>1–9</sub> ), plag (An <sub>8–25</sub> )	Metamorphosed chondrites from IAB body	Krot <i>et al.</i> (2014)

\* Source: Meteoritical Bulletin Database (<http://www.lpi.usra.edu/meteor/metbull.php>).

<sup>†</sup> Abbreviations: ol = olivine, pyx = pyroxene, plag = plagioclase; Fa = fayalite mol.%; Fs = ferrosilite mol.%; Wo = wollastonite mol.%; An = anorthite mol. %.

Not listed are the ungrouped irons (~100), ungrouped pallasites (~5), and ungrouped achondrites (~50).

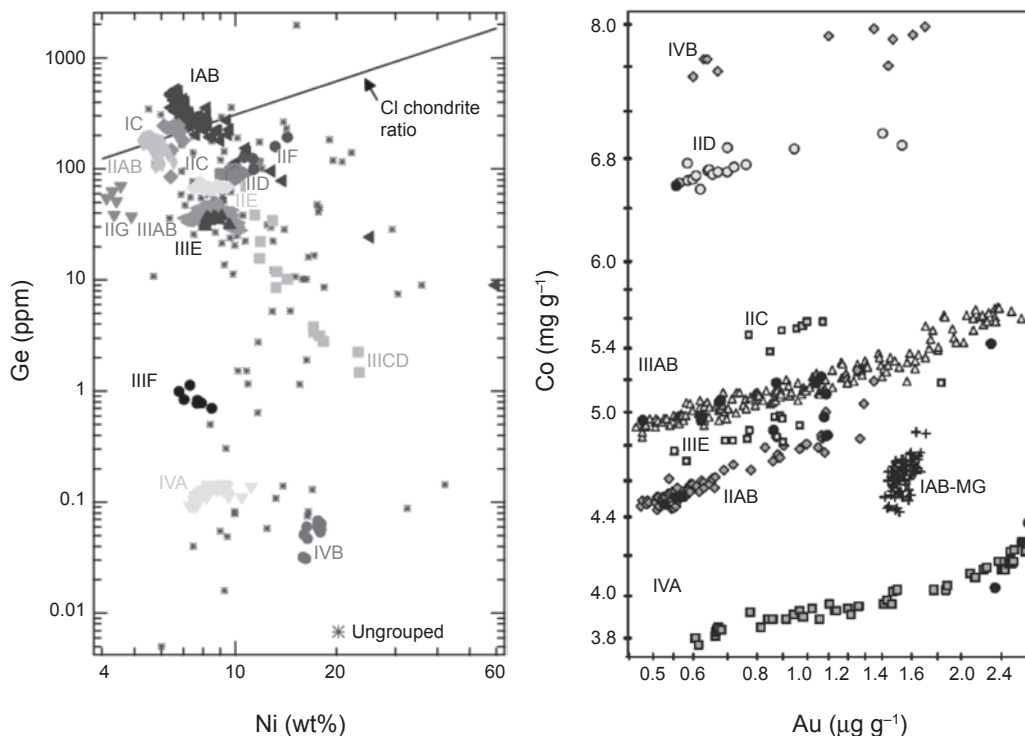


**Fig. 4.** Logarithmic plots showing the bulk compositions of iron meteorites. (a) Ge vs. Ni for grouped and ungrouped iron meteorites. Reproduced from Goldstein *et al.* (2009) by permission; image courtesy N. Chabot. (b) Co vs. Au for seven major groups of irons, which are thought to be derived from asteroidal cores that fractionally crystallized, and the group IAB-MG, which is rich in silicates and shows very different chemical trends. Reproduced from Wasson (2011) by permission.

Except for groups IAB, IIE, and IIICD, which show very different chemical trends from the other groups, chemical variations within each group can be explained by fractionation between solid and liquid Fe-Ni during solidification of a single large metallic magma, probably core material from a melted asteroid (Chabot, 2004; Goldstein *et al.*, 2009). The elements Au, As, Ni, Co, and P prefer liquid to solid Fe-Ni, whereas Ir, Re, and Os are concentrated preferentially in the solid, and Ge and Ga are scarcely fractionated. Chemical trends in fractionally crystallized groups, which are sometimes called “magmatic groups,” are largely consistent with those calculated using fractional crystallization models and experimentally determined solid-liquid partition coefficients. The nonmetals, S, P, and C, which are largely excluded from the crystallizing Fe-Ni so they become enriched in the residual melts, can drastically modify the partition coefficients of the metallic elements. Iron meteorites mostly contain 0.02–2 wt.% S in the form of troilite (FeS), although S is relatively insoluble in solid Fe-Ni (Buchwald, 1975). Troilite nodules in irons, which may have diameters of a centimeter or more, probably formed from melt that was trapped during crystallization. Fractional crystallization modeling suggests that group IVB irons crystallized from a melt that contained <1 wt.% S as the linear trends on log-log interelement plots can be modeled with fixed partition coefficients (Chabot,

2004). However, groups IIAB, IID, IIIAB, IVA appear to have crystallized from magmas with ~5–20 wt.% S and typically show nonlinear trends on log-log plots. The near absence of such S-rich irons is attributed to the low strength of troilite relative to Fe-Ni. Many iron meteoroids survived in space for hundreds of million years as meter-sized objects. Their cosmic-ray exposure ages are roughly 10× longer than nearly all stony meteorites (Herzog and Caffee, 2014).

#### 4.2.1. Formation of fractionally crystallized groups.

Three large groups of iron meteorites, IVA, IIIAB, and IVB, have chemical properties consistent with formation in a large metallic core, but other properties indicating they did not cool in a core surrounded by a silicate mantle. For the IVA irons, there are three pieces of evidence. First, their metallographic cooling rates at ~500°C vary from 100° to 6000°C m.y.<sup>-1</sup>, whereas samples from a well-insulated metallic core should have essentially uniform cooling rates at ~1200°C. Second, the ancient Pb-Pb age of troilite in one IVA iron of 4564 Ma (Blichert-Toft *et al.*, 2010) (Fig. 1) is far too old for a core sample from a large asteroid, which would take ~100 m.y. or more to cool. Third, two IVA irons contain abundant silicates with anomalously rapid cooling rates (Haack *et al.*, 1996; Ruzicka, 2014). Although the non-uniform metallographic cooling rates in IVA have been questioned (Wasson and Hoppe, 2012), several features support

a wide range of cooling rates among the IVA irons. These include the dimensions of the submicrometer intergrowth called, “cloudy taenite,” and the composition of the kamacite and taenite and their interface (Goldstein *et al.*, 2014).

The thermal history and age of group IVA irons can be explained if the original IVA asteroid was disrupted after melting to form a metallic body with a radius of  $150 \pm 50$  km surrounded by  $<1$  km of silicate mantle (Yang *et al.*, 2007, 2008). Thermal and fractional crystallization modeling shows a good match between calculated and observed cooling rates for a body that crystallized radially inward (Fig. 5). Separation of core from silicate mantle was probably caused by hit-and-run impacts as conventional hypervelocity impacts are very inefficient at separating core and mantle material (Asphaug *et al.*, 2006; Asphaug and Reufer, 2014) (see section 5).

Group IIIAB, which is the largest group of iron meteorites with over 200 members, has a cooling rate range of  $60^\circ\text{--}300^\circ\text{C m.y.}^{-1}$  and phosphates that cooled through  $\sim 750^\circ\text{C}$  about 4 m.y. after CAI formation (Sugiura and Hoshino, 2003; Yang and Goldstein, 2006) (Fig. 1). These constraints can be accommodated by a metallic body with a radius of several tens of kilometers that cooled with only a few kilometers of silicate mantle (Goldstein *et al.*, 2009). Cosmic-ray exposure ages of IIIAB and IVA irons cluster around 650 and 400 Ma, respectively (Herzog and Caffee, 2014). These ages were previously interpreted as the breakup events for the entire IIIAB and IVA metallic cores (Keil *et al.*, 1994), but it is possible that they date the destruction of relatively small but representative rubble piles of metal fragments (Yang *et al.*, 2008).

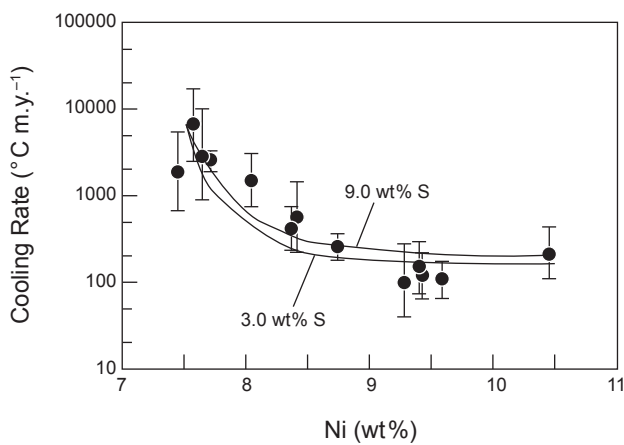


**Fig. 5.** Metallographic cooling rates at  $500^\circ\text{C}$  for 13 group IVA irons decrease with increasing bulk Ni. The curves show calculated cooling rates for a metallic body of radius 150 km that lacks a silicate mantle. The depth of each iron in the metallic body is inferred from its Ni concentration and fractional crystallization modeling assuming bulk S contents of 3 or 9 wt.%. The original IVA parent body, which would have had a minimum radius of  $300 \pm 100$  km, is thought to have been disrupted by a hit-and-run collision  $\sim 2$  m.y. after CAI formation. After Yang *et al.* (2008).

Group IVB irons cooled through  $600^\circ\text{--}400^\circ\text{C}$  at rates of  $500^\circ\text{--}5000^\circ\text{C m.y.}^{-1}$  that increase with increasing bulk Ni (Yang *et al.*, 2010b). They appear to be derived from a metallic body that crystallized outward and was  $65 \pm 15$  km in radius when cooling without a silicate mantle. Separation of the mantle from a solid core may have occurred after the core was largely solid and could have been aided by a thin layer of residual metallic melt between core and mantle. In this case, the IVB irons may have crystallized in a mantled core that was somewhat larger ( $70 \pm 15$  km in radius). Group IVB irons are unrelated to any other meteorite type (Krot *et al.*, 2014).

**4.2.2. Formation of silicate-rich irons.** Iron meteorites in groups IAB, IIE, and IIICD, which have very different chemical trends from the fractionally crystallized groups, contain numerous silicate inclusions. Textural and mineralogical evidence suggests they formed by impact-mixing of previously heated silicate and molten metal (Ruzicka, 2014). Group IAB irons contain angular fragments of chondritic material, except for Caddo County and Ocotillo, which contain highly differentiated silicates. The chemical and oxygen isotopic composition of the silicates in IAB and IIICD irons closely match those of silicates in winonaites, which are strongly metamorphosed and partly melted chondrites (Table 2), suggesting they come from the same asteroid. The low degree of silicate melting of winonaites and most silicate inclusions in IAB irons suggests that temperatures were not high enough to allow a metallic core to form in their parent body (Benedix *et al.*, 2014). The time of impact mixing of metal and silicate was inferred by Vogel and Renne (2008) from Ar-Ar ages to be  $\sim 4480$  Ma, but Hf-W and Pd-Ag isotopic systematics favor several impacts  $\sim 2\text{--}10$  m.y. after CAI formation (Schulz *et al.*, 2012; Theis *et al.*, 2013). Low shock levels in the IAB silicates and winonaites suggest that low-speed accretionary impacts mixed metal and silicate, although impacts at the current mean asteroidal impact speed of  $\sim 5$  km s $^{-1}$  are not efficient at creating shocked and melted rock (Marchi *et al.*, 2013) and cannot be excluded.

Group IIE irons have relatively uniform Fe-Ni compositions and diverse silicate inclusions that range from chondritic in composition and texture to highly differentiated basaltic and glassy inclusions. The oxygen isotopic composition and the mineralogy of the chondritic inclusions resemble those of H chondrites, although the IIE silicates appear to be slightly more reduced. They were probably formed by impacts onto an H-like chondritic body, which experienced significantly more melting than the IAB-winonaite body (Ruzicka, 2014). Since most of the IIE irons have highly differentiated silicates, it is possible that the IIE metal was derived from a molten metal core in a body with a chondritic crust (Weiss and Elkins-Tanton, 2013; see also the chapter by Scheinberg *et al.* in this volume). The impact that mixed metal and silicate occurred at  $\sim 4.5$  Ga. During the late heavy bombardment at  $\sim 4$  Ga, the IIE body was presumably still very large as many IIE irons have strongly shocked silicate inclusions with Ar-Ar ages of 3.7–4.0 Ga (Bogard, 2011) (see section 4.4.1).

### 4.3. Stony-Iron Meteorites

Two major types of stony-irons — pallasites and mesosiderites — are known (Table 2). Both appear to have formed in impacts that mixed largely unshocked silicate and molten metallic Fe-Ni (Benedix et al., 2014; Krot et al., 2014). Pallasites, which formed by impact mixing of core metal with mantle olivine, are largely from the so-called “main group.” Five Eagle Station types constitute a second group and there are another ~5–7 ungrouped pallasites.

Diverse cooling rates and paleomagnetic properties show that the main-group pallasites did not cool at the core-mantle boundary of an asteroid (Yang et al., 2010a; Tarduno et al., 2012). Metal and possibly some olivine were probably extracted by a low-velocity impact with a larger body (Asphaug et al., 2006) and deposited in the mantle of the larger body that contained a core-dynamo. Interestingly, there are no iron or olivine-rich meteorites that are genetically related to the main-group or Eagle Station pallasites. [IIIAB irons were once thought to be related to the main group, but their cooling rates and chemical compositions suggest they crystallized inward, whereas the metal in main-group pallasites was probably derived from a core that crystallized outward (Yang et al., 2010a)]. Metal was efficiently mixed with olivine so that olivine-free metal regions are  $\leq 1$  m in size, and olivine mantle chunks without metallic armor were fractured along grain boundaries and are too weak to survive as meteorites. The time of metal-olivine mixing is not well constrained, but Mn-Cr systematics suggest 4558 Ma or possibly earlier for the main group (Lugmair and Shukolyukov, 1998).

Mesosiderites formed by mixing of basaltic and gabbroic silicate from a Vesta-like body with molten Fe-Ni, probably from the core of a second asteroid (Benedix et al., 2014). They cooled through 500°C slower than any other meteorites at  $\sim 0.5^\circ\text{C m.y.}^{-1}$  for  $\sim 700$  m.y. (Goldstein et al., 2014). Argon-argon ages of 3.7–4.0 Ga reflect slow cooling, not impact reheating or excavation (Bogard, 2011). The anomalous mesosiderite Chaunskij contains cordierite, which formed at a pressure of 6 Kbar, probably in a body that was  $>400$  km in radius (Petaev et al., 2000). The time of metal-silicate mixing was previously thought from Sm-Nd ages of clasts to have been  $\sim 100$ –150 m.y. after CAIs (Stewart et al., 1994), but a reinterpretation of these ages by Ganguly and Tirone (2001) suggests that they date slow cooling and that molten metal and silicate were mixed at 4.56 Ga. The low shock levels in pallasites and mesosiderites and the efficient mixing of molten metal with silicate suggest that mixing occurred during accretion in a low-velocity impact.

### 4.4. Achondrites

**4.4.1. Eucrites.** The largest group of achondrites — the howardites, eucrites, and howardites, which are eucrite-diogenite breccias — are almost certainly from (4) Vesta (McCord et al., 1970; Keil, 2002; see also the chapter by Russell et al. in this volume). Vesta is a unique body as it appears to be the only differentiated asteroid that has retained

its core, mantle, and basaltic crust. [For a contrary view, see Consolmagno et al. (2015).] Although the effects of early impacts are commonly neglected, impacts were common during igneous processing, as many diogenites and eucrites have excessively high concentrations of siderophiles. Dale et al. (2012) attribute these high siderophile concentrations and those in other achondrites to chondritic projectiles. However, differentiated projectiles with molten cores and mantles cannot be excluded, as they also have chondritic bulk compositions.

Most eucrites and diogenites were strongly shocked and brecciated at 3.7–4.1 Ga during the late heavy bombardment (Bogard, 2011; Marchi et al. 2013), but a small group of pristine unshocked eucrites with Ar-Ar ages of 4.48 Ga may have been removed from Vesta long before the other eucrites. (This Ar-Ar age should be increased by  $\sim 0.03$  Ga to allow for half-life and other corrections.) Bogard and Garrison (2003) suggested that they were extracted from Vesta by a hypervelocity impact at that time and stored in a small body. Small asteroids that survived the late heavy bombardment intact lack shock-heated meteorites from this era. Large asteroids preferentially retain shocked rocks more efficiently and sustain larger, high-velocity impacts that deposit vastly more impact energy per kilogram of target (see also Marchi et al., 2013).

At least two ungrouped eucrites, NWA 011 and Ibitira, and possibly several others, are isotopically and chemically so different from normal eucrites that they probably come from other bodies (Mittlefehldt, 2005; Scott et al., 2009; Sanborn and Yin, 2014). These bodies were probably  $>100$  km in radius, as smaller bodies would probably have lost their basalts during explosive volcanism (Wilson and Keil, 1991). The ungrouped eucrites, unlike normal eucrites, appear to have escaped the effects of the late heavy bombardment and may have been extracted from their parent bodies before 4.0 Ga, like the 4.48-Ga-old unbrecciated eucrites. The ungrouped eucrites are not related to other types of achondrites or iron meteorites and are plausibly fragments from the small V-type asteroids that orbit far beyond Vesta (section 3.1).

**4.4.2. Angrites.** Angrites are unbrecciated and substantially unshocked igneous rocks of roughly basaltic composition that have preserved a record of early igneous activity in a large asteroid and paleomagnetic evidence for a core dynamo (Weiss et al., 2008; Keil, 2011). Hafnium-tungsten isotopic data show that the core formed  $<2$  m.y. after CAIs but not in a single event from a homogeneous magna ocean. Kleine et al. (2012) infer that planetesimals impacted the angrite parent body during core formation. The lack of shock and breccia features in angrites suggests they were removed from their parent asteroid before the late heavy bombardment (Scott and Bottke, 2011), like the unbrecciated eucrites (Bogard and Garrison, 2003).

**4.4.3. Aubrites.** Aubrites, which are enstatite achondrites, are regolith or fragmental breccias and are probably derived from one or more E-type asteroids in the Hungaria region (section 3.4). The absence of associated metal-rich meteorites or asteroids suggests that these asteroids may

have been emplaced in the Hungaria region after disruption of their parent asteroid. One ungrouped aubrite, Shallowater, which contains about ~15% of inclusions of enstatite chondrite material, provided the first meteorite evidence for very early major impacts that involved a molten planetesimal. *Keil et al.* (1989) inferred that Shallowater formed after a chondritic projectile had disrupted a molten aubritic body during a low-velocity impact. The chondritic material may also have been derived from an unmelted crust on the molten body. The ancient I-Xe age of Shallowater of 4561 Ma (Fig. 1) shows that this impact occurred about 5 m.y. after CAI formation. The thermal history of the metal grains suggests that the parent asteroid suffered two other catastrophic impacts as it cooled (*Keil et al.*, 1989).

**4.4.4. Ureilites.** Ureilites are coarse-grained carbon-bearing ultramafic rocks that formed as residues from partial melting at temperatures of ~1100°C (*Krot et al.*, 2014). The presence of uninverted pigeonite, or nanometer-scale augite exsolution lamellae (*Mikouchi et al.*, 2010), and high-Ca olivine shows that ureilites rapidly cooled from ~1100°C to <650°C in hours, and the high level of shock effects in silicates suggests that this resulted from a hypervelocity catastrophic impact (*Goodrich et al.*, 2004, 2015). To cool in hours, the fragments must have been meter-sized prior to reaccretion. The energy for dispersing the fragments was not solely kinetic as the effect of the impact was analogous to removing the cork from a champagne bottle. The reduction in lithostatic pressure allowed carbon to react with silicates, forming a CO-CO<sub>2</sub> mixture and leaving tiny Fe metal grains on the edges of the olivine grains. Release of gas helped to catastrophically fragment the rock and temporarily disperse the fragments. The impact probably occurred 5 m.y. after CAIs (Fig. 1), as this is the age of basaltic fragments from ureilite breccias containing feldspar crystals and glass (*Goodrich et al.*, 2010, 2015).

#### 4.5. Primitive Achondrites

Several groups of meteorites experienced low degrees of melting and mobilization of silicate and FeNi-FeS phases. They are commonly called primitive achondrites and include acapulcoites, lodranites, brachinites, and winonaites (Table 2) (*Krot et al.*, 2014). The least-metamorphosed acapulcoites and winonaites still contain rare relict chondrules but most primitive achondrites have recrystallized, granular textures and are typically enriched or depleted in low-temperature silicate and metallic melts. None of these meteorites are fragmental breccias and most are unshocked or only lightly shocked (stages S1–S2). Note that there are no clear-cut divisions between achondrites and primitive achondrites. Brachinites, for example, are considered by some authors to be achondrites, and ureilites have also been classed as primitive achondrites.

**4.5.1. Acapulcoites and lodranites.** Acapulcoites have near-chondritic chemical compositions whereas lodranites were heated to higher temperatures and are commonly richer in metal. They clearly formed in close proximity, as some

meteorites contain both types of material due to mixing and rewelding of hot material, and others have intermediate characteristics. These meteorites have two unusual characteristics. First, metallographic cooling rates of seven acapulcoites and lodranites are 10<sup>3</sup>–10<sup>4</sup>°C m.y.<sup>-1</sup> (*McCoy et al.*, 1996, 1997) — one or more orders of magnitude higher than maximum rates for material in undisturbed asteroids heated by <sup>26</sup>Al (*Scott et al.*, 2014). Second, Ar-Ar ages of seven of these meteorites are remarkably similar: 4512 ± 9 Ma (*Bogard*, 2011). Since their diverse textures require different formation locations, their common age and rapid cooling rate suggests they were all extracted from depth by an impact, possibly a catastrophic one, before their parent body had cooled significantly. Given the well-determined Pb-Pb age of Acapulco phosphate of 4556 ± 0.5 Ma (*Göpel and Manhes*, 2010), and the required increase in the Ar-Ar ages by 30–40 m.y. due to errors in the <sup>40</sup>K decay rate (*Bogard*, 2011), it is likely that this large impact occurred 11 m.y. after CAI formation. Thermal models that assume that cooling was undisturbed by impacts (e.g., *Golabek et al.*, 2014) can only provide very approximate constraints on parent-body size and burial depth.

**4.5.2. Brachinites.** Brachinites are ancient unbrecciated and essentially unshocked rocks that are largely composed of FeO-rich olivine and pyroxene (Table 2) with heterogenous  $\Delta^{17}\text{O}$  values consistent with low degrees of melting (*Greenwood et al.*, 2012; *Keil*, 2014). There are no firm constraints on their cooling rates, but CaO concentrations in olivine are 0.08–0.3 wt.%, higher than in acapulcoite-lodranites but not as high as in ureilites (*Krot et al.*, 2014). Thus brachinites cooled rapidly enough to prevent Ca diffusing out of olivine suggesting that, like ureilites and acapulco-lodranites, they were excavated from depth by impact before they had cooled below ~1000°C.

#### 4.6. Differentiated Meteorite Parent Bodies

There are few genetic relationships among differentiated meteorites apart from the link between winonaites and IAB irons, which are probably not derived from core metal. We lack mantle or crust material from the 60-odd parent bodies of the grouped and ungrouped iron meteorites and we lack core material from the parent bodies of the various groups of achondrites and the numerous ungrouped achondrites, such as the ungrouped eucrites, Graves Nunataks (GRA) 06128 and Divnoe, which are listed in the Meteoritical Bulletin Database (see <http://www.lpi.usra.edu/meteor/metbull.php>). Our collection of differentiated meteorites resembles a collection of 1000 pieces from ~100 different jigsaw puzzles with 1–100 pieces from each puzzle. Notably missing are the olivine-rich mantle meteorites from the parent bodies of irons, stony-irons, and achondrites.

Early impacts during the first few million years are needed to remove mantles from core material or mix molten metal and silicate and to explain the properties of IIIAB, IVA, and IVB irons, pallasites, mesosiderites, and the Shallowater aubrite. Disruption of the ureilite body and

formation of CB chondrules require later hypervelocity impacts  $\sim 5$  m.y. after CAI. The IAB irons, acapulcoites and lodranites, brachinites, angrites, and anomalous eucrites were involved in major early impacts that left little evidence for shock consistent with accretionary impacts. However, some of these impacts could have occurred after asteroid accretion given that typical asteroidal impacts at current impact speeds of  $\sim 5$  km s $^{-1}$  create relatively little shocked material (Marchi et al., 2013).

Interestingly, the metal-bearing meteorites that cooled slowest at  $\sim 500^\circ\text{C}$  are the IAB irons, the pallasites, and the mesosiderites. In each case, cooling rates are rather uniform although the meteorites are not from asteroidal cores. Iron meteorites that are probably derived originally from core material, like IIIAB, IVA, and IVB irons, cooled faster than the stony-irons and silicate-rich IAB irons, and each group shows a wide range of cooling rates. This is the exact opposite of what conventional models predict. If the core samples had cooled *in situ*, their cooling rates would be uniform in each group and generally slower than those that cooled in smaller metallic pools. These cooling rates may be understood, however, if differentiated bodies were torn apart during accretion by hit-and-run collisions when the cores were still molten or partly molten (Asphaug et al., 2006). Below, we review how these impacts differ from conventional hypervelocity impacts in the current asteroid belt and how they might explain the meteoritic evidence for early low-speed impacts between planetesimals.

## 5. HIT-AND-RUN COLLISIONS

Conventional hypervelocity impacts are not effective at excavating core material from differentiated asteroids and liberating iron meteoroids as they require exceptionally large projectiles having half the target's size and, in the case of Vesta-sized bodies, exceptionally fast impact speeds (Asphaug, 2010). By contrast, grazing impacts during early planet formation at velocities comparable to the escape velocities of the colliding bodies are remarkably effective at disrupting differentiated bodies (Agnor and Asphaug, 2004; Asphaug et al., 2006; Stewart and Leinhardt, 2012). These collisions result in a very odd assortment of relics by introducing a mechanism for winnowing or stripping the lower-density mantle, crustal, and hydrospheric components from the denser deep mantle and iron core components, forming bodies whose compositions can depart substantially from the chondritic average (Asphaug and Reufer, 2014).

### 5.1. Self-Stirred Populations

Although we do not yet know how planetesimals formed, the modern assumption is that there was a phase of rapid growth that formed bodies 100 km in diameter or larger (Weidenschilling and Cuzzi, 2006; see also the chapter by Johansen et al. in this volume). This means that a population of similar-sized protoplanets or planetary embryos was accreting early on. Similar-sized collisions ( $R_1 \sim R_2$ ) are

remarkably different from cratering impacts, there being no locus to the collision. Due to geometrical effects, most of them are grazing events where the colliding matter continues downrange (Asphaug, 2010).

According to classic theories (Safronov, 1972; Wetherill, 1980), in the absence of damping by nebula gas such a population becomes gravitationally stirred by close mutual encounters, to random relative velocities  $v_{\text{rel}}$  comparable to the escape velocity  $v_{\text{esc}}$  of the largest bodies. The impact velocity  $v_{\text{imp}} = \sqrt{(v_{\text{rel}}^2 + v_{\text{esc}}^2)}$  where  $v_{\text{esc}} = \sqrt{2G(M_1 + M_2)/(R_1 + R_2)}$  is the escape velocity, the speed at which two spherical planets of masses  $M_1 > M_2$  and radii  $R_1$  and  $R_2$  collide if falling from "infinity" with zero relative velocity. It is about equal, in meters per second, to the diameters of the colliding bodies, in kilometers, thus around 100 m s $^{-1}$  during planetesimal accretion and around 10 km s $^{-1}$  during late-stage planet formation. Impacts occurring during planetesimal accretion would not generally have involved shocks.

Relative motions are damped by smaller planetesimals and gas, and are excited by larger embryos and by resonant gravitational perturbations by large planets outside the protoplanetary region. There is always some random relative velocity, so that impacts are always somewhat faster than  $v_{\text{esc}}$ . Accretion is never completely efficient, but the surprising thing is that only a modest random velocity,  $\sim(2/3)v_{\text{esc}}$ , is sufficient to reduce accretion efficiency so that hit-and-run collisions are as frequent as coagulation (Agnor and Asphaug, 2004; Asphaug, 2010). Moreover, it makes the disruption behave in a systematically biased sort of way, as we shall see.

Disruption in turn feeds back into the population of small particles that can damp velocities, so that accretion efficiency can go back and forth as early planet formation continues. Meteorites that constitute the record of this epoch are therefore expected to represent this wide range of outcomes: effective coagulation, and more energetic mantle-stripping impacts. The outcomes that do not ultimately result in accretion into planets are those that are sampled by the meteorite collection.

The accretion efficiency  $\xi$  is defined as  $(M_F - M_1)/M_2$  where  $M_F < M_1 + M_2$  is the mass of the final largest body (Asphaug, 2009). For velocities characteristic of late-stage planet formation,  $0.7 \leq v_{\text{rel}}/v_{\text{esc}} \leq 2.5$ , it has been shown that about half of similar-sized collisions are hit and run ( $\xi \approx 0$ ), in which  $M_2$  bounces off or plows through  $M_1$ , becoming a mantle-stripped relic or chain of iron-rich bodies (Agnor and Asphaug, 2004; Asphaug et al., 2006; O'Brien et al., 2006; Asphaug, 2009; Chambers, 2013).

Higher-velocity collisions with  $v_{\text{rel}}/v_{\text{esc}} \geq \sim 3$  erode increasing fractions of the target ( $\xi < 0$ ). But catastrophic disruption of  $M_1$  requires  $v_{\text{imp}} \gg v_{\text{esc}}$ , so does not occur during accretion. Catastrophic disruption of  $M_2$ , on the other hand, is an intimate aspect of pairwise accretion, even under low relative velocities. The sensitivity of  $\xi$  over the expected velocity range leads to spectacularly diverse non-accretionary outcomes, and to the evolution, by attrition, of a highly varied assortment of unaccreted objects — mantles segregated from cores by hit-and-run events and partial accretions.

## 5.2. Mantle Stripping During Accretion

Mantle stripping during accretion has little to do with blasting material from the target into orbit or into escaping trajectories. This is especially the case for planetesimal accretion, where the collisional velocities are too slow to induce shocks. Rather, it is the two-body interaction that causes mantle material to be lost. It is not blasted off the target; it is unaccreted from the projectile.

Lower-density materials at or near the surface of  $M_2$  (i.e., the mantle, crust, hydrosphere, and atmosphere) are slung onto noncapture trajectories, while higher-density materials can be stopped effectively and sink to join the target core, or can skip off the target and be segregated into chains of iron-rich clumps and iron-poor debris. Before we present simulations of examples of such events, here we simply notice two facts: (1) the diversity of outcomes is enormous, and (2) to first order, hit and run is as common as accretion.

One very important dynamical fact is that mantle stripping by hit and run provides a permanent sink for these “lost” (unaccreted) silicates that are missing from our meteorite collections. Following a hit-and-run collision, the target  $M_1$  is orbiting the Sun along with  $M_2$  on crossing orbits. The collisional cross section of  $M_1$  is larger than  $M_2$  by approximately the geometric cross section  $\sim R_2 \times$  the gravitational focusing  $f = 1 + (v_{\text{esc}}/v_{\text{rel}})^2$ , the latter increasing with  $R \propto v_{\text{esc}}$ . Consequently  $M_1$  accretes most of the stripped mantle from  $M_2$  during the thousands of orbits following a collision.

While  $M_1$  sweeps up most of the debris, it will likewise sweep up  $M_2$  in one or more subsequent collisions, causing  $M_2$  to disappear unless gravitational perturbations or tidal migrations or other collisions isolate it from  $M_1$ . This has sometimes been regarded by dynamical modelers as discounting the relevance of hit-and-run collisions, since eventually all the mess gets swept up by  $M_1$ .

But when one considers the statistics of survivors — i.e., the attrition bias of the relics of planet formation (*Asphaug and Reufer, 2014*) — one finds that in fact survivors of multiple hit-and-run collisions will not only be present, but will be common in typical pairwise-accretion scenarios. If a population of  $N$  bodies accretes forming planets and leaves behind  $N_{\text{final}}$  unaccreted original bodies, then the average number of hit-and-run collisions experienced by the unaccreted remnants will be approximately  $h \sim \ln(N/N_{\text{final}})$ . The stronger the attrition (the smaller  $N_{\text{final}}/N$ ), not only the greater the average  $h$ , but the wider the spread in  $h$  — i.e., the greater the diversity.

On this basis, *Asphaug and Reufer (2014)* argue that Mars and Mercury, if original remnants of an original  $\sim 20$  bodies that accreted to form Earth and Venus, would be expected to have one survivor of  $\sim 2$  hit-and-run collisions, and one survivor that is relatively unperturbed by unaccretionary collisions. If tens of thousands of planetesimals accreted to form a few thousand asteroid progenitors, then  $h = \sim 3$ . Bodies like (16) Psyche and the stripped cores of the iron meteorite parent bodies could have experienced several hit-and-run collisions as the accretionary mergers

took place, while Vesta would be a survivor of few if any hit-and-run collisions.

While it may seem far-fetched to invoke multiple hit-and-run collisions for mantle stripping of planetesimals and planetary embryos, the theoretical basis for this idea has been established, and is in fact validated to some extent in the latest dynamical models. In the first N-body integrations to track the remnants of hit-and-run collisions, *Chambers (2013)* finds cases where terrestrial protoplanets experience multiple hit-and-run collisions and then become dynamically isolated. Obviously there is much work to be done on understanding the influence of imperfect accretion on the dynamics of planet formation; here we now look more closely at the aftermath of such encounters between planetesimals.

## 5.3. Subsonic Hit-and-Run

Subsonic hit-and-run collisions between planetesimals are as effective at removing mantle silicates as their hypervelocity counterparts between embryos, but do so differently as illustrated by comparison simulations (Fig. 6), where  $M_2/M_1 = 0.20$ ,  $\theta = 30^\circ$ ,  $v_{\text{imp}} = 3 v_{\text{esc}}$ , but one is subsonic, the other supersonic. In each case the core and mantle are effectively segregated, but the collision on the right, into an Earth-mass target, induces strong shocks that vaporize the escaping material and cause its dispersal. The smaller collision on the left, into a target  $0.0091 M_\oplus$  but otherwise similar in scale, shreds  $M_2$  according to subsonic mechanical and gravitational interactions, segregating it by density into chains of metal-rich and metal-free clumps, without shock heating.

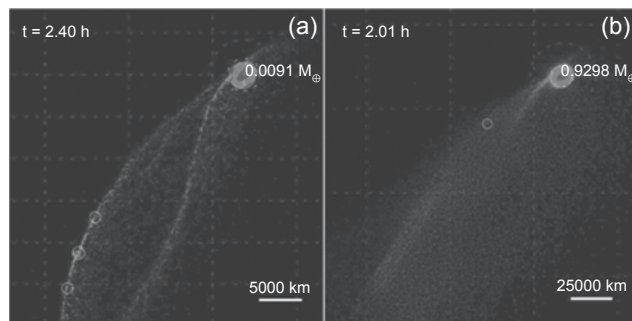


**Fig. 6.** See Plate 19 for color version. Simulations of two collisions with the same  $M_2/M_1 = 0.2$ ,  $\theta = 30^\circ$ ,  $v_{\text{imp}} = 3 v_{\text{esc}}$ , but differing in mass by a factor of 100. Both are shown at  $\sim 10$  collision times,  $\tau_{\text{coll}} = 2(R_1 + R_2)/v_{\text{imp}}$ . Silicates (red) are segregated from metals (blue) in the remnants of  $M_2$  and are dispersed downrange in both hit-and-run collisions. The subsonic collision (left;  $R_1 = 1400$  km,  $R_2 = 800$  km) leads to a chain of iron-dominated clumps (white circles) stripped gravitationally and mechanically from a sheet of lower-density mantle material. The supersonic collision (right;  $M_1 = M_\oplus$ ,  $v_{\text{imp}} \approx 30$  km s $^{-1}$ ), produces intense global shocks and fine dispersal of the plume. After *Asphaug and Reufer (2014)*.

Subsonic hit-and-run collisions among accreting planetesimals provide an evolutionary pathway that is perhaps highly relevant to the major asteroids such as Psyche that appear metallic and the parent asteroids of iron meteorites that also lost their mantles (Yang et al., 2007; Goldstein et al., 2009) (section 4.2.1). Removal of mantles from cores by conventional hypervelocity impacts (e.g., Burbine et al., 1996) is a long-standing problem, as it requires repeated giant impacts from projectiles with half the target's size, while leaving Vesta's crust intact (Davis et al., 1985).

Iron fraction and diversity in this scenario are not an aspect of the planetesimals' starting compositions — they all might start out chondritic — but a consequence of varying the number and type of hit-and-run collisions experienced by each survivor. It is unlikely for an asteroid parent body to have suffered repeated hit-and-run collisions during terrestrial planet formation, but it is even less likely for it to have not been accreted. This motivates the attrition bias argument (Asphaug and Reufer, 2014) for the preponderance of hit-and-run relics among asteroids. To not be accreted means to either be dynamically isolated from the accretionary swarm from the beginning ( $h = 0$ ), or to be lucky (unaccreted; hit and run) every time there is a collision with a larger body. So in the end, this selection bias strongly influences the surviving population.

The timing of all these collisions would have been very early, within the first few million years when the planetesimals were growing into protoplanetary embryos. Multiple mantle-stripping impacts while the bodies were solidifying would be the right recipe for a thin-skinned solidifying core such as is inferred from modeling of the IVA iron cooling rates (section 4.2.1). However, detailed modeling is needed that feeds the output of the first hit-and-run collision, into a second hit-and-run collision, and a third.

Of course, as Fig. 6 makes clear, not all the hit-and-run remnants are iron-rich clumps. Some hit-and-run collisions swallow the core and leave the mantle escaping downrange (Reufer et al., 2012). Such impacts could account for the formation of stony-irons (section 4.3). Subsonic hit-and-run collisions leave behind surviving blobs of silicate relics subject to varying degrees of deformation and pressure release (Asphaug et al., 2006), whose genetic relationship to irons would be complex — a topic of further study.

## 6. COLLISION AND DYNAMICAL EVOLUTION MODELS

If differentiated asteroids were derived from numerous Vesta-like bodies as a result of impacts in the asteroid belt, the distribution of differentiated asteroids would be very different from what we observe today. Collision and dynamical evolution modeling indicates the asteroid belt has experienced a limited amount of collisional evolution over its history (see the chapter by Bottke et al. in this volume). The existence of a very small number of differentiated asteroid families in the current main belt, the survival of Vesta's crust, and the fact that Vesta only has two very large basins collectively

suggest that comminution in the asteroid belt has been insufficient to disrupt numerous differentiated bodies down to their cores and erase silicate fragments. It appears likely that only a modest number of large fully and partially differentiated bodies ever existed in the main belt, and most of these (like Vesta) were large enough to survive intact to recent times.

To test this assertion, we have explored a scenario where Vesta once had "sister" objects in the main belt (Bottke, 2014). The idea would be that the asteroid belt once had considerably more mass in its primordial era, including several Vestas, but that most of this material was eliminated by a dynamical depletion process, such as sweeping resonances associated with planet migration, ejection of material by interaction with planetary embryos, or Jupiter migrating across the asteroid belt in the Grand Tack model (Walsh et al., 2011, 2012; see also the chapter by Morbidelli et al. in this volume). This would potentially allow ancient cratering events on Vesta's long-lost sisters to explain the V-types seen in the central and outer main belt.

Our simulations used *Boulder*, a collisional code capable of simulating the dynamical depletion and collisional fragmentation of multiple planetesimal populations using a statistical particle-in-the-box approach (Morbidelli et al., 2009). We input into *Boulder* an estimate of the primordial main-belt size distribution stretched across many semimajor axis zones as well as a preset number of Vesta-like objects. The primordial main belt was assumed to be  $N$  times larger than the currently observed population and simulations were run with 1, 2, 3, . . . ,  $N$  Vestas in that population. We tracked these populations and their fragments for hundreds of millions of years until the putative time of late giant planet migration at  $\sim 4$  Ga. At that time, we assumed that a dynamical depletion event took place that removed most of the main belt's excess mass. From that point, collisional grinding over the next 4 G.y. was set to reproduce the current main-belt population. Over all this, we assumed that impacts on Vesta-like objects would produce fragments that were distinct (in spectroscopic signatures, colors, and albedos) from background asteroids, as the V-types are today in the main belt. When the model reached the current time, a successful run was one that was able to reproduce the current main belt and the observed V-type size distributions in the inner and central/outer main belt within tolerance limits.

Our results, while still preliminary, suggest the history of Vesta and her putative sisters can be used to constrain main-belt history. We find that an excited primordial main belt with more than 3–4 Vestas after the first few million years of its history produces too many V-type fragments compared to observations; collisional and dynamical evolution over 4.5 G.y. cannot get rid of all the evidence. Accordingly, it is likely that fewer than 3–4 Vestas existed in the main-belt region after the first few million years of its history. Collisions on these bodies prior to their dynamical removal are a plausible way to explain the V-types seen in the central/outer main belt, provided dynamical mechanisms allow one to get rid of Vesta's sisters at a later time. These results are also consistent with dynamical work indicating that the

primordial asteroid belt only lost, at best, a factor of  $\sim 1\text{--}4 \times$  its population during giant planet migration as described by the Nice model (see the chapter by Morbidelli et al. in this volume). Perhaps more importantly, this scenario shows how difficult it is for collisional evolution in the main belt to produce the putative core and mantle fragments observed today; if impacts could easily extract this material from the depths of differentiated asteroids like Vesta, one would also expect to see many more V-type and related asteroids.

### 6.1. Differentiated Planetesimals and Their Fragments from the Terrestrial Planet Region

To glean insights into the origin of the differentiated material in the asteroid belt, it is useful to take a step back and consider this issue from the perspective of planetesimal formation, namely accretion timescales and planetesimal heating mechanisms.

While precise accretion timescales for planetesimals forming all across the inner solar system are unknown (see the chapter by Johansen et al. in this volume), modeling work suggests they probably vary with swarm density and semimajor axis, such that accretion timescales become longer with increasing heliocentric distance, at least until the so-called “snowline” is reached. Given that  $^{26}\text{Al}$  was the major heat source for melting asteroids (section 2.2), the earliest planetesimals would have formed in the terrestrial planet region and they are more likely to be heavily metamorphosed or differentiated compared to same-sized bodies forming in the asteroid belt. Interestingly, this internal heating trend is largely consistent with trends observed among large main-belt asteroids: S-complex asteroids, believed to be analogous to metamorphosed but unmelted ordinary chondrites, dominate the inner main belt, while C-complex asteroids, many analogous to more primitive carbonaceous chondrites, dominate the outer main belt (see the chapter by DeMeo et al. in this volume).

The best place to form large differentiated planetesimals may also be the most likely location for them to undergo hit-and-run collisions. In the first few million years of solar system history, the terrestrial planet region was filled with planetary embryos and differentiated planetesimals (see the chapter by Morbidelli et al. in this volume). Collisions between these bodies would have been common, with the outcome leading to terrestrial planets. Hit-and-run collisions between differentiated planetesimals and larger protoplanets in the interim would have led to numerous aggregates made up of diverse proportions of crust, mantle, and core, as well as a sea of smaller fragments. These bodies would then undergo their own collisional and dynamical evolution, with the vast majority lost by comminution, by accretion with larger bodies in the terrestrial planet region, or by being ejected out of the inner solar system via a Jupiter encounter. Only the largest, strongest, or most fortunate bodies would survive for very long. We speculate that the population of objects left behind by hit-and-run collisions includes the M-type asteroids, some which are exposed core material, and others of which may be a “hodgepodge” of crust, mantle, and core (referred to here

as hodgepodge worlds). In addition, these collisions would have generated A-type asteroids and possibly some S-types that are also hodgepodge bodies. (We infer that V-types have deep spectral features with little space weathering because they lack metal and troilite, and that metal/troilite mixed with differentiated material will be space weathered so that it has spectral properties like S-type asteroids.)

*Bottke et al.* (2006) argued on these grounds that some fraction of the differentiated planetesimals made their way into the main belt region via early dynamical processes. Subsequent evidence for the early destruction of molten or semimolten parent bodies of iron meteorites (section 4.2) suggests that the flux of material from the terrestrial planet region into the asteroid belt may have been dominated by debris from differentiated planetesimals. This process helps to explain why the asteroid belt has a larger-than-expected number of fragments that appear to come from differentiated planetesimals, yet could still be dominated by nondifferentiated material. The wide variety of parent bodies represented in iron meteorites would also be naturally explained as a byproduct of collisional and dynamical evolution of planetesimals and protoplanets in the terrestrial planet region. We infer that the parent bodies of non-Vestan differentiated meteorites were largely disrupted before they were inserted into the asteroid belt, rather than “battered to bits” *in situ* within the asteroid belt (*Burbine et al.*, 1996).

### 6.2. Dynamical Scenarios for Captured Assemblages of Differentiated Materials

Here we present several dynamical scenarios that could plausibly move material from the terrestrial planet zone to stable orbits within the main-belt region.

The first, and arguably the simplest, involves gravitational scattering among planetary embryos (*Bottke et al.*, 2006). Here planetesimals and their fragments evolved amid a swarm of Moon- to Mars-sized bodies spread between Mercury’s current location to within the asteroid belt. In this scenario, the S- and C-complex asteroid populations that dominate the various zones of the asteroid belt (e.g., *Petit et al.*, 2002; *DeMeo and Carry*, 2014) were assumed to form more or less *in situ*, such that only a rather limited amount of material was scattered outward from the terrestrial planet region into the asteroid belt.

Numerical runs show that even a few million years is sufficient to scatter a small fraction of terrestrial planet material onto stable orbits within the main-belt zone, provided the planetary embryos are distributed as suggested by *Bottke et al.* (2006) (Figs. 7 and 8). A compelling element to these runs is that they are consistent with the limited degree of semimajor axis mixing of large S- and C-type asteroids in the main belt (i.e., no exceptional process is needed here). Some key questions for this model, however, are whether planetary embryos ever existed in the asteroid belt, and if they did, how long they resided there before being dispersed by the formation and/or migration of Jupiter (see the chapter by Morbidelli et al. in this volume).

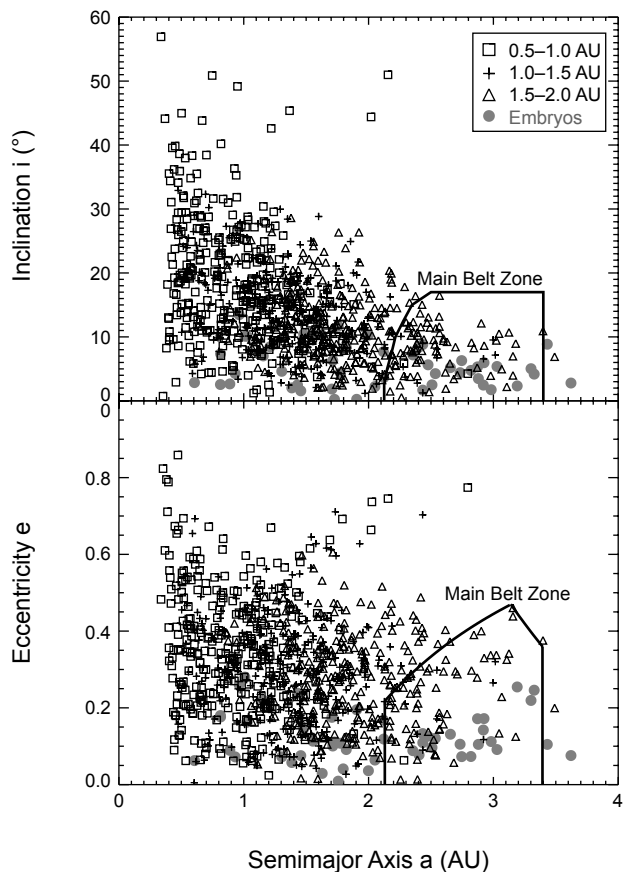


**Fig. 7.** Inclinations, eccentricities, and semimajor axes of planetesimals and planetary embryos in the inner solar system after 10 m.y. of dynamical evolution (Bottke et al., 2006). The planetesimals were given uniform semimajor axis between 0.5 and 2.0 AU and low random eccentricities and inclinations. The squares, crosses, and triangles show what happens to 1000 planetesimals started with semimajor axes of 0.5–1.0 AU, 1.0–1.5 AU, and 1.5–2.0 AU, respectively. The black line shows the location of the main asteroid belt. Numerous planetary embryos, which are shown as gray dots, are distributed between 0.5 and 3.6 AU. We see that numerous planetesimals from different zones were driven into the main belt by gravitational interactions with planetary embryos. After Bottke et al. (2006).

A second scenario involves scattering/capture opportunities within the so-called Grand Tack model, which assumes that Jupiter interacted with the nebular disk and migrated across the primordial asteroid belt within the first few million years of solar system history (Walsh et al., 2011, 2012; see also the chapter by Morbidelli et al. in this volume). Here planetesimals and fragments from the terrestrial planet region would have had the opportunity to reach stable main-belt orbits via interactions with Jupiter. As Jupiter migrated inward across the asteroid belt, main-belt planetesimals would have been scattered onto highly eccentric orbits within the terrestrial planet region, mixing with planetesimals scattered by planetary embryos. When Jupiter turned around and migrated back outward toward its current orbit, many eccentric

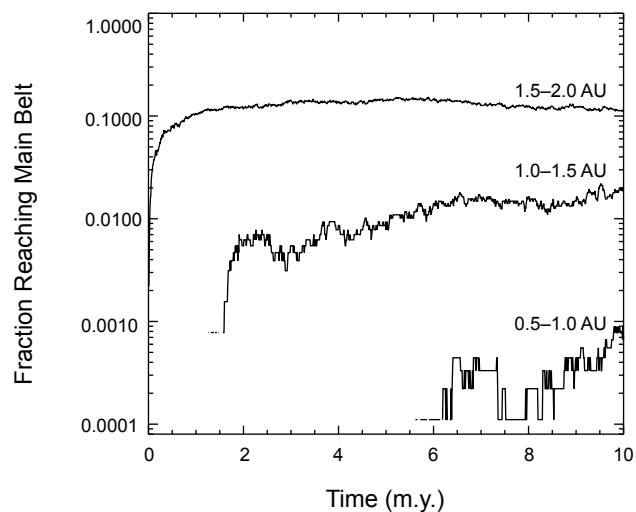


**Fig. 8.** The fraction of inner solar system planetesimals from 0.5–1.0 AU, 1.0–1.5 AU, and 1.5–2.0 AU scattered into the main belt by gravitational interactions with planetary embryos (see Fig. 7) (Bottke et al., 2006). The largest proportion of test bodies reaching the main belt is from the adjacent 1.5–2.0-AU zone. For the 1.0–1.5-AU zone, 0.8–2% are injected into the main belt after a delay of 2 m.y., while for 0.5–1.0 AU we find that 0.01–0.1% enter after 6 m.y. This shows that material from the terrestrial planet region may be found in the main belt today. Key factors here are the existence of planetary embryos in all zones of interest and the formation time of Jupiter, which is assumed to have had a hand in eliminating embryos from the main belt. Note that giant planets are neglected in this model. After Bottke et al. (2006).

planetesimals would have been implanted in the main-belt zone, thereby providing a source for differentiated material. Jupiter's migration also implants planetesimals from the Jupiter-Saturn zone into the main-belt zone, where they potentially would make up the C-complex population. Finally, the Grand Tack model allows planetary embryos to reside in the primordial main belt prior to Jupiter's early migration. This means the implantation scenario discussed above would also be active until Jupiter scattered the planetary embryos out of the main-belt region.

A key question here is whether the implantation of differentiated material can be used to test the Grand Tack; too much material, or too little, could place constraints on this putative planet-formation mechanism. An addendum to this model would be to consider how much terrestrial planet material was placed into the main belt prior to the migration of Jupiter via the first scenario, which presumably took place a few million years after CAI formation.

In a third scenario, we present promising but preliminary work within the context of the Nice model (see the chapter by Morbidelli et al. in this volume). Here the giant planets were assumed to reside for hundreds of millions of years on nearly circular, coplanar orbits in a much more compact configuration than they have today (all between 5 and 12 AU). This not only means that their mean-motion resonances were

once in different locations than we see them today, but also that they once may have been stabilizing for objects trapped inside [e.g., Neptune's mean-motion resonances are stabilizing for Pluto and other resonant Kuiper belt objects (*Levison et al.*, 2008)]. This could also explain why primordial “Kirkwood gaps” associated with the original locations of the giant planets have not yet been found in the main-belt region. By simulating how planetary perturbations affected test bodies started outside the primordial main-belt region, we found that a small fraction of bodies scattering off Mars were able to enter into the primordial main belt on low-eccentricity, low-inclination orbits via “fossil” mean-motion resonances, where they stayed for hundreds of millions of years. These bodies become permanently captured when the host resonances moved during late giant planet migration.

An intriguing method to test this hypothesis may involve the M-type asteroids. Let us assume for the moment that the M-types are remnants of planetesimals that went through hit-and-run collisions, as discussed above. Thus we will assume that these bodies include both exposed core material [e.g., (16) Psyche] as well as core-enriched gravitational accumulations of leftover debris referred to as hodgepodge worlds [e.g., we speculate that (21) Lutetia might be an example]. Much of the other crust and mantle would have been pulverized or altered beyond recognition by the associated effects (i.e., hydrostatic unloading, shock, reduction, and depletion) and/or subsequent collisional evolution in the terrestrial planet region.

As described above, a few M-types might survive by finding a dynamical pathway onto stable orbits within the main-belt region. This could result from any of the three scenarios discussed above. The first two, gravitational scattering among planetary embryos (*Bottke et al.*, 2006) and the Grand Tack model, would predict that M-types should be distributed in modestly random fashion across the main belt, with perhaps the highest concentrations in the inner main belt near the adjacent terrestrial planet region. In contrast, the 26 M-types with diameter  $D > 50$  km (see *Neese*, 2010) appear to be located at preferential values of semimajor axis  $a$ , and almost none are found in the inner main belt (Fig. 9). In addition, of the eight M-types with  $i < 5^\circ$ , three are at  $a = 2.42$  AU and four more are at  $a = 2.67$  AU. None show signs of coming from a family-forming collision at either locale (i.e., no clustered orbits; no associated fragment size distributions).

These values instead suggest that the third scenario related to the Nice model may be the most preferable solution. To check this idea, we performed proof-of-concept simulations that track how these kinds of planetary perturbations affect test bodies approaching the primordial main-belt region (Fig. 9). Interestingly, for particles initially scattered off Mars, we found that a small but notable fraction not only entered into the primordial main belt via these “fossil” mean-motion resonances, but they also stayed there until the end of the simulation 300 m.y. later. Additional evidence for this scenario comes from the orbits of all our large M-type asteroids (Fig. 9). If we assume Jupiter was originally located at 5.55 AU prior to the onset of late giant planet migration, we can explain why many M-types are found near primordial

Jovian mean-motion resonances like the J3:1 (2.67 AU) and others in the central/outer main belt. The ones we cannot yet fit also show signs of promise (i.e., the J7:2 “stalactite” at 2.4 AU in Fig. 9 is close to the M-types there).

These results do not yet fit all the M-types, possibly because we lack the appropriate initial conditions for our captured asteroids as well as the starting orbits of the giant planets. Getting all the giant planets in the correct primordial configuration, while including effects like the possibility of lost giant planets (*Nesvorný*, 2011; *Nesvorný and Morbidelli*, 2012), will require a suite of careful and numerically expensive simulations.

In summary, we consider it plausible that some M-types, A types, V-types, and possibly other exotic asteroids were captured within the primordial main belt by the mechanisms discussed above. In fact, we cannot yet rule out the possibility that a large differentiated body like Vesta formed elsewhere as well, although we caution that low capture probabilities make it difficult to construct a compelling case for this idea at this time. Future studies of these scenarios, and any new ones that may arise, will be useful because they may eventually provide us with constraints on the timing and nature of planetesimal and planet formation as well as the initial orbits of the giant planets prior to early migration.

## 7. SUMMARY AND FUTURE WORK

Given the difficulties that conventional collisional processes have in explaining the differentiated meteorite record, our

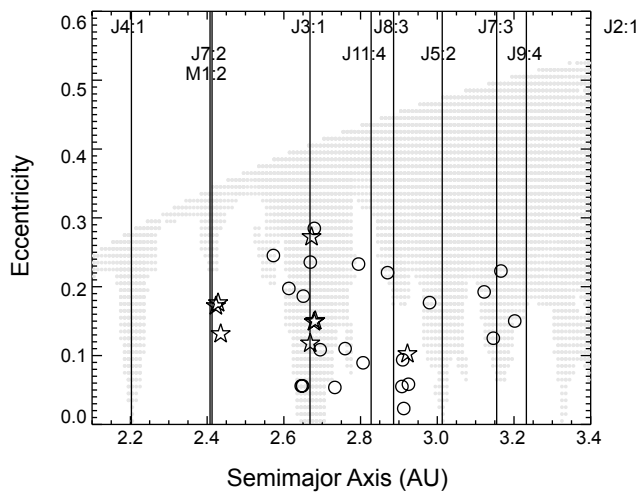


**Fig. 9.** M-type asteroids ( $D > 50$  km) in the main belt are shown next to the putative primordial location of Jupiter's resonances. Here we assumed Jupiter's initial semimajor axis was 5.5 AU. The stars are M-types with  $i < 5^\circ$ , and the circles are those with  $i > 5^\circ$ . The gray dots show the orbits of scattered test bodies started in the terrestrial planet region that entered the main-belt zone with  $i < 20^\circ$ . Some were captured on long-lived orbits within the putative locations of primordial dynamical resonances; this created the stalagmite-like features. Note that the match is interesting but imperfect, probably because the orbits of the giant planets are improperly positioned.

scenario for forming differentiated asteroids and meteorites by early accretion and disaggregation of melted planetesimals in the terrestrial planet region by hit-and-run impacts offers a new road map for explaining many of their anomalous properties and puzzling origin. In particular, it helps to explain why our collection of differentiated meteorites seems to resemble handfuls of pieces from numerous different jigsaw puzzles that cannot be reassembled into meaningful pictures. This scenario can be tested with detailed field work on differentiated asteroids by spacecraft, spectral studies of smaller asteroids, improved techniques for deriving mineral abundance and composition from spectra, better chronological constraints on the formation times of differentiated meteorites, and more detailed impact and dynamical models. We are optimistic that constraints from asteroids and meteorites can be used to discriminate between different dynamical models that have been proposed to account for the low mass of the asteroid belt and the small size of Mars (e.g., *Walsh et al.*, 2011, 2012).

We attribute much of the dunite shortage among meteorites and asteroids to preferential loss of mantle material from differentiated planetesimals by hit-and-run impacts during accretion. Mixing of molten metal and silicate by accretionary impacts may account for the formation of stony-iron meteorites, and their greater strength helps to explain the lack of complementary silicate. Silicate magma in differentiated planetesimals may also have been splashed out to form chondrules, as suggested by *Asphaug et al.* (2011) and *Sanders and Scott* (2012). Formation times of chondrules are well accounted for in this model, and chondrites, except CIIs, are substantially depleted in Fe.

We have focused on one aspect of the origin and evolution of the asteroid belt during accretion but to make more progress we require a better understanding of the effects of impacts during subsequent epochs, viz., the formation of the Moon and the late heavy bombardment. We also need a better understanding of the impact history of chondrites. Did their parent bodies escape early disruption during accretion and metamorphism, as the onion-shell model requires (*Trifeloff et al.*, 2003), or were they disrupted and disaggregated when hot like the differentiated planetesimals (*Ganguly et al.*, 2013; *Scott et al.*, 2014; *Van Niekerk et al.*, 2014)?

**Acknowledgments.** We thank numerous colleagues for helpful discussions and for sharing their insights and G. Consolmagno and D. O'Brien for helpful reviews. This research was supported by the NASA cosmochemistry program through grants NNX12AK68G (E.S.) and NN08AG53G and NNX11AF62G (J.I.G.). W.F.B. was supported by NASA's Solar System Evolution Research Virtual Institute (SSERVI) program through a grant to the Institute for the Science of Exploration Targets at the Southwest Research Institute in Boulder, Colorado. Sadly, Joseph Goldstein passed away on June 27, 2015, before this book was published. We are grateful for his contribution to this chapter.

## REFERENCES

- Agnor C. and Asphaug E. (2004) Accretion efficiency during planetary collisions. *Astrophys. J. Lett.*, **613**, L157–L160.
- Amelin Y., Ghosh A., and Rotenberg E. (2005) Unraveling the evolution of chondrite parent asteroids by precise U-Pb dating and thermal modeling. *Geochim. Cosmochim. Acta*, **69**, 505–518.
- Asphaug E. (2009) Growth and evolution of asteroids. *Annu. Rev. Earth Planet. Sci.*, **37**, 413–448.
- Asphaug E. (2010) Similar-sized collisions and the diversity of planets. *Chem. Erde–Geochem.*, **70**, 199–219.
- Asphaug E. and Reufer A. (2014) Mercury and other iron-rich planetary bodies as relics of inefficient accretion. *Nature Geosci.*, **7**, 564–568.
- Asphaug E., Agnor C. B., and Williams Q. (2006) Hit and run planetary collisions. *Nature*, **439**, 155–160.
- Asphaug E., Jutzi M., and Movshovitz N. (2011) Chondrule formation during planetesimal accretion. *Earth Planet. Sci. Lett.*, **308**, 369–379.
- Baker J. A., Schiller M., and Bizzarro M. (2012)  $^{26}\text{Al}$ - $^{26}\text{Mg}$  deficit dating ultramafic meteorites and silicate planetesimal differentiation in the early solar system? *Geochim. Cosmochim. Acta*, **77**, 415–431.
- Barucci M. A., Fornasier S., Dotto E., Lamy P. L., Jorda L., Groussin O., Brucato J. R., Carvano J., Alvarez-Candal A., Cruikshank D., and Fulchignoni M. (2008) Asteroids 2867 Steins and 21 Lutetia: Surface composition from far infrared observations with the Spitzer Space Telescope. *Astron. Astrophys.*, **477**, 665–670.
- Barucci M. A., Belskaya I. N., Fornasier S., Fulchignoni M., Clark B. E., Coradini A., Capaccioni F., Dotto E., Birlan M., Leyrat C., Sierks H., Thomas N., and Vincent J. B. (2012) Overview of Lutetia's surface composition. *Planet. Space Sci.*, **66**, 23–30.
- Bell J. F., Davis D. R., Hartmann W. K., and Gaffey M. J. (1989) Asteroids: The big picture. In *Asteroids II* (R. P. Binzel et al., eds.), pp. 921–945. Univ. of Arizona, Tucson.
- Benedix G. K., Haack H., and McCoy T. J. (2014) Iron and stony-iron meteorites. In *Treatise on Geochemistry, Vol 1: Meteorites and Cosmochemical Processes, Second edition* (A. M. Davis, ed.), pp. 267–285. Elsevier, Oxford.
- Binzel R. P. and Xu S. (1993) Chips off of asteroid 4 Vesta: Evidence for the parent body of basaltic achondrite meteorites. *Science*, **260**, 186–191.
- Bizzarro M., Baker J. A., Haack H., and Lundgaard K. L. (2005) Rapid timescales for accretion and melting of differentiated planetesimals inferred from  $^{26}\text{Al}$ - $^{26}\text{Mg}$  chronometry. *Astrophys. J.*, **632**, L41–L44.
- Blichert-Toft J., Moynier F., Lee C.-T. A., Telouk P., and Albarede F. (2010) The early formation of the IVA iron meteorite parent body. *Earth Planet. Sci. Lett.*, **296**, 469–480.
- Bogard D. D. (2011) K-Ar ages of meteorites: Clues to parent body thermal histories. *Chem. Erde–Geochem.*, **71**, 207–226.
- Bogard D. D. and Garrison D. H. (2003)  $^{39}\text{Ar}$ - $^{40}\text{Ar}$  ages of eucrites and the thermal history of asteroid 4 Vesta. *Meteoritics & Planet. Sci.*, **38**, 669–710.
- Bottke W. F. (2014) On the origin and evolution of Vesta and the V-type asteroids. In *Vesta in the Light of Dawn: First Exploration of a Protoplanet in the Asteroid Belt*, Abstract #2024. LPI Contrib. No. 1773, Lunar and Planetary Institute, Houston.
- Bottke W. F., Nesvorný D., Grimm R. E., Morbidelli A., and O'Brien D. P. (2006) Iron meteorites as remnants of planetesimals formed in the terrestrial planet region. *Nature*, **439**, 821–824.
- Bottke W. F., Vokrouhlický D., Minton D., Nesvorný D., Morbidelli A., Brasser R., Simonson B., and Levison H. F. (2012) An Archaean heavy bombardment from a destabilized extension of the asteroid belt. *Nature*, **485**, 78–81.
- Brennecke G. and Wadhwa M. (2012) Uranium isotope compositions of the basaltic angrite meteorites and the chronological implications for the early solar system. *Proc. Natl. Acad. Sci.*, **109**, 9299–9303.
- Buchwald V. F. (1975) *Handbook of Iron Meteorites*. Univ. of California, Oakland. 1418 pp. Available online at <http://evols.library.manoa.hawaii.edu/handle/10524/33750>.
- Burbine T. H. (2014) Asteroids. In *Treatise on Geochemistry, Vol. 2: Meteorites and Cosmochemical Processes, Second edition* (A. M. Davis, ed.), pp. 365–414. Elsevier, Oxford.
- Burbine T. H., Meibom A., and Binzel R. P. (1996) Mantle material in the main belt: Battered to bits? *Meteoritics & Planet. Sci.*, **31**, 607–620.
- Burbine T. H., Buchanan P. C., Binzel R. P., Bus S. J., Hiroi T., Hinrichs J. L., Meibom A., and McCoy T. J. (2001) Vesta, vestoids, and the howardite, eucrite, diogenite group: Relationships and the origin of spectral differences. *Meteoritics & Planet. Sci.*, **36**, 761–781.
- Carruba V., Michchenko T. A., Roig F., Ferraz-Mello S., and Nesvorný D. (2005) On the V-type asteroids outside the Vesta family I. Interplay of nonlinear secular resonances and the Yarkovsky

- effect: The cases of 956 Elisa and 809 Lundia. *Astron. Astrophys.*, **441**, 819–829.
- Carry B. (2012) Density of asteroids. *Planet. Space. Sci.*, **73**, 98–118.
- Chambers J. E. (2013) Late-stage planetary accretion including hit-and-run collisions and fragmentation. *Icarus*, **224**, 43–56.
- Chabot N. L. (2004) Sulfur contents of the parental metallic cores of magmatic iron meteorites. *Geochim. Cosmochim. Acta*, **68**, 3607–3618.
- Chapman C. R. (1986) Implications of the inferred compositions of asteroids for their collisional evolution. *Mém. Soc. Astron. Ital.*, **57**, 103–114.
- Ciesla F. J., Davison T. M., Collins G. S., and O'Brien D. P. (2013) Thermal consequences of impacts in the early solar system. *Meteoritics & Planet. Sci.*, **48**, 2559–2576.
- Clark B. E., Bus S. J., Rivkin A. S., Shepard M. K., and Shah S. (2004) Spectroscopy of X-type asteroids. *Astron. J.*, **128**, 3070–3081.
- Clark B. E., Ockert-Bell M. E., Cloutis E. A., Nesvorný D., Mothe-Diniz T., and Bus S. J. (2009) Spectroscopy of K-complex asteroids: Parent bodies of carbonaceous meteorites? *Icarus*, **202**, 119–133.
- Cloutis E. A., Binzel R. P., Burbine T. H., Gaffey M. J., and McCoy T. J. (2006) Asteroid 3628 Boznemcova: Covered with angrite-like basalts? *Meteoritics & Planet. Sci.*, **41**, 1147–1161.
- Connelly J. N., Bizzarro M., Krot A. N., Norlund A., Wielandt D., and Ivanova M. (2012) The absolute chronology and thermal processing of solids in the solar protoplanetary disk. *Science*, **338**, 651–655.
- Consolmagno G. J. and Drake M. J. (1977) Composition and evolution of the eucrite parent body: Evidence from rare earth elements. *Geochim. Cosmochim. Acta*, **41**, 1271–1282.
- Consolmagno G. J., Golabek G., Turrini D., Jutzi M., Sironi S., Svetsov V., and Tsiganis K. (2014) Is Vesta an intact and pristine protoplanet? *Icarus*, **254**, 190–201.
- Cruikshank D. P., Tholen D. J., Hartmann W. K., Bell J. F., and Brown R. H. (1991) Three basaltic Earth-approaching asteroids and the source of the basaltic meteorites. *Icarus*, **89**, 1–13.
- Dale C. W., Burton K. W., Greenwood R. C., Gannoun A., Wade J., Wood B. J., and Pearson D. G. (2012) Late accretion on the earliest planetesimals revealed by the highly siderophile elements. *Science*, **336**, 72–75.
- Davis A. M. and McKeegan K. D. (2014) Short-lived radionuclides and early solar system chronology. In *Treatise on Geochemistry, Vol. 1: Meteorites and Cosmochemical Processes, Second edition* (A. M. Davis, ed.), pp. 361–395, Elsevier, Oxford.
- Davis D. R., Chapman C. R., Weidenschilling S. J., and Greenberg R. (1985) Collisional history of asteroids — Evidence from Vesta and the Hirayama families. *Icarus*, **62**, 30–53.
- Davis D. R., Farinella P., and Marzari F. (1999) The missing Psyche family: Collisionally eroded or never formed? *Icarus*, **137**, 140–151.
- Davison T. M., Ciesla F. J., and Collins G. S. (2012) Post-impact thermal evolution of porous planetesimals. *Geochim. Cosmochim. Acta*, **95**, 252–269.
- Davison T. M., O'Brien D. P., Ciesla F. J., and Collins G. S. (2013) The early impact histories of meteorite parent bodies. *Meteoritics & Planet. Sci.*, **48**, 1894–1918.
- Delbo M., Gai M., Lattanzi M. G., Ligori S., Loreggia D., Saba L., Cellino A., Gandolfi D., Licchelli D., Blanco C., Cigna M., and Wittkowski M. (2006) MIDI observations of 1459 Magnya: First attempt of interferometric observations of asteroids with the VLTI. *Icarus*, **181**, 618–622.
- DeMeo F. E. and Carry B. (2013) The taxonomic distribution of asteroids from multi-filter all-sky photometric surveys. *Icarus*, **226**, 723–741.
- DeMeo F. E. and Carry B. (2014) Solar system evolution from compositional mapping of the asteroid belt. *Nature*, **505**, 629–634.
- DeMeo F. E., Binzel R. P., Slivan S. M., and Bus S. J. (2009) An extension of the Bus asteroid taxonomy into the near-infrared. *Icarus*, **202**, 160–180.
- De Sanctis M. C., Ammannito E., Migliorini A., Lazzaro D., Capria M. T., and McFadden L. (2011) Mineralogical characterization of some V-type asteroids, in support of the NASA Dawn mission. *Mon. Not. R. Astron. Soc.*, **412**, 2318–2332.
- Descamps P., Marchis F., Berthier J., Emery J. P., Duchene G., de Pater I., Wong M. H., Lim L., Hammel H. B., Vachier F., Wiggins P., Teng-Chuen-Yu J.-P., Peyrot A., Pollock J., Assafin M., Vieira-Martins R., Camargo J. I. B., Braga-Ribas F., and Macomber B. (2011) Triplicity and physical characteristics of asteroid (216) Kleopatra. *Icarus*, **211**, 1022–1033.
- D'Orazio M., Folco L., Chaussidon M., and Rochette P. (2009) Sahara 03505 sulfide-rich iron meteorite: Evidence for efficient segregation of sulfide-rich metallic melt during high-degree impact melting of an ordinary chondrite. *Meteoritics & Planet. Sci.*, **44**, 221–231.
- Duffard R. and Roig F. (2009) Two new V-type asteroids in the outer main belt? *Planet. Space Sci.*, **57**, 229–234.
- Duffard R., Lazzaro D., Licandro J., De Sanctis M. C., Capria M. T., and Carvano J. M. (2004) Mineralogical characterization of some basaltic asteroids in the neighborhood of (4) Vesta: First results. *Icarus*, **171**, 120–132.
- Farquhar R., Kawaguchi J., Russell C. T., Schwehm G., Veverka J., and Yeomans D. (2002) Spacecraft exploration of asteroids: The 2001 perspective. In *Asteroids III* (W. F. Bottke Jr. et al., eds.), pp. 367–376. Univ. of Arizona, Tucson.
- Fieber-Beyer S. K., Gaffey M. J., and Abell P. A. (2011a) Mineralogical characterization of near-Earth asteroid (1036) Ganymed. *Icarus*, **212**, 149–157.
- Fieber-Beyer S. K., Gaffey M. J., Kelley M. S., Reddy V., Reynolds C. M., and Hicks T. (2011b) The Maria asteroid family: Genetic relationships and a plausible source of mesosiderites near the 3:1 Kirkwood gap. *Icarus*, **213**, 524–537.
- Ganguly J. and Tirone M. (2001) Relationship between cooling rate and cooling age of a mineral: Theory and application to meteorites. *Meteoritics & Planet. Sci.*, **36**, 167–175.
- Ganguly J., Tirone M., Chakraborty S., and Domanik K. (2013) H-chondrite parent asteroid: A multistage cooling, fragmentation and re-accretion history constrained by thermometric studies, diffusion kinetic modeling, and geochronological data. *Geochim. Cosmochim. Acta*, **105**, 206–220.
- Golabek G. J., Bourdon B., and Gerya T. V. (2014) Numerical models of the thermomechanical evolution of planetesimals: Application to the acapulcoite-lodranite parent body. *Meteoritics & Planet. Sci.*, **49**, 1083–1099.
- Goldstein J. I., Scott E. R. D., and Chabot N. L. (2009) Iron meteorites: Crystallization, thermal history, parent bodies, and origin. *Chem. Erde–Geochem.*, **69**, 293–325.
- Goldstein J. I., Yang J., and Scott E. R. D. (2014) Determining cooling rates of iron and stony-iron meteorites from measurements of Ni and Co at kamacite-taenite interfaces. *Geochim. Cosmochim. Acta*, **140**, 297–320.
- Goodrich C. A., Scott E. R. D., and Fioretti A. M. (2004) Ureilitic breccias: Clues to the petrologic structure and impact disruption of the ureilite parent asteroid. *Chem. Erde–Geochem.*, **64**, 283–327.
- Goodrich C. A., Hutchison I. D., Kita N. T., Huss G. R., Cohen B. A., and Keil K. (2010)  $^{53}\text{Mn}$ - $^{53}\text{Cr}$  and  $^{26}\text{Al}$ - $^{26}\text{Mg}$  ages of a feldspathic lithology in polymict ureilites. *Earth Planet. Sci. Lett.*, **295**, 531–540.
- Goodrich C. A., Hartmann W. K., O'Brien D. P., Weidenschilling S. J., Wilson L., Michel P., and Jutzi M. (2015) Origin and history of ureilitic material in the solar system: The view from asteroid 2008 TC<sub>3</sub> and the Almahata Sitta meteorite. *Meteoritics & Planet. Sci.*, **50**, 782–809.
- Göpel C. and Manhes G. (2010) The thermal history of the Acapulco meteorite and its parent body deduced from U/Pb systematics in mineral separates and bulk rock fragments. *Compt. Rend. Geosci.*, **342**, 53–59.
- Greenwood R. C., Franchi I. A., Gibson J. M., and Benedix G. K. (2012) Oxygen isotope variation in primitive achondrites: The influence of primordial, asteroidal, and terrestrial processes. *Geochim. Cosmochim. Acta*, **94**, 146–163.
- Haack H., Scott E. R. D., Love S. G., Brearley A. J., and McCoy T. J. (1996) Thermal histories of IVA stony-iron and iron meteorites: Evidence for asteroid fragmentation and reaccretion. *Geochim. Cosmochim. Acta*, **60**, 3103–3113.
- Harden P. S., Gaffey M. J., and Abell P. A. (2004) Mineralogy of asteroid 1459 Magnya and implications for its origin. *Icarus*, **167**, 170–177.
- Herzog G. F. and Caffee M. W. (2014) Cosmic-ray exposure ages of meteorites. In *Treatise on Geochemistry, Vol. 1: Meteorites and Cosmochemical Processes, Second edition* (A. M. Davis, ed.), pp. 419–453. Elsevier, Oxford.
- Hevey P. J. and Sanders I. S. (2006) A model for planetesimal meltdown by  $^{26}\text{Al}$  and its implications for meteorite parent bodies. *Meteoritics & Planet. Sci.*, **41**, 95–106.
- Hiroi T. and Sasaki S. (2001) Importance of space weathering simulation products in compositional modeling of asteroids: 349 Dembowska

- and 446 Aeternitas as examples. *Meteoritics & Planet. Sci.*, 36, 1587–1596.
- Keil K. (2002) Geological history of asteroid 4 Vesta: The “smallest terrestrial planet.” In *Asteroids III* (W. F. Bottke Jr. et al., eds.), pp. 573–584. Univ. of Arizona, Tucson.
- Keil K. (2010) Enstatite achondrite meteorites (aubrites) and the histories of their asteroidal parent bodies. *Chem. Erde–Geochem.*, 70, 295–317.
- Keil K. (2011) Angrites, a small but diverse suite of ancient, silica-undersaturated volcanic-plutonic mafic meteorites, and the history of their parent asteroid. *Chem. Erde–Geochem.*, 72, 191–218.
- Keil K. (2014) Brachinitic meteorites: Partial melt residues from an FeO-rich asteroid. *Chem. Erde–Geochem.*, 74, 311–329.
- Keil K., Ntaflos Th., Taylor G. J., Brearley A. J., and Newsom H. E. (1989) The Shallowater aubrite — Evidence for origin by planetesimal impacts. *Geochim. Cosmochim. Acta*, 53, 3291–3307.
- Keil K., Haack H., and Scott E. R. D. (1994) Catastrophic fragmentation of asteroids: Evidence from meteorites. *Planet. Space Sci.*, 42, 1109–1122.
- Keil K., Stöffler D., Love S. G., and Scott E. R. D. (1997) Constraints on the role of impact heating and melting in asteroids. *Meteoritics & Planet. Sci.*, 32, 349–363.
- Kita N. T. and Ushikubo T. (2012) Evolution of protoplanetary disk inferred from  $^{26}\text{Al}$  chronology of individual chondrules. *Meteoritics & Planet. Sci.*, 47, 1108–1119.
- Kleine T., Mezger K., Palme H., Scherer E., and Münker C. (2005) Early core formation in asteroids and late accretion of chondrite parent bodies: Evidence from  $^{182}\text{Hf}$ - $^{182}\text{W}$  in CAIs, metal-rich chondrites, and iron meteorites. *Geochim. Cosmochim. Acta*, 69, 5805–5818.
- Kleine T., Toublou M., Van Orman J. A., Bourdon B., Maden C., Mezger K., and Halliday A. N. (2008) Hf-W thermochronometry: Closure temperature and constraints on the accretion and cooling history of the H chondrite parent body. *Earth Planet. Sci. Lett.*, 270, 106–118.
- Kleine T., Hans U., Irving A. J., and Bourdon B. (2012) Chronology of the angrite parent body and implications for core formation in protoplanets. *Geochim. Cosmochim. Acta*, 84, 186–203.
- Kleine T., Hans U., Irving A. J., and Bourdon B. (2013) Chronology of the angrite parent body and implications for core formation in protoplanets. *Geochim. Cosmochim. Acta*, 84, 186–203.
- Kring D. A., Hill D. H., Gleason J. D., Britt D. T., Consolmagno G. J., Farmer M., Wilson S., and Haag R. (1999) Portales Valley: A meteoritic sample of the brecciated and metal-veined floor of an impact crater on an H-chondrite asteroid. *Meteoritics & Planet. Sci.*, 34, 663–669.
- Krot A. N., Amelin Y., Cassen P., and Meibom A. (2005) Young chondrules in CB chondrites from a giant impact in the early solar system. *Nature*, 436, 989–992.
- Krot A. N., Nagashima K., Yoshitake M., and Yurimoto H. (2010) Oxygen isotopic compositions of chondrules from the metal-rich chondrites Isheyev (CH/CB<sub>b</sub>), MAC 02675 (CB<sub>b</sub>) and QUE 94627 (CB<sub>b</sub>). *Geochim. Cosmochim. Acta*, 74, 2190–2211.
- Krot A. N., Makide K., Nagashima K., Huss G. R., Ogliore R. C., Ciesla F. J., Yang L., Hellebrand E., and Gaidos E. (2012) Heterogeneous distribution of  $^{26}\text{Al}$  at the birth of the solar system: Evidence from refractory grains and inclusions. *Meteoritics & Planet. Sci.*, 47, 1848–1979.
- Krot A. N., Keil K., Scott E. R. D., Goodrich C. A., and Weisberg M. K. (2014) Classification of meteorites and their genetic relationships. In *Treatise on Geochemistry, Vol. 1: Meteorites and Cosmochemical Processes, Second edition* (A. M. Davis, ed.), pp. 1–63. Elsevier, Oxford.
- Kruijer T. S., Sprung P., Kleine T., Leya I., Burkhardt C., and Wieler R. (2012) Hf-W chronometry of core formation in planetesimals inferred from weakly irradiated iron meteorites. *Geochim. Cosmochim. Acta*, 99, 287–304.
- Kruijer T. S., Fischer-Gödde M., Kleine T., Sprung P., Leya I., and Wieler R. (2013) Neutron capture on Pt isotopes in iron meteorites and the Hf-W chronology of core formation in planetesimals. *Earth Planet. Sci. Lett.*, 361, 162–172.
- Kruijer T. S., Kleine T., Fischer-Gödde M., Burkhardt C., and Wieler R. (2014) Nucleosynthetic W isotopic anomalies and the Hf-W chronometry of Ca-Al-rich inclusions. *Earth Planet. Sci. Lett.*, 403, 317–327.
- Lazzaro D., Michtchenki T., Carvano J. M., Binzel R. P., Bus S. J., Burbine T. H., Mothe-Diniz T., Florczak M., Angelis C. A., and Harris A. W. (2000) Discovery of a basaltic asteroid in the outer main belt. *Science*, 288, 2033–2035.
- Levison H., Morbidelli A., VanLaerhoven C., Gomes R., and Tsiganis K. (2008) Origin of the structure of the Kuiper belt during a dynamical instability in the orbits of Uranus and Neptune. *Icarus*, 196, 258–273.
- Lugmair G. W. and Shukolyukov A. (1998) Early solar system timescales according to  $^{53}\text{Mn}$ - $^{53}\text{Cr}$  systematics. *Geochim. Cosmochim. Acta*, 62, 2863–2886.
- Marchi S. and 11 colleagues (2012) The violent collisional history of asteroid 4 Vesta. *Science*, 336, 690–694.
- Marchi S. and 10 colleagues (2013) High-velocity collisions from the lunar cataclysm recorded in asteroidal meteorites. *Nature Geosci.*, 6, 303–307.
- Marsh C. A., Della-Giustina D. N., Giacalone J., and Lauretta D. S. (2006) Experimental tests of the induction heating hypothesis for planetesimals. *Lunar Planet. Sci. XXXVII*, Abstract #2078. Lunar and Planetary Institute, Houston.
- Masiero J. R. and 17 colleagues (2011) Main belt asteroids with WISE/NEOWISE. I. Preliminary albedos and diameters. *Astrophys. J.*, 741, 68.
- Masiero J. R., Mainzer A. K., Bauer J. M., Grav T., Nugent C. R., and Stevenson R. (2013) Asteroid family identification using the hierarchical clustering method and WISE/NEOWISE physical properties. *Astrophys. J.*, 770, 22.
- Mayne R. G., Sunshine J. M., McSween H. Y. Jr., Bus S. J., and McCoy T. J. (2011) The origin of Vesta's crust: Insight from spectroscopy of the vestoids. *Icarus*, 214, 147–160.
- McCord T. B., Adams J. B., and Johnson T. V. (1970) Asteroid Vesta: Spectral reflectivity and compositional implications. *Science*, 168, 1445–1447.
- McCoy T. J. and 9 colleagues (1996) A petrologic, chemical, and isotopic study of Monument Draw and comparison with other acapulcoites: Evidence for formation by incipient partial melting. *Meteoritics & Planet. Sci.*, 60, 2682–2708.
- McCoy T. J., Keil K., Clayton R. N., Mayeda T. K., Bogard D. D., Garrison D. H., and Wieler R. (1997) A petrologic and isotopic study of lodranites: Evidence for early formation as partial melt residues from heterogeneous precursors. *Geochim. Cosmochim. Acta*, 61, 623–637.
- McSween H. Y. and 11 colleagues (2013) Dawn; the Vesta-HED connection; and the geologic context for eucrites, diogenites, and howardites. *Meteoritics & Planet. Sci.*, 48, 2090–2104.
- Mikouchi T., Zolensky M. E., Ohnishi I., Suzuki T., Takeda H., Jenniskens P., and Shaddad M. H. (2010) Electron microscopy of pyroxene in the Almahata Sitta ureilite. *Meteoritics & Planet. Sci.*, 45, 1812–1820.
- Michel P., Benz W., and Richardson D. C. (2004) Catastrophic disruption of pre-shattered parent bodies. *Icarus*, 168, 420–432.
- Milani A., Knezevic Z., Novakovic B., and Cellino A. (2010) Dynamics of the Hungaria asteroids. *Icarus*, 207, 769–794.
- Mittlefehldt D. W. (2005) Ibitira: A basaltic achondrite from a distinct parent asteroid and implications for the Dawn mission. *Meteoritics & Planet. Sci.*, 46, 665–677.
- Morbidelli A., Bottke W. F., Nesvorný D., and Levison H. F. (2009) Asteroids were born big. *Icarus*, 204, 558–573.
- Moskovitz N. A. and Gaidos E. (2009) Differentiation of planetesimals and the thermal consequences of melt migration. *Meteoritics & Planet. Sci.*, 46, 903–918.
- Moskovitz N. A., Lawrence S., Jedicke R., Willman M., Haghighipour N., Bus S. J., and Gaidos E. (2008) A spectroscopically unique main-belt asteroid: 10537 (1991 RY16). *Astrophys. J.*, 682, L57–L60.
- Moskovitz N. A., Willman M., Burbine T. H., Binzel R. P., and Bus S. J. (2010) A spectroscopic comparison of HED meteorites and V-type asteroids in the inner main belt. *Icarus*, 208, 773–788.
- Mothe-Diniz T. and Carvano J. M. (2005) 221 Eos: A remnant of a partially differentiated parent body? *Astron. Astrophys.*, 442, 727–729.
- Mothe-Diniz T., Carvano J. M., Bus S. J., Duffard R., and Burbine T. H. (2008) Mineralogical analysis of the Eos family from near-infrared spectra. *Icarus*, 195, 277–294.
- Nathues A. (2010) Spectral study of the Eunomia asteroid family. Part II: The small bodies. *Icarus*, 208, 252–275.
- Nathues A., Mottola S., Kaasalainen M., and Neukum G. (2005) Spectral study of the Eunomia asteroid family. I. Eunomia. *Icarus*, 175, 452–463.
- Neese C., ed. (2010) *Asteroid Taxonomy V6.0*. EAR-A-5-DDR-TAXONOMY-V6.0, NASA Planetary Data System.

- Neeley J. R., Clark B. E., Ockert-Bell M. E., Shepard M. K., Conklin J., Cloutis E. A., Fornasier F., and Bus S. J. (2014) The composition of M-type asteroids II: Synthesis of spectroscopic and radar observations. *Icarus*, 238, 37–50.
- Nesvorný D. (2011) Young solar system's fifth giant planet? *Astrophys. J. Lett.*, 742, L22.
- Nesvorný D. and Morbidelli A. (2012) Statistical study of the early solar system's instability with four, five, and six giant planets. *Astrophys. J.*, 144, 117.
- Nesvorný D., Roig F., Gladman B., Lazzaro D., Carruba V., and Mothe-Diniz T. (2008) Fugitives from the Vesta family. *Icarus*, 193, 85–95.
- Neumann W., Breuer D., and Spohn T. (2012) Differentiation and core formation in accreting planetesimals. *Astron. Astrophys.*, 543, A141.
- O'Brien D. P., Morbidelli A., and Levison H. F. (2006) Terrestrial planet formation with strong dynamical friction. *Icarus*, 184, 39–58.
- Ockert-Bell M. E., Clark B. E., Shepard M. K., Isaacs R. A., Cloutis E. A., Fornasier F., and Bus S. J. (2010) The composition of M-type asteroids: Synthesis of spectroscopic and radar observations. *Icarus*, 210, 674–692.
- Petaev M. I., Clarke R. S. Jr., Jarosewich E., et al. (2000) The Chaunskij anomalous mesosiderite: Petrology, chemistry, oxygen isotopes, classification, and origin. *Geochim. Int'l.*, 38, S322–S350.
- Petit J. M., Chambers J., Franklin F., and Nagasawa M. (2002) Primordial excitation and depletion of the main belt. In *Asteroids III* (W. F. Bottke Jr. et al., eds.), pp. 711–723. Univ. of Arizona, Tucson.
- Reufer A., Meier M. M. M., Benz W., and Wieler R. (2012) A hit-and-run giant impact scenario. *Icarus*, 221, 296–299.
- Rivkin A. S., Howell E. S., Lebofsky L. A., Clark B. E., and Britt D. T. (2000) The nature of M-class asteroids from 3 micron observations. *Icarus*, 145, 351–368.
- Roig F., Nesvorný D., Gil-Hutton R., and Lazzaro D. (2008) V-type asteroids in the middle main belt. *Icarus*, 194, 125–136.
- Rubin A. E., Ulff-Møller F., Wasson J. T., and Carlson W. D. (2001) The Portales Valley meteorite breccia: Evidence for impact-induced melting and metamorphism of an ordinary chondrite. *Geochim. Cosmochim. Acta*, 65, 323–342.
- Ruzicka A. (2014) Silicate-bearing iron meteorites and their implications for the evolution of asteroidal parent bodies. *Chem. Erde-Geochem.*, 74, 3–48.
- Safronov V. S. (1972) *Evolution of the Protoplanetary Cloud and Formation of the Earth and Planets*. NASA TM F-677, Washington, DC.
- Sanborn M. E. and Yin Q. Z. (2014) Chromium isotopic composition of the anomalous eucrites: An additional geochemical parameter for evaluating their origin. *Lunar Planet. Sci. XLV*, Abstract #2018. Lunar and Planetary Institute, Houston.
- Sanchez J. A., Reddy V., Kelley M. S., Cloutis E. A., Bottke W. F., Nesvorný D., Lucas M. P., Hardersen P. S., Gaffey M. J., Abell P. A., and Le Corre L. (2014) Olivine-dominated asteroids: Mineralogy and origin. *Icarus*, 228, 288–300.
- Sanders I. S. and Scott E. R. D. (2012) The origin of chondrules and chondrites: Debris from low-velocity impacts between molten planetesimals. *Meteoritics & Planet. Sci.*, 47, 2170–2192.
- Schulz T., Upadhyay D., Münker C., and Mezger K. (2012) Formation and exposure history of non-magmatic iron meteorites and winonaites: Clues from Sm and W isotopes. *Geochim. Cosmochim. Acta*, 85, 200–212.
- Scott E. R. D. and Bottke W. F. (2011) Impact histories of angrites, eucrites, and their parent bodies. *Meteoritics & Planet. Sci.*, 46, 1878–1887.
- Scott E. R. D., Greenwood R. C., Franchi I. A., and Sanders I. S. (2009) Oxygen isotopic constraints on the origin and parent bodies of eucrites, diogenites, and howardites. *Geochim. Cosmochim. Acta*, 73, 5835–5853.
- Scott E. R. D., Krot T. V., Goldstein J. I., and Wakita S. (2014) Thermal and impact history of the H chondrite parent asteroid during metamorphism: Constraints from metallic Fe-Ni. *Geochim. Cosmochim. Acta*, 136, 13–37.
- Shepard M. K., Kressler K. M., Clark B. E., Ockert-Bell M., Nolan M. C., Howell E. S., Magri C., Giorgini J. D., Benner L. A. M., and Ostro S. J. (2008) Radar observations of E-class asteroids 44 Nysa and 434 Hungaria. *Icarus*, 195, 220–225.
- Shepard M. K., Clark B. E., Ockert-Bell M., Nolan M. C., Howell E. S., Magri C., Giorgini J. D., Benner L. A. M., Ostro S. J., Harris A. W., Warner B. D., Stephens R. D., and Mueller M. (2010) A radar survey of M- and X-class asteroids. II. Summary and synthesis. *Icarus*, 208, 221–237.
- Solontoi M. R., Hammargren M., Gyuk G., and Puckett A. (2012) AVAST survey 0.4–1.0 micron spectroscopy of igneous asteroids in the inner and middle main belt. *Icarus*, 220, 577–585.
- Stewart B. W., Papanastassiou D. A., and Wasserburg G. J. (1994) Sm–Nd chronology and petrogenesis of mesosiderites. *Geochim. Cosmochim. Acta*, 58, 3487–3509.
- Stewart S. T. and Leinhardt Z. M. (2012) Collisions between gravity-dominated bodies. II. The diversity of impact outcomes during the end stage of planet formation. *Astrophys. J.*, 751, 32.
- Sugiura N. and Fujiya W. (2014) Correlated accretion ages and  $\epsilon^{54}\text{Cr}$  of meteorite parent bodies and the evolution of the solar nebula. *Meteoritics & Planet. Sci.*, 49, 1–16.
- Sugiura N. and Hoshino H. (2003) Mn-Cr chronology of five IIIAB iron meteorites. *Meteoritics & Planet. Sci.*, 38, 117–143.
- Sunshine J. M., Bus S. J., McCoy T. J., Burbine T. H., Corrigan C. M., and Binzel R. P. (2004) High-calcium pyroxene as an indicator of igneous differentiation in asteroids and meteorites. *Meteoritics & Planet. Sci.*, 39, 1343–1357.
- Sunshine J. M., Bus S. J., Corrigan C. M., McCoy T. J., and Burbine T. H. (2007) Olivine-dominated asteroids and meteorites: Distinguishing nebular and igneous histories. *Meteoritics & Planet. Sci.*, 42, 155–170.
- Tang H. and Dauphas N. (2012) Abundance, distribution, and origin of  $^{60}\text{Fe}$  in the solar protoplanetary disk. *Earth Planet. Sci. Lett.*, 359–360, 248–263.
- Tarduno J. A., Cottrell R. D., Nimmo F., Hopkins J., Voronov J., Erickson A., Blackman E., Scott E. R. D., and McKinley R. (2012) Evidence for a dynamo in the main group pallasite parent body. *Science*, 338, 939–942.
- Theis K. J., Schönbächler M., Benedix G. K., Rehkämper M., Andreassen R., and Davies C. (2013) Palladium-silver chronology of IAB iron meteorites. *Earth Planet. Sci. Lett.*, 361, 402–411.
- Tholen D. J. (1984) Asteroid taxonomy from cluster analysis of photometry. Ph.D. thesis, Univ. of Arizona, Tucson.
- Trieloff M., Jessberger E. K., Herrwerth I., Hopp J., Fiéni C., Ghélis M., Bourot-Denise M., and Pellas P. (2003) Structure and thermal history of the H-chondrite parent asteroid revealed by thermochronometry. *Nature*, 422, 502–506.
- Van Niekerk D., Scott E. R. D., and Taylor G. J. (2014) Constraints on the thermal and impact history of ordinary chondrites from two-pyroxene equilibration temperatures. *Lunar Planet. Sci. XLV*, Abstract #2374. Lunar and Planetary Institute, Houston.
- Vernazza P., Brunetto R., Binzel R. P., Perron C., Fulvio D., Strazzulla G., and Fulchignoni M. (2009) Plausible parent bodies for enstatite chondrites and mesosiderites: Implications for Lutetia's fly-by. *Icarus*, 202, 477–486.
- Vernazza P., Zanda B., Binzel R. P., Hiroi T., DeMeo F. E., Birlan M., Hewins R., Ricci L., Barge P., and Lockhart M. (2014) Multiple and fast: The accretion of ordinary chondrite parent bodies. *Astrophys. J.*, 791, 120.
- Vogel N. and Renne P. R. (2008)  $^{40}\text{Ar}$ - $^{39}\text{Ar}$  dating of plagioclase grain size separates from silicate inclusions in IAB iron meteorites and implications for the thermochronological evolution of the IAB parent body. *Geochim. Cosmochim. Acta*, 72, 1231–1255.
- Wadhwa M. (2014) Solar system timescales from long-lived radioisotopes in meteorites and planetary materials. In *Treatise on Geochemistry, Vol. 1: Meteorites and Cosmochemical Processes, Second edition* (A. M. Davis, ed.), pp. 397–418. Elsevier, Oxford.
- Wadhwa M., Amelin Y., Bogdanovski O., Shukolyukov A., Lugmair G. W., and Janney P. (2009) Ancient relative and absolute ages for a basaltic meteorite: Implications for timescales for planetary accretion. *Geochim. Cosmochim. Acta*, 73, 5189–5201.
- Walsh K. J., Morbidelli A., Raymond S. N., O'Brien D. P., and Mandell A. M. (2011) A low mass for Mars from Jupiter's early gas-driven migration. *Nature*, 475, 206–209.
- Walsh K. J., Morbidelli A., Raymond S. N., O'Brien D. P., and Mandell A. M. (2012) Populating the asteroid belt from two parent source regions due to the migration of giant planets — “The Grand Tack.” *Meteoritics & Planet. Sci.*, 47, 1941–1947.
- Warner B. D., Harris A. W., Vokrouhlický D., Nesvorný D., and Bottke W. F. (2009) Analysis of the Hungaria asteroid population. *Icarus*, 204, 172–182.

- Wasson J. T. (2011) Relationship between iron-meteorite composition and size: Compositional distribution of irons from North Africa. *Geochim. Cosmochim. Acta*, 75, 1757–1772.
- Wasson J. T. and Hoppe P. (2012) Co/Ni ratios at taenite/kamacite interfaces and relative cooling rates in iron meteorites. *Geochim. Cosmochim. Acta*, 84, 508–524.
- Wasson J. T. and Kallemeyn G. W. (2002) The IAB iron-meteorite complex: A group, five subgroups, numerous grouplets, closely related, mainly formed by crystal segregation in rapidly cooling melts. *Geochim. Cosmochim. Acta*, 66, 2445–2473.
- Weidenschilling S. J. and Cuzzi J. N. (2006) Accretion dynamics and timescales: Relation to chondrites. In *Meteorites and the Early Solar System II* (D. S. Lauretta and H. Y. McSween Jr., eds.), pp. 473–485. Univ. of Arizona, Tucson.
- Weiss B. P. and Elkins-Tanton L. T. (2013) Differentiated planetesimals and the parent bodies of chondrites. *Annu. Rev. Earth Planet. Sci.*, 41, 529–560.
- Weiss B. P., Berdahl A. S., Elkins-Tanton L. T., Stanley S., Lima E. A., and Carporzen L. (2008) Magnetism on the angrite parent body and the early differentiation of planetesimals. *Science*, 322, 713–716.
- Weiss B. P. and 12 coauthors (2012) Possible evidence for partial differentiation of asteroid Lutetia from Rosetta. *Planet. Space Sci.*, 66, 137–146.
- Wetherill G. W. (1980) Formation of the terrestrial planets. *Annu. Rev. Astron. Astrophys.*, 18, 77–113.
- Wilson L. and Keil K. (1991) Consequences of explosive eruptions on small solar system bodies: The case of the missing basalts on the aubrite parent body. *Earth Planet. Sci. Lett.*, 104, 505–512.
- Yang J. and Goldstein J. I. (2006) Metallographic cooling rates of the IIIAB iron meteorites. *Geochim. Cosmochim. Acta*, 70, 3197–3215.
- Yang J., Goldstein J. I., and Scott E. R. D. (2007) Iron meteorite evidence for early formation and catastrophic disruption of protoplanets. *Nature*, 446, 888–891.
- Yang J., Goldstein J. I., and Scott E. R. D. (2008) Metallographic cooling rates and origin of IVA iron meteorites. *Geochim. Cosmochim. Acta*, 72, 3043–3061.
- Yang J., Goldstein J. I. and Scott E. R. D. (2010a) Main-group pallasites: Thermal history, relationship to IIIAB irons, and origin. *Geochim. Cosmochim. Acta*, 74, 4471–4492.
- Yang J., Goldstein J. I., Michael J. R., Kotula P. G. and Scott E. R. D. (2010b) Thermal history and origin of the IVB iron meteorites and their parent body. *Geochim. Cosmochim. Acta*, 74, 4493–4506.



# Asteroid Surface Alteration by Space Weathering Processes

Rosario Brunetto

*Institut d'Astrophysique Spatiale (IAS), Université Paris-Sud*

Mark J. Loeffler

*NASA Goddard Space Flight Center*

David Nesvorný

*Southwest Research Institute*

Sho Sasaki

*Osaka University*

Giovanni Strazzulla

*Istituto Nazionale di Astrofisica (INAF)–Osservatorio Astrofisico di Catania*

Micrometeorite bombardment and irradiation by solar wind and cosmic-ray ions cause variations in the optical properties of small solar system bodies surfaces, affecting efforts to draw connections between specific meteorites and asteroid types. These space weathering processes have been widely studied for the Moon and S- and V-type asteroids, and they are currently being investigated for other asteroid types. Here we review the laboratory studies performed by several groups on meteorites and asteroid surface analogs, aimed at simulating space weathering by using ion irradiation and laser ablation. Together with direct evidence of weathering of particles from asteroid Itokawa acquired by the Hayabusa mission, these results have provided a fundamental contribution to the spectral interpretation of asteroid observations, to establish a solid asteroids–meteorites link, and to understand the energetic processes affecting the surfaces of minor bodies. A general scheme for asteroid optical maturation is thus emerging. Slope trends from large surveys and in particular of young asteroid families have confirmed that solar wind is the main source of rapid ( $10^4$ – $10^6$  yr) weathering, and that a number of rejuvenating processes (impacts by small meteorites, planetary encounters, regolith shaking, etc.) efficiently counterbalance the fast weathering timescales.

## 1. INTRODUCTION

Space weathering (SW) processes affect airless bodies in the solar system. These processes include irradiation by solar ion populations (solar wind, flares, solar-energetic-particle events), galactic cosmic rays, electrons, UV and X-rays, and bombardment by micrometeorites. The surface alteration varies not only as a function of the surface composition, but also location in the solar system. Generally, SW processes have been widely studied for the Moon and S- and V-type asteroids, and they are currently being investigated for other asteroid types. Fundamental reviews on SW have been published, and the reader is invited to refer to Hapke (2001), Clark et al. (2002), and Chapman (2004) for a comprehensive view of the state of the art approximately 10 years ago. At that time, the main effects of SW and the basics of the asteroid–meteorite connection had already been settled, mainly thanks to lunar studies, asteroid remote

sensing spectroscopy, and observations by the Galileo and Near Earth Asteroid Rendezvous (NEAR) spacecraft. For a more recent review on SW, the reader is referred to Gaffey (2010) and Bennett et al. (2013).

The Moon is the most-studied airless body and best-known case where SW is observed. Lunar SW has been investigated for decades (Gold, 1955; Hapke, 2001, and references therein). Its main driver is nanophase metallic iron ( $\text{npFe}^0$ ), which is produced from solar wind bombardment (Keller and McKay, 1997), and causes the reflectance spectra to become sloped (reddened) and darken in the visible–near-infrared (VIS-NIR) (Pieters et al., 2000; Taylor et al., 2001; Hapke, 2001). Inspired by the lunar SW work, investigators have wondered to what extent the same mechanisms were operating on asteroids (Chapman, 2004). Asteroidal SW has often been regarded to be important for explaining potential matches (or mismatches) between asteroid taxonomical classes and meteorite classes [see Krot et al. (2005) for a

review on the classification of meteorites, and *DeMeo et al.* (2009) for the most recent asteroid taxonomy].

The most studied case for asteroids concerns whether S-type asteroids are the parent bodies of ordinary chondrites. Numerous works have compared the mineralogy of S-types with ordinary chondrites (OCs) and have discussed implications for possible bias in the meteorite collections (see, e.g., *Gaffey et al.*, 1993; *Meibom and Clark*, 1999; and references therein). Later studies demonstrated that a VIS-NIR reddening spectral trend can be established by comparing OCs to main-belt S-types through near-Earth asteroids (NEAs) (*Binzel et al.*, 2004). This suggested that, in general terms, lunar-style SW could also be valid for asteroids. Evidence for darkening and reddening were observed on asteroids visited by spacecraft (NEAR, Galileo), but the albedo and 1- $\mu\text{m}$  band depth dependence on the surface age/morphology for (433) Eros and (243) Ida were found to be different than that observed on the Moon (*Chapman*, 1996; *Murchie et al.*, 2002; *Gaffey*, 2010). Strong evidence for a reddening trend with respect to space exposure has been found thanks to the study of young silicate-rich asteroid families. The latter confirms the major role played by the solar wind ions and the collisional resurfacing scenario in the case of S-type objects (*Brunetto et al.*, 2006a; *Marchi et al.*, 2006a; *Willman et al.*, 2008; *Vernazza et al.*, 2009a).

Some SW processes can be simulated in the laboratory using various approaches and analytical techniques (see, e.g., *Bennett et al.*, 2013). The silicate reddening and darkening spectral trends have been measured in many SW experiments performed by different groups on terrestrial silicates and OCs for application to S-types (*Hapke*, 1965; *Moroz et al.*, 1996; *Sasaki et al.*, 2001; *Strazzulla et al.*, 2005; *Marchi et al.*, 2005; *Brunetto et al.*, 2006b; *Loeffler et al.*, 2008a, 2009; *Fu et al.*, 2012). Although some differences arise between ion irradiation and laser irradiation/ablation experiments, the general SW trend is similar. Asteroid spectral modeling has been developed using laboratory SW results; the main result is that SW does not affect band center and relative areas of VIS-NIR silicate absorptions (although the area of each silicate band decreases). Little is known about the response to SW by other classes of meteorites. For instance, SW trends become more complicated and controversial when the case of dark asteroids (C-complex) is considered. Weak reddening trends have been observed by some investigators (*Lazzarin et al.*, 2006), while other studies have found a blueing effect (*Nesvorný et al.*, 2005; *Lantz et al.*, 2013; *Vernazza et al.*, 2013).

The common view of asteroid SW given in the *Asteroids III* volume (*Clark et al.*, 2002) was that studies of lunar rocks and soils were the most important basis on which to build an understanding of asteroidal SW. At that time it was not possible to directly measure asteroid surfaces in the laboratory. But in the recent years, extraordinary results have been obtained by the Japan Aerospace Exploration Agency (JAXA) Hayabusa mission, which visited and returned samples from asteroid (25143) Itokawa. Hayabusa spectrometers showed that SW effects develop on different regions (*Hiroi*

*et al.*, 2006), and returned Itokawa grains, later analyzed in the laboratory, showed multi-layered structures related to SW effects, including amorphized silicates and npFe<sup>0</sup> and iron sulfide inclusions (*Noguchi et al.*, 2011, 2014). Thus, although many questions are still open, Hayabusa results seem to confirm the general scenario of reddening and darkening first observed on the Moon and later on asteroid families.

In this chapter we will review the laboratory studies performed in the last decade on meteorites and asteroid surface analogs that were aimed at simulating SW (Table 1). We will also discuss the direct evidence of weathering observed on Itokawa samples and the spectral slope trends determined from observational surveys taken in the last decade. Open points for future investigations will be identified and discussed.

## 2. LABORATORY STUDIES ON SPACE WEATHERING

### 2.1. Overview of Laboratory Techniques

**2.1.1. Conditions and limitations considered for laboratory studies.** A complete simulation of an asteroid surface environment (including relevant pressures, temperatures, textures, and compositions) is not feasible, and thus much of the focus in laboratory studies is on trying to simulate the most important factors that are believed to contribute to SW. Three of the main characteristics regarding an asteroid's surface are its composition, temperature, and pressure.

The composition will vary from asteroid to asteroid, so laboratory experiments utilize data taken from remote sensing to try and pick a suitable sample material. Laboratory studies often focus on a single component (e.g., olivine, pyroxene, etc.) among the many associated with the asteroid to test its affinity to weathering. From a practical point of view, this will give insight into whether some of the minerals present may be more susceptible to weathering than others. The mineral is usually crushed down to a grain size relevant to the regolith, which is typically <100  $\mu\text{m}$ . The crushed grains are then pressed into a pellet (e.g., *Sasaki et al.*, 2001; *Brunetto et al.*, 2006b), so that it can be mounted at any geometry to be irradiated and analyzed.

To simulate the low-pressure environment that exists on most asteroids ( $10^{-15}$  Torr), the prepared sample is placed into a contaminant-free vacuum system, which typically ranges between  $10^{-5}$  and  $10^{-10}$  Torr (e.g., *Sasaki et al.*, 2001; *Loeffler et al.*, 2009). Finally, laboratory experiments on SW are typically performed at room temperature, even though the surfaces of asteroids can be at significantly lower temperatures and there is the potential that the irradiation effects produced in the minerals could depend on temperature. The lack of attention to this aspect is likely a result of the increased complexity involved with cooling of the sample. However, as one spectral study found that relevant mineral (olivine) reflectance spectra did vary with temperature (*Lucey et al.*, 1998), it is important to at least consider performing some of these SW studies at more relevant temperatures in the future.

TABLE 1. Summary of SW experiments performed on terrestrial and extraterrestrial materials.

Material	Ion Irradiation		Laser Irradiation	VIS-NIR Spectral Effects	Physical Mechanisms
<i>High albedo</i>					
Terrestrial olivine	Species: H, He, N, Ar; Energies = 1–400 keV	$\lambda = 193, 248, 1064 \text{ nm}$ ; Dose $\leq 800 \text{ J cm}^{-2}$ *	"	Strong spectral reddening and darkening	Formation of npFe <sup>0</sup> , structural modifications
Terrestrial pyroxene	"	"	"	Same as olivine but weaker	"
Ordinary chondrites	"	"	"	"	"
Enstatite chondrites	Ar 200 keV	Not performed		Very weak darkening	Structural modifications?
HED meteorites	C, Ar; 60, 200, 400 keV	$\lambda = 1064 \text{ nm}$		Same as OCs	Same as OCs
<i>Low albedo</i>					
Terrestrial bitumens	Same as olivine	Not performed		Very strong spectral flattening, weak brightening	H/C and gap decrease, aromaticity increase
Organic residues from C-rich ices	"	"	"	Reddening and darkening	Formation of refractory molecular solid
Organics covering silicates	H 200 keV, Ar 400 keV	"	"	"	Same as bitumens
"Bright" CC (Allende)	He, Ar 40 keV; Ar 400 keV	$\lambda = 1064 \text{ nm}$ ; pulse 0.5–1 $\mu\text{s}$		Weak reddening-darkening	OC-like?
"Dark" CC (Tagish Lake)	He, Ar 4 keV; He 200 keV	$\lambda = 1064 \text{ nm}$ ; D $\leq 10 \text{ J/}$ $\text{cm}^2$	Flattening		Bitumen-like?

\*The dose is usually provided as  $0.05\text{--}2 \text{ J cm}^{-2}$  per pulse (duration 5–10 ns or 0.5–1  $\mu\text{s}$ ) and then repeated on several shots.

References for high- and low-albedo materials are given in sections 2.2 and 2.3 respectively.

**2.1.2. Radiation processing.** An equally important characteristic to consider is the type of radiation that is going to be driving SW. For asteroids, one of the main drivers is believed to be ions (solar wind and cosmic rays). The solar wind consists of mostly hydrogen and helium ions (>99%), which have a mean energy of 1 keV per atomic mass unit (Gosling, 2007), and thus most studies have focused on using either of these ions. The other ion components of the solar wind could also potentially contribute to SW, but these are typically neglected as their flux is so low. Cosmic rays, mainly consisting of hydrogen ions, also impact the surface, albeit at a much lower flux than the solar wind ions. However, since they are more energetic, they can penetrate much deeper than the solar wind ions, and thus even though their flux may be lower, there is the potential that they may also contribute to SW. When considering ions and their interaction with the mineral samples, they can alter the surface by depositing energy as they pass through the grain, which may induce sputtering or structural and chemical changes. To first order, the degree to which these changes occur is going to depend on the stopping power of the ion, which is typically described as energy transfer through elastic (nuclear) and inelastic (electronic) collisions with the atoms in the solid. Although the two forms of energy transfer are different, both produce alteration in the target material and thus are relevant for SW.

In addition to ion irradiation, the surfaces of asteroids are also bombarded with micrometeorites, which can alter the regolith significantly. The fast ones (approximately kilometers per second) are believed to be able to slow down so quickly

that they can partially or even completely vaporize some of the surface grains. Interestingly, nanosecond-pulsed lasers at fluences higher than the ablation threshold have been used as an analog for micrometeorite impacts (Sasaki et al., 2001; Brunetto et al., 2006b; Loeffler et al., 2008a), as they are effective for depositing large amounts of energy over short amounts of time and can yield power densities similar to those estimated for micrometeorite impacts (Kissel and Krueger, 1987). Using a pulsed laser is appealing, because it can be purchased commercially, is typically small, can easily produce many pulses in a very short amount of time, and has pulses that can be rastered uniformly over a large sample area. The other more direct simulation of micrometeorite impacts is using a dust accelerator (e.g., Cintala and Hötz, 2008), yet the instrument's large size and low particle flux have made it less appealing for these types of studies; however, we note that a new facility capable of producing dust at much higher fluences is now in operation (Shu et al., 2012) that could potentially be useful for SW studies.

As an asteroid is exposed to radiation processing over timescales that are orders of magnitude longer than what is attainable in the laboratory, a critical step for the ions is that the effects depend on the total fluence ( $\text{ions cm}^{-2}$ ) and not on the actual flux ( $\text{ions cm}^{-2} \text{ s}^{-1}$ ) used in experiments. This is obtained by using ion currents [typically 1–2  $\mu\text{A}$  (microamperes)] that do not cause macroscopic heating of the sample. For laser irradiation experiments, the total energy deposited by the impacts that are fast enough to cause vaporization are compared with the total energy deposited by the laser

(e.g., Sasaki *et al.*, 2001; Loeffler *et al.*, 2009). However, this ends up being more of a qualitative comparison, as the vaporization of the surface minerals will be nonlinear and therefore how the energy is deposited (in one impact vs. many impacts) is critical.

**2.1.3. Analytical methods.** The main technique used for analysis of space-weathered samples in the laboratory has been VIS-NIR reflectance spectroscopy (Moroz *et al.*, 1996; Hapke, 2001, and references therein; Sasaki *et al.*, 2001; Brunetto and Strazzulla, 2005; Loeffler *et al.*, 2009), which have been performed both *in situ* and *ex situ* (i.e., in the same vacuum chamber where the alteration is performed, or outside of it). Other complementary *in situ* measurements have been used to probe the structure [Raman spectroscopy (Vernazza *et al.*, 2009b)] and surface composition [X-ray photoelectron spectroscopy (Dukes *et al.*, 1999; Davoisne *et al.*, 2008; Loeffler *et al.*, 2009)], while a number of *ex situ* techniques have been employed to look for structural and chemical changes in the grains: scanning electron microscopy SEM (Yamada *et al.*, 1999; Moroz *et al.*, 1996), transmission electron microscopy (TEM) (Sasaki *et al.*, 2001, 2003; Loeffler *et al.*, 2008a; Noble *et al.*, 2011), energy dispersive spectroscopy (EDS) (Sasaki *et al.*, 2001), and electron spin resonance (ESR) (Kurahashi *et al.*, 2002). These techniques can provide insight into the identifying characteristics of SW and when combined can provide complementary information that can help to unravel the underlying mechanisms driving SW.

## 2.2. Bright Objects

**2.2.1. Experiments on high-albedo meteorites and silicate analogs.** Many laboratory studies investigating SW relevant to asteroids have focused on the alterations produced in silicates, namely pyroxene and olivine. Most of the studies have been performed on single-component terrestrial minerals (e.g., Sasaki *et al.*, 2001; Brunetto *et al.*, 2006b; Loeffler *et al.*, 2009; Fu *et al.*, 2012), yet there have also been a number of experiments on meteorites (OCs and HEDs) that contain varying amounts of these silicates as well (e.g., Strazzulla *et al.*, 2005; Fulvio *et al.*, 2012). These silicates are of particular interest in that they can easily be identified by remote sensing spectra from their diagnostic absorption bands near 1  $\mu\text{m}$  and 2  $\mu\text{m}$  (pyroxene only). Laboratory studies show that irradiation by ions and pulsed lasers can darken (lower reflectance) and redden (cause a slope change) their spectra, as shown in Fig. 1; these findings are similar to what has been observed on lunar samples and lunar analogs and are consistent with the explanation that the spectral mismatch between OCs and their presumed parent bodies, S-type asteroids, may be explained by SW processes.

The mechanism behind the SW trends observed in these silicates has been proposed to be either due to the formation of metallic iron, e.g., iron nanoparticles, as is observed on lunar analogs (Hapke, 2001), and/or due to structural modifications/damage (Brunetto and Strazzulla, 2005). It is important to note that in all experiments the spectral changes observed for silicates and meteorites are similar and are consistent with

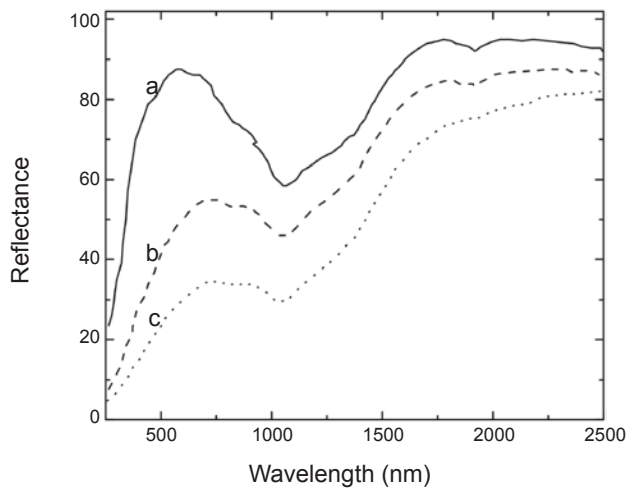


**Fig. 1.** Reflectance spectra of a <75- $\mu\text{m}$  San Carlos olivine pellet sample before (line marked "a") and after (line marked "b") one and five laser pulses from a 1064-nm laser with a fluence of 24  $\text{J cm}^{-2}$ . Spectra are adapted from Sasaki *et al.* (2001). The overall drop in reflectance is referred to as darkening, while the increase in slope, e.g., more drastic drop in reflectance at lower wavelengths, is referred to as reddening. From Sasaki *et al.* (2001), reprinted with permission of Macmillan Publishers Ltd.

the darkening and reddening mentioned previously. The presence of  $\text{npFe}^0$  (formed from oxide bound to iron) is evident through a number of studies on silicates. Sasaki *et al.* (2001) was the first to show the correlation in olivine using TEM (see Fig. 2) and he and other groups confirmed these findings using ESR (Kurahashi *et al.*, 2002). Later studies focusing on evaporated deposits produced from a pulsed laser showed that the deposits also contain metallic iron and can darken and redden the spectral reflectance (Loeffler *et al.*, 2008a). Interestingly, evaporated deposits made from iron-free forsterite ( $\text{Mg}_2\text{SiO}_4$ ) showed little spectral modification. In addition, studies using 4-keV He ions to irradiate San Carlos olivine used *in situ* XPS to correlate the formation of metallic iron with spectral reddening (Loeffler *et al.*, 2009).

Structural modification induced by bombardment has the potential to contribute to SW as well, as previous studies have shown that both olivine (Brucato *et al.*, 2004; Carrez *et al.*, 2002) and pyroxene (Demyk *et al.*, 2004; Jager *et al.*, 2003) samples are amorphized under ion bombardment. Furthermore, more recent experiments on olivine show that different crystal planes amorphize at different rates (Li *et al.*, 2013). However, in comparing experiments that used the same ion (He), the fluences needed for amorphization (Carrez *et al.*, 2002) are much lower than what was needed to observe reddening for San Carlos olivine (Loeffler *et al.*, 2009). In addition, when iron-free forsterite was irradiated well past the fluence needed for amorphization, no changes were observed in the near-infrared reflectance spectrum (Loeffler *et al.*, 2009).

The contribution of structural modification to SW for silicates may be more important in samples that have been

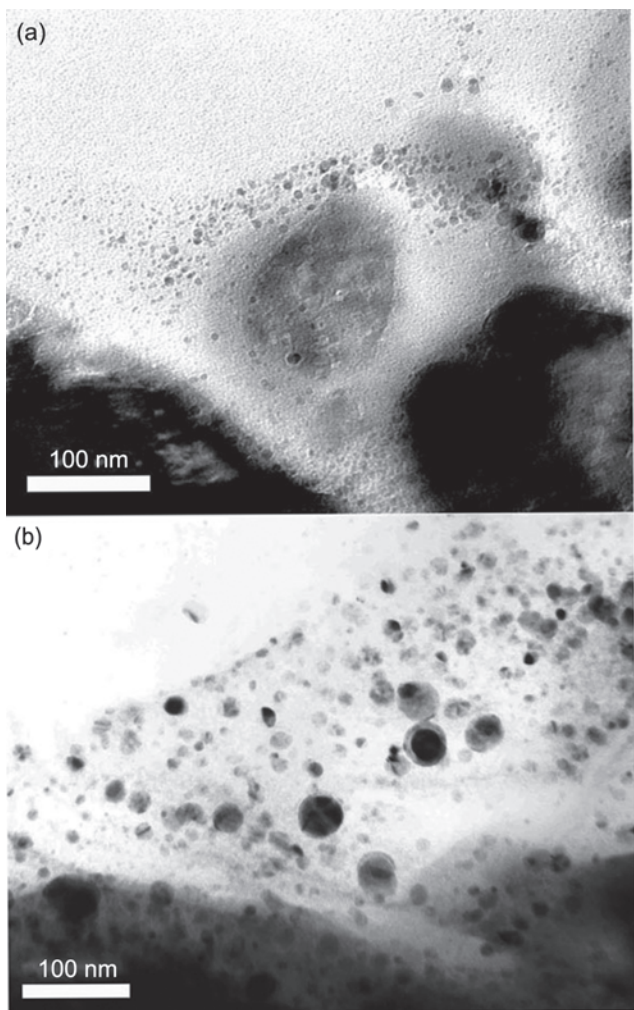


**Fig. 2.** Transmission electron microscope images of San Carlos olivine after irradiation with a 1064- $\mu\text{m}$  pulsed laser. The presence of npFe<sup>0</sup> are easily seen after 5 pulses (top), and are more evident and slightly larger after 20 pulses (bottom). In both cases, the laser fluence was 24 J cm<sup>-2</sup>. From Sasaki et al. (2001), reprinted with permission of Macmillan Publishers Ltd.

directly irradiated with a pulsed laser (Brunetto et al., 2006b), as the rapid melting of the sample may not only change the phase of the silicates but could also induce irregular structures that may contribute to changes in the scattering properties of the minerals. Regardless of whether alteration of the physical structure/morphology of the sample contributes to SW, it is possible that the mineral chemical structure (olivine vs. pyroxene), not simply the presence of iron bound to an oxide, may matter as laser irradiation experiments (1064 nm wavelength) showed that olivine was more easily altered by the laser than was pyroxene that contained a similar amount of iron bound to oxide (Yamada et al., 1999). However, comparing the susceptibility of different minerals to laser irradiation is complicated, as a small difference in the absorption coefficient at a given wavelength between two minerals may translate into larger

differences in the ablation, since it is a nonlinear process. For instance, a similar study using a UV laser (Brunetto et al., 2006b) showed that the reddening (slope change) induced in clinopyroxene was only 15% less than that for olivine. Thus, the importance of chemical structure on SW needs to be studied in more detail to determine whether it is a real effect or whether it is simply a consequence of the laser wavelength.

Finding evidence of weathering in samples either taken directly from extraterrestrial bodies (the Moon, asteroids) or believed to originate from them (meteorites) is a great way to substantiate that SW is an important process active on asteroid surfaces. Space weathering is clearly active on the Moon (Hapke, 2001) and on Itokawa (section 3). However, microscopy studies on meteorites have also shown characteristics expected from SW. For instance, Noble et al. (2011) used SEM and TEM to examine two meteorites (Kapoeta and Fayetteville) and found that both exhibit some glass characteristics indicative of SW products. Furthermore, Kapoeta also had an amorphous rim similar to those found on lunar grains and another region that contained npFe<sup>0</sup>, both of which are consistent with SW processing.

**2.2.2. Connection to bright asteroids (*A, Q, S, E, V*) and timescales.** Laboratory results have been applied to spectral modeling and used to interpret observations from large surveys and space missions with the high-albedo classes of asteroids [see Bus and Binzel (2002) and DeMeo et al. (2009) for a complete discussion of differences among taxonomic classes] receiving the most attention. The large number of observations obtained in the past decades combined with laboratory experiments allow the identification of a few general SW spectral trends for asteroids:

1. It had been suggested for decades that SW can be responsible for the puzzling and significant mismatch between the VIS-NIR spectra of the most populous class of meteorites (OCs) and the surface spectra of S-type near-Earth objects (NEOs) and main-belt asteroids (MBAs), their presumed asteroidal parent bodies (see Chapman, 1979, 2004; Clark et al., 2002). The reason for this mismatch has become clearer thanks to several SW experiments and to the Itokawa sample return (see section 3). For example, reflectance spectra measured after irradiating an OC meteorite with increasing ion fluence exhibit a progressive reddening that is similar to the spread of spectra observed for S-type NEAs (Fig. 3).

2. Analysis of the VIS-NIR spectra of a large sampling of OCs, MBAs, and NEOs showed a similar mineralogy between most asteroids and meteorites, but different distributions of spectral slopes (Marchi et al., 2005), as shown in Fig. 4. This was interpreted as a SW effect induced by solar wind ion irradiation. Experimental results can explain the shift of the OC distribution toward asteroid distributions. Spectra of unaltered and irradiated silicates have slopes that span a wider range than that observed in NEOs and MBAs. Asteroids exhibit an asymmetrical slope distribution, possibly due to a different rate of weathering between olivine-rich and pyroxene-rich asteroids, a behavior that needs to be tested by laboratory experiments.

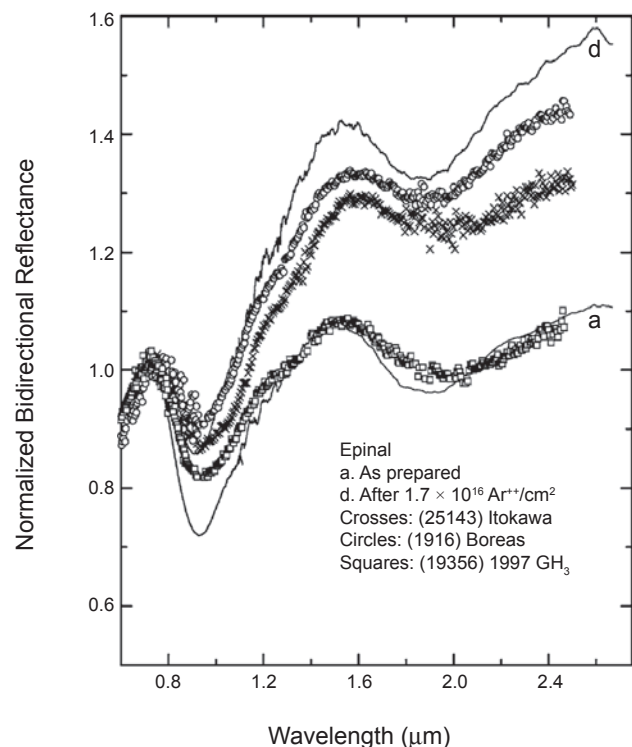


**Fig. 3.** The initial reflectance spectrum of OC Epinal and that obtained after ion irradiation (with 60 keV Ar<sup>++</sup>; only the maximum dose is shown) are shown normalized to 1 at 0.7 μm. The normalized observed spectra of three NEOs are also shown for comparison. From Strazzulla *et al.* (2005), reprinted with permission of Elsevier.

3. Studying the slope-diameter correlation for NEOs, a size-dependent transition from OC-like (Q-type) objects to S-type asteroids over the size range of 0.1–5 km (Binzel *et al.*, 2004) was observed, as reported in Fig. 5. A VIS-NIR reddening spectral trend can thus be established comparing OCs to main-belt S-types through NEAs [although an important fraction of unweathered OC-like objects may also be found among MBAs (e.g., Mothé-Diniz *et al.*, 2010; Rivkin *et al.*, 2011; Thomas *et al.*, 2012)]. The 0.1–5-km size range appears to be critical for understanding the processes, timescales, and conditions under which a regolith conducive to SW is generated, retained, and refreshed.

4. As discussed by Marchi *et al.* (2012), “the spectral reddening of an individual object can be considered as the sum of three terms, one (which is relevant for statistical analyses) depending on the exposure of the object to SW during its lifetime, a second one due to the original surface composition, and a third one (a noise term) due to the combination of poorly constrained effects (e.g. structure and texture of the surface)”. In addition, the spectral reddening induced by SW can be confused with other effects, such as surface texture or phase reddening (see, e.g., Sanchez *et al.*, 2012; Beck *et al.*, 2012). Nevertheless, it was possible to find a general correlation between the visible spectral slope of asteroids and the exposure to solar wind (Marchi *et al.*,

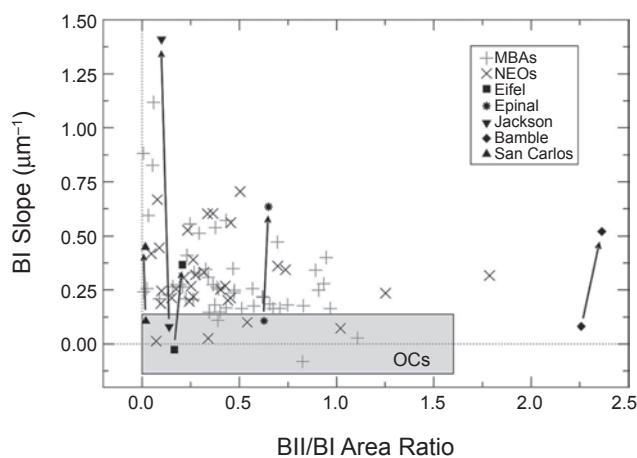


**Fig. 4.** Spectral slope around BI (broadband at about 1 μm due to the presence of ferrous iron Fe<sup>2+</sup> in olivine crystals but is also present in pyroxene) as a function of the BII/BII area ratio (where BII is the broad 2-μm band that is characteristic of pyroxene but not olivine) for main-belt asteroids (MBAs) and near-Earth objects (NEOs). Vertical arrows show the trend from unirradiated to irradiated silicates determined by laboratory experiments. The shaded box contains 95% of OCs; symbol dimensions correspond to error bars. From Marchi *et al.* (2005), reprinted with permission of ESO.

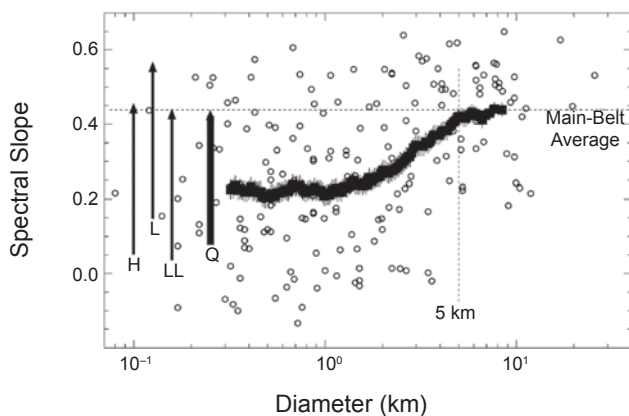


**Fig. 5.** VIS-NIR spectral slopes vs. diameter (open circles) for near-Earth and Mars-crossing objects residing within the S, Sq, and Q classes. A running box mean is shown by filled squares (box size = 50, with error bars depicting the standard deviation of the mean). The running box trend asymptotically approaches the mean slope (dashed line) for SMASSII main-belt S-type asteroids, reaching this limit at a size of 5 km. The evolution from typical OC-like (Q-type) to S-type surfaces is depicted by the Q-S vector. The vectors labeled “H,” “L,” and “LL” show the effects of a reddening model for OC meteorites resulting from the addition of 0.05% submicroscopic iron. The magnitude of the transition for the meteorites is comparable to the magnitude of the Q-S vector for the asteroids; see Binzel *et al.* (2004) for more details. Consistent results were obtained by Thomas *et al.* (2012) for the Koronis family. From Binzel *et al.* (2004), reprinted with permission of Elsevier.

2006a,b; Paolicchi et al., 2007), defined as the age times the inverse squared mean distance from the Sun (function of the semimajor axis and of the eccentricity). The relevance of the exposure parameter requires the dominance, at least for distances smaller than about 3–4 AU, of SW effects connected to the Sun. In other words, this suggests that solar ion flux is the main source of the asteroidal SW.

5. Finally, the color of asteroid families becomes redder with increasing dynamical age. This will be largely discussed in section 4, together with the estimation of the observational and experimental timescales for SW processes.

Inspired by the OC meteorites vs. Q-type and S-type paradigm, a few studies have been conducted to explore SW of other asteroid classes, such as A-types (Sasaki et al., 2001; Brunetto et al., 2007a; Fu et al., 2012), E-types (Vernazza et al., 2009b), and V-types (Fulvio et al., 2012). Strong reddening and darkening have been reported for A-type analogs, whereas little effects are observed on E-type analogs. The presence of iron and the nature of the target silicate seem to play a major role in determining the spectral effects. Unfortunately, there is still a lack of laboratory SW simulations on meteorites relevant to these asteroids, and many issues are open for future studies. The case of V-types seems particularly intriguing: Although SW effects (reddening and darkening) have been reported both in laboratory and observational studies (see, e.g., Marchi et al., 2010, and references therein), asteroid (4) Vesta (the parent body of vestoids and HED meteorites) is not reddened and shows peculiar signs of SW, as revealed by groundbased observations and by the recent Dawn mission (see, e.g., Pieters et al., 2012, and references therein).

### 2.3. Dark Objects

**2.3.1. Experiments on low-albedo meteorites and organic analogs and connection to dark asteroids.** Recent investigations have shown that primitive dark material (C-, P-types) accounts for more than half of the main-belt and Trojan asteroids by mass (DeMeo and Carry, 2013). From the astronomical point of view, SW trends become more complicated and controversial when we consider the case of dark asteroids. Weak reddening trends have been observed by some investigators (Lazzarin et al., 2006) while other authors have found a blueing effect (Nesvorný et al., 2005). Lantz et al. (2013) assumed that CM meteorites and Ch/Cgh asteroids are the same material (fresh subsurface and weathered surface materials respectively). They found a neutralization of the spectral slopes possibly due to SW, with few albedo and band modifications. It has been suggested many times that carbonaceous chondrites (CCs) are connected with specific classes of dark asteroids (C, D, P, B), although an unambiguous correspondence between single CC and asteroid classes has proven to be arduous.

The few irradiation experiments of dark CCs have shown what appear to be contradictory trends. Spectral reddening (and the presence of abundant silicates causing the band at about 1 μm) was observed in ion and/or laser irradiation ex-

periments of the Allende (CV3) meteorite, a CO3 meteorite, and CM Mighei (Moroz et al., 1996, 2004a; Lazzarin et al., 2006; Brunetto et al., 2014), while a flattening effect was observed in the case of the ion- or laser-irradiated Tagish Lake meteorite (Hiroi et al., 2004, 2013; Vernazza et al., 2013). In both cases, the spectral variations of irradiated CCs are much smaller than those observed on H-rich organics (see below) and also smaller than variations associated with the heterogeneity of the original composition. However, these differences may simply imply that these meteorites are at a different stage in the weathering process. To test the validity of these and other hypothesis, it is critical to perform laboratory studies on materials that are considered “analogs” of those present in astrophysical environments during different evolution phases of the solid matter.

Numerous SW experiments have been performed on different classes of carbon-bearing materials:

1. Carbon-bearing frozen gases ( $\text{CH}_4$ ,  $\text{CH}_3\text{OH}$ ,  $\text{C}_6\text{H}_6$ ) (Brunetto et al., 2006c), a reasonable analog for the icy surfaces of small objects in the outer solar system [e.g., (5145) Pholus)], have been irradiated, and it is found that the initially transparent layers exhibit a strong reddening of the spectra due to the formation of a “red” molecular solid similar to some terrestrial materials (e.g., bitumen). Further prolonged irradiation drives the material toward a spectrally flat and dark organic (C-rich) refractory residue. The color is preserved during annealing and sublimation of the residual volatiles produces a refractory material that has been called ion-produced hydrogenated amorphous carbon (IPHAC). Such a polymer-like cross-linked solid has a flat and dark spectrum, is mostly insoluble, and represents a “fully weathered material.” The experiments on ices are directly related to the icy objects in the outer solar system (Trojans, transneptunian objects, Oort cloud comets). However, they are also connected to asteroids, as some asteroids are likely remnants of icy objects and because asteroids are being continuously bombarded with interplanetary dust and micrometeorites, which may have come from icy objects. This latter hypothesis has been recently supported by the finding of dark material on Vesta (McCord et al., 2012) (see section 4.3).

2. Natural bitumens (asphaltite, kerite) (Moroz et al., 2004b) have very red spectra that resemble those obtained after moderate irradiation of the C-rich ices. Also, irradiation of these bitumens causes their spectra to become flatter and darker. Such spectral flattening is attributed to a specific modification of the carbonaceous component: a loss of hydrogen from the carbonaceous structure, an increase in aromaticity, and a consequent variation of the optical gap. These imply that the absorption coefficient increases so much that the molecules become optically thick and their spectral behavior changes from a volume-scattering regime into a surface-scattering regime. This may even induce an increase in the UV-VIS albedo.

The role of the optical gap change and hydrogen loss has been discussed in the context of SW of transneptunian objects, where dark inclusions in a transparent matrix (ice) play a major role (see, e.g., Dalle Ore et al., 2011, and

references therein). In the case of dark meteorites, silicates may play the role of semitransparent matrix for both carbon and npFe<sup>0</sup> inclusions. The chemical effects dominate the processing of carbon-based materials. The C/H (as well C/O or C/N) ratios all increase, producing a carbonization of the target. Carbon skeleton structural modifications after ion irradiation have also been observed, and they correlate with the elastic energy loss in the sample (Brunetto *et al.*, 2009). The spectral modifications observed by Moroz *et al.* (2004b) also scaled with the elastic energy loss. Figure 6a compares the spectrum of asphaltite, scaled at 0.55 μm, as deposited (the reddest spectrum) and after different ion fluences (for details, see Moroz *et al.*, 2004b). For comparison, the spectra of two asteroids, (1542) Schalen (D-type) and (5145) Pholus (Centaur), are also shown. The colors of both asteroids are similar to an initially red material (asphaltite) that has been ion irradiated.

3. Recently, polystyrene, deposited on a silicate (olivine), has been studied as an analog for “fresh” organics (Kaňuchová *et al.*, 2010). The spectra of the unirradiated and irradiated samples are shown and compared to asteroids (1542) Schalen (D-type) and (1951) Lick (A-type) in Fig. 6. Deposited polystyrene is a transparent polymer, unlike asphaltite, which is initially red. Polystyrene exhibits a progressive spectral reddening and darkening during irradiation. At high irradiation doses, the reddening reaches a maximum, while the sample continues to darken and starts to flatten. Interestingly, the spectral shape of the irradiated material at different doses can reproduce some asteroid spectra. It is also noted that the material is insoluble after irradiation. On the basis of these experimental results, a reddening-blueing loop has been proposed by Kaňuchová *et al.* (2012): Irradiated organics, initially exhibiting a flat spectrum and a high albedo, are progressively reddened while the albedo decreases. At very high doses, the spectra are flattened (blueing) while the albedo continues to decrease. A fully weathered organic will then have a flat and dark spectrum.

The results from irradiation experiments and the diversity of spectral slopes among carbon-rich asteroids suggest that many asteroids may contain organic materials that are not fully weathered. This material could have been produced by ion bombardment of more complex organic material originally present on the asteroid surface, such as organic ices (e.g., benzene, methane, methanol), very red materials (e.g., bitumens), or other organic molecular solids. Alternatively, this material could also be the relic of presolar material processed in the placental molecular cloud.

In summary, experiments indicate that ion bombardment of H-rich organic materials can explain the large color differences observed among dark asteroids. However, it is more difficult to determine trends in the small color differences that are observed for the high weathered asteroids with dark and flat spectra, as the observed spectral variations are comparable to variations due to sample preparation and other effects (grain size, etc.). Also, opposition effects (relative) are stronger for dark meteorites (Beck *et al.*, 2012), and these can be comparable to albedo variations induced by

irradiation. All this may explain why a clear and general SW trend for dark asteroids has not yet been found and why SW is neither necessary nor ruled out as an explanation of spectral differences between primitive asteroid families (Ziffer *et al.*, 2011).

**2.3.2. Synthesis and survival of C-H and O-H on space-weathered asteroids.** In the ion implantation process, reactive ions, such as H, C, N, O, and S, have the potential to directly

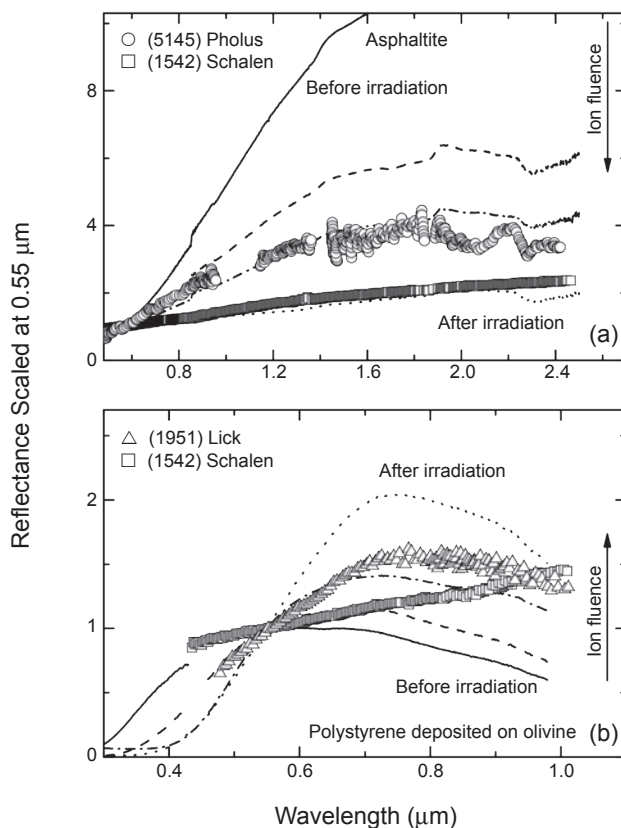


**Fig. 6.** The observed spectra of asteroids (1951) Lick [triangles, A-type, albedo 0.09 (Brunetto *et al.*, 2007a)], (1542) Schalen [squares, D-type (Bus and Binzel, 2002)], and (5145) Pholus [circles, Centaur, albedo 0.05 (Cruikshank *et al.*, 1998)] are compared with the reflectance spectra of laboratory materials before and after ion irradiation: (a) asphaltite [bitumen, for details see Moroz *et al.* (2004b)] and (b) olivine pellet with 34.4 μm of polystyrene deposited (for details, see Kaňuchová *et al.*, 2010). Schalen is chosen as an example of a primitive and possibly organic-rich surface. Pholus has one of the reddest slopes among solar system small bodies. Lick exhibits a strong silicate absorption, which suggests that the slope may be a result of SW of silicates (Brunetto *et al.*, 2007a), although the presence on the surface of a coloring organic material cannot be ruled out. A comparison between the red asteroids and irradiated asphaltite shown in (a) shows that SW of an extremely red material causes a decrease of the spectral slope that can reproduce the observed slopes. Irradiation of an olivine sample covered by an organic transparent material (polystyrene) causes a progressive reddening shown in (b) that can also reproduce some observed asteroidal slopes.

alter the target material, but they also can react with the target to produce new molecules. This phenomenon has been well studied for implantation of reactive ions in different ices (e.g., Strazzulla, 2011). As an example, the presence of sulfuric acid on Jupiter's moon Europa has been explained as due to magnetospheric sulfur ion implantation (Strazzulla et al., 2007).

The presence of organic materials on solar system objects has been inferred by the observation of C-H bonds in the reflectance spectra. However, laboratory experiments have demonstrated that C-H bonds can both be created and destroyed by radiation processes: keV-MeV ion bombardment of hydrogenated amorphous carbons causes a loss of hydrogen (Mennella et al., 2003; Godard et al., 2011), while exposing carbonaceous material to a flux of very low energy (thermal) protons produces new C-H bonds (Muñoz Caro et al., 2001). These experimental results have been applied to the dust life cycle in the interstellar medium, yet it has not been possible to apply this to asteroids, mainly because the flux of thermal protons impinging on their surface is not known. At present, the observation of surface C-H bonds suggests that the organic material on the surface is not fully weathered.

Irradiation experiments on relevant meteorites would determine the stability of organics (probed by CH stretching bands) on asteroid surfaces: Cross sections for CH destruction have been measured for ion irradiation in electronic energy loss regime [cosmic rays (Godard et al., 2011, and references therein)], but constraining CH survival timescale on inner solar system small bodies requires solar wind simulations and diffuse reflectance probes. These studies will help us to understand whether the CHs observed on asteroids (e.g., Campins et al., 2010b) correspond to a young or an old terrain.

Less numerous and more controversial are the experiments of implantation of reactive ions in silicates. In particular, it has been suggested that the bands attributed to water ice (or to hydrated silicates) observed on the Moon (Pieters et al., 2009; Basilevsky et al., 2012) and on some asteroids (Campins et al., 2010b; Rivkin et al., 2010) are produced by implantation of energetic solar protons. However, laboratory experiments have provided controversial results. While some authors have found that hydroxyl radicals are induced by proton implantation in silicates (Djouadi et al., 2011; Ichimura et al., 2012), others have found the contrary (Burke et al., 2011). In the future, experiments focusing on the implantation of reactive ions in silicates and solid carbonaceous material are necessary to obtain a more complete understanding of their potential relevance for the evolution of asteroid surfaces.

### 3. EVIDENCE FOR SPACE WEATHERING FROM SAMPLE RETURN

#### 3.1. Asteroid (25143) Itokawa: Evidence from Remote Sensing and *In Situ* Observations

Prior to observation by the Hayabusa mission (2003–2010), groundbased visible and infrared spectroscopic observations showed that (25143) Itokawa was an S (IV)-type asteroid mainly composed of olivine and pyroxene with

apparent 1- and 2- $\mu\text{m}$  absorption bands (Binzel et al., 2001). Disk-integrated visible-infrared spectra compared best with lightly reddened LL5/6 chondrites. In addition, a fairly large thermal inertia of  $750 \text{ J m}^{-2} \text{ s}^{-0.5} \text{ K}^{-1}$  was estimated, suggesting a paucity of fine regolith particles (Müller et al., 2005). In the following, we focus on the Hayabusa results that are most relevant for SW. For a complete review of the Hayabusa results, see the chapter by Yoshikawa et al. in this volume.

As shown in Fig. 7a, the surface of Itokawa is divided into rough terrain (about 80% of the surface), mostly consisting of numerous boulders, and smooth terrain, which is composed of millimeter- to centimeter-sized grains (Yano et al., 2006). Even though Itokawa's surface is deficient in fine (less than millimeter-sized) regolith particles, the observed strong opposition effect suggests that Hapke's scattering model can be applied (Hapke, 1993). Itokawa also has surface heterogeneity in both visible brightness and color. The brightness difference is approximately 10–20% on distant images and as high as 30% (up to 40%) on close-up images in the v-band (553 nm). This difference is too large to be explained by photometric effects. In the rough terrain, brighter areas are observed at some of the elevated zones, gravitationally steep zones, and structures that are presumably of impact origin (Saito et al., 2006; Hirata et al., 2009). Asteroid Multiband Imaging Camera (AMICA) observations show significant variations in brightness and color in the visible bands: ul (381 nm), b (429 nm), v (553 nm), and w (700 nm) (Ishiguro et al., 2007) and are correlated with each other: Brighter areas are bluer in color and darker areas are redder.

The near-infrared spectrometer (NIRS) confirmed previous disk-integrated results that suggested Itokawa's spectrum closely matched a weakly weathered LL5/6 chondrite (Binzel et al., 2001; Hiroi et al., 2006). Spectral variations were observed that can be explained by Hapke's SW model (Hapke, 2001), where the amount of npFe<sup>0</sup> controls spectral reddening (Fig. 8a; see section 3.3 for more details). Recent analysis of the AMICA NIR wavelengths (Ishiguro et al., 2014) shows that Itokawa's surface exhibits a good correlation between R<sub>w</sub>/R<sub>b</sub> (700 nm/429 nm reflectance ratio) and R<sub>p</sub>/R<sub>w</sub> (980 nm/700 nm reflectance ratio) (Fig. 8b). In other words, bluer and more immature regions (with moderate slope between 0.43  $\mu\text{m}$  and 0.70  $\mu\text{m}$ ) show the apparent deeper 1- $\mu\text{m}$  bands, which is consistent with NIRS results. The spectra of the rough terrains vary considerably in its degree of SW, while the smooth terrains have, on average, spectra that are lightly weathered.

It should be noted that disk-integrated reflectance between the ul-band (381 nm) and p-band (980 nm) at different rotational phases of Itokawa agree well with continuous reflectance spectra by groundbased observations (Binzel et al., 2001; Lowry et al., 2005).

The rough terrain on Itokawa contains both dark (and red) and bright (and blue) areas (Ishiguro et al., 2007, 2014). The darker areas are more abundant in boulders, while the larger (a few tens of meters) angular blocks, such as Yoshinodai, appear brighter than the smaller boulders. Figure 7a is a v-band (553 nm) image of rough terrain on the western side

of Itokawa, centered at Ohsumi Regio. The inset shows detailed images obtained in the b-band (430 nm). The bright spot (“A”) is one of the brightest points on Itokawa; it is likely that a very recent impact removed parts of the rocks’ weathered surface. Exposed bedrock zones are situated west of Ohsumi (“C”); the slope of the NIRS spectra taken in this region was blue. On the lefthand side of Fig. 7a, the area labeled “E” shows a patched dark thin layer ( $\leq 1$  m) covering the underlying brighter zone. Some boulders may have moved here after the bedrock was exposed. Kamoi (“D”) is a distinct bright circular and slightly depressed

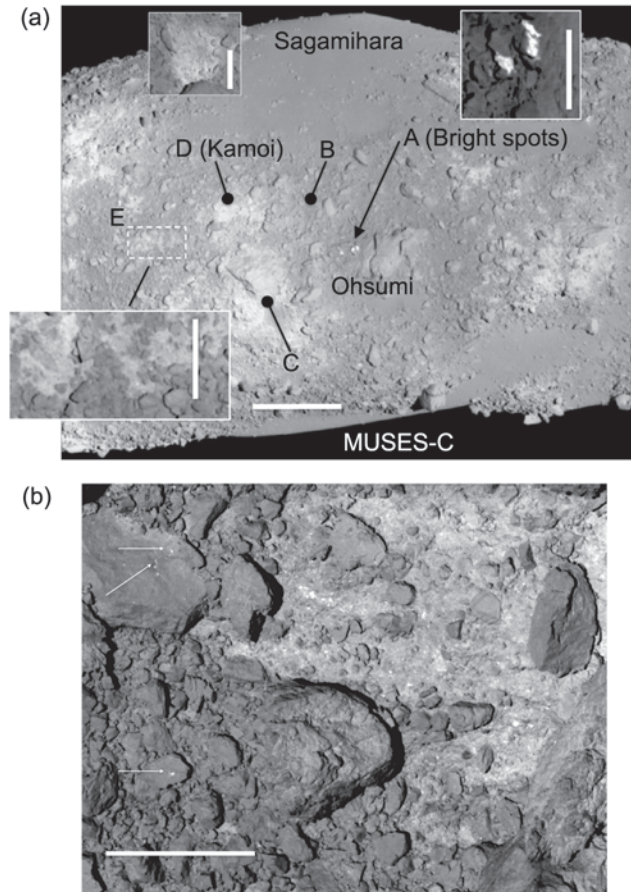


**Fig. 7.** (a) A v-band AMICA image around Ohsumi (Tsukuba) Regio in the western hemisphere of Itokawa image ST\_2494991986. Scale bar (white line) is 50 m. The dark boulder-rich zone is centered between brighter or patched areas. The arrow labeled “A” indicates “bright spots,” one of the brightest surfaces on Itokawa. Labels “B” and “C” correspond to the positions of redder and bluer NIRS spectra, which were obtained and discussed in Hiroi *et al.* (2006) (courtesy of H. Kitazato and N. Hirata). Kamoi (“D”) is a possible impact structure, where a relatively fresh surface was exposed. Inset figures (scale bars 10 m) are from a detailed b-band (429-nm) strip image ST\_2572086065. (b) ST\_2539451609 (v-band) after filtering. The original brightness difference between the basement brecciated rock and darker boulders is about 10%. Scale bar is 2 m. Small bright spots on dark boulders are shown by arrows.

area, suggesting it has an impact origin (Hirata *et al.*, 2009). Furthermore, Kamoi also looks relatively dark in the p-band (Fig. 8b), which suggests the surface is relatively fresh and unweathered (Ishiguro *et al.*, 2007, 2014). The difference in the average brightness (A, D, C, and E in order of brightness) observed in the surface features shown in Fig. 7a is consistent with each surface region having different SW exposure times. However, within bright zones of each inset image (A, D, E), finer ( $< 1$  m) brightness variations are recognized.

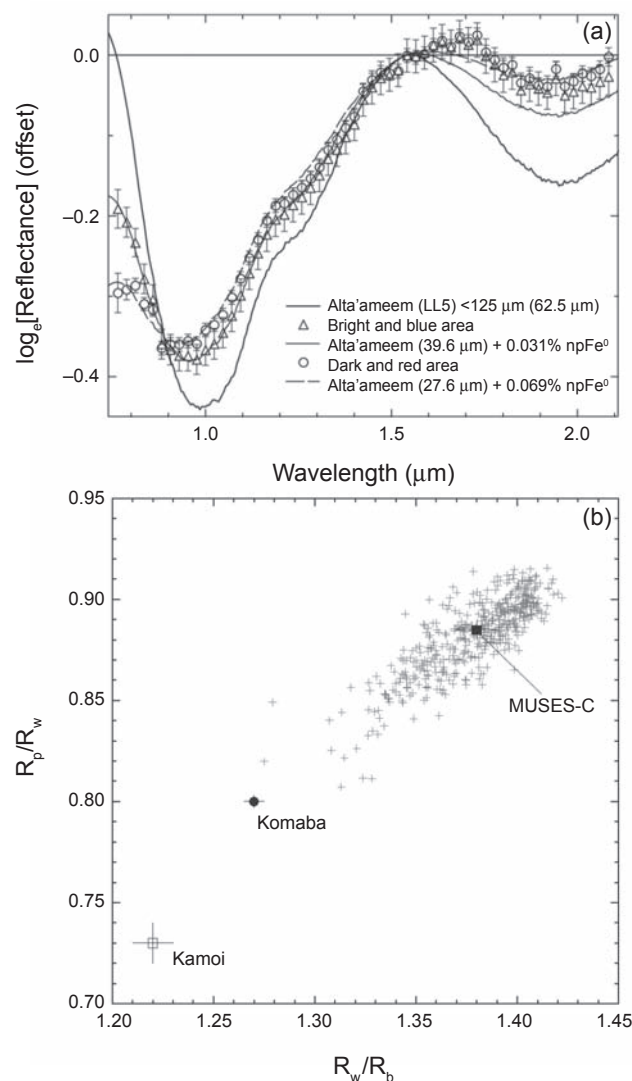


**Fig. 8.** (a) Estimation of the degree of space weathering for two areas on Itokawa. Reflectance spectra of a dark and red area (“B” in Fig. 7a) and a bright and blue area (“C” in Fig. 7a) of Ohsumi Regio are fitted with the spectrum of Alta'ameem (LL5, 125-mm sample), by optimizing the mean optical path length (MOPL) and volume percentage of npFe<sup>0</sup> particles. From Hiroi *et al.* (2006), reprinted with permission of Macmillan Publishers Ltd. (b) Correlation between  $R_p/R_w$  and  $R_b/R_w$  (courtesy of M. Ishiguro). The overall trend from the lower left to upper right can be explained by SW (Chapman, 2004). In addition to values at the Komaba crater and Hayabusa sampling site (MUSES-C Regio), the value at Kamoi is shown.

Close-up images of boulders and pebbles were obtained in the eastern hemisphere of Itokawa. Figure 7b shows the boundary area between the dark boulder-rich zone and the bedrock zone. The heterogeneous features observed in the brighter zone can be explained if the bedrock of Itokawa is breccia that was lithified on the parent body, as lithified breccias have mineralogical and petrological heterogeneity for various scales, which would affect the degree of SW. Brightness variations in the inset images (A, D, and E in Fig. 7a) can also be explained in the same manner. The two types of boulders observed on Itokawa are shown in Fig. 7b: rounded boulders with rounded edges and angular boulders with sharp edges and relatively flat surfaces (Noguchi et al., 2010). The features of the rounded boulders with undulated surfaces (10-cm-scale protrusions and patches being observed) are compatible with breccia with hardness heterogeneity. The fraction of angular rocks increases for the submeter-sized rocks. As seen in Fig. 7b, both type of boulders have weathered surfaces and may have experienced movement. It is likely that the hidden sides of boulders have experienced weathering as well. There are no significant color variations between the large rounded and angular boulders, but the smaller angular boulders do show some albedo variations. No fine (less than centimeter-sized) regolith is observed in this image of the rough terrain. Furthermore, centimeter-sized pebbles appear to have been moved out of this area into the low-lying smooth region (see the chapter by Murdoch et al. in this volume).

Distinct bright speckles are observed on some of the boulders (Miyamoto et al., 2007). In Fig. 7b, white arrows highlight the bright spots on the dark boulders. These speckles are mainly formed by high-velocity impact of small meteoroids, because 90% of bright speckles are quasicircular and the size-frequency distribution can be compared with that of craters (Takeuchi et al., 2010). The weathered surface layer is thin but appears to be resistant to alteration by rock-regolith movements.

### 3.2. Returned Itokawa Samples

**3.2.1. Laboratory analyses.** After orbiting Itokawa for two months, Hayabusa touched down onto the surface (MUSES-C Regio) for two sample collections on November 20 and 26, 2005, and then returned to the Earth on June 13, 2010. More than 2000 particles have been recovered from the returned capsule of Hayabusa. Detailed analyses of many of those particles were first described in a series of papers that appeared in *Science* in 2011 (vol. 333, issue 6046) (e.g., Nakamura et al., 2011; Noguchi et al., 2011; Tsuchiyama et al., 2011) and more recently in *Meteoritics & Planetary Science* (vol. 49, issue 2) (e.g., Noguchi et al., 2014). See also the chapter by Yoshikawa et al. in this volume for a more detailed discussion.

Analysis of mineral assemblies and the composition of Itokawa particles supports Itokawa having an LL-chondrite composition. The olivine, low-Ca pyroxene, and kamacite composition of most Itokawa particles fall within the nar-

row range that matches LL chondrites (Nakamura et al., 2011); compositional homogeneities would suggest early thermal metamorphism. The triaxial shape distribution of Itokawa particles suggests mechanical disruption as a primary source. In addition, while most Itokawa particles have angular edges compatible with their disruption origin, some have rounded edges, suggesting mechanical abrasion after particle formation (Tsuchiyama et al., 2011) (see also the chapter by Yoshikawa et al. in this volume). It should be noted that none of the textures of Itokawa particles is consistent with lunar agglutinates, caused by high-velocity meteoroid impacts.

**3.2.2. Space weathering rims and nanophase iron and iron sulfide.** Some pebbles and rocks located in the MUSES-C area have bright surfaces and may have come from the nearby bright steep area of Shirakami and Yatsugatake. It is also possible that mechanical abrasion and/or thermal fatigue may have removed some of the weathered surface. Regardless, the brightness variation in this region led to the correct hypothesis that samples taken from this region would have varying degrees of SW (Noguchi et al., 2014; Bonal et al., 2015).

The first detailed microscopic analysis of Itokawa particles found that half the particles analyzed showed surface modification (Noguchi et al., 2011). Later studies found that even the particles that appeared to be unaltered did contain very thin (~5 nm) rims (Noguchi et al., 2014). These rims lack npFe<sup>0</sup> but contain elements that were not found in the underlying bulk grain, suggesting that they were formed from vapor redeposition (Noguchi et al., 2014). The most telling indicator of surface modification for the weathered grains is the presence of an amorphous rim that contains npFe<sup>0</sup> (Noguchi et al., 2011, 2014; Matsumoto, 2014). This rim, categorized as Zone II by Noguchi et al. (2014), is relatively thick (30–60 nm), partially amorphous, and contains 2–3 nm npFe<sup>0</sup> (Fig. 9a). Given that the thickness of the rim is comparable to the penetration depth of the He solar wind ions, it seems likely that this rim was formed by solar wind irradiation.

In some of the analyzed particles, Zone II contains vesicles, which is probably due to trapping of implanted He [composite vesicular rim (Noguchi et al., 2014)]. In fact, larger vesicles were identified in 11 out of 20 Itokawa regolith particles analyzed by Matsumoto (2014). It was confirmed that a blister corresponds to a vesicle in the npFe<sup>0</sup>-bearing amorphous layer (Fig. 9b). These vesicles are heterogeneously distributed even in one particle. Sometimes they are observed in opposite surfaces of the same particle, which is strong evidence of regolith mixing. So far, there is no correlation between the vesicle distribution and surface morphologies such as the roundness of particles.

Like the unaltered particles, the outermost surface of the weathered grains contains a region distinct from the partially amorphized Zone II region. This thin amorphous (~5–15 nm) surface layer, characterized as Zone I (Fig. 9a) by Noguchi et al. (2014), contains npFe<sup>0</sup>, nanophase FeS (and MgS), and elements not present in the underlying minerals. The

presence of npFeS in asteroidal regolith is compatible with the observation of regolith breccia meteorites (*Noble et al.*, 2011). Furthermore, the difference in composition between the Zone I and II layers, which has also been confirmed in studies of other Itokawa particles (*Thompson et al.*, 2014), suggests that Zone I is formed by redeposition of impact-generated vapors or sputter deposits (*Keller and Berger*, 2014).

Based on solar flare densities, it has been estimated that the Zone II regions could have formed in less than  $10^3$  yr, while the npFe<sup>0</sup> may have formed on even shorter timescales (*Noguchi et al.*, 2014). Regolith mixing processes (discussed

in the following section) may prolong the timescale of optical maturation on smooth regions of Itokawa. Another estimate of the cosmic-ray (galactic and solar) exposure age using <sup>21</sup>Ne was obtained for an olivine-rich grain (RA-QD02-0035),  $1.5 \pm 0.4$  Ma (*Meier et al.*, 2014), which is compatible with the upper limit of 8 Ma estimated by *Nagao et al.* (2011). The timescale for the formation of the thin surface redeposition region (Zone I) must be significantly shorter than that of Zone II, as Zone I deposits are found on both the altered partially amorphous grains and the pristine crystalline surfaces. However, as there is much less npFe<sup>0</sup> found in Zone I compared with Zone II, this thin region should have little contribution to the optical properties of the weathered surface.

Finally, analysis of Itokawa samples suggests that the composition of the grain may affect the degree of weathering that occurs. This hypothesis is not new, as previous laser irradiation studies on pyroxene and olivine also suggested this (*Sasaki et al.*, 2002; *Brunetto et al.*, 2006b). However, the pyroxene grains found in the Itokawa samples appeared to be more weathered than the olivine (T. Matsumoto, personal communication), which is in contrast to previous laser irradiation studies. This apparent discrepancy is interesting and may suggest that laser irradiation produces different compositional effects than found on Itokawa, and that young asteroids are likely dominated by solar wind processing. However, more laboratory studies that focus on how the SW rates of pyroxenes and olivines induced by ion irradiation compare are needed to determine whether this is a viable explanation. In addition, it is possible that compositional differences may also explain why plagioclase grains found in Itokawa particles lack the vesicles that were easily identified on adjacent pyroxene particles (T. Matsumoto, personal communication). More experiments are also necessary to elucidate the role of FeS in SW (see, e.g., *Okazaki et al.*, 2014).

### 3.2.3. Spectral models: Lessons learned from Itokawa.

Several experimental studies (see section 2) have shown that while SW alters the reflectance spectra of minerals, the changes mainly involve alteration of the spectral continuum, as the absorption band positions and relative areas of VIS-NIR silicate absorptions are not significantly changed (see, e.g., *Gaffey*, 2010, and references therein). Thus, by computing the ratio between laboratory spectra of weathered and unweathered materials, the silicate absorption bands can essentially be removed, leaving only the continuum curve (e.g., *Brunetto et al.*, 2006a). This curve can be parameterized by a coefficient and related to the SW exposure time. This approach has also been used to remove SW effects from S-type asteroid reflectance spectra, so that the surface composition could be extracted in a more straightforward manner (*Popescu et al.*, 2012).

Modeling described in *Hapke* (2001) and *Ueda et al.* (2002) clearly shows that optical alteration depends on wavelength, thus changing the 1- and 2-μm bands in different ways. More precisely, the “weathered” spectral continuum is a nonlinear function of the optical constants of the silicate host matrix and the inclusions produced by the energetic alteration (*Hapke*, 2001; *Hiroi and Sasaki*, 2001;

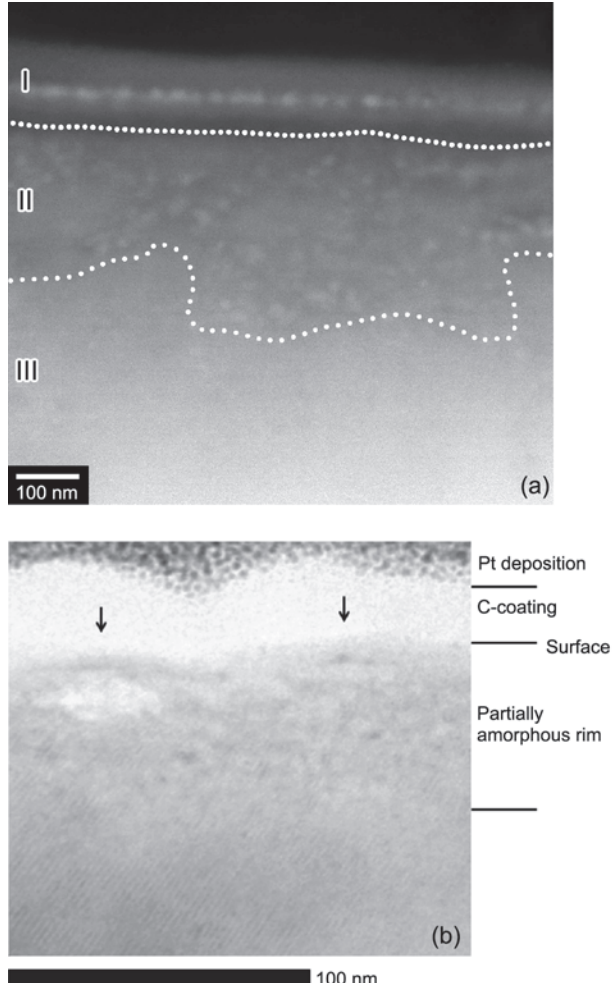


**Fig. 9.** (a) High-angle-annular-dark-field (HAADF) STEM image of the surface zone of a low-Ca pyroxene in particle RA-QD02-0042. The partially amorphous zone (I) is a vapor-deposited layer containing npFe, npFeS, and npMgS (appearing as brighter spots), depleted in Si. Zone (II) is an amorphous layer containing abundant npFe. Zone (III) retains the crystal characteristics. Figure courtesy of T. Noguchi. (b) A TEM image of a blistered surface on low-Ca pyroxene particle (QD-RB-0043) shows the npFe<sup>0</sup>-bearing rim layer associated with voids (arrows). The FIB-TEM sample was prepared to allow observation of the cross section and the structure underneath blisters. Figure courtesy of T. Matsumoto.

*Hiroi et al.*, 2006; *Brunetto et al.*, 2006b, 2007b; *Noble et al.*, 2007). Considering the inclusions to be metallic iron particles (smaller than the wavelength) in vapor-deposited coatings on soil particle surfaces and inside agglutinates, *Hapke* (2001) used the Maxwell-Garnett effective medium theory to calculate the absorption coefficient of a silicate host medium containing inclusions of small metallic iron spheres. This model can thus be used to estimate the surface abundance of nanophase iron.

*Hiroi et al.* (2006) used Hapke's SW model to estimate the abundance of npFe<sup>0</sup> for different regions on Itokawa, confirming that the asteroid is subject to SW. Now that Itokawa's samples can be studied directly in the laboratory, future studies should be able to improve these estimates as well as increase the general understanding of how SW alters asteroids. This improvement has already been realized with the recent discovery of the multilayer structure on Itokawa particles that appears to be associated with SW (*Noguchi et al.*, 2014). Furthermore, *Bonal et al.* (2015) explored the possibility of performing VIS-NIR diffuse reflectance studies on isolated Itokawa particles, which could be compared directly with remote sensing spectral data. Finally, in addition to direct laboratory measurements, improvements to the existing Hapke model, such as that developed by *Nimura et al.* (2008), and additions to take into account other possible alterations caused by SW, such as textural changes (*Moroz et al.*, 2014), will also be critical for analyzing SW effects in the near future.

#### 4. ESTIMATES FOR SPACE WEATHERING RATES ON ASTEROIDS

One of the main advantages of laboratory studies is that they can establish what spectral trends are a result of SW. These results can be used to determine whether SW could cause the variations observed between terrestrial analogs and asteroids or simply the variations between asteroids of similar composition. The spectral changes observed in the laboratory have also been used to estimate the timescale for which these spectral alterations may occur in the space environment. For example, timescales in the inner solar system have been estimated previously by comparing laboratory spectra of irradiated silicates and meteorites with remotely acquired spectra of silicate-rich asteroids, and scaling the fluences used in the laboratory to the fluxes of the solar wind ions. These estimates suggest that the effects caused by ion bombardment will saturate between 10<sup>4</sup> and 10<sup>6</sup> yr (*Hapke*, 2001; *Strazzulla et al.*, 2005; *Loeffler et al.*, 2009), while for micrometeorite bombardment, estimates are on the order of 10<sup>8</sup> yr (*Sasaki et al.*, 2001; *Brunetto et al.*, 2006b). In some cases [e.g., asteroid (832) Karin (*Brunetto et al.*, 2006a)], the irradiation timescales are in agreement with the dynamical timescales [in the case of (832) Karin, this is the age of the catastrophic impact that rejuvenated the surface about 5.8 × 10<sup>6</sup> yr ago].

However, even though the SW induced by ions is a relatively efficient process, there are many asteroids that are

not fully weathered, even though they are likely older than the above estimated timescale. This apparent discrepancy likely indicates that some rejuvenating process is able to partially resurface the asteroid, which effectively lowers the SW rate. As the average collisional lifetime of asteroids larger than several kilometers is much longer than these estimated weathering timescales, other processes such as small (nondestructive) impacts (e.g., *Shestopalov et al.*, 2013) or planetary encounters (section 4.2) are likely responsible for rejuvenating the surfaces. In the following sections, we will discuss another approach to estimate SW rates (section 4.1), as well as a few other processes that may be important to consider when estimating SW rates for asteroid surfaces.

Finally, we point out that nearly all the laboratory data used to determine SW rates focused on the reflectance spectra taken in the VIS-NIR regions. However, since the thickness probed by reflected solar photons is a function of wavelength, it is desirable to have an estimate of SW effects in another wavelength region. In this respect, it is interesting to observe that SW produces a blueing of the spectrum at near-UV wavelengths, in contrast to the reddening in the VIS-NIR. Such UV blueing occurs with a lower amount of weathering than the VIS-NIR reddening (*Hendrix and Vilas*, 2006). This implies that the UV range is highly promising to better constrain the SW timescale in future studies.

#### 4.1. Space Weathering Rates Inferred from Studies of Dynamical Families

An asteroid family is a group of fragments (the so-called family "members") produced by collisional disruption of a larger parent body. Several dozens of asteroid families have been identified in the main belt (see the chapter by Nesvorný et al. in this volume; physical properties of asteroid families are discussed by Masiero et al. in this volume). The disruption itself is a violent process that should erase the preexisting surface of a parent body (weathered or not) and expose new material, mainly from the parent body interior, on the newly created surfaces. Initially, this material should be predominantly unweathered, but it will be altered by SW processes over subsequent time.

Ideally, the asteroid families could therefore be used to empirically measure the rate of SW. The basic method consists of characterizing the surface properties of members of a single family, and then correlating them with the family age ( $t_{age}$ ), defined as the time elapsed since the family formation, and across a dataset of at least several families with different  $t_{age}$ . In practice, it is challenging to distinguish between the effects of age and composition, which is obviously significant, because the composition influences the optical properties of a surface, and because SW effects depend on composition. Also, the empirically measured rates will include the counterbalancing effects of the regolith gardening by impacts (e.g., *Willman et al.*, 2010).

The first prerequisite for this method is to have an independent estimate of  $t_{age}$ . In the past decade, several different approaches have been used: a direct integration of orbits

back in time (*Nesvorný et al.*, 2002), modeling the Yarkovsky effect on the dynamical structure of a family (*Vokrouhlický et al.*, 2006), and modeling the size distribution of small family members as it evolves by collisions (*Marzari et al.*, 1999). The dynamical methods generate credible results for the youngest families ( $t_{\text{age}} \leq 10$  Ma), while their precision degrades with increasing  $t_{\text{age}}$ , mainly because various processes acting on the longest timescales are poorly understood. The estimates for  $t_{\text{age}} > 1$  Ga are only tentative at best.

To properly characterize the average surface properties of each family and their uncertainties, several members of each family need to be observed. This first became possible with a large dataset of asteroid colors obtained by the Sloan Digital Sky Survey (SDSS) (*Ivezić et al.*, 2001). More recently, the spectroscopic surveys of young and old families generated enough data that the spectroscopic properties of families can be reasonably well established (e.g., slope, depth of the absorption bands). This is an important improvement because the SDSS colors are known to be somewhat unreliable for a precise physical characterization in specific cases. Furthermore, we now also have a large dataset of the asteroid albedo measurements from the WISE telescope (*Masiero et al.*, 2013).

The interpretation of the results obtained by correlating colors/spectroscopy with  $t_{\text{age}}$  has been subject to controversy. The initial results indicated that the characteristic timescale of SW was long (*Jedicke et al.*, 2004; *Nesvorný et al.*, 2005; see also *Willman et al.*, 2008, 2010). Specifically, *Nesvorný et al.* (2005) found that the spectral slope (at 0.35–0.9 μm) of aging surfaces of the S-type asteroids increases with time  $t$  as  $0.1 \mu\text{m}^{-1} \times \log_{10}(t/1 \text{ Ma})$ . This fit is valid only for  $2.5 \leq t \leq 3000$  Ma, because no families younger than  $\approx 2.5$  Ma were known at the time.

Correcting the spectral slopes for differential effects presumably caused by compositional differences, *Vernazza et al.* (2009a) found that the slope-time profile is essentially flat for  $t > 1$  Ma (see Fig. 10). From Fig. 3 of *Vernazza et al.*, we estimate the SW rate of  $\sim 0.3 \mu\text{m}^{-1} \times \log_{10}(t/1 \text{ Ma})$  for  $t > 1$  Ma, which is about 3× faster than the previous estimate. Comparing the spectral slope at  $t \sim 1$  Ma with that of the OC meteorites, whose spectral properties were measured in the laboratory, *Vernazza et al.* pointed out that asteroid surfaces should evolve from unweathered (as represented by OCs and Q-type NEAs; see section 4.2) to nearly completely weathered in  $\sim 1$  m.y.

However, this result is largely dependent on the differential correction that *Vernazza et al.* applied to the spectral slopes. With this correction, the Karin family, with  $t_{\text{age}} = 5.8 \pm 0.2$  Ma, appears to be  $\sim 80\%$  space-weathered but without the correction, it appears only  $\sim 40\%$  space-weathered. To apply the differential correction, *Vernazza et al.* (2009a) opted to use the Flora family as a reference composition, but showed earlier (*Vernazza et al.*, 2008) that the Flora family is incompatible in composition with the L- and H-chondrites, which together represent  $\approx 80\%$  of meteorite falls. If, instead, the Gefion family, which is thought to be the source of L-chondrites (*Nesvorný et al.*, 2009), were

chosen for a reference composition, the differential correction would have been less dramatic.

Regardless, these estimates using asteroid families suggest that the reddening trend of the visible spectral slope of an average OC-like surface in the main belt probably proceeds to reach a 50% completion in  $\sim 1$ –10 m.y., and that the following stage to reach a fully weathered surface lasts much longer. The transition between the first and second stages can be sharp or more gradual. More work will be needed to understand whether the transition really represents a switch from faster, solar-wind-induced reddening (*Vernazza et al.*, 2009a), to slower reddening at later times where other effects become important as well [e.g., regolith gardening (*Willman et al.*, 2010)]. In this respect, young families are very important because they should show the most obvious SW effects. Interestingly, some young families (Karin, Datura) seem to indicate that the  $\sim 1\text{-}\mu\text{m}$  band suppression could proceed faster than the slope reddening (*Nesvorný et al.*, 2006; *Takato*, 2008). With that much said, it has to be pointed out that the existing observational record for young families is mixed (e.g., *Mothé-Diniz and Nesvorný*, 2008) and more observations will be needed to gain some confidence in these results and separate them from other effects (i.e., grain size, etc.). In the future, additional input shall also be obtained from spectroscopic observations of the asteroid pairs (e.g., *Polishook et al.*, 2014).

#### 4.2. Unweathered Small Near-Earth Asteroids and Effects of Planetary Encounters

While only a few unweathered OC-like spectra were detected in the main belt (e.g., *Mothé-Diniz and Nesvorný*, 2008; *Polishook et al.*, 2014), they are relatively common among the small NEAs (*Binzel et al.*, 1996, 2004). While this may simply be a consequence of the difficulty of obtaining a reliable reflectance spectrum for a small faint main-belt asteroid, this may also be attributed to some special process affecting the NEAs. Using the standard asteroid taxonomy, where the unweathered OC-like spectrum is denoted by the letter Q, *Binzel et al.* (2004) showed that the number ratio of Q- to S-type NEAs is  $\sim 20\%$  for  $D \sim 1$  km. The fraction of Q-types drops with increasing diameter, and there is no known Q-type among about two dozen NEAs with  $D > 5$  km (see Fig. 5).

Previously, the appearance of Q-types among the small NEAs has been attributed to short collisional lifetimes of small asteroids, but this appears to be unlikely because the collisional lifetimes of kilometer-sized asteroids are presumably  $> 10$  m.y. (*Bottke et al.*, 2005), while the SW timescales are probably shorter. It appears, instead, that this issue can be related to the regolith retention, because small asteroids have weaker gravity and weathered regolith layers can be more efficiently stripped from them by small impacts. In addition, small asteroids undergo the so-called YORP cycles (see the chapter by Vokrouhlický et al. in this volume), which can remove or redistribute surface regolith when the asteroid is spun up beyond the critical spin rate, and the centrifugal

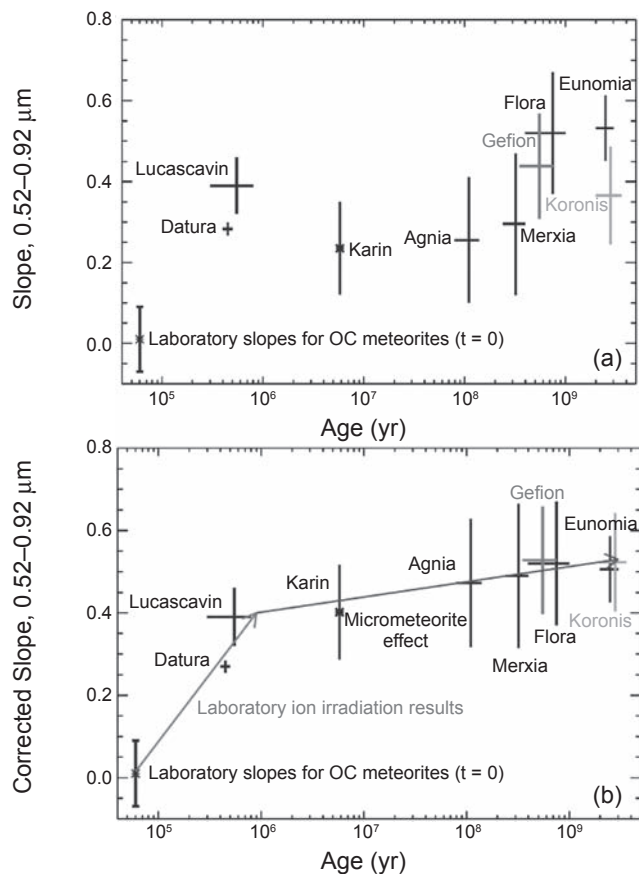


**Fig. 10.** The mean spectral slopes for both OC meteorites and S-type asteroid families vs. the age of the family. Laboratory spectra for OCs form the baseline assumption for fresh ( $t = 0$  yr) “unweathered” asteroid surfaces. The slope domain for OCs is placed at  $t = 4.6 \times 10^4$  yr. (a) Uncorrected data. (b) Data corrected for different composition. As explained by Vernazza et al. (2009a), composition can vary the outcome of a SW slope value by almost a factor of 2. Thus a comparison between weathered spectral slope and surface age requires a correction for composition. To perform this correction, Vernazza et al. (2009a) chose the composition of the Flora family as a reference. To estimate the slope deficit or excess for each family vs. the slope of the Flora family, they fitted the slopes of the S-type sample (0.52–0.92 μm range) by a straight line, providing the mean slope for a given composition. To correct the slope distribution for composition, they calculated the slope deficit or excess for all families and shifted (up or down) their mean slope values by the calculated amount. The two arrows in (b) stress two different regimes. First, the slope of an unweathered surface (at exposure time  $t = 0$ ) starts in the middle of the slope domain of OCs and reaches the 0.4 slope value of the Lucascavin family in less than 0.5 m.y. This represents a slope variation of ~0.4 in just ~0.5 m.y., which is consistent with the very rapid reddening trend observed during laboratory ion irradiation experiments. Such a rapid trend appears to be required within the first  $\sim 10^6$  yr for newly formed asteroid families. Second, the slope evolution over the interval  $t = 0.5$ –5 Ma to  $t = 2500$  Ma appears more gradual (gray line). Gradual weathering processes such as micrometeorite impacts may account for the continuing slope increase throughout the following  $2 \times 10^9$  yr. From Vernazza et al. (2009a), reprinted with permission of Macmillan Publishers Ltd.

force on the surface exceeds gravity (see the chapter by Walsh and Jacobson in this volume).

Recently, Binzel et al. (2010) found evidence that planetary encounters of NEAs with the Earth can refresh surfaces. The evidence is based on the orbital distribution of Q-type NEAs, which shows, according to Binzel et al. (2010), a sharp transition beyond the Earth-crossing limit, where Q-types cease to be found. Adopting the short, 0.5-m.y. SW timescale from Vernazza et al. (2009a), they estimated that for the planetary encounters to be significant, the optical properties of an average NEA’s surface may be refreshed for an encounter distance of up to 16 planetary radii ( $R_{pl}$ ). DeMeo et al. (2014), using a larger database of spectroscopic observations, found that Q-type NEAs also exist on orbits beyond the Earth-crossing limit.

The effect of encounters of NEAs with all terrestrial planets has been considered in Nesvorný et al. (2010), who used the SW timescale,  $\tau_{sw}$ , and the encounter radius below which the refreshing effect occurs,  $r^*$ , as free parameters (see Fig. 11). Here  $\tau_{sw}$  is defined as the timescale to bring an initially unweathered, average Q-type spectrum to appear as average S. They found that  $\tau_{sw} \sim 10^6$  yr (at 1 AU) and  $r^* \sim 5 R_{pl}$  best fit the data. Values  $\tau_{sw} < 10^5$  yr would require that  $r^* > 20 R_{pl}$ , which seems implausible because

these very distant encounters should be irrelevant. Also, the fraction of Q-type NEAs would be much larger than observed if  $\tau_{sw} > 10^7$  yr. While these results are broadly consistent with those discussed in section 4.1, they need to be validated by direct detection of the hypothesized effects. Some very close encounters of NEAs to Earth, such the encounter of 99942 Apophis at  $\approx 6 R_{pl}$  in 2029, may offer such an opportunity, i.e., to have an independent estimate of  $r^*$ .

Finally, a recent experimental work has suggested that thermal fatigue fragmentation (and the consequent production of regolith) may be an important process for the rejuvenation of the surfaces of NEAs (Delbó et al., 2014). This result deserves further investigation.

#### 4.3. Mass Accretion and Loss by Micrometeorite Impacts and Solar Wind Ion Implantation

Resurfacing agents can excavate “fresh layers” and/or add exogenous material. The exogenous material could have been processed in different environments, such as in the presolar nebula, in the solar nebula during the early phases of the solar system formation, or after prolonged permanence in the outer solar system, e.g., comets. In fact, objects in the solar system, including asteroids, receive a continuous flux

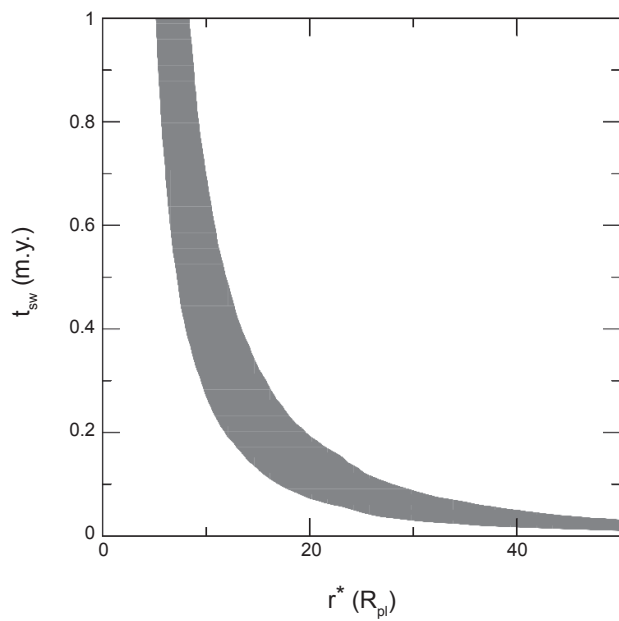


**Fig. 11.** The observed fraction of Q-type NEAs can be used to constrain parameters  $r^*$  and  $t_{sw}$  discussed in the main text (Nesvorný *et al.*, 2010). The best-fit solutions are located along a hyperbola-shaped region in  $(r^*, t_{sw})$  space. This relationship can be qualitatively explained as follows: If the distance from the planet  $r^*$  necessary to rejuvenate the asteroid is small, then the resurfacing efficiency of planetary encounters must be small as well, which implies that the weathering timescale  $t_{sw}$  must be higher, in order to account for the observed fraction of Q-type NEAs. Since planetary tides during encounters with  $r > r^* = 20 R_{pl}$  should be negligible, this implies that  $t_{sw} > 0.1$  m.y. This result holds unless Earth's magnetospheric effects are important at  $r > 35 R_{\oplus}$ , which is unlikely. From Nesvorný *et al.* (2010), reprinted with permission of Elsevier.

of mass from the interplanetary medium. There are two main sources of mass accretion: (1) dust and meteoroids and (2) solar energetic particles (solar wind and energetic events).

The flux of dust is not well known. Values consistent with that estimated for the Moon, Mars, and outer objects would be on the order of  $2 \times 10^{-17}$ – $2 \times 10^{-16}$  g cm $^{-2}$  s $^{-1}$  (see Table 3 in Bennett *et al.*, 2013). Estimates for the micrometeorite impact flux on asteroidal surfaces can be obtained from dynamical models of the zodiacal cloud (ZC). These models calibrate the populations of small particles in interplanetary space based on infrared observations of the ZC, performed by space telescopes such as the Infrared Astronomical Satellite (IRAS) and Cosmic Background Explorer (COBE), on the measurements of the impact detectors, such as the Long Duration Exposure Facility (LDEF), and on meteor observations from the ground. The main result obtained from these studies is that the ZC has a predominantly cometary origin, with perhaps as much as 90% of grains in space sampling disrupted Jupiter-family comets (Nesvorný *et al.*, 2010).

The estimated mass influx of micrometeoroids on (1) Ceres, which has a rather typical orbit in the middle of the main belt,

is  $\sim 3.5$  tons/yr. This is only a small fraction of the terrestrial impact flux [ $\sim 30,000$  tons/yr from LDEF (Love and Brownlee, 1995)], which is mainly due to a relatively small collisional cross-section of Ceres. Using these fluxes, we estimate that a square meter in the asteroid belt should be exposed to an average mass flux of  $\sim 5$  g m.y. $^{-1}$ , mainly in  $\sim 100$ - $\mu$ m cometary particles. The typical impact speeds inferred from the model are  $\sim 10$  km s $^{-1}$  (Nesvorný *et al.*, 2010).

However, this material is itself a weathering agent that influences the properties of the local regolith and the reflectance spectra of the regions where it is deposited. A recent example comes from the localized dark materials found on Vesta's surface that have been attributed to the infall of carbonaceous volatile-rich material (McCord *et al.*, 2012; Pieters *et al.*, 2012). Such a material would be similar to that present in interplanetary dust particles. These materials can be lost from comets and weathered in the interplanetary medium as simulated in the laboratory (e.g., Baratta *et al.*, 2004) and then are delivered to the surfaces of different objects, including Earth (e.g., Dartois *et al.*, 2013).

The amount of material due to energetic solar particles that impinge the surface of an airless body scales with the inverse of the squared distance from the Sun. At 1 AU the total flux of solar protons (that obviously dominate) is about  $4\text{--}6 \times 10^8$  cm $^{-2}$  s $^{-1}$  depending on the phase of the solar cycle. This corresponds to a mass infall (at 2.5 AU) of  $1\text{--}1.6 \times 10^{-16}$  g cm $^{-2}$  s $^{-1}$  ( $\sim 40$  g m $^{-2}$  m.y. $^{-1}$ ) that is competitive with the mass delivered by dust. In addition, the energy range (keV-MeV) is such that solar ions penetrate the surface and then release their energy by elastic and inelastic interactions, and most of them (those that are not backscattered) remain implanted in the object at a depth that depends on the energy and mass of the ion. As an example, the flux of C ions (average energy of about 12 keV) that hits an asteroid at 2.5 AU is on the order of  $9 \times 10^3$  cm $^{-2}$  s $^{-1}$ . Thus the time necessary to accumulate a fluence of  $10^{17}$  carbon ions cm $^{-2}$  is on the order of  $3.5 \times 10^5$  yr. It has been demonstrated that after that fluence, the wide range of colors of most of the asteroids can be reproduced by the C-ion-induced weathering of HED meteorites (Fulvio *et al.*, 2012).

Finally, a last point to mention is the possibility of surface mass loss induced by ion sputtering and meteorite bombardment. This subject can be linked to the search for exospheres around asteroids [e.g., the case of asteroid Eros (Loeffler *et al.*, 2008b)]. More experimental and observational studies will be necessary in the future. Information about surface ion sputtering can be found in Bennett *et al.* (2013) and references therein.

## 5. SUMMARY

In the past decade, new ion irradiation and laser ablation experiments on meteorites and asteroid surface analogs, together with unambiguous proofs of SW effects on particles from asteroid Itokawa, have provided a fundamental contribution to the spectral interpretation of asteroid observations, to establish a solid asteroids–meteorites link, and

to understand the energetic processes affecting the surfaces of minor bodies. Laboratory analyses of Itokawa samples in particular have revealed for the first time direct evidence and a multiplicity of new details on asteroidal SW. Returned samples contained silicate particles compatible with an LL origin, half of which revealed the presence of two types of SW rims on their surfaces: a vapor-deposited rim (~10 nm) containing nanophase Fe, FeS, and MgS particles, and a 30–60-nm-thick radiation-damaged amorphous rim containing nanophase Fe. The fundamental role played by solar wind irradiation has been established. A general scheme for asteroid optical maturation is thus emerging.

From the observational point of view, slope trends from large surveys and in particular of young asteroid families have confirmed that solar wind is the main source of rapid ( $10^4$ – $10^6$  yr) weathering, and that a number of rejuvenating processes efficiently counterbalance the fast weathering timescales. This implies that the spectral properties of asteroids depend on the relative efficiencies of resurfacing and SW agents.

The diversity and mechanisms of asteroid SW need to be investigated further. For many asteroid classes we still do not know precisely how SW acts and what effects are produced, which hampers efforts to draw connections between specific meteorites and asteroid types. In particular, VIS-NIR slope variations are still controversial for dark asteroids and contradictory trends have been observed, making future experiments that simulate micrometeorite bombardment and irradiation by solar wind and cosmic ray ions critical. In addition, establishing a solid SW trend on dark objects can provide valuable support to the selection of sampling/landing sites for future sample return missions [e.g., the Origins Spectral Interpretation Resource Identification and Security-Regolith Explorer (OSIRIS-REx) (Campins et al., 2010a) or Hayabusa 2 (Takagi et al., 2011)], and will also help interpret mission results. Inspired by the extraordinary results obtained by Hayabusa, we anticipate that these new sample return missions will enhance our knowledge about the microphysical and chemical processes affecting weathered extraterrestrial materials, and help us to solve some of the open questions about SW, similar to what has previously been achieved for the Moon and S-type asteroids.

New important information on asteroid SW will be available soon from the observations of instruments onboard Gaia, a space mission of the European Space Agency (ESA) that will survey the entire sky. In particular, Gaia is expected to observe about 400,000 asteroids, for which high-precision astrometry and photometry will be obtained (Cellino and Dell’Oro, 2012). It has been estimated that spectral characterization will be obtained for at least 100,000 asteroids from the low-resolution spectra (0.35–0.95  $\mu\text{m}$ ) obtained by Gaia (Delbó et al., 2012). These observations will provide the possibility of a new taxonomy [present taxonomy is based on the observation of a few hundred objects in the NIR (DeMeo et al., 2009) or a few 10,000 in the visible (DeMeo and Carry, 2013)], and a larger and statistically stronger view of asteroid SW.

**Acknowledgments.** We are grateful to B. E. Clark, F. E. DeMeo, T. Hiroi, and P. Michel for useful comments and suggestions. R.B. has been supported by the French national program “Programme National de Planologie” (PNP), INGMAR project.

## REFERENCES

- Baratta G. A., Mennella V., Brucato J. R., Colangeli L., Leto G., Palumbo M. E., and Strazzulla G. (2004) Raman spectroscopy of ion-irradiated interplanetary carbon dust analogues. *J. Raman Spectrosc.*, **35**, 487–496.
- Basilevsky A. T., Abdralkhimov A. M., and Dorofeeva V. A. (2012) Water and other volatiles on the Moon: A review. *Solar System Res.*, **46**, 89–107.
- Beck P., Pommerol A., Thomas N., Schmitt B., Moynier F., and Barrat J.-A. (2012) Photometry of meteorites. *Icarus*, **218**, 364–377.
- Bennett C. J., Pirim C., and Orlando T. M. (2013) Space-weathering of solar system bodies: A laboratory perspective. *Chem. Rev.*, **113**, 9086–9150.
- Binzel R. P., Bus S. J., Burbine T. H., and Sunshine J. M. (1996) Spectral properties of near-Earth asteroids: Evidence for sources of ordinary chondrite meteorites. *Science*, **273**, 946–948.
- Binzel R. P., Rivkin A. S., Bus S. J., Sunshine J. M., and Burbine T. H. (2001) MUSES-C target asteroid (25143) 1998 SF36: A reddened ordinary chondrite. *Meteoritics & Planet. Sci.*, **36**, 1167–1172.
- Binzel R. P., Rivkin A. S., Stuart J. S., Harris A. W., Bus S. J., and Burbine T. H. (2004) Observed spectral properties of near-Earth objects: Results for population distribution, source regions, and space weathering processes. *Icarus*, **170**, 259–294.
- Binzel R. P., Morbidelli A., Merouane S., DeMeo F. E., Birlan M., Vernazza P., Thomas C. A., Rivkin A. S., Bus S. J., and Tokunaga A. T. (2010) Earth encounters as the origin of fresh surfaces on near-Earth asteroids. *Nature*, **463**, 331–334.
- Bonal L., Brunetto R., Beck P., Dartois E., Dionnet Z., Djouadi Z., Duprat J., Fri E., Kakazu Y., Oudayer P., Quirico E., and Engrand C. (2015) Visible-IR and Raman micro-spectroscopic investigation of three Itokawa particles collected by Hayabusa: Mineralogy and degree of space weathering based on non-destructive analyses. *Meteoritics & Planet Sci.*, in press.
- Bottke W. F., Durda D. D., Nesvorný D., Jedicke R., Morbidelli A., Vokrouhlický D., and Levison H. F. (2005) Linking the collisional history of the main asteroid belt to its dynamical excitation and depletion. *Icarus*, **179**, 63–94.
- Brucato J. R., Strazzulla G., Baratta G., and Colangeli L. (2004) Forsterite amorphisation by ion irradiation: Monitoring by infrared spectroscopy. *Astron. Astrophys.*, **413**, 395–401.
- Brunetto R. and Strazzulla G. (2005) Elastic collisions in ion irradiation experiments: A mechanism for space weathering of silicates. *Icarus*, **179**, 265–273.
- Brunetto R., Vernazza P., Marchi S., Birlan M., Fulchignoni M., Orofino V., and Strazzulla G. (2006a) Modeling asteroid surfaces from observations and irradiation experiments: The case of 832 Karin. *Icarus*, **184**, 327–337.
- Brunetto R., Romano F., Blanco A., Fonti S., Martino M., Orofino V., and Verriente C. (2006b) Space weathering of silicates simulated by nanosecond pulse UV excimer laser. *Icarus*, **180**, 546–554.
- Brunetto R., Barucci M. A., Dotto E., and Strazzulla G. (2006c) Ion irradiation of frozen methanol, methane, and benzene: Linking to the colors of Centaurs and trans-neptunian objects. *Astrophys. J.*, **644**, 646–650.
- Brunetto R., de León J., and Licandro J. (2007a) Testing space weathering models on A-type asteroid (1951) Lick. *Astron. Astrophys.*, **472**, 653–656.
- Brunetto R., Roush T. L., Marra A. C., and Orofino V. (2007b) Optical characterization of laser ablated silicates. *Icarus*, **191**, 381–393.
- Brunetto R., Pino T., Dartois E., Cao A.-T., d’Hendecourt L., Strazzulla G., and Brichignac Ph. (2009) Comparison of the Raman spectra of ion irradiated soot and collected extraterrestrial carbon. *Icarus*, **200**, 323–337.
- Brunetto R. and 15 colleagues (2014) Ion irradiation of Allende meteorite probed by visible, IR, and Raman spectroscopies. *Icarus*, **237**, 278–292.
- Burke D. J., Dukes C. A., Kim J.-H., Shi J., Fam M., and Baragiola R. A. (2011) Solar wind contribution to surficial lunar water: Laboratory investigations. *Icarus*, **211**, 1082–1088.

- Bus S. J. and Binzel R. P. (2002) Phase II of the Small Main-Belt Asteroid Spectroscopic Survey: The observations. *Icarus*, 158, 106–145.
- Campins H., Morbidelli A., Tsiganis K., de León J., Licandro J., and Lauretta D. (2010a) The origin of asteroid 101955 (1999 RQ36). *Astrophys. J. Lett.*, 721, L53–L57.
- Campins H., Hargrove K., Pinilla-Alonso N., Howell E. S., Kelley M. S., Licandro J., Mothé-Diniz T., Fernández Y., and Ziffer J. (2010b) Water ice and organics on the surface of the asteroid 24 Themis. *Nature*, 464, 1320–1321.
- Carrez P., Demyk K., Cordier P., Gengembre L., Grimblot J., D'Hendecourt L., Jones A. P., and Leroux H. (2002) Low-energy helium ion irradiation-induced amorphization and chemical changes in olivine: Insights for silicate dust evolution in the interstellar medium. *Meteoritics & Planet. Sci.*, 37, 1599–1614.
- Cellino A. and Dell'Oro A. (2012) The derivation of asteroid physical properties from Gaia observations. *Planet. Space Sci.*, 73, 52–55.
- Chapman C. R. (1979) The asteroids: Nature, interrelations, origin, and evolution. In *Asteroids* (T. Gehrels, ed.), pp. 25–60. Univ. of Arizona, Tucson.
- Chapman C. R. (1996) S-type asteroids, ordinary chondrites, and space weathering: The evidence from Galileo's fly-bys of Gaspra and Ida. *Meteoritics & Planet. Sci.*, 31, 699–725.
- Chapman C. R. (2004) Space weathering of asteroid surfaces. *Annu. Rev. Earth Planet. Sci.*, 32, 539–567.
- Cintala M. J. and Hörz F. (2008) Experimental impacts into chondritic targets, Part I: Disruption of an L6 chondrite by multiple impacts. *Meteoritics & Planet. Sci.*, 43, 771–803.
- Clark B. E., Hapke B., Pieters C., and Britt D. (2002) Asteroid space weathering and regolith evolution. In *Asteroids III* (W. F. Bottke Jr. et al., eds.), pp. 585–599. Univ. of Arizona, Tucson.
- Cruikshank D. P. and 14 colleagues (1998) The composition of Centaur 5145 Pholus. *Icarus*, 135, 389–407.
- Dalle Ore C. M. and 19 colleagues (2011) Organic materials in planetary and protoplanetary systems: Nature, or nurture? *Astron. Astrophys.*, 533, A98.
- Dartois E. and 16 colleagues (2013) Ultra-carbonaceous Antarctic micrometeorites, probing the solar system beyond the nitrogen snow-line. *Icarus*, 224, 243–252.
- Davoisne C. et al. (2008) Chemical and morphological evolution of a silicate surface under low-energy ion irradiation. *Astron. Astrophys.*, 482, 541–548.
- Delbò M., Gayon-Markt J., Busso G., Brown A., Galluccio L., Ordenovic C., Bendjoya P., and Tanga P. (2012) Asteroid spectroscopy with Gaia. *Planet. Space Sci.*, 73, 86–94.
- Delbò M., Libourel G., Wilkerson J., Murdoch N., Michel P., Ramesh K. T., Ganino C., Verati C., and Marchi S. (2014) Thermal fatigue as the origin of regolith on small asteroids. *Nature*, 508, 233–236.
- DeMeo F. E. and Carry B. (2013) The taxonomic distribution of asteroids from multi-filter all-sky photometric surveys. *Icarus*, 226, 723–741.
- DeMeo F. E., Binzel R. P., Slivan S. M., and Bus S. J. (2009) An extension of the Bus asteroid taxonomy into the near-infrared. *Icarus*, 202, 160–180.
- DeMeo F. E., Binzel R. P., and Lockhart M. (2014) Mars encounters cause fresh surfaces on some near-Earth asteroids. *Icarus*, 227, 112–122.
- Demyk K. et al. (2004) IR spectroscopic study of olivine, enstatite and diopside irradiated with low energy H<sup>+</sup> and He<sup>+</sup> ions. *Astron. Astrophys.*, 420, 233–243.
- Djouadi Z., Robert F., Le Sergeant d'Hendecourt L., Mostefaoui S., Leroux H., Jones A. P., and Borg J. (2011) Hydroxyl radical production and storage in analogues of amorphous interstellar silicates: A possible “wet” accretion phase for inner telluric planets. *Astron. Astrophys.*, 531, A96.
- Dukes C. A., Baragiola R. A., and McFadden L. A. (1999) Surface modification of olivine by H<sup>+</sup> and He<sup>+</sup> bombardment. *J. Geophys. Res.*, 104, 1865–1872.
- Fu X., Zou Y., Zheng Y., and Ouyang Z. (2012) Effects of space weathering on diagnostic spectral features: Results from He<sup>+</sup> irradiation experiments. *Icarus*, 219, 630–640.
- Fulvio D., Brunetto R., Vernazza P., and Strazzulla G. (2012) Space weathering of Vesta and V-type asteroids: New irradiation experiments on HED meteorites. *Astron. Astrophys.*, 537, L11.
- Gaffey M. J. (2010) Space weathering and the interpretation of asteroid reflectance spectra. *Icarus*, 209, 564–574.
- Gaffey M. J., Burbine T. H., Piatek J. L., Reed K. L., Chaky D. A., Bell J. F., and Brown R. H. (1993) Mineralogical variations within the S-type asteroid class. *Icarus*, 106, 573.
- Godard M. and 10 colleagues (2011) Ion irradiation of carbonaceous interstellar analogues. Effects of cosmic rays on the 3.4 μm interstellar absorption band. *Astron. Astrophys.*, 529, A146.
- Gold T. (1955) The lunar surface. *Mon. Not. R. Astron. Soc.*, 115, 585.
- Gosling J. T. (2007) The solar wind. In *Encyclopedia of the Solar System, 2nd edition* (L.-A. McFadden et al., eds.), pp. 99–116. Academic/Elsevier.
- Hapke B. (1965) Effects of a simulated solar wind on the photometric properties of rocks and powders. *Ann. New York Acad. Sci.*, 123, 711–721.
- Hapke B. (1993) Combined theory of reflectance and emittance spectroscopy. In *Remote Geochemical Analysis: Elemental and Mineralogical Composition* (C. M. Pieters and P. A. J. Englert, eds.), pp. 31–42. Cambridge Univ., New York.
- Hapke B. (2001) Space weathering from Mercury to the asteroid belt. *J. Geophys. Res.*, 106, 10039–10074.
- Hendrix A. R. and Vilas F. (2006) The effects of space weathering at UV wavelengths: S-class asteroids. *Astron. J.*, 132, 1396–1404.
- Hirata N. and 10 colleagues (2009) A survey of possible impact structures on 25143 Itokawa. *Icarus*, 200, 486–502.
- Hiroi T. and Sasaki S. (2001) Importance of space weathering simulation products in compositional modeling of asteroids: 349 Dembowska and 446 Aeternitas as examples. *Meteoritics & Planet. Sci.*, 36, 1587–1596.
- Hiroi T., Pieters C. M., Rutherford M. J., Zolensky M. E., Sasaki S., Ueda Y., and Miyamoto M. (2004) What are the P-type asteroids made of? In *Lunar Planet. Sci. XXXV*, Abstract #1616. Lunar and Planetary Institute, Houston.
- Hiroi T., Abe M., Kitazato K., Abe S., Clark B. E., Sasaki S., Ishiguro M., and Barnouin-Jha O. S. (2006) Developing space weathering on the asteroid 25143 Itokawa. *Nature*, 443, 56–58.
- Hiroi T., Sasaki S., Misu T., and Nakamura T. (2013) Keys to detect space weathering on Vesta: Changes of visible and near-infrared reflectance spectra of HEDs and carbonaceous chondrites. In *Lunar Planet. Sci. XLIV*, Abstract #1276. Lunar and Planetary Institute, Houston.
- Ichimura A. S., Zent A. P., Quinn R. C., Sanchez M. R., and Taylor L. A. (2012) Hydroxyl (OH) production on airless planetary bodies: Evidence from H<sup>+</sup>/D<sup>+</sup> ion-beam experiments. *Earth Planet. Sci. Lett.*, 345, 90–94.
- Ishiguro M. (2014) Scattered light correction of Hayabusa/AMICA data and quantitative spectral comparisons of Itokawa. *Publ. Astron. Soc. Japan*, 66, 55.
- Ishiguro M. and 18 colleagues (2007) Global mapping of the degree of space weathering on asteroid 25143 Itokawa by Hayabusa/AMICA observations. *Meteoritics & Planet. Sci.*, 42, 1791–1800.
- Ivezic Ž. and 32 colleagues (2001) Solar system objects observed in the Sloan Digital Sky Survey commissioning data. *Astron. J.*, 122, 2749–2784.
- Jager C., Fabian D., Schremppel F., Dorschner J., Henning Th., and Wesch W. (2003) Structural processing of enstatite by ion bombardment. *Astron. Astrophys.*, 401, 57–65.
- Jedicke R., Nesvorný D., Whiteley R., Ivezic Ž., and Jurić M. (2004) An age-colour relationship for main-belt S-complex asteroids. *Nature*, 429, 275–277.
- Kaňuchová Z., Baratta G. A., Garozzo M., and Strazzulla G. (2010) Space weathering of asteroidal surfaces. Influence on the UV-Vis spectra. *Astron. Astrophys.*, 517, A60.
- Kaňuchová Z., Brunetto R., Melita M., and Strazzulla G. (2012) Space weathering and the color indexes of minor bodies in the outer solar system. *Icarus*, 221, 12–19.
- Keller L. P. and Berger E. L. (2014) A transmission electron microscope study of Itokawa regolith grains. *Earth Planets Space*, 66, 71.
- Keller L. P. and McKay D. S. (1997) The nature and origin of rims on lunar soil grains. *Geochim. Cosmochim. Acta*, 61, 2331–2341.
- Kissel J. and Krueger F. R. (1987) Ion formation by impact of fast dust particles and comparison with related techniques. *Appl. Phys.*, A42, 69–85.
- Krot A. N., Keil K., Goodrich C. A., Scott E. R. D., and Weisberg M. K. (2005) Classification of meteorites. In *Meteorites, Comets and Planets: Treatise on Geochemistry, Vol. 1* (A. M. Davis, ed.), p. 83. Elsevier, Amsterdam.

- Kurahashi E., Yamanaka C., Nakamura K., and Sasaki S. (2002) Laboratory simulation of space weathering: ESR measurements of nanophase metallic iron in laser-irradiated materials. *Earth Planets Space*, **54**, e5–e7.
- Lantz C., Clark B. E., Barucci M. A., and Lauretta D. S. (2013) Evidence for the effects of space weathering spectral signatures on low albedo asteroids. *Astron. Astrophys.*, **554**, A138.
- Lazzarin M., Marchi S., Moroz L. V., Brunetto R., Magrin S., Paolicchi P., and Strazzulla G. (2006) Space weathering in the main asteroid belt: The big picture. *Astrophys. J. Lett.*, **647**, L179–L182.
- Li Y., Li X., Wang S., Li S., Tang H., and Coulson I. M. (2013) Crystal orientation results in different amorphization of olivine during solar wind implantation. *J. Geophys. Res.–Planets*, **118**, 1974–1982.
- Loeffler M. J., Baragiola R. A., and Murayama M. (2008a) Laboratory simulations of redeposition of impact ejecta on mineral surfaces. *Icarus*, **196**, 285–292.
- Loeffler M. J., Dukes C. A., Chang W. Y., McFadden L. A., and Baragiola R. A. (2008b) Laboratory simulations of sulfur depletion at Eros. *Icarus*, **195**, 622–629.
- Loeffler M. J., Dukes C. A., and Baragiola R. A. (2009) Irradiation of olivine by 4 keV He<sup>+</sup>: Simulation of space weathering by the solar wind. *J. Geophys. Res.–Planets*, **114**, 3003.
- Love S. G. and Brownlee D. E. (1995) A direct measurement of the terrestrial mass accretion rate of cosmic dust. *Science*, **262**, 550–553.
- Lowry S. C., Weissman P. R., Hicks M. D., Whiteley R. J., and Larson S. (2005) Physical properties of asteroid (25143) Itokawa — Target of the Hayabusa sample return mission. *Icarus*, **176**, 408–417.
- Lucey P. G. et al. (1998) The influence of temperature on the spectra of the A-asteroids and implications for their silicate chemistry. *J. Geophys. Res.*, **103**, 5865–5871.
- Marchi S., Brunetto R., Magrin S., Lazzarin M., and Gandolfi D. (2005) Space weathering of near-Earth and main belt silicate-rich asteroids: Observations and ion irradiation experiments. *Astron. Astrophys.*, **443**, 769–775.
- Marchi S., Paolicchi P., Lazzarin M., and Magrin S. (2006a) A general spectral slope-exposure relation for S-type main belt and near-Earth asteroids. *Astron. J.*, **131**, 1138–1141.
- Marchi S., Magrin S., Nesvorný D., Paolicchi P., and Lazzarin M. (2006b) A spectral slope versus perihelion distance correlation for planet-crossing asteroids. *Mon. Not. R. Astron. Soc.*, **368**, L39–L42.
- Marchi S., De Sanctis M. C., Lazzarin M., and Magrin S. (2010) On the puzzle of space weathering alteration of basaltic asteroids. *Astrophys. J. Lett.*, **721**, L172–L176.
- Marchi S., Paolicchi P., and Richardson D. C. (2012) Collisional evolution and reddening of asteroid surfaces — I. The problem of conflicting time-scales and the role of size-dependent effects. *Mon. Not. R. Astron. Soc.*, **421**, 2–8.
- Marzari F., Farinella P., and Davis D. R. (1999) Origin, aging, and death of asteroid families. *Icarus*, **142**, 63–77.
- Masiero J. R., Mainzer A. K., Bauer J. M., Grav T., Nugent C. R., and Stevenson R. (2013) Asteroid family identification using the hierarchical clustering method and WISE/NEOWISE physical properties. *Astrophys. J.*, **770**, 7.
- Matsumoto T. et al. (2014) Surface micromorphologies of regolith particles from asteroid Itokawa and its implication to space weathering. *77th Annual Meteoritical Society Meeting*, Abstract #5130.
- McCord T. B. and 28 colleagues (2012) Dark material on Vesta from the infall of carbonaceous volatile-rich material. *Nature*, **491**, 83–86.
- Meibom A. and Clark B. E. (1999) Invited review: Evidence for the insignificance of ordinary chondritic material in the asteroid belt. *Meteoritics & Planet. Sci.*, **34**, 7–24.
- Meier M. and 16 colleagues (2014) A Precise cosmic-ray exposure age for an olivine grain from the surface of near-Earth asteroid (25143) Itokawa. In *Lunar Planet. Sci. XLV*, Abstract #1247. Lunar and Planetary Institute, Houston.
- Mennella V., Baratta G. A., Esposito A., Ferini G., and Pendleton Y. J. (2003) The effects of ion irradiation on the evolution of the carrier of the 3.4 micron interstellar absorption band. *Astrophys. J.*, **587**, 727–738.
- Miyamoto H. and 14 colleagues (2007) Regolith migration and sorting on Asteroid Itokawa. *Science*, **316**, 1011.
- Moroz L. V., Fisenko A. V., Semjonova L. F., Pieters C. M., Korotaeva N. N. (1996) Optical effects of regolith processes on S-asteroids as simulated by laser shots on ordinary chondrite and other mafic materials. *Icarus*, **122**, 366–382.
- Moroz L. V., Hiroi T., Shingareva T. V., Basilevsky A. T., Fisenko A. V., Semjonova L. F., and Pieters C. M. (2004a) Reflectance spectra of CM2 chondrite Mighei irradiated with pulsed laser and implications for low-albedo asteroids and martian moons. In *Lunar Planet. Sci. XXX*, Abstract #1279. Lunar and Planetary Institute, Houston.
- Moroz L., Baratta G., Strazzulla G., Starukhina L., Dotto E., Barucci M. A., Arnold G., and Distefano E. (2004b) Optical alteration of complex organics induced by ion irradiation: 1. Laboratory experiments suggest unusual space weathering trend. *Icarus*, **170**, 214–228.
- Moroz L. V., Starukhina L. V., Rout S. S., Sasaki S., Helbert J., Baither D., Bischoff A., and Hiesinger H. (2014) Space weathering of silicate regoliths with various FeO contents: New insights from laser irradiation experiments and theoretical spectral simulations. *Icarus*, **235**, 187–206.
- Mothé-Diniz T. and Nesvorný D. (2008) Visible spectroscopy of extremely young asteroid families. *Astron. Astrophys.*, **486**, L9–L12.
- Mothé-Diniz T., Jasmin F. L., Carvano J. M., Lazzaro D., Nesvorný D., and Ramirez A. C. (2010) Re-assessing the ordinary chondrites paradox. *Astron. Astrophys.*, **514**, A86.
- Müller T. G., Sekiguchi T., Kaasalainen M., Abe M., and Hasegawa, S. (2005) Thermal infrared observations of the Hayabusa spacecraft target asteroid 25143 Itokawa. *Astron. Astrophys.*, **443**, 347–355.
- Muñoz Caro G., Ruiterkam R., Schutte W. A., Greenberg J. M., and Mennella V. (2001) UV photodestruction of CH bonds and the evolution of the 3.4 μm feature carrier. I. The case of aliphatic and aromatic molecular species. *Astron. Astrophys.*, **367**, 347.
- Murchie S. and 10 colleagues (2002) Color variations on Eros from NEAR multispectral imaging. *Icarus*, **155**, 145–168.
- Nagao K. and 25 colleagues (2011) Irradiation history of Itokawa regolith material deduced from noble gases in the Hayabusa samples. *Science*, **333**, 1128.
- Nakamura T. and 21 colleagues (2011) Itokawa dust particles: A direct link between S-type asteroids and ordinary chondrites. *Science*, **333**, 1113.
- Nesvorný D., Bottke W. F. Jr., Dones L., and Levison H. F. (2002) The recent breakup of an asteroid in the main-belt region. *Nature*, **417**, 720–771.
- Nesvorný D., Jedicek R., Whiteley R. J., Ivezić Ž. (2005) Evidence for asteroid space weathering from the Sloan Digital Sky Survey. *Icarus*, **173**, 132–152.
- Nesvorný D., Vokrouhlický D., and Bottke W. F. (2006) The breakup of a main-belt asteroid 450 thousand years ago. *Science*, **312**, 1490.
- Nesvorný D., Vokrouhlický D., Morbidelli A., and Bottke W. F. (2009) Asteroidal source of L chondrite meteorites. *Icarus*, **200**, 698–701.
- Nesvorný D., Bottke W. F., Vokrouhlický D., Chapman C. R., and Rafkin S. (2010) Do planetary encounters reset surfaces of near Earth asteroids? *Icarus*, **209**, 510–519.
- Nimura T., Hiroi T., and Pieters C. M. (2008) An improved scheme for modeling the reflectance spectra of space-weathered regoliths. *Earth Planets Space*, **60**, 271–275.
- Noble S. K., Pieters C. M., and Keller L. P. (2007) An experimental approach to understanding the optical effects of space weathering. *Icarus*, **192**, 629–642.
- Noble S. K., Keller L. P., and Pieters C. M. (2011) Evidence of space weathering in regolith breccias II: Asteroidal regolith breccias. *Meteoritics & Planet. Sci.*, **45**, 2007–2015.
- Noguchi T. and 13 colleagues (2010) Surface morphological features of boulders on asteroid 25143 Itokawa. *Icarus*, **206**, 319–326.
- Noguchi T. et al. (2011) Incipient space weathering observed on the surface of Itokawa dust particles. *Science*, **333**, 1121–1124.
- Noguchi T. and 23 colleagues (2014) Space weathered rims found on the surfaces of the Itokawa dust particles. *Meteoritics & Planet. Sci.*, **332**, 49, 188–214.
- Okazaki M., Sasaki S., Tsuchiyama A., Miyake A., Matsumoto T., Hirata T., and Hiroi T. (2014) Effect of iron sulfides on space weathering: Lessons from the Itokawa particles and laboratory simulations. *Asteroids Comets Meteors 2014*, Helsinki, Abstract #5F2D.
- Paolicchi P., Marchi S., Nesvorný D., Magrin S., and Lazzarin M. (2007) Towards a general model of space weathering of S complex asteroids and ordinary chondrites. *Astron. Astrophys.*, **464**, 1139–1146.
- Pieters C. M., Taylor L. A., Noble S. K., Keller L. P., Hapke B., Morris R. V., Allen C. C., McKay D. S., and Wentworth S. (2000) Space weathering on airless bodies: Resolving a mystery with lunar samples. *Meteoritics & Planet. Sci.*, **35**, 1101–1107.

- Pieters C. M. et al. (2009) Character and spatial distribution of OH/HO<sub>2</sub> on the surface of the Moon seen by M<sup>3</sup> on Chandrayaan-1. *Science*, 326, 568.
- Pieters C. M. and 16 colleagues (2012) Distinctive space weathering on Vesta from regolith mixing processes. *Nature*, 491, 79–82.
- Polishook D., Moskovitz N., Binzel R. P., DeMeo F. E., Vokrouhlický D., Žižka J., and Oszkiewicz D. (2014) Observations of “fresh” and weathered surfaces on asteroid pairs and their implications on the rotational-fission mechanism. *Icarus*, 233, 9–26.
- Popescu M., Birlan M., and Nedelcu D. A. (2012) Modeling of asteroid spectra — M4AST. *Astron. Astrophys.*, 544, A130.
- Rivkin A. S. and Emery J. P. (2010) Detection of ice and organics on an asteroidal surface. *Nature*, 464, 1322–1323.
- Rivkin A. S., Thomas C. A., Trilling D. E., Enga M.-T., and Grier J. A. (2011) Ordinary chondrite-like colors in small Koronis family members. *Icarus*, 211, 1294–1297.
- Saito J. and 33 colleagues (2006) Detailed images of asteroid 25143 Itokawa from Hayabusa. *Science*, 312, 1341–1344.
- Sanchez J. A., Reddy V., Nathues A., Cloutis E. A., Mann P., and Hiesinger H. (2012) Phase reddening on near-Earth asteroids: Implications for mineralogical analysis, space weathering and taxonomic classification. *Icarus*, 220, 36–50.
- Sasaki S., Nakamura K., Hamabe Y., Kurahashi E., and Hiroi T. (2001) Production of iron nanoparticles by laser irradiation in a simulation of lunar-like space weathering. *Nature*, 410, 555–557.
- Sasaki S., Hiroi T., Nakamura K., Hamabe Y., Kurahashi E., and Yamada M. (2002) Simulation of space weathering by nanosecond pulse laser heating: Dependence on mineral composition, weathering trend of asteroids and discovery of nanophase iron particles. *Adv. Space Res.*, 29, 783–788.
- Sasaki S., Kurahashi E., Yamanaka C., and Nakamura K. (2003) Laboratory simulation of space weathering: Changes of optical properties and TEM/ESR confirmation of nanophase metallic iron. *Adv. Space Res.*, 31, 2537–2542.
- Shestopalov D. I., Golubeva L. F., and Cloutis E. A. (2013) Optical maturation of asteroid surfaces. *Icarus*, 225, 781–793.
- Shu A. et al. (2012) 3 MV hypervelocity dust accelerator at the Colorado Center for Lunar Dust and Atmospheric Studies. *Rev. Sci. Instrum.*, 83, 075108.
- Strazzulla G. (2011) Cosmic ion bombardment of the icy moons of Jupiter. *Nucl. Instr. Meth. Phys. Res.*, B269, 842–851.
- Strazzulla G., Dotto E., Binzel R., Brunetto R., Barucci M. A., Blanco A., and Orofino V. (2005) Spectral alteration of the meteorite Epinal (H5) induced by heavy ion irradiation: A simulation of space weathering effects on near-Earth asteroids. *Icarus*, 174, 31–35.
- Strazzulla G., Baratta G. A., Leto G., and Gomis O. (2007) Hydrate sulfuric acid after sulfur implantation in water ice. *Icarus*, 192, 623–628.
- Takagi Y. and 14 colleagues (2011) Hayabusa 2, C-type asteroid sample return mission. *AGU Fall Meeting*, Abstract #P21E-04.
- Takato N. (2008) Rotation-resolved spectroscopy of a very young asteroid, (1270) Datura. *Astrophys. J. Lett.*, 685, L161–L163.
- Takeuchi H., Miyamoto H., and Maruyama S. (2010) Origins of bright spots on the surface of boulders covering asteroid Itokawa. In *Lunar Planet. Sci. XLVI*, Abstract #1578. Lunar and Planetary Institute, Houston.
- Taylor L. A., Pieters C. M., Keller L. P., Morris R. V., and McKay D. S. (2001) Lunar mare soils: Space weathering and the major effects of surface-correlated nanophase Fe. *J. Geophys. Res.*, 106, 27985–28000.
- Thomas C. A., Trilling D. E., and Rivkin A. S. (2012) Space weathering of small Koronis family asteroids in the SDSS Moving Object Catalog. *Icarus*, 219, 505–507.
- Thompson M. S., Christoffersen R., Zega T. J., and Keller L. P. (2014) Nanoscale analysis of space-weathering features in soils from Itokawa. In *Lunar Planet. Sci. XLV*, Abstract #2121. Lunar and Planetary Institute, Houston.
- Tsuchiya A. and 32 colleagues (2011) Three-dimensional structure of Hayabusa samples: Origin and evolution of Itokawa regolith. *Science*, 333, 1125.
- Ueda Y., Hiroi T., Pieters C. M., and Miyamoto M. (2002) Changes of band i center and band ii/band i area ratio in reflectance spectra of olivine-pyroxene mixtures due to the space weathering and grain size effects. In *Lunar Planet. Sci. XXXIII*, Abstract #2023. Lunar and Planetary Institute, Houston.
- Vernazza P., Binzel R. P., Thomas C. A., DeMeo F. E., Bus S. J., Rivkin A. S., and Tokunaga A. T. (2008) Compositional differences between meteorites and near-Earth asteroids. *Nature*, 454, 858–860.
- Vernazza P., Binzel R. P., Rossi A., Fulchignoni M., and Birlan M. (2009a) Solar wind as the origin of rapid reddening of asteroid surfaces. *Nature*, 458, 993–995.
- Vernazza P., Brunetto R., Binzel R. P., Perron C., Fulvio D., Strazzulla G., and Fulchignoni M. (2009b) Plausible parent bodies for enstatite chondrites and mesosiderites: Implications for Lutetia's fly-by. *Icarus*, 202, 477–486.
- Vernazza P. and 10 colleagues (2013) Paucity of Tagish Lake-like parent bodies in the asteroid belt and among Jupiter Trojans. *Icarus*, 225, 517–525.
- Vokrouhlický D., Brož M., Bottke W. F., Nesvorný D., and Morbidelli A. (2006) Yarkovsky/YORP chronology of asteroid families. *Icarus*, 182, 118–142.
- Willman M., Jedicke R., Nesvorný D., Moskovitz N., Ivezić Ž., and Fevig R. (2008) Redetermination of the space weathering rate using spectra of Iannini asteroid family members. *Icarus*, 195, 663–673.
- Willman M., Jedicke R., Moskovitz N., Nesvorný D., Vokrouhlický D., and Mothé-Diniz T. (2010) Using the youngest asteroid clusters to constrain the space weathering and gardening rate on S-complex asteroids. *Icarus*, 208, 758–772.
- Yamada M. et al. (1999) Simulation of space weathering of planet-forming materials: Nanosecond pulse laser irradiation and proton implantation on olivine and pyroxene samples. *Earth Planets Space*, 51, 1255–1265.
- Yano H. and 19 colleagues (2006) Touchdown of the Hayabusa spacecraft at the Muses Sea on Itokawa. *Science*, 312, 1350–1353.
- Ziffer J., Campins H., Licandro J., Walker M. E., Fernandez Y., Clark B. E., Mothé-Diniz T., Howell E., and Deshpande R. (2011) Near-infrared spectroscopy of primitive asteroid families. *Icarus*, 213, 538–546.

# The Formation and Evolution of Ordinary Chondrite Parent Bodies

Pierre Vernazza

*Aix Marseille Université and Laboratoire d’Astrophysique de Marseille*

Brigitte Zanda

*Muséum National d’Histoire Naturelle and Observatoire de Paris*

Tomoki Nakamura

*Tohoku University*

Edward Scott

*University of Hawaii*

Sara Russell

*Natural History Museum (London)*

---

Ordinary chondrites (OCs) are by far the most abundant meteorites (80% of all falls). Their origin has long been the matter of a heated debate. About 30 years ago (e.g., *Pellas*, 1988), it was proposed that OCs should originate from S-type bodies (the most abundant asteroid spectral types in the inner part of the asteroid belt), but the apparent discrepancy between S-type asteroid and OC reflectance spectra generated what was known as the S-type/OC conundrum. This paradox has gradually been resolved over the years. It is now understood that space weathering processes are responsible for the spectral mismatch between S-type bodies and OCs. Furthermore, both telescopic observations and the first asteroid sample return mission (*Hayabusa*) indicate that most S-type bodies have mineralogies similar to those of OCs. Importantly, the S-type/OC link, which has remained sterile for more than 30 years, has been delivering fundamental constraints on the formation and evolution of planetesimals over the recent years.

## 1. INTRODUCTION

Observations of main-belt asteroids (MBAs) performed between the early 1970s and the late 1990s, along with meteorite measurements, led to the determination of a preliminary version of the compositional distribution in the asteroid belt (see the chapter by DeMeo et al. in this volume; *Gradie and Tedesco*, 1982; *Mothé-Diniz et al.*, 2003; *DeMeo and Carry*, 2013, 2014):

1. Two main asteroid populations were identified: the so-called S-types [comprising mostly but not only ordinary chondrite (OC)-like asteroids] and C-types [comprising mostly but not only carbonaceous chondrite (CC)-like asteroids], accounting for more than 50% of all MBAs, and several minor populations (comprising the parent bodies of the remaining meteorite classes and possibly compositions presently unsampled by meteorites).

2. A heliocentric gradient was recognized (*Gradie and Tedesco*, 1982) with water-poor S-type asteroids being pref-

erentially located in the inner belt while water-rich C-types are the dominant population in the outer belt.

3. The existence of a compositional overlap was established (e.g., a large number of C-types are currently located where S-types are the most abundant and vice versa).

Since the early 2000s, we have entered a new era of asteroid exploration, mainly because of the emergence of numerous high-quality spectroscopic measurements in the near-infrared [obtained essentially with the NASA Infrared Telescope Facility (IRTF) groundbased telescope], but also because of the Hayabusa asteroid sample return mission (*Nakamura et al.*, 2011). Near-infrared spectra for several hundreds of near-Earth asteroids (NEAs) (see chapter by Binzel et al. in this volume; *Thomas et al.*, 2014) and MBAs (e.g., *DeMeo et al.*, 2009; *Vernazza et al.*, 2014) have now been collected. These new datasets allowed us to enter the second phase of the exploration of the compositional distribution of the asteroid belt and of the compositional characterization of the NEA population. While previous

measurements in the visible allowed us to establish, for example, that ordinary chondrites (OCs) formed closer to the Sun than CCs, measurements in the near-infrared — which offer significantly more constraints on asteroid compositions than in the visible range alone (see the chapter by Reddy et al. in this volume) — allow us to constrain the respective formation location of the various meteorite classes (H, L, LL, CI, CM, etc.) within these broad groups (OCs, CCs), namely whether, for example, H chondrites formed closer to the Sun than LL chondrites or vice versa (*Vernazza et al.*, 2014). Near-infrared measurements also allow us to attack important questions such as determining the source regions of both meteorites and NEAs (e.g., *Vernazza et al.*, 2008; *Thomas and Binzel* 2010).

In parallel, samples of the S-type asteroid (25143) Itokawa were brought back to Earth by the Hayabusa mission, which demonstrated that OCs originate from S-type asteroids and validated the numerous laboratory space weathering experiments that had been performed on various meteorite classes (including OCs). In particular, these experiments had predicted that space weathering processes were responsible for the observed spectral mismatch between OCs and S-type asteroids. As a matter of fact, this work resolved the S-type/OC conundrum (*Chapman*, 2004) that lasted for more than 30 years, and demonstrated that S-type asteroids are mostly OCs or OC-like and not differentiated asteroids, as was advocated by *Bell et al.* (1989) and *Gaffey et al.* (1993).

The aim of the present chapter is to summarize the evidence concerning the origin of OCs and discuss the constraints that have been accumulated over the years regarding the formation and evolution of their parent bodies (S-type asteroids). While we give appropriate space to the resolution of the S-type/OC conundrum, the main emphasis of the chapter is placed on what was learned from the recently established spectroscopic links between specific OC classes (H, L, and LL) and their S-type asteroid parent bodies. We will show that these links, along with new laboratory work on OCs, have not only allowed us to gain a better knowledge of the formation mechanism of OC parent bodies and planetesimals in general, but they also boosted our understanding of the collisional and dynamical evolution of asteroids.

The structure of this review chapter is as follows. We start by reviewing in section 2 the most important constraints on the formation and early evolution of the OC parent bodies and sometimes, more generally, of the solar system, that were derived from laboratory studies of OCs. Then, in section 3, we will review the outstanding efforts that have been accomplished over the last 40 years by a large fraction of the asteroid-meteorite community to unambiguously identify the parent bodies of OCs. In section 4, we will review the constraints on the formation and evolution of OC parent bodies that were obtained from telescope observations of S-type asteroids and that nicely complement the laboratory constraints presented in section 2. In section 5, we will review the remaining issues in the S-type/OC field that require critical new data.

## 2. CONSTRAINTS DERIVED FROM ORDINARY CHONDRITE STUDIES ON THE FORMATION AND EARLY EVOLUTION OF THEIR PARENT BODIES

Ordinary chondrite meteorites (OCs) are silicate-rich meteorites composed mostly of olivine and low-calcium pyroxene that are by far the most abundant meteorites [80% of all falls (*Hutchison*, 2004)]. They have been subdivided into three groups (H, L, and LL) based on variations in bulk composition, such as molecular ratios [ $\text{FeO}/(\text{FeO} + \text{MgO})$ ] in olivine and pyroxene (*Mason*, 1963; *Keil and Fredriksson*, 1964) and the ratio of metallic Fe to total Fe (*Dodd et al.*, 1967) (Table 1). The L group slightly outnumbers the H group among falls (Table 1), but the reverse is true among finds. The LL group is distinctly less abundant than either group (*Hutchison*, 2004).

H chondrites have the highest total abundance of Fe (and the highest Fe/Si atomic ratio) among OCs (H stands for «High» Fe). They are also the most reduced OCs, their iron being mostly in metallic form. When equilibrated, they exhibit the lowest FeO contents in their silicates. At the other extreme, LL chondrites contain the least total Fe, corresponding to the lowest Fe/Si atomic ratio, and they are the most oxidized OCs, with little metal and with the silicates that have the highest FeO contents when equilibrated. They are «Low» in total iron and «Low» in metal, hence the LL denomination. H and LL chondrites also differ in terms of oxygen isotopes, with LL chondrites containing a very small but measurable depletion of  $^{16}\text{O}$  with respect to the other two isotopes compared to H chondrites. L chondrites («Low» in total iron) are intermediate between H and LLs in all these properties — somewhat closer to LLs in terms of total Fe.

TABLE 1. Properties of equilibrated ordinary chondrites.

	H	L	LL
Fall statistics (%)	34	37	9
Fe (wt%)	28	22	19
Fe/Si (atomic)	0.81	0.57	0.52
Metal (vol%)	8.4	4.1	2
Fa content of olivine*	16–20	21–26	27–31
Fs content of pyroxene*	15–17	18–22	22–30
$\sim\Delta^{17}\text{O}^\dagger$ (‰)	0.7	1.1	1.3
Ol/(Ol + Px)*	51–60	60–67	70–82

\* Olivine (Ol) is  $(\text{Fe}, \text{Mg})_2\text{SiO}_4$ ; pyroxene (Px) is  $(\text{Fe}, \text{Mg}, \text{Ca})_2\text{Si}_2\text{O}_6$ . Fayalite (Fa) content of olivine and ferrosilite (Fs) content of pyroxene correspond to the relative abundance of Fe atoms compared to other cations:  $\text{Fe}/(\text{Fe} + \text{Mg})$  and  $\text{Fe}/(\text{Fe} + \text{Mg} + \text{Ca})$  respectively. Ol/(Ol + Px) values are after *Vernazza et al.* (2008) and *Dunn et al.* (2010). The properties listed above are those of equilibrated (metamorphosed) ordinary chondrites. Fa content of olivine and Fs content of pyroxenes are highly variable in unequilibrated chondrites.

†  $\Delta^{17}\text{O}$  measures the distance to the terrestrial fractionation line in the oxygen three-isotope plot. It is defined as  $\Delta^{17}\text{O} = \delta^{17}\text{O} - 0.52 \times \delta^{18}\text{O}$ , where  $\delta^{17}\text{O}$  and  $\delta^{18}\text{O}$  measure respectively the excess of  $^{17}\text{O}$  and  $^{18}\text{O}$  with respect to  $^{16}\text{O}$  and to a standard (Standard Mean Ocean Water), multiplied by 1000.

Textural variations and corresponding mineral and chemical trends indicate that differing degrees of thermal metamorphism (heating) took place within each OC group (*Van Schmus and Wood*, 1967; *Dunn et al.*, 2010). Based on these variations, a petrologic classification scheme (*Van Schmus and Wood*, 1967) for OCs was developed (H, L, and LL groups are further subdivided into four groups — from 3 to 6), which consisted in distinguishing the less metamorphosed (heated) chondrites [type 3, called unequilibrated ordinary chondrites (UOCs)] from chondrites that have undergone higher degrees of thermal metamorphism [types 4 to 6, called equilibrated ordinary chondrites (EOCs); see *Huss et al.* (2006) for a review] (Fig. 1). Type 3s are further divided into 3.0–3.9 based on induced thermoluminescence properties (*Sears et al.*, 1980), but also by textures of opaque minerals (*Bourot-Denise et al.*, 1997) and the structure of organics as seen in Raman spectroscopy (*Bonal et al.*, 2006, 2007). An even finer division of petrographic types <3.2 was defined based on the distribution of Cr<sub>2</sub>O<sub>3</sub> within olivine (*Grossman and Brearley*, 2005).

The study of OCs and of other chondrite classes has provided numerous constraints on the formation and early evolution of planetesimals, including (1) the processes that occurred in the protoplanetary disk prior to primary accretion (i.e., planetesimal formation) and their associated timescales (*Cuzzi et al.*, 2001; *Cuzzi and Weidenschilling*, 2006), (2) the heating mechanisms at the origin of metamorphism in planetesimals (*Ghosh et al.*, 2006), and (3) the post- (and syn-) accretional heating and collisional events (*Haack et al.*, 1996, and references therein; *Hutchison*, 2004; *Huss et al.*, 2006; *Ghosh et al.*, 2006; *Scott et al.*, 2014).

## 2.1. Constraints on the Processes that Occurred in the Protoplanetary Disk Prior to Accretion

Unequilibrated ordinary chondrites, which represent ~15% of all OCs (*Hutchison*, 2004), are the most primitive OCs. Several thermometers indicate that a number of UOCs did not experience metamorphic temperatures (*Hutchison*, 2004) > ~370°C and that all were < ~600°C. As such, UOCs give us the best indication of the initial material (a sort of snapshot of the protoplanetary disk) from which their parent asteroids accreted, as well as key constraints on the events that occurred in the protoplanetary disk prior to primary accretion.

Unequilibrated ordinary chondrites are mainly aggregates of high-temperature (>1600°C) components, including chondrules (~80% of the volume), which are millimeter-sized silicate spherules that formed through rapid melting and cooling of precursor material via a still-elusive mechanism (*Connolly and Desch*, 2004; *Jacquet et al.*, 2012), as well as metal and sulfide grains. All these components are set in a fine-grained interchondrule matrix (10–15 vol% of the rock) (*Hutchison*, 2004), which is believed to have always remained at low temperature (<200°C) in the disk.

As of today, the most likely explanation for the simultaneous presence in OCs of low-temperature and high-tem-

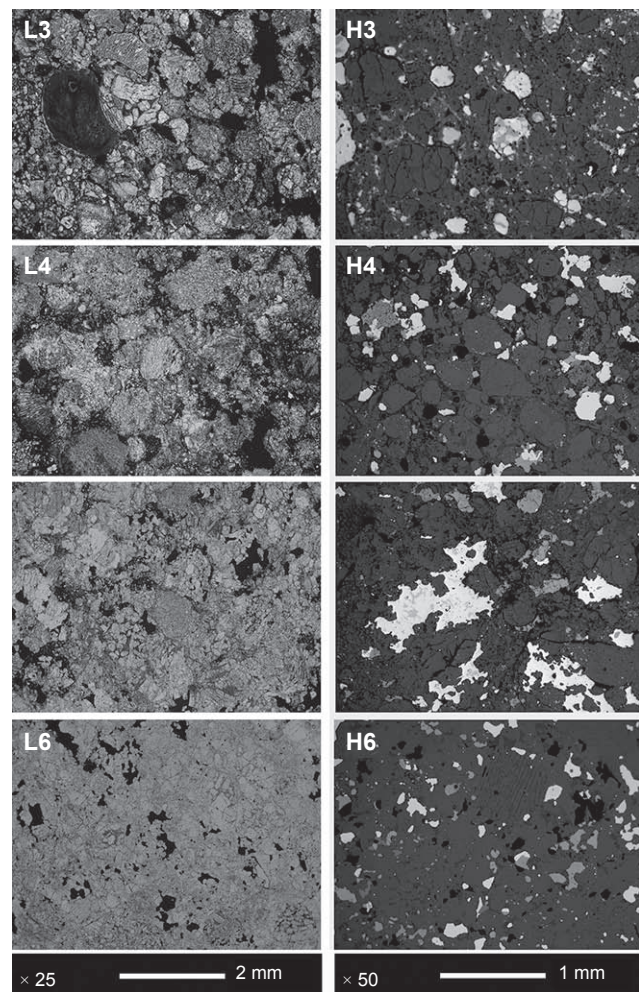


**Fig. 1.** Compositional and textural evolution of H and L chondrites as a function of petrologic type (silicate textures seen in transmitted light in L3–L6 chondrites and opaque mineral textures seen in reflected light in H3–H6 chondrites). Metamorphic heating in OCs results in chemical and textural changes, the most spectacular of which is the progressive disappearance of chondrules and matrix from petrologic type 3 (least heated) to 6 (most heated). As a result of long-duration heating (millions of years), the mineralogy of the rock is modified. Elemental diffusion allows minerals in chemical disequilibrium at the onset to react with one another. Minerals thus “equilibrate,” e.g., all olivine grains in one given rock end up with the same (FeO-rich) composition (Table 1). Glass disappears while feldspar grows. Textures also tend to equilibrate with the disappearance of the smaller grains (Ostwald ripening). This makes chondrule outlines become blurry and the typical chondritic texture hence tends to disappear.

perature components believed to have formed respectively far from and close to the Sun is that radial mixing was extensive in the solar nebula and thus played a prominent role in shaping the composition of these chondrites and that of planetesimals overall. Indeed, evidence of the simultaneous presence of low-temperature and high-temperature

components is also observed in other chondrite classes (*Hutchison*, 2004, and references therein) and in comets (*Kelley and Wooden*, 2009, and references therein).

Further evidence of the importance of radial mixing in all classes of chondrites, and OCs in particular, is provided by (1) the “universal shape” of the size distribution of chondrules that is centered at different sizes from chondrite class to chondrite class (*Grossman et al.*, 1989, and references therein; *Cuzzi et al.*, 2001, 2008), indicative of size-sorting; and (2) the simultaneous presence in a given chondrite of various proportions of two different types of chondrules [reduced type I and oxidized type II chondrules, which are made in different environments (*Zanda et al.*, 2006)].

Recently, *Fu et al.* (2014) have provided new constraints on the early evolution of the solar system by measuring the remnant magnetization in olivine-bearing chondrules from the primitive Semarkona meteorite (LL3.0). They report that these chondrules were magnetized in a nebular field of  $54 \pm 21 \mu\text{T}$ . This intensity supports chondrule formation by nebular shocks or planetesimal collisions rather than by electric currents, the x-wind, or other mechanisms near the Sun. This implies that background magnetic fields in the terrestrial planet-forming region were likely  $5\text{--}54 \mu\text{T}$ , which is sufficient to account for measured rates of mass and angular momentum transport in protoplanetary disks.

## 2.2. Heating Mechanisms Leading to Metamorphism in Chondrites

Whereas petrographic types were first discovered and described in OCs, it appears that most chondrites show evidence of metamorphism. Indeed, most enstatite chondrites have petrologic types that range from 4 to 6 with only two unequilibrated objects among observed falls (EH3). Carbonaceous chondrites also show evidence of metamorphism: CK chondrites have petrologic types that range from 3 to 6 and a few CO and CV chondrites may be somewhat metamorphosed, although most of them are ranked type 3s.

Several heat sources have been proposed to explain the thermal evolution (including metamorphism and/or differentiation) of planetesimals (see the chapter by Scott et al. in this volume for a more detailed discussion) and thus the existence of the different petrologic types (3 to 6) within each OC class (for reviews, see *McSween et al.*, 2002; *Ghosh et al.*, 2006; *Sahijpal et al.*, 2007). These include the decay of short-lived radioactive nuclides (*Urey*, 1955), which is now considered the most likely heat source; the decay of long-lived radioactive elements (*Yomogida and Matsui*, 1984); electromagnetic induction heating (*Sonnett et al.*, 1968; *Menzel and Roberge*, 2013); and impact heating (e.g., *Rubin*, 1995, 2003, 2004). Recent work has shown that neither electromagnetic induction nor impacts alone can explain the thermal processing of planetesimals [see *Marsh et al.* (2006) concerning electromagnetic induction and *Keil et al.* (1997) and *Ciesla et al.* (2013) for impact heating]. There is also no coherent scenario that could favor the decay of long-lived radioactive elements as the only heat source.

More specifically, substantial isotopic evidence suggests that  $^{26}\text{Al}$  was the major source of heat for melting early formed planetesimals and heating bodies that accreted later (e.g., *Bizzarro et al.*, 2005; *Kleine et al.*, 2005; *Hevey and Sanders*, 2006; *Ghosh et al.*, 2006; *Kruijer et al.*, 2012; *Sanders and Scott*, 2012). However, there is also evidence in chondrites for localized impact heating during metamorphism (*Rubin*, 1995, 2004). Impact heating of asteroids, even porous ones, is very inefficient (*Keil et al.*, 1997), but *Davison et al.* (2012) inferred that large projectiles impacting into highly porous chondritic targets could have buried enough impact melt at depth to cause localized slow cooling. In addition, impacts during metamorphism may have excavated hot chondritic rock so that it cooled more rapidly and mixed hot and cold material (*Davison et al.*, 2013; *Ciesla et al.*, 2013).

Over the last ~30 years, several groups have developed a wide range of thermal models of planetesimals based primarily on  $^{26}\text{Al}$  heating (e.g., *Miyamoto et al.*, 1981; *Miyamoto*, 1991; *Grimm and McSween*, 1993; *Bennett and McSween*, 1996; *Akridge et al.*, 1998; *Merk et al.*, 2002; *Ghosh et al.*, 2003; *Tachibana and Huss*, 2003; *Trieloff et al.*, 2003; *Bizzarro et al.*, 2005; *Baker et al.*, 2005; *Mostefaoui et al.*, 2005; *Hevey and Sanders*, 2006; *Sahijpal et al.*, 2007; *Harrison and Grimm*, 2010; *Elkins-Tanton et al.*, 2011; *Henke et al.*, 2012a,b; *Neumann et al.*, 2012; *Monnereau et al.*, 2013). Some authors have included additional heating effects due to  $^{60}\text{Fe}$ , which has a half-life of 2.6 m.y., compared to 0.72 m.y. for  $^{26}\text{Al}$ . However, the abundance of  $^{60}\text{Fe}$  is now thought to have been too low to provide any significant heating (*Tang and Dauphas*, 2012).

If the parent bodies of the OCs had been heated by  $^{26}\text{Al}$  and cooled without impact disturbance, they would have formed an onion-shell structure in which the most metamorphosed type 6 material occupying the central region surrounded by successive shells of less-metamorphosed type 5 through 3 material (*Trieloff et al.*, 2003; *Ghosh et al.*, 2006; *Henke et al.*, 2012a,b, 2013, and references therein).

## 2.3. Thermal and Impact History of the Ordinary Chondrite Parent Bodies

In this section we summarize the evidence that has been accumulated over the years regarding both the thermal and impact history of OC parent bodies.

**2.3.1. Evidence for impact from breccias and cosmic-ray exposure ages.** About 20–30% of all OCs are fragmental breccias composed of various petrologic types (*Bischoff et al.*, 2006). Regolith breccias, which are fragmental breccias containing a small fraction of grains with solar wind gases that were exposed on the surface of the parent asteroid, account for 15%, 3%, and 5% of H, L, and LL chondrites, respectively. Fragmental breccias that lack solar wind gases account for 5%, 22%, and 23% of H, L, and LL chondrites, respectively (*Rubin et al.*, 1983). The fraction of LL chondrites that are breccias may be much higher as *Binns* (1967) found that 62% of LLs were breccias. These breccias show that each OC parent body contains both unequilibrated and

equilibrated petrologic type material and that type 3–6 material can be found in a single body.

Regolith breccias and gas-poor fragmental breccias are dominated by clasts of equilibrated material. Although a few OC regolith breccias contain predominantly type 3 materials, most are largely composed of equilibrated, type 4–6 material. A typical regolith breccia contains clasts of equilibrated type 4–6 material, with rare impact melt clasts in a dark matrix that is mostly fine equilibrated material with a small amount of type 3 material including some unequilibrated chondrules (e.g., Metzler et al., 2011). This suggests that the surfaces of the OC parent bodies are dominated by equilibrated material and that each body contains a variety of different types. Few breccias contain more than a tiny fraction of foreign material. This is mostly CC material, presumably from projectiles.

Interestingly, the range of composition of olivine grains in a section of matrix from a regolith breccia [e.g., Fa<sub>10–29</sub> in the Northwest Africa 869 L chondrite (Metzler et al., 2011) is comparable to the range observed in the Itokawa sample, Fa<sub>24–31</sub> (Nakamura et al., 2011)]. In both cases more than 90% of the grains are derived from equilibrated material.

The presence of solar wind gas and solar-flare tracks in the regolith breccias shows that these breccias were formed after metamorphism of the parent bodies, which would have removed both features. Some gas-poor fragmental breccias may have formed earlier during metamorphism. The L breccia Mezö-Madaras, which contains L4 clasts in a predominantly L3 matrix, probably formed at this time (Scott et al., 2014).

Clues to the recent impact history of the OC parent bodies can be obtained from their cosmic-ray exposure ages, which range from ~1 to 100 m.y. (Herzog and Caffee, 2014). Cosmic rays penetrate a meter of rock, so these ages date the time when meter-sized meteoroids were formed by impacts on much larger bodies. The spectra of ages for OCs are dominated by a few peaks showing that the production of meteorites is dominated by a very small number of impact events on a correspondingly small number of parent bodies (Herzog and Caffee, 2014). H, L, and LL chondrites have different peaks in their age spectra, but petrologic types of the same group show similar peaks, and regolith breccias have similar distributions to other chondrites. These features, together with the abundance and nature of breccias, suggest that the OC parent bodies were well mixed internally by impacts with all types jumbled up. If the OC parent bodies did once have onion-shell structures, this is no longer the case. This conclusion is consistent with the results of Vernazza et al. (2014) discussed below, which show metamorphosed material to be present at the surface of H-chondrite parent bodies.

Finally, about half of all H chondrites have exposure ages of 6–10 m.y. This peak in the cosmic-ray exposure age spectrum is broader than other OC peaks and it may result from multiple impacts. Another group of meteorites, the acupulcoites and lodranites, have a similar cosmic-ray exposure age range of 5–10 m.y. (Terribilini et al., 2000; Herzog and Caffee, 2014). Numerous impacts on different

bodies during this period may result from a nearby major impact that produced a family of fragments that peppered nearby asteroids. Thus the 6–10-m.y. H-chondrite peak should not be taken as evidence that all these meteorites come from one body.

### 2.3.2. Constraints on the thermal evolution and impact history of the H-chondrite parent body from cooling rates.

Here we summarize what has been learned about the metamorphic and early impact histories of the H chondrites in relatively unshocked H3–6 chondrites.

Pellas and Storzer (1981) found that cooling rates for six H4–6 chondrites derived from Pu fission track thermometry decreased with increasing petrologic type. They concluded that the parent body of the H chondrites had been heated by <sup>26</sup>Al decay and had cooled with an onion-shell structure.

Cooling rates of more than 30 OCs have also been inferred from Ni concentrations at the centers of zoned taenite grains (Wood, 1967; Willis and Goldstein, 1981, 1983). Scott and Rajan (1981) and Taylor et al. (1987) found no evidence that the parent bodies had cooled with an onion-shell structure, as cooling rates did not decrease systematically from type 3 to type 6. They concluded that either the parent bodies never had onion-shell structures or their interiors were rearranged by impacts, possibly by catastrophic disruption and reassembly, as Grimm (1985) suggested, prior to cooling below ~600°C when taenite grains start to develop Ni concentration gradients. Because metallographic cooling rates for the six H chondrites studied by Pellas and Storzer (1981) were consistent with fission-track cooling rates, Taylor et al. (1987) suggested that the apparent conflict between the two techniques was merely a result of the small sample size of the fission track dataset.

The most detailed evidence for the onion-shell model was presented by Trieloff et al. (2003), who measured Ar-Ar ages and fission-track cooling rates for nine H chondrites and compared them with the Pb-Pb ages of Göpel et al. (1994). Both sets of radiometric ages were found to correlate inversely with petrologic type and closely matched ages calculated for various depths in a 100-km-radius asteroid that was heated by <sup>26</sup>Al to 850°C in its central regions and cooled without disturbance by impact to ~100°C in ~150 m.y. Trieloff et al. (2003) did not discuss the conflicting metallographic cooling rates of Taylor et al. (1987), but suggested that the samples studied by these authors had been modified by shock or impact heating. Wood (2003) concluded that Trieloff et al. (2003) had resolved the controversy in favor of the onion-shell model.

Subsequent studies of the radiometric ages of H chondrites or thermal modeling of their parent body have largely endorsed the conclusions of Trieloff et al. (2003). Kleine et al. (2008) found that Hf-W ages of five H4–6 chondrites, including four of those studied by Trieloff et al. (2003), decreased with increasing petrologic type. They concluded that the parent body had cooled with an onion-shell structure after heating by <sup>26</sup>Al. Harrison and Grimm (2010) used radiometric ages and metallographic cooling rates for H chondrites to constrain various thermal models and concluded that nearly

all data could be accounted for by an onion-shell body with a radius of 75–130 km. They questioned the accuracy and validity of some metallographic cooling rates and suggested that the relatively small number of nonconforming data might be attributed to impacts that left the parent body largely intact. Finally, *Henke et al.* (2012b) and *Monnereau et al.* (2013) focused on the eight H chondrites for which precise radiometric ages are available at three different closure temperatures (*Trieloff et al.*, 2003). They concluded that an onion-shell body with a radius 110–130 km that accreted rapidly (in <0.2 m.y.) around 1.8–2.1 m.y. after CAI formation could successfully reproduce their cooling histories without invoking any disturbance by impacts.

Constraints on the thermal histories of OCs from silicates and oxides suggest that the parent bodies did not cool with an onion-shell structure. Cation ordering temperatures in orthopyroxene in eight H4–6 chondrites indicated similar cooling rates at ~400°–500°C (*Folco et al.*, 1996). Olivine-chromite thermometry gave similar mean temperatures for H4, H5, and H6 chondrites of ~690°–770°C (*Wlotzka*, 2005). *Kessel et al.* (2007) also found several inconsistencies with the onion-shell model. *Ganguly et al.* (2013) measured compositional profiles across coexisting orthopyroxene-clinoptyroxene, olivine-spinel, and orthopyroxene-spinel grains in five H4–6 chondrites and found all grains to be essentially homogeneous. From calculated compositional profiles, they inferred that the chondrites cooled very rapidly above 700°C at rates of 25°–100°C k.y.<sup>-1</sup>, several orders of magnitude faster than the rates generally inferred from radiometric ages and metallography. *Ganguly et al.* (2013) concluded that the H-chondrite parent body had been fragmented and then reaccreted prior to cooling below 700°C.

Recently, *Scott et al.* (2014) have studied cloudy taenite, metallographic cooling rates, and shock effects in 30 H3–6 chondrites to elucidate the thermal and early impact history of the H-chondrite parent body. They focused on H chondrites with old Ar-Ar ages (>4.4 G.y.) and unshocked and mildly shocked H chondrites, as strongly shocked chondrites with such old ages are very rare. They found that cooling rates for most H chondrites at 500°C are 10°–50°C m.y.<sup>-1</sup> and do not decrease systematically with increasing petrologic type (see Fig. 2), as predicted by the onion-shell model, in which types 3–5 are arranged in concentric layers around a type 6 core. Some type 4 chondrites cooled slower than some type 6 chondrites and type 3 chondrites did not cool faster than other types, contrary to the onion-shell model. The three H4 chondrites that were used to develop the onion-shell model (*Trieloff et al.*, 2003), Ste. Marguerite, Beaver Creek, and Forest Vale, cooled through 500°C at >5000°C m.y.<sup>-1</sup>, at least 50× faster than any sample in a body that was heated by <sup>26</sup>Al and cooled without impact disturbance. Since such fast-cooled H4 chondrites are rare and cooling rates of types 3–6 overlap considerably, *Scott et al.* (2014) infer that the suite of chondrites studied by *Trieloff et al.* (2003) are simply not representative of unheated H4–6 chondrites. To explain their metallographic data, *Scott et al.* (2014) rely on recent work by *Ciesla et al.*

(2013) and propose that several early impacts punctured the H-chondrite parent body (bodies) to type 6 depths (assuming an onion-shell structure) while it was cooling, causing disturbances in the thermal histories of many H chondrites and leading to surfaces containing rocks that originated at a wide range of depths. They stress that the metallographic data do not require catastrophic disruption by impact during cooling. Considering the conflicting results reported above, it is reassuring that their results are coherent with the observed surface composition of large S-type asteroids (*Vernazza et al.*, 2014) (see section 4.2).

**2.3.3. Constraints on the thermal evolution and impact history of the L-chondrite parent body.** About two-thirds of L-chondrite meteorites were heavily shocked and degassed with <sup>39</sup>Ar–<sup>40</sup>Ar ages near 470 m.y. (*Korochantseva et al.*, 2007), suggesting that the L-chondrite parent body suffered a major impact ~470 m.y. ago and catastrophically disrupted (see also *Heymann*, 1967; *Haack et al.*, 1996, and references therein). Metallographic cooling rates of lightly shocked or unshocked L chondrites are in the range 1°–10°C m.y.<sup>-1</sup> (*Taylor et al.*, 1987). These slow cooling rates imply that the original parent body had a diameter >100 km (*Haack et al.*, 1996).

It is striking that the timing of the shock event coincides with the stratigraphic age ( $467 \pm 2$  m.y.) of the mid-Ordovician strata where abundant fossil L chondrites, meteorite-tracing chromite grains, and iridium enrichment were found in the active marine limestone quarry in southern Sweden (*Schmitz et al.*, 1997, 2003, 2007; *Greenwood et al.*, 2007). The recent shocked and fossil L chondrites may thus apparently record the same event, a catastrophic disruption of a large MBA that produced an initially intense meteorite bombardment of Earth and at least ≈30% of the OC falls today.

**2.3.4. Thermal history of the (25143) Itokawa parent body.** On the basis of the mineralogy and mineral chemistry of ~50 Itokawa dust particles, we will briefly summarize the current understanding of the thermal history of the Itokawa parent asteroid, Itokawa likely being a collisional fragment from a once larger body (*Nakamura et al.*, 2011). Mineralogical evidence indicates that Itokawa's parent body experienced thermal metamorphism and slow cooling (*Nakamura et al.*, 2014). It reached a peak metamorphic temperature of ~800°C (*Nakamura et al.*, 2011), which is lower by ~100°C than the peak temperature obtained for LL6 chondrites (*Slater-Reynolds and McSween*, 2005), suggesting that the most abundant material among Itokawa dust particles is likely LL5 material. In addition, the temperature during cooling appears to have remained higher than 700°C for 7.6 m.y. after CAI formation based on the absence of radiogenic <sup>26</sup>Mg in plagioclase (*Yurimoto et al.*, 2011a,b).

Both constraints have been used by *Wakita et al.* (2014) to reproduce the thermal evolution of the Itokawa parent asteroid via numerical simulations. They found that the Itokawa parent body appears to have formed with a radius greater than 20 km and accreted between 1.9 and 2.2 m.y. after CAI formation. Further modeling work by *Nakamura et al.* (2014) shows that a 50-km-sized body formed around

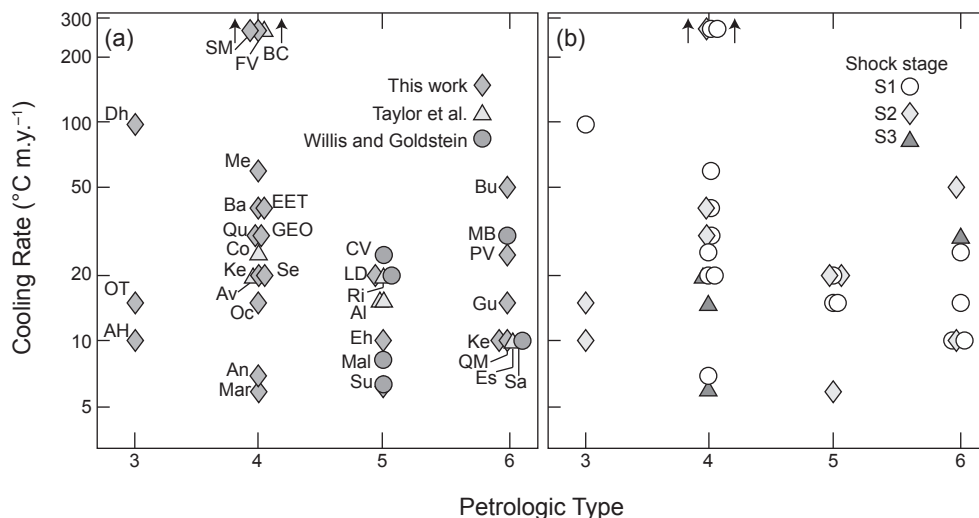


**Fig. 2.** Metallographic cooling rate vs. petrologic type for 35 H3–6 chondrites: **(a)** source of data; **(b)** shock stage of chondrites. Cooling rate ranges in types 3–6 overlap considerably, contrary to the onion-shell model, and are not correlated with shock stage. Most cooling rates have a precision of a factor of 2. From Scott et al. (2014).

~2.2 m.y. after CAIs is one of the best formation models for the Itokawa parent asteroid. In short, both papers infer that the parent body was 20–50 km in radius or larger and that it accreted 1.9–2.2 m.y. after CAI formation. However, since most LL chondrites and asteroids with LL chondrite spectral characteristics probably come from the large Flora family of asteroids, which dominates the inner part of the asteroid belt (section 5), it is likely that the Itokawa asteroid does as well and is simply deficient in type 6 material. The parent body of the Flora family of asteroids was ~100 km in radius, judging from the inferred size of the known family members (Durda et al., 2007).

### 3. IDENTIFICATION OF THE PARENT BODIES OF ORDINARY CHONDRITES

In this section, we describe the outstanding efforts that have been accomplished by a large fraction of the asteroid-meteorite community to unambiguously identify the parent bodies of OCs. These efforts include 4 decades of telescopic observations, more than 20 years of laboratory measurements and experiments, and the first asteroid sample return mission.

#### 3.1. Ordinary Chondrite Parent Bodies Among S-Type Asteroids?

The parent bodies of OCs have been searched for via visible and near-infrared photometric and/or spectroscopic observations for more than 40 years. Early photometry of asteroids based on photoelectric sensors (Chapman et al., 1971; Hapke 1971) revealed two predominant colorimetric groups: (1) those with slightly reddish sloping reflectance spectra throughout the visible out to 1 μm and with an absorption feature starting longward of 0.7 μm and with a band

minimum around 0.95 μm (such asteroids are commonly in the inner half of the belt), and (2) those with flat reflectance spectra [commonly located in the outer half of the main belt (Chapman, 2004)]. Chapman et al. (1975) introduced the taxonomy that called the reddish, moderate-albedo first group the “S-type” (mnemonic for silicaceous because the 0.95-μm band had been interpreted as being due to silicate minerals), and called the neutral-colored, low-albedo second group the “C-type” (mnemonic for carbonaceous, by analogy with carbonaceous meteorites). Thus began the C-, S-, and, later, M-, etc., asteroid taxonomy (Chapman, 2004), which has now been expanded to include most letters of the alphabet and has been further refined by many researchers [the latest taxonomy is from DeMeo et al. (2009); for a review, see the DeMeo et al. chapter in this volume]. More recent surveys, including the Sloan Digital Sky Survey (SDSS), which surveyed more than 100,000 asteroids in the visible (DeMeo and Carry, 2013, 2014), have not changed the global view presented in Chapman et al. (1975), i.e., most asteroids can still be regarded as being S or C.

Early comparisons between meteorite and asteroid optical reflectance spectra (e.g., Chapman and Salisbury, 1973) suggested that only S-type asteroids have spectral characteristics (e.g., absorption band near 0.95 μm) compatible with those seen in OCs, although S-type asteroids have a redder reflectance. Subsequent measurements in the near-infrared range have not altered this picture (e.g., Gaffey et al., 1993; Vernazza et al., 2008, 2009, 2014; DeLeon et al., 2010; Thomas and Binzel, 2010; Dunn et al., 2013). The spectral slope difference between OC and S-type spectra (see Fig. 3), however, has for more than 30 years been an obstacle to establishing a definite link between both groups and has constituted one of the greatest conundrums in the asteroid-meteorite field [see Chapman (2004) for an extensive review

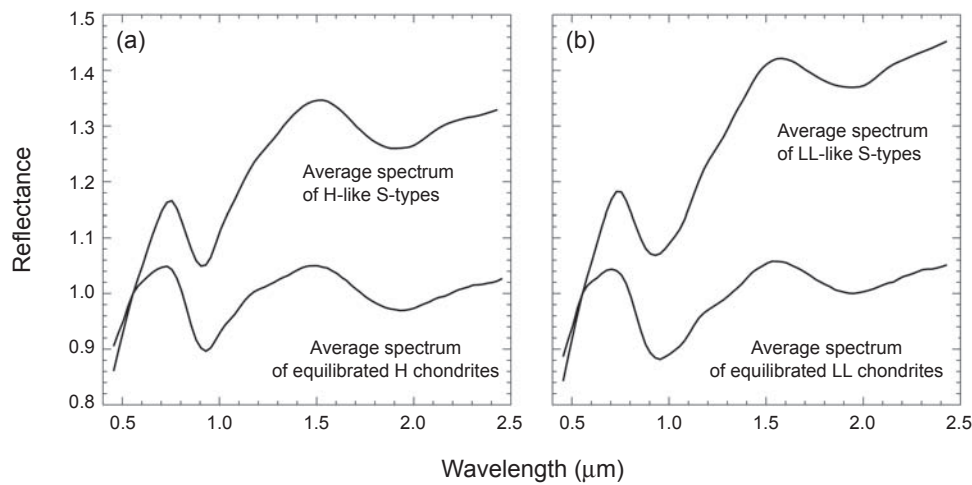


**Fig. 3.** Spectral comparisons of S-type asteroids and ordinary chondrite meteorites. Comparison between the visible to near-infrared spectral signatures of main-belt S-type asteroids [(a) asteroids with H-like compositions; (b) asteroids with LL-like compositions] and the average spectra of equilibrated (type 4–6) H- and LL-chondrite meteorites. Space weathering processes similar to those acting on the Moon (e.g., Pieters *et al.*, 2000) redden the ordinary chondrite-like spectrum of a fresh asteroid surface, giving it the appearance of an S-type spectrum (e.g., Vernazza *et al.*, 2008, and references therein). Adapted from Vernazza *et al.* (2014).

on this subject]. The conundrum was even reinforced on the basis of mineralogical arguments (Gaffey *et al.*, 1993) that were suggesting that a large fraction of S-type asteroids are partly differentiated and thus not OC-like (Abell *et al.*, 2007). This view was held by a small fraction of the community until the Itokawa sample return (Abell *et al.*, 2007).

### 3.2. Hayabusa Confirms a Linkage Between S-Type Asteroids and Ordinary Chondrites

The Japanese spacecraft Hayabusa was launched onboard an M-V-5 rocket on May 9, 2003. The aims of the Hayabusa mission were to (1) confirm a linkage between S-type asteroids and OCs, and (2) uncover the mechanisms of space weathering, responsible for the mismatch of reflectance spectra between S-type asteroids and OCs (see the chapter by Yoshikawa *et al.* in this volume for an overview of the mission and its main results). Hayabusa arrived at the S-type asteroid (25143) Itokawa (Fig. 4) in September 2005 and observed its surface using a variety of onboard apparatus (Fujiwara *et al.*, 2006). The results of the *in situ* measurements indicated that the reflectance spectra (Abe *et al.*, 2006) are similar to those of equilibrated LL chondrites, thus confirming Binzel *et al.*'s (2001) earlier prediction. Hayabusa touched down twice on smooth terrain at "MUSES-C Regio" (Fig. 4a) and tried to recover surface samples from the asteroid. Although projectiles that planned to hit the asteroid surface did not fire, the sampling horn of the spacecraft touched the surface several times, which likely stirred up the Itokawa particles captured by the spacecraft (Yano *et al.*, 2006). The spacecraft finally came back to Earth in June 2010, five years after the touchdown.

Numerous small particles mostly less than 50 μm in size were found in the Hayabusa sample container and were recovered one by one by electrostatic manipulator operation in a pure nitrogen atmosphere (Nakamura *et al.*, 2011; Yada *et al.*, 2014). The initial analysis for basic characterization of approximately 60 Itokawa dust particles showed that the mineralogy and mineral chemistry of the Itokawa dust particles were identical to those of equilibrated LL chondrites (Nakamura *et al.*, 2011) (see Fig. 5). Oxygen-isotope ratios of silicates also indicate the similarity to equilibrated LL chondrites (Yurimoto *et al.*, 2011a,b; Nakashima *et al.*, 2014). Minor and major elemental abundances were found to be similar to those of OCs (Ebihara *et al.*, 2011). In addition, the modal abundance of minerals, bulk density, porosity, and grain size of the Itokawa particles were found to be similar to those of LL chondrites (Tsuchiyama *et al.*, 2014).

Figures 6a,b show typical Itokawa particles. Olivine is the most abundant mineral, as is the case for LL chondrites. Most of the olivine particles have compositions equilibrated around Fa<sub>29</sub> (Fig. 5), which is within the compositional range of equilibrated LL chondrites, but some olivines show Mg-rich compositions, suggesting that they were on the way to final equilibration (Nakamura *et al.*, 2011). The next most abundant minerals are — as usually observed among equilibrated LL chondrites — low- and high-Ca pyroxenes and plagioclase, and their compositions are also almost homogeneous.

In summary, all measurements performed on Itokawa both *in situ* and in terrestrial laboratories indicate that the asteroid has an LL-like composition. This result confirms what many researchers had predicted (e.g., Pellas, 1988), namely that S-type asteroids comprise the parent bodies of

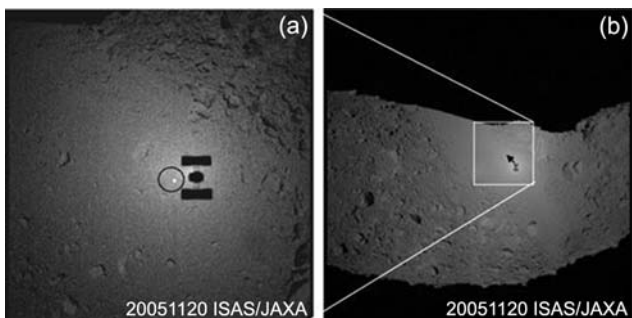


**Fig. 4.** Itokawa's landing site. **(a)** Hayabusa is descending toward MUSES-C Regio and the shadow of the spacecraft is projected on the surface. **(b)** A whole view of the MUSES-C region. JAXA digital images P-043-15285.

OCs. This fact implies that space weathering processes are generally responsible for the spectral mismatch between OCs and S-type asteroids (e.g., *Sasaki et al.*, 2001; *Strazzulla et al.*, 2005; see the chapter by Brunetto et al. in this volume for a detailed review), which we summarize in the next subsection.

### 3.3. Space Weathering Processes Responsible for the Spectral Mismatch Between Ordinary Chondrites and S-Type Asteroids

Over the last 15 years, laboratory experiments simulating space weathering effects on OCs and its main minerals (olivine, pyroxene) (e.g., *Sasaki et al.*, 2001; *Strazzulla et al.*, 2005; *Marchi et al.*, 2005; *Brunetto et al.*, 2006; see the chapter by Brunetto et al. in this volume for more information) have established unambiguously that OC-like material naturally reddens (spectrally) in space under both bombardment by micrometeorites and irradiation by solar wind particles, a conclusion that was reinforced by the analysis of both the images and near-infrared spectra of Itokawa's surface collected by Hayabusa as well as the S-type samples that Hayabusa brought back to Earth (*Nakamura et al.*, 2011).

Spatially resolved images and near-infrared spectra of Itokawa's surface by Hayabusa (*Hiroi et al.*, 2006) revealed developing space weathering on Itokawa's surface. Specifically, *Hiroi et al.* (2006) showed that dark areas on Itokawa possess on average redder spectra than bright areas, in agreement with space weathering spectral trends predicted by laboratory experiments (e.g., *Sasaki et al.*, 2001; *Strazzulla et al.*, 2005; see the chapter by Brunetto et al.).

Subsequent laboratory measurements of the three-dimensional structure of the Itokawa particles determined by X-ray microtomography suggested that they have been impacted by meteoroids (*Tsuchiyama et al.*, 2011); the discovery of microcraters on the surface of some Itokawa particles reinforced the evidence of interplanetary dust particles impacting asteroid surfaces (*Nakamura et al.*, 2012). Large amounts of solar wind noble gases were also detected within the Itokawa

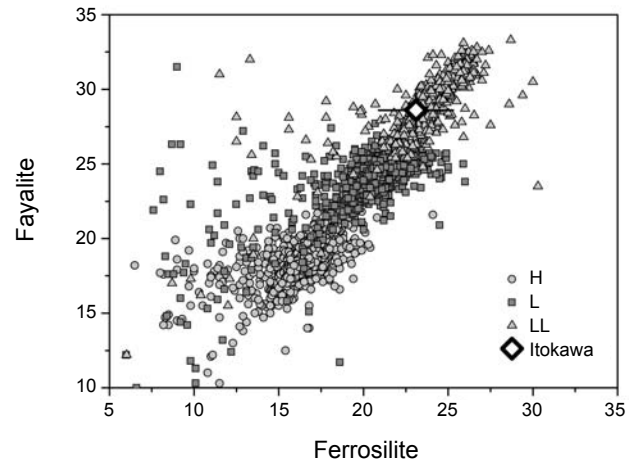


**Fig. 5.** Comparison between the mineral chemistry of the Itokawa particles and that of H, L, and LL chondrites. From *Nakamura et al.* (2011).

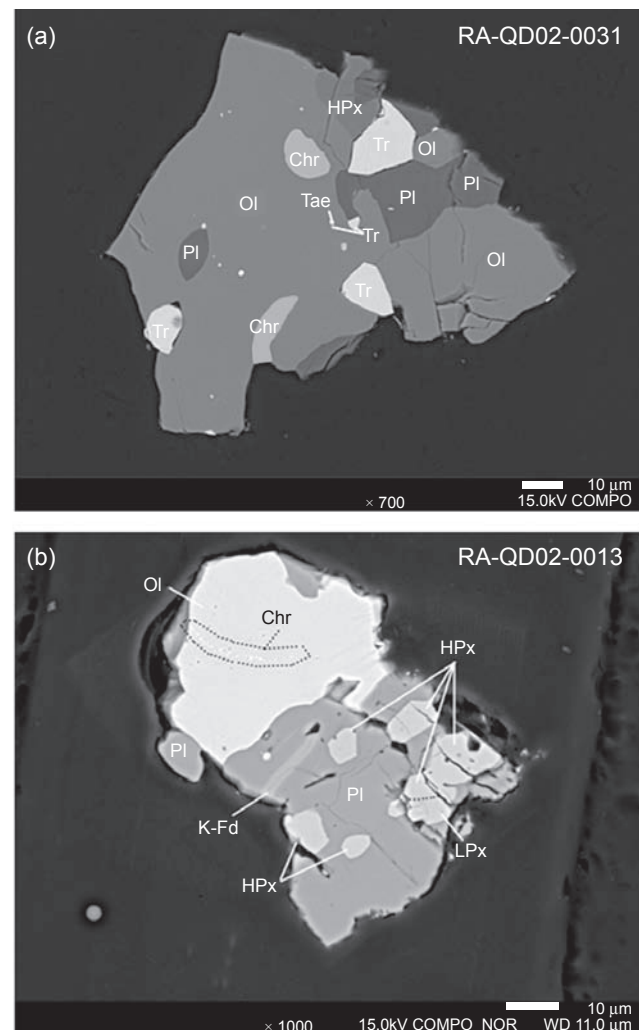


**Fig. 6.** Backscattered electron images of polished sections of typical Itokawa particles: **(a)** RA-QD02-0031; **(b)** RA-QD02-0013. OI = olivine, PI = plagioclase, Tae = taenite, Tr = troilite, Chr = chromite, LPx = low-Ca pyroxene, HPx = high-Ca pyroxene, K-fd = K feldspar.

particles, implying that solar wind implantation into the regolith particles is a common process (Nagao *et al.*, 2011). In parallel, a careful inspection of the Itokawa surface samples revealed sulfur-bearing and sulfur-free Fe-rich nanoparticles at the outermost layers of the Itokawa particles (Noguchi *et al.*, 2011), thus identifying the reddening agent responsible for the color difference between S-types and OCs. The results of further TEM analysis identified three types of particle surface modifications induced by space weathering processes (Noguchi *et al.*, 2014). In summary, all these results indicate that the Itokawa dust particles — recovered from the space-weathered area MUSES-C Regio — record intensive interactions between the asteroid regolith and incoming particles such as solar wind ions and interplanetary dust. The Hayabusa mission has thus confirmed what was suspected for a long time, namely that OCs originate from S-type asteroids and that the spectral mismatch between OCs and S-types is mainly due to space weathering processes.

As a consequence (and ironically, considering how long the S-type/OC conundrum lasted), the *normal* appearance of an OC-like asteroid is an S-type asteroid (spectral mismatch between OCs and their parent bodies), while the *anomalous* appearance of an OC-like asteroid is a Q-type asteroid (spectral match between OCs and their parent bodies)! The existence of Q-type asteroids, which indicates that rejuvenating processes do occur on some asteroids (see the chapter by Brunetto *et al.*), has offered us the opportunity to unveil a new physical process in asteroid science, namely seismic shaking during planetary encounters (Nesvorný *et al.*, 2005; Marchi *et al.*, 2006; Binzel *et al.*, 2010; DeMeo *et al.*, 2014; see also the chapter by Binzel *et al.* in this volume). Note that thermal fatigue (Delbo *et al.*, 2014) and spin-up due to the YORP effect (see the chapter in this volume by Vokrouhlický *et al.* and references therein) may also play a role in refreshing asteroid surfaces.

### 3.4. How Many S-Type Asteroids Actually Have Ordinary-Chondrite-Like Mineralogies?

At a time when it was still not fully accepted that S-type asteroids comprise the parent bodies of OCs, researchers started comparing the surface mineralogy of S-type asteroids with that of OCs to test a possible link between the two groups of objects (e.g., Gaffey *et al.*, 1993). Such compositional investigation could not be performed in the visible domain only: It required extended wavelength coverage into the near-infrared (ideally, a spectral coverage over the 0.4–2.5  $\mu\text{m}$  range; see the chapter by Reddy *et al.* in this volume). In this extended wavelength range, both S-types and OCs possess prominent 1- and 2- $\mu\text{m}$  spectral features due to the presence of olivine and pyroxene in the two populations (see Fig. 6).

Gaffey *et al.* (1993) were the first to perform this type of mineralogical investigation for a large number of S-type asteroids (39 objects; it actually turns out that only 32 of these objects are S-type MBAs). They used a classification scheme (see Fig. 7) based on band area ratios (BAR) (area

of Band II divided by area of Band I) and Band I centers to break the S-types into seven subtypes [from S(I) to S(VII)], corresponding to varying ratios of olivine to pyroxene. The BAR value tends to increase and the Band I center value tends to decrease as the subtype number increases in value, which indicates an increasing pyroxene concentration (Burbine, 2014). Their S(I) type has an olivine-dominated mineralogy, and in the new classification by DeMeo *et al.* (2009) corresponds mostly to A-types (and thus not to S-types anymore), while the S(IV) subtype has an olivine-pyroxene mineralogy similar to that of OCs. Both the S(II) and S(III) subtypes were interpreted as having olivine-dominated mineralogies with a high-Ca pyroxene component, while the S(V) and S(VII) were interpreted as having a higher and significant high-Ca pyroxene component.

The main conclusion of Gaffey *et al.*'s (1993) investigation is that few S-type asteroids have silicate mineralogies consistent with those of OCs, and that the diversity within the S-class arises from several sources, including the coexistence of undifferentiated, partially differentiated, and fully differentiated bodies within the general S-type population.

Concerning the few objects that were considered OC-like, Gaffey *et al.* (1993) noticed that they are concentrated near the 3:1 Kirkwood gap at 2.5 AU and proposed that their favorable location close to this resonance might explain why OCs are so abundant among meteorite falls. A few years later, Gaffey and Gilbert (1998) proposed asteroid (6) Hebe as the probable parent body of H-type OCs and, since then, many authors have relied on this association in their studies (e.g., Akridge *et al.*, 1998; Ghosh *et al.*, 2003; Bottke *et al.*, 2010; Henke *et al.*, 2012, 2013). In the early 2000s, the idea that several S-type asteroids have high fractions of

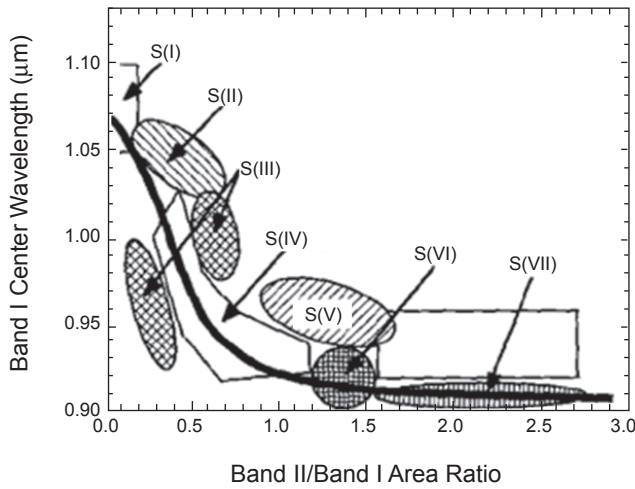


**Fig. 7.** Distribution of Gaffey *et al.* (1993) S subtypes on a plot of Band Area Ratio vs. Band I center. The thick black line is the olivine-orthopyroxene mixing line. The ordinary chondrite region is the same as the S(IV) region. The HED region (rectangle above SVII) is also plotted. From Gaffey *et al.* (1993).

high-Ca pyroxene on their surfaces, which is an indication that these bodies have undergone either melting or partial melting and thus cannot be linked to OCs, was brought up again by Sunshine et al. (2004), Hardersen et al. (2006), and Abell et al. (2007) in the case of Itokawa.

During the following years, the emergence of numerous high-quality spectroscopic measurements in the near-infrared (obtained essentially with the NASA IRTF), along with the growing utilization within the community of new spectral analysis tools [modified Gaussian method (MGM) and radiative transfer model; see the chapter by Reddy et al. in this volume] has progressively overturned the view by Gaffey et al. (1993) that many S-types are compositionally unconnected to OCs. Using both MGM and a radiative transfer model to constrain the mineralogy of a large sample of S-type NEAs, Vernazza et al. (2008) showed that most of these objects have silicate mineralogies that are compatible with those of OCs. Their findings were later confirmed by DeLeon et al. (2010), Dunn et al. (2013), and Thomas et al. (2014) for even larger samples of S-type NEAs, and by Vernazza et al. (2009), De Leon et al. (2010), and Vernazza et al. (2014) for large samples of S-type MBAs. Various authors derived the mineralogy of smaller samples of S-types and found OC-like mineralogies in most cases (Binzel et al., 2001, 2009; Reddy et al., 2009, 2011a,b, 2012; Fieber-Beyer and Gaffey, 2011, 2014; Fieber-Beyer et al., 2012; Gietzen et al., 2012; Sanchez et al., 2013).

### 3.5. Are There Meteorites Other than the Ordinary Chondrites Derived from S-Type Asteroids?

S-type asteroids are a diverse group of objects, and one cannot exclude that some meteorites other than the OCs could also originate from them (e.g., Burbine et al., 2002). Possibilities include differentiated meteorites, as proposed by Sunshine et al. (2004), such as pallasites, brachinites, ureilites, lodranites, winonaites, IAB irons, and mesosiderites (Gaffey et al., 1993).

Primitive achondrites (including winonaites, lodranites, acapulcoites, and brachinites) are meteorites with affinities to chondrites. They have undergone partial melting but the silicate and metal portions have not segregated, and so they retain their chondritic bulk composition; they are therefore likely to have spectral similarities to chondrites. Indeed, it appears that both lodranites and acapulcoites have spectral properties and ol/(ol + low Ca-px) ratios that are very similar to OCs and H chondrites in particular (see Fig. 8), although they are on average slightly more pyroxene-rich than H chondrites. However, there are two reasons as to why most H-like S-type asteroids may not be linked to either of these meteorite classes. The first is that the center of Band II for both lodranites and acapulcoites is located between 1.8 and 1.9  $\mu\text{m}$ , while the band center for H chondrites [and H-like S-types (see Vernazza et al., 2014)] and other OCs is located between 1.9 and 2  $\mu\text{m}$ , indicating differences in terms of pyroxene composition between the two groups. The second reason is that both lodranites and acapulcoites together

represent ~0.2% of the falls, implying that they are ~150× less abundant than H chondrites among falls (and ~400× less abundant than OCs in general). Although it is clear that even at similar densities and tensile strength (which is typically the case for the H, L, and LL chondrites but also for lodranites and acapulcoites), meteorite falls are not exactly representative of the compositional diversity of the asteroid belt (Vernazza et al., 2014), they still are within a factor of ~10, implying that lodranite-like and acapulcoite-like bodies should be rare among S-types.

Mesosiderites are complex brecciated meteorites consisting of metal-rich and silicate-rich portions. Their spectra (Burbine et al., 2007) are at odds with those of S-type asteroids and/or OCs (see Fig. 8). The same applies to ureilites, which are igneous meteorites composed of olivine and pyroxene with notably large amounts of carbon (several percent). The possibility that ureilites could have an S-type asteroid source could be tested when the Almahatta Sitta ureilite breccia fell near Nahr an Nil in Sudan in 2008. The

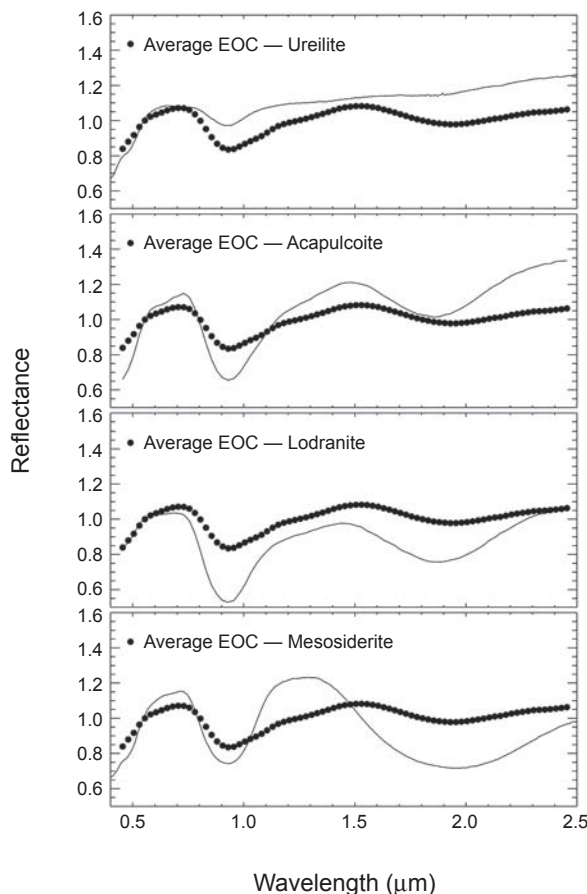


**Fig. 8.** Comparison between an average spectrum of equilibrated H, L, and LL chondrites and the spectra of ureilites, acapulcoites, lodranites, and mesosiderites (data taken from the RELAB database). While the spectra of both ureilites and mesosiderites appear quite different from the OC spectra, both lodranites and acapulcoites have similar spectra with respect to OCs.

spectroscopic features of the parent asteroid for Almathatta Sitta, 2008 TC<sub>3</sub>, were determined by Jenniskens *et al.* (2010). They concluded that the asteroid most closely resembled an F-type asteroid, and that this asteroid type is more likely to be the parent to ureilites than S-type asteroids.

Brachinites, whose spectra are not described here, are far more olivine-rich than LLs. Their spectra are great analogs for A-type asteroids but certainly not for S-type ones (Sunshine *et al.*, 2007). Finally, pallasites are also olivine-rich meteorites. As in the case of brachinites, their parent asteroids should be hidden among A-type asteroids (Sunshine *et al.*, 2007).

#### 4. CONSTRAINTS ON THE FORMATION AND EVOLUTION OF ORDINARY CHONDRITE PARENT BODIES FROM TELESCOPE OBSERVATIONS

The ability to link specific OC classes (H, L, and LL) to specific S-type asteroids via visible and near-infrared spectroscopy has not only provided us with a better understanding of the formation mechanism of OC parent bodies and planetesimals in general, it has also boosted our understanding of asteroid dynamics and in particular the delivery process of meteorites and NEAs from the main belt to near-Earth space.

##### 4.1. What Have We Learned from S-Type Near-Earth Asteroids?

Spectroscopic observations of more than 400 NEAs in visible wavelengths show that 65% of NEAs have S- and Q-type spectral properties (Binzel *et al.*, 2004). When corrected for discovery biases (Stuart and Binzel, 2004), the near-Earth population of S- and Q-type asteroids is estimated to be 36% of the total NEA population. Vernazza *et al.* (2008) used both MGM and a radiative transfer model to analyze the visible and near-infrared spectra of 38 S- and Q-type NEAs from Binzel *et al.* (2004) and reported that most NEAs (approximately two-thirds) have spectral properties similar to LL chondrites (see Fig. 9). This result is surprising, because LL chondrites are the least-abundant OCs (they represent only 10% of all OCs, and 8% of all meteorites). Vernazza *et al.* (2008) argued that the NEAs we sample telescopically (with radii of 0.3 km to 10 km) are not the immediate parent bodies of smaller objects that fall to Earth as meteorites (i.e., preatmospheric meteorite parent bodies having radii on the order of meters) and that different dynamical mechanisms (mainly a size-dependent process such as the Yarkovsky effect) and/or main-belt source regions may be responsible for supplying these two sample populations. They further proposed the Flora family (near the v<sub>6</sub> secular resonance) as the source region for NEAs with LL-like compositions.

Thomas and Binzel (2010) used MGM to determine meteorite analogs for a sampling of S-type NEAs and then used the Bottke *et al.* (2002) dynamical model to determine the probable source region for each of those NEAs. They

found that H chondrites have a higher than average delivery preference though the 3:1 mean-motion resonance, whereas LL chondrites are mostly injected in the near-Earth space via the v<sub>6</sub> resonance. De León *et al.* (2010) and Dunn *et al.* (2013) also concluded that the Flora family is the dominant source of NEAs and LL chondrites, based on inferred mineralogies of large samples of NEAs. A more recent study by Thomas *et al.* (2014) of an even larger sample of S-type NEAs (109 objects) concluded that NEAs have elevated percentages of potential LL OCs compared to the meteorite fall statistics. However, they also concluded that the relative proportions among NEAs of the OC spectral types lie somewhere between the H- and L-chondrite dominant meteorite fall statistics and the LL-chondrite spectral types

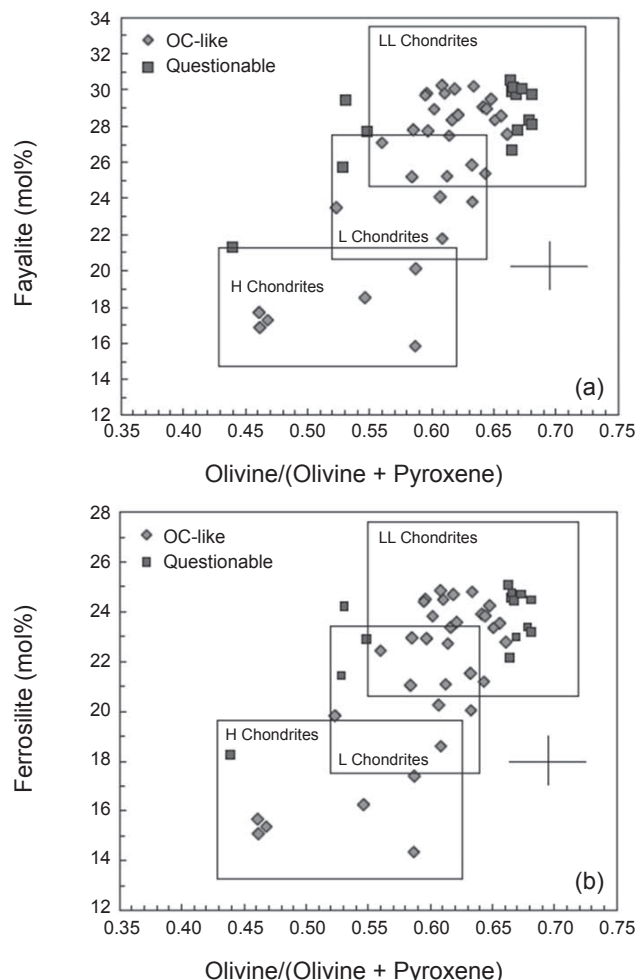


**Fig. 9.** Comparison between the mineralogies of 47 NEAs and those of ordinary chondrites. NEAs are plotted as (a) ol/(ol + px) vs. mol% Fa in olivine and (b) ol/(ol + px) vs. mol% Fs in low-Ca pyroxene. Compositional regions for the H, L, and LL chondrites were defined by Dunn *et al.* (2010). NEAs with definitive OC-like spectral parameters are represented by boxes, while NEAs with questionable spectral classification are represented by diamonds. Error bars represent the least-mean-square error of spectrally derived mineralogies: 0.03 for ol/ol + px, 1.3 for mol% Fa, and 1.4 for mol% Fs. From Dunn *et al.* (2013).

dominant NEA statistics as calculated by Dunn *et al.* (2013) and seen in Vernazza *et al.* (2008) and De León *et al.* (2010).

#### 4.2. What Have We Learned from S-Type Main-Belt Asteroids?

As stated above, Gaffey *et al.* (1993) observed 32 main-belt S-types and found that most of these objects do not have OC-like mineralogies. They suggested that most of the non-OC-like S-type asteroids originate from partially or fully differentiated bodies. More recently, Vernazza *et al.* (2014) revisited this question by conducting an extensive spectroscopic survey of 83 main-belt S-type asteroids and 3 S-type families, and obtaining the biggest spectral dataset yet assembled for the largest S-type asteroids (95% of all objects larger than 60 km). In parallel, they built up the existing database of OC laboratory spectral measurements by collecting spectra for 53 unequilibrated OCs (i.e., for the most primitive OCs). Thus the database now spans a much broader range of temperature history (from unheated to significantly metamorphosed) than previously analyzed. On the basis of these two spectral surveys, they reach the following conclusions:

1. Most S-type asteroids, including large ones ( $D \approx 100\text{--}200$  km), although not members of one family, are distributed into two well-defined compositional groups (see Fig. 10), Hebe-like and Flora-like (H-like and LL-like). This indicates that identical compositions among multiple asteroids are a natural outcome of planetesimal formation, making it possible that meteorites within a given class originate from multiple parent bodies.

2. The surfaces of nearly all these asteroids (up to 200 km) show the same compositional characteristics as high-temperature meteorites (type 4–6 OCs) that were metamorphosed in their interiors, these exposed interiors being a likely consequence of impacts by small asteroids ( $D < 10$  km) in the early solar system (Ciesla *et al.*, 2013).

3. The lack of compositional variation within both H-like asteroid families and the surfaces of the family members showing the same compositional characteristics as high-temperature meteorites (type 4–6 OCs) is consistent with their parent bodies having been metamorphosed throughout, which implies — following current thermal models — that their formation process must have been rapid. Note that such a short duration of accretion as implied by the observations of Vernazza *et al.* (2014) is consistent with current models of planet formation through streaming and gravitational instabilities (Youdin and Goodman, 2005; Johansen *et al.*, 2007; Chiang and Youdin, 2010) that show that bodies of several hundred kilometers in size form on the timescale of a few orbits (Johansen *et al.*, 2011; Youdin, 2011; Johansen *et al.*, 2012).

4. LL-like bodies formed closer to the Sun than H-like bodies, a possible consequence of radial mixing and size sorting of chondrules in the protoplanetary disk prior to accretion.

5. LL-like bodies formed on average with larger sizes than H-like bodies.

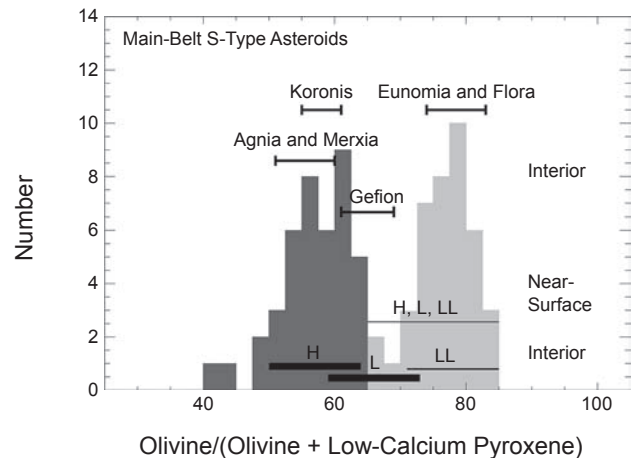


**Fig. 10.** Bimodal compositional distribution of main-belt S-type asteroids. The S-type sample comprises 83 objects, including 54 of the 56 main-belt S-types with  $D > 60$  km. Objects belonging to collisional families are not included in the histogram counts. Instead, the compositional range for the six main asteroid families (Agnia, Merxia, Koronis, Gefion, Eunomia, Flora) are shown at the top. The compositional ranges for the individual ordinary chondrite classes of «interior» samples (H, L, and LL having petrologic types  $>3.5$ ; temperature histories  $>400^\circ\text{C}$ ) are shown at the bottom. Above, we display the compositional range for the least-metamorphosed OCs (types 3.0–3.5; temperatures  $<400^\circ\text{C}$ ) that are interpreted as surface samples. The thickness of the various compositional ranges for meteorites is proportional to their fall statistics. Finally, the diversity of S-type asteroids includes compositions outside the range of ordinary chondrites, as seen for the two objects having  $\text{ol}/(\text{ol} + \text{low-Ca px}) < 45\%$ . From Vernazza *et al.* (2014).

#### 5. SUMMARY AND CONCLUSIONS

The nature of the parent bodies of OCs is no longer a mystery (Nakamura *et al.*, 2011). It has now been clearly established that the parent bodies of OCs are hidden among the S-type asteroids. Actually, most S-type asteroids are plausible OC parent bodies as they share similar spectral properties and thus similar mineralogies (Vernazza *et al.*, 2014).

Spectroscopic surveys have allowed determining rather precisely the compositional distribution among S-type NEAs and S-type MBAs. It appears that the majority of the S-type NEAs have LL-like mineralogies, implying important compositional differences between NEAs and meteorites (Vernazza *et al.*, 2008; De León *et al.*, 2010; Dunn *et al.*, 2013; Thomas *et al.*, 2014) and therefore different source regions for both populations. Concerning S-type MBAs, it appears that most S-type asteroids, including large ones ( $D \approx 100\text{--}200$  km), are distributed into two well-defined compositional groups, Hebe-like and Flora-like (H-like and LL-like), with Flora-like bodies being located — on average — closer to the Sun than Hebe-like bodies (Vernazza *et al.*, 2014). In addition, the surfaces of nearly all these asteroids (up

to 200 km) show the same compositional characteristics as high-temperature meteorites (type 4–6 OCs) that were metamorphosed in their interiors, suggesting that impacts may have played an important role in their structural evolution (Vernazza *et al.*, 2014). Interestingly, the metallographic cooling rates of H chondrites are in agreement with those observations, as they suggest that several early impacts punctured the H-chondrite parent body (or bodies) while it was cooling, causing disturbances in the thermal histories of many H chondrites and leading to surfaces containing rocks that originated at a wide range of depths (Taylor *et al.*, 1987; Scott *et al.*, 2011, 2013, 2014).

Although significant progress has been made since the *Asteroids III* book in linking OCs to S-types, there are several issues remaining that require critical new data:

1. The source regions of the individual OC classes remain to be determined. Currently, we only have predictions for the source regions of both L and LL chondrites; namely, the Gefion family is predicted, based on dynamical and compositional aspects (Nesvorný *et al.*, 2009; Vernazza *et al.*, 2014), to be the source of L chondrites, while the Flora family is proposed to be the source of most LL chondrites (e.g., Vernazza *et al.*, 2008). The source of H chondrites is currently unknown; Vernazza *et al.* (2014) have shown that several prominent S-type families could be the source of these meteorites.

Over the next decade, the ongoing development and installation of several fireball observation networks across the world [e.g., the Fireball Recovery and InterPlanetary Network (FRIPON), <http://ceres.geol.u-psud.fr/fripo/>] will help solve this long-standing issue. These camera networks will observe a statistically significant number of falls within the next 10 years and thus allow the determination of precise orbits (and hence directly the source region) for a large number of meteoroids. Hopefully, they will also allow us to recover a nonnegligible number of meteorites. Recent successful meteorite recoveries include the Tagish Lake, Almahata Sitta, Maribo, Kosice, Bunburra Rockhole, and Sutter's Mill falls (see the chapters by Borovička *et al.* and Jenniskens in this volume).

2. It remains to be explained why there are so few LL chondrites and so many H and L chondrites among falls (Vernazza *et al.*, 2008) given that the prominent LL-like Flora family is located next to the most prolific (in terms of delivery) resonance (namely, v<sub>6</sub>). In other terms, the observed compositional difference between meteorites and NEAs (Vernazza *et al.*, 2008) has yet to be explained.

3. It remains to be established whether the individual OC classes (H, L, LL) originate from one or several parent bodies. Spectroscopic surveys have opened the possibility that the individual OC classes can come from several parent bodies (Vernazza *et al.*, 2014). A new generation of meteorite measurements may shed light on this issue. Fireball observation networks will also help provide answers to this question.

4. The diversity of the fall statistics between H, L, and LL chondrites as a function of petrologic type remains to be explained [62% of H chondrites are type 4 and 5, while

type 6 represents only 21%, 68% of Ls are type 5 and 6, and 59% of LLs are type 5 and 6 (Hutchison, 2004)]. Modeling the thermal evolution of OC parent bodies as a function of the parent body's size may certainly help to shed light on this issue. [With Hebe not necessarily being the parent body of H chondrites, a D ~ 100-km-sized parent body should be envisioned along with a D ~ 200-km-sized one for H chondrites, while larger parent bodies should be considered for the L- and LL-chondrite parent bodies (see Vernazza *et al.*, 2014)]. Determining whether all meteorites within a given OC class (e.g., H chondrites) come from the same parent body via both fireball observation networks and refined measurements on OCs will also help explain the diversity of the fall statistics.

5. Spectroscopic surveys have revealed that the parent bodies of LL chondrites formed on average larger than that of H chondrites (Vernazza *et al.*, 2014). An explanation of this observation remains to be found.

6. The parent bodies of lodranites and acapulcoites are likely hidden among S-type asteroids. A careful spectral analysis of these meteorites will help to pinpoint their possible parent bodies.

7. The nature of the parent bodies of HH (Burnwell and Willaroy), H/L, and L/LL chondrites remains to be understood. The paucity of H/L and L/LL chondrites may hint at a rather clear separation between the H, L, and LL rings in the disk during accretion.

**Acknowledgments.** We thank T. Dunn, T. Burbine, and F. DeMeo for their careful reviews.

## REFERENCES

- Abe M., Takagi Y., Kitazato K., Abe S., Hiroi T., et al. (2006) Near-infrared spectral results of asteroid Itokawa from the Hayabusa spacecraft. *Science*, *312*, 1334–1338.
- Abell P. A., Vilas F., Jarvis K. S., Gaffey M. J., and Kelley M. S. (2007) Mineralogical composition of (25143) Itokawa 1998 SF36 from visible and near-infrared reflectance spectroscopy: Evidence for partial melting. *Meteoritics & Planet. Sci.*, *42*, 2165–2177.
- Akridge G., Benoit P. H., and Sears D. W. G. (1998) Regolith and mega-regolith formation of H-chondrites: Thermal constraints on the parent body. *Icarus*, *132*, 185–195.
- Baker J., Bizzarro M., and Wittig N. (2005) Early planetesimal melting from an age of 4.5662 Gyr for differentiated meteorites. *Nature*, *436*, 1127–1131.
- Bell J. F., Davis D. R., Hartmann W. K., and Gaffey M. J. (1989) Asteroids — The big picture. In *Asteroids II* (R. P. Binzel *et al.*, eds.), pp. 921–945. Univ. of Arizona, Tucson.
- Bennett M. E. III and McSween H. Y. Jr. (1996) Revised model calculations for the thermal histories of ordinary chondrite parent bodies. *Meteoritics & Planet. Sci.*, *31*, 783–792.
- Binns R. A. (1967) Structure and evolution of non-carbonaceous chondritic meteorites. *Earth Planet. Sci. Lett.*, *2*, 23–28.
- Binzel R. P., Rivkin A. S., Bus S. J., Sunshine J. M., and Burbine T. H. (2001) MUSES-C target asteroid (25143) 1998 SF36: A reddened ordinary chondrite. *Meteoritics & Planet. Sci.*, *36*, 1167–1172.
- Binzel R. P. *et al.* (2004) Observed spectral properties of near-Earth objects: Results for population distribution, source regions, and space weathering processes. *Icarus*, *170*, 259–294.
- Binzel R. P. *et al.* (2009) Spectral properties and composition of potentially hazardous asteroid (99942) Apophis. *Icarus*, *200*, 480–485.
- Binzel R. P. *et al.* (2010) Earth encounters as the origin of fresh surfaces on near-Earth asteroids. *Nature*, *463*, 331–334.

- Bischoff A., Scott E. R. D., Metzler K., and Goodrich C. A. (2006) Nature and origins of meteoritic breccias. In *Meteorites and the Early Solar System II* (D. S. Lauretta and H. Y. McSween Jr., eds.), pp. 679–712. Univ. of Arizona, Tucson.
- Bizzarro M., Baker J. A., Haack H., and Lundgaard K. L. (2005) Rapid time scales for accretion and melting of differentiated planetesimals inferred from  $^{26}\text{Al}$ - $^{26}\text{Mg}$  chronometry. *Astrophys. J. Lett.*, 632, L41–L44.
- Bonal L., Quirico E., Bourot-Denise M., and Montagnac G. (2006) Determination of the petrologic type of CV3 chondrites by Raman spectroscopy of included organic matter. *Geochim. Cosmochim. Acta*, 70, 1849–1863.
- Bonal L., Bourot-Denise M., Quirico E., et al. (2007) Organic matter and metamorphic history of CO chondrites. *Geochim. Cosmochim. Acta*, 71, 1605–1623.
- Bottke W. F. Jr., Morbidelli A., Jedicke R., Petit J.-M., Levison H. F., Michel P., and Metcalfe T. S. (2002) Debiased orbital and absolute magnitude distribution of the near-Earth objects. *Icarus*, 156, 399–433.
- Bottke W. F., Vokrouhlický D., Nesvorný D., and Shrebeny L. (2010) (6) Hebe really is the H chondrite parent body. *Bull. Am. Astron. Soc.*, 42, #46.06.
- Bourot-Denise M., Zanda B., and Hewins R. (1997) Metamorphic transformations of opaque minerals in chondrites. In *Workshop on Parent-Body and Nebular Modification of Chondritic Materials*, Abstract #4040, p. 5. LPI Technical Report 97-02, Lunar and Planetary Institute, Houston.
- Brunetto R., Romano F., Blanco A., Fonti S., Martino M., Orofino V., and Verriente C. (2006) Space weathering of silicates simulated by nanosecond pulse UV excimer laser. *Icarus*, 180, 546–554.
- Burbine T. H. (2014) Asteroids. In *Treatise on Geochemistry* (H. Holland and K. Turkian, eds.), pp. 365–415. Elsevier Pergamon, San Diego.
- Burbine T. H., McCoy T. J., Meibom A., Gladman B., and Keil K. (2002) Meteoritic parent bodies: Their number and identification. In *Asteroids III* (W. F. Bottke Jr. et al., eds.), pp. 653–667. Univ. of Arizona, Tucson.
- Burbine T. H., Greenwood R. C., Buchanan P. C., Franchi I. A., and Smith C. L. (2007) Reflectance spectra of mesosiderites: Implications for asteroid 4 Vesta. In *Lunar Planet. Sci. XXXVIII*, Abstract #2119. Lunar and Planetary Institute, Houston.
- Chapman C. R. (2004) Space weathering of asteroid surfaces. *Annu. Rev. Earth Planet. Sci.*, 32, 539–567.
- Chapman C. R. and Salisbury J. W. (1973) Comparisons of meteorite and asteroid spectral reflectivities. *Icarus*, 19, 507–522.
- Chapman C. R., Johnson T. V., and McCord T. B. (1971) A review of spectrophotometric studies of asteroids. In *Physical Studies of Minor Planets* (T. Gehrels, ed.), pp. 51–65. IAU Colloq. 12, Univ. of Sydney, Sydney.
- Chapman C. R., Morrison D., and Zellner B. (1975) Surface properties of asteroids: A synthesis of polarimetry, radiometry, and spectrophotometry. *Icarus*, 25, 104–130.
- Chiang E. and Youdin A. N. (2010) Forming planetesimals in solar and extrasolar nebulae. *Annu. Rev. Earth Planet. Sci.*, 38, 493–522.
- Ciesla F. J., Davison T. M., Collins G. S., and O'Brien D. P. (2013) Thermal consequences of impacts in the early solar system. *Meteoritics & Planet. Sci.*, 48, 2559–2576.
- Connolly H. C. Jr. and Desch S. J. (2004) On the origin of the “kleine Kugelchen” called chondrules. *Chem. Erde–Geochem.*, 64, 95–125.
- Cuzzi J. N. and Weidenschilling S. J. (2006) Particle-gas dynamics and primary accretion. In *Meteorites and the Early Solar System II* (D. S. Lauretta and H. Y. McSween Jr., eds.), pp. 353–381. Univ. of Arizona, Tucson.
- Cuzzi J. N., Hogan R. C., Paque J. M., and Dobrovolskis A. R. (2001) Size-selective concentration of chondrules and other small particles in protoplanetary nebula turbulence. *Astrophys. J.*, 546, 496–508.
- Cuzzi J. N., Hogan R. C., and Shariff K. (2008) Toward planetesimals: Dense chondrule clumps in the protoplanetary nebula. *Astrophys. J.*, 687, 1432–1447.
- Davison T. M., Ciesla F. J., and Collins G. S. (2012) Post-impact thermal evolution of porous planetesimals. *Geochim. Cosmochim. Acta*, 95, 252–269.
- Davison T. M., O'Brien D. P., Ciesla F. J., and Collins G. S. (2013) The early impact histories of meteorite parent bodies. *Meteoritics & Planet. Sci.*, 48, 1894–1918.
- Delbo M., Libourel G., Wilkerson J., Murdoch N., Michel P., Ramesh K. T., Ganino C., Verati C., and Marchi S. (2014) Thermal fatigue as the origin of regolith on small asteroids. *Nature*, 508, 233–236.
- DeMeo F. E., Binzel R. P., Slivan S., and Bus S. J. (2009) An extension of the Bus asteroid taxonomy into the near-infrared. *Icarus*, 202, 160–180.
- DeMeo F. E., Binzel R. P., and Lockhart M. (2014) Mars encounters cause fresh surfaces on some near-Earth asteroids. *Icarus*, 227, 112–122.
- De León J., Licandro J., Serra-Ricart M., Pinilla-Alonso N., and Campins H. (2010) Observations, compositional, and physical characterization of near-Earth and Mars-crosser asteroids from a spectroscopic survey. *Astron. Astrophys.*, 517, Article ID A23.
- DeMeo F. E. and Carry B. (2013) The taxonomic distribution of asteroids from multi-filter all-sky photometric surveys. *Icarus*, 226, 723–741.
- DeMeo F. E. and Carry B. (2014) Solar system evolution from compositional mapping of the asteroid belt. *Nature*, 505, 629–634.
- Dodd R. T. Jr., Koffman D. M., and van Schmus W. R. (1967) A survey of the unequilibrated ordinary chondrites. *Geochim. Cosmochim. Acta*, 31, 921–934.
- Dunn T. L., McSween H. Y. Jr., McCoy T. J., and Cressey G. (2010) Analysis of ordinary chondrites using powder X-ray diffraction: 2. Applications to ordinary chondrite parent-body processes. *Meteoritics & Planet. Sci.*, 45, 135–156.
- Dunn T. L., Burbine T. H., Bottke W. F., and Clark J. P. (2013) Mineralogies and source regions of near-Earth asteroids. *Icarus*, 222, 273–282.
- Durda D. D., Bottke W. F., Nesvorný D., Enke B. L., Merline W. J., Asphaug E., and Richardson D. C. (2007) Size-frequency distributions of fragments from SPH/N-body simulations of asteroid impacts: Comparison with observed asteroid families. *Icarus*, 186, 498–516.
- Ebihara M., Sekimoto S., Shirai N., Hamajima Y., and Yamamoto M., et al. (2011) Neutron activation analysis of a particle returned from asteroid Itokawa. *Science*, 333, 1119–1121.
- Elkins-Tanton L. T., Weiss B. P., and Zuber M. T. (2011) Chondrites as samples of differentiated planetesimals. *Earth Planet. Sci. Lett.*, 305, 1–10.
- Fieber-Beyer S. K. and Gaffey M. J. (2011) Near-infrared spectroscopy of 3:1 Kirkwood gap asteroids: (3760) Poutanen and (974) Lioba. *Icarus*, 214, 645–651.
- Fieber-Beyer S. K. and Gaffey M. J. (2014) Near-infrared spectroscopy of 3:1 Kirkwood gap asteroids II: Probable and plausible parent bodies; primitive and differentiated. *Icarus*, 229, 99–108.
- Fieber-Beyer S. K., Gaffey M. J., Hardersen P. S., and Reddy V. (2012) Near-infrared spectroscopy of 3:1 Kirkwood gap asteroids: Mineralogical diversity and plausible meteorite parent bodies. *Icarus*, 221, 593–602.
- Folco L., Mellini M., and Pillinger C. T. (1996) Unshocked equilibrated H-chondrites: A common low-temperature record from orthopyroxene iron-magnesium ordering. *Meteoritics & Planet. Sci.*, 31, 388–393.
- Fu R. R., Weiss B. P., Lima E. A., et al. (2014) Solar nebula magnetic fields recorded in the Semarkona meteorite. *Science*, 28, 1089–1092.
- Fujiiwara A., Kawaguchi J., Yeomans D. K., Abe M., Mukai T., et al. (2006) The rubble-pile asteroid Itokawa as observed by Hayabusa. *Science*, 312, 1330–1334.
- Gaffey M. J. and Gilbert S. L. (1998) Asteroid 6 Hebe: The probable parent body of the H-type ordinary chondrites and the IIE iron meteorites. *Meteoritics & Planet. Sci.*, 33, 1281–1295.
- Gaffey M. J., Bell J. F., Brown R. H., Burbine T. H., Piatek J., Reed K. L., and Chaky D. A. (1993) Mineralogic variations within the S-type asteroid class. *Icarus*, 106, 573–602.
- Ganguly J., Tirone M., Chakraborty S., and Domanik K. (2013) H chondrite parent asteroid: A multistage cooling, fragmentation and re-accretion history constrained by thermometric studies, diffusion kinetic modeling and geochronological data. *Geochim. Cosmochim. Acta*, 105, 206–220.
- Ghosh A., Weidenschilling S. J., and McSween H. Y. Jr. (2003) Importance of the accretion process in asteroidal thermal evolution: 6 Hebe as an example. *Meteoritics & Planet. Sci.*, 38, 711–724.
- Ghosh A., Weidenschilling S. J., McSween H. Y., and Rubin A. (2006) In *Meteorites and the Early Solar System II* (D. S. Lauretta, and H. Y. McSween Jr., eds.), pp. 555–566. Univ. of Arizona, Tucson.
- Gietzen K. M., Lacy C. H. S., Ostrowski D. R., and Sears D. W. G. (2012) IRTF observations of S complex and other asteroids: Implications for surface compositions, the presence of clinopyroxenes, and their relationship to meteorites. *Meteoritics & Planet. Sci.*, 47, 1789–1808.

- Göpel C., Manhès G., and Allègre C. J. (1994) U-Pb systematics of phosphates from equilibrated ordinary chondrites. *Earth Planet. Sci. Lett.*, **121**, 153–171.
- Gradie J. and Tedesco E. (1982) Compositional structure of the asteroid belt. *Science*, **216**, 1405–1407.
- Greenwood R. C., Schmitz B., Bridges J. C., Hutchison R., and Franchi I. A. (2007) Disruption of the L chondrite parent body: New oxygen isotope evidence from Ordovician relict chromite grains. *Earth Planet. Sci. Lett.*, **262**, 204–213.
- Grimm R. E. (1985) Penecontemporaneous metamorphism, fragmentation, and reassembly of ordinary chondrite parent bodies. *J. Geophys. Res.*, **90**, 2022–2028.
- Grimm R. E. and McSween H. Y. Jr. (1993) Heliocentric zoning of the planetesimal belt by aluminum-26 heating. *Science*, **259**, 653–655.
- Grossman J. N. and Brearley A. J. (2005) The onset of metamorphism in ordinary and carbonaceous chondrites. *Meteoritics & Planet. Sci.*, **40**, 87–122.
- Grossman J. N., Rubin A. E., Nagahara H., and King E. A. (1989) Properties of chondrules. *Meteorites and the Early Solar System* (J. F. Kerridge and M. S. Matthews, eds.), pp. 619–659. Univ. of Arizona, Tucson.
- Haack H., Farinella P., Scott E. R. D., and Keil K. (1996) Meteoritic, asteroidal, and theoretical constraints on the 500 Ma disruption of the L chondrite parent body. *Icarus*, **119**, 182–191.
- Hapke B. (1971) Inferences from optical properties concerning the surface texture and composition of asteroids. In *Physical Studies of Minor Planets* (T. Gehrels, ed.), pp. 67–77. IAU Colloq. 12, Univ. of Sydney, Sydney.
- Hardersen P. S., Gaffey M. J., Cloutis E. A., Abell P. A., and Reddy V. (2006) Near-infrared spectral observations and interpretations for S-asteroids 138 Tolosa, 306 Unitas, 346 Hermentaria, and 480 Hansa. *Icarus*, **181**, 94–106.
- Harrison K. P. and Grimm R. E. (2010) Thermal constraints on the early history of the H-chondrite parent body reconsidered. *Geochim. Cosmochim. Acta*, **74**, 5410–5423.
- Henke S., Gail H.-P., Tieloff M., Schwarz W. H., and Kleine T. (2012a) Thermal evolution and sintering of chondritic planetesimals. *Astron. Astrophys.*, **537**, Article ID A45.
- Henke S., Gail H.-P., Tieloff M., Schwarz W. H., and Kleine T. (2012b) Thermal history modelling of the H chondrite parent body. *Astron. Astrophys.*, **545**, Article ID A135.
- Henke S., Gail H.-P., Tieloff M., and Schwarz W. H. (2013) Thermal evolution model for the H chondrite asteroid-instantaneous formation versus protracted accretion. *Icarus*, **226**, 212–228.
- Herzog G. F. and Caffee M. W. (2014) Cosmic-ray exposure ages of meteorites. In *Treatise on Geochemistry* (H. Holland and K. Turekian, eds.), pp. 419–454. Elsevier Pergamon, San Diego.
- Hevey P. J. and Sanders S. (2006) A model for planetesimal meltdown by  $^{26}\text{Al}$  and its implications for meteorite parent bodies. *Meteoritics & Planet. Sci.*, **41**, 95–106.
- Heymann D. (1967) On the origin of hypersthene chondrites: Ages and shock effects of black chondrites. *Icarus*, **6**, 189–221.
- Hiroi T., Abe M., Kitazato K., Abe S., Clark B. E., et al. (2006) Developing space weathering on the asteroid 25143 Itokawa. *Nature*, **443**, 56–58.
- Huss G. R., Rubin A. E., and Grossman J. N. (2006) Thermal metamorphism in chondrites. In *Meteorites and the Early Solar System II* (D. S. Lauretta and H. Y. McSween Jr., eds.), pp. 567–586. Univ. of Arizona, Tucson.
- Hutchison R. (2004) *Meteorites: A Petrologic, Chemical and Isotopic Synthesis*. Cambridge Univ., Cambridge.
- Jacquet E., Gounelle M., and Fromang S. (2012) On the aerodynamic redistribution of chondrite components in protoplanetary disks. *Icarus*, **220**, 162–173.
- Jenniskens P. et al. (2010) Almahata Sitta (=asteroid 2008 TC<sub>3</sub>) and the search for the ureilite parent body. *Meteoritics & Planet. Sci.*, **45**, 1590–1617.
- Johansen A., Oishi J. S., Mac Low M.-M., Klahr H., Henning T., and Youdin A. (2007) Rapid planetesimal formation in turbulent circumstellar disks. *Nature*, **448**, 1022–1025.
- Johansen A., Klahr H., and Henning Th. (2011) High-resolution simulations of planetesimal formation in turbulent protoplanetary discs. *Astron. Astrophys.*, **529**, Article ID A62.
- Johansen A., Youdin A. N., and Lithwick Y. (2012) Adding particle collisions to the formation of asteroids and Kuiper belt objects via streaming instabilities. *Astron. Astrophys.*, **537**, Article ID A125.
- Keil K. and Fredriksson K. (1964) The iron, magnesium, and calcium distribution in coexisting olivines and rhombic pyroxenes of chondrites. *J. Geophys. Res.*, **69**, 3487–3515.
- Keil K., Stöffler D., Love S. G., and Scott E. R. D. (1997) Constraints on the role of impact heating and melting in planetesimals. *Meteoritics & Planet. Sci.*, **32**, 349–363.
- Kelley M. S. and Wooden D. H. (2009) The composition of dust in Jupiter-family comets inferred from infrared spectroscopy. *Planet. Space Sci.*, **57**, 1133–1145.
- Kessel R., Beckett J. R., and Stolper E. M. (2007) The thermal history of equilibrated ordinary chondrites and the relationship between textural maturity and temperature. *Geochim. Cosmochim. Acta*, **71**, 1855–1881.
- Kleine T., Mezger K., Palme H., Scherer E., and Munker C. (2005) Early core formation in asteroids and late accretion of chondrite parent bodies: Evidence from  $^{182}\text{Hf}$ – $^{182}\text{W}$  in CAIs, metal-rich chondrites, and iron meteorites. *Geochim. Cosmochim. Acta*, **69**, 5805–5818.
- Kleine T., Toublou M., Van Orman J. A., Bourdon B., Maden C., Mezger K., and Halliday A. N. (2008) Hf-W thermochronometry: Closure temperature and constraints on the accretion and cooling history of the H chondrite parent body. *Earth Planet. Sci. Lett.*, **270**, 106–118.
- Korochantseva E. V., Tieloff M., Lorenz C. A., Buykin A. I., Ivanova M. A., Schwarz W. H., Hopp J., and Jessberger E. K. (2007) L-chondrite asteroid breakup tied to Ordovician meteorite shower by multiple isochron  $^{40}\text{Ar}$ – $^{39}\text{Ar}$  dating. *Meteoritics & Planet. Sci.*, **42**, 113–130.
- Kruijer T. S., Sprung P., Kleine T., Leya I., Burkhardt C., and Wieler R. (2012) Hf-W chronometry of core formation in planetesimals inferred from weakly irradiated iron meteorites. *Geochim. Cosmochim. Acta*, **99**, 287–304.
- Marchi S., Brunetto R., Magrin S., Lazzarin M., and Gandolfi D. (2005) Space weathering of near-Earth and main belt silicate-rich asteroids: Observations and ion irradiation experiments. *Astron. Astrophys.*, **443**, 769–775.
- Marchi S., Magrin S., Nesvorný D., Paolicchi P., and Lazzarin M. A. (2006) Spectral slope versus perihelion distance correlation for planet-crossing asteroids. *Mon. Not. R. Astron. Soc.*, **368**, 39–42.
- Marsh C. A., Della-Giustina D. N., Giacalone J., and Lauretta D. S. (2006) Experimental tests of the induction heating hypothesis for planetesimals. In *Lunar Planet. Sci. XXXVII*, Abstract #2078. Lunar and Planetary Institute, Houston.
- Mason B. (1963) Olivine composition in chondrites. *Geochim. Cosmochim. Acta*, **27**, 1011–1023.
- McSween H. Y. Jr., Ghosh A., Grimm R. E., Wilson L., and Young E. D. (2002) Thermal evolution models of planetesimal. In *Asteroids III* (W. F. Bottke Jr. et al., eds.), pp. 559–571. Univ. of Arizona, Tucson.
- Menzel R. L. and Roberge W. G. (2013) Reexamination of induction heating of primitive bodies in protoplanetary disks. *Astrophys. J.*, **776**, Article ID 89.
- Merk R., Breuer D., and Spohn T. (2002) Numerical modeling of  $^{26}\text{Al}$ -induced radioactive melting of planetesimals considering accretion. *Icarus*, **159**, 183–191.
- Metzler K., Bischoff A., Greenwood R. C., Palme H., Gellissen M., Hopp J., Franchi I. A., and Tieloff M. (2011) The L3–6 chondritic regolith breccia Northwest Africa (NWA) 869: (I) Petrology, chemistry, oxygen isotopes, and Ar-Ar age determinations. *Meteoritics & Planet. Sci.*, **46**, 652–680.
- Miyamoto M. (1991) Thermal metamorphism of CI and CM carbonaceous chondrites: An internal heating model. *Meteoritics*, **26**, 111–115.
- Miyamoto M., Fujii N., and Takeda H. (1981) Ordinary chondrites parent body: An internal heating model. *Proc. Lunar Planet. Sci. Conf. 12B*, pp. 1145–1152.
- Monnerie M., Toplis M. J., Baratoux D., and Guignard J. (2013) Thermal history of the H-chondrite parent body: Implications for metamorphic grade and accretionary time-scales. *Geochim. Cosmochim. Acta*, **119**, 302–321.
- Mostefaoui S., Lugmair G. W., and Hoppe P. (2005)  $^{60}\text{Fe}$ : A heat source for planetary differentiation from a nearby supernova explosion. *Astrophys. J.*, **625**, 271–277.
- Mothé-Diniz T., Carvano J. M., and Lazzaro D. (2003) Distribution of taxonomic classes in the main belt of asteroids. *Icarus*, **162**, 10–21.
- Nagao K., Okazaki R., Nakamura T., Miura Y. N., Osawa T., et al. (2011) Irradiation history of Itokawa regolith material deduced from noble gases in the Hayabusa samples. *Science*, **333**, 1128–1131.

- Nakashima D., Kita N. T., Ushikubo T., Noguchi T., Nakamura T., and Valley J. W. (2014) Oxygen three-isotope ratios of silicate particles returned from asteroid Itokawa by the Hayabusa spacecraft: A strong link with equilibrated LL chondrites. *Earth Planet. Sci. Lett.*, **379**, 127–136.
- Nakamura T., Noguchi T., Tanaka M., Zolensky M. E., Kimura M., et al. (2011) Itokawa dust particles: A direct link between S-type asteroids and ordinary chondrites. *Science*, **333**, 1113–1116.
- Nakamura E., Makishima A., Moriguti T., Kobayashi K., Tanaka R., et al. (2012) Space environment of an asteroid preserved on micrograins returned by the Hayabusa spacecraft. *Proc. Natl. Acad. Sci.*, **109**, E624–E629.
- Nakamura T., Nakate A., Ishida H., Wakita S., Noguchi T., et al. (2014) Mineral chemistry of MUSES-C Regio inferred from analysis of dust particles collected from the first and second touchdown sites on asteroid Itokawa. *Meteoritics & Planet. Sci.*, **49**, 215–227.
- Naraoka H., Mita H., Hamase K., Mita M., Yabuta H., et al. (2011) Preliminary organic compound analysis of microparticles returned from asteroid 25143 Itokawa by the Hayabusa mission. *Geochem. J.*, **46**, 61–72.
- Nesvorný D., Jedicke R., Whiteley R. J., and Ivezić Z. (2005) Evidence for asteroid space weathering from the Sloan Digital Sky Survey. *Icarus*, **173**, 132–152.
- Nesvorný D., Vokrouhlický D., Morbidelli A., and Bottke W. F. (2009) Asteroidal source of L chondrite meteorites. *Icarus*, **200**, 698–701.
- Neumann W., Breuer D., and Spohn T. (2012) Differentiation and core formation in accreting planetesimals. *Astron. Astrophys.*, **543**, A141.
- Noguchi T., Nakamura T., Kimura M., Zolensky M. E., Tanaka M., et al. (2011) Incipient space weathering observed on the surface of Itokawa dust. *Science*, **333**, 1121–1125.
- Noguchi T., Kimura M., Hashimoto T., Konno M., Nakamura T., et al. (2014) Space weathered rims found on the surfaces of the Itokawa dust particles. *Meteoritics & Planet. Sci.*, **49**, 188–214.
- Pellas P. (1988) Ordinary-chondrite-type asteroids in the main-belt: Can we believe the zero abundance found by spectral studies from Earth-based telescopes? *Chem. Geol.*, **70**, 23.
- Pellas R. and Storzer D. (1981)  $^{244}\text{Pu}$  fission track thermometry and its application to stony meteorites. *Proc. R. Soc. Lond. Ser. A*, **374**, 253–270.
- Pieters C., Taylor L., Noble S., Keller L., Hapke B., et al. (2000) Space weathering on airless bodies: Resolving a mystery with lunar samples. *Meteoritics & Planet. Sci.*, **35**, 1101–1107.
- Reddy V., Emery J. P., Gaffey M. J., Bottke W. F., Cramer A., and Kelley M. S. (2009) Composition of 298 Baptistina: Implications for the K/T impactor link. *Meteoritics & Planet. Sci.*, **44**, 1917–1927.
- Reddy V., Nathues A., Gaffey M. J., and Schaeff S. (2011a) Mineralogical characterization of potential targets for the ASTEX mission scenario. *Planet. Space Sci.*, **59**, 772–778.
- Reddy V., Carvano J. M., Lazzaro D., Michtchenko T. A., et al. (2011b) Mineralogical characterization of Baptistina asteroid family: Implications for K/T impactor source. *Icarus*, **216**, 184–197.
- Reddy V., Sanchez J. A., Gaffey M. J., Abell P. A., Corre L., and Hardersen P. S. (2012) Composition of near-Earth asteroid (4179) Toutatis. *Icarus*, **221**, 1177–1179.
- Rubin A. E. (1995) Petrologic evidence for collisional heating of chondritic asteroids. *Icarus*, **113**, 156–167.
- Rubin A. E. (2003) Chromite-plagioclase assemblages as a new shock indicator; implications for the shock and thermal histories of ordinary chondrites. *Geochim. Cosmochim. Acta*, **67**, 2695–2709.
- Rubin A. E. (2004) Postshock annealing and postannealing shock in equilibrated ordinary chondrites: Implications for the thermal and shock histories of chondritic asteroids I. *Geochim. Cosmochim. Acta*, **68**, 673–689.
- Rubin A. E., Peterson E., Keil K., Rehfeldt A., and Jarosewich E. (1983) Fragmental breccias and the collisional evolution of ordinary chondrite parent bodies. *Meteoritics*, **18**, 179–196.
- Sahijpal S., Soni P., and Gupta G. (2007) Numerical simulations of the differentiation of accreting planetesimals with  $^{26}\text{Al}$  and  $^{60}\text{Fe}$  as the heat sources. *Meteoritics & Planet. Sci.*, **42**, 1529–1548.
- Sanchez J. A., Michelsen R., Reddy V., and Nathues A. (2013) Surface composition and taxonomic classification of a group of near-Earth and Mars-crossing asteroids. *Icarus*, **225**, 131–140.
- Sanders I. S. and Scott E. R. D. (2012) The origin of chondrules and chondrites: Debris from low-velocity impacts between molten planetesimals. *Meteoritics & Planet. Sci.*, **47**, 2170–2192.
- Sasaki S., Nakamura K., Hamabe Y., Kurahashi E., and Hiroi T. (2001) Production of iron nanoparticles by laser irradiation in a simulation of lunar-like space weathering. *Nature*, **410**, 555–557.
- Schmitz B., Peucker-Ehrenbrink B., Lindstrom M., and Tassinari M. (1997) Accretion rates of meteorites and cosmic dust in the Early Ordovician. *Science*, **278**, 88–90.
- Schmitz B., Haggstrom T., and Tassinari M. (2003) Sediment-dispersed extraterrestrial chromite traces a major asteroid disruption event. *Science*, **300**, 961–964.
- Schmitz B. and 8 colleagues (2007) Asteroid breakup linked to the Great Ordovician Biodiversification Event. *Nature Geosci.*, **1**, 49–53.
- Scott E. R. D. and Rajan R. S. (1981) Metallic minerals, thermal histories, and parent bodies of some xenolithic, ordinary chondrites. *Geochim. Cosmochim. Acta*, **45**, 53–67.
- Scott E. R. D., Krot T. V., Goldstein J. I., and Taylor G. J. (2011) Thermal and impact history of H chondrites: Was the onion-shell punctured by impacts during metamorphism? In 74th Annual Meteoritical Society Meeting, *Meteoritics & Planet. Sci.*, Abstract #5516.
- Scott E. R. D., Krot T. V., Goldstein J. I., and Herzog G. F. (2013) Impact and thermal history of the H chondrite parent body inferred from Fe-Ni metal and Ar/Ar ages. In 76th Annual Meteoritical Society Meeting, *Meteoritics & Planet. Sci.*, Abstract #5346.
- Scott E. R. D., Krot T. V., Goldstein J. I., and Wakita S. (2014) Thermal and impact history of the H chondrite parent asteroid during metamorphism: Constraints from metallic Fe-Ni. *Geochim. Cosmochim. Acta*, **136**, 13–37.
- Sears D. W. G., Grossman J. N., Melcher C. L., Ross L. M., and Mills A. A. (1980) Measuring metamorphic history of unequilibrated ordinary chondrites. *Nature*, **287**, 791–795.
- Slater-Reynolds V. and H. Y. McSween (2005) Peak metamorphic temperatures in type 6 ordinary chondrites: An evaluation of pyroxene and plagioclase geothermometry. *Meteoritics & Planet. Sci.*, **40**, 745–754.
- Sonnett S. P. and Colburn D. (1968) Electrical heating of meteorite parent bodies and planets by dynamo induction from a pre-main sequence T Tauri “solar wind”. *Nature*, **219**, 924–926.
- Sprung P., Göpel C., Kleine T., Van Orman J. A., and Maden C. (2011) The high-temperature history and primary structure of the L chondrite parent body. In *Lunar Planet. Sci. XLII*, Abstract #1850. Lunar and Planetary Institute, Houston.
- Strazzulla G., Dotto E., Binzel R., Brunetto R., Barucci M. A., Blanco A., and Orofino V. (2005) Spectral alteration of the meteorite Epinal (H5) induced by heavy ion irradiation: A simulation of space weathering effects on near-Earth asteroids. *Icarus*, **174**, 31–35.
- Stuart J. S. and Binzel R. P. (2004) Bias-corrected population, size distribution, and impact hazard for the near-Earth objects. *Icarus*, **170**, 295–311.
- Sunshine J. M., Bus S. J., McCoy T. J., Burbine T. H., Corrigan C. M., and Binzel R. P. (2004) High calcium pyroxene as an indicator of igneous differentiation in asteroids and meteorites. *Meteoritics & Planet. Sci.*, **39**, 1343–1357.
- Sunshine J. M., Bus S. J., Corrigan C. M., McCoy T. J., and Burbine T. H. (2007) Olivine-dominated asteroids and meteorites: Distinguishing nebular and igneous histories. *Meteoritics & Planet. Sci.*, **42**, 155–170.
- Tachibana S. and Huss G. R. (2003) The initial abundance of  $^{60}\text{Fe}$  in the solar system. *Astrophys. J. Lett.*, **588**, L41–L44.
- Tang H. and Dauphas N. (2012) Abundance, distribution, and origin of  $^{60}\text{Fe}$  in the solar protoplanetary disk. *Earth Planet. Sci. Lett.*, **359**, 248–263.
- Taylor G. J., Maggiore P., Scott E. R. D., Rubin A. E., and Keil K. (1987) Original structures, and fragmentation and reassembly histories of asteroids — Evidence from meteorites. *Icarus*, **69**, 1–13.
- Terribilini E., Eugster O., Herzog G. F., and Schnabel C. (2000) Evidence for common breakup events of the acapulcoites-lodranites and chondrites. *Meteoritics & Planet. Sci.*, **35**, 1043–1050.
- Thomas C. A. and Binzel R. P. (2010) Identifying meteorite source regions through near-Earth object spectroscopy. *Icarus*, **205**, 419–429.
- Thomas C. A., Emery J. P., Trilling D. E., Delbó M., Hora J. L., and Mueller M. (2014) Physical characterization of warm Spitzer-observed near-Earth objects. *Icarus*, **228**, 217–246.
- Trieloff M., Jessberger E. K., Herrwerth I., Hopp J., Fieni C., Ghelis M., Bourot-Denise M., and Pellas P. (2003) Structure and thermal history of the H-chondrite parent asteroid revealed by thermochronometry. *Nature*, **422**, 502–506.

- Tsuchiyama A., Uesugi M., Matsushima T., Michikami T., Kadono T., and Nakamura T., et al. (2011) Three-dimensional structures of Hayabusa sample: Origin and evolution of Itokawa regolith. *Science*, **333**, 1125–1128.
- Tsuchiyama A., Uesugi M., Uesugi K., Nakano T., Noguchi R., et al. (2014) Three-dimensional microstructure of samples recovered from asteroid 25143 Itokawa: Comparison with LL5 and LL6 chondrite particles. *Meteoritics & Planet. Sci.*, **49**, 172–187.
- Urey H. C. (1955) The cosmic abundances of potassium, uranium, and thorium and the heat balances of the Earth, the Moon, and Mars. *Proc. Natl. Acad. Sci.*, **41**, 127–144.
- Van Schmus W. R. and Wood J. A. (1967) A chemical-petrologic classification for the chondritic meteorites. *Geochim. Cosmochim. Acta*, **31**, 747–765.
- Vernazza P. et al. (2008) Compositional differences between meteorites and near-Earth asteroids. *Nature*, **454**, 858–860.
- Vernazza P., Binzel R. P., Rossi A., Fulchignoni M., and Birlan M. (2009) Solar wind as the origin of rapid weathering of asteroid surfaces. *Nature*, **458**, 993–995.
- Vernazza P., Zanda B., Binzel R. P., Hiroi T., DeMeo F. E., Birlan M., Hewins R., Ricci L., Barge P., and Lockhart M. (2014) Multiple and fast: The accretion of ordinary chondrite parent bodies. *Astrophys. J.*, **791**, Article ID 120.
- Wakita S., Nakamura T., Ikeda T., and Yurimoto H. (2014) Thermal modeling for a parent body of Itokawa. *Meteoritics & Planet. Sci.*, **49**, 228–236.
- Willis J. and Goldstein J. I. (1981) A revision of metallographic cooling rate curves for chondrites. *Proc. Lunar Planet. Sci. 12B*, pp. 1135–1143.
- Willis J. and Goldstein J. I. (1983) A three-dimensional study of metal grains in equilibrated, ordinary chondrites. *Proc. Lunar Planet. Sci. Conf. 14th*, in *J. Geophys. Res.*, **88**, B287–B292.
- Wlotzka F. (2005) Cr spinel and chromite as petrogenetic indicators in ordinary chondrites: Equilibration temperatures of petrologic types 3.7 to 6. *Meteoritics & Planet. Sci.*, **40**, 1673–1702.
- Wood J. A. (1967) Chondrites: Their metallic minerals, thermal histories, and parent planets. *Icarus*, **6**, 1–49.
- Wood J. A. (2003) Planetary science: Of asteroids and onions. *Nature*, **422**, 479–481.
- Yada T., Fujimura A., Abe M., Nakamura T., Noguchi T., et al. (2014) Hayabusa return sample curation in the Planetary Material Sample Curation Facility of JAXA. *Meteoritics & Planet. Sci.*, **49**, 135–153.
- Yano H., Kubota T., Miyamoto H., Okada T., Scheeres D., et al. (2006) Touchdown of the Hayabusa spacecraft at the Muses Sea on Itokawa. *Science*, **312**, 1350–1353.
- Yomogida K. and Matsui T. (1984) Multiple parent bodies of ordinary chondrites. *Earth Planet. Sci. Lett.*, **68**, 34–42.
- Youdin A. N. (2011) On the formation of planetesimals via secular gravitational instabilities with turbulent stirring. *Astrophys. J.*, **731**, Article ID 99.
- Youdin A. N. and Goodman J. (2005) Streaming instabilities in protoplanetary disks. *Astrophys. J.*, **620**, 459–469.
- Yurimoto H., Abe K., Abe M., Ebihara M., Fujimura A., et al. (2011a) Oxygen isotopic compositions of asteroidal materials returned from Itokawa by the Hayabusa mission. *Science*, **333**, 1116–1119.
- Yurimoto H., Abe K., Abe M., Ebihara M., Fujimura A., et al. (2011b) Oxygen and magnesium isotopic compositions of asteroid 25143 Itokawa returned by the Hayabusa mission. *74th Annual Meteoritical Society Meeting*, Abstract #5320.
- Zanda B., Hewins R. H., Bourot-Denise M., Bland P. A., Albarède F. (2006) Formation of solar nebula reservoirs by mixing chondritic components. *Earth Planet. Sci. Lett.*, **248**, 650–660.

# Sources of Water and Aqueous Activity on the Chondrite Parent Asteroids

**Alexander N. Krot and Kazuhide Nagashima**

*University of Hawai'i at Mānoa*

**Conel M. O'D. Alexander**

*Carnegie Institution*

**Fred J. Ciesla**

*University of Chicago*

**Wataru Fujiya**

*Max Planck Institute for Chemistry (now at College of Science, Ibaraki University)*

**Lydie Bonal**

*Institut de Planétologie et d'Astrophysique de Grenoble*

---

Most chondrite parent bodies accreted water ice together with anhydrous minerals and subsequently experienced aqueous/hydrothermal alteration and fluid-assisted thermal metamorphism, resulting in formation of a diverse suite of secondary minerals. The  $^{53}\text{Mn}$ - $^{53}\text{Cr}$  chronology of datable secondary minerals indicates aqueous activity on the ordinary (OC) and carbonaceous chondrite (CC) parent bodies started  $\sim$ 3–5 m.y. after the beginning of the solar system formation ( $t_0$ ), consistent with  $^{26}\text{Al}$  being the major heat source of these bodies. The  $^{53}\text{Mn}$ - $^{53}\text{Cr}$  ages of aqueous alteration, the  $^{26}\text{Al}$ - $^{26}\text{Mg}$  ages of chondrule formation, and the peak metamorphic temperatures reached by the OC and CC parent bodies suggest that they accreted  $\sim$ 2.0–4 m.y. after  $t_0$ . There are significant variations in the degree of aqueous alteration within and between different chondrite groups, possibly due to the heterogeneous distribution of water ice in their parent bodies. The CI (Ivuna-type) carbonaceous chondrites that are composed almost entirely of aqueously formed minerals are the only exception. The estimated water ice-to-rock mass ratios in OC and CC parent bodies range from  $<0.1$  to  $\sim0.6$  (could be higher in CIs), which is significantly lower than the solar value of 1.2. We suggest that most chondrite parent bodies accreted close to the snow line; CIs may have accreted further away from the Sun than other chondrite groups. Because the snow line for the 2.5–4-m.y.-old disk is expected to be within 2–3 AU of the Sun, we conclude that chondrite parent bodies are sampled by meteorites accreted in the main asteroid belt, consistent with the inferred deuterium/hydrogen (D/H) ratio of asteroidal water. The existing meteorite observations provide no clear evidence supporting the predictions of the Grand Tack and Nice dynamical models of the solar system evolution, wherein hydrated asteroids formed between and beyond giant planets and were subsequently implanted into the main asteroid belt during migration of the giant planets. We note, however, that there could be other types of hydrated or water-ice-bearing planetesimals that were implanted into the main asteroid belt, but have not been sampled by the known meteorites.

## 1. INTRODUCTION

In this paper, we address the nature of aqueous activity in and the sources of water ice accreted by the chondrite parent bodies. We also discuss how these observations could be used for testing some of the predictions of the recently proposed Nice (Gomes *et al.*, 2005; Morbidelli *et al.*, 2005; Tsiganis *et al.*, 2005; Levison *et al.*, 2009) and Grand Tack (Walsh *et al.*, 2011) dynamical models of the evolution of the solar system. This chapter is organized as follows: In section 2, we

describe the modern classification of chondritic meteorites, emphasizing the large chemical and isotopic diversity among the carbonaceous chondrites. In section 3, we summarize the current views about the location (nebular vs. parent body) and conditions (temperature and water/rock ratio) of aqueous alteration of chondritic meteorites, and list the major minerals produced during aqueous alteration of different chondrite groups. In section 4, we review the structural and compositional modifications of chondrite organics during aqueous alteration. In section 5, we summarize recent results

on  $^{53}\text{Mn}$ - $^{53}\text{Cr}$  dating of aqueously formed minerals in several chondrite groups. In section 6, we discuss the cosmochemical constraints on the timing of accretion of hydrated chondrite parent bodies, including the  $^{53}\text{Mn}$ - $^{53}\text{Cr}$  ages of aqueous alteration, the  $^{26}\text{Al}$ - $^{26}\text{Mg}$  ages of chondrule formation, the peak metamorphic temperatures reached by these bodies, and the results of physical modeling of their thermal evolution. In section 7, we discuss the results of hydrogen- and oxygen-isotopic measurements of cometary water ice, the estimates of hydrogen- and oxygen-isotopic compositions of chondritic water, and the results of astrophysical modeling of the spatial and temporal evolution of oxygen and hydrogen-isotopic compositions of the protoplanetary disk water. In section 8, we discuss the cosmochemical constraints on the accretion regions of the chondrite parent bodies, and their implications for testing the predictions of the Grand Tack and Nice models. In section 9, we summarize our main conclusions and outline future research.

## 2. CLASSIFICATION OF CHONDRITIC METEORITES

Chondritic meteorites (chondrites) consist of four major components: chondrules, refractory inclusions [Ca, Al-rich inclusions (CAIs) and amoeboid olivine aggregates (AOAs)], and fine-grained matrix. CI (Ivuna-type) chondrites, which are composed almost entirely of matrix material, are the only exception. It is generally accepted that refractory inclusions and chondrules formed in the protoplanetary disk by high-temperature processes that included evaporation, condensation, and melting during transient heating events of a poorly known nature; the currently discussed mechanisms include shock waves, planetary collisions, and current sheets (e.g., Joung *et al.*, 2004; Alexander *et al.*, 2008; Krot *et al.*, 2009; Morris *et al.*, 2010; McNally *et al.*, 2013; Asphaug *et al.*, 2011; Johnson *et al.*, 2015). Matrix escaped melting, but a significant fraction of it may have experienced evaporation and condensation prior to and/or during chondrule formation (e.g., Huss *et al.*, 2005; Scott and Krot, 2014, and references therein).

Based on bulk chemistry, bulk oxygen-isotopic compositions, mineralogy, and petrography (e.g., chondrule/matrix ratio, chondrule sizes and textures), 14 chondrite groups (+ a grouplet of two Kakangari-type chondrites) are currently recognized (Krot *et al.*, 2014a). They comprise three major chondrite classes: carbonaceous [CI (Ivuna-type), CM (Mighei-type), CR (Renazzo-type), CV (Vigarano-type), CK (Karoonda-type), CO (Ornans-type), CB (Bencubbin-type), CH (high metal abundance)], ordinary (H, L, LL) plus R (Rumuruti type) chondrites, and enstatite (EH, EL) chondrites. Several chondrites are mineralogically and/or chemically unique and defy classification into the existing chondrite groups; these are referred to as ungrouped (e.g., Tagish Lake and Acfer 094).

The term carbonaceous is somewhat of a misnomer, because only the CI, CM, and CR chondrites are significantly enriched in carbon ( $\sim 1\text{--}10\text{ wt\%}$ ) compared to other

chondrite groups ( $<1\text{ wt\%}$ ) (Fig. 5 in Krot *et al.*, 2014a). Instead, the carbonaceous and noncarbonaceous chondrites can be resolved (with some exceptions) by several characteristics, including (1) mean refractory lithophile/silicon abundance ratios relative to CI chondrites —  $\geq 1.00$  in carbonaceous chondrites, and  $\leq 0.95$  in noncarbonaceous chondrites (Fig. 1); (2) bulk oxygen-isotopic compositions (Fig. 2) — on a three-isotope oxygen diagram, most carbonaceous chondrite groups (except CI chondrites) plot below the terrestrial fractionation line, whereas noncarbonaceous chondrites (except EH and EL chondrites) plot above it; and (3) bulk chromium- and titanium-isotopic compositions — carbonaceous chondrites are enriched in  $^{54}\text{Cr}$  and  $^{50}\text{Ti}$ , whereas noncarbonaceous chondrites are depleted in these isotopes relative to Earth (Fig. 1 in Warren, 2011).

It is commonly assumed that each chondrite group sampled a single parent body. Based on the similar bulk chemical and oxygen-isotopic compositions, it has been recently suggested that CK and CV chondrites may represent different lithologies of the same parent body that experienced aqueous/hydrothermal alteration to different degrees, and were subsequently thermally metamorphosed (Greenwood *et al.*, 2010; Wasson *et al.*, 2013).

Once the chondrite parent bodies formed, they experienced different levels of alteration driven by fluids and heating by the decay of short-lived (half-life  $<10\text{ m.y.}$ ) radionuclides. To provide a guide to the degree of thermal and aqueous alteration experienced by chondrites, they are divided into six petrologic types (1–6). The sequence type 3 to type 6 represents an increasing degree of chemical equilibrium and textural recrystallization due to thermal metamorphism. Type 3 chondrites are commonly called “unequilibrated.” The type 3 ordinary, CO, and CV chondrites are subdivided into 10 subtypes (3.0–3.9), of which 3.0 is the least metamorphosed (e.g., Grossman and Brearley, 2005; Bonal *et al.*, 2006, 2007). Types 1 and 2 represent a higher degree of aqueous alteration compared to type 3. In one classification scheme, the CM and CR chondrites are divided into 10 subtypes (2.9–2.0), of which 2.0 is the most aqueously altered (Rubin *et al.*, 2007; Harju *et al.*, 2014). In this scheme, type 1 is reserved for CI chondrites. The classification scheme for aqueously altered chondrites is not universally accepted. In the past, nearly completely hydrated CM and CR chondrites have been referred to as CM1 and CR1, respectively, and an alternative classification scheme uses a 1–3 alteration scale for all chondrite groups (e.g., Alexander *et al.*, 2013; Beck *et al.*, 2014; Howard *et al.*, 2015).

## 3. PLACE AND CONDITIONS OF AQUEOUS/HYDROTHERMAL ALTERATION

Refractory inclusions, chondrules, and matrices of the most primitive chondrite known, Acfer 094, show little evidence for preterrestrial aqueous alteration (Greshake, 1997; Abreu and Brearley, 2010), and thus nearly completely avoided this process on its parent body. Mineralogical and petrographic observations of aqueously altered chondrites

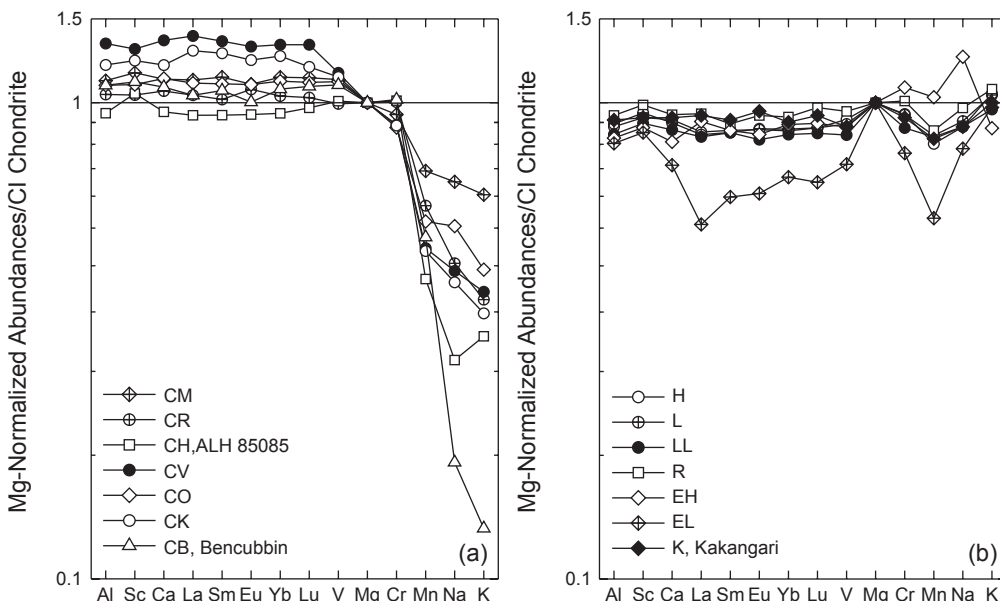


**Fig. 1.** Magnesium- and Cl-normalized bulk lithophile-element abundances of the (a) carbonaceous and (b) noncarbonaceous chondrite groups. The elemental abundances of bulk CI chondrites are viewed as a measure of average solar system abundances and are used as a reference composition. In carbonaceous and noncarbonaceous chondrites, mean refractory lithophile/Mg abundance ratios relative to CI chondrites are  $\geq 1.00$  and  $\leq 0.95$ , respectively. From Krot et al. (2014a).

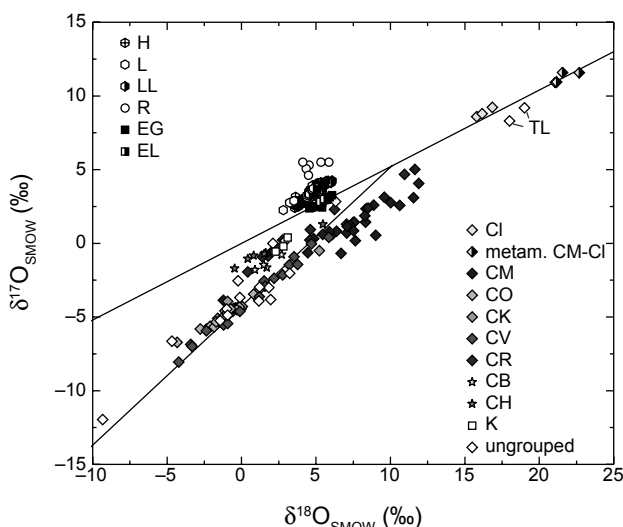


**Fig. 2.** See Plate 20 for color version. Bulk oxygen-isotope compositions of chondrite groups and ungrouped chondrites. Terrestrial fractionation line (TFL) and carbonaceous chondrite anhydrous mineral (CCAM) line are shown for reference. Oxygen-isotopic compositions are reported as  $\delta^{17}\text{O}$  and  $\delta^{18}\text{O}$ , deviations from Vienna Standard Mean Ocean Water (SMOW) [ $^{17}\text{O}/^{16}\text{O}_{\text{SMOW}} = 0.000380$ ;  $^{18}\text{O}/^{16}\text{O}_{\text{SMOW}} = 0.002005$  (De Laeter et al., 2003)] in parts per thousand:  $\delta^{17,18}\text{O}_{\text{SMOW}} = [(^{17,18}\text{O}/^{16}\text{O}_{\text{sample}})/(^{17,18}\text{O}/^{16}\text{O}_{\text{SMOW}}) - 1] \times 1000$ . Carbonaceous chondrites, except CIs, plot below the TFL; noncarbonaceous chondrites, except EHs and ELs, plot above it. After Krot et al. (2014a). Data for Tagish Lake (TL) are from Brown et al. (2000).

(e.g., Brearley, 2006; Zolensky et al., 2008; Brearley and Krot, 2012, and references therein) and the slow kinetics of hydration reactions in the solar nebula (Fegley, 2000) suggest that aqueous alteration occurred exclusively on the chondrite parent bodies. Although Ciesla et al. (2002) suggested that hydration of micrometer-sized olivine and formation of serpentine



might have occurred in icy-rich regions of the solar nebula that experienced shock-wave heating, it is generally agreed that aqueous alteration resulted from melting of water ice that accreted together with anhydrous silicates into chondrite parent bodies. The presence of veins crosscutting chondrite matrices (Fig. 3), for instance, provides clear evidence for *in situ* aqueous alteration.

With the exception of enstatite chondrites, at least some members of all known chondrite groups show evidence for aqueous alteration, but to various degrees and under variable physicochemical conditions, such as temperature and water/rock ratio. Figures 4 and 5 illustrate combined X-ray elemental maps in Mg (red), Ca (green), and Al (blue) of representative members of the major chondrite groups (CI, CM, CR, CV, CO, and LL) and the ungrouped carbonaceous chondrite Tagish Lake, which experienced aqueous alteration. In these maps, CAIs and chondrules have bluish and bright red colors, respectively; interstitial matrix has different colors reflecting variations in mineralogy and chemical compositions.

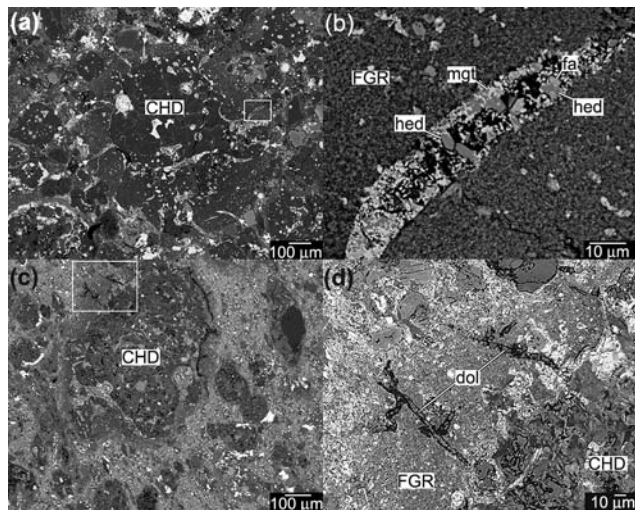


**Fig. 3.** Backscattered electron images of aqueously formed veins. (a,b) Magnesian porphyritic olivine-pyroxene chondrule (CHD) surrounded by a fine-grained rim (FGR) in MAC 88107 (CO3.1). The fine-grained rim is crosscut by veins composed of fayalite (fa), hedenbergite (hed), and magnetite (mgt). Fe,Ni-metal nodules in the chondrule are replaced by magnetite. (c,d) Porphyritic chondrule surrounded by a fine-grained rim and pseudomorphically replaced by phyllosilicates in Sutter's Mill (CM2.1). The fine-grained rim is crosscut by dolomite (dol) veins.

The CIIs, CMs, CRs, and different lithological units of Tagish Lake experienced various but often high degrees of aqueous alteration. The major secondary minerals produced during the alteration are phyllosilicates, carbonates, magnetite, and sulfides (Table 1). The CI chondrites consist almost entirely of aqueously formed minerals (Fig. 4d), and probably never contained abundant chondrules (Huss and Lewis, 1995); rare chondrule fragments (<5 vol%) have been reported in CIs by Leshin *et al.* (1997). Like CI chondrites, several CMs and CRs experienced nearly complete aqueous alteration (Zolensky *et al.*, 1997; Weisberg and Huber, 2007). In contrast to CIs, these CM and CR chondrites contain abundant chondrule pseudomorphs (Figs. 3c, 4b). Most CMs and CRs, however, experienced incomplete aqueous alteration (Rubin *et al.*, 2007; Abreu and Brearley, 2010; Harju *et al.*, 2014; Hewins *et al.*, 2014); the CM chondrites, on average, being more aqueously altered than CR chondrites. Modal mineralogy of CM chondrites measured by X-ray diffraction has been recently reported by Howard *et al.* (2009, 2011, 2015), who showed that the abundance of phyllosilicates increases and their chemical compositions change with increasing degree of aqueous alteration. Based on thermodynamic modeling (e.g., Zolensky *et al.*, 1989; Zolotov and Mironenko, 2008; Berger *et al.*, 2011; Zolotov, 2012), experimentally determined phase diagrams of the Fe-Ni-Co-S system (Bullock *et al.*, 2005; Berger *et al.*, 2011), and oxygen-isotopic compositions of aqueously formed minerals (e.g., Leshin *et al.*, 1997; Clayton and Mayeda, 1999; Benedix *et al.*, 2003; Guo and Eiler, 2007; Schrader *et al.*, 2011), it is inferred that the CIIs, CMs,

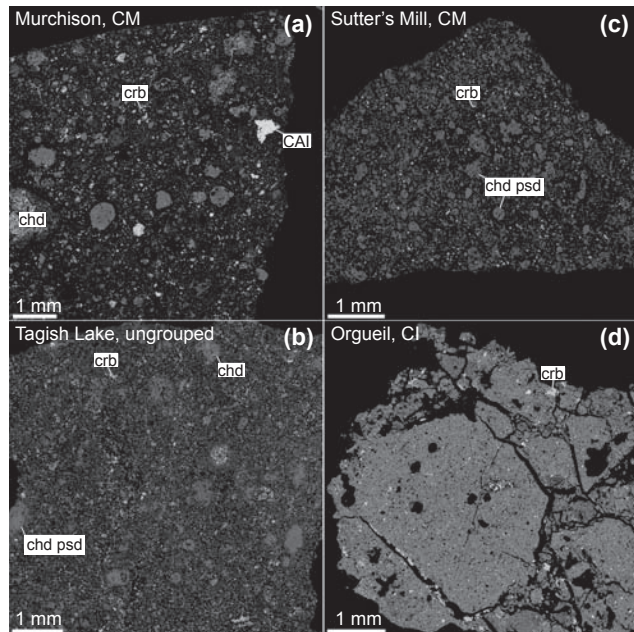


**Fig. 4.** See Plate 21 for color version. Combined elemental maps (Mg = red, Ca = green, Al = blue) of extensively aqueously altered chondrites: (a) Murchison (CM2.5), (b) ungrouped carbonaceous chondrite Tagish Lake, (c) Sutter's Mill (CM2.1), and (d) Orgueil (CI1). Murchison contains abundant magnesian chondrules (chd, red), CAIs (bluish), and heavily hydrated matrix (purple) containing relatively rare grains of carbonate (crb, green). In Sutter's Mill, CAIs, chondrules, and matrix are nearly completely replaced by phyllosilicates and carbonates; chondrule pseudomorphs (chd psd) are common. Tagish Lake contains a higher proportion of heavily hydrated matrix and carbonates, and fewer chondrules and CAIs than Murchison; incompletely altered chondrules are common; some chondrules are nearly completely replaced by phyllosilicates. Orgueil consists entirely of hydrated matrix material; chondrule pseudomorphs are absent.

CRs, and Tagish Lake experienced relatively low-temperature aqueous alteration (~20–150°C) under variable but generally high water/rock (W/R) mass ratio (up to 0.6; could be higher for CIs). Dry asteroids would have W/R = 0, whereas those that formed outside the snow line are expected to have W/R = 1.2 (Lodders, 2003).

The CV3, CO3, and unequilibrated ordinary chondrites (UOCs) experienced a much lower degree of aqueous alteration than CI, CM, and CR chondrites, and contain only minor amounts of hydrated silicates (e.g., Howard *et al.*, 2010; Brearley and Krot, 2012, and references therein); they are all classified as petrologic type  $\geq 3.0$ . It is inferred that aqueous alteration of CVs, COs, and UOCs took place at relatively high temperatures (100°–300°C) and low W/R mass ratios (<0.1–0.2) (e.g., Zolotov *et al.*, 2006; Krot *et al.*, 2013; Doyle *et al.*, 2015). Subsequently, most meteorites from these groups were heated to higher temperatures (>400°C) and experienced fluid-assisted thermal metamorphism. These processes resulted in the formation of a diverse suite of

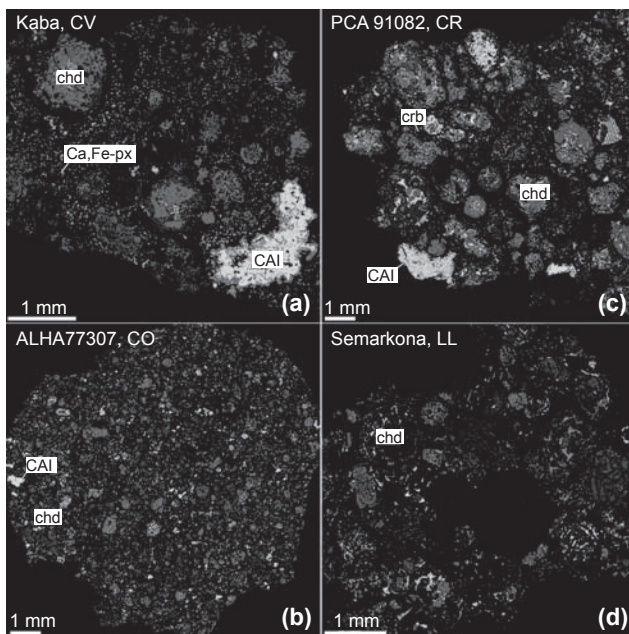


**Fig. 5.** See Plate 22 for color version. Combined elemental maps (Mg = red, Ca = green, Al = blue) of weakly aqueously altered chondrites: (a) Kaba (CV3.1), (b) ALH A77307 (CO3.1), (c) PCA 91082 (CR2), and (d) Semarkona (LL3.0). Chondrules (chd) and CAIs in these meteorites show little evidence for aqueous alteration; matrices are more aqueously altered and contain phyllosilicates, magnetite, and fayalite (except PCA 91082). The Kaba matrix contains abundant Ca,Fe-rich pyroxenes (Ca,Fe-px); the PCA 91082 matrix contains rare carbonate (crb) grains.

secondary minerals; most of them are anhydrous (Table 1) (Brearley and Krot, 2012, and references therein; Jones et al., 2014). The major secondary minerals include magnetite, ferroan olivine ( $Fa_{50-100}$ ), and hedenbergite.

Most R chondrites experienced extensive thermal metamorphism (petrologic types  $>3.6$ ) and, as a result, preserved little evidence for aqueous alteration. The important exception is the R5 chondrite LaPaz Ice Field (LAP) 04840, which contains abundant OH-rich silicate minerals: ferri-magnesiohornblende and phlogopite (Table 1) (McCanta et al., 2008). Based on their stabilities, it is estimated that these minerals formed at  $670^\circ \pm 60^\circ\text{C}$  and  $\text{H}_2\text{O}$  pressures of 250–500 bar (McCanta et al., 2008). Treiman and McCanta (2010) pointed out that even this low water pressure is problematic to generate inside a typical asteroid ( $\sim 75$  km in radius), because it could exceed the tensile strength of a rock ( $\sim 100$  bar) (Grimm and McSween, 1989). Treiman and McCanta (2010) suggested that the high water pressure recorded by LAP 04840 may have been produced in the interior of a relatively large asteroid that was sealed by an impermeable water-ice-filled regolith.

The oxygen-isotopic compositions of aqueously formed minerals (see section 7.4 for details) and bulk chondrites (Fig. 1) have been used to argue for both open-system (in the presence of a fluid flow) and closed-system (with a stagnant

TABLE 1. Aqueously formed minerals in CI, CM, CR, CV, CO, R, and ordinary chondrites.

Mineral	Composition
<i>CI, CM, and CR chondrites</i>	
serpentine	$\text{Mg}_3\text{Si}_2\text{O}_5(\text{OH})_4$
cronstedtite	$\text{Fe}_{2+}\text{Fe}^{3+}(\text{Si},\text{Fe}^{3+})_2\text{O}_5(\text{OH})_4$
saponite	$\text{Ca}_{0.25}(\text{Mg},\text{Fe})_3(\text{Si}_4\text{O}_{10})(\text{OH})_2 \cdot n\text{H}_2\text{O}$
tochilinite	$2[(\text{Fe},\text{Mg},\text{Cu},\text{Ni})\text{S}] \cdot 1.57-1.85[(\text{Mg},\text{Fe},\text{Ni},\text{Al},\text{Ca})(\text{OH})_2]$
calcite	$\text{CaCO}_3$ (trigonal)
aragonite	$\text{CaCO}_3$ (orthorhombic)
dolomite	$\text{CaMg}(\text{CO}_3)_2$
siderite	$\text{FeCO}_3$
breunnerite	$(\text{Mg},\text{Fe},\text{Mn})\text{CO}_3$
troilite	$\text{FeS}$
pyrrhotite	$\text{Fe}_{1-x}\text{S}$
pentlandite	$(\text{Fe},\text{Ni})_9\text{S}_8$
magnetite	$\text{Fe}_3\text{O}_4$
cubanite	$\text{CuFe}_2\text{S}_3$
sphalerite	$(\text{Fe},\text{Zn})\text{S}$
<i>CV, CO, R, and ordinary chondrites</i>	
saponite	$\text{Ca}_{0.25}(\text{Mg},\text{Fe})_3(\text{Si}_4\text{O}_{10})(\text{OH})_2 \cdot n\text{H}_2\text{O}$
phlogopite	$\text{KMg}_3\text{AlSi}_3\text{O}_{10}(\text{OH})_2$
amphibole	$(\text{Ca},\text{Na})_{2-3}(\text{Mg},\text{Fe}^{2+},\text{Al})_5(\text{Si},\text{Al},\text{Fe}^{3+})_8\text{O}_{22}(\text{OH},\text{F},\text{Cl})_2$
magnetite	$\text{Fe}_3\text{O}_4$
fayalite	$\text{Fe}_3\text{SiO}_4$
hedenbergite	$\text{CaFeSi}_2\text{O}_6$
andradite	$\text{Ca}_3\text{Fe}_2\text{Si}_3\text{O}_{12}$
kirschsteinite	$\text{CaFeSiO}_4$
Fe,Ni-carbides	$(\text{Fe},\text{Ni})_3\text{C}; (\text{Fe},\text{Ni})_{23}\text{C}_6$
pentlandite	$(\text{Fe},\text{Ni})_9\text{S}_8$
pyrrhotite	$\text{Fe}_{1-x}\text{S}$
Ni-rich metal	$\text{FeNi}; \text{FeNi}_3$
whitlockite	$\text{Ca}_9(\text{Mg},\text{Fe})(\text{PO}_4)_6(\text{PO}_3\text{OH})$
merrillite	$\text{Ca}_{18}\text{Na}_2\text{Mg}_2(\text{PO}_4)_{14}$
anorthite	$\text{CaAl}_2\text{Si}_2\text{O}_8$ (triclinic)
dmisteinbergite	$\text{CaAl}_2\text{Si}_2\text{O}_8$ (hexagonal)
corundum	$\text{Al}_2\text{O}_3$
forsterite	$\text{Mg}_2\text{SiO}_4$
grossular	$\text{Ca}_3\text{Al}_2\text{Si}_3\text{O}_{12}$
kushiroite	$\text{CaAl}_2\text{SiO}_6$
monticellite	$\text{CaMgSiO}_4$
Na-melilite	$(\text{CaNa})_2(\text{Al},\text{Mg})[(\text{AlSi})_2\text{O}_7]$
nepheline	$\text{NaAlSiO}_4$
sodalite	$\text{Na}_8\text{Al}_6\text{Si}_6\text{O}_{24}\text{Cl}_{12}$
wadelite	$\text{Ca}_6(\text{Al},\text{Si},\text{Mg})_7\text{O}_{16}\text{Cl}_3$
wollastonite	$\text{CaSiO}_3$
calcite	$\text{CaCO}_3$

fluid) aqueous alteration, and for constraining water/rock ratios in hydrated chondrites (Young et al., 1999; Clayton and Mayeda, 1999). The estimated low permeability of chondritic meteorites (Bland et al., 2009) and the lack of clear evidence for variations in bulk chemical compositions between meteorites with different degrees of aqueous alteration within chondrite groups appear to be consistent with the closed-system alteration. The closed-system alteration, however, is just an

approximation of reality: Highly diffusive gases (e.g., H<sub>2</sub>) at least partly escaped from the altered regions; in addition, collisions between planetesimals must have resulted in their fracturing and sudden release of the fluids (see the chapter by Wilson et al. in this volume). Given the variable degrees of aqueous alteration experienced by most chondrite groups, there probably was a heterogeneous distribution of water ice in the chondrite parent bodies at the time of alteration. This heterogeneity may be a primary (as a result of heterogeneous accretion of water ice) or a secondary (early redistribution of water ice in the chondrite parent bodies) feature. It has been suggested that carbonaceous chondrite parent bodies were not lithified during accretion and, after melting of ice, fluids and solids would have moved together as a viscous but convective mud (Bland et al., 2013; Bland and Travis, 2014). Chondrules in this scenario would have behaved as a suspended load in the mud, and would have settled out, resulting in a coarse core and a mud ocean mantle above. In this “mudball” model, convective mixing moderated internal temperature and alteration was necessarily isochemical. However, it is unclear whether the variation in the degrees of alteration observed for CM and CR chondrites could be produced in a well-mixed mud mantle.

#### 4. MODIFICATIONS OF CHONDRITE ORGANICS DURING AQUEOUS ALTERATION AND THERMAL METAMORPHISM

The organic matter present in chondrites was originally derived from precursors that formed and/or were modified in the presolar molecular cloud, the protosolar nebula, and the chondrite parent bodies. The relative importance of these different sources and processes is a matter of intense debate among cosmochemists. The organics are found in the matrix, where they are intimately intermixed with both unaltered and aqueously altered minerals (e.g., Le Guillou and Brearley, 2014; Le Guillou et al., 2014; Volmer et al., 2014). While the mineralogical effects of aqueous alteration in matrix are well documented (e.g., Brearley, 2006; Zolensky et al., 2008; Brearley and Krot, 2012), there has been a long-standing debate about the extent to which the altering fluids have modified the soluble and insoluble organic matter (SOM and IOM, respectively). Recent *in situ* studies indicate that aqueous alteration resulted in some redistribution, oxidation, and aromatization of organic matter (Le Guillou and Brearley, 2014; Le Guillou et al., 2014; Volmer et al., 2014). However, a detailed understanding of how and to what extent alteration has modified the organic matter in chondrites is still some way off. Insights into conditions of aqueous alteration gained from the study of organics are currently very limited.

There is clear evidence that aqueous alteration has modified the absolute and relative abundances of amino acids in CM and CR chondrites and Tagish Lake (Martins et al., 2007; Glavin and Dworkin, 2009; Glavin et al., 2010a,b; Herd et al., 2011; Pizzarelli et al., 2012; Elsila et al., 2012; Hilts et al., 2014). Most striking is the decrease in the abundance of  $\alpha$ -amino acids and the development of

increasing L-enantiomeric excesses in isovaline with increasing aqueous alteration. Pizzarelli et al. (2012) reported large L-enantiomeric excesses in one of the least-altered CRs and suggested that the excesses are primary rather than secondary, but their results have been challenged (Elsila et al., 2012; Pizzarelli and Munroe, 2012). The effects of alteration on other components of the soluble organic fractions in chondrites have been less well studied, but monocarboxylic acids at least do seem to have been affected by alteration (Aponte et al., 2011). Hilts et al. (2014) suggested that the variations in carboxylic acid compositions between differently altered lithologies in the Tagish Lake meteorite reflected oxidative cleavage of side chains from the IOM during alteration. Cody and Alexander (2005) and Callahan et al. (2011) have suggested this may be the case for most or all chondrites, although Aponte et al. (2011) found no evidence for this in the CM chondrites.

The origin of carboxylic acids notwithstanding, the role of aqueous alteration in the post-accretionary evolution of IOM is also a matter of debate. There are considerable variations in the elemental, isotopic, and functional group compositions of the IOM within and between the different chondrite groups. Alexander et al. (2007, 2013) proposed that these variations are primarily the result of secondary processes in the chondrite parent bodies acting on a common precursor that most closely resembled the IOM found in CR chondrites. Support for this comes from the Tagish Lake lithologies because their widely varying IOM compositions change systematically with the extent of alteration (Herd et al., 2011; Alexander et al., 2014). Comparisons with hydrothermal experiments suggest that the extent of the IOM transformations in the Tagish Lake lithologies, and by inference other chondrites, reflect differences in the temperature and/or duration of alteration. Based on a systematic characterization of IOM by Raman and IR spectroscopy, Quirico et al. (2014) and Orthous-Daunay et al. (2013) also found evidence that their Tagish Lake sample had been heated, probably by impact. However, to explain the differences in compositions of IOM from apparently unheated meteorites from different chondrite groups, these and other authors (e.g., Rémusat et al., 2006, 2010) favor variations in the accreted organic precursors. Nevertheless, there is agreement on the relative temperatures during aqueous alteration of the carbonaceous chondrite groups CR < CM < CI < CV (Alexander et al., 2014; Quirico et al., 2014), although experiments will be needed to constrain the absolute temperatures and timescales of alteration.

The effects of thermal metamorphism on the structure of the IOM are described in several papers (e.g., Quirico et al., 2003; Bonal et al., 2006, 2007; Busemann et al., 2007; Yabuta et al., 2010).

#### 5. DATING OF AQUEOUS ALTERATION

In this section, we explain the main principles and uncertainties of Mn-Cr isotope dating of aqueously formed minerals using secondary ion mass spectrometry (SIMS). We then summarize recent results of <sup>53</sup>Mn-<sup>53</sup>Cr dating of

fayalite ( $\text{Fe}_2\text{SiO}_4$ ), kirschsteinite ( $\text{CaFeSiO}_4$ ), and different carbonates [calcite,  $\text{CaCO}_3$ ; dolomite,  $\text{CaMg}(\text{CO}_3)_2$ ; siderite,  $\text{FeCO}_3$ ; and breunnerite,  $(\text{Mg},\text{Fe},\text{Mn})\text{CO}_3$ ] in several chondrite groups.

### 5.1. Principles of Manganese-Chromium Isotope Dating of Aqueously Formed Minerals by Secondary Ion Mass Spectrometry

The short-lived radionuclide  $^{53}\text{Mn}$  decays to  $^{53}\text{Cr}$  with a half-life of  $\sim 3.7$  m.y. and appears to have been uniformly distributed in the protoplanetary disk (Trinqueir *et al.*, 2008; Yin *et al.*, 2009). Aqueously formed fayalites [ $\text{Fa}_{>95}$ , where  $\text{Fa} = (\text{atomic ratio}) \text{Fe}/(\text{Fe} + \text{Mg}) \times 100$  in olivine] in L, LL, CO, and CV chondrites of low petrologic types ( $\leq 3.1$ ) and carbonates in CI, CM, and CR chondrites contain high MnO contents (several weight percent) and low concentrations of  $\text{Cr}_2\text{O}_3$  ( $\ll 0.1$  wt%), and therefore are suitable for age dating using  $^{53}\text{Mn}-^{53}\text{Cr}$  isotope chronology. The excess of radiogenic  $^{53}\text{Cr}$  ( $\delta^{53}\text{Cr}^*$ ) in 5–10- $\mu\text{m}$ -sized fayalite and carbonate grains can be measured *in situ* by SIMS. Excess  $^{53}\text{Cr}$  relative to stable  $^{52}\text{Cr}$ , correlated with the  $^{55}\text{Mn}/^{52}\text{Cr}$  ratio, indicates *in situ* decay of  $^{53}\text{Mn}$ , and the initial  $^{53}\text{Mn}/^{55}\text{Mn}$  ratio [ $(^{53}\text{Mn}/^{55}\text{Mn})_0$ ] during crystallization of these minerals can be calculated from the slope of the correlation (Fig. 6).

Manganese-53–chromium-53 dating is a relative chronometer, and the  $^{53}\text{Mn}-^{53}\text{Cr}$  ages are typically calculated relative to CV CAIs, which are the oldest solar system solids to have been dated [ $4567.30 \pm 0.16$  Ma (Connelly *et al.*, 2012)], and in cosmochemistry are considered to represent the beginning of the solar system formation ( $t_0$ ). The time of mineral formation after CV CAIs is given by

$$\Delta t_{\text{min-CAIs}} = 1/\lambda_{^{53}\text{Mn}} \times \ln[(^{53}\text{Mn}/^{55}\text{Mn})_{\text{CAIs}}/(^{53}\text{Mn}/^{55}\text{Mn})_{\text{min}}]$$

where  $\lambda_{^{53}\text{Mn}}$  is the decay constant of  $^{53}\text{Mn}$ .

The initial  $^{53}\text{Mn}/^{55}\text{Mn}$  ratio in CAIs has not been measured due to the lack of minerals having high Mn/Cr ratios as well as post-crystallization disturbance of their Mn-Cr isotope systematics (e.g., Papanastassiou *et al.*, 2002). Instead, the initial  $^{53}\text{Mn}/^{55}\text{Mn}$  ratio in CAIs,  $\sim 6.8 \times 10^{-6}$ , is estimated using the measured  $(^{53}\text{Mn}/^{55}\text{Mn})_0$  in the D'Orbigny angrite (basaltic meteorite),  $(3.24 \pm 0.04) \times 10^{-6}$  (Glavin *et al.*, 2004), its U-corrected Pb-Pb absolute age of  $4563.4 \pm 0.3$  Ma (Brennecke and Wadhwa, 2012), and the U-corrected Pb-Pb absolute age of CV CAIs,  $4567.30 \pm 0.16$  Ma (Connelly *et al.*, 2012).

Secondary ion mass spectrometry measurements of Mn-Cr isotope systematics in a mineral require the use of a proper standard to correct for the relative ionization efficiencies of  $^{55}\text{Mn}^+$  and  $^{52}\text{Cr}^+$  ions in order to determine accurate  $^{55}\text{Mn}/^{52}\text{Cr}$  abundance ratios. It has been recently shown for both fayalitic olivine (Sugiura *et al.*, 2005; McKibbin *et al.*, 2013; Doyle *et al.*, 2013, 2015) and carbonates (Sugiura *et al.*, 2010; Fujiya *et al.*, 2012; Steele and McKeegan, 2014) that past studies [fayalite (Hutcheon *et al.*, 1998; Krot *et al.*, 2000; Hua *et al.*, 2005; Jogo *et al.*, 2009) and carbonates (En-

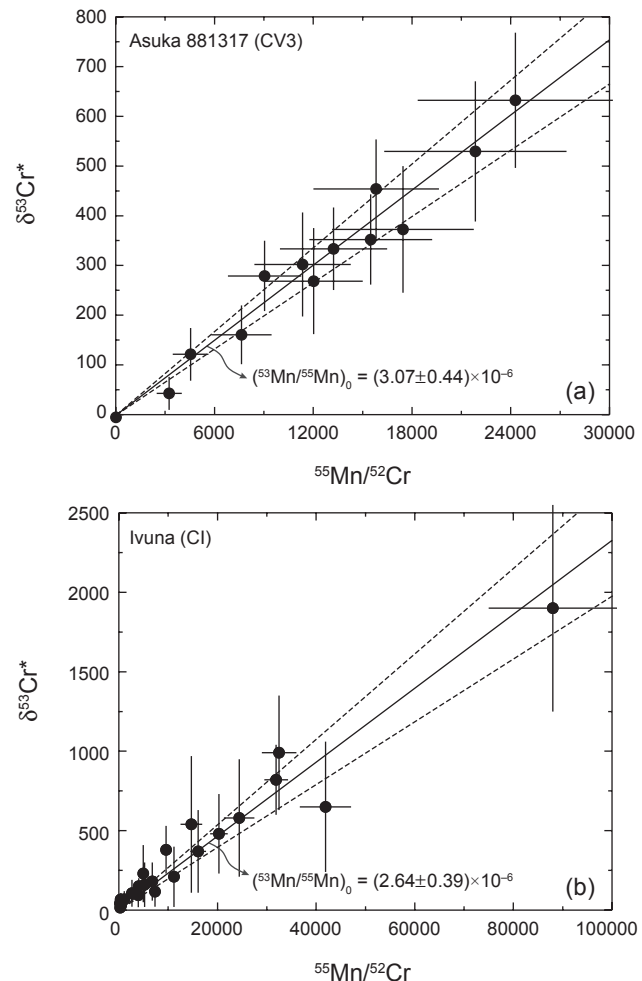


**Fig. 6.** Manganese-chromium evolutionary diagrams of (a) fayalite in Asuka 881317 (CV3) and (b) dolomite in Ivuna (CI1).  $\delta^{53}\text{Cr}^* = [(^{53}\text{Cr}/^{52}\text{Cr})_{\text{fa}} \text{ or dol} / (^{53}\text{Cr}/^{52}\text{Cr})_{\text{terrestrial}} - 1] \times 1000$ , where  $(^{53}\text{Cr}/^{52}\text{Cr})_{\text{terrestrial}} = 0.113459$ . Excess of  $\delta^{53}\text{Cr}^*$  is well correlated with  $^{55}\text{Mn}/^{52}\text{Cr}$  ratios, indicative of *in situ*  $^{53}\text{Mn}$  decay to  $^{53}\text{Cr}$ . The initial  $(^{53}\text{Mn}/^{55}\text{Mn})_0$  are indicated; all uncertainties including error envelope are  $2\sigma$ . Data from Doyle *et al.* (2015) and Fujiya *et al.* (2013).

dress *et al.*, 1996; Hoppe *et al.*, 2007; Petitet *et al.*, 2009a,b; de Leuw *et al.*, 2009; Lee *et al.*, 2012)] used inappropriate standards, rendering their inferred ages unreliable.

### 5.2. Manganese-53–Chromium-53 Ages of Fayalite Formation in Type 3 Ordinary, CO, and CV Chondrites

The  $^{53}\text{Mn}-^{53}\text{Cr}$  ages of aqueously formed fayalite measured with a proper standard have been reported so far for only three meteorites: Elephant Moraine (EET) 90161 (L3.05), Asuka 881317 (CV3), and MacAlpine Hills (MAC) 88107 (CO3-like), with ages of  $2.4^{+1.8}_{-1.3}$ ,  $4.2^{+0.8}_{-0.7}$ , and  $5.1^{+0.5}_{-0.4}$  m.y. after CV CAIs, respectively (Doyle *et al.*, 2015). Mineralogical observations and thermodynamic analysis suggest that fayalite formation occurred during the initial stages

of aqueous alteration, contemporaneously or slightly later than formation of magnetite and phyllosilicates (Krot *et al.*, 1998; Jogo *et al.*, 2009; Zolotov *et al.*, 2006; Doyle *et al.*, 2015). As a result, the  $^{53}\text{Mn}$ - $^{53}\text{Cr}$  ages of fayalite formation roughly marks the beginning of aqueous alteration of the L, CO, and CV chondrite parent bodies.

### 5.3. Manganese-53-Chromium-53 Ages of Kirschsteinite Formation in CV Chondrites

*MacPherson et al.* (2015) reported preliminary results of SIMS measurements of  $^{53}\text{Mn}$ - $^{53}\text{Cr}$  ages of secondary kirschsteinite in matrices of several CV chondrites (Vigarano, Efremovka). Synthetic Cr- and Mn-doped glass with a composition that is intermediate between kirschsteinite and fayalite was used as a standard. The  $^{53}\text{Mn}$ - $^{53}\text{Cr}$  age of kirschsteinite,  $3.7^{+0.7}_{-0.6}$  m.y. after CV CAIs, is indistinguishable from that in CV fayalite,  $4.2^{+0.8}_{-0.7}$  m.y. after CV CAIs, and in combination with mineralogical observations suggests contemporaneous formation of these minerals during aqueous/ hydrothermal alteration on the CV parent body.

### 5.4. Manganese-53-Chromium-53 Ages of Carbonate Formation in CI, CM, CR, and Lithic Clasts in CH Chondrites

The CI, CM, and CR chondrites lack fayalite but contain carbonates (dolomite, calcite, siderite, and breunnerite) that are often enriched in manganese and depleted in chromium, making them suitable for  $^{53}\text{Mn}$ - $^{53}\text{Cr}$  age dating with SIMS. Using synthetic Mn- and Cr-doped calcite (*Sugiura et al.*, 2010) as a standard, *Fujiya et al.* (2012, 2013) and *Jilly et al.* (2014a) reported  $^{53}\text{Mn}$ - $^{53}\text{Cr}$  ages of calcite and dolomite in CI and CM chondrites. The calcite and dolomite have a narrow range of ages of  $\sim 4\text{--}5$  m.y. after CV CAIs (Fig. 9). We note, however, that the lack of an appropriate standard for dolomite makes  $^{53}\text{Mn}$ - $^{53}\text{Cr}$  ages of its formation uncertain (*Steele and McKeegan*, 2014). The duration of aqueous alteration on the CM and CI parent bodies is not known. There is some correlation between the  $^{53}\text{Mn}$ - $^{53}\text{Cr}$  ages of carbonate formation and the degrees of aqueous alteration experienced by the host meteorites (Fig. 7). Mineralogical observations, chemical compositions, and carbon- and oxygen-isotope data suggest the presence of multiple generations of carbonates in CM and CI chondrites (e.g., *Brearley*, 2006; *Rubin et al.*, 2007; *Tyra et al.*, 2012; *Lee et al.*, 2012, 2013). The crystallization sequence of different carbonates are not well understood (*Petitat et al.*, 2009b, 2010; *Lee et al.*, 2012), and no reliable differences in age between the different types of carbonates have been reported. An  $\sim 7$ -m.y. age difference has been reported between dolomites and breunnerites in CI chondrites (*Endress et al.*, 1996; *Hoppe et al.*, 2007; *Petitat et al.*, 2009b), but the use of improper standards for both minerals makes these chronological inferences uncertain (*Steele and McKeegan*, 2014).

*Jilly et al.* (2013) reported  $^{53}\text{Mn}$ - $^{53}\text{Cr}$  ages of calcite in two CR chondrites, Renazzo and Grosvenor Mountains (GRO) 95577. The  $^{53}\text{Mn}$ - $^{53}\text{Cr}$  age of calcite in Renazzo is

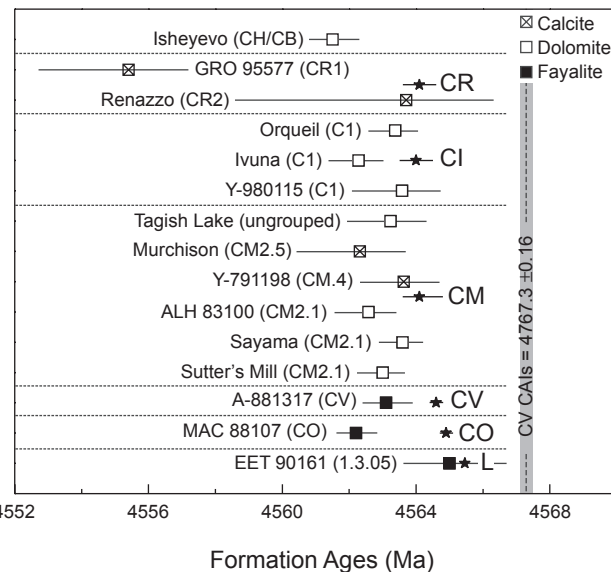


**Fig. 7.**  $^{53}\text{Mn}$ - $^{53}\text{Cr}$  ages of calcite, dolomite, and fayalite in unequilibrated ordinary (L) and carbonaceous chondrites (CV, CO, CM, CI, CR, and hydrated clasts in CH/CB) anchored to the U-corrected Pb-Pb age of the D'Orbigny angrite and CV CAIs. Data from *Fujiya et al.* (2012, 2013), *Jilly et al.* (2013, 2014a), *van Kooten et al.* (2014), and *Doyle et al.* (2015). The U-corrected Pb-Pb absolute age of CV CAIs is from *Connelly et al.* (2012). Note that *Fujiya et al.* (2012, 2013) used U-uncorrected absolute ages of a CV CAI reported by *Bouvier and Wadhwa* (2010), which is different from that reported by *Connelly et al.* (2012), and an LEW 86010 angrite anchor (*Amelin*, 2008) to calculate carbonate ages. As a result, the carbonate ages reported by *Fujiya et al.* (2012, 2013) are systematically younger, by  $\sim 0.7$  m.y., than those plotted here. The estimated accretion ages (indicated by stars) of the L, CO, CV, CI, CM, and CR chondrite parent bodies are from *Sugiura and Fujiya* (2014).

indistinguishable from those of calcite and dolomite in CM and CI chondrites. Calcite in the more aqueously altered GRO 95577 has a much younger age,  $\sim 12 \pm 2$  m.y. after CV CAIs. In addition, siderite in GRO 95577 shows no resolvable excess of  $\delta^{53}\text{Cr}^*$  (*Tyra et al.*, 2010), suggesting a very late formation of  $>23$  m.y. (with San Carlos olivine as a standard) after CV CAIs. Together with the reported  $^{53}\text{Mn}$ - $^{53}\text{Cr}$  age of calcite in GRO 95577, these observations imply prolonged aqueous alteration on the CR parent body.

Although CH and CB chondrites avoided aqueous alteration, they contain extensively hydrated chondrite lithic clasts that may represent fragments of separate parent body(ies) that were accreted after collisions disrupted their original parent bodies (*Greshake et al.*, 2002; *Bonal et al.*, 2010). Dolomite grains in the lithic clasts from the Isheyev (CH/CB) chondrite have a  $^{53}\text{Mn}$ - $^{53}\text{Cr}$  age of  $5.8^{+0.8}_{-0.7}$  m.y. after CV CAIs, similar to or slightly younger than  $^{53}\text{Mn}$ - $^{53}\text{Cr}$  ages of carbonates in CI and CM chondrites (*van Kooten et al.*, 2014).

## 5.5. Manganese-53-Chromium-53 Ages of Aqueously Formed Minerals in Ordinary and Carbonaceous Chondrites: Summary

The  $^{53}\text{Mn}$ - $^{53}\text{Cr}$  ages of carbonates in CI, CM, CR, and CH chondrites, and of fayalite in CO, CV, and L chondrites, are summarized in Fig. 7. The  $^{53}\text{Mn}$ - $^{53}\text{Cr}$  ages of fayalite and carbonates in several groups of carbonaceous chondrites are similar, suggesting that aqueous alteration on their parent bodies started within a narrow range in time,  $\sim 3.5\text{--}5$  m.y. after CV CAIs. The beginning of aqueous alteration on the L-chondrite parent body may have predated aqueous activity on the carbonaceous chondrite parent bodies by  $\sim 1$  m.y., but the uncertainties are large. The early and nearly contemporaneous onset of aqueous activity on the chondrite parent bodies is consistent with the short-lived radionuclide  $^{26}\text{Al}$  (decays to  $^{26}\text{Mg}$  with a half-life of  $\sim 0.7$  m.y.) being their major heat source.

## 6. ACCRETION AGES OF CHONDRITE PARENT BODIES

The duration and mechanism(s) of accretion of chondrite parent bodies are poorly understood: Prolonged accretion by grain coagulation (Brauer et al., 2008) and rapid accretion after chondrule formation through turbulent concentration (Cuzzi et al., 2010; Chambers, 2010) and streaming and gravitational instability in a dusty midplane (Youdin and Shu, 2002; Johansen and Klar, 2011) are currently being debated. Rapid accretion after chondrule formation appears to be consistent with the high dust/gas ratios inferred for the regions where chondrules formed (e.g., Alexander et al., 2008); it may also explain the unique chemical, isotopic, and mineralogical characteristics of known chondrite groups, and the relatively narrow ranges of  $^{26}\text{Al}$ - $^{26}\text{Mg}$  ages of chondrules in an individual chondrite group (Fig. 8). Note that rapid accretion after chondrule formation is model-dependent, because (1) mechanisms of chondrule formation are still poorly understood, and the idea of chondrule formation by collisions between planetesimals becomes quite popular (e.g., Krot et al., 2005; Alexander et al., 2008; Asphaug et al., 2011; Johnson et al., 2015), and (2) CI chondrites appear to have accreted without a significant abundance of chondrules.

The accretion ages of chondrite parent bodies can be constrained using (1) the  $^{53}\text{Mn}$ - $^{53}\text{Cr}$  ages of aqueous alteration, (2) the  $^{26}\text{Al}$ - $^{26}\text{Mg}$  ages of chondrules, and (3) the peak metamorphic temperatures reached by these bodies.

1. Because aqueous alteration occurred exclusively in the chondrite parent bodies (see section 3), the inferred  $^{53}\text{Mn}$ - $^{53}\text{Cr}$  ages of aqueously formed minerals (Fig. 7) provide the upper limits on the chondrite accretion ages.

2. Formation of chondrules predated their accretion into their host meteorites. Therefore, chondrule ages provide the lower limits on the chondrite accretion ages. This approach cannot be used for CM and CI chondrites, because (a) due to extensive aqueous alteration of CM chondrules, the  $^{26}\text{Al}$ - $^{26}\text{Mg}$  ages of their chondrules are not known, and (b) chondrules are absent in CI chondrites.

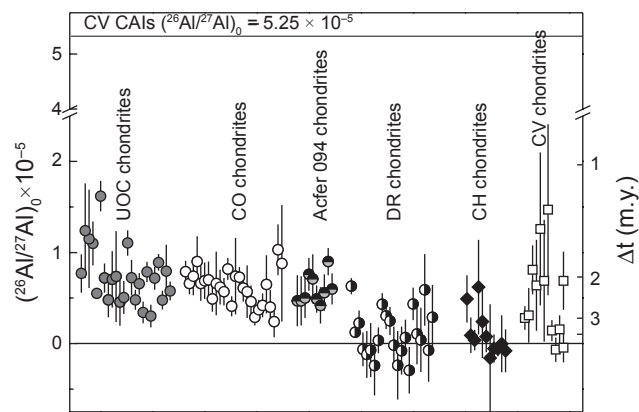


**Fig. 8.** Inferred initial  $^{26}\text{Al}/^{27}\text{Al}$  ratios  $[(^{26}\text{Al}/^{27}\text{Al})_0]$  and  $^{26}\text{Al}$ - $^{27}\text{Al}$  relative ages of porphyritic chondrules (relative to CV CAIs) from unequilibrated ordinary [UOC, Semarkona (LL3.0)], Y-81020 (CO3.0), Acfer 094 (type 3.0 ungrouped), CR2-3, CH3.0, and CV3.1-3.6 chondrites [data for Semarkona from Hutcheon and Hutchison (1989), Kita et al. (2000), Mostefaoui et al. (2002), and Rudraswami et al. (2008); for Y-81020 from Kunihiro et al. (2004) and Kurashiki et al. (2008); for CVs from Hutcheon et al. (2009); for Acfer 094 from Ushikubo et al. (2013); for CRs from Nagashima et al. (2014) and Schrader et al. (2013); for CHs from Krot et al. (2014b)]. The inferred initial  $^{26}\text{Al}/^{27}\text{Al}$  ratio in CV CAIs is from Jacobsen et al. (2008).

Chondrule ages have been measured by SIMS using  $^{26}\text{Al}$ - $^{26}\text{Mg}$  relative chronology (e.g., Kita and Ushikubo, 2012), and by thermal ionization mass spectrometry (TIMS) using U-Pb absolute chronology (e.g., Connelly et al., 2012). The U-Pb ages of chondrules are very limited: Less than 10 individual chondrules from CV3, CB3, and L3 chondrites have been measured so far (Amelin et al., 2002; Connelly et al., 2012; Bollard et al., 2014). These ages provide clear evidence that chondrule formation started almost contemporaneously with CAIs and lasted for at least 5 m.y. However, because of the limited number of chondrules measured, use of their U-Pb absolute ages for constraining the accretion time of chondrite parent bodies is premature.

It is commonly assumed that by the end of a brief epoch of CAI formation, characterized by a heterogeneous distribution of  $^{26}\text{Al}$  (e.g., Krot et al., 2012, and references therein),  $^{26}\text{Al}$  became uniformly distributed in the protoplanetary disk at the canonical level,  $(^{26}\text{Al}/^{27}\text{Al})_0 \sim 5.2 \times 10^{-5}$  (Jacobsen et al., 2008; Villeneuve et al., 2009; Kruijer et al., 2014); for an alternative view, i.e., possible evidence for heterogeneous distribution of  $^{26}\text{Al}$  in the protoplanetary disk, see Larsen et al. (2011) and Bizzarro et al. (2014). The canonical  $^{26}\text{Al}/^{27}\text{Al}$  ratio was defined on the basis of high-precision Al-Mg isotope measurements of bulk CAIs from CV chondrites by multicollector inductively coupled plasma mass spectrometry (MC-ICPMS) (Jacobsen et al., 2008; Larsen et al., 2011) and of individual CAIs by SIMS (MacPherson et al., 2011).

The  $^{26}\text{Al}$ - $^{26}\text{Mg}$  ages of chondrules are calculated relative to the canonical CAIs

$$\Delta t_{\text{chd-CAIs}} = 1/\lambda_{^{26}\text{Al}} \times \ln[(^{26}\text{Al}/^{27}\text{Al})_{\text{CAIs}}/(^{26}\text{Al}/^{27}\text{Al})_{\text{chd}}]$$

where  $\lambda_{^{26}\text{Al}}$  is the decay constant of  $^{26}\text{Al}$ .

The reported  $^{26}\text{Al}$ - $^{26}\text{Mg}$  ages of chondrules from Se-markona (LL3.0), Yamato (Y)-81020 (CO3.0), Acfer 094 (ungrouped type 3.0 carbonaceous chondrite), CR2-3, CH3.0, and CV3.1–3.6 chondrites are summarized in Fig. 8. Chondrules in most chondrite groups, except chondrules in thermally metamorphosed CV3.1–3.6 chondrites, show relatively narrow ranges of the initial  $^{26}\text{Al}/^{27}\text{Al}$  ratios. Thermal metamorphism of the CV chondrules could have disturbed their Al-Mg isotope systematics, and may explain the observed large range of  $^{26}\text{Al}$ - $^{26}\text{Mg}$  ages of the CV chondrules (Fig. 8). The mean values  $\pm$  one standard deviation of  $(^{26}\text{Al}/^{27}\text{Al})_0$  in chondrules from the least-metamorphosed chondrites — Se-markona, Y-81020, and Acfer 094 — are  $(0.78 \pm 0.3) \times 10^{-5}$ ,  $(0.62 \pm 0.19) \times 10^{-5}$ , and  $(0.57 \pm 0.15) \times 10^{-5}$ , respectively, which correspond to  $1.9 \pm 0.4$ ,  $2.2 \pm 0.3$ , and  $2.3 \pm 0.3$  m.y. after CV CAIs. These age uncertainties cannot be considered as estimates for the duration of chondrule formation recorded by these chondrite groups, because they all may contain multiple generations of chondrules (e.g., Connolly *et al.*, 2012; Bollard *et al.*, 2014). Instead, these ages may provide the upper limits of the formation age of a dominant generation of chondrules within a chondrite group. Alexander and co-workers argue that the spread in the measured  $^{26}\text{Al}$ - $^{26}\text{Mg}$  ages of chondrules within a chondrite group largely reflects measurement uncertainties and possibly resetting by alteration and thermal metamorphism (Alexander and Ebel, 2012; see also the chapter by DeMeo *et al.* in this volume). It is also possible that some of the chondrules within a chondrite group formed by impacts (e.g., Johnson *et al.*, 2015) after accretion of the chondrite parent body. Such chondrules, if they exist, are expected to have a lower  $^{26}\text{Al}/^{27}\text{Al}$  ratio than the chondrules predating the accretion.

If  $^{26}\text{Al}$  was uniformly distributed in the protoplanetary disk and was the major heat source of planetesimals, as is currently believed, the accretion time of the ordinary, CO, and CV parent bodies can be constrained using the estimated peak metamorphic temperatures they have experienced: ordinary chondrites  $\sim 950^\circ\text{C}$ , and CO and CV chondrites  $\sim 600^\circ$ – $700^\circ\text{C}$  (e.g., Huss *et al.*, 2006, and references therein; Cody *et al.*, 2008). Assuming instantaneous accretion of the L, CO, and CV parent bodies composed a homogeneous mixture of anhydrous silicates and water ice/rock volume ratio of 0.2, Doyle *et al.* (2015) modeled thermal evolution of these bodies, and concluded that they accreted  $\sim 1.8$ ,  $\sim 2.4$ , and  $\sim 2.6$  m.y. after CV CAIs, respectively (Fig. 9). Using slightly different initial parameters, Sugiura and Fujiya (2014) inferred that the accretion ages of the ordinary, CO, and CV chondrite parent bodies are  $\sim 2.1$ ,  $\sim 2.7$ , and  $\sim 3.0$  m.y. after CV CAIs, respectively. The inferred accretion ages of the enstatite, R, and CK chondrite parent bodies are  $\sim 1.8$ ,  $\sim 2.1$ , and  $\sim 2.6$  m.y. after CV CAIs, respectively (Sugiura

and Fujiya, 2014). Note that if known meteorites have not sampled the innermost regions of these bodies, the peak metamorphic temperatures reached by these bodies could be higher and the estimated accretion ages may provide only the upper limits. For example, it has suggested that the CV chondrites are the unmelted crust of a differentiated body (Elkins-Tanton *et al.*, 2011), in which case at least the central portion of the CV chondrite parent body accreted prior to the ordinary chondrites.

The accretion ages of the CI and CM chondrite parent bodies can be constrained using the formation temperatures and  $^{53}\text{Mn}$ - $^{53}\text{Cr}$  ages of carbonates, and the peak metamorphic temperatures reached by these bodies (Fujiya *et al.*, 2012, 2013). Based on the oxygen-isotope compositions of calcite and dolomite (Clayton and Mayeda, 1984; Guo and Eiler, 2007) and thermodynamic modeling (Zolensky *et al.*, 1989), it is estimated that these minerals precipitated in the earliest stages of aqueous alteration of the CM and CI chondrite parent bodies, at  $\sim 20^\circ$ – $70^\circ\text{C}$  and  $100^\circ$ – $150^\circ\text{C}$ , respectively. These estimates are model-dependent, and it is possible that both groups may have experienced similar peak metamorphic temperatures,  $\sim 100^\circ\text{C}$ . For example, the organic matter in CM and CI chondrites is structurally similar, suggesting similar peak-alteration temperatures (Alexander *et al.*, 2014). Alexander *et al.* (2014) found that the CM and CR organic matter is more aromatic than that in CR chondrites, and, as a result, suggested that CMs and CIs experienced higher peak-alteration temperatures than CRs. Based on the oxygen-isotopic compositions of carbonates and magnetite in CR chondrites, the alteration temperature of CRs was separately estimated to be  $\sim 50^\circ\text{C}$  (Jilly *et al.*, 2014b). Fujiya *et al.* (2012, 2013) modeled the thermal evolution of the CM and CI parent bodies, assuming that these bodies were  $\sim 60$ – $100$  km in diameter; that they accreted instantaneously; that they consisted of a homogeneous mixture of anhydrous silicates, water ice (W/R volume ratio of 0.56 and 1.0 for CM and CI bodies, respectively), and pore space; and that they were heated both by the decay of  $^{26}\text{Al}$  and by the hydration reactions. The thermal histories of these bodies were successfully reproduced only if they accreted  $\sim 3$ – $4$  m.y. after CV CAIs (Figs. 10, 11).

## 7. HYDROGEN AND OXYGEN-ISOTOPIC COMPOSITIONS OF COMETARY AND CHONDRITIC WATER

### 7.1. Measured Deuterium/Hydrogen Ratio of Cometary Water

While the genetic relationships between asteroids and comets remains unclear, they are both considered to represent leftover planetesimals from the formation of the solar system. As such, comparisons of their bulk properties allow us to better understand the types and ranges of processes that shaped primitive materials in the solar nebula.

Before discussing deuterium/hydrogen (D/H) values of cometary water, we note that all D/H isotope ratios reported

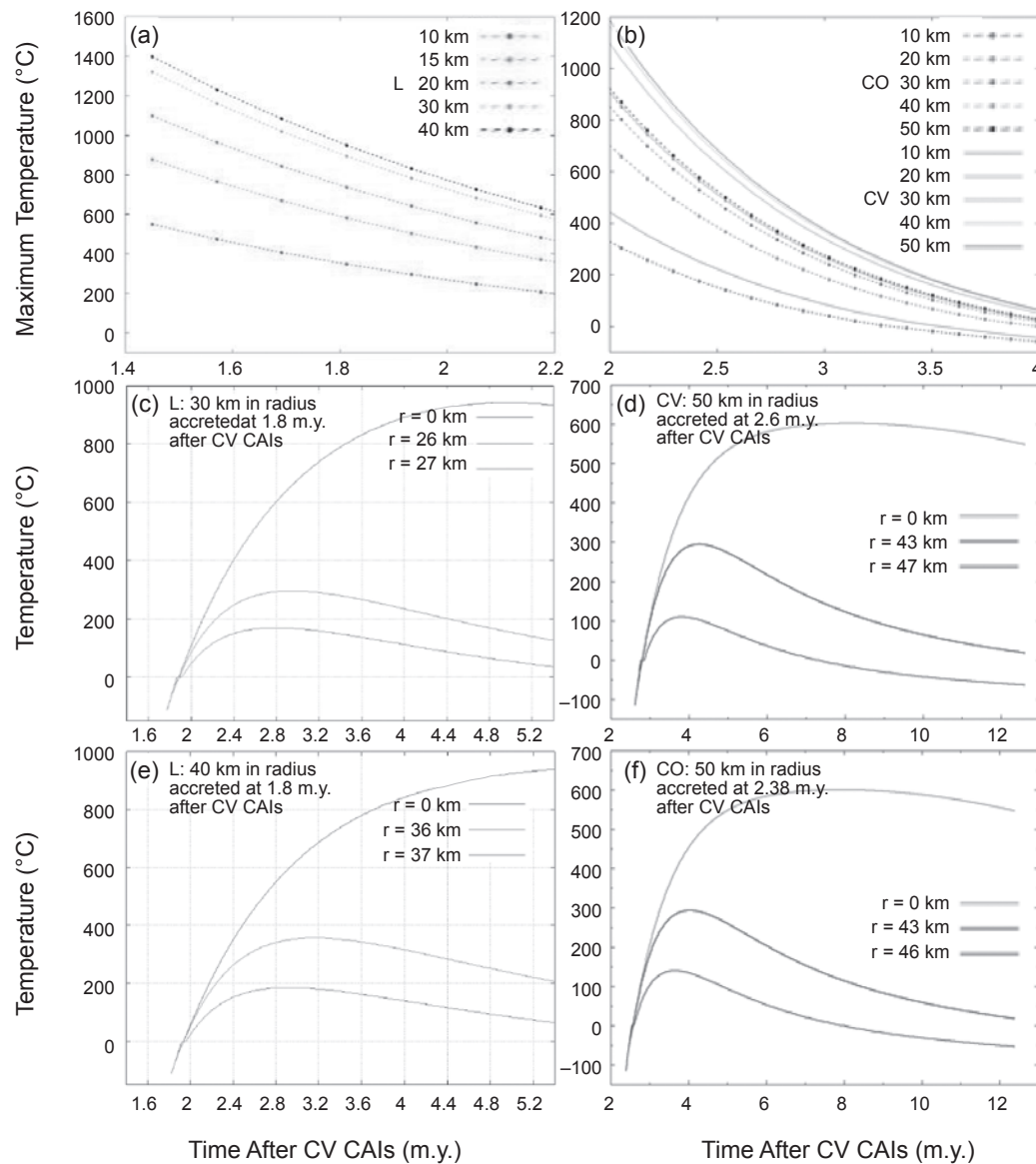


**Fig. 9.** See Plate 23 for color version. (a,b) Modeled peak metamorphic temperature for L-, CV-, and CO-like chondrite parent bodies ranging from 10 to 50 km in radius as a function of time after CV CAIs. (c–f) Temperature evolution diagrams at different depths shown for (c,e) L-like chondrite parent body of 30 and 40 km in radius, (d) CV-like chondrite parent body of 50 km in radius, and (e) CO-like chondrite parent body of 50 km in radius. Blue and green lines in (c) and (e) and blue and red lines in (d) and (f) correspond to regions where thermal conditions ( $\sim 100\text{--}300^\circ\text{C}$ ) would be suitable for the formation of fayalite at the time inferred from  $^{53}\text{Mn}$ - $^{53}\text{Cr}$  relative chronology. Figure from Doyle et al. (2015).

for comets to date have been done only on cometary comae (e.g., Balsiger et al., 1995; Eberhardt et al., 1995; Hartogh et al., 2011; Bockelée-Morvan et al., 2012; Altweegg et al., 2014); there are no direct measurements of the icy portions of cometary nuclei. Brown et al. (2012) reported on the experimental and theoretical simulations of ice sublimation at  $10^{-7}\text{--}10^{-9}$  bar pressure. They observed quasiperiodic sublimation cascades on timescales of hours to days, that the D/H ratio in the vapor issuing from the sample is in general

different from that of the sample, and in many cases, that quasiperiodic changes in the D/H ratio of the vapor accompany the sublimation cascades. Brown et al. (2012) suggested that vacuum sublimation of water ice is a diffusive process that works to leave behind the most strongly bound molecules. Therefore, it is highly unlikely that the D/H ratio in cometary comae is representative of the bulk D/H ratio in the nucleus. Subsequently, Moores et al. (2012) carried out water-ice-sublimation experiments to determine the effect of the

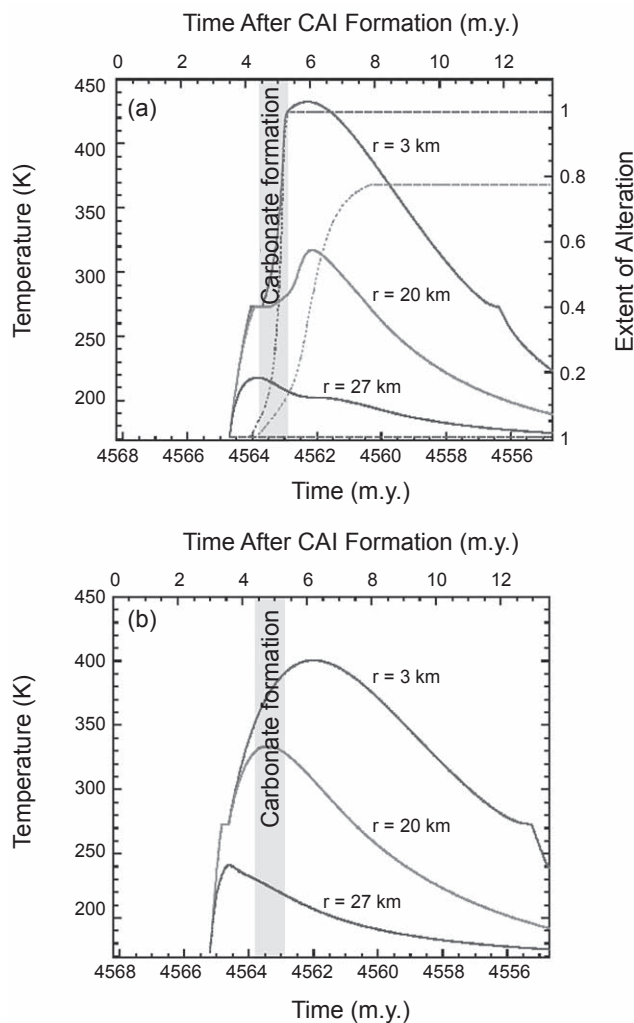


**Fig. 10.** Temperature (solid lines) and the extent of alteration (dotted lines) are given at three depths ( $r$ : distance from the center) in an asteroid with a radius of 30 km. The vertical gray band shows the  $^{53}\text{Mn}$ - $^{53}\text{Cr}$  age of CM carbonates. (a) Accretion at 3.5 m.y. after CV CAIs; the heat of hydration reaction is included. The extent of alteration is defined by  $(1 - \text{olivine}_{\text{res}}/\text{olivine}_{\text{ini}})$ , where  $\text{olivine}_{\text{res}}$  and  $\text{olivine}_{\text{ini}}$  are the moles of the residual and initial olivine, respectively. (b) Accretion at 3.0 m.y. after CV CAIs; the heat of hydration reaction is not included. Figure from Fujiya *et al.* (2012). Note the simulation was based on the  $^{53}\text{Mn}$ - $^{53}\text{Cr}$  carbonate ages with LEW 86010 angrite anchor (Amelin, 2008) and CAI from Bouvier and Wadhwa (2010).

mineral dust content of porous ice on the isotopic composition of the sublimated gas over days to weeks. They reported that if dust was present, the D/H ratio of the sublimated gas decreased with time from the bulk ratio. The more dust was added to the mixture, the more pronounced was this effect. Adsorption onto the dust grains is able to explain the low D/H ratios in the sublimate gas if adsorption favors retention of HDO over  $\text{H}_2\text{O}$ . This leads to significant isotopic enrichment of HDO on the dust over time and depletion in the amount of HDO escaping the system as sublimate gas. Moores *et al.*

(2012) suggested that this effect was significant for water-ice-bearing bodies with dust-rich surfaces through which water moves mainly in vapor phase, such as in comets. However, it remains unclear whether such fractionation affected the D/H ratio of cometary water.

Almost all the Oort cloud comets (OCCs) measured have water ice that is enriched in deuterium ( $\text{D}/\text{H} \sim 3 \times 10^{-4}$ ) relative to Earth's oceans ( $\text{D}/\text{H} \sim 1.5 \times 10^{-4}$ ) by a factor of  $\sim 2$ , although an intermediate D/H ratio,  $\sim 2 \times 10^{-4}$ , has been recently reported in the OCC C/2009 P1/Garradd (Bockelée-Morvan *et al.*, 2012). On the other hand, water ice in the Jupiter-family comet (JFC) 103P/Hartley 2 has a D/H ratio of  $\sim 1.6 \times 10^{-4}$  (Hartogh *et al.*, 2011), which is close to the terrestrial value (Fig. 12). In another JFC, 5P/Honda-Mrkos-Pajdusáková, only an upper limit of D/H ratio in water ice,  $< 2 \times 10^{-4}$ , was reported (Lis *et al.*, 2013). Finally, in the recently measured JFC 67P/Churyumov-Gerasimenko, the D/H ratio was found to be  $(5.3 \pm 0.7) \times 10^{-4}$  (Altweegg *et al.*, 2014). These observations indicate a diversity of D/H ratios of water ice in both comet populations.

## 7.2. Estimated Deuterium/Hydrogen Ratio of Chondritic Water

Chondrites have not retained water ice, and therefore the hydrogen-isotopic composition of chondritic water cannot be measured directly. The major carriers of hydrogen in chondrites are organics and phyllosilicates (e.g., Alexander *et al.*, 2010). Although the phyllosilicates resulted from water-rock interaction on the chondrite parent bodies, determining the original D/H of chondritic water is problematic, because of (1) the physically intimate association between organics and hydrated phyllosilicates, (2) the similar release temperature for hydrogen-bearing organics and water/OH in phyllosilicates, (3) the hydrogen-isotopic exchange between water and organics during parent-body alteration and metamorphism, and (4) the hydrogen-isotopic fractionation associated with oxidation of iron by water during aqueous alteration and metamorphism (Alexander *et al.*, 2010; Bonal *et al.*, 2013).

Assuming that bulk hydrogen-isotope compositions of chondrites are a two-component mixture of deuterium-rich organics and deuterium-poor phyllosilicates, in a plot of the D/H vs. C/H abundance ratio, the compositions of bulk chondrites that experienced various degrees of aqueous alteration should form a line with the D/H intercept representing the composition of the chondritic water. Using this approach, Alexander *et al.* (2012) estimated the D/H ratio of water in CI, CM, CR, CO, CV, R, and ordinary chondrites and Tagish Lake (Fig. 13). These estimates for CIs, CMs, COS, CVs, and Tagish Lake fall between the terrestrial value ( $\sim 1.5 \times 10^{-4}$ ) and the estimated protosolar value [ $\sim 2 \times 10^{-5}$  (Geiss and Gloeckler, 2003)]; the CR water is slightly heavier than the terrestrial value, while the water in ordinary and R chondrites is highly deuterium-enriched (Fig. 13). The estimated D/H ratios of chondritic water provide the upper limits of the initial compositions of accreted water ice because of possible isotopic fractionations associated with iron oxidation on the

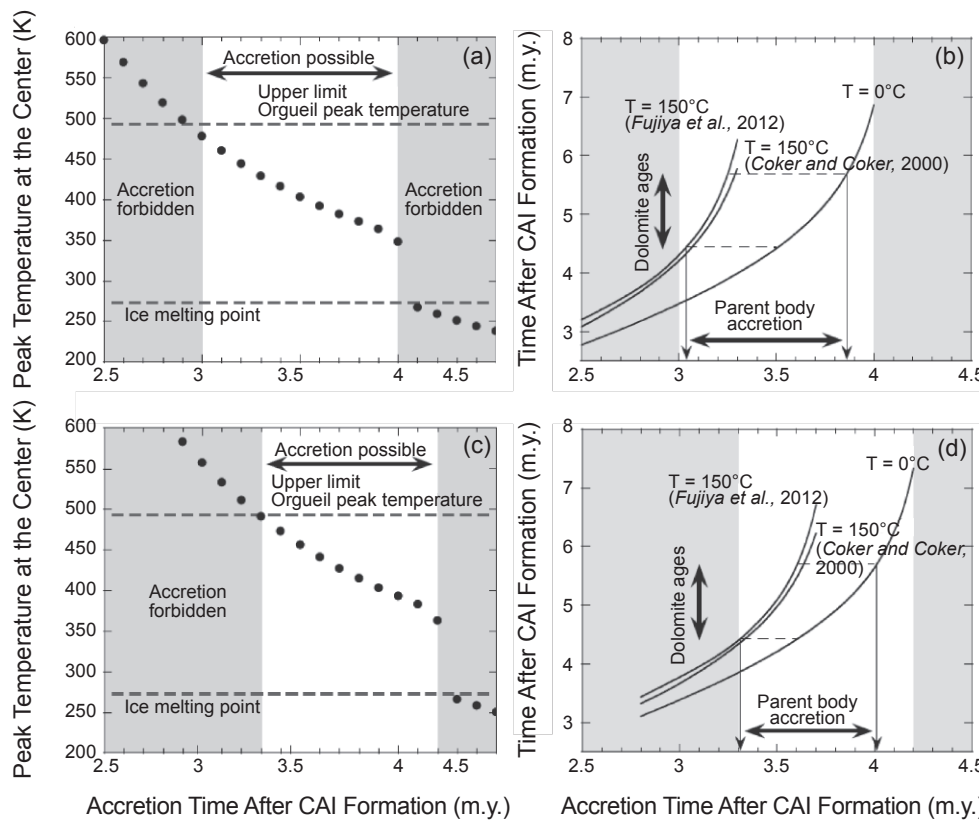


**Fig. 11.** (a,b) Peak temperatures of a CI-like asteroid with a 50-km radius as a function of accretion time; W/R volume ratio is 1 in (a) and 0.56 in (b). The accretion time between 3 and 4 in (a) and between 3.3 and 4.2 m.y. after CV CAIs in (b) is constrained by a peak metamorphic temperature of Orgueil (Busemann et al., 2007) and melting temperature of water ice. (c,d) Accretion time of the CI-like parent body vs. the time when the temperature goes up to 0°C or 150°C at the center (temperature range when CI dolomites may have crystallized) of a CI-like asteroid with W/R ratio of 1 in (c) and 0.56 in (d). The estimated accretion time of the CI parent body is 3.0–3.9 in (c) and 3.3–4.0 m.y. after CV CAIs in (d). Note that the time when temperature reaches 150°C depends on the hydration reaction rate. Two values of the hydration reaction are considered, from Cohen and Coker (2000) and from Fujiya et al. (2012). Figure from Fujiya et al. (2013). Note the simulation was based on the  $^{53}\text{Mn}$ - $^{53}\text{Cr}$  carbonate ages with LEW 86010 angrite anchor (Amelin, 2008) and CAI age from Bouvier and Wadhwa (2010).

chondrite parent bodies (Alexander et al., 2010). Alexander et al. (2010, 2012) suggested that this fractionation was very significant in ordinary and R chondrites that contained very little water.

Because water in the molecular clouds has high D/H ratios [up to  $10^{-2}$  (e.g., Rodgers and Millar, 1996; Bergin et al., 2010; Coutens et al., 2012)] compared to the estimated protosolar hydrogen-isotopic composition ( $\sim 2 \times 10^{-5}$ ), these observations suggest that the inferred D/H ratio of chondritic water must have recorded varying degrees of reequilibration between the primordial (molecular cloud) water with protosolar H<sub>2</sub> at different times and at different radial distances from the Sun. Both the temporal and the spatial distributions of the D/H ratio of water in the solar system have been recently modeled (Yang et al., 2013; Jacquet and Robert, 2013; Furuya et al., 2013; Albertsson et al., 2014) and are discussed in the next section.

### 7.3. Modeling of the Evolution of the Deuterium/Hydrogen Ratio of Water in the Protoplanetary Disk

Yang et al. (2013) developed a one-dimensional viscous disk model for the transport and mixing of water within a forming and evolving protoplanetary disk, and combined it with a kinetic study of D/H-isotopic exchange among gas-phase molecules to explore the isotopic evolution of the initially highly deuterated molecular cloud water (D/H =  $1 \times 10^{-3}$ ) in the disk. In this model, viscous expansion and radial diffusion carry high-temperature inner disk materials outward. Their calculations show that the (D/H)<sub>water</sub> is low ( $\sim 2 \times 10^{-5}$ ) in the warm ( $T > 300$  K) inner disk due to rapid isotopic exchange with molecular hydrogen, and then increases toward the cold ( $T < 300$  K) outer disk where deuterated molecular cloud water was added, and the exchange reactions are sluggish (Fig. 14). Contrary to

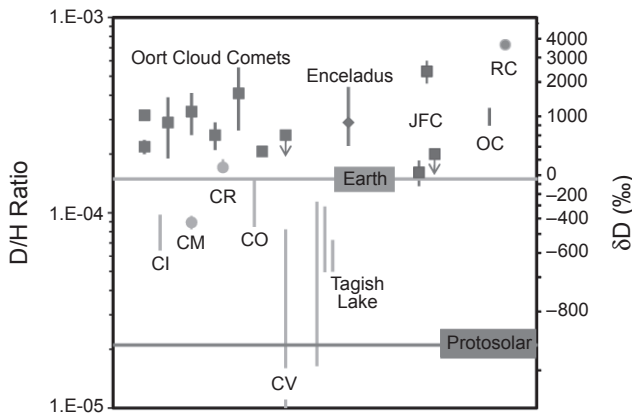


**Fig. 12.** Comparison of the estimated hydrogen isotopic compositions of water in various chondrite groups with those measured in Oort cloud comets, Jupiter-family comets (JFCs), and Saturn's icy moon Enceladus. After Alexander *et al.* (2012). Additional data for comets are from Bockelée-Morvan *et al.* (2012) and Altwegg *et al.* (2014).

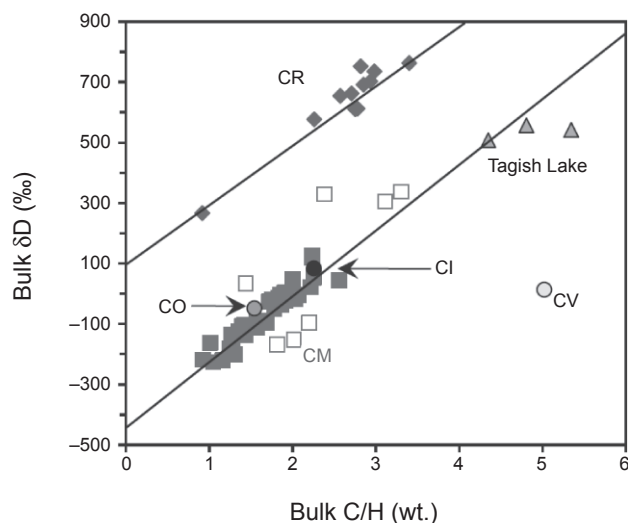


**Fig. 13.** Bulk hydrogen isotopic compositions vs. bulk C/H elemental ratio of the ungrouped carbonaceous chondrite Tagish Lake and CR, CM, CI, CO, and CV chondrites. Figure from Alexander *et al.* (2012).

the previous studies (Drouart *et al.*, 1999; Mousis *et al.*, 2000; Horner *et al.* 2007, 2008), in the outer regions of the disk, the  $(D/H)_{\text{water}}$  decreases again because water that been exchanged at high temperatures near the young star would have been transported outward during the early evolution of the disk. While the exact model results vary depending on the choice of the initial parameters for the molecular cloud and the disk, the nonmonotonic distribution in the D/H ratio of water is robust. This nonmonotonic gradient in D/H may help to explain the observations showing that the  $(D/H)_{\text{water}}$  of JFC 103P/Hartley 2,  $\sim 1.6 \times 10^{-4}$  (Hartogh *et al.*, 2011), is close to the terrestrial water value ( $\sim 1.5 \times 10^{-4}$ ) and lower than that of previously measured OCCs ( $\sim 3 \times 10^{-4}$ ). We note, however, that the accretion ages and radial-formation regions of comets are poorly known.

The model calculations of Yang *et al.* (2013) suggest that there would have been a strong radial gradient in water ice

D/H ratio in the inner solar nebula at the beginning of the solar system formation. The gradient will rapidly smooth out within 1 m.y. of the disk evolution, and a plateau with a D/H ratio of  $\sim 3 \times 10^{-4}$  would be reached. An even shallower gradient should be expected for a 2–4-m.y.-old disk, the time when the chondrite parent bodies appear to have accreted (see section 6). Model calculations for this late disk evolution were reported by Jacquet and Robert (2013). They find that the D/H ratios of carbonaceous chondrite water can be accounted for by radial mixing between water with Oort cloud cometary D/H values ( $\sim 3 \times 10^{-4}$ ) and deuterium-poor water ( $D/H \sim 2 \times 10^{-5}$ ) produced by isotopic exchange in the warm inner disk. If mixing was very efficient, the D/H ratio in nebular water even at a few tens of astronomical units (depending on time) could have been significantly lower than the plateau value of  $\sim 3 \times 10^{-4}$  (Fig. 15), and may also explain the low D/H ratios of water in the JFC 103P/Hartley 2.

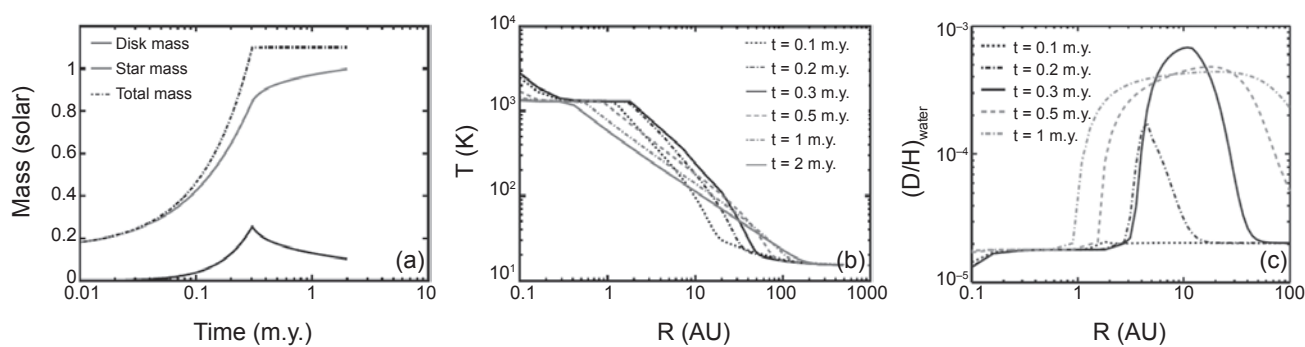


**Fig. 14.** Evolution of the (a) disk mass, star mass, and total mass, and (b) disk midplane temperature with time. (c) The radial distribution of D/H ratio of water in the disk at different times. Turbulent viscosity parameter  $\alpha$  in the disk is  $10^{-3}$ . The initial parameters for the molecular cloud are mass = 1.1× solar; T = 15 K;  $H_2O/H_2 = 2 \times 10^{-4}$ ; D/H ratio of water ice and  $H_2$  gas =  $1 \times 10^{-3}$  and  $2 \times 10^{-5}$ , respectively. Black lines represent times when infall continues while gray lines are for times after infall has ceased (at  $\sim 0.3$  m.y.). Coagulation and migration of dust aggregates have not been considered. From Yang *et al.* (2013).

#### 7.4. Oxygen Isotopic Compositions of Aqueously Formed Minerals and Estimated Oxygen Isotopic Composition of Chondritic Water

The oxygen-isotopic compositions of chondrule olivines and pyroxenes, and aqueously formed minerals (carbonates, magnetite, fayalite, etc.) in different chondrite groups (CI, CM, CO, CV, and ordinary) and Tagish Lake, are shown in Figs. 16 and 17. Magnetite and carbonates in CIs, CMs, and Tagish Lake plot within 1–2‰ of the terrestrial fractionation line (TFL), but show a large range of  $\delta^{18}\text{O}$  values; the similarly large range of  $\delta^{18}\text{O}$  values has been reported by carbonates and magnetite in CR chondrites (Jilly et al., 2014b). The observed range is consistent with mass-dependent isotope fractionation between the aqueously formed minerals and the fluid at a relatively low temperature (~20°–150°C) (Zolensky et al., 1989; Zolotov and Mironenko, 2008; Zolotov, 2012). The secondary minerals have systematically larger  $\Delta^{17}\text{O}$  values ( $\Delta^{17}\text{O}$ , deviation from the TFL,  $\delta^{17}\text{O} - 0.52 \times \delta^{18}\text{O}$ ) than those of chondrule olivines and pyroxenes, which in Figs. 16 and 17 plot along the ~slope-1 [carbonaceous chondrite anhydrous mineral (CCAM)] line. These observations indicate a lack of oxygen-isotopic equilibrium between the primary high-temperature minerals formed in the nebula and the secondary minerals precipitated from aqueous solutions. There are also small differences in  $\Delta^{17}\text{O}$  values of magnetite, calcite, and dolomite within individual

CI and CM chondrites, possibly reflecting an evolution of oxygen-isotopic composition of aqueous solutions as a result of exchange between the relatively  $^{16}\text{O}$ -poor altering fluids and the more  $^{16}\text{O}$ -rich primary anhydrous minerals during progressive aqueous alteration.

In type 3 ordinary and CO chondrites (Fig. 16d), fayalite and magnetite plot parallel to the TFL, above and below it respectively. These observations suggest that oxygen-isotopic compositions of the fluids from which fayalite and magnetite formed were different in ordinary and CO chondrite parent bodies ( $\Delta^{17}\text{O} \sim +4\text{\textperthousand}$  and  $\sim -1\text{\textperthousand}$ , respectively). The range of  $\delta^{18}\text{O}$  values between fayalite and magnetite in ordinary and CO chondrites is significantly smaller than those between magnetite and carbonates in CIs, CMs, and CRs, consistent with the inferred high-temperature aqueous alteration (100°–300°C) experienced by ordinary and CO chondrites (Zolotov et al., 2006; Krot et al., 2013; Doyle et al., 2015).

In CV chondrites, the  $\Delta^{17}\text{O}$  values of secondary minerals range from  $-4\text{\textperthousand}$  to  $-2\text{\textperthousand}$ , and are similar (uncertainties are quite large) to those of aqueously formed minerals in CO chondrites (Figs. 16, 17).

The oxygen-isotopic compositions of secondary minerals that either precipitated from aqueous solutions (e.g., carbonates, fayalite, kirschsteinite, hedenbergite, andradite) or formed by oxidation of oxygen-free Fe,Ni-metal and sulfides (e.g., magnetite) recorded the  $\Delta^{17}\text{O}$  values of these aqueous solutions. These values, ranging from  $\sim -4\text{\textperthousand}$  to  $+4\text{\textperthousand}$ , are slightly higher than those of chondrule olivines and pyroxenes in their host meteorites (Figs. 16, 17), and significantly higher than the measured  $\Delta^{17}\text{O}$  value of the solar wind ( $-26 \pm 2\text{\textperthousand}$ ) returned by the Genesis spacecraft (McKeegan et al., 2011). If aqueous solutions in the chondrite parent bodies experienced limited oxygen-isotope exchange with anhydrous silicates during alteration, the  $\Delta^{17}\text{O}$  values of carbonates, fayalite, and magnetite ( $-4\text{\textperthousand}$  to  $+4\text{\textperthousand}$ ) can be used as proxies for  $\Delta^{17}\text{O}$  values of water ice that accreted into chondrite parent bodies. Note that the extent of oxygen-isotope exchange during fluid-rock interaction is poorly constrained and model-dependent (e.g., Clayton and Mayeda, 1999; Young et al., 1999; Young, 2001). The oxygen-isotopic compositions of water ice in the outer solar system are not known, but are hypothesized to be very heavy ( $\Delta^{17}\text{O} \sim +100\text{\textperthousand}$ ) (Yurimoto and Kuramoto, 2004). If correct, the inferred near-terrestrial  $\Delta^{17}\text{O}$  values of chondritic water may indicate its local, inner solar system origin.

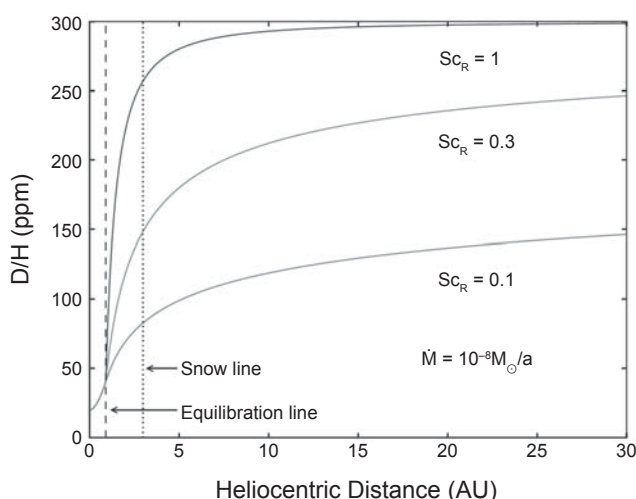


**Fig. 15.** D/H ratio, expressed in parts per million (ppm), of nebular water as a function of heliocentric distance in a steady disk for three values of the radial Schmidt number  $\text{Sc}_R$ , which ratios the efficiencies of angular momentum transport and turbulent diffusion. In the “reaction zone,” delimited by a vertical dashed line (“equilibration line”), equilibrium isotopic fractionation with hydrogen gas is assumed; beyond, mixing with cometary water controls the D/H ratio. The low value of  $\text{Sc}_R$  enhances outward transport of equilibrated water and results in decrease of D/H ratio up to tens of astronomical units. The position of the snow line is indicated by a vertical dotted line. From Jacquet and Robert (2013).

#### 7.5. Modeling of Oxygen-Isotope Evolution of the Protoplanetary Disk Water

There are three major oxygen-bearing components in the solar system: CO,  $\text{H}_2\text{O}$ , and silicates. Although the  $\Delta^{17}\text{O}$  value of the Sun ( $\sim -26 \pm 2\text{\textperthousand}$ ) has been recently inferred (McKeegan et al., 2011), the initial compositions of CO,  $\text{H}_2\text{O}$ , and silicates in the solar nebula are not known. Cosmochemical studies show that the first solids known to have formed in the disk, refractory inclusions, have a range of  $\Delta^{17}\text{O}$  values that bracket the solar value (e.g., Gounelle et al., 2009;

Krot et al., 2010; Ivanova et al., 2012). Based on these data, it is inferred that at least two isotopically distinct oxygen-isotope reservoirs,  $^{16}\text{O}$ -enriched and  $^{16}\text{O}$ -depleted relative to the Sun, coexisted in the early solar system.

In the currently favored CO self-shielding models, the ultraviolet photolysis preferentially dissociates  $\text{C}^{17}\text{O}$  and

$\text{C}^{18}\text{O}$  in certain zones of the protoplanetary disks (Clayton, 2002; Lyons and Young, 2005) or in the molecular clouds (Yurimoto and Kuramoto, 2004; Lee et al., 2008). If this process occurred in the stability field of water ice, the released atomic  $^{17}\text{O}$  and  $^{18}\text{O}$  were incorporated into water ice, while the residual CO gas became enriched in  $^{16}\text{O}$ . Subsequent

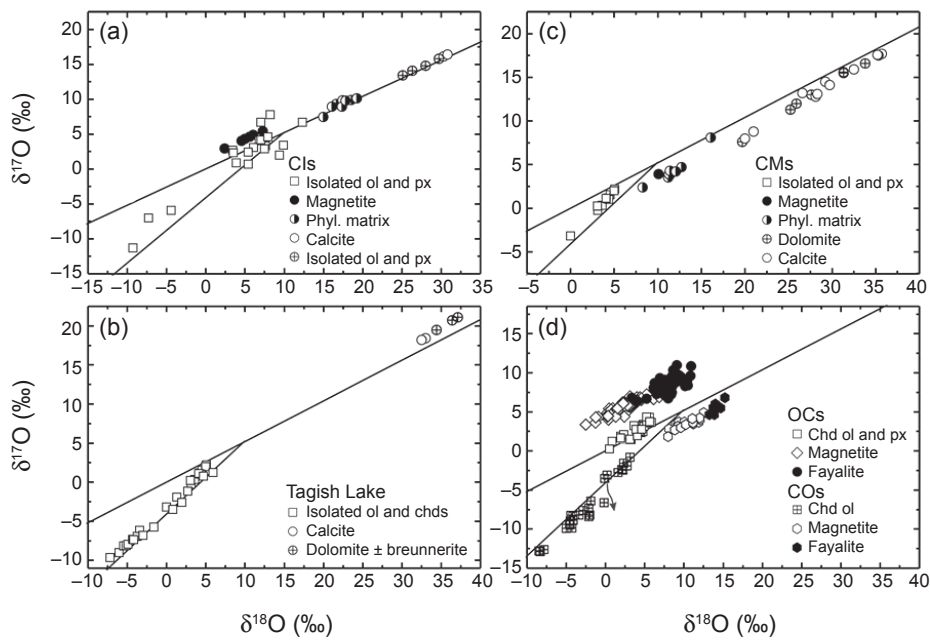


**Fig. 16.** Three-isotope oxygen diagrams of isolated olivine (ol) and pyroxene (px) grains, chondrule (chd) olivines and pyroxenes, and aqueously formed minerals: calcite, dolomite + breunnerite, fayalite, magnetite, and phyllosilicate-rich matrix in (a) CI chondrites ( $1\sigma$  uncertainties for isolated olivines and pyroxenes), (b) Tagish Lake (ungrouped), (c) CM chondrites, and (d) ordinary and CO chondrites. The terrestrial fractionation line (TFL) and carbonaceous chondrite anhydrous mineral (CCAM) line are shown for reference. Data from Rowe et al. (1994), Leshin et al. (1997), Clayton and Mayeda (1999), Benedix et al. (2003), Jabeen and Hiyagon (2003), Russell et al. (2010), Jenniskens et al. (2012), Krot et al. (2014b), and Doyle et al. (2015).

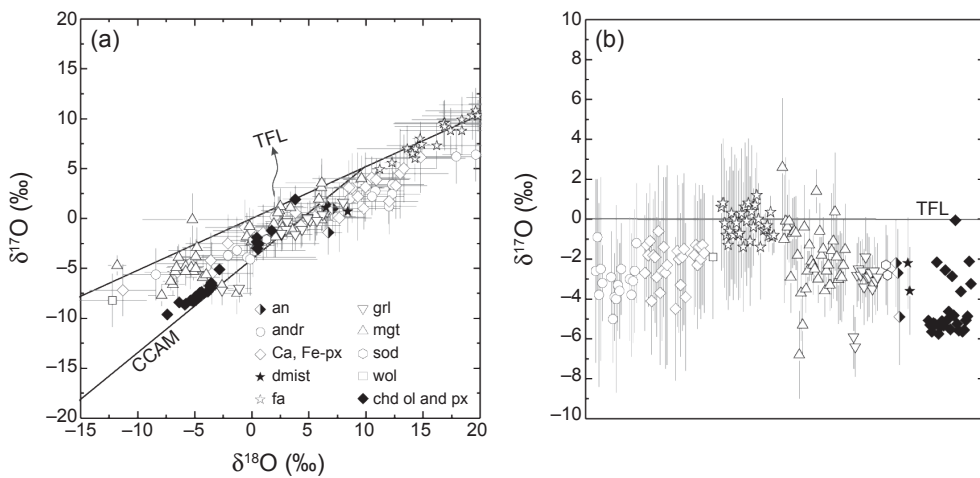


**Fig. 17.** (a) Three-isotope oxygen diagram and (b)  $\Delta^{17}\text{O}$  values of chondrule olivines and pyroxenes and aqueously formed minerals in CV chondrites. Most of the secondary minerals (except fayalite, magnetite, and anorthite) were measured by SIMS without proper standards. As a result, only  $\Delta^{17}\text{O}$  values of these minerals [(b)] can be trusted. an = anorthite; andr = andradite; Ca,Fe-px = salite-hedenbergite pyroxenes; dmist = dmisteinbergite; fa = fayalite; grl = grossular, mgt = magnetite; ol = olivine; px = pyroxene; sod = sodalite; wol = wollastonite. The terrestrial fractionation line (TF) and carbonaceous chondrite anhydrous mineral (CCAM) line are shown for reference. From Brearley and Krot (2012).

$\text{H}_2\text{O}$  ice–CO gas fractionation followed by evaporation of water ice and isotope exchange could have resulted in the generation of the  $^{16}\text{O}$ -enriched and  $^{17,18}\text{O}$ -enriched gaseous reservoirs in the inner solar system. *Sakamoto et al.* (2007) described isotopically heavy magnetite grains ( $\delta^{17,18}\text{O} \sim +180\text{\textperthousand}$ ) in the ungrouped carbonaceous chondrite Acfer 094 and suggested that these grains recorded the oxygen-isotopic compositions of the primordial (molecular cloud) water in the protoplanetary disk, consistent with the prediction from the CO self-shielding model.

Following the same formalism as in *Yang et al.* (2013), but using different initial parameters, *Yang et al.* (2011) reported preliminary results for the evolution of the oxygen-isotopic composition of water in the protoplanetary disk. In this study, the concentrations and oxygen-isotopic compositions of CO and  $\text{H}_2\text{O}$ , produced via self-shielding photodissociation of CO in the protosolar molecular cloud and modeled by *Lee et al.* (2004, 2008) were used as the input parameters for the dynamical model of the disk evolution. The results of their calculations are illustrated in Fig. 18. *Yang et al.* (2011) find that the  $\delta^{18}\text{O}$  of  $\text{H}_2\text{O}$  varies with time and location in the disk. During the epoch with large mass infall from the protosolar molecular cloud, there are strong spatial and temporal variations in the isotopic composition of water due to the changing isotopic compositions of materials being added to the disk. Once the infall ceases, radial transport and oxygen-isotope exchange smooth out these variations, leading to a more homogenized disk (Fig. 18). Subsequently, *Yang et al.* (2013) considered both oxygen- and hydrogen-isotopic exchange between  $\text{H}_2\text{O}$  and other gas species in the disk. They find that the D-H exchange proceeds much faster than the  $^{18}\text{O}-^{16}\text{O}$  exchange, implying that the initially high D/H signature of the molecular cloud water would be erased more efficiently compared to its initial high  $\delta^{18}\text{O}$  value.

## 8. ACCRETION REGIONS OF CHONDRITE PARENT BODIES: IMPLICATION FOR THE DYNAMICAL MODELS OF THE SOLAR SYSTEM EVOLUTION

### 8.1. Chondrite-Asteroid Linkages and the Presence of Hydrated Asteroids in the Main Belt

Most chondrites are thought to come from the main asteroid belt. Although the spectral reflectance properties in the range of 0.4–2.4  $\mu\text{m}$  have been recently collected for different chondrite groups (*Clark et al.*, 2011; *Cloutis et al.*, 2011a,b, 2012a,b,c,d,e,f), the connections between chondrite groups and asteroid classes are still poorly known. Spectroscopically, the ordinary chondrites have been linked to the S-type asteroids, and the carbonaceous chondrites to multiple taxonomic groups: C-, D-, P-, B-, and K-type asteroids (e.g., *Bell et al.*, 1989; *Hiroi et al.*, 2001; *Burbine et al.*, 2002; *Clark et al.*, 2010, 2011; *Cloutis et al.*, 2011a,b, 2012a,b,c,d,e,f). The linkage of L chondrites to S-type asteroids has been confirmed by the Hayabusa sample return mission from asteroid (25143) Itokawa (*Nakamura et al.*, 2011). No samples have

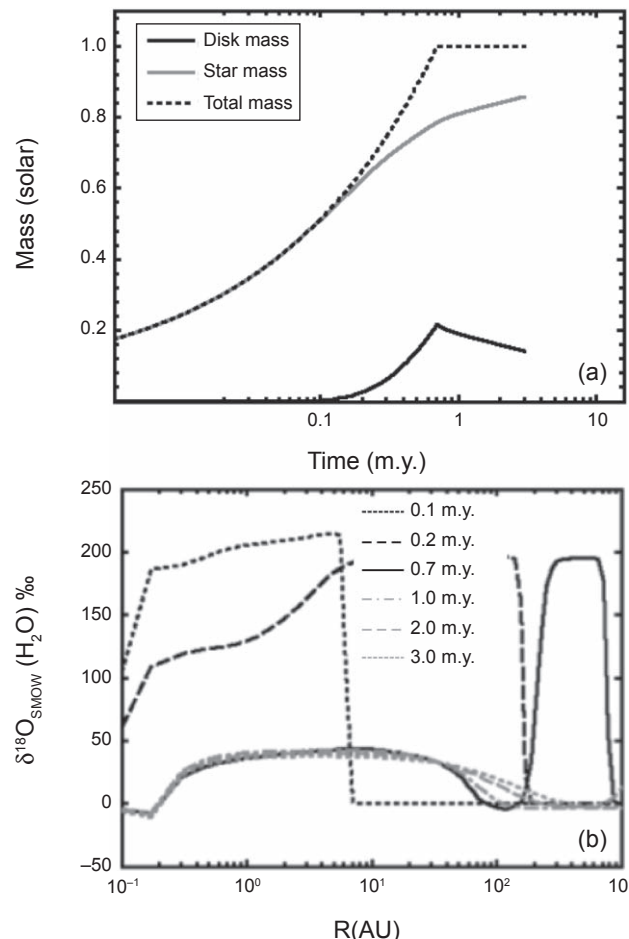


**Fig. 18.** (a) Evolution of the disk mass, stellar mass, and total mass with time. (b) The radial distribution of  $\delta^{18}\text{O}$  of water in the disk at different times. Turbulent viscosity parameter  $\alpha$  in the disk is  $10^{-3}$ . The initial parameters for the molecular cloud are mass = 1  $\times$  solar;  $T = 10\text{ K}$ ; duration of infall is 0.7 m.y. Coagulation and migration of dust aggregates have not been considered. From *Yang et al.* (2011).

yet been returned from other types of asteroids, although two recent carbonaceous chondrite falls, Tagish Lake (ungrouped) and Sutter's Mill (CM), may represent fragments of D-type (*Hiroi et al.*, 2001) and C-type asteroids (*Zolensky et al.*, 2014), respectively. Some B-type asteroids exhibit selected spectral properties consistent with CI chondrites; however, perfect spectral matches have not been found (*Cloutis et al.*, 2011a). *Clark et al.* (2011) linked the B-type asteroid (101955) Bennu (provisional designation 1999 RQ<sub>36</sub>) to the CIs and/or heavily altered CMs; however, a comparison of RQ<sub>36</sub> to other B-type asteroids measured by *Clark et al.* (2010) shows that this link is inconclusive. Some K-class asteroids exhibit spectral properties similar to CO chondrites; however, unmetamorphosed CO chondrites are difficult to distinguish from the least-altered CMs (*Cloutis et al.*, 2012c). The Hayabusa-2 and Origins Spectral Interpretation Resource Identification and Security-Regolith Explorer (OSIRIS-REx) sample return missions will target carbonaceous chondrite

asteroids 1999 JU<sub>3</sub> (C-type) and (101955) Bennu (B-type), respectively (*Tachibana et al.*, 2014; *Lauretta et al.*, 2014), which will allow us to explore the meteorite-parent body connection in greater detail.

It is estimated that about 70% of C-complex asteroids show spectroscopic evidence for the presence of hydrated minerals (e.g., *Rivkin*, 2012). Water ice has been recently detected on the C-type asteroid (24) Themis (*Campins et al.*, 2010; *Rivkin and Emery*, 2010). The presence of water ice was also inferred for some of the active asteroids, including (1) Ceres, 133P/Elst-Pizarro, and 238P/Read, named “main belt comets” (*Hsieh and Jewitt*, 2006; *Jewitt*, 2012; *Kuipers et al.*, 2014; see also the chapter by Jewitt et al. in this volume). The survival of ice in the asteroids provide a unique opportunity to study their chemical and isotopic compositions and compare them with those of OCCs and JFCs.

## 8.2. Dynamical Models of Solar System Evolution and Accretion Regions of Hydrated Asteroids

It is currently being debated whether hydrated asteroids formed in the main asteroid belt (*Alexander et al.*, 2012) or whether they formed further away from the Sun and were subsequently implanted into the main belt during dynamical evolution of the solar system (*Levison et al.*, 2009; *Walsh et al.*, 2011). Many dynamical models of solar system evolution fail to reproduce the small mass of Mars at its current location. This issue is commonly referred to as the “small Mars” problem (e.g., *Chambers*, 2001; *Raymond et al.*, 2009; *Morbidelli et al.*, 2012; *Kobayashi and Dauphas*, 2013; *Izidoro et al.*, 2014; *Raymond and Morbidelli*, 2014). According to the Grand Tack model (*Walsh et al.*, 2011), proposed to explain the small mass of Mars, Jupiter accretes at ~3.5 AU from the Sun within the first several million years of solar system formation, migrates inward to about 1.5 AU, and truncates the disk of planetesimals at ~1 AU, at which point Saturn catches up with it, and then the two planets migrate outward again to about 5 and 7 AU, respectively. Uranus and Neptune are also forced to migrate to greater distances (roughly 10 and 13 AU, respectively) as Jupiter and Saturn moved outward. As a result of this migration, not only are the planetesimals at ~1.5–3 AU depleted, but the planetesimals between 4 and 13 AU are strongly perturbed, and some of them are scattered into the inner solar system and become trapped in the outer asteroid belt. According to this model, the dry, S-type asteroids formed close to the main asteroid belt, whereas the wet, C-, P-, D-, B-, and K-type asteroids formed either between the giant planets or in the transneptunian region (>13 AU).

The Grand Tack model reproduces two important aspects of the inner solar system: the strong depletion of the main asteroid belt in mass, and its mixed structure (*DeMeo and Carry*, 2014). The major unknowns of this model are the time and place of Jupiter formation, and the timing of its migration (*Walsh et al.*, 2011; *Raymond and Morbidelli*, 2014). If this model explains the small size of Mars, the migration may have started very early, as Hf-W-Th age dating suggests that 50% of Mars’ mass accreted by 2 m.y. after t<sub>0</sub> (*Dauphas*

*and Pourmand*, 2011). The early migration of Jupiter would conflict with the estimated 2.5–4-m.y. accretion ages of most carbonaceous chondrites, since in the Grand Tack model they must predate the onset of giant planet migration.

In the model of *Izidoro et al.* (2014), the small mass of Mars resulted from a local depletion in the solar nebula density, and giant planet migration was not involved (see also *Jin et al.*, 2008). Therefore this model predicts accretion of dry and wet asteroids close to their current locations, i.e., in the main asteroid belt. Finally, in the “standard” (without giant-planet migration) model of *Fischer and Ciesla* (2014), a Mars-sized object forms in ~5–10% of simulations. In this case, the architecture of the inner solar system is simply an unusual (but not rare) outcome of a stochastic process.

According to the Nice model, proposed to explain the current solar system architecture, including the giant-planet orbits, Trojan asteroids, and origin from late heavy bombardment (*Gomes et al.*, 2005; *Morbidelli et al.*, 2005; *Tsiganis et al.*, 2005; *Levison et al.*, 2011), additional implantation of transneptunian objects (spectrally D- and P-types) into the main asteroid belt took place at ~4 Ga, when the orbits of the giant planets became unstable (*Levison et al.*, 2009).

## 8.3. Cosmochemical Constraints on Accretion Regions of Chondrite Parent Bodies

The estimated oxygen- and hydrogen-isotopic compositions of chondrite water ice, and the chondrite accretion ages combined with the inferred water/rock ratios on the aqueously altered chondrite parent bodies, can potentially be used for constraining the disk regions where these bodies accreted and therefore for testing the predictions of the dynamical models of solar system evolution.

**8.3.1. Oxygen isotopes.** Making the assumption that oxygen-isotope exchange between aqueous solutions and anhydrous silicates during alteration of chondritic meteorites was insignificant, the inferred oxygen-isotope compositions of chondritic water are close to Earth’s ocean,  $-4\text{\textperthousand} < \Delta^{17}\text{O} < +4\text{\textperthousand}$  (Figs. 15, 16). The oxygen-isotope compositions of water ice in the outer part of the solar system are hypothesized to be significantly heavier, with  $\Delta^{17}\text{O} \sim +100\text{\textperthousand}$  (*Yurimoto and Kuramoto*, 2004). Although these observations can be interpreted as evidence for a local, inner solar system origin of chondritic water, they cannot be unambiguously used for constraining the chondrite accretion regions (inner vs. outer solar system) because (1) the extent of oxygen-isotope exchange during fluid-rock interaction is poorly constrained and model-dependent (e.g., *Clayton and Mayeda*, 1999; *Young et al.*, 1999; *Young*, 2001), (2) the evolution of the oxygen-isotope compositions of disk water is not well enough understood (e.g., *Lyons and Young*, 2005; *Yang et al.*, 2011), and (3) the uncertainties in the oxygen-isotopic compositions of OCC and JFC water are too large to be useful. For example, the  $^{18}\text{O}/^{16}\text{O}$  ratios of water measured for the OCCs 1P/Halley [ $(1.9 \pm 0.2) \times 10^{-3}$  (*Balsiger et al.*, 1995)] and C/2009 P1 (Garradd) [ $(1.9 \pm 0.3) \times 10^{-3}$  (*Bockelée-Morvan et al.*, 2012)] cannot be distinguished from the standard mean

ocean water (SMOW) value of  $2.01 \times 10^{-3}$ ;  $^{17}\text{O}/^{16}\text{O}$  ratios were not measured. Both  $^{18}\text{O}/^{16}\text{O}$  and  $^{17}\text{O}/^{16}\text{O}$  ratios of water have been reported for the JFC 67P/Churyumov-Gerasimenko (*Altwegg et al.*, 2014),  $(1.8 \pm 0.2) \times 10^{-3}$  and  $(3.7 \pm 0.9) \times 10^{-4}$ , respectively; however, they also cannot be distinguished from the SMOW values ( $^{17}\text{O}/^{16}\text{O}_{\text{SMOW}} = 3.8 \times 10^{-4}$ ). More precise measurements of oxygen isotopes in the water ice of primitive bodies are required in order to deconvolve the birth regions of comets and asteroids.

**8.3.2. Hydrogen isotopes.** Comparison of the inferred D/H ratios of chondritic water (*Alexander et al.*, 2012) with the ratios reported for the OCC and JFC water provide a hint for a possible linkage between CR chondrites and comets; no such connection can be inferred for the CIIs, CMs, and ungrouped carbonaceous chondrite Tagish Lake, which all had water ice with lower D/H ratios than comets measured so far [Fig. 14; but see *Moores et al.* (2012)]. However, there are only a limited number of comets with the measured D/H ratio of water ice, and even among these there are large variations (*Hartogh et al.*, 2011; *Bockelée-Morvan et al.*, 2012; *Lis et al.*, 2013; *Altwegg et al.*, 2014). As a result, a direct comparison of the inferred D/H ratio of chondritic water with the measured D/H ratios of cometary water to constrain the accretion regions of the chondrite parent bodies (*Alexander et al.*, 2012) may be inconclusive; understanding of the temporal and spatial evolution of hydrogen-isotope compositions of the protoplanetary disk water is required. The inferred hydrogen-isotopic evolution of the disk water, however, is model-dependent (e.g., *Drouart et al.*, 1999; *Mousis et al.*, 2000; *Hersant et al.*, 2001; *Yang et al.*, 2011, 2013; *Jacquet and Robert*, 2013), and cannot be unambiguously used for constraining the chondrite-accretion regions. To further test the Grand Tack model, direct hydrogen-isotope measurements of water ice in asteroids, including main-belt comets (*Jewitt*, 2012; see also the chapter by *Jewitt et al.* in this volume) are required. If some of the wet asteroids are in fact implanted comets, their water ice may have D/H ratios similar to those reported for comets. Additional measurements of D/H ratios in water of OCCs and JFCs would be also important.

**8.3.3. Chondrite-accretion ages, water/rock ratio, and position of the snow line.** The majority of hydrated chondrite parent bodies accreted  $\sim 2\text{--}4$  m.y. after CV CAIs and had W/R mass ratios significantly lower than the solar value,  $<0.1\text{--}0.6$  (see section 3) vs. 1.2 (*Lodders*, 2003), respectively. Members of the same chondrite group often experienced quite different degrees of aqueous alteration. This, in combination with the apparently isochemical nature of the alteration (*Bland et al.*, 2005) and the low fluid permeability of chondrites (*Bland et al.*, 2009; see the chapter by *Wilson et al.* in this volume), might indicate heterogeneous accretion of chondrite water ice. If correct, one explanation for these heterogeneities and the low inferred W/R ratios would be that chondrite parent bodies accreted close to the snow line, possibly slightly inside it, where only relatively large water-ice-bearing particles could have avoided instantaneous evaporation and survived prior to accretion (*Cyr et al.*, 1998). However, it should be born in mind that there are alternative explanations for the

variation in the degree of alteration within chondrite groups that invoke fluid flow (e.g., *Young et al.*, 1999; *Young*, 2001).

The location of the snow line in the solar nebula is uncertain, and depends on the mechanisms responsible for depositing heat in the disk. The snow line likely did not reside at a single location in the solar nebula, but rather migrated with time as the luminosity of the pre-main-sequence star, mass transport rate through the disk, and opacity of the nebula all evolved with time. In viscous disks, where mass accretion occurs throughout the disk, energy from internal dissipation can keep the inner disk warm for much of the lifetime of the disk. As mass-accretion rates diminished with time, the viscous dissipation would slow, causing the snow line to migrate inward with time. While specific details vary with the assumed disk structure and viscosity, models suggest that the snow line would be located beyond 5 AU early in disk evolution, but is likely to have been present at 2–3 AU 2–4 m.y. into the lifetime of the disk (e.g., *Ciesla and Cuzzi*, 2006; *Kennedy and Kenyon*, 2008; *Min et al.*, 2011; *Martin and Livio*, 2012), when most chondrite parent bodies accreted (see section 6). If viscous dissipation was not strong or was limited to the surface of the disk, the temperature structure of the disk would have been determined solely by radiative heating from the young Sun, which would have put the snow line at no further than 1–2 AU during the accretion of chondrite parent bodies (*Sasselov and Leclar*, 2000; *Kennedy and Kenyon*, 2008; *Martin and Livio*, 2012).

If the snow line for a 2–4-m.y.-old protoplanetary disk was at  $\sim 1\text{--}3$  AU from the Sun, then most of the hydrated asteroids could have formed in the main asteroid belt and need not have been implanted from the outer solar system, as predicted by the Grand Tack model. Based on these observations, we suggest that the majority of hydrated chondrite parent bodies sampled by meteorites (CM, CO, CV, CK, H, L, LL, R) accreted in the inner solar system, close to the main asteroid belt, consistent with the conclusion of *Alexander et al.* (2012). Therefore these chondrite groups provide no support for the predictions of the Grand Tack and Nice dynamical models that hydrated asteroids formed between and beyond the giant planets and were implanted into the main asteroid belt during migration of the giant planets. We cannot exclude the possibility that there are other types of hydrated or water-ice-bearing asteroids that were implanted into the main asteroid belt, but have not been sampled by the known meteorites (e.g., did not survive atmospheric entry).

Cosmochemical data identify CI chondrites as the best candidates for being cometary meteorites (*Gounelle et al.*, 2008). In contrast to the other chondrite groups, (1) CI chondrites provide the best match to the bulk chemical composition of the solar photosphere (*Palme et al.*, 2014); (2) high-temperature chondritic components — chondrules, which are commonly attributed to transient heating events in the inner solar system — are virtually absent in CI chondrites; (3) CI chondrites have the highest abundances of presolar grains that are resistant to aqueous alteration [e.g., SiC and graphite (*Huss and Lewis*, 1995)]; and (4) CI chondrites appear to have accreted the highest abundances of water ice.

These observations may indicate that CI precursor materials largely avoided thermal processing in the inner solar system and accreted further away from the Sun than other chondrite groups. Although CI chondrites may have accreted outside the snow line, it remains unclear whether they accreted inside Jupiter's orbit, in the outer part of the main asteroid belt, or they accreted outside Jupiter's orbit and were subsequently implanted into the main asteroid belt during migration of the giant planets. The inferred low D/H ratio of water in CI chondrites (Alexander *et al.*, 2012) provides no support for the latter scenario.

## 9. CONCLUSIONS

Most chondrite parent bodies accreted water ice together with anhydrous silicates, and subsequently experienced aqueous/hydrothermal alteration and fluid-assisted thermal metamorphism under variable conditions (e.g., temperature and W/R ratios) that resulted in the formation of a diverse suite of secondary minerals. There are significant variations in the degree of aqueous alteration within and between different chondrite groups. These observations in combination with the apparently isochemical nature of aqueous alteration and the low fluid permeability of chondrites may indicate heterogeneous accretion of water ice.

The aqueous activity in the carbonaceous chondrite parent bodies started almost contemporaneously, ~3.5–5 m.y. after CAIs, which is assumed to mark the time of formation of the solar system, consistent with  $^{26}\text{Al}$  being the major heat source of these bodies. The initial stages of aqueous alteration of ordinary chondrites appear to have predated those of carbonaceous chondrites, although the uncertainties are large.

The  $^{53}\text{Mn}$ - $^{53}\text{Cr}$  ages of aqueous alteration, the  $^{26}\text{Al}$ - $^{26}\text{Mg}$  ages of chondrule formation, and the peak metamorphic temperatures reached by the ordinary and carbonaceous chondrite parent bodies suggest that they accreted ~2–4 m.y. after CAIs. The estimated water-ice-to-rock mass ratios in ordinary and carbonaceous chondrite parent bodies range from <0.1 to 0.6 (could be higher in CI chondrites), which is significantly lower than the solar value of 1.2. We suggest that ordinary and most carbonaceous chondrite parent bodies accreted close to the position of the snow line, possibly inside it. Because the position of the snow line in a 2–4-m.y.-old protoplanetary disk is estimated to be within 2–3 AU from the Sun, we infer that the majority of hydrated chondrite parent bodies sampled by meteorites (CI, CM, CO, CV, CK, H, L, LL, R) accreted in the inner solar system, close to the main asteroid belt. The estimated D/H ratios of water in CI, CM, CV, and CO chondrites are consistent with their accretion in the inner solar system. The estimated D/H ratio of water in CR chondrites is similar to the D/H ratio in some of the JFCs, but the accretion region of the CR parent body remains poorly constrained.

We conclude that most chondrite groups provide no evidence for the predictions of the Grand Tack and Nice dynamical models that hydrated asteroids formed between and beyond giant planets and were implanted into the main

asteroid belt during migration of these planets. We cannot, however, exclude the possibility that there are other types of hydrated or water-ice-bearing asteroids that may have been implanted into the main asteroid belt, but have not been sampled by the known meteorites (e.g., did not survive atmospheric entry). Additional studies of meteorites, asteroids, and comets are required to confirm or refute the Grand Tack model, including *in situ* measurements of hydrogen- and oxygen-isotopic compositions of water ice in the main-belt asteroids and comets, along with sample return missions to comets and asteroids.

Continued exploration of the diversity of primitive bodies in the early solar system and the processes that shaped the minerals they contained, coupled with detailed predictive models for the dynamic evolution of the main asteroid belt, will allow us to better refine our understanding of the processes that shaped the solar system we see today.

**Acknowledgments.** Reviews and helpful suggestions by D. S. Lauretta and anonymous reviewers, as well as editorial handling by F. DeMeo, are highly appreciated. This work was supported by NASA grants NNX12AH69G (A. N. Krot, P.I.), NNX14AJ54G (C. M. O'D. Alexander, P.I.), NNX14AN98G (F. J. Ciesla, P.I.), and NASA's Astrobiology Institute. This is Hawai'i Institute of Geophysics and Planetology publication 2175 and School of Ocean and Earth Science and Technology publication 9511.

## REFERENCES

- Abreu N. M. and Brearley A. J (2010) Early solar system processes recorded in the matrices of two highly pristine CR3 carbonaceous chondrites, MET 00426 and QUE 99177. *Geochim. Cosmochim. Acta*, 74, 1146–1171.
- Albertsson T., Semenov D., and Henning Th. (2014) Chemodynamical deuterium fractionation in the early solar nebula: The origin of water on Earth and in asteroids and comets. *Astrophys. J.*, 784, 39.
- Alexander C. M. O'D. and Ebel D. S. (2012) Questions, questions: Can the contradictions between the petrologic, isotopic, thermodynamic, and astrophysical constraints on chondrule formation be resolved? *Meteoritics & Planet. Sci.*, 47, 1157–1175.
- Alexander C. M. O'D., Fogel M., Yabuta H., and Cody G. D. (2007) The origin and evolution of chondrites recorded in the elemental and isotopic compositions of their macromolecular organic matter. *Geochim. Cosmochim. Acta*, 71, 4380–4403.
- Alexander C. M. O'D., Grossman J. N., Ebel D. S., and Ciesla F. J. (2008) The formation conditions of chondrules and chondrites. *Science*, 320, 1617–1619.
- Alexander C. M. O'D., Newsome S. D., Fogel M. L., Nittler L. R., Busemann H., and Cody G. D. (2010) Deuterium enrichments in chondritic macromolecular material — Implications for the origin and evolution of organics, water and asteroids. *Geochim. Cosmochim. Acta*, 74, 4417–4437.
- Alexander C. M. O'D., Bowden R., Fogel M. L., Howard K. T., Herd C. D. K., and Nittler L. R. (2012) The provenances of asteroids, and their contributions to the volatile inventories of the terrestrial planets. *Science*, 337, 721–723.
- Alexander C. M. O'D., Howard K. T., Bowden R., and Fogel M. L. (2013) The classification of CM and CR chondrites using bulk H, C and N abundances and isotopic compositions. *Geochim. Cosmochim. Acta*, 123, 244–260.
- Alexander C. M. O'D., Cody G. D., Kebukawa Y., Bowden R., Fogel M. L., Kilcoyne A. L. D., Nittler L. R., and Herd C. D. K. (2014) Elemental, isotopic, and structural changes in Tagish Lake insoluble organic matter produced by parent body processes. *Meteoritics & Planet. Sci.*, 49, 503–525.

- Altweig K., Balsiger H., Bar-Nun A., et al. (2014) 67P/Churyumov-Gerasimenko, a Jupiter family comet with a high D/H ratio. *Science*, 347, 1–3.
- Amelin Y. (2008) U-Pb ages of angrites. *Geochim. Cosmochim. Acta*, 72, 221–232.
- Amelin Y., Krot A. N., Hutcheon I. D., and Ulyanov A. A. (2002) Pb isotopic ages of chondrules and Ca,Al-rich inclusions. *Science*, 297, 1678–1683.
- Aponte J. C., Alexandre M. R., Wang Y., Brearley A. J., Alexander C. M. O.’D., and Huang Y. (2011) Effects of secondary alteration on the composition of free and IOM-derived monocarboxylic acids in carbonaceous chondrites. *Geochim. Cosmochim. Acta*, 75, 2309–2323.
- Asphaug E., Jutzi M., and Movshovitz M. (2011) Chondrule formation during planetesimal accretion. *Earth Planet. Sci. Lett.*, 308, 369–379.
- Balsiger H., Altweig K., and Geiss J. (1995) D/H and  $^{18}\text{O}/^{16}\text{O}$  ratio in the hydronium ion and in neutral water from *in situ* ion measurements in Comet Halley. *J. Geophys. Res.*, 100, 5827–5834.
- Beck P., Garenne A., Quirico E., Bonal L., Montes-Hernandez G., Moynier F., and Schmitt B. (2014) Transmission infrared spectra (2–25  $\mu\text{m}$ ) of carbonaceous chondrites (CI, CM, CV-CK, CR, C2 ungrouped): Mineralogy, water, and asteroidal processes. *Icarus*, 229, 263–277.
- Bell J. F., Davis D. R., Hartmann W. K., and Gaffey M. J. (1989) Asteroids — The big picture. In *Asteroids II* (R. P. Binzel et al., eds.), pp. 921–945. Univ. of Arizona, Tucson.
- Benedix G. K., Leshin L. A., Jackson T., and Thiemens M. H. (2003) Carbonates in CM2 chondrites: Constraints on alteration conditions from oxygen isotopic compositions and petrographic observations. *Geochim. Cosmochim. Acta*, 67, 1577–1588.
- Berger E. L., Zega T. J., Keller L. P., and Lauretta D. S. (2011) Evidence for aqueous activity on Comet 81P/Wild 2 from sulfide mineral assemblages in Stardust samples and CI chondrites. *Geochim. Cosmochim. Acta*, 75, 3501–3513.
- Bergin E. A., Phillips T. G., Comito C., et al. (2010) Herschel observations of Extra-Ordinary Sources (HEXOS): The present and future spectral surveys with Herschel/HIFI. *Astron. Astrophys.*, 521, L20.
- Bizzarro M., Olsen M., Itoh S., Kawasaki N., Schiller M., Bonal L., and Yurimoto H. (2014) Evidence for a reduced initial abundance of  $^{26}\text{Al}$  in chondrule forming regions and implications for the accretion timescales of protoplanets. *Meteoritics & Planet. Sci. Suppl.*, 49, Abstract #5125.
- Bland P. A. and Travis B. J. (2014) More mudballs: Simulating primordial planetesimals as unconsolidated mixtures of mud and chondrules. *Meteoritics & Planet. Sci. Suppl.*, 49, Abstract #5295.
- Bland P. A., Alard O., Benedix G. K., Kearsley A. T., Menzies O. N., Watt L. E., and Rogers N. W. (2005) Volatile fractionation in the early solar system and chondrule/matrix complementarity. *Proc. Natl. Acad. Sci.*, 102, 13755–13760.
- Bland P. A., Jackson M. D., Coker R. F., et al. (2009) Why aqueous alteration in asteroids was isochemical: High porosity ≠ high permeability. *Earth Planet. Sci. Lett.*, 287, 559–568.
- Bland P. A., Travis B. J., Dyl K. A., and Schubert G. (2013) Giant convecting mudballs of the early solar system. *Lunar Planet. Sci. XLIV*, Abstract #1447. Lunar and Planetary Institute, Houston.
- Bockelée-Morvan D., Biver N., Swinyard B., et al. (2012) Herschel measurements of the D/H and  $^{16}\text{O}/^{18}\text{O}$  ratios in water in the Oort-cloud comet C/2009 P1 (Garradd). *Astron. Astrophys.*, 544, L15.
- Bollard J., Connally J. N., and Bizzarro M. (2014) The absolute chronology of the early solar system revisited. *Meteoritics & Planet. Sci. Suppl.*, 49, Abstract #5234.
- Bonal L., Quirico E., Bourou-Denise M., and Montagnac G. (2006) Determination of the petrologic type of CV3 chondrites by Raman spectroscopy of included organic matter. *Geochim. Cosmochim. Acta*, 70, 1849–1863.
- Bonal L., Bourou-Denise M., Quirico E., Montagnac G., and Lewin E. (2007) Organic matter and metamorphic history of CO chondrites. *Geochim. Cosmochim. Acta*, 71, 1605–1623.
- Bonal L., Huss G. R., Krot A. N., and Nagashima K. (2010) Chondritic lithic clasts in the CB/CH-like meteorite Isheyeyo: Fragments of previously unsampled parent bodies. *Geochim. Cosmochim. Acta*, 74, 2500–2522.
- Bonal L., Alexander C. M. O’D., Huss G. R., Nagashima K., Quirico E., and Beck P. (2013) Hydrogen isotopic composition of water in CR chondrites. *Geochim. Cosmochim. Acta*, 106, 111–133.
- Bouvier A. and Wadhwa M. (2010) The age of the solar system redefined by the oldest Pb-Pb age of a meteoritic inclusion. *Nature Geosci.*, 3, 637–641.
- Brauer F., Henning Th., and Dullemond C. (2008) Planetesimal formation near the snow line in MRI-driven turbulent protoplanetary disks. *Astron. Astrophys.*, 487, L1–L4.
- Brearley A. J. (2006) The action of water. In *Meteorites and the Early Solar System II* (D. S. Lauretta and H. Y. McSween Jr., eds.), pp. 584–624. Univ. of Arizona, Tucson.
- Brearley A. J. and Krot A. N. (2012) Metasomatism in the early solar system: The record from chondritic meteorites. In *Metasomatism and the Chemical Transformation of Rock — Lecture Notes in Earth System Sciences* (D. E. Harlov and H. Austrheim, eds.), pp. 659–789. Springer-Verlag, Berlin.
- Brennecke G. A. and Wadhwa M. (2012) Uranium isotope compositions of the basaltic angrite meteorites and the chronological implications for the early solar system. *Proc. Natl. Acad. Sci.*, 109, 9299–9303.
- Brown P. G., Hildebrand A. R., Zolensky M. E., et al. (2000) The fall, recovery, orbit, and composition of the Tagish Lake meteorite: A new type of carbonaceous chondrite. *Science*, 290, 320–325.
- Brown R. H., Lauretta D. S., Schmidt B., and Moore J. (2012) Experimental and theoretical simulations of ice sublimation with implications for the chemical, isotopic, and physical evolution of icy objects. *Planet. Space Sci.*, 60, 166–180.
- Bullock E. S., Gounelle M., Lauretta D. S., Grady M. M., and Russell S. S. (2005) Mineralogy and texture of Fe-Ni sulfides in CI1 chondrites: Clues to the extent of aqueous alteration on the CI1 parent body. *Geochim. Cosmochim. Acta*, 69, 2687–2700.
- Burbine T. H., McCoy T. J., Meibom A., Gladman B., and Keil K. (2002) Meteoritic parent bodies: Their number and identification. In *Asteroids III* (W. F. Bottke Jr. et al., eds.), pp. 653–667. Univ. of Arizona, Tucson.
- Busemann H., Alexander C. M. O’D., and Nittler L. R. (2007) Characterization of insoluble organic matter in primitive meteorites by microRaman spectroscopy. *Meteoritics & Planet. Sci.*, 42, 1387–1416.
- Callahan M. P., Smith K. E., Cleaves H. J., Ruzicka J., Stern J. C., Glavin D. P., House C. H., and Dworkin J. P. (2011) Carbonaceous meteorites contain a wide range of extraterrestrial nucleobases. *Proc. Natl. Acad. Sci.*, 108, 13995–13998.
- Camps H., Hargrove K., Pinilla-Alonso N., et al. (2010) Water ice and organics on the surface of the asteroid 24 Themis. *Nature*, 464, 1320–1321.
- Chambers J. E. (2001) Making more terrestrial planets. *Icarus*, 152, 205–224.
- Chambers J. E. (2010) Planetesimal formation by turbulent concentration. *Icarus*, 208, 505–517.
- Ciesla F. J. and Cuzzi J. N. (2006) The evolution of the water distribution in a viscous protoplanetary disk. *Icarus*, 181, 178–204.
- Ciesla F. J., Lauretta D. S., Cohen B. A., and Hood L. L. (2002) A nebular origin for chondritic fine-grained phyllosilicates. *Science*, 299, 549–552.
- Clark B. E., Ziffer J., Nesvorný D., et al. (2010) Spectroscopy of B-type asteroids: Subgroups and meteorite analogs. *J. Geophys. Res.*, 115, 1–22.
- Clark B. E., Binzel R. P., Howell E. S., Cloutis E. A., Ockert-Bell M., and Christensen P. (2011) Asteroid (101955) 1999 RQ36: Spectroscopy from 0.4 to 2.4  $\mu\text{m}$  and meteorite analogs. *Icarus*, 216, 462–475.
- Clayton R. N. (2002) Solar system: Self-shielding in the solar nebula. *Nature*, 415, 860–861.
- Clayton R. N. and Mayeda T. K. (1984) The oxygen isotope record in Murchison and other carbonaceous chondrites. *Earth Planet. Sci. Lett.*, 67, 151–161.
- Clayton R. N. and Mayeda T. K. (1999) Oxygen isotope studies of carbonaceous chondrites. *Geochim. Cosmochim. Acta*, 63, 2089–2104.
- Cloutis E. A., Hiroi T., Gaffey M. J., Alexander C. M. O’D., and Mann P. (2011a) Spectral reflectance properties of carbonaceous chondrites: 1. CI chondrites. *Icarus*, 212, 180–209.
- Cloutis E. A., Hudon P., Hiroi T., Gaffey M. J., and Mann P. (2011b) Spectral reflectance properties of carbonaceous chondrites: 2. CM chondrites. *Icarus*, 216, 309–346.
- Cloutis E. A., Hudon P., Hiroi T., and Gaffey M. J. (2012a) Spectral reflectance properties of carbonaceous chondrites: 3. CR chondrites. *Icarus*, 217, 389–407.
- Cloutis E. A., Hudon P., Hiroi T., and Gaffey M. J. (2012b) Spectral reflectance properties of carbonaceous chondrites 4: Aqueously altered and thermally metamorphosed meteorites. *Icarus*, 220, 586–617.

- Cloutis E. A., Hudon P., Hiroi T., Gaffey M. J., and Mann P. (2012c) Spectral reflectance properties of carbonaceous chondrites — 5: CO chondrites. *Icarus*, 220, 466–486.
- Cloutis E. A., Hudon P., Hiroi T., Gaffey M. J., Mann P., and Bell J. F. (2012d) Spectral reflectance properties of carbonaceous chondrites: 6. CV chondrites. *Icarus*, 221, 328–358.
- Cloutis E. A., Hudon P., Hiroi T., and Gaffey M. J. (2012e) Spectral reflectance properties of carbonaceous chondrites: 7. CK chondrites. *Icarus*, 221, 984–1001.
- Cloutis E. A., Hudon P., Hiroi T., and Gaffey M. J. (2012f) Spectral reflectance properties of carbonaceous chondrites: 8. “Other” carbonaceous chondrites: CH, ungrouped, polymict, xenolithic inclusions, and R chondrites. *Icarus*, 221, 911–924.
- Cody G. D. and Alexander C. M. O’D. (2005) NMR studies of chemical structural variation of insoluble organic matter from different carbonaceous chondrite groups. *Geochim. Cosmochim. Acta*, 69, 1085–1097.
- Cody G. D., Alexander C. M. O’D., Yabuta H., et al. (2008) Organic thermometry for chondritic parent bodies. *Earth Planet. Sci. Lett.*, 272, 446–455.
- Cohen B. A. and Coker R. F. (2000) Modeling of liquid water on CM meteorite parent bodies and implications for amino acid racemization. *Icarus*, 145, 369–381.
- Connelly J. N., Bizzarro M., Krot A. N., Nordlund Å., Wielandt D., and Ivanova M. A. (2012) The absolute chronology and thermal processing of solids in the solar protoplanetary disk. *Science*, 338, 651–655.
- Coutens A., Vastel C., Caux E., et al. (2012) A study of deuterated water in the low-mass protostars IRAS 16293-2422. *Astron. Astrophys.*, 539, 132–143.
- Cuzzi J. N., Hogan R. C., and Bottke W. F. (2010) Towards initial mass functions for asteroids and Kuiper belt objects. *Icarus*, 208, 518–538.
- Cyr K. E., Sears W. D., and Lunine J. I. (1998) Distribution and evolution of water ice in the solar nebula: Implications for solar system body formation. *Icarus*, 135, 537–548.
- Dauphas N. and Pourmand A. (2011) Hf-W-Th evidence for rapid growth of Mars and its status as a planetary embryo. *Nature*, 473, 489–492.
- De Laeter J. R., Böhlke J. K., de Bievre P., Hidaka H., Peiser H. S., Rosman K. J. R., and Taylor P. D. P. (2003) Atomic weights of the elements: Review 2000 (IUPAC Technical Report). *Pure Appl. Chem.*, 75, 683–800.
- De Leuw S., Rubin A. E., Schmitt A. K., and Wasson J. T. (2009)  $^{53}\text{Mn}$ - $^{53}\text{Cr}$  systematics of carbonates in CM chondrites: Implications for the timing and duration of aqueous alteration. *Geochim. Cosmochim. Acta*, 73, 7433–7442.
- DeMeo F. E. and Carry B. (2014) Solar system evolution from compositional mapping of the asteroid belt. *Nature*, 505, 629–634.
- Doyle P. M., Nagashima K., Jogo K., and Krot A. N. (2013) Relative sensitivity factor defined for  $^{53}\text{Mn}$ - $^{53}\text{Cr}$  chronometry of secondary fayalite. *Lunar Planet. Sci. XLIV*, Abstract #1792. Lunar and Planetary Institute, Houston.
- Doyle P. M., Jogo K., Nagashima K., Krot A. N., Wakita S., Ciesla F. J., and Hutcheon I. D. (2015) Early aqueous activity on the chondrite parent asteroids recorded by fayalite. *Nature Commun.*, 6, 7444.
- Drouart A., Dubrulle B., Gautier D., and Robert F. (1999) Structure and transport in the solar nebula from constraints on deuterium enrichment and giant planets formation. *Icarus*, 140, 129–155.
- Eberhardt P., Reber M., Krankowsky D., and Hodges R. R. (1995) The D/H and  $^{18}\text{O}/^{16}\text{O}$  ratios in water from Comet P/Halley. *Astron. Astrophys.*, 302, 301–316.
- Elkins-Tanton L. T., Weiss B. P., and Zuber M. T. (2011) Chondrites as samples of differentiated planetesimals. *Earth Planet. Sci. Lett.*, 305, 1–10.
- Elsila J. E., Glavin D. P., Dworkin J. P., Martins Z., and Bada J. L. (2012) Inconclusive evidence for nonterrestrial isoleucine enantiomeric excesses in primitive meteorites. *Proc. Natl. Acad. Sci.*, 109, E3288.
- Endress M., Zinner E., and Bischoff A. (1996) Early aqueous activity on primitive meteorite parent bodies. *Nature*, 379, 701–703.
- Fegley B. Jr. (2000) Kinetics of gas-grain reactions in the solar nebula. *Space Sci. Rev.*, 92, 177–200.
- Fischer R. A. and Ciesla F. J. (2014) Dynamics of the terrestrial planets from a large number of N-body simulations. *Earth Planet. Sci. Lett.*, 392, 28–38.
- Fujiya W., Sugiura N., Hotta H., Ichimura K., and Sano Y. (2012) Evidence for the late formation of hydrous asteroids from young meteoritic carbonates. *Nature Commun.*, 3, 1–6.
- Fujiya W., Sugiura N., Sano Y., and Hiyagon H. (2013) Mn-Cr ages of dolomites in CI chondrites and the Tagish Lake ungrouped carbonaceous chondrite. *Earth Planet. Sci. Lett.*, 362, 130–142.
- Furuya K., Aikawa Y., Nomura H., Hersant F., and Wakelam V. (2013) Water in protoplanetary disks: Deuteration and turbulent mixing. *Astrophys. J.*, 779, 11.
- Geiss J. and Gloeckler G. (2003) Isotopic composition of H, He and Ne in the protosolar cloud. *Space Sci. Rev.*, 106, 3–18.
- Glavin D. P. and Dworkin J. P. (2009) Enrichment of the amino acid L-isovaline by aqueous alteration on CI and CM parent bodies. *Proc. Natl. Acad. Sci.*, 106, 5487–5492.
- Glavin D. P., Kubny A., Jagoutz E., and Lugmair G. W. (2004) Mn-Cr isotope systematics of the D’Orbigny angrite. *Meteoritics & Planet. Sci.*, 39, 693–700.
- Glavin D. P., Aubrey A. D., Callahan M. P., Dworkin J. P., Elsila J. E., Parker E. T., Bada J. L., Jenniskens P., and Shaddad M. H. (2010a) Extraterrestrial amino acids in the Almahata Sitta meteorite. *Meteoritics & Planet. Sci.*, 45, 1695–1709.
- Glavin D. P., Callahan M. P., Dworkin J. P., and Elsila J. E. (2010b) The effects of parent body processes on amino acids in carbonaceous chondrites. *Meteoritics & Planet. Sci.*, 45, 1948–1972.
- Gomes R. S., Levison H. F., Morbidelli A., and Tsiganis K. (2005) Origin of the cataclysmic late heavy bombardment period of the terrestrial planets. *Nature*, 435, 466–469.
- Gounelle M., Morbidelli A., Spurny P., Young E. D., and Sephton M. (2008) Meteorites from the outer solar system? In *The Solar System Beyond Neptune* (M. A. Barucci et al., eds.), pp. 525–541. Univ. of Arizona, Tucson.
- Gounelle M., Krot A. N., Nagashima K., and Kearsley A. (2009) Extreme  $^{16}\text{O}$ -enrichment in refractory inclusions from the Isheyevo meteorite: Implication for oxygen isotope composition of the Sun. *Astrophys. J. Lett.*, 698, L18–L22.
- Greenwood R. C., Franchi I. A., Kearsley A. T., and Alard O. (2010) The relationship between CK and CV chondrites. *Geochim. Cosmochim. Acta*, 74, 1684–1705.
- Greshake A. (1997) The primitive matrix components of the unique carbonaceous chondrite Acfer 094: A TEM study. *Geochim. Cosmochim. Acta*, 61, 437–452.
- Greshake A., Krot A. N., Meibom A., Weisberg M. K., and Keil K. (2002) Heavily-hydrated matrix lumps in the CH and metal-rich chondrites QUE 94411 and Hammadah al Hamra 237. *Meteoritics & Planet. Sci.*, 37, 281–294.
- Grimm R. E. and McSween H. Y. Jr. (1989) Water and the thermal evolution of carbonaceous chondrite parent bodies. *Icarus*, 82, 244–280.
- Grossman J. N. and Brearley A. J. (2005) The onset of metamorphism in ordinary and carbonaceous chondrites. *Meteoritics & Planet. Sci.*, 61, 437–452.
- Guo W. and Eiler J. M. (2007) Temperatures of aqueous alteration and evidence for methane generation on the parent bodies of the CM chondrites. *Geochim. Cosmochim. Acta*, 71, 5565–5575.
- Harju E. R., Rubin A. E., Ahn I., Choi B.-G., Ziegler K., and Wasson J. T. (2014) Progressive aqueous alteration of CR carbonaceous chondrites. *Geochim. Cosmochim. Acta*, 71, 5565–5575.
- Hartogh P., Lis D. C., Bockelée-Morvan D., et al. (2011) Ocean-like water in the Jupiter-family comet 103P/Hartley 2. *Nature*, 478, 218–220.
- Herd C. D. K., Blinova A., Simkus D. N., et al. (2011) Origin and evolution of prebiotic organic matter as inferred from Tagish Lake meteorite. *Science*, 332, 1304–1307.
- Hersant F., Gautier D., and Huré J.-M. (2001) A two-dimensional model for the primordial nebula constrained by D/H measurements in the solar system: Implications for the formation of giant planets. *Astrophys. J.*, 554, 391–407.
- Hewins R. H., Bourot-Denise M., Zanda B., et al. (2014) The Paris meteorite, the least altered CM chondrite so far. *Geochim. Cosmochim. Acta*, 124, 190–222.
- Hilts R. W., Herd C. D. K., Simkus D. N., and Slater G. F. (2014) Soluble organic compounds in the Tagish Lake meteorite. *Meteoritics & Planet. Sci.*, 49, 526–549.
- Hiroi T., Zolensky M. E., and Pieters C. M. (2001) The Tagish Lake meteorite: A possible sample from a D-type asteroid. *Science*, 293, 2234–2236.

- Hoppe P., Macdougall J. D., and Lugmair G. W. (2007) High spatial resolution ion microprobe measurements refine chronology of carbonate formation in Orgueil. *Meteoritics & Planet. Sci.*, 42, 1309–1320.
- Horner J., Mousis O., and Hersant F. (2007) Constraints on the formation regions of comets from their D/H ratios. *Earth Moon Planets*, 100, 43–56.
- Horner J., Mousis O., Alibert Y., Lunine J. I., and Blanc M. (2008) Constraints from deuterium on the formation of icy bodies in the jovian system and beyond. *Planet. Space Sci.*, 56, 1585–1595.
- Howard K. T., Benedix G. K., Bland P. A., and Cresssey G. (2009) Modal mineralogy of CM2 chondrites by X-ray diffraction (PSD-XRD). Part 1: Total phyllosilicate abundance and the degree of aqueous alteration. *Geochim. Cosmochim. Acta*, 73, 4576–4589.
- Howard K. T., Benedix G. K., Bland P. A., and Cresssey G. (2010) Modal mineralogy of CV3 chondrites by X-ray diffraction (PSD-XRD). *Geochim. Cosmochim. Acta*, 74, 5084–5097.
- Howard K. T., Benedix G. K., Bland P. A., and Cresssey G. (2011) Modal mineralogy of CM chondrites by X-ray diffraction (PSD-XRD): Part 2. Degree, nature and settings of aqueous alteration. *Geochim. Cosmochim. Acta*, 75, 2735–2751.
- Howard K. T., Alexander C. M. O'D., Schrader D. L., and Dyl K. A. (2015) Classification of hydrous meteorites (CR, CM and C2 ungrouped) by phyllosilicate fraction: PSD-XRD modal mineralogy and planetesimal environments. *Geochim. Cosmochim. Acta*, 149, 206–222.
- Hsieh H. H. and Jewitt D. (2006) A population of comets in the main asteroid belt. *Science*, 312, 561–563.
- Hua X., Huss G. R., Tachibana S., and Sharp T. G. (2005) Oxygen, silicon, and Mn-Cr isotopes of fayalite in the Kaba oxidized CV3 chondrite: Constraints for its formation history. *Geochim. Cosmochim. Acta*, 69, 1333–1348.
- Huss G. R. and Lewis R. S. (1995) Presolar diamond, SiC, and graphite in primitive chondrites: Abundances as a function of meteorite class and petrologic type. *Geochim. Cosmochim. Acta*, 59, 115–160.
- Huss G. R., Alexander C. M. O'D., Palme H., Bland P. A., and Wasson J. T. (2005) Genetic relationships between chondrules, fine-grained rims, and interchondrule matrix. In *Chondrites and the Protoplanetary Disk* (A. N. Krot et al., eds.), pp. 701–731. ASP Conf. Ser. 341, Astronomical Society of the Pacific, San Francisco.
- Huss G. R., Rubin A. E., and Grossman J. N. (2006) Thermal metamorphism in chondrites. In *Meteorites and the Early Solar System II* (D. S. Lauretta and H. Y. McSween Jr., eds), pp. 567–586. Univ. of Arizona, Tucson.
- Hutcheon I. D. and Hutchison R. (1989) Evidence from the Semarkona ordinary chondrite for  $^{26}\text{Al}$  heating of small planets. *Nature*, 337, 238–241.
- Hutcheon I. D., Krot A. N., Keil K., Phinney D. L., and Scott E. R. D. (1998)  $^{53}\text{Mn}$ - $^{53}\text{Cr}$  dating of fayalite formation in the CV3 chondrite Mokoia: Evidence for asteroidal alteration. *Science*, 282, 1865–1867.
- Hutcheon I. D., Marhas K., Krot A. N., Goswami J. N., and Jones R. H. (2009)  $^{26}\text{Al}$  in plagioclase-rich chondrules in carbonaceous chondrites: Evidence for an extended duration of chondrule formation. *Geochim. Cosmochim. Acta*, 73, 5080–5100.
- Ivanova M. A., Nagashima K., Krot A. N., and MacPherson G. J. (2012) Calcium-aluminum-rich inclusions with relict ultra-refractory inclusions rich in Zr, Y, and Sc from Efremovka and North West Africa 3118 CV3 carbonaceous chondrites: Evidence for multistage formation in oxygen isotopic reservoirs of variable composition. *Meteoritics & Planet. Sci.*, 47, 2107–2127.
- Izidoro A., Haghhighipour N., Winter O. C., and Tsuchida M. (2014) Terrestrial planet formation in a protoplanetary disk with a local mass depletion: A successful scenario for the formation of Mars. *Astrophys. J.*, 782, 1–20.
- Jabeen I. and Hiayagon H. (2003) Oxygen isotopes in isolated and chondrule olivines of Murchison. *Lunar Planet. Sci. XXXIV*, Abstract #1551. Lunar and Planetary Institute, Houston.
- Jacobsen S., Yin Q.-Z., Moynier F., Amelin Y., Krot A. N., Nagashima K., Hutcheon I. D., and Palme H. (2008)  $^{26}\text{Al}$ - $^{26}\text{Mg}$  and  $^{207}\text{Pb}$ - $^{206}\text{Pb}$  systematics of Allende CAIs: Canonical solar initial  $^{26}\text{Al}$ / $^{27}\text{Al}$  ratio reinstated. *Earth Planet. Sci. Lett.*, 272, 353–364.
- Jacquet E. and Robert F. (2013) Water transport in protoplanetary disk and the hydrogen isotopic composition of chondrites. *Icarus*, 223, 722–732.
- Jenniskens P., Fries M. D., Yin Q.-Zhu, et al. (2012) Radar-enabled recovery of the Sutter's Mill meteorite, a carbonaceous chondrite regolith breccia. *Science*, 338, 1583–1587.
- Jewitt D. (2012) The active asteroids. *Astron. J.*, 143, 66.
- Jilly C. E., Huss G. R., and Nagashima K. (2013) Mn-Cr dating of secondary carbonates in CR chondrites. *Lunar Planet. Sci. XLIV*, Abstract #2474. Lunar and Planetary Institute, Houston.
- Jilly C. E., Huss G. R., Krot A. N., Nagashima K., Yin Q.-Z., and Sugiyama N. (2014a)  $^{53}\text{Mn}$ - $^{53}\text{Cr}$  dating of aqueously formed carbonates in the CM2 lithology of the Sutter's Mill carbonaceous chondrite. *Meteoritics & Planet. Sci.*, 49, 2104–2117.
- Jilly C. E., Huss G. R., Nagashima K., and Schrader D. L. (2014b) Oxygen isotopes and geothermometry of secondary minerals in CR chondrites. *Meteoritics & Planet. Sci. Suppl.*, 49, Abstract #5395.
- Jin L., Arnett W. D., Sui N., and Wang X. (2008) An interpretation of the anomalously low mass of Mars. *Astrophys. J. Lett.*, 674, L105–L108.
- Jogo K., Nakamura T., Noguchi T., and Zolotov M. Y. (2009) Fayalite in the Vigaranjo CV3 carbonaceous chondrite: Occurrences, formation age and conditions. *Earth Planet. Sci. Lett.*, 287, 320–328.
- Johansen A. and Khlar H. (2011) Planetesimal formation through streaming and gravitational instabilities. *Earth Moon Planets*, 108, 39–43.
- Johnson B. C., Minton D. A., Melosh H. J., and Zuber M. T. (2015) Impact jetting as the origin of chondrules. *Nature*, 517, 339–341.
- Jones R. H., McCubbin F. M., Dreeland L., Guan Y., Burger P. V., and Shearer C. K. (2014) Phosphate minerals in LL chondrites: A record of the action of fluids during metamorphism on ordinary chondrite parent bodies. *Geochim. Cosmochim. Acta*, 132, 120–140.
- Joung M. K. R., Mac Low M.-M., and Ebel D. S. (2004) Chondrule formation and protoplanetary disk heating by current sheets in nonideal magnetohydrodynamic turbulence. *Astrophys. J.*, 606, 532–541.
- Kennedy G. M. and Kenyon S. J. (2008) Planet formation around stars of various masses: The snow line and the frequency of giant planets. *Astrophys. J.*, 673, 505–512.
- Kita N. T. and Ushikubo T. (2012) Evolution of protoplanetary disk inferred from  $^{26}\text{Al}$  chronology of individual chondrules. *Meteoritics & Planet. Sci.*, 43, 1108–1119.
- Kita N. T., Nagahara H., Togashi S., and Morishita Y. (2000) A short duration of chondrule formation in the solar nebula: Evidence from  $^{26}\text{Al}$  in Semarkona ferromagnesian chondrules. *Geochim. Cosmochim. Acta*, 64, 3913–3922.
- Kobayashi H. and Dauphas N. (2013) Small planetesimals in a massive disk formed Mars. *Icarus*, 225, 122–130.
- Krot A. N., Petaev M. I., Scott E. R. D., Choi B.-G., Zolensky M. E., and Keil K. (1998) Progressive alteration in CV3 chondrites: More evidence for asteroidal alteration. *Meteoritics & Planet. Sci.*, 33, 1065–1085.
- Krot A. N., Brearley A. J., Petaev M. I., Klemme S., Sears D. W. G., Benoit P. H., Hutcheon I. D., Zolensky M. E., and Keil K. (2000) Evidence for *in situ* growth of fayalite and hedenbergite in MacAlpine Hills 88107, ungrouped carbonaceous chondrite related to CM-CO clan. *Meteoritics & Planet. Sci.*, 35, 1365–1387.
- Krot A. N., Amelin Y., Cassen P., and Meibom A. (2005) Young chondrules in CB chondrites from a giant impact in the early solar system. *Nature*, 436, 989–992.
- Krot A. N., Amelin Y., Bland P., et al. (2009) Origin and chronology of chondritic components: A review. *Geochim. Cosmochim. Acta*, 73, 4963–4998.
- Krot A. N., Nagashima K., Ciesla F. J., Bradley M. S., Hutcheon I. D., Davis A. M., Huss G. R., and Scott E. R. D. (2010) Oxygen isotopic composition of the Sun and mean oxygen isotopic composition of the protosolar silicate dust: Evidence from refractory inclusions. *Astrophys. J.*, 713, 1159–1166.
- Krot A. N., Makide K., Nagashima K., Huss G. R., Ogliore R. C., Ciesla F. J., Yang L., Hellebrand E., and Gaidos E. (2012) Heterogeneous distribution of  $^{26}\text{Al}$  at the birth of the solar system: Evidence from refractory grains and inclusions. *Meteoritics & Planet. Sci.*, 47, 1948–1979.
- Krot A. N., Doyle P. M., Nagashima K., Jogo K., Wakita S., Ciesla F. J., and Hutcheon I. D. (2013) Origin of asteroidal water: Constraints from isotopic compositions of aqueously formed minerals. *Meteoritics & Planet. Sci.*, 48, Abstract #5161.

- Krot A. N., Keil K., Goodrich C., Weisberg M. K., and Scott E. R. D. (2014a) Classification of meteorites. In *Treatise on Geochemistry, Vol. 1: Meteorites and Cosmochemical Processes* (A. M. Davis, ed.), pp. 1–63. Elsevier, Oxford.
- Krot A. N., Nagashima K., and Bizzarro M. (2014b) Aluminum-magnesium isotope systematics of porphyritic chondrules and plagioclase fragments in CH carbonaceous chondrites. *Lunar Planet. Sci. XLV*, Abstract #2142. Lunar and Planetary Institute, Houston.
- Kruijer T. S., Kleine T., Fischer-Gödde M., Burkhardt C., and Wieler R. (2014) Hf-W isochron for bulk CAI: Evidence for homogeneity of  $^{26}\text{Al}$  and  $^{182}\text{Hf}$ . *Lunar Planet. Sci. XLV*, Abstract #1786. Lunar and Planetary Institute, Houston.
- Kunihiro T., Rubin A. E., McKeegan K. D., and Wasson J. T. (2004) Initial  $^{26}\text{Al}/^{27}\text{Al}$  in carbonaceous chondrite chondrules: Too little  $^{26}\text{Al}$  to melt asteroids. *Geochim. Cosmochim. Acta*, 68, 2947–2957.
- Küppers M., O'Rourke L., Bockelée-Morvan D., et al. (2014) Localized sources of water vapour on the dwarf planet (1) Ceres. *Nature*, 505, 525–528.
- Kurahashi E., Kita N. T., Nagahara H., and Morishita Y. (2008)  $^{26}\text{Al}-^{26}\text{Mg}$  systematics of chondrules in a primitive CO chondrite. *Geochim. Cosmochim. Acta*, 72, 3865–3882.
- Larsen K., Trinquier A., Paton C., Schiller M., Wielandt D., Ivanova M., Connelly J., Nordlund A., Krot A. N., and Bizzarro M. (2011) Evidence for magnesium-isotope heterogeneity in the solar protoplanetary disk. *Astrophys. J. Lett.*, 735, L37–L40.
- Lauretta D. S., Bartels A. E., Barucci M. A., et al. (2014) The OSIRIS-REx target asteroid (101955) Bennu: Constraints on its physical, geological, and dynamical nature from astronomical observations. *Meteoritics & Planet. Sci.*, 49, 1–16.
- Lee J.-E., Bergin E. A., and Evans N. J. II (2004) Evolution of chemistry and molecular line profiles during protostellar collapse. *Astrophys. J.*, 617, 360–383.
- Lee J.-E., Bergin E. A., and Lyons J. R. (2008) Oxygen isotope anomalies of the Sun and the original environment of the solar system. *Meteoritics & Planet. Sci.*, 43, 1351–1362.
- Lee M. R., Lindgren P., Sofa M. R., Alexander C. M. O'D., and Wang J. (2012) Extended chronologies of aqueous alteration in the CM2 carbonaceous chondrites: Evidence from carbonates in Queen Alexandra Range 93005. *Geochim. Cosmochim. Acta*, 92, 148–169.
- Lee M. R., Sofe M. R., Lindgren P., Starkey N. A., and Franchi I. A. (2013) The oxygen isotope evolution of parent body aqueous solutions as recorded by multiple carbonate generations in the Lonewolf Nunataks 94101 CM2 carbonaceous chondrite. *Geochim. Cosmochim. Acta*, 121, 452–466.
- Le Guillou C. and Brearley A. J. (2014) Relationships between organics, water and early stages of aqueous alteration in the pristine CR3.0 chondrite MET00426. *Geochim. Cosmochim. Acta*, 131, 344–367.
- Le Guillou C., Bernard S., Brearley A. J., and Remusat L. (2014) Evolution of organic matter in Orgueil, Murchison and Renazzo during parent body aqueous alteration: *In situ* investigations. *Geochim. Cosmochim. Acta*, 131, 368–392.
- Leshin L. A., Rubin A. E., and McKeegan K. D. (1997) The oxygen isotopic composition of olivine and pyroxene from CI chondrites. *Geochim. Cosmochim. Acta*, 61, 835–845.
- Levison H. F., Bottke W. F., Gounelle M., Morbidelli A., Nesvorný D., and Tsiganis K. (2009) Contamination of the asteroid belt by primordial trans-neptunian objects. *Nature*, 460, 364–366.
- Levison H. F., Morbidelli A., Tsiganis K., Nesvorný D., and Gomes R. (2011) Late orbital instabilities in the outer planets induced by interaction with a self-gravitating planetesimal disk. *Astrophys. J.*, 142, 1–11.
- Lis D. C., Biver N., Bockelée-Morvan D., et al. (2013) A Herschel study of D/H in water in the Jupiter-family comet 45P/Honda-Mrkos-Pajdusáková and prospects for D/H measurements with CCAT. *Astrophys. J. Lett.*, 774, L3.
- Lodders K. (2003) Solar system abundances and condensation temperatures of the elements. *Astrophys. J.*, 591, 1220–1247.
- Lyons J. R. and Young E. D. (2005) CO self-shielding as the origin of oxygen isotope anomalies in the early solar nebula. *Nature*, 435, 317–320.
- MacPherson G. J., Bullock E. S., Janney P. E., Kita N. T., Ushikubo T., Davis A. M., Wadhwa M., and Krot A. N. (2011) Early solar nebula condensates with canonical, not supracanonical, initial  $^{26}\text{Al}/^{27}\text{Al}$  ratios. *Astrophys. J. Lett.*, 711, L117–L121.
- MacPherson G. J., Nagashima K., Krot A. N., Doyle P. M., and Ivanova M. A. (2015)  $^{53}\text{Mn}-^{53}\text{Cr}$  systematics of Ca-Fe silicates in CV3 chondrites. *Lunar Planet. Sci. XLVI*, Abstract #2760. Lunar and Planetary Institute, Houston.
- Martin R. G. and Livio M. (2012) On the evolution of the snow line in protoplanetary disks. *Mon. Not. R. Astron. Soc.*, 425, L6–L9.
- Martins Z., Alexander C. M. O'D., Orzechowska G. E., Fogel M. L., and Ehrenfreund P. (2007) Indigenous amino acids in primitive CR meteorites. *Meteoritics & Planet. Sci.*, 42, 2125–2136.
- McCanta M. C., Treiman A. H., Dyar M. D., Alexander C. M. O'D., Rumble D. III, and Essene E. J. (2008) The LaPaz Icefield 04840 meteorite: Mineralogy, metamorphism, and origin of an amphibole- and biotite-bearing R chondrite. *Geochim. Cosmochim. Acta*, 72, 5757–5780.
- McKeegan K. D., Kallio A. P. A., Heber V. S., et al. (2011) The oxygen isotopic composition of the Sun inferred from captured solar wind. *Science*, 332, 1528–1532.
- McKibbin S. J., Ireland T. R., Amelin Y., O'Neill H. S. C., and Holden P. (2013) Mn-Cr relative sensitivity factors for secondary ion mass spectrometry analysis of Mg-Fe-Ca olivine and implications for the Mn-Cr chronology of meteorites. *Geochim. Cosmochim. Acta*, 110, 216–228.
- McNally C. P., Hubbard A., Mc Low M.-M., Ebel D. S., and D'Alessio P. (2013) Mineral processing by short circuits in protoplanetary disks. *Astrophys. J. Lett.*, 767, L2.
- Min M., Dullemond C. P., Kama M., and Dominik C. (2011) The thermal structure and the location of the snow line in the protosolar nebula: Axisymmetric models with full 3-D radiative transfer. *Icarus*, 212, 416–426.
- Moores J. E., Brown R. H., Lauretta D. S., and Smith P. H. (2012) Experimental and theoretical simulations of ice sublimation with implications for the chemical, isotopic, and physical evolution of icy objects. *Planet. Sci.*, 1:2, 1–30.
- Morbidelli A., Levison H. F., Tsiganis K., and Gomes R. (2005) Chaotic capture of Jupiter's Trojan asteroids in the early solar system. *Nature*, 435, 462–465.
- Morbidelli A., Lunine J. I., O'Brien D. P., Raymond S. N., and Walsh K. J. (2012) Building terrestrial planets. *Annu. Rev. Earth Planet. Sci.*, 40, 251–275.
- Morris M. A., Boley A. C., Desch S. J., and Athanassiadou T. (2010) Chondrule formation in bow shocks around eccentric planetary embryos. *Astrophys. J.*, 752, 1–17.
- Mostefaiou S., Kita N. T., Togashi S., Tachibana S., Nagahara H., and Morishita Y. (2002) The relative formation ages of ferromagnesian chondrules inferred from their initial  $^{26}\text{Al}/^{27}\text{Al}$  ratios. *Meteoritics & Planet. Sci.*, 37, 421–438.
- Mousis O., Gautier D., Bockelée-Morvan D., Robert F., Dubrulle B., and Drouart A. (2000) Constraints on the formation of comets from D/H ratios measured in  $\text{H}_2\text{O}$  and HCN. *Icarus*, 148, 513–525.
- Nagashima K., Krot A. N., and Huss G. R. (2014)  $^{26}\text{Al}$  in chondrules from CR2 chondrites. *Geochim. J.*, 48, 561–571.
- Nakamura T., Noguchi T., Takaaki M., et al. (2011) Itokawa dust particles: A direct link between S-type asteroids and ordinary chondrites. *Science*, 333, 1113–1116.
- Orthous-Daunay F. R., Quirico E., Beck P., Brissaud O., Dartois E., Pino T., and Schmitt B. (2013) Mid-infrared study of the molecular structure variability of insoluble organic matter from primitive chondrites. *Icarus*, 223, 534–543.
- Palme H., Lodders K., and Jones A. (2014) Solar system abundances of the elements. In *Treatise on Geochemistry, Vol. 1: Meteorites and Cosmochemical Processes* (A. M. Davis, ed.), pp. 15–36. Elsevier, Oxford.
- Papanastassiou D. A., Bogdanovski O., and Wasserburg G. J. (2002)  $^{53}\text{Mn}-^{53}\text{Cr}$  systematics in Allende refractory inclusions. *Meteoritics & Planet. Sci. Suppl.*, 37, A114.
- Petitat M. and Gounelle M. (2010) Magnetite content and carbonate mineralogy as constraints for parent body hydrothermal alteration. *Lunar Planet. Sci. XLI*, Abstract #1673. Lunar and Planetary Institute, Houston.
- Petitat M., Gounelle M., McKeegan K. D., Mostefaiou S., Marrocchi Y., Meibom A., and Zolensky M. E. (2009a) Kaidun carbonates: Re-examining the  $^{53}\text{Mn}-^{53}\text{Cr}$  systematics. *Lunar Planet. Sci. XL*, Abstract #1666. Lunar and Planetary Institute, Houston.

- Petitat M., McKeegan K. D., Gounelle M., Mostefaoui S., Marrocchi Y., Meibom A., and Leshin L. A. (2009b) Duration and sequence of carbonate crystallization on the Orgueil protolith:  $^{53}\text{Mn}$ - $^{53}\text{Cr}$  systematics of their evolution in O and C isotopic composition. *Lunar Planet. Sci. XL*, Abstract #1657. Lunar and Planetary Institute, Houston.
- Pizzarello S. and Monroe A. A. (2012) Reply to Elsila et al.: Large enantiomeric excesses in primitive meteorites, an analytical and computational supplement. *Proc. Natl. Acad. Sci.*, *109*, E3289.
- Pizzarello S., Schrader D. L., Monroe A. A., and Lauretta D. S. (2012) Large enantiomeric excesses in primitive meteorites and the diverse effects of water in cosmochemical evolution. *Proc. Natl. Acad. Sci.*, *109*, 11949–11954.
- Quirico E., Raynal P. I., and Bourot-Denise M. (2003) Metamorphic grade of organic matter in six unequilibrated ordinary chondrites. *Meteoritics & Planet. Sci.*, *38*, 795–811.
- Quirico E., Orthous-Daunay F.-R., Beck P., et al. (2014) Origin of insoluble organic matter in type 1 and 2 chondrites: New clues, new questions. *Geochim. Cosmochim. Acta*, *136*, 80–99.
- Raymond S. N. and Morbidelli A. (2014) The Grand Tack model: A critical review. *Proc. IAU*, *9*, 194–203. DOI: 10.1017/S1743921314008254.
- Raymond S. N., O'Brien D. P., Morbidelli A., and Kaib N. A. (2009) Building the terrestrial planets: Constrained accretion in the inner solar system. *Icarus*, *203*, 644–662.
- Rémusat L., Palhol F., Robert F., Derenne S., and France-Lanord C. (2006) Enrichment of deuterium in insoluble organic matter from primitive meteorites: A solar system origin? *Earth Planet. Sci. Lett.*, *243*, 15–25.
- Rémusat L., Guan Y., Wang Y., and Eiler J. M. (2010) Accretion and preservation of D-rich organic particles in carbonaceous chondrites: Evidence for important transport in the early solar system nebula. *Astrophys. J.*, *713*, 1048–1058.
- Rivkin A. S. (2012) The fraction of hydrated C-complex asteroids in the asteroid belt from SDSS data. *Icarus*, *221*, 744–752.
- Rivkin A. S. and Emery J. P. (2010) Detection of ice and organics on the asteroidal surface. *Nature*, *464*, 1322–1323.
- Rodgers S. D. and Millar T. J. (1996) The chemistry of deuterium in hot molecular cores. *Mon. Not. R. Astron. Soc.*, *280*, 1046–1054.
- Rowe M. W., Clayton R. N., and Mayeda T. K. (1994) Oxygen isotopes in separated components of CI and CM meteorites. *Geochim. Cosmochim. Acta*, *58*, 5341–5347.
- Rubin A. E., Trigo-Rodríguez J. M., Huber H., and Wasson J. T. (2007) Progressive aqueous alteration of CM carbonaceous chondrites. *Geochim. Cosmochim. Acta*, *71*, 2761–2782.
- Rudraswami N. G., Goswami J. N., Chattopadhyay B., Sengupta S. K., and Thapliyal A. P. (2008) Al-26 records in chondrules from unequilibrated ordinary chondrites: II. Duration of chondrule formation and parent body thermal metamorphism. *Earth Planet. Sci. Lett.*, *274*, 93–102.
- Russell S. D. J., Longstaffe F. J., King P. L., and Larson T. E. (2010) The oxygen-isotope composition of chondrules and isolated forsterite and olivine grains from the Tagish Lake carbonaceous chondrite. *Geochim. Cosmochim. Acta*, *74*, 2484–2499.
- Sakamoto N., Seto Y., Itoh S., Kuramoto K., Fujino K., Nagashima K., Krot A. N., and Yurimoto H. (2007) Oxygen isotope evidence for remnants of the early solar system primordial water. *Science*, *317*, 231–233.
- Sasselov D. D. and Lecar M. (2000) On the snow line in dusty protoplanetary disks. *Astrophys. J.*, *528*, 995–998.
- Schrader D. L., Franchi I. A., Connolly H. C. Jr., Greenwood R. C., Lauretta D. S., and Gibson J. M. (2011) The formation and alteration of the Renazzo-like carbonaceous chondrites I: Implications of bulk-oxygen isotopic composition. *Geochim. Cosmochim. Acta*, *75*, 308–325.
- Schrader D. L., Nagashima K., Krot A. N., Ogliore R. C., Yin Q.-Z., and Amelin Y. A. (2013) Testing the distribution of  $^{26}\text{Al}$  in the protoplanetary disk using CR chondrules. *Meteoritics & Planet. Sci. Suppl.*, *48*, Abstract #5141.
- Scott E. R. D. and Krot A. N. (2014) Chondrites and their components. In *Treatise on Geochemistry, Vol. 1: Meteorites and Cosmochemical Processes* (A. M. Davis, ed.), pp. 65–137. Elsevier, Oxford.
- Steele R. C. J. and McKeegan K. D. (2014) Aqueous alteration on the CI parent body: Mn-Cr ages of secondary carbonate formation. *Meteoritics & Planet. Sci. Suppl.*, *49*, Abstract #5438.
- Sugiura N. and Fujiya W. (2014) Correlated accretion ages and  $^{54}\text{Cr}$  of meteorite parent bodies and the evolution of the solar nebula. *Meteoritics & Planet. Sci.*, *49*, 772–787.
- Sugiura N., Miyazaki A., and Yanai K. (2005) Widespread magmatic activities on the angite parent body at 4562 Ma ago. *Earth Planets Space*, *57*, E13–E16.
- Tachibana S., Watanabe S., and Fujimoto M. (2014) Hayabusa 2 sample return from 1999 JU3: Initial analysis plan. *Meteoritics & Planet. Sci.*, *49*, Abstract #5278.
- Treiman A. H. and McCanta M. C. (2010) Amphibole-rich R chondrite LAP 04840 — From an icy asteroid or main-belt comet? *Meteoritics & Planet. Sci. Suppl.*, *45*, Abstract #5389.
- Trinquier A., Birck J.-L., Allegre C. J., Göpel C., and Ulfbeck D. (2008)  $^{53}\text{Mn}$ - $^{53}\text{Cr}$  systematics of the early solar system revisited. *Geochim. Cosmochim. Acta*, *72*, 5146–5163.
- Tsiganis K., Gomes R. S., Morbidelli A., and Levison H. F. (2005) Origin of the orbital architecture of the giant planets of the solar system. *Nature*, *435*, 459–461.
- Tyra M. A., Brearley A. J., Matzel J., and Hutcheon I. D. (2010) Types and timescales of secondary carbonates in CR1 chondrite GRO 95577. *Lunar Planet. Sci. XL*, Abstract #2614. Lunar and Planetary Institute, Houston.
- Tyra M. A., Farquhar J., Guan Y., and Leshin L. A. (2012) An oxygen isotope dichotomy in CM2 chondritic carbonates — A SIMS approach. *Geochim. Cosmochim. Acta*, *77*, 383–395.
- Ushikubo T., Nakashima D., Kimura M., Tenner T. J., and Kita N. T. (2013) Contemporaneous formation of chondrules in distinct oxygen isotope reservoirs. *Geochim. Cosmochim. Acta*, *109*, 280–295.
- van Kooten E. M. M. E., Nagashima K., Thomen A., Wielandt D., Schiller M., Krot A. N., and Bizzarro M. (2014) Mn-Cr isotope systematics of Isheyevo lithic clasts and implications for CH/CB chondrite formation and accretion. *Meteoritics & Planet. Sci. Suppl.*, *49*, Abstract #5129.
- Villeneuve J., Chaussidon M., and Libourel G. (2009) Homogeneous distribution of  $^{26}\text{Al}$  in the solar system from the Mg isotopic composition of chondrules. *Science*, *325*, 985–988.
- Vollmer C., Kepaptsgoulou D., Leitner J., Busemann H., Spring N. H., Ramasse Q. M., Hoppe P., and Nittler L. R. (2014) Fluid-induced organic synthesis in the solar nebula recorded in extraterrestrial dust from meteorites. *Proc. Natl. Acad. Sci.*, *111*, 15338–15343.
- Walsh K. J., Morbidelli A., Raymond S. N., O'Brien D. P., and Mandell A. M. (2011) A low mass for Mars from Jupiter's early gas-driven migration. *Nature*, *475*, 206–209.
- Warren P. H. (2011) Stable isotopes and the non-carbonaceous derivation of ureilites, in common with nearly all differentiated primary materials. *Geochim. Cosmochim. Acta*, *75*, 6912–6926.
- Wasson J. T., Isa J., and Rubin A. E. (2013) Compositional and petrographic similarities of CV and CK chondrites: A single group with variations in textures and volatile concentrations attributable to impact heating, crushing and oxidation. *Geochim. Cosmochim. Acta*, *108*, 45–62.
- Weisberg M. K. and Huber H. (2007) The GRO 95577 CR1 chondrite and hydration of the CR parent body. *Meteoritics & Planet. Sci.*, *42*, 1495–1503.
- Yabuta H., Alexander C. M. O'D., Fogel M. L., Kilcoyne A. L. D., and Cody G. D. (2010) A molecular and isotopic study of the macromolecular organic matter of the ungrouped C2 WIS 91600 and its relationship to Tagish Lake and PCA 91008. *Meteoritics & Planet. Sci.*, *45*, 1446–1460.
- Yang L., Ciesla F. J., Lyons J. R., Lee J.-E., and Bergin E. A. (2011) Oxygen isotope anomalies in the solar nebula inherited from the proto-solar cloud. *Lunar Planet. Sci. XLII*, Abstract #1602. Lunar and Planetary Institute, Houston.
- Yang L., Ciesla F. J., Alexander C. M. O'D. (2013) The D/H ratio of water in the solar nebula during its formation and evolution. *Icarus*, *226*, 256–267.

- Yin Q. Z., Amelin Y., and Jacobsen B. (2009) Project milestones: Testing consistent chronologies between extinct  $^{53}\text{Mn}$ - $^{53}\text{Cr}$  and extant U-Pb systematics in the early solar system. *Lunar Planet. Sci. XL*, Abstract #2060. Lunar and Planetary Institute, Houston.
- Youdin A. N. and Shu F. (2002) Planetesimal formation by gravitational instability. *Astrophys. J.*, 580, 494–505.
- Young E. D. (2001) The hydrology of carbonaceous chondrite parent bodies and the evolution of planet progenitors. *Philos. Trans. R. Soc. London, Ser. A*, 359, 2095–2110.
- Young E. D., Ash R. D., England P., and Rumble D. III (1999) Fluid flow in chondritic parent bodies: Deciphering the compositions of planetesimals. *Science*, 286, 1331–1335.
- Yurimoto H. and Kuramoto K. (2004) Molecular cloud origin for the oxygen-isotope heterogeneity in the solar system. *Science*, 305, 1763–1766.
- Zolensky M. E., Bourcier W. L., and Gooding J. L. (1989) Aqueous alteration on the hydrous asteroids — Results of EQ3/6 computer simulations. *Icarus*, 78, 411–425.
- Zolensky M. E., Mittlefehldt D. W., Lipschutz M. E., Wang M.-S., Clayton R. N., Mayeda T. K., Grady M. M., Pillinger C., and Barber D. (1997) CM chondrites exhibit the complete petrologic range from type 2 to 1. *Geochim. Cosmochim. Acta*, 61, 5099–5115.
- Zolensky M. E., Krot A. N., and Benedix G. (2008) Record of low-temperature alteration in asteroids. In *Oxygen in the Solar System* (G. J. MacPherson, ed.), pp. 429–463. Reviews in Mineralogy, Vol. 68, Mineralogical Society of America, Washington.
- Zolensky M. E., Mikouchi T., Fries M., et al. (2014) Mineralogy and petrography of C asteroid regolith: The Sutter's Mill CM meteorite. *Meteoritics & Planet. Sci.*, 49, 1997–2016.
- Zolotov M. Yu. (2012) Aqueous fluid composition in CI chondritic materials: Chemical equilibrium assessments in closed systems. *Icarus*, 220, 713–729.
- Zolotov M. Y. and Mironenko M. V. (2008) Aqueous alteration of CM2 chondrites evaluated with kinetic models. *Meteoritics & Planet. Sci., Suppl.*, 33, A177.
- Zolotov M. Y., Mironenko M. V., and Shock E. L. (2006) Thermodynamic constraints on fayalite formation on parent bodies of chondrites. *Meteoritics & Planet. Sci.*, 41, 1775–1796.

# Global-Scale Impacts

Erik Asphaug

*Arizona State University*

Gareth Collins

*Imperial College, London*

Martin Jutzi

*University of Bern*

---

Global-scale impacts modify the physical or thermal state of a substantial fraction of a target asteroid. Specific effects include accretion, family formation, reshaping, mixing and layering, shock and frictional heating, fragmentation, material compaction, dilatation, stripping of mantle and crust, and seismic degradation. Deciphering the complicated record of global-scale impacts in asteroids and meteorites will lead us to understand the original planet-forming process and its resultant populations, and their evolution in time as collisions became faster and fewer. We provide a brief overview of these ideas, and an introduction to models.

## 1. INTRODUCTION

The most important parameter governing the global extent of an impact is the mass ratio of the projectile to the target,  $\gamma = M_2/M_1$ . In the case of a cratering event this ratio is small, and there is a well-defined geometric locus. Crater scaling then becomes a powerful tool (e.g., *Housen et al.*, 1983) that allows simple analytical approaches to be applied to determine whether an impact “goes global”—for instance, whether the surface is shaken everywhere to the escape velocity, or whether the target is shattered or melted.

At the other extreme, as  $M_2 \rightarrow M_1$ , there is no impact locus, so the mechanics and dynamics are complex (*Asphaug*, 2010). Crater scaling does not apply, even though the impact physics are fundamentally the same. By definition, these similar-sized collisions (SSCs) are global events. Unlike most cratering impacts, they involve substantial downrange or even escaping motion of the projectile  $M_2$ , depending on the impact velocity  $v_{\text{imp}}$  and the impact angle  $\theta$ .

Impact velocity is the next most important parameter, because of its dynamical and thermodynamical consequences. In order for an asteroid to be eroded in a cratering impact, for example, one projectile mass of material must be ejected to  $v_{\text{ej}} > v_{\text{esc}}$ , where  $v_{\text{ej}}$  is the ejecta velocity and  $v_{\text{esc}}$  is the escape velocity described below. The ejection velocity in turn scales with  $v_{\text{imp}}$ , so that a cratering projectile has to strike at a few times  $v_{\text{esc}}$  in a competent rocky target if it is to cause net escape of material, and an order of magnitude faster to cause net mass loss from a highly porous target

(*Housen and Holsapple*, 2011). This implies a very different impact evolution depending on porosity.

Impact velocity also represents a specific collisional kinetic energy  $Q = \frac{1}{2}(M_1 v_1^2 + M_2 v_2^2)/(M_1 + M_2)$  where  $v_1 < v_2$  are the velocities of the target and projectile in the center of mass frame. If the energy is sufficiently intense,  $Q > Q_S^*$ , then shattering occurs, breaking the solid bonds of the asteroid into pieces no larger than  $M_1/2$ . If gravitationally bound (ejected at  $< v_{\text{esc}}$ ) then shattering produces a rubble pile as defined below; otherwise, if fragments are escaping, the result is a collection of new asteroids. This is the classic example of hitting something so hard that you break it. Catastrophic disruption requires a collision of greater energy  $Q > Q_D^* > Q_S^*$ , to break any solid bonds and also to overcome internal friction (see below), and to exceed the gravitational binding energy, thereby dispersing the fragments to  $v_{\text{ej}} > v_{\text{esc}}$ . For massive bodies, intermediate energy collisions  $Q_D^* > Q > Q_S^*$  can lead to complicated (altered and reassembled) geologies.

These are idealizations because impact energy is not deposited uniformly inside a target. Much of this chapter is to study how this deposition occurs, and what it does. The impact angle  $\theta$  is especially important in this regard, especially for similar colliding masses, since only a limited amount of angular momentum can be accreted in a collision, and because objects of comparable diameter tend to suffer grazing collisions more often than not. And finally, two asteroids of masses  $M_1$  and  $M_2$  cannot be thought of as colliding in isolation, even if one ignores all the other asteroids and planets: Both bodies orbit the Sun and their

fragments continue orbiting on intersecting orbits, so their interaction extends long after the original collision.

### 1.1. Mass Effects

Generally speaking, impacts slower than  $v_{\text{esc}}$  cause accretion, and impacts faster than  $v_{\text{esc}}$  cause erosion, with the specific boundary depending on the impact angle  $\theta$ . This is effectively the case for cratering impacts and for similar-sized collisions, so we consider the governing parameter  $v_{\text{imp}}/v_{\text{esc}}$ . But  $v_{\text{imp}}$  can be no slower than  $v_{\text{esc}}$ , the impact velocity of two spheres falling from infinity with initial relative velocity  $v_{\text{rel}} = 0$

$$v_{\text{esc}} = \sqrt{2G(M_1 + M_2)/(R_1 + R_2)} \quad (1)$$

where  $R_1$  and  $R_2$  are the corresponding radii. As a rule of thumb,  $v_{\text{esc}} = R_{\text{km}}/t$ , in meters per second, where  $R_{\text{km}}$  is the radius of a spherical asteroid in kilometers; this holds exactly true for bulk density  $\rho = 1.9 \text{ g cm}^{-3}$ .

For a two-body encounter in the absence of gas or other drag effects, conservation of energy implies that

$$v_{\text{imp}} = \sqrt{v_{\text{rel}}^2 + v_{\text{esc}}^2} \quad (2)$$

Concerning accretion and erosion, whether by cratering or SSC, it is consequently this relative velocity above  $v_{\text{esc}}$  that matters most

$$\phi = v_{\text{rel}}/v_{\text{esc}} \quad (3)$$

The magnitude of  $\phi$  defines the dynamical “kick” that drives material out of the gravitational potential of the target.

Dynamical studies of planet formation have tended to ignore the substantial differences between a collision (two objects’ radii intersecting) and an accretion. A collision at  $v = v_{\text{imp}}$  at a separation distance  $r < R_1 + R_2$  at contact angle  $\theta$  is a geophysically and astrophysically complicated event, so that even the slowest merger ( $v_{\text{imp}} \sim v_{\text{esc}}, \phi \sim 0$ ) is an imperfect accretion. Yet most N-body simulations to date implicitly assume that whenever two planetary bodies touch each other, they become a single object orbiting the Sun. This is generally an invalid assumption (Agnor *et al.*, 1999).

Accretion efficiency  $\xi$  is defined as the fraction of the projectile mass  $M_2$  acquired by the target  $M_1$ . Perfect accretion  $\xi = 1$  makes a final merged body  $M_F = M_1 + M_2$ , so in general

$$\xi = (M_F - M_1)/M_2 \quad (4)$$

Accretion efficiency is always a few percent less than 1, even in  $v_{\text{rel}} = 0$  collisions, because mergers release a substantial fraction of the gravitational binding energy compared to two contacting spheres. Mass is further lost by angular momentum redistribution, flung out by the spiraling, merging protoplanets. Mass loss in otherwise “perfect mergers” can lead to satellite formation (e.g., Canup, 2004) and percentage

losses of escaping remnants (Asphaug and Reufer, 2013).

In cratering collisions,  $\xi(\phi)$  is a relatively smooth function, becoming negative for  $\phi \sim 1$ , except in the case for highly porous bodies, where  $\xi$  may remain positive (accretionary) to velocities tens of  $v_{\text{esc}}$  in a process of compaction cratering (Housen and Holsapple, 2011). Similar-sized collisions ( $\gamma \geq 0.03$ ) are substantially different because of geometrical effects, and this leads to generally low accretion efficiency. For SSCs, accretion efficiency is a sensitive function of velocity  $\xi(\phi)$  that starts near  $\xi(\phi) \leq 1$ . At moderately off-axis angles (only  $\sim 15^\circ$ – $30^\circ$ ) SSCs are grazing, in the sense that most of the colliding material does not physically intersect. The colliding bodies can “bounce,” with outcomes very sensitive to  $\phi$  and  $\theta$ .

As reviewed by Asphaug (2010), there is an abrupt transition in accretion efficiency from  $\xi(0) \sim 1$ , to  $\xi \approx 0$  (little mass change to the target, but huge transformation to the impactor) over the velocity range  $1.2 \leq \phi \leq 2$ – $3$ . We call these “hit-and-run” collisions (see the chapter by Scott *et al.* in this volume). And finally, erosion and disruption ( $\xi < 0$ ) occur over the range  $\phi \geq 2$ – $3$ . The exact boundaries of these curves depend on the composition and degree of differentiation of the colliding bodies, as explored in further detail by Stewart and Leinhardt (2012).

One of the major unknowns of planet formation is the kind of collision that dominated the accretion of mass by asteroid parent bodies. If it was accretion of myriad much smaller objects (cratering,  $\gamma \rightarrow 0$ ), then effective compaction might facilitate accretion, with highly porous planetesimals acting as “sponges” to sweep up much smaller objects. Truly primitive bodies would contain a record of compaction events (e.g., Belton *et al.*, 2007). If SSCs dominated ( $\gamma \rightarrow 1$ ), then small planetesimals would be unlikely to accrete further once random velocities were excited to faster than  $v_{\text{esc}}$ . Turbulent stirring of the nebula would lead to their disruption (Benz, 2000), one of several “size barriers” to primary accretion (Weidenschilling and Cuzzi, 2006).

One possible solution is to bypass these bottlenecks during the gas phase, for example, by streaming instabilities followed by pebble accretion as described in the chapter by Johansen *et al.* in this volume. Such models indicate the rapid formation of  $\sim 100$ – $1000$ -km-diameter asteroid progenitors in the presence of the nebula. These bodies would be well sorted by mass, so that their further collisional interaction would be dominated by SSCs. Another implication is that many of these bodies (those containing chondritic abundances of active radiogenic  $^{26}\text{Al}$ ) would likely be melted by radionuclide decay during the timeframe of their collisional interaction. The surviving original bodies would include a preponderance of hit-and-run relics according to Asphaug and Reufer (2014), by the attrition of a population that is mostly accreted into growing planets.

### 1.2. Thermodynamical Effects

Impact heating is also sensitively dependent on velocity. In addition to radiogenic heating, shock and frictional heat-

ing were common throughout early solar system history, as recorded in meteorites, with shocks being particularly (but not uniquely) effective at dissipating impact kinetic energy  $Q$  into heat (Ahrens and O'Keefe, 1994; Melosh, 1989).

Shocks are produced when the impact velocity exceeds the sound speed,  $v_{\text{imp}} \geq c_s$ . Essentially, impact momentum is added to the medium faster than it can be transported away as a pressure wave, leading to a discontinuous “jump” that causes irreversible thermodynamical effects (heating, compression, momentum deposition). Because impacts are generally faster than  $v_{\text{esc}}$ , this means that planet-scale collisions always involve shocks ( $v_{\text{esc}}$  of tens of kilometers per second), whereas asteroid-scale impacts must be stirred up externally to high random velocity to produce shocks.

Random velocities in the main belt are excited by gravitational interactions with the terrestrial and giant planets, to velocities that are typically  $v_{\text{rel}} \sim 2\text{--}8 \text{ km s}^{-1}$ , exceeding  $v_{\text{esc}}$  by orders of magnitude. Although we have no direct measurements of asteroid sound speed, an upper limit is probably that of the lunar mantle,  $c_s \sim 7\text{--}8 \text{ km s}^{-1}$ . A more representative sound speed may be that measured by Flynn (2005) and others for competent fragments of chondrite meteorites,  $c_s \sim 1\text{--}3 \text{ km s}^{-1}$ . Thus a great deal of shock processing occurs on small bodies in the evolving and modern solar system. But unlike planet-scale collisions that retain their shock-melted materials, the shocked ejecta in asteroid-asteroid collisions are generally lost as interplanetary dust.

The sound speed is much slower in rubble piles and near-surface regoliths, perhaps only on the order of  $\sim 100 \text{ m s}^{-1}$ , so in this crushable zone it is possible to form melted materials that could be retained in place, or at least, be ejected at  $< v_{\text{esc}}$ . Housen and Holsapple (2011) find that crater ejection velocities in highly porous silicate material can be more than an order of magnitude slower than crater ejection velocities in competent materials. This means that in addition to being more prone to shock melting and compaction melting, the melted material may be less prone to escaping on highly porous bodies.

### 1.3. Velocity Relationships

Impact velocity relative to escape velocity,  $v_{\text{imp}}/v_{\text{esc}}$ , governs accretion efficiency and its mass effects, while impact velocity relative to sound speed,  $v_{\text{imp}}/c_s$ , governs the formation of shocks and its thermodynamical effects. Accordingly, there are four quadrants of global-scale impacts, as summarized in Fig. 1.

Shock-forming impacts are to the right of the diagonal band, represented here by a wide possible range  $0.5 \text{ km s}^{-1} < v_{\text{imp}} < 8 \text{ km s}^{-1}$ . Mass loss and catastrophic disruption ( $\xi < 0$ ) occur above the horizontal band, broadly the range  $v_{\text{imp}} \geq 2$  to  $20 v_{\text{esc}}$  (competent or highly porous target; cratering or SSC). Asteroid family formation, reviewed in the chapter by Michel et al. in this volume, occupies the upper right quadrant, while parent-body accretion occupies the lower left.

The transitions across quadrants (gray shaded zones) are just as important as the end-member scenarios, perhaps

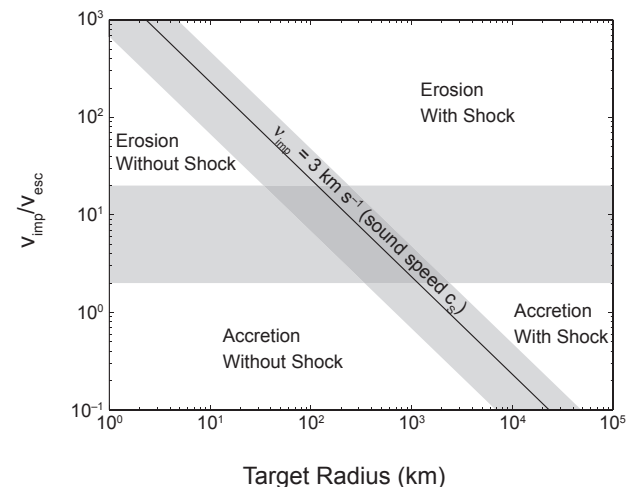


**Fig. 1.** Global-scale impacts span four quadrants in a graph of impact velocity normalized to target escape velocity,  $v_{\text{imp}}/v_{\text{esc}}$ , vs. target radius. The horizontal band marks the approximate transition from accretionary to erosive/disruptive impacts, a few times  $v_{\text{esc}}$ . The diagonal band defines impact speeds comparable to the sound speeds for a wide range of solar-system materials. Planetesimal-scale accretion (bottom left) does not involve shocks, while planet-scale accretion (bottom right) does. On small bodies, mass loss and disruption do not require shocks. Large  $v_{\text{imp}}/v_{\text{esc}}$  requires gravitational stirring by larger bodies, so that events to the right of the graph tend to be damped (no larger bodies; gravitational drag by smaller bodies), while events to the left tend to be excited, e.g., the modern main belt.

more so. Consider the horizontal band: Most collisions will have  $v_{\text{imp}}$  equal to a few times  $v_{\text{esc}}$  in a self-stirred population, because the random velocities grow to be proportional to the escape velocities of the largest members (e.g., Safronov, 1972).

As for the sound speed transition, it appears to be coincidence that the range of  $c_s$  for asteroid materials overlaps the expected collisional velocities. Random velocities are slower in the outer solar system,  $\sim 1\text{--}2 \text{ km s}^{-1}$ , but so is the sound speed of icy bodies. So in both regions, collisions are expected to occur on either side of the “shock zone,” at least in the present solar system.

During parent-body accretion, most events were at or near this line (low velocities) and toward the left (small sizes). As planets grew and stirred things up, events stayed near the line at large sizes, but rose to high above the line for small sizes, grinding down that population into today's generation of asteroids.

In the first 10–100 m.y. after dissipation of the dust and gas in the solar nebula, when collision probabilities were substantially higher than they are today, the average collision speed in the asteroid belt grew from  $< 1 \text{ km s}^{-1}$  to several kilometers per second. Hence, impacts straddled the shock transition zone when impacts were most influential in defining asteroid parent-body geology.

#### 1.4. Overlapping Timescales and Linked Models

Global-scale impacts involve a diverse range of overlapping processes and timescales, making it important to understand and utilize linked models. Because asteroidal targets vary from tens of meters to hundreds of kilometers in diameter, global-scale impacts can take place in less than a second, on the ballistic timescale

$$\tau_b \sim 2r/v_{imp} \quad (5)$$

where  $r$  is the radius of the projectile and  $v_{imp}$  is the impact velocity; or in seconds to minutes, on the stress propagation timescale

$$\tau_s \sim 2R/c \quad (6)$$

where  $2R$  is the target diameter and  $c$  is the sound speed (or shock speed); or in hours to days, on the gravity timescale

$$\tau_g \sim \sqrt{3\pi/G\rho} \quad (7)$$

where  $G$  is the gravitational constant and  $\rho$  is the asteroid bulk density.

In the end-member regimes (e.g., self-gravitating planets without strength, or monolithic rocks without gravity) key variables can be eliminated and simple models or scaling predictions can be viable. Similarly, if one can bypass a complex phase or timescale of a collision using an effective approximation, then a simpler analysis can be available — for instance, skipping the self-gravity phase by applying an escape-energy approximation, or replacing the hypervelocity impact calculation with a “z-model” velocity field derived from impact-cratering experiments (cf. Melosh, 1989). It is an open question whether these and other simplifications are well justified for modeling global-scale asteroid impacts, when the balance of force is so subtle.

Another approach is to use end-to-end linked numerical models. For asteroids up to tens of kilometers in diameter,  $\tau_b$ ,  $\tau_s$ ,  $\tau_g$  are distinct, making it possible to consider three separable regimes of impact, using one calculation as input for the next. This of course makes the assumption that not a lot of physics happen in the intermediate regimes, which as we shall see is not always the case.

Consider the example of forming an ~10-km crater on an ~20-km-diameter asteroid [e.g., Stickney on the martian satellite Phobos, or Shoemaker on asteroid (433) Eros]. Here  $\tau_b \sim 10^{-2}$  s,  $\tau_s$  is seconds, and  $\tau_g$  is hours. An impact hydrocode (Anderson, 1987) is a versatile simulation tool (see below and the chapter by Jutzi et al. in this volume) that can be run for several  $\tau_b$  to compute the shock pressures, energies, and temperatures and the initial momentum distribution emplaced by the projectile. The accuracy of this step is limited by our understanding of asteroid target geology, which in even the best codes is represented simplistically (equations of state and crush models). For example, rate-dependent effects are not typically included in hydrocodes.

After the impact-coupling phase is complete, shock pressures and stress states can be evolved using a wave propagation code (e.g., Richardson et al., 2004; Blitz et al., 2009), or using the hydrocode itself within the limitations and caveats discussed below. Hydrocodes are not generally designed for seismic-wave propagation, although as discussed further below, the most modern codes are beginning to do a good job on the equation of state (EOS) aspects of the problem, and the fracture mechanics parts of the problem, and also the granular physics, which is intimately connected to the acoustics and flow of disrupted material. Simpler approaches are also feasible, and sometimes recommended, especially those that are anchored in laboratory and field data. A power law of stress attenuation with distance (Cooper and Sauer, 1977) can be applied (e.g., Ryan and Melosh, 1998; Asphaug, 2008), as well as direct comparison with nuclear explosions (Asphaug and Melosh, 1993).

If  $\tau_g$  is orders of magnitude longer than the other timescales, then the earlier phases of a collision, establishing the pressure evolution, can be calculated with no gravity at all, or with gravity expressed as an overburden term and constant gravity. The largest-scale events conclude with a gravitational and rotational-mechanical evolution over several  $\tau_g$ , as modeled by Michel et al. (2003), Durda et al. (2004), Leinhardt and Stewart (2012), and others; see the chapter by Michel et al. in this volume.

While gravity can be ignored below some small size, it is not clear what size this is — gravity being a long-range force and strength, friction, and cohesion being short-range forces. The escape velocity of a 100-m-diameter rubble pile is a few centimeters per second, so massive debris evolution on a small asteroid can perhaps be astrophysically similar to much-larger-scale events.

On the other hand, the central pressure inside a 100-m asteroid is only ~1 Pa (10 dyn cm<sup>-2</sup>), and while not zero, it is 100× smaller than the cohesions measured for the upper lunar regolith. That is, granular cohesion may well dominate over gravity, inside of asteroids up to kilometers in diameter, as discussed further in the chapter by Scheeres et al. in this volume.

To make matters worse, granular materials can be cohesive in the absence of internal vibrations, and fluidized by the acoustic energy of a global-scale collision, respond like a mobilized global landslide (e.g., Collins and Melosh, 2003). Anyone who has played with sand is familiar with the solid liquid behavior of granular media. Models are just barely catching up to our awareness of the complex physics that can be at play in a global-scale asteroid collision.

#### 1.5. Small Giant Impacts

For large planetary collisions a separation of timescales is generally not possible. In the Moon-forming giant impact,  $\tau_b$ ,  $\tau_s$ ,  $\tau_g$  are all ~10<sup>3</sup> s, so all processes must be calculated simultaneously. Fortunately, giant-impact computations are greatly simplified by two facts: Planets can be treated as idealized fluids on these timescales, and the computational

timestep  $dt$  can be long, requiring fewer hydrocode iterations, as described in section 2.

For numerical accuracy,  $dt$  must be substantially shorter than the wave-crossing-timescale  $dx/c_s$ , where  $dx$  is the spatial resolution and  $c_s$  is the sound speed; or in the case of shock-forming impacts,  $dx/v_{imp}$ . Otherwise, information travels faster than the physical propagation velocity in a computation. In medium-resolution simulations of the Moon-forming giant impact  $dt \geq 10$  s, which is large enough that an all-in-one three-dimensional hydrocode approach is feasible for the phases leading to the capture of protolunar materials.

Although we do not consider giant impacts in this chapter, we do consider what might be called “small giant impacts,” i.e., planetesimal-scale SSCs at speeds proportional to the bodies’ mutual escape velocity. Like giant impacts, these straddle the erosion-accretion transition in Fig. 1. This is thought to be the regime where the parent bodies of asteroids were accreted (see the chapter by Johansen et al. in this volume). Modeling small giant impacts is most challenging computationally, because of the short timestep combined with complex physics. Consider a three-dimensional impact simulation of 10-km planetesimals colliding;  $dt < 0.1$  s so that it requires  $\geq 100\times$  more computational effort than a comparable Moon-forming calculation. For well-subsonic collisions the timestep can be sped up by artificially softening the EOS, thus reducing the sound speed (cf. Asphaug et al., 2011) while not greatly changing the response so long as the collision remains subsonic.

Although similar in scale to giant impacts, there is usually no shock when the colliding bodies are smaller than about 1000 km in diameter (Asphaug and Reufer, 2014). This makes the physics quite different, although there is still substantial heating, shear alteration, and melting, all ultimately compensating for the loss of gravitational binding energy. The slowest possible collisions between  $\sim 100$ -km planetesimals occur at  $\sim 100$  m s $^{-1}$ , like two high-speed trains colliding, so friction and compaction do a great amount of work. It is a cutting-edge problem in computational modeling, one that cannot easily be remedied using linked models on separate timescales, and therefore is in need of experimental work on representative bodies.

## 1.6. Rubble Piles

The consequences of accretionary collisions may thus dominate the geologic records of the largest asteroids and primary planetesimals. In small asteroids, on the other hand, this record has probably been beaten down. Because their relative collisional energies are more disruptive, compared to their binding energies (larger  $Q$ , stirred up by planets), they are second generational or further, as represented by asteroid family formation (see the chapter by Michel et al. in this volume).

Today most asteroid mutual collisions are erosive or disruptive,  $v_{rel} \gg v_{esc}$ . Impacts produce craters, sometimes with hemispheric morphologies (megacraters). If cratering “goes global,” as discussed below, the result is global-scale resur-

facing of the asteroid, by ejecta deposition and by shaking down of preexisting topography. And of course, impacts contribute great energy from heating, melting, fragmentation, and other forms of material transformation.

Strength is partly a material property, and partly a property of the scale and the dynamics of the collision (Holsapple, 2009). Size- and rate-dependent dynamic strength effects (Grady and Kipp, 1980; Melosh et al., 1992; Housen and Holsapple, 1999) make large bodies much easier to destroy, mechanically, than smaller ones. However, gravitationally large objects are harder to destroy. This means that it is much easier to create a rubble pile, breaking rocks to pieces, than to destroy it, sending half of its mass onto escaping trajectories (reviewed in Davis et al., 2002). In the 1990s it was demonstrated in computer simulations (e.g., Benz and Asphaug, 1999) that asteroids larger than a few hundred meters in diameter are likely to be pulverized completely, several times over, before they are likely to be destroyed. But as noted by Davison et al. (2013), this does not mean that a given subcatastrophic event is inevitable — just that comminution is much more likely than disruption,  $Q_S^* \ll Q_D^*$ .

According to this analysis, asteroids larger than a few hundred meters in a collisionally evolved population become rubble piles. How rapidly or completely they do so is an open question. It does not mean that asteroids larger than 100 m can be treated as liquid bodies in simulations, or that smaller asteroids are necessarily hard rocks (Holsapple, 2009). Indeed, it has become obvious in recent years that there is a broad transition regime, rather than a transition size, that spans perhaps  $\sim 0.1$ –100 km diameter, where mechanical, gravitational, and impact momentum stresses need to be calculated simultaneously altogether. This includes all but the very smallest asteroids.

## 1.7. Giant Craters

Giant craters are principal probes of interior geology. They excavate deep inside the asteroid and produce reverberating stresses that cause global surface modification, massive faulting, and overturn. Asteroids with giant craters (most of the  $\sim 10$ -km ones evidently) must be “strong” in some sense, in order to survive the megacratering events themselves. On (253) Mathilde, several hemisphere-sized simple craters were excavated [or crushed (Housen and Holsapple, 1999)] without destroying the preexisting craters, not even their steep walls and rim structures (so far as we can tell at flyby resolution; Fig. 2). For an unconsolidated material one might expect sustained reverberations that would trigger an asteroid to relax into a spheroid, but Mathilde did not; this large asteroid retained some of the most spectacular topography in the solar system.

To sustain this kind of dramatic topography, one might expect that a solid target structure is required. But this presents a paradox: Breaking holes this large into a competent asteroid will catastrophically disrupt the asteroid, according to strength-scaling rules and hydrocode models with strength (Melosh et al., 1992). So we get backed into a corner, in that



**Fig. 2.** NASA's NEAR Shoemaker mission obtained flyby images of the 50-km-diameter asteroid (253) Mathilde (Veverka *et al.*, 2000). The image at left was obtained as the spacecraft approached in the direction of the Sun; the image on the right is from greater distance at much lower phase angle (43°). Mathilde is a great puzzle for the study of global-scale impacts: Each giant crater should have reset the asteroid's global shape, according to simulations. Instead, each crater seems to have formed in isolation, without degrading the preexisting craters. If coming in at random angles, these successive global scale impacts would have spun Mathilde into fast rotation, if even a fraction of the incoming momentum was accreted (Asphaug *et al.*, 2002). But the asteroid is one of the slowest-rotating bodies in the solar system,  $P_{\text{rot}} = 418$  h.

these large craters cannot have formed in the strength regime. This does not automatically mean they are gravity-regime craters, as we shall see.

Of known asteroid craters, only Rheasilvia and Veneneia, the two largest on (4) Vesta (Schenk *et al.*, 2012; see also the chapter by Russell *et al.* in this volume) show clear evidence for gravitational rebound and central peak formation. These two giant basins overlap in Vesta's southern hemisphere, the ~500-km-diameter Rheasilvia basin overprinting the earlier ~400-km Veneneia, offset by some 40°, on an asteroid only somewhat larger (~530 km average diameter). Like Mathilde, Vesta provides an example of the interaction of younger and older giant craters overlapping, but in this case their interaction is notable. Unlike Mathilde, it is easy to recognize the sequence of events, in part because of the much more detailed global imaging, but also due to the fundamentally different cratering mechanics on a body 10× larger.

A number of past (Asphaug, 1997) and recent (Jutzi and Asphaug, 2011; Ivanov and Melosh, 2013; Bowling *et al.*, 2013; Stickle *et al.*, 2015) numerical impact modeling studies of Vesta have investigated the formation of its megacraters and their resulting global effects, and the potential for producing ejecta [the V-type asteroids (Binzel and Xu, 1993)]. Modeling two overlapping megacraters is challenging, and scientifically interesting, because of Vesta's nonspherical shape and gravity potential, rapid rotation, and differentiated structure. In addition, a three-dimensional approach is required, since the problem is strongly non-axisymmetric.

Jutzi *et al.* (2013) studied the sequential formation of Veneneia followed by Rheasilvia using a three-dimensional smooth particle hydrodynamics (SPH) impact code described below. The goal of these simulations was to start with a non-rotating differentiated  $d = 550$ -km sphere, impact it once (to form Veneneia), then place the resulting megacrater on axis, spin it to period  $P_{\text{vesta}} \sim 5.3$  h, and finally impact the rotating cratered body 40° off-axis to end up with the observed topography of Vesta. Thus Vesta's topography is created by a complex process of ejection and deposition, requiring a realistic treatment of the ejecta gravitational dynamics and the post-impact rheological response. A pressure-dependent strength model, a tensile fracture model, a friction model, and self-gravity were included. Finally, to "freeze in" the central peak structures, a block-model approximation of acoustic fluidization was used. The result (Fig. 3) is in good agreement with the shape and topography of Vesta (see the chapter by Russell *et al.* in this volume).

Understanding the formation of Vesta's giant craters and the provenance and specific distribution of ejecta is key to understanding the observed properties of Vesta, such as the topography and the surface mineralogy. The proper interpretation of surface materials [and exhumed V-type asteroids and howard-eucrite-diogenite (HED)-type meteorites] lead to important constraints on models of internal structure (McSween *et al.*, 2013; Clenet *et al.*, 2014). Jutzi *et al.* (2013) found that a significant fraction of the rocks exposed in the south pole region should come from >50 km deep, and up to ~60–100 km deep in the central mound of Rheasilvia and in the region where the two basins overlap. Also, according to the model, a significant fraction of the material that escapes Vesta during the more recent impact, which would be the dominant source for HEDs, comes from greater than 40 km deep (Clenet *et al.*, 2014). This is puzzling because olivine-rich mantle rock has not been detected in the Veneneia/Rheasilvia region on Vesta, and there is also a lack of mantle samples among the HED meteorites.

The rapid rotation of Vesta and other asteroids can lead to curious megacratering results. In the course of reproducing Rheasilvia on an already-spinning Vesta, Jutzi and Asphaug (2011) found that ejecta from megacraters would be draped back on the asteroid in complex overlapping lobes, falling back in the rotating frame. Since for Vesta the crater rebound timescale is comparable to the rotation timescale, the Rossby number of the flow  $R_o \sim 1$ , and the result is actually "Coriolis topography" as shown in Fig. 4 — i.e., crater-rebound morphologies that form a spiral pattern relative to the impact locus. This provides a potential window to further explore megacratering mechanics, especially in materials not covered beneath impact melt (Schenk *et al.*, 2012).

### 1.8. Seismic Erasure

There is a strong correlation between the normalized diameter of the largest undegraded crater  $D_{\max}$  seen on an asteroid, and the diameter  $D$  of the asteroid.  $D_{\max}$  is well defined for most imaged asteroids, and for a number of

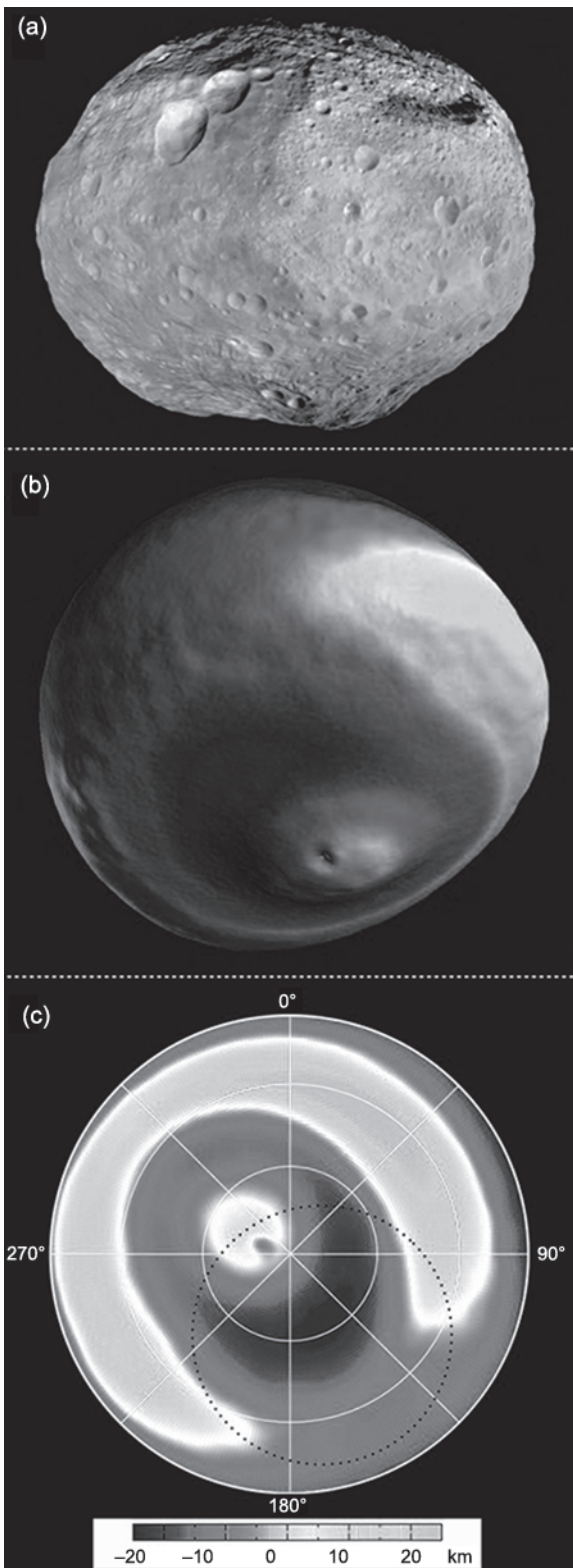


**Fig. 3.** (a) Asteroid Vesta as seen by Dawn. Credit: NASA/JPL/UCLA/MPS/DLR/IDA. (b) Final result of the simulation of two large impacts in the southern hemisphere. (c) Lambert azimuthal projection (equal area) of the southern hemisphere in the model. Shading indicates the elevation (in km) with respect to a reference ellipsoid; for color see Jutzi et al. (2013).

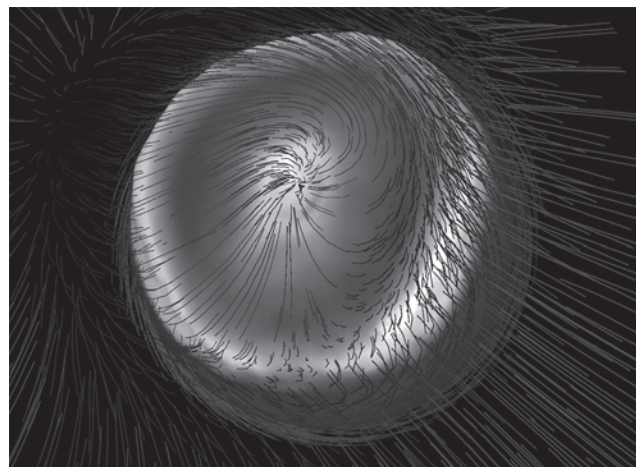


**Fig. 4.** Simulating the opening and collapse of the Rheasilvia complex crater on asteroid Vesta; from Jutzi et al. (2013). The rapid rotation of the asteroid leads to strong Coriolis forces in the rebounding ejecta, as indicated by the vectors and in agreement with the patterns on the crater floor. Outward vectors plot the distant and escaping ejecta.

the best-resolved radar-imaged asteroids (see the chapter by Benner et al. in this volume). Define  $\chi = D_{\max}/D$ . The smallest asteroid seen up close in high detail, Itokawa (mean diameter  $D = 330$  m) has a largest crater  $D_{\max} \sim 30$  m, i.e.,  $\chi \sim 0.1$ . The crater is not obvious to see. For (253) Mathilde ( $D \sim 53$  km),  $\chi \sim 0.6$  — and is reasonably well determined even from medium-resolution images. For (433) Eros ( $D \sim 20$  km),  $\chi \sim 0.4$ . The trend of  $\chi$  varying inversely with  $D$  appears to generally hold (Asphaug, 2008). Either global-spanning craters do not form on small asteroids, or they are unable to retain them.

Shoemaker Crater on Eros shows a different kind of evidence (and so perhaps would Mathilde if imaged at good resolution). The formation of this 7-km recent basin appears to have shaken down regional preexisting ~100-m-scale topography, both next to and opposite the crater (Thomas and Robinson, 2005). The seismic erasure may have been impulsive (as seems to be the evidence), taking seconds to minutes as the initial pulse radiated from the impact, or else diffusive, as acoustic energy remained trapped inside the asteroid for many  $\tau_s$ .

If seismic erasure is efficient, then why has wholesale seismic degradation not shaken down the early giant craters of Mathilde? One approach (Asphaug, 2008) is to define a self-consistent critical crater diameter  $D_{\text{crit}}$  for which the above is true, and to show that  $D_{\text{crit}}$  increases with asteroid diameter  $D$ . Craters larger than  $D_{\text{crit}}$  shake down all preexisting topography smaller than  $D_{\text{crit}}$ . The giant crater that is forming continues its excavation long after the seismic impulse attenuates, at least in this scenario, because the crater-formation timescale in the gravity regime is many times  $\tau_s$ . A crater forms as a solitary feature if it has shaken down preexisting craters of its size. Craters smaller than  $D_{\text{crit}}$

do not cause global resurfacing at their own scale. Craters larger than  $D_{\text{crit}}$  stand out as solitary undegraded craters. In this framework one can interpret that  $D_{\text{crit}}$  has never been achieved on Mathilde (there is no one solitary crater), and that  $D_{\text{crit}}$  would require something larger than Shoemaker Crater to globally erase the craters of that scale on Eros.

A normalized critical crater diameter  $\chi_{\text{crit}} = D_{\text{crit}}/D$  can be solved as a function of asteroid diameter and target properties [gravity, density, and scaling constants (cf. *Housen et al.*, 1983)]. Assume that the seismic impulse created by an impacting projectile decays in amplitude with distance  $r$  from the impact. This impulse is required to shake down topography to a scale equal to the diameter of the crater that is forming,  $D_{\text{crit}}$ , out to a maximum distance  $r = D$ . If seismic decay with distance takes the form of a simple power law (e.g., *Cooper and Sauer*, 1977), then particle velocity  $v_p \propto r^{-\beta}$ . Crater diameter  $D_{\text{crit}}$  is then calculated (*Asphaug*, 2008) according to gravity-regime crater scaling, and is substituted into the above, thus solving for  $\chi_{\text{crit}}$ .

For physically reasonable target parameters,  $\chi_{\text{crit}}$  is proportional to  $D$ , accounting for the trend in crater sizes. On a case by case basis, matching the largest undegraded craters observed on spacecraft or radar-imaged asteroids to their theoretical maximum does a good job at fitting the data if one assumes a seismic attenuation with distance  $\beta \sim 1.2\text{--}1.3$  for most asteroids. While a power-law attenuation is only an approximation to seismic dissipation, this value is comparable to seismic attenuations of  $\sim 0.1\text{--}10\text{-m s}^{-1}$  particle velocities in unconsolidated terrestrial materials.

For Mathilde-sized asteroids, the predicted  $D_{\text{crit}}$  is larger than the asteroid, consistent with the handful of non-interacting craters greater than half the asteroid diameter. For (25143) Itokawa, assuming the same seismic attenuation as Mathilde, it turns out that  $\chi_{\text{crit}} = 0.1$  — the small crater seen on Itokawa would have resurfaced the asteroid down to that scale. It is an inexpensive if approximate kind of seismology: An Itokawa-sized asteroid exhibiting larger craters would have substantially greater seismic attenuation. The different behavior is in this case not because of material differences, but because of the differences in scale: Itokawa next to Mathilde would be analogous to a refrigerator next to the Empire State Building.

## 2. NUMERICAL MODELING OF GLOBAL IMPACTS

When extrapolations lead to curious results, one turns to direct experimentation; when that is unavailable, one resorts to the brute force of computer simulations. These techniques are featured in the chapter by Jutzi et al. in this volume, and their application to global-scale impacts is summarized here. These techniques include hydrocodes (reviewed in *Anderson et al.*, 1987), particle codes (e.g., *Richardson et al.*, 2002), and linked models. These codes rely on models, implemented as part of a time-stepped evolution, describing the material behavior — such as friction, compaction, viscoelastic properties, and EOS.

Hydrocodes integrate the hydrodynamic equations describing the conservation of mass, momentum, and energy. They relate intrinsic scalar variables — the density  $\rho$ , internal energy  $U$ , and pressure  $P$ , at position  $x, y, z$  — to the velocity field  $v_x, v_y, v_z$  as determined by accelerations (forces). They integrate a time-evolving solution to a set of partial differential equations. If deviatoric stresses are considered, then body forces are evolved according to the stress tensor, introducing six additional variables in three dimensions; in practice a simplified approach is often made.

The resulting partial differential equations are integrated forward in time (*Benz*, 1990; *Collins et al.*, 2013) according to accuracy requirements on the spatial resolution and the timestep  $dt$ . Time-evolution is cast in either a Lagrangian reference frame, which follows the material, or in an Eulerian frame that is fixed in space, advecting material properties (density, momentum, energy, composition) through a grid. These have advantages and disadvantages; for more detailed background and benchmark comparison see *Pierazzo et al.* (2008).

### 2.1. Smooth Particle Hydrodynamics

In smooth particle hydrodynamics (SPH) the continuous fluid is represented as a Lagrangian set of particles (*Benz*, 1990; *Monaghan*, 2012) that move with the flow. The properties at particle  $i$  are averaged over its  $\sim 50$  nearest neighbors, weighted according to their distance from particle  $i$  relative to the smoothing length  $h$ . So  $h$  is the grid resolution. Particle density, for example, is the weighted contribution of mass over its neighbors (hence “smoothed”). The mass and momentum conservation equations are approximated to second order as kernel sums. The most commonly used SPH code in asteroid research is by *Benz and Asphaug* (1994, 1995); this includes elastic strength and fracture damage in addition to the hydro-equations. This code has been modified by *Jutzi et al.* (2008, 2013) to include friction and compaction.

The SPH method is mostly applied in three dimensions, requiring million-particle calculations to resolve colliding bodies  $\sim 100$  particles across. A fast parallel cluster is needed for production investigations. Nonetheless, SPH is popular because it is relatively simple and numerically robust. It is straightforward to add new physics, and the purely Lagrangian description (all variables co-located at particle centers, co-moving with the fluid) makes it easy to hand off to other codes, visualizations, and analytical reductions. Unlike the grid-based codes described below, the problem domain is completely described by the particles themselves, so there is no need to grid up empty space into which the problem can evolve.

### 2.2. Grid-Based Codes

For computation of shocks, and for resolving boundary conditions and abrupt material contrasts, a grid-based calculation generally has greater fidelity than a particle mesh. However, in grid-based Lagrangian hydrocodes mesh entanglement can result. Eulerian hydrocodes avoid mesh

entanglement by maintaining a fixed grid, optimized for the problem. Each timestep advects density, internal energy, momentum, and material type from cell to cell, according to the velocity and pressure differential. Material histories and interface positions are recorded using “tracer particles” whose position moves with the mass flux from cell to cell.

Advection of material type is problematic. Imagine iron flowing into a pure olivine cell, whose composition has just become 1% iron. What EOS do we use in the next timestep? It is not trivial; e.g., what if one material is vapor at the computed pressure and temperature, and the other is liquid? There are many approaches to handling mixed materials in a cell. As for the mass flux from a mixed cell, do we assume 1% iron applies instantaneously everywhere in the cell (faster than any physical velocity), or do we concentrate iron near the donor cell, holding it “upstream” according to some criterion? Eulerian codes usually require techniques for limiting this artificial diffusion.

Grid-based codes have one overwhelming advantage compared to SPH: They allow accurate calculations in two-dimensional (axisymmetric or planar) or one-dimensional (planar or spherical) symmetrical geometries. High-definition two-dimensional computations, for instance, where a spherical asteroid is impacted on axis, can be done on a modest workstation, enabling careful research exploring many kinds of hypotheses. Parameter exploration in three dimensions is much more limited.

One popular grid-based code for asteroid collisional modeling is iSALE (Collins et al., 2004; Wünnemann et al., 2006), the successor to SALE (Amsden et al., 1980; Melosh et al., 1992; Ivanov et al., 1997). This code is maintained in a community forum, and includes both two-dimensional and three-dimensional versions and associated analytical and visualization tools, as well as several of the most relevant EOS models. Another popular code is CTH (McGlaun et al., 1990; Crawford et al., 2006), although like other sophisticated defense-related packages, its foreign access restriction can limit its utility in academic collaborations.

Which hydrocode to use depends on the problem. An intrinsically axisymmetric problem, such as impact cratering within about 45° of vertical, can be prototyped in a two-dimensional code before serious computer effort is expended looking at the three-dimensional details. If projectile-target contact and compression are of greatest interest, then a two-dimensional or even one-dimensional planar calculation will allow for the highest resolution. If the downrange momentum of massive ejecta is of key interest, then an axisymmetric model at any resolution is almost useless.

To study the long-term self-gravitational interaction following megacratering or disruption, the hydrocode simulation can be handed off to a particle method such as we now describe.

### 2.3. Discrete-Element Models

At low velocity, impacts can be modeled approximately according to Newton’s laws using discrete-element methods

(DEMs). These do not model shocks or stress waves, but represent collisions by piles of immutable, self-gravitating, idealized solids with contact and restitutive forces [e.g., PKDGRAV (Stadel, 2001; Richardson et al., 2002)]. Soft-sphere codes (Sanchez and Sheeres, 2011; see the chapter by Murdoch et al. in this volume) further represent contact forces according to a viscoelastic “dashpot” model (not to be confused with SPH).

Resolution in a DEM does not mean the same thing as it does in a hydrocode. In a hydrocode, the finer the resolution, the more accurate the solution. In a DEM there is a correct resolution for the problem, because every element represents a discrete body. Infinitesimal particle size in a DEM results in infinite strength, and for physical reasons: Fine powders are strongly cohesive due to their high specific contact area. In practice, however, DEMs struggle to resolve the physical scale; a 10<sup>6</sup> element simulation of Itokawa would have a finest block size of several meters. While sufficient to mimic the granular nature of a rubble pile, the contact area per unit volume is a billion times less than if we had a finest block size of centimeters, meaning that we must represent the surface physics parametrically.

Polyhedral rubble-pile codes (Korycansky and Asphaug, 2006; Movshovitz et al., 2012) are more challenging to implement than sphere-based DEMs due to the complexity of contact detection and the variety of contacts (face, vertex, edge), and they have even worse resolution. But the physical insights are important. Polyhedral DEMs exhibit substantially different behavior than sphere-based DEMs because of the dilatancy and grain-locking effects that are only partially captured by sphere-based approaches. For example, Korycansky and Asphaug (2009) find a systematically higher value of  $Q_D^*$  in planetesimal collisions at tens of meters per second, compared with results derived using sphere-based DEMs (Leinhardt and Stewart, 2009).

For collisions faster than ~10 m s<sup>-1</sup>, DEMs are not appropriate without special handling, because they do not account for realistic mechanical behavior and thermodynamic effects. Comparable to a train wreck, or the collapse of a skyscraper, large planetesimal collisions are transformative events involving fragmentation, crushing, shear friction, and shocks — they are not piles of bouncing marbles.

Although the science is still in its early stages, a linked model (e.g., Michel et al., 2003; Leinhardt and Stewart, 2012) has proven versatile, where SPH (or another hydrocode) evolves the high-velocity collision for a few  $\tau_s$ , which is handed off as particle positions and velocities to a DEM. But even if the handoff is perfectly achieved, we caution, as shown below, that the result may depend on unknown aspects of asteroid dynamical rheology.

### 2.4. Strength and Damage

Strength describes a material’s response to volume-conserving deformation and to tensile pressure. Volumetric compaction is included in the EOS and the porosity model, described below. The strength model can be simple,

requiring no material history, or can be a complicated evolution of strain, strain rate, temperature, and pressure.

Asteroid strength modeling used to be based around concepts of brittle fragmentation and fracture damage. While these approaches are still valuable, asteroid strength modeling now revolves more around concepts of cohesion, friction, and compaction — the subtle strengths of granular rubble piles and regoliths, in microgravity.

A small strength or cohesion can exert a major influence on the asteroid impact process, especially during the final stages, which govern how the feature will appear geologically in spacecraft images. Cohesion as small as that of fresh dry snow can dominate global-scale events on ~100-m asteroids, making the difference between a cratering event “going global” or remaining local.

A shear-strength model dependent on confining pressure  $P$  is employed in iSALE (Collins *et al.*, 2004) and in SPH (Jutzi *et al.*, 2013; Jutzi, 2015). In this simple approach the shear stress is limited by a yield stress, which increases with  $P$  due to grain interlocking and friction

$$Y_i = Y_0 + \frac{\mu_i P}{1 + \mu_i P / (Y_M - Y_0)} \quad (8)$$

where  $Y_0$  is the shear strength at  $P = 0$  (measured in the lab),  $Y_M$  is the asymptotic shear strength at infinite pressure (the Hugoniot elastic limit), and  $\mu_i$  is the coefficient of internal friction.

In elastic solid materials, a damage  $D$  can be accumulated either as a tensor  $D_{ij}$  or a scalar (isotropic damage). Damage reduces the deviatoric stress, leaving behind (when  $D = 1$ ) only the granular cohesive properties. To account for thermal softening,  $Y$  may be further reduced by a factor  $1 - U/U_{melt}$  where  $U_{melt}$  is the specific melting energy, so that a molten material has zero strength.

An approach used in iSALE is to accumulate shear damage as a nonlinear function of the equivalent plastic strain (Collins *et al.*, 2004). There is no rate dependence to this function; rate-dependent fragmentation requires a dynamic fracture model (Melosh *et al.*, 1992; Benz and Asphaug, 1994, 1995).

Completely damaged material has some cohesion; lunar regolith has  $Y_0 \sim 10^3$  Pa. Cohesion of only tens of pascals can dominate the structural geology of small asteroids (Asphaug, 2009; Holsapple, 2009; Sanchez and Scheeres, 2011). This cohesion can be further weakened by granular dynamical processes, as discussed in the chapter by Jutzi *et al.* in this volume.

Acoustic fluidization has been simulated using a block model (Melosh and Ivanov, 1999) to freeze in the central peaks of the largest craters on Vesta (Jutzi *et al.*, 2013). Although it has not yet been implemented so far for small asteroid collisions, the attenuation of random motions responsible for fluidization might lock in global-scale shapes and structures of rubble-pile asteroids.

## 2.5. Size and Rate Dependence

The number of flaws  $n$  per unit volume  $V$  in a solid is often described as a power law

$$n(\varepsilon) = k\varepsilon^m \quad (9)$$

In this equation a few flaws  $n$  will become active in  $V$  for a given volumetric strain  $\varepsilon$ . There will be one single weakest flaw,  $\varepsilon_{min} = kV^{-1/m}$ , so that an asteroid’s strength decreases with size, as the power  $R^{-1/2}$  (Farinella *et al.*, 1982) for  $m \sim 6$  (a typical value). This is the static threshold, but dynamic strength increases with strain rate in a closely related manner. The overall effect is a negative slope when plotting  $Q_S^*$  vs.  $R$ , where  $R$  is asteroid radius — larger asteroids are weaker.

On the other hand, larger asteroids are harder to disrupt, because the gravitational binding energy per unit volume (equivalently, the internal hydrostatic pressure  $\sim G\rho^2R^2$ ) is proportional to the escape velocity squared. Setting gravitational binding energy equal to the rock strength  $Y$  gives a transition diameter above which it is more likely for an asteroid to be beaten into rubble many times over, than to be dispersed.

One of the remarkable discoveries of the previous decade was that the strength-gravity transition would occur around 100–300-m-diameter asteroids. This result was predicted in simple analyses and is confirmed in advanced numerical models, but the implications are still the subject of considerable debate, as reviewed in the chapter by Michel *et al.* in this volume.

## 2.6. Equations of State

The hydro-equations are closed using an EOS relating energy, density, and pressure. For impact modeling, the EOS defines the material response to changes in volume, often in collaboration with a porosity model. The EOS is called by the hydrodynamics integrator (sometimes iteratively) as  $P(\rho, U)$  to obtain the “righthand side” terms that drive evolution of the momentum equation.

One popular model is ANEOS (Thompson and Lauson, 1972; Melosh, 2007), whose thermodynamics variables are derived from the Helmholtz free energy. As a result, all data in an ANEOS table are thermodynamically consistent, something that is especially important in the detailed modeling of shocks. ANEOS returns temperature, pressure, and state of the material, mapping polymorphic and liquid/solid-phase transitions, specific heats, and vapor/liquid fraction. But thermodynamical consistency is not the same as accuracy, and Kraus *et al.* (2012) find that the shock vaporization energy of silicate rocks may be a factor of 2–3 lower than reported by ANEOS, of fundamental importance to the study of high-velocity events and giant impacts.

Another popular EOS model is that of Tillotson (1962), effectively a stitched-together polytrope defining a cold condensed state and a hot expanded state. With only five parameters Tillotson is easily modified to new materials; one

avoids the tabular precomputations and interpolations and possible version-inconsistencies that can plague calculations. Tillotson is poorly suited to problems where vapor-melt interactions are expected to dominate, such as the post-impact protolunar “flying magma ocean” (Stevenson, 1987). Even so, Canup (2004) finds that Tillotson gives comparable results to more sophisticated EOS models for the initial characteristics of the protolunar disk.

There is a practical advantage to Tillotson: It is simply defined, easily computed, and easily understood in a calculation. Because it derives from the particle-velocity shock-velocity relation (Melosh, 1989), it is highly suitable to producing the post-shock particle velocities, and that is what is most important in most asteroid collisions. Melt is not produced in Tillotson (there are no “phases”), but melt and vapor produced in asteroid collisions are usually ejected to escaping velocity anyway, as discussed further below.

## 2.7. Porosity

The realization that asteroids and planetesimals contain a large volume of pore space (e.g., Housen and Holsapple, 1999; Consolmagno and Britt, 1998) has driven a recent advance in modeling dissipative properties of porous media (e.g., Wünnemann et al., 2006; Jutzi et al., 2008; Collins et al., 2011). To the extent that resolution allows, macroporosity can be modeled explicitly using solid materials described above, as cavernous voids (Asphaug et al., 1998; Jutzi et al., 2008). But the idea of a loosely packed dust rich structure for asteroids (Asphaug, 2009) requires porosity to be modeled at the subresolution, in addition to the compressibility of a fully compacted material that is defined by the EOS.

Porosity is associated with a crushing strength. One approach [the P- $\alpha$  model (Herrmann, 1969; Carroll and Holt, 1972)] computes a distention  $\alpha = \rho_s/\rho$ , where  $\rho$  is the bulk density of the porous material and  $\rho_s$  is the density of the nonporous matrix corresponding to the EOS. The pressure  $P$  and internal energy  $U$  in the porous material, at the grid resolution, is what is needed by the hydrocode, but the EOS only knows how to compute these for the nonporous material,  $P_s$  and internal energy  $U_s$ .

The P- $\alpha$  model uses the approximation

$$P = \frac{1}{\alpha} P_s (\rho_s, U_s) = \frac{1}{\alpha} P_s (\alpha \rho, U) \quad (10)$$

In this manner the EOS model for nonporous rock is converted into an EOS model for porous rock, whose pressure gradients at the grid scale then drive material accelerations and shocks. The distention varies with pressure according to a “crush curve” derived from uniaxial laboratory experiments, as described in the chapter by Jutzi et al. in this volume.

## 2.8. Self-Gravity

For modeling global-scale impacts into small asteroids, self-gravity can be neglected during the impact phase and

applied later, since  $\tau_g \gg \tau_s$ . Otherwise, self-gravity can be approximated using a constant radial gravity field inside a spherically symmetric asteroid. The modern hydrocodes described above can also calculate gravity explicitly (e.g., Jutzi et al., 2013; Davison et al., 2013), although this adds considerably to the computational expense.

Precompression must be included along with self-gravity, otherwise the first phenomenon is the asteroid shrinking and overshooting its central pressure. For small asteroids an analytical precompression is acceptable (Asphaug and Melosh, 1993). For larger asteroids or more sensitive studies, gravitational stresses must be iteratively solved prior to the impact simulation.

Following a global-scale collision, gravitational evolution must be computed over the orbital timescale of days. This is many thousands of hydrotimescales at the resolution of an asteroid, and thus prohibitive. This evolution is best computed after pressures and velocities have equilibrated, by mapping the hydrocode results into N-body codes or self-gravitating DEMs as described above.

## 3. THERMAL EFFECTS

Following its accretion in the first few million years, a typical  $\approx 200$ -km-diameter meteorite parent body likely experienced several hundred impacts by asteroids larger than 300 m during the first 100 m.y. of solar system history. This is about half the impacts expected during its lifetime (Davison et al., 2013). Over the same period, impact speeds increased from an average  $< 1$  km s $^{-1}$  to as fast as  $\sim 10$  km s $^{-1}$  (O’Brien and Greenberg, 2005).

According to Davison et al. (2013), post-accretion collisions were only capable of catastrophically destroying at most a few percent of the finished asteroids. Of the remainder, most were subjected more than one collision with an object one-twentieth its diameter, and a few percent experienced a collision with an object one-fifth its diameter.

It is therefore no surprise that evidence for impact processing is common in meteorites (e.g., Sharp and DeCarli, 2006), including shock effects, compaction, and frictional heating. However, as we now review, impact heating appears to be inefficient at the global parent-body scale, because the same violent impact that heats and melts the material ultimately causes the asteroid to disperse ( $Q > Q_D^*$ ). The fate of dispersed shocked material is another question — whether it finds its home back to the target asteroid, or another asteroid, or becomes ground into fine dust and disappears, or is sampled as meteorites.

### 3.1. Global Impact Heating of Asteroids

Widespread heating and melting of asteroids is evident in meteorites (e.g., Bizzarro et al., 2005) and one of the primary debates has been whether the source of this heating is by early accretion of radiogenic  $^{26}\text{Al}$  or by impact processes.

Keil et al. (1997) combined simple theoretical arguments with observational evidence and numerical impact

simulations to conclude that the globally averaged effect of impact heating on a nondisrupted asteroid was equivalent to a global temperature increase of less than a few degrees. Others (e.g., Rubin, 1995) maintained that shocks from high-velocity collisions, especially into porous primitive targets, could be the source of melting, and that the meteorite collection itself would be biased to include the more highly shocked and melted surface materials.

Davison *et al.* (2013) revisited the question of impact heating, using a Monte Carlo simulation that accounted for the effect of asteroid porosity and impact velocity on the disruption threshold (Jutzi *et al.*, 2010; Housen and Holsapple, 1990) and for the evolving impactor size- and velocity-frequency distribution (using a simulation by O'Brien and Greenberg, 2005). For a 200-km-diameter, 20% porous asteroid, Davison *et al.* (2013) found that the maximum specific impact energy that could be imparted, without disrupting the target, is  $\sim 0.1\text{--}0.7 \text{ MJ kg}^{-1}$ . This corresponds to a globally averaged temperature increase of 100–700 K, depending on the impact velocity, substantially greater than the Keil *et al.* (1997) estimate.

However, an impact just below the catastrophic threshold is not representative of the largest collision that is expected. This just gives the maximum heating that is theoretically possible, without also dispersing the heated mass. Davison *et al.* (2013) followed the collisional evolution during the first 100 m.y. of solar system formation, assuming an approximately inverse square size-frequency distribution of impactors. They found that in most cases, the most energetic impact experienced by a 200-km-diameter asteroid that was not disrupted was only a few percent of  $Q_D^*$ . They concluded that significant impact heating on an  $\sim 200$ -km-diameter parent body is unlikely, and in the end obtained a result similar to Keil *et al.* (1997), that in the most typical scenario the maximum specific impact energy delivered to a nondisrupted asteroid amounts to a globally averaged temperature increase of only a few degrees.

Larger asteroids have much greater specific binding energy and can therefore withstand collisions that deposit far more heat. An analogous situation is true of planetary cratering, where the largest craters are the most melt rich. But a maximal event is less likely to occur on a larger target than on a smaller target, for an approximately inverse square size distribution. On this basis, Davison *et al.* (2013) found that both the maximum specific impact energy and the total impact energy were rather constant for asteroids 100–500 km in diameter, a few tens of degrees of heating at most. These estimates assume that all the heated materials of impact are retained in the nondisrupted asteroid. A fraction of the hottest material actually escapes the asteroid, so that these global heating estimates are upper limits.

### 3.2. Localized and Buried Heat

These globally averaged estimates suggest that short-lived radionuclide decay ( $^{26}\text{Al}$ ) was a far more effective global heat source than impact. However, impact heating is trans-

sient, local, and non-uniform. In events where the projectile is much smaller than the target, impact energy is converted into heat within the proximal, near-surface volume that is highly shocked, a few projectile radii, and zero appreciable heating occurs far from the impact. For small asteroids with low escape velocity, much of this melted material escapes, while on large asteroids it can be retained, requiring a different sort of calculation.

Temperature increases attenuate with shock pressure, rapidly with distance, and so do ejection velocities. Only in rare, disruptive collisions between objects of similar mass can impact heating be considered to be nearly uniform (Davison *et al.*, 2010). The accretionary collisions described above (“small giant impacts”) are global in consequence, but too slow to result in shock heating. Frictional and compaction heating during early accretion (the first  $\sim 3$  m.y.) may be of global consequence, but are thought to be insignificant in magnitude compared to the prevalence of  $^{26}\text{Al}$ .

Using the same dynamical and population framework described above, Davison *et al.* (2013) computed the volumetric significance of impact heating on 200-km-diameter meteorite parent bodies during the first 100 m.y. of solar system history (Fig. 5). Less than 1% by mass of a typical undisrupted parent body experiences heating of more than a few hundred Kelvins, volumetrically equivalent to a surface layer  $<300$  m thick. However, of the few percent of asteroids

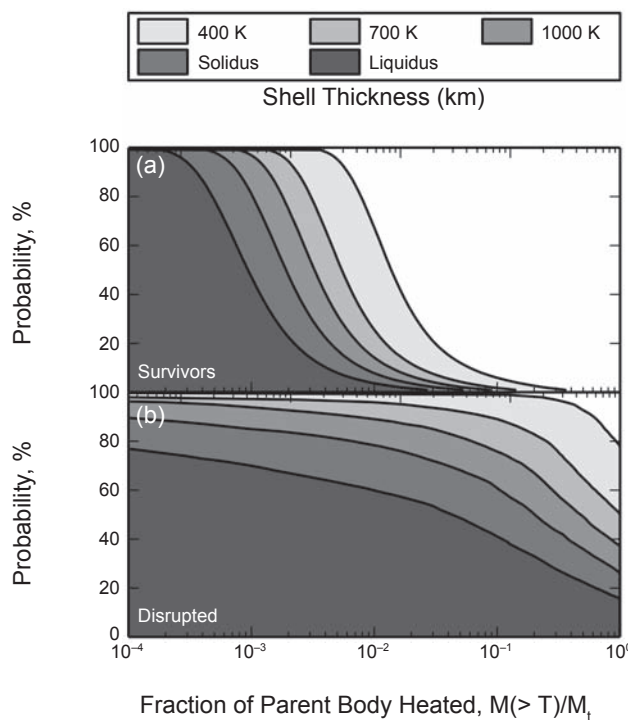


**Fig. 5.** The probability that a given mass fraction of a meteorite parent body will be heated to a range of temperatures, for (a) those asteroids that survive the first 100 m.y. of solar system history without being disrupted and (b) those bodies that are disrupted. Modified from Davison *et al.* (2013).

that are disrupted, most experience a near-global temperature increase of a few hundred Kelvins, and one-fifth are expected to undergo (near) complete melting.

The main influence of asteroid porosity on impact heating is to modify the distribution of heat. Shock heating is more extreme, but much more localized, in porous-body collisions compared to impact on a nonporous body. More shock energy is absorbed close to the impact site on a porous asteroid by permanent crushing of pore space; the excess heating from pore collapse leads to higher proximal temperatures (Asphaug et al., 2002; Davison et al., 2010).

The localized heating by subcatastrophic collisions, and the distribution of heated materials beneath and around the crater, imply that a single impact can produce materials with a remarkable range in peak temperature and cooling rates. According to Davison et al. (2012), impacts on porous asteroids can produce large amounts of melting at speeds as low as  $4 \text{ km s}^{-1}$ , and material heated up to  $\sim 1200 \text{ K}$  (petrologic type 6) is expected for most impacts in the first 100 m.y. (Davison et al., 2013).

Numerical simulations of crater formation in large subcatastrophic impacts also suggest that heated impactor and target material, and exhumed hot material from the deep mantle, is rapidly buried beneath an insulating lens of porous breccia. The structure of these lobate/hemispheric deposits, for the specific case of the global-scale impacts Rheasilvia and Vennenia on asteroid (4) Vesta, is studied by Jutzi and Asphaug (2011) and Jutzi et al. (2013). Buried impact-heated or impact-exhumed material cools slowly, consistent with the wide range of metallographic cooling rates inferred for chondritic materials (Davison et al., 2012).

While the volumetric significance of impact-heated material appears to be consistent with the limited constraints on meteorite thermal metamorphism, compared to  $^{26}\text{Al}$  decay, it appears that localized impact heating is an important secondary effect, even when considering the cumulative effect of multiple impacts over the lifetime of a parent body. There is of course a bias, that the proximity of impact-heated material to the parent body's surface makes it most accessible for excavation and meteorite delivery by subsequent collisions.

### 3.3. Accelerated Cooling by Impact Overturning

If internal heating by short-lived radioactivity was dominant, then subcatastrophic collisions would have played an additional important role in regulating thermal evolution. Ciesla et al. (2013) showed how a single large impact can have an enormous influence on the cooling of planetesimals heated internally by radioactivity.

In their models (Fig. 6), hot, thermally softened material is brought up from the deep interior to flow out and over the surface of the planetesimal, turning the asteroid "inside out." The direct exposure to space of deeply exhumed molten silicates would lead to rapidly accelerated cooling and degassing; more generally, it is a considerable source of enthalpy for materials brought to the surface, something Asphaug et al. (2011) proposed as an origin of chondrules.

In general, a much larger fraction of an internally heated planetesimal experienced enhanced cooling than is heated by the impact, implying the non-intuitive result, that the major effect of subcatastrophic collisions was to accelerate the loss of heat, rather than to deposit heat (Ciesla et al., 2013).

The rapid cooling of iron meteorites is a longstanding problem (e.g., Wood, 1964) that could perhaps be solved if melted core material buried deep inside a differentiated asteroid could be exhumed by this mechanism, so that the iron might cool rapidly. But from many simulations (Love and Ahrens, 1996, and thereafter) it appears that an iron core, once buried, is almost impossible to blast out by impact overturning. Furthermore, it would sink back to the core, cooling there instead of at the surface. So the above process, of "breaking open the pie crust," would affect mostly the thermodynamics of meteorites from the upper to mid-mantle of a melted planetesimal, not the core.

It is possible, on the other hand, to achieve greatly accelerated cooling of iron planetesimals if we consider the exhumation of the projectile rather than the target. As noted above, planetesimal projectiles (but not targets) during SSCs can be ripped apart into beads of iron-rich objects during hit-and-run collisions involving larger embryos (Asphaug et al., 2006; Asphaug, 2010). The mechanism of mantle stripping of hit-and-run projectiles is discussed in more detail in the chapter by Scott et al. in this volume, including its implications for the history and evolution of the asteroid-parent-body population.

While mantle stripping by hit and run has been simulated dynamically in a number of studies, the thermal consequences of abruptly exposing interior materials to space awaits the kind of detailed study that Ciesla et al. (2013) have given to large-scale cratering. Asphaug et al. (2011) consider exhumation in a more specific context to explain the cooling rates of chondrules, which are formed according to their model by inefficient accretion of incompletely differentiated melted planetesimals. For the general case, it is apparent that the accelerated-cooling scenarios defined above for megacratering would have comparable, more accentuated aspects if applied to the aftermath of hit-and-run collisions, which typically rip off half the mantle of a differentiated body without producing shocks (Asphaug, 2010). Yang et al. (2007) invoke hit-and-run mantle stripping to explain the rapid cooling rates of the IVA iron meteorites, in a scenario that requires almost complete mantle stripping to leave behind only a thin rind of insulating silicates. This would require repeated hit-and-run collisions while the body was still molten — something that Asphaug and Reufer (2014) argue would have been probable for at least a few of the unaccreted bodies that became the progenitors of asteroids.

## 4. RHEOLOGY AND DISRUPTION

One goal of current numerical modeling is a unified simulation of asteroid collision including fracture, crushing, dilatancy, friction, and debris flow. The physical modeling borrows equally from dynamics, seismology, geomorphology,

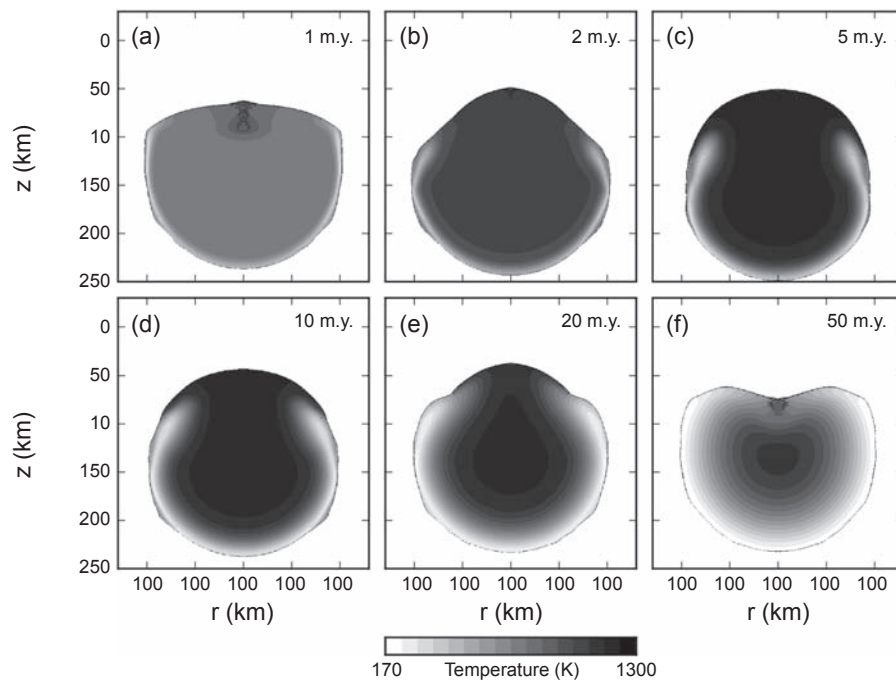


**Fig. 6.** Post-impact temperature distribution within planetesimals internally heated by radioactive decay of  $^{26}\text{Al}$  for a single impact that occurs at different times during thermal evolution. At early and late times, the impact occurs on a relatively cool planetesimal, resulting in a recognizable crater with a localized, impact-heated region at its center. In contrast, impacts that occur during the period of high internal temperatures ( $\sim 2\text{--}20$  Ma for this size planetesimal) result in uplift and overturn of deeply derived, hot and thermally softened material. From Ciesla *et al.* (2013).

and impact cratering. Only recently has it been possible to look at the additional effects of friction, porosity, and cohesion, at least on a global scale, so this represents a frontier of computational geophysics.

Jutzi (2015) used SPH to model colliding bodies in an exploration of the threshold for catastrophic disruption. Below we show a subset of those calculations: colliding asteroids that are the same size in each simulation ( $R_t = 100$  km,  $R_p = 27$  km), and the same mass (initial bulk density  $\rho = 1.3 \text{ g cm}^{-3}$ ), and the same impact parameter ( $v_{\text{imp}} = 3 \text{ km s}^{-1}$ ,  $\theta = 45^\circ$ ). What is different between the four simulations in Fig. 7 are the material properties: (1) no friction, no crushing, no cohesion; (2) friction, no crushing, no cohesion; (3) friction and crushing, no cohesion; (4) friction, crushing, and cohesion.

For the two cases with crushing, a crush curve with parameters for pumice is applied (Jutzi *et al.*, 2009). For the case with cohesion, an internal friction  $\mu_i = 1.5$  and cohesion  $Y_0 = 100 \text{ MPa}$  are applied, which is reduced to  $Y_0 = 0$ ,  $\mu_d = 0.8$  and  $Y_m = 3.5 \text{ GPa}$  following damage. The first case in Fig. 7 is a fluid, the second is a fluid resisted by friction, the third is a crushable fluid resisted by friction, and the last is a cohesive porous body like pumice.

Based on a suite of such models, Jutzi (2015) found the catastrophic disruption energy  $Q_D^*$  to be  $\sim 5\text{--}10\times$  higher when friction is included. The disruption threshold further

increases by a factor of  $\sim 2\text{--}3$  when the energy dissipation by compaction (pore crushing) is taken into account. (Surprisingly, there is not much difference between the cases

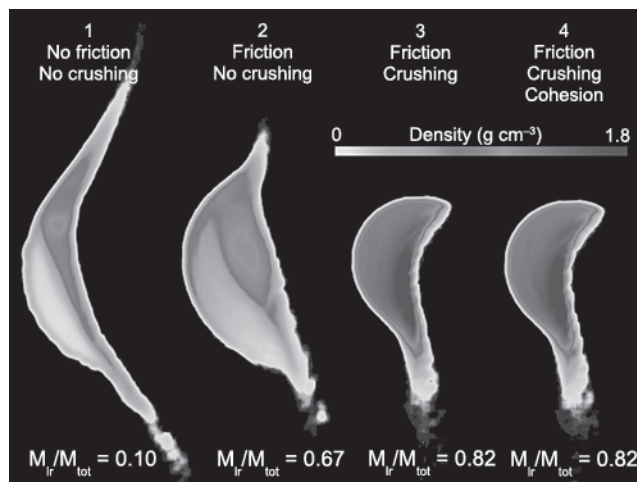


**Fig. 7.** Cross-sections of four SPH simulations of collisions between targets  $R_t = 100$  km and projectiles  $R_p = 27$  km, at relative velocity  $3 \text{ km s}^{-1}$  and  $45^\circ$  impact angle. Four different rheologies are investigated. The degree of disruption, the size of the largest remnant ( $M_{lr} = M_{tot}$ ), and the increase in density strongly depend on the target properties. From Jutzi (2014).

with or without cohesion.) This implies that many events previously thought of as catastrophically disruptive are more likely global-scale impacts that leave behind a completely transformed asteroid, but do not disperse it.

These simulations are consistent with previous models, that cohesion and tensile strength are negligible in potentially disruptive impacts involving bodies larger than a few hundred meters in diameter. But it is a misnomer to speak of this as the “strength-gravity transition,” because gravity is not the controlling aspect for the response either. For example, collisions involving partially melted silicate targets up to  $\sim 1000$  km in diameter may be limited by viscosity (Asphaug et al., 2006). For solid asteroids and planetesimals up to hundreds of kilometers in diameter that have been beaten into rubble, friction and compaction are expected to dominate, according to these calculations. Although gravity cannot be ignored, there may be no simple “gravity regime” for asteroid impacts.

## 5. CONCLUSIONS

Global-scale impacts on asteroids and their parent bodies are in many respects similar to the giant impacts that created the terrestrial planets, and there is great scientific value in making the connection. But at asteroid scales, we cannot ignore the internal stresses and their associated rheological responses — the breaking of rock, the flow of rubble, the opening of faults, the seismological vibration — in addition to the self-gravitational complexities.

Gravity is subtle, and so are the other forces. Approximations or even small numerical errors can overwhelm the accurate calculation of an asteroid impact. In recent years computer modeling has begun to catch up with the physics, and progress on this front defines much of the modern science of global-scale impacts. In the coming decade, we can look forward to ever more sophisticated simulations; for now, it is too early to say whether the models are sufficient to be predictive.

Meanwhile, every new mission to an asteroid — and in particular, every new mission to a different size or class of asteroid — has revealed a solar system process not previously envisioned, and has turned our previous understanding of small bodies on its head. Flyby missions are of great value, as are the increasingly impressive radar shape models (Ostro et al., 2002) and adaptive optics models (see the chapter by Marchi et al. in this volume) obtained so far for dozens of near-Earth asteroids (see the chapter by Benner et al. in this volume). While lacking the fidelity of a spacecraft flyby, radar images are sufficiently detailed to play a fundamental role in resolving the geophysical debates that have been summarized in this chapter.

Rendezvous missions provide a much more thorough examination of a smaller subset — three asteroids so far, with three more on the near horizon: the sample return missions Hayabusa 2 and Origins Spectral Interpretation Resource Identification and Security-Regolith Explorer (OSIRIS-REx) to small near-Earth objects, and the Dawn mission continuing to Ceres. Hayabusa 2 will conduct the

first impact experiment on an asteroid, and although it is almost certainly too small in scale to result in any of the global-scale phenomena described above, it will no doubt shed light on some of the open questions concerning microgravity impact physics at several meters scale.

Efforts are ongoing to study the effect of a small spacecraft colliding into an asteroid using a mission approach like that of the Lunar Crater Observation and Sensing Satellite (LCROSS) (Colaprete et al., 2010), which depending on the asteroid could cause global accelerations greater than local gravity, rearranging the global topography. Such a mission would elucidate the many factors that dictate whether a cratering event has global consequences or is local to one hemisphere — an understanding that in turn will allow us to put the more readily attainable cratering observations from radar and flyby missions into context.

And the last front is meteorites, including the samples that are collected by missions. Meteorites have a way of presenting us with seemingly contradictory information, leading to a spectrum of contested hypotheses for their origin. But there is a chance, through collisional and thermal modeling and geochemistry, to understand their most basic physical properties and the processes they have experienced, from the formative collisions to the catastrophic disruptions that have populated the main belt and near-Earth space.

**Acknowledgments.** E.A. acknowledges NASA PGG grant NNX13AR66G. G.S.C. acknowledges STFC grant ST/J001260/1. M.J. acknowledges the Ambizione program of the Swiss National Science Foundation. We are grateful to T. Davison for helpful discussion and access to unpublished data, and acknowledge the careful work of two referees to improve the clarity and balance of the paper.

## REFERENCES

- Agnor C. B., Canup R. M., and Levison H. F. (1999) On the character and consequences of large impacts in the late stage of terrestrial planet formation. *Icarus*, 142, 219–237.
- Ahrens T. J. and O’Keefe J. D. (1994) Impact-induced melting of planetary surfaces. In *Large Meteorite Impacts and Planetary Evolution* (B. O. Dressler et al., eds.), pp. 103–109. GSA Spec. Paper 283, Geological Society of America, Denver.
- Amsden A., Ruppel H., and Hirt C. (1980) *SALE: A Simplified ALE Computer Program for Fluid Flow at All Speeds*. Los Alamos National Laboratories Report LA-8095, Los Alamos, New Mexico, 101 pp.
- Anderson C. E. (1987) An overview of the theory of hydrocodes. *Int. J. Impact Eng.*, 5, 33–59.
- Asphaug E. (1997) Impact origin of the Vesta family. *Meteoritics & Planet. Sci.*, 32, 965–980.
- Asphaug E. (2008) Critical crater diameter and asteroid impact seismology. *Meteoritics & Planet. Sci.*, 43, 1075–1084.
- Asphaug E. (2009) Growth and evolution of asteroids. *Annu. Rev. Earth Planet. Sci.*, 37, 413–448.
- Asphaug E. (2010) Similar-sized collisions and the diversity of planets. *Chem. Erde–Geochem.*, 70, 199–219.
- Asphaug E. and Melosh H. J. (1993) The Stickney impact of Phobos — A dynamical model. *Icarus*, 101, 144–164.
- Asphaug E. and Reufer A. (2013) Late origin of the Saturn system. *Icarus*, 223, 544–565.
- Asphaug E. and Reufer A. (2014) Mercury and other iron-rich planetary bodies as relics of inefficient accretion. *Nature Geosci.*, 7, 564–568, DOI: 10.1038/ngeo2189.

- Asphaug E., Ostro S. J., Hudson R. S., Scheeres D. J., and Benz W. (1998) Disruption of kilometre-sized asteroids by energetic collisions. *Nature*, 393, 437–441.
- Asphaug E., Ryan E. V., and Zuber M. T. (2002) Asteroid interiors. In *Asteroids III* (W. F. Bottke Jr. et al., eds.), pp. 463–484. Univ. of Arizona, Tucson.
- Asphaug E., Agnor C. B., and Williams Q. (2006) Hit-and-run planetary collisions. *Nature*, 439, 155–160.
- Asphaug E., Jutzi M., and Movshovitz N. (2011) Chondrule formation during planetesimal accretion. *Earth Planet. Sci. Lett.*, 308, 369–379.
- Belton M. J. S. et al. (2007) The internal structure of Jupiter family cometary nuclei from Deep Impact observations: The talps or layered pile model. *Icarus*, 187, 332–344.
- Benz W. (1990) Smooth particle hydrodynamics: A review. In *Numerical Modeling of Nonlinear Stellar Pulsation: Problems and Prospects* (J. R. Buchler, ed.), Kluwer, Dordrecht.
- Benz W. (2000) Low velocity collisions and the growth of planetesimals. *Space Sci. Rev.*, 92, 279–294.
- Benz W. and Asphaug E. (1994) Impact simulations with fracture. I — Method and tests. *Icarus*, 107, 98–116.
- Benz W. and Asphaug E. (1995) Simulations of brittle solids using smooth particle hydrodynamics. *Comp. Phys. Commun.*, 87, 253–265.
- Benz W. and Asphaug E. (1999) Catastrophic disruptions revisited. *Icarus*, 142, 5–20.
- Blitz C., Lognonné P., Komatitsch D., and Baratoux D. (2009) Effects of ejecta accumulation on the crater population of asteroid 433 Eros. *J. Geophys. Res.—Planets*, 114, E06006.
- Binzel R. P. and Xu S. (1993) Chips off of asteroid 4 Vesta — Evidence for the parent body of basaltic achondrite meteorites. *Science*, 260, 186–191.
- Bizzarro M., Baker J. A., Haack H., and Lundgaard K. L. (2005) Rapid timescales for accretion and melting of differentiated planetesimals inferred from  $^{26}\text{Al}$ - $^{26}\text{Mg}$  chronometry. *Astrophys. J. Lett.*, 632, L41–L44.
- Bowling T. J., Johnson B. C., Melosh H. J., Ivanov B. A., O'Brien D. P., Gaskell R., and Marchi S. (2013) Antipodal terrains created by the Rheasilvia basin forming impact on asteroid 4 Vesta. *J. Geophys. Res.—Planets*, 118(9), 1821–1834.
- Canup R. M. (2004) Dynamics of lunar formation. *Annu. Rev. Astron. Astrophys.*, 42, 441–475.
- Carroll M. M. and Holt A. C. (1972) Suggested modification of the P- $\alpha$  model for porous materials. *J. Appl. Phys.*, 43, 759–761.
- Ciesla F. J., Davison T. M., Collins G. S., and O'Brien D. P. (2013) Thermal consequences of impacts in the early solar system. *Meteoritics & Planet. Sci.*, 48, 2559–2576.
- Clenet H., Jutzi M., Barrat J.-A., Asphaug E., Benz W., and Gillet P. (2014) A deep crust-mantle boundary in the asteroid 4 Vesta. *Nature*, 511, 303–306.
- Colaprete A. et al. (2010) Detection of water in the LCROSS ejecta plume. *Science*, 330, 463–467.
- Collins G. S. and Melosh H. J. (2003) Acoustic fluidization and the extraordinary mobility of sturzstroms. *J. Geophys. Res.—Solid Earth*, 108, DOI: 10.1029/2003JB002465.
- Collins G. S., Melosh H. J., and Ivanov B. A. (2004) Modeling damage and deformation in impact simulations. *Meteoritics & Planet. Sci.*, 39, 217–231.
- Collins G. S., Melosh H. J., and Wünnemann K. (2011) Improvements to the  $\epsilon$ - $\alpha$  porous compaction model for simulating impacts into high-porosity solar system objects. *Int. J. Impact Eng.*, 38, 434–439.
- Collins G. S., Wünnemann K., Artemieva N., and Pierazzo E. (2013) Numerical modelling of impact processes. In *Impact Cratering: Processes and Products* (G. R. Osinski and E. Pierazzo, eds.), pp. 254–270. Wiley-Blackwell, New York.
- Consolmagno S. J. and Britt D. T. (1998) The density and porosity of meteorites from the Vatican collection. *Meteoritics & Planet. Sci.*, 33(6), 1231–1241.
- Cooper H. F. Jr. and Sauer F. M. (1977) Crater-related ground motions and implications for crater scaling. In *Impact and Explosion Cratering* (D. J. Roddy et al., eds.), pp. 1133–1163. Pergamon, New York.
- Crawford D. A., Taylor P. A., Bell R. L., and Hertel E. S. (2006) Adaptive mesh refinement in the CTH shock physics hydrocode. *Russ. J. Phys. Chem. B*, 25(9), 85–90.
- Davis D. R., Durda D. D., Marzari F., Campo Bagatin A., and Gil-Hutton R. (2002) Collisional evolution of small-body populations. In *Asteroids III* (W. F. Bottke Jr. et al., eds.), pp. 545–558. Univ. of Arizona, Tucson.
- Davison T. M., Collins G. S., and Ciesla F. J. (2010) Numerical modelling of heating in porous planetesimal collisions. *Icarus*, 208, 468–481.
- Davison T. M., Ciesla F. J., and Collins G. S. (2012) Post-impact thermal evolution of porous planetesimals. *Geochim. Cosmochim. Acta*, 95, 252–269.
- Davison T. M., O'Brien D. P., Ciesla F. J., and Collins G. S. (2013) The early impact histories of meteorite parent bodies. *Meteoritics & Planet. Sci.*, 48, 1894–1918.
- Durda D. D. et al. (2004) The formation of asteroid satellites in large impacts: Results from numerical simulations. *Icarus*, 170, 243–257.
- Farinella P., Paolicchi P., and Zappalá V. (1982) The asteroids as outcomes of catastrophic collisions. *Icarus*, 52, 409–433.
- Flynn G. J. (2005) Physical properties of meteorites and interplanetary dust particles: Clues of the properties of meteors and their parent bodies. *Earth Moon Planets*, 95, 361–374.
- Grady D. E. and Kipp M. E. (1980) Continuum modelling of explosive fracture in oil shale. *Int. J. Rock Mech. Min. Sci. Geomech. Abstr.*, 17, 147–157.
- Herrmann W. (1969) Constitutive equation for the dynamic compaction of ductile porous materials. *J. Appl. Phys.*, 40, 2490–2499.
- Holsapple K. A. (2009) On the “strength” of the small bodies of the solar system: A review of strength theories and their implementation for analyses of impact disruptions. *Planet. Space Sci.*, 57, 127–141.
- Housen K. R. and Holsapple K. A. (1990) On the fragmentation of asteroids and planetary satellites. *Icarus*, 84, 226–253.
- Housen K. R. and Holsapple K. A. (1999) Scale effects in strength-dominated collisions of rocky asteroids. *Icarus*, 142, 21–33.
- Housen K. R. and Holsapple K. A. (2011) Ejecta from impact craters. *Icarus*, 211, 856–875.
- Housen K. R., Schmidt R. M., and Holsapple K. A. (1983) Crater ejecta scaling laws — Fundamental forms based on dimensional analysis. *J. Geophys. Res.*, 88, 2485–2499.
- Ivanov B. A. and Melosh H. J. (2013) Two-dimensional numerical modeling of the Rheasilvia impact formation. *J. Geophys. Res.—Planets*, 118(7), 1545–1557.
- Ivanov B. A., Deniem D., and Neukum G. (1997) Implementation of dynamic strength models into 2D hydrocodes: Applications for atmospheric breakup and impact cratering. *Int. J. Impact Eng.*, 20, 411–430.
- Jutzi M. (2015) SPH calculations of asteroid disruptions: The role of pressure dependent failure models. *Planet. Space Sci.*, 107, 3–9, DOI: 10.1016/j.pss.2014.09.012.
- Jutzi M. and Asphaug E. (2011) Mega-ejecta on asteroid Vesta. *Geophys. Res. Lett.*, 38, 1102.
- Jutzi M., Benz W., and Michel P. (2008) Numerical simulations of impacts involving porous bodies. I. Implementing subresolution porosity in a 3D SPH hydrocode. *Icarus*, 198, 242–255.
- Jutzi M., Michel P., Hiraoka K., Nakamura A. M., and Benz W. (2009) Numerical simulations of impacts involving porous bodies. II. Comparison with laboratory experiments. *Icarus*, 201, 802–813.
- Jutzi M., Michel P., Benz W., and Richardson D. C. (2010) Fragment properties at the catastrophic disruption threshold: The effect of the parent body's internal structure. *Icarus*, 207, 54–65.
- Jutzi M., Asphaug E., Gillet P., Barrat J.-A., and Benz W. (2013) The structure of the asteroid 4 Vesta as revealed by models of planet-scale collisions. *Nature*, 494, 207–210.
- Keil K., Stoeffler D., Love S. G., and Scott E. R. D. (1997) Constraints on the role of impact heating and melting in asteroids. *Meteoritics & Planet. Sci.*, 32, 349–363.
- Korycansky D. G. and Asphaug E. (2006) Low-speed impacts between rubble piles modeled as collections of polyhedra. *Icarus*, 181, 605–617.
- Korycansky D. G. and Asphaug E. (2009) Low-speed impacts between rubble piles modeled as collections of polyhedra, 2. *Icarus*, 204, 316–329.
- Kraus R. G., Stewart S. T., Swift D. C., Bolme C. A., Smith R. F., Hamel S., Hammel B. D., Spaulding D. K., Hicks D. G., Eggert J. H., and Collins G. W. (2012) Shock vaporization of silica and the thermodynamics of planetary impact events. *J. Geophys. Res.—Planets*, 117(E9), DOI: 10.1029/2012JE004082.
- Leinhardt Z. M. and Stewart S. T. (2009) Full numerical simulations of catastrophic small body collisions. *Icarus*, 199, 542–559.
- Leinhardt Z. M. and Stewart S. T. (2012) Collisions between gravity-dominated bodies. I. Outcome regimes and scaling laws. *Astrophys. J.*, 745, 79–106.

- Love S. G. and Ahrens T. J. (1996) Catastrophic impacts on gravity dominated asteroids. *Icarus*, *124*, 141–155.
- McGlaun J. M., Thompson S. L., and Elrick M. G. (1990) CTH: A 3-dimensional shock-wave physics code. *Intl. J. Impact Eng.*, *10*, 351–360.
- McSween H. J. et al. (2013) Composition of the Rheasilvia basin, a window into Vesta's interior. *J. Geophys. Res.*, *118*, 335–346.
- Melosh H. J. (1989) *Impact Cratering: A Geologic Process*. Oxford, New York. 253 pp.
- Melosh H. J. (2007) A hydrocode equation of state for SiO<sub>2</sub>. *Meteoritics & Planet. Sci.*, *42*, 2079–2098.
- Melosh H. J. and Ivanov B. A. (1999) Impact crater collapse. *Annu. Rev. Earth Planet. Sci.*, *27*, 385–415.
- Melosh H. J., Ryan E. V., and Asphaug E. (1992) Dynamic fragmentation in impacts: Hydrocode simulation of laboratory impacts. *J. Geophys. Res.*, *97(E9)*, 14735–14759.
- Michel P., Benz W., and Richardson D. C. (2003) Disruption of fragmented parent bodies as the origin of asteroid families. *Nature*, *421*, 608–611.
- Monaghan J. J. (2012) Smoothed particle hydrodynamics and its diverse applications. *Annu. Rev. Fluid Mech.*, *44*, 323–346.
- Movshovitz N., Asphaug E., and Korycansky D. (2012) Numerical modeling of the disruption of Comet D/1993 F2 Shoemaker-Levy 9 representing the progenitor by a gravitationally bound assemblage of randomly shaped polyhedra. *Astrophys. J.*, *759*, 93.
- O'Brien D. P. and Greenberg R. (2005) The collisional and dynamical evolution of the main-belt and NEA size distributions. *Icarus*, *178*, 179–212.
- Ostro S. J. et al. (2002) Asteroid radar astronomy. In *Asteroids III* (W. F. Bottke Jr. et al., eds.), pp. 151–168. Univ. of Arizona, Tucson.
- Pierazzo E., Artemieva N., Asphaug E., Baldwin E. C., Cazamias J., Coker R., Collins G. S., Crawford D., Elbeshausen D., Holsapple K. A., Housen K. R., Korycansky D. G., and Wünnemann K. (2008) Validation of numerical codes for impact and explosion cratering. *Meteoritics & Planet. Sci.*, *43*, 1917–1938.
- Richardson D. C., Leinhardt Z., Melosh H. J., Bottke W. F., and Asphaug E. (2002) Gravitational aggregates: Evidence and evolution. In *Asteroids III* (W. F. Bottke Jr. et al., eds.), pp. 501–516. Univ. of Arizona, Tucson.
- Richardson J. E., Melosh H. J., and Greenberg R. (2004) Impact-induced seismic activity on asteroid 433 Eros: A surface modification process. *Science*, *306*, 1526–1529.
- Rubin A. E. (1985) Impact melt products of chondritic material. *Rev. Geophys.*, *23*, 277–300.
- Ryan E. V. and Melosh H. J. (1998) Impact fragmentation: From the laboratory to asteroids. *Icarus*, *133*, 1–24.
- Safronov V. S. (1972) *Evolution of the Protoplanetary Cloud and Formation of the Earth and Planets*. Translated in English as NASA TT F-677, Washington, DC.
- Sánchez P. and Scheeres D. J. (2011) Simulating asteroid rubble piles with a self-gravitating soft-sphere distinct element method model. *Astrophys. J.*, *727(2)*, 120.
- Schenk P. et al. (2012) The geologically recent giant impact basins at Vesta's south pole. *Science*, *336*, 694–697.
- Sharp T. G. and de Carli P. S. (2006) Shock effects in meteorites. In *Meteorites and the Early Solar System II* (D. S. Lauretta and H. Y. McSween Jr., eds.), pp. 653–677. Univ. of Arizona, Tucson.
- Stadel J. G. (2001) Cosmological N-body simulations and their analysis. Ph.D. thesis, Univ. of Washington, Seattle.
- Stevenson D. J. (1987) Origin of the Moon — The collision hypothesis. *Annu. Rev. Earth Planet. Sci.*, *15*, 271–315.
- Stewart S. T. and Leinhardt Z. M. (2012) Collisions between gravity-dominated bodies. II. The diversity of impact outcomes during the end state of planet formation. *Astrophys. J.*, *751*, 32–49.
- Stickler A. M., Schultz P. H., and Crawford D. A. (2015) Subsurface failure in spherical bodies: A formation scenario for linear troughs on Vesta's surface. *Icarus*, *247*, 18–34.
- Thomas P. C. and Robinson M. S. (2005) Seismic resurfacing by a single impact on the asteroid 433 Eros. *Nature*, *436*, 366–369.
- Thompson S. L. and Lauzon H. S. (1972) *Improvements in the Chart-D Radiation Hydrodynamic Code III: Revised Analytical Equation of State*. Report SC-RR-710714, Sandia National Laboratories, Albuquerque.
- Tillotson J. H. (1962) *Metallic Equations of State for Hypervelocity Impact*. General Atomic Report GA-3216.
- Neverka J. et al. (2000) NEAR at Eros: Imaging and spectral results. *Science*, *289*, 2088–2097.
- Weidenschilling S. J. and Cuzzi J. N. (2006) Accretion dynamics and timescales: Relation to chondrites. In *Meteorites and the Early Solar System II* (D. S. Lauretta and H. Y. McSween Jr., eds.), pp. 473–485. Univ. of Arizona, Tucson.
- Wood J. A. (1964) The cooling rates and parent planets of several iron meteorites. *Icarus*, *3*, 429–459.
- Wünnemann K., Collins G. S., and Melosh H. J. (2006) A strain based porosity model for use in hydrocode simulations of impacts and implications for transient crater growth in porous targets. *Icarus*, *180*, 514–527.
- Yang J., Goldstein J. I., and Scott E. R. D. (2007) Iron meteorite evidence for early formation and catastrophic disruption of protoplanets. *Nature*, *446*, 888–891.



## *Color Section*



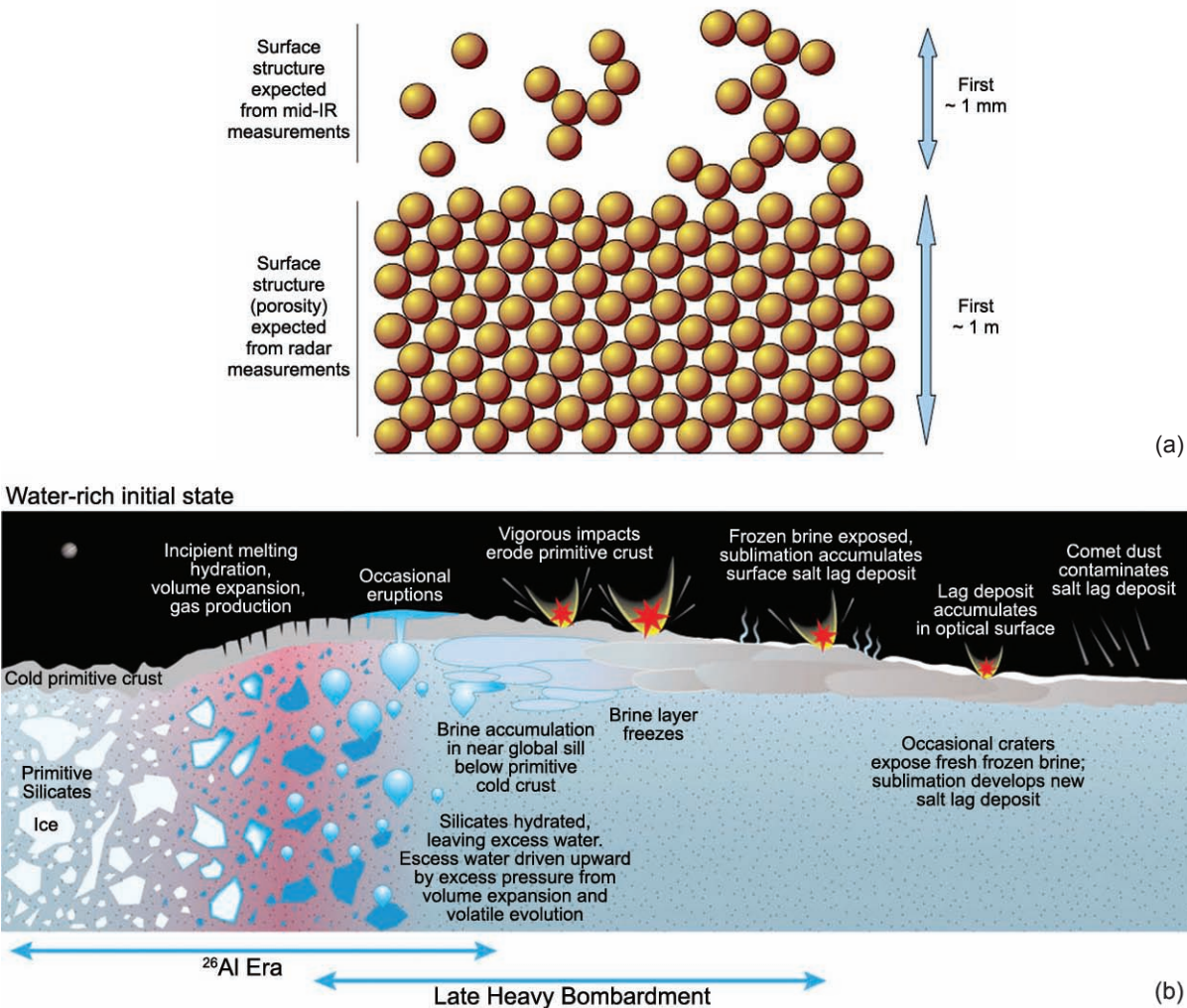


**Plate 1. (a)** Schematic model of an underdense, "fairy-castle" regolith on Trojan asteroids deduced from comparisons between MIR emissivity spectra of Trojans and laboratory measurements of powdered meteorites mixed with KBr. From Vernazza *et al.* (2012). **(b)** Evolutionary scenario that might produce salt-rich surfaces, in which embedded fine-grained silicate dust could explain measured MIR emissivity spectra of Trojans. From Yang *et al.* (2013).

Accompanies chapter by Emery *et al.* (pp. 203–220).

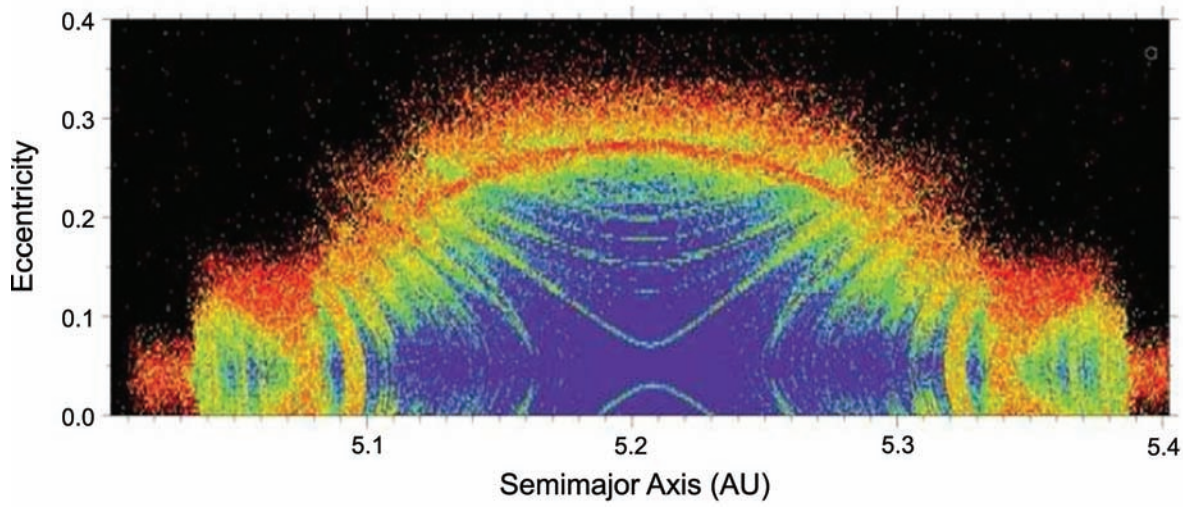


**Plate 2.** Diffusion map around  $L_4$  for an N-body model including the outer four planets. Blue indicates stable orbits while red corresponds to highly chaotic motion. The black zone marks trajectories that lead to ejection from  $L_4$  on a short timescale. From *Robutel and Gabern* (2006).

Accompanies chapter by Emery et al. (pp. 203–220).

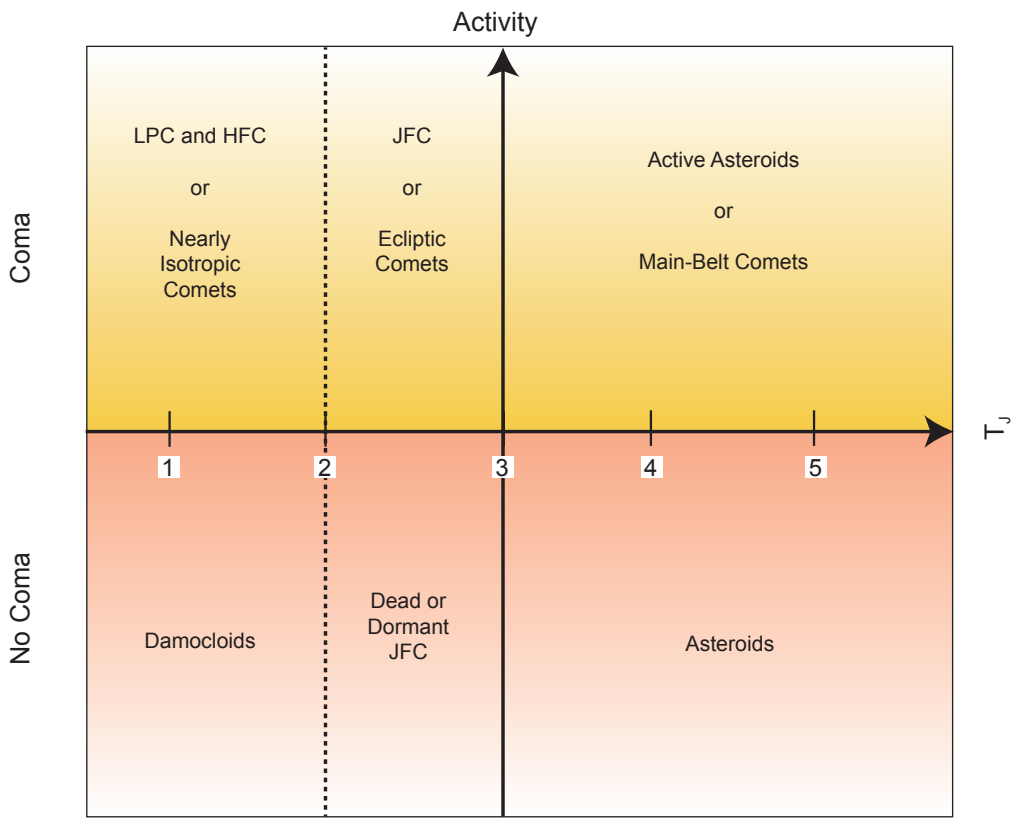


**Plate 3.** Empirical classification of small bodies based on the Tisserand parameter,  $T_J$  (x-axis), and the presence or absence of coma (y-axis). JFC, LPC, and HFC are the Jupiter-family, long-period, and Halley-family comet subtypes, distinguished by their dynamics. From Jewitt (2012).

Accompanies chapter by Jewitt et al. (pp. 221–241).

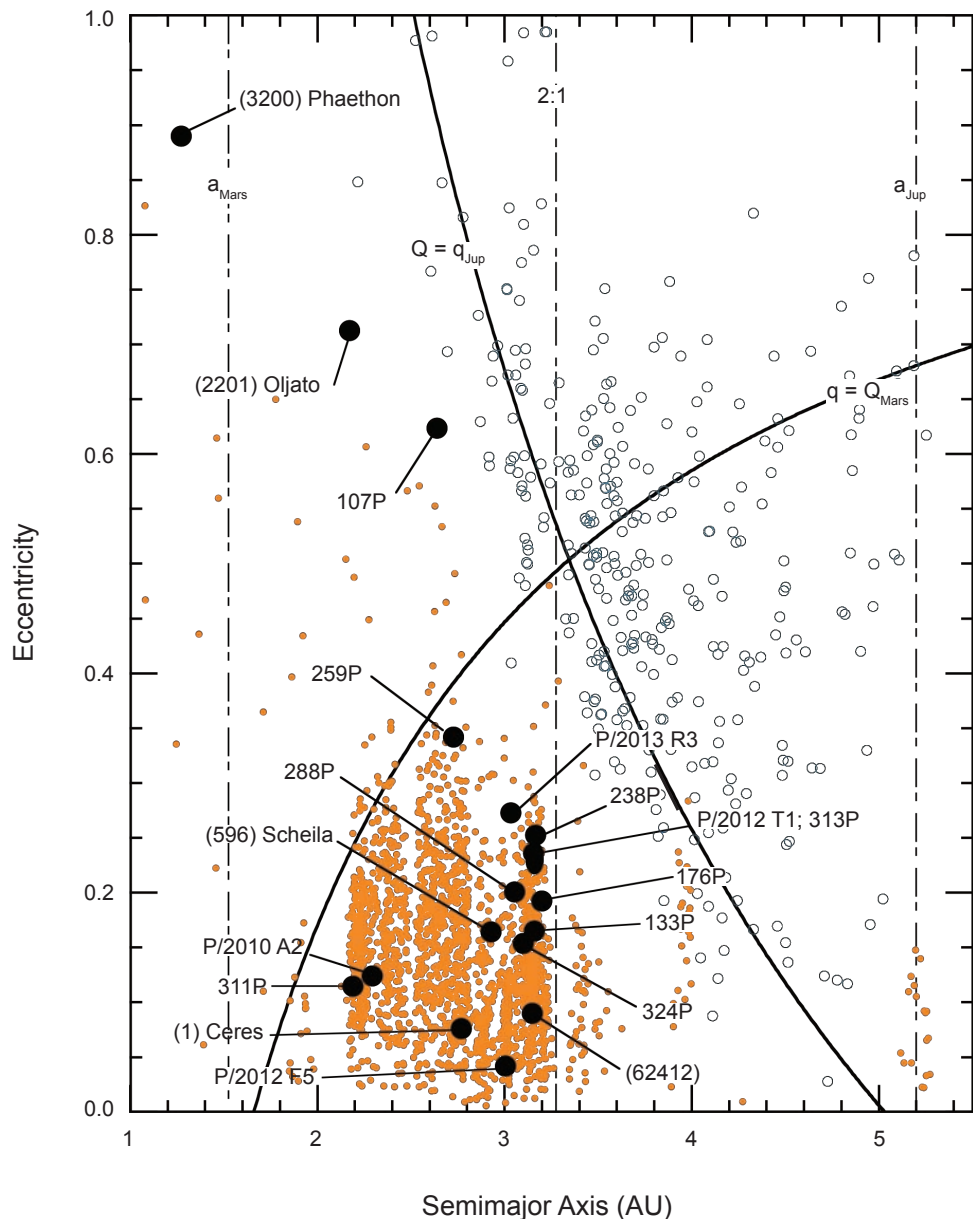


**Plate 4.** Distribution of the active asteroids in the semimajor axis vs. orbital eccentricity plane. Dynamical asteroids are shown as filled orange circles, comets as empty blue symbols, and the active asteroids as black circles, each labeled with the object name (cf. Table 1). Objects plotted above the diagonal arcs cross either the orbit of Mars or Jupiter.

Accompanies chapter by Jewitt et al. (pp. 221–241).

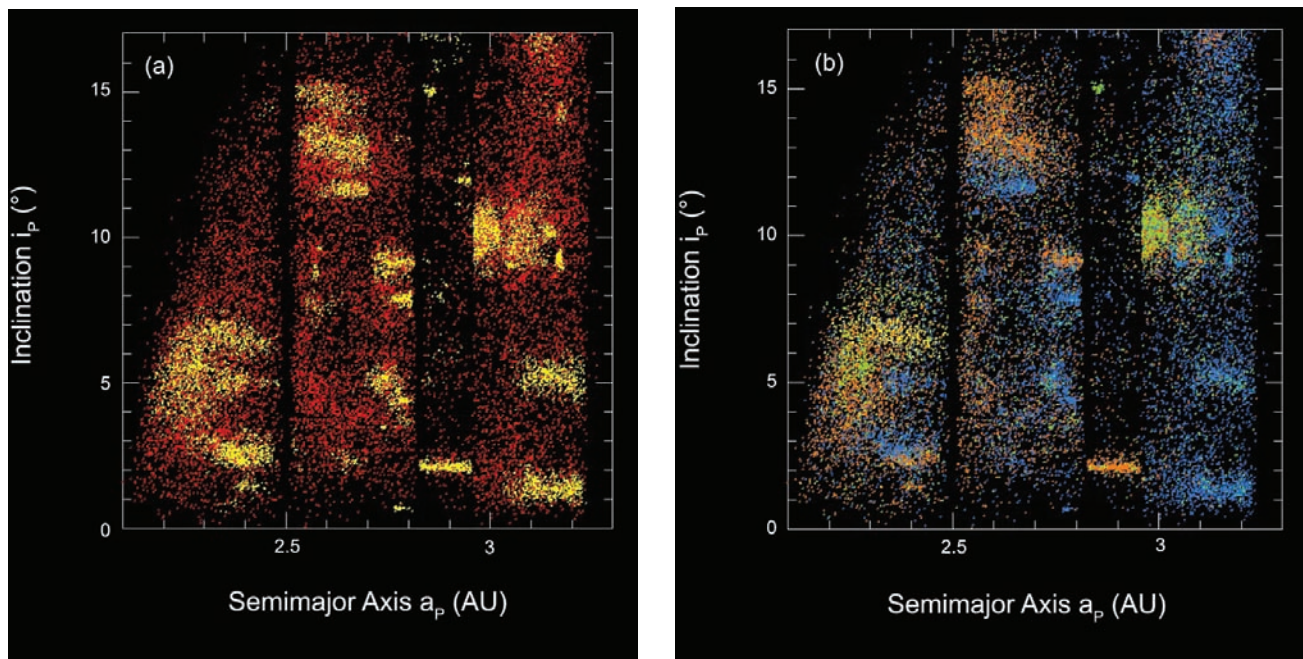


**Plate 5.** (a) Clustering algorithm applied to the asteroid belt separates dynamical families (yellow) from the background (red). (b) Variation in reflectance properties of main-belt asteroids. Here we plot  $\approx 25,000$  asteroids that were observed by both SDSS and WISE. The color code was chosen to highlight the albedo/color contrast of different families.

Accompanies chapter by Nesvorný et al. (pp. 297–321).



**Plate 6.** The Dawn spacecraft depicted as it left Earth on September 27, 2007.

Accompanies chapter by Russell et al. (pp. 419–432).

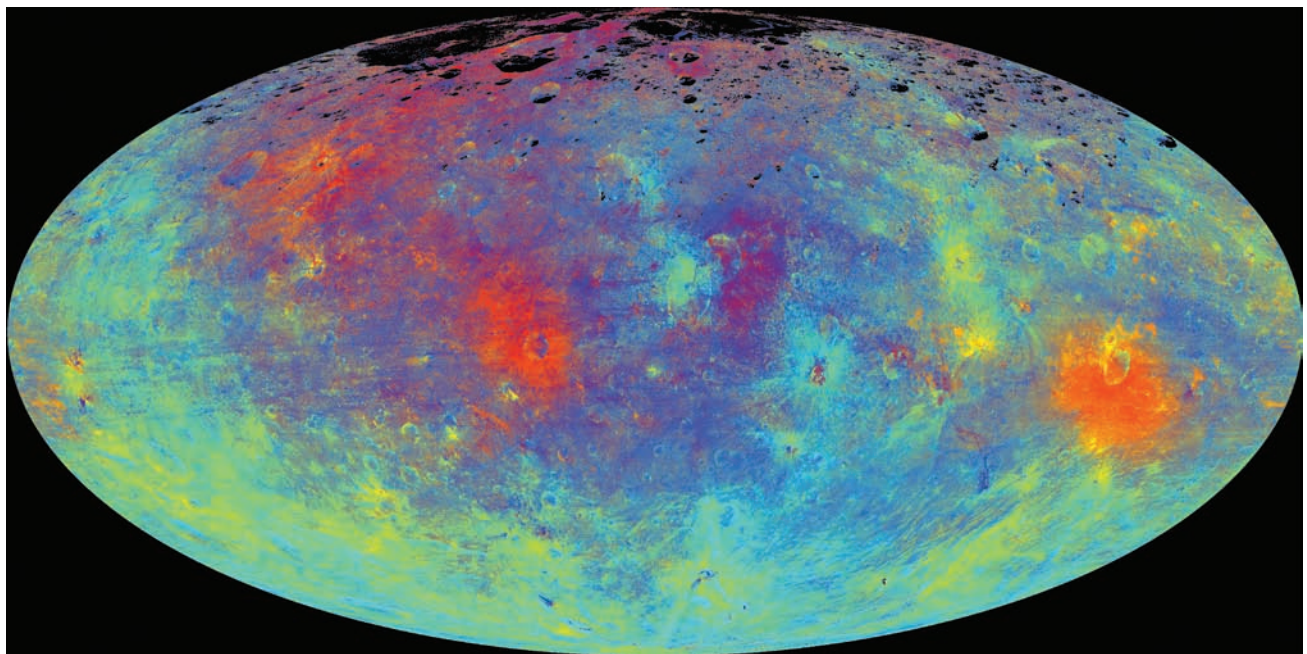


**Plate 7.** Mollweide projection of FC color mosaic using Clementine ratios (A. Nathues, personal communication, 2014).

Accompanies chapter by Russell et al. (pp. 419–432).

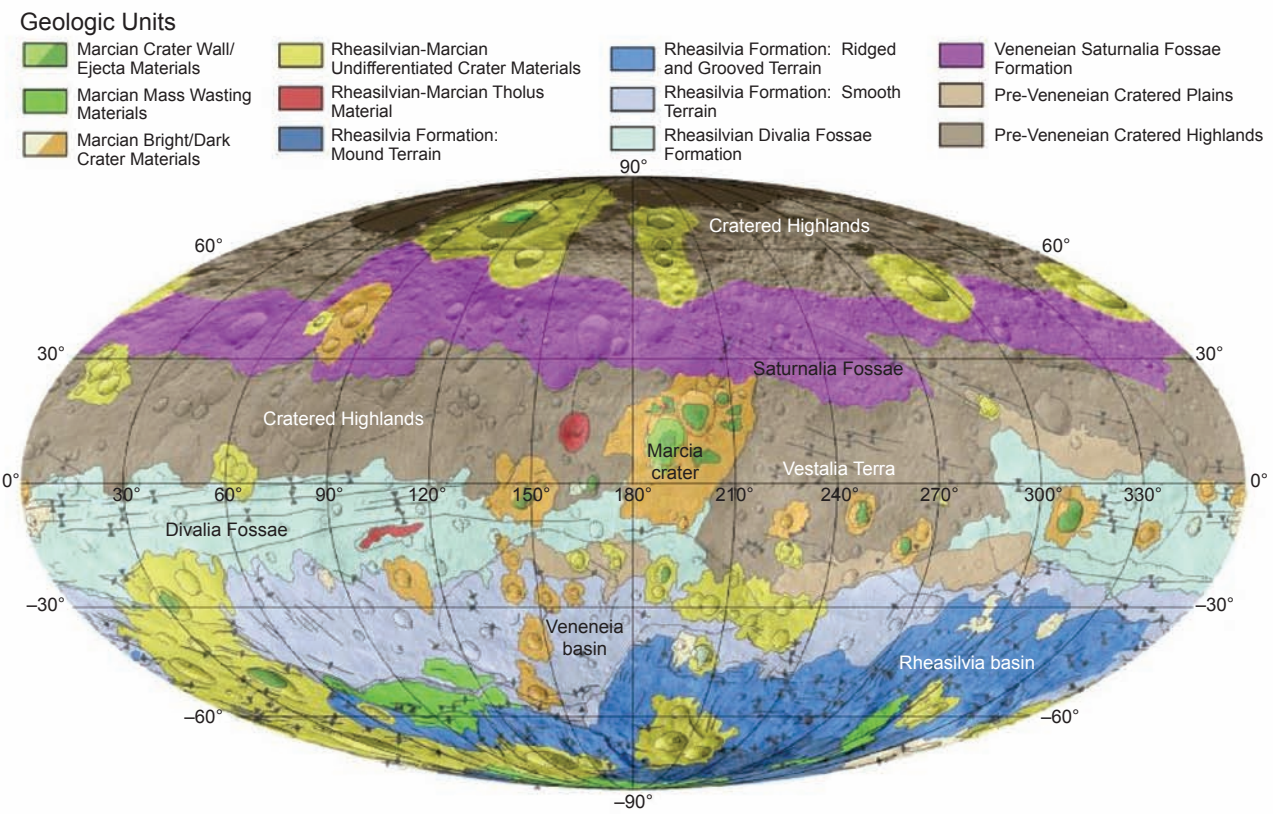


**Plate 8.** Geologic map of Vesta using Mollweide projection. Major terrains are identified here. From Jaumann *et al.* (2012) and Williams *et al.* (2014a).

Accompanies chapter by Russell *et al.* (pp. 419–432).

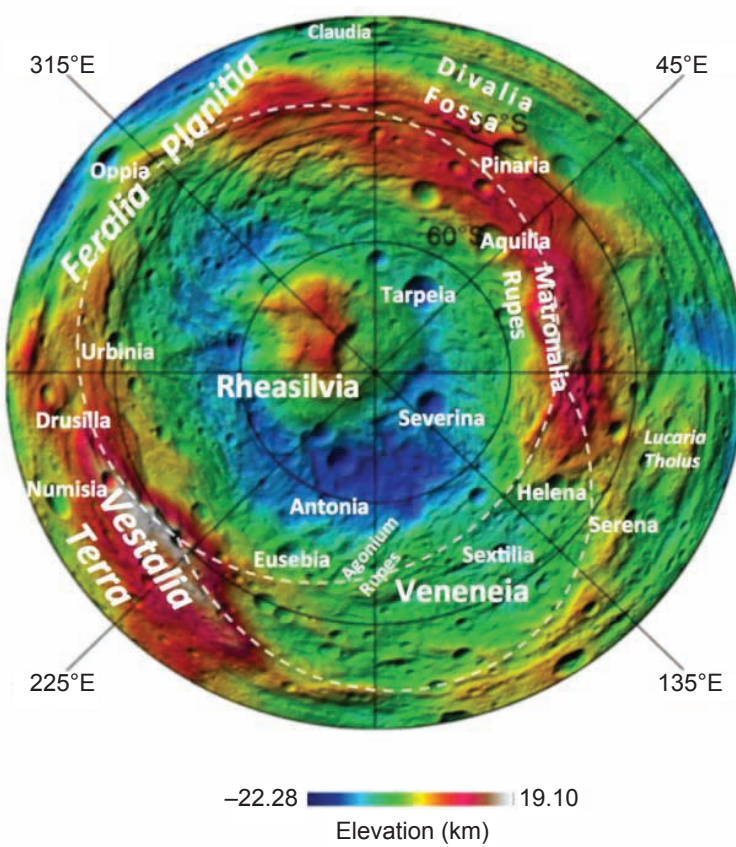


**Plate 9.** The Veneneia and Rheasilvia south polar basins and their geological environment. From Jaumann *et al.* (2012).

Accompanies chapter by Russell *et al.* (pp. 419–432).

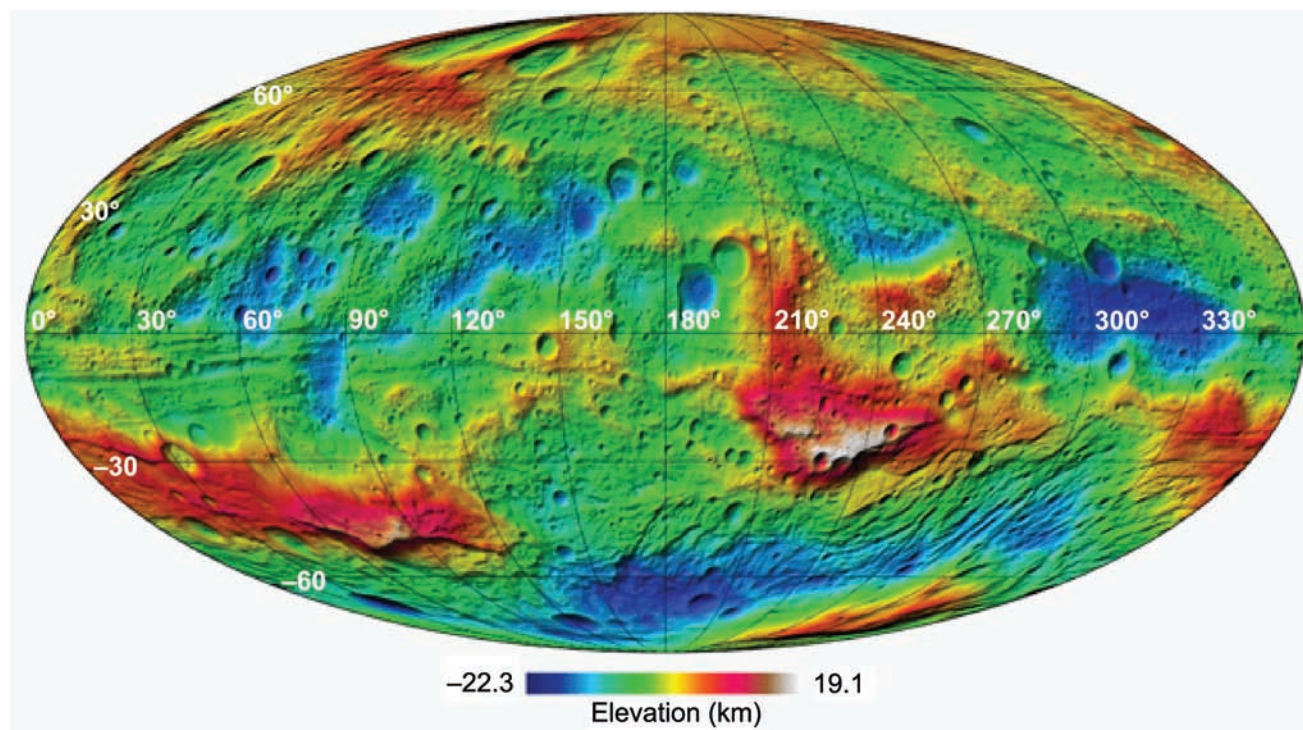


**Plate 10.** Mollweide projection of Dawn topography data.

Accompanies chapter by Russell et al. (pp. 419–432).

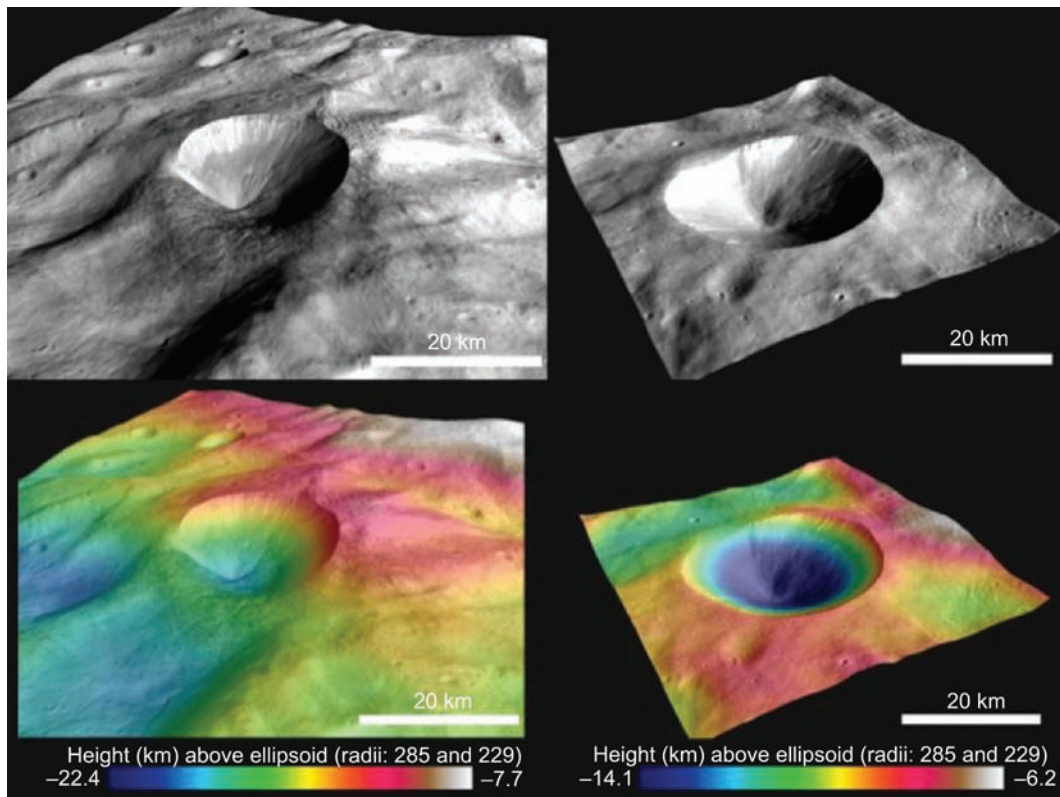


**Plate 11.** Typical impact crater on Vesta: Antonia ( $200.8^{\circ}\text{E}$ ,  $58.7^{\circ}\text{S}$ ; diameter  $16.75\text{ km}$ ) is an impact on a slope of asymmetric shape with the ejecta mainly concentrated downhill also covering the downslope crater rim; Sextilia ( $145.9^{\circ}\text{E}$ ,  $39^{\circ}\text{S}$ ; diameter  $19.48\text{ km}$ ) is of approximately the same size, located on a more gentle slope, and circular in shape but exposing significant mass wasting inside the crater on the uphill rim (Jaumann *et al.*, 2012; Krohn *et al.*, 2014b).

Accompanies chapter by Russell *et al.* (pp. 419–432).

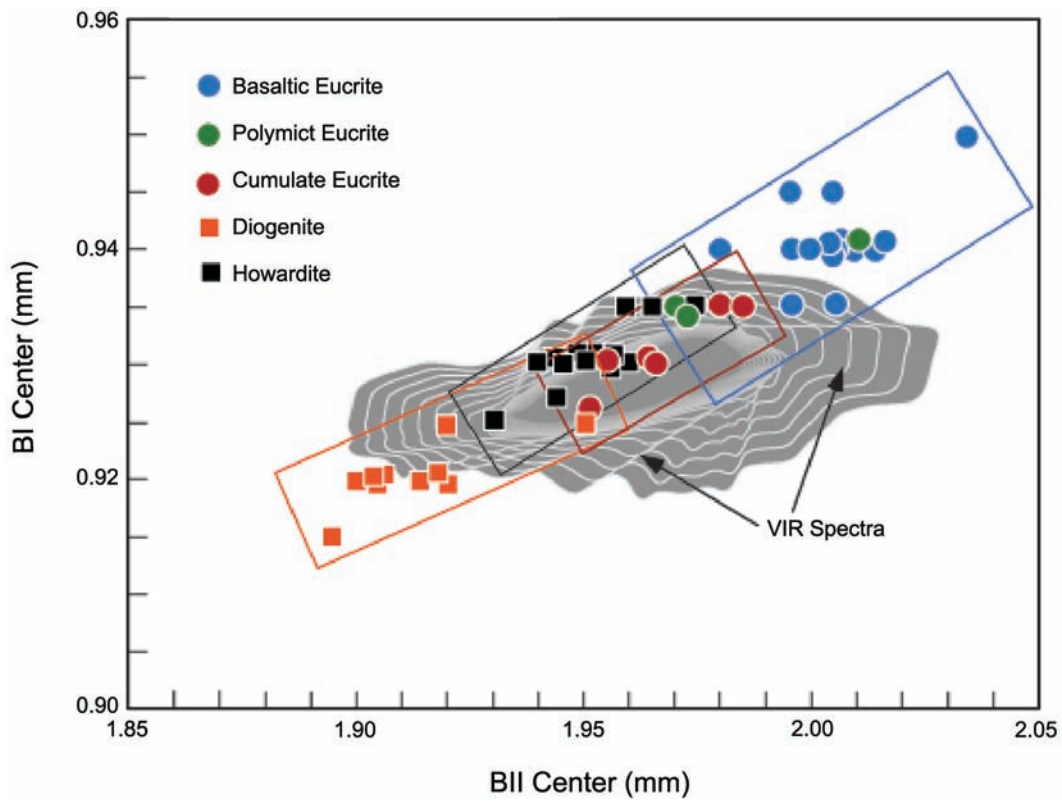


**Plate 12.** BI vs. BII for VIR data and HEDs (De Sanctis et al., 2012a, 2013).

Accompanies chapter by Russell et al. (pp. 419–432).

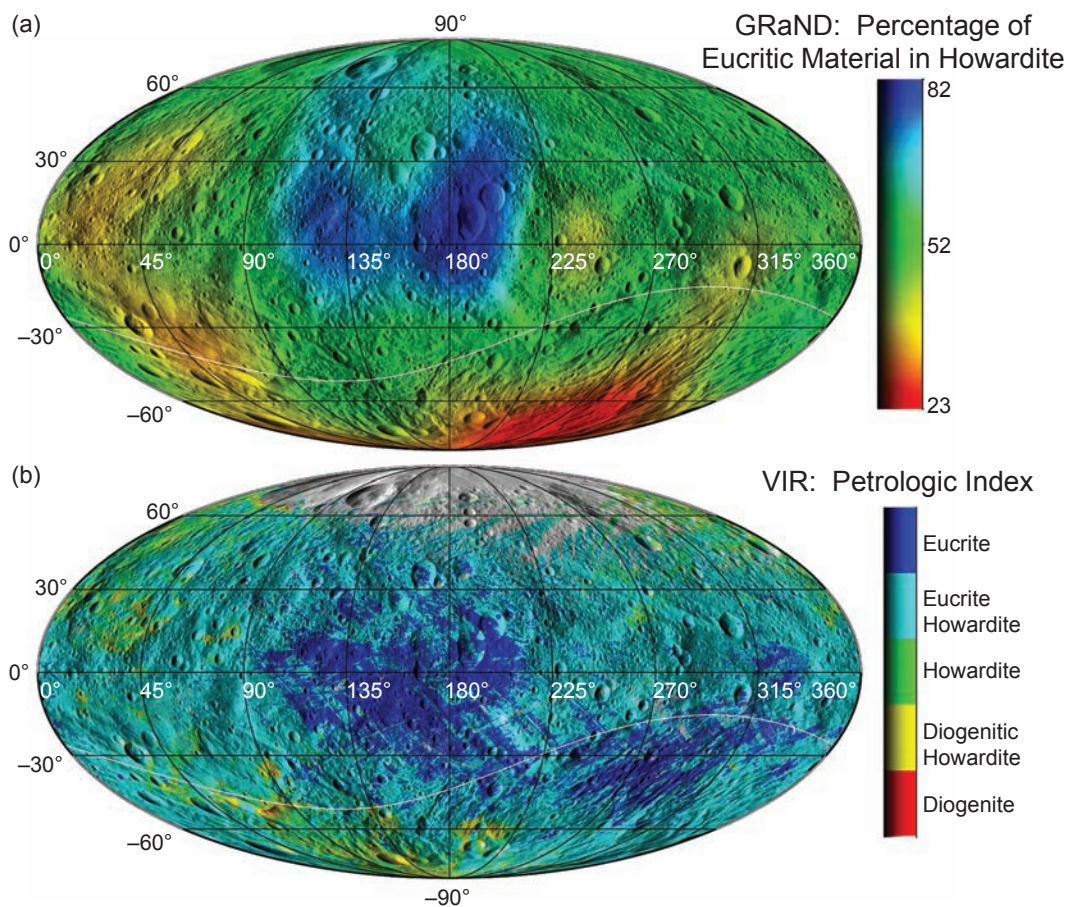


**Plate 13.** Lithologic maps of Vesta remapped in Mollweide projection. (a) Map of HED distribution mapped by VIR (Ammannito et al., 2013). (b) Map of the percentage of eucritic material from GRaND data (Prettyman et al., 2013). Eucritic regions appear as blue, whereas regions that are more diogenitic appear as red.

Accompanies chapter by Russell et al. (pp. 419–432).

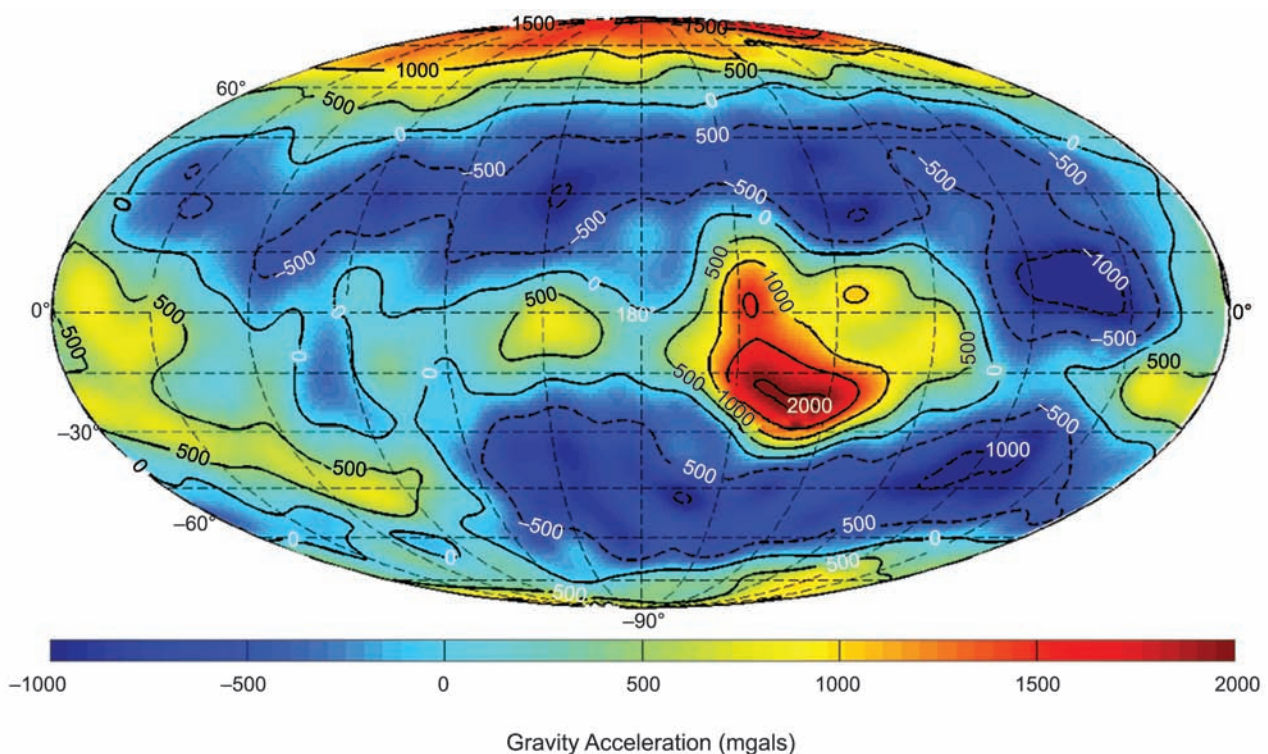


**Plate 14.** The Vesta radial gravity solution mapped to a 290 × 265-km ellipsoid surface through degree 20. The  $J_2$  coefficient has been removed. The maximum and minimum range is given by 2100 mgal at the large equatorial high near 126°W longitude and -1270 mgal, also near the equator at 44°W. From Konopliv et al. (2013).

Accompanies chapter by Russell et al. (pp. 419–432).

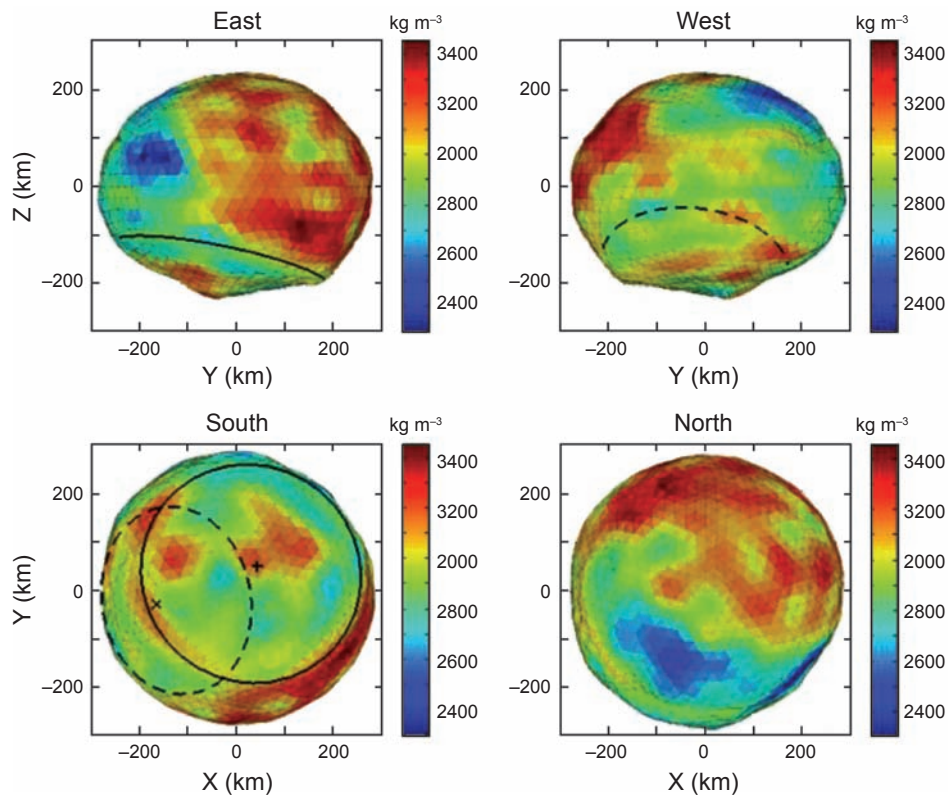


**Plate 15.** The lateral crustal density estimation of the three-layer Vesta (257 × 207-km mantle and 117 × 105-km core). Solid black and dashed black circles represent Rheasilvia and Veneneia impact basins, respectively. The lateral crustal density variation ranges from 2310 to 3440  $\text{kg m}^{-3}$ , which is required to remove the gravity anomaly. From R. S. Park (personal communication, 2014).

Accompanies chapter by Russell et al. (pp. 419–432).

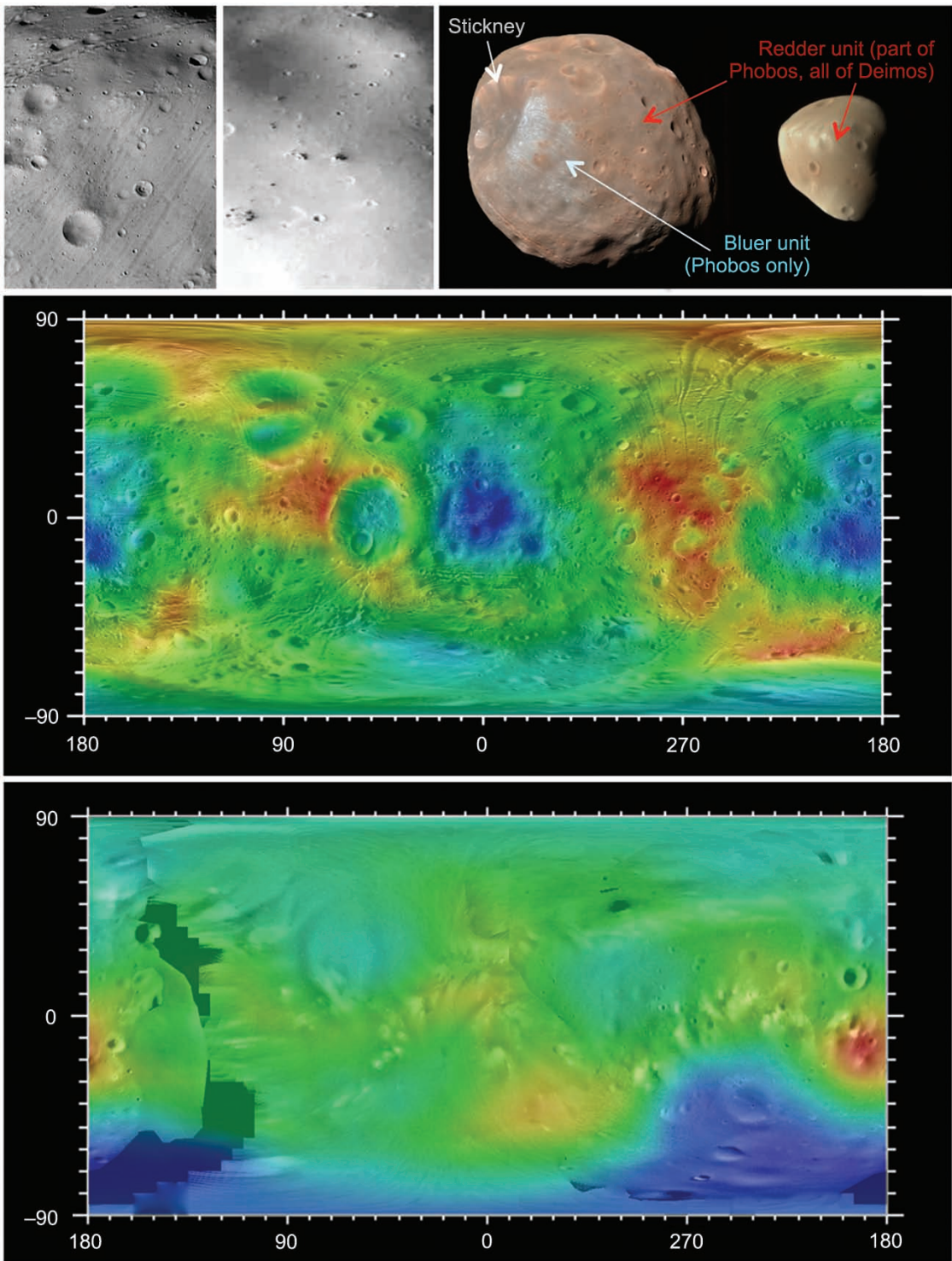


**Plate 16.** Spacecraft exploration reveals global properties of Phobos and Deimos, and basic differences between them. *Top left:* Viking images revealed that Phobos' surface is relatively rough, with well-preserved craters, and parallel topographic grooves. *Top center:* Deimos' surface is smooth with craters infilled by regolith. *Top right:* Multispectral and hyperspectral imaging from Phobos 2, Mars Express, and the Mars Reconnaissance Orbiter (shown, centered on the sub-Mars hemispheres) reveal spatial variations in Phobos' spectral properties, especially associated with Stickney. Deimos' brightness variations are accompanied by less color variation. *Middle:* Phobos simple cylindrical image map and dynamical height, using shape model from Gaskell (2011) and image mosaic from Stooke (2011). Red is high, blue low, with a range of heights of 1.8 km. *Bottom:* Deimos simple cylindrical image map and dynamical heights, using shape model and image mosaic updated from Thomas (1993). Red is high, blue low, with a range of heights of 1.9 km.

Accompanies chapter by Murchie et al. (pp. 451–467).

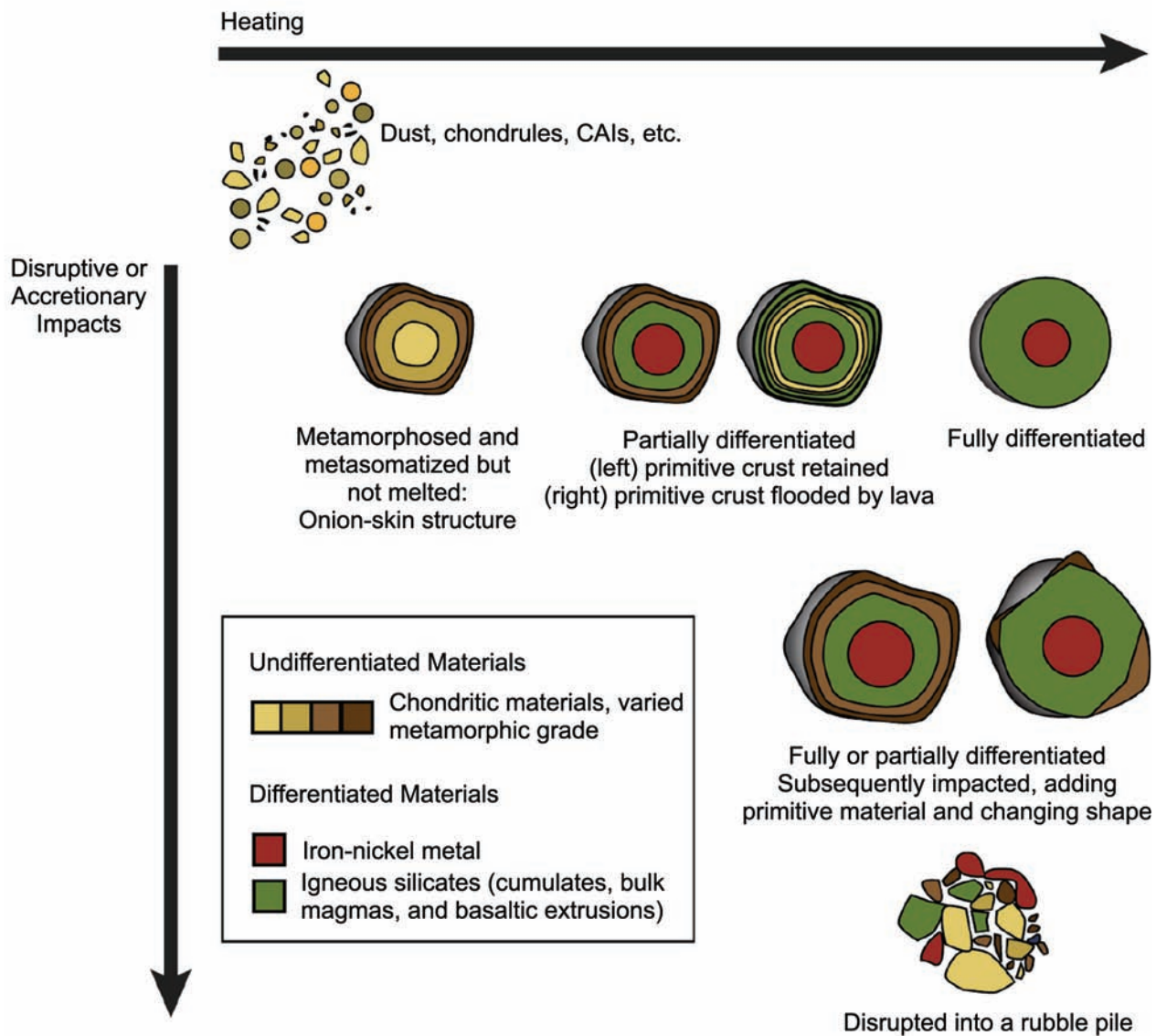


**Plate 17.** Three possible end-states of asteroid differentiation. *Left:* Unmelted but variably metamorphosed and aqueously altered body composed of chondritic materials. *Middle:* Partially differentiated body with melted interior and unmelted surface layer. *Right:* Fully differentiated body with metallic core and igneous silicate mantle. *Bottom:* Partially or fully differentiated bodies disrupted and coated by later impacts, disrupted even to the point of internal disorganization into a rubble pile.

Accompanies chapter by Scheinberg et al. (pp. 533–552).

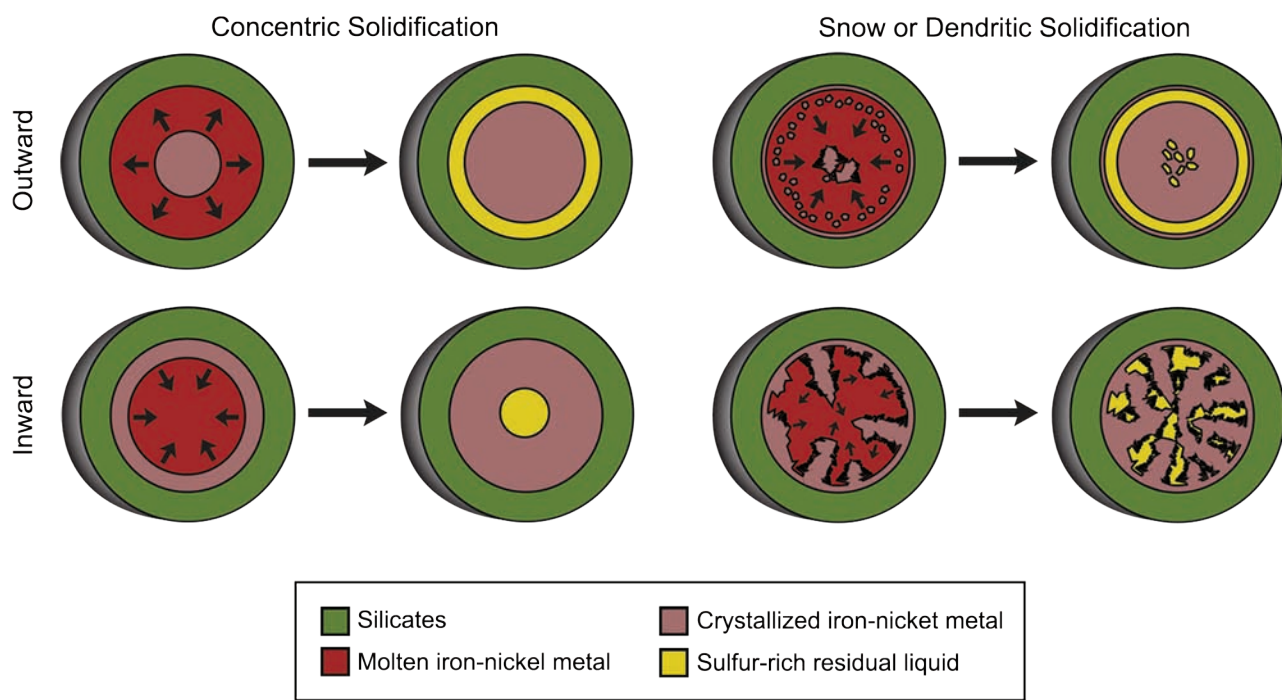


**Plate 18.** Four possible core solidification scenarios and potentially resulting end-states. *Top left:* Outward (Earth-like) solidification. *Bottom left:* Concentric inward solidification. *Top right:* Outward solid core growth due to accumulated iron “snow” and/or destabilized dendrites. *Bottom right:* Dendritic inward solidification.

Accompanies chapter by Scheinberg et al. (pp. 533–552).

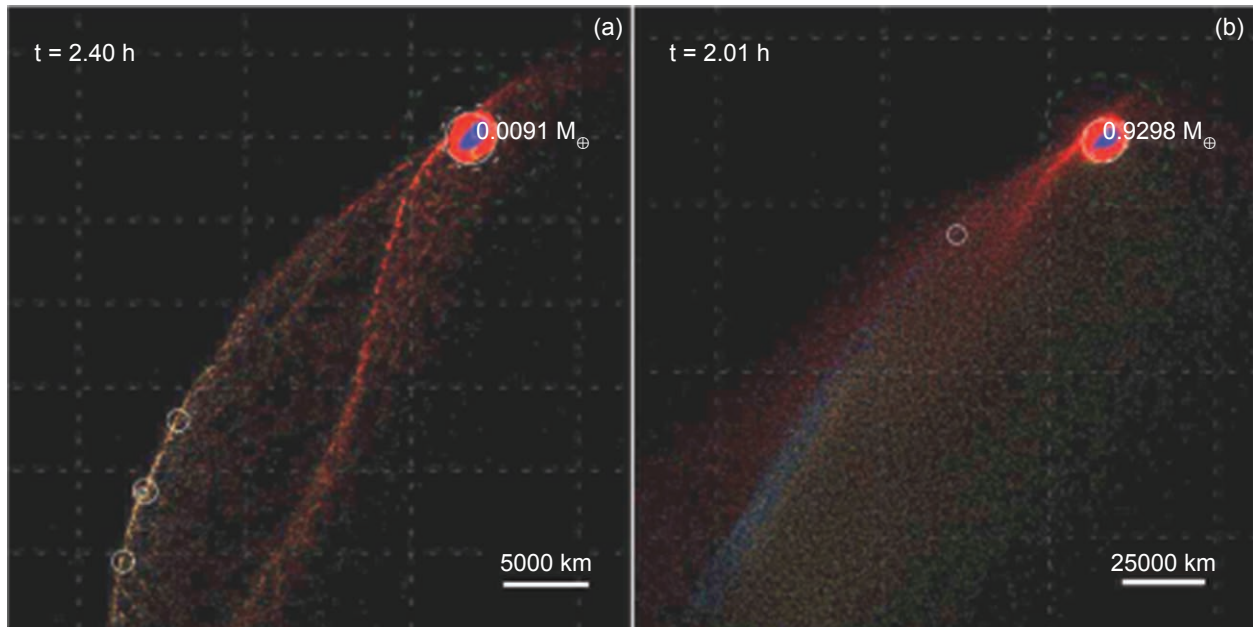


**Plate 19.** Simulations of two collisions with the same  $M_2/M_1 = 0.2$ ,  $\theta = 30^\circ$ ,  $v_{\text{imp}} = 3 v_{\text{esc}}$ , but differing in mass by a factor of 100. Both are shown at  $\sim 10$  collision times,  $\tau_{\text{coll}} = 2(R_1 + R_2)/v_{\text{imp}}$ . Silicates (red) are segregated from metals (blue) in the remnants of  $M_2$  and are dispersed downrange in both hit-and-run collisions. The subsonic collision (left;  $R_1 = 1400$  km,  $R_2 = 800$  km) leads to a chain of iron-dominated clumps (white circles) stripped gravitationally and mechanically from a sheet of lower-density mantle material. The supersonic collision (right;  $M_1 = M_\oplus$ ,  $v_{\text{imp}} \approx 30$  km s $^{-1}$ ), produces intense global shocks and fine dispersal of the plume. After Asphaug and Reufer (2014).

Accompanies chapter by Scott et al. (pp. 573–595).

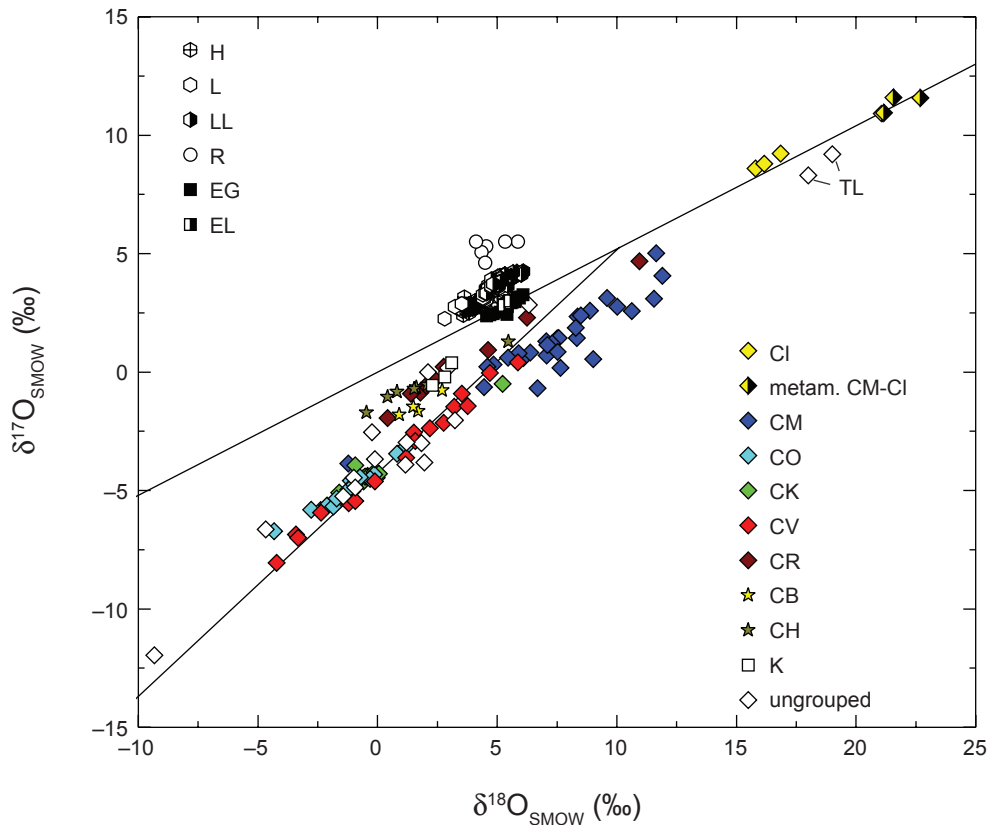


**Plate 20.** Bulk oxygen-isotope compositions of chondrite groups and ungrouped chondrites. Terrestrial fractionation line (TFL) and carbonaceous chondrite anhydrous mineral (CCAM) line are shown for reference. Oxygen-isotopic compositions are reported as  $\delta^{17}\text{O}$  and  $\delta^{18}\text{O}$ , deviations from Vienna Standard Mean Ocean Water (SMOW) [ $^{17}\text{O}/^{16}\text{O}_{\text{SMOW}} = 0.000380$ ;  $^{18}\text{O}/^{16}\text{O}_{\text{SMOW}} = 0.002005$  (*De Laeter et al.*, 2003)] in parts per thousand:  $\delta^{17,18}\text{O}_{\text{SMOW}} = [(^{17,18}\text{O}/^{16}\text{O}_{\text{sample}})/(^{17,18}\text{O}/^{16}\text{O}_{\text{SMOW}})-1] \times 1000$ . Carbonaceous chondrites, except Cls, plot below the TFL; noncarbonaceous chondrites, except EHs and ELs, plot above it. After *Krot et al.* (2014a). Data for Tagish Lake (TL) are from *Brown et al.* (2000).

Accompanies chapter by Krot et al. (pp. 635–660).

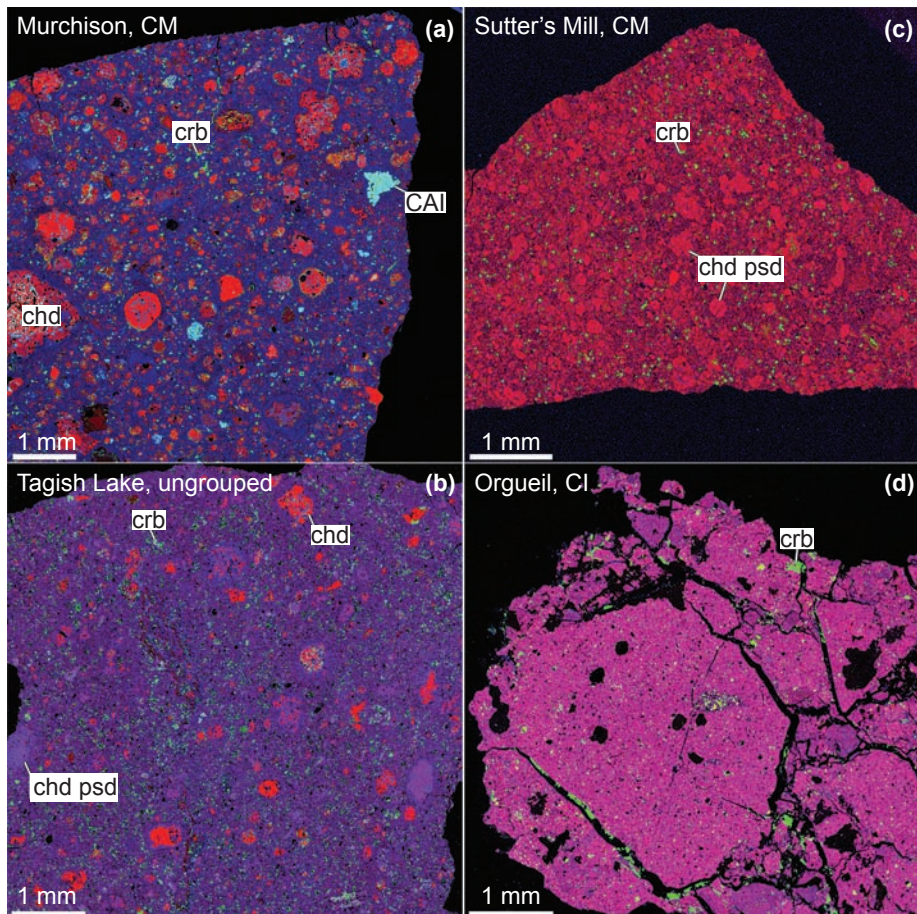


**Plate 21.** Combined elemental maps ( $\text{Mg} = \text{red}$ ,  $\text{Ca} = \text{green}$ ,  $\text{Al} = \text{blue}$ ) of extensively aqueously altered chondrites: **(a)** Murchison (CM2.5), **(b)** ungrouped carbonaceous chondrite Tagish Lake, **(c)** Sutter's Mill (CM2.1), and **(d)** Orgueil (CI1). Murchison contains abundant magnesian chondrules (chd, red), CAIs (bluish), and heavily hydrated matrix (purple) containing relatively rare grains of carbonate (crb, green). In Sutter's Mill, CAIs, chondrules, and matrix are nearly completely replaced by phyllosilicates and carbonates; chondrule pseudomorphs (chd psd) are common. Tagish Lake contains a higher proportion of heavily hydrated matrix and carbonates, and fewer chondrules and CAIs than Murchison; incompletely altered chondrules are common; some chondrules are nearly completely replaced by phyllosilicates. Orgueil consists entirely of hydrated matrix material; chondrule pseudomorphs are absent.

Accompanies chapter by Krot et al. (pp. 635–660).

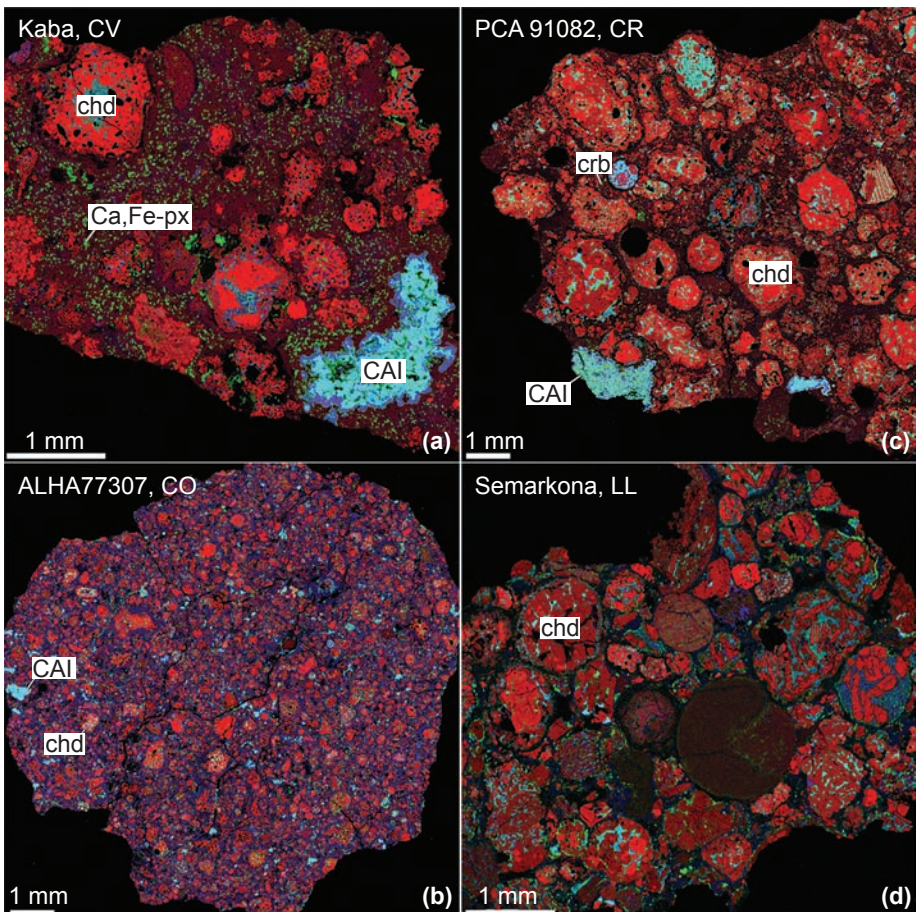


**Plate 22.** Combined elemental maps (Mg = red, Ca = green, Al = blue) of weakly aqueously altered chondrites: (a) Kaba (CV3.1), (b) ALH A77307 (CO3.1), (c) PCA 91082 (CR2), and (d) Semarkona (LL3.0). Chondrules (chd) and CAIs in these meteorites show little evidence for aqueous alteration; matrices are more aqueously altered and contain phyllosilicates, magnetite, and fayalite (except PCA 91082). The Kaba matrix contains abundant Ca,Fe-rich pyroxenes (Ca,Fe-px); the PCA 91082 matrix contains rare carbonate (crb) grains.

Accompanies chapter by Krot et al. (pp. 635–660).

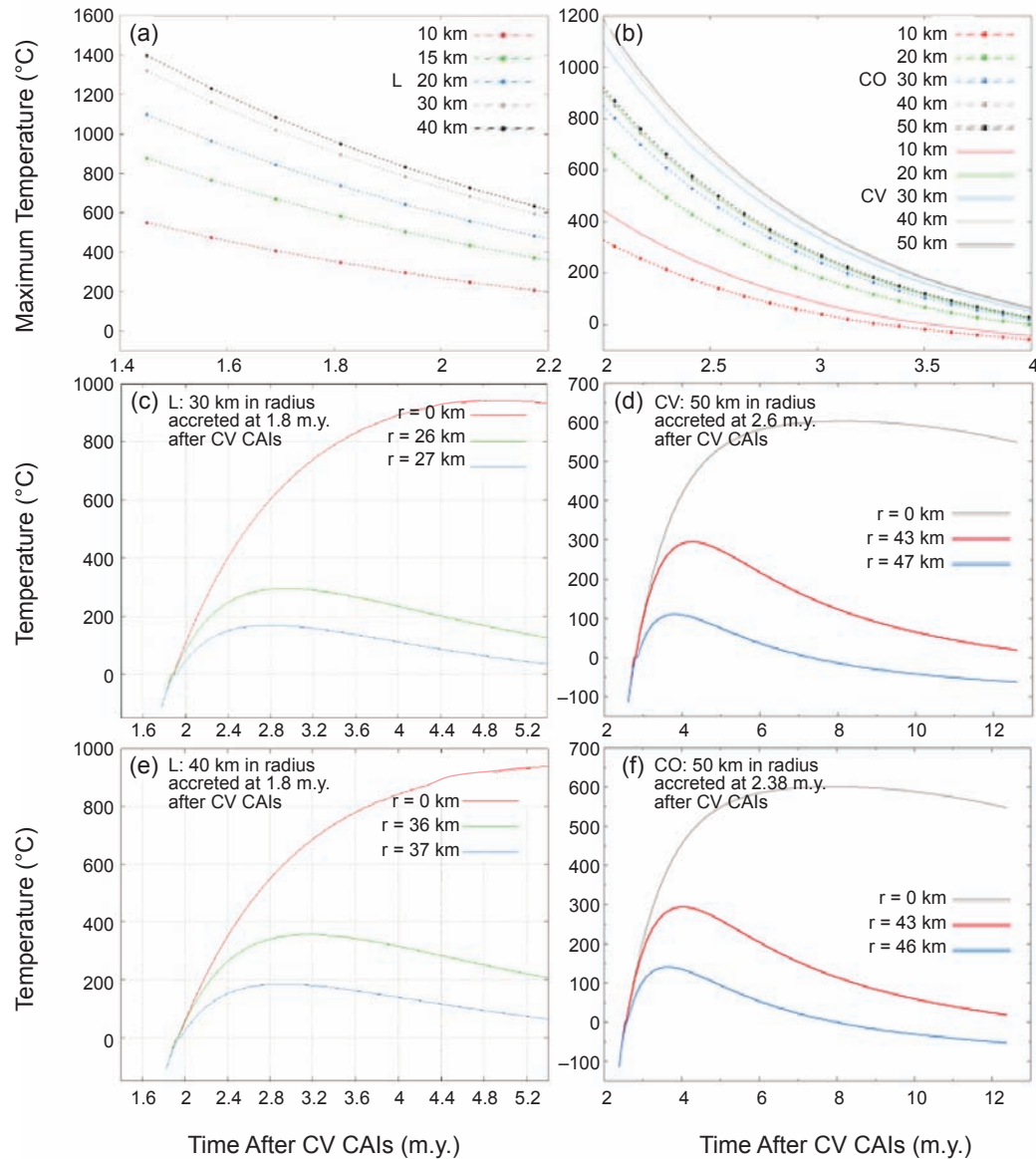


**Plate 23.** **(a,b)** Modeled peak metamorphic temperature for L-, CV-, and CO-like chondrite parent bodies ranging from 10 to 50 km in radius as a function of time after CV CAIs. **(c–f)** Temperature evolution diagrams at different depths shown for **(c,e)** L-like chondrite parent body of 30 and 40 km in radius, **(d)** CV-like chondrite parent body of 50 km in radius, and **(e)** CO-like chondrite parent body of 50 km in radius. Blue and green lines in **(c)** and **(e)** and blue and red lines in **(d)** and **(f)** correspond to regions where thermal conditions ( $\sim 100^\circ\text{--}300^\circ\text{C}$ ) would be suitable for the formation of fayalite at the time inferred from  $^{53}\text{Mn}$ - $^{53}\text{Cr}$  relative chronology. Figure from Doyle *et al.* (2015).

Accompanies chapter by Krot *et al.* (pp. 635–660).

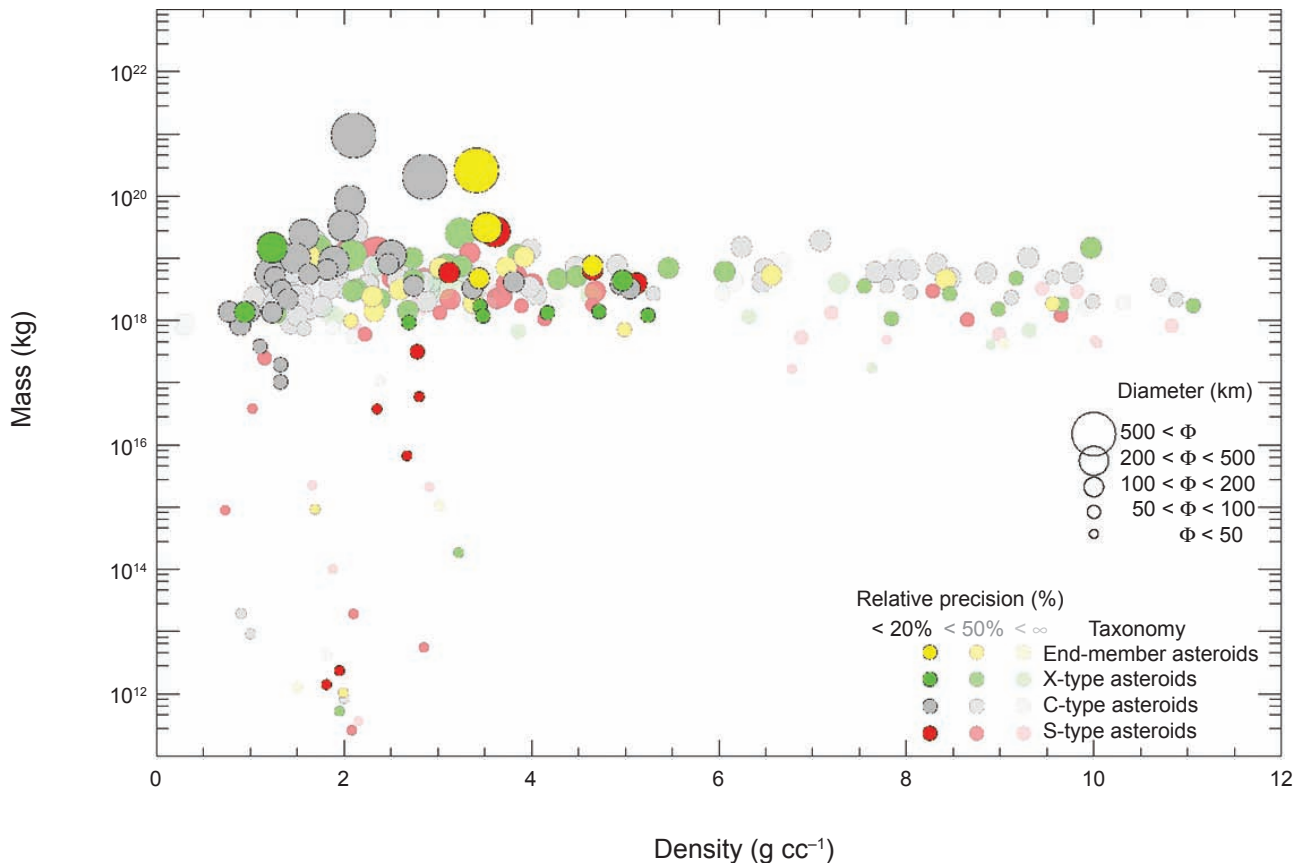


**Plate 24.** Density vs. mass. Asteroids are divided into four taxonomic groups (from DeMeo et al., 2009): S-complex in red, C-complex in gray, X-complex in green, and end members in yellow. The size of the symbols indicates the asteroid diameter, below 50 km, between 50 and 100 km, 100 and 200 km, 200 and 500 km, and above 500 km. The three different levels of contrast correspond to three cuts of relative accuracy: <20%, <50%, and regardless of precision (<∞).

Accompanies chapter by Scheeres et al. (pp. 745–766).

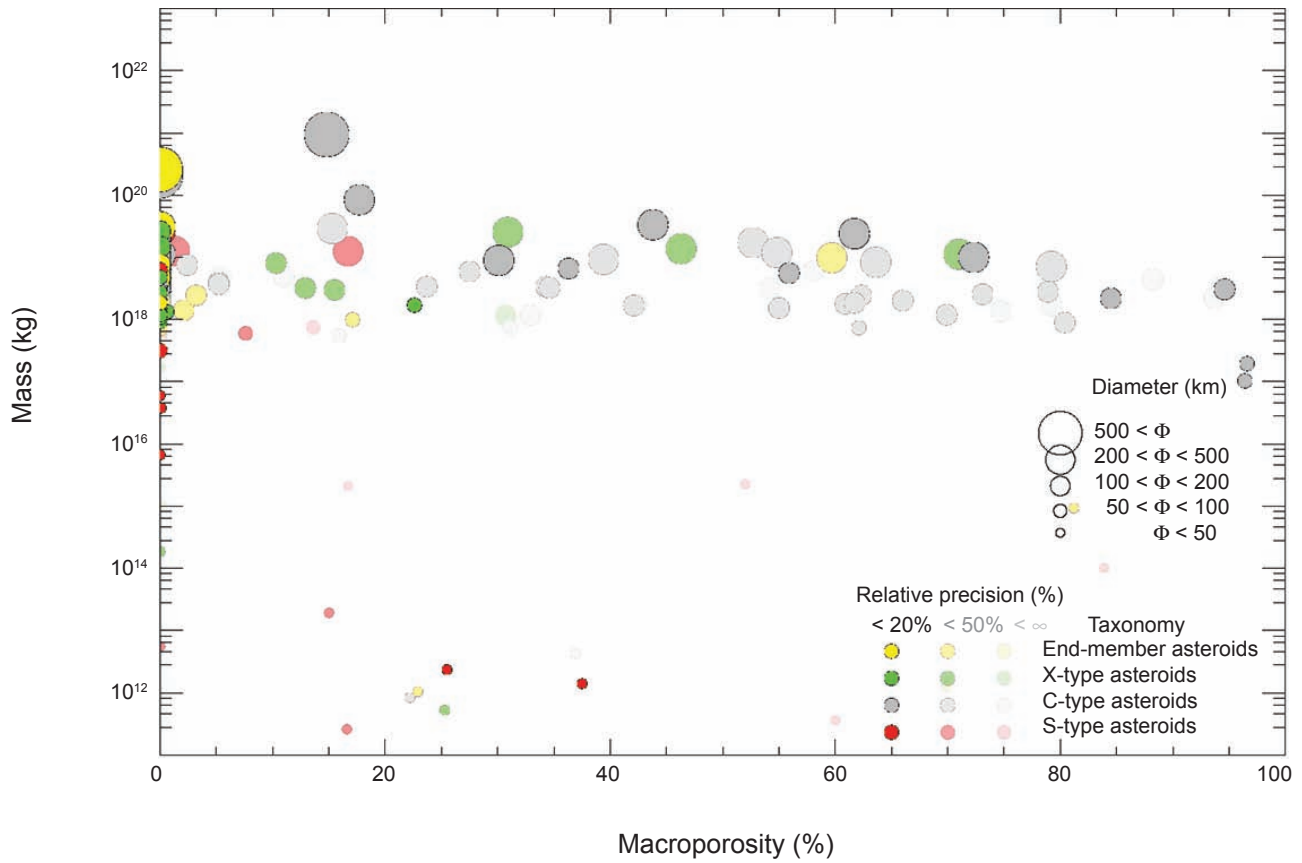


**Plate 25.** Macroporosity vs. mass. See Plate 24 for the explanation of symbols.

Accompanies chapter by Scheeres et al. (pp. 745–766).

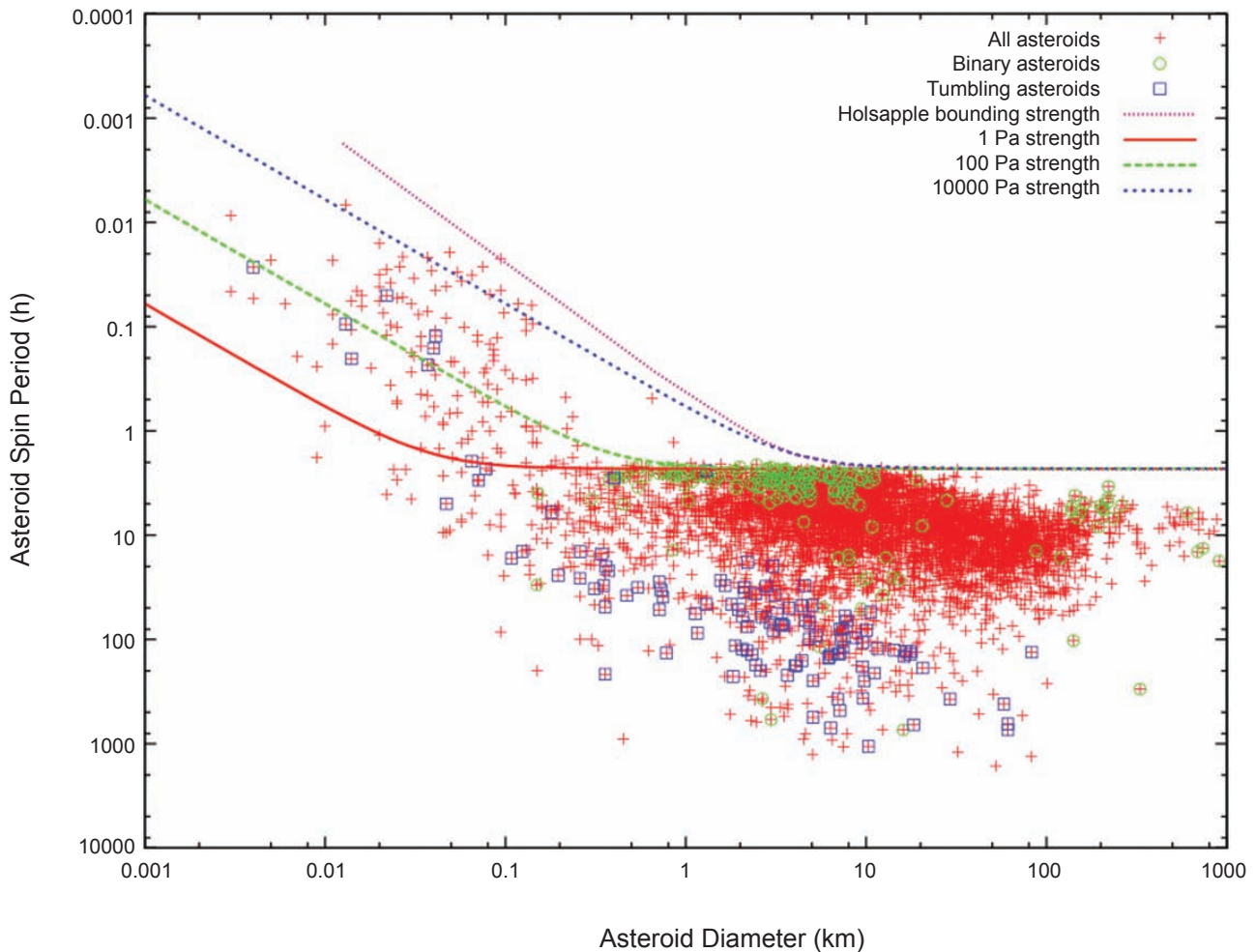


**Plate 26.** Asteroid size vs. spin period, with binaries and tumblers called out specifically. All others are assumed to be single, uniform rotators. Only bodies with periods deemed to be reliable (see Warner *et al.*, 2009) are shown. The plot shows distinct structures. No object larger than a kilometer in diameter spins faster than an ~2.4-h period, now known as the gravity spin barrier and that is understood to not be an indicator of cohesionless material by itself. Instead it is simply that at these size scales the gravity effects dominate any strength effect. A number of smaller bodies spin faster; those must experience tensile stress and must have some cohesive strength to hold together. Typically, the observed maximum spins are larger for smaller sizes. Also plotted are spin limits as a function of diameter for levels of asteroid strength. Data shown is as of August 2014.

Accompanies chapter by Scheeres *et al.* (pp. 745–766).

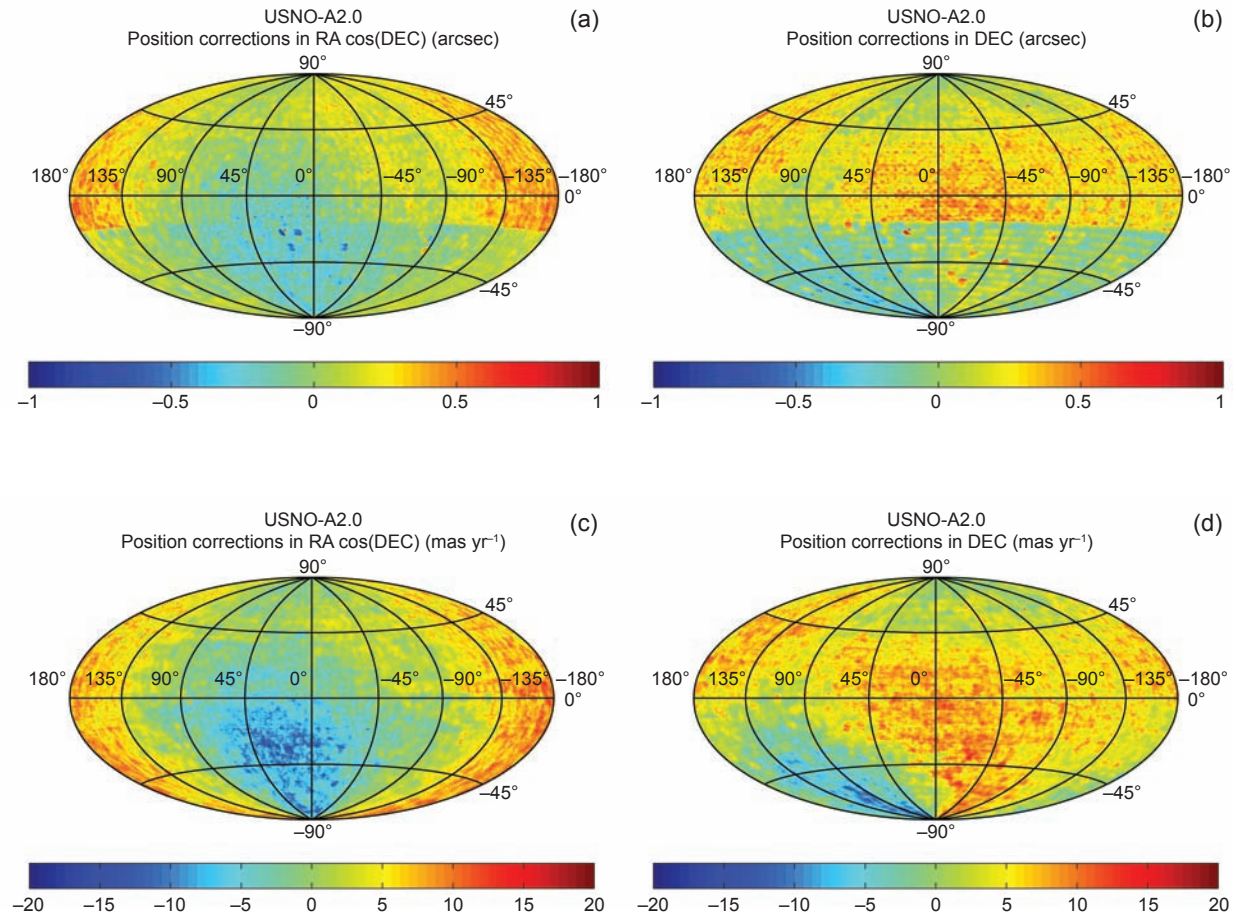


**Plate 27.** Sky map of position corrections in (a)  $\alpha \cos \delta$  and (b)  $\delta$  for USNO-A2.0. Sky map of proper motion corrections in (c)  $\alpha \cos \delta$  and (d)  $\delta$  for USNO-A2.0. Reprinted from *Star Catalog Position and Proper Motion Corrections in Asteroid Astrometry*, January 1, 2015, with permission from Elsevier.

Accompanies chapter by Farnocchia et al. (pp. 815–834).







# Modeling Asteroid Collisions and Impact Processes

**Martin Jutzi**  
*University of Bern*

**Keith Holsapple**  
*University of Washington*

**Kai Wünneman**  
*Museum für Naturkunde*

**Patrick Michel**  
*Lagrange Laboratory, Université Côte d'Azur, Observatoire de la Côte d'Azur, CNRS*

---

As a complement to experimental and theoretical approaches, numerical modeling has become an important component to study asteroid collisions and impact processes. In the last decade, there have been significant advances in both computational resources and numerical methods. We discuss the present state-of-the-art numerical methods and material models used in “shock-physics codes” to simulate impacts and collisions and give some examples of those codes. Finally, recent modeling studies are presented, focusing on the effects of various material properties and target structures on the outcome of a collision.

## 1. INTRODUCTION

The modeling of impact processes can be based upon mathematical synthesis of experimental results, on direct theoretical application of the principles of physics, or on the use of those principles in numerical codes.

The direct application of experimental results is not usually possible, because the experiments cannot be performed at the actual conditions of interest. To bridge the gap, scaling theories are developed using physical principles to extrapolate experimental results to the actual conditions of interest. For some time, principal scaling theories have been based upon the physical concept of a “point source,” wherein the genesis of an impact process is considered to occur instantaneously at a negligibly small region on the surface of the target object. Prior to 1982, point-source scaling was assumed to be governed by the kinetic energy of the impactor, but *Holsapple and Schmidt* (1982) showed that such an assumption was not warranted, and extended the analysis to arbitrary point sources. Their general approach has been followed in numerous subsequent papers by Holsapple, Housen, and Schmidt; one can refer to the review of those scaling approaches in *Holsapple* (1993). That scaling theory continues with applications to date.

In principle, the physics that govern such processes are known, at least in the continuum approach. Those physics include the balance laws of mass, momentum, and energy, augmented by mathematical descriptions of the material be-

havior. Material behavior commonly includes the “equation of state,” which models the hydrostatic components of the stress histories and the principal thermodynamics, as well as equations describing the deviatoric (shear) components of the response. The latter descriptions include stress-strain-temperature-relations and also include models for failure, flow, and fracture. That material behavior is the source of the primary uncertainties about the correct way to model these processes. However, there has been much progress in the last couple of decades, so that direct numerical solutions using time- and space-stepping increments are becoming increasingly sophisticated and important.

The codes used in those numerical approaches are commonly called “hydrocodes,” a remnant of the early days when they were used in the military industry to make calculations of weapons effects, and the modeling only included the hydrodynamic aspects of the processes. Nowadays those codes are better called “shock-physics codes” (*Pierazzo et al.*, 2008).

Just within the last decade, another approach has been applied to asteroid processes. That approach has been borrowed from the fields of particle mechanics and of “n-body” studies. They model the material of the body as a large number of individual, discrete, usually spherical, usually mono-sized, indestructible particles. With those simplifications the balance of momentum alone determines the motions of the particles. Balance of mass is automatic, and there is no accounting for energy balance and heating. The interactions of the particles are modeled using combinations of concepts of restitution,

friction, and most recently cohesive forces, with a number of interaction parameters. These approaches have only been made possible because of the extensive growth of computing power. However, because of the extreme complications of the interactions of real particles at high energies and stresses, those approaches will most likely be restricted to cases where the stresses remain low, and the discrete particle nature of the process can identify processes not contained in the continuum approaches.

In this chapter, we give an overview of the important asteroid properties that determine the outcome of a collision and discuss the physical processes involved. We then present recent experimental results and the theoretical approaches to describe the outcome of an impact. The main part of this chapter is devoted to a detailed discussion of the current state-of-the-art numerical models — shock-physics codes — which are used in the field to simulate impacts and collisions. Some examples of those codes are presented and the various approaches to model the important properties and processes are detailed here, including hybrid hydrocode-particle code computations. Finally, some examples of recent modeling are presented. In these studies, the effects of various material properties and target structures on the outcome of a collision are discussed.

## 2. IMPORTANT PROPERTIES AND PROCESSES

Asteroids have complex shapes, internal structures, and material properties. The impact response and mechanical behavior of such objects is naturally difficult to model. In this section, we present some of the important internal asteroid properties that determine the outcome of a collision and discuss late-stage processes. Asteroid interiors, morphologies and surface geophysics are further discussed in the chapters by Scheeres et al., Murdoch et al., and Marchi et al. in this volume.

### 2.1. Porosity

The fact that the bulk density of many asteroids is well below the grain density of their likely meteorite analogs indicates that many have significant porosity (Britt et al., 2002). In particular, several lines of evidence point to the presence of a high degree of porosity for asteroids belonging to the C taxonomic class, as indicated by the very low bulk density ( $\sim 1.3 \text{ g cm}^{-3}$ ) estimated for some of them, such as the asteroid (253) Mathilde encountered by the Near Earth Asteroid Rendezvous (NEAR) Shoemaker spacecraft (Yeomans et al., 1997), and as inferred from meteorite analysis (Britt et al., 2006). Porosity might be a result of a rubble-pile structure, as suggested, for instance, by spacecraft observations of asteroid (25143) Itokawa (Fujiwara et al., 2006). The various forms of structures and porosities of asteroids were discussed in *Asteroids III* (Britt et al., 2002; Richardson et al., 2002; Asphaug et al., 2002).

It is useful to distinguish between “microporosity” and “macroporosity.” The distinction is primarily a matter of

scale. The terminology arose in the study of meteorites, wherein porosity not apparent to the naked eye was called microporosity, and visually obvious voids between a grain structure or other identifiable particles was called macroporosity. But in the context of numerical modeling those terms can take on different meanings, because there are three different ways to model void space. In the first way, which is appropriate when the void space is very small compared to any length scale of interest, the porosity is considered a continuum material property and modeled as part of the equations of state. That continuum approach to porosity modeling is discussed below. In the second way, some codes allow a single numerical cell to contain both material and void, and the resulting behavior is determined by a mixture theory. In both of these first two approaches, the porosity scale is smaller than a calculation cell. In the third way, the void can be so large as to encompass an entire numerical zone, and zones without material can be scattered throughout a problem domain in some defined way. The differences between the approaches will depend on the length scale of the modeled phenomena compared to the length scale of the porosity.

The response of an asteroid to an impact is strongly affected by the presence of porosity. In the outgoing shock wave, a porous material can undergo significant permanent compression and become hot, which creates a significant energy sink (see the chapter by Asphaug et al. in this volume) (Davison et al., 2010). That effect will be included in any numerical model where the size scale of the porosity is smaller than the width of the initial outgoing compression pulse. Since it is typical in a code to numerically smear a shock over several calculation zones, even the third of the above porosity models can model significant crush up and energy loss, depending on the resolution of the calculation. In large-scale collisions (say between 100-km bodies), a shock wave can lead to compression of porous bodies even if they contain large (~kilometer-sized) voids, as long as these voids are smaller than the relevant scale (e.g., the impactor size).

In addition to the effects at the shock, porosity and the material’s resulting crushability can also have a dramatic effect on the entire cratering process. Rather than an excavation process, an entire crater can be formed by a downward flow crushing the material beneath the crater floor (K. Housen and K. Holsapple, 2014, in preparation).

Recent experiments and the scaling theory for the regime of cratering dominated by target porosity will be discussed in section 3. The different approaches proposed to model the various effects of porosity described above will be presented in section 4.4.4.

### 2.2. Strength

The outcome of an impact into an asteroid, whether a crater or a disruption, will ultimately be determined by gravity and some strength measure of the material of the object. There are many measures of strength for a geological material, and, over the last decade or so, that variety has

been identified and is often included in our scaling theories and in numerical calculations. Strength measures can include tensile strength, compressive strength, shear strength, crush strength, and others; each governs the ability of a material to withstand a different kind of stress state. In the usual continuum approach, each of those strengths is characterized by a different portion of a single “strength envelope”: a boundary defined in stress space between elastic and inelastic (permanent) deformation. An additional part of the modeling (flow rules) then describes the nature of the inelastic deformation from flow or fracture. In addition, the prior shock history can modify or “damage” the material, and that also must be accounted for. *Holsapple* (2009) presented a review of strength theories appropriate for geological materials. The interested reader can refer to that reference, in addition to further details below (section 4.4).

### 2.3. Late-Stage Processes

Since the time of the early lunar studies it is been observed that large craters and basins have a substantially lower depth-to-diameter ratio than the smaller ones. For the large craters, the slopes of the outer walls are typically well below the angle of repose expected for soils and rocks. These were judged to be puzzling because the angle of repose typically determines the static equilibrium slope angles of soils and rocks. *Melosh* (1979) proposed that the effect was due to the dynamic weakening of rock in the latter stages of crater formation by the action of acoustic vibrations. Since then, many other calculators include a “late-time” period of crater formation using rheological models that suppose the presence of that acoustic fluidization. Those methods are common today. An alternative viewpoint was presented by *Holsapple* (2004a), but his approach has yet to be fully developed.

These approaches are presented below in section 4.4.5. An application of a dynamic weakening model in the case of large-scale collisions on asteroid (4) Vesta (*Jutzi et al.*, 2013) is discussed in the chapter by Asphaug et al. in this volume.

## 3. SCALING LAWS

As mentioned in section 1, the experiments we can make on Earth are not at the size scale, gravity levels, or impact velocities of interest to most solar system impact events. For that reason, the results of experiments in the laboratory must be extrapolated, often over many decades, to predict the results of impacts into asteroids. How does a 10-km asteroid behave compared to a 10-cm laboratory sample?

The physical assumption forming the foundation of modern scaling theories is that of a general “point source.” Any impactor has three fundamental independent measures: radius,  $a$ ; velocity,  $U$ ; and mass density,  $\delta$ . The three independent measures can be taken equally well as the diameter, momentum, and kinetic energy or any other three independent combinations. In any case, they contain the three independent units of length, mass, and time. Then, when that impactor collides at high velocity with an asteroid, it sets

up a highly dynamic event affecting a region much larger than the impactor size, and over a timescale much longer than that of the initial deposition of energy into the surface. Physically, an appropriate assumption is that the deposition of momentum and energy is instantaneous into a region of vanishing dimensions compared to any length scale of interest such as the final crater. Of course, that assumption cannot be made for very low speed impacts or other cases where a final crater may be only slightly larger than the impactor.

For a point source, the governing impactor measures cannot retain a length scale or a timescale. From that assumption it follows that the individual values for the size, velocity, and mass density do not affect the outcome. Instead, there can be at most one single combination of those three variables that “measures” the impactor. That measure is then used in conjunction with those defining the material behavior of the target object to develop the scaling theory.

The earliest point source solutions for impacts simply assumed that the correct measure was the kinetic energy of the impactor that defined what is now called “energy scaling.” *Dienes and Walsh* (1970) noticed in code calculations of impacts into metals that the same crater was obtained for different impacts having the same  $aU^\mu$  where  $\mu = 0.58$ . They did not identify that result as the signature of a point source, nor did they recognize that the general form is quite universal, but with different exponents depending on material type. The Z model of cratering by *Maxwell* (1977) was essentially another early point-source model, but again it was not identified as such, and was only applied to the geometry of the cratering flow field. *Holsapple and Schmidt* (1982) developed crater scaling from the assumption of a general point source, measured by what they called a “coupling parameter.” They showed that it must always have the power-law form  $C = aU^\mu\delta^\nu$ , but the governing exponents  $\mu$  and  $\nu$  cannot be immediately predicted, because they depend in a complicated way on the material of the target. However, it was proved that  $1/3 < \mu < 2/3$  (*Holsapple and Schmidt*, 1982). They also applied the same measure to a variety of outcomes of cratering and determined definite interrelations between the power laws for all outcomes of a given event.

Over the years, the implications of that theory have been applied to many different impact outcomes from both experiments and numerical simulations, including crater size, crater formation time, shock wave propagation time, catastrophic disruptions, ejecta characteristics from the impact, momentum transfer to asteroids, etc. From that variety of applications it is been well determined that the point-source predictions work surprisingly well, and, for moderately porous materials,  $\mu \sim 0.4$ , while for nonporous materials  $\mu \sim 0.55$ , with only small variations found. And in many cases, the use of that assumption leads to simple power-law scaling for many features of interest. Well-known examples are the power laws for crater dimensions when a crater size is determined by the surface gravity (“gravity regime”) or when it is entirely determined by a strength (“strength regime”), power laws for ejecta amounts and velocities, for stress decay, and others.

The reader interested in the details and earlier applications might begin with the scaling review article in *Holsapple* (1993). A review and several applications, including catastrophic disruption cases, were presented in the chapter by *Holsapple et al.* (2002) in the *Asteroids III* volume.

In addition to the now well-known strength and gravity regimes for impacts, two new regimes for cratering have recently been introduced. First, *Holsapple and Housen* (2013b) defined a “spall” cratering regime for small craters on rocky bodies, those dominated by the tensile spall strength, and not the more common shear strength that determines excavation craters. Those have been well known for explosive craters smaller than a meter or so in rocky targets on Earth and in laboratory experiments in competent rocks (e.g., *Gault*, 1973), although that regime has usually been ignored for planetary applications. But at the low gravity on an asteroid, that regime can include much larger craters. The extent of that regime as a function of surface gravity is depicted by the shaded region in Fig. 1 from *Holsapple and Housen* (2013b). For a body such as (433) Eros (16 km) all craters smaller than about 1 km are predicted to be spall craters. They would be flatter and shallower than excavation craters, and would eject blocks, not ejecta with more uniform smaller particles. These analyses are new and require more thorough experimental and numerical investigation.

Second, *Housen and Sweet* (2013) presented experiments and scaling of impacts into highly porous materials. Large porosity also adds a new regime, as illustrated in the schematic shown on a plot of scaled volume vs. the gravity-scaled  $\pi^2$  parameter (Fig. 2).

As indicated above, the point-source-scaling theory has also been applied to catastrophic disruptions (e.g., since

*Housen and Holsapple*, 1990). Recently, *Leinhardt and Stewart* (2012) extended this approach to define “general” scaling laws that included collisions between gravity-dominated bodies of comparable sizes. While this approach was shown to work well for some specific regimes (*Leinhardt and Stewart*, 2012), its general applicability still remains to be validated.

A great number of experimental studies in either the cratering or the disruptive regime have been performed since the publication of *Asteroids III*. This chapter is focused on the modeling of collisions, and therefore we will not review this experimental work. We just give a few references to the interested reader, noting that these experiments greatly contributed to our understanding of the collisional process at small laboratory scales and always give a necessary point of reference to test numerical methods (see section 4.6). In particular, various kinds of target materials have been considered, such as targets made of sintered glass beads (e.g., *Setoh et al.*, 2010; *Hiraoka et al.*, 2011); pumice (*Jutzi et al.*, 2009); porous gypsum, sometimes admixed with small pebbles or glass beads (*Okamoto and Arakawa*, 2009; *Leliwa-Kopystynski and Arakawa*, 2014; *Yasui and Arakawa*, 2011); dense (soda lime or quartz) cores and porous (gypsum) mantles (*Okamoto and Arakawa*, 2008); and other porous materials (e.g., *Housen and Sweet*, 2013; *Nakamura et al.*, 2015). Moreover, meteorites (e.g., *Flynn et al.*, 2008; *Kimberley and Ramesh*, 2011) have been used as well as 1-m-diameter granite spheres to check the effect of size on the cratering outcome (*Walker et al.*, 2013). In some cases, scaling parameters allowing an extrapolation at larger scales were also investigated. *Holsapple and Housen* (2012) study experiments and scaling for the momentum coupling of impacts as related to the deflection of

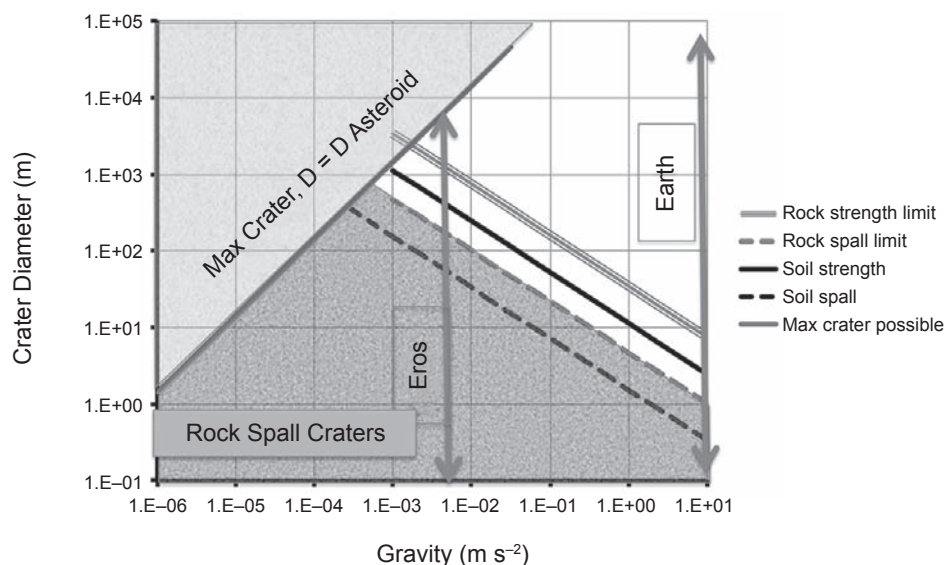


**Fig. 1.** Cratering on rocky asteroids can be dominated by surface spall phenomena when gravity and the crater are small. The lower shaded region of this plot shows the extent of that region; it includes all possible craters on kilometer-sized bodies and all craters smaller than 200 m on Eros.

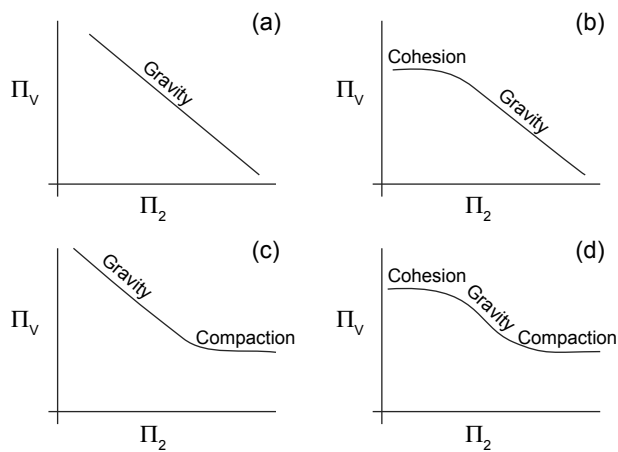


**Fig. 2.** The scaled-size  $\Pi_V$  depends upon the gravity-scaled-size  $\Pi_2$  in different ways for different materials. **(a)** For a cohesionless soil with low or moderate porosity such as dry sand, standard “gravity scaling” applies at all size scales; for increasing size or gravity, there is a reduction in cratering efficiency. **(b)** For a small or moderately porous material with cohesion, the cohesion is the dominant contribution to the shear strength at small crater-sized scales, so that the cratering efficiency is constant. But for increasing size, there is a transition to the gravity-dominated regime. **(c)** A cohesion-less material with high porosity is gravity scaled at small sizes, but at large sizes is created by compaction, independent of gravity, so  $\Pi_V$  approaches a horizontal asymptote. **(d)** A material with both cohesion and high porosity potentially shows all three of the cohesion, gravity, and compaction regimes.

Earth-threatening asteroids by impacts (see also section 5.2.). A comprehensive review of experiments and ejecta scaling has been published by *Housen and Holsapple* (2011).

The increasingly more sophisticated material modeling in shock-physics code allows “numerical experiments” to be conducted for a much larger parameter space than it is possible to cover experimentally. Moreover, the effect of individual properties such as friction and porosity can be investigated in detail. The first results of this promising approach for the cratering regime have been presented in *Wünnemann et al.* (2010) and are summarized in section 5.1.1. Recent numerical studies of asteroid disruptions will be discussed in section 5.1.2.

## 4. NUMERICAL MODELING

### 4.1. Introduction

As a complement to experimental and theoretical approaches, numerical modeling has become an important component to study the outcome of collisions. In the last decade, advances in both computational resources and numerical methods have allowed the properties and processes involved (see section 2) to be modeled more and more realistically.

Here we present the principles of numerical impact modeling. We show some examples of codes used in the field and discuss the various model approaches.

### 4.2. Numerical Techniques

The two most common approaches to simulate impacts and collisions use shock-physics codes (“hydrocodes”) and particle codes.

Shock-physics computer programs use continuum theory, and can calculate the entire dynamical process including the propagation of shock waves and resulting fields of displacement, velocity, strain, stress, etc., as function of time and position (e.g., *Anderson*, 1987). They rely on mathematical constitutive models for the thermodynamics, which often includes melt and vaporization; for the deformation processes; and for the failure, fracture, and flow. Those material equations are the outcomes of testing of materials at the various states of interest. The equations are solved in a time-stepping manner on a geometrical computational grid (or interpolation points), usually with zones much smaller than the impactor dimension. The allowable timestep size must be shorter than the time for the passage of a shock wave across the smallest zone (“Courant-Friedrichs-Levy” stability criterion). Depending on the numerical method used, additional timestep restrictions are required (e.g., *Anderson*, 1987). It is not uncommon in two-dimensional applications to include hundreds ( $n$ ) of space zones in each direction, for a total of  $n^2 \sim 10^5$  and runs for several  $10^6$  timesteps. In three-dimensional problems, many more zones ( $n^3$ ) are required, so generally  $n$  must be much smaller. That illustrates the great advantage of codes that can calculate in two dimensions. However, many problems are inherently three-dimensional.

In contrast, particle codes (including “discrete element codes”) assume a collection of simple interacting particles. These codes generally only perform three-dimensional calculations. Their collisions are modeled using heuristic descriptions for restitution, friction, and viscosity, and their interactions include mutual interparticle gravitational forces. The balance of linear and angular momentum is all that is required to calculate their motions and rotations, so there is no use of mass balance or energy balance concepts. They do not include crushing, melting, vaporization, or other phenomena occurring in high-speed impacts, so these models are limited to low-velocity, low-stress events. The number of particles might be millions, but that is still many orders of magnitude less than the actual number in a soil-like structure in any problem of interest. Thus, it is inherently assumed that there are “enough” particles to approach the “infinite number” continuum limit. And, to date, it appears that the governing parameters need be chosen on a case-by-case basis.

There are two classes of particle models. The simpler and earlier approaches are the so-called “hard sphere” models in which particle collisions, which are assumed to occur instantaneously, are predicted in advance and are governed entirely by coefficients of restitution chosen by the user.

Such a model has been implemented in the N-body hard-sphere discrete element code *pkdgrav* (*Richardson et al.*, 2000), which has been used for different applications in planetary science (see the chapter by Michel et al. in this volume for an application to asteroid family formation) and which has been adapted to enable dynamic modeling of granular materials in the presence of a variety of boundary conditions (*Richardson et al.*, 2011). Other examples of such codes are polyhedral rubble-pile codes (*Korycansky and Asphaug*, 2006; *Movshovitz et al.*, 2012).

The hard-sphere approach is equivalent to the early attempts to model fluid mechanics by a collection of very sparse interacting atoms or molecules. It works well for rarefied gas dynamics, and it is well known that averaging across many particles leads to the classical continuum equations of perfect fluids. However, dense systems involving multiple collisions and enduring contacts require another approach, such as the “soft-sphere” discrete element method. In this approach, the particles are allowed to have finite interaction times governed by elastic concepts, and in principle even static cases of enduring contact can be included, relying upon modest penetration between particles. The soft-sphere approach was recently included in the code *pkdgrav* (*Schwartz et al.*, 2012); it is also used in other codes (e.g., *Sanchez and Scheeres*, 2011). Moreover, these discrete approaches can include bonding forces between particles, as a first analog of cohesive materials (see, e.g., *Schwartz et al.*, 2013; *Sanchez and Scheeres*, 2014). Such capability is also now available in the commercial finite-element code, LS-Dyna.

But this soft-sphere extension generally comes at a price. In effect, although the soft-sphere approach has the advantage of not requiring collisions to be predicted in advance, it comes at the expense of much smaller integration timesteps than the hard-sphere approach, which can limit the integration timescale. That is similar to the timestep restrictions for the continuum codes. On the other hand, because it can be implemented into codes, like *pkdgrav*, that are fully and efficiently parallelized, it is currently possible to follow the evolution of millions of particles over a fairly large range of conditions. The chapter by Murdoch et al. in this volume provides a review of discrete element methods and continuum approaches applied to the dynamics of granular materials at the surface of asteroids.

The use of particle codes to simulate rubble-pile collisions at low speeds (below the sound speed of the materials) was discussed in *Asteroids III* (*Richardson et al.*, 2002). In a recent study, *Ballouz et al.* (2014, 2015) used the particle code *pkdgrav* to simulate low-velocity collisions between rotating rubble piles in order to measure the effect of the initial rotation of colliding bodies on the outcome.

In situations where the whole process of a large-scale asteroid collision is investigated, including both the initial shock passages, heating, fragmentation, and the subsequent reaccumulation of fragments, a hybrid approach is often used (e.g., *Michel et al.*, 2001) (see the chapter by Michel et al. in this volume). There the fragmentation is computed with a shock-physics code and the gravitational reaccumulation

with a particle code. This approach is limited by the numerical resolution that fixes the minimum size of tractable fragments (typically down to  $\sim 10$  m for simulations involving kilometer-sized bodies).

In the fragmentation phase of a hypervelocity asteroid collision, self-gravity can usually be neglected because (1) the overburden pressure is small compared to the amplitude of the shock wave, and (2) the fragmentation timescale is much smaller than the reaccumulation timescale. (For large asteroids, however, it may be important to include fracture shielding due to compression.) The fragmentation timescale is given by the time it takes for a shock wave to travel through the whole target  $\tau_f \sim R_t/c_s$ , where  $R_t$  is the target radius and  $c_s$  a wave speed. On the other hand, gravitational reaccumulation proceeds on a timescale of  $\tau_{dyn} \sim (G_p)^{-1/2} \sim 2200$  s (for a bulk density  $\rho = 3000$  kg m $^{-3}$  and the gravitational constant  $G = 6.67 \times 10^{-11}$  m $^3$  kg $^{-1}$  s $^{-2}$ ). For small bodies ( $R_t \lesssim$  a few 100 km),  $\tau_f \ll \tau_{dyn}$  and gravity does not affect the dynamics of the fragments during the fragmentation phase. However, it is important to note that for very low velocity collisions, gravity has to be computed during the whole process, even for small bodies. This is typically the case in accretionary collisions (see the chapter by Asphaug et al. in this volume) where the impact velocity  $v_{imp}$  is on the order of the mutual escape velocity  $v_{esc} = \sqrt{2G(M_p + M_t)/(R_p + R_t)}$ , where  $M_p$  is the mass of the projectile,  $M_t$  the mass of the target, and  $R_p$  the projectile radius. For 10 (100)-km-diameter bodies,  $v_{esc} \sim 5$  (50) m s $^{-1}$  (assuming a density of  $\rho = 3000$  kg m $^{-3}$ ).

The hybrid hydrocode-particle code approach is detailed in the chapter by Michel et al. in this volume, which presents the newest collision models in particle codes. Here we focus on shock-physics codes.

#### 4.3. Basic Equations

Shock-physics codes solve the system of partial differential equations that describe the conservation of mass, momentum and energy for a continuous, compressible medium (see e.g., *Collins et al.*, 2013 for a recent review). Examples and a description of such codes used in the field [smoothed particle hydrodynamics (SPH), CTH, iSALE, SOVA] will be given in section 4.5.

The stress tensor is symmetric and is often divided into isotropic (hydrostatic) and deviatoric parts

$$\sigma^{ij} = S^{ij} - P\delta^{ij} \quad (1)$$

where the pressure  $P$  is the hydrostatic pressure,  $S^{ij}$  is the (traceless) deviatoric stress tensor, and  $\delta^{ij}$  is the Kronecker symbol. Using a Lagrangian reference frame, the conservation equations (mass, momentum, and internal specific energy) can then be written using an indicial summation convention as

$$\frac{dp}{dt} + p \frac{\partial v^i}{\partial x^i} = 0 \quad (2)$$

$$\frac{dv^i}{dt} = \frac{1}{\rho} \frac{\partial \sigma^{ij}}{\partial x^j} + g^i \quad (3)$$

$$\frac{dE}{dt} = -\frac{P}{\rho} \frac{\partial}{\partial x^i} v^i + \frac{1}{\rho} S^{ij} \bar{\epsilon}^{ij} \quad (4)$$

where  $d/dt$  is the Lagrangian time derivative,  $\rho$  the density,  $v$  the velocity,  $E$  the specific internal energy,  $x$  the position, and  $\bar{\epsilon}$  the deviatoric part of the strain rate tensor. The term  $g$  on the righthand side of equation (3) accounts for any external acceleration, e.g., due to gravity forces.

To complete the set of equations, equations describing the material response are required. For the hydrostate components an equation of state (EOS) is required, which relates pressure, density, and internal energy (or temperature, if its inclusion is convenient). And constitutive equations relating the deviatoric components are used. Both of these can be very complex, but have been developed over the years, often by the military community. The specifics are discussed in section 4.4.

For many problems, the acceleration due to self-gravity is important and has to be taken into account in equation (3). The components of the gravity acceleration can be computed by solving the Poisson equation for the gravitational potential. In particle-based approaches (including SPH), the gravity acceleration for a particle  $k$  is directly given by

$$\vec{g}_k = -G \sum_{k \neq l} \frac{m_l \vec{r}_{kl}}{r_{kl}^2} \quad (5)$$

where  $G$  is the gravity constant,  $m$  the mass of the particles, and  $r = |\vec{r}|$  the distance between the particles. For  $N$  particles, the direct summation method leads to a complexity of  $O(N^2)$  and is only practical when computers that are designed to solve such problems [e.g., graphics processing units (GPUs)] are used. A method often applied for the self-gravity computation is the Barnes-Hut tree algorithm (Barnes and Hut, 1986), which allows reduction of the complexity to  $O(N \log N)$ .

#### 4.4. Material Models

An EOS relates density, internal energy, and pressure, and may also include porosity effects. A stiffness and strength model is needed to determine the deviatoric stress due to strains and possible material failure (sections 4.4.2 and 4.4.3).

Various processes occur during an impact on an asteroid and these have to be modeled in a suitable way. Those may include (1) effects due to porosity and other nonlinearities (including energy dissipation by compaction, damping of shock wave, and reduction of wave speed in highly porous materials); (2) (post-impact) flow of granular material in the case of shattered asteroids or rubble piles; and (3) dynamical state weakening (e.g., important to model the collapse of large craters).

**4.4.1. Equations of state.** An often-used form for the EOS is

$$P = P(\rho, E) \quad (6)$$

This form is convenient because in most hydrocodes, the specific internal energy (rather than the temperature) is computed directly. In fact, temperature is not required to solve the conservation equations. However, it may be useful to account for phase transitions and the thermal softening when deviatoric stresses are included (section 4.4.2).

The most simple EOSs have no thermodynamic coupling and the pressure is solely a function of density (e.g., the Murnaghan EOS). A more sophisticated and widely used analytical equation is the Tillotson EOS, which was derived for high-speed impact computations (Tillotson, 1962). One of the major advantages of this EOS is its efficiency. However, the Tillotson EOS does not provide information about how to compute the temperature or the entropy of a material. Furthermore, the treatment of vaporization is not very sophisticated. For these reasons, the Tillotson EOS is mostly used to study impacts involving specific energies that do not lead to significant melting or vaporization.

A more complex and thermodynamically consistent analytical EOS model is ANEOS (M-ANEOS) (Thompson and Lauson, 1972; Melosh, 2007). In this model, the thermodynamics variables are derived from the Helmholtz free energy. ANEOS includes a more accurate treatment of both melting and vaporization than the Tillotson approach and allows for other polymorphic and liquid/solid phase transitions.

There are also complete tabular databases such as the SESAME library, developed by the Livermore National Laboratory. Those are efficient to use, valid over vast density ranges, and commonly include complete thermodynamics, including phase changes of melt and vapor. Often those are tabular compilations of the analytical forms.

**4.4.2. Strength models.** The strength model is fundamental for modeling impacts and collisions involving small bodies. It determines the “impact strength” in disruptive collisions; the size, final shape, and characteristics of the crater in an impact; and so on.

It is important to note that, depending on the loading conditions, various forms of “strength” exist (section 2). Here we give an overview of some strength models that are included in impact codes used in the field.

A simple strength model commonly used is the von Mises model developed for ductile metals. In this model, plastic flow occurs at stresses larger than a single constant yield strength  $Y_0$ . The von Mises criterion is implemented in shock codes by reducing the deviator stress (see, e.g., Benz and Asphaug, 1994; 1995) by

$$S^{ij} \rightarrow f S^{ij} \quad (7)$$

where  $f$  is computed by

$$f = \min \left[ \frac{Y_0^2}{3J_2}, 1 \right] \quad (8)$$

This is commonly called the “radial return method” and is also, for the von Mises case, the direction of the “associated flow rule” of plasticity theories. Here, the second invariant of the deviatoric stress tensor  $J_2 = \frac{1}{2}S^{ij}S_{ij}$  is used as a scalar measure of the maximal shear stress.

Although this model was developed for ductile materials, it was commonly used in impact calculations in geological materials in the past. In combination with a tensile fracture model (see section 4.4.3), it gives reasonably accurate results in disruptive collisions. *Jutzi* (2015) gives a comparison between this approach and more sophisticated strength models in simulations of disruptive collisions.

However, common geological materials such as soils, rocks, and ices have more complex behavior than ductile metals. An important characteristic of their strength is a substantial increase of shear strength with increasing confining pressure. That is the common feature of more sophisticated failure criterion used for geologic materials. The general form for geological strength models is as indicated in Fig. 1 of *Holsapple* (2009). There is a region in “shear-pressure” space delimited by a closed curve at which “failure” or “flow” can occur. The “shear” can either be measured by the maximum shear stress  $\tau$  on any plane, or by the average shear given by the stress invariant  $\sqrt{J_2}$ . The “pressure” can as well be the actual average normal stress  $P$  or the maximum normal stress  $\sigma$  on any plane. The Drucker-Prager model uses  $P$  and  $\sqrt{J_2}$ , while the Mohr-Coulomb model uses  $\sigma$  and  $\tau$ . For small pressure, failure occurs at the upper-limit pressure-dependent shear envelope defining the largest admissible shear. For large pressures, that shear envelope flattens. Then, at the right is a constraint for the maximum pressure where compaction can occur with compressive pressure. This limit is particularly important for porous material for which “crushing” can start at very low pressures. Models for that rightmost porous limit are described below.

The initial slope of the shear envelope at low or tensile pressures is commonly called the “friction coefficient,” because the form is similar to that used for friction between solid sliding blocks. But that is in fact a misnomer; the actual mechanism is a result of the fact that a pressure impedes the movement of irregular-shaped grains up and over each other in a shearing flow. That slope then reduces at larger pressures.

The Mohr-Coulomb and Drucker-Prager models include that pressure-dependent yield strength and are the simplest failure models commonly used in soil and rock mechanics (e.g., *Holsapple*, 2009).

One strength model (*Collins et al.*, 2004) uses the following pressure-dependent shear strength for the intact material  $Y_i$

$$Y_i = Y_0 + \frac{\mu_i P}{1 + \mu_i P / (Y_M - Y_0)} \quad (9)$$

where  $Y_0$  is the shear strength at  $P = 0$ ,  $Y_M$  is the shear strength at  $P = \infty$ , and  $\mu_i$  is related to the coefficient of internal friction for the intact material. Here the “shear” is measured by  $\sqrt{J_2}$ . This model is implemented in a number

of codes (e.g., *Collins et al.*, 2004; *Senft and Stewart*, 2007; *Jutzi*, 2015). Other nonlinear functions including powers and exponentials are common (e.g., *Hoek and Brown*, 1980).

To describe the yield strength of fully damaged rock, which includes granular material

$$Y_d = \mu_d P \quad (10)$$

is used, where  $\mu_d$  is related to the coefficient of friction of the damaged material. [For modeling regoliths in low-gravity environments, it is not uncommon to add a (small) cohesion.]

In addition, the model must specify how a stress exceeding the limit is mapped back to the failure surface in each timestep (the “return method”) and also the resulting plastic flow increment during the timestep (the “flow rule”). The yield strength  $Y$  is often used to simply reduce the deviatoric stress (represented by  $\sqrt{J_2}$ ) by a factor of  $Y/\sqrt{J_2}$ . That is again the “radial return method.” The plastic strain increment is often assumed to be in shear only (no volume change). But in general plasticity theories, the “associated flow rule” is more common; it is assumed to be in the direction perpendicular to the failure envelope. That case includes the important phenomena of the dilatancy of a granular material when flowing. Such details are not yet included in most planetary code simulations, although such an approach has been implemented recently in the iSALE code (*Collins*, 2014). Much more study and use of such models is warranted.

One might note the occurrence of two characteristic strength measures in such equations. The strength  $Y_0$  at zero pressure is commonly called the cohesion. It may be zero for dry sands, or on the order of a few kilopascals to several megapascals or more for cohesive materials, and even hundreds of megapascals for small solid rocks. Then the shear strength increases with pressure to a maximum value of  $Y_M$ , a characteristic of the strength of individual grains, which may be as much as a few gigapascals. The importance of these values depends on the other pressure scales in the problem, and especially on the gravity-induced lithostatic stress  $\rho gh$  at a depth  $h$ . If that gravitational stress is much larger than the cohesion, but still less than  $Y_M$ , then the cohesion can be ignored, but a dependence on the angle of friction will still occur. That is the case in what is called the “gravity regime” of cratering, which holds, e.g., for large craters on Earth. In the gravity regime, there remains a dependence on that angle of friction, but not on any other strength measure. That dependence will emerge from any calculation including the strength equation. But for extremely large events, the gravity stress will be larger even than  $Y_M$ . For example, for collisions between planetary-sized bodies, that will be the case. Therefore, in giant impact simulations, e.g., to study the Moon-forming impact (e.g., *Benz et al.*, 1989; *Canup and Asphaug*, 2001; *Reufer et al.*, 2012), any form of strength is typically ignored.

There are additional factors that must be accounted for in the construction of any strength envelope. It is not static, but changes according to the present state of the material at any point. For example, it can depend on the instantaneous strain

rate, or on the temperature, and can change size and shape as the material is strained. The community is just beginning to include all known effects in our mathematical models.

For example, to account for the thermal softening of geologic materials for extreme impacts,  $Y$  may be further reduced according to

$$Y \rightarrow Y \tanh \left\{ \xi \left( \frac{T_{melt}}{T} - 1 \right) \right\} \quad (11)$$

(Collins et al., 2004), or using a similar function of specific internal energy  $E$

$$Y \rightarrow Y \left( 1 - \frac{E}{E_{melt}} \right) \quad (12)$$

where  $E$  is the specific internal energy and  $E_{melt}$  the specific melting energy. It is important to note that the temperature and energy at which melt occurs are strongly pressure dependent and not simply a constant, and that fact should be included in any thermal softening equation. A possible approach is to use the location of the present thermodynamic state compared to the melt boundary in the EOS space to soften the material.

**4.4.3. Fracture (or damage) models.** There is an additional complexity when a rock fractures. When a rock is stressed to failure, it breaks and becomes granular; the failure envelope should then ultimately change from one with cohesion to one appropriate for a fully granular material such as a dry sand or gravel. Some approaches in the past did not do that, but simply assumed zero strength (as water) when damaged. A scalar damage parameter  $D$  describing the accumulation of tensile and/or shear fractures and/or pore crushing from undamaged ( $D = 0$ ) to totally damaged ( $D = 1$ ) is often used to interpolate between the intact (equation (9)) and the damaged (equation (10)) strength

$$Y = (D - 1) Y_i + D Y_d \quad (13)$$

where  $Y$  is limited such that  $Y \leq Y_i$ . The damage parameter is computed using a fracture model and it may also be related to porosity models (e.g., Jutzi et al., 2008).

Continuum fracture models (e.g., Grady and Kipp, 1980) often use an underlying structure with a preexisting Weibull distribution (Weibull, 1939) of cracks that grow and coalesce under tensile loading. In these models, cracks grow at a fixed speed  $c_g$  once a flaw becomes active. This finite speed of crack growth naturally leads to a rate-dependent failure of the material, as is observed for rocks [see, e.g., Housen and Holsapple (1990) for the application to disruptions]. In *Asteroids III* (Asphaug et al., 2002), various aspects of the rate- and size-dependent fracture models were discussed. The implementation of the fracture models in shock-physics codes are discussed in, e.g., Benz and Asphaug (1994, 1995), Collins et al. (2004), and Jutzi et al. (2008). These models are generally overlaid in addition to the strength envelopes discussed above.

Damage can also increase due to pore crushing during the compression of a porous material. This effect can be taken into account using a (linear) relation between distension  $\alpha$  and damage  $D$  (e.g., Jutzi et al., 2008).

Damage is usually treated as a scalar parameter. However, others have introduced tensor measures of damage (e.g., Lubarda and Krajcinovic, 1993). Due to their complexity, those have not yet made their way into impact studies, although tensor damage has been included in some recent codes (e.g., Owen, 2010).

**4.4.4. Porosity models.** In section 2 we discussed the various scales of porosity and the effects of porosity during an impact, such as the absorption of energy due to compaction or the reduction of the wave speed.

Depending on the scale of porosity, it can be modeled as either macroscopic voids (macroporosity) or by using a continuum, subresolution material model (microporosity), or as a combination of both as discussed in section 2. Here the size scale for demarcation is a computational cell size.

A widely used continuum model is the “P- $\alpha$ ” model (Herrmann, 1969; Carroll and Holt, 1972), which uses the distension  $\alpha$  defined by

$$\alpha = \rho_s / \rho \quad (14)$$

where  $\rho$  is the bulk density of the porous material and  $\rho_s$  is the density of the corresponding solid (matrix) material. A crucial assumption in this model is that it is the density and specific internal energy of the matrix material that determines the pressure. That is true when ignoring any energy content related to the porosity such as surface energy. Therefore, the bulk pressure of the porous material  $P$  is then related to the pressure in the solid component (matrix)  $P_s$

$$P = \frac{1}{\alpha} P_s (\rho_s, E_s) = \frac{1}{\alpha} P_s (\alpha \rho, E) \quad (15)$$

A significant feature of this model is that any existing EOS for a nonporous material  $P_s(\rho_s, E_s)$  can be used as the solid component of a porous material of the same composition.

A compaction model is required to determine the history of distension as a function of the history of pressure change. It is often assumed that the crush-up is independent of shear stress, although Jutzi et al. (2008) relate the changing rate of the distension and of the deviatoric stress tensor. The form of the model for the historic P- $\alpha$  Herrmann form includes a crush curve  $\alpha = \alpha_c(P)$ , at which pressure increases will decrease the distension, defining the crush-up of the material. In addition, the porous model defines unloading elastic curves. Those apply until the stress state again reaches a failure boundary. Herrmann (1969) does not discuss that feature. The curves for loading and unloading are obtained by pressure tests that load and unload the material and are defined in the model with appropriate algebraic forms. The quadratic form assumed by Herrmann (1969) is not well suited to geological materials, but is easily changed. For instance, Jutzi et al. (2008, 2009) use a combination of two power-law functions to successfully reproduce the crush curve of pumice (Fig. 1 in Jutzi et al., 2009).

Since the EOS has the underlying density as a function of both the pressure and the internal energy, the crush curve should include that also, so *Holsapple* (2008) suggests that  $\alpha = \alpha_c(P, E)$ . In particular, the crush strength should become zero when the thermodynamic state is at melt. That feature is not yet common in models.

Elastic unloading only occurs until the stress state reaches some other point on the enclosing failure envelope. When shear stress is present, that can occur at positive pressure, but it will be at pure tensile pressure if the shear is zero and cohesion is present. At those states, increasing porosity will occur: The occurrence with shear is the physical process of dilation in shear flow. Such an approach has been implemented recently in the iSALE code (*Collins*, 2014).

The Herrmann approach to solving the history of distension following these paths used a time subcycling that was essentially a forward differencing. The difficulties in that numerical method motivated an alternative model that determines the distension as a function of volumetric strain; it was presented by *Wünnemann et al.* (2006). The so-called “ $\epsilon$ - $\alpha$ ” model addresses the above-mentioned problem of the iterations in the “P- $\alpha$ ” model due to the interdependency of pressure P and distension  $\alpha$ . When implementing equation (15) and the crushing curve  $\alpha = \alpha(P)$  into a hydrocode for a given timestep t,  $\alpha_{t+1}$  must be known to derive  $P_{t+1}$ , but  $\alpha_{t+1} = f(P_{t+1})$ . A common solution is to use small subcycles to iterate the new  $P(t+1)$  value. This method requires extra computation time and may be numerically unstable under certain circumstances. The problem is solved in the “ $\epsilon$ - $\alpha$ ” model using the volumetric strain  $\epsilon_V$  to determine the crushing of pore space:  $\alpha = \alpha(\epsilon_V)$ . The “ $\epsilon$ - $\alpha$ ” model distinguishes four compaction regimes, where the rate of compaction  $d\alpha/d\epsilon_V$  is calculated according to elastic compaction ( $\epsilon_V < \epsilon_e$ ), exponential compaction ( $\epsilon_e < \epsilon_V < \epsilon_x$ ), power-law compaction ( $\epsilon_x < \epsilon_V < \epsilon_c$ ), and the fully consolidated state ( $\epsilon_V > \epsilon_c$ ).

The improved model (*Collins et al.*, 2011) removed two shortcomings of the initial model. First, it accounts for the fact that the speed of sound of the pristine porous material can be substantially lower than the elastic wave speed in the solid material. A simple linear relationship for  $c(\alpha)$  interpolating between the speed of sound of the fully compacted material and the initial porous material is assumed. Second, the improved version distinguishes between thermal and mechanical strains. The improvement uses an approximation about the EOS, so further calls to the EOS subroutine are not needed. In contrast to the original “ $\epsilon$ - $\alpha$ ” model the improved version is also applicable for highly porous material where material is heated extremely due to the compaction of pore space (PdV-work) resulting in thermal expansion of the solid component.

An alternative idea that retains the P- $\alpha$  form was outlined in *Holsapple* (2008). It is based on a Newton-Raphson approach rather than the forward differencing and eliminates the numerical problems in the original formulation.

**4.4.5. Fluidization models.** In the opinion of some researchers, the constitutive models describing the strengths of rocks cannot explain the formation of complex crater

structures with central peaks, where originally deep-seated material was uplifted several kilometers. And they do not explain the shallow outer wall slopes that are well below the angle of repose of the models. It is assumed that an almost fluid-like rheology of matter during crater formation is required, and it is from some weakening mechanism that lasts only temporarily. The latter is an important constraint as steep, almost vertically standing flanks of central peaks can only be explained if rocks almost return to their initial strength.

A successful approach to solve the problem of a temporary fluid-like rheology of rocks during crater formation was suggested by *Melosh* (1979). He proposed that heavily fractured and brecciated rocks behave like a granular flow excited by acoustic vibrations that have been interpreted to be observed in the ground motions generated by nuclear explosions. The fluid-like nonlinear rheology decays as the amplitude of the vibration attenuates. The model requires that the wavelength of the acoustic signal is comparable to the size of the fragments. The original acoustic fluidization model has been simplified in the so-called block model where the acoustically fluidized material behavior is described by a Bingham model (*Melosh and Ivanov*, 1999). The Bingham viscosity is proportional to the block size and the Bingham cohesion depends on the amplitude of the vibration. The latter is a function of time as the amplitude of the acoustic wave decays. A shortcoming of the acoustic fluidization or block model is the fact that neither block size nor decay time are known and can only be estimated for the size of a given structure. *Wünnemann and Ivanov* (2003) suggested a heuristic linear relationship for both block size and decay time with the size of the impactor. They assume that larger impactors produce larger blocks and longer waves that attenuate slower than in case of smaller impacts where material is fractured into smaller fragments and the acoustic signal vanishes much quicker. The linear scaling of the block model parameters has been calibrated against the observed depth-to-diameter ratios of the cratering record of the Moon (*Wünnemann and Ivanov*, 2003) and on satellites (*Bray et al.*, 2014).

Figure 3 shows a simulation of the gradual transition with increasing crater size from simple to complex crater morphology, using that model. The parameter S is given by the ratio between strength Y and the hydrostatic pressure at maximum crater depth  $d_{max}$ :  $S = Y/(pgd_{max})$ . The diagram illustrates the increasing crater depth while the transient cavity is growing and the decrease of crater depth when the crater floor collapses and starts to rise, forming a complex crater with a central peak. According to some simple estimates by *Melosh* (1979), the critical value for crater collapse is given by  $S = 0.25$ , which corresponds to strength of the rocks of a few megapascals, approximately one order of magnitude smaller than typical values for rocks. The application of the block model allows the assumption of realistic strength values for crater collapse at the observed transition diameter between simple and complex crater morphology on different planets.

The approach described above is well established and was successfully applied in many studies in the past to model the formation of complex craters. However, there is an ongoing

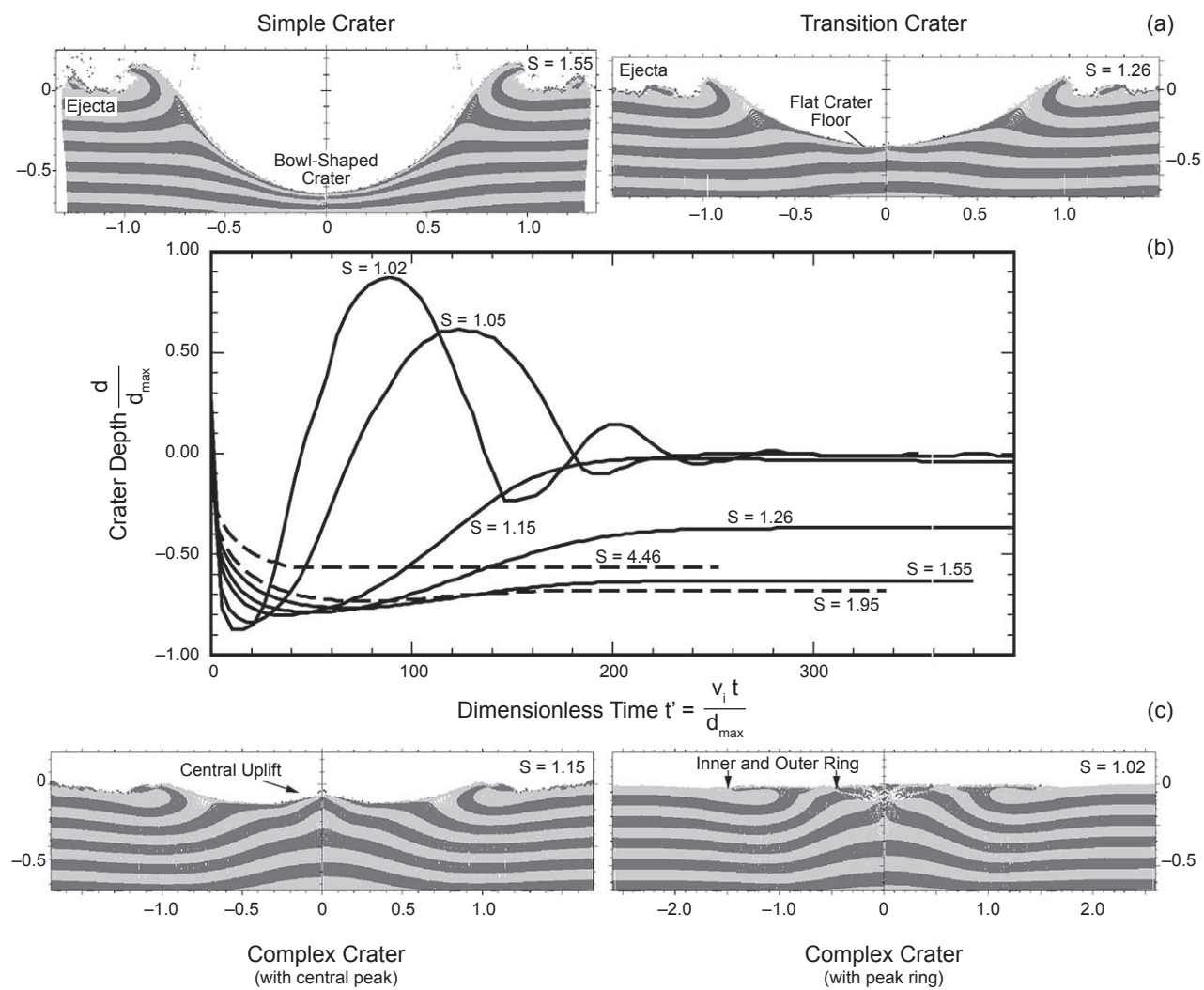


**Fig. 3.** Crater depth vs. time for different impact conditions ( $S = 1.02\text{--}4.46$ ). The length parameter is normalized by the maximum crater depth  $d_{\max}$ ; time is scaled by the ratio of impact velocity  $v_i$  and  $d_{\max}$ . The no-fluidized rheology is given by a Drucker-Prager yield strength envelope where  $Y = Y_0 + \phi p$ , with  $Y_0 = 25$  GPa and  $\phi = 0.1$ . Examples of the resulting crater morphology for different  $S$  values (different projectile sizes) are shown above and below the diagram. Note: All length scales are normalized by  $d_{\max}$  (taken from Wünnemann and Ivanov, 2003).

debate about the actual underlying physical mechanism that causes the temporary weakening. Holsapple (2004a, 2013) suggested that existing strength theories, in their complete form, can model the late-time readjustments discussed above, but his approach has not yet been fully vetted. Some important evidence for the related problem of the collapse and runout of a granular cliff is given in section 4.6.3 below.

#### 4.5. Examples of Hydrocodes

Various approaches are used in shock-physics codes to solve the continuum system of partial differential equations detailed in section 4.3. The equations may be cast in a “Lagrangian” reference frame that follows the material or in an “Eulerian” reference frame that is fixed in space. The continuum codes include finite-difference, finite-element,

and SPH methods. Each numerical method has its own strengths and weaknesses. In a recent review by Collins *et al.* (2013), the various methods are presented and numerical issues such as resolution, the treatment of shocks, multi-material approaches, etc., are discussed. Here we present a few examples of commonly used hydrocodes. For each method, the specific material models used and the pros and cons are indicated.

**4.5.1. Grid-based codes.** Most numerical simulations of planetary collision processes use Eulerian grids, because large deformations are difficult to track in the Lagrangian approach.

Grid-based codes typically use a two-step approach, where the first step is the Lagrangian step where the deformation of the grid according to a given velocity field is calculated, and then there is a second step that maps the grid back on its original location in space. The remapping

requires special treatment of material boundaries, which is usually solved by tracking or reconstructing the interface between different matter [for a discussion of different methods of interface tracking/reconstruction see *Elbeshausen and Wünnemann (2010)*]. There are several advantages to grid-based codes: (1) Lagrangian, Eulerian, or an arbitrary spatiotemporal transition between both reference frames is possible; (2) high resolution, which may be increased locally by the adaptive mesh refinement (AMR) method (*Berger and Oliger, 1984; Berger and Colella, 1989*) employed in CTH; (3) adequate treatment of solid-state deformation, liquid flow, and gas expansion including appropriate rheology models; (4) coupling of the grid-based methods with massless Lagrangian tracer particles to track the spatiotemporal thermodynamic history of matter; and (5) relatively straightforward implementation of a variety of EOS models.

Grid-based models come also with some disadvantages: (1) In Eulerian mode, material interfaces are not tracked perfectly and bulk properties must be defined for mixed cells. (2) Matter is treated as continuum, which makes it difficult to treat fragmentation properly. Separate fragments tend to be underresolved unless AMR is employed. (3) Although multi-material handling is possible, mostly the codes do not deal with multi-phase processes where each phase moves at its own speed resulting in mixing of matter. Such processes are in particular important for the interaction of solid-state fragments with an expanding vapor plume.

In this paper we mention three shock-physics codes widely used in planetary science. A much more complete overview of available hydrocodes is given in *Pierazzo et al. (2008)*.

The most advanced software package among those is the Sandia National Laboratories CTH code (*McGlaun et al., 1990*); however, because of its military uses, this code is limited in its availability to U.S. citizens. Besides highly advanced material models, it also includes AMR and self-gravity. For disruptive large-scale collision processes such as the Moon-forming impact event, self-gravity is essential (*Canup et al., 2013*). Canup et al. also compare results produced by different approaches such as grid-based models (CTH) and mesh-free codes (SPH, see below). Other widely used hydrocodes are SOVA (*Shuvalov, 1999*) and iSALE (*Amsden et al., 1980; Collins et al., 2004; Wünnemann et al., 2006; Elbeshausen et al., 2009*), which are (with some limitations) freely available for scientific purpose. SOVA contains a specific routine to deal with the interaction of lithic and molten ejecta and the vapor plume. As mixing of all phases occurs, it may be better called ejecta plume. This process requires so-called multi-phase hydrodynamics where at least two different phases (ejecta and vapor) travel at different speeds, interacting and mixing with each other. SOVA addresses this problem by introducing representative tracer particles where each tracer represents a certain number of fragments of a given size. The tracers exchange momentum and energy with the surrounding gas, but not with each other. The approach only works if the volume of fragments is small relative to the volume of the gas. The method has been successfully applied to model dusty flows (*Shuvalov,*

*1999*), tektite formation and deposition (*Stöffler et al., 2002*), and the development of Chicxulub distal ejecta (*Artemieva and Morgan, 2009*). The iSALE hydrocode is based on the SALE hydrocode solution algorithm (*Amsden et al., 1980*). To simulate hypervelocity impact processes in solid materials, SALE was modified to include an elastoplastic constitutive model, fragmentation models, various EOSs (Tillotson and ANEOS), and multiple materials (*Melosh et al., 1992; Ivanov et al., 1997*). More recent improvements include a modified strength model (*Collins et al., 2004*) and a porosity compaction model (*Wünnemann et al., 2006; Collins et al., 2011*). The three-dimensional version uses a numerical solver as described in *Hirt et al. (1974)*. The development history of iSALE-3D is described in *Elbeshausen et al. (2009)*. iSALE has been used to model the collision of highly porous planetesimals (*Davison et al., 2012*), impacts on the surface of (4) Vesta (*Krohn et al., 2014*), and the formation of large craters on (21) Lutetia (*Cremonese et al., 2012*), as well as the effect of an oblique impact angle on crater formation (*Elbeshausen et al., 2009, 2013*).

**4.5.2. Smoothed particle hydrodynamics codes.** Smoothed particle hydrodynamics is a meshless continuum Lagrangian approach (and in spite of its name is not a “particle” code). In the basic SPH method, approximate numerical solutions of the fluid-dynamics equations are obtained by replacing the fluid with a set of particles (see, e.g., *Gingold and Monaghan, 1977; Monaghan, 2012*). The properties of these particles are smoothed over a certain length  $h$  by a kernel function. That provides the link to a continuum approach. As the flow evolves, material mass moves with the particle and local density is calculated based on the proximity of nearby particles. The main advantages of this mesh-free method are: (1) SPH is a very robust scheme, and it is “straightforward” to add new physics. (2) Large deformations of the simulated objects are handled easily. (3) The description of free surfaces is trivial. (4) Due to the particle nature of the method, fragmentation is modeled naturally by the separation of particle clusters.

Disadvantages of the SPH method include: (1) The spatial resolution is typically lower than in grid-based simulations. (2) Boundary conditions and discontinuities (e.g., material interfaces) are complicated to handle. (3) It is mostly applied in three dimensions, which often requires computationally expensive million-particle calculations.

In the past years, the range of applications of the SPH algorithm has increased significantly. A number of SPH codes have been recently developed to study problems in planetary sciences. Examples are a SPH code for the modeling of pre-planetesimals (*Geretschauser et al., 2011*), SPHERAL (*Shapiro et al., 1996; Owen, 2010*), GADGET (*Springel, 2005; Marcus et al., 2009*), SPHLATCH (*Reufer et al., 2012*), or a GPU-based SPH code (*Kaplinger et al., 2013*).

A widely used SPH code to model collisions among rocky bodies was developed by *Benz and Asphaug (1994, 1995)*. This code was further extended by *Jutzi et al. (2008, 2013)* with the goal of realistically modeling rocky bodies with various internal structures (see section 4.5 for a comparison

to laboratory experiments). The most recent version of this code (see *Jutzi*, 2015) includes a pressure-dependent strength model as outlined in section 4.4.2, a tensile fracture model (section 4.4.3), and a porosity model based on the P- $\alpha$  model (section 4.4.5) and self-gravity. Friction is modeled either using the Coulomb dry friction law (equation (10)) or the rate-dependent model suggested by *Jop et al.* (2006). Self-gravity (section 4.3) is included as well. Recent applications of this code in asteroid studies are presented in section 5 and in the chapter by Asphaug et al. in this volume.

#### 4.6. Comparison to Laboratory Experiments

An important step in the development of numerical methods (which includes the implementation of complex material models) is the validation against laboratory experiments. As rigorous testing is limited by the availability of appropriate experiments, including measurements during the highly dynamic processes, a preliminary step is benchmarking of different codes against each other. An example for a very successful benchmark and validation study is given in *Pierazzo et al.* (2008), in which the modeling results of specific test problems from eight different hydrocodes were compared against each other and validated against laboratory cratering experiments, but only for water and aluminum.

Here we provide some additional examples dealing with the fracturing and fragmentation resulting from collisional processes, as well as a granular flow problem.

##### 4.6.1. Modeling the fragmentation of porous pumice.

Figure 4 shows a comparison of an SPH code calculation (using the SPH method as described in section 4.5.2) to laboratory impact experiments. The target used in the experiments is porous pumice with a porosity of ~70%. The fragment-sized distributions resulting from the impacts with velocities ranging from 2–4 km s<sup>-1</sup> could be well reproduced in the SPH code calculations (see *Jutzi et al.*, 2009, for details). This example illustrates the capabilities of the SPH method to model impact fragmentation.

**4.6.2. Fracturing in cratering experiments.** Fracturing caused by hypervelocity impact does not necessarily result in a complete disruption of the target. Figure 5 shows the cross-section of the crater that was formed by the 5.4 km s<sup>-1</sup> impact of a 1-cm-diameter iron projectile in ~20% porous sandstone. The experiment was carried out in the framework of the so-called Multidisciplinary Experimental and Modeling Impact Research Network (MEMIN) project, aiming at the validation of hydrocode modeling of hypervelocity impact processes (see *Kenkmann et al.*, 2013, and references therein). Figure 5a shows a snapshot of the iSALE cratering model at 750  $\mu$ s. The model includes the  $\epsilon$ - $\alpha$  porosity compaction model and a strength and damage model as described in *Collins et al.* (2004). Some static strength parameters of the sandstone were available (*Kenkmann et al.*, 2011); others, such as the crushing strength of the porous sandstone, were estimated or adjusted to match the observed crater depth.

A more detailed calibration and validation of the crushing of pore space and sandstone is presented in *Güldemeister et*

*al.* (2013) and *Kowitz et al.* (2013). The crater in the experiment is enlarged by spallation. Modeling of the actual spall of material from the surface is not included in the iSALE model; however, the spall zone is indicated by cells that have experienced failure.

The damage zone in the model (gray contours represent the damage parameter as introduced above) underneath the crater shows some qualitative similarities with the flaws indicated by the thin gray lines on the cross-section of the cratering experiment. On the scale of individual grains it was shown that the zone where pore space was crushed or fracturing occurs in grains extends approximately to the same distance as in the model.

**4.6.3. Cliff collapse problem.** The cliff collapse problem is a useful test case for the pressure-dependent models used in code calculations, at least for low pressure. In that problem, an initial vertical “cliff” of material is suddenly released, and the mass falls and flows out to considerable lengths. This problem is of special interest for cratering because the same requirements of temporary fluidization mechanisms have been asserted as necessary for the mechanics of landslides. The final angles of the runouts are typically <10°, far below the angle of repose of geological materials.

*Holsapple* (2013) presented detailed theoretical arguments and numerical calculations of that landslide problem, using only the standard Drucker-Prager soil model with a

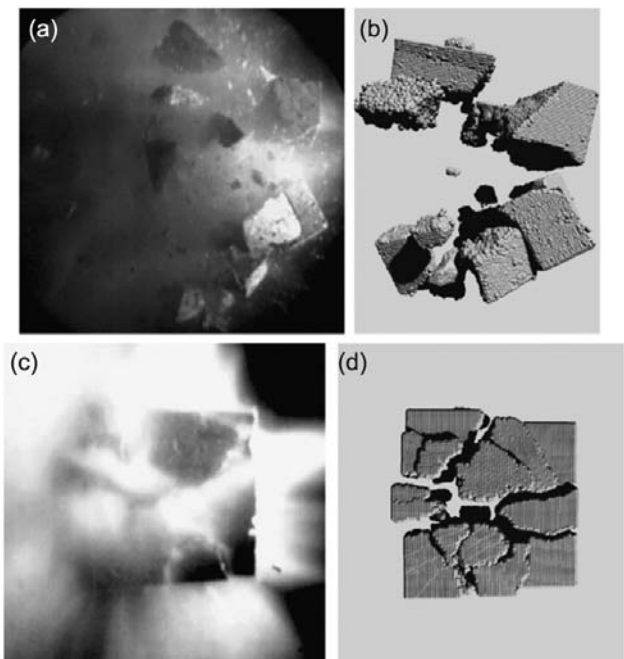


**Fig. 4.** Comparison between (a,c) laboratory impact experiments and (b,d) SPH code calculations. The targets are pumice cubes 7 cm in size with a porosity of ~70%. The impact experiments were performed at the Institute of Space and Astronautical Science (ISAS) of the Japan Aerospace Exploration Agency (JAXA) using a two-stage light-gas gun. Two impacts are shown at different times: (a,b)  $t = 8$  ms and (c,d)  $t = 1.5$  ms. From *Jutzi et al.* (2009).

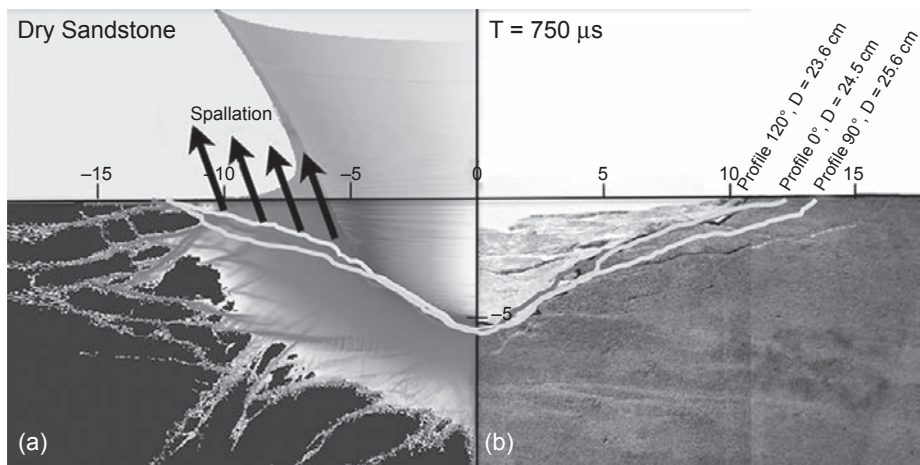


**Fig. 5.** Comparison between (a) iSALE simulation and (b) laboratory cratering experiments. The target was a  $100 \times 100 \times 50$ -cm sandstone block with 20% porosity. The so-called Seeberger sandstone is composed of 97 wt.% SiO<sub>2</sub> with an unconfined compressive strength of  $\sim 60$  MPa. The projectile was a 1-cm iron sphere impacting at  $5.4 \text{ km s}^{-1}$  (for further details see Kenkmann *et al.*, 2011). (a) A snapshot of the numerical model showing contours of the damage parameter. The black lines indicate the zone where tensile failure occurs and material spalls off the surface. (b) The thin gray lines indicate macroscopic flaws; the thick gray lines indicate crater profiles in different directions. Courtesy of the Multidisciplinary Experimental and Modeling Impact Crater Research Network (MEMIN) Team.

35° angle of friction. He concludes that no additional *ad hoc* models are required to reproduce observed laboratory results. Specifically, his numerical simulations correctly reproduce laboratory experiments with final slopes  $< 10^\circ$ . A detailed investigation of those simulations explains the reason. It lies in the fact that the “slopes” allowed by the angle of repose argument are not violated, it is just that during the highly dynamic flows, the “slopes” must be measured relative to the combination of the local gravity direction and the direction of the inertial forces.

Jutzi (2015) also presented SPH calculations of that problem. He compared two models, one with a constant coefficient of friction (equation (10)) and one using a rate-dependent and particle-size-dependent relation defined in an “inertial number” as suggested by Jop *et al.* (2006). It was found that both models reproduce the experiments very well. The two models lead to the same results because in this granular flow regime, the inertial number stays small and therefore the rate dependency is negligible. This finding provides further evidence that the global outcome of such events is well reproduced by using a simple Coulomb dry friction law with a single parameter  $\mu_d$ , although at higher pressures a nonlinear model is undoubtedly necessary.

These examples show that the cliff-collapse problem and the resulting runouts (at laboratory conditions) can be well reproduced with continuum codes using conventional rock mechanics. However, there is evidence that additional weakening mechanisms (section 4.4.6) are necessary to explain other cases, such as the very long runout slides observed on Mars (e.g., Lucas and Mangeney, 2007; Harrison and Grimm, 2003).

## 5. APPLICATIONS

In this section, some examples of recent modeling are presented that illustrate the various the effects of the material properties, target structures, and impact conditions on the outcome of a collision.

### 5.1. Scaling Laws from Numerical Modeling

**5.1.1. Cratering regime.** Simple power-law relationships, so-called scaling laws, have been proposed to relate the size of the transient crater with impact parameters such as the mass and velocity of the impactor (see section 3). Those have been shown to be a theoretical consequence of the point-source assumption, as mentioned above. The scaling parameters in these equations (the so-called velocity exponent  $\mu$  and a proportionality factor that may be called K) have been determined by laboratory experiments, mainly in sand or other granular materials. One way to determine the scaling parameters is to vary the so-called gravity-scaled size of an impact event  $\pi_2 = (Lg)/v^2$ , with the diameter L of the impactor, or the gravity g, or the impact velocity v, over as large a range as possible. For example, one can increase the gravity using a geotechnic centrifuge and decrease the gravity using drop towers. The geotechnic centrifuge method was developed both for explosive cratering and hypervelocity impact cratering by Schmidt (1977) and by Schmidt and Holsapple (1980). Since gravity can be varied over 2 orders of magnitude, a 500-G centrifuge test models 1-G events with a 500× larger scale. A meter-sized test at 500 G has the same physics

as a 0.5-km event at 1 G. However, there is no effect of the increased gravity at those magnitudes except for materials with very little cohesion, so studies are primarily limited to granular materials such as sand. Although the properties of the target material such as porosity or internal friction are somewhat under the experimenter's control, independently varying these parameters is difficult.

An alternative approach is to use numerical simulations to carry out numerical experiments that are not limited by experimental constraints in the laboratory. Of course, due to the numerous modeling questions mentioned above, those are not without their own uncertainties. And, as long as the point-source approximation is valid, they cannot contradict the theoretical scaling forms, but they can identify the unknown scaling coefficients. Also, they allow extensions of the parameter space from laboratory scale to natural dimensions under any given gravity regimes of planets, moons, and asteroids. The effect of material properties of the target such as porosity, friction, and cohesion can be independently investigated (Wünnemann et al., 2010), and the effect of the angle of incidence can be investigated as well (Elbeshausen et al., 2009). In these studies it was shown that the velocity exponent  $\mu$  depends on the coefficient of friction  $f$  of the target material (Fig. 6) and the scaling factor  $K$  may be expressed as a function of porosity  $\phi$ .

To incorporate the angle of impact  $\theta$  into the scaling equations, it was suggested by Chapman and McKinnon (1986) and others based on impact experiments in sand to replace the impact velocity  $v_\theta$  by the vertical component of the impact velocity  $v_\perp$ . For example, in this case, crater volume scales with the sine of the impact angle raised to the power  $2\gamma$  where  $\gamma = 3\mu/(2 + \mu)$ . Extensive parameter studies using models of impacts at different angles into granular targets with varying coefficient of friction (Fig. 7a) show that this approximation holds true only for a typical coefficient of friction of  $f = 0.7$  (Fig. 7c) (Elbeshausen et al., 2009). The vertical velocity component approximation also provides good estimates of crater volume and diameter for strength-dominated craters in cohesive ductile targets such as metals (Davison et al., 2011). For impacts in granular targets with a smaller coefficient of friction than is typical for sand, the size of the resulting crater is underestimated by this simple assumption (Fig. 7b). Details of the impact may not be so easily matched using this assumption.

**5.1.2. Disruption regime.** To characterize the outcome of a disruptive collision, the critical specific impact energy  $Q_D^*$ , which results in the escape of half the target's mass in a collision, is often used. The parameter  $Q_D^*$  is called the catastrophic impact energy threshold (also called the dispersion threshold). The specific impact energy is often defined as  $Q = 0.5m_p v_p^2/M_T$ , where  $m_p$ ,  $v_p$ , and  $M_T$  are the mass and speed of the projectile and the mass of the target, respectively. The catastrophic disruption threshold  $Q_D^*$  is then given by the specific impact energy leading to a largest (reaccumulated) fragment  $M_{lr}$  containing 50% of the original target's mass. In recent studies (e.g., Stewart and Leinhardt, 2009; Leinhardt and Stewart, 2012), a more general definition of

the specific impact energy was proposed that also takes into account the mass of the impactor, which can be substantial in very-low-velocity impacts of near-equal-sized bodies. The corresponding radius  $R_{C1}$  is then defined as the spherical radius of the combined projectile and target masses at a density of  $1 \text{ g cm}^{-3}$ . According to this new definition, the catastrophic disruption threshold is then called  $Q_{RD}^*$ .

Values of  $Q_D^*$  (or  $Q_{RD}^*$ ) have been estimated using both laboratory and numerical hydrocode experiments (see, e.g., Holsapple et al., 2002; Asphaug et al., 2002). For high-velocity asteroid collisions, the first suite of numerical calculations aimed at characterizing the catastrophic disruption threshold in both the strength regime and the

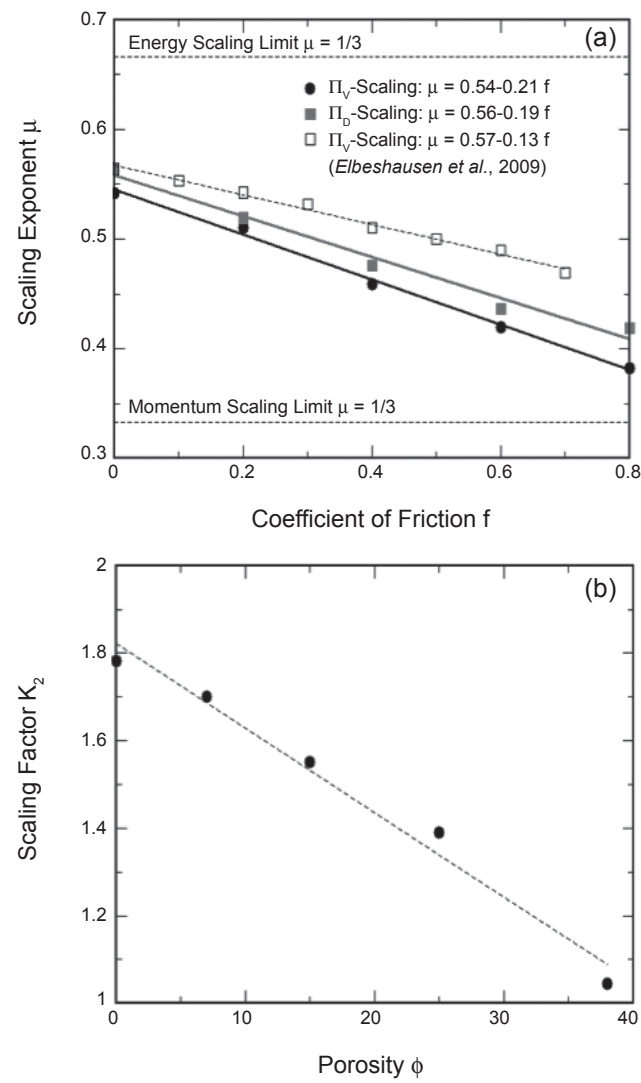


**Fig. 6.** Scaling parameters  $\mu$  and  $K_2$  as a function of coefficient of friction  $f$  and porosity  $\phi$ . (a) The scaling exponent  $\mu$  was determined by numerical impact experiments into material with different coefficient of friction, zero cohesion, and zero porosity. The dashed line was taken from Elbeshausen et al. (2009). (b) The scaling factor  $K_2$  was determined by numerical impact experiments into material with different porosities, a coefficient of friction  $f = 0.8$ , and zero cohesion.

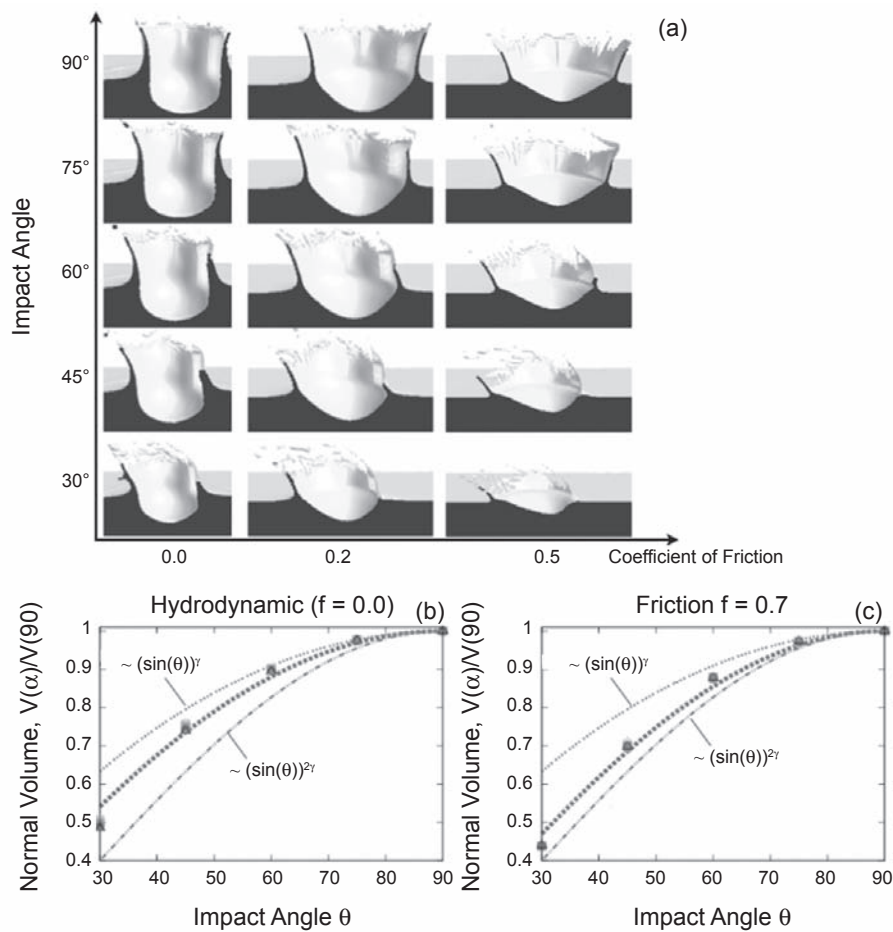


**Fig. 7.** Snapshots of the approximate transient crater for different impact angle and coefficient of friction. Relative change of the crater volume  $V_\theta$  normalized by crater volume for an equivalent 90° impact  $V_{90}$  with impact angle for (b)  $f = 0$  (fluid-like target rheology) and (c)  $f = 0.7$  (sand-like target rheology). Note: The results from numerical models over a range of different  $\pi_2$  values fall in between two lines calculated according to the vertical velocity component approximation [ $\sim -\sin(\theta)^{2\gamma}$ ; lower curve] and another line [ $\sim -\sin(\theta)^\gamma$ ]. Taken from Elbeshausen et al. (2009).

gravity regime was performed by Benz and Asphaug (1999), who used an SPH code (Benz and Asphaug, 1994, 1995) to simulate the breakup of basalt and icy bodies from centimeter scale to hundreds of kilometers in diameter. More recently, Leinhardt and Stewart (2009) computed  $Q_D^*$  curves using the hydrocode CTH (McGlaun, 1990) to compute the fragmentation phase and the N-body code *pdkgrav* to compute the subsequent gravitational evolution of the fragments. In this study, the dependency of  $Q_D^*$  on the strength of the target was investigated. In a recent study by Jutzi et al. (2010), the effect of target porosity on  $Q_D^*$  was investigated using an extended version of the SPH code (Jutzi et al., 2008). In this study, the size and velocity distribution of the fragments was computed as well, using the *pdkgrav* code. Benavidez et al. (2012) performed a study of a large number of collisions among  $R_t = 50$ -km rubble-pile bodies using the original SPH code by Benz and Asphaug (1994, 1995). As discussed in section 3, Leinhardt and Stewart (2012) proposed general scaling laws for collisions among gravity-dominated bodies.

In the chapter by Asphaug et al. in this volume, a recent systematic study of the relative effects of various asteroid properties on the disruption threshold  $Q_D^*$  (Jutzi, 2015) is presented.

## 5.2. Momentum Transfer in Small Impacts

The study of the momentum transferred in an specific impact on an asteroid as a function of impact conditions and the internal structure is crucial for performance assessment of the kinetic impactor concept of deflecting a potentially hazardous asteroid from its trajectory (see the chapter by Harris et al. in this volume). The momentum transfer is characterized by the so-called momentum multiplication factor  $\beta$ , which has been introduced to define the momentum imparted to an asteroid in terms of the momentum of the impactor

$$\beta = 1 + p_{ej} / (M_p v_p) \quad (16)$$

where  $p_{ej}$  is the escaping ejecta momentum, and  $M_p$  and  $v_p$  are the mass and velocity of the impactor, respectively (see,

e.g., *Holsapple*, 2004b). In the limiting case of an impact that produces no escaping ejecta,  $\beta = 1$ , and the momentum transferred corresponds to the momentum of the projectile (inelastic collision). However, in the case of an impact that produces a lot of material (ejected in the opposite direction) with velocities larger than the escape velocity, we can have  $\beta \gg 1$  due to the contribution of  $p_{ej}$ . Using the  $\beta$  factor, the resulting momentum of the target  $\Delta P_t$  (along the impact direction) can be obtained by

$$\Delta P_t = \beta P_p \quad (17)$$

where  $P_p = m_p v_p$  is the momentum of the projectile.

It is important to note that only fragments with ejection velocities larger than the escape velocity of the target asteroid,  $v_{eject} > v_{esc}$ , escape the body and contribute to the momentum transfer. Moreover, the ejected material is slowed down during its escape and its trajectory is changed due to the gravitational attraction of the target. Therefore, to compute the escaping ejecta momentum, the value and angle of the velocity at infinity have to be used (see, e.g., *Holsapple and Housen*, 2012; *Cheng*, 2012; *Jutzi and Michel*, 2014).

*Holsapple and Housen* (2012) presented scaling laws to extrapolate measurements of the momentum transfer in laboratory experiments to asteroid scales. Recent code calculations of the momentum transfer efficiency in impacts on asteroids for conditions typical for a kinetic impactor were performed by *Holsapple and Housen* (2013a) and *Jutzi and Michel* (2014). *Holsapple and Housen* (2013a) presented numerical simulations both for porous and non-porous materials, and obtained very good agreement with their laboratory results.

In the study by *Jutzi and Michel* (2014), the effect of different degrees and scales of porosity on the momentum multiplication factor  $\beta$  was investigated for a range of impact conditions.

Two kinds of porous target structures were considered by *Jutzi and Michel* (2014): (a) homogeneous — microporous only, and (b) heterogeneous — both micro- and macroporous. For both structures, the microporous part of the material has a porosity of 50%. For structure (b), in addition to the microporosity, macroscopic cracks with a size scale of  $\sim 0.3$  m are randomly distributed in the target. The resulting total macroscopic void fraction is 10%.

The impact simulations were performed using an SPH impact code (e.g., *Benz and Asphaug*, 1994, 1995; *Jutzi et al.*, 2008; *Jutzi*, 2015) as presented in section 4.5.2.

In Fig. 8, the outcome (in terms of damage) of an impact at  $10 \text{ km s}^{-1}$  is shown for the two target structures.

In Fig. 9, the results of the calculations of  $\beta$  are shown for the considered range of impact velocities ( $0.5\text{--}15 \text{ km s}^{-1}$ ) and the two target structures. At low-impact velocities, the amount of momentum transferred is smaller using structure (b) than structure (a). However, these differences disappear at high velocities. This means that for porous targets, inhomogeneities at the scales considered here have negligible effects on the amount of transferred momentum

for velocities  $\geq 5 \text{ km s}^{-1}$ . That confirms the view expressed earlier that the exact form of the modeling of porosity will not matter for any phenomena with scales that are large compared to the size scale of that porosity.

While the effect of target inhomogeneities on the momentum multiplication factor  $\beta$  appears to be quite small, the effect of various material properties such as tensile or crushing strength was found to be more significant (*Jutzi and Michel*, 2014).

The results of this study verify that the momentum multiplication factor  $\beta$  is small even for very-high-impact velocities ( $\beta < 2$  for  $v_{imp} \leq 15 \text{ km s}^{-1}$ ) in the case of porous targets (with  $\sim 50\%$  porosity). This is consistent with scaling laws (section 3), which, in combination with the results of laboratory experiments, predict a small value of  $\beta \sim 1\text{--}2$  for porous materials and comparable impact velocities (see Table 3 in *Holsapple and Housen*, 2012). It is also consistent with the numerical simulations performed by *Holsapple and Housen* (2013a).

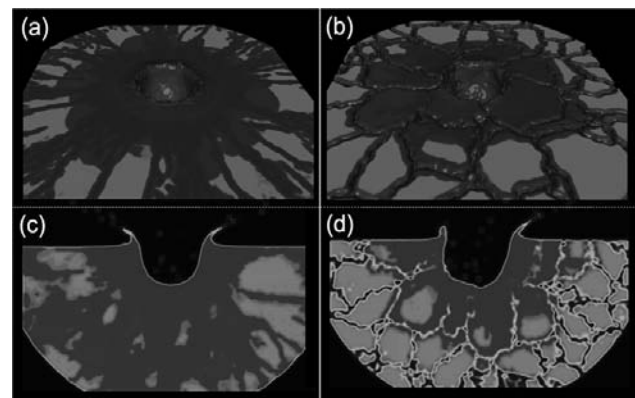


**Fig. 8.** (a,c) Damage (dark gray zones) produced by the impact at  $10 \text{ km s}^{-1}$  on a microporous target; (a) and (b) show the target from above, while (c) and (d) show a vertical slice. (b,d) Same for a target containing both microporosity and macroporosity. From *Jutzi and Michel* (2014).

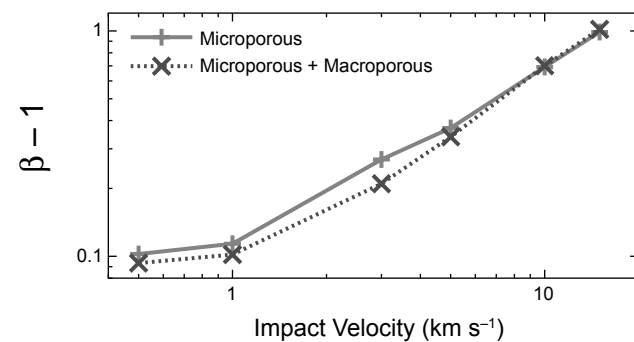


**Fig. 9.** Momentum multiplication factor  $\beta - 1$  as a function of impact velocity for the two considered structures: (1) homogeneous microporous and (2) heterogeneous, microporous, and macroporous. From *Jutzi and Michel* (2014).

However, that is not true for nonporous targets. Values of  $\beta$  as large as 5 have been directly measured at impact velocities of  $v_{\text{imp}} \leq 5 \text{ km s}^{-1}$  (*Holsapple and Housen*, 2013a) for rocky targets. Furthermore, the scaling predicts a marked increase like  $U^{0.5}$  for those targets, so at  $v_{\text{imp}} \leq 20 \text{ km s}^{-1}$  those values might reach as much as  $\beta \sim 10$ . If so, that would significantly facilitate deflections by impacts.

An important question is how to scale strength (tensile strength and crush-curve parameters) of a porous material to larger sizes. The strength properties of real asteroid materials and their size dependency are not well constrained (e.g., what is the crush-curve of a 300-m asteroid with 50% porosity?), while they have a significant effect on the momentum transfer efficiency.

### 5.3. Selective Sampling in Catastrophic Disruptions

The catastrophic disruption of a large asteroid as a result of a collision with a smaller projectile and the subsequent reaccumulation of fragments as a result of their mutual gravitational attractions have been simulated numerically during the last decades, which allowed the formation of asteroid families to be successfully reproduced (see the chapter by Michel et al. in this volume). It is generally found that most large bodies formed during a catastrophic disruption consist of aggregates formed by reaccumulation of smaller fragments (e.g., *Michel et al.*, 2001). The original location within the parent body of the small pieces that eventually reaccumulate to form the largest offspring of a disruption as a function of the original internal structure of the disrupted asteroid is interesting to determine for several reasons. If reaccumulation is a random process, we expect the particles of a given large fragment to originate from uncorrelated regions within the parent body. Conversely, if the initial velocity field imposed by the fragmentation process determines the reaccumulation phase, the particles belonging to the same fragment should originate from well-defined areas inside the parent body. In addition, the position and extent of these regions provide indications about the mixing occurring as a result of the reaccumulation process. Motivated by the question of the origin of ureilites, which, in some petrogenetic models, are inferred to have formed at particular depths within their parent body, *Michel et al.* (2014) started to investigate this problem by simulating the fragmentation (and reaccumulation) of a large body with a diameter fixed at 250 km. This study was performed using a hybrid approach with an SPH shock-physics code (*Benz and Asphaug*, 1994, 1995; *Jutzi et al.*, 2008; *Jutzi*, 2015) and the n-body code *pkdgrav* as described in section 4. They considered four kinds of internal structures that may represent the internal structure of a large body in various early stages of the solar system evolution: fully molten, half-molten (i.e., a 26-km-deep outer layer of melt containing half the mass), solid except for a thin molten layer (8 km thick) centered at a 10-km depth, and fully solid. The properties of basaltic material were assumed for the solid component. They focused on the three largest offspring that had enough reaccumulated pieces to consider.

As found by *Michel et al.* (2004), who considered fully solid and preshattered bodies in the context of family formation, they found that the particles that eventually reaccumulate to form the largest reaccumulated bodies retain a memory of their original locations in the parent body. In other words, most particles in each reaccumulated body are clustered from the same original region, even if their reaccumulations take place far away. However, they also found that the extent of the original region varies considerably depending on the internal structure of the parent (Fig. 10). In particular, it seems to shrink with the solidity of the body. Although the covered parameter space in this first study was limited, this sort of investigation can provide some constraints on the internal structure of the parent bodies of some meteorites.

## 6. CONCLUSIONS

Numerical simulations provide an important tool that allows us to probe regimes unreachable by experimental methods. Collisions among asteroids take place in those regimes. To realistically model these events, the combined effects of gravity, strength, porosity, as well as shape and structural properties need to be taken into account. Therefore, high-fidelity physical models are required, and modeling asteroid collisions is extremely complex.

Our knowledge of the asteroid properties that are relevant in terms of impact modeling is still quite limited. Moreover,

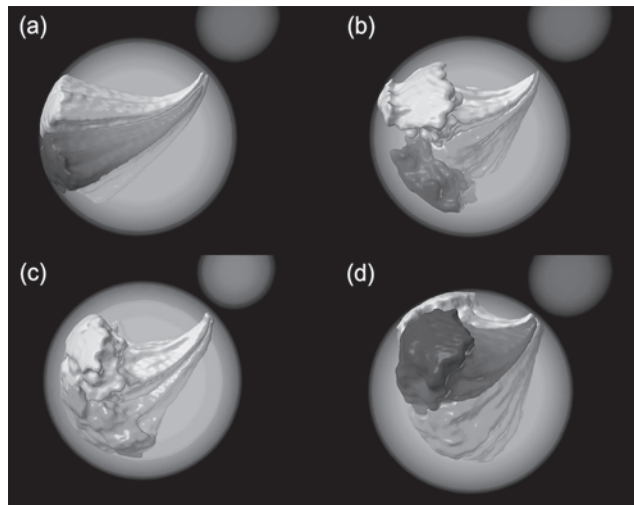


**Fig. 10.** Original positions of the material that will reaccumulate and form the largest, second-largest, and third-largest fragments (plume-shaped objects shown in different levels of gray). The results for four different internal structures are (a) fully molten, (b) half-molten, (c) with a thin molten layer (10% of the total mass) at a 10-km depth (the third largest is hidden behind the visible two largest), and (d) fully solid. The transparent gray bodies indicate the original target and impactor, respectively. The impactor moves vertically down. In the investigated greatly disruptive regimes, all the material that is not in the largest fragments (i.e., the largest fraction of the parent body) is blown away, i.e., it will not reaccumulate (or only in very small fragments). Inspired by *Michel et al.* (2015).

there are known important shortcomings in the modeling that has been used to date, although that modeling is improving. It is important to keep that in mind in assessing the meaning of any numerical simulation.

An important step in the development of numerical methods (which includes the implementation of complex material models) is the validation against laboratory experiments. Although only very briefly mentioned in this chapter, experimental studies greatly contributed to our understanding of the collisional process at small laboratory scales and always give a necessary point of reference to test numerical methods. However, in comparisons to experiments, it is important to include more than one single scalar value, such as the crater size or the fragment mass from one experiment. In order for a numerical model to be a predictive tool, it should be able to reproduce multiple experiments in different regimes without adjusting any parameters.

Since the publication of *Asteroids III* a decade ago, there have been major advances in the modeling of asteroid collisions and impact processes. The numerical simulations will undoubtedly become of higher fidelity as our models improve, guided by experimental, theoretical, and scaling results.

**Acknowledgments.** M.J. acknowledges the support of the Swiss National Science Foundation through the Ambizione program. K.H. acknowledges support from NASA grant NNX10AG51G. K.W. acknowledges support through DFG grant WU355/6-1/2. P.M. acknowledges support from the French space agency CNES and the French National Program of Planetology. We thank G. Collins and B. Ivanov for their insightful reviews.

## REFERENCES

- Amsden A., Ruppel H., and Hirt C. (1980) *SALE: A Simplified ALE Computer Program for Fluid Flow at All Speeds*. Los Alamos National Laboratories Report LA-8095, Los Alamos, New Mexico. 101 pp.
- Anderson C. E. (1987) An overview of the theory of hydrocodes. *Int. J. Impact Eng.*, 5, 33–59.
- Artemieva N. and Morgan J. (2009) Modeling the formation of the K-Pg boundary layer. *Icarus*, 201, 768–780.
- Asphaug E., Ryan E. V., and Zuber M. T. (2002) Asteroid interiors. In *Asteroids III* (W. F. Bottke Jr. et al., eds.), pp. 463–484. Univ. of Arizona, Tucson.
- Ballouz R.-L., Richardson D. C., Michel P., and Schwartz S. R. (2014) Rotation-dependent catastrophic disruption of gravitational aggregates. *Astrophys. J.*, 789, 158.
- Ballouz R.-L., Richardson D. C., Michel P., Schwartz S. R., and Yu Y. (2015) Numerical simulations of collisional disruption of rotating gravitational aggregates: Dependence on material properties. *Planet. Space Sci.*, 107, 29–35.
- Barnes J. and Hut P. (1986) A hierarchical O(N log N) force-calculation algorithm. *Nature*, 324, 446.
- Benavidez P. G. et al. (2012) A comparison between rubble-pile and monolithic targets in impact simulations: Application to asteroid satellites and family size distributions. *Icarus*, 219, 57–76.
- Benz W. and Asphaug E. (1994) Impact simulations with fracture. I — Method and tests. *Icarus*, 107, 98.
- Benz W. and Asphaug E. (1995) Simulations of brittle solids using smooth particle hydrodynamics. *Comp. Phys. Comm.*, 87, 253–265.
- Benz W. and Asphaug E. (1999) Catastrophic disruptions revisited. *Icarus*, 142, 5–20.
- Benz W., Cameron A. G. W., and Melosh H. J. (1989) The origin of the Moon and the single-impact hypothesis III. *Icarus*, 81, 113–131.
- Berger M. J. and Colella P. (1989) Local adaptive mesh refinement for shock hydrodynamics. *J. Comp. Phys.*, 82, 64.
- Berger M. J. and Oliger J. (1984) Adaptive mesh refinement for hyperbolic partial differential equations. *J. Comp. Phys.*, 53, 484.
- Bray V. J., Collins G. S., Morgan J. V., Melosh H. J., and Schenck P. M. (2014) Hydrocode simulation of Ganymede and Europa cratering trends — How thick is Europa's crust? *Icarus*, 231, 394–406.
- Britt D. T., Yeomans D., Housen K., and Consolmagno G. J. (2002) Asteroid density, porosity, and structure. In *Asteroids III* (W. F. Bottke Jr. et al., eds.), pp. 485–500. Univ. of Arizona, Tucson.
- Britt D. T., Consolmagno G. J., and Merlin W. J. (2006) Small body density and porosity: New data, new insights. *Lunar Planet. Sci. XXXVII*, Abstract #2214. Lunar and Planetary Institute, Houston.
- Canup R. M. and Asphaug E. (2001) Origin of the Moon in a giant impact near the end of the Earth's formation. *Nature*, 412, 708–712.
- Canup R. M., Barr A. C., and Crawford D. A. (2013) Lunar-forming impacts: High-resolution SPH and AMR-CTH simulations. *Icarus*, 222, 200–219.
- Carroll M. M. and Holt A. C. (1972) Suggested modification of the P- $\alpha$  model for porous materials. *J. Appl. Phys.*, 43, 759–761.
- Chapman C. R. and McKinnon W. B. (1986) Cratering of planetary satellites. In *Satellites* (J. A. Burns and M. S. Matthews, eds.), p. 492–580. Univ. of Arizona, Tucson.
- Cheng A. F. (2012) Asteroid deflection by spacecraft impact. *Asteroids, Comets, Meteors 2012*, Abstract #6414. LPI Contribution No. 1667, Lunar and Planetary Institute, Houston.
- Collins G. S. (2014) Numerical simulations of impact crater formation with dilatancy. *J. Geophys. Res.–Planets*, 119(12), 2600–2619, DOI: 10.1002/2014JE004708.
- Collins G. S., Melosh H. J., and Ivanov B. A. (2004) Modeling damage and deformation in impact simulations. *Meteoritics & Planet. Sci.*, 39, 217–231.
- Collins G. S., Melosh H. J., and Wünnemann K. (2011) Improvements to the  $\epsilon$ - $\alpha$  porous compaction model for simulating impacts into high-porosity solar system objects. *Intl. J. Impact Eng.*, 38, 434–439.
- Collins G. S., Wünnemann K., Artemieva N., and Pierazzo E. (2013) Numerical modelling of impact processes. In *Impact Cratering: Processes and Products* (G. R. Osinski and E. Pierazzo, eds.), pp. 254–270. Wiley-Blackwell, New York.
- Cremonese G., Martellato E., Marzari F., Kuhrt E., Scholten F., Preusker F., Wünnemann K., Borin P., Massironi M., Simioni E., and Ip W. (2012) Hydrocode simulations of the largest crater on the asteroid Lutetia. *Planet. Space Sci.*, 66, 147–154.
- Davison T. M., Collins G. S., and Ciesla F. J. (2010) Numerical modelling of heating in porous planetesimal collisions. *Icarus*, 208(1), 468–481.
- Davison T. M., Collins G. S., Elbeshausen D., Wünnemann K., and Kearsley A. (2011) Numerical modeling of oblique hypervelocity impacts on strong ductile targets. *Meteoritics & Planet. Sci.*, 46(10), 1510–1524.
- Davison T. M., Ciesla F. J., and Collins G. S. (2012) Post-impact thermal evolution of porous planetesimals. *Geochim. Cosmochim. Acta*, 95, 252–269.
- Dienes J. K. and Walsh J. M. (1970) Theory of impact: Some general principles and the method of Eulerian codes. In *High Velocity Impact Phenomena* (R. Kinslow, ed.), pp. 45–104. Academic, New York.
- Elbeshausen D., Wünnemann K., and Collins G. S. (2009) Scaling of oblique impacts in frictional targets: Implications for crater size and formation mechanisms. *Icarus*, 204(2), 716–731, DOI: 10.1016/j.icarus.2009.07.018.
- Elbeshausen D. and Wünnemann K. (2010) iSALE-3D: A three-dimensional, multi-material, multi-rheology hydrocode and its applications to large-scale geodynamic processes. In *Proceedings of the 11th Hypervelocity Impact Symposium* (F. Schäfer and S. Hiermaier, eds.), pp. 287–301.
- Elbeshausen D., Wünnemann K., and Collins G. S. (2013) The transition from circular to elliptical impact craters. *J. Geophys. Res.–Planets*, 118(11), 2295–2309, DOI: 10.1002/2013JE004477.
- Flynn G. J., Durda D. D., Sandel L. E., Kreft J. W., and Strait M. M. (2008) Dust production from the hypervelocity impact disruption of the Murchison hydrous CM2 meteorite: Implications for the disruption of hydrous asteroids and the production of interplanetary dust. *Planet. Space Sci.*, 57, 119–126.
- Fujiiwara A. et al. (2006) The rubble-pile asteroid Itokawa as observed by Hayabusa. *Science*, 312, 1330–1334.
- Gault D. E. (1973) Displaced mass, depth, diameter, and effects of oblique trajectories for impact craters formed in dense crystalline rocks. *Moon*, 6, 32–44.

- Geretshauser R. J., Speith R., and Kley W. (2011) Collisions of inhomogeneous pre-planetesimals. *Astron. Astrophys.*, 536, A104.
- Gingold R. A. and Monaghan J. J. (1977) Smoothed particle hydrodynamics — Theory and application to non-spherical stars. *Mon. Not. R. Astron. Soc.*, 181, 375–389.
- Grady D. E. and Kipp M. E. (1980) Continuum modelling of explosive fracture in oil shale. *Intl. J. Rock Mech. Min. Sci. Geomech.*, 17, 147–157.
- Güldemeister Ni., Wünnemann K., Durr N., and Hiermaier S. (2013) Propagation of impact-induced shock waves in porous sandstone using mesoscale modeling. *Meteoritics & Planet. Sci.*, 48(1), 115–133.
- Harrison K. and Grimm R. (2003) Rheological constraints on martian landslides. *Icarus*, 163, 347–362.
- Herrmann W. (1969) Constitutive equation for the dynamic compaction of ductile porous materials. *J. Appl. Phys.*, 40, 2490–2499.
- Hiraoka K., Hakura S., Nakamura A. M., Suzuki A., and Hasegawa S. (2011) Impact cratering experiments on porous sintered targets of different strengths. *Meteoritics & Planet. Sci. Suppl.*, 74, 53–63.
- Hirt C. W., Amsden A. A., and Cook J. L. (1974) An arbitrary Lagrangian-Eulerian computing method for all flow speeds. *J. Comp. Phys.*, 14(3), 227–253.
- Hoek E. and Brown E. T. (1980) Empirical strength criterion for rock masses. *J. Geotech. Eng. Div. ASCE*, 106, 1013–1025.
- Holsapple K. A. (1993) The scaling of impact processes in planetary sciences. *Annu. Rev. Earth Planet. Sci.*, 21, 333–373.
- Holsapple K. A. (2004a) From simple to complex craters: The mechanics of late-time crater adjustments. *Lunar Planet. Sci. XXXV*, Abstract #1937. Lunar and Planetary Institute, Houston.
- Holsapple K. A. (2004b) About deflecting asteroids and comets. In *Mitigation of Hazardous Comets and Asteroids* (M. J. S. Belton et al., eds.), p. 113. Cambridge Univ., Cambridge.
- Holsapple K. A. (2008) Porous material models for impact studies. *Lunar Planet. Sci. XXXIX*, Abstract #2257. Lunar and Planetary Institute, Houston.
- Holsapple K. A. (2009) On the “strength” of the small bodies of the solar system: A review of strength theories and their implementation for analyses of impact disruptions. *Planet. Space Sci.*, 57, 127–141.
- Holsapple K. A. (2013) Modeling granular material flows: The angle of repose, fluidization and the cliff collapse problem. *Planet. Space Sci.*, 82/83, 11–26.
- Holsapple K. A. and Housen K. R. (2012) Momentum transfer in asteroid impacts. I. Theory and scaling. *Icarus*, 221, 875–887.
- Holsapple K. A. and Housen K. R. (2013a) Mitigation by impacts: Theory, experiments, and code calculations. In *Proceedings of the IAA Planetary Defense Conference 2013*, Flagstaff, USA.
- Holsapple K. A. and Housen K. R. (2013b) The third regime of cratering: Spall craters. *Lunar Planet. Sci. XLIV*, Abstract #2733. Lunar and Planetary Institute, Houston.
- Holsapple K. and Schmidt R. M. (1982) On the scaling of crater dimensions. II — Impact processes. *J. Geophys. Res.*, 87, 1849–1870.
- Holsapple K. A., Giblin I., Housen K., Nakamura A., and Ryan E. (2002) Asteroid impacts: Laboratory experiments and scaling laws. In *Asteroids III* (W. F. Bottke Jr. et al., eds.), p. 443. Univ. of Arizona, Tucson.
- Housen K. R. and Holsapple K. A. (1990) On the fragmentation of asteroids and planetary satellites. *Icarus*, 84, 226.
- Housen K. R. and Holsapple K. A. (2011) Ejecta from impact craters. *Icarus*, 211, 856–875.
- Housen K. R. and Sweet W. J. (2013) Experimental simulation of large-scale impacts on porous asteroids. *Lunar Planet. Sci. XLIX*, Abstract #1993. Lunar and Planetary Institute, Houston.
- Ivanov B. A., Deniem D., and Neukum G. (1997) Implementation of dynamic strength models into 2D hydrocodes: Applications for atmospheric breakup and impact cratering. *Intl. J. Impact Eng.*, 20, 411–430.
- Jop P., Forterre Y., and Pouliquen O. (2006) A constitutive law for dense granular flows. *Nature*, 441, 727–730.
- Jutzi M. (2015) SPH calculations of asteroid disruptions: The role of pressure dependent failure models. *Planet. Space Sci.*, 107, 3–9.
- Jutzi M. and Michel P. (2014) Hypervelocity impacts on asteroids and momentum transfer I. Numerical simulations using porous targets. *Icarus*, 229, 247–253.
- Jutzi M., Benz W., and Michel P. (2008) Numerical simulations of impacts involving porous bodies. I. Implementing subresolution porosity in a 3D SPH hydrocode. *Icarus*, 198, 242–255.
- Jutzi M., Michel P., Hiraoka K., Nakamura A. M., and Benz W. (2009) Numerical simulations of impacts involving porous bodies. II. Comparison with laboratory experiments. *Icarus*, 201, 802–813.
- Jutzi M., Michel P., Benz W., and Richardson D. C. (2010) Fragment properties at the catastrophic disruption threshold: The effect of the parent body's internal structure. *Icarus*, 207, 54–65.
- Jutzi M., Asphaug E., Gillet P., Barrat J.-A., and Benz W. (2013) The structure of the asteroid 4 Vesta as revealed by models of planet-scale collisions. *Nature*, 494, 207–210.
- Kaplinger B., Premaratne P., Setzer Ch., and Wie B. (2013) *GPU Accelerated 3-D Modeling and Simulation of a Blended Kinetic Impact and Nuclear Subsurface Explosion*. Planetary Defense Conference 2013 IAA-PDC13-04-06.
- Kenkmann T., Wünnemann K., Deutsch A., Poelchau M. H., SchLfer F., and Thoma K. (2011) Impact cratering in sandstone: The MEMIN pilot study on the effect of pore water. *Meteoritics & Planet. Sci.*, 46(6), 890–902.
- Kenkmann T., Deutsch A., Thoma K., and Poelchau M. (2013) The MEMIN research unit: Experimental impact cratering. *Meteoritics & Planet. Sci.*, 48(1), 1–2.
- Kimberley J. and Ramesh K. T. (2011) The dynamic strength of an ordinary chondrite. *Meteoritics & Planet. Sci.*, 46(11), 1653–1669.
- Korycansky D. G. and Asphaug E. (2006) Low-speed impacts between rubble piles modeled as collections of polyhedra. *Icarus*, 181(2), 605–617, DOI: 10.1016/j.icarus.2005.10.028.
- Kowitz A., Schmitt R. T., Uwe R. W., and Hornemann Ul. (2013) The first MEMIN shock recovery experiments at low shock pressure (5–12.5 GPa) with dry, porous sandstone. *Meteoritics & Planet. Sci.*, 48(1), 99–114.
- Krohn K. et al. (2014) Asymmetric craters on Vesta: Impact on sloping surfaces. *Planet. Space Sci.*, 103, 36–56, DOI: 10.1016/j.pss.2014.04.011.
- Leinhardt Z. M. and Stewart S. T. (2009) Full numerical simulations of catastrophic small body collisions. *Icarus*, 199, 542, DOI: 10.1016/j.icarus.2008.09.013.
- Leinhardt Z. M. and Stewart S. T. (2012) Collisions between gravity-dominated bodies. I. Outcome regimes and scaling laws. *Astrophys. J.*, 745(1), Article ID 79.
- Leliwa-Kopystynski J. and Arakawa M. (2014) Impacts experiments onto heterogeneous targets simulating impact breccia: Implications for impact strength of asteroids and formation of the asteroid families. *Icarus*, 235, 147–155.
- Lubarda V. and Krajcinovic D. (1993) Damage tensors and the crack density distribution. *Intl. J. Solid Structures*, 30, 2859–2877.
- Lucas A. and Mangeney A. (2007) Mobility and topographic effects for large Valles Marineris landslides on Mars. *Geophys. Res. Lett.*, 34, L10201, DOI: 10.1029/2007GL029835.
- Marcus R. A., Stewart S. T., Sasselov D., and Hernquist L. (2009) Collisional stripping and disruption of super-Earths. *Astrophys. Lett.*, 700, L118, DOI: 10.1088/0004-637X/700/2/L118.
- Maxwell D. E. (1977) Simple Z model for cratering, ejection, and the overturned flap. In *Impact and Explosion Cratering: Planetary and Terrestrial Implications* (D. J. Roddy et al., eds.), pp. 1003–1008. Pergamon, New York.
- McGlaun J. M., Thompson S. L., and Elrick M. G. (1990) CTH: A 3-dimensional shock-wave physics code. *Intl. J. Impact Eng.*, 10, 351–360.
- Melosh H. J. (1979) Acoustic fluidization: A new geologic process? *J. Geophys. Res.*, 84, 7513–7520.
- Melosh H. J. (2007) A hydrocode equation of state for SiO<sub>2</sub>. *Meteoritics & Planet. Sci.*, 42, 2079–2098.
- Melosh H. J. and Ivanov B. A. (1999) Impact crater collapse. *Annu. Rev. Earth Planet. Sci.*, 27, 385–415.
- Melosh H. J., Ryan E. V., and Asphaug E. (1992) Dynamic fragmentation in impacts: Hydrocode simulation of laboratory impacts. *J. Geophys. Res.*, 97(E9), 14735–14759.
- Michel P., Benz W., Tanga P., and Richardson D. C. (2001) Collisions and gravitational reaccumulation: Forming asteroid families and satellites. *Science*, 294, 1696–1700.
- Michel P., Benz W., and Richardson D. C. (2004) Disruption of pre-shattered parent bodies. *Icarus*, 168, 420–432.

- Michel P., Jutzi M., Richardson D. C., Goodrich C. A., Hartmann W. K., and O'Brien D. P. (2015) Selective sampling during catastrophic disruption: Mapping the location of reaccumulated fragments in the original parent body. *Planet. Space Sci.*, *107*, 24–28.
- Monaghan J. J. (2012) Smoothed particle hydrodynamics and its diverse applications. *Annu. Rev. Fluid Mech.*, *44*, 323–346.
- Movshovitz N., Asphaug E., and Korycansky D. (2012) Numerical modeling of the disruption of Comet D/1993 F2 Shoemaker-Levy 9 representing the progenitor by a gravitationally bound assemblage of randomly shaped polyhedra. *Astrophys. J.*, *759*(2), 93, DOI: 10.1088/0004-637X/759/2/93.
- Nakamura A., Yamane F., Okamoto T., and Takasawa S. (2015) Size dependence of the disruption threshold: Laboratory examination of millimeter-centimeter porous targets. *Planet. Space Sci.*, *107*, 45–52.
- Okamoto C. and Arakawa M. (2008) Experimental study on the impact fragmentation of core mantle bodies: Implications for collisional disruption of rocky planetesimals with sintered core covered with porous mantle. *Icarus*, *197*, 627–637.
- Okamoto C. and Arakawa M. (2009) Experimental study on the collisional disruption of porous gypsum spheres. *Meteoritics & Planet. Sci.*, *44*, 1947–1954.
- Owen J. M. (2010) ASPH modeling of material damage and failure. In *Proceedings of the Fifth International SPHERIC Workshop*, pp. 297–304.
- Pierazzo E., Artemieva N., Asphaug E., Baldwin E. C., Cazamias J., Coker R., Collins G. S., Crawford D., Elbeshausen D., Holsapple K. A., Housen K. R., Korycansky D. G., and Wünnemann K. (2008) Validation of numerical codes for impact and explosion cratering. *Meteoritics & Planet. Sci.*, *43*(12), 1917–1938.
- Reufer A., Meier M. M. M., Benz W., and Wieler R. (2012) A hit-and-run giant impact scenario. *Icarus*, *221*(1), 296–299, DOI: 10.1016/j.icarus.2012.07.021.
- Richardson D. C., Quinn T., Stadel J., and Lake G. (2000) Direct large-scale N-body simulations of planetesimal dynamics. *Icarus*, *143*, 45–59.
- Richardson D. C., Leinhardt Z. M., Melosh H. J., Bottke W. F. Jr., and Asphaug E. (2002) Gravitational aggregates: Evidence and evolution. In *Asteroids III* (W. F. Bottke Jr. et al., eds.), pp. 501–515. Univ. of Arizona, Tucson.
- Richardson D. C., Walsh K., Murdoch N., and Michel P. (2011) Numerical simulations of granular dynamics. I. Method and tests. *Icarus*, *212*, 427–437.
- Sanchez P. and Scheeres D. J. (2011) Simulating asteroid rubble piles with a self-gravitating soft-sphere distinct element method model. *Astrophys. J.*, *727*, 120.
- Sanchez P. and Scheeres D. J. (2014) The strength of regolith and rubble pile asteroids. *Meteoritics & Planet. Sci.*, *49*, 788–811.
- Schmidt R. M. (1977) A centrifuge cratering experiment: Development of a gravity-scaled yield parameter. In *Impact and Explosion Cratering: Planetary and Terrestrial Implications* (D. J. Roddy et al., eds.), pp. 1261–1278. Pergamon, New York.
- Schmidt R. M. and Holsapple K. A. (1980) Theory and experiments on centrifuge cratering. *J. Geophys. Res.*, *85*, 235–252.
- Schwartz S. R., Richardson D. C., and Michel P. (2012) An implementation of the soft-sphere discrete element method in a high-performance parallel gravity tree-code. *Granular Matter*, *14*, 363–380, DOI: 10.1007/s10035-012-0346-z.
- Schwartz S. R., Michel P., and Richardson D. C. (2013) Numerically simulating impact disruptions of cohesive glass bead agglomerates using the soft-sphere discrete element method. *Icarus*, *226*, 67–76.
- Senft L. E. and Stewart S. T. (2007) Modeling impact cratering in layered surfaces. *J. Geophys. Res.*, *112*, E11002, DOI: 10.1029/2007JE002894.
- Setoh M., Nakamura A. M., Michel P., Hiraoka K., Yamashita Y., Hasegawa S., Onose N., and Okuidara K. (2010) High and low-velocity impact experiments on porous sintered glass bead targets of different compressive strengths: Outcome sensitivity and scaling. *Icarus*, *205*, 702–711.
- Shapiro P., Martel H., Villumsen J., and Owen J. (1996) Adaptive smoothed particle hydrodynamics, with application to cosmology: Methodology. *Astron. J. Suppl.*, *103*, 269–330.
- Shuvalov V. V. (1999) Multi-dimensional hydrodynamic code SOVA for interfacial flows: Application to the thermal layer effect. *Shock Waves*, *9*, 381–390.
- Springel V. (2005) The cosmological simulation code GADGET-2. *Mon. Not. R. Astron. Soc.*, *364*, 1105, DOI: 10.1111/j.1365-2966.2005.09655.x.
- Stewart S. T. and Leinhardt Z. M. (2009) Velocity-dependent catastrophic disruption criteria for planetesimals. *Astrophys. J. Lett.*, *691*, L133–L137.
- Stöffler D., Artemieva N. A., and Pierazzo E. (2002) Modeling the Ries-Steinheim impact event and the formation of the moldavite strewn field. *Meteoritics & Planet. Sci.*, *37*, 1893–1907.
- Thompson S. L. and Lauson H. S. (1972) *Improvements in the Chart-D Radiation Hydrodynamic Code III: Revised Analytical Equation of State*. Report SC-RR-710714, Sandia National Laboratories, Albuquerque, New Mexico.
- Tillotson J. H. (1962) *Metallic Equations of State for Hypervelocity Impact*. General Atomic Report GA-3216.
- Walker J. D., Chocran S., Durda D. D., Grosch D. J., Movshovitz N., Richardson D. C., and Asphaug E. (2013) Momentum enhancement from aluminum striking granite and the scale size effect. *Int. J. Impact Eng.*, *56*, 12–18.
- Weibull W. (1939) A statistical theory of strength of materials. *R. Swedish Inst. Eng. Res.*, *151*, 1–45.
- Wünnemann K. and Ivanov B. A. (2003) Numerical modelling of impact crater depth-diameter dependence in an acoustically fluidized target. *Planet. Space Sci.*, *51*, 831–845.
- Wünnemann K., Collins G. S., and Melosh H. J. (2006) A strain-based porosity model for use in hydrocode simulations of impacts and implications for transient crater growth in porous targets. *Icarus*, *180*, 514–527.
- Wünnemann K., Nowka D., Collins G. S., Elbeshausen D., and Bierhaus M. (2010) Scaling of impact crater formation on planetary surfaces insights from numerical modeling. In *Proceedings of the 11th Hypervelocity Impact Symposium* (F. Schäfer and S. Hiermaier, eds.), pp. 1–13.
- Yasui M. and Arakawa M. (2011) Impact experiments of porous gypsum-glass bead mixtures simulating parent bodies of ordinary chondrites: Implications for re-accumulation processes related to rubble-pile formation. *Icarus*, *214*, 754–765.
- Yeomans D. K. and 12 colleagues (1997) Estimating the mass of asteroid 253 Mathilde from tracking data during the NEAR flyby. *Science*, *278*, 2106–2109.



# The Collisional Evolution of the Main Asteroid Belt

**William F. Bottke**

*Southwest Research Institute/Institute for the Science of Exploration Targets (ISET)*

**Miroslav Brož**

*Charles University*

**David P. O'Brien**

*Planetary Science Institute*

**Adriano Campo Bagatin**

*Universidad de Alicante*

**Alessandro Morbidelli**

*Lagrange Laboratory, Université Côte d'Azur, Observatoire de la Côte d'Azur, CNRS*

**Simone Marchi**

*Southwest Research Institute/Institute for the Science of Exploration Targets (ISET)*

---

Collisional and dynamical models of the main asteroid belt allow us to glean insights into planetesimal- and planet-formation scenarios as well as how the main belt reached its current state. Here we discuss many of the processes affecting asteroidal evolution and the constraints that can be used to test collisional model results. We argue the main belt's wavy size-frequency distribution for diameter  $D < 100$ -km asteroids is increasingly a byproduct of comminution as one goes to smaller sizes, with its shape a fossil-like remnant of a violent early epoch. Most  $D > 100$ -km asteroids, however, are primordial, with their physical properties set by planetesimal formation and accretion processes. The main-belt size distribution as a whole has evolved into a collisional steady state, and it has possibly been in that state for billions of years. Asteroid families provide a critical historical record of main-belt collisions. The heavily depleted and largely dispersed “ghost families,” however, may hold the key to understanding what happened in the primordial days of the main belt. New asteroidal fragments are steadily created by both collisions and mass shedding events via YORP spinup processes. A fraction of this population, in the form of  $D < 30$  km fragments, go on to escape the main belt via the Yarkovsky/YORP effects and gravitational resonances, thereby creating a quasi-steady-state population of planet-crossing and near-Earth asteroids. These populations go on to bombard all inner solar system worlds. By carefully interpreting the cratering records they produce, it is possible to constrain how portions of the main-belt population have evolved with time.

## 1. INTRODUCTION

The main asteroid belt is a living relic. It contains a record of what happened to the solar system in terms of bombardment since the planet-formation epoch. Ongoing collisional and dynamical evolution processes, however, are slowly obscuring the traces left behind. The goal of modeling efforts is to use all possible observational data to discern the initial conditions and evolution processes that occurred during and after the planet-formation epoch. For example, the questions one can probe with main-belt constraints include the nature

and mass of planetesimals inside Jupiter’s orbit, the timing of Jupiter’s formation, the distribution of volatiles in the inner solar system, the size distribution produced during planetary accretion, the presence of planetary embryos inside Jupiter’s orbit, the migration of the giant planets and whether sweeping resonance ever crossed the main belt, the degree of material mixing that occurred between the feeding zones, etc.

The problem is that our uncertainties about planet-formation processes and giant planet migration feed back into the assumptions made for our collisional-evolution models of the asteroid belt. If we do not know what happened when, it

is often difficult to impossible to find unique solutions. On the other hand, the main belt provides powerful constraints, and sometimes even order-of-magnitude solutions are useful at testing planet-formation scenarios. As a result, many main-belt-evolution scenarios have been investigated over the last several decades. The latest thinking on the primordial dynamical evolution of the main belt is discussed in the chapter by Morbidelli et al. in this volume.

A key issue for many evolution models concerns the so-called mass deficit of the main belt (e.g., Morbidelli et al., 2009). Consider that the total mass of the main asteroid belt, which is dominated by the masses of the largest asteroids, is  $\sim 5 \times 10^{-4} M_{\oplus}$  (Krasinsky et al., 2002; Somenzi et al., 2010; Kuchynka and Folkner, 2013). This value is tiny compared to the mass of solids thought to exist in the same region at the time of planetesimal formation. For example, the minimum mass solar nebula (Weidenschilling, 1977) suggests that 1–2.5  $M_{\oplus}$  of solid material once existed between 2 and 3 AU. If most of the solids ended up in planetesimals, the main-belt region could potentially be deficient in mass by a factor of >1000. These values have been used to argue that the asteroid belt has lost more than 99.9% of its primordial mass (e.g., Morbidelli et al., 2009). The critical unknown here is the efficiency and nature of planetesimal formation itself, which is discussed in the chapter by Johansen et al. in this volume.

If so much mass once existed in the primordial main-belt region, collisional evolution, dynamical removal processes, or some combination of the two were needed to get rid of it and ultimately produce the current main-belt population. For some time, many attempts were made to account for the mass deficit by collisions alone; see Davis et al. (2002) for a review of work up to the time of *Asteroids III*. Essentially, there are two key problems with this scenario. First, it is difficult for collisions alone to grind away the main-belt size distribution predicted by accretion models without blasting away Vesta's basaltic crust or producing size-frequency distributions (SFDs) that are inconsistent with the observed main-belt SFD (e.g., Davis et al., 1985). Second, collisional models employing disruption scaling laws based on numerical hydrocode simulations of asteroid collisions (e.g., Benz and Asphaug 1999) cannot break up enough  $D > 100$ -km asteroids to reproduce the observed population; too many large objects are left behind (e.g., Bottke et al., 2005a,b). Taken together, these outcomes suggest that either dynamical removal of asteroids has played a powerful role in allowing the population to reach its current state (see the chapter by Morbidelli et al. in this volume), or that the main-belt SFD for the largest asteroids has not changed very much since planetesimal formation.

For the former, several dynamical scenarios have been suggested to remove most of the primordial main belt's mass (see the chapter by Morbidelli et al. in this volume). For example, planetary embryos may have initially formed in the main-belt region (e.g., Petit et al., 2002, for a review; see also Chambers and Wetherill, 1998, 2001; O'Brien et al., 2006, 2007). As they gravitationally excited themselves and the surrounding planetesimals, most of these bodies escaped,

thereby naturally creating much of the main-belt mass deficit. In a second example, Jupiter gravitationally interacts with the gas disk and migrates across the main-belt region (Walsh et al., 2011). This so-called Grand Tack scenario allows Jupiter to do the job of scattering embryos and planetesimals out of the main-belt region. The key similarity of both examples is that planetesimals dynamically excited out of the main belt have the opportunity to slam into the survivors left behind (along with leftover planetesimals already on planet-crossing orbits) (Bottke et al., 2005b; O'Brien and Greenberg, 2005; O'Brien et al., 2006; Davidson et al., 2013). This allows these dynamical models to be at least partially tested against main-belt asteroid and meteoritical constraints.

An alternative scenario is to assume that planetesimal and planet formation works differently than has been assumed in existing scenarios, and that the quantity of planetesimals in the main-belt region was never more than a few times the present-day population (e.g., Levison et al., 2015a,b). This would remove the need for a mass deficit. This new scenario invokes a process called "pebble accretion" that describes how planetesimal growth rates are governed by the way in which small particles are affected by gas drag in the solar nebula near a growing body (see the chapter by Johansen et al. in this volume). In brief, planetesimals embedded in a population of "pebbles," whose sizes are debated, can grow very quickly because of a newly discovered mode of accretion aided by aerodynamic drag on the pebbles themselves. If a pebble's aerodynamic drag stopping time is less than or comparable to the time for it to encounter a growing body, such as a planetary embryo, then it is decelerated with respect to the planetary embryo and becomes gravitationally bound. After capture, the pebble spirals inward and is accreted. If pebble-accretion scenarios are found to be valid, early collisional evolution in a low-mass main belt might be dominated by leftover planetesimals that strike from planet-crossing orbits.

Beyond the earliest times, one must also consider whether the main-belt population was affected by giant planet migration taking place after the solar nebula had completely dissipated. In a popular suite of scenarios referred to as the Nice model (see the chapter by Morbidelli et al. in this volume), the giant planets undergo a gravitational instability long after the formation of the first solids. Ice giants like Uranus and Neptune migrate across a massive primordial disk of comets, scattering most across the solar system. Some of these bodies will slam into main-belt asteroids (Brož et al., 2013). As the gas giants migrate to their current orbits, secular resonances produced by the giant planets also jump to new positions, and some will interact with the primordial main-belt population. This may cause the primordial main belt to lose some of its mass (Gomes et al., 2005; Brasser et al., 2009; Morbidelli et al., 2010; Minton and Malhotra, 2009, 2011). At the same time, it may also trap some destabilized comets within this region on stable orbits (Levison et al., 2009). The new home for certain secular resonances may even destabilize a putative stable extension of the main belt that once existed between 1.7 and 2.2 AU (Bottke et al.,

2012). It is likely that evidence for or against these possibilities can still be found in the asteroidal impact record, provided we know what to look for there.

The question is how to test these concepts with what we know about asteroids and the main belt itself, and whether the constraints we know about today are sufficient to eliminate various planet-formation and evolution scenarios. To answer this, we first must examine the processes affecting asteroidal collisional evolution, and what would need to be incorporated into a comprehensive collisional-evolution model (section 2). Next, we need to discuss the constraints that can be reasonably brought to bear on this problem (section 3). Only then can we discuss what we have learned from existing models (section 4). We also refer the interested reader to the excellent reviews of historical collisional evolution work provided in previous *Asteroids* volumes by *Davis et al.* (1979, 1989, 2002), and to a much more limited literature review in *Bottke et al.* (2005a). As much as possible, we have tried to avoid duplication with these works while keeping this chapter self-contained.

## 2. PROCESSES AFFECTING MAIN-BELT EVOLUTION

At the most basic level, main-belt collisional-evolution models involve the solution of a straightforward differential equation, although the details can become complicated and somewhat messy from an accounting standpoint. The input is an initial SFD for the asteroid belt denoted as  $N(D,t)$ , with the bodies binned in logarithmic intervals as a function of diameter. The goal of the solution is to compute the time rate of change in the population per unit volume of space over a size range between diameter  $D$  and  $D + dD$ . In a schematic form, it can be written as

$$\frac{\partial N}{\partial t}(D,t) = -I_{\text{COLL}} + I_{\text{FRAG}} - I_{\text{DYN}} \quad (1)$$

Here  $I_{\text{COLL}}$  is the net number of bodies that leave between  $D$  and  $D + dD$  per unit time from collisions (i.e., it is a “sink” for bodies in the SFD). The net number of collisions taking place at every time step is calculated by determining how many projectiles from other size bins are capable of producing either a cratering or a catastrophic disruption event among bodies between  $D$  and  $D + dD$ . Note that other mass loss processes can be included here as well, such as the loss of material via nongravitational YORP torques, which can spin up asteroids fast enough that they shed mass (see the chapter by Vokrouhlický et al. in this volume and section 2.5 below).

The results of the  $I_{\text{COLL}}$  calculation are sent to the function  $I_{\text{FRAG}}$ , which describes the number of bodies entering a given size bin per unit time that were produced by the fragmentation of larger bodies (i.e., it is a “source” for bodies in the SFD). This allows large asteroids to act as a reservoir for smaller bodies, with collisional evolution or some other process liberating fragments over time.

Finally, the equation accounts for  $I_{\text{DYN}}$ , which is the number of bodies lost from a given size bin via dynamical processes, such as an object escaping through a dynamical resonance (i.e., it is a “sink” for bodies in the SFD). Note that  $I_{\text{DYN}}$  is often enacted over the entire main-belt SFD, which is reasonable for global dynamical mechanisms like sweeping resonances or migrating planets but is less accurate for bodies escaping from specific main-belt regions via dynamical resonances (e.g., the  $v_6$  secular resonance along the inner edge of the main belt; the 3:1 mean-motion resonance with Jupiter at 2.5 AU).

In the sections below, we discuss the many parameters and mechanisms needed to understand and create these functions within a collision evolution model.

### 2.1. Asteroid Collision Probabilities

A necessary component to determining the collisional evolution of a population is to compute the impact probabilities and relative velocities between all possible pairs of bodies. These values are used to estimate the interval between targets and projectiles of different sizes striking one another as well as the effects of those collisions. The most common value used in these cases is the intrinsic collision probability  $P_i$ , defined as the likelihood that a single projectile will hit the target over a unit of time and cross-sectional area, and the mean impact velocity  $V_{\text{imp}}$  between the pair (e.g., *Öpik*, 1951; *Wetherill*, 1967; *Farinella and Davis*, 1992; *Bottke et al.*, 1994).

To get these values for the present-day main belt, *Bottke et al.* (1994) took a representative sample of main-belt asteroids [e.g., 682 asteroids with  $D > 50$  km as defined by *Farinella and Davis* (1992)] and calculated  $P_i$  and  $V_{\text{imp}}$  between all possible pairs of asteroids, assuming fixed values of semimajor axis, eccentricity, and inclination ( $a, e, i$ ). A common approximation made here is that the orbits can be integrated over uniform distributions of longitudes of apsides and nodes because secular precession randomizes their orbit orientations over  $\sim 10^4$ -yr timescales. After all possible orbital intersection positions for each projectile-target pair were evaluated and weighted, they found that main-belt objects striking one another have  $P_i \sim 2.9 \times 10^{-18} \text{ km}^{-2} \text{ yr}^{-1}$  and  $V_{\text{imp}} \sim 5.3 \text{ km s}^{-1}$ . These values are fairly reasonable given what we know about the main-belt population today, and comparable values can be found in many works (e.g., *Farinella and Davis*, 1992; *Vedder*, 1998; *dell’Oro and Paolicchi*, 1998; *Manley et al.*, 1998). Estimates for different portions of the main-belt population striking one another have been reported as well (e.g., *Levison et al.*, 2009; *Cibulkova et al.*, 2014).

To model collisional evolution in the primordial asteroid belt requires that certain assumptions be made about the excitation of asteroid belt bodies at that time. For example, the process that caused the main-belt population to become dynamically excited (see the chapter by Morbidelli et al. in this volume) should have also driven many primordial main-belt asteroids onto planet-crossing orbits. While their orbits

were short lived, their higher eccentricity and inclinations would have allowed them to strafe the surviving main belt asteroids at  $V_{\text{imp}} > 10 \text{ km s}^{-1}$  for tens of millions of years (e.g., Bottke et al., 2005b; Davidson et al., 2013; Marchi et al., 2013). Moreover, if the primordial main belt once had considerably more mass, as discussed in section 1, these departed bodies could be responsible for a considerable amount of collisional evolution in the main belt.

A related issue is that the primordial main belt has likely been struck by sizable but transient populations on planet-crossing orbits, such as leftover planetesimals (Bottke et al., 2006, 2007), ejecta from giant impacts in the terrestrial planet region (Bottke et al., 2015b), comet-like planetesimals dispersed from the primordial disk during giant planet migration (Brož et al., 2013), and Jupiter–Saturn-zone planetesimals pushed into the inner solar system via giant planet migration and/or evolution (Walsh et al., 2011; Turrini et al., 2011, 2012). Most of these dramatic events are thought to take place during the first 500 m.y. of solar system history. The nature and evolution of these populations is uncertain, such that dynamical models are needed to set limits on what they were plausibly like (see the chapter by Morbidelli et al. in this volume). Under certain conditions, they could also account for abundant collisional grinding in the main belt.

In all cases, dynamical models are needed to allow the computation of  $P_i$  and  $V_{\text{imp}}$  between the impacting bodies and the main-belt targets. From there, it is a matter of estimating the initial sizes of the populations, how fast they disperse, and how the populations undergo collisional evolution among themselves.

## 2.2. Asteroid Disruption Scaling Laws

A second key issue to modeling asteroid collisional evolution concerns the disruption scaling law. This is commonly referred to as the critical impact specific energy  $Q_D^*$ , the energy per unit target mass delivered by the projectile required for catastrophic disruption of the target (i.e., such that one-half the mass of the target body escapes). A considerable amount has been written about the value of  $Q_D^*$  (e.g., reviews in Holsapple et al., 2002; Asphaug et al., 2002; Davis et al., 2002; see also Leinhardt and Stewart, 2009; 2012), and the latest on the computation of this value can be found in the chapters in this volume by Jutzi et al. and Michel et al. For these reasons, we only briefly review the main issues here.

Using  $Q_D^*$ , the diameter of a projectile  $d_{\text{disrupt}}$  capable of disrupting a target asteroid ( $D_{\text{target}}$ ) can be estimated as

$$d_{\text{disrupt}} = \left( 2Q_D^*/V_{\text{imp}}^2 \right)^{1/3} D_{\text{target}} \quad (2)$$

where  $V_{\text{imp}}$  is the impact velocity. We assume here that the target and projectile have the same bulk density, although that is by no means assured. Small asteroids are considered part of the “strength-scaling” regime, where the fragmentation of the target body is governed by its tensile strength,

while large asteroids are considered part of the “gravity scaling” regime, where fragmentation is controlled by the self-gravity of the target (see section 4.1). Laboratory experiments and hydrocode modeling work discussed in the references above suggest the transition between the regimes occurs in the range  $100 < D < 200 \text{ m}$  (Fig. 1).

Testing what impacts do to undamaged targets with basalt-like physical properties, Benz and Asphaug (1999) found that the mass of the largest remnant  $M_{\text{LR}}$  after a collision can be fitted as a function of  $Q/Q_D^*$ , where the kinetic energy of the projectile per unit mass of the target is denoted by  $Q$

$$M_{\text{LR}} = \left[ -\frac{1}{2} \left( \frac{Q}{Q_D^*} - 1 \right) + \frac{1}{2} \right] M_T \quad (3)$$

for  $Q < Q_D^*$ , and

$$M_{\text{LR}} = \left[ -0.35 \left( \frac{Q}{Q_D^*} - 1 \right) + \frac{1}{2} \right] M_T \quad (4)$$

for  $Q > Q_D^*$ , where  $M_T$  is the target mass. Whenever  $M_{\text{LR}}$  in equation (3) turns out to be negative, one can assume that the target has been pulverized, such that all its mass is lost below some minimal mass threshold.

A missing aspect of this discussion is that asteroids have a wide range of physical properties and therefore may disrupt very differently than the idealized bodies used in numerical hydrocode runs. We refer the reader to the chapters in this

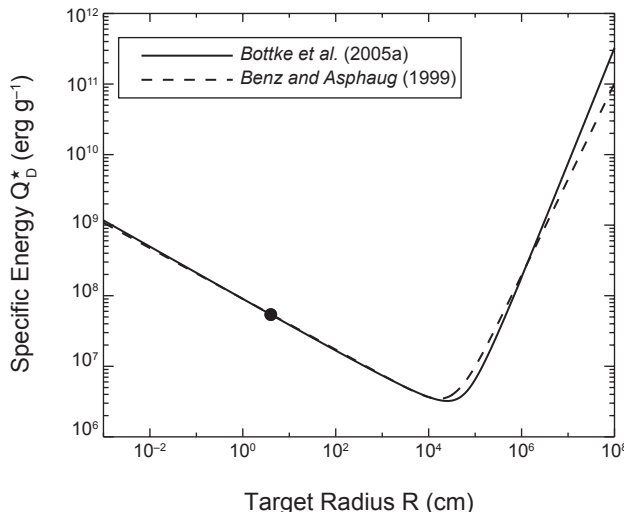


**Fig. 1.** The critical impact specific energy  $Q_D^*$  defined by Benz and Asphaug (1999). This function is the energy per unit target mass delivered by the projectile that is required for catastrophic disruption of the target, such that one-half the mass of the target body escapes. The dashed line is the function derived by Bottke et al. (2005a) for their modeling results. Both functions pass through the normalization point ( $Q_D^*, D$ ) set to  $(1.5 \times 10^7 \text{ erg g}^{-1}, 8 \text{ cm})$ , which was determined using laboratory impact experiments (e.g., Durda et al., 1998).

volume by Jutzi et al. and Michel et al., who discuss recent advances made in this area. Here we point out that all collisional models must, by necessity, make approximations to deal with complicated systems. This has led many modelers to assume that all asteroids (e.g., monoliths, rubble piles, etc.) follow the exact same  $Q_D^*$  functions for disruption. While this approach may be more accurate than one might expect (see results in the chapters in this volume by Jutzi et al. and Michel et al.), future collision evolution models will need to consider how specific asteroid types react to impacts. In addition, the influence of asteroid spin on  $Q_D^*$  has not been investigated so far in the hypervelocity impact regime, and it is likely that a spinning asteroid responds differently to an impact than a nonspinning one, as found in low-speed impacts between self-gravitating aggregates (e.g., Ballouz et al., 2014).

In practice, this will mean sorting all asteroids into broad categories that can be treated by individual  $Q_D^*$  functions. One possible way to divide them up would be by spectral signatures, such as the S-, C-, and X-complexes (see the chapter by DeMeo et al. in this volume). Within the complexes, bodies might share similar albedos (see chapters by Mainzer et al. and Masiero et al.), bulk densities and porosities (see chapter by Scheeres et al.), compositions, and so on. Differences between categories could then be dealt with in a logical fashion. For example, we know that C-complex bodies often have lower bulk densities and higher porosities than S-complex bodies, and studies of primitive carbonaceous chondrites suggest many are structurally weaker and have different grain structures as well (e.g., Britt et al., 2002). Whether this affects their  $Q_D^*$  function will then need to be determined by laboratory impact experiments and numerical hydrocode simulations of asteroid collisions. There will also be the issue of how to treat the exceptional cases (e.g., the X-complex include a wide range of asteroid types, internal structures, compositions, and bulk densities).

The hope is that this kind of work will eventually lead us to an understanding of the SFDs of different asteroid complexes and how they have changed over time. By getting the details right, it may be possible to ask more interesting questions about how the main belt reached its current state. Even the assumption that all asteroids should be placed into the S- or C-complexes, where their physical properties would be treated differently, would be an advance over current model assumptions.

### 2.3. Asteroid Fragmentation

One of the most difficult issues to deal with in any collisional evolution model is the treatment of the fragment SFD created when two bodies slam into one another. Given the wide range of parameters that could be involved in any collision, such as impact velocity, projectile and target sizes, impact angle, projectile and target properties, etc., it is a somewhat quixotic task to try to generate a “one size fits all” recipe capable of reproducing the outcomes of all meaningful cratering and catastrophic disruption events that could have ever taken place in the asteroid belt.

Comprehensive experimental work has been carried out over the last several decades on this subject. Studies based on hypervelocity laboratory impacts have provided threshold specific energies for shattering ( $Q_S^*$ ) among a wide range of materials, and scaling theories including strain-rate and gravity-scaling effects allow one to extrapolate those results to multi-kilometer-sized asteroids (Holsapple et al., 2002; chapter by Michel et al. in this volume). They show that  $Q_S^*$  and  $Q_D^*$  coincide in the strength regime, but  $Q_S^* < Q_D^*$  in the gravity regime and the minimum energy to disperse a given target can be expressed as the sum of the energy needed to shatter the body and the energy required to disperse the fragments. In this way, once the comparison between the impact specific energy and the value of  $Q_S^*$  is made, it is possible to determine whether the impact will be a cratering or a disruption event. In both cases the size distribution of the new fragments can potentially be calculated (e.g., Petit and Farinella, 1993). The critical quantity that discriminates cratering from shattering is the mass fraction between the largest fragment ( $M_{LR}$ ) and the target ( $M_T$ ), which is given by

$$f_{LF} = \frac{M_{LF}}{M_T} = 0.5 \left( \frac{Q_S^*}{E/2} \right)^{1.24} \quad (5)$$

In the case of a barely shattering impact event,  $f_{LF} = 0.5$ . Using  $Q_S^*$  instead of  $Q_D^*$  has the advantage of allowing one to calculate how many fragments are reaccumulated by the self-gravity of the non-escaping fragments (Campo Bagatin et al., 1994b).

One must also consider that many  $D < 100$ -km asteroids are likely to be second-generation gravitational aggregates. Campo Bagatin et al. (2001) tracked this aspect of collisional evolution, and found that the amount of reaccumulated mass for each object was enough that it could affect both the target body’s  $Q_D^*$  function as well as the fragment SFD created in an impact. Note that the lower size limit on gravitational aggregates is unknown; some meter-sized bodies may possibly be held together by cohesive forces (see the chapter by Scheeres et al. in this volume). Ultimately, little is known about the mass distribution of the fragments — aggregates themselves or single coherent components — coming out of a disrupting impact on a gravitational aggregate, although insights into this can potentially be gleaned from numerical hydrocode experiments of collisions on rubble-pile asteroids (Benavidez et al., 2012; see the chapter by Michel et al. in this volume).

Gravitational aggregates may also be produced by multiple subcatastrophic collisions, which may lead to the same result as a single shattering collision, provided their total energy is equivalent to the energy of the shattering event (Housen, 2009). This could mean some second-generation asteroids are gravitational aggregates with limited macro-porosity, due to the fact that fragments did not get enough kinetic energy to be jumbled and reshuffled. How these results feed into the creation of new fragment SFDs are uncertain. Improvements in this area, along the lines of an

updated *Campo Bagatin et al.* (2001) model, could help to better characterize collisional evolution in the main belt.

These issues influence the internal structure of asteroids. This may explain why mass and volume measurements of asteroids indicate a wide range of internal macroporosities for S- and C-complex asteroids (see the chapter by Scheeres et al. in this volume). Unfortunately, porosity is only a partial indicator of internal structure, as it is largely independent of the sizes of components. Porosity also hides the absolute sizes of components and their distribution. A porous gravitational aggregate might have a substantial microporosity (e.g., individual constituents with a fairy-castle structure) and/or a sizable macroporosity (e.g., large fragments and empty space near the contact points covered by regolith). The fact that many main-belt asteroids may have unusual internal structures makes it imperative that we obtain more ground truth on how real asteroids are affected by collisions.

Beyond this, it is important to recognize that our asteroid belt has been subject to an enormous number of stochastic events, and information about the fragments produced by ancient collisions has been lost by subsequent collisional and dynamical processes. This means the initial conditions for ancient family-forming events or even large cratering events (see the chapters by Asphaug et al. and Nesvorný et al. in this volume) may never be precisely known (see the chapters by Jutzi et al. and Michel et al.). A good example of this is the impact event that created the 400-km Veneneia basin on (4) Vesta; the basin has been partially buried/destroyed by the nearby Rheasilvia basin-formation event (*Schenk et al.*, 2012; see the chapter by Russell et al.).

Given these limitations, realistic modelers do the best they can with what they have. This means choosing parameters and formalism that are reasonable within the bounds of what is known and testing their results against the available constraints. The interpretation of even good matches, though, must always be met with some skepticism and wariness. Moreover, a careful modeler must also run simulations over numerous trials in an attempt to characterize how outcomes may have been affected by chance events (e.g., the disruption of a large asteroid at a strategic time or place may allow a model run to match constraints, yet this kind of event may not have happened in our asteroid belt).

To this end, modern collisional-evolution models have folded into their codes outcomes of numerical smoothed particle hydrocode (SPH) simulations that account for at least some of the parameters described above. For example, *Morbidelli et al.* (2009) constructed an algorithm that reproduced the fragment size distribution of the SPH results determined by *Durda et al.* (2004, 2007), who conducted a large number of collision simulations of projectiles of various masses and velocities striking 100-km-diameter asteroids. They found that most catastrophic collisions produce fragment SFDs that have a continuous, steep power-law size distribution starting from a single large fragment that is well separated in size from that of the largest remnant of the target.

The mass of the largest fragment and the slope of the power-law SFD in each of the experiments from *Durda et al.*

(2007) was described as a function of the ratio  $Q/Q_D^*$  that characterized each experiment

$$M_{LF} = 8 \times 10^{-3} \left[ \frac{Q}{Q_D^*} \exp^{-\left(\frac{Q}{4Q_D^*}\right)^2} \right] (M(i) + M(j)) \quad (6)$$

for the mass of the largest fragment and

$$q = -10 + 7 \left( \frac{Q}{Q_D^*} \right)^{0.4} \exp^{-\frac{Q}{7Q_D^*}} \quad (7)$$

for the slope of the cumulative power-law size distribution of the fragments. These equations represent empirical fits to the numerical hydrocode data. Note that comparable functions were created by *Cibulková et al.* (2014) from the rubble-pile impact simulation results of *Benavidez et al.* (2012). These equations were incorporated into their collisional-evolution models.

For fragment SFDs with very steep slopes, equations (5) and (6) can easily exceed the mass of the projectile and target, which is nonphysical. To avoid this problem, it is assumed that the fragment SFDs bend to shallower slopes at small sizes, although the precise diameter where this takes place is unknown; it is beyond the resolution limit of existing numerical hydrocode impact simulations.

It can be shown that the derived fragment SFDs from these simulations reproduce many attributes of observed asteroid families (*Durda et al.*, 2007). With that said, however, collisional outcomes and fragment SFDs are strongly affected by the target's gravitational forces; this means the impact outcomes onto 400-km targets differ from those of 100-km targets in terms of  $Q/Q_D^*$  (P. Benavidez, personal communication). The same is probably true for smaller targets as well. Major advances in this area will therefore come from those modelers who employ fragment SFDs appropriate for their target sizes.

A final interesting issue here is that analytical and numerical results suggest the final equilibrium main-belt SFD is often found to be relatively insensitive to the details of the fragmentation law (e.g., *Davis et al.*, 2002; *O'Brien and Greenberg*, 2003, 2005; *Bottke et al.*, 2005a,b; *Morbidelli et al.*, 2009). This statement is mainly based on experience, and it needs to be better quantified by modeling work. We suggest that while the fragmentation laws used are important, many are unlikely to dramatically change the equilibrium results. On the other hand, the choice of fragment SFD for given breakups will be important for investigating asteroid families and transient perturbations to the main-belt SFD.

## 2.4. Dynamical Depletion of Main-Belt Asteroids by the Yarkovsky Effect

As described in the chapter in this volume by Vokrouhlický et al.,  $D < 30$ -km asteroids in the main belt slowly drift inward toward or outward away from the Sun in semimajor

axis by Yarkovsky thermal forces. This allows some of them to reach resonances with the planets that drive them onto planet-crossing orbits, thereby allowing them to escape the main-belt region altogether. Additional mobility is provided by encounters with big asteroids like (1) Ceres and (4) Vesta, although the net effect of this mechanism is fairly modest (e.g., Carruba et al., 2003, 2013).

The Yarkovsky effect, working in concert with resonances, can therefore be considered a “sink” for small main-belt asteroids. Their depletion should feed back into the collisional evolution of the main belt itself (i.e., fewer smaller bodies means fewer cratering and disruption events among larger bodies). It also means that the near-Earth asteroid (NEA) population could be considered an short-lived component of the main-belt population. This allows the NEA SFD to constrain collisional and dynamical evolution within the main belt, provided the modeler understands the translation between the main belt and NEA SFDs (e.g., Morbidelli and Vokrouhlický, 2003).

The challenging part of this is to quantify the nature of small-body populations lost over time via the Yarkovsky effect and resonances. Consider the following:

- Every major main-belt resonance has a different character in its ability to produce long-lived near-Earth objects (NEOs) (e.g., Gladman et al., 1997; Bottke et al., 2006).
- The flux of asteroids reaching dynamical resonances may change over time as a consequence of asteroid family-forming events. Large asteroid families can produce enormous numbers of fragments, while smaller ones that disrupt in strategic locations next to key “escape hatches” may also influence the planet-crossing population for some interval (Nesvorný et al., 2002).
- The dynamical evolution of  $D < 1$ -km asteroids is poorly constrained because these bodies are below the observational detection limit of most surveys (e.g., Jedicke et al., 2002; see also the chapter by Jedicke et al. in this volume). Moreover, these bodies are also the most susceptible to YORP thermal torques, which can strongly affect their drift direction and evolution (see next section).

So far, no one has yet attempted to model all these factors and include them into an algorithm suitable for insertion into a collisional evolution code. It is a necessary but daunting task to do this correctly, given the current state of our knowledge of how the Yarkovsky/YORP effects modify the orbits, sizes, and shapes of small asteroids.

Instead, the best that has been done to date has been to generate loss rates for the asteroid belt that produce a steady-state population of NEOs (Bottke et al., 2005a; O’Brien and Greenberg, 2005; Cibulková et al., 2014) (Fig. 2). This approximation can provide interesting insights; for example, not including the Yarkovsky/resonance “sink” for small bodies may have a substantial affect on the collisional evolution of the main belt, with more projectiles left behind that can disrupt large main-belt asteroids (Cibulková et al., 2014).

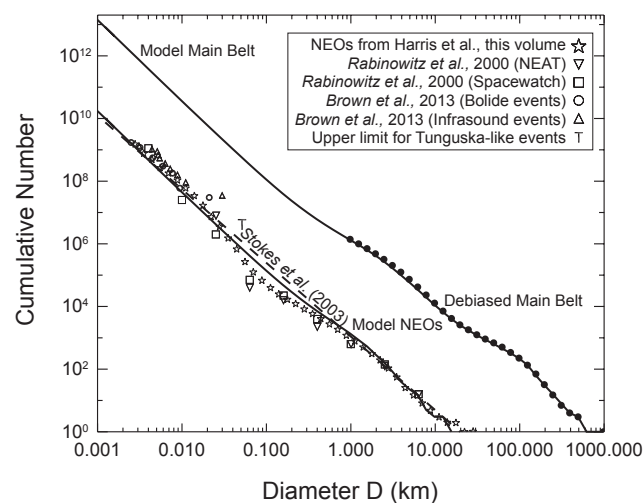


**Fig. 2.** The estimated present-day main belt and NEO populations according to Bottke et al. (2005b) model runs (solid lines). For reference, we plot our results against an estimate of the NEA population made by Stokes et al. (2003), who assumed the  $D < 1$ -km size distribution was a power-law extension of the  $D > 1$ -km size distribution, and a population discussed in the chapter by Harris et al. in this volume. Our model main-belt population provides a good match to the observed main belt (solid black dots). Most diameter  $D \leq 100$ -km bodies are fragments (or fragments of fragments) derived from a limited number of  $D \geq 100$ -km breakups (Bottke et al., 2005a). Our NEO model population is compared to estimates derived from telescopic surveys (Rabinowitz et al., 2000), as well as satellite and infrasound detections of bolide detonations in Earth’s atmosphere (Brown et al., 2013). For reference, we also include an upper limit estimate of 50-m NEAs based on the airblast explosion that occurred over Tunguska, Siberia, in 1908. A mismatch between the NEA model and data is seen near  $D \sim 0.1$  km.

## 2.5. Asteroid Disruption by YORP Torques

The Yarkovsky-O’Keefe-Radzievskii-Paddack (YORP) effect is a thermal torque that, complemented by a torque produced by scattered sunlight, can modify the spin vectors of small asteroids (see the chapter by Vokrouhlický et al. in this volume). As an asteroid’s obliquity evolves, its orientation can strongly affect a body’s drift rate across the main belt, and therefore how quickly it reaches a resonance that can take it out of the main belt. YORP can also spin asteroids up or down. If the body has substantial unconsolidated material, or is a rubble pile, it must reconfigure itself to adjust to its new rotational angular momentum budget. In certain cases, this can cause the body to shed mass, potentially creating a satellite or an asteroid pair. Many of the latest aspects of the YORP effect are discussed in the chapters by Vokrouhlický et al. and Walsh and Jacobson in this volume.

YORP spinup may be so efficient at causing small asteroids to shed mass that this mechanism may dominate the production and elimination of bodies for  $D < 1$  km. This prospect is exciting, and we believe warrants continued

investigation using a wide range of models in the future. Indeed, recent main-belt modeling work that included collisional disruption and YORP mass-shedding mechanisms show the latter could explain the shape of the main belt SFD for subkilometer- and kilometer-sized bodies (*Marzari et al.*, 2011; *Jacobson et al.*, 2014; see also *Penco et al.*, 2004).

The goal of main-belt collisional models is to include all the major processes that affect mass loss from small bodies — collisions, Yarkovsky-driven removal of bodies, and YORP-driven mass shedding — in a self-consistent manner. So far, the models of *Bottke et al.* (2005a,b) and *Cibulková et al.* (2014) include the first two, while the models of *Marzari et al.* (2011) and *Jacobson et al.* (2014) include the first and third. Future models will have to include all these effects in the most accurate way possible, with their relative contributions sorted out using constraints. While this sounds straightforward, in practice the modeler must deal with numerous uncertainties, as well as all the feedbacks they produce.

As an example, consider the mismatch between the model and observed SFDs seen in Fig. 2. While a better fit is possible, and it should be a byproduct of the processes above, which one of them, if any, should dominate?

One could argue that varying the Yarkovsky depletion rates of asteroids from the main belt should solve the problem. Unpublished test runs performed by *Bottke et al.* (2005a,b) have shown that the shape of the main-belt SFD for subkilometer-sized bodies can be reproduced by assuming more asteroids escape over time than previously predicted. The central problem here is that the loss rates of subkilometer-sized bodies from the main belt are highly uncertain, with the coupling between Yarkovsky drift and the frequency/nature of so-called YORP-cycles only modestly well understood at this time (e.g., *Bottke et al.*, 2015a).

Alternatively, the mismatch might be readily fixed by including YORP-driven mass shedding, as suggested by *Marzari et al.* (2011) and *Jacobson et al.* (2014). We find this highly plausible, yet there is also much we do not yet understand when it comes to the details of YORP-driven mass shedding (see the chapter by Vokrouhlický et al. in this volume).

Consider that careful explorations of the YORP effect show there is a preference for asteroidal spinup vs. spindown (e.g., *Rozitis and Green*, 2012; *Golubov and Krugly*, 2012; *Golubov et al.*, 2014; see also the chapter by Vokrouhlický et al.). With this said, however, spindown must also exist in order to explain the relatively flat spin frequency distribution of small asteroids as well as why numerous very slow rotators exist (e.g., *Bottke et al.*, 2015a). There is also important work that shows that YORP torques are affected by small topographic changes on an asteroid. For example, *Statler* (2009) used numerical simulations to demonstrate that minor changes in an asteroid's shape, such as the formation of a small crater or even the movement of a boulder from one place to another, could modify the YORP torques enough to change the magnitude and sign of the spin rate. These changes produce a random walk in an asteroid's spin rate,

and has been coined the “stochastic YORP” effect. While more work is needed, stochastic YORP may prevent some small asteroids from undergoing mass shedding as often as predicted (*Cotto-Figueroa*, 2013; *Cotto-Figueroa et al.*, 2015; *Bottke et al.*, 2015a). This may explain why some small asteroids have shapes that suggest they have largely avoided substantial mass-shedding events. Conversely, certain bodies may return again and again to spinup-driven mass shedding, which may rapidly turn them into top-like shapes (see the chapter by Walsh and Jacobson in this volume). Probing the asteroidal shape dichotomy using numerical modeling work is an intriguing project for the future.

In the end, all these Yarkovsky and YORP-related issues will need to be better explored and quantified if we are to formulate superior main-belt-evolution models in the future.

## 2.6. Additional Processes

Some processes that affect planetesimal and planet formation have yet to be implemented into main-belt collisional evolution models. Key examples include (1) the implications of hit-and-run collisions, defined as the disruption and escape of portions of large projectiles striking still larger bodies (see the chapters by Scott et al. and Asphaug et al. in this volume); (2) planetesimal collisional evolution taking place side by side with accretion onto protoplanets/planetary embryos with all the appropriate dynamics and fragmentation events modeled correctly (e.g., *Levison et al.*, 2015a,b); (3) the effects of collisions on the dynamical evolution of an asteroid or planetesimal; and (4) the bombardment of main-belt asteroids by planetesimals forming and evolving within the terrestrial planet and gas giant regions (e.g., see the chapters by Morbidelli et al. and Scott et al. in this volume).

Some of these processes are difficult to include in a model until their effects have been evaluated, although they are almost certainly important for particular issues [e.g., hit-and-run collisions may explain the exposed core-like nature of (16) Psyche and (212) Kleopatra; see the chapters by Asphaug et al. and Scott et al. in this volume]. For other processes, their importance is still unclear because planet-formation models are incomplete and/or are lacking in key constraints (e.g., how much net collisional evolution is produced on indigenous main-belt asteroids via planetesimals from the terrestrial planet region?). We believe an exploration of processes (1)–(4) discussed above and their inclusion in future models will greatly improve the state of the art.

## 3. CONSTRAINTS ON COLLISIONAL-EVOLUTION MODELS

Given the large number of “knobs” that exist in collisional-evolution models, and the fact that these codes may provide the user with non-unique solutions, it is imperative to test results against as many constraints as possible. Given the breadth of predictions for such codes, this means accounting for how individual asteroids, asteroid families, and different asteroid populations have taken on their current

status. With sufficient constraints, bad parameter choices can be eliminated from contention.

On the other hand, it is important that one recognizes that our understanding of main-belt evolution is still limited, and the inclusion of faulty constraints into a code can also produce inaccurate results and poor predictions. Accordingly, most constraints should be treated with some caution, with the modeler and interpreter cognizant that both data and interpretation can and often do change with time.

With these caveats, we present a list of many of the constraints that should be considered when modeling the collisional evolution of the main belt.

### 3.1. Wavy Main-Belt Size-Frequency Distribution

One of the primary constraints for collisional-evolution models comes from the main-belt SFD. Improved estimates since the review chapter of *Jedicke et al.* (2002) were provided by pencil-beam studies of the main-belt population (*Gladman et al.*, 2009), the addition of asteroids colors from the Sloan Digital Sky Survey (SDSS) (e.g., *Parker et al.*, 2008), and new infrared data of many main-belt asteroids (see the chapters by *Mainzer et al.* and *Masiero et al.* in this volume). The inclusion of all these datasets into a single debiased SFD, however, has yet to be attempted, and it is beyond the scope of this chapter.

For basic purposes, one can derive an approximate main-belt SFD using the absolute magnitude H distribution provided by *Jedicke et al.* (2002), who combined results from the Sloan Digital Sky Survey (SDSS) for  $H > 12$  (*Ivezic et al.*, 2001) with the set of known main-belt asteroids with  $H < 12$ . To transform the H distribution into a size distribution, one can use the relationship between asteroid diameter D, absolute magnitude H, and visual geometric albedo  $p_v$  provided by *Fowler and Chillemi* (1992)

$$D = \frac{1329}{\sqrt{p_v}} 10^{-H/5} \quad (8)$$

A model main-belt SFD was made by *Bottke et al.* (2005a), who set  $p_v$  to 0.092 in order to match the observed asteroids described cited in *Farinella and Davis* (1992). This population is shown in Fig. 2. Overall, the observed and debiased main-belt SFD is wavy, with “bumps” near  $D \sim 3$  km and one near  $D \sim 100$  km. The reason for these bumps will be discussed in section 4.

For more precise constraints, and more model variables, one can treat different regions of the main belt separately. For example, *Cibulková et al.* (2014) divided the main-belt population into six distinct components: inner, middle, pristine, outer, Cybele, and high-inclination regions. This allowed them to track how each different regional SFD evolved in response to various collisional and dynamical processes. The observed SFDs in each region, however, have yet to be debiased, which means they must be treated as lower limits for modeling constraints.

### 3.2. Asteroid Families

Asteroid families provide another powerful way to constrain asteroid collisional models. As discussed in the chapter by *Nesvorný et al.* in this volume, these remnants of cratering and catastrophic disruption events are identified in the main belt by their clustered values of proper semimajor axes  $a_p$ , eccentricities  $e_p$ , and inclinations  $i_p$ . The problem with using them to test our model runs is that estimates of ancient family ages can be imprecise and small families can also be eliminated over time by collisional and dynamical processes.

For this reason, the best starting constraints come from families where the parent body was large enough that their fragments could not be erased over 4 G.y. of evolution. We assume families formed prior to 4 G.y. ago were erased by sweeping/jumping resonances produced by late giant planet migration (see the chapter by *Morbidelli et al.* in this volume). Using results discussed in *Durda et al.* (2007) (see also *Cibulková et al.*, 2014), there are approximately 20 observed families created by catastrophic disruptions of parent bodies with sizes  $D_{PB} > 100$  km, where the ratio of the largest fragment’s mass to the parent body mass is  $M_{LR}/M_{PB} < 0.5$  (Fig. 3).

It is also useful to use the distribution of family parent body sizes to compare model to data. In one case, *Bottke et al.* (2005a,b) used results later published in *Durda et al.* (2007) to argue that the number of families formed over the last 3.5 G.y. from catastrophic breakups of parent bodies whose sizes were within incremental logarithmic-separated bins centered on diameters  $D = 123.5, 155.5, 195.7, 246.4, 310.2$ , and  $390.5$  km were 5, 5, 5, 1, 1, 1, respectively. New family identifications discussed in the chapter by *Nesvorný et al.* in this volume can be used to update these values.

Ideally, a good collisional model must account for all types of collisions, even relatively small cratering events. For the purpose of comparison with observations, one has to carefully select synthetic events that would still be observable. Even

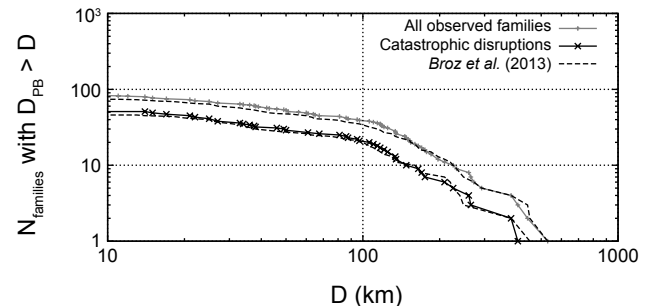


**Fig. 3.** A production function [i.e., the cumulative number  $N(>D)$  of families with parent-body size  $D_{PB}$  larger than D] for all observed families (gray) and families corresponding to catastrophic disruptions (black), i.e., with largest remnant/parent body mass ratio lower than 0.5. Adapted from *Brož et al.* (2013) and updated according to the chapter by *Nesvorný et al.* in this volume. The families were assumed to form prior to 4 G.y. ago (see Fig. 4).

though this number ( $N_{\text{fam}} \sim 20$ ) appears well defined above, it is difficult to assess its uncertainty for the following reasons:

- Determining the size of the parent of an asteroid family depends on the observed fragment distribution, which has experienced collisional and dynamical evolution, and the nature of the precise breakup involved, which may be uncertain. The existence of interlopers within the family can also be hard to exclude.
- There are overlapping families that are difficult to separate unambiguously [e.g., several families exist in the Nysa/Polana region (M. Dykhuis, personal communication)].
- The method used for the parent body size determination in *Durda et al.* (2007) may exhibit some systematic issues since it involves a number of assumptions.

Taken together, the uncertainty of  $N_{\text{fam}}$  is at least the order of a few, if not more.

The distribution of the dynamical ages and sizes of families, as derived using the methods discussed in the chapter by Nesvorný et al. in this volume, may also provide another metric to estimate family completeness. For example, Fig. 4 shows estimates of the ages of cratering and catastrophic disruption events for families derived from different parent body sizes (Brož et al., 2013). We caution the reader that discerning these values for heavily evolved ancient families is problematic, and large uncertainties exist. We therefore use Fig. 4 as a guide to glean insights into interesting possibilities, not as the last word on this topic.

We focus here on asteroid families with parent body diameters  $D_{\text{PB}} > 100$  km; they are presumably more difficult to eliminate by collisional and dynamical processes. For families formed over the last 2 G.y., we find several with  $100 < D_{\text{PB}} < 200$  km and few with  $D_{\text{PB}} > 200$  km. The opposite is found for families older than 2 G.y.; only a few  $100 < D_{\text{PB}} < 200$ -km families exist, while several  $D_{\text{PB}} > 200$  km are found.

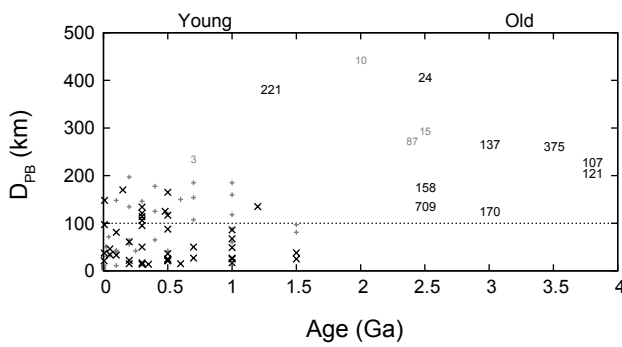


**Fig. 4.** The relationship between dynamical ages of families and the sizes of their parent bodies. Black labels, shown as x's and numbers, correspond to catastrophic disruptions, while cratering events, shown as crosses and numbers, are labeled in gray. Some of the families are denoted by the designation of the largest member. Adapted from Brož et al. (2013) and updated according to the chapter by Nesvorný et al. in this volume.

The difference between the two sets warrants additional study, but statistics of small numbers prevents us from saying they are highly unusual. The probability that two  $D_{\text{PB}} > 200$ -km families formed in the last 2 G.y. out of the seven identified with ages  $< 4$  G.y. is 23%. The number of  $100 < D_{\text{PB}} < 200$ -km families that formed at different times are also not unusual from a statistical standpoint. Overall, there are also approximately the same number of young ( $t_{\text{age}} < 2$  G.y.) and old ( $> 2$  G.y.) families produced by the catastrophic disruptions of  $D_{\text{PB}} > 100$ -km bodies.

The most intriguing issue here is that there are no identified  $D_{\text{PB}} < 100$ -km families that are  $> 2$  G.y. old. This hints at the possibility that some  $100 < D_{\text{PB}} < 200$ -km families older than 2 G.y. are so evolved that they escaped detection. If true, one could argue that something interesting was going on that was producing  $D_{\text{PB}} > 100$ -km families in the billion years or so after the completion of the major dynamical depletion events  $> 4$  G.y. (see section 1 and the chapter by Morbidelli et al. in this volume.).

Along these lines, one way to account for the unusual distribution of families in Fig. 4 is to assume that some small families are actually remnants, or “ghosts,” of much larger older families. A possible example might be the cluster of asteroids near asteroid (918) Itha (Brož et al., 2013). It exhibits a very shallow SFD, which could be a possible outcome of comminution and dynamical evolution by the size-dependent Yarkovsky effect. An excellent place to look for ghost families would be the narrow portion of the main belt with semimajor axis  $a$  between 2.835 and 2.955 AU. This pristine zone, which is bounded by the 5:2 and 7:3 mean-motion resonances with Jupiter, has a limited background population of small asteroids. We postulate it could resemble what the primordial main belt looked like prior to the creation of many big families.

An independent calibration of collisional models might also be based on very *young* families, namely younger (and larger) than some carefully estimated upper limit for which the respective sample is complete. Indeed, there are many examples of young families with well-determined ages: Veritas ( $8.3 \pm 0.5$ ) m.y. (Nesvorný et al., 2003), Karin ( $5.8 \pm 0.2$ ) m.y. (Nesvorný and Bottke, 2004), Lorre ( $1.9 \pm 0.3$ ) m.y. (Novaković et al., 2012), P/2012 F5 (Gibbs) ( $1.5 \pm 0.1$ ) m.y. (Novaković et al., 2014), etc. A collisional model then would have to reproduce the number of these events in the last  $\approx 10$  m.y. or so of the simulation.

### 3.3. Impact Basins on (4) Vesta

(4) Vesta is one of the most unique asteroids in the main belt. Not only is it among the largest asteroids, with a diameter of 525 km, but it is also has a largely intact basaltic crust that was put in place shortly after it differentiated some 2–3 m.y. after CAIs (see the chapter by Russell et al. in this volume). Decades of groundbased observations, combined with *in situ* observations of Vesta by the Dawn spacecraft, have shown that the spectral signatures found in Vesta’s crust are a good match to the howardite, eucrite, and diogenite

(HED) meteorite classes (see the chapter by Russell et al.). We do not consider the impact record on Vesta prior to the formation of this crust, although Vesta's abundance of highly siderophile elements may eventually allow us to infer what happened during this ancient period (e.g., Dale et al., 2012).

Vesta also has two enormous basins that dominate its southern hemisphere: Rheasilvia, a 505-km-diameter crater with an estimated crater retention age of 1 G.y., and Veneneia, a 395-km-diameter crater with a crater retention age of  $>2$  G.y. (Marchi et al., 2012). Rheasilvia, being younger, overlaps with and has largely obscured Veneneia (Schenk et al., 2012; Jaumann et al., 2012). The formation of each basin is also thought to have produced a set of fracture-like troughs, or graben, near Vesta's equator (Buczkowski et al., 2012). Studies of each trough group show they form planes that are orthogonal to the basin centers. Recent simulations of the formation of the Veneneia and Rhealsilvia basins using numerical hydrocodes suggest they were created by the impact of 60–70-km-diameter projectiles hitting Vesta near  $5 \text{ km s}^{-1}$  (Jutzi et al., 2013; see the chapters by Asphaug et al. and Jutzi et al. in this volume). These same events likely produced the majority of the observed Vesta family, a spread out swarm of  $D < 10$ -km asteroids in the inner main belt with inclinations and spectral properties similar to Vesta itself (see the chapter by Scott et al. in this volume).

Vesta shows no obvious signs that basins similar in size to Rheasilvia or Veneneia were ever erased or buried after its basaltic crust was emplaced; nothing notable is detected in Vesta's topography, and there are no unaccounted sets of troughs that could be linked with a missing or erased basin. This means Vesta is probably complete in Rheasilvia- or Veneneia-sized basins. This constrains both the size of many primordial populations as well as how long they could have lasted on Vesta-crossing orbits (e.g., main-belt asteroids, leftover planetesimals from terrestrial and giant planet formation, the putative late heavy bombardment (LHB) population, Jupiter-family comets, etc.).

As a working example, consider that if we use the main-belt asteroid population described in Bottke et al. (1994), where there are 682 main-belt asteroids with  $D > 50$  km, we find that the probability that Vesta has 0, 1, 2, or 3+ Rheasilvia/Veneneia formation events over the last 4 G.y. is 50%, 35%, 12%, and 3%, respectively. If Rheasilvia and Veneneia are actually both  $<2$  G.y. old, however, these values change to 70%, 25%, 4%, and 0.5%, respectively. The 4% probability for the observed situation is surprisingly small, and it suggests two possibilities: Veneneia's crater retention age was strongly affected by the Rheasilvia formation event, and its formation age is older than its crater retention age (Schenk et al., 2012), or the basins on Vesta's surface beat the odds. Note that testing modestly smaller projectiles to make the basins, such as  $D > 35$ -km asteroids (Asphaug et al., 1997), only increases the probabilities above by a factor of 2 or so.

These calculations become even more interesting if we assume the main-belt population was larger in its early history, and/or that it was hit by objects from outside the main

belt (see the chapter by Morbidelli et al. in this volume). Bottke et al. (2005a) argued the main belt experienced the equivalent of  $\sim 7.5$ – $9.5$  G.y. of collisional evolution over the last 4.56 G.y. (i.e., roughly translated as the number of impacts Vesta would get if it resided in the current main-belt population for this time; see section 4). For simplicity, we round this value to 10 G.y., which makes the probability of getting 0, 1, 2, or 3+ basins at any time in Vesta's history 17%, 30%, 27%, and 20%, respectively. This would place the Rheasilvia/Veneneia combination near the center of the probability distribution. If Rheasilvia/Veneneia formed  $<2$  G.y. ago, however, we not only have to explain their existence, but also the absence of ancient basins; large primordial populations are more likely to create ancient basins than young ones. The probability of these events taking place is only  $\sim 1\%$ .

Therefore, from a purely statistical point of view, one could argue that the main belt was probably more massive in the past, and that Veneneia's minimum age of  $\sim 2$  G.y. is not its formation age. An older age for Veneneia would also allow it to be the source for numerous Vesta family members with low inclinations, which need billions of years to reach these orbits via Yarkovsky drift and resonances (Nesvorný et al., 2008). Further work will be needed to see if the "facts on the ground" confirm or reject these predictions.

### 3.4. Near-Earth Asteroids, Asteroid Craters, and Lunar Craters

Asteroids in the main belt have struck other asteroids throughout the lifetime of the solar system. This means that projectile SFDs ranging from a few meters to multi-kilometer sizes can be constrained over hundreds of millions to billions of years by craters found on asteroids imaged by spacecraft missions (see the chapter by Marchi et al. in this volume). The main-belt SFD also produces planet-crossing asteroids via the combined Yarkovsky/YORP effects (see the chapter by Vokrouhlický et al.). This means that the observed planet-crossing asteroid population can also be used to provide main-belt SFD constraints. We focus here on the best-understood component of the population, namely the NEAs (see the chapter by Harris et al.). Finally, Earth-crossing asteroids in the NEA population have slammed into Earth and the Moon over billions of years, which means the crater SFDs and impact byproducts on these worlds can help us determine how the main-belt SFDs have evolved over these times.

The key issue for all these data is interpretation; the ages and SFDs of cratered terrains are often uncertain or complicated, and short-term changes in the flux or shape of impacting SFDs can be hard to decipher amid the integrated histories of cratered surfaces. For this reason, a full discussion of all cratering issues is beyond the scope of this section. Instead, we provide a brief summary of how asteroid and lunar craters, together with the debiased NEA population, can be used as constraints for main-belt collisional models, provided appropriate caution is employed by the reader.

The crater histories of the asteroids visited by spacecraft are reviewed in the chapters by Marchi et al. and Barucci et al. in this volume. They found that the crater SFDs that do the best job of showing off the main-belt production population are found on (951) Gaspra and (4) Vesta. Crater data for Vesta is shown in Fig. 5, while Gaspra crater data can be found in the chapter by Marchi et al. The cumulative crater SFD found on or near Vesta's Rheasilvia basin shows, from large to small craters, a wavy shape: a steep slope up to an inflection point at 20 km, a shallow slope to a roundoff near 4 km, an even shallower slope to 0.8 km, and a steep slope to 0.01 km, where the resolution limit is reached. The craters superposed on Vesta's Marcia crater and on Gaspra's surface have the same slope as that found on Rheasilvia for <0.8-km craters. If we assume the scaling relationship between asteroids and craters is a simple factor of 10 (Bottke and Chapman, 2006; Marchi et al., 2013), these values yield a wavy asteroid SFD with inflection points at ~2 km, 0.4 km, and 0.08 km. As a caveat, it is also possible that some aspects of the wavy crater SFD on Vesta are a byproduct of terrain properties (Marchi et al., 2012, 2014).

The nature of the NEA SFD is thoroughly discussed in this volume in the chapter by Harris et al., so we only discuss a few aspects of it here. Their best estimate of the NEA population is shown in Fig. 2. Its wavy shape is broadly similar to a scaled version of the crater SFD found on Vesta in Fig. 5,

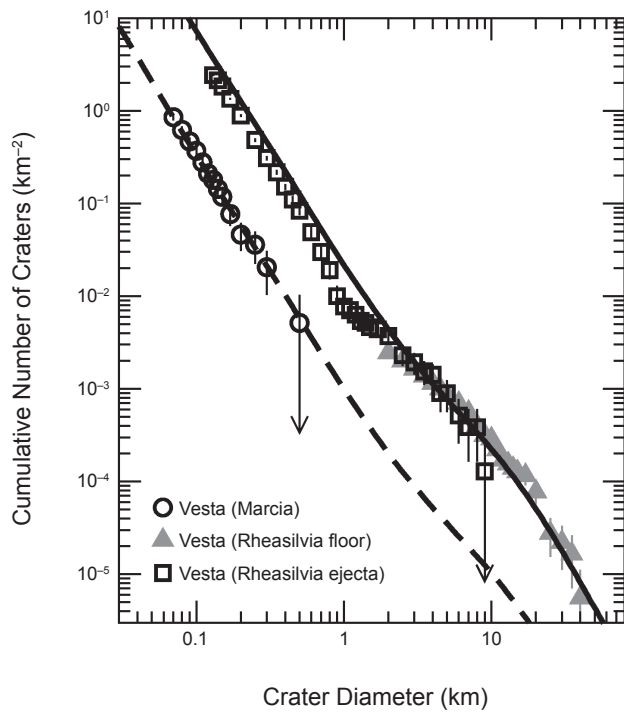


**Fig. 5.** The crater SFDs found on the young terrains of Marcia crater and the floor and ejecta blanket of the basin Rheasilvia. Details can be found in the chapter by Marchi et al. in this volume. The fit is good except near  $0.7 < D < 2$  km, where the model steepens too quickly.

although some differences exist; recall that the main-belt SFD is modified en route to the NEA population by Yarkovsky/YORP-driven asteroid migration (e.g., Morbidelli and Vokrouhlický, 2003). The inflection points for the NEA population in Fig. 2, however, are at approximately the same sizes as derived above: ~2, 0.4, and 0.1 km. Our interpretation is that the broad shapes of the main-belt and NEA population have not been strongly modified for an extended period.

A similar analysis can be performed on the lunar crater SFD plotted in Fig. 1 of Ivanov et al. (2002). The broad shapes are the same as that above, with crater diameter inflection points at 64 km, 1.4 km, and 0.3 km. The middle inflection point at 1.4 km possibly straddles a slowly bending region between 1 and 3.5 km. Using crater-scaling-law relationships from Melosh (1989), these values roughly correspond to 2–3 km, 0.03–0.16 km, and 0.009–0.014 km. As before, these compare well to the values above.

In summary, the scaled asteroid and lunar crater data, together with the NEA population, all suggest a wavy main-belt SFD with inflection points near ~2–3, 0.4, and 0.1 km. Collectively, these results imply that the shape of the main-belt SFD for asteroid sizes smaller than 5–10 km has not substantially changed for billions of years.

If the shape of the main-belt SFD has remained the same over time, what can be said about the size of the population? Here we turn once again to the Moon, our benchmark for solar system chronology. Many nearside lunar terrains have been dated by returned samples. The crater populations found on these surfaces give us a sense of how the Earth-crossing impactor flux has changed with time (e.g., Stöffler and Ryder, 2001; Morbidelli et al., 2012). Given that this flux is fed by the main-belt population, changes in the lunar impactor flux over time should correspond at some level to what took place in particular regions of the main belt.

Studies of small lunar craters ( $D < 1$  km) on specific Copernican and Eratosthenian-era terrains suggest the impact flux of very small impactors has been fairly constant, within a factor of 2 or so, for the last 3.2 G.y. (e.g., Ivanov et al., 2002; Marchi et al., 2009; Hiesinger et al., 2012; but see also Robbins, 2014). For reference, the ages of the former era are often considered to be roughly 1 G.y. old, while those of the latter are defined by the ages of samples returned by the Apollo 12 astronauts (Stöffler and Ryder, 2001). This implies the main-belt population in the inner and central main belt feeding  $D < 0.05$ -km bodies to resonances may have been reasonably stable as well.

For larger impactors, the lunar data is more difficult to interpret, although it also hints at a steady state flux. For example, the best available crater SFD of the largest Copernican- and Copernican and Eratosthenian-era craters on the Moon are shown in Fig. 6 (McEwen et al., 1997; Ivanov et al., 2002). The Copernican and Eratosthenian-era craters are roughly a factor of 3 higher than the Copernican-era craters. If the ages of these eras suggested above are reasonable, these data would indicate there have been a fairly steady supply of kilometer-sized main-belt asteroids to the NEA population and the Moon over 3 G.y. (to a factor of 2 or so).

We caution that this interpretation may be subject to revision in the near future once data from the Lunar Reconnaissance Orbiter has been fully evaluated (e.g., Kirchoff *et al.*, 2013; Robbins, 2014). For example, asteroid-family-forming events in strategic locations could potentially affect the lunar impact flux for some period of time (Nesvorný *et al.*, 2002; Bottke *et al.*, 2007, 2015). Given our present state of knowledge, however, it is fair to say that deviations from a steady state over long time spans may be modest for most projectile sizes.

There are two main reasons these results are of critical importance for collision models:

1. Collisional models of the main-belt and NEA SFD need to achieve a quasi-steady-state for the last several billions of years (or have an alternative way to explain the above constraints). This likely rules out scenarios where a very large main-belt SFD is ground down over billions of years of comminution, with the observed SFD only achieved near the present time (see Davis *et al.*, 2002). Such models should produce strongly decaying lunar impact fluxes over the last 3 G.y., and they are not observed.

2. A steady-state main-belt SFD allows modelers to predict the ages of asteroid surfaces with reasonable accuracy, although caution should still be employed (see the chapter by Marchi *et al.* in this volume).

### 3.5. Main-Belt Binaries Formed by Impacts

The population of certain types of asteroid binaries may also constrain the collisional evolution of the main belt. Using numerical hydrocode simulations to model asteroid impacts on  $D = 100$ -km target bodies, Durda *et al.* (2004) found that large-scale cratering events can create fragments whose trajectories can be changed by particle-particle interactions and by the reaccretion of material onto the remnant target body. Under the right circumstances, impact debris can enter into orbit around the remnant target body, which is a gravitationally reaccreted rubble pile, to form a SMashed Target Satellite (SMATS).

Here we only discuss SMATS made by subcatastrophic collisions. We expect those SMATS to be rather isolated in space; while their formation events produce asteroid families dominated by small fragments, most of these bodies are readily removed or dispersed by collisional and dynamical evolution. As of a few years ago, detection limits of groundbased adaptive optics searches limited the discovery of SMATS to primary-to-secondary diameter ratios smaller than 25 (e.g., Merline *et al.*, 2002). This population is thought to be complete, so we focus on these binaries here. In a survey of 300 large main-belt asteroids, Merline *et al.* (2002) reported four  $D > 140$ -km bodies that had relatively large satellites (i.e.,  $D > 10$  km) that were not in asteroid families produced by catastrophic disruption events: (22) Kalliope, (45) Eugenia, (87) Sylvia, and (762) Pulcova.

Additions since that time to the SMATS record could include (216) Kleopatra and (283) Emma, whose primaries have diameters that are nearly 140 km. The secondary

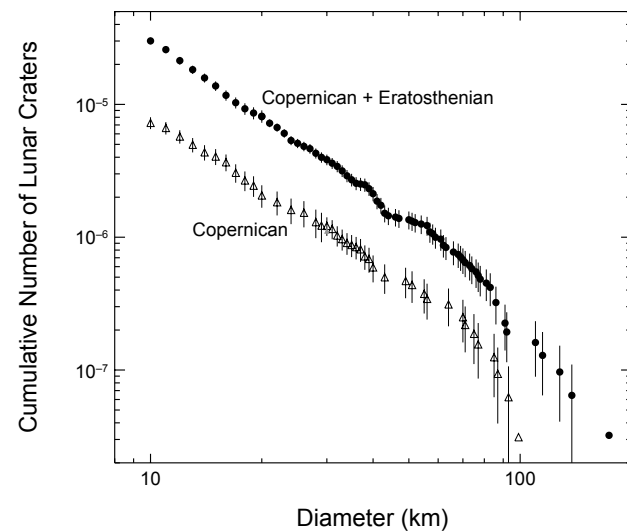


**Fig. 6.** Lunar craters in the Copernican and Copernican and Eratosthenian eras as defined by Wilhelms *et al.* (1978) and McEwen *et al.* (1997). The absolute ages of these craters are often considered  $<1$  and  $<3.2$  G.y. old (Stöffler and Ryder 2001), although the age of the former is debated (e.g., Ryder *et al.*, 1991). The plotted Copernican-era craters are a combination of nearside craters (Wilhelms, 1987) and far-side rayed craters (McEwen *et al.*, 1997). These estimates may be revised using Lunar Reconnaissance Orbiter data in the near future.

sizes of Eugenia and Emma, however, are very close to our primary-to-secondary diameter ratio limit, and Kleopatra appears to have an iron rather than stony composition, such that the results of Durda *et al.* (2004) may not be applicable. This leaves the net value somewhere in the range of 3–6. The binary (90) Antiope is excluded here because it is a likely byproduct of the catastrophic disruption that produced the Themis family.

Using their runs, Durda *et al.* (2004) estimated that the expected frequency of SMATS-forming events by non-catastrophic collisions in the present-day main belt was  $f = 0.9\text{--}1.7 \times 10^{-11}$  yr $^{-1}$ . If one then assumes that the current population of  $D > 140$ -km bodies,  $N = 94$ , is similar to that from 4 G.y. ago, we would expect these production rates to yield 3–6 SMATs on average. These results are an excellent match to the 3–6 SMATs discussed above.

These results place upper limits on what happened during the primordial phase of the asteroid belt, depending on the planet formation evolution model invoked. For example, as described in the chapter by Morbidelli *et al.* in this volume, the main belt potentially had an early massive phase, where numerous SMATS should have been made. A dynamical depletion event at the end of this phase would then remove most of the excess mass as well as most of the newly formed SMATS. Effectively, this would make the remnant number of primordial SMATS the product of  $f$ ,  $N$ , and the time interval that the excess population existed in the main belt. For Nice model simulations (see the chapter by Morbidelli *et al.*),

where the main belt is only a few times more massive than the current population for  $\sim 0.5$  G.y., this would yield  $\sim 1$  extra SMAT on average, not enough to affect the results above.

On the other hand, SMATS provide powerful constraints against evolution scenarios where collision grinding alone removes most of the primordial mass of the main belt. This scenario is already problematic, as discussed above, but numerous collisions may produce a net amount of SMATS that exceeds observations. Similarly, massive planetesimal populations on terrestrial planet-crossing orbits may create numerous SMATS. Given that we see little evidence for an abundance of primordial SMATS, these models can potentially be tested on this basis.

### 3.6. Asteroid Spin Rates and Spin States

Asteroid spin rates are affected by collisions, so it is plausible they can be used as constraints on main-belt evolution. A problem with this is that many  $D > 50\text{--}100$ -km bodies may still have spins that were largely put in place by the planetesimal accretion process. A review of the spin rate literature for the largest asteroids can be found in *Bottke et al.* (2005a). For smaller bodies, the spin rates and obliquities of  $D < 30\text{--}40$ -km asteroids are likely dominated by the effects of YORP thermal torques (e.g., *Pravec et al.*, 2002; see the chapter by Vokrouhlický et al. in this volume). Given this, an unambiguous signal of collisions affecting spin vectors in the main belt may be limited to bodies whose evolutionary context is well understood.

The interested reader can consider the spin-evolution models of *Farinella et al.* (1992) and *Marzari et al.* (2011) for their views on this topic. They should also examine results from the numerical hydrocode simulations of *Love and Ahrens* (1997), who argued that small erosive collisions have a minimal effect on an object's spin, while catastrophic disruption events essentially destroy all "memory" of the target body's initial spin. The collisional signal we are looking for, therefore, may be limited to specific remnants of certain family-forming events.

An alternative way to obtain a model constraint may be found in the spin vectors of asteroids in the Koronis asteroid family. The Koronis family is thought to be one of the asteroid belt's most ancient families, with an estimate age of 2–3 G.y. (see the chapter by Nesvorný et al. in this volume). After years of painstaking observations of Koronis family members, including 21 of the 25 brightest Koronis family members, *Slivan et al.* (2003, 2009), *Slivan* (2002), and *Slivan and Molnar* (2012) reported that nearly all of the observed 15–40-km-diameter Koronis family members with prograde spins have clustered spin periods between 7.5 and 9.5 h and spin obliquities between  $39^\circ$  and  $56^\circ$ . Those with retrograde spins have obliquities larger than nearly  $140^\circ$  with periods either  $< 5$  h or  $> 13$  h. *Vokrouhlický et al.* (2003) demonstrated that all these spin states were a byproduct of YORP thermal torques. The prograde cluster was created by an interaction between YORP torques and spin orbit resonances, and are now called "Slivan states."

The predicted timescales for these objects to reach these spin states is several billions of years. During that time, collisions did not strongly affect their spin periods or their obliquities; if they had, we would see at least a few bodies with random spin vector values. Limits on this come from (243) Ida, a member of the prograde cluster with dimensions of  $53.6 \times 24.0 \times 15.2$  km; it was apparently unaffected by the formation of two  $\sim 10$ -km-diameter craters formed on its surface.

Statistically, we would expect catastrophic disruptions to be more rare than smaller, less-energetic impact events that can modify an asteroid's spin state. In the ancient Koronis family, however, the spin vectors of many large objects show no evidence that collisions have affected them. This presents a key challenge to collisional models that assume disruption events among 20–40-km bodies are relatively common; can this outcome be reconciled with the spin states of Koronis family members? A similar argument could potentially be developed regarding the anisotropic obliquities found among  $D < 30$ -km asteroids residing in the background main-belt population (e.g., *Hanus et al.*, 2013).

### 3.7. Additional Constraints

The constraints discussed above are far from complete, and many other datasets could be brought to bear in a collisional model. For space reasons, we do not include a discussion of (1) the cosmic-ray-exposure ages of stony meteorites (e.g., *Eugster*, 2003); (2) the orbital distribution of fireballs (e.g., *Morbidelli and Gladman*, 1998); (3) the population of V-type asteroids across the main belt (see the chapter by Scott et al. in this volume); (4) the crater records found on Mercury, Venus, Earth, and Mars (e.g., *Ivanov et al.*, 2002); (5) all asteroid families not discussed here (see the chapter by Nesvorný et al. in this volume); and (6) the shock degassing ages of meteorites (e.g., *Marchi et al.*, 2013). In fact, the subject of collisional evolution in the main belt is rich enough that data from numerous *Asteroids IV* chapters could probably be employed as well.

## 4. INSIGHTS FROM MODELING RESULTS

Existing collisional modeling work has provided us with insights into the nature of planetesimal formation, asteroid fragmentation and evolution, planet-formation processes, and the bombardment history of the inner solar system. Here we summarize some of those findings.

### 4.1. The Relationship Between the Main-Belt Size-Frequency Distribution and Asteroid Disruption Scaling Laws

The bump in the main-belt SFD near  $D \sim 2\text{--}3$  km (Fig. 2) is a byproduct of collisional evolution (*Campo Bagatin et al.*, 1994; see *Davis et al.*, 2002), and is driven by a change in the  $Q_D^*$  function near  $D \sim 0.2$  km. To trace its origin, we start with the classic work of *Dohnanyi* (1969) (later

expanded by *Williams and Wetherill*, 1994, and *Tanaka et al.*, 1996), who analytically modeled collisions among a SFD of self-similar bodies and found the steady-state SFD should follow a differential power law with an exponent of  $-3.5$ . Dohnanyi assumed that the strength per unit mass of the colliding bodies is independent of size. In reality, though, for bodies smaller than  $\sim 0.2$  km in diameter, material properties cause strength to decrease with increasing size, while for larger bodies, self-gravity makes it more difficult to shatter a body and disperse its fragments, leading to an increase in strength with increasing size (e.g., *Asphaug et al.*, 2002; *Holsapple et al.*, 2002; *Davis et al.*, 2002). This provides us with the classic  $Q_D^*$  function discussed above.

The dependence of the power-law index of the size distribution on these parameters was explored analytically by *O'Brien and Greenberg* (2003), and we repeat the main results here. First consider the steady-state of a colliding population of bodies whose strength is described by a single power law. The population is described by the power law

$$dN = BD^{-p} dD \quad (9)$$

where  $dN$  is the incremental number of bodies in the interval  $(D, D + dD)$ . While  $B$  should technically be negative as there are more small bodies than large bodies, it is defined to be positive here to avoid the physically unrealistic result of having negative numbers of bodies in a given size interval.  $p$  is the power-law index of the population. Equation (9) would plot as a line with a slope of  $-p$  on a log-log plot.

*O'Brien and Greenberg* (2003) considered the case where the impact strength  $Q_D^*$  is given by a power law

$$Q_D^* = Q_0 D^s \quad (10)$$

where  $Q_0$  is a normalization constant and  $s$  is the slope of equation (10) on a log-log plot. They find that, in collisional equilibrium, the power-law index  $p$  in equation (9) is given by

$$p = \frac{7 + s/3}{2 + s/3} \quad (11)$$

For  $s = 0$ , which corresponds to size-independent strength  $Q_D^*$ , this gives the classical Dohnanyi steady-state solution of  $p = 3.5$ . For the more realistic case where  $Q_D^*$  decreases with increasing size for small bodies and increases for larger bodies once gravity becomes important (as schematically shown in Fig. 1), *O'Brien and Greenberg* (2003) show that the strength- and gravity-scaled portions of the size distribution have power-law indices  $p_s$  and  $p_g$  that are only dependent on the slope of  $Q_D^*$  in the strength and gravity-scaled regimes  $s_s$  and  $s_g$ , respectively. The power-law index of the size distribution in the strength-scaled regime  $p_s$  has no dependence on the slope  $s_g$  of  $Q_D^*$  in the gravity-scaled regime, and vice versa;  $p_s$  is found by using  $s_s$ , and  $p_g$  is found by using  $s_g$ . Because  $s_s$  is usually negative and  $s_g$  is usually positive, equation (11) yields  $p_s > 3.5$  and  $p_g < 3.5$ .

While the general slope of the size distribution in the gravity regime is unaffected by  $Q_D^*$  in the strength regime,

the transition in slope of the size distribution will lead to waves that propagate through the size distribution in the gravity regime. In the derivation of  $p_g$ , it is implicitly assumed that all asteroids were disrupted by projectiles whose numbers were described by the same power law. However, for those targets just larger than the transition diameter  $D_t$  between the strength- and gravity-scaled regimes (i.e., near the small end of the gravity-scaled regime), projectiles are mostly smaller than  $D_t$ , and hence are governed by the strength-scaled size distribution. As these projectiles will be stronger and hence more numerous than would be expected by assuming that all bodies are gravity-scaled, they will lead to a depletion of bodies of diameter  $D_t$ . This underabundance of bodies of diameter  $D_t$  (a “valley”) leads to an overabundance of bodies that impactors of diameter  $D_t$  are capable of destroying (a “peak”), which in turn leads to another “valley” and so on. This results in a wave that propagates through the large-body size distribution, as can be seen in Fig. 2. The average power-law index  $p_g$  of the population in the gravity-scaled regime will not be significantly changed by the initiation of this wave; the wave oscillates about a power law of slope  $p_g$ . Analytical expressions for the amplitude of the waves, as well as the approximate positions of the “peaks” and “valleys” in the size distribution, are derived in *O'Brien and Greenberg* (2003). The waves will not continue on to larger bodies if they have long collisional lifetimes. The origin of the bump for  $D > 100$ -km bodies is discussed in the next section.

Finally, we note that removing all small bodies instantaneously from the population (i.e., creating a small body cutoff) can also launch a wave into the size-frequency distribution (*Campo-Bagatin et al.*, 1994; *Penco et al.*, 2004). The effect is minimized, however, if removal is more gradual. This was demonstrated by both *O'Brien* (2009), who found the depletion expected from Yarkovsky removal is too small to significantly perturb the main-belt size distribution (section 2.4), and by *Durda et al.* (1997), who found the same result when they modeled the expected dust distribution created by the main belt collisions and Poynting-Robertson drag.

#### 4.2. Large Asteroids as Byproducts of Planetary Formation

One of the most difficult issues to deal with concerning main-belt evolution is estimating the initial SFD created by planetary formation mechanisms. Given the current uncertainties surrounding planet formation, a enormous range of starting SFDs are theoretically plausible. This has caused many groups to winnow these possibilities down using collisional models.

For example, *Bottke et al.* (2005a,b) tested a wide range of initial SFDs and  $Q_D^*$  functions to determine which combinations work the best at reproducing the observational constraints discussed in section 3. They found that  $Q_D^*$  functions similar to those derived in numerical SPH experiments of asteroid breakup events (*Benz and Asphaug*, 1999)

tended to work the best (Fig. 1), although this made their  $D > 100$ -km asteroids very difficult to disrupt. Accordingly, they inferred that the shape of the main-belt SFD for  $D > 100$ -km asteroids was probably close to its primordial shape (Fig. 2). Interestingly, this prediction is consistent with several pioneering papers from the 1950s and 1960s (Kuiper *et al.*, 1958; Anders, 1965; Hartmann and Hartmann, 1968).

Next, they tested initial main-belt SFDs where the incremental power law slope of  $-4.5$  between  $100 < D < 200$  km had been extended to  $D < 100$ -km bodies (Fig. 7). This eliminated the observed bump near  $D \sim 100$  km. They found bodies in this size range were so difficult to disrupt that initial SFDs with these shapes could not reproduce constraints. They argued from this that the bump near 100 km in the main-belt SFD is primordial and that  $D < 100$ -km bodies probably had a shallow power law slope. Accordingly, this would indicate the planetesimal-formation process favors the creation of bodies near 100 km (or larger), with smaller bodies increasingly fragments produced by the disruption of large asteroids. These results may act as a guide for those studying planetesimal-formation processes (e.g., Morbidelli *et al.*, 2009; see the chapter by Johansen *et al.* in this volume).

### 4.3. Collisional Evolution of the Primordial Main Belt

To understand the history of the main belt, it is important to quantify how much collisional evolution has taken place there over its history. This means choosing a starting SFD and then evaluating what it takes to reach its present-day

state. The problem is there are many different ways to get from start to finish, and the available constraints may be insufficient to tell us which pathways are favored.

In order to glean insights into this, one can adopt a simplistic but useful metric that can help us evaluate what different evolutionary paths might do. First, let us assume that the main belt is roughly self-contained in terms of collisions, such that we can largely ignore impacts from external sources like escaped main-belt asteroids, leftover planetesimals, comets, etc. Second, we assume the intrinsic collision probabilities and impact velocities of main-belt asteroids hitting one another have remained unchanged over its history. Third, we assume the main belt's SFD has been close to its current shape throughout its history, although it may have been larger in the past. We define this size to be a factor  $f_{MB}$ , the ratio of the main belt's SFD during some past interval of time defined as  $\Delta T$  over the present-day main-belt SFD. Together, these values allow us to estimate the degree of collisional evolution experienced by the main belt in terms of the time exposed to different population sizes.

This metric allows to play with evolution scenarios. The simplest example is the nominal case where the current main-belt SFD ( $f_{MB} = 1$ ) undergoes collisional evolution over its lifetime ( $\Delta T = 4.56$  G.y.). The two values multiplied together yield 4.56 G.y. of collisional grinding. In a more complicated example, we assume a dynamically excited primordial main belt had  $f = 300$  for 3 m.y. (0.003 G.y.). At that point, most of the population was lost via escaping embryos or a migrating Jupiter, which reduced it to  $f_{MB} \sim 5$  for  $\sim 0.5$  G.y. Then, at  $\sim 4$  G.y., 80% of the bodies were lost via sweeping resonances driven by late giant planet migration, which left the surviving population close to its current state ( $f = 1$ ) for the next  $\sim 4$  G.y. Taking all of the multiples, one can say that collectively the survivors experienced  $(0.9 + 2.5 + 4) = 7.4$  G.y. of collisional evolution. This pseudo-time tells us that this main belt roughly experienced the collisional evolution equivalent of a  $f_{MB} = 1$  main belt going through 7.4 G.y. of comminution.

Using a collisional model that took advantage of these concepts, as well as the constraints above, Bottke *et al.* (2005a) found median pseudo-times of 7.5–9.5 G.y. for their best-fit runs, with error bars of a few million years on each end of this range. An example of one of their runs is shown in Fig. 8. Their interpretation was that the main-belt SFD obtained its wavy shape by going through an early time interval where the main-belt survivors were exposed to many more projectiles than are observed today, with most of those bodies due lost to dynamical processes. Thus, the wavy main-belt SFD could be considered a “fossil” produced in part by early collisional evolution in the primordial main belt.

This pseudo-time range above can be used to explore dynamical-evolution scenarios, particularly those that create abundant main-belt populations. For example, using our simple metric, one could replace the middle component, which roughly corresponds to the “Jumping Jupiter” version of the Nice model (Morbidelli *et al.*, 2010; Marchi *et al.*, 2013; see also Nesvorný, 2011; Nesvorný and Morbidelli, 2012),

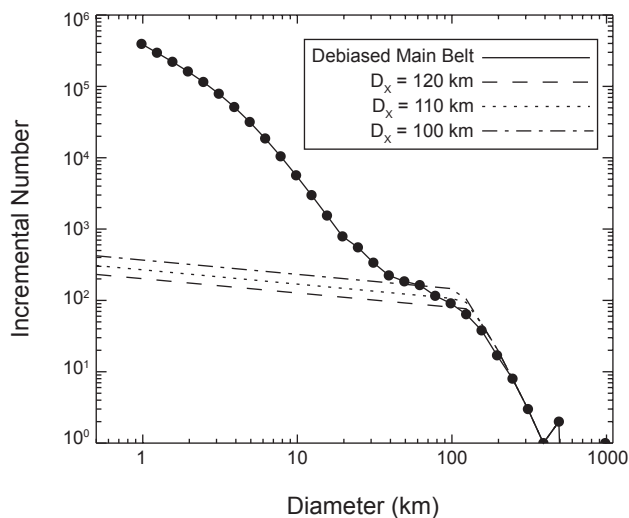


**Fig. 7.** The debiased main-belt size-frequency distribution as defined in the main text (solid line). The dashed curves show possible initial shapes of the primordial main belt SFD (Bottke *et al.*, 2005a). They found a best fit in their runs for an elbow near  $D_x \sim 110$ – $120$  km. It is likely that the primordial population was larger than the SFDs shown here, with most of the mass eliminated by dynamical processes.

with the original Nice model, where  $f_{MB} \sim 20$  for  $\sim 0.5$  G.y. (Gomes et al., 2005). This change yields  $(0.9 + 10 + 4) = 14.9$  G.y., a pseudo-time outside the favored range. While it cannot be ruled out statistically, it does suggest that collisional evolution needs to be explored in greater depth here.

Another interesting property of Fig. 8 is that once it achieves the shape of the current main belt's SFD, it tends to keep that shape for an extended time. This would explain why the main-belt SFD could remain in a near-steady-state condition for billions of years. While it would be constantly changing and losing bodies by collisional, dynamical, and

YORP spinup processes, it would also be steadily replenished by new large breakup events. This means the vast majority of disruption events produce too few fragments to push the main-belt SFD out of equilibrium for very long. This result also explains why the nonsaturated crater populations on Gaspra, Vesta (i.e., the Marcia and Rheasilvia terrains), and the Moon appear to have been hit by a projectile population with a similarly shaped SFD for an extended period (see section 3.4).

#### 4.4. Processes Affecting Small Asteroids

A comparison between the model predictions of Bottke et al. (2005b) and the observed NEO population discussed in the chapter in this volume by Harris et al. (Fig. 2) is intriguing for a different reason (see also O'Brien and Greenberg, 2005). The model does a reasonable job of fitting the observed data for small and larger NEOs, but there is a distinct mismatch near  $D \sim 0.1$  km. The same kind of discrepancy is found between the model main belt and small craters on Vesta at the same approximate location when the craters are scaled back to projectiles (see chapter by Marchi et al. in this volume) (Fig. 5).

This difference suggests the model may be missing something (see section 2.5):

1. YORP spinup torques produce such efficient mass shedding as asteroids sizes approach  $D \sim 0.1$  km that they can influence the shape of the main-belt SFD (Marzari et al., 2011; Jacobson et al., 2014). This same mechanism, however, would need to shut off for  $D < 0.1$  km. The reason why YORP mass shedding approaches termination is unknown, but we can think of several possibilities: (i) the physical nature and/or internal structure of small asteroids may be different from large asteroids, with smaller bodies less likely to be rubble-piles; (ii) small asteroids may be more susceptible to being held together by non-gravitational cohesive forces; or (iii) the thermal properties of the small asteroids are different than those of large asteroids and/or small asteroids become isothermal enough that the YORP mass shedding is less pronounced.

2. The Yarkovsky effect is more efficient at delivering small main belt asteroids to resonances than predicted by Bottke et al. (2005b). As more  $D \sim 0.1$  km objects are evacuated from the main-belt population, a steady-state deficit of small bodies may be created in both the main belt and NEO populations near this size. The reason for this increased delivery efficiency may be related to the YORP shut down discussed above. If YORP becomes less efficient, bodies may become less likely to experience YORP cycles that can cause them to random walk in semimajor axis. In turn, this would enhance their escape rate out of the main belt.

These possibilities illustrate the importance of understanding all the physical processes that affect small bodies in the inner solar system; they feed back in interesting ways, and they may ultimately affect how we interpret the ages of surfaces on both asteroids and the terrestrial planets. We look forward to seeing this investigated in the future.

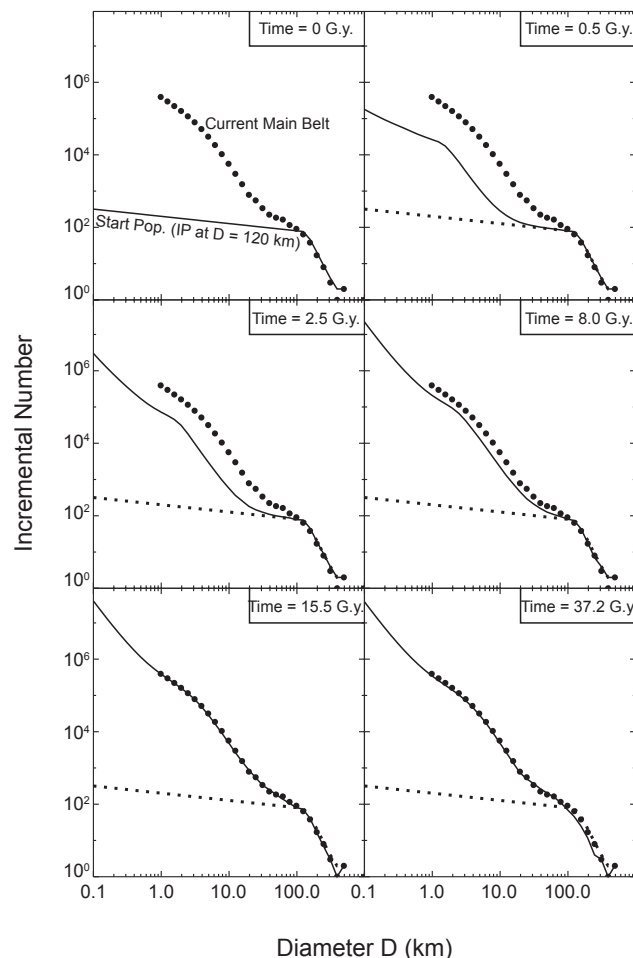


**Fig. 8.** Six snapshots from a representative run where Bottke et al. (2005a) tracked the collisional evolution of the main-belt size distribution for a pseudo-time of 50 G.y. This run uses a starting population with  $D_x = 120$  km. The bump near  $D \sim 120$  km is a leftover from accretion, while the bump at smaller sizes is driven by the transition at  $D \sim 0.2$  km between strength and gravity scaling regimes in  $Q_D^*$ . The model main belt achieves the same approximate shape as the observed population at  $t_{pseudo} = 9.25$  G.y. (not shown). The model closely adheres to the observed population for many gigayears after this time. Eventually, comminution eliminates enough  $D > 200$ -km bodies that the model diverges from the observed population.

#### 4.5. Monolithic vs. Rubble-Pile Structures

Recent collisional modeling work by *Cibulková et al.* (2014) has also taken a more sophisticated look at the evolution of six different main-belt regions (Fig. 9): inner, middle, “pristine,” outer, Cybele zone, and high inclination. Their goal was to fit the SFDs and asteroid families formed in all these zones. The observed SFDs in these regions were computed from the available WISE satellite data (*Masiero et al.*, 2011; see the chapter by Mainzer et al. in this volume). They also assumed the bodies were either monolithic asteroids or rubble piles, with the fragment SFDs derived from *Durda et al.* (2007) and *Benavidez et al.* (2012), respectively. Their model also allows for dynamical depletion due to the Yarkovsky effect.

*Cibulková et al.* (2014) found a number of intriguing results. First, treating all asteroids as weak rubble piles as defined by *Benavidez et al.* (2012) led to SFDs that are too shallow below  $D < 10$  km, as well as a factor of 2 more large families produced than are observed. This does not necessarily mean that asteroids are not rubble piles; an alternative would be that their disruption law is close to that derived for monolithic objects. New models of how porous rubble-pile asteroids break up suggest this may be the most likely answer (see the chapter by Jutzi et al. in this volume). Second, *Cibulková et al.* (2014) also found that individual breakups are unlikely to change the SFDs of the regions they investigated because small fragments, while numerous, were

quickly destroyed on a  $\sim 100$ -m.y. timescale. This is consistent with the main belt staying close to an equilibrium state.

Finally, even at the current limit of observational completeness (3 to 6 km, depending on the main belt zone), the frequency of collisions becomes comparable to the dynamical removal of bodies by the Yarkovsky effect and major mean-motion resonances (*Bottke et al.*, 2005a,b) or rotational disruption induced by the YORP effect (*Jacobsen et al.*, 2014). Regarding the former effect, removal rates used by *Bottke et al.* (2005b) or those in *Cibulková et al.* (2014) seem to be compatible with observations, namely the observed SFDs of main-belt asteroids and NEAs. The same may also be true for the latter process, although this will need to be examined in greater detail with the implications of *Statler* (2009) included. At this time, it is not clear which process dominates.

#### 4.6. Connections Between Asteroid Families and Meteorites

One of the most perplexing issues involving meteorite delivery concerns the fact that we currently have many tens of thousands of meteorites in worldwide collections, yet this population could represent as few as  $\sim 100$  different asteroid parent bodies:  $\sim 27$  chondritic,  $\sim 2$  primitive achondritic,  $\sim 6$  differentiated achondritic,  $\sim 4$  stony-iron,  $\sim 10$  iron groups, and  $\sim 50$  ungrouped irons (e.g., *Burbine et al.*, 2002). If we remove the stony-iron, iron, and differentiated meteorites,

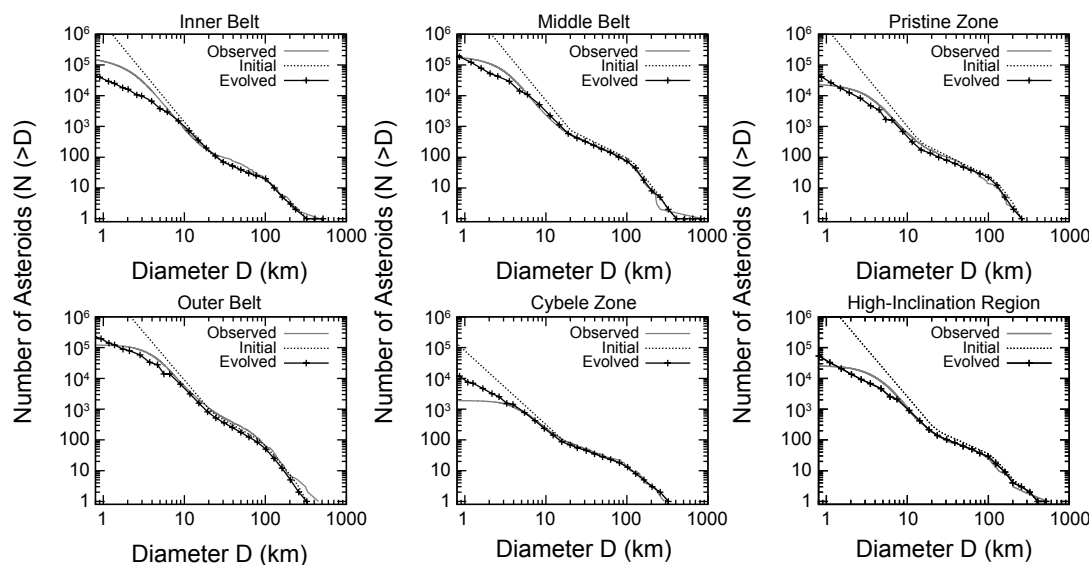


**Fig. 9.** Observed size-frequency distributions (gray lines) for six parts of the main belt compared to simulated initial (dashed) and final SFDs (black), after 4 G.y. of collisional evolution. This particular simulation shows the best-fit model out of more than 200,000 models started with various initial conditions. We assumed the scaling law of *Benz and Asphaug* (1999) and a monolithic structure of bodies. The largest differences can be seen for the inner and outer belt; they can be attributed to a dynamical removal of small bodies ( $D < 0.1$  km) caused by the Yarkovsky effect, which then cannot serve as projectiles for larger bodies ( $\approx 1$  km). Note that it is not easy to improve these results (e.g., by increasing the normalization of the outer belt; this would feed back and affect the other subpopulations). Figure adapted from *Cibulková et al.* (2014).

this number is reduced to as few as  $\sim 30$  parent bodies. This large difference in numbers is even more puzzling given current meteorite delivery scenarios, where nearly any small main-belt fragment can potentially reach a resonance capable of taking it into the terrestrial planet region via the Yarkovsky effect (see the chapter by Vokrouhlický et al. in this volume). Presumably, this would suggest that our meteorite collections should have samples from thousands upon thousands of distinct parent bodies.

An important missing component here is information on how collisional evolution has shaped meteorite delivery in the asteroid belt. Using the models discussed above, it is useful to apply what we have learned to the issue of stony meteoroid production, evolution, and delivery to Earth. First, one can consider what happens when a body undergoes a cratering or catastrophic disruption event. A fragment SFD is created ranging from meteoroid-sized bodies all the way to multi-kilometer-sized asteroids (or more). Subsequent collisions onto bodies in the SFD act as a source for new meteoroids that are genetically the same as those created in the previous generation. This collisional cascade guarantees that some meteoroids from this family, representing a single parent body, will be provided to the main-belt population, resonances, and possibly to Earth for an extended interval. At the same time, dynamical processes and collisions onto the newly created meteoroids act as a sink to eliminate them from the main belt.

An example of this process is shown in Fig. 10. It shows what happens when fragment SFDs produced by  $D = 30$ -km and 100-km parent bodies are placed in the main belt

$\sim 3.1$  G.y. ago. For fragments derived from the 30-km body, the initial meteoroid population (i.e., the population of meter-sized bodies) drops by a factor of 100 and  $10^5$  within 130 m.y. and within 3.1 G.y., respectively. Thus, meteoroid production by  $D < 30$ -km parent bodies decays away so quickly that breakup events of this size from billions of years ago are unlikely to deliver meaningful numbers of meteoroids to Earth today. For the 100-km parent body, the decay rate is significantly slower, with the meteoroid population only dropping by a factor of 100 over 2–3 G.y. This suggests that many meteoroids reaching Earth today could come from prominent asteroid families with sizable SFDs, even if those families were created billions of years ago.

Bottke et al. (2005c) used these ideas to estimate how many stony meteorite classes should be in our collection. They did this by computing the meteoroid decay rates taken from different parent body sizes (Fig. 11) and combining them with the estimated production rates of asteroid families over the last  $\sim 4$  G.y. This calculation made many simplifying assumptions: (1) meteoroids from all parts of the main belt have an equal chance of reaching Earth, (2) all  $D > 30$ -km asteroids disrupted over the last several billion years have the capability of producing a distinct class of meteorites, and (3) once a family's meteoroid production rate drops by a factor of 100, an arbitrary choice, it was unlikely to produce enough terrestrial meteorites to be noticed in our collection.

They found that asteroid families produced by the breakup of  $D > 100$ -km bodies have such slow meteoroid decay rates that most should be providing some meteoroids today, regardless of their disruption time over the last 3 G.y. Among the

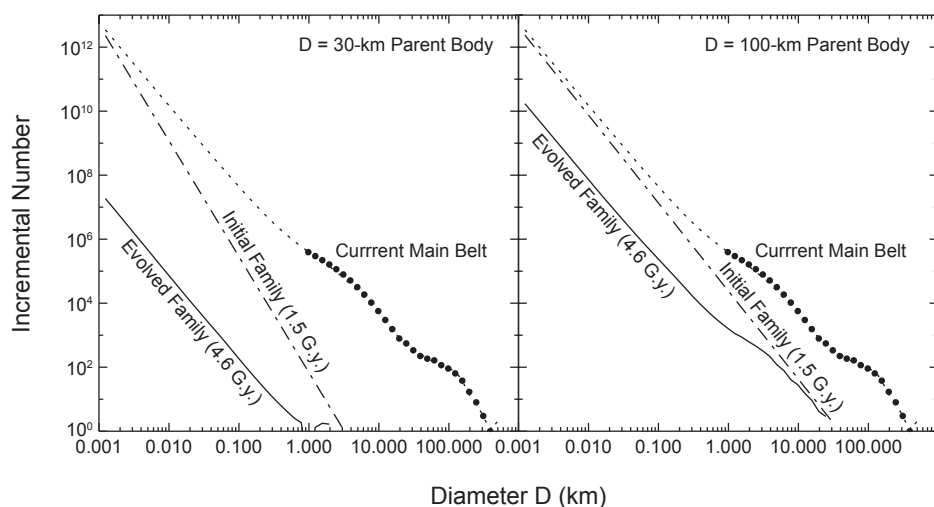


**Fig. 10.** The collisional and dynamical evolution of two asteroid families with simple fragment SFDs produced by the disruption of  $D = 30$ - and 100-km parent bodies (Bottke et al., 2005c). Both were inserted into the collision evolution model at 1.5 G.y. after solar system formation. The meteoroid population is represented by the number of bodies in the  $D \sim 0.001$ -km size bin. The solid lines show the families at present (4.6 G.y.). The smaller family has decayed significantly more than the larger family. Note the shallow slope of the  $D = 100$ -km family for  $0.7 \leq D \leq 5$  km. This shape mimics that of the background main-belt population over the same size range.

smaller parent bodies ( $30 < D < 100$  km), they found that, on average, the interval between disruption events across the main belt was short enough that many have disrupted over the last billion years or so, enough to provide some meteoroids as well. They did not examine large cratering events, such as the Rheasilvia formation event on Vesta, but presumably they would factor into this as well, with the biggest events acting like the disruption of a sizable parent body.

Overall, they found that stony meteorites were plausibly coming from  $\sim 45$  different parent bodies. This value is fairly close to the actual value of  $\sim 30$  parent bodies. A few reasons that the model estimate may be on the high side include (1) some disruption events must occur within existing families, so no unique meteorite class would be created; (2) some outer main-belt meteoroids may have great difficulty reaching Earth because they only have access to resonances that are orders of magnitude less efficient at delivering meteoroids to Earth than inner-main-belt resonances (Gladman *et al.*, 1997; Bottke *et al.*, 2006); and (3) we have not factored in the different fragment SFD actual families can have. We conclude that most stony meteorites are byproducts of a collisional cascade, with some coming from asteroid families produced by the breakup of  $D > 100$ -km bodies over the last several billion years and the remainder coming from smaller, more recent breakup events among  $D < 100$ -km asteroids that occurred over recent times (i.e.,  $\ll 1$  G.y.).

#### 4.7. Cometary Impacts on Main-Belt Asteroids During the Late Heavy Bombardment

An interesting quandary comes from the predicted bombardment of comets on main-belt asteroids during the Nice model (see the chapter by Morbidelli *et al.* in this volume). Ac-

cording to Brož *et al.* (2013), a massive  $25 M_{\oplus}$  disk of transneptunian comets might contain  $10^{12}$   $D > 1$ -km comets. Using numerical simulations of Vokrouhlický *et al.* (2008), they estimated the collision probabilities and impact velocities for a comet hitting main-belt asteroids to be  $P_i \sim 6 \times 10^{-18} \text{ km}^{-2} \text{ yr}^{-1}$  and  $V_{\text{imp}} \sim 10 \text{ km s}^{-1}$ . Coupled with models describing the loss of asteroids during resonance sweeping (Minton and Malhotra, 2010), they estimated that the LHB could potentially disrupt more than 100 parent bodies with  $D_{\text{PB}} > 100$  km, depending on the assumptions made (Fig. 12).

These values would violate many of the constraints provided in section 3, and they present an intriguing challenge to the main tenets of the Nice model. One option here would be to reject the Nice model altogether, although this would also mean giving up the successes it has had in explaining various solar system attributes (see the chapter by Morbidelli *et al.* in this volume).

The other possibility is that there are aspects of the Nice model or our collision models that need revision. For example, the disk of transneptunian comets may have different initial conditions and/or evolution properties than have been previously assumed, such that the collision probabilities between comets and asteroids are lower than expected (D. Nesvorný, personal communication). It is also possible that numerous transneptunian comets disrupt when they enter the inner solar system (e.g., Levison *et al.*, 2001), with possible mechanisms being volatile pressure buildup, amorphous/crystalline phase transitions, spinup by jets, etc. Brož *et al.* (2013) examined this possibility by arbitrarily assuming that all comets disrupt at perihelion distance,  $q_{\text{crit}} < 1.5$  AU. On average, this led to the correct number of catastrophic disruptions for  $D_{\text{PB}} = 200$ – $400$ -km bodies, but it still pro-

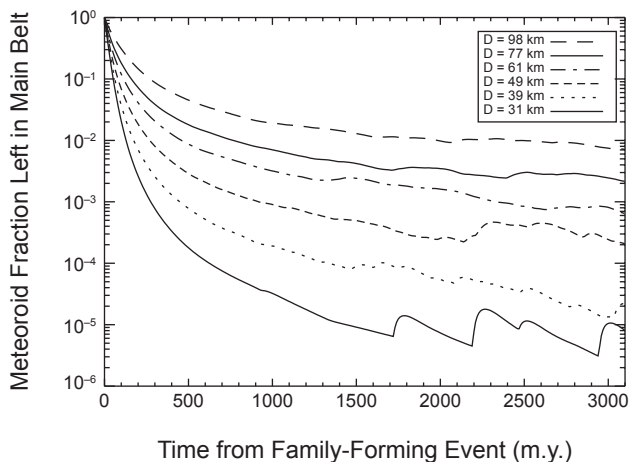


**Fig. 11.** Decay rates of meteoroid populations from asteroid families with simple power-law fragment SFD produced from parent bodies between  $30 < D < 100$  km. All families were inserted in the collisional model at 3.1 G.y. ago. The meteoroid population in the smallest families decrease by a factor of 100 over a few 0.1 G.y. while the largest take several gigayears to decay by the same factor.

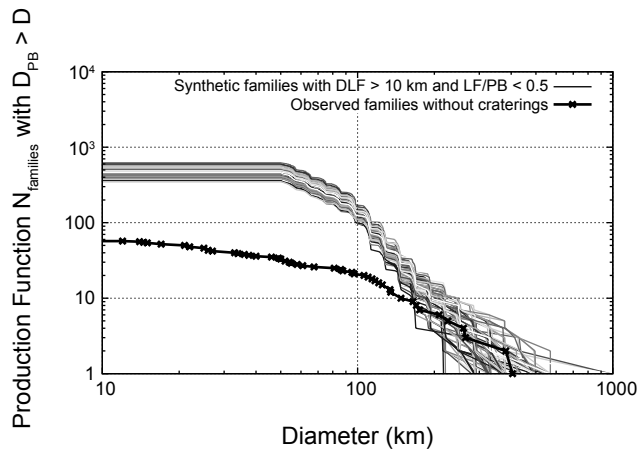


**Fig. 12.** The outcomes of the bombardment of the main asteroid belt by transneptunian comets, as modeled by Brož *et al.* (2013). The plot shows the family production functions [i.e., the cumulative number  $N_{\text{fam}}(>D)$  of families with parent-body size  $D_{\text{PB}}$  larger than  $D$ ] and a comparison to the observed one. Here we show 100 individual simulations (differing only by random-seed values) using different grayscale colors.

duced a factor of 2–3 more disruptions for  $D_{PB} \approx 100$ -km bodies than observed. It is possible that this excess could be removed by subsequent collisional and dynamical evolution. All these values assume, of course, that collisions between low-density porous comets and asteroids are understood, when in reality no hydrocode simulations have ever been run using this set up. Finally, it could be that the main belt can accommodate more early collisions than predicted here. The constraints we have on the early era are extremely limited. All these topics remain exciting areas for future research.

## 5. CONCLUSIONS

Considerable progress has been made over the last several decades in interpreting how the main belt reached its current state by collisional and dynamical evolution, but there is still much work to do. At this time, no model has yet included all the important processes affecting asteroid evolution. Even after this accomplished, these models will still have to be successfully tested against all the known constraints, including new ones that are discussed in other chapters. Still, it is fair to say that many existing models have done a good job of matching the constraints discussed in section 3, and their predictions have made it possible to glean insights into how the main-belt population reached its current state (see section 4).

We expect that major advances will also come from the inclusion of new and better constraints that can help modelers rule out solutions. A few of the entries on our wish list for new data, beyond advances in the fields of planetesimal and planet formation, include (1) increased information on the main-belt population for  $D < 1$ -km bodies (e.g., albedos, colors, spectroscopy, sizes, etc.); (2) a substantiated chronology for lunar and terrestrial crater populations, with crater SFD information verified for a wide range of surface ages; (3) a thorough examination of the main belt for ghost families; (4) more information on small asteroids that enable better predictions of Yarkovsky drift rates and YORP torques for  $D < 1$ -km asteroids; (5) additional nonsaturated crater SFDs from asteroid surfaces; (6) more discoveries of very young families, enough that we convince ourselves we have a complete set for a given time period.

In regard to modeling work, the next major steps forward will probably come from next-generation codes that can track how asteroid populations move across the main belt via Yarkovsky/YORP forces while also undergoing comminution and YORP-driven mass shedding. This would allow the collisional cascade in the main belt to be treated as accurately as possible, from disruption all the way to the fragments reaching resonances. Additional information on asteroid collisions at all sizes from numerical hydrocode simulations would be extremely useful, as would laboratory and numerical experiments completed on a wide range of asteroid compositions and internal structures. This would allow new codes to accurately account for the varying  $Q_D^*$  functions and fragment SFDs that asteroid families of different composition might have.

Finally, it is imperative that collisional models employ the best estimates of how the main-belt and external small-body populations have dynamically evolved with time. The history of our solar system is etched into the main-belt population in enumerable ways, and the only way to read these markings and tell the story of our home is to unite models of collisional and dynamical evolution from the formation of the first solids all the way to the present day.

**Acknowledgments.** We thank reviewers E. Asphaug and F. Marzari for their helpful and constructive comments. Research funds for W.F.B. and S.M. were provided by NASA's Solar System Evolution Research Virtual Institute (SSERVI) as part of the Institute for the Science of Exploration Targets (ISET) at the Southwest Research Institute (NASA grant no. NNA14AB03A). The work of M.B. was supported by the Czech Grant Agency (grant no. P209-12-01308S).

## REFERENCES

- Anders E. (1965) Fragmentation history of asteroids. *Icarus*, 4, 399–408.
- Asphaug E. (1997) Impact origin of the Vesta family. *Meteoritics & Planet. Sci.*, 32, 965–980.
- Asphaug E., Ryan E. V., and Zuber M. T. (2002) Asteroid interiors. In *Asteroids III* (W. F. Bottke Jr. et al., eds.), pp. 463–484. Univ. of Arizona, Tucson.
- Ballouz R.-L., Richardson D. C., Michel P., and Schwartz S. R. (2014) Rotation-dependent catastrophic disruption of gravitational aggregates. *Astrophys. J.*, 789, 158.
- Benavidez P. G., Durda D. D., Enke B. L., Bottke W. F., Nesvorný D., Richardson D. C., Asphaug E., and Merline W. J. (2012) A comparison between rubble-pile and monolithic targets in impact simulations: Application to asteroid satellites and family size distributions. *Icarus*, 219, 57–76.
- Benz W. and Asphaug E. (1999) Catastrophic disruptions revisited. *Icarus*, 142, 5–20.
- Bottke W. F. and Chapman C. R. (2006) Determining the main belt size distribution using asteroid crater records and crater saturation models. *Lunar Planet. Sci. XXXVII*, Abstract #1349. Lunar and Planetary Institute, Houston.
- Bottke W. F., Nolan M. C., Greenberg R., and Kolvord R. A. (1994) Velocity distributions among colliding asteroids. *Icarus*, 107, 255–268.
- Bottke W. F., Durda D. D., Nesvorný D., Jedicke R., Morbidelli A., Vokrouhlický D., and Levison H. (2005a) The fossilized size distribution of the main asteroid belt. *Icarus*, 175, 111–140.
- Bottke W. F., Durda D. D., Nesvorný D., Jedicke R., Morbidelli A., Vokrouhlický D., and Levison H. F. (2005b) Linking the collisional history of the main asteroid belt to its dynamical excitation and depletion. *Icarus*, 179, 63–94.
- Bottke W. F., Durda D. D., Nesvorný D., Jedicke R., Morbidelli A., Vokrouhlický D., and Levison H. F. (2005c) The origin and evolution of stony meteorites. In *Dynamics of Populations of Planetary Systems* (Z. Knežević and A. Milani, eds.), pp. 357–374. Cambridge Univ., Cambridge.
- Bottke W. F., Nesvorný D., Grimm R. E., Morbidelli A., and O'Brien D. P. (2006) Iron meteorites as remnants of planetesimals formed in the terrestrial planet region. *Nature*, 439, 821–824.
- Bottke W. F., Levison H. F., Nesvorný D., and Dones L. (2007) Can planetesimals left over from terrestrial planet formation produce the lunar late heavy bombardment? *Icarus*, 190, 203–223.
- Bottke W. F., Vokrouhlický D., Minton D., Nesvorný D., Morbidelli A., Brasser R., Simonson B., and Levison H. F. (2012) An Archaean heavy bombardment from a destabilized extension of the asteroid belt. *Nature*, 485, 78–81.
- Bottke W. F. et al. (2015a) In search of the source of asteroid (101955) Bennu: Applications of the stochastic YORP model. *Icarus*, 247, 191–271.
- Bottke W. F., Vokrouhlický D., Marchi S., Swindle T., Scott E. R. D., Weirich J., and Levison H. (2015b) Dating the Moon-forming impact event with asteroidal meteorites. *Science*, 348, 321–323.

- Brasser R., Morbidelli A., Gomes R., Tsiganis K., and Levison H. F. (2009) Constructing the secular architecture of the solar system II: The terrestrial planets. *Astron. Astrophys.*, 507, 1053–1065.
- Britt D. T., Yeomans D., Housen K., and Consolmagno G. (2002) Asteroid density, porosity, and structure. In *Asteroids III* (W. F. Bottke Jr. et al., eds.), pp. 485–500. Univ. of Arizona, Tucson.
- Brown P. G., et al. (2013) A 500-kiloton airburst over Chelyabinsk and an enhanced hazard from small impactors. *Nature*, 503, 238–241.
- Brož M., Morbidelli A., Bottke W. F., Rozehnal J., Vokrouhlický D., and Nesvorný D. (2013) Constraining the cometary flux through the asteroid belt during the late heavy bombardment. *Astron. Astrophys.*, 551, A117.
- Buczkowski D. L. et al. (2012) Large-scale troughs on Vesta: A signature of planetary tectonics. *Geophys. Res. Lett.*, 39, L18205.
- Burbine T. H., McCoy T. J., Meibom A., Gladman B., and Keil K. (2002) Meteoritic parent bodies: Their number and identification. In *Asteroids III* (W. F. Bottke Jr. et al., eds.), pp. 653–667. Univ. of Arizona, Tucson.
- Carruba V., Burns J. A., Bottke W., and Nesvorný D. (2003) Orbital evolution of the Gefion and Adeona asteroid families: Close encounters with massive asteroids and the Yarkovsky effect. *Icarus*, 162, 308–327.
- Carruba V., Huaman M., Domingos R. C., and Roig F. (2013) Chaotic diffusion caused by close encounters with several massive asteroids. II. The regions of (10) Hygiea, (2) Pallas, and (31) Euphrosyne. *Astron. Astrophys.*, 550, A85.
- Campo Bagatin A., Cellino A., Davis D. R., Farinella P., and Paolicchi P. (1994) Wavy size distributions for collisional systems with a small-size cutoff. *Planet. Space Sci.*, 42, 1079–1092.
- Campo Bagatin A., Petit J.-M., and Farinella P. (2001) How many rubble piles are in the asteroid belt? *Icarus*, 149, 198–209.
- Cibulková H., Brož M., and Benavidez P. G. (2014) A six-part collisional model of the main asteroid belt. *Icarus*, 241, 358–372.
- Cotto-Figueroa D. (2013) Radiation recoil effects on the dynamical evolution of asteroids. Ph.D. thesis, Ohio University, Athens, Ohio.
- Cotto-Figueroa D., Statler T. S., Richardson D. C., and Tanga P. (2015) Coupled spin and shape evolution of small rubble-pile asteroids: Self-limitation of the YORP effect. *Astrophys. J.*, 803, 25.
- Chambers J. E. and Wetherill G. W. (1998) Making the terrestrial planets: N-body integrations of planetary embryos in three dimensions. *Icarus*, 136, 304–327.
- Chambers J. E. and Wetherill G. W. (2001) Planets in the asteroid belt. *Meteoritics & Planet. Sci.*, 36, 381–399.
- Dale C. W., Burton K. W., Greenwood R. C., Gannoun A., Wade J., Wood B. J., and Pearson D. G. (2012) Late accretion on the earliest planetesimals revealed by the highly siderophile elements. *Science*, 336, 72–75.
- Davison T. M., O'Brien D. P., Ciesla F. J., and Collins G. S. (2013) The early impact histories of meteorite parent bodies. *Meteoritics & Planet. Sci.*, 48, 1894–1918.
- Davis D. R., Chapman C. R., Greenberg R., Weidenschilling S. J., and Harris A. W. (1979) Collisional evolution of asteroids — populations, rotations, and velocities. In *Asteroids* (T. Gehrels, ed.), pp. 528–557. Univ. of Arizona, Tucson.
- Davis D. R., Chapman C. R., Weidenschilling S. J., and Greenberg R. (1985) Collisional history of asteroids: Evidence from Vesta and the Hirayama families. *Icarus*, 63, 30–53.
- Davis D. R., Weidenschilling S. J., Farinella P., Paolicchi P., and Binzel R. P. (1989) Asteroid collisional history — effects on sizes and spins. In *Asteroids II* (R. P. Binzel et al., eds.), pp. 805–826. Univ. of Arizona, Tucson.
- Davis D. R., Durda D. D., Marzari F., Campo Bagatin A., and Gil-Hutton R. (2002) Collisional evolution of small body populations. In *Asteroids III* (W. F. Bottke Jr. et al., eds.), pp. 545–558. Univ. of Arizona, Tucson.
- Dell'Oro A. and Paolicchi P. (1998) Statistical properties of encounters among asteroids: A new, general purpose, formalism. *Icarus*, 136, 328–339.
- Dohnanyi J. W. (1969) Collisional models of asteroids and their debris. *J. Geophys. Res.*, 74, 2531–2554.
- Durda D. D. and Dermott S. F. (1997) The collisional evolution of the asteroid belt and its contribution to the zodiacal cloud. *Icarus*, 130, 140–164.
- Durda D. D., Greenberg R., and Jedicke R. (1998) Collisional models and scaling laws: A new interpretation of the shape of the main-belt asteroid size distribution. *Icarus*, 135, 431–440.
- Durda D. D., Bottke W. F., Enke B. L., Merline W. J., Asphaug E., Richardson D. C., and Leinhardt Z. M. (2004) The formation of asteroid satellites in large impacts: Results from numerical simulations. *Icarus*, 170, 243–257.
- Durda D. D. et al. (2007) Size-frequency distributions of fragments from SPH/N-body simulations of asteroid impacts: Comparison with observed asteroid families. *Icarus*, 186, 498–516.
- Eugster O. (2003) Cosmic-ray exposure ages of meteorites and lunar rocks and their significance. *Chem. Erde*, 63, 3–30.
- Farinella P. and Davis D. R. (1992) Collision rates and impact velocities in the main asteroid belt. *Icarus*, 97, 111–123.
- Farinella P., Davis D. R., Paolicchi P., Cellino A., and Zappala V. (1992) Asteroid collisional evolution — an integrated model for the evolution of asteroid rotation rates. *Astron. Astrophys.*, 253, 604–614.
- Fowler J. W. and Chillemi J. R. (1992) IRAS asteroid data processing. In *The IRAS Minor Planet Survey* (E. F. Tedesco, ed.), pp. 17–43. Tech. Report PL-TR-92-2049, Phillips Laboratory, Hanscom Air Force Base, Massachusetts.
- Golubov O. and Krugly Y. N. (2012) Tangential component of the YORP effect. *Astrophys. J. Lett.*, 752, L11.
- Golubov O., Scheeres D. J., and Krugly Y. N. (2014) A three-dimensional model of tangential YORP. *Astrophys. J.*, 794, 22.
- Gomes R., Levison H. F., Tsiganis K., and Morbidelli A. (2005) Origin of the cataclysmic late heavy bombardment period of the terrestrial planets. *Nature*, 435, 466–469.
- Gladman B. J., Migliorini F., Morbidelli A., Zappala V., Michel P., Cellino A., Froeschle C., Levison H. F., Bailey M., and Duncan M. (1997) Dynamical lifetimes of objects injected into asteroid belt resonances. *Science*, 277, 197–201.
- Gladman B. J. et al. (2009) On the asteroid belt's orbital and size distribution. *Icarus*, 202, 104–118.
- Hanuš J. et al. (2013) Asteroids' physical models from combined dense and sparse photometry and scaling of the YORP effect by the observed obliquity distribution. *Astron. Astrophys.*, 551, A67.
- Hartmann W. K. and Hartmann A. C. (1968) Asteroid collisions and evolution of asteroidal mass distribution and meteoritic flux. *Icarus*, 8, 361–381.
- Hiesinger H., van der Bogert C. H., Pasckert J. H., Funcke L., Giacomini L., Ostrach L. R., and Robinson M. S. (2012) How old are young lunar craters? *J. Geophys. Res.—Planets*, 117, E00H10.
- Holsapple K., Giblin I., Housen K., Nakamura A., and Ryan E. (2002) Asteroid impacts: Laboratory experiments and scaling laws. In *Asteroids III* (W. F. Bottke Jr. et al., eds.), pp. 443–462. Univ. of Arizona, Tucson.
- Housen K. (2009) Cumulative damage in strength-dominated collisions of rocky asteroids: Rubble piles and brick piles. *Planet. Space Sci.*, 57, 142–153.
- Ivezic Ž. et al. (2001) Solar system objects observed in the Sloan digital sky survey commissioning data. *Astron. J.*, 122, 2749–2784.
- Ivanov B. A., Neukum G., Bottke W. F., and Hartmann W. K. (2002) The comparison of size-frequency distributions of impact craters and asteroids and the planetary cratering rate. In *Asteroids III* (W. F. Bottke Jr. et al., eds.), pp. 90–101. Univ. of Arizona, Tucson.
- Jacobson S. A., Marzari F., Rossi A., Scheeres D. J., and Davis D. R. (2014) Effect of rotational disruption on the size frequency distribution of the main belt asteroid population. *Mon. Not. R. Astron. Soc.*, 439, L95–L99.
- Jaumann R. et al. (2012) Vesta's shape and morphology. *Science*, 336, 687–690.
- Jedicke R., Larsen J., and Spahr T. (2002) Observational selection effects in asteroid surveys. In *Asteroids III* (W. F. Bottke Jr. et al., eds.), pp. 71–88. Univ. of Arizona, Tucson.
- Jutzi M., Asphaug E., Gillet P., Barrat J.-A., and Benz W. (2013) The structure of the asteroid 4 Vesta as revealed by models of planet-scale collisions. *Nature*, 494, 207–210.
- Kirchoff M. R., Chapman C. R., Marchi S., Curtis K. M., Enke B., and Bottke W. F. (2013) Ages of large lunar impact craters and implications for bombardment during the Moon's middle age. *Icarus*, 225, 325–341.

- Krasinsky G. A., Pitjeva E. V., Vasilyev M. V., and Yagudina E. I. (2002) Hidden mass in the asteroid belt. *Icarus*, **158**, 98–105.
- Kuchynka P. and Folkner W. M. (2013) A new approach to determining asteroid masses from planetary range measurements. *Icarus*, **222**, 243–253.
- Kuiper G. P., Fugita Y. F., Gehrels T., Groeneveld I., Kent J., van Biesbroeck G., and van Houten C. J. (1958) Survey of asteroids. *Astrophys. J. Suppl.*, **3**, 289.
- Leinhardt Z. M. and Stewart S. T. (2009) Full numerical simulations of catastrophic small body collisions. *Icarus*, **199**, 542–559.
- Leinhardt Z. M. and Stewart S. T. (2012) Collisions between gravity dominated bodies. I. Outcome regimes and scaling laws. *Astrophys. J.*, **745**, 79.
- Levison H. F., Dones L., Chapman C. R., Stern S. A., Duncan M. J., and Zahnle K. (2001) Could the lunar “late heavy bombardment” have been triggered by the formation of Uranus and Neptune? *Icarus*, **151**, 286–306.
- Levison H. F., Bottke W. F., Gounelle M., Morbidelli A., Nesvorný D., and Tsiganis K. (2009) Contamination of the asteroid belt by primordial trans-Neptunian objects. *Nature*, **460**, 364–366.
- Levison H. F., Kretke K. A., Walsh K., and Bottke W. F. (2015a) Growing the terrestrial planets from the slow accumulation of sub-meter-size objects. *Proc. Natl. Acad. Sci.*, in press.
- Levison H. F., Kretke K. A., and Duncan M. J. (2015b) Growing the gas giant planets from the slow accumulation of centimeter- to meter-size objects. *Nature*, **524**, 322–324.
- Love S. G. and Ahrens T. J. (1997) Origin of asteroid rotation rates in catastrophic impacts. *Nature*, **386**, 154–156.
- Manley S. P., Migliorini F., and Bailey M. E. (1998) An algorithm for determining collision probabilities between small solar system bodies. *Astronomy Astrophys. Suppl.*, **133**, 437–444.
- Marchi S., Mottola S., Cremonese G., Massironi M., and Martellato E. (2009) A new chronology for the Moon and Mercury. *Astron. J.*, **137**, 4936–4948.
- Marchi S. et al. (2012) The violent collisional history of asteroid 4 Vesta. *Science*, **336**, 690–693.
- Marchi S. et al. (2013) High-velocity collisions from the lunar cataclysm recorded in asteroidal meteorites. *Nature Geosci.*, **6**, 303–307.
- Marchi S. et al. (2014) Small crater populations on Vesta. *Planet. Space Sci.*, **103**, 96–103.
- Marzari F., Rossi A., and Scheeres D. J. (2011) Combined effect of YORP and collisions on the rotation rate of small main belt asteroids. *Icarus*, **214**, 622–631.
- Masiero J. et al. (2011) Main belt asteroids with WISE/NEOWISE I: Preliminary albedos and diameters. *Astrophys. J.*, **741**, 68.
- McEwen A. S., Moore J. M., and Shoemaker E. M. (1997) The phanerozoic impact cratering rate: Evidence from the far side of the Moon. *J. Geophys. Res.*, **102**, 9231–9242.
- Melosh H. J. (1989) *Impact Cratering: A Geologic Process*. Oxford Univ., New York. 253 pp.
- Merline W. J., Weidenschilling S. J., Durda D. D., Margot J. L., Pravec P., and Storrs A. D. (2002) Asteroids do have satellites. In *Asteroids III* (W. F. Bottke Jr. et al., eds.), pp. 289–312. Univ. of Arizona, Tucson.
- Minton D. A. and Malhotra R. (2009) A record of planet migration in the main asteroid belt. *Nature*, **457**, 1109–1111.
- Minton D. A. and Malhotra R. (2010) Dynamical erosion of the asteroid belt and implications for large impacts in the inner solar system. *Icarus*, **207**, 744–757.
- Minton D. A. and Malhotra R. (2011) Secular resonance sweeping of the main asteroid belt during planet migration. *Astrophys. J.*, **732**, 53.
- Morbidelli A. and Gladman B. (1998) Orbital and temporal distributions of meteorites originating in the asteroid belt. *Meteoritics & Planet. Sci.*, **33**, 999–1016.
- Morbidelli A. and Vokrouhlický D. (2003) The Yarkovsky-driven origin of near-Earth asteroids. *Icarus*, **163**, 120–134.
- Morbidelli A., Bottke W. F., Nesvorný D., and Levison H. F. (2009) Asteroids were born big. *Icarus*, **204**, 558–573.
- Morbidelli A., Brasser R., Gomes R., Levison H. F., and Tsiganis K. (2010) Evidence from the asteroid belt for a violent past evolution of Jupiter’s orbit. *Astron. J.*, **140**, 1391–1401.
- Morbidelli A., Marchi S., Bottke W. F., and Kring D. A. (2012) A sawtooth-like timeline for the first billion years of lunar bombardment. *Earth Planet. Sci. Lett.*, **355**, 144–151.
- Nesvorný D. (2011) Young solar system’s fifth giant planet? *Astrophys. J. Lett.*, **742**, L22.
- Nesvorný D. and Bottke W. F. (2004) Detection of the Yarkovsky effect for main-belt asteroids. *Icarus*, **170**, 324–342.
- Nesvorný D. and Morbidelli A. (2012) Statistical study of the early solar system’s instability with four, five, and six giant planets. *Astron. J.*, **144**, 117.
- Nesvorný D., Morbidelli A., Vokrouhlický D., Bottke W. F., and Brož M. (2002) The Flora family: A case of the dynamically dispersed collisional swarm? *Icarus*, **157**, 155–172.
- Nesvorný D., Bottke W. F., Levison H., and Dones L. (2003) Recent origin of the solar system dust bands. *Astrophys. J.*, **591**, 486–497.
- Nesvorný D., Roig F., Gladman B., Lazzaro D., Carruba V., and Mothé-Diniz T. (2008) Fugitives from the Vesta family. *Icarus*, **193**, 85–95.
- Novaković B., Dell’Oro A., Cellino A., and Knežević Z. (2012) Recent collisional jet from a primitive asteroid. *Mon. Not. R. Astron. Soc.*, **425**, 338–346.
- Novaković B., Hsieh H. H., Cellino A., Micheli M., and Pedani M. (2014) Discovery of a young asteroid cluster associated with P/2012 F5 (Gibbs). *Icarus*, **231**, 300–309.
- O’Brien D. P. (2009) The Yarkovsky effect is not responsible for small crater depletion on Eros and Itokawa. *Icarus*, **203**, 112–118.
- O’Brien D. P. and Greenberg R. (2003) Steady-state size distributions for collisional populations: Analytical solution with size dependent strength. *Icarus*, **164**, 334–345.
- O’Brien D. P. and Greenberg R. (2005) The collisional and dynamical evolution of the main-belt and NEA size distributions. *Icarus*, **178**, 179–212.
- O’Brien D. P., Morbidelli A., and Levison H. F. (2006) Terrestrial planet formation with strong dynamical friction. *Icarus*, **184**, 39–58.
- O’Brien D. P., Morbidelli A., and Bottke W. F. (2007) The primordial excitation and clearing of the asteroid belt — revisited. *Icarus*, **191**, 43–452.
- Öpik E. J. (1951) Collision probability with the planets and the distribution of planetary matter. *Proc. R. Irish Acad.*, **54**, 165–199.
- Parker A., Ivezić Ž., Jurić M., Lupton R., Sekora M. D., and Kowalski A. (2008) The size distributions of asteroid families in the SDSS Moving Object Catalog 4. *Icarus*, **198**, 138–155.
- Penco U., Dell’Oro A., Paolicchi P., Campo Bagatin A., La Spina A., and Cellino A. (2004) Yarkovsky depletion and asteroid collisional evolution. *Planet. Space Sci.*, **52**, 1087–1091.
- Petit J. M. and Farinella P. (1993) Modelling the outcomes of high-velocity impacts between small solar system bodies. *Cel. Mech. Dyn. Astron.*, **57**, 1–28.
- Petit J., Chambers J., Franklin F., and Nagasawa M. (2002) Primordial excitation and depletion of the main belt. In *Asteroids III* (W. F. Bottke Jr. et al., eds.), pp. 711–738. Univ. of Arizona, Tucson.
- Pravec P., Harris A. W., and Michalowski T. (2002) Asteroid rotations. In *Asteroids III* (W. F. Bottke Jr. et al., eds.), pp. 113–122. Univ. of Arizona, Tucson.
- Rabinowitz D. L., Helin E., Lawrence K., and Pravdo S. (2000) A reduced estimate of the number of kilometre-sized near-Earth asteroids. *Nature*, **403**, 165–166.
- Robbins S. J. (2014) New crater calibrations for the lunar craterage chronology. *Earth Planet. Sci. Lett.*, **403**, 188–198.
- Rozitis B. and Green S. F. (2012) The influence of rough surface thermal-infrared beaming on the Yarkovsky and YORP effects. *Mon. Not. R. Astron. Soc.*, **423**, 367–388.
- Ryder G., Bogard D., and Garrison D. (1991) Probable age of Autolycus and calibration of lunar stratigraphy. *Geology*, **19**, 143–146.
- Schenk P. et al. (2012) The geologically recent giant impact basins at Vesta’s south pole. *Science*, **336**, 694–697.
- Slivan S. M. (2002) Spin vector alignment of Koronis family asteroids. *Nature*, **419**, 49–51.
- Slivan S. M. and Molnar L. A. (2012) Spin vectors in the Koronis family: III. (832) Karin. *Icarus*, **220**, 1097–1103.
- Slivan S. M., Binzel R. P., Crespo da Silva L. D., Kaasalainen M., Lyndaker M. M., and Krčo M. (2003) Spin vectors in the Koronis family: Comprehensive results from two independent analyses of 213 rotation light curves. *Icarus*, **162**, 285–307.

- Silivani S. M., Binzel R. P., Kaasalainen M., Hock A. N., Klesman A. J., Eckelman L. J., and Stephens R. D. (2009) Spin vectors in the Koronis family. II. Additional clustered spins, and one stray. *Icarus*, 200, 514–530.
- Statler T. S. (2009) Extreme sensitivity of the YORP effect to small-scale topography. *Icarus*, 202, 502–513.
- Stöffler D. and Ryder G. (2001) Stratigraphy and isotope ages of lunar geologic units: Chronological standard for the inner solar system. *Space Sci. Rev.*, 96, 9–54.
- Stokes G. H., Yeomans D. K., Bottke W. F., Chesley S. R., Evans J. B., Gold R. E., Harris A. W., Jewitt D., Kelso T. S., McMillan R. S., Spahr T. B., and Worden S. P. (2003) *Report of the Near-Earth Object Science Definition Team: A Study to Determine the Feasibility of Extending the Search for Near-Earth Objects to Smaller Limiting Diameters*. NASA OSS-Solar System Exploration Division, Washington, DC.
- Somenzi L., Fienga A., Laskar J., and Kuchynka P. (2010) Determination of asteroid masses from their close encounters with Mars. *Planet. Space Sci.*, 58, 858–863.
- Tanaka H., Inaba S., and Nakazawa K. (1996) Steady-state size distribution for the self-similar collision cascade. *Icarus*, 123, 450–455.
- Turri D., Magni G., and Coradini A. (2011) Probing the history of solar system through the cratering records on Vesta and Ceres. *Mon. Not. R. Astron. Soc.*, 413, 2439–2466.
- Turri D., Coradini A., and Magni G. (2012) Jovian early bombardment: Planetesimal erosion in the inner asteroid belt. *Astrophys. J.*, 750, 8.
- Vedder J. D. (1998) Main belt asteroid collision probabilities and impact velocities. *Icarus*, 131, 283–290.
- Vokrouhlický D., Nesvorný D., and Bottke W. F. (2003) The vector alignments of asteroid spins by thermal torques. *Nature*, 425, 147–151.
- Vokrouhlický D., Nesvorný D., and Levison H. F. (2008) Irregular satellite capture by exchange reactions. *Astron. J.*, 136, 1463–1476.
- Walsh K. J., Morbidelli A., Raymond S. N., O'Brien D. P., and Mandell A. M. (2011) A low mass for Mars from Jupiter's early gas-driven migration. *Nature*, 475, 206–209.
- Weidenschilling S. J. (1977) The distribution of mass in the planetary system and solar nebula. *Astrophys. Space Sci.*, 51, 153–158.
- Wetherill G. W. (1967) Collisions in the asteroid belt. *J. Geophys. Res.*, 72, 2429–2444.
- Wilhelms D. E. (1987) *The Geologic History of the Moon*. U.S. Geol. Surv. Prof. Paper 1348, 302 pp. Available online at <http://ser.sese.asu.edu/GHM/>.
- Wilhelms D. E., Oberbeck V. R., and Aggarwal H. R. (1978) Size-frequency distributions of primary and secondary lunar impact craters. *Lunar Planet. Sci. IX*, pp. 1256–1258. Lunar and Planetary Institute, Houston.
- Williams D. R. and Wetherill G. W. (1994) Size distribution of collisionally evolved asteroidal populations — analytical solution for self-similar collision cascades. *Icarus*, 107, 117–125.

# Cratering on Asteroids

**Simone Marchi and Clark R. Chapman**  
*Southwest Research Institute*

**Olivier S. Barnouin**  
*The Johns Hopkins University Applied Physics Laboratory*

**James E. Richardson**  
*Arecibo Observatory*

**Jean-Baptiste Vincent**  
*Max-Planck Institute for Solar System Research*

---

Impact craters are a ubiquitous feature of asteroid surfaces. On a local scale, small craters puncture the surface in a way similar to that observed on terrestrial planets and the Moon. At the opposite extreme, larger craters often approach the physical size of asteroids, thus globally affecting their shapes and surface properties. Crater measurements are a powerful means of investigation. Crater spatial and size distributions inform us of fundamental processes, such as asteroid collisional history. A paucity of craters, sometimes observed, may be diagnostic of mechanisms of erasure that are unique on low-gravity asteroids. Byproducts of impacts, such as ridges, troughs, and blocks, inform us of the bulk structure. In this chapter we review the major properties of crater populations on asteroids visited by spacecraft. In doing so we provide key examples to illustrate how craters affect the overall shape and can be used to constrain asteroid surface ages, bulk properties, and impact-driven surface evolution.

## 1. INTRODUCTION

Until the space age, craters had only been observed on a single astronomical body, the Moon. It was only with the analysis of the first lunar samples, however, that it finally became clear that the vast majority of lunar craters (and a recognizable minority of terrestrial craters) were caused by cosmic impacts and were not generally of volcanic or other endogenic origin (e.g., Wilhelms, 1993). Three decades later, when the Galileo spacecraft flew past (951) Gaspra, then a few years later past (243) Ida, craters were found on asteroids. During the subsequent two decades, spacecraft flybys and dedicated orbital missions have recorded crater populations on many additional asteroids.

While hypervelocity impact by asteroids and comets or by their debris will produce impact craters on any solar system body with a solid surface, there is a fundamental difference between craters on small bodies and those on larger planets and satellites: Instead of cratering on semi-infinite surfaces, asteroidal cratering occurs on smaller bodies generally with minimal gravity. So the ejecta from an impact explosion travel far and often escape into independent orbits around the Sun, becoming individual small asteroids.

Collisional fragmentation and cratering are major evolutionary processes for asteroids since the earliest epochs of solar system history and learning about the visible record of surficial cratering can provide vital clues about their evolution and interactions with the space environment. Cratered terrains provide snapshots of collisions that occurred eons ago, and in turn, inform us about the origin of the impactor populations that have shaped the surfaces of all but the most geologically active bodies. Moreover, craters excavate deep to reveal underlying layers, perhaps differing from surface materials, while some of the escaped material can eventually land on Earth as meteorites.

The fundamental observable property of a crater is its size, and the fundamental property of a population of craters concerns the ratio of the number of small craters to large craters, i.e., the size-frequency distribution (SFD). As with crater populations on larger planets and satellites, there are additional factors that interfere with a direct inference of the projectile population from the observed crater SFD. These include *saturation* of craters (the maximum number of craters that can be accommodated on a given surface), formation of *secondary* craters (craters made by impact of ejecta rather than from the *primary* cosmic projectile impacts), as well

as often size-dependent processes that erase craters or alter their morphology (downslope mass wasting, pit-formation by volatile release, etc). Crater SFDs are also affected by the properties of the target material (e.g., hard rock, rubbly megaregolith, icy or volatile-rich material); these can vary not only spatially across the target body's surface but also in the vertical dimension, so that scaling of impactor size to crater size may actually vary across the surface and with impactor size. Furthermore, energetic collisions may drastically alter the bulk properties of asteroids and scramble their surfaces by producing surface features such as troughs, ridges, and grooves.

All these issues may initially manifest themselves as problems due to our limited knowledge of asteroid properties, but, if one regards them as potentially decipherable challenges, they may eventually enable crater studies to reveal many properties of asteroid interiors, surfaces, and geological processes.

In this chapter, we attempt to summarize the most up-to-date understanding of asteroidal cratering processes, emphasizing presentation and interpretation of the more recent spacecraft data [e.g., from (4) Vesta, (21) Lutetia, and (25143) Itokawa], while also updating interpretations of earlier results from Gaspra, Ida, (253) Mathilde, (433) Eros, and some smaller targets of opportunity.

## 2. CRATER STATISTICS

The identification of impact craters is a challenging process. One may think that craters should resemble nice, sharp bowls, but observations of craters on terrestrial bodies and asteroids readily show that this is naive. In reality, cratered landscapes evolve over time under various forces, such as cratering itself, mass wasting, and other endogenic geological processes, which especially hamper our ability to identify old, degraded craters. Furthermore, there is no unanimously accepted standard procedure to map craters, and researchers need to rely on their own bag of tricks. For instance, when a group of experienced mappers were given the same image from which to count craters, it was found that the results could differ by a factor of 2 (Robbins *et al.*, 2014).

In this section we introduce the topic of crater statistics, and crater SFDs, which are a primary diagnostic tool for understanding cratering. Furthermore, we discuss how crater SFDs can reveal important processes that modify or alter the *production* population of craters — i.e., the crater SFD per unit time that results from the mainly asteroidal projectile population — and are a powerful tool to infer relative and absolute ages of various terrains along with aspects of their bulk mechanical properties.

### 2.1. Crater Size-Frequency Distributions

In this section we review crater SFDs of asteroids visited by spacecraft. As mentioned above, the identification of impact craters can be cumbersome, particularly when they are degraded and heavily modified by post-formation

processes. In addition, oddly shaped asteroids often show large facets that sometimes are interpreted to be the result of impact sculpting or to be a consequence of their rubble-pile structure. Here we take the approach of showing selected examples from the various asteroids to illustrate key processes, rather than presenting a global compilation of every measured crater SFD. In doing so we opt to show crater SFDs from selected references along with some newly measured crater SFDs, and remind readers that there are additional, and sometimes different, counts in the published literature (e.g., Schmedemann *et al.*, 2014). An important and often neglected factor that makes cratering on asteroids different from cratering of terrestrial body surfaces is the fact that the physical sizes of visited asteroids vary by more than 3 orders of magnitude. As a result, craters form and evolve under very different conditions. Here we start our discussion with the largest bodies and continue with smaller asteroids.

**2.1.1. Large asteroids.** Vesta is the largest asteroid so far visited by a spacecraft (see the chapter by Russell *et al.* in this volume). The NASA Dawn mission orbited Vesta for more than one year, gathering images of 98% of the surface. The large surface and coverage makes Vesta the best example so far to study cratering on a large asteroid. In addition, Vesta formed within a few million years after the first solar system solids (e.g., McSween and Huss, 2010), implying that its surface has been subject to extensive cratering throughout nearly all of solar system evolution. As anticipated, the surface of Vesta exhibits an extremely diverse set of crater populations. The significant population of craters (~10–15) larger than 50 km, including a few old degraded structures, witnesses the heavy collisional history, recorded primarily in the northern hemisphere (Marchi *et al.*, 2012a). The southern hemisphere, on the contrary, has been obliterated by the two largest impact structures, the ~400-km Veneneia and ~500-km Rheasilvia basins. As a result, the overall spatial distribution of craters is rather heterogeneous and shows a marked north-south asymmetry. This is easily seen in the global crater distribution, and in the resulting global average crater density (Fig. 1). The formation of Veneneia and Rheasilvia had major effects on the whole surface, as manifested by the extensive troughs and voluminous ejecta blanketing (Schenk *et al.*, 2012; Buczkowski *et al.*, 2012; Yingst *et al.*, 2014). Mapping of these and other geological features led to the development of a well-defined time-stratigraphic system (Williams *et al.*, 2014). In this system, the youngest epoch — Marcian — begins with the time of formation of the freshest of the large craters, the ~70-km Marcia. The second youngest epoch — Rheasilvian — begins with the formation of the Rheasilvia basin. The relative youthfulness of Marcian and Rheasilvian terrains offers a unique opportunity among asteroids to study the least-processed populations of craters produced by asteroidal bombardment (Marchi *et al.*, 2014) and also reveals the small main-belt asteroid SFDs. Figure 2a shows the crater SFDs of selected Marcian and Rheasilvian terrains.

The crater SFDs of older vestan terrains are not easily interpretable because they exhibit odd shapes (for details,

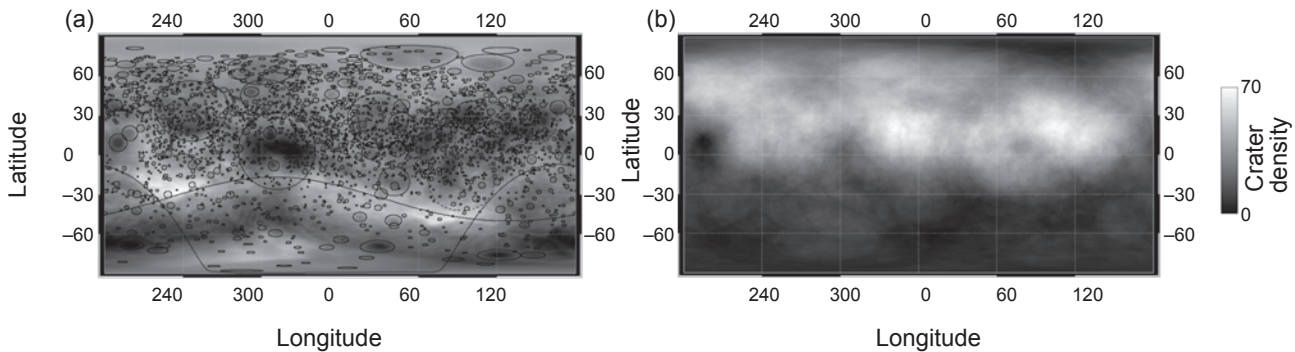


**Fig. 1.** Vesta's global crater catalog. (a) The map shows a cylindrical projection of all mapped craters larger than 4 km in diameter (more than 2500 are shown on the map) overlaid on a digital terrain model. The two lines encompassing the south pole are the projections of best-fit circles to Rheasilvia and Veneneia basins. (b) Crater areal density (in units of number of craters per  $10^4 \text{ km}^2$ ). The map is produced averaging craters over a radius of 80 km. Due to limited imaging coverage at high northern latitudes, the map is not reliable for latitudes above  $\sim 75^\circ\text{N}$ .

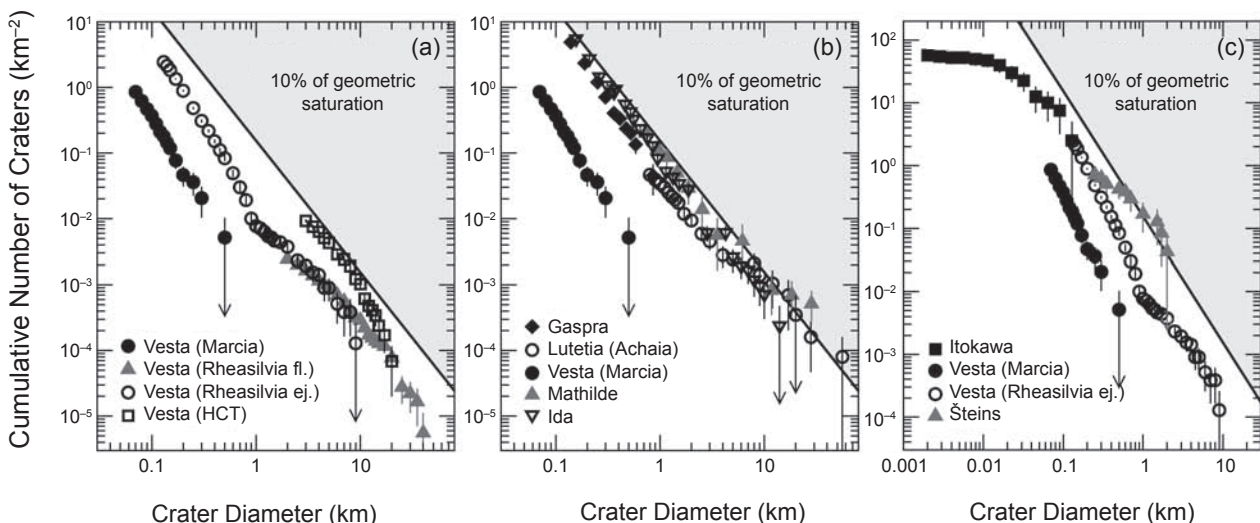


**Fig. 2.** Selected crater SFDs of various asteroids. The data are shown in the form of cumulative numbers of craters per unit area as a function of crater diameter. The thick black lines indicate the level of empirical saturation corresponding to 10% of geometric saturation (Gault, 1970; Melosh, 1989, p. 192) (see section 2.2). (a) Crater SFDs of representative terrains within the Marcian and Rheasilvian units on Vesta. Marcia crater SFD is obtained from high-resolution counts within the rim of Marcia crater (from Marchi et al., 2014). The SFDs for craters on the floor of Rheasilvia basin and on its proximal ejecta blanket update those presented by Marchi et al. (2014). (b) A comparative view of crater SFDs of Lutetia [Achaia region, from Marchi et al. (2012b)], Ida (Chapman et al., 1996a), Gaspra (Chapman et al., 1996b), Mathilde (Chapman et al., 1999), and the Vesta heavily cratered terrain (HCT) [count updated from Marchi et al. (2012a)]. For a better comparison with (a), Marcia crater SFD is plotted here again. (c) Crater SFDs of Itokawa (Hirata et al., 2009), and Šteins (Marchi et al., 2010). For a comparison with crater counts shown in (a) and (b), the crater SFDs of Marcia and Rheasilvia are also shown.

see Yingst et al., 2014), and also differ from the arguably more pristine Marcian and Rheasilvian crater SFDs. It is probable that the formation of large basins such as Rheasilvia and Veneneia (and possibly also older ones) altered crater populations on older terrains (see section 2.2). Here we present data from just a relatively small region where the highest crater density has been observed, the so-called heavily cratered terrain (HCT) (Fig. 2b). The plot also indicates a curve corresponding to empirical crater saturation, i.e.,

approximately the highest crater density that can be accumulated on a given surface (Hartmann, 1984) (see also section 2.2). Therefore, Vesta HCT seems to be close to or has reached the empirical saturation level.

Interestingly, asteroid Lutetia provides some similarities with Vesta. First, given its large size ( $\sim 100 \text{ km}$ ), it may be a primordial object (i.e., not a fragment of some still larger body) according to models of collisional evolution of the main belt (Morbidelli et al., 2009). Furthermore, its surface

shows significant features that were used to map and develop a time-stratigraphic system (*Thomas et al.*, 2012; *Massironi et al.*, 2012). However, the relatively small size and partial surface imaged (40%) did not permit detailed investigations of most of the surface. An exception is the relatively flat, coherent unit, called Achaia (Fig. 2b), which has a crater SFD showing a peculiar kink at crater sizes between ~5 and 8 km (*Marchi et al.*, 2012b; see the chapter by Barucci et al. in this volume). Craters larger than ~8 km are close to the Vesta HCT and saturation, while craters smaller than ~5 km are significantly depleted. The latter has been interpreted as due to resurfacing or a variation of the mechanical properties with depth (see the chapter by Barucci et al.).

The smooth appearances of Achaia and Vesta HCT — suggesting the presence of significant regolith — resemble the surface of asteroid Ida, although on a very different size scale. The Ida crater SFD is also close to the saturation curve, over the size range from ~0.2 to 10 km. A similar conclusion applies to asteroid Mathilde for craters smaller than ~10 km, while for craters larger than ~10 km the crater density is well above the empirical saturation curve. A comparative plot of their crater SFDs is given in Fig. 2b. In conclusion, except for large craters on Mathilde, heavily cratered surfaces of mid- to large-sized asteroids seem to cluster in proximity to the empirical saturation density.

In between the two extremes of low crater density represented by Marcian and Rheasilvian terrains on Vesta and the most heavily cratered terrains, we find a range of other terrains. Examples are the asteroid Gaspra (excluding the large facets of uncertain origin), or the Achaia region on Lutetia for craters smaller than 5 km. All these distributions (except for the kinked Achaia crater SFD) share relatively similar slopes, if one considers the statistical uncertainties associated with the measurements.

**2.1.2. Small asteroids.** Smaller asteroids, however, do not fit the above picture. Consider for instance the well-studied case of Itokawa (a similar discussion about Eros can be found in section 2.2.4). The crater SFD at sizes larger than ~0.02 km has a characteristic slope somewhat shallower than the slopes observed on other asteroids (see Fig. 2c). Unexpectedly, however, the crater SFD has a considerably shallower slope at smaller sizes (<0.02 km) than both that of nonsaturated terrains (e.g., Marcia and Rheasilvia on Vesta), and likely saturated ones (Ida, Mathilde). Moreover, craters become increasingly rare on Itokawa at smaller sizes and, indeed, the surface becomes dominated by boulders. As a result, the Itokawa crater SFD becomes almost flat in a cumulative plot below ~0.01 km (see Fig. 2c). Eros exhibits a similar behavior, with slight shallowing of the crater SFD below ~0.1 km and more pronounced shallowing below ~0.05 km (see section 2.3 for more details on Eros). Several possible interpretations for the lack of small craters were discussed by *Chapman et al.* (2002) for Eros and by *Michel et al.* (2009) and *Michel and Richardson* (2013) for Itokawa, including a decrease in the slope of main-belt asteroids' SFD, erasing of small craters, armoring by boulders, and a cratering hiatus. Similar decreasing frequencies of smaller craters were also

seen on (2867) Šteins and (4179) Toutatis, although with poorer imaging resolution (*Besse et al.*, 2012; see the chapter by Barucci et al. in this volume). The shallow sloped crater SFDs do not match those of the relatively pristine Marcia and Rheasilvia craters, suggesting that one or more specific processes on small asteroids are responsible. Although several of the ideas listed above may be partly applicable, the dominant cause is likely to be seismic shaking, discussed in detail below (section 2.2.4). Unfortunately, image resolutions of larger asteroids (e.g., Vesta, Lutetia) do not allow for a comparison with Eros and Itokawa high-resolution counts (<0.1 km). However, there is a hint that the Marcia crater SFD does not start bending to a shallower slope near 0.1 km diameter. The main-belt SFD at these impactor sizes (<0.01 km) is unconstrained by direct observations, although there are some indirect arguments against the shallow slope being an attribute of the asteroidal SFD. *Marchi et al.* (2014) showed that a current model main belt SFD matches reasonably well the Marcia crater SFD, and such a model does not yield a significant change in slope for smaller asteroids (*Bottke et al.*, 2005). Furthermore, according to recent evolution models (e.g., see the chapter by Bottke et al. in this volume), the near-Earth objects (NEO) SFD slope at this size is roughly similar to that of the main belt, and the observed NEO SFD (see the chapter by Harris et al. in this volume) does not show such a shallower slope.

## 2.2. Temporal Evolution of Crater Size-Frequency Distributions

Cratered surfaces provide time-integrated snapshots of the accumulation of craters over a certain period. Therefore, the total number of craters superposed on a given terrain should monotonically increase over time. Thus, the number of observed craters — in ideal conditions — constrains the age of the terrain (see section 2.3). In practice, however, crater topography is reduced over time by a number of surface processes, and eventually old, degraded craters fade away. As a result, the temporal evolution of a cratered terrain is rather complex and its correct interpretation involves considering various production and obliterating mechanisms.

The production of craters is primarily due to the flux of incoming asteroids and, as such, is susceptible to temporal variations reflecting variation in the impact rates and/or impactor SFD. Crater obliteration is a natural result of the degradation of the topography over time. Contrary to what is observed on geologically active terrestrial bodies, the primary cause for obliteration on asteroids is related to the bombardment itself. Basically, a newly formed crater obliterates smaller previously existing craters. Additional processes tend to magnify the erasure and extend it to larger distances. An interesting aspect is crater saturation, as anticipated in the previous section.

A newly formed crater obliterates smaller previously existing craters, or parts of larger craters, by geometrical overlap (cookie cutting), by spreading ejecta on top of them, by seismic shaking, and by sandblasting. As the integrated areas

of superposed craters approach the surface area, the chances that an earlier crater can still be recognized drop toward zero. A steady-state is eventually reached (“saturation” in jargon) where the crater spatial density cannot further increase. The manner of saturation depends on the slope of the SFD of the crater production function, reflecting that of the impactor population (cf. Richardson, 2009). A shallow-sloped impactor SFD destroys preexisting craters primarily by resetting of the surface by the creation of very large craters and their ejecta deposits, as well as by seismic shaking, whereas a steeply sloped impactor SFD erodes the topography of preexisting craters in a kind of sandblasting effect dominated by tiny projectiles. We expand on these mechanisms below.

Numerical codes simulating the random formation of craters on a surface and the various obliterating mechanism have been developed (Chapman and McKinnon, 1986; O’Brien et al., 2006; Richardson, 2009; Marchi et al., 2012c). Here we present a series of global- and regional-scale cratering simulations to illustrate the basic processes. In these simulations old craters are obliterated by the four primary mechanisms mentioned above.

### 2.2.1. Crater erasure mechanisms: Cookie cutting.

Cookie cutting describes the most direct way that new craters destroy old craters, by overprinting and geometric overlap (Woronow, 1977). When an impactor strikes a cratered surface, any preexisting smaller craters within the excavation and collapse regions of the new crater are totally obliterated. For cookie cutting to occur, however, the new crater (or a few of them) must be a sizable fraction of, or larger than, the preexisting crater. If the overlapping craters are too small, an original large crater may still be recognized as a topographic depression and counted, although its rim and other short-wavelength topography are gone.

If a production function SFD of craters has a shallow cumulative power-law slope with exponent that is larger than  $-2$ , then large-crater cookie cutting tends to dominate the crater erasure process and crater density steady-state values will continue to reflect, or follow, the shape of the production population, as large regions are continuously reset and then repopulated with small craters (Richardson, 2009). In this case, the terrain reaches what Chapman and McKinnon (1986) described as a *quasi-equilibrium* state, one in which large portions of the surface are frequently reset by the formation of large craters, and thus the newer cratering continues to reflect the production population, even after a long period of bombardment (Woronow, 1977; Chapman and McKinnon, 1986). In this process, the crater population will gradually approach *empirical saturation* levels of  $\sim 5\text{--}10\%$  geometric saturation (Gault, 1970) as small craters accumulate on the surface, only to be suddenly pushed back down again by the cookie-cutting effect of the next large crater to form (see Fig. 3).

### 2.2.2. Crater erasure mechanisms: Sandblasting.

The term sandblasting can be used to describe the process by which many small impacts can gradually erode away topographic features (Chapman, 1976), such that the numerous small craters degrade larger craters to the point that they are

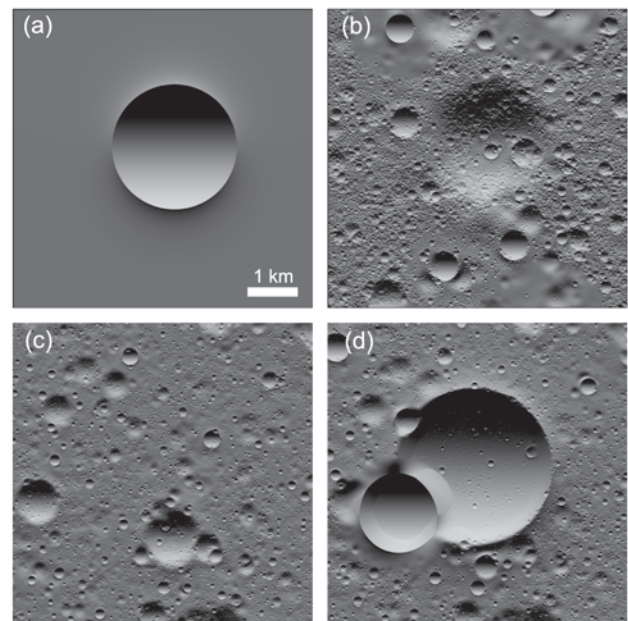


**Fig. 3.** A demonstration of (a),(b) crater sandblasting and (c),(d) cookie-cutting in a small-scale lunar surface simulation. Beginning with a pristine, large crater in (a), the surface is bombarded with a steeply sloped impactor population rich in small impactors. Individual impacts have very little effect on the large crater’s topography and visibility. However, over time and cumulative impacts (b), the large crater is eroded and filled in, as the numerous small impacts redistribute the material making up the walls and rim of the large crater. In (d), a pair of large, simple craters have cookie-cut out (erased) all of the much smaller craters that previously occupied their location in (c). In this manner, large craters can severely alter small crater populations and counts over the affected region.

not recognizable as a crater by a crater counter (Soderblom, 1970). The multiple small craters rearrange the material that had formed the topography of the larger old crater so that its topography relaxes back toward the mean elevation of the terrain.

If a production function SFD of craters has a steep cumulative power-law slope with exponent less than  $-2$ , then small-crater sandblasting tends to dominate the crater-erasure process (Richardson, 2009). In this case, the terrain will display classic behavior (Gault, 1970), with the smallest craters reaching crater-density equilibrium conditions first at between 5 and 10% of geometric saturation (with a cumulative power-law slope of about  $-2$ ), and with successively larger crater sizes reaching equilibrium over time (see Fig. 3).

**2.2.3. Crater erasure mechanisms: Ejecta burial.** The ejecta from a fresh crater can obliterate old craters beyond its rim by burying them. In other words, if the newly produced ejecta blanket is thicker than the depth of a preexisting crater at that location, the crater will be buried, and thus will be invisible to a crater counter. This concept has been employed to estimate the thickness of ejecta deposits from lunar craters (Moore et al., 1974). On a low-gravity asteroid

this process may be less efficient because ejecta are more widespread, but Vesta and Lutetia clearly show significant ejecta reaccumulation (Schenk *et al.*, 2012; Thomas *et al.*, 2012). On Eros, however, Cheng *et al.* (2001, 2002) consider the presence of ejecta, especially for small craters, as minimal, whereas Blitz *et al.* (1999) consider ejecta from larger craters as a major contributor to the several tens of meters of regolith on many parts of Eros. Associated with ejecta burial is the poorly understood scouring process of ballistic sedimentation (Oberbeck, 1975). Ballistic sedimentation involves high-energy deposition of ejecta onto the surface beyond the crater rim that mobilizes regolith where the ejecta land (Melosh, 1989).

**2.2.4. Impact-induced seismic shaking on asteroid surfaces.** The Ranger images of the Moon revealed downslope flow of material on lunar slopes in the form of slides, slumps, and creep processes, and impact-induced seismic effects were proposed as a potential cause (Titley, 1966). Cintala *et al.* (1978) published two of the primary reasons why impact-induced seismic shaking of a small body is an important surface modification mechanism. First, the small volume of the target body concentrates seismic energy from an impact within the body even though it has dispersed throughout the body. Second, the low surface gravity  $g_a$  of asteroids (frequently less than one-thousandth that of Earth) permits relatively small seismic accelerations to destabilize material resting on slopes, where destabilization begins at 0.2–0.5  $g_a$  for loose regolith (Lambe and Whitman, 1979).

Elastic stresses and seismic effects of large impacts on small bodies were first modeled by Fujiwara (1991) and Ivanov (1991), who investigated the formation of the Stickney impact crater on Phobos. Asphaug and Melosh (1993) also performed hydrocode modeling of the impact that produced the Stickney crater, and as a byproduct estimated the resulting velocities imparted to a hypothetical regolith layer resting on the surface, an effect called *seismic jolt* (Nolan *et al.*, 1996). More extensive seismic jolt estimates for large impacts on small asteroids [e.g., Gaspra (Greenberg *et al.*, 1994) and Ida (Greenberg *et al.*, 1996)] indicated that they can severely affect their cratering records, erasing most craters below a few hundred meters in diameter when a loose, mobile regolith layer exists.

The high-resolution, global-coverage of Eros by the Near Earth Asteroid Rendezvous (NEAR)-Shoemaker spacecraft greatly advanced studies of seismic shaking. In addition to clear indications of downslope regolith motion, the Eros cratering record also showed a particularly large number of degraded craters, along with a severe paucity of small craters ( $<0.1$  km in diameter), that were thought to possibly be the result of seismic shakedown (Veverka *et al.*, 2001; Chapman *et al.*, 2002). Richardson *et al.* (2004, 2005) used a series of linked seismic and geomorphic models to investigate the detailed process of impact-induced seismic shaking on Eros-like bodies. They developed a basic theory for propagating seismic energy in a highly fractured asteroid, drawing upon previous lunar crust seismic propagation theory (Toksöz *et al.*, 1974). Synthetic seismograms were then applied to a model

of regolith resting on a slope, and the resulting downslope motion computed for a full range of impactor sizes. This computed downslope regolith flow was then used in a fully three-dimensional model of the body's surface, with craters formed by impacts and then erased by the effects of superposing craters, ejecta coverage, and seismic shakedown. These simulations agreed with the observed Eros cratering record, including the observed paucity of small craters (see section 2.3). More recent simulations (Richardson, 2013) showed that for an Itokawa-like body with an extremely small gravity field ( $<0.1$  mm s $^{-2}$ ), impact-induced seismic shaking is especially effective at degrading and erasing craters on very short timescales, such that the surface for an asteroid like Itokawa should be maintained clean of all but the very most recent impact craters, with all others reduced to little more than a collection of vague, filled circular features, as observed (Abe *et al.*, 2006).

An important feature of impact-induced seismic shakedown is its extreme dependence on the size and surface gravity of the asteroid under bombardment, a direct result of the fact that seismic accelerations of greater than about 0.2–0.5  $g_a$  are required in order to effectively produce downslope regolith flow. Lesser seismic accelerations are incapable of breaking the bonds of particle friction and cohesion and causing movement under the force of gravity. Richardson *et al.* (2005) examined this feature in detail, showing that for a body less than 5 km in diameter, impactors of less than a few centimeters in diameter (at typical asteroid impact speeds) are capable of producing a global seismic event producing accelerations larger than  $g_a$  across the asteroid's surface. For a body in the size range of 10–30-km mean diameter (like Eros), a global seismic event requires an impactor of a few meters in diameter. There is an upper limit on asteroid size for experiencing global, surface-modifying, seismic effects from individual impacts; it is about 70–100 km (depending upon asteroid seismic properties). Larger asteroids will experience only localized (regional) seismic effects from individual impacts.

Beyond effects on small craters, there are catastrophic seismic effects of large impacts, exemplified on Eros and Šteins. NEAR-Shoemaker images of Eros (Thomas and Robinson, 2005) revealed differences in crater densities and scattered boulder densities that pointed to Shoemaker, the most recent large impact crater on Eros (~7.6 km diameter), as the source of these disparities. In particular, craters smaller than ~0.6 km in diameter showed a proportional decrease in numbers as the straight-line, chord distance (through the interior of the asteroid) decreased, a decrease that could not be fully attributed to visible ejecta coverage as a result of the impact. This gradient in crater density as a function of linear distance from the center of Shoemaker crater indicated that (1) the interior of Eros was coherent enough to permit the efficient passage of seismic energy to broad regions on the surface of the body, and (2) this energy was sufficient to produce noticeable degradation and/or erasure of craters smaller than ~0.6 km in diameter as a function of seismic proximity to the large impact.

As a second example, Šteins is particularly interesting from the standpoint of seismic shaking in that it lies midway in size (at ~7 km long) between the ~34-km-long Eros studied by NEAR-Shoemaker, and the ~0.5-km-long Itokawa studied by Hayabusa. As described earlier, the surface of Šteins shows a noticeable paucity of small craters below about ~0.6 km in diameter, increasingly so as one moves to smaller sizes. Marchi et al. (2010) ascribed this general paucity of small craters to one or a combination of two possibilities, either the cumulative effects of (small) impact-induced seismic shaking, or the gradual reshaping of the asteroid due to spinup and spindown caused by the Yarkovsky-O'Keefe-Radzievskii-Paddack (YORP) effect (Rubincam, 2000). In addition, observed heterogeneities in the small crater distribution may be due to a singular impact event: the formation of the relatively fresh ~2-km-diameter Diamond crater, which had disruptive effects for the rest of the surface (Jutzi et al., 2010a), probably similar to those the formation of Shoemaker crater apparently had on the surface of Eros.

### 2.3. Model Production Function and Age Determination

We provide crater-retention age estimates for some of the crater SFDs presented in section 2.1, and discuss the effects of crater obliteration (section 2.2) for selected cases (see the chapter by Barucci et al. in this volume for additional examples).

The assessment of cratering ages requires knowledge of impactor SFD, impact rate, and a crater-scaling law (i.e., a relationship between impactor sizes and crater sizes). These inputs are used to derive the model production function (MPF), i.e., the number of craters per unit time per unit surface (O'Brien et al., 2006; Marchi et al., 2010, 2011, 2012a,b). Among the available crater-scaling laws, we implemented the one by Holsapple and Housen (2007). The advantage of this formulation is that it is of general purpose and can be applied to both strength and gravity regimes. Furthermore, it allows full control of target physical properties, which may differ among various asteroids and across a body. On the other hand, crater size may depend strongly on input parameters (mostly the strength of the target,  $Y$ ), so the cratering-retention age may vary depending on the assumptions. Here we restrict our analysis to outline how to obtain crater-retention ages and how they depend on the assumed parameters. An important aspect to bear in mind is that assessing crater-retention ages is a multiple-step problem and, whenever possible, geological analyses need to be implemented to narrow down the possible range of target properties.

We consider two main cases. The first is the so-called *hard rock* (HR) case. The crater-scaling law for hard rock has been extensively applied to terrestrial planets and asteroids (Mosh, 1989), and therefore offers a good term of comparison. Here we adopt a rock strength of 20 MPa (Asphaug et al., 1996). There is little doubt, however, that the HR scaling does not generally apply to asteroids, particularly for small

craters formed in regolith or craters formed on a rubble-pile asteroid that are much larger than the components of the rubble. For this reason, we also implement an additional crater scaling for weaker materials; we adopt a scaling [for so-called *cohesive soils* in Holsapple and Housen (2007)] that has been calibrated using impact experiments on various weaker terrestrial materials, including alluvium, whose strength is below or on the order of 100 kPa at most. Here we assume that this scaling is applicable to craters in the size range of tens to hundreds of meters, and we adopt a nominal strength of 2 MPa, justified by the fact that the craters under analysis reach a significant depth where an increased strength with respect to laboratory experiments is expected (we also use different strength values for specific cases). This choice seems reasonable given that lunar regolith has a strength of ~1 kPa (at 2 m depth), and the strength increases with depth. Larger craters, however, reach a much greater depth, and it is uncertain whether both the hard rock or weaker scaling — or neither — apply. Our current understanding of asteroid evolution suggests that all except large ones undergo major collisional evolution during their lifetimes (Bottke et al., 2005), to the point that most are probably rubble piles. Larger asteroids (such as Vesta) are certainly not rubble piles; however, their upper layers may well be moderately to highly fractured, like megaregolith on the Moon. We generally refer to these situations, as well as to the loose-material case, as *rubbly material* (RM), for which we apply the cohesive soil expression by Holsapple and Housen (2007) for various values of strength as indicated.

Impact rates and velocities were specifically computed for each asteroid, using a model main-belt population from Bottke et al. (2005). Current impact rates have been extrapolated back in time following a recent model of main-belt evolution (O'Brien et al., 2014). In the following discussion we will not consider Mathilde, because the crater-scaling law for highly porous bodies is highly uncertain. Also, for the sake of simplicity we will not provide error bars for the best-fit ages. The formal analytical best-fit age uncertainties are typically on the order of a few percent. However, the uncertainty resulting from the impactor population and crater-scaling law can be as low as ~20–30% for statistically robust crater SFDs (such as Rheasilvia), and it can be even larger for oddly shaped crater SFDs and/or with low statistics (such as Šteins).

**Cratering retention ages** — For the interesting case of Vesta, we obtain an age of ~1 Ga for Rheasilvia floor's crater SFD. This age is obtained both using the HR and RM ( $Y = 2$  MPa) scaling laws. The quality of the fit is almost identical and only one of them is shown in Fig. 4. The MPF slightly overestimates the number of craters on the smooth ejecta unit. This is not surprising because of the different crater size range and nature of the terrains. The difference can be entirely due to variation in the properties of the terrains. It is also possible that the assumed impactor SFD overestimates the real main-belt population. The dip at crater sizes ~0.7–2 km is interesting and may represent a real feature in the impactor SFD. Applying the same scaling laws, we

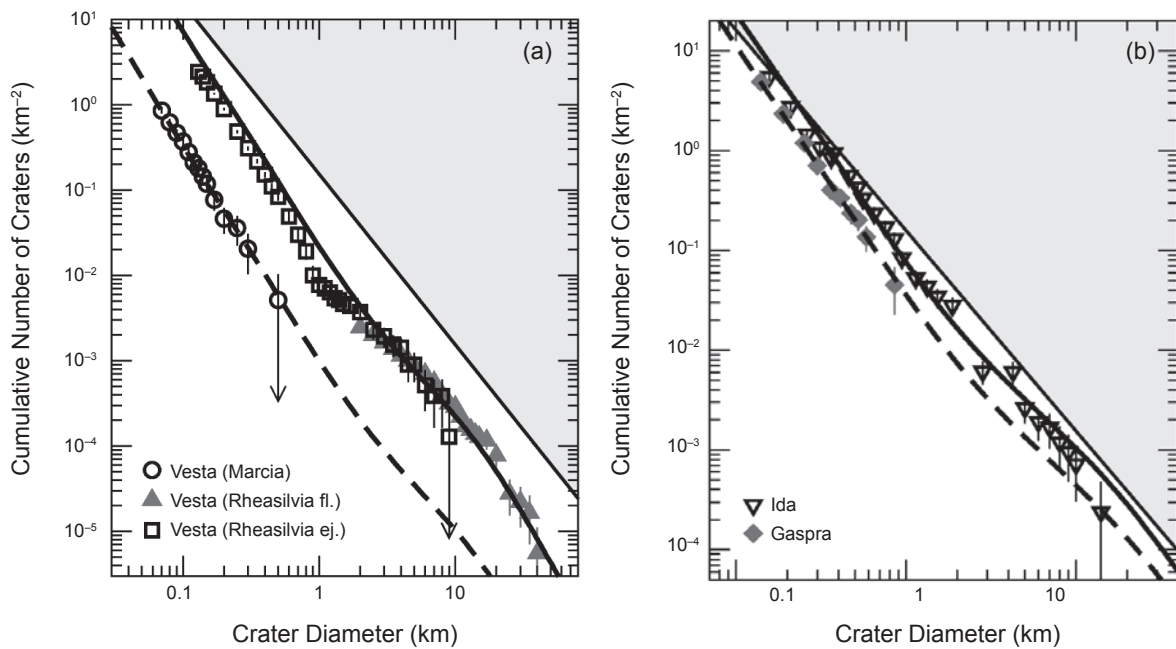


**Fig. 4.** Examples of model production function (MPF) best fits (solid and dashed thick black curves) for some of the crater SFDs presented in Fig. 2. (a) Vestan terrains, (b) Ida and Gaspra. Note that the change in slope of the MPF is primarily due to similar changes in slope in the assumed impactor SFD. The crater-scaling law may also introduce minor modifications in the MPF from one asteroid to another depending on the target strength and gravity, particularly for large craters on large asteroids that may approach the gravity regime. For details on the parameters used for the fits see the text. The thick solid line that bounds the gray area defines the empirical saturation level as in Fig. 2.

derive an age of  $\sim 50$  Ma for the Marcia smooth unit (Fig. 4). It should be noted that the target strength has a significant effect on small crater formation (crater size  $\sim Y^{(0.2-0.3)}$ ), and a strength variation of a factor of 10 results in a factor of 2–3 variation in the cratering age.

It is more difficult to derive an age for the heavily cratered terrain. A nominal fit using RM ( $Y = 2$  MPa) scaling law gives an age of  $\sim 4.2$  Ga. This should be regarded as a lower limit, given that crater obliteration is expected to be important for old terrains. An attempt to correct for this process, following the numerical approach outlined by O'Brien *et al.* (2006), gives an age of  $\sim 4.4$  Ga. These ages are certainly very uncertain; nevertheless, it is possible that much of the collisional history of Vesta may still be recorded in its HCT.

For Gaspra, we obtain an age of  $\sim 1.5$  Ga for both HR and RM ( $Y = 2$  MPa) scaling laws, which may increase to  $\sim 1.8$  Ga if crater obliteration is considered (Fig. 4). In the case of Ida we obtain an age of 3.3 Ga (HR) and 2.8 Ga (RM,  $Y = 2$  MPa), ignoring crater obliteration. Both ages become  $\sim 3.5$  Ga if we correct for crater obliteration, and the crater SFD seems to be close to or in saturation (Fig. 4).

The case of Eros is interesting for several reasons. First, it is a near-Earth object, yet it is generally believed that most observed craters formed while Eros was in the main belt, prior to being deflected into a near-Earth orbit. Here we assume, therefore, average main-belt impact rates, and derive an age of about 1.5 Ga for both HR and RM ( $Y = 2$  MPa) scaling

laws. This age is derived without crater obliteration and it is based on the fit of craters  $>0.4$  km (using the global catalog shown in Fig. 5a). Figure 5a also provides two additional crater SFDs: (1) a highly cratered terrain ( $D \sim 0.1\text{--}2$  km), and (2) a high-resolution count on a smaller area ( $D \sim 0.01\text{--}0.2$  km). Interestingly, the global crater SFD lies below the heavily cratered crater SFD for craters in the size range  $\sim 0.2\text{--}1$  km. This depletion has been ascribed to erasure due to the formation of Shoemaker crater, as mentioned in section 2.2.4 (Thomas and Robinson, 2005). The global crater SFD is used here for age dating because it provides better statistics at large crater sizes, but it should be noted that the Eros surface is not uniform. The difference between our age estimate with a previous age estimate (Richardson *et al.*, 2005) of  $\sim 0.4$  Ga can be understood in light of the different assumptions. In particular, they implemented a different scaling law that results in a much larger crater for the same impactor. Therefore, the resulting age is younger. In fact, we obtain a similar age implementing RM scaling and  $Y = 200$  kPa. On the other hand, Richardson *et al.* (2005) also argued (based on the largest craters) that the cratering age may be as old as 1–2 Ga. The second aspect of interest is the availability of high-resolution measurements that allow validation of the seismic models. Figures 5b,c show that the downslope regolith migration resulting from impact-induced seismic shaking can explain the paucity of small craters. A similar model also provides a good fit to Itokawa crater SFDs.

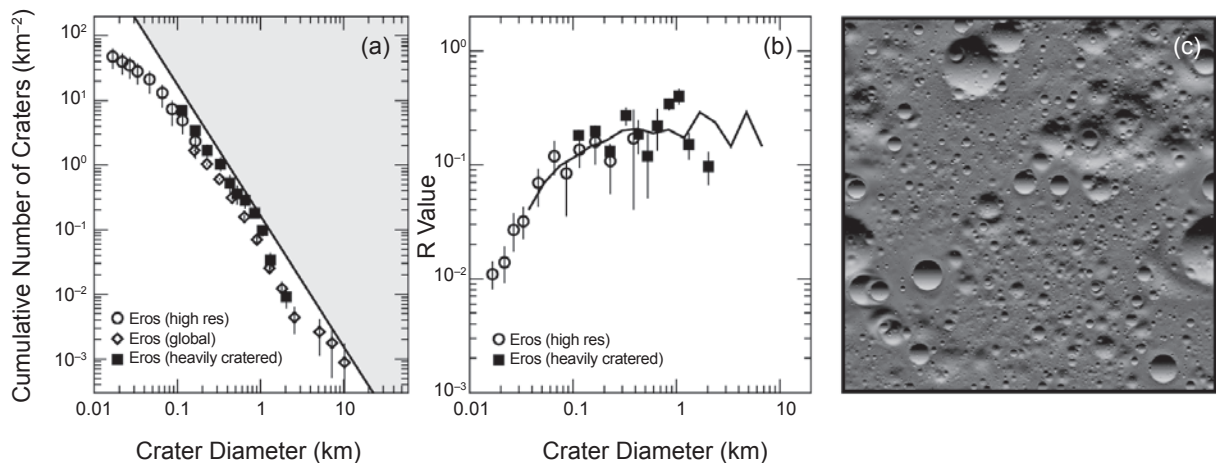


**Fig. 5.** (a) Various Eros cumulative crater SFDs from Chapman et al. (2002) (high resolution), Veverka et al. (2001) (heavily cratered), and Thomas and Robinson (2005) (global). The latter is an average over the whole surface, including regions where small craters were erased by formation of Shoemaker, and therefore it contains fewer craters than the heavily cratered counts in the size range 0.1–1 km. The thick solid line that bounds the gray area defines the empirical saturation level as in Fig. 2. (b) Same distribution as in (a) but now depicted in relative-density plot fashion (*Crater Analysis Techniques Working Group*, 1979), which is better suited to show fine-scale variations in the distributions, showing the increased paucity of small craters as one goes below about 0.1 km crater diameter. The solid curve shows the crater counts for the model simulation shown in (c).

### 3. CRATER MORPHOLOGICAL PROPERTIES

Crater morphological properties, e.g., depth-to-diameter ratio, can be used to address degradation processes operating on asteroids. Early observations of lunar terrains (Gilbert, 1893) revealed that craters with diameters below a few tens of kilometers (so-called *simple* craters) have bowl-shaped profiles with the maximum depth at the center of symmetry of the crater. Larger craters (so called *complex* craters) show progressively higher raised central peaks surrounded by flatter crater floors. The final crater shapes are attained during the so-called *modification* stage (e.g., Gault et al., 1968) that takes place when the excavation cavity has reached its maximum radial extension, and surrounding highly fractured rocks collapse within the cavity pulled by gravity. The transition from simple to complex craters scales as  $\sim 1/g_a$  (Pike, 1980); therefore, on asteroids it takes place at much larger crater sizes (see section 2) compared with terrestrial bodies. Due to the low gravity of asteroids, the crater-modification stage is probably largely affected by target mechanical properties (e.g., strength) and the asteroid's overall shape. Once a crater is formed, additional degradation processes are responsible for the evolution of its morphology, as discussed in section 2.

In general, crater morphologies on asteroids are not fundamentally different from the ones observed on terrestrial bodies, except that craters on all but the largest asteroids generally form in the strength regime, and they are also simple craters (except the largest craters on the largest asteroids, e.g., Rheasilvia basin on Vesta). Also, the morphology of a crater approaching the physical size of the asteroid

significantly differs from the final shape described above. We review key morphologic parameters of asteroidal craters, such as depth-to-diameter ratios, which can be measured from individual images or from digital terrain models. Additional useful data are the ellipticity, particularly for craters on slopes, and the overall shape of large depressions that approach an asteroid's physical size.

#### 3.1. Crater Depth-to-Diameter Ratio

Here we discuss in detail asteroid crater morphology by presenting selected examples from Itokawa, Eros, Lutetia, and Vesta. For all these bodies, crater morphologies are assessed from imaging. Crater diameter is obtained by fitting an ellipse to the crater rim and taking the length of the largest axis (in case of nongeoreferenced images) or the average of the two axes (for georeferenced images). It can be measured very precisely, with a typical uncertainty of twice the spatial resolution. Depth can be obtained directly if the spacecraft carried an altimeter, i.e., the NEAR-Shoemaker mission at Eros and the Hayabusa mission at Itokawa. However, in most cases, depth is measured with less-accurate indirect techniques such as measuring the length of rim shadows cast inside the crater, or using a digital terrain model (DTM) reconstructed by stereo-photogrammetry (e.g., Vesta) or stereo-photoclinometry (e.g., Lutetia) from the images. Comparisons of the different imaging-based methods show that the shadow technique tends to overestimate the depth while photoclinometry underestimates the depth, especially for the smallest craters. Stereo-photogrammetry is the most accurate technique, but requires multi-imaging of the surface with

very specific illumination conditions, not always achievable (especially during flybys).

In addition, for oddly shaped asteroids it is important to try to take into account preexisting topography under the crater when measuring the depth. Due to the non-equilibrium shape of most asteroids, their topographic excursions are generally significant with respect to the radius of the body.

Craters on asteroids display a wide range of shapes, from sharp bowls to very subdued and degraded depressions. This translates into a wide range of crater depths ( $h$ ). For simple craters this ratio follows a near linear law,  $h/D \sim k$ , where  $k$  for asteroids is approximately 0.15 (Grieve, 2007). Figure 6 shows an example of this linear relationship for Eros, Lutetia, and Vesta. Variations are generally interpreted as reflecting different states of degradation of the surfaces, but different physical properties of the target may also play a role. Consider two examples: target properties (porosity, strength), and impact velocity. Craters in highly porous material generally have a higher depth-to-diameter ratio than those in low-porosity material [e.g., Mathilde (Housen and Holsapple, 2003)]. An interesting characteristic of craters on asteroids, as distinct from the Moon and terrestrial planets, is that they appear deprived of impact melts due to the lower average impact speeds (e.g., Keil et al., 1997; Marchi et al., 2013); therefore, they better show the morphology of the floor and walls.

**3.1.1. Small craters.** For asteroids visited by space missions, the overall properties of  $h/D$  distributions (weighted toward fresher craters, but including somewhat degraded craters, as well) look very similar. Ranging from  $\sim 0.12$  to  $\sim 0.20$  (excepting Itokawa), their mean values are centered

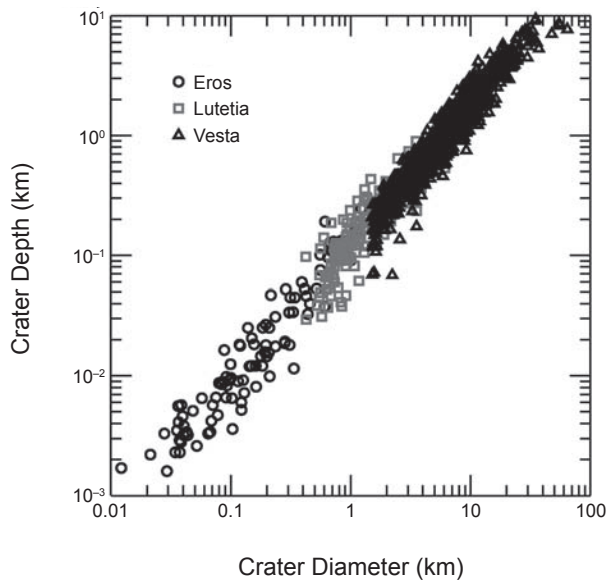


**Fig. 6.** Distributions of crater depth vs. crater diameter for asteroids Eros, Lutetia, and Vesta. Although the three asteroids are very different, one can notice similar behavior in their crater morphologies. The average relation between crater depth and diameter is close to a linear law with a slope of  $\sim 0.15$ , although degradation state is an important contributor.

close to  $\sim 0.15$  (Carr et al., 1994; Sullivan et al., 1996; Veverka et al., 1999, 2000; Besse et al., 2012; Vincent et al., 2012, 2014), slightly below the canonical value of  $\sim 0.2$  for planetary surfaces (Melosh, 1989, and references therein). Smaller, rubble-pile asteroids (e.g., Itokawa) tend to have shallower craters than larger bodies (e.g., Lutetia, Vesta).

Small craters exhibit a range of measured  $h/D$ , while larger craters tend to have similar  $h/D$  ratios. In general, the dispersion in  $h/D$  values decreases with increasing crater diameter. This may be the result of several factors: (1) Measurement uncertainty is larger for smaller craters, especially when their diameters are only a few times the image resolution, but the dispersion in  $h/D$  is still visible when removing craters smaller than  $10\times$  the resolution; (2) fresh craters are more likely to be found among small craters than larger ones, thus small craters can be found in all states of degradation while very young large craters are generally absent; and finally (3) small craters are most efficiently altered, even to the point of erasure, by post-formation processes, such as ejecta blanketing from nearby craters or seismic shaking (see section 2), whereas the largest craters remain visible, despite degradation, throughout the history of the asteroid's surface (unless large craters are saturated).

Relationships between strength, gravity, and formation regime were tested on Vesta by Vincent et al. (2014). The transition between strength and gravity regime is given by  $D_{\text{trans}} = 0.8 Y/(\rho g_a)$  (Asphaug et al., 1996), or  $D_{\text{trans}} \sim 25$  km for Vesta ( $Y = 20$  MPa,  $\rho = 2600$  kg m $^{-3}$ ,  $g_a = 0.25$  m s $^{-2}$ ), typically where we start to see a narrowing of the  $h/D$  distribution toward the typical ratio of 0.15. The transition between simple and complex craters scales with the inverse of the gravity, so simple craters should transition to complex craters for  $D \sim 160$  km for Vesta. The transition size is fuzzy and, indeed, a crater as small as the  $\sim 70$ -km-diameter crater Marcia shows evidence of incipient central peak formation.

If the average initial  $h/D$  is similar for all asteroids, recent work on high-resolution images and DTMs has shown that this picture might be too simple, either because of the low resolution of previous studies or the limited number of craters observed. While the overall distribution is generally peaked near a particular value, more complete statistics show that the average  $h/D$  can differ from region to region. This is very prominent on Vesta, where a double peak is visible in the global distribution of  $h/D$  (Vincent et al., 2014) with about a 25% difference between the peaks at 0.15 and 0.19. The same effect can be seen on Lutetia, with up to a 40% difference in average  $h/D$  between different regions (Vincent et al., 2012).

It is also valuable to compare the cumulative probability distribution of  $h/D$  for different regions and bodies. Figure 7 shows an example of such comparison for Lutetia and Vesta. On both bodies measurements were obtained on the oldest, heavily cratered regions found on the northern hemisphere and on younger regions of Vesta mostly from the southern hemisphere, as well. By comparing the cumulative probability distributions of these broadly different terrains we find that the oldest regions of Vesta and Lutetia display very similar distributions, while younger vestan areas significantly

lack shallow craters. Overall, *Vincent et al.* (2014) found a very good correlation between h/D variations and vestan geologic units (*Yingst et al.*, 2014). This is interpreted as evidence of the resurfacing event triggered by the giant impacts in the southern hemisphere of Vesta, which reset the polar surface and partially erased craters even approaching the equatorial regions.

Although most small craters on asteroids resemble those observed on rocky planets, there are a few peculiar morphologies that seem more common on asteroids. For instance, many examples of what are termed bimodal craters were discovered and analyzed on Eros (*Mantz et al.*, 2004), Lutetia (*Vincent et al.*, 2012), and Vesta (*Krohn et al.*, 2014). They are characterized by a sharp rim on one side and a less-defined rim on the other, often associated with important mass wasting. Those craters are typically found on slopes with respect to the gravity field, with the sharper rim always on the more elevated side. This peculiar morphology is explained by slumping of material from the upper rim toward the lower

rim combined with failure of the lower rim. Material accumulates on the lower edge of the impact feature, smoothing the topography. As discussed earlier, such features are more common on asteroids due to the stronger changes in topography and gravity with respect to the general curvature of the body. Figures 8a,b present a few examples of these craters.

In areas with relatively homogeneous physical properties, variations in crater morphology cannot be due to variations in such properties. Additionally, for surfaces unaffected by a massive, local resurfacing event, we can assume that differences in h/D for craters of similar sizes can measure the degradation rate, as the variation of degradation state is only a function of age. For instance, the dispersion of h/D for small craters on regions of similar physical properties on Vesta implies a degradation rate of  $\sim 10^{-7}$  m yr<sup>-1</sup> (*Vincent et al.*, 2014), comparable with an estimate of boulder erosion on Lutetia (*Kueppers et al.*, 2012), but considerably higher than for the Moon (*Fassett and Thomson*, 2014).

The morphologies of craters on Eros have been investigated by several authors (*Veverka et al.*, 2000; *Chapman et al.*, 2002; *Robinson et al.*, 2002). Measurements that make use of the NEAR Laser Rangefinder data and a careful assessment of crater freshness indicate that many of the freshest craters on Eros typically possess h/D near 0.2 for D > 100 m (Fig. 6). These ratios match results reported on the Moon (*Pike*, 1977) and Ida (*Sullivan et al.*, 1996). For D < 100 m, fresh craters on Eros are shallower than those on the Moon. The average h/D of all craters on Eros indicate that most are degraded (Fig. 8c) and follow a pattern akin to what is observed on Vesta, Šteins, and Lutetia.

Craters on Itokawa are very different from most other asteroidal craters. The best defined craters (*Hirata et al.*,

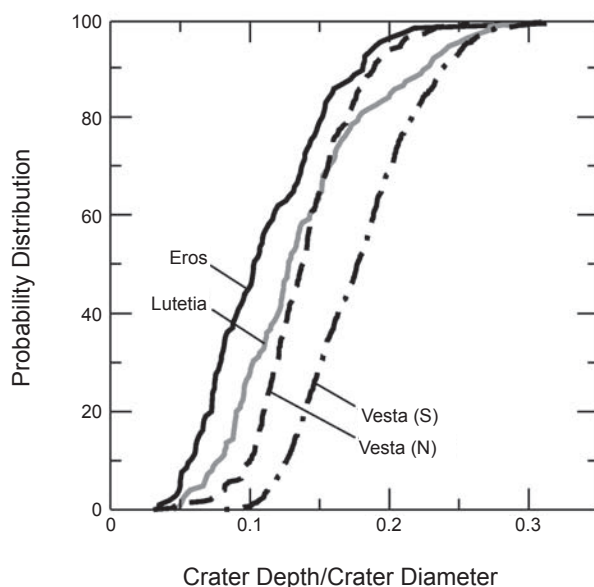


**Fig. 7.** Cumulative distribution function of h/D on Eros, Lutetia, and Vesta (N: northern hemisphere, S: southern hemisphere), emphasizing the relative differences in the distribution of depth to diameter ratios. One can see that old surfaces like Lutetia or the northern hemisphere of Vesta tend to have significantly more shallow craters than recently reset areas such as the southern hemisphere of Vesta. This degradation with age is even more pronounced in the case of Eros where additional effects such as seismic shaking smooth the topography. About 80% of Eros' craters have h/D less than the typical value of 0.15, 70% on Lutetia and Vesta N, and only 20% in Vesta S. Asteroidal h/D average values are 0.12 for Gaspra (*Carr et al.*, 1994), 0.15 for Ida (*Sullivan et al.*, 1996), 0.2 for Mathilde (*Veverka et al.*, 1999), 0.14 for Eros (*Veverka et al.*, 2000), 0.08 for Itokawa (*Hirata et al.*, 2009), 0.12 for Šteins and Lutetia (*Besse et al.*, 2012; *Vincent et al.*, 2012), and 0.15 and 0.19 for Vesta N and Vesta S, respectively (*Vincent et al.*, 2014).

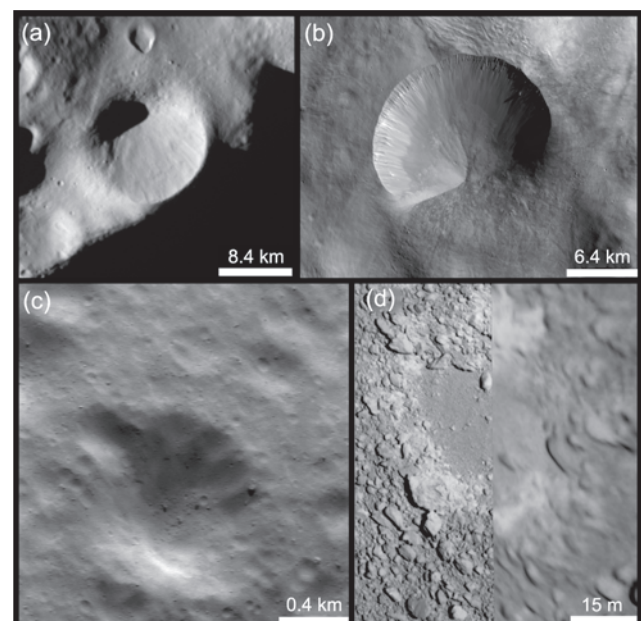


**Fig. 8.** Peculiar crater morphologies on asteroids. (a) Bi-modal crater on Lutetia and (b) Vesta. (c) Eroded impact crater on Eros, and (d) a shallow impact feature on Itokawa.

2009) are generally very shallow, with h/D ratios below 0.1 (Fig. 8d). Seismic shaking on this small body, as discussed in the previous section, would surely rapidly degrade any craters that formed on its surface. But, in addition, two other factors might contribute to causing these low h/D ratios: (1) The presence of numerous large blocks can depress crater formation as the impact energy fractures a boulder rather than excavating a depression (Chapman *et al.*, 2002) or otherwise leading to formation of flat shallow craters (e.g., Güttsler *et al.*, 2012), and (2) the large curvature of Itokawa relative to some of the diameters of the large candidate craters proposed by Hirata *et al.* (2009) can yield very shallow craters, with the crater floor exceeding the height of the crater rims in some rare instances (Fujiwara *et al.*, 1993; Asphaug *et al.*, 1996). The shallow nature of many of Itokawa's craters can therefore be attributed in part to factors influencing their initial formation as well as to subsequent degradation by seismic shaking.

Finally, it is worth considering the spatial variation of crater morphologies across small body surfaces. Most of the differences can be linked to aging processes (erosion, infilling, rim collapse, seismic shaking). However, when statistics are significant enough to build a map of h/D or measure it on various regions of an asteroid, it appears that regions of similar age can show different average h/D. This was determined on Lutetia and Vesta (Vincent *et al.*, 2012, 2014), where a link between variations of crater morphologies and geological units might indicate differences in their physical properties.

**3.1.2. Large craters.** The largest craters on asteroids can have diameters approaching or even exceeding the asteroid's radius (see Fig. 9). Most of these craters can be grossly approximated as simple bowl-shaped craters, with a few exceptions (e.g., the Rheasilvia basin on Vesta). For these simple giant craters where their h/D can be measured, this ratio is typically less than 0.2 (Thomas *et al.*, 1999). An important reason why many of these giant craters are shallow is illustrated by measurements of h/D of three giant Eros craters both along and perpendicular to the greatest radius of curvature of the asteroid. For example, Himeros crater has an h/D of 0.17 along the long axis of Eros, but a much

shallower h/D of 0.1 when measured perpendicular to the long axis of the asteroid. These craters are shallower when the local radius of curvature is more important.

The asteroid Mathilde is unique in that it possesses five giant craters on its imaged side, none of which have led to its disruption. Equally remarkable, given what is now apparent on Eros and Vesta, none of these craters seem to disturb their neighbor. These observations have been attributed to Mathilde's high porosity of 50% (Cheng and Barnouin, 1999; Housen *et al.*, 1999), which can better absorb the energy of these impacts, making the asteroid harder to disrupt and each crater less likely to influence its neighbor.

The  $500 \pm 20$ -km Rheasilvia basin is unique among asteroidal craters (Thomas *et al.*, 1997; Schenk *et al.*, 2012). It possesses a broad central uplift whose height is similar to its rims. The central uplift is remarkably broad compared with other craters on the Moon or Mercury and exhibits extensive slumping and sliding in its interior. In addition, radial curved ridges near the central mound may be the result of Coriolis forces acting on inward-collapsing material during the modification stage (Otto *et al.*, 2013). However, unlike similar-sized craters on other planets, little impact melt is observed, probably due to the comparatively low impact velocities in the asteroid belt, which do not efficiently generate melt (e.g., Keil *et al.*, 1997; Marchi *et al.*, 2013).

To date only the relatively recent, giant craters Rheasilvia on Vesta and Shoemaker on Eros show quantitative evidence for resurfacing a significant fraction of the surface of either asteroid. In the case of Rheasilvia, its ejecta have hidden most craters within tens of kilometers of its rim and influenced the crater SFD and h/D of craters further beyond (see Fig. 1) (Marchi *et al.*, 2012a; Schenk *et al.*, 2012). Unlike Rheasilvia, Shoemaker crater probably removed craters mainly by seismic shaking (Thomas and Robinson, 2005). Indeed the density of craters ranging from  $\sim 0.2$  to  $\sim 1$  km diameter increases with radial distance from the center of Shoemaker crater rather than with distance from the crater rim, as would be expected for ejecta. Furthermore, the density of the largest blocks seen on Eros that have been attributed to ejecta from Shoemaker crater (Thomas *et al.*, 2001) do not correspond with the locations where the dearth of craters on Eros has been observed.

#### 4. LINEAR SURFACE STRUCTURES AND BLOCKS

Asteroids possess various types of linear surface structures (Jaumann *et al.*, 2012; Pockter *et al.*, 2002; Sullivan *et al.*, 1996; Thomas *et al.*, 2012; Thomas *et al.*, 1979; Veverka *et al.*, 1994). They have been identified on most asteroids visited by spacecraft with the possible exception of Šteins (Besse *et al.*, 2012; see the chapter by Barucci *et al.* in this volume) and Mathilde, which possess some limited evidence for them (Thomas *et al.*, 1999), although those two asteroids were imaged with relatively poor resolution. In most cases, when sufficiently good image resolution is available, the genesis of these lineaments can be attributed in part, and

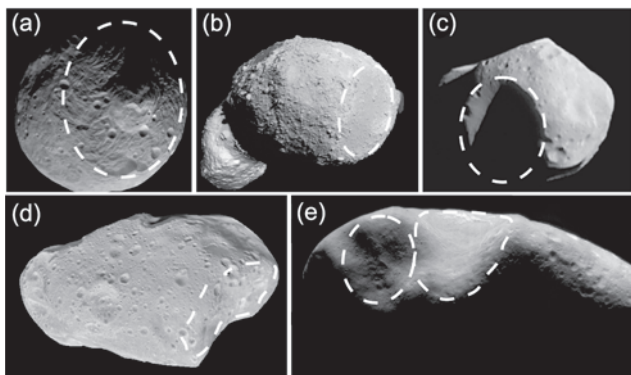


**Fig. 9.** Examples of larger features on asteroids. (a) Vesta, (b) Itokawa, (c) Mathilde, (d) Gaspra, (e) Eros.

sometimes entirely, to a source crater. Lineaments can concur to obliterate preexisting topography, including craters (Prockter et al., 2002; Jaumann et al., 2012), indicating that the formation of lineaments by large impacts can drastically reset the surface of an asteroid (see section 2). The large extent of many lineaments, and their link to the largest craters on asteroids, even when these lineaments are located far from these craters, indicate that internal properties of most of the asteroids visited must be capable of transmitting sufficient impact energy through their interior to cause near-surface failure that can be linked to a parent crater.

#### 4.1. Types of Lineaments

Lineaments on asteroids have various styles (Fig. 10). The most common are shallow troughs, grooves, and pit chains (Thomas and Prockter, 2010). Shallow troughs are linear depressions, with a flat floor and no raised rim. Grooves are usually V-shaped, while pit chains comprise a series of small depressions that are somewhat circular, with uniform sizing and spacing. Less commonly observed lineaments include fractures and broad flat troughs (Figs. 10e,f). Fractures have been reported only on Eros, perhaps because the imaging resolution for other asteroids did not easily permit their identification. The morphology of the observed fractures looks like a fan of cracks emanating from a ridge (Buczkowski et al., 2008; Prockter et al., 2002). On Vesta, broad troughs appear to be graben, with their floor tilting toward the dominant fault (Buczkowski et al., 2012). Such tilting is fairly common for graben that form in sedimentary environments on Earth, and may reflect the abundance of regolith on Vesta.

Ridges are another linear structure seen on asteroids that is also less common than negative relief linear features (Fig. 10d) indicative of extension. Ridges, however, appear to have formed through some displacement along a preexisting

zone of weakness, either because of translation and/or compression. Rahe Dorsum on Eros is one of the best examples of such a structure.

Shallow troughs have been observed on Ida, Gaspra, Eros, Lutetia, and Vesta. Grooves have been reported on Gaspra, Eros, Lutetia, and Vesta, while pit chains have been found on Steins, Eros, Lutetia, and — with extraordinary richness — on Vesta (Carsenty et al., 2013). Broad flat troughs are on Eros, Lutetia, and Vesta, while ridges are on Gaspra, Eros, Lutetia, Vesta, and even rubble-pile asteroid Itokawa. In the latter case, these appear to be very limited in length (Barnouin et al., 2014).

#### 4.2. Cratering Origin of Lineaments

Studies of the asteroids Eros, Vesta, and Lutetia show that there is a close correlation between the observed lineaments and craters, as had been suspected but not easily confirmed by earlier investigations of Ida and Gaspra (Thomas and Prockter, 2010). A detailed mapping of more than 1500 lineaments on Eros indicates that the longest, dominant set of lineaments is likely associated with the formation of large craters. Most of these long lineaments, sometimes in excess of tens of kilometers, are circumferential about impacts in the regions separating Himeros from Psyche crater. Fitting planes to the surface expressions of these lineaments provides the normal vectors to these planes, which preferentially point to either Himeros or Psyche crater (Fig. 11). It is difficult to assign which crater is directly responsible for most of the lineaments because they are essentially 180° away from each other on the opposite sides of the asteroid. Interestingly, many of the circumferential lineaments appear subdued, and are probably not very young. Although it is impossible to distinguish whether or not Himeros crater formed before Psyche, the large size of Himeros, and its degraded appearance relative to Psyche, suggest that it might have formed first. In such a scenario, it is plausible that Himeros could have initially generated most of the long circumferential lineaments, probably due to impact-generated tensile hoop stresses (Asphaug et al., 1996). Later craters such as Psyche, and perhaps Shoemaker, may have only reactivated them, causing the subdued appearance of many of the lineaments. Such a possibility is consistent with a recent numerical study, which models self-consistent dynamically interacting crack distributions and pressure-dependent granular flow of a highly damaged material (Tonge and Ramesh, 2015). These calculations investigate the evolution of porosity and damage in an asteroid. Damage is usually expressed on the surface of an asteroid as cracks. These calculations show for the simplest case where Eros is assumed to be a basaltic monolith that Himeros could easily create a 20–25% porous Eros, and generate lineament distributions comparable to those we see today. Furthermore, the model indicates that subsequent formation of Psyche and Shoemaker craters would have had minor global effects, with little change to the overall asteroid porosity and global surface cracking. These later craters limit their damage to local regions near the craters. However, the

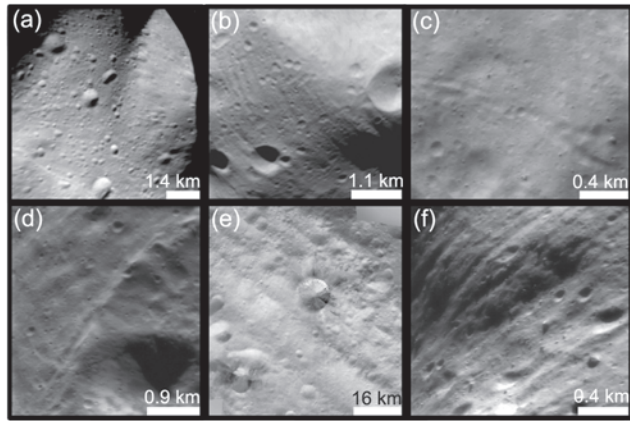


**Fig. 10.** Common lineaments observed on asteroids: (a) grooves on Ida, (b) pit chains on Eros, (c) shallow troughs on Lutetia. Less common linear structures: (d) ridges seen on Eros, (e) broad troughs on Vesta, and (f) heavy modification of topography (a crater rim) on Eros by grooves and fractures.

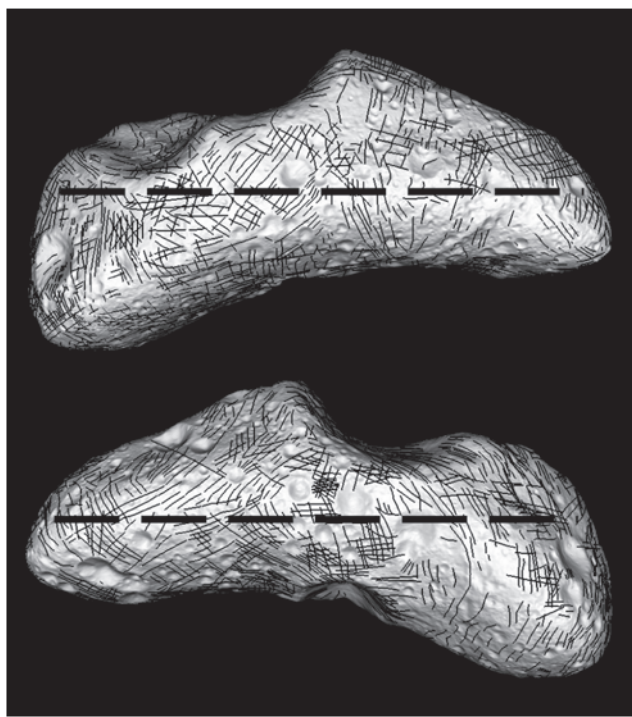


**Fig. 11.** Global distribution of lineaments on Eros. The dashed black line indicates the average planes derived from a subset of about 1500 lineaments. Perpendicular to the dashed lines are seen the large craters Himeros (above line) and Psyche (below line), which are possible sources for some of the lineaments. The two views correspond to a rotation of 180° in longitude.

calculations also indicate that for a rubble-pile Eros struck by a projectile with the same size and speed as employed for the strong case, any global link between surface cracks to Himeros' formation is lost. Cracks are formed at all scales and in all directions, with little directional connection to the parent crater.

The internal structure of Eros is, however, not known. The largest lineament on Eros, Rahe Dorsum, along with two other sets of smaller lineaments that are either parallel or in conjugate orientation to Rahe Dorsum, seem to have no parent crater and could be a remnant from Eros' original parent body (Buczkowski *et al.*, 2009). Their presence suggests that Eros must have been somewhat damaged to begin with, perhaps as the result of the collision on a larger parent body. Such a view is substantiated by analyses that indicate that Eros is probably best represented by a lunar-like megaregolith covered by a regolith, but with some large interlocking aggregates or fragments, to account for the low measured porosity (Robinson *et al.*, 2002). Such large-scale fragments may also explain the presence of the long lineaments described above. Support for this scenario may come from a smaller subset of lineaments that are radial to many of the smaller ( $\leq 5$  km) craters (Buczkowski *et al.*, 2008), indicating that the characteristic size for the putative internal rubbles is likely to be comparable to or larger than

these craters. Therefore, although a monolithic Eros seems unlikely, it still may have significant internal coherence to explain some of the surface features.

The analysis of the three-dimensional orientation used to understand the origin of structural lineaments on Eros was also employed on Vesta and Lutetia. In the case of Vesta, the two main sets of impressive circumferential lineaments are related to the formation of the two south polar basins Rheasilvia and Veneneia (Jaumann *et al.*, 2012) (Fig. 12a). The older set is clearly related to the older Veneneia, while the younger features are associated with the younger Rheasilvia. These faults are much more impressive than on Eros, with absolute vertical and horizontal displacements comparable with the size of Eros itself. Preliminary numerical investigations (Buczkowski *et al.*, 2012) suggest that these likely reflect the differentiated internal structure of Vesta, which results in shock impedance differences that can accentuate the formation of large surface faults. Furthermore, a stronger metallic interior core may also contribute to localize seismic energy (Bowling *et al.*, 2014). The formation of circumferential lineaments on Vesta was also investigated with the help of laboratory experiments and three-dimensional CTH simulations (Stickler *et al.*, 2015). The results show that large impacts induce widespread subsurface damage, and that surface lineaments may be the manifestation of faulting due to shear localization in subsurface failure planes. Furthermore, the offset of the pole of the lineaments to the crater center can be used to constrain the geometry of the impact, such as the impact angle, which for the case of Rheasilvia was inferred to be at least  $\sim 50^\circ$  from the normal to the surface (Stickler *et al.*, 2015). This process may also explain the set of pit chains seen prevailing in the east-west direction that is parallel to the major set of faults due to the formation of Rheasilvia basin.

On Lutetia, the analysis of the lineaments (Besse *et al.*, 2014) shows that both radial and circumferential lineaments observed can be attributed to craters, as proposed in recent modeling (Jutzi *et al.*, 2013). Most of the circumferential features can be attributed to the north crater complex (formed by two to four overlapping large craters; see the chapter by Barucci *et al.* in this volume), but two other sets of lineaments have also been identified (Figs. 12b,c). One set can be linked to the 60-km Massilia crater, and the other to the southern region of the asteroid not imaged by the Rosetta mission (roughly corresponding to Massilia's antipodes). Given the apparent link between many of these lineaments and craters on Eros, Vesta, and Lutetia, this last set of lineaments on Lutetia could indicate the presence of another sizable crater in the southern hemisphere, although we cannot rule out its association with Massilia crater.

Asteroidal ridges do not seem to be directly related to any particular craters. While some studies have invoked an internal process for their formation (Greenberg, 2008), others indicate that these might be the result of collisional processes that are associated with the formation of the asteroids. As mentioned previously, Buczkowski *et al.* (2009) show that on Eros, the Rahe Dorsum has a set of conjugate fractures that are likely formed coevally with the Dorsum. Neither one

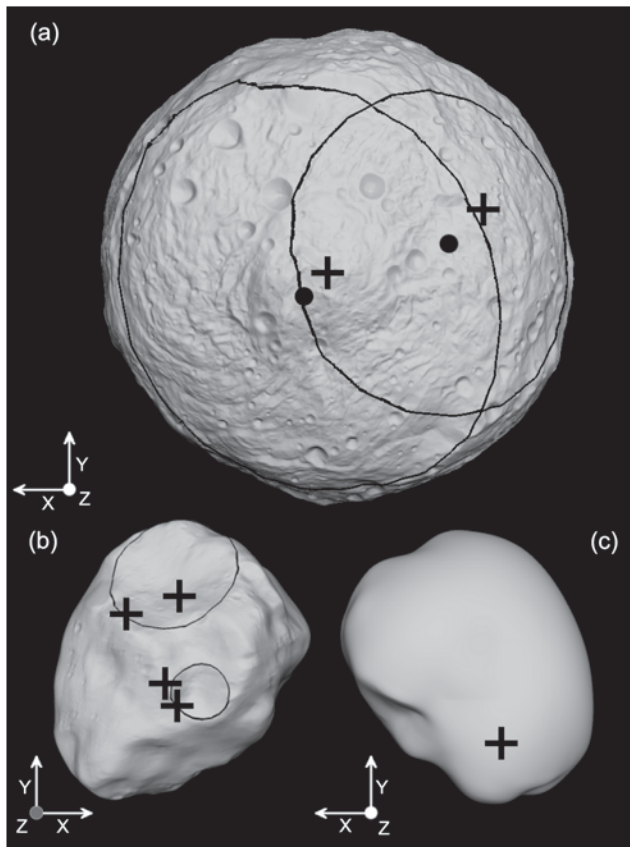


**Fig. 12.** Location of poles (black pluses) defined by best fit planes to circumferential lineaments seen on (a) Vesta (modified from Jaumann et al., 2012) and (b),(c) Lutetia (modified from Besse et al., 2014). The black lines mark major craters. The center of the large Rheasilvia and Veneneia basins on Vesta are also indicated (black dots) to highlight the slight misalignment with the poles of the equatorial troughs system associated with both basins.

of these features is obviously associated with any surface crater, which may suggest that they resulted from cracking during the disruption of Eros' parent body. Itokawa has a set of ridges that circumscribe the large lobe (but not the small lobe) that also do not have any obvious association with any of the known candidate craters located on the surface of the asteroid (Barnouin et al., 2008, 2014). These ridges may reflect some displacement along the edges of interior chunks in the body of Itokawa that were mobilized at some point in Itokawa's formation and evolution.

#### 4.3. Impact-Derived Surface Blocks

Besides forming craters and contributing to lineament formation, impacts also generate blocks on the surfaces of most small bodies. While large cratering events are the sources of many blocks on asteroids, some surface blocks may result from the disruptive origins of the asteroids, creating rubble piles, and may provide additional constraints on their makeup (Lee et al., 1986, 1996; Thomas et al., 2012; Kueppers et al.,

2012; Thomas et al., 2001; Nakamura et al., 2008; Michikami et al., 2008; Mazaroei et al., 2014; Carsenty et al., 2014).

High-resolution imaging data (<100 m/pixel) from asteroids Vesta, Lutetia, and Eros confirm the assumptions made in earlier efforts at Ida (Lee et al., 1996) that blocks on asteroids are the result of impact cratering. In many instances, the SFDs of blocks found to be associated with craters (e.g., Chapman et al., 2002; Kueppers et al., 2012), possess similar cumulative power-law exponents (slopes) with an average value of about  $-4$ . Although a preliminary analysis of the block distributions on Itokawa's surface (Michikami et al., 2008) found a shallow slope of  $-3$ , a recent more complete evaluation of all the largest blocks ( $>5$  m) on Itokawa (Mazrouei et al., 2014) show little difference from distributions derived from crater ejecta. The range of observed slopes on asteroids is comparable to that found for the block distributions of lunar impact craters, which cluster between  $-3$  and  $-4$  (e.g., Bart and Melosh, 2010). However, the blocks on Itokawa may more likely be the result of impact disruption and reaccretion (e.g., Fujiwara et al., 2006) rather than crater ejecta, despite the similar sloped SFDs. Despite the overall agreement, it is important to realize that lunar block SFDs often exhibit slopes as shallow as  $-2$  and, in a few cases, also as steep as  $-5$  (Bart and Melosh, 2010). Such a significant spread in the slope can be due to differences in terrain properties and/or preservation. In fact, it should be noted that once blocks are exposed on the surface, they undergo erosion and breakup as a result of a number of processes, such as small impacts and thermal fatigue (e.g., Delbo et al., 2014), which may alter their SFD.

The overall similarity of the asteroidal block SFDs likely reflects a common formation process, a similar range of material properties, and similar preservation. Most of these blocks appear to be derived by impact cratering (Lutetia, Eros) or disruption (Itokawa) of preexisting regolith and rubble that was created by brittle fracture. That some individual fragments fail brittlely is suggested by several studies (Nakamura et al., 2008; Michikami et al., 2010) that show that the blocks on Itokawa possess morphologies, shapes, and aspect ratios very similar to fragments generated in small-scale laboratory experiments produced by brittle failure of individual rocks (Tsuchiyama et al., 2011). Once blocks are exposed on the surface they follow similar evolutionary pathways, probably as a consequence of thermal fatigue and impacts, so they maintain similarities in their size distributions.

#### 4.4. Implications for the Internal Structures

The analyses of lineaments on Vesta, Lutetia, and perhaps Eros indicate that these objects must possess some internal ability to transfer impact energy over long global distances. Even the rubble-pile asteroid Itokawa has ridges, which indicate the presence of localized aggregates that have slid past each other, although not at the global scales seen elsewhere. Blocks observed on Vesta, Lutetia, Eros, and Itokawa provide further evidence for the presence of subsurface rocks that have been broken brittlely by impacts. Gaspra and

Ida also possess lineaments, and the latter also has surface blocks. Ida's measured density of  $2600 \pm 500 \text{ kg m}^{-3}$  is similar to that for Eros given its proposed composition, and suggests that its interior is capable of transferring impact energy over long distances (Asphaug *et al.*, 1996). These observations are consistent with their interiors — at least to the depth reached by cratering — being structured and made of materials that are connected and can fail brittlely. Of course, Vesta, and possibly Lutetia, are large enough to be primordial differentiated objects that have not been fully damaged and are surely competent (e.g., Pätzold *et al.*, 2011; Russell *et al.*, 2012; Park *et al.*, 2014).

However, collisional-evolution models strongly suggest that smaller asteroids, like Eros and Ida, should be rubble piles (Michel *et al.*, 2001; Durda *et al.*, 2007). The low observed porosity and global lineament patterns observed for some asteroids might be indicators of rubble piles with good internal connectivity. Numerical simulations of impacts into loosely bound aggregates show that well-connected aggregates are probably necessary to generate the stresses that produce lineament patterns like those observed on Eros (Crawford and Barnouin-Jha, 2003). Alternatively, Asphaug (2009) proposed that the surface morphology and density of Eros could be explained by a cohesive sand pile, although the apparent relationship of many of the lineaments to large craters (in the same way lineaments are related to large craters on Vesta and Lutetia) casts doubt on a sand-pile model. Furthermore, surface roughness assessments indicate that some bedrock could be protruding through regolith on slopes (Cheng *et al.*, 2001, 2002), which suggests that these asteroids have competent components that may even retain some memory of their relationships on their parent bodies from which they were liberated by catastrophic collisions (see the chapter by Michel *et al.* in this volume).

Mathilde is an exception to what we observe for many of the other asteroids. Unlike Eros and Ida, as well as many of the larger bodies, this C-type asteroid has a limited number of lineaments identified (perhaps due to poor imaging resolution) and high porosity (~50%) (Yeomans *et al.*, 1997). Mathilde also possesses an inordinate number of large craters relative to other asteroids (e.g., Cheng and Barnouin, 1999; Chapman *et al.*, 1999). It is well known that high porosity limits the extent to which impact-derived shocks can travel through an asteroid (Love *et al.*, 1993; Cheng and Barnouin, 1999; Housen and Holsapple, 2003; Schultz *et al.*, 2007; Jutzi *et al.*, 2010b). This can limit the extent of lineament formation (Jutzi *et al.*, 2010b), and permit the formation of many large craters without disrupting Mathilde. This difference might be a reflection of the physical differences between ordinary and carbonaceous chondrites (Britt *et al.*, 2002).

## 5. CONCLUSIONS

Our knowledge of cratering of asteroids increased greatly after 1991, when the Galileo spacecraft imaged the asteroid Gaspra during a close flyby. Continuing opportunistic flybys

as well as dedicated missions to asteroids have now revealed numerous asteroids, all of whose surfaces are cratered to varying degrees. Future missions already launched or under development [such as Hayabusa-2 and the Origins Spectral Interpretation Resource Identification and Security-Regolith Explorer (OSIRIS-REx)], and higher-resolution radar delay-Doppler mapping, promise to provide a continuing source of cratering data.

Given the lack of endogenic geological activity on most asteroids, it is no surprise that the dominant evolutionary process influencing the surface of asteroids is impacts by other asteroids and comets. These result in cratered surfaces, although larger impacts penetrate the interiors of asteroids, giving rise to a variety of linear features, ridges, and trenches, also expressed on the observed surfaces. Large impacts can also trigger mass wasting and, in other ways, degrade and eventually erase preexisting craters and landforms. Asteroids imaged at submeter resolutions (Itokawa, Eros) present boulder-strewn surfaces with fewer obvious craters as the inherent rubble-pile constituents and more effective crater-destruction processes tend to dominate over formation and retention of craters.

Size-frequency distributions of craters tend to vary not only from asteroid to asteroid, but also on different geological units on the same asteroid. Nevertheless, crater SFDs tend to initially reflect a single MPF (that of the collisionally relaxed SFD for the main-belt asteroid population; see the chapter by Bottke *et al.* in this volume), subsequently modified by formation of secondary craters in some cases and by crater-degradation processes. The degree to which these crater SFDs are undersaturated or instead approach or reach saturation enables us to not only date relative age differences on an individual asteroid, like Lutetia and Vesta, but also to approximately provide absolute ages for surfaces of different asteroids. Such absolute ages depend heavily on model parameters, including models for the rate of decline of the impact flux from the earliest times, assumed crater-scaling laws, and assumed target properties (strength, density, porosity). Given the uncertainties involved in cratering ages, it is important to compare with other methods whenever possible.

On Vesta, crater-retention ages of major units range from ~1 Ga for terrain associated with the Rheasilvia basin to perhaps as much as ~4.4 Ga for the most heavily cratered terrains, although the older estimate is highly uncertain. There have been arguments from studies of the dynamics of the Vesta asteroid family (see the chapter by Nesvorný *et al.* in this volume) that Rheasilvia, presumably the scar from the impact that created the family, has an age of ~1 Ga (Marzari *et al.*, 1996; Milani *et al.*, 2014), although other analyses pose a lower limit of ~0.5 Ga (see the chapter by Nesvorný *et al.* in this volume). The case of Vesta is particularly important because we have samples of this asteroid in our meteorite collections: the howardite, eucrite, and diogenite (HED) meteorites. Meteorites can retain a record of their parent body's collisional history in their isotopic signatures (e.g., Bogard, 2011). Particularly useful for this purpose is the K-Ar system,

which can be reset during collisions. The HED meteorites show a characteristic K-Ar age spectrum indicating numerous resetting events older than  $\sim 3.5$  Ga (Bogard, 2011; Marchi et al., 2013). Most HEDs are thought to originate from the formation of the Rheasilvia basin on Vesta, although older basins may also contribute. Interestingly, a recent high-spatial-resolution analysis of feldspar grains in Kapoeta, a howardite, yielded ages ranging from 0.8 to 1.2 Ga (Lindsay et al., 2015), compatible with Rheasilvia's cratering age.

We find ages for Gaspra and Ida of  $\sim 1.8$  Ga and  $\sim 3.5$  Ga, respectively (the age estimate for Ida would be a lower limit if Ida's surface were saturated with craters). Since Gaspra is probably a member of the Flora family [here we assume it is of rocky composition, and not metallic as suggested by Chapman (1996)] and Ida is quite certainly a member of the Koronis family, it is interesting to compare our results with dynamical ages for those families,  $\sim 1$  Ga and  $\sim 2.5$  Ga, respectively (Dykhuis et al., 2014; see the chapter by Nesvorný et al. in this volume); these are reasonably consistent, given the approximate nature of both cratering and dynamical ages. We have no independent check on our estimate of  $\sim 1.5$  Ga for the crater retention age on Eros, since Eros cannot be linked to a specific family. Age estimates for other nonfamily asteroids (Lutetia, Steins, Toutatis), based on the same methodology, are presented in the chapter by Barucci et al. in this volume. Because of great uncertainty about the applicable crater-scaling law for Mathilde and the strength of that C-type asteroid, we do not propose a cratering age for it.

We have described depth-diameter measurements for craters on several asteroids. The great diversity of crater morphologies exhibited on asteroids imaged up close (e.g., the bimodal craters formed on steep slopes on Lutetia and Vesta) suggest that more complete analyses than have been done to date of the statistics of craters of different morphologies (e.g., across the range of degradational states) may illuminate issues of crater formation, degradation, and obliteration, which are the dominant processes shaping asteroid surfaces. In a similar way, studies of impact-induced lineaments, such as ridges and trenches, can help to reveal aspects of the bulk structure of asteroids by providing constraints on how shock waves travel through asteroids.

As Dawn approached (1) Ceres in early 2015, there were ideas that this dwarf planet might exhibit large craters, like those on Vesta and Lutetia, or might not, because of its different composition, which may affect the formation, preservation, and/or survivability of craters. For example, Tyre on Europa and palimpsests on Callisto show little relief. Approach images of Ceres suggest a complex cratering history.

Impact cratering on asteroids appears to be a very complex process for which many facets are not yet fully understood despite the significant progress made over the last decade. As we have indicated, craters and impact-induced surface features potentially hold a great wealth of information about the past evolution and internal structures of asteroids. Future missions will certainly improve our understanding of these processes and undoubtedly provide new challenges.

**Acknowledgments.** We thank reviewers K. Housen and D. Minton for their helpful and constructive comments. Research funds for S.M. and C.R.C. were provided by NASA's Solar System Evolution Research Virtual Institute (SSERVI) as part of the Institute for the Science of Exploration Targets (ISET) at the Southwest Research Institute (NASA grant no. NNA14AB03A).

## REFERENCES

- Abe S., Mukai T., Hirata N., et al. (2006) Mass and local topography measurements of Itokawa by Hayabusa. *Science*, **312**, 1344–1349.
- Asphaug E. (2009) Growth and evolution of asteroids. *Annu. Rev. Earth Planet. Sci.*, **37**, 413–448.
- Asphaug E. and Melosh H. J. (1993) The Stickney impact of Phobos — A dynamical mode. *Icarus*, **101**, 144–164.
- Asphaug E., Moore J. M., Morrison D., Benz W., Nolan M. C., and Sullivan R. J. (1996) Mechanical and geological effects of impact cratering on Ida. *Icarus*, **120**, 158–184.
- Barnouin O. S., Noviello J. L., and Ernst C. M. (2014) Are there structural lineaments on Itokawa? *Lunar Planet. Sci. XLV*, Abstract #2221. Lunar and Planetary Institute, Houston.
- Barnouin-Jha O. S., Cheng A. F., Mukai T., et al. (2008) Small-scale topography of 25143 Itokawa from the Hayabusa laser altimeter. *Icarus*, **198**, 108–124.
- Bart G. D. and Melosh H. J. (2010) Distributions of boulders ejected from lunar craters. *Icarus*, **209**, 337–357.
- Besse S., Lamy P., Jorda L., Marchi S., and Barbieri C. (2012) Identification and physical properties of craters on asteroid (2867) Steins. *Icarus*, **221**, 1119–1129.
- Besse S., Kuppers M., Barnouin O. S., Thomas N., and Benkhoff J. (2014) Lutetia's lineaments. *Planet. Space Sci.*, **101**, 186–195.
- Blitz C., Lognonné P., Komaititsch D., and Baratoux D. (2009) Effects of ejecta accumulation on the crater population of asteroid 433 Eros. *J. Geophys. Res.*, **114**, E06006.
- Bogard D. D. (2011) K-Ar ages of meteorites: Clues to parent-body thermal histories. *Chem. Erde-Geochem.*, **71**, 207–226.
- Bottke W. F., Durda D. D., Nesvorný D., Jedicke R., Morbidelli A., Vokrouhlický D., and Levison H. F. (2005) Linking the collisional history of the main asteroid belt to its dynamical excitation and depletion. *Icarus*, **179**, 63–94.
- Bowling T. J., Johnson B. C., and Melosh H. J. (2014) Formation of equatorial graben on 4 Vesta following the Rheasilvia basin forming impact. In *Vesta in the Light of Dawn: First Exploration of a Protoplanet in the Asteroid Belt*, Abstract #2018. LPI Contribution No. 1773, Lunar and Planetary Institute, Houston.
- Britt D. T., Yeomans D., Housen K., and Consolmagno G. (2002) Asteroid density, porosity, and structure. In *Asteroids III* (W. F. Bottke Jr. et al. eds.), pp. 485–500. Univ. of Arizona, Tucson.
- Buczkowski D. L., Barnouin-Jha O. S., and Prockter L. M. (2008) 433 Eros lineaments: Global mapping and analysis. *Icarus*, **193**, 39–52.
- Buczkowski D. L., Barnouin-Jha O. S., Wyrick D., and Prockter L. M. (2009) Further analyses of the 433 Eros global lineament map. *Lunar Planet. Sci. XL*, Abstract #1187. Lunar and Planetary Institute, Houston.
- Buczkowski D. L., Wyrick D. Y., Iyer K. A., et al. (2012) Large-scale troughs on Vesta: A signature of planetary tectonics. *Geophys. Res. Lett.*, **39**, L18205.
- Carr M. H., Kirk R. L., McEwen A., Veverka J., Thomas P., Head J. W., and Murchie S. (1994) The geology of Gaspra. *Icarus*, **107**, 61.
- Carsenty U., Wagner R. J., Boczkowski D. L., et al. (2013) The “Swarm” — A peculiar crater chain on Vesta. *Lunar Planet. Sci. XLIV*, Abstract #1492. Lunar and Planetary Institute, Houston.
- Carsenty U., Wagner R. J., Jaumann R., et al. (2014) Boulders on the surface of Vesta — The southern hemisphere. In *Vesta in the Light of Dawn: First Exploration of a Protoplanet in the Asteroid Belt*, Abstract #1492. LPI Contribution No. 1773, Lunar and Planetary Institute, Houston.
- Chapman C. R. (1976) Asteroids as meteorite parent-bodies — The astronomical perspective. *Geochim. Cosmochim. Acta*, **40**, 701–719.
- Chapman C. R. (1978) Asteroid collisions, craters, regoliths, and lifetimes. In *Asteroids: An Exploration Assessment*, pp. 145–160. NASA CP-2053, Washington, DC.

- Chapman C. R. (1996) S-type asteroids, ordinary chondrites, and space-weathering: The evidence from Galileo's fly-bys of Gaspra and Ida. *Meteoritics & Planet. Sci.*, 31, 699–725.
- Chapman C. R. and McKinnon W. B. (1986) Cratering of planetary satellites. In *Satellites* (J. A. Burns and M. S. Matthews eds), pp. 492–580. Univ. of Arizona, Tucson.
- Chapman C. R., Ryan E. V., Merline W. J., Neukum G., Wagner R., Thomas P. C., Veverka J., and Sullivan R. J. (1996a) Cratering on Ida. *Icarus*, 120, 77–86.
- Chapman C. R., Veverka J., Belton M. J. S., Neukum G., and Morrison D. (1996b) Cratering on Gaspra. *Icarus*, 120, 231–245.
- Chapman C. R., Merline W. J., and Thomas P. (1999) Cratering on Mathilde. *Icarus*, 140, 28–33.
- Chapman C. R., Merline W. J., Thomas P. C., Joseph J., Cheng A. F., and Izenberg N. (2002) Impact history of Eros: Craters and boulders. *Icarus*, 155, 104–118.
- Cheng A. F. and Barnouin-Jha O. S. (1999) Giant craters on Mathilde. *Icarus*, 140, 34–48.
- Cheng A. F., Barnouin-Jha O. S., Zuber M. T., Veverka J., Smith D. E., Neumann G. A., Robinson M., Thomas P., Garvin J. B., Murchie S., Chapman C., and Prockter L. (2001) Laser altimetry of small-scale features on 433 Eros from NEAR-Shoemaker. *Science*, 292, 488–491.
- Cheng A. F., Barnouin-Jha O. S., Prockter L., Zuber M. T., Neumann G., Smith D. E., Garvin J., Robinson M., Veverka J., and Thomas P. C. (2002) Small-scale topography of 433 Eros from laser altimetry and imaging. *Icarus*, 155, 51–74.
- Cintala M. J., Head J. W., and Veverka J. (1978) Characteristics of the cratering process on small satellites and asteroids. *Proc. Lunar Sci. Conf. 9th*, pp. 3803–3830.
- Crater Analysis Techniques Working Group (1979) Standard techniques for presentation and analysis of crater size-frequency data. *Icarus*, 37, 467–474.
- Crawford D. A. and Barnouin-Jha O. S. (2003) Application of adaptive mesh refinement to the simulation of impacts in complex geometries and heterogeneous materials. In *Impact Cratering: Bridging the Gap Between Modeling and Observations*, Abstract #8011. LPI Contribution No. 1155, Lunar and Planetary Institute, Houston.
- Delbo M., Libourel G., Wilkerson J., Murdoch N., Michel P., Ramesh K. T., Ganino C., Verati C., and Marchi S. (2014) Thermal fatigue as the origin of regolith on small asteroids. *Nature*, 508, 233–236.
- Dykhuis M. J., Molnar L., Van Kooten S. J., and Greenberg R. (2014) Defining the Flora family: Orbital properties, reflectance properties and age. *Icarus*, 243, 111–128.
- Durda D. D., Bottke W. F., Nesvorný D., Enke B. L., Merline W. J., Asphaug E., and Richardson D. C. (2007) Size-frequency distributions of fragments from SPH/N-body simulations of asteroid impacts: Comparison with observed asteroid families. *Icarus*, 186, 498–516.
- Fassett C. I. and Thomson B. J. (2014) Crater degradation on the lunar maria: Topographic diffusion and the rate of erosion on the Moon. *J. Geophys. Res.-Planets*, 119, 2255–2271.
- Fujiwara A. (1991) Stickney-forming impact on Phobos — Crater shape and induced stress distribution. *Icarus*, 89, 384–391.
- Fujiwara A., Kadono T., and Nakamura A. (1993) Cratering experiments into curved surfaces and their implication for craters on small satellites. *Icarus*, 105, 345.
- Fujiwara A., Kawaguchi J., Yeomans D. K., et al. (2006) The rubble-pile asteroid Itokawa as observed by Hayabusa. *Science*, 312, 1330–1334.
- Gault D. E. (1970) Saturation and equilibrium conditions for impact cratering on the lunar surface: Criteria and implications. *Radio Sci.*, 5, 273–291.
- Gault D. E., Quaide W. L., and Oberbeck V. R. (1968) Impact cratering mechanics and structures. In *Shock Metamorphism of Natural Materials* (B. M. French and N. M. Short, eds.), pp. 87–90. Mono, Baltimore.
- Gilbert G. K. (1893) The Moon's face, a study of the origin of its features. *Bull. Philos. Soc. Wash.*, 12, 241–292.
- Greenberg R. (2008) Eros' Rahe Dorsum: Implications for internal structure. *Meteoritics & Planet. Sci.*, 43, 435–449.
- Greenberg R., Nolan M. C., Bottke W. F., Kolvoord R. A., and Veverka J. (1994) Collisional history of Gaspra. *Icarus*, 107, 84–97.
- Greenberg R., Bottke W. F., Nolan M., Geissler P., Petit J., Durda D. D., Asphaug E., and Head J. (1996) Collisional and dynamical history of Ida. *Icarus*, 120, 106–118.
- Grieve R. A. F., Cintala M. J., and Tagle R. (2007) Planetary impacts. In *Encyclopedia of the Solar System, 2nd edition* (L.-A. McFadden et al., eds.), p. 813–828. Academic, San Diego.
- Güttler C., Hirata N., and Nakamura A. M. (2012) Cratering experiments on the self armoring of coarse-grained granular targets. *Icarus*, 220, 1040–1049.
- Hartmann W. K. (1984) Does crater 'saturation equilibrium' occur in the solar system? *Icarus*, 60, 56–74.
- Hirata N., Barnouin-Jha O. S., Honda C., Nakamura R., Miyamoto H., Sasaki S., Demura H., Nakamura A. M., Michikami T., Gaskell R. W., and Saito J. (2009) A survey of possible impact structures on 25143 Itokawa. *Icarus*, 200, 486–502.
- Holsapple K. A. and Housen K. R. (2007) A crater and its ejecta: An interpretation of deep impact. *Icarus*, 187, 345–356.
- Housen K. R. and Holsapple K. A. (2003) Impact cratering on porous asteroids. *Icarus*, 163, 102–119.
- Housen K. R., Holsapple K. A., and Voss M. E. (1999) Compaction as the origin of the unusual craters on the asteroid Mathilde. *Nature*, 402, 155–157.
- Ivanov B. A. (1991) Mechanical consequences of impact formed crater Stickney on Phobos. *Lunar Planet. Sci. XXII*, pp. 619–620. Lunar and Planetary Institute, Houston.
- Jaumann R., Williams D. A., Buckowski D. L., et al. (2012) Vesta's shape and morphology. *Science*, 336, 687.
- Jutzi M., Michel P., and Benz W. (2010a) A large crater as a probe of the internal structure of the E-type asteroid Steins. *Astron. Astrophys.*, 509, L2–L6.
- Jutzi M., Michel P., Benz W., and Richardson D. C. (2010b) Fragment properties at the catastrophic disruption threshold: The effect of the parent body's internal structure. *Icarus*, 207, 54–65.
- Jutzi M., Thomas N., Benz W., Maarry El M. R., Jorda L., Kührt E., and Preusker F. (2013) The influence of recent major crater impacts on the surrounding surfaces of (21) Lutetia. *Icarus*, 226, 89–100.
- Keil K., Stoeffler D., Love S. G., and Scott E. R. D. (1997) Constraints on the role of impact heating and melting in asteroids. *Meteoritics & Planet. Sci.*, 32, 349–363.
- Krohn K., Jaumann R., Elbeshausen D., et al. (2014) Asymmetric craters on Vesta: Impact on sloping surfaces. *Planet. Space Sci.*, 103, 36–56.
- Kueppers M., Moissl R., Vincent J.-B., Besse S., Hvistendahl K., Carry B., Grieger B., Siersch H., Keller H. U., Marchi S., and the OSIRIS Team (2012) Boulders on Lutetia. *Planet. Space Sci.*, 66, 71–78.
- Lambe T. W. and Whitman R. V. (1979) *Soil Mechanics, SI edition*. Wiley, New York. 570 pp.
- Lee P., Veverka J., Thomas P. C., Helfenstein P., Belton M. J. S., Chapman C. R., Greeley R., Pappalardo R. T., Sullivan R., and Head J. W. (1996) Ejecta blocks on 243 Ida and on other asteroids. *Icarus*, 120, 87–105.
- Lee S. W., Thomas P., and Veverka J. (1986) Phobos, Deimos, and the Moon — Size and distribution of crater ejecta blocks. *Icarus*, 68, 77–86.
- Lindsay F. N., Delaney J. S., Turpin B. D., Herzog G. F., Park J., and Swisher C. C. (2015) Rheasilvia provenance of the Kapoeta howardite inferred from ~1 Ga  $^{40}\text{Ar}/^{39}\text{Ar}$  feldspar ages. *Earth Planet. Sci. Lett.*, 413, 208–213.
- Love S. G., Friedrich H., and Brownlee D. E. (1993) Target porosity effects in impact cratering and collisional disruption. *Icarus*, 105, 216–224.
- Mantz A., Sullivan R., and Veverka J. (2004) Regolith transport in craters on Eros. *Icarus*, 167, 197–203.
- Marchi S., Barbieri C., Kueppers M., Marzari F., Davidsson B., Keller H. U., Besse S., Lamy P., Mottola S., Massironi M., and Cremonese G. (2010) The cratering history of asteroid (2867) Steins. *Planet. Space Sci.*, 58, 1116–1123.
- Marchi S., Massironi M., Cremonese G., Martellato E., Giacomini L., and Pockter L. (2011) The effects of the target material properties and layering on the crater chronology: The case of Raditladi and Rachmaninoff basins on Mercury. *Planet. Space Sci.*, 59, 1968.
- Marchi S., McSween H. Y., O'Brien D. P., Schenk P., De Sanctis M. C., Gaskell R., Jaumann R., Mottola S., Preusker F., Raymond C. A., Roatsch T., and Russell C. T. (2012a) The violent collisional history of asteroid 4 Vesta. *Science*, 336, 690.
- Marchi S., Massironi M., Vincent J.-B., et al. (2012b) The cratering history of asteroid (21) Lutetia. *Planet. Space Sci.*, 66, 87–95.

- Marchi S., Bottke W. F., Kring D. A., and Morbidelli A. (2012c) The onset of the lunar cataclysm as recorded in its ancient crater populations. *Earth Planet. Sci. Lett.*, 325, 27–38.
- Marchi S., Bottke W. F., Cohen B. A., Wuenemann K., Kring D. A., McSween H. Y., De Sanctis M. C., O'Brien D. P., Schenk P., Raymond C. A., and Russell C. T. (2013) High velocity collisions from the lunar cataclysm recorded in asteroidal meteorites. *Nature Geosci.*, 6, 303–307.
- Marchi S., Bottke W. F., O'Brien D. P., Schenk P., Mottola S., De Sanctis M. C., Kring D. A., Williams D. A., Raymond C. A., and Russell C. T. (2014) Small crater populations on Vesta. *Planet. Space Sci.*, 103, 96–103.
- Marzari F. et al. (1996) Origin and evolution of the Vesta asteroid family. *Astron. Astrophys.*, 316, 248–262.
- Massironi M., Marchi S., Pajola M., et al. (2012) Geological map and stratigraphy of asteroid (21) Lutetia. *Planet. Space Sci.*, 66, 125–136.
- Mazrouei S., Daly M. G., Barnouin O. S., Ernst C. M., and DeSouza I. (2014) Block distributions on Itokawa. *Icarus*, 229, 181–189.
- McSween H. Y. and Huss G. R. (2010) *Cosmochemistry*. Cambridge Univ., Cambridge. 549 pp.
- Melosh H. J. (1989) *Impact Cratering*. Oxford Univ., New York. 245 pp.
- Michel P. (2001) Collisions and gravitational reaccumulation: Forming asteroid families and satellites. *Science*, 294, 1696–1700.
- Michel P. and Richardson D. C. (2013) Collision and gravitational reaccumulation: Possible formation mechanism of the asteroid Itokawa. *Astron. Astrophys.*, 554, L1–L4.
- Michel P., O'Brien D. P., Abe S., and Hirata N. (2009) Itokawa's cratering record as observed by Hayabusa: Implications for its age and collisional history. *Icarus*, 200, 503–513.
- Michikami T., Nakamura A. M., Hirata N., Gaskell R. W., Nakamura R., Honda T., Honda C., Hiraoka K., Saito J., Demura H., Ishiguro M., and Miyamoto H. (2008) Size-frequency statistics of boulders on global surface of asteroid 25143 Itokawa. *Earth Planet. Space*, 60, 13–20.
- Michikami T., Nakamura A. M., and Hirata N. (2010) The shape distribution of boulders on asteroid 25143 Itokawa: Comparison with fragments from impact experiments. *Icarus*, 207, 277–284.
- Milani A., Cellino A., Knežević Z., Novaković B., Spoto F., and Paolicchi P. (2014) Asteroid families classification: Exploiting very large datasets. *Icarus*, 239, 46–73.
- Moore H. J., Hodges C. A., Scott D. H. (1974) Multiringed basins—Illustrated by Orientale and associated features. *Proc. Lunar Sci. Conf. 5th*, pp. 71–100.
- Morbidelli A., Bottke W. F., Nesvorný D., and Levison H. F. (2009) Asteroids were born big. *Icarus*, 204, 558–573.
- Nakamura A. M., Michikami T., Hirata N., et al. (2008) Impact process of boulders on the surface of asteroid 25143 Itokawa—fragments from collisional disruption. *Earth Planets Space*, 56, 448–472.
- Nolan M. C., Asphaug E., Melosh H. J., and Greenberg R. (1996) Impact craters on asteroids: Does gravity or strength control their size? *Icarus*, 124, 359–371.
- Oberbeck V. R. (1975) The role of ballistic erosion and sedimentation in lunar stratigraphy. *Rev. Geophys. Space Phys.*, 13, 337–362.
- O'Brien D. P., Greenberg R., and Richardson J. E. (2006) Craters on asteroids: Reconciling diverse impact records with a common impacting population. *Icarus*, 183, 79–92.
- O'Brien D. P., Marchi S., Morbidelli A., Bottke W. F., Schenk P. M., Russell C. T., and Raymond C. A. (2014) Constraining the cratering chronology of Vesta. *Planet. Space Sci.*, 103, 131–142.
- Otto K. A., Jaumann R., Krohn K., et al. (2013) Mass-wasting features and processes in Vesta's south polar basin Rheasilvia. *J. Geophys. Res.—Planets*, 118, 2279–2294.
- Park R. S., Konopliv A. S., Asmar S. W., et al. (2014) Gravity field expansion in ellipsoidal harmonic and polyhedral internal representations applied to Vesta. *Icarus*, 240, 118–132.
- Pätzold M., Andert T. P., Asmar S. W., et al. (2011) Asteroid 21 Lutetia: Low mass, high density. *Science*, 334, 491.
- Pike R. J. (1977) Apparent depth/apparent diameter relation for lunar craters. *Proc. Lunar Sci. Conf. 8th*, pp. 3427–3436.
- Pike R. J. (1980) Control of crater morphology by gravity and target type—Mars, Earth, Moon. *Proc. Lunar Planet. Sci. Conf. 11th*, pp. 2159–2189.
- Prockter L. and Barnouin O. S. (2003) Fine-scale fractures on the surface of 433 Eros: Implications for structural control and tectonic resurfacing of craters. *AGU Fall Meeting Abstracts*, 31, #P31C-05.
- Prockter L., Thomas P., Robinson M., Joseph J., Milne A., Bussey B., Everka J., and Cheng A. (2002) Surface expressions of structural features on Eros. *Icarus*, 155, 75–93.
- Richardson J. E. (2009) Cratering saturation and equilibrium: A new model looks at an old problem. *Icarus*, 204, 697–715.
- Richardson J. E. (2013) Three-dimensional modeling of crater degradation via the effects of impact induced seismic shaking, with comparison to crater count data. *Lunar Planet. Sci. XLIV*, Abstract #2397. Lunar and Planetary Institute, Houston.
- Richardson J. E., Melosh H. J., and Greenberg R. (2004) Impact-induced seismic activity on asteroid 433 Eros: A surface modification process. *Science*, 306, 1526–1529.
- Richardson J. E., Melosh H. J., Greenberg R. J., and O'Brien D. P. (2005) The global effects of impact induced seismic activity on fractured asteroid surface morphology. *Icarus*, 179, 325–349.
- Robbins S. J., Antonenko I., Kirchoff M. R., et al. (2014) The variability of crater identification among expert and community crater analysts. *Icarus*, 234, 109–131.
- Robinson M. S., Thomas P. C., Everka J., Murchie S. L., and Wilcox B. B. (2002) The geology of 433 Eros. *Meteoritics & Planet. Sci.*, 37, 1651–1684.
- Rubincam D. P. (2000) Radiative spin-up and spin-down of small asteroids. *Icarus*, 148, 2–11.
- Russell C. T., Raymond C. A., Coradini A., et al. (2012) Dawn at Vesta: Testing the protoplanetary paradigm. *Science*, 336, 684.
- Schenk P., O'Brien D. P., Marchi S., Gaskell R., Preusker F., Roatsch T., Jaumann R., Buczkowski D., McCord T., McSween H. Y., Williams D., Yingst A., Raymond C. A., and Russell C. T. (2012) The geologically recent giant impact basins at Vesta's south pole. *Science*, 336, 694.
- Schmedemann N., Kneissl T., Ivanov B. A., et al. (2014) The cratering record, chronology and surface ages of (4) Vesta in comparison to smaller asteroids and the ages of HED meteorites. *Planet. Space Sci.*, 103, 104–130.
- Schultz P. H., Eberhardt C. A., Ernst C. M., A'Hearn M. F., Sunshine J. M., and Lisse C. M. (2007) The deep impact oblique impact cratering experiment. *Icarus*, 190, 295–333.
- Soderblom L. A. (1970) A model for small-impact erosion applied to the lunar surface. *J. Geophys. Res.*, 75, 2655–2661.
- Stickle A. M., Schultz P. H., and Crawford D. A. (2015) Subsurface failure in spherical bodies: A formation scenario for linear troughs on Vesta's surface. *Icarus*, 247, 18–34.
- Sullivan R., Greeley R., Pappalardo R., et al. (1996) Geology of 243 Ida. *Icarus*, 120, 119–139.
- Thomas N., Barbieri C., Keller H. U., et al. (2012) The geomorphology of (21) Lutetia: Results from the OSIRIS imaging system onboard ESA's Rosetta spacecraft. *Planet. Space Sci.*, 66, 96–124.
- Thomas P. and Prockter L. (2010) Tectonics of small bodies. In *Planetary Tectonics* (T. Watters and R. Schultz, eds.), pp. 234–264. Cambridge Univ., Cambridge.
- Thomas P. C. and Robinson M. S. (2005) Seismic resurfacing by a single impact on the asteroid 433 Eros. *Nature*, 436, 366–369.
- Thomas P. C., Everka J., Bloom A., and Duxbury T. (1979) Grooves on Phobos—Their distribution, morphology and possible origin. *J. Geophys. Res.*, 84, 8457–8477.
- Thomas P. C., Binzel R. P., Gaffey M. J., Storrs A. D., Wells E. N., and Zellner B. H. (1997) Impact excavation on asteroid 4 Vesta: Hubble Space Telescope results. *Science*, 277, 1492–1495.
- Thomas P. C., Everka J., Bell J. F., Clark B. E., Carich B., Joseph J., Robinson M., McFadden L. A., Malin M. C., Chapman C. R., Merline W., and Murchie S. (1999) Mathilde: Size, shape, and geology. *Icarus*, 140, 17–27.
- Thomas P. C., Everka J., Robinson M. S., and Murchie S. (2001) Shoemaker crater as the source of most ejecta blocks on the asteroid 433 Eros. *Nature*, 413, 394–396.
- Titley S. R. (1966) Seismic energy as an agent of morphologic modification on the Moon. In *Astrogeol. Studies Ann. Prog. Rept. July 1, 1965–July 1, 1966, Part A*, pp. 87–103. U.S. Geol. Survey Open-File Report, Flagstaff.

- Toksöz M. N., Dainty A. M., Solomon S. C., and Anderson K. R. (1974) Structure of the Moon. *Rev. Geophys. Space Phys.*, *12*, 539–567.
- Tonge A. L. and Ramesh K. T. (2015) Multi-scale defect interactions in high-rate brittle material failure, Part I: Model formulation and application to AION. *J. Mech. Phys. Solids*, in press.
- Tsuchiyama A., Uesugi M., Matsushima T., et al. (2011) Three-dimensional structure of Hayabusa samples: Origin and evolution of Itokawa regolith. *Science*, *333*, 1125.
- Vererka J., Thomas P., Simonelli D., Belton M. J. S., Carr M., Chapman C., Davies M. E., Greeley R., Greenberg R., and Head J. (1994) Discovery of grooves on Gaspra. *Icarus*, *107*, 72.
- Vererka J., Thomas P. C., and Bell J. F. III (1999) Imaging of asteroid 433 Eros during NEAR's flyby reconnaissance. *Science*, *285*, 562–564.
- Vererka J., Thomas P., Harch A., et al. (2000) NEAR encounter with asteroid 253 Mathilde: Overview. *Icarus*, *140*, 3–16.
- Vererka J., Thomas P. C., Robinson M., et al. (2001) Imaging of small-scale features on 433 Eros from NEAR: Evidence for a complex regolith. *Science*, *292*, 484–488.
- Vincent J.-B., Besse S., Marchi S., and the OSIRIS Team (2012) Physical properties of craters on asteroid (21) Lutetia. *Planet. Space Sci.*, *66*, 79–86.
- Vincent J.-B., Schenk P., Nathues A., et al. (2014) Crater depth-to-diameter distribution and surface properties of (4) Vesta. *Planet. Space Sci.*, *103*, 57–65.
- Wilhelms D. E. (1993) *To a Rocky Moon: A Geologist's History of Lunar Exploration*. Univ. of Arizona, Tucson. 477 pp.
- Williams D. A., Jaumann R., McSween H. Y., Marchi S., Schmedemann N., Raymond C. A., and Russell C. T. (2014) The chronostratigraphy of protoplanet Vesta. *Icarus*, *244*, 158–165.
- Woronow A. (1977) Crater saturation and equilibrium — A Monte Carlo simulation. *J. Geophys. Res.*, *82*, 2447–2456.
- Yeomans D. K., Barriot J. P., Dunham D. W., Farquhar R. W., Giorgini J. D., Helfrich C. E., Konopliv A. S., McAdams J. V., Miller J. K., Owen W. M., Scheeres D. J., Synnott S. P., Williams B. G. (1997) Estimating the mass of asteroid 253 Mathilde from tracking data during the NEAR flyby. *Science*, *278*, 2106–2109.
- Yingst R. A., Mest S. C., Berman D. C., et al. (2014) Geologic mapping of Vesta. *Planet. Space Sci.*, *103*, 2–23.

# Asteroid Interiors and Morphology

D. J. Scheeres

*The University of Colorado Boulder*

D. Britt

*University of Central Florida*

B. Carry

*Institut de Mécanique Céleste et de Calcul des Éphémérides*

K. A. Holsapple

*University of Washington*

---

The geophysical study of asteroids has moved from the realm of speculation and constraint to a more data rich environment where observations can be directly used to understand and probe the physical nature of these bodies. While many broad questions were posed in the *Asteroids III* chapter on asteroid interiors, in the current setting we are now able to probe more deeply into these questions, taking advantage of many different observations of asteroids across their entire size scale. The current chapter will take a very broad survey of what constraints currently exist in this area, what progress has been made in understanding these bodies analytically and through simulations, and what current theories can inform and guide future observations and tests of our understanding. The following topics are covered in this chapter: the strength of asteroid materials as inferred from meteors and meteorites, the density and porosity of asteroids as inferred from remote observations, global constraints on asteroid strength and morphology based on ground- and spacebased observations, analytical theories of asteroid strength and evolution, and the current state of numerical simulation techniques of asteroid interiors and morphology.

## 1. INTRODUCTION

The past decade has seen an astonishing array of advances across a wide spectrum of important inputs to the problem and mystery of asteroid interiors. These include the development of a large database concerning asteroid component strengths, as evidenced by meteors and meteorites (section 2); the compilation of extensive densities and inferred porosities for asteroids based on groundbased observations (section 3); the development of new computational techniques for the simulation of how asteroid rubble piles deform and fission or shed mass when subject to extreme rotation rates (section 4); and the development of crucial insights into the unique geophysics of specific asteroidal bodies (section 6). This chapter will review these different areas of advancements in an attempt to unify these disparate topics and show where future progress can be made in this field.

Knowledge about asteroid interiors is a crucial aspect for understanding these bodies, as it provides clues about their evolutionary history, in turn providing strong constraints on the history of the solar system. Unlike asteroid surfaces, it is impossible to peer directly within or easily take a sample

measurement from within a body. Thus the study of asteroid interiors must rely on a combination of measurement and theory to develop constraints on the interior environment. Given these restrictions, previous investigations have studied observable characteristics that may be related to the nature of their interiors. This being said, there are measurement techniques that can probe the interior properties of bodies, in particular through seismic and radar sounding measurements. These are discussed in section 5 and represent a potential source for future advancements in this field.

The most accessible features of an asteroid that are related to their interior structure are the mass, density, shape, and spin. These are strongly constrained by the interior structure, and by the strength and mechanical properties of that structure. By focusing on these specific observables, we can start to answer basic questions about these bodies: How strong are they? What is the nature of that strength? Are the interiors rubble piles full of voids at various size scales, or are they solid coherent structures? How do these properties depend on composition, shape, spin, size, or location?

Important steps in answering the above questions have occurred since the publication of the *Asteroids III* volume

(e.g., Asphaug *et al.*, 2002; Britt *et al.*, 2002). These advances are related to the accumulation of fundamental data on these bodies through meteor falls and groundbased observations, analytical studies of the shapes of rubble piles, and ever more precise numerical simulations that probe the mechanics of rubble-pile interactions. We do note that our discussion will be more focused on the smaller asteroid bodies and rubble-pile structures, as this is where much of the progress has occurred in the last decade. This is not to discount the important results from the European Space Agency (ESA) Rosetta mission to asteroid (21) Lutetia or the NASA Dawn mission to asteroid (4) Vesta; however, we refer the interested reader to the chapters in this volume by Russell *et al.* and Barucci *et al.* for a detailed discussion of those scientific results.

The topic of asteroid interiors has been dealt with previously in the *Asteroids III* chapter by Asphaug *et al.* (2002). That chapter serves as a fundamental starting point for the current survey, and we assume that the interested reader is familiar with that work. The current chapter takes a different approach from that earlier work, reflecting the current thinking about what aspects of observations can be directly applied to understanding asteroid interiors. Another important resource from the *Asteroids III* book is the chapter on gravitational aggregates by Richardson *et al.* (2002). The current chapter extends that descriptive chapter in the direction of geophysics, striving to link the possible granular nature of asteroids with fundamental physical processes that occur for aggregates. The goal of that chapter was to distinguish the different ways in which a shattered body could exist, from a random assemblage to a coherent collection of components shattered in place from an initial monolithic body. The current chapter does not deal much with this distinction, although its implications do arise when discussing observations of macroporosity. What is new in the current chapter, with regard to gravitational aggregates, is the realization that such assemblages may have a small level of cohesion, which changes the dynamical evolution of these bodies in a significant and observable way. Additionally, not considered in that chapter was the size distribution of the particles of these aggregates, which has now been theorized to be a crucial aspect of their geophysics (Sánchez and Scheeres, 2014). Observations have not conclusively identified which of the many types of gravitational aggregates discussed in Richardson *et al.* (2002) might in fact exist in nature; however, many different observations (as discussed in this chapter) seem to fit best with their definition of “rubble pile,” stated verbatim as: “*This structure is literally a pile of rubble, with the organization that you might expect from a bunch of rocks dumped from a truck. A body that has been completely shattered and reassembled may fit into this category.*”

The outline of the chapter is as follows. In section 2 we focus on what we know about the fundamental strength and mechanical properties of the constituent pieces of asteroids as represented in the meteorite collection and meteor observations. From this study we find that there remain interesting and significant disconnects between the measured strength of meteorites and the inferred strength that they have based

on the altitude at which they fail, which is expected to be related to their possible rubble-pile structure. This data provides insights into bodies up to several meters in size, but not beyond this limit.

In section 3 we use groundbased observations, and some spacecraft observations, to develop a wide range of constraints on how the constituent components of asteroids are assembled by computing their density and porosity. The implications are that some asteroids are highly porous bodies, in general, supporting the idea that these can be rubble piles. From this data there is also a clear progression of larger bodies having lower porosities, indicating the importance of gravitational compression. From this data we gain insight into the structure of bodies at the larger scale, ranging up to several hundreds of kilometers in size.

Section 4 applies and interprets the size-spin data for insight and motivation into an understanding of asteroid morphology and strength. From this data we can place constraints on the properties of the asteroid population and expose areas of uncertainty and ambiguity. Linking these observations with modeling and theories of asteroid strength has provided new insights and constraints on the global strength of asteroids, and provided clues as to their internal morphology. Theory and data from this section also help address the gap between the insights from meteorites on smaller bodies and from the groundbased studies of larger bodies.

Section 5 discusses the insights that can be inferred on asteroid interiors using the visible geology of asteroid surfaces, constraints on the transmission of seismic energy, and by an improved understanding of the rate of dissipation that may occur in asteroids. These methods indicate a potential pathway for better probing and determining the unique geophysical environment within small rubble-pile bodies.

Finally, section 6 focuses on a number of specific asteroids that have been observed with some level of precision since *Asteroids III*, with the exception of (4) Vesta. These include the targets of spacecraft missions, (433) Eros and (25143) Itokawa; the unique case of 2008 TC<sub>3</sub>, which was analyzed both with groundbased observations and on the ground with meteorite falls; and a number of ground observed asteroids including (216) Kleopatra, (29075) 1950 DA, (66391) 1999 KW<sub>4</sub>; and two active asteroids, P/2013 P5 and P/2013 R3. Many of these bodies are discussed in detail elsewhere in this book, but our discussions are focused specifically on what these bodies tell us about asteroid interiors and strength. Finally, overall conclusions are drawn and future areas where additional research and observations are needed are highlighted.

## 2. MATERIAL CONSTRAINTS

Meteorites and meteors are samples of materials from small bodies in near-Earth space, albeit transported from all regions of the solar system (see the chapter by Binzel *et al.* in this volume). Note that a meteorite and a meteor can be just different manifestations of the same object; a meteor is the visual and sonic phenomena of the small body transit-

ing Earth's atmosphere, while a meteorite is the surviving material that can be collected on the surface of Earth. As small bodies encounter Earth, their interaction with Earth's atmosphere, their mass loss on entry, the characteristics of their fall, and analysis of recovered fragments all provide clues about the structure, cohesion, and mineralogical homogeneity of the parent small bodies. This subsection is focused on summarizing and collecting in one place information on the strength of these bodies, both as individual components and as agglomerations when they first enter the atmosphere. For more information, see also the chapters by Borovička et al. and Jenniskens in this volume.

## 2.1. Meteorite Strength

An individual recovered meteorite is a direct sample of the material properties and strength of the components of small bodies. However, the samples that survive the stress of deceleration and atmospheric entry are necessarily biased toward the strongest and most coherent materials in the parent object. Weak and volatile-rich material tends to be destroyed on entry. Shown in Table 1 are the compressive strengths of a number of meteorites along with common materials for comparison [taken from Popova et al. (2011); see also Kimberley and Ramesh (2011) for additional data].

Natural materials can be very strong, such as individual crystals of quartz (1100 MPa). Single mineral strengths derive from the inherent strength of the crystal structure. Rocks are collections of minerals and their strength derives from a mixture of their mineral crystal strengths, their formation conditions, and the nature of the bonding between minerals. Igneous rocks like granite, for example (100–140 MPa), are composed of a substantial amount of quartz, but as a whole the bonding between their minerals makes the rock much less

strong than the individual minerals. Unreinforced concrete at 20 MPa compressive strength is a good comparison standard.

Like rocks, there are substantial variations in the inherent strength of meteorites. Most ordinary chondrites (the most abundant type of meteorite fall) are much stronger than concrete. Volatile-rich carbonaceous chondrites are much weaker, and in some cases, e.g., the Tagish Lake meteorite (meteorites are named for the localities where they are recovered and in this chapter they will be often referred to by their meteorite name), their measured strengths are on the order of weakly consolidated soils (dirt clods).

Why are ordinary chondrites so strong? In general, they are conglomerates of chondrules (millimeter-sized spheres of minerals formed in the solar nebula), chondrule fragments, dusty matrix, and iron-nickel metal that have been welded together by varying levels of grain-boundary melting. In addition to welding in the silicates, the metal in ordinary chondrites provides a natural reinforcing mesh that is often interconnected in some ordinary chondrites that have been subjected to higher temperatures and thus have undergone some degree of remelting and metamorphic processing referred to as having higher metamorphic grades. As a result, high-metamorphic-grade ordinary chondrites can have many of the strength properties and reactions to stress of steel-reinforced concrete. However, there are some very weak ordinary chondrites. The Holbrook meteorite (Table 1) is a high-metamorphic-grade ordinary chondrite but is very weak and friable. Weston is also a high-grade chondrite but the individual chondrules are so poorly cemented that it falls apart with handling. The best analogy for this sample is a loosely glued collection of millimeter-sized spheres. However, the individual chondrules that are weakly held in Weston are individually quite strong.

The major exception to the story of relatively weak ordinary chondrite bolides is the large and well-studied Chelyabinsk

TABLE 1. Meteorite and material strength.

Material	Meteorite Type	Compressive Strength (MPa)	Tensile Strength (MPa)
Concrete — Unreinforced	Typical sidewalk	20	
Quartz	Single crystal	1100	55
Granite		100–140	
Medium dirt clod		0.2–0.4	
Holbrook, Arizona	L6 (OC)	6.2	
La Lande, New Mexico	L5 (OC)	373.4	
Tsarev	L5 (OC)	160–420	16–62
Covert	H5 (OC)	75.3	
Kunashak	L5 (OC)	265	49
Elenovka	L5 (OC)	20	2
Krymka	LL3 (OC)	160	22
Seminole	H4 (OC)	173	22.5
Plutusk	H5 (OC)	21.3	31
Hoba	Iron — ataxite	700	
Sikhote-Alin	Iron — octahedrite	410	44
Tagish Lake	C2 (CC)	0.25–1.2	
Murchison bolides	CM (CC)	~50	0.1–1

OC = ordinary chondrite; CC = carbonaceous chondrite. Data from Popova et al. (2011).

bolide and meteorite (*Borovička et al.*, 2013). While its first breakup was at high altitude (~45 km and 0.7 MPa), it underwent a series of fragmentation events. This included 11 fragmentations between 39 and 29 km under atmospheric dynamic pressure loads of 1–5 MPa and several boulders breaking off at 26–24 km under loads of 10–13 MPa. Interestingly, the main body remained relatively intact down to 22 km until its massive disaggregation at 18 MPa. This is probably due to the heterogeneities and highly shocked nature of the Chelyabinsk meteorite and the presence of extensive melt veins that welded portions of the meteorite.

Volatile-rich materials like the Tagish Lake meteorite are much different than the ordinary chondrite bolides. In this case the strength of the individual cobbles is roughly what is seen in the atmospheric breakup phenomena and this is the only case where the maximum compressive strength inferred in the atmosphere is greater than the compressive strength of the measured meteorite. This may be due to the presence of ice surviving in Tagish Lake. Recovered samples often expressed significant amounts of water when brought above freezing temperatures (*Brown et al.*, 2002), and samples of Tagish Lake that have been kept at freezing temperatures show lower porosity than samples that have been allowed to warm (*Ralchenko et al.*, 2014). It may be that ice-filled pore space within the meteorite provided extra strength for the bolide during atmospheric entry.

The meteorites listed in Table 1 are samples of hand- and cobble-sized survivors of atmospheric entry, which are the strongest and most coherent materials of the original small body. The vast majority of bolides do not survive entry as anything other than widely dispersed ablation dust. Typically the minority of small bodies that do survive entry lose approximately >95% of their preatmospheric mass (*Popova et al.*, 2011). Only a handful of bolides have been tracked to delivering material to the surface with that material recovered. Shown in Table 2 are bolides with recovered meteorites (*Popova et al.*, 2011).

TABLE 2. Select bolides with recovered meteorites (*Popova et al.*, 2011; *Borovička et al.*, 2013).

Meteorite (type)	Compressive Strength (MPa)		
	Range for Met. Type	First Breakup	Max.
Pribram (H5)	77–247	0.9	
Lost City (H5)	77–247	0.7	2.8
Innisfree (L5)	20–450	0.1	3
Chelyabinsk (LL5)	0.7	18	
Tagish Lake (C2)	0.25–1.2	0.3	2.2
Moravka (H5–6)	77–327	<0.9	5
Neuschwanstein (EL6)	3.6	9.6	
Park Forest (L5)	20–450	0.03	7
Villalbeto de la Pena (L6)	63–98	5.1	
Bunburra Rockhole (Ach)	0.1	0.9	
Almahata Sitta (Ure, OC)	0.2–0.3	1	
Jesenice (L6)	63–98	0.3	3.9
Grimsby (H4–6)	77–327	0.03	3.6

## 2.2. Bolides and Boulders

A bolide is roughly defined as a large, bright meteor that is typically brighter than the full Moon during its brief peak brightness. The physical phenomena are the result of a small body entering the atmosphere at hypersonic speeds [in the case of near-Earth asteroids (NEAs), velocities are in the range of ~12–20 km s<sup>-1</sup>) and rapidly shedding their orbital kinetic energy into visible and thermal energy from friction with the atmosphere. As the body comes apart the initially compact mass fragments, exposing a larger surface area to rapid deceleration. This is seen as bright flashes within the bolide as smaller fragments rapidly heat, ablate, and decelerate. This typically occurs at altitudes ranging over 70–23 km and the small body's response to the atmospheric ram pressure can be used to estimate the body's coherent strength under compression (*Popova et al.*, 2011). These bolides are typically recorded on specialized optical tracking networks, but for the brightest objects security cameras and even dashcams are a valuable source of data (*Brown et al.*, 2002). Table 2 shows strength data from bolides with recovered meteorites. This permits a direct comparison of the strength of the surviving fragments with the strength estimated during the breakup of the small body on atmospheric entry.

Several points are readily apparent from Table 2. While most recovered meteorites are very strong, the initial breakup of the entering small body occurs at very low compressive stress. Initial breakup altitudes can be very high, as much as 70 km in some cases for the weakest bodies in Table 2, and the maximum compressive stress in Table 2 may occur at what are also substantial altitudes typically in the range of 35–20 km. For the initial breakup, these altitudes represent relatively low stresses, creating failures within weakly bound materials.

A question that has yet to be fully addressed is whether these stresses are consistent with some small asteroids being rubble piles, potentially held together by weak cohesive forces (see section 4.5). Examples of low-coherent-strength objects from Table 2 would include the Grimsby and Park Forest meteorites. However, while the first breakup provides insight into the strength of the entering body, the bolide phenomenon continues as the individual large pieces of the body break up under rising compressive stresses. Essentially these are the cobbles and boulders within the body shattering under rising stresses, and represent the state of fracturing and cohesion within individual components of the small body. For example, Park Forest started to fail under low compressive stress of 0.03 MPa, but the last major breakup was at more than 2 orders of magnitude greater stress. One possible explanation would be that the weak breakup occurred for a boulder within the rubble pile that failed along zones of preexisting weakness. While the basic material of ordinary chondrites is very strong, these objects are often pervasively fractured from a long impact and shock history and would be much weaker along their existing fractures. Indeed, that is the primary reason for multiple observations that large bodies are globally much weaker than smaller ones. However,

not all entering bolides fail under the stress of atmospheric entry. There are a number of examples of coherent “boulders” impacting the ground with little or no apparent fragmentation during entry. A recent example was the meter-sized boulder Carancas (H4–5) that created a 13-m-wide crater near Lake Titicaca in 2007 (*Borovička and Spurný*, 2008).

### 2.3. Meteorite Showers

While coherent boulders occasionally do survive atmospheric entry, a much more typical case is the meteorite shower. These are small bodies that break up in the atmosphere similarly to the observed bolides. Table 3 includes a list of selected large meteorite falls (meteorites that were observed to fall from space) and finds (meteorites that were found some time after they fell). The discussion of atmospheric breakup and observed bolides has focused on stony meteorites, since so far no iron meteorite falls have been instrumentally recorded. On the other hand, irons are much stronger under compression and tension than stones and recovered irons are typically much larger than stones. Most of the recovered mass of meteorites are irons and the 15 largest meteorites are all irons. There are strong positive selection effects in finding irons since they are clearly unusual in the terrestrial environment. That said, note that of the largest irons, only two are single bodies. The largest meteorite in total mass is Campo del Cielo, which fell in at least 30 fragments. Most of the fragments are buried so the mass and fragment count is a rough estimate. The largest single body to reach the ground is either Hoba, which was found in a single mass, or Sikhote-Alin, which fragmented on impact (producing a 60-m-diameter crater and more than 9000 fragments).

For stony meteors, almost all the large mass meteorites are showers. Some of the more famous showers are listed in Table 3. With stones, the entry phenomena make it more likely that they will shatter in the atmosphere, producing a literal shower of rocky fragments. These fragments tend to

be largely homogeneous. Investigations of several showers have, with one notable exception, not found significant mineralogical variation within the shower (*Consolmagno et al.*, 2008). The major exception is the Almahata Sitta fall, which was primarily ureilite material with a significant component of ordinary chondrite (see the chapter by Jenniskens in this volume). Heterogeneity within meteorites is not unknown and it is not uncommon to find xenoliths (different meteorite types, literally “foreign rock”) incorporated into meteorite breccias (*Brearley and Jones*, 1998); however, the level of heterogeneity is typically pretty small. Xenoliths are usually confined to single or a few clasts within a much larger homogeneous matrix. The shower data suggests that an Almahata Sitta level of heterogeneity is rare. For discussion about Kaidun, see the chapter by Borovička et al. in this volume.

### 2.4. Summative Discussion

The data presented here on meteorites, bolides, and showers provides some basic insights on the structure of meteorite parent bodies up to several meters in size. For stony bodies of even a few meters in diameter, rubble piles seem to be the norm. The relatively low stresses on breakup seen in most of the bolides and the prevalence of showers for large stones point to a rubble-pile structure being very common. The individual components of these aggregates can be very strong, ranging up to an order of magnitude stronger than concrete, but the overall body is very weak. Volatile-rich bodies are both individually and collectively very weak.

Mineralogical homogeneity seems to be the general rule in small bodies. While there are significant exceptions and xenoliths are not uncommon, the shower data point to largely homogenous small bodies. Finally, for small bodies, irons are easily the strongest and most-coherent materials. Their large compressive and tensile strengths and apparent relatively low fracturing result in irons being by far the largest meteorites that survive atmospheric entry. However, they are relatively rare in the fall population, and the selection effects of their large strength suggest they are overrepresented in the fall population relative to their share of the NEA population.

## 3. ASTEROID BULK PROPERTIES

The next section probes the interiors of asteroids through a different approach, based on determining their bulk densities and bulk porosities. This takes us beyond the strength of the individual components of asteroidal bodies, either determined by measurements on meteorite falls or through inferred strengths in the upper atmosphere. The bulk densities are found by comparing mass estimates to volume or size estimates for these bodies. Bulk porosities are estimated by comparing the bulk densities to the asteroid spectral type, to determine likely grain densities and hence bulk porosities

The fundamental data compiled here concerning asteroid densities and macroporosities are presented in Figs. 1 and 2. Details on how the data were compiled are given in *Carry* (2012), and are not repeated here. While the previous section

TABLE 3. Selected large meteorites and showers (*Grady*, 2000).

Meteorite	Date (dd/mm/yyyy)	Mass (kg)	No. Fragments
Campo del Cielo (IAB Iron)	Find	100,000	30
Sikhote-Alin (IIAB Iron)	12/02/1947	70,000	9000
Hoba (IVB Iron)	Find	60,000	1
Cape York (IIIAB Iron)	Find	58,000	8
Willamette (IIIA Iron)	Find	14,500	1
Pultusk (H5)	30/01/1868	8863	70,000
Allende (CV3)	08/02/1969	5000	1000
Jilin City (H5)	08/03/1976	4000	100
Tsarev (L5)	06/12/1922	1132	40
Knyahinya (L5)	09/06/1866	500	1000
Mocs (L6)	03/02/1882	300	3000
Homestead (L5)	12/02/1875	230	
Holbrook (L/LL6)	09/06/1866	218	14,000
Forest City (H5)	02/05/1890	122	2000

was focused on meter-sized bodies, the focus in this section is necessarily on the other end of the scale, with most of the reliable data on densities and porosity existing for larger bodies, up to hundreds of kilometers. Only in a few situations are there good data on smaller bodies.

The first evidence on asteroid interiors was derived from meteorites, with identification of differentiated and nondif-

ferentiated internal structures (see section 2). Dynamical families, originating from catastrophic disruptive collisions, provide another way to study asteroid interiors. Clumps of asteroids identified dynamically (e.g., *Bendjoya and Zappalà*, 2002) also share common surface properties, which are in turn used to discriminate genuine family members from the background population (*Parker et al.*, 2008; *Carruba*

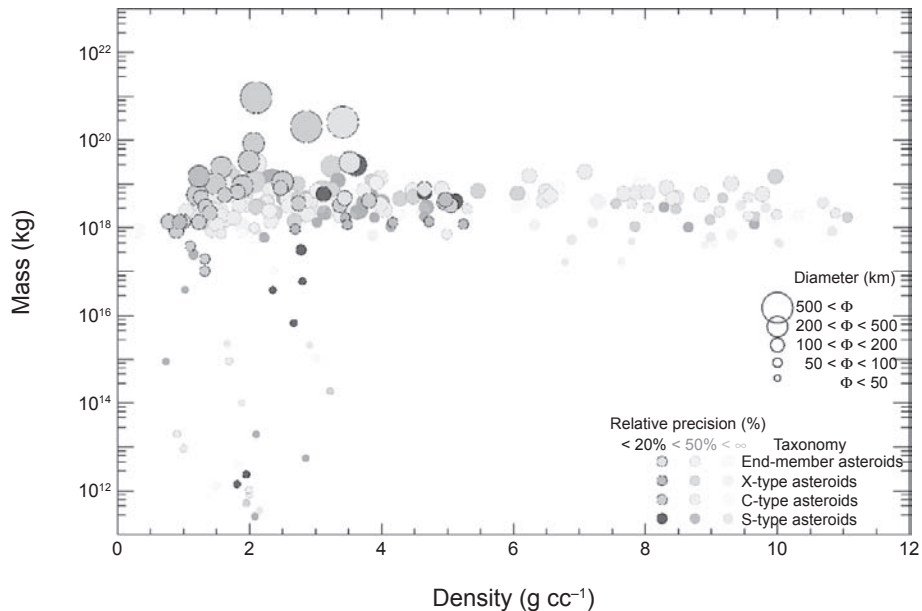


**Fig. 1.** See Plate 24 for color version. Density vs. mass. Asteroids are divided into four taxonomic groups (from *DeMeo et al.*, 2009): S-complex in red, C-complex in gray, X-complex in green, and end members in yellow. The size of the symbols indicates the asteroid diameter, below 50 km, between 50 and 100 km, 100 and 200 km, 200 and 500 km, and above 500 km. The three different levels of contrast correspond to three cuts of relative accuracy: <20%, <50%, and regardless of precision (< $\infty$ ).

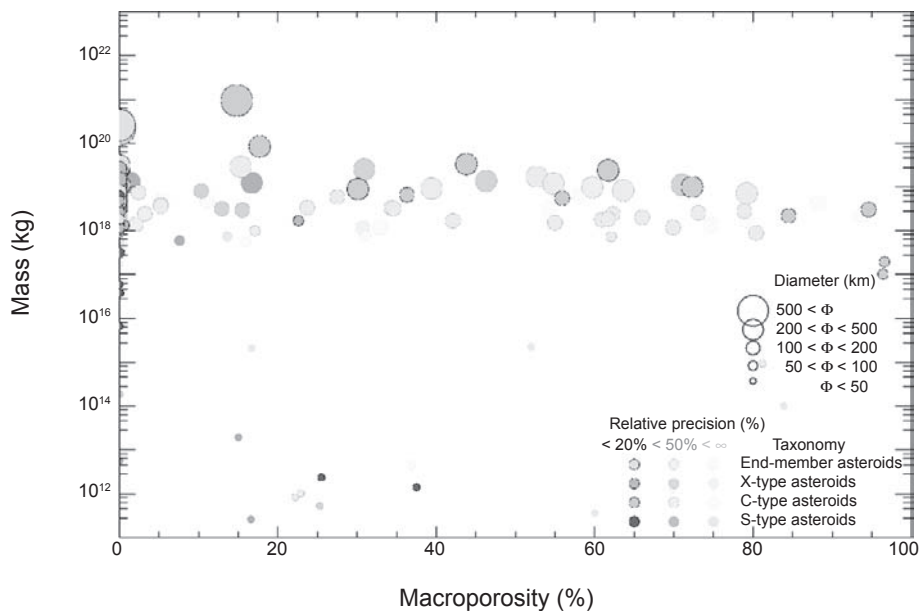


**Fig. 2.** See Plate 25 for color version. Macroporosity vs. mass. See Fig. 1 for the explanation of symbols.

*et al.*, 2013). Such similarities are suggestive of a homogeneous interior for the parent bodies of these families (see the chapter by Michel *et al.* in this volume).

### 3.1. Density

Density is perhaps the most fundamental property for discriminating the composition and internal structure of asteroids (Britt *et al.*, 2002). It is also extremely difficult to measure, and the number of precisely measured asteroid densities is still very limited. This is because both mass and volume are required to determine the density of an asteroid.

Estimating any mass at all is a challenge, owing to the relatively low mass of asteroids as compared to other planetary objects. The exception is for binary asteroids, for which the total mass can be easily estimate (see the chapter by Margot *et al.* in this volume). The number of mass determinations thus limits the number of density estimates. The precision of these estimates is, however, limited by the uncertainty on asteroid diameters (Carry, 2012).

Any determination of the mass relies on measurements of the gravitational interaction between the target asteroids and other objects. The most accurate estimates (at a few percent accuracy) are derived from radio science experiments during spacecraft encounters [orbit or flyby (e.g., Yeomans *et al.*, 2000; Abe *et al.*, 2006; Pätzold *et al.*, 2011)] and studies of binary asteroids (see the chapter by Margot *et al.*). The vast majority of asteroids, however, have never been visited by spacecraft nor possess satellites [only a handful of large asteroids possess satellites, albeit the fraction is higher at smaller size; about 15% of near-Earth asteroids have satellites (Margot *et al.*, 2002)]. It is nevertheless possible to determine their mass from the gravitational pull they exert on other planetary objects: asteroids, planets and their satellites, and interplanetary spacecrafs (see, e.g., Hilton, 2002; Fienga *et al.*, 2008; Kuchynka and Folkner, 2013; Goffin, 2014).

Methods based on long-range influence rely heavily on the modeling of all relevant gravitational effects and interactions in the solar system (e.g., asteroid ephemerides, planets, general relativity) and are therefore more prone to systematic errors, and current precision is still limited to date [often above 50%, see the dispersion of estimates, together with the discussion on the accuracy and biases affecting mass estimates, in Carry (2012)]. Current samples of asteroid masses are therefore strongly biased. First, the best determinations are for binaries, but there may be differences between binary and single asteroid internal structures and thus extrapolating the density determined from binary asteroids to the whole population may introduce biases. Second, only large asteroids are massive enough to perturb the orbits of other objects. Thus this sample is mainly limited to asteroids larger than 100 km, while there is evidence for a size-dependence of the density owing to a different level of macroporosity [see Fig. 2 below and Fig. 9 in Carry (2012)].

The situation for diameter estimates is less dramatic. There are many techniques to measure the apparent size or surface area of an asteroid, and diameter estimates are available for

tens of thousands of objects (e.g., Masiero *et al.*, 2011). Although diameter estimates are less prone to systematics than mass estimates [values generally agree to within measurement uncertainties (see Carry, 2012)], their contribution to the density uncertainty overwhelms that of mass. Diameter determinations have to be as accurate as 2–3% to allow density estimates to be more precise than 20%, a level over which density estimates hardly provide constraints. While simple modeling can have systematics above this level, realistic descriptions of asteroids, including knowledge of spin and three-dimensional shape, can provide this level of accuracy (see the chapter by Durech *et al.* in this volume).

Despite these limitations, the field of asteroid density has seen a revolution since the time of *Asteroids III* (Britt *et al.*, 2002). There has been a tenfold improvement in sample numbers (from 20 to 320), spanning many different taxonomic classes (and hence composition), diameters, and heliocentric distance (Carry, 2012). The upcoming decade will certainly provide many more determinations with a high level of accuracy. First, the stellar catalog at the microarcsecond level provided by the ESA Gaia mission should improve the precision on asteroid astrometry by an order of magnitude. Mass determinations from orbital perturbations should therefore become more precise. The observation of asteroids by Gaia will also allow the determination of the mass of about 150 asteroids with a relative precision better than 50%. It is even expected that 50 of these determinations will be more precise than 10% (Mouret *et al.*, 2007). The number of known binaries is also constantly increasing, adding to the number of high accuracy density estimates (see the chapter by Margot *et al.*).

### 3.2. Macroporosity

A density estimate by itself can restrict the list of possible components of an asteroid's composition. For example, a low-density asteroid such as (617) Patroclus [ $\rho \approx 1 \text{ g cm}^{-3}$  (Marchis *et al.*, 2006; Mueller *et al.*, 2010)] cannot host large fractions of dense material or even silicates. The internal structure can be constrained using a comparison of the asteroid bulk density ( $\rho_A$ ) with the grain density of its most likely constituents ( $\rho_C$ ), as determined from study of the surface composition (see the chapter by Reddy *et al.* in this volume).

If  $\rho_A \ll \rho_C$ , the asteroid is underdense. This points toward large-scale voids or the presence of low-density material (i.e., volatiles) in its interior. While this is a typical case for comets, many asteroids are also seen to have porous internal structure. The porosity  $p$ , i.e., the fraction of volume occupied by empty space ( $p = 1 - \rho_A/\rho_C$ ), provides a measure of these structures. Because meteorites have microporosity (empty spaces at the grain-size scale, noted  $p_m$ ), the macroporosity  $P$  has been defined as the fraction of volume occupied by large voids, i.e.,  $P = p - p_m$ . The question of the distribution of these volatiles or voids inside the asteroid remains open (Britt *et al.*, 2002). Following the terminology of Richardson *et al.* (2002), we can ask whether they are the results of cracks within a shattered monolith,

or interstices of a rubble pile formed through gravitational reagglomeration after a disruptive collision.

If  $\rho_A \gg \rho_C$ , the asteroid is overdense, and some high-density material must be present in its interior. This could be due to gravitational self-compression, differentiation (e.g., Russell *et al.*, 2012), or the result of the collision between two bodies of different densities. Most asteroids with a mass above  $10^{19}$  kg are overdense, while the majority of asteroids below that threshold present some level of macroporosity. This is consistent with large bodies having enough internal energy from accretion and radioactive decay to differentiate.

If  $\rho_A \approx \rho_C$ , no clear conclusions can be made. However, given the comparable spectral properties observed among members of dynamical families, it may be reasonable to assume that the body is homogeneous.

### 3.3. What Can Be Concluded

Based on the data presented in Table 4 and Figs. 1 and 2, and more fully discussed in Carry (2012), there are a number of overall conclusions that can be drawn from these compilations, listed below.

- Asteroids in the S-complex are on average more dense than those in the C-complex.
- Asteroids in the C-complex seem to have larger macroporosity than those in the S-complex, hinting at a looser structure.
- The density of asteroids from both the S-complex and the C-complex seems to increase with the mass, apparently resulting from a decreasing macroporosity.
- In both the C and S-complex, NEAs (with masses from  $10^{11}$  to  $10^{16}$  kg) seem to have a lower density than main-belt asteroids, following the trend between mass and density observed for large asteroids.
- At comparable sizes, B-types appear significantly denser ( $\rho \sim 2.4$  g cm $^{-3}$ ) than the other types of the C-complex that gather around  $\rho \sim 1.4$  g cm $^{-3}$ .

- While asteroids in both C- and S-complexes have narrow density ranges (with a few exceptions), asteroids in the X-complex covers a larger range, from the most dense Xc-types with  $\rho \sim 4.9$  g cm $^{-3}$  to X-types with  $\rho \sim 1.8$  g cm $^{-3}$ .
- Dwarf-planets (with masses above  $10^{20}$  kg) apparently have little macroporosity, contrary to small bodies whose masses are inferior to  $\approx 10^{20}$  kg (Consolmagno *et al.*, 2008).
- With the exception of NEAs, the dispersion in density and macroporosity is huge.

### 3.4. Future Prospects

As discussed above, the accuracy and reliability of density estimates have seen dramatic improvement since the time of *Asteroids III*. Even though many estimates still suffer from mild inaccuracy, the techniques are constantly being refined, and the next decade will provide more, increasingly reliable density measurements. A major issue still to be resolved is, how certain are the link between asteroids and meteorites? Based on their spectral properties, asteroids are classed within taxonomies (e.g., Tholen and Barucci, 1989; Tedesco *et al.*, 1989; Bus and Binzel, 2002). The latest to date by DeMeo *et al.* (2009) defines 26 classes, but analog minerals and meteorites have been identified for only 50% of them (see the chapters in this volume by DeMeo *et al.* and Reddy *et al.*). In other words, we have no reference density for half the taxonomic classes among asteroids. Discovering this meteorite-asteroid link is crucial for future interpretations of asteroid interiors.

## 4. ASTEROID STRENGTH AND FAILURE LIMITS

In addition to the constraints on asteroid density and porosity that can be determined from the population of ob-

TABLE 4. Average density, porosity, and macroporosity for the 12 (out of 26) taxonomic classes where density determinations more accurate than 20% are available ( $N$  determinations).

Class	Met.	$N$	Density (g cm $^{-3}$ )	Porosity (%)	Macroporosity (%)
S	OC	11	$2.72 \pm 0.54$	$30.88 \pm 8.76$	$25.28 \pm 31.67$
Sq	OC	2	$3.43 \pm 0.20$	$3.79 \pm 0.35$	$-1.81 \pm 2.16$
B	CV	2	$2.38 \pm 0.45$	$38.66 \pm 10.63$	$16.86 \pm 6.81$
C	CI	5	$1.33 \pm 0.58$	$84.96 \pm 52.43$	$49.96 \pm 43.61$
Cb	CI	3	$1.25 \pm 0.21$	$96.80 \pm 23.11$	$61.80 \pm 20.86$
Ch	CI	9	$1.41 \pm 0.29$	$74.47 \pm 21.73$	$39.47 \pm 16.29$
X	EL	8	$1.85 \pm 0.81$	$90.81 \pm 56.70$	$86.91 \pm 147.58$
Xc	Mes	2	$4.86 \pm 0.81$	$-9.47 \pm 2.49$	$-14.47 \pm 28.74$
Xe	EH	1	$2.60 \pm 0.20$	$40.00 \pm 4.42$	$36.20 \pm 47.49$
Xk	Mes	3	$4.22 \pm 0.65$	$4.27 \pm 1.05$	$-0.73 \pm 1.46$
K	CV	1	$3.54 \pm 0.21$	$-6.78 \pm 0.72$	$-28.58 \pm 5.31$
V	HED	3	$1.93 \pm 1.07$	$68.39 \pm 53.72$	$57.39 \pm 71.55$

The analog meteorite of each class is listed. A negative porosity is indicative of an “overdense” structure.  
Table adapted from Carry (2012).

served asteroids, there are also significant constraints that can be gleaned from the combined data on asteroid spin rates, spin states, morphology, and sizes, filling the gap between meter-sized meteors (section 2) and kilometer-sized asteroids (section 3). The significant data for these inferences are summarized in Fig. 3, which shows asteroid diameters and spin rates taken from the database described by Warner *et al.* (2009). Also indicated on this figure are those asteroids that are tumbling or are binary asteroids, and a number of spin-limit curves as a function of different cohesive strength theories (all to be discussed later). Over the last few decades these observations have accumulated to the point where useful inferences on asteroid morphology can be made. In Fig. 3 we only show those bodies that have a quality measure of 2<sup>-</sup> or higher, meaning that these observations are deemed reliable. It is interesting to note that there are a number of unconfirmed observations of spin periods (i.e., of quality measured less than 2<sup>-</sup> and thus not shown in the figure) that could be significant if shown to be true. These are discussed later, in the hopes of motivating additional observations.

This data has motivated several different theories for the strength and morphology of asteroids. Significant among

these is a better understanding that the spin limits do not require the rubble-pile hypothesis for almost all asteroids, the cohesion hypothesis in rubble-pile bodies, and the existence of tidal dissipations within such bodies. In the following subsections we discuss these issues in more detail, trying to integrate the physical and mathematical theories used to explain certain aspects of this data alongside a discussion of the data itself.

The precursor to these studies was given almost 20 years ago by Harris (1996), in which he noted that no asteroid had a spin period shorter than about 2.2 h and that the spin periods of objects in a given size range abruptly truncate at that value. He noted that this limit is essentially the spin rate  $\omega_s = \sqrt{4\pi G\rho/3}$ , where  $G$  is the gravitational constant and  $\rho \sim 2.2$  is the bulk density, at which internal tensile stresses would be present within a spherical, constant density object (the actual spin rate for a body also depends strongly on its elongation). This spin rate also corresponds to local circular speed at the surface of the body, at which centrifugal forces equal the gravitational attraction of the body. From that connection he concluded that all or most asteroids must have a rubble-pile structure, as defined earlier, although that is not

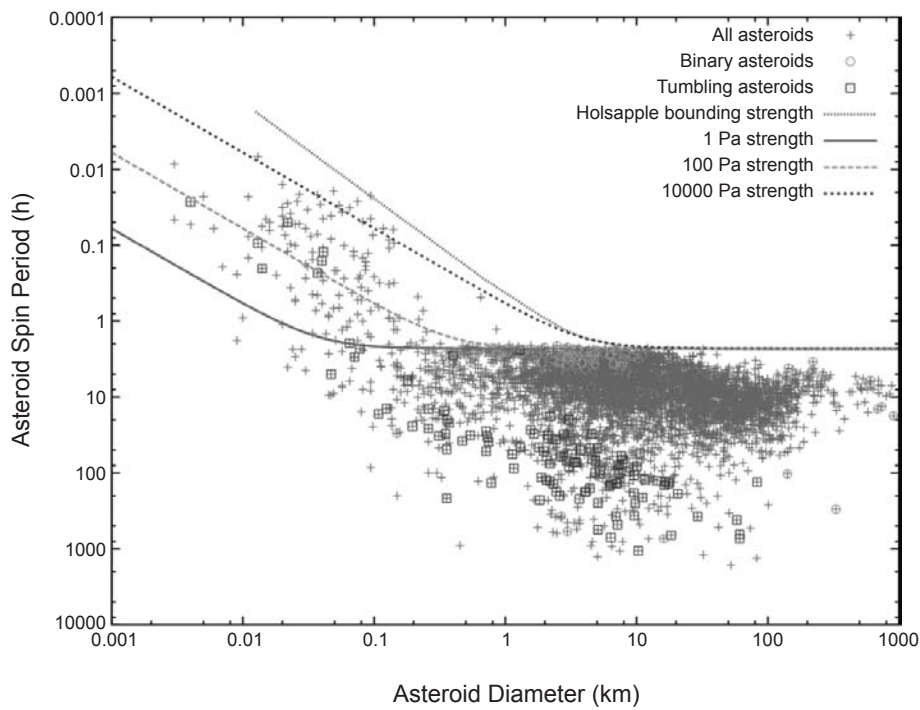


**Fig. 3.** See Plate 26 for color version. Asteroid size vs. spin period, with binaries and tumblers called out specifically. All others are assumed to be single, uniform rotators. Only bodies with periods deemed to be reliable (see Warner *et al.*, 2009) are shown. The plot shows distinct structures. No object larger than a kilometer in diameter spins faster than an ~2.4-h period, now known as the gravity spin barrier and that is understood to not be an indicator of cohesionless material by itself. Instead it is simply that at these size scales the gravity effects dominate any strength effect. A number of smaller bodies spin faster; those must experience tensile stress and must have some cohesive strength to hold together. Typically, the observed maximum spins are larger for smaller sizes. Also plotted are spin limits as a function of diameter for levels of asteroid strength. Data shown is as of August 2014.

the current interpretation. In addition, he also predicted that asteroids could spin faster than this limit if they had some strength, although no such asteroids were known at that time. He suggested there would be two regimes for spin, a gravity-dominated regime for larger asteroids and a strength-dominated regime for smaller asteroids. He suggested that in the strength regime their spin could increase inversely proportional to the diameter of the object. Since that paper, these ideas have been essentially verified and expanded, but with clarifications and new interpretations. A number of “fast spinners” have been found with shorter periods; however, they are all less than 1 km in diameter. And there have been detailed modeling studies deriving the relation between asteroid shape, maximum spin, and internal properties.

#### 4.1. Analytical and Numerical Models of Rubble Piles

We first provide a brief review of current and past methods used to model asteroids, their interiors, and their morphologies. Studies of relations between shape, density, and spin of isolated self-gravitational bodies dates back several centuries, but mainly in application to fluid bodies. In those cases, the nature of the bodies was assumed to be fluid, the spin was known, and the goal was to determine the permissible shape. In 1687, Isaac Newton determined that the shape of a fluid Earth with gravitational and rotational forces is a slightly oblate spheroid. In 1742, Colin Maclaurin extended the work to discover the existence of equilibrium oblate spheroidal shapes with large ellipticity for rotating bodies with self-gravity, now called the “Maclaurin spheroids.” Jacobi (1834) discovered the “Jacobi ellipsoids”: equilibrium ellipsoidal shapes with three unequal axes. Roche (1850) added tidal forces during an orbit around a parent body and determined that there is a limit to the orbit radius, the famous Roche limit, inside of which there are no equilibrium solutions. Poincaré (1885) discovered other pear-shaped, non-ellipsoidal possibilities for equilibrium. Chandrasekhar (1969) gives a complete exposition of these classical works. A number of authors have used those fluid limits to infer limits on the mass density or density distribution of solar system bodies, although the mass density dependence can be swamped by other factors, the most important of which is the nonfluid composition. A separate approach to analyzing the internal stress properties of a nonfluid gravitating ellipsoid was given by Chree (1895), using linear elastic response from an initial stress-free state to model the mechanics of a self-gravitating body. This approach has motivated some modern study as well, discussed later.

Just as for a fluid, an ideal rubble-pile body can be assumed to have no tensile strength. But that does not mean that it behaves as a fluid. Consider an idealized rubble-pile body consisting of dry sand. Sand is an assemblage of relatively rigid, angular, submillimeter-sized grains that must interact during deformations. In a shearing deformation, the grains must move up and over adjacent grains. That motion is suppressed if the sand is subjected to a compressive pressure such as from gravity. That simple physical idea is the basis for the standard continuum soil mechanics models of

failure, the Mohr-Coulomb and the Drucker-Prager criteria. In those models, the shearing strength is strongly increased by a compressive pressure in a relation that is assumed to be linear. The coefficient of that linear form is called the “angle of friction,” although its presence is due to the interlocking of grains, not surface friction. These criterion have similar results, although Mohr-Coulomb is considered to be more accurate while Drucker-Prager is easier to handle analytically. It is the basis for the important difference between the behavior of water and the behavior of sand. The shearing resistance of water is independent of the confining pressure so that the angle of friction is zero. From this example it is clear that a material with no tensile strength can certainly have other strengths, including shear strength.

For that reason, the classical fluid theories relating shape and spin do not apply to rubble-pile, asteroid objects. Holsapple (2001, 2004) presented a comprehensive study of the relations between shape, spin, and internal properties for rubble-pile objects as a direct generalization of the historical fluid theories, and includes them as special cases. He assumed constant mass density, a general ellipsoidal shape, and in Holsapple (2001) a Mohr-Coulomb and in Holsapple (2004) a Drucker-Prager failure model. He was able to derive specific algebraic relations for the maximum spin allowable as a function of internal density, ellipsoidal shape, and angle of friction. Sharma *et al.* (2009) and Sharma (2013) analyze the problem following a somewhat different methodology and find similar results. Other studies on the stability of a continuum model of asteroids have also been made more in line with the classical approach developed by Chree (1895). In particular, Dobrovolskis (1982) studied internal stresses in Phobos; Washabaugh and Scheeres (2002) study the energetics of nonfluid, self-gravitating ellipsoids using a linear elastic model with a Young’s modulus and Poisson ratio; and Kadish *et al.* (2005, 2008) studied stresses in bodies grown by accretion.

In the analytical realm Scheeres has also pursued the understanding of how a collection of self-gravitating rigid bodies evolves when subject to increasing spin rates. These studies have mainly focused on the dynamical stability of fissioned bodies (Scheeres, 2002a, 2009b), conditions for when bodies will transition from resting to orbiting configurations (Scheeres, 2002b, 2009a), and identification of different possible resting states that bodies may have when in contact (Scheeres, 2002b, 2012). These analyses are, by default, somewhat simple, although there are a few general results that can be discerned.

Over this same time period a number of researchers have pursued the modeling of cohesionless asteroid rubble piles using numerical methods, primarily with discrete element method (DEM)-based approaches. There have been two major modeling directions that have been used, the so-called hard-sphere DEM (HSDEM) and soft-sphere DEM (SSDEM) models. An HSDEM code models all particle interactions as impulsive, and thus does not directly determine or track forces. This is a computational simplification that allows for relatively rapid combined dynamical and interaction

computations, but makes it difficult to track or determine interior stress states or conditions. An SSDEM code allows for particle deformation (using an analytical model), and thus directly computes contact forces between the grains. This provides a more natural and realistic way for computing rubble piles in a condensed phase, as the grains are then allowed to come to complete rest with each other (which is impossible in an HSDEM as it only models two-body interactions), form force chains, and enable the internal stress state of the modeled body to be computed. The chapter by Murdoch et al. in this volume provides a more detailed discussion of HSDEM and SSDEM codes as applied to asteroids.

Some representative initial studies in this area for modeling asteroids were done by Richardson's group using an HSDEM code (Richardson et al., 1998, 2005; Walsh and Richardson, 2006). They studied the ability of a collection of same-sized grains with a given level of spin to form a stable configuration, with the use of classical Jacobi or Maclaurin ellipsoids used as a measure of stability, and explored how such bodies would deform and fission following a planetary flyby or when subject to a rapid rotation rate. The mechanical properties of the grains are not directly controlled in these studies; in particular, the friction angle is simulated by having the grains either fall into a crystalline-packed matrix or through the use of a bimodal grain size distribution to promote a loss of friction (Walsh et al., 2012).

Sánchez and Scheeres introduced a self-gravitating SSDEM model for describing the global behavior of rubble-pile bodies (Sánchez and Scheeres, 2011, 2012), in part to overcome such limitations. These models used grains with a size dispersion to avoid crystallization. The friction angle of the rubble pile is controlled by surface friction and interlocking. With this approach it becomes possible to track the internal stress and failure conditions using a granular mechanics code. Relevant results are given below.

An additional approach to the modeling of asteroid rubble piles was introduced in Hirabayashi and Scheeres (2014) and applied in Hirabayashi (2014) and Hirabayashi and Scheeres (2015). In this approach a detailed asteroid shape model can be used and the interior stress states computed by using commercial finite-element-analysis methods. This approach has the significant capability of being able to develop detailed models for the failure of asteroids when subject to gravitational and inertial forces. The use of a general approach enables the detailed analysis of plastic deformation modes and inclusion of detailed continuum model parameters such as Poisson ratio, cohesion, and angle of friction.

#### 4.2. Rubble-Pile Shapes

Using the methods outlined above, the most fundamental question to be asked is what the expected shape of a rubble pile should be. Some insight can be gained by observing the surface slopes of asteroids, as these can indicate if there are regions that are clearly beyond the angle of repose for geological granular material; however, this cannot always be clearly linked to the internal processes. A number of different

asteroid slopes have been computed in the past for specific shapes, and a recent analysis by Richardson and Bowling (2014) shows that most asteroids with known shapes have the majority of their surfaces beneath a typical angle of repose for granular material of  $\sim 35^\circ$ . While there are some specific bodies that have significant regions of their surface that are clearly beyond these angles, such as (6489) Golevka (Hudson et al., 2000) and (4179) Toutatis (Hudson et al., 2003), such situations have not been commonly found in the estimated asteroid shapes described to date.

There have been some attempts at approaching the stability of rubble-pile asteroids through analysis of their shapes alone. Harris et al. (2009) and Minton (2008) approached the problem by analyzing the expected shapes of an asteroid where the surface slopes are constrained to be less than or equal to a certain limit. These analyses were used to explore the likely surface environment of rotationally symmetric, spheroidal asteroids commonly found to be the primaries of binary systems. The poster child of such asteroid shapes is (66391) 1999 KW<sub>4</sub>-Alpha, which exhibits many peculiar features that are indicative of this body to be at or near its failure limit. More recently, Scheeres (2015) has studied these bodies using an approach that is fundamentally motivated by the surface slopes and combines some of the methodology from Harris et al. (2009) along with orbital dynamics considerations.

Such analyses are limited, however, in that they do not consider the totality of the mechanical principles that must be accommodated in order to say with certainty whether a given shape is stable or not. Indeed, it is possible for a given shape to have low slopes across its surface (even zero slope, and much less than the angle of repose), yet be structurally unstable as viewed from a mechanics point of view, which also considers its internal stress field and common failure theories. The necessary approach for that sort of analysis requires the development of a stress field within the body that accounts for all internal forces and that vanishes at the surface. The development of such stress fields is not in general unique. However, if one assumes linear elasticity, an ideal ellipsoidal shape, and a stress-free initial state, then a unique stress field can be derived. Given such a stress field, it is then possible to evaluate it against a failure theory, with the most commonly used ones being the Mohr-Coulomb or Drucker-Prager theory. For a cohesionless body these are simply specified as a function of their interior stress field for a given internal friction angle. Furthermore, there is only one stress state that is in equilibrium and also at the failure limit at each interior point. That occurs at a higher spin than for the elastic solutions, and provides the maximum possible spins among all possible stress fields.

In a series of papers, Holsapple (2001, 2004) applied this basic approach and evaluated the limit spins as a function of the ellipsoidal shape of a large range of asteroids modeled as ellipsoids of axes  $a \geq b \geq c$ . A representative result is given in Fig. 4, which depicts the maximum equilibrium spin as a function of the aspect ratio  $b/a$ , for a prolate object ( $a > b = c$ ), along with data for a number of asteroids. The limit

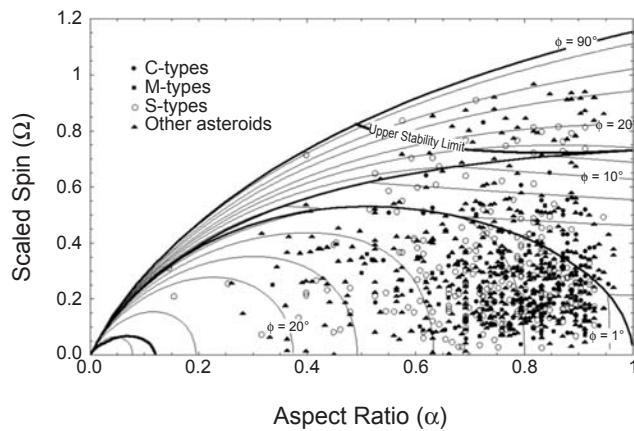


**Fig. 4.** Maximum equilibrium spin limits ( $\Omega$ ) for a prolate rubble pile body as a function of its aspect ratio defined as its polar extent over its total length, ( $\alpha = c/a$ ). The spin limit is normalized to be independent of density and depends upon the angle of friction, ( $\phi$ ), and for each angle of friction there is an upper spin limit and a lower spin limit. At the upper limit equilibrium cannot be achieved for a larger spin and at the lower limit equilibrium cannot be achieved for a smaller spin. Under the dictates of the theory all the asteroid objects plotted, even if not exactly ellipsoidal, must have some nonzero angle of friction arising from a particulate structure. See Holsapple (2001) for a more complete discussion of this figure.

spin is found to depend explicitly on the angle of friction, as is shown in the curves, which for most soils is on the order of  $35^\circ$ . (A fluid body with spin cannot be exactly prolate, but instead must have a Jacobi shape. Therefore it does not appear on this figure.)

Spherical asteroids are represented at the right abscissa of Fig. 4. As an example computation, assume a  $35^\circ$  angle of friction and a mass density of  $2.5 \text{ g cm}^{-3}$ . From this analysis the body cannot have a period shorter than 2.5 h before it begins to deform. However, the period at which a loose surface particle would spin off that spherical object is  $p_s = 2\pi = (\omega_s 3600) = 2.08 \text{ h}$ , the case noted by Harris (note that the surface speed for escape from a spherical asteroid is a factor of  $\sqrt{2}$  faster than the spin-off speed, so a particle would not escape after spin-off unless the spin period was shorter than 1.5 hr). Between these limits loose particles spun off could remain around the asteroid for some period of time. A similar elongated ellipsoidal object with an aspect ratio of 0.5 has a deformation spin period limit of 4.2 h and the particle spin-off limit of 2.9 h.

These theoretical results add detail to the basic idea that rubble-pile asteroids cannot spin faster than some well-defined limit, with specific results about the dependence of that limit spin on the actual shape, density, and internal strength of an object. For the idealized ellipsoidal case, elongation lowers the spin limit, but not as much as the linear decrease as suggested in Harris (1996).

On a case-by-case basis these analyses can be compared to calculations with numerical codes. A particle-based analysis

of equilibrium shape was presented by Richardson *et al.* (2005) using an HSDEM code with 1000 total particles. They considered a spinup of an initial shape and the subsequent reformation to an equilibrium shape. Those reformed equilibrium shapes were roughly consistent with the Holsapple continuum limits discussed above, but for an angle of friction of  $\sim 40^\circ$ . Subsequent analysis by Walsh *et al.* (2012) indicated that the effective friction angle of their stacked hard-spheres was on the order of  $40^\circ$ , leading to consistency with this result. It is also relevant to note that Washabaugh and Scheeres (2002) showed that the total energy of ellipsoidal shapes at a given level of angular momentum was minimized in a broad region in the vicinity of the Jacobi and Maclaurin ellipsoids. While not providing specific failure conditions, their analysis did include the effect of Poisson's ratio in their stress field, accounting for a non-incompressible condition that has been associated with granular materials. In another study, Tanga *et al.* (2009) demonstrate the ability of rubble piles modeled with HSDEM to evolve toward the fluid equilibrium shapes of Jacobi and Maclaurin ellipsoids when subject to intermittent "shaking" due to relatively small impacts.

#### 4.3. Deformation of Rubble Piles

A natural follow-on question regards the expected shape deviation of a rubble-pile body when subject to a changing angular momentum. For asteroids such changes in angular momentum are known to occur for smaller bodies due to the Yarkovsky-O'Keefe-Radzievskii-Paddack (YORP) effect (see the chapter by Vokrouhlický *et al.* in this volume) and for larger bodies due to impacts. The outcomes of such evolutionary questions can only be addressed through theory and simulation; however, such studies are important as they provide predictions for what may occur in actual asteroid systems.

This question of the fate of an object as its spin limit is slowly subjected to additional angular momentum was analyzed using a continuum model in Holsapple (2010). Such an object must globally change shape once it reaches the limiting failure condition outlined above in order to remain stable. Holsapple assumed that the body transitions through a sequence of evolving ellipsoidal shapes. The dynamical theory leads to an ordinary differential equation for the axis ratios of the ellipsoid (Holsapple, 2010, equation (45)), which can be numerically integrated. A typical result is presented in Fig. 5, which plots the axis ratios along level sets of solutions to the differential equations.

For an object starting in the upper right corner of this figure, which represents a slightly oblate initial shape, the body will flatten, becoming more oblate. It can ideally approach a very flat shape with thickness only a fraction of its diameter before then deforming to a prolate shape. For a body initially at a shape near the center of this plot, it will become more prolate, eventually approaching a very long shape, with  $a/c$  of 5.1 or more. As it deforms, although its angular momentum increases, in most cases its spin decreases because its moment of inertia increases. The implication of this is important for

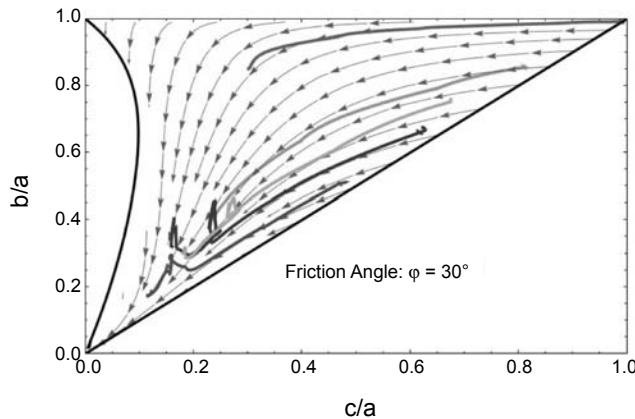


**Fig. 5.** Figure showing the deformation path of the semi-major axis ratios of an ellipsoid as its angular momentum is increased. An object with the angle of friction of  $30^\circ$  can be at its limit spin at any point along one of the curves in this figure. If the angular momentum is slowly increased, e.g., by YORP, the object deforms and traces a path in the direction indicated along the curves shown. The overlaid lines show results of numerical simulations using a SSDEM model. From Sánchez and Scheeres (2012). These curves terminate when the body fissions, which is not modeled in the analytical theory.

interpreting the spin limit in Fig. 3. It predicts that bodies that lie at the minimum spin period line may not necessarily be at the limit of their angular momentum, but may be starting to go through a deformation that may actually decrease their spin rate as their angular momentum increases.

These deformational dynamics have also been seen in numerical simulations. Walsh *et al.* (2008) analyzed the effect of spinup on initially spheroidal rubble piles modeled with an HSDEM code. They found that as spin increased, components of the body would migrate to the equator, both causing a bulge to form and leading to loss of components into orbit about the body. These studies indicated a link between the expected shape deformation from YORP spinup and with these bodies being linked to binary formation. Sánchez and Scheeres (2012) also analyzed such spinup deformations using an SSDEM code. Their numerically computed deformations are plotted in Fig. 5 and are seen to closely follow the analytical curves derived by Holsapple (2010). However, we note that these simulations are only started in ellipsoidal shapes and are not constrained to be ellipsoidal (unlike the Holsapple computations). Thus as the angular momentum becomes large enough, the collections of grains are seen to undergo deformation beyond the classical ellipsoid shape. This is seen as the sequence of ideal ellipsoid deformations end once they become unstable and sensitive to collapse, which occurs at extreme elongations. The manner in which such systems fail range from surface shedding to fission, and is largely driven by the morphology of the mass distribution. Specifically, in the Sánchez and Scheeres (2012) simulations, initially ellipsoidal bodies are found to separate due to fission while initially spherical bodies are seen to shed material from

their surface. Another possible outcome of deformation is a change in the body's YORP coefficient, which can cause a body's spin evolution to change sign, as initially noted in Scheeres *et al.* (2007) and recently studied in detail in Statler (2009) and Cotto-Figueroa *et al.* (2015).

Strongly oblate shapes have been found in several asteroids, some of which are fast rotating, such as (66391) 1999 KW<sub>4</sub>, (341843) 2008 EV<sub>5</sub>, (367943) Duende (formerly 2012 DA<sub>14</sub>), (101955) Bennu (formerly 1999 RQ<sub>36</sub>), (65803) Didymos, (2867) Šteins, and others. The equators of these objects generally protrude outside the equivalent oblate ellipsoidal shape, and therefore loose particles at their equator can spin off (Scheeres, 2015). Such shed particles are found to eventually escape (Jacobson and Scheeres, 2011a), although if sufficient numbers are shed in a short period, they may also form into a secondary (Walsh *et al.*, 2008, 2012). Analytical studies of such spunup shapes have been published by Harris *et al.* (2009), Minton (2008), and most recently Scheeres (2015). These studies seek to tie surface deformation to the overall shape of the body, with a particular focus on the oblate, fast-spinning shapes that have been associated with primaries of binary asteroids.

#### 4.4. Evidence for Fission

One predicted outcome for rapidly spinning bodies is that they can undergo a shape bifurcation and separation into multiple components. This outcome is to be compared to the loss of material directly from the surface — a distinction that has been studied to some extent in Walsh *et al.* (2008), Hirabayashi and Scheeres (2014), and Hirabayashi (2014). Analytical methods applied to simplified studies have been able to model such fission mechanics. In Scheeres (2009a) it was shown that the first components to fission in a non-uniform body will be those whose mass centers are the furthest from each other. For simple models of ellipsoids resting on each other, this corresponds to the distinct bodies fissioning first. Under this assumption, it is possible to show that the dynamical evolution of a fissioned body can be directly related to the relative mass fraction between the components (Scheeres, 2007, 2009b). Specifically, if the mass ratio between the bodies is less than  $\sim 0.2$ , the resulting system has positive total energy and can escape [albeit not immediately (Jacobson and Scheeres, 2011a)], while for mass ratios larger than this the bodies are gravitationally bound and cannot escape without exogenous forcing.

This theory was specifically supported with the observations from Pravec *et al.* (2010) on asteroid pairs, which are asteroids that have had an extremely close passage to each other at an extremely slow speed ( $<1 \text{ m s}^{-1}$ ) at some point in the past (Vokrouhlický and Nesvorný, 2008). In the Pravec survey the relative sizes of asteroid pairs were determined and the spin period of the primary measured (see Fig. 6). This survey showed the predicted relation between mass ratio and formation of asteroid pairs, as there is a cut-off in asteroid pairs for mass ratios larger than  $\sim 0.2$ . As a secondary confirmation, the analysis also showed that the spin rates of

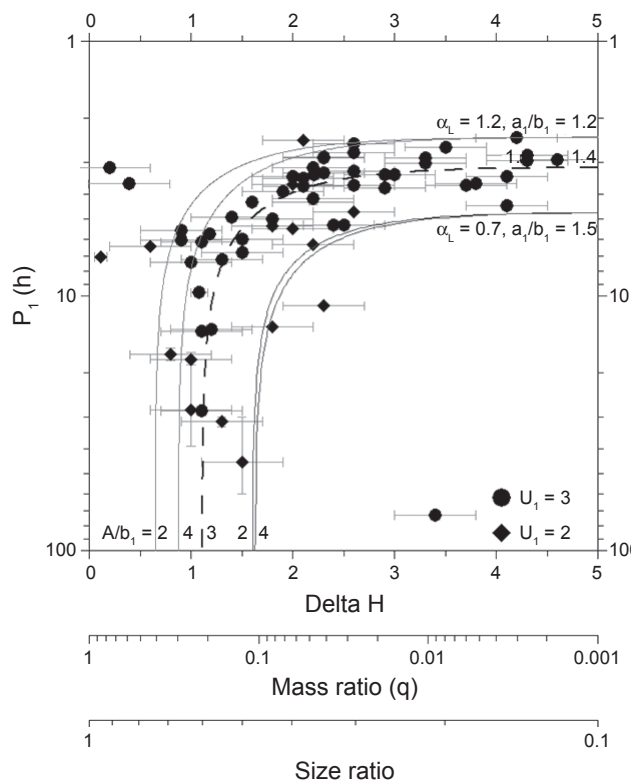


**Fig. 6.** Asteroid pairs showing the mass ratio and spin period of the primary with data through September 2014 (Pravec, 2014). There are a few significant outliers that do not fit with the theory, although the majority of added pairs is consistent with the initial interpretation in Pravec *et al.* (2010), where the parameters and detailed models used are described.

primaries decrease as the mass ratio limit is approached, which is the predicted mechanism for ejection, where energy for escape is taken from the spin rate of the primary. Additional observations of asteroid pairs have largely been consistent, although there are a few bodies that do not follow this rule and thus may be asteroid pairs formed by another mechanism (cf. Vokrouhlický and Nesvorný, 2008). There have also been spectroscopic studies of these asteroid pairs by Polishook *et al.* (2014), which have also been interpreted to support the fission hypothesis. This is significant as it has direct bearing on the manner in which rubble-pile bodies fail, even though there is not much detail. The implications of such fissioning have been investigated in Jacobson and Scheeres (2011a), which is described more fully in the chapter by Walsh and Jacobson in this volume.

#### 4.5. Spin Limits for Cohesive Objects

Since *Asteroids III*, a significant number of small asteroids spinning above the limits derived for a cohesionless rubble pile have been discovered. Those objects, whose existence was predicted in Harris (1996), must have sufficient internal strength to withstand their internal tensile stresses. The ques-

tion these bodies raise is what physics provide the source of that strength, what magnitude of strength is needed, and whether these can still be thought of as rubble-pile bodies.

That question was first addressed in Holsapple (2007), where the rubble-pile analysis outlined above was expanded to include strength models with cohesive strength, and it was found that the limit spins could be substantially faster if the internal material was capable of withstanding some level of tensile stress. However, that is true only for smaller asteroids, as can be seen in Fig. 3, as all the strength-limit curves fall back to the nominal spin limit for increasing size (which is the reason why the gravity spin limit does not necessarily imply cohesionless rubble piles). Holsapple derived specific limit curves for two strength cases. First, for a constant strength it is found that the maximum spin rate decreases linearly as the asteroid diameter increases, as noted in Harris (1996). Second, it was assumed that the strength of meter- to kilometer-sized objects will decrease with increasing size, to the  $-1/2$  power, and in this way accounting for increasing planes of weakness in a larger body. Then the limits of spin vs. size decrease with the power of  $-5/4$ . The resulting curve is the upper, bounding curve plotted in Fig. 3. This curve furnishes an upper bound to all the present data and is for a material that has a tensile strength of only 100 kPa in a 10-cm specimen, and then decreasing as  $1/\sqrt{r}$  with size  $r$ . That value is more than an order of magnitude less than measured for typical meteorites (see section 2). Therefore, whether these data are really constrained by a strength limit or not remains an open question, as the limit may only indicate a lack of mechanism to further increase spin rates. A related question is also whether this represents the strength of individual components.

Sánchez and Scheeres (2014) have investigated the question of what minimum level of strength could exist between rubble-pile components. It is an important distinction that they are not considering the strength of all components, but are probing for the presence of possible cohesive strength between rubble-pile components. Their theory notes that van der Waals attractions between the finest material present in the rubble pile (in sufficient quantities to form an underlying matrix of material) should hold larger components in place, in the same way that cement holds rocks within a matrix. Using data from the Apollo lunar experiments and samples, and information on size distributions inferred from observations and samples from Itokawa, they predict the possible strength of this regolith to be on the order of 100 Pa, with their preferred value stated as 25 Pa (it should be noted that this value depends on an assumed density, angle of friction, and other shape parameters). This model probes the lower end of the strength envelope to determine whether there is any evidence for such cohesive strength in rubble-pile asteroids.

Sánchez and Scheeres (2014) point to a few aspects of the asteroid size, spin, and morphology database represented in Fig. 3, in addition to some specific asteroids, as evidence for their theory. First they note that cohesive strength between rubble-pile components greater than  $\sim 100$  Pa should

lead to a more filled-in population below the strength line in the intermediate size range of 0.1–1 km. However, only when total effective strength (which is actually a function of density and shape assumptions as well) falls below the 100-Pa limit is the visual gap less significant. Another prediction from this theory is that binaries should not form when less than a certain size, as the spin rate required for fission to overcome cohesion would cause the resulting fragments to separate at speeds in excess of their mutual gravitational escape speed. They use this to explain the sharp drop-off in binaries below a few hundred meters, which has been shown to be statistically significant (see the chapter by Margot et al. in this volume). Finally, the presence of small and rapidly spinning tumbling asteroids at the strength limit is also consistent with the failure of rubble-pile asteroids with cohesion, as such a failure will generally induce tumbling in the separated bodies, which will also immediately escape from each other (Scheeres et al., 2010). There are also a few specific bodies that provide additional support for this weak level of strength being present in a rubble-pile body. These are P/2013 R3, (29075) 1950 DA, and 2008 TC<sub>3</sub>, which are discussed in the final section.

Before continuing it is important to note that the apparent gap between strengths greater than 100 Pa and the observed bodies in the 0.1–1-km range has been challenged by a number of observations that show the existence of objects that fill in the region beneath the upper bound. These are noted in Holsapple (2007) and reported in Masiero et al. (2009), Chang et al. (2014), and Urakawa et al. (2014). These observations have not been deemed sufficiently reliable in the lightcurve database (Warner et al., 2009) to include in the confirmed cases. It is important that these objects be viewed in future apparitions to confirm them. Confirmation of these bodies' size and spin rates would have a significant impact on our understanding of the possible strength of asteroids.

## 5. PROBING ASTEROID INTERIORS

Although the previous models and interpretations take the interior properties of asteroids into account, they do not directly sense or constrain the interior properties or geophysics. This is because they still rely on external measures of the asteroid stability state, such as its shape, size, and spin. This section discusses approaches that are currently being developed to probe the interior properties of an asteroid, taking advantage of fundamental geophysical properties and observable effects. There are three main recent advances in this area, the first of which is the classical interpretation of surface geological structures to make inferences on the interior of an asteroid. Second is the analysis of the interior seismic properties of rubble-pile bodies. Third is the analysis of tidal dissipation effects within small rubble-pile bodies. A fourth advance that can be mentioned in passing is the use of radar to probe the interior of a rubble-pile body. However, there have not been definitive analyses of this approach for asteroidal bodies, although such analyses will be performed for the first time at a comet by the Rosetta spacecraft.

### 5.1. Geological Interpretation

The classical approach to interpreting the interior structure of an asteroid was pioneered at the asteroid (433) Eros, although it has also been applied to interpret the interior of Phobos (see the chapter by Marchi et al. in this volume). The underlying theory is outlined in Prockter et al. (2002) and interprets surface features as expressions of subsurface strength. The key focus was on the lineaments and global structures such as Rahe Dorsum on Eros. Buczkowski et al. (2008) studied the lineaments across Eros to determine whether there was clear evidence for internal strength or structures. While certain correlations seem to exist, along with evidence for some subsurface structure, it is also difficult to independently confirm what these structures may be, whether they arise from the mechanical properties of the regolith itself, or how they could be uniquely estimated (Robinson et al., 2002). The approach has also had limited use at (25143) Itokawa, where there are no specific global geographic features that could be used to make interior interpretations other than the component shapes themselves. On the other hand, such an approach can be very valuable at a larger body such as (4) Vesta, which has many global features that could be used as constraints on the interior of the body (reviewed in the chapter by Russell et al. in this volume).

### 5.2. Seismic Effects

The importance of seismic effects was underlined by the Near Earth Asteroid Rendezvous (NEAR) observations of Eros. While craters were present on that body, they became more sparse at smaller sizes, with the surface dominated by a thick layer of regolith (Chapman et al., 2002). This was explained using a statistical and global analysis of crater erasure due to seismic shaking as a result of impacts on Eros (Richardson et al., 2004). In a subsequent analysis, Thomas and Robinson (2005) were able to positively correlate the erasure of small craters with a single large impact, thus linking the transmission of seismic energy from an impact to the surface motion of regolith and not due to regolith created in the impact itself. The chapter by Marchi et al. in this volume reviews this material in more detail.

Motivated by, and contemporaneous with, this physical correlation there were many different studies of the effects of impacts on the redistribution of regolith. These include the use of particle hydrodynamic codes for simulating impacts (Nolan et al., 2001), coupled models of seismic transmission and granular motion (Richardson et al., 2004; Richardson and Bowling, 2014), and the application of Earth geophysical models of seismic-energy transmission to rubble-pile bodies (Martin et al., 2008; Blitz, 2009).

A culmination of these analyses is the realization that the mechanical properties of a rubble-pile body can be linked with the observed crater distributions and levels of erasure. Asphaug (2008) proposes a methodology to directly estimate the attenuation of seismic energy within a rubble pile using the observed largest crater on that body. This basic idea has

also migrated beyond the use of naturally occurring impacts to include the application of controlled and induced cratering blasts or impacts on the surface of a rubble-pile asteroid. By controlling the energy and deposition of the blast, it is possible to infer the seismic transmission of energy at distal points of a rubble-pile body by comparing before and after images of the surface. This can be enhanced by the deployment of instrumented devices across the surface, where they can record the sensed seismic energy or, in the extreme case if they are lofted from the surface, determine the strength of the seismic wave by tracking the length of their ballistic phase. Such ideas were proposed in Scheeres *et al.* (2003) and have subsequently appeared as a concept in a number of space science missions, with the combination of calibrated blasts and sensing measuring devices proposed in the Discovery mission Binary Asteroid In-Situ Explorer (BASiX) (Robert *et al.*, 2010). Similar concepts have also been subsequently proposed in the mission concepts of MarcoPolo-R (Michel *et al.*, 2014) and Asteroid Impact and Deflection Assessment (AIDA) (Galvez *et al.*, 2013). This approach to seismic inference will be realized with the currently planned Hayabusa-2 mission to primitive asteroid 1999 JU<sub>3</sub>. This mission concept calls for using an explosive device to accelerate an impactor into the surface of the body, creating a crater and seismic energy source that can then be tracked by observing modifications of the surface (Tsuda *et al.*, 2013).

### 5.3. Tidal Dissipation

Another measure that can be used to peer into the interior of a rubble-pile body is related to energy dissipation due to tidal deformations. There are two main ways in which rubble-pile bodies can dissipate excess kinetic energy via this method. One occurs if the body is in a non-uniform rotation state, as this induces traveling waves of alternating accelerations, which can cause stress and strains that dissipate energy. This effect has been linked to the fact that the vast majority of asteroids are in or near a rotation state about their maximum moment of inertia (Burns and Safronov, 1973). Harris (1994) showed that the vast majority of known tumbling asteroids had an overall slow rotation rate, meaning that the time for them to relax to uniform rotation could be long, although these estimates depend on assuming that the geophysical properties of larger planetary bodies and satellites are similar to rubble-pile bodies.

To better constrain and understand how the observed tumblers should be interpreted in terms of their internal geophysics of tidal dissipation, there have been several analytical and numerical studies of how asteroids could enter complex rotation states and what the frequency of them entering such states should be. This would allow for the comparison of the population with different dissipation rates. The trend of tumbling with greater spin period implicitly indicates that asteroids are dissipative bodies. The degree of dissipation is not fully understood, and depends on the assumed parameters of rigidity,  $\mu$ , which measures the stiffness of the body; the quality factor,  $Q$ , which is inversely proportional to the rate

of energy dissipation due to non-uniform deformations; and the rate at which tumblers are created. We note that tumblers can be created in several ways: catastrophic disruptions (Asphaug and Scheeres, 1999; Scheeres *et al.*, 2000b), planetary flybys (Scheeres *et al.*, 2000b, 2005; Pravec *et al.*, 2014), YORP-induced fission (Sánchez and Scheeres, 2014), and, potentially, YORP spindown effects either in isolation (Vokrouhlický *et al.*, 2007) or in combination with impacts (Marzari *et al.*, 2011; Henych and Pravec, 2013).

On the other hand, the application of standard planetary theory geophysics to rubble-pile asteroids made in earlier studies may not be appropriate. This has motivated researchers to develop improved mathematical models and to carry out geophysical analyses that are relevant for this environment. Efroimsky and Williams (2009) considered the effect of frequency dependent terms in tidal dissipation, while Sharma *et al.* (2005) and Breiter *et al.* (2009) have developed novel mathematical expressions for tidal dissipation. Perhaps most fundamental, however, is the study by Goldreich and Sari (2009), which shows that rubble-pile bodies are expected to behave distinctively relative to the classical planetary satellite theory. In their analysis they show that the functional relationship between the quality factor,  $Q$ , and the Love number of an object,  $k$  (related to the rigidity of the body and how the shape responds to tidal stress), should follow a variation where  $Q/k \propto r$ , the radius of the body, which is distinctly different than the classical relationship. Specifically, they show that the effective dimensionless rigidity of a rubble pile is smaller than that of a monolithic body of the same size, with the reduction arising from the concentration of stresses due to the presence of voids. Using this result they show that it is likely that a rubble-pile secondary in a binary asteroid system should circularize, which cannot be necessarily concluded if the secondary is monolithic and follows the classical planetary relation. The implications of their analysis for the relaxation time for tumbling asteroids has not been made as of yet.

The Goldreich and Sari analysis has been applied to develop a more detailed model for the expected evolution of binary asteroid systems. In Jacobson and Scheeres (2011b) they analyze the joint evolutionary dynamics of tidal dissipation and the binary YORP (BYORP) effect (see the chapter by Vokrouhlický *et al.* in this volume) in light of the Goldreich and Sari theory for tidal dissipation. They find that there should exist a so-called BYORP and tide equilibrium where a contractive BYORP effect acting on the synchronous secondary is balanced by an expansive tidal effect due to dissipation in the rapidly rotating primary. The existence of this equilibrium is significant for a number of reasons, described elsewhere in this volume in the chapters by Walsh and Jacobson and Vokrouhlický *et al.* In the context of this chapter the significance is that this provides a direct way in which to constrain and indirectly measure the rigidity of the primary in a rubble-pile binary asteroid. Once a binary asteroid is known or suspected to lie in such an equilibrium, it also provides a way to evaluate the functional relationship between a body's size and its quality factor and tidal

Love number. The existence of this equilibrium has been recently validated for binary asteroid 1996 FG<sub>3</sub> (Scheirich et al., 2015). From that study there is an inferred value of rigidity times quality factor of  $\mu Q \sim 2.7 \times 10^9$  Pa, which is orders of magnitude less than that expected for a monolithic body and for what has been bounded in the past for binary asteroids (Margot et al., 2002). This result is significant, as it is the first “measured” value of this parameter for a rubble-pile body, albeit there are a number of significant sources of uncertainty that are discussed in that paper.

A significant next step in analysis will be to start to blend these results to better understand the dissipation rate within rubble-pile bodies. This will require additional theoretical, observational, and ultimately numerical computations to fully understand. It also provides motivation for a space science mission to a binary asteroid in a BYORP-tide equilibrium, since obtaining a precise estimate of the rigidity requires that the secondary body be fully mapped.

## 6. SPECIFIC ASTEROID OBSERVATIONS

In addition to the insights obtained by analyzing the asteroid population database, there have been significant insights from analyzing specific asteroids. There have been a number of dramatic and unprecedented observations of single bodies that provide deep insight into the morphology and, in some cases, the mechanical properties of these asteroids. In the following we discuss some of the more significant of these bodies. As some of these bodies are discussed in more detail elsewhere, in some cases we only draw on a few aspects of the analysis and indicate the appropriate chapter for more details. Instead of grouping these bodies by how they were observed, which could be done, we just list them in order of their alphabetical names and designations.

### 6.1. (433) Eros

At the time the *Asteroids III* book was being completed, significant, but incomplete, data on asteroid (433) Eros taken by the NEAR-Shoemaker spacecraft was already included. The definitive analysis of the gravity field of this asteroid had not been published, however, and is what we focus on here. Initial data indicated that the asteroid’s gravity field was homogeneous at the few-kilometers scale (Asphaug et al., 2002). Subsequent analysis of the gravity field was made and reported in two papers (Miller et al., 2002; Konopliv et al., 2002). Both papers included a comparison between the measured gravity field and a homogenous gravity field computed from the shape with a constant density assumption. Density variations can be detected through the comparisons of measured and computed gravity field coefficients (cf. Scheeres et al., 2000a; Takahashi and Scheeres, 2014). Gravity field comparisons in both papers showed differences at the relative level of less than  $10^{-3}$  through the 6th degree-and-order gravity terms. At higher degree and order the uncertainty in the gravity-field coefficients was greater than this relative level, meaning that at these higher levels the differences were

indistinguishable from noise. This provides a strong constraint on the density homogeneity within this asteroid. We also note that the bulk density of this body was determined to be  $2.67 \pm 0.03$  g cm<sup>-3</sup> (Miller et al., 2002), indicating a relatively low level of macroporosity of approximately 20% assuming the S-type asteroid had a grain density of ordinary chondrites (Yeomans et al., 2000). The Miller et al. (2002) paper also made an accurate rotation-state estimate for the body, and was unable to observe any complex rotation except that driven by solar torques. This indicates that the body had fully relaxed to principle-axis rotation.

### 6.2. (25143) Itokawa

The asteroid (25143) Itokawa was visited by the Hayabusa spacecraft in 2005 (see the chapter by Yoshikawa et al. in this volume). The greatest achievement of that mission was the collection of a small but valuable sample of regolith from the surface. However, several important observations and measurements of the asteroid were also taken during the few months that the spacecraft was in close proximity to that body. There were several important determinations with regard to the geophysics of this asteroid. These include the total bulk density of the body, measured to be  $1.9 \pm 0.13$  g cm<sup>-3</sup>, corresponding to a macroporosity of 41% for this S-type asteroid (Fujiwara et al., 2006). As the spacecraft never spent significant time in ballistic motion close to the asteroid, the gravity field determination was not able to progress beyond the total mass. Subsequent to the mission it has been speculated that the density distribution within the body is heterogeneous. This idea was first proposed in Scheeres and Gaskell (2008) to explain the apparent disconnect between the predicted YORP torque (which was computed to be negative based on several different computations) and the lack of a detected change in its spin. This theory predicted that either the head or neck region of the body should have a greater density. Lowry et al. (2014) were able to detect a measurable acceleration in the spin rate of Itokawa. Based on the theory outlined in Scheeres and Gaskell (2008) and Breiter et al. (2009) it was determined that the density disparity between the head and body would need to be 2.85 and 1.75 g cm<sup>-3</sup>, respectively, for this effect alone to account for the disparity. Such a drastic disparity between densities, 62%, is not out of the question given that the secondary and primary of (66391) 1999 KW<sub>4</sub> have a large density disparity, although for that body it is only 42% for the nominal values (see below). However, as discussed in the chapter by Vokrouhlický et al. in this volume, there are other effects besides a density disparity that could have caused the acceleration of Itokawa, making the result somewhat uncertain.

Beyond the mass, bulk density, macroporosity, and possible density heterogeneity, important information was obtained regarding the size distribution of rocks, boulders, and grains on Itokawa. Based on images taken while in close proximity to the body, the size distribution of boulders and rocks across its surface was measured and found to follow a size distribution with an exponent of  $-3.1 \pm 0.1$  down to

5 m (*Michikami et al.*, 2008). A more recent paper revisits the Itokawa data and focuses on the difference between the head and body of this asteroid, as well as discussing several possible hypotheses for its formation (*Mazrouei et al.*, 2013). They find a somewhat steeper size distribution down to 6 m, albeit changing depending on where on the body one looks. Ultimately their general conclusions on the distribution of larger blocks are consistent with *Michikami et al.* (2008). Using the returned samples, a size-distribution analysis was also made by *Tsuchiyama et al.* (2011). Across the grain sizes ranging from 0.5 to 100  $\mu\text{m}$  they found a size distribution with an exponent between  $-2.8$  and  $-2$  (steeper at the smaller sizes). While these two size distributions (from the observations and the samples) cannot be easily combined, they do present some insight into the size distribution of grains and boulders within a rubble-pile asteroid. *Tsuchiyama et al.* present the hypothesis that the size distribution may break to a shallower level at millimeter- to centimeter-sized grains, which may explain why they were viewed as the dominant grain size on the body [at least in the Muses-Sea region (*Yano et al.*, 2006)]. These measurements of size distribution are important as they speak directly to the presumed size distributions that all rubble-pile bodies may have. Also, the recent theory on cohesive strength in rubble piles (*Sánchez and Scheeres*, 2014) depends explicitly on the presence of fine regolith grains for its physical realization.

### 6.3. (216) Kleopatra

The asteroid (216) Kleopatra is a strangely shaped main-belt asteroid with a total length on the order of 250 km and with a very narrow “neck” (*Ostro et al.*, 2000). This asteroid has already been distinguished by its rapid rotation and odd shape. *Descamps et al.* (2011) reported the discovery of two satellites about this asteroid, enabling a precise mass of the asteroid to be determined. However, while their observations were also consistent with the *Ostro et al.* (2000) radar-based shape, they reported finding a significantly larger size for this body, approximately 25% larger in mean diameter than the *Ostro et al.* radar shape. A different set of observations by *Marchis et al.* (2012) reported an even larger size, raising the interesting situation of knowing the mass and shape of the body but not its size and hence density. The rapid rotation of this object and its shape mean that the stability of this body is highly sensitive to its bulk density and size. *Hirabayashi and Scheeres* (2014) took advantage of this size ambiguity to probe the stability of this body across a range of sizes, from the *Ostro et al.* (2000) size to the *Marchis et al.* (2012) size. Based on an averaged stress analysis, essentially applying the averaging method of Holsapple to a non-ideal shape, they were able to determine that the *Descamps et al.* (2011) size requires the lowest angle of friction to keep the body stable. This analysis has also been confirmed using a finite-element plastic-deformation analysis that shows that the smaller *Ostro et al.* (2000) size will tend to collapse, the larger *Marchis et al.* (2012) size will tend to separate, and the *Descamps et al.* (2011) size seems to be the most

stable again, and is only susceptible to surface failures that could be related to inaccuracies in the detailed shape of the body (*Hirabayashi*, 2014). This analysis is listed here as it represents a unique use of continuum and failure theory to help resolve an inconsistency in measurements.

### 6.4. (29075) 1950 DA

The asteroid (29075) 1950 DA is well known as one of the most hazardous bodies for Earth in the solar system, due to its relatively high impact probability of 1 in 4000 (albeit in the year 2880) and its relatively large size, on the order of 1 km (see the chapter by Harris et al. in this volume). In *Rozitis et al.* (2014) the body’s density is determined by using the measured Yarkovsky acceleration of the body and analyzing the thermal inertia. This allowed them to infer that the body was a rubble pile, that the rotation of the body was retrograde, and that the corresponding shape model for this rotation pole could be used (*Busch et al.*, 2007). Based on these measurements, *Rozitis et al.* (2014) determined that the body was spinning beyond the failure limit at which both loose material would be shed from its surface and it would undergo global deformation. Due to this they concluded that the body required cohesion to stay intact, and applied basic techniques (*Holsapple*, 2001) to determine the level of cohesive strength needed. Based on a Drucker-Prager failure model they were able to identify a minimum necessary strength of approximately 65 Pa for the body to hold together, which they note is comparable to the level of strength for rubble-pile bodies hypothesized in *Sánchez and Scheeres* (2014). A detailed finite-element analysis was performed by *Hirabayashi and Scheeres* (2015) that confirmed this strength as a lower bound and found that for uniform strength, the center of the body should fail prior to the surface. They note that should this occur, it could result in a less-dense core, which could be detected with an orbiting spacecraft.

### 6.5. (66391) 1999 KW<sub>4</sub>

The binary asteroid (66391) 1999 KW<sub>4</sub> was observed with range-Doppler radar at a number of epochs, enabling a detailed model of the shapes of each of its components and their relative orbital and rotational dynamics (*Ostro et al.*, 2006; *Scheeres et al.*, 2006). These papers provided the first, and to date most accurate, insight into the morphology of a binary asteroid system, and it is of interest to briefly review the results here. First, it is important to note that in the nominal model the primary rotates just shy of where loose material should be shed from its surface, implying that its interior may also be close to a failure limit. At the lower end of density for the primary the surface may require cohesive strength to stay together. Thus this body exhibits and showcases the traits of the rapidly rotating oblate bodies discussed earlier in this chapter and has been used as the motivating example of this class of body (*Harris et al.*, 2009; *Scheeres*, 2015).

The primary has an obliquity of about 3° with respect to the orbit plane of the binary and the secondary has relative

librations of several degrees. Thus the system is not in a fully relaxed state. Based on the shape of the secondary we note that the predicted BYORP coefficient is positive, meaning that this system could be undergoing expansion (the system is currently being monitored for BYORP expansion, as described in the chapter by Vokrouhlický et al. in this volume). As this system has not settled into a fully relaxed state it introduces the interesting possibility that it could be tracked over longer time periods to possibly determine or detect effects associated with either tidal relaxation or with BYORP expansion.

There is a large density disparity between the primary and secondary body. The primary density is determined to be  $1.97 \pm 0.24 \text{ g cm}^{-3}$  and the secondary to be  $2.81^{+0.82}_{-0.63} \text{ g cm}^{-3}$ , a relative factor of 42%. Possible reasons for such a disparity are discussed in Scheeres et al. (2006), and involve the compaction of the secondary by continuous shaking and the expansion of the primary due to the extremely rapid rotation rate.

## 6.6. 2008 TC<sub>3</sub>

Now we consider asteroid 2008 TC<sub>3</sub>, which became the Almahata Sitta meteorite (Jenniskens et al., 2009). This asteroid was observed prior to entering Earth's atmosphere during the brief period after its discovery. Lightcurve observations of this body showed that it was spinning with a period of 100 s and also was in a tumbling rotation state (Scheirich et al., 2010). It can be found on Fig. 3, where it is the smallest known tumbler and only requires approximately 100 Pa of cohesive strength to withstand disruption. Based on analysis of the meteorite fall, this body consisted of several different mineralogical types that constituted separate components in the parent asteroid (see the chapter by Jenniskens in this volume), with one possible interpretation being that it could be described as a rubble pile (Jenniskens et al., 2009). Analysis of the preentry observations and the meteorite falls also indicate that the body had significant macroporosity (Kohout et al., 2011). The meteor was observed to break up high in the atmosphere, indicating a weak body (Borovička and Charvat, 2009; Popova et al., 2011). Furthermore, Borovička and Charvat (2009) note the presence of an abundance of micrometer- and larger-sized dust associated with the meteor, consistent with this dust composing a “substantial part” of the total mass of the object. These disparate observations related to this asteroid were linked together in the recent theory proposed in Sánchez and Scheeres (2014), and described earlier in section 4.5, although there remain questions about that interpretation (see discussion in the chapter by Borovička et al. in this volume).

## 6.7. P/2013 P5

Body P/2013 P<sub>5</sub> was initially catalogued as a comet, yet now seems to more properly identified as an asteroid (see the chapter by Jewitt et al. in this volume; Jewitt et al., 2013; Hainaut et al., 2014). This body has exhibited periodic shedding over a number of different observational epochs. Material

shed from its surface has been seen to consist of fine grains down to 10 μm in size at least. A clear explanation for its periodic shedding has not been found, although some initial analysis of this phenomenon has occurred (Scheeres, 2015).

## 6.8. P/2013 R3

Finally, we mention another active asteroid, P/2013 R<sub>3</sub> (Jewitt et al., 2014). This body was seen to fail in an entirely different morphological fashion, splitting repeatedly into smaller components that escaped from each other. Hirabayashi et al. (2014) analyzed the main components of this body and estimated the initial spin rate of the protobody by mapping estimates of size and speed backward to the inferred epoch of disruption. Based on this analysis they predicted a range of possible strengths for the progenitor rubble-pile body prior to breakup, from 40 to 200 Pa, with the range of values accounting for uncertainties in size, density, and relative speed.

## 7. CONCLUSIONS

In this chapter we bring together disparate material on the strength, mechanics, and morphology of asteroids based on meteors and meteorites, groundbased observations, spacebased observations, analysis, and numerical simulation. While there has been significant progress on all fronts since *Asteroids III*, many new issues and questions have been exposed as well. A main issue that arises is the wide variation in strength determinations of asteroids and their constituents. While direct comparisons of meteor strengths as parameterized by dynamic pressure and strength parameterized by spin rate cannot be naively made, there must be some underlying connection between these. Elucidation of this should be a priority, as it would enable a clear application of meteor data to the interpretation of strength of rubble-pile bodies. Another area that is ripe for progress is an improved theory of tidal dissipation within rubble-pile bodies, coupled with new ways in which the fundamental parameters of rubble piles can be estimated. This involves a better understanding of how asteroids are made to tumble, modified theories for tidal dissipation of rubble-pile bodies, and estimation of improved values for rigidity, tidal Love number, and quality factors of rubble piles. Finally, the continued advancement in analytical and numerical simulation tools will be essential for continued progress in this difficult and fundamental issue of asteroid mechanics.

**Acknowledgments.** D.J.S. acknowledges support from the NASA Near Earth Object Observations Program through grant NNX14AL16G. The authors appreciate the thorough reviews from two expert referees.

## REFERENCES

- Abe S., Mukai T., Hirata N., et al. (2006) Mass and local topography measurements of Itokawa by Hayabusa. *Science*, **312**, 1344–1347.
- Asphaug E. (2008) Critical crater diameter and asteroid impact seismology. *Meteoritics & Planet. Sci.*, **43**, 1075–1084.

- Asphaug E. and Scheeres D. J. (1999) Deconstructing Castalia: Evaluating a postimpact state. *Icarus*, 139(2), 383–386.
- Asphaug E., Ryan E. V., and Zuber M. T. (2002) Asteroid interiors. In *Asteroids III* (W. F. Bottke Jr. et al., eds.), pp. 463–484. Univ. of Arizona, Tucson.
- Bendjoya P. and Zappalà V. (2002) Asteroid family identification. In *Asteroids III* (W. F. Bottke Jr. et al., eds.), pp. 613–618. Univ. of Arizona, Tucson.
- Blitz C. (2009) Modélisation de la propagation des ondes sismiques et des éjecta dans les astéroïdes : Application à l'érosion des cratères de la Léthoïde (433) Eros. Ph.D. thesis, Institut de Physique du Globe de Paris, Paris.
- Borovička J. and Charvat Z. (2009) Meteosat observation of the atmospheric entry of 2008 TC3 over Sudan and the associated dust cloud. *Astron. Astrophys.*, 507(2), 1015.
- Borovička J. and Spurný P. (2008) The Carancas meteorite impact — Encounter with a monolithic meteoroid. *Astron. Astrophys.*, 485(2), L1–L4.
- Borovička J., Spurný P., Brown P., et al. (2013) The trajectory, structure and origin of the Chelyabinsk asteroidal impactor. *Nature*, 503, 235–237.
- Brearley A. J. and Jones R. H. (1998) Chondritic meteorites. *Rev. Mineral. Geochem.*, 36(1), 3–1.
- Breiter S., Bartczak P., Czechaj M., et al. (2009) The YORP effect on 25143 Itokawa. *Astron. Astrophys.*, 507(2), 1073.
- Britt D. T., Yeomans D. K., Housen K. R., and Consolmagno G. J. (2002) Asteroid density, porosity, and structure. In *Asteroids III* (W. F. Bottke Jr. et al., eds.), pp. 485–500. Univ. of Arizona, Tucson.
- Brown P. G., Revelle D. O., Tagliaferri E., and Hildebrand A. R. (2002) An entry model for the Tagish Lake fireball using seismic, satellite and infrasound records. *Meteoritics & Planet. Sci.*, 37(5), 661–675.
- Buczkowski D. L., Barnouin-Jha O. S., and Prockter L. M. (2008) 433 Eros lineaments: Global mapping and analysis. *Icarus*, 193(1), 39–52.
- Burns J. A. and Safronov V. S. (1973) Asteroid nutation angles. *Mon. Not. R. Astron. Soc.*, 165, 403.
- Bus S. J. and Binzel R. P. (2002) Phase II of the Small Main-Belt Asteroid Spectroscopic Survey: A feature-based taxonomy. *Icarus*, 158, 146–177.
- Busch M. W., Giorgini J. D., Ostro S. J., et al. (2007) Physical modeling of near-Earth asteroid (29075) 1950 DA. *Icarus*, 190(2), 608–621.
- Carruba V., Domingos R. C., Nesvorný D., et al. (2013) A multidomain approach to asteroid families' identification. *Mon. Not. R. Astron. Soc.*, 433, 2075–2096.
- Carry B. (2012) Density of asteroids. *Planet. Space Sci.*, 73, 98–118.
- Chandrasekhar S. (1969) *Ellipsoidal Figures of Equilibrium*. Dover, New York.
- Chang C.-K., Waszczak A., Lin H.-W., et al. (2014) A new large superfast rotator: (335433) 2005 UW163. *Astrophys. J. Lett.*, 791(2), L35.
- Chapman C. R., Merline W. J., Thomas P. C., et al. (2002) Impact history of Eros: Craters and boulders. *Icarus*, 155(1), 104–118.
- Chree C. (1895) The equilibrium of an isotropic elastic solid ellipsoid under the action of normal surface forces of the second degree, and bodily forces derived from a potential of the second degree. *Q. J. Pure Appl. Math.*, 27, 338–353.
- Consolmagno G. J., Britt D. T., and Macke R. J. (2008) The significance of meteorite density and porosity. *Chem. Erde—Geochem.*, 68(1), 1–29.
- Cotto-Figueroa D., Statler T. S., Richardson D. C., and Tanga P. (2015) Coupled spin and shape evolution of small rubble-pile asteroids: Self-limitation of the YORP effect. *Astrophys. J.*, 803, 25.
- DeMeo F. E., Binzel R. P., Slivan S. M., and Bus S. J. (2009) An extension of the Bus asteroid taxonomy into the near-infrared. *Icarus*, 202, 160–180.
- Descamps P., Marchis F., Berthier J., et al. (2011) Triplicity and physical characteristics of asteroid (216) Kleopatra. *Icarus*, 211(2), 1022–1033.
- Dobrovolskis A. R. (1982) Internal stresses in Phobos and other triaxial bodies. *Icarus*, 52(1), 136–148.
- Efroimsky M. and Williams J. G. (2009) Tidal torques: A critical review of some techniques. *Cel. Mech. Dyn. Astron.*, 104(3), 257–289.
- Fienga A., Manche H., Laskar J., and Gastineau M. (2008) INPOP06: A new numerical planetary ephemeris. *Astron. Astrophys.*, 477(1), 315–327.
- Fujiwara A., Kawaguchi J., Yeomans D. K., et al. (2006) The rubble-pile asteroid Itokawa as observed by Hayabusa. *Science*, 312, 1330–1334.
- Galvez A., Carnelli I., Michel P., et al. (2013) AIDA: The asteroid impact and deflection assessment mission. In *European Planetary Science Congress*, 8, EPSC2013-1043. Available online at <http://meetings.copernicus.org/epsc2013>.
- Grady M. M. (2000) *Catalogue of Meteorites, 5th edition*. Cambridge Univ., Cambridge.
- Goffin E. (2014) Astrometric asteroid masses: A simultaneous determination. *Astron. Astrophys.*, 565, A56.
- Goldreich P. and Sari R. (2009) Tidal evolution of rubble piles. *Astrophys. J.*, 691, 54–60.
- Hainaut O. R., Boehnhardt H., Snodgrass C., et al. (2014) Continued activity in P/2013 P5 PanSTARRS. Unexpected comet, rotational break-up, or rubbing binary asteroid? *Astron. Astrophys.*, 563, 75.
- Harris A. W. (1994) Tumbling asteroids. *Icarus*, 107(1), 209–211.
- Harris A. W. (1996) The rotation rates of very small asteroids: Evidence for 'rubble pile' structure. *Lunar Planet. Sci. XXVII*, p. 493. Lunar and Planetary Institute, Houston.
- Harris A. W., Fahnestock E. G., and Pravec P. (2009) On the shapes and spins of rubble pile asteroids. *Icarus*, 199(2), 310–318.
- Henych T. and Pravec P. (2013) Asteroid rotation excitation by sub-catastrophic impacts. *Mon. Not. R. Astron. Soc.*, 432(2), 1623–1631.
- Hilton J. M. (2002) Asteroid masses and densities. In *Asteroids III* (W. F. Bottke Jr. et al., eds.), pp. 103–112. Lunar and Planetary Institute, Houston.
- Hirabayashi M. (2014) Structural stability of asteroids. Ph.D. thesis, University of Colorado, Boulder.
- Hirabayashi M. and Scheeres D. J. (2014) Analysis of asteroid (216) Kleopatra using dynamical and structural constraints. *Astrophys. J.*, 780(2), 160.
- Hirabayashi M. and Scheeres D. J. (2015) Stress and failure analysis of rapidly rotating asteroid (29075) 1950 DA. *Astrophys. J. Lett.*, 798, L8.
- Hirabayashi M., Scheeres D. J., Sánchez D. P., and Gabriel T. (2014) Constraints on the physical properties of main belt Comet P/2013 R3 from its breakup event. *Astrophys. J. Lett.*, 789, L12.
- Holsapple K. A. (2001) Equilibrium configurations of solid cohesionless bodies. *Icarus*, 154(2), 432–448.
- Holsapple K. A. (2004) Equilibrium figures of spinning bodies with self-gravity. *Icarus*, 172(1), 272–303.
- Holsapple K. A. (2007) Spin limits of solar system bodies: From the small fast-rotators to 2003 EL61. *Icarus*, 187, 500–509.
- Holsapple K. A. (2010) On YORP-induced spin deformations of asteroids. *Icarus*, 205(2), 430–442.
- Housen K. R., Holsapple K. A., and Voss M. E. (1999) Compaction as the origin of the unusual craters on the asteroid Mathilde. *Nature*, 402, 155–157.
- Hudson R. S., Ostro S. J., Jurgens R. F., et al. (2000) Radar observations and physical model of asteroid 6489 Golevka. *Icarus*, 148(1), 37–51.
- Hudson R. S., Ostro S. J., and Scheeres D. J. (2003) High-resolution model of asteroid 4179 Toutatis. *Icarus*, 161, 346–355.
- Jacobi C. G. J. (1834) Ueber die figur des gleichgewichts. *Ann. Phys.*, 109(8–16), 229–233.
- Jacobson S. A. and Scheeres D. J. (2011a) Dynamics of rotationally fissioned asteroids: Source of observed small asteroid systems. *Icarus*, 214, 161–178.
- Jacobson S. A. and Scheeres D. J. (2011b) Long-term stable equilibria for synchronous binary asteroids. *Astrophys. J. Lett.*, 736(1), L19.
- Jenniskens P., Shaddad M. H., Numan D., et al. (2009) The impact and recovery of asteroid 2008 TC3. *Nature*, 458(7237), 485–488.
- Jewitt D., Agarwal J., Weaver H., et al. (2013) The extraordinary multi-tailed main-belt comet P/2013 P5. *Astrophys. J. Lett.*, 778(1), L21.
- Jewitt D., Agarwal J., Li J., et al. (2014) Disintegrating asteroid P/2013 R3. *Astrophys. J. Lett.*, 784(1), L8.
- Kadish J., Barber J. R., and Washabaugh P. D. (2005) Stresses in rotating spheres grown by accretion. *Int. J. Solids Structures*, 42(20), 5322–5334.
- Kadish J., Barber J. R., Washabaugh P. D. and Scheeres D. J. (2008) Stresses in accreted planetary bodies. *Int. J. Solids Structures*, 45(2), 540–550.
- Kimberley J. and Ramesh K. T. (2011) The dynamic strength of an ordinary chondrite. *Meteoritics & Planet. Sci.*, 46(11), 1653–1669.
- Kohout T., Kiuru R., Montonen M., et al. (2011) Internal structure and physical properties of the asteroid 2008 TC3 inferred from a study of the Almahata Sitta meteorites. *Icarus*, 212(2), 697–700.

- Konopliv A. S., Miller J. K., Owen W. M., et al. (2002) A global solution for the gravity field, rotation, landmarks, and ephemeris of Eros. *Icarus*, 160, 289–299.
- Kuchynka P. and Folkner W. M. (2013) A new approach to determining asteroid masses from planetary range measurements. *Icarus*, 222, 243–253.
- Lowry S. C., Weissman P. R., Duddy S. R., et al. (2014) The internal structure of asteroid (25143) Itokawa as revealed by detection of YORP spin-up. *Astron. Astrophys.*, 562, 48.
- Marchis F., Hestroffer D., Descamps P., et al. (2006) A low density of 0.8 g cm<sup>-3</sup> for the Trojan binary asteroid 617 Patroclus. *Nature*, 439, 565–567.
- Marchis F., Enriquez J. E., Emery J. P., et al. (2012) Multiple asteroid systems: Dimensions and thermal properties from Spitzer Space Telescope and ground-based observations. *Icarus*, 221(2), 1130–1161.
- Margot J. L., Nolan M. C., Benner L. A. M., et al. (2002) Binary asteroids in the near-Earth object population. *Science*, 296(5572), 1445–1448.
- Martin R., Komatitsch D., Blitz C., and Le Goff N. (2008) Simulation of seismic wave propagation in an asteroid based upon an unstructured mpi spectral-element method: Blocking and non-blocking communication strategies. In *High Performance Computing for Computational Science — VECPAR 2008* (J. M. Laginha et al., eds.), pp. 350–363. Springer-Verlag, Berlin.
- Marzari F., Rossi A., and Scheeres D. J. (2011) Combined effect of YORP and collisions on the rotation rate of small main belt asteroids. *Icarus*, 214(2), 622–631.
- Masiero J., Jedicke R., Dürsch J., et al. (2009) The thousand asteroid light curve survey. *Icarus*, 204(1), 145–171.
- Masiero J. R., Mainzer A. K., Grav T., et al. (2011) Main belt asteroids with WISE/NEOWISE. I. Preliminary albedos and diameters. *Astrophys. J.*, 741, 68.
- Mazrouei S., Daly M. G., Barnouin O. S., et al. (2013) Block distributions on Itokawa. *Icarus*, 229, 181–189.
- Michel P., Barucci M. A., Cheng A. F., et al. (2014) MarcoPolo-R: Near-Earth asteroid sample return mission selected for the assessment study phase of the ESA program cosmic vision. *Acta Astronaut.*, 93, 530–538.
- Michikami T., Nakamura A. M., Hirata N., et al. (2008) Size-frequency statistics of boulders on global surface of asteroid 25143 Itokawa. *Earth Planets Space*, 60(1), 13–20.
- Miller J. K., Konopliv A. S., Antreasian P. G., et al. (2002) Determination of shape, gravity, and rotational state of asteroid 433 Eros. *Icarus*, 155, 3–17.
- Minton D. A. (2008) The topographic limits of gravitationally bound, rotating sand piles. *Icarus*, 195(2), 698–704.
- Mouret S., Hestroffer D., and Mignard F. (2007) Asteroid masses and improvement with Gaia. *Astron. Astrophys.*, 472, 1017–1027.
- Mueller M., Marchis F., Emery J. P., et al. (2010) Eclipsing binary Trojan asteroid Patroclus: Thermal inertia from Spitzer observations. *Icarus*, 205, 505–515.
- Nolan M. C., Asphaug E., Greenberg R., and Melosh H. J. (2001) Impacts on asteroids: Fragmentation, regolith transport, and disruption. *Icarus*, 153(1), 1–15.
- Ostro S. J., Scott R., Nolan M. C., et al. (2000) Radar observations of asteroid 216 Kleopatra. *Science*, 288(5467), 836–839.
- Ostro S. J., Margot J. -L., Benner L. A. M., et al. (2006) Radar imaging of binary near-Earth asteroid (66391) 1999 KW4. *Science*, 314, 1276–1280.
- Parker A., Ivezic Ž., Jurić M., et al. (2008) The size distributions of asteroid families in the SDSS Moving Object Catalog 4. *Icarus*, 198, 138–155.
- Pätzold M., Andert T., Asmar S. W., et al. (2011) Asteroid 21 Lutetia: Low mass, high density. *Science*, 334, 491.
- Poincaré H. (1885) Sur l'équilibre d'une masse fluide animée d'un mouvement de rotation. *Acta Mathemat.*, 7(1), 259–380.
- Polishook D., Moskovitz N., Binzel R. P., et al. (2014) Observations of fresh and weathered surfaces on asteroid pairs and their implications on the rotational-fission mechanism. *Icarus*, 233, 9–26.
- Popova O., Borovička J., Hartmann W. K., et al. (2011) Very low strengths of interplanetary meteoroids and small asteroids. *Meteoritics & Planet. Sci.*, 46(10), 1525–1550.
- Pravec P. (2014) Asteroid spin-up fission systems. In *Asteroids, Comets, Meteors 2014, Book of Abstracts* (K. Muinonen et al., eds.), p. 451. University of Helsinki, Finland.
- Pravec P., Vokrouhlický D., Polishook D., et al. (2010) Formation of asteroid pairs by rotational fission. *Nature*, 466(7310), 1085–1088.
- Pravec P., Scheirich P., Dürsch J., et al. (2014) The tumbling spin state of (99942) Apophis. *Icarus*, 233, 48–60.
- Prockter L., Thomas P., Robinson M., et al. (2002) Surface expressions of structural features on eros. *Icarus*, 155(1), 75–93.
- Ralchenko M., Britt D. T., Samson C., et al. (2014) Bulk physical properties of the Tagish Lake meteorite frozen pristine fragments. *Lunar Planet. Sci. XLV*, Abstract #1021. Lunar and Planetary Institute, Houston.
- Richardson J. E. and Bowling T. J. (2014) Investigating the combined effects of shape, density, and rotation on small body surface slopes and erosion rates. *Icarus*, 234, 53–65.
- Richardson D. C., Bottke W. F., Love S. G., et al. (1998) Tidal distortion and disruption of Earth-crossing asteroids. *Icarus*, 134(1), 47–76.
- Richardson D. C., Leinhardt Z. M., Melosh H. J., et al. (2002) Gravitational aggregates: Evidence and evolution. In *Asteroids III* (W. F. Bottke Jr. et al., eds.), pp. 501–515. Univ. of Arizona, Tucson.
- Richardson J. E., Melosh H. J., and Greenberg R. (2004) Impact-induced seismic activity on asteroid 433 Eros: A surface modification process. *Science*, 306(5701), 1526–1529.
- Richardson D. C., Elankumaran P., and Sanderson R. E. (2005) Numerical experiments with rubble piles: Equilibrium shapes and spins. *Icarus*, 173(2), 349–361.
- Robert O., Lognonné P., Scheeres D. J., et al. (2010) Seismology on a small body: Expected results for the BASiX Discovery mission proposal. Abstract U51B-0044 presented at 2010 Fall Meeting, AGU, San Francisco, California, 13–17 Dec.
- Robinson M. S., Thomas P. C., Veverka J., et al. (2002) The geology of 433 Eros. *Meteoritics & Planet. Sci.*, 37(12), 1651–1684.
- Roche E. (1850) La figure dune masse fluide soumise la traction dun point loign. *Acad. Sci. Montpellier*, 1, 1847–1850.
- Rozitis B., MacLennan E., and Emery J. P. (2014) Cohesive forces prevent the rotational breakup of rubble-pile asteroid (29075) 1950 DA. *Nature*, 512(7513), 174–176.
- Russell C. T., Raymond C. A., Coradini A., et al. (2012) Dawn at Vesta: Testing the protoplanetary paradigm. *Science*, 336, 684–686.
- Sánchez P. and Scheeres D. J. (2011) Simulating asteroid rubble piles with a self-gravitating soft-sphere distinct element method model. *Astrophys. J.*, 727, 120.
- Sánchez P. and Scheeres D. J. (2012) DEM simulation of rotation-induced reshaping and disruption of rubble-pile asteroids. *Icarus*, 218, 876–894.
- Sánchez P. and Scheeres D. J. (2014) The strength of regolith and rubble pile asteroids. *Meteoritics & Planet. Sci.*, 49(5), 788–811.
- Scheeres D. J. (2002) Stability in the full two-body problem. *Cel. Mech. Dyn. Astron.*, 83(1), 155–169.
- Scheeres D. J. (2007) Rotational fission of contact binary asteroids. *Icarus*, 189, 370–385.
- Scheeres D. J. (2009a) Minimum energy asteroid reconfigurations and catastrophic disruptions. *Planet. Space Sci.*, 57(2), 154–164.
- Scheeres D. J. (2009b) Stability of the planar full 2-body problem. *Cel. Mech. Dyn. Astron.*, 104(1), 103–128.
- Scheeres D. J. (2012) Minimum energy configurations in the n-body problem and the celestial mechanics of granular systems. *Cel. Mech. Dyn. Astron.*, 113(3), 291–320.
- Scheeres D. J. (2015) Landslides and mass shedding on spinning spheroidal asteroids. *Icarus*, 247, 1–17.
- Scheeres D. J. and Gaskell R. W. (2008) Effect of density inhomogeneity on YORP: The case of Itokawa. *Icarus*, 198(1), 125–129.
- Scheeres D. J., Khushalani B., and Werner R. A. (2000a) Estimating asteroid density distributions from shape and gravity information. *Planet. Space Sci.*, 48, 965–971.
- Scheeres D. J., Ostro S. J., Werner R. A., et al. (2000b) Effects of gravitational interactions on asteroid spin states. *Icarus*, 147(1), 106–118.
- Scheeres D. J., Asphaug E. I., Colwell J., et al. (2003) Asteroid surface science with pods. *Lunar Planet. Sci. XXXIV*, Abstract #1444. Lunar and Planetary Institute, Houston.
- Scheeres D. J., Benner L. A. M., Ostro S. J., et al. (2005) Abrupt alteration of asteroid 2004 MN4's spin state during its 2029 Earth flyby. *Icarus*, 178(1), 281–283.
- Scheeres D. J., Farnestock E. G., Ostro S. J., et al. (2006) dynamical configuration of binary near-Earth asteroid (66391) 1999 KW4. *Science*, 314, 1280–1283.

- Scheeres D. J., Abe M., Yoshikawa M., et al. (2007) The effect of YORP on Itokawa. *Icarus*, 188, 425–429.
- Scheeres D. J., Hartzell C. M., Sánchez P., and Swift M. (2010) Scaling forces to asteroid surfaces: The role of cohesion. *Icarus*, 210, 968–984.
- Scheirich P., Urech J. D., Pravec P., et al. (2010) The shape and rotation of asteroid 2008 TC3. *Meteoritics & Planet. Sci.*, 45(10–11), 1804–1811.
- Scheirich P., Pravec P., Jacobson S. A., et al. (2015) The binary near-Earth asteroid (175706) 1996 FG3 — an observational constraint on its orbital stability. *Icarus*, 245, 56–63.
- Sharma I. (2013) Structural stability of rubble-pile asteroids. *Icarus*, 223, 367–382.
- Sharma I., Burns J. A., and Hui C.-Y. (2005) Nutational damping times in solids of revolution. *Mon. Not. R. Astron. Soc.*, 359(1), 79–92.
- Sharma I., Jenkins J. T., and Burns J. A. (2009) Dynamical passage to approximate equilibrium shapes for spinning, gravitating rubble asteroids. *Icarus*, 200(1), 304–322.
- Statler T. S. (2009) Extreme sensitivity of the YORP effect to small-scale topography. *Icarus*, 202(2), 502–513.
- Tanga P., Comito C., Paolicchi P., et al. (2009) Rubble-pile reshaping reproduces overall asteroid shapes. *Astrophys. J. Lett.*, 706(1), L197.
- Takahashi Y. and Scheeres D. J. (2014) Morphology driven density distribution estimation for small bodies. *Icarus*, 233, 179–193.
- Tedesco E. F., Williams J. G., Matson D. L., et al. (1989) Three-parameter asteroid taxonomy classifications. In *Asteroids II* (R. P. Binzel et al., eds.), pp. 1151–1161. Univ. of Arizona, Tucson.
- Tholen D. J. and Barucci M. A. (1989) Asteroid taxonomy. In *Asteroids III* (R. P. Binzel et al., eds.), pp. 298–315. Univ. of Arizona, Tucson.
- Thomas P. C. and Robinson M. S. (2005) Seismic resurfacing by a single impact on the asteroid 433 Eros. *Nature*, 436, 366–369.
- Tsuchiyama A., Uesugi M., Matsushima T., et al. (2011) Three-dimensional structure of Hayabusa samples: Origin and evolution of Itokawa regolith. *Science*, 333(6046), 1125–1128.
- Tsuda Y., Yoshikawa M., Abe M., Minamino H., and Nakazawa S. (2013) System design of the Hayabusa 2 asteroid sample return mission to 1999 JU3. *Acta Astronaut.*, 91, 356–362.
- Urakawa S., Ohtsuka K., Abe S., Ito T., and Nakamura T. (2014) Fast rotation of a subkilometer-sized near-Earth object 2011 XA3. *Astron. J.*, 147(5), 121.
- Vokrouhlický D. and Nesvorný D. (2008) Pairs of asteroids probably of a common origin. *Astron. J.*, 136(1), 280.
- Vokrouhlický D., Breiter S., Nesvorný D., and Bottke W. F. (2007) Generalized YORP evolution: Onset of tumbling and new asymptotic states. *Icarus*, 191(2), 636–650.
- Walsh K. J. and Richardson D. C. (2006) Binary near-Earth asteroid formation: Rubble pile model of tidal disruptions. *Icarus*, 180(1), 201–216.
- Walsh K. J., Richardson D. C., and Michel P. (2008) Rotational breakup as the origin of small binary asteroids. *Nature*, 454(7201), 188–191.
- Walsh K. J., Richardson D. C., and Michel P. (2012) Spinup of rubble-pile asteroids: Disruption, satellite formation, and equilibrium shapes. *Icarus*, 220(2), 514–529.
- Warner B. D., Harris A. W., and Pravec P. (2009) The asteroid lightcurve database. *Icarus*, 202(1), 134–146.
- Washabaugh P. D. and Scheeres D. J. (2002) Energy and stress distributions in ellipsoids. *Icarus*, 159(2), 314–321.
- Yano H., Kubota T., Miyamoto H., et al. (2006) Touchdown of the Hayabusa spacecraft at the Muses Sea on Itokawa. *Science*, 312(5778), 1350–1353.
- Yeomans D. K., Antreasian P. G., Barriot J.-P., et al. (2000) Radio science results during the NEAR-Shoemaker spacecraft rendezvous with Eros. *Science*, 289, 2085–2088.

# Asteroid Surface Geophysics

**Naomi Murdoch**

*Institut Supérieur de l'Aéronautique et de l'Espace (ISAE-SUPAERO)*

**Paul Sánchez**

*University of Colorado Boulder*

**Stephen R. Schwartz**

*Lagrange Laboratory, Université Côte d'Azur, Observatoire de la Côte d'Azur, CNRS*

**Hideaki Miyamoto**

*University of Tokyo*

---

The regolith-covered surfaces of asteroids preserve records of geophysical processes that have occurred both at their surfaces and sometimes also in their interiors. As a result of the unique microgravity environment that these bodies possess, a complex and varied geophysics has given birth to fascinating features that we are just now beginning to understand. The processes that formed such features were first hypothesized through detailed spacecraft observations and have been further studied using theoretical, numerical, and experimental methods that often combine several scientific disciplines. These multiple approaches are now merging toward a further understanding of the geophysical states of the surfaces of asteroids. In this chapter we provide a concise summary of what the scientific community has learned so far about the surfaces of these small planetary bodies and the processes that have shaped them. We also discuss the state of the art in terms of experimental techniques and numerical simulations that are currently being used to investigate regolith processes occurring on small-body surfaces and that are contributing to the interpretation of observations and the design of future space missions.

## 1. INTRODUCTION

Before the first spacecraft encounters with asteroids, many scientists assumed that the smallest asteroids were all monolithic rocks with a bare surface, although there had been a few articles suggesting possible alternative surface properties and internal structures (e.g., *Dollfus et al.*, 1977; *Housen et al.*, 1979; *Michel et al.*, 2001; *Harris*, 2006). Given the low gravitational acceleration on the surface of an asteroid, it was thought that regolith formation would not be possible; even if small fragments of rock were created during the impact process, nothing would be retained on the surface (e.g., *Chapman*, 1976). However, the NASA Galileo, Near Earth Asteroid Rendezvous (NEAR)-Shoemaker (hereafter simply NEAR), and Japan Aerospace Exploration Agency (JAXA) Hayabusa space missions revealed a substantial regolith covering (951) Gaspra, (243) Ida, (433) Eros (*Sullivan et al.*, 2002; *Robinson et al.*, 2002), and (25143) Itokawa (*Fujiwara et al.*, 2006). In addition to finding each of these bodies to be regolith-covered, there is strong evidence that this regolith has very complex and active dynamics. In fact, it was due to the NEAR observations of Eros that the local gravity was first

understood to be of importance to asteroid surface processes (*Robinson et al.*, 2002). The importance of gravity for regolith dynamics was emphasized even further when the first images were received from the Hayabusa probe.

Over the course of these space missions and others, a wide range of geological features have been observed on the surfaces of asteroids and other small bodies, such as the nucleus of Comet 103P/Hartley 2 (*Thomas et al.*, 2013). However, we do not have direct access to the properties of the granular material that led to these features. Although constitutive equations exist for granular interactions on Earth, the inferred scaling to the gravitational and environmental conditions on other planetary bodies such as asteroids is currently untested. Understanding the dynamics of granular materials in the small-body gravitational environment is vital for the interpretation of their surface geology and is also critical for the design and/or operation of any device planned to interact with their regolith-covered surfaces.

Regolith was originally defined as “a layer of fragmented debris of relatively low cohesion which overlies a more coherent substratum” (*Shoemaker et al.*, 1968), although this definition runs into difficulties when there is no clear interface

separating the fragmented debris and the coherent substrate (*Robinson et al.*, 2002). Here we will use the term regolith to describe, in general terms, the “loose unconsolidated material that comprises the upper portions of the asteroid” (as defined in *Robinson et al.*, 2002). However, we note that self-gravitating aggregates like Itokawa, often referred to as “rubble piles” (*Richardson et al.*, 2002), are composed of rubble — boulders on the order of tens of meters and less — held together by gravity and cohesive forces instead of being a monolithic body (*Fujiwara et al.*, 2006). As such they are essentially made of regolith throughout. Therefore, although not discussed in this chapter, understanding how granular materials behave in these extremely low-gravity environments can also improve our understanding of the interiors of these bodies.

This chapter will start by presenting our current knowledge of the surfaces of asteroids (433) Eros, (25143) Itokawa, (21) Lutetia, and (4) Vesta. After a short introduction to granular materials, we will then introduce the unique asteroid environment and suggest how this may influence the regolith dynamics. Next, we discuss in detail the underlying physical mechanisms behind the geological processes observed to occur on the surfaces of asteroids. Finally, a discussion of the experimental techniques that can be used to simulate the asteroid environment and the recent advances in modeling regolith dynamics is provided.

## 2. IN SITU OBSERVATIONS OF ASTEROID SURFACES

In this section we will briefly discuss the *in situ* observations of four asteroids: (433) Eros, (25143) Itokawa, (21) Lutetia, and (4) Vesta. For more detailed reviews about these bodies the readers are referred to *Cheng* (2002) and the chapters in this volume by *Yoshikawa et al.*, *Barucci et al.*, and *Russell et al.* Additionally, detailed reviews of the geology of other asteroids such as (951) Gaspra, (243) Ida, and (253) Mathilde are available elsewhere (e.g., *Carr et al.*, 1994; *Sullivan et al.*, 1996; *Thomas et al.*, 1999).

### 2.1. Asteroid (433) Eros

(433) Eros (hereafter simply Eros; Fig. 1, Table 1), the second largest near-Earth asteroid (NEA), shows a subdued,

gently undulating and complex regolith-covered surface, characterized by abundant, but not uniformly distributed, ejecta blocks and conspicuously degraded craters (*Veverka et al.*, 2000, 2001a; *Cheng et al.*, 1997). The effective topography on Eros has a range of about 2 km and the slopes, calculated relative to the local gravity vector, vary over the surface of the asteroid [for an explanation of how elevation is defined on irregular bodies, see section 5 of *Cheng et al.* (2002a)] with an average slope of ~8° to 10° (*Zuber et al.*, 2000; *Thomas et al.*, 2002).

**2.1.1. Evidence of regolith motion on Eros.** In general, Eros is very bland in terms of color and albedo variations. However, visible variations, such as several bright features typically with sharp boundaries, can be seen in regions that have steep slopes (see Fig. 2) (*Veverka et al.*, 2000; *Robinson et al.*, 2001; *Cheng*, 2002; *Mantz et al.*, 2004; *Murchie et al.*, 2002). As all the NEAR data indicate global compositional homogeneity, the brighter surfaces imply freshly exposed material that has not yet been subjected to space weathering (*Chapman*, 2004; see also the chapter by *Brunetto et al.* in this volume). In contrast, dark soils are typically located at the bases of bright streaks and display both diffuse and sharp boundaries (*Thomas et al.*, 2002; *Riner et al.*, 2008). These observations, and morphological data, indicate that the bright streaks are the results of preferential downslope movement or a landslide of mature regolith, revealing immature material beneath (e.g., *Robinson et al.*, 2002; *Thomas et al.*, 2002; *Riner et al.*, 2008; *Murchie et al.*, 2002).

Indeed, on closer inspection, accumulations of granular material that have been gravitationally transported away from topographic highs can be seen on Eros (Fig. 20 (*Thomas et al.*, 2002; *Veverka et al.*, 2001b; *Robinson et al.*, 2002)). These granular deposits appear to result from low-momentum downslope movements and some observations suggest that mobilized regolith may even be halted by frictional or other effects before reaching the foot of the slope (*Mantz et al.*, 2004; *Thomas et al.*, 2002). Downslope motion has also been observed on slopes that are well below the expected angle of repose for granular materials. Whether this indicates the necessity for a triggering mechanism or not is a subject currently under debate (*Cheng*, 2002; *Holsapple*, 2013).

**2.1.2. Craters and crater morphology on Eros.** Further evidence for regolith motion is that, despite the large number of craters on the surface of Eros, there is a deficiency of small

TABLE 1. Characteristics of the asteroids discussed in detail in this chapter.

Asteroid	Space Mission	Mean Diameter (km)	Bulk Density (g cm <sup>-3</sup> )	Rotation Period (h)	Surface Acceleration (cm s <sup>-2</sup> )	Escape Speed (m s <sup>-1</sup> )
(433) Eros	NASA NEAR <sup>[1]</sup>	~17 <sup>[2]</sup>	2.7 <sup>[2]</sup>	5.3 <sup>[3]</sup>	0.23–0.56 <sup>[3]</sup>	~1 <sup>[4]</sup>
(25143) Itokawa	JAXA Hayabusa <sup>[5]</sup>	~0.32 <sup>[5]</sup>	1.9 <sup>[6]</sup>	12.1 <sup>[7]</sup>	2.4e-3–8.6e-3 <sup>[7]</sup>	0.1–0.2 <sup>[5]</sup>
(21) Lutetia	ESA Rosetta <sup>[8]</sup>	~99 <sup>[9]</sup>	3.4 <sup>[9]</sup>	8.2 <sup>[10]</sup>	~5 <sup>[11]</sup>	~70 <sup>[11]</sup>
(4) Vesta	NASA Dawn <sup>[12]</sup>	~526 <sup>[13]</sup>	3.5 <sup>[13]</sup>	5.3 <sup>[13]</sup>	~25	~363

References: [1] *Cheng et al.* (1997); [2] *Yeomans et al.* (2000); [3] *Miller et al.* (2002); [4] *Veverka et al.* (2000); [5] *Fujiwara et al.* (2006); [6] *Abe et al.* (2006); [7] *Scheeres et al.* (2006); [8] *Schulz et al.* (2012); [9] *Sierks et al.* (2011); [10] *Lamy et al.* (2010); [11] *Thomas et al.* (2012); [12] *Russell and Raymond* (2011); [13] *Russell et al.* (2012).



**Fig. 1.** Global images of asteroids (433) Eros (top left), (25143) Itokawa (top right), (21) Lutetia (bottom left), and (4) Vesta (bottom right). Images courtesy of NEAR/NASA, Hayabusa/JAXA, Rosetta/ESA, and Dawn/NASA, respectively.

(<2-km-diameter) craters (Veverka et al., 2000, 2001b). As there are sufficient projectiles in near-Earth space to produce small craters, there must therefore be a process that either covers or erodes small craters on Eros (Veverka et al., 2001b). It has been suggested that impact-induced seismic shaking (see section 5), which causes the regolith to move, may erase small crater features and thus explain their paucity compared to predictions of dynamical models of projectile populations (e.g., Richardson et al., 2004; Michel et al., 2009). However, alternative degradation mechanisms have also been suggested, including microcratering and thermal creep (Cheng, 2002). For a detailed discussion of cratering on asteroids, see the chapter by Marchi et al. in this volume.

Additional evidence of resurfacing and modification is visible in the interiors and the subdued rims of several craters (Robinson et al., 2002; Zuber et al., 2000). The depth-to-diameter ratio of craters on Eros is, on average, ~0.13, but the freshest and youngest craters approach lunar values of ~0.2 (Robinson et al., 2002). Many of the topographic lows are filled with deposits of fine granular material (Fig. 2) (e.g., Veverka et al., 2001a). These features, referred to as “ponds,” are characterized by smooth, level surfaces that are sharply delineated (Robinson et al., 2001; Cheng et al., 2002b). They are found preferentially at low latitudes and in the bottom of small (<1 km) craters or other topographic lows (Robinson et al., 2001; Cheng et al., 2002b); however, this may be due to observational biases (Roberts et al., 2014b). The bottoms of the ponds are often offset in a direction toward the downslope of the crater (Veverka et al., 2001b), and recent results have found that the pond floors are not as flat as originally believed (Roberts et al., 2014a).

**2.1.3. Linear features on Eros.** On the surface of Eros several lineations can be observed, including chains of craters,

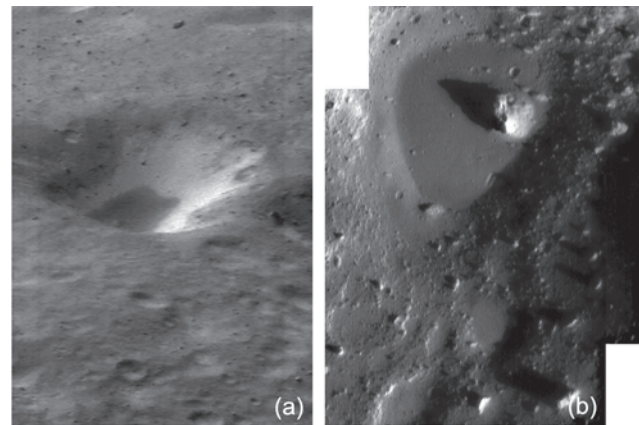


**Fig. 2.** Evidence of regolith transport on Eros. (a) Bright, freshly exposed material on a large crater wall, as the darker material moves downslope (PIA03134). (b) An example of a dust pond (2001\_028\_5\_eros.png from <http://ser.sese.asu.edu/near.html>).

sinuous and linear elongated depressions, and topographic ridges (Veverka et al., 2000). Such lineations are similar to those observed on the martian satellite Phobos (Thomas et al., 1979). Prockter et al. (2002) explain that, on Eros, these linear features, or grooves, exist on a global scale (prominent wide troughs and ridges several kilometers in length), a regional scale (chains of craters and straight-edged grooves several hundreds of meters long), and also on very local scales (closely spaced ridge and trough terrains tens of meters in scale). The large variations in directions, patterns, and relative ages of the lineations indicate that they were formed during many different and unrelated events (see section 5, the chapter by Marchi et al. in this volume, and also Veverka et al., 2000; Prockter et al., 2002; Thomas et al., 2002; Robinson et al., 2002). For a full map and analyses of the linear features on Eros, see Buczkowski et al. (2008).

**2.1.4. Depth and character of Eros’ regolith.** Eros has a widespread unconsolidated regolith of depths that are typically several tens of meters in thickness, but not uniform over the surface (Cheng, 2002; Barnouin-Jha et al., 2001; Veverka et al., 2001a; Robinson et al., 2002). The heterogeneity of the regolith depth distribution is probably caused partially by the asymmetric nature of crater ejecta blankets [a consequence of the asteroid’s rotation; see section 5 and Geissler et al. (1996)] and is further accentuated by the irregular spacing of craters and the subsequent downslope motion and regolith transport that, as discussed above, appears to occur commonly on the surface of Eros (Robinson et al., 2002).

The surface of Eros is extremely rough and the surface roughness is approximately self-affine from scales of a few meters to hundred of meters (Cheng, 2002). The regolith particles range in size from the fine (much less than centimeter-sized) dust particles found in the ponds to the numerous ( $>10^4$ ) large ( $>10$  m) ejecta blocks of boulders at the extreme large end of the particle size distribution (Thomas et al., 2002). The morphology of these blocks ranges from angular to fractured

to disaggregated (Robinson *et al.*, 2002), and their size distribution is described adequately by a power law with a slope of about  $-3$  on a cumulative plot (Fig. 3). For more information about the nature of these boulders, see the chapter by Marchi *et al.* in this volume.

## 2.2. Asteroid (25143) Itokawa

Compared to Eros, the NEA (25143) Itokawa (hereafter simply Itokawa; Fig. 1, Table 1) was found, astonishingly, to have entirely different structural and surface properties despite their similar taxonomic class. The reason for these different properties is not clearly understood, but perhaps this shouldn't have been surprising; because of their size (mass) difference, if gravity is the discriminator, then Itokawa is expected to be as different from Eros, geologically, as Eros is from the Moon (Asphaug, 2009).

One of the most remarkable features of Itokawa is the global shape, which seems to consist of two parts: a small "head" and a large "body" separated by a constricted "neck" region [Fig. 1 (Fujiwara *et al.*, 2006; Demura *et al.*, 2006)]. It is highly likely that Itokawa is a rubble-pile asteroid rather than a monolithic body (Fujiwara *et al.*, 2006). The low bulk density of Itokawa (Table 1) provides further evidence for the rubble-pile interior structure, with estimates suggesting that Itokawa's macroporosity may be as high as  $\sim 41\%$  (Fujiwara

*et al.*, 2006). However, these density measurements do not rule out the presence of a core on the order of 100 m in size.

**2.2.1. Depth, character and migration of Itokawa's regolith.** Two different types of terrain — rough and smooth — are observed on Itokawa (Saito *et al.*, 2006). The rough deposits consist of numerous boulders (Fujiwara *et al.*, 2006) and typically exhibit variations in elevation that range from 2 to 4 m over small lateral distances (Barnouin-Jha *et al.*, 2008). The very highest and roughest parts of the asteroid are covered in large gravel and boulders and are completely devoid of all particles smaller than 1 cm in size (Barnouin-Jha *et al.*, 2008). The smooth terrains — Muses Sea and Sagamihara — coincide with the low-gravitational potentials and are generally homogeneous, featureless, and relatively flat (slopes  $<8^\circ$ ). This is consistent with a loose granular layer that has been allowed to seek out its minimum energy configuration after the formation of the asteroid (Miyamoto *et al.*, 2007; Fujiwara *et al.*, 2006; Yano *et al.*, 2006; Riner *et al.*, 2008). This idea is further reinforced by the close-up images and measurements taken during the touchdown of the Hayabusa spacecraft; these indicate that small regolith particles are being transported into the Muses Sea region and are gradually covering up the boulder-rich surface (Miyamoto *et al.*, 2007; Barnouin-Jha *et al.*, 2008). The regolith depth in the smooth regions on Itokawa is estimated to be approximately 2.5 m (Barnouin-Jha *et al.*, 2008; Cheng *et al.*, 2007).

In general, Itokawa's regolith appears to be dominated by grains  $>1$  mm in size (Miyamoto *et al.*, 2007). That said, the regolith particles that were returned to Earth are fine-grained [size range between 3 and 180  $\mu\text{m}$ , but most  $<10 \mu\text{m}$  (Nakamura *et al.*, 2011)]. The apparent absence, or at least the small quantity, of fines on the surface of Itokawa may be explained by processes such as electrostatic levitation combined with solar radiation pressure (Lee, 1996; Scheeres, 2005); segregation of the fines toward the interior of the body (Asphaug, 2007; Miyamoto *et al.*, 2007); or simple higher-ejection velocities following impacts, making reaccumulation difficult (Nakamura *et al.*, 1994). Some of these processes will be discussed later in sections 4 and 5.

The size distribution of boulders on Itokawa's surface is estimated to be a power law with a slope of  $-2.8$  to  $-3.0$  on a cumulative plot (Fig. 3). It is possible, however, that the observed distributions on Itokawa may be related to the preferential displacement of some block sizes relative to others, and the settling locations of differing-sized blocks. The abundance of meter-sized boulders [particularly on the western side (Fujiwara *et al.*, 2006)], and the fact that decameter-sized boulders exist [the length of the largest boulder is approximately one-tenth of the length of Itokawa itself (Saito *et al.*, 2006)], indicate that they may have been produced during a catastrophic disruption event, consistent with the rubble-pile structure (Fujiwara *et al.*, 2006; Michel *et al.*, 2001).

**2.2.2. Further evidence for an active regolith on Itokawa.** At the boundary of the Muses Sea region with the rough terrain, boulders are typically piled on top of each other without being buried by fines. The larger-sized gravels tend

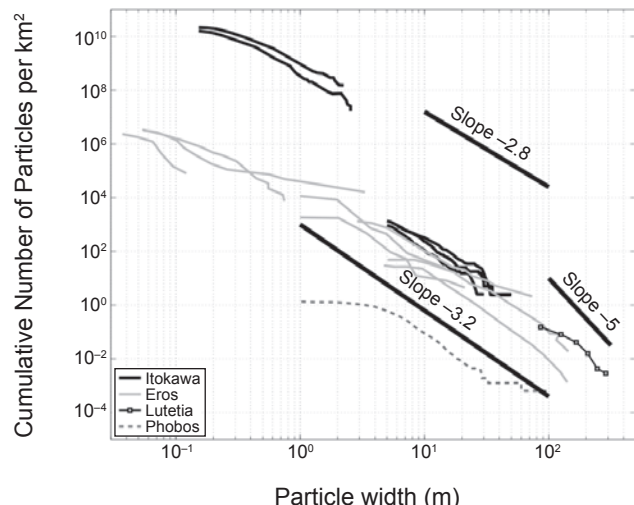


**Fig. 3.** Measured cumulative size distribution as a function of particle size on the surfaces of asteroids and Phobos. Data combined from several papers. Itokawa: Miyamoto *et al.* (2007), Saito *et al.* (2006), Michikami *et al.* (2008), Mazrouei *et al.* (2012); Eros: Thomas *et al.* (2001); Lutetia: Küppers *et al.* (2012); Phobos (a martian satellite with a mean diameter of  $\sim 22$  km): Thomas *et al.* (2002). For the papers in which the cumulative number of particles was given, this has been approximately converted to cumulative number per square kilometer using the information provided in the respective papers. A shallower slope may indicate that boulders have experienced less processing, including breaking, sorting, and transporting (Thomas *et al.*, 2002).

to overlie the smaller particles and are aligned with directions coincident with the local gravity slope (*Miyamoto et al.*, 2007). This type of organization of gravels is referred to as imbrications, in this case with the longest axes of the gravel being preferentially orientated transverse to the granular flow. The positions and orientations of all the particles indicate that they are stable against local gravity and that the migrations were gravity-induced (*Miyamoto et al.*, 2007).

Evidence of landslide-like deposits can be seen in Fig. 4. There are large boulders that have blocked the migration of smaller particles, resulting in piles of smaller particles on the uphill sides of the boulders (*Miyamoto et al.*, 2007). Unlike the surface of Eros, Itokawa is very heterogeneous in color and albedo, with brighter surfaces being found in three main areas: areas with steeper slopes; areas of local high terrain; and apparently eroded areas, e.g., crater rims (*Saito et al.*, 2006). *Saito et al.* (2006) suggest that this dichotomy is due to dark surfaces being removed, leaving the fresh regolith newly exposed at the surface, as observed on Eros.

All these observations provide a strong indication that regolith on the surface of Itokawa has been relocated since the initial accumulation or deposition.

**2.2.3. Craters and crater morphology on Itokawa.** Itokawa has very few craters in general (the total number of craters on Itokawa is <100 over the entire surface, including indefinite candidates) and absolutely no distinct craters <1 m in diameter (*Saito et al.*, 2006; *Fujiwara et al.*, 2006). Those craters that do exist on the rough and transitional terrains, and that retain their regolith, are filled with finer particles, similar to the “ponds” seen on Eros. The best example of a crater on the surface of Eros — Komaba — is located near the edge of the highlands. It has a small depth-to-diameter ratio

(0.09) consistent with crater formation in a coarse granular target, a flat floor, and is surrounded by brighter rims (*Saito et al.*, 2006; *Barnouin-Jha et al.*, 2008). In addition, there appears, unusually, to be no apparent correlation between the locations of boulders and craters (*Michikami et al.*, 2008). These observations are further evidence of regolith motion and suggest that a mechanism is filling in and erasing the craters on the surface of Itokawa. Such a mechanism may well be seismic shaking, as proposed to explain the paucity of small craters on Eros (see section 5). Alternatively, it is also possible that Itokawa could have been generated relatively recently in the main belt before being moved to its current orbit (*Saito et al.*, 2006).

**2.2.4. Linear features on Itokawa.** Unlike Eros, there are no global lineaments on Itokawa (*Fujiwara et al.*, 2006). However, on the body of Itokawa, subtle local linear features can be observed. These features, caused by the alignment of boulders (*Cheng et al.*, 2007), are not as tall as other structures such as large boulders. Nonetheless, they are an important contributor to the topography of Itokawa due to their large lateral extent (*Barnouin-Jha et al.*, 2008).

### 2.3. Asteroid (21) Lutetia

The main-belt asteroid (21) Lutetia (hereafter simply Lutetia; Fig. 1, Table 1) has a highly complex surface geology with significant interactions between ancient and more recent structures (*Sierks et al.*, 2011; *Thomas et al.*, 2012).

**2.3.1. Craters and crater morphology on Lutetia.** The higher gravity and escape velocity on Lutetia have provided an environment for continuous ejecta patterns with obvious relations to the impact from which they formed (*Massironi et al.*, 2012). The typical depth-to-diameter ratio of craters on Lutetia is 0.12, but values have been observed ranging from 0.05 to 0.3 (*Vincent et al.*, 2012). The distribution of depth-to-diameter ratios varies depending on the region of Lutetia’s surface, indicating that not only are there variations of physical properties across the surface, but there are also differences in the surface evolutionary processes (*Vincent et al.*, 2012).

*Thomas et al.* (2012) divide the craters on Lutetia into four different categories: standard craters, buried or partially filled craters, distorted or cut craters that have been disturbed by lineament formation, and morphologically nonstandard impact structures. By the latter they refer to craters that are not typically bowl-shaped and/or do not have a round rim, and the strange form is not obviously linked to linear features. Such unusually shaped craters (for examples, see *Thomas et al.*, 2012) could be the result of oblique impacts (*Thomas et al.*, 2012; *Herrick and Hessen*, 2006; *Krohn et al.*, 2014), but other mechanisms have also been proposed (*Vincent et al.*, 2012).

Similarly to the surface of Eros, Lutetia’s surface exhibits a paucity of small (<1 km) craters. This could perhaps be explained by seismic shaking; however, there is also a depletion in craters of sizes up to 8 km, which is more difficult to attribute to seismic shaking. The craters that have been deformed by linear features are additional evidence that the

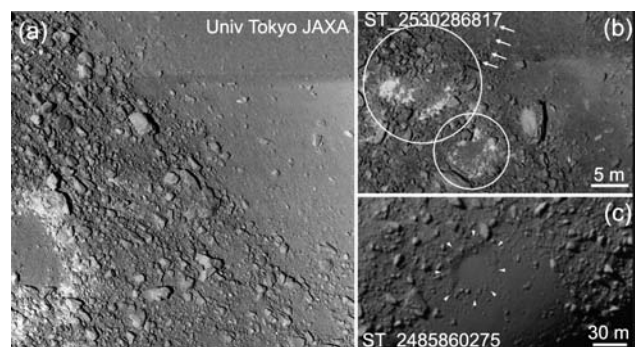


**Fig. 4.** Evidence of regolith transport on Itokawa. **(a)** High-resolution image of the boundary area between Muses Sea and the rough terrains. Piles of gravel can be seen on the uphill sides of boulders. Such a characteristic is similar to terrestrial landslides. **(b)** Image of the “neck” area of Itokawa (13 cm/pixel) showing piles of angular boulders at the lower part of the image. Crater-like depressions are shown by the circles and the arrows indicate the debris, which appears to have drained from the rim of the upper crater toward the smooth terrain. **(c)** A circular depression that appears to be filled with finer particles.

surface has been modified since the crater formation (*Sierks et al.*, 2011).

**2.3.2. Depth and character of Lutetia's regolith.** The surface of Lutetia is covered by an extensive regolith, similar to that of the Moon (*Coradini et al.*, 2011). Nonetheless, Lutetia's surface is very heterogeneous. Images taken during the close approach of the European Space Agency's (ESA) Rosetta spacecraft allowed Lutetia's surface to be separated into several distinct regions [for a detailed map of the Lutetia regions, see *Sierks et al.* (2011) and *Massironi et al.* (2012)]. Some regions are very old and heavily cratered with significant deformation by linear features, while others exhibit sharp morphological boundaries. The Baetica (north pole) region contains a cluster of craters, created from a series of superposed impacts (*Massironi et al.*, 2012); this is one of the most prominent features imaged on Lutetia's surface. The extremely low crater density and lack of linear features in this region can perhaps be attributed to the covering of smooth regolith material, probably the ejecta blanket from the crater cluster (*Sierks et al.*, 2011; *Vincent et al.*, 2012).

Lutetia's regolith is estimated to be up to ~600 m in depth (*Vincent et al.*, 2012). This estimate is based on the thickness of the ejecta blanket of the largest crater assuming a uniform gravity field, and may therefore be improved with a more detailed study of regional ejecta geophysics, taking into account the complex gravitational field of Lutetia. Surface slopes can exceed 30° in some places but are generally less than this (*Sierks et al.*, 2011; *Thomas et al.*, 2012). The size distribution of blocks on Lutetia is reported to be a steep power law of -5 (Fig. 3) (*Küppers et al.*, 2012). It is noted, however, that the method used by Küppers et al. for binning the boulders is different to the method used by other research groups.

**2.3.3. Evidence for an active regolith on Lutetia.** Diverse evidence for regolith motion was observed inside the large crater cluster in the Baetica region. The observations include albedo variations with bright regions on the steep slopes indicative of relatively recent landslides (as observed inside craters on Eros and on Itokawa), deposits of smooth and fine particles with boulders, and apparent landslide deposits (*Sierks et al.*, 2011). In addition, observations show craters that have poorly defined rims as a consequence of multiple landslides (e.g., Fig. 5 of *Thomas et al.*, 2012). Rocky outcrops are also visible at what appears to be the source of the landslides (*Thomas et al.*, 2012).

**2.3.4. Linear features on Lutetia.** Lutetia displays a huge number of lineaments (e.g., Fig. 5) that can be found over the entire imaged surface, with the exception of two young regions (*Thomas et al.*, 2012). The orientation of these linear features, which are similar in appearance to those on Eros discussed in section 2.1, has been linked to three impact craters (*Besse et al.*, 2014). The linear structures have been classified into several types by *Thomas et al.* (2012): irregular troughs, large faults and tectonic troughs, organized linear reflectance variations and narrow faults, rows of coalesced pits (known as pit-chains), intracrater trenches, intracrater layers and ejecta layers, and finally scarps and ridges. The

most striking linear feature on Lutetia's surface is the very long (~10 km) and wide (~1.2 km maximum width) groove in the Noricum region (*Thomas et al.*, 2012). This groove is situated on a local topographic high and is approximately 100 m in depth (*Sierks et al.*, 2011). For a complete discussion of the lineaments on Lutetia, including multiple examples, see *Thomas et al.* (2012).

## 2.4. Asteroid (4) Vesta

(4) Vesta (hereafter simply Vesta; Fig. 1, Table 1) is the second most massive main-belt asteroid and is one of the fastest rotators of the large asteroids. Vesta's surface has a complex topography at all spatial scales (*Jaumann et al.*, 2012). One of the most dramatic discoveries on the surface of Vesta is an 18-km-high mountain in the center of a huge (460-km-wide) crater named the Rheasilvia basin. This peak is the second highest in the solar system after Olympus Mons on Mars.

**2.4.1. Depth and character of Vesta's regolith.** The thickness of Vesta's regolith is estimated to be approximately 800 m (*Jaumann et al.*, 2012). The surface slopes on Vesta can exceed 40° and there are a considerable number of steep slopes that may be indicative of intact bedrock beneath or the presence of cohesive forces in the regolith. Dark materials, of likely exogenic origin (carbon-rich low-speed impactors), are distributed unevenly across Vesta's surface [(Fig. 6a (*Jaumann et al.*, 2014))].

**2.4.2. Craters and crater morphology on Vesta.** Craters on Vesta display a wide range of degradation states, from fresh craters with unmodified rims to impact crater ruins showing almost no visible rims (*Jaumann et al.*, 2012).

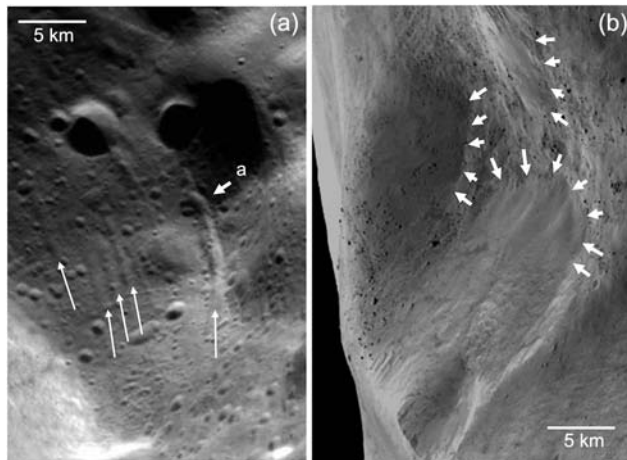


**Fig. 5.** Closeup images of Lutetia. **(a)** Curvilinear features. Some linear features cut crater rims (arrow labeled "a"), implying that these features post-date the craters (ID 224598, ESA 2010 MPS for OSIRIS Team MPS/UPD/LAM/IAA/RSSD/INTA/UPM/DASP/IDA). **(b)** The central crater cluster in Baetica showing landslides (arrows) and numerous boulders (ID 216820, ESA 2010 MPS for OSIRIS Team MPS/UPD/LAM/IAA/RSSD/INTA/UPM/DASP/IDA).

Depth-to-diameter ratios are similar to Lutetia, varying from 0.05 to 0.4 with a mean of 0.17 (Jaumann et al., 2012; Vincent et al., 2012, 2013). The northern hemisphere is observed to be heavily cratered, whereas the southern hemisphere shows comparatively fewer craters, most probably due to the relatively recent basin-forming impacts near the south pole (Vincent et al., 2013). Shallower craters are found in the oldest regions on the surface of Vesta, as would be expected due to progressive crater degradation. The deep, loose regolith in the younger southern hemisphere may also aid the formation of deeper craters (Vincent et al., 2013).

Topography plays a much more important role in crater formation and evolution on small bodies and moons than on terrestrial planets. For example, Vesta's ratio of observed relief to size [15% (Williams et al., 2013)] is significantly greater than for terrestrial planets [1% (Jaumann et al., 2012)]. Strongly asymmetric craters have been seen on the many steep surfaces of Vesta (Fig. 6c). During impacts on

steep slopes, ejecta is prevented from being deposited in the uphill direction and slumping material superimposes the deposit of ejecta on the downhill side (Krohn et al., 2014). This leads to craters with a smoothed downslope rim that is often covered by the asymmetric ejecta (Jaumann et al., 2012). Resurfacing due to impacts, gravitational modifications, and seismic shaking are important geophysical processes that not only add to the complexity of Vesta's surface evolution, but also substantially alter Vesta's morphology (Jaumann et al., 2012). Young bright and dark-rayed craters and their ejecta field are superposed across the surface of Vesta (Fig. 6b) (Williams et al., 2014; Yingst et al., 2014). Pond-like deposits are also seen on the surface of Vesta. Similarly to those on Eros, they tend to have a downslope asymmetry within craters on slopes, and show no evidence for regolith flows into the craters and depressions (Jaumann et al., 2012; Cheng et al., 2002b). However, given the more important gravity on Vesta (compared to Eros) and the larger size of such pond-like features, their formation may simply be due to standard crater slumping, rather than a process by which external material is transported into the crater.

**2.4.3. Evidence for an active regolith on Vesta.** As on the surfaces of the other asteroids discussed so far, extensive evidence of regolith mobility has been observed on Vesta; slumps of material, scarps beginning at the top of a slope, and dark and bright material emanating from the rims or walls of impact craters or running downslope into the crater bowl (Fig. 6d) (Jaumann et al., 2012; Williams et al., 2013; Yingst et al., 2014). Lobate, flow-like features are generally observed in close proximity to impact craters or in steep slopes (Williams et al., 2013). These features are interpreted as gravity-driven mass flow deposits, impact ejecta deposits, or, for a small number of features, impact melt deposits (Jaumann et al., 2012; Williams et al., 2013).

On Vesta, the seismic shaking created by the giant basin-forming impacts probably contributed to smoothing and erasure of small features well beyond the extent of the ejecta blankets (Vincent et al., 2013). Mixing of regolith materials (e.g., the dark exogenic materials with impact ejecta) is evident on Vesta's surface (Jaumann et al., 2014; Pieters et al., 2012). There is also a dearth of large-scale volcanic features on the surface of Vesta, compared to what was expected (e.g., Wilson and Keil, 1996; McSween et al., 2011). Jaumann et al. (2012) suggest that the lack of such features may be due to extensive cratering, regolith formation, and resurfacing that has removed the evidence of large-scale volcanism that ceased early in Vesta's history (Williams et al., 2013; Jaumann et al., 2012). This will be discussed further in section 5.

**2.4.4. Linear features on Vesta.** Large equatorial and northern troughs appear on Vesta's surface (Fig. 1). The equatorial troughs are wide, flat-floored, and bounded by steep scarps along ~240° of longitude, while in the remaining longitude muted troughs, grooves, and pit crater chains are evident (Jaumann et al., 2012). The northern troughs display gentler slopes, rounded edges, and considerable infilling. This, combined with the heavy cratering, suggests that they

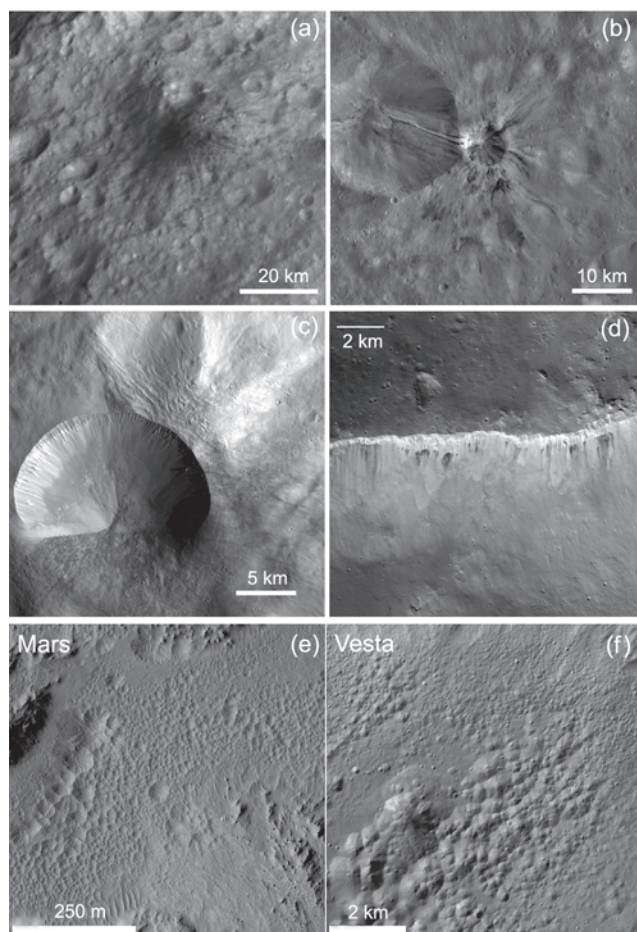


**Fig. 6.** Surface processes on Vesta. (a) Dark hill (PIA14689, modified). (b) Fresh crater (center) with bright and dark rays (PIA15045, modified). (c) Crater on a slope with a sharp crest uphill and slumping material covering the lower rim (PIA15495). (d) Dark and bright material at the rim of Marcia crater (NASA/JPL-Caltech/UCLA/MPS/DLR/IDA/LPI/ASU). (e) Pitted terrains on Mars (PIA16185, modified). (f) Pitted terrains on Vesta (PIA16185, modified).

are much older than the equatorial troughs (*Jaumann et al.*, 2012). The center positions of these circular troughs correspond to the center of Vesta's two southern basins, indicating that the formation of the troughs and the basins are very likely related (see Fig. 2 of *Jaumann et al.*, 2012).

### 3. AN INTRODUCTION TO GRANULAR MATTER

Granular materials are unlike solids in that they can conform to the shape of the vessel containing them, thereby exhibiting fluid-like characteristics. On the other hand, they cannot be considered a fluid, as they can be heaped (*Gudhe et al.*, 1994). The study of granular dynamics is incredibly complex and constitutes an entire field of research by itself. In fact, P. G. De Gennes, a French physicist and Nobel Prize laureate, said that, “*For physicists, granular matter is a new type of condensed matter; as fundamental as liquid, or solid; and showing in fact two states: one liquid-like, one solid-like. But, there is yet no consensus on the description of these two states. Granular matter, in 1998, is at the level of solid state physics in 1930*” (*de Gennes*, 1999). This is not to say that granular matter has not been studied; ancient Egyptians did indeed know how to work with it, at least at an empirical level (*Fall et al.*, 2014); Ernst Chladni (*Chladni*, 1787) and Michael Faraday (*Faraday*, 1831) studied the interaction of grains and fluids; and researchers in the field of geosciences have also long dealt with its complexities on the surface of Earth.

On Earth, we can observe granular materials involved in dramatic avalanches and rockslides, as well as active sand dunes moving across deserts. Industries also handle several different types of granular materials. Some examples are tablets or powders in the pharmaceutical trades as well as agricultural products such as wheat, oats, rice, and other cereals and sands in the construction industry. Theoretical models of granular dynamics are also widely employed to understand traffic flow and even crowd dynamics.

#### 3.1. What is Granular Material?

The term granular material is most often used to describe a material containing a large number of particles that interact with each other through dissipative contact forces (*Richard et al.*, 2005; *Jaeger et al.*, 1996). In these aggregates, although each individual grain can be adequately described by Newtonian physics, a collection of grains offers complex behavior that is often extremely sensitive to external conditions (such as external forcing). Granular material is a material for which the relevant energy scale is the potential energy rather than the thermal energy; i.e., particles in granular material are massive enough for their potential energy to be orders of magnitude larger than their thermal energy (*Schroter et al.*, 2005). For example, a typical grain of sand of mass  $m$ , raised by its own diameter  $d$ , in Earth's gravity,  $g$ , will have potential energy,  $mgd$ , that is at least  $10^{12}$  times the thermal energy  $k_B T$  at room temperature on Earth (*Jaeger et al.*, 1996).

The size of the constituent particles is closely linked to the type of interactions between the particles that will dominate the behavior of the aggregate. On Earth the approximate size at which dissipative contact interactions dominate is 100  $\mu\text{m}$ ; at grain sizes  $<100 \mu\text{m}$ , humidity and van der Waals forces will influence the particle interactions. Additionally, if present, interstitial fluid will also influence the dynamics of the grains depending on the density of the fluid and the grain size (*Burtally et al.*, 2002; *Biswas et al.*, 2003). We will discuss in section 4 how the importance of some of these forces changes in the low-gravity environment of an asteroid.

#### 3.2. Basic Characteristics of Granular Material

Granular materials exhibit several characteristics that make them interesting but equally very difficult to model and understand. From the definitions presented above, some characteristics can be extracted, while others come from observation: (1) the grains that form a granular material are solid; (2) grain-grain interactions are highly dissipative; (3) potential energy, more than temperature, of the system is the relevant parameter; (4) granular materials are thixotropic, meaning they exhibit solid-, liquid-, and gas-like behavior; and (5) friction, globally understood to be a combination of surface-surface friction and geometrical interlocking that prevents motion, makes aggregates able to sustain shear stress and contribute to the dissipative nature of grain-grain interactions.

From these basic characteristics, some phenomena result. For example, Fig. 7b shows the solid-, liquid-, and gas-flow regimes obtained in an avalanche-like situation. In a solid-like state, such as a heap or pile, the material is said to be “quasistatic” as the individual particles are in a stable mechanical equilibrium with their local neighbors. In the liquid-like and gas-like states, the material is said to “flow.” Dense flows (liquid-like state) are dominated by many-body interactions and occur when particles have long-lived contacts with many neighbors. In rapid or dilute flows (the gas-like state) there are no enduring contacts and the collision time is much smaller than the time between collisions [*Andreotti et al.* (2013) provide a thorough exposition of these topics].

Flowing granular materials can segregate according to particle properties (size, density, shape, and more), making granular media highly heterogeneous (Fig. 7a). The phenomenon of segregation is a continued source of frustration for industries (*McCarthy*, 2009); however, segregation may help us to explain several geological features observed on the surface of asteroids and discussed at the beginning of this chapter.

The final, but very important, property of granular materials is the nonlinear transmission of force between particles via force chains. A force acting on a granular material is distributed through a complex force distribution network that depends on the positioning and packing of the individual particles. This grain network resists reorganization when stressed and imposes a granular drag force when a solid object is pushed through the material (*Costantino et al.*,

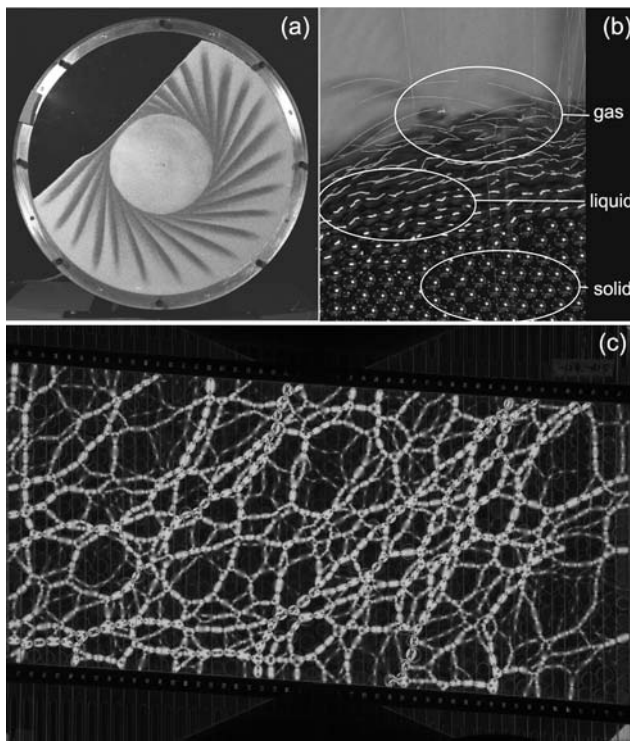


**Fig. 7.** (a) Segregation of particles in a tumbler. The large sugar crystals (white) and small iron particles (black) segregate in the tumbler as described in Gray and Chugunov (2006). Credit: N. Gray, University of Manchester. (b) Solid, liquid or gas? An illustration of the solid- (bottom), liquid- (middle), and gas- (top) flow regimes obtained by pouring steel beads on a pile. Credit: O. Pouliquen and Y. Forterre. (c) Force chains in a granular material. Photoelastic image of a system that has been jammed by applying simple shear strain from an initially force-free state. The apparatus used here applies shear from the boundaries and also from the base, which consists of individual slats that deform affinely with the boundary. Credit: J. Ren and R. P. Behringer, Duke University.

2008). Figure 7c shows the force chains inside a granular material. The presence of force chains can induce complex stresses at the sides of grain silos (Schwartz et al., 2012), preventing explosions at the bottom and instead leading to ruptures at the sides (Janssen, 1895; Jaeger et al., 1996). This can be linked to the nonlocal effects granular materials exhibit (Nichol et al., 2010) and may even cause asteroids to experience long-range consequences of small events such as meteoroid impacts (Murdoch et al., 2013b).

### 3.3. Theoretical Framework

As shown above, granular matter can present solid-, liquid-, and gas-like behaviors, all at the same time. Although a complete theory to describe each behavior simultaneously has yet to be proposed (e.g., Jop et al., 2006; GDR-MiDi, 2004), different regimes (or states) can be modeled within certain frameworks. Depending on which of these theo-

retical frameworks is best suited to the regime at hand, the properties of the grains will be described by different sets of parameters, e.g., friction, elastic moduli, viscosity, and restitution coefficients among others.

The elasticity-perfect plasticity models can be used for the static case (e.g., Holsapple, 2004; Holsapple and Michel, 2006). These models belong to the field of continuum mechanics and, as the name would suggest, they treat a granular media as continuous. This can be done under one assumption: the size of the grains that form the media (or soil) are very small compared with the typical length scale or size of the sample. The dynamics of the media is modeled through yield criteria such as Mohr-Coulomb or Drucker-Prager, in which the main parameters are angle of friction and cohesive strength. The pressure and shear stress (both derived from the principal stresses of the stress tensor) define the stress state of the media and are average quantities that in reality result from the contacts between particles and the interactions between their surfaces.

Fluid mechanics equations are used for dense flows, or for when grains begin to flow like a liquid (e.g., Haff, 1983; Forterre and Pouliquen, 2008). Within this framework, the dynamics of the medium is described through a continuity equation, derived from the conservation of mass principle; a momentum equation, derived from the conservation of momentum principle (in the case of granular materials, a description of viscosity must be included); an energy equation, derived from the conservation of energy principle; and an equation of state relating the three conservation equations.

Kinetic theory (e.g., Jenkins and Zhang, 2002; Brilliantov and Pöschel, 2010), used for dilute, highly dynamical (gas-like) systems, makes the assumption that the particles only have binary collisions. Of course, in a real system this is not the case, as multi-particle collisions may also occur; however, they are determined to be too rare to be taken into account. The validity of the assumption is related to the density of the granular system (must be safely below the jamming density) and the duration of the collisions (must be short in order to avoid the occurrence of three or more particles in simultaneous contact). Thus, the particles of this system are idealized as hard spheres (instantaneous collisions). In this particular regime, the concept of granular temperature can be defined. A “granular temperature” can be defined in multiple ways, but essentially it is some measure of the average of energy fluctuations exhibited by a collection of grains. An example of one such definition, for a collection of  $N$  grains of average velocity  $\bar{v}$  and average spin  $\bar{\omega}$ , with each grain having a mass  $m_i$ , velocity  $v_i$ , moment of inertia  $I_i$ , and spin  $\omega_i$ , the granular temperature may be defined as

$$T_g = \frac{1}{2Nk_B} \sum_{i=1}^N \left( m_i |\mathbf{v}_i - \bar{\mathbf{v}}|^2 + I_i |\boldsymbol{\omega}_i - \bar{\boldsymbol{\omega}}|^2 \right) \quad (1)$$

This quantity does not include, but is analogous to, the thermodynamic temperature (Walton and Braun, 1986). One important difference between a granular gas and a molecular gas is the inelastic nature of the collisions of the former, which

leads to clumping and effectively serves to distinguish the behavior of granular material.

#### 4. THE ASTEROID SURFACE ENVIRONMENT

By now it should be clear that asteroid surfaces are formed by regolith of various shapes, sizes, materials, and, therefore, material properties. In a granular aggregate, these material properties are intrinsically related to the size and shape of the grains, their atomic and electronic structure, and the gravitational field to which they are subjected, to mention the most important factors. These properties will also play a role in how asteroid surfaces, and asteroids as a whole, react to external agents such as gravitational fields of other planetary bodies, solar radiation pressure [the Yarkovsky and Yarkovsky-O'Keefe-Radzievskii-Paddack (YORP) effects, particle transport, and levitation] or impacts. In what follows, we will explore these aspects of the surfaces of asteroids. Note that SI units should be assumed in all expressions in this section.

##### 4.1. Surface Characterization

**4.1.1. Materials.** Different mineral compounds form the regolith that is present in asteroid surfaces; they provide their spectral, thermal, and some mechanical characteristics. The first two are obvious as they have to do with the absorption, transmission, and reemission of energy (*Masiero et al.*, 2009); the third comes from how regolith is formed, as that would be a reflection of the hardness of the material, the crystalline structure, and forces between the surfaces of grains in contact (adhesion, cohesion, and friction).

At the moment, what is known about the materials that make up asteroids comes from the meteorites that have crashed on Earth, from spectral observations, and, more recently, from the samples returned from asteroid Itokawa by the Hayabusa mission. Through the research carried out on the available samples, it has been found that asteroids are formed mainly by pyroxene, olivine, plagioclase, and iron compounds. These materials have crystalline structures, and their detailed study belongs to the field of solid-state physics or condensed-matter physics.

**4.1.2. Observed regolith characteristics.** Section 2 has already summarized the main observations and interpretations made about the slopes and grain size distributions on asteroid surfaces.

**4.1.3. Surface gravity.** Up to this point, in the description and characterization of the surface regolith of asteroids, there are no big differences from what can be found on Earth. However, it is here where the similarities end, as one of the most important factors affecting the dynamics of the regolith on asteroids is the ambient gravity, i.e., the sum of the local gravitational field and centrifugal forces due to the rotation of the asteroid. The calculated surface gravity of asteroids such as Itokawa and 1999 KW<sub>4</sub> can be found in the chapters by Yoshikawa et al. and Scheeres et al. in this volume, *Scheeres et al.* (2010), and *Hartzell and Scheeres* (2013).

These surface gravity calculations show some important features that are not common in our terrestrial experience: (1) gravity is 10<sup>3</sup>–10<sup>6</sup> times smaller than Earth's gravitational field, g; (2) the gravitational field is not always perpendicular to the terrain; and (3) relatively small displacements on the surface of a small body could mean big changes in the gravitational field. Among the main implications are that escape speeds are in the order of centimeters per second, micrometeoroid impacts could transfer enough energy to generate surface or even global changes, and stepping or landing on one of these aggregates could generate an ejecta field that could damage the instruments of a spacecraft or generate a local avalanche.

**4.1.4. Friction.** Intuitively, the idea of friction is that of a force that resists the relative motion of two bodies that are in contact. This resistance may appear in various ways; the work carried out by *Bowden and Leben* (1939), *Bowden and Tabor* (1939), and *Bowden et al.* (1943) and later summarized by *Rao et al.* (2008) suggested that asperities or projections on the surfaces of the bodies adhere to form junctions. Therefore work must be done to deform and break these junctions, and this is accompanied by wear or erosion of material in the interfacial region. Additional work is associated with the deformation of the material in a larger region near the interface (plowing).

The first attempt to formulate a macroscopic friction coefficient is attributed to *Coulomb* (1776), who equated it to the tangent of the angle of repose, by defining it to be the ratio of shear and normal stresses on an inclined pile of sand. The seminal work of *Bagnold* (1954, 1966) found that the frictional force varied as the square of the shear rate for grain-inertial flow in the regime of rapid shear. On the other hand, *GDR-MiDi* (2004) made it clear that the rheological properties of granular flows (friction, viscosity) depend on the shear rate, i.e., on the dynamics, thus putting the work of Bagnold and collaborators into context.

*Mehta* (2007) recognizes that the proper microscopic formulation of intergrain friction remains an outstanding theoretical problem. In a granular material, it is not only the grain-grain surface friction that will determine the resistance of a grain to movement, or the resistance of the aggregate to be sheared and deform, but also the grains' shapes, geometrical interlocking, packing, and size distribution; all these factors are usually pulled together in a single term: the angle of (internal) friction that appears in the Mohr-Coulomb or Drucker-Prager yield criteria.

Within the Mohr-Coulomb yield criterion, the angle of internal friction is defined as the arctangent of the ratio of shear to normal compressive stress at the stability limit (see Fig. 8). The Mohr-Coulomb criterion prescribes that shearing along any plane in a granular material cannot occur unless the shear stress ( $\sigma_s$ ) on that plane reaches a value proportional to the normal (compressive) stress on that plane:  $\sigma_s = \mu\sigma_n$ . The proportionality constant  $\mu$ , the friction coefficient, is written as the tangent of the friction angle  $\phi$ :  $\mu = \tan(\phi)$ . Thus, the friction angle is a material property. The Drucker-Prager criterion is based on similar physical ideas, but uses a linear

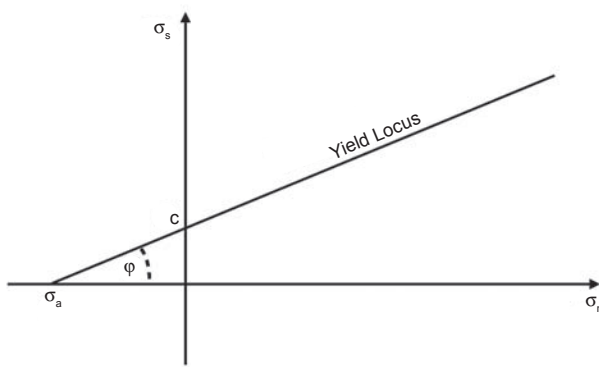


**Fig. 8.** Mohr-Coulomb yield criterion: normal stress ( $\sigma_n$ ), shear stress ( $\sigma_s$ ), cohesive strength (c), tensile strength ( $\sigma_a$ ), and friction angle ( $\varphi$ ).

dependence of an average shear stress, as measured by the  $J_2$  stress invariant, on the pressure (Holsapple, 2013; Chen and Han, 1988). Theoretically, if a material is cohesionless, the angle of repose corresponds to the angle of internal friction. On the other hand, for a cohesive aggregate, the angle of repose has to be such that is related to the cohesive strength of the material [see Nedderman (2005) for an indepth explanation].

Cohesive forces (electrostatic and van der Waals are among the best known interactions) are kept in a different term and, within either criteria, do not affect the angle of friction, but only the angle of repose. Figure 8 shows the relation between the normal stress ( $\sigma_n$ ), shear stress ( $\sigma_s$ ), cohesive strength (c), tensile strength ( $\sigma_a$ ), and friction angle ( $\varphi$ ). If cohesive strength is defined as the shear stress at zero normal stress, then tensile strength is the normal stress at zero shear stress.

On Earth, a well-known experimental fact is that angles of internal friction of cohesionless granular materials vary from  $25^\circ$  for smooth spherical particles to  $45^\circ$  for rough angular particles (Carryg, 1970; Pohlman et al., 2006; Kleinhans et al., 2011). Calculations made on asteroids Eros and Ida and martian satellites Phobos and Deimos show that only Ida has more than 2% (by area) of gravitational slopes above typical repose angles ( $35^\circ$ ). At this point it is worth explaining that the static angle of repose is the maximum slope that can be supported before the formation of an avalanche, and a dynamic angle of repose is the slope that results after this avalanche has taken place. The maximum angle of stability, critical angle, and static angle of repose are the same; angle of repose and dynamic angle of repose are also the same. The static angle of repose may be related to cohesive forces, including van der Waals forces, electrostatic forces, and capillary forces in the case of microscopic fluid pockets between the particles. Using a parabolic flight experiment, Kleinhans et al. (2011) concluded that for decreasing gravity, the static angle of repose increased while the dynamic angle of repose decreased for all tested materials.

**4.1.5. Electrostatic forces and cohesion.** As mentioned before, any kind of cohesive force between the grains of

an aggregate is going to increase the value of its angle of repose. This includes van der Waals, capillary, electrostatic, and magnetic forces. The effects of these cohesive forces can be clearly seen in powders on Earth (flour, toner, pollen, and chalk are common examples). How they appear and when they are apparent in the behavior of granular aggregates will be discussed in the next sections.

## 4.2. Cohesive and Adhesive Forces

Cohesive and adhesive forces have the same origin, the only difference being that the term cohesive applies to the attractive force between molecules of the same material and the term adhesive applies to molecules of different materials. For example, liquid water molecules attract one another and form water droplets with surface tension (this is cohesion); water molecules and silica molecules also attract one another and water can make a glass wet (this is adhesion). These attractive forces are electromagnetic in nature and are appreciable when the electronic clouds of the atoms that form the surfaces of two bodies are within a few angstroms. The term van der Waals forces is used here very loosely and refers to the totality of nonspecific attractive or repulsive intermolecular forces other than those responsible for ionic and covalent molecular bonds (McNaught and Wilkinson, 1997). These interactions are often modeled by the Lennard-Jones potential (Jones, 1924)

$$V_{LJ} = 4\epsilon \left[ \left( \frac{\gamma}{r} \right)^{12} - \left( \frac{\gamma}{r} \right)^6 \right] \quad (2)$$

where  $\epsilon$  is the depth of the potential well,  $\gamma$  is the finite distance at which the interparticle potential is zero, and  $r$  is the distance between the two particles (neutral atoms or molecules). Although other, more accurate forms of the potential exist, this one is usually used in computer simulations due to its simplicity. The  $r^{-12}$  term describes the Pauli exclusion principle due to overlapping electron orbitals and the  $r^{-6}$  term describes the long-range attraction (van der Waals force, or dispersion force).

Johnson et al. (1971), Heim et al. (1999), and Hughes et al. (2008) theoretically and experimentally studied the characteristics of the van der Waals force in granular materials. The cohesion between two spherical particles (radii  $r_1$  and  $r_2$ ) can be approximately described by (Castellanos, 2005; Perko et al., 2001; Rognon et al., 2008)

$$F_c = \frac{A}{48(t+d)^2} \frac{r_1 r_2}{r_1 + r_2} \quad (3)$$

where  $A$  is the Hamaker constant for the grains ( $4.3 \times 10^{-20}$  J for lunar soil),  $t$  is the minimum distance between the particle surfaces due to adsorbed molecules, and  $d$  is the width of any additional separation between the particles beyond that caused by the presence of the adsorbed molecules. In the extreme environment of space, the minimum distance between the materials can be much closer than possible on

Earth, where atmospheric gases, water vapor, and relatively low temperatures allow for significant contamination of surfaces ( $d = 0$ ). These much cleaner surfaces and closer contacts allow for increased cohesion (Perko *et al.*, 2001; Scheeres *et al.*, 2010).

Perko *et al.* (2001) define a cleanliness factor  $S$  as  $\Omega/t$ , where  $\Omega$  is the diameter of an oxygen ion ( $O^{2-}$ ) and  $t$  is defined as above. This being so, the cohesive force between a grain (radius,  $r$ ) and a flat surface (or a much larger grain) is

$$F_c = \frac{AS^2}{48\Omega^2} r \quad (4)$$

### 4.3. Electrostatic Forces

Electrostatic forces have been hypothesized to play an important role on the surfaces of asteroids, and have been specifically invoked as one means by which small dust grains can be transported across a body's surface. The first evidence of electrostatic lofting was the lunar horizon glow observed by the Surveyor spacecraft (Rennison and Criswell, 1974) at the terminator region. A second discovery contributing to this hypothesis was the existence of ponds on Eros and other asteroids, even though it has been found that their apparent distribution could have an observational bias. Finally, there is also the fact that the Hayabusa mission was able to bring back samples of grains from asteroid Itokawa despite the malfunctioning of the sampling mechanism (Yano *et al.*, 2006). It has been proposed that the electrostatic interaction between charged particles and a possibly charged sampler horn helped collect the sample (Tsuchiyama *et al.*, 2011). Whether or not dust levitation occurs on asteroids is still an open question, although it is undoubttable that surface grains on these bodies are subject to electrostatic forces. Unfortunately, as of yet, this is still not fully understood.

The electrostatic force felt by a particle on the surface of an asteroid is related to its location on the surface. The charge density at any point on the surface is the result of the difference between the number of electrons that are deposited on it by the solar wind and those that leave the surface due to photoemission. These two vary with the location of the surface and with time as the asteroid rotates and solar wind influences different areas of the surface. Photoemission and solar wind interaction depend on the solar incidence angle and a variety of plasma-related phenomena that vary with solar longitude, respectively. The resulting charge on the surface of the asteroid then influences the charging of the particle in question and influences the plasma environment (photoelectron and plasma sheaths) that will be experienced by the particle if it is lofted above the asteroid's surface (Scheeres *et al.*, 2010).

If grains are idealized as spherical, and we make the same assumptions as Colwell *et al.* (2005) about the plasma sheet, it is then possible to demonstrate that for a particle of radius  $r$  (surface area,  $\Lambda = 4\pi r^2$ ), the electrostatic force that would provide lofting is:

$$F_{es} = \epsilon_0 E^2 \Lambda \approx 4\pi\epsilon_0 E^2 r^2 \Rightarrow F_{es} \approx 9 \times 10^{-9} r^2 \quad (5)$$

where  $\epsilon_0$  is the permittivity of vacuum and  $E$  is the electric field.

Recent theoretical analysis and experiments have shown that cohesion will play a role in dust levitation (Hartzell and Scheeres, 2011; Hartzell *et al.*, 2013), and that cohesion will dictate the electric field required for lofting for particles smaller than 1 mm on Itokawa (100  $\mu m$  on Eros and 10  $\mu m$  on the Moon). Furthermore, these experiments have also shown that a balance between cohesive, gravitational, and electrostatic forces is needed to ensure levitation.

### 4.4. Link Between Surface Environment and Geophysical Features

In the previous sections we have tried to account for and describe the origin of the main forces that could affect grains on the surface of an airless planetary body. However, an even more interesting aspect is the interplay of these forces, as this determines the dynamics of the grains and the landscape of the surface as a whole. With this in mind, and following the notation used by Scheeres *et al.* (2010), we define something called a bond number as

$$B = \frac{F_c}{W} \quad (6)$$

where  $F_c$  is the cohesive force acting on a grain and  $W$  is its weight. For an ambient gravitational acceleration of  $g_A$  the ambient weight of a grain is defined as  $W = mg_A$ , where  $m$  is the particle's mass.

On small planetary bodies, self-gravity between individual grains is much more important than on Earth and should be taken into account in calculations. For two equal-sized particles of radius  $r$  and density  $\rho_g = 3500 \text{ kg m}^{-3}$  (larger than the asteroid's bulk density), the bond number is

$$B_{self} = G \frac{4\pi\rho_g}{3g_A} r \approx 1 \times 10^{-6} \frac{r}{g_A} \quad (7)$$

For the electrostatic force due to photoelectric emission alone, using equation (5)

$$B_{es} = 6 \times 10^{-13} \frac{1}{g_A r} \quad (8)$$

We note that triboelectric charging and other (not yet understood) mechanisms in the terminator regions could increase the electrostatic force to  $F_{es} \approx 0.1 r^2$ . This would, therefore, increase the electrostatic bond number to

$$B_{es} \approx 7 \times 10^{-6} \frac{1}{g_A r} \quad (9)$$

For cohesive forces and for material parameters of lunar regolith

$$B_c = 2.5 \times 10^{-6} \frac{S^2}{g_A r^2} \quad (10)$$

where S is the cleanliness factor defined earlier.

On small planetary bodies, for sufficiently small grain sizes, these bond numbers can easily attain values greater than 1, meaning that the grain's own weight can be overcome. Strong cohesive forces give rise to highly porous structures first called "fairy castles" by *Hapke and van Hoen* (1963). Back then they attributed the existence of such structures to adhesive and long-range electrostatic forces that act between grains during deposition and influence their trajectories. After that, the work of *Matson and Nash* (1983), *Kreslavsky and Shkuratov* (2003), and *Cassidy and Johnson* (2005) shed more light on how these structures affect photometric anomalies of the Moon. Anomalous halos around small bright impact craters have been associated with changes in porosity probably related to some geologically recent damage of the equilibrium regolith structure.

Additionally, the scaling of cohesive forces with ambient gravity means that centimeter-sized grains in a microgravity environment may behave as micrometer-sized grains in Earth's gravity. Keeping this in mind, *Mériaux and Triaudafillou* (2008) and *Durda et al.* (2013) have begun research to understand the dynamics of cohesive powders under vacuum as a proxy to regolith-covered granular surfaces on asteroids. Simulations carried out by *Sánchez and Scheeres* (2014) and *Hirabayashi* (2014) have shown that modest values of cohesive strength (25–150 Pa) and a heterogeneous structure can drastically modify the maximum spin rates, disruption patterns, and the existence (or lack) of surface flow. The results obtained by *Rozitis et al.* (2014), *Hirabayashi et al.* (2014), and *Scheeres* (2014) about 1950 DA and P/2013 R3 also seem to agree with the models, showing that values of cohesive strength under 100 Pa and angles of friction similar to those found on granular aggregates on Earth (35°–45°) are enough to explain the elevated spin rates of these asteroids.

## 5. GEOPHYSICAL PROCESSES ACTING ON ASTEROIDS

As we have already discussed, asteroids observed by spacecraft preserve records of geophysical processes that have operated at their surfaces and sometimes in their interiors. Here, these processes are classified into the following three categories: (1) exogenic phenomena, which are outer geophysical processes including impact cratering and slope failures/collapses; (2) endogenic phenomena, which are inner geophysical processes including ridges, faulting, and possible volatile and volcanic activities; and (3) other origins, including tidal and YORP effects. Note that some processes dominantly acting on one asteroid might not necessarily act on other asteroids because the physical, especially mechanical, environments of asteroids vary significantly (for example,

Vesta is considered to have been volcanically active because its mass is significantly large, 10 orders of magnitude larger than that of Itokawa, which is simply a pile of rubble).

### 5.1. Exogenic Phenomena

Because of the lack of an atmosphere, an asteroid is directly exposed to solar wind, cosmic and solar rays, and influxes of meteoroids of varying sizes. An impact can largely modify the shape of an asteroid and even its arrangement (such as impact-induced breakup of an asteroid). This will not be discussed here; rather, we focus on surface processes resulting from impacts.

On small bodies, regolith is traditionally believed to result from repetitive impacts that excavate the surface and distribute ejecta materials. However, speeds of ejecta are typically greater than several tens of centimeters per second (*Housen et al.*, 1979; *Housen and Holsapple*, 2011), which corresponds to the gravitational escape speed of kilometer-sized asteroids. Impact debris reaccumulation therefore may not be solely responsible for the ubiquitous presence of regolith on small asteroids. Other regolith-formation processes have been proposed, including during contact-binary forming collisions of asteroids, by tidal forces, as well as due to the retention of regolith from a parent body (*Barnouin-Jha et al.*, 2008; *Scheeres et al.*, 2007). Using laboratory experiments and numerical simulations, *Delbo et al.* (2014) have shown that thermal fragmentation induced by diurnal temperature variations breaks up rocks larger than a few centimeters more quickly than comminution by micrometeoroid impacts. The latter was demonstrated by adapting the lunar impact-induced comminution rates of *Hoerz et al.* (1975) to asteroids. Because thermal fragmentation is independent of asteroid size, this process can also contribute to regolith production on larger asteroids. Production of fresh regolith originating in thermal fatigue fragmentation may therefore be an important process for the rejuvenation of the surfaces of NEAs (*Delbo et al.*, 2014).

Once formed, resultant deposits of loose debris will be affected by the gravity in a longer timescale, where repeated disturbances cause overall slow motion in the downhill direction. The disturbances may be caused by processes such as small impacts and severe thermal cycling, while many of the surface processes are in some aspects similar to those terrestrial phenomena resulting from expansion and contraction processes, heating and cooling, wetting and drying, and freezing and thawing. We note here that there are many important temperature-related processes occurring on asteroid surfaces and these are discussed in the chapter by Delbo et al. in this volume.

**5.1.1. Impact ejecta mantling.** An impact will excavate the surface and create impact ejecta, which usually results in a deposit of debris surrounding the impact crater except for the cases in which the target has too little gravity to retain ejecta or too much porosity to produce it. The ejecta deposits normally affect at least the area within 5 crater radii by blanketing the original surface (*Melosh*, 1989). In

the case of gravity-dominated cratering, the thickness of the deposit,  $H_b$ , is given by

$$H_b = 0.14R_c^{0.74} \left[ \frac{r_c}{R_c} \right]^{-3} \quad (11)$$

where  $r_c$  is the distance from the crater center and  $R_c$  is the crater radius (McGetchin *et al.*, 1973). As suggested in this equation, the ejecta deposit is thickest at the crater rim and thins with increasing distance away from the crater. Impact-ejecta mantling may account for the absence of discernible surface features near craters on bodies such as Lutetia.

When the ejecta deposit is continuous and clearly recognized to be the result of the cratering event, it is called an ejecta blanket. However, such a blanket is not recognized on the surface of a small asteroid. Considering the low gravity, as well as the often irregular shapes, the above equation might not be directly applicable for small asteroids. In fact, other than the local gravity, spin parameters, especially the rotational period, can significantly affect the situation and cause very asymmetric ejecta blankets as observed on Eros. For example, a three-dimensional smoothed-particle hydrodynamics (SPH) simulation of a hemispheric-scale impact onto Vesta, which spins every 5.3 h, shows that variably shaped, multiply folded deposits can be formed (Jutzi and Asphaug, 2011) rather than a simple ejecta mantling.

The presence of boulders adjacent to an impact site on Lutetia suggests that boulder generation is a common feature of large impacts on this asteroid (Sierks *et al.*, 2011). In fact, the fragments of ejecta deposits can be size-sorted through an impact event. Even though some interaction may occur between ejecta fragments in the denser parts of the ejecta curtain, general motion of the fragments is likely dominated by ballistics and thus follows a nearly parabolic trajectory above the asteroid before falling back to the surface. The size of the ejecta fragments near the base of the ejecta curtain is expected to be larger than the fragments higher in the curtain.

One may wonder if ejecta may selectively escape from the surface of an asteroid never to return to mantle its original surface. This idea has been tested against the observations of Itokawa, for which 530 boulders larger than 5 m in size have been identified on its surface (Michikami *et al.*, 2008). Assuming the slope value on the cumulative plot (Fig. 3) from Saito *et al.* (2006), the cumulative number ( $N$ ) of boulders may be approximated as

$$N(>d) = 4.8 \times 10^4 d^{-2.8} \quad (12)$$

where  $d$  is the diameter of a boulder. If we assume that the above size distribution is continuous down to the size of a pebble, the volume of pebbles (4 mm to 6.4 cm in size) can be estimated as  $1.9 \times 10^5 \text{ m}^3$ . Note, however, that smaller particles that exist on the asteroid surface are difficult to observe, because they are overlapped by larger boulders; the size distribution may therefore be different from that observed for larger boulders by 0.2–0.3 in the slope of log-

log plot. This estimate is nonetheless on the same order as that estimated from the areas and depths of smooth terrains [ $2.3 \times 10^5 \text{ m}^3$  (Miyamoto *et al.*, 2007)]. It might therefore be appropriate to assume that no particular pebble-sized blocks have selectively escaped or accumulated (Miyamoto, 2014).

**5.1.2. Seismic shaking.** Crater excavation resulting from an impact onto an asteroid is associated with a shock wave that severely shakes the terrain. Such shaking may induce local movements that cause a net downslope movement of loose surface material (Richardson *et al.*, 2005b), and this effect can be more important for a smaller asteroid because the seismic energy is unable to attenuate over a large volume.

Indeed, the first evidence for such seismic shaking on an asteroid was presented by Thomas and Robinson (2005). They showed that the formation of a relatively young crater (7.6 km in diameter) on asteroid Eros resulted in the removal of other craters as large as 0.5 km over nearly 40% of the asteroid's surface. As burial by ejecta cannot explain the observed pattern of crater removal, and the areas with low small-crater densities correlate well with radial distance from the Shoemaker crater, they conclude that seismic shaking is the most probable mechanism.

Assuming that the seismic energy is completely supplied by the kinetic energy of an impactor, the ratio of the maximum acceleration to the surface gravity,  $a/g$ , can be written as

$$\frac{a}{g} = \frac{3fv_i}{G} \sqrt{\eta \frac{\rho_i D_i^3}{\rho_a^3 D_a^5}} \quad (13)$$

where  $f$  is the seismic frequency in Hertz,  $v_i$  is the velocity of the impactor,  $G$  is the gravitational constant,  $\eta$  is the seismic efficiency factor (the fraction of the original kinetic energy converted to seismic energy),  $\rho_i$  is the bulk density of the impactor,  $\rho_a$  is the bulk density of the asteroid,  $D_i$  is the radius of the impactor, and  $D_a$  is the diameter of the asteroid. For the case of a rubble pile, the seismic energy may attenuate significantly. In this case, a diffusive scattering theory as adopted by Richardson *et al.* (2005b) might be a realistic approach. In this theory,  $a/g$  on a diffusive body may be written as in equation (13) but multiplied by the scale factor

$$\exp\left(-\frac{fD_a^2}{K\pi Q}\right)$$

where  $K$  is the seismic diffusivity and  $Q$  is the seismic quality factor. Note that the exact values of some of the parameters for the above equations, such as  $f$ ,  $K$ ,  $Q$ , and  $\eta$  are difficult to properly obtain. However, most importantly, both models show that the size of an asteroid is an important factor in determining the surface acceleration against the gravity; smaller asteroids vibrate easier than larger asteroids. Although it is difficult to constrain reasonable ranges of values for many parameters, the above equations generally suggest that very small impactors may produce global shaking. Thus, repetitive impacts on asteroids may cause significant shaking, believed

to be responsible for the depletion of craters on Itokawa and small craters on Eros.

**5.1.3. Mass movements.** Once an asteroid is seismically shaken, reverberation continues until internal friction and collisions finally convert it entirely into heat. Similarly, some other disturbances such as heating and cooling may occur. When the formation of faults, rapid landslides, or other processes occur, releasing horizontal stress, such disturbances generally make the ground surface expand perpendicularly to the slope. When the disturbance ceases, the ground surface contracts along the direction of gravity, which is not necessarily parallel to that of the above surface expansion (especially on a surface inclined against the local gravity). When such expansion and contraction occur cyclically, the materials covering the surface show overall migrations, which are essentially downslope displacements. This kind of downslope mass movement of dry, unconsolidated material is a common geological process on terrestrial planets (Meunier et al., 2013). However, geophysically, that on terrestrial planets is generally interpreted in terms of the competition between gravity or inertia and intergranular friction. Naturally, for the case of a relatively smaller asteroid, the situation may be more complicated, since other forces such as cohesive forces can play a significant role, as discussed in section 4.

A slow and cyclic creep process is not the only type of mass movement on an asteroid. More rapid examples include landslides, which take place when the acceleration due to the ambient gravity exceeds the ability of a rock on a slope to resist. Roughly speaking, the conditions for this phenomenon to occur can be described by Coulomb's equation,  $\sigma_s = c + \sigma_n \tan \varphi$  (see Fig. 8). If the shear of a block of rock exceeds the maximum sustainable shear stress, the block slips and may be recognized as a landslide. This kind of mass movement can be found as small-scale, streak-like features such as observed on crater walls of Vesta (section 2). Indeed, mass movements can expose an interior, often recognized through differences in color, as described in section 2.

When a block of rock slips on a slope, sometimes the balance of shear stress and sustainable shear stresses inside the block changes. This causes a flow-like phenomenon, sometimes referred to as a debris flow or granular flow (Legros, 2002). Some of the above-mentioned mass movements may be better explained by this process.

When we consider a case in which a block of rock is resting on a slope at angle  $\alpha$ ,  $\sigma_s = \left(\frac{mg}{A}\right) \sin \alpha$ , where  $m$  is the mass of the block and  $A$  is its basal area. Similarly,  $\sigma_n = \left(\frac{mg}{A}\right) \cos \alpha$ . Assuming the case in which the sliding rock is actually loose debris (a case in which cohesion is negligible in a terrestrial environment, and thus flow occurs rather than simply sliding), the largest shear stress in the block is achieved at the base of the rock. In this situation,  $\sigma_s = \sigma_n \tan \varphi$ , which gives the condition of  $\alpha = \varphi$ . In other words, in this case, the angle of repose is the same as the angle of internal friction and is independent of the gravitational acceleration.

The overall migrations of such flows are sometimes considered as gravity flows, whose speed  $U$  may be described

as  $U \sim D(\rho gh)^{1/2}$ , where  $D$  is a coefficient of drag force,  $\rho$  is the density of the flow, and  $h$  is the thickness of the flow. The speed of the flow therefore depends on the square root of gravity (Jop et al., 2006), indicating that the flow can be much slower than typical ones on Earth.

Another type of mass movement is electrostatic dust levitation (see also section 4), which is proposed to be responsible for particle migrations on airless bodies exposed to both direct sunlight and the solar wind (Lee, 1996). Smaller levitated particles on an asteroid may escape into space through the solar wind, but larger particles may settle back onto the surface. This may explain the smooth ponds on the surface of Eros (Robinson et al., 2001), the formation of which clearly involves the settling of fines (much less than centimeter-sized particles) in gravitational lows by a secondary process, after crater formation [section 2 (Cheng et al., 2002b; Robinson et al., 2002)].

Cheng et al. (2002b) suggest, however, that the pond material derives from the flanks of the bounding depression seismically shaken down to the bottom of the depression. Another idea for the formation of ponds is eroding of boulders; repeated day/night cycling causes material fatigue leading to erosion of the boulders (Dombard et al., 2010). However, recent morphological analyses indicate that the deposited material most likely originates from a source external to the ponds themselves (Roberts et al., 2014a). In addition, the morphology, geography, color, and albedo of the ponds may be consistent with formation by electrostatic levitation rather than seismic shaking (Riner et al., 2008; Richardson et al., 2005b).

**5.1.4. Regolith segregation.** In addition to the size segregation that occurs during impact ejecta mantling, in granular flows where particles have different physical properties, particle segregation also occurs (as discussed in section 3). One example of such segregation is in a granular avalanche. The dominant mechanism for segregation in granular avalanches is kinetic sieving (Bridgwater, 1976) rather than the effects of diffusive remixing, particle-density differences, or grain inertia (Thomas et al., 2000). As the grains avalanche downslope, there are fluctuations in the void space and the smaller particles are more likely to fall, under gravity, into gaps that open up beneath them because they fit more easily into the available space than the coarse grains. The fine particles, therefore, percolate toward the bottom of the flow, and force imbalances squeeze the large particles toward the surface (Gray and Chugunov, 2006).

A further example of regolith segregation, which may be responsible for the presence of large boulders on the surface of asteroids such as Itokawa and Eros (Asphaug et al., 2001; Miyamoto et al., 2007), is the "Brazil-nut effect" (Rosato et al., 1987). The idea is that seismic shaking may cause the larger regolith particles to move up to the surface. If this is the case, the interiors of rubble-pile asteroids having experienced this kind of evolution are likely to be composed of smaller particles than those observed at the surface. This may also lead to some variations of macroporosity with depth inside the asteroid.

The mechanism driving the Brazil-nut segregation is still under debate (Kudrolli, 2004). It has been suggested that the segregation may result from the percolation of small particles in a similar fashion to the kinetic-sieving mechanism, but here the local rearrangements are caused only by the vibrations (e.g., Rosato *et al.*, 1987; Williams, 1976). However, other experimental results from Knight *et al.* (1993) have shown that vibration-induced size segregation may arise from convective processes within the granular material and not always from local rearrangements.

Granular convection is in fact a process often invoked by the community of small-body scientists to interpret the surface geology of asteroids (Miyamoto *et al.*, 2007; Asphaug, 2007). However, as discussed in Murdoch *et al.* (2013b), kinetic sieving and granular convection are strongly dependent on the gravitational acceleration (Thornton, 2005; Murdoch *et al.*, 2013c). A weak gravitational acceleration may therefore reduce the efficiency of particle size segregation. Indeed, recent numerical simulations and parabolic flight experiments of the Brazil-nut effect have shown that the speed at which a large intruder in a granular material rises is reduced as the external gravity decreases (Tancredi *et al.*, 2012; Güttsler *et al.*, 2013; Matsumura *et al.*, 2014). Therefore, all convective and particle segregation processes in a granular material on or near the surface of a small body may require much longer timescales than the same processes would require in the presence of a strong gravitational field.

## 5.2. Endogenic Phenomena

For terrestrial planets, “endogenic processes” are geological processes associated with energy originating from the interior of the planet, including tectonics, magmatism, metamorphism, and seismic activities. However, in the case of asteroids, the ultimate cause of tectonics or seismic activities may be difficult to clearly separate.

Internal magmatism and volcanic processes are not often expected to occur on asteroids. However, differentiated early-forming asteroids should have experienced various kinds of volcanic activity, especially as a result of incorporating the heat-generating isotope  $^{26}\text{Al}$ . The howardite-eucrite-diogenite (HED) class of meteorites, whose parent body is believed to be the asteroid Vesta, have been studied in detail, and the magmatic origins of these rocks and their compositions as surface lavas or intrusions are well understood (e.g., Taylor, 1993). Nevertheless, observations of Vesta show no conclusive evidence of volcanic features. The surface of Vesta, particularly the northern hemisphere, appears to be saturated with craters  $>10$  km in diameter (Marchi *et al.*, 2012). This indicates that the surface regolith to depths of more than 1 km is significantly overturned. On the other hand, Wilson (2013) predicted that typical lava flow dimensions are  $\sim 10$  m thick, much shallower than the thickness of overturned regolith, which might be the reason for the lack of clear evidence of lava flows or pyroclastics on the surface of Vesta.

Even though volcanism is not a common process on an asteroid, some features indicate phase-changing of materi-

als and their transportation to the surface. Possible melting flows identified on Vesta might be good examples. Also, more than 10 active (mass-shedding) asteroids have been reported (Jewitt, 2012), and the possible mechanisms for producing mass loss include dehydration stresses and thermal fracture. Although comets are not the focus of this chapter, we note that, in fact, strange features exist in the nuclei of both Tempel 1 and Wild 2. These features are interpreted as pits and scarp retreats resulting from venting of subsurface volatiles (Veverka *et al.*, 2013).

Some pitted terrains of Vesta (Fig. 6f) are also believed to be related to subsurface volatiles; morphologic similarities of pitted terrains between Mars and Vesta suggest volatile release as an origin. However, because meteorites thought to originate from Vesta indicate low endogenic volatile content, it has been suggested that the volatiles have been delivered to Vesta’s surface and are not endogenic. The source may be carbonaceous chondrites, which have been observed as clasts in howardites (meteorites most likely originating from the surface of Vesta), or perhaps comets. Later impacts into this water-bearing regolith would result in devolatilization due to impact heating and melting (Denevi *et al.*, 2012).

Tectonic features are surface features created by internal stresses that fracture or deform the surface layer. Numerous tectonic features are documented on asteroids. For example, Vesta displays examples similar to those found on small saturnian satellites such as Iapetus. Also, Rahe Dorsum on Eros is a ridge extending for about 18 km around the asteroid that resembles thrust fault structures on the terrestrial planets (Prockter *et al.*, 2002). Tectonic deformation cannot occur without forces to drive it. However, many sources of tectonic stress exist of both internal and external origin, and a clear separation and exclusive classification is difficult.

For example, on Eros, the large “spiral” pattern southwest of Psyche is suggestive of extensional tectonics, whereas the spatial distributions of other ridge systems, as well as its estimated shear strength, indicate that the ridges are in fact thrust faults that were formed by impact-induced compression (Watters *et al.*, 2011; Cheng *et al.*, 2002b; Veverka *et al.*, 2000). However, the ridge system on asteroid (2867) Šteins (hereafter simply Šteins), which is the most prominent feature recognized on its surface, may be formed through the change in rotation rate due to the effect of solar radiation known as the YORP effect. The effect spins Šteins, making the surface seek for the object’s potential-energy minimum, which may cause tectonic arrangements or landslide-like surface modifications toward the equator (Harris *et al.*, 2009). Either process can explain the formation of the ridge at the equator. A similar origin is proposed for an equatorial ridge of 1999 KW<sub>4</sub> (Walsh *et al.*, 2008).

Grabens or linear depressions are found on many asteroids (see section 2), which may seem strange given the fact that asteroids are covered by loose fragmental debris. It is possible that these fractures are evidence of competent rock below the regolith. It has been suggested that they result from stresses from large impact events, which have refocused and caused fracture far from the crater (Fujiiwara

and Asada, 1983; Asphaug et al., 1996), or that they are due to thermal stresses (Dombard and Freed, 2002) and/or body stresses induced by changes in spin. However, faulting can occur even in a granular matrix when it is cohesive relative to the applied stress.

Grooves have been reported on Gaspra, Eros, Šteins, Lutetia, and many other asteroids observed at high resolution. A subset of the grooves appear to be chains of pits (or crater-like indentations) in an almost linear arrangement. The global extent of a series of pitted chains found on Steins indicates these are not impact craters, because the chances of formation of many chains of these craters of similar size is highly improbable. Instead, partial drainage of loose surface material into a fracture within stronger, deeper material is considered as a likely origin (Richardson et al., 2002; Keller et al., 2010). This explanation of how pitted grooves form was suggested to explain the features seen on Phobos (Thomas et al., 1979). Experiments have demonstrated that, in such a model, the spacing of the pits along the groove is equal to the thickness of the regolith in which they form and is independent of regolith bulk density, grain size, shape, angularity, and angle of repose (Melosh, 1989; Prockter et al., 2002). Short and well-defined grooves can also be caused by a boulder that has bounced and rolled a short distance, but very few (<5) such tracks have been positively identified on the surface of Eros (Prockter et al., 2002; Robinson et al., 2001).

### 5.3. Tidal and Rotational Effects

There might be some morphological or even larger modifications of asteroids due to tidal forces. Modest influences are expected to include exposing layers of surface materials; to explain the fact that the laboratory spectra of ordinary chondrite meteorites are a good match to Q-type asteroids, Binzel et al. (2010) and Nesvorný et al. (2010) pointed out the possibility that Q-type NEAs underwent recent encounters with the terrestrial planets and the tidal force exposed fresh ordinary chondrite material on the surface. More considerable outcomes may include splitting the asteroid into a binary (Walsh and Richardson, 2008) or even catastrophically disrupting it in a manner similar to Comet Shoemaker-Levy 9 at Jupiter. Such tidal effects by a terrestrial planet are considered as one of the most likely creation scenarios for asteroid families (Fu et al., 2005). Also, strange shapes of some NEAs as revealed by radar images may have resulted from the tidal disruption processes and reaccumulations of disrupted fragments (e.g., Bottke et al., 1999).

YORP can modify both the rotation rate and the spin-axis orientation of small asteroids and has been identified as an important process driving their physical and dynamical evolution (Vokrouhlický et al., 2003). Asteroids of 5 km and smaller in radius in near-Earth orbits and a few tens of kilometers in the inner main belt are subject to the YORP effect. The spinup of asteroids can have dramatic consequences (Scheeres et al., 2007; Walsh et al., 2008). For example, the deficiency in small craters on Steins is attributed to surface reshaping (through landslides) due to

spinup by the YORP effect (Keller et al., 2010). The shape of the northern hemisphere of Steins is reminiscent of that of the NEA 1999 KW<sub>4</sub>, which has been attributed to spinup by the YORP effect. A plausible scenario is that Šteins was spun up by YORP, leading to material sliding toward the equator to form the typical top-shape (Keller et al., 2010). Mass shed from the equator of a critically spinning asteroid can accrete into a satellite (Walsh et al., 2008). Alternatively, an asteroid may spin up by the YORP effect until it reaches its fission spin limit and the components enter orbit about each other (Scheeres et al., 2007). Asteroid pairs may be formed by the rotational fission of a parent asteroid into a protobinary system, which subsequently disrupts under its own internal system dynamics (Pravec et al., 2010). These binary asteroid formation mechanisms may explain the fact that asteroid pairs ubiquitously exist. For more information on asteroid binaries, see the chapter by Walsh and Jacobson in this volume.

## 6. INVESTIGATING REGOLITH DYNAMICS

Regolith processes on asteroid surfaces may not have ready terrestrial analogs. In order to study regolith dynamics in the unique asteroid environment described in section 4, both experimental methods and numerical simulations can be used.

### 6.1. Experimental Methods

**6.1.1. Creating reduced-gravity conditions.** One of the major challenges for investigating the behavior of regolith at the surface of an asteroid is to recreate the proper gravitational conditions. Microgravity, the condition of relative near weightlessness, can only be achieved on Earth by putting an object in a state of free-fall. Here we introduce some of the techniques used to perform experiments in reduced-gravity conditions.

Drop towers have been extensively used for microgravity experiments related to dust and regolith dynamics [e.g., Hofmeister et al. (2009) studying granular flow under reduced-gravity, and Schräpler et al. (2012) and Beitz et al. (2011) investigating low-velocity collisions between dust agglomerates]. Parabolic flights can also provide a microgravity environment for regolith experiments [e.g., Murdoch et al. (2013a,c) performing experiments of granular shear and granular convection, Güttinger et al. (2013) investigating granular convection and the Brazil-nut effect, and Dove and Colwell (2013) investigating particle charging and the dynamics of charged particles on the surfaces of airless bodies]. Such flights are normally operated using modified commercial aeroplanes, but smaller aircraft have also been used (e.g., Kleinhans et al., 2011). Other ways of achieving microgravity are using a sounding rocket [e.g., Krause and Blum (2004) studying the formation of dust agglomerates] or flying an experiment on the International Space Station [e.g., Colwell (2003) investigating low-speed impacts into dust]. Additional methods of simulating microgravity exist as well, such as magnetic levitation and neutral buoyancy. However,

in order to perform an experiment with particles using these techniques, every particle in the experiment would have to be neutrally buoyant or magnetically levitated. If, for example, only the experiment container is levitated or buoyant, the individual grains would still feel the gravitational field.

**6.1.2. Creating the electrostatic environment.** The electrostatic part of the asteroid environment is provided by the solar wind, which is essentially a stream of plasma (electrons and protons) that originates in the upper atmosphere of the Sun. The energy of this plasma ranges between 1.5 and 10 keV. Although there are many ways to obtain plasma, the one technique that is chiefly employed to study lunar and asteroid environments uses an emissive filament within a cylindrical stainless steel vacuum chamber. Argon plasma is created by the impact ionization using electrons emitted from a negatively biased and heated filament in the bottom of the chamber (Wang *et al.*, 2012; Hartzell *et al.*, 2013). However, the experiments have a higher density and lower temperature than the solar wind.

Efforts are being made to improve these experimental techniques so that the obtained results are not only *qualitatively* but also *quantitatively* correct, and so they can be directly translated to the asteroid environment. In spite of this, they come with size, time, and cost constraints, and even in the best possible conditions, sometimes fall short of the real environments that are the object of study. These constraints are what make computer simulations and their development and understanding attractive from a scientific point of view. Of course, computer simulations also have a cost, as there are many simplifications and assumptions that have to be made (see section 6.2). This means that there must be a trade off between their complexity and their realism. A trade off that calls for a very careful look at the results and their interpretations as computational artifacts must be distinguished from fact. If research is carefully conducted, simulations can be used to guide better experiments and predictions of simulations can be tested so that nature is understood.

## 6.2. Numerical Methods

With advances in computer hardware and software, numerical modeling has become increasingly important to the study of granular systems in general, and to granular systems in exotic environments such as the surfaces of small bodies, where conditions are difficult to replicate experimentally. The different types of numerical approaches can be divided into the broad categories of continuum and discrete. In the realm of numerical simulation, continuum approaches and discrete approaches have relative advantages and disadvantages that depend on the specific investigation at hand. In general, discrete approaches attempt to treat material as individual particles, sometimes with large particles as proxies for groupings of smaller ones. Continuum approaches average the physics of nearby particles, and use smooth transitions to account for variance. Continuum approaches are particularly well suited for high-speed collisions, where material phase changes and the finite propagation speed of sound waves are

important. In low-speed granular regimes, however, discrete approaches have the advantage of being able to capture the inherently discrete nature of granular systems and being able to describe in great detail the properties of individual grains. These properties are then used to solve for the frictional and cohesive forces that arise when grains come into contact with each other. Discrete codes are also much better suited toward capturing the physics of slowly evolving granular systems such as those that take place on the surfaces of small bodies.

**6.2.1. Numerical modeling of granular systems in planetary science.** For many years, numerical continuum approaches have been used to address issues related to granular dynamics in the field of planetary science [e.g., Holsapple (1993) investigating scaling laws for impact-induced catastrophic disruption, and Benz *et al.* (1994) investigating different classes of two-body collisions]. Continuum approaches have since grown significantly in sophistication [some in current use for the modeling of asteroid shapes and the scaling laws for disruption are, e.g., Holsapple and Michel (2008), Holsapple (2009), and Sharma *et al.* (2009)]. Discrete numerical approaches, described below, have been in use in the field of planetary science since, e.g., Brahic (1975, 1977), who simulated Saturn's rings; Asphaug and Benz (1994), who simulated the breakup of Comet Shoemaker-Levy 9 using a soft-sphere discrete element method (SSDEM); and Richardson *et al.* (1998), who conducted a more generalized numerical investigation into tidal breakups of small bodies using a hard-sphere discrete element method (HSDEM). In light of advances in computer processor speeds, only quite recently have robust versions of SSDEM begun to be applied to the realm of planetary science, and specifically to the study of regolith dynamics in microgravity environments. SSDEM granular physics codes are now developed or adapted specifically for planetary applications by various groups (e.g., Wada *et al.*, 2006; Sánchez and Scheeres, 2011; Schwartz *et al.*, 2012; Tancredi *et al.*, 2012) using various integration schemes and strategies to account for the types of friction between grains. Other codes, using continuum approaches, have also been developed to investigate, for instance, collisions between porous aggregates (Sirono, 2004; Jutzi *et al.*, 2013). However, owing to the granular nature of the relevant dynamical processes involved, the regolith surfaces of small bodies are more commonly modeled using discrete-element methodologies, specifically (although not exclusively) SSDEM.

**6.2.2. The continuum approach to regolith modeling.** Continuum numerical modeling of granular material usually begins by defining a systematic approach to averaging the physics across many particles (and thereby treating the granular material as a continuum). The approach typically will involve dividing a parameter space or dimensional space into regions, and then integrating the system forward in time.

In describing fluid mechanics equations for dense flows, relevant conservation laws are followed, often in a Navier-Stokes framework (e.g., Haff, 1983). At minimum, these conservation laws should include mass conservation, momentum conservation, and the conservation of energy together with the first law of thermodynamics. These regions may be

described in Eulerian terms, where a volume in space is held constant, with material passing in and out of this volume, or in Lagrangian terms, where a region is described by the material itself as it moves around in space [e.g., see *Springel and Hernquist* (2002) for a fully conservative derivation of a Lagrangian treatment in a SPH code]. The numerical viscosity problems that stem from continuum codes [a known problem since *von Neumann and Richtmyer* (1950), a result of the homogenization of material properties] are somewhat easier to mitigate in Eulerian approaches (*Springel*, 2010), whereas the principle advantage to the Lagrangian approach is that the resolution of the system adjusts automatically to the movement of the material [see, e.g., the *Benz et al.* (1994) handling of two-body collisions]. Sophisticated codes have been developed that use hybrids of Eulerian and Lagrangian descriptions together with complex physical laws and computational parameters [see *Monaghan* (1988) for an early perspective]. In addition, there have been significant advances in continuum coding approaches that mitigate some of the problems of numerical viscosity, including sophisticated differencing schemes (see, e.g., *Marti and Mulet*, 2014).

In the modeling of granular media, the continuum approach often treats the material as a deformable solid and models it with some chosen finite-element [e.g., *Crosta et al.* (2009), who make use of the definition of bulk plastic and elastic moduli] or mesh-free (Lagrangian) method suited for the particular situation at hand (e.g., *Elaskar et al.*, 2000). Stability problems (e.g., the stability of granular piles or cliffs) require an elastoplastic framework that defines, at minimum, some type of yield criterion (consider the simple one-dimensional Coulomb yield criterion — conditions are static until the tangential force exceeds the product of the coefficient of static friction and the normal force).

Depending on the system, a continuum approach could incorporate viscosity in some useful form (e.g., *Lagréé et al.*, 2011) and treat the material as a fluid and use computational fluid dynamics (useful in describing outflows from, e.g., crater walls). However, since successful simulations of asteroid surface dynamics entail the capturing of the discrete nature of individual particles, the effects of such homogenization must be examined thoroughly. *Haff* (1983), in his article describing his efforts to treat granular media as a fluid analytically, considers many of the potential hazards and payoffs of using fluid dynamics from his analytical approach. These same considerations that arise analytically (i.e., the sharp boundary conditions on grain surfaces, including the complex frictional forces at play on these surfaces), also arise numerically.

**6.2.3. The discrete approach to regolith modeling.** The discrete-element method (DEM) is a general term applied to the class of discrete approaches to the numerical simulation of particle motion, where particles usually represent actual grains (or collections of grains), unlike the continuum approach, which uses averages to homogenize the material. However, as continuum approaches use homogenization schemes to simplify the complex and rapidly varying physical quantities within a material, in discrete approaches, the physics within individual particles are averaged, and thus the

particles are defined only by their *effective* behavior, described by quantitative parameters. Nevertheless, these parameters are typically borrowed directly from continuum mechanics, either by explicitly defining quantities such as Poisson's ratio and Young's, bulk, and shear moduli, or by using derived quantities including spring constants and friction coefficients.

Discrete-element-method collisional routines are typically built off an N-body routine. In an N-body framework, at the beginning of each timestep, forces on each of the N number of particles (bodies) in a given simulation are solved for and used to advance the simulation ahead through time in small quantized steps. These forces can include, e.g., external gravity or electromagnetic fields, and can incorporate the effects that the particles themselves have on the field (e.g., interparticle gravity). The collisional routines are then built on top of this framework, and define a new set of forces to account for the physical interactions that particles have with each other (of course these interactions are also electric at the molecular level).

In the standard implementation, particles are approximated as having perfect spherical geometry (more complex geometries are also possible). Since DEMs tend to compute the motions of large numbers of individual particles, it is relatively computationally intensive, which tends to limit either the length of a simulation or the number of particles in the simulation.

**6.2.3.1. Hard-sphere discrete-element method (HSDEM):** The numerical approach to solving the equations of motion in HSDEM is to discretize the simulation in time, with variables progressing in small steps (timesteps) by forward-advancing along derivatives. Collisions are predicted in advance by analyzing particle motion and checking for potential contacts that may occur within the current timestep. Particles are not allowed to penetrate each other (overlaps are not allowed). HSDEM codes carry out collisions between spheres by treating collisions as instantaneously occurring at a single point of contact that lies on the particles' surfaces; the sound speed through a particle is also instantaneous. Thus this methodology treats motions and mutual interactions of nondeformable, indestructible (hard) particles. The assumption of hard particles allows collisions to be carried out analytically, with post-collision velocities and rotations given by, e.g., *Richardson* (1994, 1995).

**6.2.3.2. Soft-sphere discrete element method (SSDEM):** The SSDEM is commonly used in the study of granular materials, and has often been applied to industrial problems (e.g., *Tsuji et al.*, 1992; *Cleary and Sawley*, 2002; *Kosinski and Hoffmann*, 2009). The methodology is known in other disciplines of physics, such as chemical physics, as molecular dynamics (MD), where it is used to compute motions of atoms and molecules and interactions between them [in fact, this application and nomenclature predates SSDEM's use in granular physical contexts (*Alder and Wainwright*, 1959)]. In the complex case of simulating regolith dynamics, one must treat each of the relevant frictional forces by generalizing and applying the rules of interaction between grains. The basic methodology having been developed by *Cundall and Strack*

(1979), SSDEM treats macroscopic particles as deformable spheres, allowing overlaps between particles to act as proxies for actual deformation. Particles are taken to be in contact if and only if their surfaces are touching or mutually penetrating. The greater the extent of this penetration, the more repulsive the force that is generated. The majority of codes either assume a linear force dependence or a Hertzian dependence on penetration depth ( $F \propto x$  or  $F \propto x^{3/2}$ , where  $x$  is the penetration in units of length). Once a contact is established, particles are subject to frictional forces, often making use of material parameters based on continuum mechanical theory; these forces will vary depending on the specific SSDEM code [see *Radjai and Dubois* (2011) for a comprehensive overview of the different classes of SSDEM codes and common variations].

**6.2.4. Benefits and drawbacks between these numerical approaches.** In contrast to HSDEM, where collisions are solved for analytically, based on the positions and momentum states of the particles along with some basic material parameters to describe the behavior, SSDEM must resolve each collision numerically. As such, collisions typically require dozens of timesteps to resolve. In HSDEM, however, since collisions are predicted in advance and then treated as instantaneous, it is the external dynamics (e.g., gravity) that drives the choice in step size rather than the collision handling; although the timestep may also be limited by concerns over missing a collision, timesteps in SSDEM can often be smaller than those used in identical HSDEM simulations by factors of  $10^2$ . In dense regimes, however, the speed of the integration in HSDEM is typically limited by collisional bottlenecks owing to the fact that collisions must typically be computed one at a time in sequence, limiting the efficiency of parallel processing.

During the finite amount of time that it takes for two real particles to collide, the particles are in contact, exchanging energy and momentum. In sufficiently dense regimes, a third particle may intrude on this collision by making contact with either particle or with both particles, changing the outcome. This exposes another drawback of HSDEM's treatment of collisions between particles: Multiple contact effects are not taken into account in HSDEM, where collisions are separate and instantaneous. Multi-contact systems of rigid, indestructible particles can, however, be solved using an algorithm known as contact dynamics (CD), which treats these rigid particles as subject to Coulomb static frictional forces (*Moreau*, 1994). The HSDEM methodology also must account for the problem of inelastic collapse, which occurs when a group of particles collides infinitely often in a finite time, causing the simulation to grind to a halt [see, e.g., *Petit and Henon* (1987) and *Bernu and Mazighi* (1990) for early numerical encounters of this effect, and, e.g., *McNamara and Young* (1992) and *McNamara* (2000) for more complete quantitative descriptions]. Although sophisticated collision-handling schemes have been tailored to help mitigate this problem (*Petit and Henon*, 1987; *Luding and McNamara*, 1998), the simplest way to avoid the finite-time singularity in HSDEM is straightforward: It requires setting some minimum impact speed or energy under which the coefficient of

restitution is unity (no dissipation). This results in particles, even those in “stable” configurations, always maintaining some minimum energy state (temperature), which may not appropriately capture certain low-energy granular regimes. Problems of inelastic collapse do not arise in SSDEM or CD methodologies.

Nevertheless, SSDEM is the appropriate choice over CD in very dense regimes of large numbers of particles because CD must solve, through iteration between each timestep, the contact forces between each particle in a contact chain. Still, HSDEM and CD can be a more appropriate collisional routine in more dilute regimes, where collisions do not involve networks consisting of large numbers of particles (e.g., higher energy, “granular gas” regimes; see section 3 of this chapter), and where sound propagation speed is unimportant (the sound speed can be controlled in soft-sphere methodologies via a stiffness parameter). However, even in two-body collisions, HSDEM can make errors. Particles can rotate significantly during realistic, finite, oblique collisions, altering the outcome of the collision — an effect that does not occur between perfectly rigid particles (*Müller and Pöschel*, 2012). In addition to CD, attempts have been made to use HSDEM with added analytical corrections to account for rotations of the multi-body system while particles are colliding (*Müller and Pöschel*, 2013), and to account for finite collision times (by “pausing” collisions). These are most effective in regimes when (third-) particle intruders can be safely ignored. Also, when two real (deformable) grains just “graze” each other, depending on the rigidity of the grains, they may interact very weakly; however, these types of contacts are given too much significance when using hard spheres (the assumption of grain incompressibility in HSDEM and CD leads to the exchange of too much energy and momentum during oblique impacts).

Despite these drawbacks, HSDEM and/or CD can be the appropriate choice in certain dilute/ballistic regimes (cf. *Richardson et al.*, 2011; *Murdoch et al.*, 2012), where they are advantageous over continuum models for their speed and accuracy, and often over SSDEM for their speed given the ability to handle large timesteps. These are regimes where collisional timescales may be long compared to other dynamical timescales (the “granular gas” regime; see section 3 of this chapter), where contacts between grains do not persist and thus complex frictional forces are less relevant, and where the propagation of disturbance waves (material sound speeds) are unimportant.

For the simulation of dense environments, however, including many granular regimes in which grain deformation, finite sound speed, multicontact physics, and the complexity of higher-order frictional forces during contact cannot be neglected, SSDEM is the better choice. Although the use of small timesteps can limit its speed, it is well suited for true parallelization (without the HSDEM drawback of having to compute collisions in serial order). Presently it is possible to follow the evolution of millions of grains in close contact and over a fairly large range of simulation conditions, something not possible with HSDEM.

The search for contacts in SSDEM is a simpler task than the search for contacts (collisions) in HSDEM. Before integrating over the next timestep, HSDEM must ask, will there be a collision at any moment during the following timestep? In contrast, SSDEM needs only to ask if there are any overlaps presently occurring. Effectively, this means that contact searches are a four-dimensional problem in HSDEM (three spatial dimensions and one temporal dimension) and a three-dimensional problem in SSDEM (three spatial dimensions). More complex wall boundary geometries are more easily included in SSDEM [the SSDEM code implemented in *pdkgrav*, for example, allows for a wider set of wall boundaries; these include the triangle, which can allow for sophisticated three-dimensional polyhedral shapes, along with those discussed in *Schwartz et al.* (2012)].

As a direct comparison of the two DEM collisional methodologies, HSDEM and SSDEM, simulations of low-speed rubble-pile collisions were performed using both SSDEM and HSDEM in the same numerical code (*Richardson et al.*, 2012b). In the tests, self-gravitating rubble piles (without friction or cohesive forces) were collided together at low speed. The results from the two collisional routines were generally similar; SSDEM often, but not in all cases, showed a somewhat higher final ellipticity of the largest collisional remnant, suggesting a higher shear strength that may arise from its more careful treatment of contact forces and finite collisional times.

In terms of computational efficiency, continuum codes in general are inherently conducive to parallelization, especially fixed-grid continuum codes. Several DEM codes also take advantage of parallel processing capabilities to scale up the number of particles or length of the simulation (e.g., *Richardson et al.*, 2000; *Cleary and Sawley*, 2002; *Kacianauskas et al.*, 2010; *Schwartz et al.*, 2012); HSDEM codes that have to compute collisions one at a time face more challenges in this regard, whereas SSDEM codes, like continuum codes, can accommodate true parallelization.

Due to the nonzero angle of repose exhibited by granular materials, which is the case even when the grains are cohesionless and support no grain-grain surface friction, perfect rubble piles (no cohesion) can maintain nonspherical shapes without bulk spin, unlike a fluid. Rubble piles can also spin faster than a perfect fluid before shedding mass. A study was performed by *Richardson et al.* (2005a) using HSDEM to compare the results of rubble-pile equilibrium shapes in simulation to continuum theory. Investigated were the shape and spin limits of self-gravitating rubble piles that consist of identical HSDEM particles in a hexagonal-close-pack configuration and no sliding friction, and this entirely discrete approach was found to be consistent with the theory for the more general continuum rubble-pile model as analyzed by *Holsapple* (2004) for a friction angle of 40°. Rubble piles that reassembled following a catastrophic disruption reconfigured themselves to lie within stability limits predicted by the continuum theory. In the Holsapple model, the Mohr-Coulomb prescription was used to describe pressure-dependent yield to obtain rubble-pile stability limits; later, the same analysis was performed using the Drucker-Prager relation, giving

very similar results (*Holsapple and Michel*, 2006). As an additional follow-up to these continuum studies, a comprehensive analysis was performed that extended the continuum theory for (cohesionless) rubble piles to give an upper bound on actual load limits of bodies with cohesion (*Holsapple and Michel*, 2008). To compare with these results, preliminary work was performed that included gravitational aggregates with and without cohesion (*Richardson et al.*, 2008) using a portion of the numerical tools described in *Schwartz et al.* (2013). This work expanded upon the discrete numerical work from *Richardson et al.* (2005a). More recently, SSDEM has been used to analyze equilibrium shapes of rubble piles without the use of cohesion (*Sánchez and Scheeres*, 2012), and compared their results with the Holsapple analyses and HSDEM models of *Walsh et al.* (2012).

In general, SSDEM approaches are inherently well suited to capturing the discrete nature of granular systems, and tend to rely upon fewer free parameters to reproduce the correct behavior of many granular systems. Also, continuum codes typically have a difficult time conserving angular momentum due to the effects of numerical viscosity (section 6.2.2). This can particularly be a problem in certain planetary science applications when considering isolated bodies in space. However, in comparison with the continuum approach, DEM is not well suited to the treatment of supersonic motion, particle fragmentation, or phase-changing material.

**6.2.5. The use of numerical simulation in the field of regolith dynamics.** Several DEM numerical codes have been written with the specific aim of investigating and solving for regolith dynamics. *Walsh et al.* (2008, 2012) used the HSDEM collisional routine in *pdkgrav* (*Stadel*, 2001; *Richardson et al.*, 2000) to study grain displacements and lofting due to YORP spinup. Soft-sphere collisional methodologies have been used to study regolith dynamics in low-gravity environments, which include subsonic impact cratering into regolith (*Wada et al.*, 2006; *Schwartz et al.*, 2014), the Brazil-nut effect (*Tancredi et al.*, 2012; *Matsumura et al.*, 2014), and regolith motion due to tidal forces (*Yu et al.*, 2014). Also in the realm of asteroid surface science, several numerical investigations to study avalanche run-outs and angles of repose of regolith have been performed using both continuum codes [e.g., *Holsapple* (2013), using a finite-differencing method] and using DEM [e.g., *Richardson et al.* (2012a), using soft-sphere].

The inclusion of cohesion in numerical coding can be adapted to many different granular dynamics applications in planetary science, including the study of regolith dynamics [e.g., in SSDEM (*Schwartz et al.*, 2013; *Sánchez and Scheeres*, 2014)]. Attractive interparticle forces may be used to treat ionic or covalent molecular bonds, weaker intermolecular dipole-dipole bonds such as hydrogen bonds and London dispersion forces, or electrostatic forces. Recently, *Sánchez and Scheeres* (2014) performed a simulation using two spherical, meter-sized particles (boulders) with small (approximately a few centimeters) cohesive particles (regolith) between them, and measured the force necessary to pull the large particles apart. The cohesion conforms to Hamaker's

generalized van der Waals force law for interacting spheres (equation (3)). These intermolecular cohesive forces, of regolith especially, may be of importance in low-gravity environments and could be helpful to explain the rotation rates of some of the smallest asteroids catalogued by *Pravec et al.* (2005) and, more recently, *Statler et al.* (2013) and *Rozitis et al.* (2014). It is beyond a doubt that many fast rotators spin in excess of what gravity alone could hold together. Some could be monoliths, but it has been shown that a small amount of cohesion is sufficient to explain these rotation rates (*Holsapple*, 2007; *Richardson et al.*, 2008; *Sánchez and Scheeres*, 2014; *Hirabayashi and Scheeres*, 2015).

Innovative uses of numerical tools have had the capacity to advance the field of planetary science in general, and, more recently, the specific realm of small-body regolith dynamics. Part of what it will take to push this area of research forward will inevitably entail recognizing creative applications and the usage of new techniques, aided by further bridging between the research communities of planetary science and granular dynamics, the latter of which continues to expand and develop (e.g., *Luding and Tomas*, 2014).

## 7. CONCLUSIONS

In this chapter we have presented a brief overview of the observations of granular surfaces of asteroids, our current understanding of the geophysical processes that may have occurred, and the state-of-the-art experimental and computational methods used to study them and make new predictions. The field of regolith dynamics in varying gravitational environments, including the study of NEAs as self-gravitating aggregates, is a new field of planetary science that will continue to evolve with the development of better computational tools and experimental techniques, refinements in the theoretical models, and new *in situ* observations from upcoming space missions such as the NASA's Origins Spectral Interpretation Resource Identification and Security-Regolith Explorer (OSIRIS-REx) and JAXA's Hayabusa-2.

**Acknowledgments.** We would like to thank D. C. Richardson and D. J. Scheeres for their comments on our chapter and L. Staron and O. Barnouin for their very helpful reviews.

## REFERENCES

- Abe S., Mukai T., Hirata N., et al. (2006) Mass and local topography measurements of Itokawa by Hayabusa. *Science*, *312*(5778), 1344–1347.
- Alder B. J. and Wainwright T. E. (1959) Studies in molecular dynamics. I. General method. *J. Chem. Phys.*, *31*, 459–466.
- Andreotti B., Forterre Y., and Pouliquen O. (2013) *Granular Media: Between Fluid and Solid*. Cambridge Univ., Cambridge (e-Book).
- Asphaug E. (2007) The shifting sands of asteroids. *Science*, *316*(5827), 993–994.
- Asphaug E. (2009) Growth and evolution of asteroids. *Annu. Rev. Earth Planet. Sci.*, *37*(1), 413–448.
- Asphaug E. and Benz W. (1994) Density of Comet Shoemaker-Levy 9 deduced by modelling breakup of the parent ‘rubble pile.’ *Nature*, *370*, 120–124.
- Asphaug E., Moore J. M., Morrison D., et al. (1996) Mechanical and geological effects of impact cratering on Ida. *Icarus*, *120*(1), 158–184.
- Asphaug E., King P., Swift M., and Merrifield M. (2001) Brazil nuts on Eros: Size-sorting of asteroid regolith. *Lunar Planet. Sci. XXXII*, Abstract #1708. Lunar and Planetary Institute, Houston.
- Bagnold R. A. (1954) Experiments on a gravity-free dispersion of large solid spheres in a newtonian fluid under shear. *Proc. R. Soc. London, Ser. A: Math. Phys. Sci.*, *225*(1160), 49–63.
- Bagnold R. (1966) The shearing and dilatation of dry sand and the ‘singing’ mechanism. *Proc. R. Soc. London, Ser. A: Math. Phys. Sci.*, *295*(1442), 219–232.
- Barnouin-Jha O. S., Garvin J. B., Cheng A. F., et al. (2001) Preliminary impact crater dimensions on 433 Eros from the NEAR laser rangefinder and imager. *Lunar Planet. Sci. XXXII*, Abstract #1786. Lunar and Planetary Institute, Houston.
- Barnouin-Jha O. S., Cheng A. F., Mukai T., et al. (2008) Small-scale topography of 25143 Itokawa from the Hayabusa laser altimeter. *Icarus*, *198*, 108–124.
- Beitz E., Gütter C., Blum J., et al. (2011) Low-velocity collisions of centimeter-sized dust aggregates. *Astrophys. J.*, *736*, 34.
- Benz W., Asphaug E., and Ryan E. V. (1994) Numerical simulations of catastrophic disruption: Recent results. *Planet. Space Sci.*, *42*, 1053–1066.
- Bernu B. and Mazighi R. (1990) One-dimensional bounce of inelastically colliding marbles on a wall. *J. Phys. A: Math. Gen.*, *23*(24), 5745.
- Besse S., Küppers M., Barnouin O., et al. (2014) Lutetia’s lineaments. *Planet. Space Sci.*, *101*, 186–195.
- Binzel R. P., Morbidelli A., Merouane S., et al. (2010) Earth encounters as the origin of fresh surfaces on near-Earth asteroids. *Nature*, *463*, 331–334.
- Biswas P., Sánchez P., Swift M. R., and King P. J. (2003) Numerical simulations of air-driven granular separation. *Phys. Rev. E*, *68*, 050301.
- Bottke W. F. Jr., Richardson D. C., Michel P., and Love S. G. (1999) 1620 Geographos and 433 Eros: Shaped by planetary tides? *Astron. J.*, *117*, 1921–1928.
- Bowden F. and Leben L. (1939) The nature of sliding and the analysis of friction. *Proc. R. Soc. London Ser. A: Math. Phys. Sci.*, *371*–391.
- Bowden F. and Tabor D. (1939) The area of contact between stationary and between moving surfaces. *Proc. R. Soc. London Ser. A: Math. Phys. Sci.*, *391*–413.
- Bowden F. P., Moore A. J. W., and Tabor D. (1943) The ploughing and adhesion of sliding metals. *Appl. Phys.*, *14*(2), 80–91.
- Brahic A. (1975) A numerical study of a gravitating system of colliding particles: Applications to the dynamics of Saturn’s rings and to the formation of the solar system. *Icarus*, *25*(3), 452–458.
- Brahic A. (1977) Systems of colliding bodies in a gravitational field: I — Numerical simulation of the standard model. *Astron. Astrophys.*, *54*, 895–907.
- Bridgwater J. (1976) Fundamental powder mixing mechanisms. *Powder Tech.*, *15*(2), 215–236.
- Brilliantov N. V. and Pöschel T. (2010) *Kinetic Theory of Granular Gases*. Oxford Univ., Oxford.
- Buczkowski D. L., Barnouin-Jha O. S., and Prockter L. M. (2008) 433 Eros lineaments: Global mapping and analysis. *Icarus*, *193*, 39–52.
- Burtally N., King P. J., and Swift M. R. (2002) Spontaneous air-driven separation in vertically vibrated fine granular mixtures. *Science*, *295*(5561), 1877–1879.
- Carr M. H., Kirk R. L., McEwen A., et al. (1994) The geology of Gaspra. *Icarus*, *107*, 61.
- Carrigy M. A. (1970) Experiments on the angles of repose of granular materials I. *Sedimentology*, *14*(3–4), 147–158.
- Cassidy T. and Johnson R. (2005) Monte Carlo model of sputtering and other ejection processes within a regolith. *Icarus*, *176*(2), 499–507.
- Castellanos A. (2005) The relationship between attractive interparticle forces and bulk behaviour in dry and uncharged fine powders. *Adv. Phys.*, *54*(4), 263–376.
- Chapman C. R. (1976) Asteroids as meteorite parent-bodies — The astronomical perspective. *Geochim. Cosmochim. Acta*, *40*, 701–719.
- Chapman C. R. (2004) Space weathering of asteroid surfaces. *Annu. Rev. Earth Planet. Sci.*, *32*(1), 539–567.
- Chen W. and Han D. (1988) *Plasticity for Structural Engineers*. Springer, New York.
- Cheng A. F. (2002) Near Earth asteroid rendezvous: Mission summary. In *Asteroids III* (W. F. Bottke Jr. et al., eds.), pp. 351–366. Univ. of Arizona, Tucson.

- Cheng A. F., Santo A. G., Heeres K. J., et al. (1997) Near-Earth asteroid rendezvous: Mission overview. *J. Geophys. Res.*, *102*, 23695–23708.
- Cheng A. F., Barnouin-Jha O., Prockter L., et al. (2002a) Small-scale topography of 433 Eros from laser altimetry and imaging. *Icarus*, *155*, 51–74.
- Cheng A. F., Izenberg N., Chapman C. R., and Zuber M. T. (2002b) Ponded deposits on asteroid 433 Eros. *Meteoritics & Planet. Sci.*, *37*, 1095–1105.
- Cheng A. F., Barnouin-Jha O., Hirata N., et al. (2007) Fundamentally distinct outcomes of asteroid collisional evolution: Itokawa and Eros. *Geophys. Res. Lett.*, *34*, L09201.
- Chladni E. (1787) *Entdeckungen über die theorie des klanges*. Bey Weidmanns erben und Reich, Leipzig.
- Cleary P. W. and Sawley M. L. (2002) DEM modelling of industrial granular flows: 3D case studies and the effect of particle shape on hopper discharge. *Appl. Math. Model.*, *26*, 89–111.
- Colwell J. E. (2003) Low velocity impacts into dust: Results from the COLLIDE-2 microgravity experiment. *Icarus*, *164*, 188–196.
- Colwell J. E., Gulbis A. A., Horányi M., and Robertson S. (2005) Dust transport in photoelectron layers and the formation of dust ponds on Eros. *Icarus*, *175*(1), 159–169.
- Coradini A., Capaccioni F., Erard S., et al. (2011) The surface composition and temperature of asteroid 21 Lutetia as observed by Rosetta/VIRTIS. *Science*, *334*, 492.
- Costantino D. J., Scheidemantel T. J., Stone M. B., et al. (2008) Starting to move through a granular medium. *Phys. Rev. Lett.*, *101*, 108001.
- Coulomb C. A. (1776) *Essai sur une application des règles de maximis et minimis à quelques problèmes de statique, relatifs à l'architecture*. De l'Imprimerie Royale, Paris.
- Crosta G. B., Imposimato S., and Roddeman D. (2009) Numerical modeling of 2-D granular step collapse on erodible and nonerodible surface. *J. Geophys. Res.–Earth Surface*, *114*, F3.
- Cundall P. A. and Strack O. D. L. (1979) A discrete numerical model for granular assemblies. *Géotechnique*, *29*, 47–65.
- de Gennes P. G. (1999) Granular matter: A tentative view. *Rev. Mod. Phys.*, *71*, S374–S382.
- Delbo M., Libourel G., Wilkerson J., et al. (2014) Thermal fatigue as the origin of regolith on small asteroids. *Nature*, *508*, 233–236.
- Demura H., Kobayashi S., Nemoto E., et al. (2006) Pole and global shape of 25143 Itokawa. *Science*, *312*(5778), 1347–1349.
- Denevi B. W., Blewett D. T., Buczkowski D. L., et al. (2012) Pitted terrain on Vesta and implications for the presence of volatiles. *Science*, *338*, 246.
- Dollfus A., Geake J. E., Mandeville J. C., and Zellner B. (1977) The nature of asteroid surfaces, from optical polarimetry. In *Comets, Asteroids, Meteorites: Interrelations, Evolution and Origins* (A. H. Delsemmre, ed.), pp. 243–251, IAU Colloq. 39, Univ. of Toledo, Toledo.
- Dombard A. J. and Freed A. M. (2002) Thermally induced lineations on the asteroid Eros: Evidence of orbit transfer. *Geophys. Res. Lett.*, *29*, 16.
- Dombard A. J., Barnouin O. S., Prockter L. M., and Thomas P. C. (2010) Boulders and ponds on the asteroid 433 Eros. *Icarus*, *210*(2), 713–721.
- Dove A. and Colwell J. E. (2013) Investigations of charged particle motion on the surfaces of dusty, airless solar system bodies (invited). Abstract P53F-01 presented at 2013 Fall Meeting, AGU, San Francisco, California, 9–13 Dec.
- Durda D., Devaud G., Scheeres D., et al. (2013) Laboratory investigation of asteroid regolith properties. *EPSC Abstracts*, *8*, EPSC2013-1050.
- Elaskar S. A., Godoy L. A., Gray D. D., and Stiles J. M. (2000) A viscoplastic approach to model the flow of granular solids. *Intl. J. Solids Struct.*, *37*, 2185–2214.
- Fall A., Weber B., Pakpour M., et al. (2014) Sliding friction on wet and dry sand. *Phys. Rev. Lett.*, *112*, 175502.
- Faraday M. (1831) On a peculiar class of acoustical figures; and on certain forms assumed by groups of particles upon vibrating elastic surfaces. *Philos. Trans. R. Soc. London*, *121*, 299–340.
- Forsterre Y. and Pouliquen O. (2008) Flows of dense granular media. *Annu. Rev. Fluid Mech.*, *40*(1), 1–24.
- Fu H., Jedicke R., Durda D. D., et al. (2005) Identifying near-Earth object families. *Icarus*, *178*, 434–449.
- Fujiwara A. and Asada N. (1983) Impact fracture patterns on phobos ellipsoids. *Icarus*, *56*(3), 590–602.
- Fujiwara A., Kawaguchi J., Yeomans D. K., et al. (2006) The rubble-pile asteroid Itokawa as observed by Hayabusa. *Science*, *312*(5778), 1330–1334.
- GDR-MiDi (2004) On dense granular flows. *Eur. Phys. J. E*, *14*(4), 341–365.
- Geissler P., Petit J. M., and Greenberg R. (1996) Ejecta reaccretion on rapidly rotating asteroids: Implications for 243 Ida and 433 Eros. In *Completing the Inventory of the Solar System* (T. Rettig and J. M. Hahn, eds.), pp. 57–67. ASP Conf. Ser. 107, Astronomical Society of the Pacific, San Francisco.
- Gray J. M. N. T. and Chugunov V. A. (2006) Particle-size segregation and diffusive remixing in shallow granular avalanches. *J. Fluid Mech.*, *569*, 365–398.
- Gudhe R., Yalamanchili R., and Massoudi M. (1994) Flow of granular materials down a vertical pipe. *Intl. J. Non-Linear Mech.*, *29*(1), 1–12.
- Güttler C., von Borstel I., Schräpler, R., and Blum J. (2013) Granular convection and the Brazil nut effect in reduced gravity. *Phys. Rev. E*, *87*, 044201.
- Haff P. (1983) Grain flow as a fluid-mechanical phenomenon. *J. Fluid Mech.*, *134*(1), 401–430.
- Hapke B. and van Hoen H. (1963) Photometric studies of complex surfaces, with applications to the moon. *J. Geophys. Res.*, *68*(15), 4545–4570.
- Harris A. W. (2006) The surface properties of small asteroids from thermal-infrared observations. In *Asteroids, Comets, Meteors* (L. Daniela et al., eds.), pp. 449–463. IAU Symp. 229, Cambridge Univ., Cambridge.
- Harris A. W., Fahnestock E. G., and Pravec P. (2009) On the shapes and spins of “rubble pile” asteroids. *Icarus*, *199*, 310–318.
- Hartzell C. M. and Scheeres D. J. (2011) The role of cohesive forces in particle launching on the moon and asteroids. *Planet. Space Sci.*, *59*(14), 1758–1768.
- Hartzell C. M. and Scheeres D. J. (2013) Dynamics of levitating dust particles near asteroids and the Moon. *J. Geophys. Res.–Planets*, *118*(1), 116–125.
- Hartzell C., Wang X., Scheeres D., and Horányi M. (2013) Experimental demonstration of the role of cohesion in electrostatic dust lofting. *Geophys. Res. Lett.*, *40*(6), 1038–1042.
- Heim L. O., Blum J., Preuss M., and Butt H. J. (1999) Adhesion and friction forces between spherical micrometersized particles. *Phys. Rev. Lett.*, *83*, 3328–3331.
- Herrick R. R. and Hessen K. K. (2006) The planforms of low-angle impact craters in the northern hemisphere of Mars. *Meteoritics & Planet. Sci.*, *41*, 1483–1495.
- Hirabayashi M. (2014) Structural failure of two-densitylayer cohesionless biaxial ellipsoids. *Icarus*, *236*, 178–180.
- Hirabayashi M. and Scheeres D. J. (2015) Stress and failure analysis of rapidly rotating asteroid (29075) 1950 DA. *Astrophys. J. Lett.*, *798*(1), L8.
- Hirabayashi M., Scheeres D. J., Sánchez, D. P., and Gabriel T. (2014) Constraints on the physical properties of main belt comet P/2013 R3 from its breakup event. *Astrophys. J. Lett.*, *789*(1), L12.
- Hoerz F., Schneider E., Gault D. E., et al. (1975) Catastrophic rupture of lunar rocks — A Monte Carlo simulation. *Moon*, *13*, 235–258.
- Hofmeister P. G., Blum J., and Heißelmann D. (2009) The flow of granular matter under reduced-gravity conditions. In *Powders and Grains 2009: Proceedings of the 6th International Conference on Micromechanics of Granular Media* (M. Nakagawa and S. Luding, eds.), pp. 71–74. AIP Conf. Ser. 1145, American Institute of Physics, Melville, New York.
- Holsapple K. A. (1993) The scaling of impact processes in planetary sciences. *Annu. Rev. Earth Planet. Sci.*, *21*, 333–373.
- Holsapple K. A. (2004) Equilibrium figures of spinning bodies with self-gravity. *Icarus*, *172*, 272–303.
- Holsapple K. A. (2007) Spin limits of solar system bodies: From the small fast-rotators to 2003 EL<sub>61</sub>. *Icarus*, *187*, 500–509.
- Holsapple K. A. (2009) On the “strength” of the small bodies of the solar system: A review of strength theories and their implementation for analyses of impact disruptions. *Planet. Space Sci.*, *57*, 127–141.
- Holsapple K. A. (2013) Modeling granular material flows: The angle of repose, fluidization and the cliff collapse problem. *Planet. Space Sci.*, *82*–83, 11–26.
- Holsapple K. A. and Michel P. (2006) Tidal disruptions: A continuum theory for solid bodies. *Icarus*, *183*, 331–348.

- Holsapple K. A. and Michel P. (2008) Tidal disruptions. II. A continuum theory for solid bodies with strength, with applications to the solar system. *Icarus*, 193, 283–301.
- Housen K. R. and Holsapple K. A. (2011) Ejecta from impact craters. *Icarus*, 211, 856–875.
- Housen K. R., Wilkening L. L., Chapman C. R., and Greenberg R. (1979) Asteroidal regoliths. *Icarus*, 39, 317–351.
- Hughes A. L., Colwell J. E., and DeWolfe A. W. (2008) Electrostatic dust transport on Eros: 3-D simulations of pond formation. *Icarus*, 195(2), 630–648.
- Jaeger H. M., Nagel S. R., and Behringer R. P. (1996) Granular solids, liquids, and gases. *Rev. Mod. Phys.*, 68, 1259–1273.
- Janssen H. A. (1895) Versuche über Getreidedruck in Silozellen. *Z. Vereines deutscher Ingenieure*, 39(35), 1045–1049.
- Jaumann R., Williams D. A., Buczkowski D. L., et al. (2012) Vesta's shape and morphology. *Science*, 336, 687.
- Jaumann R., Nass A., Otto K., et al. (2014) The geological nature of dark material on Vesta and implications for the subsurface structure. *Icarus*, 240, 3–19.
- Jenkins J. T. and Zhang C. (2002) Kinetic theory for identical, frictional, nearly elastic spheres. *Phys. Fluids*, 14(3), 1228–1235.
- Jewitt D. (2012) The active asteroids. *Astron. J.*, 143, 66.
- Johnson K. L., Kendall K., and Roberts A. D. (1971) Surface energy and the contact of elastic solids. *Proc. R. Soc. London Ser. A: Math. Phys. Sci.*, 324(1558), 301–313.
- Jones J. E. (1924) On the determination of molecular fields. I. From the variation of the viscosity of a gas with temperature. *Proc. R. Soc. London Ser. A: Math. Phys. Sci.*, 106(738), 441–462.
- Jop P., Forterre Y., and Pouliquen O. (2006) A constitutive law for dense granular flows. *Nature*, 441, 727–730.
- Jutzi M. and Asphaug E. (2011) Mega-ejecta on asteroid Vesta. *Geophys. Res. Lett.*, 38, L01102.
- Jutzi M., Asphaug E., Gillet P., et al. (2013) The structure of the asteroid 4 Vesta as revealed by models of planet-scale collisions. *Nature*, 494, 207–210.
- Kacianauskas R., Maknickas A., Kaceniauskas A., et al. (2010) Parallel discrete element simulation of polydispersed granular material. *Adv. Eng. Software*, 41, 52–63.
- Keller H. U., Barbieri C., Koschny D., et al. (2010) E-type asteroid (2867) Steins as imaged by OSIRIS on board Rosetta. *Science*, 327, 190.
- Kleinmans M. G., Markies H., de Vet S. J., et al. (2011) Static and dynamic angles of repose in loose granular materials under reduced gravity. *J. Geophys. Res.–Planets*, 116, E11.
- Knight J. B., Jaeger H. M., and Nagel S. R. (1993) Vibration-induced size separation in granular media: The convection connection. *Phys. Rev. Lett.*, 70(24), 3728–3731.
- Kosinski P. and Hoffmann A. C. (2009) Extension of the hard-sphere particle-wall collision model to account for particle deposition. *Phys. Rev. E*, 79(6), 061302.
- Krause M. and Blum J. (2004) Growth and form of planetary seedlings: Results from a sounding rocket microgravity aggregation experiment. *Phys. Rev. Lett.*, 93(2), 021103.
- Kreslavsky M. A. and Shkuratov Y. G. (2003) Photometric anomalies of the lunar surface: Results from Clementine data. *J. Geophys. Res.–Planets*, 108, E3.
- Krohn K., Jaumann R., Elbeshausen D., et al. (2014) Asymmetric craters on Vesta: Impact on sloping surfaces. *Planet. Space Sci.*, 103, 36–56.
- Kudrolli A. (2004) Size separation in vibrated granular matter. *Rept. Prog. Phys.*, 67(3), 209.
- Küppers M., Moissl R., Vincent J.-B., et al. (2012) Boulders on Lutetia. *Planet. Space Sci.*, 66, 71–78.
- Lagré P.-Y., Staron L., and Popinet S. (2011) The granular column collapse as a continuum: Validity of a two-dimensional Navier–Stokes model with a  $\mu(i)$ -rheology. *J. Fluid Mech.*, 686, 378–408.
- Lamy P. L., Faury G., Jorda L., et al. (2010) Multi-color, rotationally resolved photometry of asteroid 21 Lutetia from OSIRIS/Rosetta observations. *Astron. Astrophys.*, 521, A19.
- Lee P. (1996) Dust levitation on asteroids. *Icarus*, 124, 181–194.
- Legros F. (2002) The mobility of long-runout landslides. *Eng. Geol.*, 63(34), 301–331.
- Luding S. and McNamara S. (1998) How to handle the inelastic collapse of a dissipative hard-sphere gas with the TC model. *Granular Matter*, 1(3), 113–128.
- Luding S. and Tomas J. (2014) Particles, contacts, bulk-behavior. *Granular Matter*, 16(3), 279–280.
- Mantz A., Sullivan R., and Veverka J. (2004) Regolith transport in craters on Eros. *Icarus*, 167, 197–203.
- Marchi S., McSween H. Y., O'Brien D. P., et al. (2012) The violent collisional history of asteroid 4 Vesta. *Science*, 336, 690.
- Marti M. and Mulet P. (2014) Some techniques for improving the resolution of finite difference component-wise WENO schemes for polydisperse sedimentation models. *Appl. Num. Math.*, 78, 1–13.
- Masiero J., Hartzell C., and Scheeres D. J. (2009) The effect of the dust size distribution on asteroid polarization. *Astron. J.*, 138(6), 1557.
- Massironi M., Marchi S., Pajola M., et al. (2012) Geological map and stratigraphy of asteroid 21 Lutetia. *Planet. Space Sci.*, 66, 125–136.
- Matson D. L. and Nash D. B. (1983) Io's atmosphere: Pressure control by regolith cold trapping and surface venting. *J. Geophys. Res.–Space Physics*, 88(46), 4771–4783.
- Matsumura S., Richardson D. C., Michel P., et al. (2014) The Brazil nut effect and its application to asteroids. *Mon. Not. R. Astron. Soc.*, 443, 3368–3380.
- Mazrouei S., Daly M., Barnouin O., et al. (2012) Distribution of boulders on asteroid 25143 Itokawa. *Lunar Planet. Sci. LXIII*, Abstract #2404. Lunar and Planetary Institute, Houston.
- McCarthy J. J. (2009) Turning the corner in segregation. *Powder Tech.*, 192(2), 137–142.
- McGetchin T., Settle M., and Head J. (1973) Radial thickness variation in impact crater ejecta: Implications for lunar basin deposits. *Earth Planet. Sci. Lett.*, 20(2), 226–236.
- McNamara S. (2000) Inelastic collapse. In *Dynamics: Models and Kinetic Methods for Non-Equilibrium Many-Body Systems* (J. Karkheck, ed.), pp. 267–277. Kluwer, Dordrecht.
- McNamara S. and Young W. R. (1992) Inelastic collapse and clumping in a one-dimensional granular medium. *Phys. Fluids A*, 4, 496–504.
- McNaught A. D. and Wilkinson A. (1997) *IUPAC Compendium of Chemical Terminology*, 2nd edition. Blackwell Scientific, Oxford. (Updated version available online at <http://goldbook.iupac.org/>.)
- McSween H. Y., Mittlefehldt D. W., Beck A. W., et al. (2011) HED meteorites and their relationship to the geology of Vesta and the Dawn mission. *Space Sci. Rev.*, 163, 141–174.
- Mehta A. (2007) *Granular Physics*. Cambridge Univ., Cambridge.
- Melosh H. J. (1989) *Impact Cratering: A Geologic Process*. Oxford Univ., Oxford.
- Mériaux C. and Triantaifillou T. (2008) Scaling the final deposits of dry cohesive granular columns after collapse and quasi-static fall. *Phys. Fluids*, 20(3), 033301.
- Meunier P., Uchida T., and Hovius N. (2013) Landslide patterns reveal the sources of large earthquakes. *Earth Planet. Sci. Lett.*, 363, 27–33.
- Michel P., Benz W., Tanga P., and Richardson D. C. (2001) Collisions and gravitational reaccumulation: Forming asteroid families and satellites. *Science*, 294, 1696–1700.
- Michel P., O'Brien D. P., Abe S., and Hirata N. (2009) Itokawa's cratering record as observed by Hayabusa: Implications for its age and collisional history. *Icarus*, 200, 503–513.
- Michikami T., Nakamura A. M., Hirata N., et al. (2008) Size-frequency statistics of boulders on global surface of asteroid 25143 Itokawa. *Earth Planets Space*, 60, 13–20.
- Miller J. K., Konopliv A. S., Antreasian P. G., et al. (2002) Determination of shape, gravity, and rotational state of asteroid 433 Eros. *Icarus*, 155, 3–17.
- Miyamoto H. (2014) Unconsolidated boulders on the surface of Itokawa. *Planet. Space Sci.*, 95, 94–102.
- Miyamoto H., Yano H., Scheeres D. J., et al. (2007) Regolith migration and sorting on asteroid Itokawa. *Science*, 316(5827), 1011–1014.
- Monaghan J. J. (1988) An introduction to SPH. *Comp. Phys. Commun.*, 48(1), 89–96.
- Moreau J. J. (1994) Some numerical methods in multibody dynamics: Application to granular materials. *Eur. J. Mech. A: Solids*, 13, 93–114.
- Müller P. and Pöschel T. (2012) Oblique impact of frictionless spheres: On the limitations of hard sphere models for granular dynamics. *Granular Matter*, 14(2), 115–120.
- Müller P. and Pöschel T. (2013) Event-driven molecular dynamics of soft particles. *Phys. Rev. E*, 87(3), 033301.
- Murchie S., Robinson M., Clark B., et al. (2002) Color variations on Eros from NEAR multispectral imaging. *Icarus*, 155, 145–168.
- Murdoch N., Michel P., Richardson D. C., et al. (2012) Numerical simulations of granular dynamics II. Particle dynamics in a shaken granular material. *Icarus*, 219(1), 231–335.

- Murdoch N., Rozitis B., Green S., et al. (2013a) Granular shear flow in varying gravitational environments. *Granular Matter*, 15(2), 129–137.
- Murdoch N., Rozitis B., Green S. F., et al. (2013b) Simulating regoliths in microgravity. *Mon. Not. R. Astron. Soc.*, 433(1), 506–514.
- Murdoch N., Rozitis B., Nordstrom K., et al. (2013c) Granular convection in microgravity. *Phys. Rev. Lett.*, 110, 018307.
- Nakamura A. M., Fujiwara A., and Kadono T. (1994) Velocity of finer fragments from impact. *Planet. Space Sci.*, 42, 1043–1052.
- Nakamura T., Noguchi T., Tanak M., et al. (2011) Itokawa dust particles: A direct link between S-type asteroids and ordinary chondrites. *Science*, 333, 1113.
- Nedderman R. M. (2005) *Statics and Kinematics of Granular Materials*. Cambridge Univ., Cambridge.
- Nesvorný D., Bottke W. F., Vokrouhlický D., et al. (2010) Do planetary encounters reset surfaces of near Earth asteroids? *Icarus*, 209, 510–519.
- Nichol K., Zanin A., Bastien R., et al. (2010) Flow-induced agitations create a granular fluid. *Phys. Rev. Lett.*, 104, 078302.
- Perko H., Nelson J., and Sadeh W. (2001) Surface cleanliness effect on lunar soil shear strength. *J. Geotech. Geoenvir. Eng.*, 127(4), 371–383.
- Petit J.-M. and Henon M. (1987) A numerical simulation of planetary rings. I — Binary encounters. *Astron. Astrophys.*, 173, 389–404.
- Pieters C. M., Ammannito E., Blewett D. T., et al. (2012) Distinctive space weathering on Vesta from regolith mixing processes. *Nature*, 491, 79–82.
- Pohlman N. A., Severson B. L., Ottino J. M., and Lueptow R. M. (2006) Surface roughness effects in granular matter: Influence on angle of repose and the absence of segregation. *Phys. Rev. E*, 73, 031304.
- Pravec P., Harris A. W., Scheirich P., et al. (2005) Tumbling asteroids. *Icarus*, 173, 108–131.
- Pravec P., Vokrouhlický D., Polishook D., et al. (2010) Formation of asteroid pairs by rotational fission. *Nature*, 466, 1085–1088.
- Prockter L., Thomas P., Robinson M., et al. (2002) Surface expressions of structural features on Eros. *Icarus*, 155(1), 75–93.
- Radjaï F. and Dubois F. (2011) *Discrete-Element Modeling of Granular Materials*. Wiley-ISTE, Berlin. 448 pp.
- Rao K. K., Nott P. R., and Sundaresan S. (2008) *An Introduction to Granular Flow*. Cambridge Univ., New York. 512 pp.
- Rennilson J. and Criswell D. (1974) Surveyor observations of lunar horizon-glow. *Moon*, 10(2), 121–142.
- Richard P., Nicodemi M., Delannay R., et al. (2005) Slow relaxation and compaction of granular systems. *Nature Materials*, 4, 121–128.
- Richardson D. C. (1994) Tree code simulations of planetary rings. *Mon. Not. R. Astron. Soc.*, 269, 493.
- Richardson D. C. (1995) A self-consistent numerical treatment of fractal aggregate dynamics. *Icarus*, 115, 320–335.
- Richardson D. C., Bottke W. F., and Love S. G. (1998) Tidal distortion and disruption of Earth-crossing asteroids. *Icarus*, 134, 47–76.
- Richardson D. C., Quinn T., Stadel J., and Lake G. (2000) Direct large-scale N-body simulations of planetesimal dynamics. *Icarus*, 143, 45–59.
- Richardson D. C., Leinhardt Z. M., Melosh H. J., et al. (2002) Gravitational aggregates: Evidence and evolution. In *Asteroids III* (W. F. Bottke Jr. et al., eds.), pp. 501–515. Univ. of Arizona, Tucson.
- Richardson J. E., Melosh H. J., and Greenberg R. (2004) Impact-induced seismic activity on asteroid 433 Eros: A surface modification process. *Science*, 306(5701), 1526–1529.
- Richardson D. C., Elankumaran P., and Sanderson R. E. (2005a) Numerical experiments with rubble piles: Equilibrium shapes and spins. *Icarus*, 173, 349–361.
- Richardson J. E., Melosh H. J., Greenberg R. J., and O'Brien D. P. (2005b) The global effects of impact-induced seismic activity on fractured asteroid surface morphology. *Icarus*, 179(2), 325–349.
- Richardson D. C., Schwartz S. R., Michel P., and Walsh K. J. (2008) Modeling cohesion in gravitational aggregates. *Bull. Am. Astron. Soc.*, 40, 498.
- Richardson D. C., Walsh K. J., Murdoch N., and Michel P. (2011) Numerical simulations of granular dynamics: I. Hard-sphere discrete element method and tests. *Icarus*, 212, 427–437.
- Richardson D. C., Blum J., Weinhart T., et al. (2012a) Numerical simulations of landslides calibrated against laboratory experiments for application to asteroid surface processes. *AAS Division for Planetary Sciences Meeting Abstracts*, 44, 105.06.
- Richardson D. C., Munyan S. K., Schwartz S. R., and Michel P. (2012b) Comparison of discrete element methods for simulating low-speed rubble pile collisions: First results. *Lunar Planet. Sci. XLIII*, Abstract #2195. Lunar and Planetary Institute, Houston.
- Riner M. A., Robinson M. S., Eckart J. M., and Desch S. J. (2008) Global survey of color variations on 433 Eros: Implications for regolith processes and asteroid environments. *Icarus*, 198, 67–76.
- Roberts J. H., Kahn E. G., Barnouin O. S., Ernst C. M., Pockter L. M., and Gaskell R. W. (2014a) Origin and flatness of ponds on asteroid 433 Eros. *Meteoritics & Planet. Sci.*, 49, 1735–1748.
- Roberts J. H., Barnouin O. S., Kahn E. G., and Pockter L. M. (2014b) Observational bias and the apparent distribution of ponds on Eros. *Icarus*, 24, 160–164.
- Robinson M. S., Thomas P. C., Veveka J., et al. (2001) The nature of ponded deposits on Eros. *Nature*, 413(6854), 396–400.
- Robinson M. S., Thomas P. C., Veveka J., et al. (2002) The geology of 433 Eros. *Meteoritics & Planet. Sci.*, 37, 1651–1684.
- Rognon P. G., Roux J.-N., Naaim M., and Chevoir F. (2008) Dense flows of cohesive granular materials. *J. Fluid Mech.*, 596, 21–47.
- Rosato A., Strandburg K. J., Prinz F., and Swendsen R. H. (1987) Why the Brazil nuts are on top: Size segregation of particulate matter by shaking. *Phys. Rev. Lett.*, 58(10), 1038–1040.
- Rozitis B., MacLennan E., and Emery J. P. (2014) Cohesive forces prevent the rotational breakup of rubble-pile asteroid (29075) 1950 DA. *Nature*, 512(7513), 174–176.
- Russell C. T. and Raymond C. A. (2011) The Dawn mission to Vesta and Ceres. *Space Sci. Rev.*, 163, 3–23.
- Russell C. T., Raymond C. A., Coradini A., et al. (2012) Dawn at Vesta: Testing the protoplanetary paradigm. *Science*, 336, 684.
- Saito J., Miyamoto H., Nakamura R., et al. (2006) Detailed images of asteroid 25143 Itokawa from Hayabusa. *Science*, 312(5778), 1341–1344.
- Sánchez P. and Scheeres D. J. (2011) Simulating asteroid rubble piles with a self-gravitating soft-sphere distinct element method model. *Astrophys. J.*, 727, 120.
- Sánchez P. and Scheeres D. J. (2012) DEM simulation of rotation-induced reshaping and disruption of rubble-pile asteroids. *Icarus*, 218(2), 876–894.
- Sánchez P. and Scheeres D. J. (2014) The strength of regolith and rubble pile asteroids. *Meteoritics & Planet. Sci.*, 49, 788–811.
- Scheeres D. J. (2005) Solar radiation pressure and transient flows on asteroid surfaces. *Lunar Planet. Sci. XXXVI*, Abstract #1919. Lunar and Planetary Institute, Houston.
- Scheeres D. J. (2014) Solar system: Sandcastles in space. *Nature*, 512(7513), 139–140.
- Scheeres D., Gaskell R., Abe S., et al. (2006) The actual dynamical environment about Itokawa. In *AIAA/AAS Astrodynamics Specialist Conference and Exhibit*, AIAA 2006-6661. American Institute of Aeronautics and Astronautics.
- Scheeres D. J., Abe M., Yoshikawa M., et al. (2007) The effect of YORP on Itokawa. *Icarus*, 188, 425–429.
- Scheeres D., Hartzell C., Sánchez P., and Swift M. (2010) Scaling forces to asteroid surfaces: The role of cohesion. *Icarus*, 210(2), 968–984.
- Schräpler R., Blum J., Seizinger A., and Kley W. (2012) The physics of protoplanetesimal dust agglomerates. VII. The low-velocity collision behavior of large dust agglomerates. *Astrophys. J.*, 758, 35.
- Schröter M., Goldman D. I., and Swinney H. L. (2005) Stationary state volume fluctuations in a granular medium. *Phys. Rev. E*, 71(3), 030301.
- Schulz R., Sierks H., Küppers M., and Accomazzo A. (2012) Rosetta fly-by at asteroid (21) Lutetia: An overview. *Planet. Space Sci.*, 66, 2–8.
- Schwartz S. R., Richardson D. C., and Michel P. (2012) An implementation of the soft-sphere discrete element method in a high-performance parallel gravity tree-code. *Granular Matter*, 14, 363–380.
- Schwartz S. R., Michel P., and Richardson D. C. (2013) Numerically simulating impact disruptions of cohesive glass bead agglomerates using the soft-sphere discrete element method. *Icarus*, 226, 67–76.
- Schwartz S. R., Michel P., Richardson D. C., and Yano H. (2014) Low-speed impact simulations into regolith in support of asteroid sampling mechanism design I: Comparison with 1-g experiments. *Planet. Space Sci.*, 103, 174–183.
- Sharma I., Jenkins J. T., and Burns J. A. (2009) Dynamical passage to approximate equilibrium shapes for spinning, gravitating rubble asteroids. *Icarus*, 200, 304–322.
- Shoemaker E. M., Batson R. M., Holt H. E., et al. (1968) Television observations from Surveyor 3. *J. Geophys. Res.*, 73, 3989.

- Sierks H., Lamy P., Barbieri C., et al. (2011) Images of asteroid 21 Lutetia: A remnant planetesimal from the early solar system. *Science*, 334, 487.
- Sirono S.-I. (2004) Conditions for collisional growth of a grain aggregate. *Icarus*, 167, 431–452.
- Springel V. (2010) Smoothed particle hydrodynamics in astrophysics. *Annu. Rev. Astron. Astrophys.*, 48(1), 391–430.
- Springel V. and Hernquist L. (2002) Cosmological smoothed particle hydrodynamics simulations: The entropy equation. *Mon. Not. R. Astron. Soc.*, 333(3), 649–664.
- Stadel J. G. (2001) Cosmological N-body simulations and their analysis. Ph.D. thesis, Univ. of Washington, Seattle.
- Statler T. S., Cotto-Figueroa D., Riethmiller D. A., and Sweeney K. M. (2013) Size matters: The rotation rates of small near-Earth asteroids. *Icarus*, 225, 141–155.
- Sullivan R., Greeley R., Pappalardo R., et al. (1996) Geology of 243 Ida. *Icarus*, 120, 119–139.
- Sullivan R. J., Thomas P. C., Murchie S. L., and Robinson M. S. (2002) Asteroid geology from Galileo and NEAR Shoemaker data. In *Asteroids III* (W. F. Bottke Jr. et al., eds.), pp. 331–350. Univ. of Arizona, Tucson.
- Tancredi G., Maciel A., Heredia L., et al. (2012) Granular physics in low-gravity environments using discrete element method. *Mon. Not. R. Astron. Soc.*, 420, 3368–3380.
- Taylor G. J. (1993) Rapid magma migration in asteroids. *Meteoritics*, 28, 447–448.
- Thomas N., Barbieri C., Keller H. U., et al. (2012) The geomorphology of (21) Lutetia: Results from the OSIRIS imaging system onboard ESA's Rosetta spacecraft. *Planet. Space Sci.*, 66, 96–124.
- Thomas P. C. and Robinson M. S. (2005) Seismic resurfacing by a single impact on the asteroid 433 Eros. *Nature*, 436, 366–369.
- Thomas P., Veveka J., Bloom A., and Duxbury T. (1979) Grooves on Phobos: Their distribution, morphology and possible origin. *J. Geophys. Res.*, 84, 8457–8477.
- Thomas P. C., Veveka J., Bell J. F., et al. (1999) Mathilde: Size, shape, and geology. *Icarus*, 140, 17–27.
- Thomas P. C., Veveka J., Sullivan R., et al. (2000) Phobos: Regolith and ejecta blocks investigated with Mars orbiter camera images. *J. Geophys. Res.*, 105, 15091–15106.
- Thomas P. C., Veveka J., Robinson M. S., and Murchie S. (2001) Shoemaker crater as the source of most ejecta blocks on the asteroid 433 Eros. *Nature*, 413, 394–396.
- Thomas P. C., Joseph J., Carcich B., et al. (2002) Eros: Shape, topography, and slope processes. *Icarus*, 155, 18–37.
- Thomas P. C., A'Hearn M. F., Veveka J., et al. (2013) Shape, density, and geology of the nucleus of Comet 103P/Hartley 2. *Icarus*, 222, 550–558.
- Thornton A. (2005) A study of segregation in granular gravity driven free surface flows. Ph.D. thesis, Univ. of Manchester, Manchester.
- Tsuchiyama A., Uesugi M., Matsushima T., et al. (2011) Three-dimensional structure of Hayabusa samples: Origin and evolution of Itokawa regolith. *Science*, 333(6046), 1125–1128.
- Tsuji Y., Tanaka T., and Ishida T. (1992) Lagrangian numerical simulation of plug flow of cohesionless particles in a horizontal pipe. *Powder Tech.*, 71, 239–250.
- Veveka J., Robinson M., Thomas P., et al. (2000) NEAR at Eros: Imaging and spectral results. *Science*, 289(5487), 2088–2097.
- Veveka J., Thomas P. C., Robinson M., et al. (2001a) Imaging of small-scale features on 433 Eros from NEAR: Evidence for a complex regolith. *Science*, 292, 484–488.
- Veveka J., Farquhar B., Robinson M., et al. (2001b) The landing of the NEAR-Shoemaker spacecraft on asteroid 433 Eros. *Nature*, 413, 390–393.
- Veveka J., Klaasen K., A'Hearn M., et al. (2013) Return to Comet Tempel 1: Overview of Stardust-NExT results. *Icarus*, 222(2), 424–435.
- Vincent J.-B., Besse S., Marchi S., et al. (2012) Physical properties of craters on asteroid (21) Lutetia. *Planet. Space Sci.*, 66, 79–86.
- Vincent J.-B., Schenck P., Nathues A., et al. (2013) Crater depth-to-diameter distribution and surface properties of (4) Vesta. *Planet. Space Sci.*, 103, 57–65.
- Vokrouhlický D., Nesvorný D., and Bottke W. F. (2003) The vector alignments of asteroid spins by thermal torques. *Nature*, 425, 147–151.
- von Neumann J. and Richtmyer R. D. (1950) A method for the numerical calculation of hydrodynamic shocks. *J. Appl. Phys.*, 21(3), 232–237.
- Wada K., Senshu H., and Matsui T. (2006) Numerical simulation of impact cratering on granular material. *Icarus*, 180, 528–545.
- Walsh K. J. and Richardson D. C. (2008) A steady-state model of NEA binaries formed by tidal disruption of gravitational aggregates. *Icarus*, 193, 553–566.
- Walsh K. J., Richardson D. C., and Michel P. (2008) Rotational breakup as the origin of small binary asteroids. *Nature*, 454, 188–191.
- Walsh K. J., Richardson D. C., and Michel P. (2012) Spinup of rubble-pile asteroids: Disruption, satellite formation, and equilibrium shapes. *Icarus*, 220, 514–529.
- Walton O. R. and Braun R. L. (1986) Viscosity, granular temperature, and stress calculations for shearing assemblies of inelastic, frictional disks. *J. Rheology*, 30, 949.
- Wang X., Horányi M., and Robertson S. (2012) Characteristics of a plasma sheath in a magnetic dipole field: Implications to the solar wind interaction with the lunar magnetic anomalies. *J. Geophys. Res.–Space Physics*, 117, A6.
- Watters T. R., Thomas P. C., and Robinson M. S. (2011) Thrust faults and the near-surface strength of asteroid 433 Eros. *Geophys. Res. Lett.*, 38, L02202.
- Williams D. A., O'Brien D. P., Schenk P. M., et al. (2013) Lobate and flow-like features on asteroid Vesta. *Planet. Space Sci.*, 103, 24–35.
- Williams D. A., Yingst R. A., and Garry W. B. (2014) Introduction: The geologic mapping of Vesta. *Icarus*, 244, 1–12.
- Williams J. (1976) The segregation of particulate materials. A review. *Powder Tech.*, 15(2), 245–251.
- Wilson L. (2013) Volcanism on differentiated asteroids (invited). Presented at AGU Fall Meeting, San Francisco, California, 9–13 December.
- Wilson L. and Keil K. (1996) Volcanic eruptions and intrusions on the asteroid 4 Vesta. *J. Geophys. Res.*, 101, 18927–18940.
- Yano H., Kubota T., Miyamoto H., et al. (2006) Touchdown of the Hayabusa spacecraft at the Muses Sea on Itokawa. *Science*, 312(5778), 1350–1353.
- Yeomans D. K., Antreasian P. G., Barriot J.-P., et al. (2000) Radio science results during the NEAR-Shoemaker spacecraft rendezvous with Eros. *Science*, 289(5487), 2085–2088.
- Yingst R., Mest S., Berman D., et al. (2014) Geologic mapping of Vesta. *Planet. Space Sci.*, 103, 2–23.
- Yu Y., Richardson D. C., Michel P., et al. (2014) Numerical predictions of surface effects during the 2029 close approach of asteroid 99942 Apophis. *Icarus*, 242, 82–96.
- Zuber M. T., Smith D. E., Cheng A. F., et al. (2000) The shape of 433 Eros from the NEAR-Shoemaker laser rangefinder. *Science*, 289(5487), 2097–2101.

*Part 5:*

*Groundbased Surveys, Hazards,  
and Future Exploration*



# Surveys, Astrometric Follow-Up, and Population Statistics

**Robert Jedicke**  
*University of Hawai'i*

**Mikael Granvik**  
*University of Helsinki*

**Marco Micheli**  
*European Space Agency Near Earth Object Coordination Centre*

**Eileen Ryan**  
*Magdalena Ridge Observatory*

**Timothy Spahr**  
*Minor Planet Center*

**Donald K. Yeomans**  
*Jet Propulsion Laboratory*

---

Asteroid surveys are the backbone of asteroid science, and with this in mind we begin with a broad review of the impact of asteroid surveys on our field. We then provide a brief history of asteroid discoveries so as to place contemporary and future surveys in perspective. Surveys in the United States (U.S.) have discovered the vast majority of the asteroids, and this dominance has been consolidated since the publication of *Asteroids III*. Our descriptions of the asteroid surveys that have been operational since that time are focused on those that have contributed the vast majority of asteroid observations and discoveries. We also provide some insight into upcoming next-generation surveys that are sure to alter our understanding of the small bodies in the inner solar system and provide evidence to untangle their complicated dynamical and physical histories. The Minor Planet Center, the nerve center of the asteroid discovery effort, has improved its operations significantly in the past decade so that it can manage the increasing discovery rate, and ensure that it is well-placed to handle the data rates expected in the next decade. We also consider the difficulties associated with astrometric follow-up of newly identified objects. It seems clear that both of these efforts must operate in new modes in order to keep pace with expected discovery rates of next-generation ground- and spacebased surveys.

## 1. INTRODUCTION

Without asteroid surveys there would be no asteroid science. The cumulative efforts of more than 200 years of asteroid surveying has resulted in the discovery of over half a million asteroids in the inner solar system that range from just a tenth of an astronomical unit from the Sun to beyond Jupiter's orbit. The surveys have identified asteroids that are the targets of spacecraft missions, that are the remnants of larger asteroids that were catastrophically disrupted long ago, and that allow us to untangle the complicated processes that formed our solar system billions of years ago. The surveys' capabilities have improved over the decades as they took advantage of every new available technology to push their performance in area coverage, limiting magnitude, and data rates. Their efforts have enabled our community to advance our understanding of the past, current, and future interactions

of both the small and large objects in our solar system. This chapter provides a historical perspective on asteroid surveys, then focuses on their current capabilities and discoveries since *Asteroids III*, discusses the importance of targeted astrometric follow-up for critical objects, and concludes with a speculative forecast on how the next decade of asteroid surveying will unfold.

The benefits of a database containing a large number of asteroid orbit elements and basic physical properties have mostly been achieved over the past couple decades as a result of the NASA-funded near-Earth object (NEO) surveys (Table 1). They attempt to optimize their surveying for the discovery of unknown NEOs but, in the process, discover and recover known asteroids throughout the solar system. While it seems obvious that “more is better,” it is not necessarily straightforward to justify the argument for different asteroid populations — How many asteroids are necessary

for science? Is a complete survey required, or is a statistical sample sufficient?

The first decade of intensive asteroid surveying at the end of the last century was motivated by NASA's goal of detecting NEOs that are larger than 1 km in diameter. The impact on Earth of one of those objects is expected to have global consequences and the set of about 1000 NEOs of that size or larger was thought to incorporate 90% of the impact risk (e.g., Morrison, 1992; Harris, 2008). Thus, the surveys had a relatively well-defined goal that was motivated by planetary defense rather than science: Identify most of the largest hazardous asteroids that could threaten Earth. Progress toward achieving that goal could be measured against the derived population size or by the rediscovery rate (e.g., Jedicke et al., 2003; Harris, 2007). It is possible that there remain undiscovered large objects on an impact trajectory with Earth, but the probability is small.

The last decade of asteroid discovery, roughly since *Asteroids III*, has mostly retired the risk of an unanticipated impact of a globally devastating asteroid (e.g., Harris, 2008; Mainzer et al., 2011b). Having achieved that goal, the surveys are now focusing on detecting even smaller asteroids with the goal of discovering >90% of the potentially hazardous objects (PHOs) larger than 140 m diameter because they (1) represent the lower limit of those that can cause serious regional ground destruction and (2) contribute roughly 90% of the residual hazard to Earth from unknown impactors. The discovery rate for objects less than 140 m in diameter is currently about 400 per year, so *Asteroids VII* could potentially be published before the goal is reached unless new technologies are brought to bear in the coming decades.

Thus, for PHOs, there are well-defined and clearly motivated practical goals for discovering a specific number of objects, but the situation is not so clear for other asteroid populations in the inner solar system. How many main-belt

asteroids are necessary? To what absolute magnitude should we strive to be complete for Jupiter's Trojan asteroids? Without the NEO surveys driving the discovery of asteroids to fainter apparent magnitudes and smaller sizes, we would not have discovered, for example, extremely young asteroid families that can be traced back in time to their collision origin (e.g., Nesvorný et al., 2006; see also the chapter by Nesvorný et al. in this volume), widely separated asteroid pairs on nearly identical orbits that point to Yarkovsky-O'Keefe-Radzievskii-Paddack (YORP) spinup and tidal disruptions of large asteroids (e.g., Vokrouhlický and Nesvorný, 2008; see the chapters by Walsh and Jacobson and Vokrouhlický et al. in this volume), main-belt comets that provide evidence of a water reservoir that may have allowed life to thrive on Earth (e.g., Hsieh and Jewitt, 2006; Jewitt, 2012; see the chapter by Jewitt et al. in this volume), and contemporary catastrophic disruptions of main-belt asteroids that suggest that YORP driven rotational spinup might be the dominant cause of their breakup (e.g., Jewitt et al., 2010; Denneau et al., 2015). In addition, we would not have been able to measure the ages of main-belt asteroid families through fitting the characteristic Yarkovsky/YORP-induced "V" shape of the families' absolute magnitude vs. proper semimajor axes distributions (e.g., Vokrouhlický et al., 2006; see the chapter by Vokrouhlický et al. in this volume) to constrain the dynamical and collisional evolution of the main belt since its formation (e.g., O'Brien and Greenberg, 2005; see the chapters by Morbidelli et al. and Bottke et al. in this volume).

The surveys' capabilities are now so synoptic that most slow-moving objects brighter than about  $V = 21$  are routinely detected multiple times in a lunation, and will be re-detected regularly in the future, so that they require no specific allocation of resources for targeted follow-up observations. Indeed, 80% of the known main-belt asteroids with  $H < 16.5$

TABLE 1. Top 10 NEO surveys (2003–2014).

Rank	NEOs	Survey	Location	P.I.	Aperture (m)	f-Ratio	FOV (deg $^2$ )	Pixel Scale ('/pix)	Obs. Code
1	2,910	CSS	Mt. Lemmon, AZ, USA	E. Christensen	1.50	2.0	1.2	1.0	G96
2	1,952	CSS	Mt. Lemmon, AZ, USA	E. Christensen	0.68	1.8	8.2	2.5	703
3	1,364	LINEAR	White Sands, NM, USA	G. Stokes	1.0	2.2	2.0	2.25	704
4	1,303	Pan-STARRS1	Haleakala, HI, USA	R. Wainscoat	1.8	4.0	7	0.26	F51
5	574	Spacewatch	Kitt Peak, AZ, USA	R. McMillan	0.9	3.0	2.9	1.0	691
6	462	CSS	Siding Spring, Australia	S. Larson	0.5	3.5	4.2	1.8	E12
7	166	LONEOS	Anderson Mesa, AZ, USA	E. Bowell	0.6	1.8	8	2.6	699
8	162	NEOWISE	Earth polar orbit	A. Mainzer	0.4	3.375	0.6	2.75/5.5*	C51
9	119	NEAT/AMOS	Palomar, CA, USA	E. Helin	1.2/1.2	3/2.0	5/2.0	1/1.25	644/608
10	95	La Sagra Sky Survey	Granada, Spain	J. Nomen	3 × 0.45	2.8	1.5	2 × 1.5 and 2	J75

\*2.75"/pix in the 3.4, 4.6, and 12-μm channels and 5.5"/pix in the 22-μm channel.

The top 10 NEO surveys discovered >96% of all NEOs identified during the time period from January 1, 2003, through November 18, 2014. Columns are the rank and number of NEOs discovered, survey name or acronym, location of the survey site, name of the original or current principal investigator (P.I.), telescope aperture in meters, f-ratio (focal length of primary mirror divided by its aperture), FOV in square degrees, image scale in arcseconds per pixel, and site's IAU observatory code.

are now numbered, meaning that their orbits are good enough to predict their future ephemerides to within 2" for at least the next decade. On the other hand, rapidly moving, nearby NEOs that may pose an Earth impact hazard in the future usually require rapid follow-up to measure their astrometric positions (Ticha et al., 2002) over as long an arc as possible during their discovery opposition to (1) accurately assess their Earth impact hazard (e.g., Milani et al., 2005; see the chapter by Harris et al. in this volume) and (2) increase the probability that detections of the object in future apparitions can be associated with the discovery apparition observations (e.g., Milani et al., 2012; see the chapter by Farnocchia et al. in this volume).

We think that continued asteroid survey efforts in the next decades are justified in order to expand upon the rich asteroid science yield of the past decades, to provide exciting new discoveries that will generate unexpected insights into our solar system's formation and continuing evolution, and to further reduce the NEO impact hazard risk. The remainder of this chapter provides an introduction to the history of asteroid surveys before *Asteroids III*, the continuing survey improvements and their current status as of publication of this volume, the importance and state of the art of follow-up efforts, and our perspective on upcoming surveys and technologies as we look forward to *Asteroids V*.

## 2. A BRIEF HISTORY OF ASTEROID DISCOVERY (PRIOR TO ASTEROIDS III)

The first asteroid to be discovered, (1) Ceres, was visually identified by Father Giuseppe Piazzi, director of the

Palermo Observatory, on the morning of January 1, 1801, the first day of the nineteenth century. Piazzi was identifying and correcting the positions of stars in an existing catalog when he noticed that one "star" in Taurus shifted position from night to night. He followed the object until February 11, 1801, but his discovery was not announced until the summer of that year. It was recovered on December 7, 1801, only after Karl Gauss, with characteristic genius, provided an elliptic orbit for (1) Ceres that allowed an accurate-enough ephemeris prediction. Three more asteroids were discovered shortly thereafter: Heinrich Olbers identified the second and fourth asteroids, (2) Pallas and (4) Vesta, in 1802 and 1807 respectively, while Karl Harding discovered (3) Juno in 1804. It was another 41 years until (5) Astraea was discovered in 1845, and the discovery rate would remain less than about one per month until about the time of the advent of astrophotography. There were only 10 known asteroids by mid-century and 447 by 1900 (see Fig. 1).

The era of photographic asteroid discovery began in 1891 when Max Wolf compared the images on three successive photographic plates to detect the motion of (323) Brucia, the first of Wolf's 321 asteroid discoveries. Trailed detections of asteroids on single long-exposure photographic plates were also used to identify asteroids and Gustav Witt discovered the trailed image of the first near-Earth object, (433) Eros, at the Urania Observatory in Berlin in 1898.

The pioneering photographic asteroid surveys in the 1970s and early 1980s marked the beginning of the modern NEO discovery era (see Fig. 1). Gene Shoemaker and Eleanor Helin began using the 18-inch Palomar Schmidt telescope in southern California for finding NEOs in 1973

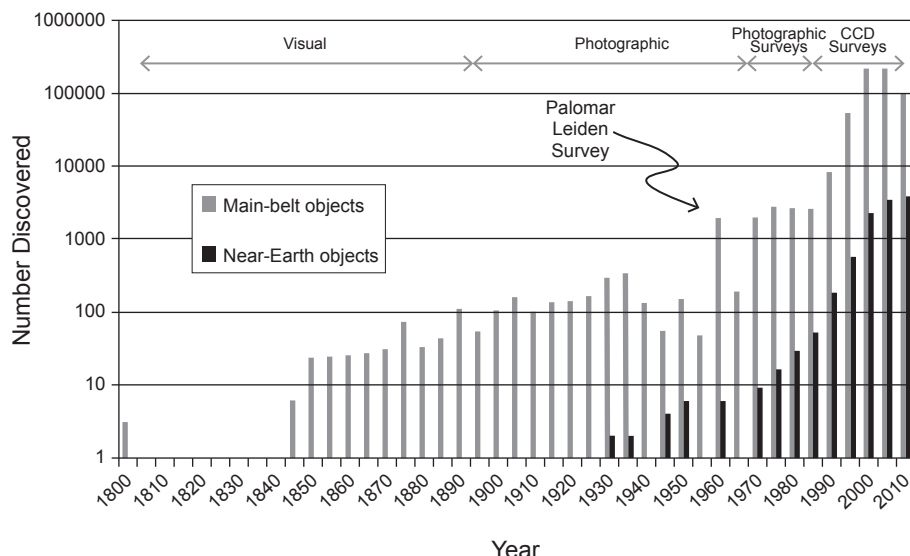


**Fig. 1.** Main-belt and near-Earth object discovery statistics since 1800 in five-year intervals. The time periods corresponding to serendipitous visual and photographic asteroid discovery is indicated, as are the time periods for photographic and CCD surveys. The Palomar-Leiden Survey (PLS) (Van Houten et al., 1970) in 1960 was particularly ahead of its time as it discovered  $>10\times$  more asteroids in a few months than were being discovered over five years at the time. It took another decade before the discovery rates regularly matched the PLS rate.

and were joined by Carolyn Shoemaker in the early 1980s (*Helin and Shoemaker*, 1979). Their early photographic surveys identified asteroids using manually-operated blink comparators and stereomicroscopes that enabled visual comparison of images of the same portion of sky taken several minutes apart. The vast majority of the objects in the images were stationary stars and galaxies, but a moving NEO would be in a slightly different position on each photograph so that it would appear to jump back and forth when each image was quickly viewed in turn with the blink comparator. Alternately, the NEO's image would appear to "float" above the background stars when two different images were examined at the same time with a stereomicroscope. [For more details concerning these pioneering NEO search efforts, see, e.g., *Cunningham* (1988), *Stokes et al.* (2002), and *Yeomans* (2013)].

The surveys entered the modern era in 1984 when the Spacewatch telescope (see section 3.1) became the first survey to employ a camera with a charge-coupled device (CCD) focal plane (see Fig. 1). Their first  $320 \times 512$ -pixel CCD detector was replaced in 1989 with a large format  $2048 \times 2048$  CCD that was used for three years until they obtained a high-efficiency (~70%) thinned  $2048 \times 2048$  CCD. The system was operated for about 23 nights per month with the CCD read out in a time-efficient "drift-scanning" mode in which the right ascension axis was stationary so that the star field would drift through the telescope's field-of-view (FOV) while the CCD detector was read out at the same rate. This technique allowed the survey to image about  $200 \text{ deg}^2$  each month to a limiting V-band magnitude of  $\geq 21$ . Each scan was repeated three times with about 30 minutes separation and automated software identified moving objects in the field (*Rabinowitz*, 1991).

The NEO discovery rate increased dramatically in the late 1990s (see Fig. 1) when NASA increased the funding available for NEO surveys, partly in response to impact awareness generated by the 1994 impact of Comet Shoemaker-Levy 9 with the planet Jupiter. The perfect storm of increased funding coupled with the decreasing cost of CCDs and the availability of frame-transfer CCDs enabled the rise of the LINEAR (section 3.4) and Catalina (section 3.5) NEO surveys that dominated the modern survey era for about two decades leading up to and through *Asteroids III*.

*Stokes et al.* (2002) provides more details of the history and state of asteroid surveys leading up to *Asteroids III*.

### 3. ASTEROID SURVEYS (SINCE ASTEROIDS III)

All contemporary asteroid surveys use extremely efficient CCDs to record digital images of the sky. While CCD detectors are far more sensitive and accurate than film, their application to asteroid discovery is similar. Three or more CCD images are taken of the same region of the sky with successive images separated in time by about 30 minutes. The images are then compared in software to identify detections that have systematically moved to different positions from one image to the next. The rate of motion of the detec-

tions from one image to the next, the direction they appear to be traveling, and their apparent brightness are helpful in identifying interesting objects and can provide first-order estimates of an object's distance from Earth, its size, and its general orbital characteristics. For example, an object that appears to be moving very rapidly from one image to the next ( $>1^\circ/\text{day}$ ) is almost certainly an NEO. New NEO discoveries are usually still verified with the human eye even though sophisticated and automated software analyses of the CCD images have replaced manual identification of moving objects.

In 1998, NASA established the goal of discovering 90% of NEOs larger than 1 km in diameter, and in 2005 Congress extended that goal to include 90% of the NEOs larger than 140 m (George E. Brown, Jr. Near-Earth Object Survey Act). There are thought to be about 1000 NEOs larger than 1 km in diameter and roughly 26,000 larger than 140 m (e.g., *Granvik et al.*, 2014); see the chapter by Harris et al. in this volume). The desire to meet the NEO goals has enabled the funding and driven the success of the asteroid surveys over nearly the past two decades.

Asteroid surveys that search the largest area of sky each month will discover the most NEOs (*Bowell and Muinonen*, 1994), all other things being equal. How much sky each telescope surveys depends upon several factors, including the number of clear nights available for observing, the telescope aperture and FOV, and the sensitivity and efficiency of the CCD detector. That being said, not all regions of the sky are equally productive for discovering new NEOs (e.g., *Bowell and Muinonen*, 1994; *Chesley and Spahr*, 2004; *Vereš et al.*, 2009). Once the most effective regions are fully surveyed, it is important to extend the search to greater distances from Earth or, in other words, to fainter limiting magnitudes.

Spacebased asteroid surveys have advantages over groundbased observing in that they are not hindered by weather, can search continuously, and can observe in the infrared where asteroids are brighter and there are fewer background sources; in addition, space telescopes can observe NEOs when they are much closer to the Sun (see the chapter by Mainzer et al. in this volume). A case in point is the ~18-m-diameter asteroid that injured more than 1500 people when it airburst over Chelyabinsk, Russia, on February 15, 2013, that was not detected by groundbased surveys since it came from a sunward direction (e.g., *Brown et al.*, 2013). Of course, spacebased surveys are expensive, risky, can be data-rate-limited due to the availability and limitations of the downlink from the spacecraft to the ground, and are not repairable in the event of a major failure.

The asteroid surveys have discovered about 90% of the NEOs larger than 1 km in diameter since NASA's initiation of its NEO Observations (NEOO) program in 1998 (*Mainzer et al.*, 2011b), and a good fraction of those larger than 140 m. Progress toward meeting the goals can be monitored on the NEO discovery statistics page at <http://neo.jpl.nasa.gov/stats/>. The vast majority of those NEO discoveries were made by NASA-supported groundbased telescopic surveys,

and in the following subsections we briefly describe the major surveys that were or are operational since *Asteroids III* in roughly chronological order by start date [the Jet Propulsion Laboratory (JPL) maintains a list of NASA-supported NEO survey programs at <http://neo.jpl.nasa.gov/programs/>].

### 3.1. Spacewatch (1983–Present)

The Spacewatch team was a pioneer in digital detection of NEOs (e.g., Rabinowitz, 1991). They discovered the first NEO on digital images in 1989 and reported the first automated (software) discovery in 1990. They led the effort to automate the discovery and follow-up of NEOs, culminating in the modernization of their 0.9-m and 1.8-m telescopes, which can both be operated from a single control room by a single observer.

They began using their custom-built 1.8-m-aperture telescope for NEO surveying and follow-up in 2002. Later that same year their 0.9-m telescope was instrumented with a large-scale mosaic camera consisting of four  $4608 \times 2048$  CCDs to take advantage of its new optical system, which provides a  $2.9\text{-deg}^2$  FOV. The 0.9-m telescope's new optical configuration required that it operate in the conventional "stare" mode, whereas the 1.8-m telescope continued to be operated in the "drift-scan" mode until 2011. From 2005 through 2008, Spacewatch gradually shifted its emphasis from NEO surveying to follow-up as other surveys began to dominate NEO discovery. Finally, the imaging detector on the 1.8-m telescope was replaced in October 2011 with a stare-mode CCD with finer pixel resolution, faster readout, and flatter focus. The new camera allowed Spacewatch to increase their NEO follow-up rate by more than 50% while at the same time halving the astrometric residuals. The Spacewatch 1.8-m telescope is currently among the world's leaders in faint-object follow-up, especially in terms of critical follow-up of the most challenging faint objects.

### 3.2. Near-Earth Asteroid Tracking (NEAT) (1995–2007)

Beginning in 1995, the JPL NEAT program (Pravdo et al., 1999) operated survey telescopes on the summit of Haleakala, Hawaii, in cooperation with the Air Force. The Ground-based Electro-Optical Deep Space Surveillance (GEODSS) 1-m telescope was equipped with a  $4k \times 4k$  CCD and initially utilized 12 nights per month centered on new Moon (December 1995 to December 1996), subsequently reduced to 6 nights per month (January 1997 to February 1999). In February 2001 NEAT began using a modified 1.2-m telescope, part of the U.S. Air Force Space Surveillance System in Maui, Hawaii. Nightly pointing lists were generated at JPL for the telescope control computer in Maui and small subimages of candidate NEOs were transferred back to JPL for inspection by JPL scientists. In 2001 the NEAT program transitioned to the 1.2-m Schmidt telescope at Palomar Mountain in southern California before ceasing operations in 2007.

### 3.3. Lowell Observatory Near Earth Object Survey (LONEOS) (1993–2008)

LONEOS (Bowell et al., 1995) operated from 1993 through 2008 using the Lowell Observatory 0.6-m Schmidt telescope at Anderson Mesa near Flagstaff, Arizona. The relatively small aperture telescope was competitive because it had a large FOV of about  $8\text{ deg}^2$  instrumented with two  $2k \times 4k$  cooled CCDs. LONEOS collected four 45-s exposures of each field that were automatically searched for moving objects down to  $V \sim 19.3$ . The LONEOS system's productivity eventually declined due to competition with larger-aperture survey telescopes, so they switched their primary objective to photometric observations of NEOs and finally ceased operations in 2008.

### 3.4. Lincoln Near-Earth Asteroid Research (LINEAR) Program (1996–2013)

The LINEAR survey (Stokes et al., 2000) was operated out of Socorro, New Mexico, by the Massachusetts Institute of Technology (MIT) Lincoln Laboratory team, which was based in Lexington, Massachusetts. The legacy 1-m LINEAR telescope system is located at Lincoln Laboratory's Experimental Test Site near Stallion Range Center on the U.S. Army's White Sand Missile Range in central New Mexico. It began operations in early 1996 but was in routine use from March 1998 through May 2013. The survey used two 1-m-aperture telescopes originally designed as prototypes for Earth-orbiting debris tracking. LINEAR's success was driven by the application of electro-optical sensor technology, originally developed for U.S. Air Force Space Surveillance, to the problem of discovering near-Earth asteroids and comets. Their frame transfer CCDs allowed large areas of sky to be surveyed extremely efficiently because the camera required effectively zero readout time. Furthermore, the rapid-readout CCDs and access to fast-computing resources allowed them to apply an advanced image processing technique involving generating a median of five images of the same field and subtracting the median from the sum of the same five images to generate difference images that contained only transients and relatively few artifacts. The differenced images were then searched for transient detections moving in roughly straight lines (tracklets). During the late 1990s and early 2000s they could survey several thousand square degrees per night to  $V \sim 19$ , enabling the program to single-handedly discover more than one-third of all NEOs 1 km in diameter or larger. Lincoln Laboratory discontinued use of the 1-m system in 2013 while it transitions to the use of the 3.5-m Space Surveillance Telescope (SST) (see section 7.2).

### 3.5. Catalina Sky Survey (CSS) (1992–Present)

The University of Arizona's CSS (Larson et al., 1998) has been the primary NEO discovery system over much of the time since *Asteroids III* and has done so while remaining cost-competitive. Their success can be traced to remaining

focused on their primary objective of discovering NEOs; employing dedicated, professional, skillful observers; and standardizing equipment and software across their different sites. For instance, all the cameras at their three sites are identical, thinned,  $4\text{k} \times 4\text{k}$  back-illuminated detectors packaged by Spectral Instruments, Inc., of Tucson, Arizona, that are cooled with a closed-cycle cryocooler. The use of identical cameras has minimized hardware and software development as well as maintenance and operations costs. Their dedication to continual improvement, comprehensive sky coverage, human vetting of candidate discoveries, and onsite recovery capability have further contributed to their success over the last decade.

The CSS was preceded by the Bigelow Sky Survey (BSS), which photographically searched for new asteroids and comets between 1992 and 1996 (*Spahr et al.*, 1993, 1996). The experience gained in operating the BSS informed and motivated modifications to the telescope, camera, and software beginning in 1997 so that the CSS's CCD survey began producing observations in 1998.

The CSS has used 3 different telescopes in the past 10 years and in 2013 alone discovered 603 NEOs, easily making it the top survey program that year. Their 2 primary telescopes are the Catalina Schmidt and the Mt. Lemmon telescopes, but their third site, the Siding Spring Schmidt in Australia, has delivered enough NEOs to place it in the top 6 NEO discovery sites in each of the past 10 years. About 20% of CSS observing time is devoted to post-discovery follow-up observations (see section 5).

The Catalina Schmidt in the mountains north of Tucson, Arizona, was upgraded to a f/1.8, 0.7-m telescope from 2003 to 2004, which increased their sensitivity to  $V \sim 20.0$ . Its  $8.2\text{-deg}^2$  FOV enabled the site to survey 1000 to 1500 deg $^2$  per night and vaulted the CSS program into the lead in terms of annual discoveries.

In 2004–2005 the CSS team procured a  $4\text{k} \times 4\text{k}$  CCD and then built and installed a prime-focus camera that delivers a  $1.2\text{-deg}^2$  FOV on their Mt. Lemmon 1.5-m telescope. Its limiting magnitude reaches  $V \sim 21.5$  under good conditions and they can survey  $\sim 200$  deg $^2$  on an average night. This survey excels at finding very small objects that are very close to Earth (*Jedicke et al.*, in preparation) and demonstrates the need to shift to larger optical systems in order to complete the inventory of smaller, yet still threatening, NEOs. For example, the CSS identified the only two Earth impactors that were discovered in advance of impact [2008 TC (*Kowalski et al.*, 2008) and 2014 AA (*Kowalski et al.*, 2014)].

The 0.5-m Uppsala Schmidt telescope at Siding Spring, Australia, was operated by the CSS for several years when it was the only NEO survey in the southern hemisphere. However, in 2013 the Australian dollar became much stronger relative to the U.S. dollar-based funding from the NASA NEOO program compared to when the survey was established. The combination of the exchange rate shift and the telescope's modest aperture and FOV reduced the cost-effectiveness of the survey compared to the CSS's northern

hemisphere assets, and the decision was made to end support for this facility.

### 3.6. Panoramic Survey Telescope and Rapid Response System (Pan-STARRS) (2010–Present)

The 1.8-m Pan-STARRS1 (PS1) (*Wainscoat et al.*, 2013) telescope on Haleakala, Hawaii, was developed by the University of Hawaii's Institute for Astronomy and operated by the PS1 Science Consortium (PS1SC) until early 2014. It was the prototype telescope for the four-telescope Pan-STARRS system (*Kaiser et al.*, 2002), which was supposed to be operational late in the last decade but may never be completed. The PS1 CCD camera was the largest in the world when it was originally built, with a focal plane consisting of an almost complete  $8 \times 8$  array of CCDs (the four corner CCDs were left out of the focal plane) with a total of about 1.4 gigapixels. The large focal plane combined with the system's f/4 optics yields an  $\sim 7\text{-deg}^2$  FOV that has moved PS1 to be the leading PHO discovery site beginning in calendar year 2012. In 2014 it will discover about 4× more PHOs than the second most successful site.

The first PS1 NEO discoveries were recorded in the second half of 2010 but only about 5% of the observing time was devoted to NEO discoveries at that time. The NEO survey time fraction was increased to 11% beginning in November 2012. In addition, 56% of the observing time was used for a “ $3\pi$ ” sky survey in three filters that was also executed in a manner that led to the discovery of NEOs. The time devoted to the NEO search was increased to 100% beginning in April 2014 with funding provided by NASA's NEOO program after the end of the PS1SC.

PS1's strength lies in having the faintest magnitude limit of any active NEO survey, reaching  $V \sim 22$  under good conditions. This allows the team to discover NEOs that are too faint to be detected by the other systems. Their excellent site in the middle of the Pacific Ocean allows PS1 to survey the “sweet spots” near the Sun where the sky-plane PHO density is highest if the system can reach fainter than  $V \sim 21$  (*Chesley and Spahr*, 2004; *Vereš et al.*, 2009).

PS1 developed a sophisticated image processing pipeline (IPP) (*Magnier*, 2006) that feeds transient detections to the Moving Object Processing System (MOPS) (*Denneau et al.*, 2013), which uses kd-trees to quickly link transient detections into tracklets (*Kubica et al.*, 2007). The final observations are extremely accurate with astrometry good to  $\lesssim 0.1''$  (*Milani*, 2012), which allows the MPC to tightly constrain NEO orbital solutions and uncertainty maps to facilitate the recovery of PS1 NEO candidates.

### 3.7. Near Earth Object Wide-field Infrared Survey Explorer (NEOWISE) (2010–Present)

The NEOWISE program (e.g., *Mainzer et al.*, 2011a; see also the chapter by Mainzer et al. in this volume) observes and discovers NEOs and other asteroids in the near-infrared

(IR) with the 0.4-m telescope onboard the Wide-field Infrared Survey Explorer (WISE) spacecraft (e.g., *Cutri et al.*, 2012; *Wright et al.*, 2010). The spacecraft was launched on December 14, 2009, into a “Sun-synchronous” polar orbit around Earth (the spacecraft’s orbital plane is always roughly perpendicular to the Earth-Sun line) and as it orbited it continuously surveyed a 47'-wide strip of sky in the opposite direction from Earth. WISE operated for 10 months in 2010, performing an all-sky astronomical survey in four bands centered at 3.4, 4.6, 12, and 22  $\mu\text{m}$ . When the hydrogen coolant for the two longest wavelength detectors was exhausted, a secondary post-cryogenic mission continued for four more months using just the two shorter-wavelength detectors, and then the spacecraft was decommissioned and hibernated on February 17, 2011. After more than two-and-a-half years the spacecraft was awakened from hibernation and NEOWISE was reactivated in September 2013 for a planned three-year observing period using just the 3.4- $\mu\text{m}$  and 4.6- $\mu\text{m}$  passbands (*Mainzer*, 2014). Its first NEO discovery in the new operational phase, 2013 YP<sub>139</sub>, occurred on December 29, 2013.

NEOWISE’s Sun-synchronous survey mode imposes a time limit of about 36 hours during which images at a specific location can be acquired. Hence, the program requires groundbased NEO candidate follow-up by a dedicated network of amateur and professional astronomers to secure their orbits (see section 5). NEOWISE also detected tens of thousands of known asteroids in the IR that allowed diameter measurements of thousands of objects, thus enabling a range of studies of the origins and evolution of the small bodies in our solar system [e.g., NEOs (*Mainzer et al.*, 2011b), main-belt objects (MBOs) (*Masiero et al.*, 2014), and Jupiter Trojans (*Grav et al.*, 2012; see also the chapter by Mainzer et al. in this volume)].

### 3.8. Other Contributions

Amateur astronomers have historically played a role in advancing the astronomical fields, but their contribution to NEO discovery has been limited due to their access to telescopes of relatively modest apertures. From 1998 through 2013 only about 1.8% of the 10,044 discovered NEOs were found by the amateur community. The most productive team was the Las Sagra Survey (LSS) operated in Spain by J. Nomen, R. Stoss, and others. They discovered 79 NEOs prior to being funded professionally by the European Space Agency (ESA) for space debris tracking. During the same time period only 99 other NEOs were discovered by amateurs from the rest of the world combined.

A small number of asteroids are discovered serendipitously by professional observers or other astronomical surveys in the course of their work that is not always primarily associated with asteroids. For instance, the International Scientific Optical Network (ISON) (*Molotov*, 2010) is designed to identify and track Earth-orbiting space-debris, but its capabilities naturally serve asteroid identification pro-

cesses, as illustrated by their discovery of the spectacular Comet ISON (C/2012 S1). Similarly, the Palomar Transient Factory (PTF) (e.g., *Polishook and Ofek*, 2011) is an all-sky astronomical survey designed to identify transient and variable objects that has also identified many asteroids and NEOs.

## 4. THE MINOR PLANET CENTER (MPC)

All the candidate detections of minor planets identified by the surveys are delivered to the Minor Planet Center (MPC) (<http://minorplanetcenter.net>) — the IAU’s official international repository and distributor of asteroid astrometric observations, minor planet orbits, and identifications. The MPC’s goal is to identify and/or link all reported minor planet observations in nearly real time. This is a challenging process because the MPC has experienced a 7 $\times$  increase in reported observations over the time since *Asteroids III* (see Fig. 1) and the time required for orbit determination and linking increases faster-than-linearly with the number of observations in the database. Fortunately, Moore’s Law and the implementation of improved operational procedures have allowed the MPC to handle the increased data and analysis rate. Today, the MPC can automatically and seamlessly receive and process a few million observations of a few hundred thousand minor planets each day from both ground- and spacebased observatories.

The MPC concentrates on expeditiously processing NEO discoveries and observations because they are of interest to NASA and the public. Ephemerides need to be provided promptly so that follow-up telescope facilities can quickly recover the objects. The MPC checks all reported NEO candidate “tracklets” (sets of detections that are claimed to be of the same object) for identification with known objects, computes the likelihood that unknown objects are new NEOs, and posts the best candidates on the NEO Confirmation Page (NEOCP) for follow-up (the NEOCP is available at <http://www.minorplanetcenter.net/iau/NEO/ToConfirm>; follow-up efforts are described in section 5). The ESA’s NEO Coordination Centre also maintains a parallel and prioritized follow-up list at <http://neo.ssa.esa.int/web/guest/priority-list>.

The NEOCP was handily validated in October 2008 when the MPC identified a CSS discovery that would impact Earth only 20 hours after discovery (*Kowalski and Chesley*, 2008). The international network of observers monitoring the NEOCP quickly responded (see section 5) and reported more than 800 astrometric observations, multiple light curves, and even a spectrum, over a timespan of less than a day. As a result of this coverage JPL predicted that the object now known as 2008 TC<sub>3</sub> would impact in a small desert area in northern Sudan. This prediction was subsequently confirmed by visual and satellite reports and with the collection of meteorite fragments on the ground (e.g., *Jenniskens et al.*, 2009; see also the chapter by Jenniskens in this volume).

The MPC’s database (see Table 2) mostly contains optical observations of main-belt asteroids even though much of the MPC’s time and effort is devoted to dealing with

TABLE 2. Minor Planet Center holdings as of November 6, 2014.

Type	Objects
Numbered	415,688
Multi-opposition	133,306
Single-opposition	115,042
Two-night	~165,000
One-night	$\mathcal{O}(3,000,000)$

The MPC data files contained a total of 118,328,160 observations as of November 6, 2014.

NEOs. As of this writing there are almost 400,000 minor planets classified as “numbered” (most of them in the main belt), meaning that their orbits are of sufficient accuracy that their ephemeris uncertainties in the next decade are no more than a few arcseconds. To be numbered, an object usually needs to be observed over a period of at least four oppositions with detections on more than one night in most of the apparitions. This rule of thumb applies to MBOs that typically have only optical sky-plane positions — NEOs may have secure orbits with just two apparitions of data because of the power of parallax for nearby objects to reduce the uncertainty on the orbit elements. Similarly, the range and range-rate accuracy available with radar may be combined with optical observations from just a single apparition to yield good orbits (e.g., Ostro *et al.*, 2004). In total, the numbered objects have increased by more than a factor of 10 since *Asteroids III* and about 90% of those objects were discovered by just 10 surveys or sites (see Table 3). Many of the objects that are now numbered were discovered more than a decade ago, before *Asteroids III*, because it requires about 10 years before a typical MBO has been detected in enough apparitions to allow it to be numbered. Thus, the tremendous number of new discoveries by contemporary NEO surveys (see section 3) will only be numbered as this decade progresses toward the publication of *Asteroids V*.

The unfortunate reality of the difference between the capabilities of professional and amateur facilities is that only 0.6% of the numbered objects in the top 10 list were contributed by amateur observatories. Eight of the top 10 most productive programs are, or were, funded directly by NASA specifically for discovery or follow-up of NEOs. Thus, it is clear that the discovery of minor planets is almost uniquely a NASA-funded survey effort based in the U.S. Indeed, fully 80% of the discoveries were realized at just a handful of NASA-funded NEO search programs led by the LINEAR program (see section 3.4).

The MPC database contains observations and orbits of objects that were detected in multiple oppositions, a single opposition, and even on only two nights. The sum total of all these objects is currently comparable to the number of numbered objects (see Table 2). The accuracy of the ephemerides for each successive class of objects decreases dramatically such that single-opposition orbits might be suitable for predicting the location of the object for only

TABLE 3. Top 10 asteroid discovery surveys (of all time).

Rank	Survey or Observer	Obs. Code	Discoveries	Operations
1	LINEAR	704	141,577	1997–2010
2	Spacewatch	691	85,338	1985–present
3	NEAT/AMOS	644/608	31,116	1995–2007
4	Mt. Lemmon Survey	G96	30,422	2004–present
5	CSS	703	20,664	1998–present
6	LONEOS	699	19,856	1998–2012
7	Haleakala-AMOS	608	7475	1995–2003
8	PLS/T-1,T-2,T-3	675	6796	1960–1977
9	E. Elst*	809	5650	1983–2012
10	Pan-STARRS 1	F51	4684	2010–present

\*Belgian professional astronomer.

Rankings are from September 14, 2014. Columns are the rank of the survey in terms of the number of asteroid discoveries credited to the survey; survey name, acronym, or observer, site’s IAU observatory code; current number of asteroid discoveries credited to the survey; and time period of survey operations.

another 1 or 2 years while objects observed on only 2 nights can typically only be used for about 10 days.

Finally, the MPC maintains a publicly available file of all single-night detections that currently cannot be linked or identified with other minor planets. This file, pejoratively dubbed “One Night Stand” (ONS) by Brian Marsden in the mid 1990s, now contains over eight million observations. While it is likely that many of the observations in this file represent duplicates, false detections, and errors, it is also likely that the file includes several hundred thousand uncatalogued minor planets. The MPC currently employs a graduate student (J. Myers, University of Arizona) who is developing advanced linking techniques to extract as many objects as possible from the ONS file, but it will always contain a high fraction of unlinkable and likely false detections.

One challenge at the MPC is linking and processing datasets of very different observational quality. For example, the mean astrometric residual for observations prior to the CCD era (ca. 1995) is about 1–2”, while residuals from the modern Pan-STARRS program (section 3.6) are ~0.1” — an improvement of a factor of 10 to 20! Even today, the mean residuals for survey data from the professional surveys range from about 0.05” to 0.7”.

## 5. ASTROMETRIC FOLLOW-UP, RECOVERY, AND PRECOVERY

Modern survey telescopes are specifically designed to have a wide FOV and rapid readout in order to image as much sky as possible, so using them for targeted follow-up of specific objects is an inefficient use of their capabilities. Instead, the surveys identify and report likely asteroid tracklets to the MPC on a nearly real-time or nightly basis and then continue to survey the sky for other candidates. They rely on other “follow-up” facilities to obtain more observations of the objects for verification and to secure their orbits. Follow-

up usually refers to obtaining astrometric and photometric observations of an object to secure its orbit and determine its absolute magnitude, but may also include various types of “physical characterization,” including obtaining an object’s light curve to determine its rotation rate and, perhaps, shape, or spectra to determine its taxonomy (and mineralogy). This chapter and subsection will concern itself almost exclusively with astrometric follow-up.

The most challenging follow-up is for the NEOs. More distant objects tend to move slowly so that their ephemeris uncertainties are relatively small and, in any event, they will be redetected in the course of normal ongoing survey operations. The first detections of a new candidate NEO typically span a temporal arc of less than an hour and represent just the beginning of the lengthy and complex discovery process. First, the candidate must be confirmed as being a real and unknown object — it is not uncommon for reported candidates to be false because of processing errors such as mislinking of two different asteroids or combining false detections in an image into a false tracklet. Once an object is established as being real and recoverable, discovery observations must be followed by an observational campaign to establish the object’s orbit with enough accuracy to enable it to be “recovered” in the future. (Recovery is the process of obtaining new observations that can be attributed to an object.) The extension of the observed arc is essential for more accurate orbit determination, which leads to a better understanding of the object’s dynamics either because of its scientific interest or because of its possible impact threat to Earth (e.g., Milani *et al.*, 2000). Some candidate NEOs may be real but are moving so fast that they are effectively unrecoverable due to timing considerations, weather, and/or ephemeris uncertainties.

The most critical follow-up takes place within about three days of discovery because the initial observations are usually insufficient to even broadly identify the orbital properties of the new object. This is because a small number of observations by a single observatory over a short timespan do not contain enough information to determine the geocentric distance of the object — they contain very little parallax information and, as a result, ephemerides rapidly become extremely uncertain or useless. Obtaining follow-up observations of an asteroid is so essential that only those with confirmatory observations are eligible for official designation and assignment of discovery credit by the MPC.

An illustration of the need for rapid follow-up is asteroid 2014 JR<sub>24</sub>, which was discovered at magnitude V ~ 17.2 on May 6, 2014, by the CSS. Its diameter is in the 4–8-m range (based on its absolute magnitude, H = 29.3), and it made a close approach to Earth of about 0.3 lunar distances on May 7, 2014, when it reached a peak magnitude of V ~ 15.6. Although some astrometric follow-up was obtained, there was no physical characterization of this interesting close flyby and potential radar target, and its apparent magnitude dropped to V ~ 27 within three days of discovery, thereby eliminating the opportunity for further follow-up. It will not have a favorable apparition for more than a decade, at which time the recovery will necessarily be serendipitous because the ephemeris uncertainty will be large.

There are a variety of assets for follow-up of recently discovered asteroids ranging from self-funded, highly-productive, submeter-class telescopes (e.g., *Birtwhistle*, 2009), to NASA-funded 1–2-m-class telescopes, and, increasingly common, even access to “big glass” in the 4–8-m range (*Abell*, 2013) for characterization studies (Table 4). FOVs for the facilities extend from arcminute scales to about a

TABLE 4. Top 10 asteroid astrometric follow-up sites (2011–2014).

Observatory	Obs. Code	Location	Lead(s)	Telescope(s) Aperture	Limiting V mag	NEOs Total 2011–2014	NEOs V > 20 2011–2014
ARO	H21	Illinois, USA	R. Holmes	0.5 m; 1.4 m	22	3418	2112 (62%)
Cerro Tololo	807	Chile	T. Linder, R. Holmes	0.41 m	20–21	2563	1659 (65%)
Spacewatch II	291	Arizona, USA	R. McMillan	0.9 m; 1.8 m	20–23	2511	2149 (86%)
Schiaparelli	204	Italy	L. Buzzi	0.38 m; 0.6 m	22	1821	567 (31%)
Sandlot	H36	Kansas, USA	G. Hug	0.56 m	22	1040	437 (42%)
Great Shefford	J95	England	P. Birtwhistle	0.4 m	20–21	968	388 (40%)
Mauna Kea	568	Hawaii, USA	D. Tholen, R. Wainscoat	2.2 m; 3.6 m	>23	937	827 (88%)
Desert Moon	448	New Mexico, USA	B. Stevens, J. Stevens	0.3 m	20–21	896	314 (35%)
Magdalena Ridge	H01	New Mexico, USA	W. Ryan, E. Ryan	2.4 m	24	854	573 (67%)
Tenagra II	926	Arizona, USA	M. Schwartz	0.8 m	18–21	782	402 (51%)

The sites are ranked and listed by total number of NEOs observed at each observatory from June 2011 through June 2014. Columns are the observatory name or acronym; site’s IAU observatory code; site’s location; name of the current lead, observer, or principal investigator; telescope aperture in meters; limiting magnitude in the V band; total number of NEOs observed during the four years from 2011 to 2014 inclusive; and number of NEOs observed at each facility with V > 20 (and fraction of NEOs with V > 20). The last column is provided to illustrate that some facilities excel at faint object follow-up.

degree; bigger fields facilitate astrometric follow-up when ephemeris uncertainties are large. The Astronomical Research Observatory (ARO), located in Westfield, Illinois, currently tops the NEO follow-up list while at the same time contributing to astronomical education and public outreach by involving amateur astronomers and students. They have recently included a southern hemisphere site at Cerro Tololo, Chile, to follow up objects that are too far south for most of the follow-up facilities that are located in the northern hemisphere. Large-aperture telescopes with faint limiting magnitudes that can gather good signal-to-noise detections even through thin clouds are valuable tools for faint objects or when weather conditions are less than optimal (e.g., Mauna Kea and Magdalena Ridge in Table 4). Unfortunately, these large-aperture observatories are typically only available for follow-up on a few nights per lunation because they are not dedicated NEO facilities. The researchers and sites within the University of Hawaii network (*Tholen et al.*, 2013; *Wainscoat et al.*, 2013) give preference to follow-up of NEO candidates discovered with the PS1 telescope using their 2-m-class and larger telescopes on Mauna Kea, a big advantage for follow-up of the smaller/fainter objects being discovered by PS1. The Magdalena Ridge Observatory's (MRO) fast-tracking 2.4-m telescope (*Ryan et al.*, 2002), located in New Mexico, has the ability to accurately track rapidly moving targets that is essential for follow-up of challenging faint objects or for physical characterization (i.e., to keep the moving object on the spectrograph's slit). MRO performs follow-up astrometry and real-time characterization (spin rates and composition), achieves subarcsecond point spread functions (PSFs) even close to the horizon (pushing the limits to lower declinations than typical for the northern hemisphere), and can have multiple instruments mounted simultaneously (for rapid switching between photometry and spectroscopy).

It is common, natural, and unfortunate that a recently discovered object receives a lot of attention primarily during the few days after discovery when often hundreds of astrometric and physical observations are collected by professional and amateur observers. The attention is explicable because objects tend to be discovered near a maximum in apparent brightness so that all aspects of follow-up are easier. However, the major determinant in orbit-element accuracy is the temporal coverage, not the number of observations; i.e., there is an opportunity cost of too many observations because most of them will not contribute to improving the orbit. It is therefore desirable that observers that have access to large-aperture telescopes obtain astrometric measurements of the most important targets down to the limiting magnitude of their instrumentation [e.g., V ~ 26 for 8–10-m-class telescopes such as that achieved in the ESA's efforts with the Very Large Telescope (VLT) (*Micheli et al.*, 2014) and Large Binocular Telescope (LBT)]. Only this additional optical and orbital-arc coverage will make it possible to determine an orbit accurate enough to recover the object in its next apparition, which may be many years or even decades in the future, unless radar data are available (e.g.,

*Ostro et al.*, 2004). The wasted effort and lack of temporal coverage for important objects suggest that there is a need in our community for an enhanced follow-up coordination effort beyond the current capability of the NEOCP. A centralized scheduling site that assigns available observing sites to specific targets based on weather, limiting magnitude, location, etc., could increase the efficiency of the overall follow-up effort (we note that this effort could be a component of the “Management Action” called out by NASA’s Office of Inspector General’s report on the NEO effort; IG-14-030, September 15, 2014). The ESA NEO Coordination Centre is already coordinating follow-up observations of high-relevance targets by a worldwide network of cooperating observatories by providing them with rapid triggers when an observational opportunity arises appropriate for their systems. Over the past year their coordination efforts have contributed to the removal of 20 high-rated virtual impactors from their impact risk list.

The subsequent recovery of an object in a future apparition, enabled by a well-orchestrated follow-up effort in the discovery apparition, would result in a dramatic decrease in its orbit-element uncertainty and correspondingly extend the ephemeris accuracy for decades into the future. However, in some (rare) cases an object’s dynamics may be so complex that, even then, predicting its motion is nontrivial. This often occurs when there are future close encounters with major planets or when nongravitational forces become relevant. In these cases, observational coverage extending over multiple apparitions is often necessary to model the phenomena to a sufficient level of accuracy to accurately predict the object’s future behavior (e.g., *Farnocchia et al.*, 2013; *Chesley et al.*, 2014; see also the chapter by Farnocchia et al. in this volume).

The rationale for, and scientific benefits of, observations of asteroids at the Arecibo radar facility (Puerto Rico) and Goldstone Deep Space Network (California) are unassailable, but radar follow-up and characterization is expensive in time and resources. Radar directly and uniquely provides range, range-rate, shape, spin, and size data that complement the optically derived physical information (e.g., *Ostro and Giorgini*, 2004) and enables computation of asteroid ephemerides much further into the future than ephemerides derived from optical-only astrometry because of radar’s exquisite precision in measuring the object’s range and range-rate. However, the only way that a radar facility can detect an object is with an accurate orbit provided by optical assets. Thus, radar is typically employed only for the most “interesting” objects.

The follow-up effort is more complicated for spacebased discoveries (e.g., from NEOWISE; see the chapter by Mainzer et al. in this volume). Delays in posting the candidate NEO’s ephemerides caused by scheduling the Deep Space Network for data transmission from the spacecraft (by several days) can result in untenable ephemeris errors. Furthermore, if an NEO has been discovered in a passband that is not a groundbased standard (e.g., an IR space telescope), then the transformation from the spacecraft’s passband to groundbased passbands can generate significant errors in the predicted apparent magnitudes. The apparent magnitude can

be much fainter than expected if the object is of low albedo (dark), such that acquiring good signal-to-noise detections for the object is difficult or impossible from the ground. Future wide or deep spacebased surveys will need to carefully consider groundbased follow-up requirements or build self-follow-up into their survey strategy.

The future needs for asteroid follow-up and rapid physical characterization are clear — neither will keep pace with the expected discovery rates of future surveys (see section 7). The mean V-magnitude of asteroids at discovery is now about 20, which limits follow-up and characterization sites to professional telescopes or a handful of the most advanced amateur astronomers. As the capabilities of the ground- and spacebased survey telescopes continue to improve, pushing the mean discovery magnitude to even fainter values, the follow-up contribution from the amateur community will drop. This will require the survey telescopes to adopt self-follow-up survey strategies that reacquire their own discoveries several times per month. Indeed, the advent of deep *and* wide surveys has changed the cost-benefit analysis of separating surveying and follow-up such that it may now simply be more efficient to do both with the same system in an integrated discovery and follow-up survey program. The reobserving strategy will reduce the possible discovery rate, but the good news is that the strategy will extend the main-belt minor planet catalog to much smaller sizes.

In many important cases it has been possible to dramatically increase the known arclength for an object that has become unobservable by identifying “precovery” observations in historical images. Over the last decade most professional observatories and surveys have developed online repositories of all their astronomical images, including digitizing very old photographic plates with associated astrometry and photometry of all sources in the images. Most of the images were acquired for projects unrelated to asteroids, but some of them contain unrecognized detections of known asteroids. The most obvious example is the MPC’s ONS file (section 4), which is automatically searched by the MPC for precoveries when feasible. In other cases, and increasingly more commonly, a survey’s archival detection database can provide precovery observations. Although the survey’s images were already inspected for moving objects, there may be cases where an object was too faint to be detected or reported with confidence, but a precovery tracklet can be identified given a new object’s ephemeris. The success of the precovery efforts coupled with the relatively modest cost of archiving images suggests that surveys should “save all the bits,” i.e., every bit of every pixel of every image should be stored and, even better, searchable and accessible in an online repository.

## 6. POPULATION STATISTICS

We tend to think of distinct populations of asteroids in the inner solar system even though we know that they are actually interrelated. For instance, the NEOs are fragments created in the collisions of main-belt asteroids that have been

transported to near-Earth space by orbital evolution driven by gravitational dynamics and thermal recoil forces (e.g., see the chapter by Binzel et al. in this volume). Furthermore, we are now beginning to understand that many main-belt asteroids may be implanted objects that were originally formed elsewhere in the protosolar system. Thus, in this section we attempt to address inner solar system asteroids holistically, providing orbit-element distributions of NEOs, MBOs, and Jupiter’s Trojans on the same scales and figures and touch upon the transfer of objects between them (Fig. 2). That being said, we cannot avoid the conventional nomenclature for the populations, so when we refer to NEOs, we explicitly mean those objects with perihelion  $q \leq 1.3$  AU and

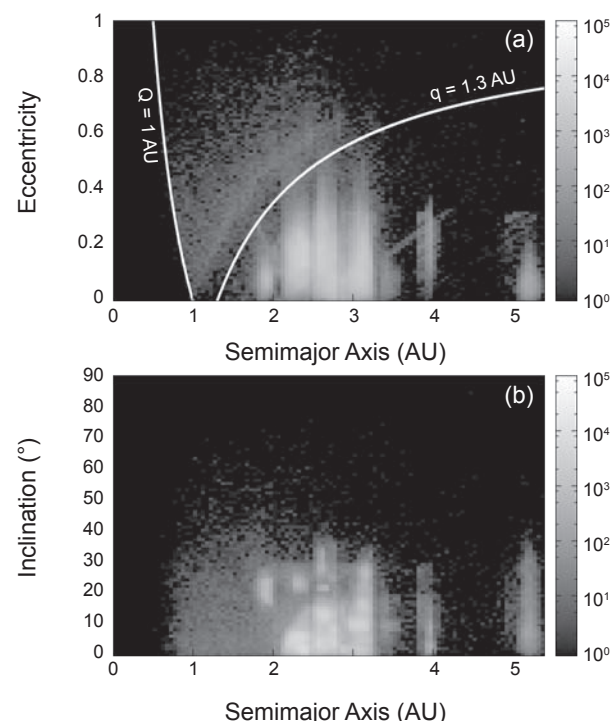


**Fig. 2.** (a) Eccentricity and (b) inclination vs. semimajor axis for all known asteroids in the inner solar system available in the MPC database as of June 8, 2014. Note that the completeness, the fraction of the actual population that is known, varies as a function of semimajor axis, so these images do not provide a good representation of the actual distribution of asteroids (see Fig. 3). The clump of objects with  $2 \text{ AU} \leq a \leq 3.5 \text{ AU}$  are the main-belt objects and the clump just under  $4 \text{ AU}$  are the dynamically separated Hilda population. The group just beyond  $5 \text{ AU}$  are the Jupiter Trojan objects (JTO). The near-Earth objects are those above the (solid white)  $1.3\text{-AU}$  perihelion line in (a). Objects on the left of the aphelion line at  $1 \text{ AU}$  in (a) have orbits entirely inside Earth’s orbit. The enhancement of NEOs along the  $q \sim 1 \text{ AU}$  curve in (a) is an observational selection effect that makes it easier to detect those objects from Earth. The “diagonal feature” in (a) near  $a = 3.7 \text{ AU}$  and  $e = 0.2$  are all WISE spacecraft discoveries that lack proper follow-up observations and only have a very rough, eccentricity-assumed orbit.

semimajor axis  $a < 4.2$  AU. The MBOs are defined as those with  $q > 1.3$  AU and  $a < 4.8$  AU, while jovian Trojan objects (JTO) have  $q > 4.2$  AU and  $4.8 \text{ AU} < a < 5.4$  AU.

In what follows we will frequently refer to “unbiased” and “debiased” distributions. We use the term “unbiased” to refer to the true distributions, whereas “debiased” means that the observed distributions have been corrected for observational selection effects. A perfect debiasing procedure would lead to identical unbiased and debiased distributions. We can only provide unbiased distributions in circumstances for which there is evidence that the entire population is already known, e.g., main-belt asteroids larger than 10 km in diameter. A good introduction to various types of selection effects is given by Jedicke *et al.* (2002) and recent advances for quantifying these effects are described by Jedicke *et al.* (in preparation).

We will present the asteroid’s absolute-magnitude ( $H$ ) distributions in terms of their cumulative number,  $N(< H) \propto 10^{\alpha H}$ , where  $\alpha$  is referred to as the “slope.” When available or appropriate, we may provide the diameter ( $D$ ) number distribution, where  $N(> D) \propto D^{-b}$  and  $b$  is also called the “slope.” Both the  $H$  and  $D$  versions are often colloquially referred to as the “size” distribution. The slopes are generally not constant with  $H$  or  $D$  but are often approximately constant over some intervals. The two slope parameters are related by  $b = 5\alpha$  under the assumption of a constant albedo within a population.

## 6.1. Near-Earth Objects

The Bottke *et al.* (2002) NEO population model has been extremely successful for the past 12 years, especially considering that it was calibrated with only 137 known NEOs. Their modeling approach utilized dynamical constraints provided by the orbital-element “residence-time” distributions for NEOs originating in different source regions (essentially likelihood maps in orbital-element space). The only notable improvement to the model was the recalculation of the residence-time distributions by Greenstreet *et al.* (2012a) using smaller timesteps and more particles to reduce the statistical noise and provide an improved orbital model. They did not refit the observed NEO population but provided an improved NEO model using the Bottke *et al.* (2002) source weights and slope ( $\alpha = 0.35$ ) of the  $H$  distribution. The Greenstreet *et al.* (2012b) NEO model suggested that there exist dynamical pathways from prograde MBO orbits to retrograde NEO orbits and estimated that there are about four  $H < 18$  NEOs on retrograde orbits at any time. They also concluded that one of the currently known retrograde NEOs is likely an asteroid rather than a comet.

Preliminary results from the WISE mission suggested that there are  $981 \pm 18$  NEOs with  $D > 1$  km and that the cumulative diameter distribution could be represented by a broken power-law with  $b = 5$  for  $D > 5$  km,  $b = 2.1$  for  $1.5 < D < 5$  km, and  $b = 1.32 \pm 0.14$  for  $D < 1.5$  km (Mainzer *et al.*, 2011b). Their subsequent preliminary analysis (Mainzer *et al.*, 2012) of the four NEO subpopulations

(Atiras, Atens, Apollos, and Amors) suggested that there are fewer high-inclination Aten asteroids than predicted by Bottke *et al.* (2002), a result that was soon verified by Greenstreet *et al.* (2013).

Zavodny *et al.* (2008) derived the absolute-magnitude and orbit distribution for Atiras — objects orbiting the Sun entirely inside the orbit of Earth (IEO) — using data obtained by the CSS. They found that the Bottke *et al.* (2002) NEO orbit distribution is consistent with the CSS observations and derived a nearly independent measurement of the slope of the absolute magnitude distribution ( $\alpha = 0.44^{+0.23}_{-0.22}$ ), again, consistent with both Bottke *et al.* (2002) and Stuart (2001).

Temporarily captured natural Earth satellites are a recently recognized NEO subpopulation (Granvik *et al.*, 2012). The average length of capture in the Earth-Moon system is about 9 months for these “minimoons” and the largest object at any given time has a diameter of about 1 to 2 m assuming that their size distribution follows that observed for small Earth-impacting asteroids (Brown *et al.*, 2002, 2013). Only one minimoon has been positively identified [2006 RH<sub>120</sub> (Kwiatkowski *et al.*, 2009)] due to their small sizes and rapid sky-plane motions, but the discovery rate will most likely increase in the future as the next generation of asteroids surveys come online (Bolin *et al.*, 2014) (see section 7).

Figures 3 and 4 illustrate the orbit and absolute-magnitude distributions for NEOs from the preliminary work of Granvik *et al.* (2014) because (1) they used the largest currently available single-survey NEO dataset (from CSS) and (2) their work is an independent data product in the sense that its development did not rely on any other NEO models; i.e., the WISE measurements were debiased assuming the orbital distribution by Bottke *et al.* (2002), and Greenstreet *et al.* (2012b) also used the source ratios and size distributions from Bottke *et al.* (2002). The Granvik *et al.* (2014) estimate for the number of  $H < 18$  NEOs agrees with Stuart (2001), and the number of  $H < 17.75$  NEOs is consistent with the number of  $D > 1$ -km NEOs predicted by Stuart and Binzel (2004) and Mainzer *et al.* (2011b). The advantage of using the results of Granvik *et al.* (2014) is that they provide (1) the debiased ( $a, e, i$ ) orbital-element distributions and (2) an extended range in the debiased absolute magnitude number distribution to  $H = 25$ . The functional form of their  $H$  distribution allows for a “wave” (a nonconstant slope) as suggested by, e.g., Harris (2013), but does not require it. They also allow a different  $H$  distribution for each of their seven source regions so that the observable NEO  $H$  distribution is the sum of seven analytic functions and the NEO orbit distribution changes slightly as a function of  $H$ .

## 6.2. Main-Belt Objects

It is challenging to develop debiased size and orbit distributions for MBOs that extend to sizes smaller than the completeness level [currently about  $H \sim 17$  (Denneau *et al.*, 2015)] because asteroid families induce discontinuities into the distributions and, contrary to NEOs, MBOs are not replenished from outside sources. In other words, the MBO

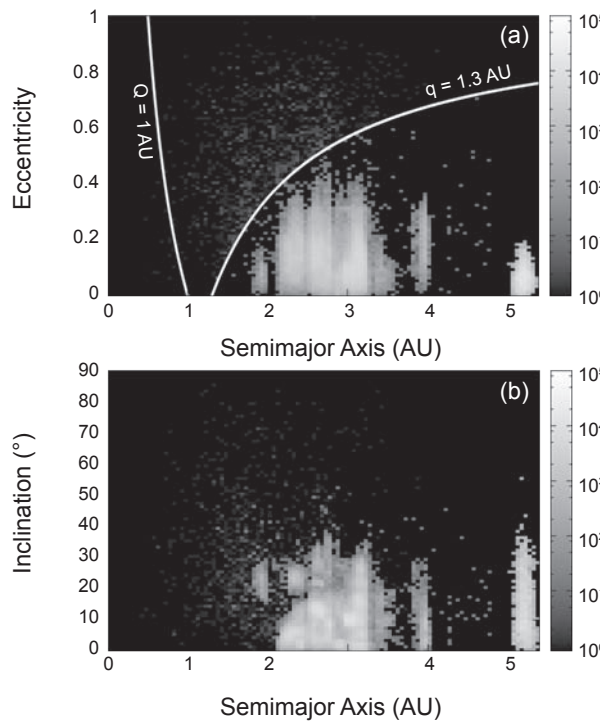


**Fig. 3.** Debiased (a) eccentricity and (b) inclination vs. semimajor axis for asteroids with  $H < 18$  in the inner solar system. For NEOs we use the Granvik et al. (2014) model. For MBOs and JTOs we assume a negligible correlation between orbital elements and size, and extrapolate the orbit distribution from the assumed completeness levels of  $H = 15$  and  $H < 12.5$ , respectively, using the slopes shown in Fig. 4. The total number of NEOs, MBOs, and JTOs with  $H < 18$  are predicted to be about 1500, 1,300,000, and 600,000, respectively. The near-Earth objects are those above the 1.3-AU solid white perihelion line in (a). Objects on the left of the aphelion line at 1 AU in (a) have orbits entirely inside Earth's orbit.

population is not in a steady state — it continues to erode through collisional grinding, and dynamical- and radiation-induced orbit evolution. There are two population models for the MBO orbit and absolute-magnitude distributions: the Statistical Asteroid Model (SAM) (Tedesco et al., 2005) and the Pan-STARRS Synthetic Solar System Model (S3M-MBO) (Grav et al., 2011a). Both models were developed by starting from the unbiased orbital-element distribution of large MBOs. The MBOs were extrapolated to smaller sizes assuming a negligible correlation between size and orbit, and that the slope of the H-distribution is constant beyond the H completeness limit at the time of the model's development. The S3M-MBO uses a single slope for all subcomponents of the main asteroid belt, whereas SAM employs different slopes for each of 15 families and 3 background populations. The maximum absolute magnitude in the S3M is correlated with perihelion distance so that it only contains synthetic objects that can reach  $V < 24.5$  at perihelion at opposition, i.e., those that might be detectable by the four-telescope

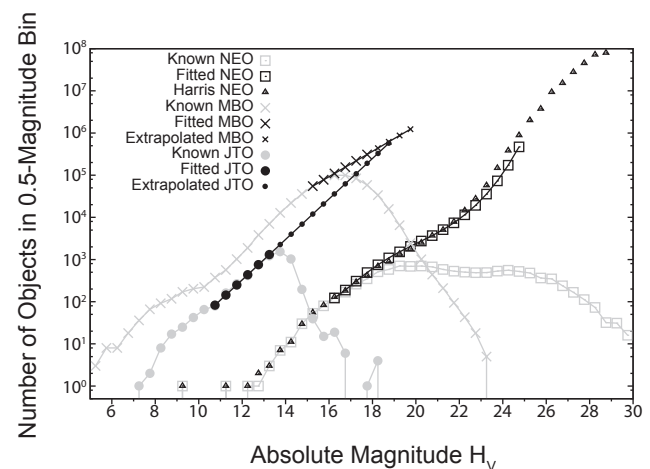


**Fig. 4.** Known, fit, and extrapolated H-distributions of NEOs, MBOs, and JTOs. The “known” population is the number of objects in the MPC database as of June 8, 2014. The “fitted” populations represent the debiased distributions over specific H ranges for NEOs and MBOs as derived by Granvik et al. (2014) and Gladman et al. (2009), respectively. The “Harris” NEO HFD is provided for reference and described in the chapter by Harris et al. in this volume. For JTOs we use a slope of  $\alpha = 0.48$  and assume that there are  $10^6$  JTOs with  $H < 18.5$  — the slope is slightly shallower but still in statistical agreement with that derived by Szabo et al. (2007). The NEO H-distribution has to become shallower for  $H > 25$  to match the bolide data (Brown et al., 2013). The “extrapolated” populations for MBOs and JTOs are simple linear extensions of the HFD to larger H (smaller diameters) for the purpose of comparison with the other populations in an extended H range.

Pan-STARRS, equivalent to modeling all objects in the main belt with  $D \geq 300$  m but including objects as small as 100 m in diameter on the inner edge. SAM attempted to reproduce the distribution of all MBOs with  $D > 1$  km.

While these models are the most comprehensive MBO models to date, they represent only the first steps in modeling this complex population. The actual population at the smallest sizes and most extreme orbits cannot be simply extrapolated from larger objects and more common orbits, as demonstrated by:

- *Subkilometer Main-Belt Asteroid Survey (SMBAS):* The SMBAS (Yoshida et al., 2003) with the Subaru telescope demonstrated that the cumulative size distribution slope is shallower for subkilometer MBOs ( $0.5 \text{ km} < D < 1 \text{ km}$ ) than for  $D > 5 \text{ km}$  MBOs,  $b \sim 1.2$  vs. 1.8, respectively. The depletion of subkilometer MBOs is more pronounced in the outer belt ( $a > 2.5$  AU) than the inner belt ( $a < 2.5$  AU).
- *Sub-Kilometer Asteroid Diameter Survey (SKADS):* The pencil-beam-type SKADS (Gladman et al., 2009) derived a debiased H-magnitude distribution of  $\alpha = 0.30 \pm 0.02$  throughout the main belt in the range  $15 < H_R < 18$ . Limiting the analysis to the inner main

belt allowed them to extend the absolute magnitude interval to  $15 < H_R < 19.5$ , for which the slope is marginally shallower with  $\alpha = 0.23 \pm 0.04$ . A fit to the SKADS dataset does not *require* a decrease in the slope for  $H \geq 18$  but cannot rule it out.

- *Terai et al. (2013)*: Terai et al. suggest that high- and low-inclination MBOs have different size-frequency distributions based on observational data collected with the Subaru telescope. They interpret this as a consequence of the larger impact speed for high-inclination asteroids.

### 6.3. Trojan Asteroids

Trojan asteroids orbit the Sun in a 1:1 mean-motion resonance with a planet and populate two distinct “clouds” leading or trailing the planet by  $\sim 60^\circ$ , the Lagrange 4 ( $L_4$ ) and Lagrange 5 ( $L_5$ ) clouds, respectively. In what follows we will primarily discuss JTOs but also touch upon Trojans of other planets in the inner solar system.

The Nice model (e.g., *Morbidelli et al.*, 2005) suggests that the JTOs originated in the outer reaches of the protoplanetary disk with semimajor axes in the range  $15 \text{ AU} < a < 30 \text{ AU}$  and were dynamically captured by Jupiter during the repositioning of the planets after the formation of the solar system. Interestingly, the number of JTOs in the clouds appears to be unequal: *Szabo et al.* (2007) estimated that the  $L_4:L_5$  number ratio is  $1.6 \pm 0.1$  based on SDSS data, whereas *Grav et al.* (2011b) derived an independent ratio of  $1.4 \pm 0.2$  using WISE measurements. Assuming that the two values are truly independent, the error-weighted ratio of  $1.58 \pm 0.08$  is more than  $7\sigma$  from unity. The combined clouds have an H-distribution with a slope of  $\alpha = 0.64 \pm 0.05$  in the range

$9 < H < 13.5$  (*Szabo et al.*, 2007). The equivalent slope of the cumulative size distribution is  $b = 2.2 \pm 0.25$ , in agreement with the preliminary result from WISE of  $b \sim 2$  (*Grav et al.*, 2011b). Similar slopes have recently also been obtained by *Yoshida and Nakamura* (2005) using a substantially smaller sample size.

Trojan objects have also been discovered for Mars (MTO) [see *de la Fuente Marcos and de la Fuente Marcos* (2013) and *Christou* (2013) for the most recent tally], Venus (VTO) (*de la Fuente Marcos and de la Fuente Marcos*, 2014) and Earth (ETO) (*Connors et al.*, 2011). Based on the uneven distribution of objects in the Mars  $L_4$  and  $L_5$  clouds (1 vs. 7), and the compactness of the orbital distribution in  $L_5$ , both *de la Fuente Marcos and de la Fuente Marcos* (2013) and *Christou* (2013) suggest that the objects in  $L_5$  have a common origin in either a collisional or a rotational breakup event. Whereas the eight known MTOs are on orbits that are stable on gigayear timescales, the known ETOs and VTOs appear to be transient captures of NEOs with kiloyear lifetimes.

## 7. ANTICIPATING THE FUTURE

The next decade of NEO discovery will likely be dominated by the large-aperture, wide-FOV, groundbased telescopes or the spacebased near-IR discovery systems described below, with details provided in Table 5. But this NEO-centric viewpoint belies the important contributions to the detection and monitoring, follow-up, and characterization of all the asteroids in the inner solar system. Some or all of these efforts might still be dominated by smaller-aperture and visible-light groundbased systems. Furthermore, we specifically address an emerging new camera technology that could impact the way we detect all types of asteroids — early tests

TABLE 5. Anticipated improved and new sky surveys.

Survey	Site	Lead(s)	Aperture (m)	f-Ratio	FOV (deg <sup>2</sup> )	Pixel Scale ("/pix)	IAU Obs Code
ATLAS	Haleakala, Hawaii, USA	J. Tonry	0.5	2.0	30	1.86	TBD
ATLAS	Mauna Loa, Hawaii, USA	J. Tonry	0.5	2.0	30	1.86	T08
CSS	Schmidt, Arizona, USA	E. Christensen	0.68	1.8	8.2	2.5	703
CSS	Mt. Lemmon, Arizona, USA	"	1.50	2.0	1.2	1.0	G96
Gaia	Earth-Sun L2	ESA, T. Prusti	1.45 × 0.5	n/a	0.42	0.059 × 0.18	TBD
Fly-Eye	TBD	ESA SSA-NEO D. Koschny and G. Drolshagen	1.1	2.0	45	1.5	TBD
LSST	Cerro Pachon, Chile	LSSTC*	8.4 (6.4 <sup>†</sup> )	1.2	9.6	0.22	TBD
Pan-STARRS2	Haleakala, Hawaii, USA	R. Wainscoat	1.8	4.0	7	0.26	F51
Spacewatch	Kitt Peak, Arizona, USA	R. McMillan	0.9	3.0	2.9	1.0	691
Spacewatch	"	"	1.8	2.7	0.6	1.0	291
SST	Atom Peak, New Mexico, USA	G. Stokes	3.5	1.0	6	0.89	G45

\* LSST is operated by the LSST Corporation.

<sup>†</sup> LSST will have an unusually large secondary mirror and “dual-purpose” primary mirror, so we also provide the system’s effective aperture.

Listed in alphabetical order by survey name. Fly-Eye, Gaia, LSST, and SST are not focused on NEO or asteroid discovery but could make major contributions to the inventory. We provide site-specific information even for surveys that use multiple sites and/or telescopes. The list includes only funded surveys as the time of this writing. The columns are survey, site, P.I., telescope aperture in meters, f-ratio (focal length of primary mirror divided by its aperture), FOV in square degrees, image scale in arcseconds per pixel, and IAU observatory code.

are promising, but its actual implementation awaits funding and verification.

This section is divided into three subsections that present our current understanding of upcoming improvements and expected new ground- and spacebased assets. The facilities in each subsection are presented alphabetically.

## 7.1. Upgrades to Existing Facilities

**7.1.1. Catalina Sky Survey (CSS).** The CSS team has distinguished itself in their ability to constantly improve their systems, and are currently in the process of installing monolithic  $10k \times 10k$  CCD cameras on both the CSS Schmidt and MLS telescopes. This will effectively double the surveying capability of the CSS Schmidt, allowing 3000 to 5000 deg $^2$  of sky to be surveyed nightly to V  $\sim$  20. The MLS telescope will enjoy a factor of 5 increase in area coverage through the addition of reducing optics, and will be capable of surveying  $\sim$ 1000 deg $^2$ /night to V  $\sim$  21.5. It is possible that the CSS Schmidt will be used to survey most of the observable sky over the course of a night or two. The repeated survey coverage will yield a more complete main-belt minor planet catalog because it will be easier to link asteroid detections from night to night, and then to other apparitions.

Further improvements will be realized by pushing the capability of linking detections to faster rates and nonlinear motion. Most surveys currently require that detections on a single night follow a linear trajectory even though the closest object's paths will be curved on the sky plane; since most surveys ignore the curvature, it implies that many nearby, perhaps even geocentric, objects are not being identified by the current surveys. Yet another seemingly mundane  $\sim$ 30% reduction in the time required for the telescope to step + settle + readout will yield a 10–12% increase in overall area coverage and, presumably, discovery rate.

The combined CSS and MLS telescopes should extend the completeness of the main-belt minor planet catalog to an absolute magnitude well beyond the current 17.5 (Denneau et al., 2015), perhaps as deep as H  $\sim$  19 (about 800 m diameter). The increased discovery rate is not expected to have any impact on the MPC processing of the reported observations.

**7.1.2. Panoramic Survey Telescope and Rapid Response System (Pan-STARRS).** Beginning in March 2014 and continuing through at least March 2015, PS1 has been dedicated 100% to the NEO survey, after which it will continue to devote 90% of its time to the search. It will be joined in late 2015 by a second, nearly identical, telescope, Pan-STARRS2, and both telescopes will be used for the NEO survey at the 90% level through at least September 2017. Doubling the number of telescopes will not double the NEO discovery rate because not all areas of the sky are equally rich in unknown NEOs.

Upgrading the CCDs in both telescopes has the potential to dramatically increase the NEO discovery rate, but is dependent on whether funding can be identified. The existing CCDs each have a cell structure consisting of an  $8 \times 8$  grid of  $600 \times 600$  pixels, which makes the system less efficient

for finding faster-moving objects because they can move over the cell gaps (which are not sensitive to light), dividing the asteroid's trail in two. Larger monolithic commercial-grade low-noise CCDs will eliminate this problem, correct cosmetic problems in the existing CCDs that decrease the effective fill factor, and allow deeper NEO searches due to lower noise.

The IPP (Magnier, 2006) and MOPS (Denneau et al., 2013) (see section 3.6) are both being continually tuned and improved to enhance the NEO detection efficiency.

## 7.2. Exciting New Facilities and Technologies

**7.2.1. Asteroid Terrestrial-impact Last Alert System (ATLAS).** The University of Hawaii's ATLAS project (Tonry, 2011) is expected to be operational in 2015 when it will begin robotically surveying the entire sky multiple times each night. The system will have two identical 50-cm Wright-Schmidt telescopes, each located in separate domes: one on Mauna Loa, Hawaii, and the other on Haleakala, Maui. The telescopes will have 7.4° FOVs instrumented with STA-1600 110-megapixel CCDs. They expect to identify asteroids roughly in the range  $13 < r < 20$  with each primary system and to identify asteroids in the  $6 < r < 14$  range with auxiliary cameras co-mounted on each of the primary telescopes. (The r wavelength band is similar to the Johnson-Cousins R band.) Thus this system could monitor the entire main belt visible in the night sky to about r = 20 multiple times each night.

**7.2.2. Fly-Eye.** The ESA is planning a network of small telescopes with a novel "Fly-Eye" optical concept to completely scan the sky each night to identify space debris and NEOs (Cibin et al., 2012). The system's name captures the idea that the optics create 16 subimages of a field that are seamlessly stitched together to create a composite image with a 100% "fill-factor" [the fraction of the image plane or sky that is actively instrumented; e.g., the PS1 mosaic camera system has a fill factor of  $\sim$ 75% (Denneau et al., 2013)]. A prototype system is currently being built that has a  $6.7^\circ \times 6.7^\circ$  FOV (about 45 deg $^2$ ) with performance equivalent to a 1-m-diameter telescope.

**7.2.3. Gaia.** The ESA's Gaia mission (e.g., Lindegren et al., 2008) will measure the positions of about a billion stars spanning the entire sky to about 24 parsec precision. As of June 13, 2014, there were already over 260 published, refereed articles about the Gaia mission despite the fact that the primary survey had not even begun; 35 of those papers had both Gaia in the title and "asteroid" as a keyword. There is no doubt that Gaia's astrometric and photometric catalog will transform our ability to measure an asteroid's position and brightness, and the spacecraft should provide spectrophotometry of asteroids with V  $<$  20. Gaia is expected to detect about 350,000 asteroids and yield spectral classifications for about a quarter of that sample (e.g., Delbo et al., 2012; Mignard et al., 2007).

**7.2.4. Large Synoptic Survey Telescope (LSST).** The LSST has the potential to be an extremely powerful asteroid

detection and discovery telescope. With an expected limiting magnitude of  $R \sim 24$ , it could discover millions of new MBOs and hundreds of thousands of NEOs during its operational lifetime. The system is expected to repeat the same fields every four nights, thus providing its own follow-up. A system this robust could obviate most other groundbased observing systems for discovery (but asteroids brighter than  $R \sim 18$  would saturate the system and probably not be reported). Its actual performance for discovering asteroids will remain to be demonstrated because LSST intends to acquire only two frames per night separated by a small time interval. This strategy should pose little difficulty for linking detections to known objects, but its application to discovering new objects could be limited by the false detection rate.

**7.2.5. Space Surveillance Telescope (SST).** The U.S. Defense Advanced Research Projects Agency's (DARPA) SST has a 3.5-m-diameter mirror and an  $f = 1.0$  Mersenne-Schmidt optical system that is currently located on Atom Peak in New Mexico, at 2400 m elevation within the White Sands Missile Range, but is scheduled to be moved to Australia. The extremely fast telescope has a curved focal plane instrumented with *curved* CCDs developed specifically for the purpose. It is capable of covering several thousand square degrees per night to  $V > 20$ . The SST's primary goal is to survey the geosynchronous belt, but DARPA is considering providing some of the survey time to an asteroid survey (Monet *et al.*, 2013), much like the LINEAR system (Stokes *et al.*, 2000) was tasked for NEO surveying when not searching for satellites. LINEAR set the performance bar when it joined the NEO search and there is little doubt that the SST could do the same if it brings its new-technology, large-aperture, large-field, fast-optics, and rapid-readout system to bear on the NEOs.

**7.2.6. Synthetic tracking.** Shao *et al.* (2014) describe the application of two new technologies to asteroid detection that might, if successful, advance the field over the next decade. They combine new low-noise fast-readout CCDs with the computational power of graphics processing units (GPU). Their CHIMERA camera, with a  $2.5' \times 2.5'$  FOV, has already been tested on the Palomar 5-m telescope where they obtained images at 2 Hz (much faster rates will be used in standard operations) and then implemented the standard shift-and-add technique on their GPU to "synthetically track" an asteroid. They hope to upgrade their camera to a  $8' \times 8'$  FOV in the next couple of years, which will enable rapid searching, albeit over limited areas, for fast-moving asteroids to as faint as  $V \sim 25$ .

### 7.3. Possible Future Spacebased Missions

**7.3.1. Near-Earth Object Camera (NEOCam).** NEOCam is a proposed NASA Discovery-class mission whose goal is to survey for NEOs from a spacebased platform operating from near the Earth-Sun  $L_1$  point. Given the success of the NEOWISE mission (Mainzer *et al.*, 2011a), we expect that the substantially larger telescope surveying 100% of the time

for NEOs will be extremely successful. NEOCam should excel at detecting NEOs due to strong emission in the proposed 6–10- $\mu\text{m}$  band. Loosely translating this to the R-band suggests that the NEOCam survey could reach a groundbased equivalent depth of  $R \sim 24$ –25, making it an extraordinarily powerful survey capable of discovering hundreds of thousands of NEOs and more than  $10^6$  MBOs. NEOCam plans to adopt a self-follow-up cadence such that each field will be imaged at least  $4\times$  per day and each field will be visited every  $\sim$ 6 nights. Preliminary tests of the observing cadence have already been accomplished with the MPC and their existing software can easily link NEOs observed in this fashion.

**7.3.2. Sentinel.** The philanthropic nonprofit B612 organization (<https://b612foundation.org>) is attempting to raise private donations to fund the construction, launch, and operations of a spacecraft specifically designed to identify "threatening asteroids whose orbits approach Earth," i.e., PHOs, and identify many other NEOs and MBOs in the process. They hope to launch the spacecraft in 2017–2018 into a Venus-like elliptical orbit for its 6.5-yr mission. The orbit is particularly effective for identifying PHOs since they must pass through a torus of 0.05 AU diameter centered on Earth's orbit that is always exterior to the spacecraft's orbit. They expect to survey  $\sim$ 165 deg $^2$ /h with a 24-million-pixel IR camera (5–10.2  $\mu\text{m}$ ) with an 11-deg $^2$  FOV.

## 8. SUMMARY AND CONCLUSIONS

The NEO surveys have improved dramatically since publication of *Asteroids III*, yielding 8 $\times$  more NEOs and 10 $\times$  more MBOs in the last five years than in the five years leading up to *Asteroids III*. This accomplishment is all the more impressive considering that none of the current survey telescopes was designed with NEO observations in mind — they are all repurposed instruments originally designed for entirely different operations.

The situation could change in the next decade with the introduction of new groundbased and/or spacebased surveys specifically designed for NEO observations (e.g., ATLAS, NEOCam, Sentinel). These new facilities suggest that we can expect an increased discovery rate of asteroids in the near future, but they will require a concomitant operational evolution. For instance, existing NEO surveys still rely on human vetting of asteroid tracklet candidates, but this process might not be tenable if the discovery rate increases another order of magnitude. It seems clear that the surveys will need to implement regular self-follow-up, improved software processing, and coordination of surveying and follow-up efforts through a centralized organization (cf. NASA's Office of Inspector General's report on the NEO effort; IG-14-030, September 15, 2014).

Improvements to the existing surveys and the development of the next-generation surveys will push the completeness limits of all the inner solar system's asteroid subpopulations to ever smaller sizes to allow us to study the unbiased orbit and size distributions. Debiasing the populations to even

smaller sizes requires attention to the surveying plan and measuring the system's detection efficiency from the outset. Indeed, the limiting factor in generating good debiased models of the inner solar system's asteroid populations is the lack of well-calibrated survey data, e.g., detection efficiencies, per detection astrometric and photometric uncertainties, etc.

Most of the largest, globally devastating PHOs larger than 1 km diameter are now known, but there remains a residual impact risk from the remaining unknown ~10% and sporadic long-period comets. Perhaps surprisingly, that risk is now comparable to that of <100-m-diameter objects because of (1) the reduced slope of the NEO SFD in the 100-m to 1-km-diameter range and (2) the partial discovery of some of the objects in the intermediate range. In any event, there are active plans and funding to address the residual risk in the next decade, mostly funded by NASA and mostly based in the U.S. The scientifically interesting and spacebased resource utilization options for the much more numerous objects of <100 m diameter remains to be explored. About one-third of the discovered NEO population is <100 m in diameter (almost 4000 objects!), but about three-fourths of them have a minimum orbit intersection distance (MOID) of <0.05 AU, placing them in the sub-PHO category only by virtue of their mass. These objects may be discovered days to weeks before impact by groundbased surveys like the upcoming ATLAS and LSST projects, but the maximum groundbased detection efficiency for objects on the scale of the Chelyabinsk impactor is only about 50% because about half of them will approach Earth from the direction of the Sun — like the Chelyabinsk impactor. The only way to detect and characterize these objects before impact is with a spacebased detection system like NEOCam or Sentinel.

It is likely that physical characterization of asteroids will lag ever farther behind their discovery simply because of the much larger phase-space of possible “physical characterization” and the dedicated resources that must be applied for each measurement to individual asteroids. It seems that the only solution is to continue the process of limiting physical characterization to the most interesting targets and developing new systems that allow characterization in a multi-object mode. For instance, NEOWISE, NEOCam, and Sentinel have or plan to measure accurate asteroid diameters in the IR while they survey for unknown NEOs. Similarly, the already operational Gaia mission will measure main-belt asteroid masses, densities, shapes, pole orientations, and the impact of the Yarkovsky effect on their orbital evolution.

In closing, the only certainty about the future of asteroid discovery, characterization, and exploration is that we can expect great progress in the next decade leading to the publication of *Asteroids V*.

**Acknowledgments.** We wish to thank E. Christensen (CSS), L. Denneau (Pan-STARRS), R. McMillan (Spacewatch), G. Stokes (LINEAR), and R. J. Wainscoat (Pan-STARRS) for providing information and perspective on their surveys. C. Hergenrother and A. W. Harris (U.S.) provided helpful feedback as reviewers.

## REFERENCES

- Abell P. and 13 colleagues (2013) The Mission Accessible Near-Earth Objects Survey (MANOS). *AAS/Division for Planetary Sciences Meeting Abstracts*, 45, #208.30.
- Birtwhistle P. (2009) Lightcurves for five close approach asteroids. *Minor Planet Bulletin*, 36, 186–187.
- Bolin B., Jedicke R., Granvik M., Brown P., Howell E., Nolan M. C., Jenniskens P., Chyba M., Patterson G., and Wainscoat R. (2014) Detecting Earth's temporarily-captured natural satellites — Minimoons. *Icarus*, 241, 280–297.
- Bottke W. F., Morbidelli A., Jedicke R., Petit J.-M., Levison H. F., Michel P., and Metcalfe T. S. (2002) Debiased orbital and absolute magnitude distribution of the near-Earth objects. *Icarus*, 156, 399–433.
- Bowell E. and Muinonen K. (1994) Earth-crossing asteroids and comets: Groundbased search strategies. In *Hazards Due to Comets and Asteroids* (T. Gehrels, ed.), p. 149. Univ. of Arizona, Tucson.
- Bowell E., Koehn B. W., Howell S. B., Hoffman M., and Muinonen K. (1995) The Lowell Observatory near-Earth-object search: A progress report. *Bull. Am. Astron. Soc.*, 27, 1057.
- Brown P., Spalding R. E., ReVelle D. O., Tagliaferri E., and Worden S. P. (2002) The flux of small near-Earth objects colliding with the Earth. *Nature*, 420, 294–296.
- Brown P. G. and 32 colleagues (2013) A 500-kiloton airburst over Chelyabinsk and an enhanced hazard from small impactors. *Nature*, 503, 238–241.
- Chesley S. R. and Spahr T. B. (2004) Earth impactors: Orbital characteristics and warning times. In *Mitigation of Hazardous Comets and Asteroids* (M. J. S. Belton et al., eds.), pp. 22–37. Cambridge Univ., Cambridge.
- Chesley S. R. and 15 colleagues (2014) Orbit and bulk density of the OSIRIS-REx target asteroid (101955) Bennu. *Icarus*, 235, 5–22.
- Christou A. A. (2013) Orbital clustering of martian Trojans: An asteroid family in the inner solar system? *Icarus*, 224, 144–153.
- Cibin L., Chiarini M., Milani Comparetti A., Bernardi F., Ragazzoni R., Pinna G. M., Zayer I., Besso P. M., Rossi A., and Villa F. (2012) Wide Eye Debris telescope allows to catalogue objects in any orbital zone. *Mem. Soc. Astron. Ital. Suppl.*, 20, 50.
- Connors M., Wiegert P., and Veillet C. (2011) Earth's Trojan asteroid. *Nature*, 475, 481–483.
- Cunningham C. J. (1988) *Introduction to Asteroids: The Next Frontier*. Willmann-Bell, Richmond, Virginia.
- Cutri R. M. and 41 colleagues (2012) *Explanatory Supplement to the WISE All-Sky Data Release Products*. Available online at <http://wise2.ipac.caltech.edu/docs/release/allsky/expsup/>.
- de la Fuente Marcos C. and de la Fuente Marcos R. (2013) Three new stable L5 Mars Trojans. *Mon. Not. R. Astron. Soc.*, 432, L31.
- de la Fuente Marcos C. and de la Fuente Marcos R. (2014) Asteroid 2013 ND15: Trojan companion to Venus, PHA to the Earth. *Mon. Not. R. Astron. Soc.*, 439, 2970–2977.
- Delbó M., Gayon-Markt J., Busso G., Brown A., Galluccio L., Ordenovic C., Bendjoya P., and Tanga P. (2012) Asteroid spectroscopy with Gaia. *Planet. Space Sci.*, 73, 86–94.
- Denneau L. and 43 colleagues (2013) The Pan-STARRS Moving Object Processing System. *Publ. Astron. Soc. Pac.*, 125, 357–395.
- Denneau L. and 17 colleagues (2015) Observational constraints on the catastrophic disruption rate of small main belt asteroids. *Icarus*, 245, 1–15.
- Farnocchia D., Chesley S. R., Chodas P. W., Micheli M., Tholen D. J., Milani A., Elliott G. T., and Bernardi F. (2013) Yarkovsky-driven impact risk analysis for asteroid (99942) Apophis. *Icarus*, 224, 192–200.
- Gladman B., Davis D., Neese C., Jedicke R., Williams G., Kavelaars J. J., Petit J.-M., Scholl H., Holman M., Warrington B., Esquerdo G., and Tricarico P. (2009) On the asteroid belt's orbital and size distribution. *Icarus*, 202, 104–118.
- Granvik M., Vaubaillon J., and Jedicke R. (2012) The population of natural Earth satellites. *Icarus*, 218, 262–277.
- Granvik M. and 10 colleagues (2014) Unbiased dynamical and physical characteristics of the near-Earth-object population. In *Asteroids, Comets, Meteors 2014, Book of Abstracts* (K. Muinonen et al., eds.), p. 180. Univ. of Helsinki, Finland.
- Grav T., Jedicke R., Denneau L., Chesley S., Holman M. J., and Spahr T. B. (2011a) The Pan-STARRS synthetic solar system model: A

- tool for testing and efficiency determination of the moving object processing system. *Publ. Astron. Soc. Pac.*, 123, 423–447.
- Grav T. and 16 colleagues (2011b) WISE/NEOWISE observations of the jovian Trojans: Preliminary results. *Astrophys. J.*, 742, 40.
- Grav T., Mainzer A. K., Bauer J. M., Masiero J. R., and Nugent C. R. (2012) WISE/NEOWISE observations of the jovian Trojan population: Taxonomy. *Astrophys. J.*, 759, 49.
- Greenstreet S. and Gladman B. (2013) High-inclination Atens are indeed rare. *Astrophys. J.*, 767, L18.
- Greenstreet S., Ngo H., and Gladman B. (2012a) The orbital distribution of near-Earth objects inside Earth's orbit. *Icarus*, 217, 355–366.
- Greenstreet S., Gladman B., Ngo H., Granvik M., and Larson S. (2012b) Production of near-Earth asteroids on retrograde orbits. *Astrophys. J. Lett.*, 749, L39.
- Harris A. W. (2007) An update of the population of NEOs and impact risk. *Bull. Am. Astron. Soc.*, 39, 511.
- Harris A. (2008) What Spaceguard did. *Nature*, 453, 1178–1179.
- Harris A. W. (2013) The value of enhanced NEO surveys. *Planetary Defence Conference*, IAAPDC130509. International Academy of Astronautics, Paris.
- Helin E. F. and Shoemaker E. M. (1979) The Palomar planet-crossing asteroid survey, 1973–1978. *Icarus*, 40, 321–328.
- Hsieh H. H. and Jewitt D. (2006) A population of comets in the main asteroid belt. *Science*, 312, 561–563.
- Jedicke R., Larsen J., and Spahr T. (2002) Observational selection effects in asteroid surveys. In *Asteroids III* (W. F. Bottke Jr. et al., eds.), pp. 71–87. Univ. of Arizona, Tucson.
- Jedicke R., Morbidelli A., Spahr T., Petit J.-M., and Bottke W. F. (2003) Earth and space-based NEO survey simulations: Prospects for achieving the spaceguard goal. *Icarus*, 161, 17–33.
- Jenniskens P. and 34 colleagues (2009) The impact and recovery of asteroid 2008 TC3. *Nature*, 458, 485–488.
- Jewitt D. (2012) The active asteroids. *Astron. J.*, 143, 66.
- Jewitt D., Weaver H., Agarwal J., Mutchler M., and Drahus M. (2010) A recent disruption of the main-belt asteroid P/2010 A2. *Nature*, 467, 817–819.
- Kaiser N. and 25 colleagues (2002) Pan-STARRS: A Large Synoptic Survey Telescope array. In *Survey and Other Telescope Technologies and Discoveries* (J. A. Tyson and S. Wolff, eds.), pp. 154–164. SPIE Conf. Ser. 4836, Bellingham, Washington.
- Kowalski R. A. (2008) 2008 TC3. *Minor Planet Electronic Circular 2008-T50*.
- Kowalski R. A. (2014) 2014 AA. *Minor Planet Electronic Circular 2014-A02*.
- Kowalski R. A. and Chesley S. (2008) 2008 TC3. *IAU Circular 8990*.
- Kubica J., Denneau L., Grav T., Heasley J., Jedicke R., Masiero J., Milani A., Moore A., Tholen D., and Wainscoat R. J. (2007) Efficient intra- and inter-night linking of asteroid detections using kd-trees. *Icarus*, 189, 151–168.
- Kwiatkowski T. and 14 colleagues (2009) Photometry of 2006 RH<sub>120</sub>: An asteroid temporarily captured into a geocentric orbit. *Astron. Astrophys.*, 495, 967–974.
- Larson S., Brownlee J., Hergenrother C., and Spahr T. (1998) The Catalina Sky Survey for NEOs. *Bull. Am. Astron. Soc.*, 30, 1037.
- Lindgren L. and 13 colleagues (2008) The Gaia mission: Science, organization and present status. In *A Giant Step: From Milli- to Micro- Arcsecond Astrometry* (W. Jin et al., eds.), pp. 217–223. IAU Symp. 248, Cambridge Univ., Cambridge.
- Magnier E. (2006) The Pan-STARRS PS1 Image Processing Pipeline. In *The Advanced Maui Optical and Space Surveillance Technologies Conference* (S. Ryan, ed.), p. E50. Maui Economic Development Board, Maui, Hawaii.
- Mainzer A. and 34 colleagues (2011a) Preliminary results from NEOWISE: An enhancement to the Wide-field Infrared Survey Explorer for solar system science. *Astrophys. J.*, 731, 53.
- Mainzer A. and 36 colleagues (2011b) NEOWISE observations of near-Earth objects: Preliminary results. *Astrophys. J.*, 743, 156.
- Mainzer A. and 12 colleagues (2012) Characterizing subpopulations within the near-Earth objects with NEOWISE: Preliminary results. *Astrophys. J.*, 752, 110.
- Mainzer A. and 34 colleagues (2014) Initial performance of the NEOWISE reactivation mission. *Astrophys. J.*, 792, 30.
- Masiero J. R., Grav T., Mainzer A. K., Nugent C. R., Bauer J. M., Stevenson R., and Sonnett S. (2014) Main-belt asteroids with WISE/NEOWISE: Near-infrared albedos. *Astrophys. J.*, 791, 121.
- Micheli M., Koschny D., Drolshagen G., Hainaut O., and Bernardi F. (2014) An ESA NEOCC effort to eliminate high Palermo scale virtual impactors. *Earth Moon Planets*, 113, 1–13.
- Mignard F. and 10 colleagues (2007) The Gaia mission: Expected applications to asteroid science. *Earth Moon Planets*, 101, 97–125.
- Milani A., Chesley S. R., and Valsecchi G. B. (2000) Asteroid close encounters with Earth: Risk assessment. *Planet. Space Sci.*, 48, 945–954.
- Milani A., Chesley S. R., Sansaturo M. E., Tommei G., and Valsecchi G. B. (2005) Nonlinear impact monitoring: Line of variation searches for impactors. *Icarus*, 173, 362–384.
- Milani A. and 11 colleagues (2012) Identification of known objects in solar system surveys. *Icarus*, 220, 114–123.
- Molotov I., Elenin L., Krugly Y., and Ivaschenko Y. (2010) ISON Near-Earth asteroids project. *38th COSPAR Scientific Assembly*, 38, 688.
- Monet D. G., Axelrod T., Blake T., Claver C. F., Lupton R., Pearce E., Shah R., and Woods D. (2013) Rapid cadence collections with the Space Surveillance Telescope. *AAS Meeting Abstracts*, 221, #352.17.
- Morbidelli A., Levison H. F., Tsiganis K., and Gomes R. (2005) Chaotic capture of Jupiter's Trojan asteroids in the early solar system. *Nature*, 435, 462–465.
- Morrison D. (1992) *The Spaceguard Survey: Report of the NASA International Near-Earth-Object Detection Workshop*. NASA STI/Recon Technical Report No. 92, 34245.
- Moskovitz N. and 19 colleagues (2013) The near-Earth flyby of asteroid 2012 DA<sub>14</sub>. *AAS Division for Planetary Sciences Meeting Abstracts*, 45, #101.03.
- Nesvorný D., Vokrouhlický D., and Bottke W. F. (2006) The breakup of a main-belt asteroid 450 thousand years ago. *Science*, 312, 1490.
- O'Brien D. P. and Greenberg R. (2005) The collisional and dynamical evolution of the main-belt and NEO size distributions. *Icarus*, 178, 179–212.
- Ostro S. J. and Giorgini J. D. (2004) The role of radar in predicting and preventing asteroid and comet collisions with Earth. In *Mitigation of Hazardous Comets and Asteroids* (M. J. S. Belton et al., eds.), pp. 38–65. Cambridge Univ., Cambridge.
- Polishook D. and Ofek E. O. (2011) Asteroid science with the Palomar Transient Factory Survey. *EPSC-DPS Joint Meeting 2011*, 872.
- Pravdo S. H., Rabinowitz D. L., Helin E. F., Lawrence K. J., Bambery R. J., Clark C. C., Groom S. L., Shaklan S. B., Kervin P., Africano J. A., Sydney P., and Soohoo V. (1999) The Near-Earth Tracking (NEOT) Program: An automatic system for telescope control, wide-field imaging and object detection. *Astron. J.*, 117, 1616–1633.
- Rabinowitz D. L. (1991) Detection of Earth-approaching asteroids in near real time. *Astron. J.*, 101, 1518–1529.
- Ryan E. V., Ryan W. H., Romero V. D., and Magdalena Ridge Observatory Consortium Collaboration (2002) Magdalena Ridge Observatory (MRO) as a tool for asteroid science. *Bull. Am. Astron. Soc.*, 34, 898.
- Shao M., Nemati B., Zhai C., Turyshev S. G., Sandhu J., Hallinan G., and Harding L. K. (2014) Finding very small near-earth asteroids using synthetic tracking. *Astrophys. J.*, 782, 1.
- Spahr T. B., Hergenrother C., and Larson S. M. (1993) High ecliptic latitude asteroid and comet search. *Bull. Am. Astron. Soc.*, 25, 1059.
- Spahr T. B., Hergenrother C. W., Larson S. M., and Campins H. (1996) High ecliptic latitude asteroid and comet surveying with the Catalina Schmidt. In *Completing the Inventory of the Solar System* (T. W. Rettig and J. M. Hahn, eds.), pp. 115–122. ASP Conf. Ser. 107, Astronomical Society of the Pacific, San Francisco.
- Stokes G. H., Evans J. B., Viggh H. E. M., Shelly F. C., and Pearce E. C. (2000) Lincoln Near-Earth Asteroid Program (LINEAR). *Icarus*, 148, 21–28.
- Stokes G. H., Evans J. B., and Larson S. M. (2002) Near-Earth asteroid search programs. In *Asteroids III* (W. F. Bottke Jr. et al., eds.), pp. 45–54. Univ. of Arizona, Tucson.

- Stuart J. S. (2001) A near-Earth asteroid population estimate from the LINEAR survey. *Science*, *294*, 1691–1693.
- Stuart J. S. and Binzel R. P. (2004) Bias-corrected population, size distribution, and impact hazard for the near-Earth objects. *Icarus*, *170*, 295–311.
- Szabó G. M., Ivezić Ž., Jurić M., and Lupton R. (2007) The properties of jovian Trojan asteroids listed in SDSS Moving Object Catalogue 3. *Mon. Not. R. Astron. Soc.*, *377*, 1393–1406.
- Tedesco E. F., Cellino A., and Zappalá V. (2005) The statistical asteroid model. I. The main-belt population for diameters greater than 1 kilometer. *Astron. J.*, *129*, 2869–2886.
- Terai T., Takahashi J., and Itoh Y. (2013) High ecliptic latitude survey for small main-belt asteroids. *Astron. J.*, *146*, 111.
- Tholen D. J., Micheli M., Bauer J., and Mainzer A. (2013) 2009 BD as a candidate for an asteroid retrieval mission. *AAS/Division for Planetary Sciences Meeting Abstracts*, *45*, #101.08.
- Tichá J., Tichý M., and Kočer M. (2002) The recovery as an important part of NEO astrometric follow-up. *Icarus*, *159*, 351–357.
- Tony J. L. (2011) An early warning system for asteroid impact. *Publ. Astron. Soc. Pac.*, *123*, 58–73.
- van Houten C. J., van Houten-Groeneveld I., Herget P., and Gehrels T. (1970) The Palomar-Leiden survey of faint minor planets. *Astron. Astrophys. Suppl. Ser.*, *2*, 339.
- Vereš P., Jedicke R., Wainscoat R., Granvik M., Chesley S., Abe S., Denneau L., and Grav T. (2009) Detection of Earth-impacting asteroids with the next generation all-sky surveys. *Icarus*, *203*, 472–485.
- Wainscoat R. J., Veres P., Denneau L., Jedicke R., Micheli M., and Chastel S. (2013) The Pan-STARRS search for near-Earth objects: Recent progress and future plans. *AAS/Division for Planetary Sciences Meeting*, *45*, #401.02.
- Vokrouhlický D. and Nesvorný D. (2008) Pairs of asteroids probably of a common origin. *Astron. J.*, *136*, 280–290.
- Vokrouhlický D., Brož M., Bottke W. F., Nesvorný D., and Morbidelli A. (2006) Yarkovsky/YORP chronology of asteroid families. *Icarus*, *182*, 118–142.
- Wright E. L. and 37 colleagues (2010) The Wide-field Infrared Survey Explorer (WISE): Mission description and initial on-orbit performance. *Astron. J.*, *140*, 1868–1881.
- Yeomans D. K. (2013) *Near-Earth Asteroids: Finding Them Before They Find Us*. Princeton Univ., Princeton, New Jersey.
- Yoshida F. and Nakamura T. (2005) Size distribution of faint jovian L4 Trojan asteroids. *Astron. J.*, *130*, 2900–2911.
- Yoshida F., Nakamura T., Watanabe J.-I., Kinoshita D., Yamamoto N., and Fuse T. (2003) Size and spatial distributions of sub-km main-belt asteroids. *Publ. Astron. Soc. Japan*, *55*, 701–715.
- Zavodny M., Jedicke R., Beshore E. C., Bernardi F., and Larson S. (2008) The orbit and size distribution of small solar system objects orbiting the Sun interior to the Earth's orbit. *Icarus*, *198*, 284–293.



# Orbits, Long-Term Predictions, and Impact Monitoring

Davide Farnocchia and Steven R. Chesley

*Jet Propulsion Laboratory/California Institute of Technology*

Andrea Milani and Giovanni F. Gronchi

*University of Pisa*

Paul W. Chodas

*Jet Propulsion Laboratory/California Institute of Technology*

---

In this chapter we review the methods currently in use to compute asteroid orbits and make ephemeris predictions. Despite a well-consolidated theory, the increasing number and ever higher quality of observational data, together with the goal of pushing forward the horizon for ephemeris predictions, pose new challenges in estimating asteroid trajectories. We discuss how to develop a realistic statistical error model for astrometric observations by removing star catalog systematic errors and suitably weighting astrometric data. Moreover, since the dynamical model has to be accurate enough to fit the observational data and reliably predict an asteroid's position in the future, we analyze the relevance of the different components of the force model. In particular, we show that nongravitational forces can be relevant at a high level of precision. We also address the problem of estimating asteroid orbits when only a short arc of observations is available. Solving this problem has relevant implications for modern surveys, where the amount of observational data requires innovative methods to compute an orbit catalog avoiding an excessive computational load. Finally, we discuss the Earth impact hazard assessment. We describe the standard methods that have been in use for the last 15 years as well as newer techniques that allow long-term impact monitoring, including going beyond scattering planetary encounters and accounting for nongravitational perturbations.

## 1. INTRODUCTION

Determining asteroid orbits is a challenging problem that the scientific community has faced since 1801, when Piazzi discovered (1) Ceres, the first main-belt object. Shortly after discovery Ceres was heading for conjunction, thus making it impossible to keep collecting observations. To prevent Ceres from being lost, Gauss computed its orbit using the observations collected by Piazzi and successfully predicted where Ceres would be observable after emerging from the Sun. Interestingly, the orbit determination of Ceres represents the first remarkable application of the famous method of least squares, which since then has been one of the most used mathematical tools with applications in disciplines such as statistics, physics, biology, geodesy, economics, and indeed every physical science.

One of the reasons why, after more than two centuries, orbit determination continues to be a fascinating branch of celestial mechanics is that it strikes an impressive fusion between a scientifically sound theory and several relevant applications. Celestial mechanics rigorously describes the motion of celestial bodies and the large number of observations of space bodies allows one to extensively test

the validity of the theory. In particular, for asteroid orbit determination we have a rigorous mathematical theory to compute trajectories and more than 650,000 asteroids (as of September 2014) whose observations continuously serve as validation of the theoretical computations. Just to give an idea of the level of accuracy that can be reached, there are asteroids for which the available observational data reveal accelerations with a precision of a few  $\text{fm s}^{-2}$  ( $10^{-15} \text{ m s}^{-2}$ ).

Asteroid orbit determination has several important applications. By computing an orbit along with its uncertainty, we can inform astronomers on when and where they should observe the night sky so that they can collect additional observations. If a mission to an asteroid is planned, estimating trajectories is important to select a viable target, and reliable ephemerides are required to successfully navigate the spacecraft to the asteroid. When two asteroids get close enough we can measure the gravitational interaction between them and obtain an estimate of an asteroid's mass. Perhaps the most interesting application is planetary defense. When an asteroid's orbit is computed we can figure out where the object will be in the future and whether or not there are upcoming planetary encounters. In particular, it is possible to compute the probability of an Earth impact and contribute

to the study of mitigation measures, such as deflection, in case they are deemed necessary.

## 2. BASIC THEORY

### 2.1. Orbits

The equations of motion for celestial bodies are ordinary differential equations with a smooth righthand side. An orbit is defined by the evolution of the Cartesian heliocentric position  $\mathbf{r}$  and velocity  $\mathbf{v}$  of the asteroid, which is determined by the initial conditions  $(\mathbf{r}_0, \mathbf{v}_0)$  at a time  $t_0$ . In fact, the initial Cartesian state can be integrated to any given time according to the accelerations  $\mathbf{a}$  acting on the asteroid

$$\dot{\mathbf{r}} = \mathbf{v}, \quad \dot{\mathbf{v}} = \mathbf{a}(t, \mathbf{r}, \mathbf{v}, \psi) \quad (1)$$

The main component of the righthand side  $\mathbf{a}$  is the Newtonian attraction of the Sun. Therefore, as a first approximation, asteroids follow Keplerian motion (e.g., Roy, 2005). However, as discussed in section 4.1, there are several other accelerations contributing to  $\mathbf{a}$  such as the Newtonian attraction from other bodies (planets, Moon, Pluto) and relativistic perturbations. In some cases the orbit also depends on dynamical parameters  $\psi$ , e.g., parameters defining nongravitational perturbations acting on the asteroid (see section 4.2). In general,  $\mathbf{a}$  is a function of time  $t$ , current Cartesian state  $(\mathbf{r}, \mathbf{v})$ , and some dynamical parameters  $\psi$ .

### 2.2. Observations

Observations are the data needed to compute the orbit of an asteroid. There are primarily two kinds of observations used in asteroid orbit determination: optical and radar.

Optical observations provide the angular position of an asteroid in the sky. The information is expressed by spherical coordinates, typically right ascension ( $\alpha$ ) and declination ( $\delta$ ), in an inertial reference frame, e.g., J2000 (Kaplan, 2005). Optical observations can be obtained from groundbased observatories as well as spacebased telescopes, provided that their position is accurately known.

Radar observations provide the distribution of echo power in time delay and Doppler frequency. Besides giving valuable information on an asteroid's physical properties, the superior precision of radar observations puts exceptional constraints on asteroid orbits, thus allowing reliable predictions over longer time intervals (Ostro *et al.*, 2002) (see also the chapter by Benner *et al.* in this volume).

If the initial Cartesian state is available and  $\mathbf{a}$  is known, observations can be predicted by an explicit computation. Theoretical predictions and measured observations do not generally coincide and the differences O–C, observed minus computed, form the vector of residuals  $\mathbf{v}$ .

### 2.3. Differential Corrections

The first step in orbit determination is to select a list of parameters  $\mathbf{x}$  defining the orbit to be determined from the

available observations. The most common case is when  $\mathbf{x}$  is given by the asteroid's Cartesian position  $\mathbf{r}_0$  and velocity  $\mathbf{v}_0$  at the initial epoch  $t_0$ . However,  $\mathbf{x}$  can also include some of the dynamical parameters  $\psi$ . Note that the number of parameters to be determined can be no larger than the number of scalar observations (optical observations give two scalar observations), otherwise the problem is underdetermined and cannot be solved.

The basic tool of the classical theory of orbit determination (Gauss, 1809) is the definition of a cost function

$$Q = \mathbf{v}^T \mathbf{W} \mathbf{v}$$

where  $\mathbf{W}$  is the weight matrix, i.e., the inverse of the observational covariance matrix. For instance,  $\mathbf{W}$  can be a diagonal matrix whose elements are  $1/\sigma_i^2$ , where  $\sigma_i$  is the uncertainty of the corresponding observation. The cost function  $Q$  measures how close the orbital solution is to the observations. Therefore, the nominal solution  $\bar{\mathbf{x}}$  for  $\mathbf{x}$  corresponds to the minimum of  $Q$ , i.e.,  $\bar{\mathbf{x}}$  satisfies the equation

$$0 = \frac{\partial Q}{\partial \mathbf{x}} = 2\mathbf{v}^T \mathbf{W} \mathbf{B}, \quad \mathbf{B} = \frac{\partial \mathbf{v}}{\partial \mathbf{x}} \quad (2)$$

The matrix  $\mathbf{B}$  is called the design matrix. Equation (2) generally has no explicit solutions but can iteratively be solved as follows

$$\mathbf{x}_{k+1} - \mathbf{x}_k = -\Gamma \mathbf{B}^T \mathbf{W} \mathbf{v}, \quad \Gamma = \mathbf{C}^{-1}, \quad \mathbf{C} = \mathbf{B}^T \mathbf{W} \mathbf{B} \quad (3)$$

This iterative scheme is essentially a Newton method that is applied to equation (2) where  $\partial^2 Q / \partial \mathbf{x}^2$  is approximated with  $2\mathbf{C}$ . The matrix  $\mathbf{C}$  is called the normal matrix (or information matrix). Equation (3) can be solved by using standard linear algebra algorithms such as singular value decomposition or Cholesky factorization. If the sequence  $\mathbf{x}_k$  converges to  $\bar{\mathbf{x}}$ , the limit has to be a (local) minimum of  $Q$ . This method is called differential corrections and is applied by asteroid data processing centers such as the Minor Planet Center (MPC), the Jet Propulsion Laboratory (JPL), and the Near Earth Objects Dynamic Site (NEODyS) thousands of times per day to determine the orbits of asteroids and comets.

There are several methods to determine a preliminary orbit to be used as a starting estimate for differential corrections, e.g., the methods of Gauss, Laplace, Vaisala, and Herget. A description of these methods is beyond the scope of this chapter and can be found in textbooks such as Dubyago (1961) and Escobal (1965).

### 2.4. Probabilistic Interpretation

Since observations come with an uncertainty, the orbit observational uncertainty maps to the orbital uncertainty.

If we assume that the observation errors are normally distributed, with zero mean and uncertainty expressed by the observational covariance matrix  $\mathbf{W}^{-1}$ , then the probability density function of the residuals is

$$f_v = \frac{1}{\sqrt{(2\pi)^{n_{\text{obs}}} \det W^{-1}}} \exp\left(-\frac{1}{2} v^T W v\right) \quad (4)$$

where  $n_{\text{obs}}$  is the number of scalar observations. In the case of independent observation errors the observational covariance matrix is a diagonal matrix whose elements are the squares of observation uncertainties  $\sigma_i$ . (We discuss the validity of these assumptions in section 3.)

If we linearize around  $\bar{x}$ , we have that  $\Delta v = B\Delta x$ , where  $\Delta v = v - \bar{v}$ ,  $\Delta x = x - \bar{x}$ , and  $\bar{v} = v(\bar{x})$ ; the variation of  $Q$  around its minimum is

$$\Delta Q = \Delta v^T W \Delta v = \Delta x^T C \Delta x \quad (5)$$

Since  $v$  is normally distributed with zero mean and covariance matrix  $W^{-1}$ ,  $x$  is normally distributed with mean  $\bar{x}$  and covariance matrix  $\Gamma_x = \Gamma$ . [For a rigorous proof, see section 5.7 of Milani and Gronchi (2010).] The level curves of  $\Delta Q$  correspond to the boundary of the confidence ellipsoids for different values of  $\sigma$ . The probability that the actual orbit is within a given ellipsoid can be computed by using the distribution of  $\chi^2$  with the number of determined parameters as degrees of freedom. For instance, if  $x = (r_0, v_0)$  we have six degrees of freedom and the probability of being inside the  $3\sigma$  ellipsoid, i.e.,  $\Delta Q < 9$ , is 82.64%.

## 2.5. Predictions

Once an orbit is determined, we want to make predictions. For example, we want to compute the ephemerides in the sky so that observers can collect additional observations or we may want to compute the probability that an asteroid strikes Earth. In any case, the prediction  $p$  is going to be a function of our parameters  $x$ . Therefore, from the nominal orbit  $\bar{x}$  we can compute a nominal prediction  $\bar{p}$ . As an example, if we want to predict the Cartesian state of an asteroid in the future, we take the initial state and integrate the equations of motion to the desired epoch.

Since orbits are determined along with an uncertainty, we need to compute the resulting uncertainty in the prediction. In the linear approach we have that  $\Delta p = A\Delta x$ , where  $A = \partial p / \partial x$ . Since  $\Delta p$  is a linear combination of  $\Delta x$ , and  $\Delta x$  is normally distributed,  $\Delta p$  is normally distributed, too. If we indicate the normal matrix of  $p$  with  $C_p$ , we have that:

$$\Delta p^T C_p \Delta p = \Delta x^T A^T C_p A \Delta x = \Delta x^T C \Delta x$$

Therefore,  $C = A^T C_p A$  or, equivalently, the covariance matrix of  $p$  is  $\Gamma_p = A \Gamma A^T$ . [Again, for a rigorous proof, see section 7.5 of Milani and Gronchi (2010).]

For example, we can map the uncertainty of the initial Cartesian state  $(r_0, v_0)$  at epoch  $t_0$  to the uncertainty of the Cartesian state  $(r, v)$  at a different epoch  $t$ . All we need are the partial derivatives

$$A = \begin{pmatrix} D & E \\ \dot{D} & \dot{E} \\ \ddot{D} & \ddot{E} \end{pmatrix}$$

where  $D = \partial r / \partial r_0$ ,  $\dot{D} = \partial v / \partial r_0$ ,  $E = \partial r / \partial v_0$ , and  $\dot{E} = \partial v / \partial v_0$ . These matrices can be computed by solving the classical variational equation

$$\begin{cases} \ddot{D} = \frac{\partial \mathbf{a}}{\partial v} \dot{D} + \frac{\partial \mathbf{a}}{\partial r} D, \quad D(t_0) = \mathbb{I}, \quad \dot{D}(t_0) = 0 \\ \ddot{E} = \frac{\partial \mathbf{a}}{\partial v} \dot{E} + \frac{\partial \mathbf{a}}{\partial r} E, \quad E(t_0) = 0, \quad \dot{E}(t_0) = \mathbb{I} \end{cases}$$

where  $\mathbb{I}$  is the identity matrix of rank 3 and  $\mathbf{a}$  represents the acceleration acting on the asteroid as in equation (1). Note that the variational equation was already needed to compute the design matrix  $B$  of equation (2).

When  $x$  includes some of the dynamical parameters  $\psi$ , we also need the partials  $F = \partial r / \partial \psi$  and  $\dot{F} = \partial v / \partial \psi$ , which can be obtained by solving

$$\ddot{F} = \frac{\partial \mathbf{a}}{\partial v} \dot{F} + \frac{\partial \mathbf{a}}{\partial r} F + \frac{\partial \mathbf{a}}{\partial \psi}, \quad F(t_0) = 0, \quad \dot{F}(t_0) = 0$$

## 3. TREATMENT OF THE ASTROMETRY

The computation of an asteroid's orbit as described in section 2 relies on the accuracy of the observational error model. Thus, possible limitations arise from making simplified assumptions on the observational error model. In particular, observation errors are usually assumed to be distributed according to a Gaussian distribution with zero mean. Moreover, the astrometric uncertainty is often taken as a simple function of the epoch of the observation only (e.g., 3" before 1890, 2" between 1890 and 1950, 1" after 1950) (see Baer et al., 2011a), and observation errors are assumed to be uncorrelated. The above assumptions are unrealistic as shown by Carpino et al. (2003), who proved the presence of biases, non-Gaussian statistics, and correlations between observations close in time. Moreover, the accuracy of the astrometry depends not only on the epoch of observation, but also on the observer. For instance, the Panoramic Survey Telescope and Rapid Response System (Pan-STARRS) PS1 (Hodapp et al., 2004) telescope achieves  $\sim 0.1''$  quality, thus its data cannot be assumed to have the same accuracy of any other observation made since 1950. Unrealistic assumptions compromise the orbital solution and the interpretation of the probabilistic distribution of the orbit within the uncertainty region.

### 3.1. Systematic Errors Due to Star Catalogs

The vast majority of asteroid astrometry is given by optical observations describing the position of an asteroid on the celestial sphere at a specified time. The corresponding

angular measurements are obtained with respect to nearby reference stars, whose positions are provided by a star catalog. Therefore, the presence of systematic errors in the star catalog affects the quality of the observation. *Chesley et al.* (2010) showed that some of the most widely used star catalogs can have position biases up to 1''–2'', which are comparable to (if not larger than) the expected quality of the data. Moreover, *Tholen et al.* (2013) show that even the lack of proper motion information can produce significant systematic errors for Pan-STARRS PS1, one of the best surveys in terms of data quality (*Milani et al.*, 2012).

To correct for systematic errors due to star catalogs, one can select a reference catalog to which the other catalogs are compared. The reference catalog has to be dense, accurate, and include proper motions. *Chesley et al.* (2010) used Two Micron All Sky Survey (2MASS) (*Skrutskie et al.*, 2006) as reference catalog because of its accuracy and density, but 2MASS does not include proper motions. A possible choice would be the Position and Proper Motion Extended-L (PPMXL) catalog (*Roeser et al.*, 2010), which includes proper motions and is a merge of 2MASS and U.S. Naval Observatory (USNO)-B1.0 (*Monet et al.*, 2003) obtained after a critical reprocessing of the data. However, the astrometric position of the PPMXL stars selected from USNO-B1.0 are not sufficiently accurate. Therefore, *Farnocchia et al.* (2015a) select the subset of PPMXL corresponding to 2MASS-based stars as a reference catalog. This set of stars is dense, has accurate star positions, and includes proper motions.

To compare the different star catalogs to the selected reference catalog we map the star positions at epoch J2000.0 and divide the celestial sphere in 49,152 equal-area tiles by using the JPL Hierarchical Equal Area isoLatitude Pixelisation (HEALPix) package (*Górski et al.*, 2005). For each tile we find stars in common by using a 2'' radius and compute the average position and proper motion differences in right ascension  $\alpha$  and declination  $\delta$ . As an example, Figs. 1a,b show the position corrections for the USNO-A2.0 catalog (*Monet*, 1998), which as of September 2014 has been the most widely used catalog to reduce asteroid astrometry. Position errors are as large as 1'' and are therefore extremely relevant at the expected level of uncertainty of asteroid astrometric observations. The transition around  $\delta = -20^\circ$  shows how USNO-A2.0 splits in its northern and southern parts (*Assafin et al.*, 2001). Figures 1c,d show the proper-motion corrections to be applied to observations reduced with USNO-A2.0, which does not include proper motions. It is easy to see that astrometric observations can be significantly affected if the catalog used for the astrometric reduction has large proper motion errors, as in the case of Pan-STARRS PS1 (*Tholen et al.*, 2013). Each observation can be corrected by subtracting the quantities

$$\begin{aligned}\Delta\alpha &= \Delta\alpha_{2000} + \Delta\mu_\alpha \Delta t \\ \Delta\delta &= \Delta\delta_{2000} + \Delta\mu_\delta \Delta t\end{aligned}$$

where  $\Delta t$  is the observation time with respect to epoch J2000.0,  $\Delta\alpha_{2000}$  and  $\Delta\delta_{2000}$  are the position corrections,

and  $\Delta\mu_\alpha$  and  $\Delta\mu_\delta$  are the proper-motion corrections for the tile corresponding to the catalog used for the astrometric reduction and the observed  $\alpha$  and  $\delta$ . For more details, see *Farnocchia et al.* (2015a).

### 3.2. Astrometric Weighting

Each observation should be weighted according to its expected quality. Ideally, observers should provide rigorous and reliable uncertainty information. For instance, this information is available for radar observations (<http://ssd.jpl.nasa.gov/?radar>). However, optical observations are distributed by the MPC without including uncertainty information (<http://www.minorplanetcenter.net/iau/info/OpticalObs.html>). Therefore, to infer what the data quality is, one needs to analyze the statistics of astrometric errors.

The  $\alpha$  and  $\delta$  accuracy,  $\sigma_\alpha$  and  $\sigma_\delta$ , of an optical astrometric observation can be easily seen as dependent on (1) epoch of the observation; (2) observation type, e.g., charge-coupled device (CCD) or photographic (see <http://www.minorplanetcenter.net/iau/info/OpticalObs.html> for the list of observation types); (3) observer (see <http://www.minorplanetcenter.net/iau/lists/-ObsCodesF.html> for the list of observatories and their codes); and (4) star catalog used to reduce the astrometry (see <http://www.minorplanetcenter.net/iau/info/CatalogueCodes.html> for the list of catalogs and their codes).

*Chesley et al.* (2010) analyzed the observation quality for different observatories, star catalogs, etc., by computing the root mean square (RMS) of the  $\alpha$  and  $\delta$ . Table 1 shows examples of station-specific expected accuracies for CCD observations according to the star catalog used for the astrometric reduction. The reported  $\sigma_\alpha$  and  $\sigma_\delta$  can be converted to weights as  $w = 1/\sigma^2$ . Note that  $\sigma_\alpha$  includes the spherical metric factor  $\cos \delta$ . For a more comprehensive list of weighting rules, see *Farnocchia et al.* (2015a).

### 3.3. Correlations

The statistics of the residuals shows that observation errors are not independent, especially for single-station observations closely spaced in time (*Carpino et al.*, 2003). The presence of correlations is in large part due to unresolved biases. As a matter of fact, *Chesley et al.* (2010) demonstrate that correcting for star catalog position biases significantly reduces correlations. Although star catalog errors are the most important source of systematic errors in asteroid astrometry, there are other possible sources of systematic errors. For instance, a well-known problem is due to timing errors. If the reported observation epoch is wrong, there is a corresponding positional error along the direction of the angular motion of the asteroid. Correcting for all sources of systematic errors can be extremely difficult (if not impossible), and yet the error model needs to account for them.

*Baer et al.* (2011a) develop an error model that accounts for correlations between same-station observations. Given two observations, the correlation coefficient is computed as a linear combination of exponential functions that decrease as

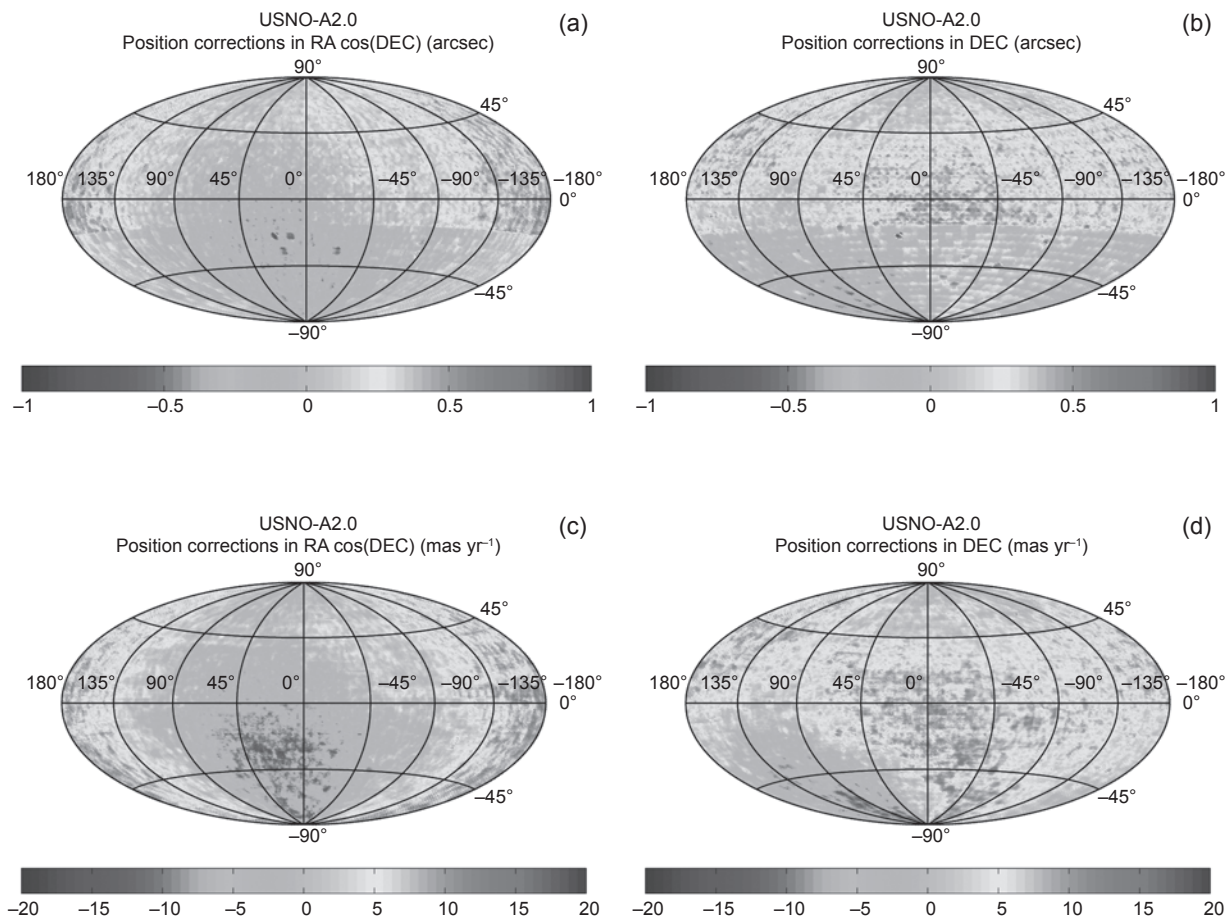


**Fig. 1.** See Plate 27 for color version. Sky map of position corrections in (a)  $\alpha \cos \delta$  and (b)  $\delta$  for USNO-A2.0. Sky map of proper motion corrections in (c)  $\alpha \cos \delta$  and (d)  $\delta$  for USNO-A2.0. Reprinted from *Star Catalog Position and Proper Motion Corrections in Asteroid Astrometry*, January 1, 2015, with permission from Elsevier.

the time separation between the two observations increases: The farther in time the observations, the smaller the correlation. The coefficients defining the linear combination are empirically derived for different stations and different observation epochs. These correlation coefficients can be used to populate the nondiagonal elements of the observational covariance matrix  $W^{-1}$  defined in section 2.

Since correlations are mostly due to unresolved biases and the computation of the correlation coefficients is cumbersome, an alternative approach is to mitigate the effect of

unresolved systematic errors and correlations by relaxing the weights. This simple approach is conservative and allows one to keep the observational covariance matrix diagonal. Chesley et al. (2010) already found that applying a safety factor 2 to the  $\sigma$  values listed in Table 1 results in more statistically consistent predictions, i.e., the prediction error distribution is closer to that of a theoretical normal distribution. As discussed in Farnocchia et al. (2015a), a better way to mitigate unresolved systematic errors is to account for the number  $N$  of observations from the same station in

TABLE 1. Examples of station specific weighting rules for CCD observations.

Station	Catalog	$\sigma_\alpha$	$\sigma_\delta$	Station	Catalog	$\sigma_\alpha$	$\sigma_\delta$
644	USNO-A2.0	0.24"	0.28"	644	USNO-B1.0	0.18"	0.17"
691	USNO-A2.0	0.32"	0.34"	691	USNO-B1.0	0.25"	0.28"
699	USNO-A2.0	0.47"	0.39"	699	USNO-B1.0	0.42"	0.41"
703	USNO-A2.0	0.62"	0.57"	703	UCAC	0.49"	0.46"
704	USNO-A2.0	0.62"	0.60"	F51	2MASS	0.15"	0.15"
G96	UCAC	0.25"	0.21"	E12	UCAC	0.41"	0.43"

the same night. Since the error in the mean decreases with  $\sqrt{N}$ , the larger the number of observations, the more systematic errors affect the orbit computation. To compensate for that, the weights can be relaxed by a factor  $N$ , i.e.,  $w = 1/(N\sigma^2)$ , which is equivalent to inflating  $\sigma$  by  $\sqrt{N}$ . It is worth pointing out that for a typical survey observation batch  $N = 4, 5$  and thus the  $\sqrt{N}$  factor is similar to the *Chesley et al.* (2010) safety factor of 2.

### 3.4. Outlier Rejection

The observational dataset of an asteroid can be contaminated by “bad” observations (outliers) that may corrupt the orbital computation. The presence of outliers may arise from unusual circumstances such as human error, software bugs, and difficult observing conditions. Therefore, these outliers have to be identified and removed from the orbital fit. There are several techniques to reject outliers, e.g., Chauvenet’s criterion (*Taylor*, 1997) and Pierce’s criterion (*Gould*, 1855). These techniques reject all the observations whose residuals are beyond a fixed number of standard deviations. A more sophisticated outlier rejection algorithm is that of *Carpino et al.* (2003), which not only accounts for the residuals with respect to the fitted model, but also for the *a posteriori* prediction uncertainty.

Following the *Carpino et al.* (2003) approach, we indicate the initial orbital parameters with  $\mathbf{x}_0$ , the convergent solution with  $\bar{\mathbf{x}}$ , the prefit residuals with  $\mathbf{v}_0$ , and the postfit residuals with  $\bar{\mathbf{v}}$ . From equation (3), in the linear approximation we have that

$$\bar{\mathbf{x}} - \mathbf{x}_0 = -\Gamma \mathbf{B}^T \mathbf{W} \mathbf{v}_0$$

The first-order Taylor expansion for the residuals is

$$\bar{\mathbf{v}} = \mathbf{v}_0 + \mathbf{B}(\bar{\mathbf{x}} - \mathbf{x}_0) = (\mathbf{I} - \mathbf{B}\Gamma\mathbf{B}^T \mathbf{W}) \mathbf{v}_0$$

Therefore, since  $\mathbf{W}^{-1}$  is the observational covariance matrix, the covariance of the postfit residuals is

$$\Gamma_{\bar{\mathbf{v}}} = \mathbf{W}^{-1} - \mathbf{B}\Gamma\mathbf{B}^T \quad (6)$$

For a given observation one can compute a  $\chi^2$  value as

$$\chi_i^2 = \mathbf{v}_i^T \gamma_i^{-1} \mathbf{v}_i$$

where  $\gamma_i$  is the block of  $\Gamma_{\bar{\mathbf{v}}}$  corresponding to that observation. Similarly,  $\mathbf{v}_i$  is a subset of  $\bar{\mathbf{v}}$  corresponding to the considered observation. For optical observations,  $\gamma_i$  has rank 2 and  $\mathbf{v}_i$  is a two-element vector. For radar observations, both  $\gamma_i$  and  $\mathbf{v}_i$  are scalar. In a similar way, the covariance matrix for discarded observations is obtained by adding (rather than subtracting)  $\mathbf{B}\Gamma\mathbf{B}^T$  to  $\mathbf{W}^{-1}$  in equation (6). At this point, one can select a threshold  $\chi_{\text{rej}}^2$  and reject observations with  $\chi_i^2 > \chi_{\text{rej}}^2$ . Similarly, a threshold  $\chi_{\text{rec}}^2$  is used to recover the observations previously excluded if  $\chi_i^2 < \chi_{\text{rec}}^2$ . The selection of the parameters  $\chi_{\text{rec}} < \chi_{\text{rej}}$  is not obvious, although the theoretical distribution of  $\chi^2$  can serve as a reference. Our current

choices for these parameters are  $\chi_{\text{rej}} = 3$  and  $\chi_{\text{rec}} = 2.8$ . For more details on the implementation of this algorithm, see *Carpino et al.* (2003).

## 4. DYNAMICAL MODEL

### 4.1. Gravitational Perturbations

To make reliable predictions the force model needs to be accurate enough. In particular, when an orbit is very well constrained, it may be impossible to match the observational data unless all the relevant perturbations are accounted for.

While the main acceleration acting on asteroids is the Newtonian attraction of the Sun, one certainly needs to include the contribution of the planets. These perturbations are usually based on precomputed ephemeris tables from which the Cartesian states of the planets, Pluto, and the Moon can be retrieved. We use JPL’s planetary ephemerides (<http://ssd.jpl.nasa.gov/?ephemerides>), but other planetary ephemerides are available as well, such as the ones provided by the Institut de Mécanique Céleste et de Calcul des Éphémérides (<http://www.imcce.fr/langues/en/ephemerides>). As an example, Fig. 2a shows the Newtonian attraction of the Sun, Earth, Jupiter, and Uranus acting on asteroid (6489) Golevka computed using JPL’s DE431 ephemerides (*Folkner et al.*, 2014).

The gravity of large bodies in the main belt, such as (1) Ceres, (2) Pallas, and (4) Vesta, can also be relevant. Therefore, we include the Newtonian attraction of the 16 most massive main belt objects (see Table 2). These accelerations are based on mutually perturbed trajectories for these 16 objects computed starting from DE431. As an example, Fig. 2a shows the contribution of (1) Ceres and (15) Eunomia for Golevka.

Relativity is an important component of the force model. For most objects a general relativistic model for the Sun [see equation (2.5) in *Damour and Deruelle* (1985)] is enough

$$\mathbf{a}_{\text{REL}} = \frac{GM_{\odot}}{c^2 |\mathbf{r}|^3} \left[ \left( \frac{4GM_{\odot}}{|\mathbf{r}|} - |\mathbf{v}|^2 \right) \mathbf{r} + 4(\mathbf{r} \cdot \mathbf{v}) \mathbf{v} \right]$$

where  $G$  is the gravitational constant and  $M_{\odot}$  the mass of the Sun. However, for asteroids experiencing planetary encounters, it can be important to include the relativistic contribution of the planets (see Fig. 2b). For instance, *Chesley et al.* (2014) show that the Earth relativistic term causes a  $3\sigma$  change in the orbital solution of asteroid (101955) Bennu due to the significant short range effect during Earth encounters. Thus, for these asteroids one can use the Einstein-Infeld-Hoffman formulation for relativity (*Moyer*, 2003, section 4.4.1), which is an N-body relativistic model that accounts for the contribution of the planets.

For objects experiencing Earth close encounters there are more stringent requirements on the accuracy of the force model. In fact, when observing these objects from the ground, their angular velocity in the sky is usually larger and therefore observations have more leverage. Moreover,

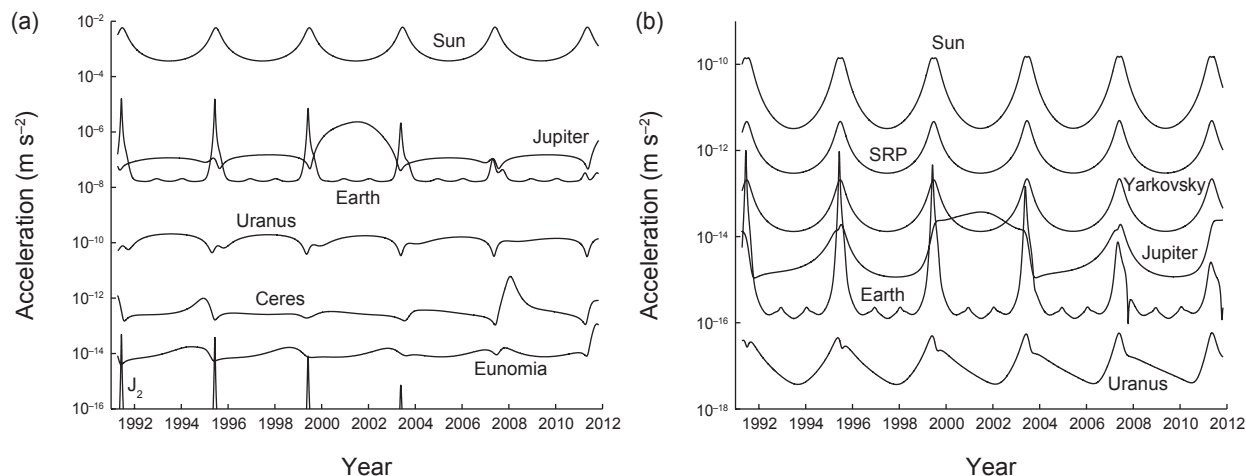


**Fig. 2.** Magnitude of the accelerations acting on asteroid (6489) Golevka. **(a)** Newtonian attraction of the Sun, Earth, Jupiter, Uranus, Ceres, and Eunomia, as well as the contribution of the Earth oblateness ( $J_2$ ). **(b)** Nongravitational perturbations, i.e., solar radiation pressure (SRP) and the Yarkovsky effect, and the Einstein-Infeld-Hoffman relativistic terms due to Sun, Earth, Jupiter, and Uranus.

objects passing close to Earth are more likely to be observed by radar telescopes, which provide observations of extremely high quality. For these objects it can be important to include the effect of the nonspherical shape of Earth. As an example, asteroid 2011 MD experienced an Earth encounter in 2011 at a geocentric distance of 19,000 km, and it is not possible to fit the data before and after the close approach unless the  $J_2$  term of the Earth geopotential (Battin, 1987, chapter 8) is accounted for. Thus, whenever an object is close enough to Earth [e.g., within 0.1 AU of Earth (see Chesley et al., 2014)] one should add the perturbation due to the second-degree zonal harmonics of Earth. The  $J_2$  parameter can be obtained by the JPL ephemerides or the EGM96 geopotential model (Lemoine et al., 1998). Figure 2a shows the  $J_2$  contribution for asteroid Golevka.

#### 4.2. Nongravitational Perturbations

Despite their small size, nongravitational perturbations can be significant in modeling asteroid trajectories. Solar radiation pressure (Vokrouhlický and Milani, 2000) is due to energy and linear momentum carried by light and transferred

to an asteroid upon impact of photons on the surface. This perturbation is along the radial direction  $\hat{r}$ , i.e., the Sun-to-asteroid direction. The Yarkovsky effect (Bottke et al., 2006; see the chapter by Vokrouhlický et al. in this volume) arises from the anisotropic reemission at thermal wavelengths of absorbed solar radiation. The Yarkovsky perturbation has a component in the along-track direction  $\hat{t}$  and therefore causes asteroids to undergo a secular variation in semimajor axis.

Nongravitational perturbations are intrinsically different from the other accelerations described in section 4.1. As a matter of fact, they depend on the individual physical properties of the asteroid we are dealing with and thus they are generally unknown. As an example, nongravitational perturbations are proportional to the asteroid's area-to-mass ratio and therefore inversely proportional to the diameter  $d$ . A possible approach is to model nongravitational perturbations as follows (Farnocchia et al., 2013a)

$$\mathbf{a}_{\text{NG}} = (A_1 \hat{\mathbf{r}} + A_2 \hat{\mathbf{t}}) g(r) , \quad g(r) = (1 \text{ AU}/r)^2$$

where  $r$  is the heliocentric distance and  $A_1$  and  $A_2$  are free parameters to be determined through the orbital fit to the

TABLE 2. The 16 most massive main belt perturbers and their gravitational parameters.

Name	GM (km <sup>3</sup> s <sup>-2</sup> )	Reference		Name	GM (km <sup>3</sup> s <sup>-2</sup> )	Reference
(1) Ceres	$63.13 \pm 0.10$	Baer et al. (2011b)		(16) Psyche	$1.81 \pm 0.50$	Carry (2012)
(2) Pallas	$13.73 \pm 0.34$	Konopliv et al. (2011)		(29) Amphitrite	$0.86 \pm 0.13$	Carry (2012)
(3) Juno	$1.82 \pm 0.19$	Carry (2012)		(52) Europa	$1.59 \pm 0.39$	Carry (2012)
(4) Vesta	$17.2903 \pm 0.0001$	Russell et al. (2012)		(65) Cybele	$0.91 \pm 0.21$	Carry (2012)
(6) Hebe	$0.93 \pm 0.07$	Carry (2012)		(87) Sylvia	$0.99 \pm 0.14$	Carry (2012)
(7) Iris	$0.86 \pm 0.14$	Carry (2012)		(88) Thisbe	$1.02 \pm 0.21$	Carry (2012)
(10) Hygiea	$5.78 \pm 0.10$	Baer et al. (2011b)		(511) Davida	$2.26 \pm 0.68$	Carry (2012)
(15) Eunomia	$2.10 \pm 0.12$	Carry (2012)		(704) Interamnia	$2.19 \pm 0.30$	Carry (2012)

observations as dynamical parameters, i.e.,  $\psi = (A_1, A_2)$ .  $A_1$  accounts for solar radiation pressure and the radial component of the Yarkovsky effect, while  $A_2$  models the tangential component of the Yarkovsky effect. The dependence on the heliocentric distance is contained in the  $1/r^2$  factor, which matches the level of absorbed radiation. In case of other effects such as outgassing,  $g(r)$  can be replaced with a different function (e.g., Marsden *et al.*, 1973). Figure 2b shows the magnitude of nongravitational perturbations acting on (6489) Golevka. Solar radiation pressure and the Yarkovsky effect are computed according to Chesley *et al.* (2003).

Determining  $A_1$  from the orbital fit is complicated. Because of the  $1/r^2$  dependency, the radial component of  $\mathbf{a}_{NG}$  essentially reduces the size of solar gravity. Since the orbital period is constrained by the observational data,  $A_1$  and the semimajor axis  $a$  are strongly correlated and they adapt to match the observed orbital period. Therefore,  $A_1$  is observable only for small objects ( $A_1 \propto 1/d$ ) experiencing close approaches, which break Keplerian motion around the Sun and thus the correlation between  $A_1$  and  $a$ : 2009 BD (Micheli *et al.*, 2012; Mommert *et al.*, 2014a), 2011 MD (Micheli *et al.*, 2014; Mommert *et al.*, 2014b), and 2012 LA (Micheli *et al.*, 2013).

The Yarkovsky effect is generally more relevant than solar radiation pressure, although solar radiation pressure is larger in magnitude (see Fig. 2b). In fact, the Yarkovsky-related semimajor axis drift causes a run-off in longitude that accumulates quadratically with time. For asteroids (6489) Golevka (Chesley *et al.*, 2003) and (101955) Bennu (Chesley *et al.*, 2014), the availability of three radar apparitions clearly reveals the action of the Yarkovsky effect. For (152563) 1992 BF (Vokrouhlický *et al.*, 2008) the Yarkovsky effect is needed in order to match the precovery observations from 1953. Moreover, there are few tens of objects for which the Yarkovsky-related semimajor axis drift is detected from the orbital fit (Nugent *et al.*, 2012; Farnocchia *et al.*, 2013a) (see the chapter by Vokrouhlický *et al.* in this volume).

Figure 3 shows how important it can be to include non-gravitational perturbations in the model to make reliable predictions. Asteroid (101955) Bennu was observed by radar in 2011 (Chesley *et al.*, 2014). Since the observed arc before the 2011 radar observations can be fit with a gravity-only orbit, it is possible to make two different predictions for the radar delay measurements: either with or without the Yarkovsky effect in the model. By using a gravity-only solution we obtain a prediction with a small uncertainty of 3  $\mu$ s. If the Yarkovsky effect is included in the model, we obtain a significantly different prediction, shifted by 700  $\mu$ s with respect to the gravity-only prediction. Moreover, the prediction uncertainty is much larger, i.e., 150  $\mu$ s, as it accounts for the  $A_2$  uncertainty obtained by fitting the observed arc before the 2011 radar observations. The comparison between the actual delay measurements, whose reported uncertainty is 2  $\mu$ s, and the gravity-only prediction results in a  $170\sigma$  discrepancy. On the other hand, the radar measurements and the prediction obtained including the Yarkovsky effect

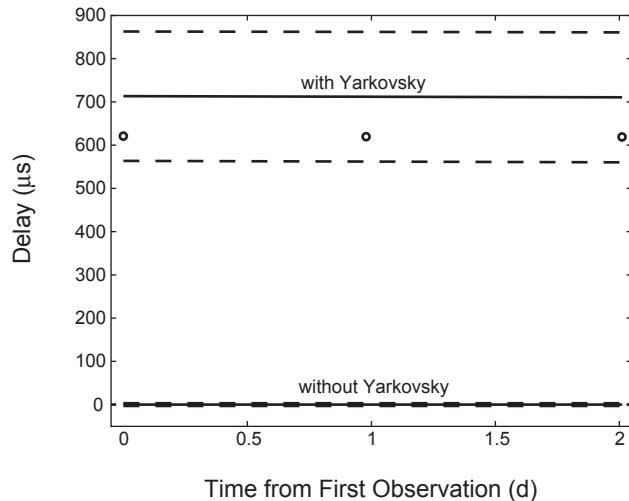


**Fig. 3.** Comparison between predictions and 2011 radar delay measurement for asteroid Bennu. Circles represent radar measurements, whose uncertainty is 2  $\mu$ s. Solid lines are prefit predictions with and without Yarkovsky effect in the model. Dashed lines correspond to the  $1\sigma$  prediction uncertainties, 3  $\mu$ s without Yarkovsky, and 150  $\mu$ s with Yarkovsky in the model. The origin of the y-axis corresponds to the gravity-only prediction.

in the model agree at the  $0.6\sigma$  level. The significantly better agreement between prediction and observations is due to both a much better nominal prediction and a larger uncertainty that accounts for the uncertainty in the Yarkovsky effect. This example shows that, although one can fit the available data without nongravitational perturbations, the inclusion of nongravitational perturbations may be important (if not necessary) to provide accurate predictions.

#### 4.3. Nonlinearity in Propagation

The main difficulty in asteroid trajectory estimation is nonlinearity, which restricts the validity of the linear methods of section 2 to local approximations. There are three main causes of nonlinearity.

The first source of nonlinearity is when the confidence region  $\Delta Q \leq \sigma^2$  becomes too large. This situation occurs when the normal and covariance matrices have a large condition number, which results in confidence ellipsoids with a very elongated shape: If  $\lambda_j$  are the eigenvalues of the normal matrix  $C$ , the lengths of the semiaxes of the confidence ellipsoid are  $\sigma_j = 1/\sqrt{\lambda_j}$ , and the ratio of the longest to the shortest is  $\sqrt{\text{cond}(C)}$ . It is common to find ratios  $10^5 \approx 10^6$ , thus some of the points in the confidence ellipsoid are far from the nominal solution.

When the quadratic approximation of  $\Delta Q$  fails, the shape of the actual confidence regions is very different from the ellipsoid given by equation (5). The boundaries of the confidence region are level manifolds of the probability density

function (PDF). Because of the exponential dependence on  $\chi^2$ , the probability estimates from the linearly propagated normal distributions fail. The PDF of the orbital elements cannot be computed from the covariance matrix. This has serious implications in the orbit determination for asteroids with few observations (see section 5).

The second cause of nonlinearity is the propagation of the orbit to some time well separated from the observed arc. This situation occurs even for Keplerian motion and is therefore relevant even for orbits weakly perturbed by planets, e.g., main-belt asteroids. The mean-motion  $n$  is a nonlinear function of the semimajor axis  $a$ ,  $n \propto a^{-3/2}$ . Since  $n(a)$  is a convex function, even a perfectly elliptic confidence region at the initial epoch is converted into a banana-shaped region in Cartesian space (see Fig. 5.2 in Milani and Gronchi, 2010), and the PDF is not normal anymore. The condition number of the normal matrix grows proportionally to the square of the time interval, so that even well-constrained initial conditions have badly conditioned normal matrices when propagated far in time.

The third cause is chaos, i.e., the exponential increase in the largest semimajor axis of the confidence ellipsoid as a function of time. The Lyapunov time is the time interval in which the longest axis increases, on average over long times, by a factor  $\exp(1)$ . For main-belt asteroids Lyapunov times can be on the order of thousands to tens of thousands of years (Holman and Murray, 1996). Because of planetary encounters, for near-Earth asteroids (NEAs) (perihelion smaller than 1.3 AU) Lyapunov times can range from years to decades (Whipple, 1995). As an example, for asteroid 2009 FD (Spoto et al., 2014) the Lyapunov time in the time interval 2009–2185 is about 15 yr: The longest axis of the confidence ellipsoid grows by a factor  $\approx 10^5$ . Although the current uncertainty is well approximated by an ellipsoid, the prediction uncertainty for 2185 has a very long banana shape. Note that the increase of size of the uncertainty region does not occur in all directions (also because the flow is volume preserving in phase space, in the purely gravitational case): The predominant direction in which the uncertainty grows is along-track, as a consequence of changes in the semimajor axis due to close approaches. After a time long with respect to the Lyapounov time, the uncertainty region appears like a wire bending and winding around the orbit and therefore impact monitoring is difficult for chaotic orbits (see section 6).

## 5. SHORT-ARC ORBIT DETERMINATION

When the observed arc is short, perhaps only a few hours or less, the standard technique of iterative differential corrections often fails due to nonconvergence, and even if there is convergence it is hard to rule out the possibility of other local minima of  $Q$  that may actually be closer to the true orbit. Nor is it obvious how to assess the prediction uncertainty when the linear theory presented in section 2 clearly does not apply and indeed some of the elements may be substantially unconstrained.

### 5.1. Bayesian Orbit Determination

To remove the assumption of linearity, one can use the Bayesian inversion theory as described by Muinonen and Bowell (1993). Given the orbital elements  $\mathbf{x}$ , their probability density is proportional to the product of the distribution of the observation residuals and a prior distribution

$$f_{\mathbf{x}}(\mathbf{x}) \propto f_v(v(\mathbf{x}))f_{\text{prior}}(\mathbf{x}) \quad (7)$$

The prior distribution  $f_{\text{prior}}$  can be non-informative, e.g., a uniform distribution in Cartesian coordinates, or informative, e.g., based on asteroid population models such as Grav et al. (2011). See Farnocchia et al. (2015b) for a discussion on the choice of  $f_{\text{prior}}$ .

When the linear approximation fails, the probability distribution of the orbital elements  $\mathbf{x}$  given by equation (7) can be very complicated. Therefore, Monte Carlo methods are suitable to generate orbital samples compatible with the available observations. Since optical observations constrain the angular position and rates, ranging methods are preferred. These methods originate in the plane-of-sky spherical coordinate frame, where the observer is at the origin and the asteroid state is given by the position and rates in right ascension, declination and range  $(\alpha, \delta, \dot{\alpha}, \dot{\delta}, \rho, \dot{\rho})$ , and they sample the space of  $\rho$  and  $\dot{\rho}$  in some way so as to explore a reasonable extent of line-of-sight position and velocity.

**5.1.1. Statistical ranging.** The idea of statistical ranging (Virtanen et al., 2001) is to randomly sample the topocentric range, i.e., the distance  $\rho$  between observer and asteroid. The first step is choosing the interval  $[\rho_{\min}, \rho_{\max}]$  of plausible values of the topocentric range. Then, orbital samples are generated as follows: (1) Noise is added to the observations according to the observational error model (e.g., see section 3). (2) Two observations  $(\alpha_A, \delta_A)$  and  $(\alpha_B, \delta_B)$  are randomly selected. (3) The topocentric distances  $\rho_A$  and  $\rho_B$  are randomly generated in the chosen interval and, coupled with the selected observations, yield two Cartesian states  $\mathbf{r}_A$  and  $\mathbf{r}_B$  at epochs  $t_A$  and  $t_B$ . (4) From  $\mathbf{r}_A$  and  $\mathbf{r}_B$ , one computes an orbit (e.g., see Dubyago, 1961) and the observation residuals. (5) The probability density function for the computed orbit is obtained from equation (7).

**5.1.2. Systematic ranging.** The systematic ranging technique (Chesley, 2005; Farnocchia et al., 2015b) relies on the fact that a series of astrometric positions over a short time interval gives an excellent constraint on the sky-plane position and motion. The range and range-rate are only weakly constrained, if at all, but if one were to fix the values of  $(\rho, \dot{\rho})$  the result would be a complete orbit, with small uncertainty. Thus, the systematic ranging concept scans a suitably dense grid in  $(\rho, \dot{\rho})$ , computing at each grid point the constrained best-fitting orbit. Then, the corresponding observation residuals provide the marginal probability in  $\mathbf{x} = (\rho, \dot{\rho})$  through equation (7).

**5.1.3. Markov-Chain Monte Carlo ranging.** The Markov-Chain Monte Carlo ranging (Oszkiewicz et al., 2009) is based on statistical ranging but allows one to generate an

unbiased sequence of orbital samples distributed according to equation (7). Statistical ranging is used to generate candidate orbits. However, a candidate orbit  $\mathbf{x}'$  is not always accepted. If  $\mathbf{x}_m$  is the last accepted solution, the acceptance of  $\mathbf{x}'$  depends on the ratio

$$\tau = \frac{f_{\mathbf{x}}(\mathbf{x}')}{f_{\mathbf{x}}(\mathbf{x}_m)}$$

The candidate orbit is accepted, i.e.,  $\mathbf{x}_{m+1} = \mathbf{x}'$ , with probability  $\min(1, \tau)$ . If the orbit is rejected, then  $\mathbf{x}_{m+1} = \mathbf{x}_m$ .

## 5.2. Linkage

Modern surveys produce a large number of observations belonging to many different moving objects. In general, one can initially identify only a very short arc of observations, also called tracklet, as belonging to the same physical object. When the arc length is small enough so that the curvature is not significant with respect to the astrometric uncertainties, the information contained in the short arc can be compressed through a linear fit in an attributable (Milani and Knežević, 2005)

$$\mathcal{A} = (\alpha, \delta, \dot{\alpha}, \dot{\delta})$$

which represents the angular position and velocity of the object in the sky. Given an attributable  $\mathcal{A}$ , the radial distance  $\rho$  and the radial velocity  $\dot{\rho}$  between the moving object and the observer are completely undetermined. If  $\rho$  and  $\dot{\rho}$  were known, it would be possible to compute the Cartesian state, and therefore the orbit, of the object

$$\begin{aligned} \mathbf{r} &= \mathbf{q} + \rho \hat{\mathbf{p}}, \\ \mathbf{v} &= \dot{\mathbf{q}} + \dot{\rho} \hat{\mathbf{p}} + \rho \dot{\alpha} \partial \hat{\mathbf{p}} / \partial \alpha + \rho \dot{\delta} \partial \hat{\mathbf{p}} / \partial \delta \end{aligned} \quad (8)$$

where  $\hat{\mathbf{p}} = (\cos \alpha \cos \delta, \sin \alpha \cos \delta, \sin \delta)$  is the line of sight, and  $\mathbf{q}$  and  $\dot{\mathbf{q}}$  are the observer's heliocentric position and velocity, respectively.

As the amount of data that can immediately be assigned to a single object is not enough to compute an orbit, we need to solve the identification problem, i.e., finding among independent observations those belonging to the same physical object. On the other hand, an identification can be considered reliable only if an orbit can be consistently fit to all the data believed to be of the same physical object. Thus, orbit determination and identification have to be solved by a single algorithm. Moreover, the computational complexity of the algorithm is a key consideration: Efficient methods capable of computing preliminary orbits using a low number of observations are desirable.

A comprehensive discussion of the process to solve the identification problem is beyond the scope of this chapter and can be found in chapter 11 of Milani and Gronchi (2010). Here we only discuss the linkage, i.e., joining together two or more short arcs of observations to form an orbit fitting all the data. First, we quickly describe the Kubica

*et al.* (2007) kd-tree algorithm and then we focus on other two methods to perform the linkage: The first method is based on the admissible region theory (Milani *et al.*, 2004), while the second method relies on the prime integrals of Keplerian motion (Gronchi *et al.*, 2010, 2011).

**5.2.1. kd-trees.** Kubica *et al.* (2007) present a technique based on kd-trees that has been successfully used by the Pan-STARRS PS1 Moving Object Pipeline System (MOPS) (Denneau *et al.*, 2013). kd-trees are hierarchical data structures that can be used to efficiently answer a variety of spatial queries (Bentley, 1975) and their structure provides fast and scalable performance. The first step is linking tracklets with a quadratic fit for the plane-of-sky motion, then preliminary orbit determination methods are used to find orbits compatible with the linked tracklets (Milani *et al.*, 2008).

**5.2.2. Admissible region.** Given an attributable  $\mathcal{A}$ , the possible values of  $\rho, \dot{\rho}$  can be constrained by making some hypotheses.

Using equation (8), the heliocentric two-body energy is an explicit function of  $(\rho, \dot{\rho})$

$$\begin{aligned} 2\mathcal{E}(\rho, \dot{\rho}) &= |\mathbf{v}(\rho, \dot{\rho})|^2 - 2GM_{\odot}/|\mathbf{r}(\rho)| \\ &= \dot{\rho}^2 + c_1 \dot{\rho} + W(\rho) - 2GM_{\odot}/\sqrt{S(\rho)} \end{aligned} \quad (9)$$

where  $c_1$  is a constant and  $W$  and  $S$  are quadratic functions of  $\rho$  (Milani *et al.*, 2004).

The first condition defining the admissible region is to select only those values of  $(\rho, \dot{\rho})$  for which the orbit is bounded, i.e.,  $\mathcal{E} < 0$ . The region of the  $(\rho, \dot{\rho})$  plane satisfying this condition has at most two connected components (Milani *et al.*, 2004).

A difficulty in the practical usage of the region defined above is that it is not a compact set, i.e., the observed object could be at an arbitrarily small distance from the observer. Thus, we need to define an inner boundary. A solution to assign a lower limit to the distance is to impose the constraint that the object is not very small and very close to Earth. The size can be controlled by setting a maximum value for the absolute magnitude  $H \leq H_{\max}$ . If an average value  $V$  of the apparent magnitude is available, then  $H$  can be computed as

$$H = V - 5 \log_{10} \rho - g(\rho, \phi)$$

where the correction  $g(\rho, \phi)$  accounts for the distance from the Sun and the phase angle  $\phi$  (owell *et al.*, 1989). For small values of  $\rho$ ,  $g(\rho, \phi)$  can be approximated with a constant  $g_0$ . However, this approximation is also acceptable for larger values of  $\rho$ . Thus, the upper bound on  $H$  yields

$$\log_{10} \rho \geq \frac{V - H_{\max} - g_0}{5} = \log_{10} \rho_H$$

Therefore, given the apparent magnitude  $V$ , we have a minimum distance  $\rho_H = \rho(H_{\max})$  for the object to be of significant size. Other conditions to define the inner boundary can be found in Milani *et al.* (2004).

Figure 4 shows the admissible region for asteroid (60558) Echeclus using the negative heliocentric energy and the upper bound on the magnitude ( $H_{\max} = 30$ ), which results in a lower bound on  $\rho$  of 0.34 AU.

Once the admissible region for a given attributable is computed, one can generate samples  $(\rho_i, \dot{\rho}_i)$  by constructing a Delaunay's triangulation (Bern and Eppstein, 1995) (see Fig. 4). Each node of the admissible region corresponds to an orbit to which we can assign a covariance matrix resulting from the attributable uncertainty. This orbit can be considered as a virtual asteroid (VA), i.e., one of the possible orbits compatible with the given attributable.

Each computed orbit and its covariance can be propagated to the time of a second attributable  $\mathcal{A}_2$  to compute a predicted attributable  $\mathcal{A}_p$  with covariance  $\Gamma_p$ . If  $\Gamma_2$  is the covariance of  $\mathcal{A}_2$  we can compute an attribution penalty (see chapter 7 of Milani and Gronchi, 2010) as

$$K = (\mathcal{A}_p - \mathcal{A}_2)^T (\Gamma_p^{-1} - \Gamma_p^{-1} \Gamma_0 \Gamma_p^{-1}) (\mathcal{A}_p - \mathcal{A}_2)$$

where

$$\Gamma_0 = (\Gamma_p^{-1} + \Gamma_2^{-1})^{-1}$$

If  $K$  is below some maximum value  $K_{\max}$ , the orbit is kept as candidate orbit to be confirmed by adding additional observational data (see chapter 11 of Milani and Gronchi, 2010). The distribution of  $\chi^2$  with 4 degrees of freedom can be used as a reference to select  $K_{\max}$ , although some margin might be necessary to account for nonlinearity.

**5.2.3. Keplerian integrals.** Another method to compute orbital solutions from two attributables  $\mathcal{A}_1$  and  $\mathcal{A}_2$  is based on the use of the conservation of the orbital energy  $\mathcal{E}$  and

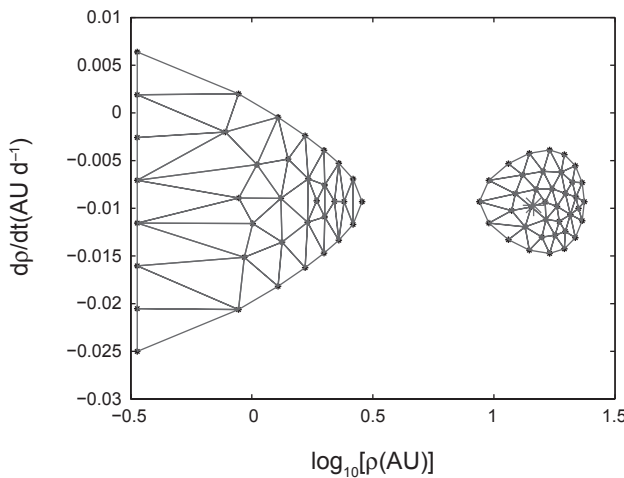


**Fig. 4.** An example of admissible region for asteroid (60558) Echeclus. The attributable is computed from the Spacewatch observations of February 5, 2000. The Delaunay's triangulation is indicated by the solid lines and the nodes are marked with dots. The actual solution for  $(\rho, \dot{\rho})$  is marked with an asterisk.

angular momentum  $\mathbf{c}$ .  $\mathcal{E}$  can be expressed as a function of  $(\rho, \dot{\rho})$  (see equation (9)). The same holds for  $\mathbf{c}$

$$\mathbf{c}(\rho, \dot{\rho}) = \mathbf{r} \times \mathbf{v} = \mathbf{D}\dot{\rho} + \mathbf{E}\rho^2 + \mathbf{F}\rho + \mathbf{G}$$

where  $\mathbf{D}$ ,  $\mathbf{E}$ ,  $\mathbf{F}$ , and  $\mathbf{G}$  only depend on the attributable and the observer's position and velocity (Gronchi et al., 2010). By imposing the conservation of  $\mathcal{E}$  and  $\mathbf{c}$  at the time of the two attributables we obtain a system of four equations in four unknowns

$$\begin{cases} \mathcal{E}_1(\rho_1, \dot{\rho}_1) = \mathcal{E}_2(\rho_2, \dot{\rho}_2) \\ \mathbf{c}_1(\rho_1, \dot{\rho}_1) = \mathbf{c}_2(\rho_2, \dot{\rho}_2) \end{cases} \quad (10)$$

By eliminating  $\dot{\rho}_1$  and  $\dot{\rho}_2$ , we are left with two equations  $p_1(\rho_1, \rho_2) = 0$ ,  $p_2(\rho_1, \rho_2) = 0$ . As an example, the corresponding curves are shown for asteroid (243) Ida in Fig. 5. By using the resultant (Cox et al., 2007) and other algebraic manipulations it is possible to obtain a polynomial equation in either  $\rho_1$  or  $\rho_2$  of degree  $\leq 48$  (Gronchi et al., 2010). It is possible to lower the maximal degree of the polynomial equation down to 20 if the conservation of the energy is replaced by the conservation of the eccentricity vector projected on a suitable direction (Gronchi et al., 2011).

Some of the solutions of the polynomial equation are unphysical, e.g.,  $\rho_1 < 0$ . Other solutions are spurious, i.e., they have been introduced by algebraic manipulations. Thus, each solution of the polynomial equation has to be tested to make sure it is a solution of system (10) as well. For the solutions passing the test we obtain  $(\rho_1, \dot{\rho}_1)$  and  $(\rho_2, \dot{\rho}_2)$ , and so the Cartesian states of the orbit at the epochs of the two attributables  $t_1$  and  $t_2$ . Still, one needs to make sure that the

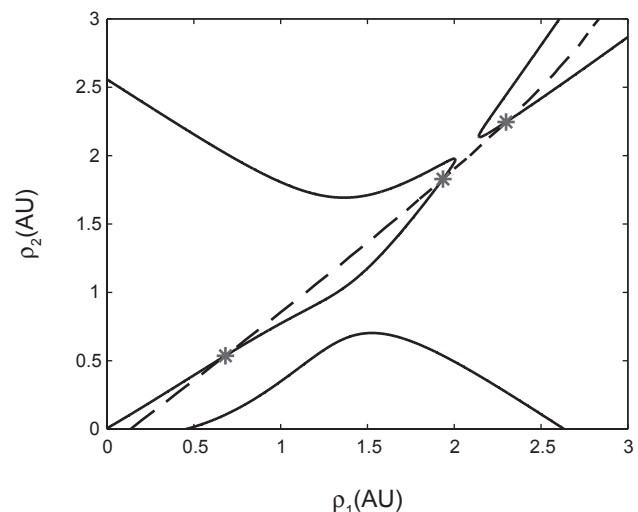


**Fig. 5.** Projection of system (10) on the  $(\rho_1, \rho_2)$  plane for asteroid (243) Ida. The attributables used are from February 17 and March 27, 1993. The asterisks mark the possible solutions for  $(\rho_1, \rho_2)$ . The solution  $(\rho_1, \rho_2) = (1.9, 1.8)$  AU is compatible with the actual orbit of Ida.

corresponding orbits are compatible. The conservation of the energy and the angular momentum ensures that semimajor axis, eccentricity, inclination, and longitude of node are the same. However, argument of perihelion and mean anomaly may well be incompatible.

As described in Gronchi *et al.* (2011), by solving system (10), one can map  $(\mathcal{A}_1, \mathcal{A}_2)$  to  $(\mathcal{A}_1, p_1, \dot{p}_1)$ . Thus, one can map the known covariances  $\Gamma_{\mathcal{A}_1}$  and  $\Gamma_{\mathcal{A}_2}$  of the two attributables to the covariance of the orbit at the epoch of  $\mathcal{A}_1$ . Finally, one can check the compatibility of the orbit and  $\mathcal{A}_2$  as described at the end of section 5.2.2. Again, the orbits passing this test can be used to find additional observations compatible with the computed orbital solution.

## 6. IMPACT MONITORING

A high-profile application of asteroid orbit estimation and ephemeris prediction is Earth impact monitoring. This area of work has obvious relevance to the public, requiring great care to make sure results are transparent and accurate. Moreover, the imperative to make impact hazard assessments as far in advance as possible — and thereby allowing the maximum time for deflection or other mitigation efforts — leads to severe technical challenges.

The b-plane frame, sometimes also known as the target plane or Öpik plane, is a common and convenient framework for conducting Earth-asteroid impact hazard analyses (Vals-ecchi *et al.*, 2003; Öpik, 1951, 1976). In this formalism, the b-plane includes the geocenter at the origin and is oriented orthogonal to the incoming asymptote of the asteroid's geocentric orbit. For hazard assessment we are interested in the b-plane position  $\mathbf{b}$  of the inbound asymptote. As important is the uncertainty in  $\mathbf{b}$ , which in the simplest case is normally

distributed and can thus be described as an ellipse centered at  $\mathbf{b}$ . For the trajectory unperturbed by Earth,  $\mathbf{b}$  marks the encounter distance; however, due to gravitational focusing, close flyby trajectories can impact even if the asymptote does not intersect the figure of Earth. The b-plane distance of a grazing trajectory is given by  $b_{\oplus} = R_{\oplus}\sqrt{1 + v_e^2/v_{\infty}^2}$ , where  $R_{\oplus}$  is Earth radius,  $v_{\infty}$  is hyperbolic excess velocity, and  $v_e$  is Earth escape velocity ( $v_e^2 = 2GM_{\oplus}/R_{\oplus}$ ). For a spherical Earth, trajectories for which  $b < b_{\oplus}$  will impact.

The classical Öpik formulation of the b-plane establishes coordinate axes  $\mathbf{b} = (\xi, \zeta)$  so that the projection of Earth's heliocentric velocity onto the b-plane defines the negative  $\zeta$ -axis. Thus, the  $\zeta$  coordinate defines how early or late the asteroid is for the minimum orbital intersection distance (MOID) (Gronchi, 2005), which is well approximated by the absolute value of the  $\xi$  coordinate. Because in the most challenging cases the uncertainty in the time of arrival strongly dominates over the uncertainty in the other orbital elements, this decoupling of the miss distance into timing and orbital separation allows an intuitive perspective from which one can analyze encounters. As example, Fig. 6a shows the uncertainty region of (101955) Bennu mapped onto the b-plane of the 2135 Earth encounter. The uncertainty is mostly stretched along  $\zeta_{2135}$  and reflects the time of arrival uncertainty. The inner circle at the origin corresponds to Earth radius, while the outer circle corresponds to Earth capture radius.

The preferred approach to detecting potential impacts and assessing the hazard posed by potential impactors varies depending on the uncertainty in the estimated orbit, the time span of interest, and the intervening dynamics between the time of the observations and that of the potential impact. As we discuss below, linear methods are fast and therefore

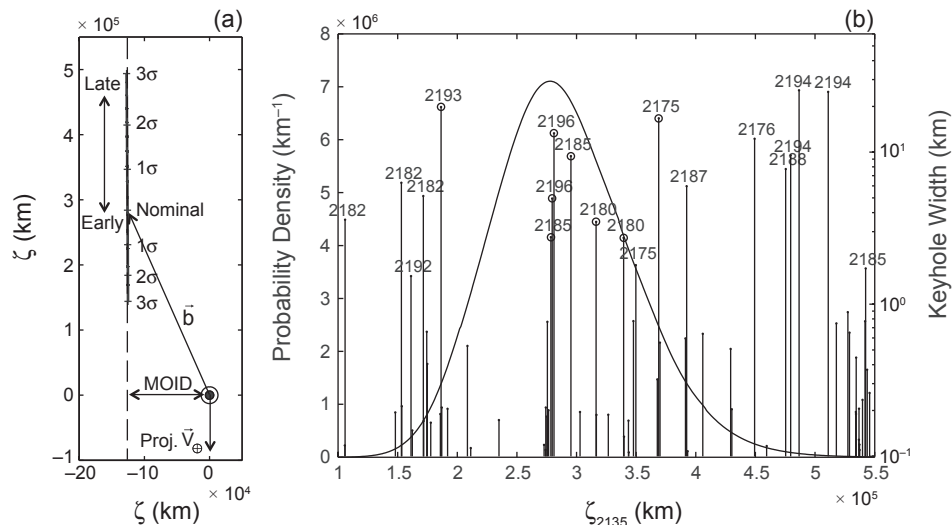


**Fig. 6.** (a) Map of the Bennu  $3\sigma$  uncertainty region onto the b-plane of the 2135 Earth encounter. The inner circle at the origin corresponds to the Earth radius, while the outer circle corresponds to the Earth capture radius. (b) Distribution of  $\zeta_{2135}$  for asteroid Bennu. The vertical bars correspond to the keyholes for post-2135 impacts and their height is proportional to the keyhole width. Reprinted from Chesley *et al.* (2014), with permission of Elsevier.

preferred when linear approximations are reliable for both the orbit determination and propagation. In cases where the linear assumption is inappropriate, an array of more computationally intensive nonlinear tools is available, such as Monte Carlo or line of variations (LOV) methods. One can picture this as a sort of cascade of computational tools that apply as the problem becomes progressively more nonlinear and less constrained.

## 6.1. Linear Methods

Linearity is a strong assumption for the impact monitoring problem and must be met in both the mapping from the observation residuals  $v$  to the orbital parameters  $x$  at the time of the observations, and in the mapping of  $x$  to orbital state  $x_{\text{ENC}}$  at the time of potential encounter. Following the notation of section 2 the assumption requires  $\Delta x \approx B\Delta v$  and  $\Delta x_{\text{ENC}} \approx A\Delta x$ . In such cases the observational uncertainty can be mapped directly to the future position uncertainty through the chain rule  $\Delta x_{\text{ENC}} \approx AB\Delta v$ .

The final step is to map the encounter state  $x_{\text{ENC}}$  and its uncertainty to the b-plane according to the linear mapping  $\Delta b = J\Delta x_{\text{ENC}}$ , where  $J = \partial b / \partial x_{\text{ENC}}$ . Here again the question of nonlinearity must be addressed, because for cases with large uncertainty and distant encounters, the curvature of Earth's orbit induces subtle nonlinearities that can corrupt results.

In the event that the linearity assumptions are valid, the uncertainty on the b-plane can be represented by the  $2 \times 2$  b-plane covariance matrix  $\Gamma_b = JABW^{-1}B^T A^T J^T$ , with probability density

$$f_b = \frac{1}{\sqrt{4\pi^2 \det \Gamma_b}} \exp\left(-\frac{1}{2}(\mathbf{b} - \bar{\mathbf{b}})^T \Gamma_b^{-1} (\mathbf{b} - \bar{\mathbf{b}})\right)$$

where  $\bar{\mathbf{b}}$  is the nominal b-plane prediction. From here the impact probability  $\mathcal{P}$  is simply the integral over the impact cross-section of Earth

$$\mathcal{P} = \int_{b < b_{\oplus}} f_b db$$

This is a fast numerical computation, but can only be used in cases where the numerous linearity assumptions hold. As a rough rule of thumb, the linear method is reliable when the impact probability increases above  $\sim 10^{-3}$ ; lower probabilities imply that the uncertainty region is too large to be adequately represented by a normal distribution. An optical data arc that extends over several days or more will generally allow linearity in the orbit determination so that  $\Gamma_x$  can represent the uncertainty. Generalizations are more difficult for the propagation to the prediction epoch, but the state transition matrix  $A$  will often prove adequate if the data arc is at least several days and the propagation time is at most a few years. For multi-apparition datasets propagations up to a century are often linear, though intervening close approaches may introduce nonlinearities far earlier.

## 6.2. Nonlinear Methods

When the foregoing linearity assumptions are invalid, one must resort to more cumbersome and computationally intensive techniques to properly characterize the prediction uncertainty at a potentially threatening close encounter. These techniques can be grouped into three general categories, namely Monte Carlo, ranging, and LOV methods. Each approach has its own advantages and disadvantages, and yet each has a regime where it is best suited to provide accurate and efficient results.

**6.2.1. Monte Carlo methods.** Monte Carlo methods are the most accurate and the most computationally intensive approach. The basic idea is to take randomly distributed orbital samples and for each sample compute the Earth miss distance at the epoch of interest. The estimated impact probability is simply the number of impacts divided by the number of samples  $N$ .

The most robust approach is to sample in the space of observations, i.e., to add normally distributed noise to the observation to model the observational uncertainty. The sampling can be done according to the probability density function  $f_v$  of the residuals (see equation (4)). The sampled  $v$  is added to the observations and these synthetic observations are used in the orbit estimation process to derive a sample least-squares orbit, which is then propagated to the time horizon of interest.

A somewhat more efficient approach can be used if the orbital variations are linear in the observation residuals over the range of uncertainty. In that case one can directly sample the orbit with the covariance  $\Gamma_x$  around the nominal orbital solution  $\bar{x}$ .

The uncertainty  $\sigma_{\mathcal{P}}$  in the impact probability estimate is given by  $\sigma_{\mathcal{P}}^2 = \mathcal{P}(1-\mathcal{P})/N$ . Thus, to find most potential impacts with probabilities greater than  $\mathcal{P}_{\text{lim}}$ , one needs to propagate  $\geq 4/\mathcal{P}_{\text{lim}}$  samples. For instance, for  $\mathcal{P}_{\text{lim}} \approx 10^{-6}$  we require  $N \approx 4 \times 10^6$  samples to obtain a 50% relative precision in our Monte Carlo result. With current computer technology, one can accurately propagate asteroid orbits at the rate of a few million years per hour, and so if we desire to identify all potential impacts with  $\mathcal{P} > 10^{-6}$  for a given asteroid for the next 100 yr we would need to integrate a total of  $4 \times 10^8$  yr, which would require roughly a week of time on a single processor. Reaching  $\mathcal{P} > 10^{-7}$  would require a few months of computing. Even with parallelization this technique can be impractical to implement in the framework of monitoring all NEAs for potential impact and updating the search whenever new observations become available.

Despite these limitations, the technique can be reasonably fast for potential impacts taking place within a few years if the probabilities are not too small. More importantly, the Monte Carlo techniques allow a robust uncertainty propagation where other methods falter or fail, and they can serve as an important validation tool in critical cases that require more careful analyses.

**6.2.2. Ranging methods.** A particularly challenging case arises with the need to provide short-term warning

for newly discovered objects that may impact within a few days of discovery. One might consider using the Monte Carlo approach in observation space if differential corrections converge successfully, but the question of sampling at other (potentially unknown) local minima could compromise the result. Since for newly discovered objects we generally only have a short arc of observations, the ranging methods described in section 5.1 are the most reliable means to perform the hazard assessment. Whichever ranging approach is used, the final result is an assessment of the element-space probability density and an estimate of the impact probability, whose reliability depends on obtaining enough samples to properly cover the orbital element phase-space. Because of the large uncertainty regions and computational cost, ranging techniques are particularly well-suited for single-night datasets and for impact monitoring up to a few weeks into the future.

For example, Fig. 7 shows the application of systematic ranging (see section 5.1.2) to 2014 AA, a small 2–4-m-sized asteroid. 2014 AA was discovered 21 h before striking Earth and only seven optical observations over 69 min were collected prior to the impact (<http://neo.jpl.nasa.gov/news-news182.html>). Despite the limited amount of data available, the astrometric RMS level curves bound the possible orbits and clearly suggest that 2014 AA is on a collision course.

**6.2.3. Line of variations methods.** The LOV method takes advantage of the fact that the orbital uncertainty grows with time in a peculiar way, by stretching into a long slender ellipsoid in Cartesian space. Small variations in most of the elements lead to periodic variations in the future position prediction, and by the same token, modest uncertainties in these elements lead to prediction uncertainties that do not grow with time. However, the uncertainty in semimajor

axis  $a$  is unique in this context because small variations in  $a$  produce variations in orbital period that cause the orbital anomaly to drift steadily away from the nominal orbit, a process referred to as Keplerian shear. The effect is to steadily stretch the uncertainty region along the orbit track, and so even for modest uncertainties in semimajor axis the uncertainty region can grow to cover the entire orbit. As an example, for an asteroid with semimajor axis  $1 \pm 0.05$  AU the mean anomaly uncertainty can increase to  $\pm 180^\circ$  in less than 7 yr, meaning that the asteroid could be anywhere along, although probably not far from, its nominal orbit.

The tendency of the uncertainty region to grow long and slender as time passes suggests the possibility of a one-dimensional parameterization of the orbital uncertainty region. In the LOV method we only sample the spine, or LOV, of the confidence region, and if all orbits are sufficiently close to the LOV, then we obtain tremendous computational savings over higher-dimensional sampling methods without sacrificing reliability. The LOV method begins by computing the orbit at intervals along the LOV, forming a set of ordered multiple solutions (Milani *et al.*, 2005a), each of which is propagated to a time horizon of interest while recording all close approaches within a selected distance, which may be, say, 0.1 AU. By sorting and collating the recorded close approaches, while preserving the order implied from the multiple solutions, one can identify simply connected loci of points on the b-plane of a given encounter and perform an impact hazard assessment for every identified route to impact.

The LOV method is unmatched in its ability to reliably detect low probability events deep in the nonlinear regime with a minimum of computational effort. Milani *et al.* (2005b) define the generic completion level of the search as the greatest impact probability that can escape detection if the LOV is reasonably well behaved on the target plane. The finding is that generic completion levels of  $10^{-7}$  can be readily obtained with the propagation of only  $\sim 10^4$  multiple solutions, leading to compute times 3–4 orders of magnitude below those required for similar completeness in Monte Carlo simulations. Such speeds are clearly a tremendous advantage; however, the disadvantage of the method is that the LOV analysis can grow quite complex after it has been stretched and folded by multiple close planetary encounters, leaving open the possibility of missing pathological cases, which is a lower risk for Monte Carlo methods.

A more complete discussion of LOV methods is presented by Milani *et al.* (2002), while a complete implementation of the LOV method, which can be fairly involved, is described in detail by Milani *et al.* (2005b).

### 6.3. Keyholes and Hazard Assessment

The trajectory of a potential impactor will have by definition a very small MOID relative to Earth's orbit. Given enough time, asteroids on such trajectories will therefore likely experience multiple close approaches to our planet. Consider the case in which an asteroid misses Earth during one close approach, but the gravitational perturbation of the

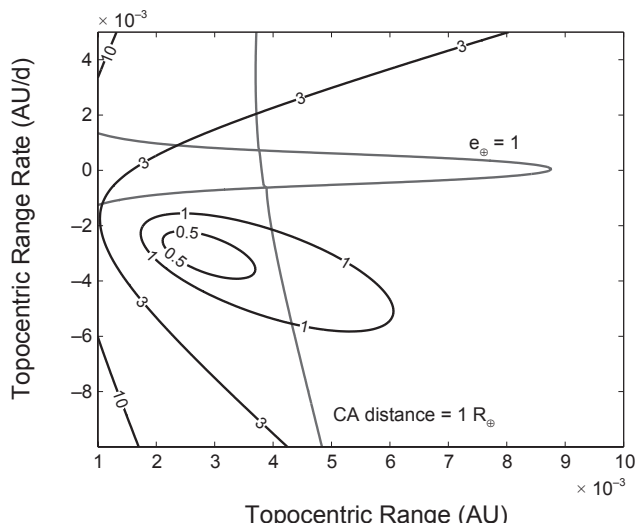


**Fig. 7.** Contour levels of the astrometric RMS ("") for asteroid 2014 AA based on the seven optical observations obtained before the impact. The labeled curves show the limits for bounded geocentric orbits ( $e_\oplus = 1$ ) and impacting orbits (CA distance =  $1 R_\oplus$ ).

encounter places the object on a near-resonant trajectory that causes it to impact during a later encounter. The term keyhole was introduced by Chodas (1999) to describe the small region in the b-plane of the initial encounter encompassing the trajectories that impact at the later encounter.

Early Monte Carlo explorations of uncertainty regions in a b-plane revealed keyholes as long narrow gateways that led to later impacts. All trajectories that pass through a keyhole will impact the planet at a subsequent encounter. Each keyhole is generally associated with an orbital resonance: The keyhole for a 7:6 resonance, for example, would place an object on an orbit that makes six complete revolutions about the Sun while Earth makes seven. Since there are many possible resonances, there can be many keyholes created by a close approach. Valsecchi *et al.* (2003) outline the mathematical theory behind keyholes and describe how their approximate locations can be predicted as a function of the heliocentric orbit and the particular keyhole resonances. As a first approximation, the coordinates on the b-plane corresponding to a given resonant return form a circle. The intersection between this circle and the uncertainty region gives the keyhole. As an example, Fig. 8a shows the 2029 b-plane for asteroid (99942) Apophis and the Valsecchi circle corresponding to the 2036 resonant return. The intersection between the LOV and the Valsecchi circle corresponds to the 2036 keyhole. It should be noted that nonresonant returns are also possible (Milani *et al.*, 1999) and that some resonances will not have associated keyholes because of perturbations from other planets.

Keyhole widths range from less than a kilometer to hundreds of kilometers or more. The 2036 keyhole in the 2029 b-plane of Apophis, for example, is very narrow, only about 600 m wide (Chesley, 2006). The narrow width is due to the fact that close approaches tend to scatter initially neighboring trajectories, because of the differential gravita-

tional perturbation. Slight differences in the close approach distance produce differences in the post-encounter semimajor axis, leading to a secular spreading apart of the different trajectories along the orbit path. A sequence of initially close neighboring points can be stretched apart by the close approach, and the points can become widely separated by the time of a potential impact. Keyholes can be thought of as pre-images of Earth mapped back to the pre-impact b-plane: When the stretching is reversed, the Earth disk at impact compresses down to the width of the keyhole in the pre-impact plane. Note that closer pre-impact encounters with Earth will lead to larger rates of spreading, and therefore to narrower keyholes. As a matter of fact, the 2036 keyhole for Apophis is narrow because of the small Earth encounter distance in 2029 of about 38,000 km.

Statistical studies have shown that about 15% of potential impactors will pass through a keyhole of several hundred kilometers or less in the 50-yr period before impact (Chodas, 2012). These studies also address the question of how close an object needs to approach Earth to form a keyhole: For a close approach within 50 yr of impact, the close approach distance must be less than about 0.10 AU in order to form a keyhole. Interestingly, distant pre-impact close approaches can have an effect opposite to that of keyhole encounters: Instead of spreading neighboring trajectories apart, encounters at distances of roughly 0.10 AU to 0.15 AU can actually focus neighboring trajectories (Chodas, 2012).

A systematic analysis of keyhole locations and widths along the length of the uncertainty region in a pre-impact b-plane forms the basis of another approach for estimating the impact hazard. A key step in this analysis is the creation of what we call a keyhole map. The map is formed using an LOV method very similar to that described in section 6.2.3, but with more finely spaced steps: Typically, hundreds of

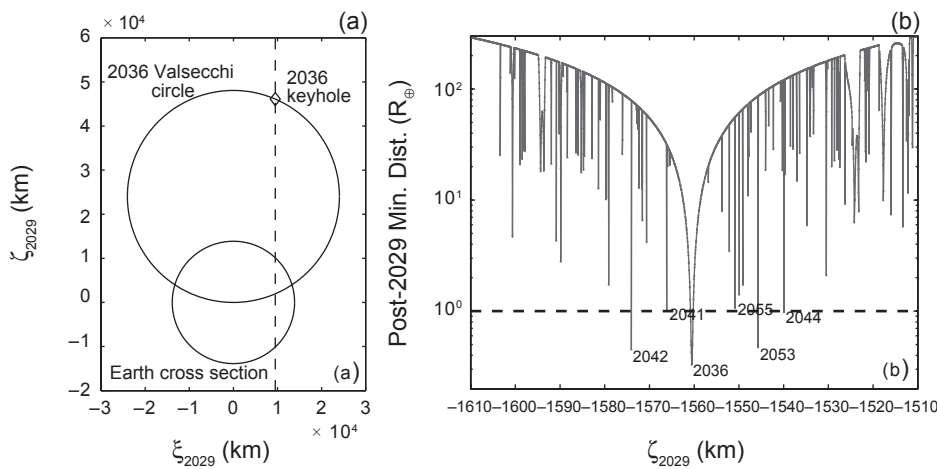


**Fig. 8.** (a) The 2029 b-plane for asteroid Apophis. The two circles are the cross section of the Earth and the Valsecchi circle corresponding to a resonant return in 2036. The dashed line represents the LOV direction and the diamond the 2036 keyhole. (b) A segment of the Apophis keyhole map, i.e., the minimum post-2029 Earth distance as a function of  $\zeta_{2029}$ . Encounters distances smaller than  $1.1 R_\oplus$  are labeled with the corresponding year. The  $\zeta_{2029}$ -axis origin is set to 47677 km to match Fig. 9.

thousands of samples are used along the LOV. The trajectories are all propagated forward in time, first to the primary encounter where the keyholes will be mapped, and then forward to a time horizon of interest, while recording the close approach distances of the subsequent, secondary Earth encounters, within a threshold distance such as 0.15 AU. The Öpik coordinates are also computed in the secondary b-planes. The keyhole map is formed by plotting the minimum secondary close approach distance for each trajectory against the  $\zeta$ -component in the primary b-plane.

Figure 8b shows a close-up of the keyhole map for Apophis in the region surrounding the 2036 keyhole in the 2029 b-plane. Each downward spike represents a close approach sometime between the years 2029 and 2100. The dashed horizontal line marks the radius of Earth, and points below it indicate trajectories that impact, with the year of the impact noted. The 600-m width of the 2036 keyhole can be clearly seen as the horizontal width of the portion of the curve below the dashed line. The downward spikes on either side of the main keyhole are secondary returns spawned by the 2036 encounter. Just as the Earth capture disk in a b-plane is surrounded by primary keyholes, primary keyholes are in turn surrounded by secondary keyholes. And since they are produced by two consecutive close approaches, there are two levels of trajectory stretching, and the secondary keyholes are therefore even narrower than primary keyholes, often only meters or tens of meters across.

Special efforts are made to interpolate between points in the often sparsely populated secondary b-planes, and the closest approach point of the LOV from the origin is computed; the corresponding minimum close approach distance is then included in the keyhole map. If the LOV happens to cut across the Earth capture cross section in the secondary b-plane, there must be a keyhole in the primary b-plane. To get the width of the keyhole, the first step is to compute the chord length of the LOV intersection in the secondary b-plane, and then scale it down by the stretching factor between the b-planes. The stretching is computed by examining the trajectories that bracket the keyhole and taking the ratio of separation between the trajectories in the two b-planes.

The impact probability associated with each keyhole is estimated by integrating the  $\zeta$  PDF in the primary b-plane across the keyhole. Keyholes are usually narrow enough that one can assume a constant probability density across the keyhole. For instance, Fig. 6b shows an alternative representation of a keyhole map, with the probability distribution of  $\zeta$  in 2135 for Bennu as well as the locations and width of the keyholes corresponding to potential later impacts. The impact probability for each of these impacts can be easily computed as the product of the PDF at the keyhole center and the keyhole width.

#### 6.4. Yarkovsky-Driven Impact Monitoring

The impact monitoring discussion so far has implicitly assumed gravity-only orbital dynamics and that an asteroid orbit only requires six estimable parameters. And yet, as

discussed in section 4.2, we know that asteroids can be significantly perturbed by nongravitational accelerations. In particular, the Yarkovsky effect can be a crucial part of an asteroid's impact hazard assessment, although this generally applies only to well-observed asteroids with precise orbits. The reason is that the Yarkovsky effect is such a slight perturbation to the orbit that it cannot rise above the overwhelming uncertainty seen in a new discovery, or even a typical multi-apparition orbit. The semimajor axis drift  $da/dt$  of a typical half-kilometer NEA may be only on the order of  $10^{-9}$  AU yr $^{-1}$ , i.e., 100 m yr $^{-1}$  or less, far below the uncertainties in most NEA orbits, where the uncertainty is completely dominated by astrometric uncertainties. As a result, the Yarkovsky effect generally remains unimportant for uncertainty propagation until decades of observations are available, although radar astrometry can require Yarkovsky consideration far sooner.

The generic case of a Yarkovsky-driven impact hazard assessment is centered upon a scattering encounter where the b-plane uncertainty is significantly enhanced by uncertainties in the Yarkovsky acceleration. Consider for instance the 2029 encounter of Apophis, which is nominally at a geocentric distance of 38,000 km. By neglecting the Yarkovsky effect and assuming gravity-only dynamics we find a b-plane uncertainty of only a few kilometers (see dashed line in Fig. 9b) and no meaningful probability of impact. However, the available physical characterization of Apophis (Binzel *et al.*, 2009; Pravec *et al.*, 2014; Müller *et al.*, 2014) suggests a reasonable range of the Yarkovsky effect. Specifically,  $A_2$  could be between  $-6 \times 10^{-14}$  AU d $^{-2}$  and  $-1 \times 10^{-14}$  AU d $^{-2}$  (see Fig. 9a), which corresponds to  $da/dt$  between  $-400$  m yr $^{-1}$  and  $-70$  m yr $^{-1}$  (Vokrouhlický *et al.*, 2015). Thus, the Yarkovsky effect leads to b-plane dispersions of several hundred kilometers and numerous keyholes fall within the b-plane uncertainty footprint. Figure 9b shows a keyhole map of the 2029 encounter where the large difference between the gravity-only and Yarkovsky uncertainty regions is apparent. After the scattering encounter, the Yarkovsky effect may again be negligible because the range of scattered orbits dominates over post-scattering Yarkovsky drift. The only effect of the post-scattering drift is a slight shift of the keyhole locations, typically by a distance that is similar to the actual size of the keyhole. Similarly, there is the possibility that the scattering encounter could induce a change in the spin state, for instance, by exciting a non-principal axis rotation state that could change the Yarkovsky drift rate. Again, this has only a small effect of shifting the keyhole locations on the b-plane, but does not appreciably alter the hazard assessment.

Most detected potential impacts are associated with recently discovered objects with large orbital uncertainties for which the impact probabilities are correspondingly low. The best approach to resolving these cases lies with obtaining more astrometric data to extend the data arc and eliminate the possibility of impact. For Yarkovsky-driven cases the situation is much different because the uncertainty at the scattering encounter is dominated by Yarkovsky dispersions,

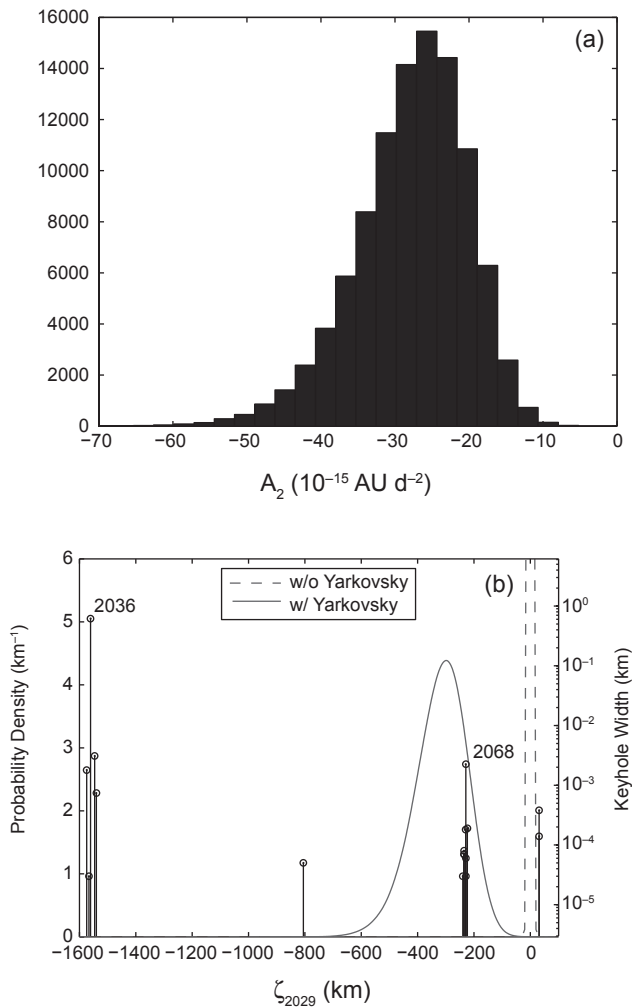


**Fig. 9.** (a) Distribution of the Yarkovsky parameter  $A_2$  for Apophis. (b) Apophis distribution on the 2029 b-plane and keyhole map. Both the distribution without the Yarkovsky effect (gravity-only) and the one with the Yarkovsky effect are shown. The  $\zeta_{2029}$ -axis origin is arbitrarily set to 47,677 km, i.e., the nominal  $\zeta_{2029}$  value of the gravity-only solution.

and gathering additional astrometry will have a small or negligible effect on the hazard analysis.

When the Yarkovsky effect is relevant to the hazard assessment, there are two distinct approaches: either modeling or estimating the Yarkovsky effect. The most widely applicable technique is to model the range of the Yarkovsky effect by considering the thermophysical characteristics that drive it. We can model the Yarkovsky effect (Bottke et al., 2006; see the chapter by Vokrouhlický et al. in this volume) as

$$A_2 \propto \frac{\cos \gamma}{\rho d} f(I, \omega, A)$$

where  $\gamma$  is the obliquity of the asteroid equator,  $\rho$  is the bulk density,  $I$  is the surface thermal inertia,  $\omega$  is the rotation rate, and  $A$  is the Bond albedo. All these quantities can be con-

strained to some extent depending on what is known about the specific asteroid, or the asteroid population in general, and from that a distribution of  $A_2$  can be derived. Farnocchia et al. (2013b) and Farnocchia and Chesley (2014) provide a more detailed description of this approach, while Fig. 9a shows the example of Apophis where its nonprincipal axis rotation is accounted for (Vokrouhlický et al., 2015). This  $A_2$  distribution can be used as a basis of a Monte Carlo method to perform the hazard assessment: We randomly select  $A_2$  from its distribution, we compute a best-fit orbital solution corresponding to that value of  $A_2$ , we sample the orbital elements within the uncertainty region, and we propagate the orbit to the desired epoch. For instance, by doing so we obtain the  $\zeta_{2029}$  distribution for Apophis as shown in Fig. 9b. Finally, the  $\zeta_{2029}$  distribution can be compared to the keyholes to compute the impact probabilities by multiplying the  $\zeta_{2029}$  PDF and the keyhole widths.

With this technique the best way to resolve the impact hazard situation is to reduce the Yarkovsky dispersions by refining the asteroid physical model through direct observations of albedo, spin state, thermal inertia and shape, etc. Any new information on these characteristics feeds further refinements to the Yarkovsky model and reductions in the b-plane uncertainty.

When the signal for the Yarkovsky drift is visible in the astrometric dataset, often due to the availability of radar astrometry, we can work in the other direction, i.e., direct estimation. The usual strategy is to estimate  $A_2$  as a part of the orbit-determination process and use that directly to reduce the uncertainty at the encounter. In this case the orbit determination is a straightforward seven-parameter estimation process with a  $7 \times 7$  covariance matrix. The prediction problem still requires mapping to the b-plane, but now with seven parameters. This mapping may not be linear due to two-body dynamics and N-body perturbations, but Monte Carlo or LOV methods are readily extended to the seven-parameter case. Direct estimation of the Yarkovsky effect is preferred when available because there is less reliance on inference of sometimes poorly known physical properties. In this scenario, resolving Yarkovsky-driven impact problems calls for additional astrometry that can help to constrain the Yarkovsky effect, irrespective of thermophysical modeling. For instance, the mapping of the uncertainty region of Bennu on the 2135 b-plane (see Fig. 6b) was obtained by using a seven-dimensional orbital solution where  $A_2$  is determined with 0.5% precision (Chesley et al., 2014).

## 7. FUTURE WORK

Computing asteroid trajectories is a 200-yr-old problem. Despite the work that has been done so far, the quality and amount of observational data still call for continuous research and ever more accurate models.

While the star catalog debiasing and weighting schemes presented in section 3 represent a significant step forward in the statistical treatment of astrometric observations, there is still plenty of room for improvement. The Gaia star catalog

(Perryman *et al.*, 2001) will be released in the near future with its unprecedented accuracy for star positions and proper motions. Therefore, the Gaia catalog will allow better astrometric solutions for asteroid observations as well as a better reference to remove biases due to systematic errors in the other star catalogs. For the astrometric weights we plan a more indepth analysis to account not only for observation type and observatory code but also for specific observers, timing errors, correlations between right ascension and declination, angular rates, and observational signal-to-noise ratio.

The force model discussed in section 4 is accurate enough for most asteroids. We have seen how minor perturbations such as planetary relativistic accelerations, second-order spherical harmonics of Earth, and nongravitational forces can be critical to fit observational data and to make accurate predictions. In the near future, with more and more accurate astrometric data collected, we might find that other terms need to be added to the force model. In particular, the Origins Spectral Interpretation Resource Identification and Security-Regolith Explorer (OSIRIS-REx) mission (Lauretta *et al.*, 2012) will push the presented dynamical model to its limits. For instance, OSIRIS-REx will provide an independent measurement of the Yarkovsky effect acting on (101955) Bennu, thus serving as a validation for the current  $200\sigma$  detection (Chesley *et al.*, 2014). Moreover, OSIRIS-REx's ranging, together with the three radar apparitions already available, will put exceptional constraints on Bennu's orbit and reveal possible inaccuracies in the observation and force models.

The rapid increase of the quantity of asteroid astrometry could result in an excessive accumulation of unidentified single-night observations. Therefore, the short-arc orbit determination methods described in section 5 are important for present and future asteroid surveys. For instance, Bayesian-inversion orbit determination is planned for the asteroid observations obtained by Gaia (Mignard *et al.*, 2007). The linkage methods presented in section 5.2 and their improvement will be useful to efficiently compute orbits for surveys producing a large amount of data, such as the survey foreseen as part of ESA's Space Situational Awareness program (Drolshagen *et al.*, 2012), the Asteroid Terrestrial-Impact Last Alert System [ATLAS (Tonry, 2011)], and the Large Synoptic Survey Telescope (LSST) survey (LSST Science Collaboration and LSST Project, 2009).

In section 6 we described the current techniques to compute the probabilities of potential asteroid impacts. Whereas for most objects the impact monitoring is handled with methods that have been in use for the last 15 yr, there are nonstandard cases for which additional effort is required. In these cases we need to estimate the dispersion due to nongravitational perturbations, explore beyond scattering planetary encounters, and extend the impact-prediction horizon. Although we described methods to successfully compute impact probabilities for these cases, we are still far from having a fully automated procedure.

Another field of future work is the hazard assessment for short-term impactors. When a potential NEA is observed for the first time, the MPC places the corresponding informa-

tion on the NEO Confirmation Page (NEOCP) (<http://www.minorplanetcenter.net/iau/NEO/ToConfirm.html>) so that other astronomers can collect additional observations and confirm that it is indeed a NEA. When an object is on the NEOCP the orbit is only weakly constrained by the observations and the theory of least squares does not always apply. Still, we would like to be able to identify those objects that not only are potential NEAs but also potential short-term impactors. This way, astronomers would give priority to potentially hazardous objects on the NEOCP and provide additional astrometry to refine the trajectory before a possible impact occurs. While the ranging methods described in section 5.1 are suitable to identify hazardous asteroids, their implementation for automated short-term impact monitoring of all new detections is an ongoing project.

**Acknowledgments.** The authors thank G. B. Valsecchi and an anonymous referee for their useful comments. D.F., S.R.C., and P.W.C. conducted this research at the Jet Propulsion Laboratory, California Institute of Technology, under a contract with the National Aeronautics and Space Administration. A.M. and G.F.G. were partially supported by the Marie Curie Initial Training Network Stardust, FP7-PEOPLE-2012-ITN, Grant Agreement 317185, and by the University of Pisa, Department of Mathematics internally funded project "Dynamics of Populations of Celestial Bodies." Copyright 2015 California Institute of Technology.

## REFERENCES

- Assafin M., Andrei A. H., Martins R. V., da Silva Neto D. N., Camargo J. I. B., Teixeira R., and Benevides-Soares P. (2001) Investigation of USNO-A2.0 Catalog Positions. *Astrophys. J.*, **552**, 380–385.
- Baer J., Chesley S. R., and Milani A. (2011a) Development of an observational error model. *Icarus*, **212**, 438–447.
- Baer J., Chesley S. R., and Matson R. D. (2011b) Astrometric masses of 26 asteroids and observations on asteroid porosity. *Astron. J.*, **141**, 143.
- Battin R. H. (1987) *An Introduction to the Mathematics and Methods of Astrodynamics*. AIAA Education Series, New York. 799 pp.
- Bentley J. L. (1975) Multidimensional binary search trees used for associative searching. *Commun. ACM*, **18**(9), 509–517.
- Bern M. and Eppstein D. (1995) Mesh generation and optimal triangulation. In *Computing in Euclidean Geometry* (D.-Z. Duand and F. K. Hwang, eds.), pp. 23–90. World Scientific, Singapore.
- Binzel R. P., Rivkin A. S., Thomas C. A., Vernazza P., Burbine T. H., DeMeo F. E., Bus S. J., Tokunaga A. T., and Birlan M. (2009) Spectral properties and composition of potentially hazardous asteroid (99942) Apophis. *Icarus*, **200**, 480–485.
- Bottke W. F., Vokrouhlický D., Rubincam D. P., and Nesvorný D. (2006) The Yarkovsky and YORP effects: Implications for asteroid dynamics. *Annu. Rev. Earth Planet. Sci.*, **34**, 157–191.
- Bowell E., Hapke B., Domingue D., Lumme K., Peltoniemi J., and Harris A. W. (1989) Application of photometric models to asteroids. In *Asteroids II* (R. P. Binzel et al., eds.), pp. 524–556. Univ. of Arizona, Tucson.
- Carpino M., Milani A., and Chesley S. R. (2003) Error statistics of asteroid optical astrometric observations. *Icarus*, **166**, 24–270.
- Carry B. (2012) Density of asteroids. *Planet. Space Sci.*, **73**, 98–118.
- Chesley S. R. (2005) Very short arc orbit determination: The case of asteroid 2004 FU<sub>162</sub>. In *Dynamics of Populations of Planetary Systems* (Z. Knezević and A. Milani, eds.), pp. 255–258. IAU Colloq. 197, Cambridge Univ., Cambridge.
- Chesley S. R. (2006) Potential impact detection for near-Earth asteroids: The case of 99942 Apophis (2004 MN<sub>4</sub>). *Asteroids, Comets, Meteors*, **229**, 215–228.
- Chesley S. R., Ostro S. J., Vokrouhlický D., Čapek D., Giorgini J. D., Nolan M. C., Margot J.-L., Hine A. A., Benner L. A. M., and

- Chamberlin A. B. (2003) Direct detection of the Yarkovsky effect by radar ranging to asteroid 6489 Golevka. *Science*, 302, 1739–1742.
- Chesley S. R., Baer J., and Monet D. G. (2010) Treatment of star catalog biases in asteroid astrometric observations. *Icarus*, 210, 158–181.
- Chesley S. R., Farnocchia D., Nolan M. C., et al. (2014) Orbit and bulk density of the OSIRIS-REx target asteroid (101955) Bennu. *Icarus*, 235, 5–22.
- Chodas P. W. (1999) Orbit uncertainties, keyholes, and collision probabilities. *Bull. Am. Astron. Soc.*, 31, 1117.
- Chodas P. W. (2012) Keyholes and Jabbas: The role of pre-impact close approaches in asteroid deflection. In *Asteroids, Comets, Meteors (ACM) 2012*, Abstract #6471. LPI Contribution No. 1667, Lunar and Planetary Institute, Houston.
- Cox D. A., Little J. B., and O’Shea D. (2007) *Ideals, Varieties and Algorithms*. Springer, New York. 553 pp.
- Damour T. and Deruelle N. (1985) General relativistic celestial mechanics of binary systems. I. The post-Newtonian motion. *Annu. Inst. Henri Poincaré Phys. Théor.*, 43, 107–132.
- Denneau L., Jedicke R., Grav T., et al. (2013) The Pan-STARRS moving object processing system. *Publ. Astron. Soc. Pac.*, 125, 357–395.
- Drolshagen G., Bassano E., Bernardi F., Hahn G., Koschny D., Milani A., Perozzi E., Sanchez N., Valsecchi G., and Weikert S. (2012) Precursor services for a near-Earth object segment of ESA’s Space Situational Awareness Programme. In *Asteroids, Comets, Meteors (ACM) 2012*, Abstract #6229. LPI Contribution No. 1667, Lunar and Planetary Institute, Houston.
- Dubyago A. D. (2010) *The Determination of Orbits*. The MacMillan, New York. 434 pp.
- Escobal P. R., ed. (1965) *Methods of Orbit Determination*. Wiley, New York. 500 pp.
- Farnocchia D., Chesley S. R., Vokrouhlický D., Milani A., Spoto F., and Bottke W. F. (2013a) Near Earth asteroids with measurable Yarkovsky effect. *Icarus*, 224, 1–13.
- Farnocchia D., Chesley S. R., Chodas P. W., Micheli M., Tholen D. J., Milani A., Elliott G. T., and Bernardi F. (2013b) Yarkovsky-driven impact risk analysis for asteroid (99942) Apophis. *Icarus*, 224, 192–200.
- Farnocchia D. and Chesley S. R. (2014) Assessment of the 2880 impact threat from asteroid (29075) 1950 DA. *Icarus*, 229, 321–327.
- Farnocchia D., Chesley S. R., Chamberlin A. B., and Tholen D. J. (2015a) Star catalog position and proper motion corrections in asteroid astrometry. *Icarus*, 245, 94–111.
- Farnocchia D., Chesley S. R., and Micheli M. (2015b) Systematic ranging and late warning asteroid impacts. *Icarus*, 258, 18–27.
- Folkner W. M., Williams J. G., Boggs D. H., Park R. S., and Kuchynka P. (2014) The planetary and lunar Ephemerides DE430 and DE431. *Interplanetary Network Progr. Rept.*, 196, 1.
- Gauss K. F. (1809) *Theoria motus corporum coelestium in sectionibus conicis solem ambientium*. Sumtibus F. Perthes et I. H. Besser, Hamburgi.
- Górski K. M., Hivon E., Banday A. J., Wandelt B. D., Hansen F. K., Reinecke M., and Bartelmann M. (2005) HEALPix: A framework for high-resolution discretization and fast analysis of data distributed on the sphere. *Astrophys. J.*, 622, 759–771.
- Gould B. A. (1855) On Peirce’s criterion for the rejection of doubtful observations with tables for facilitating its application. *Astron. J.*, 4, 81–87.
- Grav T., Jedicke R., Denneau L., Chesley S., Holman M. J., and Spahr T. B. (2011) The Pan-STARRS synthetic solar system model: A tool for testing and efficiency determination of the moving object processing system. *Publ. Astron. Soc. Pac.*, 123, 423–447.
- Gronchi G. F. (2005) An algebraic method to compute the critical points of the distance function between two Keplerian orbits. *Cel. Mech. Dyn. Astron.*, 93, 295–329.
- Gronchi G. F., Dimare L., and Milani A. (2010) Orbit determination with the two-body integrals. *Cel. Mech. Dyn. Astron.*, 107, 299–318.
- Gronchi G. F., Farnocchia D., and Dimare L. (2011) Orbit determination with the two-body integrals. II. *Cel. Mech. Dyn. Astron.*, 110, 257–270.
- Hodapp K. W., Kaiser N., Aussel H., et al. (2004) Design of the Pan-STARRS telescopes. *Astron. Nachr.*, 325, 636–642.
- Holman M. J. and Murray N. W. (1996) Chaos in high-order mean resonances in the outer asteroid belt. *Astron. J.*, 112, 1278.
- Kaplan G. H. (2005) The IAU resolutions on astronomical reference systems, time scales, and Earth rotation models: Explanation and implementation. *U.S. Naval Observatory Circular* 179.
- Konopliv A. S., Asmar S. W., Folkner W. M., Karatekin Ö., Nunes D. C., Smrekar S. E., Yoder C. F., and Zuber M. T. (2011) Mars high resolution gravity fields from MRO, Mars seasonal gravity, and other dynamical parameters. *Icarus*, 211, 401–428.
- Kubica J., Denneau L., Grav T., Heasley J., Jedicke R., Masiero J., Milani A., Moore A., Tholen D., and Wainscoat R. J. (2007) Efficient intra- and inter-night linking of asteroid detections using kd-trees. *Icarus*, 189, 151–168.
- Lauretta D. S., Barucci M. A., Bierhaus E. B., et al. (2012) The OSIRIS-REx mission — Sample acquisition strategy and evidence for the nature of regolith on asteroid (101955) 1999 RQ<sub>36</sub>. In *Asteroids, Comets, Meteors (ACM) 2012*, Abstract #6291. LPI Contribution No. 1667, Lunar and Planetary Institute, Houston.
- Lemoine F., Pavlis N., Kenyon S., Rapp R., Pavlis E., and Chao B. (1998) New high-resolution model developed for Earth’s gravitational field. *Eos Trans. AGU*, 79, 113–118.
- LSST Science Collaboration and LSST Project (2009) *LSST Science Book, Version 2.0*. 596 pp. ArXiv e-prints, arXiv:0912.0201.
- Marsden B. G., Sekanina Z., and Yeomans D. K. (1973) Comets and nongravitational forces. *V. Astron. J.*, 78, 211.
- Micheli M., Tholen D. J., and Elliott G. T. (2012) Detection of radiation pressure acting on 2009 BD. *New Astron.*, 17, 446–452.
- Micheli M., Tholen D. J., and Elliott G. T. (2013) 2012 LA, an optimal astrometric target for radiation pressure detection. *Icarus*, 226, 251–255.
- Micheli M., Tholen D. J., and Elliott G. T. (2014) Radiation pressure detection and density estimate for 2011 MD. *Astrophys. J. Lett.*, 788, L1.
- Mignard F., Cellino A., Muinonen K., et al. (2007) The Gaia mission: Expected applications to asteroid science. *Earth Moon Planets*, 101, 97–125.
- Milani A. and Gronchi G. F. (2010) *Theory of Orbit Determination*. Cambridge Univ., Cambridge. 392 pp.
- Milani A. and Knežević Z. (2005) From astrometry to celestial mechanics: Orbit determination with very short arcs. *Cel. Mech. Dyn. Astron.*, 92, 1–18.
- Milani A., Chesley S. R., and Valsecchi G. B. (1999) Close approaches of asteroid 1999 AN<sub>10</sub>: Resonant and non-resonant returns. *Astron. Astrophys.*, 346, L65–L68.
- Milani A., Chesley S. R., Chodas P. W., and Valsecchi G. B. (2002) Asteroid close approaches: Analysis and potential impact detection. In *Asteroids III* (W. F. Bottke Jr. et al., eds.), pp. 55–69. Univ. of Arizona, Tucson.
- Milani A., Gronchi G. F., de’Micheli Vitturi M., and Knežević Z. (2004) Orbit determination with very short arcs. I. Admissible regions. *Cel. Mech. Dyn. Astron.*, 90, 59–87.
- Milani A., Sansaturo M. E., Tommei G., Arratia O., and Chesley S. R. (2005a) Multiple solutions for asteroid orbits: Computational procedure and applications. *Astron. Astrophys.*, 431, 729–746.
- Milani A., Chesley S. R., Sansaturo M. E., Tommei G., and Valsecchi G. B. (2005b) Nonlinear impact monitoring: Line of variation searches for impactors. *Icarus*, 173, 362–384.
- Milani A., Gronchi G. F., Farnocchia D., Knežević Z., Jedicke R., Denneau L., and Pierfederici F. (2008) Topocentric orbit determination: Algorithms for the next generation surveys. *Icarus*, 195, 474–492.
- Milani A., Knežević Z., Farnocchia D., et al. (2012) Identification of known objects in solar system surveys. *Icarus*, 220, 114–123.
- Mommert M., Hora J. L., Farnocchia D., Chesley S. R., Vokrouhlický D., Trilling D. E., Müller M., Harris A. W., Smith H. A., and Fazio G. G. (2014a) Constraining the physical properties of near-Earth object 2009 BD. *Astrophys. J.*, 786, 148.
- Mommert M., Farnocchia D., Hora J. L., Chesley S. R., Trilling D. E., Chodas P. W., Müller M., Harris A. W., Smith H. A., and Fazio G. G. (2014b) Physical properties of near-Earth asteroid 2011 MD. *Astrophys. J. Lett.*, 789, L22.
- Monet D. G. (1998) The 526,280,881 objects in the USNO-A2.0 catalog. *Bull. Am. Astron. Soc.*, 30, #120.03.
- Monet D. G., Levine S. E., Canzian B., et al. (2003) The USNO-B catalog. *Astron. J.*, 125, 984–993.
- Moyer T. D. (2003) *Formulation for Observed and Computed Values of Deep Space Network Data Types for Navigation*. Wiley-Interscience, Hoboken. 372 pp.
- Muunonen K. and Bowell E. (1993) Asteroid orbit determination using Bayesian probabilities. *Icarus*, 104, 255–279.
- Müller T. G., Kiss C., Scheirich P., Pravec P., O’Rourke L., Vilenius E., and Altieri B. (2014) Thermal infrared observations of asteroid (99942) Apophis with Herschel. *Astron. Astrophys.*, 566, A22.

- Nugent C. R., Margot J. L., Chesley S. R., and Vokrouhlický D. (2012) Detection of semimajor axis drifts in 54 near-Earth asteroids: New measurements of the Yarkovsky effect. *Astron. J.*, 144, 60.
- Öpik E. J. (1951) Collision probability with the planets and the distribution of planetary matter. *Proc. R. Irish Acad. Sect. A*, 54, 165–199.
- Öpik E. J. (1976) *Interplanetary Encounters: Close-Range Gravitational Interactions*. Elsevier, Amsterdam. 155 pp.
- Ostro S. J., Hudson R. S., Bennér L. A. M., Giorgini J. D., Magri C., Margot J. L., and Nolan M. C. (2002) Asteroid radar astronomy. In *Asteroids III* (W. F. Bottke Jr. et al., eds.), pp. 151–168. Univ. of Arizona, Tucson.
- Oszkiewicz D., Muinonen K., Virtanen J., and Granvik M. (2009) Asteroid orbital ranging using Markov-Chain Monte Carlo. *Meteoritics & Planet. Sci.*, 44, 1897–1904.
- Pravec P., Scheirich P., Dürrech J., et al. (2014) The tumbling spin state of (99942) Apophis. *Icarus*, 233, 48–60.
- Perryman M. A. C., de Boer K. S., Gilmore G., Høg E., Lattanzi M. G., Lindegren L., Luri X., Mignard F., Pace O., and de Zeeuw P. T. (2001) GAIA: Composition, formation and evolution of the galaxy. *Astron. Astrophys.*, 369, 339–363.
- Roeser S., Demleitner M., and Schilbach E. (2010) The PPMXL catalog of positions and proper motions on the ICRS. Combining USNO-B1.0 and the Two Micron All Sky Survey (2MASS). *Astron. J.*, 139, 2440–2447.
- Roy A. E. (2005) *Orbital Motion*. Institute of Physics, Bristol. 526 pp.
- Russell C. T., Raymond C. A., Coradini A., et al. (2012) Dawn at Vesta: Testing the protoplanetary paradigm. *Science*, 336, 684.
- Skrutskie M. F., Cutri R. M., Stiening R., et al. (2006) The Two Micron All Sky Survey (2MASS). *Astron. J.*, 131, 1163–1183.
- Spoto F., Milani A., Farnocchia D., Chesley S. R., Micheli M., Valsecchi G. B., Perna D., and Hainaut O. (2014) Nongravitational perturbations and virtual impactors: The case of asteroid (410777) 2009 FD. *Astron. Astrophys.*, 572, AA100.
- Taylor J. (1997) *Introduction to Error Analysis, the Study of Uncertainties in Physical Measurements*. University Science Books, New York. 327 pp.
- Tholen D. J., Micheli M., and Elliott G. T. (2013) The effect of proper motion on Pan-STARRS asteroid astrometry. *Icarus*, 223, 625–627.
- Tony J. L. (2011) An early warning system for asteroid impact. *Publ. Astron. Soc. Pac.*, 123, 58–73.
- Valsecchi G. B., Milani A., Gronchi G. F., and Chesley S. R. (2003) Resonant returns to close approaches: Analytical theory. *Astron. Astrophys.*, 408, 1179–1196.
- Virtanen J., Muinonen K., and Bowell E. (2001) Statistical ranging of asteroid orbits. *Icarus*, 154, 412–431.
- Vokrouhlický D. and Milani A. (2000) Direct solar radiation pressure on the orbits of small near-Earth asteroids: Observable effects? *Astron. Astrophys.*, 362, 746–755.
- Vokrouhlický D., Chesley S. R., and Matson R. D. (2008) Orbital identification for asteroid 152563 (1992 BF) through the Yarkovsky effect. *Astron. J.*, 135, 2336–2340.
- Vokrouhlický D., Farnocchia D., Čapek D., Chesley S. R., Pravec P., Scheirich P., and Müller T. G. (2015) The Yarkovsky effect for 99942 Apophis. *Icarus*, 252, 277–283.
- Whipple A. L. (1995) Lyapunov times of the inner asteroids. *Icarus*, 115, 347–353.

# Asteroid Impacts and Modern Civilization: Can We Prevent a Catastrophe?

**Alan W. Harris**

*German Aerospace Center (DLR) Institute of Planetary Research*

**Mark Boslough**

*Sandia National Laboratories*

**Clark R. Chapman**

*Southwest Research Institute*

**Line Drube**

*German Aerospace Center (DLR) Institute of Planetary Research*

**Patrick Michel**

*Lagrange Laboratory, Université Côte d'Azur, Observatoire de la Côte d'Azur, CNRS*

**Alan W. Harris**

*MoreData! Inc.*

---

We are now approaching the level of technical expertise necessary to deflect a near-Earth asteroid (NEA) capable of destroying a large urban area, if not a small country. The current level of activity in the field, including search programs, physical characterization, and international initiatives to assess mitigation strategies, is unprecedented. However, we have only just started to explore the relevant properties of the small end of the NEA population (diameter <300 m), of which the next major impactor is most likely to be a member. The Chelyabinsk event has reminded us that objects as small as 20 m, about which we know very little, impact frequently and are a serious threat to life and property. Political awareness and international response efforts are still at a very primitive stage. For a global guarantee of protection, advances in scientific and technical competence must be matched by improvements in international coordination, as well as preparedness at the political level.

## 1. INTRODUCTION

The planets of the solar system started out as clumps of material, so-called planetesimals, with diameters of around 1–100 km, which grew by accreting particles and small bodies from the cloud of gas and dust that surrounded the newly formed Sun. Some planetesimals enjoyed rapid growth and quickly developed significant gravitational fields, thereby attracting and absorbing more and more small bodies to become fully fledged planets. Others were destroyed in violent collisions that produced clouds of fragments. A large fraction of the asteroids present in the solar system today are collisional fragments, orbiting the Sun in the main asteroid belt between the orbits of Mars and Jupiter. As a result of gradual orbital evolution due to the recoil effect of thermal radiation emission (the Yarkovsky effect; see the chapter

by Vokrouhlický et al. in this volume) and perturbations by large planets, primarily Jupiter, there is a continual leakage of asteroids from the main belt into the inner solar system. The resulting populations of so-called Mars crossers and near-Earth asteroids (NEAs) have orbits that give rise to occasional collisions with the terrestrial planets. The orbits of periodic comets can also evolve to cross Earth's orbit. The population of near-Earth objects (NEOs, a term embracing both asteroids and comets) contains a wide variety of bodies with diverse physical and dynamical properties (see the chapter by Jedicke et al. in this volume), and presents a permanent threat to our civilization and a serious challenge to those involved in developing mitigation strategies. While the term "NEO" is often used in texts on the impact hazard, comets are much less numerous than asteroids in Earth's neighborhood and represent only a minor fraction of potential

impactors. In this chapter we use the term “NEA” when referring primarily to the asteroid component of the NEO population (e.g., in discussions of population statistics and deflection techniques).

Awareness of the threat presented by NEOs has grown rapidly during the past few decades as a result of, for example, the first observation in real time of a large-scale impact on a planet, i.e., the impact of Comet Shoemaker-Levy 9 on Jupiter in 1994 (e.g., see *Noll et al.*, 1996); observations of fresh craters appearing on the Moon and Mars (e.g., *Buratti and Johnson*, 2003; *Malin et al.*, 2006); the discovery, with search programs of ever-increasing sophistication, of thousands of NEOs, some of which make uncomfortably close approaches to Earth; and the realization that the Tunguska event of 1908 was not a freak phenomenon after the blast waves from the Chelyabinsk superbolide of February 15, 2013, injured some 1500 people and damaged thousands of buildings (*Popova et al.*, 2013) (see section 2). The rather unsettling coincidence of the anticipated close approach at an altitude of only 28,000 km *on that very same day* of (367943) Duende (known at the time by its provisional designation of 2012 DA<sub>14</sub>), an asteroid with an extent of about 20 × 40 m unrelated to the Chelyabinsk object, ensured that asteroids made the headlines in most major news media at the time.

While this chapter concentrates on developments since the publication of *Asteroids III*, readers interested in earlier developments in this field are referred to, e.g., *Chapman and Morrison* (1994), *Toon et al.* (1997), and the books edited by *Gehrels* (1994), *Belton et al.* (2004), and *Bobrowsky and Rickman* (2007). In nearly all aspects of the impact hazard there have been major advances since the publication of the predecessor chapter to this one (*Morrison et al.*, 2002) in *Asteroids III*. In terms of our knowledge of the threat, the number of NEAs of all sizes discovered has risen from around 2000 at the end of 2002 to some 11,000 at the time of this writing (section 3). Surveys carried out by spacebased infrared telescopes, such as the Wide-Field Infrared Survey Explorer (WISE) (*Wright et al.*, 2010) and the Spitzer Space Telescope (*Werner et al.*, 2004), have provided diameters and albedos for many hundreds of NEAs, in contrast to the few tens of NEAs for which this information was available in 2002 (see section 5 and the chapter by *Mainzer et al.* in this volume). There has been a significant increase in efforts by observers and modelers to physically characterize the NEA population in terms of spin vectors, taxonomy, thermal properties, binarity, shape, surface structure, etc., and investigate properties particularly relevant to deflection considerations, such as porosity and internal structure, although these efforts have not kept pace with the dramatic increase in the discovery rate. Three NEAs have been visited by spacecraft, revealing very different small worlds, despite similarities in taxonomic type. The NASA Near Earth Asteroid Rendezvous (NEAR)-Shoemaker spacecraft visited the second largest NEA, (433) Eros, for one year starting in February 2000, revealing a peanut-shaped body with rich geological features such as large craters but a lack of small ones, boulders, “ponds,” and a fine regolith-covered surface (*Cheng*, 2002). The Japan

Aerospace Exploration Agency’s (JAXA) Hayabusa spacecraft visited the small NEA (25143) Itokawa and returned a surface sample to Earth (*Nakamura et al.*, 2011). Images of Itokawa suggest that even a body of just a few hundred meters in size can have a rubble-pile structure and be covered with large boulders and coarse regolith (*Fujiwara et al.*, 2006; see also the chapter by *Yoshikawa et al.* in this volume). The Chinese Chang’e-2 lunar mission flew by (4179) Toutatis just 800 m above its surface when Toutatis came within 18 lunar distances of Earth in December 2012. The images obtained show a contact binary NEA of 4.75 × 1.95 km and details of the distribution of boulders and regolith (*Huang et al.*, 2013). Radar observations have provided information on the shapes of some NEAs passing close to Earth (see the chapter by *Benner et al.* in this volume), including small binary NEAs, which constitute about 15% of the NEA population.

The Chelyabinsk event (Fig. 1 and section 2) taught us that an Earth-bound object large enough to cause considerable destruction of property, if not life, can be small enough to escape detection, especially if its final approach is in the daylit sky. While new wide-field, rapid-scan telescopes are currently planned to detect small impactors, the days to weeks of warning time they might provide would be inadequate for any mitigation action, apart from advising the relevant communities, who might organize evacuation if considered appropriate and feasible. The size of the threatening NEO that will trigger the first spaceborne deflection attempt is a matter of debate. Due to the steep size distribution of NEOs there are many more small objects than large ones, and consequently many more sightings of fireballs than crater-forming impacts. However, in this respect it is informative to compare the airburst of a stony object, such as the Tunguska event, which flattened 2000 km<sup>2</sup> of forest but left no other obvious trace on the ground, with the impact of a similarly sized metallic object, which produced the 1.2-km-diameter Barringer Crater in Arizona. In both cases the diameter of the impactor is estimated to be 30–50 m. Clearly the potential of a threatening NEO to cause damage depends not only



**Fig. 1.** The trail left by the Chelyabinsk bolide. The left part of the image shows two contrarotating vortices formed by heating and buoyancy effects in the horizontal cylinder of air in which kinetic energy of the asteroid was deposited. Credit: Wikimedia Commons.

on its size but also on its composition, density, and ability to survive passage through the atmosphere. The asteroid 2008 TC<sub>3</sub> lost 99.9% of its mass during its passage through the atmosphere, which suggests that this meter-sized body probably consisted of fragile material, as well as more solid but weakly aggregated pieces. Nevertheless, a few hundred fragments with a surprising range of lithologies were recovered in Sudan (see, for example, the chapters by DeMeo et al. and Borovička et al. in this volume). It seems that the lower size threshold for considering spaceborne deflection action should be around 30–50 m (see the discussion in section 6), although with current and foreseeable search programs it is highly unlikely that an object of this size would be detected far enough in advance for any deflection action to be feasible. At the other end of the size scale, it would seem difficult to justify spending taxpayers' money at present investigating how to deal with an object of more than 300 m in diameter, given that the impact probability per year of such objects is estimated to be around one in 70,000. In any case, given the size-frequency distribution of NEOs, it is probable that we will gain some experience in deflecting smaller ones before being confronted by a large potential impactor.

Serious effort is now being spent on investigating realistic asteroid deflection techniques (section 4). The main contenders at present are impulsive techniques, such as kinetic and explosive methods, and so-called "slow-push" techniques, such as those based on laser or ion-beam devices. The gravity tractor is a viable contender as a "slow-pull" technique. An interesting concept is the use of a slow technique directly after an impulsive deflection has taken place, in order to make fine corrections to the new orbit of the deflected NEA and provide some insurance against malfunction of the impulse transfer.

In recent years not only have the scientific and space-technology communities begun to pay more attention to impact-hazard issues, but some national space agencies and international organizations are now investing significant funding in various endeavors, motivated by the increased awareness of the problem.

NASA now funds the International Astronomical Union's Minor Planet Center and has recently significantly increased its funding of NEO search programs such as Lincoln Near Earth Asteroid Research (LINEAR), the Catalina Sky Survey, and the Panoramic Survey Telescope and Rapid Response System (Pan-STARRS) (see the chapter by Jedicke et al. in this volume). NASA also funds several groups to carry out research into aspects of NEA deflection options, such as those at Iowa State University's Asteroid Deflection Research Center. In total NASA allocated about 3% of its 2013 NEO funding to mitigation studies. The European Space Agency (ESA) is currently developing a program devoted to NEO defense in the framework of its Space Situational Awareness (SSA) initiative, including establishing a European NEO Coordination Centre. A collaborative mission concept currently under study in the U.S. and Europe is the Asteroid Impact and Deflection Assessment (AIDA) mission, the goal of which is to demonstrate the kinetic impactor concept by impacting the moon of a binary NEA (see section 4).

The European Commission's Seventh Framework Programme for Research and Technological Development (FP7) issued a call for proposals in 2010 entitled "Prevention of impacts from near-Earth objects on our planet." A consortium of 13 partners from 6 countries, including Russia and the U.S., responded with a proposal for the project NEOShield (<http://www.neoshield.net>), which succeeded in gaining 5.8 million euros of funding from January 2012 to May 2015. The NEOShield partners are investigating mitigation-relevant NEO physical properties and potential mitigation techniques (Harris et al., 2013). A further call for proposals for similar research projects was issued by the Commission in 2013; funding for a second phase of NEOShield, until 2017, was granted while this chapter was in preparation.

In a complementary initiative to those mentioned above, the United Nations (UN) has authorized the establishment of two new bodies (see section 7), the International Asteroid Warning Network (IAWN) and the Space Mission Planning Advisory Group (SMPAG).

While it seems the stage is now set for coordinated international activities in pursuit of solutions to the NEO impact threat, it remains to be seen if the momentum built up over the past few years can be maintained. The activities to be overseen by the IAWN and SMPAG will require significant and continuous funding, which will have to be made available by the participating countries. The recent Chelyabinsk event has served to focus attention on the impact hazard, but it is a fact of life that political interest in an area of public concern tends to wane if not regularly stimulated. Furthermore, we are still far removed from having an international agreement on who would do what, who would pay for what, and who would take responsibility for failure, in the event of a deflection action becoming necessary.

## 2. THE CHELYABINSK EXPERIENCE

On February 15, 2013, at the crack of dawn, a glowing object appeared in the clear southeastern sky seen from the industrial Russian city of Chelyabinsk. As it streaked nearly sideways across the sky, it grew brighter until it was a blinding white light that cast eerie moving shadows. It radiated high-intensity light for several seconds as it elongated and grew into a larger source, then gradually slowed, dimmed, and changed color from white to yellow, orange, and then a dull red. The sources of light continued along the original path as the main body stopped, forming the roiling head, rising like thunderclouds from a long, puffy trail that traced its entire path across the heavens. As residents looked on in wonder, the trail split neatly into two parts that seemed like mirror images of one another with a sharp line between them (Fig. 1). The columns silently drifted apart and grew upward, attracting early morning office workers and students to windows to observe and snap photos with their smart phones.

Suddenly, just under a minute and a half after the brightness of the fireball peaked, an unexpected blast wave ripped through the city, blowing out windows and showering spectators with high-speed shards of glass and falling ceiling

tiles. Nobody anticipated a blast following so long after the spectacle in the sky, the delay being due to the time it took the blast wave to travel at the speed of sound some 29 km down to the city. Fifteen hundred people would have to be treated for their injuries. Out on the streets, startled residents screamed and shouted expletives as the concussion hit them and set off car alarms. After the main boom, smaller explosions continued in rapid succession like artillery fire. The blasts lofted years of accumulated dust from old factories, creating a thick black pall over parts of the city as the booms continued. Power lines and mobile phone towers bounced and shook from the succession of blasts, leading to outages. To the south of the city, small black rocks rained down on villages and snow-covered fields.

Across the city and surrounding countryside, dashboard-mounted digital cameras captured the event from every angle. Within minutes, computer-savvy Russians were uploading images and videos to the internet. The Russian media initially reported the event as an unidentified flying object (UFO), and these reports were forwarded across the world by users of social media. Scientists at the Jet Propulsion Laboratory (JPL) in Pasadena first learned of the event from Twitter, and only because a dedicated JPL media specialist monitors her feed after hours. Others found out from Facebook because a late-night chess-playing Canadian shared a story posted by his early morning Russian counterparts.

U.S. government satellites with instruments designed to detect nuclear explosions recorded the bright flash as it happened, but did not automatically report it because it did not have the characteristics of a weapon. Seismometers in Russia recorded the shaking ground, which resembled an earthquake. Slower-moving low-frequency sound waves in the air (infrasound), which carried the first atmospheric news of the event, had not yet reached the western border of Russia by the time the international wire services picked up the story, albeit with sketchy anecdotal descriptions.

In the western hemisphere, most relevant experts were blissfully asleep, either on the U.S. east coast, where it was after midnight, or in pre-dawn Europe. Ironically, many were prepared for what was expected to be the big news event of the day, the close passage of asteroid (367943) Duende. With interviews and press conferences scheduled, they had no way of knowing that the Chelyabinsk event had just occurred. NASA does not have a system to detect atmospheric explosions, and the International Monitoring System only puts out alerts when explosions are nuclear, so nobody's pager went off. Without fortuitous social media connections, it is possible that officials would have been caught entirely off guard when asked by reporters if the Chelyabinsk event was related to (367943) Duende, or if NASA's calculations were wrong.

Those who had already seen the YouTube videos knew immediately that this was pure coincidence. The Chelyabinsk asteroid came from the direction of the Sun in the northern hemisphere, and Duende was arriving from the southern nightside. Nevertheless, if a few scientists in western time zones hadn't had their attention drawn to it and alerted their colleagues to the east, it could have created an unfortunate

embarrassment (even though it was not NASA's job to know about it, the public, media, and politicians may have perceived it differently).

Embarrassment, however, is not the worst-case scenario. If it had been cloudy in Chelyabinsk that morning, it may not have been immediately apparent to locals or outsiders that this was a cosmic airburst. The bright flash and huge blast, followed by the sound of heavy artillery, and parts of the city shrouded in dark smoke, could have been misperceived as an act of aggression. Snezhinsk, to the north, is the Russian equivalent of Lawrence Livermore National Laboratory in the U.S., and the region is of nuclear strategic importance. Russia, unlike its neighbor Kazakhstan in the direction from which the asteroid came, is still a nuclear-armed state. It is hard to know what would happen in the heat of the moment when there is great uncertainty about the cause of a half-megaton explosion over a Russian city.

If the same asteroid had come from a different direction it may have had far worse consequences on the ground. It was lucky that it arrived on a near-grazing trajectory, because its energy was spread out over a large distance, and was deposited high enough in the atmosphere to diverge and disperse before it reached the ground. A steeply descending asteroid would explode much lower and its downward momentum would carry it closer to the ground, causing much more severe damage (Kring and Boslough, 2014). It is almost certain that there would have been massive casualties under just slightly different conditions.

Thanks to the plethora of data collected from the dashboard cameras, seismometers, infrasound detectors, and satellites, we have a very good understanding of what happened. The best estimate of the kinetic yield (explosive energy) is 400–500 kt, making Chelyabinsk the most powerful such event observed since the 1908 Tunguska explosion [3–5 Mt (Boslough and Crawford, 2008)]. Analysis of video combined with subsequent onsite stellar calibrations enable reliable estimates of entry velocity ( $19 \text{ km s}^{-1}$ ), angle ( $17^\circ$  elevation), and altitude of peak brightness (29 km). This implies a preentry diameter of  $\sim 20 \text{ m}$  and mass of  $\sim 12,000 \text{ t}$ . Satellite sensors recorded the emission peak at 03:20:33 UT, with a total radiated energy of  $3.75 \times 10^{14} \text{ J}$  ( $\sim 90 \text{ kt}$ ). A typical bolide luminous efficiency of 20% implies a total energy of  $\sim 450 \text{ kt}$ , consistent with infrasound and other observations. The maximum radiant intensity was  $2.7 \times 10^{13} \text{ W sr}^{-1}$ , corresponding to an absolute magnitude (referenced to a distance of 100 km) of  $-28$ , or more than  $30\times$  brighter than the Sun as seen by an observer located directly below (Brown *et al.*, 2013).

The shallow entry angle led to a long bolide duration (16.5 s) and energy was deposited over hundreds of kilometers, leading to an extended, near-horizontal, linear explosion. The blast was distributed over a large area, and was much weaker than it would have been in the case of a steep entry and a more concentrated explosion closer to the surface. The orientation also led to different phenomena than expected for a more vertical entry. There was no ballistic plume as observed in the case of the Shoemaker-Levy 9 impacts into Jupiter ( $45^\circ$ ), or calculated for Tunguska [ $\sim 35^\circ$ ] (Boslough

and Crawford, 1997)]. Instead, buoyant instabilities grew into mushroom clouds and bifurcated the trail into two counterrotating vortices (Kring and Boslough, 2014).

Hydrodynamic models can now be initialized with extremely accurate energy depositions at correct locations, and results can be compared with observations (such as timing and distribution of blast energy at the surface, and evolution of the trail) to validate the models and better understand the physical phenomena associated with airbursts. Models suggest that airbursts are more damaging than nuclear explosions of the same yield (traditionally used to estimate impact risk, although nuclear radiation is not produced by the impact of a NEO). On the basis of recent observation-based size-frequency data, Chelyabinsk was estimated to be a once-per-century event while Tunguska was about once-per-millennium. These two events suggested that the size-frequency data underestimated the frequency of large airbursts. However, one of us (Harris of MoreData! Inc.) has updated the size-frequency estimates and determined that Chelyabinsk is a 50-year event. Chelyabinsk can no longer be considered an outlier as it is the only observed event of its size in the last 50 years. On the other hand, Tunguska is now estimated to be a 500-year event, so its occurrence just over 100 years ago can still be considered a statistical outlier. The new size-frequency data are presented and discussed in section 3 (see also Table 1). The risk from airbursts is greater than previously thought, but still highly uncertain.

There are several approaches that can be employed to reduce the uncertainty in the risk, and also to reduce the risk itself. One way to reduce uncertainty is to improve the monitoring and quantification of bolides. There are extensive records of past bolides seen by U.S. government satellites, and these data have been used by Brown *et al.* (2002, 2013) to estimate the flux of 1-m- to 10-m-diameter asteroids (permission has now been granted for the scientific community to access more recent data; see <http://neo.jpl.nasa.gov/fireball>). Another approach would be to launch dedicated satellites with missions optimized to observe and quantify bolides. Such a system would also provide immediate notice and location of an airburst event, which would aid in communication to the public as well as recovery of meteorites.

The best way to reduce the risk from Chelyabinsk-class asteroids would be to implement a short-warning survey, with groundbased telescopes optimized to search the entire night sky on a roughly daily basis, which would find even asteroids and meteoroids much smaller than Chelyabinsk as they brighten during the last days or weeks of their final encounters with Earth (see section 5). An alternative or complementary measure could be an infrared space telescope with a position and cadence optimized to find small objects within days or weeks of impacts. Such systems would also find smaller objects that are not a threat, but that would be a potential boon to science, and could even be commercialized with costs recouped by the recovery of meteorites and high-end adventure tourism (Boslough, 2014). If such a system had existed in 2013, the storyline of Chelyabinsk might read differently:

*On February 15, 2013, at the crack of dawn, a glowing object appeared as expected in the clear southeastern sky seen from the industrial Russian city of Chelyabinsk. As it streaked nearly sideways across the sky it was tracked with scientific instruments, including telescopes, spectrometers, high-definition cameras, radar, and calibrated radiometers. Optical pyrometers determined the temperature of the fireball as it cooled and changed color. As the spark-like fragments continued to fade out and fall in dark flight, they were still glowing in the thermal infrared and were tracked all the way to the ground, where they were immediately recovered and taken to meteorite laboratories that had been prepared for them.*

*Residents who had been warned to stay away from windows and to watch from a safe distance looked on in wonder. Hotels in outlying areas were filled with adventure tourists who had come from all over the world to see this once-in-a-lifetime spectacle. Some had volunteered to join scientific expeditions to scour the fall area for meteorites.*

*Researchers were able to use the wealth of high-quality, calibrated data to improve models of ablation, fragmentation, breakup, and explosion, improving their understanding of the high deformation-rate processes that will ultimately improve risk assessment, as well as facilitate the design of more effective impulsive deflection methods if a larger hazardous asteroid is discovered with sufficient advance warning.*

### 3. CURRENT UNDERSTANDING OF THE IMPACT HAZARD

Although the impact frequencies for NEAs with diameters, D, larger than 100 m are known quite well, and about 90% of NEAs with D > 1 km have been discovered, smaller NEAs are less well characterized. Relative to astronomical surveys of NEAs, actual impact events like Chelyabinsk (although small in number), and recalibration of infrasonic airwave data (Silber *et al.*, 2009), suggest that the frequencies of impacts by bodies tens of meters in diameter may be several times higher than those estimated earlier from optical survey data.

Our present understanding of the numbers of NEAs and impact probabilities is summarized in Fig. 2, in which the curve traced by the circles represents current best estimates of the cumulative number of NEAs larger than a given diameter. For a given H-value interval, optical survey population estimates are derived by counting the number of redetections of previously discovered objects compared to the total number of detections (new discoveries plus redetections) in the most recent survey period of two years. As the ratio of redetections to all detections approaches 100%, so does the survey completion. However, since some asteroids are easier to find than others, and the easy ones are discovered first, the estimated completion is actually always less than the redetection ratio. A correction to the completion estimate is derived using a realistic model of the NEA population and

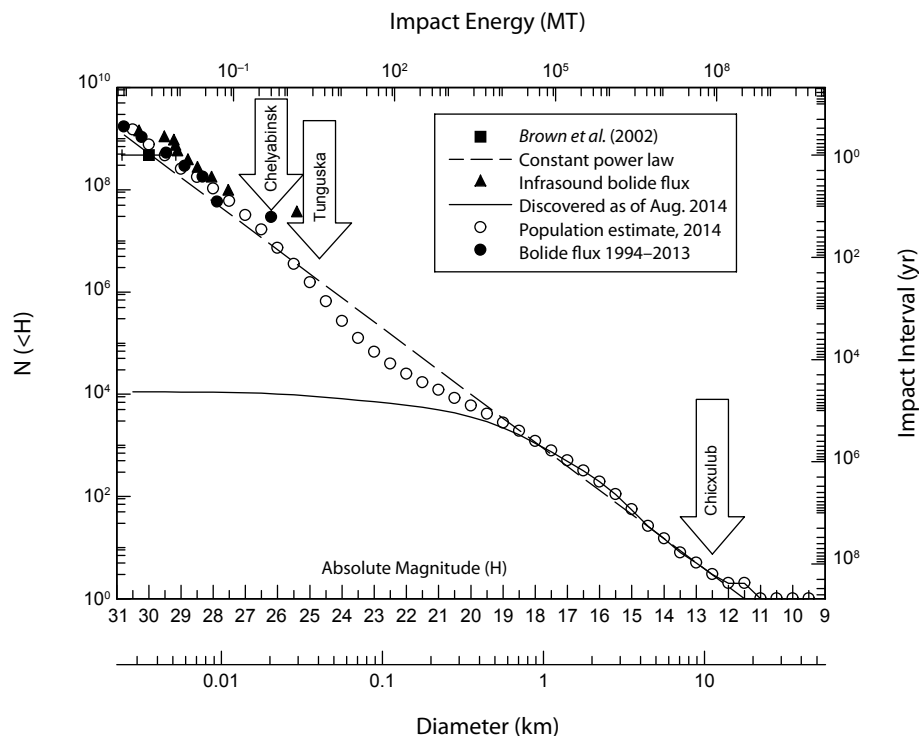


**Fig. 2.** Estimated number of NEAs larger than a given diameter/brighter than a given absolute magnitude. The continuous curve represents discoveries as of August 2014; the curve traced by the circles represents the estimated total number of objects in the NEA population, derived from computer modeling of discovery and redetection rates by optical telescope surveys over the two-year period to August 2014. The population estimated in this way appears to be in excellent agreement with population estimates from bolide and infrasound data. The estimated mean interval between impacts of objects larger than a given diameter can be read off on the righthand scale using the curve traced by the circles. The conversion from H to diameter assumes an albedo of  $p_V = 0.14$ . The uncertainty in the estimated population curve in the range  $D = \sim 10$  to  $\sim 100$  m from all errors, observational, model, and the albedo assumption is probably less than a factor of 3. At larger sizes, the uncertainty is even less, diminishing to only a few percent for  $D \sim 1$  km and larger.

a computer simulation of a hypothetical optical telescope survey over the same time period, in this case 20 years.

The latest update of the NEA population, presented in Fig. 2, appears to largely resolve the above-mentioned discrepancy in population estimates between astronomical surveys and bolide frequencies (Brown *et al.*, 2013; Silber *et al.*, 2009). Earlier population estimates from astronomical surveys obtained a population in the tens of meters size range about a factor of 3–4 lower than estimated from bolide and infrasound data (see, e.g., Harris, 2014). However, the most recent population estimate falls within the scatter over the size range of the bolide estimates.

To the best of our knowledge there is no current threat from any NEA larger than about 4 km in diameter, since they have probably all been found and none are on a threatening trajectory during the next century. There remains a very small but uncertain threat from large comets. Objects originating in the Oort cloud are discovered typically only about two years prior to perihelion, precluding any effective spaceborne de-

flection action in these cases. For example, Comet C/2013 A1 (Siding Spring) was discovered in January 2013 on its way into the inner solar system from the Oort cloud. Early orbit calculations revealed a small probability that the comet would impact Mars on October 19, 2014, with a velocity of some 56 km s<sup>-1</sup>. Even with a diameter of around 500 m, at the lower end of initial size estimates, an impact of the comet on Mars would have had dramatic, possibly global, effects, not to mention the potentially disastrous consequences for the valuable scientific assets on its surface and in orbit around it. Later refinements of the orbit of C/2013 A1 ruled out an impact but showed it would pass within around 20 martian diameters of the planet (Farnocchia *et al.*, 2014).

Apart from the frequency of impacts by cosmic bodies of various sizes, a major question concerns the scale of damage such an impact might cause. The Chicxulub (K-Pg boundary) impact at 66 Ma presents a qualitative example of how very infrequent impacts by large NEOs can greatly change the global ecosphere and biosphere of Earth. Near-

Earth objects with  $D = 2\text{--}3 \text{ km}$ , and possibly as small as 1 km, could destroy civilization as we know it, although the degree to which that civilization is robust or vulnerable to the multiple environmental effects of such impacts remains speculative. Impacts of bodies only 500 m in diameter could, for example, severely damage or destroy the ozone layer (Birks et al., 2007). Near-Earth objects of such sizes impacting in the ocean could also produce very destructive tsunami, although a number of studies (e.g., Gisler et al., 2011; Wünnemann et al., 2007; Korycansky and Lynett, 2005; and references therein) suggest that such waves would largely disperse before reaching coastlines, unless the impact were rather close to the coastline. The environmental consequences of damage from a ground explosion are simulated in the online program Impact Earth [<http://www.purdue.edu/impactearth/> — for details, including assumptions and uncertainties, see Collins et al. (2005)]; how much infrastructure would be destroyed or how many lives would be lost would depend on proximity to the impact (see, e.g., Garbolino and Michel, 2011) and how much advance warning there was to strengthen infrastructure or evacuate the region.

Recently there has been emphasis on the effects of the smaller but much more frequent impacts of NEOs several tens of meters in diameter and smaller. A big issue has been, what is the smallest NEO that would be damaging? The NASA NEO Science Definition Team study (NASA SDT) (Stokes et al., 2003) concluded that NEOs with  $D < 40 \text{ m}$  would explode rather harmlessly in the upper atmosphere, but that conclusion has been undercut for several reasons. First, Boslough and Crawford (2008) realized that downward momentum of a NEO through the atmosphere would be more damaging than a stationary explosion, and concluded that the great damage at Tunguska could have been produced by a body only  $\sim 40 \text{ m}$  in diameter (a few megatons of equivalent energy). Second, we have learned that some types of smaller projectiles can be more damaging than the average, such as nickel-iron objects, which are relatively dense, and objects that can reach the ground by virtue of unusual aerodynamic shapes. Low cosmic velocities ( $12\text{--}14 \text{ km s}^{-1}$ ) and shallow entry angles also contribute to reducing aerodynamic stress and may allow meter-sized stony meteoroids to reach the ground, such as the object that caused the 13-m-diameter impact crater near the Peruvian village of Carancas in 2007 (Kenkmann, et al., 2009; Tancredi et al., 2009). The Chelyabinsk event (section 2) could have been even more destructive at ground zero if it had entered the atmosphere at a less shallow angle. On the other hand, the impact was unfortunately close to a major city, which would not usually be the case. One factor that needs to be recognized is that any nominal estimate of size (and associated damage potential) has uncertainties that could be very great for a body discovered only shortly before impact. Asteroids have diverse compositions and shapes, wide ranges of albedo and bulk density, and other uncertain attributes, which could be difficult or impossible to assess before impact but conceivably could result in the nominal estimate of destructive energy being in error by an order of magnitude in either direction.

Thus, even if a body just 10 m in diameter or smaller were predicted to strike a locality, a prudent civil defense official might well warn people to evacuate, or at least stay indoors in structurally sound buildings well clear of windows (to avoid flying glass), to cover their ears (to avoid eardrum rupture), and, where possible, to open all windows and doors (to minimize damage by the overpressure of the blast waves).

The general approach to dealing with the NEO hazard is to (1) search the skies for NEOs that may strike Earth; (2) plan and carry out a deflection spacecraft mission if there is sufficient time and the threat is sufficiently great (high probability of damaging impact); and/or (3) evacuate or otherwise prepare to mitigate the effects of an impact.

Telescopic searches for NEOs are of several kinds (see the chapter by Jedicke et al. in this volume). The Spaceguard Survey was designed to find  $>90\%$  of NEOs  $>1 \text{ km}$  in size, and it has accomplished that task, although taking some years longer than the mandated decade. As a byproduct, the Survey has found many NEOs down to hundreds of meters in diameter, and a statistical sample of those down to  $\sim 10 \text{ m}$  in diameter. The Survey continues, although with modifications. The NASA NEO Science Definition Team report and the subsequently passed law by the U.S. Congress (George E. Brown, Jr. NEO Survey) recommend finding 90% of NEOs with diameters larger than 140 m within the near term. Various groundbased, e.g., the Large Synoptic Survey Telescope (LSST), and spacebased, e.g., the NEOCam and Sentinel, projects are designed to meet this goal, although the timeframe for the surveys keeps slipping into the future. Yet another approach is to use dispersed small telescopes to cover the sky on a nightly basis and find NEOs as they approach Earth for the last time before striking. The Catalina Sky Survey, for example, found the tiny asteroid/meteoroid 2008 TC<sub>3</sub> just over 20 hours before it struck in the Sudanese desert. Several systems are under development [e.g., the University of Hawaii's Asteroid Terrestrial-impact Last Alert System (ATLAS) or ESA's Fly-Eye concepts — see section 5] that could find up to half of potential impactors during the days to months before impact — those coming from the night sky rather than from the daylit sky — providing adequate time for evacuation warnings.

If a sizeable NEA is discovered to be on a possible impact trajectory years or a decade or two before impact, then a spacecraft mission designed to deflect the asteroid is technically feasible. Direct deflection of a hazardous NEA so that it passes several Earth radii away from Earth instead of striking Earth may be necessary in the worst case. However, an asteroid may closely approach Earth on a previous apparition so that the perturbation by Earth's gravitational field is just the right amount to cause its orbit to enter a resonance condition with Earth's orbit and impact Earth on a later approach. The small region of space through which the NEA has to pass to enter a resonance is called a gravitational (or resonance) "keyhole" (see the chapter by Farnocchia et al. in this volume). A recent prominent example was the prediction of a keyhole only about 600 m wide in the case of the 2029 approach to within 35,000 km of Earth's surface of

(99942) Apophis, a NEA with a diameter of some 325 m. If Apophis were to pass through the keyhole an impact with Earth would follow in the year 2036 (see, e.g., *Yeomans et al.*, 2009). Fortunately, recent observations have ruled out a possible passage of Apophis through the keyhole. Accurate knowledge of an asteroid's orbit allows the existence of keyholes for the object to be predicted well in advance. It is much easier to deflect the asteroid from passing through a small keyhole than having to deflect it by several Earth radii.

Studies of deflection missions are in their infancy (see section 4) but there appear to be no fundamental issues preventing existing technology from being put together rapidly to build a deflection mission, should the need arise. Similarly, the disaster response community has little familiarity with asteroid impact as a natural disaster, but the kinds of environmental effects arising from the atmospheric explosion or ground impact of a NEO are similar to those of more common natural disasters (*Garshnek et al.*, 2000) so that, provided a predicted impact is properly communicated to relevant officials in the relevant nations or localities, it seems likely that appropriate responses to a predicted impact would result in most cases. There will always be, though diminishing with time as surveys advance, the chance that an unpredicted impact will occur, as in the case of Chelyabinsk.

#### 4. NEAR-EARTH ASTEROID DEFLECTION TECHNIQUES

Many ideas have been proposed to deflect an asteroid from an Earth-bound trajectory or to disrupt it. However, to date none has been tested in space and the feasibility of proposed techniques given present technology differs greatly.

Three apparently realistic methods have emerged from the numerous studies devoted to this topic, namely the kinetic impactor, the gravity tractor, and blast deflection, which are described below. Other suggested techniques include directing a laser beam at the asteroid's surface to expel (ablate) material from it, thereby creating a force that moves the object so as to conserve linear momentum (*Gibbins et al.*, 2013). Similarly, the use of large mirrors or lenses to concentrate the Sun's energy onto an asteroid using single or multiple spacecraft has been advocated. Another idea would be to exploit the momentum transmitted by a collimated beam of ions impacting the asteroid surface (*Bombardelli et al.*, 2013). Ion thrusters attached to a hovering spacecraft could be used for this purpose. The spacecraft, placed at a distance of a few asteroid diameters, would also need an ion thruster pointed in the opposite direction of the asteroid to balance the spacecraft's reaction to the deflecting thrust and keep a constant distance between the asteroid and the shepherd spacecraft. A more speculative idea is to paint the surface of an asteroid to increase its albedo, thereby enhancing the solar radiation pressure acting upon it (*Paek*, 2012). These methods require much *a priori* knowledge of the asteroid and/or they involve technologies that require significant further development. In particular, providing adequate power for deploying beams of light or ions to deflect a threatening NEA to a safe

trajectory, developing systems that can operate continuously and reliably over periods of years, and the requirement for autonomous guidance and control of the deflecting spacecraft are all major technical challenges.

Most recent studies (e.g., *Shapiro et al.*, 2010) find that the most reasonable approach in the vast majority of cases, especially for NEAs with diameters above about 100 m (see section 6), is deflection by hypervelocity kinetic impact by a massive spacecraft, while an observer spacecraft (preferably with a slow push or pull capability, such as a gravity tractor, as discussed below) looks on to assess the success and magnitude of the deflection. The impact of the artificial projectile (spacecraft) transfers momentum to the NEA, causing a small change in velocity. If a large amount of ejecta is produced by the impact event then the momentum transferred can be greatly enhanced, as dictated by the law of conservation of momentum, resulting in a larger deflection of the object's course. The production of ejecta increases the effectiveness of impulsive deflection techniques but the amount of ejecta produced depends strongly on the subsurface properties of the asteroid. A series of kinetic impactors should suffice for threatening NEAs possibly up to 1 km in size.

The NASA Deep Impact mission (*A'Hearn et al.*, 2005) successfully caused an impactor to collide with the nucleus of Comet 9P/Tempel 1 on July 4, 2005. Due to the large mass of the 6-km-diameter nucleus, and nongravitational forces acting on it, it was not possible to measure a change in the comet's trajectory resulting from the impact, so the experiment did not provide a measurement of momentum transfer to the comet. Nevertheless, the mission successfully impacted its target and highlighted the complex autonomous guidance necessary to do so.

The kinetic impactor technique has been the subject of a number of studies carried out by major space agencies. In 2006 the European Space Agency funded and coordinated detailed studies of a kinetic impactor concept called Don Quijote, which consisted of an orbiter and a small impactor spacecraft arriving several months later than the orbiter (e.g., see *Wolters et al.*, 2011, and references therein). The orbiter would first characterize the target and measure the deflection due to the impact of the second spacecraft. While the Don Quijote concept as such has not been funded to date, it has served as the inspiration for aspects of the NEOShield program and European participation in the AIDA concept. In early 2010, ESA, Johns Hopkins University's Applied Physics Laboratory, NASA, the Côte d'Azur Observatory, and the German Aerospace Center initiated a study of AIDA, the aim of which is to deflect the small secondary of a binary asteroid, chosen so that the perturbation to the orbit of the secondary can be observed from groundbased facilities in 2022. The target is the binary asteroid (65803) Didymos. The mission (*Cheng et al.*, 2015; *Michel et al.*, 2015) has two independent components: the projectile spacecraft, "Double Asteroid Redirection Test" (DART), which would be developed in the U.S., and the European rendezvous spacecraft Asteroid Impact Mission (AIM). DART would serve as a test of our ability to impact a small (150-m-diameter) object, while

AIM would allow it to be characterized in detail by observing the target before, during, and after the impact event. The advantage of the AIDA concept, compared to a mission to deflect a normal NEA, lies in the relative ease with which the orbit of a small binary moon around the primary can be changed to a measurable extent, and the fact that in the case of Didymos, due to the favorable observation geometry, the change can be measured by groundbased telescopes monitoring the variability of reflected sunlight caused by eclipses and occultations in the binary system. While groundbased observations would complement the observations made by AIM and provide a vital backup, AIM would measure the resulting change in orbit of the moon with greater accuracy, and would provide detailed *in situ* reconnaissance of the system's physical characteristics. The results of the AIDA mission would allow the detailed verification of impact models on a realistic size scale. At the time of this writing AIDA is the only deflection mission concept that is actively under study by major space agencies. If funded for launch, the impact would occur in October 2022.

An alternative, relatively inexpensive, test of the kinetic impactor concept, under consideration in ongoing NEOShield work, would be to impact a NEA far from its rotation axis, thus causing a change in its rotation rate, which, depending on the choice of the target, could be measurable with ground-based telescopes (NEOTwIST, Drube et al., in preparation). The change in rotation rate would provide insight into the same near-surface structural characteristics on which the efficiency of the kinetic impactor deflection concept depends. A possible target for such a test would be the NEA (25143) Itokawa, which has been well studied by the Japanese Hayabusa mission. The payload of the impactor spacecraft could include an ejectable science package to allow the impact to be observed and provide information on the crater formation, and ejecta mass and velocity distributions. While any type of deflection test would be very instructive, given the diverse properties of NEAs we should bear in mind that the responses to impacts could be very different for other NEAs.

In the case of the gravity tractor (*Lu and Love*, 2005), a spacecraft under power hovers near an asteroid and uses the gravitational attraction between it and the asteroid to tow the asteroid off course. Multiple spacecraft flying in formation could be deployed to expedite the gravity tractor maneuver and/or provide redundancy (*Foster et al.*, 2013). Given the very small tractor/asteroid mass ratio, this technique is only useful for small objects, but since small NEAs are more numerous than larger ones, a gravity tractor might suffice for the most likely scenarios in which deflection seems to be warranted, depending on the available time before the predicted impact. How small is still a matter of debate, but the current practical upper diameter limit suggested by recent (as yet unpublished) NEOShield results is around 50 m for a direct impact trajectory [*Shapiro et al.* (2010) give roughly 100 m for the same limit]. The main difficulty is developing reliable autonomous control systems able to keep the tractor at a fixed distance from a small, rotating, irregularly shaped asteroid, possibly for a period of many

years. If time is insufficient for the use of a gravity tractor as sole deflector, a currently realistic scenario is deployment of the gravity tractor as a secondary deflection technique to an impulsive primary strike. For example, an appropriately designed and instrumented spacecraft could first act in a reconnaissance capacity and study the NEA in advance of the impact, subsequently remain in place to monitor the deflection, and have the capability to finally act as a gravity tractor to adjust the post-impact trajectory of the NEA, if necessary. Alternatively, if the threatening object were due to pass through a keyhole, then a relatively small deflection, which could be performed by a gravity tractor alone, would suffice to cause the object to miss the keyhole. In fact, in the case of keyhole avoidance, the gravity tractor alone may suffice to deflect much larger asteroids.

While the gravity tractor appears to be feasible with current technology, the slow-push alternatives, such as the ion-beam shepherd and laser ablation mentioned above, may in time prove to be more practical and effective per kilogram of launch mass in many cases, depending on future developments of the relevant technologies and the details of the hazard scenario. An important advantage of the gravity tractor is that few characteristics of the NEA need to be known in advance. However, gravity tractors and the alternative slow-push techniques are weak, so depending on the time available and the circumstances of the NEA's orbit (presence of keyholes), the much more powerful capability of a kinetic impactor may be desirable or necessary.

In the very unlikely case of a very large hazardous asteroid and/or inadequate time for the deployment of other deflection techniques, "blast deflection" with a nuclear device may offer the only technically feasible solution: This technique requires the use of an explosive close to, on the surface of, or buried beneath the surface of the NEA. Complete disruption of the threatening object would be an option if it were small enough so that the largest pieces of debris would not present a hazard on impact. Otherwise, the blast should be designed to deflect the asteroid, not break it up. The blast from a nuclear device would cause the outer layers of the NEA to evaporate and be expelled from the surface. The effect would be similar to rocket propulsion, thus altering the asteroid's trajectory. Burying an explosive on the asteroid before setting it off, or delivering the device by means of a surface penetrator, would probably be most effective at ejecting surface material, but this method would require prior knowledge of the material properties and subsurface structure of the object. A deflection mission concept study supported by NASA's Innovative Advanced Concepts Program combines a kinetic impactor mission with a nuclear device for deflection of large asteroids, or for cases in which there is very little warning time. In the very unlikely case of a large comet, deflection would be very challenging at best due to the likely short lead time and nongravitational forces affecting the comet's trajectory. In any case, political and legal objections, not to mention technical issues, would have to be overcome before nuclear explosive devices could be used for NEA deflection.

## 5. CURRENT PRIORITIES AND INITIATIVES

At the time of this writing there are a number of ground-based telescopes under development with the goal of discovering very small NEOs to provide advance warning of about one week for objects with diameters in the range 30–50 m, and longer times for larger objects. Examples of such wide-field, rapid-scan search programs currently under development are ESA's Fly-Eye (*Farnocchia et al.*, 2012) and NASA's ATLAS (*Tonry*, 2011). Plans for ATLAS include up to eight small telescopes, each fitted with cameras of up to 100 megapixels. According to the ATLAS team, the system should offer a warning of about 1 week in the case of a 50-m-diameter asteroid or “city killer,” and 3 weeks for a 150-m “small country killer.” Such wide-field survey systems will complement the established surveys, such as the Catalina Sky Survey and Pan-STARRS, in being able to provide warning of small objects in the final phase of their plunge to Earth, thereby enabling measures on the ground, such as evacuation, to be carried out.

Apart from the work to discover and track NEOs, there is much ongoing groundbased effort to investigate their physical properties. Observations in the visible and infrared spectral regions of light reflected from asteroid surfaces are a powerful means of studying their compositions and assigning them to taxonomic classes. For reviews of earlier work the reader is referred to *Binzel et al.* (2002), and for more recent developments, to the chapters in this volume, such as those by Binzel et al. and DeMeo et al. Efforts to derive information on the physical properties of asteroids by observing absorption features in reflected sunlight are complemented by observations of thermally emitted infrared radiation and radar investigations. The latter two approaches, briefly discussed here, have brought major advances relevant to the impact hazard since the publication of *Asteroids III*.

A survey of the sizes and albedos of more than 100,000 asteroids has been carried out by the NASA WISE space telescope (*Wright et al.*, 2010). WISE was launched to Earth orbit in December 2009 carrying a 40-cm-diameter telescope and infrared detectors. WISE surveyed the sky for 12 months and the objects observed included a total of at least 584 NEOs, of which more than 130 were new discoveries (*Mainzer et al.*, 2011). The specially funded Near-Earth Object Wide-field Infrared Survey Explorer (NEOWISE) program analyzed images collected by the WISE spacecraft to derive information on the NEOs detected. The fact that the cryogenic phase of the WISE mission measured asteroid thermal emission in up to four infrared bands, centered on 3.4, 4.6, 12, and 22  $\mu\text{m}$ , allowed reliable values of diameter, albedo, and other parameters to be derived for many of the asteroids observed. *Mainzer et al.* (2011) report that after debiasing with a synthetic NEO population, the NEOWISE results imply a total of some 980 for the number of NEOs larger than 1 km. These results mean that the Spaceguard goal of detecting 90% of all NEOs with diameters larger than 1 km has now been met (see the chapter by Mainzer et al. in this volume). A complementary program to NEOWISE,

“ExploreNEOs” (*Trilling et al.*, 2010; see also the chapter by Mainzer et al. in this volume), has used the Spitzer Space Telescope to observe some 600 previously detected NEOs to study the size and albedo distributions of the NEO population, and identify NEOs that may have a cometary origin or that could serve as accessible and scientifically interesting targets for future robotic or manned space missions.

Following in the footsteps of the successful Infrared Astronomical Satellite (IRAS) mission in 1983, the WISE and Spitzer missions have highlighted the value of spacebased infrared telescopes for basic physical characterization of the asteroid population. In addition to size and albedo information, application of thermal models to thermal-infrared observations has revealed their potential to provide information on thermal inertia and mineralogy, including the presence of metal on the surfaces of asteroids (*Harris and Drube*, 2014). A threatening NEA containing a large amount of metal would presumably be relatively robust and massive, depending on its internal structure, factors that would require careful consideration by deflection-mission planners and/or those mandated to manage mitigation, e.g., evacuation and other activities on the ground in advance of a possible impact. Moreover, the identification of NEAs with high metal content is an important task for endeavors in the field of planetary resources. Metal-rich asteroids could provide a vast reservoir of vital materials for future interplanetary space activities and perhaps eventually for use on Earth.

The success of NEOWISE suggests that future missions with more sensitive spacebased infrared telescopes, designed specifically for NEO detection, would bring major advances in our knowledge of the mitigation-relevant small end of the NEO size distribution, and may even provide a useful guide for interplanetary prospectors. Examples of such spacebased infrared telescopes currently under study are the Near-Earth Object Camera (NEOCam) and Sentinel (see the chapter by Jedicke et al. in this volume). In particular, a spacebased infrared telescope on a heliocentric orbit inside that of Earth, such as the Sentinel spacecraft, would have an advantage over Earth-based telescopes in detecting Aten asteroids and inner-Earth objects (Atiras), which spend much of their time in the daylit sky as seen from Earth.

Radar is a crucial means of obtaining very accurate astrometric data for NEOs. Radar observations can provide enormous improvements in the precision of a NEO's orbit and allow the position of the object to be projected much further into the future than allowed by optical monitoring alone. The uncertainty in the prediction of a future impact can be dramatically reduced with the help of radar data or, much more likely, a possible impact can be ruled out (*Ostro and Giorgini*, 2004). Radar is also a powerful method for the characterization of NEOs, especially their sizes, shapes, and surface structure. A radar echo contains information not only on the position and velocity of a NEO, but also on a number of mitigation-relevant physical parameters. Radiation transmitted at a single frequency is returned from a rotating asteroid with a spread of (Doppler-shifted) frequencies, each component frequency being associated with a particular time

delay depending on the distance to the reflecting surface element. The “delay-Doppler” distribution of echo power is determined by the size, spin rate, orientation, and shape of the target asteroid, and radar reflectivity of the surface material. Given a suitable transmission coding, the information in a radar echo can be processed to provide resolved radar “images” of asteroids. The strength of the echo, normalized to the size and distance of the target (“radar albedo”), can provide information on the mineralogy of the asteroid surface, in particular its metal content. A circularly polarized transmission will give rise to a mix of “opposite sense” (OC) and “same sense” (SC) polarized radiation in the echo, depending on the number of reflections taking place at the surface. The ratio of SC/OC polarization in the echo is an indicator of the roughness of the surface at the scale of the radar wavelength (typically 3–13 cm). In particular, radar observations have observed a large number of binary NEAs, and have taught us that small asteroids can have very irregular shapes but also that some NEAs are surprisingly round, with equatorial bulges, suggestive of loose agglomerates of boulders and gravel that change shape as the spin rate exceeds a critical value, presumably preceding the spinning off of material that may then accumulate to form a moon (see the chapter by Walsh and Jacobson in this volume). For an overview of radar observations of asteroids, see the chapter by Benner et al. in this volume.

Rendezvous missions are a valuable source of mitigation-relevant physical information on particular NEAs. A concept under study by NASA at the time of writing is the Asteroid Redirect Mission (ARM), in which either an asteroid with a diameter of less than 10 m is captured whole, or a 2–3-m boulder from a larger NEA is collected, and brought into lunar orbit (see the chapter by Abell et al. in this volume). For the second option, NASA is considering a test of the gravity-tractor concept by using the combined mass of the spacecraft and the boulder to slightly change the orbit of the mother NEA. In general, regardless of which option is chosen, experience gained with ARM in the rendezvous and approach phases, and in capturing and maneuvering large masses with a solar-electric powered spacecraft, will be of direct benefit to mission planning for planetary defense.

While their primary aim is to contribute to our understanding of solar system history, sample-return missions to asteroids also provide valuable information for planetary defense. The Japanese Hayabusa mission was the first mission to return samples of an asteroid to Earth. The micrometer-sized grains returned by Hayabusa from the NEA (25143) Itokawa allowed a direct link to be demonstrated between asteroids of S taxonomic type and the LL class of meteorites (Nakamura et al., 2011). JAXA launched the Hayabusa-2 mission (see, e.g., Tsuda et al., 2013) on December 3, 2014, with the aim of returning a sample from the primitive (i.e., relatively unprocessed) C-class NEA (162173) Ryugu (1999 JU<sub>3</sub>), which has a diameter of about 750 m. The payload includes a small copper projectile designed to impact the surface of the NEA at about 2 km s<sup>-1</sup>, and a small camera to observe the event. Observations in real time of the production of a crater

would provide data of direct relevance to deflection studies. In addition, a small European lander, the Mobile Asteroid Surface Scout (MASCOT), will perform *in situ* compositional measurements. NASA is also developing a sample-return mission called the Origins Spectral Interpretation Resource Identification and Security-Regolith Explorer (OSIRIS-REx) (Lauretta et al., 2012). Launch is currently scheduled for September 2016. The sample mechanism is designed to collect between 60 g and a few kilograms, depending on the surface properties of the target, namely the primitive B-type NEA (101955) Bennu, which has a diameter of ~450 m.

It is important not only to improve our understanding of the mitigation-relevant physical properties of small NEAs, but also to develop technically and financially realistic test missions to enable deflection concepts to be tried out on real NEA targets, representative of the sort of objects that could threaten Earth in the not-too-distant future. Given the diverse observed shapes and mineralogies, and strong evidence for relatively low bulk densities, high porosities, and loose rubble-pile structures among NEAs, demonstrating that we can actually measurably change the orbit of a NEA is a vital step in building confidence that we can defend our civilization from a natural hazard that will otherwise cause serious loss of life and property in the future, if not threaten our long-term survival on planet Earth. The NEOShield project has performed industrial studies of test missions for the kinetic impactor, gravity tractor, and blast deflection concepts, as well as studies of the future evolution of NEA orbits after deflection attempts. While an actual deflection demonstration mission was financially beyond the scope of the NEOShield project, the aim was to provide the first designs of appropriate demonstration missions, sufficiently detailed to facilitate the rapid development of such a mission in subsequent rounds of project funding in a European/international frame.

Results from the type of studies carried out by NEOShield and similar programs obviously also serve to reduce the scientific and technical preparatory work required to bring an appropriate and viable deflection mission to the launch pad in an emergency situation.

## 6. WHAT WE DO NOT KNOW: PRESSING AREAS OF CONCERN

Although it will happen one day, the likelihood of any generation being confronted with a threatening object with a diameter, D, of around 300 m or larger is extremely small. In any case, NEO survey programs may provide several decades of warning time in which to prepare a response, although at present an estimated 40% of such objects remain to be discovered. Therefore, in the case of large objects, we should normally have sufficient time between hazard identification and the predicted time of impact to physically characterize the NEO using Earth-based telescopes and rendezvous missions, and prepare and test an appropriate deflection mission. The lower size threshold below which we could safely ignore an approaching object is subject to debate (see below). Even a NEO with a diameter of just 20 m can

cause serious damage, impacting on average about once or twice per century. It would therefore seem prudent to take precautionary measures well in advance, and not wait until a threatening object is identified. Apart from civil defense planning in case a late detection precludes a deflection attempt, appropriate measures include investigations of the mitigation-relevant physical properties of small NEOs, such as composition, density, porosity, internal structure, spin rate, and shape, and the development and testing of appropriate and reliable deflection techniques. Unfortunately, our current knowledge of the NEO population is very biased toward the large end of the size range, since large NEOs are brighter and more readily detected and observed. Relatively little is known about the small members of the population and much work remains to be done in exploring their deflection-relevant physical properties.

At present we have no clear idea of how the international community would respond to the announcement of a credible threat from a NEO identified as significantly hazardous. After discovery of the NEO in question and initial orbit refinement, the threat could be expressed only as a probability for those parts of Earth lying on the “risk corridor” (the track of possible impact points allowed by imperfect knowledge of the object’s trajectory; see Fig. 3). We would not know for sure whether the object would impact or not

due to the observational uncertainties in the orbit and factors influencing its evolution, and we would only have a poor idea of what damage it would cause if it did. If, for example, the probability of impact somewhere on Earth in 15 years’ time were to be estimated at 5%, politicians could argue that with a 95% probability of a miss there is hardly any justification for action to be taken (depending, perhaps, on whether their part of the world were in the risk corridor!). Indeed, one would normally expect the impact probability to suddenly drop, after initially rising, as further observations reduce the uncertainty region so that Earth is no longer within it (see, e.g., Chesley and Spahr, 2004). However, if Earth were to remain within the uncertainty region as more observational data are gathered, the probability might rise to levels at which an international consensus for action builds, regardless of other circumstances, and valuable time would have been lost for characterizing the object and preparing a spaceborne deflection mission. One of the most difficult challenges faced by astronomers and scientists involved in impact-hazard assessment is ensuring that politicians and decision makers are adequately informed of, and understand, the level of the risk at each stage and how it might develop with time, i.e., how to interpret evolving impact probabilities based on uncertain observational data and incomplete knowledge of factors influencing a NEO’s orbit. Critical decisions

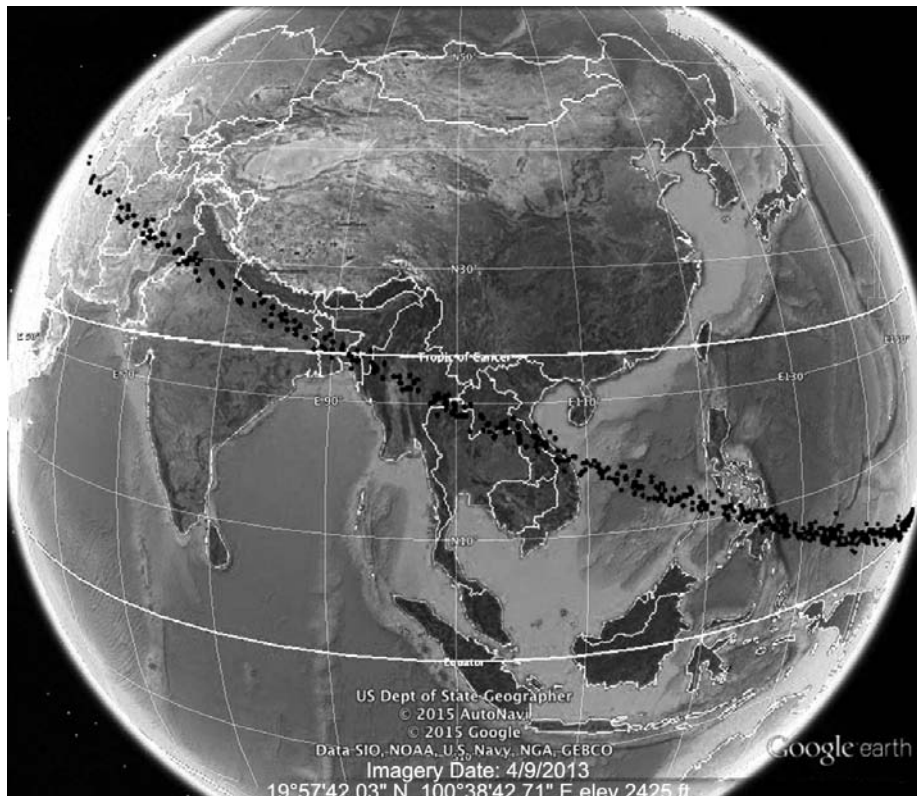


**Fig. 3.** Example of a hypothetical impact-risk corridor, traced by the black dots extending from the eastern Pacific Ocean, through the Philippines, Southeast Asia, India, to Turkey. In the event the fictional asteroid were to impact Earth, it would do so somewhere within the region traced by the dots. Credit: P. Chodas, NASA/JPL [emergency response exercise conducted during the International Academy of Astronautics (IAA) 2015 Planetary Defense Conference in Frascati, Italy, April 13–17, 2015].

would have to be made as a threatening impact scenario evolves concerning what type(s) of mitigation or deflection measure(s) need to be implemented, depending on the size, hence potential destructive power, of the threatening NEO. The answers necessarily depend on some other aspects of the specific scenario, such as duration of advance warning, whether the predicted impact will be in or over an ocean or instead will involve a populated land region, or the availability of heavy-lift launch vehicles.

From a politician's point of view the consequences of "getting it wrong" would be a prime consideration in the decision-making process. Spending the equivalent of hundreds of millions, or billions, of dollars on a deflection campaign, only to learn at a later stage that new observational data imply that the hazardous object will in fact just miss Earth, or that its potential for damage had been grossly overestimated, could lead to serious loss of credibility in the eyes of the public, not only for the politicians involved but also for the scientific community. On the other hand, ignoring a threat that turns out to have more serious consequences than nominally assumed from the available observational data and estimated probabilities would be a far worse outcome. In any case, civil defense planning should always be considered when a threatening object is identified, not only in the case of small objects, e.g., on the scale of Chelyabinsk, but also for larger objects as a back-up measure in case a deflection mission fails. At least in the next couple of decades, it is most likely that predicted impacts by small NEAs will involve days to weeks, or possibly months, of warning, because in general small NEAs would be detected during their final plunges to Earth (see section 5). Such warning times are typical of, or longer than, warning times for evacuation of cities or coastlines in the cases of other natural disasters, such as hurricanes/typhoons. But in most cases, such as those resembling, or smaller than, Chelyabinsk, sheltering in place and staying away from windows is preferable to evacuation. As a precaution against unusual circumstances or early uncertainties about the mass of a recently discovered NEA, such warnings might even be given for predicted impacts by bodies estimated to be as small as a few meters in diameter.

Above what size of impactor would a deflection mission be called for? Since development and execution of such a mission takes years to perhaps a decade, the question of whether or not to seriously embark on such an endeavor will most likely arise well before the magnitude of the threat is well known. In particular, how large an impactor can be allowed to strike without a deflection? And does a spacefaring nation start spending money on such a mission when the probability of striking Earth is just 1%, or must it be 50% or greater? If the probability of striking Earth were only a few percent, it seems unlikely that society would fund such an ambitious project. Perhaps 10% or 30% is a more appropriate threshold for action, although it would certainly depend on the specifics of the threat, and it would be influenced by public attitudes and political and economic considerations. In almost all cases, the risk corridor will be known soon after discovery of the threat, even though the probability of

actually impacting may be very low. Assuming, as is probable, that the risk corridor does cross populated regions, it is unlikely (despite the Chelyabinsk example) that it will threaten a major population area or truly critical infrastructure, in which case allowing a Tunguska-sized object to enter the atmosphere, and employing civil defense measures only, should be a reasonable response (unless it is known in advance that the object has a metallic composition; see section 5). It is more problematic to allow a 50–100-m-diameter NEA strike without a deflection attempt, but surely above 100 m diameter a deflection would seem to be mandatory, if feasible.

In terms of the development of appropriate deflection techniques, we have only just started to consider realistic possibilities; indeed, the choice of deflection technique will depend on knowledge of the physical properties of the threatening object (see, e.g., Michel, 2013). There are many schools of thought on how asteroids could be deflected (section 4). The kinetic impactor appears to offer a realistic approach for objects in the size range 100–500 m. Sending a spacecraft to collide with an asteroid at high relative velocity appears to be feasible, although this method and its associated technology remain to be verified in a test mission. Studies, such as those of the Don Quijote and AIDA concepts (see section 4), imply that the technique could provide an impulse of sufficient magnitude to deflect an object in the aforementioned size range (the secondary of a binary object in the case of AIDA), given some years of warning time, depending on the size and orbit of the asteroid. However, there are many outstanding questions associated with the kinetic impactor technique: How much impactor kinetic energy may be wasted in compaction and restructuring, rather than excavating momentum-enhancing ejecta? How does the target NEA's momentum change depend on parameters such as its bulk density, porosity, mineralogy, and subsurface/internal structure, and the velocity vector of the impactor relative to the NEA (see the chapter by Jutzi et al. in this volume)? Can ejecta production be characterized in terms of mineralogy and taxonomic type? If so, such knowledge would greatly increase the value of groundbased observations for deflection mission planning. Preliminary work carried out within the European-funded NEOShield project suggests that the momentum transferred by an artificial projectile to a nonporous body is significantly greater (by up to 10× the momentum of the projectile) than to a porous body (Jutzi and Michel, 2014), a result that is consistent with laboratory impact experiments using scaling laws to extrapolate the results to asteroid scales (e.g., Holsapple and Housen, 2012). However, much work remains to be done to enable reliable predictions to be made as to how a NEA with a particular set of physical parameters would respond to an impacting spacecraft.

Furthermore, there are a number of important issues relating to the targeting accuracy achievable with current technology. The efficiency of momentum transfer from the impactor to the hazardous NEA depends crucially on the impact accuracy. While linear momentum is conserved, a

spacecraft impacting near the end of an elongated object would waste kinetic energy in changing the spin state of the object rather than producing momentum-enhancing ejecta. The most effective collision trajectory would be aimed at the center of mass of the asteroid. How would the necessary camera resolution and autonomous control-loop response time depend on the approach velocity, target size, thruster sizing, and required accuracy of the impact location? What is the trade-off between impactor approach trajectory, impact accuracy, and potentially unfavorable illumination conditions (e.g., approach from a high solar phase angle)? These are examples of questions that need to be addressed before we could be confident that a kinetic-impactor mission would have the desired effect. It is clear from the above discussion that not only does the kinetic impactor technique have an upper size limit on its applicability due to current limitations on launch mass, but also a lower size limit given by the targeting accuracy achievable with current autonomous guidance, navigation, and control systems.

Other currently favored deflection techniques that may be more suited to smaller bodies, or cases in which only a small deflection is required (such as avoidance of a “keyhole” — see section 3), include the so-called slow-push (or -pull) techniques, such as those involving the use of lasers or ion beams and the gravity tractor (see section 4). Such techniques differ considerably in terms of their maturity. The gravity tractor concept has the advantage of relative simplicity and, given current technology (but as yet without the benefit of practical experience), is considered to be the most reliable option in the class of non-impulsive techniques.

If the discovery of a threatening NEA leads to the decision to develop a deflection mission, which kind of deflection technique would be most appropriate? Here we assume currently available launch vehicle capabilities, a few decades of warning, a NEA bulk density of  $2 \text{ g cm}^{-3}$ , and that populated regions are near ground zero or near the risk corridor. We assume that the purpose of deflection is to miss Earth by a comfortable margin ( $2.5 R_{\oplus}$  from Earth’s center), although there will be cases where the much easier task of deflection — to miss a small keyhole — is all that is required. These issues were evaluated by *Shapiro et al.* (2010). It is anticipated that one or a series of kinetic impactors could reasonably deflect an NEA of 500 m to  $\leq 1 \text{ km}$  in diameter. For most scenarios involving larger bodies, a nuclear device is the only sufficiently energetic approach for deflection. A gravity tractor acting for a decade could deflect a NEA of up to  $\sim 50 \text{ m}$  in diameter. So the kinetic impactor approach to deflection would be appropriate for most of the truly dangerous scenarios for which deflection is mandatory in order to prevent a regional catastrophe (e.g., an impact that could lay waste to land areas the size of a country or a U.S. state). Such an approach, for NEAs mainly in the diameter range of 100 to 500 m, would necessarily require a high degree of reliability, which could be assured by appropriate physical characterization of the threatening body by precursor investigation, supplemented by an observer spacecraft to witness the deflection operation and assess its success, and

finally, if necessary, function as a gravity tractor. It would, of course, be desirable to have backup kinetic impactors and gravity tractors in case the first ones fail.

One can question whether a deflection technique with excessive capability might be used on a smaller NEA. For example, a nuclear device could surely deflect or even destroy a NEA much smaller than 0.5–1 km. We suggest that such possible use is not realistic because of the serious ancillary political issues involving development of such a capability, legal issues concerning practicing such a capability in outer space, and expected widespread public objection to using such a technique, except perhaps as a measure of last resort. On the other hand, there is the concern that procrastination in approving and implementing feasible nonnuclear deflection missions might leave nuclear as the only last-minute option, which would pose a serious geopolitical dilemma.

Should kinetic impactors be used even for NEAs smaller than 100 m, where a slow-push/pull method could be sufficient? Here, the answer may be “yes.” Of course, the kinetic impactor approach is inherently less precise because it involves direct interaction with the possibly heterogeneous surface of the NEA for which the momentum enhancement factor may be very uncertain. However, a kinetic impactor can accomplish its task with an instantaneous strike rather than having to operate reliably for many years.

In Table 1 we give an overview of our current state of knowledge (or perhaps ignorance!) of the impact hazard for different sizes of impactor and appropriate mitigation strategies given current technology. Some knowledge of the physical properties of a threatening NEA is necessary to ensure the successful outcome of a deflection attempt. The type of knowledge required depends on the deflection technique in question (see, e.g., *Michel*, 2013): A gravity tractor has to operate for long periods of time in close vicinity to the NEA, but does not physically interact with the surface; in this case, therefore, accurate information on the mass, shape, and rotation vector of the object are required, which can be obtained by the spacecraft after it arrives at the object, but other physical properties are largely irrelevant. On the other hand, in the case of a kinetic impactor, knowledge of density, porosity, and internal structure would also be important for a predictable outcome. In the case of a deflection mission based on a laser, ion-beam, or explosive device, knowledge of the mineralogical composition of the surface material would also be relevant.

The NEOShield consortium, among others, has performed studies of observational data on NEAs (see, e.g., *Harris and Drube*, 2014) and laboratory experiments, including hypervelocity impacts on asteroid surface analog materials, and carried out related computer simulations (see, e.g., *Jutzi and Michel*, 2014). While our knowledge of NEA properties has grown significantly over the past decade, our knowledge of the deflection-relevant internal structures of NEAs is still seriously lacking. Available data on the distribution of lightcurve amplitudes and spin rates (Fig. 4) suggest that many fast-spinning objects take on more symmetrical shapes, presumably due to restructuring caused by spin-induced movement and relocation

TABLE 1. Estimated near-Earth asteroid numbers, impact intervals, impact consequences, and mitigation possibilities.

NEA Diameter, D (m)	Estimated Total Number* with Diameter $\geq D$ in the NEA Population	Indicative Impact Interval (yr)* for NEAs with Diameter $\geq D$	Possible Consequences of Impact Near Populated Region†	Appropriate Mitigation/Deflection Strategy Assuming Current Technology
10	100 million	5	Meteorite falls; crater unlikely	Civil defense only
30	3 million	150	Chelyabinsk/Tunguska-type airburst; crater, depending on composition; some injuries and deaths	Civil defense only
50	500,000	1000	Violent Tunguska-type airburst; crater, depending on composition; potentially many injuries and deaths	Slow push/pull (e.g., gravity tractor) or kinetic impactor, if feasible, civil defense only if not
100	50,000	10,000	Crater 1–2 km in diameter; local destruction; tsunami risk from near-shore impacts; many deaths likely	Civil defense; slow push/pull or kinetic impactor — slow push/pull combination
300	7000	70,000	Crater several kilometers in diameter; regional/national destruction; tsunami risk; potentially millions of deaths	Kinetic impactor — slow push/pull combination if feasible, explosive impulse if not, plus civil defense if practical
500	3500	140,000	Crater some 10 km in diameter; international catastrophe; tsunami risk; potentially millions of deaths	Kinetic impactor — slow push/pull combination if feasible; several kinetic impactors may be necessary. Explosive impulse if no alternative
1000	1000	500,000	Global effects; partial disruption of civilization	Series of kinetic impactors or large explosive impulse
10,000	3‡	100 million	End of present civilization	Series of large explosive impulses; deflection may not be feasible with current technology

\* Estimated from current detections (see Fig. 2).

† The effects listed are rough estimates based on incomplete knowledge of NEA physical characteristics and impact processes in the atmosphere and on the ground. The actual outcome of an impact could differ considerably, depending on parameters such as composition and density of the impactor, impact velocity, impact angle, and the nature of the surface impacted.

‡ The remaining risk is dominated by long-period comets; deflection would not be possible with any foreseeable technology (see section 3).

of material in a rubble-pile-like structure with little cohesion. The fact that binary objects cluster just below the spin barrier for gravity-dominated bodies with diameters larger than about 300 m (spin period  $\sim 2$  h) also suggests that many objects in this size category have insufficient cohesion or strength to withstand faster rotation (Figs. 4 and 5); on the other hand, many of the asteroids smaller than 300 m rotate much faster, implying they must have a cohesive structure, even if just a small amount of cohesion appears to be sufficient for them to survive (Holsapple, 2007). Sánchez and Scheeres (2014) hypothesize that van der Waals forces acting between small dust grains in a rubble pile can give rise to cohesion: Boulders and pebbles of diverse sizes could be held in place by a surrounding matrix of finer material. In this picture even very small objects with large lightcurve amplitudes (and therefore probably elongated shapes) could exist as rubble piles but spin more rapidly than the spin barrier for gravity-dominated objects. For example, work by Rozitis *et al.* (2014) implies that

the fast-spinning kilometer-sized NEA (29075) 1950 DA is a rubble pile held together by weak cohesive forces comparable to, or less than, the forces between grains in lunar regolith. However, if the spin rate of a rubble pile is increased, as a result of the Yarkovsky-O’Keefe-Radzievskii-Paddack (YORP) effect or a close planetary encounter, then the object could disintegrate, giving rise to small monolithic bodies. While observational data and modeling results are consistent with rubble-pile structures being common among NEAs, the fact that numerous small objects spin at rates above the Sánchez and Scheeres (2014) disruption limit (Fig. 5) suggests the possible existence of monolithic asteroids at the small end of the size distribution.

In any case, the fact that small asteroids can have very high rotation rates (some measurements exceed 1 rev/min) is an important consideration for a deflection mission. In the case of a kinetic impactor, fast rotation, combined with imperfect knowledge of the target’s shape, and rapid approach from a

high solar phase angle could significantly increase the risk of a navigation error and failure to impact at the required position. In the case of a gravity tractor, maneuvering and station keeping close to the surface of an irregularly shaped

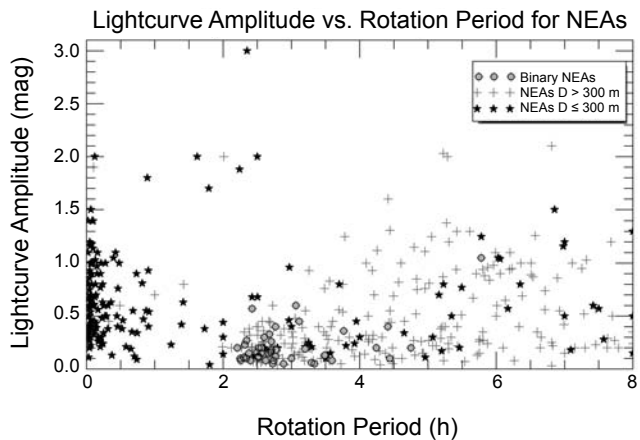


**Fig. 4.** Lightcurve amplitude vs. spin period for NEAs. Data are from the European Asteroid Research Node (EARN) database (<http://earn.dlr.de/>). The data suggest that many fast-spinning objects with diameters larger than 300 m take on more symmetrical shapes (and thus have smaller lightcurve amplitudes), presumably due to restructuring caused by spin-induced movement and relocation of material in a rubble-pile-like structure with little cohesion. On the other hand, many of the asteroids smaller than 300 m rotate much faster, implying they must have a somewhat cohesive structure.

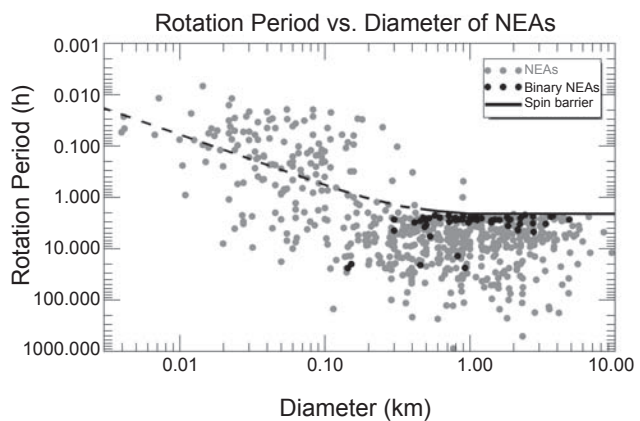


**Fig. 5.** Rotation period vs. size for NEAs. Data are from the EARN database (<http://earn.dlr.de/>). The “spin barrier” for gravity-dominated bodies (spin period ~2 h, diameters larger than about 300 m) is shown merging into the disruption limit (dashed line) of Sánchez and Scheeres (2014) for smaller bodies. The plotted disruption limit corresponds to a cohesion strength of 25 Pa, which is consistent with available data according to Sánchez and Scheeres (2014). It should be noted, however, that a higher strength is required to enclose the super-fast rotators among smaller (<100-m-diameter) objects. Thus, the internal strength of many smaller NEOs must be greater than that of the larger ones.

asteroid with an irregular gravity field become more difficult at high rotation rates. Since fast-rotating NEAs appear to be common, and deflecting a fast-rotating target is likely to be technically challenging, a deflection demonstration mission targeting a representative relatively fast rotator would provide a revealing test of current NEA deflection capabilities.

Studies of NEA physical properties, including laboratory work, numerical modeling, and computer simulations, are essential aspects of a program to develop deflection technology, but they are not sufficient to enable robust predictions to be made of the outcome of a deflection attempt. We may one day be faced with having to decide on a risky deflection mission without having time to acquire adequate information on the physical properties of the threatening object. We would obviously obtain the best knowledge of the body possible using available astronomical facilities, but that might still result in uncertainties of a factor of a few in the body’s mass and ignorance of other relevant characteristics. A “bang and hope” mission with an uncertain outcome would be our only option, although we could improve our chances by preparing back-up missions and taking civil defense action. In any case, to minimize the uncertainties in the outcome of a deflection mission, it would seem prudent to test our concepts and assumptions in experimental missions to deflect suitable representative NEA targets *before* we are forced to apply deflection technology in a hurry in a real impact-prevention scenario.

## 7. INTERNATIONAL COORDINATION EFFORTS AND THE POLITICAL DIMENSION

Protecting Earth from NEO impacts is a global problem and, as such, any deflection strategy should involve at least the most scientifically and technologically capable nations. However, all nations, especially those with large geographical areas or regions of high population density, should be encouraged to take part in discussions and decision-making concerning mitigation planning in general. Impact-hazard-related activities at the UN were prompted by the recommendations of the Third United Nations Conference on the Exploration and Peaceful Uses of Outer Space (UNISPACE III) held in Vienna in July 1999. Following the UNISPACE III recommendations the Action Team on Near-Earth Objects (AT-14) was established by the UN’s Committee on the Peaceful Uses of Outer Space (COPUOS), an intergovernmental body set up in 1959 to “encourage continued research and the dissemination of information on outer space matters and to study legal problems arising from the exploration of outer space.” Action Team 14, which is composed of both government and nongovernment experts, was charged with reviewing the ongoing efforts in the field of NEOs, identifying fields in which further effort is required, or where other countries/organizations could contribute, and proposing steps for the improvement of international coordination. The work of AT-14 continued until 2008 when the team presented a summary of the recommendations contained in the report *Asteroid Threats: A Call for Global Response*, prepared by the Association of Space Explorers (ASE) (<http://www.space-explorers.org>).

To accelerate the formal processing of the ASE report within the UN, the Scientific and Technical Subcommittee of COPUOS established a working group at the government level for the purposes of formally receiving and assessing the recommendations of the report. Subsequently, in the light of the ASE/AT-14 recommendations, the focus of AT-14 changed to reviewing policies and proposing procedures for handling the NEO threat on the international stage. As a direct result of the work of AT-14 and the ASE, the establishment of two new groups (Fig. 6) was endorsed by the sixty-eighth session of the UN General Assembly in December 2013: the IAWN and the SMPAG. The purpose of the IAWN is to link together institutions carrying out discovery, monitoring, and physical characterization of potentially hazardous NEOs with other relevant organizations, and promote an internationally recognized clearinghouse to manage NEO observations and impact predictions. While some of these functions are already covered by existing bodies, such as the Minor Planet Center at the Smithsonian Astrophysical Observatory, which operates under the auspices of the International Astronomical Union, the IAWN is intended to enhance cooperation between relevant organizations and to be the *UN-mandated international portal* for accurate and validated information on the NEO population, as well as to provide recommendations for communication strategies for governments and other relevant bodies in the event of an emerging impact threat. NASA has agreed to be the initial coordinator of the IAWN.

The IAWN is also charged with establishing collaboration with international disaster response agencies in order to develop emergency plans in response to an impact threat in a populated area. NASA sponsored a tabletop exercise in April 2013 to simulate an impact on Earth for the U.S. Federal Emergency Management Agency (FEMA). A further impact simulation exercise was held during the Planetary Defense Conference in Flagstaff, Arizona, also in 2013 (Carnelli et al., 2014), at which FEMA participated. A scenario in which the probability of impact of a 200–300-m NEA increased over a period of 15 years was simulated. More than 200 exercise participants were allocated to groups to take charge of different aspects of mitigation planning (e.g., NEO discovery and follow-up, mitigation techniques and missions, impact effects, media and risk communication, launch capability of space agencies, etc.). FEMA and NASA have recently established a NEO Impact Working Group, to be responsible for reviewing disaster response and recommend future exercises. In 2014, ESA also held an information meeting and similar tabletop exercise for representatives of the European emergency response community. Further information meetings involving emergency coordination agencies, including those of the UN, are planned and will help to establish a dialog between the scientific and technical impact hazard community and those that would be responsible for disaster management in the event of an impact emergency.

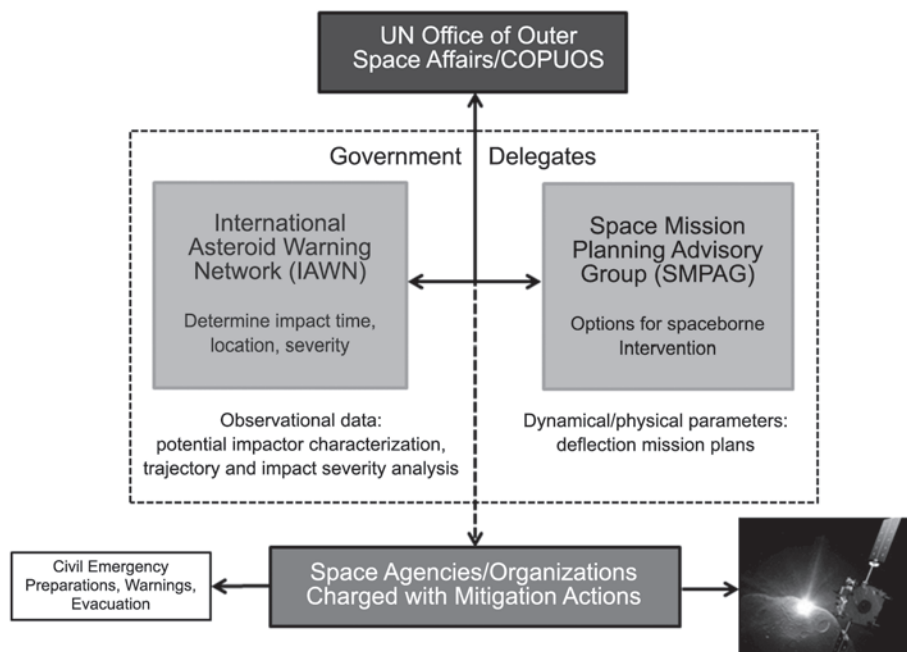


**Fig. 6.** Draft scheme of the organization of NEO impact hazard activities under the auspices of the United Nations. Details of the tasks, responsibilities, and funding of the IAWN and SMPAG, and the assignment of mandates to take action in an emergency situation, are under discussion at the present time. The vertical dashed arrow represents channels that have yet to be formally established. Contacts with civil defense organizations are currently being developed. Present membership of the SMPAG includes space agencies that would be capable of contributing to a spaceborne deflection attempt. Kinetic impactor illustration courtesy of ESA-AOES Medialab.

The SMPAG was established to promote opportunities for international collaboration on research and development work relating to NEO deflection and to develop a framework, timeline, and options for initiating and executing space-mission-response activities. The SMPAG should also develop a set of reference missions, addressing a variety of potential NEO impact scenarios and deflection/disruption possibilities, to facilitate realistic technical and resource planning. Whenever a credible impact threat is established by the IAWN, the SMPAG is charged with proposing options for spaceborne intervention to divert the threatening object. Membership in the SMPAG is open to all national space agencies or governmental or intergovernmental entities that coordinate and fund space activities and are capable of carrying out, or contributing to, a spaceborne NEO deflection campaign. The first chair of the SMPAG is ESA; the chairmanship will rotate around the members at intervals of two years.

Information on the history, development, and status of UN activities relating to NEOs and the impact threat is available from <http://www.oosa.unvienna.org/oosa/en/COPUOS/stsc/wgneo/index.html>.

The IAWN and SMPAG are asked to work together on recommendations for criteria and thresholds for mitigation action, such as notification of a significant impact risk or the initiation of observation/mitigation campaigns. Both groups are currently still in their infancy and questions regarding such details as their ultimate tasks and responsibilities, schedule of activities, etc., are still open at the time of this writing. A pressing current concern with regard to the initiatives of the UN is financial provision for the tasks involved. The work of both the IAWN and SMPAG has to be carried out at no cost to the UN budget. Consequently, the states and organizations making up the membership of the two UN groups have to fund their involvement from their own resources. A model for the support of the activities of the groups might be the current funding of the NEOShield project by the European Commission. While 11 of NEOShield's 13 partner organizations are from European Union countries, two are from non-EU countries, namely Russia and the U.S., but they also receive funding from the European Union. Therefore NEOShield is a truly international project. Taking the SMPAG, for example, statements or "white papers" on future research and development requirements in the field could be issued by the SMPAG on a regular basis, carrying the authority of the UN. Calls for proposals from funding agencies, such as the European Commission or national agencies, could refer to the SMPAG statements, and proposers could orient their work plans accordingly. A plausible vision for the future would be coordinated calls for mitigation-related proposals from a combination of international and national funding bodies, based on the recommendations of the UN-backed groups.

## 8. SUMMARY AND CONCLUSIONS

The period since the publication of *Asteroids III* has seen rapid progress in many fields related to impact hazards. Optical search programs benefiting from advances in detector

technology and sophisticated automated detection routines are currently enjoying increased funding from NASA. The rate of discovery of NEOs has increased to an average of some 3 per day and the number of NEOs discovered of all sizes has risen from around 2000 at the end of 2002 to some 11,000 at the time of this writing. While endeavors in the field of physical characterization have not kept up with the rate of new discoveries, the NEOWISE and ExploreNEO projects have provided size and albedo data for many hundreds of NEOs and demonstrated the value of spacebased telescopes sensitive in the thermal infrared for NEO risk assessment.

Unfortunately, the unanticipated Chelyabinsk event on February 15, 2013, has demonstrated that the blast waves from even relatively small (diameter ~20 m) asteroids exploding in the atmosphere can cause serious injuries and damage to property. Chelyabinsk has also taught us that a potentially serious impact can occur with no prior warning if the orbit of the NEO happens to be unfavorable for detection from the ground.

A number of initiatives suggest that the NEO impact threat is attracting increasing attention in political circles not only in the U.S. The European Commission funded the NEO-Shield project from 2012 to 2015, enabling 13 academic and industrial organizations from 6 countries, including the U.S. and Russia, to collaborate on investigating NEO physical characteristics and deflection options. European activities also include the NEO segment of ESA's Space Situational Awareness program, which is currently under development and includes plans to build the "Fly-Eye" telescope system with the aim of providing sufficient warning of small impactors to allow civil defense measures to be taken. A U.S. project with similar aims is the ATLAS system. New groups have been established under the auspices of the UN to help to coordinate astronomical NEO survey and characterization activities (IAWN) and to advise on deflection-related space mission planning (SMPAG). The UN initiatives demonstrate that concern about the NEO impact hazard is increasing worldwide.

Despite the encouraging progress made during the past decade or so, there is still much to be done before we can be confident of our ability to deflect a threatening NEO. Evidence from observations, laboratory impact experiments, and theoretical work suggest that NEOs differ widely in the nature of their near-surface structure, and the outcome of impulsive techniques, such as the kinetic impactor, would be difficult to predict in the absence of information on bulk density, porosity, tensile strength, etc. While alternative slow-push or -pull techniques, such as the gravity tractor, may be suitable in certain circumstances, such as keyhole avoidance, it seems at present that the most likely scenario in which a deflection mission is called for would involve an impulsive technique, perhaps together with a combination observer/gravity tractor spacecraft to provide reconnaissance data and the opportunity to adjust the post-impulse trajectory of the target.

While studies of a number of deflection techniques have been carried out, no technique has yet been tested in space on a real NEA. In order to minimize the uncertainties in the outcome of a deflection mission, it would certainly be

prudent to test our concepts and assumptions in experimental missions to deflect suitable representative NEA targets before we are forced to apply deflection technology in a hurry in a real impact-prevention scenario.

**Acknowledgments.** We thank L. Johnson, Program Executive for NASA's NEO Observations Program, for information on the status of NASA NEO initiatives. We thank our referees, D. Morrison and D. Yeomans, for their thorough reviews, which have led to significant improvements in the presentation of this work. Some of the research described in this article has received funding from the European Union's Seventh Framework Program (FP7/2007–2013) under grant agreement No. 282703 (NEOShield).

## REFERENCES

- A'Hearn M. F., Belton M. J. S., Delamere W. A., et al. (2005) Deep impact: Excavating comet Tempel 1. *Science*, *310*, 258–264, DOI: 10.1126/science.1118923.
- Belton M. J. S., Morgan T. H., Samarasinha N., and Yeomans D. K., eds. (2004) *Mitigation of Hazardous Comets and Asteroids*. Cambridge Univ., Cambridge. 414 pp.
- Binzel R. P., Lupishko D. F., Di Martino M., Whiteley R. J., and Hahn G. (2002) Physical properties of near-Earth objects. In *Asteroids III* (W. F. Bottke Jr. et al., eds.), pp. 255–271. Univ. of Arizona, Tucson.
- Birks J. W., Crutzen P. J., and Roble R. G. (2007) Frequent ozone depletion resulting from impacts of asteroids and comets. In *Comet/Asteroid Impacts and Human Society* (P. Bobrowsky and H. Rickman, eds.), pp. 225–245. Springer-Verlag, Berlin.
- Bobrowsky P. and Rickman H., eds. (2007) *Comet/Asteroid Impacts and Human Society*. Springer-Verlag, Berlin. 546 pp.
- Bombardelli C., Urrutxa H., Merino M., Peláez J., and Ahedo E. (2013) The ion beam shepherd: A new concept for asteroid deflection. *Acta Astronaut.*, *90*, 98–102, DOI: 10.1016/j.actaastro.2012.10.019.
- Boslough M. (2014) Airburst warning and response. *Acta Astronaut.*, *103*, 370–375, DOI: 10.1016/j.actaastro.2013.09.007.
- Boslough M. B. E. and Crawford D. A. (1997) Shoemaker-Levy 9 and plume forming collisions on Earth. In *Near-Earth Objects* (J. L. Remo, ed.), pp. 236–282. Annals of the New York Academy of Sciences, Vol. 822, New York, DOI: 10.1111/j.1749-6632.1997.tb48345.x.
- Boslough M. B. E. and Crawford D. A. (2008) Low altitude airbursts and the impact threat. *Intl. J. Impact Eng.*, *35*, 1441–1448, DOI: 10.1016/j.ijimpeng.2008.07.053.
- Brown P., Spalding R. E., ReVelle D. O., Tagliaferri E., and Worden S. P. (2002) The flux of small near-Earth objects colliding with the Earth. *Nature*, *420*, 294–296, DOI: 10.1038/nature01238.
- Brown P. G., Assink J. D., Astiz L. et al. (2013) A 500-kiloton airburst over Chelyabinsk and an enhanced hazard from small impactors. *Nature*, *503*, 238–241, DOI: 10.1038/nature12741.
- Buratti B. J. and Johnson L. L. (2003) Identification of the lunar flash of 1953 with a fresh crater on the Moon's surface. *Icarus*, *161*, 192–197, DOI: 10.1016/S0019-1035(02)00027-1.
- Carnelli I., Ailor W., and Tremayne-Smith R. (2014) NEO Planetary Defense 2013: Gathering for impact. *Acta Astronaut.*, *103*, 307–308, DOI: 10.1016/j.actaastro.2014.08.004.
- Chapman C. and Morrison D. (1994) Impacts on the Earth by asteroids and comets: Assessing the hazard. *Nature*, *367*, 33–40, DOI: 10.1038/367033a0.
- Cheng A. F. (2002) Near Earth Asteroid Rendezvous: Mission summary. In *Asteroids III* (W. F. Bottke Jr. et al., eds.), pp. 351–366. Univ. of Arizona, Tucson.
- Cheng A. F., Atchison J., Kantsiper B., Rivkin A. S., Stickle A., Reed C., Galvez A., Carnelli I., Michel P., and Ulamec S. (2015) Asteroid Impact and Deflection Mission. *Acta Astronaut.*, *115*, 262–269, DOI: 10.1016/j.actaastro.2015.05.021.
- Chesley S. R. and Spahr T. B. (2004) Earth impactors: Orbits and warning times. In *Mitigation of Hazardous Comets and Asteroids* (M. J. S. Belton et al., eds.), pp. 22–37. Cambridge Univ., Cambridge.
- Collins G. S., Melosh H. J., and Marcus R. A. (2005) Earth impact effects program: A web-based computer program for calculating the regional environmental consequences of a meteoroid impact on Earth. *Meteoritics & Planet. Sci.*, *40*, 817–840, DOI: 10.1111/j.1945-5100.2005.tb00157.x.
- Farnocchia D., Bernardi F., and Valsecchi G. B. (2012) Efficiency of a wide-area survey in achieving short- and long-term warning for small impactors. *Icarus*, *219*, 41–47, DOI: 10.1016/j.icarus.2012.02.014.
- Farnocchia D., Chesley S. R., Chodas P. W., Tricarico P., Kelley M. S. P., and Farnham T. L. (2014) Trajectory analysis for the nucleus and dust of Comet C/2013 A1 (Siding Spring). *Astrophys. J.*, *790*, 114, DOI: 10.1088/0004-637X/790/2/114.
- Foster C., Bellerose J., Mauro D., and Jaroux B. (2013) Mission concepts and operations for asteroid mitigation involving multiple gravity tractors. *Acta Astronaut.*, *90*, 112–118, DOI: 10.1016/j.actaastro.2012.10.010.
- Fujiwara A., Kawaguchi J., Yeomans D. K., et al. (2006) The rubble-pile asteroid Itokawa as observed by Hayabusa. *Science*, *312*, 1330–1334, DOI: 10.1126/science.1125841.
- Garbolino E. and Michel P. (2011) Proposal of a spatial decision support system architecture to estimate the consequences and costs of small meteorites impacts. *Nat. Hazards Earth Syst. Sci.*, *11*, 3013–3021, DOI: 10.5194/nhess-11-3013-2011.
- Garshnek V., Morrison D., and Burkle F. M. (2000) The mitigation, management, and survivability of asteroid/comet impact with the Earth. *Space Policy*, *16*, 213–222, DOI: 10.1016/S0265-9646(00)00025-4.
- Gehrels T., ed. (1994) *Hazards Due to Comets and Asteroids*. Univ. of Arizona, Tucson. 1300 pp.
- Gibbings A., Vasile M., Watson I., Hopkins J.-M., and Burns D. (2013) Experimental analysis of laser ablated plumes for asteroid deflection and exploitation. *Acta Astronaut.*, *90*, 85–97, DOI: 10.1016/j.actaastro.2012.07.008.
- Gisler G., Weaver R., and Gittings M. (2011) Calculations of asteroid impacts into deep and shallow water. *Pure Appl. Geophys.*, *168*, 1187–1198, DOI: 10.1007/s00024-010-0225-7.
- Harris A. W. (2014) Near-Earth-object survey progress and population of small near-Earth asteroids. In *Asteroids, Comets, Meteors 2014, Book of Abstracts* (K. Muinonen et al., eds.), Helsinki, Finland. Available online at <http://www.helsinki.fi/acm2014/pdf-material/Day-2/Session-3/Room-3/HARRIS-6E69.pdf>.
- Harris A. W. and Drube L. (2014) How to find metal-rich asteroids. *Astrophys. J. Lett.*, *785*, L4, DOI: 10.1088/2041-8205/785/1/L4.
- Harris A. W., Barucci M. A., Cano J. L., Fitzsimmons A., Fulchignoni M., Green S. F., Hestroffer D., Lappas V., Lork W., Michel P., Morrison D., Payson D., and Schäfer F. (2013) The European Union funded NEOShield project: A global approach to near-Earth object impact threat mitigation. *Acta Astronaut.*, *90*, 80–84, DOI: 10.1016/j.actaastro.2012.08.026.
- Holsapple K. A. (2007) Spin limits of solar system bodies: From the small fast-rotators to 2003 EL61. *Icarus*, *187*, 500–509, DOI: 10.1016/j.icarus.2006.08.012.
- Holsapple K. A. and Housen K. R. (2012) Momentum transfer in asteroid impacts. I. Theory and scaling. *Icarus*, *221*, 875–887, DOI: 10.1016/j.icarus.2012.09.022.
- Huang J., Ji J., Ye P., et al. (2013) The ginger-shaped asteroid 4179 Toutatis: New observations from a successful flyby of Chang'e-2. *Scientific Reports*, *3*, 3411, DOI: 10.1038/srep03411.
- Jutzi M. and Michel P. (2014) Hypervelocity impacts on asteroids and momentum transfer: I. Numerical simulations using porous targets. *Icarus*, *229*, 247–253, DOI: 10.1016/j.icarus.2013.11.020.
- Kenkmann T., Artemieva N. A., Wünnemann K., Poelchau M. H., Elbeshausen D., and Núñez Del Prado H. (2009) The Carancas meteorite impact crater Peru: Geologic surveying and modeling of crater formation and atmospheric passage. *Meteoritics & Planet. Sci.*, *44*, 985–1000, DOI: 10.1111/j.1945-5100.2009.tb00783.x.
- Korycansky D. G. and Lynett P. J. (2005) Offshore breaking of impact tsunami: The Van Dorn effect revisited. *Geophys. Res. Lett.*, *32*, L10608, DOI: 10.1029/2004GL021918.
- Kring D. and Boslough M. (2014) Chelyabinsk: Portrait of an asteroid airburst. *Phys. Today*, *67*, 32–37, DOI: 10.1063/PT.3.2515.
- Lauretta D. S. and the OSIRIS-REx Team (2012) An overview of the OSIRIS-REx asteroid sample return mission. *Lunar Planet. Sci. XLIII*, Abstract #2491. Lunar and Planetary Institute, Houston.
- Lu E. T. and Love S. G. (2005) Gravitational tractor for towing asteroids. *Nature*, *438*, 177–178, DOI: 10.1038/438177a.
- Mainzer A., Grav T., Bauer J., et al. (2011) NEOWISE observations of near-Earth objects: Preliminary results. *Astrophys. J.*, *743*, 156, DOI: 10.1088/0004-637X/743/2/156.

- Malin M. C., Edgett K. S., Posiolova L. V., McColley S. M., and Noe Dobrea E. Z. (2006) Present-day impact cratering rate and contemporary gully activity on Mars. *Science*, *314*, 1573–1577, DOI: 10.1126/science.1135156.
- Michel P. (2013) Physical properties of near-Earth objects that inform mitigation. *Acta Astronaut.*, *90*, 6–13, DOI: 10.1016/j.actaastro.2012.07.022.
- Michel P., Cheng A. F., Küppers M., and the AIDA Team (2015) Asteroid Impact and Deflection Assessment (AIDA) mission: Science investigation of a binary system and mitigation test. *EPSC Abstracts*, *10*, EPSC2015-123, available online at <http://meetingorganizer.copernicus.org/EPSC2015/EPSC2015-123.pdf>.
- Morrison D., Harris A. W., Sommer G., Chapman C. R., and Carusi A. (2002) Dealing with the impact hazard. In *Asteroids III* (W. F. Bottke Jr. et al., eds.), pp. 739–754. Univ. of Arizona, Tucson.
- Nakamura T., Noguchi T., Tanaka M., et al. (2011) Itokawa dust particles: A direct link between S-type asteroids and ordinary chondrites. *Science*, *333*, 1113–1116, DOI: 10.1126/science.1207758.
- Noll K., Weaver H., and Feldman P., eds. (1996) *The Collision of Comet Shoemaker-Levy 9 and Jupiter*. IAU Colloq. 156, Cambridge Univ., Cambridge.
- Ostro S. J. and Giorgini J. D. (2004) The role of radar in predicting and preventing asteroid and comet collisions with Earth. In *Mitigation of Hazardous Comets and Asteroids* (M. J. S. Belton et al., eds.), pp. 38–65. Cambridge Univ., Cambridge.
- Paek S. W. (2012) A multi-functional paintball cloud for asteroid deflection. *63rd International Astronautical Congress*, Naples, Italy, IAC-12-A3.4.13.
- Popova O. P., Jenniskens P., Emel'yanenko V., et al. (2013) Chelyabinsk airburst, damage assessment, meteorite recovery, and characterization. *Science*, *342*, 1069–1073, DOI: 10.1126/science.1242642.
- Rozitis B., MacLennan E., and Emery J. P. (2014) Cohesive forces prevent the rotational breakup of rubble-pile asteroid (29075) 1950 DA. *Nature*, *512*, 174–176, DOI: 10.1038/nature13632.
- Sánchez P. and Scheeres D. J. (2014) The strength of regolith and rubble pile asteroids. *Meteoritics & Planet. Sci.*, *49*, 788–811, DOI: 10.1111/maps.12293.
- Shapiro I. I., Vilas F., A'Hearn M., et al. (2010) *Defending Planet Earth: Near-Earth Object Surveys and Hazard Mitigation Strategies*. National Academies, Washington DC.
- Silber E. A., ReVelle D. O., Brown P. G., and Edwards W. N. (2009) An estimate of the terrestrial influx of large meteoroids from infrasonic measurements. *J. Geophys. Res.*, *114*, E08006, DOI: 10.1029/2009JE003334.
- Stokes G. H., Yeomans D. K., Bottke W. F., et al. (2003) *Study to Determine the Feasibility of Extending the Search for Near-Earth Objects to Smaller Limiting Diameters*. Report of the Near-Earth Object Science Definition Team at the Request of NASA's Office of Space Science, Solar System Exploration Division, available online at <http://neo.jpl.nasa.gov/neo/neoreport030825.pdf>.
- Tancredi G., Ishitsuka J., Schultz P. H., Harris R. S., Brown P., Revelle D. O., Antier K., Le Pichon A., Rosales D., Vidal E., Varela M. E., Sánchez L., Benavente S., Bojorquez J., Cabezas D., and Dalmau A. (2009) A meteorite crater on Earth formed on September 15, 2007: The Carancas hypervelocity impact. *Meteoritics & Planet. Sci.*, *44*, 1967–1984, DOI: 10.1111/j.1945-5100.2009.tb02006.x.
- Tony J. L. (2011) An early warning system for asteroid impact. *Publ. Astron. Soc. Pac.*, *123*, 58–73, DOI: 10.1086/657997.
- Toon O. B., Zahnle K., Morrison D., Turco R. P., and Covey C. (1997) Environmental perturbations caused by the impacts of asteroids and comets. *Rev. Geophys.*, *35*, 41–78, DOI: 10.1029/96RG03038.
- Trilling D. E., Mueller M., Hora J. L., Harris A. W., Bhattacharya B., Bottke W. F., Chesley S., Delbo M., Emery J. P., Fazio G., Mainzer A., Penprase B., Smith H. A., Spahr T. B., Stansberry J. A., and Thomas C. A. (2010) ExploreNEOs. I. Description and first results from the warm Spitzer near-Earth object survey. *Astron. J.*, *140*, 770–784, DOI: 10.1088/0004-6256/140/3/770.
- Tsuda Y., Yoshikawa M., Abe M., Minamino H., and Nakazawa S. (2013) System design of the Hayabusa 2 — Asteroid sample return mission to 1999 JU3. *Acta Astronaut.*, *91*, 356–362, DOI: 10.1016/j.actaastro.2013.06.028.
- Werner M. W., Roellig T. L., Low F. J., et al. (2004) The Spitzer Space Telescope mission. *Astrophys. J. Suppl.*, *154*, 1–9, DOI: 10.1086/422992.
- Wolters S. D., Ball A. J., Wells N., Saunders C., and McBride N. (2011) Measurement requirements for a near-Earth asteroid impact mitigation demonstration mission. *Planet. Space Sci.*, *59*, 1506–1515, DOI: 10.1016/j.pss.2011.06.015.
- Wright E. L., Eisenhardt P. R. M., Mainzer A. K., et al. (2010) The Wide-field Infrared Survey Explorer (WISE): Mission description and initial on-orbit performance. *Astron. J.*, *140*, 1868–1881, DOI: 10.1088/0004-6256/140/6/1868.
- Wünnemann K., Weiss R., and Hoffmann K. (2007) Characteristics of oceanic impact-induced large water waves — Re-evaluation of the tsunami hazard. *Meteoritics & Planet. Sci.*, *42*, 1893–1903, DOI: 10.1111/j.1945-5100.2007.tb00548.x.
- Yeomans D. K., Bhaskaran S., Broschart S. B., Chesley S. R., Chodas P. W., and Sweetser T. H. (2009) Deflecting a hazardous near-Earth object. *1st IAA Planetary Defense Conference: Protecting Earth from Asteroids*, Granada, Spain, available online at [http://neo.jpl.nasa.gov/neo/pdc\\_paper.html](http://neo.jpl.nasa.gov/neo/pdc_paper.html).

# Human Exploration of Near-Earth Asteroids

**P. A. Abell**

*NASA Johnson Space Center*

**B. W. Barbee**

*NASA Goddard Space Flight Center*

**P. W. Chodas**

*Jet Propulsion Laboratory, California Institute of Technology*

**J. Kawaguchi**

*Japan Aerospace Exploration Agency*

**R. R. Landis**

*NASA Wallops Flight Facility*

**D. D. Mazanek**

*NASA Langley Research Center*

**P. Michel**

*Lagrange Laboratory, Université Côte d'Azur, Observatoire de la Côte d'Azur, CNRS*

---

Due to a number of factors, including a recent U.S. presidential directive, the successful return of an asteroid sample by the Japanese spacecraft Hayabusa in 2010, and the high-visibility airburst impact event over Chelyabinsk, Russia, in 2013, scientific and exploration interest in near-Earth asteroids (NEAs) has never been greater. In particular, NASA and the Japanese and European space agencies have begun expending serious effort to discover and identify appropriate NEA targets for a wide variety of spaceflight activities, including both robotic and human missions. These missions are particularly attractive as they will yield an unprecedented amount of knowledge about the formation of the solar system, provide a stepping-stone approach for future human exploration missions to Mars and beyond, identify materials for *in situ* resource utilization (ISRU), and test techniques for deflecting potentially hazardous objects that threaten Earth.

## 1. INTRODUCTION

Asteroids have generated significant worldwide interest in recent years as a result of flyby, rendezvous, and sample return missions. Robotic missions to near-Earth asteroids (NEAs) have already been completed by several space agencies, and subsequent robotic missions to these bodies are under development or consideration. In addition, human-led exploration missions to these destinations are now also being seriously considered. In 2009, the Review of the United States Human Spaceflight Plans Committee, also known as the Augustine Commission, identified NEAs as high-profile destinations for human exploration missions beyond the Earth-Moon system as part of the “Flexible Path” approach ([http://www.nasa.gov/pdf/384767main\\_SUMMARY%20REPORT%20-%20FINAL.pdf](http://www.nasa.gov/pdf/384767main_SUMMARY%20REPORT%20-%20FINAL.pdf),

pdf, accessed July 19, 2015). In response to these findings, President Barack Obama directed NASA to include NEAs as destinations for future human exploration with the goal of sending astronauts to an NEA in the mid to late 2020s. This directive became part of the official *National Space Policy of the United States of America* as of June 28, 2010. More recently, on June 18, 2013, President Obama gave NASA a Grand Challenge to “find all asteroid threats to human populations and know what to do about them.” This Grand Challenge, combined with the directive for a human NEA mission, forms the basis of NASA’s Asteroid Initiative (<http://www.nasa.gov/asteroidinitiative>, accessed June 10, 2015) (Fig. 1).

Near-Earth asteroid targets suitable as destinations for human exploration tend to have orbits very similar to Earth’s, and also have a statistically greater chance of impacting our

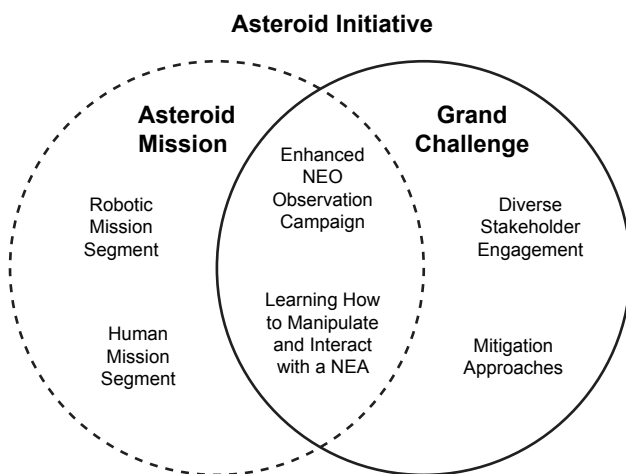


**Fig. 1.** NASA's Asteroid Initiative.

planet. Therefore, one of the major goals for NASA's human spaceflight program and the Asteroid Initiative is to identify these NEAs both from the standpoint of human exploration and planetary defense. Ideally, once suitable targets have been identified, NASA would send astronauts beyond the Earth-Moon system to NEAs within the coming decades. These missions, and the activities required to identify and characterize suitable targets, would pave the way for exploration of the martian system, and would have the added benefit of finding potentially threatening objects and increasing our knowledge about the physical characteristics that will be necessary to develop future NEA hazard mitigation techniques.

Human-led missions to NEAs will undoubtedly provide a great deal of technical and engineering data on spacecraft operations for future human deep-space exploration and planetary defense while simultaneously conducting in-depth scientific examinations of these primitive objects. Information obtained during a human mission to an NEA, combined with ground- and spacebased observations and robotic spacecraft investigations of asteroids and comets, will also provide a real measure of ground truth to data obtained from samples within the worldwide extraterrestrial material collections (e.g., meteorites and cosmic dust) and those collected directly from spacecraft sample-return missions [e.g., Stardust, Hayabusa, Hayabusa2, and the Origins Spectral Interpretation Resource Identification and Security-Regolith Explorer (OSIRIS-REx)]. Major advances in the areas of geochemistry, impact history, thermal history, isotope analyses, mineralogy, space weathering, formation ages, thermal inertias, volatile content, source regions, solar system formation, etc., can be expected from human NEA missions. Samples directly returned from a primitive body would lead to the same kind of breakthroughs for understanding NEAs that the Apollo samples provided for understanding the Earth-Moon system and its formation history.

Prior to sending human explorers to NEAs, however, robotic investigations of these bodies will be required in

order to maximize operational efficiency and reduce mission risk. These precursor missions will help fill crucial strategic knowledge gaps (SKGs) (see section 6.1.2) concerning the physical characteristics of NEAs that are relevant for human exploration of these relatively unknown destinations.

One such SKG that is considered critical for future human spaceflight is the identification of resources that could be utilized *in situ*. Some NEAs have been identified via spectroscopic observations as having affinities with volatile- and organic-rich carbonaceous chondrite mineralogies, which contain significant amounts of OH and other volatiles bound within their geologic structures (Brearley, 2006; Pizzarello *et al.*, 2006; Weisberg *et al.*, 2006; Burton *et al.*, 2012). Successful identification of these types of materials and the subsequent extraction and utilization of the resources contained within them will enable human missions to leverage these resources and essentially "live off the land." This will reduce mission risk and allow more aggressive approaches for conducting exploration missions beyond low-Earth orbit (LEO). Such missions would not have to carry all the necessary supplies that would normally be used in a round-trip mission, thus freeing up extra mass that could be used for additional payloads and systems. This could eventually aid in the development of alternative mission architectures to Mars and other solar system destinations.

In addition, robotic precursor and human exploration missions to NEAs would allow NASA and its international partners to gain operational experience in performing complex tasks (e.g., sample collection, deployment of payloads, retrieval of payloads, etc.) with crew, robots, and spacecraft under low-gravity or microgravity conditions at or near the surface of a small body. This would provide an important synergy between the worldwide science and exploration communities, which will be crucial for development of future international deep-space exploration architectures and has potential benefits for future exploration of other destinations beyond LEO. This experience would be directly applicable to the moons of Mars, Phobos and Deimos, and could be leveraged to enable an eventual landing on Mars itself.

Among all human spaceflight destinations currently under consideration, only NEAs encompass all the following critical themes: exploration, science, resource utilization, and planetary defense. The scientific, *in situ* resource utilization (ISRU), and hazard mitigation benefits, along with the operational benefits of a human venture into deep space, make a human mission to an NEA a compelling prospect that has the potential to inspire future generations of scientists, engineers, and explorers on an international level for decades to come.

## 2. HISTORICAL BACKGROUND

The impetus for asteroid exploration is scientific, political, and pragmatic, and the idea of sending human explorers to asteroids is not new. Piloted missions to these primitive bodies were first discussed in the 1960s, pairing Saturn V rockets with enhanced Apollo spacecraft to explore what were then called "Earth-approaching asteroids" (Cole, 1963;

(*Cole and Cox*, 1964; *Smith*, 1966). The difference today, compared to nearly a half-century ago, is that the science and engineering communities are now much more aware of the small bodies in the vicinity of Earth. Prerequisite steps must be taken before mounting a robotic precursor mission, let alone piloted missions. The first such step, and the lynchpin of such an architecture, is a spacebased near-Earth object (NEO) survey (see section 6.1.1).

## 2.1. Apollo Applications Program/Post-Apollo

Arguably, the first realistic notions of human missions to asteroids were imagined in the 1960s by *Cole* (1963), *Cole and Cox* (1964), and *Smith* (1966). While Cole was a futurist, he was also an aerospace engineer who suggested a number of innovative scenarios for exploring the inner solar system by utilizing Apollo hardware to reach NEAs. For the most part, however, these ideas were general rather than specific. *Smith* (1966) examined the technical feasibility of implementing a human flyby mission to (433) Eros. Smith suggested that the 1975 close approach of (433) Eros (within 0.15 AU of Earth), coupled with the descending node of the asteroid's orbit, would enable an opportunity for a relatively low-energy interplanetary mission (post-Earth escape  $\Delta v = 4.2 \text{ km s}^{-1}$ ). In the 1960s, Mars and even Venus were considered primary targets for initial human missions. Smith pointed out that missions to asteroids would complement the as-yet only conceptual missions to Mars and beyond, and that a flyby mission of (433) Eros could be accomplished by a single, upgraded Saturn V along with derivatives of the Manned Orbital Research Laboratory (MORL) and the Apollo capsule. The MORL was a concept for a 5-metric-ton space station lofted by a Saturn 1B, with Gemini or Apollo capsules utilized for crew transport. For the Eros mission concept, Smith surmised that an adapted MORL could serve as a habitation module, while the Apollo capsule would be used as a launch and Earth reentry vehicle for the crew. MORL was never launched, as NASA had more ambitious plans with the Apollo Applications Orbital Workshop, which later became Skylab.

The mission architecture considered by *Smith* (1966) in his analysis began with injecting an S-IVB/Interstage Unit (with the crew and habitation module) into a two-day geocentric elliptical orbit. The S-IVB evolved from the upper stage of the Saturn 1, and was the third stage of the Saturn V rocket, which for lunar missions was ignited twice: once to place the combined Apollo Command and Service Modules and Lunar Lander (the Apollo "stack") into LEO after second-stage cutoff, and again for translunar injection (TLI). Upon completing spacecraft and systems checkout, the spacecraft "stack" would depart with a second impulse on a 270-day journey outbound toward Eros. Then, 257 days after the closest approach to the asteroid, the crew would return to Earth. A 500+-day round-trip mission with upgraded Apollo and Saturn V hardware was an audacious concept at best. However, this was the first feasibility study of its kind that examined what might be possible for missions beyond the

Moon. This was before NASA Headquarters established the Apollo Applications Program (AAP) in 1968; its intent was to develop a detailed planning guideline for the Manned Spacecraft Center [now the Johnson Space Center (JSC)] and Marshall Space Flight Center (MSFC) for piloted missions utilizing the hardware developed for the Moon. The proposed flight schedule was ambitious, calling for 13 Saturn 1B and 16 Saturn V missions, but none of these concepts imagined NEA missions. NEA human mission feasibility concepts using Apollo hardware were analyzed in more detail in 1971, but none of these concepts matured beyond the study phase (*Hall*, 1971).

## 2.2. Space Exploration Initiative

*O'Leary* (1977) discussed mining asteroids in the late 1970s, but it would be more than a decade later before NASA examined the idea of visiting NEAs as part of the Space Exploration Initiative (SEI) (*Nash et al.*, 1989). *Davis et al.* (1993) pointed out that given the large investment, as part of the SEI, in a Mars landing mission, a program of robotic and human exploration missions to NEAs would result in additional return by (1) providing a precursor to a Mars mission (with flight testing of hardware and mission operations); (2) providing a highly visible program milestone and thus sustaining momentum for the SEI in the interval between a return to the Moon and a Mars mission; (3) providing a large science return via *in situ* observations and macroscopic sample return; and (4) carrying out an assessment of the resources available in the NEA population.

None of the ancillary SEI studies on asteroids and asteroid exploration specified or even suggested a particular architecture toward achieving the human exploration of these primitive bodies. However, the variety of overview studies did begin to search the asteroid database for potential low propulsive change in velocity (low  $\Delta v$ ) targets in order to develop preliminary "suggestive" lists of possible targets, including but not limited to 1989 ML, 1989 UQ, 1991 VG, and 1991 JW (*Davis et al.*, 1993; *Jones et al.*, 1994).

By 1992, SEI had largely faded from view, suffering from a flawed, defective decision-making process (*Hogan*, 2007). As NASA acknowledged budgetary realities, notions of human exploration beyond LEO were abandoned. A new emphasis was placed on "faster, better, cheaper" robotic missions while maintaining the status quo on human spaceflight activities; this mantra referred to the Discovery program, begun in 1992, that was intended to spur proposals, subject to a competitive peer-review process, for low-cost, high-impact robotic science missions to explore the solar system. The Near Earth Asteroid Rendezvous (NEAR) mission to (433) Eros (later renamed NEAR-Shoemaker in honor of the late Eugene "Gene" Shoemaker) was the first Discovery mission launched. In addition, by 1996, the National Space Policy had removed human spaceflight exploration from the U.S. national agenda. As a result, it would be 15 years before NASA would again consider piloted missions to asteroids.

### 2.3. NASA Near-Earth Object Observations Program

In 1998, NASA established a goal to discover 90% of the NEAs larger than 1 km in diameter and in 2005, Congress extended that goal to include 90% of the NEAs larger than 140 m. There are thought to be approximately 1000 NEAs larger than 1 km and roughly 15,000 larger than 140 m. The progress toward meeting these goals can be monitored on the NEO Discovery page at <http://neo.jpl.nasa.gov/stats/> (accessed October 6, 2015). The NEO Observations program has functioned as a key foundational source for the asteroid identification and characterization activities of NASA.

Since NASA's initiation of the NEO Observations program in 1998, NEO surveys have been extremely successful, reaching the goal of finding more than 90% of the estimated NEAs larger than 1 km and a significant fraction of the estimated NEAs larger than 140 m. The vast majority of these discoveries have been made by NASA-supported groundbased telescopic surveys, including the Catalina Sky Survey (CSS) and Spacewatch near Tucson, Arizona (<http://www.lpl.arizona.edu/css/> and <http://spacewatch.lpl.arizona.edu/>, both accessed October 6, 2015); the Lincoln Near Earth Asteroid Research (LINEAR) project near Socorro, New Mexico (<http://www.ll.mit.edu/mission/space/linear/>, accessed October 6, 2015); the Panoramic Survey Telescope and Rapid Response System (Pans-STARRS) 1 on Haleakala, Maui, Hawai'i (<http://pan-starrs.ifa.hawaii.edu/public/>, accessed October 6, 2015); Lowell Observatory Near-Earth-Object Search (LONEOS) near Flagstaff, Arizona (<http://asteroid.lowell.edu/asteroid/loneos/loneos.html>, accessed October 6, 2015); and the Near-Earth Asteroid Tracking (NEAT) project run by NASA's Jet Propulsion Laboratory (JPL) (<http://neo.jpl.nasa.gov/programs/neat.html>, accessed October 6, 2015). The Near-Earth Object Wide-field Infrared Survey Explorer (NEOWISE), a near-infrared space telescope in an Earth polar orbit, discovered and characterized NEOs for 10 months in 2010 before its cryogens were exhausted, and is operating now in a post-cryogenic mission (<http://neowise.ipac.caltech.edu/>, accessed October 6, 2015). The LINEAR survey has transitioned to a new facility, LONEOS and NEAT have been discontinued, and Spacewatch now operates primarily in a follow-up capacity.

### 2.4. Constellation Program

NASA's Constellation Program (CxP) was formulated as a response to the goals laid out in the Vision for Space Exploration (VSE) ([http://www.nasa.gov/pdf/55583main\\_vision\\_space\\_exploration2.pdf](http://www.nasa.gov/pdf/55583main_vision_space_exploration2.pdf), accessed October 6, 2015). The milestones for the CxP were to (1) complete the International Space Station (ISS); (2) return to the Moon by 2020; and (3) place humans on Mars as the end goal. During the CxP's existence from 2005 to 2009, two studies examined the feasibility of reaching a number of NEAs utilizing CxP hardware elements (i.e., Ares 5 and Ares 4 launch vehicles; Ares 4 with an Atlas V and Centaur upper stage; Ares 5 with a modified Altair lunar lander as a habitation module; etc.).

In the first CxP study related to NEAs, *Mazanek et al.* (2005) looked at relatively short round-trip missions (45–90 days) and the hardware that might enable such missions. This study conducted a top-level mission analysis of a “2.5 launch Earth-orbit rendezvous architecture,” which required two Ares 5 upper-stage Earth-departure stages (EDS) for Earth departure and arrival at the asteroid, and one Ares 1 vehicle for the crew. As CxP was rolled out, the nominal architecture for the return to the Moon was the “1.5 launch” scenario, or one Ares 5 and the Ares 1 vehicle for the crew. The 1.5 launch architecture was intended to initially place its payload into LEO (parking orbit) and to be reignited to depart Earth on a translunar trajectory, very much akin to the S-IVB stage of the Saturn V. The *Mazanek et al.* (2005) concept involved a double rendezvous in LEO with the first EDS providing the departure  $\Delta v$  from the Earth-Moon system, while the second EDS, along with the lunar lander's descent stage, would provide the braking  $\Delta v$  for rendezvous, proximity, and surface operations at the asteroid. Following surface exploration operations, including collection of samples, the Orion service module would perform the  $\Delta v$  maneuver (trans-Earth injection) to return to Earth.

The second CxP study also focused on utilizing hardware developed for the return to the Moon, but with a slight difference. It examined the feasibility of adapting that hardware within the then-planned launch vehicle infrastructure with minimal modifications to the Orion vehicle [e.g., only flying two or three astronauts, inclusion of a science instrument module (SIM) bay on the service module section of the Orion, etc.]. Four launch options were assessed: (1) Ares 1/Orion and an evolved expendable launch vehicle (EELV) such as the Atlas V and Delta IV rockets; (2) Orion atop an Ares 4 rocket; (3) Orion atop an Ares 5 rocket; and (4) Ares 1/Orion and Ares 5 (with a modified Altair lunar lander).

These feasibility studies were based upon anticipated CxP hardware performance and primarily addressed the orbital mechanics (i.e., based on low  $\Delta v$  targets and their accessibility). Coincident to and following the CxP studies, a more exhaustive examination of asteroid exploration via the Orion spacecraft was led by *Hopkins* (2009) and *Hopkins and Dissel* (2010) at Lockheed Martin Space Systems; the latter study was called “Plymouth Rock.”

Based on the expected launch vehicle development schedules (ca. 2009) and the assumption of a long-duration test flight, the Plymouth Rock concept looked at several candidate NEA targets before settling on 2008 EA<sub>9</sub> and 2000 SG<sub>344</sub> for possible missions in the 2019–2030 timeframe (Fig. 2).

The Plymouth Rock concept went to greater depth than previous studies. It proposed utilization of Orion capsules; mission durations of 4–7 months; sufficient habitable volume and life support consumables for at least two and preferably three crew members over this time span; a spacecraft propulsion system with at least 1.5 km s<sup>-1</sup> of  $\Delta v$  capability for major course maneuvers in deep space; extravehicular activities (EVAs) or at least minimal telerobotic capability to collect macroscopic samples in geological context; and a

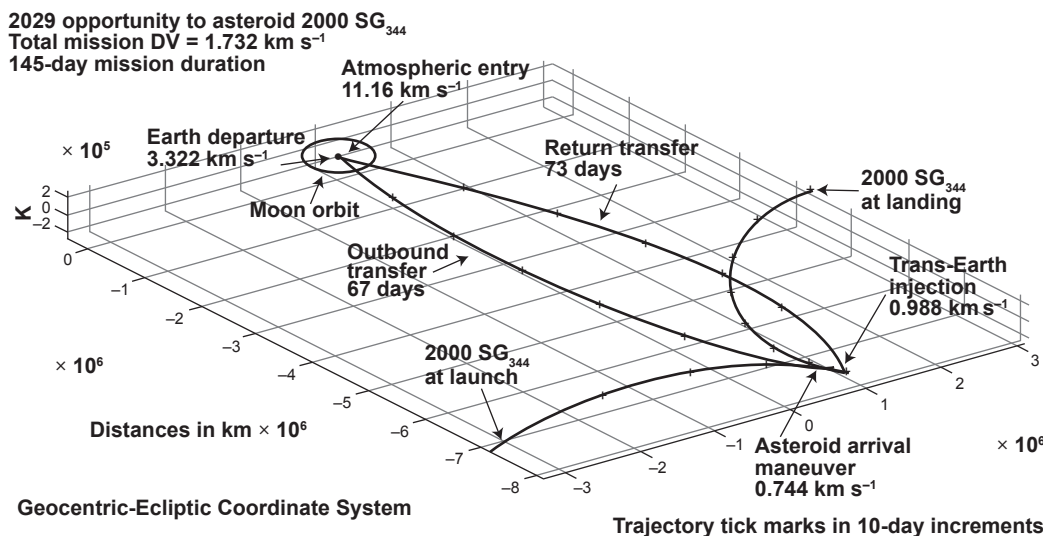


**Fig. 2.** Plymouth Rock mission to 2000 SG<sub>344</sub> (*Hopkins and Dissel, 2010*).

reentry thermal protection system to withstand  $\sim 12 \text{ km s}^{-1}$  (*Hopkins and Dissel, 2010*).

Plymouth Rock considered a dual-Orion launch by an unmanned Ares 5 with the supplemental Orion “deep-space vehicle” and EDS on a Delta IV heavy (or Ares 1) rocket with the crew. After rendezvous in LEO, the EDS would place the combined “stack” on an Earth departure trajectory to the asteroid. *Hopkins and Dissel* (2010) evaluated life support consumables (i.e., food, water, CO<sub>2</sub> removal, O<sub>2</sub> generation, etc.) and acknowledged that even with the quasi-dual Orion (a standard Orion crew cabin capable of reentry and the enhanced Orion deep-space vehicle, not capable of reentry, with a stretched cabin), this would be a minimalistic mission.

The majority of the mission concept studies that have been conducted to date [i.e., CXP, NASA’s “Human Exploration Framework Team” (HEFT)] have not considered the benefit that NEO surveys would provide by finding more accessible targets to enable mission durations on par with ISS expeditions (i.e.,  $\sim 180$  days). The current low discovery level of viable candidate NEAs as potential human destinations is largely due to the fact that the world’s NEO observing assets are currently confined to the vicinity of Earth. Analyses of past trajectory opportunities to known NEOs have shown that some were highly accessible during the timeframes of their discovery, because they had to closely approach Earth in order to be detected. Many of these have synodic periods of several decades and longer, and would be more easily detected by a deep-space telescopic NEO infrared (IR) survey mission at, for instance, the Sun-Earth Lagrange L<sub>1</sub> point (SEL<sub>1</sub>), where such a telescope could focus on the so-called “sweet spots” in order to find human-accessible NEOs leading and trailing Earth’s orbit (*Mainzer et al., 2015*).

### 3. TARGET POPULATION DYNAMICS

The population of NEAs that may be accessible for human space flight missions is defined by the Near-Earth Object

Human Space Flight Accessible Targets Study (NHATS). NHATS is an automated system designed to monitor the accessibility of, and particular mission opportunities offered by, the NEA population. This is analogous to systems that automatically monitor the impact risk posed to Earth by the NEA population. The NHATS system identifies NEAs that are potentially accessible for future round-trip human space flight missions and provides rapid notification to asteroid observers so that crucial follow-up observations can be obtained following discovery of accessible NEAs. NHATS was developed in 2010 and was automated by early 2012. NHATS data are provided via an interactive website (<http://neo.jpl.nasa.gov/nhats/>, accessed June 9, 2015), and daily NHATS notification emails are transmitted to a mailing list (<https://lists.nasa.gov/mailman/listinfo/nhats>, accessed June 9, 2015); both resources are available to the public.

Automation of the NHATS processing was motivated by the fact that newly discovered NEAs are often only detectable for several days or weeks surrounding their discovery epochs because of their faintness in the night sky and tendency to both approach and depart Earth’s vicinity relatively quickly. The brief window of time surrounding discovery is therefore critical to obtain follow-up observations that can provide information about the NEA’s physical characteristics and improve estimates of its orbit. The automated NHATS system supports those efforts by rapidly identifying those NEAs that are particularly accessible and quickly notifying observers.

An NEA is classified as NHATS-compliant if there exists at least one round-trip trajectory solution to the NEA that satisfies NHATS key analysis constraints: (1) the total propulsive change in velocity ( $\Delta v$ ) required for the round-trip mission must be  $\leq 12 \text{ km s}^{-1}$ ; (2) the total round-trip mission duration must be  $\leq 450$  days; (3) the stay time at the NEA must be  $\geq 8$  days; and (4) Earth departure must occur sometime during the years 2015 through 2040. These constraints are discussed in greater detail later in section 3.4.

The discussions presented hereinafter regarding NEA population estimates and dynamical considerations are largely driven and framed by NHATS data, because NHATS provides a comprehensive accessibility assessment for the entire NEA population.

### 3.1. Astrodynamics Background

The accessibility of an NEA is largely framed in terms of the total  $\Delta v$  and round-trip mission duration required to visit it. The other related consideration is what range of Earth departure dates offer feasible (e.g., low  $\Delta v$ /low mission duration) missions to the NEA. Mission  $\Delta v$  is largely influenced by whether the NEA will approach Earth with low relative heliocentric velocity, while mission duration is largely influenced by how closely the NEA will approach Earth. Thus, the most favorable mission opportunities occur when an NEA approaches Earth at close distance with low relative speed. For reference, in this context “close distance” is generally  $<0.1$  AU and “low relative speed” is generally  $<2$  km s $^{-1}$ .

NEAs that will approach Earth at relatively close distances and with slow relative speeds generally have so-called “Earth-like orbits,” meaning that the NEA’s heliocentric orbit has a semimajor axis near 1 AU, eccentricity near zero, and inclination near zero. Efforts have been made to construct analytical formulations based on these fundamental considerations, for the purpose of identifying accessible NEAs based on their osculating heliocentric Keplerian orbital elements (e.g., Adamo *et al.*, 2010). However, the subtle complexities of astrodynamics, especially with regard to constrained optimization of round-trip trajectories, limit the utility of analytical formulations based on NEA orbital elements. Such approaches are not capable of identifying all members of the NEA population that meet specific mission design criteria. The empirical approach taken by the aforementioned NHATS system, on the other hand, provides complete identification of those observed NEAs that meet specific mission design constraints.

One challenging aspect of observing NEAs with very Earth-like orbits is that, much like two cars traveling at nearly the same speed around a race track, NEAs with heliocentric orbit semimajor axis near that of Earth ( $\sim 1$  AU) will be traveling around the Sun at nearly the same rate as Earth and, therefore, have very long synodic periods relative to Earth (decades or, in some cases, centuries). The synodic period is the amount of time required for the orbital geometry between Earth and the NEA to repeat. Thus, while an NEA with a very Earth-like orbit may spend substantial time loitering in Earth’s vicinity, it will then spend much more time slowly pulling ahead of or falling behind Earth as both objects orbit the Sun. Such an NEA will then spend a long period of time very far from Earth, during which it is neither observable via Earth-based telescopes nor readily accessible for spacecraft missions. Thus, one of the factors that makes an NEA very accessible (semimajor axis near 1 AU) during certain favorable time windows (when the NEA is near Earth) also makes that NEA unobservable and inaccessible for long

periods of time between the comparatively brief seasons of observability and mission accessibility.

### 3.2. Near-Earth Asteroid Population Estimates

As of June 9, 2015, the number of known NEAs is 12,697, and the current rate of NEA discovery is approximately 1000 to 1500 per year. NEAs are further classified according to both composition and orbit (see the chapters by Binzel *et al.* and Mainzer *et al.* in this volume). The four NEA orbital groups are Amors (exterior to Earth’s orbit), Apollos (Earth-crossing, semimajor axis  $>1$  AU), Atens (Earth-crossing, semimajor axis  $<1$  AU), and Atiras (interior to Earth’s orbit). Some NEAs are also classified as “potentially hazardous” based on minimum orbit intersection distance (MOID) to Earth of  $\leq 0.05$  AU and their estimated diameters (see the chapters by Binzel *et al.* and Farnocchia *et al.* in this volume). The number of known potentially hazardous asteroids (PHAs) as of June 9, 2015, is 1592.

Current estimates for the NEO population survey completeness are based on work published by Mainzer *et al.* (2011), wherein the NEOWISE results lead to debiased NEO population estimates. Based on those results (see the chapter by Jedicke *et al.* in this volume), the total number of NEAs  $>1$  km in diameter is  $\sim 1000$ , of which  $\sim 70$  remain undiscovered, and the total number of NEAs 100 to 1000 m in diameter is  $\sim 19,500$ , of which  $\sim 15,000$  remain undiscovered. Insufficient data are available to precisely estimate the total number of NEAs  $<100$  m in diameter. However, previous modeling suggests that there are on the order of  $10^6$ – $10^8$  undiscovered NEAs  $<100$  m in diameter.

The subpopulation of potential NEA exploration targets may be considered in relation to the entire NEA population by examining the set of NHATS-compliant NEAs and its relationship to the overall population. There are currently 1245 known NHATS-compliant NEAs (11% of known NEAs). Table 1 presents their distribution among the four NEA orbit groups, while Fig. 3 shows the relationships between orbit semimajor axis, eccentricity, and inclination for the NHATS-compliant NEAs according to orbit group. Note that the term semilatus rectum,  $p$ , represents a property of the elliptical path followed by an orbit. It is a function of the orbit semimajor axis,  $a$ , and eccentricity,  $e$ , as follows:  $p = a(1-e^2)$ . In terms of the ellipse geometry, the semilatus rectum is half the length of the chord passing through the

TABLE 1. Currently known NHATS-compliant NEAs by orbit group.

NEA Orbit Group	All NEAs	NHATS NEAs	NHATS Portion of Orbit Group	Orbit Group Portion of NHATS
Atiras	14	0	0	0
Atens	864	289	23%	33%
Apollos	6112	742	60%	12%
Amors	4370	214	17%	5%

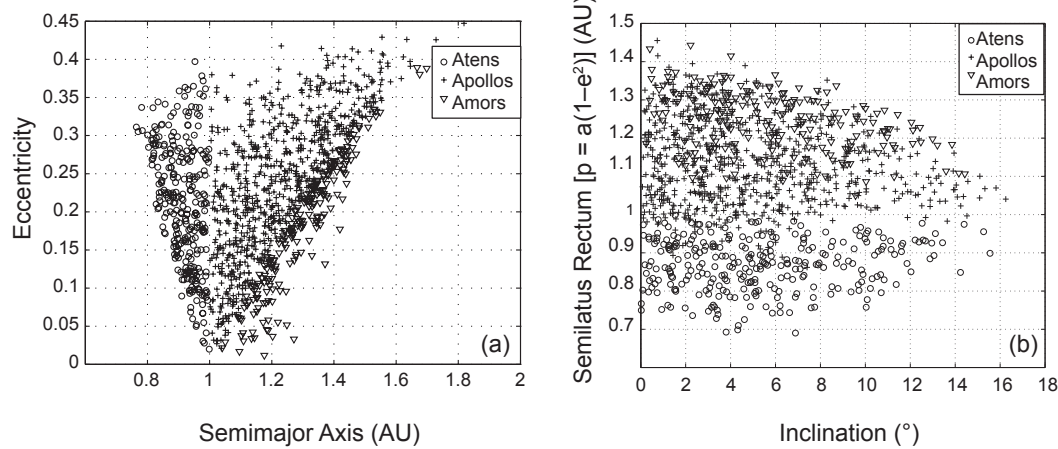


**Fig. 3.** Semimajor axis vs. eccentricity and inclination vs. semilatus rectum for the NHATS-compliant NEAs by orbit group.

ellipse focus, running perpendicular to the line of apsides. Because it is a function of semimajor axis and eccentricity, the semilatus rectum also describes the energy of the orbit. Note that asteroids with Earth-like orbits will have a value of  $p$  near 1 AU.

The majority of the currently known NHATS-compliant NEAs (60%) are Apollos, yet only 12% of the currently known Apollos are NHATS-compliant. Furthermore, 33% of Atens are NHATS-compliant, yet Atens are currently a minority among NEAs at ~8% of the known NEA population. This phenomenon is investigated in *Adamo and Barbee* (2011) and may lead to an improved understanding of where the most accessible NEAs tend to reside in orbital element space.

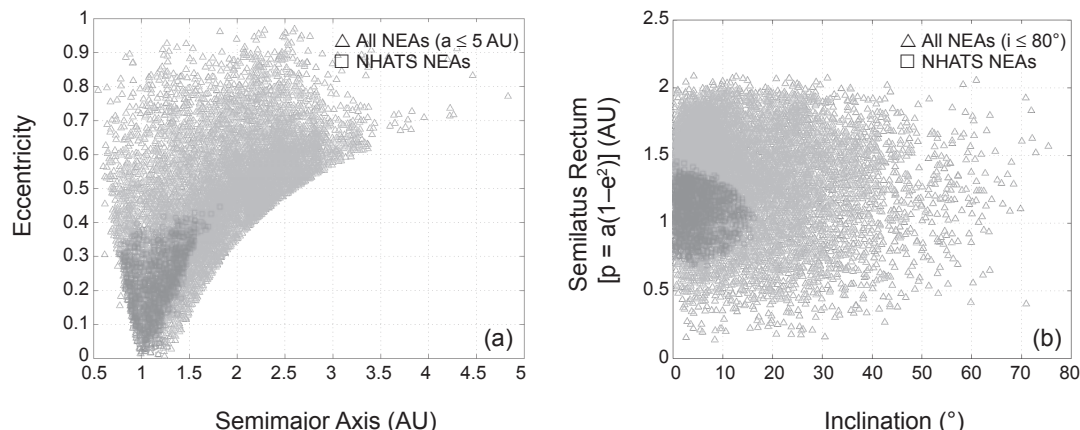
Figure 4 presents the relationships between semimajor axis, eccentricity, and inclination for the NHATS-compliant NEAs in comparison to all known NEAs. Note that seven NEAs are excluded from Figs. 4a,b because their orbit semimajor axis is  $>5$  AU, and/or their orbit inclination is  $>80^\circ$ , which would adversely affect the scales of the plots. While the NHATS-compliant NEAs have more Earth-like orbits

TABLE 2. Uncorrelated statistics for NHATS-compliant NEA orbital elements.

Orbital Element	Minimum	Mean	Maximum
Semimajor axis (AU)	0.764	1.163	1.819
Eccentricity	0.012	0.224	0.447
Inclination	0.021°	5.180°	16.253°

than other NEAs, as expected, the extent to which NHATS-compliant NEA orbits can deviate from being Earth-like is notable. Table 2 summarizes the uncorrelated minimum, mean, and maximum values for NHATS-compliant NEA orbit semimajor axes, eccentricities, and inclinations.

Table 2 clearly indicates that the mean NHATS-compliant NEA orbit is rather Earth-like, although the mean orbital inclination of  $5.180^\circ$  is displaced from the ecliptic plane where Earth's mean orbit plane resides. Orbit inclination is a significant driver of the total  $\Delta v$  required for a spacecraft to visit an NEA, so the maximum NHATS-compliant NEA



**Fig. 4.** Semimajor axis vs. eccentricity and inclination vs. semilatus rectum for the NHATS-compliant NEAs and all known NEAs.

inclination of  $16.253^\circ$  is noteworthy. However, this must be considered in the context of Figs. 3b and 4b, which show that NHATS-compliant NEAs with high inclination have semilatus rectum values near 1 AU; this value is commensurate with the energy level of Earth's orbit (as determined by semimajor axis and eccentricity). Thus, the higher NEA orbit inclinations can only be tolerated by the  $\Delta v$  budget when the NEA's semimajor axis and eccentricity are quite Earth-like.

Figure 5 presents histograms showing the distributions of orbit semimajor axis, orbit eccentricity, orbit inclination, and absolute magnitude for the known NHATS-compliant NEAs and all known NEAs; these distributions add context to the abbreviated statistics presented in Table 2.

Figure 5d shows the distribution of absolute magnitudes,  $H$ , of the known NHATS-compliant NEAs vs. that for all known NEAs. The mean value of  $H$  is 21.823 for all known NEAs and 24.796 for the known NHATS-compliant NEAs. Since  $H$  can be used as a proxy for asteroid size, the known NHATS-compliant NEAs tend to be smaller, on average, than the overall known NEA population, assuming that the distribution of geometric albedo is similar in the two populations. If the geometric albedo is assumed to be 0.14 (considered representative for the average NEA), the mean diameter of the known NHATS-compliant population is 39 m, while that of all known NEAs is 153 m. However, the ability to draw conclusions about the physical characteristics

of the *total* NHATS-compliant NEA population (including objects not yet discovered) from the currently available data is limited because the data are likely influenced by observational bias; accessible NEAs will tend to closely approach Earth, and smaller (less bright) NEAs are often only detectable when near Earth.

### 3.3. Dynamical Considerations for the Entire Near-Earth Asteroid Population

The aforementioned role of observational bias may also be evident in the relationship between minimum round-trip  $\Delta v$  for the NHATS-compliant NEAs and their absolute magnitudes, shown in Fig. 6a, which indicates that the more accessible (lower  $\Delta v$ ) NEAs also tend to be smaller (i.e., have larger absolute magnitudes). Nevertheless, Fig. 6a also shows that there are some rather bright ( $\sim 100$ -m-class) NEAs for which the round-trip  $\Delta v$  requirements are modest.

A consequence of accessible NEAs occupying Earth-like orbits is that the synodic period between such NEAs and Earth can be large. This is shown in Fig. 6b, which presents the minimum round-trip  $\Delta v$  for the NHATS-compliant NEAs vs. their synodic periods relative to Earth. Figure 6b shows only synodic periods  $< 30$  years so that the plot scale allows the fine structure of interest to be visible. Not included in Fig. 6b are the several dozen NHATS-compliant NEAs with

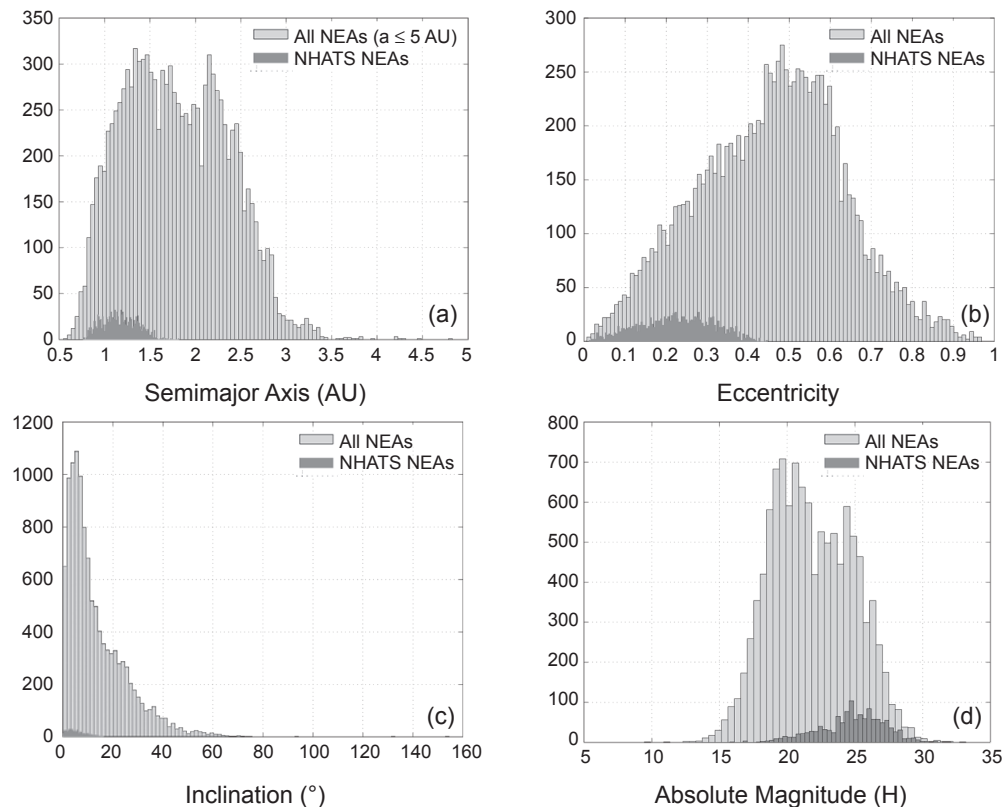


**Fig. 5.** Distributions of orbit semimajor axis, orbit eccentricity, orbit inclination, and absolute magnitude for the known NHATS-compliant NEAs and all known NEAs.

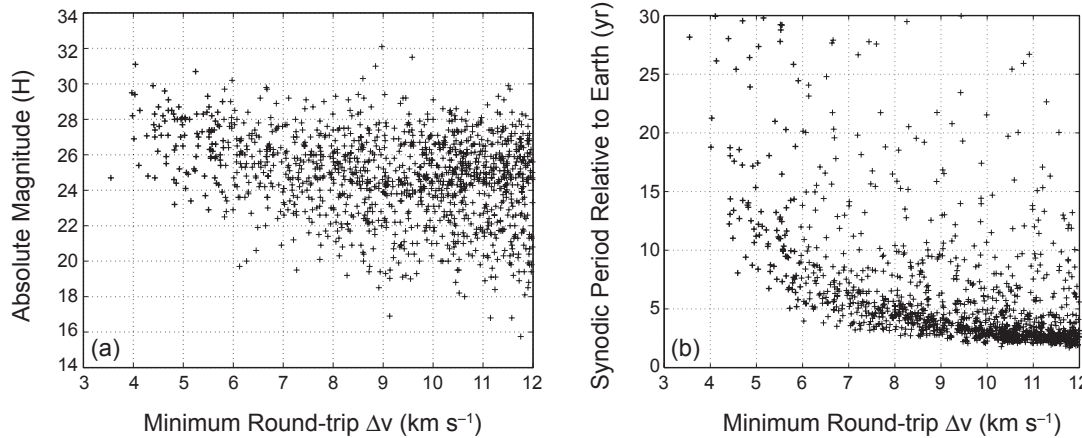


**Fig. 6.** NHATS-compliant NEA minimum round-trip  $\Delta v$  vs. (a) absolute magnitude and (b) synodic period relative to Earth.

synodic periods  $>30$  years; approximately one-third of those have a synodic period between one and several centuries, although the synodic period calculation can be misleading for such cases (Adamou, 2013). Care must be exercised when computing the synodic period relative to Earth for NEAs with very Earth-like orbits. For example, NEAs on “horseshoe” orbits, which are oscillating orbits as seen from Earth, will tend to have effective synodic periods (i.e., the elapsed time between close encounters with Earth) that are much smaller than what the typical synodic period calculation reports using the standard equation based on Keplerian orbit dynamics. Figure 6b shows that the most accessible NEAs have relatively large synodic periods, on the order of one to several decades.

However, Fig. 6b also shows that there are a number of NEAs with low to modest round-trip  $\Delta v$  requirements and relatively small synodic periods approaching five years or less. Note that the NEAs with large synodic periods *and* large  $\Delta v$  requirements are NEAs with very Earth-like semimajor axes (near 1 AU), but high orbit inclinations and/or orbit eccentricities. Large synodic periods mean that accessible NEAs discovered when they are near Earth will not return to Earth’s vicinity for a considerable amount of time after departing; this clearly complicates efforts to deploy missions to such NEAs. A spacebased survey telescope stationed far from Earth would be capable of discovering accessible NEAs before they closely approach Earth, potentially affording enough advance notice to plan and execute human and/or robotic missions to those NEAs.

The tendency of known NHATS-compliant NEAs to closely approach Earth is further illustrated by comparing them to known PHAs. An NEA is classified as a PHA if its MOID with Earth’s orbit is  $\leq 0.05$  AU and its absolute magnitude H is  $\leq 22$ . Currently, 1034 of the known NHATS-compliant NEAs (83%) have Earth MOID  $\leq 0.05$  AU and compose 21% of all known NEAs with Earth MOID  $\leq 0.05$  AU. However, only 178 known NHATS-compliant NEAs (14%) have H  $\leq 22$ . The number of known NHATS-compliant NEAs that are classified as PHAs (both Earth MOID  $\leq 0.05$  AU and H  $\leq 22$ ) is 115.

Thus, only 9% of the currently known NHATS-compliant NEAs are also classified as PHAs, but this is largely based on their H values rather than their Earth MOID values, meaning these asteroids are too small to be formally classified as PHAs.

Additionally, although the NHATS analysis is specifically designed to identify NEAs that are particularly accessible for round-trip human space flight missions, it also has a more general use. NHATS-compliant NEAs will tend to be generally accessible for other types of missions, including one-way or round-trip robotic missions involving longer mission durations and more complicated flight plans (e.g., incorporating additional deep-space maneuvers, gravity assist planetary flybys, etc.). For example, almost every NEA that has been visited, is currently scheduled to be visited, or has been seriously considered as a potential target for funded robotic science missions has turned out to be NHATS-compliant. Examples include (25143) Itokawa (1998 SF<sub>36</sub>), (101955) Bennu (1999 RQ<sub>36</sub>), (162173) Ryugu (1999 JU<sub>3</sub>), and (341843) 2008 EV<sub>5</sub>, all of which are also classified as PHAs. Itokawa was visited by JAXA’s Hayabusa (samples returned in 2010), Bennu will be visited by NASA’s OSIRIS-REx (launch in 2016 with samples to be returned in 2023), and Ryugu will be visited by the Japan Aerospace Exploration Agency’s (JAXA) Hayabusa2 (launched on December 3, 2014, with samples to be returned in 2020). In addition, 2008 EV<sub>5</sub> was the target of the European Space Agency’s (ESA) proposed MarcoPolo-R sample return mission, but the mission was not selected for funding. In summary, the subpopulation of NHATS-compliant NEAs provides an excellent starting point for identifying low- $\Delta v$  candidate targets for a wide variety of possible mission types.

Table 3 summarizes the properties of selected accessible NEAs. These NEAs were selected by querying NASA’s NHATS website for NEAs offering mission opportunities that meet the following criteria:  $\Delta v \leq 6 \text{ km s}^{-1}$ , total mission duration  $\leq 360$  days, stay time at NEA  $\geq 8$  days, and Earth departure dates between the years 2020 and 2030. These criteria are considered notionally representative of an accessible NEA. As expected, these NEAs all occupy relatively Earth-like orbits

TABLE 3. Selected accessible NEAs and their physical, orbital, and accessibility properties.

NEA	H	Est. Diameter (m)	OCC	a (AU)	e	i	Minimum $\Delta v$ Solution		Minimum Duration Solution		Spectral Type	Rot. Period (h)	Radar Observed
							$\Delta v$ (km s <sup>-1</sup> )	Duration (d)	$\Delta v$ (km s <sup>-1</sup> )	Duration (days)			
2007 YF	24.8	19–85	5	0.953	0.120	1.652°	5.89	258	5.965	250	?	?	No
2013 WA <sub>44</sub>	23.7	32–142	3	1.100	0.060	2.302°	5.936	354	5.936	354	?	?	No
2012 BB <sub>14</sub>	25.0	17–78	3	1.064	0.099	2.645°	5.453	354	5.985	338	?	?	No
2009 HC	24.7	20–89	4	1.039	0.126	3.778°	4.627	354	5.975	306	?	?	No
2001 CQ <sub>36</sub>	22.5	68	0	0.938	0.178	1.261°	5.824	354	5.993	338	?	?	Yes
2012 PB <sub>20</sub>	24.9	18–81	4	1.054	0.095	5.839°	5.82	354	5.969	346	?	?	No
2000 SG <sub>344</sub>	24.7	20–89	2	0.978	0.067	0.111°	3.556	354	5.973	114	?	?	No
2015 JD <sub>3</sub>	25.7	12–55	4	1.058	0.009	2.730°	5.048	354	5.983	306	?	?	No
2014 KF <sub>39</sub>	25.3	15–68	2	1.041	0.079	3.644°	5.634	354	5.978	338	?	?	No
2011 UX <sub>275</sub>	25.8	12–54	6	1.035	0.076	4.541°	5.903	354	5.903	354	?	?	No
2011 BP <sub>40</sub>	25.4	14–65	7	1.121	0.151	0.913°	5.848	330	5.964	306	?	?	No
2015 BG <sub>92</sub>	25.1	17–74	3	1.050	0.057	7.744°	5.218	178	5.911	162	?	?	Yes
2014 JV <sub>54</sub>	25.8	12–54	2	1.043	0.060	7.746°	5.978	354	5.978	354	?	?	No

and their optimal mission opportunities tend to involve flight times of approximately six months to one year. Note that only two of these NEAs have been observed by radar, and none of them have a known spectral type or rotation period; additional characterization of these and other accessible NEAs is greatly needed, though challenging to accomplish using only groundbased observing assets. That said, the diligence of the current groundbased surveys is evidenced by the fact that most of these accessible NEAs have an orbit condition code (OCC)  $\leq 5$ . The OCC is a 0 to 9 integer scale measuring how well an NEA's orbit is known, and numerous high-quality observations are needed to provide good knowledge of an NEA's orbit. An OCC  $\leq 5$  is accepted as a notional threshold for an NEA not being "lost" (not locatable in the sky at what should be its next apparition). Note that it is generally required that OCC = 0 before launching a spacecraft to an NEA. Finally, not shown in Table 3 are the departure declinations associated with the mission trajectory solutions. For the trajectories given in Table 3, the associated Earth departure declinations vary between 8° and 62°, with an average of approximately 33°. The departure declination is a significant mission parameter because if the absolute value of the declination is larger than the launch site latitude, then additional out-of-plane  $\Delta v$  will be required to reach the Earth departure hyperbola, thus reducing the mass performance of the launch vehicle. For reference, the latitude of NASA's Kennedy Space Center (KSC) is 28.5°.

Even though the NHATS analysis system was designed and implemented prior to the conception of NASA's proposed Asteroid Redirect Mission (ARM), which seeks to capture and return a multi-ton boulder from a large NEA and place it in a lunar distant retrograde orbit (LDRO) for human visitation, the mission accessibility of NEAs classified as NHATS-compliant is sufficiently general that candidate ARM targets also tend to be NHATS-compliant.

Figure 7 illustrates the concepts described above by comparing the round-trip mission accessibility of selected NHATS-compliant NEAs to the accessibility of an object in LDRO (see section 5 for a discussion of ARM robotic mission options). For reference, the  $\Delta v$  and round-trip duration requirements for visiting the LDRO are approximately 4.5 km s<sup>-1</sup> and 25 days, respectively, where 5 of the 25 days are spent at the NEA. The data in Fig. 7 demonstrate that the most accessible of the NHATS-compliant NEAs have mission accessibility approaching that of an NEA in LDRO. However, this comparison can be extended and tied to the discussion of NEA accessibility during discovery epochs by applying the NHATS algorithm to selected NHATS-compliant NEAs during the timeframe surrounding their discovery epochs. That analysis was performed for 2006 RH<sub>120</sub> and 2009 BD, the former of which was discovered when it was temporarily captured by Earth from approximately September 2006 through June 2007.

The results show that 2006 RH<sub>120</sub> could have been visited using a total  $\Delta v$  of only 4.451 km s<sup>-1</sup> and a round-trip mission duration of only 58 days in mid-January 2007, while 2009 BD could have been visited for a total  $\Delta v$  of 5.998 km s<sup>-1</sup> and a round-trip mission duration of 50 days in mid-April 2011.

Thus, both 2006 RH<sub>120</sub> and 2009 BD were at their most accessible locations near the times when they were discovered, and their accessibilities during those times, especially that of 2006 RH<sub>120</sub>, rival that of an NEA in LDRO. Note that the mid-April 2011 launch for 2009 BD would have come about two years after its discovery and so a sufficiently long observation arc could have been obtained to characterize its orbit and ascertain that it was not an artificial object. However, 2006 RH<sub>120</sub> did not even receive its minor planet designation until February 2008, so January 2007 would have been much too early to launch a mission to the NEA.

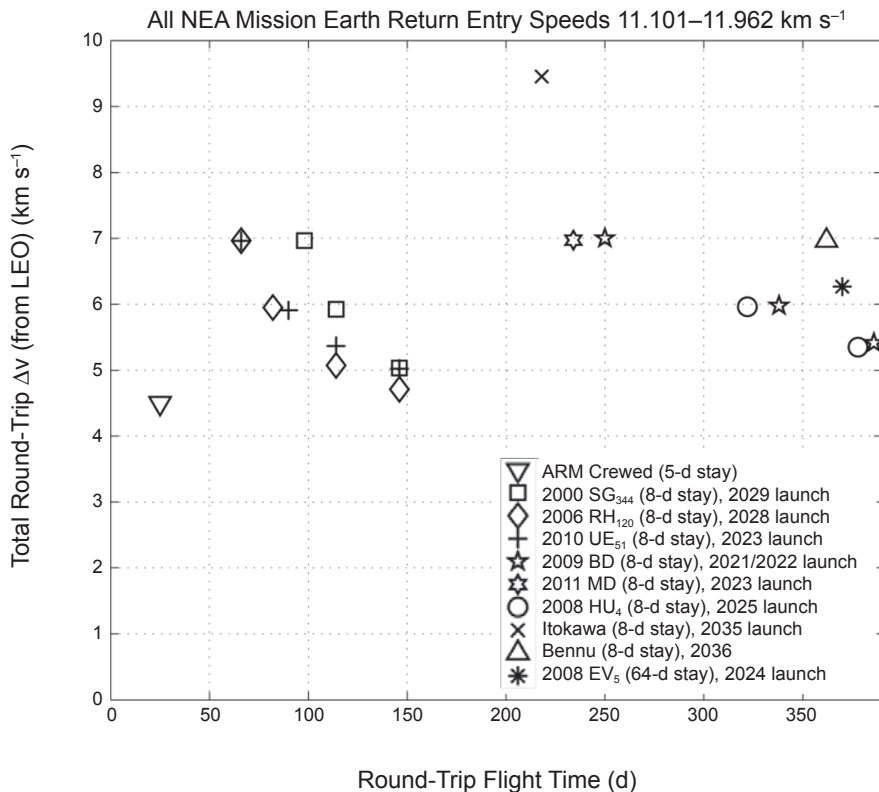


**Fig. 7.** Comparison of round-trip mission accessibility for selected NHATS-compliant NEAs and an entire small NEA or captured boulder in LDRO.

These results serve to emphasize (1) how accessible NEAs can be in their natural orbits, and (2) that a spacebased telescope stationed far from Earth would be needed to discover and characterize NEAs sufficiently far in advance of their peak mission accessibility seasons to enable missions for which we would otherwise not have enough advance notice.

### 3.4. Near-Earth Object Human Spaceflight Accessible Targets Study Algorithm

The NHATS algorithm uses the method of embedded trajectory grids (Barbee et al., 2010, 2011, 2013) to perform a comprehensive analysis of available round-trip trajectories to a particular NEA. The notional mission sequence is depicted in Fig. 8, which illustrates the four key parameters that must be varied in order to identify optimal round-trip trajectories to an NEA: (1) Earth departure epoch, (2) time of flight to reach the NEA, (3) stay time at the NEA, and (4) duration of return flight to Earth. The method of embedded trajectory grids is utilized to efficiently compute solutions for all combinations of those parameters within a four-dimensional parameter space and locate optimal solutions (e.g., minimum total mission  $\Delta v$  or minimum total mission duration). Each of the four key parameters are stepped through at eight-day intervals.

The NHATS trajectory constraints are shown in Table 4. These constraints were developed in 2010 by a human exploration committee, and the constraint values were selected

such that any mission meeting the constraints would be less demanding (e.g., in terms of  $\Delta v$  and/or duration) than any round-trip mission to Mars (e.g., conjunction class, opposition class, short stay, long stay, or Mars free-return flyby; all with or without Venus gravity assist).

The Earth departure  $C_3$  is twice the specific (per unit mass) energy of the spacecraft with respect to Earth. The total mission  $\Delta v$  is the sum of the following  $\Delta v$  maneuvers: (1) departure from a circular 400-km-altitude LEO; (2) NEA arrival (matching NEA's heliocentric velocity at the time of arrival); (3) NEA departure; and (4) reduction of Earth atmospheric entry speed if necessary (the atmospheric entry speed reduction  $\Delta v$  is modeled as being performed at Earth's gravitational sphere of influence for conservatism; some trajectories will naturally have Earth atmospheric entry speed  $\leq 12 \text{ km s}^{-1}$ ). These calculations use a value of  $3.986004415 \times 10^5 \text{ km}^3 \text{ s}^{-2}$  for Earth's gravitational parameter and a value of  $6378.136 \text{ km}$  for Earth's radius. The total round-trip mission duration is the sum of (1) the time of flight required to reach the NEA from Earth, (2) the stay time at the NEA, and (3) the time of flight required to return to Earth from the NEA.

The trajectories to/from the NEAs are computed by solving Lambert's problem with precise ephemeris files for Earth and NEAs obtained from the JPL Horizons system (<http://ssd.jpl.nasa.gov/?horizons>, accessed June 9, 2015), and using a value of  $1.32712440018 \times 10^{11} \text{ km}^3 \text{ s}^{-2}$  for the Sun's gravitational parameter. The Lambert trajectory solutions

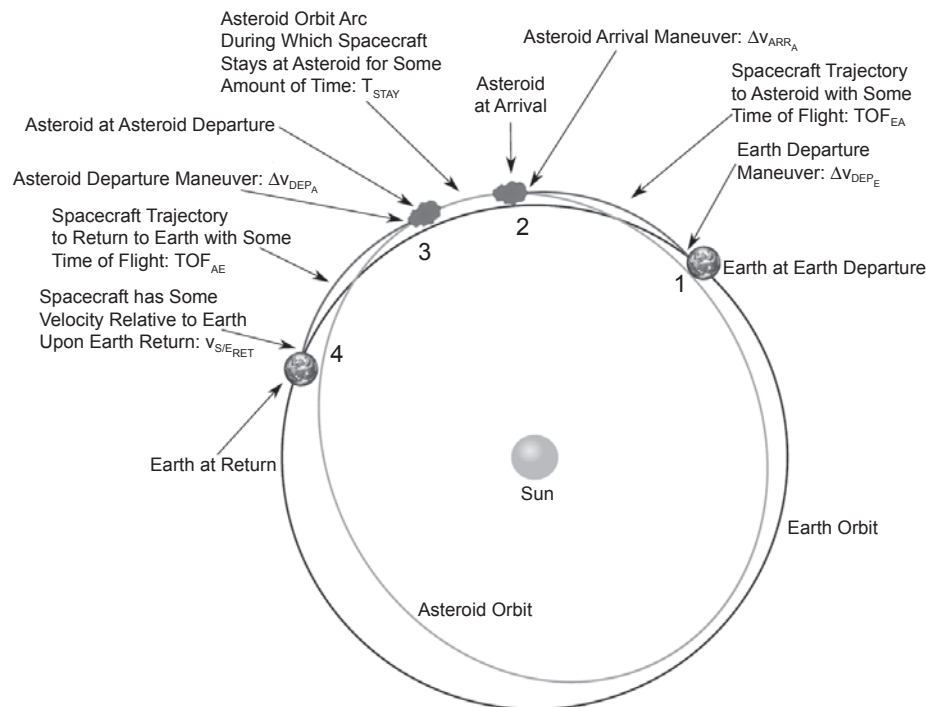


**Fig. 8.** Round-trip mission profile assumed in NHATS.

TABLE 4. NHATS trajectory analysis parameter constraints.

Parameter	Constraint
Earth departure date	2015-01-01 to 2040-12-31
Earth departure $C_3$ ( $\text{km}^2 \text{ s}^{-2}$ )	$\leq 60$
Total mission $\Delta v$ ( $\text{km s}^{-1}$ )	$\leq 12$
Total round-trip mission duration (d)	$\leq 450$
Stay time at NEA (d)	$\geq 8$
Earth atmospheric entry speed ( $\text{km s}^{-1}$ )	$\leq 12$

omit mid-course maneuvers and gravity assists, but those trajectory design techniques are unlikely to be useful when total round-trip mission duration is limited to no more than 450 days. Additionally, the Lambert solutions have been found to be quite accurate when compared to precision trajectory solutions obtained via differential corrections and high-fidelity force models for the spacecraft (Barbee *et al.*, 2011).

The NHATS criteria are defined such that any NHATS-compliant NEA is more dynamically accessible than Mars (and, therefore, the martian moons Phobos and Deimos). Table 5 illustrates this by providing a summary comparison of mission parameters for NHATS NEAs and Mars in various modalities: round-trip visits to the surface of Mars, round-trip visits to a highly elliptical orbit around Mars (no landing) with and without a Venus flyby, and free-return round-trip missions to Mars that neither enter orbit around Mars nor land on the surface of Mars (with and without a Venus flyby). Table 5 shows that no possible Mars mission opportunity of any kind requires both round-trip  $\Delta v \leq$

$12 \text{ km s}^{-1}$  and round-trip duration  $\leq 450$  days. Furthermore, the most aggressive Mars mission options are only sparsely available during particular Earth departure years and entail close approaches to the Sun (Venus orbit distance or less).

It is important to recognize that while the NHATS criterion for  $\Delta v$  extends up to  $12 \text{ km s}^{-1}$ , the most desirable NEA mission opportunities involve total mission  $\Delta v$  of only  $6\text{--}7 \text{ km s}^{-1}$ . Thus, the fact that >1000 NHATS-compliant NEAs are currently known should not be misconstrued to imply that an enhanced survey for additional target NEAs is unnecessary. On the contrary, additional enhanced NEA survey efforts are very much needed.

Thus far a number of NEAs have been discovered that offer very low- $\Delta v$  and short-duration mission opportunities. This point must be kept in mind when considering the NHATS analysis criteria in the context of Table 5. Although these criteria extend up to  $\Delta v$  of  $12 \text{ km s}^{-1}$  and mission duration of 450 days, some NEAs offer mission opportunities requiring much less  $\Delta v$  and shorter mission duration. This is seen in Fig. 9, which depicts the 62,138 round-trip trajectory solutions available in the NHATS website database for the 1245 known NHATS-compliant NEAs. The grid-like nature of the data points is simply an artifact of the binning scheme used within the NHATS website database to keep the data volume manageable (many millions of trajectory solutions are in fact computed and stored outside of the website database). The data points in Fig. 9 represent optimal (minimum  $\Delta v$  and minimum mission duration) round-trip solutions that satisfy NHATS analysis constraints. The solid line in Fig. 9 indicates the minimum  $\Delta v$  from LEO to barely reach Earth escape conditions; the  $\Delta v$  requirement for any viable NEA mission

TABLE 5. Comparison of mission parameters for NHATS NEAs and Mars.

Destination	Round-Trip $\Delta v$ (km s <sup>-1</sup> )	Round-Trip Duration (d)	Stay Time at Destination (d)	Closest Approach to Sun	Earth Departure Year(s)	Notes
NHATS NEAs	$\leq 12$	$\leq 450$	$\geq 8$	Usually near 1 AU	2015–2040	
Lowest $\Delta v$ Mars surface visit	12.530	923	500	Usually near 1 AU	2035	Round-trip to Mars surface
Lowest $\Delta v$ visit to Mars orbit	6.290	923	500	Usually near 1 AU	2035	No landing; stay in elliptical Mars orbit
Very short visit to Mars orbit	12.136	422	7	~0.72	2034	No landing; stay in elliptical Mars orbit
Short visit to Mars orbit (with Venus flyby)	12.813	485	45	0.70	2035	No landing; stay in elliptical Mars orbit
Short visit to Mars orbit (with Venus flyby)	8.120	588	45	0.62	2033	No landing; stay in elliptical Mars orbit
Mars free-return flyby	9.010	501	0	0.73	2018	No landing; no stay in Mars orbit
Mars free-return (with Venus flyby)	6.065	582	0	0.70	2021	No landing; no stay in Mars orbit

Mars mission data taken from NHATS summary chart available at [http://www.lpi.usra.edu/sbag/science/NHATS\\_Accessible\\_NEAs\\_Summary.png](http://www.lpi.usra.edu/sbag/science/NHATS_Accessible_NEAs_Summary.png) (accessed September 12, 2014).

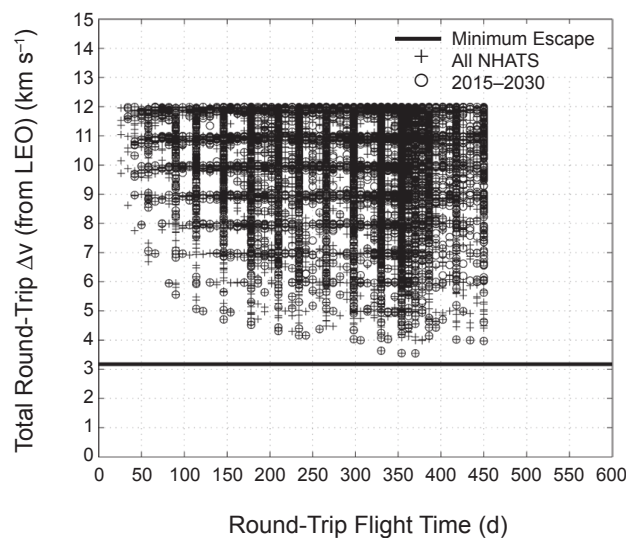


**Fig. 9.** Round-trip  $\Delta v$  and mission duration for selected mission opportunities to the NHATS-compliant NEAs.

trajectory will always be at least slightly higher. Note that several mission opportunities identified by NHATS closely approach this threshold. Also, the data markers in Fig. 9 indicate when particular mission opportunities are available with Earth departure dates between 2025 and 2030; that particular range of years may be programmatically desirable, and marking the data in that way illustrates the concept that NEA missions must launch during certain Earth departure seasons.

For added context, when examining Fig. 9, consider that round-trip missions to a low-altitude circular lunar orbit or the lunar surface require a total mission  $\Delta v$  of 5 or 9 km s<sup>-1</sup>, respectively, and one to several weeks of mission duration. Some of the NHATS mission solutions have durations that begin to approach lunar mission duration, but a substantial number of NHATS mission solutions require less  $\Delta v$  than a lunar mission. Specifically, as of September 12, 2014, there are 522 NHATS-compliant NEAs that can be visited round-trip for less total  $\Delta v$  than a round-trip mission to the lunar surface ( $\Delta v \leq 9$  km s<sup>-1</sup>), and 44 NHATS-compliant NEAs that can be visited round-trip for less total  $\Delta v$  than a round-trip mission to a low-altitude circular lunar orbit ( $\Delta v \leq 5$  km s<sup>-1</sup>). Finally, it is also useful to compare the data points shown in Fig. 9 to the Mars mission data contained in Table 5.

It is illustrative to further examine a particular mission opportunity to an exemplar NEA. Consider NEA 2000 SG<sub>344</sub>, which is currently regarded as the most accessible of the NHATS-compliant NEAs because it offers the overall lowest mission  $\Delta v$  and the largest number of mission trajectory solutions within the NHATS analysis interval. A round-trip mission opportunity to spend 16 days at 2000 SG<sub>344</sub> is available with an Earth departure date of July 14, 2029, a total mission  $\Delta v$  of 4.989 km s<sup>-1</sup>, and a total mission duration of 154 days. The Earth atmospheric entry speed upon return would be 11.157 km s<sup>-1</sup> (nearly as low as the fastest atmospheric entry ever logged by humans: 11.069 km s<sup>-1</sup> during Apollo 10), the minimum distance to the Sun would be 0.976 AU, the maximum distance from the Sun would be 1.027 AU, and the maximum distance from Earth would be only 0.055 AU.

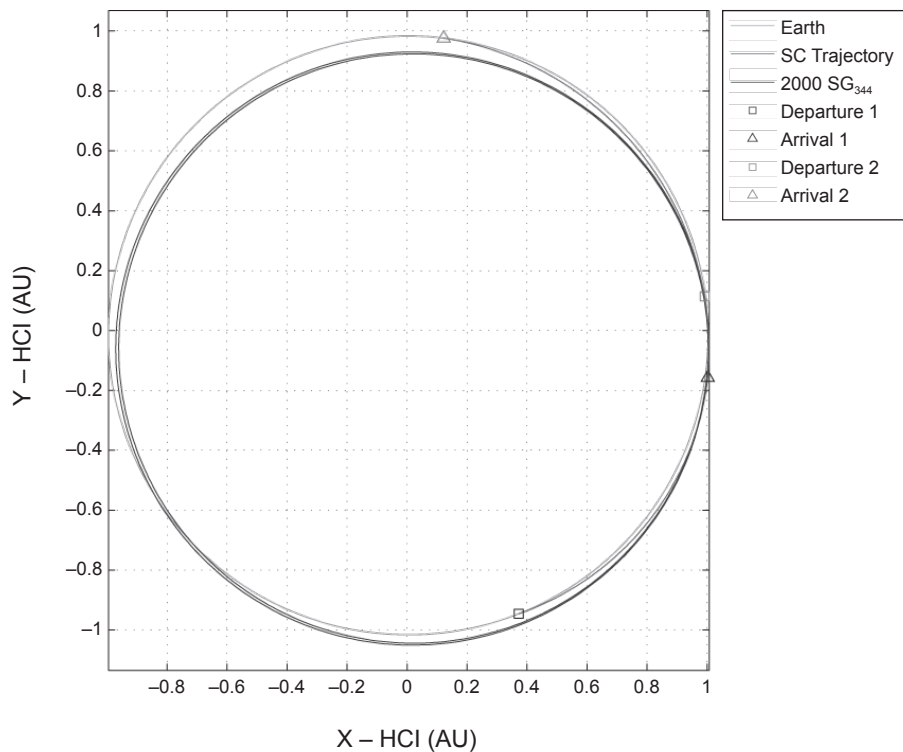


**Fig. 10.** Heliocentric inertial view of a 154-day round-trip mission to NEA 2000 SG<sub>344</sub>.

(21.226 lunar distances). Figure 10 depicts a heliocentric inertial view of the mission trajectory.

#### 4. INTERNATIONAL EFFORTS AND CONTRIBUTIONS

##### 4.1. Japanese Perspective

**4.1.1. Hayabusa and Hayabusa2 missions.** Asteroid sample return missions are regarded as one of the most important space goals for space-related science and engineering in Japan. The successful Hayabusa mission (see the chapter by Yoshikawa et al. in this volume), conducted by JAXA, was the world's first attempted asteroid sample return mission. The second such mission, Hayabusa2, is currently underway (Yoshikawa et al., 2014).

Hayabusa was launched in May 2003, arrived at its target asteroid (25143) Itokawa in September 2005, and returned to Earth in June 2010. After its seven-year voyage, the Hayabusa spacecraft successfully returned asteroidal surface material from Itokawa, although much less than was originally hoped for. The curation facility, located at JAXA's Sagamihara Campus, has retrieved approximately 400 particles from the spacecraft's sample catcher to date. In 2012 and 2013, two international Announcements of Opportunity (AOs) related to Itokawa particles were issued, and the samples were distributed to approximately 30 research groups all over the world. Many sample analysis results have already been reported and the analyses are still ongoing (e.g., Yurimoto et al., 2011).

A few years before the return of the Hayabusa spacecraft, JAXA began planning its next asteroid sample return mission, Hayabusa2. Hayabusa was considered an engineering demonstration mission, but Hayabusa2 will primarily focus on science, with a goal of furthering understanding of the origin and evolution of the solar system, particularly as relates to water and organic matter. It is generally understood that C-type asteroids contain more organic matter and hydrated minerals than S-type asteroids such as Itokawa. Therefore, C-type asteroid (162173) Ryugu (1999 JU<sub>3</sub>) was selected as Hayabusa2's target. From a technological point of view, the purpose of Hayabusa2 is to develop more reliable and robust systems for sample return exploration. The scale of the spacecraft is similar to Hayabusa, but many parts have been modified or redesigned to prevent most of the difficulties experienced by the Hayabusa spacecraft. The Hayabusa2 spacecraft will carry new instrumentation as well, such as an impactor that will create a small crater on the surface of the asteroid. The spacecraft launched in December 2014 and is scheduled to arrive at Ryugu in June 2018. It will remain at the asteroid for approximately 18 months, departing in December 2019 and arriving at Earth in December 2020.

**4.1.2. Solar sail missions.** Hayabusa and Hayabusa2 are both considered challenging missions, but JAXA is currently considering an even more challenging mission in which a spacecraft powered by a solar power sail will return a sample from a Jupiter Trojan asteroid (e.g., an asteroid located in the L<sub>4</sub> or L<sub>5</sub> Lagrange points that precede or follow Jupiter in its orbit) (Kawaguchi, 2004). A solar sail is a large mem-

brane that uses the pressure of sunlight to propel a spacecraft; it therefore has no need to consume any propellant as long as it can obtain enough energy from sunlight. A solar power sail is an original Japanese concept in which electrical power is additionally generated by thin-film solar cells on the sail membrane. This power can be used for electrical propulsion to supplement the thrust from photon pressure, thus turning the spacecraft into a hybrid propulsion vehicle. JAXA completed the world's first demonstration of a solar power sail by the Interplanetary Kite-craft Accelerated by Radiation of the Sun (IKAROS), which was launched on an interplanetary voyage in May 2010. IKAROS achieved its primary mission goals during its first seven months, and then entered an extended operation phase at the beginning of 2011 (*Mori et al.*, 2010).

For JAXA's proposed asteroid sample return mission using a solar power sail, the target asteroid will be much further away than either Itokawa or Ryugu. The science purpose of this mission will be to study a D-type asteroid, which is a more primitive asteroid type than Itokawa (S-type) and Ryugu (C-type). JAXA believes that sample return missions from primitive bodies are very important for both the science of the solar system and space mission engineering in general.

Another advantage of the solar power sail concept is that it will allow a deep-space probe powered by the hybrid propulsion of solar photon acceleration and ion engines to explore the outer planetary regions of the solar system without relying on nuclear technology. JAXA is currently planning an outer solar system exploration mission using the demonstrated solar power sail technology. The spacecraft will travel first to Jupiter, where it will perform a flyby of a Trojan asteroid. According to a preliminary mission analysis, a sail ~50 m wide should be deployed for this mission. JAXA plans to initiate the project within the next few years, with the launch occurring in or around 2020. In order to extend the mission's output, the feasibility of an optional sample return mission by a small probe is being studied. That part of the mission would be considered in the extra success category; it is defined as an engineering mission and could take almost 30 years to complete its round trip back to Earth.

**4.1.3. Future activities.** A number of countries, including Japan, have participated in the International Space Exploration Coordination Group (ISECG), which studies human exploration missions from a global perspective. The group released the Global Exploration Roadmap, which identified two representative types of missions to the Moon and the NEAs. The discussion that follows is the preliminary study of JAXA's proposed human missions to the NEAs (JAXA, 2010). This study of human exploration of NEAs looks at the currently known NEO population as accessible targets in the 2015 to 2035 timeframe. All known NEAs are initially considered as potential targets, to keep the initial population as large as possible. The target size is restricted to absolute magnitudes  $H \leq 21.5$ , which corresponds to a diameter range of 130–300 m, thereby minimizing the probability that the target is a superfast rotator (*Pravec et al.*, 2002; Pravec, personal communication, 2015). A restriction of the departure

orbits to free-return trajectories is also considered to provide some amount of safety for the spacecraft crew. The results are evaluated by on-orbit mass requirement, mission duration, target properties, and the overall accessibility of the target. Within these constraints, only a fraction of the 8049 known NEAs (as of May 2011) fulfill the mission requirements imposed by safety considerations and scientific value without exceeding the already high on-orbit mass limit of 500 metric tons. The number of accessible target asteroids in the next 20 years is thereby limited to a total of three, with the asteroid (99942) Apophis being the most likely candidate.

Removing the restriction to free-return trajectories can be another option to reduce mass and increase the number of available targets, although the increased risk must be taken into account and possibly mitigated by additional safety features. Other mission scenarios, going beyond the scope of the presented baseline mission, have yet to be investigated in detail. These scenarios include the launch of supplies and payloads to the asteroid ahead of the crewed spacecraft, as well as the use of a Deep-Space Port (DSP) at the Sun-Earth or Earth-Moon Lagrange points.

Japan and JAXA intend to take part in NASA's proposed ARM (see section 5) by making robotic and/or human architecture contributions to the mission. In addition, JAXA intends to collaborate with international partners to contribute to the planetary defense activity represented by either NASA's Grand Challenge initiative or the activities proposed by the Technical Subcommittee of the United Nations Committee on the Peaceful Uses of Outer Space (COPUOS). For this purpose, JAXA will continue its efforts to discover new NEAs. In turn, the increasing discovery rates of NEAs in recent years will increase the chances of finding better targets than those that are currently available, in addition to improving the identification of possibly hazardous objects.

## 4.2. European Perspective

ESA has performed several studies of space missions to asteroids in the last decade and has successfully conducted two asteroid flybys (one in 2008, the other in 2010) with its probe Rosetta. Rosetta reached its final target, Comet 67P/Churyumov-Gerasimenko, in August 2014, and for the first time performed the successful deployment of a lander, called Philae, on a comet's surface in November 2014.

**4.2.1. Mitigation missions to near-Earth asteroids.** In July 2002, the general studies program of ESA funded preliminary studies of six space missions, three observational and three rendezvous and/or deflection missions, that could make significant contributions to our knowledge of NEAs. Following the presentation of the study results, ESA's Near-Earth Object Mission Advisory Panel (NEOMAP) was established in January 2004. NEOMAP, which consists of six European scientists active in studies of NEAs, was charged with the task of advising ESA on cost-effective options for ESA participation in an asteroid space mission to contribute to the understanding of the terrestrial impact hazard and the physical nature of NEAs. In particular, NEOMAP was charged with:

- identifying the advantages of, and defining a solid rationale for, the utilization of space missions for the assessment of the impact hazard;
- identifying which of those advantages would best complement groundbased observations and data;
- revising the scientific rationale for the six missions studied in the light of current knowledge and international initiatives; and
- producing a set of prioritized recommendations for observatory and rendezvous missions in an international context.

Taking all factors into account, NEOMAP unanimously agreed that the proposed rendezvous mission concepts were of significantly higher priority in terms of risk assessment and mitigation than the observatory mission concepts. At the time of the NEOMAP work, it was expected that ground-based facilities, such as Pan-STARRS, would be operational before any of the considered space observatory missions were launched. Therefore, it was expected that an 80–90% discovery rate for  $H < 20.5$  bodies would have been achieved within the next decade even without space observatory missions. For that reason, NEOMAP decided to reconsider a spacebased NEO observatory mission in 10–15 years once the residual hazard of NEOs that are unobservable from groundbased surveys has become better defined. In particular, NEOMAP noted that the ability to change the orbit of an NEO has not yet been demonstrated, so a vital link in the chain from threat identification to threat mitigation is missing.

Of the three rendezvous missions reviewed, NEOMAP considered the Don Quijote mission concept to be most compatible with the criteria and priorities established in their report. This concept involves an orbiter that would characterize the asteroid target, followed six months later by a hypervelocity vehicle that would impact the target. The orbiter would then observe the event and measure the deflection resulting from the impact. Don Quijote was considered to have the potential to discover a great deal, not only about the internal structure of an NEO, but also how to mechanically interact with it; it was also judged capable of providing the vital missing link between threat identification and mitigation. NEOMAP also felt that the Don Quijote concept could readily attract the attention of potential partners outside of ESA. A Phase A study was performed in 2007 but no actual plan was made to study the concept further, despite the recommendation from the international community to perform such a test (*National Research Council of the National Academies*, 2010; *International Academy of Astronautics*, 2013).

In 2011, ESA, NASA, the Applied Physics Laboratory (APL) of The Johns Hopkins University (JHU), the Côte d'Azur Observatory, and the German Space Agency (DLR) began a study of a mission similar to the Don Quijote concept called the Asteroid Impact and Deflection Assessment (AIDA) mission. This mission would be the first to actually demonstrate asteroid impact hazard mitigation by using a kinetic impactor to deflect an asteroid.

At the time of this writing, AIDA is a joint ESA-NASA cooperative project, which includes the ESA Asteroid Impact Mission (AIM) rendezvous spacecraft and the NASA Double Asteroid Redirection Test (DART) mission. AIM is equipped with a visual imaging system, a small lander, a thermal infrared imager, a high-frequency (decimeter-wave) radar, and a low-frequency (60-MHz) radar, to measure surface and subsurface physical properties and to study internal structures. AIM also includes an interplanetary optical communication demonstration that can be used as a laser altimeter and an intersatellite link with its deployed CubeSat payloads. The DART payload consists of a high-resolution visible imager to support the primary mission objective of impacting the target body through its center. The DART imager is required to support optical navigation on approach and autonomous navigation in the terminal phase.

The AIM study entered Phase A/B1 at ESA in early 2015 and will proceed through summer 2016. The DART study should enter NASA Phase A in early fall 2015 and will also proceed through summer 2016. ESA and NASA will decide whether to proceed to the next phases of AIM and DART, respectively, in early 2017.

The primary goals of AIDA are to (1) investigate the binary NEA (65803) Didymos, (2) test our ability to impact its moon with a hypervelocity projectile in 2022, and (3) measure and characterize the impact deflection both from space with AIM and from groundbased observatories. AIM is not meant to be a purely scientific mission but rather a demonstration of several technologies that can then be applied to future missions. However, AIM will drastically improve our scientific knowledge of small asteroids in terms of asteroid geophysics, granular mechanics, impact processes, and thermal effects/properties. It is worth noting that because none of the medium- or large-class missions identified by ESA's Cosmic Vision Program are devoted to asteroids, AIM provides the only opportunity for ESA to conduct an asteroid mission for the next 20 years.

If selected for launch in 2020, AIDA will return fundamental new information on a binary asteroid system; on its mechanical response; on the impact cratering process; and consequently on the collisional evolution of asteroids with implications for planetary defense, human spaceflight, and solar system science. AIDA will be the first fully documented impact experiment at real asteroid scale, allowing numerical codes and modeling to be tested and used for similar and other scientific applications at those scales (see the chapters by Jutzi et al. and Harris et al. in this volume).

**4.2.2. Science missions to asteroids.** In 2004, ESA launched the space mission Rosetta. The primary goal of this mission was to land on Comet 67P/Churyumov-Gerasimenko and obtain data on its physical and compositional properties by performing *in situ* measurements. The spacecraft reached its target in August 2014, and the resultant images quickly showed that the comet's shape and morphology were completely different than anything previously observed. The deployment of the lander Philae was successfully accomplished, although it bounced off the surface and then landed

in a different zone on the comet's surface; its precise location has not been determined at the time of this writing.

In addition, given the current high interest in small bodies, ESA chose a trajectory that allowed multiple asteroid flybys before reaching the final destination. In October 2008, Rosetta encountered the asteroid (2867) Šteins, and in July 2010 it encountered the asteroid (21) Lutetia (see the chapter by Barucci et al. in this volume). With a diameter of approximately 100 km, (21) Lutetia was the largest visited asteroid at that time, before Dawn visited one year later the second largest asteroid in the main belt, (4) Vesta, which is approximately 540 km in diameter (see the chapter by Russell et al. in this volume).

In 2007, the Marco Polo mission was selected by ESA, along with a few other mission concepts, for the assessment study phase of the first medium-class missions of its program Cosmic Vision 2015–2025. Marco Polo's goal was to return a sample from a primitive asteroid in partnership with JAXA. The scientific rationale was highly ranked by ESA committees but the mission was not selected for the next phase because the estimated cost was higher than the allotted amount for a medium-class mission. In 2011, ESA selected a second proposal, called MarcoPolo-R, for the assessment study phase of the third medium-class competition. Thanks to collaboration with APL/JHU and JPL, the new concept, with a lower budget, was proposed for coordination with ESA's Cosmic Vision Call for Proposal. The original target was the primitive binary asteroid 1996 FG<sub>3</sub> (Barucci et al., 2011; Michel et al., 2014). The scientific objectives were similar to those of two other sample return missions in development, namely OSIRIS-REx (NASA) and Hayabusa2 (JAXA), but the selection of a binary target would allow the mission to acquire additional information on the geophysics of such systems, which represent 15% of the NEO population. The target was later changed to asteroid 2008 EV<sub>5</sub>, which is not a binary system. Contrary to the OSIRIS-REx and Hayabusa2 targets, which have albedos below 0.05, 2008 EV<sub>5</sub>'s albedo is moderate for a primitive asteroid, with a value about 0.12, while its spectrum is characteristic of a primitive body (Reddy et al., 2012). In effect, spectroscopic observations strongly suggest that 2008 EV<sub>5</sub> is a particularly primitive object that may have accreted in a volatile-rich region. Its spectrum shares similarities with CI carbonaceous chondrite meteorites, such as Orgueil, believed to represent the most primitive material available on Earth (Reddy et al., 2012). 2008 EV<sub>5</sub> is expected to contain water in the form of hydrated minerals, as well as organics such as amino acids, and may correspond to a transitional object between asteroids and comets. With this target, MarcoPolo-R could therefore make a unique contribution to our better understanding of the origin and evolution of the solar system, Earth, and life itself. Unfortunately, although MarcoPolo-R was ranked first by the ESA Solar System and Exploration Working Group, the ESA Space Science Advisory Committee instead elected to move forward with the PLAnetary Transits and Oscillations of stars (PLATO) mission, which is devoted to the discovery of extrasolar planets. Nevertheless,

both the ESA internal studies as well as industrial studies related to MarcoPolo-R that have been conducted since 2007 have generated valuable information about and experience on small-body sample return missions that will prove useful in the future. In fact, part of the knowledge gained regarding various payloads and operations, particularly as related to guidance, navigation, and technology, is being used in the study of the AIM spacecraft (see section 4.2.1.).

**4.2.3. Human exploration.** Asteroids are not considered a priority destination in ESA's human spaceflight program; the program is primarily focused on the ISS, where significant technological and research achievements have already been realized. Human-tended operations in LEO have enabled Europe to develop critical capabilities in human spaceflight, first with Spacelab in the early 1980s and then through its participation in the ISS program. Major technological achievements include the development and operations of the Columbus laboratory, as well as the development and implementation of the Automated Transfer Vehicle (ATV) cargo supply vehicle. Exploitation of the ISS is foreseen by the ISS partners until at least 2020 and possibly until 2028. The decision of the ESA Council in March 2011 paved the way for European participation in ISS exploitation up to 2020. Moreover, the approval of the development of the European Service Module (ESM) for the NASA Multi-Purpose Crew Vehicle (MPCV), within the framework of an ISS barter agreement, created for the first time a role on the critical path for Europe in human space transportation. This decision not only helps stabilize ESA activities on the ISS up to 2020 but also opens up new perspectives for Europe's role in human missions targeting destinations beyond LEO.

Whereas international space agencies agree that the ultimate goal in this century is to land humans on Mars, the route to achieving this goal is under discussion and a clear international political commitment is still lacking. Current ESA programs aim to advance European exploration goals and developing perspectives for strong European participation in international exploration scenarios beyond 2020.

ESA's strategic interests are realized through cooperation with international partners, in particular NASA and Roscosmos, and in the future possibly also the Chinese Manned Space Agency (CMSA). Considering their already proven or quickly developing capabilities in human space transportation, these partners are in a position to take initiatives in the field of space exploration. Regarding ESA's cooperation with NASA, based on the development of the ESM of the MPCV, a continued production of the ESM for future crew missions could be envisioned. In parallel, ESA could start the development of complementary transportation and technology elements, leveraging its lunar robotic exploration activities, technology demonstrators, and all of the European ISS program elements with the post-2020 LEO exploitation scenario. The ultimate goal is to generate a role for Europe in human missions to the Moon and eventually to Mars. ESA's cooperation with Roscosmos has been formalized in relation to ESA's current contribution to Mars exploration with the ExoMars program. The success of the two ExoMars

missions to be launched in 2016 and 2018 will enable ESA and Europe to fully engage in future robotic exploration missions with their Russian partners. Through the Mars Robotic Exploration Program, ESA is studying post-ExoMars candidate missions designed as technology precursors for Mars sample return missions. ESA is also currently defining and developing, using a step-wise approach, a European contribution to the Russian-led Luna-Resurs (2019) and Lunar Polar Sample Return (2021+) missions, enabling participation in a potential future international lunar human exploration program. Regarding cooperation with China, in recent months ESA and CMSA have been attempting to identify opportunities for collaboration, particularly in the areas of astronaut training and crewed missions.

In conclusion, ESA's Agenda 2015 defines LEO, the Moon, and Mars as its three strategic destinations. On this basis, integrated planning for human spaceflight activities post-2020 is under review, addressing both future engagement in LEO exploitation and participation in human missions beyond LEO. Near-term preparatory activities are currently focused on engaging with international partners in determining future mission scenarios, identifying and defining potential future roles for ESA, and advancing and demonstrating technologies for securing such roles. In particular, the development of the service module for the NASA Orion crew vehicle, implemented in the context of the ISS program, opens further perspectives for European roles in human transportation. Asteroids are viewed with great interest by ESA's science program but are not a priority or even an explicit goal in the exploration program. However, participation in an asteroid mission is not explicitly excluded, due to the collaboration with NASA concerning the development of the ESM for NASA's MPCV. In this context, technologies developed by ESA may be used in NASA human missions to asteroids, which would open the possibility for additional European participation.

## 5. ASTEROID REDIRECT MISSION

A major element of NASA's Asteroid Initiative is ARM, which is a capability demonstration mission that combines robotic and crewed segments to develop, test, and utilize a number of key capabilities that will be needed for future exploration of Mars and other solar system destinations, as well as providing other broader benefits. ARM will develop a high-power solar electric propulsion (SEP) spacecraft and capture a multi-ton boulder (minimum-maximum extent of 1–6 m) from a large NEA 100–1000 m in size (*Mazanek et al.*, 2014), and move the boulder into an LDRO, where it would be accessible for human exploration via flights of the Orion crew vehicle. *Brophy et al.* (2012) originally proposed a robotic mission concept to capture an entire small asteroid (4–10 m in size) to leverage several of NASA's key ongoing activities in human exploration, space technology, and planetary defense, with the collection of a boulder from a large asteroid as an alternate approach. NASA evaluated both mission approaches, designated the Small Asteroid

Capture Option (Option A) and the Robotic Boulder Capture Option (Option B), to determine their feasibility, identify the important differences between them, and evaluate the key risks and figures of merit (FOMs) for each concept. On March 25, 2015, NASA announced the selection of Option B for the robotic segment of ARM.

A major focus of ARM is the development and flight demonstration of a multi-purpose, next generation SEP vehicle. This propulsive element, known as the Asteroid Redirect Vehicle (ARV), will feature higher power levels than ever used before (~40 kW available to the electric propulsion system), test new high-efficiency magnetically shielded electric propulsion Hall thrusters, and provide an essential capability for moving large payloads around the solar system. For the robotic segment, the ARV will be outfitted to enable boulder capture for this first demonstration mission (Fig. 11), but could also become, with minor modifications, a general-purpose tug for deploying cargo modules in support of future human missions to deep-space destinations, such as NEAs and Mars. The ARV is currently planned to launch at the end of 2020 and the duration will be approximately five years between departure and return to the Earth-Moon system. After the boulder has been collected from the parent asteroid and secured, the ARV will demonstrate a planetary defense technique known as an Enhanced Gravity Tractor (EGT). During the EGT phase, the ARV will operate in a halo orbit around the parent asteroid, using the mass of the vehicle and captured boulder to slowly alter the asteroid's orbit (*Mazanek et al.*, 2013, 2015).

Once the ARV, along with its asteroidal payload, has been successfully returned to the Earth-Moon system and maneuvered into the LDRO, the crewed segment of the mission will be conducted. This will consist of an Orion capsule with a two-person crew launched in late 2025 using NASA's Space Launch System (SLS). Orion will first fly by the Moon and then maneuver into the LDRO, where it will rendezvous and dock with the ARV and the captured boulder. The crew will then perform two EVAs to collect asteroid samples and deploy instruments before returning to Earth (Fig. 12). The crewed portion of the mission will last approximately 25 days, and will represent the longest-duration human mission beyond LEO since the Apollo program. Subsequent human and robotic missions to the asteroidal material will also be facilitated by its presence in cislunar space and will benefit scientific and partnership interests, expanding our knowledge of small celestial bodies and enabling the demonstration of mining asteroid resources for commercial and exploration needs.

### 5.1. Rationale and Objectives

To achieve its long-term goal of sending humans to Mars, NASA plans to proceed in a series of incrementally more complex human spaceflight missions. Sending humans on shorter deep-space missions to explore accessible asteroids is a compelling intermediate step toward Mars, but even those missions are a significant leap beyond current capabilities.

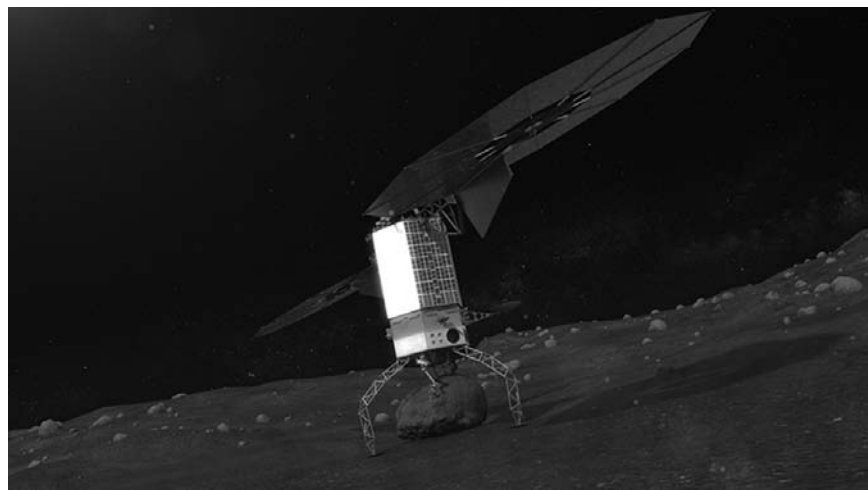


**Fig. 11.** Illustration of ARM robotic segment with ARV on the surface of the parent asteroid.

Today, human flight experience extends only to LEO, from which a crew can return to Earth in a matter of minutes to hours should problems arise during a mission. The next logical step for human spaceflight is to gain flight experience in the vicinity of the Moon. These cislunar missions provide a “proving ground” for the testing of systems and operations while still accommodating an emergency return path to Earth that would last only several days. Cislunar mission experience will be essential for more ambitious human missions to NEAs and eventually Mars, which will require weeks, months, or even years of transit time. Flight hardware to support cislunar Orion missions is already under development, and those missions are scheduled to be launched as early as 2021. The additional habitation modules and crew

propulsive stages needed to support multi-month human missions into deep space are only in the proposal stage, and those flights are clearly many years farther down the road than the proving-ground cislunar flights.

A principle objective of ARM is the development of a high-power SEP vehicle, and the demonstration that it can operate for many years in interplanetary space. NASA has long had plans for developing and demonstrating a next generation “SEP tug” vehicle that would offer a more efficient cargo transportation capability and would be critical for affordable deep-space exploration missions. In particular, current NASA architectures for human missions to Mars or its moons will require large SEP tugs to predeploy support modules, habitation modules, and propulsive stages not

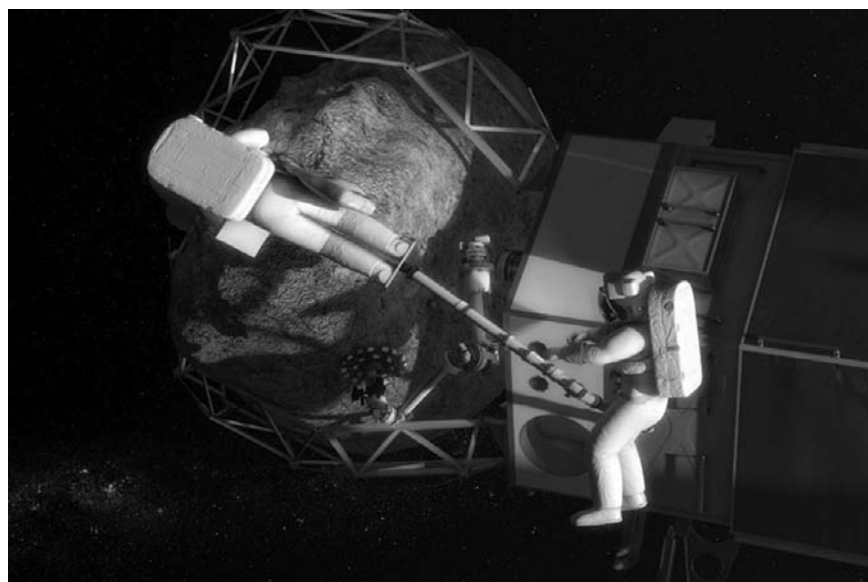


**Fig. 12.** Illustration of ARM crewed segment with astronauts performing an EVA to collect samples from the returned asteroid boulder.

only into cislunar space, but also into Mars orbit (*Price et al.*, 2014).

The ARV developed for ARM will include a general-purpose SEP Module (SEPM) and Mission Module (MM). The majority of ARM's development cost is for the SEPM and MM rather than the asteroid Capture Module (CM), which current estimates predict would only be a minor part of ARM's total cost, and significantly less than the cost of a typical NASA Discovery-class mission. The SEP demonstration could be performed with only cargo modules or ballast, but ARM will allow collection of many tons of asteroidal material and the demonstration of planetary defense techniques at comparatively little additional cost.

A second prime objective of ARM is to conduct a human spaceflight mission involving in-space interaction with a natural object, in order to provide the systems and operational experience that will be required for eventual human exploration of Mars, including the martian moons Phobos and Deimos. ARM provides a compelling science focus for the early flights of the Orion program, which will take place before the infrastructure for more ambitious flights will be available. Astronauts will participate in the scientific in-space investigation of nearly pristine asteroid material, at most only minimally altered by the capture process. ARM will provide the opportunity for human explorers to work in space with unaltered asteroid material, testing the activities that would be performed and tools that would be needed for later exploration of primitive body surfaces in deep space. The operational experience would be gained close to our home planet, with a relatively quick return to Earth if problems should arise. There will also be opportunities to revisit the returned boulder, to further refine asteroid exploration techniques.

Another important objective for ARM is the demonstration of some basic planetary defense techniques that would inform future strategies for impact hazard mitigation. The EGT will use the mass of the spacecraft enhanced by that of the boulder to move the asteroid through mutual gravitational attraction. The acceleration imparted on the parent asteroid will be very small, and the spacecraft will be able to approach the center of mass of the asteroid to within a few hundred meters. Approximately two months of ARV operation will be required to impart a measurable velocity change on the parent asteroid. The tracting duration would likely be much longer if this technique were required for an actual deflection mission, but this amount of time would depend on the size of the impactor and the mass that can be collected. Since the material would not need to be returned to cislunar space for a deflection mission, the collected mass could be much greater, which would significantly enhance the gravitational acceleration. The operational experience gained from performing the EGT technique would be the main benefit of the demonstration.

A final objective for ARM is to pursue a target of opportunity to examine the possible uses of small celestial bodies for *in situ* resource extraction and utilization. The possibility of extracting water and/or oxygen from asteroids has been proposed as the key that might enable affordable expansion of humankind throughout the solar system. Hydrated miner-

als are likely abundant in certain types of carbonaceous (C-type) asteroids, and it is therefore highly desirable to target an asteroid of this class. Because it is easier to obtain high signal-to-noise spectra for large as opposed to small NEAs, it is therefore easier to confirm the presence of volatiles. This definitive spectral information is critical for achieving ARM's resource utilization objectives.

## 5.2. Mission Benefits

ARM provides the ability for the science community to select a well-characterized multi-ton boulder with geological context that astronauts can explore and from which they can return samples. The robotic segment enables centimeter-level characterization over an entire large NEA and the ability to identify the NEA's compositional type (e.g., a water/volatile-rich carbonaceous target), while also being robust to programmatic uncertainties by allowing the return mass to be varied. The robotic segment also provides additional experience operating at a low-gravity planetary body, including extended surface contact critical to future human and robotic missions and the ability to demonstrate one or more planetary defense deflection techniques on an NEA of hazardous size, which will inform planetary defense strategies. The ARV capture module comprises multiple, complementary robotic systems. The Contact and Restraint Subsystem (CRS) consists of three "legs" that facilitate the low-gravity landing (LGL) of the ARV on the asteroid surface, and can be directly extended to enable missions to a wide range of low-gravity, airless bodies. After the LGL is completed, two seven-degree-of-freedom robotic arms will capture the boulder using an innovative microspine gripper and anchoring mechanism. After boulder capture, the CRS will perform the ascent maneuver by mechanically pushing off the asteroid, and later will provide the restraint of the boulder during the ARV's return to cislunar space. The CM robotic elements will demonstrate key capabilities that can be used on many future missions, including delivery of surface assets to NEAs or the martian moons, robotic servicing of spacecraft, and mobility options for exploring other destinations. For example, the robotic arms will include a tool change-out mechanism that allows both for mission-specific tools to be mated to the multi-mission arms, and for tools to be changed during the mission. The microspine gripper could also demonstrate a novel approach for collecting samples on a variety of future human and robotic missions (e.g., anchoring with low-gravity drilling, climbing lava tubes or canyon walls, etc.).

In addition, ARM can change the paradigm of ISRU by delivering many tons of water/volatile-rich carbonaceous asteroidal material to cislunar space where ISRU techniques and equipment can be tested and refined on an industrial scale. These demonstrations can be performed teleoperatedly in this region, with very little latency, from Earth or a crewed spacecraft in cislunar space, and the associated equipment could be serviced by astronauts when needed.

Much of the planetary science community's interest in asteroids is focused on primitive, water/volatile-rich car-

bonaceous targets that could provide valuable information on the formation of our solar system and the origins of life on Earth. ARM allows the return of a well-characterized sample with geological context from an NEA of a known compositional type (e.g., a large carbonaceous boulder and one or more parent-body surface samples). The mission also provides numerous opportunities for mission enhancements to support science objectives, including robotic arm sample collection (e.g., drilling, coring, surface sample collection, and caching), the ability to host and deploy free-flyers or surface rovers/hoppers, and additional scientific instrumentation for *in situ* or remote observation of a large NEA. Additionally, the advanced SEP technologies, instrumentation, and low-gravity-body autonomous operations required for the robotic segment will help enable more capable future robotic missions.

### 5.3. Candidate Near-Earth Asteroid Targets

Four NEAs are currently being considered as selectable targets for ARM: (341843) 2008 EV<sub>5</sub>, (101955) Bennu (1999 RQ<sub>36</sub>), (162173) Ryugu (1999 JU<sub>3</sub>), and (25143) Itokawa (1998 SF<sub>36</sub>). Precursor reconnaissance is planned for two candidate carbonaceous asteroids, Bennu and Ryugu, while one stony asteroid, Itokawa, was visited by JAXA's Hayabusa spacecraft in 2005 (see section 4.1.1 and the chapter by Yoshikawa et al. in this volume). Bennu will be visited by NASA's OSIRIS-REx spacecraft and Ryugu will be visited by JAXA's Hayabusa2 spacecraft; both will

rendezvous with their respective targets in 2018 and provide detailed mapping and characterization of their targets' physical properties. 2008 EV<sub>5</sub> has been well characterized by groundbased radar (signal-to-noise ratio >5000) (Busch et al., 2011) and in the infrared wavelengths with the Wide-field Infrared Survey Explorer (WISE) spacecraft. Groundbased measurements of 2008 EV<sub>5</sub>, Bennu, and Ryugu show that these NEAs are carbonaceous chondrite targets (C-types) that are believed to be water/volatile-rich, possibly containing significant amounts of organic materials (Clark et al., 2011; Reddy et al., 2012; Moskovitz et al., 2013). The physical and orbital properties of the current ARM candidate targets are summarized in Table 6.

It is possible that additional candidate targets for ARM could be identified and sufficiently characterized using radar observations prior to launch of the ARV. A preliminary scan using a ranking parameter and a thrust-limited, multi-revolution Lambert's solver identified numerous asteroids that could be reached with ballistic trajectories and a low enough velocity change ( $\Delta v$ ) needed for significant mass return. Trajectories to over 60 target NEAs with upcoming radar observations were identified, but opportunities for observations with high signal-to-noise ratios to confirm or infer the existence of boulders are limited. But even without additional targets, the existence of three high-value carbonaceous targets (two with planned precursor missions) and the knowledge of a well-characterized target (Itokawa) provide a robust set of candidate NEAs for ARM.

TABLE 6. Physical and orbital characteristics of ARM target NEAs.

Parameter	2008 EV <sub>5</sub>	(101955) Bennu	(162173) Ryugu	(25143) Itokawa
<i>Physical properties</i>				
Dimensions	420 × 410 × 390 m	492 × 508 × 546 m	870 m diameter	535 × 294 × 209 m
Shape	Spheroid	Spheroid	Spheroid	Kidney bean
Volume	0.0352 km <sup>3</sup>	0.0623 km <sup>3</sup>	0.3448 km <sup>3</sup>	0.0184 km <sup>3</sup>
Surface area	0.5195 km <sup>2</sup>	0.786 km <sup>2</sup>	2.37 km <sup>2</sup>	0.393 km <sup>2</sup>
<i>Surface properties</i>				
Taxonomic class	C	B	C	S
Geometric albedo	0.05–0.20	0.03–0.06	0.06–0.08	0.53
Thermal inertia	—	310 J m <sup>-2</sup> K <sup>-1</sup> s <sup>-1/2</sup>	—	750 J m <sup>-2</sup> K <sup>-1</sup> s <sup>-1/2</sup>
<i>Mass properties</i>				
Mass	7.03E+10 kg	7.79E+10 kg	6.90E+11 kg	3.51E+10 kg
Density	2 g cm <sup>-3</sup>	1.3 g cm <sup>-3</sup>	1.0–1.7 g cm <sup>-3</sup>	3.2 g cm <sup>-3</sup>
GM	4.687 m <sup>3</sup> s <sup>-2</sup>	5.20 m <sup>3</sup> s <sup>-2</sup>	46.0 m <sup>3</sup> s <sup>-2</sup>	2.34 m <sup>3</sup> s <sup>-2</sup>
<i>Rotational properties</i>				
Rotation period	3.725 h	4.297 h	7.627 h	12.132 h
Direction of rotation	Retrograde	Retrograde	—	Retrograde
Pole position	77.6°, -82.3°	45°, -88°	—	355°, -84° ± 5°
<i>Orbital properties</i>				
Apoapsis	1.038 AU	1.3558877 AU	1.416 AU	1.695 AU
Periapsis	0.878 AU	0.89689433 AU	0.963 AU	0.953 AU
Inclination	7.4369°	6.0349°	5.884°	1.622°
Orbital period	342.658 d	436.649 d	211.437 d	556.355 d
Orbital condition code (OCC)	0	0	0	0

## 6. HUMAN MISSIONS TO NEAR-EARTH ASTEROIDS

### 6.1. Target Identification and Characterization

**6.1.1. Near-Earth object (NEO) survey telescope.** The most suitable targets for human missions are NEAs in Earth-like orbits with long synodic periods. This makes these objects difficult to detect from groundbased telescopes because their orbits place them in viewing geometries that are close to the Sun as viewed from Earth. Hence these objects often spend much of their time in daytime skies, and are only observable during their close approaches to Earth. However, these NEAs are often not observable from Earth until the timeframe of their most favorable human mission opportunities, which does not provide enough time for target characterization and future mission development.

A spacebased infrared survey telescope could find these targets in a more efficient, timely, and affordable manner. Such a system will not only be able to discover new objects, but will also be able to track and characterize objects of interest for human space flight consideration. Those objects with characteristic signatures representative of volatile-rich or metallic materials will be considered as top candidates for further investigation due to their potential for resource utilization and scientific interest.

The best targets for the initial piloted missions would be those NEAs that:

- have Earth-like orbits (low eccentricity and low inclination);
- make very close Earth approaches (i.e., within ~0.05 AU of Earth);
- are principal-axis “slow” rotators (i.e., not tumbling with a rotation period of several hours);
- are single, solitary objects (~one-sixth of all NEAs are binary or ternary bodies; see the chapter by Margot et al. in this volume); and
- are asteroidal in nature (i.e., not an extinct or dormant comet)

Based on these high-level parameters, in order to find potential targets for human exploration, a preliminary filter began to emerge, based on semimajor axis ( $a$ ), eccentricity ( $e$ ), and inclination ( $i$ ) (with respect to the ecliptic):  $0.5 \text{ AU} < a < 1.5 \text{ AU}$ ,  $e < 0.5$ , and  $i < 4^\circ$ . Only a very small fraction of the current NEA catalog in the NHATS subset deemed “human-accessible” have inclinations  $<2^\circ$ . Nearly every degree of orbital inclination requires  $\sim 0.5 \text{ km s}^{-1}$  of post-Earth escape  $\Delta v$ ; therefore, for the first piloted missions to these bodies, potential asteroid targets must truly have Earth-like orbits about the Sun. As a result, the NHATS effort continues to identify potential targets that fit within the accessibility filter constraints. The first tier characteristics for accessibility include short round-trip mission length (ideally  $\sim 30\text{--}180$  days), slower rotation rate (i.e.,  $>2$  h), and

larger size ( $>30$  m in diameter). Second-tier characteristics preclude binary systems or potential volatiles and surface activity, and perhaps indicate a preference for certain mineralogical compositions and internal structures. To date, the various sets of studies have identified only a few potential NEA targets for human missions, all of which are small (i.e.,  $<30$  m across).

Hence the most pertinent knowledge needed to prepare for any human exploration missions to NEAs is to discover a sufficient number of suitable candidate targets. Such detailed knowledge of the NEA population would also have the ancillary benefit of informing planetary defense initiatives, since those targets that are the most accessible also present the greatest impact threat to Earth. Identification of human-accessible NEAs will not be met in a timely manner by existing or planned groundbased surveys (Abell et al., 2009; Adamo et al., 2010; Cheng et al., 2011). This point has also been the recent focus of the small-bodies scientific community, which has repeatedly called for the rapid development and operation of a spacebased infrared survey telescope as a foundational asset for future space exploration initiatives.

**6.1.2. Strategic knowledge gaps (SKGs).** For the past several years NASA has been interested in identifying the key SKGs related to future human destinations. These SKGs highlight the various unknowns and/or data gaps of targets that the science and engineering communities would like to have filled in prior to committing crews to explore the solar system. An action team from the NASA-chartered Small Bodies Assessment Group (SBAG) was formed specifically to identify the small body SKGs under the direction of the Human Exploration and Operations Missions Directorate (HEOMD), given NASA’s recent interest in NEAs and the martian moons as potential human destinations (Rivkin and Sykes, 2013). The action team organized the SKGs into four broad themes: (1) identify human mission targets; (2) understand how to work on and interact with the small-body surface; (3) understand the small-body environment and its potential risks/benefits to crew, systems, and operational assets; and (4) understand the small-body resource potential.

Each of these themes was further subdivided into categories to address specific SKG issues. Robotic reconnaissance missions should be able to address specific aspects related to SKG themes 1 through 4. Theme 1 deals with the identification of human mission targets within the NEA population. The current guideline indicates that human missions to fast-spinning, tumbling, or binary asteroids may be too risky to conduct successfully from an operational perspective. However, no spacecraft mission has been to any of these types of NEAs before, so further knowledge of objects with these attributes would be desired in order to fully understand the suite of potentially available targets for human exploration.

Theme 2 addresses the concerns about interacting on the small-body surface under microgravity conditions, and how the surface and/or subsurface properties affect or restrict the interaction for human exploration. A robotic precursor with remote sensing instruments combined with *in situ* payloads (e.g., rovers, landers, penetrators, impactors, etc.) will pro-

vide key insights into the asteroid's surface and near-surface physical properties. Knowledge of these physical properties is necessary in order to inform and develop the correct tools, instruments, and operational procedures required to fully investigate and explore the NEA safely and efficiently.

SKG theme 3 deals with the environment in and around the small body that may present a nuisance or hazard to any assets operating in close proximity or on the surface of the NEA. Impact and surface experiments will help address issues related to particle size, particle longevity, internal structure, and the near-surface mechanical stability of the asteroid. Understanding or constraining these physical characteristics is important for mission planning given that multiple assets may be operating in the vicinity of the NEA. It would be useful to identify those characteristics that could result in nonbenign failure modes that would jeopardize the mission and/or crew.

Theme 4 addresses the resource potential of small bodies. This is a particularly important aspect of human exploration since the identification and utilization of resources is a key aspect for deep-space mission architectures to the martian system and other destinations. There is good evidence from the analysis of meteorite samples and remote sensing data that a significant number of NEAs may contain useful resources (e.g., water and volatile materials). Identification of such resources, their locations, and their relative accessibility with respect to NEAs is something that could be readily achieved through precursor spacecraft.

**6.1.3. Robotic precursors.** Robotic precursor reconnaissance of small bodies can provide a wealth of information relevant to the science of NEAs as well as planetary defense. However, such missions can also provide key insights into small-body SKGs and contribute to the overall success for human exploration missions to asteroids. Ideally, robotic precursor missions to potential NEA targets would be implemented since this would significantly reduce operational risk to the crewed mission. NEAs may have small satellite(s) or complex surface morphologies that may not be detectable from prior groundbased observations. These prior missions would be useful in identifying any potential hazards to the astronauts, their spacecraft, and any deployable assets/instruments. Such in-depth examinations by small robotic spacecraft would help identify the surface and interior physical characteristics of a potential NEA selected for study. A robotic precursor mission to an NEA would be akin to the Ranger and Surveyor probes that preceded the crewed Apollo missions. Knowledge of the NEA's gravitational field, shape, surface topography, and general composition would aid in planning for later proximity operations. Additionally, the information obtained about the NEA's basic physical characteristics would be crucial for planning operational activities, designing in-depth scientific/engineering investigations carried by the spacecraft and its astronauts, and identifying sites on the NEA for sample collection.

One of the more interesting aspects of employing a robotic precursor is its usefulness during crew activities at the NEA, and also after the crew departs the asteroid for the return to

Earth. During crew activities it can provide enhanced situational awareness and act as a communication relay for the crew and assets performing operations out of the line of sight. Once the crew departs the NEA, the robotic precursor could remain behind to observe a high kinetic energy experiment at the NEA to investigate cratering excavation and formation, ejecta processes, seismic propagation, interior composition, and momentum transfer [similar to the activities planned in 2022 by the NASA/ESA joint AIDA mission (see section 4.2.1)]. Such information would not only be extremely valuable in terms of science, but would also provide crucial data relevant for hazard mitigation and planetary defense. The precursor spacecraft could also continue to relay data from any science or engineering packages left on the surface of the NEA, while at the same time monitoring the asteroid and refining the orbital motion (e.g., Yarkovsky effect) and rotation rate changes [e.g., Yarkovsky-O'Keefe-Radzievskii-Paddack (YORP) effects] over time.

## 6.2. Human Near-Earth Asteroid Missions Beyond the Earth-Moon System

Human missions to NEAs would be the first human expeditions to interplanetary bodies beyond the Earth-Moon system and would prove useful for testing technologies required for human missions to Mars, Phobos and Deimos, and other solar system destinations. Current analyses of operational concepts suggest that stay times of 15 to 30 days may be possible at an NEA with total mission duration limits of 180 days or less. Hence these missions would undoubtedly provide a great deal of technical and engineering data on spacecraft operations for future human space exploration while simultaneously conducting detailed investigations of these primitive objects with instruments and equipment that exceed the mass and power capabilities delivered by robotic spacecraft. All these activities will be vital for refinement of resource characterization and identification as well as development of extraction and utilization technologies to be used on airless bodies under low- or microgravity conditions. In addition, gaining enhanced understanding of an NEA's geotechnical properties and its gross internal structure will assist in the development of hazard mitigation techniques for planetary defense.

The spacecraft would require several basic capabilities in order to complete the scientific and technical objectives of the mission. These would involve equipment and techniques supporting remote sensing, telerobotic operations, multiple crewmember EVAs, deployment/redeployment of surface experiment packages, and surface/subsurface sampling. Previous groundbased observations and precursor mission data of the target should have adequately characterized the surface and local space environment to reduce the risk to the crew, spacecraft, and other mission assets (e.g., EVA tools and equipment, science and engineering packages, etc.). Hence the majority of the operations should be able to take place in close proximity (approximately a few to several hundred meters) from the NEA. Such operations have been found

to be challenging for remotely controlled spacecraft due to round-trip light delay times of several tens of seconds or minutes, but should be much more tractable for the crew. Based on previous Apollo and space shuttle experience, the crew should be able to match the rotation of the NEA, or hover over its surface, while maintaining a stable attitude from which to conduct detailed investigations of the target.

One of the more attractive aspects of human missions to NEAs is having the ability to adapt to specific situations in real time, and adjust operations with much more flexibility than possible when operating a robotic spacecraft. Furthermore, a crewed mission would have the capability via EVA to precisely place, adjust, redeploy, and retrieve relatively small scientific or engineering packages on the surface. Packages such as remotely operated or autonomous rovers/hoppers could greatly increase the amount of data obtained, helping to refine site selection for subsequent sample collection and enhancing the diversity of samples to be collected from the surface. *In situ* experiments designed to test such technologies as surface anchors/tethers, drills/excavation equipment, or resource extraction equipment could also be deployed and recovered.

Arguably, the main scientific goal of such a mission would be to collect macroscopic samples from various terrains on the NEA's surface. The crew's ability to land, traverse the NEA, and collect the samples [e.g., the Muses Sea region or the Little Woomera terrain on asteroid Itokawa (*Fujiwara et al.*, 2006)] would bring a wealth of information on physical characteristics and geotechnical properties of the asteroid such as particle size, space weathering, composition, regolith depth, cohesion, compaction, density, and porosity. The flexibility of the crew's mobility during NEA proximity operations would enable sample collection in geological context to ensure that profiles (i.e., top, middle, and bottom) could be maintained. Intact samples of the optical surface would also be used to evaluate space weathering/surface alteration effects in a deep-space environment. In addition, supplemental telerobotic collection of samples from different or difficult to reach sites on the NEA could expand the sample suite. It would also be useful to identify and collect materials that may not be indigenous to the NEA, or that may have undergone alteration processes [i.e., black boulders on the surface of Itokawa (*Fujiwara et al.*, 2006)].

Another primary goal of this mission would be to investigate and determine the interior characteristics of the target NEA. This would place some constraints on the macroporosities that may be found among this population of objects and help scientists understand the impact history of the early solar system. Such investigations could be combined with a detailed examination of any features/structures associated with crater formation in microgravity environments (crater morphology, crater internal structures, fractures, ejecta movement/secondary impacts, effects of surface topography/curvature on crater morphology, etc.) to further refine impact physics models appropriate for these primitive objects and understand NEA internal structures. Active detonation of a kinetic energy experiment after deployment of a seismic

network would also serve to characterize the interior of the NEA while gaining insights into the effects of crater excavation. Such information also has important benefits for future hazard mitigation scenarios.

### 6.3. Recent and Current Analog Activities

Since the earliest days of the Apollo program, NASA has used analog activities to test operations and procedures at various levels of fidelity in order to gain understanding, under controlled and safe conditions, of operational requirements for future space operations. In more recent years, NASA has developed a variety of analog activities specific to future NEA operations.

**6.3.1. Neutral Buoyancy Lab (NBL).** NASA's Neutral Buoyancy Lab (NBL), located at the Sonny Carter Training Facility near Johnson Space Center, has been used to simulate nearly all of NASA's EVA activities since the inception of the shuttle program. Regarding potential crewed missions to NEAs, including ARM, the NBL has been used to test the speeds and accuracy with which astronauts may be able to collect samples under the microgravity conditions that will exist in the NEA environment. Astronauts conducted tests while attached to the end of a robotic arm that was translated at various rates across two simulated NEA surfaces. In the first instance astronauts had to target specific rock samples that were attached to a rock wall and place them into a sample bag either by hand or with a simulated collection tool. The second test involved a similar approach, but instead of targeting specific samples, the astronauts collected bulk regolith samples as they translated across the surface.

**6.3.2. NASA Extreme Environment Mission Operations (NEEMO).** The NASA Extreme Environment Missions Operation (NEEMO) is a program that sends astronauts, scientists, and engineers to live in Aquarius, currently the world's only permanent undersea research station, located approximately 3.5 miles off of Key Largo in Florida. To date, NEEMO has conducted operations lasting up to three weeks intended to simulate missions to the Moon, the martian system, and NEAs (*Chappell et al.*, 2013a,b). Astronaut crews have simulated three types of EVA: tethered, jetpack, and robotic arm attached to a submersible intended to represent a free-flying spacecraft. Additionally, crews have tested communication protocols that incorporate the signal delays that would occur between Mission Control and a spacecraft during missions to NEAs or the martian system.

**6.3.3. NASA Research and Technology Studies (RATS).** NASA's Research and Technology Studies (RATS) team runs simulations at both Johnson Space Center and selected remote environments, such as desert regions located in Arizona. In particular, RATS has simulated crew activity in rovers meant to represent small two-person excursion vehicles that would conduct *in situ* investigations during NEA missions (*Abercromby et al.*, 2013a,b). RATS has also employed a virtual reality wall displaying detailed images of Itokawa based on data supplied by Hayabusa; two crew members in the simulated excursion vehicle interacted with the reproduced

environment while communicating with a science officer, including the appropriate signal delay, back at Mission Control. The crew were able to “visit” various sites on Itokawa and simulate sample collection and instrument deployment.

## 7. SUMMARY

The collective human spaceflight experience of the Apollo, space shuttle, Salyut, Mir, and ISS programs underscores the world’s space agencies’ capability to meet operational challenges and solve problems in the space environment. Despite the current uncertainty surrounding the future of human exploration beyond LEO, humanity could be poised to execute historic missions of exploration and discovery by reaching for the resources and knowledge of NEAs, which are the nearest waypoints in interplanetary space. Such missions would represent humanity’s first forays beyond the Earth-Moon system and would pave the way for future missions to Mars and other solar system destinations (Fig. 13). Exploration of NEAs with robotic and human missions would also provide a wealth of information about the formation of the solar system and the Earth-Moon system, while simultaneously aiding the development of planetary defense strategies. The critical themes of exploration, science, resource utilization, and planetary defense are what make NEAs such intriguing and compelling future destinations for humanity.



**Fig. 13.** Conceptual human mission to an NEA located several million kilometers from Earth. Note the Earth-Moon system in the lower right of the image. Courtesy of William Hartmann.

## REFERENCES

- Abell P. A., Korsmeyer D. J., Landis R. R., Jones T. D., Adamo D. R., Morrison D. D., Lemke L. G., Gonzales A. A., Gershman R., Sweetser T. H., Johnson L. L., and Lu E. (2009) Scientific exploration of near-Earth objects via the Orion Crew Exploration Vehicle. *Meteoritics & Planet. Sci.*, **44**, 1825–1836.
- Abercromby A. F. J., Chappell S. P., and Gernhardt M. L. (2013a) Desert RATS 2011: Human and robotic exploration of near-Earth asteroids. *Acta Astronaut.*, **91**, 34–48.
- Abercromby A. F. J., Chappell S. P., Litaker H. L. Jr., Reagan M. L., and Gernhardt M. L. (2013b) NASA Research and Technology Studies (RATS) 2012: Virtual simulation and evaluation of human and robotic systems for exploration of near-Earth asteroids. *43rd International Conference on Environmental Systems*, Vail, Colorado.
- Adamo D. R. (2013) The “horseshoe” orbit of near-Earth object 2013 BS<sub>45</sub>. *Horizons*, AIAA Houston Section, March/April 2013, pp. 20–26. Available online at [http://www.aiaahouston.org/wp-content/uploads/2012/07/Horizons\\_2013\\_03\\_and\\_04\\_page\\_20\\_to\\_26\\_Adamo\\_2\\_of\\_3.pdf](http://www.aiaahouston.org/wp-content/uploads/2012/07/Horizons_2013_03_and_04_page_20_to_26_Adamo_2_of_3.pdf) (accessed September 12, 2014).
- Adamo D. R. and Barbee B. W. (2011) Why Atens enjoy enhanced accessibility for human space flight. *Adv. Astronaut. Sci.*, **142**, 709–728.
- Adamo D. R., Giorgini J. D., Abell P. A., and Landis R. R. (2010) Asteroid destinations accessible for human exploration: A preliminary survey in mid-2009. *J. Spacecraft Rockets*, **47**, 994–1002.
- Barbee B. W., Esposito T., Piñon E. III, Hur-Diaz S., Mink R. G., and Adamo D. R. (2010) A comprehensive ongoing survey of the near-Earth asteroid population for human mission accessibility. *Proc. AIAA/AAS Guidance, Navigation, and Control Conference*, #2010-8368. Toronto, Canada.
- Barbee B. W., Mink R. G., Adamo D. R., and Alberding C. M. (2011) Methodology and results of the Near-Earth Object (NEO) Human Space Flight (HSF) Accessible Targets Study (NHATS). *Adv. Astronaut. Sci.*, **142**, 613–632.
- Barbee B. W., Abell P. A., Adamo D. R., Alberding C. M., Mazanek D. D., Johnson L. N., Yeomans D. K., Chodas P. W., Chamberlin A. B., and Friedensen V. P. (2013) The Near-Earth Object Human Space Flight Accessible Targets Study: An ongoing effort to identify near-Earth asteroid destinations for human explorers. *Proc. IAA Planet. Defense Conf.*, Flagstaff, Arizona.
- Barucci A. M., Cheng A. F., Michel P., Benner L. A. M., Binzel R. P., Bland P. A., Böhnhardt H., Brucato J. R., Campo Bagatin A., Cerroni P., Dotto E., Fitzsimmons A., Franchi I. A., Green S. F., Lara L.-M., Licandro J., Marty B., Muinonen K., Nathues A., Oberst J., Rivkin A. S., Robert F., Saladino R., Trigo-Rodriguez J. M., Ulamec S., and Zolensky M. (2011) MarcoPolo-R near Earth asteroid sample return mission. *Exp. Astron.*, **33**, 645–683.
- Brearley A. J. (2006) The action of water. In *Meteorites and the Early Solar System II* (D. S. Lauretta and H. Y. McSween Jr., eds.), pp. 587–622. Univ. of Arizona, Tucson.
- Brophy J., Culick F., Friedman L., and the Asteroid Retrieval Feasibility Study Team (2012) *Asteroid Retrieval Feasibility Study*. Keck Inst. for Space Studies, Pasadena, California.
- Burton A. S., Stern J. C., Elsila J. E., Glavin D. P., and Dworkin J. P. (2012) Understanding prebiotic chemistry through the analysis of extraterrestrial amino acids and nucleobases in meteorites. *Chem. Soc. Rev.*, **41**, 5459–5472.
- Busch M. W., Ostro S. J., Benner L. A. M., Brozovic M., Giorgini J. D., Jao J. S., Scheeres D. J., Magri C., Nolan M. C., Howell E. S., Taylor P. A., Margot J.-L., and Brisken W. (2011) Radar observations and the shape of near-Earth asteroid 2008 EV5. *Icarus*, **212**, 649–660.
- Chappell S. P., Abercromby A. F. J., and Gernhardt M. L. (2013a) NEEMO 15: Evaluation of human exploration systems for near-Earth asteroids. *Acta Astronaut.*, **89**, 166–178.
- Chappell S. P., Abercromby A. F. J., Todd W. L., Reagan M. L., and Gernhardt M. L. (2013b) NEEMO 16: Evaluation of systems for human exploration of near-Earth asteroids. *43rd International Conference on Environmental Systems*, Vail, Colorado.
- Cheng A. F., Rivkin A. S., Hibbard K. E., Mink R. G., Barbee B. W., Garvin J. B., Abell P. A., Mazanek D. D., and Landis R. R. (2011) Near-Earth asteroid survey precursor to human exploration. *Lunar Planet. Sci. XLII*, Abstract #1820. Lunar and Planetary Institute, Houston.
- Clark B. E., Binzel R. P., Howell E. S., Cloutis E. A., Ockert-Bell M., Christensen P., Barucci M. A., DeMeo F., Lauretta D. S., Connolly H., Soderberg A., Hergenrother C., Lim L., Emery J., and Mueller M. (2011) Asteroid (101955) 1999 RQ36: Spectroscopy from 0.4 to 2.4 μm and meteorite analogs. *Icarus*, **216**, 462–475.
- Cole D. F. (1963) Asteroids stir growing interest. *Missiles and Rockets*, Feb. 24, 43–54.
- Cole D. F. and Cox D. W. (1964) *Islands in Space: The Challenge of the Planets*. Chilton, Philadelphia. 276 pp.
- Davis D. R., Friedlander A. L., and Jones T. D. (1993) The role of near-Earth asteroids in the Space Exploration Initiative. In *Resources*

- of Near Earth Space (J. Lewis et al., eds), pp. 619–655. Univ. of Arizona, Tucson.
- Fujiwara A., Kawaguchi J., Yeomans D. K., Abe M., Mukai T., Okada T., Saito J., Yano H., Yoshikawa M., Scheeres D. J., Barnouin-Jha O., Cheng A. F., Demura H., Gaskell R. W., Hirata N., Ikeda H., Kominato T., Miyamoto H., Nakamura A. M., Nakamura R., Sasaki S., and Uesugi K. (2006) The rubble-pile asteroid Itokawa as observed by Hayabusa. *Science*, *312*, 1330–1334.
- Hall H. (1971) Manned mission to an asteroid. In *Physical Studies of Minor Planets* (T. Gehrels, ed.), pp. 539–541. NASA SP-267, Washington, DC.
- Hogan T. (2007) *Mars Wars: The Rise and Fall of the Space Exploration Initiative*. NASA SP-2007-4410, Washington, DC.
- Hopkins J. B. (2009) Plymouth Rock: An early human asteroid mission using Orion. *2nd Small Bodies Assessment Group (SBAG) Meeting*, November 19, 2009, Boulder, Colorado.
- Hopkins J. B. and Dissel A. F. (2010) Plymouth Rock: Early human missions to near-Earth asteroids using Orion spacecraft. *AIAA Space 2010 Conference*, Anaheim, California.
- International Academy of Astronautics (IAA) (2013) 2013 IAA Planetary Defense Conference white paper. IAA, Paris. Available online at <http://www.hse.ru/data/2013/06/13/1284344245/2013%20PDC%20White%20Paper.pdf> (accessed June 10, 2015).
- JAXA (Japan Aerospace Exploration Agency) (2010) *International Manned Spacecraft Investigation Team: Manned Spacecraft System Investigation Report*. JAXA Technical Report, Tokyo, Japan.
- Jones T. D., Eppler D. B., Davis D. R., Friedlander A. L., McAdams J., and Krikalev S. (1994) Human exploration of near-Earth asteroids. In *Hazards Due to Comets and Asteroids* (T. Gehrels, ed.), pp. 683–708. Univ. of Arizona, Tucson.
- Kawaguchi J. (2004) A power sailer mission for a jovian orbiter and Trojan asteroid flybys. In *35th COSPAR Scientific Assembly*, Abstract #COSPAR04-A-01655. COSPAR Scientific Assembly, Paris.
- Mainzer A., Grav T., Bauer J., Masiero J., McMillan R. S., Cutri R. M., Walker R., Wright E., Eisenhardt P., Tholen D. J., Spahr T., Jedicke R., Denneau L., DeBaun E., Elsbury D., Gautier T., Gomillion S., Hand E., Mo W., Watkins J., Wilkins A., Bryngelson G. L., Del Pino Molina A., Desai S., Gómez Camus M., Hidalgo S. L., Konstantopoulos I., Larsen J. A., Maleszewski C., Malkan M. A., Mauduit J.-C., Mullan B. L., Olszewski E. W., Pforr J., Saro A., Scotti J. V., and Wasserman L. H. (2011) NEOWISE observations of near-Earth objects: Preliminary results. *Astrophys. J.*, *743*, 156.
- Mainzer A., Grav T., Bauer J., Conrow T., Cutri R. M., Dailey J., Fowler J., Giorgini J., Jarrett T., Masiero J., Spahr T., Statler T., and Wright E. L. (2015) *Astron. J.*, *149*, 172.
- Mazanek D. D., Angster S., Earle K., Garn M., Karlgaard C., Keyes J., Korte J., Lepsch R., Lucas V., Merrill G., Paschal K., and Qu M. (2005) *The Near-Earth Object Crewed Mission Concept Status*. Internal Constellation/ESMD study, NASA Langley Research Center, Hampton, Virginia.
- Mazanek D. D., Brophy J. R., and Merrill R. G. (2013) Asteroid Retrieval Mission concept — trailblazing our future in space and helping to protect us from Earth impactors. *Planetary Defense Conference 2013*, Abstract #IAA-PDC13-04-14.
- Mazanek D. D., Merrill R. G., Belbin S. P., Reeves D. M., Earle K. D., Naasz B. J., and Abell P. A. (2014) Asteroid redirect robotic mission: Robotic boulder capture option overview. *AIAA/AAS Astrodynamics Spec. Conf.*, San Diego.
- Mazanek D. D., Reeves D., Hopkins J., Wade D., Tantardini M., and Shen H. (2015) Enhanced gravity tractor technique for planetary defense. *4th IAA Planetary Defense Conference (PDC 2015)*, Frascati, Roma, Italy.
- Michel P., Barucci M. A., Cheng A. F., Böhnhardt H., Brucato J. R., Dotto E., Ehrenfreund P., Franchi I. A., Green S. F., Lara L.-M., Marty B., Koschny D., and Agnolon D. (2014) MarcoPolo-R: Near-Earth asteroid sample return mission selected for the assessment study phase of the ESA program cosmic vision. *Acta Astronaut.*, *93*, 530–538.
- Mori O., Tsuda Y., Sawada H., Ryu F., Takayuki Y., Takanao S., Katsuhide Y., Hirokazu H., Hiroyuki M., Tatsuya E., and Junichiro K. (2010) World's first mission of solar power sail by IKAROS. *Intl. Conf. Space Aero. and Nav. Elec.*, Abstract #ICSANE2010-95. Jeju, Korea.
- Moskovitz N. A., Abe S., Pan K.-S., Osip D. J., Pefkou D., Melita M. D., Elias M., Kitazato K., Bus S. J., DeMeo F. E., Binzel R. P., and Abell P. A. (2013) Rotational characterization of Hayabusa II target asteroid (162173) 1999 JU3. *Icarus*, *224*, 24–31.
- Nash D. B., Plescia J., Cintala M., Levine J., Lowman P., Mancinelli R., Mendell W., Stoker C., and Suess S. (1989) *Science Exploration Opportunities for Manned Missions to the Moon, Mars, Phobos, and an Asteroid*. NASA Document Z-13-001, Pasadena, California.
- National Research Council of the National Academies (2010) *Defending Planet Earth: Near-Earth Object Surveys and Hazard Mitigation Strategies*. National Academies, Washington, DC. Available online at [http://www.nap.edu/openbook.php?record\\_id=12842](http://www.nap.edu/openbook.php?record_id=12842) (accessed June 10, 2015).
- O'Leary B. T. (1977) Mining the Apollo and Amor asteroids. *Science*, *197*, 363–366.
- Pizzarello S., Cooper G. W., and Flynn G. J. (2006) The nature and distribution of the organic material in carbonaceous chondrites and interplanetary dust particles. In *Meteorites and the Early Solar System II* (D. S. Lauretta and H. Y. McSween Jr., eds.), pp. 625–652. Univ. of Arizona, Tucson.
- Pravec P., Harris A. W., and Michalowski T. (2002) Asteroid rotations. In *Asteroids III* (W. F. Bottke Jr. et al., eds.), pp. 113–122. Univ. of Arizona, Tucson.
- Price H. W., Baker J. D., Strange N. J., and Woolley R. C. (2014) Human missions to Mars orbit, Phobos, and Mars surface using 100-kWE-class solar electric propulsion. *AIAA Space 2014 Conf. Expo.*, Abstract #4446. AIAA, San Diego, California.
- Reddy V., Le Corre L., Hicks M., Lawrence K., Buratti B. J., Abell P. A., Gaffey M. J., and Hardersend P. S. (2012) Composition of near-Earth asteroid 2008 EV5: Potential target for robotic and human exploration. *Icarus*, *212*, 678–681.
- Rivkin A. S. and Sykes M. V. (2013) *Small Bodies Assessment Group Special Action Team Report on Small Body Strategic Knowledge Gaps*. Available online at [http://www.lpi.usra.edu/sbag/meetings/jan2013/presentations/sbag8\\_presentations/MON\\_1330\\_Sykes\\_SBAD\\_SKG\\_SAT\\_report.pdf](http://www.lpi.usra.edu/sbag/meetings/jan2013/presentations/sbag8_presentations/MON_1330_Sykes_SBAD_SKG_SAT_report.pdf) (accessed June 10, 2015).
- Smith E. A. (1966) A manned flyby mission to (433) Eros. *Third Space Cong. Proc.*, pp. 137–155. Northrop Space Laboratories, Hawthorne, California.
- Weisberg M. K., McCoy T. J., and Krot A. N. (2006) The nature and distribution of the organic material in carbonaceous chondrites and interplanetary dust particles. In *Meteorites and the Early Solar System II* (D. S. Lauretta and H. Y. McSween Jr., eds.), pp. 19–52. Univ. of Arizona, Tucson.
- Yoshikawa M., Watanabe S., Tsuda Y., Kuninaka H., and the Hayabusa2 Project Team (2014) Hayabusa2 — the next asteroid sample return mission of Japan. *Trans. JSASS Aerospace Tech. Japan*, *12*(29), 29–33.
- Yurimoto H., Abe K., Abe M., Ebihara M., Fujimura A., Hashiguchi M., Hashizume K., Ireland T. R., Itoh S., Katayama J., Kato C., Kawaguchi J., Kawasaki N., Kitajima F., Kobayashi S., Meikel T., Mukai T., Nagao K., Nakamura T., Naraoka H., Noguchi T., Okazaki R., Park C., Sakamoto N., Seto Y., Takei M., Tsuchiyama A., Uesugi M., Wakaki S., Yada T., Yamamoto K., Yoshikawa M., and Zolensky M. E. (2011) Oxygen isotopic compositions of asteroidal materials returned from Itokawa by the Hayabusa mission. *Science*, *333*, 1116–1119.

# Index

- Ablation 259  
Ablation coefficient 259  
Ablation equation 259  
Absolute ages 740  
Absolute magnitude cutoff 300  
Absolute magnitude H 304, 312  
Absorption feature 14  
Accretion 533ff, 555, 573ff, 643  
age 23, 556, 643, 644  
efficiency 585, 662  
energy 535  
layered 472, 478, 479, 484, 487  
Acoustic fluidization 670, 681, 688  
Action Team on Near-Earth Objects (AT-14) 850  
Active asteroids 6, 77, 99, 221ff, 275, 283, 337, 782  
Active asteroids, individual  
  107P/(4015) Wilson-Harrington 229  
  133P/(7968) Elst-Pizarro 227, 303, 333  
  176P/(118401) LINEAR 228  
  238P/Read 228  
  259P/(Garradd) (P/2008 R1) 226  
  288P/(300163) 2006 VW139 227  
  311P/PanSTARRS 223, 224, 229, 230, 232, 236  
  313P/Gibbs (2014 S4) 229  
  324P/2010 R2 (La Sagra) 229  
  P/2010 A2 337  
  P/2010 A2 (LINEAR) 224  
  P/2012 F5 (Gibbs) 226, 303  
  P/2012 T1 (PanSTARRS) 228  
  P/2013 P5 763  
  P/2013 R3 763  
  P/2013 R3 (Catalina-PanSTARRS) 227  
Activity 333  
Adaptive optics (AO) 171, 362, 363, 379  
Adiabatic invariance 384  
Admissible region 824, 825  
Advanced Research Projects Agency (ARPA) 290  
Aerodynamic sorting 473  
Age 308, 495, 709ff, 717, 721  
Aggregates (*see also* Rubble piles) 344, 345, 346, 349, 351, 406, 414, 480, 696, 738, 739, 749, 768, 774, 776, 777, 779  
Airburst frequency 839  
AKARI All-Sky Survey 297  
AKARI space telescope 91, 193, 206, 312, 326  
Albedo 16, 46, 98, 131, 158, 206, 224, 226, 297, 305, 310, 323ff, 327, 509, 610  
Albedo, single-scattering 51  
Aluminum-26 21, 419, 473ff, 486, 533ff, 555, 574, 620  
Amino acids 640
- Amoeboid olivine aggregates (AOAs) 22  
Angle of friction 754, 756  
Angle of repose 388, 681, 691, 755, 768, 776, 781  
Angular momentum 230, 359ff, 363, 367, 369, 377, 380, 383ff, 387, 756, 757  
Apollo Applications Program (AAP) 857  
Aqueous alteration 6, 22, 24, 69, 71, 79, 473, 475, 635ff  
Aqueous alteration, hydrothermal alteration 556  
Arecibo Observatory 165ff, 193, 290, 357, 457, 516  
Armoring 406  
Association of Space Explorers (ASE) 850  
Asteroid belt 493ff, 701ff  
  collisional history 319  
  mass 495  
  primordial 494ff  
  radial mixing 16, 19, 20, 66, 494, 495, 497, 619  
Asteroid dust band 304  
Asteroid families, general 5, 238, 297ff, 380, 381, 477, 479, 487, 505, 523, 609, 709, 718  
age 298, 302, 303, 305, 310, 311, 317ff, 347ff, 524  
albedo 299, 301, 308, 312, 326, 328ff  
albedo cutoff 311, 312  
anisotropic distribution of spin poles 327  
color 299, 301, 308, 324, 328ff  
composition 325, 351  
cutoff distance 299, 300, 311  
diameter 326  
dynamical ages 710, 714  
dynamical evolution 307  
dynamical families 504  
family identification number (FIN) 311ff  
formation 341ff, 381, 663, 665  
halo 301, 310, 311  
homogeneity 328  
infrared space surveys 326  
interlopers 297, 298, 300, 301, 304  
light/phase curves 327  
non-Maxwellian rotation rate distribution 327  
parent bodies 301, 304, 307, 312, 317ff, 325, 327, 333, 342, 344ff, 409, 709ff  
physical properties 301, 323ff  
polarimetric surveys 327  
shape criterion 311  
shape distribution 324  
size distribution 304, 328, 334, 345ff  
size-frequency distribution (SFD) 310, 326  
spectral properties 308, 328ff  
spectroscopic surveys 325  
spin pole direction 327  
synthesis 311ff  
thermal inertia 326  
V-shape criterion 305, 307
- Asteroid families, individual  
  Adeona 309

Page numbers refer to specific pages on which an index term or concept is discussed. "ff" indicates that the term is also discussed on the following pages.

- Asteroid families, individual (*continued*)
- Agnia 306, 307, 326, 578
  - Baptistina 306, 325, 332
  - Barbara 327
  - Beagle 286, 304
  - Burdett 333
  - Centaurs, (10199) Chariklo 365
  - Cybele 97, 326, 334, 494
  - Datura 302, 306
  - Eos 50, 304ff, 318, 324, 327, 334, 479, 578
  - Erigone 306, 525
  - Eulalia 301, 332, 524
  - Eunomia 318, 325, 326, 342, 345, 347, 479, 578
  - Euphrosyne 309, 326
  - Eurybates 208, 216
  - Flora 57, 197, 223, 224, 300, 308, 310, 325ff, 332, 342, 523, 579, 610, 628, 741
  - Gefion 309, 326, 523
  - Hertha 332
  - Hilda 27, 97, 311, 335, 494
  - Hungaria 17, 311, 327, 332, 334, 578
  - Hygiea 227, 309
  - Karin 286, 298, 300, 302ff, 306, 307, 325, 327, 346, 610
  - Koronis 118, 299, 300, 304, 308, 310, 311, 324, 326, 327, 342, 345, 346, 348, 352, 377, 524, 527, 579, 714, 741
  - Levin 332
  - Lixiaohua 229
  - Maria 325, 327
  - Massalia 306, 332
  - Merxia 306, 326, 578
  - Nysa 326
  - Nysa-Polana 301, 310, 327, 332
  - Padua 306
  - Pallas 284, 309, 326
  - Polana 301, 326, 332
  - (new) Polana 332
  - Schubart 335
  - Sylvia 333
  - Themis 80, 228, 304, 324ff, 333, 380, 713
  - Tina 306
  - Trojans 19, 27, 52, 78, 97, 203ff, 212, 311, 335, 336, 363, 365, 369, 380, 494, 502, 504, 603, 808  
capture model 212
  - Veritas 286, 290, 303, 304, 306, 307, 325, 347ff
  - Vesta 17, 300, 306, 308ff, 318, 324, 326, 327, 332ff, 577, 740
  - Watsonia 327, 334
- Asteroid follow-up 802
- Asteroid Impact and Deflection Assessment (AIDA) 10, 760, 837, 842, 843, 847, 870
- Asteroid Impact Mission (AIM) 842, 843, 870
- Asteroid initiative 855
- Asteroid Lightcurve Database 185
- Asteroid pairs (*see also* Split pairs) 8, 355ff, 378, 524, 757, 758
- Asteroid precovery 802
- Asteroid recovery 802
- Asteroid Redirect Mission (ARM) 845, 864, 872, 873, 875
- Asteroid Redirect Vehicle (ARV) 872ff
- Asteroid strength 752ff
- Asteroid systems 8, 355
- evolution 355
  - formation 355
- Asteroid Terrestrial-impact Last Alert System (ATLAS) 187, 809, 841, 844, 852
- Asteroids 3ff
- Asteroids, binaries 8, 171, 173, 190ff, 194, 209, 355ff, 375ff, 514, 527, 759ff
- asynchronous 356, 357, 360, 369, 378, 379
  - component 356ff
  - doubly synchronous 356, 357, 360, 362, 379, 527
  - evolution 375ff
  - formation 375ff, 757
  - main belt 713
  - mass ratio 357, 358, 367
  - primary 356ff
  - radii 375ff
  - secondaries 356ff, 375ff
  - synchronous 356, 359, 378, 383, 386, 387, 514, 515, 521, 527
  - thermophysical models 116
- Asteroids, general
- albedo 90
  - basaltic 505
  - basaltic crust 561
  - bulk properties 749
  - collisions 693
  - color 230, 238, 610
  - composition 175
  - core 533ff, 555, 561, 573ff
  - core formation 539ff, 560, 576
  - crust 533ff, 553ff, 573
  - interiors 745ff
  - internal structure 706, 717
  - mantle 542, 573ff,
  - metallic 505
  - mineralogy 6
  - monolithic 718
  - morphology 745ff, 753
  - satellites (*see* Asteroids, binaries)
  - shape 168
  - size distribution 477, 486
  - spin rate 377, 385, 387, 388, 714, 753, 754
  - spin state 714
  - tumbling 514
- Asteroids, individual
- (1) Ceres 19, 78, 100, 117, 141, 146, 224, 235, 298, 308, 309, 419ff, 501, 504, 652, 741
  - (2) Pallas 222, 275, 309, 545
  - (4) Vesta 7, 27, 29, 54, 67, 117, 143, 252, 306, 308, 309, 318, 419ff, 540, 544, 561, 565, 576, 667, 673,

- Asteroids, individual, (4) Vesta (*continued*)  
 710ff, 717, 726, 732, 734, 735, 737ff, 769, 772,  
 773, 780, 782  
 Albalonga Catena 566  
 basaltic crust 318, 477, 702, 710  
 basin (crater) 333  
 Brumalia Tholus 566  
 chronology 422, 423  
 composition 426, 427  
 coordinate system 421  
 crater-retention ages 740  
 craters 421, 422, 773, 782  
 dark material 425  
 differentiation 427  
 ejecta 773  
 geology 422  
 gravity 427  
 gullies 424  
 impact basin 710  
 interior 427  
 Leslie feature 55  
 Marcia crater 712, 726ff, 732  
 nomenclature 421  
 Oppia crater 55  
 physical properties 421  
 pits 424  
 Rheasilvia basin 7, 55, 308, 333, 421, 567, 577,  
 666, 673, 706, 711, 726ff, 731, 736, 738ff, 772  
 tectonics 422  
 topography 772  
 Veneneia basin 7, 333, 422, 577, 666, 673, 706,  
 711, 726, 727, 738, 739  
 Vestalia Terra 566
- (7) Iris 171  
 (8) Flora 332  
 (16) Psyche 116, 170, 578, 708  
 (21) Lutetia 29, 113, 118, 143, 153, 171, 187, 350,  
 437, 544, 547, 565, 578, 727, 734, 735, 737ff, 769,  
 771, 772, 780, 783  
 boulders 440  
 Corduba 437  
 craters 771  
 ejecta blanket 772  
 Gades 437  
 groove 772  
 landslides 440, 772  
 lineaments 438, 772  
 Massilia crater 437, 738  
 north polar crater cluster (NPCC) 437
- (22) Kalliope 365, 376, 713  
 Linus 365  
 (24) Themis 229, 333, 652  
 (41) Daphne 188, 362  
 (44) Nysa 51, 332  
 (45) Eugenia 356, 369, 379, 713  
 (64) Angelina 51  
 (65) Cybele 230, 501
- (87) Sylvia 362, 369, 378, 379, 713  
 Remus 378  
 Romulus 365, 378  
 (90) Antiope 195, 360, 362, 365, 369, 380, 713  
 (216) Kleopatra 170, 171, 190, 192, 362, 365, 379,  
 578, 708, 713, 762  
 (243) Ida 29, 54, 356, 362, 376, 378, 380, 446, 547,  
 565, 579, 714, 725ff, 732, 735, 737, 767, 777  
 age 732  
 Dactyl 356, 378, 380  
 (253) Mathilde 565, 665ff, 680, 728, 736, 740  
 (283) Emma 713  
 (298) Baptista 332  
 (349) Dembowska 578  
 (354) Eleonora 579  
 (379) Huenna 363, 365  
 (433) Eros 7, 29, 51, 118, 350, 351, 353, 402, 420,  
 547, 555, 565, 667, 733, 735, 737, 738, 759, 761,  
 767ff, 777, 780, 782, 783, 857  
 age 732  
 craters 768, 769, 780  
 ejecta blankets 769  
 fracture 737  
 grooves 350, 769  
 Himeros crater 736ff  
 lineations 769  
 Psyche crater 737, 738  
 Rahe Dorsum 737, 738  
 Shoemaker crater 667, 730, 736, 737  
 (434) Hungaria 17, 51  
 (490) Veritas 303, 304, 347  
 (596) Scheila 226, 227, 236, 337  
 (617) Patroclus 204, 216, 363, 365, 369, 380  
 (624) Hektor 52, 204, 216, 363  
 (758) Mancunia 170  
 (762) Pulcova 713  
 (785) Zwetana 170  
 (809) Lundia 308  
 (832) Karin 307, 346  
 (854) Frostia 379  
 (951) Gaspra 54, 446, 547, 565, 579, 712, 717,  
 725ff, 732, 737, 767, 783  
 age 732, 741  
 (956) Elisa 308  
 (1036) Ganymed 172  
 (1338) Duponta 359  
 (1459) Magnya 505, 561, 579  
 (1580) Betulia 178  
 (1620) Geographos 172, 520, 522  
 (1862) Apollo 145, 171, 520, 522  
 (1866) Sisyphus 356  
 (1904) Massevitch 561  
 (2100) Ra-Shalom 517  
 (2201) Oljato 225  
 (2867) Šteins 7, 142, 434, 547, 565, 578, 727, 730,  
 737, 757, 782, 783  
 thermal inertia 437

Asteroids, individual (*continued*)  
 (3200) Phaethon 122, 222ff, 230, 233, 275, 284, 288  
 (3628) Boznemcova 578  
 (3749) Balam 359, 379, 381  
 (4179) Toutatis 169, 170, 196, 443, 514, 517, 518,  
     728, 755  
     boulders 444  
 (4507) 1990 FV 346  
 (4660) Nereus 176  
 (4709) Ennomos 207, 208  
 (4769) Castalia 173  
 (6070) Rheinland 524  
 (6489) Golevka 8, 171, 516, 755  
 (8306) Shoko 359, 379  
 (9969) Braille 547  
 (25143) Itokawa 6, 7, 29, 45, 48, 118, 119, 141, 168,  
     169, 248, 350, 377, 397ff, 448, 512, 520, 565, 601,  
     605, 622, 624, 651, 667, 668, 680, 727, 735, 737,  
     739, 761, 767, 769, 770, 780, 843, 845, 875  
     age 404  
     albedo 405  
     blisters 412  
     body 402, 404, 520, 770  
     boulders 351, 402ff  
     bulk chemical composition (samples) 411  
     Itokawa, bulk density 402, 405, 406, 761  
     Itokawa, color 405  
     craters 403, 404, 411, 771  
     density 520  
     density heterogeneity 761  
     dynamical origin 414  
     exotic materials 413  
     formation scenario 409  
     global properties 401  
     head 402, 404, 520, 770  
     landslide 771  
     macroporosity 406, 761, 770  
     mass 401  
     materials 409  
     minerals 409  
     Muses Sea 770  
     MUSES-C Regio 402  
     neck 404, 770  
     particles (samples) 406ff  
     potential model 405  
     regolith 405, 409  
     rotation period 405  
     rough terrain 402  
     sample collection 406  
     sample mass 407  
     sample return 397ff  
     shape 402, 405  
     shock features 409  
     size distribution of boulders 761  
     smooth terrain 402  
     space weathering 404, 411, 412  
     spectral properties 404

Asteroids, individual, (25143) Itokawa (*continued*)  
     strength 405  
     surface abrasion 411, 412  
     surface history 413  
     thermal inertia 406  
     topography 771  
     Yoshinobu 404  
     Yoshinodai 402  
 (33342) 1998 WT<sub>24</sub> 177  
 (35107) 1991 VH 357  
 (54509) YORP 172, 518, 520  
 (54827) 2001 NQ<sub>8</sub> 524  
 (62412) 2000 SY<sub>178</sub> 227  
 (65803) Didymos 10, 357ff, 757, 842, 870  
 (66391) 1999 KW<sub>4</sub> 174, 358, 382ff, 387, 388, 514,  
     515, 521, 755, 757, 761, 762  
     density 763  
 (69230) Hermes 357, 360, 376, 379, 527  
 (99942) Apophis 113, 172, 196, 514, 518, 611,  
     829ff, 842, 869  
     2029 encounter 10, 249  
 (100085) 1992 UY<sub>4</sub> 178  
 (101955) Bennu 10, 113, 117, 147, 171, 175, 176,  
     358, 379, 382, 516, 522, 651, 757, 820, 822, 826,  
     830ff, 845, 875  
 (118401) LINEAR (1999 RE<sub>70</sub>) 228, 238, 333  
 (136617) 1994 CC 174  
 (136849) 1998 CS<sub>1</sub> 174, 175  
 (152563) 1992 BF 516, 517  
 (155140) 2005 UD 222  
 (162173) Ryugu (1999 JU<sub>3</sub>) 117, 414, 845, 868, 875  
 (162421) 2000 ET<sub>70</sub> 176  
 (175706) 1996 FG<sub>3</sub> 359, 384, 386, 387, 389, 521  
 (185851) 2000 DP<sub>107</sub> 174, 384  
 (192642) 1999 RD<sub>32</sub> 173  
 (214869) 2007 PA<sub>8</sub> 176  
 (225416) 1999 YC 223  
 (285262) 1998 QE<sub>2</sub> 357  
 (29075) 1950 DA 171, 177, 178, 379, 387, 522, 762,  
     849  
     impact probability 762  
 (300163) P/2006 VW<sub>139</sub> 303  
 (308635) 2005 YU<sub>55</sub> 167, 176  
 (311066) 2004 DC 174  
 (341843) 2008 EV<sub>5</sub> 177, 358, 757, 875  
 (363599) 2004 FG<sub>11</sub> 518  
 (367943) Duende 178, 757, 838  
 1991 VH 366  
 1996 FG<sub>3</sub> 761  
 1996 HW<sub>1</sub> 173  
 1999 JU<sub>3</sub> 9, 652  
 1999 KW<sub>4</sub> 195, 360, 366, 379, 782, 783  
 1999 RD<sub>32</sub> 175  
 2000 DP<sub>107</sub> 358, 365, 366, 381  
 2000 ET<sub>70</sub> 177  
 2000 SG<sub>344</sub> 859, 867  
 2000 SY<sub>178</sub> 388

- Asteroids, individual (*continued*)
   
2000 UG<sub>11</sub> 358
   
2002 FC 173
   
2004 RF<sub>84</sub> 173
   
2005 YU<sub>55</sub> 114, 174
   
2006 RH<sub>120</sub> 172, 806, 864
   
2008 EV<sub>5</sub> 174, 379, 871
   
2008 TC<sub>3</sub> (*see also* Meteorites, individual, Almahata Sitta) 9, 28, 48, 56, 196, 253, 258, 269, 270, 763, 837
   
2009 BD 516, 864
   
2009 BR<sub>60</sub> 359, 379
   
2011 SR<sub>158</sub> 359, 379
   
2013 EC<sub>20</sub> 172
   
2013 ET 178
   
2013 JR<sub>28</sub> 173
   
2013 WT<sub>44</sub> 174
   
2014 BY<sub>57</sub> 175
   
2014 HQ<sub>124</sub> 167, 177
   
107P/(4015) Wilson-Harrington 229
   
133P/(7968) Elst-Pizarro 227, 303, 333
   
176P/(118401) LINEAR 228, 238, 333
   
238P/Read 228
   
259P/(Garradd) (P/2008 R1) 226
   
288P/(300163) 2006 VW139 227
   
311P/PanSTARRS 223, 224, 229, 230, 232, 236
   
313P/Gibbs (2014 S4) 229
   
324P/2010 R2 (La Sagra) 229
   
P/2010 A2 337
   
P/2010 A2 (LINEAR) 224
   
P/2012 F5 (Gibbs) 226, 303
   
P/2012 T1 (PanSTARRS) 228
   
P/2013 P5 763
   
P/2013 R3 763
   
P/2013 R3 (Catalina-PanSTARRS) 227
   
Asteroids, numbered 802
   
AstOrb database 327
   
Astrometric observations 818, 831
   
Astronomical Research Observatory (ARO) 804
   
Atacama Large Millimeter Array (ALMA) 185, 366
   
Augite 47
   
Ballistic sedimentation 730
   
Band area analysis 248
   
Band area ratio (BAR) 45, 48, 626
   
Barbarian 327
   
Barringer crater 836
   
Basaltic crust 308, 541, 576
   
Beaming parameter 94, 99, 109
   
Bias 237, 330, 359, 378, 521
   
Binary Asteroid In-Situ Explorer (BASiX) (Discovery mission) 760
   
Binary YORP (BYORP) 8, 359, 366, 368, 369, 381, 383ff, 388, 389, 514, 515, 521, 527, 528, 760
   
coefficient 383, 384, 386, 514, 515, 521, 527, 763
   
Blake-Kozeny-Carman equation 559
   
Blast 838
   
Blast deflection 842, 843
   
Blast wave 260
   
Bolides 258, 260
   
Bolides, source energies 263
   
Bolides, strength 748
   
Bolides, terminal mass 263
   
Bond albedo 94, 111, 132, 510
   
Bond number 778
   
Bondi radius 485
   
Boulders 175
   
coherent 749
   
strength 748
   
Bouncing 480
   
Bouncing barrier 473, 478, 480, 481
   
Brazil-nut effect 781, 782
   
Breccias 22, 553, 564, 583
   
Bulk densities 108, 171, 226, 269, 305, 336, 358, 363, 406, 522, 544, 680, 749ff
   
estimate 751
   
Bulk porosities 108, 749
   
Bulk viscosity 561
   
Bus taxonomy 14
   
Bus-DeMeo taxonomy 14
   
Cameras for Allsky Meteor Surveillance (CAMS) 284
   
Canadian Meteor Orbit Radar (CMOR) 285
   
Capture 367
   
Carbonates 557, 642
   
Castastrophic disruption 284
   
Catalina Sky Survey (CSS) 95, 187, 799, 809, 844
   
Catastrophic disruption 8, 259, 297, 323, 336, 342, 345, 349, 351, 361, 379ff, 405, 406, 585, 661, 674, 681, 682, 696, 703, 709, 713, 714, 719, 739, 770
   
energy threshold 5
   
impact energy threshold ( $Q^*_D$ ) 661, 665, 671, 672, 674, 693, 704ff, 715ff, 721
   
shattering impact energy threshold ( $Q^*_S$ ) 661, 665, 670, 705
   
Chang'e-2 mission 170, 196, 434
   
Chaos 366
   
Chaotic chronology 303
   
Chicxulub 503, 840
   
Christiansen feature 52
   
Chronology 476
   
Circular polarization ratio 170, 175
   
Circulating tides 385, 386
   
Coagulation 643
   
Coefficient of restitution 343
   
Coherent-backscattering mechanism (CBM) 157
   
Cohesion 178, 358, 367, 387, 388, 664, 670, 674, 686, 759, 777, 778, 781, 787, 849
   
Cohesive forces 367, 387, 522, 680, 777ff, 781
   
Cohesive strength 230ff, 270, 753, 758, 775, 777, 779
   
Collision (*see also* Impacts) 5, 19, 24, 174, 207, 230, 249, 275, 289, 297, 305, 309, 310, 328, 341, 343ff, 349, 350, 353, 356, 369, 380, 382, 385, 477, 478, 480, 555, 586, 661ff, 679, 696, 701ff, 725

- Collision probability 500, 703  
 Collisional evolution 4, 215, 344, 477, 505, 701ff  
 Collisional grinding 704  
 Collisional history 495  
 Collisional lifetimes 28  
 Collisional-evolution model 701ff  
 Color 98, 297, 324  
 Comets, general 26  
   dust 274  
   dust composition 282  
   Jupiter-family comets 237, 282, 288  
   nuclei 645  
   Oort cloud comets 500, 502, 504, 646  
 Comets, individual  
   2P/Encke 274, 275, 282, 285, 288  
   9P/Tempel 1 842  
   21P/Giacobini-Zinner 275  
   67P/Churyumov-Gerasimenko 500  
   81P/Wild 2 274, 282  
   96P/Machholz 286  
   103P/Hartley 2 282, 501, 505  
   133P/(7968) Elst-Pizzaro 228, 230, 237, 303, 504  
   209P/Linear 283  
   238P/Read 229, 237, 504  
   259P/Garradd 237  
   503D/Pigott 237  
   D/1993 F2 (Shoemaker-Levy 9) 381  
   P/2010 A2 (LINEAR) 225, 230, 236  
   C/2013 A1 (Siding Spring) 840  
   P/2013 R3 (Catalina-PanSTARRS) 228, 230, 232, 236  
 Compaction 5, 665, 670, 672, 674, 683, 685ff, 690, 691  
 Compaction cratering 662  
 Constellation program 858  
 Contact binaries 173  
   abundances 173  
   formation 174  
 Continuous flow 259  
 Continuum (asteroids, comets) 500, 501  
 Continuum approach 679ff, 690, 756, 784, 785, 787  
 Continuum mechanics 754, 775, 785  
 Cooling 673  
 Co-orbital objects 100, 244  
 Coriolis topography 666  
 Corolis forces 736  
 Cosmic Background Explorer (COBE) 612  
 Cosmic-ray exposure (CRE) 264, 272, 547, 581, 582, 621  
 Cosmic-rays 264  
 Crater retention ages 711  
 Crater scaling 661, 668, 681  
   point source 679, 682, 692, 693  
 Crater seismic coupling 272  
 Cratering 725ff  
 Cratering regime 682, 683, 692  
 Cratering retention ages 731  
 Craters 7, 435, 666, 667, 711ff, 725ff  
 Craters (*continued*)  
   ages 731  
   bimodal 735, 741  
   complex 733  
   cookie cutting 729  
   degradation 735  
   depth-to-diameter ratio 733ff  
   ejecta burial 729  
   empirical saturation 727, 728  
   erasure mechanisms 729  
   giant 665, 666  
   modification stage 733  
   morphological properties 733, 735, 741  
   obliteration 728, 731  
   population 726  
   sandblasting 729  
   saturation 725, 729  
   secondary 725  
   shape 734  
   simple 733  
   simple-complex crater transition 734  
   size-frequency distribution (SFD) 725ff, 740  
   statistics 726  
   strength-gravity regime transition 734  
 Critical crater diameter 667  
 Critical disruption spin limit 230, 360, 366, 369, 376, 378, 383, 753, 756, 758  
 Critical disruption spin-up 367  
 Crushing 671, 673, 674, 680, 683, 686ff, 691, 695  
 Crystallization age 472, 473  
 Crystallization-remanent magnetization 545  
 CTH code 342, 669, 684, 690  
 Damage 669, 670, 687, 691, 692, 737  
 Darcy flow 560  
 Dark flight 260, 271  
 Dark fusion crust 260  
 Database of Asteroid Models from Inversion Techniques (DAMIT) 186  
 Dawn mission 7, 29, 54, 67, 81, 117, 141, 143, 333, 419ff, 501, 545, 675, 726  
 D-criterion 318  
 Debris disk 31  
 Deceleration 263  
 Deconvolution 188  
 Deep Impact mission 282, 842  
 Deep Space 1 mission 547  
 Deimos 7, 79, 451ff, 777  
   mass wasting 457  
 Density 197, 209  
 Depletion 497  
 Desiccation 233, 234  
 Deuterium/hydrogen ratio 26, 30, 500, 505, 644  
 Diameter estimates 751  
 Diameters 90  
 Differential precession 302  
 Differentiated 333, 337, 740

- Differentiation 5, 29, 475, 476, 479, 533ff, 553ff, 556, 576  
 Digital terrain model (DTM) 733  
 Direct imaging 362  
 Discrete approach 784, 785  
 Discrete element method (DEM) 669, 683, 785  
   Hard Sphere Discrete Element Method (HSDEM) 388, 683, 684, 754, 784, 785  
   Soft Sphere Discrete Element Method (SSDEM) 344, 388, 669, 684, 754, 755, 757, 784, 785  
 Disk-integrated photometry 133, 183, 185  
 Disks, lifetime 653  
 Disruption 283, 691, 707  
 Disruption limit 850  
 Disruption regime 693  
 Disruption scaling laws 704  
 Don Quijote mission concept 842, 847, 870  
 Double Asteroid Redirection Test (DART) 842, 870  
 Drag equation 259  
 Drucker-Prager 342, 686, 689, 691, 754, 755, 762, 775, 776, 787  
 Dust growth 479  
 Dynamic pressure 259, 264, 265  
 Dynamic strength 665  
 Dynamical depletion 706  
 Dynamical excitation 494ff, 496, 499, 504, 505  
 Dynamical fraction 502  
 Dynamical properties 297ff  
 Dynamical resonance 707  
 Dynamics 222, 237, 366, 380, 382, 388  
 Dynamos 24, 545
- Earth departure declination 864  
 Eccentricities 19, 363, 384, 386, 388, 494ff, 499, 503, 514  
 Effective temperature 117  
 Eight Color Asteroid Survey (ECAS) 72  
 Ejecta 232, 380, 780  
 Ejecta blanket 729, 780  
 Ejecta blocks 768, 769  
 Ejecta deposits 729  
 Ejecta mantling 779  
 Ejecta velocity 661  
 Ejection velocity 298, 302, 304, 305, 307, 310, 342, 347, 348, 672  
 Elastic modulus 386  
 Electric Delta-V Earth Gravity Assist (EDVEGA) 398  
 Electrophonic sounds 260  
 Electrostatic forces 235, 778  
 Encounter 172, 174, 284, 357, 361, 366, 369, 381  
 Enhanced gravity tractor (EGT) 872, 874  
 Entry velocity 258  
 Ephemeris predictions 815, 826  
 Equation of state (EOS) 342, 664, 665, 669ff, 679, 685, 687, 688  
 Equatorial bulge 174, 358, 367, 369, 387, 757, 845  
 Equatorial ridge 174, 175, 177, 379, 382, 387ff, 435
- Erosion 739  
 Eruptions 561  
 Escape velocity 297, 662, 664, 665, 684, 695  
 European Commission 837, 852  
 European Extremely Large Telescope (E-ELT) 10, 363  
 European Southern Observatory (ESO) 363  
 Excited rotation 196  
 Exhalation flow 539  
 Exoasteroid 31  
 ExploreNEO 844, 852  
 Explosive eruption 564  
 Extended belt (E-belt) 503  
 Extrasolar super-Earth 505
- Failure limits 752ff  
 Fast rotator 208  
 Faults 738  
 Fill-factor 809  
 Finite-element-analysis methods 755  
 Fireball networks 258  
 Fireball Recovery and InterPlanetary Network (FRIPON) 630  
 Fireballs 258, 260ff  
   apparent ablation coefficient 264  
   intrinsic ablation coefficient 264  
   PE criterion 263, 264  
   statistics 273  
 Fission 359, 363, 367ff, 382, 388, 527, 757ff  
 Flate 260  
 Fluid flow 538, 553ff  
 Fluidization 688, 691  
 Fly-Eye Telescope (ESA) 809, 841, 844, 852  
 Follow-up 795ff  
 Force chains 774, 775  
 Force model 820, 832  
 Formation 4  
 Formation age 479  
 Fourier transform 116  
 Fractional crystallization models 581  
 Fractionation 23  
 Fragmentation 480  
 Fragmentation phase 342  
 Fragmentation threshold 480  
 Free energy 361, 368, 383  
 Friction 224, 230, 344, 664, 665, 670, 674, 680, 683, 691, 693, 755, 774, 776  
   angle of 387, 388, 686, 692, 755, 775ff, 781  
   coefficient 686, 692ff, 776  
   forces 786  
   time 473, 480, 482
- Gaia mission 10, 13, 31, 187, 217, 336, 366, 751, 809  
 Galileo mission 29, 356, 767  
 Gardening 235  
 Gauss equation 307  
 Gaussian image 186  
 Gemini Planet Imager (GPI) 363

- Geminids (*see also* Meteor streams, Geminids) 649  
 Genesis mission 649  
 Geometric albedo 132  
 George E. Brown, Jr. Near-Earth Object Survey 798, 841  
 Giant Magellan Telescope (GMT) 10  
 Giant planet instability 502ff, 505  
 Giant planet migration 19, 210, 238, 337, 497, 498, 501, 504, 505, 701, 702, 704, 709  
 Goldstone Observatory 193  
 Goldstone Solar System Radar 165ff  
 Grain size 16  
 Grand challenge 855  
 Grand Tack model 4, 20, 24, 26, 66, 282, 334, 497ff, 502ff, 587, 589, 652, 702  
 Granular material 404, 686, 687, 693, 755, 768, 769, 774ff  
 Granular temperature 775  
 Gravitational aggregates 5, 342, 352, 387, 705, 706, 787  
 Gravitational phase 342ff  
 Gravity, ambient 776, 779, 781  
 Gravity regime 666, 667, 675, 681, 682, 686, 693, 704, 715  
 Gravity tractor 842, 850  
 Grooves 737, 783  
 Groundbased interferometer 366
- H, G magnitude system 94, 114, 138  
 Hapke model 51, 134, 139, 145, 605, 609  
 Hayabusa mission 6, 7, 29, 54, 119, 141, 248, 397ff, 448, 598, 605, 624, 651, 767, 868  
 Hayabusa2 mission 9, 31, 58, 81, 108, 117, 253, 389, 414, 651, 675, 760, 788, 845, 868, 875  
 Heat 663, 672, 673  
 Heat capacity 511  
 Heat conduction 110  
 Heat source 554  
 Heavily cratered terrain (HCT) 727, 728  
 Helium-3 concentration 290  
 Herschel Space Observatory 93, 193, 442  
 Herschel Space Telescope 229  
 Hierarchical clustering method (HCM) 299ff, 310, 330  
 High-Contrast Coronographic Imager for Adaptive Optics (HiCIAO) 363  
 Hit-and-run collision 26, 349, 585, 662, 673, 708  
 Horseshoe orbits 863  
 Hubble Space Telescope (HST) 55, 188, 362, 363, 379  
 Human exploration 855ff  
 Hydrated minerals 67, 73, 76, 78  
 Hydration features 171  
 Hydrocodes 342, 344, 664, 665, 668, 669, 671, 679, 683ff, 688ff, 693, 706, 711, 713, 721  
 Hydrothermal alteration 636  
 Hydroxyl 67, 463  
 Hypervelocity impact 222, 342, 480, 691, 692, 705, 848  
 Iapetus (Saturn) 502
- Ice 221ff, 333, 478, 480, 748  
 Identification 297ff  
 Impact hazard 9, 839ff  
 Impact heating 473, 536, 576, 662, 671  
 Impact monitoring 823, 826ff, 830, 832  
 Impacts (*see also* Collision) 222, 224, 226, 227, 232, 234, 236, 297, 337, 342, 343, 345, 346, 350, 351, 353, 365, 367, 383, 403, 405, 477, 479, 536, 555, 573ff, 661ff, 679ff, 704ff, 711, 713, 714, 716, 720  
 age 502, 503  
 craters 174, 272, 739  
 cross-section 827  
 giant 664  
 Impulsive technique 837, 852  
*In situ* resource utilization (ISRU) 874  
 Inclination 19, 494ff, 499, 503  
 Infrared Astronomical Satellite (IRAS) 90, 153, 192, 206, 612  
 Infrared Telescope Facility (IRTF) 14, 43, 72, 325, 461, 617  
 Infrasound 260  
 Insoluble organic matter (IOM) 640  
 Interferometry 184, 190  
 Interior 7, 8  
 Interlocking 755  
 Internal heating 479, 486, 673  
 Internal structure 344, 345, 349, 352, 358, 721  
 International Asteroid Warning Network (IAWN) 837, 851, 852  
 International Space Exploration Coordination Group (ISECG) 869  
 Interplanetary dust particles (IDPs) 281, 282  
 Interplanetary Kite-craft Accelerated by Radiation Of the Sun (IKAROS) 869  
 Intrusion 562, 563  
 Invariable plane 496  
 Inverse problem 184, 185, 188  
 Inversion angle 153, 159  
 Ion engine 398  
 Ion irradiation 598, 608  
 Ion-beam shepherd 843  
 Ionization 260  
 Iron meteorite 673  
 Iron-60 473ff, 533ff, 555, 576  
 Irregular satellites 502  
 iSAGE code 669, 670, 684, 686, 688, 690ff  
 Isotopes  
   hydrogen 653  
   manganese-chromium 640  
   nitrogen 501, 505  
   oxygen 21, 539, 636, 649, 652  
   signatures 740
- Jacobi ellipsoids 754  
 James Webb Space Telescope (JWST) 10, 71, 81, 217  
 Japan Aerospace Exploration Agency (JAXA) 397  
 Jet Propulsion Laboratory (JPL) Horizons system 865

- Jumping-Jupiter scenario 210, 212  
*Jupiter-family comets* (*see* Comets, Jupiter-family comets)
- Ka-Band Objects Observations and Monitoring (KaBOOM) 179  
 Keck telescope 229  
 Keplerian integrals 825  
 Keplerian shear 301  
 Keyhole 826, 828ff, 841, 842, 843  
 Kinetic impactor 353, 837, 842, 843, 847ff, 852  
 Kirchhoff's Law 70  
 Kozai cycle 284  
 Kozai effect 388  
 Kuiper Airborne Observatory (KAO) 54  
 Kuiper belt 19, 213, 477, 500, 504
- La Sagra Sky Survey 796  
 Labile 539  
 Lagrange points 203ff, 335  
 Lagrange regions 203ff  
 Landslide 406, 691, 768, 781  
 Large Binocular Telescope (LBT) 804  
 Large Binocular Telescope Interferometer (LBTI) 191  
 Large Synoptic Survey Telescope (LSST) 10, 13, 124, 179, 187, 217, 809  
 Laser ablation 843  
 Laser irradiation 598, 601, 608  
 Late heavy bombardment (LHB) 502, 711, 720  
 Least squares 815, 827, 832  
 Librational tides 384ff  
 Light curves 207  
 Lightcurve inversion 186, 196  
 Lightcurve observations 358, 361  
 Limb brightening 121  
 Limb darkening 133  
 Lincoln Near-Earth Asteroid Research (LINEAR) 95, 799  
 Line of variations (LOV) 827, 828  
 Lineaments 565, 566, 736, 738, 739, 741  
 Linkage 824, 832  
 Lithophiles 21  
 Lithosphere 564  
 Long-Range Tracking and Instrumentation Radar (ALTAIR) 290  
 Love number 385, 386, 760  
 Lowell Observatory Near Earth Object Survey (LONEOS) 799  
 Luminosity equation 259  
 Luminous efficiency 263  
 Lumme-Bowell model 145  
 Lunar basins 503, 681  
 Lunar bombardment 503  
 Lunar Crater Observation and Sensing Satellite (LCROSS) 675  
 Lunar craters 712, 713  
 Lunar distant retrograde orbit (LDRO) 864, 865, 872
- Machholz complex 286  
 Maclaurin spheroids 754  
 Macroporosity 358, 671, 680, 687, 695, 706, 750, 752 estimate 751  
 Magdalena Ridge Observatory (MRO) 804  
 Magma 537  
 Magma ocean 25, 541ff, 561  
 Magma reservoir 563, 564  
 Magma transport 563  
 Magmatism 566  
 Main-belt asteroids (MBA) 165ff, 323, 355ff, 375ff, 477, 752 source 290  
 Main-belt comets (MBC) 77, 222, 237, 303, 504, 652  
 Manned Orbital Research Laboratory (MORL) 857  
 Mantle stripping 586, 673  
 Marco Polo mission 871  
 MarcoPolo-R mission 177, 760, 871  
 Mariner 7 mission 452  
 Mariner 9 mission 452  
 Mars Express mission 454, 457, 459  
 Mars Reconnaissance Orbiter mission 454  
 Mass depletion 19, 20, 495, 496, 499ff, 504, 505  
 Mass estimate 751  
 Mass ratio 361, 363  
 Mass shedding 224, 231, 236, 367, 382, 388, 708, 717, 757  
 Mass survival fraction 271  
 Mass transport 653  
 Massive stars, winds 474, 475  
 Matrix 486, 561  
 Maximum compatibility estimate (MCE) 184  
 Mean-motion resonance 19, 226, 228, 237, 284, 301, 307ff, 327, 333, 348, 497, 522ff  
 Melting 663, 665, 670, 671, 673, 683, 685, 687  
 Melts, volatile-depleted melts (dry melts) 541
- Metallic 170  
 Metamorphism 553, 619  
 Meteor showers 273, 275, 281, 283, 285  
 Meteor streams  
   Draconids 275  
   Geminids 222, 275, 284, 288  
 Meteorites, mass 263  
 Meteorite showers 749  
 Meteorite streams 275  
 Meteorite-asteroid link 752  
 Meteorites 257ff, 663, 671, 675, 718  
 Meteorites, general  
   achondrites 269, 472, 475  
   age 472, 475, 476, 485, 486, 574  
   angrites 583  
   aubrites 583  
   breccias 620  
   calcium-aluminum-rich inclusions (CAIs) 22, 23, 419, 472ff, 486, 533ff, 554, 573ff, 641

Meteorites, general (*continued*)

- carbonaceous chondrites 26, 271, 318, 325, 453, 459, 473, 476, 478, 481, 486, 494, 500, 501, 504, 505, 538, 545, 603, 635
- CB-type 23, 556
- CH-type 556, 636
- CI-type 21, 25, 68, 274, 282, 476, 494, 501, 556, 636
- CK-type 333, 556, 578, 636
- CM-type 68, 121, 274, 282, 476, 556, 636
- CO-type 23, 333, 556, 578, 636
- CR-type 23, 282, 476, 556, 636
- CV-type 23, 333, 479, 538, 556, 636
- chondrites 257, 472, 473, 475, 486
- chondrules 22, 25, 257, 472ff, 476, 481, 484ff, 486, 534, 556, 574ff, 636, 643, 673
- accretion 485, 486
- aggregates 481, 484
- matrix complementarity 486
- cometary origin 274
- cooling rates 574, 581
- differentiated meteorites 472
- enstatite chondrites 25, 269, 473, 476, 478, 479, 636
- EH-type 479, 556
- EL-type 479, 556
- eucrites 583
- falls 257, 269ff, 272, 651
- finds 257
- howardite-eucrite-diogenite (HED) 7, 27, 45, 252, 333, 419, 545, 666, 710, 740, 782
- irons 23, 257, 337, 472, 475, 580, 749
- IIAB 24
- IIIAB 24
- IVA 24, 673
- matrix 22, 473, 476, 481, 485, 539, 636
- mesosiderites 22, 325, 583
- micrometeorites 501
- composition 282
- ordinary chondrites 6, 23, 25, 27, 247, 248, 269, 270, 325, 326, 473, 478, 486, 494, 500, 556, 598, 601, 618, 636, 624, 651, 747
- paradox 29
- H-type 47, 224, 475, 479, 556, 610, 618, 628
- L-type 47, 270, 479, 523, 556, 610, 618, 628
- LL-type 47, 223, 325, 332, 405ff, 409, 475, 479, 485, 523, 556, 618, 628, 845
- LL5/6-type 605
- pallasites 22, 583
- parent bodies 265, 270
- physical properties 264
- polymict ureilites 270
- refractory inclusions 636
- Rumuruti-type chondrites 25, 473, 556, 636
- source regions 265
- stony 257, 749
- stony-iron meteorites 583
- strength 747, 748

Meteorites, general (*continued*)

- unequilibrated 636
- ureilites 269, 270, 584
- xenolith 749
- Meteorites, individual
- Acfer 094 24, 558
- Allan Hills (ALH) A81001 545
- Allende 29, 473, 479, 485, 545, 557
- Almahata Sitta (*see also* Asteroids, individual, 2008 TC<sub>3</sub>) 9, 28, 56, 253, 258, 265, 269, 627, 749, 763
- Angra dos Reis 545
- Benesov 270
- Bunburra Rockhole 57
- Campo del Cielo 749
- Carancas 749
- Chelyabinsk 8, 28, 57, 254, 265, 272, 275, 282, 326, 332, 747, 836, 837, 852
- parent body atmospheric fragmentation 272
- parent body mass and size 272
- Galim 270
- Grimsby 748
- Hoba 749
- Holbrook 747
- Kaidun 28, 271
- Kapoeta 741
- Maribo 271, 274, 282
- Neuschwanstein 271, 275
- Orgueil 274, 282, 501
- Park Forest 748
- Příbram 258, 271, 275
- Sainte Marguerite 475
- Semarkona 24, 558
- Sikhote-Alin 749
- Sutter's Mill 271, 274, 282, 651
- Tagish Lake 24, 54, 265, 271, 494, 640, 651, 748
- Meteoroid streams 281ff
- asteroidal, epsilon Pegasids 284
- evolution 283
- formation 283
- main belt asteroid source 284
- mass 288
- Meteoroids 9, 257ff, 281ff, 523, 719
- asteroidal 273
- atmosphere entry 258
- atmospheric flight 264, 265
- bulk density 259, 264
- dynamic data 265
- dynamic mass 262
- fragmentation 259, 262
- iron 264
- mass 262
- mass influx to Earth 281
- physical properties 272
- plasma 260
- production 719
- stony 264
- strength 259

- Meteors 257, 258, 281  
 observation 286
- Meter-sized barrier 478, 482
- Micrometeorites 9, 257  
 impact 599, 612
- Microporosity 5, 344, 347, 680, 687, 695, 706, 751
- Microporous structure 347
- Mid-infrared spectroscopy 6
- Mineralogical characterization 44
- Mineralogical modeling 248
- Minimoons 806
- Minimum orbit intersection distance (MOID) 863
- Minkowski stability 186
- Minor Planet Center (MPC) 95, 312, 801
- Missing dunite problem 28
- Missing mantle problem 28
- Mobile Asteroid Surface Scout (MASCOT) 9, 845
- Model production function (MPF) 731, 732, 740
- Modified Gaussian model (MGM) 49, 251, 627
- Mohr-Coulomb 342, 686, 754, 755, 775ff, 787
- Molecular hydrogen 647
- Molecular strength 367
- Momentum transfer 694, 696, 842, 847
- Monolithic 344, 849
- Monolithic structure 345
- Monte Carlo method 827ff, 831
- Mudball model 640
- Mutual events 360
- Nanophase iron 66, 597, 604, 607
- NASA Extreme Environment Mission Operations (NEEMO) 878
- Natural Earth satellites 806
- Near Earth Asteroid Rendezvous (NEAR) mission 29, 51, 118, 347, 420, 759, 761, 767
- Near-Earth Asteroid Thermal Model (NEATM) 69, 94, 109
- Near-Earth Asteroid Tracking (NEAT) 799
- Near-Earth asteroids (NEAs) (*see also* Near-Earth objects) 8, 165ff, 243, 257ff, 332, 335, 355ff, 375ff, 522, 526, 711ff, 752, 768, 835ff, 855ff  
 Amors 860  
 Apollos 860  
 Atens 860  
 Aturas 860  
 deflection techniques 842  
 impact consequences 849  
 impact effect 841  
 impact intervals 849  
 mitigation possibilities 849  
 NHATS-compliant 859  
 numbers 849  
 shapes 172  
 size-frequency distribution (SFD) 728, 840  
 spin properties 172
- Near-Earth Object Camera (NEOCam) 810, 844
- Near-Earth Object Confirmation Page (NEOCP) 801, 832
- Near-Earth Object Human Space Flight Accessible Targets Study (NHATS) 178, 859, 865, 876
- Near-Earth Object Mission Advisory Panel (NEOMAP) 869, 870
- Near-Earth Object Observations (NEOO) Program 798
- Near-Earth Object Wide-field Infrared Survey Explorer (NEOWISE) 206, 217, 326, 328, 479, 800, 844, 852, 860
- Near-Earth objects (NEOs) (*see also* Near-Earth asteroids) 243, 323, 835ff  
 observations 858
- NEOShield 837, 843, 845, 847, 848, 852
- Neutral Buoyancy Lab (NBL) 876
- Nice model 4, 21, 24, 26, 66, 204, 210, 333, 337, 496, 497, 501ff, 588, 589, 652, 702, 714, 716, 720, 808
- Nongravitational perturbations 821, 822, 832
- Numerical modeling 668, 680, 683, 692, 784
- Obliquity 512, 515, 521, 522, 524ff
- Octantoid 184, 185
- Olivine 14, 28, 44, 210, 539, 542, 579, 600, 601, 618, 641
- Olivines 649
- One night stand file 802
- Onion-shell model 536, 591, 621
- Oort cloud comets (OCCs) (*see* Comets, Oort cloud comets)
- Opposition effect (OE) 131, 146, 208, 604
- Optical constants 248, 608
- Orbit condition code (OCC) 864
- Orbit determination 815, 816, 823, 824, 827, 831, 832
- Orbital distribution 20
- Orbits, Earth-like 860
- Organic material 69, 209, 605
- Organic matter 640, 644
- Organics 646
- Origin of lineaments 737
- Origins Spectral Interpretation Resource Identification and Security-Regolith Explorer (OSIRIS-REx) mission 9, 31, 58, 70, 82, 108, 117, 147, 171, 176, 253, 382, 389, 448, 522, 651, 675, 788, 832, 875
- Osculating orbital angles 301
- Osculating orbital elements 298
- Outgassing 221, 229, 230, 238
- Oxygen fugacity 540
- Paleomagnetism 545
- Palomar Transient Factory (PTF) 801
- Panoramic Survey Telescope and Rapid Response System (Pan-STARRS) 95, 124, 187, 217, 800, 809, 817, 818, 824, 844  
 Pan-STARRS1 survey telescope 227
- Partial differentiation 537, 547
- Pebbles 19, 21, 477, 478, 483, 702  
 accretion 662, 702
- Permeability 539, 559, 639
- Petrologic types 636

- Phase angle 145, 444  
 Phase curve 95  
 Phase reddening 45, 130, 145, 602  
 Phobos 7, 79, 451ff, 777, 783  
   blocks 457  
   grooves 452ff, 458  
   Stickney crater 452ff  
 Phobos 2 mission 454, 460, 461  
 Photometric correction 130, 142, 144  
 Photometry 6, 129ff, 185, 544  
 Phyllosilicates 14, 68, 71, 73, 461, 557, 638, 646  
 Physical characterization 43  
 Physical properties 94  
 Pioneer 225  
 Pit chains 737  
 Pit crater 565  
*pkdgrav* code 343, 344, 351, 669, 684, 694, 696, 787  
 Planetary Data System (PDS) 298, 312  
 Planetary embryos 496ff, 504, 505  
 Planetary encounters 249  
 Planetary migration 27  
 Planetesimals 494, 497ff, 502, 503  
   accretion 475  
   formation 471, 473, 475, 483, 486, 714ff, 721  
   heating 473  
 Planets, migration 587  
 Plymouth Rock mission concept 858, 859  
 Point source 681  
 Point spread function (PSF) 188  
 Polarimetry 6, 151  
 Polarization 327  
 Polarization phase curve 153, 154  
 Population 840  
 Population estimates 860  
 Porosity 5, 347, 554, 555, 671, 673, 680, 682, 683, 687, 691, 693ff, 706, 740, 751, 779  
 Porosity model 669, 680, 687, 691  
 Porous aggregates 485  
 Porous material 680ff, 687, 688, 696  
 Post-fission dynamics 369  
 Potentially hazardous asteroids (PHAs) 8, 860  
 Poynting-Robertson (P-R) 285, 289, 291  
 Pre-impact heliocentric orbits 274  
 Pre-shattered 344, 345  
 Presolar molecular cloud 640  
 Pressure bumps 472, 481ff  
 Projections, generalized 184, 193  
 Proper elements 18, 297, 298, 300, 301, 303, 308, 310, 311  
   analytic 298, 299, 312  
   synthetic 299  
 Protosolar nebula 640  
 Pyroclast 563  
 Pyroxene 14, 28, 44, 49, 542, 579, 600, 601, 618, 649  
 Quality factor 760, 761  
 Quasi random level (QRL) 300, 317  
 Radar albedo 170  
 Radar facilities 179  
 Radar observations 165, 193, 356, 844  
   ground-truth 168  
 Radar speckle tracking 167  
 Radial drift 480, 481  
 Radiation pressure 223, 224, 226, 229, 230, 234, 236, 284  
 Radiative heating 653  
 Radiative transfer model 145  
 Radiogenic heating 536, 555  
 Range-Doppler 184, 193  
 Rapid isotopic exchange 647  
 Ray-tracing 184  
 Reaccumulation 5, 8, 297, 323, 328, 336, 342, 345, 349ff, 353, 380, 405, 406, 684, 696, 739  
 Recrystallization 553  
 Reflectance spectroscopy 43  
 Regolith 7, 114, 233, 245, 325, 405, 425, 452, 456, 513, 730, 738, 759, 767ff  
   fairy-castle 211  
 Regularization function 184, 185  
 Remanent magnetization 545  
 Research and technology studies (RATS) 878  
 Resetting 741  
 Residence-time 806  
 Resources 856  
 Restrahlen bands 52  
 Resurfacing 728, 735, 736, 769, 773  
 Retrograde rotation 522  
 Ridges 737ff  
 Rigidity 760, 761  
 Risk corridor 846  
 Robotic boulder capture option 872  
 Roche limit 358, 359, 382, 388, 754  
 Rosetta mission 29, 113, 118, 142, 153, 433, 772, 869, 870  
 Rotation period 850  
 Rotation rate 512, 525  
 Rotational disruption 8, 222, 232, 236, 369, 377, 381, 382, 386  
 Rotational fission 356, 361, 366ff, 380ff, 383, 384, 388  
 Rotational instability 222, 224, 226, 230ff, 236  
 Roughness 513  
 Rubble piles (*see also* Aggregates) 7, 8, 174, 176, 208, 230, 232, 269, 284, 342, 344ff, 349ff, 358, 359, 377, 381, 382, 384, 386, 388, 406, 435, 444, 473, 479, 513, 515, 521, 527, 555, 663, 669, 707, 713, 717, 718, 731, 740, 748, 749, 753ff, 758ff, 768, 770, 780, 787, 848, 849  
   deformation 756  
   gravitational aggregates 273  
   shape 755  
 Scaling laws 4, 681, 692, 694, 695, 712, 731, 732  
 Scaling theories 679ff  
 Secondary ion mass spectrometry (SIMS) 640

- Secular perturbation 284  
 Secular resonances 19, 226, 299, 308, 309, 326, 332, 333, 348, 494ff, 502, 503, 522, 523, 526, 702  
 sweep 496, 502  
 Sedimentation 480, 482, 484, 486  
 Segregation 770, 774, 775, 781, 782  
 Seismic accelerations 730  
 Seismic erasure 666, 667  
 Seismic limit 249  
 Seismic shaking 249, 404, 405, 728ff, 736, 759, 769, 771, 773, 780  
 Self-gravity 664, 671  
 Self-heating 513, 514  
 Semilatus rectum 860, 861  
 Semimajor axis 386, 510, 514  
 Sentinel 810, 844  
 Shadowing 512, 513  
 Shape factor 259  
 Shape model 186, 188, 190, 193, 196  
 Shape support 184, 185  
 Shark darkening 426  
 Shear localization 738  
 Shear strength 356, 366, 388, 754  
 Shkuratov model 51, 134  
 Shock darkening 28, 252, 326, 332, 333, 337  
 Shock-physics code 679, 680, 683, 684, 687, 689, 690, 696  
 Shocks 663, 668  
 Short-lived 5  
 Short-lived radionuclides 473, 486, 641, 672  
 Siderophile 21  
 Silicates 14, 44, 66, 71, 210, 471ff, 478ff, 542, 553, 598ff, 618ff, 649  
 melting 556  
 Size distribution 204  
 Size-frequency distribution (SFD) 4, 96, 108, 702ff, 711ff, 721  
 wavy 709, 712, 716  
 Slivan states 527  
 Sloan Digital Sky Survey (SDSS) 13, 297, 299, 311, 312, 318, 342ff, 610, 623  
 Slow rotator 207  
 Slow-push/pull techniques 837, 848, 852  
 Small asteroid capture option 872  
 Small Mars problem 652  
 Smoothed particle hydrodynamics (SPH) 342, 344, 380, 438, 666, 668, 674, 684, 685, 689ff, 694ff, 706, 716, 780  
 Snowline 6, 65, 221, 333, 478, 494, 497, 498, 501, 505, 556, 588, 653  
 Solar electric propulsion (SEP) 872, 873  
 Solar nebula 637, 653  
 Solar sail 868  
 Solar Terrestrial Relations Observatory (STEREO) 223  
 Solar wind 67, 601, 602, 607  
 Soluble organic matter (SOM) 640  
 Sound speed 344, 663, 665  
 SOVA code 684, 690  
 Space exploration initiative 857  
 Space Mission Planning Advisory Group (SMPAG) 837, 851, 852  
 Space Situational Awareness (SSA) program 837, 852  
 Space Surveillance Telescope (SST) 810  
 Space weathering 6, 27, 29, 45, 66, 249, 325, 327, 336, 452, 457, 460, 597, 601, 625  
 rates 609  
 Spaceguard survey 841  
 Spacewatch 799  
 Spatial resolution 167  
 Speckle interferometry 188  
 Spectral observations 361, 363  
 Spectral reddening 45, 602, 604, 625  
 Spectral reflectance 600  
 Spectral slope 610  
 Spectro-Polarimetric High-contrast Exoplanet REsearch (SPHERE) 363  
 Spectropolarimetry 152  
 Spin axis obliquity 510  
 Spin barrier 207, 245, 360  
 Spin rates 173, 230, 526  
 Spin vector 113, 187, 207, 245  
 Spin-orbit coupling 366, 368, 381, 384  
 Spin-orbit resonance 383, 527  
 Spitzer Space Telescope 71, 124, 192, 193, 206, 326, 365, 442, 844  
 Split pairs (*see also* Asteroid pairs) 377, 379, 380, 380, 382, 383  
 Sputtering 258  
 Standard mean ocean water (SMOW) 652  
 Standard thermal model (STM) 69, 94, 109  
 Standing-wave polarization mechanism (SWM) 157  
 Stardust mission 274  
 Statistical asteroid model (SAM) 807  
 Statistical ranging 823, 824  
 Stellar occultation 186, 189, 365  
 Sticking 479  
 Stokes number 480  
 Strategic knowledge gaps (SKGs) 856, 876  
 Stratospheric Observatory for Infrared Astronomy (SOFIA) 71, 81  
 Streaming instability 472, 481ff, 486, 643, 662  
 Strength 5, 8, 233, 263, 265, 272, 273, 344, 351, 664, 665, 669, 670, 680ff, 685, 686, 694, 696, 715, 731, 732, 753, 754, 758, 759, 762, 850  
 Strength model 342, 685, 686, 690, 691  
 Strength regime 666, 681, 693, 704, 715  
 Subaru telescope 363  
 Sub-Kilometer Asteroid Diameter Survey (SKADS) 807  
 Subkilometer Main-Belt Asteroid Survey (SMBSA) 807  
 Sublimation 222ff, 227ff, 234ff, 283, 333  
 Sulfur 543  
 Surface blocks 739  
 size-frequency distribution (SFDS) 739  
 Surface conductivity 305

- Surface gravity 730, 776  
 Surface morphology 740  
 Surface roughness 94, 109, 112, 130, 146  
 Surface slopes 755  
 Synodic periods 860, 862, 863  
 Synthetic Solar System Model (S3M) 807  
 Synthetic tracking 810  
 Systematic errors 817ff, 832
- Tadpole orbit 210  
 Target plane 826, 828  
 Taurid complex 275, 285, 286, 288, 291  
 Taxonomic classes, spectral 14, 45, 145, 154, 246, 312, 318, 494, 576, 610  
 A-type 15, 27, 577  
 B-type 15, 76, 651, 752, 845  
 C-type 15, 27, 75, 133, 146, 154, 170, 206, 227, 238, 246, 252, 301, 305, 310, 325, 334ff, 365, 414, 479, 494, 497, 498, 500, 501, 504, 603, 651, 752, 845  
 Cb-type 15  
 Cg-type 15  
 Cgh-type 15, 75  
 Ch-type 15, 75  
 D-type 15, 27, 52, 133, 170, 206, 335, 336, 494, 504, 651  
 E-type 7, 15, 27, 133, 146, 170, 332, 436, 578  
 F-type 154, 170, 270  
 G-type 170  
 K-type 15, 50, 154, 305, 310, 333, 578, 651  
 L-type 15, 27, 155, 327  
 M-type 7, 15, 27, 67, 76, 170, 578  
 O-type 15, 578  
 P-type 15, 27, 76, 133, 170, 206, 334ff, 494, 504, 603, 651  
 Q-type 15, 47, 145, 248, 602, 610, 628, 783  
 R-type 15, 578  
 S-type 6, 15, 27, 45, 47, 50, 133, 145, 170, 223, 238, 246, 248, 301, 310, 325, 326, 332ff, 342, 397, 404, 407, 479, 494, 497, 499, 500, 504, 578, 598, 601, 602, 623, 624, 628, 651, 752, 845  
 Sa-type 15  
 Sq-type 15  
 Sr-type 15  
 Sv-type 15  
 T-type 15  
 V-type 15, 45, 133, 146, 252, 308, 318, 326, 333, 576, 666  
 X-type 15, 170, 301, 332, 752  
 Xc-type 15  
 Xe-type 15  
 Xk-type 15  
 Taxonomic distribution 20  
 Taxonomy 623  
 Tectonic processes 565  
 Tectonics 782  
 Temperature gradient 233
- Tensile strength 356, 361, 366, 681, 682, 695, 696, 754, 758  
 Terrestrial cumulativ impact flux 273  
 Terrestrial fractionation line (TFL) 649  
 Thermal 553  
 Thermal ablation 259, 260  
 Thermal conductivity 107ff, 114, 511  
 Thermal cracking 6, 122  
 Thermal diffusivity 233  
 Thermal disintegration 230, 233, 234  
 Thermal effects 383, 389  
 Thermal emission 14, 69, 94, 110, 112, 205, 216  
 Thermal expansion 233  
 Thermal fatigue 122, 405, 411, 739, 779  
 Thermal fracture 233, 782  
 Thermal fragmentation 779  
 Thermal history 555  
 Thermal inertia 94, 99, 108ff, 171, 209, 245, 365, 510, 511, 513, 522  
 Thermal infrared spectroscopy 325  
 Thermal metamorphism 21, 22, 473, 474, 639, 673  
 Thermal radiation 234, 509ff  
 Thermal skin depth 233, 511, 513  
 Thermal strain energy 233  
 Thermophysical models 6, 107ff, 198, 510, 515  
 Thermoremanent magnetization 545  
 Thirty Meter Telescope (TMT) 10, 363  
 Tholen taxonomy 14  
 Tidal bulge 384ff  
 Tidal disruption 381, 783  
 Tidal dissipation 8, 384ff, 515, 527, 753, 760  
 Tidal effects 783  
 Tidal saltation 387  
 Tidally locked 357  
 Tides 368, 383, 384, 386, 389, 515, 527  
 Timescale 223, 231, 523, 664, 667  
 Timestep 665  
 Tisserand parameter 18, 221ff, 265, 274, 284, 285  
 Top shape 358, 367, 379, 389  
 strongly oblate shapes 757  
 Top-like shape 360  
 Topography 8, 513, 729, 735, 768, 773  
 Torque 230, 231, 359, 366, 368, 379, 383ff, 511, 513, 518, 520, 526  
 Trails 260  
 Transneptunian disk 500, 501, 504  
 Transneptunian objects (TNOs) 333, 336, 355, 369  
 Trinary (see Triples)  
 Triples 174, 355, 356, 379ff, 456  
 Troughs 737  
 Tumbler 760, 763  
 Tunguska event 272, 836  
 Turbulence 472, 478, 480ff  
 Turbulent concentration 481, 482, 486

- Turbulent viscosity and diffusion ( $\alpha$ ) 476, 480ff  
 Two Micron All Sky Survey (2MASS) 818
- U.S. Naval Observatory (USNO) 818, 819  
 United Nations (UN) 837, 852  
   Committee on the Peaceful Uses of Outer Space (COPUOS) 850
- van der Waals forces 230, 232, 270, 273, 522, 758, 777, 788
- Venus Express mission 225
- Very Large Telescope (VLT) 188, 363, 804
- Viewing geometry 16
- Viking Orbiter mission 453, 456, 458
- Viscous deformation 561
- Viscous dissipation 653
- Volatiles 222, 238, 333, 337, 537, 558, 580
- Volcanism 562, 565
- Vortices 472, 482
- Water 478, 494, 498, 500, 501, 504
- Water vapor 224, 235
- Wavelet Analysis Method (WAM) 318
- Wide-field Infrared Survey Explorer (WISE) 13, 93, 124, 192, 198, 297, 299, 301, 311, 312, 318, 610, 844
- Widmanstätten pattern 576
- Wollastonite 47
- Yarkovsky effect 8, 18, 27, 109, 114, 118, 171, 172, 176ff, 197, 210, 230, 236, 298ff, 303ff, 309, 310, 327, 335, 348, 357, 377, 387, 504, 509ff, 706, 707, 711, 712, 717ff, 796, 821, 822, 830ff  
   diurnal 510  
   seasonal 510
- Yarkovsky-O'Keefe-Radzievskii-Paddack (YORP) effect 8, 27, 109, 118, 168, 172, 195, 207, 224, 231, 305, 306, 327, 356, 359, 360, 367ff, 375ff, 381, 382, 405, 412, 414, 435, 509ff, 610, 703, 707, 708, 711, 712, 714, 718, 731, 756, 782, 783, 796, 849
- spinup 174, 232, 283, 284, 356, 360, 367, 381, 382, 388, 707, 717, 757, 783
- timescale 232
- torque 222, 230
- Zodiacal cloud 9, 281ff, 612  
   comet breakup source 288  
   Kuiper belt and interstellar dust source 291  
   models 289, 290  
   source of Jupiter-family comets 288  
   source of Oort cloud comets 290  
 Zodiacal light 501